PTB

OTTO VON GUERICKE
UNIVERSITÄT
MAGDEBURG

13th International Symposium on Hazards, Prevention and Mitigation of Industrial Explosions

Proceedings

ISHPMIE2020
Braunschweig, Germany

Physikalisch-Technische Bundesanstalt

Otto von Guericke Universität Magdeburg

13th Symposium International Symposium on Hazards, Prevention and Mitigation of Industrial Explosions

Proceedings

DOI: 10.7795/810.20200724

Citation Template:

Author 1, Author 2, ... : "Title of article", pp. n1 - n2 . In: "Proceedings of the 13th International Symposium on Hazards, Prevention and Mitigation of Industrial Explosions (ISHPMIE 2020)", Braunschweig, Germany, 2020. DOI: 10.7795/810.20200724

Herausgeber:
Physikalisch-Technische Bundesanstalt
Bundesallee 100
38116 Braunschweig, Germany
Dr. Michael Beyer
Dr. Arnas Lucassen
3.7 | Fundamentals of Explosion Protection
phone: +49 531 592-3700
e-mail: michael.beyer@ptb.de
ishpmie2020.ptb.de
ishpmie2020@ptb.de

DOI: 10.7795/810.20200724

Contents

Session 04: Electro-chemical energy carriers *(Frank Lienesch)*

Session 05: Explosion modelling and simulation (1) *(Ulrich Krause)*

Session 06: Explosion modelling and simulation (2) *(Josué Melguizo-Gavilanes)*

Session 07: Explosion modelling and simulation (3) *(Holger Großhans)*

Session 08: Explosion modelling and simulation (4) *(Paola Russo)*

DOI: 10.7795/810.20200724

Session 13: Explosion testing *(Robert Zalosh)*

Session 14: Explosions of sprays and vapors *(Olivier Dufaud)*

Session 15: Flame propagation and acceleration (1) *(Wookyung Kim)*

DOI: 10.7795/810.20200724

Session 16: Flame propagation and acceleration (2) *(Jennifer Wen)*

Session 17: Gas, dust, and hybrid mixture explosions (1) *(Dieter Gabel)*

Session 18: Gas, dust, and hybrid mixture explosions (2) *(Jérôme Taveau)*

Session 19: Gas, dust, and hybrid mixture explosions (3) *(Wei Gao)*

Session 23: Ignition phenomena (2) *(Ritsu Dobashi)*

Session 24: Ignition phenomena (3) *(Robert Schießl)*

DOI: 10.7795/810.20200724

Greetings from the President of PTB, the host organization

Dear participants,

Welcome to the "13th international Symposium on Hazards, Prevention and Mitigation of Industrial Explosions" hosted by the Physikalisch-Technische Bundesanstalt in Braunschweig.

As Germany’s National Metrology Institute, PTB is the nation’s highest authority when it comes to correct and reliable measurements. Since its foundation in 1887 by Werner von Siemens and Hermann von Helmholtz, PTB has supported industry with the precise realization of units and with knowledge of how to measure appropriately and precisely. Over the years, PTB and its scientists have contributed many important metrological achievements to society and industry. The safety-related tasks, as one important area, were added “only” 70 years ago to PTB’s portfolio. Like in any technical area, safety technology fundamentally relies on correct and reliable measurement results. With the efforts of PTB, the industry gets both from a single source.

Your major concern as a scientist is to understand the underlying physics of safety and to use this knowledge for a safe implementation of industrial processes. Looking at its international economic relevance, this undertaking is certainly also a worthwhile goal on a global scale. New technologies generally create new potential hazards and we should have an answer to these safety challenges. In my view, hydrogen technology poses a very recent and prominent example of such a challenge. It has left the laboratory environment and large-scale applications are being set up in Germany to tackle climate change. Apart from the technological aspects, social acceptance may be at stake in the event of serious accidents causing massive individual tragedies and possibly also the entire hydrogen technology along with the associated climate targets.

These prospects are compelling reasons for an exchange of knowledge throughout the world. Unfortunately, a conference held in person is not possible this year due to safety considerations of a different kind. We are thus happy to see that the PTB organization team has quickly set up a virtual discussion forum instead, which enables an appropriate scientific discussion of the articles that have already been completed.

PTB is proud to offer the forum for this as a host. Well over 550 participants from all over the world are registered for the virtual event. In my view, this is a great success for bridging the gap between science and industry. It shows that this type of conference is important and willingly accepted. Thank you for your interest and participation in this symposium.

I wish all authors and the organizers fruitful and enlightening discussions. We are very much looking forward to hosting the next symposium and hope to welcome you all in Braunschweig in 2022.

Joachim Ullrich
President of the Physikalisch-Technische Bundesanstalt

Address from the International Organizing Committee

10th August 2020

Due to the situation with the COVID-19 pandemic, the 13th *International Symposium on Hazards, Prevention and Mitigation of Industrial Explosions* (ISHPMIE) was organised as an online event on 27-31 July 2020. The Local Organising Committee did a tremendous job putting together a virtual event with an online forum where a record number of 575 registered participants could discuss the 87 peer-reviewed papers in the technical program.

The 13th ISHPMIE symposium was hosted by the Physikalisch-Technische Bundesanstalt (PTB), with support from the Otto-von-Guericke-Universität Magdeburg (OVGU). The same organisations will organise the 14th ISHPMIE, scheduled for 11-15 July 2022 in Braunschweig. The International Organising Committee would like to congratulate the Local Organising Committee with the successful completion of 13th ISHPMIE.

We look forward to meeting you at 14th ISHPMIE in Braunschweig in 2022.

Yours sincerely,
Trygve Skjold

On behalf of the International Organising Committee:
Isabelle Sochet
Jérôme Taveau
Masaharu Nifuku
Michael Pegg
Michael Beyer
Paul Amyotte
Ritsu Dobashi
Rolf Kristian Eckhoff
Sergey Frolov
Trygve Skjold (Chair)
Ulrich Krause
Wei Gao

DOI: 10.7795/810.20200724

Greetings form the Local Organizing Committee Chair

July 27, 2020

Dear participants,

I welcome you to the 13th international Symposium on Hazards, Prevention and Mitigation of Industrial Explosions. The host is the Physikalisch-Technische Bundesanstalt in Braunschweig together with the Otto von Guericke University Magdeburg in the week from July 27 to 31, 2020.

The series of International Symposia on Hazards, Prevention and Mitigation of Industrial Explosions has a long tradition. 12 symposia could be held undisturbed and as planned. For the first time and because of the corona pandemic, this year's symposium cannot take place as a face-to-face conference. We are very sorry, because all aspects of the conference were already organized when we had to stop the invitation to Braunschweig.

We have now endeavored to create a replacement with the ISHPMIE 2020 Forum, which at least makes it possible to appreciate the completed articles and put them up for discussion in the community. Please apologize that it is not perfect and that there may arise problems in some places. As in the previous symposia, selected articles will be proposed for publication in a special volume of the Journal of Loss Prevention in the Process Industries.

In contrast, many elements of our symposia had to be left behind: the personal presentations and discussions in the sessions, the plenary lectures, the 'industry meets science' session, the social events such as the welcome reception and the farewell reception, the young researchers 's night, the banquet, the experimental demonstrations, the best paper awards and last but not least the most important thing of all, the many personal contacts and conversations. Now we must wait another two years. I would like to thank the International Organizing Committee for giving us the opportunity to do this at the 14th ISHPMIE 2022 in Braunschweig.

I am now looking forward to discussing the topics in our ISHPMIE 2020 Forum. 575 registered participants are a great success and I and believe that it was the right decision to hold the symposium in this form. It allows all participants in the different time zones to contribute to the discussion at a time that is comfortable for them. Please note also the podcasts of the authors. Most of the authors followed our request and present their papers in less than 5 minutes.

Finally, I would like to thank all my colleagues for their support. Without them, the preparation and holding of such a symposium would not be possible: first of all the ISHPMIE 2020 Organization Team, the ISHPMIE 2020 Forum Team and the many helping hands from PTB and Otto von Guericke University Magdeburg, my co-chair Detlev Markus, the program chairs Ulrich Krause and Holger Großhans together with the authors, reviewers and session chairs, the supporting organizations of the symposium mentioned on the website as well as Trygve Skjold and the International Organizing Committee. Thank you very much!

I wish all participants an interesting conference week.

Michael Beyer
Local Organizing Committee Chair

DOI: 10.7795/810.20200724

Foreword of the Proceeding Editors

It is our pleasure to present the proceedings of the 13th International Symposium on Hazards, Prevention, and Mitigation of Industrial Explosions (ISHPMIE). The publication of these proceedings was heavily affected by the global situation. We received many messages from authors who were not able to submit their manuscripts in time because they could not enter their laboratories for months. Also, the reviewers faced the situation of not having full access to their scientific infrastructure.

In light of these challenges, we are happy to compile proceedings consisting of 84 high-quality papers that reflect the scientific state-of-the-art. All articles in this volume have been subject to a peer review process administered by the proceeding editors. We are thankful to the 71 expert referees who guaranteed the professional and scientific standards expected of ISHPMIE. After the conference, Elsevier will publish selected papers from 13th ISHPMIE in a special issue of the Journal of Loss Prevention in the Process Industries.

Overall, we firmly believe that the special format of this year’s conference continues the tradition of ISHPMIE in benefiting all participants in many ways.

Prof. Ulrich Krause
University of Magdeburg

Dr. Holger Grosshans
Physikalisch-Technische Bundesanstalt

DOI: 10.7795/810.20200724

Symposium Committees

International Organizing Committee

T. Skjold (Norway, Chair), P. Amyotte (Canada), R. Dobashi (Japan), R. K. Eckhoff (Norway), S. Frolov (Russia), W. Gao (P. R. China), M. Nifuku (Japan), M. Pegg (Canada), I. Sochet (France), J. R. Taveau (USA)

Honorary Members
R. Klemens (Poland), K. Lebecki (Poland), P. Wolanski (Poland)

Local Organizing Committee

Michael Beyer (PTB, Chair), Ulrich Krause (OvGU, Co-Chair), Detlev Markus (PTB, Co-Chair), Carola Lotz-Foerster, Tanja Eckert, Arnas Lucassen, Christian Lehrmann, Thomas Stolz, Tim Krause, Irina Mulyasch, Dieter Gabel, Holger Großhans, Martin Thedens, Carola Schierding, Florian Baumann, Dirk Frobese, Thekla Kiffmeyer, Christine Werner, Martin Tränker, Julia Mildner, Frank Lienesch, Michael Hilbert, Sabine Zakel

Program Committee Chairs

Ulrich Krause, Holger Großhans

ISHPMIE 2020 Forum Team

Tobias Schäfer, Christian Lehrmann, Michael Beyer, Holger Großhans, Detlev Markus, Arnas Lucassen, Ulrich Krause, Dieter Gabel

DOI: 10.7795/810.20200724

Laboratory Development and Pilot-scale Deployment of a Two-part Foamed Rock Dust

Connor B. Brown [a], Inoka E. Perera [a], Marcia L. Harris [a], Linda L. Chasko [a], James D. Addis [a] & Scott Klima [a]

[a] National Institute for Occupational Safety and Health (NIOSH), Pittsburgh, PA, USA

E-mail: CBBrown1@cdc.gov

Abstract

U.S. Code of Federal Regulations 30 CFR 75.402 and 75.403 require 80% total incombustible content to be maintained within 40 feet of the coal mine face via the liberal application of rock dust. Unfortunately, this application of rock dust limits miners' visibility downwind and can increase the miners' exposures to a respirable nuisance dust. Wet rock dust applied as a slurry is, at times, used to negate these negative effects. Although this aids in meeting the total incombustible limits, the slurry forms a hard cake when dried and no longer effectively disperses as needed to suppress a coal dust explosion. As a result, a dry rock dust must be reapplied to maintain a dispersible layer. Therefore, researchers from the National Institute for Occupational Safety and Health (NIOSH) have been working towards finding and testing a foamed rock dust formulation that can be applied wet on mine surfaces and remain dispersible once dried which minimizes the likelihood of mine disasters, including mine explosions. The initial tests were aimed at discerning dispersion characteristics of three different foamed rock dusts via the NIOSH-developed dispersion chamber and led to identification of a two-part foam with adequate dispersion characteristics. The current study was conducted to assess the robustness of the two-part foamed rock dust. Through a series of laboratory-scale experiments using the dispersibility chamber, the effects of testing conditions and product formulations on the foam's dispersibility was determined. Some of the tested variables include: exposing the foam to high humidity, varying the component levels of the foamed rock dust, altering the rock dust size distribution, and varying the rock dust types. Further pilot-scale tests examined the atmospheric concentrations of dust via personal dust monitors downwind of foamed rock dust production and application. Additionally, product consistency was recorded during pilot-scale testing at key points in the formulation and application. The results of these experiments will be discussed in this paper.

Keywords: *dust dispersibility, foamed rock dust, coal mining, explosion prevention*

1. Introduction

The impetus for developing a dispersible rock dust slurry came from the two requirements placed on underground coal mines. The first requirement, from 30 CFR § 75.2 (Mandatory Safety Standards–Underground Coal Mines) and 30 CFR § 75.403 (Maintenance of incombustible content of rock dust), is the application of dispersible rock dust in sufficient quantities. The second requirement, 30 CFR § 70.100 (Respirable dust standards), is the time-weighted average limit of mine workers' exposure to airborne dust.

Rock dust acts as a physical heat sink during an explosion (Cybulski, 1975; Richmond, et al., 1975; Nagy, 1981) and is the primary technique used to supress the reaction. Therefore, application of rock dust in sufficient quantities is essential to inert coal dust and to prevent continued flame propagation. Current rock dusts wick moisture, forming a nondispersible wet paste that stiffens to a cake when dried, thereby significantly reducing or inhibiting the rock dust's ability to effectively disperse. Coal dust, due to its hydrophobicity, can remain dispersible under these conditions, thereby permitting its involvement in a propagating dust explosion. The presence of moisture in the mine can lead to the condition in which the coal dust can be dispersed and participate in the explosion while the rock dust becomes ineffectual.

Additionally, there have been continuing concerns of respirable diseases among coal miners resulting in another requirement limiting the total respirable dust to which coal miners are exposed. The respirable size fraction of rock dust used to inert a coal dust explosion can contribute to the total dust being measured. As a result, some mines have turned to applying a wet rock dust to minimize the miner's exposure to respirable dust. The wet application of the rock dust allows the mine to place dust in key locations, such as the roof and ribs, and cover the exposed coal without exposing the workers to respirable dust. However, a side effect of the wet application of the rock dust is that the rock dust no longer is dispersible due to caking and is subsequently ineffective. Currently, MSHA requires an application of dry rock dust on top of the wet-applied rock dust once the wet rock dust dries (MSHA, 2015) and becomes caked.

A possible solution to this problem is a foamed rock dust (FRD). The hope is that the FRD has the benefits of a normal rock dust slurry while remaining dispersible when dry. Currently, the ability of the FRD to fracture from a passing pressure wave and disperse into individual particles to inert a dust explosion is not known. Prior laboratory testing has, however, led to promising results showing favourable dispersion characteristics with a few specific formulations. Hierarchically, the resulting engineering control of respirable dust through the application of foam dust would foster better health for coal miners, while keeping them safe from coal dust explosions. The FRD also has the potentially additional benefit of better adherence to elevated surfaces in the mine entry leading to increased effectiveness of the inert material. Past studies have shown that rock dust located on the roof, ribs and other elevated surfaces is more readily dispersed than dust on the floor (Hartmann, 1957).

To this end, laboratory experiments were conducted on a previously tested rock dust which incorporated a two-part foam (TPF). Past studies showed promising results when compared to other foam products currently on the market (Brown et al., 2018). However, the unique formulation and application properties of the TPF with rock dust are still not understood. Therefore, NIOSH researchers conducted a series of laboratory-scale experiments using the NIOSH-developed dispersibility chamber to examine the effects of testing conditions and product formulations on foam dispersibility. The insights gained were then applied during the pilot-scale testing in the Bruceton Experimental Mine (BEM) at the Pittsburgh Mining Research Center. Again, a series of tests were conducted to investigate the impact of various factors on the dispersion characteristics of the foam. Additionally, the airborne dust levels were measured during the production and application of the foam dust to confirm the benefits of the wet-applied method.

2. Experiments

The test series had two main environments where the samples were prepared—in the laboratory at the benchtop scale and in the BEM at the pilot scale. The bulk of the sample preparations were conducted under laboratory conditions. The main method of discerning the performance of the rock dust was its dispersion performance in the NIOSH dispersion chamber (Perera et al., 2016). The samples were compared on a relative basis to the reference rock dust used by NIOSH at the Lake Lynn Experimental Mine (LLEM) in large-scale explosions testing.

2.1 Experimental materials

This section describes the two experimental materials used in the testing. These materials include the various rock dusts and a foam.

2.1.1 Rock dust

Several rock dusts were used in these series of experiments, including the reference limestone rock dust, a set of classified rock dusts that used the reference rock dust as input, and five other

DOI: 10.7795/810.20200724

commercially available rock dusts. The reference rock dust has been extensively used in previous experiments at the LLEM, most notably in experiments which lead to the implementation of the 80% incombustible rule in the United States (Cashdollar et al., 2010). The classified rock dust used the same reference rock dust but was sieved through either a 200-mesh or a 400-mesh sieve. The resulting oversized and undersized material was later used in the experiments.

2.1.2 Foam

Previous experiments were conducted with various commercially available foams that could incorporate rock dust. These tests had the similar aim of creating a wet-applied material which when dried was dispersible via a "light blast of air" (30 CFR § 75.2). These experiments showed that the use of a TPF in this application provided a promising solution. The TPF used in this series of tests consisted of water, a foaming agent, and a stabilizing agent (Brown et al., 2018).

2.2 Experimental apparatuses

This section describes three experimental apparatuses used during in the testing. These apparatuses allowed researchers to measure the dispersion characteristics, size distribution and airborne dust concentrations.

2.2.1 Dispersion chamber

The FRD samples produced in the lab or in the BEM were tested in NIOSH's dispersion chamber. The chamber sends a pulse of air across a sample bed of rock dust, dispersing a quantity of the dust and sending it across a dust probe as seen in Figure 1.

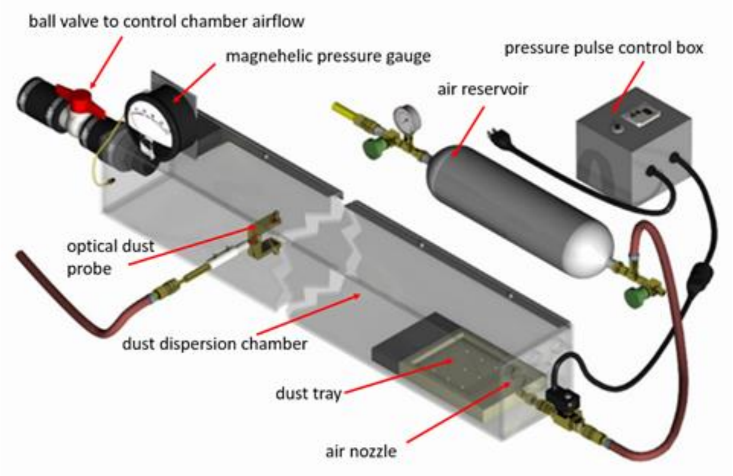

Fig. 1. *Dispersion chamber schematic (Perera et al., 2016)*

Passage of the dust across the probe causes the obscuration of a light beam which is measured and recorded (Cashdollar, et al., 1981). The obscuration caused by these entrained particles is used as a means of assessing the dispersibility of the sample. The pulse of air used to initiate the test was based on the dynamic pressure measurements of a near-limit propagating coal dust explosion conducted at LLEM, as shown in Figure 1 and, as such, provides the reproducible "light blast of air" described in 30 CFR § 75.2.

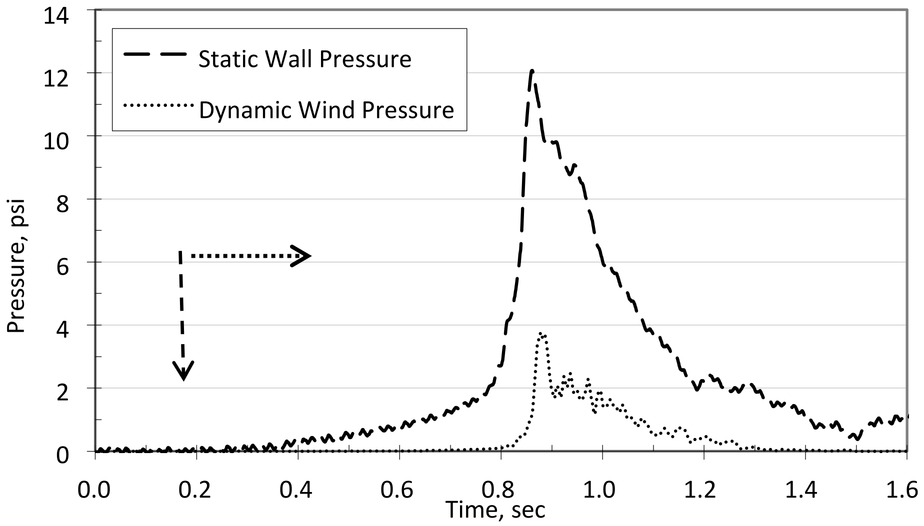

Fig. 2. *Horizontal and vertical components of dust explosion pressures measured during LLEM shot #517*

The test procedure, notably, does not simulate a shockwave but, rather, creates a similar pressure history per the rapid release of the air pulse. Use of this method is described in greater detail by Perera et al. (2016).

As shown from the aforementioned large-scale testing at LLEM in Figure 2, vertical or static forces are created due to the passing of a shock wave. The static pressure in Figure 2 is about three times greater than the dynamic pressure. It is reasonable to assume that the overpressure may destroy the cohesive foam matrix, freeing individual particles or particle agglomerations for dispersion. Computational models have observed these vertical forces in addition to reflected compaction waves in the dust layer just behind the shockwave (Lai et al., 2018). As a result of these findings, samples were tested using the additional 45° nozzle orientation (Figure 3). The change in orientation allowed the researchers to add a vertical force component.

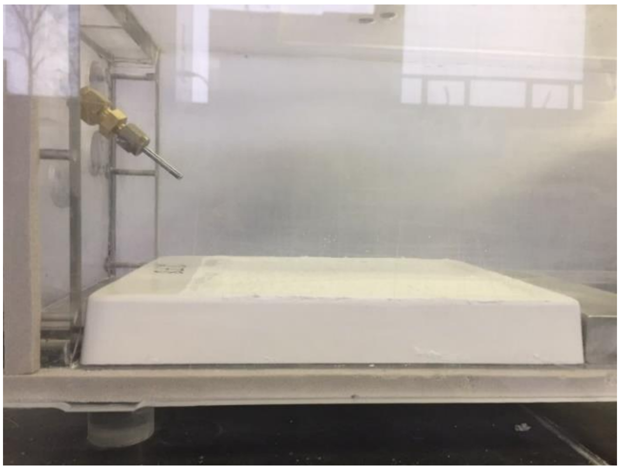

Fig. 3. *45° nozzle orientation*

2.2.2 Particle size

The particle size distributions of rock dusts were determined using a Beckman-Coulter LS 13 320 laser scattering size analyser. The Beckman-Coulter instrument measures the scattering of a 780-nm laser beam by the entrained dust at various angles with respect to the beam direction. The instrument returns the particle size distribution in terms of the spherical equivalent via Mie scattering.

2.2.3 Dust concentration monitor

Dust concentrations were monitored and measured during the production and application of the foam rock dust in the BEM. The gravimetric samples were collected on pre-weighed filters using the standard Zefon Escort ELF personal air sampling pumps after the respirable size fraction was separated from the oversized dust by a 10-mm Dorr-Oliver cyclone. Additionally, a continuous personal dust monitor from Thermo Scientific, the PDM 3600, was used to monitor dust concentrations during the test via a tapered element oscillating microbalance (Page et al., 2008).

2.3 Experimental sample preparation

This section describes the process of sample preparation in the lab and in the pilot-scale test facility. In addition this section details the changes made to the sample variables.

2.3.1 Laboratory sample prep

The dry rock dust samples, used for the relative comparison, were prepared in accordance with the standard operation procedures of the NIOSH-developed dispersion chamber (Perera et al., 2016). To prepare the FRD samples, the TPF was prepared first by combining 300 g of water and 15 g of the foaming agent. This solution was whipped with a mixer until a consistent foam matrix was established. A stabilizing agent was then slowly added to the foam matrix. Once blended, the stabilized TPF was combined with the rock dust. The samples were then placed under two drying conditions. The fast-drying condition was the ambient lab environment. The slow-drying condition placed the samples in sealed chambers with high humidity and no airflow. After a week in the chamber, the samples were taken out and allowed to dry under ambient lab conditions. All samples were dispersed using a 45-degree nozzle.

Initial rounds of testing examined the effects of changing the amount of stabilizer and the amount of rock dust used in the formulation. The amounts of stabilizer tested were 10 g and 21 g. The amounts of rock dust tested were 600 g, 900 g, and 1,500 g.

Other FRD samples were made by adding water to the rock dust prior to being mixed with a different blend of foam. The TPF in these cases kept the ratio of stabilizer and foaming agent at 1:1. The stabilizer levels were 6.5 g, 5 g, and 3.5 g per batch while keeping the rock dust mass at 1,500 g and the additional water at 400 g. The amount of pre-wet rock dust also varied, but the ratios of rock dust to water and the amounts of stabilizer and foaming agent (5 g) remain the same.

Five total sample sets were run with different commercially available rock dusts using the same FRD formulation. The formulation consisted of 300 g of water, 5 g of foaming agent, 5 g of stabilizer, 1,500 g of rock dust, and 400 g of water to pre-wet the rock dust.

The final sample set produced in the lab used the same previous formulation except with four classified batches of the reference rock dust. The reference rock dust was sieved through either a 200-mesh or a 400-mesh sieve. In both cases, 1,500 g of the oversized or undersized material was used in the FRD, keeping all other ingredients the same. Each combination of drying condition and formulation tested a total of five samples. A tabulation of the various sample sets is shown in Table 1 below.

***Table 1:** Laboratory tests examining the impact of various components on the dispersibility of foamed rock dust*

Sample set	FOAM			ROCK DUST			Drying Conditions
	Water (g)	Foaming Agent (g)	Stabilizer (g)	Base rock dust	Amount (g)	Water (g)	

1	300	15	10	Reference	600	-	Fast & Slow
2	300	15	21	Reference	600	-	Fast & Slow
3	300	15	10	Reference	900	-	Fast & Slow
4	300	15	21	Reference	900	-	Fast & Slow
5	300	15	10	Reference	1500	-	Fast & Slow
6	300	15	21	Reference	1500	-	Fast & Slow
7	300	6.5	6.5	Reference	1500	400	Fast & Slow
8	300	5	5	Reference	1500	400	Fast & Slow
9	300	3.5	3.5	Reference	1500	400	Fast & Slow
10	300	5	5	Reference	1275	340	Fast & Slow
11	300	5	5	Reference	1725	460	Fast & Slow
12	300	5	5	Commercial RD 1	1500	400	Fast
13	300	5	5	Commercial RD 2	1500	400	Fast
14	300	5	5	Commercial RD 3	1500	400	Fast
15	300	5	5	Commercial RD 4	1500	400	Fast
16	300	5	5	Commercial RD 5	1500	400	Fast
17	300	5	5	- 400 mesh Reference	1500	400	Fast
18	300	5	5	- 200 mesh Reference	1500	400	Fast
19	300	5	5	+ 400 mesh Reference	1500	400	Fast
20	300	5	5	+ 200 mesh Reference	1500	400	Fast

2.3.2 BEM sample preparation

Anemometers were placed upwind and downwind of the test area to monitor airflow velocities. Additionally, the dust sampling equipment was placed 100 ft downwind of the test area. The mortar mixer used to blend and apply the FRD was turned on and allowed to run to collect a baseline level of diesel particulate matter (DPM). The test matrix is tabulated in Table 2.

Table 2: *Test matrix for pilot-scale testing two-part foamed rock dust in the BEM*

Test Conditions	Test Number	Dust, kg	Water, l	Amount of foam
Triplicate	1	45.4	11.4	40 second of foam
Triplicate	2	45.4	11.4	40 second of foam
Triplicate	3	45.4	11.4	40 second of foam
+15% rock dust	4	52.2	11.4	40 second of foam
-15% rock dust	5	38.6	11.4	40 second of foam
-15% water	6	45.4	9.7	40 second of foam
+15% water	7	45.4	13.1	40 second of foam

All the tests used the reference rock dust as the base inert material. The first three tests were a set of triplicates that emulated the laboratory formulations. The following four tests looked at variations of the formulation to see how the foam would be impacted if a mine worker would improperly mix the inputs to the system. The first two tests changed the amount of rock dust by ±15%, and the other two tests varied the water used to pre-wet the rock dust by ± 15%. The parameters for the foam generator would be initially set and not altered by the machine operator. Once the instrumentation was in place, a premeasured amount of dust was placed into the mixing hopper of the mortar mixer. The premeasured amount of water was then added to the rock dust and allowed to mix. At this point, the calibrated foam generator was turned on, and a foam was added to the slurry for a predetermined amount of time. This was mixed until the mixture was homogenous. When the mixer was stopped, a sample was taken with a 1-qt container and weighed to get a density measurement. Additional material was taken from the mixer and used to fill trays for later testing in the dispersion chamber. The initial weight of the trays with the fresh samples was taken at this point for use in later calculations to determine the FRD density and measured water content. Once the samples were taken out of the mixer, the rest of the material was dumped into the hopper and the auger pump was turned on. A 1-qt sample was then taken as the material left the application nozzle. This was then weighed for a density measurement. Additional material was also taken from the end of the nozzle for the dispersion trays. These trays also had their mass recorded. Once the last sample of material was taken, the FRD was applied to the roof and ribs of the mine. This continued until there was no more FRD left for the pump to move. The area was then marked with spray paint to denote the test number, and the application equipment and dust monitoring equipment were then moved to the next testing location. The tray samples were kept in the mine under the same drying conditions until the sample weights stabilized, just over one week. The dispersion testing in the lab began about 2 weeks after the application.

3. Results and discussion

3.1 Lab results

3.1.1 Dispersibility of the reference rock dust (dry powder)

The relative dispersibility of the dry reference rock dust was tested using the 45° nozzle instead of the horizontal nozzle. The resulting average (Figure 4) was used as a benchmark to compare the relative dispersibilities of the foamed dusts. The average integral optical densities (IOD) of the FRD is compared to that of the dry rock dust powder. After all data was normalized, the relative IOD for the reference rock dust was 1 ± 0.11.

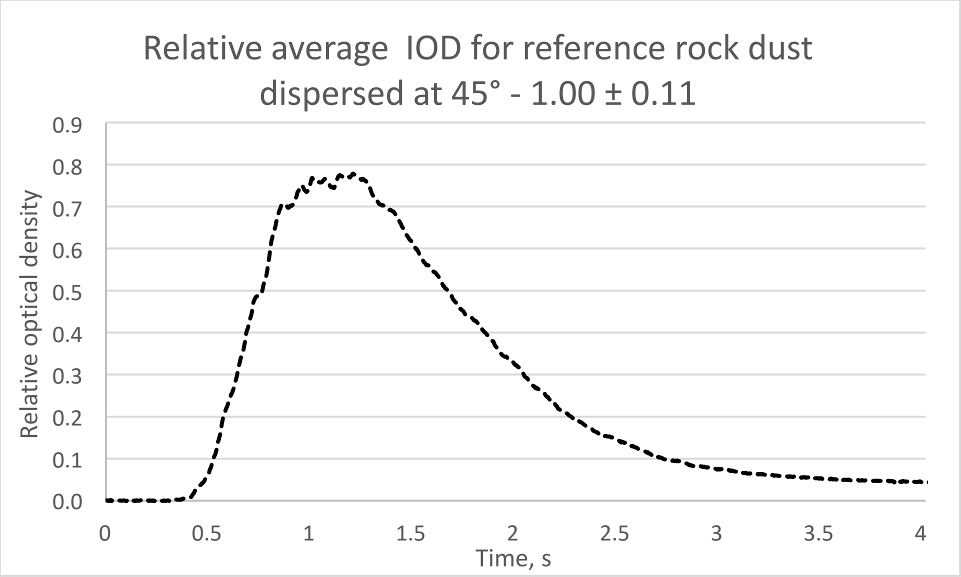

Fig. 4. *Relative average optical density trace of dry reference rock dust*

3.1.2 Environmental/testing conditions of the foam

The effects of high humidity exposure did show a marked negative difference in the dispersibility of the foams when comparing the combined averages from sample sets 1 through 11 (Figure 5). Although a number of samples did disperse after being placed in the humidity cabinets, it was to a lesser extent than when the samples were dried quickly in the laboratory environment.

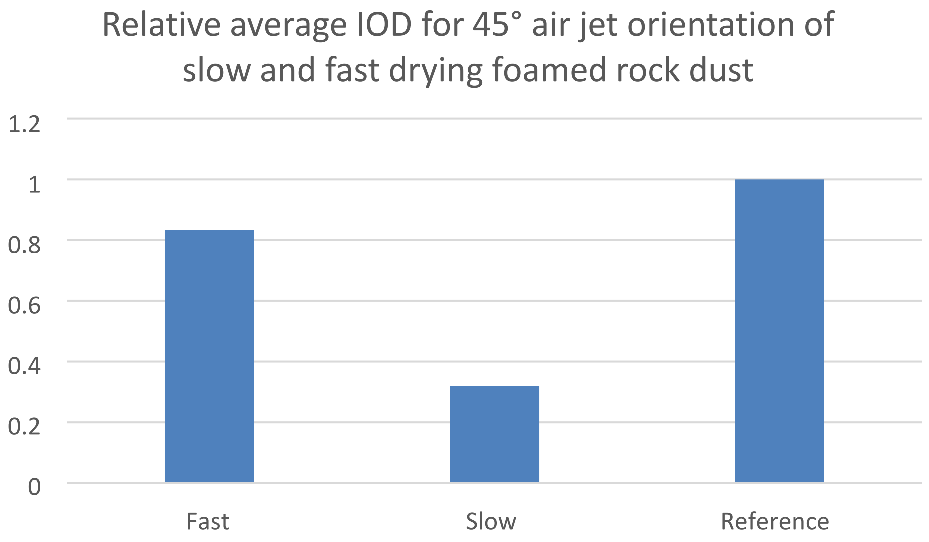

Fig. 5. *Relative average IOD of fast and slow-drying FRDs compared to the reference rock dust*

In some cases, the bubbles in the slow-drying foams began to agglomerate, which stiffened its lattice. These resulting agglomerations remained cohesive enough that when the bulk material broke, the agglomerations fell out of suspension very quickly and did not reach the dust probe, resulting in poorer performance.

3.1.3 Variation in formulation

Using sample sets 1 through 6, researchers found that the increased amount of stabilizer, while aiding in the foam's rigidity during longer periods of high humidity, negatively affected the dispersion characteristics by reinforcing the cohesive characteristics of the dust. Conversely, the lower levels of stabilizer allowed for a rigid yet friable structure which more readily dispersed. Another important note was that few samples collapsed due to insufficient amounts of material being present as the samples dried. Conversely, better dispersion characteristics were seen with samples containing 900 g or 1,500 g of rock dust per batch. These results may be due to the changing ratio of water to rock dust, which, could be affecting the rate of drying per unit volume. The additional material also could be simply translating to more material being entrained and, therefore, more obscuration at the dust probe. Lastly, the formulations which used higher amounts of rock dust had a decreased ratio of stabilizer in the formulation. All these factors may have led to the increases in performance. The results of these variations to the formulation under the fast- and slow-drying conditions can be seen in Figure 6 and Figure 7, respectively.

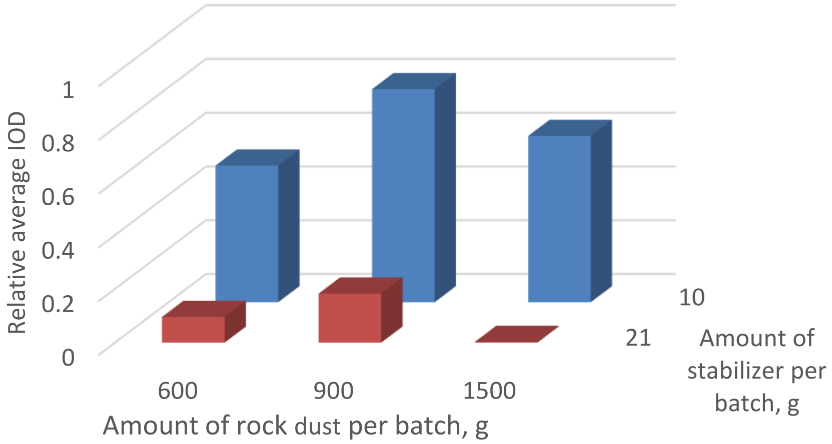

Fig. 6. *Relative average IOD for fast-drying foam formulations from samples 1-6*

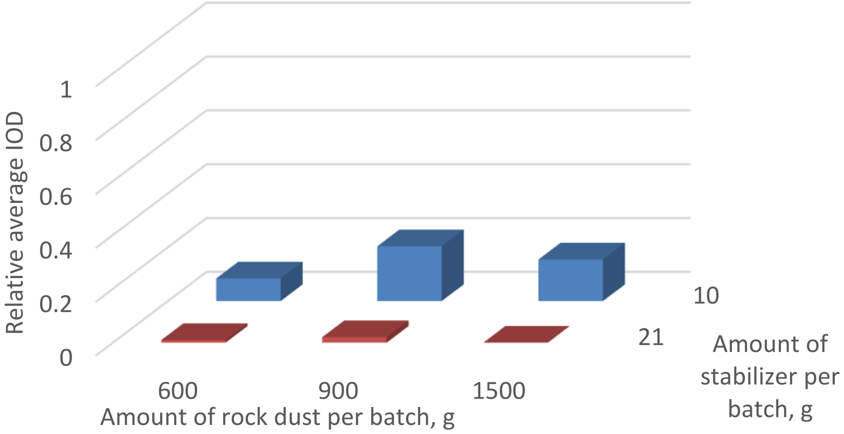

Fig. 7. *Relative average IOD for slow-drying foam formulations from samples 1-6*

The performance of the foam seemed to be most sensitive to levels of stabilizer in the formulation when considering variations to the components of the FRD. Additional efforts were made to keep the amount of rock dust high while decreasing the levels of stabilizer further without causing adverse effects to the foam. To achieve these aims, water was added to the rock dust before being blended into the foam. This practice prevented the rock dust from absorbing too much water out of the foams' lattice, which could have produced negative effects. The results from sample sets 7 through 11 can be seen in Figure 8 for fast-drying samples and Figure 9 for slow-drying samples.

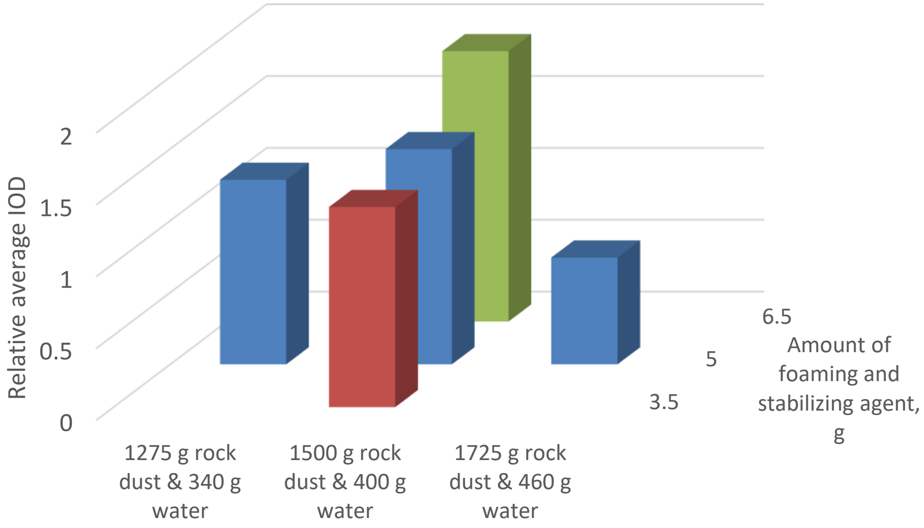

Fig. 8. Relative average IOD for fast-drying foam formulations from samples 7-11

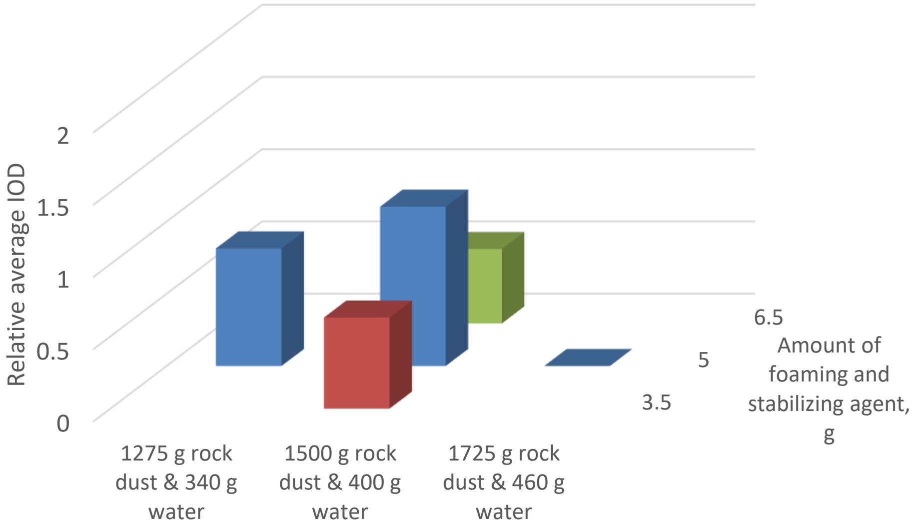

Fig. 9. Relative average IOD for slow-drying foam formulations from samples 7-11

The most consistent formulation that performed well in both the fast- and slow-drying conditions used 1,500 g of rock dust with 400 g of water, while the stabilizer and foaming agent were held at 5 g per batch. This formulation was then compared to the original dry reference rock dust. The obscuration traces are shown in Figure 10.

DOI: 10.7795/810.20200724

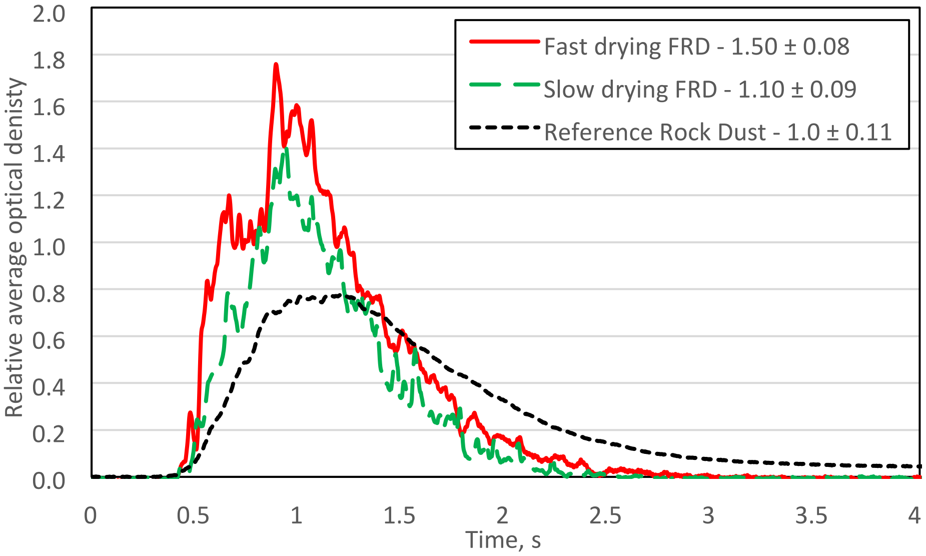

Fig. 10. *Impacts of environmental conditions on the formulation from sample set 8 compared to the dry reference rock dust when dispersed with a 45° nozzle*

The robustness of the foam was then tested using samples sets 12 through 16 where the formulations were held the same, but the rock dust was replaced using other commercially available rock dusts. These tests were conducted to ensure the FRD formulation was applicable with various dusts and that the formulation was not over-optimized for the reference rock dust. The test results are shown in Figure 11 where the relative average IODs are plotted against their respective specific surface areas (SSA).

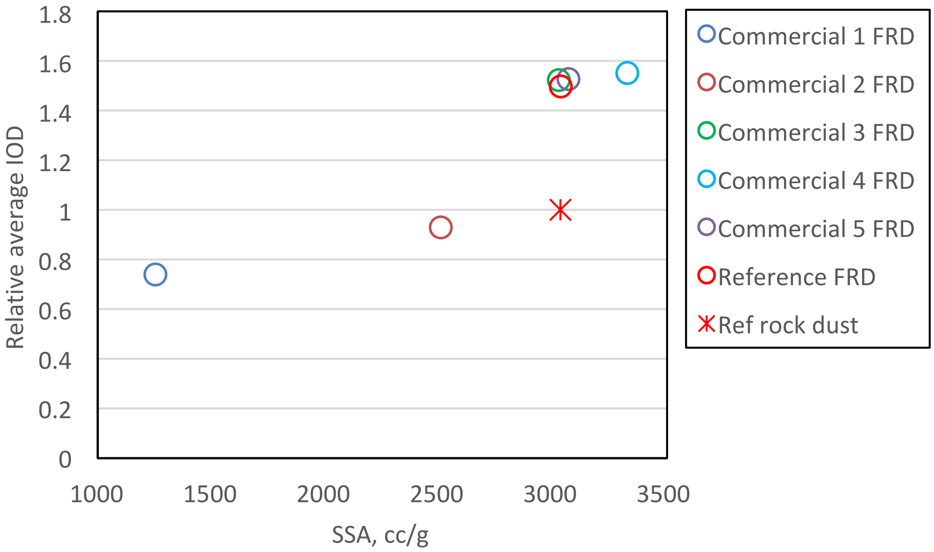

Fig. 11. *The impact of various commercial rock dusts on the foam formulation and the relationship with the rock dusts' SSA.*

When compared to the reference rock dust, the FRD that used a coarser commercial rock dust, commercial rock dusts 1 and 2, did not perform as well as the other rock dusts that had a similar SSA to the reference rock dust. It should also be noted that the coarser dusts also have a larger fraction of particles that fall out of suspension sooner, leading to a drop in performance. To test this, the reference rock dust was classified using a 200- and 400-mesh sieve resulting in the sample sets 17 through 20.

The formula ratios were kept the same for all tests, and the results were plotted in Figure 12 along with the data from sample sets 12 through 16.

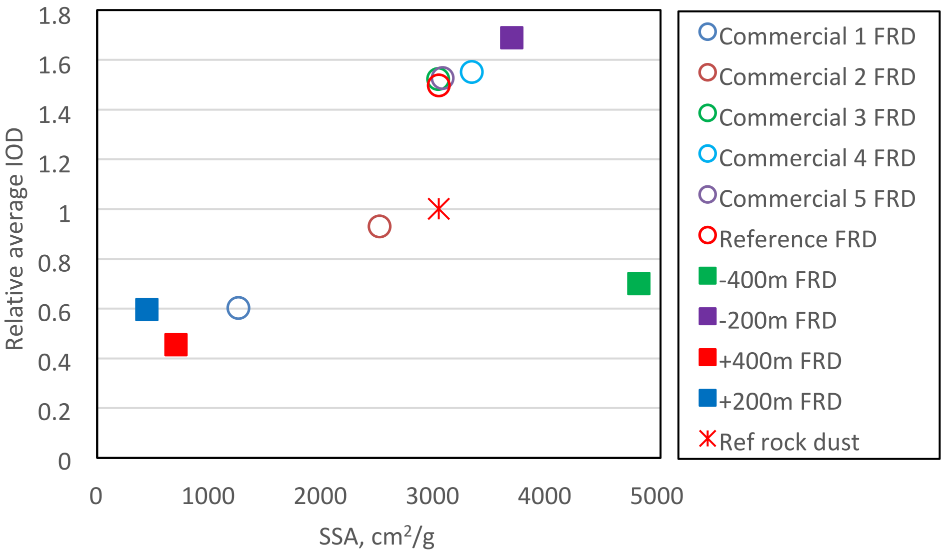

Fig. 12. *The impact of classified rock dusts on the foam formulation and the relationship with the rock dusts' SSA.*

The coarser rock dust size fractions performed as expected with less relative average obscuration at the dust probe. The fine size fraction (-200 mesh) closest to the reference rock dust was found to show good performance. The poor results for the -400 mesh material was, however, unexpected. The initial thought was that the finer size fraction would allow for more particles to be entrained and obscure the dust probe. From this initial data set, it looks like the range of SSA for utilizing this formulation is about 2,500 – 3,500 cm^2/g. The lack of performance from the -400 mesh FRD does not suggest the avoidance of fine material in the mixture but, rather, suggests that the formulation should be altered to better incorporate the ultra-fine dust. The larger surface area allows the ultra-fine material to adsorb more water. This could be alleviated by increasing the amount of water in the formulation that is added to the rock dust before the foam is added so that the rock dust does not draw water out of the foam matrix. It is, however, unlikely that mine operators would choose to use a cut of dust with such a high respirable dust fraction.

3.2 BEM results

3.2.1 Respirable content

During the application of the FRD, the respirable dust content was being recorded. The dust levels were so low that the DPM and gravimetric samples were found to be below the limit of detection. This can sometimes result in negative dust totals, and therefore the gravimetric samples were excluded. The results shown in Table 3 depict the levels during the testing using the personal dust monitors (PDMs). The levels ranged from 0.1 to 0.5 mg/m^3. These levels include the DPM and could be deemed negligible during the production and application of the FRD.

Table 3: *Dust concentrations during the production and application of the FRD 100 ft from the test location in the BEM using PDMs*

	Dust Conc. Total, mg/m^3
Test #1	0.473

Test #2	0.485
Test #3	0.366
Test #4	0.100
Test #5	0.319
Test #6	0.398
Test #7	0.386

The PDM, located 100 ft from the FRD application area, shows higher start and stop concentrations compared to the totals for each test. This is due to the PDM's continuous sampling. These levels accumulated and account for dust that was re-entrained into the mine atmosphere during the activities and movement of personnel and equipment, and not during the production and application of the foam.

3.2.2 Tray samples

During the application process, tray samples were collected and allowed to dry in the same mine environment as the material on the mine roof and ribs. The resulting stabilized weights were used to calculate the dry bulk density of the foam samples. The dry samples were dispersed in the same manner as the lab samples and compared to the reference rock dust. The results are shown in Table 4.

Table 4: *Bulk density and relative average IOD of samples collected during the pilot-scale testing of FRD in the BEM.*

Test	Sample location	Bulk Density, g/cm^3		Relative Average IOD	
		$\bar{X}$	σ	$\bar{X}$	σ
1	Hopper	0.31	0.01	0.82	0.18
	Nozzle	0.46	0.02	0.34	0.07
2	Hopper	0.28	0.03	0.52	0.09
	Nozzle	0.36	0.04	1.20	0.10
3	Hopper	0.23	0.00	1.88	0.10
	Nozzle	0.36	0.02	1.52	0.13
4	Hopper	0.32	0.03	0.86	0.24
	Nozzle	0.44	0.03	0.91	0.21
5	Hopper	0.26	0.01	1.29	0.18
	Nozzle	0.40	0.02	0.75	0.26
6	Hopper	0.28	0.01	1.38	0.48
	Nozzle	0.42	0.02	1.23	0.24
7	Hopper	0.24	0.00	1.31	0.21
	Nozzle	0.24	0.01	1.45	0.17

A discernible trend appears when comparing the dry bulk density of the foam as it moves from the hopper to the nozzle. The increase in density is likely due to the shearing effect of the auger pump, which would cause the matrix to degrade. The only case where there is no difference in the bulk density is the instance where an additional 15% water was added to the rock dust before adding the foam. Similar results would have been expected from the samples that received 15% less rock dust, but the cause of the improved foam stability in this case is not known.

When examining the IOD of the foam samples, no discernible trend is evident. Although the resulting average of all hopper or nozzle samples outperform the reference rock dust, the distribution of the data is too large to make any conclusions. This is clearly seen in the wide variation of the triplicate results. More consideration should be given to selecting the pilot-scale mixing and pumping equipment with an emphasis on the repeatability of foam characteristics.

4. Conclusions

The series of laboratory-produced foamed rock dust (FRD) yielded a wet-applied formulation that performed as well as the dry reference rock dust in the dispersion chamber. The foam's dispersion characteristics were satisfactory under both fast- and slow-drying conditions. The formulation yielded acceptable results when commercially available rock dusts were used in lieu of the reference rock dust. These successes were, however, restricted to rock dusts with a similar specific surface area (2,500 – 3,500 cm^2/g) of the reference rock dust. The pilot-scale testing yielded mixed results with the largest concern being the repeatability of the foams' performances. Future work should focus on selecting more appropriate pumps and mixers to decrease the degradation of the foam during application. Additional testing should focus on producing consistent results from the foam before variations to the formulation are made. Additional research should be conducted with regards to the longevity of the foam. This testing series has shown that degradation occurs in an atmosphere with high humidity, but it is unknown how fast the degradation occurs or how long the foam can be left before a new application is necessary. Lastly, extensive full-scale testing needs to occur to determine the capability of foamed rock dust to suppress a propagating coal dust flame front. Current and future tests are aimed at fulfilling these research needs in conjunction with NIOSH's overarching research aims of minimize the likelihood of mine disasters, including mine explosions.

Disclaimer

The findings and conclusions in this paper are those of the authors and do not necessarily represent the official position of the National Institute for Occupational Safety and Health (NIOSH), Centers for Disease Control and Prevention. Mention of any company or product does not constitute endorsement by NIOSH.

References

Brown C. B., Harris M. L., Perera I. E., and Sapko M. J. (2018). Laboratory Assessment Of Various Rock Dust Foams. 12th ISHPMIE conference, Kansas City, MO.

Cashdollar, K. L., Liebman, I., & Conti, R. S. (1981). Three Bureau of Mines optical dust probes. NASA STI/Recon Technical Report N, 82.

Cashdollar K. L., Sapko M. J., Weiss E. S., Harris M. L., Mann C. K., Harteis S. P., Green G. M. (2010). Recommendations for a New Rock Dust Standard to Prevent Coal Dust Explosions in Intake Airways. Pittsburgh, PA: U.S. Department of Health and Human Services, Public Health Service, Centers for Disease Control and Prevention, National Institute for Occupational Safety and Health, DHHS (NIOSH) Publication No. 2010–151, RI 9679.

Cybulski, W. (1975). Coal dust explosions and their suppression (Vol. 73, No. 54001). Bureau of Mines, US Department of the Interior and the National Science Foundation, Washington, DC

Hartmann, I. (1957). Studies on the Development and Control of Coal-dust Explosions in Mines (Vol. 7785). US Department of the Interior, Bureau of Mines.

Lai, S., Houim, R., & Oran, E. (2018). Effects of Particle Size on Dispersion of Stratified Dust Layers. 12th ISHPMIE conference, Kansas City, MO.

MSHA (2015, July). Retrieved February 26, 2020, Program Policy Manual VOLUME V – COAL MINES https://arlweb.msha.gov/REGS/COMPLIAN/PPM/PMVOL5E.HTM

Nagy, J. (1981). The explosion hazard in mining. US Department of Labor, Mine Safety and Health Administration.

Page, S. J., Volkwein, J. C., Vinson, R. P., Joy, G. J., Mischler, S. E., Tuchman, D. P., & McWilliams, L. J. (2008). Equivalency of a personal dust monitor to the current United States coal mine respirable dust sampler. Journal of Environmental Monitoring, 10(1), 96-101.

Perera, I. E., Sapko, M. J., Harris, M. L., Zlochower, I. A., & Weiss, E. S. (2016). Design and development of a dust dispersion chamber to quantify the dispersibility of rock dust. *Journal of Loss Prevention in the Process Industries*, 39, 7-16.

Richmond, J. K., Liebman, I., & Miller, L. F. (1975). Effect of rock dust on explosibility of coal dust (Vol. 8077). US Department of the Interior, Bureau of Mines.

U.S. Code of Federal regulation (2019). Title 30 CFR, Part 75, Section 75.2, Mandatory Safety Standards—Underground Coal Mines.

U.S. Code of Federal regulation (2019). Title 30 CFR, Part 75, Section 75.402, Rock dusting, and 75.403, Maintenance of incombustible content of rock dust.

U.S. Code of Federal regulation (2019). Title 30 CFR, Part 70, Section 70.100, Respirable dust standards.

DOI: 10.7795/810.20200724

Assessment of Release Mitigation of Water-Reactive Chemicals by Absorbents

Ting-Jia Kao [a], Thanh-Trung Nguyen [a], Yu-Jhen Lin [a], Zhi-Xuan Lin [a], Hsiao-Yun Tsai [a],
Jenq-Renn Chen [a*]

[a] Department of Safety, Health and Environmental Engineering,
National Kaohsiung University of Science and Technology, Kaohsiung, Taiwan

E-mail: *jrc@nkust.edu.tw*

Abstract

Phosphorus oxychloride ($POCl_3$) is a water-reactive and aggressive chemical whose major hazard comes from the clouds of hydrogen chloride (HCl) and the phosphorus compound produced when they escape from containment and exposed to moisture. In this work, we investigated the application of different absorbent for suppressing the fuming from $POCl_3$. A small-scale evaporating chamber was used to facilitate the measurement and evaporation of $POCl_3$ liquid with controlled ventilation. A Fourier-transform infrared (FT-IR) spectroscopy was employed to measure the gases from the exit of the chamber which were then used as an indicator for efficacy of absorbent to suppress the fuming. It was found that the suppression efficiency depends on the amount of PetroGuard®. With increase quantity, the PetroGuard® covered and isolated the $POCl_3$ liquid from evaporation and reacting with moisture. In contrast, neutralization agent Trivorex® will rapidly react with $POCl_3$ releasing excessive heat which in turns vaporize $POCl_3$. About 40% of the $POCl_3$ was vaporized or reacted into HCl and vented into air. The remaining 60 % of $POCl_3$ was neutralized into solid waste. The results are crucial for developing best practices for mitigating the release of water-reactive chemicals.

Keywords: *water-reactive, release mitigation, absorbents*

1. Introduction

Accidental releases or spill of chemicals have been a major contributing factor for fire, explosion and toxic release in chemical process plants and transportation. Effective control and mitigation of the release are crucial for minimizing the dispersion impact and reduce potential fire and explosion. Frequently, water spray or mist have been used as the common means for release mitigation. This is however not a preferred option as added water will increase the final volume of liquid chemical spills. Also, water is also not allowed for water-reactive chemicals such as chlorosilanes and phosphorus oxychloride.

$POCl_3$ has been widely used in manufacture of phosphate esters for plasticizers, flame retardants, hydraulic fluids and other applications (Muller, 2000; Ullmann et al., 1985). It is an aggressive material and described as a skin or sense organ toxicant with the threshold limit value (TLV) of 0.1 ppm or 0.63 mg/m3 (Barsan, 2007). Additionally, the clouds of hydrogen chloride (HCl) is also a major hazard arising from the reaction of $POCl_3$ and water. In reality, liquid pools will be created due to the spillage of $POCl_3$ which will react with water and trigger the exothermic reaction. The energy produced by the reaction increases thus increases the vapor evolution rate. In the period 1990-1999, there were 15 reported incidents in the USA involving spillage of $POCl_3$ causing 144 injuries (Kapias et al., 2001). Unfortunately, there are no detailed reports of any accidents relating to spill of $POCl_3$.

The ASTM F716-09 and ASTM F726-12 standards have been developed for absorbent/adsorbent performance and uptake capacity testing. However, the ASTM standards have some shortcomings that make them unattractive for researchers to use (Bazargan et al., 2015). In particular, they all focused on the uptake capacity testing without reference to vaporization or fuming from the liquid.

It is clear that there is a lack of studies conducted to examine the absorbents in suppressing the fumes generated from the spill of water-reacting/fuming liquids which may affect human health. Tests were conducted in this study by means of a small-scale evaporating chamber and real-time FTIR analysis with the goal of evaluating the different forms of absorbents in terms of their capability to suppress the fuming.

2. Experiments

2.1 Materials

The phosphorous Oxychloride used in this work was obtained from J. T. Baker Chemical Company, Phillips burg, New Jersey with a stated purity of greater than 99.97%. Sorbents with different properties were used including PetroGuard® chemical spill absorbent and Trivorex® neutralizing absorbent. PetroGuard® is a sponge, soft polymeric materials as shown in Fig. 6 that solidifying chemical and oil spill. It is also claimed that with PetroGuard®, most common water reactive chemicals, hazardous hydrocarbons and silicone-based chemicals are absorbed, encapsulated, solidified, immobilized, and stabilized quickly and effectively absorbent (Guardian Environmental Technologies, 2020). Trivorex® is a neutralizing absorbent which may neutralize acids, bases, oxidizing agents, reducing agents, and solvents (Prevor, 2020). It is also claimed that the neutralization process will help to suppress the emission of hazardous gases from corrosive chemicals. There is however no report with quantifying efficacy on both absorbents.

2.2 Equipment

The experimental equipment consisted essentially of evaporating chamber and a FTIR spectroscopy. Fig. 1 shows the configuration of the small-scale evaporating chamber used in this work to facilitate the measurement of vaporization and fuming from a liquid pan with controlled ventilation. This chamber is made of stainless steel and equipped with 3 removable sight glasses to facilitate visual check. The ventilation rate was controlled by a mass-flow-controlled air stream to a fixed 20 slm with a known dew point temperature of 10.2±0.4 °C. A hood was mounted to the exit of the chamber having an area of 100 × 100 mm to capture the vented gases for subsequent gas treatment.

The stainless-steel evaporating pan had an area of 200 × 200 mm and was 20 mm deep. During the test, the weight of the pan containing $POCl_3$ liquid and sorbent was recorded by using a precision scale; the temperature was monitored by means of a type K thermocouple immersed in the test substance.

A FT-IR instrument with a 10 cm light path gas cell was employed to measure the concentration of gasses from the exit of the chamber which was used as the indicator for efficacy of the absorbent to suppress the fuming. The wave number range considered was from 600 to 4000 cm^{-1}. Spectra were obtained every 2.14 seconds with a resolution of 1 cm^{-1}.

The chemical functional groups of the sorbents were determined by a Smiths IdentifyIR Attenuated Total Reflection (ATR) Fourier transform infrared spectrometer with a scan range of 650–4000 cm^{-1}.

DOI: 10.7795/810.20200724

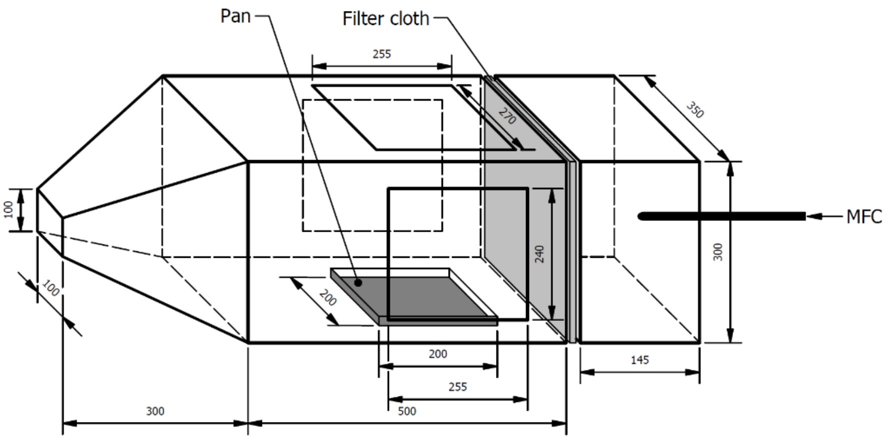

Fig. 1. Detail drawing of evaporating chamber

2.3 Experimental procedure

After the evaporating pan was filled with around 170 g of liquid $POCl_3$, the system was then allowed to come to equilibrium. The time required to come to equilibrium in the first stage was usually 10 to 20 minutes. The system was considered to be in equilibrium when the concentration of the vented gases stays constant.

Once the equilibrium of the first stage had been established, the top sight glass was dismantled and a given amount of absorbent was then applied and spread evenly over the surface of the liquid $POCl_3$. The sight glass was quickly reassembled. The experiment ended when the system was in equilibrium which took 45 to 230 minutes depending on the testing sorbent.

All tests were performed at room temperature. The temperature and weight of the substance were recorded, along with the concentrations of vented gases. The identification and quantification of gases were confirmed by IR spectra of gaseous $POCl_3$, HCl and CO_2.

3. Results and discussion

3.1 The characterization of test sorbents

According to Fingas and Fieldhouse (2011), styrene-butadiene and related polymers have been the most common materials of polymer sorbents. The IR spectrum of PetroGuard® (Fig. 2) is similar to that of butadiene styrene polymer observed in several studies (Liu et al., 2019; Luna et al., 2020; Zieba-Palus, 2017) that the band at 697 and 755 cm^{-1} are attributed to CH deformation vibrations in styrene aromatic rings; the weak bands at 1491 and 1599 cm^{-1} can be assigned to ring vibrations of styrene; the weak bands at 745, 963, and 907 cm^{-1} can be assigned to 1,4 cis-butadiene, 1,4 trans-butadiene and 1,2-butadiene segment, respectively; the bands at 1377 and 1452 cm^{-1} can be attributable to CH_3 deformation vibrations; the bands at 2848, 2917, and 2955 cm^{-1} can be assigned to C-H stretching vibrations; and the bands at 2917 and 2848 cm^{-1} can also be assigned to elongation of CH groups in styrene aromatic rings. The integration of these peaks indicates that PetroGuard® contains mainly butadiene styrene polymer.

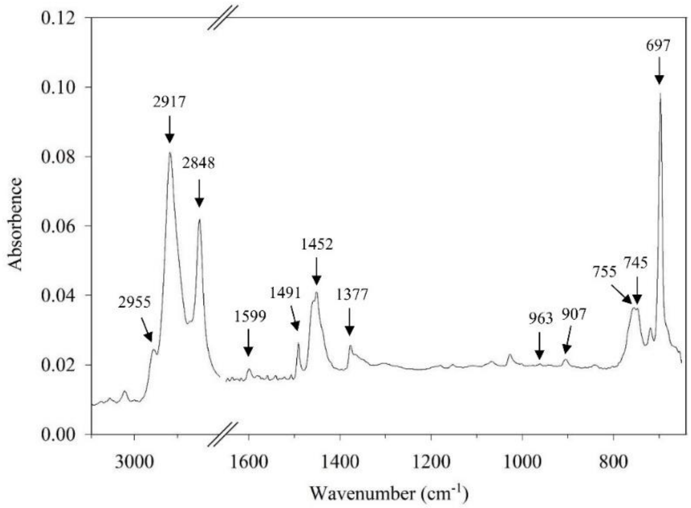

Fig. 2. *IR spectrum of PetroGuard® absorbent*

Fig. 3 compares the IR spectrum of Trivorex® and sodium bicarbonate ($NaHCO_3$). As a result, Trivorex® contains significant amount of sodium bicarbonate due to the obvious similarities at 687, 829, 1393, 1609, and 1905 cm^{-1}. In addition, the band at 1085 cm^{-1} may be due to the Si-O-Si asymmetric vibrational mode of stoichiometric silica (SiO_2) (Tolstoy et al., 2003). These observations are in agreement with Mathilde et al. (2019). These peaks confirm that Trivorex® contains mainly $NaHCO_3$ which is a common neutralizing agent.

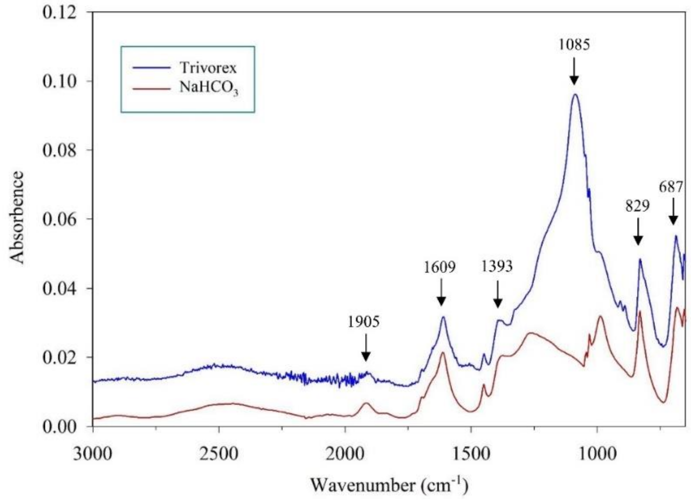

Fig. 3. *IR spectra of Trivorex® neutralizing absorbent and sodium bicarbonate ($NaHCO_3$)*

3.2 *The efficacy of PetroGuard®*

The effectiveness of PetroGuard® applied to $POCl_3$ was quantitatively judged by performing the test with different amount of absorbent. In the first test, 129.59 g of PetroGuard® was applied to 164.92 g $POCl_3$. Fig. 4 shows the concentration of $POCl_3$ and HCl of the gases measured at the exit of the chamber. It shows that after 6 minutes $POCl_3$ liquid was poured into the pan, the system was in equilibrium with the average $POCl_3$ and HCl concentration of 798.5 and 803.3 ppm, respectively and the temperature of the liquid increase slightly from 30 to 31.4 °C. During this period, the average weight loss is 0.311 g/min.

Immediately after applying the PetroGuard®, fuming was stopped with no detectable $POCl_3$ or HCl. However, HCl appeared again after 2 min and $POCl_3$ also reappear for another 2 minutes. After 50 minutes of applying PetroGuard® to the pan containing $POCl_3$, the concentration of $POCl_3$ and HCl were found to be steady at 447.9 ppm and 967.0 ppm, respectively; the temperature slightly increased from 30.5 to 33.2 °C. During this period, the average weight loss is 0.166 g/min. According to Fingas and Fieldhouse (2011), the disadvantage of this type of solidifier, styrene-butadiene-containing absorbent, is that the absorbate can be released, especially under some pressure. Therefore, right after coming into contact, $POCl_3$ was quickly absorbed by PetroGuard® that can explain for the period of 2 minutes without fuming and detectable $POCl_3$ or HCl. $POCl_3$ was then released slowly and reacted with moisture to form HCl leading to a significant decrease of 44% of $POCl_3$ concentration (from 798.5 to 447.9 ppm) while 20% increase in HCl concentration was observed (from 803.3 to 967.0 ppm). Based on the experimental observation, we presumed that there was no chemical reaction between $POCl_3$ and PetroGuard®. Therefore, the hydrolysis reaction of $POCl_3$ and moisture yielding HCl is responsible for the temperature rise in this test. Abatement efficiencies based on measured drops in $POCl_3$ concentration and weight loss rate are 43.3% and 46.6%, respectively. The same reduced weight loss rate and reduced $POCl_3$ concentration suggests that the PetroGuard® helps to suppress the vaporization of $POCl_3$ liquid through absorbing the liquid. Nevertheless, the surface of the absorbed materials remains continued to emit vapor as well undergo hydrolysis with moisture.

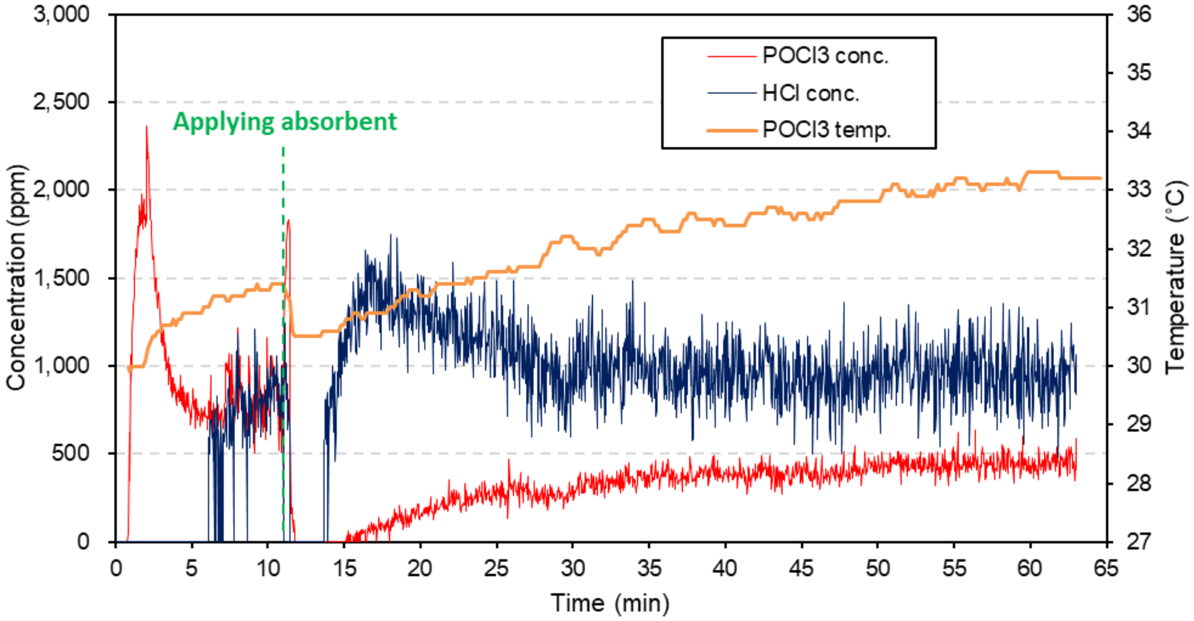

Fig. 4. Results for suppressing 164.92 g of $POCl_3$ with 129.59 g of PetroGuard® absorbent

In the second test, 251.5 g of PetroGuard® was applied to 168.1 g of $POCl_3$. Fig. 5 shows that after 35 minutes applying PetroGuard® to $POCl_3$, the average steady concentrations of $POCl_3$ and HCl decreased significantly from 813.1 ppm to 196.9 ppm and from 1072.4 ppm to 558.5 ppm, respectively with a higher the abatement efficiency of 75.3 % compared to 43.3 % in the first test. The steady weight loss rate was decreased from 0.322 g/min to 0.062 g/min, giving an abatement efficiency of 80.7% which is comparable to the abatement efficiency based on reduced $POCl_3$ concentration. Therefore, with increase quantity the PetroGuard® may covered and isolated the $POCl_3$ liquid from evaporation and reacting with moisture. Fig. 8 shows the $POCl_3$ liquid, $POCl_3$ liquid covered with PetroGuard®, and absorbed PetroGuard®. The absorbed PetroGuard® was soft, wet and still emitting vapor. Thus, PetroGuard® may provide a rapid vapor suppression of the fuming liquid right after the spills. The rapid suppression is useful for evacuating the nearby community but the complete removal or abatement still requires other response actions as the absorbed materials remain fuming.

DOI: 10.7795/810.20200724

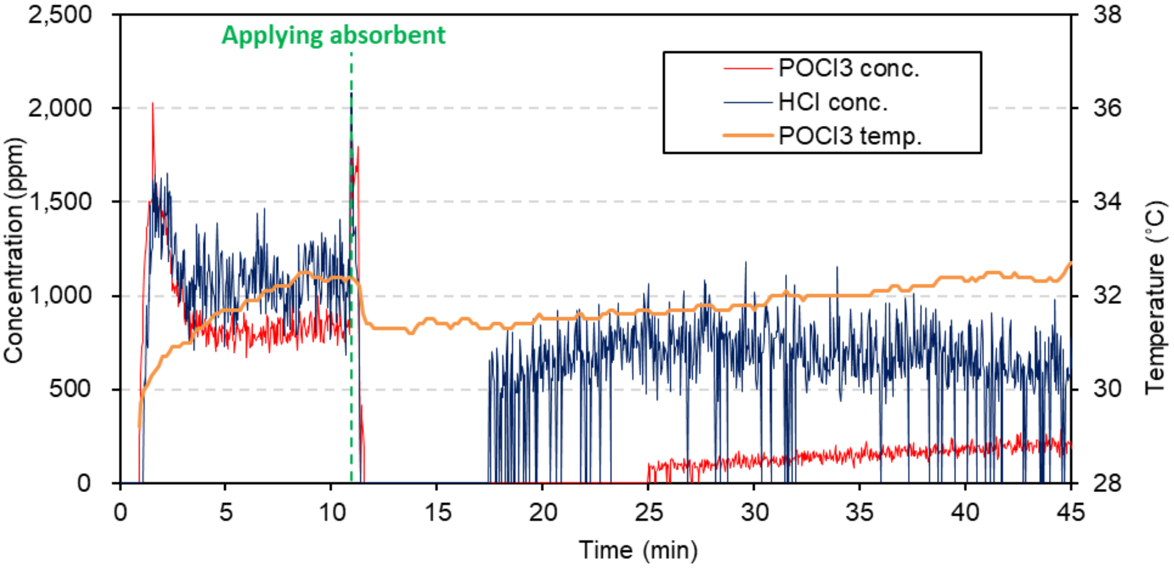

Fig. 5. *Results for suppressing 168.10 g of $POCl_3$ with 251.1 g of PetroGuard® absorbent.*

3.3 The efficacy of Trivorex®

In this test, 128.24 g of Trivorex® was applied into 172.92 g of $POCl_3$. In the first stage, the system was in equilibrium after 15 minutes with a steady weight loss rate of 0.304 g/min. The reaction behavior between $POCl_3$ and Trivorex®, however, was much different from that of PetroGuard®. In particular, an immediately violent reaction with vigorous boiling took place when Trivorex® and $POCl_3$ came into contact. The temperature soared quickly from 32.3 to 108.5 °C in 3 minutes accompanied by a large amount of gaseous $POCl_3$, HCl and CO_2 as shown in Fig. 6. After around 210 minutes applying Trivorex®, the temperature then gradually dropped to 34.1°C and the $POCl_3$ concentration was found to be less than the limit of detection of it to FT-IR (50~60 ppm). Sodium bicarbonate containing in Trivorex® as a neutralizing agent which may trigger highly exothermic reactions and the evolution of CO_2 according to the following schemes:

$$NaHCO_3 + HCl \rightarrow NaCl + H_2O + CO_2 \tag{1}$$

$$3NaHCO_3 + POCl_3 \rightarrow H_3PO_4 + 3NaCl + 3CO_2 \tag{2}$$

Fig. 7 shows the real weight of $POCl_3$ and absorbent monitored by the precision scale during the experiment. It is clear that the real weight loss was divided into two apparent parts. In the first part, after 40 seconds applying Trivorex®, the weight loss was 71.12 g (decreased from 302.62 to 231.5 g). In the second part, the weight loss continued gradually from 231.5 g to 208.45 g before slightly increased again. The total weight loss after applying Trivorex® was 94.16 g.

The rapid weight loss is accompanied by spikes in CO_2 and $POCl_3$ concentration to more than 60,000 and 30,000 ppm, respectively. The spikes were however dropped quickly in 30 s to less than half of these peak values. In addition, CO_2 was completely diminished by 8 min after the application. The presence of CO_2 is a direct evidence of neutralization according to scheme (2). The spikes in CO_2 and $POCl_3$ concentrations and weight loss confirm that the weight loss is a direct consequence of neutralization and vaporization of $POCl_3$. However, the measured concentration of CO_2 and $POCl_3$ are far less than the corresponding weight loss which indicates that the FTIR concentration measurement is incapable to cope with such high concentration. The ratio of measured peak concentration of CO_2 and $POCl_3$ is about 2 which may provide an indication of relative contribution of neutralization and vaporization. The weight fraction of CO_2 in the total weight loss can thus be calculated to around 0.36 based on molar ratio of CO_2 to $POCl_3$. Thus, approximately 25.6 g of the weight loss can be attributed to neutralization reactions while the remaining 45.52 g is attributed to the vaporization of $POCl_3$. The second part of the weight loss was purely vaporization which is 23.05 g. Total vaporization of $POCl_3$ is 45.54+23.05 = 68.59 g which accounts for 40% of the total liquid spilled in the pan. Thus, an estimation of the gross efficacy of abatement by Trivorex® is approximately 60%.

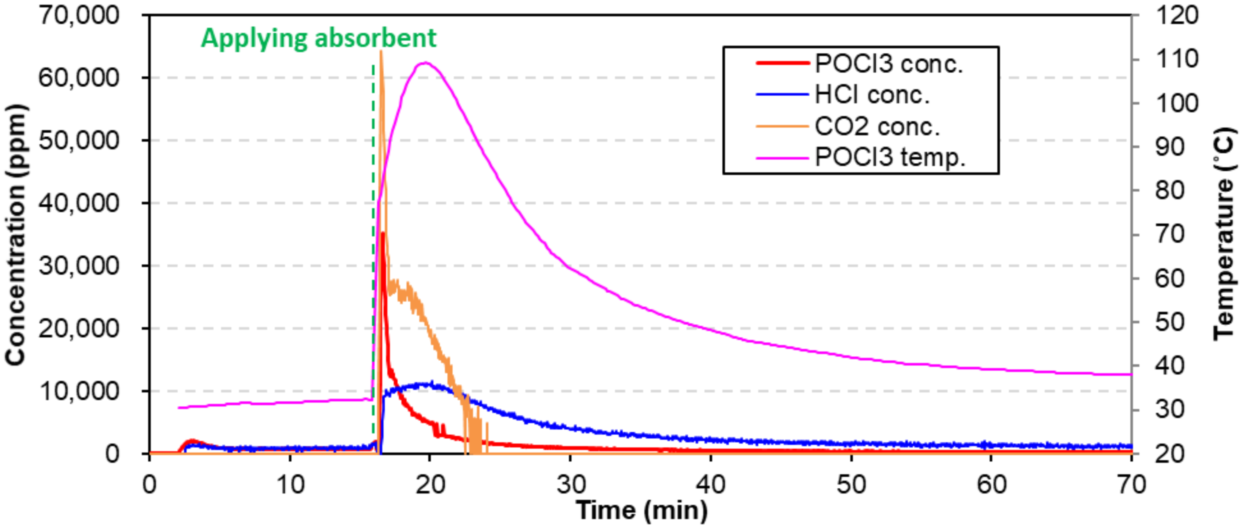

Fig. 6. *Results for suppressing 172.92 g of $POCl_3$ with 128.24 g of Trivorex® neutralizing absorbent*

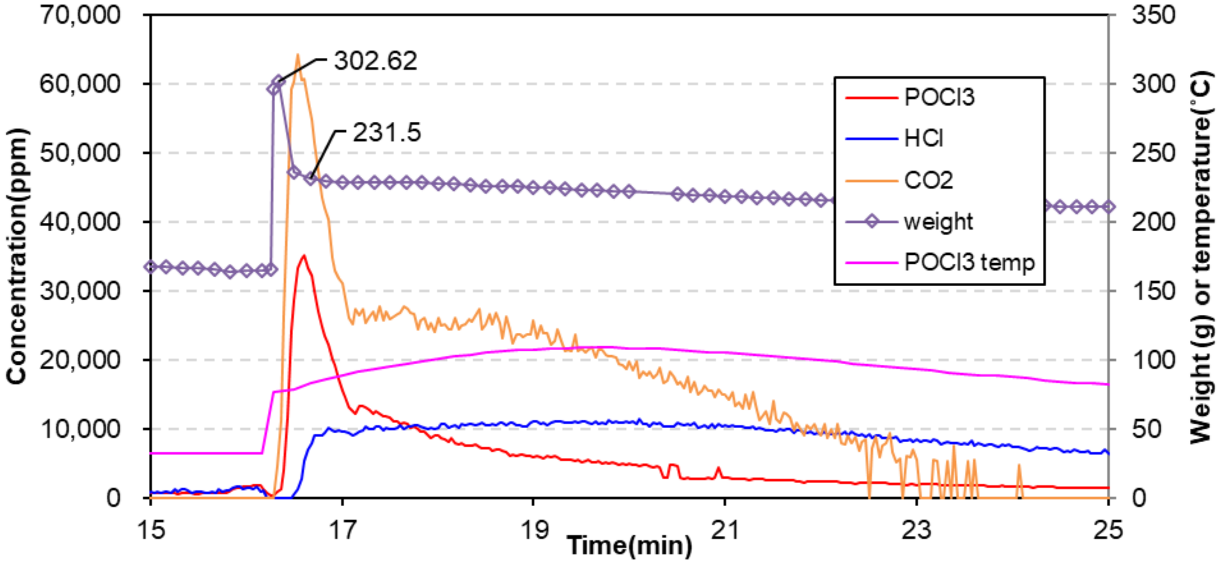

Fig. 7. *The weight of liquid $POCl_3$ and absorbent during the experiment*

3.4 Discussions

Fig. 8 shows the photos of $POCl_3$ liquid, $POCl_3$ liquid covered with PetroGuard®, and absorbed PetroGuard®. The absorbed PetroGuard® was soft, wet and still emitting vapor. Thus, PetroGuard® may provide a rapid vapor suppression of the fuming liquid right after the spills. The rapid suppression is useful for evacuating the nearby community but the complete removal or abatement still requires other response actions as the absorbed materials remain fuming.

Fig. 8. *Photos from left to right: $POCl_3$ liquid, $POCl_3$ liquid covered with PetroGuard®, and absorbed PetroGuard®.*

Fig. 9 shows the photos of $POCl_3$ liquid before and after neutralized with Trivorex®. Although the neutralized Trivorex® is no longer fuming with very limited HCl detected, care must be taken due to the violent exothermic reaction with vigorous boiling leading to a significantly higher evaporation rate of $POCl_3$ and evolution of HCl. Without doubt, the vaporization will create a large impact on the nearby communities. In fact, it will be a challenging task even for emergency responders in applying Trivorex® owing the excessive heat.

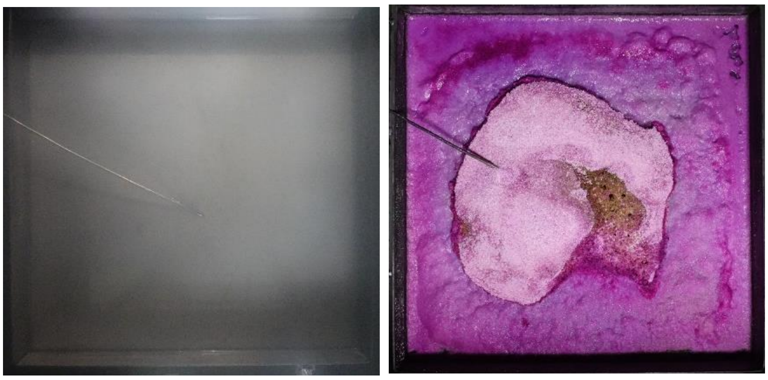

Fig. 9. *Photos from left to right: $POCl_3$ liquid before and after neutralized with Trivorex®.*

In comparison of the two absorbents, one being temporarily suppressing vaporization while the other one provides ultimate abatement through neutralization, both suffer different drawbacks and great cares are required for applying both absorbents. More work is certainly needed to develop a better material and/or method for abating the spill of water-reactive/fuming chemicals. Finally, the current design of chamber provides a consistent and insightful way to assess the risks associated with the abatement of chemical spills.

4. Conclusions

We have developed a chamber method to investigate the efficacies of different commercial absorbents including PetroGuard® and Trivorex® for suppressing the fuming from $POCl_3$ spills. Excessive amount of PetroGuard® will absorb and suppress the fuming effectively. In contrast, neutralization agent Trivorex® will react violently with $POCl_3$ releasing excessive heat leading to the higher evaporation rate of $POCl_3$ and the evolution of HCl gas. The results are crucial for developing best practices for mitigating the release of water-reactive chemicals.

References

Barsan, M.E., 2007. NIOSH pocket guide to chemical hazards.

Bazargan, A., Tan, J., McKay, G., 2015. Standardization of oil sorbent performance testing. *Journal of Testing and Evaluation,* 43, 1271-1278.

Fingas, M., Fieldhouse, B., 2011. Review of solidifiers. in: *Oil spill science and technology*. Elsevier, 2011, pp. 713-733.

Kapias, T., Griffiths, R., Stefanidis, C., 2001. REACTPOOL: a code implementing a new multi-compound pool model that accounts for chemical reactions and changing composition for spills of water reactive chemicals. *Journal of hazardous materials,* 81, 1-18.

Liu, J., Min, X., Zhang, X., Zhu, X., Wang, Z., Wang, T., Fan, X., 2019. A novel synthetic strategy for styrene–butadiene–styrene tri-block copolymer with high cis-1, 4 units via changing catalytic active centres. *Royal Society open science,* 6, 190536.

Luna, C.B.B., Araújo, E.M., Siqueira, D.D., Morais, D.D.d.S., Filho, E.A.d.S., Fook, M.V.L., 2020. Incorporation of a recycled rubber compound from the shoe industry in polystyrene: effect of SBS compatibilizer content. *Journal of Elastomers & Plastics,* 52, 3-28.

Mathilde, N., Mathieu, L., Blomet, J., Meyer, M.-C., 2019. Pollution removal composition and use thereof. in: Google Patents.

Muller, T.L., 2000. Sulfuric acid and sulfur trioxide. *Kirk-Othmer Encyclopedia of Chemical Technology*.

Prevor Trivorex®. https://www.prevor.com/us/trivorex.

Tolstoy, V.P., Chernyshova, I., Skryshevsky, V.A., 2003. *Handbook of infrared spectroscopy of ultrathin films*. John Wiley & Sons.

Ullmann, F., Gerhartz, W., Yamamoto, Y.S., Campbell, F.T., Pfefferkorn, R., Rounsaville, J.F., 1985. *Ullmann's encyclopedia of industrial chemistry*. VCH publishers.

Zieba-Palus, J., 2017. The usefulness of infrared spectroscopy in examinations of adhesive tapes for forensic purposes. *Forensic Sci. Criminol.,* 2, 1-9.

DOI: 10.7795/810.20200724

Modeling of Explosion Dynamics in Vessel-Pipe Systems to Evaluate Performance Limitations of Explosion Isolation Systems

Lorenz R. Boeck, C. Regis Bauwens & Sergey B. Dorofeev
FM Global, Research Division, Norwood, MA, USA
E-mail: lorenz.boeck@fmglobal.com

Abstract

Explosion isolation systems provide critical protection for interconnected vessels and work areas, preventing the spread of explosions through interconnecting pipes and ducts. These systems not only prevent propagating events, but also mitigate the elevated explosion hazards of interconnected vessels, caused by pressure piling and enhanced turbulence. Explosion isolation systems can, however, fail catastrophically if they are not properly designed for a use case.

Evaluating the performance limitations of explosion isolation systems includes assessing their pressure resistance, flame-barrier efficacy, and appropriate installation distances, which typically requires extensive testing. To predict the performance of a system for use cases outside the tested conditions, models are needed that reliably predict both the explosion dynamics and isolation system response.

In this study, a previously developed physics-based model for explosions in vented vessel-pipe systems is further extended and validated. Large-scale validation experiments were performed at an 8-m^3 vessel with attached pipes, varying the pipe dimensions, ignition location, and mixture reactivity. It is found that the model captures the effects of the experimentally varied parameters, and accurately predicts the time available for isolation systems to form a flame barrier. These results show how this model can help predict installation distances as part of the overall performance limitations of explosion isolation systems, extending the range of use cases and reducing the number of tests needed for system evaluation.

Keywords: *experiments, explosion isolation, modeling, vessel-pipe systems*

Nomenclature

Symbol	Description	Units	Values
a	Flame cone base radius	(m)	
D_P	Pipe diameter	(m)	
h	Flame cone height	(m)	
k_V	Calibration parameter for flame advection	(-)	0.35
L_P	Pipe length	(m)	
p	Vessel pressure	(Pa)	
R	Vessel radius	(m)	
r_f	Flame radius	(m)	
R_V	Vent radius	(m)	
u_x	Advection velocity at the leading flame-tip position	(m/s)	
X	Fuel concentration, by volume	(%)	
x_f	Flame tip position	(m)	
x_f*	Flame tip position in coordinates of the virtual origin	(m)	
α	Flame cone angle	(rad)	
γ_V	Ratio of heat capacities of vented gases	(-)	
ρ_V	Density of vented gases	(kg/m^3)	
ζ	Ignition location parameter	(-)	0.25; 1; 2

1. Introduction

Explosion isolation is a key element of explosion protection that mitigates the effects of explosions in interconnected vessels (Hattwig and Steen, 2008). Figure 1 illustrates an explosion originating in a primary vessel or piece of equipment and propagating through an interconnecting pipe toward a secondary vessel. Compared to isolated vessels, interconnected vessels present a more severe explosion hazard: As combustion occurs in the primary vessel, pressure increases in both vessels; pressure is elevated in the secondary vessel when the flame enters, and the peak explosion pressure increases proportionally. This effect is known as pressure piling. In addition, turbulence is enhanced in the pipe and in the secondary vessel due to the flow generated ahead of the flame, leading to higher rates of pressure rise, which may overwhelm explosion protection designed to protect individual vessels. A highly turbulent flame-jet entering the secondary vessel similarly enhances the rate of pressure rise. (Bartknecht, 2012; Eckhoff, 2016; Taveau, 2017)

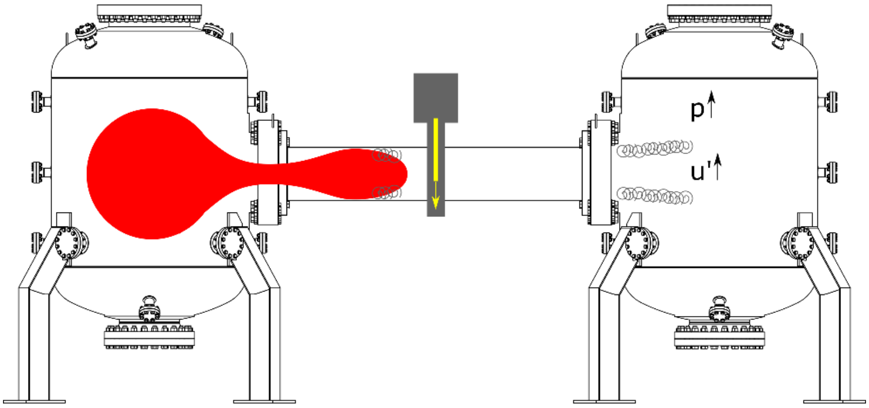

Fig. 1. *Illustration of explosion in interconnected vessels. Combustion produces turbulence ahead of the flame and elevates pressure, resulting in pressure piling and high rate of pressure rise. Explosion isolation valve closes pipe cross-section to prevent flame spread.*

To prevent these hazardous effects, and prevent flame spread, explosion isolation systems are installed at interconnecting pipes to form a flame barrier in the event of an explosion. Both active and passive systems are commonly used, which activate electronically based on pressure or flame detection, or are triggered by pressure waves and flow ahead of the flame, respectively.

To successfully isolate an explosion, an isolation device must satisfy three criteria, including:

(i) pressure resistance: the isolation device must withstand the explosion overpressure;
(ii) barrier efficacy: the flame barrier formed by the device must prevent transmission of flame and/or hot gases/material that may cause re-ignition downstream;
(iii) rapid barrier formation: an effective flame barrier must be formed before the flame arrives at the device location and maintained for the duration of the explosion.

As all isolation systems require some finite time to respond, the third requirement translates into a minimum necessary installation distance for an isolation system, the distance along the pipe between vessel and isolation device, which allows time for the barrier to develop prior to flame arrival. The installation distance depends on the specific use case, determined by parameters such as vessel and pipe dimensions, mixture reactivity, ignition location, and the presence of additional explosion protection measures such as venting or suppression. To determine installation distances, existing testing standards, such as EN 15089, *Explosion Isolation Systems*, require a significant number of tests. Such tests can only be performed in a narrow parameter range, limited by available experimental facilities and cost. As a result, testing in large vessels, representative of installations such as spray dryers with volumes of several hundred cubic meters, is typically infeasible. In order to economically assess the performance of these devices over a wide range of scenarios, dedicated methods are needed to scale the results from tested configurations to practical use cases. Currently, the methods used by manufacturers to accomplish such scaling are largely proprietary.

The objective of the present work is to develop a method that determines the performance limitations of explosion isolation systems that can accommodate a wide range of use cases, reducing the number of physical tests needed to establish performance limitations compared to current testing standards. A combined testing and physics-based modeling approach is pursued: Testing assesses the pressure resistance and flame-barrier efficacy of the device, as well as the actuation dynamics of the isolation system. A physics-based model is then used to predict explosion dynamics for a wide range of use cases. The actuation dynamics measured for a specific isolation system are then combined with the model predictions to determine appropriate installation distances.

This paper extends and validates a previously developed physics-based explosion dynamics model (Boeck et al., 2018), using data from large-scale explosion tests in vented vessel-pipe systems. The paper describes the experiments performed, reviews the explosion dynamics model at a high level, and compares model predictions with experiments, demonstrating the capability of the model to determine installation distances.

2. Experiments

Experiments and model validation for confined and vented explosions were presented in previous work (Boeck et al., 2018; Boeck et al., 2019). The present paper focuses on experiments and modeling of vented vessel-pipe systems. The experimental setup used for these tests included an 8-m^3 vessel and pipes with different dimensions.

While propane-air, methane-air and dust explosion experiments were performed for this study, this paper exclusively focuses on the results of propane-air mixtures. It should be noted that while dust explosion mitigation is a primary application of explosion isolation systems, gas mixtures provide well-defined initial conditions and can be modeled using intrinsic mixture properties. In contrast, the dynamics of dust explosions depend largely on the dust injection parameters of the individual experimental setup. In the present study, gas explosions serve as model validation, which will be extended in a future study to reproduce dust explosions.

2.1 Setup

Figure 2 shows a schematic of the 8-m^3 vessel used for the present experiments, with a pipe attached to the side-flange of the vessel. Two pipe lengths, L_P = 4.88 m and L_P = 9.75 m, and three pipe diameters, D_P = 0.1 m, D_P = 0.2 m, and D_P = 0.4 m, were examined.

The vessel was vented through its top flange to prevent deflagration-to-detonation transition and excessive overpressure in the experiments, which is consistent with typical explosion protection used in practical applications. Aluminum foil with a thickness of 0.076 mm was used as the vent material, providing well-defined vent deployment pressures. By varying the number of foil layers, the deployment pressure was adjusted to properly vent each test, as will be discussed further in Sec. 4.

DOI: 10.7795/810.20200724

Non-reactive, quasi-steady pressurization tests were used to determine the static vent deployment pressures and associated uncertainties as a function of the number of foil layers, given in Table 1.

Table 1: *Static vent deployment pressure as a function of the number of foil layers.*

Number of foil layers	1	2	3	4
Static deployment pressure (kPa)	9.5±0.3	17.8±0.5	25.8±0.8	33.5±1.0

The pipe exit was sealed by a steel plate during mixture preparation, held in place with electromagnets, and removed one second prior to ignition. Thus, the pipe exit was fully open at the time of ignition.

A weak electric spark was used to ignite the mixtures at different locations along the horizontal centerline of the vessel ($y = 0$ m). Ignition was affected at one of three locations in each test: the vessel center ($x = 0$ m); the back-wall opposite of the pipe entrance ($x = -0.95$ m); or near the pipe entrance ($x = 0.95$ m).

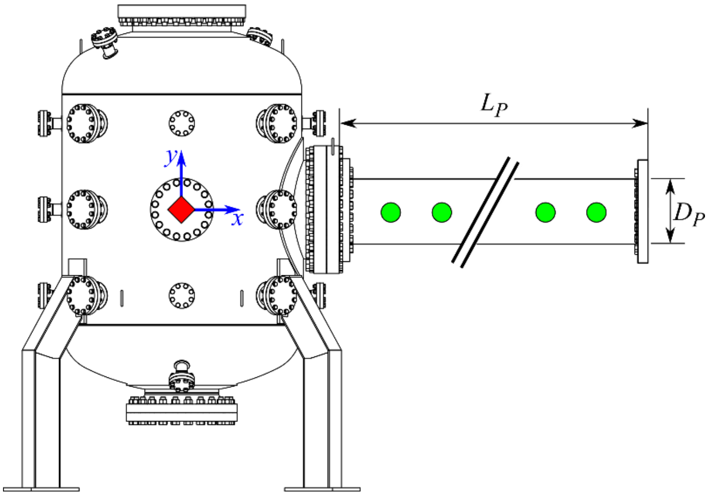

Fig 2. *Experimental test setup used, showing 8-m^3 vessel and pipe dimensions. The red marker depicts the vessel pressure transducer location; green markers depict locations of pipe transducers.*

2.2 Diagnostics

The diagnostics used to characterize each test included pressure transducers, flame detectors, and a high-speed video camera. Three piezoresistive pressure transducers, type Kistler 4260A 0-350 kPa, measured pressures in the vessel. The vessel pressure traces reported in this paper were taken from the transducer located at the side flange marked in Fig. 2 with a red diamond, and the other two signals taken at different flanges were used to verify the measurement. Pipe instrumentation included piezoelectric pressure transducers, type Kistler 211B 0-350 kPa, and flame detectors, type Thorlabs PDA36A2, connected to the pipe via optical fibers. At each axial location given in Table 2, both a pressure transducer and a flame detector were installed, although pressure data from the pipe will not be discussed in the present paper. All data was acquired at a rate of 20 kHz, and pressure data was post-processed with a low-pass filter (3rd order Butterworth, 2 kHz cut-off, applied forward/backward for zero phase shift). A high-speed video camera (Phantom Flex) operating at 1 kHz captured the times of vent deployment and flame exit from the vent and the pipe, and high-speed video was used to determine the vent deployment pressures in each test, along with the pressure measurements.

Table 2: *Sensor locations along the pipe, relative to vessel flange.*

Pipe length L_P = 4.88 m

Sensor number	1	2	3	4	5	6	7	8	9
Sensor location (m)	0.30	0.61	1.22	1.83	2.44	3.05	3.66	4.27	4.57

Pipe length L_P = 9.75 m

Sensor number	1	2	3	4	5	6	7	8	9	10
Sensor location (m)	0.30	0.61	1.83	3.05	4.27	5.49	6.71	7.92	9.14	9.45

A gas sampling and analysis system verified the mixture composition before each test. Samples were pulled from the vessel and analyzed using independent speed-of-sound (SRS BGA244) and infrared absorption measurements (custom-built system including 3.39 µm laser, chopper wheel, and InAsSb detectors for measurement and reference). The measurement accuracy of the combined gas analysis system was ±0.05% by volume.

2.3 Procedure

The procedure for conducting a test was as follows: (1) vessel and pipe were flushed with dry compressed air; (2) the pipe exit was electromagnetically sealed using a steel plate; (3) fuel was added to the vessel; (4) gases in both vessel and pipe were mixed using a circulation pump; (5) the mixture composition was verified by gas analysis and adjusted by addition of fuel or air as needed; (6) the seal plate was released and the mixture ignited. All acquired data was referenced to the time of ignition.

3. Physics-based model

To capture explosion dynamics in vented vessel-pipe systems, a previously developed physics-based model (Boeck et al., 2018) was extended. As the mathematical model definition was provided in the previous work, the present paper will focus on a high-level summary of the physics considered by the model, and highlight modifications made to extend its capabilities.

The model is divided into three parts, corresponding to the components of a vented vessel-pipe system: (1) the vessel; (2) the vent; (3) the pipe. For each component, equations are solved that describe flame propagation and advection, compression/expansion of gases, and the flow generated through openings such as the vent or the pipe. The system of equations is integrated in time using a Runge-Kutta method, resulting in a time-resolved solution for pressure, flame position, and flow velocities. A brief description is given in the following for each model component:

1) In the vessel, a mass balance is solved for burned and unburned mixture where combustion, venting, and flow through the pipe are considered as sources and sinks. Combustion rates are computed from spherical flame propagation theory, including the effects of pressure, temperature, and the Landau-Darrieus instability. Isentropic compression/expansion determines the time-resolved vessel pressure. In the presence of openings in the vessel wall, such as a vent or a pipe, flame advection is considered toward the opening. There, the leading flame tip is advected toward the opening at a rate that satisfies the conservation of mass exiting the opening.
2) The vent deploys at a specified pressure. After vent deployment, the mass flow rate through the vent is computed as a function of vessel pressure, where the vent discharge coefficient is given as a model constant, and gas inertia is neglected.

3) Flow in the pipe is described by the incompressible momentum equation, accounting for flow resistance due to wall friction, inlet/outlet losses, and gas inertia. Combustion in the pipe is modeled using a turbulent burning velocity relation, which establishes the important feedback between the flow generated ahead of the flame, and the turbulent burning rate.

The model is extended in the present work to consider ignition locations other than the vessel center. For ignition at the vessel back-wall or front-wall, hemispherical flame propagation is assumed, and the flame surface area is calculated as

$$A_f = \underbrace{0.5 * 4\pi {r_f}^2}_{hemisphere} - \underbrace{2\pi {r_f}^2(1-\cos\alpha)}_{spherical\ cap} + \underbrace{\pi a\sqrt{\left(x_f - r_f + h\right)^2 + a^2}}_{cone}\ . \tag{1}$$

Equation (1) includes terms for the surface area of a conical flame section extending toward an opening due to flame advection. The flame volume is determined accordingly:

$$V_f = \underbrace{0.5 * 4{r_f}^3\pi/3}_{hemisphere} - \underbrace{\pi h^2\left(3r_f - h\right)/3}_{spherical\ cap} + \underbrace{\pi a^2(x_f - r_f + h)/3}_{cone}\ . \tag{2}$$

Equation (3) describes the relation between the mass flow rate exiting through a pipe or vent, $\dot{m}_v$, and the flow velocity at the flame tip in the vessel facing the pipe entrance, u_x, which advects the flame toward the opening,

$$\dot{m}_v = 2k_v u_x {x_f^*}^2 \pi \rho_v \left(1 - \frac{u_x^2}{2\dfrac{\gamma_v}{\gamma_v - 1}\dfrac{p}{\rho_v}}\right)^{1/(\gamma_v - 1)}, \tag{3}$$

where k_v is a calibration parameter, equal to 0.35 in present comparisons with experiments, that is needed to account for the simplifications made in the description of flame advection. The distance of the flame tip from the opening is defined in terms of a distance to a virtual origin, x_f^*, where all mass flow converges. The definition of this virtual distance is modified in this work to accommodate front and back-wall ignition,

$$x_f^* = R - x_f/\zeta + R_v/\sqrt{2}, \tag{4}$$

where x_f is the physical position of the flame tip, and ζ assumes a value of 1 for center ignition, a value of 2 for back-wall ignition, and a calibrated value close to 0 for front ignition, depending on the exact ignition location with respect to the pipe entrance ($\zeta = 0.25$ is used to compare with the present experiments). For the case of front ignition, all of the mixture entering the pipe after the flame arrives is assumed to be burned.

Mixture properties required by the model are computed using Cantera (Goodwin et al., 2017) and thermochemical data included in the GRI mechanism (Smith et al.). Laminar burning velocities and flame-instability parameters for propane-air mixtures are taken from Lowry et al., 2010 and Bauwens et al., 2015.

Further aspects of practical installations such as pneumatic conveying through the system at a nominal flow velocity, or the presence of elbows in the pipe, can be accounted for by modifying the initial model conditions and turbulence levels in the pipe. These aspects are not discussed in this paper.

4. Experimental results and model comparison

Previous work validated the explosion dynamics model for confined and vented explosions and verified that the effects of vessel volume (Boeck et al., 2018) and vent size (Boeck et al., 2019) are captured accurately. The following sections validate the overall model, including modeling of flow and combustion in the pipe, using experiments in vented vessel-pipe systems. Parameters are explored that govern the explosion dynamics, including pipe dimensions, mixture reactivity, and ignition location. Vessel pressure traces and flame-arrival times at the sensor locations along the pipe are used for experiment-model comparison.

It is important to note, that the number of vent foil layers, N_V, varies between different tests throughout this section, and is shown in each pressure plot. In general, the number of layers was adjusted such that the flame exited from the pipe before the vent deployed. This ensured that flame propagation through the pipe was unaffected by vent deployment. For less severe tests, a smaller number of layers was generally used. As the peak pressure in most tests was entirely dependent on the vent deployment, peak pressures should not be compared between tests with a different number of foil layers.

4.1 Effect of pipe dimensions

Figure 3 shows pressure traces and flame-arrival times along the pipe for two configurations with different pipe lengths, $L_P = 4.88$ m and $L_P = 9.75$ m, for center ignition. As the pipe length increases, flame propagation from the ignition location to the pipe entrance is slightly delayed (+20 ms in flame-arrival time at the pipe entrance) due to increased friction losses and gas inertia in the pipe. The model reproduces this small difference with a relative accuracy of ±1 ms. Flame propagation through the longer pipe takes proportionally more time, compared to the shorter pipe. As the flame enters the pipe, the rate of vessel pressure rise increases sharply, which is a common behavior in all tests. As the flame enters the pipe, and thermal expansion occurs in the pipe at a high turbulent burning rate, this expansion impedes the venting of gases from the vessel through the pipe, leading to an accelerated pressure rise in the vessel. The flow velocity at the pipe entrance can reverse for short periods, shortly after flame arrival at the pipe entrance, which has been observed in previous studies (Ferrara et al., 2008; Molkov, 1994; Poinzy and Leyer, 1999) and is reproduced by the model.

Figure 4 shows the effect of pipe diameter on center ignition cases. While it should be noted that differences in peak pressure are due to different vent deployment pressures, these results clearly illustrate how the pipe diameter significantly affects both pressure transients and flame propagation. For a larger pipe diameter, the flame arrives at the pipe entrance earlier due to lower flow resistance and enhanced flame advection toward the larger opening. Pressure initially increases more rapidly for smaller pipes, due to smaller mass flow rates exiting through the pipe. Once the flame enters the pipe, flame speeds within the pipe are highest for the smallest pipe diameter, due to the higher flow velocity associated with higher vessel pressure and higher resulting turbulent burning velocity in the pipe.

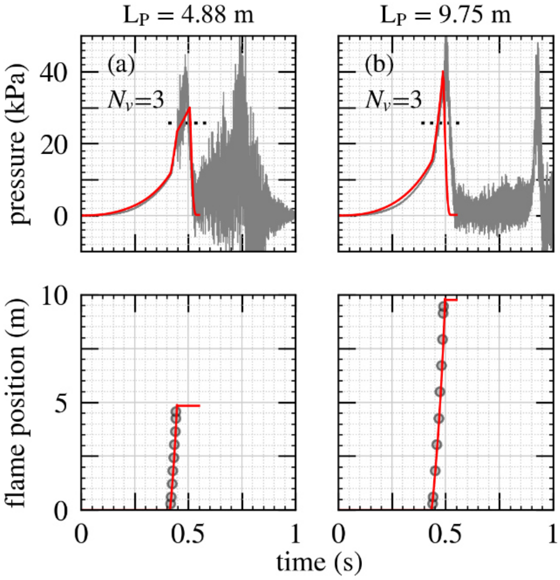

Fig. 3. Effect of pipe length L_P on pressure (top) and flame arrival (bottom). Experiments (grey lines and markers) and model predictions (red lines). Dotted lines mark static vent deployment pressure for each test. $X = 3.0\%$, $D_P = 0.2$ m, center ignition.

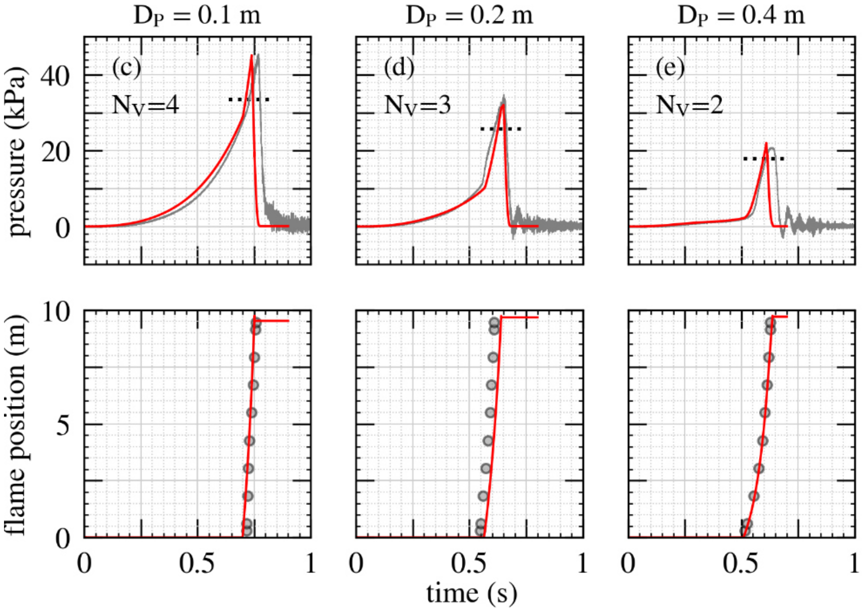

Fig. 4. Effect of pipe diameter D_P on pressure (top) and flame arrival (bottom). Experiments (grey lines and markers) and model predictions (red lines). Dotted lines mark static vent deployment pressure for each test. $X = 2.8\%$, $L_P = 9.75$ m, center ignition.

4.2 Effect of mixture reactivity

Figure 5 shows experiments and model predictions for propane concentrations of 2.8% ($\Phi = 0.69$), 3.0% ($\Phi = 0.74$), and 3.5% ($\Phi = 0.86$), for center ignition and a pipe with 9.75 m length and 0.4 m diameter. Increasing the propane concentration leads to an increase in mixture reactivity (higher laminar burning velocity and expansion ratio), which results in significantly faster pressure rise, earlier flame arrival at the pipe entrance, and faster flame propagation through the pipe. As a secondary effect, flame-acoustics are enhanced in richer mixtures due to lower Markstein numbers, manifesting as high-frequency pressure oscillations at late times.

DOI: 10.7795/810.20200724

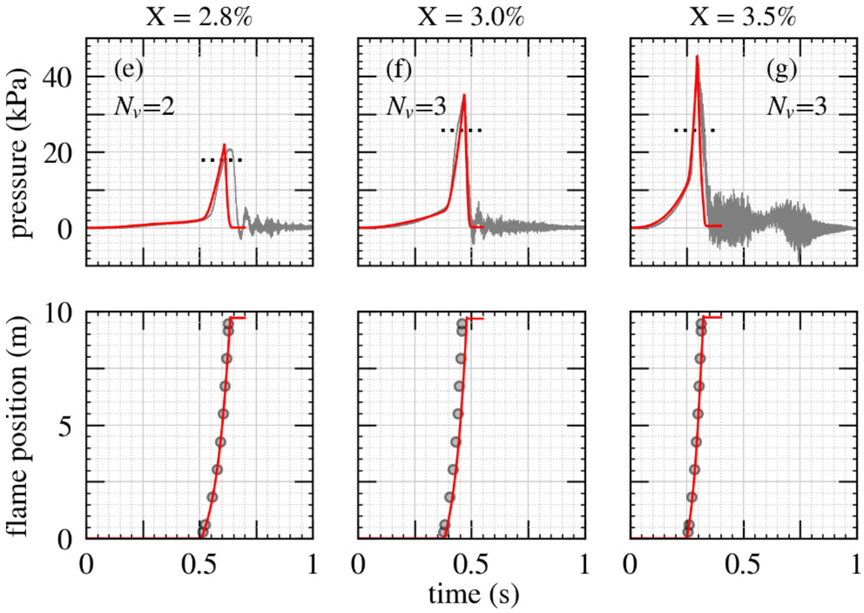

__Fig. 5.__ Effect of mixture reactivity (propane concentration X) on pressure (top) and flame arrival (bottom). Experiments (grey lines and markers) and model predictions (red lines). Dotted lines mark static vent deployment pressure for each test. L_P = 9.75 m, D_P = 0.4 m, center ignition.

The peak pressures at both $X = 3.0\%$ and $X = 3.5\%$ clearly exceed the static deployment pressure of the vent, indicated with black dotted lines. This is due to rapid pressure rise in both cases: The pressure exceedance above the static vent deployment pressure increases as the rate of pressure rise increases with increasing mixture reactivity. It was observed that the presence of a pipe can lead to higher dynamic vent deployment pressures compared to simply vented explosions, without pipes attached to the vessel.

4.3 Effect of ignition location

Figure 6 shows experimental results and model predictions for different ignition locations. For front ignition, the flame shape inside the vessel is approximately hemispherical, leading to a moderate rate of combustion and pressure rise. For this case, the model over-predicts the early pressure peak, but still captures flame propagation through the pipe accurately. Cases with front ignition and lean mixtures are typically the most challenging from a modeling perspective, as small model deviations integrate over longer times and flame speeds are highly sensitive to mixture composition. Center ignition shows faster initial pressure rise due to a spherical flame shape and higher rate of combustion. After flame arrival at the pipe, pressure rises rapidly, which is attributed to higher flow velocity in the pipe, increasing the turbulent burning rate in the pipe, and a larger flame surface area inside the vessel at this time, producing faster pressure rise. For back-wall ignition, initial pressure rise is slow due to the hemispherical flame geometry. As the flame arrives at the pipe, higher vessel pressure and resulting higher flow velocity in the pipe, compared to center ignition, lead to high turbulent burning rates in the pipe and the sharpest rise in vessel pressure among the three tests. Back-wall ignition generally produces the highest peak pressures and flame speeds in the pipe, unless early vent deployment mitigates the explosion severity.

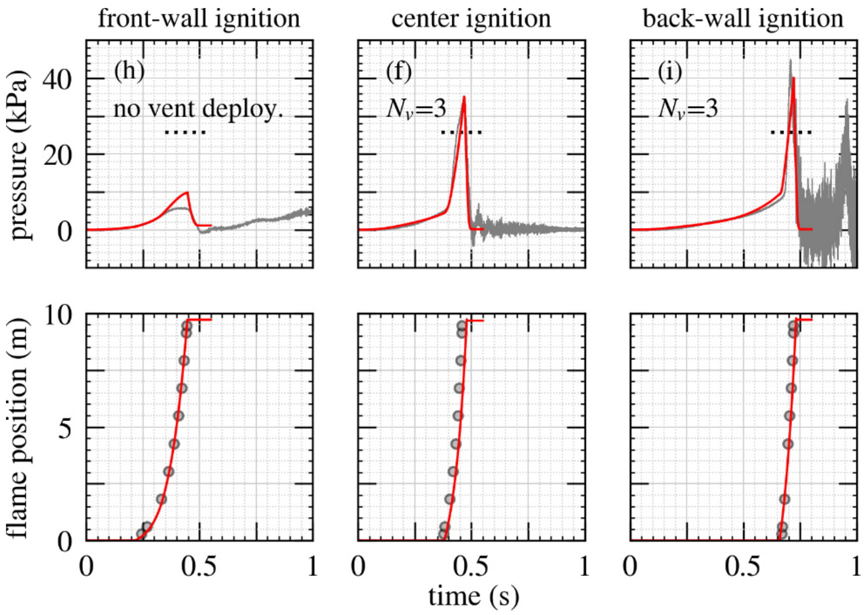

Fig. 6. *Effect of ignition location (front; center; back) on pressure (top) and flame arrival (bottom). Experiments (grey lines and markers) and model predictions (red lines). Dotted lines mark static vent deployment pressure for each test.* $L_P = 9.75$ *m,* $D_P = 0.4$ *m,* $X = 3.0\%$.

5. Discussion of predictive model capability

Experiment-model comparisons in Sec. 4 demonstrated that the model predicts time-resolved vessel pressure and flame progress well and captures the critical effects of geometry and mixture parameters. For broader validation, a total of 20 experiments with different combinations of parameters are used in the following for comparison against model results. Figure 7 summarizes the various combinations of parameters covered by these tests.

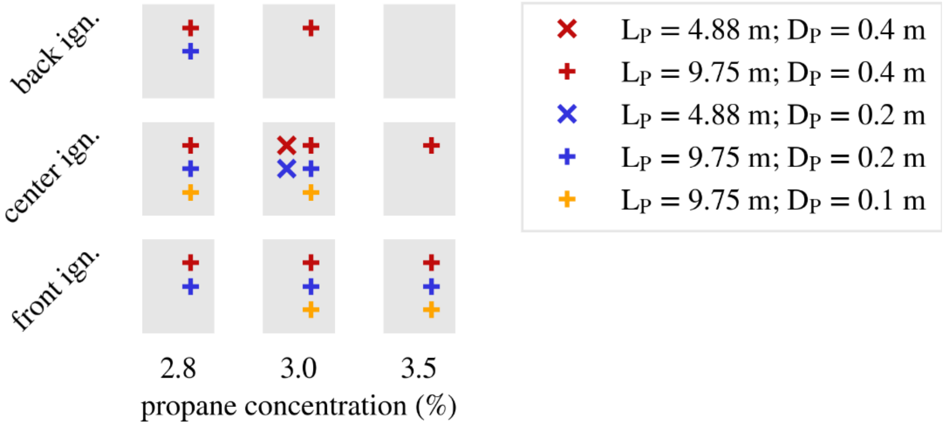

Fig. 7. *Matrix of parameters used for model validation in Fig. 8. Marker color indicates pipe diameter; marker shape indicates pipe length.*

Figure 8, upper left panel, compares experimental and modeled flame-arrival times (relative to ignition) for all flame detector positions along the pipe. Model predictions capture all experimental results within an accuracy of ±10%, which is comparable to the scatter of the experimental results.

The next step is to evaluate the predictive capability of the model from the perspective of explosion isolation. Active explosion isolation systems typically activate based on a pressure measurement using a set pressure threshold. Once the vessel pressure reaches this threshold, the system control unit triggers the explosion isolation device. Once the device is triggered, it takes a finite time for the device to form an effective flame barrier, i.e., to close the pipe cross-section if the device is a mechanical valve, or to establish a sufficient concentration of suppressant in the pipe in the case of chemical isolation systems. The explosion dynamics model can be used to predict the time of flame arrival, relative to the time of crossing a set vessel-pressure threshold, at various locations along the pipe. These arrival times can then be compared to the time a specific isolation system requires to form a barrier, to determine the minimum installation distance for the specific system and use case.

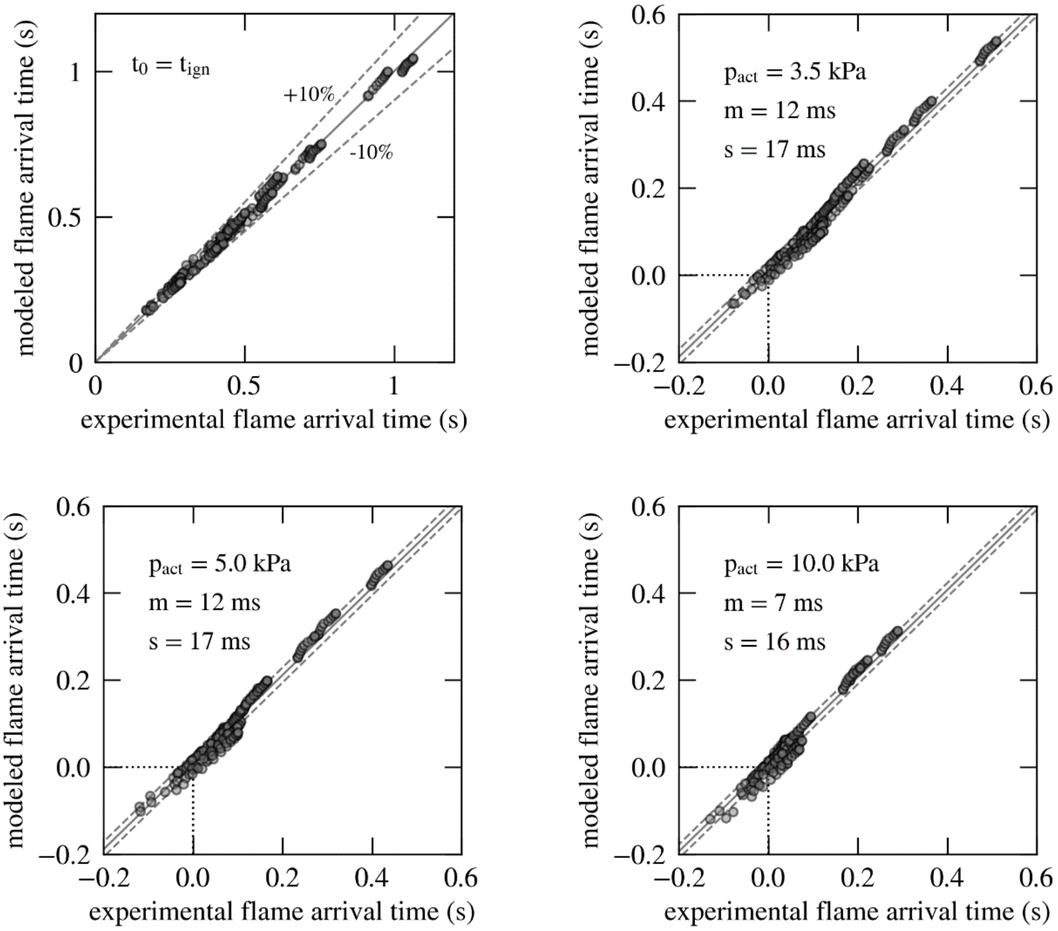

Fig. 8. *Comparison of experimental and modeled flame-arrival times along the pipe. Top left: time from ignition; Top right: time from reaching p = 3.5 kPa; Bottom left: time from reaching p = 5.0 kPa; Bottom right: time from reaching p = 10.0 kPa.*

Figure 8, upper right and lower panels, show comparisons of experimental and modeled flame-arrival times along the pipe, relative to the time a given activation pressure threshold is reached in the vessel in each test. Typical activation pressure thresholds are evaluated, i.e., 3.5 kPa, 5.0 kPa, and 10.0 kPa. For each plot, the mean deviation, *m*, between model and experiments (solid line), and the standard deviation, *s* (dashed lines), are given. These comparisons show good agreement between the model predictions and experimental results throughout the entire range of parameters studied. This indicates that the model accurately captures both the early phase of flame propagation within the vessel and its associated pressure rise, which would activate the isolation system, as well as the later high-speed flame propagation through the pipe. The non-zero mean and standard deviations can be considered for practical applications as part of safety margins for installation distances. The slight over-prediction of flame-arrival time by 7–12 ms relative to pressure-based activation, is fairly consistent between different configurations. This may be a result of the simplified treatment for flame-entrance into the pipe, where forward-jetting of the flame along the centerline of the pipe is not considered. Note, that arrival times for some cases and pipe locations are negative in both experiments and model, which shows that pressure-based detection cannot detect all explosions before the flames enter the pipe. This is particularly relevant for front-ignition cases, low mixture reactivities, and large ratios of pipe diameter to vessel volume. Optical flame detection at the pipe entrance or large installation distances may be needed to resolve such situations.

For explosion isolation systems activating by means other than pressure detection, the model can provide similar predictions. Active systems may use flame detectors at the pipe entrance, which can be simulated based on the model predictions for flame progress. Passive systems such as flap or float valves activate based on flow velocity in the pipe, which can also be predicted by the model.

While these results can be used to determine the minimum installation distances, it is important to mention that installation distances are also bounded by upper limits to prevent deflagration-to-detonation transition (DDT) and excessive over-pressure. Model predictions, experimental results, and literature studies will be used in future work to establish such upper limits, using maximum permissible values for flame speed and pressure build-up that elevate the likelihood of DDT.

6. Conclusions and future work

This study validated a physics-based model for explosion dynamics in vented vessel-pipe systems using large-scale experimental data. Large-scale explosion tests were performed in an 8-m^3 vessel that provide a wide range of validation cases and varied parameters that govern the explosion dynamics, including: pipe lengths of 4.88 m and 9.75 m; pipe diameters of 0.1 m, 0.2 m, and 0.4 m; ignition locations at the center of the vessel, at the back-wall, and at the pipe entrance; and propane concentrations in air of 2.8% (Φ = 0.69), 3.0% (Φ = 0.74), and 3.5% ($\Phi = 0.86$).

It was shown that the model predicts pressure transients closely and captures flame-arrival times along the pipe at an accuracy better than ±10%, over the full range of parameters studied. The model can be used to predict the time available for an explosion isolation system to actuate and form a flame barrier, which can be compared with the activation dynamics of the specific system. The explosion dynamics model can support analyses that determine whether isolation systems will perform as needed in applications, including the prediction of minimum installation distances, while reducing the number of tests needed to determine the performance limitations of isolation systems.

Additional work is needed to develop comprehensive installation guidance for various types of explosion isolation systems. Practical test methods are currently being developed that determine the isolation system pressure-resistance and flame-barrier efficacy, and measure activation dynamics.

Acknowledgements

This work was funded entirely by FM Global and performed within the framework of the FM Global Strategic Research Program on Explosions and Material Reactivity.

References

Bartknecht, W. (2012). *Explosions: course, prevention, protection*. Springer Science & Business Media.

Bauwens, C. R., Bergthorson, J. M., & Dorofeev, S. B. (2015). Experimental study of spherical-flame acceleration mechanisms in large-scale propane-air flames. *Proceedings of the Combustion Institute*, 35, 2059–2066.

Boeck, L.R., Bauwens, C.R., & Dorofeev, S.B. (2018). A physics-based model for explosions in vented vessel-pipe systems. *12th ISHPMIE, Kansas City, USA.*

Boeck, L.R., Bauwens, C.R., & Dorofeev, S.B. (2019). Propane-air explosions in an 8-m^3 vessel with small vents: Dynamics of pressure and external flame-jet. *9th ISFEH, St. Petersburg, Russia.*

Eckhoff, R. K. (2016). *Explosion hazards in the process industries*. Gulf Professional Publishing.

EN 15089 (2009). *Explosion Isolation Systems.*

Ferrara, G., Willacy, S. K., Phylaktou, H. N., Andrews, G. E., Di Benedetto, A., Salzano, E., & Russo, G. (2008). Venting of gas explosion through relief ducts: Interaction between internal and external explosions. *Journal of Hazardous Materials*, 155, 358-368.

Goodwin, D. G., Moffat, H. K., & Speth, R. L. (2017). *Cantera: An object-oriented software toolkit for chemical kinetics, thermodynamics, and transport processes, version 2.3*.

Hattwig, M., & Steen, H. eds. (2008). *Handbook of explosion prevention and protection*. John Wiley & Sons.

Lowry, W., de Vries, J., Krejci, M., Petersen, E.L., Serinyel, Z., Metcalfe, W., Curran, & H., Bourque, G. (2010). Laminar flame speed measurements and modeling of pre alkanes and alkane blends at elevated pressures. *Journal of Engineering for Gas Turbines and Power*, 133 (9) 091501.

Molkov, V. V. (1994). Venting of deflagrations: Dynamics of the process in systems with a duct and receiver. *Fire Safety Science*, 4, 1245-1254.

Ponizy, B., & Leyer, J. C. (1999). Flame dynamics in a vented vessel connected to a duct: 1. Mechanism of vessel-duct interaction. *Combustion and Flame*, 116, 259-271.

Smith, G. P., Golden, D. M., Frenklach, M., Moriarty, N. W., Eiteneer, B., Goldenberg, M., Bowman, T., Hanson, R. K., Song, S., Gardiner Jr., W. C., Lissianski, V. V. & Qin, Z. GRI-Mech 3.0. http://www.me.berkeley.edu/gri_mech/.

Taveau, J. (2017). Dust explosion propagation and isolation. *Journal of Loss Prevention in the Process Industries*, 48, 320–330.

DOI: 10.7795/810.20200724

CEQAT-DGHS interlaboratory tests for chemical safety: Validation of laboratory test methods by determining the measurement uncertainty and probability of incorrect classification including so-called "Shark profiles"

Peter Lüth [a], Steffen Uhlig [b], Kirstin Frost [c], Marcus Malow [a], Heike Michael-Schulz [a], Martin Schmidt [a] & Sabine Zakel [d]

[a] Bundesanstalt für Materialforschung und -prüfung (BAM), Berlin, Germany
[b] QuoData GmbH, Berlin, Germany
[c] QuoData GmbH, Dresden, Germany
[d] Physikalisch-Technische Bundesanstalt (PTB), Braunschweig, Germany

E-mail: peter.lueth@bam.de

Abstract

Laboratory test results are of vital importance for correctly classifying and labelling chemicals as "hazardous" as defined in the UN Globally Harmonized System (GHS) / EC CLP Regulation or as "dangerous goods" as defined in the UN Recommendations on the Transport of Dangerous Goods. Interlaboratory tests play a decisive role in assessing the reliability of laboratory test results. Interlaboratory tests performed over the last 10 years have examined different laboratory test methods. After analysing the results of these interlaboratory tests, the following conclusions can be drawn:

1. There is a need for improvement and validation for all laboratory test methods examined.
2. To avoid any discrepancy concerning the classification and labelling of chemicals, the use of validated laboratory test methods should be state of the art, with the results accompanied by the measurement uncertainty and (if applicable) the probability of incorrect classification.

This paper addresses the probability of correct/incorrect classification (for example, as dangerous goods) on the basis of the measurement deviation obtained from interlaboratory tests performed by the *Centre for quality assurance for testing of dangerous goods and hazardous substances* (CEQAT-DGHS) to validate laboratory test methods. This paper outlines typical results (e.g. so-called "Shark profiles" – the probability of incorrect classification as a function of the true value estimated from interlaboratory test data) as well as general conclusions and steps to be taken to guarantee that laboratory test results are fit for purpose and of high quality.

Keywords: *interlaboratory test, validation, measurement uncertainty, incorrect classification*

1. Introduction

Accidents such as explosions in chemical plants and fires on dangerous goods vessels can be caused in several ways. Prevention starts in the laboratory, where chemicals are tested for their hazardous properties in order to be able to assess the risks involved in their handling. For this purpose, laboratory test methods have been developed and published (see e.g. laboratory test methods published by the European Union (2008) and by the United Nations (2019)); these methods are currently applied throughout the world. Laboratory test results (amongst others) are used to correctly classify and label chemicals as “hazardous” as defined in the UN Globally Harmonized System (GHS) / EC CLP Regulation or as “dangerous goods” as defined in the UN Recommendations on the Transport of Dangerous Goods.

Safety experts, manufacturers, suppliers, importers, employers and consumers must be able to rely on the validity of safety-related laboratory test methods and on the accuracy of laboratory test results and assessments. Interlaboratory tests play a decisive role in assessing the reliability of laboratory test results. Participation in interlaboratory tests is a crucial element of the quality assurance of laboratories; for this reason, it is explicitly recommended in ISO/IEC 17025 (2017) (assuming such interlaboratory tests are available). Interlaboratory tests are used in laboratory test method development and validation and can be used to determine measurement uncertainties (Hässelbarth, 2004; ISO 21748:2017-04, 2017).

Over the past 10 years, the Bundesanstalt für Materialforschung und -prüfung (BAM) and the Physikalisch-Technische Bundesanstalt (PTB) in cooperation with QuoData GmbH have carried out interlaboratory comparisons to evaluate various laboratory test methods (Lueth et al., 2019). Significant differences between the results of the participating laboratories were observed in all interlaboratory tests. The deviations in the laboratory test results were caused not only by malfunctions in the laboratory equipment and laboratory faults but also by deficiencies in the different laboratory test methods (see interlaboratory test reports of the *Centre for quality assurance for testing of dangerous goods and hazardous substances* (CEQAT-DGHS), www.ceqat-dghs.bam.de).

After analysing the results of these interlaboratory tests, the following conclusions can be drawn:

- To avoid any discrepancies in the classification and labelling of chemicals, the use of validated laboratory test methods should be state of the art, with the results accompanied by the measurement uncertainty and (if applicable) the probability of incorrect classification.
- There is a need for improvement and validation for all laboratory test methods examined. Thus, interlaboratory tests should initially focus on the development, improvement and validation of the laboratory test methods (including the determination of the measurement uncertainty) and not on proficiency tests.
- Laboratory management and the practical execution of laboratory tests need to be improved in many laboratories.
- The term “experience of the examiner” must be seen critically; long-term experience involving many laboratory tests does not necessarily guarantee correct results.

However, it is not currently clear whether the measurement uncertainty is sufficiently considered in practice when a chemical is classified as a particular packing group (PG) or as a hazard class based on the measurement results combined with the measurement uncertainties. Statistical methods and graphical tools must therefore be developed which will clearly define how the measurement uncertainty should be used in practice.

This paper addresses so-called “Shark profiles”, graphical indicators of the probability of incorrect classification of dangerous goods and hazardous substances on the basis of the measurement uncertainty obtained from special interlaboratory tests performed by CEQAT-DGHS to validate laboratory test methods. “Shark profiles” were developed to characterize the quality and suitability of the laboratory test method(s) with respect to the laboratory test objective, i.e. the classification of chemicals based on specific classification criteria (Antoni et al., 2010, Antoni et al., 2011 and Kunath et al., 2011). This objective is particularly important when there are several classification levels (e.g. packing groups PG or hazard classes) and the question of the reliability of the classification arises.

The principle of the calculation of “Shark profiles” for interlaboratory tests is explained by means of quantitative laboratory test results. This paper outlines typical results as well as general conclusions and steps to be taken to guarantee that laboratory test results are fit for purpose and of high quality.

2. Experiments

2.1 CEQAT-DGHS interlaboratory tests and minimum number of participating laboratories

As part of the CEQAT-DGHS programme, interlaboratory tests were carried out on various laboratory test methods and either qualitative or quantitative test results were obtained and evaluated.

An overview of the laboratory test methods currently listed in the CEQAT-DGHS interlaboratory test programme is shown in Fig. 1. This figure also indicates interlaboratory tests already performed by CEQAT-DGHS as well as the number of laboratories interested in taking part in these interlaboratory tests.

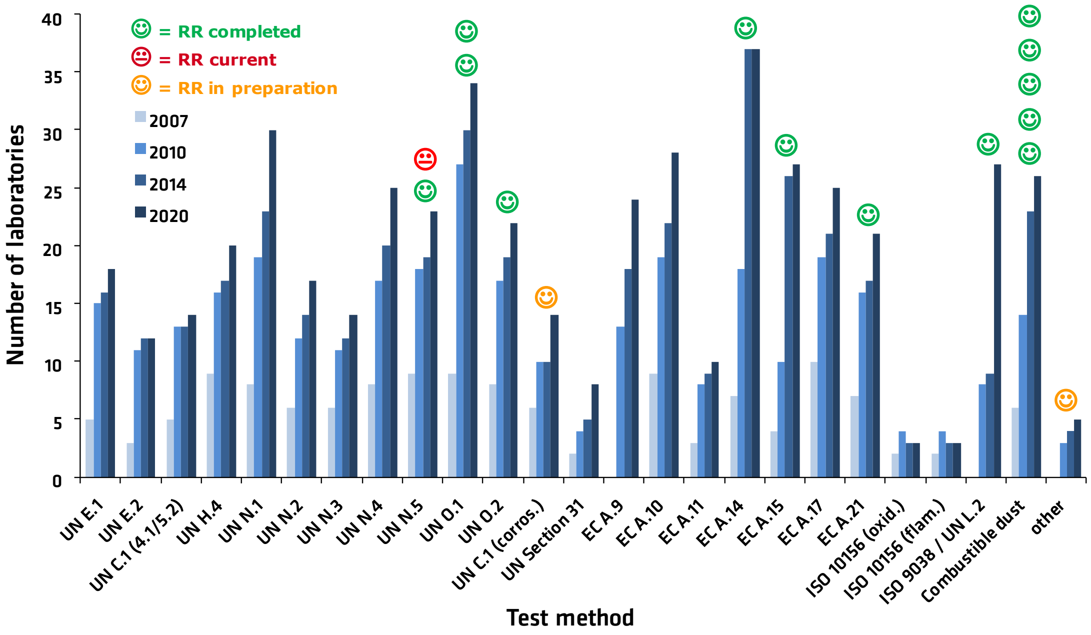

Fig. 1. *Laboratory test methods listed in the CEQAT-DGHS interlaboratory test programme, number of laboratories with interest in participation in CEQAT-DGHS interlaboratory tests and interlaboratory tests performed by CEQAT-DGHS since 2007 (RR = interlaboratory test)*

Since CEQAT-DGHS was founded in 2007, the number of laboratories interested in taking part in interlaboratory tests has steadily increased to about 98. The minimum number of participating laboratories required for statistically meaningful interlaboratory tests (i.e. for statistical reliability) has been met for almost all laboratory test methods. Hence, interlaboratory tests can now be carried out for almost all laboratory test methods listed in in Fig. 1.

2.1.1 Data verification (inspection upon receipt) in interlaboratory tests for method validation

A special feature of the CEQAT-DGHS interlaboratory comparison programme for method validation is that the data supplied by the laboratories are subjected to a strict verification before being evaluated. This is necessary to ensure data quality.

The specific review of the data submitted by the laboratories includes the following points (Antoni et al., 2010, Antoni et al., 2011, Kunath et al., 2011, Frost et al., 2016 and Lueth et al., 2019):

- Completeness of the data – check for missing data
- Conformity – check for irregular deviations from the laboratory testing method and/or from the interlaboratory test instructions
- Plausibility – check for obvious incorrectness of the data submitted (e.g. distorted data)
- Consistency – check the correctness of the values in the data input form submitted (e.g. by comparing them to raw data)

The data were verified/validated by different experts independently directly after receiving the data from the laboratory and before starting the statistical analysis. If necessary and possible, faulty data were corrected after consulting the respective laboratory; laboratories were also asked to submit any missing data. A statistical evaluation including the determination of the measurement uncertainty and the probability of incorrect classification with corresponding “Shark profiles” was carried out on this specially validated data. The test results constituted an adequate basis for the statistical evaluation and for reliable conclusions.

2.2 Probability of incorrect classification and corresponding “Shark profiles”

The probability of incorrect classification of a tested substance, as defined by the European Union (2008) and by the United Nations (2019), depends on the measurement uncertainty of the test result(s) and the difference between the test result and the classification criterion. However, the percentage of laboratories which have incorrectly classified the test samples may be only a very rough estimate of the actual probability of the incorrect classification. Therefore, statistical methods and graphical indicators must be developed which can provide the probability of incorrect classification regardless of the substance and characterize the quality and the suitability of the laboratory test method(s) with regard to the test objective (i.e. the classification of chemicals based on special classification criteria). For this reason, the concept of the probability of incorrect classification and the visual shark profiles explained below were developed. The methods and development relevant to this topic are demonstrated below using several examples.

During the development of the “Shark profiles” the focus was on laboratory test methods whose quantitative test results are used to classify substances based on classification criteria defined by the European Union (2008) and the United Nations (2019). The interlaboratory tests evaluated the laboratory test methods listed in Table 1:

Table 1: *Quantitative laboratory test methods of the CEQAT-DGHS interlaboratory tests, year in which each interlaboratory test was performed and name of report published*

Laboratory test method	**Year of the interlaboratory test**	**Report of the interlaboratory test**
UN Test O.1 “Test for oxidizing solids”	2005-2006	Antoni et al., (2010)
UN Test N.5 “Substances which in contact with water emit flammable gases”/EC A.12 “Flammability (contact with water)”	2007	Kunath et al., (2011)
UN Test O.2 “Test for oxidizing liquids”/ EC A.21 “Oxidizing Properties (Liquids)”	2009-2010	Antoni et al., (2011)

The laboratory test methods shown in Table 1 were examined in interlaboratory tests for the improvement and validation of laboratory test methods (i.e. there were no proficiency tests). For reasons of simplification and better readability, an alternative packing group designation – PG 1, PG 2 and PG 3 – is used in the following instead of the legally correct designation – PG I, PG II and PG III.

2.2.1 Measurement uncertainty of laboratory test methods

The measurement uncertainty of the laboratory test methods can be determined efficiently via interlaboratory tests for method validation (Hässelbarth, 2004, ISO, 2017-04), and can be expressed as shown in eq (1).

‘Laboratory result’ = ‘Measurement result’ ± U,

where U denotes the expanded measurement uncertainty $U = k * u$ with $u = s_R$ (1)

The factor k corresponds to the coverage factor k defined in GUM (Guide to Uncertainty in Measurement, Joint Committee for Guides in Metrology, 2008) and the factor s_R denotes the reproducibility standard deviation obtained in the interlaboratory tests for method validation.

The reproducibility standard deviation s_R is determined by means of standardized procedures and statistical methods (Antoni et al., 2011). These standardized statistical calculations are commonly used by statistical experts in proficiency testing and therefore do not require any further explanation at this point. However, detailed information on the calculation methods can be found in the respective interlaboratory test reports (Antoni et al., 2010, Antoni et al., 2011, Kunath et al., 2011).

2.2.2 Calculation of the probability of incorrect classification and "Shark profiles"

The procedure used to calculate the probability of incorrect classification and the "Shark profiles" is similar to statistical testing with a null hypothesis (e.g. the test sample belongs to PG 1) and with an alternative hypothesis (e.g. the test sample belongs to PG 2). In general, the objective of a statistical test is to keep the probability of a false positive result (rejection of null hypothesis and acceptance of alternative hypothesis) below a certain limit (statistical significance level), whereas the probability of the false negative error (acceptance of null hypothesis) can only be controlled with great difficulty. These probabilities always depend on the "true" value of the measurand (e.g. combustion time) for the specific test sample.

Using interlaboratory test data, the percentage of laboratories which incorrectly classified test samples provides only a very rough estimate of the actual probability of incorrect classification. A more reliable estimation of this probability can be obtained using the quantitative properties of the data. Here, the probability of incorrect classification of the test samples is derived by evaluating the ratios between the laboratory results of the test sample and the classification criterion (e.g. a firmly defined threshold value taken from a legal regulation or a laboratory test value obtained by testing a reference substance which characterizes the classification criterion (threshold value)). The procedure is as follows (and is initially carried out for each PG separately):

Step 1: Calculation of the characteristic statistical values and determination of the true value

Based on interlaboratory test data, the mean value and the standard deviation of the laboratory-specific ratios between the test results of the test sample and those of the reference sample are determined using the robust Q/Hampel method (described e.g. in ISO 13528:2015). Thus, with the interlaboratory test data, a robust estimate of the "true" ratio value (which is typically not exactly known) will be obtained as well as the respective reproducibility standard deviation regarding the ratios. The advantage of using robust methods is that no special outlier tests are required. Especially the Hampel estimator is a weighted arithmetic mean, with lower weights for the outlying values. Obvious "outliers" have a weight of zero and no influence on the mean value.

Step 2: Calculation of the probability of incorrect classification

Based on the "true" ratio value (i.e. the robust mean value), and the corresponding reproducibility standard deviation obtained in Step 1 above), the expected reproducibility standard deviation for the ratio between the test results of an arbitrary test sample and those of the reference sample (which characterizes the classification limit) can be estimated. Based on this estimation, the probability of the test sample being classified in a PG for more dangerous substances can be calculated as a function of the ratio of the "true" value of the measurand (see Fig. 2). Here, the "decision direction" (i.e. from a PG for less dangerous substances to a PG for more dangerous substances) must be taken into account. For the packaging groups, the order from PG 3 to PG 2 to PG 1 means an increase in the dangerousness of the substance. Once a certain classification threshold value (criterion for classification) has been reached, the substance is to be classified as a defined PG and then remains in this PG until the next higher classification criterion (i.e. for more dangerous substances) has been reached. Once the next higher criterion value (for the next PG for more dangerous substances) has been reached, the substance is classified in the next PG for more dangerous substances. Below, Fig. 2 shows the probability of incorrect classification of the measured value for which the next-higher classification (i.e. for more dangerous substances, ratio < 1) is required.

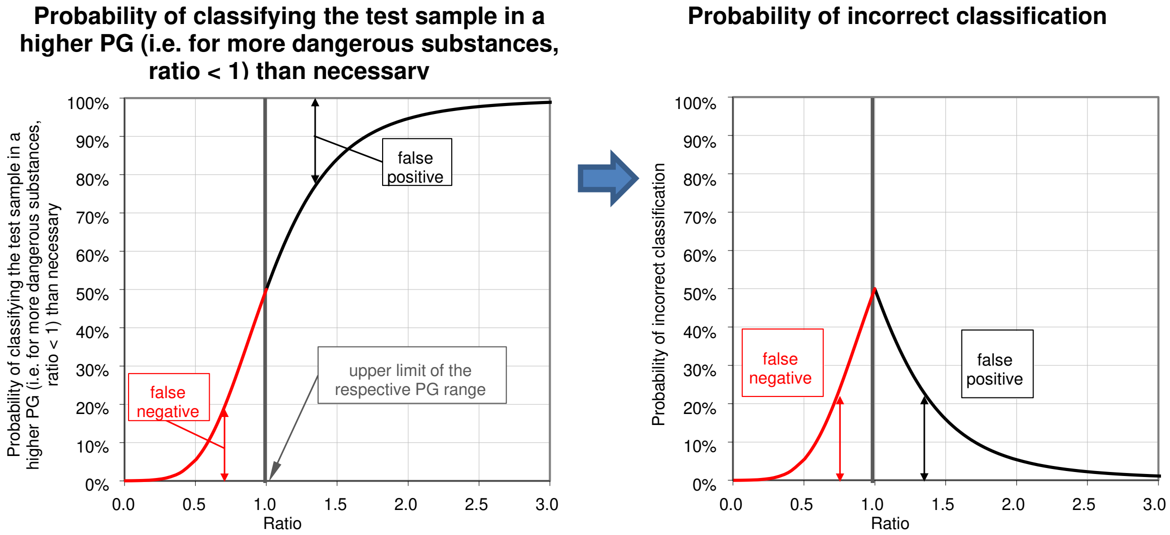

Fig. 2 Probability of classifying the test sample in a higher PG (i.e. for more dangerous substances, ratio < 1) than necessary as well as the resulting false negative and false positive error (left diagram) and the resulting probability of incorrect classification (right diagram), (ratio = ratio between the laboratory results of the test sample and the reference substance/classification criterion)

As given in Fig. 2 (left diagram), for a ratio less than 1, the resulting probability indicates the probability of a false negative classification, while for a ratio greater than 1, the probability of the false positive classification can be calculated by subtracting the given probability from 100 % (see Fig. 2, right diagram). For a ratio of exactly 1, the probability of both the false negative and the false positive classifications are equal to 50 %.

Step 3: Transformation of the ratio-based diagram into a “Shark profile” diagram

For the resulting “Shark profile”, the y-axis indicates the probability of false negative classification for arbitrary test samples with a value less than that of the reference sample as well as the false positive classification for arbitrary test samples with a value greater than that of the reference sample, which creates a shape like a shark’s dorsal fin. Instead of the ratios, the x-axis shows the value of the measurand as a continuous scale. The robust mean value of the reference sample (depending on the PG) is used for the transformation. It is therefore possible to depict the results in one figure for all PGs considered (see Fig. 3).

A laboratory can generally assess the test result of an arbitrary sample using the “Shark profile” as follows: Assume that the sample has been characterized as PG 2 in the measurement (see Fig. 3). Then, the corresponding right arm of the curve of PG 1 (red curve) can be interpreted as the probability that the sample was incorrectly classified as PG 2, although it belongs to PG 1. This probability naturally depends on the “true” value of the test sample (e.g. combustion time). If the probability is less than 5 %, it can be argued that the classification based on the test result is statistically significant (i.e. the assumption that the sample belongs to PG 1 would be rejected at a statistical significance level of 5 %). The level at which the 5% limit is attained can be considered the lower limit of the measurement uncertainty (k = 2) when the test result belongs to PG 2.

Conversely, in Fig. 3, the corresponding left arm of the curve from PG 2 (blue curve) can be interpreted as the probability that the sample is incorrectly assigned to PG 2, although it belongs to

PG 3. The statistical significance level at which the 5 % limit is attained can be considered the upper limit of measurement uncertainty (k = 2) when the test result belongs to PG 2.

The probability of incorrect classification and the corresponding "Shark profiles" were calculated in three different CEQAT-DGHS interlaboratory tests. The interlaboratory tests on the methods given in Table 1 were used. The procedure for and calculation of the probability and the corresponding "Shark profiles" have been explained in greater detail in the respective interlaboratory test reports (Antoni et al., 2010, Antoni et al., 2011, Kunath et al., 2011). Examples of the “Shark profiles” are explained in the next chapter.

3. Results and discussion

In the following, it is assumed that a false positive classification indicates that the test sample mixture has been classified by a laboratory in a PG for more dangerous substances, although a PG for less dangerous substances would have been correct because this is the “true” packing group. A false negative classification, however, indicates that the test sample mixture is classified by a laboratory in a PG for less dangerous substances, although a PG for more dangerous substances would have been correct.

3.1 Example 1: Probability of incorrect classification and “Shark profiles” of the UN Test O.1 interlaboratory test for an arbitrary test sample mixture

The probability of incorrect classification can be calculated for the test sample mixtures used in the interlaboratory test as well as for an arbitrary test sample mixture. For example, in Fig. 3 below, the “Shark profiles” calculated on the basis of the UN Test O.1 interlaboratory test, “Test for oxidizing solids” (Antoni et al., 2010), are shown. Due to its curves, the profile in Fig. 3 is also referred to as a “Shark profile”. “Shark profiles” of incorrect classification as packing groups are to be interpreted in accordance with Table 2. The colours of the different curves represent the probability of incorrect classification according to the respective classification criteria of PG 1 (red curve), PG 2 (blue curve) and PG 3 (green curve). The probability of incorrect classification depends on the measurement uncertainty.

Table 2: *Interpretation of the curves of the probability of incorrect classification (“Shark profiles”) of the CEQAT-DGHS interlaboratory test of the UN Test O.1 method (Antoni et al., 2010)*

Arm of the “Shark profile” *	Classification	Classification error
Left arm of PG 1 (red)	Probability that a laboratory has classified the test sample as PG 2 although PG 1 would have been correct (i.e. the true classification is PG 1 for more dangerous substances)	false negative classification
Right arm of PG 1 (red)	Probability that a laboratory has classified the test sample as PG 1 although PG 2 would have been correct (i.e. the true classification is PG 2 for less dangerous substances)	false positive classification
Left arm of PG 2 (blue)	Probability that a laboratory has classified the test sample as PG 3 although PG 2 would have been necessary (i.e. the true classification is PG 2 for more dangerous substances)	false negative classification
Right arm of PG 2 (blue)	Probability that a laboratory has classified the test sample as PG 2 although PG 3 would have been correct (i.e. the true classification is PG 3 for less dangerous substances)	false positive classification
Left arm of PG 3 (green)	Probability that a laboratory has not classified the test sample although PG 3 would have been necessary (i.e. the true classification is PG 3 for more dangerous substances)	false negative classification
Right arm of PG 3 (green)	Probability that a laboratory has classified the test sample as PG 3 although no classification for less (no) dangerous substances would have been correct (i.e. the true classification is “no” PG)	false positive classification

*…Curve of the probability of incorrect classification according to the respective PG criterion

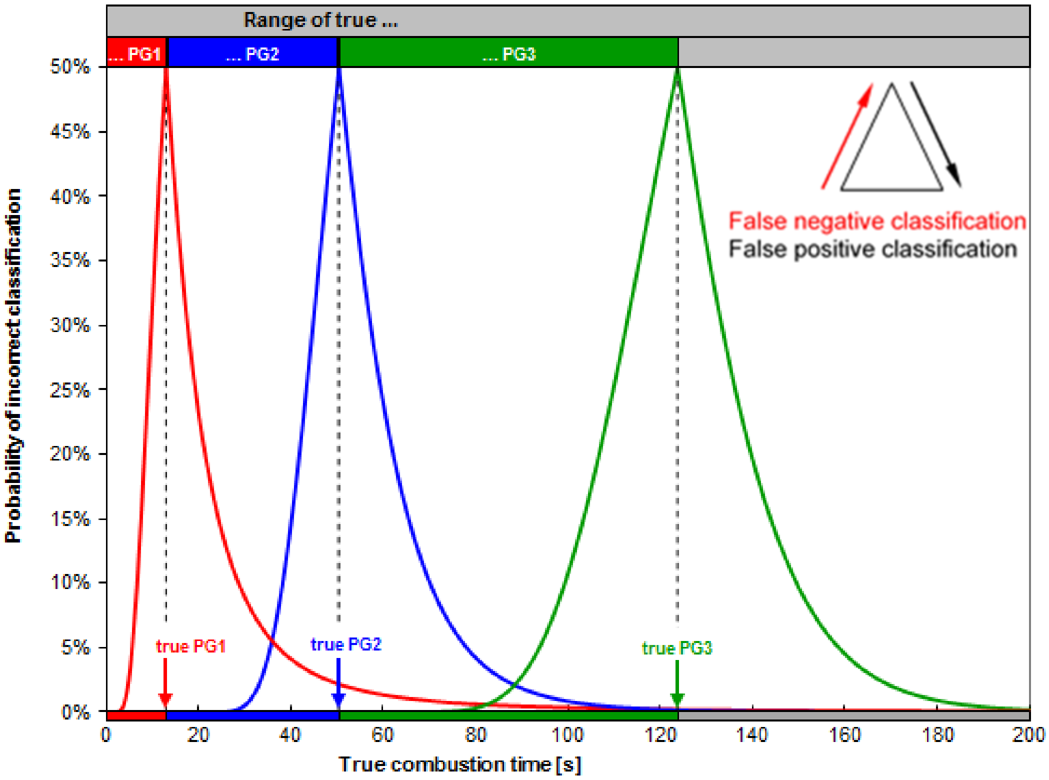

Fig. 3 *"Shark profiles" calculated for the UN Test O.1 interlaboratory test – probability of incorrect classification as PG 1, PG 2 or PG 3 or no classification as a function of the "true" combustion times of an arbitrary sample mixture (PG=packing group) (Antoni et al., 2010)*

If the curves in Fig. 3 do not overlap, only one kind of incorrect classification can occur. Therefore, in a range where two or more curves overlap, more than one type of error must be taken into account.

If, for example, the "true" combustion time of an arbitrary test sample mixture equals 40 s, the probability of a false positive classification with regard to PG 1 (i.e. the probability of the test sample mixture being classified as PG 1 instead of the "true" PG 2 due to the measurement uncertainty) equals about 4 % (value of red curve for 40 s). At the same time, for a mean combustion time of 40 s, there is the possibility of a false negative error as well: the probability of a false negative classification (i.e. the probability of the test sample mixture being classified as PG 3 instead of the "true" PG 2) equals about 15 % (value of blue curve for 40 s).

3.2 Example 2: Probability of incorrect classification and "Shark profiles" of the UN Test O.2/EC A.21 interlaboratory test for the "aqueous solution of sodium nitrate" test sample and for an arbitrary test sample mixture

The significance and advantage of the "Shark profiles" can be seen particularly well in UN Test O.2 interlaboratory test because, in this interlaboratory test for method improvement, two different series of tests (see Table 3) were carried out with the same interlaboratory test sample, "aqueous solution of sodium nitrate" (mass fraction 44.6 % g/g (checked by gravimetry)/44.7 % g/g to 45.0 % g/g (checked by means of ion chromatography)). Sodium nitrate (45 % aqueous solution) is listed in Table 34.4.2.5, "Examples of result", of UN Test O.2 as an example of an oxidizing liquid which must be classified as Division 5.1, PG 3 according to the UN Manual of Tests and Criteria (United Nations, 2019).

Table 3: *Test series in UN Test O.2/EC A.21 (Antoni et al., 2011)*

Test series	**Test method**	**Instruction for the mixing procedure (short description)**
1	UN O.2/EC A.21 (without modification)	No special recommendation* ("should be applied as usual in your laboratory")
2 (optional)	Modification of UN Test O.2/EC A.21	Modified mixing procedure: 1. Use a ceramic mortar and a pestle 2. Homogenize with only very little force 3. Homogenize within exactly 2 minutes

The current application of UN Test O.2 in different laboratories and the classification error were assessed in the first part of the interlaboratory test (test series 1). The influence of the mixing procedure on the test results/classification was evaluated using a second, optional test (test series 2) the participating laboratories were requested to perform. The mixing procedure in this test series was standardized with regard to the mixing equipment and the mixing duration. The modification of the mixing procedure in test series 2 was based on a proposal by BAM.

The probabilities of a false positive classification of the “aqueous solution of sodium nitrate” interlaboratory test sample are given in Table 4 with regard to all classifications/packing groups in both test series.

Table 4: *Probability of a false positive classification as PG 1, PG 2 or PG 3 of the “aqueous solution of sodium nitrate” interlaboratory test sample depending on the test series (see Table 3) of UN Test O.2/EC A.21 (PG=packing group) (Antoni et al., 2011)*

Test series	**Packing group**	**Probability of incorrect positive classification**
1	PG 1	7 %
1	PG 2	19 %
1	PG 3	27 %
2	PG 2	10 %
2	PG 3	5 %

Additionally, for test series 1 and test series 2, the probability of incorrect classification can also be predicted for an arbitrary test sample mixture (see Fig. 4 and Fig. 5). The “Shark profile” curves for test series 1 in Fig. 4 should be read as follows:

If, for example, in test series 1, the "true" pressure rise time of an arbitrary test sample mixture equals 500 ms, the probability of a false positive classification with regard to PG 1 (i.e. the probability of the test sample mixture being classified as PG 1 instead of as the “true” PG 2) is about 30 % (value of red curve for 500 ms). At the same time, there is the possibility of a false negative error of classification for a mean pressure rise time of 500 ms as well: the probability of a false negative classification (i.e. the probability of the test sample mixture being classified as PG 3 instead of the “true” PG 2) is about 15 % (value of blue curve for 500 ms).

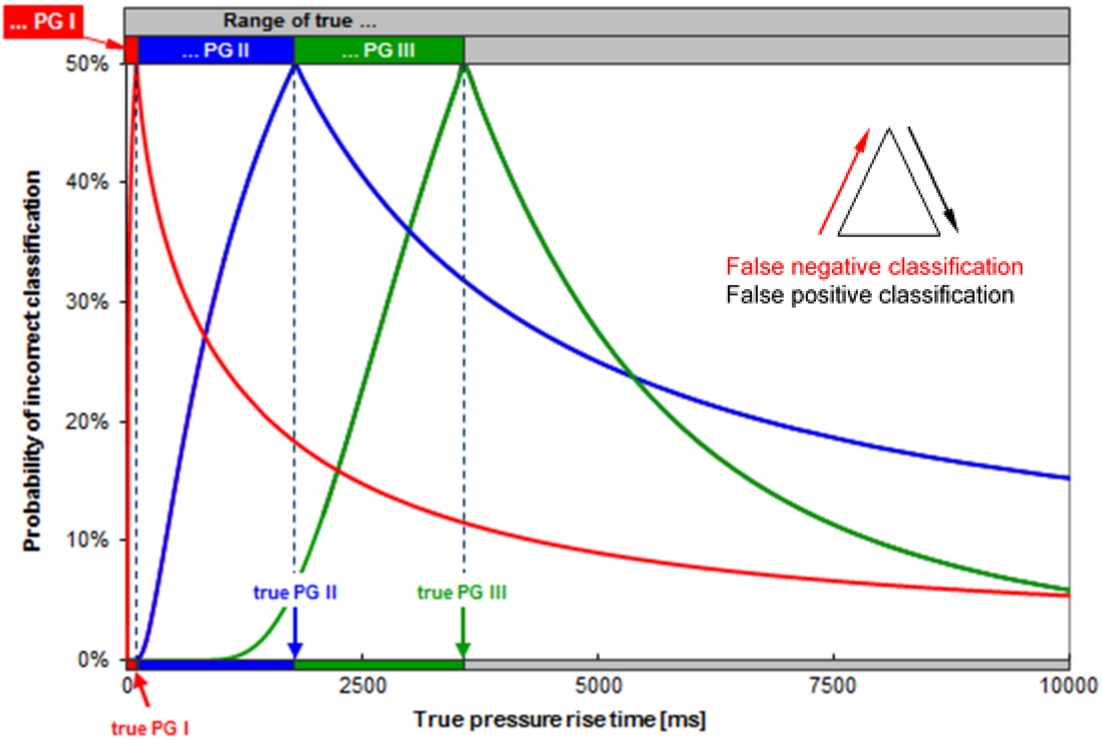

Fig. 4 *“Shark profiles” of test series 1 of the UN Test O.2/EC A.21 interlaboratory test – probability of incorrect classification as PG 1, PG 2 or PG 3 or no classification as a function of the "true" pressure rise time of an arbitrary sample mixture (Antoni et al., 2011)*

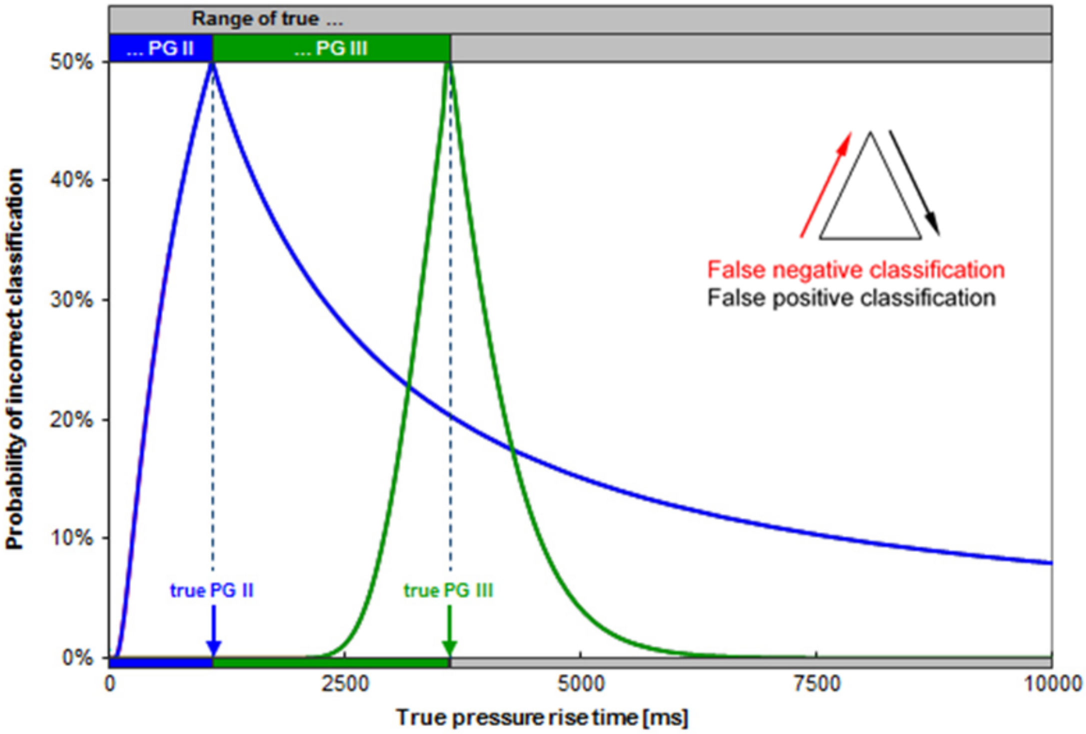

Fig. 5 *“Shark profiles” of test series 2 of the UN Test O.2/EC A.21 interlaboratory test – probability of incorrect classification as PG 2 or PG 3 or no classification as a function of the "true" pressure rise time of an arbitrary sample mixture (Antoni et al., 2011)*

As can be seen in Fig. 4, the “Shark profiles” of the UN Test O.2 /EC A.21 interlaboratory test in test series 1 are rather blunt; thus, the classification error (i.e. the probability of incorrect classification) is relatively high and a clear distinction between the packing groups is not possible with acceptable certainty.

However, as shown in Fig. 5, in test series 2 of the interlaboratory test, the “Shark profile” curve of the probability of incorrect classification as PG 3 has become significantly narrower and more pointed, which supports the idea of better selectivity between the packing groups. This means that, even if the given laboratory test method is not yet optimal, the modifications in test series 2 (see Table 3) have already led to a significant improvement of the laboratory test method: “Shark profiles” are a useful graphic tool for clarifying the safety level of classification as a particular packing group or for deciding whether classification of a chemical substance in a particular packing group is safe.

4. Conclusion

A sound database is a prerequisite for the reliable evaluation of interlaboratory tests and for the correct validation of laboratory test methods. Within the scope of interlaboratory tests, the laboratory data submitted must be verified in order to validate laboratory test methods. Although it is very labour-intensive and time-consuming, this validation must not be neglected, as doing so will minimize the impact of deficiencies in the data on test conclusions. The comprehensive database compiled within the scope of the interlaboratory test, together with the verification of the data, created a clear overview of the probability of incorrect classification to be obtained and the corresponding “Shark profiles” to be determined.

Based on the results obtained to date regarding the probability of incorrect classification and the corresponding “Shark profiles”, the following conclusions can be drawn:

1. “Shark profiles” are a good graphic tool for clarifying the accuracy of classification and for deciding whether the classification of a chemical substance is accurate.
2. The probability of incorrect classification and the corresponding “Shark profiles” can be calculated via different laboratory test methods.
3. To avoid any discrepancy concerning the classification and labelling of chemicals, using validated laboratory test methods should be state of the art, with the results accompanied by the measurement uncertainty and (if applicable) the probability of incorrect classification and the corresponding “Shark profiles”.
4. By visualizing the probability of incorrect classification in “Shark profiles”, the quality of the laboratory test methods (and ultimately the quality of the classification of chemical substances as defined by the European Union (2008) and the United Nations (2019)) can be assessed in a simple manner. This statistical tool should be used in further method development tests and method validation.
5. The probability of incorrect classification and the corresponding “Shark profiles” can be used to discuss general quality requirements for classification rules in a simple manner. The probability can be used to define specific requirements for the quality of the laboratory test methods and for the corresponding classification (e.g. maximum permissible measurement uncertainties of the laboratory test method, tolerable probability, target measurement uncertainties and target probabilities of incorrect classification). The application of the measurement uncertainty of laboratory test results to the classification of chemical substances should be investigated in greater detail.

Continued efforts are necessary to further develop interlaboratory test programmes such as CEQAT-DGHS and to improve the corresponding laboratory test methods and the accuracy of the classification of chemical substances. Currently, the CEQAT-DGHS interlaboratory test programme is operated by BAM in collaboration with PTB and QuoData GmbH. Method validation by means of interlaboratory tests requires considerable effort with regard to time, money and personnel; the resources available at the CEQAT-DGHS competence centre limit the number of interlaboratory tests that can be offered to approximately one per year.

Interested laboratories can obtain detailed information and register for interlaboratory tests at the CEQAT-DGHS website (www.ceqat-dghs.bam.de).

Acknowledgements

The authors gratefully acknowledge the personnel and financial support provided by the Bundesanstalt für Materialforschung und -prüfung (BAM), Physikalisch-Technische Bundesanstalt (PTB), QuoData GmbH and by the laboratories participating in the interlaboratory tests.

References

Antoni S., Kunath K., Lüth P., Schlage R., Simon K., Uhlig S., Wildner W., Zimmermann C. (2010). Evaluation of the interlaboratory test on the method UN test O.1 'Test for oxidizing solids' with sodium perborate monohydrate 2005 / 06 Final report, *BAM, Berlin.* ISBN 978-3-9814281-2-4 https://opus4.kobv.de/opus4-bam/frontdoor/index/index/docId/25091.

Antoni, S., Kunath, K., Lüth, P., Simon, K., Uhlig, S. (2011). Evaluation of the interlaboratory test on the method UN O.2 / EC A.21 Test for oxidizing liquids 2009 - 2010 Final report*, BAM, Berlin,* ISBN 978-3-9814634-0-8, https://opus4.kobv.de/opus4-bam/frontdoor/index/index/docId/25090.

European Union (2008). Commission Regulation (EC) No 440/2008 of 30 May 2008 laying down test methods pursuant to Regulation (EC) No 1907/2006 of the European Parliament and of the Council on the Registration, Evaluation, Authorisation and Restriction of Chemicals (REACH), OJ L 142, 31.5.2008, p.1.

Frost K., Lüth P., Schmidt M., Simon K., Uhlig S. (2016). Evaluation of the interlaboratory test 2015-2016 on the method DIN EN 15188:2007 "Determination of the spontaneous ignition behaviour of dust accumulations" Final report, *BAM, Berlin*. ISBN 978-3-9818270-0-2, https://opus4.kobv.de/opus4-bam/frontdoor/index/index/docId/38734.

Hässelbarth W. (2004). BAM-Leitfaden zur Ermittlung von Messunsicherheiten bei quantitativen Prüfergebnissen. *Forschungsbericht* 266. BAM, Berlin. ISBN 3-86509-212-8.

ISO 13528:2015-08 Statistical methods for use in proficiency testing by interlaboratory comparison, International Organization for Standardization, Geneva.

ISO/IEC 17025:2017-11 General requirements for the competence of testing and calibration laboratories, International Organization for Standardization, Geneva.

ISO 21748:2017-04 Guidance for the use of repeatability, reproducibility and trueness estimates in measurement uncertainty evaluation, International Organization for Standardization, Geneva.

Joint Committee for Guides in Metrology (2008) Evaluation of measurement data — Guide to the expression of uncertainty in measurement (GUM 1995 with minor corrections), BIPM <www.bipm.org/en/publications/guides/gum.html>, accessed 06.02.2020.

Kunath K., Lüth P., Uhlig S. (2011). Interlaboratory test on the method UN test N.5 / EC A.12 'Substances which, in contact with water, emit flammable gases' 2007 Short report, *BAM, Berlin*. ISBN 978-3-9814634-1-5, https://opus4.kobv.de/opus4-bam/frontdoor/index/index/docId/25094.

Lueth P., Frost K., Kurth L., Malow M., Michael-Schulz H., Schmidt M., Schulte P., Uhlig S., Zakel S. (2019). CEQAT-DGHS Interlaboratory Test Programme for Chemical Safety - Need of Test Methods Validation. *CET Chemical Engineering Transactions*, 77: 1-6. DOI: 10.3303/CET1977001.

United Nations (2019). Manual of Tests and Criteria, Seventh revised edition, *United Nations*, New York and Geneva, <www.unece.org/trans/danger/publi/manual/rev7/manrev7-files_e.html>, accessed 06.02.2020

DOI: 10.7795/810.20200724

CEQAT-DGHS Interlaboratory tests for chemical safety – A new gravimetric procedure for the gas flow measurement for flammable and toxic gases

Peter Lüth [a], Marcus Malow [a]

[a] Bundesanstalt für Materialforschung und –prüfung (BAM), Berlin, Germany

E-mail: marcus.malow@bam.de

Abstract

Testing of hazardous materials and evaluating their hazardous properties concerning transport, handling or use is essential for the prevention of incidents. For this purpose, test methods have been developed and published that are used worldwide today (European Union, 2008, United Nations, 2019). For the evaluation of test results their correct measurement is of importance. On basis of the interlaboratory tests carried out by BAM and PTB within the framework of the CEQAT-DGHS in the last years, it is shown that there is a need for improvement in all the test methods examined so far. In addition to the interlaboratory tests further quality measures are mandatory (ISO, 2017). For example, methods for verifying the test equipment used in the laboratories should be developed.

The development of a verification method is demonstrated using the test method UN Test N.5 as an example. This test method is used to evaluate substances which in contact with water emit flammable gases. The basic principle of the verification method is demonstrated by Lüth et al. (2019). Requirements and difficulties during this development are discussed.

This test procedure UN Test N.5 has now been modified at BAM so that it is possible to measure very small or large amounts of both flammable and/or toxic gases over a long period of time in a validated and verified test apparatus, utilizing the principle of a gas collector. This allows us to determine slow as well as fast gas evolution rates. The determination of the evolution rates (e.g. total gas amount or flow rate) of toxic gases is of special interest because of the ongoing discussion how to evaluate and quantify toxic gases which are formed from a substance due to contact with water. Up today no validated test procedure for the measurement of evolution rates for toxic gases is described. It is shown that the newly modified test method could help to solve this problem.

Keywords: *hazardous materials, transport regulations, flammable gases, toxic gases*

1. Introduction

The gas flow measurement procedure for substances which emit flammable gases in contact with water is described in the UN Test method N.5 (United Nations, 2019). The experiment involves the determination of the maximum gas evolution rate (GER) by means of a conical flask (Erlenmeyer flask) and a dropping funnel. The volume of the gas produced when the chemical comes into contact with water should be measured at appropriate time intervals by suitable measures. However, more precise information on measurement technique, how the GER should be determined, and corresponding quality requirements are not specified in this UN method. On basis of the calculated maximum GER, the dangerous goods classification of the chemicals is carried out according to the criteria listed in (United Nations, 2019).

On the criteria listed in Table 1, it can be stated that a relatively large measuring range must be covered by the test apparatus when determining the GER which is needed for the determination of the corresponding Packing Group (PG). It is therefore to be assumed that for this large measuring range a relatively high effort is required in the control of the test quality realized with the respective testing apparatus.

Table 1: *Criteria for Classification in Dangerous Goods Division 4.3 on the basis of the test results in accordance with UN Test N.5 (maximum GER), [PG] = Packing Group (United Nations, 2019)*

Maximum gas evolution rate	**Dangerous Goods Division**	**PG**
≥ 10 l / (kg*min)	4.3	I
≥ 20 l / (kg*h) and not ≥ 10 l / (kg*min)	4.3	II
> 1 l / (kg*h) and neither ≥ 20 l / (kg*h) nor ≥ 10 l / (kg*min)	4.3	III
≤ 1 l / (kg*h)	not 4.3	No

For example, the volume flows ("minute flow" and "hour flow") resulting in the respective PG decision criterion for a typical sample quantity of 10 g for the two evaluation intervals (1 minute or 1 hour) are shown in Table 2.

Table 2: *Criteria for Classification in Dangerous Goods Division 4.3 on the basis of the test results in accordance with UN Test N.5 (maximum GER), [PG] = Packing Group (United Nations, 2019)*

PG	**Gas evolution rate PG-Decisions criterion**	**Sample weight [g]**	**"Minute-Flow" per sample weight [ml/min]**	**"Hour-Flow" per sample weight [ml/h]**
I	10 l / (kg*min)	10	100.00	6000
II	20 l / (kg*h)	10	3.33	200
III	1 l / (kg*h)	10	0.17	10

An essential question for the acceptance and the trustworthiness of the test results according to UN test N.5 is the question of the traceability of the test results (ISO, 2017). With a gravimetric test method, the traceability of the results can be demonstrated very easily, especially in the daily laboratory routine. For this reason and because of the simplicity of the procedure, the UN Test N.5 at BAM is carried out using a gravimetric test apparatus. The results of the verification of this gravimetric apparatus are explained in (Lüth et al., 2020) and are based on a gravimetric and thus easily traceable verification process.

1.1 Gas evolution rate and total amount of gas evolution

The GER is an important safety-related parameter for the risk assessment and the selection of protective measures. According to test method UN N.5, the maximum GER is a measure of the risk of ignition and is used to classify a substance in class 4.3. However, it can be assumed that the maximum GER determined over a maximum of 5 days according to UN Test N.5 is not a safety-relevant parameter in all cases to prevent an accident (e.g. long-term transport in the container with the formation of an explosive and / or gas concentration dangerous for inhalation).

The chemical reaction usually does not run smoothly. Thus, the gas evolution rate depends on the duration of the chemical reaction with water. It has to be considered that in some cases the maximum activity of the chemical reaction is only reached after 5 days or even more.

However, it should be noted that a low gas formation rate is no guarantee for a safe situation at the workplace or during transport. Even a small gas evolution rate with a correspondingly long duration of reaction with water can lead to a dangerous gas concentration. The following factors can play a decisive role here: air exchange rate, ratio of the amount of substance to the volume of the room, chemical reaction kinetics / reaction course, reaction time, type of water (e.g. freshwater, seawater). The lower the air exchange rate and the closer the ratio of substance amount to the room volume, the faster a dangerous gas concentration is reached. This is problematic in terms of safety, e.g. during the long transport of reactive substances in containers or in ship holds and other relatively small storage rooms.

Therefore, in addition to the GER (as a limited parameter for the kinetics, velocity of the chemical reaction process), the absolute amount of gas produced, and the duration of the reaction must also be considered. The absolute amount of evolved gas can also be an important parameter for risk assessment and for the selection of protective measures. A chemical mixture with only a very small proportion, but which is a very strongly water-reactive chemical substance (with a high chemical reaction rate / kinetics with water), can e.g. show a very high maximum gas evolution rate. However, due to the small amount of substance in the mixture, the total amount of gas will tend not to be as large compared to another chemical mixture which could react completely with water, even if this other chemical mixture would react with water much more slowly. The amount of gas is also a question of the duration of exposure, i.e. how long the chemically reactive mixture has been in contact with water. In case of contact with moisture and water during long-term storage or transport (e.g. in maritime traffic over several weeks), the question of the total amount of gas generated could therefore be very important and possibly even more important than the gas evolution rate. From the BAM's perspective, both parameters (the maximum gas evolution rate and the total amount of gas) should therefore be determined for the risk assessment and the definition of protective measures. This might especially be important for toxic gas release.

Taking these aspects into account, we have therefore modified the BAM test system for the UN Test N.5 system, i.e. with the help of a solenoid valve the system automatically degasses the measuring system depending on the filling level of the measuring container. The mode of operation and some exemplary results are explained below.

2. Experimental

2.1 Modification of the testing apparatus to determinate both the gas evolution rate and the total amount of gas evolution

As discussed above, the GER at BAM is determined using a gravimetric approach as described in the following. The basic set-up continues to meet the requirements of UN Test N.5 (United Nations, 2019). The functional scheme is illustrated in Fig. 1. The reaction chamber is a closed system without direct contact to atmosphere and basically consists of a conical flask (1) and a dropping funnel (2). The evolved gas in the conical flask pressurizes the water column in the gas-water-displacement tank (4). This water column is displaced via the flexible connecting hose (5) to the water collection tank (6) (open to atmosphere), located on a balance (7). Essentially the evolved gas is detected as the corresponding weight increase on the balance and can be processed digitally. One drawback of this system is the discontinued measuring range. That means if all water is displaced into the water collection tank no additional gas evolution can be recorded. Therefore, a modification of this set-up was implemented, i.e. a solenoid valve (3) was introduced into the set-up which opens automatically when a preset weight on the balance is reached and degasses the system. After degassing and reaching a certain mass level on the balance, the valve automatically closes. Hereby the device works like a continuous gas collector, despite the short degassing intervals that must be switched on automatically when a maximum fill level in the gravimetric container is reached.

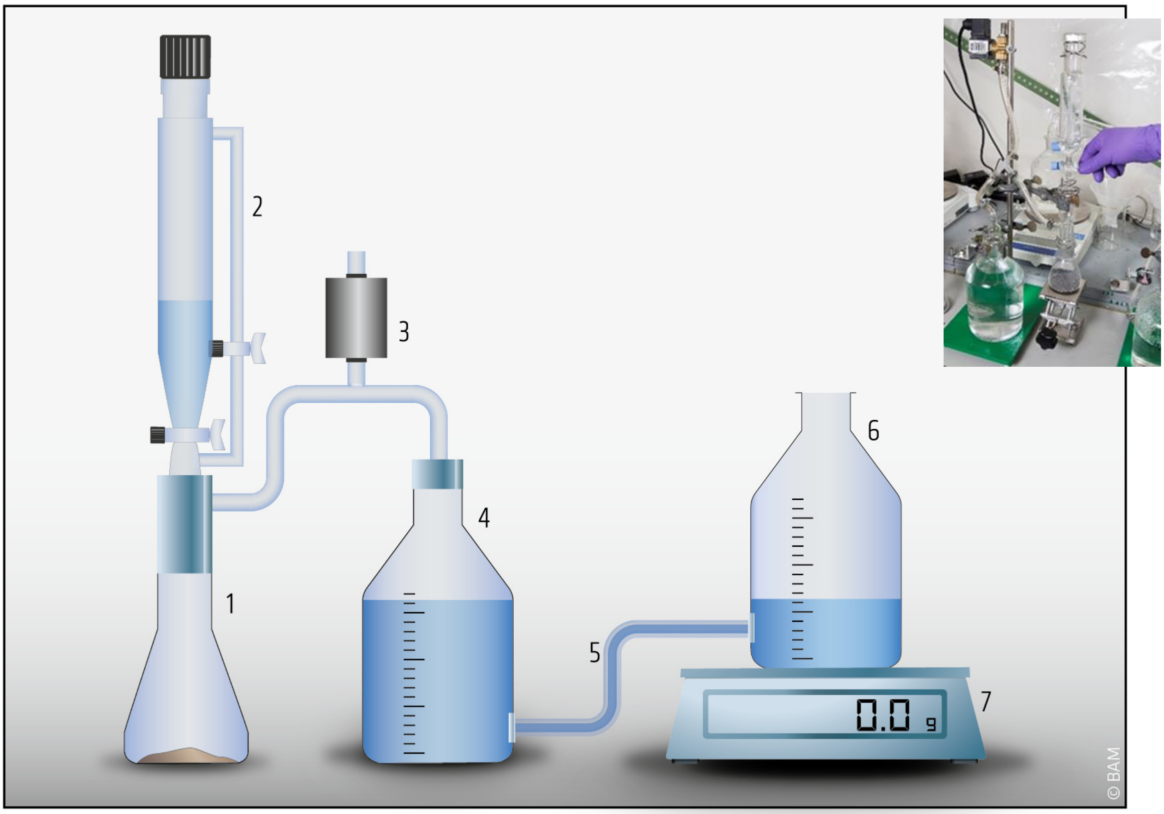

Fig. 1. *Functional scheme of the modified gravimetric method and photo of the gravimetric test apparatus and the additional solenoid valve (3) used in the BAM for the determination of the gas flow according the UN Test N.5 method with:*
1 = Erlenmeyer flask with the chemical test sample, 2 = dropping funnel, 3 = solenoid valve
4 = gas-water-displacement tank, 5 = connecting hose, 6 = water-collection tank and 7 = balance with coupling to a computer

Table 3 summarizes the main parts and important parameters of the modified set-up as shown in Fig. 1.

The changes in weight are recorded every 12 seconds using a computer. For the set-up standard laboratory glassware was used. The connecting hose (4) was a flexible PVC hose. The balance was either a Mettler Toledo model B 2002-S or a model ME2992T. The water volume in the system is about 2 l. The solenoid valve (one-way valve) automatically degasses the system when the maximum load on the balance is reached. The degassing stops and the system is closed again when the lower weight limit on the balance is reached.

Based on the gravimetric measurement results, the GER at each time point and the maximum is determined. The GER was calculated using MS Excel.

Table 3: *Special information about the devices according to Fig. 1 and operating parameters*

Number according to Fig. 1	**Device**	**Description**
1	Erlenmeyer flask	Holds the chemical test substance
2	Dropping funnel	By dropping the water onto the chemical substance, the reaction is initiated
3	Solenoid valve	Used for short degassing the system in case of maximum load on the balance is reached
4	Gas-water-displacement tank	Cylindrical* gas-water-displacement tank (may also be filled with other appropriate liquids)
5	Connecting hose	Flexible junction between the two tanks
6	Water collection tank	Cylindrical* water collection tank (may also be filled with other appropriate liquids)
7	Balance	Mettler Toledo model B 2002-S or a model ME2992T with measuring range up to 2 kg with a resolution with 2 decimal places with dynamic weighing

*…the cylindrical shape allows gas volume correction by calculating the pressure rise in the gas phase, which arises from the changes in the liquid height levels (height differences) in the containers 4 and 6 according to Fig.1.

2.2 Verification of the modified testing apparatus

The modified testing apparatus with the solenoid valve can be verified using the newly developed verification procedure (Lüth et al., 2020). This is important in order to also check the suitability of the solenoid valve or the gas-tight seal and the gas-tightness of the test system. The experimental setup for the verification of the apparatus is shown in Fig. 2.

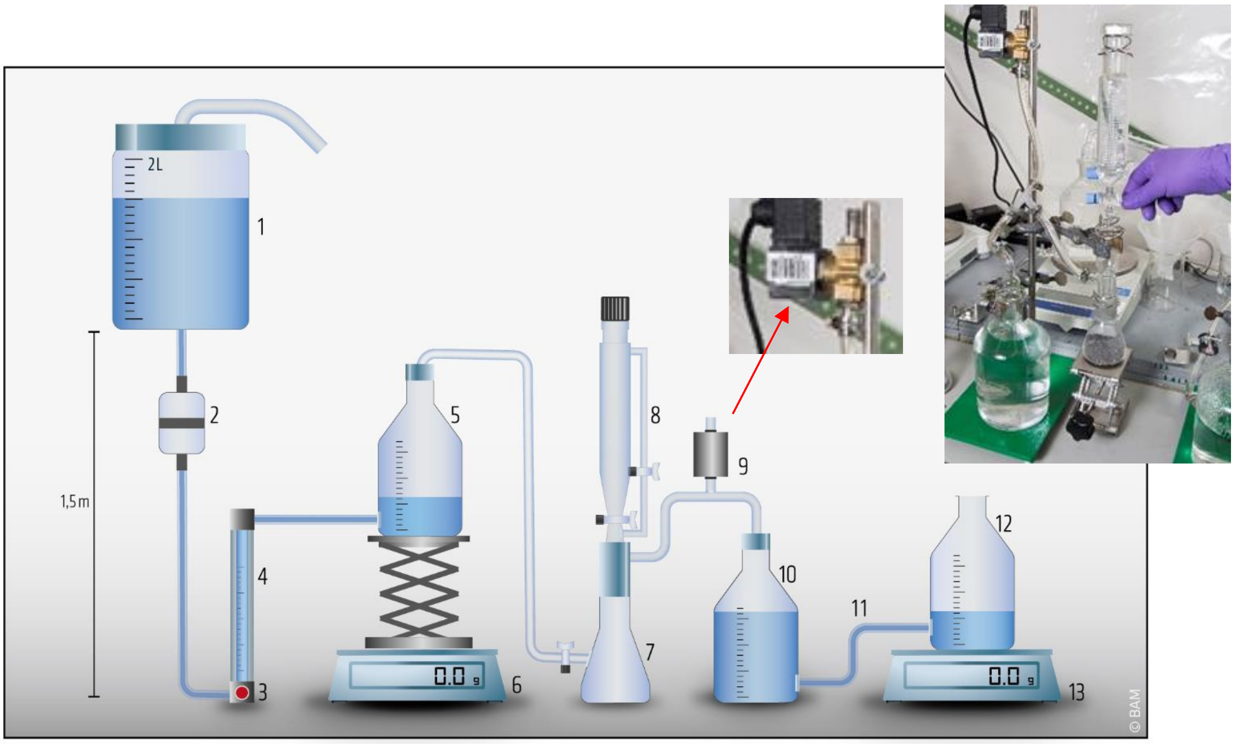

Fig. 2. *Functional scheme of the verification apparatus (left part of scheme) and test apparatus (right part of scheme) with: 1 = water reservoir, 2 = filter, 3 = needle valve, 4 = rotameter, 5 = water-gas-displacement tank, 6 = balance with coupling to a computer, 7 = Erlenmeyer flask with pipe connection, 8 = dropping funnel, 9 = solenoid valve; 10 = gas-water-displacement tank, 11 = connecting hose, 12 = water-collection tank, 13 = balance with coupling to a computer*

For more details on the verification procedure and results please see Lüth et al. (2020).

3. Results and discussion

3.1 Results of data acquisition and calculation of gas volume and gas evolution rates

The results of the data acquisition and calculation of the gas quantity and the gas evolution rates as determined with this newly modified set-up are explained using a test sample, which has been examined at BAM. The sample was an aluminum alloy which was in powder form (< 500 µm, i.e. 20-63 µm) and was examined at BAM without further processing. An amount of about 10 g was weighed into the flask and 30 ml of water were added. The examination time is approx. 333 h, i.e. almost 15 days, i.e. the time was significantly longer than required by UN Test N.5.

The following Fig. 3 shows the increase in mass on the scale for the test sample with automatic degassing of the system. In principle, the device works like a continuous gas collector, despite the short degassing intervals that are started automatically when a certain fill level (e.g. at mass 1500 g in Fig. 3) in the water-collection tank is reached.

DOI: 10.7795/810.20200724

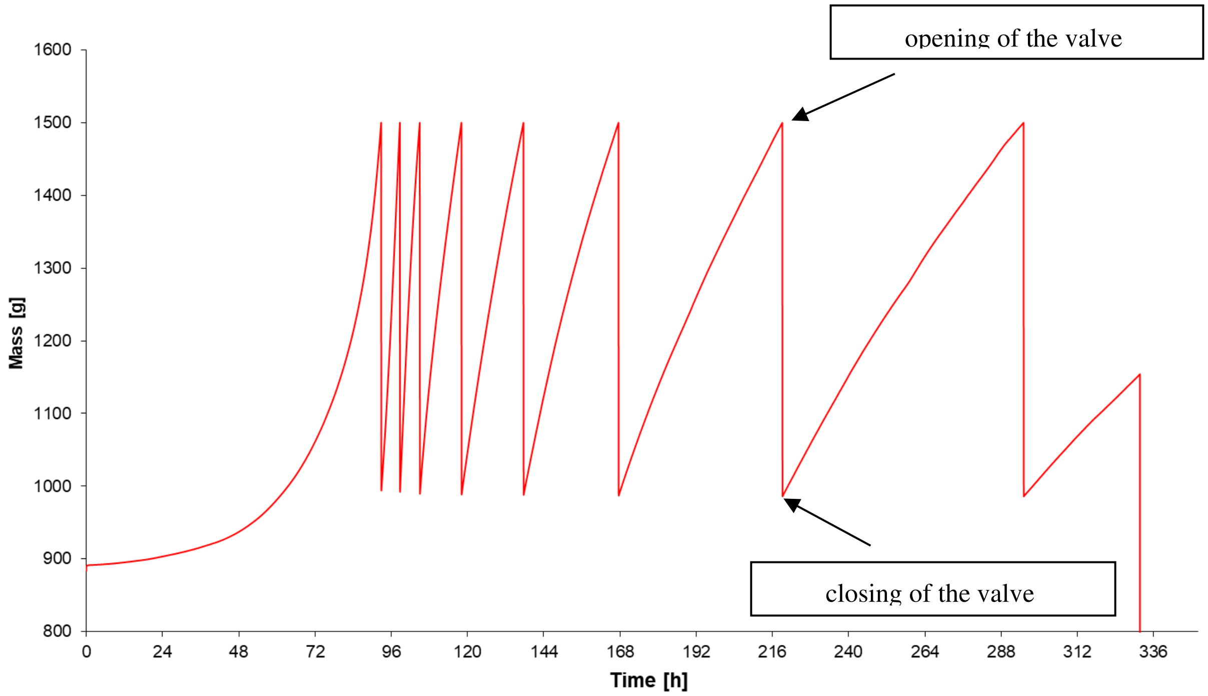

Fig. 3. Typical weight vs. time diagram of the test sample measured by balance of the test apparatus with automatic degassing of the system

The strictly vertical lines of the mass-time-curves correspond to the opening and closing of the valve and thus to the temporary degassing of the system (see marked example in Fig. 3).

3.2 Determination of the course of the developing gas volume

The gas volume is determined on the basis of the mass of the medium displaced (e.g. water), taking into account the density of the respective gravimetric medium (e.g. water) and shown in Fig. 4.

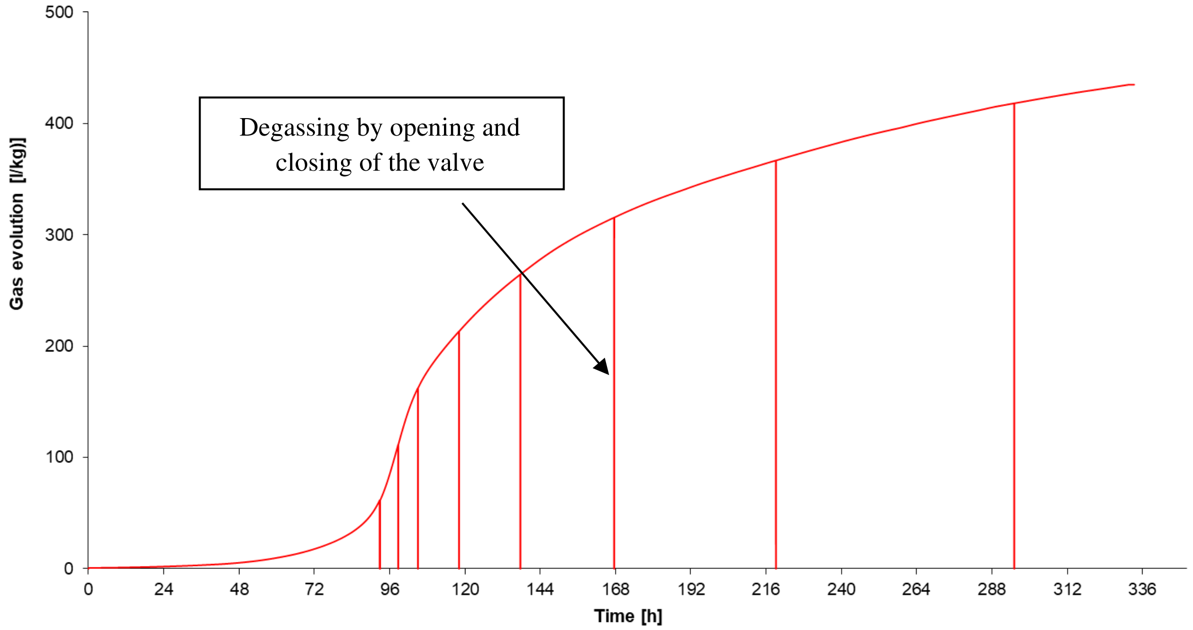

Fig. 4. Gas volume vs. time diagram of the test sample measured by balance of the test apparatus with automatic degassing of the system

As shown in Fig. 3 and Fig. 4 there were 8 automatic switching operations for degassing the system within the testing. Each degassing operation accounts to 9 intervals of 12 seconds (data acquisition rate is 12 s per data point), which, given the corresponding rate of increase, means a loss of approx. 3.8 g of the water displaced during this time by further gas formation (approx. 3.8 ml gas). Based on the 500 g measuring interval, this is a loss of less than 1% and was therefore not considered in Fig. 4.

From Fig. 4 it can be seen that the signal-to-noise ratio in relation to the total gas evolution is perfectly sufficient. The total gas evolution measured by this modified method can be used as a sufficient safety parameter for both the flammable and the toxic safety questions.

3.3 Determination of the GER

The calculation of the gas flow rate is based on the weight differences between the respective neighboring 12-second measuring intervals as shown in Fig. 5, left axis.

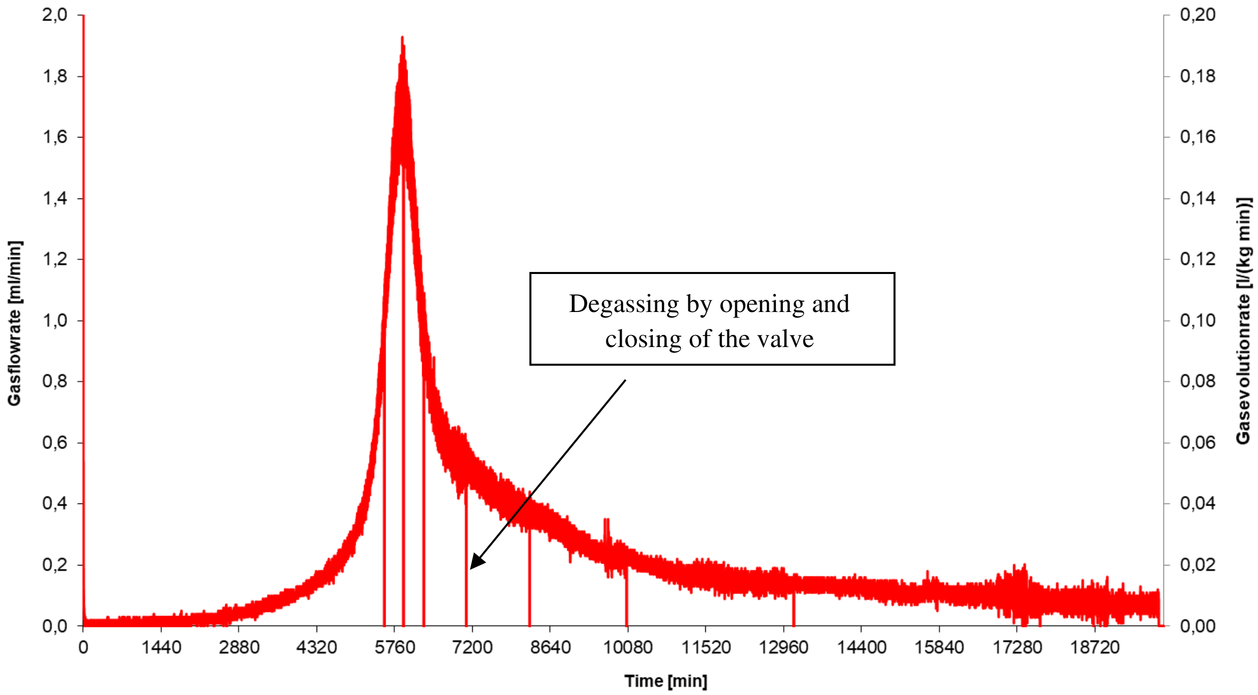

Fig. 5. *Left axis: Typical gas flow rate vs. time diagram of the test sample measured by balance of the test apparatus with automatic degassing of the system; right axis: Typical GER (minute volume) vs. time diagram of the test sample measured by balance of the test apparatus with automatic degassing of the system*

Taking into account the weight of 10 g of test substance, we calculated the normalized GER shown in Fig. 5, right axis.

From Fig. 5 it can be seen that the signal-to-noise ratio in relation to the classification criteria for PG I (10 l / (kg*min)) is perfectly sufficient and even low values of about 0.2 l / (kg*min) can be accurately determined whereby the experimental limit of detection is not reached yet.

For classification purposes it is also necessary to calculate the GER on the hour basis also. This is illustrated in Fig. 6.

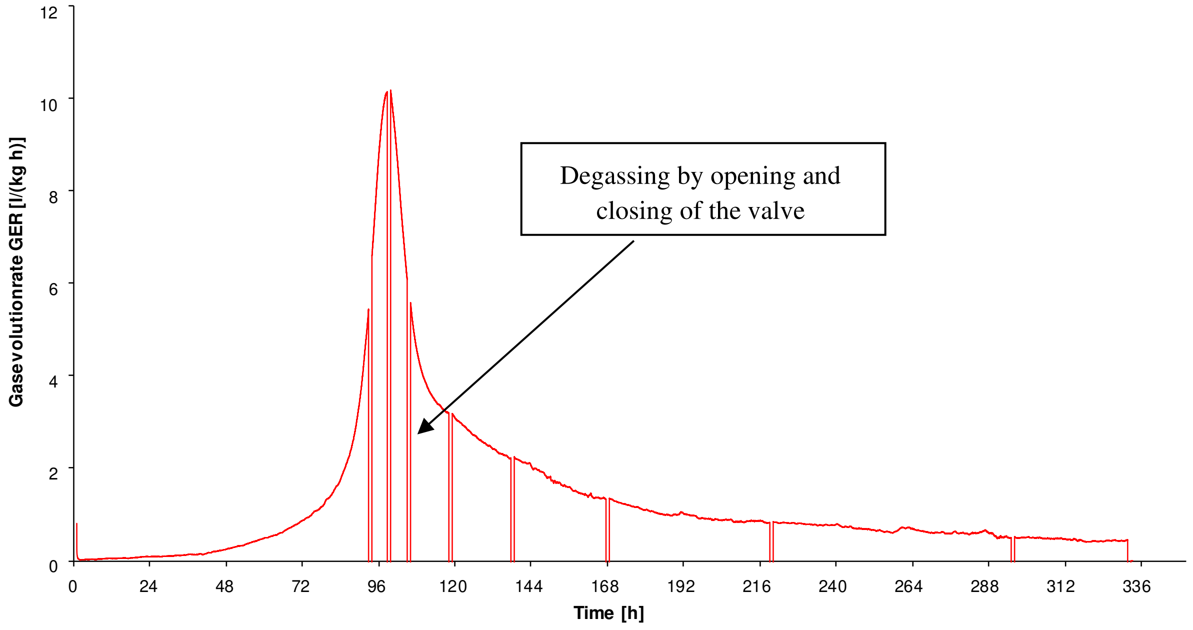

Fig. 6. *Typical GER (hour volume) vs. time diagram of the test sample measured by balance of the test apparatus with automatic degassing of the system*

The signal-to-noise ratio with regard to the classification criterion for PG III of 1 l/(kg*h) is shown graphically in Fig. 7:

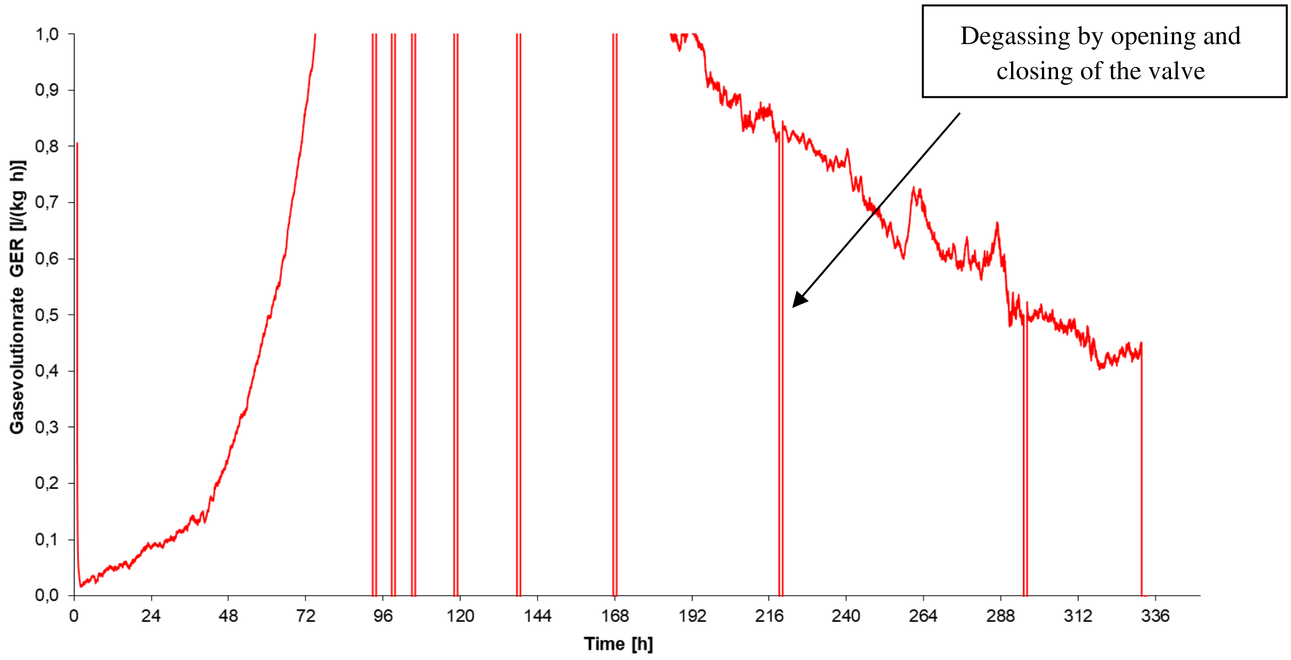

Fig. 7. *Enlarged Fig. 6 with enlarged y-axis to evaluate the signal-to-noise in relation to the classification criterion of PG III (1 l/(kg*h)*

It can be stated that also the evaluation of the GER on basis of the hour value can be performed with our modified set-up accurately. From Fig. 7 it can be seen that the signal-to-noise ratio in relation to the classification criteria for all PG is perfectly sufficient.

4. Conclusions

We introduced a new method for the detection of small or large amounts of flammable or toxic gases based on the established UN Test N.5 method. This modified test method can be used universally, it is not important whether the produced gas is toxic or flammable and it expands the possibilities of the UN Test N.5. In principle, the testing time period is unlimited and freely selectable.

The results can also be used to perform risk assessments, e.g. if the absolute gas volume generated in a certain time of interest.

A final validation including the determination of the measurement uncertainty of the modified test method should be carried out with the help of a special interlaboratory test.

References

European Union (2008). Commission Regulation (EC) No 440/2008 of 30 May 2008 laying down test methods pursuant to Regulation (EC) No 1907/2006 of the European Parliament and of the Council on the Registration, Evaluation, Authorisation and Restriction of Chemicals (REACH), OJ L 142, 31.5.2008, p.1.

ISO/IEC 17025:2017-11 General requirements for the competence of testing and calibration laboratories, International Organization for Standardization, Geneva.

Lüth, P., Frost, K., Kurth, L., Malow, M., Schmidt, M., Michael-Schulz, H., Uhlig, S. and Zakel, S. (2019). CEQAT-DGHS Ringversuchsprogramm für die Chemikaliensicherheit – Entwicklung von Verfahren zur Verifizierung der Prüfapparatur am Beispiel der Prüfmethode UN Test N.5. Physikalisch-Technische Bundesanstalt (PTB). DOI: https://doi.org/10.7795/210.20190521E

Lüth, P., Malow, M. (2020). CEQAT-DGHS Interlaboratory Test Programme for Chemical Safety – Development of a procedure for the verification of gas flow measurement devices used in UN Test N.5. To be published.

United Nations (2019). Manual of Tests and Criteria, Seventh revised edition, *United Nations*, New York and Geneva, <www.unece.org/trans/danger/publi/manual/rev7/manrev7-files_e.html>, accessed 06.02.2020

DOI: 10.7795/810.20200724

On the strength of knowledge in risk assessments for hydrogen systems

Trygve Skjold

University of Bergen, Department of Physics and Technology, Bergen, Norway

E-mail: *trygve.skjold@uib.no*

Abstract

The energy infrastructure needs a shift towards sustainable use of conventional hydrocarbons and an increased share of renewable energy sources in the global energy mix. To this end, energy forecasts from various organisations outline a future where hydrogen is widely used as an energy carrier in industry and society. However, it is not realistic to envisage widespread use of hydrogen unless the suppliers of hydrogen technologies demonstrate that the associated risk is comparable or lower than the corresponding risk for conventional energy carriers. This applies to all aspects of the energy system where it is relevant to produce, transport or use hydrogen, from industrial facilities such as reformers, electrolysers and liquefaction plants, to cars, busses, trucks, trains, ships, airplanes and domestic heating and cooking. To achieve and document the required level of safety for hydrogen systems represents a considerable technological, organisational and societal challenge. Recent developments in the area of risk analysis focus on uncertainty and strength of knowledge. This paper explores the knowledge available to support risk assessments for hydrogen systems and the implications for design and operation of hydrogen installations in society.

Keywords: *hydrogen, energy systems, risk assessment, uncertainty, strength of knowledge*

1. Introduction

Extraction, conversion, storage, transport and use of energy play a fundamental role in advancing modern societies and will continue to do so in the foreseeable future. Humankind will continue to consume energy commodities at an increasing rate due to population growth and improvements in the standard of living. While the global reserves of fossil fuels diminish, continued release of carbon dioxide on a massive scale is likely to influence the global climate. To this end, the energy infrastructure needs a shift towards increased use of renewable energy sources and sustainable use of conventional hydrocarbons. Several of the Sustainable Development Goals (SDGs) from the United Nations (UN) reflect this realisation, including SDG #7 on affordable and clean energy and SDG #13 on climate action. The variable and intermittent supply of renewable energy from solar and wind suggests a transition towards energy systems that entail widespread use of hydrogen or hydrogen-based fuels as energy carriers in industry and society (DoE, 2011; IEA, 2019; FCH 2 JU, 2019; DNV GL, 2019; Clean Sky 2 JU & FCH 2 JU, 2020). Existing technologies can convert energy from renewable or non-renewable sources into hydrogen, hydrogen can be stored and transported in compressed, liquid or chemical form, and energy converters such as turbines and fuel cells can convert hydrogen or hydrogen-based fuels into electrical or mechanical energy and heat on demand. However, sudden and uncontrolled releases of energy, such as accidental fires and explosions, represent a significant hazard to people, industries, society and the environment (Skjold *et al.*, 2017; Skjold *et al.*, 2018). Hence, it is not realistic to envisage widespread use of hydrogen in industry and society unless the suppliers of hydrogen technologies can demonstrate that the associated risk is comparable or lower than the corresponding risk associated with conventional fuels.

DOI: 10.7795/810.20200724

It is not straightforward to foresee all significant hazards in industrial facilities, nor to predict the consequences of the corresponding accident scenarios. Furthermore, there are inherent uncertainties associated with the estimation of event frequencies, especially for emerging technologies. In principle, it might be possible to derive the probability of failure of an integrated system from a fault tree analysis based on the probabilistic time to failure for individual components. However, this approach requires information that is often not readily available, and does not account for initiating events resulting from the complex interaction between people and technologically advanced systems, such as ‘human error’ during design, construction and assembling, as well as start-up, shutdown and maintenance operations. Furthermore, risk management and safety culture in organisations, or lack thereof, can explain many accidents where investigations in the past attributed the root cause to human error (DoE, 2009). Relevant experience is arguably the most reliable way to document the true level of safety for complex systems that entail close interaction between humans and technology. However, typical thresholds for individual risk suggest that it is necessary to accumulate a million years of a certain activity, such as hydrogen refuelling station years, to document a satisfactory level of safety for the public. This creates a fundamental challenge for the emerging hydrogen technologies.

2. Uncertainty in risk assessments

Sudden and uncontrolled releases of energy represent a significant hazard to people, industries, society and the environment. In the present context, safety implies control over hazards that can result in loss of life, material values, reputation, etc. Accidents are unintended and sudden events that result in losses, and risk is a measure of the expected loss for a specified system or activity. Figure 1 shows a general schematic of the processes and activities involved in risk analysis, risk assessment and risk management. A quantitative risk assessment (QRA) entails the calculation and evaluation of an expectation value (i.e. risk) that combines event frequencies and the corresponding consequences for the relevant hazards identified for a specified system.

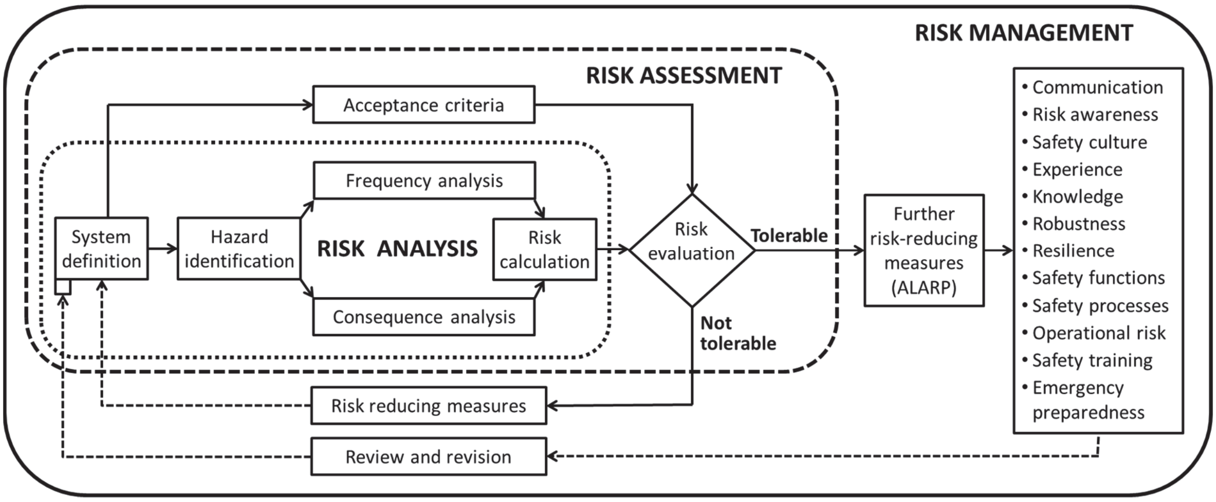

Fig. 1. *General schematic for risk analysis, risk assessment and risk management.*

The top management is ultimately responsible for the safety of the employees and material properties of an organisation, as well as any significant deterioration of the environment resulting from the activities of the organisation. Management controls the resources available for safety training and other risk-reducing measures, and management must decide whether the risk associated with an activity is acceptable or tolerable. In this context, a QRA can be a valuable tool for decision support, provided all significant hazards are identified, there is sufficient knowledge available to estimate the associated event frequencies and consequences with a reasonable degree of accuracy, and the results and inherent uncertainties are presented to the relevant stakeholders in a suitable format (Aven, 2015; Aven, 2019; Taylor, 2016).

Whether decision makers or the public perceive the risk associated with a specific energy carrier as acceptable depends on various factors, such as (Ehrenfeld, 1996; Lemkowitz & Schotte, 1999; Frewer, 1999; Flynn & Bellaby, 2007; Skjold *et al.*, 2017; Lemkowitz & Taveau, 2019):

- the benefits resulting from the development and application of the technology,
- previous accidents involving the specific energy carrier and related technologies,
- how the energy systems are constructed and maintained, including risk reducing measures,
- relevant properties of the energy carrier, such as toxicity, ignitability, flammability, etc.,
- public perception of moral or ethical aspects of the technology, including environmental concerns,
- the level of trust in relevant sources of information, especially with respect to the dimensions 'competence' and 'honesty', and
- the specific knowledge about the particular combination of the energy carrier and the associated system by the people that estimate and evaluate the risk.

This paper is primarily concerned with the last point, in particular the strength of knowledge and inherent limitations in the achievable level of accuracy in risk assessments for hydrogen systems.

Most accidents in technically advanced systems, such as electrolysers, refuelling stations, ships, airplanes and nuclear power plants, entail a more or less intricate chain of events. Furthermore, most accidents do not occur under normal operation. A disproportionally high fraction of accidents takes place in connection with start-up or shutdown operations, maintenance work, etc. Hence, it is not possible to assess the safety of a complex system based on technical specifications of its single components alone, and risk assessments based on 'normal operating conditions' have limited value.

The upper thresholds for individual risk, above which the risk is simply unacceptable and has to be reduced or eliminated regardless of the costs, are typically 10^{-3}-10^{-4} and 10^{-5}-10^{-6} fatalities or serious injuries per year for workers in industrial facilities and members of the public, respectively (Paté-Cornell, 1994). The corresponding thresholds for the transition from the domain of cost-benefit analysis to a level below regulatory or legal concern (*'de minimis'*) are typically 10^{-6} and 10^{-7}-10^{-8}. Hence, from a societal point of view, it is necessary to accumulate 10^{5}-10^{6} years of a certain activity, such as refuelling station years or nuclear reactor years, to document the level of safety. This creates a fundamental challenge for the emerging hydrogen technologies. With less than a thousand hydrogen refuelling stations operational worldwide, it would take 100-1000 years, with a limited number of serious accidents, to demonstrate an acceptable level of safety. Furthermore, an estimated average level of safety will in general not be representative for all systems. The technical and organisational solutions for a given category of energy systems, such as 'hydrogen refuelling stations' or 'hydrogen-powered ferries', may differ significantly between installations designed, owned and operated by different organisations.

The inherent lack of relevant statistical data for complex systems that entail emerging technologies does not imply that the risk is not acceptable or tolerable. It does however imply a significant source of uncertainty in the estimation of event frequencies. One of the trends in contemporary approaches to risk analysis entails increased focus on the inherent uncertainties in both frequency and consequence assessments (Aven & Kristensen, 2019). A pragmatic solution in situations with high degree of uncertainty is to implement additional safety measures to compensate for the inherent uncertainty associated with weak knowledge. In response to the growing criticism towards the classical probabilistic approach, there is also a tendency to adopt methodologies that entail design against 'worst credible events', or robust/resilient design. However, it is not straightforward to reach consensus on what the term 'credible' should imply.

Experiments are indispensable when it comes to understanding physical phenomena, e.g. whether a given ignition source can ignite a fuel-air mixture, for exploring repeatability and scaling laws, and for validating consequence models (Skjold *et al.*, 2013). However, the deterministic nature of controlled experiments implies that it does not make sense to derive event frequencies for complex systems from data obtained from tests performed under controlled conditions in simplified systems.

In addition to the challenges associated with the identification of significant hazards and estimation of event frequencies, it is not straightforward to predict the consequences of realistic accident scenarios. Figure 2 illustrates the experimental setup and summarises the experimental results and model predictions obtained with four different computational fluid dynamics (CFD) tools in a blind-prediction benchmark study conducted as part of the HySEA project (Skjold *et al.*, 2019a). Seven different modellers, or groups, submitted the model predictions M-1 to M-7. Two modellers, M-6 and M-7, submitted results for four different grid sizes, indicated by the numbers in parenthesis.

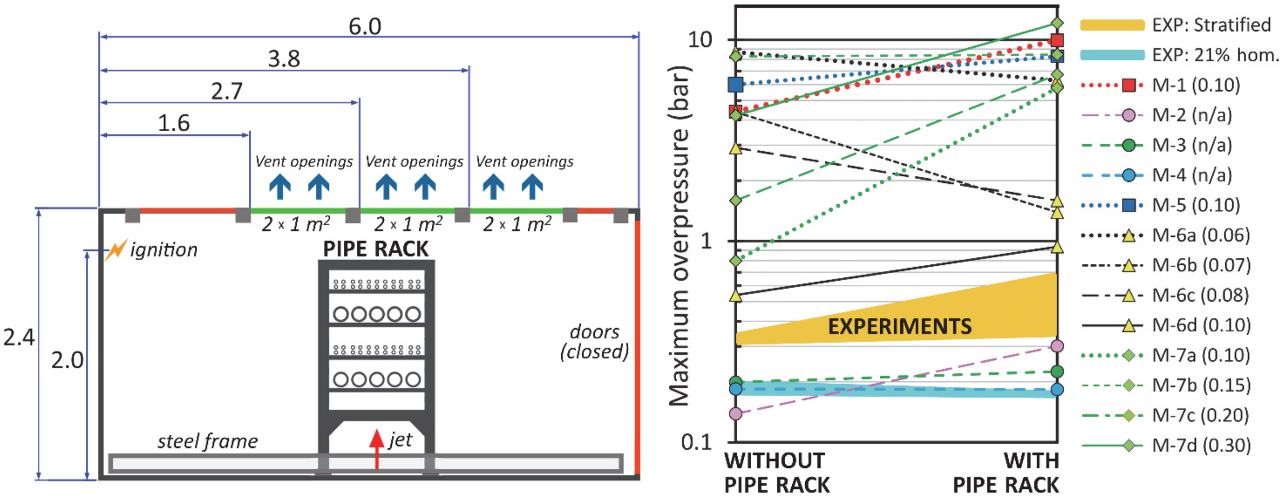

Fig. 2. *Experimental setup (left) and model predictions by CFD tools (right) from a blind-prediction benchmark study with vented hydrogen deflagrations in a 20-foot shipping container.*

The blind-prediction study focused on scenarios with release of gaseous hydrogen into a 20-foot shipping container at a constant flow rate of 56 $Nm^3\ hr^{-1}$ through a vertical pipe with inner diameter 18 mm. The duration of the releases was 450 s, corresponding to an average fuel concentration of 21.0 vol.% in the enclosure at the end of the release. The jet releases resulted in stratified layers with 25-27 vol.% hydrogen near the ceiling at the time of ignition, 30 s after the releases ended. A single-sheet bulged vent panel with vent area 1.0 m^2, nominal static opening pressure 0.100 bar, specified opening pressure 0.075-0.125 bar, and specific weight 6.8 kg m^{-2}, covered each of the six 1.0m×1.0m vent openings indicated in Figure 2. The modelling exercise included the release and dispersion process, followed by ignition and vented deflagrations, with or without the pipe rack present. The test series included reference tests with 21.0 vol.% homogeneous mixture in the enclosure. Skjold *et al.* (2019ab) describe the experimental setup, test procedures and results in detail.

The spread in the predicted maximum overpressures in Figure 2, covering two orders of magnitude, demonstrate an urgent need to improve the predictive capabilities of consequence models for vented hydrogen deflagrations, as well as the users of such models. The experiments in the HySEA project demonstrated that conventional explosion venting devices could prevent the rupturing of containers used for hydrogen energy applications during relatively severe explosions, at least for moderate levels of internal congestion (Skjold *et al.*, 2019b). However, safe design of hydrogen installations requires models that can predict the consequences of realistic accident scenarios, including the effect of mitigating measures, with a reasonable degree of accuracy. The significant spread in the results for users of the same consequence model was partly due to mistakes in the setup of the simulations. As such, further blind-prediction benchmark studies combined with certification of modellers can be an important step towards more consistent results in risk assessments for hydrogen systems.

3. Principles for risk reduction

Knowledge about hydrogen safety is relevant for a wide range of energy systems in industry and society. This includes hydrogen production from natural gas by steam reforming or electrolysis of water, carbon capture and storage (CCS), industrial production of chemical compounds such as ammonia and methanol, refinery processes, nuclear power plants, space exploration, hydrogen-powered turbines, fuel cells and batteries in transportation (cars, trucks, trains, ships and airplanes), hydrogen refuelling stations, etc. Numerous factors influence the level of safety an organisation can achieve for a given system, including the potential for loss, the maturity of the technology, safety functions and processes, safety training and emergency preparedness, the maturity and availability of relevant regulations, codes and standards, risk perception and risk awareness, and the prevailing safety culture in the organisation. Nevertheless, hard-earned lessons from industrial activities over more than two centuries have resulted in a hierarchy of principles for risk reduction (Kletz, 1999):

1. Inherent safety (Kletz, 1978), such as minimising the inventory of hazardous materials.
2. Preventive measures, including:
   a. Preventing the formation of explosive atmospheres, such as loss of containment of fuel,
   b. Preventing or controlling ignition sources.
3. Mitigative measures, including:
   a. Passive mitigation, such as passive ventilation, passive isolation/sectioning, and explosion venting devices,
   b. Active mitigation, such as forced ventilation, active suppression and active isolation/sectioning.
4. Procedural safety, such as hot work permits, mandatory use of personal protection equipment, etc.

That is, safety engineers should consider the principles for inherent safety first, and procedural safety is the last resort. In practice, it is usually necessary to combine various risk-reducing measures to achieve an acceptable level of safety.

4. Regulations, codes and standards

Various organisations provide guidelines for safe implementation of hydrogen systems, and specific regulations, codes and standards (RCS) apply, depending on location, the nature of the system, the inventory of hydrogen, etc. As part of the HyLAW project, Floristean (2019) reviewed the EU legislation that regulates production, storage, transport and use of hydrogen. Owners and operators of facilities (i.e. employers) where there is a possibility of forming an explosive atmosphere are legally obliged to comply with the ATEX workplace directive (1999/92/EC), including:

- Carrying out risk assessments for any work-related activities that involve flammable substances.
- Recording the findings of the risk assessment in an explosion protection document (EPD).
- Providing technical and organizational measures to reduce the risk to an acceptable level.
- Providing training to workers employed in locations where explosive atmospheres may occur.
- Classifying areas where explosive atmosphere may occur into hazardous area zones.
- Selecting and providing suitable equipment for use in the hazardous area zones.

Within Europe, other relevant legal requirements follow from the ATEX equipment directive (2014/34/EU), the SEVESO directive (2012/18/EU), and the pressure equipment directive (2014/68/EU). The SEVESO directive applies to storage of more than five metric tons of hydrogen, which is a considerable amount for a highly reactive fuel with high specific energy.

5. Specific challenges for hydrogen safety

It is not realistic to foresee widespread use of hydrogen in society unless the suppliers of hydrogen and hydrogen technologies can demonstrate that the associated risk is comparable or lower than the corresponding risk for conventional fuels (Hord, 1976; Cracknel *et al.*, 2002; Crowl & Jo, 2007; Rigas & Amyotte, 2013; IMO, 2016). In the present context, relevant conventional fuels include compressed natural gas (CNG), liquefied natural gas (LNG), liquefied petroleum gas (LPG), and distillate fuels such as petrol, diesel, jet fuel and marine fuel oils (in the following, safety-related properties for methane and propane will be used for CNG/LNG and LPG, respectively). To achieve and demonstrate an acceptable level of safety for hydrogen systems represents a considerable technological challenge, for various reasons:

- Hydrogen has high specific energy, about 142 and 120 MJ kg^{-1} for the higher heating value (HHV) and lower heating value (LHV), respectively, compared to hydrocarbons such as methane (55 and 50 MJ kg^{-1}), propane (50 and 46 MJ kg^{-1}), as well as diesel and jet fuel (45-46 and 43 MJ kg^{-1}). However, the low density, and hence low energy density, implies that compressed hydrogen (GH2) is stored and transported at considerably higher pressures (≈700 bar) compared to conventional energy carriers, such as CNG (≈260 bar), LPG (≈30 bar), as well as marine gas oil, heavy fuel oil, diesel and petrol (atmospheric pressure in the tank space). As such, it is not straightforward to prevent loss of containment. The pressurised vessels also represent a hazard, for instance in the event of material failure or external loads from impacts, projectiles, fires, etc. Furthermore, the low boiling point implies that liquefied hydrogen (LH2) is stored and transported at considerably lower temperatures (≈ -253 ºC) compared to conventional energy carriers, including LNG (≈ -162 ºC). This implies cryogenic hazards in the event of loss of containment.
- Hydrogen is a gas at normal temperatures and pressure, but LH2 has very low flashpoint (< -253 ºC) compared to conventional fuels such as LNG (≈ -188 ºC), LPG (≈ -104 ºC) and marine fuel oils (flashpoint > 60 ºC). Since the *flashpoint* indicates the lowest temperature at which a volatile substance evaporates to form an ignitable mixture with air, a lower flashpoint generally implies increased fire and explosion hazard. To this end, the United Nations (UN) classifies flammable liquid and vapours according to their flashpoint (UN, 2011):
  - Extremely flammable liquid and vapour: flashpoint < 23 ºC and initial boiling point ≤ 35 ºC
  - Highly flammable liquid and vapour: flashpoint < 23 ºC and initial boiling point > 35 ºC
  - Flammable liquid and vapour: flashpoint ≥ 35 ºC and ≤ 60 ºC
  - Combustible liquid: flashpoint > 60 ºC and ≤ 93 ºC
  - Non-flammable liquid: flashpoint > 93 ºC
- Hydrogen-air mixtures are flammable over a considerably wider range of concentrations (4-75 vol.%), compared to conventional fuels such as methane (5-15 vol.%) and propane (2.1-9.5 vol.%).
- Hydrogen has very low minimum ignition energy (MIE ≈0.017 mJ), compared to conventional fuels such as methane (≈0.28 mJ) and propane (≈0.26 mJ). This implies that ignition sources that otherwise do not represent a significant hazard may readily ignite hydrogen-air mixtures (Skjold & van Wingerden, 2010). Further research will presumably result in better understanding of ignition phenomena related to electrostatic discharges, mechanical impacts and the effect of external congestion and presence of dust or mist for spontaneous ignition of high-pressure releases (Wolański & Wojcicki, 1973).
- Table 1 summarises the classification of gases and vapours for equipment used in explosive atmospheres (EN IEC 60079-0, 2018). The classification is based on the parameters maximum experimental safe gap (MESG), minimum ignition current (MIC) and the auto-ignition temperature (AIT). The AIT of hydrogen (≈500 ºC) is comparable to other conventional fuels in temperature class T1, such as natural gas (≈640 ºC) and propane (≈466 ºC).

***Table 1**: Classification of selected flammable vapours and gases.*

Gas group	**Temperature class** – AIT (ºC)					
	T1	**T2**	**T3**	**T4**	**T5**	**T6**
	450 >	300 – 450	200 – 300	135 – 200	100 – 135	85 – 100
IIA MESG > 0.9 mm	Methane Propane Ammonia	Methanol Ethanol	Diesel Fuel oils Petrol	–	–	–
IIB 0.9 ≥ MESG > 0.5	Coal gas	Ethylene	–	Diethyl ether	–	–
IIC 0.5 mm > MESG	Hydrogen	Acetylene	–	–	–	Carbon disulphide

- The maximum laminar burning velocity of hydrogen-air mixtures is significantly higher ($S_L \approx 2.9$ m s^{-1}) than for most conventional fuels (Konnov *et al.*, 2018), such as methane ($S_L \approx 0.36$ m s^{-1}) and propane ($S_L \approx 0.41$ m s^{-1}). Furthermore, various hydrodynamic, thermo-diffusive and thermo-acoustic instabilities may influence the flame propagation in hydrogen-air mixtures significantly (Clavin & Searby, 2016). In particular, the role of thermo-diffusive instabilities depends on mixture composition (Sánchez & Williams, 2014) – cellular instabilities occur at sufficiently fuel-lean conditions (negative Markstein lengths), and pulsating instabilities occur at sufficiently fuel-rich conditions (positive Markstein lengths).
- Vapour cloud explosions (VCEs) in industry entail turbulent flame propagation in premixed fuel-air mixtures. The positive feedback mechanism between expansion of combustion products, turbulence generation in the unreacted mixture (e.g. in wakes behind obstacles), flame folding caused by obstacles and/or instabilities, and enhanced rate of turbulent combustion results in flame acceleration and pressure build-up, especially in congested and partly confined regions. The chain of events depends on the reactivity of the mixture, typically quantified by the laminar burning velocity mentioned above, as well as initial and boundary conditions such as the turbulent flow conditions, the size of the flammable cloud, and the degree of congestion and confinement. The extreme reactivity of hydrogen-air mixtures, relative to conventional fuels, results in a dramatic increase in flame acceleration in the presence of obstacles and/or initial turbulence, with significant potential for escalation (Skjold *et al.*, 2019b; Shirvill *et al.*, 2019ab).
- Hydrogen-air mixtures have a propensity for deflagration-to-detonation-transition (DDT) under specific conditions (Ciccarelli & Dorofeev, 2008). The detonation cell size for stoichiometric hydrogen-air is about 10 mm, compared to 300 mm for methane and 70 mm for propane. This implies that small variations in the initial and boundary conditions can have dramatic influence on the chain of events in hydrogen explosions. Extensive research in the aftermath of the Buncefield explosion has resulted in increased awareness of the critical importance of considering detonation scenarios in risk assessments and design of industrial facilities (Oran *et al.*, 2020).
- Hydrogen can cause embrittlement in certain materials, resulting in loss of physical properties, and possible loss of containment.
- Several of the risk-reducing measures frequently employed for systems with conventional energy carriers have limited applicability for hydrogen, including deflagration venting and automatic suppression.
- Many application areas for hydrogen involve emerging technologies, and hence inherent uncertainty associated with the estimation of both event frequencies and consequences.
- Hydrogen safety is an area of active research, which often addresses inherently complex phenomena and emerging technologies. As such, the strength of the knowledge available for risk assessments is inherently limited.
- Many consultants that perform risk assessments do not have specific competence on hydrogen safety, and may apply conventional consequence models and event frequencies derived from the hydrocarbon industry. This increases the uncertainty in the risk assessments considerably and can result in a false impression of safety amongst owners and operators of hydrogen systems.
- It takes time to build competence on technical safety and to develop a healthy safety culture in an organisation. Furthermore, experience shows that accidents recur in the same industry, and even in the same organisation (Kletz, 1993).
- As mentioned above, there is a fundamental difference between the required level of safety for controlled production and use of hydrogen within industrial facilities, with access control and trained employees, and widespread use of hydrogen in the public domain.

There are some favourable features of hydrogen concerning safety, at least for specific conditions:

- Buoyancy, due to the low density of hydrogen relative to air at the same temperature, can prevent the formation and limit the duration of large flammable clouds in unconfined areas. This implies that natural convection in open geometries is the preferred approach for preventing and mitigating hydrogen explosions. However, in confined geometries, buoyancy favours the formation of highly reactive stratified layers near the ceiling (Skjold *et al.*, 2019b). This implies that classical means of explosion protection are inherently difficult to implement for tunnels and parking facilities, as well as fuel preparation rooms, fuel cell rooms and machinery spaces on ships. Furthermore, in congested unconfined scenarios, a DDT event in a localised congested and/or confined region can trigger an aboveground detonation in the rising hydrogen-air plume. The interaction between the original blast wave and the blast wave reflected from the ground may result in a Mach stem.

- Pure hydrogen flames do not produce soot, which implies less transport of heat by radiation, compared to hydrocarbon flames. However, jet flames in realistic accidents may entrain components from volatile materials, such as paint, plastic, dust, etc. Without proper barriers in place, an external fire, e.g. a jet fire from an uncontrolled release of hydrogen, may compromise the tanks used for storing the fuel.

Figure 3 illustrates a typical event tree for the initiating event ‘release and dispersion’ (i.e. loss of containment) of gaseous hydrogen, with associated probabilities (*P*) and consequences (*C*) for various scenarios. A comprehensive QRA will consider multiple initiating events, representing leaks with different release rates and durations, located in various positions and pointing in different directions, for different wind conditions and/or with or without forced or natural ventilation. It is essential to account for the variation in the release rate during the event, as well as the delay between the onset of the release and ignition, since these parameters influence the size of the flammable cloud, and hence the time-dependant probability of ignition and the consequences of potential explosions. Furthermore, there can be numerous intermediate or combined scenarios, such as fires initiated by explosions or vice versa, structural collapse caused by fires and explosions, blast waves, projectiles, etc. Nevertheless, the simple event tree in Figure 3 illustrates the significant challenge of reducing the risk for hydrogen installations to a level equivalent to or below that of conventional fuels.

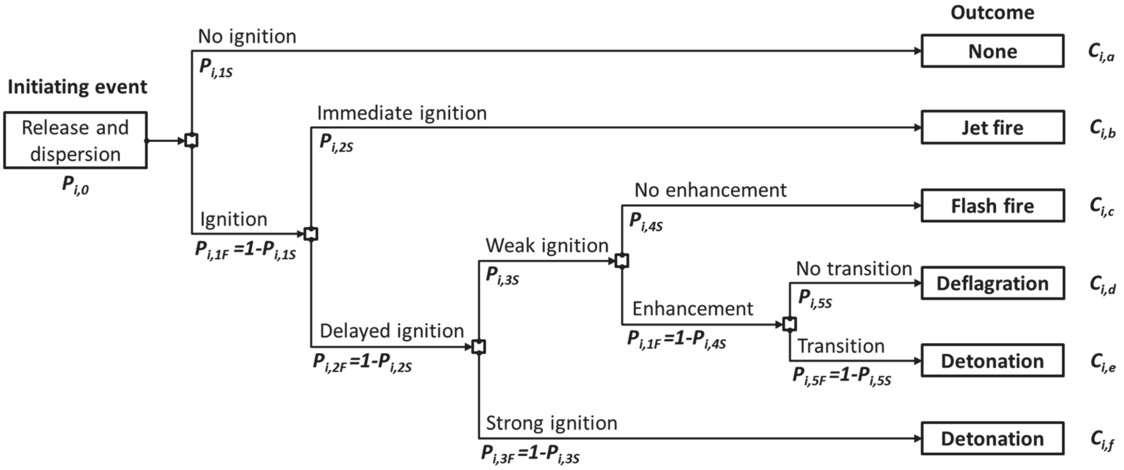

Fig. 3. *Simplified event tree for loss of containment of hydrogen.*

For comparable energy systems, i.e. facilities with similar inventory of fuel (chemical energy), similar probabilities of initiating events, similar levels of confinement and congestion, similar age and level of maintenance, etc., the safety-related properties of fuels mentioned above imply that the overall risk often will be significantly higher for hydrogen systems, compared to systems based on conventional fuels. In particular, the likely shift towards an increased fraction of accident scenarios involving strong deflagrations or detonations implies an increased likelihood of major accidents, and hence increased requirements for emergency preparedness in society. Hence, to achieve an acceptable level of safety for systems where hydrogen is the primary energy carrier, such as hydrogen refuelling stations or ferries, the design of the hydrogen systems must differ significantly from that of contemporary systems using conventional fuels. Furthermore, from the perspective of societal safety it will be increasingly important to develop appropriate infrastructure and procedures for emergency response. In summary, the specific safety-related properties of hydrogen imply that it often will be necessary to implement additional or specially designed safety measures to reduce the risk to an acceptable level in systems and infrastructure that use hydrogen as an energy carrier.

6. Learning from accidents

The accident at a hydrogen refuelling station in Sandvika, Norway, on 10 June 2019 illustrates some of the challenges associated with the safe introduction of hydrogen in society (Løkke, 2019). The accident took place around 17:30 on Pentecost/Whit Monday, a public holiday in Norway. The chain of events started with a leak from the high-pressure system (about 900 bar), followed by ignition and a strong explosions. The initial accident investigation did not identify an obvious ignition source. The accident did not result in any fatalities, and only minor injuries to people when the blast wave from the explosion triggered airbags in cars. Plates of sheet metal covered the exterior of the fire/pressure wall surrounding the compound with the process equipment for hydrogen production, compression and storage. Figure 4 illustrates how parts of the wall near the high-pressure unit and plates of sheet metal formed projectiles that landed on the opposite side of a four-lane road and a roundabout, after passing over a combined sidewalk and bicycle path. Hence, under slightly different circumstances this accident could have resulted in severe injuries and even fatalities.

Fig. 4. *The hydrogen refuelling station in Norway after the explosion on 10 June 2019 (NRK, 2019).*

Apart from the considerable material damage to the refuelling station and minor damage to nearby buildings, the accident resulted in loss of shareholder value and a considerable setback for the development of the hydrogen infrastructure, at least in Norway. The operator of the station closed down all hydrogen refuelling stations in Norway shortly after the accident, and put all plans for new stations on hold. It is difficult to predict whether this accident will influence public perception and widespread adoption of hydrogen as an energy carrier in a long-term perspective. However, the accident demonstrates several important aspects of hydrogen safety, from an industrial (commercial) as well as a societal perspective:

- Risk assessments involving explosion scenarios are often limited to pressure and thermal loads, combined with simplified criteria for effects (harm), and do not necessarily consider escalating accident scenarios that may involve structural response, fires following explosions or *vice versa*, failure of pressurised vessels due to fire loads, formation of projectiles due to explosion or blast loads, etc. Nevertheless, most fire and explosion accidents that result in considerable damage involve one or several of these aspects.
- The thresholds for individual risk for members of the public are typically two orders of magnitude lower than for onsite personnel in industry. As such, it is essential to adopt sufficiently conservative risk acceptance criteria when members of the public can access the system under consideration, such as hydrogen refuelling stations, cars, buses, trains, ferries, etc.

- The risk assessment for a given facility will not necessarily consider all the indirect losses related to an accident scenario, such as downtime, loss of production, and delayed implementation or termination of emerging technologies. A transition towards widespread use of hydrogen as an energy carrier in industry and society will require massive investments in technology and infrastructure, and the prospect of serious accidents represent a significant risk to investors and insurance companies.

There are several examples of accidents that have had widespread and long-lasting impact on the development of other industries. The Piper Alpha disaster on 6 July 1988 (167 fatalities) resulted in significant changes to the safety regulations in the offshore petroleum industry. The explosion and fire at the drilling rig Deepwater Horizon on 20 April 2010 (11 fatalities) initiated the largest marine oil spill in the history of the petroleum industry, the Macondo blowout, as well as expensive legal proceedings and sentencing for owners and operators. The accidents at Three Mile Island on 28 March 1979, Chernobyl on 26 April 1986 (42 acute and delayed fatalities) and Fukushima-Daiichi on 11 March 2011 (one delayed fatality) had severe impact on the development of the nuclear industry. Regarding hydrogen, events such as the Hindenburg disaster on 6 May 1937 (36 fatalities), the Space Shuttle Challenger disaster on 28 January 1986 (seven fatalities), and the hydrogen explosions at Fukushima-Daiichi influence public perception. Some recent accidents involving hydrogen include:

- the explosion and fire at the AB Specialty Silicones Facility in Waukegan, Illinois, on 3 May 2019 (four fatalities, one injured),
- the explosion in the Gangwon Technopark in Gangneung, South Korea, on 23 May 2019 (two fatalities, six injured),
- the explosion at the Air Products facility in Santa Clara, California, on 1 June 2019,
- the explosion and fire at the Uno-X refuelling station in Sandvika, Norway, on 10 June 2019,
- the explosion at the Airgas plant in Waukesha, Wisconsin, on 12 December 2019,
- the explosion at the OneH2 hydrogen plant in Catawba County, North Carolina, on 7 April 2020,
- the explosion at the Praxair hydrogen production plant in Texas City, Texas, on 11 June 2020 .

Although it is not possible to assess the level of safety for the emerging hydrogen technologies from a limited number of accidents, mostly in industrial facilities, there is reason for concern regarding the prospective increase in exposure to hydrogen systems for members of the public.

7. Conclusions

The inherent complexity of the physical and chemical phenomena involved in accidental fires and explosions represents a significant challenge for the communication of hazards and risks for hydrogen systems. This has implications for risk perception, in industry as well as society. The inherent lack of relevant experience data for the emerging hydrogen technologies implies significant uncertainty in the estimation of event frequencies for hydrogen systems with a non-trivial level of complexity. The level of conservatism in the design of hydrogen installations should reflect this uncertainty. However, optimal design requires reliable and efficient consequence models that reproduce important trends observed in experiments. To this end, future research on hydrogen safety should focus on developing and validation consequence models for industrial applications. Further blind-prediction benchmark studies are arguably the only reliable way of documenting the predictive capabilities of advanced model systems, as well as the users of such models. Large-scale experiments in realistic geometries are essential for model validation, as well as for supporting the blind-prediction studies. Certification of modellers can also be an effective means of reducing the uncertainty in risk assessments. A more holistic approach to risk analysis, risk assessment and risk management as tools for decision support will be required for ‘nourishing’ of the emerging hydrogen technologies through the remaining technology readiness levels, and eventually towards widespread commercial use in society. In its current state, the development of the ‘hydrogen economy’ is fragile, and new accidents, especially in the public domain, may delay or terminate further development. It is imperative that all stakeholders realise that the implications of future severe accidents in hydrogen systems will not be limited to the companies that own or operate the affected installations.

References

Aven, T. & Kristensen, V. (2019). How the distinction between general knowledge and specific knowledge can improve the foundation and practice of risk assessment and risk-informed decision-making. *Reliability Engineering and System Safety*, 191: 9 pp. DOI: https://doi.org/10.1016/j.ress.2019.106553

Aven, T. (2015). Implications of black swans to the foundations and practice of risk assessment and management. *Reliability Engineering and System Safety*, 134: 83-91. DOI: https://doi.org/10.1016/j.ress.2014.10.004

Ciccarelli, G. & Dorofeev, S.B. (2008). Flame acceleration and transition to detonation in ducts. *Progress in Energy and Combustion Science*, 34: 499-550. DOI: https://doi.org/10.1016/j.pecs.2007.11.002

Clavin, P. & Searby, G. (2016). *Combustion waves and fronts in flows*. Cambridge University Press, Cambridge.

Clean Sky 2 JU & FCH 2 JU (2019). *Hydrogen-powered aviation: a fact-based study of hydrogen technology, economics, and climate impact by 2050*. Report prepared by McKinsey for Clean Sky 2 Joint Undertaking and Fuel Cells and Hydrogen Joint Undertaking: 96 pp.

Cracknell, R.F., Alcock, J.L., Rowson, J.J., Shirvill, L.C. & Ungut, A. (2002). Safety considerations in retailing hydrogen. *SAE Technical Paper* 2002-01-1928: 922-926. DOI: https://doi.org/10.4271/2002-01-1928

Crowl, D.A. & Jo, Y.-D. (2007). The hazards and risks of hydrogen. *Journal of Loss Prevention in the Process Industries*, 20: 158-164. DOI: https://doi.org/10.1016/j.jlp.2007.02.002

Dawood, F., Anda, M. & Shafiullah, G.M. (2020). Hydrogen production for energy: an overview. *International Journal of Hydrogen Energy*, 45: 3847-3869. DOI: https://doi.org/10.1016/j.ijhydene.2019.12.059

DNV GL (2019). *Maritime forecast to 2050 – Energy transition outlook 2019*. DNV GL Report.

DoE (2009). *Human performance improvement handbook, Volume 1: concepts and principles*. US Department of Energy (DoE), Report DOE-HDBK-1020e2009, Washington DC.

DoE (2011). *The Department of Energy hydrogen and fuel cells program plan*. US Department of Energy (DoE), September 2011.

Ehrenfeld, J.R. (1996). Risk assessment and management: a critique of current practices and policy implications. *Industrial & Environmental Crisis Quarterly*, 9: 376-404. URL: https://doi.org/10.1177/108602669600900305

EN IEC 60079-0 (2018). *Explosive atmospheres – Part 0: Equipment – General requirements*. European Committee for Electrotechnical Standardization (CENELEC), Brussels, July 2018.

FCH 2 JU (2019). *Hydrogen Roadmap Europe – a sustainable pathway for the European energy transition*. FCH JU, January 2019.

Floristean, A. (2019). *HyLAW Deliverable 4.4: EU regulations and directives which impact the deployment of FCH technologies*. February 2019.

Flynn, R. & Bellaby, P. (2007). Risk and the public acceptance of new technologies. Edited by R. Flynn and P. Bellaby, Palgrave Macmillan. DOI: https://doi.org/10.1057/9780230591288

Frewer, L. (1999). Risk perception, social trust, and public participation in strategic decision making: implications for emerging technologies. *Ambio*, 28: 569-574.

Hord, J. (1976). *Is hydrogen safe?* US Department of Commerce, National Bureau of Standards Technical Note 690: 38 pp.

IEA (2019). *The future of hydrogen – seizing today's opportunities*. International Energy Agency (IEA), June 2019.

IMO (2016). *IGF Code – International code of safety for ships using gases or other low-flashpoint fuels*. IMO, London.

Kletz, T. (1993). *Lessons from disaster: How organizations have no memory and accidents recur*. Gulf Professional Publishing.

Kletz, T.A. (1978). What you don't have, can't leak. *Chemistry and Industry*, 6 May: 287–292.

Kletz, T.A. (1999). The origins and history of loss prevention. *Process Safety and Environmental Protection*, 77: 109-116. DOI: https://doi.org/10.1205/095758299529938

Konnov, A.A., Mohammad, A., Kishore, V.R., Kim, N.I., Prathap, C. & Kumar, S. (2018). A comprehensive review of measurements and data analysis of laminar burning velocities for various fuel+air mixtures. *Progress in Energy and Combustion Science*, 68: 197-267. DOI: https://doi.org/10.1016/j.pecs.2018.05.003

Lemkowitz, S.M. & Schotte, R.M. (1999). Explosion theory for dummies – Using simple theory to predict how process changes affect gas explosion risk. *NPT Procestechnologie*, March-April 1999: 19-24.

Lemkowitz, S.M. & Taveau, J.R. (2019). A model structuring dust, mist, gas/vapour and hybrid explosion behavior: the Chemical-Engineering Model. *Chemical Engineering Transactions*, 77: 961-966. DOI: https://doi.org/10.3303/CET1977161

Løkke, J.A. (2019). *The Kjørbo incident*. Presentation, press conference 28 June 2019: 22 pp.

NRK (2019). *Eksplosjon ved hydrogenstasjon* ['Explosion at hydrogen station']. Online news article from the Norwegian Broadcasting Company (NRK). In Norwegian. Available 30.06.2020: https://www.nrk.no/nyheter/eksplosjon-ved-hydrogenstasjon-1.14582944

Oran, E.S., Chamberlain, G. & Pekalski, A. (2020). Mechanisms and occurrence of detonations in vapor cloud explosions. *Progress in Energy and Combustion Science*, 77: 100804. DOI: https://doi.org/10.1016/j.pecs.2019.100804

Paté-Cornell, M.E. (1994). Quantitative safety goals for risk management of industrial facilities. *Structural Safety*, 13: 145-157. DOI: https://doi.org/10.1016/0167-4730(94)90023-X

Rigas, F. & Amyotte, P. (2013). Myths and facts about hydrogen hazards. *Chemical Engineering Transactions*, 31: 913-918. DOI: https://doi.org/10.3303/CET1331153

Sánchez, A.L. & Williams, F.A. (2014). Recent advances in understanding of flammability characteristics of hydrogen. *Progress in Energy and Combustion Science*, 41: 1-55. DOI: https://doi.org/10.1016/j.pecs.2013.10.002

Shirvill, L.C., Roberts, T.A., Royle, M., Willoughby, D.B. & Sathiah, P. (2019a). Experimental study of hydrogen explosion in repeated pipe congestion – Part 1: Effects of increase in congestion. *International Journal of Hydrogen Energy*, 44: 9466-9483. DOI: https://doi.org/10.1016/j.ijhydene.2018.04.193

Shirvill, L.C., Roberts, T.A., Royle, M., Willoughby, D.B. & Sathiah, P. (2019b). Experimental study of hydrogen explosion in repeated pipe congestion – Part 2: Part 2: Effects of increase in hydrogen concentration in hydrogen methane-air mixture. *International Journal of Hydrogen Energy*, 44: 3264-3276. DOI: https://doi.org/10.1016/j.ijhydene.2018.12.021

Skjold, T. & van Wingerden, K. (2010). *A fatal accident caused by bacterial hydrogen production in an atmospheric storage tank*. Proceedings Sixth International Seminar on Fire and Explosion Hazards (6 ISFEH), Leeds, 11-16 April 2010: 516-525.

Skjold, T., Hisken, H., Bernard, L., Mauri, L., Atanga, G., Lakshmipathy, S., Lucas, M., Carcassi, M., Schiavetti, M., Rao, V.C.M., Sinha, A., Tolias, I.C., Giannissi, S.G., Venetsanos, A.G., Stewart, J.R., Hansen, O.R., Kumar, C., Krumenacker, L., Laviron, F., Jambut, R. & Huser, A. (2019a). Blind-prediction: estimating the consequences of vented hydrogen deflagrations for inhomogeneous mixtures in 20-foot ISO containers. *Journal of Loss Prevention in the Process Industries*, 61: 220-236. DOI: https://doi.org/10.1016/j.jlp.2019.06.013

Skjold, T., Hisken, H., Lakshmipathy, S., Atanga, G., van Wingerden, M., Olsen, K.L., Holme, M.N., Turøy, N.M., Mykleby, M. & van Wingerden, K. (2019b). Vented hydrogen deflagrations in containers: effect of congestion for homogeneous and inhomogeneous mixtures. *International Journal of Hydrogen Energy*, 44: 8819-8832. DOI: https://doi.org/10.1016/j.ijhydene.2018.10.010

Skjold, T., Pedersen, H.H., Bernard, L., Middha, P., Narasimhamurthy, V.D., Landvik, T., Lea, T & Pesch, L. (2013). A matter of life and death: validating, qualifying and documenting models for simulating flow-related accident scenarios in the process industry. *Chemical Engineering Transactions*, 31: 187-192. DOI: http://dx.doi.org/10.3303/CET1331032

Skjold, T., Siccama, D., Hisken, H., Brambilla, A, Middha, P., Groth, K.M. & LaFleur, A.C. (2017). 3D risk management for hydrogen installations. *International Journal of Hydrogen Energy*, 42: 7721-7730. DOI: https://doi.org/10.1016/j.ijhydene.2016.07.006

Skjold, T., Souprayen, C. & Dorofeev, S. (2018). Fires and explosions. *Progress in Energy and Combustion Science*, 64: 2-3. DOI: http://dx.doi.org/10.1016/j.pecs.2017.09.003

Taylor, J.R. (2016). Can process plant QRA reduce risk? – Experience of ALARP from 92 QRA studies over 36 years. *Chemical Engineering Transactions*, 48: 811-816. DOI: http://dx.doi.org/10.3303/CET1648136

UN (2011). *Globally harmonized system of classification and labelling of chemicals (GHS)*. United Nations, New York and Geneva.

Wolański, P. & Wojcicki, S. (1973). Investigation into the mechanism of the diffusion ignition of a combustible gas flowing into an oxidizing atmosphere. *Proceedings from the Combustion Institute*, 14: 1217–1223.

DOI: 10.7795/810.20200724

Review of the HySEA project

Trygve Skjold [a,b], Melodia Lucas [b], Helene Hisken [b], Gordon Atanga [b], Sunil Lakshmipathy [b,k],
Laurence Bernard [b,h], Matthijs van Wingerden [a,b], Kees van Wingerden [b], Jennifer X. Wen [c],
Vendra Chandra Madhav Rao [c], Anubhav Sinha [c,l], Marco Carcassi [d], Martino Schiavetti [d],
Tommaso Pini [d], Jef Snoeys [e], Arve Grønsund Hanssen [f], Changjian Wang [g],
Simon Jallais [h], Elena Vyazmina [h], Derek Miller [i], Carl Regis Bauwens [j]

[a] University of Bergen, Bergen, Norway
[b] Gexcon, R&D Department, Bergen, Norway
[c] University of Warwick, Coventry, UK
[d] University of Pisa, Pisa, Italy
[e] Fike Europe, Herentals, Belgium
[f] Impetus Afea, Flekkefjord, Norway
[g] Hefei University of Technology, Hefei, China
[h] Air Liquide, R&D, Paris Innovation Campus, Paris, France
[i] Air Products, Central Process Safety Team, Allentown, PA, USA
[j] FM Global, Research Division, Norwood, MA, USA
[k] Jensen Hughes, Richmond, BC, USA
[l] Indian Institute of Technology, Banaras Hindu University, Varanasi, India

E-mail: *trygve.skjold@uib.no*

Abstract

Explosion protection by venting is a frequently used measure for mitigating the consequences of deflagrations in confined systems. The overall goal of the project *"Improving hydrogen safety for energy applications through pre-normative research on vented deflagrations"* (HySEA) was to provide recommendations for European and international standards on hydrogen explosion venting mitigation systems. The HySEA project received funding from the Fuel Cells and Hydrogen 2 Joint Undertaking (FCH 2 JU) under grant agreement No 671461. The official project started on 1 September 2015 and ended on 30 November 2018. The members of the HySEA consortium were Gexcon (coordinator), University of Warwick (UWAR), University of Pisa (UNIPI), Fike Europe (FIKE), Impetus Afea (IMPETUS) and Hefei University of Technology (HFUT). The research activities in the project included development of empirical and semi-empirical correlations, as well as computational fluid dynamics (CFD) and finite element (FE) models, and verification and validation of the various models against data from experiments performed in 20-foot shipping containers and smaller enclosures with industry-representative obstacles. As foreseen in the project proposal, the project resulted in a hierarchy of predictive tools for the safe design of venting devices for hydrogen deflagrations. The HySEA project demonstrated that explosion protection by venting can be a valuable means of risk reduction for hydrogen installations, isolated or in combination with measures such as natural ventilation, forced ventilation, gas detection and inerting. Projectiles generated during explosions in weak enclosures represent a significant hazard, but adequately designed venting devices can prevent rupture and fragmentation of containers, even for strong hydrogen deflagrations. This paper reviews the results from the HySEA project, including selected research activities conducted after the official end date of the project. The discussion highlights some of the practical implications of the project and suggestions for further work.

Keywords: *Vented hydrogen deflagrations, maximum reduced explosion pressure, structural response, pre-normative research, computational fluid dynamics, empirical correlations*

1. Introduction

It is common practice in the industry to install equipment for hydrogen energy applications in containers and smaller enclosures. Fires and explosions represent a significant hazard for such installations, and specific measures are generally required for reducing the risk to a tolerable level (Hord, 1976; Strehlow, 1980; Dorofeev *et al.*, 1994; Cracknel *et al.*, 2002; Crowl & Jo, 2007; Rigas & Amyotte, 2013; Skjold *et al.*, 2017a; Fuster *et al.*, 2017; Skjold *et al.*, 2018a; Moradi & Groth, 2019). Explosion venting is a frequently used measure for mitigating the consequences of hydrogen deflagrations in confined systems. This paper summarises the main results from the project *"Improving hydrogen safety for energy applications through pre-normative research on vented deflagrations"* (HySEA). The HySEA project received funding from the Fuel Cells and Hydrogen 2 Joint Undertaking (FCH 2 JU) under grant agreement No 671461. Fig. 1 shows the logo for the HySEA project.

Fig. 1. *The logo for the HySEA project (www.hysea.eu).*

The members of the HySEA consortium were Gexcon (coordinator), University of Warwick (UWAR), University of Pisa (UNIPI), Fike Europe (FIKE), Impetus Afea (IMPETUS) and Hefei University of Technology (HFUT). The project started on 1 September 2015 and ended on 30 November 2018. The research activities were organised in five work packages (WPs):

- WP1 Engineering models and standards
- WP2 Experimental campaigns
- WP3 Advanced modelling
- WP4 Exploitation, dissemination and communication
- WP5 Project management

The overall goal of the HySEA project was to conduct pre-normative research on vented hydrogen deflagrations with an aim to provide recommendations for European and international standards on hydrogen explosion venting mitigation systems. Furthermore, the members of the HySEA consortium developed and validated empirical and semi-empirical correlations, as well as computational fluid dynamics (CFD) and finite element (FE) models, and verified and validated selected models against data from experiments performed in containers and smaller enclosures with industry-representative obstacles. Additional objectives of the HySEA project included:

- To characterise different venting devices (i.e. container doors, plastic film and commercial vent panels), including measurements of the structural response of the walls of the enclosures.
- To broaden the participation in the project by inviting the scientific and industrial community engaged in hydrogen safety, and hence a variety of modellers using different models, to participate in blind-prediction benchmark studies based on full-scale experiments in vented enclosures.
- To develop, verify and validate models, including CFD-based tools, for reliable predictions of the reduced maximum overpressure in vented hydrogen deflagrations.
- To develop and validate empirical and FE-based tools for predicting the structural response of enclosures during vented hydrogen deflagrations, and derive empirical pressure-impulse (P-I) diagrams for typical hydrogen energy applications.
- To use the validated CFD models to explore vented hydrogen deflagrations in larger enclosures, such as warehouses with forklift trucks powered by hydrogen.
- To formulate recommendations to the standardising committees for EN 14994 (Europe) and NFPA 68 (USA), as well as recommendations for a harmonised international standard on hydrogen explosion venting mitigation systems.

Overall, the activities in the HySEA project progressed according to schedule. However, it took longer than expected to complete and submit several of the 80 deliverables from the project, and the final project report was not submitted to the FCH 2 JU until July 2019. The HySEA project resulted in more than 20 peer-reviewed journal publications and a considerable number of conference papers, posters and presentations. The following sections summarise the activities in the various WPs, with ample reference to relevant publications.

2. Engineering models and standards (WP1)

This section summarises the research activities in WP1 of the HySEA project.

Models based on empirical or semi-empirical correlations, such as EN 14994 (2007), NFPA 68 (2018) and HyRAM (Groth & Hecht, 2017), are often referred to as engineering models (EMs), as opposed to models that involve more elaborate numerical solutions of problems described by partial differential equations (PDEs). This practice can be somewhat misleading, since several more advanced models, in particular models based on computational fluid dynamics (CFD) and finite element (FE) methods, are undoubtedly also engineering models (e.g. FLACS and Impetus Afea developed by partners in the HySEA project). Furthermore, some researchers refer to models based on semi-empirical correlations as phenomenological models or physics-based models.

Hisken *et al.* (2016) described the model evaluation protocol (MEP) and the validation framework used by Gexcon for the development of the CFD tool FLACS. For HySEA, UWAR developed simplified MEPs for the models based on semi-empirical correlations and CFD, respectively. UWAR (Sinha *et al.*, 2017ab; Sinha *et al.*, 2019b) reviewed and evaluated various models for vented hydrogen deflagrations that include empirical or semi-empirical correlations. Modellers submitted model predictions obtained with various empirical or semi-empirical correlations for the first and second HySEA blind-prediction benchmark studies (Skjold *et al.*, 2017b; Skjold *et al.*, 2018b; Skjold *et al.*, 2019bc). UWAR (Sinha *et al.*, 2018) and GEXCON (Lakshmipathy *et al.*, 2017; Lakshmipathy *et al.*, 2019) compared predictions by CFD tools and various empirical and semi-empirical models.

UWAR developed a semi-empirical model, sometimes referred to as the external cloud model (ECM), for vented hydrogen deflagrations (Sinha & Wen, 2018ab; Sinha & Wen, 2019ab; Sinha *et al.*, 2019ab). Several aspects of the UWAR are inspired by, and resemble, the model developed by FM Global (Bauwens *et al.*, 2010; Bauwens *et al.*, 2012), including a physics-based approach for estimating the maximum pressure during vented deflagrations. Both the FM Global model and the UWAR model are extended with simplified versions based on tabulated bulk parameters to facilitate engineering calculations. The simplified UWAR model has one equation with four parameters, of which two parameters depend on tabulated fuel properties. The two other parameters are simple functions of the enclosure and obstacle geometry, and hence relatively straightforward to compute. The model from UWAR is somewhat simpler than most other models described in the open literature and relevant standards. Skjold *et al.* (2019e) includes a more detailed comparison of the UWAR and FM Global models.

The predictive capabilities of the model developed by UWAR have been assessed through comparison with results from various experiments, including tests with obstacles, initial turbulence and stratified mixtures in the enclosure. In general, the predictions from the model were found to be either more accurate than, or comparable with, other existing models (Sinha & Wen, 2019). Although the HySEA project focused on vented hydrogen deflagrations, the model is also applicable to other fuels, such as methane and propane. Fig. 2 shows examples of comparisons between model predictions and experimental results for two vented enclosures with internal obstacles: a 182 m^3 vented enclosure with natural gas (Tomlin *et al.*, 2015) and a 20-foot ISO container with hydrogen (Skjold, 2018b; Skjold *et al.*, 2019d). Tomlin *et al.* describe the geometry configurations represented by the letters in the legend in Fig. 2 (left). Permanent deformation of the container walls can be a contributing factor to the over-prediction of the maximum overpressure for the vented deflagrations in 20-foot containers. Sinha & Wen (2019) provide results for additional validation cases.

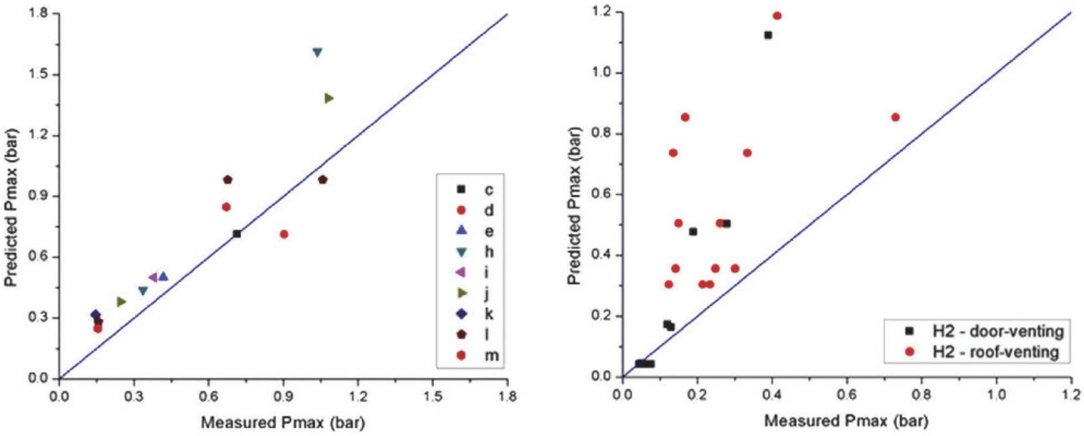

Fig. 2. *Examples of model predictions for vented enclosures with obstacles (Sinha & Wen, 2019).*

The results from the HySEA project were not available in time to be considered for the latest revision of the American standard for vented deflagrations (NFPA 68, 2018). Hence, the efforts towards regulations, codes and standards (RCS) focused on the European standard for gas explosion venting protective systems (EN 14994, 2007). UWAR, Gexcon and FIKE communicated relevant project results to the European Committee for Standardization (CEN) Technical Committee 305 (TC305) Working Group 3 (WG3) ad-hoc group on gas explosions. The model developed by UWAR will likely be included as an appendix in a revised version of EN 14994. The next section include model predictions by EN 14994 (2007), NFPA 68 (2018) and the UWAR model (Sinha & Wen, 2019) for selected experiments conducted as part of the HySEA project.

3. Experimental campaigns (WP2)

This section summarises the research activities in WP2 of the HySEA project.

Experiments by UNIPI in a 1.14 m^3 enclosure

UNIPI (Pini *et al.*, 2017; Pini *et al.*, 2019; Schiavetti *et al.*, 2017ab; Schiavetti *et al.*, 2019) designed a small-scale enclosure (SSE) for investigating vented hydrogen deflagrations, and completed 76 tests with homogeneous mixtures and 82 tests with inhomogeneous mixtures in the SSE facility. The enclosure was 0.92 m wide, 0.62 m deep and 2 m high, i.e. a total free volume of 1.14 m^3.

The tests with homogeneous mixtures explored the effect of hydrogen concentration (8-18 vol.%), obstacles inside the enclosure, ignition position, and type of venting device. Carcassi *et al.* (2018) described the experiments with inhomogeneous mixtures. Hydrogen was released through a nozzle from a 3.8-litre buffer tank at pressures up to 60 bar. The aim was to reproduce realistic accident scenarios with loss of containment from a high-pressure storage tank. The tests included releases into an empty enclosure and tests with up to three bottles inside the enclosure. The results show that the momentum generated by the jet is not sufficient to create a homogeneous mixture, with or without obstacles inside the enclosure. The parameters varied during testing include obstacle configuration, pressure in the buffer tank (15-60 bar), nozzle diameter (0.50-0.95 mm), release direction (horizontal, downward, upward), ignition location (top, centre, bottom), vent type and ignition delay. Fig. 3 compares the results for homogeneous and inhomogeneous mixtures for various release scenarios and three bottles inside the enclosure. For this configuration, homogenous mixing resulted in the highest overpressures.

Small-scale experiments by HFUT

Guo *et al.* (2015, 2017ab) and Yang *et al.* (2018) reported results from 124 vented deflagration experiments in a mini cylindrical vessel (12.3 litre). The parameters investigated included the effect of hydrogen equivalence ratio (from 0.4 to 6.0), vent area (6.12, 12.25, 24.5, 49 and 98 cm^2), the number of vent openings, ignition location (front, centre or back), and the effect of a vent duct.

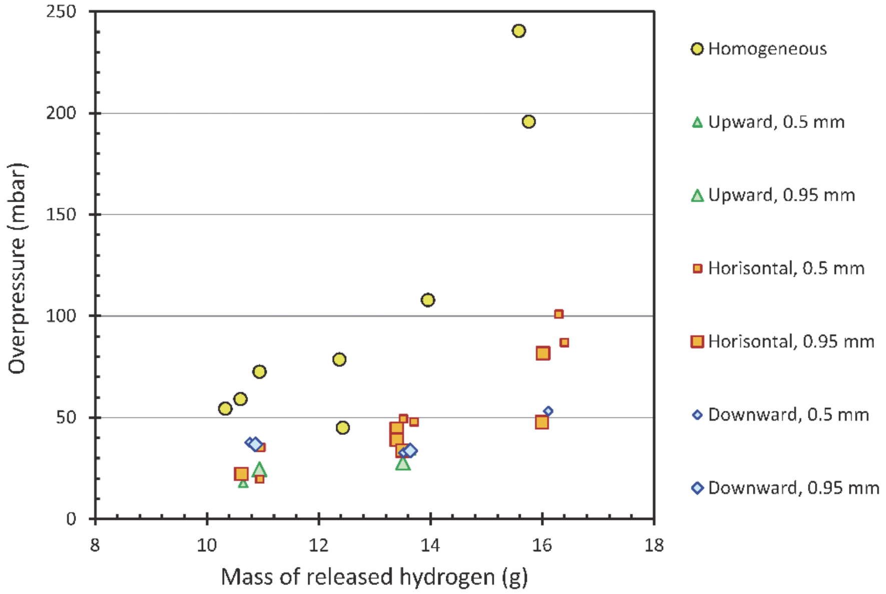

Fig. 3. *Maximum overpressure as a function of released mass with three bottles in the enclosure.*

The results from the experiments in the MCV included opening pressures and behaviour of explosion vents, maximum reduced overpressure vs. equivalence ratio, maximum reduced overpressure vs. vent area, maximum reduced overpressure vs. ignition location, the effect of one or two vent openings on the maximum reduced overpressure, the effect of a vent duct on the maximum reduced overpressure, and the length of the vented flames. Li *et al.* (2018) described experiments involving venting from a duct to a vessel. Rui *et al.* (2018) investigated the effect of the opening pressure of the venting device on hydrogen deflagrations in a 1-m^3 vessel. HFUT also performed 40 vented hydrogen deflagration tests with inhomogeneous mixtures in a cubic box with dimensions 0.5 m × 0.5 m × 0.5 m (volume 0.125 m^3). The test matrix included four average hydrogen concentrations. Five concentration gradients were considered for each of the average concentrations by changing the time for diffusive mixing. A thin plastic film covered rectangular vents with dimensions 0.1 m × 0.1 m, 0.2 m × 0.2 m or 0.3 m × 0.3 m.

Experiments by Gexcon in 20-foot containers

Gexcon designed a test rig for 20-foot ISO containers and completed 66 vented hydrogen deflagration tests with homogeneous and inhomogeneous mixtures (Skjold *et al.*, 2017bcd; Skjold, 2018ab; Skjold, 2019; Skjold *et al.*, 2019abcd). The tests with 20-foot ISO containers in the HySEA project were organised in two experimental campaigns and included:

- 42 tests with initially homogeneous and quiescent mixtures:
  - 14 tests vented through the container doors
  - 1 test with closed container (test #70)
  - 27 tests vented through openings on the roof
- 24 tests with inhomogeneous mixtures:
  - 17 tests with stratified mixtures
  - 7 tests with initial turbulence generated by either a fan or a transient jet

The total number of tests was 72, including five unignited tests and one failed test. Tab. 1 summarises the test configurations and selected results for 30 of the 66 vented deflagration tests, including the tests that resulted in the highest overpressures and the most severe structural damage. Twelve used containers from the same manufacturing series were damaged beyond repair, and the twelve test numbers marked with an asterisk in Tab. 1 represent the last tests with one of the containers, i.e. tests resulting in severe structural damage. Fig. 4 shows selected frames from test 61, illustrating the opening of the vent panels and permanent deformation of the container walls typical for relatively strong explosions (Skjold, 2019).

DOI: 10.7795/810.20200724

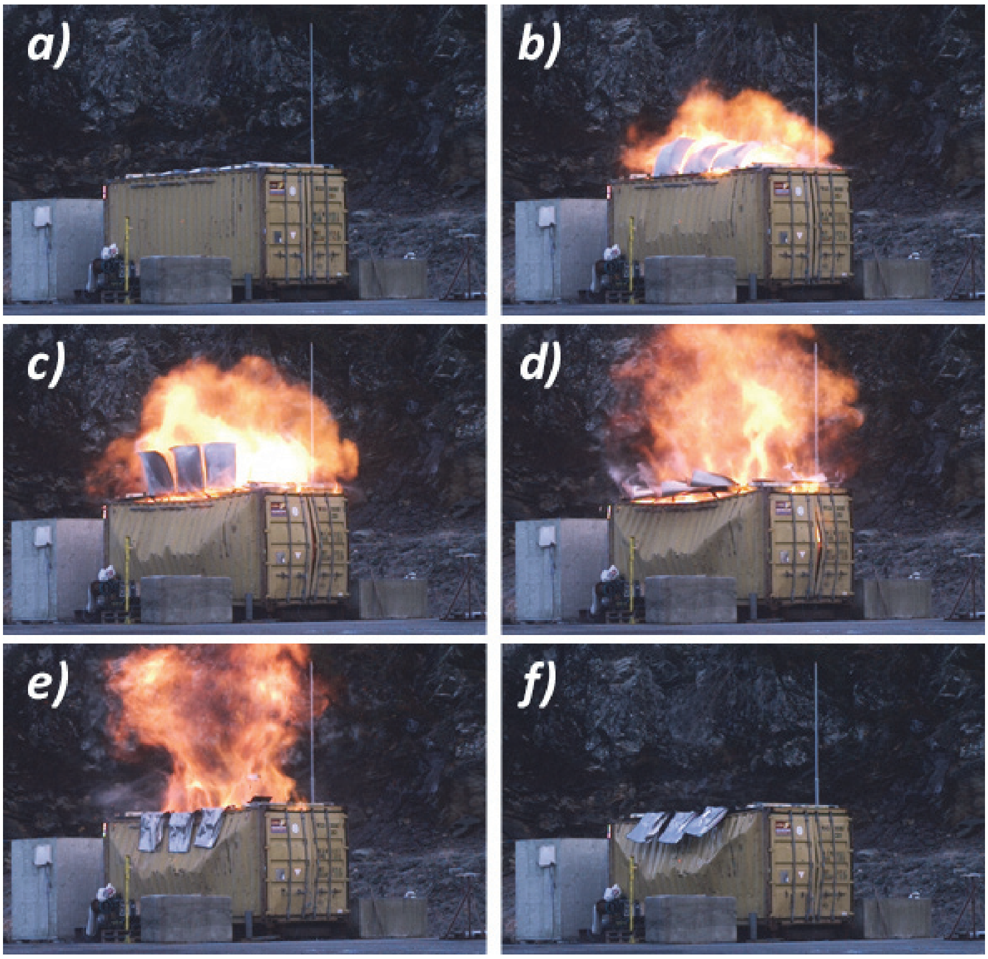

***Fig. 4:** The vented hydrogen deflagration in test no. 61.*

The venting device was either perforated polyethylene film (O) or commercial vent panels with static opening pressure 0.1 bar (P). In test no. 9, the container doors were initially closed (C) but opened during the test. The purpose of test no. 70 was to investigate the structural response resulting from a quasi-static pressure load. The doors remained closed (S) in this test, but some leakage occurred. Three ignition positions were used: back wall centre (bc), back wall upper (bu), and floor centre (fc). The obstacle configuration used in most tests involved frame only (FO), frame with bottle basket obstacle fixed in inner position (B1), frame with pipe rack obstacle fixed in inner position (P1), or frame with pipe rack obstacle fixed in centre position (P2). Test no. 14 included two obstacles: the pipe rack in inner position (P1) and the bottle basket in outer position (B3), partly blocking the venting through the door opening. Tests 71 and 72 explored the effect of significantly higher levels of congestion (HC) for lean hydrogen-air mixtures (12 and 15 vol.%). The initial conditions for the flammable mixture were either initially quiescent and homogeneous mixture (Q), or stratified mixture generated by a vertical jet (SJ) or a vertical diffusive release (SD).

Tab. 1 includes the following parameters measured in the vented deflagration experiments:

- the maximum reduced explosion pressure P_{max},
- the average maximum reduced explosion pressure P_m,
- the average maximum rate of pressure rise $(\mathrm{d}P/\mathrm{d}t)_\mathrm{m}$,
- the average pressure impulse I_m,
- the average maximum deflection D_m,
- the average permanent deformation D_p.

Skjold (2018ab) describes the data analysis and includes data for additional parameters, including the pressures measured by the external blast gauges, the time t_{stat} when the venting devices started to open, and the time it took the vent panels to open 45, 90 and 180 degrees.

Tab. 1. *Results from 30 of the 66 experiments in 20-foot ISO containers.*

Test	C_{H2} (vol.%)	A_v (m^2)	Vent	Ign.	Obst.	Flow	P_{max} (bar)	P_m (bar)	D_m (m)	D_p (m)	$(\mathrm{d}P/\mathrm{d}t)_\mathrm{m}$ (bar s^{-1})	I_m (bar ms)
70*	12	~0	S	bu	FO	Q	0.36	0.34	0.19	0.065	1.0	397
24	21	4.0	O	fc	P2	Q	0.14	0.12	0.07	0.003	4.4	5.1
29	24	4.0	O	fc	P2	Q	0.22	0.22	0.17	0.069	12	15
9*	24	5.56	C	bc	B1	Q	1.42	1.30	—	—	46	48
14*	21	5.56	D	bc	P1B3	Q	0.85	0.79	0.29	0.103	46	19
71	12	6.0	P	fc	HC	Q	0.12	0.11	0.05	0.002	1.3	11
72*	15	6.0	P	fc	HC	Q	0.54	0.46	0.36	0.278	25	14
22	21	6.0	O	fc	P2	Q	0.12	0.11	0.07	0.012	5.2	3.9
23	24	6.0	O	fc	P2	Q	0.17	0.15	0.09	0.026	7.8	4.4
27	21	6.0	P	fc	P2	Q	0.25	0.23	0.16	0.042	8.1	9.0
31	21	6.0	P	fc	P2	Q	0.25	0.22	0.15	0.016	6.7	8.2
28*	24	6.0	P	fc	P2	Q	0.45	0.31	0.17	0.081	12	8.6
17	21	8.0	O	fc	P2	Q	0.12	0.11	0.06	0.006	4.8	3.8
19	24	8.0	O	fc	P2	Q	0.13	0.12	0.06	0.014	6.1	4.1
34*	42	8.0	O	fc	P2	Q	0.53	0.42	—	—	15	32
18	21	8.0	P	fc	P2	Q	0.23	0.21	0.16	0.040	8.5	7.6
30	21	8.0	P	fc	P2	Q	0.21	0.18	—	—	6.2	7.1
20*	24	8.0	P	fc	P2	Q	0.31	0.29	0.17	0.083	11	8.9
69*	42	8.0	P	fc	P2	Q	0.68	0.58	0.59	0.476	32	13
65	15	6.0	P	bu	FO	SJ	0.16	0.16	0.10	0.000	3.9	6.7
55	18	6.0	P	bu	FO	SJ	0.16	0.15	0.09	0.009	3.5	6.6
57*	21	6.0	P	bu	FO	SJ	0.33	0.26	0.18	0.042	11	7.9
59	21	6.0	P	bu	FO	SJ	0.34	0.26	0.17	0.030	9.6	8.0
64	15	6.0	P	bu	FO	SD	0.16	0.15	0.09	0.000	3.7	6.8
56	18	6.0	P	bu	FO	SD	0.16	0.15	0.09	0.008	3.5	6.8
44*	21	6.0	P	bu	FO	SD	0.41	0.32	0.16	0.071	14	8.6
62	15	6.0	P	bu	P2	SJ	0.16	0.14	0.07	0.009	3.0	6.7
50	18	6.0	P	bu	P2	SJ	0.19	0.18	0.12	0.006	5.5	7.0
60*	21	6.0	P	bu	P2	SJ	0.36	0.28	0.19	0.064	10	10
61*	21	6.0	P	bu	P2	SJ	0.61	0.43	0.38	0.263	17	12

Fig. 5, Fig. 6 and Fig. 7 compare the maximum explosion pressures measured inside the container for the 30 vented deflagration tests summarised in Tab. 1 and model predictions according to EN 14994 (2007), NFPA 68 (2018) and the UWAR model (Sinha & Wen, 2019), respectively. The last numbers in the legends indicate the vent area in square metres. Both container doors fully open represents a vent area of about 5.56 m^2.

The empirical correlations in EN 14994 are only applicable for empty enclosures and flammable atmospheres with gas explosion constant $K_G \leq 550$ bar m s^{-1}, corresponding to the reactivity of hydrogen-air mixtures with concentrations in the range 22-28 vol.% hydrogen (Holtappels, 2006). The model predictions in Fig. 5 were obtained using published values for the maximum rate of pressure rise and the maximum explosion pressure from a 6-litre explosion vessel as input to the commercial software package WinVent 4.0. This approach implies significant uncertainty since flame wrinkling and other instabilities cause experimentally determined K_G values to vary significantly with the volume and shape of the test vessel. Furthermore, since the correlations in EN 14994 assume a static opening pressure P_{stat} of 0.10 bar, the standard over-predicts the reduced explosion pressure for tests with low reactivity mixtures and vent openings covered by polyethylene film.

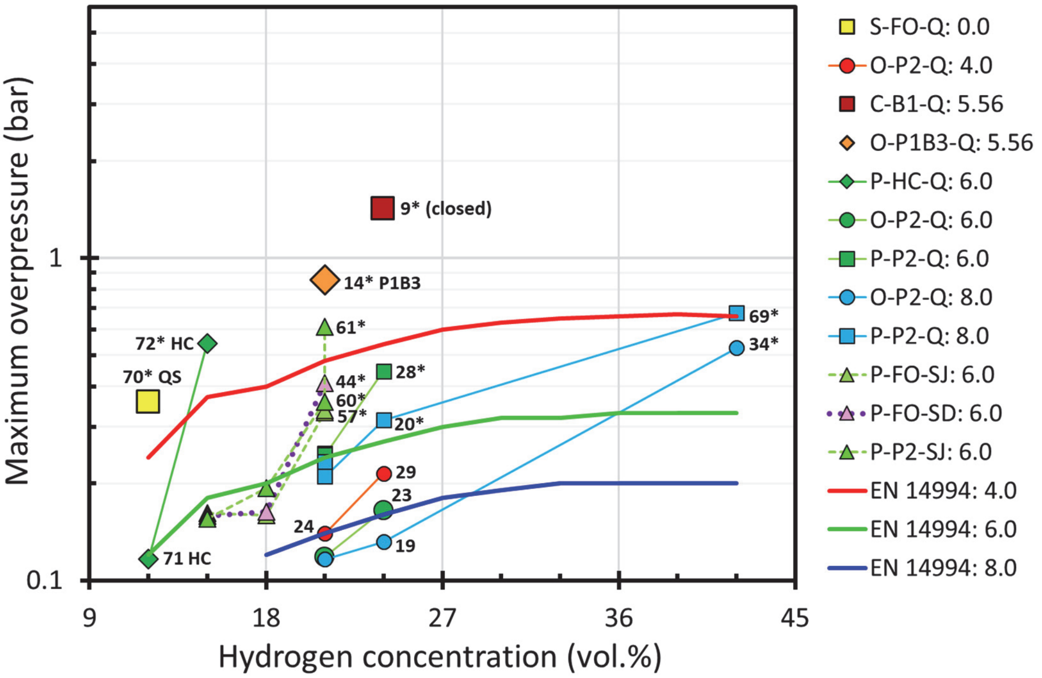

Fig. 5: *Maximum explosion pressures for 30 vented deflagration tests in 20-foot containers (Skjold, 2019) and predictions according to EN 14994 (2007) using K_G values from Holtappels (2006).*

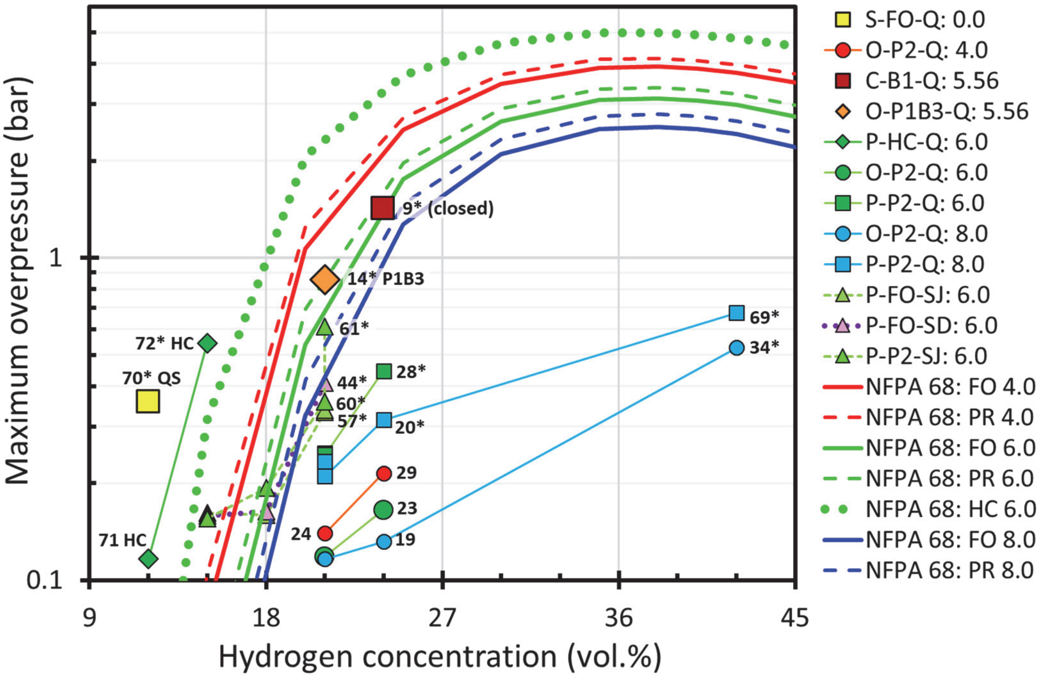

Fig. 6: *Maximum explosion pressures for 30 vented deflagration tests in 20-foot containers (Skjold, 2019) and predictions according to NFPA (2018).*

The model predictions by NFPA 68 and the model developed by UWAR in Figs. 6 and 7 incorporate the effect of internal congestion. This results in better agreement with experimental data, especially for the HC scenarios. Fig. 8 shows the geometry models for the three obstacle configurations from the CFD tool FLACS. Tab. 2 summarises the values used for the total external surface area A_{obs} in the predictions by NFPA 68, calculated by the FLACS utility program *cofile* (Version 2.1) for the geometry models in Fig. 8. The estimates by the UWAR model in Fig. 7 used a somewhat smaller surface area for the pipe rack (8.4 m^2), since this model only include external surfaces in the flame path. The estimates for the HC scenarios used the value from Tab. 2 (i.e. 83.0 m^2).

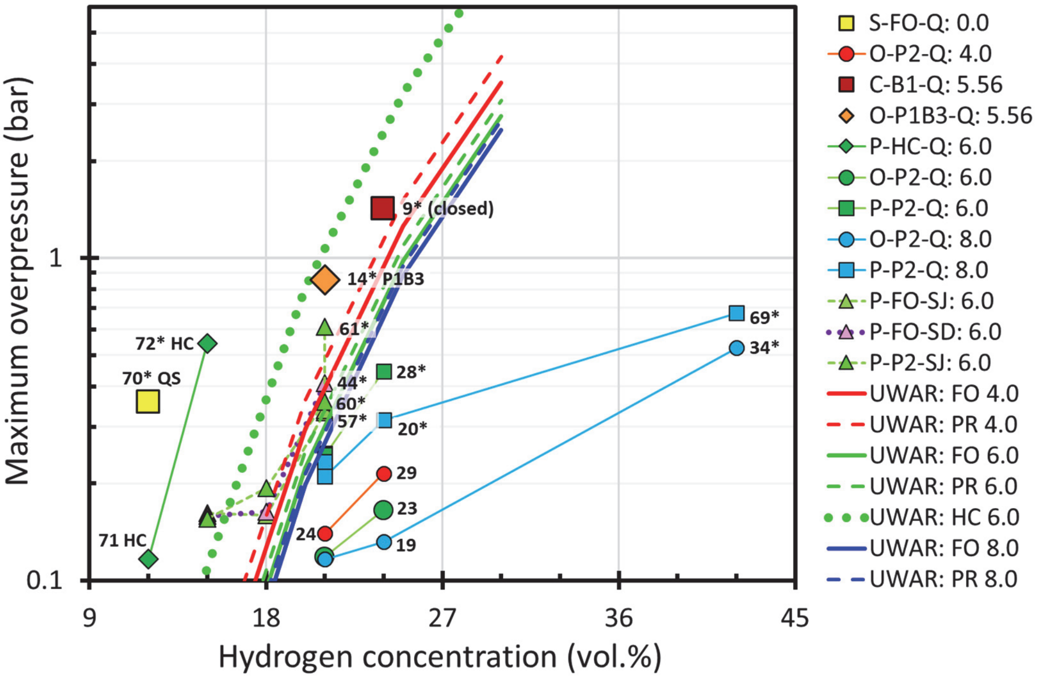

Fig. 7: *Maximum explosion pressures for 30 vented deflagration tests in 20-foot containers (Skjold, 2019) and predictions according to the UWAR model (Sinha & Wen, 2019).*

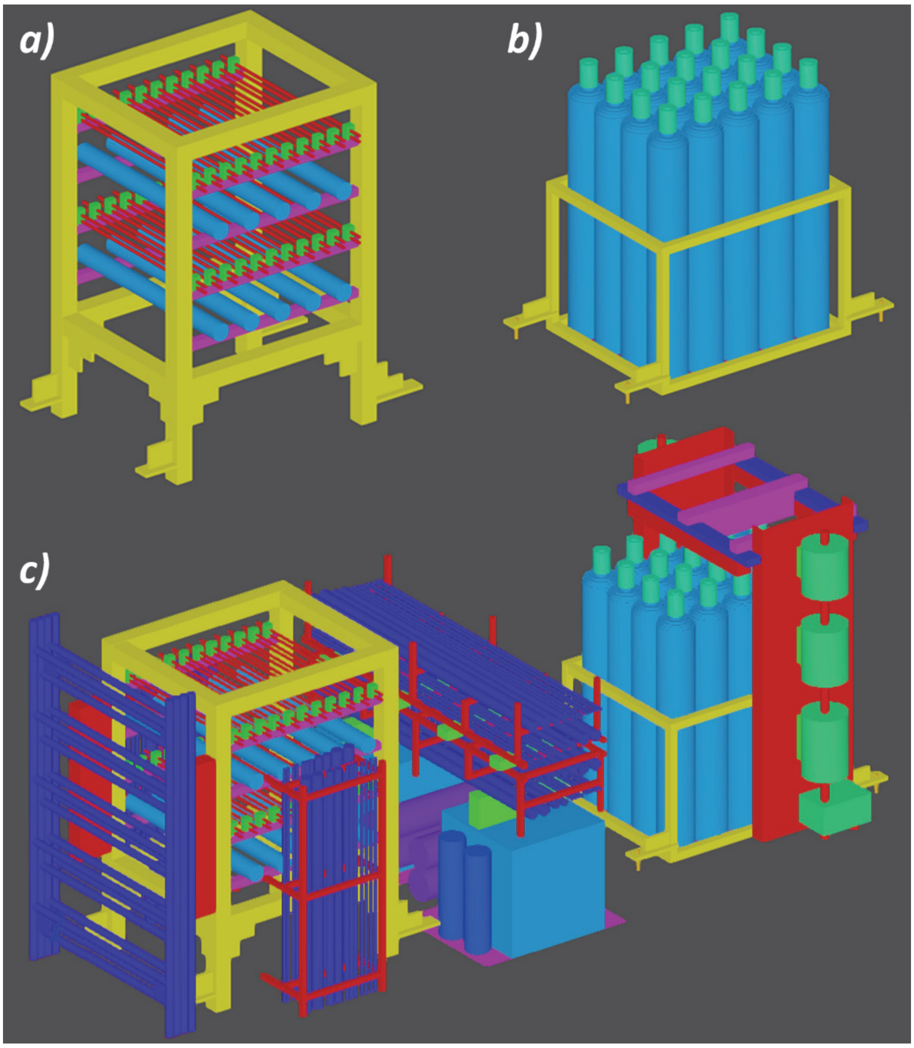

Fig. 8: *Geometry models from FLACS for a) the bottle basket obstacle, b) the pipe rack obstacle, and c) the high congestion (HC) geometry.*

***Tab. 2.** Total external surface area for the obstacle configurations in Fig. 8.*

Obstacle	Cylinders (m^2)	Boxes (m^2)	Total (m^2)
Bottle basket	18.1	4.9	23.0
Pipe rack	4.8	9.6	14.4
High congestion (HC)	4.4	3.9	83.0

Unambiguous estimates for the relevant external surface area of obstacles, or any other parameter used for representing internal congestion, represent a significant source of uncertainty in the semi-empirical correlations for the reduced explosions pressure in vented deflagrations. Other limitations include reliable prediction of the pressure impulse, as well as realistic representation of the effect of the static opening pressure P_{stat} of the explosion venting device on the reduced explosion pressure P_{red}. The latter is particularly important for weak enclosures, such as buildings, ships and containers, where even the loading resulting from the opening pressure of a commercial vent panel (typically 0.1 bar) may result in permanent deformation. The UWAR model has not been validated for hydrogen concentrations exceeding about 25 vol.% in air, and there is significant uncertainty in the estimates for concentrations exceeding this value in Fig. 7.

Fig. 9 shows examples of empirical pressure-impulse (*P-I*) diagrams for 20-foot shipping containers, where the damage criteria, i.e. the *P-I* curves, are based on specific levels of permanent deformation, as well as whether the containers were damaged beyond repair (Skjold *et al.*, 2019a). The plot on the left resembles a classical *P-I* diagram for ideal blast waves (Friedlander, 1946; Krauthammer, 2008; Dewey, 2010), while the plot on the right illustrates typical *P-I* curves that account for the effect of the finite rise time of the pressure loads (Baker *et al.*, 1983).

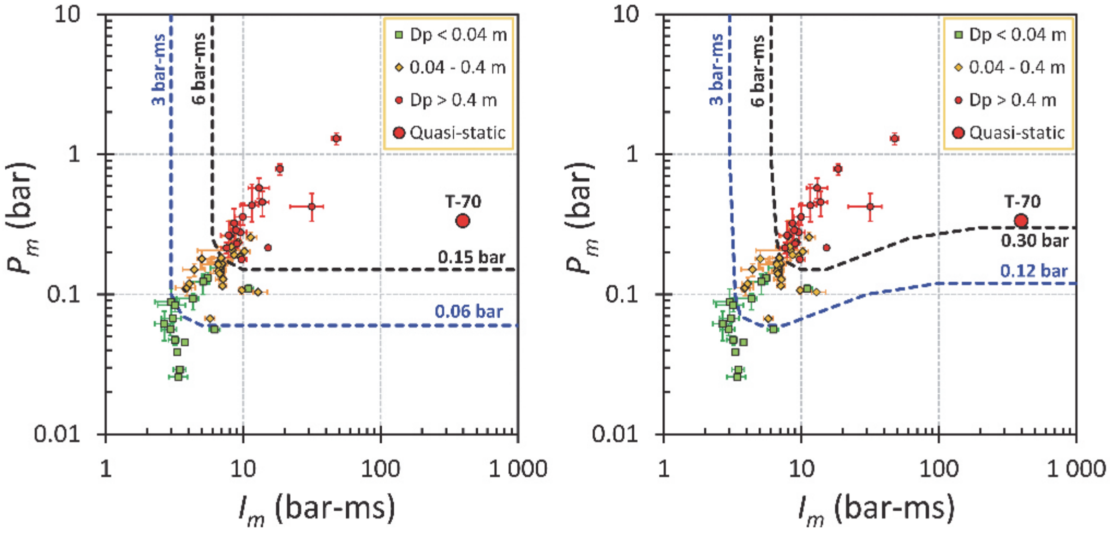

***Fig. 9:** Empirical pressure-impulse diagrams for 20-foot shipping containers.*

From the point of view of vented deflagrations, 20-foot ISO containers are relatively weak structures, and the structural response measurements reveal significant deflection of the container walls even for relatively modest pressure loads. Hence, the volume of the enclosures varied significantly during some of the tests, especially the more violent explosions. The vent panels opened simultaneously in most of the tests with commercial panels. The main structure of the container remained intact in all tests, except from test 9 where the hinges broke when the doors opened. One door bounced off the gravel on the side of the container, hit the hillside some 10 m above the ground, and landed about 30 m from the container. This observation demonstrates the hazard posed by projectiles and highlights the importance of securing attached structural elements such as doors, louvre panels and ventilators. The experiments with 20-foot containers included measurements of external blast pressures (Skjold *et al.*, 2017c; Skjold, 2018b).

The container doors do not represent proper explosion venting devices according to the European standard (EN 14797, 2006). The containers walls ruptured in some of the tests that produced high overpressures, e.g. test #9 in Fig. 5-7. The smoothing frequency used for processing the experimental pressure-time curves influenced the results (Skjold, 2018ab; Skjold *et al.*, 2019d), but primarily for the maximum rate of pressure rise. The finite rise time of the pressure loads and the high level of plasticity of the corrugated plates in the walls and roof complicate the analysis of the structural response (Baker *et al.*, 1983). Furthermore, it was not straightforward to calculate unambiguous values for pressure impulse for tests with multiple pressure peaks.

Fig. 5-7 illustrates that the maximum reduced explosion pressures increase consistently with increasing fuel concentration for all obstacle and vent configurations. This is reasonable since most tests involved lean mixtures, i.e. less than 30 vol.% hydrogen in air. Tests 34 (O) and 69 (P) with rich mixtures (42 vol.% hydrogen) were included to explore near worst-case conditions for a modest degree of congestion (P2). The maximum pressures increase more rapidly for tests with internal congestion, compared to the predictions by EN 14994 (2007). The results for tests 71 and 72 demonstrate the strong effect that higher levels of congestion (HC) can have on the maximum reduced explosion pressure, even for a modest increase in concentration (from 12 to 15 vol.%) for lean hydrogen-air mixtures. Although no detonations were observed in any of the 66 tests, tests with more reactive mixtures in the HC geometry would likely have resulted in deflagration-to-detonation-transition (DDT).

Loss of containment of gaseous hydrogen in confined spaces will typically result in buoyant releases and stratified fuel-air clouds. The significantly higher overpressures obtained for stratified mixtures, compared to lean homogeneous mixtures with the same total mass of fuel, imply that models for vented hydrogen deflagrations should account for the effect of inhomogeneous fuel-air clouds. The second blind-prediction benchmark exercise in the HySEA project explored the predictive capabilities of consequence models for simulating vented deflagrations resulting from stratified hydrogen-air mixtures ignited to deflagration in 20-foot ISO containers (Skjold *et al.*, 2018b; Skjold *et al.*, 2019b). Although some of the results were encouraging, especially for the modelling of release and dispersion scenarios, there is significant room for improving the predictive capabilities of both model systems and modellers. For well-defined vented deflagration scenarios, the spread in the explosion pressures predicted by different CFD tools covered two orders of magnitude, and none of the predictions were within a factor two of the experimental values.

Large-scale experiments by HFUT

HFUT designed a test vessel with dimensions 12.0 m × 2.5 m × 2.5 m, i.e. approximately the same dimensions as a standard 40-foot ISO container (Rui *et al.*, 2020). The walls of the enclosure were made from 25 mm steel plates, and 20 rectangular vent panels could be fitted on the roof. To accommodate tests with inhomogeneous mixtures, 20 nozzles located near the ceiling could be used for creating well-defined concentration gradients. The experimental setup allowed researchers to study the effect of the internal layout (obstructions), structural response, and the effect of mitigating measures. By July 2019, HFUT has completed 92 vented deflagration tests in the 40-foot enclosure:

- 47 tests vented through the opening at the end wall, covered by a thin plastic film
- 45 tests vented through openings in the roof, covered by a thin plastic film

HFUT has also completed 24 vented tests in the 20-foot enclosure (half of the 40-foot enclosure):

- 12 tests vented through the opening at the end wall, covered by a thin plastic film
- 12 tests vented through openings in the roof, covered by a thin plastic film.

Fig. 10 shows selected frames from a test in the 40-foot enclosure, vented through the opening at the end wall. The experimental matrix included variation in parameters such as hydrogen concentration, ignition locations, obstacles (tanks), and the number of vent openings on the roof.

DOI: 10.7795/810.20200724

Fig. 10: *Vented deflagration test in the 40-foot enclosure.*

4. Advanced modelling – CFD and FE (WP3)

This section summarises the research activities in WP3 of the HySEA project.

UWAR (Rao & Wen, 2017ab; Rao & Wen, 2019bcd), in cooperation with HFUT (Wang & Wen, 2017), developed the in-house CFD solver HyFOAM, based on the open-source solver OpenFOAM. HFUT developed and validated the CFD code ExplosionFOAM, also within the OpenFOAM framework (Wang & Wen, 2017).

Gexcon (Lakshmipathy *et al.*, 2017; Lakshmipathy *et al.*, 2019; Lucas *et al.*, 2019ab) developed the CFD solver FLACS™, including the special version FLACS-Hydrogen for simulating dispersion and explosion phenomena involving hydrogen. The two versions of FLACS-Hydrogen that were released during the project period for the HySEA project focused on validation of the Flacs-2 solver and did not include extensive changes to the model system. Lucas *et al.* (2019a) described the changes to the model system for the new CFD solver developed during the HySEA project (Flacs-3). Fig. 11 shows selected results for both solvers for two experiments with stratified mixtures.

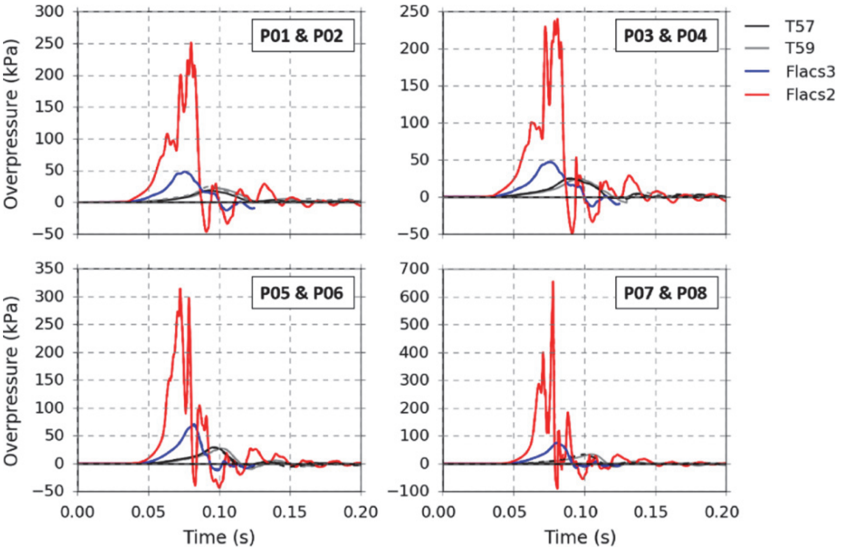

Fig. 11: *Simulated and experimental pressure-time histories for tests 57 and 59 with stratified mixtures and commercial vent panels (Lucas et al., 2019a).*

The new Flacs-3 solver includes several fundamental changes (Lucas *et al.*, 2019a), including a new two-equation Reynolds-averaged Navier Stokes (RANS) turbulence model (the *kskL* model), a new correlation for turbulent burning velocity that includes the effect of the stretch-rate Markstein number, and a transport equation for flame folding. Gexcon and UWAR used the improved model system to simulate vented hydrogen deflagrations in larger enclosures. Fig. 11 shows the geometry model for a hypothetical warehouse (Lucas *et al.*, 2019b).

In connection with the first HySEA blind-prediction study, Gexcon and IMPETUS (Atanga *et al.*, 2017; Atanga *et al.*, 2019) developed a methodology for one-way coupling between the CFD solver FLACS and the Impetus Afea FE solver. The primary limitation of this approach is the inherent uncertainty in the prediction of the transient pressure loads on the walls of the enclosure during vented hydrogen deflagrations (Skjold *et al.*, 2017b; Skjold *et al.*, 2018; Skjold *et al.*, 2019bc).

Fig. 11: *Hypothetical warehouse geometry (Lucas et al., 2019b).*

UWAR (Rao & Wen, 2017ab; Rao & Wen, 2019bcd) implemented several model improvements in HyFOAM during the HySEA project:

- Flame wrinkling computed from an algebraic model or by solving a transport equation.
- Lewis number effects for the turbulent burning velocity in lean hydrogen-air mixtures.
- An analytical expression for estimating the effect of the Darrieus–Landau and thermo-diffusive instabilities on flame propagation in lean hydrogen-air mixtures.

Rao & Wen (2018, 2019a) modelled the interaction between the pressure loads predicted by HyFOAM and the structural response of the container walls computed by fluid-structure interactions (FSI) for vented hydrogen deflagrations. To evaluate the dynamic displacement of the container walls based on the peak overpressure inside the container, a single degree of freedom model approximated the structural response observed in the experiments.

5. Exploitation, dissemination and communication (WP4)

This section summarises selected activities from WP4 of the HySEA project.

The HySEA project included extensive activities related to dissemination and communication of results – 33 of the 80 deliverables from the project addressed various aspects of dissemination. The project website (www.hysea.eu) includes a comprehensive list of various dissemination activities, including publications and newsletters. The members of the HySEA consortium made significant efforts to involve the international research community on hydrogen safety, including active interaction with the International Association for Hydrogen Safety (IA HySafe) and International Energy Agency (IEA) Hydrogen Task 37 on Hydrogen Safety. UNIPI and Gexcon organised two blind-prediction benchmark exercises during the project (Skjold *et al.*, 2017b; Skjold *et al.*, 2018; Skjold *et al.*, 2019bc). Gexcon Software released an updated version of the CFD tool FLACS for hydrogen applications in 2017 (FLACS v10.7), and an updated beta version in 2018 (FLACS v10.8 beta). Through the cooperation with UNIPI, IMPETUS and Gexcon, Fike explored innovative solutions for venting of hydrogen deflagrations in containers and smaller enclosures. UWAR released two versions of the HyFOAM software. HFUT used the network and competence acquired through the participation in the HySEA consortium to acquire research funding from the Chinese government.

The final dissemination workshop was organised in cooperation with the Fire and Blast Information Group (FABIG). Gexcon, UWAR and Air Liquide presented results from the HySEA project at the FABIG technical meetings *'Developments in Fire & Explosion Engineering towards a Hydrogen Economy'* in Aberdeen on Wednesday 26 September and in London on Thursday 27 September 2018.

The ultimate goal of the HySEA project was to provide recommendations for a harmonised international standard on vented hydrogen deflagrations, and thereby support safe and widespread introduction of hydrogen as an energy carrier in industry and society. The call explicitly mentioned the European standard EN 14994 (2007) on *"Gas explosion venting protective systems"*. To this end, UWAR and Gexcon communicated relevant results to the European Committee for Standardization (CEN) Technical Committee 305 (TC305) Working Group 3 (WG3) ad-hoc group on gas explosions.

6. Project management (WP5)

This section summarises selected activities in WP5 of the HySEA project.

Gexcon organised the kick-off meeting for the HySEA project in Bergen on 14-16 September 2015. The subsequent progress and advisory board meetings were organised by FIKE (Herentals, February 2016), Gexcon (Bergen, September 2016), UNIPI (Pisa, February 2017), Gexcon (Bergen, September 2017), Air Liquide (Paris, April 2018), HFUT (Hefei, July 2018), and finally by Gexcon (London, September 2018). Gexcon presented results from the HySEA project at the FCH 2 JU Programme Review Days in Brussels in 2016, 2017 and 2018.

7. Impact

The ultimate goal of the HySEA project was to deliver amendments on vented hydrogen deflagrations to the European standard EN 14994 *"Gas explosion venting protective systems"* and the American standard NFPA 68 *"Standard on explosion protection by deflagration venting"*, as well as a potential new international standard on *"Hydrogen explosion venting mitigation systems"* from the International Organization for Standardization (ISO). The relevant results from the HySEA project were not available in time to be considered for the latest revision of NFPA 68 (2018). Furthermore, there was no initiative within ISO for a common international standard on vented deflagrations. Hence, the efforts towards RCS focused on EN 14994 (2007). As a result of the constructive dialogue and exchange of information between members of the HySEA consortium and the ad-hoc group on gas explosions in CEN TC305 WG3, a version of the semi-empirical model developed by UWAR will likely be included as an appendix to the next revised version of EN 14994. As such, the HySEA project achieved its primary objective, at least to the extent that members of the HySEA consortium could influence the internal processes of the relevant standardising committee during the project period.

The HySEA project resulted in a hierarchy of predictive tools for the safe design of venting devices for hydrogen deflagrations. UWAR developed a semi-empirical model for vented hydrogen deflagrations (Sinha & Wen, 2019ab), and UWAR with support from HFUT developed an improved version of the CFD solver HyFOAM (Rao & Wen, 2019abcd), Gexcon developed an improved version of the commercially available software product FLACS (Atanga *et al.*, 2019; Lakshmipathy *et al.*, 2019; Lucas *et al.*, 2019ab), and IMPETUS validated the commercially available Impetus Afea FE solver for structural response calculations in connection with hydrogen explosions in enclosures (Atanga *et al.*, 2019; Pini *et al.*, 2019; Skjold *et al.*, 2019c). Although the research activities in the HySEA project resulted in improved models and model systems, it is necessary to improve the predictive capabilities of consequence models for vented hydrogen deflagrations further. In particular, there is a need for empirical and semi-empirical models that can predict both the maximum pressure and the impulse of vented hydrogen deflagrations, and at the same time account for the effect of internal congestion and the opening pressure of commercial vent panels.

The experimental data generated in the HySEA project will be of value to end-users, as well as modellers from industry and academia. Several modellers and research groups participated in the blind-prediction benchmark studies organised during the project (Skjold *et al.*, 2019bc), and the results from the vented deflagration experiments have been published extensively (Carcassi *et al.*, 2018; Pini *et al.*, 2019; Schiavetti *et al.*, 2019; Skjold, 2019; Skjold *et al.*, 2019abcd). The outcome of the blind-prediction studies is likely to increase the awareness amongst developers and users of consequence models for vented deflagrations concerning the inherent limitation and uncertainty of the model predictions. In a longer perspective it is foreseen that this awareness will result in model improvements, including more user-friendly interfaces, as well as updated documentation and guidelines, and possibly some kind of certification or approval of users of advanced model systems.

In principle, it should be possible to complement the experimental results from the HySEA project with data from CFD and FE simulations of vented deflagrations (Atanga *et al.*, 2019). However, the results from the two blind-prediction benchmark studies conducted as part of the HySEA project demonstrate that it is not straightforward to simulate vented hydrogen deflagrations in 20-foot shipping containers with internal congestion (Skjold *et al.*, 2019ac). Combustion in stratified hydrogen-air mixtures and vented deflagrations in weak enclosures are inherently complex phenomena. The laminar burning velocity of hydrogen-air mixtures is significantly higher than for most conventional and alternative fuels (Astbury, 2008; Konnov *et al.*, 2018), and various hydrodynamic, thermo-diffusive and thermo-acoustic instabilities may influence the flame (Clavin & Searby, 2016). To this end, it is necessary to further improve the predictive capabilities of advanced consequence models for vented hydrogen deflagrations. It is particularly important to improve the modelling of flame acceleration in highly congested geometries and to implement models that describe the opening of realistic explosion venting devices with sufficient accuracy.

Safe design of container-based installations for hydrogen energy applications should consider the hazard of projectiles generated from vented deflagrations. As such, the experiments with 20-foot shipping containers on the HySEA project demonstrated that the container doors do not represent suitable explosion venting devices (Skjold *et al.*, 2017c; Skjold *et al.*, 2019d). Properly installed and certified explosion venting devices shall not represent a hazard (EN 14797, 2006), but it may be necessary to secure structural elements such as louvre panels and fans for natural or forced ventilation.

The experiments performed as part of the HySEA project did not result in any DDT events. Nevertheless, the possibility of DDT and detonation should be accounted for in risk assessments for systems with significant inventory of hydrogen and high degree of congestion. In general, it can be difficult to rule out the possibility of detonations for large flammable clouds with more than 18-20 vol.% hydrogen in air if the initial and boundary conditions support significant flame acceleration. The results from the two HC scenarios in Fig. 5-7 demonstrate the extreme effect internal congestion can have on vented hydrogen deflagrations. In summary, it is not straightforward to eliminate the possibility of DDT for industrial hydrogen systems that include high levels of congestion inside the enclosure, especially in the event of high-pressure releases impinging on congestion.

The results from the blind-prediction benchmark exercises in the HySEA project (Skjold *et al.*, 2019bc) demonstrated severe limitations in the predictive capabilities of current state-of-the-art consequence models for vented hydrogen deflagrations. At the same time, modern hydrogen energy applications represent emerging technologies where there are limited statistical data to support the estimation of event frequencies. In light of the increasing awareness of the importance of reflecting knowledge and lack of knowledge in the understanding, assessment and management of risk (Aven & Kristensen, 2019), the inherent uncertainty in risk assessments for hydrogen systems should be reflected in a conservative approach to both the location and the design/layout of new installations. In this context it is important to keep in mind that the criteria for tolerable or acceptable risk for hydrogen systems located in populated areas is typically two orders of magnitude lower than for industrial facilities (Paté-Cornell, 1994). As such, robust, or resilient, design based on a credible worst-case approach should be considered as an alternative to the classical probabilistic approach.

The HySEA project demonstrated that explosion protection by venting can be a valuable addition to other means of risk reduction for hydrogen installations, such as natural ventilation, forced ventilation, gas detection and inerting. Projectiles represent a significant hazard, but adequately designed venting devices can prevent rupture and fragmentation of containers, even for strong hydrogen deflagrations. For a given mass of hydrogen, stratified mixtures result in significantly higher pressures, compared to lean homogeneous mixtures. Although it is not straightforward to predict the maximum reduced explosion pressures in vented hydrogen deflagrations, a total vent area of 8 m^2 on the roof have been shown to give reasonable protection of 20-foot ISO containers with limited internal congestion, even for highly reactive mixtures (Skjold, 2019; Skjold *et al.*, 2019ad). To this end, the results from the HySEA project have resulted in significant changes in the approach to explosion protection in relevant industries.

Acknowledgements

The HySEA project received funding from the Fuel Cells and Hydrogen 2 Joint Undertaking (FCH 2 JU) under grant agreement No 671461. This Joint Undertaking receives support from the European Union’s Horizon 2020 research and innovation programme and Hydrogen Europe and Hydrogen Europe Research. The members of the HySEA consortium gratefully acknowledge the valuable contributions from the members of the HySEA Advisory Board: Simon Jallais and Elena Vyazmina from Air Liquide, Derek Miller from Air Products and Carl Regis Bauwens from FM Global.

References

Astbury, G.R. (2008). A review of the properties and hazards of some alternative fuels. *Process Safety and Environmental Protection*, 86: 397-414. DOI: https://doi.org/10.1016/j.psep.2008.05.001

Atanga, G., Lakshmipathy, S., Skjold, T., Hisken, H. & Hanssen, A.G. (2017). Structural response for vented hydrogen deflagrations: coupling CFD and FE tools. Proceedings Seventh International Conference on Hydrogen Safety (ICHS 2017), Paper # 224, Hamburg, 11-13 September 2017: 378-387. ISBN 978-88-902391. URL: https://www.hysafe.info/wp-content/uploads/2017_papers/224.pdf

Atanga, G., Lakshmipathy, S., Skjold, T., Hisken, H. & Hanssen, A.G. (2019). Structural response for vented hydrogen deflagrations: coupling CFD and FE tools. *International Journal of Hydrogen Energy*, 44: 8893-8903. DOI: https://doi.org/10.1016/j.ijhydene.2018.08.085

Aven, T. & Kristensen, V. (2019). How the distinction between general knowledge and specific knowledge can improve the foundation and practice of risk assessment and risk-informed decision-making. *Reliability Engineering & System Safety*, 191: 9 pp. DOI: https://doi.org/10.1016/j.ress.2019.106553

Baker, W.E., Cox, P.A., Westine, P.S., Kulesz, J.J. & Strehlow, R.A. (1983). *Explosion hazards and evaluation*. Elsevier, Amsterdam.

Bauwens, C.R., Chaffee, J. & Dorofeev, S.B. (2010). Effect of ignition location, vent size, and obstacles on vented explosion overpressures in propane-air mixtures. *Combustion Science and Technology*, 182: 1915- 1932. DOI: http://dx.doi.org/10.1080/00102202.2010.497415

Bauwens, C.R., Chao, J. & Dorofeev, S.B. (2012). Effect of hydrogen concentration on vented explosion overpressures from lean hydrogen-air deflagrations. *International Journal of Hydrogen Energy*, 37: 17599-17605. DOI: https://doi.org/10.1016/j.ijhydene.2012.04.053

Carcassi. M., Schiavetti, M. & Pini, T. (2018). Non-homogeneous hydrogen deflagrations in small scale enclosure: Experimental results. *International Journal of Hydrogen Energy*, 43: 19293-19304. DOI: https://doi.org/10.1016/j.ijhydene.2018.08.172

Clavin, P. & Searby, G. (2016). *Combustion waves and fronts in flows*. Cambridge University Press, Cambridge.

Cracknell, R.F., Alcock, J.L., Rowson, J.J., Shirvill, L.C. & Ungut, A. (2002). Safety considerations in retailing hydrogen. *SAE Technical Paper* 2002-01-1928: 922-926. DOI: https://doi.org/10.4271/2002-01-1928

Crowl, D.A. & Jo, Y.-D. (2007). The hazard and risks of hydrogen. *Journal of Loss Prevention in the Process Industries*, 20: 158-164. DOI: https://doi.org/10.1016/j.jlp.2007.02.002

Dewey, J.M. (2010). The shape of the blast wave: studies of the Friedlander equation. Proceedings Twenty-first International Symposium on Military Aspects of Blast and Shock (21 MABS), Jerusalem, 3-8 October 2010: 9 pp.

Dorofeev, S.B., Kochurko, A.S., Efimenko, A.A. & Chaivanov, B.B. (1994). Evaluation of the hydrogen explosion hazard. *Nuclear Engineering and Design*, 148: 305-316. DOI: https://doi.org/10.1016/0029-5493(94)90116-3

EN 14797 (2006). *Explosion venting devices*. European Committee for Standardization (CEN), Brussels.

EN 14994 (2007). *Gas explosion venting protective systems*. European Committee for Standardization (CEN).

Friedlander, F.G. (1946). The diffraction of sound pulses I: Diffraction by a semi-infinite plate. *Proceedings of the Royal Society A*, 186: 322-344. DOI: https://doi.org/10.1098/rspa.1946.0046

Fuster, B., Houssin-Agbomson, D., Jallais, S., Vyazmina, E., Dang-Nhu, G., Bernard-Michel, G., Kuznetsov, M., Molkov, V., Chernyavskiy, B., Shentsov, V., Makarov, D., Dey, R., Hooker, P., Baraldi, D., Weidner, E., Melideo, D., Palmisano, V., Venetsanos, A. & Kinderen, J.D. (2017). Guidelines and recommendations for indoor use of fuel cells and hydrogen systems. *International Journal of Hydrogen Energy*, 2: 7600-7607. DOI: https://doi.org/10.1016/j.ijhydene.2016.05.266

Groth, K.M. & Hecht, E.S. (2017). HyRAM: A methodology and toolkit for quantitative risk assessment of hydrogen systems. *International Journal of Hydrogen Energy*, 42: 7485-7493. DOI: https://doi.org/10.1016/j.ijhydene.2016.07.002

Guo, J., Liu, X. & Wang, C.J. (2017a). Experiments on vented hydrogen-air deflagrations: the influence of hydrogen concentration. *Journal of Loss Prevention in the Process Industries*, 48:254-259. DOI: http://doi.org/10.1016/j.jlp.2017.05.013

Guo, J., Sun, X., Rui S., Cao, Y., Hu, K., & Wang, C.J. (2015). Effect of ignition position on vented hydrogen-air explosions. *International Journal of Hydrogen Energy*, 40: 15780-15788. DOI: http://doi.org/10.1016/j.ijhydene.2015.09.038

Guo, J., Wang, C.J., Liu, X. & Chen, Y. (2017b). Explosion venting of rich hydrogen-air mixtures in a small cylindrical vessel with two symmetrical vents. *International Journal of Hydrogen Energy*, 42: 7644-7650. DOI: http://doi.org/10.1016/j.ijhydene.2016.05.097

Hisken, H., Atanga, G., Skjold, T., Lakshmipathy, S. & Middha, P. (2016). Validating, documenting and qualifying models used for consequence assessment of hydrogen explosion scenarios. Proceedings Eleventh International Symposium on Hazards, Prevention and Mitigation of Industrial Explosions (11 ISHPMIE), Dalian, 24-29 July 2016: 1069-1086. DOI: https://doi.org/10.5281/zenodo.581649

Holtappels, K. (2006). Report on the experimentally determined explosion limits, explosion pressures and rates of explosion pressure rise, Part 1: methane, hydrogen and propylene, SAFEKINEX Project Deliverable No. 8, Federal Institute for Materials Research and Testing (BAM), Germany: 149 pp.
URL: https://www.morechemistry.com/SAFEKINEX/deliverables/44.Del.%20No.%208.pdf

Hord, J. (1976). *Is hydrogen safe?* US Department of Commerce, National Bureau of Standards Technical Note 690: 38 pp.

Konnov, A.A., Mohammad, A., Kishore, V.R., Kim, N.I., Prathap, C. & Kumar, S. (2018). A comprehensive review of measurements and data analysis of laminar burning velocities for various fuel+air mixtures. *Progress in Energy and Combustion Science*, 68: 197-267.
DOI: https://doi.org/10.1016/j.pecs.2018.05.003

Krauthammer, T. (2008). *Modern protective structures*. CRC Press, Boca Raton.

Lakshmipathy, S., Skjold, T., Hisken, H. & Atanga, G. (2017). Consequence models for vented hydrogen deflagrations: CFD vs engineering models. Proceedings Seventh International Conference on Hydrogen Safety (ICHS 2017), Paper # 222, Hamburg, 11-13 September 2017: 615-626. ISBN 978-88-902391.
URL: https://www.hysafe.info/wp-content/uploads/2017_papers/222.pdf

Lakshmipathy, S., Skjold, T., Hisken, H. & Atanga, G. (2019). Consequence models for vented hydrogen deflagrations: CFD vs engineering models. *International Journal of Hydrogen Energy*, 44: 8699-8710. DOI: https://doi.org/10.1016/j.ijhydene.2018.08.079

Li, H., Guo, J., Yang, F. Wang, C., Zhang, J. & Lu, A (2018). Explosion venting of hydrogen-air mixtures from a duct to a vented vessel. *International Journal of Hydrogen Energy*, 43: 11307-11313. DOI: https://doi.org/10.1016/j.ijhydene.2018.05.016

Lucas, M., Hisken, H. & Skjold, T. (2019a). Simulating vented hydrogen deflagrations: improved modelling in the CFD tool FLACS-Hydrogen. Accepted for oral presentation at Eighth International Conference on Hydrogen Safety (ICHS 2019), Adelaide, 24-26 September 2019.

Lucas, M., Skjold, T. & Hisken, H. (2019b). CFD simulations of hydrogen releases and vented deflagrations in large enclosures. Submitted to *Journal of Loss Prevention in the Process Industries.*

Moradi, R. & Groth, K.M. (2019). Hydrogen storage and delivery: review of the state of the art technologies and risk and reliability analysis. *International Journal of Hydrogen Energy*, 44: 12254-12269. DOI: https://doi.org/10.1016/j.ijhydene.2019.03.041

NFPA 68 (2018). *Standard on explosion protection by deflagration venting*. National Fire Protection Association (NFPA), Quincy, Massachusetts, USA.

Pate-Cornell, M.E. (1994). Quantitative safety goals for risk management of industrial facilities. *Structural Safety*, 13: 145-157. DOI: https://doi.org/10.1016/0167-4730(94)90023-X

Pini, T., Hanssen, A.G., Schiavetti, M. & Carcassi, M. (2017). Experimental measurements of structural displacement during hydrogen vented deflagrations for FE model validation. Proceedings Seventh International Conference on Hydrogen Safety (ICHS 2017), Paper # 292, Hamburg, 11-13 September 2017: 400-411. ISBN 978-88-902391.
URL: https://hysafe.info/wp-content/uploads/2017_papers/292.pdf

Pini, T., Hanssen, A.G., Schiavetti, M. & Carcassi, M. (2019). Small scale experiments and FE model validation of structural response during hydrogen vented deflagrations. *International Journal of Hydrogen Energy*, 44: 9063-9070.
DOI: https://doi.org/10.1016/j.ijhydene.2018.05.052

Rao, V.C.M & Wen, J.X. (2017a). Numerical modelling of vented lean hydrogen-air deflagrations using HyFOAM. Twenty-Sixth International Colloquium on the Dynamics of Explosions and Reactive Systems (26 ICDERS), Boston, 30 July – 4 August 2017, 7 pp. DOI: https://doi.org/10.5281/zenodo.1134895

Rao, V.C.M & Wen, J.X. (2017b). Vented hydrogen deflagrations in an ISO container. Proceedings Seventh International Conference on Hydrogen Safety (ICHS 2017), Paper # 154, Hamburg, 11-13 September 2017: 579-590. ISBN 978-88-902391. URL: https://hysafe.info/wp-content/uploads/2017_papers/154.pdf

Rao, V.C.M & Wen, J.X. (2018). Fluid structure interactions modelling in vented lean deflagrations. Proceedings Twelfth International Symposium on Hazards, Prevention and Mitigation of Industrial Explosions (XII ISHPMIE), ISBN 978-1-5323-8443-1, Kansas City, 12-17 August 2018: 899-914. DOI: https://doi.org/10.5281/zenodo.2602154

Rao, V.C.M & Wen, J.X. (2019a). Fluid structure interactions modelling in vented lean deflagrations. *Journal of Loss Prevention in the Process Industries*, 61: 183-194. DOI: https://doi.org/10.1016/j.jlp.2019.06.004

Rao, V.C.M & Wen, J.X. (2019b). Modelling approach for vented lean deflagrations in non-rigid enclosures. Proceedings Ninth International Seminar on Fire and Explosion Hazards (ISFEH9), 21-24 April 2019, Saint Petersburg, Russia, Vol. 1: 393-402. DOI: http://doi.org/10.18720/SPBPU/2/k19-81

Rao, V.C.M & Wen, J.X. (2019c). Numerical investigation of venting through roof for an ISO containers. Twenty-Seventh International Colloquium on the Dynamics of Explosions and Reactive Systems (27 ICDERS), Beijing, 28 July – 2 August 2019, 6 pp.

Rao, V.C.M & Wen, J.X. (2019d). Numerical modelling of vented lean hydrogen deflagrations in an ISO container. *International Journal of Hydrogen Energy*, 44: 8767-8779. DOI: https://doi.org/10.1016/j.ijhydene.2018.11.093

Rigas, F. & Amyotte, P. (2013). Myths and facts about hydrogen hazards. *Chemical Engineering Transactions*, 31: 913-918. DOI: https://doi.org/10.3303/CET1331153

Rui, S., Guo, J., Li, G. & Wang, C. (2018). The effect of vent burst pressure on a vented hydrogen-air deflagration in a 1 m^3 vessel. *International Journal of Hydrogen Energy*, 43: 21169-21174. DOI: https://doi.org/10.1016/j.ijhydene.2018.09.124

Rui, S., Wang, C., Wan, Y., Luo, X., Zhang, Z. & Li, Q. (2020). Experimental study of end-vented hydrogen deflagrations in a 40-foot container. International Journal of Hydrogen Energy, 45: 15710-15719. DOI: https://doi.org/10.1016/j.ijhydene.2020.04.036

Schiavetti, M., Pini, T. & Carcassi, M. (2017a). Homogeneous hydrogen deflagrations in small scale enclosure: experimental results. Proceedings Seventh International Conference on Hydrogen Safety (ICHS 2017), Paper # 109, Hamburg, 11-13 September 2017: 533-544. ISBN 978-88-902391. URL: https://hysafe.info/wp-content/uploads/2017_papers/109.pdf

Schiavetti, M., Pini, T. & Carcassi, M. (2017b). The role of the flow field generated by the venting process on the time history of a vented deflagration. Proceedings Seventh International Conference on Hydrogen Safety (ICHS 2017), Paper # 108, Hamburg, 11-13 September 2017: 567-578. ISBN 978-88-902391. URL: https://hysafe.info/wp-content/uploads/2017_papers/108.pdf

Schiavetti, M., Pini, T. & Carcassi, M. (2019). The effect of venting process on the progress of a vented deflagration. *International Journal of Hydrogen Energy*, 44: 9080-9088. DOI: https://doi.org/10.1016/j.ijhydene.2018.05.007

Sinha, A. & Wen, J.X. (2018a). Modelling of flow past obstacles in vented explosions. Seventh International and Forty-fifth National Fluid Mechanics and Fluid Power Conference (FMFP 2018), Mumbai, India, 10-12 December 2018. DOI: https://doi.org/10.5281/zenodo.3247026

Sinha, A. & Wen, J.X. (2018b). Phenomenological modelling of external cloud formation in vented explosions. Proceedings Twelfth International Symposium on Hazards, Prevention and Mitigation of Industrial Explosions (XII ISHPMIE), ISBN 978-1-5323-8443-1, Kansas City, 12-17 August 2018: 847-859. DOI: https://doi.org/10.5281/zenodo.2601952

Sinha, A. & Wen, J.X. (2019a). A simple model for estimating peak pressure in vented explosions of hydrogen and hydrocarbons. *FABIG Newsletter*, 76: 32-44.

Sinha, A. & Wen, J.X. (2019b). A simple model for calculating peak pressure in vented explosions of hydrogen and hydrocarbons. *International Journal of Hydrogen Energy*, 44: 22719-22732. DOI: https://doi.org/10.1016/j.ijhydene.2019.02.213

Sinha, A., Rao, V.C.M. & Wen, J.X. (2017a). Evaluation of engineering models for vented lean hydrogen deflagrations. Twenty-Sixth International Colloquium on the Dynamics of Explosions and Reactive Systems (26 ICDERS), Boston, 30 July – 4 August 2017, 6 pp. DOI: http://doi.org/10.5281/zenodo.1134925

Sinha, A., Rao, V.C.M. & Wen, J.X. (2017b). Performance evaluation of empirical models for vented lean hydrogen explosions. Proceedings Seventh International Conference on Hydrogen Safety (ICHS 2017), Paper # 155, Hamburg, 11-13 September 2017: 545-555. ISBN 978-88-902391. URL: https://hysafe.info/wp-content/uploads/2017_papers/155.pdf

Sinha, A., Rao, V.C.M. & Wen, J.X. (2018). Comparison of engineering and CFD model predictions for overpressures in vented explosions. Proceedings Twelfth International Symposium on Hazards, Prevention and Mitigation of Industrial Explosions (XII ISHPMIE), ISBN 978-1-5323-8443-1, Kansas City, 12-17 August 2018: 860-874. DOI: https://doi.org/10.5281/zenodo.2600350

Sinha, A., Rao, V.C.M. & Wen, J.X. (2019a). Modular phenomenological model for vented explosions and its validation with experimental and computational results. *Journal of Loss Prevention in the Process Industries*, 61: 8-23. DOI: https://doi.org/10.1016/j.jlp.2019.05.017

Sinha, A., Rao, V.C.M. & Wen, J.X. (2019b). Performance evaluation of empirical models for vented lean hydrogen explosions. *International Journal of Hydrogen Energy*, 44: 8711-8726. DOI: https://doi.org/10.1016/j.ijhydene.2018.09.101

Skjold, T. (2018a). Vented hydrogen deflagrations in 20-foot ISO containers. Proceedings Twelfth International Symposium on Hazards, Prevention and Mitigation of Industrial Explosions (XII ISHPMIE), ISBN 978-1-5323-8443-1, Kansas City, 12-17 August 2018: 823-846. DOI: https://doi.org/10.5281/zenodo.2603985

Skjold, T. (2018b). *Experimental investigation of vented hydrogen deflagrations in containers: homogeneous and inhomogeneous mixtures*. Report HySEA-D2-08-2018: 638 pp.

Skjold, T. (2019). Vented hydrogen deflagrations in weak enclosures: experimental results and implications for industrial practice. Accepted for presentation at Sixteenth International Symposium on Loss Prevention and Safety Promotion in the Process Industries, Delft, 16-19 June 2019. *Chemical Engineering Transactions*, 77: 685-690. DOI: https://doi.org/10.3303/CET1977115

Skjold, T., Hisken, H., Bernard, L. & Hanssen, A.G. (2019a). Structural response of 20-foot shipping containers during vented hydrogen deflagrations. Twenty-Seventh International Colloquium on the Dynamics of Explosions and Reactive Systems (27 ICDERS), Beijing, 28 July – 2 August 2019, 6 pp.

Skjold, T., Hisken, H., Bernard, L., Mauri, L., Atanga, G., Lakshmipathy, S., Lucas Pérez, M., Carcassi, M., Schiavetti, M., Rao, V.C.M., Sinha, A., Tolias, I.C., Giannissi, S.G., Venetsanos, A.G., Stewart, J.R., Hansen, O.R., Kumar, C., Krumenacker, L., Laviron, F., Jambut, R. & Huser, A. (2018b). Blind-prediction: estimating the consequences of vented hydrogen deflagrations for inhomogeneous mixtures in 20-foot ISO containers. Proceedings Twelfth International Symposium on Hazards, Prevention and Mitigation of Industrial Explosions (XII ISHPMIE), ISBN 978-1-5323-8443-1, Kansas City, 12-17 August 2018: 875-898. DOI: https://doi.org/10.5281/zenodo.2600761

Skjold, T., Hisken, H., Bernard, L., Mauri, L., Atanga, G., Lakshmipathy, S., Lucas, M., Carcassi, M., Schiavetti, M., Rao, V.C.M., Sinha, A., Tolias, I.C., Giannissi, S.G., Venetsanos, A.G., Stewart, J.R., Hansen, O.R., Kumar, C., Krumenacker, L., Laviron, F., Jambut, R. & Huser, A. (2019b). Blind-prediction: estimating the consequences of vented hydrogen deflagrations for inhomogeneous mixtures in 20-foot ISO containers. *Journal of Loss Prevention in the Process Industries*, 61: 220-236. DOI: https://doi.org/10.1016/j.jlp.2019.06.013

Skjold, T., Hisken, H., Lakshmipathy, S., Atanga, G., Carcassi, M., Schiavetti, M., Stewart, J.R., Newton, A., Hoyes, J.R., Tolias, I.C., Venetsanos, A.G., Hansen, O.R., Geng, J., Huser, A., Helland, S., Jambut, R., Ren, K., Kotchourko, A., Jordan, T., Daubech, J., Lecocq, G., Hanssen, A.G., Kumar, C., Krumenacker, L., Jallais, S., Miller, D. & Bauwens, C.R. (2017b). Blind-prediction: estimating the consequences of vented hydrogen deflagrations for homogeneous mixtures in 20-foot ISO containers. Proceedings Seventh International Conference on Hydrogen Safety (ICHS 2017), Paper # 225, Hamburg, 11-13 September 2017: 639-652. ISBN 978-88-902391.
URL: https://www.hysafe.info/wp-content/uploads/2017_papers/225.pdf

Skjold, T., Hisken, H., Lakshmipathy, S., Atanga, G., Carcassi, M., Schiavetti, M., Stewart, J.R., Newton, A., Hoyes, J.R., Tolias, I.C., Venetsanos, A.G., Hansen, O.R., Geng, J., Huser, A., Helland, S., Jambut, R., Ren, K., Kotchourko, A., Jordan, T., Daubech, J., Lecocq, G., Hanssen, A.G., Kumar, C., Krumenacker, L., Jallais, S., Miller, D. & Bauwens, C.R. (2019c). Blind-prediction: estimating the consequences of vented hydrogen deflagrations for homogeneous mixtures in 20-foot ISO containers. *International Journal of Hydrogen Energy*, 44: 8997-9008. DOI: https://doi.org/10.1016/j.ijhydene.2018.06.191

Skjold, T., Hisken, H., Lakshmipathy, S., Atanga, G., van Wingerden, M., Olsen, K.L., Holme, M.N., Turøy, N.M., Mykleby, M & van Wingerden, K. (2017c). Influence of congestion on vented hydrogen deflagrations in 20-foot ISO containers: homogeneous fuel-air mixtures. Twenty-Sixth International Colloquium on the Dynamics of Explosions and Reactive Systems (26 ICDERS), Boston, 30 July – 4 August 2017, 6 pp.
DOI: http://doi.org/10.5281/zenodo.1218170

Skjold, T., Hisken, H., Lakshmipathy, S., Atanga, G., van Wingerden, M., Olsen, K.L., Holme, M.N., Turøy, N.M., Mykleby, M. & van Wingerden, K. (2017d). Vented hydrogen deflagrations in containers: effect of congestion for homogeneous mixtures. Proceedings Seventh International Conference on Hydrogen Safety (ICHS 2017), Paper # 223, Hamburg, 11-13 September 2017: 591-603. ISBN 978-88-902391.
URL: https://www.hysafe.info/wp-content/uploads/2017_papers/223.pdf

Skjold, T., Hisken, H., Lakshmipathy, S., Atanga, G., van Wingerden, M., Olsen, K.L., Holme, M.N., Turøy, N.M., Mykleby, M. & van Wingerden, K. (2019d). Vented hydrogen deflagrations in containers: effect of congestion for homogeneous and inhomogeneous mixtures. *International Journal of Hydrogen Energy*, 44: 8819-8832.
DOI: https://doi.org/10.1016/j.ijhydene.2018.10.010

Skjold, T., Lucas, M., Hisken, H., Atanga, G., Lakshmipathy, S., Bernard, L., van Wingerden, K., Wen, J., Rao, V.C.M, Sinha, A., Carcassi, M., Schiavetti, M., Pini, T., Snoeys, J., Hanssen, A.G., Wang, C., Jallais, S., Vyazmina, E., Miller, D. & Bauwens C.R. (2019e). Summary of the HySEA project. *FABIG Newsletter*, 76: 17-31.

Skjold, T., Siccama, D., Hisken, H., Brambilla, A, Middha, P., Groth, K.M. & LaFleur, A.C. (2017a). 3D risk management for hydrogen installations. *International Journal of Hydrogen Energy*, 42: 7721-7730. DOI: http://dx.doi.org/10.1016/j.ijhydene.2016.07.006

Skjold, T., Souprayen, C. & Dorofeev, S. (2018a). Perspective: fires and explosions. *Progress in Energy and Combustion Science*, 64: 2-3. DOI: http://dx.doi.org/10.1016/j.pecs.2017.09.003

Strehlow, R.A. (1980). Accidental explosions. *American Scientist*, 68: 420-428. URL: https://www.jstor.org/stable/27849953

Tomlin, G., Johnson, D.M., Cronin, P., Phylaktou, H.N. & Andrews, G.E. (2015). The effect of vent size and congestion in large-scale vented natural gas/air explosions. *Journal of Loss Prevention in the Process Industries,* 35: 169-181. DOI: https://doi.org/10.1016/j.jlp.2015.04.014

Wang, C.J. & Wen, J.X. (2017). Numerical simulation of flame acceleration and deflagration-to-detonation transition in hydrogen-air mixtures with concentration gradients. *International Journal of Hydrogen Energy*, 42: 7657-7663. DOI: http://doi.org/10.1016/j.ijhydene.2016.06.107

Yang, F., Guo, J., Wang, C. & Lu, S.（2018). Duct-vented hydrogen-air deflagrations: The effect of duct length and hydrogen concentration. *International Journal of Hydrogen Energy*, 43: 21142-21148. DOI: https://doi.org/10.1016/j.ijhydene.2018.09.074

DOI: 10.7795/810.20200724

Influence of Geometry on Flame Acceleration and DDT in H_2-CO-Air Mixtures in a Partially Obstructed Channel

Daniel Heilbronn[a], Christoph Barfuss[a] & Thomas Sattelmayer[a]

[a] Lehrstuhl für Thermodynamik, (Technische Universität München, Garching, Germany)

E-mail: *heilbronn@td.mw.tum.de*

Abstract

Former studies of flame acceleration (FA) and deflagration-to-detonation transition (DDT) in a partially obstructed channel using a blockage ratio of 60 % and a spacing of 300 mm showed that addition of CO to H_2-air mixtures can have significant impact on FA, DDT and resulting peak pressures. In this study, the obstacle configuration of the channel is varied in order to further investigate the influence of CO on the flame dynamics. Blockage ratios are set to 30 % and 60 % while the spacing between the obstacles is varied between 100 and 300 mm. The test rig is a small-scale 6 m long channel and has a rectangular cross section. The fuel is varied from 100/0, 75/25 to 50/50 H_2/CO. The overall fuel content is varied from 15-40 vol.-% in air. Flame speeds and dynamic pressures are evaluated. Limits with regards to fuel and fuel content for DDT in homogenous H_2-CO-air mixtures are presented. Results extend the existing data on FA and DDT provided by Veser et al. (2002) and can be used for validation of numerical frameworks.

Keywords: *flame acceleration, DDT, H_2-CO-air, obstructed channel*

1 Introduction

As the need for green power supply is growing, fuel mixtures containing large amounts hydrogen (H_2) and carbon-monoxide (CO) commonly known as syngas might be used for green power generation as they can be obtained from biomass, organic waste or steam reforming (Demirbas (2005)). The use of syngas in combination with gas turbines allows for low emissions at a wider load flexibility, which is needed to back up renewable power generation (Lieuwen et al. (2009)). However the storage and use of syngas in large quantities poses a major risk for equipment and personnel due to its wide flammability limits and low ignition energies. In a worst case scenario flame acceleration (FA) and deflagration-to-detonation transitions (DDT) will lead to extensive damages (Kumar et al. (2000)).

Furthermore, syngas might be produced due to molten-core-concrete-interactions (MCCI) during the ex-vessel phase in severe accident scenarios in nuclear power plants (Kumar et al. (2000)). As numerical studies of the Fukushima-Daiichi accident by Gauntt et al. (2012) showed, large amounts of H_2 and CO were produced in Unit 1. Due to a failure of the containment seals, the mixture enters the reactor building. By mixing with the ambient air, a stratified combustible mixture is formed. Ignition of the mixture and subsequent FA can destroy the reactor building which is the last barrier between the radioactive inventory and the environment.

Despite the variety of actual and future industrial applications and the severe consequences of FA and DDT in combustible syngas-clouds, investigations of the flame dynamics in H_2-CO-air mixtures are rare (Kumar et al. (2000), Barfuss et al. (2019)). Veser et al. (2002) investigated FA and DDT of H_2-CO-air mixtures in a partially obstructed channel of 7.2 m length using a blockage ratio of $\mathrm{BR} = 30\,\%$ and a spacing of $s = 100\,\mathrm{mm}$ along the whole channel. The investigation focused on homogeneous, lean mixtures at fuel contents of $x_\mathrm{F} \leq 15\,\mathrm{vol.\text{-}\%}$. Veser found that mixtures of 50/50 H_2/CO above $x_\mathrm{F} = 12.5\,\mathrm{vol.\text{-}\%}$ are subjected to flame acceleration reaching flames speeds above the speed of sound of the products (fast flame regime). Due to the low fuel content no detonations were observed. It was concluded, that for fuel contents of $x_F > 13$ vol.-% the influence of CO addition on the terminal flame speed is weak. Unfortunately, the pressure data available in the publication is limited to a case of $x_F = 13$ vol.-%.

Experiments in a partially obstructed channel using a blockage ratio of 60 % and a spacing of $s =$ 300 mm conducted by Heilbronn et al. (2019) showed, that CO addition might lead to an extended detonation regime. Detonations of H_2/CO-fuels were observed at fuel contents between x_F =20-35 vol.-%. The results showed that peak pressures of H_2/CO-fuels in lean conditions are similar to those obtained in pure H_2. In case of fuel rich mixtures, H_2/CO-fuels showed higher peak pressures and velocities. In the present study three additional obstacle configuration are investigated in order to obtain more detailed knowledge about FA and DDT in H_2/CO-fuels. Combinations of BR = 30 % and $s = 300$ mm as well as BR = 60 % and $s = 100$ mm are investigated. Fuel mixtures containing 100/0, 75/25 and 50/50 H_2/CO are used. Fuel contents vary from 15-40 vol.-% in air. The data obtained is used for validation of numerical methods as well as for general predictions on detonations in H_2/CO-fuels (Barfuss et al., 2020).

2 Experimental Setup

2.1 Geometry

In order to investigate the influence of the obstacle configuration on FA and DDT, the modular designed GraVent test rig is used. The test rigs consists of six standard segments and one optical segment. The explosion channel has a rectangular cross section of 60 mm in height and 300 mm in width. The overall length of the channel is $L = 6$ m. As indicated in fig. 1, the length of the obstructed section is $L_{obs} = 3.95$ m, yielding an unobstructed part at the rear end of the channel of 2.05 m. The channel is partially obstructed by obstacles of a blockage ratio of BR= 60 % as well as of BR= 30 %. In both cases obstacles are mounted on the floor and the ceiling of the channel (see fig. 2). In case of BR60 obstacles, the open area in the middle of the channel has a height of 24 mm, in case of the BR30 obstacles the open area is 42 mm. Both kinds of obstacles are 12 mm thick. The spacing between the obstacles is set to $s = 100$ mm and $s = 300$ mm. The first obstacle is mounted at a distance of 50 mm to the ignition plate. The configurations are termed BR60S100L, BR30S100L and BR30S300L as listed in table 1.

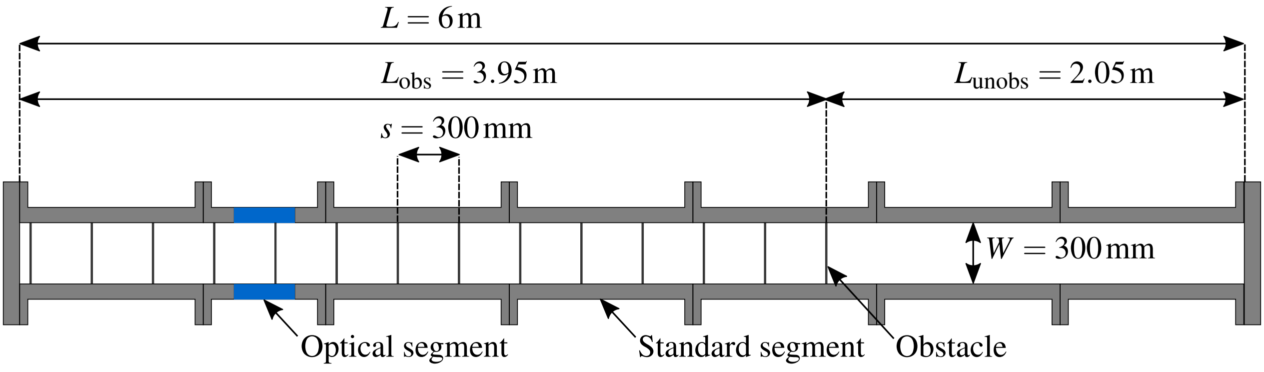

Fig. 1: Geometry of the GraVent test rig

2.2 Experimental Procedure

An external mixing unit is used in order to provide the fuel to the test rig. The fuel is mixed based on the method of partial pressures. The fuel composition was validated by gas chromatography yielding an accuracy of 0.5 %. A two stage pressure reduction valve is used to ensure a steady flow of the fuel gas into the test channel. Nozzles of 0.9 mm diameter are mounted upstream of each fuel injection

***Table 1**: Obstacle configurations of the test rig*

Blockage ratio BR in %	Spacing s in mm	Obstructed part L_{obs} in m	Abbreviation
60	100	3.95	BR60S100L
	300	3.95	BR60S300L[1]
30	100	3.95	BR30S100L
	300	3.95	BR30S300L

[1] Results for this configuration are only mentioned briefly. A more detailed discussion can be found in Heilbronn et al. (2019)

unit. Due to a pressure of 8 bar in the fuel supply system, the critical flow condition in the nozzles ensures a uniform fuel distribution along the explosion channel. The fuel is injected into the test rig through 27 holes per section in the channel ceiling.

In order to prepare the channel for one shot, the channel is evacuated to a specific sub-atmospheric pressure at first. By opening the fuel valves for a set injection time, the channel is filled with the H_2/CO-mixture until ambient pressure is reached. The inflowing gas is deflected at deflection plates which are integrated in the obstacles in the obstructed part or which are mounted at the ceiling in the unobstructed of the channel, as shown in fig. 2. At the unobstructed part of the channel the deflection plates induce a BR of about 2 %. Due to the deflection a stratified mixture is established after the injection. Diffusion allows the fuel to distribute over the channel height, mixing with air present in the channel. Since only homogenous mixtures are investigated, the diffusion time between the end of injection and ignition is set to $t_{\mathrm{D}} = 60\,\mathrm{s}$. Investigations at a model of the test rig used by Vollmer et al. (2010) showed that a uniform fuel distribution can be achieved by setting this diffusion time. The fuel content of the channel is measured based on the method of partial pressures by two static pressure transducers of type SW A09 and WIKA S20. The mixture is ignited using a conventional spark plug centred at the end plate of the channel. The spark plug is operated for approximately 15 ms. After each shot, the channel is flushed with air for 4 min.

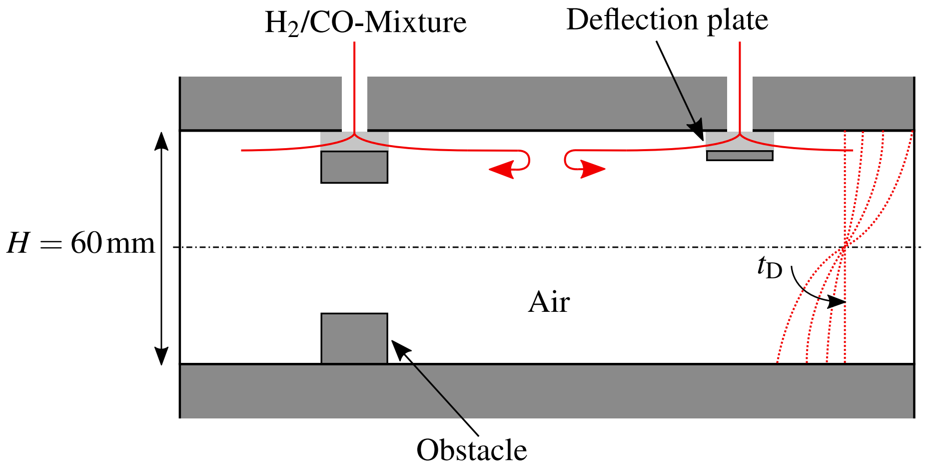

***Fig. 2**: Injection mechanism*

In order to track the flame trajectory, 36 photodiodes are located in the ceiling of the explosion channel as indicated by the red dots in fig. 3. The UV-sensitive diodes are of type Hamamatsu S1366-18BQ and are mounted slightly above the centreline. A quarz glass cover protects each photo diode from the flame, yielding an 10° angle of view. Knowing the position and time of arrival at each diode, the trajectory of the flame is obtained. The mean flame velocity u_{f} between two diodes located at positions x_1 and x_2 is evaluated from the time of arrival at each diode t_1 and t_2:

$$u_\mathrm{f}\left(\frac{x_2-x_1}{2}\right)=\frac{\Delta x}{\Delta t}=\frac{x_2-x_1}{t_2-t_1} \tag{1}$$

The dynamic pressure is recorded by eight pressure transducers of type Kistler 601A as indicated by the green squares in fig. 3. Seven transducers are mounted in the ceiling of the channel, one is mounted at the end plate. The faces of the transducers are covered by a thin layer of silicone in order to protect the transducers from thermal shocks. The pressure and photo diode signals are recorded by a data logging system operated at a sample rate of 225 kHz.

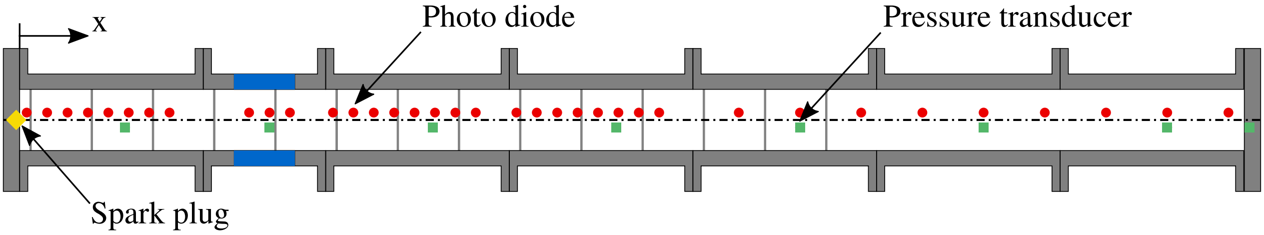

***Fig. 3**: Conventional measurement system*

3 Results

In table 2 the desired fuel contents x_F as well as the expansion ratios σ for fuel mixtures of 100/0, 75/25 and 50/50 H_2/CO are listed. The expansion ratios for an adiabatic combustion are calculated with Cantera (Goodwin et al. (2018)). The fuel content x_F is given in vol.-% in air. The fuel injection mechanism of the channel does not allow to set an exact fuel content. A variance of $\Delta x_\mathrm{F}=\pm 0.5$ vol.-% with regards to the desired fuel content is accepted. The data presented in the following section is based on the average of at least three experiments per fuel and fuel content.

***Table 2**: Expansion ratios at the desired fuel contents*

x_F [vol.-%]	15	17.5	20	22.5	25	27.5	30	35	40
$\sigma_{100/0}$	4.64	5.14	5.62	6.06	6.47	6.81	7.02	6.88	6.58
$\sigma_{75/25}$	4.73	5.24	5.72	6.16	6.55	6.85	7.02	6.93	6.62
$\sigma_{50/50}$	4.82	5.34	5.82	6.25	6.62	6.89	7.04	7.00	6.70

3.1 Relative terminal velocity

The relative terminal velocity $\tilde{u}_\mathrm{term}$ is evaluated by averaging the velocity at the unobstructed part of the channel for each experiment. The averaged velocity is normalized by the Chapman-Jouguet velocity D_CJ for the given fuel and fuel content calculated by the SD-Toolbox (Browne et al. (2008)). The obtained relative terminal velocities are averaged regarding the fuel and desired fuel content.

The relative terminal velocities $\tilde{u}_\mathrm{term}$ plotted against the fuel content for BR30S100L are shown in fig. 4. Two regimes are identified. For $\tilde{u}_\mathrm{term}\approx 1$ flames are found in the detonation regime, while flames at $\tilde{u}_\mathrm{term}\approx 0.6$ are found in the fast flame regime. For BR30S100L all fuels at a fuel content of $x_\mathrm{F}=15$ vol.-% are found in the fast flames regime. If the fuel content is increased the 100/0 H_2/CO fuel transits to the detonation regime at $x_\mathrm{F}=17.5$ vol.-%, while fuels of 75/25 and 50/50 H_2/CO are still found in the fast flame regime. If the fuel content is further increased all fuels are found in the detonation regime. As soon as the detonation regime is reached, $\tilde{u}_\mathrm{term}$ is highest for 100/0 H_2/CO with a slight decrease at the boundaries of the detonation regime at $x_\mathrm{F}=17.5$ and 30 vol.-%. In case of 75/25 and 50/50 $\tilde{u}_\mathrm{term}$ is lower than for 100/0 H_2/CO. For $x_\mathrm{F}\leq 27.5$ vol.-% the highest terminal velocities are found for 100/0 followed by 75/25 and 50/50 H_2/CO. At a fuel content of $x_\mathrm{F}\geq 30$ vol.-%

transition from the detonation to the fast flame regime is observed for 100/0, while 75/25 and 50/50 H_2/CO-fuels remain in the detonation regime. For $x_F = 40$ vol.-% only 50/50 H_2/CO-fuels are found in the detonation regime. In this case $\tilde{u}_{\text{term}}$ is slightly below the unity.

The configuration BR30S100L is similar to the one used by Veser et al. (2002) with regard to blockage ratio and spacing. As shown in fig. 4, $\tilde{u}_{\text{term}}$ for $x_F = 15$ vol.-% is similar for all fuels. This agrees well with the findings of Veser et al. (2002). Both studies show similar velocities ($u \approx 1400\,\text{m}\,\text{s}^{-1}$) in the obstructed part. The experiments conducted by Veser et al. (2002) did not feature an unobstructed section. Terminal velocities were found to be at $u_{\text{term}} \approx 1150\,\text{m}\,\text{s}^{-1}$ for 100/0, $u_{\text{term}} \approx 900\,\text{m}\,\text{s}^{-1}$ for 75/25 and $u_{\text{term}} \approx 800\,\text{m}\,\text{s}^{-1}$ for 50/50 H_2/CO. When leaving the obstructed part of the channel, the velocities in the present study are decreasing, leading to lower terminal velocities, which are in order of the speed of sound of the products.

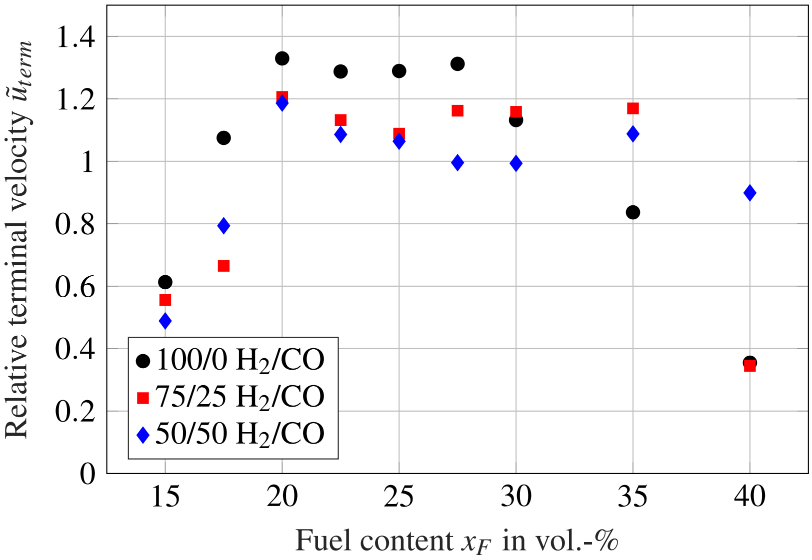

***Fig. 4**: Relative terminal velocity $\tilde{u}_{\text{term}}$ over fuel content x_F for BR30S100L*

The relative terminal velocities for BR30S300L are shown in fig. 5. Similar to BR30S100 the fast flame and the detonation regime can be distinguished. For 100/0 H_2/CO $\tilde{u}_{\text{term}}$ is found in the fast flame regime at x_F =15 vol.-%. The transition to the detonation regime is found at $x_F = 17.5$ vol.-%. In case of 75/25 H_2/CO the transition is less clear. For $x_F = 17.5$ vol.-% one out of four experiments is found in the detonation regime. For $x_F = 20$ vol.-%, three out of four experiments reached the detonation regime. For 50/50 H_2/CO-fuels a clear transition is reached at a fuel content of $x_F = 22.5$ vol.-%. In the detonation regime 100/0 H_2/CO shows the highest relative terminal velocity with little variation over the fuel content. The relative terminal velocities for 75/25 are found similar to the ones obtained for 100/0 H_2/CO. In contrast 50/50 H_2/CO show lower relative terminal velocities in the detonation regime. In case of fuel rich mixtures, the transition to a fast flame is found between 35 vol.-% $< x_F <$ 40 vol.-% for 100/0 and 75/25 H_2/CO. For 50/50 H_2/CO $\tilde{u}_{\text{term}}$ is still found in the detonation regime for $x_F = 40$ vol.-% .

DOI: 10.7795/810.20200724

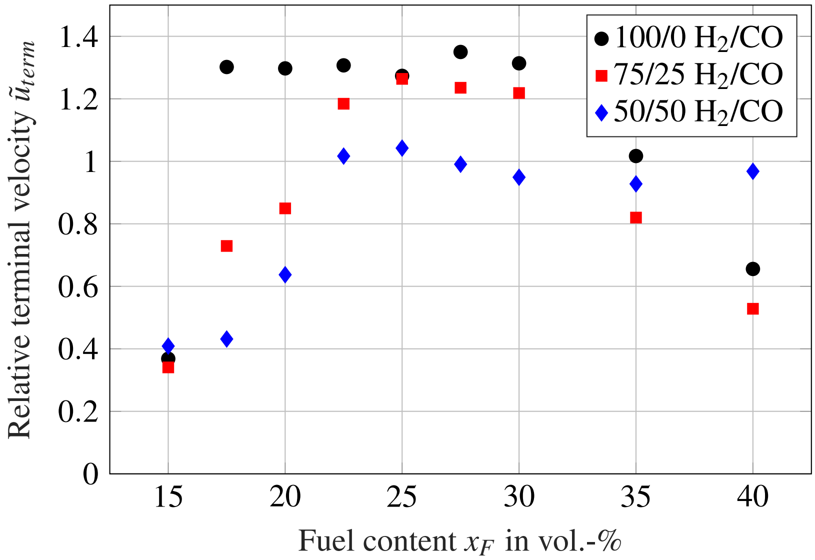

***Fig. 5**: Relative terminal velocity $\tilde{u}_{\text{term}}$ over fuel content x_{F} for BR30S300L*

In fig. 6 the relative terminal velocities $\tilde{u}_{\text{term}}$ for the configuration BR60S100L are shown. Compared to BR30S100L and BR30S300L, $\tilde{u}_{\text{term}}$ remains significantly smaller than the Chapman-Jouguet velocities for the given mixtures. In case of BR60S100L, $\tilde{u}_{\text{term}}$ ranges from $\tilde{u}_{\text{term}} = 0.14$ to 0.33. The highest terminal velocity is found at a fuel content of $x_{\text{F}} = 25\,\text{vol.-\%}$. A distinctive influence of the fuel as shown in fig. 4 and 5 is not displayed. When compared to the speed of sound of the products a_{Pr}, the results show, that almost all experiments are found in the fast flame regime in the obstructed part of the channel. In the unobstructed part the flame is found below a_{Pr}. Hence, the flame is decelerating when entering the unobstructed part. This might be linked to reflected waves from the end plate. A similar behaviour was observed by Vollmer et al. (2011) at a similar obstacle configuration.

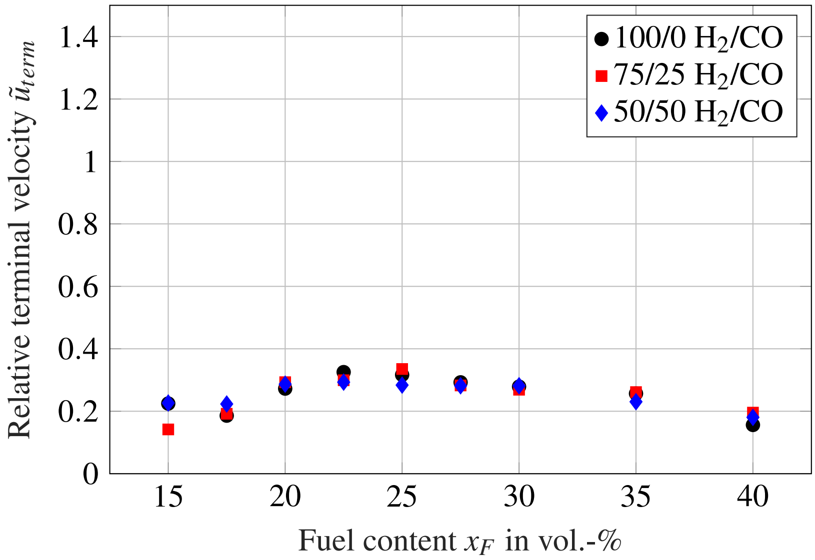

***Fig. 6**: Relative terminal velocity $\tilde{u}_{\text{term}}$ over fuel content x_{F} for BR60S100L*

3.2 Dynamic pressure

Fig. 7 shows the maximum dynamic pressure p_{max} for the configuration BR30S100L. The average peak pressure for all investigated fuel contents is found at $\bar{p}_{\text{max}} = 28.16\,\text{bar}$ for 100/0, $\bar{p}_{\text{max}} =$

24.78 bar for 75/25 and $\bar{p}_{\max} = 26.95$ bar for 50/50 H_2/CO. The lowest dynamic pressure is found at $x_F = 15$ vol.-% for 75/25 H_2/CO. As the fuel content is increased the peak dynamic pressure increases. When increasing the fuel content to $x_F = 17.5$ vol.-%, the peak pressure for 100/0 H_2/CO almost doubles, while the increase for 75/25 and 50/50 H_2/CO is small. For 75/25 and 50/50 a similar behaviour is obtained when the fuel content is increased to 20 vol.-%. The sharp increase in $p_{\max}$ matches well with the transition from fast flames to detonations as described in 3.1. The peak pressure further increases with increasing fuel content. The highest pressure is found at $p_{\max} = 49.46$ bar at $x_F = 27.5$ vol.-% for 100/0 H_2/CO. If the fuel content is further increased the peak pressure decreases. Again the transition from detonation to fast flames agress well with the decrease in the peak pressure. While 75/25 and 50/50 H_2/CO are still found in the detonation regime at $x_F = 35$ vol.-%, 100/0 H_2/CO is in the fast flame regime. This results in a lower dynamic pressure for 100/0 when compared to 75/25 and 50/50 H_2/CO. For $x_F = 40$ vol.-% a similar behaviour is observed for 75/25 and 50/50 H_2/CO.

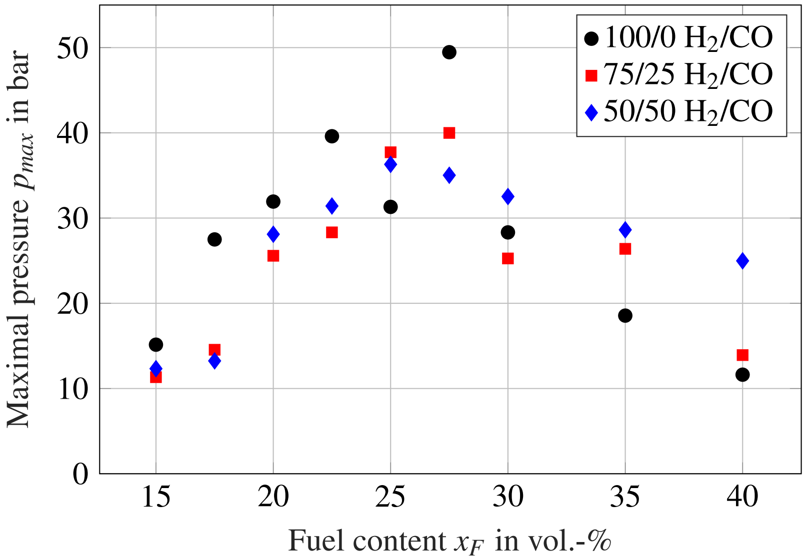

Fig. 7: Maximum dynamic pressure $p_{\max}$ over fuel content x_F for BR30S100L

In fig. 8 the maximum dynamic pressure $p_{\max}$ for the configuration BR30S300L is plotted against the fuel content x_F. The average pressure is $\bar{p}_{\max} = 24.66$ bar for 100/0, $\bar{p}_{\max} = 24.17$ bar for 75/25 and $\bar{p}_{\max} = 25.10$ bar for 50/50 H_2/CO slightly below the mean pressures obtained for BR30S100L. The lowest pressure is obtained for 75/25 H_2/CO at $x_F = 15$ vol.-% at $p_{\max} = 10.90$ bar. The peak pressure increases as the fuel content is increased. A high increase is observed between $x_F = 15$ vol.-% and $x_F = 17.5$ vol.-% for 100/0 and 75/25, which might be related to the transition from fast flames to detonations in one of the experiments leading to a strong increase in peak pressure. A similar behaviour is obtained at $x_F = 20$ vol.-% as the experiments with detonation increase the peak pressure. Within the detonation regime an increase in fuel content leads to an continuous rise in peak pressure. Compared to BR30S100L the increase in peak pressure is smaller. The highest peak pressure is found at a fuel content of $x_F = 35$ vol.-% for 50/50 H_2/CO. Although all fuels are found at the detonation regime at $x_F = 35$ vol.-% (see fig. 5), the peak pressure for 75/25 and 50/50 H_2/CO is increased when compared to $x_F = 30$ vol.-%. A similar increase in pressure was observed at the configuration BR60S300L at which a significant increase in dynamic pressure was obtained at $x_F = 35$ vol.-% for 50/50 H_2/CO. In this case 50/50 H_2/COwas the only fuel found at the detonation regime for $x_F = 35$ vol.-% (Heilbronn et al. (2019)), while for BR30S300L 75/25 H_2/CO is found in the detonation regime too.

DOI: 10.7795/810.20200724

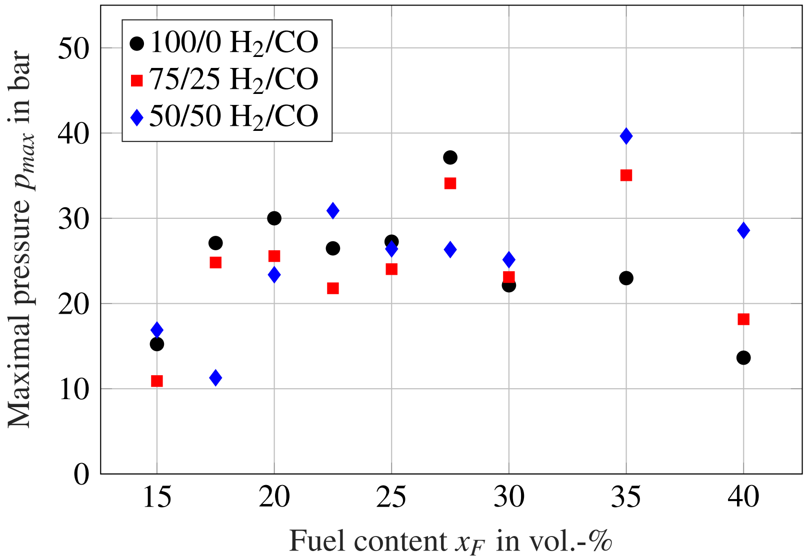

***Fig. 8**: Maximum dynamic pressure p_{max} over fuel content x_{F} for BR30S300L*

In fig. 9 the maximum dynamic pressure for the configuration BR60S100L is displayed. The average pressure is $\bar{p}_{\text{max}} = 10.17\,\text{bar}$ for 100/0, $\bar{p}_{\text{max}} = 10.06\,\text{bar}$ for 75/25 and $\bar{p}_{\text{max}} = 10.38\,\text{bar}$ for 50/50 H_2/CO. The lowest peak pressure is found at $x_{\text{F}} = 15\,\text{vol.-\%}$ for 100/0 H_2/CO. When increasing the fuel content a slight increase in the peak pressure is found. The maximum peak pressure is obtained at $x_{\text{F}} = 25\,\text{vol.-\%}$ for 75/25 H_2/CO at $p_{\text{max}} = 12.15\,\text{bar}$. Although the flames are found in the fast flame regime at short run-up distances, DDT was not observed in this configuration (see sec. 3.1). This might be related to the detonation cell width. Due to the high blockage ratio and the low spacing, no detonations are obtained within the obstructed part of the channel. Hence the pressures obtained at BR60S100L are mainly the result of FA and therefore lower compared to BR30S100L and BR30S300L.

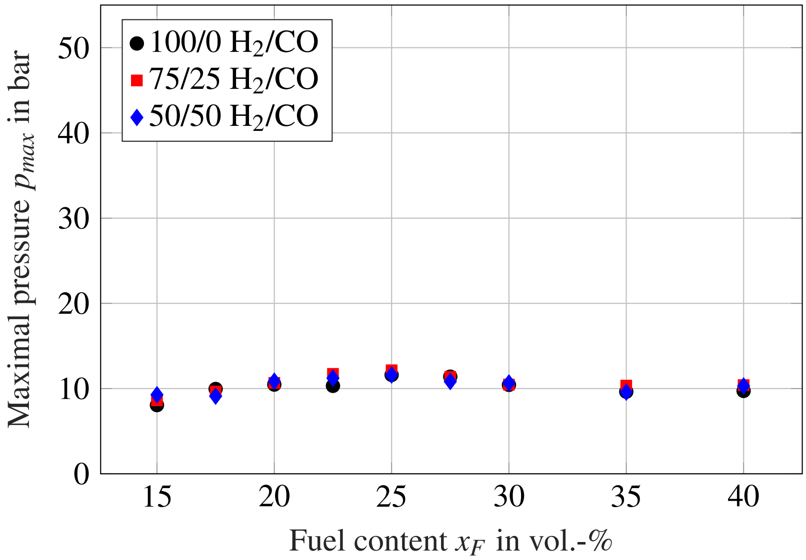

***Fig. 9**: Maximum dynamic pressure p_{max} over fuel content x_{F} for BR60S100L*

3.3 Run-up distance

Since reaching the speed of sound of the isobaric combustion products a_{pr} is one of the critical conditions for DDT, the run-up distance is a key parameter for safety applications (Ciccarelli & Dorofeev

(2008)). Fig. 10 displays the run-up distance for the BR30S100L configuration. The mean run-up distance is $\bar{x}_{a_{pr}} = 1.00\,\mathrm{m}$ for 100/0, $\bar{x}_{a_{pr}} = 1.20\,\mathrm{m}$ for 75/25 and $\bar{x}_{a_{pr}} = 1.18\,\mathrm{m}$ for 50/50 H_2/CO. For very lean mixtures of $x_F = 15$-17.5 vol.-% the run-up distance for 75/25 and 50/50 fuels is shorter than for 100/0 H_2/CO. This trend is reversed as soon as a fuel content of $x_F = 20$ vol.-% is reached. Within the range of $x_F = 20$-27.5 vol.-% the run-up distances of 75/25 and 50/50 H_2/CO are very similar and about 0.4 m longer than for 100/0 H_2/CO. For fuel rich mixtures another behaviour is observed. While for $x_F = 30$-35 vol.-% all fuels behave quite similar, the gap between the run-up distance increases at 40 vol.-%. When compared to the results obtained by Veser et al. (2002), a shorter run-up distance is obtained. While Veser found a run-up distance of $x_{a_{pr}} \approx 1.5\,\mathrm{m}$ for 100/0, 2 m for 75/25 and 2.6 m for 50/50 H_2/CO the run-up distances for the GraVent configuration are shorter. This might be related to a slightly different geometry. The tube used by Veser used orifice plates of BR= 30 %. In contrast, the obstacles in the GraVent configuration allow the flame to transit through the obstructed part through the whole channel width.

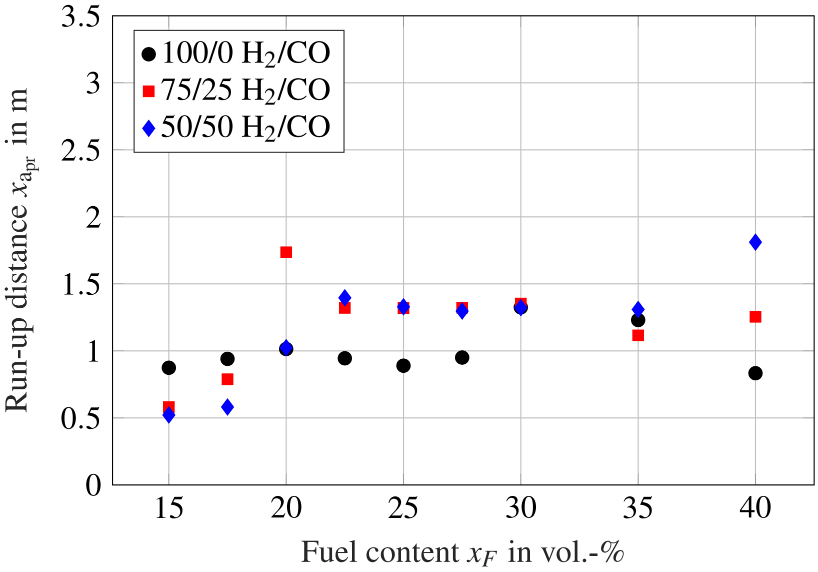

Fig. 10: *Run-up distance $x_{a_{pr}}$ to speed of sound of the products a_{Pr} over fuel content x_F for BR30S100L*

The run-up distance for BR30S300L is shown in fig 11. The mean run-up distance is $\bar{x}_{a_{pr}} = 1.42\,\mathrm{m}$ for 100/0, $\bar{x}_{a_{pr}} = 1.30\,\mathrm{m}$ for 75/25 and $\bar{x}_{a_{pr}} = 1.38\,\mathrm{m}$ for 50/50 H_2/CO. Similar to BR30S100L a shorter run-up distance compared to 100/0 is found for $x_F = 15$ vol.-% for 75/25 and 50/50 H_2/CO. The run-up distance for 75/25 and 50/50 H_2/COincreases significantly if the fuel content is increased to $x_F = 17.5$ vol.-%. For 100/0 H_2/COthe run-up distance in a range of $x_F = 15$-30 vol.-% show only very little variation. A similar trend can be observed for 75/25 and 50/50 in an range of $x_F = 22.5$-27.5 vol.-%. In the fuel rich range of $x_F = 30$-35 vol.-% an increase in the run-up distance is observed. This trend is reversed when the fuel content is further increased to $x_F = 40$ vol.-%. In total the run-up distance for BR30S300L is slightly longer than for BR30S100L, which might be related to less turbulence due to fewer obstacles. The influence of the fuel is less clear.

DOI: 10.7795/810.20200724

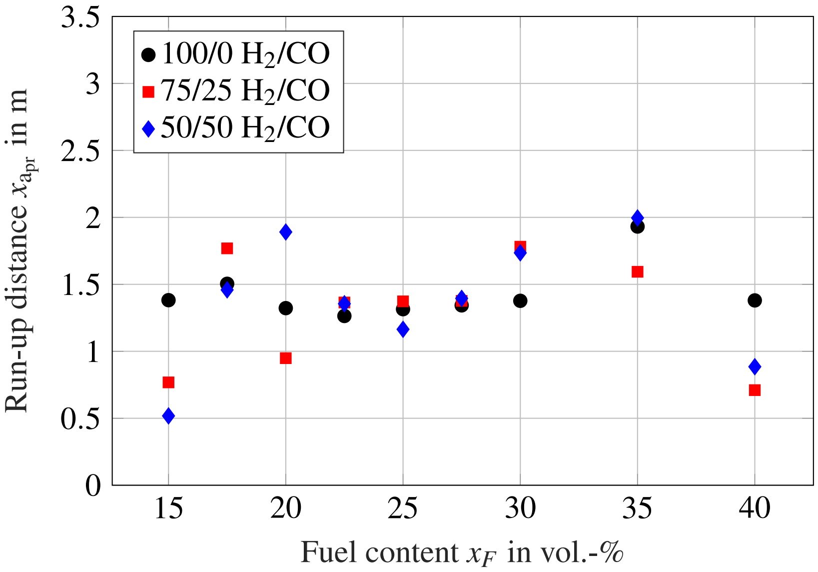

***Fig. 11**: Run-up distance $x_{a_{pr}}$ to speed of sound of the products a_{Pr} over fuel content x_F for BR30S300L*

Fig 12 displays the run-up distance for BR60S100L. The mean run-up distance is $\bar{x}_{a_{pr}} = 0.80$ m for 100/0, $\bar{x}_{a_{pr}} = 0.73$ m for 75/25 and $\bar{x}_{a_{pr}} = 0.78$ m for 50/50 H_2/CO. At $x_F = 15$ vol.-% the shortest run-up distance is found for 100/0 H_2/CO at $x_{a_{pr}} = 0.41$ m. When the fuel content is increased the run-up distance for 100/0 increases to $x_{a_{pr}} = 0.90$ m at $x_F = 27.5$ vol.-%. In fuel rich mixtures $x_{a_{pr}}$ slightly decreases before increasing sharply at $x_F = 40$ vol.-%. A similar trend is observed at 75/25 H_2/CO. The slope of the run-up distance over the fuel content seems to be slightly shifted to higher fuel contents as the local maximum of the run-up distance is observed at $x_F = 30$ vol.-%. In contrast to 100/0 a short run-up distance is found at $x_F = 40$ vol.-%.

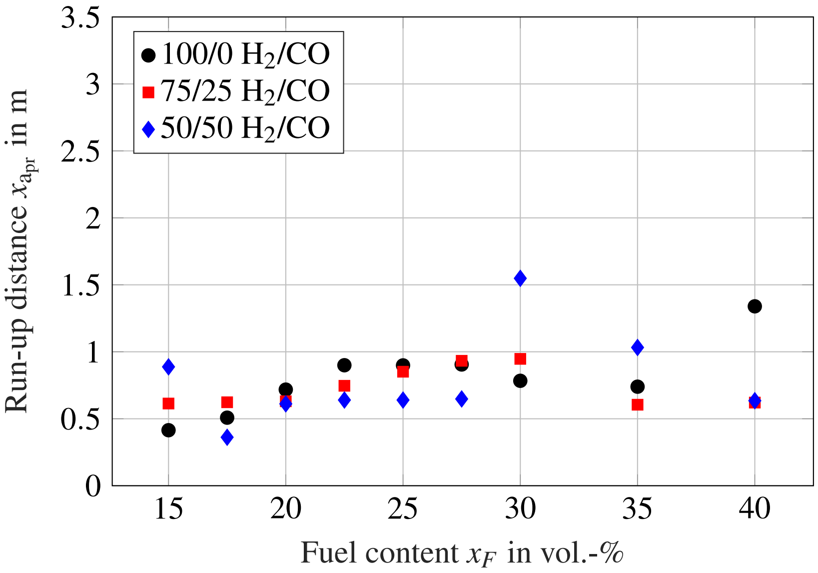

***Fig. 12**: Run-up distance $x_{a_{pr}}$ to speed of sound of the products a_{Pr} over fuel content x_F for BR60S100L*

For 50/50 the slope of the run-up distance is different than for 100/0 and 75/25 H_2/CO. A local minimum is observed at $x_F = 17.5$ vol.-%. If the fuel content is increased, a marginal increase in $x_{a_{pr}}$ is observed. In the range between $x_F = 17.5$-27.5 vol.-%, 50/50 H_2/CO-fuels have the shortest run-up distances for the investigated fuels. A sharp increase is observed at $x_F = 30$ vol.-%. By further increasing the fuel content, $x_{a_{pr}}$ decreases and is shorter than for 100/0 H_2/CO at $x_F = 40$ vol.-%. Compared to BR30S100L and BR30S300L the run-up distances at BR60S100L are the shortest, due to the high blockage ratio and the low spacing.

In general the trends of the run-up distance are different between the investigated fuels. This is true especially for very lean mixtures of $x_\mathrm{F} = 15\text{-}17.5\,\text{vol.-\%}$ at which 75/25 and 50/50 show shorter run-up distances than 100/0 H_2/CO. This can not directly be explained by thermodynamic properties of the mixtures. The Lewis-Numbers are well below unity for all investigated fuels at lean fuel contents. Hence thermo-diffusive instabilities, which lead to a higher integral fuel consumption should be present in all lean mixtures (Katzy et al., 2017). Furthermore, the total energy content as well as the expansion ratios σ are similar for each fuel at a given fuel content (compare table 2). Hence, the different behaviour might be linked to flow phenomena induced by the higher momentum of jets passing through obstacles in CO containing fuels.

4 Conclusion and Outlook

Results of experimental studies on FA and DDT in homogenous H_2-CO-air mixtures in a partially obstructed channel have been presented. Three different obstacle configurations have been investigated: a low obstruction (30 %) at a small (100 mm) and large spacing (300 mm), a high obstruction (60 %) at a small spacing in addition to the high obstruction and large spacing which was published in Heilbronn et al. (2019). Each obstacle configuration featured a 3.95 m long obstructed and a 2.05 m long unobstructed section in a rectangular explosion channel. The fuel was varied between 100/0, 75/25 and 50/50 H_2/CO. The fuel content was varied from $x_\mathrm{F} = 15\text{-}40\,\text{vol.-\%}$ in air. The experiments were analysed with regard to terminal velocity, peak pressure and run-up distance to the speed of sound of the products.

Whether detonations occur depends on the obstacle configuration, the fuel and the fuel content in air. For high obstruction and small spacing, detonations are not observed. For a lower obstruction detonations occur at slightly leaner conditions at 100/0 compared to 75/25 and 50/50 H_2/CO. A similar trend is observed at a less frequently obstructed geometry. A significant change in the detonation limits is found in fuel rich mixtures. In low obstructed obstacle configurations fuels of 75/25 and 50/50 are found in the detonation regime, while 100/0 H_2/CO remain in the fast flame regime. This supports the findings in Heilbronn et al. (2019), showing that H_2/CO-fuels show a different behaviour than 100/0 H_2/CO in fuel rich mixtures. In addition to Veser et al. (2002) it can be concluded that CO addition can have an impact in fuel rich mixtures.

The highest peak pressures are found at a low obstruction and a small spacing. For rich fuel mixtures, peak pressures of 75/25 and 50/50 H_2/COin low obstructed configurations are higher than the ones observed for the same fuel contents of 100/0 H_2/CO, hence leading to a higher potential damage. On average, peak pressures at low obstructions are slightly lower for a larger spacing. Since DDT was not observed a high obstruction and a small spacing, the measured peak pressures are very similar for all fuels and contents. Compared to a lower obstruction, the peak pressures are found to be lower.

The longest run-up distances to the speed of sound of the products were found at a low obstruction and a large spacing. In this case, all fuels showed a similar run-up distance. For a smaller spacing, run-up distances for 75/25 and 50/50 were slightly shorter than for 100/0 H_2/CO. The shortest run-up distances were found for a high obstruction and a small spacing. The influence of the CO-content in the fuel on the run-up distance could not be identified by the measurement systems used for the present study. Hence are more detailed investigation of the early stages of flame propagation using shadowgraphy and OH-PLIF will be used in order to gain further insights.

Acknowledgements

This project is funded by the German Federal Ministry of Economics and Technology (BMWi) on the basis of a decision by the German Bundestag (project no. 1504545A) which is gratefully acknowledged.

References

Barfuss, C., Heilbronn, D., Sattelmayer, T. (2019). *Simulation of deflagration-to-detonation transition of lean h2-co-air mixtures in obstructed channels*. In *International Conference on Hydrogen Safety*.

Barfuss, C., Heilbronn, D., Sattelmayer, T. (2020). *Impact of local flame quenching on the flame acceleration in h2-co-air mixtures in obstructed channels*. In *13th International Symposium on Hazards, Prevention, and Mitigation of Industrial Explosions*.

Browne, S., Ziegler, J., Shepherd, J. (2008). *Shock and detonation toolbox*. GALCIT-Explosion Dynamics Laboratory, Pasadena, CA.

Ciccarelli, G., Dorofeev, S. (2008). *Flame acceleration and transition to detonation in ducts*. Progress in energy and combustion science, 34(4):499–550.

Demirbas, A. (2005). *Potential applications of renewable energy sources, biomass combustion problems in boiler power systems and combustion related environmental issues*. Progress in Energy and Combustion Science, 31(2):171 – 192. ISSN 0360-1285.

Gauntt, R., Kalinich, D., Cardoni, J., Phillips, J., Goldmann, A., Pickering, S., Francis, M., Robb, K., Ott, L., Wang, D., et al. (2012). *Fukushima daiichi accident study (status as of april 2012)*. Sandia Report Sand, 6173.

Goodwin, D., Speth, R., H.K., M., Weber, B. (2018). *Cantera: An object-oriented software toolkit for chemical kinetics, thermodynamics, and transport processes*. https://www.cantera.org. Version 2.4.0.

Heilbronn, D., Barfuss, C., Sattelmayer, T. (2019). *Deflagration-to detonation transition in h2-co-air mixtures in a partially obstructed channel*. In *International Conference on Hydrogen Safety*.

Katzy, P., Hasslberger, J., Boeck, L. R., Sattelmayer, T. (2017). *The effect of intrinsic instabilities on effective flame speeds in under-resolved simulations of lean hydrogen–air flames*. Journal of Nuclear Engineering and Radiation Science, 3(4).

Kumar, R., Koroll, G., Heitsch, M., Studer, E. (2000). *Carbon monoxide–hydrogen combustion characteristics in severe accident containment conditions*. Organisation for Economic Co-operation and Development, Paris, France, Report No. NEA/CSNI.

Lieuwen, T., Yang, V., Yetter, R. (2009). *Synthesis gas combustion: fundamentals and applications*. CRC press.

Veser, A., Stern, G., Grune, J., Breitung, W., Burgeth, W. (2002). *Co-h2-air combustion tests in the fzk-7m-tube*. Technical report, Institut für Kern- und Energietechnik.

Vollmer, K. G., Ettner, F., Sattelmayer, T. (2010). *Influence of concentration gradients on flame acceleration in tubes*. In *8th International Symposium on Hazards, Prevention, and Mitigation of Industrial Explosions*.

Vollmer, K. G., Ettner, F., Sattelmayer, T. (2011). *Influence of concentration gradients on flame acceleration in tubes*. Science and Technology of Energetic Materials, 72(3-4):74–77.

DOI: 10.7795/810.20200724

Impact of Local Flame Quenching on the Flame Acceleration in H_2-CO-Air Mixtures in Obstructed Channels

Christoph Barfuss[a], Daniel Heilbronn[a] & Thomas Sattelmayer[a]
[a] Lehrstuhl für Thermodynamik (Technische Universität München, Garching, Germany)
E-mail: *barfuss@td.mw.tum.de*

Abstract

After weak ignition, flame acceleration preconditions the fresh gas ahead of the flame front allowing deflagration-to-detonation transition to occur. Mechanisms decreasing the acceleration, like local flame quenching in the wake of obstacles along the flame path, potentially delay the onset of detonation. Strong shear layers forming at the rear edge of obstacles isolate fresh gas pockets behind them, limiting the integral heat release. In this study, the intensity of quenching is investigated in varying geometrical configurations for H_2-CO-air mixtures. Initially, the presence of local flame quenching is shown in high fidelity simulations for a H_2-air and a H_2-CO-air mixture with 75/25 H_2/CO. Secondly, the impact of different quenching limit treatments in RANS based combustion models is investigated, varying blockage ratio and obstacle spacing. Due to the non-linear scaling of turbulence with geometry dimensions, the impact of the geometry dimension on the necessity to consider quenching is examined. The results indicate that quenching does not need to be considered in RANS based combustion models for H_2-CO-air flames in explosion scenarios. But since quenching does eventually occur at an upper limit of turbulence intensity, the authors suggest the usage of limiting flame stretch values in RANS based turbulent flame speed closure models from 1D flame simulations with detailed chemistry.

Keywords: *flame acceleration, flame quenching, H_2-CO-air, obstructed channel*

1 Introduction

The main components of technical syngas are hydrogen (H_2) and carbon monoxide (CO). It is used in the chemical industry and as carbon free fuel in the power generation sector. Independent of the technology, highly reactive fuels pose the hazard of explosions if sudden ignition occurs. As a worst case scenario, detonations might even be the consequence. In order to asses the risk of H_2-CO-air explosions, safety analysis tools based on computational fluid dynamics (CFD) with efficient combustion modeling approaches are developed at various institutes (Velikorodny et al., 2015, Xiao et al., 2017, Hasselberger, 2017).

After weak ignition, a self exciting feedback loop of the expanding flame generating flow and turbulence ahead of the flame, which in reverse increases the fuel consumption rate, continuously accelerates the flame. The flame acceleration (FA) preconditions the fresh gas until auto-ignition may lead to deflagration-to-detonation transition (DDT). Due to the importance of preconditioning for the onset of DDT, physical mechanisms decreasing the acceleration influence the probability of DDT. In realistic accident scenarios the flame path is often partially obstructed by obstacles. Vortex shedding from the obstacle edges will at first enhance turbulence and the burning rate. However, with increasing velocity the intensive turbulent mixing can lead to partial flame extinction if the smallest eddies are capable to perturb the flame's reaction zone (Poinsot and Veynante, 2005, Ciccarelli and Dorofeev, 2008).

Flame quenching occurring in fast flames has already been discussed in other studies with regard to varying fuels (Dorofeev et al., 2001). It was mentioned that the flame is more pronounced to local quenching in fuels with a positive Markstein number ($Ma_\mathrm{b} > 0$). Fuels with a negative Markstein number like H_2 or H_2-CO are less susceptible to quenching. Flame stretch resulting from turbulent structures decreases the flame thickness and enhances local gradients. Fuels with Lewis numbers less than unity, e.g. H_2-CO, are less susceptible to extinction due to their strong diffusion of fuel (Poinsot and Veynante, 2005).

In this study, direct numerical simulations demonstrate the presence of local flame quenching in the wake of obstacles for H_2-air and H_2-CO-air mixtures. More importantly for safety analysis CFD codes, the question arises whether flame quenching has to be considered in combustion modeling on the coarser meshes typically used. The impact of different quenching formulations on the H_2-CO-air flame trajectory is therefore established by means of a RANS based CFD solver (Barfuss et al., 2019). Varying obstacle configurations in a rectangular explosion channel are investigated. The run-up distance to the speed of sound in the combustion products is used for comparison. Finally, a generic scale-up by a factor ten of the previously investigated explosion channel is simulated in order to asses the necessity to consider quenching in combustion modeling approaches for large-scale geometries.

2 Quenching during flame acceleration

The flow velocities associated with fast flames are high in comparison with typical internal flows in technical applications. Hence, obstacles in the flame path generate strong shear layers with vortex shedding. The flame stretch by these vortices can eventually quench sections of the flame front convected into the vortices. Thereby, the shear layer isolates fresh gas volumes behind obstacles from the flame. Consequently, fresh gas will only be burned once the flame is convected into the fresh gas pocket by vortices further downstream of the obstacle. As a results, overall FA drops due to the limited increase of the integral heat release. If subsequent DDT occurs, flame quenching can delay the onset of detonation.

In the fast flame regime the flame speed reaches up to the speed of sound in the combustion products a_{pr}. It is within the same range for 100/0 vol.-% ($a_{\mathrm{pr}} = 904.12\,\mathrm{m/s}$) and 75/25 vol.-% ($a_{\mathrm{pr}} = 881.78\,\mathrm{m/s}$) H_2/CO fuels at 22.5 vol.-% fuel in air. Hence independent of the fuel composition, the high velocity gradients behind obstacles result in noticeable flame stretch. Key parameter is the limit of flame stretch the flame can endure before it extinguishes. In the following, the presence of partial flame quenching as a consequence of flame stretch is presented for H_2-CO-air flames in obstructed channels.

2.1 DNS simulation of H_2-CO-air mixtures

2.1.1 Solver

A 2D direct numerical simulation (DNS) of the H_2-CO-air mixture has been set up based on the *rhoReactingFoam* solver of the C++ CFD library package *OpenFOAM v7*. The unsteady compressible Navier-Stokes equations are solved on the unstructured mesh topology of *OpenFOAM*. Since this study focuses on the early stage of FA, the robust PIMPLE algorithm is used for pressure-velocity coupling. Spatial discretization is second order accurate for advection and diffusion terms. Time integration is realized with a first order implicit Euler scheme. Adjustable time stepping with an acoustic Courant number of $Co_{\mathrm{ac}} = 0.1$ is used. In order to show local flame extinction, detailed chemistry is computed with the reaction mechanism of Li et al. (2015). The varying species diffusion in H_2-CO-air mixtures is accounted for with individual Schmidt numbers Sc_k for each specie k. The Schmidt numbers are provided in table 1.

2.1.2 Computational domain and case setup

Figure 1 displays the 2D computational domain with a uniform mesh resolution of $\Delta x_{\mathrm{cell}} = 0.04\,\mathrm{mm}$. The domain has a length of 500 mm and half-channel height of 30 mm. Obstacles block 60 % of the cross-section and are installed with a spacing of 50 mm. The flame front is resolved with at least 10 cells at all times. Comparison of DNS simulations of an obstructed full-

DOI: 10.7795/810.20200724

channel and half-channel by Gamezo et al. (2007a) showed almost same results, justifying the use of symmetry. The boundaries are adiabatic, no-slip walls and symmetry at the center plane. The initial conditions are 293 K and 1.013 bar.

***Table 1**: Schmidt numbers of individual species.*

k	N_2	H	H_2	O	O_2	OH
Sc_k	0.7427	0.1318	0.2021	0.4924	0.7866	0.5019
k	H_2O	HO_2	H_2O_2	HCO	CO	CO_2
Sc_k	0.7075	0.7718	0.7772	1.0178	0.7698	1.0161

The flame is initiated as a circle of burned gas with a 7.5 mm radius. In order to achieve quick acceleration, additional energy is superposed onto the volume of burned gas. The energy is equivalent to a 2 mm thin domain over the half-channel height, which has been compressed to 3.5 bar by an according pressure wave. The case is set up following the DNS investigation of Gamezo et al. (2007a) at a similar geometrical scale. The simulations have been carried out for 22.5 vol.-% of fuel in air. Fuel compositions of 100 vol.-% H_2 and 75/25 vol.-% H_2 /CO in the fuel have been investigated.

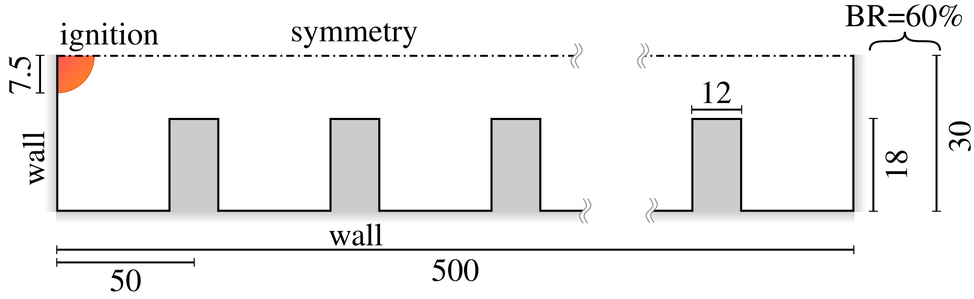

***Fig. 1**: Schematic of 2D computational domain.*

2.1.3 Simulation results

Despite turbulence being a 3D phenomenon, 2D DNS simulations of vortex-flame interaction can be carried out with sufficient accuracy, because flame turbulence interaction primarily experiences tube-shaped turbulent structures (Poinsot and Veynante, 2005). Gamezo et al. (2007b) reported only minor differences between 2D and 3D simulation results of accelerating H_2-air flames.

Figure 2 shows a sequence of images obtained in 100 vol.-% H_2 fuel. Additional to the temperature contour, the images show a blue iso-surface of regions in which flow strain reaches values above the calculated extinction flame stretch. The limiting values have been evaluated from 1D counter-flow flames in *Cantera* using the reaction mechanism of Davis et al. (2005) (Goodwin et al., 2018). The applied method to determine the extinction limit has been presented by Barfuss et al. (2019). Increasing pressures have been considered in the 1D simulation and hence, the iso-surface bounds have been adjusted according to the local pressure in the simulation.

The formation of vortices shedding from the front and back edge of the obstacle can be identified in image 1 of figure 2. While the frontal vortex causes a fresh gas pocket in the flame front in the second image, the rear vortex in image 4 shows the potential to extinguish the flame. Sections of the flame are separated from the bulk flame in the vortex. The flame is extensively stretched inside the vortex and strain rates exceed the limit values of 550000 1/s. The heat release at the flame tip close to the vortex center is efficiently reduced. This results in fresh gas islands passing the continuous flame surface without being consumed directly. Similar behavior has been reported by Gamezo et al. (2007b). In image 4, a large flame tip reaches from the right end of the image backward into the fresh gas pocket behind the obstacle. Compared to the flame in smaller vortices, this flame tip does not exhibit limiting flame stretch values. The flame tip velocity at the obstacle located at 250 mm is 372 m/s in the laboratory reference frame. The results indicate that limiting strain rates begin to occur at flame tip velocities of around 300 m/s.

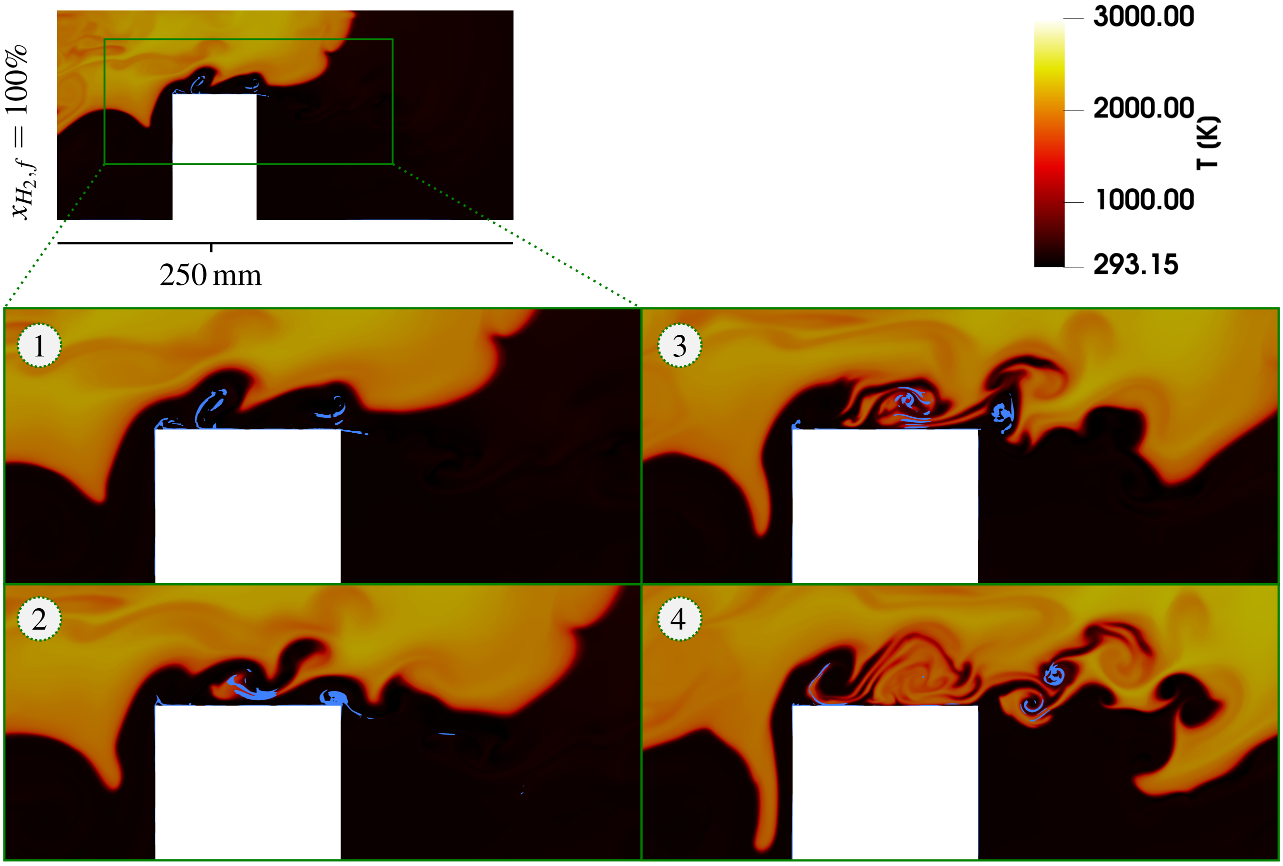

***Fig. 2**: DNS simulation of 22.5 vol.-% fuel-air mixture including iso-surface (blue) of extinction flame stretch determined from 1D simulations (100/0 H_2/CO fuel).*

In comparison to 100 vol.-% H_2, the 75/25 vol.-% H_2/CO fuel mixture reaches a lower flame tip velocity of 306 m/s at the obstacle location of 250 mm. Figure 3 shows equally intense iso-surface regions at almost the same limiting strain rate of 540000 1/s. The increased density of the gas mixture results in higher momentum. Due to the higher momentum, H_2-CO-air flames appear to be susceptible to partial flame extinction at lower flame tip velocities. As the image sequence indicates, vortices shedding at the back edge of the obstacle persist for a much longer distance than those from pure H_2 fuel. The vortices stretch the flame with increasing strain rates along the image sequence. This leads to partial flame extinction at the flame tip reducing the overall heat release. The combination of quenching and vortex shedding of the shear layer efficiently prevents the flame from entering the fresh gas pocket behind the obstacle. Even the flame in the second vortex of image 4 located further downstream is separated from the bulk. This flame section also exhibits limiting flame stretch rates, but does reach further into the fresh gas behind the obstacle than the upstream flame vortex.

It should be mentioned that not the entire spectrum of turbulent eddies can perturb the flame's reaction zone. The smallest eddies at the Kolmogorov scale dissipate too fast (Meneveau and Poinsot, 1991). Therefore, required flame stretch in the transient flow leading to flame extinction has to be even higher than determined from 1D counter-flow flame simulations with detailed chemistry. Therefore, exceeding the calculated stretch limit is not sufficient to consider a flame extinguished. But decreased reactivity allowing for unburned gas pockets to imping the flame surface and partial flame extinction can be observed in the 2D DNS simulations nonetheless.

DOI: 10.7795/810.20200724

It can be concluded that partial flame quenching exists for accelerating H_2-CO-air flames in obstructed channels. But the percentage of quenched flame surface is relatively small at flame tip velocities around 300 m/s. This percentage is assumed to increase with rising flow velocities at subsequent obstacles. The isolation of a fresh gas pocket by the shear layer cannot be contributed to quenching alone. CO containing fuels are more prone to partial flame extinction due to the increased momentum in equally fast flows. Thus, the quenching impact in RANS based modeling approaches is investigated only for a 75/25 vol.-% H_2/CO fuel composition.

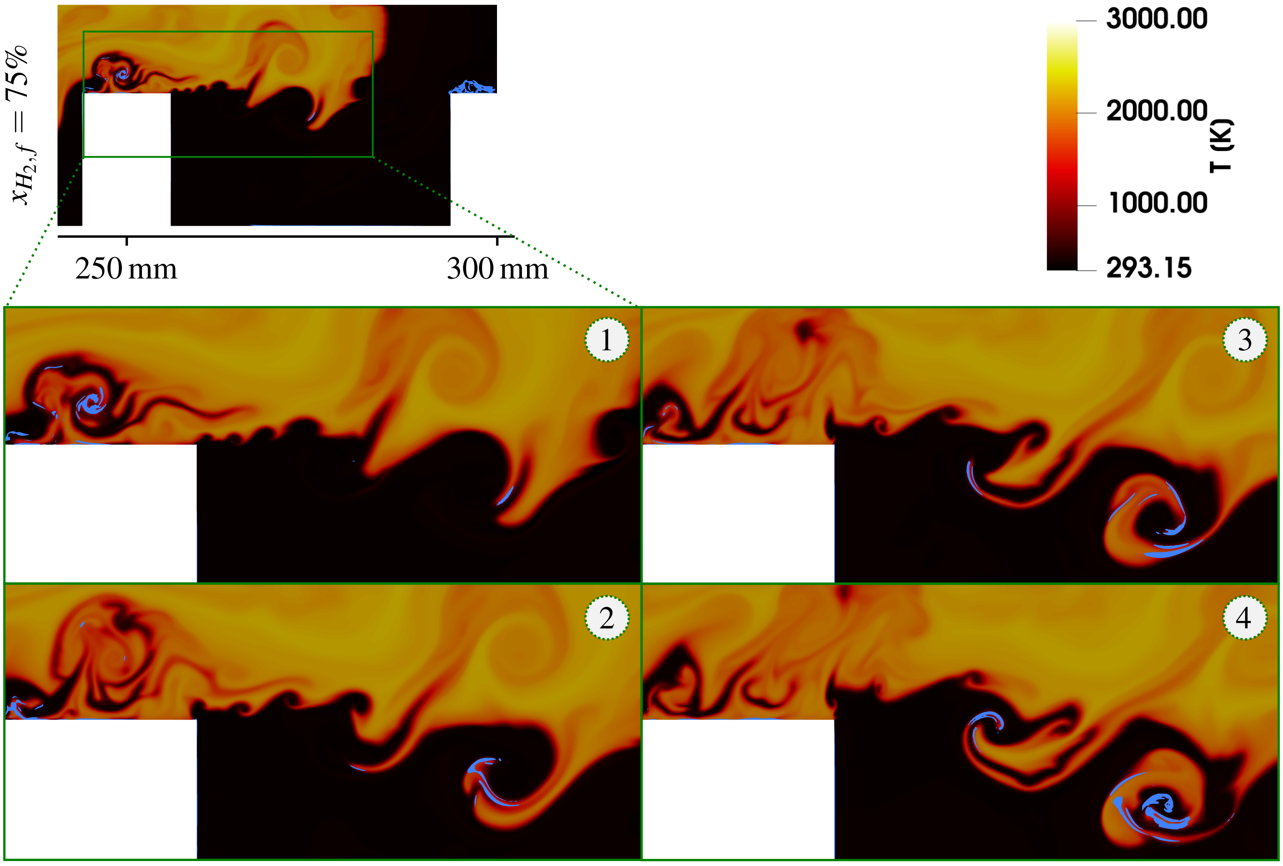

Fig. 3: *DNS simulation of 22.5 vol.-% fuel-air mixture including iso-surface (blue) of extinction flame stretch determined from 1D simulations (75/25 H_2/CO fuel).*

2.2 *Impact of flame quenching in a RANS based combustion modeling approach*

In order to investigate the impact of quenching on the flame acceleration in RANS based CFD simulations of explosions, a previously presented CFD solver based on the *OpenFOAM* framework is used (Barfuss et al., 2019). It solves the unsteady compressible Navier-Stokes equations on a density-based solver architecture. Turbulence is considered by the well-established k-ω SST turbulence model with wall functions as boundary conditions (Menter, 1994). Advection terms are computed with the Harten-Lax-van Leer contact (HLLC) scheme, an approximate Riemann solver (Toro et al., 1994). Adaptive mesh refinement in the vicinity of flames and pressure waves as well as in regions of high turbulence production is applied. Eulerian time integration scheme with adjustable time stepping based on an acoustic Courant number of $Co_{\mathrm{ac}} = 0.3$ is used. Flame propagation is considered in the transport equation of the reaction progress variable c. The equation's source term is the maximum value out of a deflagration term and detonation term. The detonation source term accounting for auto-ignition is not further explained here. A description can be found in the work of Hasselberger (2017).

Equation 1 describes the deflagration source term, which is modified from the 'turbulent flame speed closure' (TFC) model of Zimont (2000). According to Damköhler's ansatz, turbulent flame speed S_t is the product of flame wrinkling factor Ξ and the laminar flame speed S_L. The expansion of the burned gas is accounted for by the density of unburned gas ρ_u. The equation introduces flame quenching with the quenching factor G, which ranges from 0 to 1.

$$\dot{\omega}_\mathrm{def} = \rho_\mathrm{u} G \underbrace{\Xi S_\mathrm{L}}_{=S_\mathrm{t}} \left| \frac{\partial c}{\partial x_i} \right| \tag{1}$$

The quenching factor in equation 2 is derived from the log-normal distribution of the turbulent dissipation rate ε (Zimont et al., 1998). The standard deviation σ of the log-normal distribution is calculated from the ratio of integral and Kolmogorov length scale $\sigma = 0.26\ln(l_\mathrm{t}/l_\eta)$. Once the critical dissipation rate ε_cr is reached, the error function in equation 2 starts to decrease noticeably. Equation 3 estimates the critical dissipation rate from the kinematic viscosity ν and the critical velocity gradient g_cr. g_cr resembles the flow strain equivalent to the flame stretch capable of extinguishing the flame.

$$G = \frac{1}{2}\mathrm{erfc}\left\{ -\frac{1}{\sqrt{2\sigma}} \left(\ln\left(\frac{\varepsilon_\mathrm{cr}}{\varepsilon} \right) \right) + \frac{\sigma}{2} \right\} \tag{2}$$

$$\varepsilon_\mathrm{cr} = 15 \nu g_\mathrm{cr}^2 \tag{3}$$

No best practice whether to consider quenching in RANS based H_2-CO-air explosion simulations has been established so far. Thus, different approaches of treating the critical velocity gradient term are applied to a variation of obstacle configurations at small scales. Additionally, a generic scale-up of factor ten in respect of the cross-section is investigated to establish the impact of quenching in larger-scale simulations as well.

Zimont (2000) derived the formulation in the first column of table 2 by dimensional analysis. The usage of the dimensional term might not be adequate for fuels with Lewis numbers less than unity (Barfuss et al., 2019). As a second formulation for g_cr, 1D counter-flow flame simulations have been carried out in *Cantera* for varying fuel compositions, fuel-air mixtures and pressures. Obtained values are used as entries in an interpolation table providing g_cr directly to the solver. The second approach thereby resembles 1D flame simulations with detailed chemistry. Additionally, simulations neglecting quenching entirely are carried out as a reference result (third column).

***Table 2**: Different formulation for the quenching modeling approach in Zimont's TFC model.*

	Dimensional term	**Interpolation table**	**Quenching neglected**
Quenching formulation	$g_\mathrm{cr} = \frac{s_\mathrm{L}^2}{a}$	$g_\mathrm{cr} = f\left(y_\mathrm{fuel}, y_{\mathrm{H_2},\mathrm{fuel}}, T_\mathrm{u}, p\right)$	$G = 1$

2.2.1 *Variation of small-scale obstacle configurations*

The CFD solver is applied to DDT experiments in the GraVent test rig, in which homogeneous H_2-CO-air mixtures have been investigated experimentally (Heilbronn et al., 2019, 2020). The test rig is a 6 m long rectangular explosion channel at a width of 300 mm and a height of 60 mm. The first 3.95 m are partially obstructed with obstacles of varying blockage ratio (30 % or 60 %) and obstacle spacing (100 mm or 300 mm). The first obstacle is installed at 50 mm. Conventional measurement techniques (photo diodes) are used to evaluate flame trajectory data. The abbreviation *BRxxSxxxL*, filled accordingly with blockage ratio (BR) and spacing (S) for the place holder *x*, characterizes the obstacle configuration. The investigated gas mixture contains 22.5 vol.-% fuel in air with a fuel composition of 75 vol.-% H_2 in fuel.

Independent whether the flame undergoes DDT or remains in the chocked flame regime, the flame accelerates to the maximum velocity possible in a deflagrative combustion, i.e. Chapman-Jouguet condition behind the flame. The flame tip velocity in this state is close to the speed of sound in the combustion products a_{pr} (Lee, 2008). The run-up distance to the speed of sound in the products $x_{a_{\mathrm{pr}}}$ is characteristic for the flame acceleration phase (Ciccarelli and Dorofeev, 2008). It also represents the intensity of acceleration and, hence, gives an idea of the DDT probability. If the distance is shorter, waves are emitted from the flame at a higher rate and stronger accumulated pressure waves evolve leading to an earlier onset of detonation. While flame trajectory results have been reported previously for the GraVent test rig (Barfuss et al., 2019), here, the influence of varying blockage ratios and spacings shall be easily apparent. Therefore, the characteristic $x_{a_{\mathrm{pr}}}$ is used for comparison of numerical and experimental results.

In table 3 the run-up distances of the different quenching limit treatments are listed together with experimental findings from the GraVent experiments. Additionally, a relative deviation of the two approaches, dimensional term and interpolation table, is presented. The deviation is normalized by the the experimental value.

***Table 3**: Simulated run-up distances $x_{a_{\mathrm{pr}}}$ of different strain limit treatments and experimental values for 22.5 vol.-% fuel in air.*

Test rig configuration	**Dimensional term**	**Interpolation table**	**Quenching neglected**	**Rel. deviation** $g_{\mathrm{cr,Dim}} - g_{\mathrm{cr,1D}}$	**Experiment**
BR60S100L	1.012	0.9319	0.9297	10.73 %	0.7464
BR60S300L	1.133	0.9523	0.9523	17.82 %	1.0139
BR30S100L	1.252	1.2510	1,2510	0.08 %	1.3215
BR30S300L	1.280	1.3430	1.3700	4.62 %	1.3645

The experimental results in table 3 are averaged values of three repetitions with the same experimental setup (Heilbronn et al., 2020). All numerical results remain within the confidence range of the experimental findings. The run-up distances obtained with the interpolation table approach and with neglected quenching are almost identical for all obstacle configurations. This suggests that flame stretch limits from 1D simulations are almost never reached. This is due to the much coarser grid in the RANS based simulations in comparison to the DNS simulation of figure 3. In contrast, sufficient strain exists for the smaller limit from the dimensional quenching term resulting in a generally further downstream position to reach a_{pr}. As an exception, the flame tip velocity in the configuration *BR30S300L* rises above a_{pr} in the jet passing an obstacle, but drops noticeable below a_{pr} during the expansion after the obstacle. Hence, a Chapman-Jouguet deflagration has not been reached sustainably and further acceleration due to increasing heat release is still possible.

Results from varying quenching limit approaches differ most at large blockage ratios. Variation of obstacle spacing has a smaller impact on the contribution of quenching in comparison to blockage ratio variations. Since numerical results without quenching or with interpolation tables better match the experiments, it is concluded, that flame quenching can be neglected in small scale geometries. Due to the greater deviation from experiments, the evaluation of g_{cr} with the dimensional term is not considered suitable for accelerating H_2-CO-air flames with a Lewis number less than unity. The accelerating and, hence, stabilizing effects on a flame by a Lewis number less than unity are not captured sufficiently by the variables of the dimensional approach (Poinsot and Veynante, 2005). In contrast the interpolation table approach can be used, in order to maintain a threshold of maximum turbulence intensity leading to quenching, which is almost never reached in the RANS based simulations investigated in this study. Application of efficiency functions correcting for the spectrum contributing to flame stretch do not appear to be useful, because in general coarse meshes are used in safety analysis investigations (Meneveau and Poinsot, 1991).

2.2.2 *Impact of geometry dimensions*

Realistic accident scenarios often happen on much larger geometrical dimensions than the GraVent test rig. The impact of quenching has to be investigated on medium-scale or large-scale geometries also. Therefore, the GraVent configuration *BR60S100L* has been scaled-up by the factor ten in its geometrical dimensions with respect to the cross section. The dimensional scale-up is denoted with the abbreviation *BR60S1000* in the following. The length of the channel is 9 m and the obstructed section at 5.5 m. Hence, the number of obstacles reduces to 6. Simulations with the two quenching limit treatments, the dimensional term approach and the interpolation table, have been conducted with the same gas mixture of 22.5 vol.-% fuel in air (75/25 H_2/CO). The initial mesh of the scale-up consists of cubic cells with a cell size of $\Delta x_{\mathrm{cell}} = 40\,\mathrm{mm}$. This roughly relates to the initial mesh of the small-scale GraVent investigation after adaptive mesh refinement is applied twice.

Table 4 presents the evaluated run-up distances $x_{a_{\mathrm{pr}}}$. In Case *BR60S1000*, both simulations experienced a subsequent DDT after reaching a_{pr}. Because there is no experimental verification in the scale-up geometry, only the relative derivation can be discussed. The deviation is normalized here with the run-up distance obtained from the interpolation table approach.

***Table 4**: Run-up distances $x_{a_{\mathrm{pr}}}$ in the generic GraVent BR60S1000 scale-up.*

Test rig configuration	Dimensional term	Interpolation table	Relative deviation
BR60S100L	1.012	0.932	8.69 %
BR60S1000	4.055	4.005	1.25 %

The relative deviation is seven times smaller in the scale-up than in the original configuration. The smaller deviation in comparison to the original GraVent experiment can be explained by the larger averaged cell size relating to lower strain rates. Because turbulence does not scale linearly with the geometrical dimension, it can be assumed that volumes of unburned gas behind obstacles isolated by potential shear layers do not scale linearly either. According to this assumption, the impact of quenching on the flame trajectory decreases in larger geometries. The smaller deviation between the two stretch limit treatments in the scale-up is proof of that behavior. Strain rates from both modeling approaches are not high enough to result in significant flame quenching here.

3 Conclusions

In this study, the presence of local flame extinction by flame stretch has been presented for H_2-CO-air mixtures undergoing flame acceleration to fast flames. DNS simulations have been carried out for 22.5 vol.-% H_2 in air as well as for 75/25 vol.-% H_2/CO in air. The simulation results show how vortices, shedding from the obstacle edges, stretch the flame and separate sections of the flame from the bulk flame. The strain rate grows in smaller vortices leading to strong stretching of the flame. Locally the flame's reactivity is reduced or it even extinguishes. Starting from flame tip velocities of 300 m/s, first vortices were observed, which efficiently quench the flame. With increasing velocities the intensity of said vortices is assumed to grow. Furthermore, in CO containing fuels the momentum of the jet passing the same obstacles is higher than in pure H_2 fuels. The increased momentum allows for equally strong strain as in H_2 fuels at lower flame tip velocity. As a consequence, the observed impingement depth of vortices shedding from the rear edge of the obstacle is larger in comparison to pure H_2 fuel. The effect of isolating a fresh gas in a pocket behind obstacles is therefore stronger in CO containing fuel.

For the purpose of an application oriented modeling approach for safety analysis, three different approaches for evaluating critical stretch rates are investigated in an RANS based compressible CFD solver. The CFD solver has already been validated for subsequent FA and DDT of H_2-CO-air mixtures in one geometry configuration (Barfuss et al., 2019). A variation of obstacle spacing and blockage ratio allows for a more general statement on the necessity to consider quenching in efficient combustion modeling approaches.

Simulated run-up distances to the speed of sound in the combustion products have been compared with experiments. Simulations neglecting quenching show better agreement than simulations with Zimont's dimensional term for the flame stretch limit. While run-up distances of the different g_{cr} approaches significantly deviate in small-scale geometries with high blockage ratios, the differences become irrelevant on medium to large-scale geometries. Therefore, the combustion phenomenon of partial flame quenching does not need to be taken into account in TFC combustion models for accelerating H_2-CO-air flames in obstructed channels. Even though it can be neglected, the authors suggest to still apply a quenching term to maintain an upper limit of turbulent intensity as DNS data has shown general presence of partial quenching. A good practice for H_2-CO-air flames appears to be using strain rate limits of flame extinction from 1D counter-flow flame simulations with detailed chemistry, which take the increasing pressure of transient flame acceleration into account.

Acknowledgements

The presented work is funded by the German Federal Ministry of Economic Affairs and Energy (BMWi) on the basis of a decision by the German Bundestag (project no 1501545A) which is gratefully acknowledged.

References

Barfuss, C., Heilbronn, D., Sattelmayer, T. (2019). *Simulation of deflagration-to-detonation transition of lean h2-co-air mixtures in obstructed channels.* In *Proceedings of the 8th International Conference on Hydrogen Safety*. Adelaide, Australia.

Ciccarelli, G., Dorofeev, S. (2008). *Flame acceleration and transition to detonation in ducts.* Progress in Energy and Combustion Science, 34(4):499 – 550. ISSN 0360-1285. doi: https://doi.org/10.1016/j.pecs.2007.11.002.

Davis, S. G., Joshi, A. V., Wang, H., Egolfopoulos, F. (2005). *An optimized kinetic model of h2/co combustion.* Proceedings of the combustion Institute, 30(1):1283–1292.

Dorofeev, S. B., Kuznetsov, M. S., Alekseev, V. I., Efimenko, A. A., Breitung, W. (2001). *Evaluation of limits for effective flame acceleration in hydrogen mixtures.* Journal of Loss Prevention in the Process Industries, 14(6):583 – 589. ISSN 0950-4230. doi:https://doi.org/10.1016/S0950-4230(01)00050-X.

Gamezo, V. N., Ogawa, T., Oran, E. S. (2007a). *Effect of obstacle spacing on flame acceleration and ddt in obstructed channels.* 21st ICDERS.

Gamezo, V. N., Ogawa, T., Oran, E. S. (2007b). *Numerical simulations of flame propagation and ddt in obstructed channels filled with hydrogen–air mixture.* Proceedings of the Combustion Institute, 31(2):2463–2471.

Goodwin, D. G., Speth, R. L., Moffat, H. K., Weber, B. W. (2018). *Cantera: An object-oriented software toolkit for chemical kinetics, thermodynamics, and transport processes.* doi: 10.5281/zenodo.1174508. Version 2.4.0.

Hasselberger, J. (2017). *Numerical Simulation of Deflagration-to-Detonation Transition on Industry Scale.* Ph.D. thesis, TU München.

Heilbronn, D., Barfuss, C., Sattelmayer, T. (2019). *Deflagration-to detonation transition in h2-co-air mixtures in a partially obstructed channel.* In *Proceedings of the 8th International Conference on Hydrogen Safety*. Adelaide, Australia.

Heilbronn, D., Barfuss, C., Sattelmayer, T. (2020). *Influence of geometry on flame acceleration and ddt in h2-co-air mixtures in a partially obstructed channel.* In *In Proceedings of 13th International Symposium on Hazards, Prevention, and Mitigation of Industrial Explosions*. Braunschweig, Germany. In print.

Lee, J. H. S. (2008). *The Detonation Phenomenon.* Cambridge University Press, Cambridge. ISBN 978-0-521-89723-5.

Li, X., You, X., Wu, F., Law, C. K. (2015). *Uncertainty analysis of the kinetic model prediction for high-pressure h2/co combustion*. Proceedings of the Combustion Institute, 35(1):617–624.

Meneveau, C., Poinsot, T. (1991). *Stretching and quenching of flamelets in premixed turbulent combustion*. Combustion and Flame, 86(4):311–332.

Menter, F. R. (1994). *Two-equation eddy-viscosity turbulence models for engineering applications*. AIAA journal, 32(8):1598–1605.

Poinsot, T., Veynante, D. (2005). *Theoretical and numerical combustion*. RT Edwards, Inc.

Toro, E. F., Spruce, M., Speares, W. (1994). *Restoration of the contact surface in the hll-riemann solver*. Shock waves, 4(1):25–34.

Velikorodny, A., Studer, E., Kudriakov, S., Beccantini, A. (2015). *Combustion modeling in large scale volumes using europlexus code*. Journal of Loss Prevention in the Process Industries, 35:104–116.

Xiao, J., Breitung, W., Kuznetsov, M., Zhang, H., Travis, J. R., Redlinger, R., Jordan, T. (2017). *Gasflow-mpi: A new 3-d parallel all-speed cfd code for turbulent dispersion and combustion simulations: Part i: Models, verification and validation*. international journal of hydrogen energy, 42(12):8346–8368.

Zimont, V. L. (2000). *Gas premixed combustion at high turbulence. turbulent flame closure combustion model*. Experimental thermal and fluid science, 21(1-3):179–186.

Zimont, V., Polifke, W., Bettelini, M., Weisenstein, W. (1998). *An efficient computational model for premixed turbulent combustion at high reynolds numbers based on a turbulent flame speed closure*. Journal of engineering for gas turbines and power, 120(3):526–532.

DOI: 10.7795/810.20200724

Observations of DDT in narrow channels

Yves Ballossier, Josué Melguizo-Gavilanes & Florent Virot
Institut Pprime, UPR 3346 CNRS, ISAE–ENSMA, Futuroscope Chasseneuil, France
E-mail: *yves.ballossier@ensma.fr*

Abstract

Experiments are conducted in a smooth 10 × 10 mm square cross-section, 1-m long channel, closed at the ignition end and open at the other end. Simultaneous two-direction schlieren visualization is used to investigate the three-dimensional dynamics of transition to detonation for a stoichiometric H_2-O_2 mixture. Results show the existence of two distinct structures before detonation onset: (i) asymmetric, composed of an oblique shock trailed by a flame, that runs preferentially along the wall, and seems to get ignited inside the boundary layer developed by the precursor shock; (ii) symmetric, referred to as *strange wave* in literature, propagating at the speed of sound in combustion products. The combined effect of shock induced preheating and viscous heating near walls seem to be responsible for the formation of the complex flame-shock interactions observed. Furthermore, simultaneous two-direction optical access allows to map the exact location of detonation onset, showing that 78 % of cases exploded in corners, highlighting the role of corner flows and boundary layers in transition to detonation at this scale.

Keywords: *DDT, narrow smooth channels, hydrogen safety, flow visualization, strange wave*

1 Introduction

To comply with international agreements limiting CO_2 emissions, different solutions have been proposed to reduce the share of fossil fuels in electricity generation and transportation (Masson-Delmotte et al., 2018). The increased used of renewable (e.g. wind, solar) requires efficient/lasting storage solutions due to its intermittent nature. Among them battery banks or electrolyzers to produce hydrogen (H_2). H_2 has the potential to be a key player in enabling a sustainable energy transition. Its widespread use in transportation, for instance, poses risks due to leaks in refueling stations for vehicles (such as the recent accident in Sandvika, Norway) or in fuel cell/battery enclosures that can lead to strong explosions via deflagration-to-detonation transition (DDT). Note that the typical gaps in these compartments are of the order of millimeters, therefore understanding of DDT at this scale is needed to mitigate the aforementioned hazards through improved, research-based design.

Towards that goal, in general, we focus on a canonical configuration, namely a 1-m long, optically accessible, square cross-section channel (10 mm × 10 mm) to study all stages of DDT: from ignition, flame propagation and acceleration, to transition to detonation. However, here, we are only interested in characterizing the dynamics before and during detonation onset (i.e. formation of flame-shock complexes) and revealing their three dimensional structure. Studying this stage is essential to understand how to promote/mitigate DDT in narrow channels. Previous numerical and experimental work on flame-shock interaction by (Khokhlov et al., 1999, Thomas et al., 2001) have identified interesting structures that lead to DDT; Yanez and Kuznetsov (2016) also observed similar structures but using narrow channels in which very wrinkled funnel-shape flames trail behind planar shocks. These quasi-steady flame-shock complexes propagate at speeds of the order of the speed of sound in combustion products; the authors called this regime *strange wave*.

In the present work, two channels are used to study the formation of strange waves. They allow one- and two-direction simultaneous schlieren visualization, respectively.

2 Experiments

2.1 *Apparatus and procedure*

The experimental apparatus was designed to allow flexibility regarding optical access. Its total length is 1030 mm; 91 % of which is optically accessible. To switch from one-direction (1-DV) to two-direction visualization (2-DV) only the center piece of the channel needs being interchanged (see cross sectionals view in Fig. 1). In both configurations, 15-mm thick polycarbonate plates are used as windows. Aluminum flanges on top and bottom avoid bending of the polycarbonate during detonation propagation. For the two direction configuration, spacers prevent bending on the sides (one of them is visible in Fig. 8 bottom view). None of the tests performed showed signs of deformation. Structural integrity is ensured with bolts screwed on the aluminum in a "sandwich" configuration.

The experiments were conducted as follows: (i) the channel was vacuumed to an absolute pressure below 1 mbar (controlled by a MKS 220DA pressure sensor); (ii) a plastic cap, held on a servo motor's arm, sealed the open end of the channel; (iii) subsequently, the reactive mixture (stoichiometric H_2-O_2) was fed into the channel until it reached atmospheric pressure. (iv) At this point, the plastic cap was automatically removed by the servo motor; one second later the mixture is ignited ($E_{\text{ign}} < 1$ mJ) at the closed end by the electric arc that forms between the electrodes. This procedure ensured adequate control of the mixture composition ($\Phi = 1 \pm 0.01$). The waiting time between filling and ignition was also carefully controlled; 15 s were found sufficient to avoid any impact of initial flow unsteadiness on early stages of flame propagation. After each test, the channel was vacuumed for a few minutes to remove visible condensation from burned gases.

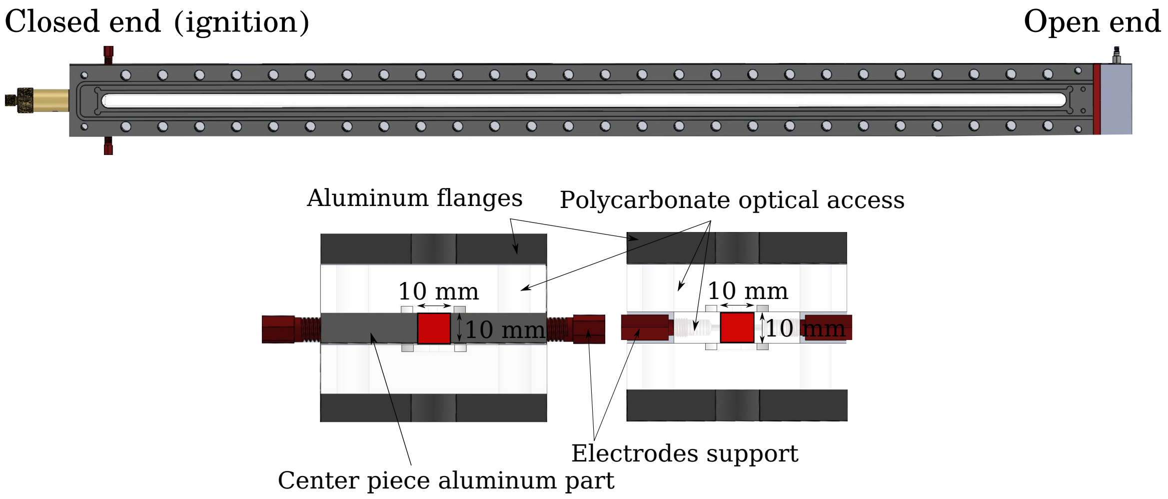

***Fig. 1**: Schematic of narrow channel (top) and cross-sections for 1-DV (bottom left) and 2-DV (bottom right). Red squares indicate effective section of the channel; white spaces optically accessible.*

2.2 *Flow visualization*

Schlieren visualization (SV) is performed on both channels. Two sets of cameras were used:
(i) Two black and white Photron FASTCAM SA-Z set at 140k frame per second (fps) (158 ns exposure), together with (248 ns exposure) for 2-DV; (ii) Shimadzu HPVX camera, with acquisition rates of 1 million (500 ns exposure) to 10 million fps (100 ns exposure), together with a Shimadzu HPV2 camera set at 1 million fps (500 ns exposure) for 2-DV.

Different light sources were utilized, two 100-mm diameter collimated LED, and a mercury light, coupled with a collimating mirror also of 100 mm in diameter. While the collimated LED offers compactness, the use of a mercury light provides a smaller focal point that results in a larger range of observable gradients (the side view in Fig. 8 is the only case using the latter). For the remaining cases shown, the collimated LED set-up is used with a razor blade occulting 50 % of the light to highlight gradients in the direction of flame propagation. Our schlieren set-up allows to visualize a section up to 100 mm; 2-DV is performed on the same section when done simultaneously. Figure 2 shows a simplified schematic of the global optical set-up. To trigger high speed camera(s), a BPW34 photo-diode, placed before the section of interest detects the arrival of the flame.

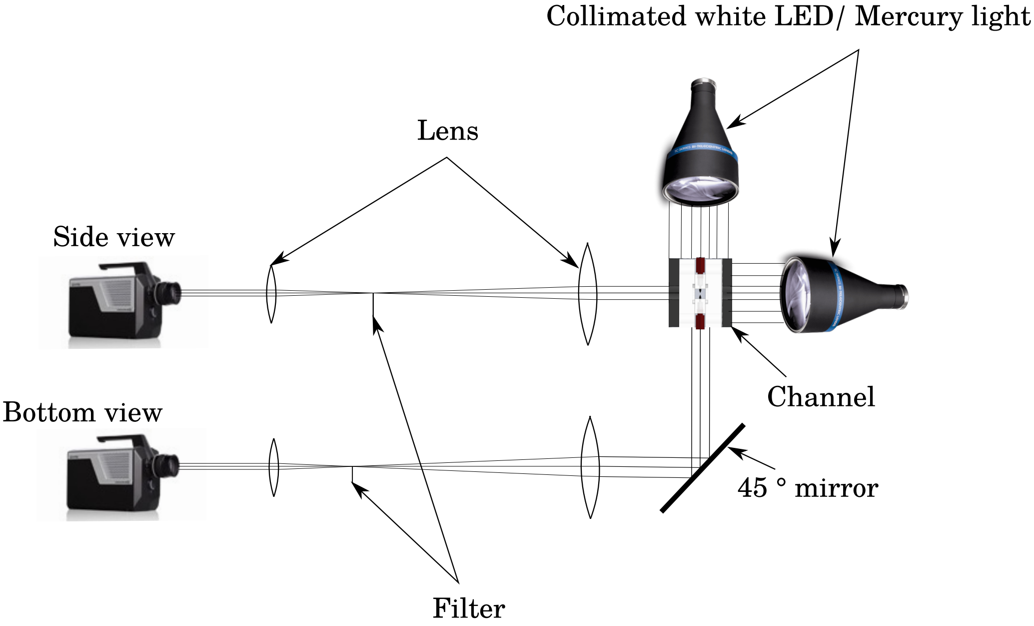

Fig. 2: *Schematic of global optical set-up for one- and two-direction visualisation.*

3 Results and discussion

For the sake of clarity in the presentation of the results that follow, Fig. 3 presents a schematic of the visualization orientations. Note that “Bottom” and “Side” faces refers to the relative position of the cameras; the actual position of the bottom face along the $z-$axis (or side face along $y-$axis) is arbitrary, as SV only provides integrated information along the line of visualization. The chosen representation is convenient when interesting dynamics occur in the lower right corner as seen from the ignition end. Post-processing typically consists of contrast adjustment, and sometimes, background subtraction to highlight important flow features. A total of 56 tests were performed of which 26 used 1-DV and 30 used 2-DV.

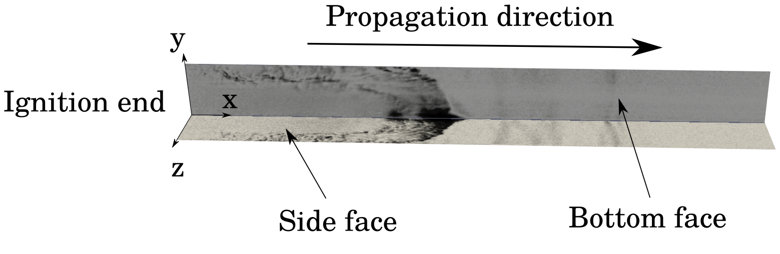

Fig. 3: *Schematic of the visualization directions. “Side” and “Bottom” faces refer to the camera position.*

3.1 Strange wave dynamics

3.1.1 Early stages and formation

Figure 4 shows the structure observed during formation of the strange wave using 1-DV. Time 0 μs is arbitrary, and simply represents the first instance in the sequence. The tip of a very corrugated flame (A) is seen to propagate from left to right at $t = 0$ μs. Expansion of burned products and the acceleration of the flame itself, generate perturbations within the fresh but shocked mixture ahead of the flame (weak (B) and strong (C) pressures waves are visible in this frame). At 27.5 μs, strengthening of flame acceleration and successive preheating from precursor shocks/pressure waves result in new, stronger shocks, forming closer to the flame. The flame starts to show a rather symmetric shape, preferentially burning near walls, resembling a funnel-shape (D) presumably filled with unburned mixture, finally, the flame catches up with the shock at 55 μs (not shown as it is outside of the viewing window). Note that an explosion emanating somewhere on the bottom face is observed, remnants of which are visible as a discontinuity traveling left (E). Not enough information is available to tell whether this local explosion lead to DDT. Front speeds computed from the images vary from 1200 – 1500 m/s for the corrugated flame, and from 700 – 1000 m/s, for the precursor shock.

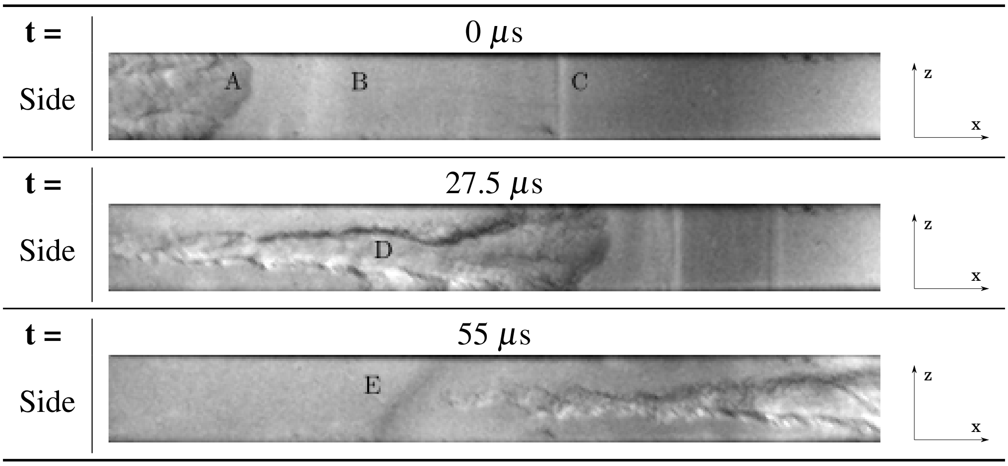

Fig. 4: *1-DV: symmetric formation of strange wave; section 454 to 544 mm from ignition; conditions: stoichiometric H_2-O_2 at $p_0 = 100$ kPa, and $T_0 = 290$ K. Raw images. A: corrugated front; B: weak pressure waves; C: precursor shock; D: funnel-shaped flame surface; E: left moving discontinuity.*

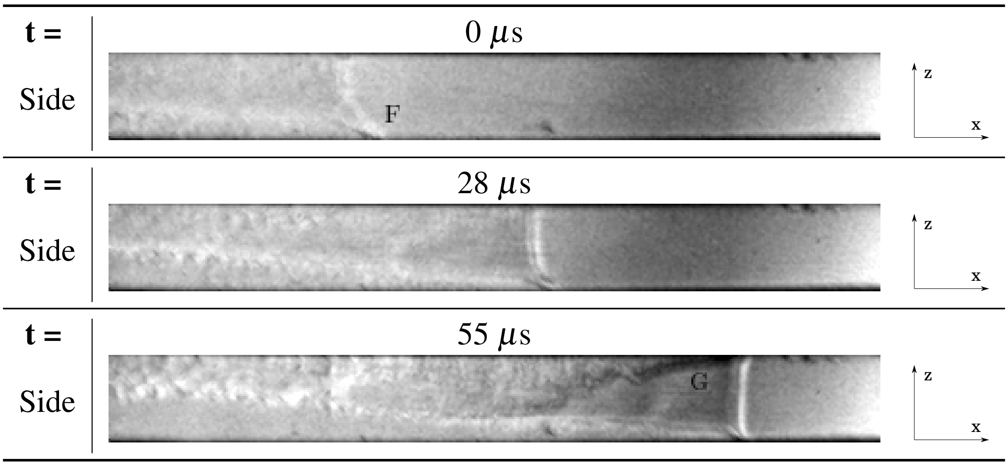

Fig. 5: *1-DV: asymmetric formation of strange wave; section 454 to 544 mm from ignition; conditions: stoichiometric H_2-O_2 at $p_0 = 100$ kPa, and $T_0 = 290$ K. Raw images. F: oblique shock; G: second ignition.*

Interestingly, in some cases using the same configuration and viewing section, another structure was observed (see Fig. 5). In this case no perturbations seem to be visible ahead of the flame, instead, a front propagating within the boundary layer at the bottom wall forms an oblique shock (F). Upon reflection from the top wall, a second ignition within the boundary layer takes place (G). On the last frame, at 55 μs, a symmetric shape starts to form. This shape is very similar to that observed experimentally by Thomas et al. (2001) and numerically by Khokhlov et al. (1999), and Oran et al. (2002) when they studied shock-flame interactions. The precursor shock in this case propagates at the same speed as that reported above.

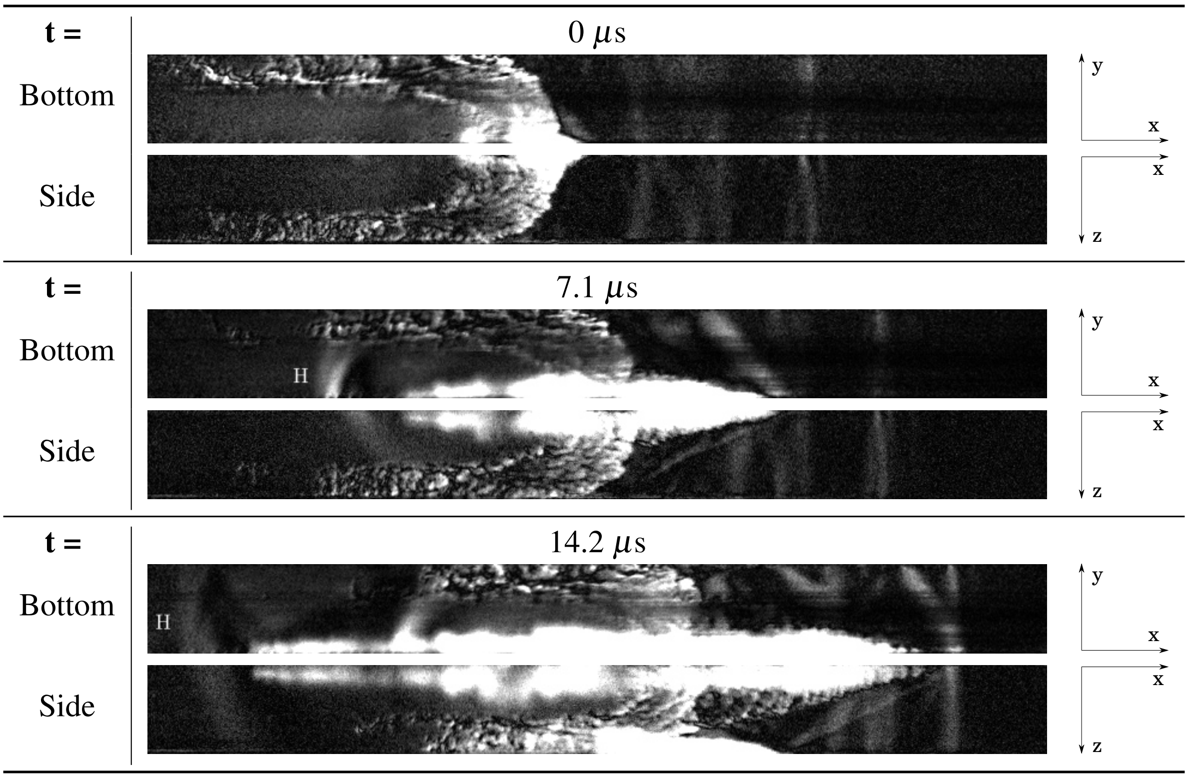

***Fig. 6**: Simultaneous 2-DV of the formation of strange wave; section 281 to 353 mm from ignition; conditions: stoichiometric H_2-O_2 at $p_0 = 100$ kPa, and $T_0 = 290$ K. Background substracted to highlight important flow features. H: left moving discontinuity.*

Figure 6 shows 2-DV during formation of the strange wave. Note that in this channel this stage of DDT occurred in a different section, 281 mm $\leq x \leq$ 383 mm, instead of 454 mm $\leq x \leq$ 544 mm. At $t = 0$ μs, this configuration shows a similar structure as in Fig. 4 preceded by a succession of pressure waves. The main difference lies on the fact that the corrugated flame does not catch up with the perturbations, instead the mixture seems to ignite within the boundary layer, likely due to a flame-boundary layer interaction, resulting in a front that propagates near the wall (similar to that seen in Fig. 5). Simultaneous SV allows to pinpoint the exact location in the channel cross-section where ignition takes place (bottom right corner looking from the ignition end). At 7.1 μs, the front in the boundary layer propagates faster than the corrugated flame ($\sim$ 3000 m/s), subsequently it decelerates to 2400 m/s, between 7.1 and 14.2 μs. In the side view, at 14.2 μs, another fast front starts to propagate within the boundary layer at the lower edge of this frame. The ignition of this front seems to be the result of an oblique shock-boundary layer interaction. However, based on a preliminary survey of all the results collected, ignition within the boundary layers arise more frequently due to flame-boundary layer interactions. The exact reason of spontaneous ignition within the corner is not clear, additional tests and analysis are currently being carried out to rule out uncertainties concerning manufacturing imperfections. The DNS of Dziemińska and Hayashi (2013) and LES of Zhao et al. (2017) present a similar scenario of DDT, but in our case, the flame-shock complex propagates more than 100 mm before it actually transits to detonation. A discontinuity (H), similar to that seen in Fig. 4 at 55 μs, is also visible at 7.1 and 14.2 μs. The overall dynamics obtained closely resembles that for 1-DV.

3.1.2 Quasi-steady propagation

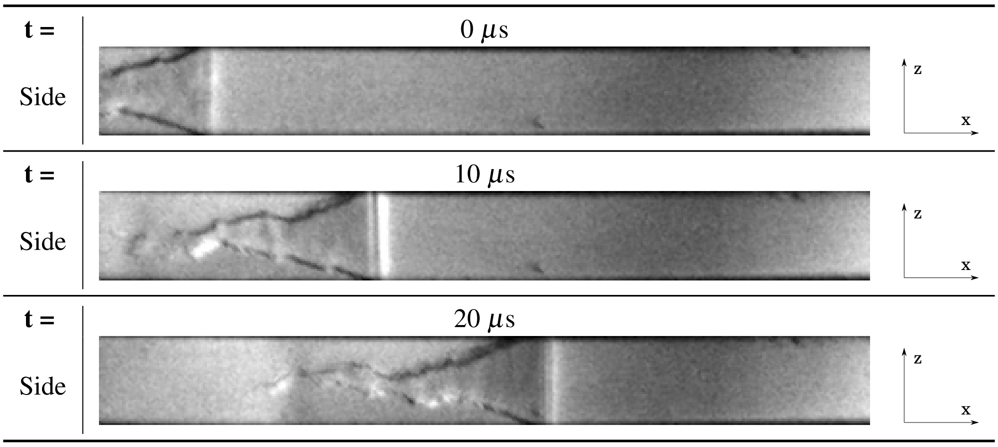

***Fig. 7**: 1-DV of strange wave; section 454 to 544 mm from ignition; conditions: stoichiometric H_2-O_2 at $p_0 = 100$ kPa, and $T_0 = 290$ K. Raw images.*

The structure of the strange wave is visible in Fig. 7. It is very similar to that observed by Yanez and Kuznetsov (2016), except that in our case it propagates at a speed $\sim$ 29% higher ($\sim$ 1800 m/s). As mentioned above, it is composed of a flat shock with a very wrinkled funnel-shaped flame surface responsible for sustaining the very high burning rates observed. The 2-DV shown in Fig. 8, reveals additional information. At 0 μs, the Bottom view and Side view exhibit very different shapes. From the side, a similar shape as that observed in the first configuration, with a planar shock ahead of a funnel-shaped flame, whereas from the bottom, only a planar shock is visible, just before the black spacer. Even though this flame-shock complex is supersonic with respect to reactants ahead, it is not the quasi-steady strange wave observed by Yanez and Kuznetsov (2016). The planar shock propagates around 1200 m/s and it is quickly caught up by the funnel-shaped flame. When they merge near the center, at 18 μs, the complex accelerates to $\sim$ 1500-1600 m/s and starts to flatten, sometimes staying curved in one corner until detonation onset. The Bottom view at 18 μs, is evidence of the convoluted three-dimensional structure that forms when both oblique flame-shock complexes merge.

3.1.3 Detonation onset

Transition to detonation systematically occurs following the strange wave structure described above. Figure 9 shows the results obtained using the 1-DV configuration. An ignition kernel develops at the bottom wall at $t = 0$ μs. The initially planar shock becomes curved, as the shock generated from the explosion travels towards the top wall, consuming the fresh shocked mixture present downstream of it. Finally, the frame at 3.2 μs, shows a quasi-planar shock of an incipient detonation. Run-up distances computed from the schlieren images (i.e. DDT location) lied between 38 - 67% of the total length of the channel (sample size: 14 tests). The high temporal resolution used allowed us to resolve the detonation onset in great detail (5 million fps).

Figure 10 shows the results obtained with 2-DV configuration, following the flattening of the complex described in Fig. 8, whose propagation speed is $\sim$ 2000 m/s, a strong explosion takes place. Note that to be consistent with the schematic in Fig. 3, the planes $x-y$ and $x-z$ were translated, and subsequently rotated over the $x-$axis; the DDT point is actually in the top left corner. Run-up distances lied between 42-47% of total length (sample size: 20 tests).

SV performed on the same section for 1-DV configuration (454-544 mm) include four different structures (Figures 4, 5, 7 and 9); fully developed detonations, as well as slower deflagrations were also observed but not included here. The 2-DV channel, on the other hand, provided repeatable results

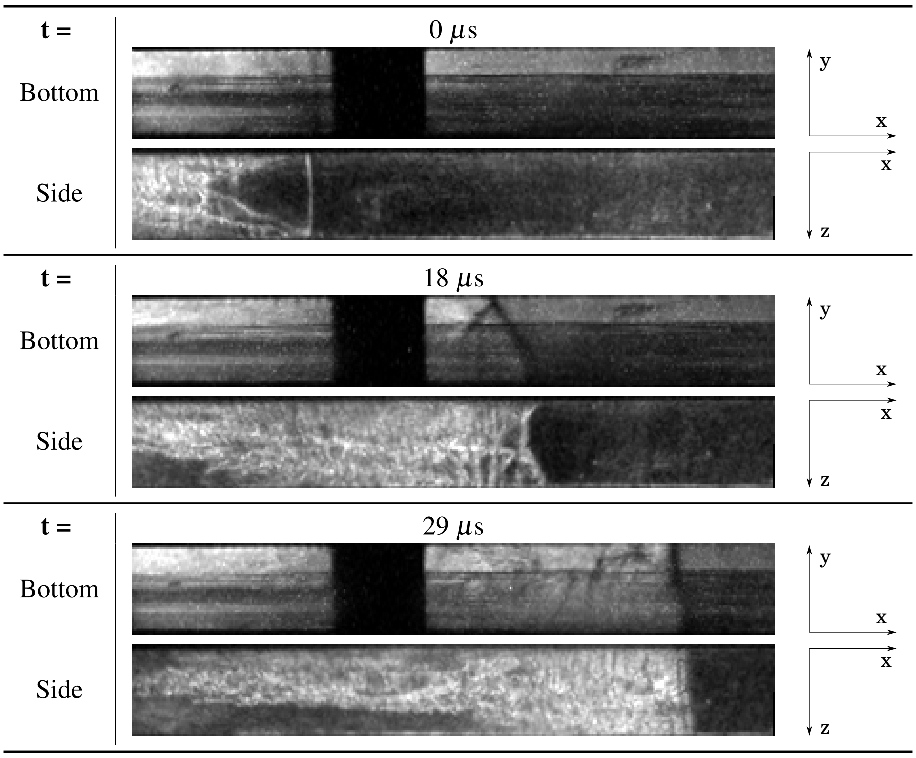

***Fig. 8**: Simultaneous 2-DV of the propagation of a complex flame-shock structure; section 352 to 423 mm from ignition; conditions: stoichiometric H_2-O_2 at $p_0 = 100$ kPa, and T_0 = 290 K. Raw images.*

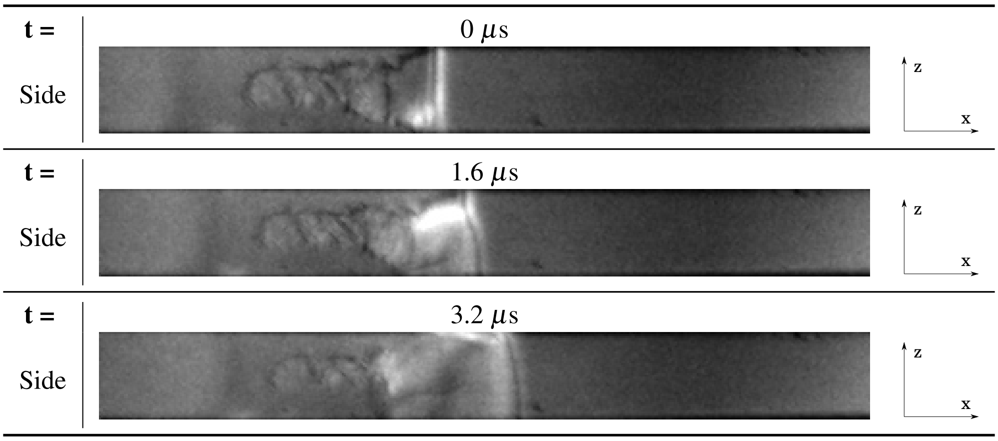

***Fig. 9**: 1-DV of transition to detonation; section: 454 to 544 mm from ignition; conditions: stoichiometric H_2-O_2 at $p_0 = 100$ kPa, and T_0 = 290 K. Raw images.*

for the same viewing window, and each figure shows different sections, as specified on the figures' captions. The discrepancies observed between 1-DV and 2-DV cases are due to manufacturing imperfections that were identified on the edges of the windows, and are currently being corrected. As a consequence, the available reactive volume is about 10% larger, as there are pockets of reactive mixture in small gaps outside the cross section that perturbs the boundary layer and corner flows. This shows the importance of geometry induced perturbations on the stochasticity of DDT; similar observations have been made for obstructed channels by Goodwin et al. (2016), Teodorczyk et al. (2009), Ren et al. (2017). Table 1 summarizes our results.

The extra information gathered from the 2-DV allows us to map the exact location of detonation onset (see Fig. 11). For 78 % of the cases ignition occurs within a corner, and always close to a wall, elucidating the crucial role played by viscous boundary layers and corner flows in detonation onset.

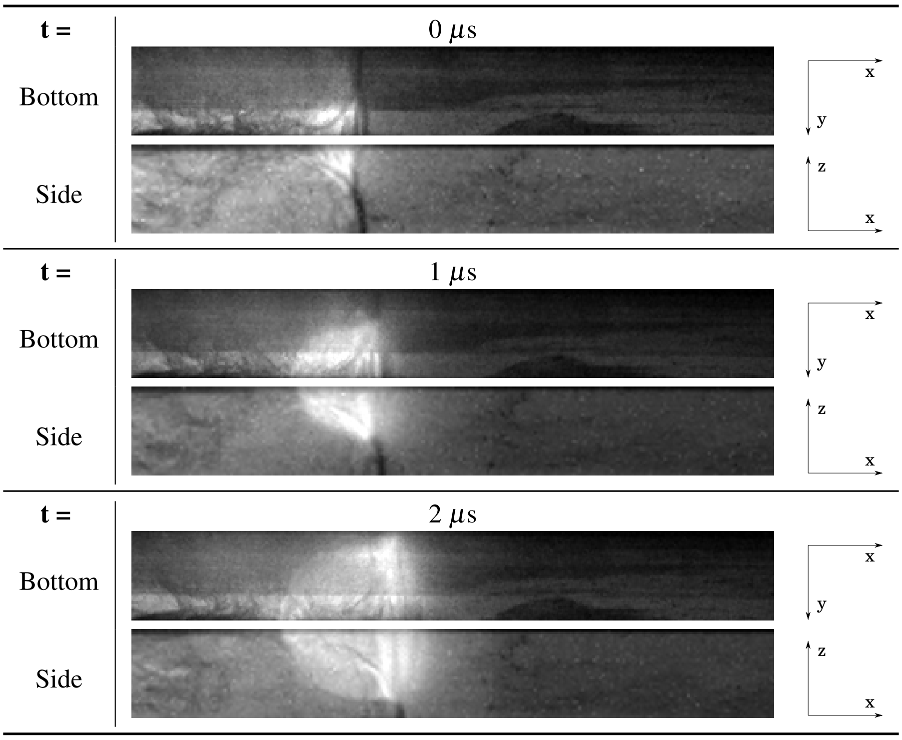

Fig. 10: *Simultaneous 2-DV of transition to detonation; section: 393 to 498 mm from ignition, rotated; conditions: stoichiometric H_2-O_2 at $p_0 = 100$ kPa, and $T_0 = 290$ K. Raw images*

Table 1: *Summary of results specifying number of occurrences and structures observed per visualization type. Total sample size: 56 tests.*

	1-DV	**2-DV**
Symmetric	4	0
Asymmetric	3	6
Funnel-shaped	5	4
DDT onset	14	20

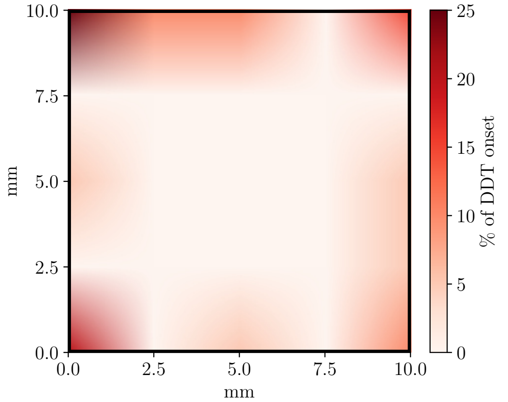

Fig. 11: *Spatial likelihood of detonation onset on the channel cross-section (looking from the ignition-end) in percentage (sample size: 20 tests). Conditions: stoichiometric H_2-O_2 at $p_0 = 100$ kPa, and $T_0 = 290$ K.*

Krivosheyev et al. (2019) built a similar map, for highly diluted acetylene-oxygen mixtures, using a different configuration (i.e. a closed, circular 6-m long tube, 60 mm in diameter). They also observed a high likelihood of DDT close to walls; bear in mind however, that the flow structures and boundary layers that develop behind precursor shocks differ significantly between square and circular cross-sections.

4 Conclusions

DDT experiments were conducted using two narrow channels to characterize the three-dimensional structure during detonation onset. One-direction and two-direction simultaneous schlieren visualization was used for that purpose.

The following structures were observed: (i) symmetric funnel-shaped flames; (ii) asymmetric shapes as a result of ignition within boundary layers upon their interactions with the accelerating flame and/or oblique shocks formed by propagating fronts near walls; (iii) quasi-steady propagation of symmetric flame-shock complexes (rather short-lived, for the 2-DV channel); and (iv) detonation onset near the channel's walls.

Notably, 2-DV allowed us to map the exact location of detonation onset on the channel's cross-section. The highly three-dimensional flows observed, shed light on the importance of understanding the complex structures that develop before DDT, as they may provide important clues regarding mitigation strategies (i.e. quenching of fast flames and suppression of DDT onset).

Future work will include enhancing the quality of the flow visualization, better control of the geometry, as well as the characterization of waves speeds (i.e. flames, shocks, etc.), as an attempt to better understand the role played by corner flows on DDT dynamics.

Acknowledgements

The authors gratefully acknowledge *l'École Doctorale SIMME*, and the contribution of the technical personnel at *l'Institut Pprime*.

References

Dziemińska, E., Hayashi, A. K. (2013). *Auto-ignition and ddt driven by shock wave–boundary layer interaction in oxyhydrogen mixture*. International Journal of Hydrogen Energy, 38(10):4185–4193.

Goodwin, G., Houim, R., Oran, E. (2016). *Effect of decreasing blockage ratio on DDT in small channels with obstacles*. Combustion and Flame, 173:16–26.

Khokhlov, A., Oran, E., Thomas, G. (1999). *Numerical simulation of deflagration-to-detonation transition: the role of shock–flame interactions in turbulent flames*. Combustion and Flame, 117(1-2):323–339.

Krivosheyev, P. N., Penyazkov, O. G., Sakalou, A. (2019). *High-speed imaging of DDT in a round tube*.

Masson-Delmotte, V., Zhai, P., Pörtner, H., Roberts, D., Skea, J., Shukla, P., Pirani, A., Moufouma-Okia, W., Péan, C., Pidcock, R., et al. (2018). *IPCC, 2018: Summary for policymakers*. Global Warming of 1.5° C Above Pre-industrial Levels and Related Global Greenhouse Gas Emission Pathways, in the Context of Strengthening the Global Response to the Threat of Climate Change, Sustainable Development, and Efforts to Eradicate Poverty.

Oran, E., Gamezo, V., Khokhlov, A. (2002). *Effects of boundary layers and wakes on shock-flame interactions and DDT*. In *40th AIAA Aerospace Sciences Meeting & Exhibit*, page 776.

Ren, K., Kotchourko, A., Lelyakin, A., Jordan, T. (2017). *Numerical reproduction of DDT in small scale channels*. In *2017 25th International Conference on Nuclear Engineering*. American Society of Mechanical Engineers Digital Collection.

Teodorczyk, A., Drobniak, P., Dabkowski, A. (2009). *Fast turbulent deflagration and DDT of hydrogen–air mixtures in small obstructed channel*. international journal of hydrogen energy, 34(14):5887–5893.

Thomas, G., Bambrey, R., Brown, C. (2001). *Experimental observations of flame acceleration and transition to detonation following shock-flame interaction*. Combustion Theory and Modelling, 5(4):573–594.

Yanez, J., Kuznetsov, M. (2016). *Experimental study and theoretical analysis of a 'strange wave'*. Combustion and Flame, 167:494–496.

Zhao, Y., Wang, C., Bi, Y. (2017). *LES of flame acceleration and DDT in small-scale channels*. Journal of Loss Prevention in the Process Industries, 49:745–752.

DOI: 10.7795/810.20200724

Explosibility Properties of Gases from Lithium-Ion Energy Storage Battery Thermal Runaways

Adam Barowy [a], Pravin Gandhi [a], Robert Zalosh [b] & Alexandra Klieger [a]

[a] UL LLC, Northbrook, USA
[b] Firexplo LLC, Wellesley, USA

E-mail: adam.barowy@ul.com

Abstract

Many lithium-ion batteries are susceptible to thermal runaways in which an internal or external fault in one cell induces uncontrolled self-heating to temperatures high enough to thermally decompose the cell materials and cause emission of flammable gases and vapors. Often, the thermal energy released by thermal runaway causes propagation to adjacent cells, thereby escalating the incident. In the case of energy-storage batteries, the gaseous thermal runaway products can accumulate within the battery enclosure, posing a gas explosion hazard.

UL 9540A, Test Method for Evaluating Thermal Runaway Fire Propagation in Battery Energy Storage Systems, has been developed to test the propensity of batteries to thermal runaways and to characterize both the fire and explosion threat associated with such runaways. The tests, which are typically initiated by flexible film heaters, are conducted on a cell level, on a module level, and larger. This paper describes the composition and explosibility properties of battery gases collected during that testing.

Closed vessel maximum explosion pressures measured for representative gas mixtures in a 5-liter test vessel show a maximum pressure of approximately 7 bar-g at a gas concentration of about 20% in air. Burning velocities measured in a 40 mm ID glass tube at room temperature using ASHRAE standard 34-2010 methodology typically have been approximately 40 cm/s. Explosion protection provisions should adjust this measured burning velocity for the battery enclosure temperatures anticipated during thermal runaway events.

Keywords: *batteries, gas explosions, explosibility, thermal runaways*

1. Introduction

Energy storage systems (ESS) are a necessary advancement to meet society's goals to implement renewable energy generation, reduce air emissions, and improve electrical grid resilience. Electrochemical ESS using lithium-ion (li-ion) cells are one approach popularly pursued because of excellent electrical performance characteristics and relatively low cost. However, li-ion batteries have demonstrated the potential for fires and explosions from the consumer product scale (Samsung, 2017) up to the grid energy storage scale (APS, 2019) through various public incidents.

DOI: 10.7795/810.20200724

1.1 *Energy storage system construction*

The primary function of ESS are to separate the generation and consumption of electrical energy. Therefore, the fundamental component is the electrochemical energy storage cell (energy storage mechanism). A block diagram from UL 9540 (Underwriters Laboratories Inc., 2016) shows the major components of the system, which include inverters and switchgear (input and output energy conversion), and battery management systems which may handle several processes such as charging/discharging, power conditions, input/output signalling, and environmental control. Faulty operation of equipment in this system can lead to internal or external faults that induce uncontrolled self-heating and thermal runaway in cells. The heat generated from these cells is often sufficient to induce cascading thermal runaway conditions within the energy storage system resulting in fires or explosions. UL 9540A, a standard for evaluating fire and explosion hazards of ESS, was developed to determine the thermal runaway propensity of ESS cells and to quantify the volume and constituents of gases released during thermal runaway at cell level (Underwriters Laboratories, Inc., 2019). Module (groups of electrically connected cells) level and unit (groups of modules) level tests are conducted to ascertain the extent of thermal runaway propagation within an ESS product and associated gas release volumes. A full set of data provides the anticipated release volume of an ESS in a propagating thermal runaway scenario and provides the properties of the gas: lower flammability limit, maximum closed vessel deflagration pressure, and burning velocity.

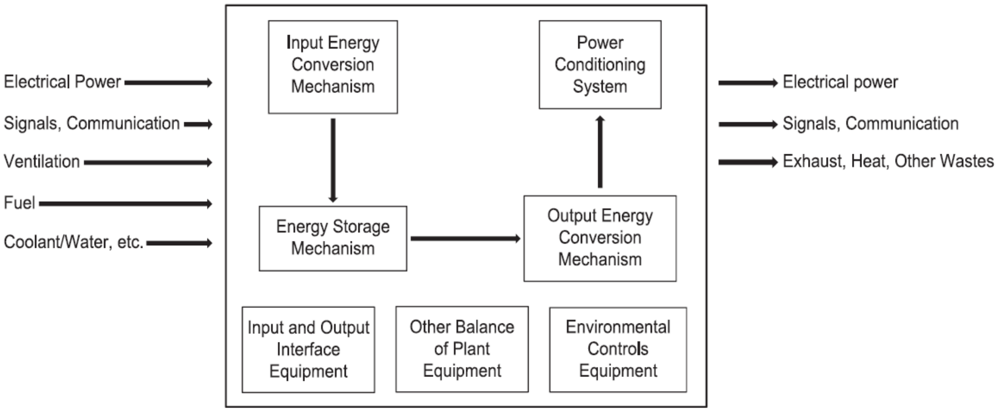

Figure 1. *Block Diagram of Electrical Energy Storage System.*

Three physical formats of li-ion cells are manufactured, and all three may be utilized in ESS: cylindrical, prismatic, and pouch formats. In all formats, the cells are comprised of anode, cathode, separators and electrolyte materials. The outer enclosure and geometry define a cell's physical format. Li-ion cells used in ESS weigh from tens of grams up to several kilograms. Figure 2 provides basic examples, though the physical dimensions of cells vary widely and increase with cell electrical capacity. Cells often include a safety vent intended to relieve internal vapor pressure.

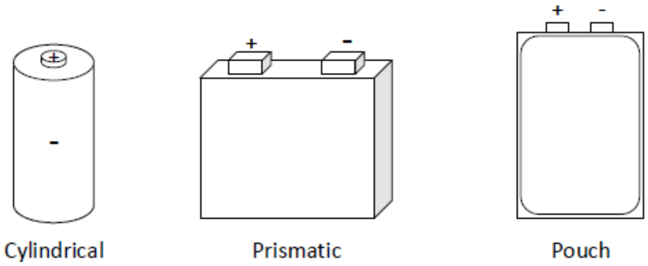

***Figure 2**. Li-ion cell physical formats.*

Energy storage specific li-ion cells tend to be physically larger than consumer cells because their size is not limited by the need to fit within consumer product enclosures, though there are manufacturers who do develop energy storage systems (ESS) from cells used in consumer products. The five material components of a common li-ion cell consist of a cathode material, an anode material, a separator material between the two electrodes, an electrolyte, and an outer case.

To manufacture a cell, cathode, separator, and anode materials are either wound together simultaneously or are assembled in a stack of alternating layers (Schröder et al., 2017). This “winding” or “jellyroll” is inserted into a case manufactured from aluminium or steel, or into metallicized polymer pouch, depending on the cell format. In order to enable winding or stacking, cathode and anode materials are coated onto substrates of aluminium and copper foil, respectively (Warner, 2015). Electrolytes are injected into any of these formats at the conclusion of assembly (Schröder et al., 2017).

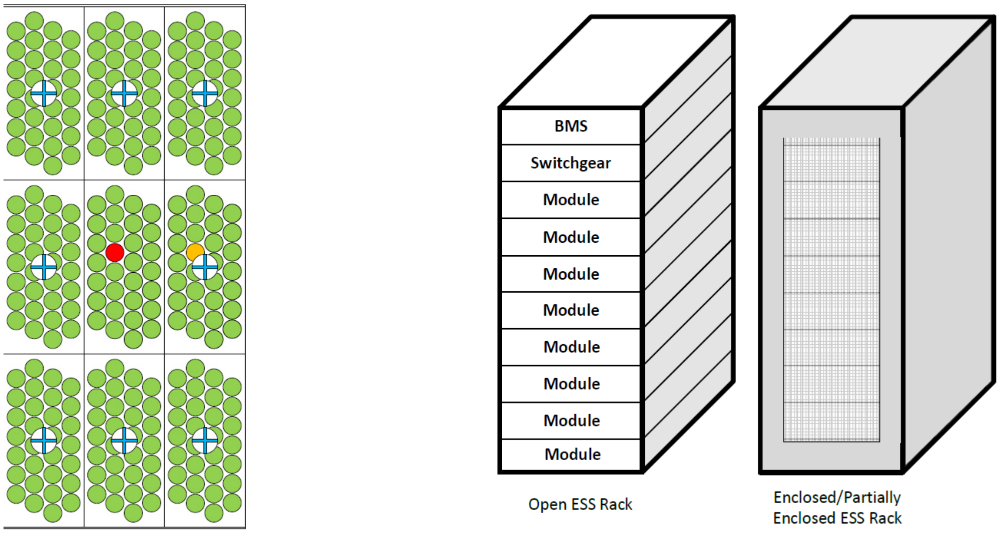

(a) (b)

***Figure 3.** a) Cells enclosed within a module housing, b) open and enclosed ESS units.*

Cells are electrically interconnected in series and parallel from several cells to thousands of cells to achieve increases in voltage and output current. A manufactured group of cells that are housed within an enclosure that typically includes hardware (e.g., fuses) and software (e.g., battery management) electrical safety features is referred to as a module. Modules contain tens to hundreds of kilograms of cells and may or may not have thermal runaway propagation mitigating features. Figure 3 (a) shows a schematic of a module with cylindrical cells designed by UL to demonstrate the potential for cell-to-cell propagation of thermal runaway, off-gassing and flaming behaviour of li-ion modules.

Complete residential ESS typically do not exceed the module scale and may include all ancillary equipment within a single housing. In commercial and industrial applications, modules are typically installed within racking physically similar to data systems and telecommunications equipment. Bus bars connect modules, to meet voltage and current design objectives. Bus bar voltage ranges from hundreds of volts DC to more than 1000 VDC. Complete racks are defined as “units” and may be unenclosed or have enclosures that aid in meeting thermal management, electrical and mechanical safety, and visual appearance objectives. Units typically weigh from tens to thousands of kilograms. Rack arrangements are shown in Figure 3 (b).

An ESS installation can consist of a single unit, especially in residences, and may be installed indoors or outdoors. Commercial and industrial installations can scale from single to hundreds of ESS units. It is common for ESS units to be installed in an intermodal shipping container which contains ancillary ESS equipment and a complete fire protection system (e.g., detection, alarm, and extinguishing systems), which enables manufacturers/installers to perform some pre-assembly before shipping. Similarly, custom large weatherproof enclosures are built to house one more ESS units. Dedicated ESS buildings constructed on-site are similar in layout to intermodal containers. Figure 4 shows the basic layout of ESS equipment commonly found at installations.

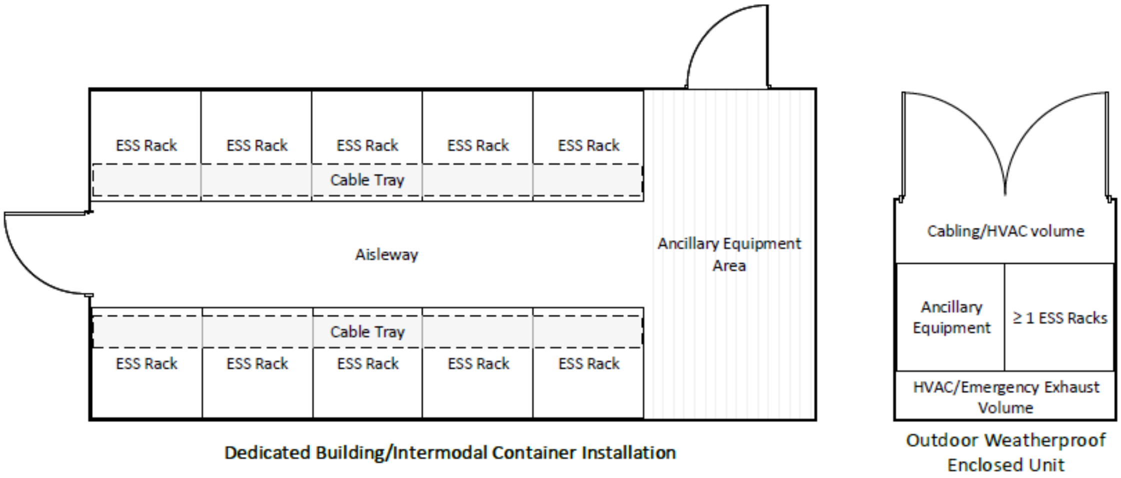

Figure 4. *Examples of outdoor ESS installations.*

The layout of ESS units in installations is like the layout of data and telecommunications equipment racking. The installation volume may be orders of magnitude larger than outdoor ESS enclosures. Indoor ESS installations are not common in North America, as codes and standards currently require indoor equipment configurations to be first tested to develop fire and explosion safety performance data using UL 9540A before an Authority Having Jurisdiction (AHJ) approves a specific installation (NFPA 855, 2019; International Code Council, 2018; Underwriters Laboratories, Inc., 2019).

1.2 *Phenomenological description of li-ion cell thermal runaway and cell materials*

The basic design of a li-ion cell is unique in terms of fire and explosion hazards in that a single product can possess all of the elements necessary to initiate and sustain the process of combustion: fuel, heat, and some of the oxygen needed for partial oxidation of combustible cell materials. Thermal runaway occurs when a li-ion cell increases its own temperature through self-heating, uncontrollably, until the rate of heat generation exceeds the rate of heat dissipation. The thermal runaway process often initiates in response to an abuse mechanism that destabilizes electrical and chemical potential energy stored by the cell. Abuse mechanisms can be thermal (e.g., external heat exposure), mechanical (e.g., crushing, penetration), electrical (e.g., external short circuit, overcharge, over discharge), or internal short circuits (e.g., formation of internal growths that compromise the separator, manufacturing defects, and contamination).

Electrical potential energy is released as part of thermal runaway when a loss of separator integrity results in an internal short circuit and Joule heating. The contribution of electrical potential energy to thermal runaway severity and heat release rate has been documented by Golubkov, et al., (2015), Said, et al. (2018), and others.

Chemical potential energy is released as part of thermal runaway when cell materials are sufficiently heated to initiate exothermic decomposition reactions, which lead to further heating and additional exothermic decomposition reactions. Feng, et al. (2018) identified six reactions that occur during a thermal runaway process. All but the separator melting are exothermic reactions. Although some reactions occur in parallel, the following order is given:

1. Decomposition of the solid-electrolyte interphase, which can happen as low as 57 °C.
2. Melting of the separator.
3. Further decomposition and regeneration of the solid-electrolyte interphase.
4. Cathode decomposition.
5. Electrolyte decomposition.
6. Decomposition of the graphite/carbon anode with electrolyte.

In terms of materials, li-ion cells used in commercial and residential energy storage applications are effectively the same as those used consumer products (Warner, 2015). Common cathode materials are: Lithium Cobalt Oxide (LCO), Lithium Iron Phosphate (LFP), Lithium Manganese Oxide (LMO), Lithium Nickel Cobalt Aluminum Oxide (NCA), Lithium Nickel Manganese Cobalt Oxide (NMC), and Lithium Titanate (LTO). Anodes typically consist of graphitic carbons, although newer anode materials now include lithium alloyed metals. (Mekonnen et al., 2016; Nitta et al., 2015; Doughty et al., 2012; Warner, 2015). Within the first few charge cycles, a coating referred to as the solid-electrolyte interphase forms on the anode surface by reactions with the electrolyte. Separator materials are made from polyethylene, polypropylene and ceramicpolyolefin composite membranes (Orendorff, 2012; Baldwin, 2009; Yang et al., 2012; Zhang et al., 2016). The thickness is typically on the order of 25 µm but may be less.

Electrolytes can be aqueous, non-aqueous, ionic liquids (salts with low boiling points), gel and solid polymers, or hybrid electrolytes. Most electrolytes used in commercial cells are non-aqueous and consist of a solution of dissociated lithium salt ($LiPF_6$) in hydrocarbon solvents (Doughty et al., 2012; Mekonnen et al., 2016). The hydrocarbon solvents are typically mixtures of ethylene carbonate, dimethyl carbonate, propylene carbonate, diethyl carbonate, and ethyl methyl carbonate (Li, et al., 2016; Aurbach, et al., 2004).

Table 1, summarized from Somandepalli et al., shows an example of the material composition of an LCO cell by mass ratio (Somandepalli et al., 2014).

Table 1. *Materials used in a lithium cobalt oxide pouch cell.*

Chemical Compound	Molecular Formula	ΔH_c (kJ · g^{-1})	Mass %	Purpose
Lithium Cobalt Oxide	$LiCoO_2$	Inorganic	42.5	Cathode
Lithium-intercalated Graphite	LiC_6	Inorganic	34.9	Anode
Diethyl Carbonate	$C_5H_{10}O_3$	21.15	7.2	Electrolyte
Nylon 6	$(C_6H_{11}NO)_n$	28.74	2.2	Case material
Ethylene Carbonate	$C_3H_4O_3$	12.3	1.1	Electrolyte
Propylene Carbonate	$C_4H_6O_3$	15.53	0.9	Electrolyte
Polypropylene	$(C_3H_6)_n$	42.66	9.0	Separator
Dimethyl Carbonate	$C_3H_6O_3$	13.4	0.3	Electrolyte
Polyester Terephthalate	$(C_{10}H_8O_4)_n$	22	2.0	Case material

Table 1 demonstrates that material composition determines cell stability and the severity of thermal runaway. For example, the temperature of internal short circuit can be increased selecting a separator material with a higher transition temperature, which can prevent breaching and distortion. A polyethylene separator material has a transition temperature of 135 °C, whereas composite separators may have transition temperatures in excess of 220 °C (Orendorff, 2012). Cathode selection can affect thermal runaway severity. Less heat is released during thermal runaway with an LFP cathode than with an LCO cathode (Feng, et al., 2018).

Material composition also determines the off-gassing constituents once thermal runaway occurs. The thermal energy generation of thermal runaway results in dissociation and vaporization of nearly all cell materials, typically leaving only residual soot, metals used for the cell case, and anode and cathode substrates. The gaseous/vapor products of thermal runaway are often released through the safety vent. The safety vent may or may not prevent catastrophic rupture of the cell case during thermal runaway. With higher energy density cell chemistries, cell material surface temperatures achieved during thermal runaway can ignite the mixture, but off-gassing can occur entirely without flaming, especially when thermal runaway occurs in confined volume such as in a module, unit or in a battery room/outdoor container.

1.3 *Thermal runaway vent gas composition and release volume*

UL 9540A has standardized a methodology for determining the thermal runaway gas composition by applying an abuse mechanism to a cell contained in an 82 L nitrogen-inerted pressure vessel, shown in Figure 5. This approach was developed from that used by Somandepalli et al. (2014).

Figure 5. 82-Liter gas composition test apparatus at UL.

Application of thermal energy to the external cell surface by flexible film heater at 4 °C/min to 7 °C/min is one of the abuse mechanisms used, as the results of the thermal abuse provide data which quantifies the surface temperature at which the cell safety vent operates, and the surface temperature of the onset of thermal runaway.

The inert environment inside the test apparatus prevents combustion during thermal runaway off-gassing, and facilitates collection of unreacted thermal runaway gases[1]. The accumulated gases are identified and quantified by gas chromatography. Table 2 provides a typical makeup of thermal runaway off-gas composition for common li-ion chemistries. The gas composition results is used to develop the synthesis of thermal runaway gas for follow-on explosibility testing, described in section 2. The volume of gas released by a cell thermal runaway in the test apparatus, assumed to follow the ideal-gas law, is given by:

$$V = \frac{n_{BVG} R T_\infty}{P_\infty} \tag{1}$$

$$n_{BVG} = \frac{P_f V}{R T_f} - \frac{P_i V}{R T_i} \cdot \left(1 - \left[\frac{\varphi_{O2}}{100}\right]\right) \tag{2}$$

---

[1] excluding reaction of thermal runaway gas components with any cathode-bound oxygen.

Where:
V is gas volume in m^3, n_{BVG} is the number of moles of battery vent gas, R is the universal gas constant in J/mol·K , P is pressure in Pa, T is temperature in °K, ω_{O2} is the oxygen volume fraction in the test chamber prior to testing, and the subscripts "i", "f", and "∞" denote test apparatus initial, final and ambient conditions at Normal Temperature and Pressure (NTP), respectively.

UL 9540A standard requires testing of energy storage modules if a cell demonstrates thermal runaway and releases flammable gas. Propagation of thermal runaway in a module testing may result in a larger release of thermal runaway vent gas. Testing of energy storage units is necessary if module level testing demonstrates that module to module thermal runaway propagation is possible. Quantification of thermal runaway gas volume release at both module and unit level testing is achieved by collecting the offgas and totalizing the product of the exhaust flow rate and concentration measurements of CO, CO_2, total hydrocarbons, and hydrogen.

1.4 *Propagation of thermal runaway within ESS*

The thermal exposure imposed on adjacent cells by cells in thermal runaway is often enough to start the decomposition reactions described by Feng et. al., cause an ISC and induce a cascading event. **Figure 6** shows the time evolution for propagation of thermal runaway in a non-electrically interconnected array of twenty-five 18650 cylindrical li-ion cells. One cell in the bottom layer was heated with a flexible film heater until thermal runaway. Within 1.5 s, thermal runaway occurred in adjacent cells and the velocity of gas release was fast enough to cause jetting and flame lift-off. After 8.5 s thermal runaway propagated to all cells in the array. From 11.5 s until after 22 seconds, the surface temperatures of the cell array are at a high enough temperature to emit visible light. Within 65 s the array was exhausted of thermal runaway gases and residual combustible material. The gas composition obtained by testing one of the cells from Figure 6 with the 82-L gas composition test apparatus using the UL 9540A cell level test methodology is shown in Table 2. Values have been rounded to the nearest integer and correspond well with values tabulated by Baird et al. (2019).

Table 2.: *Representative gas composition from cell level thermal runaway tests*

Gas	Percent
Carbon Dioxide	36
Carbon Monoxide	22
Hydrocarbons	10
Hydrogen	32
Others	< 1%

Similar thermal runaway propagation speed and severity results for 18650 cells in air have been measured by (Said et al., 2019). Said et. al. showed that the intensity of cell to cell heat transfer in arrays can support thermal runaway propagation even without flaming in a nitrogen environment.

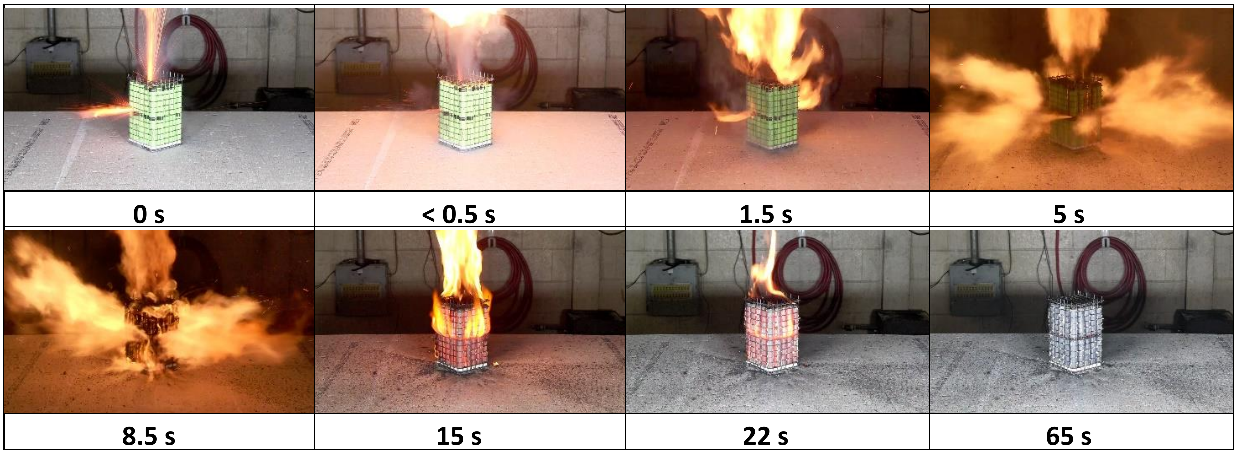

Figure 6. *Propagation of thermal runaway from one to 24 adjacent 18650 cells.*

The thermal energy generated by cell to cell thermal runaway propagation, as well as high momentum flaming combustion of thermal runaway can enable module to module thermal runaway propagation. Figure 7 shows a UL 9540A module level test demonstration conducted at UL based on the module design shown in Figure 3a. The module contained 27.2 kg of cells, with a capacity of approximately 3.2 kWh. The pressure generated within the module enclosure was high enough to vent flaming gases more than 1 m, as shown in Figure 7c.


(a) (b) (c)

Figure 7. *Demonstration of module (a) at t = 0 (b) during a 20-min period of off-gassing without flaming (c) immediately after ignition of thermal runaway gas.*

Figure 3b shows that typical rack configurations tend to have minimal air gaps between modules, which may not provide insulation enough to inhibit heat transfer and prevent propagation between adjacent modules in a unit. Propagation of thermal runaway is also possible between nearby units if spacing is not adequate to limit heat transfer from unit to unit, particularly considering the potential for jet flaming from modules in thermal runaway. Without sprinkler protection, FM Global recommends spacing units a minimum of 1.8 m – 2.7 m apart based on full-scale tests of LFP and NMC ESS units, respectively (Ditch, 2019).

1.5 *Development of an explosion hazard from accumulated battery gas*

Explosion hazards can develop where unburned thermal runaway vent gas accumulate in a confined volume. Figure 3 and Figure 4 show confined volumes defined by the module, unit and battery room enclosures. Therefore, deflagration hazards can occur at several different product levels. Figure 8 shows the volume flow rates measured during the UL 9540A module level test demonstration. Volume flow rates were determined by measuring gas concentrations within the ductwork of an oxygen consumption calorimeter that collected the gases released by the module. CO and CO_2 were measured by nondispersive infrared gas analysis and total hydrocarbons were measured using flame ionization detection. The module released a total of 1 m^3 of thermal runaway gas before flaming.

The demonstration also showed that the module enclosure forced under-ventilated conditions in which the gases were released without flaming. A release volume of 1 m^3 volume is adequate to create a mixture above the lower flammability limit (LFL) in volumes up to approximately 16 m^3, based upon a range of LFLs from 6.1 v% to 11.8 v% calculated for thermal runaway gas by Baird et al. (2019). The severity of the deflagration hazards are greater for smaller volumes, as the fuel concentration can reach a worse-case scenario near stoichiometric fuel-air conditions. The gas composition data of the cell are used to develop the deflagration parameters lower flammability limit (ASTM E-918), laminar burning velocity (ASHRAE 34), and P_{max} (EN 15967)

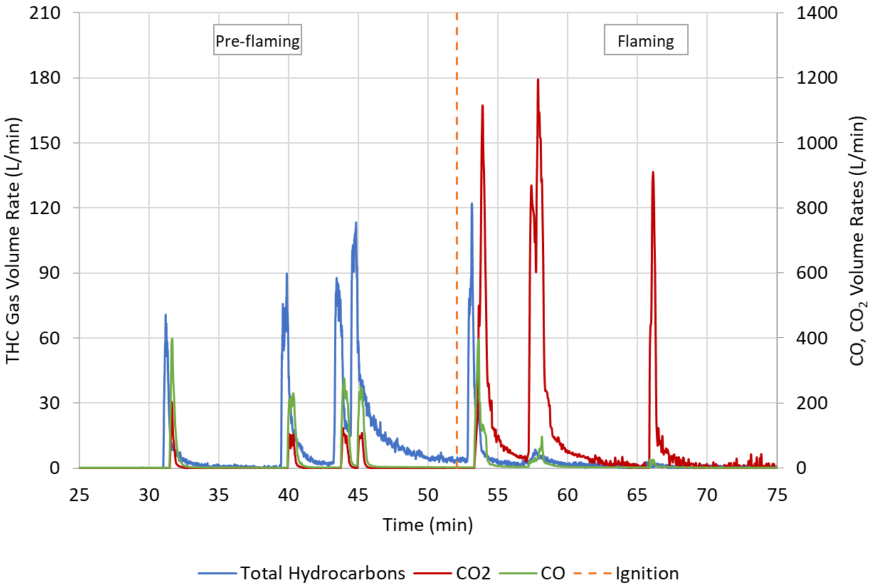

Figure 8. Volume flow rates of thermal runaway off gas.

2. Explosibility parameter values for thermal runaway gases

The gas explosibility parameters needed for explosion protection design depend on the protection method and associated design standard. The primary parameters for NFPA 68 (2018) explosion vent sizing are the gas mixture closed vessel deflagration pressure, P_{max}, the gas mixture laminar burning velocity, S_u, and the ratio of the gas mixture volume, V_{mix}, to the enclosure volume. The European normative standard for gas explosion venting, EN 14494 (2007), uses these parameters plus the gas mixture normalized rate-of-pressure rise, K_G.

In applying these explosion venting standards, the protection design is usually based on a worse-case, near-stoichiometric, gas mixture. Therefore, determinations of P_{max} and S_u require testing or calculations over a range of gas concentrations. UL 9540A testing requires determination of P_{max} and S_u over a range of fuel concentrations for the thermal runaway vent gas mixture measured at the cell level in the inerted environment.

An example of P_{max} test data obtained over a range of fuel concentrations is shown in Figure 9. Thermal runaway vent gases correspond to the mixture documented in Table 2. P_{max} data for the thermal runaway gases was obtained in a spherical 5 L test vessel using a 10-15 joule squib igniter. A P_{max} of 6.4 bar-g was measured at a fuel concentration of 29 vol%. Data from Somandepalli et al. (2014) obtained for thermal runaway vent gases from 7.7 Wh cells at 100% SOC are also shown. The Somandepalli et al. tests were conducted in a 20 L test vessel using a 250 J chemical igniter. The Somandepalli et al. data show a P_{max} of 7.0 bar-g at a fuel concentration of about 15 vol%. The slightly higher P_{max} for the smaller cell thermal runaway gases may be due to larger test vessel and more energetic igniter since the gas compositions were similar.

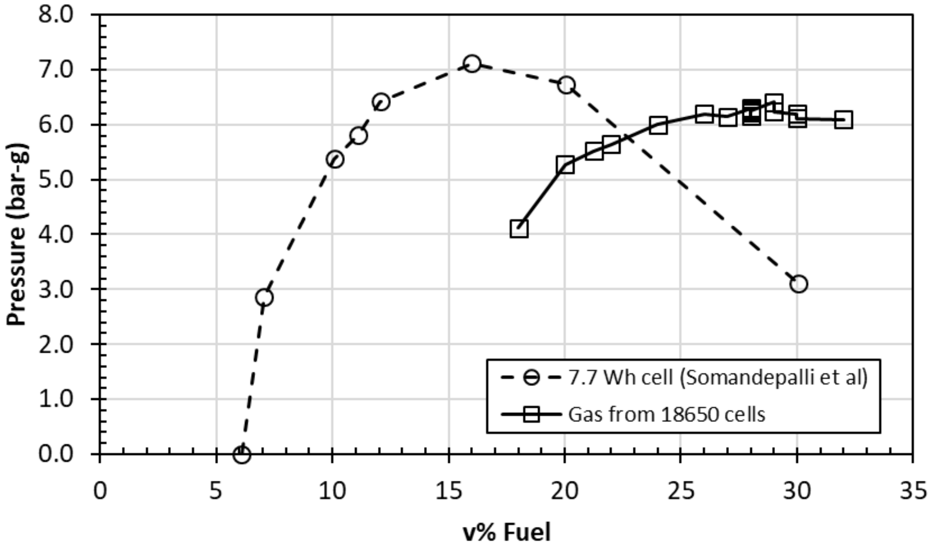

Figure 9. *Closed vessel pressure versus concentration for two different size cells.*

Gas mixture burning velocities for the UL 9540A thermal runaway gases were obtained by measuring flame propagation speeds and flame front surface areas in a 4-cm diameter, 150 cm long glass tube and adjusting the flame speed by the ratio of the flame base cross-sectional area to the flame surface area per Jabbour (2004). Data obtained for the same thermal runaway gases as used to obtain the Figure 9 data show a maximum burning velocity of roughly 35 cm/s at a fuel concentration of 26 v%, with burning velocities decreasing to about 20 cm/s at a concentration of 17 v% on the lean side and about 38 v% on the fuel rich side of the worst-case concentration. This data is not necessarily representative of results for other UL 9540A runaway gas samples, some of which have produced significantly higher burning velocities.

Johnsplass et al. (2017) have calculated burning velocities using measured thermal runaway gas compositions and widely used open-source software for chemical reactions and burning velocities. Their results for different lithium ion electrolytes show peak values of S_u in the range 35-50 cm/s at equivalence ratios of 1.1 to 1.2. The lower end of this range is about 10% higher than the peak S_u for the gas from Table 2, while the upper end of that range is roughly comparable to the higher values of S_u measured from gases produced in UL 9540A tests.

Since laminar burning velocities increase rapidly with increasing gas mixture temperature, the room-temperature measured values of S_u need to be adjusted upward for ESS explosion venting applications in which the thermal runaway produces elevated gas temperatures. Fernandes et al. (2018) have calculated values of S_u for gas compositions formed from vented Li-ion cell overcharge tests. They show the value of S_u for stoichiometric mixtures increasing from 30 cm/s to almost 110 cm/s as the gas mixture initial temperature increases from 300 K to 600 K.

Normalized rate-of-pressure rise, K_G, data are also obtained for the UL 9540A thermal runaway gases using the same test method as for P_{max} values. Data for the Table 2 gas mixtures resulted in a K_G of 84 bar-m/s at a fuel concentration of 29 v%. This is 29% greater than the K_G value measured by Somandepalli et al. of 65 bar-m/s for their tests with 100% SOC thermal runaway gases. However, the use of the 5-L and 20-L test vessels for this data may limit its applicability because of the well-known test-vessel large-volume flame acceleration effects mentioned by Somandepalli et al.

The gas mixture volume to be used for explosion venting applications can be either the entire ESS enclosure volume for worse-case scenarios, or a smaller volume for performance-based scenarios involving thermal runaway conditions represented by UL 9540A testing. In the latter case, calculations can be based on the volumes of the thermal runaway gases measured in module or larger scale UL 9540A testing. Usually, this would entail assuming the measured gas volumes from worse-case near-stoichiometric mixtures with enclosure air.

If NFPA 69 (2019) or another explosion prevention standard is to be used, the applicable explosibility parameters are either the gas mixture LFL to achieve prevention by combustible concentration reduction or the Limiting Oxygen Concentration (LOC) to achieve prevention by inerting. LFL data are obtained with gas samples from UL 9540A thermal runaway tests. An LFL value of 8.9 v% was obtained for the gas shown in Table 2, as determined using ASTM E918 with an electric arc ignition. Baird et al. (2020) report LFL values in the range 6.1% to 11.8% for gas compositions obtained from different cell chemistries and SOCs.

Thermal runaway gas LOC data are not routinely measured because they depend on the inert gas used and, so far, there have been few, if any, ESS inerting applications. Calculation methods to estimate fuel gas mixture LOC values from the gas composition and LOC values of the constituent gases are described by Britton et al. (2016) and summarized in Annex B of NFPA 69-2019.

Standardized tests, such as ASTM E2079, can be used to check estimated LOC values, particularly if there are uncertain temperature variations in ESS application scenarios.

3. Conclusions

Li-ion cells can present a unique fire and explosion hazard in that they can act as a fuel, oxidizer and ignition source. Gases that vent from lithium-ion cells have been shown to be flammable but may not always ignite, especially if housed with a product enclosure. Thermal runaway, with or without flaming, can create sufficiently intense heat transfer to propagate thermal runaway between cells, modules and units. While the cell thermal runaway data is used to develop the deflagration parameters (i.e., lower flammability limit, laminar burning velocity, P_{max}), consideration has to be given to product design that may allow accumulation of unburned thermal runaway gases in ESS rooms and containers. Total volume and volume release rates of thermal runaway gas must be quantified for designing explosion prevention and deflagration venting systems. This data is obtained from larger-scale module and unit level tests described in the UL 9540A standard.

References

ASTM E918 (2019) Standard Practice for Determining Limits of Flammability of Chemicals at Elevated Temperature and Pressure, ASTM.

ASTM E2079 (2013) Standard test methods for limiting oxygen(oxidant) concentration in gases and vapors, ASTM.APS, (2019) McMicken investigation continues, aps.com/en/About/Our-Company/Newsroom/Articles/Equipment-failure-at-McMicken-Battery-Facility.

Aurbach, D., Talyosef, Y., Markovsky, B., Markevich, E., Zinigrad, E., Asraf, L., Kim, H.-J. (2004). Design of electrolyte solutions for Li and Li-ion batteries: a review. *Electrochimica Acta*(50), 247-254.

Baird, A., Archibald, E., Marr, K., and Ezekoye, O. (2020) Explosion hazards from lithium-ion battery vent gas, J. Power Sources, v 446, 227257.

Baldwin, R. S. (2009). *A review of state-of-the-art separator materials for advanced lithium-based batteries for future aerospace missions.* Cleveland, Ohio: National Aeronautics and Space Administration.

Britton, L., et al. (2016) Limiting oxygen concentrations of gases, Process Safety Progress, v 35, pp 107-114.

Ditch, B. et al. (2019) Development of Sprinkler Protection Guidance for Lithium Ion Based Energy Storage Systems, FM Global.

Doughty, D., & Rother, E. P. (2012, Summer). A General Discussion of Li Ion Battery Safety. *Interface*, pp. 37-44.

EN 14494 (2007) Gas explosion venting protective systems, CEN.

EN 15967 (2011) Determination of maximum explosion pressure and the maximum rate of pressure rise of gases and vapours, CEN.

Feng, X., Ouyang, M., Liu, X., Lu, L., Xia, Y., & He, X. (2018). Thermal runaway mechanism of lithium ion battery for electric vehicles: A review. *Energy Storage Materials, 10*, 246-267.

Fernandes, Y., Bry, A., and de Persis, S. (2018) Identification and quantification of gases emitted during abuse tests by overcharge of a commercial Li-ion battery, J. of Power Sources, v 389, pp 106-119.

Golubkov, A., Scheikl, S., Planteau, R., Voitic, G., Wiltsche, H., Stangl, C., . Hacker, V. (2015). Thermal runaway of commercial 18650 Li-ion batteries with LFP and NCA cathodes – impact of state of charge and overcharge. *Royal Society of Chemistry - Advances*, 57171–57186.

International Code Council. (2018). *International Fire Code.* Falls Church, Va: International Code Council.

Jabbour, T. (2004) Flammable refrigerant classification based on the burning velocity, Doctoral Thesis, Ecole Des Mines De Paris.

Johnsplass, J. et al. (2017) Simulation of burning velocities in gases vented from thermal runaway lithium ion batteries, Proceedings of the 58th SIMS, DOI: 10.3384/ecp17138157.

Li, Q., Chen, J., Fan, L., Kong, X., & Lu, Y. (2016). Progress in electrolytes for rechargeable Li-based batteries and beyond. *Green Energy & Environment, 1*, 18-42.

Mekonnen, Y., Sundararajan, A., & Sarwat, A. (2016). A review of cathode and anode materials for lithium-ion batteries. *SoutheastCon 2016.* Norfolk, VA, USA.

NFPA 68 (2018) Standard for Explosion Protection by Deflagration Venting, National Fire Protection Association.

NFPA 69 (2019) Standard on Explosion Prevention Systems, National Fire Protection Association.

NFPA 855 (2019) Standard for the Installation of Stationary Energy Storage Systems, National Fire Protection Association.

Nitta, N., Wu, F., Tae Lee, J., & Yushin, G. (2015). Li-ion battery materials: present and future. *Materials Today, 18*(5), 252-264.

Orendorff, C. J. (2012, Summer). The Role of Separators in Lithium-Ion Cell Safety. *Interface*, pp. 61-65.

Said, A., et. Al., (2018). Simultaneous measurement of multiple thermal hazards associated with a failure of prismatic lithium ion battery. *Proceedings of the Combustion Institute*, 4173-4180.

Said, A., et. Al.,. (2019). Comprehensive analysis of dynamics and hazards associated with cascading failure in 18650 lithium ion cell arrays. *Applied Energy*, 415-428.

Samsung, Galaxy Note 7: What we discovered, January 23, 2017, https://news.samsung.com/global/infographic-galaxy-note7-what-we-discovered

Schröder, R., Aydemir, M., & Seliger, G. (2017). Comparatively assessing different shapes of lithium-ion battery cells. *Procedia Manufacturing*(8), 104-111.

Somandepalli, V., & Biteau, H. (2014). Cone Calorimetry as a Tool for Thermal Hazard Assessment of Li-Ion Cells. *SAE International Journal of Alternative Powertrains, 3*(2), 222-233.

Somandepalli, V., Marr, K,. and Horn, Q., Quantification of combustion hazards of thermal runaway failures in lithium-ion batteries, SAE Intl. J Alt. Power, v 3, pp 98-103.

Underwriters Laboratories Inc. (2016). *UL 9540: Standard for Energy Storage Systems and Equipment, 1st Edition.* Underwriters Laboratories Inc.

Underwriters Laboratories, Inc. (2019). *Test Method for Evaluating Thermal Runaway Fire Propagation in Battery Energy Storage Systems, 4th Edition.* Northbrook, IL: Underwriters Laboratories, Inc.

Warner, J. (2015). *The Handbook of Lithium-Ion Battery Pack Design.* Waltham, MA: Elsevier.

Yang, M., & Hou, J. (2012). Membranes in Lithium Ion Batteries. *Membranes, 2*, 367-383.

Zhang, X., et. Al.,. (2016, September 01). Li-ion Battery Separators, Mechanical Integrity and Failure Mechanisms Leading to Soft and Hard Internal Shorts. *Scientific Reports*.

DOI: 10.7795/810.20200724

Lithium-Ion Energy Storage Battery Explosion Incidents

Robert Zalosh [a], Pravinray Gandhi [b] & Adam Barowy [b]

[a] Firexplo LLC, Wellesley, USA
[b] UL LLC, Northbrook, USA

E-mail: bzalosh@firexplo.com

Abstract

Utility-scale lithium-ion energy storage batteries are being installed at an accelerating rate in many parts of the world. Some of these batteries have experienced troubling fires and explosions. There have been two types of explosions; flammable gas explosions due to gases generated in battery thermal runaways, and electrical arc explosions leading to structural failure of battery electrical enclosures. The thermal runaway gas explosion scenarios, which can be initiated by various electrical faults, can be either prompt ignitions soon after a large flammable gas mixture is formed, or delayed ignitions associated with late entry of air and/or loss of gaseous fire suppression agent. The electrical explosions have entailed inadequate electrical protection to prevent high energy arcs within electrical boxes vulnerable to arc induced high pressures and thermal loads. Estimates of both deflagration pressures and arc explosion pressures are described along with their incident implications.

Keywords: battery explosions, thermal runaways, arc flash, deflagration protection.

1. Introduction

According to the International Energy Agency (2020), worldwide energy storage system capacity nearly doubled from 2017 to 2018, to reach over 8 GWh. The total installed storage power in 2018 was about 1.7 GW. About 85% of the storage capacity is from lithium-ion batteries.

U.S. Energy Information Administration (2019) projections are that megawatt-scale battery capacity will approximately triple from 2018 to 2021. Based on current utility plans, EIA projects most of the additional capacity to come from increasingly large lithium-ion energy batteries. Many such installations are now in the range 2 MW to 20 MW, but several planned installations have capacities greater than 100 MW. A major reason for these expansions is that the cost for lithium-ion batteries lowered from approximately $1200 per kWh in 2010 to less than $200 per kWh in 2018 (Bloomberg, 2019).

Figure 1 shows a simplified layout of a utility-scale lithium-ion Energy Storage Battery (ESB) installation unit. Lithium-ion cells, which can be any one of the three different geometries shown in the diagram, are arranged in a module. These cells almost always have vents to prevent internal over-pressurization. Modules are equipped with electrical protection (fuses) and sensors for monitoring of voltages and (sometimes) temperatures, and either passive or active ventilation provisions.

Modules are placed and electrically interconnected in vertical racks as indicated in Figure 1. Each rack has a rack-level battery management system that communicates with the module sensors, and also has one or more DC connectors and fuses. A typical rack has a voltage of about 1000 VDC. The racks are installed in an enclosure, sometimes called a Battery Energy Storage Unit, equipped with system level Battery Management System (BMS) for electrical control, a Heating Ventilation Air Conditioning (HVAC) system, and a fire detection and suppression system.

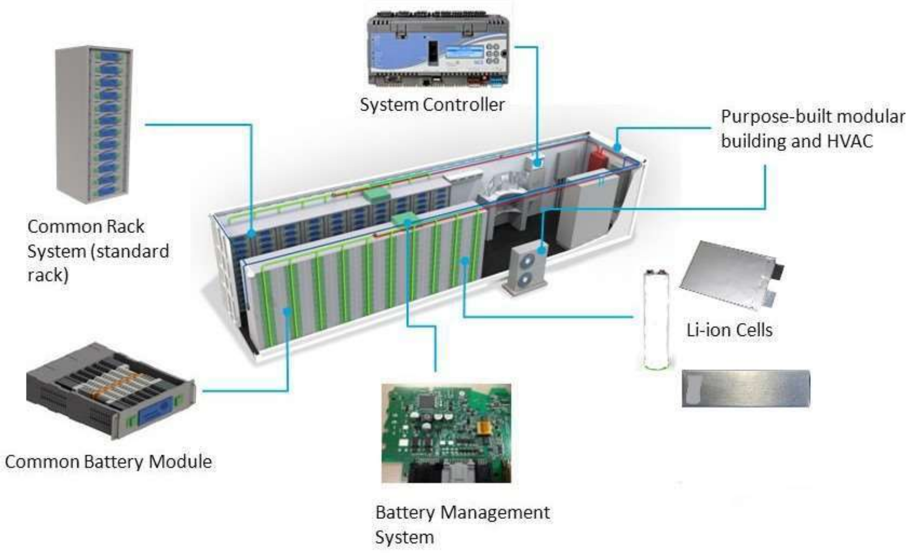

Figure 1. A simplified Battery Energy Storage Unit example.

Battery Energy Storage Units have doors for operating and maintenance personnel and for installation and replacement of equipment. A variety of Energy Storage Unit sizes have been used to accommodate the varying electrical energy and power capacities required for different applications. Several designs are variations or modifications of standard ISO freight containers, with nominal dimensions of 2.4 m x 2.4 m x 6 m, and 2.4 m x 2.4 m x 12 m. Other designs are up to 16 m in length.

Installations are being located in rural, urban, and suburban areas, often adjacent to a solar power or wind turbine generator for charging the battery. There are also many behind-the-meter installations in which the energy storage battery can be charged by the utility electricity grid and often has electrical controls to allow discharging through an inverter and utility interface back into the grid.

Unfortunately, there have been a large number of energy storage battery fires in the past few years. For example, in South Korea, which has by far the largest number of energy storage battery installations, there were 23 reported fires between August 2017 and December 2018 according to the Korea Joongang Daily (2019). A Korean government led investigation of these incidents found that one important cause of the fires was defective battery protection systems. The failure of these protection systems in some incidents caused components to explode. Other fires in South Korea and elsewhere have involved explosions from other causes, including a vulnerability of some batteries to operate at abnormally high temperatures under certain fault conditions (Yonhap News Agency, 2020).

The objectives of this paper are 1) to describe some generic scenarios of energy storage battery fire incidents involving explosions, 2) discuss explosion pressure calculations for one vented deflagration incident and some hypothesized electrical arc explosions, and 3) to describe some important new equipment and installation standards and regulations intended to prevent energy storage battery explosions.

2. Thermal Runaway Gas Explosion Incidents

Various recent papers, for example Guo et al (2018) and Li et al (2019), describe how any one of several fault conditions, including electrical faults, overcharging, and particulate/moisture contamination, can lead to an escalated temperature in one lithium-ion cell, causing deterioration and eventual failure of the cell separator, with subsequent electrolyte decomposition and elevated vapor pressure. This leads to a thermochemical runaway venting in the cell that can then propagate to many other cells in an energy storage battery module. The vented thermal runaway causes flammable gas to be emitted into the battery enclosure, where the resulting flammable mixture can be ignited by hot module casings, electrical connectors, or ejected sparks from the involved module. This generic explosion hazard has been discussed previously by Marr et al (2013) and Baird et al (2020), among others.

Two or three different runaway gas explosion hazard scenarios can occur. In one scenario, the flammable gas mixture is ignited soon after it is formed near the initiating module, such that there is only a minor deflagration and a subsequent fire. In the second scenario, batteries in thermal runaway release flammable gases without igniting initially, and a delayed explosion associated with the accumulation of additional flammable atmosphere then occurs. Another variation of the delayed explosion incident described below involves an initial fire with accumulation of incomplete combustion products and possibly fire suppression agent, until something happens, e.g. oxygen addition to the rich gas mixture, to suddenly render the mixture ignitable.

2.1 Prompt explosion incidents

One particular Korean energy storage battery incident in which a prompt thermal runaway occurred was investigated and described by Kim et al [2019]. The battery portion of the 1.0 MWh Energy Storage System (ESS) consisted of 15 racks, each containing nine modules, which in turn contained 22 lithium ion 94 Ah, 3.7 V cells. A 250 kW Power Conversion System (PCS) was connected to the battery through a Battery Control Panel. Electrical protection included module fuses and rack fuses.

The initiating event in this incident was a series of PCS faults. As indicated in Figure 2, the faults occurred shortly after the battery was fully (95%) charged and began to discharge. However, the PCS faults produced a current reversal and forced battery charging, with a thermal runaway when the battery was at a 90.8% State of Charge (SOC).

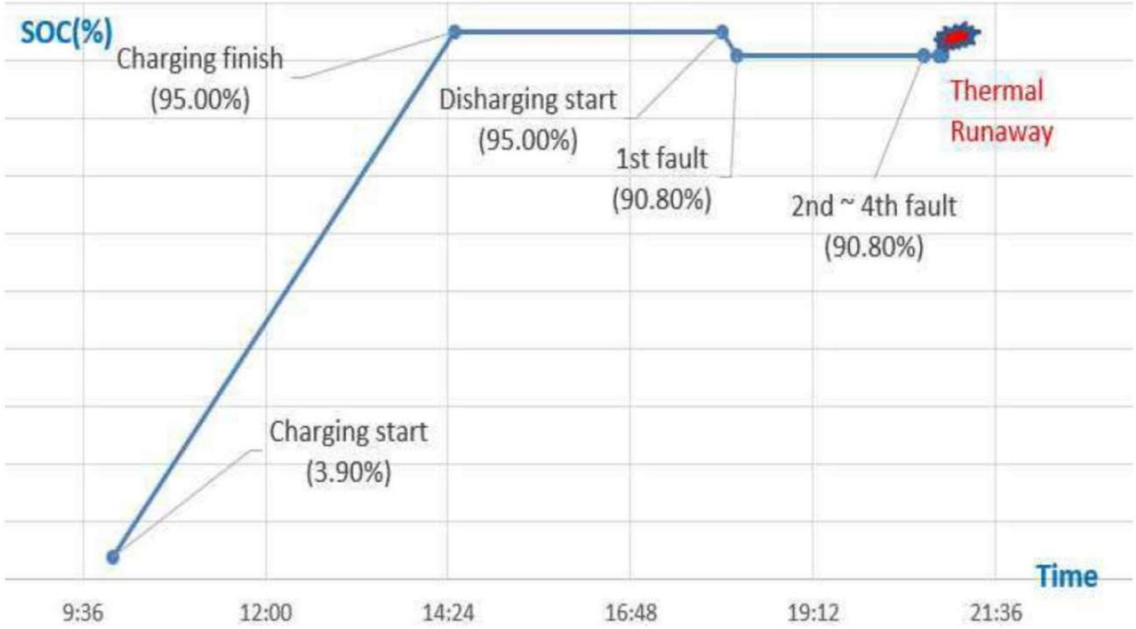

Figure 2. Battery state of charge preceding thermal runaway (from Kim et al, 2019)

The electrical faults in this incident caused a cell voltage imbalance and ground fault in one of the battery modules. Data records indicate the cell voltage imbalance rose to 3 V, whereas the battery manufacturer recommends the system be tripped when voltage imbalance exceeds 0.10 V. The corresponding recorded cell temperature rise was at least 64 ^{o}C, producing a cell temperature in excess of the 80 ^{o}C threshold for the onset of cell membrane deterioration and exothermic decomposition reactions (Guo et al, 2018). The absence of any battery data after the onset of thermal runaway suggests that the flammable electrolyte decomposition gases were ignited soon after thermal runaway in at least one module.

DOI: 10.7795/810.20200724

Recommended safety improvements in Korean ESS installations include Surge Protection Devices (Kim et al) and limitations on the charging rate and the maximum allowable State of Charge (Yonhap News, Feb 6, 2020).

In other battery ESS thermal runaway incidents, the flammable gases accumulated in the battery enclosure for a while because of inadequate enclosure ventilation. Ignitions eventually occurred producing varying levels of enclosure explosion damage.

2.2 Delayed explosion incident in Arizona

One delayed explosion battery ESS incident is particularly noteworthy because the severe firefighter injuries and unusual circumstances in this incident were widely reported (Renewable Energy World, 2019). This incident occurred at the Arizona Public Service (APS) McMicken Energy Storage facility in Surprise, Arizona, 28 miles northwest of Phoenix. As shown in Figure 3, the facility is adjacent to an APS substation. According to the APS posted updates (APS 2019), this is a 2 MW, 2MWh facility put into service in March 2017.

Figure 3. APS ESS in Surprise, Arizona

Figure 4 is a view into the APS ESS (after the incident) showing the racks and a module transporter in the aisle. Besides a HVAC system, the ESS was equipped with an automatic fire suppression system that was designed to discharge a gaseous suppression agent, probably FK-5-1-12 ($CF_3CF_2C(O)CF(CF_3)_2$), upon fire detection.

DOI: 10.7795/810.20200724

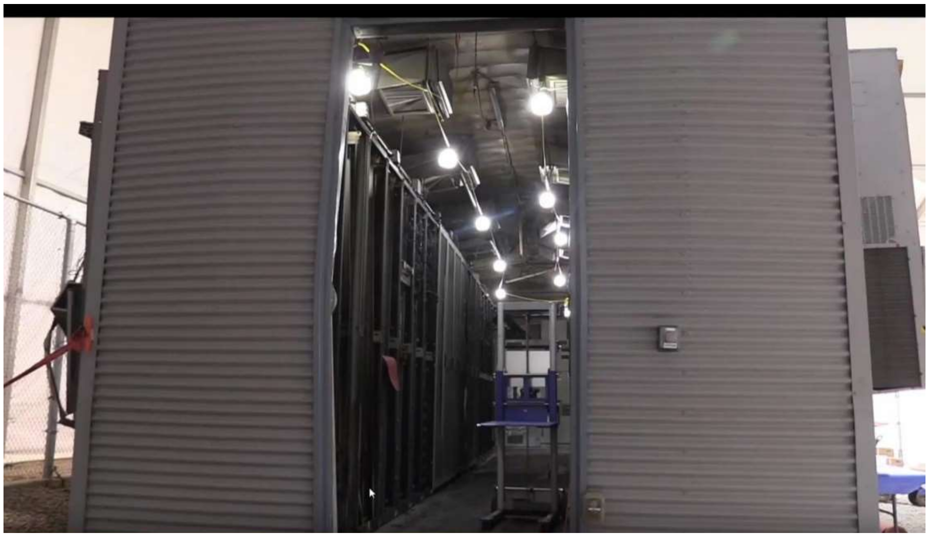

Figure 4. View into APS ESS after incident (APS, 2019).

On the afternoon of April 19, 2019, alarms triggered by the Battery Management System were received by battery monitoring personnel. At about 5 PM, smoke was seen by a passerby venting from the ESS (APS, 2019). The Surprise Fire Department was called and responded to the scene. Upon arrival, firefighters also observed a dense ground level white smoke or fog as can be seen in Figure 5.

Figure 5. Firefighters observing white smoke or fog around APS ESS in Surprise, AZ (Chief Ruiz)

The Surprise firefighters were concerned about possibility of hazardous materials inside and venting from the ESS and requested assistance from a four-man hazmat team at the nearby Peoria Fire Department. The four Peoria firefighters approached the still closed ESS structure with handheld gas detectors. The readings, including very high carbon monoxide levels, and telephone conversations with APS personnel caused them to pause for several hours before attempting entry into the ESS.

According to the Surprise Fire Department incident report, when the external gas concentration and temperature readings subsided, the firefighters did open the ESS door. Soon after the door was opened at about 8 PM, an explosion occurred! The blast wave pressures and velocities caused two firefighters to be blown approximately 23 m away from the door, passing under the chain link security fence shown in Figures 3 and 5. The emerging flames from the ESS produced severe burn injuries. All four Peoria firefighters were hospitalized, two with severe burn and trauma injuries, including facial and head injuries despite their wearing helmets and face shields. Four firefighters from the Surprise Fire Department experienced minor injuries.

Figure 6 shows the front of the APS ESS after the explosion. There is some bulging distortion of the wall and there is char above the open doorway. Pressure induced deformations of the ESS end wall and ceiling are also visible in Figure 4. A door on the end wall was blown off.

Figure 6. APS Surprise ESS after incident.

An incident investigation led by APS is still underway with occasional progress reports posted on an APS web page (APS, 2019). As of this writing, the following investigation results were posted in the most recent (November 2019) APS progress report.

- A single rack of modules was compromised by the initiating thermal event; the fire did not spread to surrounding racks.
- After the initiating event, the fire suppression agent was discharged.
- The compromised modules emitted a mixture of explosive gases, which built up in the container.
- The battery modules did not themselves explode; the gas mixture reached certain concentrations, came in contact with a thus far unidentified ignition source and subsequently exploded.

The APS updates so far have not provided an explanation for the source of the white smoke or fog seen emanating from the ESS during this incident, but there has been a lot of conjecture about this. A similar looking fog is often observed during the discharge of gaseous agent fire suppression systems. The fog induced by the gaseous agent discharge is usually due to atmospheric water vapor condensing because of the cooling effect of the gas expansion as it is discharged from the suppression system nozzles. In the APS ESS incident, the ESS atmosphere probably also contained condensable flammable vapors, such that the observed fog could be a combination of condensed flammable vapors and water droplets, possibly together with some FK-5-1-12.

The explosion analysis described below is not part of the APS investigation, nor has it been reviewed by the investigation team. The objective of this analysis is to develop an understanding of the flammable vapor mixture size and burning velocity that was ignited upon opening the door. The premise is that the ignition source had been present all along, but the concentration of FK-5-1-12 in the atmosphere had been sufficiently high to prevent re-ignition and provide some inerting. The FK-5-1-12 minimum design concentration for flammable liquid fires, per NFPA 2001 (2015) guidelines, is 5.9 %, with higher concentrations probably being needed depending on the electrolyte cup burner Minimum Extinguishing Concentration (MEC). FK-5-1-12 cup burner MECs measured by Ingram (2013) for several electrolytes ranged from 6.2% to 6.7%. Since the NFPA 2001 minimum design concentration is equal to the cup burner MEC multiplied by 1.3, it is quite possible that the FK-5-1-12 design concentration for the ABS ESS was about equal to or higher than the NFPA 2001 specified propane inerting concentration of 8.1%; thereby providing inerting to prevent re-ignition. When the APS ESU door was opened, a significant amount of FK-5-1-12 and other gases flowed out and probably were replaced with air to form a flammable mixture ignited by the still hot modules or by flame from a suddenly re-ignited fire in the rack.

Deflagration vent areas required to comply with NFPA 68-2018 have been calculated for the APS BSS enclosure using different combinations of laminar burning velocity, S_u, ratio of flammable mixture partial volume fraction, X_{pv}, i.e. ratio of flammable mixture volume to enclosure volume, and the reduced deflagration pressure, P_{red}. The NFPA 68-2018 vent sizing methodology includes adjustments for turbulence enhancement of the laminar burning velocity and partial volume effects. The calculated vent areas have been compared to the actual doorway opening (2 m^2), and also to an estimated vent area of 2.5 m^2 corresponding to the total vent area of the doorway together with partial ventilation openings. A second door was blown open at some time during the deflagration and provided some additional obstructed vent area that is difficult to estimate because of the door inertia. The normal ESS ventilation system is designed to be shut down prior to the discharge of the gaseous fire suppression agent, but there clearly was some leakage causing the emission of the observed fog before the door was opened.

Based on explosion testing with structures of similar size and construction (including ISO mobile containers), the observed damage in Figures 4 and 5 are estimated to be caused by an internal pressure in the range 0.10 bar to 0.17 bar. These P_{red} values together with various values of S_u and X_{pv} that result in a calculated required vent area of either 2 m^2 or 2.5 m^2 are shown in Table 1. The APS ESS enclosure dimensions used in these calculations are 2.1 m x 3.5 m x 6.1 m.

Table 1: NFPA 68 Parameters Resulting in Observed APS ESS A_v

P_{red} (bar)	S_u (m/s)	X_{pv}	Av (m^2)
0.10	0.20	0.17	2.00
0.10	0.25	0.063	2.00
0.10	0.20	0.5	2.51
0.10	0.25	0.122	2.49
0.14	0.20	0.36	2.01
0.14	0.31	0.046	2.00
0.14	0.28	0.063	2.00
0.14	0.22	0.19	2.00
0.14	0.31	0.075	2.50
0.17	0.20	0.60	2.00
0.17	0.22	0.31	2.00
0.17	0.22	1.0	2.49

Results in Table 1 show that NFPA 68 calculated areas are roughly equal to the actual enclosure vent area for a mixture burning velocity no greater than 0.22 m/s if most of the ESS enclosure was filled with a flammable gas mixture when the explosion occurred. A burning velocity of about 0.20 m/s has been calculated for methane-hydrogen mixtures with an equivalence ratio of about 0.60 providing the ratio of hydrogen-to-methane is less than about 0.60 (Sarli and Benedetto, 2007). It also is applicable to mixture equivalence ratios of 1.5 with hydrogen-to-methane ratios less than about 0.50. Similarly, a burning velocity of about 0.20 m/s has been calculated for vented runaway lithium ion battery gases at equivalence ratios of about 0.60 and about 1.6 to 1.8 (Johnsplass et al 2017).

If only a small fraction (less than 10%) of the enclosure had a flammable mixture at the time of the explosion, the mixture burning velocity may have been as large as 0.31 m/s, which is a representative burning velocity calculated (Johnsplass et al, 2017) for the flammable mixtures produced in lithium-ion cell runaways at equivalence ratios of about 0.7 and about 1.5 to 1.7. Since the flammable mixture was formed so soon after the door was opened, and areas away from doorway probably retained significantly higher concentrations of FK-5-1-12 so as to prevent flame propagation, it is more likely that X_{pv} is not much greater than 0.10. The results in Table 2 with values of $X_{pv} \leq 0.10$ suggest that the mixture burning velocity was in the range 0.25 to 0.31 m/s.

3. Thermal Runaway Explosion Prevention Measures

The lithium-ion energy storage battery thermal runaway issue has now been addressed in several recent standards and regulations. New Korean regulations are focusing on limiting charging to less than 90% SOC to prevent the type of thermal runaway conditions shown in Figure 2 and in more recent Korean battery fires (Yonhap News 2020). The new NFPA 855 standard for energy storage systems requires that “a listed device or other approved method shall be provided to preclude, detect, and minimize the impact of thermal runaway.” A footnote elaboration explains that the approved method can be a battery management system evaluated to UL 1973 or UL 9540.

Another NFPA 855 requirement for lithium-ion systems is for explosion control, specified to be either explosion prevention systems in accordance with NFPA 69 or deflagration venting in accordance with NFPA 68. There is an exception for systems that have had large-scale fire tests demonstrate “that flammable gas concentrations in the room, building, or walk-in unit cannot exceed 25 percent of the LFL in locations where the gas is likely to accumulate.” An NFPA 855 Annex paragraph explains that “a UL 9540A test or equivalent methodology should evaluate the fire characteristics of an ESS that undergoes thermal runaway, such as might occur due to a fault, physical damage, or exposure hazard. The data generated by the large-scale fire testing is intended to be used by manufacturers, system designers, and AHJs [Authorities Having Jurisdiction] to determine the fire and explosion protection required for an ESS installation.” Use of the UL 9540A tests for characterizing thermal runaway gas explosibility properties and release volumes is described in another paper by the authors for this symposium (Barowy, Gandhi, and Zalosh 2020).

A recent New York City (2019) Fire Department regulation for outdoor battery energy storage systems also requires thermal runaway fire testing evaluations and has two additional requirements for explosion mitigation that are analogous to the NFPA 855 requirements. It is also required that venting is positioned and oriented so that blast waves and any potential shrapnel are directed up and away from personnel. The new NYC regulation also requires a manually-operated purge system to exhaust smoke and gases by a switch installed at the fire department or utility connection. This requirement is intended to prevent firefighter injuries of the type that occurred in the APS Surprise AZ incident described above.

4. Arc Flash Explosion Incidents

Several lithium-ion battery energy storage system incidents involved electrical faults producing an arc flash explosion. The arc flash in these incidents occurred within some type of electrical enclosure that apparently could not withstand the thermal and pressure loads generated by the arc flash. One example of an electrical enclosure that is designed to withstand a limited/controlled arc flash is a DC contactor. Each rack in the ESS enclosure is usually equipped with at least one high-voltage DC contactor to make and break electrical connections to the rack modules. The Battery Management System also has a DC contactor for overall system charging and discharging current.

Figure 7 shows an example of a DC contactor design and operation. The stationary contact connectors at the top of the contactor are connected to the rack electrical circuit. The movable contact bridge position is dependent on the presence or absence of current in the contractor coil. When the contact bridge approaches or disengages from the stationary contact an electric arc is formed as shown in the diagram. Since the arc can transmit a lot of heat to the contacts, there is often a gas within the contactor housing to provide cooling. In some cases, as shown in this diagram, hydrogen is used. In other cases, nitrogen or sulfur hexafluoride is used in these contactors.

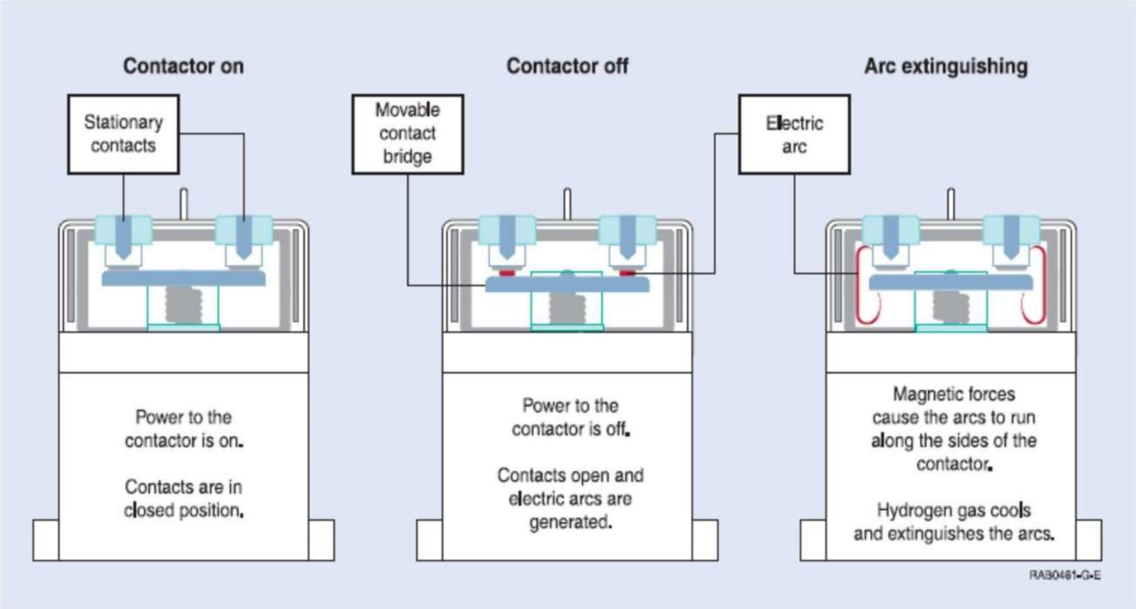

Figure 7. DC Contactor operating diagram (from www.epcos.com High-Voltage Contactors)

DC contactors are rated for their maximum operating voltage and nominal current load. They can also withstand temporary over-currents for a short period of time. Over-currents produce more energetic arcs upon opening and closing contacts, and these can challenge the strength and thermal resistance of the ceramic housing, which often has an epoxy resin sealant. Some of the Korean ESS fire incidents were reportedly attributed to catastrophic failure of DC contactors due to large electrical surges (associated with ground faults and short circuits) that fuses were not able to interrupt sufficiently fast to prevent excessive currents in the DC contactors.

The issue addressed in this section of the paper is the explosion pressures generated from energetic arcs within either a DC contactor or another electrical enclosure, such as a battery module or a rack protection enclosure (within which the DC contactors are situated). Chévrier et al (1993) have shown via Computational Fluid Dynamic modelling and experiments that the arc current causes joule heating and thermal radiation of the gas between the electrodes such that the ionized arc gas temperatures are approximately 15000 °K. A combination of expansion of the hot ionized gas and radiant heat absorption of the surrounding gas is responsible for the arc induced pressure rise in a contactor

DOI: 10.7795/810.20200724

enclosure. Chévrier et al measured and calculated a peak pressure of about 1 bar for an 8 kA arc of 9 ms duration in a thermal expansion circuit breaker.

Thoren (1962), using results reported by Hennecke and Horn (1960), derived a simple equation for estimating the peak pressure from a confined arc flash assuming half of the arc flash energy heats the air uniformly in the electrical enclosure. The equation is

$$P = \frac{2NUI_{arc}t_{arc}}{V} \tag{1}$$

where
P is the arc peak pressure in bar-g,
N is the number of arcs,
U is the voltage drop per arc in kilovolts,
I_{arc} is the arc current in kiloamps,
t_{arc} is the arc duration in seconds,
V is the enclosure volume in m^3.

Equation 1 was used by Crawford et al (1993) to calculate a pressure of 3.2 bar-g that would be generated from an 8.1 kA, 140 V, three cycle arc, in an 0.035 m^3 motor terminal box, similar to some that had experienced ruptures during several chemical plant incidents. They also estimated that the burst pressure of many motor terminal boxes is in the range 0.7 bar-g to 3 bar-g, and that the cover of one typical box would fracture at a pressure of 0.72 bar-g. Motor terminal boxes are sturdier than the electrical boxes used in energy storage systems, which would likely have lower fracture or rupture pressures.

Hoagland et al (2017) conducted arc flash tests in a 0.13 m^3 enclosure and found that their measured pressures agreed very well with pressures calculated using Equation 1. This implies that Equation 1 can also be used to estimate the arc flash pressures that can be produced in various hypothesized arcs in representative energy storage battery electrical enclosures. Table 2 shows the results of some such calculations for arc parameters that are characteristic of (albeit not directly attributable to any particular ESS) arc flash parameters specified by battery manufacturers for determining required thermal personnel protective equipment to be used by electrical service personnel working on or near circuits while the battery is near 100% SOC. The calculated pressures are conservatively high estimates for enclosures which have ventilation openings. Not shown in Table 2 are the much larger explosion pressures calculated for hypothesized arc faults in the much smaller DC contactors.

Table 2: Calculated Arc Flash Electrical Enclosure Pressures

Enclosure	V (m^3)	U (kV)	I_{arc} (kA)	t_{arc} (s)	P (bar-g)
Rack Encl. 1	0.037	0.9	2.5	0.025	3.1
Rack Encl. 2	0.036	1.1	6.5	0.021	8.4
Module 1	0.033	0.09	3.5	0.026	0.49
Module 2	0.034	0.8	0.38	0.050	0.90
Module 3	0.053	0.08	0.60	0.026	0.047

The calculated arc flash pressures for rack enclosures are an order-of-magnitude larger than those for module enclosures, and are higher than the enclosures can withstand. However, these enclosures usually are vented, which make actual arc pressures significantly lower than the values shown in Table 2. Another significant factor affecting the enclosure strength in an actual arc incident is the radiant heat transfer to the enclosure walls, thereby weakening them significantly. Therefore, it is likely that the structural integrities of both rack and module enclosures are compromised in energetic

DOI: 10.7795/810.20200724

arc explosions. This is probably why at least some of the fire incidents involved arc induced failures of electrical enclosures.

5. Conclusions

Several large-scale lithium-ion energy storage battery fire incidents have involved explosions. The large explosion incidents, in which battery system enclosures are damaged, are due to the deflagration of accumulated flammable gases generated during cell thermal runaways within one or more modules. Smaller explosions are often due to energetic arc flashes within modules or rack electrical protection enclosures. These smaller explosions can either initiate or exacerbate energy storage system fires.

Estimates of the vented deflagration pressure in one incident have been used, along with various assumptions of gas mixture volume and laminar burning velocity, to calculate NFPA 68 deflagration vent areas for the energy storage system enclosure. Comparisons of calculated and actual incident vent areas suggest that only a small fraction of the enclosure volume may have had a flammable mixture, with a laminar burning velocity in the range 0.25 to 0.31 m/s, at the time of the explosion. It is likely that the rest of the enclosure had a sufficient residual concentration of suppression agent gas to prevent more extensive flame propagation.

Recently issued standards and regulations for lithium-ion storage battery systems now explicitly require protection to prevent and/or control thermal runaways leading to possible deflagrations. Other recently imposed measures are intended to limit electrical fault energies in battery control units. By limiting the arc flash energy, these new measures may allow modules and other electrical enclosures to withstand otherwise excessive arc explosion pressures.

References

APS, (2019) McMicken investigation continues, aps.com/en/About/Our-Company/Newsroom/Articles/Equipment-failure-at-McMicken-Battery-Facility.

Baird, A., Archibald, E., Marr, K., and Ezekoye, O. (2020) Explosion hazards from lithium-ion battery vent gas, J. Power Sources, v 446, 227257.

Barowy, A., Gandhi, P., and Zalosh, R., (2020) Explosibility properties of gases from lithium-ion storage battery thermal runaways, for presentation at ISHPMIE 2020.

Bloomberg (2019) Battery Reality: There's Nothing Better Than Lithium-Ion Coming Soon, https://www.bloomberg.com/news/articles/2019-04-03/battery-reality-there-s-nothing-better-than-lithium-ion-coming-soon.

Chévrier, P., Barrault, M., and Flévet, C. (1996) Hydrodynamic model for electrical arc modelling, IEEE Trans. Power on Power Delivery, v 11, pp 1824-1829.

Crawford, K., Clark, D., and Doughty, R. (1993) Motor terminal box explosions due to faults, IEEE Trans. On Industry Applications, v 29, pp 72-81.

Di Sarli, V. and Di Benedetto, A. (2007) Laminar burning velocity of hydrogen-methane premixed flames, International Journal of Hydrogen Energy 32, pp 637-646.

Guo, D. et al, (2018) The causes of fire and explosion of lithium ion battery for Energy Storage, 2nd IEEE Conference on Energy Internet and Energy System Integration, ISBN-13: 978-1-5386-8549-5.

G. Hennecke and W. Horn, (1960) Pressure development and radiation in the case of arc short circuits in switchgears," Conti Elektro Berichte, vol. 6, no. 3, pp. 119-128.

Hoagland, E., Maurice, C., Haines, A., and Maurice, A. (2017) Arc flash pressure measurement by the physical method, effect of metal vapor on are blast, IEEE Trans. On Industry Applications, v 53, pp 1576-1582.

Ingram, J. (2013) Lithium-Ion Batteries: A Potential Fire Hazard, Power Magazine.

International Energy Agency (2020), Energy storage – Tracking Energy Integration – Analysis – IEA, https://www.iea.org/reports/tracking-energy-integration/energy-storage.

Johnsplass, J. et al (2017) Simulation of burning velocities in gases vented from thermal runaway lithium ion batteries, Proceedings of the 58th SIMS, DOI: 10.3384/ecp17138157.

Kim, H., Kim, S.H., and Song, H-Y. (2019) DC Ground fault induced fire accident in lithium ion battery ESS, Transactions Korean Institute of Electrical Engineers, v 68, pp 1470-1476.

Korea Joongang Daily, ESS units caught on fire due to bad management, June 12, 2019.

Li, W. et al (2019) Theoretical and experimental analysis of the lithium-ion thermal runaway process based on the internal combustion engine combustion theory, Energy Conversion and Management, v 185, pp 211-22.

Marr, K., Somendepalli, V., and Horn, Q. (2013) Explosion hazards due to failures of lithium-ion batteries, Proceedings AIChE Spring Meeting and 9th Global Congress on Process Safety.

NFPA 68 (2018) Explosion Prevention by Deflagration Venting, National Fire Protection Association.

NFPA 69 (2019) Standard on Explosion Prevention Systems, National Fire Protection Association.

NFPA 855 (2020) Standard for the Installation of Stationary Energy Storage Systems, National Fire Protection Association.

NFPA 2001 (2015) Standard on Clean Agent Fire Extinguishing Systems, National Fire Protection Association.

New York City Fire Department Rule 3 RCNY 608-01 (2019) Outdoor Energy Storage Systems, https://rules.cityofnewyork.us/tags/energy-storage.

Renewable Energy World (2019), APS battery energy storage facility explosion injures four firefighters; industry investigates, https://www.renewableenergyworld.com/2019/04/23/aps-battery-energy-storage-facility-explosion-injures-four-firefighters-industry-investigates/#gref.

Thoren, B. (1962) Arcs on power lines and in high voltage switchgear, Elteknik, vol. 139-143, pp. 139-143.

UL 1973 (2018) Standard for Batteries for Use in Stationary, Vehicle Auxiliary Power and Light Electric Rail (LER) Applications, Underwriters Laboratories Inc.

UL 9540 (2017) Standard for Energy Storage Systems and Equipment, Underwriters Laboratories Inc.

UL 9540A (2019) Standard for Test Method for Evaluating Thermal Runaway Fire Propagation in Battery Energy Storage Systems, Underwriters Laboratories Inc.

U.S. Energy Information Administration (July 2019) U.S. utility-scale battery storage power capacity to grow substantially by 2023, https://www.eia.gov/todayinenergy/detail.php?id=40072

Yonhap News Agency, Faulty batteries blamed for ESS fires: panel, February 13, 2020.

DOI: 10.7795/810.20200724

Li-ion batteries: characterization of the thermal runaway reactions using a DSC

Paola Russo *, Maria Luisa Mele

[a] Department of Chemical Engineering Materials Environment, Sapienza University of Rome, Rome, Italy

E-mail: paola.russo@uniroma1.it

Abstract

Lithium-ion batteries are widely used in many applications due to their formidable performance and characteristics. Numerous accidents involving lithium-ion batteries have occurred in recent years and this has led to focus on safety issues related to their extensive use. In this work the Panasonic's NCR18650 lithium-ion cylindrical cells were investigated by Differential Scanning Calorimetry. The aim is to identify and characterize the main reactions that occur at the anode under thermal abuse conditions and which can lead to thermal runaway. The kinetics of these reactions are assessed using the Kissinger and Ozawa methods. Furthermore, the results show the relationship between the initial state of charge of the cell and the progress of reactions.

Keywords: *Thermal runaway, lithium-ion batteries, kinetics, fire, explosion.*

1. Introduction

Lithium-ion batteries are now widely used in many applications, particularly in portable digital electronics-based equipment or in the automotive sector for electric vehicles (EVs) due to their high-power density, long cycle life and low self-discharge (Tarascon et al., 2001; Ping et al., 2014; Garche et al., 2019).

Despite these advantages, this technology shows some safety problems related to thermal stability, which have led to numerous accidents occurred in recent years, for example in the automotive sector or in the energy storage sector (Bandhauer et al., 2011). The presence of dangerous substances both for humans and the environment, such as flammable organic solvents, lithium heavy metal oxides, carbon and lithium salts makes these devices potentially dangerous. The fire hazard of lithium-ion batteries is related to their chemical composition and conditions of use. In fact, during normal operating conditions a failure can occur, which can lead to the ignition of a thermal runaway, an unstoppable chain reaction during which a series of uncontrolled exothermic reactions occurs (Wang et al., 2012).

In a lithium-ion cell the negative electrode is protected by a film called Solid Electrolyte Interface (SEI). This film protects the electrode from direct reaction with solvent (Garche et al., 2019), but it is metastable and can decompose exothermically at 90–130 °C. Therefore, when the temperature rises to 70–90 °C decomposition begins of the SEI. The cell then starts self-heating followed by the exothermic reaction between intercalated lithium and electrolyte, and the exothermic reaction between the fluorinated binder and the lithiated carbon at high temperature (Du Pasquier et al., 1998; Spotnitz at al., 2003; Wang et al., 2006; Chen et al., 2011; Forestier et al., 2016).

The active cathode material can also decompose exothermically with the generation of oxygen which can react with the electrolyte by oxidizing it (Spotnitz at al., 2003; Belharouak et al., 2006).

Therefore, it is necessary to evaluate the behaviour of lithium-ion batteries in abuse conditions that can help provide information for improving battery safety (Ruiz et al., 2018).

Furthermore, the development of a mathematical model to predict battery behavior in case of abuse requires knowledge of the mechanism of reactions that take place during the thermal runaway. On the other hand, it can help to reduce the number of tests to optimize the battery design.

Few studies have been carried out in the literature to evaluate the kinetic parameters of the main exothermic reactions that occur in batteries (Richard et al., 1999a, 1999b II), while others have determined the kinetic parameters of the decomposition reactions of negative and positive electrodes based on DSC tests (Wang et al., 2011), Geder, (2014), Yamaki et al., 2014; Chen et al., 2009).

In this framework this work is a preliminary study aimed at analyzing and characterizing the main reactions that occur at the anode during a thermal runaway. In particular, the mechanism of the SEI decomposition reaction (in the range 90-120 °C), which is the first step leading to a self-heating process, and of the reaction that occurs between the lithiated anode and the PVDF, which is the reaction that develops the greatest amount of heat. In addition, it is assessed how the state of charge of the batteries affects the reactions and their progress. For this purpose, the anode and cathode of the Panasonic’s NCR 18650 cells in different states of charge are analyzed using a DSC.

2. Experiments

2.1 Materials

Panasonic’s NCR18650 lithium-ion cylindrical cells (18 mm in diameter and 65 mm length) are tested. This type of cells is mostly used in the automotive sector. The active material for cathode is lithium-nickel-aluminum-cobalt oxide (NCA), while the anode is made of graphite. The binder is polyvinylidene fluoride (PVDF).

2.2 Charging procedure

Some cells are charged using a PS 8000 2U series power supply from Elektro-Automatik (EA) with a constant current of 12 A, imposing a maximum limit voltage of 4.2 V (accuracy <0.2%), which corresponds to a state of charge of the cell (SOC) equal to 100%. For other cells a maximum limit voltage of 3.7 V and 3.5 V has been set which corresponds to a SOC of 50% and 30%, respectively. SOC of 30% is the value at which lithium-ion cells are normally stored and transported.

2.3 Disassembly procedure

The cells are dismantled in a glovebox filled with argon and the collected materials are carefully sealed in sealed containers until the tests. To preserve the electrode system and not to upset it completely and to study the real system, the samples were tested including the current collector.

2.3 DSC tests

Hermetically sealed high pressure resistant stainless-steel pans are used to carry out the tests, in order to inhibit the leakage of the gaseous products formed during the test and avoid the danger of a catastrophic capsule breakage.

The mass of the samples is between 10-20 mg. The high-pressure capsules are crimped using a special sealing tool provided by the PerkinElmer, with fixed torque. All the tested samples are weighted before and after the experiment to test their effective hermetic closure.

DSC measurements are performed using Perkin Elmer DSC equipment (model 8500) in nitrogen flow (20 mL min^{-1}) at different heating rate of 5, 7, 10, 15 K min^{-1} in the temperature range 25-350 K.

3. Results and discussion

The mechanisms of some processes are often too complicated and isoconversional methods are often used to describe their kinetics. Alternatively, the non-isothermal isoconversional methods described by Kissinger (1956) and Ozawa (1970) are applied to evaluate the pre-exponential factor (A) and the activation energy (E_a) of exothermic reactions when the mechanism is unknown. These methods are based on the basic assumption that the reaction rate to a given conversion is only a function of temperature (Vyazovkin et al., 1998).

The equations can be derived from the integration of the basic kinetic equation taking into account that the tests are performed in a non-isothermal way, during which the samples are heated at a constant heating rate: $\beta = dT / dt$.

From the results of the DSC tests carried out varying the heating rates, the Kissinger's equation can be written as follows:

$$ln\left(\frac{\beta_i}{T_{p,i}^2}\right) = ln\left(\frac{A_x R}{E_{a,x}}\right) - \frac{E_{a,x}}{RT_{p,i}} \qquad i = 1, 2, 3, \dots, u \qquad 3.1$$

where β_i is the heating rate, $T_{p,i}$ is the peak temperature, and u stands for the different values of the heating rate.

A $ln\left(\frac{\beta_i}{T_{p,i}^2}\right)$ vs $\frac{1}{T_p}$ graph is then plotted, and the best-fit of experimental data is performed. The result is a straight line, the slope of which is the value of the activation energy $E_{a,x}$, while the pre-exponential factor A_x is obtained from the intercept.

In Ozawa method (Ozawa, 1970; Flynn et al. 1966, Flynn, 1983) the plot of $ln(\beta_i)$ vs $\frac{1}{T_p}$ gives a straight line, the slope of which is:

$$\ln(\beta) \cong -0.4567 \frac{E}{R} \frac{1}{T_p} \qquad 3.2$$

while the pre-exponential factor A_x is obtained from the intercept.

Fig. 1, 2 and 3 show the results of DSC, in terms of specific heat vs temperature, of the tests performed on anode of cells with different states of charge (i.e. 30%, 50% and 100% of SOC, respectively) and heating rates.

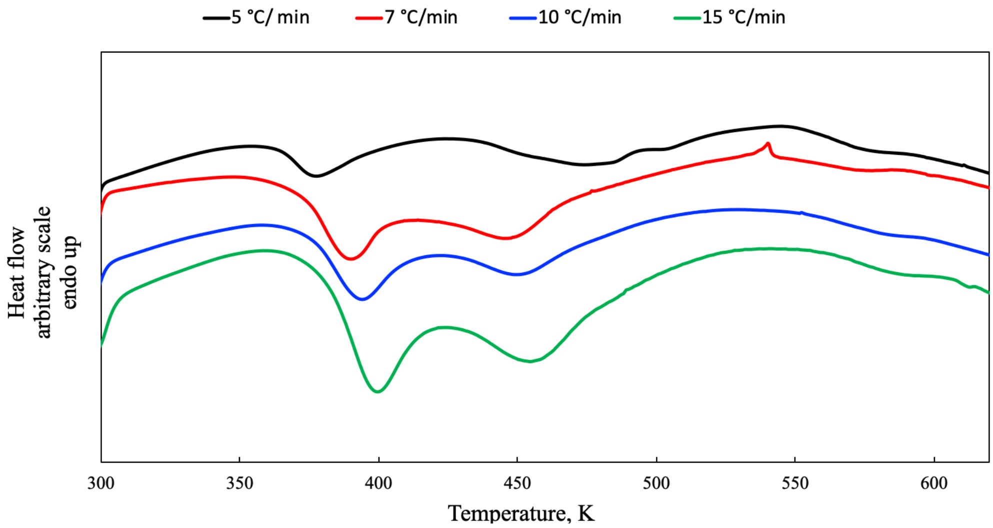

Fig. 1. *DSC curves at different heating rates of Panasonic NCR 18650 anode charged at 30% SOC*

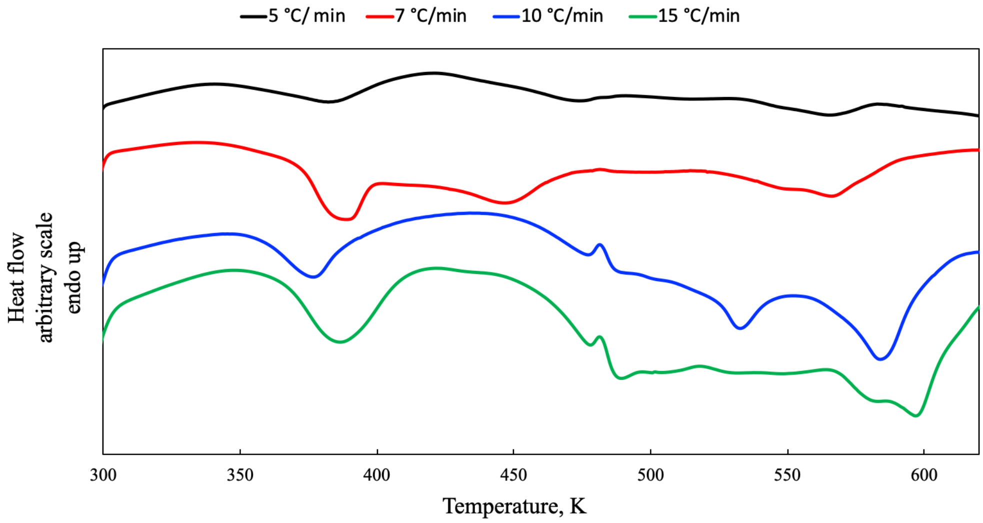

Fig. 2. *DSC curves at different heating rates of Panasonic NCR 18650 anode charged at 50% SOC*

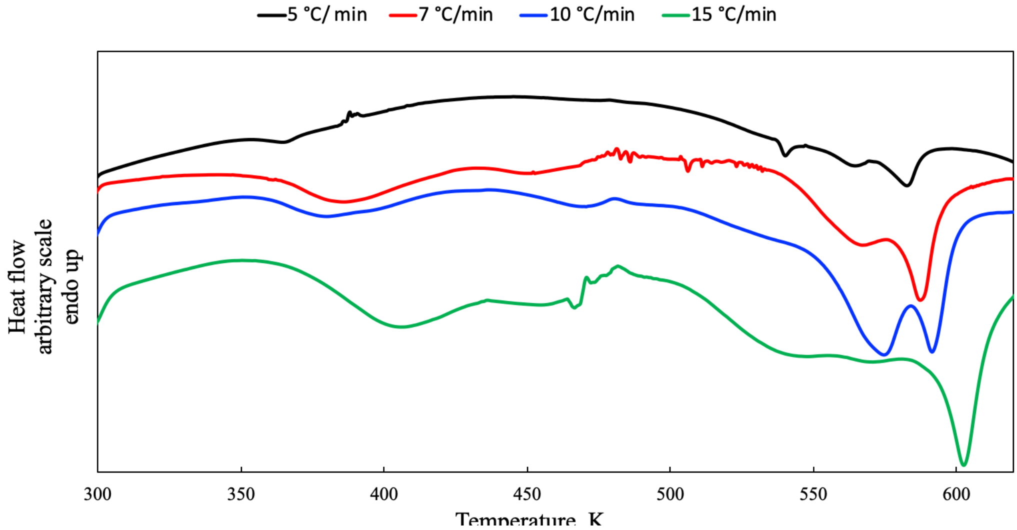

Fig. 3. *DSC curves at different heating rates of Panasonic NCR 18650 full charged*

It appears that during heating two main exothermic reactions occur: i) the decomposition reaction of the SEI layer (104 – 130 °C) and the exothermic reaction between the lithiated anode and the PVDF binder (292 – 329 °C) (Du Pasquier et al., 1998).

Table 1 reports the peak temperatures of these reactions for cells at different states of charge

***Table 1:** Peak temperatures of the exothermic reactions for cells at different states of charge*

Heating rate °C/min	**30% SOC**	**50%SOC**		**100 %SOC**		
	SEI decomposition	**SEI decomposition**	**Li_xC_6-PVDF**	**SEI decomposition**	**Li_xC_6-PVDF 1st peak**	**Li_xC_6-PVDF 2nd peak**
5	104.4 °C	108.9 °C	292.0 °C	92.2 °C	290.4°C	309.7 °C
7	115.7 °C	113.9 °C	294.2 °C	113.3 °C	290.8 °C	314.7 °C
10	120.3 °C	110.1 °C	311.3 °C	107.4 °C	300.5 °C	318.7 °C
15	125.5 °C	112.5 °C	324.8 °C	130.4 °C	/	329.5 °C

Standard uncertainty **u(T)** = ± 0.1 K.

From fig. 1-3 it is possible to note that the presence and extent of the reaction between the lithiated anode and the binder is closely related to the state of charge of the cell. In detail, the lower SOC cell does not show a peak related to this reaction (Fig.1), while the 50% SOC cell shows only a smaller peak (Fig.2) than the double peaks visible in the results of the fully charged cell (Fig.3). In general, the use of different heating rate causes the temperatures at which reactions occur to shift, in particular, higher heating rates cause the reactions to move to higher temperatures. This is evident in all the figures. Furthermore, if different reactions occur in the same temperature range, the heat flux results may overlap and the peaks may not be resolved (Gabbott, 2008). This is evident in Fig.3 for the experiment conducted at heating rate of 15 °C/min in which a single peak appears at 329.5°C compared to other heating rate where two peaks are distinguished (1st peak at 290.4-300.5 °C , 2nd peak at 309.7-329.5 °C). Instead, the lower peak at 290-300 °C at lower SOC may be attributed to a low quantity and to the unavailability of lithium in the anode at that temperature (Roth et al., 2004). In fact, lithium and PVDF are not close each other, so lithium must diffuse through the graphite to reach PVDF and react, hence, not all the lithium is available for reaction. The more the degree of lithiation increases, which means that the higher the state of charge, the greater the quantity of lithium available for the reaction (Spotnitz et al., 2003).

In addition, fig.2 shows a small endothermic peak at around 200°C, probably due to the melting of the $LiPF_6$ (Roth et al., 1999). Beside this peak, DSC traces of pure $LiPF_6$ reported in literature also shows a greater endothermic decomposition peak at 285°C which is not evident in fig.2, which can be hidden by the exothermic peaks present in the same temperature range. The appearance of the endothermic peak only in fig.2 can be due to the different availability of $LiFP_6$ near the anode which is not always ensured in the sampling procedure used. Further studies will be conducted to confirm this hypothesis.

Table 2 reports the kinetic parameters calculated with both Kissinger and Ozawa methods. In particular, Fig.4 shows the method of calculating the kinetics parameters using Ozawa's method.

***Table 2:** Kinetic parameters obtained from the Kissinger and Ozawa methods*

Sample	Reaction	A_x, s^{-1}		E_a, kJ mol^{-1}		R^2	
		Kissinger	Ozawa	Kissinger	Ozawa	Kissinger	Ozawa
30% SOC	**SEI decomposition**	2.1388×10^3	2.3744×10^9	56.50	137.78	0.91	0.93
50% SOC	**SEI decomposition**	1.2231×10^{42}	1.3310×10^{48}	340.03	758.01	0.89	0.89
	Li_xC_6-PVDF	1.0995×10^2	2.7492×10^8	73.49	181.90	0.93	0.95
100%SOC	**SEI decomposition**	2.9447	3.6953×10^5	27.93	75.07	0.87	0.91
	Li_xC_6-PVDF 1st peak	7.7594×10^7	1.8475×10^{14}	136.21	318.75	0.78	0.80
	Li_xC_6-PVDF 2nd peak	6.1677×10^{18}	1.6052×10^{15}	151.71	353.55	0.96	0.97

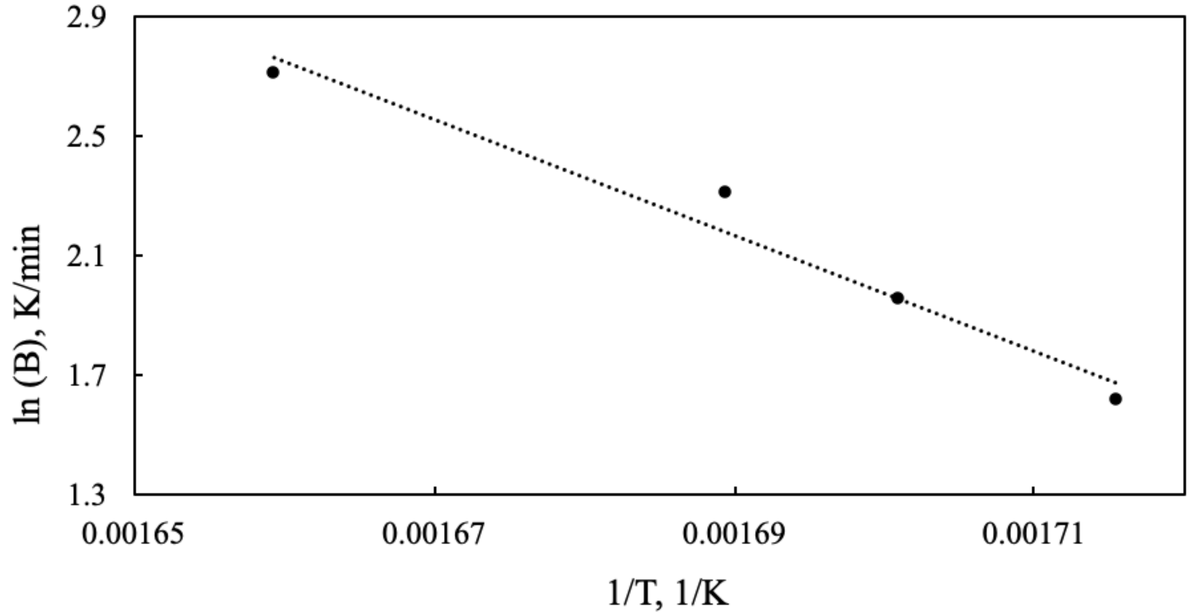

***Fig. 4.** Ozawa's method for calculation of kinetics parameters for Li_xC_6-PVDF reaction (2nd peak) using (100% SOC)*

Analyzing the results, it is clear that the correlation coefficient is in the range 0.78-0.97. This means that the assumption of an Activation energy constant throughout the reaction is not exactly true (Flynn, 1983).

By comparing the data obtained with both methods, it is also found that the Ozawa method provides values with a higher correlation coefficient. Furthermore, the activation energy and the values of the pre-exponential factor of the Ozawa method agree well with those found in the literature (Ren et al., 2018).

Conclusions

Panasonic's NCR 18650 lithium-ion cells have been tested using DSC tests at different heating rates. Two main exothermic reactions are recognized and analyzed: that at lower temperatures (104 – 130 °C) is related to the decomposition of the SEI and that, in the range 290-310°C, related to the reaction between the binder (PVDF) and the lithium intercalated in the negative electrode. These two reactions were kinetically analyzed using a non-isothermal isoconversional method developed by Kissinger and Ozawa.

The relationship between the initial state of charge of the cells and the reactions taking place is evident. As for to the SEI decomposition reaction, the activation energy for fully charged cells is significantly lower than for 30% and 50% state of charge.

The cells with lower SOC do not show the peak related to the Li_xC_6-binder reaction, while the cells with 50% SOC show only a minor peak, compared to the two peaks which is visible in the full charged cell. This is probably due to the availability of lithium during the tests, therefore the greater the state of charge and the greater the lithium available for the reaction.

The data obtained can be used as preliminary results for further and complementary analysis in order to develop a detailed mathematical model to describe all the reactions that occur during the thermal runaway.

Acknowledgements

The authors gratefully acknowledge the financial contribution from MISE-ENEA

References

Bandhauer T.M., Garimella S., Fuller T.F. (2011). A critical review of thermal issues in lithium-ion batteries. *Journal of the Electrochemical Society* 158 R1.

Belharouak I., Vissers D., Amine K. (2006). Thermal stability of the $Li(Ni_{0.8}Co_{0.15}Al_{0.05})O_2$ cathode in the presence of cell components. *Journal of the Electrochemical Society*; 153: A2030–5.

Chen Z., Qin Y., Liu J., Amine K. (2009). Lithium difluoro(oxalato)borate as additive to improve the thermal stability of lithiated graphite. *Electrochemical and Solid-State Letters*, 12: A69–72.

Chen Z., Qin Y., Ren Y., Lu W., Orendorff C., Roth E.P,. et al. (2011). Multi-scale study of thermal stability of lithiated graphite. *Energy & Environmental Science*, 4: 4023–30.

Du Pasquier A., Disma F., Bowmer T., Gozdz A. S., Amatucci G., Tarascon J. M. (1998). *Journal of the Electrochemical Society*, 145(2):472–477.

Flynn J.H. (1983). The Isoconversional Method for Determination of energy of Activation at Constant Heating rates, *Journal of Thermal Analysis and Calorimetry*, 27: 95-102.

Flynn J.H., Wall L.A. (1966). A Quick, Direct Method for the Determination of Activation energy from thermogravimetric Data, *Journal of Polymer Science Part C: Polymer Letters*, (4): 323-328.

Forestier C., Grugeon S., Davoisne C., Lecocq A., Marlair G., Armand M., et al. (2016). Graphite electrode thermal behavior and solid electrolyte interphase investigations: role of state-of-the-art binders, carbonate additives and lithium bis(fluorosulfonyl)imide salt. *Journal of Power Sources*, 330: 186–94.

Gabbott P., *Principles and Applications of Thermal Analysis*; Blackwell Publishing 2008.

Garche J., Brandt K. *Electrochemical Power Sources: Fundamentals, Systems, and Applications-Li-Battery Safety*; Elsevier 2019.

Geder J., Hoster H.E., Jossen A., Garche J., Yu D.Y.W. (2014). Impact of active material surface area on thermal stability of $LiCoO_2$ cathode. *Journal of Power Sources*, 257: 286–92.

Kissinger HE. (1956) Variation of peak temperature with heating rate in differential thermal analysis. *Journal of Research of the National Bureau of Standards,* 57: 217–21.

Ozawa T. (1970). Kinetic Analysis of Derivative Curves in thermal Analysis. *Journal of Thermal Analysis and Calorimetry*, (2):301-324.

Ping P., Wang Q., Huang P., Sun J., Chen C. (2014). Thermal behavior analysis of lithium ion battery at elevated temperature using deconvolution method. *Applied Energy*, 129: 261-73.

Ren D., Liu X., Feng X., Lu L., Ouyang M., Li J., He X. (2018). Model-based thermal runaway prediction of lithium-ion batteries from T kinetics analysis of cell components. *Applied Energy,* 228:633-644.

Richard M.N., Dahn J.R. (1999a). Accelerating rate calorimetry study on the thermal stability of lithium intercalated graphite in electrolyte. I. Experimental. *Journal of the Electrochemical Society*, 146: 2068–77.

Richard M.N., Dahn J.R. (1999b). Accelerating rate calorimetry study on the thermal stability of lithium intercalated graphite in electrolyte. II. Modeling the results and predicting differential scanning calorimeter curves *Journal of the Electrochemical Society*, 146: 2078–84.

Roth E. P., Doughty D. H., Franklin J. (2004). DSC investigation of exothermic reactions occurring at elevated temperatures in lithium-ion anodes containing PVDF-based binders. Journal of Power Sources 134: 222-234.

Roth E.P., Nagasubramanian G., Tallant D. R., Garcia M. (1999). Instability of polyvinylidene Fluoride-Based polymeric binder in lithium-ion cells: final report. Sandia Report SAND99-1164.

Ruiz V., Pfrang A., Kriston A., Omar N., Van den Bossche P., Boon-Brett L. (2018). A review of international abuse testing standards and regulations for lithium ion batteries in electric and hybrid electric vehicles. *Renewable and Sustainable Energy Reviews*, 81: 1427–52.

Simon P. (2004). Isoconversional methods - Fundamentals, meaning and application. *Journal of Thermal Analysis and Calorimetry*, Vol. 76: 123–132.

Spotnitz R., Franklin J. (2003). Abuse behavior of high-power, lithium-ion cells. *Journal of Power Sources*, 113:81–100.

Tarascon J. M., Armand M. (2001). Issues and challenges facing rechargeable lithium batteries. *Nature*, 414: 359-367.

Vyazovkin S., Wight W. (1998). Isothermal and Non-isothermal kinetics of thermally Stimulated reactions of Solids, Int. Rev. Phys. Chem., 17(3), 407-433.

Wang Q., Sun J., Yao X., Chen C. (2006). Thermal behavior of lithiated graphite with electrolyte in lithium-ion batteries. *Journal of the Electrochemical Society*, 153: A329–33.

Wang H., Tang A., Huang K. (2011). Oxygen evolution in overcharge $Li_xNi_{1/3}Co_{1/3}Mn_{1/3}O_2$ electrode and its thermal analysis kinetics. *Chinese Journal of Chemistry*, 29: 1583–8.

Wang Q., Ping P., Zhao X., Chu G., Sun J., Chen C. Chen (2012). Thermal runaway caused fire and explosion of lithium ion battery. Journal of Power Sources, 208: 210–224.

Yamaki J., Shinjo Y., Doi T., Okada S. (2014). The rate equation for oxygen evolution by decomposition of Li_xCoO_2 at elevated temperatures. *Journal of the Electrochemical Society*, 161: A1648–54.

DOI: 10.7795/810.20200724

Vortex Dynamics and Fractal Structures in Reactive Richtmyer-Meshkov Instability

M. Bambauer[a], J. Hasslberger[a], N. Chakraborty[b] & M. Klein[a]

[a] Bundeswehr University Munich, Department of Aerospace Engineering, Germany
[b] Newcastle University, School of Engineering, United Kingdom

E-mail: *maximilian.bambauer@unibw.de*

Abstract

In nuclear and process plant safety, the accurate prediction of explosion loads requires understanding of various mechanisms responsible for flame acceleration (FA) and deflagration-to-detonation transition (DDT). In confined geometries, shock-flame interactions due to shock reflections at obstacles and walls are a key contributing factor to FA and DDT. In this context, the wrinkling of the flame surface due to the production of baroclinic torque and in consequence the increase of the integral reaction rate is referred to as the reactive Richtmyer-Meshkov Instability (RMI).

With the goal of developing a RMI sub-grid model, compressible 3D-DNS of a shock-flame interaction in a lean and a stoichiometric homogeneous H2/Air mixture have been performed. The chemistry is modeled using a modified one-step Arrhenius approach, since the problem is dominated by fluid dynamic phenomena rather than complex chemical kinetics. Temporal and spatial discretization are achieved using a 3rd order Runge-Kutta method and a high-order WENO scheme respectively. The set-up consists of a planar shock propagating towards a perturbed but statistically planar flame. After interacting with the flame, the shock is reflected at the back-end of the domain, causing a second shock-flame interaction (re-shock).

The development of the RMI, measured by the evolution of the flame surface area and turbulent mixing width, is influenced by key physical parameters. One important parameter is the equivalence ratio, as it affects the Lewis number and laminar flame speed. Using the DNS database, sub-grid modeling approaches for closure of the averaged/filtered reaction rate can be quantified. For this purpose individual terms of the enstrophy transport equation are analyzed, identifying dominant mechanisms during the development of the instability. Furthermore, the fractal behavior of the RMI is analyzed in an approach of power-law based modeling of the flame wrinkling factor.

For the investigated cases it is found that the baroclinic torque is the most dominant enstrophy transport term, showing high peaks after every shock-flame interaction. The baroclinic torque is heavily dependent on the flame thickness, which varies with the chosen equivalence ratio and in time, as the flame thickness is reduced by about 50% after interacting with the shock and re-shock. Each shock interaction also causes a strong increase of the flame surface area and turbulent mixing width, with an maximum increase in area of about 400%. The final area increase of the stoichiometric case is about 30% lower than the lean case due to funnel-closure and smoothing effects, caused by the increased reaction rate. The fractal dimension D_f, as found in power law based modeling, is investigated using explicit filtering of the present DNS data. There a maximum fractal dimension of 2.92 to 2.96 is determined for both cases, before the stoichiometric and lean cases settle at a value of 2.38 and 2.67 respectively. Since the maximum fractal dimension of the flame surface is expected to be $8/3$ for a premixed flame, values of $D_\mathrm{f} > 8/3$ are a strong indicator for additional wrinkling caused by the RMI. For the lean case with an effective Lewis number $\mathrm{Le}_\mathrm{eff} < 1$, thermo-diffusive instabilities can provide an additional contribution towards flame wrinkling.

Keywords: *RMI, DNS, shock, vorticity, fractal, sub-grid model*

DOI: 10.7795/810.20200724

1 Introduction

The Richtmyer-Meshkov instability (RMI) (Richtmyer, 1960, Meshkov, 1972), like the Rayleigh-Taylor instability (RTI) (Rayleigh, 1882, Taylor, 1950), describes a form of hydrodynamic instability, that can occur at the interface between a light and heavy fluid upon interaction with a pressure gradient ∇p. In the RMI, the pressure gradient is caused by a shock wave, while in the case of RTI it is caused by constant acceleration $\mathbf{g}$ (e.g. gravity). The mechanism causing this type of instability is the production of vorticity, due to the misalignment of ∇p and the density gradient $\nabla \rho$ across the interface. Small disturbances at the fluid interface are increasingly amplified, leading to wrinkling and increased mixing of heavy and light fluid.

Two prominent occurrences for RMI and RTI in nature and technology are supernovae (Remington et al., 2000) and inertial confinement fusion (Lindl, 1995). The focus of this work lies on the RMI in the context of combustion, where it plays an important role as a mechanism for the deflagration-to-detonation transition (DDT) in geometrically confined explosions. In that context, the RMI is caused by a shock wave interacting with a flame (density gradient), after being reflected from an obstacle or wall (Ciccarelli et al., 2010). The RMI causes a heavily wrinkled flame brush region and subsequently a strong increase in the integral reaction rate, which can be a decisive factor for DDT (Dorofeev, 2011). Understanding and accurate prediction of the DDT and explosion loads is a key element in nuclear and chemical safety research (Breitung et al., 2000). Commercial applications can only provide qualitative predictions of explosion loads in large scale geometries due to the heavy computational demands posed by the wide time- and length-scale spectrum, associated with the simulation of the chemistry and turbulent flow in such cases (Ciccarelli and Dorofeev, 2008). The accuracy of large eddy simulation (LES) or unsteady Reynolds-averaged Navier-Stokes simulation (URANS) could be improved by including small-scale RMI effects via a sub-grid model (Hasslberger, 2017).

In this work direct numerical simulations (DNS) of shock-flame interactions for a lean and stoichiometric H2/Air gas mixture are presented and analyzed in regards of $A_\mathrm{f}(t)$, $\delta_\mathrm{w}(t)$, the enstrophy transport equation and fractal behavior for power law based modeling of the flame wrinkling. Sec. 2 will give an overview on the numerical methods used for the DNS simulations, which is followed by an explanation of the case set-up in sec. 3. The simulation results are presented in sec. 4 with an analysis of the enstrophy transport equation in sec. 4.1 and of the fractal flame wrinkling in sec. 4.2.

2 Numerical Methods

The SENGA solver (Jenkins and Cant, 1999) is used to carry out 3D combustion DNS of the shock-flame interactions. It solves a dimensionless form of the Navier-Stokes (NS) equations, including the total energy e_t and reaction progress variable c, given by Eqs. (1) to (4) and using the dimensionless variables defined in table 1.

$$\frac{\partial \rho}{\partial t}+\frac{\partial(\rho u_k)}{\partial x_k}=0 \tag{1}$$

$$\frac{\partial(\rho u_i)}{\partial t}+\frac{\partial(\rho u_k u_i)}{\partial x_k}=-\frac{\partial p}{\partial x_i}+\frac{1}{\mathrm{Re}_0}\frac{\partial \tau_{ki}}{\partial x_k} \tag{2}$$

$$\begin{aligned}\frac{\partial(\rho e_t)}{\partial t}+\frac{\partial(\rho u_k e_t)}{\partial x_k}=&-(\gamma-1)\mathrm{M}_0^2\frac{\partial(p u_k)}{\partial x_k}+\frac{1}{\mathrm{Re}_0}(\gamma-1)\mathrm{M}_0^2\frac{\partial(\tau_{ki}u_i)}{\partial x_k}\\&+\frac{\tau_\mathrm{h}}{\mathrm{Re}_0\mathrm{Pr}}\frac{\partial}{\partial x_k}\left[\lambda\frac{\partial T}{\partial x_k}\right]-\frac{\tau_\mathrm{h}}{\mathrm{Re}_0\mathrm{LePr}}\frac{\partial}{\partial x_k}\left[\rho D\frac{\partial c}{\partial x_k}\right]\end{aligned} \tag{3}$$

$$\frac{\partial(\rho c)}{\partial t}+\frac{\partial(\rho u_k c)}{\partial x_k}=\dot{\omega}+\frac{1}{\mathrm{Re}_0\mathrm{LePr}}\frac{\partial}{\partial x_k}\left[\rho D\frac{\partial c}{\partial x_k}\right] \tag{4}$$

The dimensioned (superscript '*') reference (subscript '0') values for density ρ_0^*, temperature T_0^*, thermal conductivity λ_0^*, mass diffusivity D_0^*, specific heat capacities $c_{\mathrm{p},0}^*$ and $c_{\mathrm{v},0}^*$, dynamic viscosity μ_0^* and the adiabatic flame temperature T_ad^* are taken from the initial state (unburned H2/Air gas-

***Table 1**: Definition of the dimensionless variables.*

variable	**definition**
density	$\rho = \rho^*/\rho_0^*$
pressure	$p = p^*/(\rho_0^* u_0^{*2})$
temperature	$T = (T^* - T_0^*)/(T_{\mathrm{ad}}^* - T_0^*)$
velocity	$u_i = u_i^*/u_0^*$
thermal conductivity	$\lambda = \lambda^*/\lambda_0^*$
mass diffusivity	$D = D^*/D_0^*$
total chemical energy	$e_{\mathrm{t}} = e_{\mathrm{t}}^*/(c_{\mathrm{p},0}^* T_0^*)$
viscous stress	$\tau = (\tau^* l_0^*)/(\mu_0^* u_0^*)$
length	$x_i = x_i^*/l_0^*$
time	$t = t^* u_0^*/l_0^*$

mixture) at $t^* = 0$. The reference velocity u_0^* and reference length l_0^* are set to the laminar burning velocity S_{L} and to $\approx 250\delta_{\mathrm{th,st}}^*$ (thermal laminar flame thickness for stoichiometric mixture at $t^* = 0$) respectively.

Using the heat capacity ratio $\gamma = c_{\mathrm{p},0}^*/c_{\mathrm{v},0}^*$ and the specific gas constant R_{s}^*, the reference speed of sound can be defined as $a_0^* = \sqrt{\gamma R_s^* T_0^*}$. This gives a reference Mach number of $M_0 = u_0^*/a_0^*$. Other dimensionless parameters such as the reference Reynolds number Re_0, Prandtl number Pr, Schmidt number Sc, Lewis number Le and heat release parameter τ_{h} are defined as:

$$\mathrm{Re}_0 = \frac{\rho_0^* u_0^* l_0^*}{\mu_0^*} \quad \mathrm{Pr} = \frac{\mu_0^* c_{\mathrm{p},0}^*}{\lambda_0^*} \quad \mathrm{Sc} = \frac{\mu_0^*}{\rho_0^* D_0^*} \quad \mathrm{Le} = \frac{\lambda_0^*}{\rho_0^* D_0^* c_{\mathrm{p},0}^*} \quad \tau_{\mathrm{h}} = \frac{T_{\mathrm{ad}}^* - T_0^*}{T_0^*} \tag{5}$$

The parameters Re_0 and M_0 are calculated using $u_0^* = S_{\mathrm{L}}$ as per definition of the reference parameter u_0^*. Since the RMI is mainly dominated by the dynamics of the shock-flame interaction and a detailed chemistry model would entail large computational costs, the chemistry (see $\dot{\omega}$ in Eq. (4)) is modeled using the following one step Arrhenius approach.

$$\dot{\omega} = B_{\mathrm{A}} \rho (1-c) \exp\left[-\frac{\beta_{\mathrm{z}}(1-T)}{1-\alpha_{\mathrm{h}}(1-T)}\right] \tag{6}$$

The Zeldovich number β_{z} and parameter α_{h} are defined as $\beta_{\mathrm{z}} = T_{\mathrm{ac}}^*(T_{\mathrm{ad}}^* - T_0^*)/T_{\mathrm{ad}}^{*2}$ and $\alpha_{\mathrm{h}} = \tau_{\mathrm{h}}/(1+\tau_{\mathrm{h}})$, where T_{ac}^* is the activation temperature. The values used in the present cases for β_{z} and the pre exponential factor B_{A} can be found in table 2. The viscous stress tensor τ_{ki} is defined as:

$$\tau_{ki} = \mu \left[\frac{\partial u_i}{\partial x_j} + \frac{\partial u_j}{\partial x_i}\right] - \frac{2}{3}\delta_{ij}\left[\frac{\partial u_k}{\partial x_k}\right] \tag{7}$$

For time discretization a low-storage third-order explicit Runge-Kutta scheme (Wray, 1990) is utilized. The spatial derivatives of all convective terms are calculated with the fifth order WENO-5 method by Jiang and Shu (1996), using the scalar Lax-Friedrichs flux splitting procedure described by Shu (1998). At the non-periodic boundaries, the scheme is gradually reduced to a one-sided 2nd order scheme. The scheme provides sharp shock capturing capabilities without numerical oscillations for the investigated cases. Figure 1 shows a comparison of the WENO-5 scheme with an analytical 1D solution of a shock at a shock Mach number of $M_{\mathrm{s}} = 1.5$, where the shock is resolved by about 2-3 nodes. All simulations presented in this work are initialized with a $M_{\mathrm{s}} = 1.5$ shock, without expansion fan and contact discontinuity.

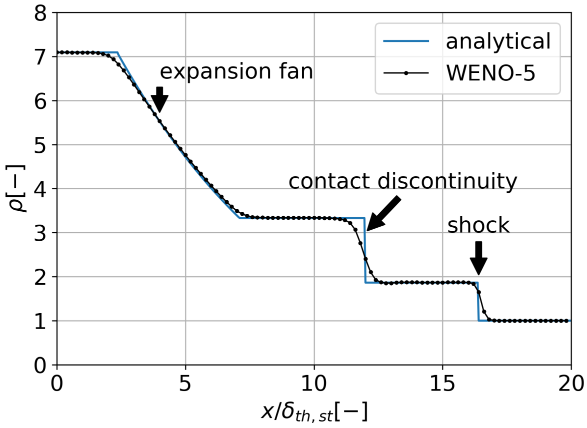

***Fig. 1**: Comparison of the numerical and analytical shock-tube solution for $M_s = 1.5$.*

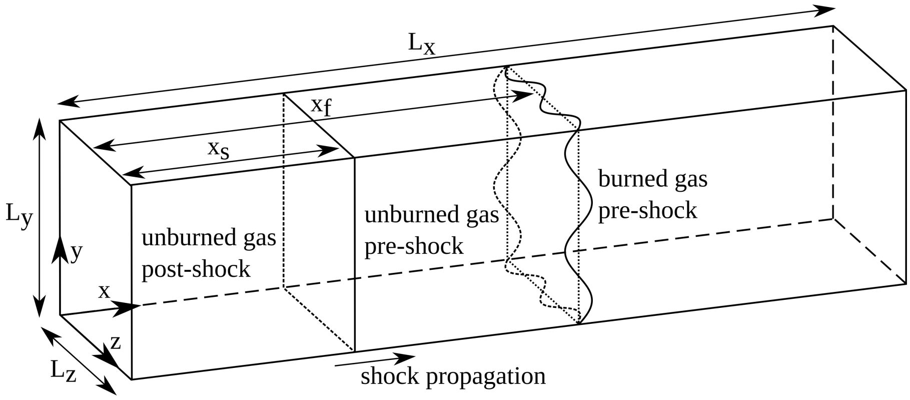

***Fig. 2**: Set-up schematic with position of shock and statistically planar flame.*

3 Simulation Set-Up

The simulation domain, consisting of a rectangular channel divided into areas of unburned and burned gas by a statistically planar flame, is schematically shown in Fig. 2. Figure 3 depicts the boundary conditions used in the set-up. A modified Navier-Stokes characteristic boundary condition (NSCBC) is implemented at $x = 0$ to allow for both outflow and inflow of fluid (Poinsot and Veynante, 2005). To enable the reflection of incoming shock waves, an adiabatic free-slip boundary is applied at $x = L_x$. The remaining boundaries in y and z-direction are periodic. The RMI can only occur if an initial disturbance is present in the flame surface. A flame disturbance method by Tritschler et al. (2013) is used for this purpose. It enables a quasi-stochastic disturbance of the flame front while still remaining reproducible on different systems, i.e. it is not based on random numbers. Across all cases in this work the initial flame disturbance was kept constant. The influence of changes in the initial flame disturbance on the development of the wrinkled flame brush was investigated in Bambauer et al. (2020) for a nonreactive medium. The disturbance field, is shown in Fig. 4, with the initial displacement in x-direction for each point of the statistically planar flame surface.

For the present work, two cases of a H2/Air gas mixture at different equivalence ratios ϕ are investigated. The set-up parameters listed in Tab. 2 for the stoichiometric case ($\phi = 1$) and the lean case ($\phi = 0.5$) were calculated using the Cantera software (Goodwin et al., 2018) and the GRI-MECH 3.0 model at $T_0^* = 298.15\,\mathrm{K}$ and $p_0^* = 1\,\mathrm{bar}$. Changing ϕ has an effect on several important parameters, such as the laminar flame speed S_L, the heat release parameter τ_h, the density gradient of the flame $\nabla\rho$ and the Lewis number. Generally, the Lewis number (see Eq. (5)) is calculated using the mass diffusion coefficient of the deficient reactant. For a very lean mixture ($\phi \ll 1$) the Hydrogen-Lewis number is $\mathrm{Le}_{H2} \approx 0.3$ and for a very fuel-rich mixture ($\phi \gg 1$) the Oxygen-Lewis number is $\mathrm{Le}_{O2} \approx 2.1$. To avoid a jump of the Lewis number at $\phi = 1$, an effective (also known as reduced) Lewis number $\mathrm{Le}_{\mathrm{eff}}$ is defined, that provides a smooth transition between Le_{H2} and Le_{O2} in the whole

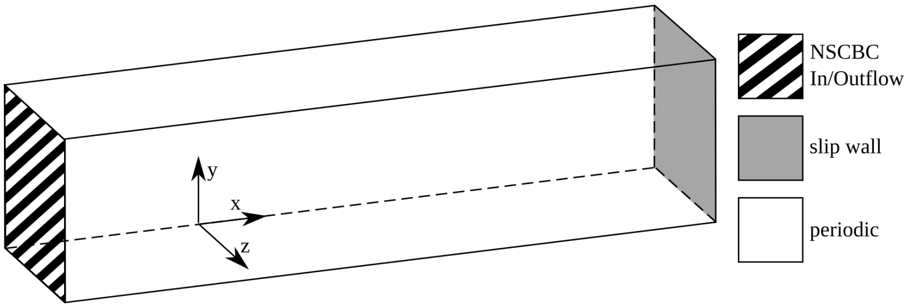

Fig. 3: Set-up schematic showing the boundary conditions.

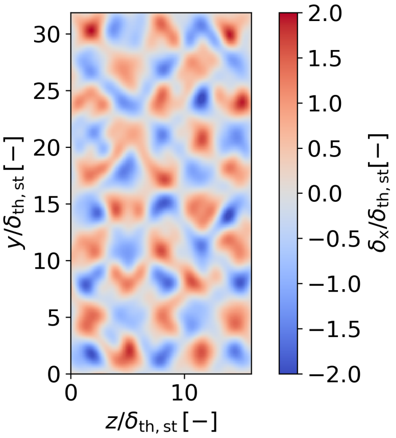

Fig. 4: Distortion δ_x of the statistically planar flame front.

ϕ range. The definition of the effective Lewis number used in this work can be found in Bechtold and Matalon (2001) and is calculated from the Cantera results with

$$\mathrm{Le}_{\mathrm{eff}} = 1 + \frac{(\mathrm{Le}_{\mathrm{H2}} - 1) + (\mathrm{Le}_{\mathrm{O2}} - 1)A_{\mathrm{Le}}}{1 + A_{\mathrm{Le}}}, \tag{8}$$

where $A_{\mathrm{Le}} = 1 + \beta_z(\Phi - 1)$ and $\Phi = \phi$ for fuel-rich mixtures and $\Phi = 1/\phi$ for lean-mixtures. For the sake of simplicity the following text will refer to the effective Lewis number only as "Lewis number" or Le.

The normalized flame area $A_f/A_{f,n}$ and the normalized turbulent mixing width $\delta_m/\delta_{m,n}$, obtained from the DNS, can be related to the wrinkling factor and turbulent diffusion, which is required for LES or URANS sub-grid modeling. There they can provide insights in modeling approaches for closure of

Table 2: Input parameters for simulation cases.

	stoichiometric	**lean**
ϕ	1.0	0.5
Le	1.1	0.5
Re_0	1093	213
Pr	0.47	0.52
Sc	0.52	0.26
τ_h	7.1	4.5
β_z	5.0	5.0
M_0	0.005609	0.001025
M_s	1.5	1.5
B_A	50000	13000

the reaction rate term, or the non-linear convective term. For A_f (Klein et al., 2020) and δ_m (Tritschler et al., 2014) the following definitions are used.

$$A_\mathrm{f} = \iiint_V |\nabla c| dV \tag{9}$$

$$\delta_\mathrm{m} = \int_0^{L_\mathrm{x}} 4\langle c\rangle(1-\langle c\rangle)dx \tag{10}$$

$$\langle c\rangle = \frac{1}{L_\mathrm{y}L_\mathrm{z}}\iint c\,dydz \tag{11}$$

With $\delta_\mathrm{th,st}$ as the thermal laminar flame thickness of the stoichiometric case, the dimensions of the domain are $L_\mathrm{x} \times L_\mathrm{y} \times L_\mathrm{z} = 128\delta_\mathrm{th,st} \times 32\delta_\mathrm{th,st} \times 16\delta_\mathrm{th,st}$ uniformly discretized by $1024 \times 256 \times 128$ grid points. The shock and flame are initialized at $x_\mathrm{s} = 3.125\delta_\mathrm{th,st}$ and $x_\mathrm{f} = 12.5\delta_\mathrm{th,st}$ respectively. The initial thermal laminar flame thickness of the lean case is $\delta_\mathrm{th,le} \approx 8\delta_\mathrm{th,st}$.

4 Results

Figure 5 shows density slices in the xy-plane at successive timesteps for the stoichiometric and lean case. The subfigures Fig. 5a to Fig. 5d show the formation of fresh gas funnels reaching into the burned side of the gas, after the first shock-flame interaction at $t \times S_\mathrm{L,st}/\delta_\mathrm{th,st} = 0.2$. Then at $t \times S_\mathrm{L,st}/\delta_\mathrm{th,st} = 0.4$, a second shock-flame interaction ('re-shock') occurs, after the shock has been reflected from the back wall of the domain. Next at $t \times S_\mathrm{L,st}/\delta_\mathrm{th,st} = 0.6$, another shock flame interaction occurs (termed 'reflection'), caused by partial transmissions and reflections of the shock between the flame surface and the back wall after re-shock. Finally another interaction with a partially reflected shock occurs at $t \times S_\mathrm{L,st}/\delta_\mathrm{th,st} = 0.8$. As time progresses differences between both cases in the development of the fresh gas funnels and later the overall structure of the flame surface become apparent. The laminar flame speed for $\phi = 1$ is about five times higher than for $\phi = 0.5$. This leads to an increased reduction in size of the fresh gas funnels for the stoichiometric case, as the funnels and other developing turbulent structures are continuously being enclosed by reacting gas. The effects of this on later development of the flame surface structure, can be seen in Fig. 5d. In the lean case the flame surface shows a variety of small scale wrinkled structures, which are not present in the stoichiometric case.

Another contributing factor to the differences in the development of the flame brush for both cases are the differences in Lewis number. In the lean case the formation of thermo-diffusive instabilities are promoted by the low Lewis number which contributes to the flame wrinkling in addition to the RMI. The shock-position offset is caused by differences in the speed of sound, due to an increased adiabatic flame temperature in the stoichiometric case and differences in the turbulent mixing width.

Figure 6 shows the temporal development of the normalized flame surface area A_f and normalized turbulent mixing width δ_m for the stoichiometric ($\phi = 1$) and lean ($\phi = 0.5$) case. The flame area is normalized with the area of the shock tube cross-section $A_\mathrm{f,n}$. For $\delta_\mathrm{m,n}$ the initial mixing width of the $\phi = 1$ case at $t \times S_\mathrm{L,st}/\delta_\mathrm{th,st} = 0$ is taken. After each shock interaction, an area increase is observed for both cases. The stoichiometric case shows a steep linear increase at the beginning of the first shock interaction, growing faster than the lean case. Since the initial flame perturbation is the same for both cases, this is caused by the increased initial density gradient across the flame due to the lower flame thickness (see Fig. 8) and the increased heat release parameter τ_h for $\phi = 1$. As is shown in sec. 4.1, this leads to a higher production of baroclinic torque and increased wrinkling. The flame surface area then reaches a maximum increase of about 300%, before decreasing slightly again until the interaction with the re-shock. The area decrease is caused by the closure of the fresh gas funnels by the burning gas and further smoothing of emerging turbulent structures. The funnel-closure and smoothing effects are far less pronounced for the lean case, therefore it surpasses the stoichiometric case in area after the re-shock. The final surface area values reached at $t \times S_\mathrm{L,st}/\delta_\mathrm{th,st} = 1$ differ by about 30% between both cases. Another effect, which is visible for both A_f and δ_m, is a short initial

DOI: 10.7795/810.20200724

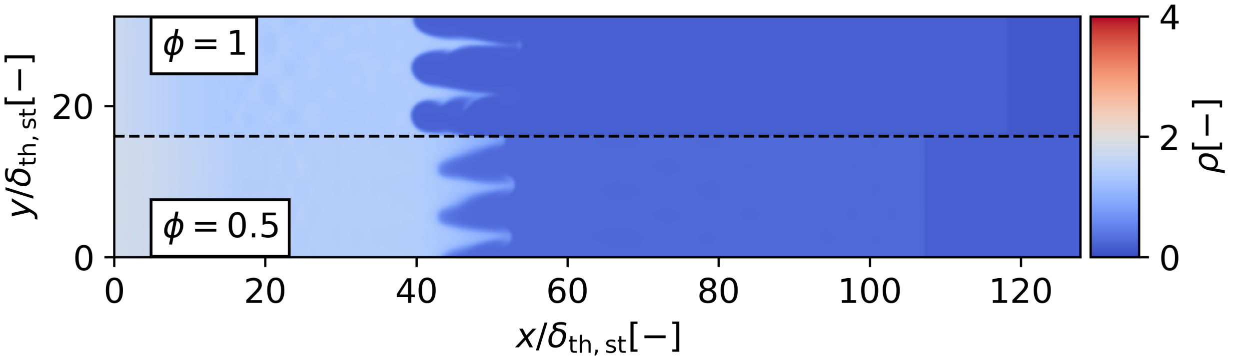

(a) Density slice at $t \times S_{\mathrm{L,st}}/\delta_{\mathrm{th,st}} = 0.2$; formation of fresh gas funnels after first shock-flame interaction.

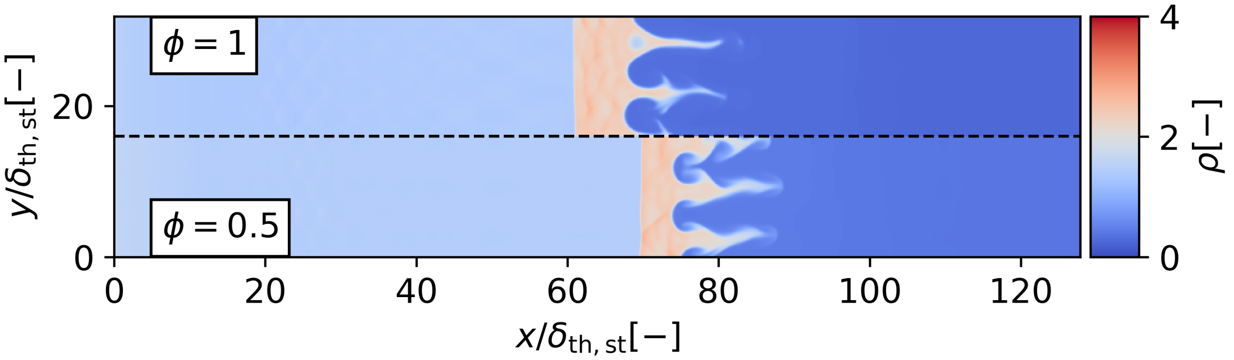

(b) Density slice at $t \times S_{\mathrm{L,st}}/\delta_{\mathrm{th,st}} = 0.4$; second shock-flame interaction (re-shock).

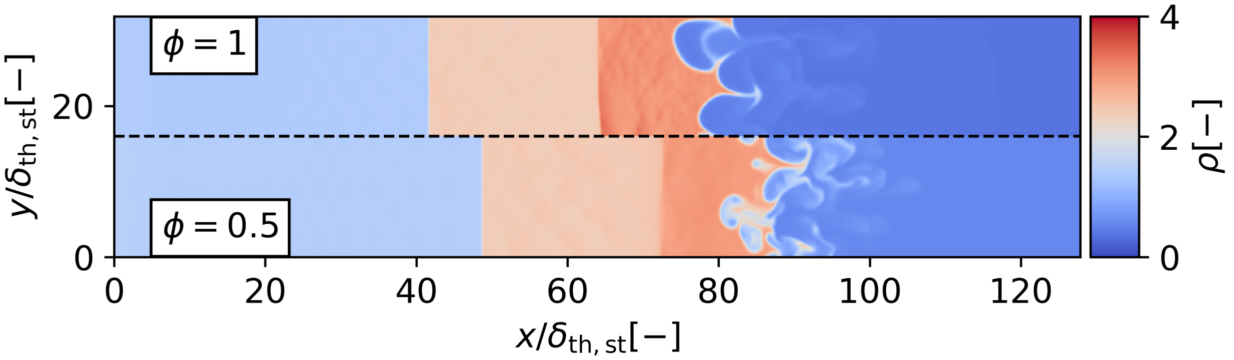

(c) Density slice at $t \times S_{\mathrm{L,st}}/\delta_{\mathrm{th,st}} = 0.6$; third shock-flame interaction (1st reflection).

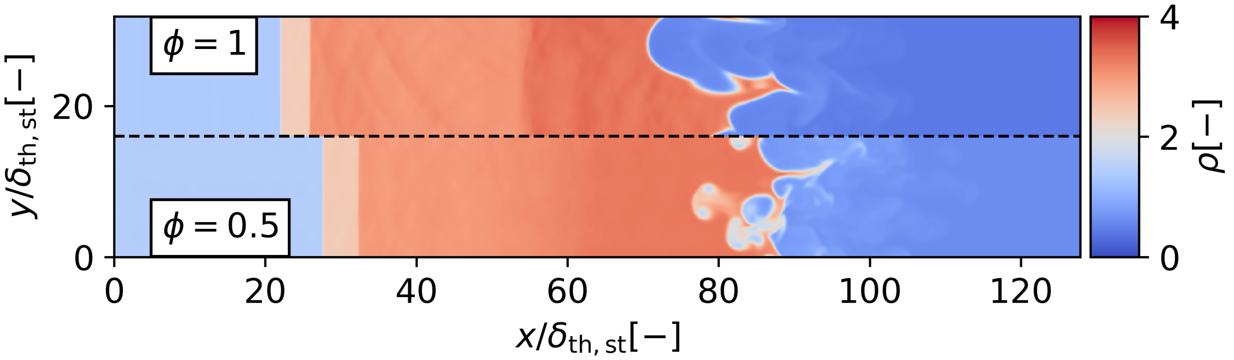

(d) Density slice at $t \times S_{\mathrm{L,st}}/\delta_{\mathrm{th,st}} = 0.8$; fourth shock-flame interaction (2nd reflection).

***Fig. 5**: Density slice of the shock tube at $z = L_z/2$ for successive timesteps. Comparison of equivalence ratio for stoichiometric ($\phi = 1$) and lean ($\phi = 0.5$) H2/Air gas mixture.*

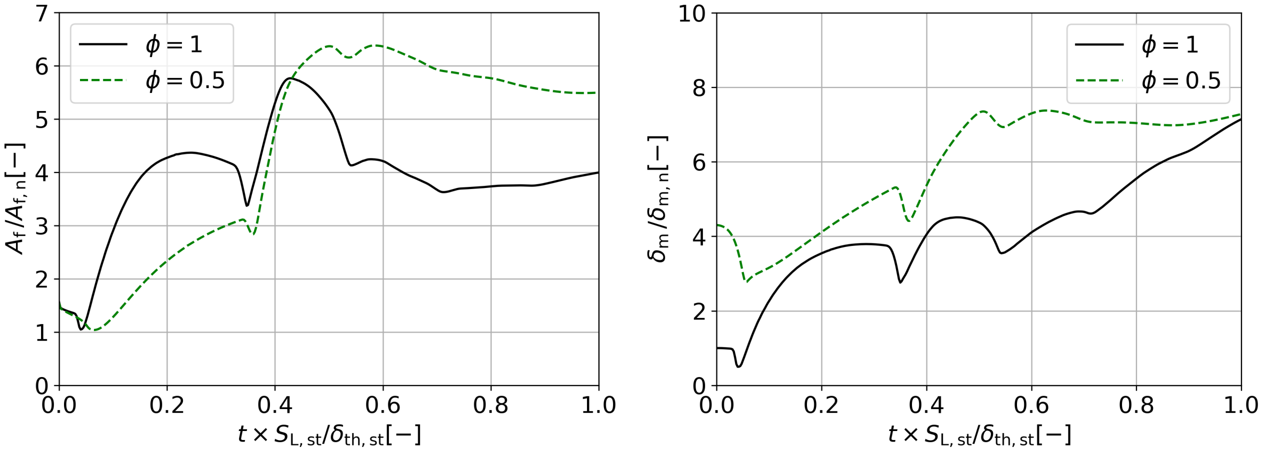

(a) Normalized flame surface area. *(b) Normalized mixing width.*

***Fig. 6**: Normalized flame surface area and normalized turbulent mixing width over time for lean and stoichiometric gas mixture.*

decline when an interaction with a shock wave occurs. This is not connected with the RMI itself, but caused by the shock interacting with the leading flame structures first, before interacting with the rest of the flame (and RMI sets on). Those structures are then flattened or pushed back, initially reducing A_f and δ_m.

Proceeding with the turbulent mixing width shown in Fig. 6b, it becomes apparent that the initial δ_m differs between both cases due to differences in flame thickness δ_f. The flame thickness δ_f is defined by $\delta_f = V_f/A_f$, where the flame volume V_f is calculated by summation of all grid points with $0.01 \leq c \leq 0.99$. The normalization parameter $\delta_{f,n}$ is taken for $\phi = 1$ and $t \times S_{L,st}/\delta_{th,st} = 0$ and $\delta_{f,n} \approx 1.76\delta_{th,st}$. Initially the flame thickness of the lean case is about eight times higher than for the stoichiometric case, resulting in an increased δ_m at the start of the simulation (see Fig. 8). In both cases the turbulent mixing width in Fig. 6b initially grows linearly after each shock flame interaction. While the lean case continues to grow in a linear fashion until the next shock interaction, the stoichiometric case reaches a maximum before it plateaus or even begins to decline (similar to Fig. 6a). Towards the end of the simulation the turbulent mixing width of the stoichiometric case keeps increasing steadily while δ_m starts to settle for the lean case. The continued growth could be explained by the increased reaction rate at $\phi = 1$, that causes large areas of burned gas to expand into the unburned gas as visible in Fig. 5d.

4.1 Enstrophy Analysis

The generation of vorticity due to baroclinic torque at the flame surface, is the main mechanism responsible for the RMI. The enstrophy $\Omega = \omega_i^2/2$ can be interpreted as a scalar energy equivalent of the vorticity $\omega_i = \varepsilon_{ijk}\partial u_k/\partial x_j$ and its transport equation is given as:

$$\frac{\partial \Omega}{\partial t} + u_k \frac{\partial \Omega}{\partial x_k} = \underbrace{\omega_i \omega_k \frac{\partial u_i}{\partial x_k}}_{\mathrm{T_I}} \underbrace{- \varepsilon_{ijk}\omega_i \frac{1}{\rho^2}\frac{\partial \rho}{\partial x_j}\frac{\partial \tau_{kl}}{\partial x_l}}_{\mathrm{T_{II}}} + \underbrace{\frac{\varepsilon_{ijk}\omega_i}{\rho}\frac{\partial^2 \tau_{kl}}{\partial x_j \partial x_l}}_{\mathrm{T_{III}}} \underbrace{-2\frac{\partial u_k}{\partial x_k}\Omega}_{\mathrm{T_{IV}}} + \underbrace{\varepsilon_{ijk}\frac{\omega_i}{\rho^2}\frac{\partial \rho}{\partial x_j}\frac{\partial p}{\partial x_k}}_{\mathrm{T_V}} \quad (12)$$

The terms on the right hand side represent the changes in enstrophy due to vortex stretching (I), viscous torque (II), diffusion (III), dilatation (IV) and baroclinic torque (V). The normalized volume integrals of the terms I to V are shown in Fig. 7 for the lean and stoichiometric case. Generally peaks in the enstrophy terms can be observed after each shock interaction. Term V (baroclinic torque) is dominating most of the time for both cases, although the peak heights differ in comparison. Term I (vortex stretching), term III (diffusion) and term IV (dilatation) show small peaks on each shock-flame interaction. Comparing the behavior of term I and term III in figs. 7a and 7b, a noticeable

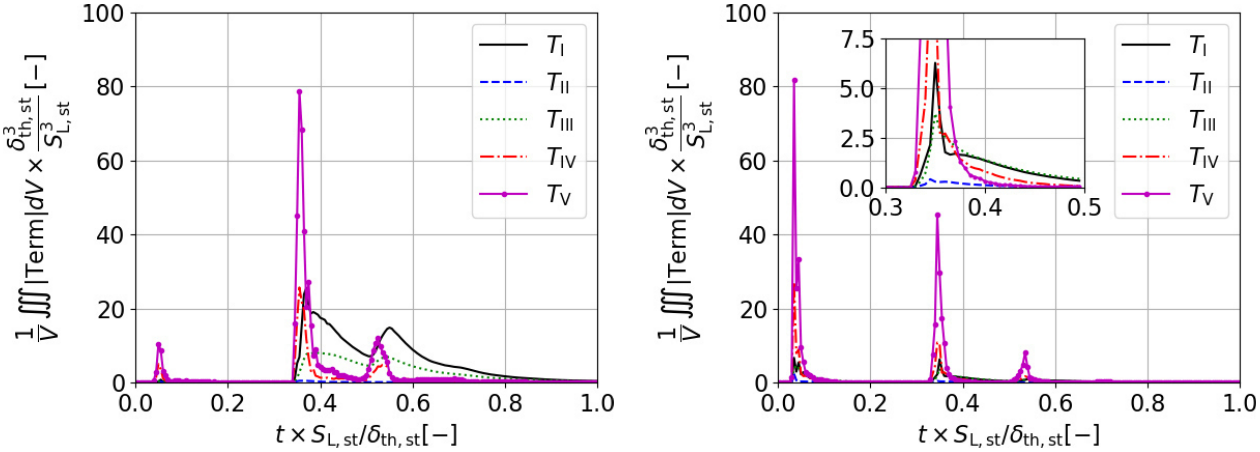

(a) $\phi = 0.5$ *(b)* $\phi = 1$

***Fig. 7**: Normalized volume integral (with* $V = \mathrm{L_x L_y L_z}$*) of the enstrophy transport terms for lean and stoichiometric gas mixture (with enlarged figure section for* $\phi = 1$*).*

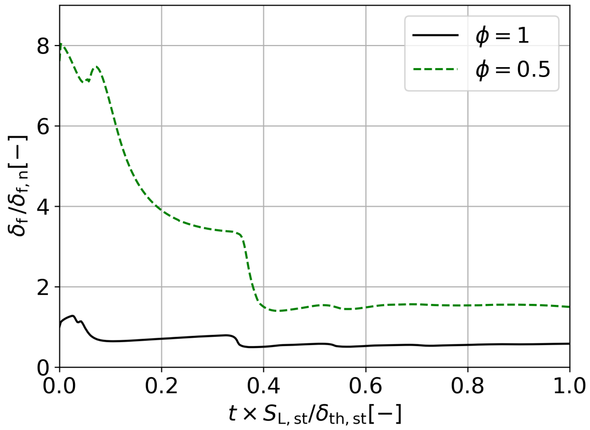

***Fig. 8**: Normalized flame thickness over time for lean and stoichiometric gas mixture.*

difference between the cases becomes apparent. After each shock interaction the terms decline again, but at a much slower rate than the baroclinic torque (term V), which causes terms I and III to become the dominant terms after the re-shock and the reflection. This can be seen for $\phi = 0.5$ and to a lesser extent for $\phi = 1$ as the values reached for term I and III are generally much smaller in this case. The influence of Term II (viscous torque) on the enstrophy production can be neglected for the investigated cases.

Focusing on term V, a significant difference in peak height between both cases can be seen after the first shock interaction. As already mentioned in the discussion of Fig. 6, this is caused by differences in initial flame thickness (see Fig. 8) and heat release τ_{h}, leading to a considerably increased density gradient for $\phi = 1$. Since the thickness of the lean flame is massively reduced after each shock interaction and the flame surface area is increased due to the formation of fresh gas funnels and other turbulent structures, the peak in baroclinic torque is massively increased at the re-shock, even surpassing the stoichiometric flame. The flame thickness decrease, is caused by the compression of the flame by the shock and the increased pressure level after passing of the shock wave. The flame thickness, which initially is about 8 times higher in the lean flame, is reduced by about 50% after interacting with the shock and re-shock (later interactions have a negligible effect on the flame thickness).

4.2 Fractal Analysis

A common approach for reaction rate closure in RANS and LES, is to model the sub-grid scale wrinkling factor $\Xi = \overline{|\nabla c|}/|\nabla \bar{c}|$ (overbar indicates RANS averaging or LES filtering) as a power-law function, giving the expression (Fureby, 2005, Knikker et al., 2004):

$$\Xi = (\eta_\mathrm{o}/\eta_\mathrm{i})^{D_\mathrm{f}-2} \tag{13}$$

The outer and inner cut-off scales η_o and η_i are taken as the LES filter width Δ and a quantity that corresponds to the smallest occurring flame structure (Gülder, 1995), respectively. The fractal dimension D_f of the premixed flame can be calculated from the present DNS data by explicit filtering (Chakraborty and Klein, 2008). With the generalized flame surface density (FSD) $\Sigma_\mathrm{gen} = \overline{|\nabla c|}$ defined by Boger et al. (1998) and using Eq. (13) the following expression for Σ_gen is obtained (Gouldin et al., 1989):

$$\Sigma_\mathrm{gen} = |\nabla \bar{c}|(\Delta/\eta_\mathrm{i})^{D_\mathrm{f}-2} \tag{14}$$

Following the method described in detail by Chakraborty and Klein (2008) and taking the volume average of Eq. (14), results in

$$\log(\langle\Sigma_\mathrm{gen}\rangle/\langle|\nabla \bar{c}|\rangle) = (D_\mathrm{f}-2)\log(\Delta) - (D_\mathrm{f}-2)\log(\eta_\mathrm{i}) \; . \tag{15}$$

Equation (15) can be interpreted as a straight line equation with a slope of $(D_\mathrm{f}-2)$. Figure 9 shows a double logarithmic plot of $\langle\Sigma_\mathrm{gen}\rangle/\langle|\nabla \bar{c}|\rangle$ over the normalized filter size Δ for the stoichiometric case at $t \times S_\mathrm{L,st}/\delta_\mathrm{th,st} = 1$. When the filter width is smaller than the stoichiometric flame thickness $\delta_\mathrm{th,st}$ (see sec. 3), the variation of $\log(\langle\Sigma_\mathrm{gen}\rangle/\langle|\nabla \bar{c}|\rangle)$ becomes increasingly non-linear. For $\Delta \gg \delta_\mathrm{th,st}$ the linear behaviour expected from Eq. (15) becomes apparent and the fractal dimension D_f can be calculated from the slope of a line fit. By repeating this procedure for successive timesteps and for all cases, the evolution of D_f over time, as shown in Fig. 10a, can be determined. Since the definition of D_f is tied to the FSD or flame surface area A_f (see Eq. (9)), it is consistent that D_f evolves similarly to A_f as shown in Fig. 6a. Initially the shock will flatten the initially disturbed (see Fig. 4) flame surface, reducing the fractal dimension to $D_\mathrm{f} \approx 2$, or $\Xi \approx 1$. The fractal dimension then steeply increases to about 2.92 for $\phi = 1$ and 2.78 for $\phi = 0.5$. After the re-shock D_f increases further for the lean case and reaches larger values than the stoichiometric mixture, with a maximum of ≈ 2.96 (≈ 2.89 for stoichiometric). Towards the end of the simulation the fractal dimension values settle at 2.38 ($\phi = 1$) and 2.67 ($\phi = 0.5$). In the flamelet regime Kerstein (1988) suggests a fractal dimension of 7/3, while the maximum D_f for a flame in the well-mixed regime (Hawkes et al., 2012) as well as a passive scalar iso-surface (Mandelbrot, 1975) is found to be 8/3. Values of $D_\mathrm{f} > 8/3$ are a strong indicator for additional wrinkling caused by the RMI and possibly thermo-diffusive instabilities for $\mathrm{Le} < 1$.

The intersection of the straight line fit with the line given by $\langle\Sigma_\mathrm{gen}\rangle/\langle|\nabla \bar{c}|\rangle = 1$ in Fig. 9 yields the inner cut-off scale η_i. The development over time of the normalized inner cut-off scale $\eta_\mathrm{i}/\delta_\mathrm{th,st}$ is shown in Fig. 10b, where the stoichiometric thermal flame thickness $\delta_\mathrm{th,st}$ is used for normalization in both cases. The values of $\eta_\mathrm{i}/\delta_\mathrm{th,st}$ are only weakly dependent on the chosen equivalence ratio, since both cases show similar normalized values of $\approx 1 \pm 25\%$. The assumption of a constant and stoichiometry-independent η_i could be useful for simplified sub-grid modelling approaches using Eq. (14), as only D_f has to be modelled.

5 Summary and Outlook

DNS of premixed lean and stoichiometric H2/Air flames interacting with a $M_\mathrm{s} = 1.5$ shock-wave are performed. Two cases are investigated that involve a lean and a stoichiometric H2/Air mixture with an equivalence ratio of $\phi = 0.5$ and $\phi = 1$. Spatial discretization and shock capturing is achieved by implementing the WENO-5 scheme. The scheme successfully avoids numerical oscillations around discontinuities, while resolving the shock with about 2-3 grid points.

During a simulation there are three significant occurrences of shock-flame interaction:

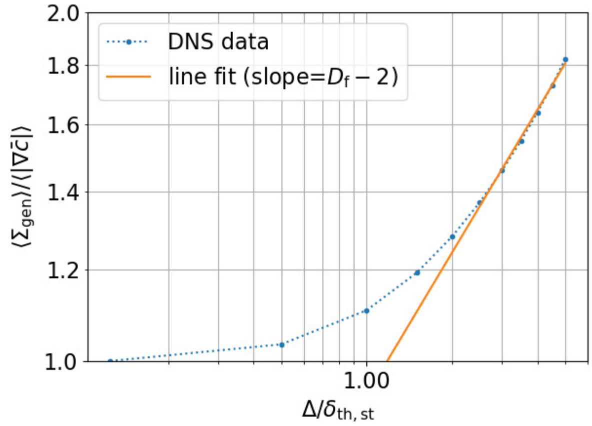

***Fig. 9**: Left: Double logarithmic plot of volume averaged wrinkling factor over normalized filter size, for* $\phi = 1$ *and* $t \times S_{L,st}/\delta_{th,st} = 1$.

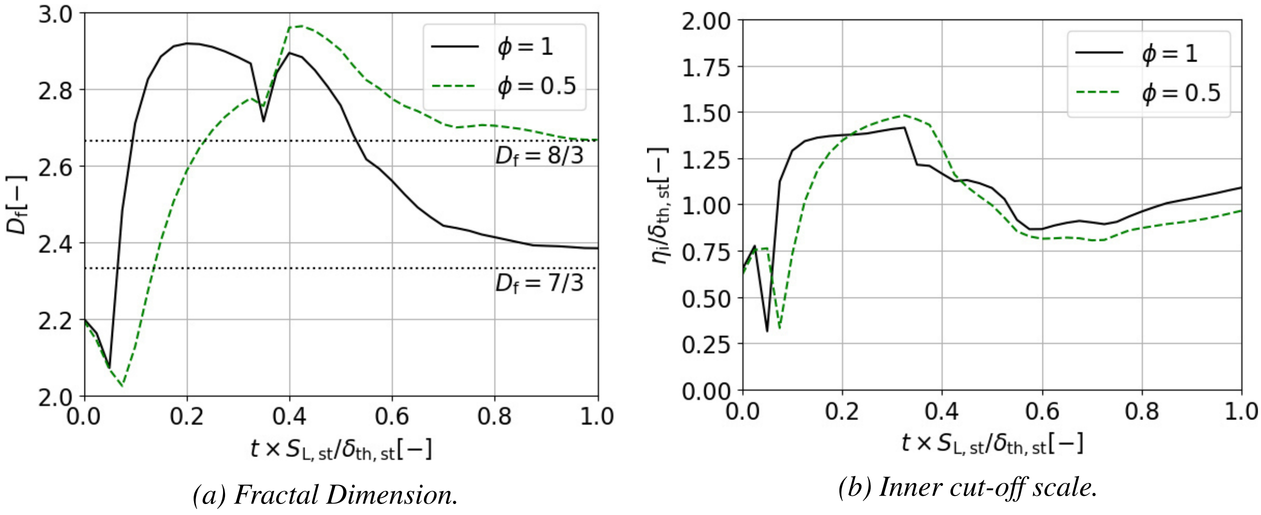

(a) Fractal Dimension. *(b) Inner cut-off scale.*

***Fig. 10**: Fractal dimension and inner cut-off scale for lean and stoichiometric gas mixture over time.*

- interaction of the shock-wave with the initially perturbed flame surface
- re-shock due to the reflection of the shock wave at the back wall
- interaction with partially reflected shock (flame surface $\leftrightarrow$ wall)

The individual terms of the enstrophy transport equation are investigated, where it is found that the baroclinic torque, which is responsible for the RMI, dominates the other terms most of the time. It is found that the vortex stretching and diffusion term surpass the baroclinic term after the re-shock. This effect is visible in the lean case and to a lesser extent in the stoichiometric case as the vortex stretching and diffusion terms are generally much smaller there. The baroclinic torque shows high peaks after each shock-flame interaction. The peak heights are heavily influenced by the flame thickness, which differs between both cases and in time due to flame compression and an increased pressure level caused by the shock wave. After the first shock-flame interaction, the peak height of the stoichiometric case is about ten times higher than for the lean case, due to the previously mentioned differences in flame thickness and also heat release ratio, leading to an increased density gradient across the flame. After the re-shock the baroclinic torque production of the lean case increases significantly as the difference in flame thickness is reduced and more flame surface area is available.

The effects of the baroclinic torque production and flame wrinkling also become apparent when investigating the temporal development of the flame surface area A_f and the turbulent mixing width δ_m. A strong increase in A_f and δ_m is observed on each shock interaction, with a maximum possible increase of about 400% for the investigated cases. Due to funnel-closure and smoothing effects of the stoichiometric case, the end values of A_f differ by about 30% between both cases. Finally the fractal behavior of the flame surface is investigated in the context of power-law based modeling of the wrinkling factor. For the stoichiometric and lean case a maximum fractal dimension of about 2.92 to 2.96 is determined (reached at different times), before settling at 2.38 respective 2.67. The inner cut-off scale is only weakly dependent on the equivalence ratio and reaches values close to the stoichiometric thermal flame thickness ($\pm 25\%$).

For the lean case ($\mathrm{Le} = 0.5$) the Lewis number is significantly smaller than unity, therefore the flame is more susceptible to thermo-diffusive instabilities in addition to the RMI. A next step would be to investigate the effect of isolated changes in the Lewis number to separate the influence on flame wrinkling of the thermo-diffusive instabilities and RMI. Furthermore the investigations on the enstrophy transport equation and fractal behavior can be used in the work towards a sub-grid model of the RMI flame wrinkling.

Acknowledgements

The presented work is funded by the German Federal Ministry of Economic Affairs and Energy (BMWi) on the basis of a decision by the German Bundestag (project no. 1501574) which is gratefully acknowledged.

References

Bambauer, M., Hasslberger, J., Klein, M. (2020). *Direct Numerical Simulation of the Richtmyer–Meshkov Instability in Reactive and Nonreactive Flows*. Combustion Science and Technology, pages 1–18.

Bechtold, J. K., Matalon, M. (2001). *The Dependence of the Markstein Length on Stoichiometry*. Combustion and Flame, 127(1-2):1906–1913.

Boger, M., Veynante, D., Boughanem, H., Trouvé, A. (1998). *Direct Numerical Simulation Analysis of Flame Surface Density Concept for Large Eddy Simulation of Turbulent Premixed Combustion*. Symposium (International) on Combustion, 27(1):917–925.

Breitung, W., Chan, C., Dorofeev, S., Eder, A., Gelfand, B., Heitsch, M., Klein, R., Malliakos, A., Shepherd, J., Studer, E., Thibault, P. (2000). *Flame Acceleration and Deflagration-to-Detonation Transition in Nuclear Safety*. NEA/CSNI/R(2000)7.

Chakraborty, N., Klein, M. (2008). *A Priori Direct Numerical Simulation Assessment of Algebraic Flame Surface Density Models for Turbulent Premixed Flames in the Context of Large Eddy Sim-*

ulation. Physics of Fluids, 20(8):085108.

Ciccarelli, G., Dorofeev, S. (2008). *Flame acceleration and Transition to Detonation in Ducts*. Progress in Energy and Combustion Science, 34(4):499–550.

Ciccarelli, G., Johansen, C. T., Parravani, M. (2010). *The Role of Shock–Flame Interactions on Flame Acceleration in an Obstacle Laden Channel*. Combustion and Flame, 157(11):2125–2136.

Dorofeev, S. B. (2011). *Flame Acceleration and Explosion Safety Applications*. Proceedings of the Combustion Institute, 33(2):2161–2175.

Fureby, C. (2005). *A Fractal Flame-Wrinkling Large Eddy Simulation Model for Premixed Turbulent Combustion*. Proceedings of the Combustion Institute, 30(1):593–601.

Goodwin, D. G., Speth, R. L., Moffat, H. K., Weber, B. W. (2018). *Cantera: An object-oriented software toolkit for chemical kinetics, thermodynamics, and transport processes*. `https://www.cantera.org`. Version 2.4.0.

Gouldin, F., Bray, K., Chen, J.-Y. (1989). *Chemical Closure Model for Fractal Flamelets*. Combustion and Flame, 77(3-4):241–259.

Gülder, O. (1995). *Inner Cutoff Scale of Flame Surface Wrinkling in Turbulent Premixed Flames*. Combustion and Flame, 103(1-2):107–114.

Hasslberger, J. (2017). *Numerical Simulation of Deflagration-to-Detonation Transition on Industry Scale*. Ph.D. thesis, Technical University Munich.

Hawkes, E. R., Chatakonda, O., Kolla, H., Kerstein, A. R., Chen, J. H. (2012). *A Petascale Direct Numerical Simulation Study of the Modelling of Flame Wrinkling for Large-Eddy Simulations in Intense Turbulence*. Combustion and Flame, 159(8):2690–2703.

Jenkins, K. W., Cant, R. S. (1999). *Direct Numerical Simulation of Turbulent Flame Kernels*. In Knight, D., Sakell, L., editors, *Recent Advances in DNS and LES*, pages 191–202. Springer Netherlands, Dordrecht.

Jiang, G.-S., Shu, C.-W. (1996). *Efficient Implementation of Weighted ENO Schemes*. Journal of Computational Physics, 126(1):202–228.

Kerstein, A. R. (1988). *Fractal Dimension of Turbulent Premixed Flames*. Combustion Science and Technology, 60(4-6):441–445.

Klein, M., Herbert, A., Kosaka, H., Böhm, B., Dreizler, A., Chakraborty, N., Papapostolou, V., Im, H. G., Hasslberger, J. (2020). *Evaluation of Flame Area Based on Detailed Chemistry DNS of Premixed Turbulent Hydrogen-Air Flames in Different Regimes of Combustion*. Flow, Turbulence and Combustion, 104(2-3):403–419.

Knikker, R., Veynante, D., Meneveau, C. (2004). *A Dynamic Flame Surface Density Model for Large Eddy Simulation of Turbulent Premixed Combustion*. Physics of Fluids, 16(11):L91–L94.

Lindl, J. (1995). *Development of the Indirect-Drive Approach to Inertial Confinement Fusion and the Target Physics Basis for Ignition and Gain*. Physics of Plasmas, 2(11):3933–4024.

Mandelbrot, B. B. (1975). *On the Geometry of Homogeneous Turbulence, with Stress on the Fractal Dimension of the Iso-Surfaces of Scalars*. Journal of Fluid Mechanics, 72(03):401.

Meshkov, E. E. (1972). *Instability of the Interface of Two Gases Accelerated by a Shock Wave*. Fluid Dynamics, 4(5):101–104.

Poinsot, T., Veynante, D. (2005). *Theoretical and Numerical Combustion*. Edwards, London.

Rayleigh (1882). *Investigation of the Character of the Equilibrium of an Incompressible Heavy Fluid of Variable Density*. Proceedings of the London Mathematical Society, s1-14(1):170–177.

Remington, B. A., Drake, R. P., Takabe, H., Arnett, D. (2000). *A review of Astrophysics Experiments on Intense Lasers*. Physics of Plasmas, 7(5):1641–1652.

Richtmyer, R. D. (1960). *Taylor Instability in Shock Acceleration of Compressible Fluids*. Communications on Pure and Applied Mathematics, 13(2):297–319.

Shu, C.-W. (1998). *Essentially Non-Oscillatory and Weighted Essentially Non-Oscillatory Schemes for Hyperbolic Conservation Laws*. In *Advanced Numerical Approximation of Nonlinear Hyperbolic Equations*, pages 325–432. Springer.

Taylor, G. (1950). *The Instability of Liquid Surfaces when Accelerated in a Direction Perpendicular to* *their Planes. I.* Proceedings of the Royal Society of London. Series A. Mathematical and Physical Sciences, 201(1065):192–196.

Tritschler, V. K., Hickel, S., Hu, X. Y., Adams, N. A. (2013). *On the Kolmogorov Inertial Subrange Developing from Richtmyer-Meshkov Instability*. Physics of Fluids, 25(7):071701.

Tritschler, V. K., Olson, B. J., Lele, S. K., Hickel, S., Hu, X. Y., Adams, N. A. (2014). *On the Richtmyer–Meshkov Instability Evolving from a Deterministic Multimode Planar Interface*. Journal of Fluid Mechanics, 755:429–462.

Wray, A. A. (1990). *Minimal Storage Time Advancement Schemes for Spectral Methods*. NASA Ames Research Center, California, Report No. MS, 202.

DOI: 10.7795/810.20200724

Physical and Mathematical Modelling of Interaction of Detonation Waves with Inert Gas Plugs

Dmitry Tropin & Igor Bedarev
Khristianovich Institute of Theoretical and Applied Mechanics SB RAS, Novosibirsk, Russia
E-mail: d.a.tropin@itam.nsc.ru

Abstract

In the paper the physical and mathematical model for the description of the processes of transition, attenuation and suppression of detonation in hydrogen-air mixture in one- and two-dimensional formulation, taking into account reduced and detailed kinetics of chemical transformations in reactive gases, by inert gas plugs was proposed. On the basis of this model calculations of the interaction of plane (in one-dimensional formulation) and cellular (in two-dimensional formulation) detonation wave propagating in hydrogen-air mixture with layer of inert gases (argon, nitrogen, carbon dioxide) were performed. It was shown that depending on the type of isolating gas and the length of the plug various flow regimes were realized after the shock wave exits from the inert gas plug: a) reinitiation of detonation wave; b) suppression of the detonation wave with the formation of a deflagration wave at the end of the inert gas layer; c) suppression of the detonation wave with the combustion zone isolation by inert gas plug. The geometric limits of detonation (minimum inert gas plug length leads to detonation suppression with combustion zone isolation) for all three types of inert gas plugs were calculated. Comparison of the effectiveness of detonation suppression by various inert gas plugs shows that the carbon dioxide is more efficient for suppressing the detonation wave, i.e. geometric limits of detonation during interaction of detonation with carbon dioxide plug is smallest compared with other two types of plugs.

Keywords: *detonation wave, detonation suppression, inert gas plug, physical and mathematical modelling*

1. Introduction

The physical and mathematical modelling of the interaction of detonation waves propagating through a hydrogen-air mixture with a layer of unreacting gas is performed in the paper. The relevance of these studies is related to issues of explosion and fire safety, namely, the problem of attenuation and suppression of detonation waves in combustible gas mixtures (Gottiparthi and Menon 2012, Liu et. al. 2016, Tropin and Fedorov 2017, 2018, 2019). Explosions of combustible industrial gases and gas suspensions are one of the main causes of technological disasters. An example of the catastrophe is the explosion in the city of Kaohsiung, Taiwan related with a propylene leak (Yang et.al. 2017). The explosion occurred during the transportation of propylene from the port to a chemical plant through a pipeline laid in underground utilities. One way to prevent the catastrophic consequences of these incidents is to use inert components, for example solid inert particles or inert gas plugs, to suppress detonation and to isolate the combustion zones.

There are a lot of works devoted to suppression the detonation waves by inert components, primarily by solid inert particles. The addition of chemically inert particles reduces the velocity of detonation (Borisov et.al. 1975, Tropin and Fedorov 2014, 2019), change the length of the chemical reaction zone of the detonation wave (Borisov et.al. 1975) and at certain conditions can lead to the splitting of detonation wave (DW) into frozen shock wave (SW) and lagging from it the combustion front (Dong et. al. 2005, Fedorov and Tropin 2013, Liu et. al. 2016). The concentration limits of detonation in various mixtures of hydrogen, methane, silane and oxidizer while suppressing DW by clouds of inert micro- and nanoparticles was defined by many authors both experimentally and numerically (Bedarev (2019), Gottiparthi and Menon (2012), Pinaev et.al. (2015), Tropin and Fedorov (2019)). Furthermore, in these papers it has been shown that the most effective in detonation suppressing the smaller diameter particles. Papalexandris (2004) and Shafiee and Djavareshkian (2014) shown that the addition of inert microparticles destroys the cellular structure of the DW in some model mixture.

There are not many papers in the literature devoted to the suppression of explosion and detonation by inert gas plugs. Yang et.al. (2019) were carried out experimental studies demonstrates the flame propagation suppression with inert gas plugs. They were found that the critical length of the inert gas section required for successful suppression of flame from the igniting the flammable section is from 0.2m to 0.9m long depending on type of inert gas.

This paper proposes the numerical study of the process of detonation wave interaction in a hydrogen-air mixture with plugs of three inert gases: carbon dioxide, argon, nitrogen.

2. Physical and Mathematical Formulation of the Problem

Let's consider a shock tube filled with the mixture of hydrogen and air at atmospheric conditions ($p_0 = 1$ atm, $T_0 = 296$ K). Plane (in one-dimensional formulation) and cellular (in two-dimensional formulation) detonation wave was used as the initial data and located at the left boundary of shock tube (Fig. 1). At some distance from the detonation wave the inert gas plug (CO_2, N_2 or Ar) is located. After the start of the calculation, the detonation wave moved from left to right and interacts with the plug.

The considered process was modeled by the Euler system of equations describing the motion of an inviscid compressible gas, taking into account the multicomponent nature of the gas mixture and chemical kinetics.

During modeling the flows with detonation waves, as in any problem with chemical reactions, arises the problem of choosing a kinetic scheme for an adequate description of the combustion process. In this paper, we will consider the reduced and detailed kinetics of combustion of a gas mixture. Detailed kinetics makes it possible to more accurately reproduce such parameters as the ignition delay time of the mixture, the distribution of the components of the gas mixture in the structure of the detonation wave, but requires a large machine time costs. To describe the chemical reactions in the reacting gas mixture we will use the following detailed kinetics model provided by Tien and Stalker (2002) and taking into account 38 reactions of 8 components. In our previous studies, this model allowed us to describe the experimentally observed ignition delay time in a hydrogen–oxygen mixture (Bedarev and Fedorov 2006, Fedorov et.al. 2010), to calculate the concentration limits of detonation (Fedorov and Tropin 2013), and to determine the geometric limits of detonation (Fedorov and Tropin 2011).

We will also use the previously developed one-stage model of chemical kinetics (Bedarev et.al. 2015). According to this model, the combustion of a stoichiometric mixture of hydrogen and oxygen will be described by one integral irreversible reaction:

$$2H_2 + O_2 + \nu N_2 \rightarrow 2H_2O + \nu N_2$$

where ν – stoichiometric coefficient depending on the degree of dilution of the mixture with nitrogen (for air $\nu = 3.82$). A detailed verification of this kinetic scheme by ignition delay times, detonation wave velocity, detonation cell size and inclined detonation wave modes, as well as an algorithm for determining the model constants are presented by Bedarev et.al. 2015, 2019.

DOI: 10.7795/810.20200724

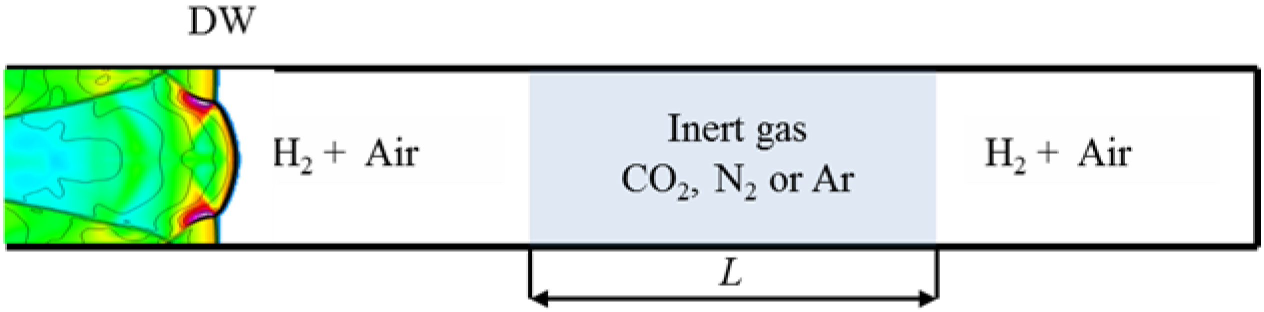

Fig. 1. *The problem statement. Flow pattern.*

3. Results and discussion

Let's consider the interaction of a one- and two-dimensional detonation wave with inert gas plug of various inert gases (argon, nitrogen, carbon dioxide).

3.1 One-dimensional detonation wave. Reduced kinetics

First of all, one-dimensional calculations using reduced kinetics mechanism were performed. Depending on the type of isolating gas and the length of the plug, various flow regimes can be realized after the shock wave leaves the inert plug: a) detonation reinitiation; b) suppression of the detonation wave with the formation of a deflagration wave; c) suppression of the detonation wave with the combustion zone isolation. Figs. 2-5 shows the examples of these regimes during interaction of detonation wave with nitrogen gas plug with various length. In figures left boundary of the plug located at coordinate $x = 0.5$ m. It can be seen that after the detonation wave enters the inert plug chemical reactions stops and detonation wave transforms into the shock wave. The latter attenuates during its propagation in inert plug. Then, if the inert plug length is not enough to reduce the shock wave parameters less than some critical, after the shock wave exits the plug behind its front chemical reactions starts again. Fig. 2 shows the propagation of the shock wave through nitrogen plug 30cm length. It can be seen that after shock wave exits from the plug behind its front the initiation of detonation wave occurs. The temperature behind the frozen shock wave before it leaves the plug is equal to 816K. So, we have the first interaction regime – re-initiation of detonation. Fig. 3 shows the propagation of the shock wave through nitrogen plug 40cm length. Here, after the shock wave exits from plug re-initiation of detonation does not occur, temperature behind the frozen shock wave is equal to 760K. Shock wave propagation and compression waves propagation from the left boundary of the plug-reacting gas interface towards the shock wave are observed. Fig. 4 shows distribution of mass concentration of water vapor in shock tube. There are 2 regions of high mass concentration of water vapor – left caused by the propagation of detonation wave before the interaction with inert gas plug and right – indicates a chemical reactions behind the shock wave front after it exits from the plug. Here we have another one interaction regime – suppression of detonation wave with formation of deflagration wave. Fig. 5 shows the propagation of the shock wave through nitrogen plug 70cm length. It can be seen that after the shock wave exits from the plug no chemical reaction are observed behind its front, only propagation of attenuated shock wave are occurs. The temperature behind the frozen shock wave before it leaves the plug is equal to 636K which is much less than hydrogen ignition temperature. So, here we have the third interaction regime – suppression of detonation with isolation of combustion zone and propagation of frozen shock wave which attenuates during its propagation in combustible gas.

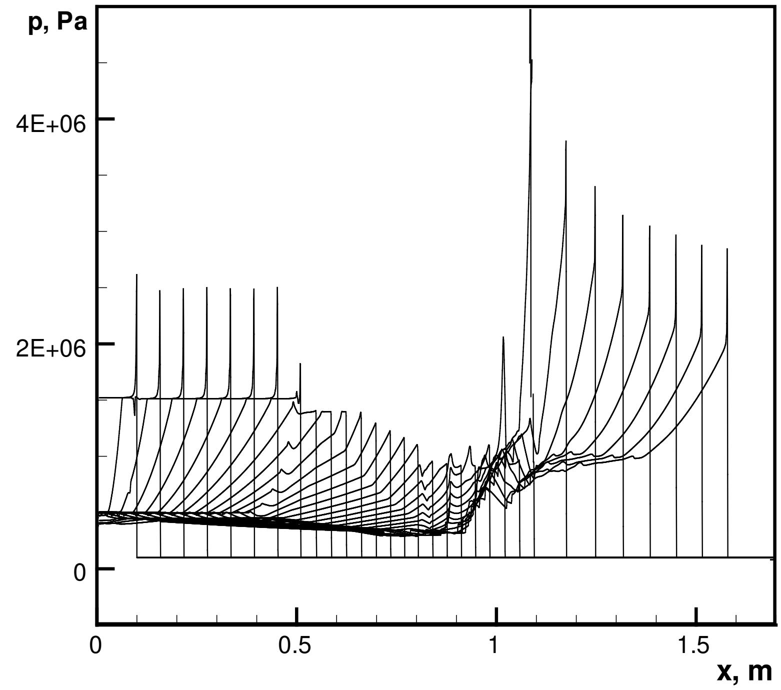

Fig. 2. *Pressure distribution in shock tube. Nitrogen gas plug 30 cm length. Reinitiation of detonation wave*

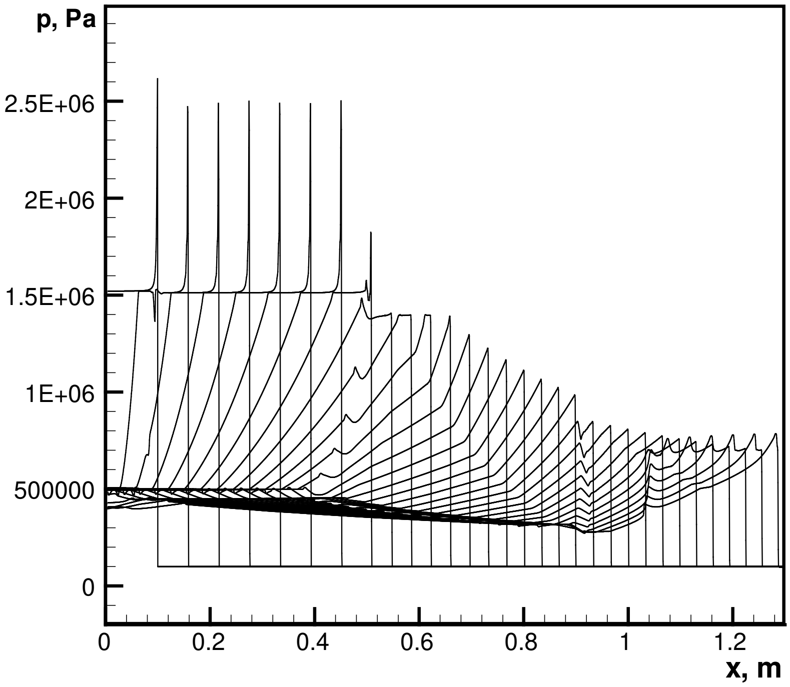

Fig. 3. *Pressure distribution in shock tube. Nitrogen gas plug 40 cm length. Detonation wave suppression with the formation of deflagration wave*

DOI: 10.7795/810.20200724

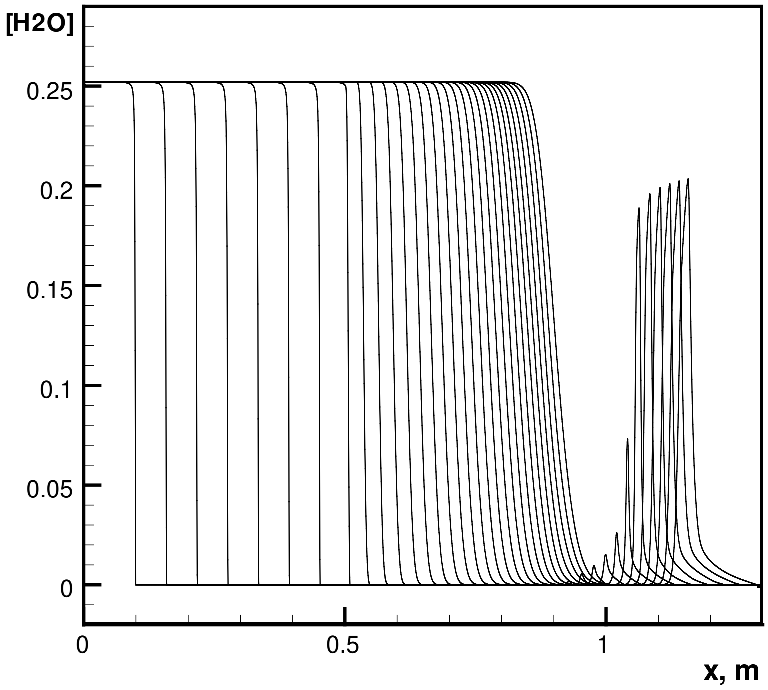

Fig. 4. Distribution of mass concentration of water vapor in shock tube. Nitrogen gas plug 40 cm length. Detonation wave suppression with the formation of deflagration wave

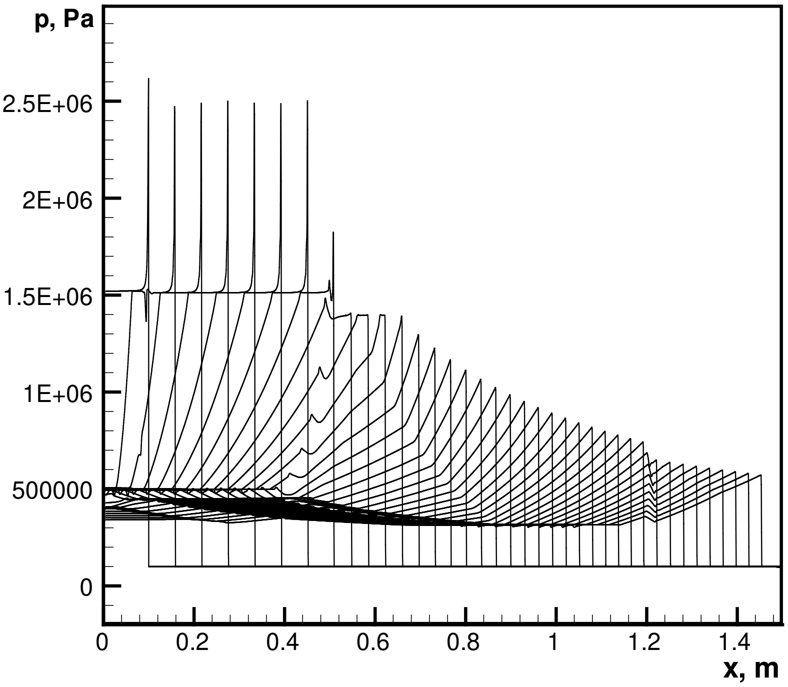

Fig. 5. Pressure distribution in shock tube. Nitrogen gas plug 70 cm length. Detonation wave suppression

In other inert gases under consideration these regimes are remains but at different plug length. The table 1 summarizes the flow regimes after the shock wave leaves the cloud of three inert gases:

carbon dioxide (CO_2), nitrogen (N_2) and argon (Ar). In the table, the regimes are indicated as follows: A –reinitiation of detonation; B - detonation wave suppression with the deflagration wave formation; C – detonation wave suppression with the combustion zone isolation. If we will compare the detonation suppressing effect of the plugs we can see that carbon dioxide is more effective for detonation suppression and the argon is less effective in this process. These difference caused by the different densities and heat capacities of the inert gases. The parameters are: carbon dioxide – $\rho = 1.764$ kg/m^3, $c_p = 843.86$ J/(kg*K), nitrogen – $\rho = 1.123$ kg/m^3, $c_p = 1040$ J/(kg*K), argon – $\rho = 1.604$ kg/m^3, $c_p = 519.65$ J/(kg*K). The energy losses of shock wave will be the greater if the multiplication of density and heat capacity of inert gas in plug will be greater. The multiplication are greater in carbon dioxide and the smallest in argon. Yang et.al. (2019) experimentally compare the effectiveness of deflagration suppression by carbon dioxide and nitrogen gas plug and obtain that the latter is less effective in this process. So our calculations are in good agreement with the experimental observations.

Table 1: *Detonation regimes*

	L = 0.3 m	*L* = 0.4 m	*L* = 0.6 m	*L* = 0.7 m	*L* = 1.2 m
CO_2	B	B	C	C	C
N_2	A	B	B	C	C
Ar	A	B	B	B	C

3.2 One-dimensional detonation wave. Detailed kinetics

Then, one-dimensional calculations using detailed kinetics mechanism were performed. All three types of detonation flows described in section 3.1 in calculations with the detailed kinetics are remains, but the length of inert gas plugs for corresponding regimes are greater. Fig. 6 shows the first realized regime – detonation reinitiation during interaction of detonation wave with nitrogen plug 75cm length. It can be seen that after shock wave leaves the plug the initiation of detonation wave behind its front occurs. The second regime – suppression of detonation with formation the deflagration wave are shown in figs. 7, 8. Here, we have a propagation of shock wave and compression waves (fig. 7) and reaction front (deflagration) behind them (fig. 8). The last regime – suppression of detonation with isolation of reaction zone are presented in fig. 9. Here, it can be seen the propagation of attenuated shock wave without any chemical reaction.

The table 2 summarizes the flow regimes after the shock wave leaves the cloud for all three inert gases under consideration. In the table, the regimes are indicated in the same form like in section 3.1. From tables 1 and 2 it can be seen that the length of inert gas plug of corresponding inert gas is greater in calculations with detailed kinetics. But qualitatively the results are similar: the argon plug has greater length for detonation suppression, the smallest one – the carbon dioxide plug. Yang et.al. (2019) were carried out experimental studies of interaction of deflagration waves with inert gas plug. In experiments they obtain that for suppression of the high velocity deflagration wave the 90cm carbon dioxide plug is needed. But the detonation is more powerful process and quite possible that for its suppression the longer plugs will be needed. Given this circumstance the cloud lengths in calculations with detailed kinetics are more appropriate compared with reduced kinetics.

Table 2: *Detonation regimes*

	L = 0.5 m	*L* = 0.75 m	*L* = 0.9 m	*L* = 1.5 m	*L* = 1.7 m	*L* = 2.6 m
CO_2	A	A	C	C	C	C
N_2	A	A	A	B	C	C
Ar	A	A	A	A	A	B

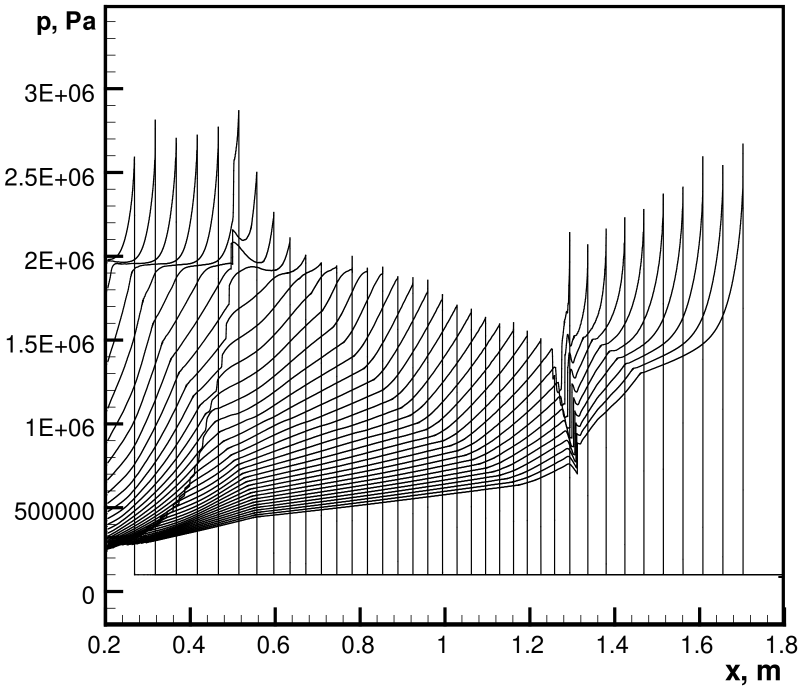

Fig. 6. Pressure distribution in shock tube. Nitrogen gas plug 75 cm length. Reinitiation of detonation wave

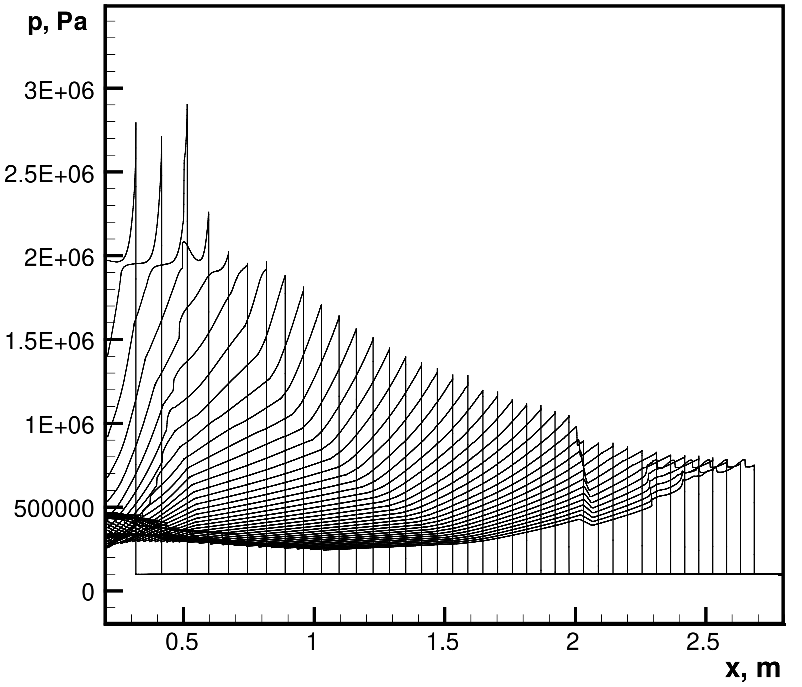

Fig. 7. Pressure distribution in shock tube. Nitrogen gas plug 150 cm length. Detonation wave suppression with the formation of deflagration wave

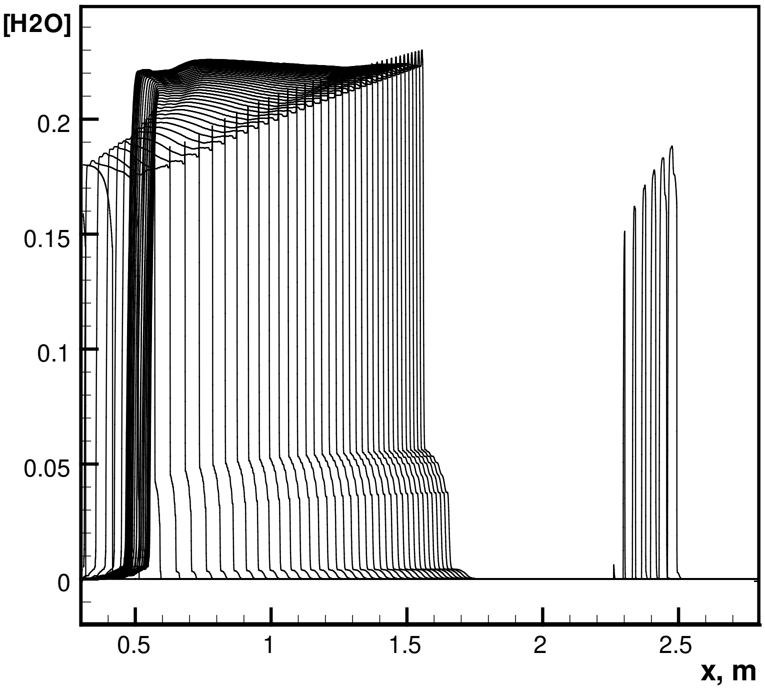

Fig. 8. Distribution of mass concentration of water vapor in shock tube. Nitrogen gas plug 150 cm length. Detonation wave suppression with the formation of deflagration wave

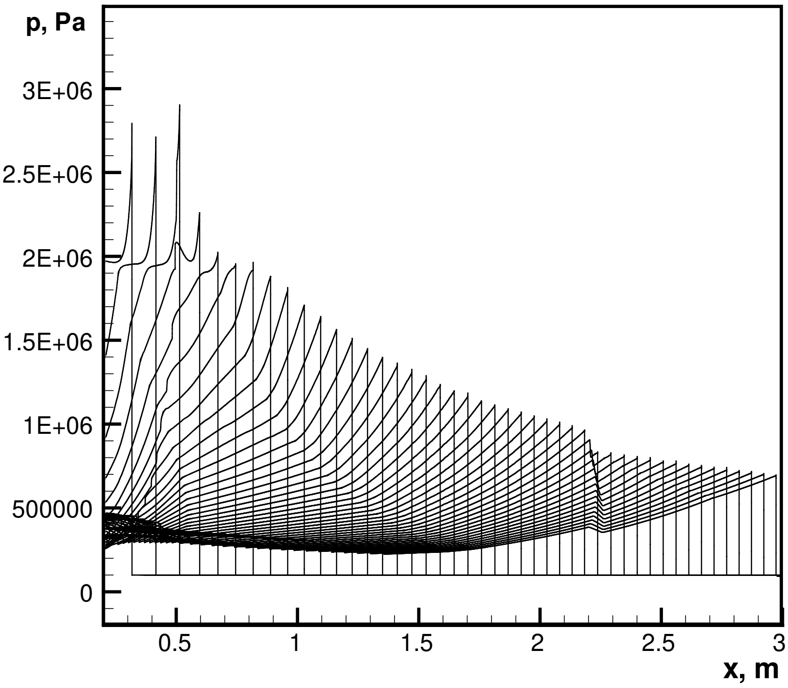

Fig. 9. Pressure distribution in shock tube. Nitrogen gas plug 170 cm length. Detonation wave suppression

DOI: 10.7795/810.20200724

3.3 Two-dimensional detonation wave. Reduced kinetics

It should be noted that detailed kinetic models are expensive in machine time. Therefore, in two-dimensional calculations, to optimize computational costs, we used the mentioned above single-stage reduced model.

In two-dimensional calculations all three types of detonation flows realized in one-dimensional calculations are remains. Fig. 10 shows these three regimes for a CO_2 plug with a length of L = 0.2 m (a), 0.3 m (b), and 0.4 m (c) in the form of the fields of density maxima in time. For a plug with a length of L = 0.2 m (fig. 10a), after the shock wave leaves the inert gas plug, the detonation wave is reinitiated with the further formation of the cellular structure. It is seen that at first the detonation cell with a small size is formed, but then the size of the detonation cell is enlarged to a value of 10-15 mm typical for a stoichiometric hydrogen-air mixture. Fig. 10b shows the fields of density maxima in time in case of detonation suppression with the formation of deflagration wave and fig. 10c shows the fields of density maxima in time in case of detonation suppression. The difference between the regimes can be seen in the fields of temperature and mass fraction of CO_2, which shown in fig. 11. Here the calculation results at time of 1.9 ms for clouds of 0.3 m (*a*, *b*) and 0.4 m (*c*, *d*) length are presented. It can be seen from the figure that for plug of inert gas with a length of 0.3 m, a combustion zone appears at its right boundary, which for a moment from 1.7 ms to 1.9 ms moves at an average velocity of about 485 m/s. Conclusions about the propagation dynamics of the combustion zone and the effect of turbulence on its behavior will allow further studies. We can also note the instability of the contact boundary of the CO_2 layer. This is Richtmayer-Meshkov instability, which is caused by the passing of reflected shock waves through the boundary between the layer of light and heavy gas.

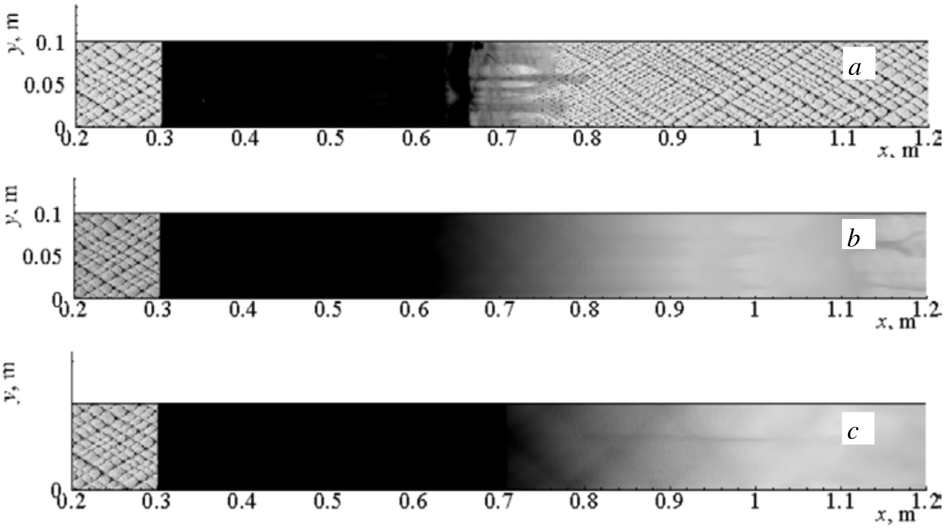

Fig. 10. Fields of density maxima in time for a CO_2 plug of length L = 0.2 m (a), 0.3 m (b), and 0.4 m (c).

DOI: 10.7795/810.20200724

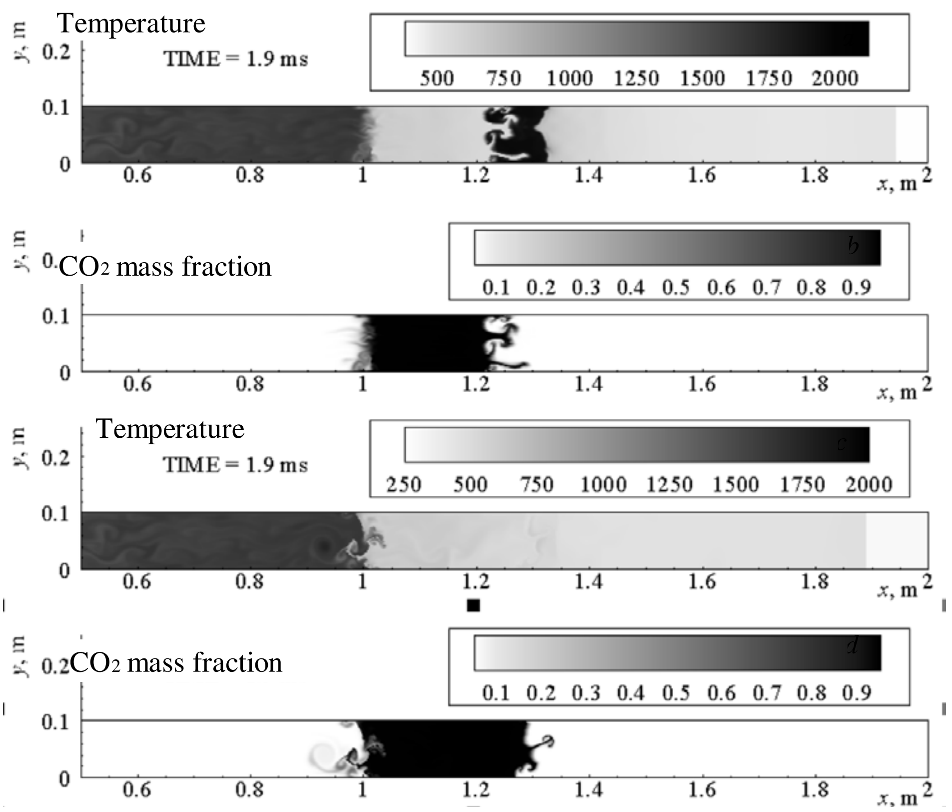

Fig. 11. *Fields of temperature and mass fraction of CO_2 for plugs of length L = 0.3 m (a, b) and 0.4 m (c, d).*

The table 3 summarizes the detonation flow regimes after the shock wave leaves the cloud for three inert gases under consideration. In the table, the regimes are indicated in the same form like in section 3.1. It is seen from comparison of the tables 1 – 3 that the two-dimensional calculations gives the smallest length of inert gas plug with corresponding inert gases compared with one-dimensional calculations with two kinetics models. This can be caused by the small width of the channel. The experiments of Yang et.al. (2019) shown that if the channel is wider than the larger inert gas plug is needed at the same gas and wave parameters.

Table 3: *Detonation regimes*

	$L = 0.2$ m	$L = 0.3$ m	$L = 0.4$ m	$L = 0.5$ m	$L = 0.75$ m
CO_2	A	B	C	C	C
N_2	A	A	A	B	C
Ar	A	A	B	C	C

4. Conclusions

Calculations of the interaction of plane (in one-dimensional formulation) and cellular (in two-dimensional formulation) detonation wave propagating in hydrogen-air mixture with plug of inert gases (argon, nitrogen, carbon dioxide), based on the physical and mathematical model for the description of the process, taking into account reduced and detailed kinetics of chemical transformations in reactive gases, were performed.

It was shown that depending on the type and the length of inert gas plug various flow regimes are realized: reinitiation of detonation wave; suppression of the detonation wave with the formation of a deflagration wave; suppression of the detonation wave with the combustion zone isolation by inert plug.

The geometric limits of detonation (minimum inert gas plug length leads to detonation suppression with combustion zone isolation) for all types of inert gas plug under consideration were calculated. Comparison of the effectiveness of detonation suppression by various inert gas plugs shows that the carbon dioxide is more efficient for suppressing the detonation wave and argon is less efficient for this process.

Acknowledgements

This work was supported by the Russian Science Foundation (project № 19-79-00096) and Program of Fundamental Scientific Research of the State Academies of Sciences for 2013-2020 (project AAAA-A17-117030610139-4).

References

Bedarev, I.A. (2019). Micro-Level Modeling of the Detonation Wave Attenuation by inert particles. *Thermal Science,* 23(2): 439-445.

Bedarev, I.A., and Fedorov, A.V. (2006) Comparative Analysis of Three Mathematical Models of Hydrogen Ignition. *Combustion, Explosion and Shock Waves,* 42(1): 19-26.

Bedarev, I.A., Rylova, K.V., Fedorov, A.V. (2015). Application of detailed and reduced kinetic schemes for the description of detonation of diluted hydrogen-air mixtures. *Combustion, Explosion and Shock Waves,* 51(5): 528-539.

Bedarev, I.A., Temerbekov, V.M., Fedorov, A.V. (2019). Simulating the regimes of oblique detonation waves arising at detonation initiation by a small-diameter projectile. *Thermophysics and Aeromechanics*, 26(1): 59-68.

Borisov, A.A., Gel'fand, B.E., Gubin, S.A., Kogarko, S.M. (1975). Effect of inert solid particles on detonation of a combustible gas mixture. *Combustion, Explosion and Shock Waves,* 11(6): 774-778.

Dong, G., Fan, B., Xie, B., Ye, J. (2005). Experimental investigation and numerical validation of explosion suppression by inert particles in large-scale duct. *Proceedings of the Combustion Institute,* 30(2): 2361-2368.

Fedorov, A.V. and Tropin, D.A. (2011). Determination of the critical size of a particle cloud necessary for suppression of gas detonation. *Combustion, Explosion and Shock Waves*, 47(4): 464-472.

Fedorov, A.V. and Tropin, D.A. (2013). Modeling of detonation wave propagation through a cloud of particles in a two-velocity two-temperature formulation. *Combustion, Explosion and Shock Waves*, 49(2): 178-187.

Gottiparthi, K.C. and Menon, S. (2012). A Study of Interaction of Clouds of Inert Particles with Detonation in Gases. *Combustion Science and Technology,* 184(3): 406-433.

Liu, Y., Liu, X., Li, X. (2016). Numerical investigation of hydrogen detonation suppression with inert particle in pipelines. *International journal of hydrogen energy* 41(46): 21548-21563.

Papalexandris, M.V. (2004) Numerical simulation of detonations in mixtures of gases and solid particles. *Journal of Fluid Mechanics,* 507: 95-142.

Pinaev, A.V., Vasil'ev, A.A., Pinaev, P.A. (2015). Suppression of gas detonation by a dust cloud at reduced mixture pressures. *Shock Waves,* 25(3): 267-275.

Shafiee, H. and Djavareshkian, M.H. (2014). CFD Simulation of Particles Effects on Characteristics of Detonation. *International Journal of Computer Theory and Engineering,* 6(6): 466-471.

Tien, J.H., and Stalker, R.J. (2002). Release of Chemical Energy by Combustion in a Supersonic Mixing Layer of Hydrogen and Air. *Combustion and Flame,* 131(3): 329-348.

Tropin, D.A. and Fedorov, A.V. (2014). Mathematical modeling of detonation wave suppression by cloud of chemically inert solid particles. *Combustion Science and Technology,* 186(10-11): 1690-1698.

Tropin, D.A. and Fedorov, A.V. (2017). Physical and mathematical modeling of ignition, combustion and detonation of silane-hydrogen-air mixtures. *Journal of Loss Prevention in the Process Industries*, 49(B): 762-768.

Tropin, D.A. and Fedorov, A.V. (2018). Attenuation and suppression of detonation waves in reacting gas mixtures by clouds of inert micro- and nanoparticles. *Combustion, Explosion and Shock Waves,* 54(2): 200-206.

Tropin, D.A. and Fedorov, A.V. (2019). Effect of inert micro- and nanoparticles on the parameters of detonation waves in silane/hydrogen - air mixtures. *Combustion, Explosion and Shock Waves,* 55(2): 230-236.

Tropin, D.A. and Fedorov, A.V. (2019). Physical and mathematical modeling of interaction of detonation waves in mixtures of hydrogen, methane, silane, and oxidizer with clouds of inert micro- and nanoparticles. *Combustion Science and Technology,* 191(2): 275–283.

Yang, H.N., Chen, J.H., Chiu, H.J., Kao, T.J., Tsai, H.Y. and Chen, J.R. (2017). Leak and explosion from an underground pipeline in Kaohsiung, Taiwan. *Loss Prevention Bulletin,* 257: 13-18.

Yang, H.N., Lin, Y.J., Liu, C.H., Chin, M.G., Wang, C.C., Tsai, H.Y., Chen, J.R. (2019). Suppression of flame propagation in a long duct by inertia isolation with inert gases. *Journal of Loss Prevention in the Process Industries*, 59: 23–34.

DOI: 10.7795/810.20200724

Boundary Conditions and Grid Dependency in CFD Simulation of Atmospheric Flow

Henry Plischka[a], Johann Turnow[a] & Nikolai Kornev[a]
[a] Chair of Modeling and Simulation (Department of Mechanical Engineering and Shipbuilding,
University of Rostock, Germany)
E-mail: *henry.plischka@uni-rostock.de*

Abstract

An analysis of boundary conditions and numerical grid dependency for the simulation of atmospheric boundary layer flow in urban environment with regard to gas propagation is presented. Although irregular terrain, buildings and other obstacles influence the flow field significantly, realistic velocity and turbulent fields upstream the area of interest is of major importance and must be reproduced by the simulation method as realistically as possible to depict all important convection and diffusion processes. In this study the consistency of inlet boundary conditions and various wall function approaches using Reynolds averaged Navier Stokes equation simulations as well as the influence of subgrid-scale models in Large Eddy Simulation are investigated with regard to numerical grid resolution and roughness length. Variations are applied for simulations over level terrain with local grid refinement, which are validated using experimental wind tunnel data.

Keywords: *CFD, LES, gas dispersion, atmospheric boundary layer*

1 Introduction

Precise prediction of dispersion of hazardous gases inside the atmospheric boundary layer for complex environment is becoming increasingly important for a proper estimation of risks connected to normal operation and accidents in different industrial objects. Particularly as formerly, pure industrial regions, get mixed with inhabited areas by growing cities. Typically simple dispersion models following the Gaussian or Lagrangian approach (e.g. Janicke (1985), Janicke and Janicke (2007)) are used for these applications. Velocity, fluctuation and dispersion fields needed in Lagrangian models are often based on logarithmic wind profiles which are altered to account obstacles. Different approximations are available for the reproduction of recirculation zones e.g. behind buildings and the turbulence induced by different obstacles (see (Hirtl and Baumann-Stanzer, 2007)). Whereas the result quality of Lagrangian models depend highly on the underlying wind and dispersion fields, Gaussian models don't resolve obstacles in the flow field, which makes them only applicable for releases in open or simple environment. Besides these methods, hazardous gas propagation can be calculated within the Euler approach using additional transport equation and results of the flow simulations. The most common approaches are Reynolds Averaged Navier-Stokes (RANS) and Large Eddy Simulation (LES) methods. In RANS time averaged velocity and dispersion fields are calculated, while LES resolves a substantial part of turbulent structures both in time and space.
All three models (Gaussian, Lagrangian and Euler approach) were tested and compared with wind tunnel measurements in a model evaluating case study for typical accidental scenarios (Baumann-Stanzer et al., 2015), where high uncertainties of the results have been revealed. For releases into an open space the first phase of dispersion can properly be predicted by all model types, whereas for sources located in complex terrain (such as street canyons) only scale resolving techniques such as LES are able to capture the strong discontinuities close to the release.

Many authors discussed horizontal homogeneity of atmospheric boundary layer flow for RANS. A short summary is given in section 2.2.1. Sensitivity to surface roughness and grid refinement at the ground has, to the authors best knowledge, not been described in the literature. For LES simulations of Atmospheric boundary layer (ABL) Porté-Agel et al. (2000) and Bou-Zeid et al. (2005) compared their dynamic scale dependent model (DSDM) with standard and dynamic Smagorinky model, where they also discussed the grid influence though only for SDDM. Stoll and Porté-Agel (2006) extended the investigation for one grid with various wall functions and roughness lengths up to 0.5 m for SDDM. Xie et al. (2015) analyzed sensitivity of three dynamic subgrid-scale (SGS) models to numerical scheme, filter size and grid resolution. Dependency on SGS modeling, atmospheric roughness and numerical grid with near-wall grading has not been described in literature for the models used in this study.

Aim of this work is to analyze rough wall boundary conditions, grid dependency and turbulence models for RANS and LES methods with focus on roughness length dependency for generating reliable atmospheric flow fields in gas propagation simulation.

2 Computational Methods

In the following section the geometrical and boundary conditions as well as the numerical setup of the simulations is described separately for RANS and LES methods. The software tool used in this work is OpenFOAM® (v1906) (Weller et al., 1998).

2.1 Computational domain

All simulations are performed in full scale. The computational domain has a size of $7H \times H \times H$ in RANS and $10H \times H \times H$ in LES, with (x-length $\times$ y-width $\times$ z-height) and $H = 600\,\text{m}$. In case of LES, a recycling or mapping approach is applied to ensure fully turbulent inlet conditions, which copies the velocity field from a mapping plane at $x = 7H$ back onto the domain inlet. The resolution in x- and y-direction (streamwise and spanwise) is 12.5 m. Three mesh refinements in vertical direction, with width of the first cell being $\Delta z_1 = 1.6\,\text{m}$, 3.2 m and 8 m are applied.

2.2 Boundary conditions

2.2.1 RANS

Vertical profiles of velocity and turbulence kinetic energy usually specified at the inlet in RANS have to be in equilibrium with driving force at the top of the computational domain and roughness characteristics of the ground to guaranty horizontal homogeneity in flow direction for each closure model (Richards and Norris, 2011)(Blocken et al., 2007). For the standard k-ε turbulence model Richards and Hoxey (1993) introduced a set of boundary conditions, widely used in wind engineering applications and thoroughly discussed (e.g. Hargreaves and Wright (2007), (Richards and Norris, 2011)). Inlet boundary conditions according to Richards and Hoxey (1993) and reading as

$$U_x = \frac{U_*}{\kappa} \ln\left(\frac{z+z_0}{z}\right), \qquad k = \frac{U_*^2}{\sqrt{C_\mu}}, \qquad \varepsilon = \frac{U_*^3}{\kappa\,(z+z_0)}, \tag{1}$$

are applied for all simulations regardless of different wall function approaches. In eq. (1) U_x is the mean axial velocity, k is the turbulence kinetic energy, ε is the dissipation rate, U_* is the friction velocity, z is the height coordinate and z_0 is the roughness height. The von Karman constant is defined as $\kappa = 0.41$ and C_μ is a common constant of the k-ε model. At the top boundary U is set to a constant value given by eq. (1) for $z = H$ appearing as driving force, whereas zero normal gradient condition (zero-gradient) is employed for the pressure p, k and ε. A fixed pressure is given at the outlet with zero-gradient for other variables. At the ground wall condition for U, zero-gradient for p and k, and wall function according to Richards and Hoxey (1993) for ε are applied. All simulations have been performed with zero normal velocity (slip) for U and zero-gradient conditions on the sides of the domain for the pressure p, turbulent kinetic energy k and turbulent dissipation rate ε.

Rough wall treatment at the ground is imposed by different wall functions for turbulent viscosity ν_t. The first wall function is based on roughness height z_0 (referred further to as the z_0-WF), where patch value of ν_t is calculated with

$$\nu_{t,w} = \frac{U_* z_1 \kappa}{\ln\left(\frac{z_1+z_0}{z_0}\right)} - \nu_w, \tag{2}$$

with friction velocity defined as $U_* = C_\mu^{0.25}\sqrt{k}$, the distance to adjacent cell midpoint z_1 and fluid viscosity at the wall ν_w. The second wall function is based on the so-called sand grain roughness k_s (k_s-WF), where

$$\nu_{t,w} = \frac{U_* z_1 \kappa}{\ln\left(\overline{E}\frac{u_* z_1}{\nu_w}\right)} - \nu_w, \qquad \text{with} \qquad \overline{E} = \frac{9.8}{\left(1+\frac{1}{2}k_s^+\right)}. \tag{3}$$

The non-dimensional sand grain roughness is defined as $k_s^+ = \frac{U_* k_s}{\nu}$, where k_s is set to $30\,z_0$.

2.2.2 LES

Tabor and Baba-Ahmadi (2010) classified LES inflow methods, to specify a time-varying turbulent velocity field, in precursor and synthetic methods. The atmospheric boundary layer profile can be provided by different treatment at the ground. In (Rodi et al., 2013) distinction is made by explicitly modeling roughness elements, applying momentum force or prescribing shear stress at the wall. In case of precursor method the inflow profile is generated upstream the area of interest. Different combinations of precursor methodologies and roughness modeling have been applied in literature. In Nakayama et al. (2011) rectangular blocks are arrayed and resolved on the surface of a separate precursor domain to produce a fully developed boundary layer flow, which is imposed to the inlet of the main domain. Nozawa and Tamura (2002) and Yang and Meneveau (2016) additionally recycled and rescaled the outlet field to inlet of precursor domain, whereas e.g. Bechmann and Sørensen (2011) and Chaudhari et al. (2018) neglected the rescaling due to assumption of fully developed boundary layer over constant roughness height upstream the area of interest. Direct recycling of the flow fields behind the obstacles (pure periodic boundary conditions) usually needs long extension in downstream direction, which can get numerically expensive (Chaudhari et al., 2018). (Xie and Castro, 2009) described that their LES results were not in reasonable agreement with wind tunnel data, when using periodic condition with short downstream extension. Other authors, especially when interested in flow over afforested regions, use momentum forces in porous media to predict atmospheric boundary layer, while in simulation of urban and suburban areas this method is rarely used.
Various models for applying shear stress at the wall to provide ABL profile are known from literature. Within this study the well known Schumann-Grötzbach (Schumann, 1975),(Grötzbach, 1987) wall function is used, where the turbulent viscosity is defined as

$$\nu_{t,w} = \frac{|\langle U\rangle|\,|\widetilde{U}|\kappa^2}{\frac{\partial|\widetilde{U}|}{\partial z}\left[\ln\left(\frac{z_1+z_0}{z_0}\right)\right]^2} - \nu_w, \tag{4}$$

where $|\langle U\rangle|$ and $|\widetilde{U}|$ are magnitude values of the horizontal averaged and the instantaneous filtered velocities of the ground adjacent cells. Comparison with the boundary condition of Thomas and Williams (1999) in time average form proposed by Vasaturo et al. (2018) was made for few cases with only minor differences to proposed results, whereas they are not shown.
Periodic boundary conditions are employed at sides of the domain and mapped fields are imposed at the inlet. Zero-gradient boundary condition is used for pressure at the top, bottom and inlet boundary whereas a fixed value is given at the outlet. Wall condition is applied for the velocity at the ground, while slip and zero-gradient conditions are employed at the top and outlet boundaries respectively. For the turbulent kinetic energy k zero-gradient conditions are enforced everywhere but inlet and sides of domain.

DOI: 10.7795/810.20200724

2.3 Numerical settings

2.3.1 RANS

All RANS simulations are run with the standard k-ε model using the SIMPLE algorithm for pressure correction. Due to numerical oscillations in velocity and pressure fields a blend of 90% second-order central differencing and 10% of the more diffusive second-order upwind differencing is imposed for convection terms. Convergence criteria for residuals is set to 10^{-4}.

2.3.2 LES

For the pressure-velocity coupling, the PISO algorithm (Issa, 1986) with two pressure correction steps and variable time step is used, where Courant-Friedrich-Lewis (CFL) number is limited to 0.4. Four LES models (Smagorinsky (SM) (Smagorinsky, 1963), dynamic Smagorinsky (DSM) (Lilly, 1992), k-equation (kEM) (Yoshizawa, 1986) and dynamic k-equation model (DOM) (Kim and Menon, 1995)) are utilized in the simulations. The Smagorinsky constant in SM is $C_s = 0.168$. All cases are initialized with flow fields of previous LES and run for about 11 flow through times to ensure a developed turbulent boundary layer. For statistical convergence a sampling of 120 flow through times is applied. Horizontal pressure gradient is imposed by scaling of the inflow velocity to a constant mean value. Second order implicit backward differences scheme is used for temporal integration, while convection terms are discretized using second order scheme.

3 Results and discussion

3.1 RANS

In Fig. 1 velocity profiles for four roughness lengths ($z_0 = 0.06\,\mathrm{m}$, $0.3\,\mathrm{m}$, $1.0\,\mathrm{m}$, $1.5\,\mathrm{m}$) with three near-wall refinements (adjacent cell center $z_1 = 0.8\,\mathrm{m}$, $1.6\,\mathrm{m}$ and $4.0\,\mathrm{m}$) and two wall functions (see section 2.2.1) are shown at the distance of 3000 m behind the inlet. Whereas a good agreement with the inlet profile is achieved for lower roughness with both wall function approaches, simulations with k_s-WF do not converge with higher roughness due to numerical instabilities. For z_0-WF increasing deviation from the inlet profile can be seen for $z_0 = 1\,\mathrm{m}$ and $z_0 = 1.5\,\mathrm{m}$ with increasing near-ground resolution. For very rough walls only the simulation with the coarse mesh is able to prevent changes in longitudinal direction, while finer meshes still give reasonable results.

It should be mentioned, that it is usually not recommended to use k_s-WF if $k_s > z_1$ (e.g. (Blocken et al., 2007),(Franke et al., 2004)), which is the case for all but one simulation presented. However, results show that with restricted violation of $k_s > z_1$ reasonable results can be achieved, while substantial exceeding the limit leads to numerical diverging simulations.

For simulations of gas propagation prediction of the turbulence level is of major importance, since dissipative processes increase with increasing turbulence. Therefore, the development of turbulent kinetic energy k in longitudinal direction must be analyzed as well. At the inlet a constant value of k is specified (see eq. 1). Vertical profiles of k for the same configurations as above are shown in Fig. 2. The turbulent kinetic energy in near ground region increase with decreasing grid refinement for all roughness lengths and wall functions. For the medium rough cases ($z_0 = 0.06\,\mathrm{m}$ and $0.3\,\mathrm{m}$) k-profiles of z_0-WF retain the inlet profile reasonably good, while for higher roughness the deviations increases. Sand grain roughness wall function (k_s-WF) over-predicts k up to 20% in near-ground region for all cases. However, since the inlet velocity profile is calculated with z_0-WF condition, improved homogeneity of z_0-WF over k_s-WF can be expected. Profiles for turbulent dissipation rate, shown in Fig. 3, indicate negligible disagreement with target profiles.

To minimize numerical effort, the inflow lengths in industrial application is much shorter than shown above, where numerical stability and blocking effects of obstacles are the only reasons for longer inflow regions in RANS. However, for gas dispersion the propagation region can easily exceed one kilometer. The development of U- and k-profiles in flow direction from the inlet is shown in Fig. 4 with additional measurement data from wind tunnel experiments, described in (Fischer et al., 2010)

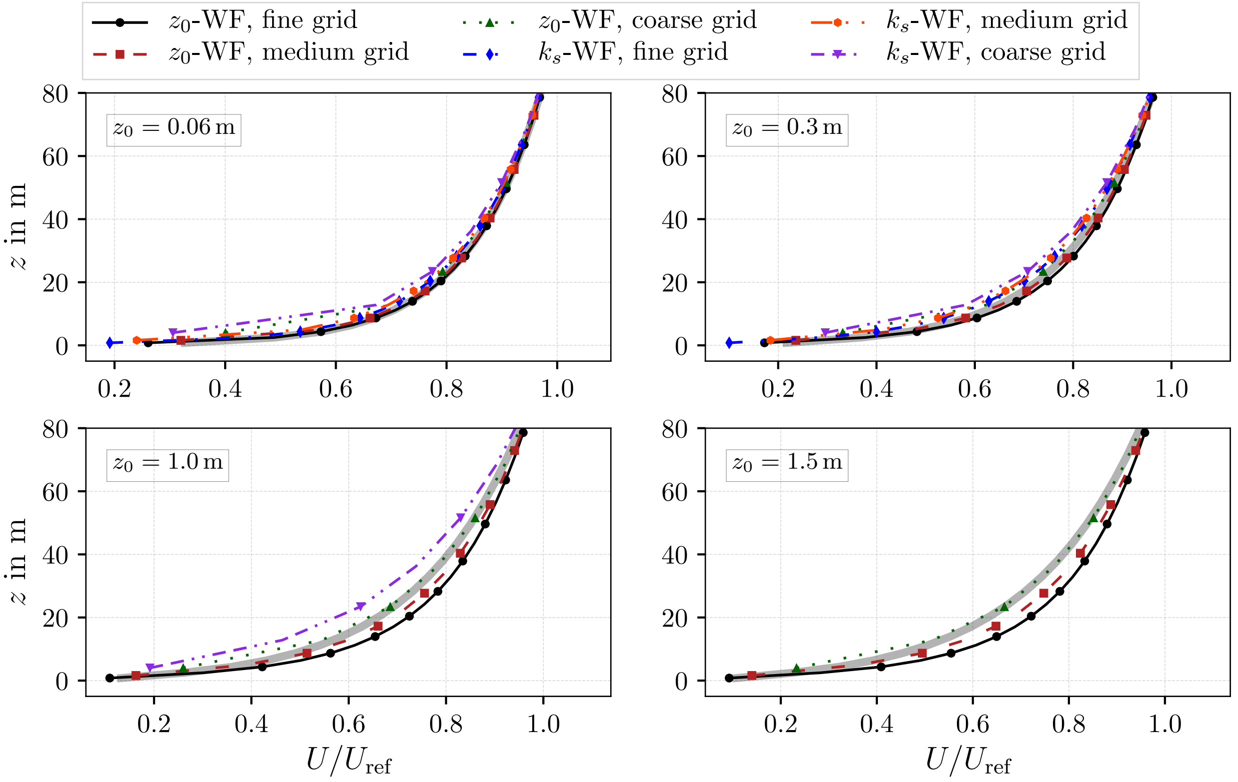

***Fig. 1**: Normalized profiles of time averaged velocity of prescribed grids and wall functions 3,000 m downstream the inlet (RANS). Thick solid line indicates inlet profile.*

[1]. Velocity and especially k-profiles immediately start diverging from inlet profile near the ground. Velocity profiles converge to a stable condition at about 3,000 m downstream the inlet. This rapid changes have to kept in mind when doing gas propagation simulations with RANS with high roughness lengths.

3.2 LES

Due to extensive numerical costs, two roughness lengths ($z_0 = 0.06\,\mathrm{m}$ and $z_0 = 1.5\,\mathrm{m}$) are considered in the LES. Since the first part of the numerical domain is used as precursor in LES, longitudinal changes do not take place in our simulations. Fig. 5 shows velocity profiles of three SGS models normalized by reference velocity (U_{ref}) at $z_{ref} = 70\,\mathrm{m}$ for minor roughness length ($z_0 = 0.06\,\mathrm{m}$). Corresponding profiles of the time averaged Reynolds normal stress in flow direction $\overline{u'u'}$ normalized with friction velocity $u_* = \kappa\, U_{ref}/\ln\left(\left(z_{ref}+z_0\right)/z_0\right)$ are shown in Fig. 6. Presented measurement data for this roughness is provided by the University of Hamburg measured in wind tunnel experiments. Compared to the logarithmic profile, SM and kEM underpredict the velocity in the near-ground region and matches the log-profile at about 20 m respectively 30 m with minor influence of the grid, whereas the progression of DOM show high dissimilarity between grid resolution for the first 50 m of boundary layer. The Velocity predicted by DOM is significantly overestimated at the ground for the two finer meshes.

SM and kEM profiles of $\overline{u'u'}$ overestimate up to 100% compared to measurement data, with minor grid dependency in near-ground region whereas sensitivity to grid resolution can be observed in the lower region ($z \leq 30\,\mathrm{m}$). The DOM shows high mesh dependency over the complete presented height with increasing values for decreasing grid resolution.

---

[1] https://mi-pub.cen.uni-hamburg.de/index.php?id=6339

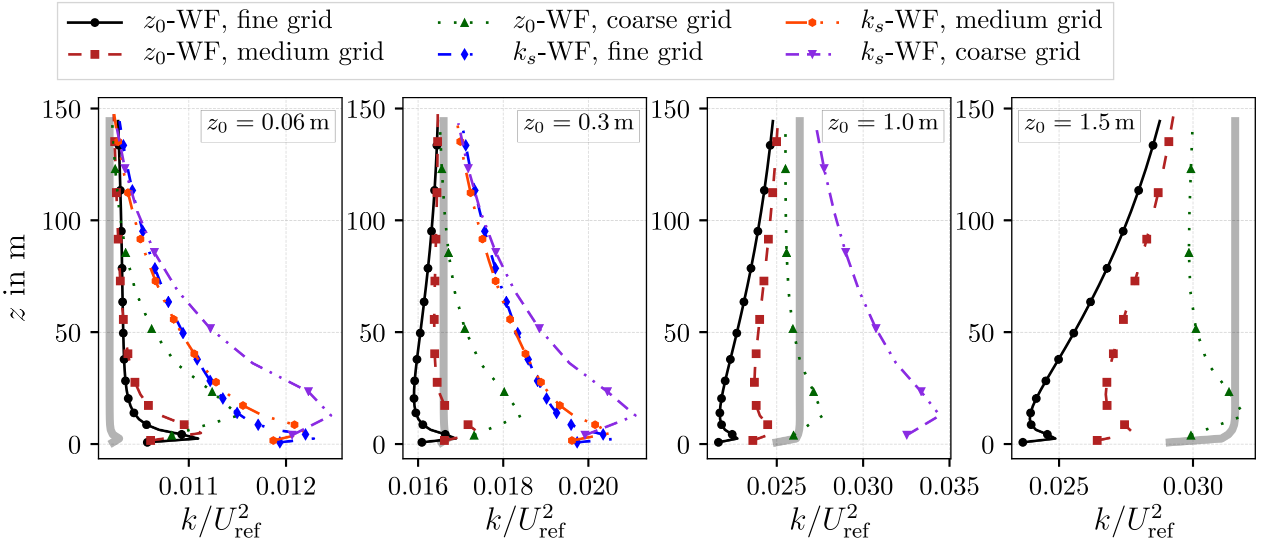

***Fig. 2**: Normalized profiles of time averaged turbulent kinetic k energy of prescribed grids and wall functions 3,000 m downstream the inlet (RANS). Thick solid line indicates inlet profile.*

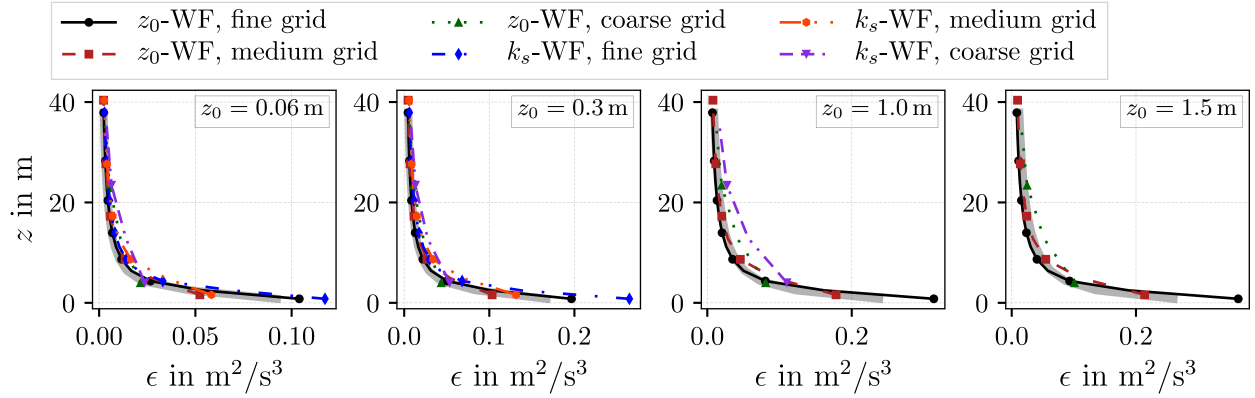

***Fig. 3**: Profiles of time averaged turbulent dissipation rate ε of prescribed grids and wall functions 3,000 m downstream the inlet (RANS). Thick solid line indicates inlet profile.*

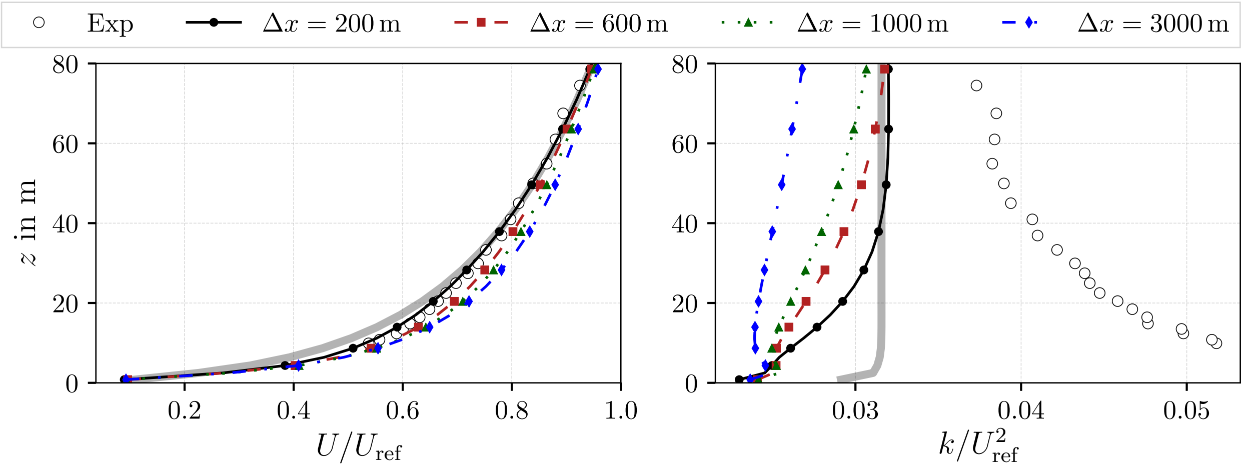

***Fig. 4**: Normalized velocity and turbulent kinetic energy profiles of fine grid and z_0-WF for $z_0 = 1.5\,m$ at various positions downstream the inlet (RANS). Thick solid line indicates inlet profile.*

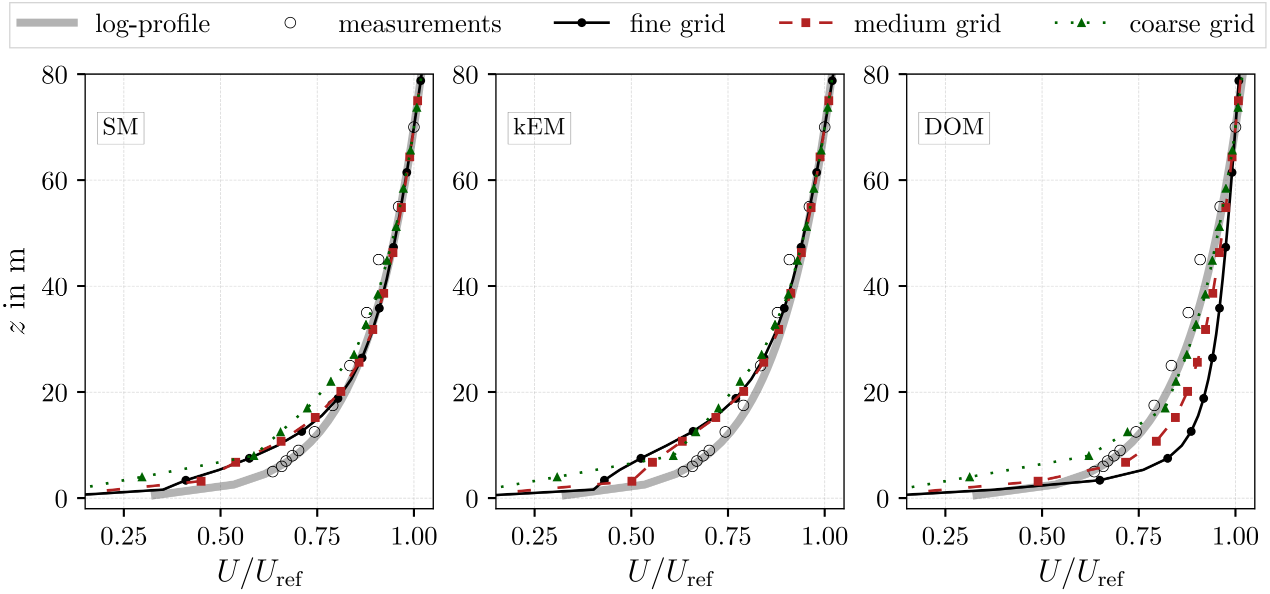

Fig. 5: Normalized velocity profiles of prescribed grids and SGS-models for $z_0 = 0.06\,\mathrm{m}$ (LES). Thick solid line indicates logarithmic velocity profile.

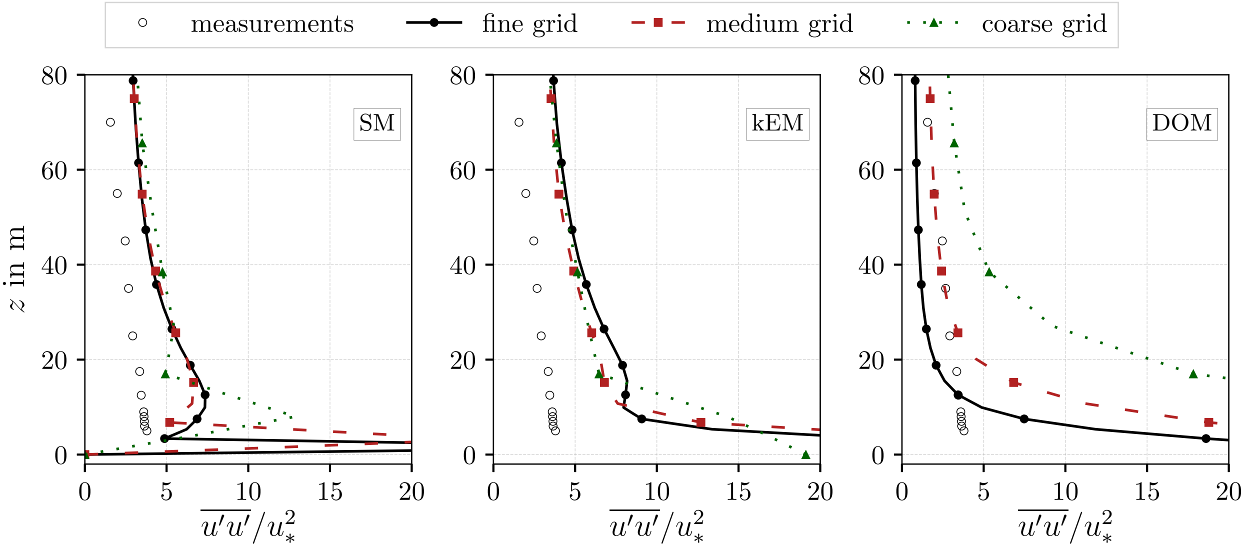

Fig. 6: Normalized profiles of Reynolds normal stress in streamwise direction of prescribed grids and SGS-models for $z_0 = 0.06\,\mathrm{m}$ (LES).

Similar behavior can be observed for U- and k-profiles in high roughness environment ($z_0 = 1.5\,\mathrm{m}$), which are shown in Fig. 7 and Fig. 8 with experimental data of (Fischer et al., 2010)[2] and an additional SGS model (DSM). Reference height in this case is $z_{ref} = 100\,\mathrm{m}$. Increasing mesh dependency is noticeable for all SGS models compared to $z_0 = 0.06\,\mathrm{m}$ with considerably high deviation in near-ground velocities for DSM and DOM. Contrary to the lower roughness the SM and kEM overestimate the velocity of log- and experimenta data near the surface for this roughness length. The coarse grid matches the experimental data reasonable well, whereas the deviation increases with mesh refinement. DSM and DOM, both using dynamic procedure for estimating the model constants Germano et al. (1991), shows high dependency with regard to grid refinement, with increasing fullness of the profile for finer meshes. Similar constraints were observed with wall-adapting local eddy-viscosity

---

[2] https://mi-pub.cen.uni-hamburg.de/index.php?id=6339

SGS model (WALE) (Nicoud and Ducros, 1999), which is not shown here.

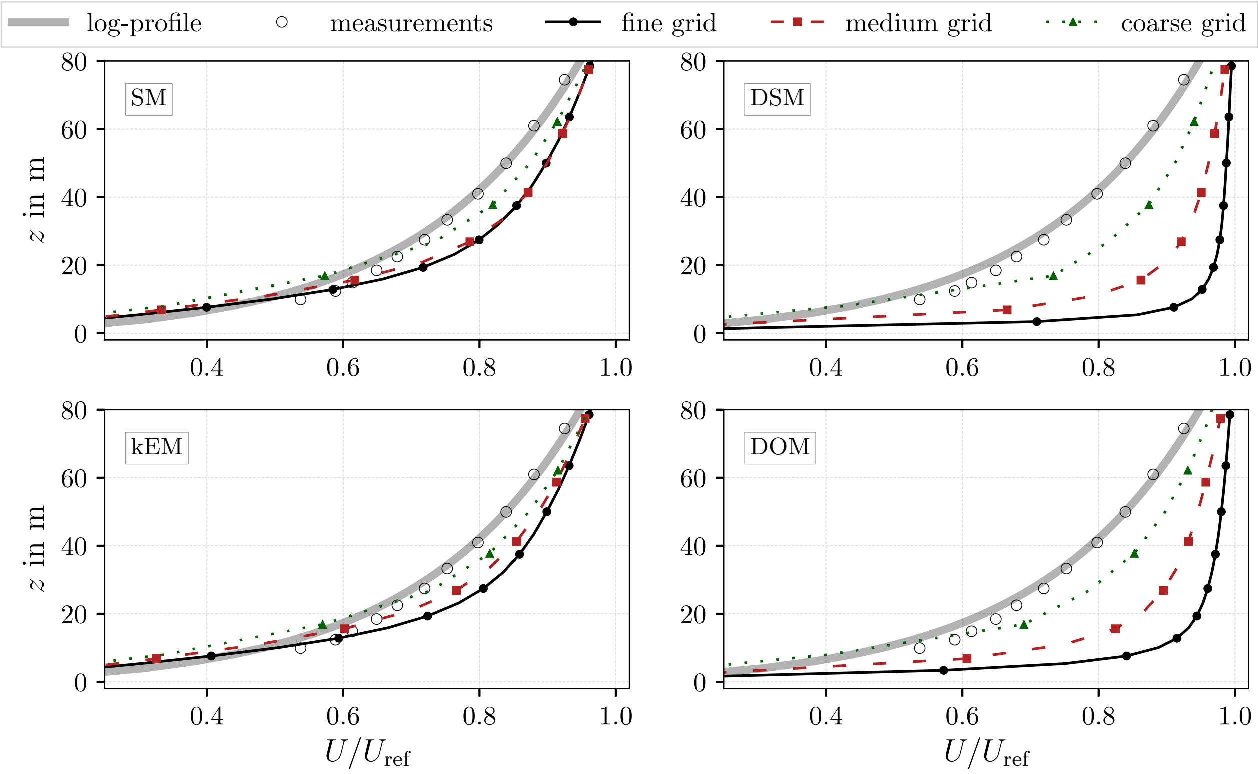

***Fig. 7**: Normalized velocity profiles of prescribed grids and SGS-models $z_0 = 1.5\,m$ (LES). Thick solid line indicates inlet profile.*

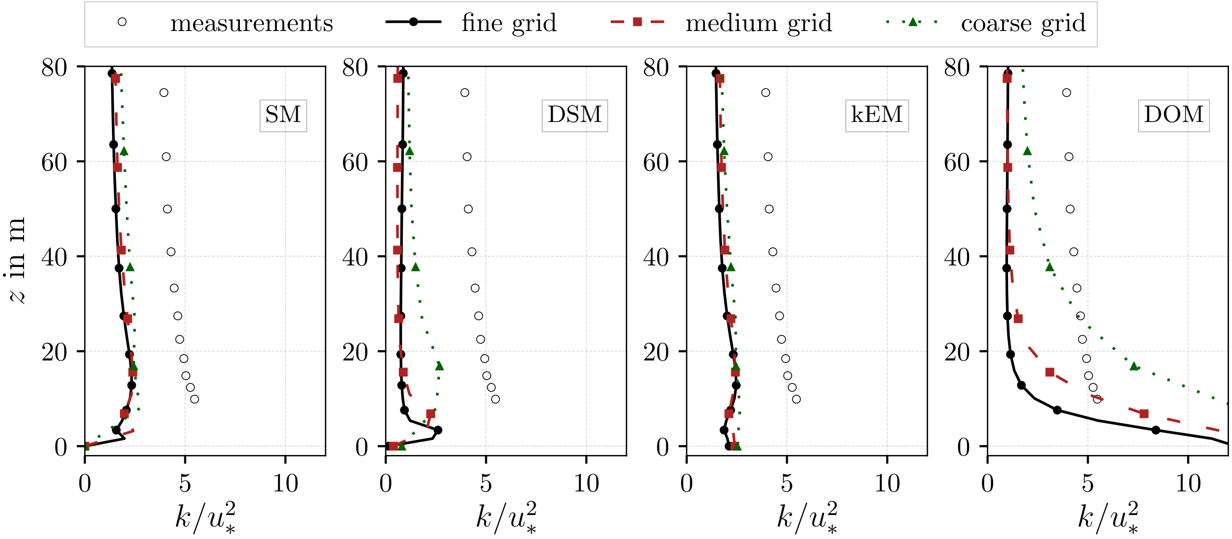

***Fig. 8**: Normalized profiles of turbulent kinetic energy of prescribed grids and SGS-models for $z_0 = 1.5\,m$ (LES).*

Theoretically, since the SM is too dissipative in the near-ground region, high damping of turbulent kinetic energy occurs which leads to less reduction of mean shear and thereby larger velocities (Porté-Agel et al., 2000). In presented simulations this is the case only for $z_0 = 1.5\,\mathrm{m}$, where k-values are under- and velocities are overestimated. For $z_0 = 0.06$ velocities of SM and kEM are lower as expected logarithmic profile. Porté-Agel et al. (2000) also mentioned a opposite effect for the dynamic

DOI: 10.7795/810.20200724

Smagorinsky model, which cannot be observed in our simulations with the DSM (and also DOM) for both roughness lengths.

A verification of LES quality with profiles of resolved and SGS turbulent kinetic energy for $z_0 = 1.5\,\mathrm{m}$ (Fig. 9) shows expectable ratios. In the upper region (above 40 m) less then 20% of the turbulence is modeled in all SGS models but DOM. The resolved part of turbulence decreases to zero at the surface, since the grid scale gets of the order of the local length scale (Porté-Agel et al., 2000). The intersection between modeled and resolved part is lowest in DSM, with strong gradients and a high mesh influence. In SM and kEM less of the near-ground turbulence is resolved. The profile is smoother and the dependency of grid refinement is less. The lowest ratio of resolved turbulence can be seen in DOM model over the complete ABL height. Highest and lowest ratio result in comparable velocity profiles, which can be seen as a hint that the ratio might not be the main reason for the high overprediction of velocity in DSM and DOM.

Considering the energy spectra of the normalized streamwise velocity for different heights (normalized with friction velocity u_* and probe height z) the results should be proportional to $(k_1 z)^{-5/3}$ for large wave numbers k_1 and to k_1^{-1} for small wave numbers (Kader and Yaglom, 1991). Perry et al. (1986) additionally mentioned a collapsing of lines when plotted against $k_1 z$. The normalized spectra of kEM and DOM for $z_0 = 1.5\,\mathrm{m}$ and $\Delta z_1 = 3.2\,\mathrm{m}$ are shown in Fig. 10. For DOM the spectra are in good agreement with the $(k_1 z)^{-1}$ slope in the near-surface region, what would indicate a correct damping, which can't be seen in the velocity profiles. The decay of kEM is faster for $(k_1 z) \leq 0.7$, which was already reported in (Porté-Agel et al., 2000) and results from too strong dissipation of kinetic energy. The $(k_1 z)^{-5/3}$-slope is well predicted by the kEM. The DOM has a more unspecific slope which roughly matches $(k_1 z)^{-5/3}$ until $k_1 z = 10$ with a significant increase of the slope at wave number greater than 10, which results in an increase of fluctuation above $z = 300\,\mathrm{m}$.

It should be noted that regarding to the high dissipation of SM in near-wall region, usually a damping function (e.g. van Driest damping (van Driest, 1956)) is applied in wall-bounded flows. Since grid refinement near the wall is coarse (even for the fine mesh) compared with typical industrial applications and the implemented version of van Driest damping is limited to dimensionless wall normal distance $y^+ \leq 50$, no damping at the ground is applied in simulations using the SM. Other damping functions as e.g. described in (Mason and Thomson, 1992) will be implemented and tested in the future.

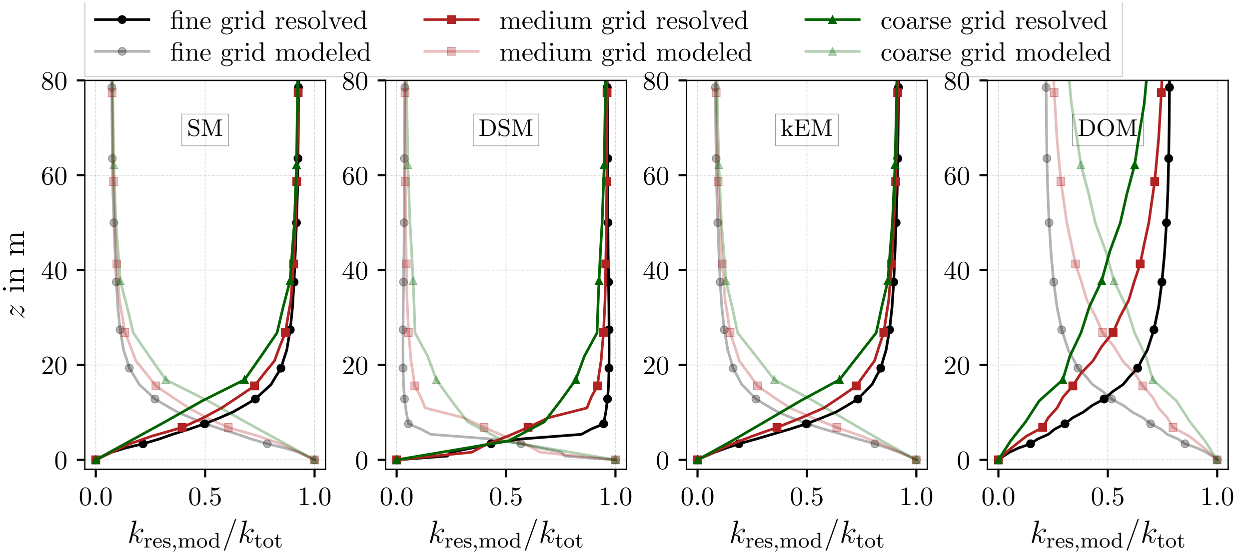

***Fig. 9**: Ratio of resolved and modeled turbulent kinetic energy for $z_0 = 1.5$.*

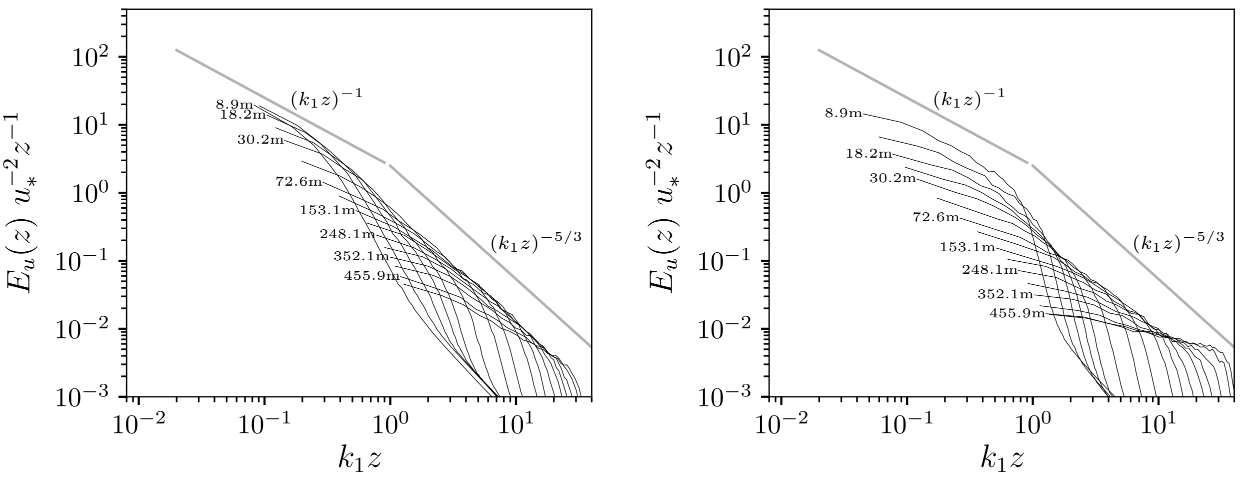

***Fig. 10**: Normalized energy spectra of streamwise velocity at various heights for kEM (left hand side) and DOM (rights hand side)*

4 Conclusions

Reynolds-averaged Navier-Stokes Simulations of atmospheric boundary layer are performed with various wall function approaches for three near-wall grid refinements and three roughness lengths. Horizontal homogeneity of velocity profiles in RANS for minor roughness is achieved with both, z_0 and k_s based wall functions. For higher roughness lengths increasing grid refinement at the ground leads to increasing velocity near the ground. Profiles of k for smoother walls are best preserved by fine grid resolution, where simulations with z_0-WF show less alteration in flow direction than k_s-WF simulations. For very rough walls k_s-WF numerically diverge for the used setup and are therefore not applicable. In summary velocity and k-profiles succeed best homogeneity with z_0-WF. A grid dependency is seen, whereas increasing grid resolution should be used for increasing roughness lengths.

In LES four SGS models are applied on two roughness lengths ($z_0 = 0.06$ m and $z_0 = 1.5$ m). Smagorinsky and k-Equation model show little dependency on grid refinement for smooth and slightly more for very rough ground, whereas for SGS models using dynamic procedure (DSM and DOM) significant variation with increasing overestimation of near-ground velocity is observed for increasing grid resolution at the surface. However, velocity profiles of SM and kEM still show deviation to theoretical log-profile in ground region, with increasing discrepancy for increasing roughness. In the profiles of turbulent kinetic energy high variations can be observed.

Future work should extend the study to the influence of spanwise and streamwise grid resolution. A thorough investigations of the interaction between dynamic model equations and rough wall function implementation might explain the high velocities of DSM in near-surface region. Also the above mentioned damping function of (Mason and Thomson, 1992) should be applied for standard Smagorinsky model to improve the results for small roughness lengths.

Acknowledgements

The authors gratefully acknowledge the financial contribution from the German Federation of Industrial Research Associations (AiF).

References

Baumann-Stanzer, K., Andronopoulos, S., Armand, P., Berbekar, E., Efthimiou, G., Fuka, V., Gariazzo, C., Gasparac, G., Harms, F., Hellsten, A., et al. (2015). *COST ES1006—model evaluation case studies: approach and results*. ISBN 987-3-9817334-2-6.

Bechmann, A., Sørensen, N. N. (2011). *Hybrid rans/les applied to complex terrain*. Wind Energy, 14(2):225–237.

Blocken, B., Stathopoulos, T., Carmeliet, J. (2007). *Cfd simulation of the atmospheric boundary* *layer: wall function problems*. Atmospheric environment, 41(2):238–252.

Bou-Zeid, E., Meneveau, C., Parlange, M. (2005). *A scale-dependent lagrangian dynamic model for large eddy simulation of complex turbulent flows*. Physics of fluids, 17(2):025105.

Chaudhari, A., Vuorinen, V., Hämäläinen, J., Hellsten, A. (2018). *Large-eddy simulations for hill terrains: validation with wind-tunnel and field measurements*. Computational and Applied Mathematics, 37(2):2017–2038.

Fischer, R., Bastigkeit, I., Leitl, B., Schatzmann, M. (2010). *Generation of spatio-temporally high resolved datasets for the validation of les-models simulating flow and dispersion phenomena within the lower atmospheric boundary layer*. In *Proc. 5th International Symposium on Computational Wind Engineering (CWE2010), Chapel Hill, North Carolina, USA*.

Franke, J., Hirsch, C., Jensen, A., Krüs, H., Schatzmann, M., Westbury, P., Miles, S., Wisse, J., Wright, N. (2004). *Recommendations on the use of cfd in wind engineering*. In *Cost action C*, volume 14, page C1.

Germano, M., Piomelli, U., Moin, P., Cabot, W. H. (1991). *A dynamic subgrid-scale eddy viscosity model*. Physics of Fluids A: Fluid Dynamics, 3(7):1760–1765.

Grötzbach, G. (1987). *Direct numerical and large eddy simulation of turbulent channel flows*. Encyclopedia of fluid mechanics, 6:1337–1391.

Hargreaves, D., Wright, N. G. (2007). *On the use of the k–ε model in commercial cfd software to model the neutral atmospheric boundary layer*. Journal of wind engineering and industrial aerodynamics, 95(5):355–369.

Hirtl, M., Baumann-Stanzer, K. (2007). *Evaluation of two dispersion models (adms-roads and lasat) applied to street canyons in stockholm, london and berlin*. Atmospheric Environment, 41(28):5959–5971.

Issa, R. I. (1986). *Solution of the implicitly discretised fluid flow equations by operator-splitting*. Journal of computational physics, 62(1):40–65.

Janicke, L. (1985). *Particle simulation of dust transport and deposition and comparison with conventional models*. In *Air Pollution Modeling and Its Application IV*, pages 759–769. Springer.

Janicke, U., Janicke, L. (2007). *Lagrangian particle modeling for regulatory purposes; a survey of recent developments in germany*. In *Proceedings of the 11th International Conference on Harmonization within Atmospheric Dispersion Modeling for Regulatory Purposes, Cambridge, England. Siehe http://www. harmo. org*.

Kader, B., Yaglom, A. (1991). *Spectra and correlation functions of surface layer atmospheric turbulence in unstable thermal stratification*. In *Turbulence and Coherent Structures*, pages 387–412. Springer.

Kim, W.-W., Menon, S. (1995). *A new dynamic one-equation subgrid-scale model for large eddy simulations*. In *33rd Aerospace Sciences Meeting and Exhibit*, page 356.

Lilly, D. K. (1992). *A proposed modification of the germano subgrid-scale closure method*. Physics of Fluids A: Fluid Dynamics, 4(3):633–635.

Mason, P. J., Thomson, D. J. (1992). *Stochastic backscatter in large-eddy simulations of boundary layers*. Journal of Fluid Mechanics, 242:51–78.

Nakayama, H., Takemi, T., Nagai, H. (2011). *Les analysis of the aerodynamic surface properties for turbulent flows over building arrays with various geometries*. Journal of applied meteorology and climatology, 50(8):1692–1712.

Nicoud, F., Ducros, F. (1999). *Subgrid-scale stress modelling based on the square of the velocity gradient tensor*. Flow, turbulence and Combustion, 62(3):183–200.

Nozawa, K., Tamura, T. (2002). *Large eddy simulation of the flow around a low-rise building immersed in a rough-wall turbulent boundary layer*. Journal of Wind Engineering and Industrial Aerodynamics, 90(10):1151–1162.

Perry, A., Henbest, S., Chong, M. (1986). *A theoretical and experimental study of wall turbulence*. Journal of Fluid Mechanics, 165:163–199.

Porté-Agel, F., Meneveau, C., Parlange, M. B. (2000). *A scale-dependent dynamic model for large-*

eddy simulation: application to a neutral atmospheric boundary layer. Journal of Fluid Mechanics, 415:261–284.

Richards, P., Hoxey, R. (1993). *Appropriate boundary conditions for computational wind engineering models using the k-ε turbulence model*. Journal of wind engineering and industrial aerodynamics, 46:145–153.

Richards, P., Norris, S. (2011). *Appropriate boundary conditions for computational wind engineering models revisited*. Journal of Wind Engineering and Industrial Aerodynamics, 99(4):257–266.

Rodi, W., Constantinescu, G., Stoesser, T. (2013). *Large-eddy simulation in hydraulics*. Crc Press.

Schumann, U. (1975). *Subgrid scale model for finite difference simulations of turbulent flows in plane channels and annuli*. Journal of computational physics, 18(4):376–404.

Smagorinsky, J. (1963). *General circulation experiments with the primitive equations: I. the basic experiment*. Monthly weather review, 91(3):99–164.

Stoll, R., Porté-Agel, F. (2006). *Dynamic subgrid-scale models for momentum and scalar fluxes in large-eddy simulations of neutrally stratified atmospheric boundary layers over heterogeneous terrain*. Water Resources Research, 42(1).

Tabor, G. R., Baba-Ahmadi, M. (2010). *Inlet conditions for large eddy simulation: A review*. Computers & Fluids, 39(4):553–567.

Thomas, T., Williams, J. (1999). *Generating a wind environment for large eddy simulation of bluff body flows*. Journal of Wind Engineering and Industrial Aerodynamics, 82(1-3):189–208.

van Driest, E. R. (1956). *On turbulent, flow near a wall*. J . Aero. Sci., page 1007–1011.

Vasaturo, R., Kalkman, I., Blocken, B., van Wesemael, P. (2018). *Large eddy simulation of the neutral atmospheric boundary layer: performance evaluation of three inflow methods for terrains with different roughness*. Journal of Wind Engineering and Industrial Aerodynamics, 173:241–261.

Weller, H. G., Tabor, G., Jasak, H., Fureby, C. (1998). *A tensorial approach to computational continuum mechanics using object-oriented techniques*. Computers in physics, 12(6):620–631.

Xie, Z.-T., Castro, I. P. (2009). *Large-eddy simulation for flow and dispersion in urban streets*. Atmospheric Environment, 43(13):2174–2185.

Xie, S., Ghaisas, N., Archer, C. L. (2015). *Sensitivity issues in finite-difference large-eddy simulations of the atmospheric boundary layer with dynamic subgrid-scale models*. Boundary-layer meteorology, 157(3):421–445.

Yang, X. I., Meneveau, C. (2016). *Recycling inflow method for simulations of spatially evolving turbulent boundary layers over rough surfaces*. Journal of Turbulence, 17(1):75–93.

Yoshizawa, A. (1986). *Statistical theory for compressible turbulent shear flows, with the application to subgrid modeling*. The Physics of fluids, 29(7):2152–2164.

DOI: 10.7795/810.20200724

Numerical modelling of the effects of vessel length-to-diameter ratio (L/D) on pressure piling

Damilare Ogungbemide,[a] Martin P. Clouthier,[a,b] Chris Cloney,[c]
Robert G. Zalosh,[d] Robert C. Ripley,[e] & Paul R. Amyotte [b]

[a] Jensen Hughes, Halifax, Canada; [b] Dalhousie University, Halifax, Canada; [c] DustEx Research Ltd., Halifax, Canada; [d] Firexplo, Wellesley, USA; [e] Lloyd's Register, Halifax, Canada
E-mail: *dogungbemide@jensenhughes.com*

Abstract

Pressure piling presents a major explosion hazard in interconnected process vessels. Pressure enhancement in the secondary vessel due to the acceleration of the flame through the connecting pipe can generate a disproportionately more violent explosion than would have been expected based on the concentration of dust in the secondary vessel. Pressure piling is a very complex phenomenon that is difficult to investigate through experimentation. Advanced computational fluid dynamics (CFD) modelling is a promising route to accurately account for all the complexities associated with pressure piling.

In this paper, the current state of knowledge concerning pressure piling is presented. Further, the effects of varying the length-to-diameter ratio (L/D) of the primary vessel (Vessel 1) on pressure piling was investigated using numerical modelling. The volumes and volume ratio of the interconnected vessels were kept constant while the L/D of Vessel 1 was varied from 0.5 to 15. The simulations of coal dust explosion were performed using the coalChemistryFoam solver from OpenFOAM version 5.0.1. It is hoped that the findings from this study provide insight into the effects of the geometrical design of interconnected vessels, particularly L/D, on pressure piling. Additionally, this work has implications for the optimal placement of explosion isolation devices intended to actuate before the flame front and pressure escape to downstream vessels.

Keywords: *pressure piling, coal, CFD, OpenFOAM, dust explosion, numerical modelling*

1 Introduction

The greatest hazard in an interconnected system is pressure piling—the behaviour of an explosion as it propagates from one vessel to the next through an interconnecting duct (Barton, 2002). A deflagration in a vessel, even if the vessel is vented, can enter a connecting duct and travel towards another vessel. The acceleration of the flame through the duct causes pre-compression of the gas in the duct and the connected vessel. If there is an ignitable concentration of dust inside the second vessel or along the length of the duct, the flame can ignite the dust. The explosion in the second vessel will be disproportionately higher than would have been expected based on the concentration of dust in it. This is due to the magnifying effect of the pre-compression of the gas from the first vessel. Pressure-piling effect depends on the explosion severity (K_{St}), the dust concentration, and the conditions inside the duct, including flow velocity and the strength of the initiating event (Barton, 2002).

Due to the limited range of available data and conflicting results from the literature, it is difficult to develop models that can be used to make definitive predictions on the limiting conditions of pressure piling in an interconnected system. Advanced computational fluid dynamics (CFD) modelling is a promising route to accurately account for the complexities associated with phenomena such as pressure piling to meet safety requirements. The phenomenon of pressure piling during combustible dust explosions in interconnected vessels have been investigated, to some extent, using the Gexcon's DustEx modelling software. However, very limited studies are available on the numerical modelling of pressure piling using the opensource software OpenFOAM.

OpenFOAM (Open-source Field Operation And Manipulation) is a free computational fluid dynamics (CFD) code developed by OpenCFD Ltd. and the OpenFOAM Foundation. OpenFOAM is gaining recognition in academic, research and industrial sectors due to its being opensource, no license fees, a comprehensive range of fluid dynamics applications, unlimited parallel computing, and no limitation of number of species in the chemistry models (Lysenko et al., 2013).

Pressure piling has not been numerically studied extensively due to the niche nature of the problem (McCarthy-Singh et al., 2019), and even when studied numerically, the focus has been more on gas explosions, with limited effort directed at dust explosions. Some experimental studies have been published on pressure piling by Gleim and Marcy (1952); Bartknecht (2012); Phylaktou and Andrews (1993); Singh (1984), Singh (1994); Lunn et al. (1996); Kanzleiter and Fischer (1994); Yan et al. (2009); Razus et al. (2003); Zhang et al. (2016); and Zhang et al. (2017).

Simulations of homogenous mixtures have, by and large, produced comparative results with experiments (Di Benedetto and Salzano, 2010); however, simulations of non-homogenous mixtures have unique challenges. Skjold (2010) discussed the challenges for model validation for studies on flame propagation in non-homogenous dust clouds. These challenges may also explain why more simulation studies have been performed for gas explosions in comparison to dust explosions. Though a few studies, such as the works of Cloney et al. (2018) and Ogungbemide and Clouthier (2020), have investigated the capabilities and limitations of the OpenFOAM software to model dust explosions, there remains a lot to be done on the simulations of non-homogenous mixtures. The current study builds on the study of Ogungbemide and Clouthier (2020), which investigated the capability and limitations of OpenFOAM to model the pressure piling effect in coal dust explosions. To date, there has been no comprehensive experimental or numerical study to investigate the role of the length-to-diameter ratio (L/D) of the primary vessel on pressure piling. It is hoped that this study improves our current understanding of flame and pressure propagation through interconnected systems of process vessels.

2 Methodology

This section describes the computational domain, case set up, multiphase discretization, and numerical solution methods used in the simulations. The CFD model employed in this work builds on the coalChemistryFoam solver from the OpenFoam toolkit version 5.0.1. The equations governing transport processes, thermophysical parameters, and reaction chemistry are given for the gas and particle phases in this section.

2.1 Model description

The Reynolds-averaged Navier-Stokes (RANS) model used in this study is based on the coalChemistryFoam solver from the OpenFOAM toolkit version 5.0.1. The coalChemistryFoam solver is a transient combustion solver for simulating turbulent, compressible flow, with coal particle clouds and an energy source term. OpenFOAM solves the compressible RANS conservation equations for mass, momentum, enthalpy and chemical species on a 3D Cartesian grid. The set of equations is closed by the ideal gas law and the effects of turbulence is included through the eddy viscosity concept by solving equations for turbulent kinetic energy (k) and its rate of decay (ε) using the standard k-ε model by Launder and Spalding (1983).

The geometry was generated using the Salome CAD and meshing software. Two sets of simulations were performed: the first set was performed with the ignition source located at the centre of Vessel 1 (central ignition), while the second set was performed with the ignition source located 0.02 m from the upper end of Vessel 1 (end ignition).

The gas-phase chemistry reaction mechanism used in the current work is the MP1 mechanism which has five species and one reaction as shown in Eqn. 1. This helped to further reduce modelling complexity and computational requirements.

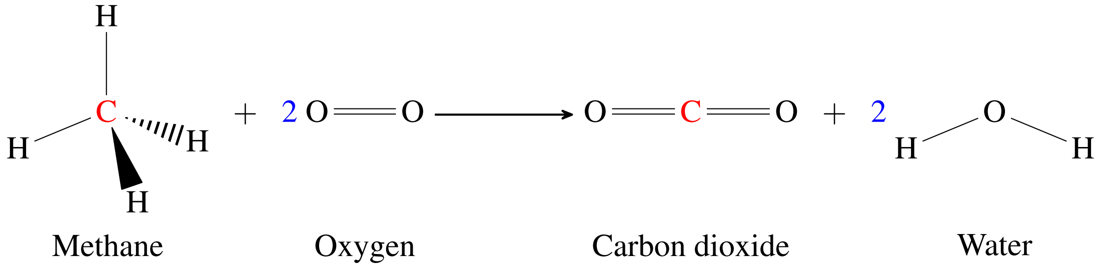

(1)

The parameters of the single-step reaction model, as implemented in OpenFOAM coalChemistryFoam are shown in Table 1.

Table 1: Single-step global reaction model parameters.

Name	A_r	n_r	$E_{a,r}/R$ (K)	Reaction Order
MP1	3.48×10^8	0.0	10063.8	$[CH_4]^1 [O_2]^{0.5}$

where A_r is the Arrhenius pre-exponential factor, n_r is the temperature coefficient, and $E_{a,r}$ is the activation energy ($\mathrm{J\,kg^{-1}}$).

The overall rate of any specific reaction ($\dot{\omega}_r$, $\mathrm{mol\,m^{-3}\,s}$) is determined based on a general Arrhenius expression for the forward and backward reaction coefficients (Eqn. 2 and Eqn. 3).

$$\dot{\omega}_r = k_r^f \prod_{k=1}^{N_k} \eta_k^{\nu'_{k,r}} - k_r^b \prod_{k=1}^{N_k} \eta_k^{\nu''_{k,r}} \tag{2}$$

$$k_r = A_r T^{n_r} e^{\left(-\frac{E_{a,r}}{RT}\right)} \tag{3}$$

Following the work of Bradley et al. (1994) and Cloney et al. (2018), the particle composition is assumed to be 40% methane and 60% carbon in this work. Particle devolatilization is described by a single-step Arrhenius expression. Heat is removed from the particle due to devolatilization. Heterogeneous combustion is specified based on a single surface reaction between oxygen molecules and carbon in the coal particle. A comprehensive model description for the OpenFOAM coalChemistryFoam solver can be found in Cloney et al. (2018).

2.2 *Numerical domain*

The simulation domain for the current model is shown in Fig. 1. The three-dimensional domain represents an interconnected system that comprises Vessel 1 (the primary vessel) with a volume of $0.025\,\mathrm{m^3}$ connected to Vessel 2 (the secondary vessel) with a volume of $0.006\,\mathrm{m^3}$ via a 1.0 m long duct with a diameter of 0.04 m. The volumes and volume ratio of the interconnected vessels were kept constant while the length-diameter ratio (L/D) of Vessel 1 was varied from 0.5 to 15. Two ignition positions (central and end) were used in the simulations. In total, sixteen simulations were performed, eight simulations for each ignition position. Ignition was initiated directly in OpenFOAM 1 ms after start of simulation and continued throughout the entire simulation period. Probes for monitoring the parameters of interest (pressure, temperature, and velocity) were positioned at several locations within the vessels and at regular intervals along the interconnecting duct.

Fig. 1 shows the geometry of the interconnected system. Each vessel was filled with a dust cloud at a concentration of $500\,\mathrm{g\,m^{-3}}$. The cellZone Injection model was used to place the dust. The duct was not filled with dust to remove the complexity of particle inertia and combustion in the duct as discussed in Ogungbemide and Clouthier (2020) and Taveau et al. (2019). A mass parcel basis type and fixed-value particle size distribution of 33 µm were used. A uniform temperature of 300 K was set for both the gas phase and the solid particles. To ensure that all mixtures could actually ignite, the modelled ignition source was set to a value of 1500 K. A summary of the simulation parameters used in the present study is shown in Table 2.

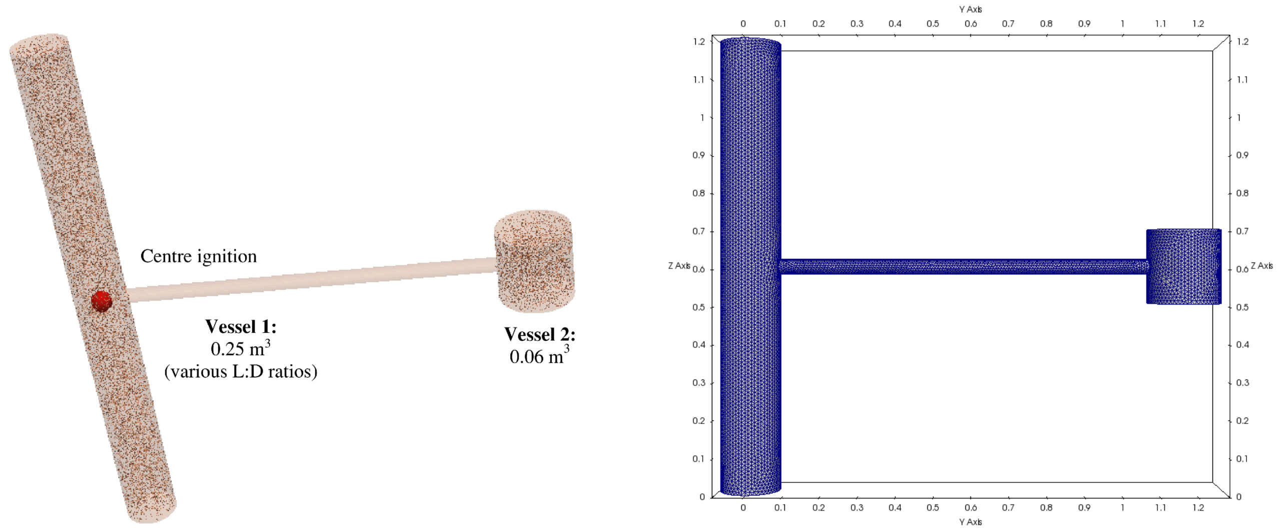

(a) Simulated dust cloud with central ignition. *(b) Mesh of interconnected system.*

Fig. 1*: Simulated dust cloud and grid mesh for one of the interconnected systems used in the current study. Two ignition positions (central and end) were used in the simulations.*

Table 2*: Simulation parameters used in the model.*

Parameter	Value
Fluid	air
Solid	coal dust
Particle size (µm)	33
Volatile content (%)	40
Volume (Vessel 1 - primary vessel) (m^3)	0.025
Volume (Vessel 2 - secondary vessel) (m^3)	0.006
Volume (Duct) (m^3)	0.00126
Dust concentration (g m^{-3})	500
Particle density (kg m^{-3})	1300
Ambient pressure (Pa)	100 000
Temperature (fluid) (K)	300
Temperature (particles) (K)	300
Ignition temperature (K)	1500
Cell (tets) size (m)	0.010 (max) & 0.001 (min)
Simulation time (ms)	300
Start of ignition (ms)	1

In this work the coal particles were discretized using the Discrete Particle Model (DPM) Lagrangian approach. Particle-wall interaction was taken into consideration, but particle–particle interaction was neglected. Interaction between the gas and particle phase was modelled using a particle-source-in-cell method (Christ, 2013, Migdal and Agosta, 1967) where the particles act as point sources and sinks within the cell in which their centre resides.

The gas phase conservation equations were solved using a segregated approach where each equation is discretized over all cells with the finite volume method. The convective terms were discretized using a bounded Gaussian upwind interpolation scheme, the diffusion terms were discretized using Gaussian linear interpolation, and the time-derivative terms were discretized with an Euler scheme. Preconditioned Conjugate Gradient (PCG) was used for symmetric matrices (pressure) and Preconditioned Bi-Conjugate Gradient (PBiCG) for asymmetric matrices (velocity). The Diagonal-based

Incomplete Cholesky (DIC) preconditioner was used with the PCG solver, while the Diagonal-based Incomplete LU preconditioner (DILU) was used with the PBiCG solver. Pressure-velocity coupling was achieved using the PIMPLE algorithm, which is a combination of PISO (Pressure Implicit with Splitting of Operator) and SIMPLE (Semi-Implicit Method for Pressure-Linked Equations). The simulation was treated as transient but used the SIMPLE (steady-state) treatment to find the steady-state solution for each time step. An advantage of using the PIMPLE algorithm is that it generally achieves better stability over the PISO algorithm and allows the Courant number to be larger than one; however, the Courant number was kept at a maximum of 0.75 for all the simulations.

The Lagrange solution method includes a fractional timestep approach as described by Macpherson et al. (2009). At each timestep, the numerical scheme loops through all Lagrange particles, updates their properties, calculates new velocities, positions, temperatures, and densities, and calculates the gas phase source terms. If the particle residence time in a cell is smaller than the overall timestep, all variables are updated using the state in that cell. However, if the particle transfers to an adjacent cell, it takes a fractional timestep to the cell face, and then a second timestep within the adjacent cell. This process occurs repeatedly until the overall outer timestep is complete. The Lagrange momentum and energy exchange equations are integrated analytically. This is completed based on the fractional timestep, where a semi-implicit Euler formulation is used to solve for velocity and an explicit exponential Euler scheme is used to solve for temperature. The particle density is updated explicitly based on the fractional timestep, and the devolatilization and surface reaction models.

The combustion model is a Partially Stirred Reactor (PaSR) model. In the PaSR approach, a computational cell is split into two different zones. In one zone all the reactions occur, while in the other zone there are no reactions. Thus, the composition changes due to mass exchange with the reacting zone. The reaction zone is treated as a perfectly stirred reactor (PSR), in which all reactants are assumed to be perfectly mixed with each other. This allows us to neglect any fluctuations when calculating the chemical source terms. A set of ordinary differential equations (ODEs) are constructed from the species and energy solution vectors, along with the details of the chemistry reaction model. A robust solver is required to integrate this stiff system of equations, and the Rosenbrock34 algorithm was used in this work due to the constant failure of the default Seulex algorithm. Coupling between the gas phase, Lagrange particles, and chemistry solutions is also completed using a segregated approach. At the start of the timestep the Lagrange position, velocity, temperature, and density are updated along with the respective gas phase source terms. The fluid velocity is calculated based on the momentum transport equation, followed by calculation of the combustion reaction source terms. The species mass fraction and energy transport equations are then solved with the updated source terms and velocity.

3 Results

Varying the L/D ratio of Vessel 1 resulted in both qualitative and quantitative differences in the pressure histories and dynamics of the simulated explosions. Results from the simulations are presented in this section. Discussion focuses on both the qualitative and quantitative trends observed in the simulation results.

3.1 General trend

The four distinct phases of coal dust explosion in fully enclosed interconnected systems previously discussed in Ogungbemide and Clouthier (2020) can be observed in the current study. The first phase involved the initial slow development of combustion in Vessel 1. The flame started to develop initially as a sphere from the point of ignition until it reached the vertical walls of Vessel 1. Afterward, the flame elongated and accelerated in the direction towards the duct opening more than in other directions. The second phase involved rapid flame propagation through the connecting duct. During this phase, the flame entered the connecting duct and burned rapidly through the unburned dust cloud ejected from the expanding dust cloud from Vessel 1. In the third phase, jet flame ignition and secondary explosion occurred in Vessel 2. Upon the flame arrival in Vessel 2, a secondary ignition of the more compressed, more turbulent, dust cloud in the vessel occurred. At the time of arrival of the

DOI: 10.7795/810.20200724

flame in Vessel 2, the initial pressure in the vessel was higher than the atmospheric pressure due to pre-compression. Fig. 2 shows typical examples of flame propagation in the interconnected system for select simulations with central and end ignition sources.

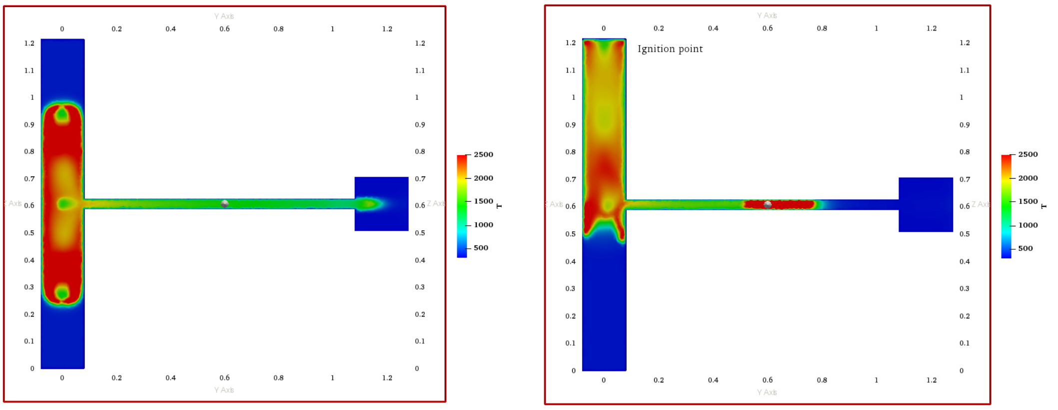

(a) L/D of 7.5, central ignition. *(b) L/D of 7.5, end ignition.*

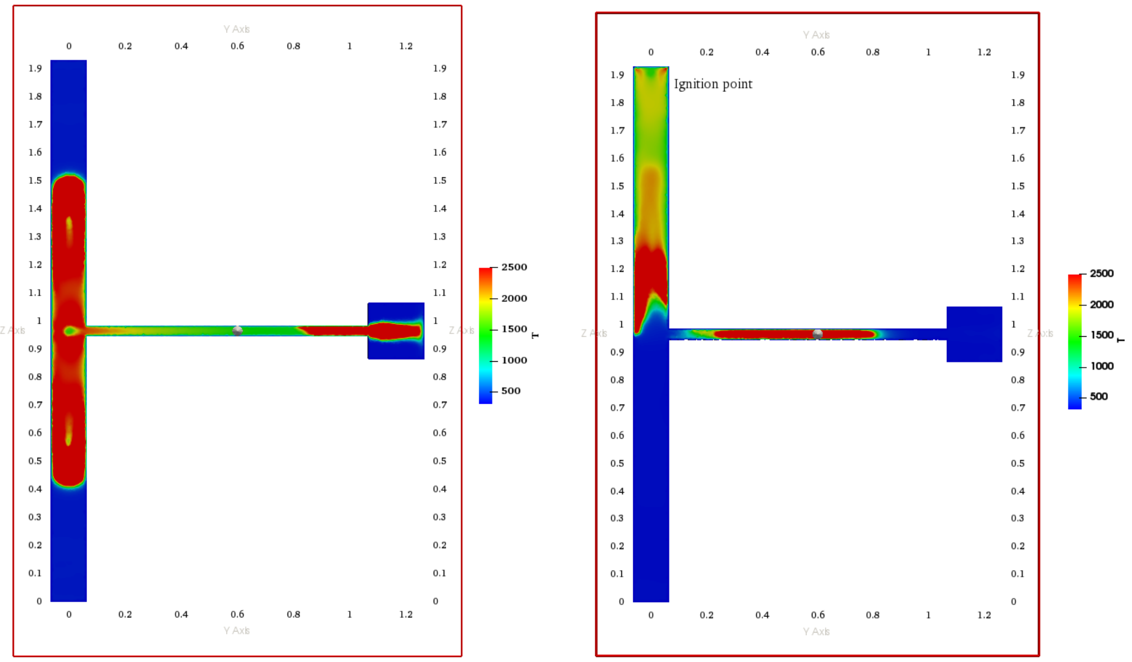

(c) L/D of 15, central ignition. *(d) L/D of 15, end ignition.*

***Fig. 2**: Behaviour of flame front propagation in interconnected system for central and end ignition sources.*

In the fourth and last phase, back venting of the secondary explosion in Vessel 2 into Vessel 1 occurred. Due to the pressure generated by the secondary explosion, a pressure differential was generated between Vessel 2 and Vessel 1. The rapid secondary explosion that occurred in Vessel 2 caused the pressure in the vessel to surpass that of Vessel 1, and the flow was reversed. As the volume of Vessel 2 is small compared to that of Vessel 1 (ratio 1:4.4), the compression in Vessel 2 was high, and it prevented the free outflow of material from Vessel 1 as the pressure gradient favoured flow from Vessel 2 to Vessel 1. The back flowing mixture contained a significant amount of expanded combustion products, which tended to increase the flame velocity. This induced additional turbulence and enhanced the combustion rate in Vessel 1. This, in turn, created a pressure gradient and caused yet another change in the direction of flow. Consequently, a strong, low frequency oscillation was set up in the system.

DOI: 10.7795/810.20200724

These oscillations indicate that the compressed combustion mixture in the vessels acted as a system of springs. This "piston" effect described by Taveau et al. (2019) is applicable to only the central ignition simulations as the explosion propagation created a symmetrical pressure system in Vessel 1. In contrast, for end ignition, there is an assymetrical pressure system in the vessel with the propagated pressure from the end ignition point branching into the duct and the opposite end of the vessel. Consequently, there are more distinct "pressure zones" in the interconnected systems for end ignition than for central ignition, due to the symmetry of the latter. As the L/D of Vessel 1 increased, it was observed that the preference of the approaching flame for the duct over the opposite end of Vessel 1 increased, with the flame failing to propagate to the opposite end of the vessel for elevated L/D values. Back venting from Vessel 2 was the more effective means of propelling the explosion in Vessel 1 to the opposite end in high L/D vessels, rather than the initial explosion in the vessel.

3.2 Pressure-time profiles

The simulated pressure-time profiles in Vessel 1 ($0.025\,\mathrm{m}^3$) and Vessel 2 ($0.006\,\mathrm{m}^3$) for end ignition are shown in Fig. 3. The difference between the pressure simulated in Vessel 1 compared to that of Vessel 2 is indicative of the pressure piling effect.

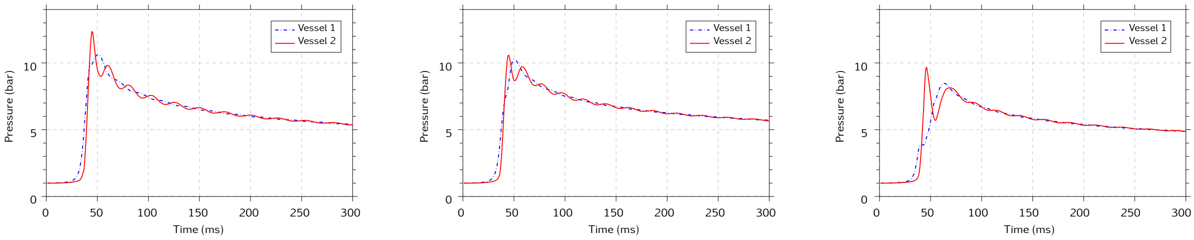

(a) L/D ratio of 0.5. *(b) L/D ratio of 1.0.* *(c) L/D ratio of 2.5.*

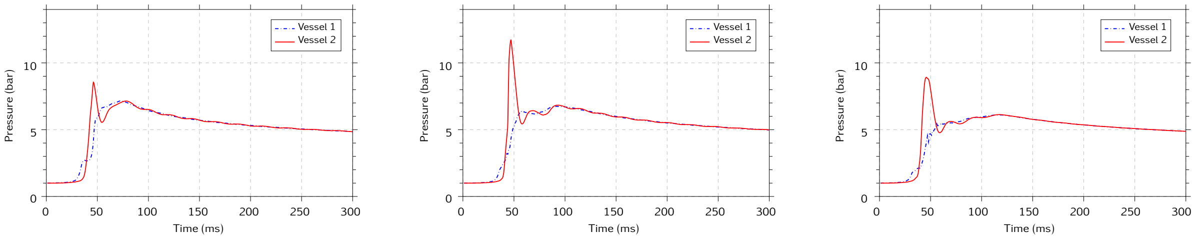

(d) L/D ratio of 5.0. *(e) L/D ratio of 7.5.* *(f) L/D ratio of 10.0.*

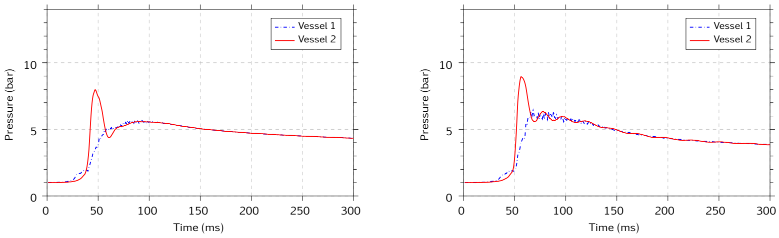

(g) L/D ratio of 12.5. *(h) L/D ratio of 15.0.*

***Fig. 3**: Pressure profiles in Vessel 1 ($0.025\,\mathrm{m}^3$) and Vessel 2 ($0.006\,\mathrm{m}^3$) for end ignition at various L/D ratios.*

For end ignition, the highest pressure enhancement (relative to Vessel 1) was observed for L/D of 7.5, which caused a relative pressure increase of 1.75 in Vessel 2. The lowest pressure enhancement was recorded for the L/D of 1.0, which had a relative pressure increase of 1.06. The highest recorded relative pressure increase for central ignition was 1.27 for L/D of 15. Overall, pressure enhancement in Vessel 2 increased with L/D, as indicated by the gap between the pressure spike in the pressure profile of Vessel 2 compared to the pressure peak of Vessel 1 as L/D increased (Fig. 3). However, this does not translate into the average pressure in the vessels increasing with L/D. In fact, except for L/D of 7.5 which has a peak pressure of 12.35 bar, the average and peak pressures recorded for the elevated L/D cases are significantly lower than the pressures recorded for L/D of 0.5 to 2.5.

The rate of pressure rise was estimated for all L/D cases. As expected, in all cases, the rate of pressure rise in Vessel 2 was higher than observed for Vessel 1 due to pressure piling effect. The highest rate of pressure rise in Vessel 1 was observed for L/D of 0.5 ($695\,\mathrm{bar\,s^{-1}}$), while the highest rate of pressure rise in Vessel 2 was recorded for L/D of 7.5 ($1155\,\mathrm{bar\,s^{-1}}$), which is slightly higher than the value obtained for L/D of 0.5 in Vessel 2 ($1068\,\mathrm{bar\,s^{-1}}$). The relatively high rate of pressure rise for L/D of 0.5 was probably due to the wider diameter (relative to height) of the vessel allowing the explosion to almost fully develop before the flame in the duct had reached Vessel 2; thus, increasing the pre-compression in Vessel 2.

3.3 Effect of L/D on pressure distribution in Vessel 1

For both central and end ignitions, the history-time profiles monitored at the centre and upper extreme of Vessel 1 are shown in Fig. 4.

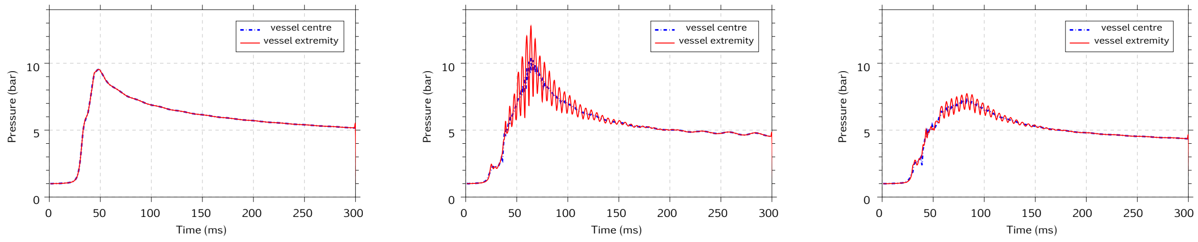

(a) L/D of 2.5, central ignition. *(b) L/D of 12.5, central ignition.* *(c) L/D of 15, central ignition.*

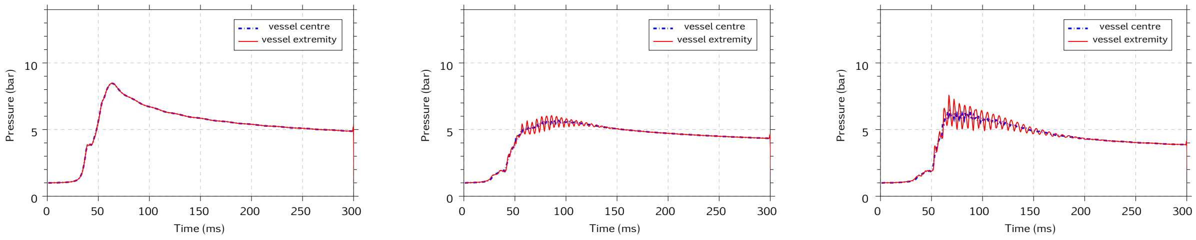

(d) L/D of 2.5, end ignition. *(e) L/D of 12.5, end ignition.* *(f) L/D of 15, end ignition.*

***Fig. 4**: Comparison of the pressure-time profiles monitored at the centre and extremity of Vessel 1 for select L/D cases.*

For L/D of 0.5 to 10, the pressure-time profiles monitored at the two points are indistinguishable; however, for L/D of 12.5 and 15, there is a distinct difference in the patterns of the pressure profiles at the two locations. High frequency pressure oscillations were observed in the vessel extremity. These pressure oscillations fluctuated rapidly between as much as $+2.9$ bar and -3.3 bar relative to the pressure at the centre for the L/D of 12.5. The oscillations, with a frequency of about 250 Hz, persisted for about 120 ms. The frequency of these oscillations may be indicative of the acoustic harmonics of the geometry. A practical implication of this observation is that a primary vessel (where ignition is initiated) with L/D of 12.5 and above could experience significant vibrations in the vessel extremities; therefore, these vibrations should be taken into consideration during the design of process vessels and their structural support. It is also important to consider the L/D of a vessel if the proposed basis for safety is pressure containment, as using the pressure measured at the centre may not be indicative of the pressure at the extremities of vessels with elevated L/D. For example, when the maximum pressure measured at the centre was 10.4 bar, the pressure monitored at the extremity was 12.8 bar.

3.4 *Effect of L/D ratio on time to reach maximum pressure*

As the maximum pressure (P_m) is expected to be developed when the explosion reaches the vessel wall, it stands to reason that the time required for an explosion to attain maximum pressure in a vessel will increase as L/D ratio increases. Table 3 shows the time required to attain maximum pressure in Vessel 1 and Vessel 2 for central and end ignition cases. It can be observed from Table 3 that the time to reach maximum pressure clearly increased with L/D in Vessel 1 for the central ignition cases. There is no clear trend for the end ignition cases for either Vessel 1 or Vessel 2.

***Table 3**: Time to reach maximum pressure in Vessel 1 and Vessel 2.*

	Central ignition		End ignition	
L/D	Vessel 1 (ms)	Vessel 2 (ms)	Vessel 1 (ms)	Vessel 2 (ms)
0.5	43	39	51	45
1.0	45	40	50	45
2.5	48	39	68	46
5.0	58	38	77	46
7.5	74	78	96	46
10.0	72	78	118	47
12.5	64	68	49	46
15.0	83	40	66	55

The relationship between time to reach maximum pressure in Vessel 1 (normalized by the time for the L/D of 1.0) and L/D is shown in Fig. 5. The best fit for the data is a power function.

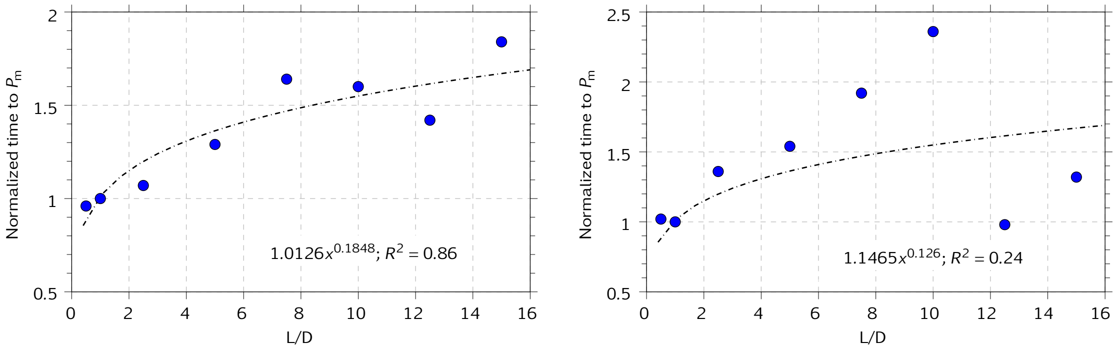

(a) central ignition *(b) end ignition*

***Fig. 5**: Normalized time to reach maximum pressure (P_m) in Vessel 1 as a power function of the L/D ratio. Time to reach P_m is normalized by the time to reach P_m for L/D of 1.*

As discussed earlier, the central ignition data has a better fit to the power function than the end ignition data which has a lot of scatter. For central ignition, if the time to attain maximum pressure in the vessel with L/D of 1 is known, the relative increase in time required to attain maximum pressure as the vessel L/D increases can be estimated from the relationship, if other factors remain constant.

3.5 *Effect of L/D on magnitude of explosion contact cones*

As the flame and pressure emerge from the duct into Vessel 2, they impact the wall directly opposite the duct opening in the shape of a “contact cone” of combusted and uncombusted materials, if the

DOI: 10.7795/810.20200724

wall is within the reach of the pressure and flame. This may be useful in explosion forensics to determine the cause and course of an explosion in an interconnected system. Roser et al. (1999), in their experiments using a 9.4 m^3 secondary vessel (Vessel 2) with L/D of 3 connected to a primary vessel (Vessel 1) of 4.25 m^3 with L/D of 2.1, observed contact cones at the points at which the inlet stream from the connecting duct impacted the wall opposite the duct opening as shown in Fig. 6a. They also observed another contact cone as Vessel 2 vented back into Vessel 1, the emergent flame impacted the wall of Vessel 1 directly opposite the duct opening (Fig. 6b).

Contact cones were observed in the current simulations as shown in Fig. 6c and Fig. 6d. As the L/D increases from 0.5 to 15, the magnitude of the explosion contact cone increases. For example, the contact cone observed at the wall of Vessel 1 opposite the duct opening for L/D of 15 is distinct compared to the simulation with L/D of 7.5, for which the contact cone, though present, is not distinct at the similar pressure scale used.

(a) Contact cone in Vessel 2 (image is from Roser et al. (1999)).

(b) Back flow contact cone in Vessel 1 (image is from Roser et al. (1999)).

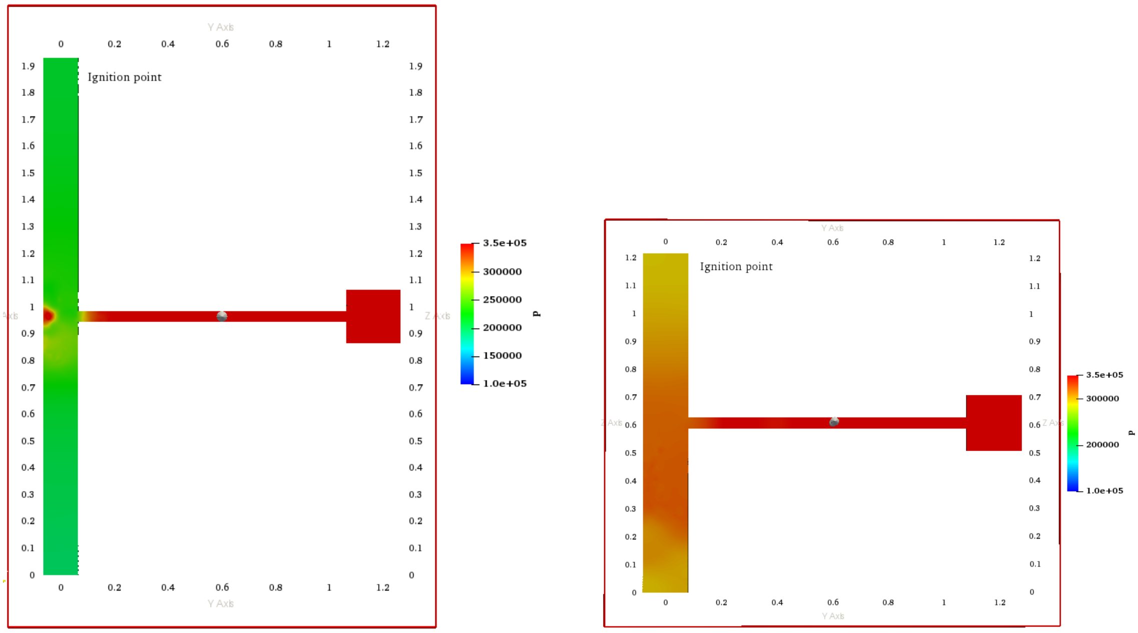

(c) Back flow contact cone in Vessel 1 for L/D of 15 (current study).

(d) Back flow contact cone is not distinct for L/D of 7.5 (current study).

***Fig. 6**: High pressure explosion contact cones from current simulations compared with contact cones from the experiments of Roser et al. (1999).*

Another notable observation from Fig. 6 is that the lower the L/D, the more uniform the pressure distribution in Vessel 1. In contrast, in vessels with elevated L/D, a high pressure contact cone is distinct at a higher pressure from the surrounding areas in the vessel, which are at pressure of about

DOI: 10.7795/810.20200724

1.5 bar less than the pressure at the contact cone. This has practical implications for process vessel designs, as the walls directly opposite the duct openings in both Vessel 1 and Vessel 2 should be designed with the contact cones in mind.

3.6 Effect of L/D ratio on flame speed within duct

The time it took for the flame front to travel through the duct was estimated for all simulations to investigate the role of L/D on flame speed within the duct. The estimated flame speeds were normalized by the flame speed estimated for L/D of 1. As shown in Fig. 7, as the L/D ratio increases, the flame speed in the duct decreases as a power function of L/D. This was probably caused by the larger flame balls formed in Vessel 1 at low L/D ratios pushing the flame through the duct at a very high speed. In contrast, as the L/D increased, the diameter of the vessel reduced and the flame ball reduced in size. The reduced flame ball forced the flame into the duct, albeit at a lower flame speed. Overall, simulation results show that it takes increasingly longer time for the flame to travel through the same length of duct as the L/D of Vessel 1 increases. A potential practical application of this relation is that if the flame speed in a duct connected to a primary vessel with L/D of 1.0 is known, the relative flame speed for other L/D cases can be estimated from the relationship.

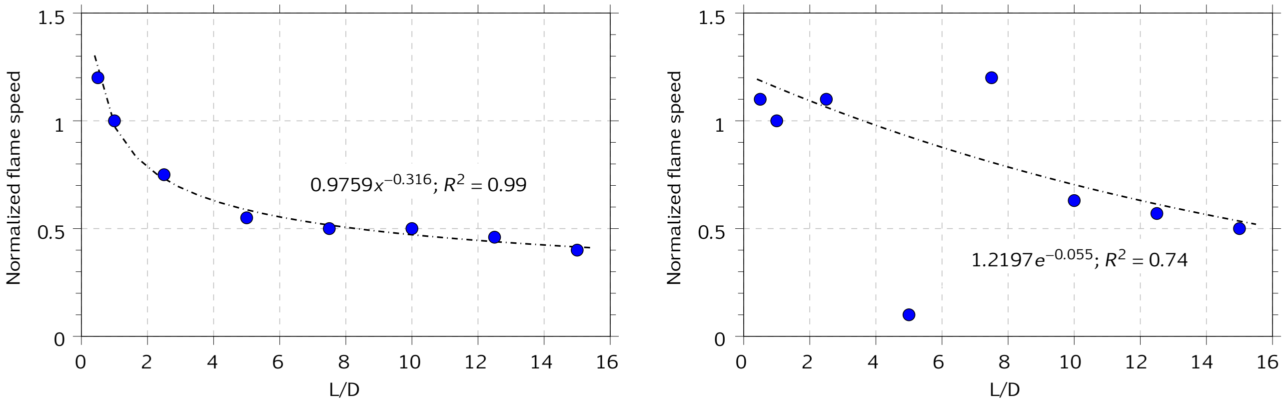

(a) central ignition

(b) end ignition

***Fig. 7**: Normalized flame speed through the duct as a power function of the L/D ratio. Flame speed is normalized by the flame speed at L/D of 1.*

3.7 Grid independence study

The grid independence analysis for this study was adopted from the grid independence study that was performed for a similar geometrical set up used in the numerical study by Ogungbemide and Clouthier (2020), on which the current study is based. The grid cells were varied from 0.005 m to 0.020 m. Grid cells of 0.005 m gave the fastest simulation progress. However, the qualitative trend, maximum explosion pressures, and rate of pressure rise were not affected by the grid sizes used in the analysis. Grid sizes ranging from 0.010 m to 0.0010 m were used in the current study to capture the geometrical variations between the vesels and the interconnecting duct.

3.8 Practical implications for industrial design

In addition to the support that this study provides to the design philosophy that it is more effective to prevent pressure piling by focusing on Vessel 1 or the duct so that a dangerous pressure build up does not occur in the first place, there are other notable practical implications for industrial design from this study. For example, this study shows that a primary vessel with L/D of 12.5 and above could experience significant vibrations in the vessel extremities; therefore, these vibrations should be taken into consideration during the design of process vessels and their structural support. It is also important to consider the L/D of a vessel if the proposed basis for safety is pressure containment, as using the pressure measured at the centre may not be indicative of the pressure at the extremities of vessels with elevated L/D. Another notable observation is that in the event of an explosion, vessels with elevated L/D will have high pressure contact cones on the walls directly opposite the duct openings, and these cones should be taken into consideration during process vessel design. Another potential practical application of this study is that if the flame speed in a duct connected to a primary vessel with L/D of 1.0 is known, the relative flame speed for other L/D cases can be estimated from the power relation developed in this study. In addition to the fundamental wisdom that requires the provision of adequate explosion protection devices on Vessel 1 and the duct to forestall the development of potentially dangerous pressures and high flame speeds in the interconnected system, the present study underscores the importance of considering the choice of the L/D ratio of Vessel 1 in the design of process vessels for handling explosible dusts.

4 Conclusion

Understanding the mechanisms of explosion flame propagation in interconnected vessels is paramount both during the design of new process plants and when installing systems for explosion mitigation. The current work investigated the effects of varying the L/D of the primary vessel (Vessel 1) on pressure piling in a system of interconnected vessels. A thorough analysis of several coal dust explosion simulations for different L/D ratios of Vessel 1 is provided. This study contributes to our understanding of the fundamental mechanisms which govern the propagation of dust flames through a system of interconnected process vessels.

The following points summarize the major findings from the current study:

- Pressure enhancement in the secondary vessel (Vessel 2) increased with the L/D of the primary vessel (Vessel 1).
- High frequency oscillations were observed in Vessel 1 extremities at elevated L/D ratios.
- The time to attain maximum pressure in Vessel 1 is a power function of the L/D ratio of the vessel.
- The magnitude of the explosion contact cone increased with increase in the L/D of Vessel 1.
- As the L/D ratio of Vessel 1 increased, the flame speed in the connected duct decreased as a power function of L/D ratio.

Acknowledgements

The authors gratefully acknowledge Jensen Hughes for logistical support.

References

Bartknecht, W. (2012). *Explosions: course, prevention, protection*. Springer Science & Business Media.

Barton, K. (2002). *Dust explosion prevention and protection: A practical guide*. Elsevier.

Bradley, D., Chen, Z., El-Sherif, S., Habik, S. E.-D., John, G., Dixon-Lewis, G. (1994). *Structure of laminar premixed carbon methane-air flames and ultrafine coal combustion*. Combustion and flame, 96(1-2):80–96.

Christ, D. M. (2013). *The effect of char kinetics on the combustion of pulverized coal under oxyfuel conditions*.

Cloney, C. T., Ripley, R. C., Pegg, M. J., Amyotte, P. R. (2018). *Laminar burning velocity and structure of coal dust flames using a unity lewis number cfd model*. Combustion and Flame, 190:87–102.

Di Benedetto, A., Salzano, E. (2010). *Cfd simulation of pressure piling*. Journal of Loss Prevention in the Process Industries, 23(4):498–506.

Gleim, E., Marcy, J. (1952). *Study to determine factors causing pressure piling in testing explosion-proof enclosures*. Report of investigations, 4904.

Kanzleiter, T., Fischer, K. (1994). *Multi-compartment hydrogen deflagration experiments and model development*. Nuclear engineering and design, 146(1-3):417–426.

Launder, B. E., Spalding, D. B. (1983). *The numerical computation of turbulent flows*. In *Numerical Prediction of Flow, Heat Transfer, Turbulence and Combustion*, pages 96–116. Elsevier.

Lunn, G., Holbrow, P., Andrews, S., Gummer, J. (1996). *Dust explosions in totally enclosed interconnected vessel systems*. Journal of loss prevention in the process industries, 9(1):45–58.

Lysenko, D. A., Ertesvåg, I. S., Rian, K. E. (2013). *Modeling of turbulent separated flows using openfoam*. Computers & Fluids, 80:408–422.

Macpherson, G. B., Nordin, N., Weller, H. G. (2009). *Particle tracking in unstructured, arbitrary polyhedral meshes for use in cfd and molecular dynamics*. Communications in Numerical Methods in Engineering, 25(3):263–273.

McCarthy-Singh, B., Gambaruto, A., Coclite, A. (2019). *Numerical modelling of pressure piling with inhomogeneous hydrogen/air mixtures*. In *Workshop on Fundamental Understanding and Modelling of High Pressure Turbulent Premixed Combustion (HPTC)*.

Migdal, D., Agosta, V. (1967). *A source flow model for continuum gas-particle flow*.

Ogungbemide, D. I., Clouthier (2020). *Numerical modelling of pressure piling using openfoam*. American Institute of Chemical Engineers 2020 Spring Meeting and 16th Global Congress on Process Safety.

Phylaktou, H., Andrews, G. (1993). *Gas explosions in linked vessels*. Journal of loss prevention in the process industries, 6(1):15–19.

Razus, D., Oancea, D., Chirila, F., Ionescu, N. (2003). *Transmission of an explosion between linked vessels*. Fire Safety Journal, 38(2):147–163.

Roser, M., Vogl, A., Radandt, S., Malalasekera, W., Parkin, R. (1999). *Investigations of flame front propagation between interconnected process vessels. development of a new flame front propagation time prediction model*. Journal of Loss Prevention in the process industries, 12(5):421–436.

Singh, J. (1984). *Gas explosions in compartmented vessels: pressure piling*. Chemical Engineering Research and Design, 62(6):351.

Singh, J. (1994). *Gas explosions in inter-connected vessels: pressure piling*. Process safety and environmental protection, 72(4):220–228.

Skjold, T. (2010). *Flame propagation in dust clouds: challenges for model validation*. Flame propagation in dust clouds. Numerical simulation and experimental investigation.

Taveau, J., Lemkowitz, S., Hochgreb, S., Roekaerts, D. (2019). *Dust explosion propagation in small diameter pipes*. Process safety progress, 38(3):e12033.

Yan, J., Jiang, J., Wang, Z. (2009). *Experimental investigation into explosion of premixed gases in linked vessels [j]*. Journal of the Chemical Industry and Engineering Society of China, 1.

Zhang, K., Wang, Z., Gong, J., Liu, M., Dou, Z., Jiang, J. (2017). *Experimental study of effects of ignition position, initial pressure and pipe length on h2-air explosion in linked vessels*. Journal of Loss Prevention in the Process Industries, 50:295–300.

Zhang, K., Wang, Z., Jiang, J., Sun, W., You, M. (2016). *Effect of pipe length on methane explosion in interconnected vessels*. Process Safety Progress, 35(3):241–247.

DOI: 10.7795/810.20200724

A computational framework for electrification of turbulent liquid flows

Mathieu Calero[a], Holger Grosshans[b] & Miltiadis V. Papalexandris[a]

[a] Institute of Mechanics, Materials and Civil Engineering, 1348 Louvain-la-Neuve, Belgium
[b] Physikalisch-Technische Bundesanstalt, 38116 Braunschweig, Germany

E-mail: *mathieu.calero@uclouvain.be*

Abstract

Flow electrification constitutes a significant hazard to operational safety in industry and for this reason it has been studied in detail over the years. It is generally accepted that the impact of turbulence on the electrification of liquids is of paramount importance. More specifically, at sufficiently high Reynolds numbers and for low-conductivity liquids such as hydrocarbons, the thickness of the hydrodynamic boundary layer can become comparable to that of the electrical double layer. This can lead to increased charge diffusion towards the bulk of the flow and, subsequently, flow electrification. However, quantitative information of the underpinning mechanisms of this phenomenon is still lacking. In this paper we present a computational framework for the study of electrification of turbulent liquid flows via numerical simulations. In the first part of the paper, we present the governing equations and describe the proposed algorithm and its implementation in pafiX, which is a computational tool for the simulation of fluid flows related to explosion protection. In the second part, we present results from numerical tests that we performed in order to access the efficiency of the proposed computational framework.

Keywords: *flow electrification, turbulent flows, dielectric liquids, numerical simulations, electrical double layer, electrohydrodynamics.*

1 Introduction

Flow electrification is the phenomenon of transport of electric charge from the interface between a flowing liquid and a solid boundary towards the bulk of the liquid. This transport is achieved via the electrical double layer that is inevitably formed at such an interface. In an electrical double layer, the first layer, also referred to as *Stern layer*, consists of ions anchored on the solid surface due to physicochemical processes (Stern, 1924). The second layer, also referred to as *diffuse layer* consists of free ions of opposite charge, the concentration of which decreases away from the solid surface. The characteristic thickness of the electrical double layer is the Debye length (Paillat et al., 2001). It has been shown that the Debye length is proportional to the square root of the electrical resistivity of the liquid. Typically, the Debye length is of the order of a few microns.

However, certain liquids of particular importance from the industrial and technological perspective have high electrical resistivity. Typical examples include liquid hydrocarbons such as benzene and heptane. In flows of such liquids, the thickness of the diffuse layer is not always negligibly small. Accordingly, under suitable conditions, ions that are initially located inside the diffuse layer can be transported towards the bulk of the flow, thereby resulting in flow electrification. For example, in turbulent flows at sufficiently high turbulent intensities, the thickness of the hydrodynamic boundary layer can become comparable to that of the diffuse layer and the turbulent structures of the flow will facilitate the transport of ions away from the diffuse layer. However, it must be mentioned that flow electrification is not exclusive to turbulent flows but can also occur in laminar flows.

On the other hand, flow electrification during the transport of highly flammable liquids such as hydrocarbons, constitutes a major safety hazard. In fact, this phenomenon is deemed responsible for a number of accidents in the petroleum industry (Paillat et al., 2009). For this reason, it has been the subject of numerous research efforts over the years. With regard to analytical or numerical studies of laminar flows, one can compute the charge density for a diffuse layer of a liquid initially at rest and then study the effect of the liquid velocity; see, for example, Touchard et al. (1996), Paillat et al. (2001), Cabaleiro et al. (2008), El-Adawy et al. (2011), Leblanc et al. (2017) and references therein. The advantage of this approach is that for simple geometries (channel, square duct, circular pipe, etc.) analytical or semi-analytical expressions for the velocity profile are readily available. Similarly, in the case of weak space charge, i.e. when the difference between the anion and cation concentrations near the interface is much smaller than their sum, the charge density profile for a fluid at rest can be found analytically; otherwise it can be computed numerically in a straightforward manner. One of the main results of these efforts was that the streaming current is a function of the mean flow velocity.

In the case of turbulent flows, the majority of theoretical and numerical studies are based on the mean velocity profile; see Touchard (1978), Dumínguez and Touchard (1997), Cabaleiro et al. (2019) as well as references provided in these papers. Following this approach, Dumínguez and Touchard (1997) proved that flow turbulence affects the diffuse layer and accelerates electrification. Moreover, it results in higher electric currents than in laminar flow. However, small-scale turbulent structures near the hydrodynamic boundary layers are expected to play a significant role in flow electrification. For this reason, the predictive capacity of approaches based solely on the mean velocity profile has certain limitations. In summary, our knowledge of electrification of turbulent flows currently remains incomplete.

On the other hand, the design of advanced flow solvers and the ever-increasing power of modern computer have made possible to study turbulent flows via numerical simulations. In fact, simulations do take into account the small-scale structures of the flow, either by resolving or by modelling them. For this reason, they can provide significant new physical insight of the underlying mechanisms of the phenomenon of interest. This approach, however, requires the design of efficient numerical algorithms for the system of governing equations which consists of three strongly coupled parts: the Navier-Stokes equations that describe the fluid flow, Gauss' law for the electric field and the balance law for the electric charge density. Numerical algorithms for electrohydrodynamics have been developed by López-Herrera et al. (2011) and Roghair et al. (2013). In those algorithms, however, mechanisms for charge generation at solid boundaries and charge diffusion away from them are not taken into account.

In this paper we present an algorithm for computational electrohydrodynamics that is well suited for the study of flow electrification and, more generally, for wall-bounded flows of dielectric liquids. This algorithm has been implemented in our recently developed computational tool pafiX (2019) for simulations of flows that involve an operational hazard. This tool is available as freeware and is developed specifically for the study of powder and fluid flows under conditions involving a hazard to operational safety.

This communication is structured as follows. In section 2, we present the governing equations for the flows of interest and in section 3, we outline the proposed algorithm. Then, in section 4, we present and analyze some of the numerical tests that we performed in order to test the efficiency and robustness of the algorithm. Finally, section 5 concludes.

2 Governing equations

In this section, we describe the governing equations of electrohydrodynamics for incompressible flows. As mentioned above, this system consists of three strongly coupled parts, namely the Navier-Stokes equations (supplemented with the Lorentz force), Gauss' law for the electric field, the balance law of the electric charge density. More specifically, the Navier-Stokes equations describe the conservation of mass and momentum of the fluid and read,

$$\nabla \cdot \boldsymbol{u} = 0 \,, \tag{1}$$

$$\frac{\partial \boldsymbol{u}}{\partial t} + (\boldsymbol{u} \cdot \nabla)\boldsymbol{u} = -\frac{1}{\rho}\nabla p + \nu \nabla^2 \boldsymbol{u} + \frac{1}{\rho}\boldsymbol{F}_{\mathrm{el}} \,, \tag{2}$$

where $\boldsymbol{u}$ is the velocity vector, ρ the (mass) density, p the dynamic pressure and ν the kinematic viscosity of the fluid. Further, $\boldsymbol{F}_{\mathrm{el}}$ stands for the Lorentz force, i.e. the volume electric force acting on the fluid. More specifically, $\boldsymbol{F}_{\text{el}}$ can be derived from the electrostatic Maxwell stress tensor (Castellanos, 1991). For nonpolar media, it is equal to the product between the electric field $\boldsymbol{E}$ and the charge density ρ_{el},

$$\boldsymbol{F}_{\text{el}} = \rho_{\text{el}}\, \boldsymbol{E}\,. \tag{3}$$

For the applications of interest, dynamic currents due to charge transport are very small so that the effects of electromagnetic induction are negligible (Saville, 1997). Accordingly, the laws of electrodynamics are simplified to those of electrostatics. In particular, the electric field $\boldsymbol{E}$ satisfies Gauss' law,

$$\nabla \cdot \boldsymbol{E} = \frac{\rho_{\text{el}}}{\epsilon}\,, \tag{4}$$

where ρ_{el} is the electric charge density and ϵ is the homogeneous electrical permittivity.

Also, since in the electrostatic approximation the electric field is irrotational, it can be written in terms of the electric potential ϕ,

$$\boldsymbol{E} = -\nabla\phi\,. \tag{5}$$

Accordingly, Gauss' law reduces to the following Poisson equation,

$$\nabla^2\phi = -\frac{\rho_{\text{el}}}{\epsilon}\,. \tag{6}$$

Concerning the charge density ρ_{el}, for the flows in hand, it is given by Dumargue (1971),

$$\rho_{\text{el}} = e_0(z_\text{P} n_\text{P} - z_\text{N} n_\text{N})\,, \tag{7}$$

where n_P and n_N are, respectively, the concentrations of cations and anions in the liquid and e_0 is the elementary charge. Further, z_P and z_N are, respectively, the valences of cations and anions. They are often set equal to unity, in which case the above equation reduces to,

$$\rho_{\text{el}} = e_0(n_\text{P} - n_\text{N})\,. \tag{8}$$

The charge density ρ_{el} satisfies a balance law of the form,

$$\frac{\partial \rho_{\text{el}}}{\partial t} + \nabla \cdot \boldsymbol{J} = 0\,. \tag{9}$$

In this equation $\boldsymbol{J}$ stands for the electric current density and is given by Dumargue (1971),

$$\boldsymbol{J} = \rho_{\text{el}}\boldsymbol{u} + \sigma\boldsymbol{E} - D\nabla\rho_{\text{el}}\,. \tag{10}$$

The first term on the right-hand side of this equation describes convective currents and the second one describes (ohmic) conductive currents. Finally, the third term stands for ionic diffusion. This term is sometimes neglected (López-Herrera et al., 2011) because it can be several orders of magnitude smaller than the other terms. However, in problems involving diffuse layers of non-negligible thickness, as is the case in flow electrification, this term is significant.

Also in equation (10), D stands for the ionic diffusion coefficient and σ for the electric conductivity of the liquid. Under constant thermodynamic conditions, these coefficients can be considered to be constant (Leblanc et al., 2017, Touchard et al., 1996). Furthermore, σ is given by Dumargue (1971),

$$\sigma = \frac{e_0^2\, D\, n_0}{K_\text{B} T}\,, \tag{11}$$

with K_B being the Boltzmann constant, T the temperature and $n_0 = n_\text{P} + n_\text{N}$ the total ionic concentration in the liquid.

By virtue of the continuity equation (1), Gauss' law (4) and the expression (10) for $\boldsymbol{J}$ the charge balance law (9) is written as,

$$\frac{\partial \rho_{\mathrm{el}}}{\partial t} + \boldsymbol{u}\cdot\nabla\rho_{\mathrm{el}} = -\frac{\sigma}{\epsilon}\rho_{\mathrm{el}} + D\nabla^2\rho_{\mathrm{el}}\,. \tag{12}$$

It is also worth mentioning that the Debye length is given by Paillat et al. (2001),

$$\lambda_D = \sqrt{\frac{\epsilon\, K_{\mathrm{B}}T}{e_0^2\, n_0}}\,. \tag{13}$$

In view of the definition (11) of the electrical conductivity, it can also be written as,

$$\lambda_D = \sqrt{\frac{\epsilon\, D}{\sigma}}\,. \tag{14}$$

Therefore the charge balance can be cast in the following form,

$$\frac{\partial \rho_{\mathrm{el}}}{\partial t} + \boldsymbol{u}\cdot\nabla\rho_{\mathrm{el}} = -\frac{D}{\lambda_D^2}\rho_{\mathrm{el}} + D\nabla^2\rho_{\mathrm{el}}\,. \tag{15}$$

3 Numerical algorithm

In this section we elaborate on the numerical procedure that we use to integrate the governing system of equations, starting with an outline of the Navier-Stokes solver. Since the dynamic pressure enters the momentum equations (2) via its gradient, its role is to constrain the fluid motion so that the continuity equation (1) is satisfied. Herein, we couple the continuity and momentum equations through the distributed Gauss-Seidel scheme, originally proposed by Brandt and Dinar (1979), but extended to three-dimensional domains and non-uniform grids. The underlying idea of this scheme is to diminish the error in the continuity equation by iteratively adjusting the velocity field. Afterwards, the pressure field is modified accordingly so that the residuals of the momentum equations at all points remain unchanged. Distributive relaxation represents an efficient and intuitive alternative to popular velocity-pressure schemes such as SIMPLE or PISO (Ferziger and Perić, 2002).

With regard to the discretization of the spatial derivatives of the flow variables, we note the following. The convective term in (2) is discretized via a fifth-order accurate Weighted Essentially Non Oscillatory, WENO, scheme (Jiang and Shu, 1996). Also, the velocity derivatives in (1) as well as the pressure gradient and viscous terms in (2) are discretized via fourth-order central differences.

Furthermore, for the simulation of wall-bounded flows, one typically introduces non-uniform grids, with refined meshing in the wall region. In the proposed algorithm, and in order to keep the high-order discretization schemes simple, the spatial derivatives of the convective terms are transformed via stretching of the spatial coordinates. For a generic flow quantity ζ, this transformation is performed with the application of the chain rule as follows,

$$\frac{d\zeta}{dx} = \frac{1}{x'(\xi)}\frac{d\zeta}{d\xi}\,, \tag{16}$$

where the prime symbol denotes the derivative of the x variable with respect to the stretched ξ variable. Thus, the non-uniform grid in physical x direction space is mapped to the uniform grid in the ξ direction on which the derivatives are then discretized.

For purposes of computational savings, we apply the deferred-correction method since it is a well-established method for the construction of high-order approximations based on lower-order numerical methods by a process of iterated corrections. According to it, the numerical approximation of a quantity ζ is expressed by,

$$\zeta = \zeta^{\mathrm{l}} + (\zeta^{\mathrm{h}} - \zeta^{\mathrm{l}})^{\mathrm{old}}\,, \tag{17}$$

where the superscript l denotes an approximation by a low-order scheme and h an approximation by a high-order scheme. The terms indicated by "old" are computed explicitly using values from the previous outer iteration. For the computational cells in the vicinity of a solid boundary there are not sufficient number of points available to form a five-point stencil for the high-order discretization of the spatial derivatives. In those computational cells, only the low-order schemes are retained.

Finally, the Navier-Stokes equations are integrated in time via an implicit second-order scheme using a variable time-step,

$$\frac{\partial \boldsymbol{u}}{\partial t} \approx \frac{\left(1+\tau^{n+\frac{1}{2}}\right)\, \boldsymbol{u}^{n+1} - \left(1+\tau^{n+\frac{1}{2}}+\tau^{n-\frac{1}{2}}\right)\, \boldsymbol{u}^{n} + \tau^{n-\frac{1}{2}}\, \boldsymbol{u}^{n-1}}{2\tau^{n+\frac{1}{2}}\, \Delta t^{n+1}}\,, \tag{18}$$

with

$$\tau^{n+\frac{1}{2}} = \frac{\Delta t^{n+1}}{\Delta t^{n+1}+\Delta t^{n}} \quad \text{and} \quad \tau^{n-\frac{1}{2}} = \frac{\Delta t^{n}}{\Delta t^{n}+\Delta t^{n-1}}\ . \tag{19}$$

In the above equations the superscript n is a label for the current time instance, t^n, i.e. the most advanced time at which the solution has been computed. Also, Δt^{n+1} is the time-step used to advance the solution from the n-th time level to the next one.

As regards the electrostatic equations, the left-hand side of the Poisson equation (6) for the electric potential is discretized via second-order central differences. This discretization results in a linear system that can be solved by standard linear solvers. Herein we apply the Jacobi method which facilitates the straightforward parallelization of the computer code.

The balance law for the charge density is integrated in time with the same time-marching scheme that is used for the velocity field of the liquid. The convective term of (12) is also discretized via a fifth-order WENO scheme and the diffusive term via second-order central differences.

It should also be mentioned that the above algorithm has been discretized in staggered grids, which are not prone to the well-known odd-even decoupling between the pressure and velocity fields. Accordingly, the dynamic pressure p, electric field $\boldsymbol{E}$, electric charge density ρ_{el} are evaluated at cell centers. Similarly, the Lorentz force in (2) and the conductive current in (12) are also evaluated at cell centers. On the other hand, the fluid-velocity vector is evaluated at the centers of the cell interfaces.

Finally, the time-advancement of the coupled Navier-Stokes and electrostatics equations is performed via Strang splitting (**?**). More specifically, the flow chart of the proposed algorithm to advance the solution from t^n to $t^{n+1} = t^n + \Delta t$ is the following.

1. The charge conservation equation (12) is integrated numerically over $\Delta t/2$, from t^n to $t^n + \Delta t/2$, by using the velocity distribution from the previous time-step.
2. The electric potential ϕ is computed by solving the Poisson equation (6), the right-hand side of which involves the values of ρ_{el} that were computed in step 1.
3. The electric field $\boldsymbol{E}$ is computed from (5).
4. The value of the Lorentz force $\boldsymbol{F}_{\mathrm{el}}$ is updated from (3).
5. The Navier-Stokes equations are integrated numerically over Δt by using the updated values of $\boldsymbol{F}_{\mathrm{el}}$. This step provides the values of the fluid velocity $\boldsymbol{u}$ and dynamic pressure p at t^{n+1}.
6. Finally, the charge conservation equation (12) is re-integrated numerically over $\Delta t/2$, this time from $t^n + \Delta t/2$ to t^{n+1}, by using the velocity distribution at t^{n+1} that was computed in step 5.

4 Numerical tests and discussion

In this section we present results from three numerical tests that we performed to test the accuracy of the proposed algorithm. The Navier-Stokes solver has already been tested for turbulent-flow simulations and the results are reported by Grosshans et al. (2020). For this reason herein emphasis is placed on the numerical treatment of the charge density equation (12). To this end, we present three

***Table 1**: Material properties of benzene.*

Symbol	**Quantity**	**Value**
ρ	Fluid density	879 Kg/m^3
ν	Fluid kinematic viscosity	7.24×10^{-7} m^2/s
ϵ	Permittivity	2.04×10^{-11} F/m
T	Temperature	298 K
D	Ionic diffusion constant	2.21×10^{-9} m^2/s
n_0	Total ionic concentration	7.97×10^{13} ions/m^3

test cases, namely, charge relaxation of benzene at rest and flow electrification of laminar flow with uniform and non-uniform charges at the boundary.

In all cases the computational domain is a duct of square cross section. Its height, H, is equal to 1 cm and its length, L , is equal to $2\pi H$. The computational domain is discretized via $60\times60\times60$ grid cells. The grid is refined close to the solid walls since the near-wall regions are the ones with the highest velocity and charge-density gradients. The distribution of grid points in the two spanwise (y and z) directions is performed in a fashion similar to that employed by Kim et al. (1987) for grid refinement in the wall-normal direction in channel flows. Thus the grid points at the y direction are located at,

$$y_j = \cos\left(\frac{j-1}{N-1}\pi\right), \qquad j = 1, \ldots, N, \tag{20}$$

where N is equal to the total number of points in the y direction. Since we investigate a square duct flow, the number of points and the grid-point distribution in the z-direction are the same as in the y-direction. At the walls of the duct, zero-slip conditions are applied for the velocity field. Also, in order to mimic a very long duct, periodic boundary conditions are applied in the streamwise x direction.

For purposes of non-dimensionalization, the half-height of the duct $H/2$ is used as the reference length-scale and the electric relaxation time, $t_e = \epsilon/\sigma$, is employed as the reference time-scale. Also, the maximum of the initial charge distribution, $(\rho_{el,0})_{max}$, is employed as the reference charge density. The dimensionless length, time and charge density are denoted by x^*, t^* and ρ^*_{el} respectively. Finally, for all the simulations presented therein the time step was determined via the CFL condition with a Courant number equal to 0.25.

4.1 Charge relaxation in benzene

In this test the working medium is benzene. We assume that it is at rest and contained in a square duct. Its material properties are provided in table 1 above. The particular value of the ionic concentration n_0, is set so as to match the electric conductivity σ of benzene on the basis of equation (11). The electric conductivity of benzene is $\sigma \approx 1.1 \times 10^{-12}$ S/m (Forster, 1962).

Initially, a specific electric charge density $\rho_{el,0}(y, z)$ is assigned to benzene. This initial condition is computed as the solution of a Poisson equation. The right-hand side of the Poisson equation is adjusted so that the maximum initial charge, $(\rho_{el,0})_{max}$, is located at the center of the square section of the duct; see figure 1. With regard to boundary conditions, zero Dirichlet conditions are prescribed for the charge density and zero Neumann conditions are prescribed for the electric potential. The objective of the test is to compute the relaxation of this electric charge with time. This problem admits an analytic solution, namely,

$$\rho^*_{el} = \rho^*_{el,0}\exp(-t^*)\,. \tag{21}$$

In figure 2 we have plotted the analytical and numerical solutions for the evolution of the charge density at the center of the cross section. From this figure we readily infer that our numerical solution

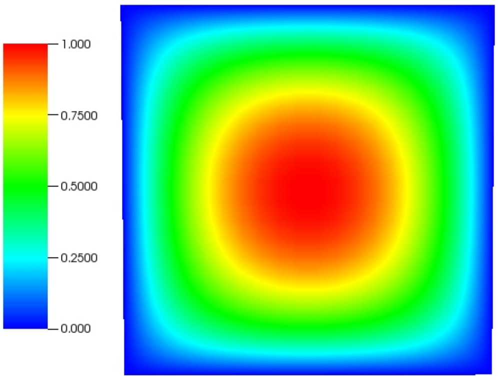

Fig. 1*: Charge relaxation in benzene. Colormap of the initial charge density* $\rho^*_{\mathrm{el},0}$ *at the cross section of the duct. The peak of the charge density,* $(\rho_{\mathrm{el},0})_{\max}$*, is located at the center of the cross section.*

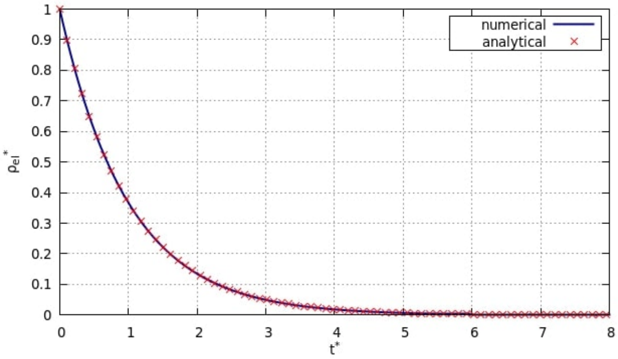

Fig. 2*: Charge relaxation in benzene. Analytical and numerical solutions for the evolution of the charge density at the center of the cross section.*

matches the analytical one. The very good accuracy of the computations was further confirmed by comparing the analytical and numerical solutions at different points in the cross section of the duct.

4.2 Laminar flow electrification - uniform charge at the boundary

In this test we consider electrification of a laminar flow in a square duct. The flow is maintained by an externally applied pressure gradient $\boldsymbol{P}$, the value of which is adjusted so that the bulk Reynolds number is $Re_{\mathrm{b}} = 2000$. The bulk Reynolds number is defined as $Re_{\mathrm{b}} = u_{\mathrm{b}}H/\nu$ with u_{b} being the bulk velocity, i.e. the mass flow rate divided by the cross-section area of the duct. At such bulk Reynolds number, the flow remains laminar.

We assume that the charge at the top and bottom walls (i.e. the walls normal to the y direction) is kept constant and equal to $(\rho_{\mathrm{el},0})_{\max} = 1$ mC/m^3. Also, we assume that initially a layer of electric charge is formed next to these walls. Inside this layer the charge decreases linearly from $(\rho_{\mathrm{el},0})_{\max}$ to zero and the thickness of this layer is $H/10$.

On the other hand, the duct walls normal to the z direction are kept free of charge. The objective of this test is to compute the diffusion of charge from the walls towards the bulk of the duct. In order to accelerate this process, we use an artificial ionic diffusion coefficient is that 100 times than that of benzene given in table 1. Also, the electric conductivity is modified according to equation (11). All other parameters have been kept the same as in table 1. With this set of parameters, the value of the Debye length for this case is $\lambda_{\mathrm{D}} = 2.02 \times 10^{-4}$ m.

In figure 3 we provide plots of the charge density along the y axis at four different time instances from

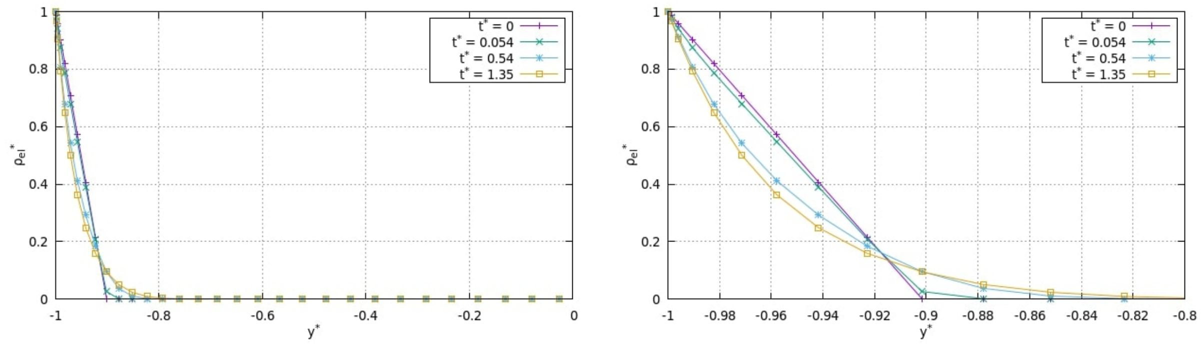

(a) (b)

***Fig. 3**: Laminar flow electrification - uniform charge at the boundary. Charge density profile along the y direction at four different times and z = 0. The right plot is a zoom near the wall.*

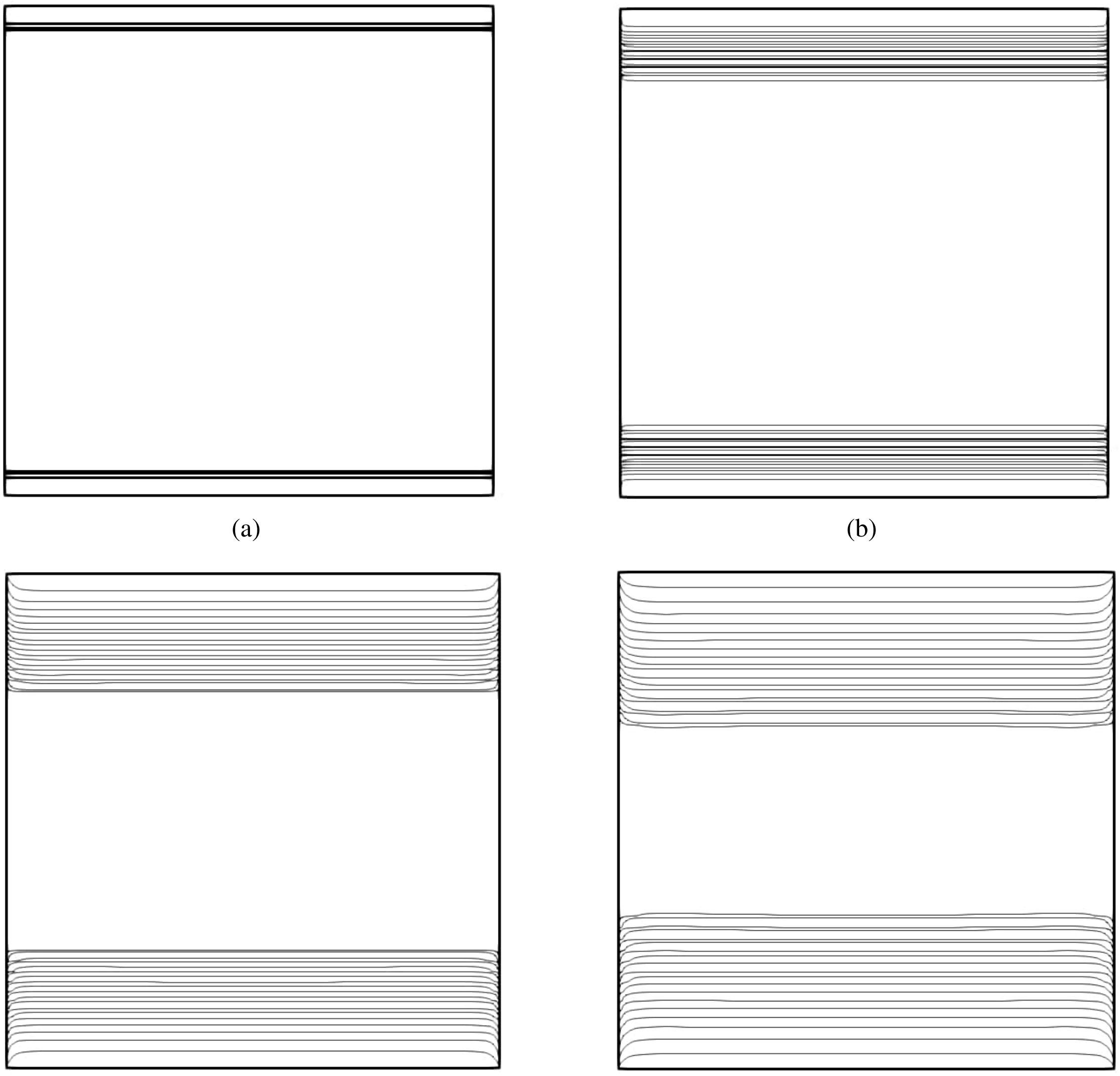

(a) (b)

(c) (d)

***Fig. 4**: Laminar flow electrification - uniform charge at the boundary. Contour plots of the charge density distribution at the cross section of the duct (yz plane) at four time instance. (a) $t^* = 0$, (b) $t^* = 0.054$, (c) $t^* = 0.54$, (d) $t^* = 1.35$. Each plot depicts 20 iso-contours distributed evenly between $\rho^*_{\text{el}} = 0$ and $\rho^*_{\text{el}} = 1$.*

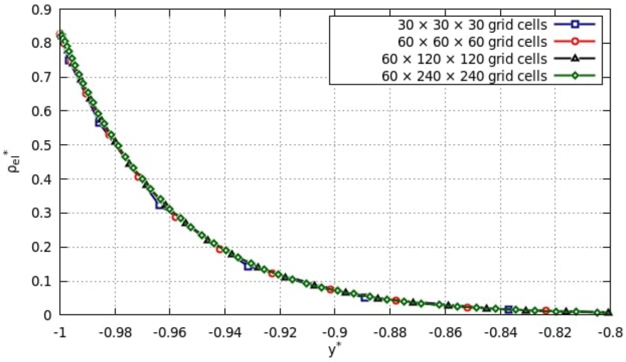

***Fig. 5**: Laminar flow electrification - uniform charge at the boundary. Profiles of the charge density along the y direction at* $t^* = 5.0$ *and* $z = 0$ *computed with four different grids.*

which we can observe the diffusion of the charge towards the bulk of the domain. Contour plots of the charge density distribution at the cross section of the duct and for the same fours instances are provided in figure 4. From these plots we confirm that in this particular case, flow electrification is dominated by charge diffusion away from the walls. Moreover, the charge density does not vary in the x direction. This is to be expected because in a fully established laminar flow the streamlines are parallel to the streamwise x direction, i.e. only the streamwise velocity component is non-zero. On the other hand, the initial charge distribution varies only along one of the spanwise directions. Consequently, the convective term in the charge density equation (12) is always equal to zero. In other words, in this particular case, there are no convective currents.

In order to test the efficiency of the proposed computational framework, we have performed a numerical grid-convergence study for this test case, the results of which are presented below. More specifically, we used four different computational meshes consisting, respectively, of $30 \times 30 \times 30$, $60 \times 60 \times 60$, $60 \times 120 \times 120$ and $60 \times 240 \times 240$ grid cells. In figure 5 we show the results for the charge-density profiles along the y direction at $t^* = 5.0$ and $z = 0$ as obtained with these grids. We observe that the numerical results are practically identical, thereby affirming the accuracy of the computations.

4.3 Laminar flow electrification - non-uniform charge at the boundary

In this test we also consider electrification of a laminar flow in a square duct. As in the previous case of subsection 4.2, we assume an initial layer of electric charge adjacent to the top and bottom walls (normal to the y direction) whose thickness is $H/10$. Inside this layer, the charge density decreases linearly away from the walls. Moreover, the walls normal to the z direction are kept free of charge.

However, this case differs from the previous one in two important aspects. The first one is that the charge at the top and bottom walls, i.e. the planes normal to the y direction, is not uniform but varies sinusoidally along the streamwise x direction. In particular, we set

$$\rho_{\mathrm{el}}(x, y = \pm H/2) \;=\; (\rho_{\mathrm{el},0})_{\max}\left(1 + 0.1\cos\frac{2\pi x}{L}\right), \tag{22}$$

with $(\rho_{\mathrm{el},0})_{\max} = 1\ \mathrm{mC/m^3}$. In this manner the velocity vector and the gradient of the charge density are no longer perpendicular and therefore, the charge density will vary along the x direction too.

The second difference is that in this test case the Debye length has been increased to $\lambda_{\mathrm{D}} = 3 \times 10^{-3}$ m. It should be mentioned that this particular value does not correspond to a real liquid and is introduced herein only for the purposes of validation of the proposed algorithm and the implemented computer code. On the other hand, the diffusion coefficient D has been kept the same as in the previous test. It can be inferred from (15) that the increase of the Debye length will result in higher levels of electrification away from the walls, i.e. in the bulk of the duct. This is due to the decrease of the amplitude

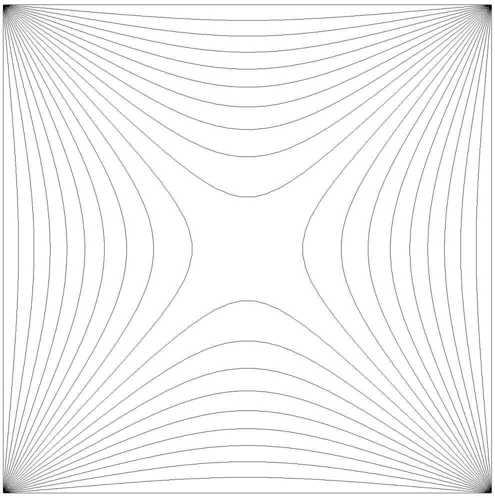

***Fig. 6**: Laminar flow electrification - non-uniform charge at the boundary. Contour plots of the charge density distribution at steady state and at the cross section (yz plane) with $x = 0$. The plot depicts 20 iso-contours uniformly distributed between $\rho^*_{\text{el}} = 0.11$ (close to the left and right walls) and $\rho^*_{\text{el}} = 0.98$ (close to the top and bottom walls).*

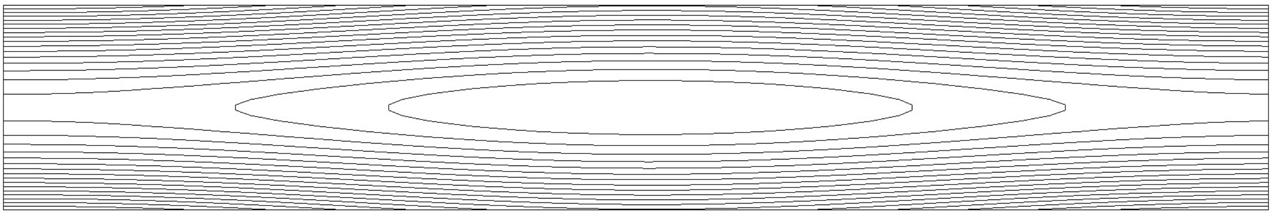

***Fig. 7**: Laminar flow electrification - non-uniform charge at the boundary. Contour plots of the charge density distribution on the x-y plane at steady-state. The plot depicts 20 iso-contours uniformly distributed between $\rho^*_{\text{el}} = 0.41$ and $\rho^*_{\text{el}} = 1$.*

of the source term on the right-hand side of (15) and the corresponding predominance of the second term that describes ionic diffusion.

Contour plots of the charge density at steady state and at the cross section with $x = 0$ are provided in figure 6. From this plot we readily infer that the initial layers of charge, adjacent to the top and bottom walls of the duct, have diffused throughout the cross section. In particular, the charge density at the center of the cross section is almost half of that at the top and bottom walls. Moreover, electric charge is also diffused along the z direction.

Also, contour plots of the charge density at steady state across the xy plane is provided in figure 7. From this figure, we can confirm the significant variation of the charge density along the streamwise x direction. As mentioned above, this is a direct consequence of the applied charge at the top and bottom boundaries, which varies along x, and the presumed increase of the Debye length.

Finally, in figure 8 we have plotted the profile of the charge density at steady state along the centerline of the duct, as well as the charge density at the top and bottom walls, $\rho_{\text{el}}(x, y = \pm H/2)$. From this plot, we readily infer that this steady-state profile at the centerline has inherited the sinusoidal variation from the wall charge.

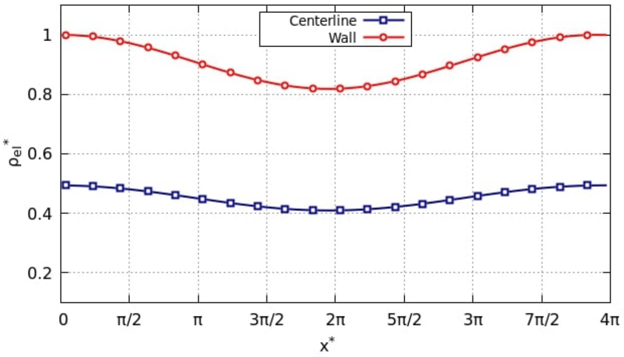

***Fig. 8**: Laminar flow electrification - non-uniform charge at the boundary. Charge density distribution at steady state along the centerline and at the top and bottom walls.*

5 Conclusions and future work

Electrification of liquid flows constitutes a major safety issue in petrochemical and process industries. In this communication we presented a computational framework for the numerical study of this phenomenon and for the study of confined flows involving dielectric fluids in general. The proposed numerical algorithm consists of three coupled components, namely, a Navier-Stokes solver for the fluid flow, a Poisson solver for the electric potential, and a solver for the charge density equation. We further presented three of the test cases that we simulated in order to assess the efficiency of the proposed numerical procedures. These tests concerned the charge relaxation in benzene at rest and the charge diffusion away from solid walls in laminar flows with two different types of charge at the wall boundaries. Our next studies will focus on electrification of turbulent duct flows involving dielectric liquids.

Acknowledgements

The first and third authors gratefully acknowledge the financial support of the National Research Fund of Belgium (FNRS) under the FLOW-CHARGE grant. The second author gratefully acknowledges the financial support from the Max Buchner Research Foundation.

References

Brandt, A., Dinar, N. (1979). *Multigrid solutions to elliptic flow problems.* Numerical methods for partial differential equations, pages 124–142.

Cabaleiro, J. M., Paillat, T., Artana, G., Touchard, G. (2019). *Flow electrification in turbulent flows of liquids—comparison of two models for one specific case.* IEEE, 55(5):5235–5238.

Cabaleiro, J. M., Paillat, T., Moreau, O., Touchard, G. (2008). *Flow electrification of dielectric liquids in insulating channels: limits to the application of the classical wall current expression.* Journal of Electrostatics, 66(1-2):79–83.

Castellanos, A. (1991). *Coulomb-driven convection in electrohydrodynamics.* IEEE Transactions on Electrical Insulation, 26(6):1201–1215.

Dumargue, P. (1971). *Perturbations des couches diffuses-I. Équations théoriques de base.* Electrochimica Acta, 16(8):1115–1128.

Dumínguez, G., Touchard, G. (1997). *Streaming current development in a rectangular channel.* Journal of Electrostatics, 40-41:153–159.

El-Adawy, M., Paillat, T., Touchard, G. (2011). *Numerical simulation of the electrical double layer development: physiochemical model at the solid and dielectric liquid interface for laminar flow electrification phenomenon.* IEEE Transactions on dielectrics and electrical insulation, 18(5):1463–1475.

Ferziger, J. H., Perić, B. (2002). *Computational Methods for Fluid Dynamics.* Springer-Verlag.

Forster, E. O. (1962). *Electric conduction in liquid hydrocarbons. I. Benzene*. The journal of chemical physics, 37(5):1021–1028.

Grosshans, H., Bissinger, C., Calero, M., Papalexandris, M. V. (2020). *The effect of electrostatic charges on particle-laden duct flows*. Under review.

Jiang, G. S., Shu, C. W. (1996). *Efficient implementation of weighted ENO schemes.* J. Comput. Phys., 126:202–228.

Kim, J., Moin, P., Moser, R. (1987). *Turbulence statistics in fully developed channel flow at low Reynolds number.* J. Fluid. Mech., 177:133–166.

Leblanc, P., Cabaleiro, J. M., Paillat, T., Touchard, G. (2017). *Impact of the laminar flow on the electrical double layer development*. Journal of Electrostatics, 88:76–80.

López-Herrera, J. M., Popinet, S., Herrada, M. A. (2011). *A charge-conservative approach for simulating electrohydrodynamic two-phase flows using volume-of-fluid.* Journal of Computational physics, 230(5):1939–1955.

pafiX (2019). `https://www.ptb.de/cms/asep`.

Paillat, T., Cabaleiro, J. M., El-Adawy, M., Moreau, O., Touchard, G. (2009). *High power transformers failures due to flow electrification: tools for understanding the electrostatic hazard.* Conference paper. RN.

Paillat, T., Moreau, E., Touchard, G. (2001). *Space charge density at the wall in the case of heptane flowing through an insulating pipe.* Journal of Electrostatics, 53(2):171–182.

Roghair, I., van den Ende, D., Mugele, F. (2013). *An OpenFOAM-based electrohydrodynamical model*. In *8th Int. Conf. Multiphase Flow*.

Saville, D. A. (1997). *Electrohydrodynamics: the Taylor-Melcher leaky dielectric model.* Annual Review of Fluid Mechanics, 29:27–64.

Stern, O. (1924). *Zur theorie der elektrolytischen doppelschicht*. Zeitschrift für Elektrochemie, 30:508.

Touchard, G. (1978). *Streaming currents developed in laminar and turbulent flows through a pipe.* J. Electrostatics, 5:463–476.

Touchard, G., Patzek, T. W., Radke, C. J. (1996). *A physiochemical explanation for flow electrification in low-conductivity liquids in contact with a corronding wall*. IEEE Trans Ind Appl. Soc., 32(5):1051–1057.

DOI: 10.7795/810.20200724

CFD-based simulation of flammable gas dispersion in a complex geometry

Miroslav Mynarz [a], Aleš Tulach [a], Petr Lepík [a] & Milada Koubkova [b]

[a] VSB – Technical University of Ostrava, Faculty of Safety Engineering, Ostrava, Czech Republic
[b] VSB – Technical University of Ostrava, Faculty of Mechanical Engineering, Ostrava, Czech Republic
E-mail: *miroslav.mynarz@vsb.cz*

Abstract

Quantification of time and spatial concentration profiles of a gas-air cloud caused by accidental leakage of flammable gas from damaged equipment can be of great importance for the correct prediction of the occurrence of dangerous situations. Knowing the extent of leakage and time dependence of generation of hazardous concentrations may be a good tool in the design of mitigation equipment (e.g., gas detection alarms) or in determining further measures (e.g., the extent and method of ventilation of the premises).

The paper describes the dispersion of leaked methane (natural gas) from a damaged low-pressure gas pipeline, in a confined space with a geometrically complex environment and the formation of local explosive concentrations at the lower explosion limit (LEL) of the methane-air mixture. The measurements were carried out in a middle-scale model of a building with a volume of approximately 2.7 m^3. A new type of sensing system has been developed for the detection of individual concentrations, allowing the required concentrations to be recorded continuously and with greater accuracy.

The velocity of propagation of leaked gas, local explosive concentrations of a gas-air mixture, and also duration of formations of these local concentrations, could be determined using successful verification of a CFD simulation with experiments. A comparison of experimental data with simulation data demonstrated that CFD technology can be an effective aid to describe the process of flammable gas dispersion and can also predict the tendency of gas dispersion and gas distribution. The key to a successful application of CFD in dispersion simulation lies in the accuracy with which the effect of turbulence is generated, due to the complex geometry of the monitored space. Within the simulations of turbulent flow, the accordance of experimentally determined values with the values calculated in dependence on the mesh density and used turbulence model was observed. RANS equations with six turbulent models were used (Laminar; k-ε Standard; k-ε RNG; k-ε Realizable; k-ω Standard and k-ω SST). The best match of the numerical simulation results with the performed experiments was achieved using the mathematical model of turbulence k-ε RNG.

Keywords: *prediction, dispersion, flammable gas, simulation, CFD*

1. Introduction

Considering flammable gases, each gas with flammable components that is used for a combustion process is taken into account. Hydrogen, gaseous hydrocarbons, and carbon monoxide become the base of the flammable part of gas fuels. Fuels formed of flammable gases are ranked among the most ecologic thermal energy sources. Their emissions of harmful oxides of carbon and nitrogen are lower compared to solid or liquid fuel; however, particular values of their physical properties are valid only for a specific state (pressure, temperature). Gas fuels have been recently used mainly for cooking, heating, and water heating; they strongly compete with electric energy. Gases are also beginning to be applied in other areas, for example, in providing heat, cooling and electric power in so-called cogeneration units (Prasad et. al., 2011; Barley et. al., 2009).

Numerical simulations using CFD software are suitable instruments for more detailed analysis of leakage and dispersion of flammable gases. Numerical simulations are focused on leakage and dispersion of flammable gases in confined space, because, according to statistics, fire or explosion of flammable gas occurs inside houses and flats.

Within the problem solving, a literature search was performed in publications focused on mathematical modelling of natural gas flow from pipelines to confined space. Priority was given mainly to calculation principles, mesh generation, and the solution of admixture spreading. Much attention has been drawn to this issue worldwide. R.P. Cleaver from the "Gas Research Centre" in Great Britain writes about CFD simulation of leakage and fire of natural gas (Cleaver, et al., 1994). His paper is concerned with mixing and generation of a gas concentration in unventilated space, as a result of various means of natural gas leakage. The paper presents the results of experiments and mathematical models and it also takes into account the possibility of using the model for leakage of different gases (for example propane-butane).

The article (Lowesmith et. al., 2009) follows experiments and mathematical models describing the accumulation of methane and methane-hydrogen mixture in ventilated space (households). Some of the researches are engaged in mathematical modelling of natural gas leakage into open space from pipelines (Gilham et. al., 1997; Wilkening et. al., 2007) or factory equipment (Swain et. al., 2003; Kassomenos et. al., 2008). Simulations can be also used for more detailed description of physical processes during liquefied natural gas leakage (Zhu et. al., 2013; Siddiqui et. al., 2012).

Numerical simulations also find application in risk analysis in confined areas of industrial enterprises, in the case of leakage of dangerous gases (García et. al., 2008; Arnaldos et. al., 1998). Other articles do not deal with the leakage of natural gas or methane, but they describe the simulation of CO_2 in the building. The authors (Gilham et al., 1997) are occupied with existing, simplified, calculation procedures that take into account total mixing of a gas mixture in a whole volume. The experiment and CFD simulation are compared. They consider a cube-shaped room with 2.4 m edges. During the literature search, many other publications concerning leakage of CO and CO_2 in households (kitchens, bathrooms, etc.) were found.

Databases also provide a huge amount of experimental and numerical research examining leakages of hydrogen from vehicles to garages and tunnel space (Gavelli et. al., 2008; Telmo Miranda et. al., 2013; Tauseef et. al., 2011; Cariteau et. al., 2011; Gupta et. al., 2009; Venetsanos et. al., 2010). The contribution (Prasad et al., 2012) presents the validation of numerical simulation in ANSYS Fluent software, on the basis of the experiment results when measurements were taken in a room with a volume of 83 m^3. Another paper demonstrates the dispersion of helium in a closed container with a volume of 1 m^3 (Papanikolaou et al., 2010). In the USA, many research projects were conducted on these problems. Risk determination connected with hydrogen leakage is described in (Swain et al., 2003). For safety reasons, hydrogen, when investigated, is replaced with helium. The contribution (Venetsanos et al., 2010) compares numerical simulation of four CFD software products (Flacs, CFX, ADRA-HF, Open FOAM, Fluent). The study in (Middha et al., 2009) analyses the amount of leakage, location of leakage source, and its huge effect on calculated results. This work uses FDS software (Fire Dynamics Simulator). The study (Tauseef et al., 2011) considers the choice of a suitable turbulent model for simulation of dispersion of toxic and flammable gases where obstructions are situated in the investigated space.

It is clear from the state of art that most of the works deal with the leakage of dangerous gases from pressure vessels (for example, leakages of flammable gases from cars in garages). Leakages from low pressure systems are addressed only in a limited range. In terms of mathematical models, they are in the area of problematic transition flow, between laminarity and turbulence. Selection and verification of mathematical models in this application requires the preparation of a quality experimental device and a special mathematical procedure.

2. Experiments

Measurements were performed with use of a measuring set, which imitated the circulating area of common block of flats, in which a leakage of gas from the main gas valve located in the basement can occur. The measuring set consisted of a staircase area and a part of the basement. It was designed with the dimensions of 1.5 x 2.0 x 2.2 m (W x D x H). The gas valve DN10 type K800, from which its cone was removed (Figure 1), was chosen as a source of methane (CH_4). Pure gas was used with a concentration 99.95 vol. % of methane. A pressure tank was used as a source of methane, which provided methane flow under a constant pressure of 75 kPa using a defined reducing valve. The flow rate of leaking natural gas flow was chosen in relation to the dimensions of the model and used range of gas detectors and was set to the constant value Q = 0.744 l/s. The value of flow was chosen in relation to dimensions of the model and used gas detectors.

Fig. 1. *Interior part of the dissected space (basement and staircase) and experimental setup*

2.1 Measurement of local methane concentrations

For monitoring and verification of basic information on the values of dangerous concentrations of individual points, five GC20-CH_4 two-stage detectors and five GI30-CH_4 three-stage detectors, calibrated to methane CH_4, were used, inserted into external walls of the measuring kit. Detectors signalled the occurrence of 0.5, 1.0 and 2.5% of the methane volume fraction at the monitored points (Tulach et al., 2013).

Detectors were equipped with non-selective hot-semiconductor sensors, which react to the presence of oxidizing or reducing gases. It concerns surface absorption detection, where exchange of electrons proceeds between the conduction and valence band.

New detectors were developed and calibrated to improve the quality of experimental measurements of dynamic behaviour of local methane concentrations. Semiconductor sensors were no longer used. They were replaced by detectors with sensors working on principle of catalytic combustion of flammable gases (detection proceeds through comparison of electric resistances of the measuring spiral). The sensor MI-02 (Figure 2) by Hankook Gas kiki comp. was chosen from available sensors.

The developed detecting system enabled the obtaining of a more detailed course of formation of local concentrations and the immediate measured concentration was recorded. The aim was to develop the detector for recognition of gas concentration within the range of lower than 1 to 5 vol. % (lower explosive limit of methane).

DOI: 10.7795/810.20200724

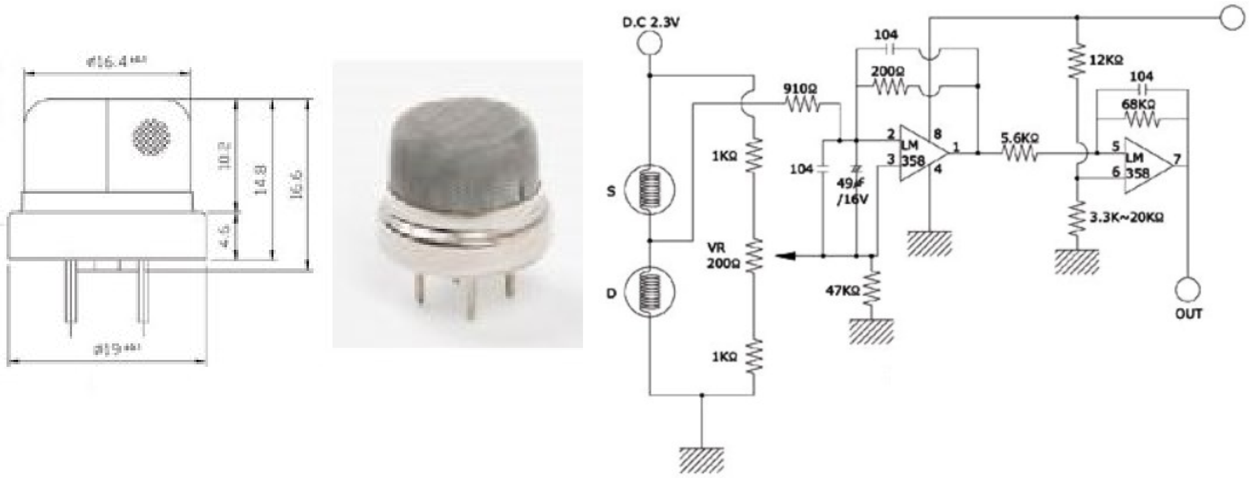

Fig. 2. *Catalytic sensor MI-02 and circuit diagram of detector*

Parameters of the sensor MI-02:

Power supply 2.3 VDC ± 10%; current lower than 210 mA ± 10%; output loss 0.46 W ± 10%; time of primary stabilization 30 s ± 10%; speed of response 10 s ± 10%; temperature at catalytic reaction 425 °C ± 10%.

The detectors developed were constructed with the help of a printed circuit (Figure 2). A total of ten measuring circuits were made. Testing of the prototype led to findings that the temperature of a cooler does affect a constructed measuring circuit and thus the resulting measured voltage (measured concentration). Therefore, more coolers were used, and they were purposely placed farther from measuring circuits. These changes (compared to the prototype) caused a decrease of temperature and minimization of influence on measuring circuits by ambient temperature. All the detectors used were connected to the data loggers, which afterwards recorded changing voltage in second intervals.

2.2 *Calibration of detectors*

Before measurement detectors were calibrated, the same gas (99.95 vol. % of methane) was used both for calibration and the physical model. The most available and exact method of calibration was to determine required methane concentration in the air, using partial pressures in the 20-liter sphere apparatus. The pressure sensor MSD100MRE was used for measurement of partial pressures. Measurement uncertainty of this sensor is ± 0.2%.

For calibration, mixtures were prepared one after another with 1 to 5 vol. % of methane with air. Calibration measurements were performed under constant initial and boundary conditions. The influence of the flow rate of the methane-air mixture was verified in steps (increments of 0.1 m/s) for individual values ranging from 0 to 0.5 m/s.

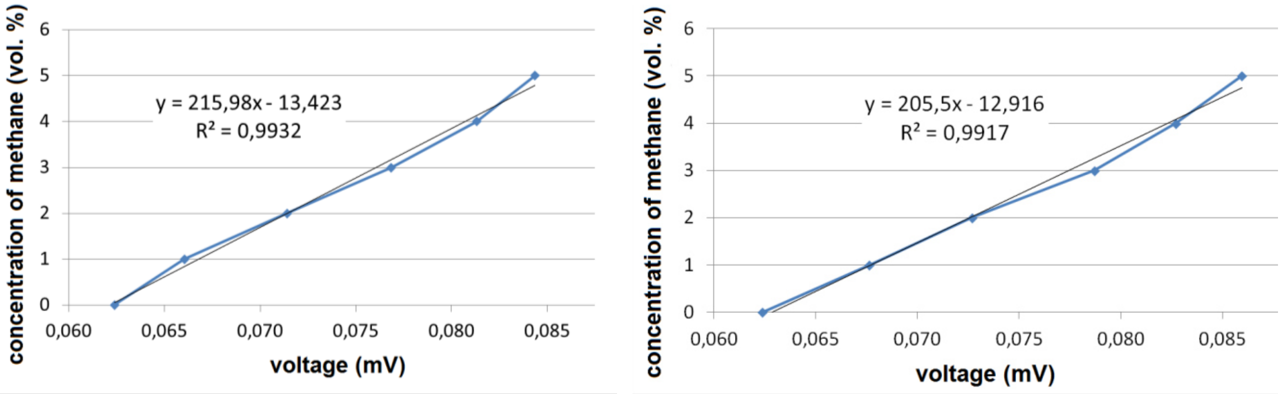

Fig. 3. *Calibration function for Detectors No. 1 and 10*

The deviations found were compensated by the introduction of a calibration constant. Measured points were interleaved with a straight (linear) line using statistical methods. On the basis of this straight line, the function for conversion between measured voltage and methane concentration was generated. The graph of calibration function shows an approximately linear course of voltage increase with concentration increase. Figure 3 shows the calibration function for Detectors No.1 and 10.

2.3 Procedure of measurement of local concentrations

Ten measurements of the local concentration of methane were taken at defined points in a confined space. The result of these measurements was to determine the time between the beginning of gas leakage and moment of occurrence of 5 vol. % of methane concentration at all monitored points. The latest time to reach 5 vol. % of methane concentration was at the monitored Points No. 2 and 5, located in the lowest and highest levels of the staircase area (Figure 4).

3. Gas dispersion modelling

The software ANSYS Fluent (ANSYS, 2013) was used for numerical modelling of physical measurements described above, as it is suitable especially for the solution of flows in the given space. The selected software used for mathematical description of the ongoing physical processes following laws:

Navier-Stokes equations (Fox et al., 2008) express the conservation law of momentum and describe the flow as follows.

$$\frac{\partial(\rho\vec{u})}{\partial t}+\nabla\cdot(\rho\vec{u}\vec{u})=-\nabla p+\nabla\cdot(\bar{\tau})+S_m \tag{1}$$

In the above three equations, four unknown quantities appear (pressure and velocity of all three components x, y, z). By adding the fourth equation, a relation of four equations with four unknown quantities is obtained. The continuity equation is the fourth equation, which deals with conservation of mass flow.

$$\frac{\partial(\rho)}{\partial t}+\frac{\partial(\rho u_x)}{\partial x}+\frac{\partial(\rho u_y)}{\partial y}+\frac{\partial(\rho u_z)}{\partial z}=S_z\,. \tag{2}$$

The molar concentration C_i is the quantity, which is used in conjunction with propagation of impurities; it is expressed in unit (kmol/m^3).

Transfer of admixtures (mass fraction) is solved by the balance equation (Kozubkova, 2008), which in a changing time computes the values of the mass fractions of admixtures Y_i. It takes into account the diffusion flux to the i-th mixture component $J_{j,i}$, the rate of production of admixtures resulting from chemical reaction R_i, and the rate of formation of increments from the distributed admixtures S_i. Distribution of admixtures varies in dependence on the diffusion flux.

$$\frac{\partial}{\partial t}(\rho Y_{i'})+\frac{\partial}{\partial x_j}\cdot(\rho u_j Y_{i'})=-\frac{\partial}{\partial x_j}J_{i',j}+R_{i'}+S_{i'} \tag{3}$$

The mass conservation law of propagation of admixtures is accepted and it is expressed by the local mass fractions of admixtures Y_i in the mixture. The mass fraction is defined as follows:

$$Y_{i'}=\frac{m_{i'}}{m}=\frac{\rho_{i'}V_{i'}}{\rho V}=\frac{\rho_{i'}}{\rho}\alpha_{i'} \tag{4}$$

where m_i is mass of admixture i, m is total mass of the mixture, α_i is a volume fraction of the admixture in the mixture.

It was a transition zone, where, in the leaking area, the turbulent flow (Re = 6,480) occurred due to a high velocity, and already, at the distance of approx. 20 cm from the leak, a nearly laminar flow took place, due to a sharp drop in velocity to approx. 0.5 m/s. In order to achieve the best possible agreement of numerical simulation with experimental measurements, three mathematical models ("Laminar", "k-ε", "k-ω") were used. Turbulence can be described using several mathematical models of turbulence, such as direct method and spatial filtering (large eddy simulation – LES method), but the most commonly used method is the Reynolds Averaged Navier-Stokes method – RANS using the Boussinesq approach. Two-equation turbulence models (k-ε, k-ω and other mathematical models) are very often used. The k-ε two-equation model determines the turbulent viscosity using two transport equations for k (turbulent kinetic energy) and ε (rate of dissipation), which defines the conversion of turbulent vortex energy to thermal energy due to the decay of the smallest turbulent eddies. Both quantities are obtained from the following transport equations:

$$\frac{\partial}{\partial t}(\rho k)+\frac{\partial}{\partial x_i}\cdot(\rho k u_i)=\frac{\partial}{\partial x_j}\left[\left(\mu+\frac{\mu_t}{\sigma_k}\right)\frac{\partial k}{\partial x_j}\right]+G_k+G_b-\rho\epsilon-Y_M+S_k \tag{5}$$

and

$$\frac{\partial}{\partial t}(\rho \varepsilon)+\frac{\partial}{\partial x_i}\cdot(\rho \varepsilon u_i)=\frac{\partial}{\partial x_j}\left[\left(\mu+\frac{\mu_t}{\sigma_\varepsilon}\right)\frac{\partial \varepsilon}{\partial x_j}\right]+C_{1\varepsilon}\frac{\varepsilon}{k}(G_k+C_{3\varepsilon}G_b)-C_{2\varepsilon}\rho\frac{\varepsilon^2}{k}+S_\varepsilon+S_k \tag{6}$$

In these equations, G_k represents the generation of turbulence kinetic energy due to the mean velocity gradients, G_b is the generation of turbulence kinetic energy due to buoyancy, Y_M represents the contribution of the fluctuating dilatation in compressible turbulence to the overall dissipation rate $C_{1\varepsilon}$, $C_{2\varepsilon}$, and $C_{3\varepsilon}$ are constants. σ_k and σ_ε are the turbulent Prandtl numbers for k and ε,. S_k and S_ε are user-defined source terms.

The main difference between the different types (k-ε Standard; k-ε RNG and k-ε Realizable) is in the way of solving k-ε equations, mainly in the process of determining the turbulent viscosity and Prandtl numbers governing turbulent diffusion.

The two-equation model k-ω was developed in parallel with the k-ε model and it is based on the equation for kinetic energy k and for the relative specific losses (dissipation) ω. These can also be understood as the ratio ε/k. The turbulence kinetic energy and the specific dissipation rate are obtained from the following transport equations:

$$\frac{\partial}{\partial t}(\rho k)+\frac{\partial}{\partial x_i}\cdot(\rho k u_i)=\frac{\partial}{\partial x_j}\left(\Gamma_k\frac{\partial k}{\partial x_j}\right)+G_k-Y_k+S_k \tag{7}$$

and

$$\frac{\partial}{\partial t}(\rho \omega)+\frac{\partial}{\partial x_i}\cdot(\rho \omega u_i)=\frac{\partial}{\partial x_j}\left(\Gamma_\omega\frac{\partial \omega}{\partial x_j}\right)+G_\omega-Y_\omega+S_\omega \tag{8}$$

In these equations, G_k represents the generation of turbulence kinetic energy due to mean velocity gradients. G_ω represents the generation of ω. Γ_k and Γ_ω represent the effective diffusivity of k and ω. Y_k and Y_ω represent the dissipation of k and ω due to turbulence. S_k and S_ω are user-defined source terms.

In Fluent software, the k-ω Standard model is the modification of Wilcox k-ω basic model that incudes low Reynolds numbers, compressibility of fluid and shear flows. Its negative feature is the sensitivity of solving of transport equations in free flow outside the shear layer. Its main advantage is accuracy near the wall, but with increasing distance the accuracy decreases.

The k-ω SST (Shear-Stress Transport) model combines the advantages of two basic models: k-ε model is characterized by higher accuracy in free flow farther from the walls, and the k-ω model is more accurate in the area close to the wall.

In the "k-ε" model, the variants k-ε Standard, k-ε RNG and k-ε Realizable were tested, and in the model "k-ω", the variants k-ω Standard and k-ω SST were tested (Fox et al., 2008).

3.1 Geometric Model

A geometry of the measuring set for the CFD simulations (Figure 4) was created, using Design Modeler software. In order to accelerate the calculation, only internal volumes of the investigated space were modelled. Afterwards, a geometry of the sample of piping with a gas cock was created. The gas cock was modelled as a source of a gas leak, i.e., with the missing inner cone. The gas leak occurred from two opposite gas cock holes with diameters of 18 and 14.6 mm.

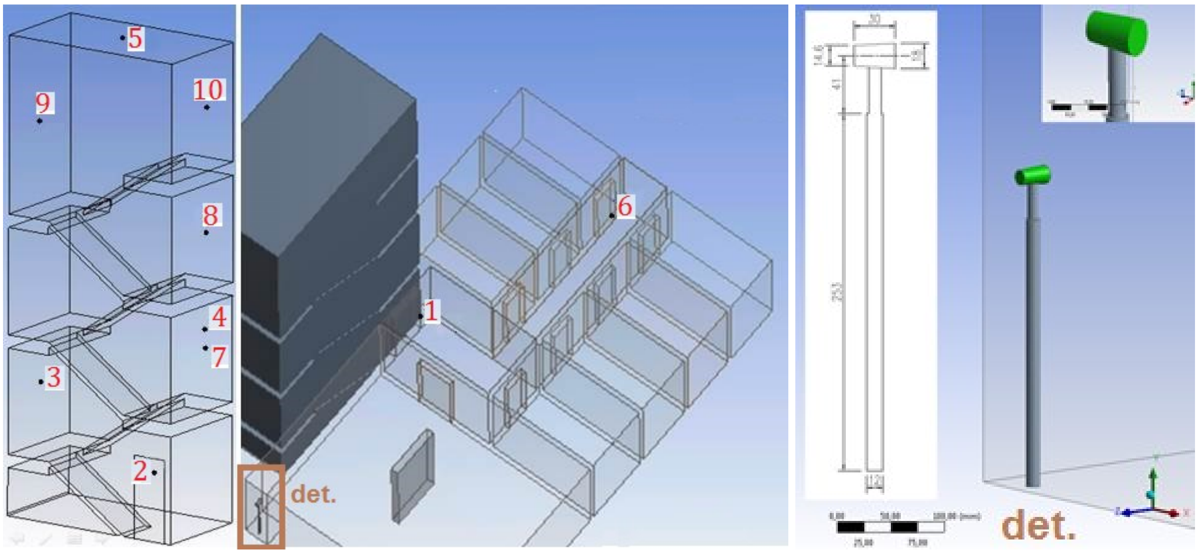

Fig. 4. *Geometric model and placement of monitoring points and pipe geometry with a gas cock*

The gas leak occurred in the basement of the closed dissected space (Figure 4) with a volume of approx. 1.5 m^3. Piping was placed in a corner (left side) of the closed space at the height of 0.25 m above the floor. The second part of created geometry consists of the internal volume of the staircase space of approx. 1.2 m^3.

The location of monitoring points was identical with the placement of detectors on the outer walls of the experimental model delimitating the space. On the basis of these points, an evaluation was made of the dependence between the duration of leakage and the methane concentration in the air mixture.

3.2 Initial and boundary conditions

Within the setting of computational processes in the modelling of gas mixtures flow, the "Double Precision" setting was used to speed up the calculation. Using a quad-core processor, the computational domain was divided into four areas of similar number of cells. The issue was solved as a transient problem for an ideal gas. The boundary conditions define fixed obstacles and the location (including the intensity), through which the gas enters and exits. Fixed obstacles were defined as a "Wall" with zero wall velocity. The input boundary condition was defined by the mass flow of methane, including the direction of flow and temperature of gas. The output boundary condition was given by the current properties of the outer space, mainly by temperature and atmospheric pressure. The turbulent intensity in the gas pipeline was set at 1 %. Within the calculation, the change in hydrostatic pressure in the calculation domain was taken into account. "Compressibility Effects" was chosen in the settings for all used turbulent models and „Standard Wall Functions“ was chosen for k-ε turbulent models.Through the "Surface Monitors" function, monitoring points were placed in the model to monitor methane concentrations in a mixture with air.

Within the solution methods, the pressure-velocity connection scheme was set to “Simple”. Gradient was computed using “Least Squares Cell Based”. The PRESTO! computing scheme was chosen for pressure and “First Order Upwind” for other variables. At the start of the calculation, a time step of 0.001 s was set. The correct convergence occurred in about the tenth time step. During the calculations, depending on the decreasing number of iterations in one time step, the time step was gradually adjusted to 0.01 s and then 0.1 s, at which it was left until the end of the calculation.

3.3 Mesh of the model

Determination of suitable computational mesh is given by important parameters for determining the accuracy of performed numerical simulations. An important criterion is not only the total number of cells in the computational mesh, but also the quality of the computational mesh (cells) itself. The main quality indicators of a computational mesh are the Skewness and Orthogonal mesh quality parameters. Table 1 shows the comparison of computational meshes, in terms of numerical simulations performed and the main quality parameters.

Table 1: *Parameters of the mesh*

Mesh	**Cells**	**SKEWNESS index**				**Orthogonal mesh quality**				**Calculation data**		
No.	No.	Min	Max	Mean	SD	Min	Max	Mean	SD	Total number of iterations	Approx. calc. time (h)	Median deviation of measurement (%)
1	895,373	1.305 E-10	0.87	0.17	0.14	0.21	1.00	0.91	0.09	26,998	40	4.17
2	1,230,620		0.90			0.13				30,708	45	6.07
3	1,869,187	1.306 E-10	0.89	0.16	0.15	0.08	1.00	0.91	0.10	27,038	62	4.18

SD - Standard deviation

Quality of the mesh is one of the most important parameters influencing the result of the calculation. Thickening and refining the shape of mesh makes it possible to achieve more accurate results, while maintaining the parameters of mathematical models. After completion of the initial calculation, three types of mesh were made. Some improvements were made directly in the software ANSYS Fluent, where mesh was refined at the places with increased flow rate of the flammable gas (monitoring of velocity gradient). According to this adaptation, the cells were automatically densified, for example, in front of the hole (Figure 5, left) from which the flammable gas leaked, or in the space below the ceiling of the basement space and upper part of doorframes, between the basement and staircase spaces.

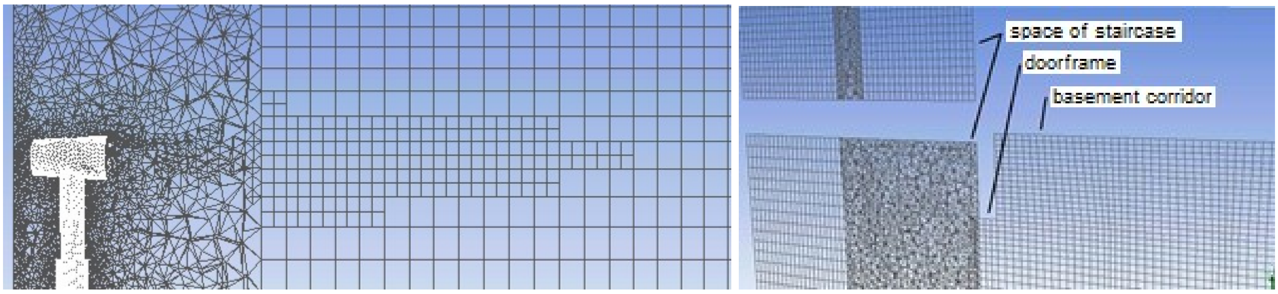

Fig. 5. *Mesh in section of the pipeline with the gas cock and basement corridor and staircase space (mesh 1,869,187 cells)*

The next improvement of the mesh was made by replacement of the part of tetrahedral elements by hexahedral elements. The mesh was created in the software ANSYS Meshing, where tetrahedral elements no longer filled the whole staircase space, but only a small part of the space next to the doors leading to the basement (Figure 5, right).

4. Results and discussion

4.1 Effect of time step

Comparison of measured and calculated values is presented in the graph (Figure 6). It describes the change of volume concentration of methane in Monitoring Point No. 5 in time. Point No. 5 is situated at the greatest distance from the gas leak point. The graph shows average values from ten measurements and values calculated (mathematical model k-ε RNG) at various time steps (1,000; 100 and 10 ms).

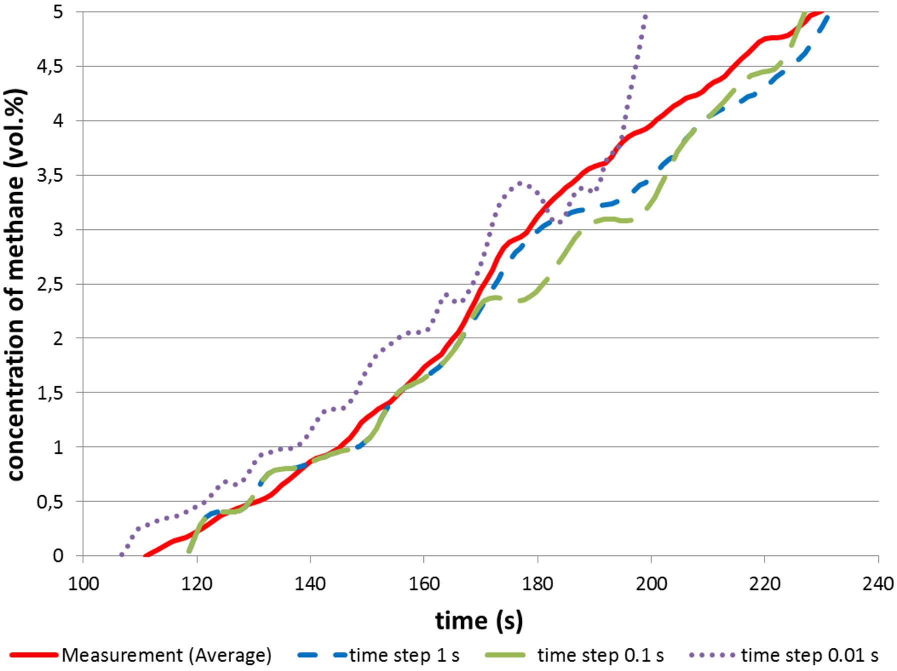

Fig. 6. *Comparative measurements with numerical simulation depending on the time step at Point No. 5*

It is apparent from the course of the curves (Figure 6) that the choice of the right time step may affect the quality of the result.

For time-dependent tasks, it is recommended to set a maximum of 20 iterations per time step. The condition for convergence to the twentieth iteration was fulfilled by specifying the appropriate time step. Each mathematical model requires a different time step. Entering the time step 0.001 s, the correct convergence occurred in approximately the tenth time step. Gradually, during the calculations, depending on the decreasing number of iterations in a single time step, the time step was adjusted to 0.01 s and 0.1 s for which it was left until the calculation was completed.

4.2 Effects of mesh density and turbulent models

In the piping (Re = 4,985) and in the valve (Re = 6,480), significant turbulent flow took place. Gradually, six mathematical models (Laminar, k-ε Standard, k-ε RNG, k ε Realizable, k-ω Standard, k-ω SST) were tested. The best match with the results of experimental measurements was achieved by numerical simulations with the mathematical models k-ε RNG and k-ω SST.

The graphs in Figures (below) show the influence of the number of cells of the mesh in selected models on the quality of the results. Mesh No. 1 includes 895,373 cells, Mesh No. 2 includes 1,230,620 cells, and Mesh No. 3 includes 1,869,187 cells. For better comparison, the following graphs show the segments put through medians of the measured concentrations. The graphs are completed with minimum and maximum measured values of concentrations in individual (second) intervals. This resulted in bounded areas that show the possible formation of local methane concentrations at defined times.

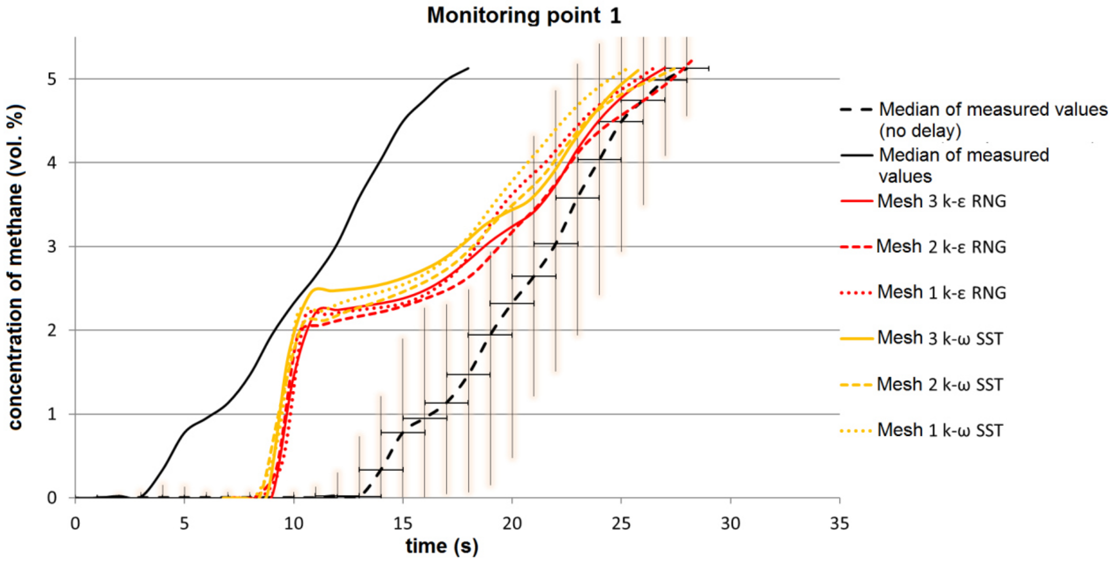

***Fig.** 7. Dependence of concentration change on time at Monitoring Point No. 1*

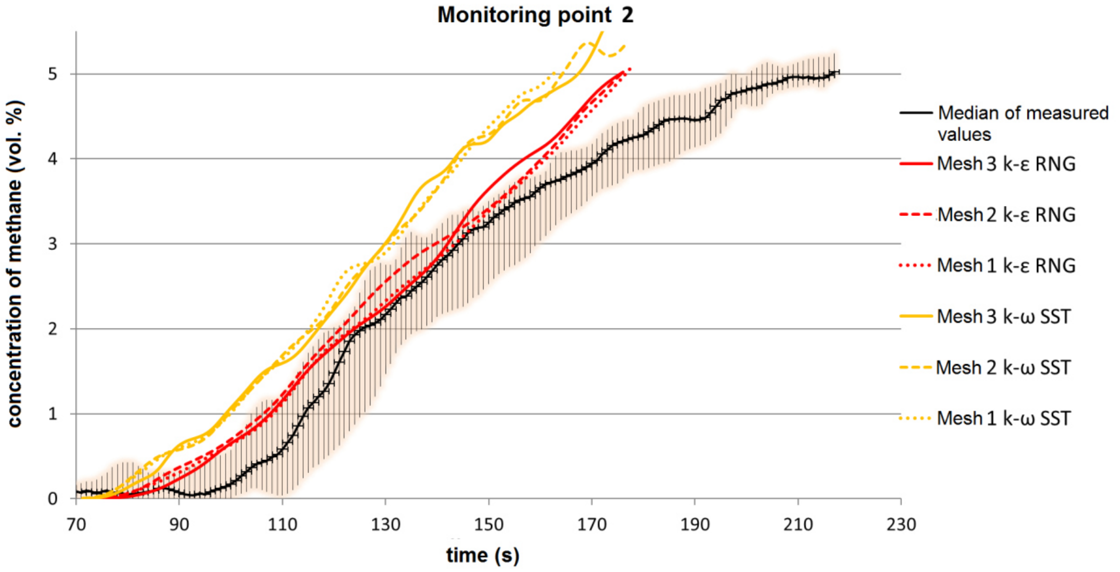

***Fig.** 8. Dependence of concentration change on time at Monitoring Point No. 2*

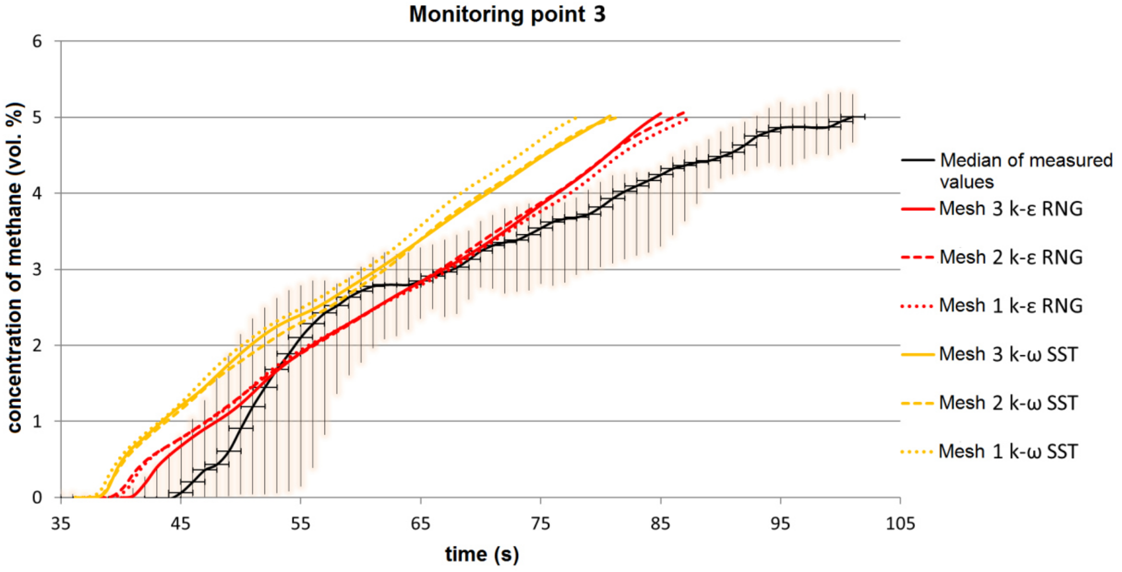

***Fig.** 9. Dependence of concentration change on time at Monitoring Point No. 3*

DOI: 10.7795/810.20200724

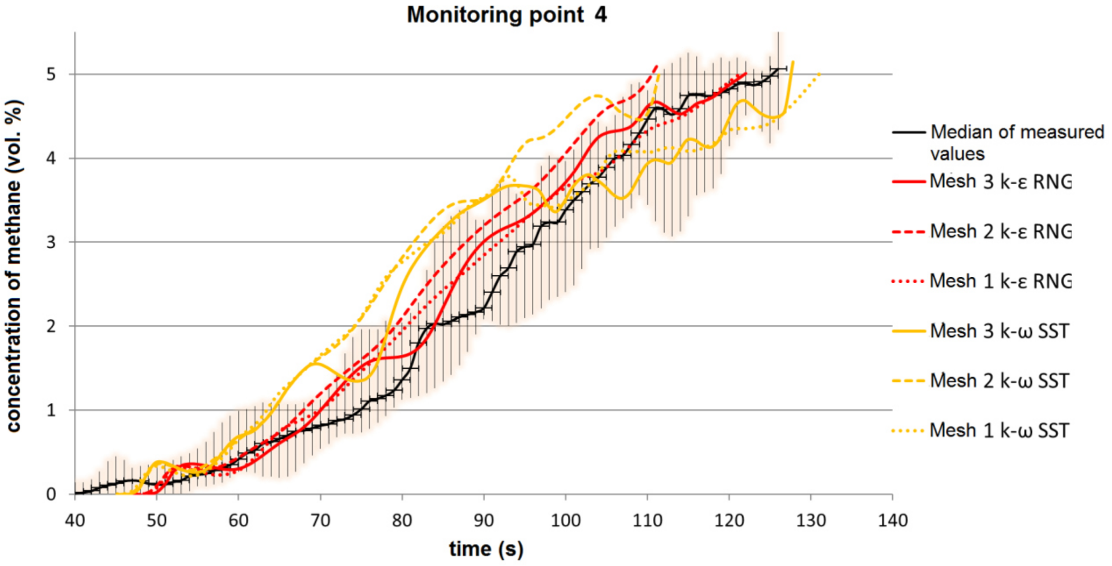

Fig. 10. Dependence of concentration change on time at Monitoring Point No. 4

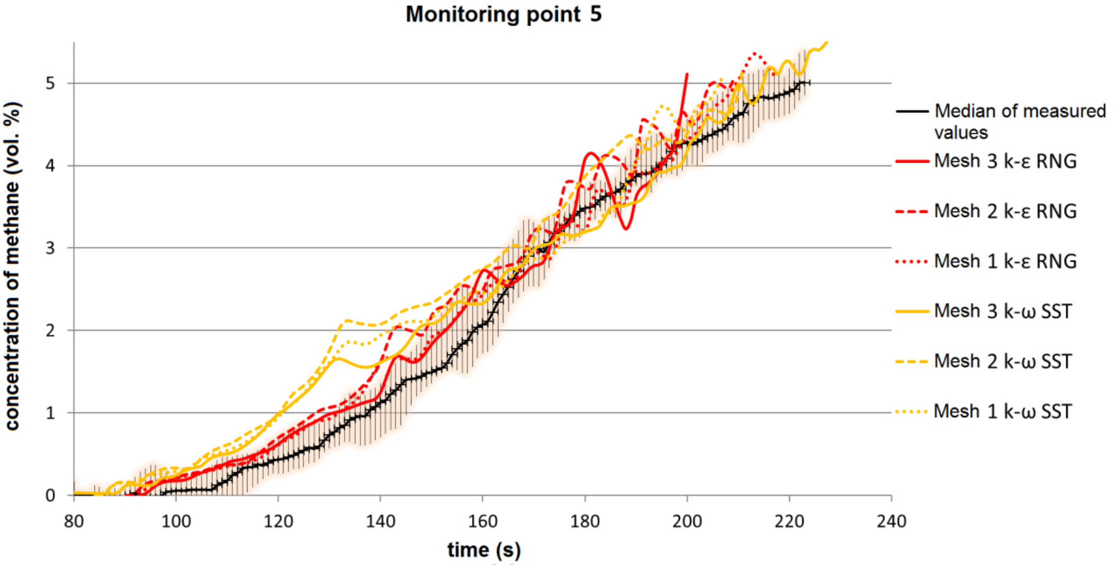

Fig. 11. Dependence of concentration change on time at Monitoring Point No. 5

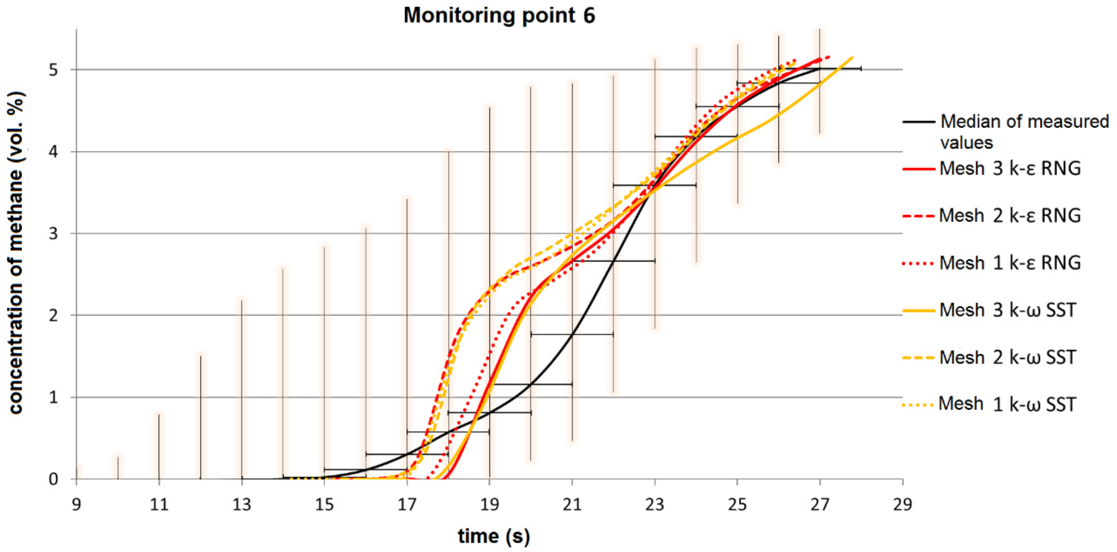

Fig. 12. Dependence of concentration change on time at Monitoring Point No. 6

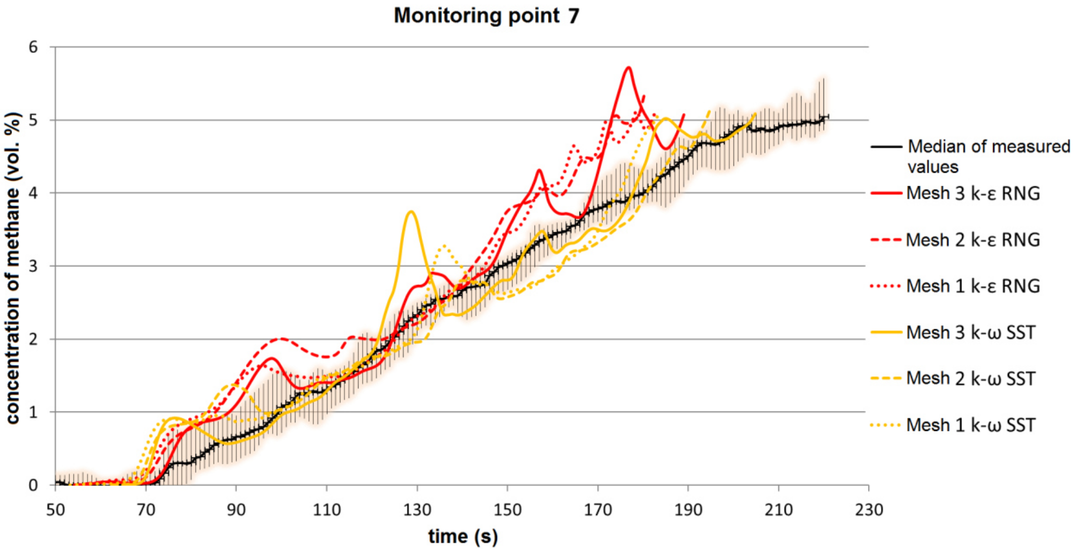

Fig. 13. *Dependence of concentration change on time at Monitoring Point No. 7*

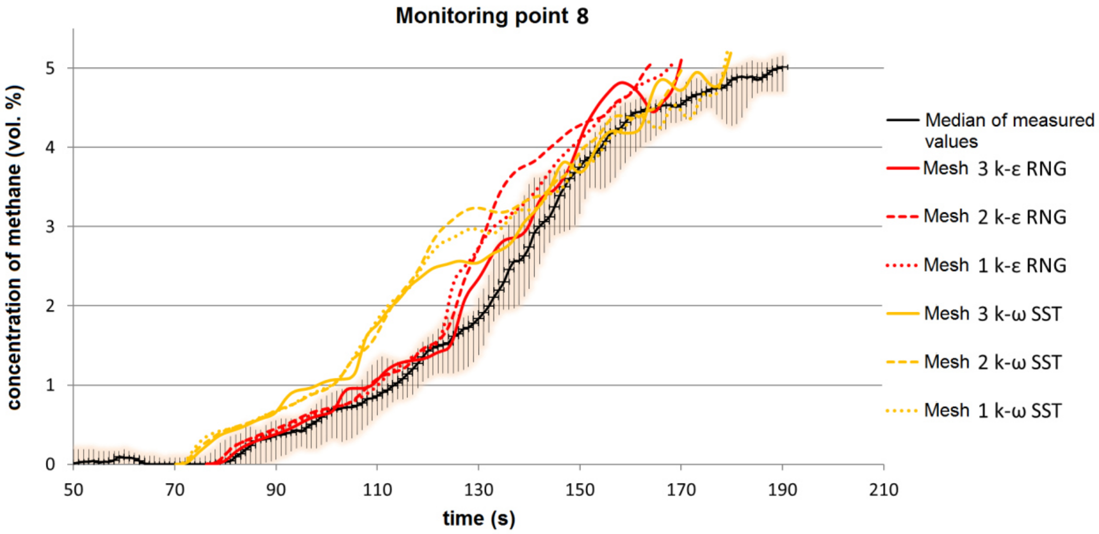

Fig. 14. *Dependence of concentration change on time at Monitoring Point No. 8*

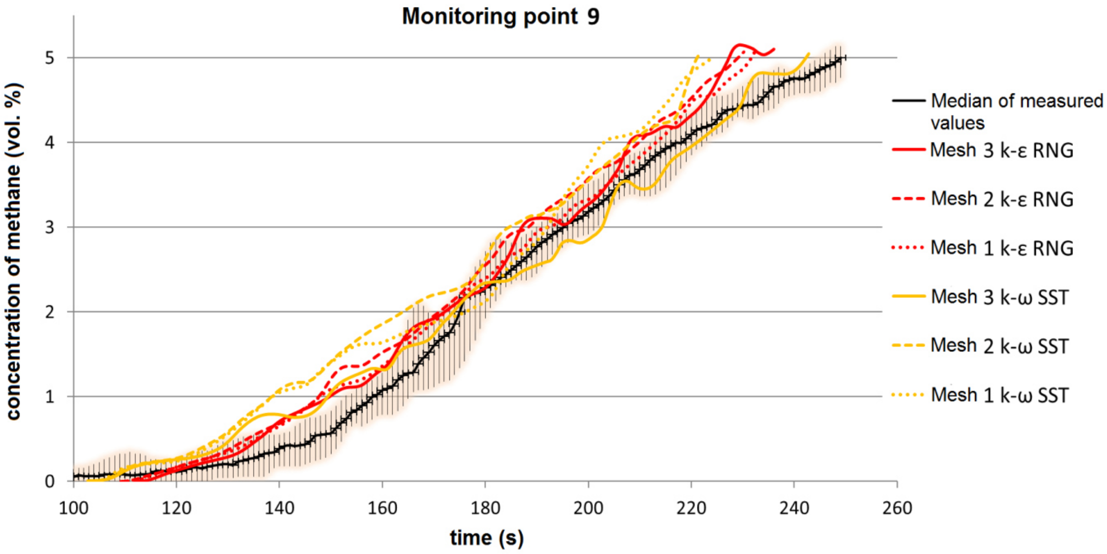

Fig. 15. *Dependence of concentration change on time at Monitoring Point No. 9*

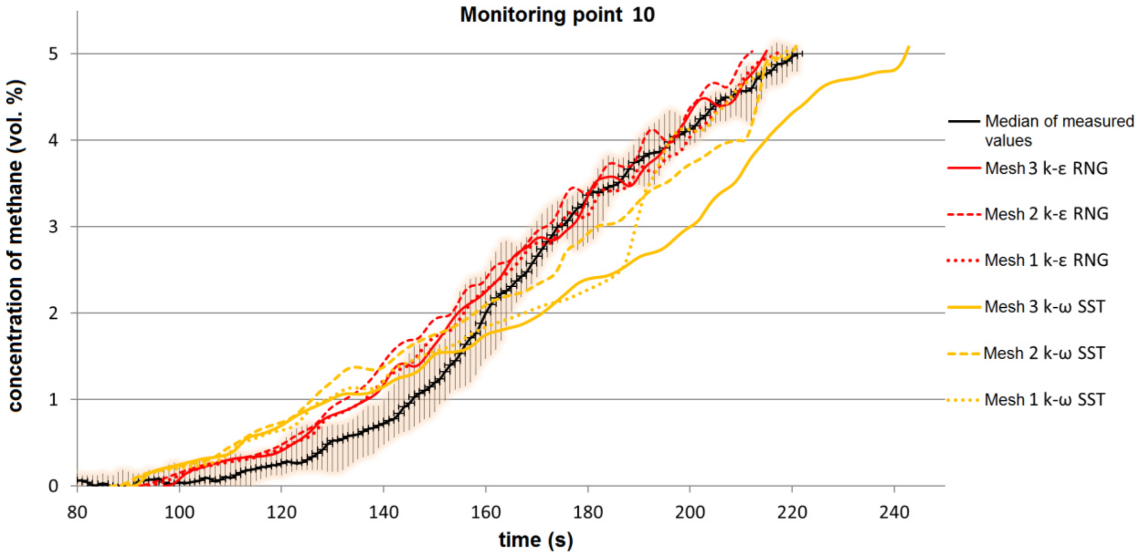

Fig. 16. *Dependence of concentration change on time at Monitoring Point No. 10*

Numerical simulation enabled the ascertaining of approximate levels of critical concentrations of methane (blue => 5 vol. %, green => 9 vol. %, red => 15 vol. %) in the gas mixture, at the time of 219 s after the gas leak from the gas cock, see Figure 17.

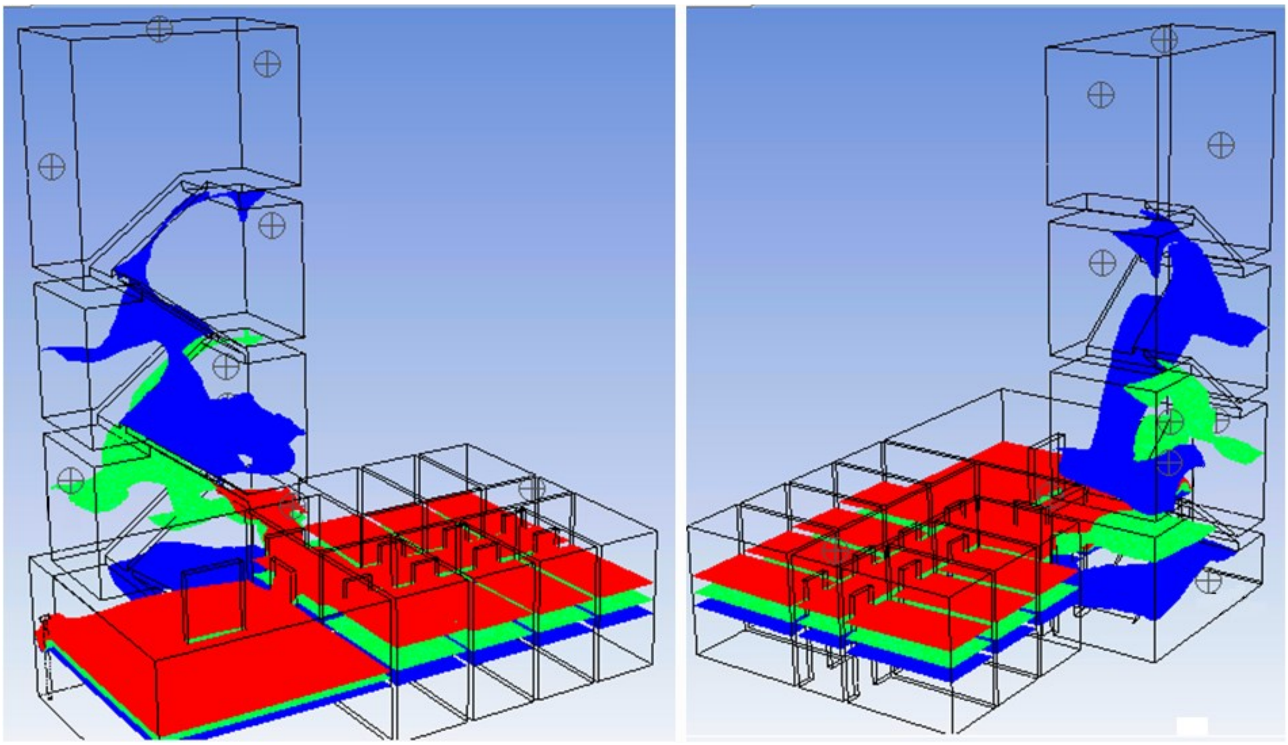

Fig. 17. *Critical concentration levels of CH_4 at the time of 3 min 39 s (219 s)*

During the filling of the staircase space, gas was spreading to the upper floors from the lower floor space along the flights. The dangerous concentration at the highest point of the model (Point No. 5) was reached approximately 219 seconds after the start of the gas leak from the gas cock. An explosive concentration occurred throughout entire basement. Concentration at the lower explosive limit (blue level) originated in three floors, and in the lower part of the staircase optimal explosive concentration (green level) appeared as well.

DOI: 10.7795/810.20200724

5. Conclusions

The best match of the numerical simulation results with the performed experiments was achieved using the mathematical model of turbulence k-ε RNG. This model is derived using the statistical method known as the renormalization group method (RNG). It is similar to the k-ε Standard model, but it improves accuracy at high strain rates, involves the effect of vortices on turbulence, and thus increases the accuracy for vortex flow. These properties make the RNG more accurate and reliable for a wider range of flow types, compared to the k-ε Standard model. The RNG method is about one-tenth slower than the classical two-equation model, but it is more accurate in the vortex regions (where the fluid slows down and there is a lower Reynolds number).

However, the quality of the computational mesh proved to be a key parameter in the calculations performed. Mesh No. 2 (1,230,620 cells) should be an enhancement of Mesh No. 1 (895,373 cells) when ANSYS Fluent automatically increased the number of cells; however, the calculations performed with this mesh were the least consistent with the results of experimental measurements, which could be due to the quality of the computational mesh. Compared to the other meshes used (Mesh No. 1 and 3), it showed the worst quality. When comparing Mesh No. 1 (895,373 cells) and Mesh No. 3 (1,869,187 cells), it was found, on the basis of the comparisons, that a double increase in the number of cells, while maintaining similar mesh quality, did not significantly improve the quality of the results. From the comparison of the calculation time and the best agreement of the calculation with the experimental measurement, Computational Mesh No. 1 seems to be the most suitable. The gradual increase in the number of computational cells did not bring the expected improvement of the results.

Testing of models has shown that, in places of very slow flow, the laminar model corresponds well with the experiment (for instance, Monitoring Point No. 2), while the turbulence models are in better agreement with the experiment in areas with higher velocity. This was probably caused by the fact that Monitoring Point No. 2 was placed outside the main directions of flow of the leaking gas. Flammable gas first filled the spaces under the flight of stairs and stair landings and only then the borders of the monitored concentrations decreased in the lower part of the staircase space, where they were detected by the sensor located in Monitoring Point No. 2. This resulted in a weak flow with a low Reynolds number.

In the case of transient flow between laminar and turbulent mode, the main problem of numerical simulation consists in the choice of a suitable turbulence model and the quality of the mesh. For verification of the results, the quality of sensors for measurement of concentrations is important. At present, development and calibration of new detectors is performed, in which catalytic sensors are used, which are in many ways (for measuring) far better than the existing semiconductor sensors. Moreover, the detectors will be capable of recording the measured values at shorter intervals, which will make it possible to determine, in an almost continuous manner, the formation of concentrations of leaking flammable gas at the monitoring points. So far, only the discrete values of concentrations were measured, depending on the type of detector used.

Acknowledgements

This paper was financially supported by a grant project of the Ministry of the Interior of the Czech Republic under ID No. VI20172020103, entitled “Safety of pressure cylinders in the work environment and the possibility of defusing pressure cylinders by shooting".

References

Arnaldos, J., et al. (1998). Design of a computer tool for the evaluation of the consequences of accidental natural gas releases in distribution pipes. *Journal of Loss Prevention in the Process Industries*, 11.2: 135-148.

ANSYS, (2013). Inc. ANSYS FLUENT 14.5 - User’s Guide.

Barley, C. D., Gawlik, K. (2009) Buoyancy-driven ventilation of hydrogen from buildings: laboratory test and model validation. *International Journal of Hydrogen Energy*, 34.13: 5592-5603.

Cleaver R.P., Marshal M.R., Linden P.F. (1994). The build-up of concentration within a single enclosed volume following a release of natural gas. *Journal of Hazardous Materials*, Volume 36.3: 209-226.

Fox R.W., McDonald A.T, Pritchard P.J. (2004). *Introduction to fluid mechanics*. Sixth edition. John Wiley & Sons Publishing, USA.

García, J., et al. (2008). Study of the dispersion of natural gas issuing from compressor stations through silencers with upper cover. *Journal of hazardous materials*, 152.3: 1060-1072.

Gilham, S., et al. (1997). Gas build-up within a single building volume—comparison of measurements with both CFD and simple zone modelling. *Journal of hazardous materials*, 53.1: 93-114.

Kassomenos, P., et al. (2008). Modelling the dispersion of a toxic substance at a workplace. *Environmental modelling & software*. 2008. 23.1: 82-89.

Kozubkova M. (2008), Modelling the flow of liquids, FLUENT, CFX. 1st edition. VŠB– TUO Publishing. Ostrava.

Lowesmith, B.J., Hankinson, G., Spataru, C., Stobbart, M. (2009). Gas build-up in a domestic property following releases of methane/hydrogen mixtures. *Journal of Hydrogen Energy*, Volume 34.14: 5932-5939.

Luketa-hanlin, A., Koopman, R.P., Ermak, D.L. (2007). On the application of computational fluid dynamics codes for liquefied natural gas dispersion. *Journal of hazardous materials*, 140.3: 504-517.

Middha, P., Hansen, O.R. (2009). CFD simulation study to investigate the risk from hydrogen vehicles in tunnels. *International Journal of Hydrogen Energy*, 34.14: 5875-5886.

Papanikolaou, E.A., et al. (2010). HySafe SBEP-V20: numerical studies of release experiments inside a naturally ventilated residential garage. *International Journal of Hydrogen Energy*, 35.10: 4747-4757.

Prasad, K., et al. (2012). Natural and forced ventilation of buoyant gas released in a full-scale garage: Comparison of model predictions and experimental data. International Journal of Hydrogen Energy, 37.22: 17436-17445.

Prasad, K., Pitts, W.M., Yang, J.C.A. (2011). Numerical study of the release and dispersion of a buoyant gas in partially confined spaces. International Journal of Hydrogen Energy, 36.8: 5200-5210.

Siddiqui, M., Jayanti, S., Swaminathan, T. (2012). CFD analysis of dense gas dispersion in indoor environment for risk assessment and risk mitigation. *Journal of hazardous materials*, 209: 177-185.

Swain, M.R., et al. (2003). Hydrogen leakage into simple geometric enclosures. *Journal of hydrogen energy*, 28.2: 229-248.

Tulach, A., Mynarz, M., Kozubkova, M. (2013). *Study of quantification and distribution of explosive mixture in a confined space as a result of natural gas leak*. In: EPJ Web of Conferences: Volume 67, EDP Sciences, Paris. p. 1-7. ISBN 978-80-260-5375-0, ISSN 2100-014X.

Venetsanos, A.G., et al. (2010). HySafe standard benchmark Problem SBEP-V11: Predictions of hydrogen release and dispersion from a CGH2 bus in an underpass. *International Journal of Hydrogen Energy*, 35.8: 3857-3867.

Wilkening, H., Baraldi, D.C.F.D. (2007). CFD modelling of accidental hydrogen release from pipelines. *Journal of hydrogen energy*, 32.13: 2206-2215.

Zhu, H., et al. (2013). The Influences of Key Factors on the Consequences Following the Natural Gas Leakage from Pipeline. *Procedia Engineering*, 62: 592-601.

DOI: 10.7795/810.20200724

A Eulerian model for dust deflagrations, including inner particle effects

Christoph Spijker [a], & Harald Raupenstrauch [a]

[a] Chair of Thermal Processing Technology (Montanuniversitaet Leoben, Leoben, Austria)

E-mail: *christoph.spijker@unileoben.ac.at*

Abstract

Previous studies (Spijker 2017) have shown that the oil evaporation rate of Lycopodium particles is dependent on the resistance for diffusive and convective transport through the pores. Based on these studies a simplified inner particle transport model was created. The model assumes that the evaporation of the oil occurs in a layer. The species and energy transport between this layer and the particle surface are modelled by algebraic equations assuming a momentary steady state condition. The evaporation rates calculated by this approach achieve similar results to the 3D fully resolved particles. In the dust deflagration of Lycopodium, pyrolysis of the lignin structure is of secondary importance, therefore a simplified one equation pyrolysis mechanism was developed. The results are compared with the results from the model excluding inner transport effects, the Eulerian flame speed model developed by Spijker (2014). Furthermore the influence of heat transfer by radiation was considered.

Keywords: *inner particle effects, dust deflagration, simulation, Eulerian approach, Lycopodium*

1. Introduction

Usually, the transport effects in the particles are neglected due to the high demand on computing resources. To model particle inner effects with discretized particles would introduce new differential equations to be solved for each particle. A radial 1-D model from Spijker (2015) with 25 layers needs 680 seconds to model 0.25 seconds real time on one core of an Intel i7-970. Using a Eulerian approach such a particle must be solved in every cell and additional transport equations have to be introduced on the fluid grid, to account the movement of the particles. When a Lagrangian approach is used, the differential equations must be solved for every parcel. The grid used to model the duct experiment from Kern (2013) has 6,3 Million cells. Pollhammer (2015) used additionally 4 million parcels, representing approx. 16 million particles for his Lagrangian approach. As shown in Fig. 1 the dominate process on the thermal conversion of Lycopodium in a dust deflagration is the evaporation of the contained oil. The 0D model, neglecting inner particle transport effects, shows higher evaporation rates than the fully resolved 3D particle model. This will result in a faster flame propagation. With an analytical model describing the transport resistance of the oil vapour in the pores of the particle, this effect can be modelled with low additional computing resources. The pyrolysis of the lignin structure is of secondary relevance and shows no difference between the 0D and 3D model.

DOI: 10.7795/810.20200724

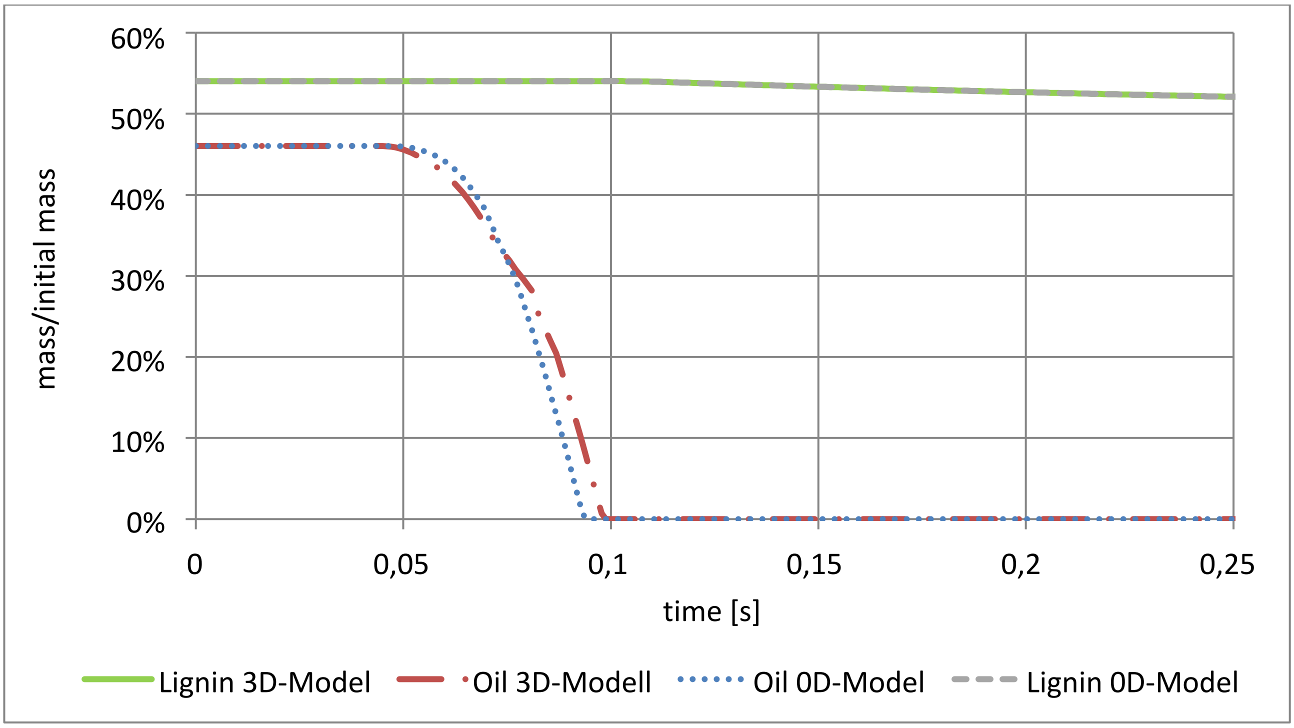

Fig. 1. *Change of mass for a Lycopodium particle in a dust deflagration (Spijker 2015)*

2. Model description

2.1 Global Eulerian Model

The global Eulerian model uses an Eulerian approach to describe multi component reacting mixtures in the gas phase, including turbulence and radiation. An additional Eulerian approach is used for the particle phase, with additional transport equations for the composition of the particles.

2.1.1 Momentum and continuity equations

Equation 1 represents the momentum equation for the gas phase. Here is $\vec{v}$ the velocity vector, ε the gas phase volume fraction calculated from the particle concertation D and density of the mixture ρ, calculated using the ideal gas equation and the molar mass of the mixture. Turbulence is considered by the effective viscosity μ_{Eff} which is the sum of the molecular viscosity, given by the Sutherland approach (Sutherland 1893) and the turbulent viscosity from the turbulence model. To consider gravitational effects, the volume forces caused by the gravitational acceleration vector $\vec{g}$ are included in the equation. The interaction forces between particle and gas phase is considered by Wen-Yu (1966) copping coefficient K (equation 2) and the relative velocity between the phases $\vec{u}-\vec{v}$. The continuity equation for the gas phase (equation 3) considers the gas phase volume fraction and the mass transfer source term Q_D, calculated using the inner particle model.

$$\frac{\partial(\varepsilon\rho\vec{v})}{\partial t} + div\left(\varepsilon\rho\,\vec{v}\,\vec{v}\right) - div\left[\varepsilon\mu_{Eff}grad(\vec{v})\right] - \varepsilon\rho\,\vec{g} - K\left(\vec{u}-\vec{v}\right) = -grad(p)\varepsilon \qquad (1)$$

$$K = \frac{3}{4}C_W\frac{\varepsilon(1-\varepsilon)\rho}{d_p\varepsilon^{2{,}65}}\left|\vec{v}-\vec{u}\right| \qquad (2)$$

$$\frac{\partial(\varepsilon\rho)}{\partial t} + div\left(\varepsilon\rho\,\vec{v}\right) = S_D \qquad (3)$$

The particle phase conservation equation (equation 4) describes the momentum of the dust, where D stands for dust mass concentration and $\vec{u}$ is velocity vector of the particle phase. Diffusive effects on the particle phase are considered by the kinetic particle viscosity μ_{kin} and the particle collision viscosity μ_{coll}. Granular pressure ps as well as μ_{kin} and μ_{coll} are calculated by an analytical approach (Syamlal 1993). The continuity equation (equation 5) is based on the mass concentration D and takes the mass transfer source term Q_D into account.

$$\frac{\partial(D\,\vec{u})}{\partial t} + div(D\,\vec{u}\,\vec{u}) - div[\varepsilon(\mu_{kin} + \mu_{coll})grad(\vec{u})] - D\,\vec{g} - K(\vec{v} - \vec{u})$$

$$= -grad(p)(1-\varepsilon) - grad(ps) \tag{4}$$

$$\frac{\partial(D)}{\partial t} + div(D\,\vec{u}) = -S_D \tag{5}$$

2.1.2 *Energy equations*

An energy equation is solved for each phase. The gas phase energy equation (equation 6) is based on the enthalpy h, using in OpenFOAM 2.4 implemented reaction and thermophysical models. The heat conduction is calculated using effective heat conductivity λ_{Eff} which is the sum of the molecular heat conductivity and the turbulent heat conductivity. The turbulent heat conductivity is calculated from the turbulent viscosity and turbulent Prandtl number. This equation considers the heat source from homogenous reactions $Q_{R,g}$, the heat transfer with the particle phase and the heat source term for radiation Q_{Rad}. This source term considers only gas absorption and wall interactions. For the heat transfer coefficient to the particle phase $\alpha_{g,p}$ the Nusselt correlation by Ranz-Marshall (Ansys 2009) is used. A_V describes the volume specific surface area of the particles, based on the dust concentration D. T_p is the particle temperature and T_g the gas temperature from the thermophysical model used in OpenFOAM.

$$\frac{\partial(\varepsilon h)}{\partial t} + div(\varepsilon\,\vec{u}\,h) - div[\varepsilon\lambda_{Eff}grad(T_g)] = Q_{R,g} + \alpha_{g,p}A_V(T_p - T_g) + Q_{Rad} \tag{6}$$

In the energy equation for the particle phase (equation 7) enthalpy is formulated using dust concentration D, temperature of the particle phase T_p and heat capacity of the particles cp_p. Heat capacity is calculated considering particle composition and temperature, based on the work of Spijker (2015). Additionally to transient and source terms the convective heat transport is considered. Heat source term for the particle reactions $Q_{R,p}$ is modelled with inner particle model. Absorption and emission from the particles are taken in account in the radiation model with a separate source term $Q_{Rad,p}$ for the particle phase.

$$\frac{\partial(DT_p cp_p)}{\partial t} + div(D\,\vec{v}\,T_p cp_p) = Q_{R,p} + \alpha_{g,p}A_V(T_g - T_p) + Q_{Rad,p} \tag{7}$$

2.1.3 Species equations and reactions

Species transport in the gas phase is given by equation 8. This equation is based on the gas phase mass fraction Y_i. Diffusive transport is modelled by an effective diffusivity d_{eff} which is the sum of the molecular diffusivity calculated from the viscosity, constant Schmidt number and the turbulent diffusivity from the turbulence model. The source term $S_{D,i}$ represents the heterogenous reaction rate for the species i in the inner particle model. S_i is the homogenous reaction rate calculated by using the Partially Steered Reactor (PaSR) model implemented in OpenFOAM 2.4. For the homogenous reactions, two combined reaction mechanisms were used. For the combustion of the pyrolysis gases the Jones-Linstedt (1988) was used, whereas for the combustion of the oil vapor in the gas phase the mechanism by Pollhammer (2015) was implemented.

$$\frac{\partial(\varepsilon\rho Y_i)}{\partial t} + div\left(\varepsilon\rho\,\vec{v}\,Y_i\right) - div\left[d_{eff}\,grad(Y_i)\right] = S_{D,i} + S_i \tag{8}$$

In the particle phase two transport equations are solved, one for the mass fraction of the liquid oil X_{oil} and one for the lignin mass fraction X_{lignin}. Only convective transport and the pyrolysis reaction rate from the inner particle model $S_{D,j}$ were considered.

$$\frac{\partial(DX_j)}{\partial t} + div\left(D\,\vec{u}\,X_j\right) = -S_{D,j} \tag{9}$$

2.1.4 Turbulence modelling

For turbulence modelling a modified standard k-ε model was used. Based on the studies of turbulence behaviour in dust deflagrations by Spijker (2014), an additional source term, based on the consistent approach of Crowe (Crowe, 2000) was implemented in the equation for the turbulent kinetic energy k (equation 10). This term models the generation of turbulent kinetic energy due to the relative velocity of the phases.

$$\frac{\partial(k\rho)}{\partial t} + \bar{v}_i\frac{\partial(k\rho)}{\partial x_i} = \frac{\partial}{\partial x_i}\left(\frac{\mu_t}{Pr_k}\frac{\partial k}{\partial x_i}\right) + \mu_t\left(\frac{\partial\overline{v_i}}{\partial x_j} + \frac{\partial\overline{v_j}}{\partial x_i}\right)\frac{\partial\overline{v_i}}{\partial x_j} - \varepsilon p\rho + \rho\frac{D}{\tau_p}\left|\vec{u} - \vec{v}\right|^2 \tag{10}$$

2.1.5 Radiation

The radiation model used is a P1-model, considering absorption and emission of gas phase and absorption, emission and uniform scattering of the particle phase. Radiation intensity G is using equation 11. Here is a the absorption coefficient of the gas phase. This coefficient will be modelled by a Weighted Sum of Gray Gases Model, based on the TNF6 Proceedings (Grosshandler 1993). This model considers temperature depended absorption of CO_2, CO and H_2O. The absorption coefficient of the particles a_p is calculated by formula 12, where ε_p is a constant emission coefficient, D the mass concertation of dust, ρ_p the density of the particle and d_p the particle diameter. In similar manner the scattering coefficient ψ_p for uniform scattering modelled (formula 13). The source term for the energy equation of each phase (formula 14) is calculated by the difference between absorption by the phase Ga and emission by the phase $4a\sigma {T_g}^4$.

$$div\left[\frac{1}{3(a + a_p + \psi_p)}grad(G)\right] + 4a\sigma {T_g}^4 + 4a_p\sigma {T_p}^4 = \left(a + a_p\right)G \tag{11}$$

$$a_p = \varepsilon_p\frac{3\,D}{\rho_p\,d_p} \tag{12}$$

$$\psi_p = \left(1 - \varepsilon_p\right)\frac{3\,D}{\rho_p\,d_p} \tag{13}$$

$$Q_{Rad} = Ga - 4a\sigma {T_g}^4 \text{ and } Q_{Rad,p} = Ga_p - 4a_p\sigma {T_{gp}}^4 \tag{14}$$

2.2 *Inner particle Models*

2.2.2 *Oil evaporation*

The numerical studies by Spijker (2017) on different forms of resolved Lycopodium particles have shown that the maximum occurring thickness of the oil evaporation region is less than 3,4 µm. So, the analytical model for the oil evaporation uses a core approach shown in figure 2. This approach is based on two radii, r_0 is the constant particle radius equal to $\frac{d_p}{2}$, whereas the second r_v is the radius of the oil saturated particle, calculated as a function of the oil mass fraction X_{oil}. To account the dens core, an averaged core radius r_c is introduced. The calculation of the radius r_v is shown in equation 15, where $X_{oil,start}$ is the oil mass fraction before evaporation.

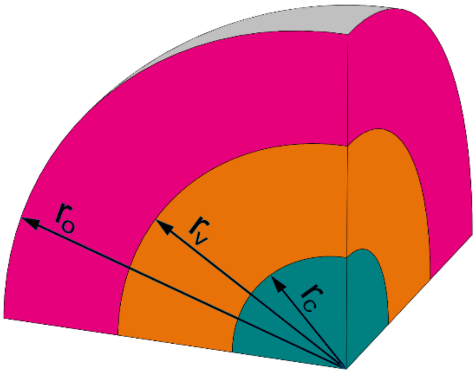

Fig. 2. *Concept of the core model for the oil evaporation*

$$r_v = \left[\frac{X_{oil}}{X_{oil,start}}\left({r_0}^3 - {r_c}^3\right) + {r_c}^3\right]^{\frac{1}{3}} \tag{15}$$

The main transport mechanism for the oil vapor from the evaporating layer to the particle surface is the convection through the pore structure. To describe the pressure gradient, the Carman Kozeny (1956) equation for a spherical coordinate system is used (equation 16). Here is u_r radial velocity, μ_{oil} viscosity of the oil vapor at evaporating temperature, ε_{eff} effective pore volume fraction, d_{pore} pore diameter and F stands for an empirical factor for the form of the pore structure.

$$\frac{\partial p}{\partial r} = -\mu_{oil}\, u_r \frac{\left(1-\varepsilon_{eff}\right)^2}{F \varepsilon_{eff} d_{pore}^2} \tag{16}$$

To obtain the radial velocity continuity equation for a spherical coordinate system is defined by equation 17 and used as the source term for the global species equations. Here is ρ_{oil} the density of the oil vapor, p^* the vapor pressure of the oil calculated by the Antoine equation and p_∞ the pressure of the computing cell.

$$S_{D,oil} = D\, \rho_{oil} \frac{\pi F \varepsilon_{eff} d_{h\,pore}^2}{4\mu_{oil}\left(1-\varepsilon_{eff}\right)^2} \frac{p^* - p_\infty}{\frac{1}{r_v} - \frac{1}{r_0}} \tag{17}$$

This equation fails numerically when $r_v \approx r_0$. For that reason, if $r_v > 0.9\, r_0$ simple enthalpy difference evaporation model is used. To avoid unphysical conditions, the source them $S_{D,oil}$ is set to zero if $p^* \leq p_\infty$ or $X_{oil}\, D < \frac{S_{D,oil}\, \Delta t}{2}$.

To evaluate the oil evaporation model, evaporation rates of the single particle models by Spijker (2015) were used. The 0D model neglects transport effects and as a consequence overestimates evaporation rate of the oil. The 3D model represents a fully resolved particle with a core structure, diffusive and convective transport though the pores. The boundary conditions are mapped from the two Lagrangian models (Particle 1, Particle 2), used for a dust deflagration in a vertical duct by Spijker (2015). As can been seen from figure 3 evaporation rates calculated using evaporation model 3D model are almost identical. The slight difference is caused by the simplified round core in the evaporation model.

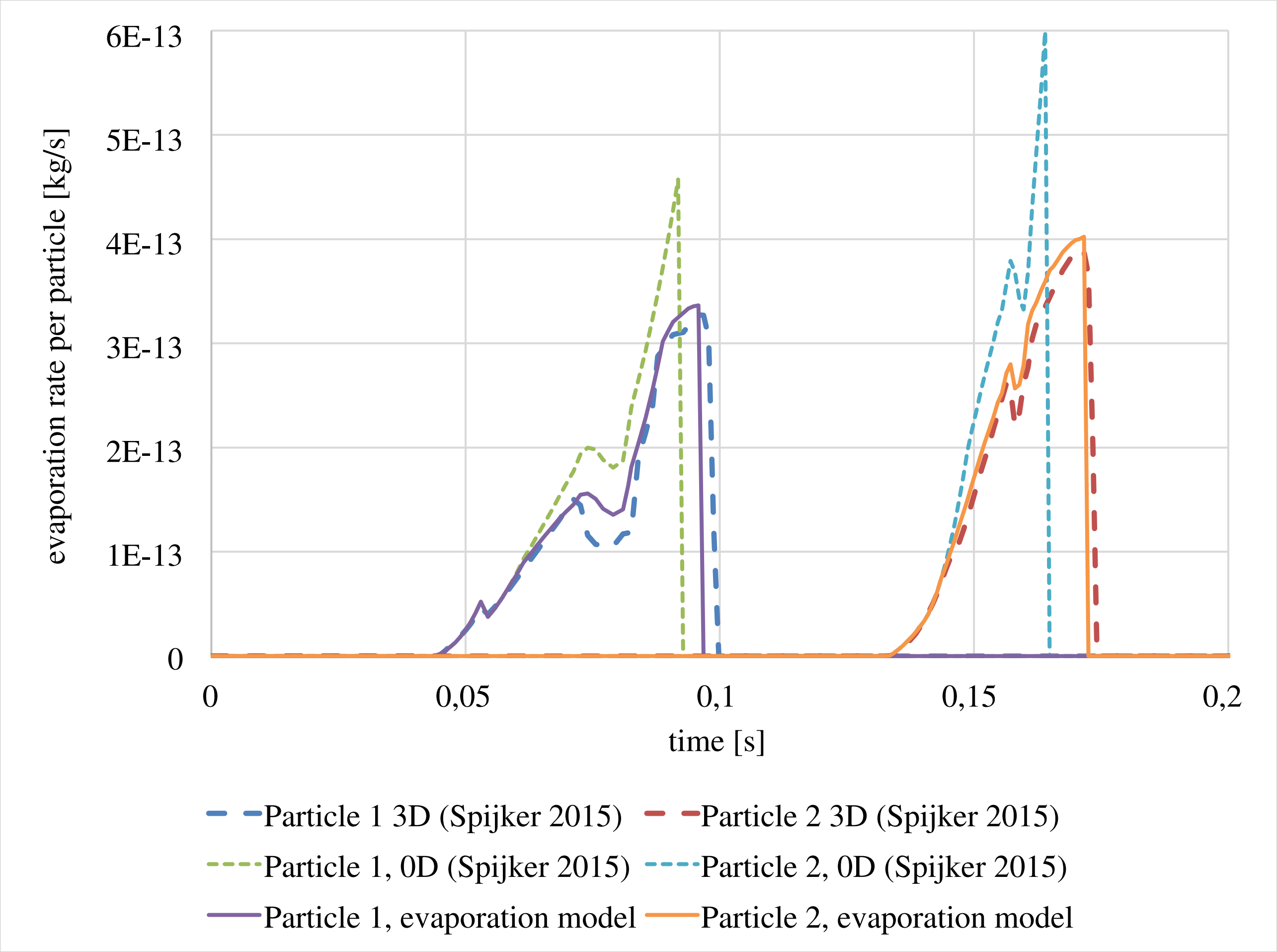

Fig. 3. *Compression of oil evaporation model to the 0D and 3D results from Spijker (2015)*

2.2.3 Pyrolysis of the Lignine

The pyrolysis rates between the 0D, 1D and 3D studies of Spijker (2015, 2017) show basically no difference. The implementation of 8 reaction pyrolysis model would require 7 additional variables in the particle phase of the global model. To simplify the pyrolysis only one averaged reaction is implemented (equation 18). The frequency factor A, the activation energy Ea and the reaction order n are averaged from the results of the studies by Spijker (2015, 2017).

$$S_{D,Lingine} = \mathrm{D}\frac{A}{{X_{Liginin,start}}^{n}} e^{-\frac{Ea}{RT_p}} \left(X_{Liginin,max} - X_{Liginin}\right)^{n} \qquad (18)$$

To provide different source terms for the gas phase, a splitting gas factors for each species ϕ_i were introduced. These provide an average composition of the pyrolysis gases, based on the studies by Spijker (2015, 2017).

$$S_{D,i} = S_{D,Lingine}\phi_i \qquad (19)$$

3. Model evaluation and results

3.1 Evaluation

The model was evaluated by the flame propagation from duct experiments by Kern (2013) and the flame temperature measurements by Wieser (2015). For both experiments the same apparatus was used. A vertical duct with an inner diameter of 140 mm and a length of 2000 mm. At the top of the duct particles were dispersed by a screw conveyer and ignited at the bottom by a spark. The first step in the modelling of dust deflagration in the duct is to achieve the initial conditions before ignition. For that purpose, the dust dispersion was modelled, until there was no significant change in the dust concertation and turbulence field. Subsequently the mixture was ignited by setting one cell to a constant gas phase temperature of 2000 K for 20 ms. The top flame position is the highest point in the duct where the flame reaches a temperature above 1000 K. In figure 4 the top flame position from the evaporation model is compared to the flame speed model by Spijker (2014) and experiments by Kern (2013) where the flame position is tracked by video analysis. For the first simulations the same grid was used as by Spijker (2014), called normal grid. This grid has a hexahedral cell length of 2.5 mm. Here is the flame velocity using the evaporation model much slower than the 0D model and adequate accordance to the measurements. The flame speed model by Spijker (2014) has the best agreement with the experiment until 200 ms. Flame velocities of the evaporation model are in good accordance to the measurements after 120 ms but overestimated at the beginning. A grid study for this model shows grid independency for a hexahedral cell length of 1 mm (fine grid). The coarser grid overestimates the flame velocity at the beginning, caused by the larger volume of the ignition cell and therefore higher ignition energy.

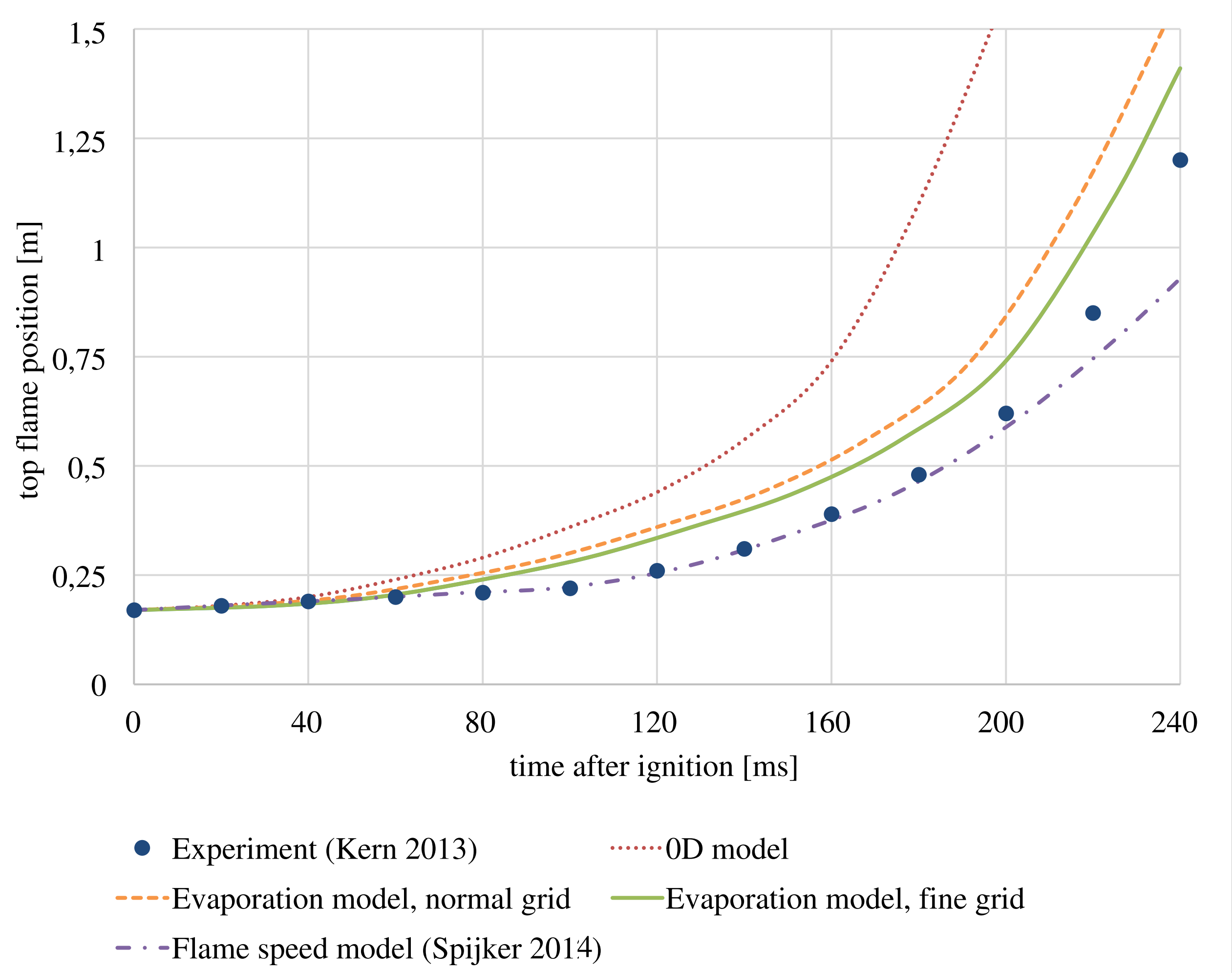

Fig. 4. *Comparison of the top flame position between different models and experimental results from Kern (2013)*

The measurements by Wieser (2015) where carried out by the analysis of the transient heat up of thermocouples. The measurements have a large spread, still all simulation results are within given range (Table 1). The temperatures of the 0D and evaporation model are close due to the limitation of oxygen. The flame speed model has a different thermophysical model, based on progress variables and calculates slightly lower temperatures.

Table 1: *Comparison of the Flame temperatures*

Hight in the duct	**Measured temperate (Wieser 2015)**	**Temperature flame speed model (Spijker 2014)**	**Temperature 0D model**	**Temperature evaporation model**
300 mm	1186 K – 1642 K (3 σ)	1205 K	1238 K	1232 K
600 mm	1222 K - 1299 K (3 σ)	1219 K	1251 K	1246 K
900 mm	1149 K – 1307 K (3 σ)	1153 K	1225 K	1213 K

3.2 *Evaporation and flame propagation*

Till approx. 120 ms the evaporation takes place in a thin layer and the flame grows in an elliptical shape, as shown in figure 5 at 100 ms. After 120 ms the flame gets influenced by the wall and stats to accelerate, where the top of the flame deforms and the thickness of the evaporation layer increases, as can be seen from figure 5 at 200 ms. This behaviour continues and the top of the flame deforms further, the volume of the evaporation zone increases, as well as the total evaporation rate in the system. At 245 ms the flame reaches the highest point. Due to the rich mixture and the lack of oxygen the flame starts to collapse, as shown at 250 ms.

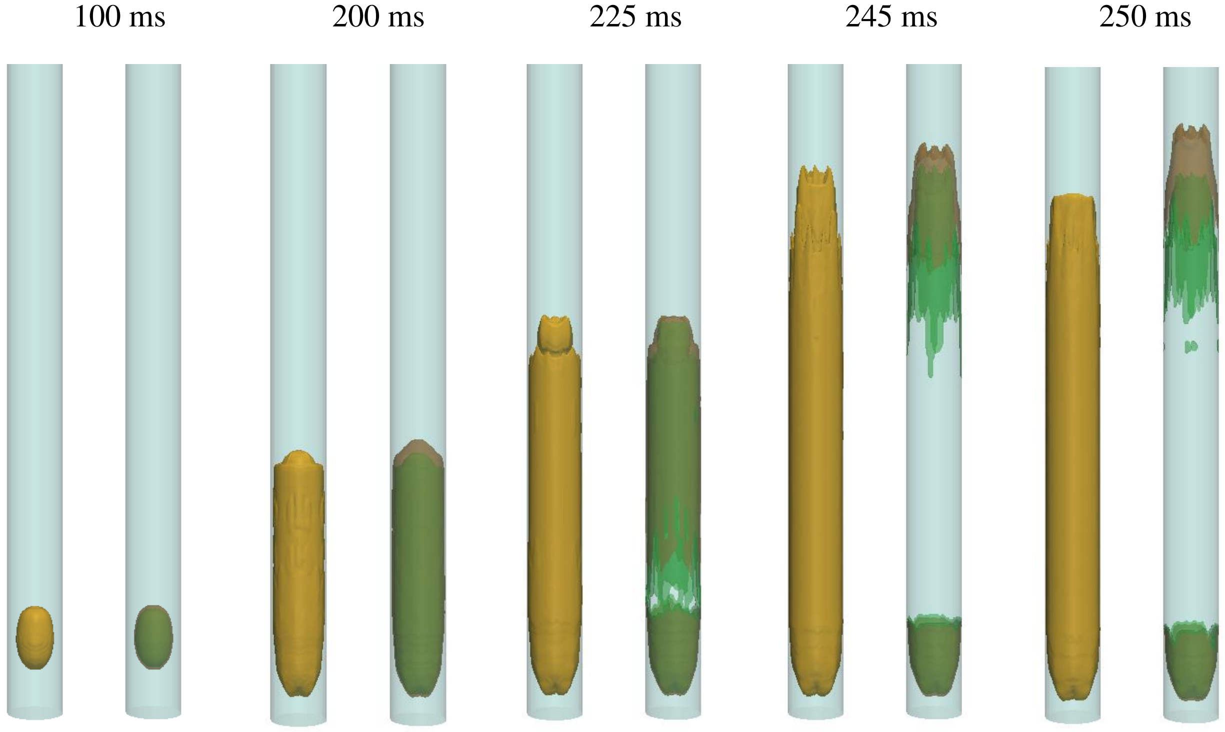

Fig. 5. *Representation of the flame position and evaporation zone. The orange iso-surface represents the flame position at the temperature of 1000 K, the green represents particles with 1 % of the initial oil content and the brown particles with 99 % of the initial oil content.*

4. Conclusions and outlook

Implementation of the evaporation model using an analytical solution for the transport resistance in the particle gives a better prediction of the flame in a Lycopodium deflagration then a 0D model, without increasing calculation time significantly. In the current form the model is applicable to large industrial geometries with reasonable calculation time and can explain the physics on a detailed level. The approach in this form is only applicable for the evaporation of fluids in the pore structures of small particles. The focus of further research is to develop simplified models for other particles, using highly resolved single particle models. A model for coal dusts is in progress.

References

Ansys Inc. (2009). Ansys Fluent 12 Theory Guide

Carman, P.C. (1956). Flow of gases through porous media, *Butterworths Scientific Publications*, London

Crowe, C. T. (2000). On models for turbulence modulation in fuid-particle fows, *International Journal of Multiphase Flow*, 26: 719-727

Grosshandler, W. L., RADCAL (1993). A Narrow-Band Model for Radiation Calculations in a Combustion Environment, *NIST technical note 1402*

Jones, W. P., Lindstedt, R. P. (1988). Global reaction schemes for hydrocarbon combustion, *Combustion and Flame* 73: 222–233

Kern, H. (2013). Brennbare Staub/Luft Gemische - Untersuchungen zur Flammenfortpflanzung unter nichtatmosphärischen Bedingungen, *PhD Thesis*, Montanuniversitaet Leoben, Leoben Austria

Pollhammer, W. (2015). Numerische Untersuchung der Mindestzündenergie sowie der Flammenfortpflanzung in Staub/Luft – Gemischen mittels eines Euler – Lagrange – Modells in OpenFOAM, *Master Thesis*, Montanuniversitaet Leoben, Leoben Austria

Spijker, C. (2014). A CFD Approace for dust explosions based on OpenFOAM, *X ISHPMIE Conference Proceedings*

Spijker, C. (2015). Numerische Untersuchung der partikelinneren Effekte bei Lykopodiumstaubdeflagrationen, *PhD Thesis*, Montanuniversitaet Leoben, Leoben Austria

Spijker, C. (2017). Numerical investigation on inner particle effects in Lycopodium/Air dust deflagrations, *Journal of Loss Prevention in the Process Industries*, 49: 870-879.

Sutherland W. (1893). The viscosity of gases and molecular force, *Philosophical Magazine*, 5: 507–531

Wen, C.-Y., Yu, Y. H. (1966). Mechanics of Fluidization, *Chem. Eng. Prog. Symp.* :100–111

Wieser, G. (2015). Einflüsse der Temperatur und der Turbulenz auf die Flammenausbreitung in Staub/Luft-Gemischen unter reduzierten Druckbedingungen, *4. Magdeburger Brand- und Explosionsschutztag*, Magdeburg

DOI: 10.7795/810.20200724

CFD Simulation of an Unconfined Vapor Cloud Explosion through obstacles using OpenFoam®

C. Langrée[a,b], E. Franquet[c], J. Reveillon[a], G. Lecocq[b] & F.X. Demoulin[a]

[a] Complexe de Recherche Interprofessionnel en Aérothermochimie (CORIA), Rouen, France
[b] Institut National de l'Environnement Industriel et des Risques (INERIS), Verneuil en halatte, France
[c] Laboratoire de Thermique, Energétique et Procédés (LaTEP), Pau, France

E-mail: *langreec@coria.fr*

Abstract

In this work, numerical simulations are carried out to characterize the impact of obstacles on flame propagation velocity to properly assess the consequences of Unconfined Vapor Cloud Explosions (UVCE). Within this scope, an UVCE within a congested environment is simulated using RANS modeling of the turbulence. Combustion phenomena are characterized through the progress variable transport equation. The simulation is done with the open source library OpenFoam®. Numerical results are compared with data from the INERIS and GDF-SUEZ experimental campaign EXJET (hydrogen-air and methane-air explosions).

Keywords: *hazards, industrial explosions, CFD, premixed combustion*

1 Introduction

Unconfined Vapor Cloud Explosion (UVCE) is one of the most devastating industrial accidents possible (J. Daubech (2016)). The loss of containment of a flammable product (e.g. methane or hydrogen) can lead to the formation of a flammable cloud all across the plant. The resulting mixture can be lit by any energy source within the cloud (e.g. sparkles, hot surfaces). The propagation of the flame front within the cloud can cause damaging pressure effects in close and long range. In order to assess these damages, CFD can be used, in parallel with widely used phenomenological tools. The open source code OpenFoam® has already been used for such purpose (Bauwens et al. (2011), Ghasemi et al. (2014), Rao et al. (2018)). The global aim of this study is to improve numerical methods for CFD simulation of industrial UVCE.

Hazardous consequences of UVCE are mainly caused by the over-pressure generated by the propagation of the flame front. In deflagration cases, this over-pressure is directly linked to the flame front propagation speed (J. Daubech (2016)). In an industrial configuration, the flame front is impacted by the various obstacles in its way (e.g. pipes, walls). One of the consequences of the presence of obstacles is an acceleration of the flame front (Moen et al. (1980), Moen et al. (1982)) and, consequently, many experiments has been conducted to evaluate this effect. The EXJET campaign (INERIS, GDF-SUEZ) has been set to study experimentally the effect of an obstacle module on the propagation of a flame front in many configurations (steady flammable mix, methane-air jet, hydrogen-air jet).

2 Description of the experimental work

The experimental work considered here has been carried out by INERIS and GDF-SUEZ (Sail et al. (2014)). The aim of the experiment was to study methane jet explosion in a congested environment. The congestion module was a medium size (3m×1m×0.45m) obstacle module, consisting of 296 steel tubes of 2cm diameter. In the framework of the EXJET experimental setup, several experiments have been carried out : methane jet dispersion within the module (without ignition), methane jet ignition within the module, and ignition of a steady methane-air mix. The steady methane-air mix ignition configuration has been simulated with OpenFoam® in this study.

To assess the pressure variations, several pressure probes are positioned in and around the obstacle module as in Fig. 1. The pressure signals from those probes will be compared to the pressures signals from virtual probes of the numerical simulation. Moreover, pictures of the experiment will be post-process to obtained experimental flame position data.

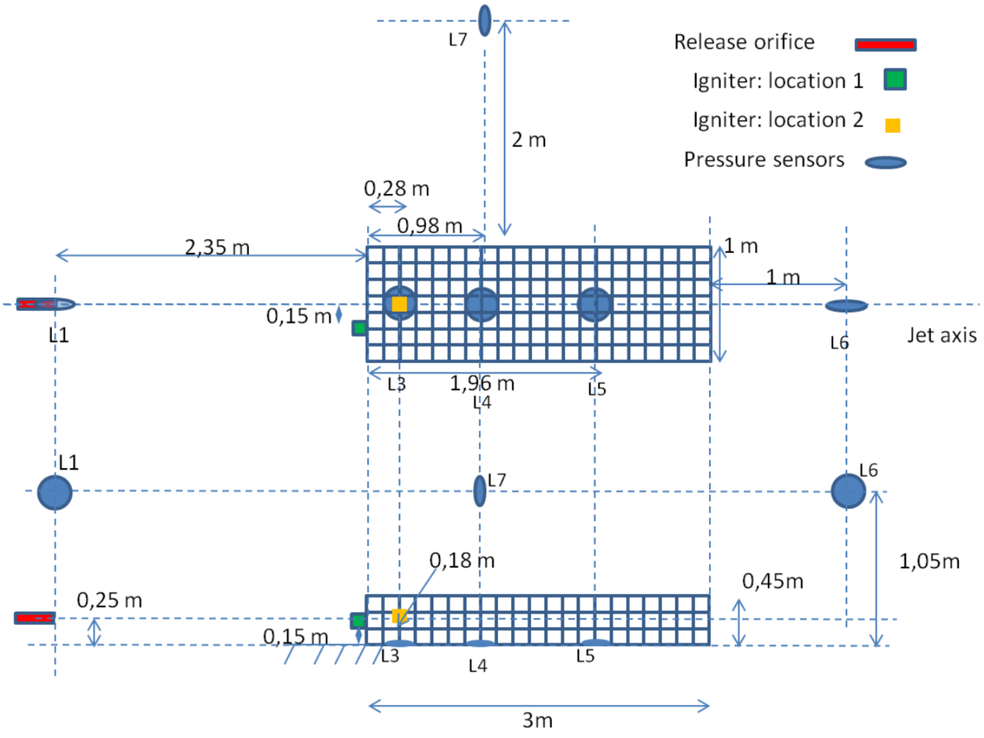

***Fig. 1**: Locations of the release orifice, pipes, igniter and pressure sensors used by INERIS and GDF SUEZ for methane jets within a 3D array of 20 mm diameter tubes (Sail et al. (2014)). Up : top view of the obstacle module ; Bottom : side view of the obstacle module.*

In the configuration that interests us, a homogeneous stoichiometric methane-air mixture is spread within the obstacle module. The mixture is kept in the obstacle area by a plastic sheet supported by steel frames. Those plastic sheets will come off with the explosion. The flammable mix is ignited by an electrical ignition device (location 1 on Fig. 1) located inside an aluminium box (19cm × 15cm × 13cm) with an opening toward the congestion module.

3 Numerical study

3.1 Equations solved

With the solver XiFoam of OpenFoam® v7.0, the Weller b-Xi model (Weller et al. (1998)) is used to model partially premixed combustion. Navier-Stokes equations (eqs. 1, 2) are solved as well as the energy equation (eq. 3).

$$\frac{\partial \overline{\rho}}{\partial t} + \nabla.(\overline{\rho}\widetilde{U}) = 0 \tag{1}$$

$$\frac{\partial \overline{\rho}\widetilde{U}}{\partial t} + \nabla.(\overline{\rho}\widetilde{U}\widetilde{U}) = -\nabla.(\overline{\rho}\widetilde{U''U''}) - \nabla\overline{p} + \nabla.(\overline{\tau}) \tag{2}$$

$$\frac{\partial \overline{\rho}\widetilde{h}_t}{\partial t} + \nabla.(\overline{\rho}\widetilde{U}\widetilde{h}_t) + \frac{\partial \overline{\rho}K}{\partial t} + \nabla.(\overline{\rho}\widetilde{U}K) + \frac{\partial p}{\partial t} + \nabla.(\alpha\nabla\widetilde{h}_t) = \dot{Q} \tag{3}$$

With K being the kinetic energy, α the thermal diffusivity, τ the viscous stress tensor and $\dot{Q}$ an external energy source term (in our case, $\dot{Q} = 0$).

In order to model the combustion, a combustion regress variable "b" is defined (4).

$$b = \frac{T_b - T}{T_b - T_u} \tag{4}$$

With T_b the burnt gases temperature, and T_u the unburnt temperature. A transport equation is solved for this regress variable (5) in order to model the propagation of the flame front.

$$\frac{\partial \overline{\rho} b}{\partial t} + \nabla.(\overline{\rho}\widetilde{U} b) - \nabla.(\alpha \nabla b) = -\rho_u S_u \Xi \mid \nabla b \mid \tag{5}$$

With Su the laminar flame speed, ρ_u the unburnt gases density, and Ξ the flame wrinkling factor (turbulent and laminar flame speed ratio). This ratio is obtained algebraically (6).

$$\Xi = 1 + 2(1-b)\Xi_{coeff}\sqrt{\frac{u'}{Su}R_\eta} \tag{6}$$

With R_η the Kolmogorov Reynolds number, u' the sub-grid turbulence intensity and Ξ_{coeff} a model constant equal, in our case, to 0.62. And finally, to take into account the inhomogeneity of the mix, an equation for a mix variable f_t is solved (7).

$$\frac{\partial \overline{\rho} f_t}{\partial t} + \nabla.(\overline{\rho}\widetilde{U} f_t) = \nabla.(\mu \nabla f_t) \tag{7}$$

With μ the dynamic viscosity. The effects of equivalence ratio inhomogeneity on the flame front propagation speed is taken into account by the S_u term in the b equation with the Gulder flame speed correlation (8) (Gulder (1984)).

$$Su(T,p,\phi) = W\phi^{\eta} e^{-\xi(\phi-\sigma)}(\frac{T}{T_0})^{\alpha}(\frac{p}{p_0})^{\beta} \tag{8}$$

With W, η, σ, α, β Weller model constant and ϕ, the equivalence ratio, being recovered from f_t and $(\frac{Y_{air}}{Y_{fuel}})_{sto}$, the stoichiometric air-fuel ratio .

$$\phi = (\frac{Y_{air}}{Y_{fuel}})_{sto}\frac{f_t}{1-f_t} \tag{9}$$

The ignition is managed via an OpenFoam® integrated module which generate, in a given duration, a spherical volume of burnt gases of a given radius, at a given location. The duration and radius of this ignition kernel has been tuned to the laminar flame speed of the mix.

The PIMPLE algorithm is used to solve the pressure-velocity coupling in XiFoam (Holzmann (2019)). The equations modeling the effect of the combustion are included in the PIMLE loop.

3.1.1 Mesh, boundary condition and numerical schemes

The meshing process has been conducted with both SALOME and the OpenFoam® utilities blockMesh and snappyHexMesh. The domain consists of 836 296 cells and the minimum dx of a cell is 6.25 mm.

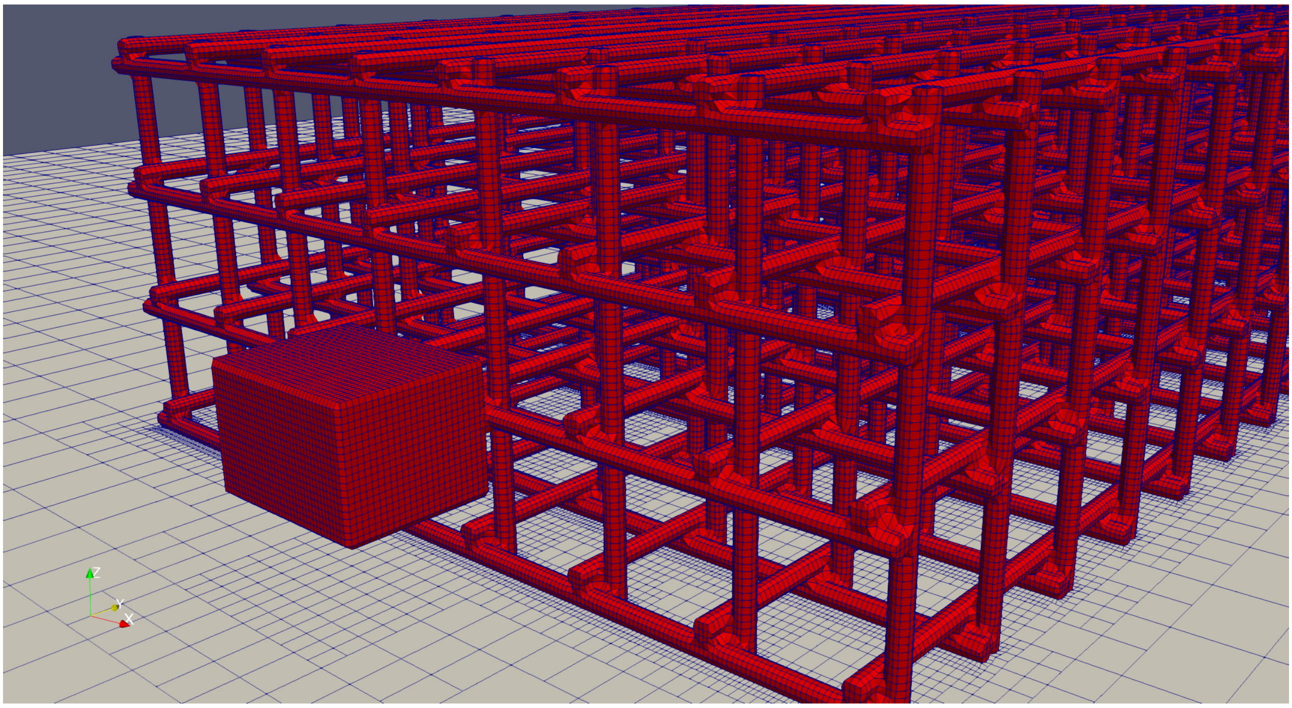

***Fig. 2**: View of the calculation mesh (ParaView)*

The boundary of the numerical domain surrounding the obstacle module is at 2.5m distance of the module in the x and y direction and at 1.5m distance of the module in the z direction.

The boundary conditions to take into account for this simulation are :

- the obstacle module
- the ground
- the ambiant air

The obstacle module and ground will be considered "wall" boundary condition whereas ambient air will be considered free outlet boundary condition. The boundary conditions used are given in Table 1.

***Table 1**: Numerical simulation boundary conditions*

Variable	**WallBC**	**AirBC**
U	fixedValue (0 0 0)	fluxCorrectedVelocity
p	zeroGradient	totalPressure
*	zeroGradient	zeroGradient

The different numerical schemes available in OpenFoam® are detailed in (Moukalled et al. (2015)). The schemes used in this simulation are given in Table 2.

***Table 2**: Simulation numerical schemes*

Variable	**ddt**	**div**	**laplacian**
U/p/k	Euler backward	Upwind	Gauss linear corrected
b/ft	Euler backward	Gauss linearlimited01	Gauss linear corrected
*	Euler backward	Gauss linearlimited	Gauss linear corrected

DOI: 10.7795/810.20200724

4 Results and discussion

As we are willing to assess for the over-pressure effects of the UVCE, we will look at two aspects of it : the propagation speed of the flame front and the resulting over-pressure.

4.1 Flame speed

A first simulation has been done to check that the solver take into account the accelerating effect of the obstacles on the flame front. A flame front has been propagated in two cases, with and without an obstacle module. The same mesh and numerical schemes has been used for the two simulation.

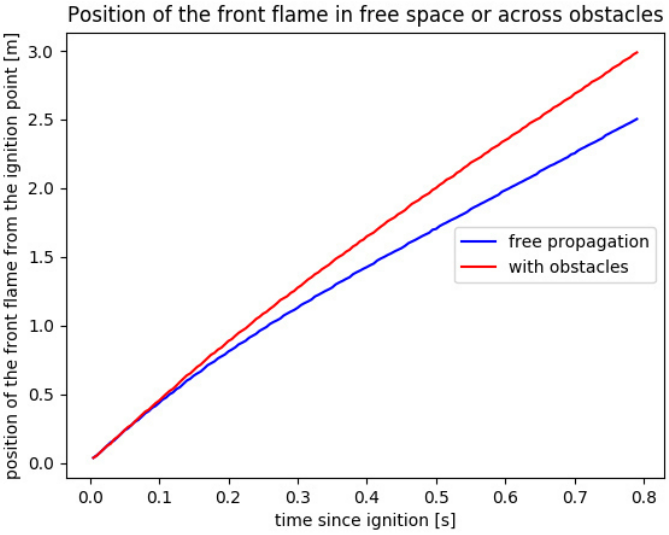

Fig. 3*: Flame front position in time with and without obstacles*

Here we can see that the flame front positions diverged. An accelerating effect of the obstacle can be observed with XiFoam. We can explain that effect by the turbulent kinetic energy generated by the obstacles. In fact, the flame front propagation, by pushing the fresh gases in front of it, generate a velocity flow normal to the flame surface. This flow, in presence of obstacles, will increase turbulent kinetic energy around those obstacles. This turbulent kinetic energy will, as we can see in (eq .6), increase the wrinkling factor and hence the flame propagation speed, as we can see in (eq. 5). The turbulent kinetic energy generation by the obstacles is illustrated in Fig. 4. There we can see that turbulent kinetic energy is generated around the obstacles crossed by the flame front.

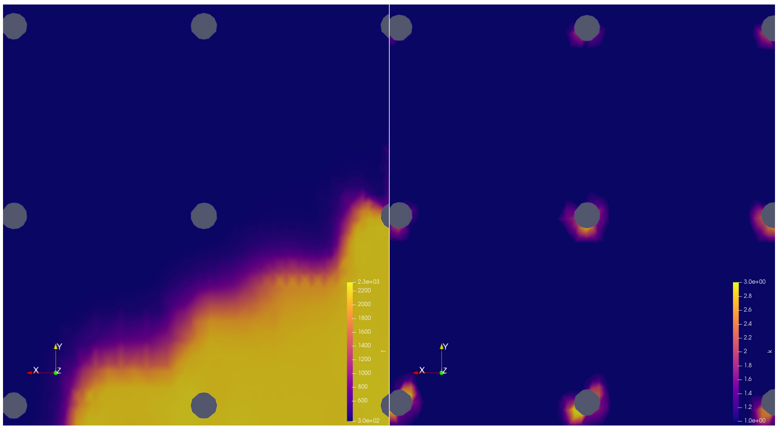

Fig. 4*: Sectional view (z axis) of the flame front propagation (Paraview). Left : temperature (K), right : turbulent kinetic energy ($m^2.s^{-2}$)*

Finally, we can compare the experimental and numerical flame speed. We observe an acceleration of the experimental flame front during the whole experiment, starting propagating at 9 m/s until it attained a speed of roughly 25 m/s. In the numerical case however, we observe a constant flame speed of approximately 12 m/s. As we are in the same magnitude in term of flame propagation speed, we fail to reconstruct the accelerating behavior of the flame front within the obstacle module. The usage of a transport equation for Ξ in further work can be a lead toward reproducing this accelerating behavior.

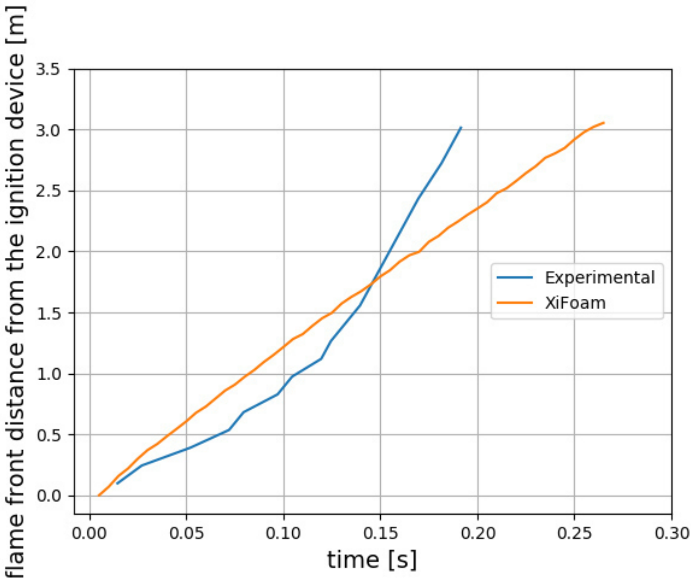

Fig. 5: Experimental and numerical flame front position from the ignition point in time

4.2 Pressure signal

For the pressure signals, the numerical simulation result in an over-pressure "wave" being pushed by the flame front, as shown on the Fig. 6. There we can observe an over-pressure "wave" just in front of the flame front. This over-pressure is the result of the unburnt gases being pushed by the flame front propagation.

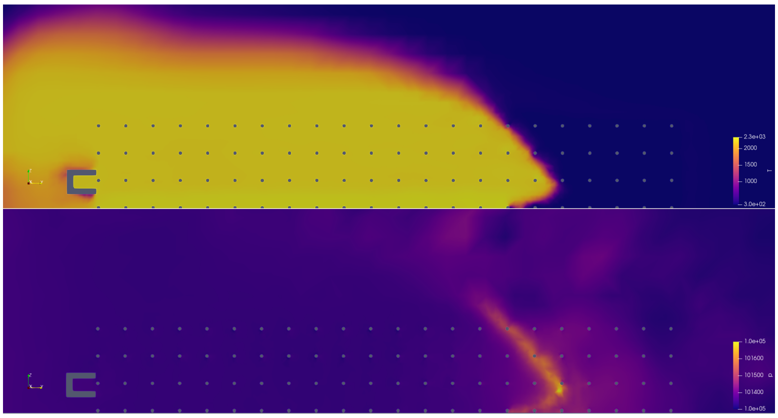

Fig. 6: Sectional view (x axis) of the flame front propagation at t = 0.2 sec (Paraview). Up : temperature (K), down : pressure (Pa)

But when comparing the signals from two pressure probes (positioned along the y axis from the ignition point) Fig. 7, both experimental and numerical, we couldn't reproduce with precision the over-pressure wave. There we can see that at 0.28 cm from the ignition point, a 4.5 mmBar over-pressure is obtained but the peak is obtained numerically at approximately 0.03sec in the numerical case, versus 0.1sec for the experimental case. However, with the over-pressure being "pushed" by the flame front, the phase between the two signal is likely to be induced by the different position of the experimental and numerical flame front.

Now at 1.96m from the ignition point, the two over-pressure peaks are occurring approximately at the same time (0.16 sec), but the magnitude is not accurately reproduced. The numerical over-pressure peak value is 1.75 mmBar and the experimental one being 6 mmBar. This difference may be explained by the flame speed difference when crossing the probe. In fact, at the moment where the flame crosses the probe at 1.96m from the ignition point, the experimental has already attained its max velocity of 25 m/s whereas the numerical one is still at the same speed of 12 m/s Fig. 5.

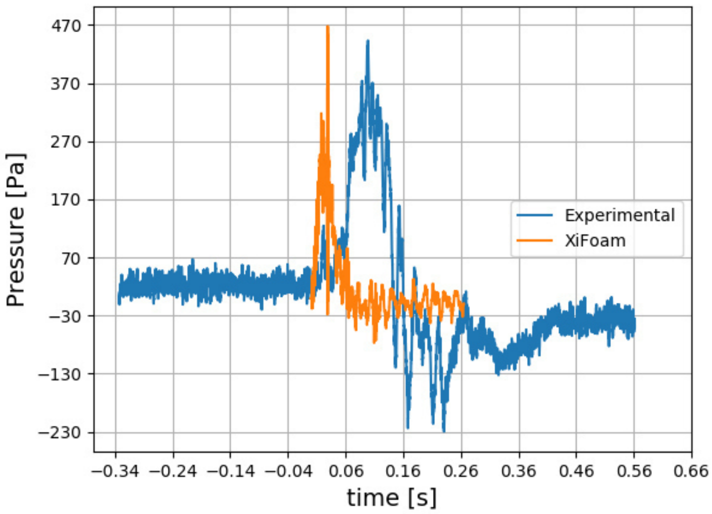

(a) Relative pressure at 0.28m from the ignition point

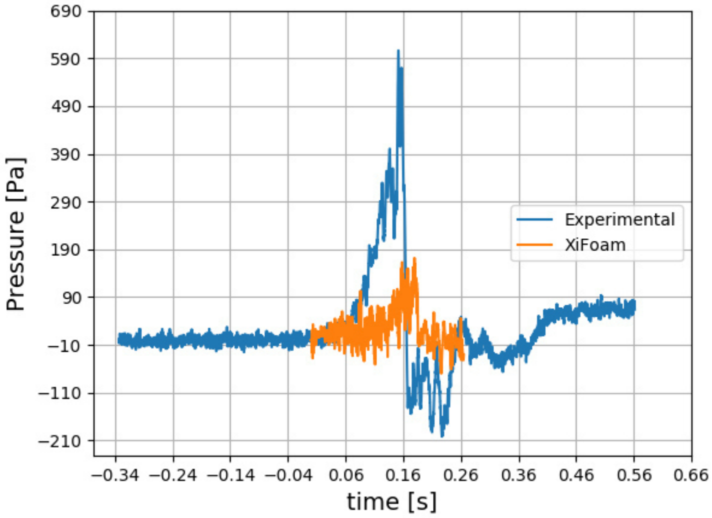

(b) Relative pressure at 1.96m from the ignition point

***Fig.** 7: Relative pressure signal in time at 2 point on the y axis*

The magnitude of the peak over-pressure is roughly the same (severals mBar), although the over-pressure is attenuated between the two probes for the numerical simulation(from 4.7 mBar to 1.8 mBar), and is enhanced in the experiment(from 4.5mBar to 6.0 mBar). This is probably explained by the acceleration of the experimental flame front Fig. 5 between the two probes, effectively generating more over-pressure in front of it.

5 Conclusions

In this study, a methane-air explosion in a confined environment has been simulated. The explosion "at rest" case of the EXJET (INERIS GDF-SUEZ) as been taken to assess for the fidelity of the simulation with OpenFoam®. So far, several aspects of the simulation have shown good agreement with the experiment : The accelerating effect of the obstacles can be reproduced, and magnitude of both flame speed and over-pressure peaks are conserved. But the study fails to reproduce the accelerating behavior of the flame front and hence the over-pressure signals obtained numerically are not accurately reproducing the experimental ones.

The key to reproduce with fidelity the over-pressure signals (and more specifically, the over pressure peak values) is to capture with fidelity the flame propagation speed. Current works on the transport equation for Ξ are carried out to take care of that aspects. Results will be updated accordingly.

References

Bauwens, C., Chaffee, J., Dorofeev, S. (2011). *Vented explosion overpressures from combustion of hydrogen and hydrocarbon mixtures*. International Journal of Hydrogen Energy, 36(3):2329 – 2336. ISSN 0360-3199. doi:https://doi.org/10.1016/j.ijhydene.2010.04.005. The Third Annual International Conference on Hydrogen Safety.

Ghasemi, E., Soleimani, S., Lin, C. (2014). *Rans simulation of methane-air burner using local extinction approach within eddy dissipation concept by openfoam*. International Communications in Heat and Mass Transfer, 54:96 – 102. ISSN 0735-1933. doi: https://doi.org/10.1016/j.icheatmasstransfer.2014.03.006.

Gulder, O. (1984). *Correlations of laminar combustion data for alternative si engine fuels*.

Holzmann, T. (2019). *Mathematics, Numerics, Derivations and OpenFOAM®*.

J. Daubech, E. Leprette, C. P. (2016). *Formalisation du savoir et des outils dans le domaine des risques majeurs (eat-dra-76) les explosions non confinées de gaz et de vapeurs - ω uvce*. Technical report, Institut National de l'Environnement Industriel et des Risques.

Moen, I., Donato, M., Knystautas, R., Lee, J. (1980). *Flame acceleration due to turbulence produced by obstacles*. Combustion and Flame, 39(1):21 – 32. ISSN 0010-2180. doi: https://doi.org/10.1016/0010-2180(80)90003-6.

Moen, I., Lee, J., Hjertager, B., Fuhre, K., Eckhoff, R. (1982). *Pressure development due to turbulent flame propagation in large-scale methaneair explosions*. Combustion and Flame, 47:31 – 52. ISSN 0010-2180. doi:https://doi.org/10.1016/0010-2180(82)90087-6.

Moukalled, F., Mangani, L., Darwish, M. (2015). *The Finite Volume Method in Computational Fluid Dynamics: An Advanced Introduction with OpenFOAM® and Matlab®*, volume 113. ISBN 978-3-319-16873-9. doi:10.1007/978-3-319-16874-6.

Rao, V. C. M., Sathiah, P., Wen, J. X. (2018). *Effects of congestion and confining walls on turbulent deflagrations in a hydrogen storage facility-part 2: Numerical study*. International Journal of Hydrogen Energy, 43(32):15593 – 15621. ISSN 0360-3199. doi: https://doi.org/10.1016/j.ijhydene.2018.06.100.

Sail, J., Blanchetiere, V., Geniaut, B., Osman, K., Daubech, J., Jamois, D., Hebrard, J. (2014). *Review of knowledge and recent works on the influence of initial turbulence in methane explosion*. In SKJOLD, T., ECKHOFF, R. K., VAN WINGERDEN, K., editors, *10. International symposium on hazards, prevention, and mitigation of industrial explosions (X ISHPMIE)*, pages 401–432. GexCon AS, Bergen, Norway.

Weller, H., Tabor, G., Gosman, A., Fureby, C. (1998). *Application of a flame-wrinkling les combustion model to a turbulent mixing layer*. Symposium (International) on Combustion, 27(1):899 – 907. ISSN 0082-0784. doi:https://doi.org/10.1016/S0082-0784(98)80487-6. Twenty-Seventh Sysposium (International) on Combustion Volume One.

DOI: 10.7795/810.20200724

Understanding the role of thermal radiation in dust flame propagation

Christophe Proust [a,b], Rim Ben Moussa[c]

E-mail: *christophe.proust@ineris.fr*

[a] Institut National de l'Environnement Industriel et des Risques, Parc Technologique ALATA, BP 2, 60550 Verneuil-en-Halatte, France
[b] Sorbonne Universités, UTC-TIMR, 1 rue Dr Schweitzer, 60200 Compiègne, France
[c] Université Paris-Est Créteil Val de Marne, UPEC-IUT de Créteil-Vitry, Bât. L1B, 61avenue du Général de Gaulle, 94010 Créteil Cedex, France

Abstract

The role of thermal radiation in premixed flame propagation has been a matter of debate for decades. And it is not only a challenging scientific point, it has significant practical implications. For instance, a proposed explanation of the Buncefield explosion (*HSL, 2009*) was tiny particles were raised by the blast and promoted flame acceleration through enhanced heat exchanges by thermal radiation through the flame front. In dust explosion protection, the flame is implicitly supposed to propagate like a in a gaseous mixtures but if it happens that thermal radiation is dominant for some dusts, many aspects concerning the way to mitigate the explosions for those particular dusts would need to be revised.

The present research team (Ben Moussa et al., 2013, 2017; Proust et al., 2017a, 2017b) and another one (Julien et al., 2015) have been working on this subject for some time. The scientific problem was settled and a significant experimental effort was done. It was shown that thermal radiation could accelerates flames possibly to a considerable extent but without any firm confirmation.

In the present paper a numerical modelling of this problem is proposed to help understanding the physics of the flames seeded with particles and especially aluminum dust flames. The code uses the discrete element method and was developed from scratch over the last years. Some information to understand how the code work is provided into the paper and the results are compared to the experiments. From this comparison it can be concluded that thermal radiation is readily capable of strongly accelerating dust flames depending on the experimental conditions. Large scale experiments are now needed which however could be complicated to perform.

Keywords: *aluminium dust explosion, thermal radiation, dust flame propagation*

1. Introduction

The role of thermal radiation in premixed flame propagation has been a matter of debate for decades. And it is not only a challenging scientific point, it has significant practical implications. For instance, a proposed explanation of the Buncefield explosion (*HSL, 2009*) was tiny particles were raised by the blast and promoted flame acceleration through enhanced heat exchanges by thermal radiation through the flame front. In dust explosion protection, the flame is implicitly supposed to propagate like a in a gaseous mixtures but if it happens that thermal radiation is dominant for some dusts, many aspects concerning the way to mitigate the explosions for those particular dusts would need to be revised.

DOI: 10.7795/810.20200724

Ben Moussa et al. (2015, 2017) and Liberman et al. (2015) claim that heat radiation enhanced flame propagation is possible especially for high temperature burning metal particles (like aluminium) : hot burnt particles in the products produce backwards heat radiation towards the cold reactants, preheat them and promotes burning . Liberman claims that very large flame acceleration may be possible.

Unfortunately, an analytical appraisal is possible only under very strong assumptions like infinitely fast combustion and/or Beer-Lambert model for radiative transfers (Ben Moussa et al., 2017; Deshaies et al., 1985; Liberman, 2015; Bidabadi et al., 2013). As shown elsewhere (Proust et al., 2017), the later assumption is not valid so that a representative theoretical analysis remains difficult.

In addition, experimental evidence is clearly still lacking. Recently Proust et al. (2017a, 2017b) showed new results aiming at illustrating the potential flame propagation promoting effect of thermal radiation and at providing measurements strategies to highlight the underlying complicated physics.

In this communication, after recalling some recent experimental data on the subject, the authors investigate the phenomenology using an accurate modelling tool based on the discrete element method. The model compares very well with experimental results. It is shown that heat radiation can greatly promote flame propagation under certain conditions.

2. Some experimental evidence

Experiments were done using the flame propagation tube (fig. 1) already used in several studies (for instance in Proust, 2006). The experimental chamber is a vertical tube (length 1.5 m and diameter 10 cm), filled with the dust cloud from the bottom using a fluidized bed device. The cloud is ignited (spark) at the bottom after having stopped the flow, shut the upper part of the tube (with a gate valve) and removed the suspension generator. The flame is then freely propagating upwards without being thrusted by the expansion of the burnt products which are vented out through the open end. The dust concentration is controlled by weighting the dust suspension generator before and after the tests and by measuring the volume of the gas.

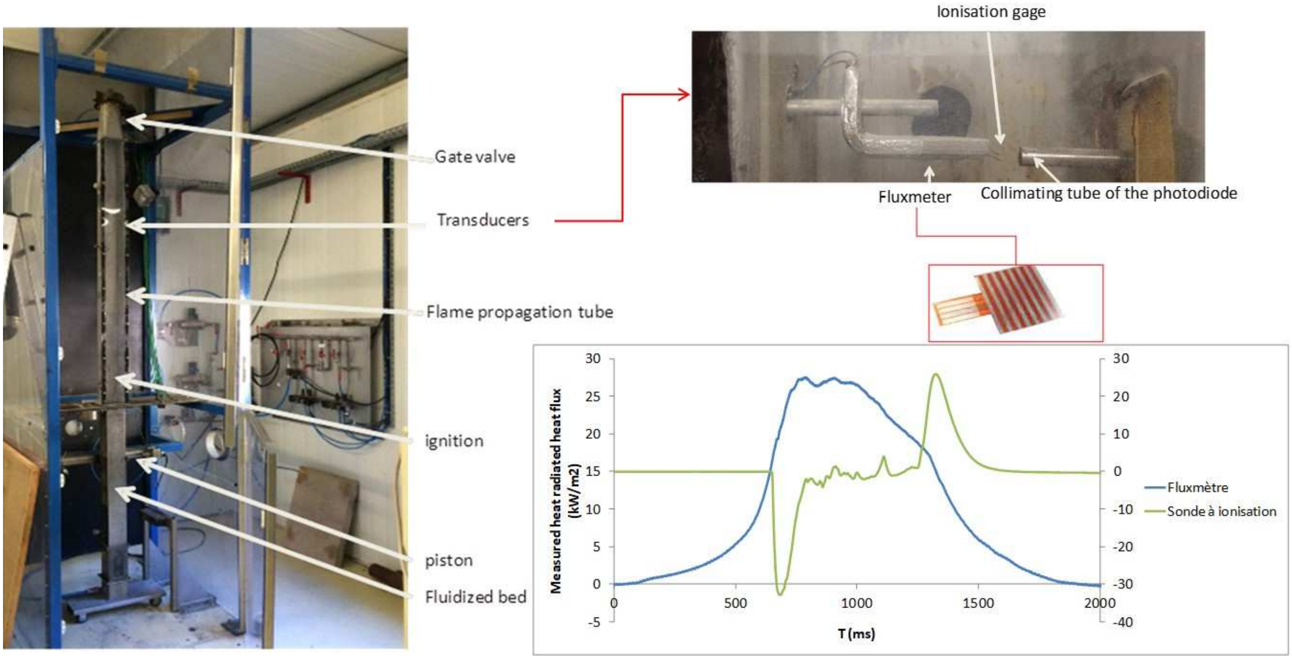

Fig. 1. Experimental setup and heat flux-ionisation gage signal for a stoichiometric CH_4-air flame

DOI: 10.7795/810.20200724

High speed video was used to obtain an accurate measurement of the flame speed and of the flame area. From this, the laminar burning velocity was obtained using the well-known "tube method" (Andrews and Bradley, 1972). Besides, a fast response fluxmeter was used (Captec technology :0.1 to 12 µm, 0.1 s response time, "looking" in the direction of the flame) coupled with an ionization gage. A typical example of the signals is shown on Fig.1 (bottom right) for a stoichiometric methane air flame (without particles). The heat flux is nearly 30 kW/m^2 (only 2-3% of the total heat release rate).

Experiments were performed using methane-air mixtures with and without particles in suspension (SiC, VMD=30 µm and SMD=15 µm). Tests were also done with aluminium dust air mixtures (VMD=20 µm and SMD=10 µm).

SiC has a rather large absorption/emission coefficient (0.7). For small particle concentrations (below 150 g/m^3), the laminar burning velocity increases so as the radiated heat flux (Fig. 2) suggesting a link between both parameters. For larger particle concentrations, the laminar burning velocity drops.

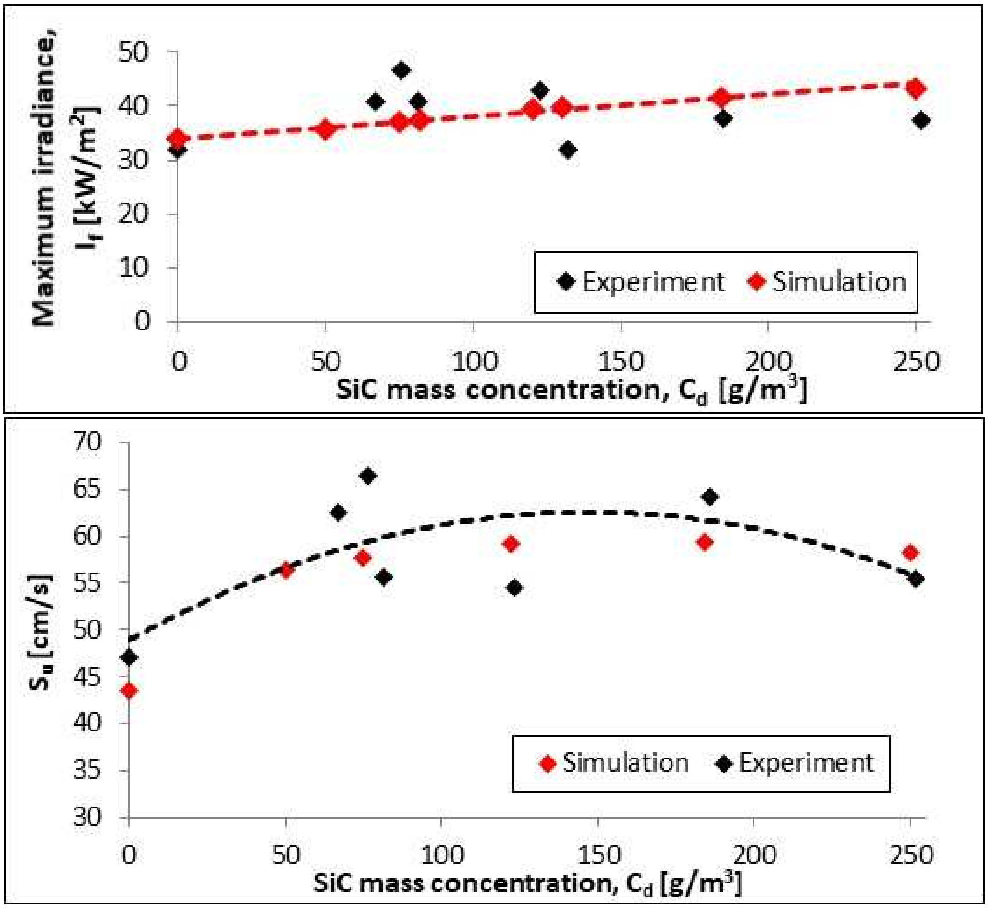

***Fig. 2:** methane air flame (stoichiometry) seeded with SiC particles*

Alumina and aluminium are poor emitters (emissivity 0.1 to 0.2) as compared with SiC but it can be expected that the much larger combustion temperature in the flame (3300°C as compared to 1900°C for methane air flames) would more than compensate the lower emissivity.

Tests were performed with aluminium dust air mixture at varying dust concentrations (Fig. 3). When the concentration of dust is low (below 500 g/m^3), the flame speed reaches a constant value, 0.4 m/s at 80 g/m^3, 0.7 m/s at 350 g/m^3, suggesting a burning velocity on the order of 0.3 m/s. But above a certain concentration threshold (above 500 g/m^3), a tremendous flame acceleration is observed : the flame speed increases from a few m/s in the ignition zone up to 50 m/s after one meter of propagation. The experimental device was significantly impaired preventing further testing.

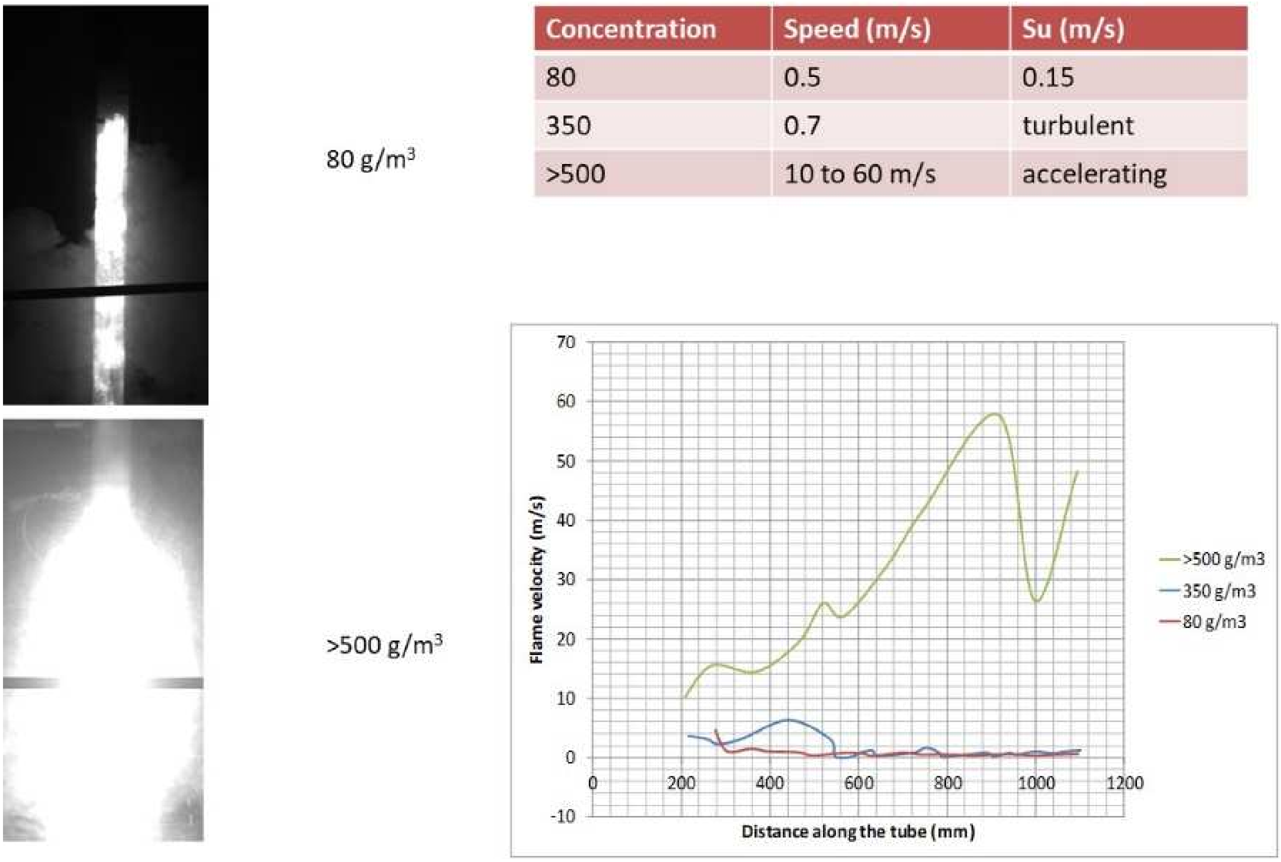

Concentration	Speed (m/s)	Su (m/s)
80	0.5	0.15
350	0.7	turbulent
>500	10 to 60 m/s	accelerating

Fig. 3 : self-acceleration of flames propagating in an aluminium dust-air cloud

3. Numerical tool (RADIAN)

The present experimental data suggest that heat radiation transfer through the flame may promote flame propagation possibly with a strong acceleration, as suggested by Liberman (2015), but a strong phenomenological approach is needed.

But many complex and non-linear phenomena intervene (combustion, heat transfer by conduction between phases, heat transfer by thermal radiation between particles, …) so that a complete analytical approach remains difficult without simplifying assumptions.

To preserve the predictive capability of the mode,l integrating most of the non-linear phenomena listed above, a Discrete Element Method (Cundall and Strack, 1983) was implemented. With this technique, the detailed mechanical interactions between the particles ("discrete elements") and between the particles and the boundaries can be described in detail. Originally, this modelling technique was developed to better represent granular flows (Munjiza and Cleary, 2009) and mechanical contacts (Nguyen et al., 2008a). Heat transfer was introduced as a natural expansion of the DEM principles (Nguyen et al., 2008b). More recently a coupling between CFD (Computational Fluid Dynamics) and DEM was established (Zhong et al., 2016) to better describe fluidized beds.

In the present situation, an accurate representation of the physics is looked for, at the expenses of the industrial representativity if needed. The interactions between the phases need to be finely described. The following assumptions (Ben Moussa, 2017) were made:

- The particles are spherical, homogeneous and monodisperse;
- The gaseous reactants are transparent to heat radiation (but not the products);
- The gaseous reaction is described using a one-step global reaction (Coffee et al., 1983);
- The combustion of the aluminium particles is described using an experimental “d^2 law “ (Ben Moussa et al., 2007);
- No velocity sliding between the phases.

Otherwise it was shown that, for particle sizes and concentrations under consideration (below 100 µm and below 10 kg/m^3), multiple scattering of the thermal radiation could be ignored, that the temperature inside the particles is homogeneous and that a Nüsselt number of 2 was a very good approximation to calculate gas-particle heat transfer. Since the particles are far from each other (10 diameters), each particle appears as a “point source” to its neighbouring particles. The point source model was thus implemented in which the Mie theory (van de Hulst, 1981) was incorporated to calculate the absorption, emission and scattering coefficients of the thermal radiation (which depend on the angle of the incident light) providing the most accurate and general description. The obscuration effect by the particles located between a source and a target is incorporated.

A tricky point is the simulation of the thermal radiation emission by the burned gases containing radiative species like water and carbon dioxide. From the work of people like Hottel and Sarofim (1967), it is possible to calculate the emissivity of a given volume of gas at a uniform temperature. In the present context, the burnt gases were discretized in small spheres in contact with each other. By trial and error, it was found that the maximum radiated heat flux was constant when the “gaseous” particles are smaller than 50 µm.

Four equations are solved simultaneously :

- The 3D transient equation of heat transfer in the gaseous phase with the one step combustion source term of Coffee, with the convective exchange with the particles and with the thermal radiation sink of the gaseous emitting species (CO2, H2O);
- The heat balance equation for each particle accounting for the net heat radiation flux (emission/absorption) with the solid and gaseous particles, for convective heat exchange with the gas phase and for combustion (“d^2 law “);
- The radiation exchange between solid particles using the DEM methodology (the “connectivity matrix”) and the point source approximation;
- The radiation exchange between “gaseous” particles using the DEM methodology and the point source approximation.

An explicit finite difference scheme is applied on a regular mesh using a small enough Fourier number to ensure the convergence (1/6). The particles are randomly distributed through the mesh. The cell size is chosen so that the various scales of the flame propagation can be represented. It was shown that the results converge with a cell size on the order of 10^{-6} m and a time step of 10^{-7} s. In practise, not more than one particle could be present in a cell.

A representation of the "gaseous particles" of the burnt gases, of the dust particles and of the mesh is shown on Fig. 4. To fully compute a propagation in the experimental conditions above requires a week on a powerful workstation. The details of the mathematics and the step by step validation procedure are out of the scope of the present paper.

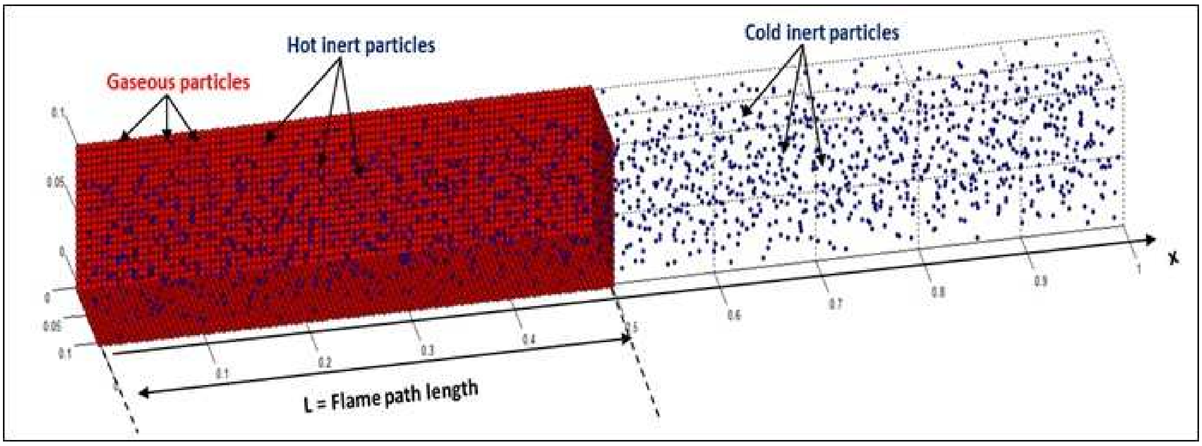

***Fig. 4 :** example of the discretization/repartition of dust particles to compute a flame propagating in a methane-air mixture seeded with inert SiC particles.*

4. Results

Preliminary results were obtained for methane air flames (without dust – Fig. 5) and for aluminium dust air flames (Fig. 6) and are compared to data from the literature. For aluminium dust air flames, since experimental results were obtained using very small-scale apparatuses (much smaller that the absorption length), thermal radiation exchanges were neglected to speed up the simulations. A good agreement is found comforting the usage of the tool.

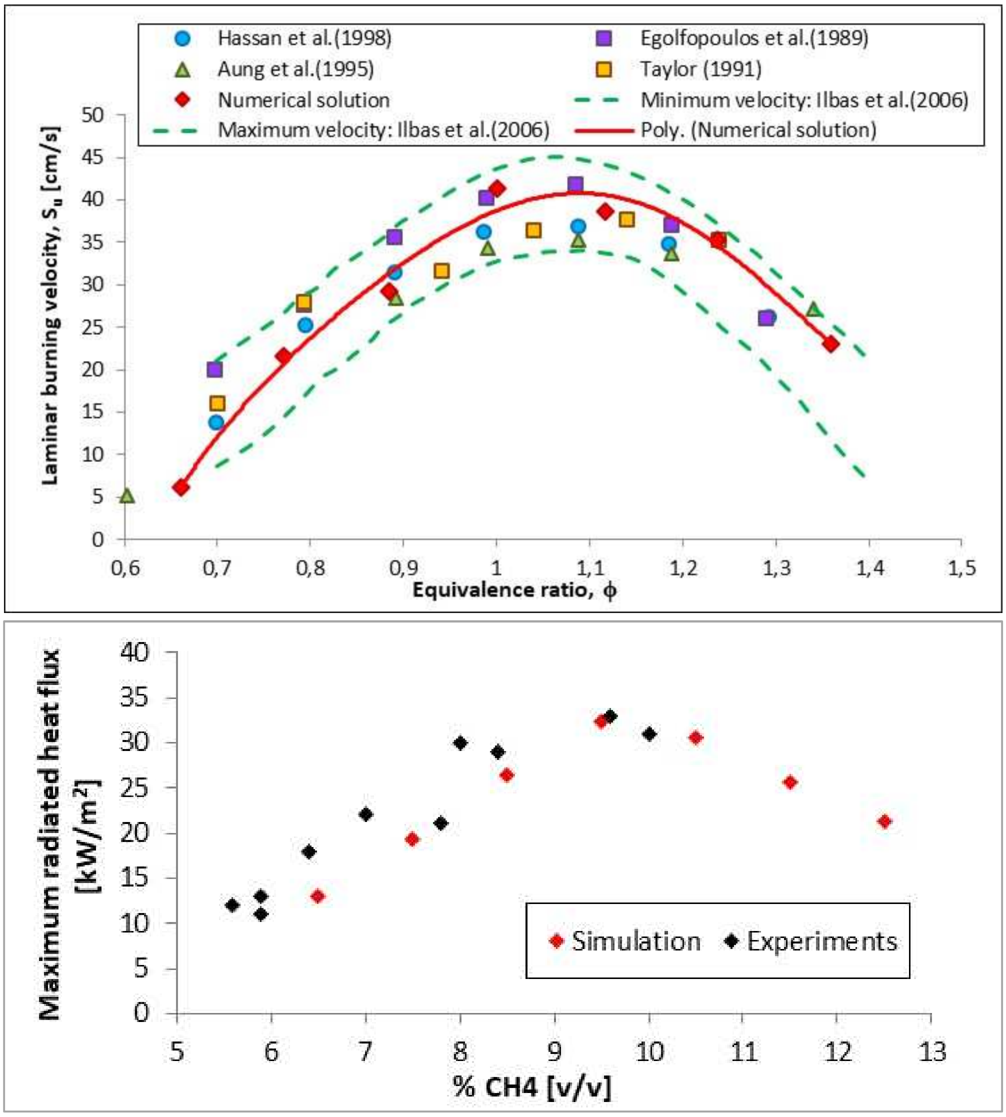

***Fig. 5** : Laminar burning velocity in methane air mixtures and maximum heat radiated flux*

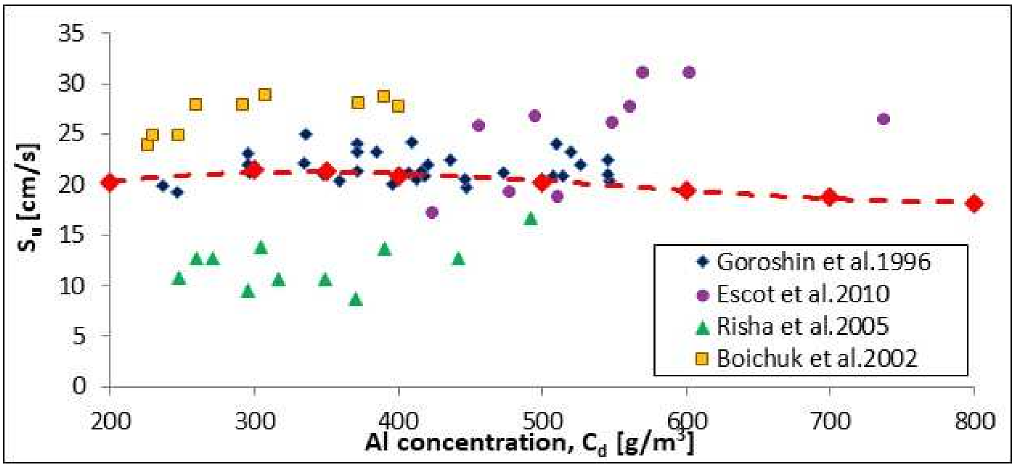

***Fig. 6** : Laminar burning velocity in aluminium dust air mixtures (very small scale)*

The simulations were also done to compare with the experimental data presented in section 2. The evolution of the thermal radiated flux in front of the burning zone is shown on Fig. 7 for a stoichiometric methane-air seeded with SiC particles. The agreement with the experiments is excellent. It may look surprising that the diffusion of the thermal radiation ahead of the flame front hardly depends on the mass particle concentration. This is due to the fact that the geometrical attenuation of the heat flux (proportional to the square of the distance to the emitter in the point source approximation) is much larger than the obscuration by the particles located between the emitter and the receiver. This explains why the Beer-Lambert's law cannot apply (at least for industrial configurations).

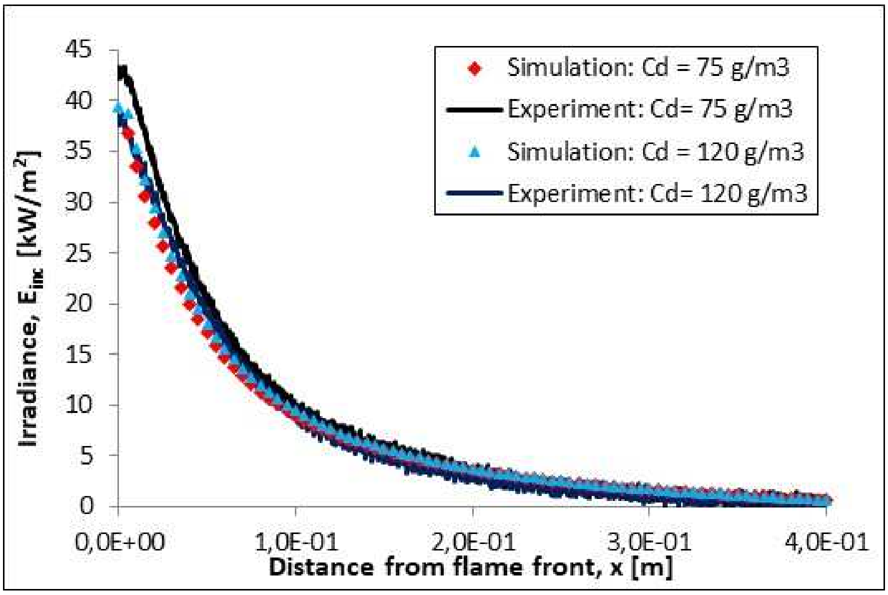

***Fig. 7** : Thermally radiated flux ahead of the burning zone of a stoichiometric methane air flame seeded with SiC particles.*

On Fig. 2 of section 2, the simulated maximum heat fluxes and laminar burning velocities are plotted together with the experimental results showing also a good agreement. The interpretation suggested by the simulations is the following. The thermally radiated flux is absorbed by the particles ahead of the flame which induces a heat up of the reactants amounting of few tens of degrees. This should favour the gaseous reaction of combustion and should accelerate the flame as shown by Joulin (1987). But simultaneously, heat is extracted by the particles from the burnt side of the flame and radiated away which is a loss for the flame and will reduce the burning velocity. So, there should be a maximum in the burning velocity curve as function of the mass particle concentration.

Similar simulations were performed for aluminium dust air flames.

First, a marked increase in irradiance with the particle mass concentration is observed (Fig. 8). This is due to the significant increase in the combustion temperature between the flammability limit conditions (2000°K at 70 g/m^3) and the stoichiometric conditions (3500°K at 300 g/m^3). The combustion temperature stays close to 3500°K up to a mass particle concentration of 500 g/m^3 (Ben Moussa et al., 2017). Experiments did not provide much information about the radiated heat flux (because of very harsh conditions) but about 20 kW/m^2 was measured at about 150 g/m^3 which is not in disagreement with the simulations.

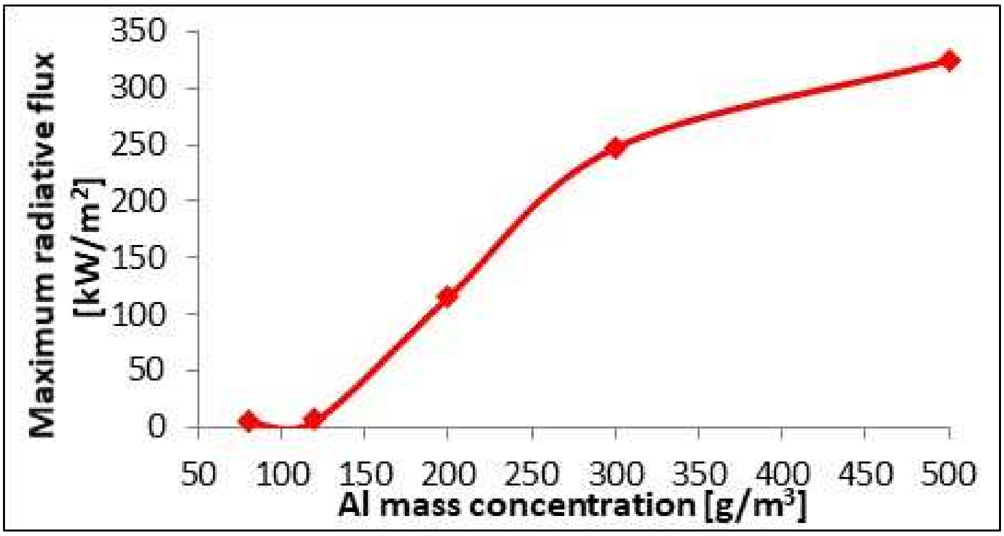

Fig. 8 : *Simulated maximum irradiance versus Al mass concentration*

The simulations also show that for mass particle concentrations smaller than 450 g/m^3, the burning velocity is constant (Fig. 9). Above, the burning velocity increases dramatically. At 700 g/m^3, the burning velocity raises by 1.5 m/s over a distance of 0.08m. All of this is in reasonable agreement with the experiments.

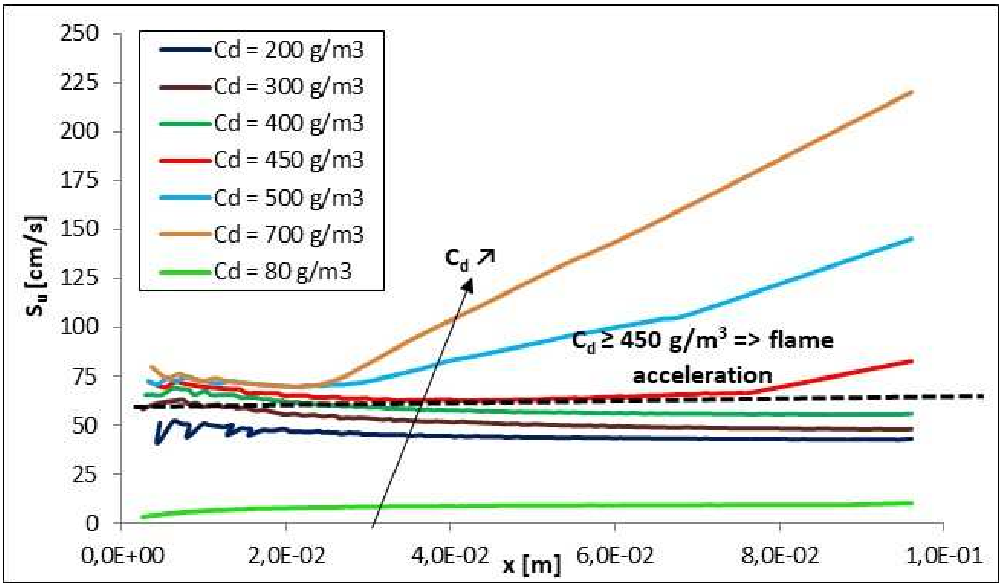

Fig. 9 : *Burning velocity VS distance across the combustion tube for different Al mass concentrations*

Further information about the structure of the flame front can be found in Fig. 10 for non- accelerating flames and in Fig. 11 for accelerating flames.

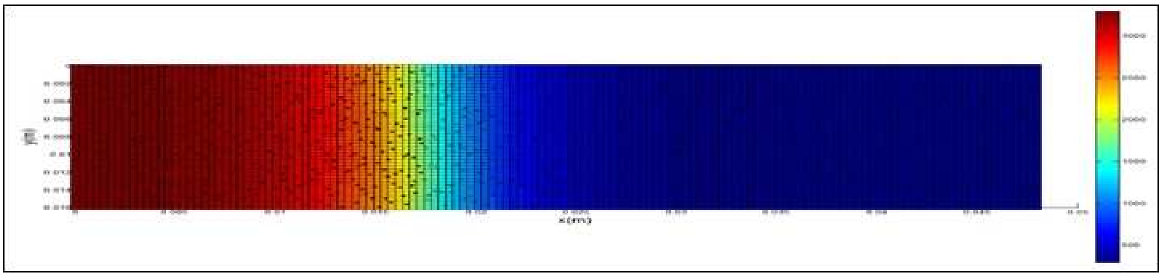

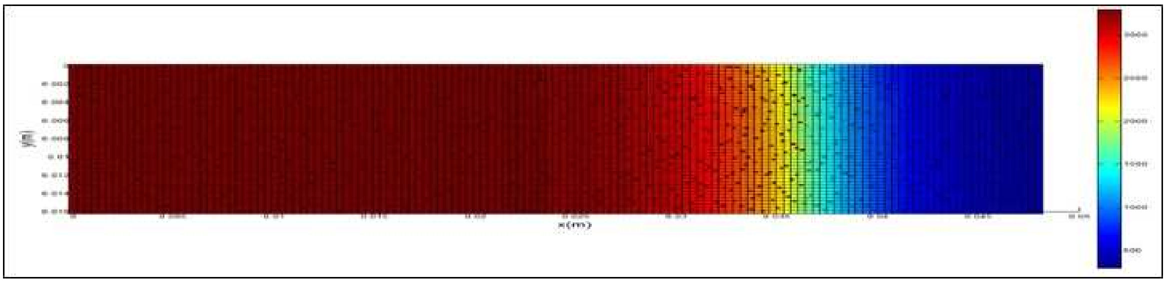

***Fig. 10**: Zoom on temperature field at two different instants, Al dust-air flame, C_d = 80 g/m^3*

In the first case (of non-accelerating flames), the structure of the front does not change and a representative flame thickness is some mm (3 mm between isotherms 1500°K and 2500°K for instance). This is a typical heat conduction/reaction flame front.

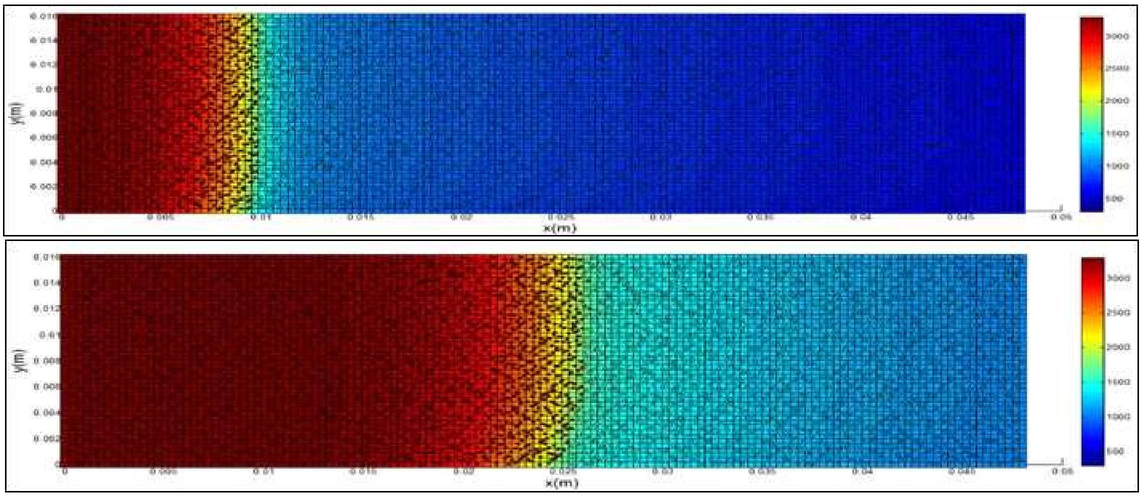

***Fig. 11:** Zoom on temperature field, Al dust-air flame, C_d = 500 g/m^3*

In the second case (of an accelerating flame), the flame thermal thickness evolves rapidly during the propagation : 3mm at the beginning of the propagation between the isotherms 1500 K-2500 K and 10 mm after 20 cm of flame propagation.

For our purpose of clarifying the role of the thermal radiation transfer in the aluminum dust flame propagation process, it might be sufficient to compare the amounts of heat absorbed by the reactants (up to the ignition temperature) by thermal conduction and by thermal radiation. The former heat transfer mechanism is always at work even in non-radiating flames.

To estimate the thermal conduction heat flux at the ignition point (1750°K in the present situation, Ben Moussa et al., 2007), the temperature maps obtained with RADIAN in situations where the irradiance is negligible were used. The temperature gradient at the ignition point is on the order of 250 000 K/m. Multiplying it by the local thermal conductivity of the gas mixture (0.1 W/m.K) provides the thermal conduction heat flux at the ignition surface : 25 kW/m^2. This should normally be the maximum heat conduction flux through the flame.

The thermally radiated heat flux ahead of the combustion zone can also be extracted from the simulations. The results are given in Fig. 12 were the origin of the abscissae is the ignition point.

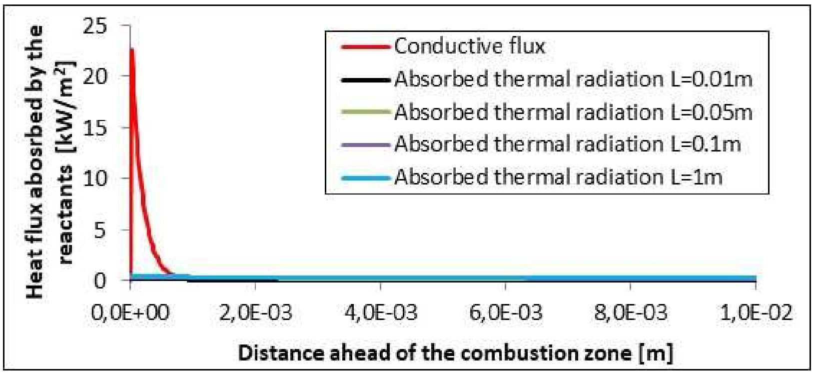

(a) $C_d = 80$ g/m^3

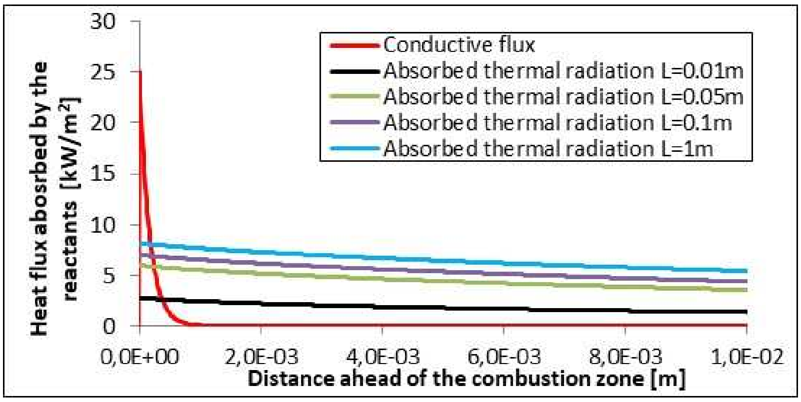

(b) $C_d = 200$ g/m^3

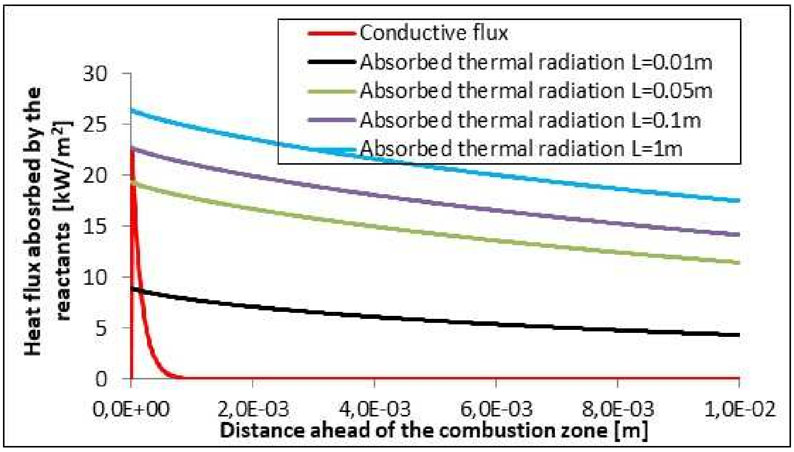

(c) $C_d = 300$ g/m^3

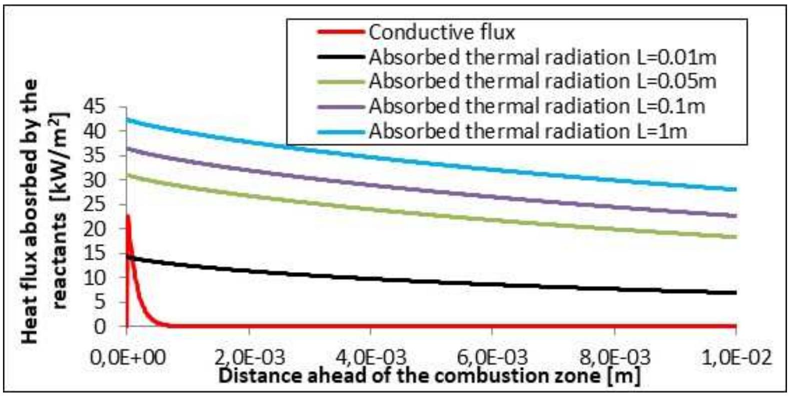

(d) $C_d = 400$ g/m^3

Fig. 12: *Comparison of the heat conductive flux and thermal radiation flux absorbed by the reactants (aluminum dust-air cloud) ahead of the ignition surface for several mass particle concentrations (L is the "flame path length" or equivalently the length of the burnt products column)*

It appears immediately that for concentrations below 200 g/m^3, the reactants are mainly heated up to the ignition point by the conductive thermal transfer. The burning regime then resembles to the standard "Le Chatelier" concept. For large enough concentrations, above 400 g/m^3, the thermal radiation flux absorbed by the reactant is well above that due to the heat conduction in all the relevant temperature domain (from ambient temperature to the ignition point). Note that this is true only when the burnt products column is large enough, typically larger than 1 to 5cm. When this occurs, since the heat flux is now larger, the laminar burning velocity must increase to keep the balance of energy through the flame:

Because of this, and because the amount of thermal energy transferred by radiation to the reactants increases with the length of the burnt product column, the flame speed is expected to increase in proportion to the propagated distance. For 400 g/m^3 dust concentration, the radiated heat flux exceeds that of the thermal conduction some cms after the start of the propagation triggering the acceleration. This observation seems in line with the simulations but also with the experimental results.

Although not included in the present paper, a very significant influence of the particle size is expected.

5. Conclusions

In the present work, a new simulation code based one the discrete element method is presented to interpret experiments perform to highlight the potential influence of thermal radiation on dust-gas flame propagation.

Although bounded by some simplifying assumption, the code (RADIAN) is close to a direct numerical tool.

Methane-air flames seeded with inert SiC particles and aluminium dust-air mixtures were studied. The simulation seems to reproduce very well the experimental results. In particular, thermal radiation may add up to the flame propagation, in the first situation, or may completely dominate in the second one.

The present, still too limited, simulations do not answer the question of the maximum burning velocity and do not give information about the behaviour of the flame towards disturbances. Additional work is needed. Nonetheless, the present information may be enough to propose in the future a semi-analytical model enabling a phenomenological analysis of flames dominated by thermal radiation.

References

HSL, (2009). Research Report RR718.

Andrews G.E, Bradley D., 1972. Determination of laminar burning velocities : a critical review. Comb. and Flame, 18.

Aung, K. T., Tseng, L. K., Ismail, L. K. & Faeth, G. M., 1995. Laminar burning velocities and Markstein numbers of hydrocarbon/air flames. Combustion and Flame, 102.

Ben Moussa R., 2017. Etude de la contribution des échanges thermiques radiatifs aux processus de propagation des flammes de poussières : application aux explosions de poussières d'aluminium, PhD thesis, Université de Technologie de Compiègne-France, defended on 21st dec 2017.

Ben Moussa R, Guessasma M, Proust C, Saleh K, Fortin J., 2015. Thermal radiation contribution to metal dust explosions. Procedia Engineering, 102.

Ben Moussa R, Proust C, Guessasma M, Saleh K, Fortin J., 2017. Physical mechanisms involved into the flame propagation process through aluminum dust-air cloud: a review., Journal of Loss Prevention in the Process Industries, 45.

Bidabadi M., Zadsirjan S., Mostafavi S. A., 2013. Radiation heat transfer in transient dust cloud flame propagation. Journal of Loss Prevention in the Process Industries, 26.

Boichuk L. V., Shevchuk V. G., Shvets A. I., 2002. Flame Propagation in Two-Component Aluminum–Boron Gas Suspensions. Combustion, Explosion and Shock Waves; 38.

Coffee, T. P., Kotlar, A. J., Miller, A. S., 1983. The overall reaction concept in premixed, laminar, steady-state flames. I. Stoichiometries. Combustion and Flame, 54.

Cundall P.A., Strack O.D.L., 1983. Modeling of Microscopic Mechanisms in Granular Material. Studies in Applied Mechanics, 7.

Deshaies B., Joulin G., 1985. Radiative transfer as a propagation mechanism for rich flames of reactive suspensions. SIAM J. of Applied Math., 46.

Escot-Bocanegra P., Davidenko D., Sarou-Kanian V., Chauveau C., Gökal I., 2010. Experimental and numerical studies on the burning of aluminum micro and nanoparticle clouds in air. Experimental Thermal and Fluid Science, 34.

Egolfopulos, F. N., Cho, P., Law, C. K., 1989. Laminar flame speeds of methane-air mixtures under reduced and elevated pressures. Combustion and Flame, Volume 76, p. 375

Goroshin S., Fomenko I., Lee J. H. S., 1996. Burning velocities in fuel-rich aluminum dust clouds. Twenty-Sixth Symposium (International) on Combustion/ The Combustion Institute.

Hassan M. I., Aung K. T., Faeth G. M., 1998. Measured and Predicted Properties of Laminar Premixed Methane/Air Flames at Various Pressures. Combustion and Flame, 115.

Hottel, H. C., Sarofim, A. F., 1967. Radiative Transfer. New York: McGraw-Hill.

Ilbas M., Crayford A.P., Yılmaz İ., Bowen P.J., Syred N., 2006. Laminar-burning velocities of hydrogen–air and hydrogen–methane–air mixtures: An experimental study. International Journal of Hydrogen Energy, 31.

Joulin G., 1987. Temperature lags and radiative transfer in particle-laden gaseous flames part I:Steady planar fronts. Combustion Science and Technology*,* 52.

Julien D., J. Vickery J., S. Whiteley S., A. Wright A., S. Goroshin S., Bergthorson J.M., Frost D.L., 2015. Effect of scale on freely propagating flames in aluminum dust clouds. Journal of Loss Prevention in the Process Industries, 36.

Liberman M.A., Ivanov M. F., Kiverin A.D., 2015. Effects of thermal radiation heat transfer on flame acceleration and transition to detonation in particle-cloud hydrogen flames. Journal of Loss Prevention in the Process Industries, 38.

Munjiza, A. and Cleary, P., 2009. Industrial particle flow modelling using discrete element method. Engineering Computations, 26.

Proust C. (2006). Flame propagation and combustion in some dust-air mixtures Journal of Loss Prevention in the Process Industries, 19.

Proust C, Ben Moussa R, Guessasma M, Saleh K, Fortin J. (2017a). Thermal radiation in dust flame propagation. Journal of Loss Prevention in the Process Industries, 49.

Proust C, Ben Moussa R, Guessasma M, Saleh K, Fortin J. (2017b). Potential accelerating effect of thermal radiation in dust flame propagation : some experimental evidence. The 26th ICDERS, july 30th-August 4th 2017, Boston, USA.

Risha G., Son S.F., Yetter R.A., Yang V., Tappan B.C., 2007. Combustion of nano-aluminum and liquid water. Proceedings of the Combustion Institute, 31.

Taylor, S. C., 1991. Burning velocity and the influence of flame stretch. University of Leeds: PhD. Thesis

Nguyen V.-D, Fortin J., Guessasma M., Bellenger E., Coorevits P., 2008a. Modelling of energy dissipation generated by friction in granular flows by using DEM. The Sixth International Conference on Engineering Computational Technology Athens, Greece from 2 to 5 September 2008.

Nguyen V.D., Fortin J., Guessasma M., Bellenger E., Cogné C., 2008b. Heat transfer modeling by Discrete Element Method. Journal of the Mechanics of Materials and Structures, 111-113.

Zhong W., Yu A., Liu X., Tong Z., Zhang H. 2016. DEM/CFD-DEM Modelling of Non-spherical Particulate Systems: Theoretical Developments and Applications. Powder Technology, 302.

DOI: 10.7795/810.20200724

Impact of photovoltaic power plants on far-field effects of UVCEs

Guillaume Lecocq [a], Antoine Dutertre [b] & Emmanuel Leprette [a]

E-mail: *guillaume.lecocq@ineris.fr*

[a] Institut National de l'Environnement Industriel et des Risques, Parc Technologique ALATA, BP 2, 60550 Verneuil-en-Halatte, France
[b] TOTAL S.A., 2 place Jean Millier, La Défense 6, 92400 Courbevoie, France

Abstract

Photovoltaic power stations are developing worldwide as they emit no greenhouse gases while producing electricity. In France, industries such as Total plan to install such stations in fields surrounding their chemical and refining plants. The risk analyses performed for these plants often highlighted Unconfined Vapor Cloud Explosions scenarios, related to heavy gases releases, for which characteristic overpressure effect distances were computed

The present work aims at quantifying the impact of the presence of a photovoltaic power station in a potential flammable cloud. It is nevertheless limited to a station geometry provided by Total.

The problem is not straightforward as two main physical trends appear: flame acceleration due to panels obstruction and flame extinction when the flame reaches the top of the flammable cloud. It has first to be determined if explosion runaway is possible, this one due to the obstacles repetition on the flame path. Then, characteristic overpressure effects distances can be computed for photovoltaic power plants of any size.

To this goal, a CFD-based method is proposed and detailed. The open-source CFD code OpenFoam is used as well as phenomenological considerations for computing characteristic overpressure effects distances.

Keywords: *photovoltaic power plants, premixed gaseous flame propagation, overpressure effects distances, CFD*

1. Introduction

Some industries such as Total own large lands surrounding their production plants such as refineries. They are often unused and free of any building and therefore perfect candidates for installing photovoltaic power plants. For some of these, scenarios of Unconfined Vapor Cloud Explosions (UVCE) were identified during risk analyses. This kind of phenomenon is related to the potential release of flammable products followed by an ignition of the generated flammable cloud. In the French regulation, the UVCE overpressure effects are quantified by the distances at which the characteristic thresholds of 200, 140, 50 mbar are reached. These distances give regulatory perimeters which constrain land-use planning. Installing photovoltaic power plants requires to check if the pre-existing overpressure effects distances would be significantly modified by the presence of rows of panels in the flammable cloud.

A study co-funded by Total and INERIS was carried out in order to develop a method for quantifying overpressure effects related to the explosion of a flammable cloud covering photovoltaic panels representative of the ones that could be installed by Total around its production plants. This partnership enabled INERIS to gain expertise for modelling dangerous phenomena appearing with the development of photovoltaic power plants and Total to develop a philosophy for their safe positioning. The paper details some elements of the study.

2. Scenario and problem description

Scenarios of massive releases of heavy hydrocarbons such as propane or equivalent medium reactivity gases could be identified for industrial plants. Due to buoyancy effects, such products when mixed with air generate "flat" flammable clouds *ie* with a maximum height about 3-4 m and a length in order of hundreds of meters. The flammable cloud size is limited by the iso-surface with a concentration that equals the lower flammability limit.

Current projects plan the installation of photovoltaic power plants around some industrial plants. A design example was supplied by Total and is shown in the Figure below. In this case, a rotation of the panels is possible. For this work, two bounding cases were considered: parallel to the ground or inclined with an angle of 45° as in Fig. 1. The panels width and the distance between the rotation point and the ground are about a few meters. A few meters also separate the panels rows.

Fig. 1. *Cross-section of a photovoltaic power plant designed by Total*

The explosion scenario deals with a flammable cloud that can theoretically cover dozens of rows of panels at full height. Before any modelling, the regarded phenomenology should be analysed.

According to experimental works, flat flammable clouds generate slow flames (*ie* the flame speed is about a few m/s) when there is no obstruction in the flammable zone (Zeeuwen, 1983). Furthermore, according to theoretical works (Daubech, 2016), two explosion phases should be distinguished in the case of an ignition source in the flammable zone: a spherical or hemispherical phase during which the burnt gases expansion contributes to the flame propagation followed by an azimuthal phase during which this effect is lost. Two theoretical expressions were derived from the work of Daubech et al. for quantifying the far-field pressure generated by each phase. In the case of flames with a constant speed, they write:

$$\text{Eq. (1) } \Delta p(r,t) \approx \rho_{atm} \frac{4H}{r}\ \tau(\tau-1)V_f^2$$

$$\text{Eq. (2) } \Delta p(r,t) \approx \rho_{atm} \frac{2H}{r}\ (\tau-1)V_f^2$$

ρ_{atm} is the atmospheric volume mass, H is the flammable cloud height, τ is the burnt gases expansion rate and $V_f$is the constant flame speed. This set of equations highlights that far from the flame the azimuthal phase pressure is about 2τ times lower than the hemispherical phase pressure.

If there are repeated obstacles in the flat cloud, it can be questioned if the relative importance of each phase in the pressure generation process is kept. In case of ignition in the power plant covered with a flammable cloud, the flame is first spherical, then interacts with the closest panel or panels leading to a distortion which is prone to increase the burned gases production rate. The flame at a given moment reaches the lower flammable concentration at the top of the cloud and a part of the flame front quenches. This latter phenomenon induces a progressive venting of the burnt gases which contributes to slow down the flame whereas in the same time, the flame keeps on propagating in the direction parallel to the ground. During the propagation across the rows of panels, there is a permanent competition between an increase in pressure generation due to flame distortion and venting due to a a flame reaching the flammable cloud limits.

DOI: 10.7795/810.20200724

Previous experiments showed the separation distance between obstacles could be a key parameter for pressure effects (Van der Berg, 2005). If the obstacles are too close, there can be a continuous acceleration from an obstacle to another leading to a runaway phenomenon. The maximum overpressure in the flammable cloud is then limited by the acceleration length for the flame *ie* the minimum length between the flammable cloud length and the photovoltaic power plant length. Both of them being about hundreds of meters, an explosion runaway cannot be excluded theoretically on this basis.

A practical consequence of the occurrence of such a phenomenon when quantifying the regulation overpressure effects distances is to account for all the flammable mass of the cloud and to assume maximum overpressure in the cloud about several bars. Such assumptions could lead to large overpressure effect distances and restrict the installation of photovoltaic plants.

A method has to be proposed to study the runaway risk and to quantify the regulation effects distances. In the current paper, a modelling approach was chosen.

3. A method mixing CFD and phenomenology

Modelling tools such as the CFD software FLACS (Hansen, 2010) were developed for addressing complex set-ups at the industrial scale. In short, it relies on a URANS approach for modelling turbulence and obstacles are partly resolved by the mesh. A sub-grid porosity accounts for unresolved obstacles. This porosity as well as other physical parameters were calibrated against a large number of explosion trials involving obstacles at large-scale.

This tool was first employed to get a first guess of the pressure effects related to a UVCE developing in a photovoltaic power plant. The related computations did not highlight a global flame acceleration phenomenon. The computed overpressure levels were not significant as they were lower than 20 mbar, except in a few points of the geometry. These punctual peaks dissipated in a few meters and had no effect on the global pressure field.

In order to confirm these results, another approach based on CFD is proposed for modelling a potential explosion in the photovoltaic power plant. For studying the risk of explosion runaway, there must be a few rows of photovoltaic panels in the computational domain whose topology should ideally be 3D. The computational domain has to be a few dozens of meters long in each direction. This first aspect if of importance as computation resources are limited. They will limit the minimum size of the cells of the mesh.

At the moment, it may appear tricky to choose a relevant set of physical sub-models when using CFD to account for large-scale explosions mechanisms. Even an explosion in a flat flame is complex as the following physical effects may appear: interaction of the flame with the wind, self-acceleration due to instabilities more or less pronounced with the fuel and local equivalence ratio and partly explained by non-unitary Lewis number and Markstein length effects. The latter physics requires a mesh fine enough to get a realistic flame thickness and a description of differential diffusion of species and temperature.

Adding obstacles in the cloud, other physical phenomena appear and have to be accounted for, especially if the solar panels rows are inclined: a Karman vortex street in the wake of obstacles, with a characteristic Reynolds number increasing as the flame approaches obstacles, an acceleration of the flame and the fresh gases in front of it between the ground and the bottom of the panels.

Concerning turbulence modelling, Large-Eddy Simulations are attractive as they tend to become the state-of-the-art for engineering problems and get more and more precise as the mesh is refined, limiting the modelled part. Nevertheless, the validity of sub-grid scale models for turbulence and flame/turbulence could be questioned for cells with a characteristic width of a dozens of centimeters. In engineering computations, the characteristic cell width is lower than a millimeter. Furthermore, even well-resolved middle-scale explosions showed a pressure field depending on the chosen turbulent/flame SGS model (Di Sarli, 2010, Quillatre, 2014). URANS modelling works were proposed for modelling a methane flame acceleration (Lecocq, 2019) in a 24-m long tube but there is no guarantee all the chosen parameters could be re-used at larger scale with a global 3D topology flame.

A modelling method grounded on CFD and phenomenological considerations is proposed and tested in what follows.

a. Modeling method

The current work does not deal with the flammable product dispersion and the flammable cloud generation. It focuses on the explosion stage only.

The 3D flame propagation is modelled with a CFD approach. The transport equations of pressure, momentum, energy, chemical species and progress variable are solved numerically by the OpenFoam code (Weller, 1998), version 5. The solver is compressible. The chemistry is addressed with a one-step reaction and only propane, oxygen, nitrogen, carbon dioxide and water mass fractions are transported. There is no turbulence model. The modelling mainly aims at obtaining a conservative wrinkling factor for the flame during its propagation.

A turbulent premixed flame can be modelled with a flame surface-density ($\bar{\Sigma}$) approach. This quantity is approximated as $\Xi|\nabla c|$, where Ξ is the wrinkling factor of the flame related to an increase of the un-resolved part of the flame surface and c is the progress variable. The chemical source terms appearing in the transport equations of the progress variable and chemical species mass fractions can be closed as (Lecocq, 2011):

$$\text{Eq. (3) } \rho\omega_c = \rho_u S_L \Xi|\nabla c|$$

$$\text{Eq. (4) } \rho\dot{\omega}_{Y_i} = \rho\omega_c(Y_i^b - Y_i^u)$$

Where ρ_u is the volume mass of the fresh gases, $S_L$is the laminar flame speed, Y_i^b (resp. Y_i^u) is the burnt (resp. fresh) gases mass fraction of the i$^{\text{th}}$ chemical species.

This model does not include differential diffusion between temperature and chemical species. If Ξ is set to 1, in case of ignition in a flammable medium at rest with an homogenous concentration, the model accounts for a spherical flame that propagates at a speed: burnt gases expansion rate times the laminar flame speed. Some un-resolved phenomena at grid scale can be included through modifications of the wrinkling factor.

According to some works (Daubech, 2016), a spherical flame propagation without obstacles can be analytically described. The flame speed V_{disf} can write as:

$$\text{Eq. (5) } V_{disf} = \tau V_f = \tau S_L \Xi_{\text{Total}}$$

Where τ is the burnt gases expansion rate and Ξ_{Total} is the wrinkling related to the wind and intrinsic flame instabilities. This latter wrinkling factor was written as: $\Xi_{\text{Total}} = \Xi_{\text{I}}\Xi_{\text{TW}}$ with Ξ_{I} the wrinkling related to instabilities solely and Ξ_{TW} the wrinkling related to the turbulence of the wind solely. This choice is cautious as recent works have shown at lab scale that depending of the flame position in the theoretical combustion diagram an effect was dominant on the other but there was no combination of the effects (Yang, 2018). For a propane flame, the asymptotic value of Ξ_{I} and predicted by theory, depends only on the burnt gases expansion rate and is about 3.5. The wind effect is computed with the Gülder correlation (Gülder, 1995) and an integral length scale for the atmospheric turbulence about 1 m and a fluctuating speed about 0.5 m leading to a value of 8 for Ξ_{TW}. Adding all these contributions, mathematically speaking by multiplying the wrinkling factors, the theoretical flame speed during the hemispherical phase of flame propagation is about 90 m/s.

Recent experimental works (Bauwens, 2015) gave for a stoichiometric spherical propane/air flame propagating on a length about 1 m, in a medium initially at rest, an increase of flame surface about 1.5 explained by Darrieus-Landau instabilities. In the target computation, the flame is interacting with photovoltaic panels roughly one meter after ignition. In order not to be too much conservative and

DOI: 10.7795/810.20200724

avoid artificial explosion runaway, in the following, Ξ_I is set to 1.5. The reference propane/air flame propagates at speed of 45 m/s when undergoing burnt gases expansion effects and 6 m/s when it is no longer the case. A case with propylene gives a minimum flame speed of 55 m/s and 7 m/s. The flame speeds for the spherical phases have the same order of magnitude as encountered with the propagation of a spherical stoichiometric hydrogen/air flame (Schneider, 1983) without wind effects. They are one order of magnitude greater than the ones measured in a propane/air explosion free of obstacles. Both observations mean the computed flame speeds remain conservative.

b. First tests

Free fields tests were performed with CFD in a 3D computational domain with 15 cm wide cells in the zone of interest (measured flame and pressure wave propagation). A flammable cloud at rest with a homogenous propane/air concentration was initialized, the height of the cloud being 4 m, the half-length of the cloud being 20 m. The wrinkling factor was tuned to get a minimum flame speed of 72 m/s during hemispherical phase. The computation was redone with another mesh made of 10 cm wide cells in the interest zone.

The results in terms of overpressure at ignition point and 30 m away, out of the flammable cloud are shown in Fig. 2. It can be seen that the same hemispherical phase is predicted at ignition point by both computations. Out of the flammable cloud, the same maximum overpressure is recovered. It means the wave propagation is weakly impacted by the mesh resolution. The azimuthal phase is nevertheless different in both cases: the maximum overpressure at ignition point is about 65 % higher with the fine mesh. Out of the flammable cloud, the same gap is retrieved. This difference between the two meshes is explained by a higher resolved flame wrinkling during the transition between the spherical and the azimuthal phase (Fig. 2b). It is explained by a limit of the proposed CFD model: the added wrinkling factor does not depend on the mesh size whereas if the mesh is refined, more wrinkling appears at the resolved level.

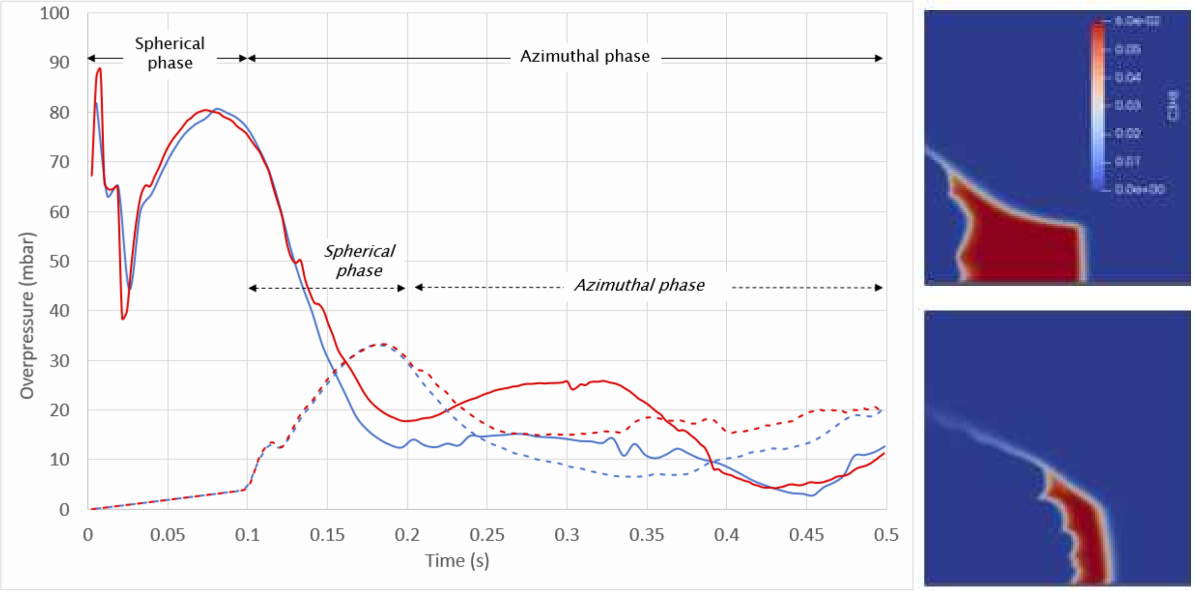

(a) ***(b)***

Fig. 2. a) *Computed pressure signals at ignition point (line) and 30 m from ignition point (dash line). Blue: reference mesh. Red: fine mesh.* ***b)*** *Propane mass fraction contours 300 ms after ignition. Top: reference mesh, bottom: fine mesh.*

The overpressure values can be compared with the theory. According to (Lannoy, 1989), for a constant flame speed flame with a flame speed lower than 120 m/s, overpressure in the burnt gases writes:

$$\text{Eq. (6) } \Delta p = \rho_{atm}\left(1-\frac{1}{\tau}\right)\left(\tau V_f\right)^2\frac{1}{2}\left(3-\frac{1}{\tau}\right)$$

For a flame propagating at 72 m/s, Eq. (6) gives 78 mbar whereas a value of 80 mbar was obtained with CFD. Eqs. (1) and (2) can be used to predict the overpressure field out of the flammable cloud. For a constant flame speed of 72 m/s (resp 9 m/s) during the hemispherical (azimuthal) flame propagation, 30 m away from ignition point, the maximum overpressure is 14 mbar (resp. 1 mbar). Both CFD computations predict larger values: the overestimation is about 100 % for the hemispherical phase and one order of magnitude for the azimuthal phase. The computation performed with a reference mesh being conservative when compared with theory, it is kept for the computations with a photovoltaic power plant.

4. CFD computations with a photovoltaic power plant

a. Parametric tests

The reference situation is the one of a stoichiometric propane/air cloud at rest covering the photovoltaic panels. Several parameters were of interest: the orientation of the photovoltaic panels (parallel to the ground or inclined), the separation distance between two rows, the height of the cloud and the reactivity of the cloud (propane/air or propylene/air mixture). The computations to be performed to investigate some trends are numerous. It was chosen to perform these computations with an assumption of a 2D-symmetry for a flame propagating perpendicularly to the rows. It implicitly means the flame is cylindrical and the width of the panels is infinite.

The cell width in these computations is 3 cm. When comparing the burnt gases pressure for a given flame speed with theory, the overestimation of the 2D mesh is about 100 %. The computations that follow give overpressures exceeding real ones but enable to identify the main trends, changing a parameter at a time. The criterion between two computations is the overpressure out of the flame. The Fig. 3 details through a zoom on the computational domain the location of main pressure probes relative to the flammable cloud and the photovoltaic panels.

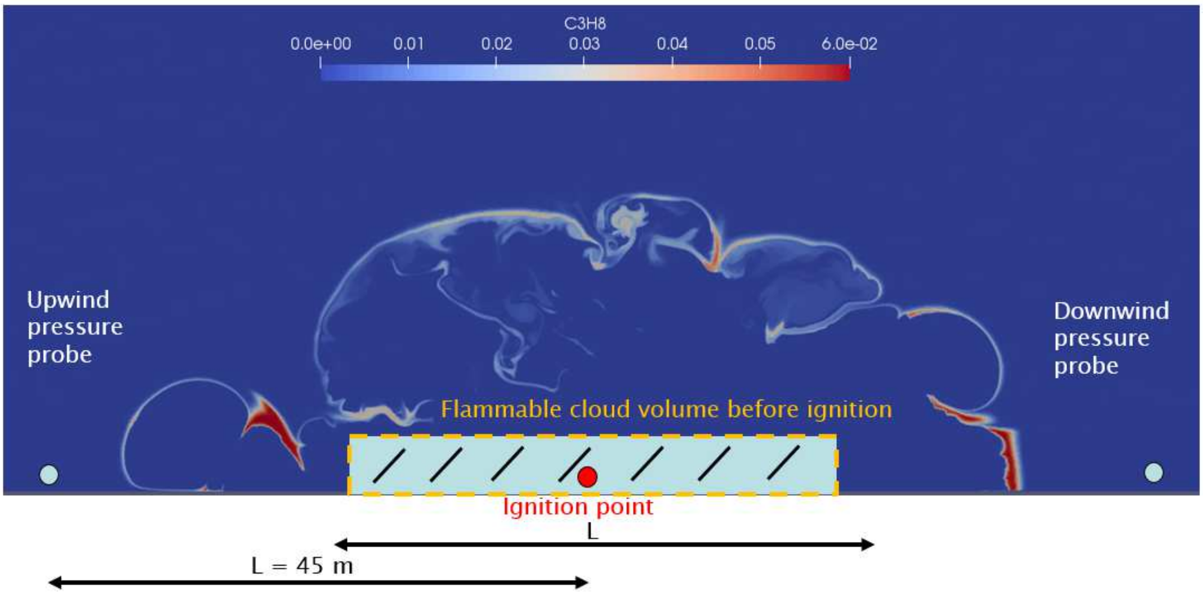

Fig. 3. Location of the pressure probes relative to the flammable cloud and the power plant.

In what follows, a 45 m/s (resp. 55 m/s) flame is a flame propagating with a speed of 45 m/s (resp. 55 m/s) during the hemispherical phase. Computations for a 55 m/s flame propagating in a power plant with either flat or inclined panels show that the far-field pressure effects are higher in the second case (Fig. 4). It tends to confirm that the obstruction and related flame acceleration have a stronger effect on the pressure field than the venting effect between two rows of panels. This result is coherent

DOI: 10.7795/810.20200724

with the experimental data of Zeeuwen (1983). A propane/air flame was propagating in a 25 m x 25 m array of regularly spaced vertical tubes with a diameter of 1 m below a full roof. In the array, despite the lack of venting at the roof a maximum pressure of 20 mbar was measured.

Another computation with inclined rows of panels highlights the stronger acceleration (Fig. 5) on a side of the power plant (towards the left in Fig. 3), giving an increase in overpressure about 50 % when compared with the other side.

A 55 m/s flame gives overpressure effects of the same order than a 45 m/s flame when it propagates in inclined rows of panels (Fig. 6). The increase in overpressure is nevertheless about 50 %.

The height of the cloud also plays a role in pressure effects. For half a cloud normally covering the power plant, the far-field pressure peak is about half the pressure peak obtained with a full height cloud (Fig. 7). The venting occurs earlier enabling to reduce pressure effects for the smallest cloud.

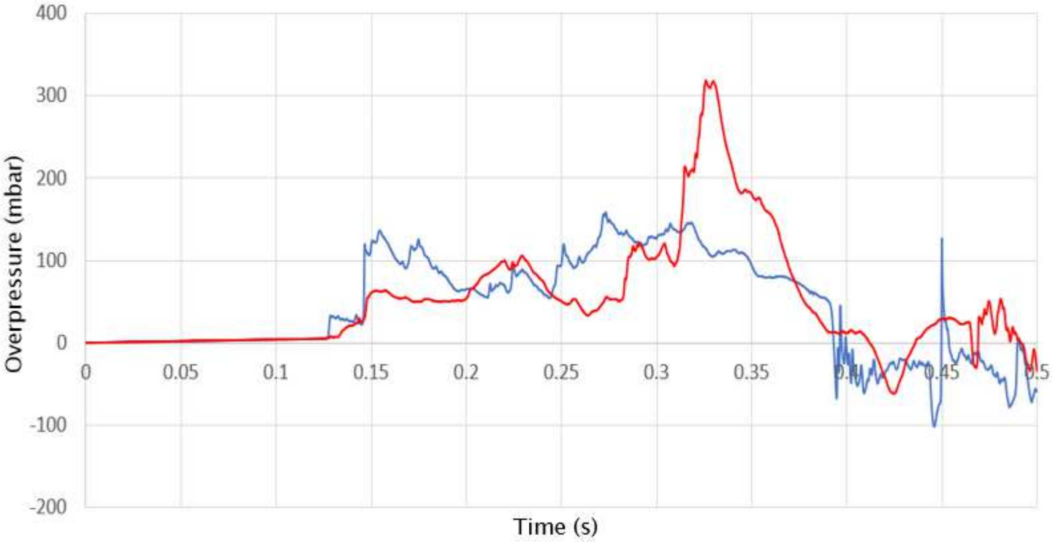

Fig. 4. *Overpressure effects 45 m on the left of ignition point. Case of a 55 m/s flame and inclined panels. Blue line: flat panels. Red line: inclined panels.*

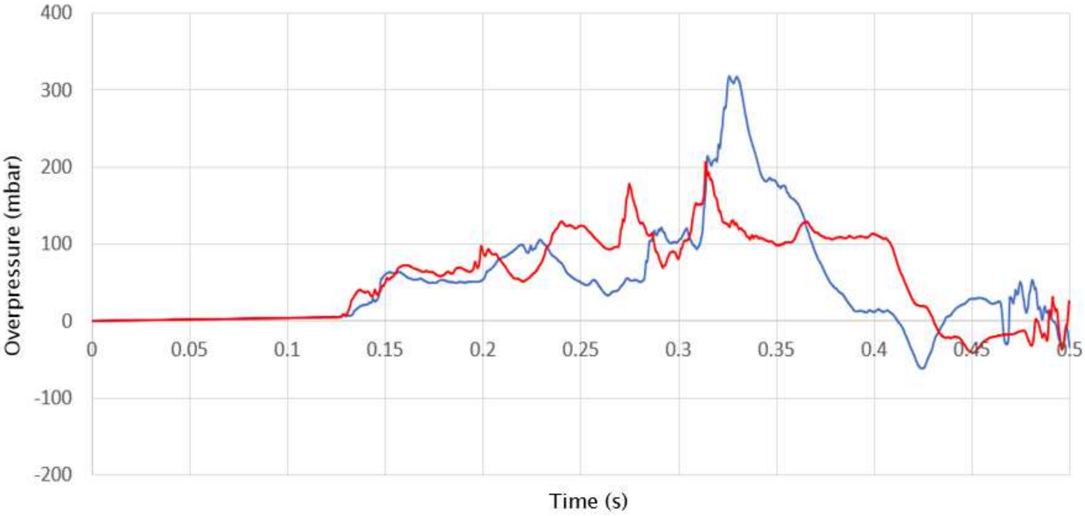

Fig. 5. *Overpressure effects on each side of the power plant for a 55 m/s flame. Blue line: upwind pressure probe. Red line: downwind pressure probe.*

Finally, the highest far-field effects are obtained in the case of a flammable cloud fully covering the power plant, with inclined panels and a quick flame propagating to the left (see Fig. 3).

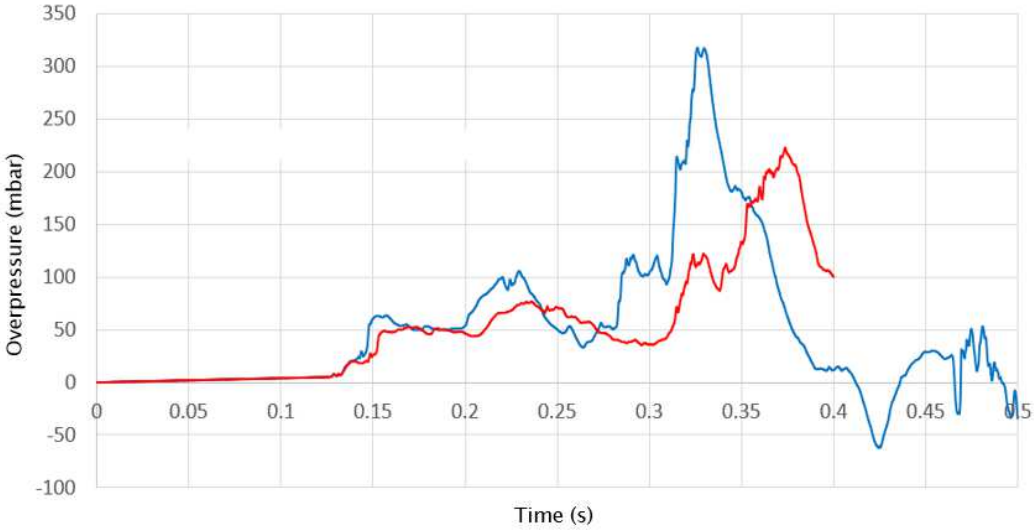

__Fig. 6.__ Overpressure effects 45 m on the left of ignition point. Case of 45 m/s and 55 m/s flames and inclined panels. Blue line: "quick" flame. Red line: "slow" flame.

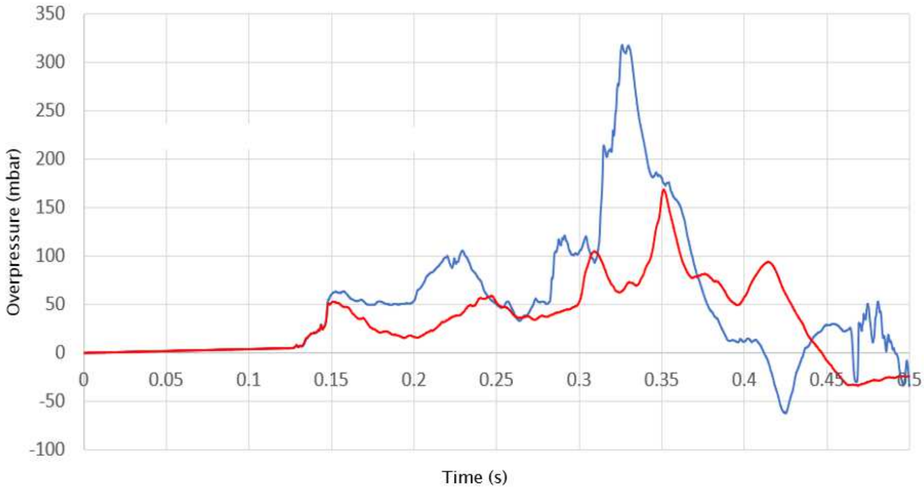

__Fig. 7.__ Overpressure effects 45 m on the left of ignition point. Case of a 55 m/s flame. Blue line: flammable cloud covering the full height of the power plant. Blue line: cloud covering half this height.

b. 3D tests and overpressure effects distances

3D CFD computations were finally performed for inclined panels fully covered by a stoichiometric flammable cloud at rest. As mentioned in the beginning of the paper, a first goal was to check if an explosion runaway can occur in the power plant. To do so, the overpressure is computed at a given distance from the side of the flammable cloud. The number of panels is increased from 4 to 6 as well as the size of the flammable cloud to keep all of them covered.

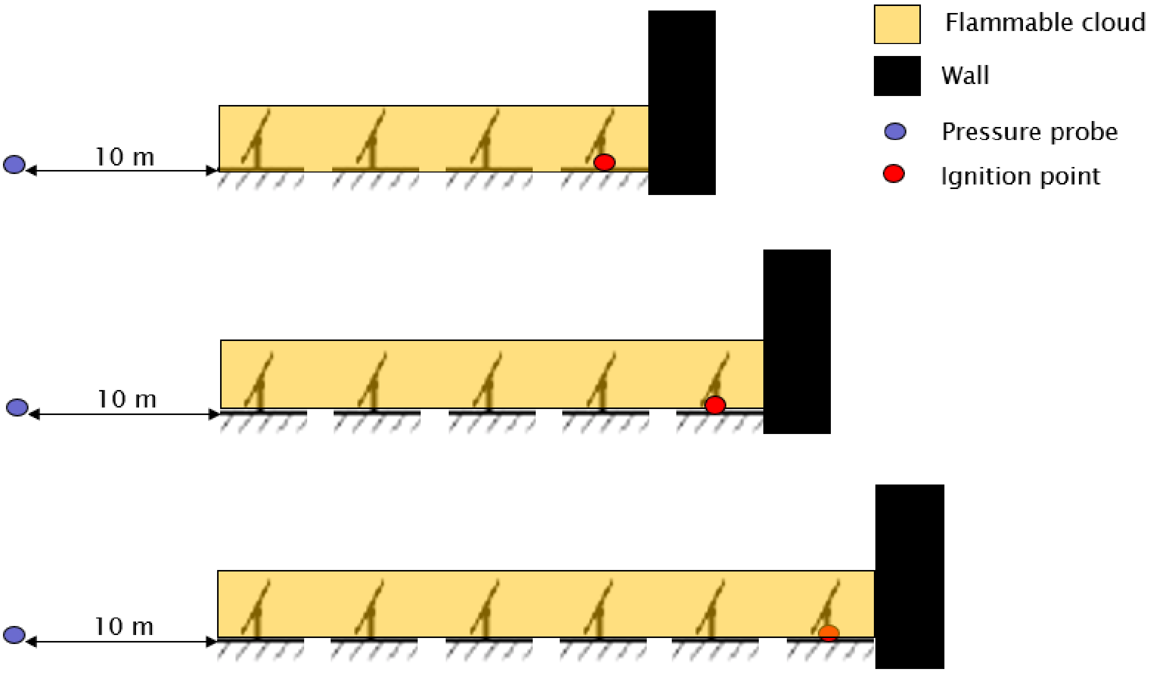

Fig. 8. *Principle of the 3D CFD computations. The number of panels the flame interacts with increases from 4 to 6.*

The cell width in the zone of interest is 15 cm. A 45 m/s flame representative of propane/air mixture and a 55 m/s flame representative of propylene/air mixture are tested (Fig. 9).

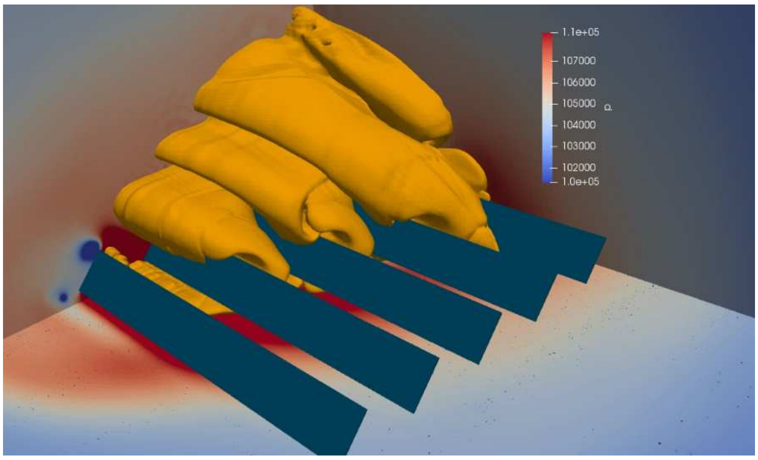

Fig. 9. Example of a CFD result related to flame/solar panels interaction. Shown: pressure fields, flame front (orange), solar panels (dark blue).

The pressure signal computed far from the flammable cloud for the case of the 45 m/s flame are shown in Fig. 10. In all cases, the first pressure peak is related to an interaction of the flame with the two first panels. This first peak is followed by N other pressure peaks where N equals the number of rows minus 2. The final pressure peak which is all the time the highest seems to reach a plateau in terms of magnitude with an increasing number of rows. An explosion runaway can be discarded regarding these aspects.

Almost the same set of characteristic curves is obtained with a 55 m/s flame (Fig. 11). The conclusions just above remain valid.

For both flames, the threshold of 50 mbar is reached about 20 m from the border of the cloud. This distance effect is higher than the one obtained without obstacle. Installing a photovoltaic power plant may have an impact on the regulatory overpressure effects distances but it remains moderate.

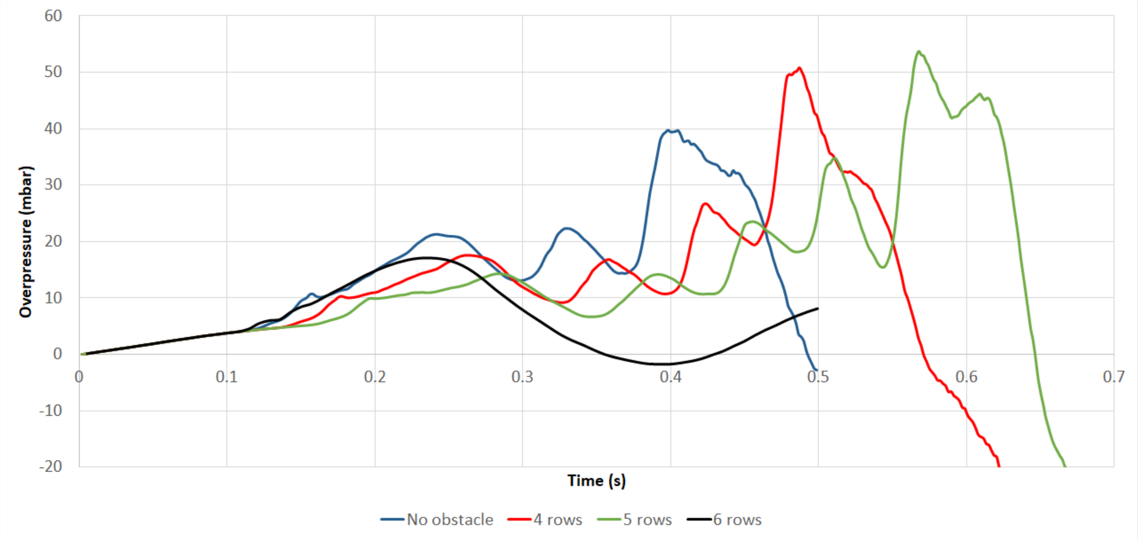

Fig. 10. *Computed overpressure 10 m from the flammable cloud border for the cases of no obstacle, 4, 5 and 6 rows of panels in the flammable cloud. Case of the "slow" flame.*

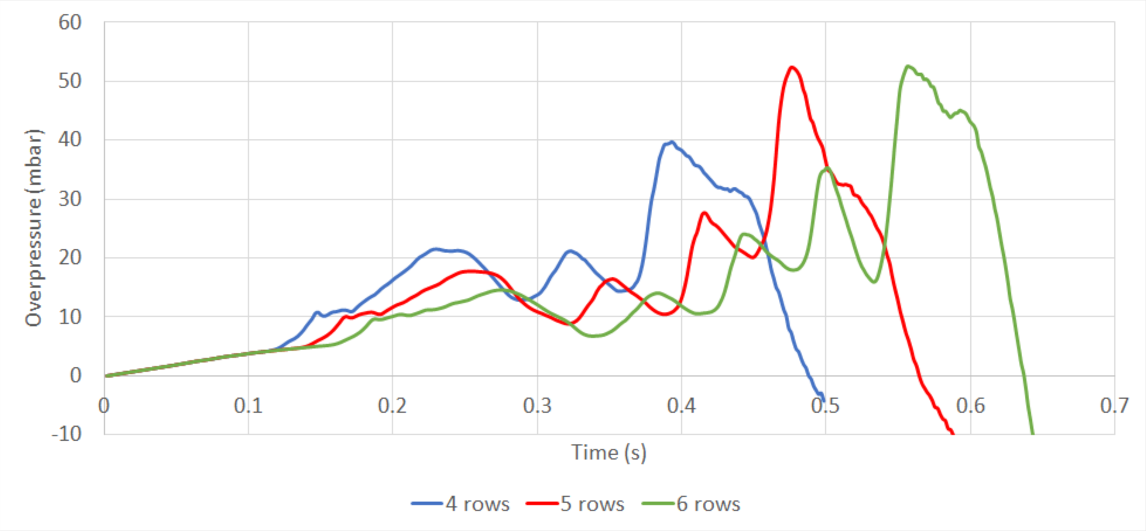

Fig. 11. *Computed overpressure 10 m from the flammable cloud border for the cases of no obstacle, 4, 5 and 6 rows of panels in the flammable cloud. Case of the "quick" flame.*

5. Conclusions

Total and INERIS worked on the topic of the potentially aggravating effect related to the presence of a photovoltaic power plant in flammable cloud in case of an UVCE. The study was limited to a geometry of a power plant supplied by Total and a flammable cloud formed with hydrocarbons such as propane and propylene.

First FLACS computations showed the pressure effects in the flammable cloud remain below 20 mbar. In order to confirm these results, a method based on phenomenological considerations and CFD was proposed. It appeared with this latter that no explosion runaway occurred for the regarded cases and the maximum distance at which an overpressure of 50 mbar was reached was 20 m from the side of the cloud. Installing a power plant, with the restrictions mentioned in the first paragraph, has an impact when compared to a situation with no obstacle but it remains moderate. These conclusions are globally in line with FLACS simulations, although a bit more restrictive.

References

Zeeuwen J.P. et al. (1983). Experimental investigation into the blast effect produced by unconfined valpour cloud explosions, *Loss Prevention and Safety Promotion* 4 1, D20

Van der Berg A.C. et al. (2005). Research to improve guidance on separation distance for the multi-energy method (RIGOS), TNO Prins Maurits Laboratory

Daubech J. et al. (2016). Les explosions non confinées de gaz et de vapeurs. Omega UVCE. INERIS technical report

Di Sarli V., Di Benedetto A., Russo G. (2010). Sub-grid scale combustion models for large eddy simulation of unsteady premixed flame propagation around obstacles, *Journal of Hazardous Materials* 180(1-3):71-8

Quillatre P. (2014). Simulation aux grandes échelles d'explosions en domaine semi-confiné, Thesis Manuscript. University of Toulouse.

Lecocq, G., Leprette, E., Daubech, J., Proust, C. (2019). Further insight into the gas flame acceleration mechanisms in pipes. Part II: numerical work. *Journal of Loss Prevention in the Process Industries* 62, 103919

Hansen, O.R., Johsnon, D.M. (2010). Improved far-field blast predictions from fast deflagrations, DDTs and detonations of vapour clouds using FLACS CFD, *Journal of Loss Prevention in the Process Industries* 35(15):293-306

Weller, H.G, Tabor, G. (1998). A tensorial approach to computational continuum mechanics using object-oriented techniques. *Computational Physics*, 12: 620-631.

Lecocq, G, Richard, S., Colin, O. & Vervisch, L. (2011). Hybrid presumed pdf and flame surface density approaches for Large-Eddy Simulation of premixed turbulent combustion Part 1: Formalism and simulation of a quasi-steady burner, *Combustion and Flame* 158: 1201-1214

Yang, S. et al. (2018). Role of Darrieus–Landau instability in propagation of expanding turbulent flames. *J. Fluid Mech.* 850, pp. 784-802

Bauwens, C.R. et al. (2015) Experimental study of spherical-flame acceleration mechanisms in large-scale propane–air flames, *Proc. Combust. Inst.* 35

Gülder, O.L., Smallwood, G.J. (1995). Inner cut-of scale of flame surface wrinkling in turbulent premixed flames, *Combustion and Flame*, vol. 103, pp. 107-114

Schneider, H, Pförtner, H. (1983) Fraunhofer-ICT Internal Report: *PNPSichcrheitssofortprogramm, Prozebgasfreisetzung-Explosion in der Gasfabrik und Auswirkungen von Druckwellen auf das Containment*

Lannoy, A., Leyer J.C., Desbordes D., St Cloud J.P. (1989). *Déflagrations sans turbulence en espace libre : expérimentation et modélisation*, Bulletin de la DER, série A, Electricité de France

Kostopoulos, D. (2019). *Evaluation des effets de surpression d'un UVCE en présence d'installations photovoltaïques*, Total internal report.

DOI: 10.7795/810.20200724

Influence of Thermal Radiation on Layered Dust Explosions

Swagnik Guhathakurta & Ryan W. Houim

University of Florida (Gainesville, Florida, USA)
E-mail: *swagnik@ufl.edu; rhouim@ufl.edu*

Abstract

Multidimensional unsteady numerical simulations were carried out to explore the influence of thermal radiation on the propagation and structure of layered coal dust explosions. The simulation solved the reactive compressible Navier-Stokes equations coupled to an Eulerian kinetic-theory-based granular multiphase model. The radiation heat transfer is modeled by solving the radiation transfer equation using the third-order filtered spherical harmonics approximation. The radiation was assumed to be gray and all boundaries of the domain are black at 300 K. The reaction mechanism is based on global irreversible reactions for each physical process including devolatilization, char burning, moisture vaporization, and methane combustion. The governing equations were solved using a high-order Godunov method. Several simulation configurations were considered: layer volume fractions of 47% and 1%, channel lengths of 10 m and 40 m, and radiative and non-radiative cases. The results show that gray radiation has a significant influence on the propagation and structure of a layered dust explosion. However, radiation can have opposite effects on different scenarios. For example, radiation promotes the propagation of the dust flame when the layer volume fraction was 1% and in the short-channel cases where reflected shock-flame interactions are important. However, radiation enhances quenching for the 47% volume fraction dust layer in the longer channel.

Keywords: *layered dust explosions, radiation heat transfer, numerical simulations*

1 Introduction

Dust explosions can occur when reactive particles are dispersed into a gaseous oxidizer. They can cause significant overpressures, which, in turn, may lead to severe structural damage as well as fatalities. Many common organic materials, such as powdered spices, sugar, coffee, etc., as well as non-organic materials such as powered metals (aluminum, magnesium and titanium) can be causes of dust explosions. Some recent notable incidents related to dust explosions include the Imperial Sugar Explosion in Port Wentworth, Georgia, USA (February, 2008) that caused 38 injuries and 6 fatalities, an aluminum dust explosion in Kunshan, China (August, 2014) which killed 146, and Benxihu Colliery coal mine explosion in Benxi, Liaoning, China (April, 1942), which is one of the worst coal mine accidents in recorded history that caused 1,549 fatalities. Thus, understanding dust explosions is essential to develop improved mitigation strategies and regulation, or, in the best case, completely avoid them.

Most data available on the combustion of dust clouds are obtained from experiments using closed bombs. These closed bomb experiments usually do not provide visual access and typically measure only pressure within the vessel. While the pressure-time history provides important information on the explosivity of dust clouds usually with the K_{st} explosion index, fundamental knowledge on the propagation mechanism and structure of the dust flame are not obtained. In addition, dust flames and explosions are often optically thick which makes visualization of their fundamental structure difficult. As a result, comprehensive mathematical and numerical models are necessary to increase fundamental understanding of the structure and propagation mechanisms of dust explosions.

Dust explosions have a significant history of study. However, there are relatively few reports available in the literature about the effects of radiative heat transfer on the flame ignition and propagation behavior. One of the reasons that thermal radiation is often neglected can be attributed to its complexity and computational cost. In cases where radiation is considered, the optically thick approximation is typically assumed (Slezak et al., 1985), which is accurate if the entire explosion is used as the characteristic length scale. However, in many cases the radiation is optically intermediate if the dust flame thickness is used as the characteristic length. In reality the radiation opacity will be somewhere in between these two limits, which makes understanding the role of radiation on dust explosions difficult due to the inherent nonlinearity if the optical thickness is in an intermediate regime. In such cases, the radiation transfer equation (RTE) must be solved because traditional RTE approximations based on optically thick or thin assumptions are not accurate.

Some of the only modeling work that consider radiation in explosion processes include Cao et al. (2014), Houim and Oran (2015a), Bidabadi and Azad (2015) and Liberman et al. (2015). While the first three concentrate on coal dust flames, the fourth article studied the effects of radiation on particle-laden hydrogen-oxygen flames. Liberman et al. (2015) assumes that the gas phase is transparent to radiation, whereas the particles can both absorb and emit radiation. Different effects were observed depending on how the particles were distributed in the hydrogen-oxygen suspension. The reactants ahead of the flame was preheated due to absorption of thermal radiation by the cold particles. This, in turn, caused either the flame to accelerate, ignite a new deflagration, or initiate a detonation ahead of the flame. Furthermore, whether the radiative preheating triggers a deflagration or a detonation ahead of the flame depends on the optical thickness of the particle suspension.

In this paper we explore the effect of thermal radiation on layered dust explosions using multidimensional numerical simulations. Scenarios where coal particles are initially placed on a thin layer on the floor of a long channel, as shown in Fig. 1, are considered. Similar to our earlier work (Houim and Oran, 2015b,c), the shock remnant of a failed gas-phase detonation disperses the coal dust into the shock-heated air where particles ignite and burn. This scenario is similar to Houim and Oran (2015b) and Houim and Oran (2015c), however, the simulations here include the effect of thermal radiation.

2 Problem Description and Numerical Methods

2.1 Physical Model

The initial and boundary conditions for the simulations are shown in Fig. 1. The domain consists of a long two-dimensional channel 5 cm in height, with a 4-mm thick layer of coal placed on the bottom. Channel lengths of 10 m and 40 m were considered. All boundaries of the domain are assumed to be symmetry planes. The diameter of the coal particles is 30 μm, which is in the middle of the explosive range for coal dust (Cashdollar, 2000). Volume fractions of 47% and 1% of particles in the dust layer were considered to explore the influence of particle packing. The volume fraction of the dense cases is based on empirical data for densely-packed coal dust layer (Edwards and Ford, 1988) and the dilute cases are based on data from Semenov et al. (2013). The domain contains a stoichiometric mixture of methane and air from the left boundary up to 2 m. After 2 m, the rest of the domain is transitioned to pure air gradually, over a distance of about 1 m, using a hyperbolic tangent function. The dust explosion is initiated by igniting a methane-air detonation on the left portion of the domain. The detonation is triggered near the left boundary using two hot pockets of unreacted methane and air at 100 atm and 1000 K.

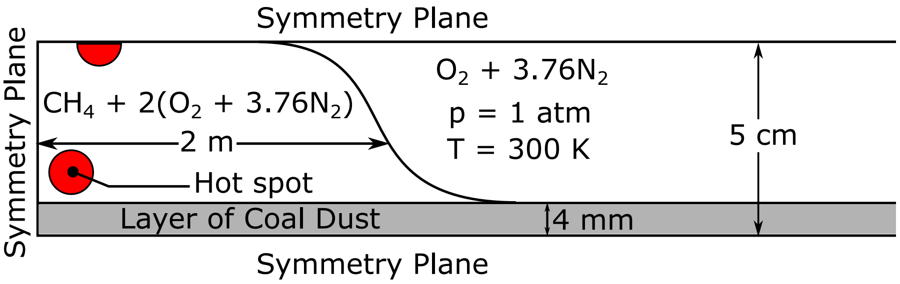

Fig. 1: *Initial and boundary conditions*

The two-dimensional simulations are computed using an in-house code, HyBurn, which solves the full set of coupled, multiphase, compressible, unsteady, partial differential equations (Houim and Oran, 2016). Kinetic theory-based solid phase reactive multiphase equations are solved. Drag, convective heat transfer, particle-particle interactions and inelastic collisions are modeled (Houim and Oran, 2016).

Magnus force is used to model the lift force, which is given by $\boldsymbol{f}_{\text{lift}} = C_l \alpha_s \rho_g (\boldsymbol{v}_s - \boldsymbol{v}_g) \times (\nabla \times \boldsymbol{v}_g)$, where $C_l = 1$. The lift coefficient was not varied in these simulations, since generally the shock-lifting of dust layers is insensitive to changes in it (Zydak and Klemens, 2007). Viscous stress, molecular diffusion, heat conduction and radiation are all considered. The ideal gas model with variable specific heat is used to relate pressure, chemical composition, temperature and density of the gas phase. The gas phase is composed of $\mathrm{CH_{4,g}}$, $\mathrm{O_2}$, $\mathrm{N_2}$, $\mathrm{H_2O_g}$ and $\mathrm{CO_2}$. Global, irreversible reactions were used to model methane combustion in high speed flows from Cloney et al. (2018), which is based on the MP1 model of CERFACS.

The dust particles are composed of dry ash-free coal (DAF), moisture ($\mathrm{H_2O}_s$), char (C_s), and inert ash. The DAF is first assumed to devolatilize in a process based on Kobayashi et al. (1977), releasing gaseous methane and solid carbon C_s (or char). The char can then react with air in a single-step process (Baek et al., 1990). The moisture is allowed to vaporize based on an Arrhenius reaction (Bradley et al., 2006).

The particles are assumed to be spherical and monodisperse, with a diameter of 30 μm, a constant specific heat of 987 J/kg.K, and material density, ρ_s, of 1200 kg/m^3 (Houim and Oran, 2015b). The coefficient of restitution used in these simulations is 0.99. The initial mass fractions of coal are 0.93 for DAF, 0.06 for ash, and 0.01 for moisture.

2.2 Reaction Mechanism for the Gas and Solid Phases

The chemical reactions used in this paper are

$$\mathrm{DAF} \xrightarrow{\mathrm{k_{DAF,1}}} \mathrm{CH_4} + \mathrm{C_s}, \tag{R1}$$

$$\mathrm{DAF} \xrightarrow{\mathrm{k_{DAF,2}}} \mathrm{CH_4} + \mathrm{C_s}, \tag{R2}$$

$$\mathrm{H_2O_s} \xrightarrow{\mathrm{k_{H_2O}}} \mathrm{H_2O_g}, \tag{R3}$$

$$\mathrm{C_s} + \mathrm{O_{2,g}} \xrightarrow{\mathrm{k_{f(C)}}} \mathrm{CO_2}, \tag{R4}$$

$$\mathrm{CH_4} + 2\,\mathrm{O_2} \xrightarrow{\mathrm{k_{CH_4}}} \mathrm{CO_2} + 2\,\mathrm{H_2O}. \tag{R5}$$

The model of Kobayashi et al. (1977) is used for the devolatilization reactions where R1 is dominant a low temperatures and R2 is dominant at higher temperatures. The rate constants are

$$k_{\mathrm{DAF,1}} = B_1 \exp(-E_1/RuT_{\mathrm{p}}), \tag{1}$$

$$k_{\mathrm{DAF,2}} = B_2 \exp(-E_2/RuT_{\mathrm{p}}), \tag{2}$$

where Ru is the universal gas constant, the pre-exponential factors B_1 and B_2 are 3.7×10^5 and 1.46×10^{13}, respectively, and activation energies E_1 and E_2 are 7.37×10^7 J and 2.51×10^8 J, respectively. The mass-based volatile yield fraction for R1 and R2 is 0.37 and 0.56, respectively.

Moisture vaporization, R3, is given as an Arrhenius reaction (Bradley et al., 2006) where

$$k_{\mathrm{H_2O}} = A_{\mathrm{H_2O}} \exp(-Ea_{\mathrm{H_2O}}/RuT_{\mathrm{p}}), \tag{3}$$

and $A_{\mathrm{H_2O}} = 1.46 \times 10^{13}$ and $Ea_{\mathrm{H_2O}} = 1.464 \times 10^8$J.

The char reaction rate R4 is based on mixed diffusion-limited and chemical-kinetic limited combustion models where

$$\frac{1}{k_{\mathrm{f(C)}}} = \frac{1}{k_{\mathrm{f(C),\,diff}}} + \frac{1}{k_{\mathrm{f(C),\,kin}}}. \tag{4}$$

The rate constant for the diffusion-limited char reaction is

$$k_{\mathrm{f(C),\,diff}} = \frac{24 T_{\mathrm{g}} D_{\mathrm{s}}}{T_{\mathrm{g}} + T_{\mathrm{p}}}, \tag{5}$$

where T_{g} is gas temperature and $D_{\mathrm{s}} = 100$ mm^2/s, which is an averaged mass diffusivity of for the char reaction (Cloney et al., 2018). The chemical-kinetic limited rate constant is

$$k_{\mathrm{f(C),\,kin}} = A_{\mathrm{C}} \exp(-Ta_{\mathrm{C}}/T_{\mathrm{p}}), \tag{6}$$

where $A_{\mathrm{C}} = 9.5 \times 10^7$ s^{-1} and activation temperature is $Ta_{\mathrm{C}} = 17{,}977$ K (Baek et al., 1990).
The volatiles are assumed to be pure CH_4 and react with oxygen in a single-step irreversible reaction R5. The rate constant is

$$k_{\mathrm{CH_4}} = A_{\mathrm{CH_4}} \exp(-Ea_{\mathrm{CH_4}}/RuT), \tag{7}$$

where $A_{CH_4} = 1.1 \times 10^{10}$ is the pre-exponential factor and $Ea_{CH_4} = 20{,}000$ cal/mol. Despite its simplicity, this single-step volatile combustion model has been shown to produce good results for laminar coal dust flames (Cloney et al., 2018).

2.3 Thermodynamic and Transport Models

The fluid model uses a variable specific heats model to preserve a high degree of accuracy. The thermodynamic and transport data for the species have been obtained from the AramcoMech2.0 library. The transport properties are assumed to be mixture-average. A generic transport property ψ for the mixture is

$$\psi_{\mathrm{mix}} = \left(\sum_{i=1}^{N_g} X_i \psi_i^{1/n} \right)^n, \tag{8}$$

where n is $1/6$ for the mixture viscosity and 4 for the mixture thermal conductivity (Ern and Giovangigli, 1994).
The Curtis-Hirschfelder approximation is used for the mixture-averaged mass diffusion coefficients (Kee et al., 2005)

$$D_{i,mix} = \frac{1 - Y_i}{\sum_{j \neq i}^{N_g} X_j / \mathscr{D}_{ij}}, \tag{9}$$

where $\mathscr{D}_{ij}$ are the binary diffusion coefficients of all pairs of species. The correction procedure of Coffee and Hiemerl (Coffee and Heimerl, 1981) is used to ensure mass conservation for the diffusion velocities.

2.4 Radiation Modeling

In this work we solve the radiation transfer equation (RTE) to compute the radiation field and the radiative heating and cooling rates for the particles. The third-order filtered spherical harmonics (FP_3) approximation to simplify the radiation transfer equation (Radice et al., 2013). The radiation is assumed to be spectrally gray with isotropic scattering. The Buckius and Hwang correlation is used to compute the Planck-mean extinction and scattering coefficients for the coal dust (Buckius and Hwang, 1980). The gray Plank-mean absorption coefficients for CH_4, O_2, CO_2 and H_2O were based on curve fits to the data from the RADCAL program (Grosshandler, 1993).

2.5 Numerical Solution Methods

An operator splitting method is used to solve the governing equations with separate solution methods for hydrodynamic terms, source terms arsing from chemical reactions, drag, etc., and thermal radiation. The hydrodynamic terms are solved using a Godunov-based method and a third-order Runge-Kutta method is used for time integration (Houim and Kuo, 2011, Houim and Oran, 2016). The FP_3 equations are marched in pseudo-time until steady-state is achieved using an approximate Riemann solver (McClarren and Hauck, 2010). The gas-phase reaction terms are integrated in time using the yet-another-stiff-solver (YASS) method (Khokhlov et al., 2012).

Adaptive mesh refinement was used to achieve the required amount of resolution, which is based on the AMReX library (Zhang et al., 2019). Four levels of refinement were used with finest resolution of $\Delta x_{\max} = 0.2$ mm, which is roughly 6.7 particle diameters in size. This computational cell size is comparable to the resolution used in our earlier work (Houim and Oran, 2015b).

3 Results

3.1 Short 10-m channel with 47% volume fraction in the dust layer

Figure 2 shows position-time diagrams for the short channel cases. These plots show the propagation of the detonation, its subsequent failure, propagation of the dust flame, and the reflection of the incident shock. The methane-air detonation fails at ∼1.5 ms. The resulting shock remnant and the dust flame propagate separately. The incident shock propagates to the right and reflects from the end wall at ∼14 ms and propagates towards the flame. After failure of the detonation, the flame decelerates until the reflected shock reaches the flame front at ∼22 ms. In the case with radiation, the dust flame accelerates to the right after the shock-flame interaction. The dust flame in the non-radiative case is much more unstable and does not accelerate to the right.

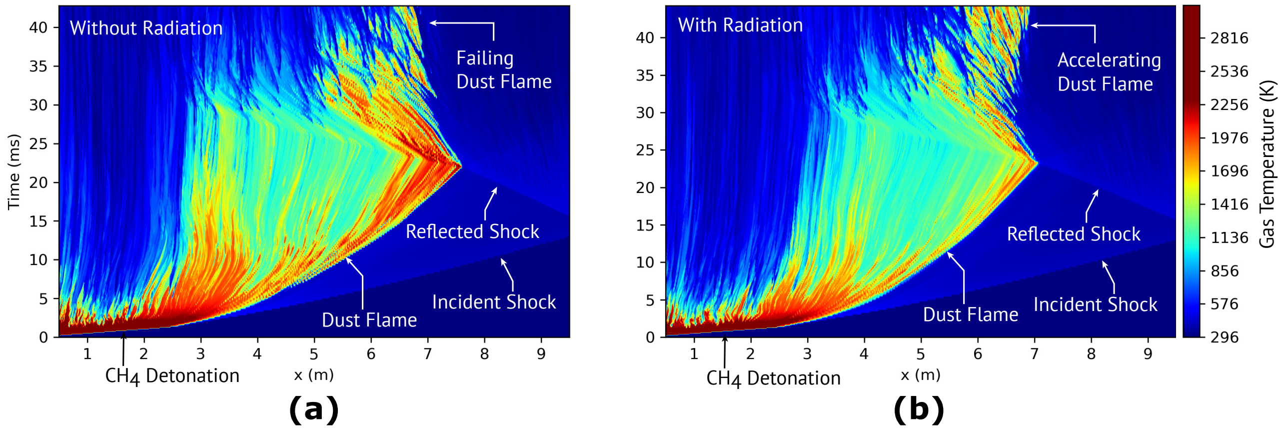

***Fig. 2**: XT plot shaded by gas phase temperature for the 10-m channel with 47% layer volume fraction for (a) without radiation and (b) with radiation.*

Fig. 3 (a) shows the heat release rates due to gas-phase chemical reactions for the cases with and without radiation. The heat release rate is ∼2 GW/m for the first 1.5 ms which is due to the propagating detonation. The heat release rate then sharply falls after the detonation fails at 1.5 ms due to lack of pre-suspended CH_4 in the air for the first two meters in the channel. After failure of the detonation, the heat release rate sharply decreases, but shortly afterwards rises continuously until ∼12 ms for both cases due to the propagating dust flame. A case with pure inert dust in the layer, does not show the continuous rise in the heat release after detonation failure as shown in Fig. 3 (b). The heat release rate increases substantially at ∼30 ms, which is likely due to effects from the shock-flame interactions enhancing mixing. After ∼36 ms, the heat release rate for the case without radiation decreases sharply and continuously until the end of the simulation while the case with radiation decreases more gradually and appears to be plateauing.

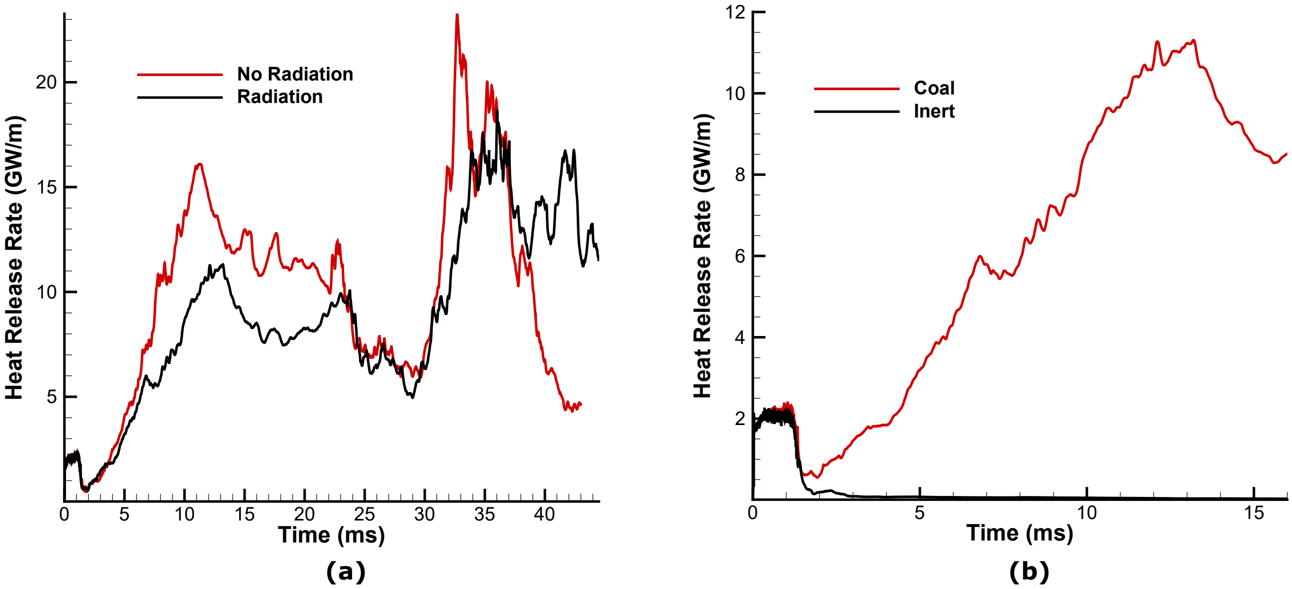

Fig. 3: *Heat release rates due to chemical reactions for the cases (a) with and without radiation; (b) with inert ash and reactive coal for the 10 m channel with a dust volume fraction of 47%.*

Fig. 4 shows a snapshot of the structure of the coal-dust flames for both cases at 45 ms. The radiative flame, at this instance, has a much broader structure and a lower peak temperature. The flame temperature predicted by the case without radiation at ∼ 20 ms is ∼2250 K, whereas for the case with radiation, it is ∼2050 K.

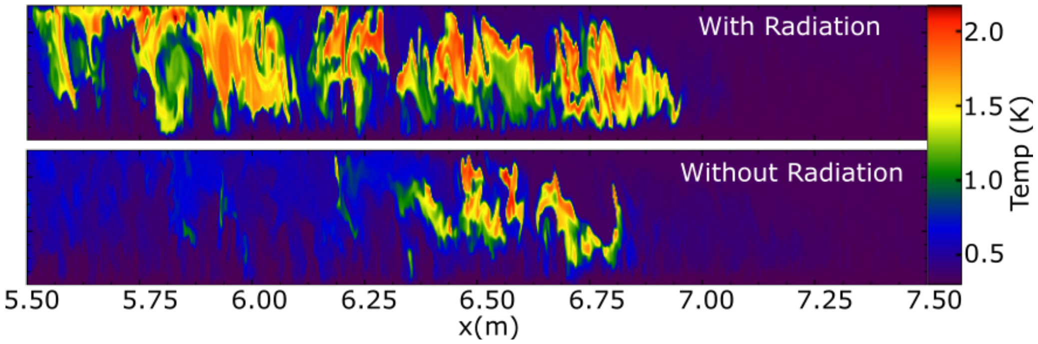

Fig. 4: *Contour plots of gas temperature for the cases with and without radiation at 45 ms for the 10-m channel the dust layer volume fraction fo 47%. Note that the plots have been stretched in the y-direction by 4 times for better visualization.*

3.2 Long 40-m channel with 47% volume fraction in the dust layer

Reflected shocks interacted with the flame in the shorter 10-m channel cases. Longer 40-m long channels were simulated to eliminate the effect of these shock-flame interactions. Here we present the results for the long-channel cases with a dust layer volume fraction of 47% volume fraction, with and without radiation. This case is nearly identical to setups discussed in Houim and Oran (2015c,b), Shimura and Matsuo (2019), but with a different reaction mechanism, different coal parameters, and a much longer simulation time.

The total heat release rates due to gas phase chemical reactions and the flame and shock velocities for these cases are shown in Fig. 5. Figure 6 shows position-time of the temperature field at $y = 2.5$ cm. Toward the end of the simulations, at ∼80 ms, both cases show that heat release is substantially decreasing. In addition, the flame velocity, shown in Fig. 5(b), continuously decreases and eventually approaches zero. However, the flame locations and velocities are different for the two cases. At the

DOI: 10.7795/810.20200724

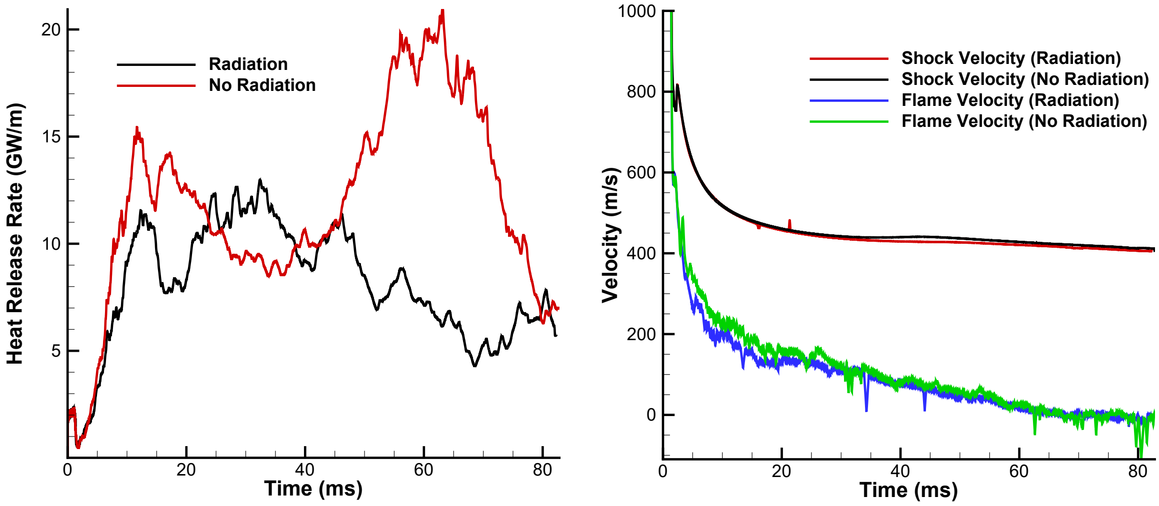

(a) **(b)**

Fig. 5: *Dense (47%) case (a) Total heat release rate due to gas phase chemical reactions and (b) Shock and flame velocities.*

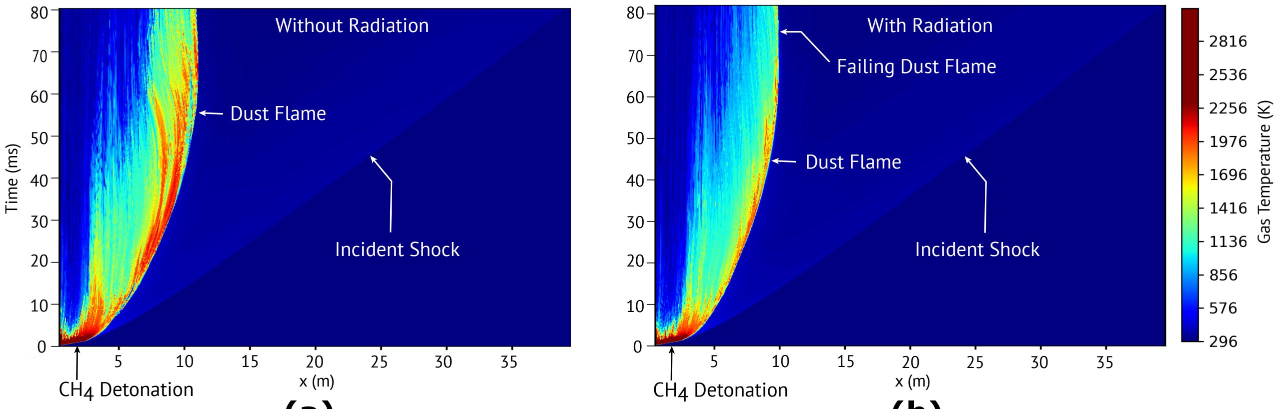

(a) **(b)**

Fig. 6: *Dense (47%) case XT plot shaded by gas phase temperature for (a) without radiation and (b) with radiation.*

end of the calculation ($t \sim 80$ ms) the flame is at 11.0 m, and 9.9 m for for non-radiative and radiative cases, respectively.

The XT diagrams shown in Fig. 6 indicate that the peak coal dust flame temperature is around 200 K lower when radiation is considered. The dust flame starts to quench for the radiative case when the peak temperature drops to ∼1200 K after 70 ms. The non-radiative flame shown in Fig. 6 (a) propagates unstably after 30 ms, with intermittent regions of high flame temperature followed by substantially lower temperatures.

3.3 Long channel with 1% volume fraction

The 40-m long channel was simulated with a volume fraction of 1% to explore the influence of dust layer packing on the simulation results. Total heat release rate due to gas-phase chemical reactions and the shock and flame velocities are shown in Fig. 7(a) and (b), respectively. The heat release rate continually increases and the flame velocity propagates stably at roughly 400 m/s for much of the calculation for these dilute cases. This is in contrast to the dense cases where the flames eventually quenched or propagating unstably.

The XT diagram in Fig. 8 shows that thermal radiation is accelerating the flame, which is indicated

DOI: 10.7795/810.20200724

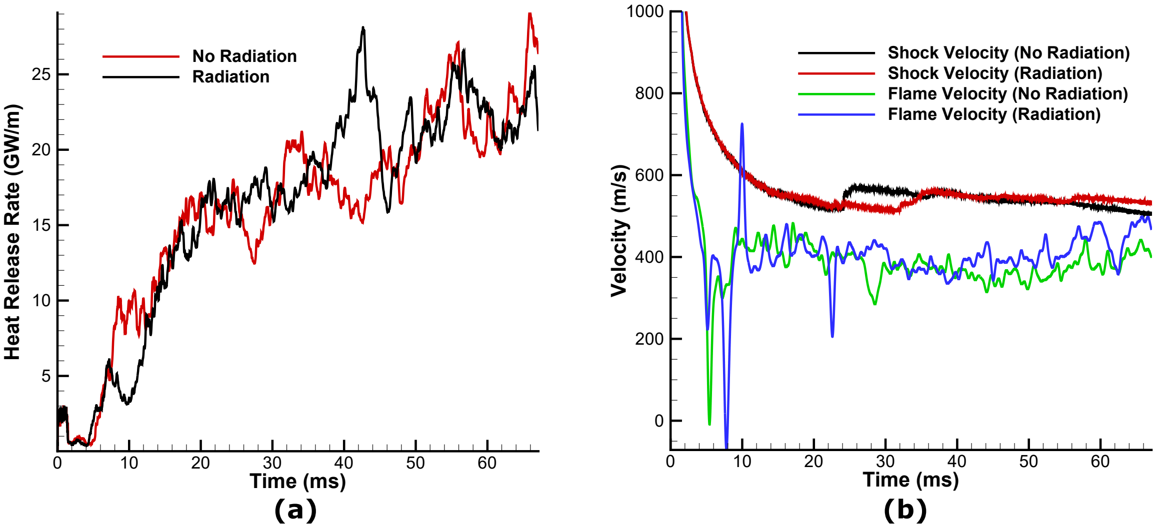

Fig. 7*: Dilute (1%) case (a) Total heat release rate due to gas phase chemical reactions; (b) Shock and flame velocities*

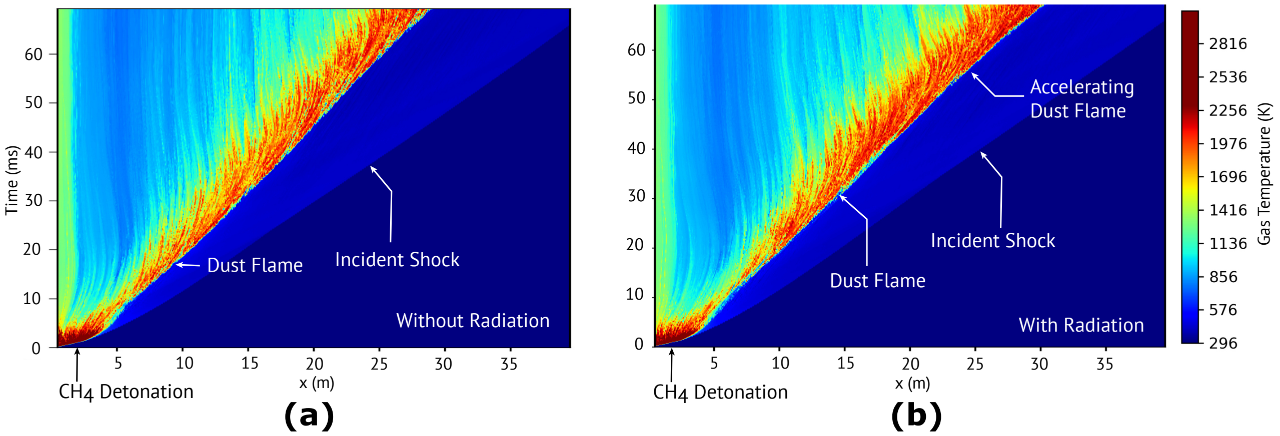

Fig. 8*: Dilute (1%) case XT plot shaded by gas phase temperature for (a) without radiation; (b) with radiation.*

by the slight kink in the flame position in Fig. 8(b), at ∼50 ms. This corresponds to the time in Fig. 7(b) where the flame with radiation begins to accelerate relative to the case without radiation. It is interesting to note that the radiative flame produces higher peak flame temperatures relative to the non-radiative flame after 40 ms, which is opposite to the previous cases.

Fig. 9 shows the flame structure for (a) radiative case and (b) non-radiative case for the dilute dust layer. It is clear that radiation has an influence on the flame structure and temperature. In particular, the radiative case shows devolatilization over a longer distance ahead of the flame, which is indicative of radiative pre-heating.

4 Discussion

The simulation results show that the influence of radiation on the bulk dust flame parameters such as velocity and peak temperatures are quite different for the scenarios presented in the paper and can even have opposite effects. For example, radiation hinders flame propagation in some cases, and assists propagation in other cases. The chemical energy release rate shown in Figs. 3, 5, and 7 show that for majority of the time in most cases the total rate of heat release is reduced by radiation. This trend can be explained by radiation losses from the flame region dominating over radiation absorption in the cold reactants. These radiation losses near the flame reduce the peak temperature relative to the non-

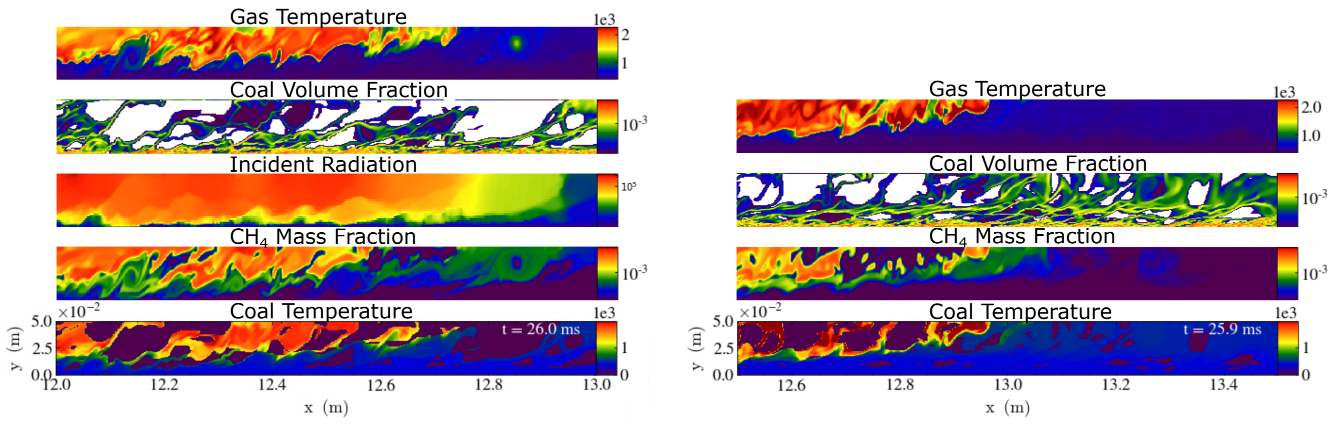

(a) **(b)**

***Fig. 9**: Plots of gas temperature, dust volume fraction, incident radiation, methane mass fraction, and coal temperature for cases (a) with radiation and (b) without radiation with the 1% volume fraction dust layer in the 40-m channel at a time of 26 ms.*

radiative simulations. A notable exception is the dilute cases where the opposite trend was observed. The radiative case with a layer volume fraction of 1% had peak flame temperatures that were ~ 20 K higher than the corresponding non-radiative case. This can be explain by the faster shock Mach 1.4 shock raising the air temperature by ~ 20 K for the radiative case compared to the Mach 1.33 shock for the non-radiative case. Another notable influence of radiation is that it produced a stably propagating flame for the shorter 10-m channel after the shock-flame interaction, while, simulations neglecting radiation produced a very unstable flame that is likely in process of quenching. This is shown most clearly in Figs. 2 and 4 which indicate a healthy flame for the radiative case and an unstable flame for the non-radiative case.

The flame is predicted to quench for both the radiative and non-radiative cases for the 40-m channel when a realistic layer volume fraction of 47% is used. Nevertheless, radiation has a significant influence on the quenching process. The radiative flame quenches much earlier than the non-radiative case due to radiation losses from flame overwhelming the radiative and conductive heating of the reactants. Quenching of the flame was an unexpected result that has not been reported in earlier literature (Houim and Oran, 2015c, Shimura and Matsuo, 2019). However, these earlier simulations considered much shorter simulation times, used different reaction mechanisms for CH_4 and coal, and used different initial mass fractions for DAF, ash, and moisture. The sensitivity of the results to the choice in reaction mechanism and other model parameters is currently ongoing.

5 Conclusions

Numerical simulations of layered coal dust explosions were performed both with and without radiation for 10 m and 40 m long channels to explore the influence of thermal radiation on the propagation of a layered dust explosion. Two particle volume fractions in the dust layer were considered. A loosely packed case with an 1% initial volume fraction and a densely packed case where the layer volume fraction was initially 47%. The results from the different cases were examined to understand the effect of radiation heat transfer on the structure and propagation of coal dust layered explosions.

Results from each of the simulations show that key dust flame parameters, such as flame temperature, velocity, and overall structure can be quite different between the radiative and non-radiative cases. However, the influence of radiation can have opposite effects for different scenarios. In some cases, radiation can lead to enhanced quenching of the explosion, while in others it can accelerate the flame and increase the severity of the explosion. For example, radiation promotes flame propagation after the reflected shock-flame interaction in the 10-m channel, and for the dilute dust layer. However, radiation quenches the flame more quickly for the long channel with the dense dust layer. The precise conditions that lead to these differences are currently being explored.

The differences on the influence of radiation are likely dependent on modeling choice such as the chemical reaction model, spectral model for radiation, absorption and scattering models for the particles and gas, and other physical constant such as the lifting coefficient. Sensitivity of the results to these modeling choices is under investigation.

Acknowledgements

This work was supported in part by the US National Science Foundation (NSF) grant 1942861 and the US National Institute for Occupational Safety and Health (NIOSH) grant 200-2015-64091. The authors also would like thank Dr. Elaine Oran of Texas A&M and Marcia Harris and Dr. Mike Sapko of NIOSH for their fruitful discussions.

References

Baek, S., Sichel, M., Kauffman, C. (1990). *Asymptotic analysis of the shock wave ignition of dust particles*. Combustion and Flame, 81(3):219 – 228. ISSN 0010-2180. doi:https://doi.org/10.1016/0010-2180(90)90020-R.

Bidabadi, M., Azad, A. V. (2015). *Effects of radiation on propagating spherical flames of dust–air mixtures*. Powder Technology, 276:45 – 59. ISSN 0032-5910. doi:https://doi.org/10.1016/j.powtec.2014.12.044.

Bradley, D., Lawes, M., Park, H.-Y., Usta, N. (2006). *Modeling of laminar pulverized coal flames with speciated devolatilization and comparisons with experiments*. Combustion and Flame, 144(1):190 – 204. ISSN 0010-2180. doi:https://doi.org/10.1016/j.combustflame.2005.07.007.

Buckius, R. O., Hwang, D. C. (1980). *Radiation Properties for Polydispersions: Application to Coal*. Journal of Heat Transfer, 102(1):99–103. ISSN 0022-1481. doi:10.1115/1.3244256.

Cao, W., Gao, W., Liang, J., Xu, S., Pan, F. (2014). *Flame-propagation behavior and a dynamic model for the thermal-radiation effects in coal-dust explosions*. Journal of Loss Prevention in the Process Industries, 29:65 – 71. ISSN 0950-4230. doi:https://doi.org/10.1016/j.jlp.2014.02.002.

Cashdollar, K. L. (2000). *Overview of dust explosibility characteristics*. Journal of Loss Prevention in the Process Industries, 13(3):183 – 199. ISSN 0950-4230. doi:https://doi.org/10.1016/S0950-4230(99)00039-X.

Cloney, C. T., Ripley, R. C., Pegg, M. J., Amyotte, P. R. (2018). *Laminar burning velocity and structure of coal dust flames using a unity lewis number cfd model*. Combustion and Flame, 190:87 – 102. ISSN 0010-2180. doi:https://doi.org/10.1016/j.combustflame.2017.11.010.

Coffee, T., Heimerl, J. (1981). *Transport algorithms for premixed, laminar steady-state flames*. Combustion and Flame, 43:273 – 289. ISSN 0010-2180. doi:https://doi.org/10.1016/0010-2180(81)90027-4.

Edwards, J., Ford, K. (1988). *Model of coal-dust explosion suppression by rock dust entrainment. report of investigations/1988*.

Ern, A., Giovangigli, V. (1994). *Multicomponent transport algorithms*, volume 24. Springer Science & Business Media.

Grosshandler, W. L. (1993). *Radcal: a narrow-band model for radiation*. Calculations in a Combustion Environment, NIST Technical Note, 1402.

Houim, R. W., Kuo, K. K. (2011). *A low-dissipation and time-accurate method for compressible multi-component flow with variable specific heat ratios*. Journal of Computational Physics, 230(23):8527 – 8553. ISSN 0021-9991. doi:https://doi.org/10.1016/j.jcp.2011.07.031.

Houim, R. W., Oran, E. S. (2015a). *Effect of radiation on the propagation of planar coal dust flames in air*.

Houim, R. W., Oran, E. S. (2015b). *Numerical simulation of dilute and dense layered coal-dust explosions*. Proceedings of the Combustion Institute, 35(2):2083 – 2090. ISSN 1540-7489. doi:https://doi.org/10.1016/j.proci.2014.06.032.

Houim, R. W., Oran, E. S. (2015c). *Structure and flame speed of dilute and dense layered coal-dust explosions*. Journal of Loss Prevention in the Process Industries, 36:214 – 222. ISSN 0950-4230.

doi:https://doi.org/10.1016/j.jlp.2015.01.015.

Houim, R. W., Oran, E. S. (2016). *A multiphase model for compressible granular–gaseous flows: formulation and initial tests*. Journal of Fluid Mechanics, 789:166–220. doi:10.1017/jfm.2015.728.

Kee, R. J., Coltrin, M. E., Glarborg, P. (2005). *Chemically reacting flow: theory and practice*. John Wiley & Sons.

Khokhlov, A., Domínguez, I., Bacon, C., Clifford, B., Baron, E., Hoeflich, P., Krisciunas, K., Suntzeff, N., Wang, L. (2012). *Three-dimensional simulations of thermonuclear detonation with alpha-network: Numerical method and preliminary results*. In *Advances in Computational Astrophysics: Methods, Tools, and Outcome*, volume 453, page 107.

Kobayashi, H., Howard, J., Sarofim, A. (1977). *Coal devolatilization at high temperatures*. Symposium (International) on Combustion, 16(1):411 – 425. ISSN 0082-0784. doi:https://doi.org/10.1016/S0082-0784(77)80341-X.

Liberman, M., Ivanov, M., Kiverin, A. (2015). *Effects of thermal radiation heat transfer on flame acceleration and transition to detonation in particle-cloud hydrogen flames*. Journal of Loss Prevention in the Process Industries, 38:176 – 186. ISSN 0950-4230. doi:https://doi.org/10.1016/j.jlp.2015.09.006.

McClarren, R. G., Hauck, C. D. (2010). *Robust and accurate filtered spherical harmonics expansions for radiative transfer*. Journal of Computational Physics, 229(16):5597 – 5614. ISSN 0021-9991. doi:https://doi.org/10.1016/j.jcp.2010.03.043.

Radice, D., Abdikamalov, E., Rezzolla, L., Ott, C. D. (2013). *A new spherical harmonics scheme for multi-dimensional radiation transport i. static matter configurations*. Journal of Computational Physics, 242:648 – 669. ISSN 0021-9991. doi:https://doi.org/10.1016/j.jcp.2013.01.048.

Semenov, I., Utkin, P., Markov, V. (2013). *Numerical modelling of dust-layered detonation structure in a narrow tube*. Journal of Loss Prevention in the Process Industries, 26(2):380 – 386. ISSN 0950-4230. doi:https://doi.org/10.1016/j.jlp.2012.04.007. Selected Papers from the Eighth International Symposium on Hazards, Prevention, and Mitigation of Industrial Explosions (Yokohama, Japan, 5–10 September 2010).

Shimura, K., Matsuo, A. (2019). *Using an extended cfd–dem for the two-dimensional simulation of shock-induced layered coal-dust combustion in a narrow channel*. Proceedings of the Combustion Institute, 37(3):3677 – 3684. ISSN 1540-7489. doi:https://doi.org/10.1016/j.proci.2018.07.066.

Slezak, S. E., Buckius, R. O., Krier, H. (1985). *A model of flame propagation in rich mixtures of coal dust in air*. Combustion and Flame, 59(3):251 – 265. ISSN 0010-2180. doi:https://doi.org/10.1016/0010-2180(85)90129-4.

Zhang, W., Almgren, A., Beckner, V., Bell, J., Blaschke, J., Chan, C., Day, M., Friesen, B., Gott, K., Graves, D., Katz, M., Myers, A., Nguyen, T., Nonaka, A., Rosso, M., Williams, S., Zingale, M. (2019). *Amrex: a framework for block-structured adaptive mesh refinement*. Journal of Open Source Software, 4(37). ISSN 2475-9066. doi:10.21105/joss.01370.

Zydak, P., Klemens, R. (2007). *Modelling of dust lifting process behind propagating shock wave*. Journal of Loss Prevention in the Process Industries, 20(4):417 – 426. ISSN 0950-4230. doi:https://doi.org/10.1016/j.jlp.2007.04.020. Selected Papers Presented at the Sixth International Symposium on Hazards, Prevention and Mitigation of Industrial Explosions.

DOI: 10.7795/810.20200724

Determination of reaction mechanisms for the gasification and explosion of organic powders

Matteo Pietraccini [a], Eloise Delon [a], Audrey Santandrea [a], Stéphanie Pacault [a],
Pierre-Alexandre Glaude [a], Anthony Dufour [a] & Olivier Dufaud [a]

[a] Université de Lorraine, CNRS, LRGP, F-54000 Nancy, France

E-mail: olivier.dufaud@univ-lorraine.fr

Abstract

Reaction kinetics is fundamental for modelling the thermal oxidation of a solid phase, in processes such dust explosions, combustion or gasification. The methodology followed in this study consists in i) the experimental identification of the reaction mechanisms involved in the explosion of organic powders, ii) the proposal of a simplified mechanism of pyrolysis and oxidation, iii) the implementation of the model to assess the explosion severity of organic dusts. Flash pyrolysis and combustion experiments were carried out on starch (22 µm) and cellulose (53 µm) at temperatures ranging from 973K to 1173K. The gases generated were collected and analyzed by chromatography. In this paper, a pyrolysis model was developed for reactive systems with low Damköhler number. It is in good agreement with the experimental data and shows that both carbon monoxide and hydrogen are mainly generated during the pyrolysis, the generation of the latter compound being greatly promoted at high temperature. In parallel, flame propagation tests were performed in a semi open tube in order to assess the burning velocity of such compounds. The laminar burning velocity of cellulose was determined to be 21 cm.s^{-1}. Finally, this model will be integrated to a predictive model of dust explosions and its validation will be based on experimental data obtained using the 20 L explosion sphere. The explosion severity of cellulose was determined and will be used to develop and adjust the predictive model.

Keywords: *pyrolysis, combustion, dust explosion, organic powders, reaction mechanisms*

1. Introduction

The importance of merging process safety and engineering design together is well known; but if inherent safety is essential (Rathnayaka et al., 2014), it is also compulsory to complement this approach by the quantitative assessment of residual risks. However, for dust explosion as for other risks, the industrial conditions are multiple, changing and can hardly be reproduced in a laboratory by a series of experiments. Supporting the tests with a numerical model able to extrapolate their results to operating conditions other than those defined by the international standards, would obviously increase the relevance and scope of a normative approach.

Developing such a model is far from being easy as various steps have to be considered: for instance, i) the dust dispersion and the potential variation of its particle size distribution, ii) the dust ignition, which is by nature a discontinuous process, iii) the flame propagation and the turbulence/combustion interactions. Among the essential bricks of this model, the chemical reaction kinetics is probably the most central input. However, at present, the proposed reaction mechanisms do not allow to represent the complexity of these phenomena. Indeed, predictive models of solid combustion exist, but are almost always based on slow heating tests of powder deposits (thermogravimetric analysis, dust layer heating test, etc.). In order to model a dust explosion phenomenon or/and a gasification process, it is thus compulsory to determine the rate-limiting mechanisms occurring during the rapid heating of a dust cloud, followed by a flash pyrolysis and an oxidation step.

In this paper, the pyrolysis/oxidation mechanisms of simple organic dusts (starch, cellulose) were studied using a Godbert-Greenwald furnace and by collecting and analyzing the gases generated at different temperatures. As the determination of a simplified mechanism and of pyrolysis/oxidation kinetics will also be useful to assess burning velocity, tests were also performed in a flame propagation tube in order to estimate a laminar flame velocity. Finally, as the final objective of this work is to model an explosion test in a 20 L chamber and assess the dust explosion severity, experiments were also carried out in this vessel. Once the combustion model elaborated and validated for cellulosic compounds, it would be extended for instance to lignocellulosic residues and food waste, for process safety purposes as well as for the optimization of gasification processes or combustion of biomass.

2. Materials and methods

2.1 Powders

Tests were performed on two powders: wheat starch (Sigma-Aldrich) and cellulose (Arbocel). They both show the same monomer molecular formula ($C_6H_{10}O_5$, glucose), but have different structure. Indeed, in a starch chain, glucose molecules are linked to each other by means of a α(1-4) and a α(16) glycosidic chemical bonds, which gives this biopolymer its characteristic branched structure. On the other hand, in a cellulose chain, glucose molecules are kept together thanks to β(1-4) glycosidic bond, which leads to a more linear molecule. The choice of these two powders was dictated by the need to compare the combustion behavior of two different compounds having a quite similar chemical formula but different physical properties. Other organic molecules will be tested later, then mixtures in order to approach the phenomenon with several levels of complexity.

Starch powder was sieved, initially in order to test the influence of the mean diameter on the combustion mechanism. In this paper, only the finest fraction will be studied. Table 1 shows the particle sizes distribution (PSD) of both samples and in particular the equivalent volume diameters d_{10}, d_{50}, d_{90}, and the Sauter mean diameter (SMD or $d_{3,2}$), i.e. the diameter of a sphere having the same volume/surface area ratio. The measurements were carried out by a laser diffraction sensor Helos (Sympatec) after dispersion of the dusts by an air-pulse in a semi-open tube. The dispersion procedure was consistent with that applied to determine the minimum ignition energy of a powder (EN 80079-20-2). It should be noted that the PSD of starch is unimodal, which is not the case of cellulose. In fact, the cellulose sample is formed by fibers of different shapes, lengths and geometric configurations. It was estimated, by optic microscopy, that their length-to- width ratio ranges from 6 to 10. Furthermore, the PSD of cellulose shows three main peaks, at about 25, 60 and 190 µm (Figure 1). Except for the first 50 ms, the PSD remains stable for dispersion times up to 300 ms, which is noteworthy as ignition delay times ranging from 60 to 300 ms will be used to observe the flame propagation.

Table 1: *Characteristics of the particle size distributions of starch and cellulose*

Sample	**d_{10} (µm)**	**d_{50} (µm)**	**d_{90} (µm)**	**SMD (µm)**
Starch	9.8	22.3	42.1	18.5
Cellulose	14.4	53.3	196.0	33.3

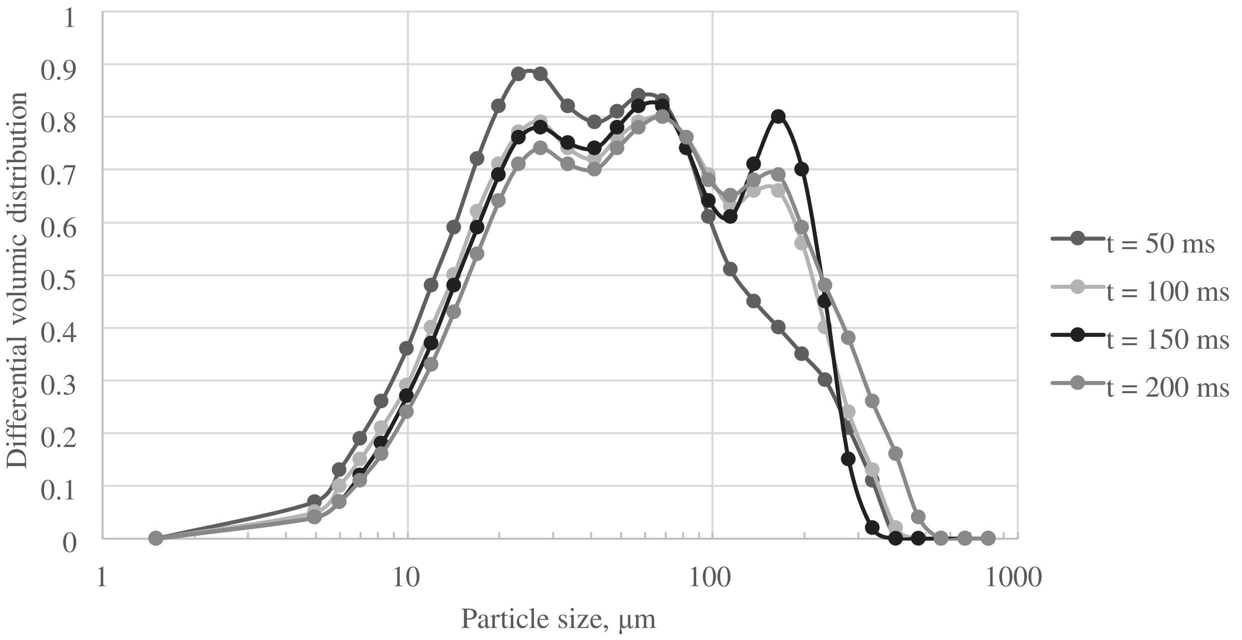

Fig. 1. *Time evolution of the PSD of cellulose for times ranging from 50 to 200 ms after a free-fall dispersion through the laser diffraction sensor.*

2.2 *Analysis of the pyrolysis and combustion gases*

The tests were carried out using a modified Godbert-Greenwald furnace similar to the one used by Dufaud et al. (2012a), used here to realize flash-pyrolysis and combustion experiments. This paper will mainly focus on the pyrolysis step. In this device, shown below in Figure 2, dust is dispersed into the vertical tubular furnace with a pulse of gas (air for combustion and argon for pyrolysis). The emitted gases are then collected in a collapsible Tedlar bag situated at the bottom of the device and are analyzed with a micro gas chromatograph (µGC, Varian, CP 4900). Tests were performed thrice to obtain results with a good reproducibility degree.

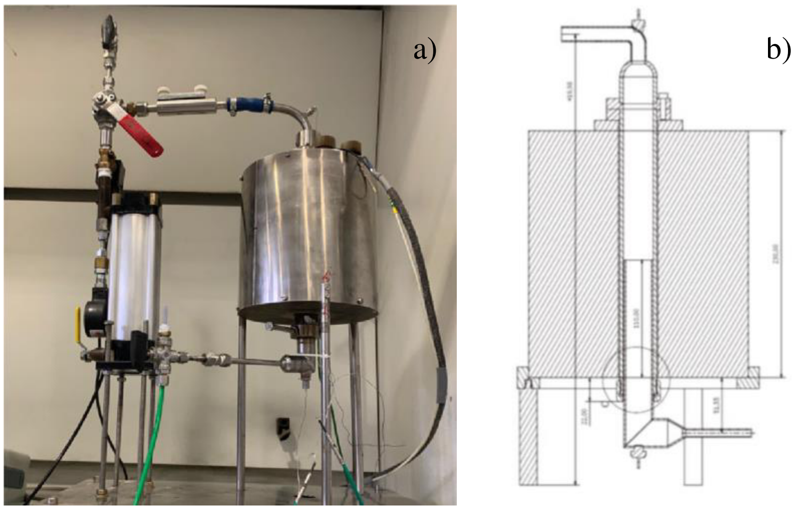

Fig. 2. *a) Experimental setup used for the combustion and pyrolysis experiments, b) focus on the modified Godbert-Greenwald furnace*

The pyrolysis and combustion products have been determined at temperatures of 973 K, 1073K and 1173 K, with masses of the samples varying between 0.1 g and 0.4 g and with an estimated residence time of 200-250 ms. This time was determined by visualizing the powder entering and exiting the furnace thanks to a high-speed video camera. For this study, the amount of powder was set at 0.2 g, corresponding to a dust concentration in the GG furnace of approximately 600 g.m^{-3}, by considering both the minimum explosive concentration (MEC) and the stoichiometric concentration of the powders.

During the pyrolysis of organic powders, permanent gases, tar and char are generated (Nowakowska et al., 2018). It should be underlined that, as the quantities of char and tar collected on small grids placed at the bottom of the tube were very small with regard to the experimental reproducibility, no reliable information could be obtained from such measurements. As a consequence, both proportions will be deduced from a mass balance.

2.3 *Determination of the unstretched flame velocity*

Flame propagation tests were carried out in a modified Hartmann tube, which is a semi-open tube of 1 m long, with a square section of 7x7 cm^2 (Cuervo, 2015; Cuervo et al., 2017). The powder is dispersed with a 7 bar compressed air pulse and then ignited with a 1 J electric spark. The electrodes are 9 cm above the dispersion nozzle. The ignition delay time tv, i.e. the time between the dispersion and the ignition was set at 180 ms. This value results from a compromise between a high tv which ensures a weak turbulence of the dust cloud and a low tv which avoids the segregation of the particles (Figure 1b). Tests were performed with 1 g of powder.

Flame propagation was recorded using a high-speed video camera (MotionBlitz EoSens mini2) and a Matlab code developed by Cuervo (2015) was used to identify both the flame front position and flame surface area. Then, assuming a linear relationship between the flame spatial velocity and the stretching factor (Karlovitz factor) (Clavin, 1985; Markstein, 1964), the unstretched 'laminar' burning velocity can be estimated (Cuervo et al., 2017).

2.4 *Dust explosion severity*

Experiments were performed using a standard 20L spherical vessel, equipped with a rebound nozzle. Two 5 kJ chemical igniters were used as ignition sources. The sphere was externally cooled with water at a temperature ranging between 20 and 30°C. The maximum pressure Pm and maximum rate of pressure rise, dP/dt_m, were determined for each test. The maxima of these parameters over a wide range of concentration will be called Pmax and dP/dt_{max}. Applying the 'cube-root law', the Kst parameter will be deduced (Bartknecht, 1989).

3. Results and discussion

The main part of this article will be focused on the determination of the pyrolysis mechanisms of starch and cellulose. Then, the results of flame propagation and explosion tests performed on cellulose will be described.

3.1 *Model development for the pyrolysis of organic powders*

As previously said, during an organic dust explosion, the combustion of the powder occurs in three main steps: first, the particle heating, then the pyrolysis/devolatilization and finally the oxidation of the gases that have been produced by the pyrolysis. It is then interesting to introduce the Damköhler number Da, which in this case represents the ratio of the characteristic time of the diffusion of the pyrolysis products (from the particle surface to the bulk of the gas phase) over the pyrolysis reaction time. The rate-limiting step of the process depends notably on the particle size distribution of the powder. In fact, the bigger the particles are, the longer it will take for the two first steps to occur. When the oxidation in gaseous phase is very fast, three limitations can be considered as a function of the particle diameter and the external temperature. In Figure 3, four different pyrolysis kinetics have been considered (Chan et al., 1985; Di Blasi & Branca, 2001; Font et al., 1990; Wagenaar et al., 1993), but it should be stressed that they were usually obtained from thermogravimetric analyses or fluidized bed experiments (Cuervo, 2015). Considering the mean particle diameter of cellulose and starch powders used in this work and a temperature range of 973 - 1173 °K, it can be seen that the pyrolysis mechanism is supposed to be mainly 'reaction-limited'. For very small particles, the oxidation can be the slowest step of the process. In this case, all the pyrolysis gases are emitted very quickly and will then react with oxygen to form the combustion products: the explosion is therefore 'diffusion limited'.

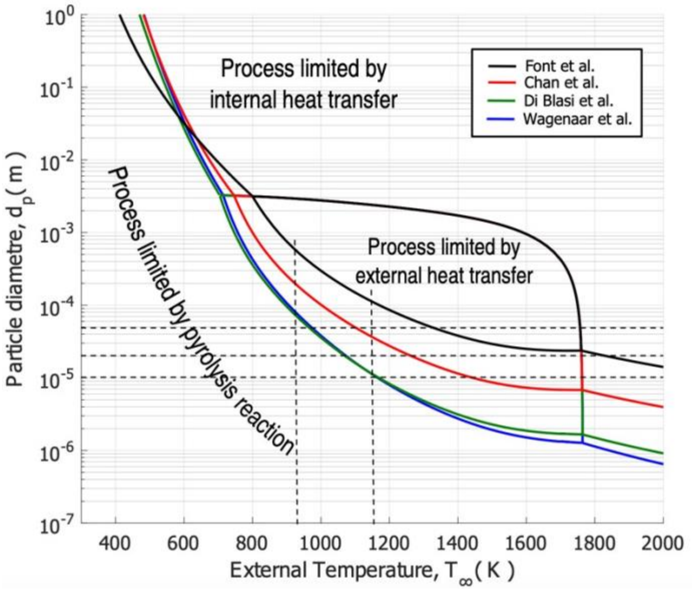

Fig. 3. *Regime limits as a function of the particle diameter and the external temperature*

It has been shown by Dufaud et al. (2012b) that the critical particle size corresponding to an intermediate regime (Da ≈ 1) for wheat starch is 30 µm. The choice has thus been made to develop two models: a first one to predict the pyrolysis products of organic compounds, which would then be implemented in a second model to represent the distribution of their combustion products. This paper will be mainly focused on the pyrolysis model, which aims to describe the solid phase devolatilization phenomena.

3.1.1 *Approach and assumptions*

A simplified model for the pyrolysis of organic compound was developed, whose aim is to predict the proportions of the different species emitted during this process. The model was based on the first experimental results carried out on starch dispersed in the furnace with argon, and is inspired by the mechanisms of biomass pyrolysis developed by Ranzi et al. (2017). For simplicity purposes, only three main reactions were considered to represent the emission of the pyrolysis products (Equations 1- 3). It should be underlined that the purpose of this model was not to represent thoroughly the pyrolysis phenomenon with all the gases potentially generated, but to present a simple alternative route based on a few reactions which will be easily integrated in a more global model.

$$C_6H_{10}O_5 \overset{k_1}{\rightarrow} n_1\,H_2 + n_2\,CO + n_3\,CO_2 + n_4\,CH_4 + n_5\,C_2H_4 + n_6\,H_2O + n_7\,C_2H_4O \quad (1)$$

$$C_6H_{10}O_5 \overset{k_2}{\rightarrow} m_1\,H_2 + m_2\,CO + m_3\,CO_2 + m_4\,CH_4 + m_5\,C_2H_4 + m_6\,H_2O + m_7\,C_2H_4O \quad (2)$$

$$C_6H_{10}O_5 \overset{k_3}{\rightarrow} 5\,H_2O + 6\,C \quad (3)$$

In this model, the two first equations represent the emission of the main pyrolysis gases as well as water and acetaldehyde (C_2H_4O). This compound should be considered as a surrogate for the tars and other permanent gases not considered here, rather than as acetaldehyde itself. Equations 1 and 2 are similar in their structure; but introducing this set of reactions in the model was necessary to explain the evolution of the different gas concentrations as a function of temperature. Indeed, experiments have shown that gas concentrations can either increase or decrease with temperature. Considering a single equation and strictly positive activation energies, as proposed by Ranzi et al. (2017), would only uniformly increase the gas concentration with temperature, which is inadequate. Equation 3 has been introduced to represent the formation of char (indicated as C in the reaction).

In addition to the simplification made on acetaldehyde generation, this model is based on the following assumptions: i) the pyrolysis takes place in an inert atmosphere (this has been verified as the amount of N_2, which would attest an air leak, was also analyzed by micro gas-chromatography), ii) both starch and cellulose are represented by the chemical formula $C_6H_{10}O_5$ and no impurity is present, iii) the powders are dried so there is no water inlet, iv) the reaction rate *i* can be written as:

$$r_i = k_i \, . [C_6H_{10}O_5] \qquad (4)$$

3.1.2 Solving method

A system of equations, based on the carbon, hydrogen and oxygen balances, was developed in order to determine the coefficients n_i, m_i and of the reaction rate constants k_i. It should be noted that the coefficients k_i are expressed using the Arrhenius law and depend on a pre-exponential factor A_i and an activation energy E_i. Rather than solving the system with the A_i and E_i as unknowns, which would introduce exponential functions, the coefficients n_i, m_i and k_i were determined for different temperatures. Then, the evolution of k_i as a function of the temperature allows the determination of A_i and E_i.

The concentrations of the following gases can be obtained directly through chromatographic measurements: carbon monoxide, hydrogen, carbon dioxide, methane and ethylene. By considering the furnace as a stirred tank reactor and expressing the products concentration as a function of the carbon monoxide content, five ratios can be expressed as, for instance:

$$\frac{[H_2]}{[CO]} = \frac{n_1\, k_1 + m_1\, k_2}{n_2\, k_1 + m_2\, k_2} \qquad (5)$$

It was unfortunately, in this study, impossible to quantify precisely the amount of char and tar. However, estimated values of two remaining ratios can be obtained by applying atomic balances (C, H and O) to the experimental results, knowing the inlet dust concentration.

The system was solved using Matlab® with the function 'lsqnonlin', which is based on the resolution of a non-linear system of equations by the least square fitting. Lower boundaries were set to zero for the stoichiometric coefficients and the reaction rate constants. With regard to the results obtained by Ranzi et al. (2017), an upper limit of 1010 was set for the reaction rate constants.

3.1.3 Results of the pyrolysis tests

The results of the pyrolysis tests are presented in Table 2 for starch and cellulose for 973 and 1173K. It should be noticed that carbon monoxide and hydrogen are the main gases (in molar proportions) produce by the pyrolysis, which is consistent with the literature (Commandre et al., 2011). Even if the orders of magnitude are close, differences are noticeable between the two products, especially at 973K. For both powders, the CO/CO_2 ratio, hydrogen, ethylene and methane contents increase with the temperature. These trends are consistent with the shift of the C/CO_2 equilibrium towards CO when temperature increases. Moreover, the significant growth of hydrogen content for cellulose is not compensate by a decrease of methane, as methane conversion to hydrogen is made difficult by steam reforming (Commandre et al., 2011). Then, H_2 evolution is certainly due to water reaction.

Table 2: *Permanent dry gases generated by pyrolysis of 0.2 g of starch or cellulose at 973 and 1173K*

Molar fraction (%)	**Starch (973 K)**	**Starch (1173 K)**	**Cellulose (973 K)**	**Cellulose (1173 K)**
H_2	26.8	23.8	12.6	28.1
CO	55.2	58.7	58.2	45.3
CO_2	15.1	8.6	20.4	12.9
CH_4	1.3	5.0	5.6	8.2
C_2H_4	1.6	3.9	3.2	5.5

By applying atomic balances to the experimental results, the concentrations of 'char' (carbon), 'tar' (represented here by acetaldehyde) and water can be determined. For instance, for both starch and cellulose, the acetaldehyde concentration is approximately divided by 2 when the temperature increases from 973 to 1173K. This trend is consistent with the fact that, at high temperatures, the final amount of tar is lower as it transforms into char and secondary gases. The water concentration seems to be rather constant for starch, but significantly decreases with temperature for cellulose, which can be coupled with the H_2 production shown in Table 2.

3.1.4 Results of the pyrolysis model

Using the resolution method previously described, the coefficients of the equations 1 and 3 have been determined as follows (Equations 6-7) for wheat starch:

$$C_6H_{10}O_5 \overset{k_1}{\rightarrow} 1.17\ H_2 + 3.4\ CO + 0.02\ CO_2 + 0.45\ CH_4 + 0.32\ C_2H_4 + 0.83\ H_2O + 0.72\ C_2H_4O \quad (6)$$

$$C_6H_{10}O_5 \overset{k_2}{\rightarrow} 0.8\ H_2 + 1.7\ CO + 0.55\ CO_2 + 0.04\ CH_4 + 0.05\ C_2H_4 + 0.4\ H_2O + 1.83\ C_2H_4O \quad (7)$$

$$C_6H_{10}O_5 \overset{k_3}{\rightarrow} 5\ H_2O + 6\ C \quad (3)$$

The activation energies and pre-exponential factors of the three reaction rate constants k_i are shown in Table 3. These values are in good agreement with those determined by Ranzi et al. (2017). It is thus possible to predict the distribution of the pyrolysis products for any given temperature between 973 K and 1173 K. A verification has been performed by running the program at 1073K and comparing the results with an additional set of experimental values. The composition of the pyrolysis products calculated with the program can be seen below in Figure 4. The gas concentrations show a satisfactory match between the model and the experimental results, which tends to validate the model.

Table 3: *Parameters of the reaction rate constants k_i determined for starch*

Reaction rate constants	**Pre-exponential factor (s^{-1})**	**Activation energy ($kJ.mol^{-1}$)**
k_1	$1.2x10^{17}$	318.6
k_2	$8.8x10^{17}$	41.0
k_3	$2.8x10^{5}$	72.6

DOI: 10.7795/810.20200724

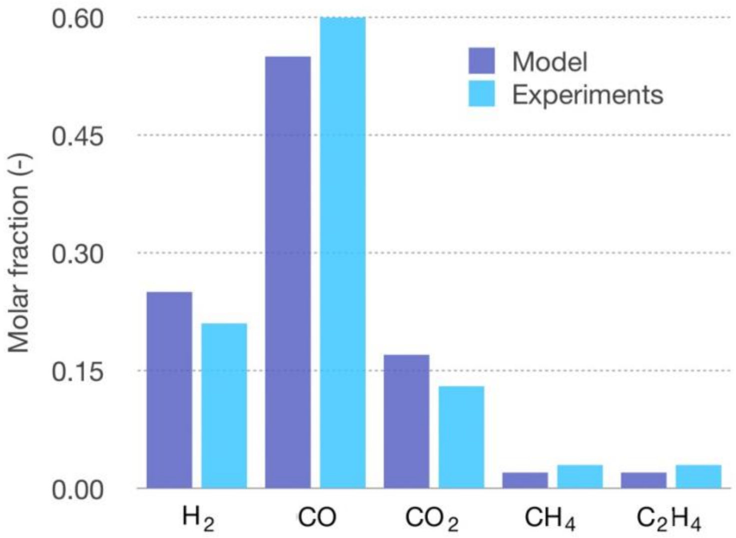

Fig. 4. *Comparison between experimental and calculated gas molar fractions for starch at 1073K*

The same development has been done for cellulose powder. Figure 5 shows the evolution of water vapor, tar (represented by acetaldehyde), char and permanent gases for cellulose powder. As observed for starch, the molar fraction of permanent gases increases with the temperature, whereas both water and char content decrease.

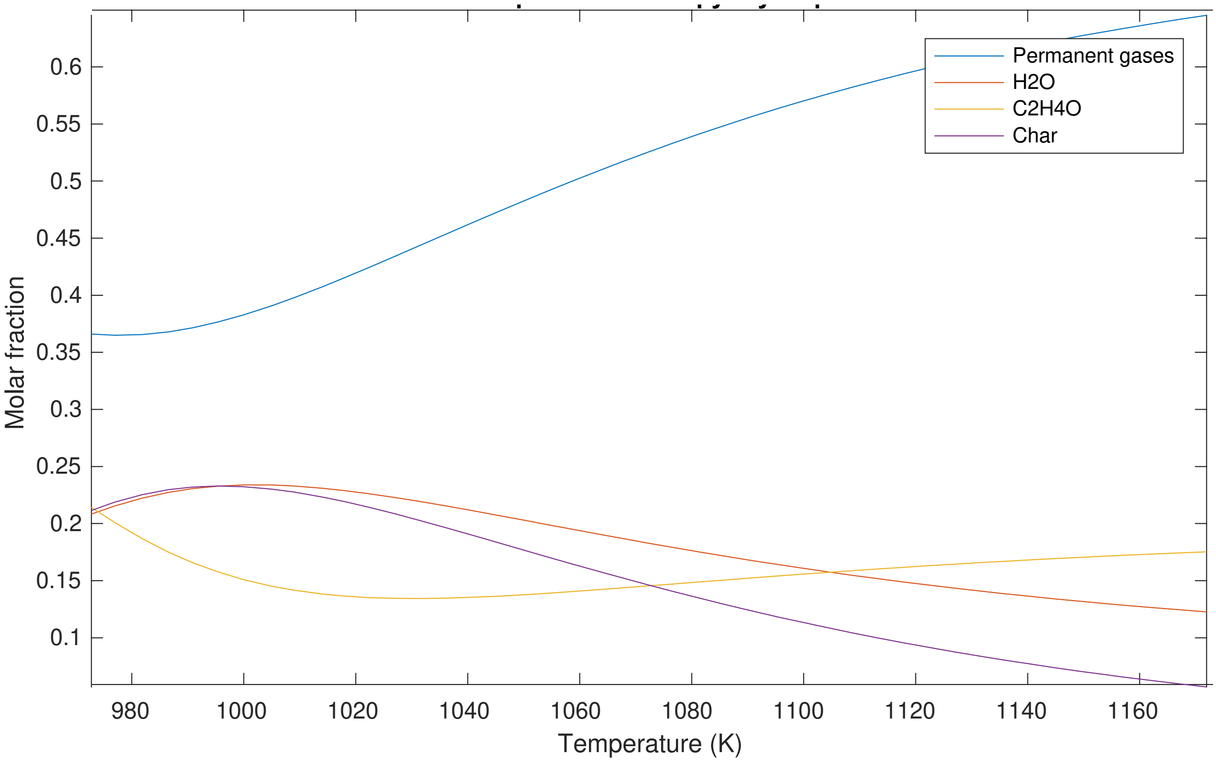

Fig. 5. *Evolution of the global composition of the pyrolysis products of cellulose from 973 to 1173K*

A similar approach has been used to model the combustion step. The results of combustion experiments performed in the Godbert-Greenwald furnace were used to fit two additional oxidation reactions complementing the global reaction mechanism. It seems that the distribution of the gases varies less with temperature than during the pyrolysis step; moreover, as expected, the concentration of carbon dioxide produced during the combustion (molar fraction of 0.51) exceeds largely the amounts created during pyrolysis.

DOI: 10.7795/810.20200724

3.4 *Towards the determination of the burning velocity*

As previously said, a simplified mechanism of a few lumped reactions can be used to assess a burning velocity (Torrado et al., 2018). The flame propagation of starch and cellulose in a semi-open tube was then studied in order to determine a spatial flame velocity and estimate the laminar flame velocity. For instance, Figure 6 illustrates the flame propagation of a cellulose dust cloud.

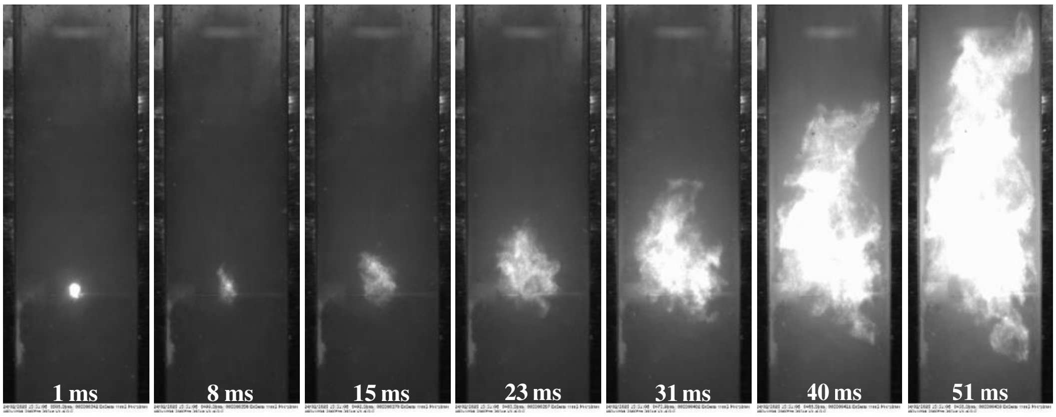

Fig. 6. *Flame propagation of cellulose: 1 J, t_v 180 ms, 1 g of powder*

Following the approach developed by Cuervo et al. (2017), the flame velocity can be plotted as a function of the stretching factor or Karlovitz factor, representing the time evolution of the flame surface area. Figure 7 shows that a linear trend can be observed for low stretching factors, the intercept corresponding theoretically to the laminar flame velocity of this cellulose/air mixture. A laminar flame velocity of 21.5 cm.s-1 is obtained for the cellulose, which is in good agreement with the laminar burning velocity of nanocellulose determined by Santandrea et al. (2020), i.e. 21 cm.s-1. Further tests should be performed to cover a wide range of conditions and the choice of a linear or non-linear regression to determine the intercept, and thus the laminar flame velocity, should be debated.

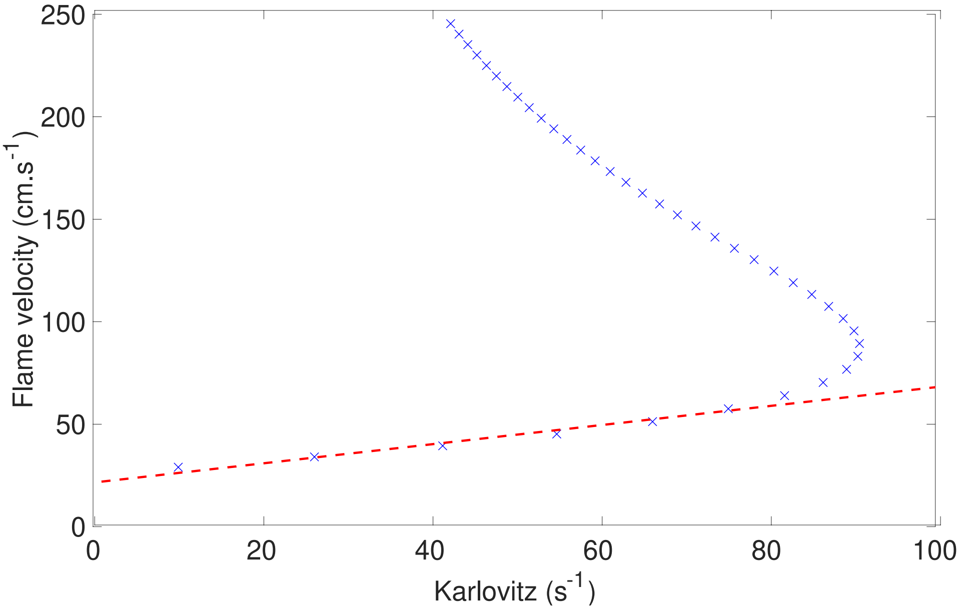

Fig. 7. *Flame velocity versus stretching factor for a cellulose explosion – t_v =180 ms, 1 J, mass 1 g*

3.5 Explosion severity of organic powders

The final objective of proposing a simplified mechanism for the combustion of organic dusts is to model the explosion severity, especially the safety parameters determined under standard conditions in a 20L vessel. Preliminary tests were carried out to assess the maximum explosion pressure and maximum rate of pressure rise of cellulose (Figure 8). By considering the average values of three tests series, P_{max} reaches 6.8 bar, whereas $(dP/dt)_{max}$ is 287 bar/s, which corresponds to a K_{St} parameter of 78 bar/m/s. This latter parameter is consistent with the literature data for cellulose powder with a mean diameter ranging from 30 to 51 µm (BGIA, 1997) and with the value obtained for microcrystalline cellulose (d_{50} = 108 µm), i.e. 86 bar/m/s (Santandrea et al., 2020). However, if P_{max} is lower than the literature values for similar diameters, the whole PSD has to be considered (Figure 1b) and additional tests should be performed between 500 and 1000 $g.m^{-3}$.

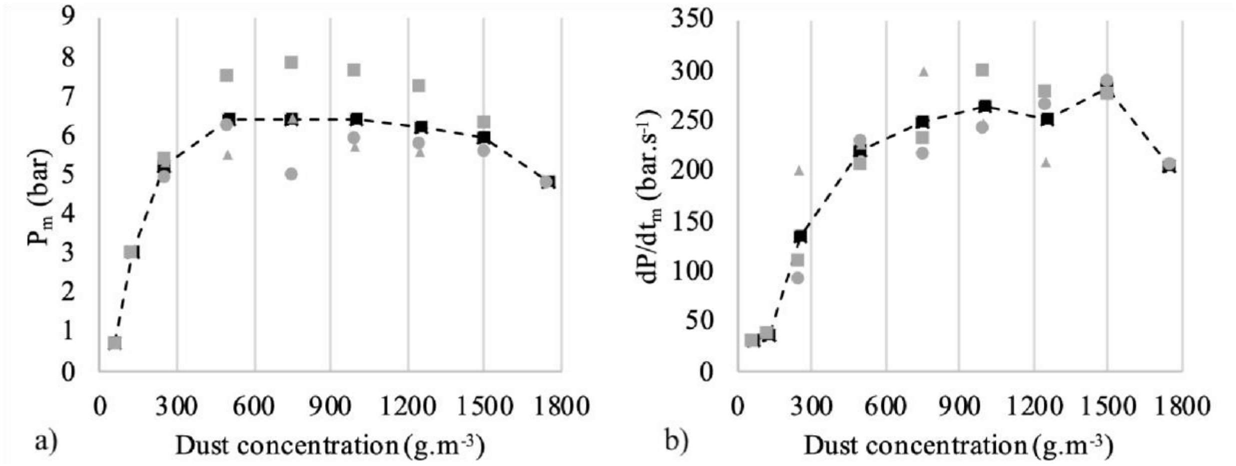

Fig. 8. *Explosion severity of cellulose (d_{50} = 53.3 µm) determined with various series of experiments (the dotted line corresponds to the average values).*

4. Conclusions

Briefly During the explosion of organic powders, the particles undergo a pyrolysis process, emitting pyrolysis gases in quantities varying with the temperature. When mixed with oxygen, the oxidation reaction leads to heat generation and a flame propagation. As a function of the Damköhler number, proposing a semi-global reaction mechanism for the pyrolysis or the oxidation step is therefore essential to develop a more global model aiming at assessing the dust explosion severity.

The pyrolysis model, developed for starch and cellulose, needs to be refined by better taking into account the ‘char’ generation, the influence of water, as well as the particle size distribution. Once validated for various PSD of starch, cellulose and mixtures of both products, the reaction mechanisms will be integrated in another existing model (Torrado et al, 2018) to estimate the laminar flame velocity and, in a second time, the maximum rate of pressure rise of organic compounds in a 20L sphere.

References

Bartknecht, W. (1989). *Dust-explosions: Course, Prevention, Protection*. Springer-Verlag, Berlin.

BGIA (1997). *Combustion and explosion characteristics of dusts*. BIA-Report 13/97 and Gestis Database, HVBG, Sankt Augustin, Germany.

Chan, W.C.R., Kelbon, M. & Krieger, B.B. (1985). Modelling and experimental verification of physical and chemical processes during pyrolysis of a large biomass particle, *Fuel,* 64(11):1505–1513.

Clavin, P. (1985). Dynamic behavior of premixed flame fronts in laminar and turbulent flows. *Progress in Energy and Combustion Science*, 11: 1–59.

Commandre, J.M., Lahmidi, H., Salvador, S. & Dupassieux, N. (2011). Pyrolysis of wood at high temperature: The influence of experimental parameters on gaseous products. *Fuel Processing Technology*, 92(5):837 - 844.

Cuervo, N. (2015). *Influences of turbulence and combustion regimes on explosions of gas-dust hydrid mixtures* (PhD Thesis). The University of Lorraine, France (in English).

Cuervo, N., Dufaud, O. & Perrin, L. (2017). Determination of the burning velocity of gas/dust hybrid mixtures. *Process Safety and Environmental Protection*, 109: 704–715.

Di Blasi, C. & Branca, C. (2001). Kinetics of primary product formation from wood pyrolysis. *Industrial & Engineering Chemistry Research*, 40(23): 5547–5556.

Dufaud, O., Poupeau, M., Khalili, I., Cuervo, N., Christodoulou, M., Olcese, R., Dufour, A. & Perrin, L. (2012a). Comparing pyrolysis gases and dusts explosivities: a clue to understanding hybrid mixtures explosions? *Industrial & Engineering Chemistry Research*, 51(22): 7656–7662.

Dufaud, O., Khalili, I., Cuervo, N., Olcese, R., Dufour, A., Perrin, L. & Laurent, A. (2012b). Highlighting the importance of the pyrolysis step on dusts explosions, *Chem. Eng. Trans.*, 2012062, 369–374.

Font, R., Marcilla, A., Verdu, E. & Devesa, J. (1990). Kinetics of the pyrolysis of almond shells and almond shells impregnated with cobalt dichloride in a fluidized bed reactor and in a pyroprobe 100. *Industrial & Engineering Chemistry Research,* 29(9): 1846–1855.

Markstein, G.H., (1964). *Non-Steady Flame Propagation*. Pergamon, New York.

Nowakowska, M., Herbinet, O., Dufour, A. & Glaude, P.A. (2018). Kinetic study of the pyrolysis and oxidation of guaiacol. *Journal of Physical Chemistry A*, 122 (39): 7894-7909.

Ranzi, E., Debiagi, P.E.A. & Frassoldati, A. (2017). Mathematical modeling of fast biomass pyrolysis and bio-oil formation. Note I: kinetic mechanism of biomass pyrolysis. *ACS Sustain. Chem. Eng.*, 5(4): 2867–2881.

Rathnayaka, S., Khan, F. & Amyotte, P. (2014). Risk-based process plant design considering inherent safety. *Safety Science*, 70:438-464.

Santandrea, A., Gavard, M., Pacault, S., Vignes, A., Perrin, L. & Dufaud, O. (2020). ‘Knock on nanocellulose’: Approaching the laminar burning velocity of powder-air flames. *Process Safety and Environmental Protection*, 134: 247–259.

Torrado, D., Pinilla, A., Amin, M., Murillo, C., Munoz, F., Glaude, P.-A. & Dufaud, O. (2018). Numerical study of the influence of particle reaction and radiative heat transfer on the flame velocity of gas/nanoparticles hybrid mixtures. *Process Safety and Environmental Protection*, 118: 211-226.

Wagenaar, B. M., Prins, W. & van Swaaij W.P.M. (1993). Flash pyrolysis kinetics of pine wood. *Fuel Processing Technology*. Third international rolduc symposium on coal science and technology and related processes, 36(1): 291– 298.

DOI: 10.7795/810.20200724

Effect of multiple vent characteristic parameters on external explosion induced by indoor premixed methane-air explosion

Lei Pang [a,b], Qianran Hu [a], Yang Hu [c], Pengfei Lv [a,b] & Kai Yang [a,b,¯]

[a] School of Safety Engineering, Beijing Institute of Petrochemical Technology, Beijing 102617, China
[b] Beijing Academy of Safety Engineering and Technology, Beijing 102617, China
[c] School of Safety Engineering, North China Institute of Science & Technology, Yanjiao 065201, China

E-mail: ycyangk@bipt.edu.cn

Abstract

In order to reveal the influence of the vent characteristic parameters on the dynamic mechanism of external explosion induced by the inner premixed methane-air explosion, based on the characteristics of typical large-scale rooms, the evolution process of external flow field such as outdoor unburned gas cloud distribution, characteristics of vented flame propagation and turbulence under different vent opening pressures, opening times and pressure relief ratios ($K_v = A_v/V^{2/3}$) were studied by means of computational fluid dynamics, and the influence laws of the external flow field parameters on the characteristics of external explosion such as the overpressure intensity, the occurrence time interval and the occurrence location of external explosion were systematically clarified. The results show that the axial distribution range of external high-concentration unburned gas cloud decreases with the increase of the vent opening pressure and opening time, and the shape of unburned gas gradually changes from jet shape to sag towards the direction of vent with the K_v increasing. The vented flame and the unburned gas cloud keep the same evolutionary trend. The vented flame speed, turbulence intensity, and turbulence range ($k > 1$ m^2·s^{-2}) all increase significantly with the increase of the opening pressure, opening time, and the decrease of the pressure relief ratio. As the vent parameters increase, the occurrence time interval of external explosion gradually shortens, and the occurrence location of external explosion more closes to the vent. The occurrence time interval is related to the flame speed, distribution range of unburned gas cloud, and flow field turbulence, while the occurrence location has a main relationship with the unburned gas cloud distribution. The correlation between the external explosion overpressure

---

[¯] Corresponding author. School of Safety Engineering, Beijing Institute of Petrochemical Technology, Beijing 102617, China.
E-mail addresses: ycyangk@bipt.edu.cn (K. Yang).

and outdoor flow field parameters under different vent characteristic parameters is complex, and any change in the flow field parameters will have a significant impact on the explosion overpressure intensity. The conclusion will provide theoretical basis for the gas explosion hazard assessment, external explosion hazard prevention and control, and explosion pressure relief design.

Keywords: *gas explosion, venting, external explosion, flow filed*

1 Introduction

Explosion venting is an effective method for controlling gas explosion hazard happening in a confined space (Yang et al., 2018). As the high-pressure unburned gas and combustion products are timely released to the outdoors during the explosion venting, the indoor explosion peak overpressure will rapidly reduce and the damage of explosion overpressure on equipment and buildings could be avoided. However, when a vented explosion occurs in a confined space, a large amount of combustible gas and high-speed flame will be discharged through the vent at the moment of the vent opening, which will cause complex changes in the outdoor flow field. Under certain special conditions, the vented flame will ignite the outdoor flammable gas cloud, and an external explosion will occur, which may induce a serious secondary disaster, and pose a potential threat to the surrounding environment, equipment and personnel (Bao et al., 2005; Chen et al., 2006; Proust and Leprette, 2010).

The external explosions will not only increase outdoor explosion hazard (Sun et al., 2018), but also cause significant changes in indoor flow field and overpressure (Harrison and Eyre, 1987; Tomlin et al., 2015; Yang et al., 2019). Therefore, more and more attention has been paid to the formation mechanism and disaster effects of external explosions in recent years. Wang et al. (2017) used numerical methods to investigate the formation process of external explosion induced by indoor gas explosion, and the results showed that the high-speed combustible gas was ejected through the vent under the effect of the indoor and outdoor pressure difference, and a combustible gas cloud was formed outdoors (Jiang et al., 2014), when the vented flame reached the outside, the external high-temperature preheating gas cloud was ignited, and a severe turbulent combustion occurred which led to a sharp rise in the outdoor pressure. Guo et al. (2015) studied the effects of ignition position and gas concentration on hydrogen explosion characteristics using a small-scale explosion experimental device, the analysis found that the external explosion overpressure caused by the rear ignition was the largest, and the overpressure increased first and then decreased with the increase of hydrogen concentration. Ye et al. (2004) found that the external maximum explosion overpressure increased with the increase of the vent opening pressure when the equivalent ratio of the methane was the same (Cao et al., 2017). Zhang et al. (2018) and Pang et al. (2019) used the computational fluid dynamics software AutoReaGas to investigate the effect of pressure relief ratio ($A_v/V^{2/3}$, where A_v is the vent area and V is the volume of the explosion chamber) and vent opening time on vented hydrogen explosion characteristics. The external explosion overpressures all increased first and then decreased with the increase of pressure relief ratio and vent opening time. Sun et al. (2019) studied the effect of aluminum plate inertia on the vented gas explosion, it was found that during the opening of aluminum plate, the vented flame first appeared on the two sides of the aluminum plate instead of directly in front, thereby the external explosion overpressure weakened. However, the process of external explosion induced by indoor gas explosion is extremely complicated, it not only involves various physical processes such as combustion, thermodynamics, and fluid dynamics, but also is very susceptible to the vent characteristic parameters such as the opening pressure, opening time, vent area, and other influencing factors such as gas concentration, ignition location, and indoor obstacles (Chen et al., 2006). Although a large number of studies have revealed the influence of the vent characteristic parameters on external explosion overpressure, they have not conducted in-depth research on the formation conditions and processes of external explosions. Relevant researches show that the occurrence of external explosions should have at least three conditions at the same time (Du et al., 2006): (1) A large amount of combustible gas; (2) Severe turbulence and vortices; (3) vented flame. Under the different vent characteristic parameters, the outdoor distribution characteristics of unburned gas cloud, the vented flame propagation speed, and the turbulence intensity of flow field all show different distribution laws, and any changes of above factors may cause significant changes in the external explosion characteristics such as the explosion overpressure intensity, the explosion occurrence time interval (The time lag between the vent rupture and the occurrence of the external explosion) and the explosion occurrence location (the distance between the center of external explosion fireball and the vent). Although, the existing literatures have conducted a detailed study of external explosion overpressure, and the characteristics of external flow field and external explosion under different vent characteristic parameters haven’t been systematically analyzed.

Therefore, this work used the computational fluid dynamics software AutoReaGas to establish a large-scale explosion physical model. Vented explosion of methane/air mixture was taken as the research object. The influences of vent characteristic parameters such as opening pressure, opening time and pressure relief ratio on the external flow field parameters such as the distribution of external unburned gas cloud, vented flame propagation and flow field turbulence, and the characteristics of external explosion such as the explosion overpressure, occurrence time interval and occurrence location were studied. And the cause and process of the external explosion induced by indoor premixed methane/air explosion was analysed deeply. The research results have important theoretical and practical significance for establishing accurate external explosion overpressure prediction models, scientifically designing explosion pressure relief facilities, and mitigating the hazardous effects of external explosions.

2 Research methods

2.1 Numerical models

The gas explosion dynamics simulation software AutoReaGas based on computational fluid dynamics technology is suitable for gas explosion and shock dynamics problems. In addition, in the PRESSURFS boundary condition in

DOI: 10.7795/810.20200724

AutoReaGas, a static threshold pressure can be set for a specific surface structure based on the actual situation to determine the transient vented explosion flow field in a confined space. Thus, the software is used to study the pre-mixed gas vented explosion in confined spaces. AutoReaGas numerically solves a series of sets of simultaneous equations, such as mass, momentum and energy conservation equations, mainly using the finite volume method. The following representations can be obtained using Cartesian tensors:

The mass-conservation equation is

$$\frac{\partial\rho}{\partial t}+\frac{\partial}{\partial x_j}\left(\rho u_j\right)=0 \tag{1}$$

The momentum-conservation equation is

$$\frac{\partial}{\partial t}\left(\rho u_i\right)+\frac{\partial}{\partial x_j}\left(\rho u_j u_i\right)=-\frac{\partial p}{\partial x_i}+\frac{\partial\tau_{ij}}{\partial x_j} \tag{2}$$

The energy-conservation equation is

$$\frac{\partial}{\partial t}\left(\rho E\right)+\frac{\partial}{\partial x_j}\left(\rho u_j E\right)=\frac{\partial}{\partial x_j}\left(\Gamma_E\frac{\partial E}{\partial x_j}\right)-\frac{\partial}{\partial x_j}\left(p u_j\right)+\tau_{ij}\frac{\partial u_i}{\partial x_j} \tag{3}$$

where x is the space coordinate, t is the time coordinate, ρ is the density, u is the velocity, p is the static pressure, and i and j are the coordinate directions. The specific internal energy is $E = C_V T + m_{fu} H_c$, where C_V is the constant-volume specific heat, T is the temperature, m_{fu} is the mass fraction of the fuel, and H_c is the heat of combustion. The turbulent-diffusion coefficient is $\Gamma_{*} = \mu_t / (\sigma)^{*}$, where $(\sigma)^{*}$ is the default value of the turbulent Prandtl constant. τ_{ij} is the viscous stress tensor; its expression is

$$\tau_{ij}=\mu_t\left(\frac{\partial u_i}{\partial x_j}+\frac{\partial u_j}{\partial x_i}\right)-\frac{2}{3}\delta_{ij}\left(\rho k+\mu_t\frac{\partial u_i}{\partial x_j}\right) \tag{4}$$

where the turbulence-viscosity coefficient $\mu_t = C_\mu \rho k^2 / \varepsilon$, where k and ε are the turbulent kinetic energy and its dissipation rate, δ_{ij} is the Kronecker delta, and the value of the model constant C_μ is 0.09 m^2/s. The turbulence in the vented gas explosion process is described by the standard k-ε turbulence model. It consists of two conservation equations for k and ε, respectively:

$$\frac{\partial}{\partial t}\left(\rho k\right)+\frac{\partial}{\partial x_j}\left(\rho u_j k\right)=\frac{\partial}{\partial x_j}\left(\Gamma_k\frac{\partial k}{\partial x_j}\right)+\tau_{ij}\frac{\partial u_i}{\partial x_j}-\rho\varepsilon \tag{5}$$

$$\frac{\partial}{\partial t}\left(\rho\varepsilon\right)+\frac{\partial}{\partial x_j}\left(\rho u_j\varepsilon\right)=\frac{\partial}{\partial x_j}\left(\Gamma_\varepsilon\frac{\partial\varepsilon}{\partial x_j}\right)+C_1\frac{\varepsilon}{k}\tau_{ij}\frac{\partial u_i}{\partial x_j}-C_2\frac{\rho\varepsilon^2}{k} \tag{6}$$

where C_1 and C_2 are constants(C_1, C_2=*1.44* and 1.79). A one-step reaction model is used to describe the combustion process of the fuel/air mixture. This is mathematically formulated as a conservation equation for the fuel mass fraction:

$$\frac{\partial}{\partial t}\left(\rho m_{fu}\right)+\frac{\partial}{\partial x_j}\left(\rho u_j m_{fu}\right)=\frac{\partial}{\partial x_j}\left(\Gamma_{fu}\frac{\partial m_{fu}}{\partial x_j}\right)+R_{fu} \tag{7}$$

The volume combustion rate $R_{fu} = C_t \rho\ (s_t^2/\Gamma_{fu})\ R_{\min}$, where R_{min} is the minimum of the mass fractions for fuel, oxygen, and the reaction product, and C_t is the combustion-model constant (C_t = 40). The turbulence combustion velocity is expressed as:

$$S_t=1.8u_t^{0.412}\cdot L_t^{0.196}\cdot S_l^{0.784}\cdot\nu^{-0.196} \tag{8}$$

Where u_t is the turbulence intensity, L_t is the characteristic length of the turbulence, S_l is the specific laminar combustion velocity, and v is the fluid dynamic viscosity.

The effective laminar burning velocity S_b can be expressed as:

$$S_b = S_l(1 + F_s R_f) \tag{9}$$

Where S_l is the specific laminar combustion velocity, R_f is the spherical flame radius, F_s is the laminar flame acceleration coefficient, and the value is 0.15.

2.2 Verification of grid independence

AutoReaGas uses an 8-node structure grid to discretize the space, while using sub-grid technology to describe the effect of small-scale entities on the flow field (Pang et al., 2011). In order to investigate the effect of grid size on the accurate capture of the explosion flow field, a room with dimensions of 5 m × 2 m × 2.5 m was selected, and there were no obstacles in the room. A vent with a size of 0.5 m × 0.5 m was set on the smaller vertical wall of the room, the vent opening pressure was 60 kPa and the opening time was 0 s. The room was filled with a static methane/air premixed gas at a volume concentration of 9.5%, and the ignition source was located at the geometric center of the rear wall. For this physical model, two sets of dimensions: 0.1 m × 0.1 m × 0.1 m (M1) and 0.05 m × 0.05 m × 0.05 m (M2) were used to mesh it, and the peak overpressures of the two examples were compared and analyzed. Table 1 showed the comparison of peak overpressures under two grid sizes. It was concluded that the relative discrepancy of the peak overpressures was less than 9%, indicating that the two grid sizes had less effect on this work and all were suitable to this study (Pang et al., 2019). Therefore, in order to save time and improve calculation efficiency, the grid M1 was used to perform numerical calculations in the following studies, and the adaptive grid technology was used to automatically adjust the grid of some computation area to improve the accuracy of numerical calculation.

Table 1: *Comparison of peak overpressures.*

Distance to the back wall/m	P_{M1} **/kPa**	P_{M2} **/kPa**	**Relative discrepancy/%**
0.5	108.08	118.71	8.95
1.5	108.04	118.20	8.60
2.5	107.94	116.64	7.46
3.5	107.96	116.44	7.28
4.5	107.49	114.16	5.84

2.3 Experimental validation of numerical model

In order to verify the applicability of the selected numerical model to this study, the results of the numerical simulation and the large-scale methane/air explosion experiment of Bao et al. (2016) were compared. Bao et al. used a 2 m × 2 m × 3 m experimental device to conduct a methane explosion study, and he analyzed the vented explosion effects of the pressure relief surface of 6 groups with different static opening pressures and the methane gas of 9 groups with different volume concentrations. The same parameters and conditions were used in this model verification as in the experiment, in which the methane volume concentration was 9.5 %, the ignition source was located at the geometric center of room. The initial environmental pressure and temperature before ignition were set to 1.01325 × 10^5 Pa and 300 K, respectively. The vent area was 0.64 m^2, and the other walls were set as rigid wall boundaries. The overpressure curve was taken from the measuring point at the geometric center of the rear wall of explosion chamber.

Based on the experiment, numerical calculations were carried out for the five groups of experimental conditions with the vent opening pressure of 1.5, 12.1, 20.6, 31.4 and 62.7 kPa, respectively. The indoor maximum peak overpressures obtained by numerical simulation and experiment under different opening pressures were shown in Fig. 1. The comparison showed that the maximum relative discrepancy of the experimental and numerical simulation data was 4.2 %. Due to the uncertainty of the experimental device itself, sensor accuracy and experimental process, the discrepancy might be caused by the combination of experimental test error and computational domain discretization. The comparison of experimental and numerical simulation results confirmed that it was feasible to solve the transient flow field problems of vented natural gas explosion with the above numerical methods.

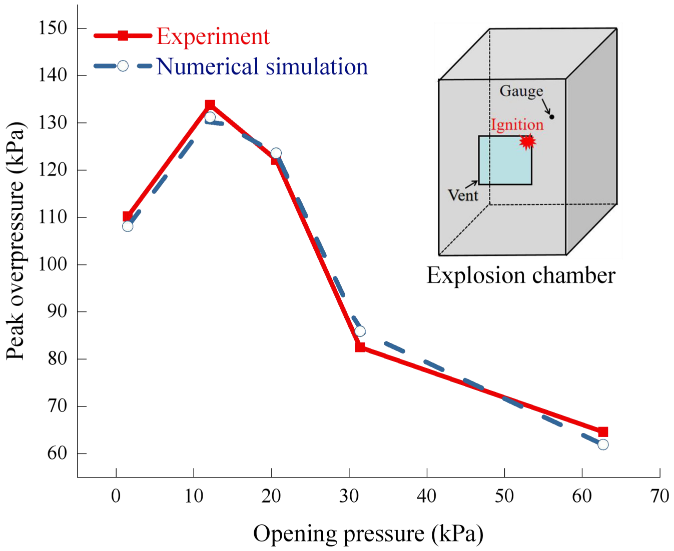

Fig. 1. *Comparison of peak overpressures between numerical and experimental results.*

3 Research plans

According to the general characteristics of gas explosion hazard in ordinary rooms, a cuboid physical model with a size of 6 m (length) × 3 m (width) × 2.5 m (height) was used. The four walls of room, the roof and the ground were all adiabatic smooth rigid walls. The vent was arranged on one of the smallest vertical walls and it was able to completely break immediately after reaching the set opening pressure or opening time. According to the relevant literature (Wang et al., 2017), a volume concentration of 10% was considered to be the best concentration for methane explosion. Thus, the static state methane/air premixed gas with a volume concentration of 10% was used in this study. The ignition location was at the geometric center of the rear wall of the room, with a radius of 0.015 m and a distance of 0.1 m from the rear wall. The influence of the ignition source on the explosion flow field was not considered. There were no obstacles in the room. In order to accurately capture the effect of external explosions on indoor overpressures, the calculation domain was extended 5.5 times the length of the room in the direction of the vent, and its size was 39 m × 3 m× 2.5 m, the extended calculation domain was set as the free outflow boundary. The outside air was in a static state, and the initial ambient pressure and temperature in the calculation domain were set to 1.01325×10^2 kPa and 300 K, respectively. All measuring points were located on the central axis of the room, and measuring point 1 was 0.5 m away from the rear wall, measuring points 7 and 8 were arranged at 0.1 m on both sides of the vent. The sketch of the room and the arrangement of some measuring points were shown in Fig. 2.

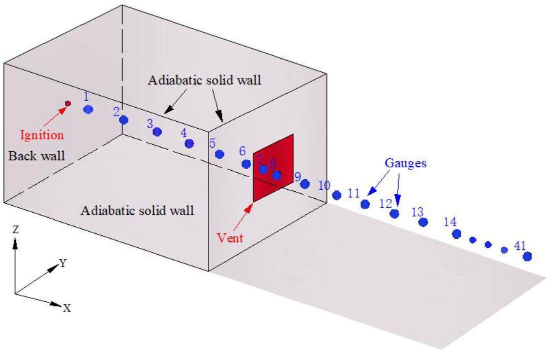

Fig. 2. *Room sketch and partial arrangement of measuring points.*

This study mainly investigated the influence of the vent opening pressure (P_v), opening time (T), and pressure relief ratio ($K_v = A_v/V^{2/3}$) on the mechanism of external explosion induced by indoor methane explosion. The vent opening pressures in this study were 20, 30, 40 and 50 kPa, respectively, because the static opening pressure of civil building window glass was generally about 7 ~ 60 kPa (Sun et al., 2018). The opening times of different materials were different, for example, the opening time of ordinary glass and calcium silicate board was between several milliseconds and tens of milliseconds, respectively (Ren et al., 2011; Liu et al., 2014). Therefore, the vent opening times in this study were 0, 0.02, 0.06, and 0.1 s, respectively. At the same time, based on the selection range of pressure relief ratio in the related literature (Zhang et al., 2018), the range of pressure relief ratio of 0.05 ~ 0.18 was used in this work.

4 Results and discussion

4.1 Effect of vent characteristic parameters on external flow field

4.1.1 Distribution characteristics of unburned gas cloud

Fig. 3 is a nephogram of the mass concentration distribution of unburned gas cloud when an external explosion occurs under different vent characteristic parameters. It can be seen from Fig. 3(a) and 3(b) that the vent opening pressure and opening time have similar effects on the distribution characteristics of outdoor unburned gas cloud. The external unburned gas cloud is generally distributed in a jet shape, and the gas cloud concentration gradually decreases radially from the center line of the vent. The radial distribution widths of the high-concentration unburned gas cloud (FUEL. M. FR. > 0.042, orange area) are the same, but as the opening pressure and opening time decrease, the axial distribution lengths of the high-concentration unburned gas cloud gradually increase. It might be due to the lower opening pressure and shorter opening time, the unburned gas cloud will be discharged earlier through the vent and experience a longer diffusion time outdoors. At the same time, it can be seen from Fig. 3(c) that the distribution and shape of external unburned gas cloud change significantly with the increase of pressure relief ratio, that is, the radial distribution widths of the high-concentration gas cloud increase and the axial distribution lengths increase first and then decrease. When K_v = 0.05, the shape of unburned gas cloud is a wrinkle-free jet, and the edges are more regular. With the K_v increasing, the radial distribution widths of high-concentration gas significantly increase, and the shape of vented gas cloud wrinkles and deforms. This is because the indoor and outdoor pressure difference reduces with the increasing of pressure relief ratio at the moment the vent rupture, and the spread speed of the vented unburned gas cloud reduces as well, and then the edge of unburned gas cloud is more susceptible to the friction and obstruction of outdoor air and gradually loses its stability. When $K_v \geqslant$ 0.13, the outflow velocity of indoor unburned gas further decreases, and so does the Helmholtz oscillation period. This may cause rapid reciprocating oscillation of the discharged unburned gas near the vent, which will prevent the gas from spreading along the axis. Thus, a high-concentration gas cloud area near the vent is formed, and the outflow gas front appears to sag into the room under the action of Helmholtz oscillation, and so does the indoor gas.

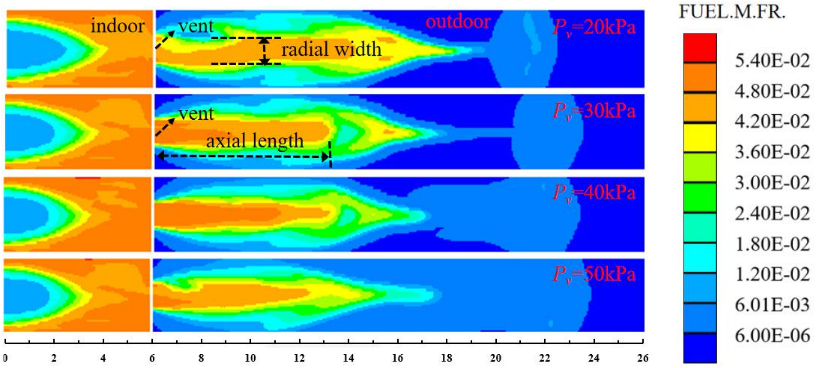

(a) Opening pressure (T = 0s, K_v = 0.08)

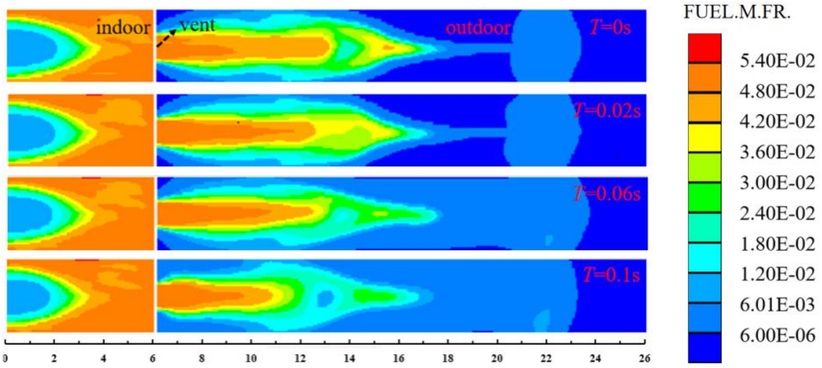

(b) Opening time (P_v = 30kPa, K_v = 0.08)

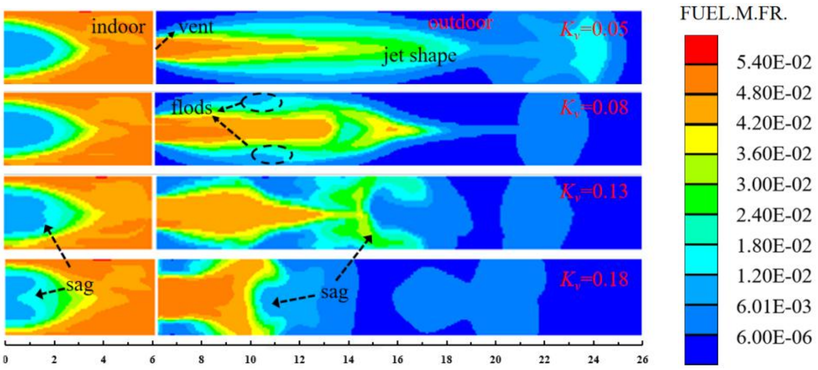

(c) Pressure relief ratio (P_v = 30kPa, T = 0s)

Fig. 3. *Unburned gas cloud mass concentration nephogram under different vent parameters.*

4.1.2 Propagation characteristics of vented flame

Fig. 4 shows a nephogram of the combustion rate distribution when an external explosion occurs under different vent characteristic parameters. The comparison between Fig. 3 and Fig. 4 shows that the shape of vented flame is consistent with the distribution characteristics of unburned gas cloud. As the vent opening pressure and opening time increase, the flame propagation distance and the burning velocity of the external gas all gradually decrease. As the pressure relief ratio increases, the flame propagation distance also gradually decreases, but due to the lumped high-concentration unburned gas cloud, the burning velocity of the external gas gradually increases (COMB.RATE > 0.036 kg/s, yellow area). In addition, the flame propagation speed is mainly composed of the gas burning velocity and the gas flow diffusion speed (Sun and Gao, 2016), and the faster the outflow velocity of vented gas, the faster the flame propagation speed. Thus, as the opening pressure and opening time increase and the pressure relief ratio decreases, the flame propagation speed near the vent increases, and the rates of increase are reached 64%, 48%, and 24%, respectively. It can be seen that the vent opening pressure and opening time have the most significant effects on the vented flame propagation speed, and the maximum flame propagation speed can reach more than 100 m/s, which may cause a severer external explosion hazard effect.

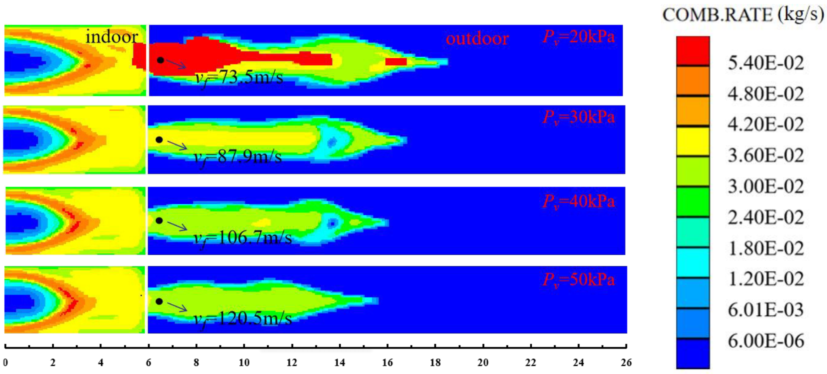

(a) Opening pressure (T = 0 s, K_v = 0.08)

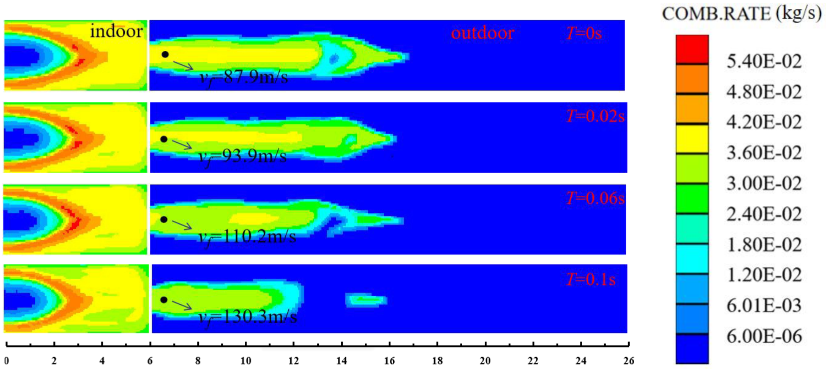

(b) Opening time ($P_v = 30$kPa, $K_v = 0.08$)

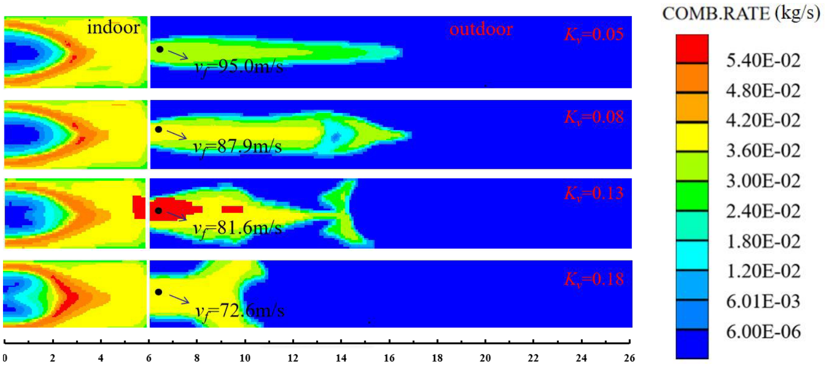

(c) Pressure relief ratio ($P_v = 30$kPa, $T = 0$s)

Fig. 4. *Vented flame propagation nephogram under different vent parameters.*

4.1.3 Turbulence intensity of external flow field

As a measure of turbulence intensity of outdoor flow field, the turbulent kinetic energy can be used to characterize turbulence degree of flow field to some extent. Fig. 5 shows the distribution of the peak turbulent kinetic energy of outdoor flow field (k) along the axial when an external explosion occurs under different vent parameters. It can be seen that all the external peak turbulent kinetic energy along the axial increases first and then decreases. Meanwhile the external turbulence intensity increases significantly with the vented gas velocity, which is influenced by the opening pressure, opening time and pressure relief ratio. Therefore, with the increase of P_v and T, the maximum peak turbulence energy of the outdoor flow field increases from 28 $m^2 \cdot s^{-2}$ to 1050 $m^2 \cdot s^{-2}$ and from 279 $m^2 \cdot s^{-2}$ to 1411 $m^2 \cdot s^{-2}$, respectively, and the rates of increase are 90 % and 80 %. As K_v decreases, the maximum change rate of turbulent kinetic energy can reach 99.5 %. Meanwhile, as P_v and T increase and K_v decreases, the outdoor turbulence area range ($k > 1$ $m^2 \cdot s^{-2}$) shows an increasing trend. As it is shown in the Fig. 5(a) and 5(c), as the P_v increases from 20 kPa to 50 kPa and K_v decreases from 0.18 to 0.05, the turbulence area ranges increase from 5 m to 17 m and from 8 m to 16 m, respectively, and the maximum increase rates are all more than 100 %. However, the maximum increase rate of turbulence area range (32.9 %) is relatively low in Fig. 5(b). Thus, the vent opening time seems to have a smaller effect on the turbulence area range.

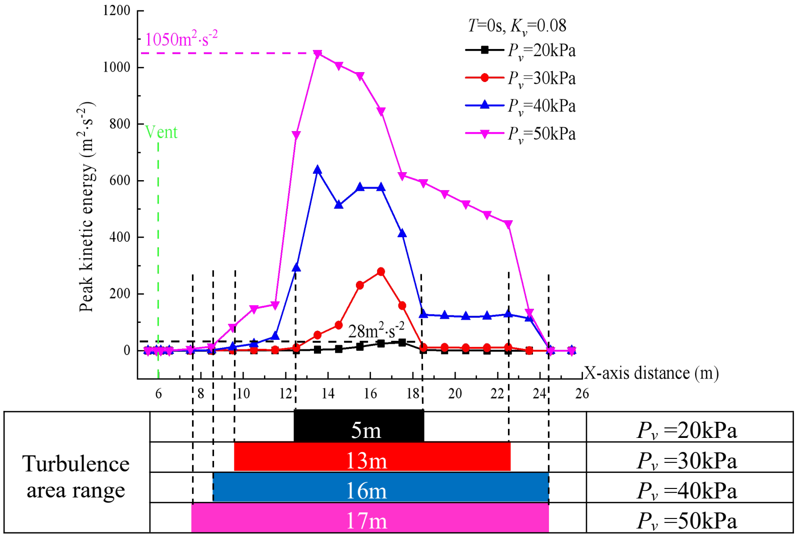

(a) Opening pressure

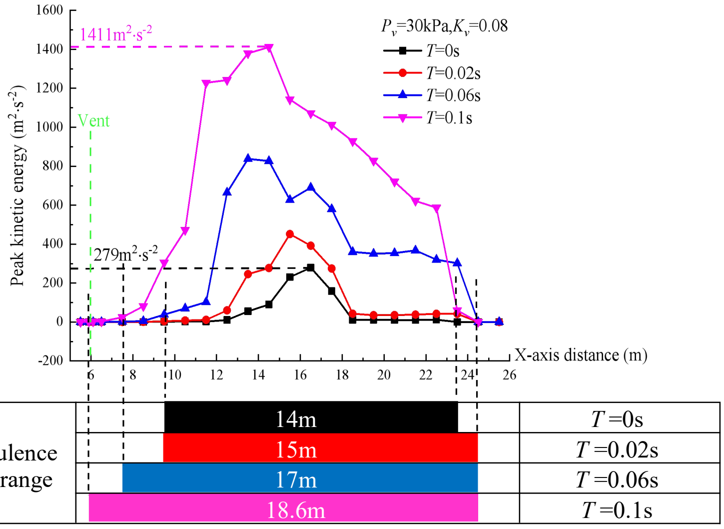

(b) Opening time

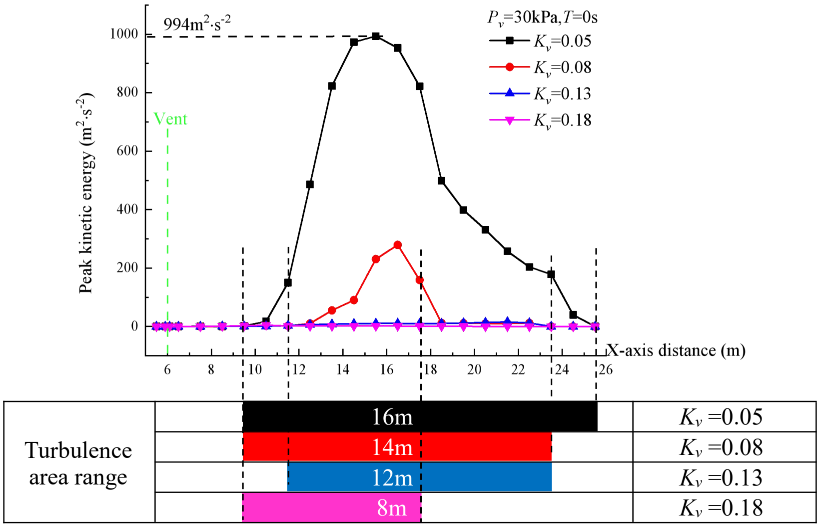

(c) Pressure relief ratio

Fig. 5. *Peak turbulent kinetic energy vs. distance under different vent parameters.*

4.2 Effect of vent characteristic parameters on external explosion

DOI: 10.7795/810.20200724

4.2.1 External explosion overpressure

The peak explosion overpressure is plotted against distance with different vent characteristic parameters in Fig. 6. It can be seen that due to the strong gas explosions outdoors, the outdoor peak overpressures (P_e) are higher than the indoor's. Fig. 6(a) shows that the maximum outdoor peak overpressure increases with the increase of the opening pressure, that is, from 42.89 kPa to 73.75 kPa; Meanwhile, Fig. 6(b) shows that the maximum outdoor peak overpressure increases first and then decreases with the increase of the opening time, and the peak overpressure reaches the maximum (P_e = 74.39 kPa) when the opening time is 0.06 s, and then the maximum peak overpressure begins to decrease as the opening time continues to increase. Due to the increase in the opening time, the indoor gas combustion time increases, which will consume a large amount of combustible gas, so that the amount of unburned gas discharged outdoors decreases, and finally the concentration of outdoor unburned gas cloud decreases and the distribution length of high-concentration unburned gas cloud reduces in the axial direction, as shown in Fig. 3(b). Fig. 6(c) shows that as the pressure relief ratio K_v increases from 0.05 to 0.18, the maximum external peak overpressure also increases first and then decreases. When K_v = 0.08, the external explosion peak overpressure reaches the maximum (P_e = 63.92 kPa). However, when K_v > 0.08, it can be seen from the comparison between the Fig. 4(c) and 5(c), the vented flame propagation speed decreases and the outdoor flow field turbulence weakens, which will cause the external explosion overpressure to decrease rapidly.

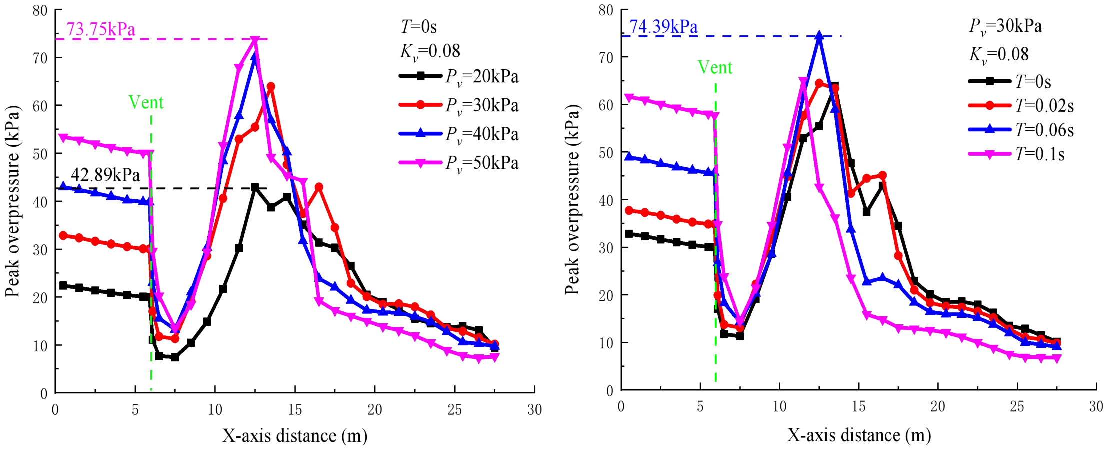

(a) Opening pressure (b) Opening time

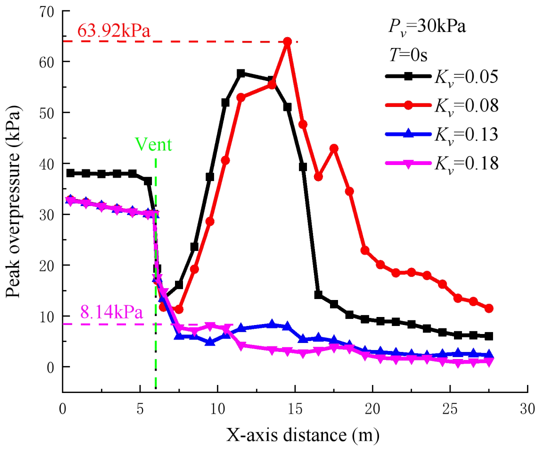

(c) Pressure relief ratio

Fig. 6. *Peak overpressure vs. distance under different vent parameters.*

4.2.2 The occurrence time interval of external explosion

In Fig. 7, the time interval curves between the moment of the vent opening and the external explosion occurring are plotted against different vent characteristic parameters. The figure shows that the occurrence time interval of external explosion gradually decreases with the increase of the opening pressure, opening time, and pressure relief ratio. The decrement of the time interval (Δt = 0.02 s) is the smallest with an increase in K_v, and its maximum relative reduction rate is only 8 %. However, all the decrements are more than 0.07 s with the increase of the opening pressure and opening time, and the maximum relative reduction rates are 34.9 % and 28.5 %, respectively. It demonstrates that the pressure relief ratio has a relatively little impact on the occurrence time interval of external explosion. As the Fig. 4(a), (b) and Fig. 7 show that the greater the vented flame propagation speed, the shorter the corresponding occurrence time interval of explosion. Therefore, the occurrence time interval of external explosion is directly related to the vented flame propagation speed under different vent characteristic parameters. The accelerating propagation mechanism of outdoor vented flame is mainly realized by the turbulence in the unburned gas cloud at the front of the flame (Salzano et al., 2002). Thus, the outdoor flow field turbulence will also have an indirect effect on the explosion time interval. Simultaneously, as it is shown in Fig. 4(c), when K_v = 0.18, the vented flame propagation speed (v_f = 72.6 m/s) is the lowest, but the occurrence time interval of explosion shortens in Fig. 7, this may be related to the fact that the distribution length of the outdoor high-concentration unburned gas cloud in Fig. 3(c) is closer to the vent in the axial direction. Thus, the influence of the outdoor distribution characteristics of unburned gas cloud on the occurrence time interval of external explosion cannot be ignored.

DOI: 10.7795/810.20200724

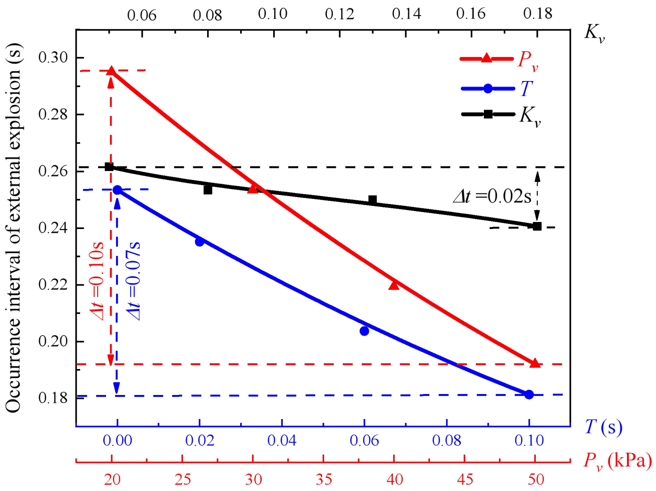

***Fig.** 7. Occurrence time interval of external explosion under different vent parameters.*

4.2.3 The occurrence location of external explosion

The peak combustion rate is plotted against distance with different vent characteristic parameters in Fig. 8. And the location where the maximum peak combustion rate occurs is considered to be where the external explosion occurred (Pang et al., 2019). It can be seen from Fig. 8(a) and 8(b) that when the opening pressure is lower or the opening time is shorter, the external explosion occurs farthest from the vent, which can reach 13.5 m. However, as the vent opening pressure or opening time continues to increase, the vented flame propagation speed near the vent is also continuously increasing, and the distribution length of the high-concentration unburned gas cloud is also closer to the vent in the axial direction at the moment of outdoor gas cloud ignited, so the location of external explosion more closes to the vent, as shown in Fig. 3(a) and 3(b). Fig. 8(c) shows that the external explosion occurs more closely to the vent as K_v increases, and the location of external explosion (14.5 m) is the farthest when K_v = 0.05. This is related with the distribution of unburned gas cloud outside the vent in Fig. 3(c). Therefore, the distribution characteristics of high-concentration unburned gas cloud have an important effect on the location of external explosion. The closer the high-concentration unburned gas cloud is to the vent, the nearer the occurrence location of external explosion is to the vent.

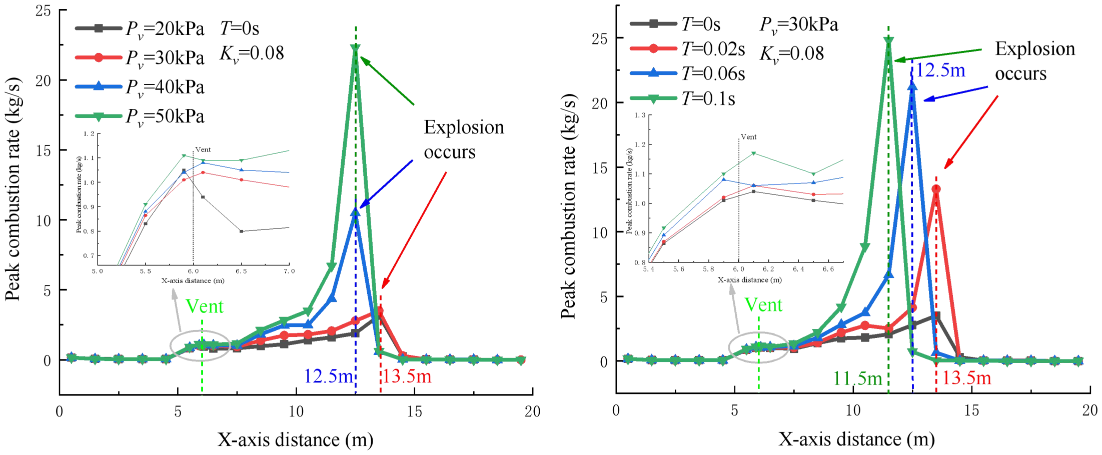

(a) Opening pressure (b) Opening time

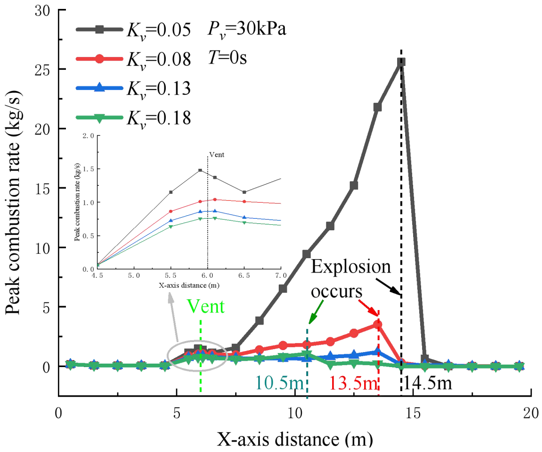

(c) Pressure relief ratio

Fig. 8. *Peak combustion rate vs. distance under different vent parameters.*

4.3 Correlation between external explosion characteristics and external flow field

Through the analysis of the flow field parameters, external explosion characteristics, and the effect of the flow field on the external explosion under different vent characteristic parameters, the qualitative influence of the outdoor flow field on the external explosion characteristics is summarized, as shown in Fig. 9.

It is shown that the characteristics of unburned gas cloud (concentration and distribution distance), vented flame propagation speed and flow field turbulence are considered to be important factors influencing the external explosion overpressure. And the occurrence location of external explosion can be determined by the distribution distance of unburned gas cloud outside the vent. That is, the unburned gas cloud with shorter axial distribution distance will lead to a closer external explosion location. The occurrence time interval of external explosion is mainly related to the vented flame propagation speed and the distribution characteristics of the external unburned gas cloud. Meanwhile the vented flame propagation speed is also affected by the flow field turbulence. Consequently, the turbulence intensity of outdoor flow field is also a key influencing factor of the occurrence time interval of external explosion. Under the conditions of stronger flow field turbulence, faster vented flame propagation speed, and closer distribution distance of unburned gas cloud to the vent, the occurrence time interval of external explosion will be shorter.

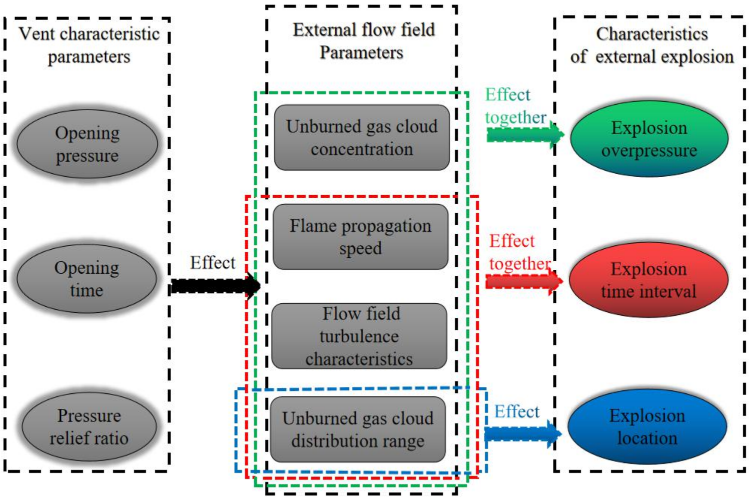

Fig. 9. *Qualitative influence of external flow field on the external explosion characteristics.*

As the most intuitive disaster parameter in the study of external explosion, the overpressure has been widely studied by scholars (Yang et al., 2019). Therefore, Fig. 10 shows the correlation between the external explosion overpressure (P_e) and the flow field parameters such as the distribution range of unburned gas cloud (axial distance d), flame propagation speed (v_f), turbulent kinetic energy of flow field (k) under different vent characteristic parameters.

It can be seen from Fig. 10(a) that the external explosion overpressure, vented flame propagation speed and turbulence intensity of flow field all increase with the increase of vent opening pressure, while the distribution range of unburned gas cloud gradually decreases. Thus, the external explosion overpressure under different opening pressure shows a strong positive correlation with the vented flame propagation speed and the turbulence intensity of flow field, and a negative correlation with the axial distribution range of the unburned gas cloud. From Fig. 10(b), when the vent opening time $T < 0.06$ s, although the distribution range of high-concentration unburned gas cloud is far ($d \geq 6.3$ m), the flame propagation speed and the turbulence intensity of the flow field are relatively low ($v_f \leq 93.9$ m/s, $k \leq 452$ $m^2 \cdot s^{-2}$), and the overpressure rise caused by external explosion is still relatively low ($P_e \leq 64.5$ kPa). Thus, the external explosion overpressure has a strong positive correlation with flame propagation speed and flow field turbulence, and a negative correlation with the axial distribution range of unburned gas cloud. However, when the opening time $T \geq 0.06$ s, this correlation is just the opposite. As the vent opening time is longer, the indoor combustion reaction consumes too much flammable gas, which will cause the concentration of outdoor unburned gas cloud to decrease, and the axial distribution of outdoor unburned gas cloud will be closer to the vent. Even if flame propagation speed and flow field turbulence all increase, a higher external explosion overpressure will not occur. Meanwhile, Fig. 10(c) shows that the external explosion overpressure seems to have a strong positive correlation with the distribution range of the unburned gas cloud under different pressure relief ratios, because they both maintain the trend of increasing first and then decreasing. When K_v

≥ 0.08, it is found that there is a positive correlation between the external explosion overpressure and the distribution range of unburned gas cloud, flame propagation speed and flow field turbulence.

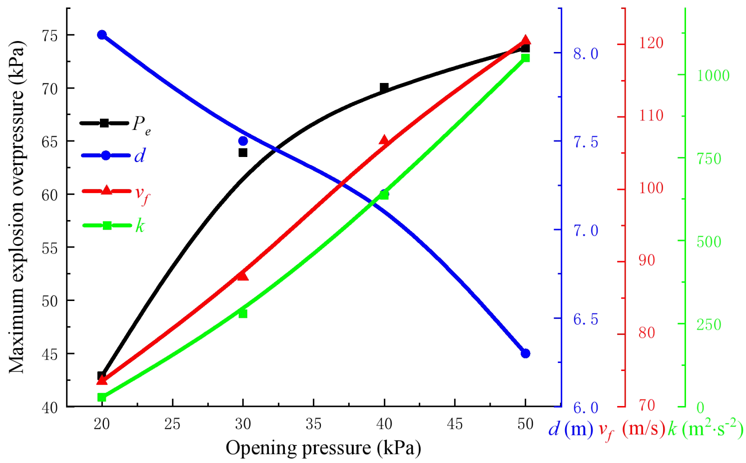

(a) Opening pressure

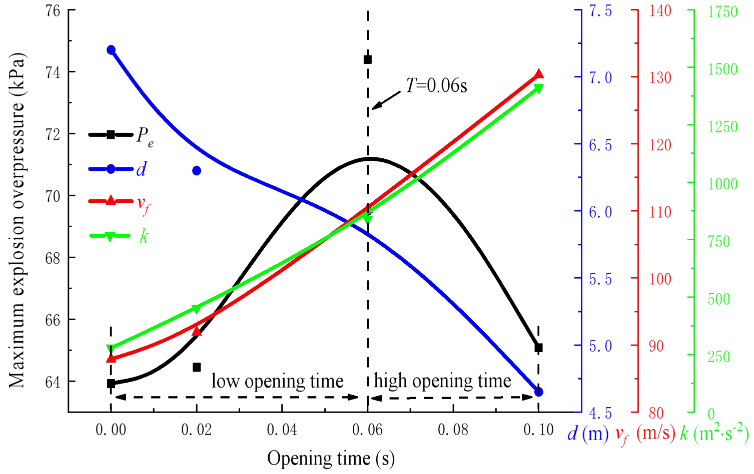

(b) Opening time

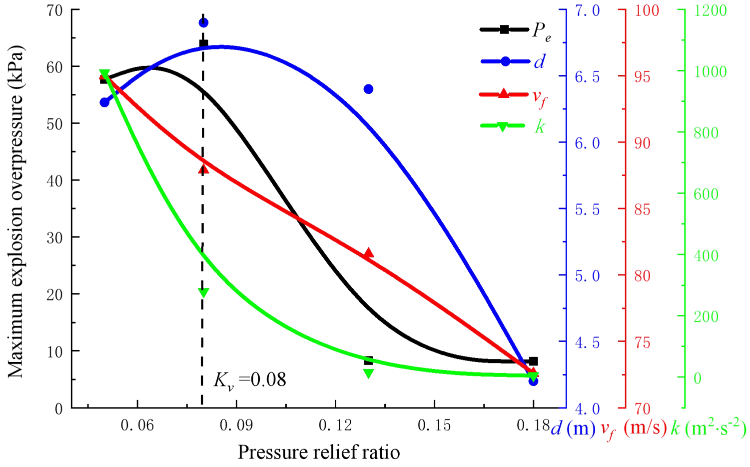

(c) Pressure relief ratio

Fig. 10. *Correlation analysis between the flow field parameters and external explosion overpressure.*

5 Conclusions

(1) The vent characteristic parameters have a significant effect on the outdoor flow field. With the increase of vent opening pressure and opening time, the radial widths of the discharged high-concentration unburned gas cloud remain unchanged, and the axial lengths tend to decrease. As the pressure relief ratio increases, the radial widths of the high-concentration unburned gas cloud increase, and the axial lengths increase first and then decrease. Under different vent characteristic parameters, the shape of vented flame is basically consistent with the distribution characteristics of unburned gas cloud, but the vented flame propagation speed near the vent varied greatly with the vent parameters, among which the opening pressure and opening time have the most significant effect. As the opening pressure and opening time increase and the pressure relief ratio decreases, the indoor and outdoor pressure difference increases, and the gas outflow velocity increases, as a result, the turbulence in the outdoor flow field is significantly enhanced, and the outdoor turbulence range also increases.

(2) The distribution characteristics of external explosion vary with the vent characteristic parameters. The external explosion overpressure tends to increase with an increase in vent opening pressure, but it increases first and then decreases with the increase of the opening time and pressure relief ratio. With the increase of the vent parameters, the occurrence location of external explosion more closes to the vent, and the occurrence time interval of external explosion gradually shortens. And the pressure relief ratio has relatively little effect on the occurrence time interval of external explosion.

(3) The characteristics of external explosion are closely related to the outdoor flow field parameters. The distribution characteristics of unburned gas cloud, flame propagation speed and flow field turbulence are the main influencing factors of the external explosion overpressure. The occurrence location of external explosion is mainly determined by the distribution range of unburned gas cloud. The shorter the axial distribution length of unburned gas cloud, the closer the occurrence location of external explosion will be to the vent. The occurrence time interval of external explosion is mainly related to the vented flame propagation speed and the distribution range of unburned gas cloud. The faster the flame propagation speed and the closer the axial distribution length of unburned gas cloud to the vent will lead to a shorter occurrence time interval. Since the vented flame propagation speed is related to the outdoor flow field turbulence, the turbulence intensity of outdoor flow field is also an important influencing factor of the occurrence time interval.

(4) The correlation between the external explosion overpressure and the outdoor flow field under different vent characteristic parameters is complex. External explosion overpressures under different vent opening pressures show a strong positive correlation with the flame propagation speed and the turbulence intensity of outdoor flow field, and a negative correlation with the axial distribution length of the high-concentration unburned gas cloud. When the opening time $T < 0.06$ s, the external explosion overpressures have a strong positive correlation with the vented flame propagation speed and flow field turbulence, and as $T \geqslant 0.06$ s, the external

explosion overpressures only have a strong positive correlation with the axial distribution length of the unburned gas cloud. The indoor explosions consume a large amount of combustible gas under the condition of the longer vent opening time, and the vented unburned gas will reduce, which ultimately leads to the decrease of external explosion overpressure. Under different pressure relief ratios, the external explosion overpressures always have a strong correlation with the axial distribution length of the high-concentration unburned gas cloud. And when $K_v \geqslant 0.08$, the external explosion overpressures maintain a strong positive correlation with the all three flow field parameters.

Acknowledgements

The authors appreciate the financial support from the Beijing Natural Science Foundation-Municipal Education Committee Joint Funding Project (No. KZ201910017020), the National Natural Science Foundation of China Project (No. 51404029), the Science and Technology Plan Project of Beijing Education Commission (No. KM202010017008), the Beijing Science and Technology Nova Program (No. Z181100006218092), the Training Funded Project of the Beijing Youth Top-Notch Talents of China (No. 2016000026833ZK05), and the Training Funded Project of the Beijing Young Backbone Talents of China (No. 2018000020124G087).

References

Bao, C.F., Xiao, H.J., Zhi, H.C., Jing, F.Y. & Gang, D. (2005). Investigation on external explosions during venting. *Fire Safety Science-Proceedings of The Eighth International Symposium*, pp: 1365-1374.

Bao, Q., Fang, Q., Zhang, Y.D., Chen, L., Yang, S.G. & Li, Z. (2016). Effects of gas concentration and venting pressure on overpressure transients during vented explosion of methane-air mixtures. *Fuel*, 175: 40-48.

Cao, Y., Guo, J., Hu, K.L., Xie, L.F. & L, B. (2017). Effect of ignition location on external explosion in hydrogen-air explosion venting. *International Journal of Hydrogen Energy*, 42(15): 10547-10554.

Chen, Z.H., Fan, B.C, Jiang, X.H. & Ye, J.F. (2006). Investigations of secondary explosions induced by venting. *Process Safety Progress*, 25(3): 255-261.

Du, Z.M., Jin, X.Q., Cui, D.M., & Ye, J.F. (2006). The investigation of correlated factors of external explosion during the venting process. *Journal of Loss Prevention in the Process Industries*, 19(4): 326-336.

Guo, J., Sun, X.X., Rui, S.C., Cao, Y. & Hu, K.L. (2015). Effect of ignition position on vented hydrogen-air explosions. *International Journal of Hydrogen Energy*, 40(45): 15780-15788.

Harrison, A.J. & Eyre, J.A. (1987). External explosions” as a result of explosion venting. *Combustion Science and Technology*, 52: 91-106.

Jiang, X.H., Fan, B.C., & Ye, J.F. (2004). Turbulence, vortex and external explosion induced by venting. *Applied Mathematics and Mechanics*, 25(12): 1271-1277.

Liu, J.C., Yu, R.Q. & Tang, D.L. (2014). Improved prediction model for failure strength and failure time of glass panels under dynamic loading-I. Theory.

Journal of Vibration and Shock, 33(13): 77-81.

Pang, L., Hu, Q.R., Zhao, J.J., Liu, P.F., Sun, S.H. & Yang, K. (2019). Numerical study of the effects of vent opening time on hydrogen explosions. *International Journal of Hydrogen Energy*, 44(29): 15689-15701.

Pang, L., Zhang, Q., Li, W., Xiang, C. & Tan, R.M. (2011). Relationship between shock wave and high-temperature flow produced by gas explosion in coal mine roadways. *Chinese Journal of High Pressure Physics*, 25(5): 457-462.

Proust, C. & Leprette, E. (2010). The dynamics of vented gas explosions. *Process Safety Progress*, 29(3): 231-235.

Ren, S.F., Chen, X.F., Wang, Y.J., Tao, M. & Chen, M. (2011). Effect of pressure-orifice ratio on dynamic behavior during gas venting. *Journal of China Coal Society*, 36(5): 830-833.

Salzano, E., Marra, F.S., Russo, G. & Lee, J.H.S. (2002). Numerical simulation of turbulent gas flames in tubes. *Journal of Hazardous Materials*, 95(3): 233-247.

Sun, S. & Gao, K.H. (2016). Study on turbulence factors of flame propagation in tube under gas explosion. *Journal of China Coal Society*, 41(S2): 441-447.

Sun, S., Wang, M.Y., Gao K.H., Zhao, T.H. & Guo, Q. (2018). Effect of vent conditions on internal overpressure time-history during a vented explosion. *Journal of Loss Prevention in the Process Industries*, 54: 85-92.

Sun, S., Wang, M.Y., Gao, K.H., Zhao, T.H. & Guo, Q. (2018). Experimental study one effect of large-scale explosion venting component on interior deglagration pressure. *Explosion and Shock Waves*, 38(2): 359-366.

Sun, S., Wang, M.Y., Qiu, Y.Y. & Gao, K.H. (2019). Effect of a hinged rotating vent cover on a vented explosion. *Journal of Loss Prevention in the Process Industries*, 57: 186-193.

Tomlin, G., Johnson, D.M., Cronin, P., Phylaktow H.W. & Andrews G.E. (2015). The effect of vent size and congestion in large-scale vented natural gas/air explosions. *Journal of Loss Prevention in the Process Industries*, 35: 169-181.

Wang, Y.X., Lian, Z., & Zhang, Q. (2017). Effect of ignition location and vent on hazards of indoor liquefied petroleum gas explosion. *Combustion science and Technology*, 189(4): 698-716.

Yang, F.Q., Guo, J., Wang, C.J. & Lu, S.X. (2018). Duct-vented hydrogen-air deflagrations: The effect of duct length and hydrogen concentration. *International Journal of Hydrogen Energy*, 43(45): 21142-21148.

Yang, K., Hu, Q.R., Sun, S.H., Liu, P.F. & Pang, L. (2019). Research progress on multi-overpressure peak structures of vented gas explosions in confine d spaces, *Journal of Loss Prevention in the Process Industries*, 62. https://doi.org/10.1016/j.jlp.2019.103969.

Ye, J.F., Jiang, X.H., Jia, Z.W., Dong, G. & FAN, B.C. (2004). Experimental investigations of external second-explosion induced by vented explosion. *Explosion and Shock Waves*, 24(4): 356-362.

Zhang, S.H. & Zhang, Q. (2018). Effect of vent size on vented hydrogen-air explosion. *International Journal of Hydrogen Energy*, 37(43): 17788-17799.

DOI: 10.7795/810.20200724

Keeping the Overview on Surface Resistivity Measurements

Aaron D. Ratschow[a], Sigrun Stein[a] & Hans-Jürgen Gross[a]

[a] Bayer AG, Leverkusen, Germany
E-mail: *hans-juergen.gross@bayer.com*

Abstract

The measurement of surface resistance is both a means of material specification and quality characterization as well as a central approach for evaluating electrostatic hazards in explosion protection assessments. The different methods given in different standards differ in design and test parameters and give different quantities as results. Permitted variances within a standardized method may lead to deviations. Also, in practical work, it may not be possible to prepare a sample geometry according to the relevant standards for example because of limitations of sample availability or shape. This paper provides an overview of established standards, information about their comparability and factors for converting results obtained by one method into another, where applicable. The method used is theoretical to avoid effects due to inaccuracies or non-isotropic sample properties: Analytical and finite element calculations of the different electrode geometries based on an isotropic material of a specific sample size which follows Ohm's law.

Keywords: *surface resistivity, surface resistance, electrostatics, test design, sample geometry*

1 Introduction

Measuring surface resistance is an important factor in safety studies including electrostatic ignition hazards dealt with in IEC 60079-0:2019-09 (2019). In view of the large number of test methods, maintaining an overview and correctly interpreting the various specifications of surface resistivity poses a challenge. It starts with the correct designation. DIN EN 60079-32-2:2015-12 (2015), table 1, gives values for "Surface Resistivity", "Surface Resistance" and "Volume Resistivity" for when a solid material is considered to be conductive, dissipative or insulating. The methods to determine surface resistivity and surface resistance differ, but the conversion factor, which is due to the different measurement setups, is given in DIN EN 60079-32-2:2015-12 (2015) by surface resistivity = 10 * surface resistance.

However, this factor of 10 can be called into question considering a simple argument: If there is enough material around two electrodes, an electric current can also occur between the backs of two electrodes, the so-called fringe fields, contributing to the conductivity respectively decreasing the measured resistance between the electrodes. It is also plausible that such an effect would be larger on a square, used for measuring surface resistivity, than on the 10:1 rectangle generally used for measuring surface resistance. In other words, an "Ohm square" measurement might be more susceptible to sample geometry outside the considered square than a 10:1 rectangle.

Other measurement methods might also be affected by fringe fields. These considerations led to the present study to investigate the effect of sample geometries on measured values for different standards. Furthermore, the sample sizes required in standards are not always available, so that a transfer of the results is desirable, or an error estimation can be done.

As the question about comparison of different measurement geometries is independent of any particular material, it is well suited to treatment by simulation. An ideal isotropic material following Ohm's law was chosen for the simulations, the contacting of the electrodes was assumed to be perfect. Since the equations to be solved are linear, results from the simulation can be scaled easily, and constant factors can be given for conversions between different sample geometries and measurement methods.

2 Calculation method

To investigate the influence of different electrode arrangements and sample sizes on measured surface resistivity, numerical simulations for the different geometries described in the literature were performed. For easy conversion of the different measurements into surface resistivity, analytical calculations were conducted.

2.1 Governing equations

In this work stationary currents in ideal isotropic conductive media are assumed to obey Ohm's law

$$\mathbf{J} = \frac{\mathbf{E}}{\rho} \tag{1}$$

with current density $\mathbf{J}\,(A/m^2)$, the electric field $\mathbf{E}\,(V/m)$ and resistivity $\rho\,(\Omega m)$. Under static conditions, the electric field is defined as

$$\mathbf{E} = -\nabla\Phi \tag{2}$$

with the electric potential $\Phi\,(V)$. By combining this and eqn. 1 with the stationary equation of continuity with no sources, the Laplace equation for the electric potential is derived.

$$\nabla^2\Phi = 0 \tag{3}$$

The Laplace equation describes the electric potential distribution in space. Electric fields and currents can then be derived from the electric potential during post processing. For sheets with constant thickness, the calculation of the electric potential reduces to a two-dimensional (2D) problem and can be described with the 2D Laplace equation. In this case Ohm's law (eqn. 1) can be integrated along the sheet thickness z. This yields

$$\int \mathbf{J} dz = \frac{\mathbf{E}}{R_s} \tag{4}$$

introducing surface resistivity $R_s\,(\Omega)$. The resistance of a square piece of material with electrodes attached to opposite edges is called Ohm square and equates to surface resistivity R_s.

2.1.1 Boundary conditions

The boundary conditions (BCs) for eqn. 3 were formulated as Dirichlet BCs at the electrodes where the potential was set to either zero, thus ground, or to the specified electrode voltage. On all other boundaries, homogeneous Neumann BCs applied which inhibit normal current at these boundaries with $\mathbf{n}\cdot\mathbf{E} = 0$.

2.2 Numerical simulations

The Laplace equation was solved numerically using the finite element method (FEM) and the commercial FEM code Comsol Multiphysics 5.5. Electric potential was discretized using quadratic Lagrangian form functions and grid independence of the solution was ensured for all geometries.

2.3 Analytical solutions

While numerical solutions allow for detailed investigations of effects like sample size, they do not provide closed form solutions in terms of geometrical parameters. Analytical solutions provide formulas for direct conversion of measurements to surface resistivity.

2.3.1 Concentric circular electrodes

For concentric circular electrodes as described in DIN EN 61340-2-3:2017-05 (2017), DIN EN 60079-32-2:2015-12 (2015), DIN EN 1149-1:2006-09 (2006) and DIN EN 62631-3-2:2016-10 (2016) the analytical solution is straightforward. Fig. 1 shows the geometry. Due to radial symmetry, the Laplace equation can be expressed in polar coordinates with only radial derivatives.

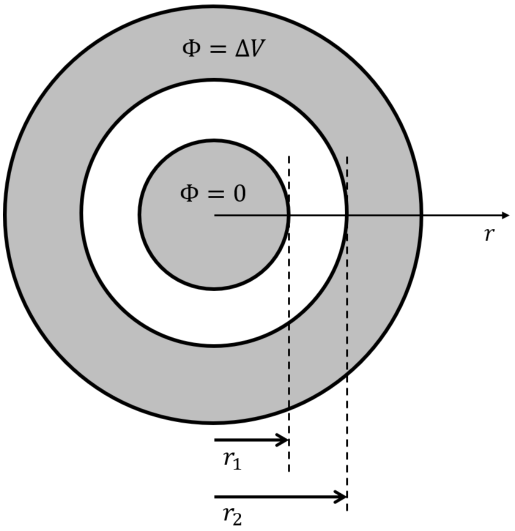

***Fig. 1**: Concentric circular electrode assembly with dimensions and applied voltages.*

$$\frac{\partial}{\partial r}\left(r\frac{\partial \Phi}{\partial r}\right) = 0 \tag{5}$$

The solution with the BCs $\Phi(r_1) = 0$ and $\Phi(r_2) = \Delta V$, ΔV being the applied voltage across the electrodes, is easily found through integration to be

$$\Phi = \frac{\Delta V}{\ln(r_2/r_1)\ln(r/r_1)}. \tag{6}$$

Using eqns. 2 and 3, surface resistivity R_s can be expressed in terms of the measured resistance $\Delta V/I$ with $I = \int_{\partial\Omega} \mathbf{n}\cdot\mathbf{J}ds$ being the total normal current across the boundary of an electrode $\partial\Omega$:

$$R_s = \frac{\Delta V}{I}\frac{2\pi}{\ln(r_2/r_1)}. \tag{7}$$

Since this mathematical problem is defined on a confined geometry, an excess sample size does not influence the result and eqn. 7 can be used to convert measurements into surface resistivity without restrictions.

2.3.2 Point electrodes

Point electrodes of defined radius and distance are described in DIN EN 61340-2-3:2017-05 (2017) and used for uneven surfaces. Mathematically this can be described as the electric field between two equipotential circles on an infinite plane. The problem is electrostatically equivalent to two infinite lines of charge λ of opposite polarity and separated by a distance $2a$. The situation is depicted in fig. 2. The equivalent problem of two infinite line charges has circular equipotential lines. The solution to this problem is well known and described in textbooks like Griffiths and Schroeter (2018), Smythe (1988):

$$\phi = \frac{\lambda}{4\pi\varepsilon_0}\ln\left[\frac{(x+a)^2+y^2}{(x-a)^2+y^2}\right] \tag{8}$$

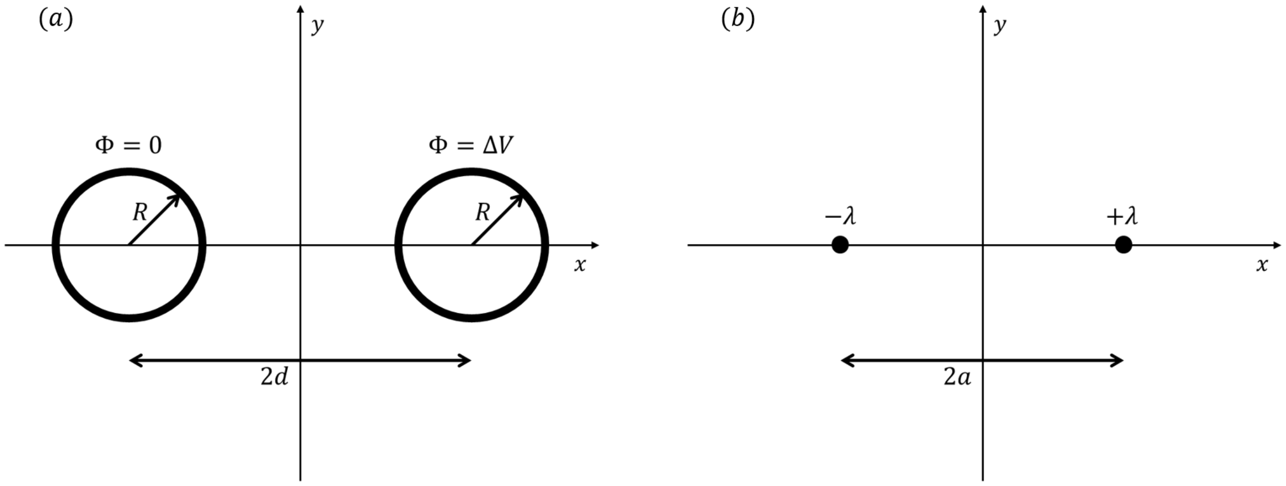

***Fig. 2**: Two-point electrodes in the x-y-plane with dimensions and applied voltages (a) and the mathematically equivalent problem of two infinite line charges (b).*

Eqn. 8 applies to the problem in fig. 2 (a) by using the following transformations

$$a = \sqrt{d^2 - R^2},$$

$$\frac{d}{R} = \cosh\left(\frac{\pi\varepsilon_0 \Delta V}{\lambda}\right) \tag{9}$$

From the electric potential the total current between the electrodes can be evaluated as

$$I = \int_{-\infty}^{\infty} -\frac{1}{R_s}\frac{\partial\Phi}{\partial x}(x=0)dy. \tag{10}$$

Combining eqns. 8-10 surface resistivity can be expressed in terms of the measured resistance $\Delta V/I$ as

$$R_s = -\frac{\Delta V}{I}\frac{\pi}{\cosh^{-1}(d/R)}. \tag{11}$$

This eqn. describes the relationship of surface resistivity and measured resistance in the limiting case of an infinitely large sample size. This refers to a case where the boundaries of the measured sample do not influence the electric field around the electrode.

2.3.3 Strip electrodes

Measuring surface resistivity with two parallel strip electrodes is described in DIN EN 60079-32-2:2015-12 (2015) and DIN EN 62631-3-2:2016-10 (2016). In the limiting case of infinitely thin electrodes and an infinitely large sample size the problem can be described as the electric potential between two parallel lines of defined length w and distance d and potential difference ΔV. Mathematically, this is equivalent to a parallel plate capacitor. Under the assumption of a homogeneous field between the electrodes the solution is trivial, and the surface resistivity can be calculated from the measured resistance with

$$R_s = -\frac{\Delta V}{I}\frac{w}{d}. \tag{12}$$

This equation is also described in the corresponding standards for conversion of measured values. However, it neglects all edge effects and fringe fields as depicted in fig. 3 which yields a systematic error in the results for surface resistivity. A more elaborate solution to the problem in fig. 3 is required for accurate conversion of the measured resistance to surface resistivity, taking into account fringe fields and electrode geometry. A closed form solution to this mathematical problem

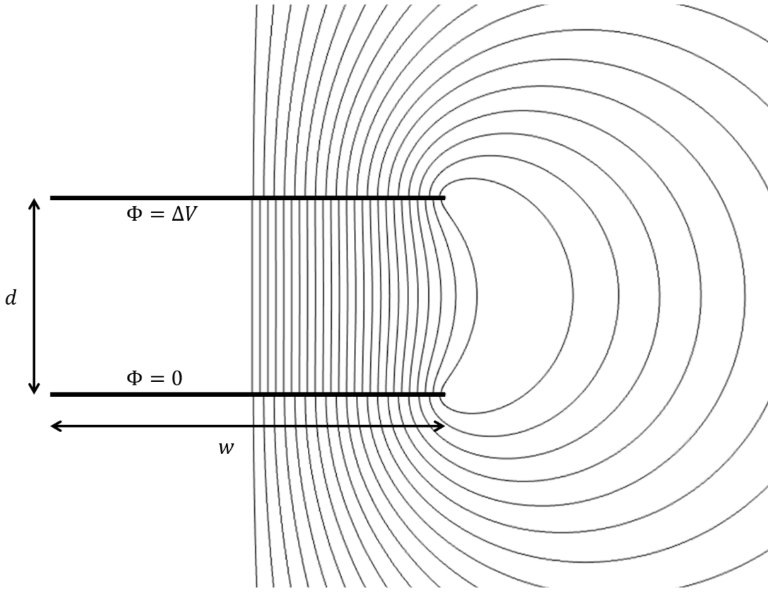

***Fig. 3**: Two strip electrodes with dimensions and applied voltages on the left and electric field lines highlighting the influence of edge effects and resulting fringe fields on the right.*

is not known to literature as analytic solutions employing the Schwartz-Christoffel-Transformation incorporate elliptic integrals (Moon and Spencer (2012), Palmer (1937)).

There are however several investigations of capacitance of parallel plate capacitors in air under consideration of fringe fields like Chen et al. (2019), Nishiyama and Nakamura (1990), Rochelle (1975). Exploiting the mathematical equivalence of the two problems it is possible to express the solution for the surface resistivity in terms of the capacity C of a parallel plate capacitor using the integral of the normal electric field along the boundary of the electrode that is according to Gauss's law and Ohm's law respectively proportional to both the charge Q on a plate capacitor (eqn. 13) as well as the total current I between the electrodes in the measurement setup (eqn. 14).

$$C = \frac{Q}{\Delta V} = \frac{\varepsilon_0}{\Delta V} \int_{\partial\Omega} \mathbf{n} \cdot \mathbf{E} ds$$

$$\int_{\partial\Omega} \mathbf{n} \cdot \mathbf{E} ds = \frac{CU}{\varepsilon_0} \tag{13}$$

$$I = \frac{1}{R_s} \int_{\partial\Omega} \mathbf{n} \cdot \mathbf{E} ds \tag{14}$$

Combining eqns. 13 and 14, surface resistivity for a two-strip electrode setup can be expressed in terms of measured resistance $\Delta V/I$ and capacitance C as well as the dielectric constant ε_0:

$$R_s = \frac{\Delta V}{I} \frac{C}{\varepsilon_0}. \tag{15}$$

Rochelle (1975) found an approximate analytical solution for the capacitance as a function of aspect ratio $A = w/d$ for an infinite sample size. Using this approximation solution together with eqn. 15 gives a formula for expressing surface resistivity in terms of measured resistance and aspect ratio A of two parallel strip electrodes.

$$R_s = \frac{\Delta V}{I} 4\pi \left[\frac{8}{A} \tan^{-1}(A) - \frac{2}{A^2} \ln(1 + A^2) + 2 \ln\left(\frac{1 + A^2}{A^2}\right) \right]^{-1} \tag{16}$$

3 Results and discussion

In the following section the simulation results are presented for different electrode configurations described in the norms. The presented surface resistivities are scaled with the values that would have been measured without systematic errors in the measuring procedures. Hence the deviation of scaled surface resistivity from 1 quantifies systematic errors. Sample size corresponds with the excess area around the electrode that was varied in size. It was quantified by a variable N called excess that is defined as the distance of the electrodes and sample boundaries divided by the distance of electrodes. A value of no excess ($N = 0$) indicates a sample the size of the electrode arrangement while large values approach the limiting case of infinitely large sample size. Sketches to describe this excess value can be found in the according diagrams (figs. 5 and 6).

3.1 Concentric circular electrodes

For concentric electrodes as depicted in fig. 1 the problem is well defined and thus eqn. 7 gives accurate results for surface resistivity without systematic errors. Sample size for concentric circular electrodes does not matter, because there are no fringe fields on the outside. When working with DIN EN 61340-2-3:2017-05 (2017) however, a different formula for calculating R_s is provided:

$$R_s = \frac{\Delta V}{I} \pi \frac{r_2 + r_1}{r_2 - r_1} \tag{17}$$

This is an approximation for eqn. 7 and produces errors of up to 4% (depending on the electrode geometry).

3.2 Point electrodes

For two-point electrodes (comp. fig. 4) DIN EN 61340-2-3:2017-05 (2017) does not provide a formula for converting the measured resistance to surface resistivity. Eqn. 11 provides a possible conversion formula and makes measurements between different measuring procedures comparable. For the specific geometry described in the norm and omitting the negative sign, the formula simplifies to $R_s = 2.4\Delta V/I$ for an infinitely large sample size.

Fig. 4 shows the simulation results for different sample sizes. For small sample sizes with scaling factor N (sample radius/electrode radius) < 10 the measured values deviate from the real value by a factor of up to 2.47 for a sample the size of the electrode arrangement. This can be explained by the sample edges affecting the fringe fields around the electrodes. With large sample sizes the method approaches a measurement without errors. Since the norm does not specify a minimum sample size, this measuring procedure yields inaccurate results for small samples.

3.3 Strip electrodes

3.3.1 Electrode thickness and sample size

Strip edge electrodes described in standards differ in geometry. DIN EN 62631-3-2:2016-10 (2016) describes several electrode assemblies, all of which have an aspect ratio of 10. Assembly D mentioned in DIN EN 62631-3-2:2016-10 (2016) is equivalent to the one mentioned in DIN EN 60079-32-2:2015-12 (2015). The difference for the two-dimensional assessment is mainly in the thickness of the electrodes. In fig. 5 the distance of the electrode was assigned 10 units of length and the electrode thickness was varied between 0.3 and 5 units. In the example of a 100 mm·10 mm electrode one unit of length is equal to 1 mm. Assuming that the electrode distance remains the same, a change in the electrode thickness only leads to a deviation in the measurement of $< 2\%$ (see Fig. 5).

Fig. 6 depicts the results for this assembly. For small sample sizes the fringe fields are affected and partially cut off by the sample edges resulting in increased resistance compared to an infinitely large sample size. This effect is apparent for both conversion formulas. The suggested formula from the

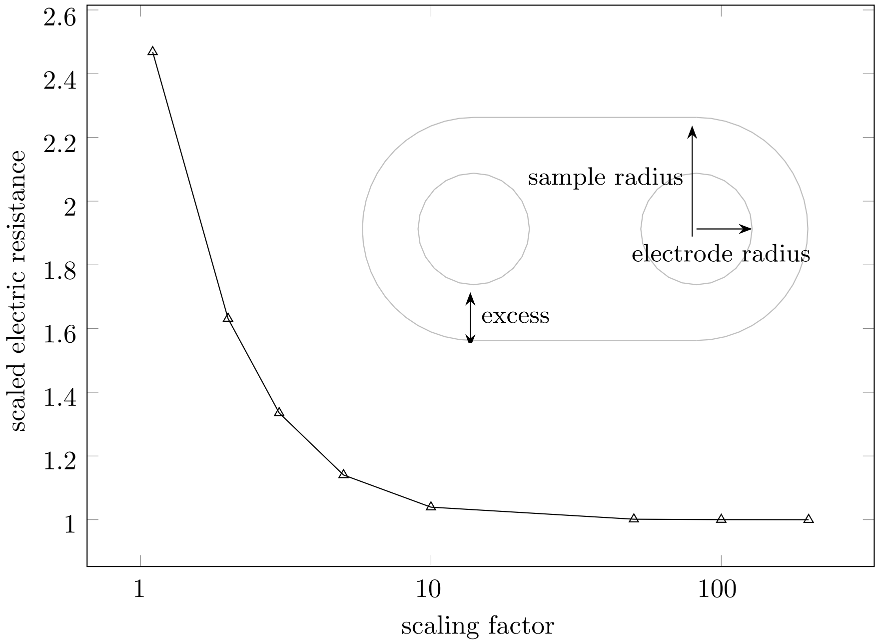

***Fig. 4**: Simulation results for two-point electrodes, measurements were converted using eqn. 11; scaling factor: sample radius/electrode radius.*

standard (eqn. 12) approaches the real value of surface resistivity for no excess area (excess 0) which corresponds to a case with no fringe fields. For larger sample sizes it shows a systematic error of -12%. The formula suggested in this paper (eqn. 15) shows less deviations for sample sizes of an excess of more than 5 units and therefore gives more accurate results. In the limiting case of infinitely large sample sizes it simplifies to $R_s = 11.8\Delta V/I$.

The proposed conversion formula (eqn. 15) still exhibits an error when approaching very large samples. This offset is explained by the finite electrode thickness that is not accounted for in either formula and introduces additional warp and distortion of the fringe fields at the edges of the assembly. To compare surface resistivity to surface resistance it is interesting to look at the different measurement values for a 10x10 to a 100x10 units electrode. The influence of the fringe fields decreases as the electrode aspect ratio increases. For a 10x10 unit length electrode the influence of the sample size is very large. The measured resistance decreases by more than 50% for large sample areas. The surface resistivity as addressed in various standards therefore always refers to the minimum sample size. It should be noted that, provided there are no surface effects that increase conductivity, the specific surface resistance for a thin layer corresponds to the specific volume resistance multiplied by the thickness.

3.3.2 Sample thickness and protection electrode

For thin samples such as foils it is reasonable to simplify the problem to two dimensions. For thicker samples however, this assumption may not hold true. Especially the introduction of a grounded protective electrode on the opposite side of the sample that covers the area of the two strip electrodes, as described in DIN EN 62631-3-2:2016-10 (2016), makes the problem three-dimensional.

The total observed surface resistivity of the sample of the measured samples comprises contributions of the bulk as well as the thin layer on the surface. Because of special properties, surfaces often show different properties than the bulk like adsorption of molecules or other interface effects. So it is likely it exhibits an increased conductivity on the surface.

The surface was modelled as a very thin layer with an additional resistivity ρ_s (Ω) and the influence was measured as the ratio ψ of theoretical contributions of surface contribution and bulk contribution

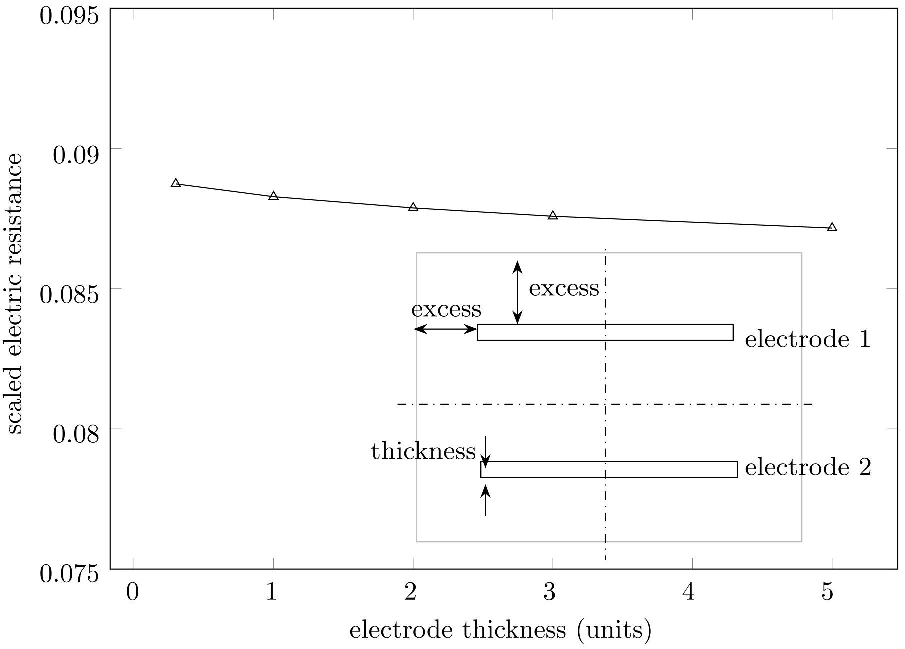

***Fig. 5**: Influence of electrode thickness on measured value for a 100x10 units electrode and a very large sample size.*

to the overall resistivity:

$$\psi = \frac{\rho}{\rho_s d}. \tag{18}$$

Fig. 8 shows the influence of sample thickness for different ratios ψ, where $\psi = 0.001$ denotes the case of no significant surface contribution. Results are scaled relative to the theoretical two-dimensional result. The influence of the sample thickness and the corresponding errors are small for thin samples of up to a thickness of 2 units. With a 100 mm · 10 mm electrode this would correspond to a thickness of 2 mm. For thicker samples, the 2D simplification and the corresponding measuring procedures described in the standards yield substantial errors of up to 368%. For higher ψ, errors due to sample thickness are reduced.

In fig. 9 an additional grounded electrode, a so-called protection electrode, on the opposite side of the sample is added. For low values of ψ this yields large errors between 4560% and 763.9% and makes the measuring procedure unsuitable for practical use. The deviations are larger for smaller sample thicknesses due to an increased current through the sample towards the protective electrode. For higher ψ the errors are smaller but only drop below 100% for $\psi > 1000$ which corresponds with dominant surface contributions and almost no bulk conduction. Therefore, the use of a protective electrode is only appropriate if the physical properties of the measured sample indicate a dominant contribution of the surface conductivity.

4 Conclusions

Different measuring procedures for surface resistivity described in standards have been compared regarding systematic geometrical errors. Conversion formulas have been presented that make different methods comparable. It was shown that sample sizes can have an impact on the accuracy of a method due to fringing effects in the electric field. These effects are present in two-point and strip electrodes. Ultimately, a method for correcting systematic errors in practical measurements has been introduced.

It could be shown that two-point electrodes are also suitable for the determination of surface resistivity; a conversion formula was introduced. The findings in this paper allow for more accurate surface resistivity measurements and better understanding of the different methods, thus helping to limit the risks of electrostatic discharges as explosion ignition sources.

DOI: 10.7795/810.20200724

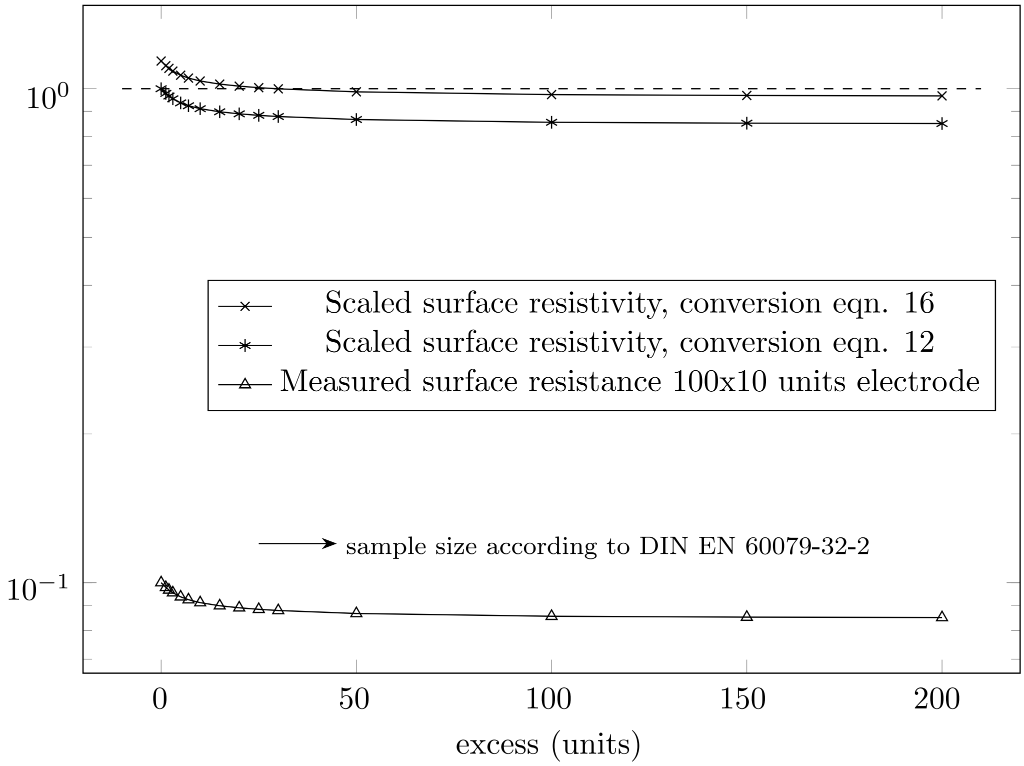

***Fig. 6**: Simulation results for strip electrode assembly (100x10 units). Conversions with eqns. 12 and 16.*

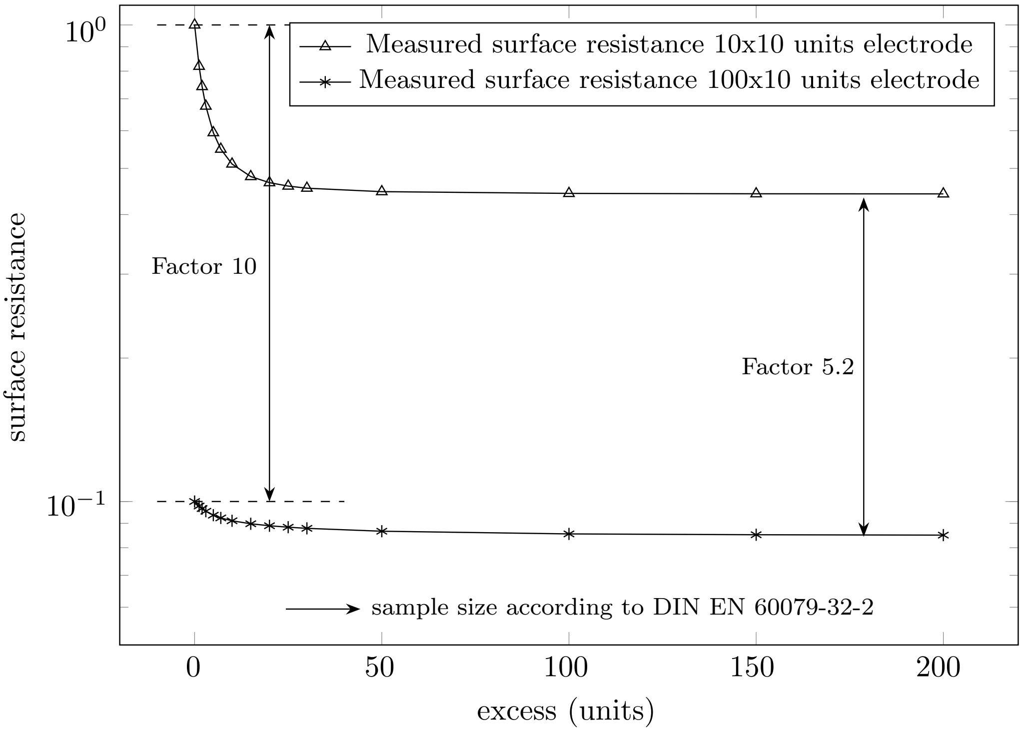

***Fig. 7**: Comparison of different aspect rations of strip electrode assemblies. Deviations due to fringing fields are stronger with smaller aspect ratios.*

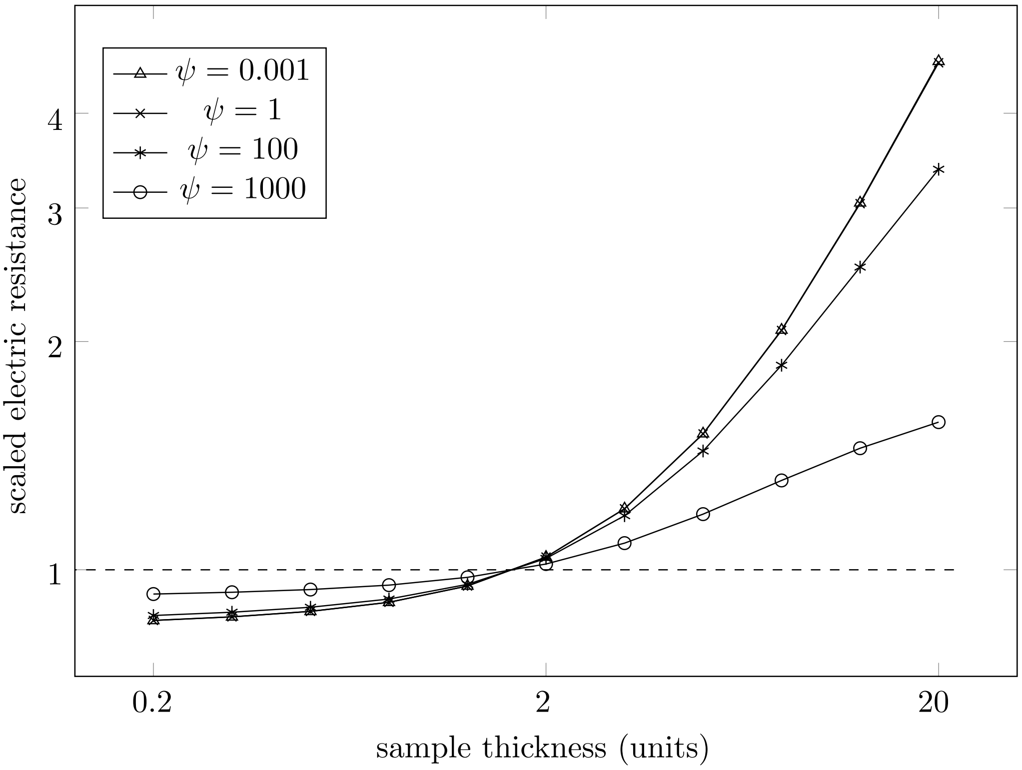

***Fig. 8**: Influence of sample thickness for 100x10 units electrode without protective electrode. ψ scales the influence of additional surface conductivity with $\psi \to 0$ denoting only volume contribution and $\psi \to \infty$ only surface contribution.*

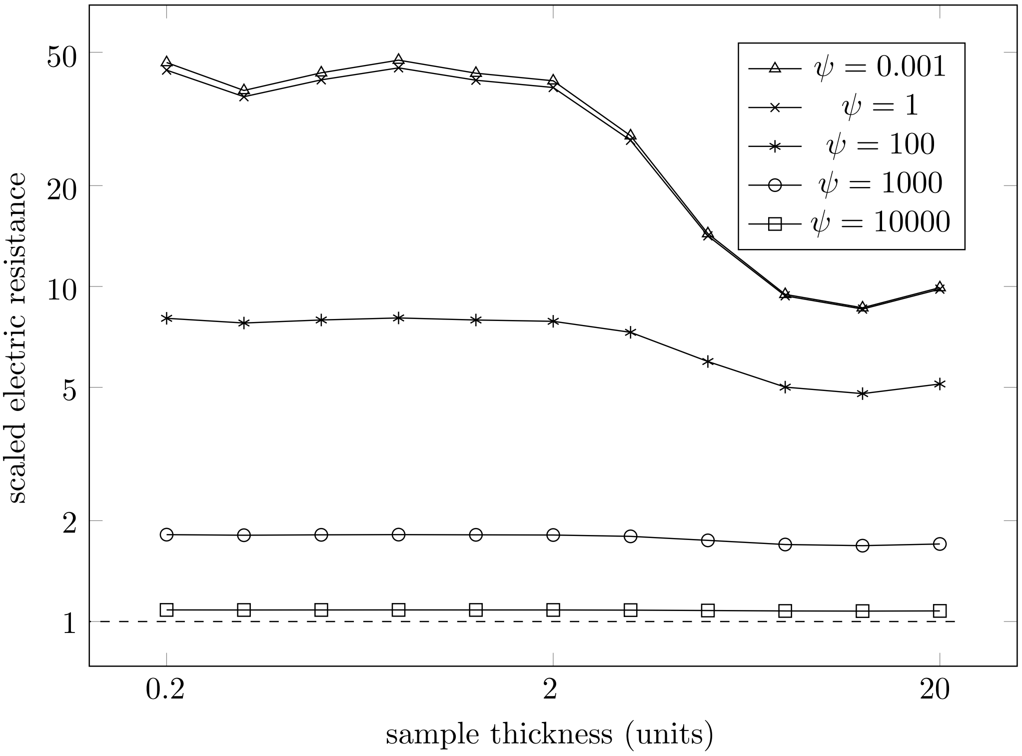

***Fig. 9**: Influence of sample thickness for 100x10 units electrode with additional grounded protective electrode. ψ scales the influence of additional surface conductivity with $\psi \to 0$ denoting only volume contribution and $\psi \to \infty$ only surface contribution.*

Acknowledgements
The authors would like to thank Anton Sperling for his assistance in this project.

References

1149-1:2006-09, D. E. (2006). *DIN EN 1149-1:2006-09, schutzkleidung_- elektrostatische eigenschaften_- teil_1: Prüfverfahren für die messung des oberflächenwiderstandes deutsche fassung EN_1149-1:2006.* doi:10.31030/9705607.

60079-0:2019-09, I. (2019). *DIN EN 60079-0:2019-09, explosionsgefährdete bereiche - teil 0: Betriebsmittel - allgemeine anforderungen (iec 60079-0:2017); deutsche fassung en iec 60079-0:2018.*

60079-32-2:2015-12, D. E. (2015). *DIN EN 60079-32-2:2015-12, explosionsgefährdete bereiche - teil 32-2: Elektrostatische gefährdungen - prüfverfahren (iec 60079-32-2:2015); deutsche fassung en 60079-32-2:2015.*

61340-2-3:2017-05, D. E. (2017). *DIN EN 61340-2-3:2017-05, elektrostatik - teil 2-3: Prüfverfahren zur bestimmung des widerstandes und des spezifischen widerstandes von festen werkstoffen, die zur vermeidung elektrostatischer aufladung verwendet werden (iec 61340-2-3:2016); deutsche fassung en 61340-2-3:2016.*

62631-3-2:2016-10, D. E. (2016). *DIN EN 62631-3-2:2016-10, dielectric and resistive properties of solid insulating materials - part 3-2: Determination of resistive properties (dc methods) - surface resistance and surface resistivity (iec 62631-3-2:2015).*

Chen, X., Zhang, Z., Yu, S., Zsurzsan, T.-G. (2019). *Fringing effect analysis of parallel plate capacitors for capacitive power transfer application.* In *4th IEEE International Future Energy Electronics Conference*. IEEE.

Griffiths, D. J., Schroeter, D. F. (2018). *Introduction to quantum mechanics.* Cambridge University Press.

Moon, P., Spencer, D. E. (2012). *Field theory handbook: including coordinate systems, differential equations and their solutions.* Springer.

Nishiyama, H., Nakamura, M. (1990). *Capacitance of a strip capacitor.* IEEE Transactions on Components, Hybrids, and Manufacturing Technology, 13(2):417–423.

Palmer, H. B. (1937). *The capacitance of a parallel-plate capacitor by the schwartz-christoffel transformation.* Electrical Engineering, 56(3):363–368.

Rochelle, J. (1975). *Approximations for the symmetrical parallel-strip transmission line.* IEEE Transactions on Microwave Theory and Techniques, 23(8):712–714.

Smythe, W. B. (1988). *Static and dynamic electricity.*

DOI: 10.7795/810.20200724

A new technique to produce well controlled electrical sparks. Application to MIE measurements

Christophe Proust [a,b]

E-mail: *christophe.proust@ineris.fr*

[a] Institut National de l'Environnement Industriel et des Risques, Parc Technologique ALATA, BP 2, 60550 Verneuil-en-Halatte, France
[b] Sorbonne Universités, UTC-TIMR, 1 rue Dr Schweitzer, 60200 Compiègne, France

Abstract

Few laboratories in the world have kept the capability of measuring minimum ignition energies (MIE). When a flammable gas needs to be allocated an ATEX group other measurements may be performed like determining the minimum experimental safety gap (MESG). However, the relationship between MESG and MIE is statistical and certainly lacks accuracy and when more accurate information is required as for instance when investigating the influence of the initial conditions on the ignitability, direct MIE measurements are required. To be able to meet such request, the author's team re-developed an expertise in this field be using up to date technologies. A brief review of the methods used in the past is first given highlighting the difficulties. Then a new technique is described with which the losses can be accurately estimated. The method was used for propane and hydrogen air.

Keywords: *minimum ignition energy, spark ignition*

1. Introduction

To implement safety in the process industries and to market flammable goods, accurate safety data are compulsory. As far as explosible mixtures are concerned, some key parameters are the minimum ignition energies (MIE), the minimum auto ignition temperatures (AIT) and the flammability limits (FL).

An intense effort was devoted by the industrialized countries during the XXth century, primarily to better define these parameters and to develop adequate testing methods, secondly to relate them to the practical ignition circumstances and thirdly to organize the market of the flammable goods (REACH directive) and of equipments to be used in dangerous areas (ATEX directives). But it seems that the technical and scientific effort related to the physics of ignition has dropped since 2 decades, the concerned laboratories having switched their core activity towards certification. Nevertheless, new flammable goods appear for which the well accepted experimental methodologies for traditional fuels may not be suited (for instance of too small size if the product is slightly flammable) and would require at least a critical appraisal.

The aim of this work is to revisit Minimum Ignition Energy measurements and (re)develop an expertise especially in view of investigating very sensitive mixtures. Below are recalled the main physical aspects and data about spark ignition. Then the technology developed is presented and results are shown and analysed.

2. Spark ignition

2.1. Some theoretical considerations

A theoretical "spark" could be defined as a punctual and instantaneous deposit of energy. Good monographs have been published along the last 50 years regarding the underlying physical mechanisms of flame development including ignition processes (Lewis and von Elbe, 1987; Glasmann, 1977; Williams, 1985; Hattwig and Steen, 2004). Extending the work of Brokaw and Gerstein (1957), the classical "thermal explosion theory" can be used to describe the phenomenology and this shows the links between the ignition and combustion parameters. Most analytical developments rely on a highly simplified chemistry and, often, the heat release is represented by a one-step chemical reaction obeying a global Arrhenius reaction rate:

F (fuel) + O (oxidant as air) -> P (products) + heat

With the volumetric heat release rate, Q_{comb} (W/m^3) in a simple form :

$$\dot{Q}_{comb} = \rho \cdot \Delta H_{comb} \cdot A \cdot e^{-\frac{E_{act}}{R \cdot T}} \qquad [1]$$

Where:

- ΔH_{comb} is the specific heat release rate per unit mass of the mixture (J/kg)
- ρ the specific mass of the mixture (kg/m^3)
- A the preexponential factor of the Arrhenius law (s^{-1})
- E_{act} the energy of activation of the reaction (J/mole)
- R the perfect gas constant (8.314 J/mole/K)
- T the temperature (K)

Note that ΔH_{comb} is a property of the mixture and is related the maximum temperature of the combustion (T_{ad}) as measured in an adiabatic system. If T_0 is the initial temperature, ρ_0 the initial specific mass and Cp the specific heat capacity then [1] reads:

$$\dot{Q}_{comb} = \rho_0 \cdot A \cdot Cp \cdot (T_{ad} - T_0) \cdot \frac{T_0}{T} \cdot e^{-\frac{E_{act}}{R \cdot T}} \qquad [2]$$

Because E_{act}/R is typically on the order of 10000 K for most fuel-air mixtures, the evolution of [2] with T is largely dominated by the exponential term as shown on figure 1. Note also that this equation is valid for T smaller or equal to T_{ad}. This expression does not include any limitation so that it may be inferred that combustion would occur at any temperature even without any ignition source. The speed of the combustion process would only depend on T. This might be true only if the process was perfectly adiabatic but not when heat losses are taken into account. Unless T is very large, gases exchange heat mainly by conduction and convection. Assuming a volume V (m^3) of the gas having a typical size D (in m, for instance $D = V^{1/3}$), then the volumetric heat lost by conduction or convection with the surrounding (Q_{comb} in W/m^3) through the external area $A_{exchange}$ (m^2) of V reads:

$$\dot{Q}_{losses} = h_{conv} \cdot \frac{A_{exchange}}{V} \cdot (T - T_0) \approx h_{conv} \cdot \frac{1}{D} \cdot (T - T_0) \qquad [3]$$

where h_{conv} is the exchange rate coefficient (unit of W/m^2K), usually approximately constant for a given geometrical configuration and flowing conditions. It appears that, for a given size D, [3] varies linearly with T as shown on figure 1. Equations [2] and [3] then describe the behavior of a pocket of reactant raised at a given temperature T (Fig. 1). Suppose a homogeneous and quiescent explosive atmosphere is prepared in the volume V. T is gradually increased. The combustion is active, but proceeds extremely slowly. If the heat losses (volumetric rate in W/m^3) are larger than the heat released by the combustion ($Q_{losses} > Q_{comb}$), the chemical reaction is dampened because T is forced to decrease. Because of the exponential temperature dependency of the reaction of combustion, there is a temperature where the heat released by the combustion becomes larger than the linear heat losses ($Q_{losses} < Q_{comb}$). Above this temperature nothing prevents the runaway of the reaction and the explosion occurs (T increases up to T_{ad}).

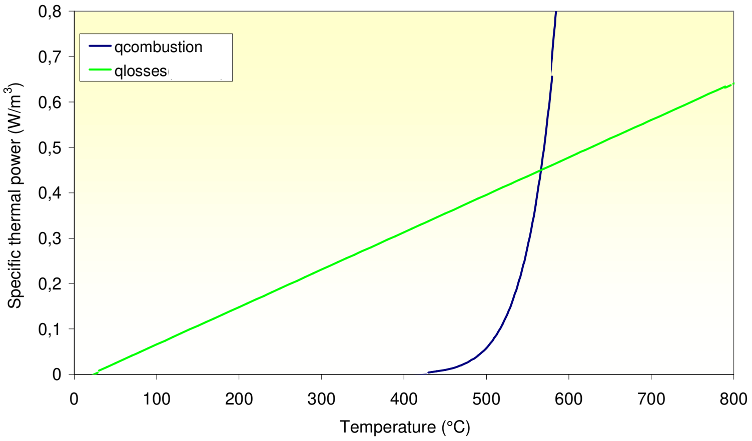

Fig. 1: *volumetric heat release rate and losses in a volume V (featuring the ASTM flash for autoignition temperature measurements) containing a homogeneous and quiescent stoichiometric hydrogen air mixture*

Although it is an over-simplified theory, it is useful to investigate the various ignition modes (Carleton and Weinberg, 1994). A well-known application, particularly fitted to this modelling concept, is the autoignition problem. The autoignition temperature of hydrogen mixture is about 550°C, measured in a 50 mm size flash. The temperature of the flash is progressively increased until the volumetric ignition. The latter occurs when the heat loss curve is tangent to the heat release curve[1]. This theory was applied in the present work to fit the combustion parameters (A and E_{act}/R). A good agreement (Fig. 2) is obtained with $A = 5.10^3$ s^{-1} and $E_{act}/R=10000$ K. Note this value for E_{act}/R is that recommended for hydrogen air mixtures (Coffee et al., 1983).

---

[1] Standard natural heat convection laws are used in [3]

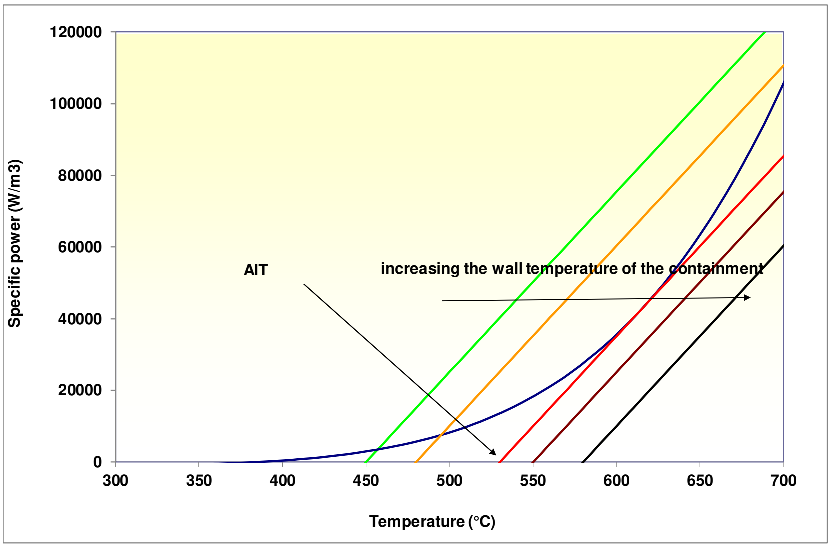

***Fig. 2 :** fitting of the combustion parameters to retrieve the autoignition temperature of hydrogen-air mixtures*

This modelling approach is now tentatively applied to spark ignition mechanisms.

In the spark gap, the heat of the ignition source, E_{spark} (in J), is delivered punctually and instantaneously. At this point, D=0 and T is infinite, so that heat losses are infinite and combustion cannot start. Some (small) amount of time is required for this initial "point" to spread out due to thermal conduction. Following, this initial amount of heat is spread by thermal conduction in the surrounding area but conserved if other thermal losses are ignored (heat radiation, thermal conduction to solid bodies). All along this "spreading" process", the spark energy is conserved according to the following expression (where D increases with time and Cp is the specific heat of the mixture in J/kg.K) which is an application of the first principle of the thermodynamics :

$$E_{spark} = \rho_0 \cdot Cp \cdot \frac{\pi}{6} \cdot D^3 \cdot (T - T_0) \quad [4]$$

The heat loss curve formulated by equation [3] (with h_{conv}~ 2.λ/D where λ is the thermal conductivity of the mixture at the spark temperature so approximately 0.1 W/mK) can now be computed using equation [4]. For each spark kernel size, a temperature and a specific heat loss can be calculated. This evolution is presented in fig. 3 for various spark energies (curves labelled "spark").

The heat release represented by expression [2] can now be plotted using the values of E_{act}/R and A found above. This curve stops at $T=T_{ad}$ with is the maximum combustion temperature. When E_{spark} is too small (E_{spark}=0.015 mJ), the « spark heat loss » curve (line+triangles) never intercepts the heat release curve and, for any value of T, $Q_{losses}(T)>Q_{comb}(T)$ and the explosion cannot occur. When E_{spark} is sufficiently large (E_{spark}=0.05 mJ), the « spark heat loss » curve (line+circles) intercepts the heat release curve and the explosion can occur since there is a domain where $Q_{losses}(T)<Q_{comb}(T)$ while $T<T_{ad}$.

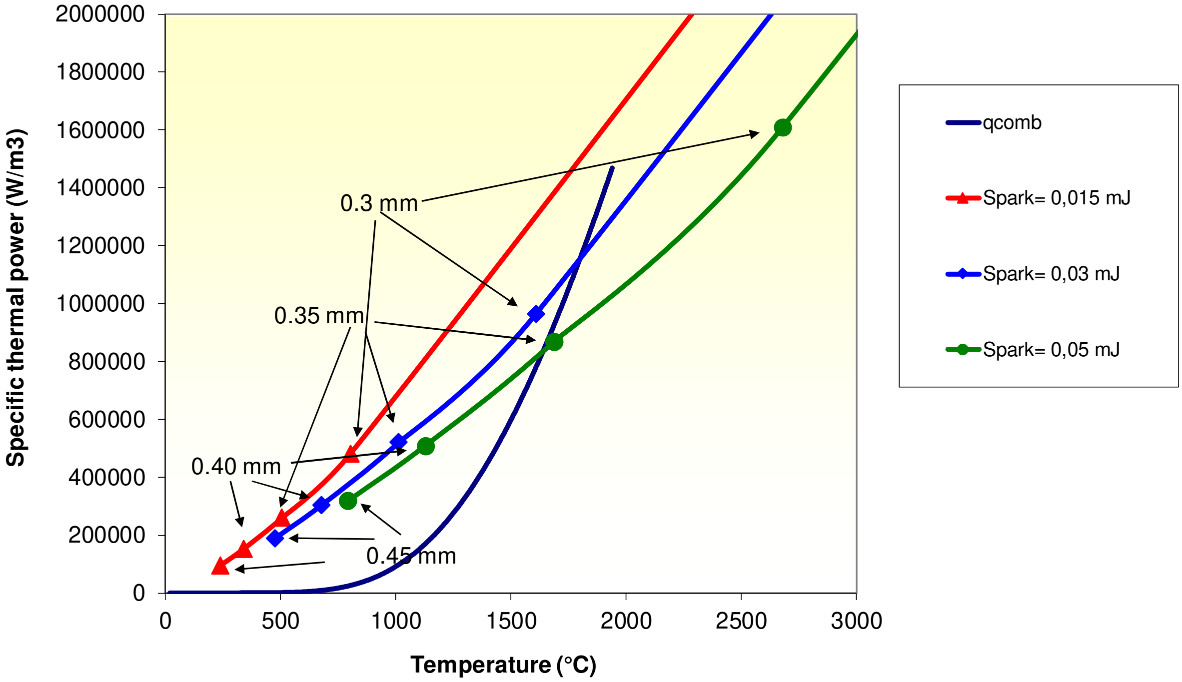

***Fig. 3:** simulated spark ignition of a hydrogen-air stoichiometric mixture for three different values of the initial spark energy (arrows and text refer to the hot pocket of gas size at different times)*

The Minimum Ignition Energy (MIE) is thus obtained when the intercept is obtained for $T=T_{ad}$, corresponding to the upper point of the heat release curve. This particular point corresponds to a specific size of the hot pocket of gas called the « minimum flame kernel », D_{crit}, which is an intrinsic property of the mixture. It is the minimum size of a flame able to develop in a cold environment. This definition is very close to that of the « minimum quenching distance »[2] (D_{quench}). Physically, both parameters can only be proportional.

The main outcomes from this simplified theory are :

- In the MIE conditions (E_{spark}=MIE), the temperature of the spark kernel is equal to T_{ad} so that equation [4] can be used to calculate the MIE;
- T_{ad}, D_{crit} (D_{quench}) and MIE are interlinked. At the ignition point, [2] and [3] are equal and $T=T_{ad}$ and $D=D_{crit}\sim D_{quench}$. In equation [3], ($T_{ad}$-$T_0$) should be replaced by a parameter proportional to MIE/($\rho_0.\pi/6.Cp.D^3$) from equation [4] so that it appears that Q_{losses} is proportional to MIE/D^4. In addition, it can be shown that $\rho_0 \cdot A \cdot Cp \cdot (T_{ad} - T_0) \cdot \frac{T_0}{T_{ad}} \cdot e^{-\frac{E_{act}}{R \cdot T_{ad}}}$ is proportional to the square of the laminar burning velocity Sl_{ad} of the mixture (Glassmann, 1977). Further, it is known (Hattwig and Steen, 2004) that D_{quench} and Sl_{ad} are correlated:

$$\boxed{Pe = \frac{Sl_{ad} \cdot D_{quench}}{a_{diff}} \approx 50} \qquad [5]$$

---

[2] the minimum quenching distance is the smallest gap between two cold parallel planes just allowing the flame to propagate steadily. If the distance is infinitesimally smaller, the flame is quenched.

where a_{diff} is the thermal diffusivity of the (cold) mixture (typically 2.10^{-5} m^2/s for ambient air). So, Q_{comb} is proportional to $1/D^2$. Since Q_{losses} is proportional to MIE/D^4, MIE should be proportional to the square of $D=D_{crit}\sim D_{quench}$.

This relationship was discussed Lewis and von Elbe (1987) and this last conclusion is fully confirmed by available data (fig. 4). MIE is approximately proportional to the square of D_{quench}.

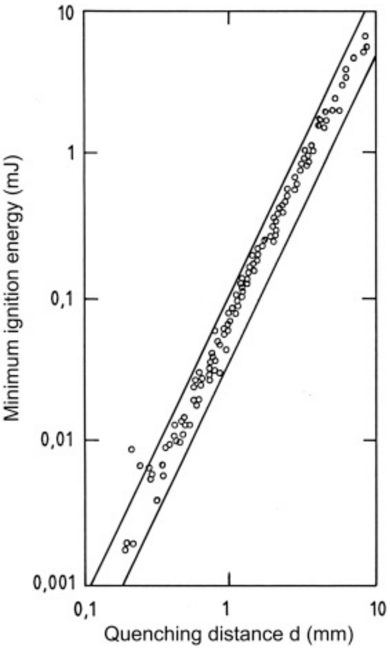

Fig. 4: *relationship between MIE and D_{quench} (from Kuchta, 1985)*

The practical conclusions are that MIE is a fundamental parameter, depending only on the physico-chemical properties of the mixtures, and that it may be deduced from other fundamental parameters like D_{quench}. D_{quench} is not easy to measure and rather the Minimum Experimental Safety Gap (MESG) is used to correlate with MIE. But these are approximate correlations, relying on several assumption like the validity of [5]. Direct measurements of MIE are preferable when some accuracy is required.

2.2. *Measuring the MIE*

If a "spark" were truly "a punctual and instantaneous deposit of energy", the temperature would be infinite which is unrealistic. In practice, the deposit is not punctual nor instantaneous. Electrical deposits (breakdown, arc) or focusses laser beams are used in which plasma temperatures up to 5000 to 10000 K are reached in nanoseconds.

Usually, capacitive spark discharges are used because of the apparent simplicity (Kumamoto et al., 2011) since the energy delivered into the circuitry cannot be larger than that stored in the capacitor[3]. This energy can be easily varied, changing the charging voltage. Most often, the MIE is the minimum <u>stored</u> energy enabling ignition. A good overview was proposed by Ngo (2009). Usually, the capacitor

---

[3] Other techniques were tried like focussed pulsed laser beams (Weinrotter et al., 2005). The energy of the pulse is known but not the quantity really absorbed in the plasma created at the local point. The major part of it is transmitted through the plasma and dissipated by absorption in other parts of the beam. Following the minimum energy pulse (MPE) appears on order of magnitude larger than the traditional MIE.

is mounted in series with the spark gap and the voltage of the capacitor is increased slowly until breakdown. In some case, a transformer is used to produce the breakdown from a low voltage capacitor. A significant body of work was performed more than 50 years ago by Lewis and von Elbe (in the edition of 1987) and Calcote et al. (1952). The influences of several parameters like the spark gap distance and of the duration of the spark were investigated. They found that the optimum spark gap distance is about D_{quench}. When it is larger, the part of the energy of the spark dissipated outside the initial flame kernel is lost and when it is smaller the quenching effect of the electrodes appears. Because of this last phenomenon, the shape and diameter of the electrodes is also important especially when the spark gap is smaller than D_{quench}. It is advised to choose a spark gap slightly larger than D_{quench} and pointed and thin electrodes. Further, a shallow minimum as function of the duration of the spark is found. This optimum amounts a few tens of microseconds. Presumably for very short spark durations, the temperature of the plasma is so large that significant losses by heat radiation occur (and some mechanical losses by the emission of a shock wave). And obviously the energy delivered by the spark after the flame has emerged from the initial kernel is also lost.

Despite the effort devoted to controlling the spark, authors generally observe a large overlap between the “ignition points” and “no ignition” points (fig. 5). Because of this, experimentalist use some statistics, like probit laws, to define an ignition threshold (Eckhoff, 2010). Then, the renown ignition threshold, as those given by Lewis and von Elbe, might then be more a statistic limit than a true physically meaningful border (Bane et al., 2010). This statistical nature may come partly from the difficulty to master the spark characteristics although the flame ball development although the complicated flow produced in the spark may disturb the flame ball growth (Kono et al., 1992).

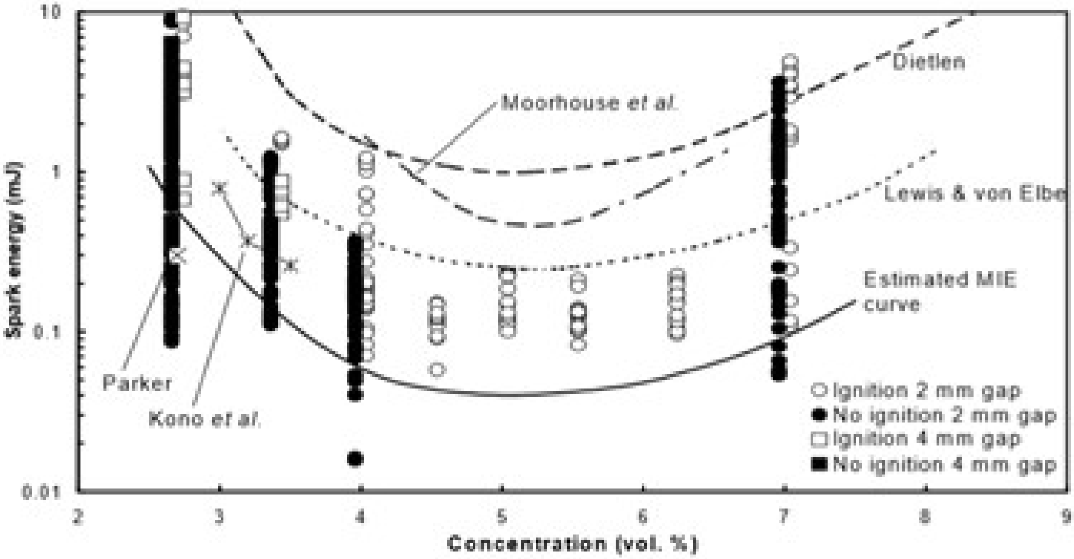

Fig. 5 : *illustration of the data scattering about the minimum ignition energy of propane-air mixtures at ambient conditions (from Randeberg and Eckhoff, 2007)*

It is believed that there is thus room to progress into the way of measuring the MIEs and, especially, in controlling the spark characteristics.

3. Experimental setup

The explosion chamber is a 7 liter transparent cylindrical chamber (figure 8) able to support a static internal pressure amounting 100 bars. It is equipped with measuring ports and feeding lines. The mixture is prepared into a small stainless-steel mixing tank (0.1 l) using mass flowmeters (fig. 6). The composition is controlled using a paramagnetic oxygen meter (SERVOMEX : O_2 % accuracy = ±0.01 % v/v) upstream of the chamber and downstream. For a targeted 5% v/v fuel/air mixture, the accuracy of the composition is : 5±0.1 % v/v. The maximum explosion (over)pressures is measured using a Kistler 10 b piezoresistive gauge. High speed video (up to 10000 fps: Photron camera) is used.

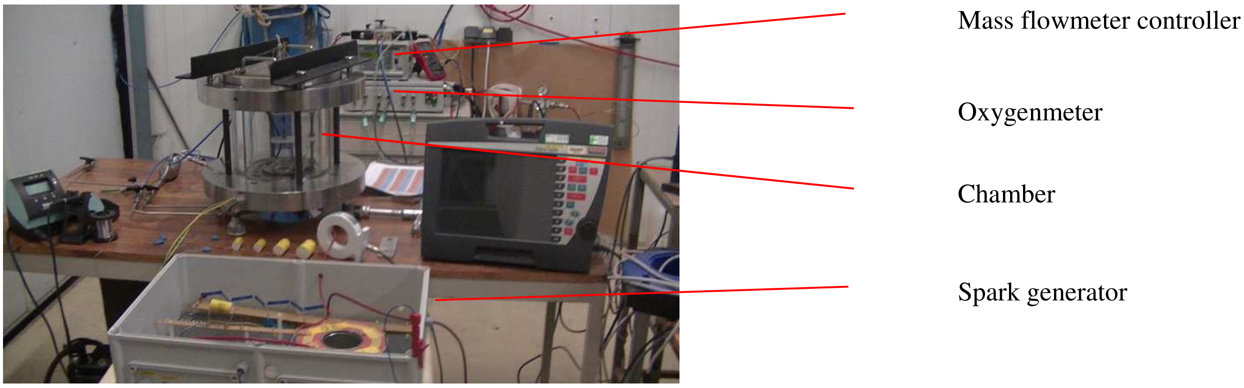

***Fig. 6 :** experimental set-up*

In the spark gap a part of the electrical energy is dissipated into heat which is the source of the ignition. But part of it is lost in producing the conditions sustaining the current stream (vaporizing the material of the electrodes, anode/cathode voltage gap,..), heat conduction towards the electrodes, shock waves, thermal radiation,… Microcalorimetric measurements (not shown here) showed that using small tungsten electrodes is a good mean for reducing the first two sources of losses. The electrodes are 0.3 mm in diameter (Tungsten) tightly screwed on steel rods in such a way that any heat loss sources (supports, walls) are cms away from the spark gap (fig. 7).

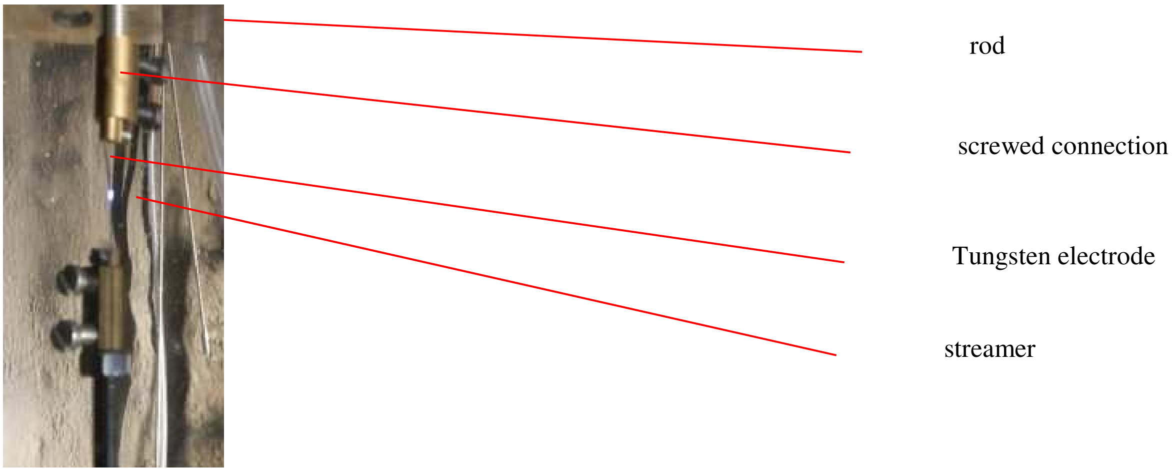

***Fig. 7** : spark gap arrangement*

But only a better control of the current and duration of the spark can reduce the two last sources of losses which supposes a flexible control of the current/voltage supply which depends on the spark generator. A large variety is described in the literature. An electrical spark is a two steps process. During the "disruption phase", a large voltage is required (typically 3000 V/mm) to ionize the atmosphere and create a "streamer" (ionized channel visible on fig. 7). The current remains very low during that phase (micro amperes). Then the electrical arc takes place during which a large current (up to tens of amperes) flows through the spark gap. The voltage amounts a few volts to several tens of volts. As said before, in many spark generators, the electrical energy is stored in a single capacitor and is used to create the disruption and the arc with considerable losses due to very large currents. The ratio energy delivered in the spark/stored energy may vary is significant proportions depending on the current, so from one test to another. This might be a reason for the statistical nature of the ignition. To obtain a better yield, the impedance of the circuit needs to be carefully controlled. This was attempted in the present work.

If a purely capacitive circuit were used with only a few meters of cables, the expected resistance would be a fraction of 1 ohm and the inductance nearly zero. Using a single high-voltage capacitor and a 2 mm spark gap, a minimum voltage of 6000 V would be required meaning a typical capacitor value of 5 pF (this is difficult to control in practice) to be able to deliver 100 µJ. The energy is dissipated into the circuit within a time scale amounting R.C= 10^{-12} s which is much too short for an efficient ignition and with a very large current (hundreds of amperes) favoring the losses. This is the reason why it is suggested, in the standards for instance, to add a rather large inductance (1 mH). Its role is to increase the impedance of the circuit without consuming much energy (which a resistor would do) to reduce the current and increase the duration of the spark. However, our initial trials showed that controlling a very low capacitance circuit is difficult and that the scattering in the disruption appearance is significant depending presumably on the electrodes (shape, surface conditions,…). This technique was rapidly abandoned.

Rather, it was decided to disconnect the two phases of the spark. A separate high voltage and high impedance circuit is used to produce the streamer. A second, low voltage and low impedance circuit, is used to produce the arc and dissipate the energy. Once the streamer is created the low voltage circuit discharges automatically. A set of Zener diodes prevents the high voltage to be transmitted to the low voltage circuit. The circuit is presented on fig. 8. The current is measured using a standard current gauge and the voltage is measured at the charge capacitor. As it stands, the total capacitance of the circuit is 20 nF (which is that of the charge capacitor but which can be varied), the inductance is 1.7 µH and the resistance is 0.1 Ω. The measured capacitance of the chamber, of the diodes and of the high voltage cable is not more than 45 pF, half of this being due to the cable. An additional 1 mH inductance can be placed close to the electrodes. The main advantage of the device is that the stored energy can be varied in very large proportions since it was verified that an arc is maintained down to voltages as low as 35 V. In theory, the stored energy can be varied between 10 and 2000 µJ without changing the capacitor. Note that it was verified that the streamer is not able to ignite the mixtures.

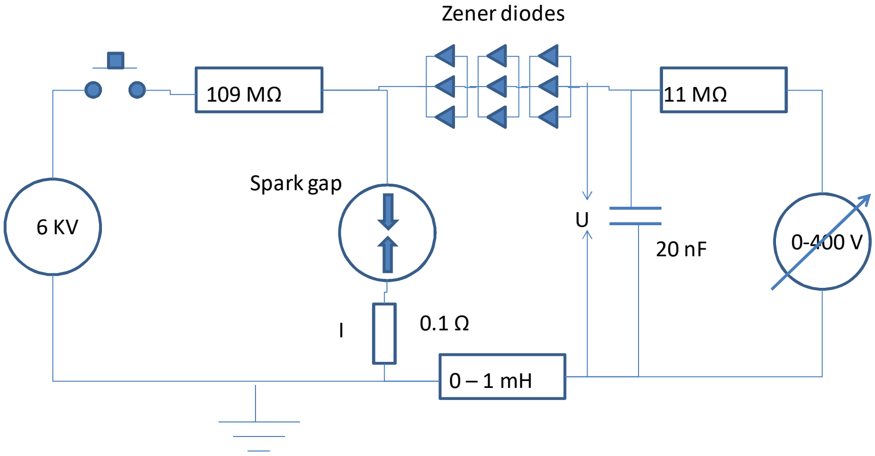

***Fig. 8 :** scheme of the electrical circuit*

Electrical tests were performed without the high voltage part (to limit the noise affecting the very beginning of the signal at the start of the breakdown). In the first test (fig. 9), the diodes were short-circuited and the discharge was obtained by short circuiting manually the electrodes. Doing this, a short spark is produced over a length amounting a fraction of a mm during some tens of microseconds.

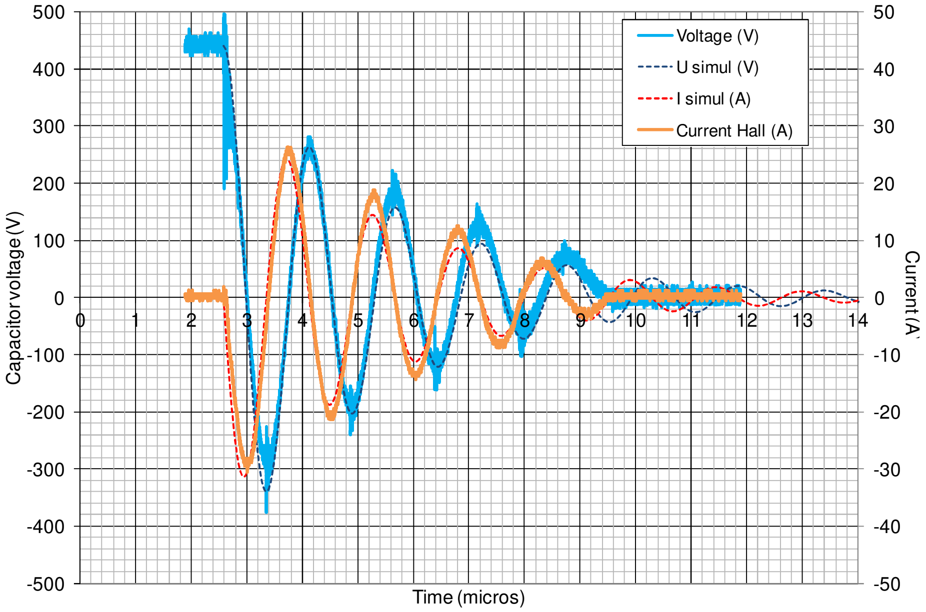

Fig. 9 : current voltage signals : no streamer, manually triggered spark, without additional inductance, 440 V in the 20 nF capacitor, without the diodes.

In the second test, the diodes were reintroduced (fig. 10).

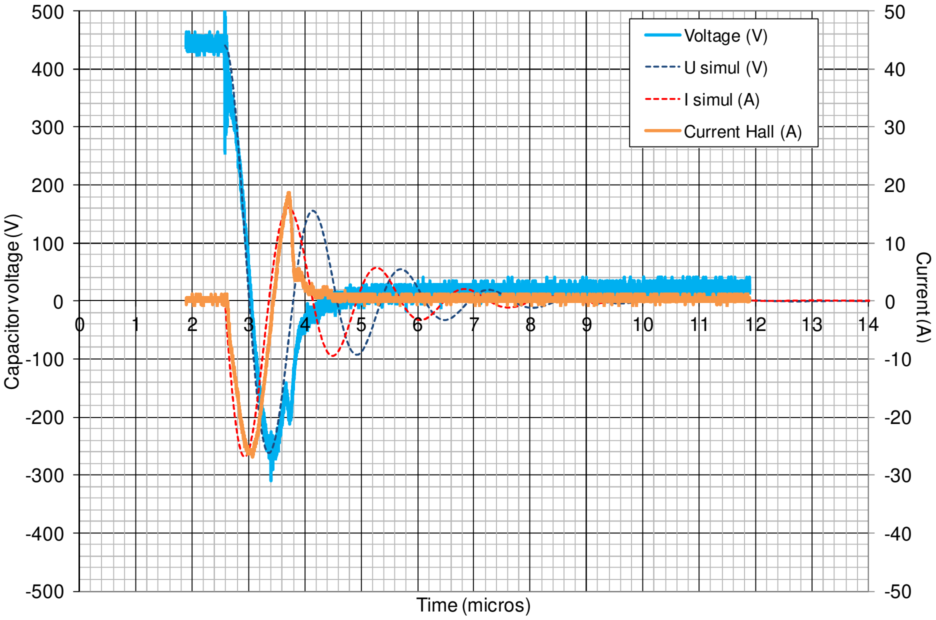

Fig. 10 : current voltage signals : no streamer, manually triggered spark, without additional inductance, 440 V in the 20 nF capacitor, with the diodes.

The dampened oscillating signal of figure 9 is a typical RLC circuit response with a moderate resistance. Clearly, the diodes have a strong influence (fig. 10) and remove a lot of energy. A simulation of the RLC circuit was performed, and the results are the dotted lines on fig. 9 and 10. The best fit is obtained with an inductance of 3 µH (capacitor=20 nF) and a resistance of 2 Ω for fig. 9

and an inductance of 3 µH (capacitor=20 nF) and a resistance of 4 Ω for fig. 10.When the diodes are short circuited, it can be verified that all the energy is consumed in the resistance. The latter is much larger than the natural resistance of the wires as measured initially. Most probably it is that of the "spark gap" (the direct contact of the electrodes). When the diodes are incorporated, the best fit is obtained with R=4Ω at least until about 3.5 µs. After this, a catastrophic change appears suggesting a strong increase of the resistance as the Zener diodes start to open the circuit. The characteristic of the circuit turns from a LC to a RC dominated. In terms of energy, the average resistance needed to close the balance would be 6 Ω. About half of the energy is dissipated in the "spark gap" and the duration is on the order of 1 microsecond.

A similar attempt was performed inserting a 1 mH inductance (added resistance=2Ω). The arc is triggered by the streamer (2 mm spark gap). The signals (fig. 11) resembles that of fig. 10 but over a larger timescale (10 µs instead of 1) as expected. The very beginning of the current signal is an artifact probably due to the Zener diodes closing the low voltage part of the circuit. The simulation shows that the best fit is obtained with L=0.4 mH (instead of 1 mH) and R=150 Ω. This value of the resistance closes the energy balance as well. This increase of the resistance as compared to figure 14 is due the spark gap which resistance increases in proportion with the electrode distance and inversely with the current intensity. From the energy remaining in the charge capacitor, current measured and model of the circuit it was possible to obtain a robust estimate of the yield of the spark. With a reduced current below 1 A, the yield is better, up to 90%. With a current of about 3 A, the yield is 70% at 10 A, it drops at about 50%. To some extent, it confirms that depending on the voltage between the electrodes when the spark appears in standard apparatuses, the yield of the spark may strongly vary.

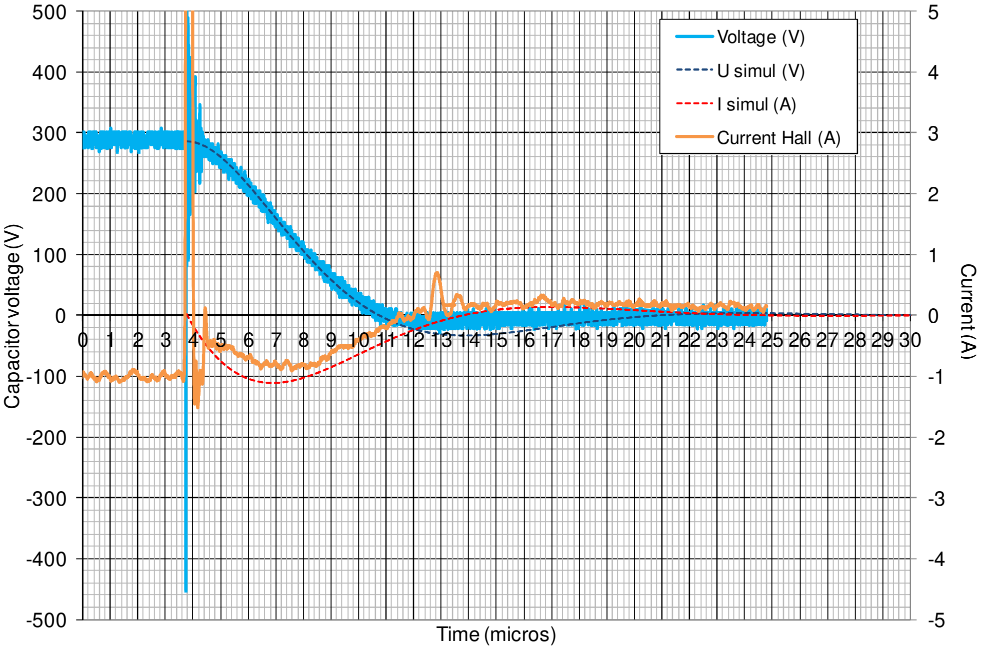

Fig. 11 : current voltage signals : streamer triggered spark, with a 1 mH additional inductance, 290 V in the 20 nF capacitor, with the diodes.

4. Results

Propane-air and hydrogen-air tests were performed.

A typical sequence is shown on fig. 12 for a 4.5% v/v propane-air mixtures. The spark gap is 2 mm. A double lobed structure appear just after the spark with seems to be a double vortex and would suggest a Maecker (1955) effect due to the flow of heavy ions between the electrode. This “jet” is mostly responsible for the energy transfer between the spark gap and the mixture. A blue flame kernel is visible at 3 ms and expands out. The expansion velocity is a few m/s.

The minimum ignition energy measurements are shown on fig. 13a (the values are three quarters the energy stored in the capacitor to account for the losses). The voltage is dropped gradually until systematic no ignition. Each test is repeated 10 times. There is some remaining overlap between the no ignition zone and the ignition zone but much less at compared to the data of fig. 5. It is possible that the remaining scattering results from the development of the flame kernel (Esmann et al., 2020). If the minimum ignition energy is in line with the standard values (0.3 mJ at stoichiometry fig. 13b), the evolution of MIE on the lean and rich side are different but in line with the most recent measurements.

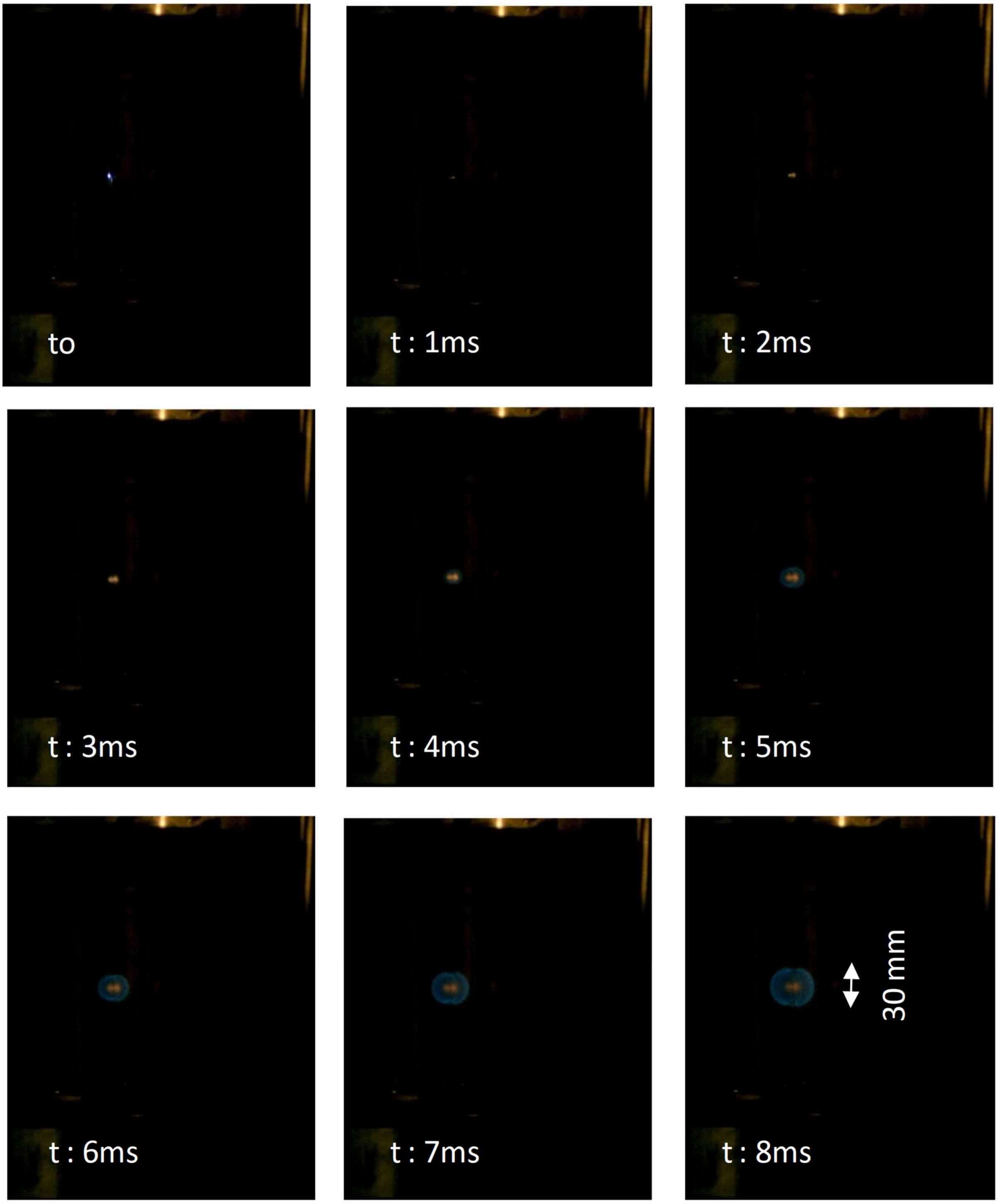

Fig.12 : *flame kernel development (4.5%* C_3H_8 *in air, 400V, 1 mH)*

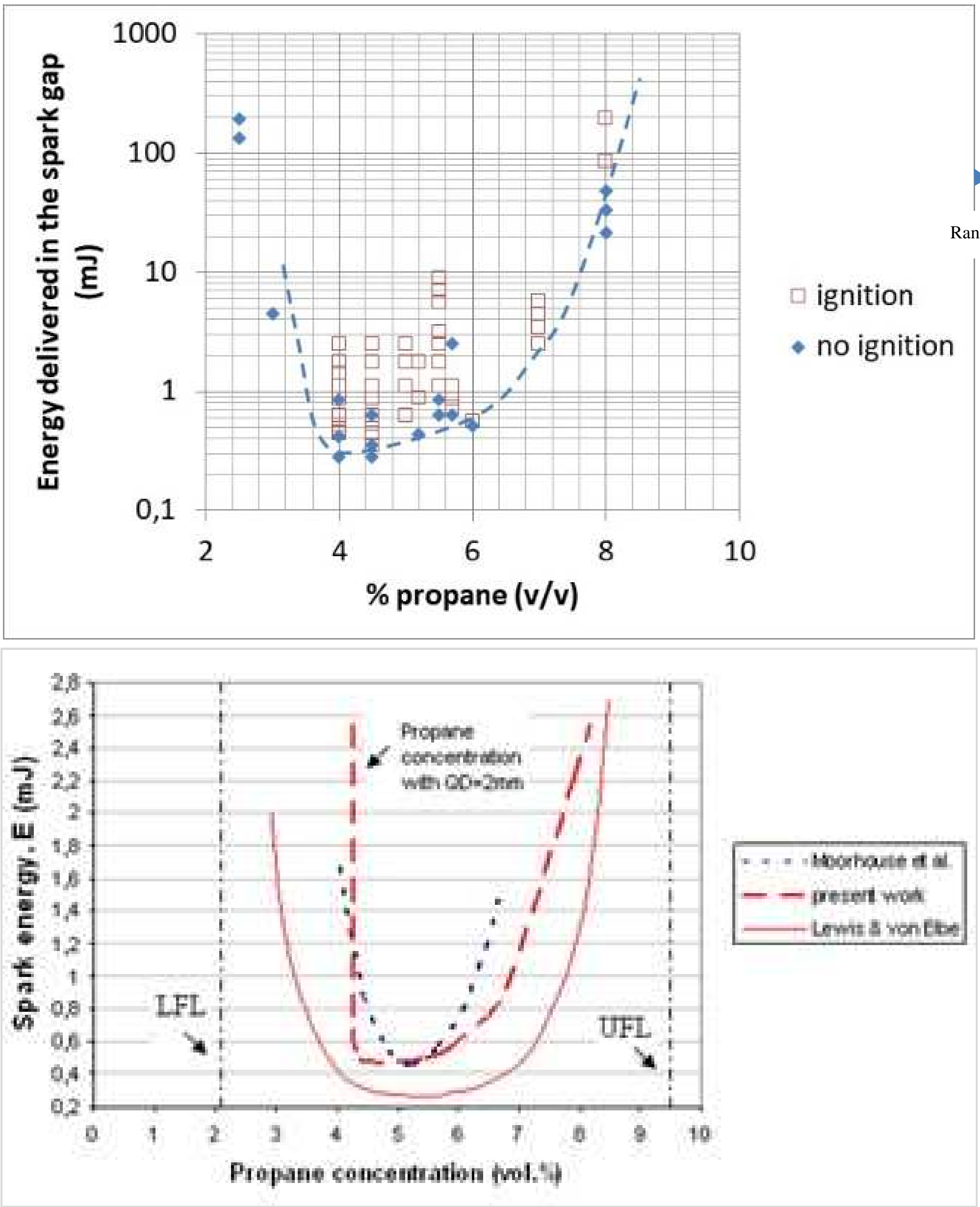

Randeberg et al.

Fig. 13 : minimum ignition energies for propane air mixtures at ambient conditions (bottom grap^h from Randeberg et al., 2007)

A typical sequence is shown on fig. 14 for a 40% v/v hydrogen-air mixtures. The spark gap is 0.5 mm. the beahaviour of the flame is similar to that of the propane air mixture.

The results of the MIE measurements for hydrogen-air mixtures are shown on fig. 15. In fig.15a are given the results obtained under exactly the same conditions than for propane-air experiments. In these tests the mixture is still. In fig15b, the same measurement obtained with a continuous flow of the flammable mixture (0.1 m/s). There is a clear influence of the experimental conditions. It was noticed during these tests the extreme sensitivity of the triggering of the spark to the presence of humidity. It is believed that when the mixture is still, the water vapor produced by the local burning of hydrogen modifies the sparking conditions especially at the easiest burning conditions (40% H_2 v/v) for which the sparks are very tiny. The present results are globally consistent with the literature (Ono et al., 2007).

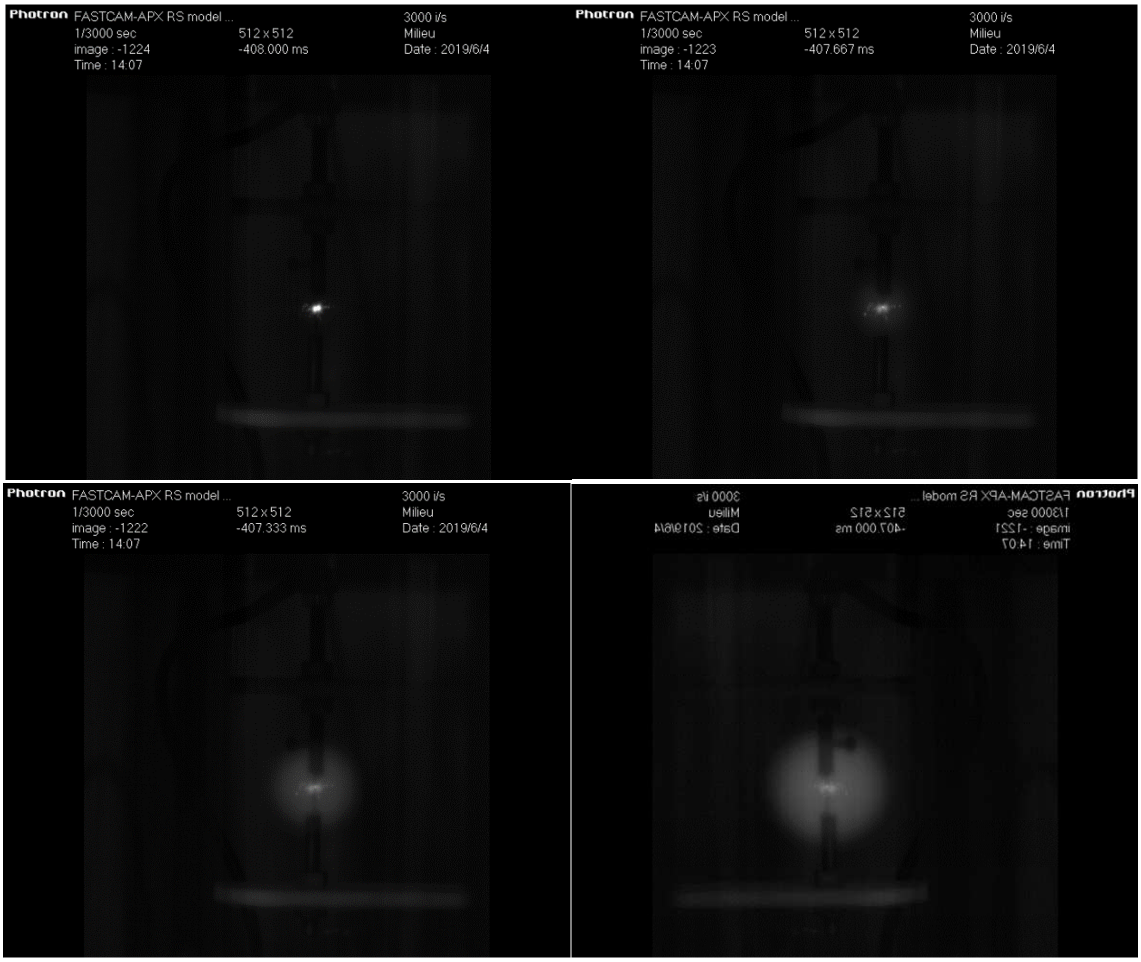

***Fig. 14 :** flame kernel development (40% H_2 in air)*

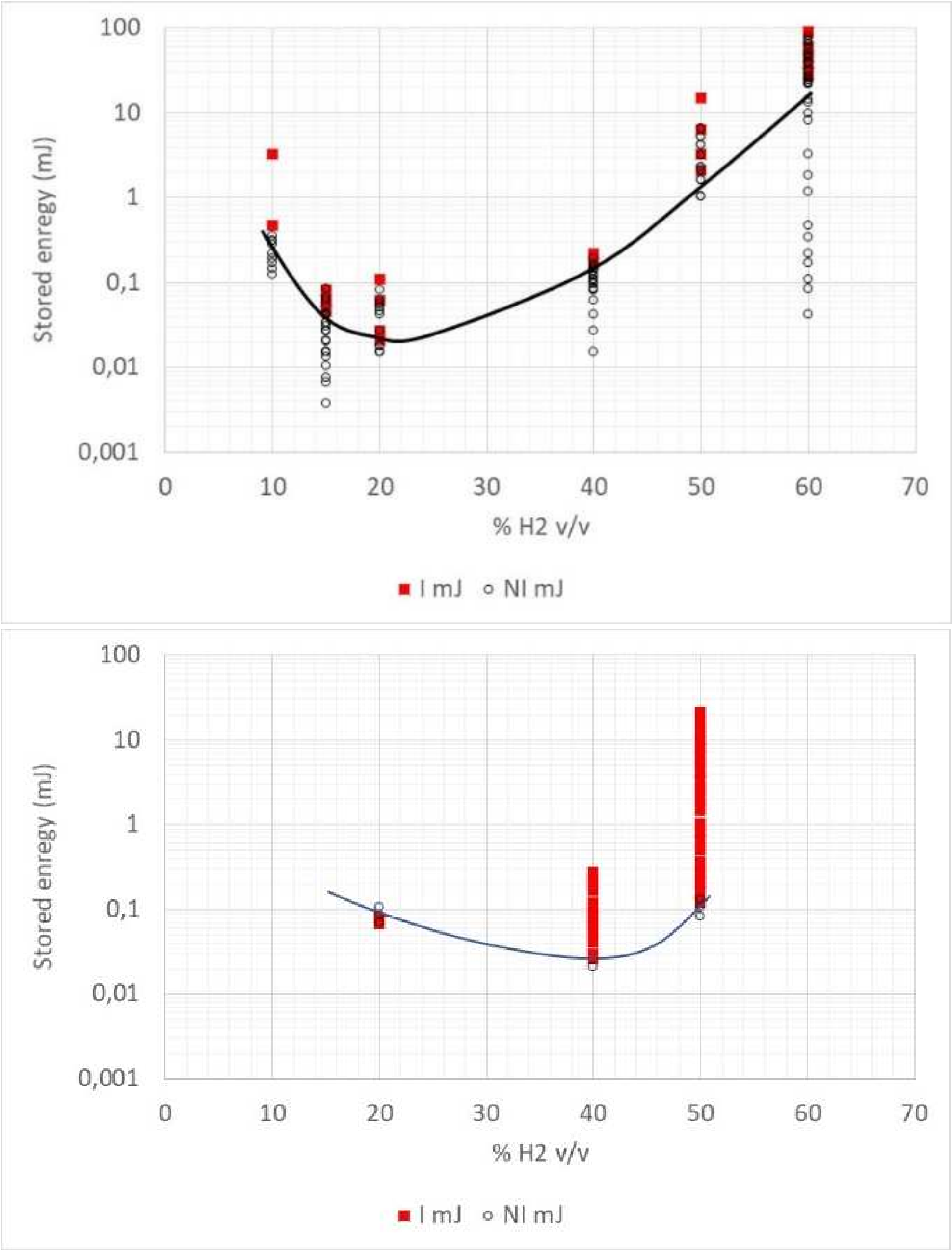

Fig. 15 : *minimum ignition energies for hydrogen air mixtures at ambient conditions (a-with a still mixture and b- with a flowing one)*

5. Conclusions

In the present document, a new device to measure minimum ignition energies of flammable gases is presented. The originality of the system lies in the triggering mechanism of the spark which promotes the reproducibility by controlling the losses.

It is shown that the scattering of the ignition/non ignition point is can be reduced as compared to other studies. However, for very low MIEs, like with hydrogen air mixtures, the ignition process seems more erratic although the sparks are reproducible. Humidity seems to be a potential explanation.

Acknowledgements

The authors gratefully acknowledge the financial contribution from the European Union via the sponsorship of PRESLY project

DOI: 10.7795/810.20200724

References

Lewis, B., Von ELBE, G., Combustion, flames and explosions of gases : 3rd edition, Academic Press, London, 1987, ISBN 0-12-446751-2.

Carleton, F.B., Weinberg, F.J., Correlating minimum ignition criteria, Proc. R. Soc. Lond. A, 447, 1994, 513-520.

Kono M., Isshii K., Tsukamoto T. and Ujiie Y. (1992): Analysis of ignition mechanism of combustible mixtures by composite sparks, Combustion and Flame, Vol. 91, 1992, 153-164.

Maecker, Plasmaströmungen in Lichtbögen infolge Eigenmagnetische Kompression, Zeitschrift für Physik, Vol.141, 1955, 198-216.

Essmann S., Markus D., Grosshans H., Maas U., Experimental investigation of the stochastic early flame propagation after ignition by a low-energy electrical discharge, Combustion and Flame, Volume 211, 2020, 44-53.

Calcote, H.R., Gregory, Jr. C.A., Barnett, C.M., Gilmer, R.B., Spark ignition. Effect of molecular structure, Ind. Eng. Chem., Vol. 44, 1952, 2656.

Kuchta, J. M., Investigation of Fire and Explosion Accidents in the Chemical, Mining, and Fuel-Related Industries A Manual, U.S. Bureau of Mines Bulletin, 1980, 680.

Kumamoto, A., Iseki, H., Ono, R., Oda, T., Measurement of minimum ignition energy in hydrogen-oxygen-nitrogen premixed gas by spark discharge, Journal of Physics: Conference Series, , 2011, 301.

Ngo M., Determination of the minimum ignition energy (MIE) of premixed propane-air, Master of Phycics, 2009, Department of Physics and Technology University of Bergen, Norway

Randeberg, E. and Eckhoff, R.K, Measurement of minimum ignition energies of dust clouds in the 1 mJ region, J. Hazardous Materials, Vol. 140, 2007, 237-244.

Ono, R., Nifuku, M., Fujiwara, S., Horiguchi, S., Oda, T., Minimum ignition energy of hydrogen–air mixture: Effects of humidity and spark duration, Journal of Electrostatics, Volume 65, 2007, 87-93.

Eckhoff R.K., Ngo M., Olsen W., On the minimum ignition energy (MIE) for propane/air, Journal of Hazardous Materials 175, 2010, 293–297.

Bane S.P.M., Shepherd J.E., Kwon E., Day A.C., Statistical analysis of electrostatic spark ignition of lean $H_2/O_2/Ar$ mixtures, International Journal of Hydrogen Energy, volume 36, 2010, 2344-2350.

Glasmann I., " Combustion ", Academic Press, London GLASSMAN I. (1977), " Combustion ", 1977, Academic Press, London

Williams F.A., " Combustion theory : 2nd edition ", Benjamin/Cummings publishing company Inc., 1985, Amsterdam, ISBN 0-8053-9801-5

Hattwig M., Steen H., Handbook of Explosion Prevention and Protection, Wiley-VCH Verlag GmbH & Co. KGaA, 2004 ,ISBN 9783527307180.

Brokaw R.M., Gerstein M., Correlations of burning velocity, quenching distances, and minimum ignition energies for hydrocarbon-oxygen-nitrogen systems, Symposium (International) on Combustion, Vol. 6, 1957, 66-74.

Coffee, T.P., Kotlar A.J., Miller, M.S., The Overall Reaction Concept in Premixed, Laminar, Steady-State Flames. I. Stoichiometries, Comb. and Flame, 54, 1983, 155-169.

DOI: 10.7795/810.20200724

25 years of ATEX directive: the real role of each stakeholder

Michał Górny [a] & Xavier Lefebvre [b]

[a] ExKontakt, Katowice, POLAND
[b] XLefebvre, Calais FRANCE

E-mail: MGorny@ExKontakt.eu

Some general conclusion may be expressed regarding categories of interest and their contribution regarding explosion prevention and protection. These elements are based on over 25 years of findings regarding Ex regulations through recent revision of ATEX Directive 94/9/CE to 2014/34/EU, standardisation development, Ex product testing and participation in various colleges, observing the whole market and organisation rules in EU.

The actual system is mainly driven by regulators and testing body side, the manufacturer impact, although officially possible, not balance the other two sides.

The delicate balance between market and required safety is illustrated through some key points due to learnt lessons, such as voluntary ATEX certification system, reaction on state of the art changes, certification of specific equipment, potential support from Ex NBs, preferring IEC standard solution instead of clearly defined requirements in ATEX directive, practically not equal market surveillance in all EU countries and some gaps required to enhance actual 1999/92/CE directive.

The start of discussion regarding this topic should be helpful mainly for manufacturers and end users to reach some practical situations and/or to solve some practical problems.

Keywords: *explosion hazards, regulation, best practice, conformity assessment*

Foreword

The scope and the objective of the ATEX Directive remain unchanged from the previous Directive 94/9/EC to the new Directive 2014/34/EU, to ensure free movement for the products to which it applies in the EU territory. Therefore, the ATEX Directive provides for harmonised requirements and procedures to establish compliance for products placed on the EU market for the first time.

The ATEX Directive carries specific obligations for the person (natural or legal) who makes products available on the market and/or puts products into service, be it the manufacturer, its authorised representative, the importer or the distributor. The Directive does not regulate the use of equipment in a potentially explosive atmosphere which is covered by different EU or national legislation: for instance, the ATEX "workplace" Directive 1999/92/EC

It is the duty of Member States to protect, on their territory, the health and safety of persons, especially workers, and, where appropriate, domestic animals and property, especially against the hazards resulting from the use of equipment and systems providing protection against potentially explosive atmospheres.

1. Introduction

The ATEX directive, initially as 94/9/CE, later as 2014/34/EU [1] was implemented or into force in 1 March 1996. Initially, it was used voluntarily (until 2003) to later (from July 1, 2003) become obligatory.

It is important to reminder that this Directive shall apply to the following, hereinafter referred to as “products”:

(a) equipment intended for use in potentially explosive atmospheres;
(b) protective systems
(c) safety devices, controlling devices and regulating devices intended for use outside potentially explosive atmospheres but required for or contributing to the safe functioning of equipment and protective systems with respect to the risks of explosion;
(d) components intended to be incorporated into equipment and protective systems.

During this time some changes took place.

For example, it turned out that the weight of the device's certificate is no longer the same as before, and that for a significant number of products, products certification is not required at all. If we look at the size of explosion hazard zones, we will notice that the largest areas are zones 2 and 22, in which certification or, speaking the language of the ATEX directive, the participation of a Notified Body is not required.

Zoning are optimised but also, they are in line with obligations and recommendations due to environmental codes and protection of workers from hazards.

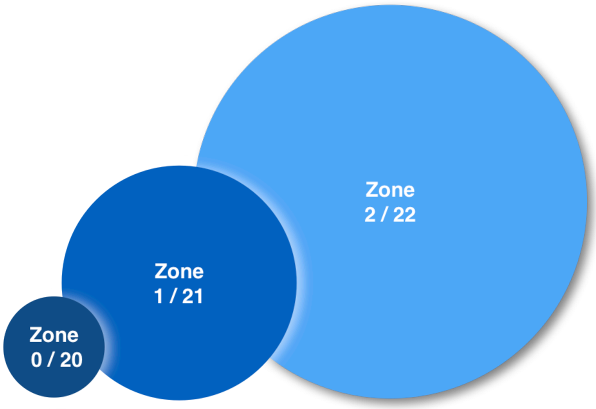

Fig. 1. An overview of the size of hazardous areas. Zones 2 and 22 are the largest areas.

2. Findings

The flow chart below indicates the conformity assessment procedures for according to ATEX directive, we can highlight that a large part of products is assessed without third party certification.

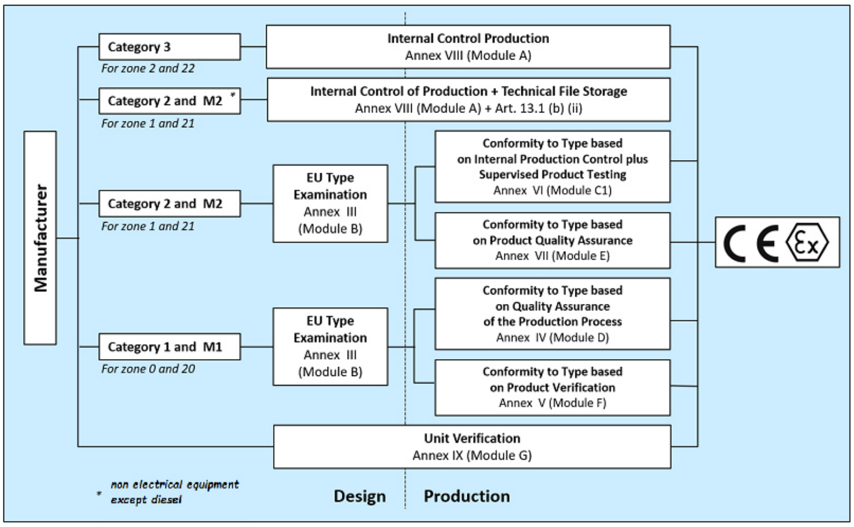

Fig. 2. An overview of ATEX conformity assessment system.

In the specific case of category 3 products intended to be used in zones 2 and/or 22, the manufacturer may make his own assessment and, on this basis, declare the conformity of the product. Therefore, manufacturers had to become proficient in the technical assessment of their products. At the same time, recipients of these products have not relinquished their expectations regarding certification, i.e. assessment by a third party. Hence the quite large "voluntary ATEX certification" market is already important.

Even if tests are used by manufacturers to demonstrate compliance, they need to respect at least principles of requirements regarding quality of tests (e.g. EN 17025) like those observed by testing houses. Rarely, manufacturers are fitted with specific tests facilities dealing with required tests linked to Ex standards.

For complex equipment like a fan, often observed as a source of ignition during accidents survey, we can highlight several cases for which hazards are delicate to prevent.

- The fan can be installed in hazardous area and handled air
- The fan can be installed in hazardous area and handled explosive fluid
- The fan can be installed in safe area and handled explosive fluid

In all cases hazards are present even hidden hazard like electrostatic charges.

In all applications the involvement of Ex agencies should be required to consider requirements of harmonized standard like EN 14986.

3. Actual situation

To harmonize the interpretation of the directive, an ATEX guide has been developed, which has taken on a new shape since the new edition of the directive and makes it easier to understand the provisions of the directive. However, it is only a guide and does not constitute a law. Legal requirements, including technical ones, are given only in the ATEX directive.

Although the technical requirements of the ATEX directives do not change (the update of Directive 94/9 / CE to 2014/34 / EU did not introduce any changes to the technical requirements), the change in the current state of knowledge takes place in the standards harmonized with the directive. Standards are replaced by newer editions, and withdrawn ones are commented that "the presumption of conformity has ceased". This approach imposes on the manufacturer (and notified bodies) the obligation to track changes in the list of harmonized standards, fortunately these changes are communicated in advance.

One of the undoubted advantages of the EU approach to conformity assessment is the increased role of the instruction manual. The requirements for the instruction are one of the essential requirements (EHSR 1.0.6). The buyer of the product agrees to the provisions in the user manual - he must comply with its provisions. If any record or requirement of the user manual is unfavourable for the buyer - it remains only not to buy this product.

The compliance assessment system is partially balanced by market surveillance, whose task is to oust the dishonest participants from the market, i.e. those who unreasonably declare the appropriate level of safety for their products.

It is worth noting, however, that although market surveillance principles are agreed at EU level, each Member State oversees its own market.

4. Actual state of knowledge

The technical requirements contained in Annex II of the ATEX Directive (EHSR) do not change from the very beginning of the Directive. Technical progress, or as the ATEX directive specifies, the

DOI: 10.7795/810.20200724

current state of knowledge is reflected in technical standards, especially in harmonized standards. Let us remind that harmonized standards are standards that were ordered by the European Commission.

The number of harmonized standards has steadily increased, especially in "new" areas, ie for non-electrical equipment and protective systems.

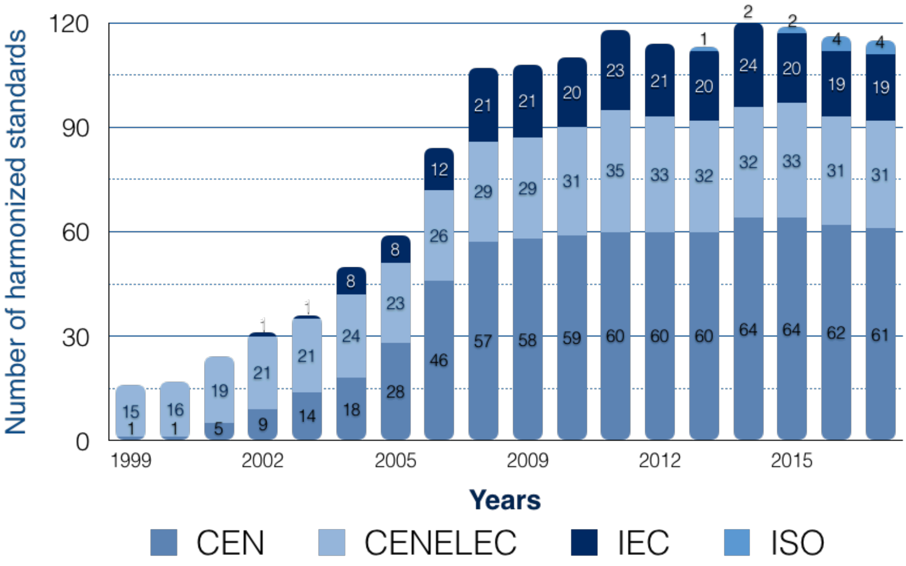

Fig. 3. *Increase in the number of standards harmonized with the ATEX directive over the years: CEN, CENELEC, IEC and ISO standards.*

The current (2020) list of harmonized standards contains 124 items [2]. Considering the average period of 5 years of review and update of standards, virtually every year a standard (or standards) changes.

A change in the current state of knowledge (change in the standard) entails the need for the manufacturer to assess whether the new provisions of the standard relate (i.e. whether they are relevant) to the product of its production.

There is the first discussion point between the manufacturer and NB who took part in the conformity assessment (if any). Does every change of the standard require a re-assessment or even acceptance of the manufacturer's assessment by NB?

Since during the EU type examination a "representative specimen" was tested, only the facts need to be assessed whether it is still "representative" in relation to the new standard. In addition, the standards contain lists of introduced changes with categorization as to whether they are significant changes. A skilled manufacturer has the opportunity to assess whether these changes are significant in relation to his product.

The documentation accompanying the EU-type examination certificate obtained from NB is also helpful for the manufacturer.

The manufacturer's own assessment may also be questioned by NB supervising production. Although, referring to the content of the ATEX directive, can be found that:

> *Conformity assessments shall be carried out in a proportionate manner, avoiding unnecessary burdens for economic operators.* (Article 29, p. 2)

And that:

> *Where, in the course of the monitoring of conformity following the issue of a certificate, a notified body finds that a product no longer complies, it shall require the manufacturer…* (Article 29, p. 4)

Moreover:

> *The EU-type examination certificate and its annexes shall contain all relevant information to allow the conformity of manufactured products with the examined type …* (Annex III, p. 6)

And finally, what is best for the manufacturer:

> *The notified body shall keep itself apprised of any changes in the generally acknowledged state of the art which indicate that the approved type may no longer comply with the applicable requirements of this Directive, and shall determine whether such changes require further investigation. If so, the notified body shall inform the manufacturer accordingly.* (Annex III, p. 7)

That is, the NB supervises the issued certificate and assesses whether it can still be used, and this is not about general supervision, but specific - for each issued certificate. Meanwhile, the generally accepted practice is only general informing by NB as a duty that a new edition of a given standard has been issued - this requirement is not treated by the ATEX directive cited above.

In addition, the unit provides all information used to issue the certificate (the costs of which were borne by the client) - see § 110 ATEX Guidelines [3] - which greatly facilitates the assessment of changes by the manufacturer with the introduction of the new standard. By querying manufacturers, it was confirmed that such documentation was not forwarded. NBs hide behind alleged confidentiality. To the manufacturer who incurred the costs?

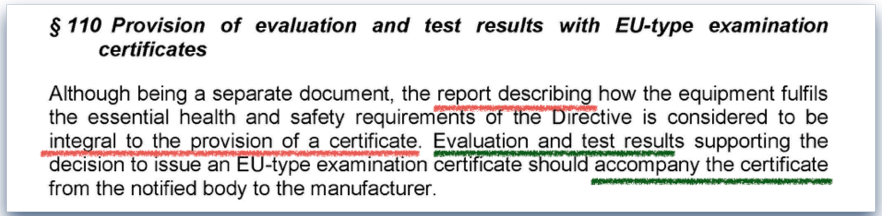

§ 110 Provision of evaluation and test results with EU-type examination certificates

Although being a separate document, the report describing how the equipment fulfils the essential health and safety requirements of the Directive is considered to be integral to the provision of a certificate. Evaluation and test results supporting the decision to issue an EU-type examination certificate should accompany the certificate from the notified body to the manufacturer.

Fig.4. *An explanation in the ATEX Guidelines on providing the manufacturer with all information (including test results and assessments) that was used to decide to issue an EU type-examination certificate.*

The gate is open for debate but it is important reminder, that state of art is mandatory. All stakeholders ask for a clarification from EU commission for this issue. To respect the last Ex standard is one of the efficient answers.

5. Manufacturer's impact on the organization of the ATEX system

All interested parties, including manufacturers, governmental bodies (regulators), notified bodies, consumer organizations and recipients, standardization organizations participate in the management of the ATEX directive. The figure below schematically shows the participants involved in managing the directive.

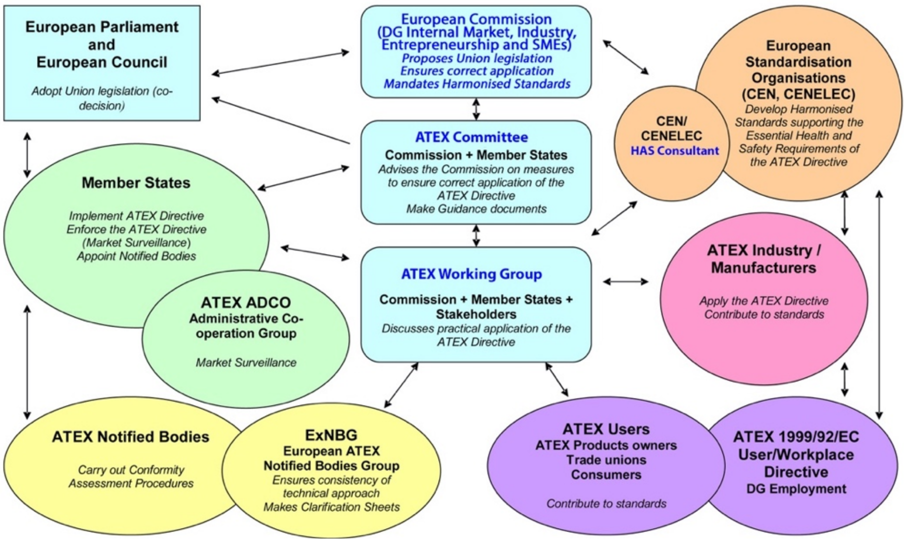

Fig.5. *Management of the ATEX directive - individual participants*

The ATEX Directive uses early (from the beginning of the 20th century) expert knowledge in the construction and testing of explosion-proof electrical equipment. Before the entry into force, these devices were tested, evaluated, certified and kept up with changes in the current state of knowledge. The introduction of the ATEX directive has expanded the area to include non-electric devices and devices for dust atmospheres.

Experts participating in particular bodies come mainly from notified and certification bodies. They participate in the ExNBG group, in the work of the ATEX committee (in support of their government delegations), in the work of the working group of the ATEX committee, in standardization work (CEN and CENELEC). These experts have specialist and unique knowledge. Most often this is their main activity. However, looking from the manufacturer's perspective, the requirements of the ATEX directive are one of the many requirements their product must meet. Hence, manufacturers are not able to match the level of involvement of experts from NB.

The system seems unbalanced, the participation of experts from NB is dominant in view of a much smaller share of manufacturer representatives. This is particularly adverse for small and medium enterprises.

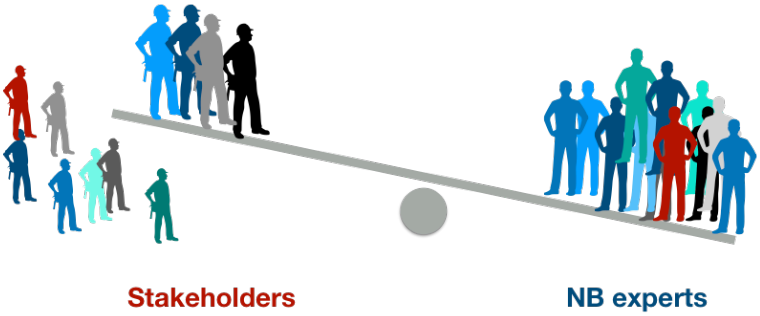

Fig.6. *System imbalance - significantly greater participation and influence of experts from notified bodies than manufacturers*

Small and medium-sized enterprises are also not properly represented in standardization work. The costs of such activity in the case of SMEs are significant. If the development of standards based on the mutual agreements of CENELEC-IEC and CEN-ISO is beneficial, then the costs of active participation in the work when meetings of committees and working groups take place in various parts of the world outside the EU are already significant.

It is important to reminder that manufacturers must follow all procedures to demonstrate compliance. As a first reminder, it is also important to apply others directives and regulations if any and industrial standards if any before Ex standards.

As a second fact, it is also important to respect routine tests even to verify periodically through internal audit the quality of equipment to put into the market. NB in charge of quality has to share responsibilities, they need to be stricter during audit but also during mandatory unexpected audit through FAT, Ex plants inspections, etc.

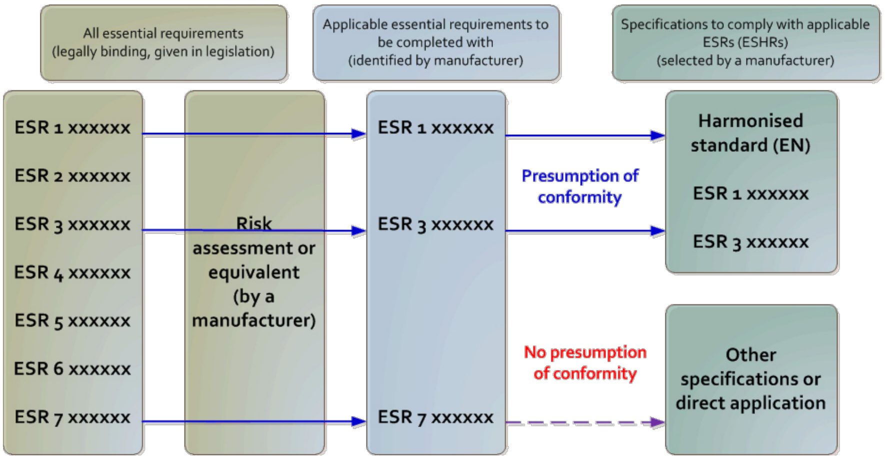

***Fig.** 7. Manufacturer's risk assessment (Blue Guide [12])*

6. Needs of participants (stakeholders)

Meetings and discussions with manufacturers allowed to indicate the most important support needs in the ATEX directive. The most important are given below.

A. Examples of EU declaration of conformity

According to the manufacturers, the ATEX Guidelines could be supplemented with examples of compliance declarations for various products. The biggest problems for manufacturers are the conformity assessment of assembly, or as defined by the directive for devices built from other devices. It is known that the declaration may take the form of a document file and the (final) manufacturer is only responsible for his part of the device's safety - he does not have to declare again the conformity of the devices used. But what if the final device is partly category 1 and does not create any new sources of ignition (potential or effective). An example of such a product may be a mixer in which all the devices used (propulsion engine, agitator assembly, other accessories) have their own appropriate declarations of conformity and the final manufacturer only assembles these devices in the tank, and each device works in the intended use. How to prepare a declaration of compliance and is NB participation required?

The situation is similar in the case of complex protective systems. Even if all parts of this assembly are already assessed. They have their declarations of conformity, or even EU type-examination certificates and NB control the production process, the function of the system (suppression of the arising explosion) appears only after the elements are interconnected. And this system should be evaluated and the manufacturer of this system should be supervised by NB. There is no place for final "suppliers" or "assemblers". Either they become manufacturers or act on behalf of the manufacturer.

B. Equipment user manual

The assessment of the manufacturer's instructions manual is not part of the EU-type[1] . Admittedly, some NBs make such an assessment, but such an assessment is outside the scope of the EU-type examination. The operating instructions are not part of the agreed documentation. However, if NB has assessed such a manual, changes to this manual make it necessary to include changes to the list of scheduled documentation.

Additionally, according to EN 60079-0, a manual should be provided which defines those parts of the user instructions which will ensure safe operation related to explosion protection, including special conditions of safe use and the requirements of EN 60079-0 for instance. Manufacturers may alter their user instructions following issue of the certificate if any provided that the changes do not detract from the requirements for safe operation as defined at the time of certification and provided that changes can be tracked for verification during audits. Any Specific Conditions of Use or Schedule of Limitations cannot be changed

In addition, as users say, copying solutions from outside the EU does not necessarily contribute to improving or maintaining an adequate level of device safety during operation.

If the manufacturer's reference manual for maintenance contains a reference to EN 60079-17 [4], this is not sufficient. The directive explicitly requires that the operating instructions should contain all necessary maintenance information. The product and thus the user will not be exposed to any mistakes resulting from incorrect classification of the product for inspection according to EN 60079-17.

Recall: point 1.06 a) of Annex II of the Directive (EHSR) requires:

> *All equipment and protective systems must be accompanied by instructions ... instructions for safe ... use, assembling and dismantling, maintenance (servicing and emergency repair), installation, adjustment ...*

So, the manufacturer should specify what maintenance (scope, when, conditions) are required for the device.

The same applies to the repair (reclamation) of equipment. If the manufacturer refers to the EN 60079-19 [5] standard in the instruction manual, does it mean that he accepts, for example, repairs that result in a lack of conformity (marking R in a triangle)?

Also, in this case, the recipients expect detailed and approved repair procedures for a given device.

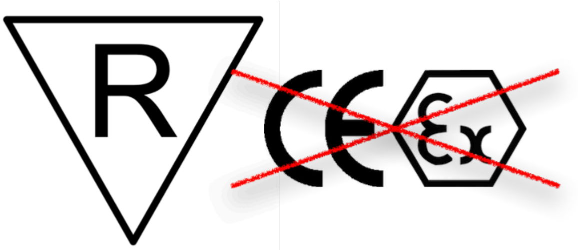

Fig.8. *A post-repair device with explicit conformity marking (R in a triangle) indicates that a significant change has been made.*

At the end, user will perform an assessment to assess the suitability of modified equipment versus zone in view to respect explosion protection document.

---

[1] Differences between IECEx conformity assessment system and ATEX system are not part of this paper.

Instructions and EU Declaration of conformity shall accompany the equipment. NB in charge of quality has to share responsibilities regarding these documents. A part of the audit must be dedicated to this issue.

C. Equipment on the borderline between MD and ATEX

The mixer described earlier is a good example of a device that not all manufacturers can handle. If the manufacturer qualifies that there is a "zone 0" inside the mixer instead of saying that the explosive mixture is often or permanently present, does this mean that the user should develop a EPD (Explosion Protection Document required by 1999/92/CE directive) even if no hazard zones are specified in the workplace of the device?

This question always raises lively discussion and it may be time to reactivate the Committee on Directive 1999/92/CE (ATEX users) [6]. Such a committee could be a forum for presenting the views of manufacturers and users. *"Non-binding guide ..."* [7] also requires refreshing after observations of learnt lessons in each European State (e.g. through a survey).

If the purpose of the ATEX users directive is, among others ensuring the absence of technical barriers to the free movement of goods, this approach should be consistent across the EU.

D. ATEX voluntary certification

Since zones 2 and 22 are the largest in terms of area, the voluntary certification market for category 3 equipment is also significant. Users often expect third party confirmation that the products are safe.

Meanwhile, apart from the reservation issued by ExNBG that notified bodies may issue so-called voluntary certificates (however, this decision is questionable from the legal side - NBs decided in the area outside the notification) no common certification program was developed.

This means that each certification body develops its own certification program. This is not an advantageous situation, hence a very good position in the field of voluntary certification of the IECEx certification scheme, in which CBs act equally.

Perhaps in this respect (voluntary certification) it would be possible to create in the EU a group of auditors and a system of mutual evaluation of CBs, as is the case with IECEx. Currently, NBs are assessed at national level using local experts, who, however, most often come from NBs in a given country. The effects of NBs activities cover the entire EU, so maybe we should also ensure the same level of assessment of the competence of individuals with the use of peer evaluation.

This proposal or approach can be tested for countries under MRA as first observation.

E. Distinguishing between modules D and E

An earlier standard EN 13980 [8] specified which areas are subject to assessment for individual modules (D or E). The current EN ISO / IEC 80079-34[2] [9] standard does not specify this requirement - it is precisely specified in the directive.

The EN ISO/IEC 80079-34 standard is used by manufacturers not only for certified products, but also applies to other products (category 3, non-electrical category 2) under voluntary basis.

So why in the scope of NB's assessment of the production system was copied the overall assessment of compliance with this standard from the IECEx certification scheme. NB should operate in a way that does not cause unnecessary burdens for the manufacturer. So, the assessment of the production system (basically technical) should consider the differences in individual modules.

Certainly, the scope of the assessment (audit) used by NB, i.e. the overall assessment of compliance with the EN ISO/IEC 80079-34 standard affects the time of assessment and thus the cost of the audit.

---

[2] The new edition soon published through annex Z indicates clearly links with directive 2014/34/EU

Table 1: *Comparison of assessment requirements according to module D and Module E. The differences are highlighted in colour*

Module D	Module E
The quality system documentation shall … in particular, contain an adequate description of:	
the quality objectives and the organisational structure, responsibilities and powers of the management with regard to product quality,	
the corresponding manufacturing, quality control and quality assurance techniques, processes and systematic actions that will be used,	-
the examinations and tests that will be carried out before, during and after manufacture, and the frequency with which they will be carried out,	the examinations and tests that will be carried out after manufacture,
the quality records, such as inspection reports and test data, calibration data, qualification reports on the personnel concerned, etc., and	
the means of monitoring the achievement of the required product quality and the effective operation of the quality system.	the means of monitoring the effective operation of the quality system.

F. Market surveillance

We expect increased market surveillance activity. ATEX products are not sold in stores, most often they are made to order. Honest manufacturers expect their efforts to ensure an appropriate level of product safety to be a market asset and not offset by cost savings in other manufacturers' production costs.

If statistically it is known what number of devices according to ATEX is assessed in a given country over a year, the dishonest manufacturer (if there are any) can estimate the risk of "control". Market surveillance has broad powers and has the right to also apply to assessments carried out by NB - it can verify the correctness of operations. Active market surveillance is also desired by users. They want to be sure that the products they use are properly designed and operated (which they declare in EPD).

According to the data presented in the report [10] in 2014-2016 in 14 EU countries market surveillance controlled 739 devices, 35 devices were subjected to laboratory tests. Unfortunately, still can be found find countries where the number of checks is 0.

Due to that national market surveillance offers a distortion of the market. Only coordination at EU level and specific national support can secure consumers and confidence on the global market.

G. Electrostatic hazards

The scope is well understood by stakeholders, therefore the specific case of ignition due to electrostatic charges is always subject of debate. Even when we know that 40% of accidents are linked to electrostatic charges. It is really the time to assess all equipment/process able to generate this type of ignition. Assessment needs to ask only tests due to the large variety of materials and process involved. A first part of the assessment will be performed under tests (e.g. charge transfer) of equipment or parts of the equipment, a second part of the assessment through tests (continuity, at workplaces described in the explosion protection document.

H. End user's role

Explosion Protection Document is well implemented to describe hazards at workplaces. The health and safety of persons will need technical and organizational measures to prevent explosion hazards. But all user's (employer) decision should be based on explosion risk assessment. As answer, training of stakeholders is the key element. COMPEX ISMATEX COPCC and other national qualification schemes are now recognized as positive contribution. This training is also a part of the Explosion Protection Document. Definitions of equipment, installation and maintenance through suitable standards EN60079-14 and -17 and national regulations will secure safety at workplaces.

7. Summary

The system of free movement of goods in the EU is guaranteed, among others, by the applicable ATEX and ATEX user directives. However, the economic freedoms of manufacturers and users should be balanced by market surveillance activity. This supervision could be particularly attentive to the attached operating instructions. In the interest of safety, they should be more specific.

It is desirable to increase the activity of product manufacturers. So far, decisions taken in the interpretation of the ATEX directive, the provisions of the ATEX Guidelines, are taken with increased influence of experts from notified bodies.

Small and medium-sized enterprises incur high costs of applying standards. Standards are changing, their number is constantly increasing, and their volume also unfortunately translates into increased costs for the purchase of standards. If the standards in some sense constitute a source of requirements (and e.g. in the case of the CPR Regulation, the CJEU has already issued a relevant judgment [11]) then perhaps the standards could be reimbursed to manufacturers in some way. Maybe it would be a good idea to read standards for free, e.g. via a specific internet connection.

As a summary in view to fuel the discussion with the relevant experts.:

a. The high technical level of assessments carried out by NB should be balanced by the activity of market surveillance and greater representation of manufacturers in the ATEX directive decision system.

b. It is expected to reactivate activity (committee) in the field of ATEX user directive 1999/92/CE.

c. Interpretative documents (ATEX Guidelines) should contain more guidelines for manufacturers and end users.

d. If ExNBG agrees on how to deal with manufacturers, the latter should influence these decisions.

e. Regular training of stakeholders will enhance dialogue between interested parts and safety at work places.

f. Complex equipment like fans, forklift, blower, gas turbine should be assessed by 3rd qualified part or certified, a specific survey made by market surveillance authorities can demonstrate the weaknesses of “self-assessment”.

g. Risks due to electrostatic charges shall be assessed by tests.

References

[1] Directive 2014/34/EU of the European Parliament and of the Council of 26 February 2014 *on the harmonisation of the laws of the Member States relating to equipment and protective systems intended for use in potentially explosive atmospheres* (OJEU L 96/309)

[2] Summary of references of harmonised standards published in the Official Journal – Directive 2014/34/EU 1 of the European Parliament and of the Council of 26 February 2014 *on the harmonisation of the laws of the Member States relating to equipment and protective systems intended for use in potentially explosive atmospheres* dated 24.10.2019

[3] *ATEX Guidelines* 2nd edition, December 2017

[4] EN 60079-17:2014 *Explosive atmospheres -- Part 17: Electrical installations inspection and maintenance*

[5] EN 60079-19:2011 *Explosive atmospheres -- Part 19: Equipment repair, overhaul and reclamation*

[6] Directive 1999/92/Ec of The European Parliament and of The Council of 16 December 1999 *on minimum requirements for improving the safety and health protection of workers potentially at risk from explosive atmospheres* (OJEU L 23 dated 28.1.2000)

[7] *Non-binding guide to good practice for implementing the European Parliament and Council Directive 1999/92/EC*

[8] EN 13980:2002 *Potentially explosive atmospheres - Application of quality systems*

[9] EN ISO/IEC 80079-34:2011 *Explosive atmospheres - Part 34: Application of quality systems for equipment manufacture (ISO/IEC 80079-34:2011)*

[10] *Summary of EU Member States and EEA EFTA States' assessment and review of the functioning of market surveillance activities according to article 18(6) of Regulation (EC) No 765/2008 for the period 2014-2016*

[11] Judgment Of The Court (Third Chamber) 27 October 2016 — CASE C-613/14

[12] The 'Blue Guide' on the implementation of EU product rules 2016 (Official Journal EU no 2016/C 272/01)

DOI: 10.7795/810.20200724

Investigation on limiting oxygen concentration of combustible gas for safety control during air injection process

Pengliang Li, Zhenyi Liu, Mingzhi Li, Yao Zhao, Xuan Li
State Key Laboratory of Explosion Science and Technology, Beijing Institute of Technology,
Beijing 100081, People's Republic of China
E-mail: zhenyiliu@bit.edu.cn

Abstract

High pressure air injection is an important method for oil recovery. In this process, due to exist of combustible gas and oxygen, the wellbore explosion accident may happen. To solve the problem, the optimal method is to control the oxygen concentration in the wellbore. Thus, it needs to investigate the limiting oxygen concentration (LOC) of combustible gas at high pressures and temperatures. In this study, experiments were carried out to investigate the LOC of combustible gas at pressures from 1 MPa to 15 MPa and temperatures from 40 °C to 120 °C. The influence of pressure and temperature on LOC was analyzed. The results showed that the LOC of combustible gas declines a lot as the initial pressure and temperature increases. At 15 MPa and 120 °C, the LOC drops up to 8.21%. The empirical formulas were also proposed to calculate the LOC at different conditions. Based on the present results, the standard for controlling the oxygen concentration in the wellbore was confirmed. As a result, the allowable oxygen concentration in the wellbore at different conditions can be determined. Therefore, the results of this study can help to avoid the wellbore explosion and ensure safety during air injection process.

Keywords: *air injection, wellbore explosion, high pressure, limiting oxygen concentration*

1 Introduction

Energy consumption is still growing in the worldwide. According to the International Energy Outlook 2018 (EIA, 2018), the total world energy consumption in 2017 is approximately 578 quadrillion Btu and is predicted to increase to approximately 726 quadrillion Btu in 2040. Also, the demand for oil is consistently higher than that of other type of energy. In view of the huge demand for oil, it is important to exploit existing reservoirs more reasonably (Hashemi et al., 2014). For the low permeability reservoirs, air injection technology is a convenient and efficient tertiary oil recovery method (Ruiz and Babadagli, 2016). In air injection process, nitrogen has a displacement effect on crude oil, and oxygen can react with crude oil to release a certain amount of heat, thus improving the fluidity of crude oil and improving the oil recovery (Montes et al., 2010). Compared to other oil recovery technologies, air injection is easier to operate and lower in cost. Most importantly, air injection can produce crude oil which is not suitable by water flooding and other oil recovery methods. However, air injection technology also has its drawbacks. During air injection process, the light hydrocarbons in the crude oil vaporize and form an explosive mixture with air in the wellbore, which is in danger of explosion. There have been several explosion accidents in different oilfields in China, resulting in casualties and economic losses (Huang et al., 2014).

At present, in order to avoid wellbore explosion accident and ensure safety of air injection process, there are two commonly used methods in oil recovery technology. One is to inject oxygen-reduced air, by reducing the proportion of oxygen in air and increasing the proportion of nitrogen, so as to inhibit the combustion or explosion of combustible gases (Liao et al., 2018). The other is air injection, such as low temperature oxidation (LTO) and in-situ combustion (ISC). In these processes, the gas composition in wellbore is regularly monitored. When the oxygen concentration is too high, inert gas such as nitrogen is injected into the wellbore, thus reducing the oxygen concentration. If the oxygen concentration is lower than LOC, explosion accident will not occur. However, in these processes, due to the lack of a clear understanding of the LOC of combustible gas at high temperature and pressure in reservoir conditions, the amount of nitrogen in oxygen-reduced air and nitrogen injected into the wellbore is not clear. If the amount of nitrogen is too little, it may bring about explosion risk. If the injection volume of nitrogen is too large, the production cost will be increased. Therefore, it is necessary to study the LOC of combustible gas at reservoir conditions.

In some oil reservoirs, the temperature can reach 100 °C and the pressure can reach 15 MPa (Wang et al., 2018). Obviously, the temperature and pressure at reservoir conditions are much higher than atmospheric pressure and ambient temperature. Most previous studies (Kondo et al., 2006; Addai et al., 2019) focused on the explosion characteristics of combustible gas at normal pressure and temperature. Razus et al. (2006) proposed a simple method to calculate LOC of fuel-air-inert mixtures at elevated temperatures and ambient pressure. In their study, based on the values of LFL and the calculated adiabatic flame temperature (CAFL) at LFL, the CAFL at LOC can be derived through a linear relationship. Thus, the LOC can be estimated by the value of CAFL. The results showed that the relative errors are within 5% and 10% in comparison to experimentally measured values. Schoor et al. (2009) experimentally investigated LOC of H_2/CO mixtures at atmospheric pressure and initial temperatures up to 200 °C through a cylindrical tube. It is found that the experimental results are higher than values calculated through LFL. Due to insufficient experimental temperature conditions, the dependence of LOC on temperature is not derived. To safely use oxygen in the pharmaceutical industry, Osterberg et al. (2014) determined LOCs of nine organic solvents with initial pressures up to 2 MPa. It is found that the LOC decreases with the increase of pressure. As the LOCs were determined at only two pressures in their study, the relationship between LOC and pressure is unclear. In summary, previous studies mainly focused on the calculation and determination of LOC at normal pressure and ambient temperature. The data on LOC at elevated pressure and temperature is limited. The dependence of LOC on pressure and temperature is unsettled. Therefore, it is indispensable to explore LOC of combustible gas at elevated pressures and temperatures.

In this study, an experimental apparatus was used to test the LOC of combustible gas at high pressures and high temperatures. By sampling and analyzing the gas in the wellbore at the oil production site, a mixture of certain components was selected. The LOC at different temperatures and pressures was studied experimentally. The dependence of LOC on pressure and temperature was determined. The results can help better understanding LOC of combustible gas at different conditions, and provide technical guidance for control of oxygen concentration in air injection process.

2 Theoretical calculation of LOC at normal pressure and ambient temperature

The data plotted in Table 1 gives the results of the measured components of combustible gas in wellbore. As shown in Table 1, the components of the combustible gas detected from the oil recovery site are mainly methane and ethane. The proportion of propane and the other alkanes is very little. Therefore, the combustible mixture used in this study consists of 97.9% of methane and 2.1% of ethane.

Table 1: *Measured composition of natural gas in wellbore.*

Gas component	percent by volume / %
Methane	96.26
Ethane	2.06
Propane	0.42
iso-Butane	0.31
n-Butane	0.45
iso-Pentane	0.17
n-Pentane	0.16
Hexane	0.14
Heptane	0.03

Basiclly, there are two methods for the calculation of LOC at normal pressure and ambient temperature. The first is the triangular method. In this method, the lower flammability limit (LFL) and upper flammability limit (UFL) of combustible mixture in air and oxygen should be determined.

The calculation of the flammability limit of the mixture at normal temperature and pressure is based on the Le Chatelier formula (Wierzba and Wang, 2006), with an UFL of 15.01% and a LFL of 4.93%. The UFL of mixture in pure oxygen is 61.10% and the LFL is 4.93%. Then, the LOC of the mixture was calculated by the triangular diagram method.

As shown in Fig. 1, vertices F, O and N of the equilateral triangle denote combustible gas, oxygen, and nitrogen, respectively. Take 21% length of the NO side to mark point A, then FA means air. The flammability limits X_1 and X_2 of the combustible mixture in air are drawn on the air line FA. The flammability limits X_{11} and X_{22} of the combustible mixture in pure oxygen are drawn on the oxygen line FO. The extension line of X_1X_{11} and X_2X_{22} intersects at point C. Draw a line over point C parallel to FN and intersect with ON at point S. Then, the length of SN is the LOC. It can be seen that the LOC of the mixture is 12.30% at normal pressure and ambient temperature.

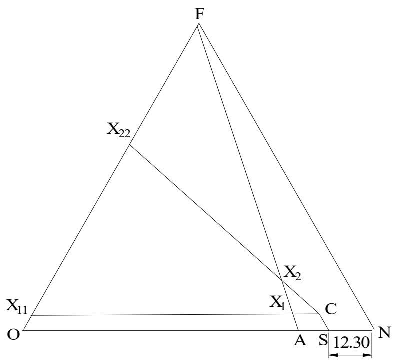

Fig. 1. *The calculating results of LOC by the triangular diagram method.*

The second one is stoichiometric method. When the combustible gas reacts completely with oxygen, the reaction equation is as follows,

$$\mathrm{C}_n\mathrm{H}_m+\left(n+\frac{m}{4}\right)\mathrm{O}_2=n\mathrm{CO}_2+\left(\frac{m}{2}\right)\mathrm{H}_2\mathrm{O} \quad (1)$$

where n and m represent the number of carbon atoms and hydrogen atoms, respectively. The oxygen concentration corresponding to the LFL of combustible gas is the LOC of combustible gas, which is given by equation (2).

$$LOC{=}LFL_{\mathrm{a}}\left(n+\frac{m}{4}\right) \quad (2)$$

with LFL_{a} the LFL of combustible mixture in air.

The volume fraction of each gas in the multicomponent mixed gas is equal to its mole fraction, so the mixed gas can be approximately regarded as a single gas containing C and H. For combustible gas used in this study,

$$n= (97.9+2\times2.1)/100=1.02$$

$$m= (4\times97.9+6\times2.1)/100=4.04$$

As a result, the LOC of combustible gas can be calculated as follows,

$$LOC{=}LFL_{\mathrm{a}}\left(n+\frac{m}{4}\right)=10.01\%$$

It is clear that there is a visible difference between results of two methods. The triangular diagram method is based upon the experimental results of previous studies. And the Le Chatelier formula is substantiated to be satisfactory for the calculation of flammability limits of combustible mixtures at ambient pressure. While the stoichiometric method based on the assumption that the LOC lies on the intersection of the LFL branch and the stoichiometric line. This assumption may cause the difference. As reported by Schoor et al. (2007) the stoichiometric method may underestimate LOC compared to the experimental results. Thus, the LOC obtained through the triangular diagram method is closer to the real value.

3 Experimental section

3.1 Experimental Apparatus

A schematic of the LOC test system is presented in Fig. 2. The system consists of high pressure reactor, ignition system, gas injection system, data acquisition system, safety protection system and so on.

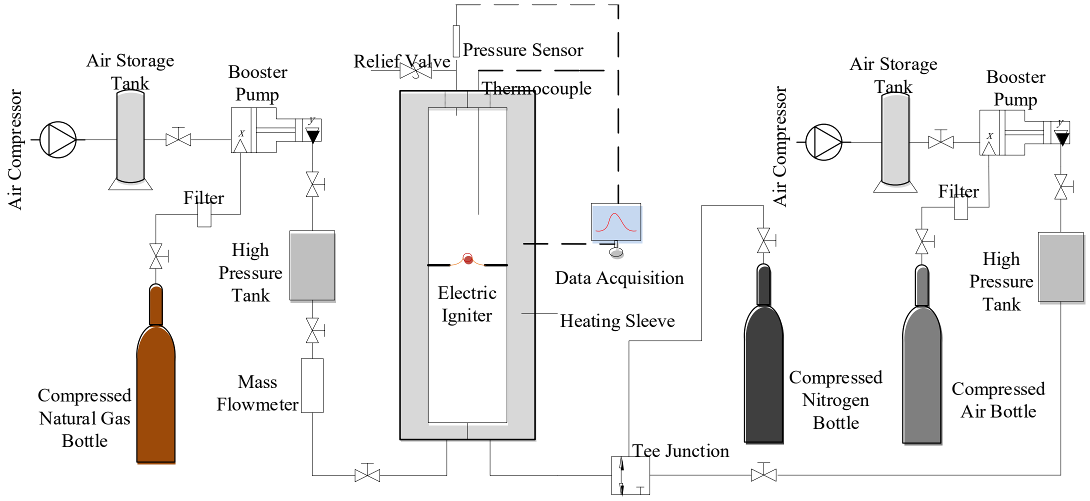

Fig. 2. *Schematic of the LOC test system.*

The reactor has a design pressure of 100 MPa and a volume of about 1 L. As recommended by ASTM E918 standard (2011), the vessel with a minimum volume of 1 L can be used for determining the flammability limits at elevated pressure and temperature. Besides, the reactor can be heated to 350 ℃ with a split heating mantle. There are two electrodes in the middle of the reactor to connect the electric ignitor. In addition, a pressure sensor and thermocouple are connected to the top of the reactor to detect the pressure and temperature inside the reactor.

The ignition system consists of the electric ignitor, ignition wire and trigger. The trigger sends a current signal to the electric ignitor through the ignition wire. Then the electric wire fuses to release heat and ignite chemical igniter.

Gas injection system is divided into air injection system, combustible gas injection system and nitrogen injection system. In air injection system, air is compressed to the air tank by air compressor. When the pressure in the air tank reaches 0.6 MPa, the drive valve is opened and the booster pump starts to work. Then, air in the high pressure air bottle is injected into the high pressure tank and the pressure can reach 60 MPa. When the valve of the high pressure tank is opened, air is injected into the reactor. In natural gas injection system, the volume of natural gas injected into the reactor is controlled by a mass flow meter. Nitrogen is directly injected into the reactor from a compressed nitrogen bottle.

The data acquisition system consists of thermocouple, pressure sensor, and computer, which can record the change of temperature and pressure in the reactor in real time.

The safety protection system realizes the safety protection of the system through a pressure gauge and a relief valve. When the pressure inside the reactor reaches the pressure value set by the pressure gauge, the pressure gauge will control the heating mantle to stop heating. The pressure is automatically released when the pressure reaches the upper pressure limit of the relief valve. The security of the system is ensured by double protection.

3.2 Experimental Conditions

The temperature of the target reservoir is 100 ℃ and the pressure is 15 MPa. Therefore, the experimental conditions selected in this study are a temperature range from 40 ℃ to 120 ℃ (40 ℃, 60 ℃, 80 ℃, 100 ℃, 120 ℃) and pressure range from 1 MPa to 15 MPa (1 MPa, 2 MPa, 5 MPa, 10 MPa, 15 MPa).

DOI: 10.7795/810.20200724

3.3 Experimental Method

During the experiment, the electrodes on the side of the reactor were firstly opened to install the electric ignitor. Secondly, air was filled into the reactor at a certain pressure and all the valves were closed to test the airtightness of the whole system. After air tightness was confirmed, intake valve and exhaust valve were opened to clean the whole circuit with dry air. Then, the intake valve and exhaust valve were closed and the air compressors were started for gas injection. Nitrogen and combustible gas were injected into the reactor according to the partial pressure method, and then air was replenished to the reactor, until the pressure of the reactor reached the required value, the intake valve was closed. After half an hour, the mixture was well mixed and then ignited. Whether the explosion occurs or not was judged according to the change of temperature and pressure in the reactor, and the data were recorded automatically in a computer.

4 Results and Discussion

4.1 Flammability Criterion

Generally, in a tube experiment, a visual criterion is used to see whether the flame propagates a certain distance from the ignition position or not, as mentioned in the ASTM E681 standard (2015). While in a closed experimental vessel, the flame is invisible, a 7% pressure rise criterion is used, as mentioned in the ASTM E2079 standard (2013). However, as early as 2000, Smedt et al. (2000) compared the results between a visual criterion of flame detachment and a 7% pressure rise criterion. It was found that visual criterion gave wider limits. Accordingly, they concluded that a 7% pressure rise is too high and recommended the use of a 2 % pressure rise criterion to bring the results of both methods in closer agreement. Similarly, Heinonen et al. (1994) compared the explosion pressure with the flame propagation criterion based on the ASTM E681 standard (2015). The results showed that the explosion pressure lies in the range of 0.5-2% of the initial pressure. Therefore, a 7% pressure rise is unsuitable for determination of ignition in closed experimental vessel, especially at high initial pressures. In the study of Vanderstraeten et al. (1997), the UFL of methane was determined with initial pressures up to 5.5 MPa. A temperature increase of 2 °C or a 1% pressure rise was used as flammability criterion. In this study, a pressure rise was used to judge whether the explosion occurred or not, and the temperature rise was also used to judge comprehensively. Because the electric igniter was used in this experiment, the pressure rise and temperature rise caused by the combustion of the electric igniter were firstly determined. The tests were carried out both in air and pure natural gas. The results showed that the pressure rise produced by electric igniter was not more than 0.05 MPa. The temperature rise was less than 5 °C in most situations. Therefore, the value of pressure rise greater than 0.05 MPa was taken as the criterion of ignition.

4.2 Test results of LOC

As shown in ASTM E2079 standard (2013), the LOC of hydrogen was tested by varying concentration of hydrogen and added nitrogen in the hydrogen-air-nitrogen system. The LOC is derived as the average value of the lowest oxygen concentration for which ignition occurs and the highest oxygen concentration for which ignition is impossible.

In this study, similar method was used. During the experiment, the LOC was tested by gradually changing the concentration of combustible gas and nitrogen. Table 2 gives the experimental results of LOC at 1 MPa and 40 °C. As can be seen from Table 2, when the concentration of fuel is 4.9% (LFL), with the increasing addition of nitrogen, the concentration of oxygen decreases gradually, but the mixture is still flammable. It means that the LFL will not be increased when the concentration of added nitrogen is between 10% and 35% at 1 MPa, 40 °C. When the amount of added nitrogen increases to 40%, the mixture cannot be ignited. Then the added nitrogen concentration remains at 40%, slightly increasing the fuel concentration to 5.3% and 5.7%, and the mixture became combustible. This phenomenon shows that when the amount of added nitrogen reaches 40%, the LFL increases. Then the concentration of natural gas stays at 5.7%, as the concentration of nitrogen increased to 49%, the mixture becomes nonflammable again. Next increase the fuel concentration, it is found that the mixture can be ignited only if the natural gas concentration is 5.8% and the added nitrogen concentration is 48%. Therefore, it can be determined that the LOC of natural gas at 1 MPa and 40 °C is 9.69%.

Table 2: *Experimental results of LOC at 1 MPa and 40 °C.*

Test No.	Added N_2 /%	Fuel /%	Oxygen /%	Flammable	Test No.	Added N_2 /%	Fuel /%	Oxygen /%	Flammable
1	10	4.9	17.87	Yes	11	48	5.7	9.72	Yes
2	15	4.9	16.82	Yes	12	49	5.7	9.51	No
3	20	4.9	15.77	Yes	13	49	6.1	9.43	No
4	25	4.9	14.72	Yes	14	48	6.1	9.64	No
5	30	4.9	13.67	Yes	15	49	5.8	9.49	No
6	35	4.9	12.62	Yes	16	48	6.5	9.56	No
7	40	4.9	11.57	No	17	48	6.2	9.62	No
8	40	5.3	11.49	Yes	18	48	5.8	9.70	Yes
9	40	5.7	11.40	Yes	19	48	5.9	9.68	No
10	45	5.7	10.35	Yes					

The test results of 1 MPa and 40 °C is clearly plotted in Fig. 3. The red triangle symbols represent flammable situations, while the blue circle symbols represent nonflammable situations. As shown in Fig. 3, ignition does not occur below the LOC line. This is consistent with the definition of LOC, the minimum oxygen concentration that supports combustion.

DOI: 10.7795/810.20200724

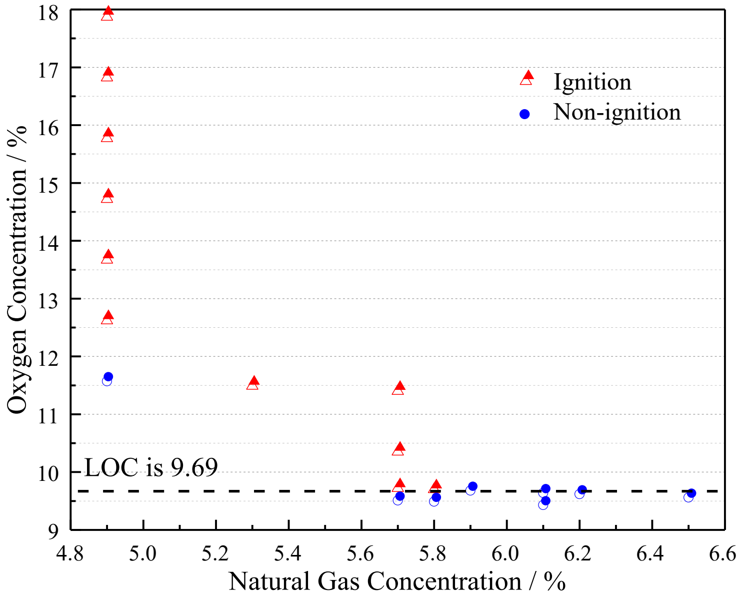

Fig.3. *Experimental results of LOC at 1 MPa and 40 °C.*

The LOCs at other conditions can be measured using the same method, as shown in Table 3. It is obvious that the LOC decreases with the increase of temperature or pressure. The LOC decreases from 9.69% of 1 MPa and 40 °C to 8.21% of 15 MPa and 120 °C. As calculated by the triangular diagram method, the LOC of combustible mixture is 12.30% at normal pressure and ambient temperature. Besides, as summarized by Kuchta (1985), the LOC of methane determined through a tube experiment is 12% at normal pressure and ambient temperature. Both values of LOC are much higher than that measured at elevated pressures and temperatures. This indicates that the explosion risk of combustible mixture increases under high temperature and high pressure. Therefore, during air injection EOR process, more nitrogen should be injected into the wellbore to make the oxygen concentration of the mixture lower than the LOC.

Table 3: *Experimental results of LOCs at all conditions in this study.*

Pressure / MPa	LOC at different temperatures / %				
	40 °C	60 °C	80 °C	100 °C	120 °C
1	9.69	9.47	9.19	8.93	8.64
2	9.45	9.22	8.98	8.75	8.51
5	9.15	8.96	8.79	8.60	8.40
10	8.93	8.76	8.60	8.44	8.27
15	8.78	8.64	8.49	8.35	8.21

4.3 Effect of pressure and temperature on LOC

To calculate the LOC more precisely at high pressures and temperatures, the relationship between the LOC and initial pressures and temperatures were fitted based on the experimental results. The traces of LOC as a function of pressure are shown in Fig. 4 for different initial temperatures. The fitting curves are also presented in Fig. 4, which can well describe the relationship between LOC and initial pressure. It can be found that the LOC is exponentially dependent on initial pressure. The corresponding equation is shown below,

$$LOC_P = a + b\exp(-P/c) \qquad (3)$$

where LOC_P is LOC of combustible gas at different initial pressures, P is initial pressure, a, b and c are coefficients that vary with temperature. The specific values of coefficients are given in Table 4.

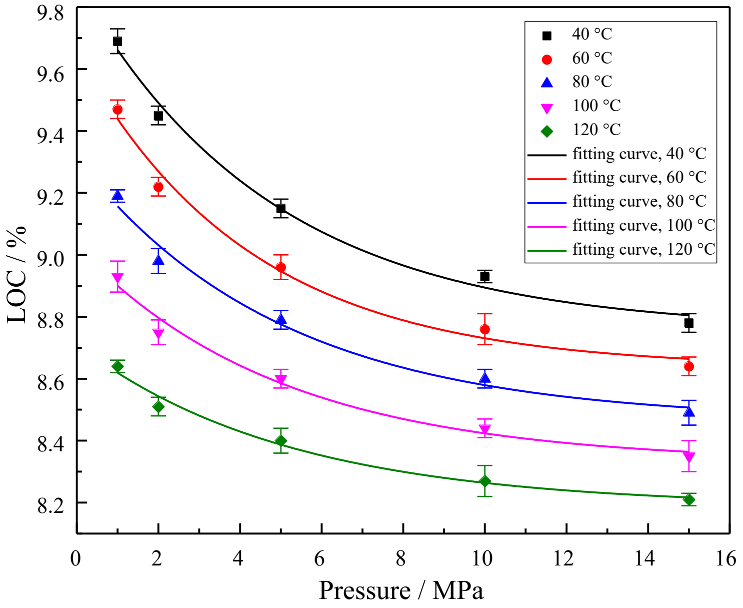

Fig. 4. *The traces of LOC as a function of pressure at different temperatures.*

Table 4: *The specific values of coefficients.*

Temperature/ °C	a	b	c	R_2
40	8.75651	1.11587	4.77905	0.99
60	8.63472	1.01801	4.23355	0.99
80	8.46470	0.84513	5.00346	0.99
100	8.32923	0.69727	4.99988	0.98
120	8.18780	0.52312	5.18077	0.99

Similarly, the traces of LOC as a function of temperature at different initial pressures were presented in Fig. 5. It is clear that with the increase of initial temperature, the LOC decreases. For example, when the pressure is 1 MPa, the LOC drops from 9.69% at 40 °C to 8.64% at 120 °C. Besides, the fitting curve of LOC as a function of initial temperature was also plotted in Fig. 6. It was found that the LOC is linearly dependent on initial temperature. With the increase of initial pressure, the absolute value of the slope of the curve gradually declines. At 1 MPa, the difference of LOC between 40 °C and 120 °C is 1.05%, and this difference drops to 0.57% at 15 MPa. It means that the influence of temperature and pressure on the LOC is interactional. With the increase of pressure, the effect of temperature on the LOC decreases slightly. The LOC as a function of initial temperature was fitted into the following equation,

$$LOC_T = d + eT \qquad (4)$$

where LOC_T is LOC of combustible gas at different initial temperatures, T is initial temperature, d and e are coefficients that vary with pressure. The specific values of coefficients are given in Table 5.

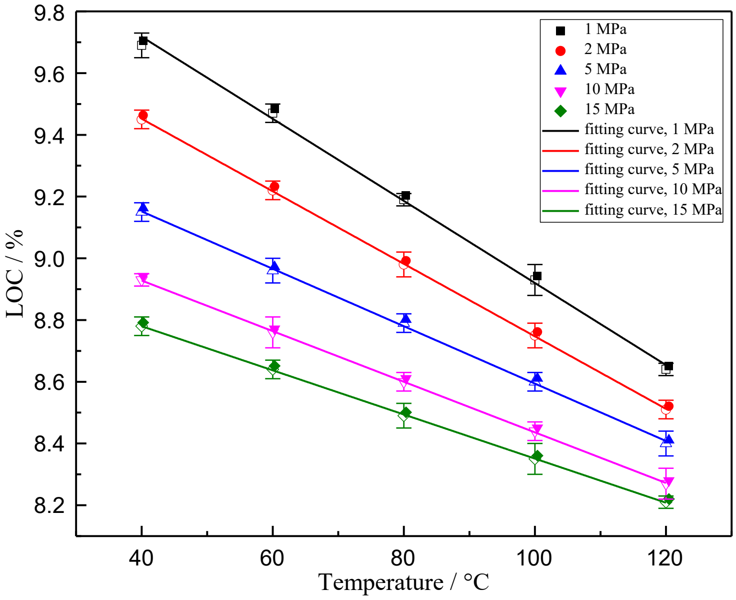

***Fig. 5.** The traces of LOC as a function of temperature at different pressures.*

***Table 5:** The specific values of coefficients.*

Pressure/ MPa	d	e	R2
1	10.250	-0.01330	0.99
2	9.922	-0.01175	0.99
5	9.524	-0.00930	0.99
10	9.256	-0.00820	0.99
15	9.066	-0.00715	0.99

4.4 Prevention of wellbore explosion

On the grounds that the conditions in the wellbore is really complex, explosion may happen in an inadvertent way. To avoid the explosion accident, the oxygen concentration in wellbore should be controlled in a low level. There are two methods to achieve this purpose. The first one is to reduce the oxygen concentration in air before injected into the wellbore. The second one is to monitor the oxygen concentration in wellbore and inject nitrogen if the oxygen concentration is in a too high level.

In order to ensure safety and cut down cost, the oxygen concentration should be controlled based on the experimental results of this study.

The oxygen concentration in the wellbore can be checked on a regular schedule. According to the standard NFPA 69 (2014), if the oxygen concentration is not continuously monitored, the following measures should be taken. For the situation where the LOC is higher than or equal to 7.5%, a safety margin of at least 4.5% below the LOC should be maintained. While the LOC is lower than 7.5%, the oxygen concentration should be controlled no more than 40% of the LOC. In this study, for the combustible mixture in which methane is the majority, the lowest LOC is 8.21% at 15 MPa and 120 °C. As mentioned above, the oxygen concentration in the wellbore needs to be restricted at least 4.5% below the LOC. For example, when the pressure is 15 MPa and temperature is 120 °C, the oxygen concentration should be controlled below 3.71%. As a result, the wellbore explosion accident can be avoided in air injection process for oil recovery. For conditions that not mentioned in this study but within the range of this study, the LOC can be approximately estimated through the equations (3) and (4).

5 Conclusion

In this study, the experiments on LOC of combustible mixture with 97.9% of methane and 2.1% of ethane were carried out. The effects of pressure (1 MPa-15 MPa) and temperature (40 °C-120 °C) on LOC were investigated. The main conclusions are drawn as follows.

1) The LOC of combustible gas is significantly influenced by both pressure and temperature. With the increase of initial pressure or temperature, the LOC declines. The LOCs at elevated pressures and temperatures are much lower than atmospheric pressure and room temperature.

2) The LOC has an exponential dependence with initial pressure. When the pressure increases, its effect on LOC gradually becomes weaker. While the LOC is linearly dependent on initial temperature. As the pressure rises, the effect of temperature on LOC slightly decreases.

3) Based on the experimental results, the oxygen concentration in the wellbore should be controlled at least 4.5% below the LOC. It can provide technical basis for safety control in air injection process for enhancing oil recovery.

Reference

Addai E K, Clouthier M, Amyotte P, et al. Experimental investigation of limiting oxygen concentration of hybrid mixtures[J]. Journal of Loss Prevention in the Process Industries, 2019, 57:120-130.

ASTM. (2011). Standard practice for determining limits of flammability of chemicals at elevated temperature and pressure. ASTM E918. American Society for Testing and Materials.

ASTM. (2013). Standard Test Methods for Limiting Oxygen (Oxidant) Concentration in Gases and Vapors. ASTM E2079. American Society for Testing and Materials.

ASTM. (2015). Standard Test Method for Concentration Limits of Flammability of Chemicals (Vapors and Gases). ASTM E681. American Society for Testing and Materials.

EIA. International energy outlook 2018. US Energy Information Administration, Jul 2018.

Hashemi R, Nassar N, Almao P. Nanoparticple technology for heavy oil in-situ upgrading and recovery enhancement: opportunities and challenges. Applied Energy, 2014, 133: 374-387.

Heinonen E W, Tapscott R E, Crawford F R. Methods development for measuring and classifying flammability/combustibility of refrigerants. Final Report DOE/CE/23810-50, Center for global environmental technologies, New Mexico Engineering Research Institute, The University of New Mexico, Albuquerque, 1994.

Huang Q, Liu ZY, Zuo Z. Study on evaluation of explosion effects of gas injection wells. Adv Mater Res, 2014, 1051: 962-966.

Kondo S, Takizawa K, Takahashi A, et al. Extended Le Chatelier\"s formula and nitrogen dilution effect on the flammability limits [J]. Fire Safety Journal, 2006, 41(5):406-417.

Kuchta, J.M. (1985). Investigation of fire and explosion accidents in the chemical, mining, and fuel-related industries – a manual. U.S. Bureau of Mines Bulletin, 680. 84 pp.

Liao G, Yang H, Jiang Y, Ren S, Li D, Wang L, et al. Applicable scope of oxygen-reduced air flooding and the limit of oxygen content [J]. Petroleum Exploration and Development, 2018, 45(1):105-110.

Montes A R, Gutierrez D, Moore R G, et al. Is High-Pressure Air Injection (HPAI) Simply a Flue-Gas Flood? [J]. Journal of Canadian Petroleum Technology, 2010, 49(2):56-63.

NFPA 69. (2014). Standard on Explosion Prevention Systems, National Fire Protection Association, Quincy, MA.

Osterberg P M , Niemeier J K , Welch C J , et al. Experimental Limiting Oxygen Concentrations for Nine Organic Solvents at Temperatures and Pressures Relevant to Aerobic Oxidations in the Pharmaceutical Industry[J]. Organic Process Research & Development, 2014, 141223071236001.

Razus D, Molnarne M, Movileanu C, et al. Estimation of LOC (limiting oxygen concentration) of fuel–air–inert mixtures at elevated temperatures by means of adiabatic flame temperatures [J]. Chemical Engineering & Processing Process Intensification, 2006, 45(3):193-197.

Ruiz J M, Babadagli T. Low temperature air injection with solvents in heavy-oil containing naturally fractured reservoirs: effects of matrix/fracture properties and temperature on recovery. Fuel, 2016, 179: 376-390.

Schoor F V D, Norman F, Vandermeiren K, et al. Flammability limits, limiting oxygen concentration and minimum inert gas/combustible ratio of H2/CO/N2/air mixtures[J]. International Journal of Hydrogen Energy, 2009, 34(4):2069-2075.

Schoor F V D, Norman F, Tangen L, et al. Explosion limits of mixtures relevant to the production of 1,2-dichloroethane (ethylene dichloride)[J]. Journal of Loss Prevention in the Process Industries, 2007, 20(3):281-285.

Smedt G D, Corte F D, Notelé R, et al. Comparison of two standard test methods for determining explosion limits of gases at atmospheric conditions[J]. Journal of Hazardous Materials, 2000, 70(3):105-113.

Vanderstraeten B, Tuerlinckx D, Berghmans J, Vliegen S, Oost EV, Smit B. Experimental study of the pressure and temperature dependence on the upper flammability limit of methane–air mixtures. J Hazard Mater 1997; 56: 237–246.

Wang H, Luo M, Lun Z, Lv C, Zhao C, Zhao Q, et al. Determination and comparison of interfacial interactions between CO_2, crude oil and brine at reservoir conditions. Energy & Fuels, 2018, 32(8): 8187-8192.

Wierzba I, Wang Q. The flammability limits of H_2-CO-CH_4 mixtures in air at elevated temperatures. International Journal of Hydrogen Energy, 2006, 31, 485-489.

DOI: 10.7795/810.20200724

Measurement of the deposit formation during pneumatic transport of polydisperse PMMA powder

Nuki Susanti[a,b], Holger Grosshans[a,b]
[a] Physikalisch-Technische Bundesanstalt (PTB), Braunschweig, Germany
[b] Institute of Apparatus- and Environmental Technology, Otto von Guericke University Magdeburg, Germany
E-mail: *holger.grosshans@ptb.de*

Abstract

Deposits which form during the pneumatic transport of particles are a frequent source of explosions in industrial facilities. Thus, to contribute to the operational safety of industrial plants, we explore the deposit formation of powder flows with our new experimental test-rig. To this end, the particle flow was analyzed optically using a square-shaped transparent pipe as a measuring section. We characterized the deposit pattern and quantified the fraction of particles that deposit depending on the flow conditions. The parameters under consideration included the flow Reynolds number, the powder loading, the duct material, and the ambient conditions (temperature, humidity). More specifically, we investigated the transport of polydisperse PMMA particles through pipes made of PMMA and PC.

Keywords: *pneumatic conveying, deposits, electrostatics, particle-laden flow, experiment*

1 Introduction

When powders are conveyed pneumatically through pipes or ducts, they form deposit layers on component surfaces. These deposits are a frequent source of explosions in industrial particle flow facilities (Eckhoff, 2003). For example, if the powder is charged by triboelectric effects, a deposit represents a local accumulation of electrostatic energy, which may lead to hazardous spark discharges. Also, an external heat source such as welding at the outside of the pipe may initiate the deposit to smolder. Moreover, it was recently observed that deposited dust in an enclosed pipeline can trigger a reverse explosion (Song and Zhang, 2019) and the re-entrainment of deposited particles can cause secondary explosions (Eckhoff, 2003). Also, particle deposition along the transporting pipeline causes a reduced cross-sectional area and blockage which might lead to a reduced operation efficiency (Klinzing, 1981, 2018). Thus, an increased understanding of the physical mechanisms involved in particle deposition will help to design safe and efficient particle transport systems.

In dilute flow pneumatic conveying, which is the focus of the present study, particles are known to adopt preferential positions due to the inhomogeneity of the flow inside the pipe (Eaton and Fessler, 1994) and electrostatic forces (Grosshans, 2018, 2020). The particle concentration becomes even more complicated when the conveying line is of a non-cylindrical shape, such as a square or rectangular duct (Noorani et al., 2016). Further, pneumatic transport is known to generate high charge due to severe particle-wall collisions (Bailey, 1984, Grosshans and Papalexandris, 2017, 2016b,a,c). Those issues make a seemingly simple process highly convoluted since a wide range of factors influences particle motion, dispersion, preferential concentration, and subsequent deposition.

Particle deposition from turbulent flow in non-cylindrical enclosures has been widely studied, both by means of numerical simulation (Wang et al., 2019, Yao and Fairweather, 2011, Winkler et al., 2006, Klahn and Grosshans, 2020, 2019) and experimental investigation (Sippola and Nazaroff, 2004, Kaftori et al., 1995, Matsusaka et al., 1998). Wang et al. (2019), as well as Yao and Fairweather (2011), used large eddy simulation (LES) combined with a Lagrangian approach of one-way coupling to simulate deposition at almost the same range of particle sizes (50 µm–500 µm) and Reynolds numbers (10 000-250 000). They found that particles have preferential deposition locations depending on size and Reynolds number, either in the center or in the corner of the duct. Sippola and Nazaroff (2004) experimentally measured small particle deposition (1 µm–16 µm) at relatively low air velocities (2.2 m/s–8.8 m/s) in a steel ventilation and an insulated duct. They pointed out the deposition rate increases due to surface roughness. The experimental work of Kaftori et al. (1995) using water as conveying fluid and particles ranging from 100 µm–900 µm revealed a relation of the particle motion and, thus, deposition with near-wall coherent vortices.

Despite its obvious importance, the detailed mechanism of deposit formation remains unknown such as which forces mainly contribute and where the deposit tends to form. This can be attributed to the complex interaction of the fluid mechanics, particle dynamics, and various adhesive forces acting on the particles. Consequently, the main objective of the present study is to design, based on our experience with a previous facility (Schwindt et al., 2017) a new experimental test-rig to investigate particle deposition in a square duct. The presented experimental facility was designed with the aim to maximize consistency with our complimentary numerical simulations (Grosshans, 2018, Grosshans et al., 2019). Then, the influence of the Reynolds number, particle mass flow rate, and relative air humidity (RH) and temperature was investigated. In this experiment, first particles and a duct of the same material (PMMA) were used to minimize the triboelectric charging effect which might influence deposition. Subsequently, in the second part of the study, a measurement is conducted to investigate the influence of particle deposition due to triboelectric charging by using a different duct material (PC).

2 Experimental set-up

The schematics of the new experimental setup at Physikalisch-Technische Bundesanstalt (PTB) Braunschweig, Germany, is depicted in Fig. 1. It consists of an air blower (Moro MHR 452) equipped with a frequency converter (Danfoss FC 51) that is connected to a square duct (PMMA ID:45 mm or PC ID: 46 mm) of a length of 1.8 m. At the end of the duct, a pitot tube anemometer (PCE-HVAC 2) is placed to measure the mean bulk air velocity using the duct traversing technique (Log-Tchebychef). Point P in the schemata represents an airflow measuring point. Particles are fed into the duct via a vibratory feeder (Retsch DR100) and transported to the bin where the particle mass leaving the duct is weighed and recorded every 60 seconds. Thus, the particle mass fraction deposited in the duct can be calculated as

$$\text{deposition fraction} = \frac{\dot{m}_{\text{in}} - \dot{m}_{\text{out}}}{\dot{m}_{\text{in}}}. \tag{1}$$

In the above equations $\dot{m}_{\text{in/out}}$ are the particle mass flow rate input and output in kg/hr.

We used the same PMMA particles provided by KFG GmbH Biebesheim which were already used in previous work (Schwindt et al., 2017). The particle size distribution is plotted in Fig. 2 The experiments were not conducted in the climate chamber, thus, the day-to-day temperature and RH were always carefully considered and recorded.

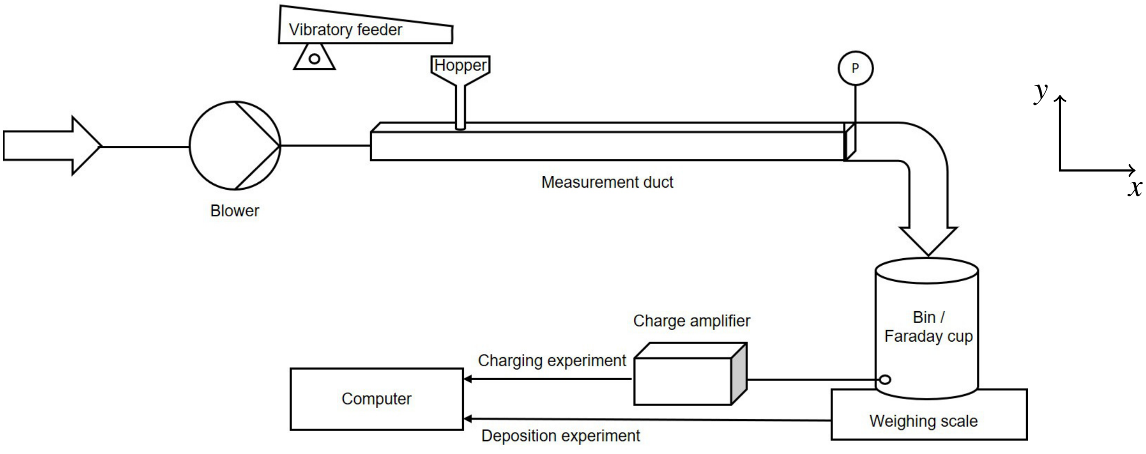

***Fig. 1**: Schematic diagram of the new experimental setup.*

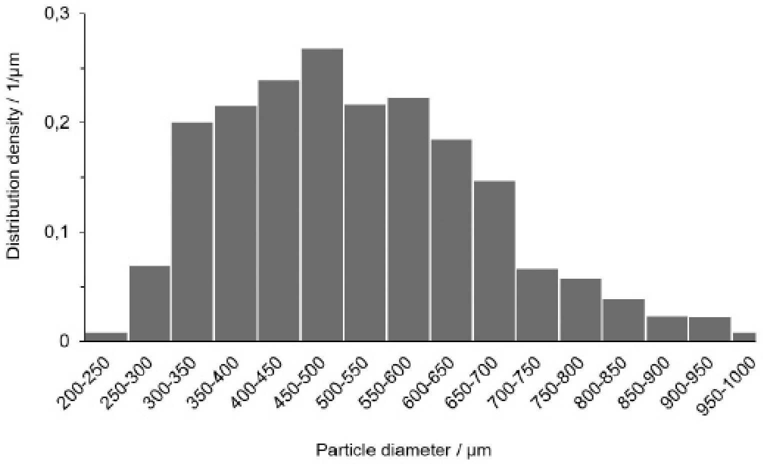

***Fig. 2**: Distribution of the volumetric frequency of the PMMA powder XP 200, reprinted from Schwindt et al. (2017).*

3 Results and discussion

3.1 Characterization of the airflow

Since a pitot tube can only measure the velocity at one particular point, a method to observe the velocity distribution and, thus, the average flow velocity is needed. To this end, we used the pitot-static traverse technique (Cheong, 2001) as proposed by ISO standard 3966. According to the Log-Tchebychef method the duct is divided into several small squares and the velocity in each corner of the small square is measured. In order to get a good average velocity, a minimum of 25 measurements is required. For a duct of a height less than 30 inches (76.2 cm), 5 traversal lines are required. Peszýnski et al. (2018) compared this method to the numerical integration curve resulting in a 2.2% difference.

The profile of the flow in the PMMA duct is plotted in Fig. 3(a) and in the PC duct in Fig. 3 (b). This air velocity measurement is taken at the end of the duct located at 1.8 m from the air inlet point respectively 1.5 m from the particle feeding point (see the experimental sketch) and expressed in terms of the time-averaged velocity. The measured streamwise air velocity, u_x, and the distance from

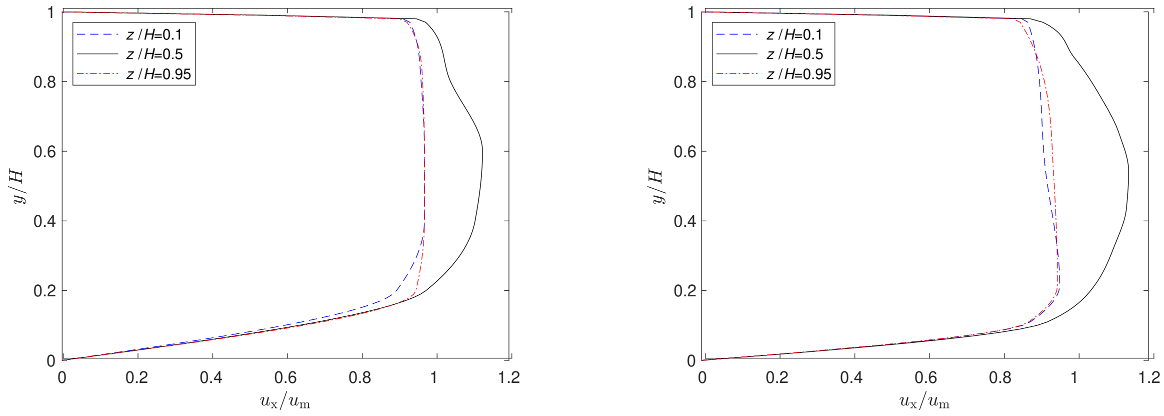

(a) (b)

***Fig. 3**: Air velocity profiles at three different cross-sections inside the (a) PMMA duct at Re = 12705 and inside the (b) PC duct at Re = 25945.*

the wall, y and z, are normalized using the mean bulk velocity, u_m, and the inner height of the duct, H, respectively. Thus, Re is given by

$$Re = \frac{H\,u_\mathrm{m}}{\nu}\,, \tag{2}$$

where ν is kinematic viscosity.

3.2 *Influence of the environmental conditions on the deposition velocity*

An important quantity in the following analysis is the deposition velocity which represents the minimum conveying air velocity required to transport particles without settling or forming any stationary or resting deposition layer. This quantity indicates the operation range of a specific conveying system. In our experiments, we defined the depoision velocity as the velocity at which particles halt within the first minute of the transport process and form a deposition layer at the bottom of the duct. We observed that at an air velocity close to this point, the flow appears to be unstable which manifests by the intermittent appearance of particle clusters. As the air velocity is further reduced, particles start to settle and form a deposition layer.

It is well known that air RH and temperature may affect particle deposition (Han et al., 2011, He and Ahmadi, 1998). Thus, we first examine the influence of RH and temperature on the deposition velocity and fraction. Experiments are initially performed to capture the general behavior. For that purpose, a constant particle flow rate of 3 kg/hr was adjusted. Three different RHs (31%, 49%, and 59%) were tested while the room temperature was 18 °C–23 °C. The results shown in Fig. 4(a) indicate that for our coarse polydisperse particles the RH is not of significant influence on the deposition velocity. Only a slight increase of the deposition velocity occurs as air RH increases drastically causing a comparable deposition fraction. To examine the temperature effect tests were performed at three temperatures (18°C, 20°C, and 23°C) at fixed RH (31%) using the PMMA duct. The constant deposition velocity plotted in Fig. 4(b) indicates a negligible effect of the temperature at least for relatively large particles. He and Ahmadi (1998) confirmed that the temperature predominantly influences particle transport and deposition in turbulent flow when the particles are rather small, namely less than 0.1 µm (1 µm according to Han et al. (2011)). Therefore, the effect of temperature will not be considered for the entire discussion of the present work.

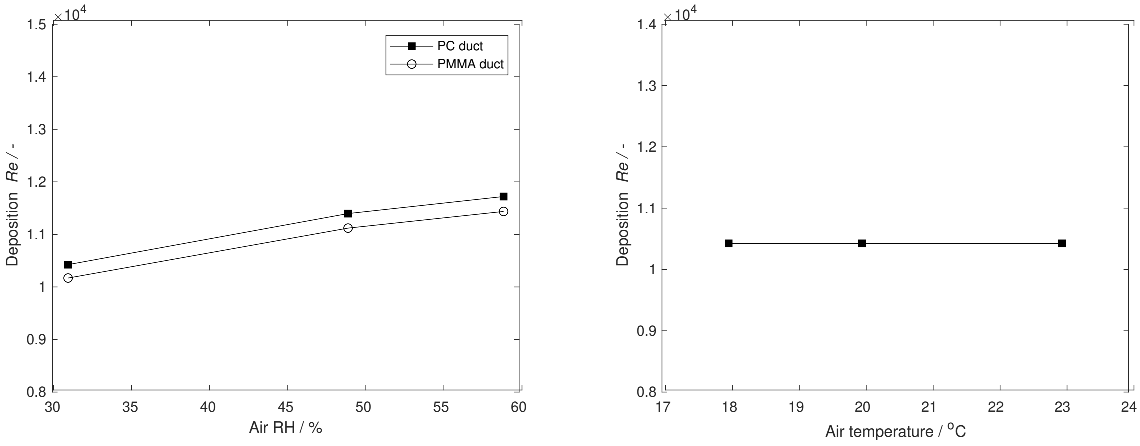

(a) (b)

Fig. 4*: Influence of the air (a) RH and (b) temperature on the deposition velocity of polydisperse particles.*

3.3 Influence of Re and the particle mass flow rate on particle deposition

For polydisperse particles, we measured the instantaneous particle deposition fraction for different flow *Re* numbers keeping the particle flow rate constant during each experiment while varying the flow rate in different experiments between 3 kg/hr and 24 kg/hr. Thus, a dilute conveying phase is present. Each test was performed for 20 min using the PMMA duct and RH ranging between 30% and 36%.

The results presented in Fig. 5 show that by reducing *Re* more particles settle at the pipe bottom and the deposition process occurs faster. Thus, a layered bed is created which at a certain time will block the cross-sectional area of the duct and prevent the particles to flow. As mentioned above, close to the deposition velocity the flow is highly unstable. This process is optically clearly observable at higher particle flow rates where the particles are no longer homogeneously distributed, but rather resemble particle clusters sliding at the bottom of the pipe.

Finally, the resulting deposition velocity for all experiments in both a PC and PMMA duct are summarized in Fig. 5(d). As expected, the deposition velocity increases with increasing particle flow rate. In essence, the more particles are present in the conveying air, the higher the required air velocity to keep the particle in suspension.

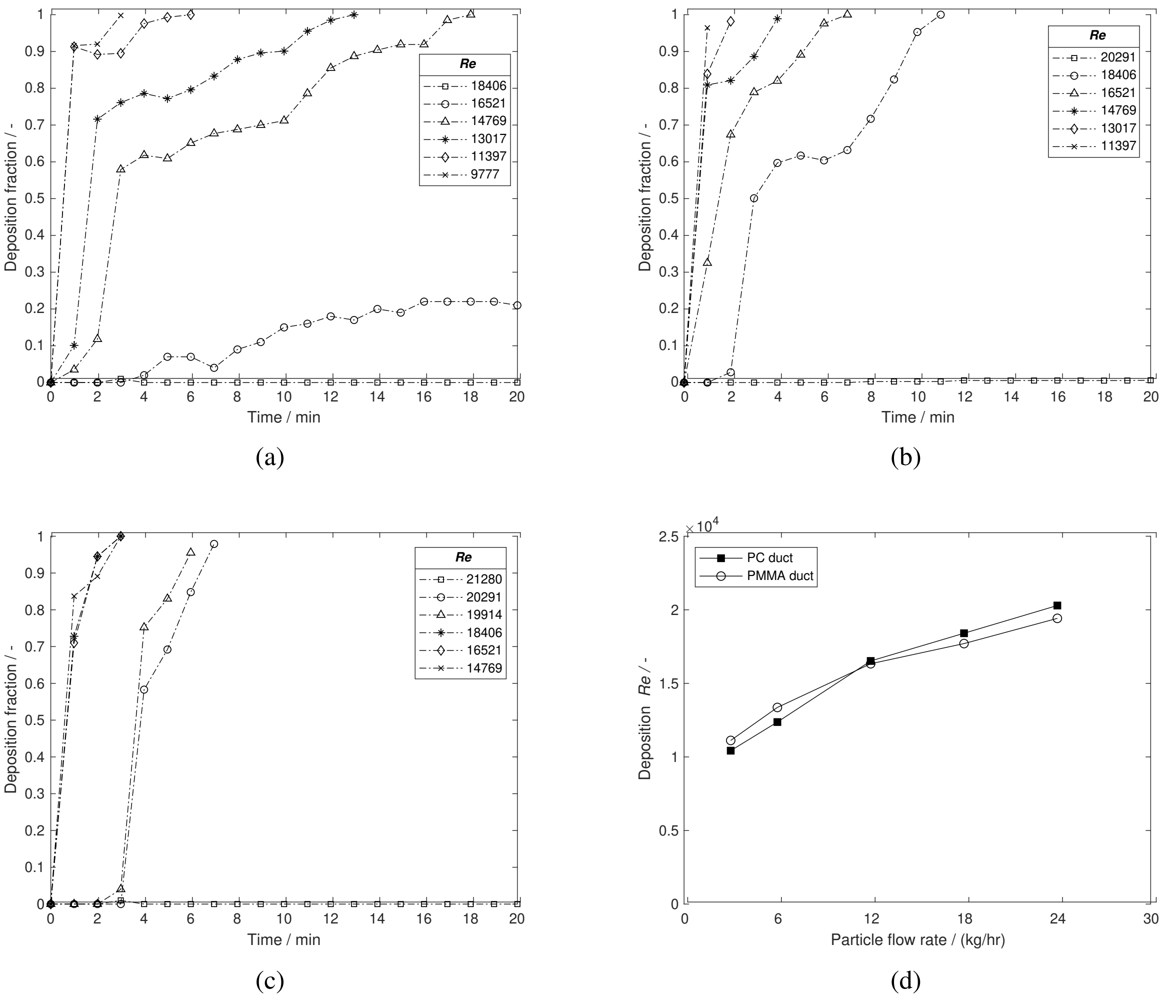

(a) (b)

(c) (d)

Fig. 5*: Particle deposition for different flow Reynolds numbers as a function of time for a particle mass flow rate of (a) 3 kg/hr, (b) 12 kg/hr, and (c) 18 kg/hr. In (d) the deposition velocity based on a conveying duration of 1 min is summarized.*

Moreover, the usage of transparent ducts enables us to ascertain that particles that do not have enough inertia to propagate to the discharge point halt once they hit the bottom wall of the duct. The following particles then hit these initially settling particles and join together resulting in a lengthwise monolayer deposit bed. Thus, the initial settling particle acts seed-like as an initial point where the deposit starts to grow. Meanwhile, the particles above the bed are still transported in the dilute phase. As the deposit bed increases its length towards the feeding point, the following particles no longer hit the bottom of the pipe, but the deposit layer. These particle collisions decrease the particle velocity. Thus, they are no longer in suspension, rather rolling above the deposit bed and slowly adding up the bed height into a multilayer deposit until it is sufficient to completely block the duct.

As can be seen in Fig. 5(a), the deposition velocity of polydisperse particle fed at a rate of 3 kg/hr is 5.0 m/s (*Re* = 14769). However, deposition is also observed at 5.6 m/s (*Re* = 16521) related to a different mechanism. Before 5 min deposition forms and afterward the particles start to drop out of suspension and generate a tail pattern of monolayer deposit at the center part of the bottom duct. The following particles hit these deposited particles; however, they do not join together as with the lower *Re*. We could observe that the airborne particles swept away the particles in the deposit and took instead their place. Thus, an equilibrium of deposited and resuspended particles is created and, in sum, the amount of deposit is constant. This type of equilibrium behavior was reported by other authors before (Adhiwidjaja et al., 2000, Matsusaka et al., 1998).

3.4 Deposition shape and location

In Fig. 6 typical deposit patterns for two different Reynolds numbers are presented. Therein, the left picture relate to a flow slightly above the respective deposition velocity and the right one slightly below. As can be seen, the particles tend to deposit at the center of the duct.

This is likely related to fluid mechanical phenomena: it is known that the concentration of particles in a wall-bounded flow is inhomogeneous due to the turbophoretic drift under the influence of near-wall coherent turbulent structures. Also, the squared-shaped duct under consideration has two inhomogeneous directions (wall-normal and spanwise) which induces a secondary flow of Prandtl's second kind (Gessner, 1973, Yao and Fairweather, 2010). As a result of this mechanism, four pairs of counter-rotating vortices are generated in the square duct (Wu et al., 2018). This secondary flow affects particle transport and dispersion, and consequently, deposition location. It enhances lateral mixing which is found stronger at the corner of the duct and supposedly responsible for the particle spanwise motion and transporting particles from the duct corner to the duct center (Sharma and Phares, 2006). However, that motion considerably weakens in the duct center. Here, streamwise turbulence dominates the flow where turbophoresis occurs and brings the particles again to the region having low turbulence intensity, which is in the duct corner. These visual evidences confirm the

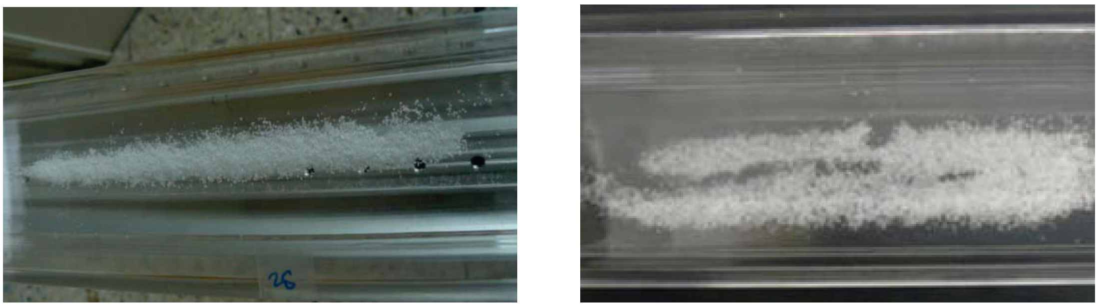

(a) Polydisperse, *Re* = 12705 (b) Polydisperse, *Re* = 11437

Fig. 6*: Deposition patterns in the PMMA duct. The airflow in (a) is slightly above the deposition velocity and in (b) slightly below.*

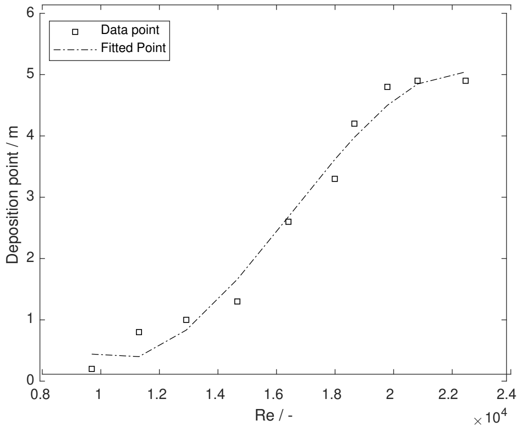

***Fig. 7**: Influence of the air velocity on the deposition point of the polydisperse particles.*

results of several numerical studies (Noorani et al., 2016, Winkler et al., 2006, Sharma and Phares, 2006, Lin et al., 2017, Zhang et al., 2015).

Further, based on the Reynolds number, the shape of the deposit appears differently. Analyzing the deposition shape of the lower flow *Re* depicted in Fig. 6(b) it can be seen that the streaky pattern looks more dispersed compared to concentrated ones of the higher *Re* case in Figs. 6(a). When the shear rate is decreased, the near-wall vortices are no longer able to eject and entrain particles. As a result, they will only be pushed aside by the sweep motion. On the contrary, when the shear rate is increased, vortices have sufficient energy to entrain particles causing the thin streaky deposition pattern (Kaftori et al., 1995).

Moreover, we investigated the influence of the air velocity on the deposition point. The deposition point is the point at which particles start to deposit and create a layer measured as the distance from the feeding point. For that analysis, a PC duct with a total length of 5.4 m was used. As shown in Fig. 7, the increasing air velocity is able to convey particles a farther distance until a constant point is reached. In other words, a higher air velocity will no longer influence the transport distance. This point is also called the boundary saltation.

4 Conclusion

The presence of particle deposits during pneumatic conveying is a potential hazard and ignition source for dust explosions. The objective of this work is to design and build a new test-rig to investigate particle deposition phenomena in squared ducts. Further, we analyzed the influence of the air conveying velocity, particle mass flow rate, relative air humidity and temperature, and duct material. It was found that the higher the particles' flow rate, the higher the required air velocity to transport the powder to the outlet. High RH caused small particles to deposit at higher air conveying velocity and increases the particle deposition fraction. These findings enhance our understanding of the detailed mechanisms underlying the formation of deposits.

Acknowledgements

The authors gratefully acknowledge the financial support from Max Buchner Research Foundation.

References

Adhiwidjaja, I., Matsusaka, S., Tanaka, H., Masuda, H. (2000). *Simultaneous phenomenon of particle deposition and reentrainment: Effects of surface roughness on deposition layer of striped pattern*. Aerosol Sci. Technol., 33(4):323–333.

Bailey, A. (1984). *Electrostatic phenomena during powder handling*. Powder Technol., 37(1):71–85.

Cheong, K. W. D. (2001). *Airflow measurements for balancing of air distribution systems - tracer-gas technique as an alternative?* Building and Environment, 36:955–964.

Eaton, J. K., Fessler, J. R. (1994). *Preferential concentration of particles by turbulence.* Int. J. Multiphase Flows, 20:169–209.

Eckhoff, R. K. (2003). *Dust Explosions in the Process Industries.* Gulf Professional Publishing, 3rd edition.

Gessner, F. (1973). *The origin of secondary flow in turbulent flow along a corner.* J. Fluid Mech., 58:1–25.

Grosshans, H. (2018). *Modulation of particle dynamics in dilute duct flows by electrostatic charges.* Phys. Fluids, 30(8):083303.

Grosshans, H. (2020). *Simulation of Turbulent Particle-laden Flows and their Electrostatic Charging.* Habilitation, Otto-von-Guericke-Universität Magdeburg.

Grosshans, H., Papalexandris, M. V. (2016a). *Evaluation of the parameters influencing electrostatic charging of powder in a pipe flow.* J. Loss Prev. Process Ind., 43:83–91.

Grosshans, H., Papalexandris, M. V. (2016b). *Large eddy simulation of triboelectric charging in pneumatic powder transport.* Powder Technol., 301:1008–1015.

Grosshans, H., Papalexandris, M. V. (2016c). *A model for the non-uniform contact charging of particles.* Powder Technol., 305:518–527.

Grosshans, H., Papalexandris, M. V. (2017). *Direct numerical simulation of triboelectric charging in a particle-laden turbulent channel flow.* J. Fluid Mech., 818:465–491.

Grosshans, H., Villafañe, L., Banko, A., Papalexandris, M. V. (2019). *Case study on the influence of electrostatic charges on particle concentration in turbulent duct flows.* Powder Technol., 357:46–53.

Han, Y., Hu, Y., Qian, F. (2011). *Effects of air temperature and humidity on particle deposition.* Chem. Eng. Res. Des., 89(10):2063–2069. ISSN 0263-8762.

He, C., Ahmadi, G. (1998). *Particle deposition with thermophoresis in laminar and turbulent duct flows.* Aerosol Sci. Tech., 29(6):525–546.

Kaftori, D., Hetsroni, G., Banerjee, S. (1995). *Particle behavior in the turbulent boundary layer. i. motion, deposition, and entrainment.* Phys. Fluids, 7(5):1095–1106.

Klahn, E., Grosshans, H. (2019). *Modeling the agglomeration of electrostatically charged particles.* In *Electrostatics 2019.* Manchester, UK.

Klahn, E., Grosshans, H. (2020). *An accurate and efficient algorithm to model the agglomeration of macroscopic particles.* J. Comput. Phys., 407:109232.

Klinzing, G. E. (1981). *Gas-solid transport.* McGraw-Hill,.

Klinzing, G. E. (2018). *A review of pneumatic conveying status, advances and projections.* Powder Technol., 333:78–90.

Lin, Z. W., Xueming, S., Yu, Z. S., Wang, L. P. (2017). *Effects of finite-size heavy particles on the turbulent flows in a square duct.* J. Hydrodynam. B, 29:272–282.

Matsusaka, S., Adhiwidjaja, I., Nishio, T., Masuda, H. (1998). *Formation of striped pattern deposition layers by an aerosol flow — analysis of thickness and interval of layers.* Adv. Powder Technol., 9(3):207–218. ISSN 0921-8831.

Noorani, A., Vinuesa, R., Brandt, L., Schlatter, P. (2016). *Aspect ratio effect on particle transport in turbulent duct flows.* Phys. Fluids, 28(11):115103.

Peszýnski, K., Olszewski, L., Smyk, E., Perczy´nski, D. (2018). *Analysis of the velocity distribution in different types of ventilation system ducts.* EPJ Web Conf., 180:02081. doi: 10.1051/epjconf/201817002081.

Schwindt, N., von Pidoll, U., Markus, D., Klausmeyer, U., Papalexandris, M. V., Grosshans, H. (2017). *Measurement of electrostatic charging during pneumatic conveying of powders.* J. Loss

Prev. Process Ind., 49:461–471.

Sharma, G., Phares, D. J. (2006). *Turbulent transport of particles in a straight square duct*. Int. J. Multiph. Flow, 32(7):823–837. ISSN 0301-9322.

Sippola, M. R., Nazaroff, W. W. (2004). *Experiments measuring particle deposition from fully developed turbulent flow in ventilation ducts*. Aerosol Sci. Technol., 38(9):914–925.

Song, Y., Zhang, Q. (2019). *Multiple explosions induced by the deposited dust layer in enclosed pipeline*. J. Hazard. Mater., 371:423–432.

Wang, Y., Zhao, Y., Yao, J. (2019). *Large eddy simulation of particle deposition and resuspension in turbulent duct flows*. Adv. Powder Technol., 30(3):656–671. ISSN 0921-8831.

Winkler, C., Rani, S. L., Vanka, S. (2006). *A numerical study of particle wall-deposition in a turbulent square duct flow*. Powder Technol., 170(1):12–25. ISSN 0032-5910.

Wu, J., Xiao, H., Paterson, E. (2018). *Physics-informed machine learning approach for augmenting turbulence models: A comprehensive framework*. Phys. Rev. Fluids, 3:74602.

Yao, J., Fairweather, M. (2010). *Inertial particle resuspension in a turbulent, square duct flow*. Phys. Fluids, 22(3):33303.

Yao, J., Fairweather, M. (2011). *Particle deposition in turbulent square duct flows*. In *J. Phys. Conf. Ser.*, volume 318, page 052005. IOP Publishing.

Zhang, H., Trias, F. X., Gorobets, A., Oliva, A., Yang, D., Tan, Y., Sheng, Y. (2015). *Effect of collisions on the particle behavior in a turbulent square duct flow*. Powder Technol., 269:320–336.

DOI: 10.7795/810.20200724

Suppression effect of inert gas on aluminum dust explosion

Shulin Zhang[a], Mingshu Bi[a], Haipeng Jiang[a], Wei Gao[a]

[a] State Key Laboratory of Fine Chemicals, Department of Chemical Machinery and Safety Engineering,
Dalian University of Technology, 2 Linggong Rd., Dalian 116024, China

E-mail: gaoweidlut@dlut.edu.cn.

Abstract

In this study, the suppression mechanism of inert gas (carbon dioxide and nitrogen) for 5 μm aluminum dust explosion was investigated experimentally and numerically in a confined cuboid chamber. The flame propagation characteristics parameters (flame propagation behavior, flame propagation velocity) and explosion severity parameters influenced by inert gas were systematically studied. The results showed that as the inerting volume fraction increased, the distribution of flame fault was enlarged, the duration time of flame and the flame propagation velocity were slowed down accordingly. The minimum inerting volume fraction of carbon dioxide was lower than that of nitrogen for 5 μm aluminum particles, indicating that the suppression effect of carbon dioxide on aluminum dust explosion was superior to that of nitrogen. The scanning electron microscopy analysis indicated that the condensed explosion product contained unburned aluminum particles with crystallized phase suppressed by inert gas. To reveal the suppression mechanism from the micro level, a kinetic model considering surface chemistry was proposed. The results revealed that as the inerting volume fraction of inert gas increased, for the sensitivity analysis of open sites, the heterogeneous elementary reactions that promoted the generation of open sites were mostly suppressed, while the heterogeneous elementary reactions that consuming open sites were facilitated.

Keywords: *suppression effect, aluminum dust explosion, inert gas, surface chemistry*

1. Introduction

As the well-recognized energetic material, aluminum particles have been widely used in metalized slurry fuel (Choudhury, 1992), propellants (Natan and Rahimi, 2001) and the solid metalized explosives (Zhang, 2006) due to its remarkable properties. Nevertheless, the endless aluminum dust explosion accidents reflected its potential explosion hazard and hindered the development of processing industry. For instance, on August 02, 2014, a disastrous aluminum dust explosion during wheel polishing process occurred in Kunshan, China, killing 146 workers, and causing economic losses of 351 million RMB (Chen et al., 2018). On July 06, 2018, an explosion occurred in an aluminum plant in Okayama, Japan, with a shock wave range as great as 100 km, leading to at least ten injuries (Taveau et al., 2018).

Thus, the study on suppression of aluminum dust explosion is desperately needed. There are several control technologies for prevention and mitigation of dust explosion, such as water mist, inert gas, and solid suppressants, each with its own applicable dominance. However, it should be pointed out that, once the aluminum dust explosion breaks out, the extremely high overpressure and flame temperature would make it more difficult for fire control facilities to suppress effectively and quickly. Moreover, the production of halogenated hydrocarbon was prohibited internationally due to its destructive effect on stratospheric ozone (Cao et al., 2016). Therefore, inert gas, as the outstanding suppressant, can offer incomparable advantages compared with the other suppressants (Pang et al., 2019).

The studies concerning the suppression effect of inert gas on dust explosion have been conducted theoretically and experimentally by scholars. Pang et al. (2019) revealed the effects of different inert gases on explosion characteristics during low density polyethylene (LDPE) dust explosion and optimized the explosion-proof process. It was found that the reduction of oxygen concentration could effectively weaken the effect of dust combustion reaction and the effect of carbon dioxide was significantly better than nitrogen in inerting. Sun et al. (2004) integrated the nitrogen circulatory system into the closed steam tube rotary drying technology. The dust explosion hazard caused by hot air in the original drying system can be reduced with this method. Going et al. (2000) conducted a series of experimental test concerning the limiting oxygen concentration of several kinds of dust (gilsonite, bituminous coal, etc) in both 20-L and 1-m^3 vessels, and a protocol for testing at different volumes was developed. Overall, the studies mentioned above have shown that the inert gas may significantly reduce the explosion intensity in a macroscopic view, but the suppression effect of inert gas on aluminum dust explosion have not been thoroughly explored or explicitly stated, and failed to give an interpretation of suppression mechanism in detail. In terms of these limitations, the flame propagation characteristics and explosion overpressure behavior of aluminum dust explosion were quantitatively studied by means of a designed experimental system with different inert gases (nitrogen, carbon dioxide). And a kinetic model based on surface chemistry was used to further clarify the suppression mechanism of inert gas for such explosion. The research results will be helpful for improving the intrinsic safety of the aluminum industry and reducing the hazards of dust explosions.

2. Experimental method

2.1 Preparation of experimental sample

Because of experimental limitations, the majority of studies were performed with relatively large particles, ranging from tens to even hundreds of microns in size (Myers, 2013). Nevertheless, the size of particles was often in the small micron-size range in practical application. Previous study pointed out that the combustion regime of aluminum particles might be different due to the reduction in particle size (Julien et al., 2014). The aluminum particles used in this study were provided by Angang Group Aluminum Powder Co., Ltd, China. Figure 1(a) shows the particle size distribution measured by Malvern Mastersizer 2000 laser particle analyzer. And the scanning electron microscope (SEM) images of aluminum particles shown in Fig. 1(b) illustrates the morphology of the particles. The aluminum particles were characterized by spheroidal shape having a Sauter mean diameter D (3,2) of about 5 μm. High purity nitrogen, carbon dioxide, and oxygen (≥99.99%) were supplied by the 40-L gas cylinder, respectively.

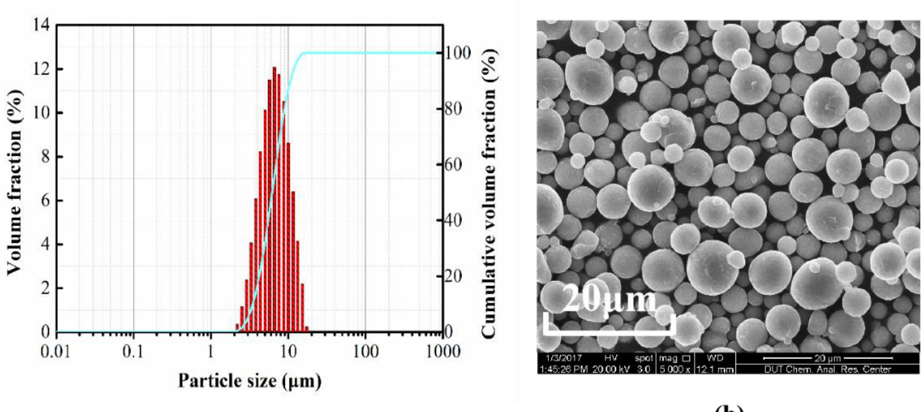

(a) **(b)**

Fig. 1. *The particle size distribution and SEM image of 5 μm aluminum particles*

DOI: 10.7795/810.20200724

2.2 Experimental system

The schematic diagram of aluminum dust explosion experimental system is shown in Fig.2. The system was composed of the following subsystems: (1) a cuboid chamber (670mm*200mm*200mm) with tempered glass window (512mm*122mm*60mm); (2) a powder spraying system; (3) a gas supply system; (4) an ignition system; (5) a high-speed camera; (6) a procedure control; and (7) a data acquisition system.

The aluminum particles were put into a hemisphere cup and the dispersed through a solenoid valve. Based on the Dalton's law of partial pressure, the pressure tank was first evacuated and then filled by a mixture of oxygen and gas inhibitor up to 0.6MPa in terms of the partial pressure method. The inhibition volume fraction (i.e., 79 %, 85 %, 90 %) was defined as the volume fraction of gas inhibitor in constant volume. After that, the cuboid chamber was evacuated and filled with the mixture to the pre-determined vacuum degree, the inhibition volume fraction of which was same as in the pressure tank. The premixed inert gas-oxygen mixture in the pressure tank was seeded with aluminum powder using the powder spraying system. Through the aforementioned process, initial pressure can obtain to 0.1 MPa for each experiment. Two electrodes were installed on the sidewall of cuboid chamber whose height was 180mm above the bottom of vessel and the gap was 2 mm. The aluminum dust cloud was ignited by a 15KV high-voltage transformer and the ignition time lasted 500ms. Moreover, a Photron high-speed camera (SA-4) equipped with a normal lens (Nikkor 50 mm f/1.2, Nikon) and an Asahi Spectra narrow band-pass filter (484nm), the radiation wavelength of which was the main intermediate product of aluminum combustion, allowed the flame propagation behavior to be monitored with a framing rate of 10000 frames per second. Besides, a micro-lens (AF Micro Nikkor 200 mm f/4D, Nikon) was used to image the microstructure of flame under different inert gas atmosphere. A PCB pressure sensor was used to record the explosion overpressure changes with time. The powder spraying duration was 500 ms, and the ignition delay time was 40 ms.

Before experiments, the aluminum particles were put into the drying oven for 24 hours to remove the influence of humidity. More than three duplicate experiments were conducted for each experimental condition to guarantee the accuracy of experimental data.

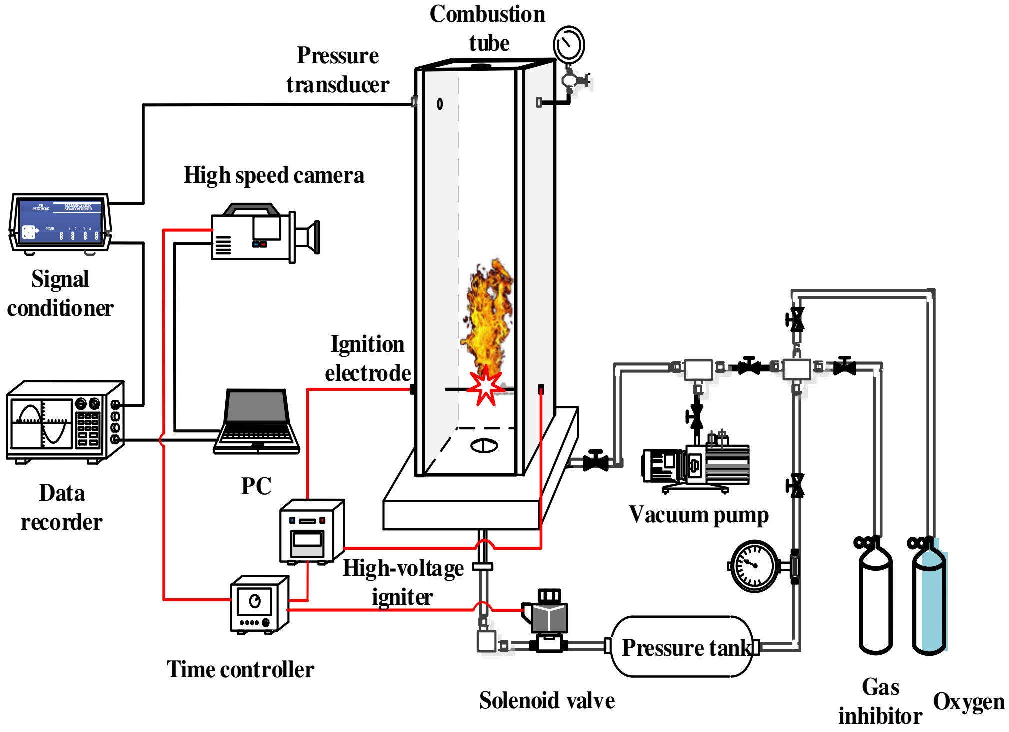

Fig. 2. Experimental apparatus

3. Kinetic model

Based on previous studies, the combustion regime of aluminum particle mainly depended on the particle's size (Beackstead, 2005). The large micron-sized particle was controlled by the diffusion-limited regime, while the small micron-sized aluminum particles (< 10 μm) were in the transition regime, the diffusion rate of oxidizer was larger than the chemical reaction rate near the surface of particle (Dreizin, 1999). That is to say, heterogeneous aluminum/oxygen interaction processes affect the combustion scenario significantly for 5 μm aluminum particles in this study. Numerical simulations were conducted on aluminum/ inert gas mixture accounting for surface kinetic mechanism, which was derived from the pioneering work of Glorian et al. (2016). The surface reaction of aluminum combustion referred to the catalytic reaction that occurred on the surface of aluminum particles during combustion. The minimum effective structural unit that catalyzed the surface of aluminum particles was called the "open site", it was a material which was used in the CHEMKIN surface chemical mechanisms presenting the type of specific material that promote the reaction, Al(L) was defined as open site on aluminum surface in this study. For clarify, (S) and (B) represented the bulk- phase species for surface species and solid species, respectively. Therefore, the surface reaction mechanism contained 34 reactions with following species (Al(L), AlO(S), AlO_2(S), O(S), C(S), CO(S), CO_2(S), N(S), AlN(S), Al_2O_2(S), Al_2O(S), Al(B), Al_2O_3(B). Since the aluminum particles were easily to form the alumina shell (Sundaram et al., 2016), the numerical model used in this study neglected the potential presence of the oxidation shell on the particle surface. Therefore, calculations were performed for combustion of aluminum particles in air with the inerting atmosphere similar with experimental conditions. The initial temperature was set as 2700K, and initial pressure was set as 1 atm.

As we know, this detailed mechanism is a tentative approach to evaluate to which extent surface chemistry can play a role in aluminum dust explosion under inert gas atmosphere.

4. Results and discussions

4.1 Suppression effect of flame propagation behaviors by inert gas

In the practical industrial production process, aluminum particles will be presented in large amounts and create a fuel- rich state (Nifuku et al., 2007). Hence, nominal dust concentration with 1000 g/m^3 was selected to carry out the suppression experiment.

As shown in Fig.3(a), in order to reveal the interaction mechanism between inert gas and aluminum dust flame, the propagation mechanism of aluminum dust explosion in air was studied. The time of ignition was defined as 0 ms. It could be found that, shortly after ignition, the aluminum particles were soon be ignited and started to propagate along the cuboid chamber. The flame front of dust flame had a continuous structure similar to gaseous flame with obviously overexposed large area of white light. As the decreasing of particle size, the specific surface area was enlarged, leading to the violence reaction between aluminum particles and oxidizer. However, as the volume fraction of nitrogen increased, both flame light intensity and flame shape changed. Fig.3 (b)-(d) show that the luminosity of flame was decreased significantly, the overexposed area of white light faded away and the flame shape became irregular. When volume fraction of nitrogen increased to 90%, fault area appeared in the middle of the flame propagation process, the duration time of flame propagated to the top of chamber was prolonged to 230 ms. The flame propagation behavior of aluminum dust cloud was distinctly suppressed with the further decreasing of oxygen concentration.

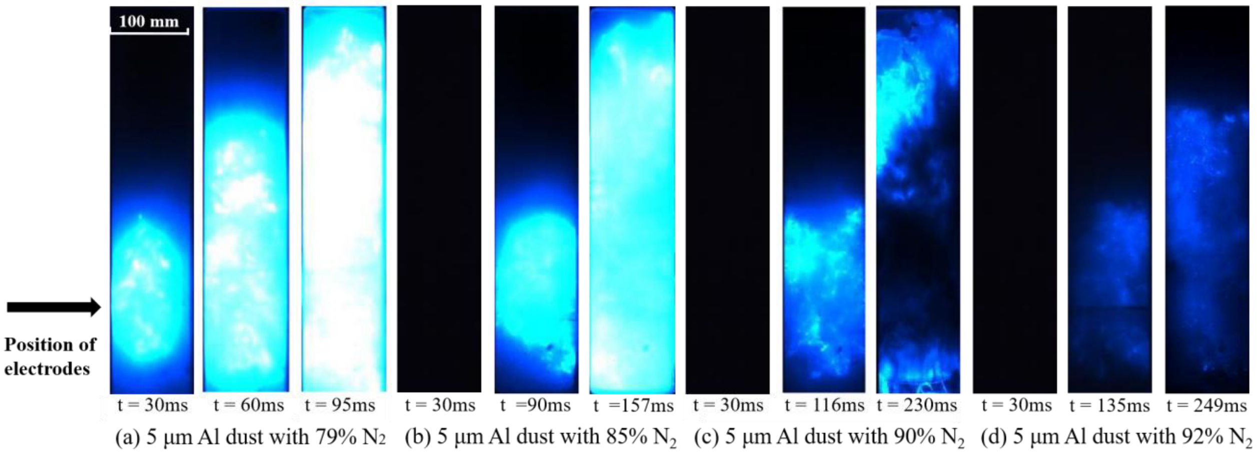

(a) 5 μm Al dust with 79% N_2 (b) 5 μm Al dust with 85% N_2 (c) 5 μm Al dust with 90% N_2 (d) 5 μm Al dust with 92% N_2

Fig. 3. *Flame propagation behaviors of 5 μm aluminum dust cloud with different volume fractions of nitrogen. Dust concentration: 1000g/m*^{3}

Fig. 4 provides the flame propagation behavior of aluminum dust explosion suppressed by different volume fractions of carbon dioxide. With the increasing inerting volume fraction of carbon dioxide, the flame front became discrete and irregular. White light area was obviously dimmed and scattered in the combustion reaction area with the occurrence of discrete clusters of flames, indicating that suppression effect of carbon dioxide was promoted with the decreasing of oxygen concentration.

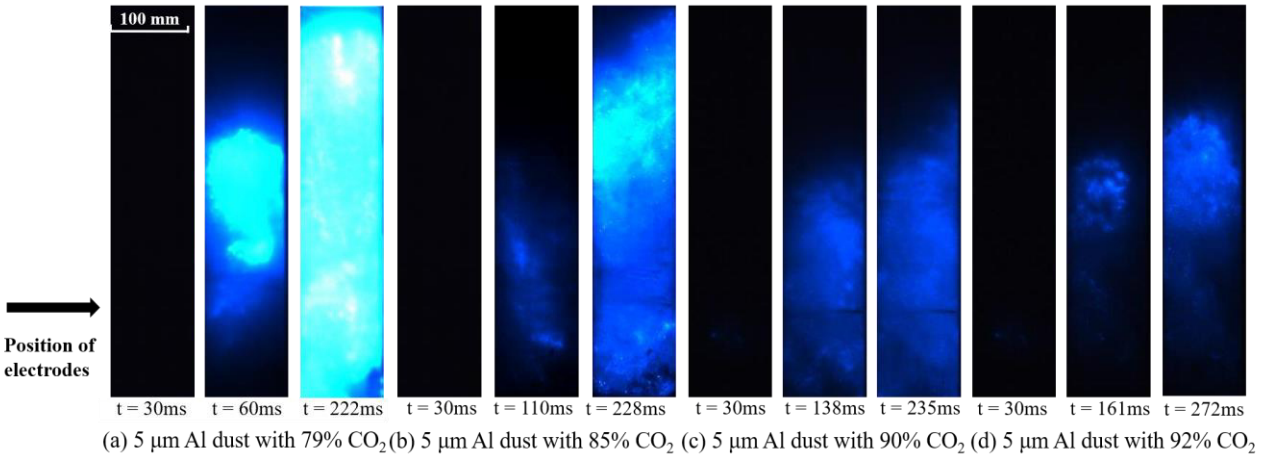

(a) 5 μm Al dust with 79% CO_2 (b) 5 μm Al dust with 85% CO_2 (c) 5 μm Al dust with 90% CO_2 (d) 5 μm Al dust with 92% CO_2

Fig. 4. *Flame propagation behaviors of 5 μm aluminum dust cloud with different volume fractions of carbon dioxide. Dust concentration: 1000g/m*^{3}

The high-speed camera with a micro-lens was used to capture the microstructures of aluminum dust flame effected by inert gases, which is illustrated in Fig.5. Based on the literature, transition regime played a role in controlling the combustion mode of small aluminum particles, which was affected by both diffusion speed and kinetic rates (Han and Sung, 2019). It can be found from Fig. 5(a), several symmetry spherical gaseous flames were formed, which encircled the aluminum particles. Nevertheless, when the inerting volume fraction of carbon dioxide was 90% (Fig. 5(b)), the diameter of the gaseous flame was evidently diminished. Moreover, the spacing between particles was increased and the continuous gaseous flame turned to nearly flame morphology with discrete propagation. The aluminum dust flames got closer to the surface of particles, signifying that the gaseous flame was suppressed. The luminosity of flame front was darkened, difficulty in observing the combustion structure characterized by spherical gaseous flame explicitly.

DOI: 10.7795/810.20200724

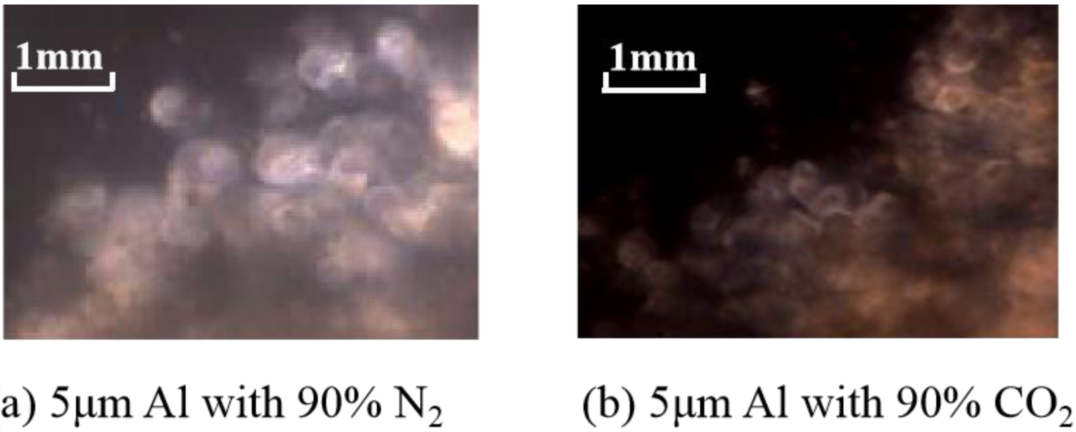

(a) 5μm Al with 90% N_2 (b) 5μm Al with 90% CO_2

Fig. 5. *Flame microstructures of 5 μm aluminum dust cloud under different inert gases atmosphere with fixed inerting volume fraction. Dust concentration: 1000g/m*^{3}

4.2 Suppression effect of flame propagation velocity by inert gas

The acquisition of flame propagation information was based on the OpenCV library (Yan, 2016), consisted of the following steps: (1) Region of interest (ROI) was designated for each frame image; (2) Adaptive threshold segmentation was applied to the gray image of ROI to distinguish the flame from the background using OTSU's method (Li and Liu, 1993); (3) The ROI was transformed from a gray scale map to a binary map after obtaining the maximum threshold; (4) The distance from ignition point and flame propagation velocity can be obtained on account of upwardly propagated, respectively. The addition of inert gases could dilute the gas environment, block the heat transfer from reaction zone to unburned zone. Moreover, the inert gases could absorb large quantity of heat released from the combustion zone, leading to the suppression of aluminum flame propagation relatively. According to previous study, radiative heat transfer process could also contribute to the heat dissipation (Julien et al., 2015).

Fig. 6 shows the flame propagation velocities of 5 μm aluminum dust cloud with different volume fractions of inert gases. Within the range of the experimental conditions, the flame propagation velocities of aluminum dust cloud all characterized by the similar development trend. With the addition of inert gases, the flame propagation velocity was decreased gradually. When inerting volume fraction of inert gases increased from 79% to 92%, the time of flame propagation from the igniter to the top of chamber was prolonged from 96 ms to 260 ms for nitrogen and from 122ms to 350 ms for carbon dioxide, respectively. Moreover, the maximum flame propagation velocity was decreased accordingly. Carbon dioxide exhibited superior inerting effect to nitrogen on flame propagation velocity.

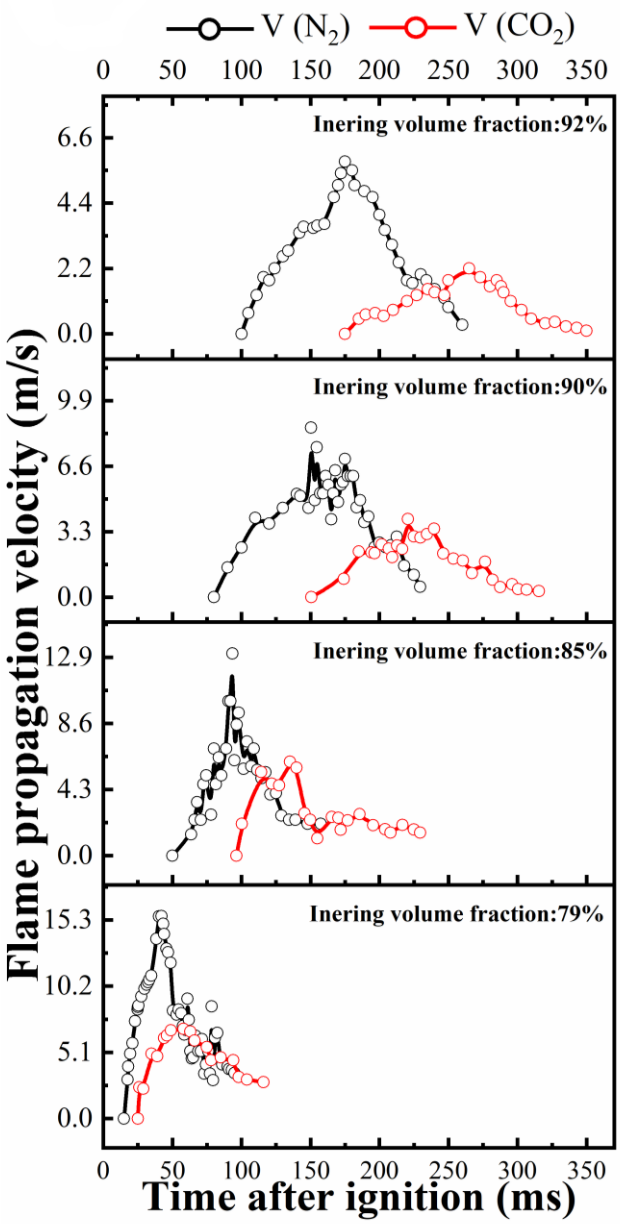

Fig. 6. *Flame propagation velocities of 5 μm aluminum dust cloud with different volume fractions of inert gas. Dust concentration: 1000g/m^3*

Maximum flame propagation velocity and acceleration speed were both chose as indicators evaluating reduction in flame propagation velocity suppressed by inert gases. As can be find in Fig.7, the indicators both presented decreasing trend with the increasing of inerting volume fraction of inert gases. Acceleration speed was a physical parameter describing how quickly the flame propagation velocity changed, illustrating that reduction of flame propagation velocity was enlarged. When inerting volume fraction of inert gases increased to 90%, the maximum flame propagation velocity was reduced by 40.6% for nitrogen and 72.7% for carbon dioxide compared with air atmosphere.

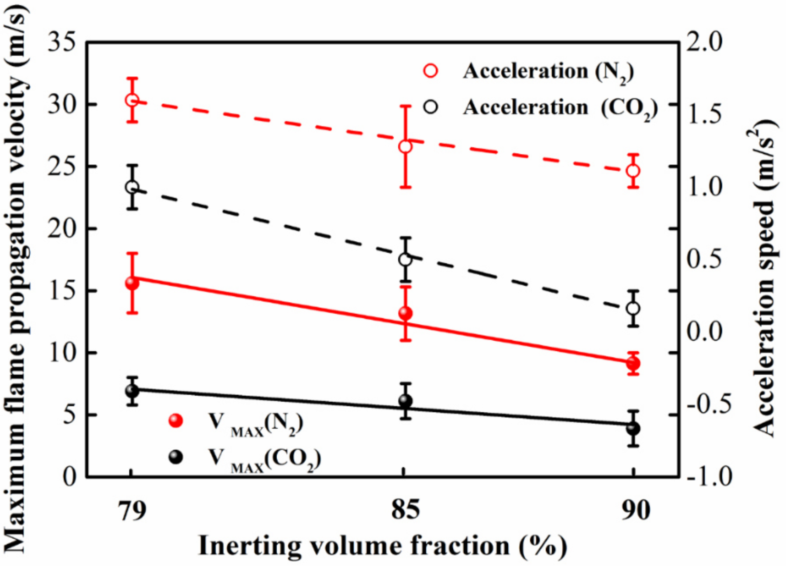

Fig. 7. *Maximum flame propagation velocity and acceleration speed of 5 μm aluminum dust cloud under different inerting volume fractions of inert gas. Dust concentration: 1000g/m^3*

As shown in Fig.8, the duration time of flame and ignition delay time of aluminum dust were both prolonged with the increasing of inert gases. The growth rate of radicals was slowed down and the consumption rate of radicals was accelerated due to the collision between free radicals and inert gases (Huang et al., 2019). The ignition difficulty was augmented and the ignition delay time was distinctly increased.

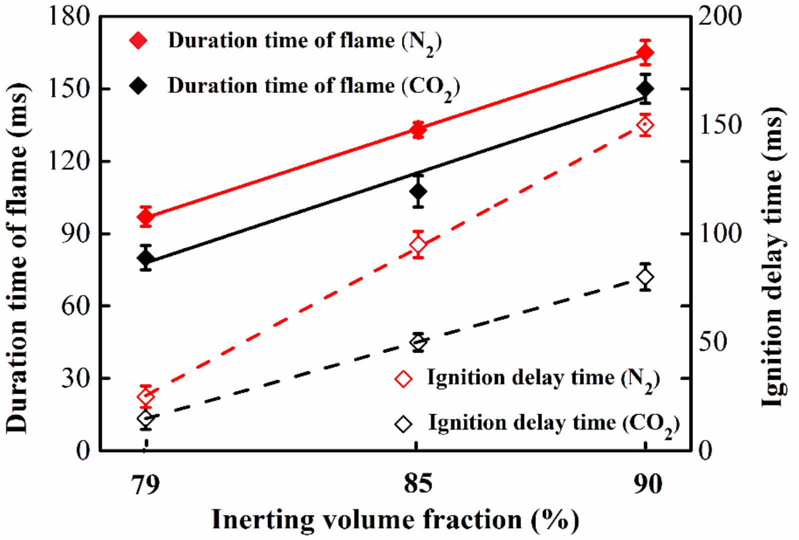

Fig. 8. *The duration time of flame and ignition delay time of flame for 5 μm aluminum dust cloud under different inerting volume fractions of inert gas. Dust concentration: 1000g/m^3*

4.3 Suppression effect of explosion overpressure by inert gas

Explosion overpressure is a crucial parameter that reflect the explosion hazard of aluminum dust, which is also an important reference for explosion protection design. After dispersion process, the premixed inert gas/ oxygen mixture was flushed into the cuboid chamber with aluminum particles, the ambient pressure was reached to 0.1 MPa before ignition.

Fig. 9 and Fig.10 presents the effect of inert gases on the explosion overpressure of 5 μm aluminum dust explosion. As the inerting volume fraction of inert gases increased, the degree that aluminum dust cloud got diluted was increased, the space between aluminum particles were enlarged, and the heat transfer generated during explosion process can be effectively hindered afterwards. Furthermore, more heat released from reaction zone can be absorbed by inert gases, the flame temperature of aluminum dust explosion was reduced accordingly. The vaporization of unburned aluminum particles in the preheating zone was impeded, the combustion rate of aluminum particles was decreased as well. In the end, the maximum explosion overpressure was reduced gradually with the increasing of inerting volume fraction of inert gases.

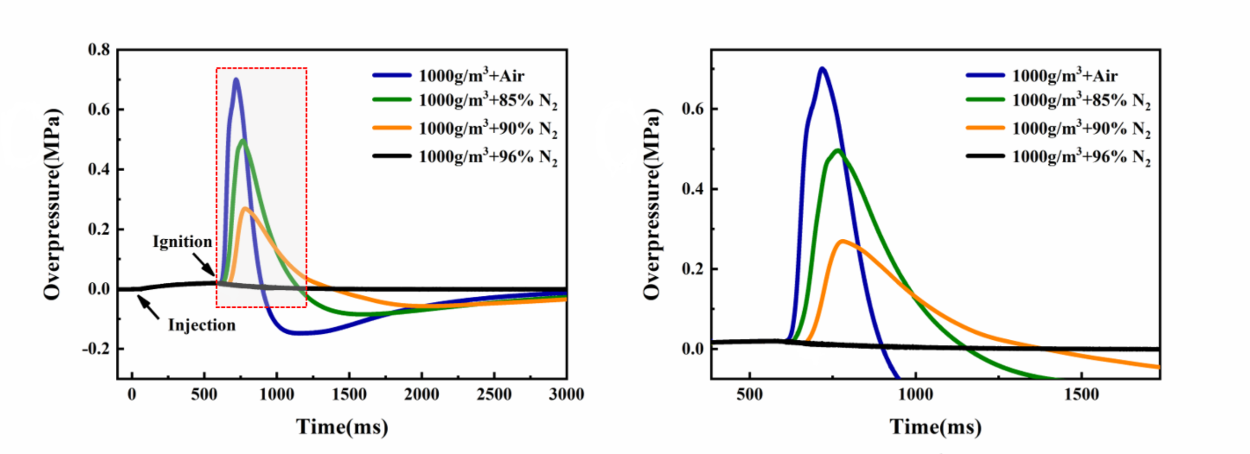

(a) (b)

Fig. 9. *The typical pressure history(a) and partial enlarged pressure history(b) of 5 μm aluminum dust cloud under different inerting volume fractions of nitrogen. Dust concentration: 1000g/m*^{3}

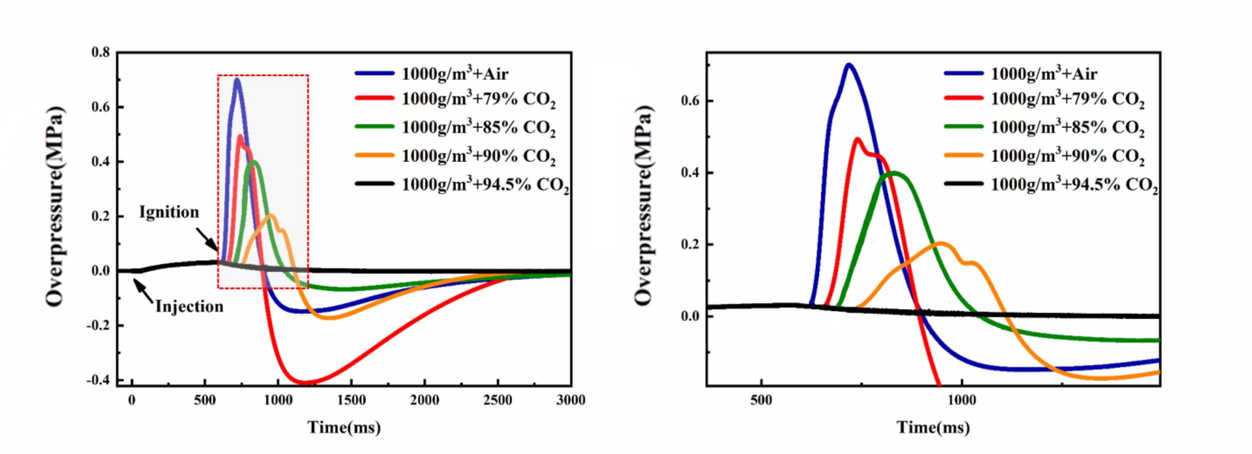

(a) (b)

Fig. 10. *The typical pressure history(a) and partial enlarged pressure history(b) of 5 μm aluminum dust cloud under different inerting volume fractions of carbon dioxide. Dust concentration: 1000g/m*^{3}

Minimum inerting volume fraction is defined as the minimum volume fraction of inert gases that required for completely inerting dust explosion. Fig. 11 provides the inerting volume fraction as a function of aluminum dust explosion. It was obviously demonstrated that carbon dioxide exhibited superior suppression effect to nitrogen for 5 μm aluminum dust explosion. The results may aid in preventing aluminum dust explosion during industrial production and reducing the harmful consequences of dust explosions.

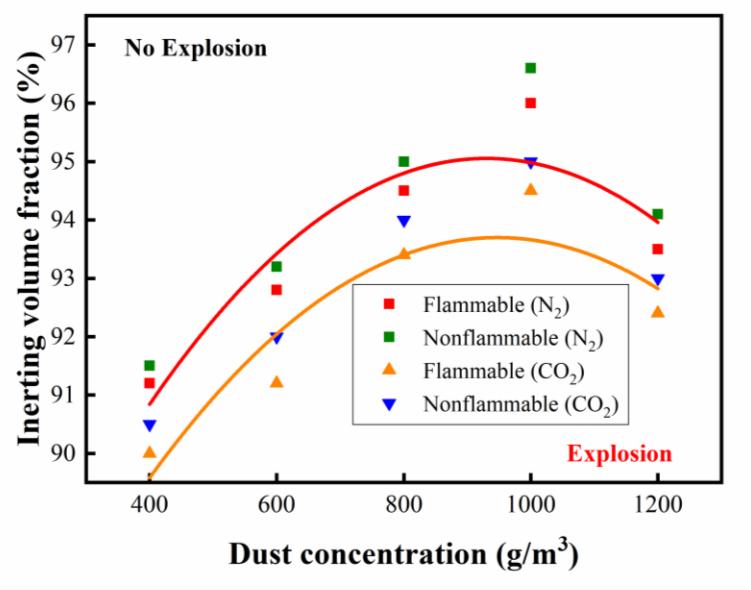

Fig. 11. *The inerting curve of 5 μm aluminum dust cloud under different inert gas with various aluminum dust concentration*

4.4 Analysis of suppression mechanism

In this study, the combustion mode of 5 μm aluminum particles was mainly controlled by transition regime as previously discussed. However, the effect of gas-phase suppression could not be ignored. The presence of unburned metallic aluminum particles in the collected condensed product (Fig.12) indicated that the reaction of aluminum particles was suppressed through gas-phase reaction, which was in accordance with literature (Jiang et al., 2020). Besides, carbon dioxide exerted better suppression effect than nitrogen in gas- phase reaction.

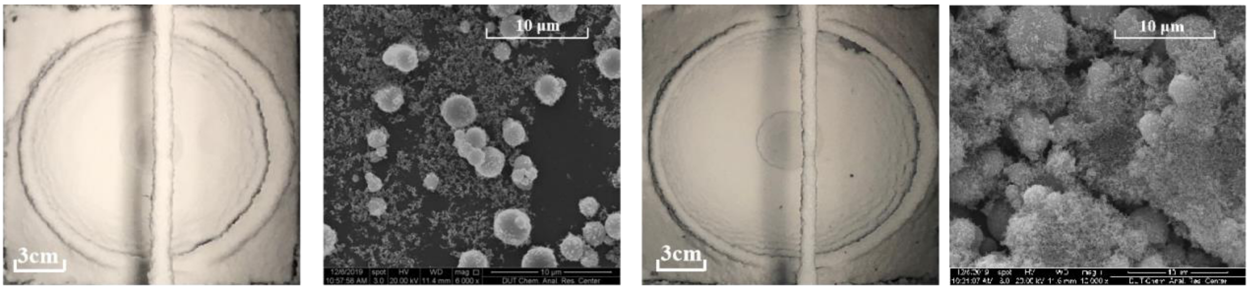

(a) 5μm Al with 90% N_2 (b) SEM image of (a) (c) 5μm Al with 90% CO_2 (d) SEM image of (c)

Fig. 12. *The photographs and SEM images of 5 μm aluminum dust explosion residues under different inert gases atmosphere with fixed volume fraction. Dust concentration: 1000g/m³*

As for the surface chemistry of aluminum particles, it is known to all that the combustion mode which attached to kinetic controlled regime followed Langmuir-Hinshelwood mechanism or Eley-Rideal mechanism. The above two mechanism present different reaction mechanism (Krazter and Brenig, 1991). The former means two adsorbed species reacted on catalyst surface, while the latter denotes adsorbed species reacted with the other species directly. In this study, the ambient temperature was set as 2700K. Thus, a virgin aluminum surface was obtained. During the explosion process, different oxidizer encircled the aluminum particle, which referred to Eley-Rideal mechanism.

Fig. 13 shows the conceptual diagram of the above-mentioned adsorption process. During a surface reaction, an oxygen molecule was adsorbed on the surface of an aluminum particle filling into two open sites and a sequence of surface reactions then occurred. Adsorption products were generated by intermediate species. The final adsorption material was desorbed from the surface of the aluminum particle to form the product molecule (Sormojai, 1994). O(S) and AlO(S) were two vital

DOI: 10.7795/810.20200724

open sites that reflected the effect of inert gases on the diffusion rate of oxidizer on particle surface in the heterogeneous reaction (Glorian et al., 2016). Therefore, sensitivity analysis of those species under different inerting volume fraction of inert gases were studied to figure out the suppression mechanism for surface reaction. As shown in Fig. 14 and Fig. 15, with the increasing of inerting volume fraction of inert gases, the heterogeneous elementary reactions that promoted the generation of open sites were mostly suppressed, while the heterogeneous elementary reactions that consuming open sites were facilitated. These results illustrated that, as the inerting volume fraction increased, the oxidizer diffusion rate was limited, and fewer gas-phase reactants were absorbed, resulting in the suppression of reaction of aluminum particles and a decrease in the generation of aluminum-containing product.

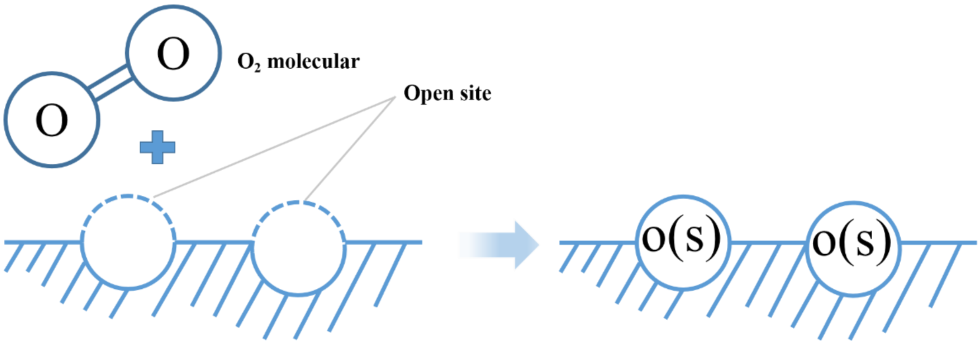

Fig.13. The conceptual diagram of adsorption process

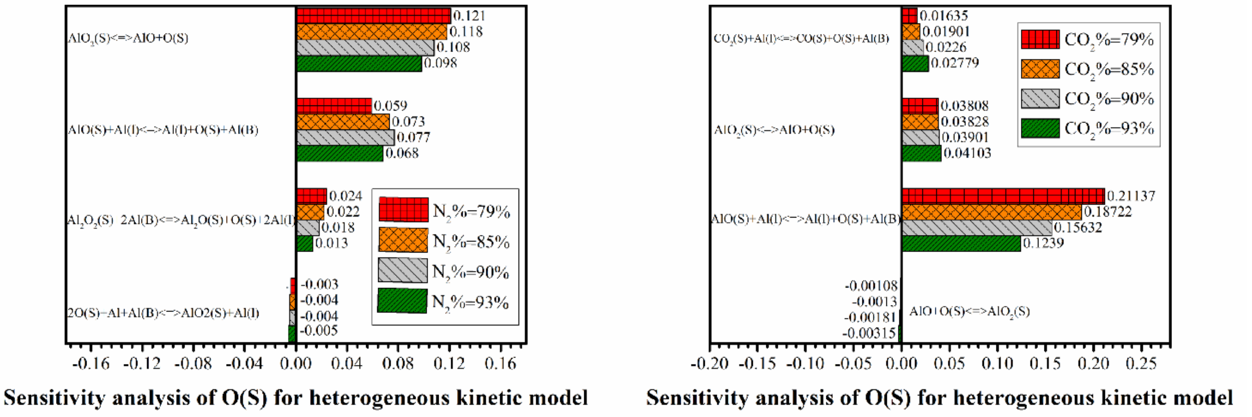

(a) (b)

Fig. 14. The sensitivity analysis of O(S) under different inerting volume fractions of nitrogen and carbon dioxide

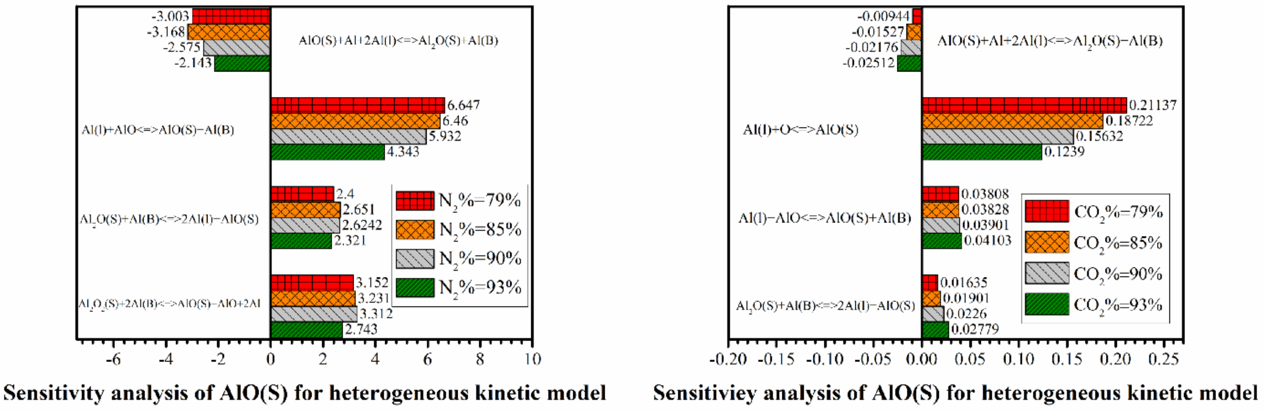

(a) (b)

Fig. 15. The sensitivity analysis of AlO(S) under different inerting volume fractions of nitrogen and carbon dioxide

Hence, creating an inert atmosphere by, for example, reducing the oxygen concentration, was probably the most feasible way to prevent aluminum explosion hazard. Although it may be costly to inject inert gas into the surface processing operation owing to its unconfined system, it could still be an appropriate way to prevent dust explosion. Moreover, the use of multiple safety systems including equipped with an automatic spraying device would be the most effective way to reduce the dust explosion hazard.

5. Conclusions

The flame propagation characteristics and explosion overpressure behavior of 5 μm aluminum dust explosion suppressed by inert gas (nitrogen, carbon dioxide) were investigated experimentally and numerically, a kinetic model concerning the kinetically- controlled mechanism was developed. The main conclusions were appended below:

(1) Flame propagation behavior and microstructures of flame were varied with the addition of different inert gases. As the inerting volume fraction increased, the distribution of flame fault was enlarged, the flame propagation velocity was reduced. The microstructures of flame indicated that the gas- phase combustion of aluminum particles was suppressed accordingly.

(2) The explosion overpressure of 5 μm aluminum particles can reach to 0.7 MPa without the addition of inert gas due to its remarkable properties. Both nitrogen and carbon dioxide exerted certain suppression effect. The minimum inerting volume fraction of inert gases were determined, it reflected that carbon dioxide was more effective than nitrogen.

(3) The suppression effect of inert gases on aluminum dust explosion was composed of gas- phase suppression, which referred to dilution, isolation and cooling process, and surface reaction suppression. The numerical calculations conducted in this study showed that, the heterogeneous elementary reactions that promoted the generation of open sites were mostly suppressed, while the heterogeneous elementary reactions that consuming open sites were facilitated with the addition of inert gases.

Acknowledgments

The authors gratefully acknowledge the financial support from the National Science Fund for Excellent Young Scholars (Grant No. 51922025), the National Natural Science Foundation of China (Grant No. 51874066), and the National Key R&D Program of China (Grant No. 2017YFC0804705).

References

Beackstead, M.W. (2005). Correlating aluminum burning times. *Combustion Explosion and Shockwaves*, 41: 533-546.

Cao, X.Y., Ren, J.J., Bi, M.S., Zhou, Y.H., Li, Y.M. (2016). Experimental research on the characteristics of methane/ air explosion affected by ultrafine water mist. *Journal of Hazardous Material*, 324: 489-497.

Chen, H.Y., Zhang, Y.S., Li, H., Meng, X.B., Dong, W.Z. (2018). Cause analysis and safety evaluation of aluminum powder explosion on the basis of catastrophe theory. *Journal of Loss Prevention in the Process Industries*, 55: 19-24.

Choudhury, P.R. (1992). Slurry fuels. Progress in Energy and Combustion Science, 18(5): 409-427.

Dreizin, E.L. (1999). On the mechanism of asymmetric aluminum particle combustion. *Combust and Flame*, 117: 841-850.

Glorian, J., Gallier, S., Catoire, L. (2016). On the role of heterogeneous reactions in aluminum combustion. *Combust and Flame*, 168: 378-392.

Going, J.E., Chatrathi, K., Cashdollar, K.L. (2000). Flammability limit measurements for dusts in 20-L and 1-m^3 vessels. *Journal of Loss Prevention in the Process Industries*, 13: 209-219.

Han, D.H., Sung, H.G. (2019). A numerical study on heterogeneous aluminum dust combustion including particle surface and gas-phase reaction. *Journal of Loss Prevention in the Process Industries*, 206: 112-122.

Huang, C.Y., Chen, X.F., Yuan, B.H., Zhang, H.M., Dai, H.M., He, S., Zhang, Y., Niu, Y., Shen, S.F. (2019). Suppression of wood dust explosion by ultrafine magnesium hydroxide. *Journal of Hazardous Material*, 378(120723).

Jiang, H.P., Bi, M.S., Gao, W. (2020). Suppression mechanism of Al dust explosion by melamine polyphosphate and melamine cyanurate. *Journal of Hazardous Material*, 358(121684).

Julien, P., Soo, M., Goroshin, G., Frost, D.L., Bergthorson, J.M. (2014). Combustion of aluminum suspensions in hydrocarbon flame products. *Journal of Propulsion and Power*, 30(4): 1047-1054.

Julien, P., Vickery J., Whiteley. S. (2015). Freely-propagating flames in aluminum dust clouds. *Combust and Flame*, 162: 4241-4253.

Krazter, P., Brenig, W., (1991). Highly excited molecules from Eley-Rideal reactions. *Surface Science*, 254: 275-280.

Li, W.Q., Liu, J.Z. (1993). Automatic thresholding using the Otsu algorithm based on the 2D gray image. *Acta Automatica Sinica*, 19: 101-105.

Myers, T.J. (2013). Reducing aluminum dust explosion hazards: case study of dust inerting in an aluminum buffing operation. *Journal of Hazardous Material*, 159: 72-80.

Nifuku, M., Koyanaka, S., Ohya, H., Barre, C., Hatori, M. (2007). Ignitability characteristics of aluminum and magnesium dusts that are generated during the shredding of post-consumer wastes. *Journal of Loss Prevention in the Process Industries*, 20: 322-329.

Natan, B., Rahimi, S. (2001). Status of gel propellants in year 2000. International Journal of Energetic Materials and Chemical Propulsion, 5: 172-194.

Pang, L., Zhao, Y., Yang, K., Zhai, H., Lv, P.F., Sun, S.H. (2019). Law of variation for low density polyethylene dust explosion with different inert gases. *Journal of Loss Prevention in the Process Industries*, 58: 42-50.

Sormojai, G.A. (1994). *Introduction to Surface Chemistry and Catalysis*. Hoboken: John Wiley and Sons.

Sun, Z.X., Zhang, Y., Zhao, X., Wang, Y., He, D.Q. (2004). A nitrogen circulation ultra-high molecular weight polyethylene steam tube rotary drying method. Chinese patent, CN1515393. 2004.07.28.

Sundaram, D.S., Puri, P., Yang,V. (2016). A general theory of ignition and combustion of nano- and micron-sized aluminum particles. *Combust and Flame,* 169: 94-109.

Taveau, J., Hochgreb, S., Lemkowitz, S., Roekaerts, D. (2018). Explosion hazards of aluminum finishing operations. *Journal of Loss Prevention in the Process Industries*, 51: 84-93.

Yan, W.G. (2016). *Investigation of flame spread behaviors of PU insulation materials coupled with building exterior wall geometry*. University of Science and Technology of China. Dissertation.

Zhang, F. (2006). Detonation in reactive solid particle-gas flow. 2006. *Journal of Propulsion and Power*, 22(6): 1289-1309.

DOI: 10.7795/810.20200724

Homogeneity of methane-air mixture in devices for the determination of explosion limits

Eliška Fišerová [a], Jan Karl [a]

[a] Technical Institute of Fire Protection in Prague, Fire Rescue Service of the Czech Republic

E-mail: *eliska.fiserova@tupo.izscr.cz, jan.karl@tupo.izscr.cz*

Abstract

The explosion characteristics of flammable gases are dependent on many factors. These factors include, for example, pressure, temperature and initiation energy – all of which can be variable. Their variability depends on the explosion characteristics and the initial conditions. The input parameters must be guaranteed during these tests; if they are not, then the correctness of the measured values cannot be relied upon. One of the parameters influencing the results is the homogeneity of the test mixture. To avoid affecting results, it is necessary to ensure a homogeneous mixture throughout the test apparatus.

This contribution describes two approaches to homogenisation of a mixture of flammable gas and air in the determination of explosion concentration limits. In the design of the device, the homogenisation of the mixture was solved by means of a nozzle, which should create sufficient gas flow against the wall of the vessel and through which the mixture should be homogenised. As 100% homogenisation of the mixture was not achieved, a second procedure was proposed consisting of creating an external forced circulation of the mixture, making the mixture blended.

This work describes the determination of methane concentration in air at the test facility by GC MS. The result is stratification and homogenisation of the methane-air mixture under the conditions of the above homogenisation procedures, followed by a description of the reliability and the effect on the determination of the explosion concentration limits.

Keywords: *autoclave, nozzle, homogeneous compound, mixing the compound*

1. Introduction

For the determination of the explosion limits under non-atmospheric conditions, a test device was developed which meets the requirements of the applicable EN 1839 standard: “Determination of explosion limits and the limiting oxygen concentration (LOC) for flammable gases and vapours”. This standard is currently undergoing revision, and a new edition is being prepared which extends the possibilities of determination even under variable initial conditions.

For correct results, it is very important that the test mixture is homogeneous at all points. This study will examine the mixing of the gaseous mixture by means of the flow generated by the gas outlet from a specially treated nozzle. The nozzle is installed in the autoclave so that the outlet is directed to the walls of the autoclave, thereby providing sufficient flow to ensure homogenisation of the mixture.

In inter-laboratory comparative tests, we found that our results differ in the measured values of lower explosion limits (LEL) and upper explosion limits (UEL) of methane. One reason could be the preparation of the test mixture itself. Unlike us, other test laboratories use equipment with integrated mixing. It is therefore a considerable difference in the design of the device itself.

DOI: 10.7795/810.20200724

The error in the preparation of the homogeneous mixture was confirmed by preliminary determination of the methane concentration after the mixture was filled into the vessel. For the purpose of this test, we used a methane concentration detector with an automatic pump.

We were able to preliminarily confirm inhomogeneity of the prepared mixture. Subsequently, it was necessary to determine the methane concentration in detail at various locations in the test facility and to assess these values. The inhomogeneity of the mixture was evaluated based on measurement results of the methane concentration using the GC-FID method.

1.1. Description of the test vessel

The test device (fig. 1) with an internal volume of 10 litres is designed as a spherical thick-walled pressure vessel. The inner diameter of this container is 270 mm and the wall thickness is at least 25 mm. It is forged with a thick circular lid attached to the body flange using six studs. This flange connection is sealed by a graphite seal which operates on the principle of self-sealing by internal pressure on the inner lid. The filling of the test pressure vessel is ensured manually, using a control panel (fig. 2).

As can be seen in fig. 3, various measuring and locking elements are also present in the test device. These include a rupture disc, pressure sensors, temperature sensors and a gas supply. We will deal with the gas supply in this study. A specially adapted nozzle should reverse the direction of gas flow into the autoclave against the vessel wall, thereby putting the gases inside the vessel into motion, and this should homogenise the mixture.

***Fig. 1.** Explosion vessel (volume 10 l)*

***Fig. 2.** Control panel of a pressurized gases filling system (TIFP FRS CR)*

DOI: 10.7795/810.20200724

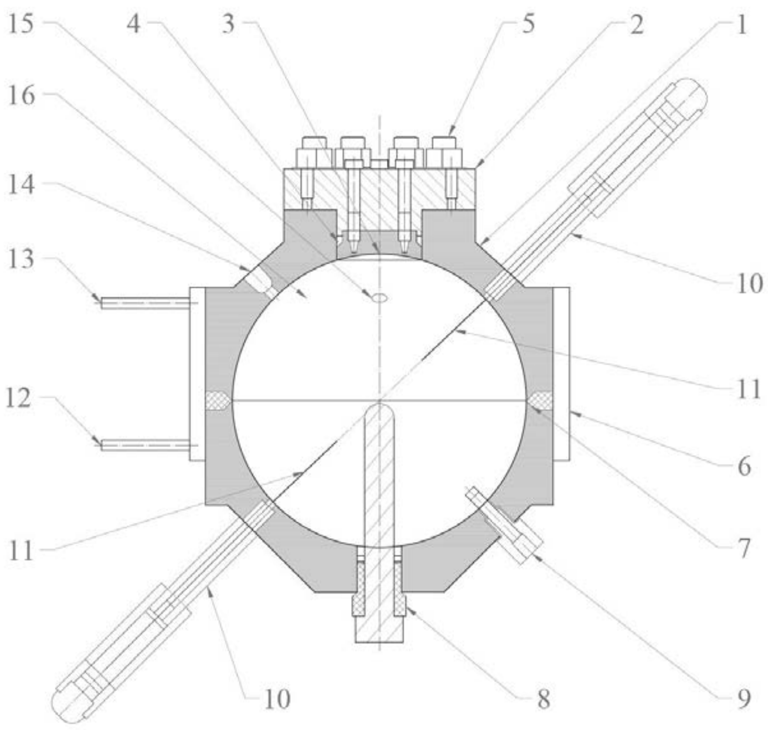

1 – 10 liter reaction vessel
2 – reaction vessel lid
3 – inner lid
4 – graphite seal
5 – screw
6 – duplicator/double shell
7 – weld
8 – electrical initiation electrode
9 – special nozzle
10 – thermowell
11 – thermocouple
12 – inlet throat of the heating medium supply
13 – outlet of the heating medium outlet
14 – rupture disc
15 – fitting for HPLC pump connection
16 – explosion pressure sensor

***Fig. 3.** Longitudinal section view of the test autoclave*

1.2. Description of special nozzle

In the production of the test vessel, a special nozzle (fig. 4) was also designed, which should help to perfect gas mixing. The nozzle is made of stainless steel as is the rest of the test vessel. It is fixed to the vessel by means of NPT thread to ensure tightness and strength in the joint. The nozzle has three 2.9 mm diameter circular orifices evenly spaced in one plane at the end of nozzle. A schematic of the nozzle, including the layout of the orifices, is shown in fig. 4.

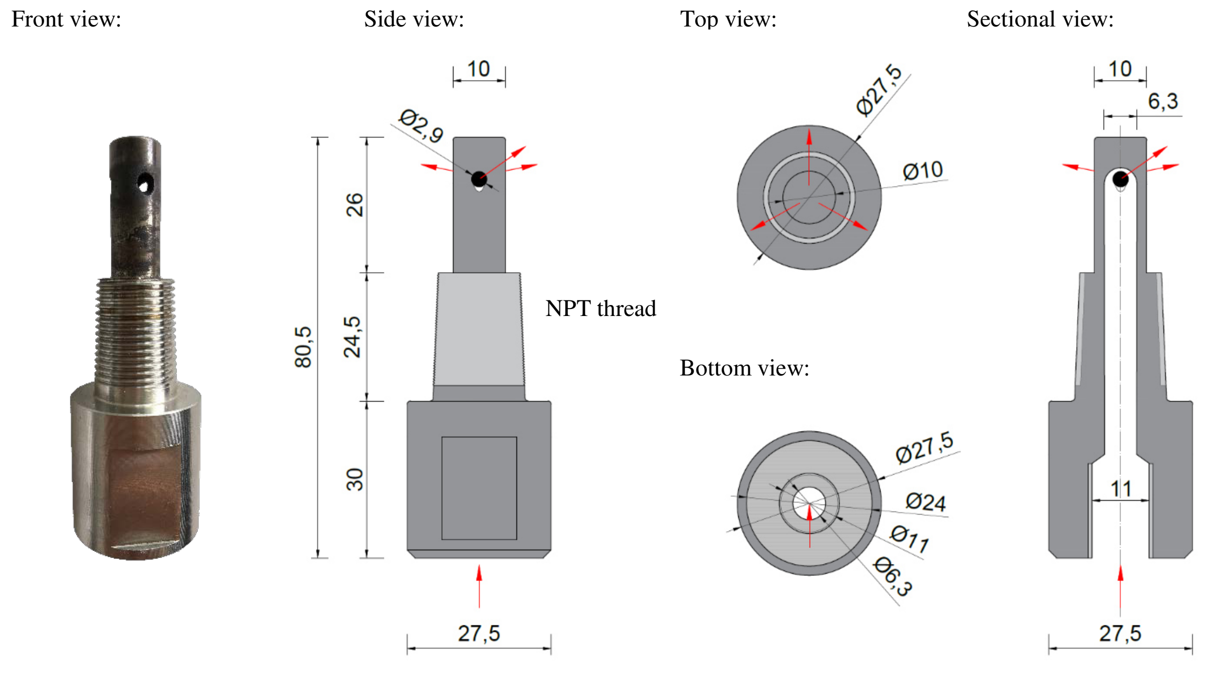

***Fig. 4.** Special nozzle*

2. Experiments

2.1. *Determination procedure*

We modified the test vessel for research purposes by removing the thermocouples and the rupture discs and replaced them with a septa. In this way, we prepared six sampling points evenly distributed throughout the autoclave (fig. 5).

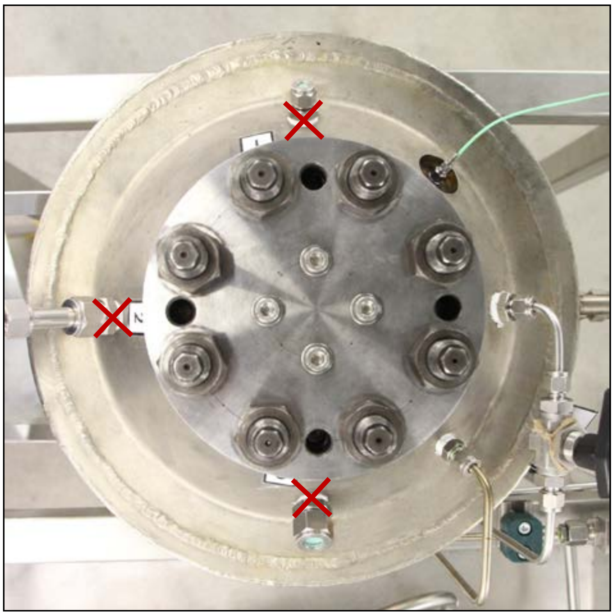

Fig. 5. *Spherical cap of autoclave with marked sampling points*

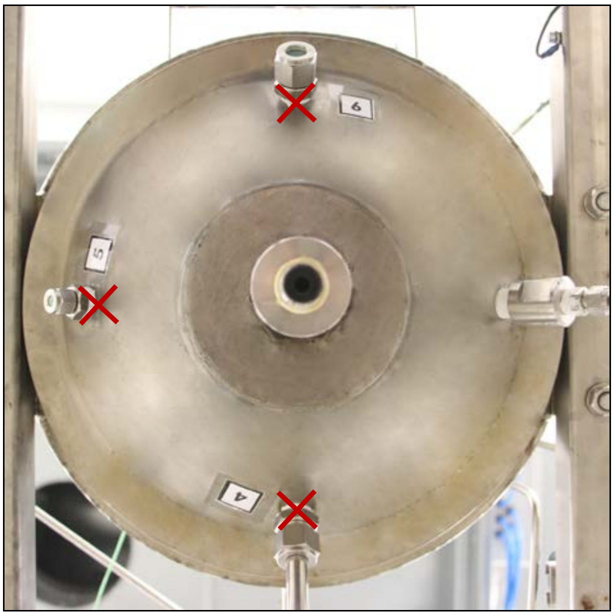

Fig. 6. *Bottom of autoclave with marked sampling points*

Prior to each test, the test vessel was filled with gases to produce the desired methane-gas mixture. This process was carried out as in standardised tests. The vessel was evacuated several times and subsequently filled with the combustible component (methane) to the required partial pressure to determine the concentration. The vessel was then filled with air to atmospheric pressure. Our aim was to consistently fill the vessel in the same manner. The task was therefore to create a similar flow and thus the same process of mixing the mixture. After filling the vessel, the mixture was allowed to stabilise for 5 minutes.

To determine the concentration of methane in the mixture, we sampled with a gas-tight syringe (50 µl volume, 200 mm needle). Such a long needle allowed us to take a sample at different depths of the vessel. We were at the center of the vessel when sampling at maximum depth. Samples were taken at depths of 5, 25, 105, 150 mm from the vessel wall. Methane concentration was monitored in the areas shown in the fig. 7.

The samples were analysed by gas chromatography with flame ionisation detector GC-FID. A TraceGC gas chromatograph was used for the analysis using a 3 mm wide liner and a Rtx-DHA-50 GC column of 50 m x 0.20 mm x 0.5 µm. The carrier gas was helium at a constant flow rate of 1 ml/min. The 25 µl sample was injected manually. Dilution was achieved using a split/splitless inlet with a split ratio of 50:1. The temperature program was set at 35 °C for 3.5 min and then a temperature increase in speed of 40 °C/min up to 120 °C. After reaching the target temperature, the analysis was terminated. The total analysis time was approximately 6 min. Evaluation of measured data was performed in Xcalibur software.

The aim of this work was to determine the stratification of the non-homogeneous mixture. Therefore, for the assessment of the measured values, it was important to determine the deviation of the individual areas from the concentration value of the filled mixture to assess the inhomogeneity in the test vessel.

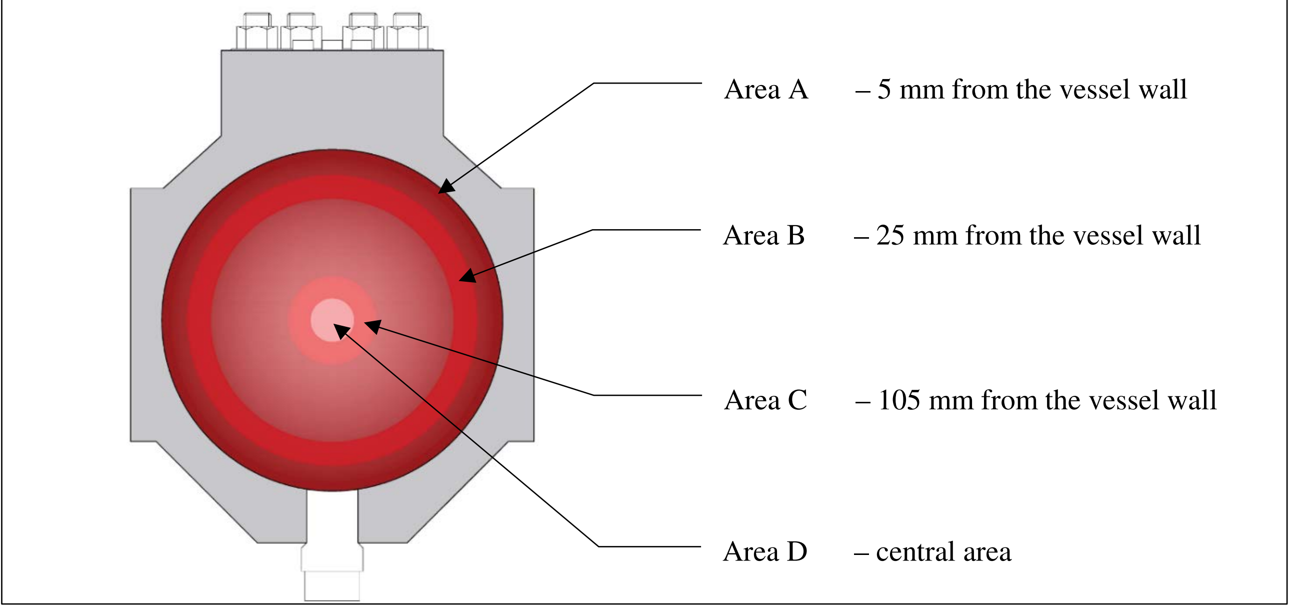

Fig. 7. *Areas for monitoring methane concentration in the test vessel*

2.2. *Mixing the filled mixture*

The mixing of the gases in the test vessel should be ensured by a special nozzle. As a result, the vessel is not designed to provide an additional design internal mixing system. In order to ensure the mixing of the gases, it was necessary to select an external circulation with a fan suitable for an explosive atmosphere and resistant to high pressures and temperatures which could be set at the beginning of the tests. The scheme of external mixing is shown in the fig. 8.

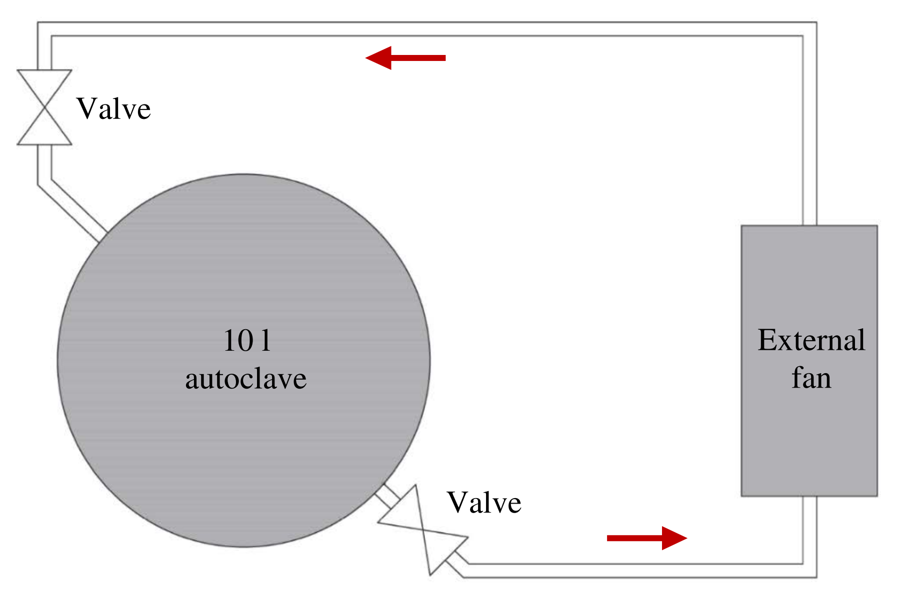

Fig. 8. *Scheme of fan mixing system*

After connecting the designed external mixing system, the tests were repeated as described in section 2.1. There was only one change: after both the flammable component and the air were filled, the mixture was stirred for 10 minutes using an external fan. It was then allowed to equilibrate for 5 minutes as in the nozzle mixing system sampling, and determination of samples was carried out using the same procedure.

3. Results and discussion

A series of tests were performed for the above-described areas to ensure repeatability of the tests. Only average values of deviations from the filled concentration are given in the results tables. A new test mixture of flammable air was prepared for each test. As a total result, the maximum difference between the assay areas was calculated.

The results of the methane-air nozzle mixing system measurement values are shown in tab. 1. Based on the measured results, we confirmed that the filled mixture is not completely homogeneous, since it creates a difference in the concentration of the methane mixture in the test vessel space of 0.36 vol. %. Such an inhomogeneous mixture may create great inaccuracy in determining the explosion concentration limits.

In order to improve the homogeneity of the impregnated mixture, we verified the homogeneity of the fan mixed system, the results of which are shown in tab. 2.

***Table 1:** Results of difference from the filled concentration in the nozzle mixing system*

Areas	**Test 1 vol. %**	**Test 2 vol. %**	**Average**	**Maximum difference**
A (5 mm)	0.16	-0.09	0.03	0.36
B (25 mm)	0.35	0.08	0.21	
C (105 mm)	-0.11	-0.08	-0.09	
D (150 mm)	-0.39	0.09	-0.15	

***Table 2:** Results of difference from the filled concentration in the fan mixing system*

Areas	**Test 1 vol. %**	**Test 2 vol. %**	**Average**	**Maximum difference**
A (5 mm)	-0.13	-0.01	-0.07	0.17
B (25 mm)	0.18	0.02	0.10	
C (105 mm)	-0.03	-0.12	-0.07	
D (150 mm)	-0.02	0.10	0.04	

4. Conclusions

The aim of this work was to verify the homogeneity of the resulting mixture when filling the vessel to determine the explosion concentration limits. In the first part, the filling was carried out by means of a special nozzle, which was designed together with the entire vessel and was intended to ensure mixing by the emerging flow. In the mixing tests, we found stratification of the methane concentration in different areas of the test vessel.

Because of the large maximum difference in deviations from the filled concentration in the nozzle mixing system, it was necessary to improve mixing to create a better homogeneity of the mixture. Therefore, we installed external mixing in the form of a fan suitable for explosive environments and resistant to high pressures and temperatures. This system provides sufficient circulation to improve the homogeneity of the filled mixture.

Based on the measured value of 0.36% vol. Of the maximum deviation from the inflow concentration for the nozzle mixing system, we improved the homogeneity of the mixture by means of an external circulation an mixing system to 0.17% vol.

References

Suchý, O. a kol. (2015). *Výzkumný projekt č. VF20112015020: Výzkum a vývoj progresivních metod stanovení požárně technických charakteristik hořlavých látek a materiálů za specifických technologických podmínek, Dílčí výzkumný úkol č. 2: Výzkum a vývoj metod zkušebního stanovení a výpočetního odhadu DMV, HMV, Pmax, brizance a KGmax hořlavých plynů a par hořlavých kapalin za podtlaku nebo přetlaku ve vzduchu, kyslíku nebo jiném plynném oxidantu,* Závěrečná výzkumná zpráva, Praha.

EN 1839 2017. *Determination of explosion limits and the limiting oxygen concentration (LOC) for flammable gases and vapours.* (European standard).

DOI: 10.7795/810.20200724

Enhanced Friction and Shock Sensitivities of Hexachlorodisilane Hydrolyzed Deposit Mixed with KOH

Thanh-Trung Nguyen[a], Yu-Jhen Lin[a], Zhi-Xuan Lin[a], Hui-Chu Tai[a], Chun-Yi Lee[a], Hsiao-Yun Tsai[a], Jenq-Renn Chen[*,a] & Eugene Y. Ngai[b]

[a] Department of Safety, Health and Environmental Engineering, National Kaohsiung University of Science and Technology, Kaohsiung, Taiwan

[b] Chemically Speaking LLC, Whitehouse Station, New Jersey 08889, United States

[*]E-mail: jrc@nkust.edu.tw

Abstract

In this work, the effect of KOH on friction and shock sensitivity of the hexachlorodisialne hydrolysate was studied. The dried mixtures containing 0.04 and 0.35% by weight were found to be extremely sensitive to impact and friction with a limiting impact energy of 0.125 J and a lowest friction force of 7 N compared to 6 J and 326 N for the sample without KOH treatment, respectively. Differential scanning calorimeter curve showed that a new small exothermic peak was observed between 80 °C and 150 °C which is also accompanied by evolution of hydrogen. It is proposed that, the presence of KOH leads to the formation of –Si–Si–OH and –Si–Si–OK groups containing unstable Si–Si bonds which are readily cleaved by mechanical friction or impact. This work provides valuable information for risk management as well as the future work regarding disposing the explosive HCDS hydrolyzed deposit.

Keywords: Hexachlorodisilane, hydrolysis, KOH, shock sensitivity, friction sensitivity

1. Introduction

Hexachlorodisilane (HCDS, Si_2Cl_6) has been widely used as an important precursor for process tools such as chemical vapor deposition (CVD) or atomic layer deposition (ALD) in semiconductor and related industries. However, HCDS has been known to generate shock sensitive deposits with moisture through hydrolysis reactions that form a complex mixture of silicon oxides and hydrogen chloride as postulated (Innocenzi, 2003; Lin et al., 2019). Besides, HCDS is also an abundant constituent in the trichlorosilane direct process residue (TCS DPR) which may form shock sensitive hydrolysis products known as "popping gels" through hydrolysis reaction when exposed to ambient air (Harder and Tselepis, 2005). In 2014, a fatal explosion occurred during the cleaning of a heat exchanger in the high-purity polycrystalline silicon manufacturing facility at the Yokkaichi Plant of Mitsubishi Materials corporation (MMC), Japan, resulting in 5 fatalities and 13 injuries (Mitsubishi Materials Corporation, 2014).

Friction and impact have long been recognized as the significant ignition sources in explosives. According to the investigative report of above-mentioned explosive accident, impact was responsible for the death toll at MMC, Japan (Mitsubishi Materials Corporation, 2014). Besides, friction has been a suspected culprit causing several fatal explosions for decades (Dickson, 2010).

The shock sensitivity of the hydrolysis products from chlorosilanes is due to the oxidation of the reactive Si–Si bonds in the materials (Hengge, 1974). A possible mechanism of this phenomenon has been proposed recently by Lin et al. (2019) as the Si–Si bond in HCDS hydrolyzed deposits can be cleaved by shock resulting in intramolecular oxidation of the neighboring silanol groups to form Si–O–Si structure with concurrent hydrogen gas revolution. Therefore, the cleavage of Si–Si bond has been the major steps in abating the polysilanes and their shock-sensitive hydrolysis products.

A few works were done lately to investigate the shock and thermal sensitivities of this explosive deposit resulting in the above-mentioned pitiful accident. Additionally, efforts have been made to safely handle and dispose the polychlorosilanes and their hydrolysis products.

Zhou et al. (2018) determined the shock and thermal sensitivities of hydrolyzed HCDS deposit (denoted as hy-HCDS) produced by both methods of adding liquid HCDS to de-ionized water and hydrolyzing HCDS on molecular sieve pellets. The dried white powder synthesized by the adding HCDS to water was found to be sensitive to heat but non-shock sensitive; in contrast, the pellets coated with the hydrolyzed solids had a high shock sensitivity igniting by quickly squeezing a tongue-and-groove pliers.

Following this in 2019, Lin et al. (2019) studied meticulously in characterization and investigation the shock sensitivity of the hydrolysis products produced by hydrolyzing liquid HCDS in the ambient conditions and vapor HCDS in a strictly moisture-controlled environment. The authors found that the liquid- and vapor-hydrolyzed deposits have a lowest recorded limiting impact energy (LIE) of 6 J and 5 J, respectively. Thermal treatment at 200 °C and above was found to be effective to remove the shock-sensitivity of HCDS hydrolyzed deposits. It is, however generally inapplicable for the pumping system. Moreover, the shock sensitivity and flammability of these deposits can be temporarily suppressed in the presence of excessive water.

In 2020, Colomb et al. (2020) investigated the sensitivity of the hydrolysis products deriving from the industrial by-products containing mainly HCDS. These highly viscous byproducts harvested within the reactor and exhausting piping of the Siemens process were added into water to yield a hydrolyzed polymer. This dried hydrolyzed polymer was found to be insensitive to impact and friction even up to 31 J of impact energy and 360 N of friction load. These results are in disagreement with those of the previous study conducted by Lin et al. (2019) and Nguyen et al. (2020). The reason for the above inconsistency in shock sensitivity may be due to the different hydrolysis conditions and the drying process. On the basis of their experimental results, the authors recommended using only water to fully hydrolyzed the viscous byproducts.

Recently, Nguyen et al. (2020) has reproduced, characterized and successfully disposed the gel-like polychlorosilane substance generated in the exhaust of ALD tool using HCDS as the precursor and its hydrolysis products. The hydrolysis products considered as moderate shock-sensitive were formed by exposing the highly viscous gel to ambient conditions. Heating the deposit to 220 °C may remove the shock sensitivity of the hydrolyzed deposit. Alcohol-based solutions were found to be effective to abate both gel and its hydrolyzed deposit because of the gentle reactions accompanied with the formation of H_2 gas and non-flammable products such as potassium silicate and silica. The aqueous solution of KOH, reacts vigorously with these substances leading to the formation of pyrophoric silane (SiH_4) resulting in an almost spontaneous explosion.

More recently, Lin et al. (2020) reported that alkaline solutions were effective to abate the HCDS vapor because the Si-Si bonds tend to be broken up during the hydrolysis reaction in an alkaline environment, the final products of the abatement were nonflammable including predominantly potassium silicate and silica gel. On the contrary, alkaline solutions were found to be ineffective even enhanced the shock sensitivity of HCDS hydrolyzed deposit which ignites at less than 5 J of impact energy after alkaline treatment. It should be noted that there was neither visual chemical reaction to the naked eye when vapor HCDS hydrolyzed deposits contacts with aqueous solution of KOH nor notable difference between the IR spectra of the deposit with and without alkaline treatment.

It is clear from the above literature that the reaction between aqueous KOH solution and different hydrolysis products of polychlorosilanes, especially HCDS hydrolysate remains highly ambiguous and there has been no any extensive work with regard to determining the sensitivity of this such explosive deposit after alkaline treatment and as well as elucidating the mechanism of this phenomenon. More importantly, it is imperative to find measures to remove/dispose this such deposit safely.

Tests were conducted in this study with the goal of determining the sensitivity of HCDS hydrolyzed deposits to friction and impact before and after KOH treatment, further characterizing their thermal decomposition behavior, and finally proposing the mechanism leading to the extremely sensitive phenomena. By doing so, the results presented in this work will provide valuable safety data for risk management and future research in disposal of this explosive solid. These are our primary objectives in this work.

2. Experiments

2.1 Materials

Semiconductor grade HCDS was supplied by Air Liquid Advanced Materials, USA, with a purity of 99.5% by gas chromatography. Potassium hydroxide (KOH) pellets were obtained from Nihon Shiyaku, Japan, with assay of 85%, a maximum of 1.5% potassium carbonate (K_2CO_3), and the remaining being water. Ultrapure nitrogen gas with a purity of 99.999% was used for sample preparation and analysis.

2.2 Hydrolysis Process of HCDS

Hydrolysis products of HCDS can be prepared by the four following methods:

- HCDS vapor hydrolyzing with water vapor (moisture)
- HCDS liquid hydrolyzing with liquid water
- HCDS liquid hydrolyzing with water vapor (moisture)
- HCDS vapor hydrolyzing with liquid water.

In this work, we focused on vapor HCDS hydrolyzed in a moist air to simulate the HCDS hydrolysis in semiconductor manufacturing process.

Test was carried out for water/HCDS molar ratio of 1 to 6 which is the stoichiometric ratio of HCDS that theoretically will react all Si–Cl bonds with water into silanol (Si–OH). The silanol condensation reaction due to the unstable silanol subsequently occurs leading to the formation of linear or cyclic siloxanes.

Fig. 1 shows a schematic diagram of the experimental setup and conditions for producing HCDS hydrolyzed deposit. The hydrolysis process was strictly control by a group of mass flow controllers (MFC) to ensure a reproducible result. Precise control of HCDS to water molar ratio was achieved by controlling the nitrogen flow rate, liquid HCDS flow rate, and moisture concentration. The flowrate of liquid HCDS was controlled accurately by using a Horiba STEC liquid MFC (MFC2), model number LV-F20PO and vaporized in a Venturi tube by a nitrogen stream with a fixed flow rate of 2 slm controlled by MFC1. The moisture source was provided by bubbling N_2 gas with a flow rate of 1.66 slm controlled by MFC4 through a water box which was placed in a recirculating cooling system to keep water temperature constant at about 24.75 °C. The moist N_2 stream was then mixed well with 1.93 slm dry N_2 delivered by MFC3 at a buffer chamber where the humidity was monitored throughout the experiment. The N_2/HCDS stream is flowed downward concurrently with the moisture-controlled N_2 stream in a vertical tube used as reactor with an internal diameter of 21.7 mm and 1 m long. The clear, transparent deposit formed on tube wall was collected to vial by gently knocking the tube. The reaction was run continuously for a period of 5 hours to produce 13.5 g of deposit with a yield of 45%.

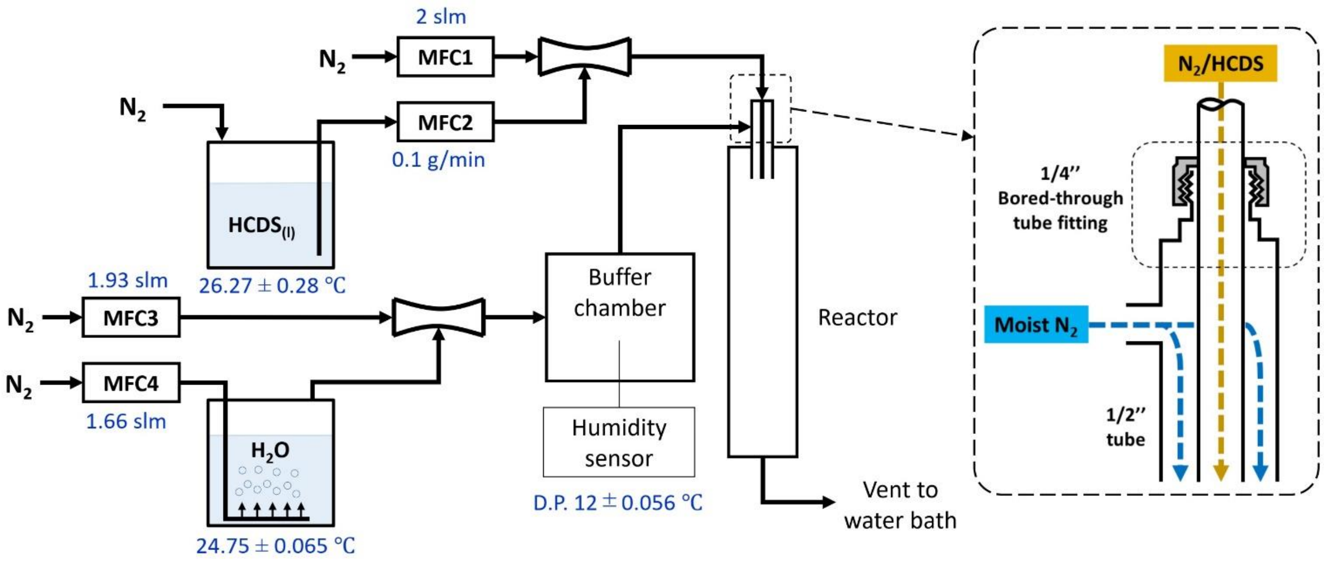

Fig. 1. Sketch of the apparatus used to produce vapor HCDS hydrolyzed deposit

2.3 Sample Preparation

The HCDS hydrolyzed deposit was gently crushed and hand sieved in glovebox under control environment to obtain different particle sizes including <0.0074 mm, 0.0074–0.177 mm, 0.177–0.297 mm, 0.297–0.420 mm and 0.420–0.500 mm to investigate the effects of particle size on the hydrogen evolution of KOH treated deposits during pyrolysis. The particle size less than 0.5 mm was used to prepare the samples for the shock and friction sensitivity testing (United Nations, 2015). The sample of KOH treated deposit with the wide range of KOH content (from 0.02 to 25% by weight) was prepared by mixing the aqueous solution of KOH with the sieved HCDS hydrolyzed deposit to create a slurry which was then nitrogen-dried in glovebox. The drying process generally took 2 to 4 hours. The water evaporation induced a packing behavior of the particle cluster; therefore, the dried samples were carefully loosened up again before performing further tests including impact and friction sensitivity testing and thermal analyses. The residual KOH-treated deposits were stored in a 5 mL sealed with nitrogen and kept in ambient temperature for further testing. Care must be taken for every single step in the sample preparation process, especially the crushing and loosening the KOH treated samples because of their extreme sensitivity that may ignite with a scratch by hand.

2.4 Determination of Impact and Friction Sensitivity

Both BAM Fall-hammer impact test and BAM friction test apparatuses from Reichel & Partner GmbH, Germany, which comply with the UN Recommendations on the Transport of Dangerous Goods (United Nations, 2015) were employed to determine the impact and friction sensitivities of the samples. In the impact sensitivity test, a sample mass of 17.5 mg was used in the testing. Limiting impact energy (LIE) is determined from the mass of the drop weight and the height giving an energy of 0.125 to 100 J. In the case of friction sensitivity test, the quantity to be tested, about 10 mm^3, was taken by means of a cylindrical measure (2.3 mm diameter and 2.4 mm depth). The lowest friction force (LFF) is determined by using different weights in different notches resulting in loads on the porcelain pin from 7 to 360 N. It should be emphasized that any substance having a LIE and/or LFF of ≤2 J and/or <80 N, respectively, is considered too dangerous for transport in the form in which it was tested, in this work, powder to be exact (United Nations, 2015).

2.5 *Thermal and Gas Evolution Analyses*

Differential scanning calorimetry (DSC) were performed using Mettler Toledo HP DSC H+, about 7 mg of the sample in an aluminium crucible was heated from 50 to 500 °C with a heating rate of 10 °C. DSC instrument was equipped with a H_2 gas detector and a humidity meter for evolved gas analysis. Nitrogen was used as purge gas with a flow rate of 20.46 mL/min controlled accurately by using MFC.

2.6 *Structural Characterization*

The chemical functional groups of the samples were determined by a Smiths IdentifyIR Attenuated Total Reflection (ATR) Fourier transform infrared spectrometer with a scan range of 650–4000 cm^{-1}. The spectrometer was placed directly inside a glovebox for the sample preparation and analysis under controlled environment due to the reaction of KOH and CO_2 in ambient environment.

3. Results and Discussion

3.1 *Impact and Friction Sensitivity of Original HCDS Hydrolyzed Deposit*

The LIE for prepared hydrolyzed deposit with water/HCDS molar ratio of 6 was determined to be 6 J. Fig. 2 shows impact sensitivity result of pure HCDS hydrolyzed deposit that 6 J of impact energy resulted in an ignition of the deposit and the combustion quickly propagated throughout the powder cloud resulting in a fire ball. This observation is consistent with that in the previous study conducted by Lin et al. (2019).

In the case of fiction testing, LFF of prepared hydrolyzed deposit was determined to be 324 N. In contrast to impact testing, the deposit was ignited accompanied by jetting and quenched quickly in all cases, as shown in Fig. 2b.

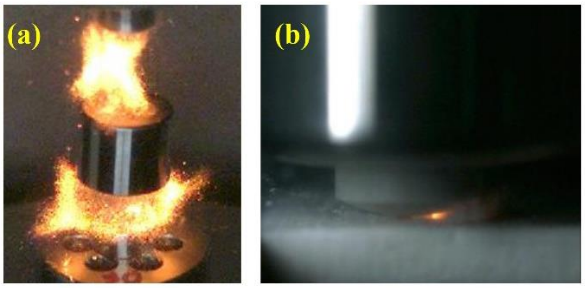

Fig. 2. *Typical ignition of HCDS hydrolyzed deposits with (a) 6 J of impact energy and (b) 324 N of friction force*

3.2 *The Effect of KOH on HCDS Hydrolyzed Deposit*

3.2.1 *Sensitivity of the Deposit*

The results of the impact and friction tests for HCDS hydrolyzed deposit before and after KOH treatment were tabulated and summarized in Table 1 and Fig. 3. It was found that both impact and friction sensitivities increased with an increase in the KOH content in the HCDS hydrolyzed deposit. Fig. 3a shows that the LIE decreases from 6 J of the original deposit to 2 J for the deposit with 0.02 wt% KOH which is considered as very sensitive to impact according to UN recommendation. Furthermore, LIE dropped to less than 0.125 J, the lowest possible impact energy for the fall–hammer apparatus, for deposit containing 0.04 wt% KOH and above considered extremely sensitive.

The friction test offers better resolution for the extremely sensitive deposits and is thus replace the fall-hammer test. The LFF decreases from 326 N of the original deposit to 80 N and less than 7 N, the lowest possible friction energy for the friction apparatus, for deposit with 0.15 and 0.35 wt% KOH and above, respectively as shown in Fig. 3b. It is important to emphasize that the LFF of less than 80 N is considered too sensitive to friction.

Table 1: *Results of LIE and LFF of HCDS hydrolyzed deposit with and without KOH treatment*

KOH content (wt%)	LIE (J)	Ignition behavior
Pure Hy-HCDS	6	Fire ball
0.02	3, 2	Fire ball
0.04	0.2, <0.125	Fire ball
0.06–1	<0.125	Fire ball
KOH content (wt%)	LFF (N)	Ignition behavior
Pure Hy-HCDS	324	Spark and weak jetting
0.02	216	Spark and jetting
0.04	168	Spark and jetting
0.05	160	Spark and jetting
0.06	120	Spark and jetting
0.08	108	Spark and jetting
0.1	80, 96	Strong spark (explosion in some cases)
0.12	80	Strong spark (explosion in some cases)
0.15	80	Explosion (fire ball)
0.2	54	Explosion (fire ball)
0.2	54	Explosion (fire ball)
0.25	18	Explosion (fire ball)
0.3	8	Explosion (fire ball)
0.35–5.07	<7	Explosion (fire ball)
15.05–25.12	<7	Spark and strong jetting

DOI: 10.7795/810.20200724

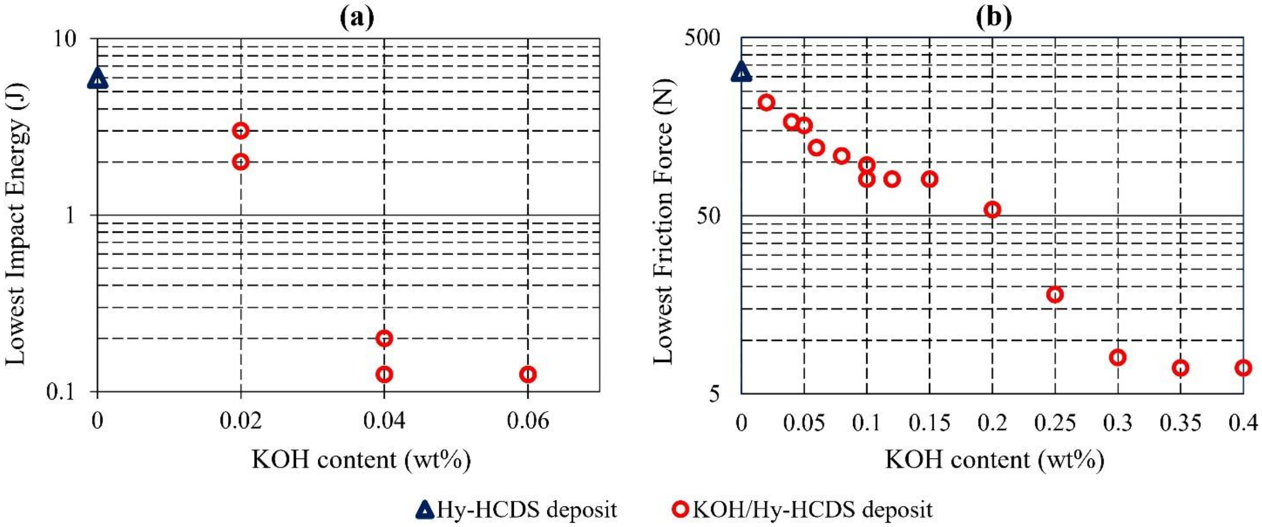

Fig. 3. *(a) Impact and (b) friction sensitivities of HCDS hydrolyzed deposit before and after KOH treatment with different KOH content*

The explosion behavior in the friction tests was found to be vastly different with the increasing KOH content in the deposit. Particularly, in the same manner of pure HCDS hydrolyzed deposit, the KOH treated sample with 0.02–0.12 wt% KOH was initiated but not able to develop a fire ball, as shown in Fig. 4a. For the deposit containing 0.15 wt% KOH, the explosion with fire ball was first observed (Fig. 4b) and big fire balls were observed for the samples containing 0.25 wt% KOH (Fig. 4c). Fig. 4d shows the ignition behavior of the deposit with very high KOH content of 15 wt% KOH and higher, the sample was initiated accompanied by a strong jetting but no fire ball was developed in all cases even at higher friction force of 216 N. Care must be taken during friction testing for KOH treated deposits due to premature initiation which usually took place when the porcelain pin rests on the sample.

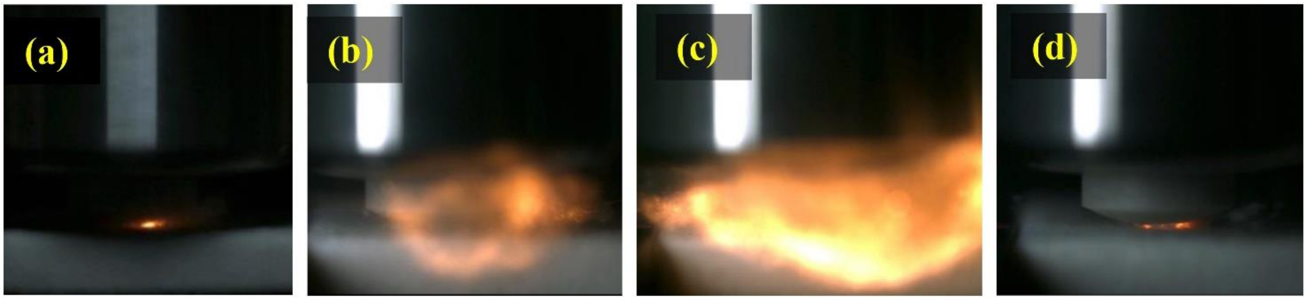

Fig. 4. *Typical ignition in fiction testing of KOH treated deposits (a) 0.04 wt% KOH with 252 N, (b) 0.15 wt%, 80 N, (c) 0.25 wt% KOH, 18 N and (d) 15 wt% KOH, 216 N*

4.2.2 Structure Characterization of the Deposit

The structure of hydrolysis products has been well studied in the previous research that is a complex silicon oxide (SiO_x) containing a large amount of Si–Si bonds (Lin et al., 2019). The absorption band at 1000 cm^{-1} corresponds to $SiO_{1.11}$ (Tolstoy et al., 2003). In particular, the 1000 cm^{-1} band is attributed to the asymmetric stretching mode of the Si–O–Si structure arising from the condensation of two silanol groups (Belot et al., 1991). The 875 cm^{-1} band was assigned by Ritter (1962) and Belot et al. (1991) as the Si_2O_3 phase. There have been some researchers used this band (875 cm^{-1}) as indicative of the Si–Si bond in the structure of HCDS hydrolyzed deposits (Lin et al., 2019; Lin et al., 2020; Nguyen et al., 2020). A weak band at 725 cm^{-1} can be assigned to Si–O–Si bending vibration (Ahsan and Mortuza, 2005).

For the KOH treated sample, the maximum of the overall asymmetric stretching mode of Si–O–Si bonds shifts to lower wavenumbers with the increasing KOH content in the deposit due to the formation of potassium silicate, which was observed clearly in Fig. 5 for the sample containing high KOH concentration of 15 wt%. The formation of potassium silicate during the drying was due to the etching process (Palik et al., 1982) and followed by the dissolution of silica in high pH solution (Iler, 1979), in which OH^- and H_2O react with the Si atoms on the surface of the deposit to form a thin layer of silicate. This potassium silicate layer covering the surface of the deposits may be responsible for the ignition phenomenon for the deposit contains 15 wt% KOH, as shown in Fig. 4d, in which the ignition is not able to propagate and develop into a fire ball. Potassium carbonate inherently being an impurity of KOH is attributable to the peak at 1400 cm^{-1} and contributes to 880 cm^{-1} band which can be observed clearly in the spectrum of the sample with 15 wt% KOH (Cerfontain and Moulijn, 1986).

Camon and Moktadir (1997) suggested that the strength of Si–Si bond decreases with an increase in the number of OH groups attached to these two Si atoms leading to the higher probability of breaking it. However, the intensity of the vibrational region from 3000 to 4000 cm^{-1} attributed to silanol groups (Smith et al., 1991) did not change markedly for the hydrolyzed deposit before and after 1 wt% KOH treatment leading to the LFF of less than 7 N, as shown in Fig. 5. Therefore, this mechanism seems to be inappropriate to explain the formation of extremely sensitive deposits.

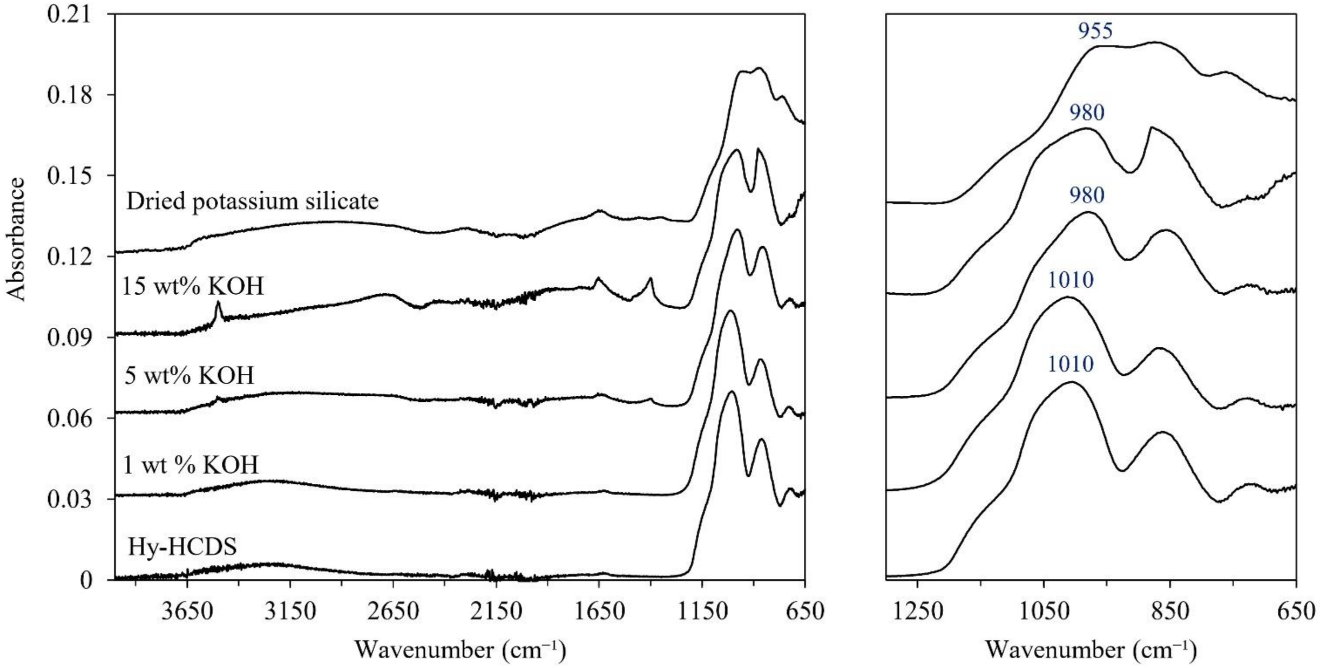

Fig. 5. *FTIR spectra for original and KOH treated hydrolyzed deposits*

3.2.3 Slow Decomposition at Ambient Temperature

At ambient temperature, a slow, continuous decomposition process occurred in the sample of KOH-treated HCDS hydrolyzed deposit. After 15-day storage, up to 360 ppm of H_2 gas was detected from the opening of a 5 mL vial storing around 50 mg of dried 15 wt% KOH-treated deposit, indicating that the Si-Si bond was slowly cleaved during the storage time. The corresponding mechanism was proposed as follows(Belot et al., 1992)

$$\mathrm{Si-Si+H_2O \rightarrow Si-OH+Si-H} \tag{1}$$

$$\mathrm{Si-H+H_2O \rightarrow Si-OH+H_2} \tag{2}$$

DOI: 10.7795/810.20200724

$$\mathrm{Si-OH+HO-Si \rightarrow Si-O-Si+H_2O} \tag{3}$$

Fig. 6 compares the IR spectra of 4 wt% KOH-treated deposit as soon as the sample was dried in glovebox and after 2 months. After 2 months, the sample was caked, the band at 3250 cm^{-1} attributed to silanol was diminished significantly due to the silanol condensation with a strong gain of the band at 1650 cm^{-1} assigned to bending vibration mode of water. These observations imply that the polymerization may occurred during the storage time as equation (3). The peaks at 980 cm^{-1} and 725 cm^{-1} of asymmetric stretching and bending Si–O–Si groups shift to 1002 cm^{-1} and 770 cm^{-1}, **indicating** the oxidation of the silicon oxide cluster (Lin et al., 2019). The cleavage of Si–Si bonding can be seen clearly through the decrease in the band at 860 cm^{-1} being Si-Si bond indicator (Nguyen et al., 2020). Besides, the band at 1400 cm^{-1} is attributable to potassium carbonate as mentioned in the section 3.2. It should be noted that although significant oxidation of Si–Si bond was experimentally observed after 2 months thought the IR result and H_2 gas evolution, the KOH-treated deposit was still very sensitive to thermal and exploded inside the vial by very gentle shaking.

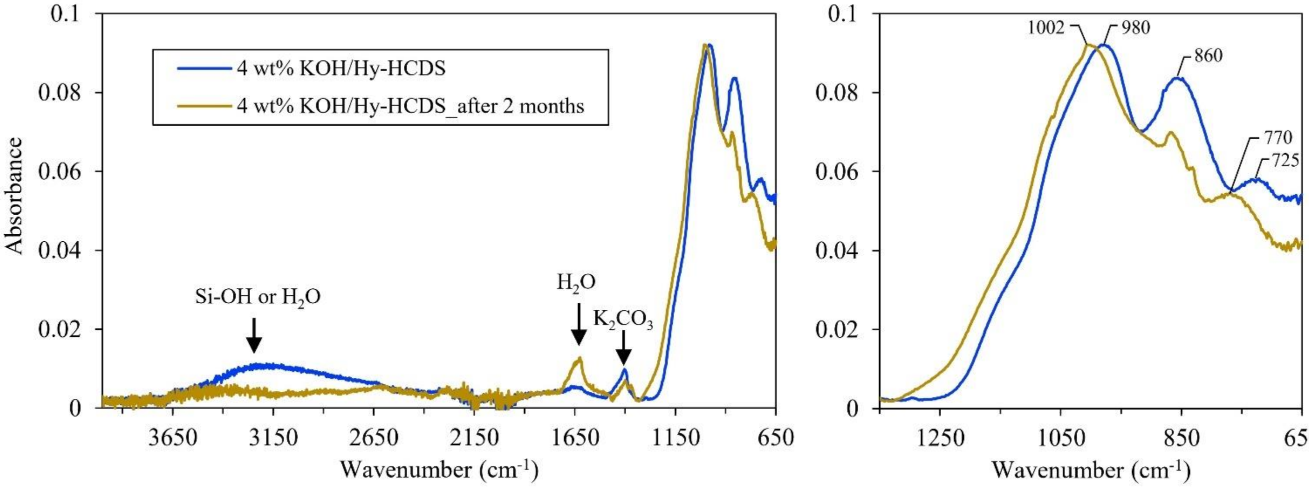

Fig. 6. *IR results of fresh and 2-month 4 wt% KOH-treated HCDS hydrolyzed deposit*

3.2.4 DSC with Gas Evolution Analysis

To further elucidate the mechanism of enhanced friction sensitivity of KOH treated HCDS hydrolyzed deposit, DSC with gas evolution analysis was performed. For the original HCDS hydrolyzed deposit, there is an endothermic reaction taking place at 135 °C, which is attributed to the evaporation of water arising from the water absorption and silanol condensation reaction. For the KOH treated sample, however, a small exothermic peak was observed between 80 °C and 150 °C (Fig. 7) accompanied by evolution of hydrogen. It was found that the hydrogen generation always accompanies by the generation of water. Therefore, the water arising from silanol condensation or absorption before the pyrolysis plays a crucial role in the cleavage of the weakened Si–Si bonds with the evolution of H_2 and the formation of the networked Si–O–Si (Belot et al., 1992).

DOI: 10.7795/810.20200724

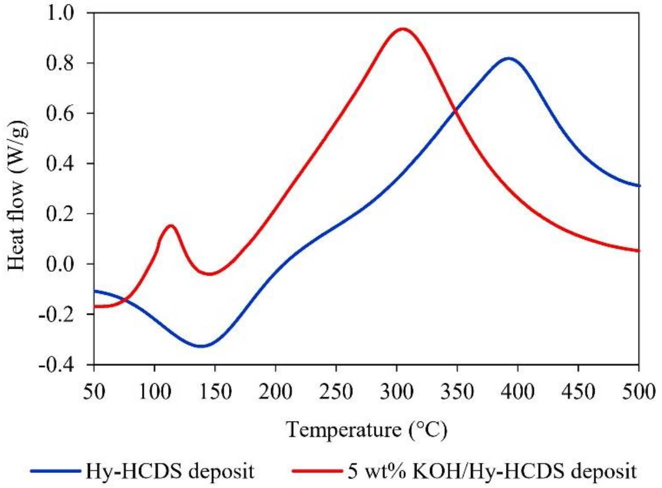

***Fig. 7.** DSC curves of HCDS hydrolyzed deposit before and after KOH treatment*

Fig. 8 shows that the amount of H_2 evolved in the temperature range of 50–150 °C was found to be proportional to the KOH content of 0.5 to 11.5 wt% in the deposit. In contrast, for high KOH content exceeding 11.5 wt%, the H_2 generation tends to slightly decrease and seems to stay constant at around 0.02 mL/mg, which is probably due to the silicate layer. According to Palik et al. (1982), the etch-stop phenomenon can be attributable to the formation of a passivation film, which is a very thin oxide or silicate layer avoiding the reaction of H_2O/OH^- and Si atoms on the surface of the deposit. For original HCDS hydrolyzed deposit, there a negligible amount of H_2 generated from the first stage of pyrolysis (50–150 °C) and significantly evolved only after 180 °C. The total evolution of H_2 at the second stage of pyrolysis (150–500 °C) of KOH treated deposit was found to be 1.3 to 2.4 times higher than that of original deposit and independent of the KOH content in the deposit; however, there is no clear correlation between the rate of H_2 evolution and KOH concentration in this pyrolysis stage.

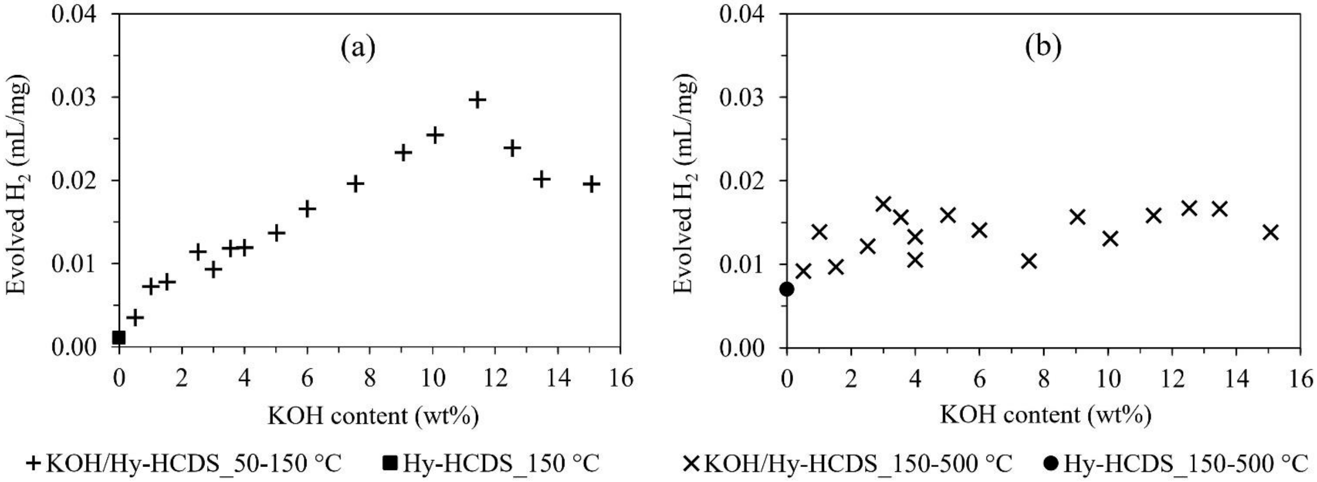

***Fig. 8.** The results of H_2 generation during pyroslysis (a) 50–150 °C, (b) 150–500 °C*

In order to better understand the emission behavior of H_2 gas during thermal treatment, especially from 150 to 500 °C, the measurement of generated H_2 gas was carried out at separate temperature ranges and the results are illustrated in Fig. 9. The rates of H_2 evolution in the temperature range of 50–150 °C of these three samples are consistent with the above results (Fig. 8a). It is interesting that the similar manner was observed in the temperature range of 150–200 °C, the rate of H_2 evolution of 1 wt% and 11 wt% KOH treated deposits was found to be 30 and 50 times higher than that of the sample without KOH treatment, respectively. This result implies that after KOH treatment, there is a new exothermic reaction taking place at the early stage of the temperature range of 150–200 °C which may also contribute to the sensitivity of KOH treated deposit. There was no drastically different rate of H_2 generated from the pyrolysis of these deposits in the annealing temperature of 200–400 °C. In the pyrolytic temperature range of 400–500 °C, there was only tiny amount of released H_2 for pure HCDS hydrolysate while no H_2 generated for KOH treated deposits. No further released H_2 gas was detected in the temperature range of 500–1000 °C for both pure and KOH treated deposits.

Impact and friction sensitivity tests were carried out for these KOH treated deposit after heat treatment at 150 °C for 1 hour by using a furnace at ambient conditions. It should be noted that with 150 °C heat treatment, both samples of 1 wt% and 11 wt% KOH treated deposits remain too sensitive to impact and friction. In particular, the 150 °C heat treated samples ignites either at impact energy of 2 J (fire ball) or friction force of 60 N (weak spark) and 0.125 J (fire ball) or 7 N (weak spark) for 1 wt% and 11 wt% KOH-containing deposits, respectively. These results suggest that not all weakened Si–Si bonds were cleaved by thermal treatment at 150 °C. Although the sensitivity and severity KOH treated deposit were somewhat decreased in the friction testing after heating at 150 °C compared to that deposit without heat treatment, the deposit was still considered extremely sensitive to transport.

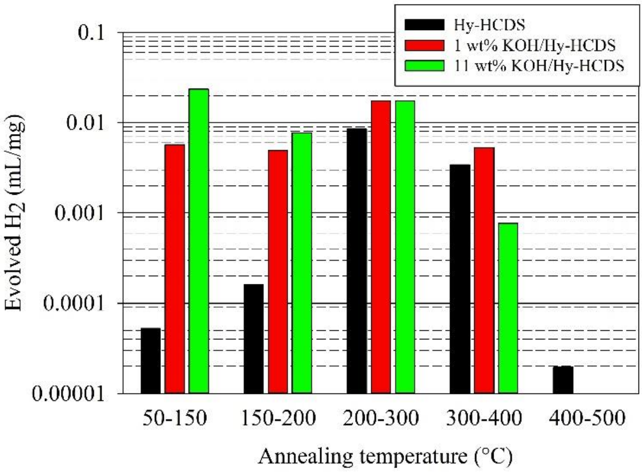

Fig. 9. *The evolution of H_2 at different annealing temperature for the HCDS hydrolyzed deposit with and without KOH treatment*

Fig. 10 shows the correlation between H_2 generation and heat release from the pyrolysis of KOH treated deposits. The volume of evolved H_2 from the first pyrolysis stage (50–150 °C) was found to be proportional to the heat release. For the second stage (150–500 °C), however, no clear correlation between the volume of H_2 generated and heat release. The results revealed that during the second stage of pyrolysis, there is additional exothermic reaction taking place without generating H_2 gas. This phenomenon maybe due to the rearrangement of oxygen atoms in the silicon oxide cluster during pyrolysis that is explained by infrared study in section 3.4.

DOI: 10.7795/810.20200724

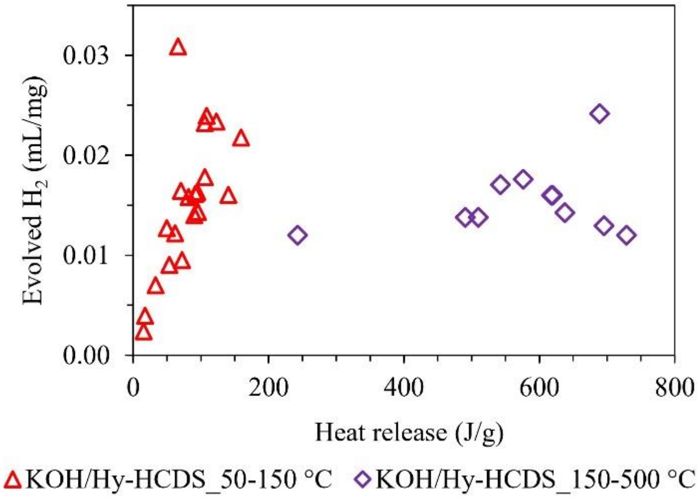

Fig. 10. *Correlation between evolved H_2 gas and heat release of treated HCDS hydrolyzed deposit*

3.3 The Effect of Particle Size on H_2 Generation

Fig. 11 shows the rate of generated hydrogen as a function of particle size during the pyrolysis of the 3.5 wt% KOH treated sample. For the <0.177 mm deposit, the volume of hydrogen evolved from the first stage of pyrolysis (50–150 °C) tends to increase significantly while it is almost constant for the 0.177–0.5 mm deposit. In particular, the rate of H_2 evolution of the <0.074 mm deposit is higher than that for >0.177 mm deposit by the factor of 2.5. The result indicates that the amount of weakened Si–Si bonds increases with a decrease in particle size. For the second pyrolysis stage (150–500 °C), it seems to be that the evolution of H_2 remains independent from the particle size. As a result, the reaction enhancing the sensitivity of HCDS hydrolyzed deposit presumably takes place on the surface of the hydrolyzed deposit.

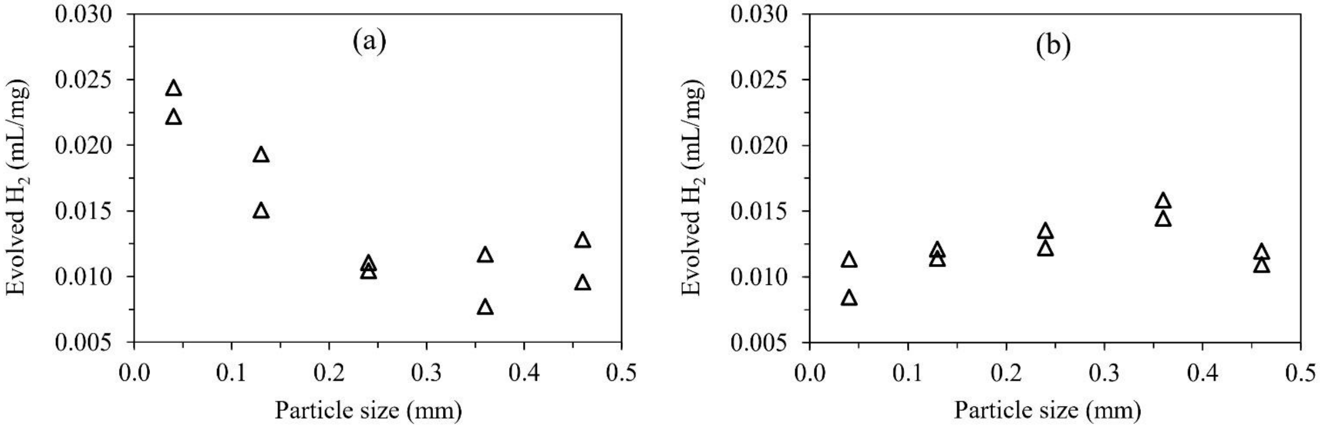

Fig. 11. *Results of H_2 gas evolution (a) 50–150 °C, (b) 150–500 °C*

3.4 Structure Characterization of the Heat-treated HCDS Hydrolyzed Deposit

To elucidate the thermal decomposition behavior of the HCDS hydrolyzed deposit, additional pyrolysis was performed at a wide range of annealing temperature from 150 to 1000 °C in nitrogen. The IR spectra of the samples show a very intense absorption band at around 1000 cm^{-1} which corresponds to the asymmetric stretching vibration of the oxygen atom in the Si–O–Si structure. With annealing treatments, the shift of the asymmetric stretching mode of Si–O–Si was observed initially from 1000 cm^{-1} for the original hydrolyzed deposit to 1090 cm^{-1} for the sample annealed at 1000 °C. This absorption band gives information about the oxidation degree of the SiO_x substance since the frequency of this mode is shifted

DOI: 10.7795/810.20200724

to the higher frequencies as a linear function of x. The absorption bands at 1000 cm^{-1} and 1090 cm^{-1} correspond to $SiO_{1.1}$ and $SiO_{2.1}$, respectively (Tolstoy et al., 2003). Simultaneously, with an increase in heating temperature up to 1000 °C, there is a shift of the Si–O–Si bending mode from 725 to 800 cm^{-1} corresponding to stoichiometric silica.

Heating up to 200 °C, the intensity of 875 cm^{-1} band being Si-Si bond indication slightly decreased and then was significantly diminished in the annealing temperature of 300–700 °C, suggesting the cleavage of Si–Si bond leading to the formation of Si–O–Si structure confirmed by the shift to higher wave number of Si–O–Si asymmetric stretching vibration.

Heating up to 300 °C the intensity of silanol band at 3250 cm^{-1} was gradually decreased and completely disappeared at the temperature of 500 °C and above. Additionally, the majority of H_2 generated was observed in the temperature range of 150–400 °C, as shown in Fig. 12. Furthermore, there is a negligible rate of H_2 evolution was measured in the annealing temperature range of 400–500 °C and no H_2 was detected for higher annealing temperature. It again supports the above-mentioned assumption that the H_2 generated during pyrolysis may be due to the cleavage of Si–Si bonds by water arising from the silanol condensation reaction. The result is in agreement with Camon and Moktadir (1997) in which the strength of Si–Si bond will be decreased with an increase in amount of OH group bonded to Si atoms. That explains why the Si–Si bonds in the hydrolyzed deposit can survive on very high annealing temperature from 500 to 700 °C in the absence of silanol.

Subsequent heating to 1000 °C causes additional profound changes in the experimental spectrum in which the weak peaks at 2260 cm^{-1} and 875 cm^{-1} attributed to Si–H and Si–Si bonds completely diminished and the spectrum matches perfectly with silica structure due to prominent peaks at 1090 and 800 cm^{-1} attributed to the Si–O–Si asymmetric stretching and bending modes of SiO_2. However, no H_2 was detected by our H_2 detector in the temperature range from 500 to 1000 °C, suggesting that the cleavage of Si–Si bond by water did not take place or occurred with very low degree.

According to Schmeisser and Schwarzmann (1956) the cleavage of Si–Si bond may take place due to the oxygen insertion, in which −Si−H can be formed from silanol without the presence of water and evolution of hydrogen

$$\mathrm{HO-Si-Si-OH \rightarrow HO-Si-O-Si-H} \tag{4}$$

However, the intensity of 2260 cm^{-1} band attributed to Si–H stretching mode did not increase during pyrolysis as shown in Fig. 12 (Pauthe et al., 1989). Therefore, this reaction may not take place or take place with a very low degree during the heating treatment.

Dřínek et al. (2001) proposed that the shift of Si–O–Si stretching mode with the increasing temperature is due to the rearrangement of oxygen atoms in the deposit. The oxygen atoms move from $Si–Si_{4-m}O_m$ bonding units (m = 1, 2, 3) to the $Si–O_4$ bonding unit (m = 4). That means the $Si–O_4$ bonding unit in the sample becomes more dominant in FTIR. In this work, all samples were heated and analyzed in inert atmosphere by using nitrogen gas and stoichiometric SiO_2 was formed at high annealing temperature (700–1000 °C). Therefore, this mechanism seems to be reasonable to explain the thermal decomposition behavior of the hydrolyzed deposit during pyrolysis.

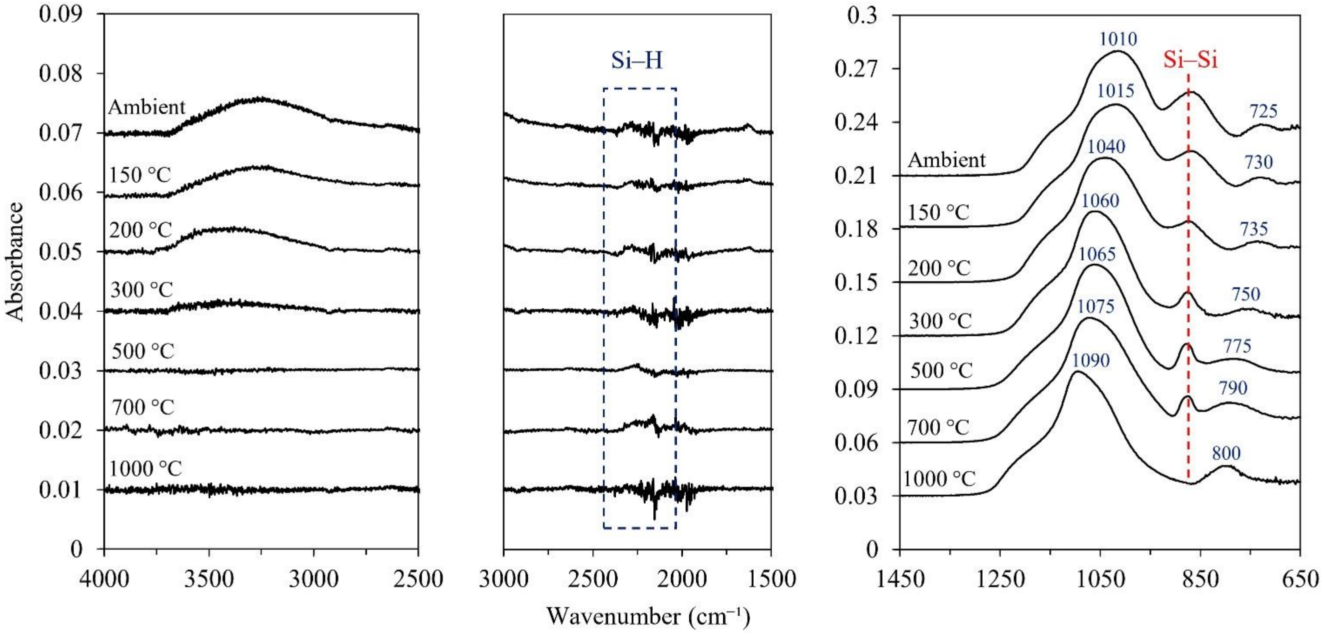

***Fig. 12.** IR spectra of vapor HCDS hydrolyzed deposits annealed at different temperature*

3.5 Proposed Mechanism of Enhancing Shock and Friction Sensitivity

On the basis of the above results, the following mechanism of enhancing shock and friction sensitivities by KOH is proposed. After mixing aqueous KOH solution with HCDS hydrolyzed deposit, the KOH was deposited on the surface of hydrolyzed deposits in which the –Si–Si–O–Si–Si– was broken down to form –Si–Si–OH and –Si–Si–OK. Once –Si–Si–OK groups were created, an electron displacement was generated leading to the weakening of the neighboring Si–Si bonds (Deleuze et al., 1995). The unstable Si–Si bonds were found to be slowly oxidized to form H_2 gas and Si–O–Si groups at ambient temperature. These reactions took place repeatedly during the storage time even in an inert atmosphere. It is evident that, the more amount of KOH was in the deposit, the more quantities of weakened Si–Si bonds were generated. Any thermal or mechanical friction or impact will lead to the cleavage of the unstable Si–Si bonds and subsequently initiated a fast chain oxidation of adjacent Si–Si bonds to form more Si–O–Si groups and H_2 gas and heat release. Cares should be taken when dealing with these deposits as they are extremely sensitive to handle plus the generated hydrogen may become a secondary hazard.

4. Conclusions

We have investigated the effects of KOH on enhancing the sensitivities of HCDS hydrolyzed deposit to impact and friction. A BAM Fall hammer and A BAM friction apparatus were used to characterize the shock and friction sensitivity of the hydrolyzed deposits before and after KOH treatment. The mixture of KOH and HCDS hydrolyzed is considered extremely sensitive that even a scratch by hand may ignite the deposit. The mechanism was proposed based on the IR studies and results of DSC with gas evolution analyses. The results of this study will be helpful for risk management and safe handling of the HCDS hydrolyzed deposits.

References

Ahsan, M.R., Mortuza, M.G., 2005. Infrared spectra of xCaO (1−x−z) SiO2zP2O5 glasses. *Journal of Non-Crystalline Solids,* 351, 2333-2340.

Belot, V., Corriu, R., Leclercq, D., Lefevre, P., Mutin, P., Vioux, A., Flank, A., 1991. Sol-gel route to silicon suboxides. Preparation and characterization of silicon sesquioxide. *Journal of Non-Crystalline Solids,* 127, 207-214.

Belot, V., Corriu, R., Leclercq, D., Mutin, P., Vioux, A., 1992. Organosilicon gels containing silicon-silicon bonds, precursors to novel silicon oxycarbide compositions. *Journal of Non-Crystalline Solids,* 144, 287-297.

Camon, H., Moktadir, Z., 1997. Simulation of silicon etching with KOH. *Microelectronics Journal,* 28, 509-517.

Cerfontain, M., Moulijn, J., 1986. The interaction of CO2 and CO with an alkali carbonate carbon system studied by in-situ Fourier transform infrared spectroscopy. *Fuel,* 65, 1349-1355.

Colomb, M.A., Straight, S.D., Hanaue, Y., 2020. Characterization and Hazards of the Silicon-Based Polymers Produced in the Manufacture of Ultrapure Polysilicon. *Industrial & Engineering Chemistry Research,* 59, 2696-2707.

Deleuze, M., Goiffon, A., Ibanez, A., Philippot, E., 1995. Solvent influence on kinetics and dissolution mechanism of quartz in concentrated basic media (NaOH, KOH, LiOH). *Journal of Solid State Chemistry,* 118, 254-260.

Dickson, P., 2010. Friction. in: *Shock Wave Science and Technology Reference Library, Vol. 5*. Springer, 2010, pp. 537-554.

Dřínek, V., Pola, J., Bastl, Z., Šubrt, J., 2001. TEA CO2 pulsed laser deposition of silicon suboxide films. *Journal of Non-Crystalline Solids,* 288, 30-36.

Harder, P.J., Tselepis, A.J., 2005. Characterization of Trichlorosilane Direct Process Residue. in: N. Auner, J. Weis (Eds.), *Organosilicon chemistry VI: from molecules to materials*. Wiley-VCH, Germany, 2005, pp. 126-130.

Hengge, E., 1974. Properties and preparations of Si-Si linkages. in: *Silicon Chemistry II*. Springer Berlin Heidelberg, 1974, pp. 1-127.

Iler, R.K., 1979. *The Chemistry of Silica: Solubility, Polymerization, Colloid and Surface Properties and Biochemistry of Silica*. Wiley.

Innocenzi, P., 2003. Infrared spectroscopy of sol–gel derived silica-based films: a spectra-microstructure overview. *Journal of Non-Crystalline Solids,* 316, 309-319.

Lin, Y.-J., Liu, C.-H., Chin, M.-G., Wang, C.-C., Wang, S.-H., Tsai, H.-Y., Chen, J.-R., Ngai, E.Y., Ramachandran, R., 2019. Characterization of Shock-Sensitive Deposits from the Hydrolysis of Hexachlorodisilane. *ACS Omega,* 4, 1416-1424.

Lin, Y.-J., Nguyen, T.-T., Chin, M.-G., Wang, C.-C., Liu, C.-H., Tsai, H.-Y., Chen, J.-R., Ngai, E.Y., Ramachandran, R., 2020. Disposal of hexachlorodisilane and its hydrolyzed deposits. *Journal of Loss Prevention in the process industries,* 104136.

Mitsubishi Materials Corporation Investigative Report by the Accident Investigation Committee for the Explosion & Fire Accident occurred in the High-Purity Polycrystalline Silicon Manufacturing Facility at Yokkaichi Plant of Mitsubishi Materials Corporation. http://www.mmc.co.jp/corporate/en/news/2014/news20140612.html (accessed June 12, 2014).

Nguyen, T.-T., Lin, Y.J., Chin, M.-G., Wang, C.-C., Tsai, H.-Y., Chen, J.-R., Ngai, E.Y., Chacon, J., Franzi, A., Fifield, C., 2020. Characterization and control of energetic deposits from hexachlorodisilane in process tool exhaust lines. *Journal of Loss Prevention in the process industries,* 104127.

Palik, E., Faust, J., Gray, H., Greene, R., 1982. Study of the Etch-Stop Mechanism in Silicon. *Journal of the Electrochemical Society,* 129, 2051-2059.

Pauthe, M., Phalippou, J., Corriu, R., Leclercq, D., Vioux, A., 1989. Silica xerogels containing a functional group at silicon. *Journal of Non-Crystalline Solids,* 113, 21-30.

Ritter, E., 1962. Zur Kenntnis der SiO-und Si2O3-Phase in Dünnen Schichten. *Optica Acta: International Journal of Optics,* 9, 197-202.

Schmeisser, M., Schwarzmann, M., 1956. Das Siliciuin-dibromid [SiBr2]x und seine Derivate. *Zeitschrift für Naturforschung B,* 11, 278-282.

Smith, A.L., Winefordner, J.D., Kolthoff, I., 1991. *The analytical chemistry of silicones*. Wiley-Interscience.

Tolstoy, V.P., Chernyshova, I., Skryshevsky, V.A., 2003. *Handbook of infrared spectroscopy of ultrathin films*. John Wiley & Sons.

United Nations, 2015. *United Nations Recommendations on the Transport of Dangerous Goods - Manual of Tests and Criteria*. 6 ed. United Nation Publication.

Zhou, X., Wanous, M.A., Wang, X., Eldred, D.V., Sanders Jr, T.L., 2018. Study on the Shock Sensitivity of the Hydrolysis Products of Hexachlorodisilane. *Industrial & Engineering Chemistry Research,* 57, 10354-10364.

DOI: 10.7795/810.20200724

Preliminary Study of Lignocellulosic biomass ignition properties estimation from Thermogravimetric Analysis

Blanca Castells[a], Isabel Amez[a], Ljiljana Medic[a] Nieves Fernandez-Anez[b] & Javier Garcia-Torrent[a]

[a] Universidad Politécnica de Madrid & Laboratorio Oficial Madariaga, Spain
[b] Department of Safety, Chemistry and Biomedical Laboratorio Sciences, HVL, Haugesund, Norway

E-mail: b.castells@upm.es

Abstract

In the last decade, the use of renewable resources has increased significantly in order to reduce the energetic dependence on fossil fuels, as they have an important contribution to the global warning and greenhouse gasses effect. Therefore, the role of biomass on the energetic mix is becoming critical nowadays, as it is the only renewable resource, whose characteristics of use match those of the conventional fuel's: solid biomass can be used instead of coals, and biodiesel could replace diesel. But in order to accomplish that goal, it is necessary to improve biomass physical-chemical properties such as high heating value, hygroscopicity, etc., but also to deep study its flammable characteristics in order to define the proper industrial safety measures.

Research on solid biomass ignition properties has been considerably developed because of the amount of industrial accidents related to the treatment and use of solid biomass (self-ignition, dust explosions, etc.). On the other hand, thermogravimetric analysis (TGA) is becoming and important characterization technique as it can be used to determine a wide spectrum of properties, such as kinetics, composition, proximate analysis, etc. This research aims to combine both by using the TGA to obtain the elemental composition of lignocellulosic biomass and compare those results to Minimum Ignition Energy (MIE) values test output, so a relation between oxygen, carbon and hydrogen content and MIE can be found; which means that further studies could develop an estimation of MIE by TGA.

To achieve this aim, biomass samples from different origins have been used: oil palm wastes (empty fruit bunches, mesocarp fiber and palm kernel shell), agricultural wastes (straw chops) and forestry wastes (wood chips and wood powder). Also, raw materials and torrefied biomass were compared Thermogravimetric analysis was carried on each sample, and so the percentages of cellulose, hemicellulose and lignin were estimated. Afterwards, MIE analysis was carried out and it was observed that torrefied samples presented lower energy values than the original samples.

Finally, the hemicellulose/cellulose ratio was calculated and compared to different flammability properties, finding out that the greater the ratio and the lower the onset temperature (temperature at which the pyrolysis reaction accelerates), the lower was the minimum ignition energy. From this basis it was possible to define "tendency areas" that grouped the samples whose MIE was similar. Three tendency areas were found: high minimum ignition energy, medium minimum ignition energy, and low ignition energy.

Keywords: *flammability, thermal analysis, biomass, minimum ignition energy*

1. Introduction

In the last decade, climate change had an important effect on the energetic regulations, increasing the use of renewable energies and trying to reduce the consume of fossil fuels (Chapman et al., 2018). This scenario promoted the research on new energetic sources or improving the ones already known, so they could replace the traditional energy resources. In this context, biomass has been studied so it could replace coal and its important role, as it is the only solid renewable energy (McKendry, 2002).

Even if biomass has been used for centuries, it is nowadays that several industries and facilities dedicate their activity to biomass production, storage, or handle, which means that its use has increased, and the safety conditions needed too. However, biomass flammability properties are still quite unknown and accidents keep happening such as fires, explosions and poisoning by carbon monoxide emissions (Gauthier et al., 2012; Hedlund, 2017). According to Moreno and Cozzani, (2015), regarding bioenergy industry, biomass accidents are more common than biogas or bioliquid accidents. It also states the equipment involved in the accidents, and most of the fires are produced when biomass is stored in piles or bulks and the smouldering process begins, such as the fire in Plevin Recycling Plant in United Kingdom, 2014 ("Plevin Hazlehead incident," 2014). On the other hand, explosions usually take place in the form of dust explosions in power plants during operations (such as material discharge, conveyor transport, etc.) that allow the dispersion of the dust into the air forming explosive atmospheres that may produce and explosion when ignition is produced as happened in Pinnacle Renewable Energy's wood pellet plan in Canada, 2019 ("Global News. Alberta energy plant suspends operations after explosion," 2019), or at Koda Energy combined power plant in USA, 2013 ("Star Tribune. Koda Energy invests in safer technology," 2013).

Because of this flammable nature of biomass, in the past years researches on biomass flammability properties have increased (Garcia-Torrent et al., 2016; Rupar-Gadd and Forss, 2018), trying to understand the mechanisms that take place during fires and dust explosions so that safety measures can be applied. The effect of particle size, compaction, moisture, dispersion, etc., has been widely studied (Fernandez-Anez et al., 2018; Luo et al., 2016; Saeed et al., 2017).

In order to define properly the flammable characteristics of a biomass sample, a lot of tests shall be carried out (minimum ignition temperature, self-ignition temperature, minimum ignition energy, explosion severity…) making it a hard task. Because of this, a lot of researchers have developed methods that allow the estimation of those parameters from other tests (Fumagalli et al., 2016; Uzun et al., 2017) in order to simplify the process. Thermogravimetric analysis (TGA) has proved to be quite useful (Garcia-Torrent et al., 2016; Janković et al., 2020; Saldarriaga et al., 2015) due to the unique information that reports, the small amount of sample that requires the test and the reproducibility of the test (human error is very low).

More precisely, the parameters that influence minimum ignition energy have been widely studied not only for solid materials but also for gas mixtures (Ballal and Lefebvre, 1975; Eckhoff, 1975; Horstmann et al., 2001; Norman et al., 2013), finding out that parameters such as oxygen concentration, turbulence or particle size, among others, have a significant effect on minimum ignition energy. The amount of researches that focus on biomass minimum ignition energy is not as great as the ones that focus on coal or gas/air mixtures; but it is increasing as the use of biomass does (Abelha et al., 2016). It is also known that minimum ignition energy can provide information about ignition parameters (Frendi and Sibulkin, 1990).

On the other hand, it is necessary to have a reliable comprehension on biomass composition, as it may have an effect on the ignition properties. Biomass includes a wide range of materials, but most of them are lignocellulosic materials (Shankar et al., 2011). It means that they are composed by three main components: cellulose (β-glucose monomers), hemicellulose (xylose, galactose, mannose, rhamnose and arabinose monomers) and lignin (substituted phenyl propane units). The composition of almost each type of lignocellulosic biomass has been previously studied, however, literature data differs from one study to another, so for the same material, different percentages of each component might be obtained (Bridgeman et al., 2008; González Martínez et al., 2019; Lewandowski, 2016). The macromolecular composition is usually obtained using an Accelerated Solvent Extractor Jacob et al., but it is also possible to obtain an estimation of the composition through TGA, technique used by several researchers (Gaitán-Álvarez et al., 2018; Hu et al., 2016; Janković et al., 2019b).

Given this background, the present study intends to find a relation between the parameters obtained from TGA and minimum ignition energy (MIE) so a preliminary estimation can be developed. To carry out this research, different biomasses were studied, all of them lignocellulosic so a compositional relation could be studied; and subjected to thermal analysis (thermogravimetry and differential scanning calorimetry) and minimum ignition energy test. All the data obtained from the tests was carefully studied so preliminary analysis of relations between thermal parameters, composition and minimum ignition energy was developed. The purpose of this study is to provide a new tool to make an early classification of materials according to their ignition properties, by using thermal analysis, which simplifies the testing process to assess flammable characteristics.

2. Experiments

In this study, six different lignocellulosic biomass samples were used, from agricultural and forestry wastes. Wood powder (WP) and wood chops (WC) come from Scots pine (Pinus Sylvestris L.), straw chops (SC) are made of reed canary grass (Phalaris Arundinacea L.), and the other samples come from palm oil wastes from Malaysia (Elaeis Oleifera). The palm oil samples come from different parts of the tree: EFB sample comes from Empty Fruit Bunches, while PKS means Palm Kernel Shell, and PMF Palm Mesocarp Fiber. As torrefaction is considered an important technique to improve biomass (Van der Stelt et al., 2011), and its effects on palm wastes has been widely studied (Uemura et al., 2011), torrefied PKS and PMF have been also studied (PKS T1, PKS T2, PMF T1 and PMF T2, where T1 and T2 represents two different dry torrefaction processes, the second one more intense than the first one). The samples were chosen in order to cover a wide range of biomass types, however no sewage sludge has been used in this study, as its composition cannot be assessed trough TGA (it is not a lignocellulosic biomass).

All the samples were prepared at particle size <1mm so the tests could be performed in the same conditions for each sample. The granulometry was assessed using laser diffraction with a Mastersizer 2000 apparatus.

The samples were first characterized through proximate analysis, so moisture, ash and volatile contents were defined. Fixed carbon content was calculated from proximate analysis data on dry basis as:

$$Fixed\ carbon = 100 - Ash\ (\%) - Volatiles\ (\%)$$

2.1 Thermogravimetric Analysis (TGA)

TGA measures the weight of the sample while it is heated from 30ºC to 800ºC at a constant heating rate (in this study the heating rate was β=5 K/min). During the whole procedure, the weight is recorded so it is possible to determine the onset temperature, which is the temperature at which the reaction accelerates, and so the weight decreases significantly. TG analysis was carried out using a TG-DSC Mettler Toledo TG-50 equipment.

From TGA it is also possible to obtain the apparent activation energy. Different methodologies to obtain activation energy have been developed in the last years (Hu et al., 2016; Radojević et al., 2018), however, Cumming's equation constitutes a good approximation of activation energy for first order kinetics and simplifies the process (Cumming, 1984).

If the first derivative of the TG curve is calculated, a second curve called DTG is obtained. This second curve provides important data such as the maximum weight loss temperature (MWL), which is the temperature at which the greatest decrease of weight takes place; but also, it is possible to obtain an estimation of the main components of lignocellulosic materials by calculating the deconvolution of the curve (Janković et al., 2019a; Perejón et al., 2011; Sronsri and Boonchom, 2018). The pseudocomponents obtained (so called because they represent an estimation instead of the precise value) will be cellulose, hemicellulose and lignin; and the area beneath those curves will represent the percentage of each component. Different deconvolution methods have been used to obtain the pseudocomponents such as Fraser-Suzuki deconvolution (Hu et al., 2016), Gaussian deconvolution

(Perejón et al., 2011), DAEM method (distribution activation energy model) (Cheng et al., 2015), etc. In this study, gaussian deconvolution was used with 3 terms, resulting into the 3 pseudocomponents mentioned above. PKS samples needed 4 terms so the approach was considered good enough (R^2 greater than 0.99), and the fourth component was found to represent carbonous matter: char after test. The mathematical treatment of the data was carried out using Matlab R2016b.

2.2 Differential Scanning Calorimetry (DSC)

DSC defines the heat exchange of the sample while heating it from 30ºC to 550ºC with a constant heating rate (in this study the heating rate was β=20 K/min). The heat exchange is recorded during the whole procedure, which means that it is possible to define the exothermic and endothermic processes that takes place during the heating. Three important parameters are obtained directly from the DSC curve: Initial Exothermic reaction Temperature (IET), which is the temperature at which the exothermic process begins; Change of Slope Temperature (CST), which is the temperature at which the reaction accelerates; and Final Exothermic reaction Temperature (FET), which is the temperature at which the exothermic reaction ends. DSC analysis was carried out using a TG-DSC Mettler Toledo TG-50 equipment.

From DSC data it is possible to estimate the specific heat capacity, which is the amount of energy that one unit of mass needs to increase its temperature in one unit. The estimation is carried out following the methodology presented by Collazo et al., (2012).

2.3 Minimum Ignition Energy (MIE)

MIE is the minimum ignition required to ignite the sample dispersed into air forming a cloud using a high voltage capacitor discharge. The procedure of the test is carried out according to the standard EN ISO/IEC 80079-20-2:2016 (European committee for standardization CEN-CENELEC, 2016), and the energy is calculated as follows:

$$MIE = \frac{1}{2} \cdot C \cdot U^2$$

Where C is the capacity of discharge expressed in Farads, and U is the applied voltage expressed in Volts. The test was carried out using a MIKE 3 apparatus that incorporates a Hartmann tube.

3. Results and discussion

The results from the proximate analysis and granulometry can be shown in Table 1. The moisture content presents the lowest values in the torrefied samples, as torrefaction reduces the hygroscopicity of the biomasses. The woody samples have the lowest ash content but the highest volatile percentage which means that an important amount of the sample has weak bonds and the onset temperature will be greater as the acceleration will take place after volatilizing most of this matter.

Table 1: *Proximate Analysis*

Sample	Moisture	Ash d.b.	Volatile d.b.	Fixed Carbon d.b.
PKS	7.0%	9.5%	66.8%	23.7%
PKS T1	0.5%	5.4%	72.1%	22.5%
PKS T2	0.9%	4.4%	73.0%	22.6%
EFB	6.5%	2.9%	72.7%	24.4%
PMF	8.8%	5.8%	62.7%	31.5%
PMF T1	1.4%	6.3%	73.8%	20.0 %
PMF T2	1.1%	6.6%	72.6%	20.8%
WC	6.2%	0.2%	85.6%	14.3%
WP	5.8%	0.2%	84.1%	15.8%

SC	5.1%	6.4%	76.5%	17.1%

3.1 Thermal Analysis (TGA and DSC)

In most of the biomass samples the IET represents the very beginning of the reaction, afterwards onset temperature indicates the moment of which it begins to accelerate, the CST would be greater than the onset temperature as indicates when the rapid exothermic reaction begins and it will be close to the MWL temperature, as when the process accelerates, the weight loss increases. Finally, the FET will define the end of the exothermic reaction, and from this point so on the sample will be mostly char. For each temperature, those temperatures are shown in table 2, also adding the apparent activation energy and the specific heat capacity.

Table 2: *Thermal Analysis: TG and DSC*

Sample	**IET (ºC)**	**Onset (ºC)**	**CST (ºC)**	**MWL (ºC)**	**FET (ºC)**	**Ea (kJ/mol)**	**Cp (J/kg·K)**
PKS	105.9	218.4	242.5	344.6	535.2	67.7	2589.6
PKS T1	220.0	250.0	334.0	350.0	545.0	67.9	1794.7
PKS T2	221.0	251.2	333.0	350.0	545.0	68.3	762.3
EFB	72.0	236.8	317.0	315.4	513.0	66.0	1235.4
PMF	80.3	222.7	289.5	310.0	527.5	65.5	2492.9
PMF T1	70.8	244.2	300.6	339.3	526.9	67.1	349.2
PMF T2	88.9	241.2	359.2	304.6	543.2	66.1	1388.0
WC	94.0	271.1	376.0	339.4	529.0	70.6	1955.1
WP	85.0	263.6	377.0	320.6	530.0	68.6	622.3
SC	94.0	239.3	375.0	328.7	530.0	67.4	578.9

Kernel shell samples (PKS) present the greatest IET temperatures, as they present strong chemical bonds (Alengaram et al., 2010) and so the exothermic reaction requires greater temperatures to start, even more after torrefaction process

Torrefied samples have lower Cp values, as torrefaction improves the energetic parameters of the biomasses besides PMF T2, whose behaviour is not as expected, and will be explained when discussing pseudocomponents results. On the other hand, the activation energy has an effect on the onset temperature, as the Ea is the minimum energy required for a system to start a process, the highest energies correspond to the highest onset temperatures as the system requires more heat to start the process. However, there is no significant relation between activation energy and CST. This fact can be due to the effect of the volatile content of the sample. In the first stage of the process, the light volatile matter will be released, and it is after this volatilization when the combustion accelerates and so the onset temperature is defined.

Table 3 shows the pseudocomponents percentage for each sample, obtained by Gaussian deconvolution. In addition, the table shows the obtained R2, which represents the quality of the fitted model; and the char percentage, which is the matter percentage that remained after the TG analysis. As it was explained above, PKS samples needed 4 terms deconvolution due to the great char amount of the samples. A great char content implies that the sample contains non-combustible matter that needs to be represented, in this case, through the carbonous matter of the sample that was estimated with the fourth component (25.14% for PKS, 23.27% for PKS T1 and 20.08% for PKS T2).

***Table 3:** Pseudocomponents from Gaussian deconvolution and char percentage*

Sample	Cellulose (%)	Hemicellulose (%)	Lignin (%)	R^2	Char (%)
PKS	13.1	8.4	13.1	0.9986	30.3
PKS T1	17.8	10.9	15.4	0.9978	31.9
PKS T2	9.2	11.0	22.8	0.9973	35.9
EFB	43.1	20.8	8.0	0.9995	19.0
PMF	45.6	29.2	14.5	0.9902	1.7
PMF T1	24.1	27.7	18.4	0.9946	27.7
PMF T2	52.7	39.0	4.0	0.9942	3.0
WC	39.6	23.4	16.2	0.9924	14.2
WP	45.2	21.5	23.7	0.9833	2.9
SC	48.0	25.2	15.3	0.9953	4.2

The deconvolution of WP did not reach the 0.99 R^2 expected, however the results of each component are consistent if compared to bibliographic data for Scots pine (Zborowska et al., 2018), so the obtained results are considered accurate enough. PMF and PKS samples show an increase of lignin after torrefaction process due to the decomposition of hemicellulose and degradation of cellulose, which can also be noticed in the results. However, PMF T2 behaves in a completely different way, reducing its lignin content and increasing the cellulose, which might be related to the thermal behaviour during the TGA. Figure 1 shows the curves from the thermal analysis for PMF, PMF T1 and PMF T2, where it is possible to see that PMF combustion decreases around 300ºC and so the slope increases. Torrefaction should correct this behaviour and so it happens when testing PMF T1, however, PMF T2 shows this "slow combustion" phenomena again, complicating the estimation of pseudocomponents through TGA.

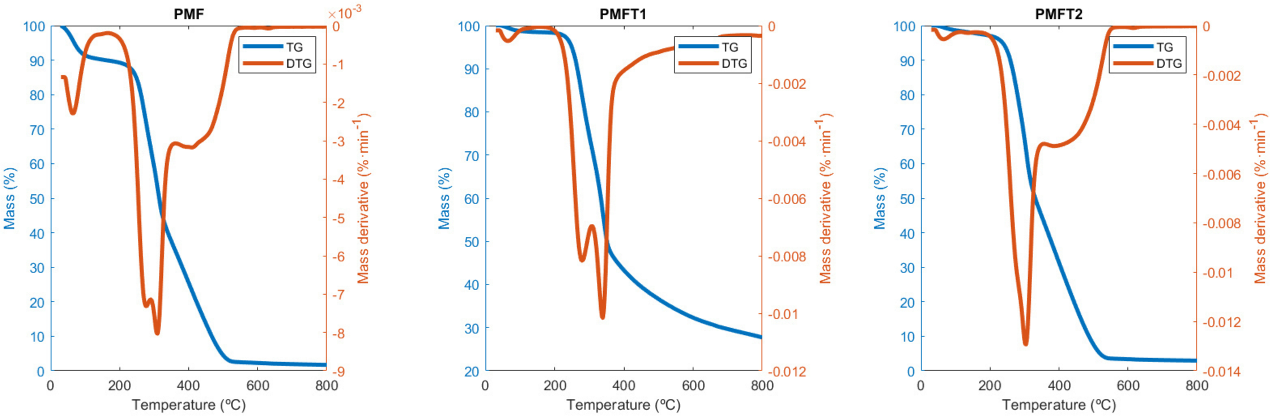

***Fig. 1.** TGA of palm mesocarp fiber samples*

3.2 *Minimum Ignition Energy*

The results obtained from the MIE test are shown in table 4. As occurred when assessing the specific heat capacity, torrefied samples present lower MIE values than their original sample. The woody samples have the same MIE value, as both are the same species and their thermal characteristics were very similar. From those results, three different groups can be made: samples with high minimum energy (PKS, EFB, WC and WP), samples with medium-low minimum energy (PKS T1, PMF and SC) and samples with low minimum energy (PKS T2, PMF T1 and PMF T2). The previous tests showed an "erratic" behaviour of PMF T2 which also manifests in MIE results as MIE increases from PMF T1 to PMF T2. However, this fact can also be explained because of its particle size distribution, which can be seen also in table 4, and shows an increase of particle size if compared to PMF T1. The fact that minimum ignition energy decreases after torrefaction has been contrasted in previous literature, however the previous studies show discordance when approaching the relation between explosivity and torrefaction (Boskovic et al., 2015; Szamosi et al., 2017; Thrän et al., 2016); which could be explained by the feedstock type. Indeed, torrefaction may present different effects depending on the chemical and physical structure of the sample. If particle size is considered, kernel shell samples increase granulometry after torrefaction, probably because the smaller particles volatilize, but, on the other hand, when mesocarp fiber is tested, granulometry decreases after torrefaction, which could be due to the bonds break in the sample structure, so the particles are weaker and break easily into smaller particles.

Table 4: *MIE and particle size distribution*

Sample	**MIE (mJ)**	**d10**	**d50**	**d90**
PKS	840	4.2	189.7	1021.6
PKS T1	200	11.6	234.0	745.0
PKS T2	55	272.4	730.9	1350.8
EFB	610	30.0	146.5	414.7
PMF	220	41.9	367.9	1354.2
PMF T1	55	7.9	125.4	337.9
PMF T2	79	32.5	103.2	1421.8
WC	610	152.7	619.4	1307.8
WP	610	171.1	613.4	1295.2
SC	220	125.9	457.6	1227.5

Lignin is a polymer that binds the fibres of the cells and vessels acting as a cementing agent, which means that this molecule is stronger than cellulose and hemicellulose. According to that, the minimum ignition will be related to the percentage of each component, as the samples with higher hemicellulose will require less energy to break the chemical bonds in the combustion. However, from the contents obtained above, no relation was found between MIE and pseudocomponents content, so the ratios hemicellulose/cellulose, hemicellulose/lignin and cellulose/lignin were calculated in order to find out if the proportion between components may produce an effect on the minimum ignition energy. From this data, it was inferred that the lignin content does not affect the MIE as much as hemicellulose and cellulose. Figure 2 plots the hemicellulose/cellulose ratio versus some of the flammability parameters explained above: fixed carbon content, specific heat capacity, apparent activation energy and onset temperature. The samples with the lowest minimum ignition energies are always located in the lower right quadrant of the plots, as their hemicellulose/cellulose ratios are higher than the ratios of the other samples. More precisely, those samples whose minimum energy was lower than 100 mJ presented ratios greater than 0.7: PMF T2 has a ratio of 0.74 (and the highest MIE from low MIE group) and PMF T1 and PKS T2 have ratios over 1 (1.15 and 1.2 respectively).

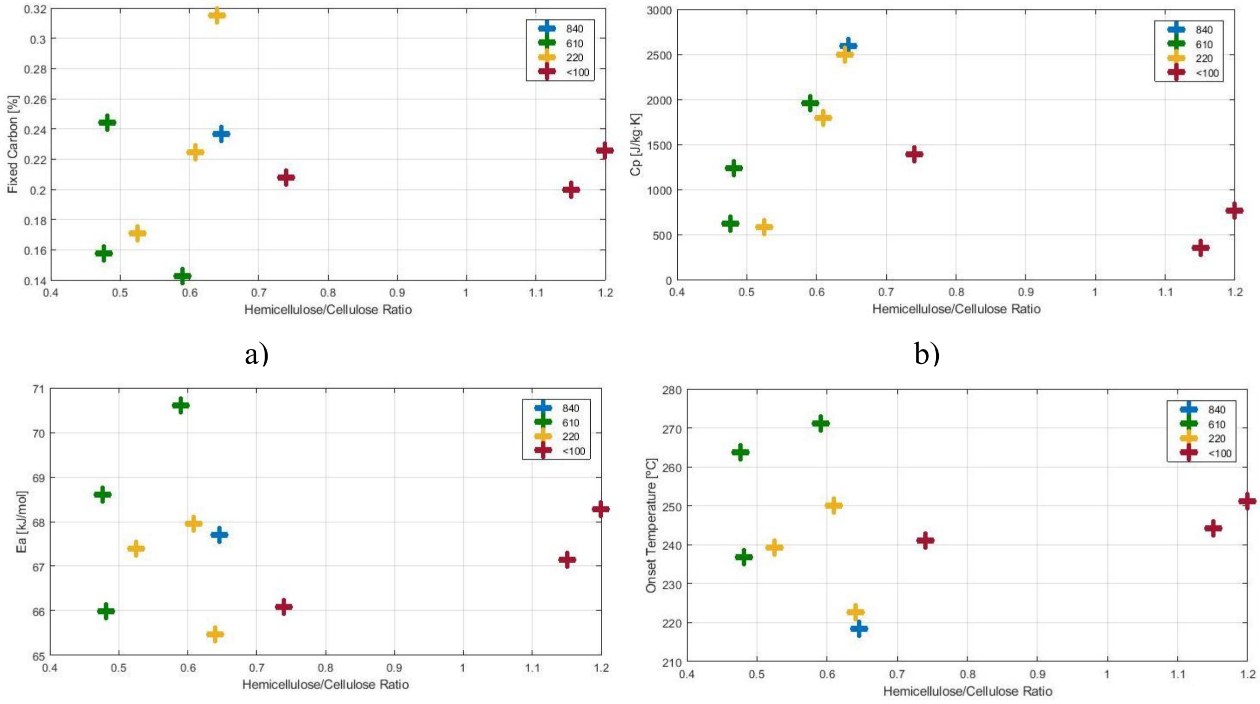

a) b)

c) d)

Fig. 2. *Hemicellulose/Cellulose Ratio Vs Flammability Parameters: a) Ratio Vs Fixed Carbon content, b) Ratio Vs Specific Heat Capacity, c) Ratio Vs Activation Energy, d) Ratio Vs Onset Temperature*

The samples with high MIE seem to have lower ratios, however PKS's (whose MIE is 840 mJ) ratio is 0.64 and behaves more similar to the medium MIE group than to the high MIE group. The fixed carbon content varies in a short range for the low MIE group (figure 2 a), however for the rest of the groups present an important dispersion. Same fact could be stated for the apparent activation energy (figure 2 c), but it could be due to the fact that the activation energy was calculated as a first order kinetics and the values are an approximation. As Ea is a parameter that have been proved useful to estimate self-ignition tendency (Garcia-Torrent et al., 2016), it can be expected that it has an effect on the minimum ignition energy, so further studies would be required in order to define the kinetics best fit in each sample, and so more accurate values would be obtained. Regarding the specific heat capacity (figure 2 b), there is no significant relation to MIE, as the lowest Cp values corresponds to samples whose MIE is 55 mJ, 220 mJ and 610 mJ.

The most significant plot is figure 2 d, in which the ratio is plotted versus the onset temperature. It seems to be a tendency that samples with great onset temperatures, and low hemicellulose/cellulose ratios have higher MIEs than the samples that locate in the opposite part of the plot. Figure 3 shows the three MIE groups (high, medium, and low), and establish around them "tendency areas". From this plot it is possible to make a preliminary classification of samples according to these tendency areas.

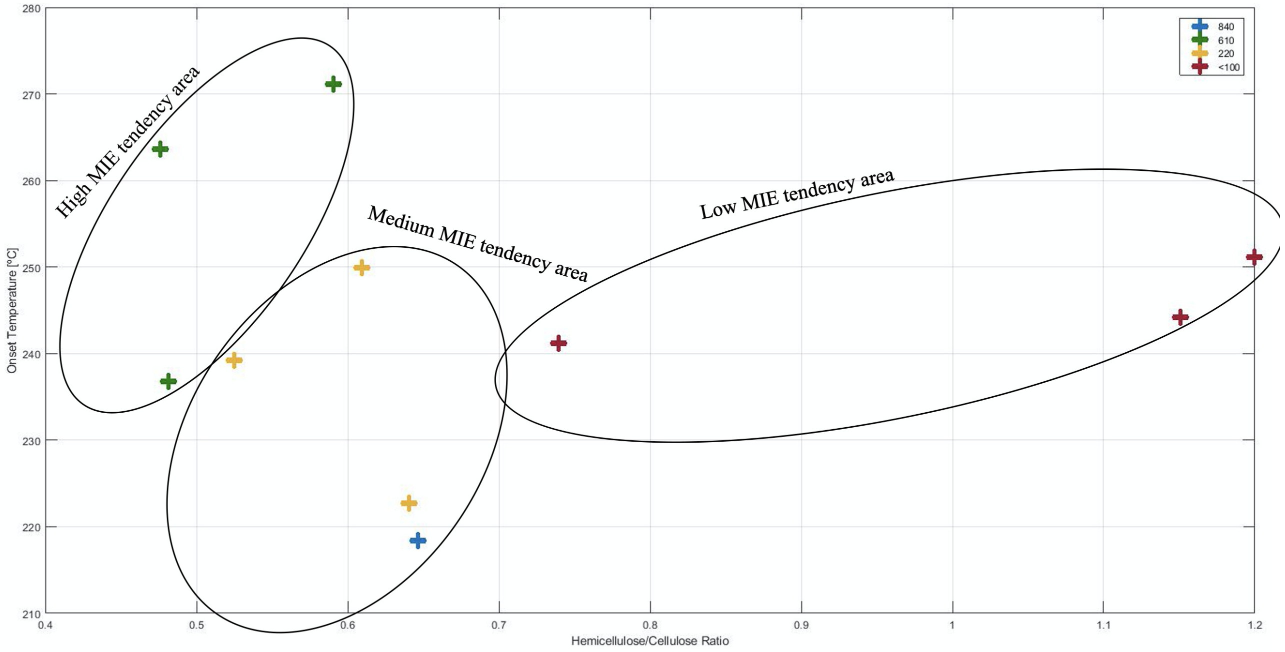

Fig. 3. *MIE Tendency Areas*

4. Conclusions

The first conclusion that can be obtained from the tests result is that torrefaction treatment may have an important effect on the flammability properties of the samples depending on the feedstock. It has been proved that palm wastes torrefied samples have lower MIE values than the original samples, but also the specific heat capacity was reduced in those samples. It means that torrefied palm oil wastes might require special safety measures as their ignition does not need great amounts of energy.

The lignin content does not have a significant effect on the flammability characteristics of the samples however, the proportion between hemicellulose and cellulose appears to group samples with similar MIE. More precisely, when evaluating the hemicellulose/cellulose ratio and the onset temperature there is a tendency to increase minimum ignition energy as the ratio decreases and the onset temperature increases. It means that if the ratio is plotted versus onset temperature, the samples that locates in the upper left part of the plot will have greater minimum ignition energy than those that locate in the lower right part.

PMF T2 sample behaves in an unexpected way, however the data evaluated in this study is not enough to state that the sample constitutes a deviation or not. It would be necessary to test similar samples (biomasses made from fibres), so a proper tendency is defined. Indeed, as this research was a preliminary study, it would require an improvement by adding samples and studying their properties so the estimation can be fully reliable, and it will be possible to define classification zones instead of tendency areas.

References

Abelha, P., Carbo, M., Cieplik, M., 2016. Explosivity properties of dusts from torrefied biomass pellets. Chem. Eng. Trans. 48, 403–408. https://doi.org/10.3303/CET1648068

Alengaram, U.J., Mahmud, H., Jumaat, M.Z., 2010. Comparison of mechanical and bond properties of oil palm kernel shell concrete with normal weight concrete. Int. J. Phys. Sci. 5, 1231–1239.

Ballal, D.R., Lefebvre, A.H., 1975. The influence of flow parameters on minimum ignition energy and quenching distance. Symp. Combust. 15, 1473–1481. https://doi.org/10.1016/S0082-0784(75)80405-X

Boskovic, A., Basu, P., Amyotte, P.R., 2015. An exploratory study of explosion potential of dust from torrefied biomass. Can. J. Chem. Eng. 93, 658–663. https://doi.org/10.1002/cjce.22153

Bridgeman, T.G., Jones, J.M., Shield, I., Williams, P.T., 2008. Torrefaction of reed canary grass, wheat straw and willow to enhance solid fuel qualities and combustion properties. Fuel 87, 844–856. https://doi.org/10.1016/j.fuel.2007.05.041

Casson Moreno, V., Cozzani, V., 2015. Major accident hazard in bioenergy production. J. Loss Prev. Process Ind. 35, 135–144. https://doi.org/10.1016/j.jlp.2015.04.004

Chapman, A.J., McLellan, B.C., Tezuka, T., 2018. Prioritizing mitigation efforts considering co-benefits, equity and energy justice: Fossil fuel to renewable energy transition pathways. Appl. Energy 219, 187–198. https://doi.org/10.1016/j.apenergy.2018.03.054

Cheng, Z., Wu, W., Ji, P., Zhou, X., Liu, R., Cai, J., 2015. Applicability of Fraser-Suzuki function in kinetic analysis of DAEM processes and lignocellulosic biomass pyrolysis processes. J. Therm. Anal. Calorim. 119, 1429–1438. https://doi.org/10.1007/s10973-014-4215-3

Collazo, J., Pazó, J.A., Granada, E., Saavedra, Á., Eguía, P., 2012. Determination of the specific heat of biomass materials and the combustion energy of coke by DSC analysis. Energy 45, 746–752. https://doi.org/10.1016/j.energy.2012.07.018

Cumming, J.W., 1984. Reactivity assessment of coals via a weighted mean activation energy,. Fuel 63, 1436–1440. https://doi.org/10.1016/0016-2361(84)90353-3

Eckhoff, R.K., 1975. Towards absolute minimum ignition energies for dust clouds? Combust. Flame 24, 53–64. https://doi.org/10.1016/0010-2180(75)90128-5

European committee for standardization CEN-CENELEC, 2016. ISO/IEC 80079-20-2:2016 Explosive atmospheres - Part 20-2: Material characteristics - Combustible dusts test methods.

Fernandez-Anez, N., Slatter, D.J.F., Saeed, M.A., Phylaktou, H.N., Andrews, G.E., Garcia-Torrent, J., 2018. Ignition sensitivity of solid fuel mixtures. Fuel 223, 451–461. https://doi.org/10.1016/j.fuel.2018.02.106

Frendi, A., Sibulkin, M., 1990. Dependence of minimum ignition energy on ignition parameters. Combust. Sci. Technol. 73, 395–413. https://doi.org/10.1080/00102209008951659

Fumagalli, A., Derudi, M., Rota, R., Copelli, S., 2016. Estimation of the deflagration index KSt for dust explosions: A review. J. Loss Prev. Process Ind. 44, 311–322. https://doi.org/10.1016/j.jlp.2016.09.011

Gaitán-Álvarez, J., Moya, R., Puente-Urbina, A., Rodriguez-Zúñiga, A., 2018. Thermogravimetric, devolatilization rate, and differential scanning calorimetry analyses of biomass of tropical plantation species of Costa Rica torrefied at different temperatures and times. Energies 11. https://doi.org/10.3390/en11040696

Garcia-Torrent, J., Ramírez, Á., Fernandez-Anez, N., Medic, L., Tascón, A., 2016. Influence of the composition of solid biomass in the flammability and susceptibility to spontaneous combustion. Fuel 184, 503–511. https://doi.org/10.1016/j.fuel.2016.07.045

Gauthier, S., Grass, H., Lory, M., Krämer, T., Thali, M., Bartsch, C., 2012. Lethal carbon monoxide poisoning in wood pellet storerooms-two cases and a review of the literature. Ann. Occup. Hyg. 56, 755–763. https://doi.org/10.1093/annhyg/mes047

Global News. Alberta energy plant suspends operations after explosion [WWW Document], 2019. . Glob. News. URL https://globalnews.ca/news/4953314/pinnacle-entwistle-energy-plant-explosion-injuries/ (accessed 12.19.19).

González Martínez, M., Ohra-aho, T., Tamminen, T., da Silva Perez, D., Campargue, M., Dupont, C., 2019. Detailed structural elucidation of different lignocellulosic biomass types using optimized temperature and time profiles in fractionated Py-GC/MS. J. Anal. Appl. Pyrolysis 140, 112–124. https://doi.org/10.1016/j.jaap.2019.02.011

Hedlund, F.H., 2017. Biomass accident investigations - Missed opportunities for learning and accident prevention. Eur. Biomass Conf. Exhib. Proc. 2017, 1804–1814. https://doi.org/10.5071/25thEUBCE2017-4AV.2.45

Horstmann, T., Leuckel, W., Maurer, B., Maas, U., 2001. Influence of turbulent flow conditions on the ignition of flammable gas/air-mixtures. Process Saf. Prog. 20, 215–224. https://doi.org/10.1002/prs.680200311

Hu, M., Chen, Z., Wang, S., Guo, D., Ma, C., Zhou, Y., Chen, J., Laghari, M., Fazal, S., Xiao, B., Zhang, B., Ma, S., 2016. Thermogravimetric kinetics of lignocellulosic biomass slow pyrolysis using distributed activation energy model , Fraser – Suzuki deconvolution , and iso-conversional method. ENERGY Convers. Manag. 118, 1–11. https://doi.org/10.1016/j.enconman.2016.03.058

Janković, B., Dodevski, V., Radović, I., Pijovi, M., 2019a. Physico-chemical characterization of carbonized apricot kernel shell as precursor for activated carbon preparation in clean technology utilization 236. https://doi.org/10.1016/j.jclepro.2019.117614

Janković, B., Manić, N.G., Dodevski, V., Popović, J., Rusmirović, J.D., Tošić, M., 2019b. Characterization analysis of Poplar fluff pyrolysis products . Multi-component kinetic study. Fuel 238, 111–128. https://doi.org/10.1016/j.fuel.2018.10.064

Janković, B., Manić, N.G., Stojiljković, D.D., Jovanović, V. V., 2020. The assessment of spontaneous ignition potential of coals using TGA–DTG technique. Combust. Flame 211, 32–43. https://doi.org/10.1016/j.combustflame.2019.09.020

Lewandowski, I., 2016. Biomass Production from Lignocellulosic Energy Crops, in: Encyclopedia of Applied Plant Sciences. Elsevier Inc., pp. 159–163. https://doi.org/10.1016/B978-0-12-394807-6.00171-4

Luo, Q., Liang, D., Shen, H., 2016. Evaluation of self-heating and spontaneous combustion risk of biomass and fishmeal with thermal analysis (DSC-TG) and self-heating substances test experiments. Thermochim. Acta 635, 1–7. https://doi.org/10.1016/j.tca.2016.04.017

McKendry, P., 2002. Energy production from biomass (part 1): Overview of biomass. Bioresour. Technol. 83, 37–46. https://doi.org/10.1016/S0960-8524(01)00118-3

Norman, F., Berghmans, J., Verplaetsen, F., 2013. The minimum ignition energy of coal dust in an oxygen enriched atmosphere. Chem. Eng. Trans. 31, 739–744. https://doi.org/10.3303/CET1331124

Perejón, A., Pedro, E.S., Criado, M., Luis, A.P., 2011. Kinetic Analysis of Complex Solid-State Reactions . A New Deconvolution Procedure 1780–1791.

Plevin Hazlehead incident [WWW Document], 2014. . News Feed - Plevin. URL http://www.plevin.co.uk/news?page=11 (accessed 12.19.19).

Radojević, Balac, M., Jovanović, V. V., Stojiljković, D.D., Manić, N.G., 2018. Thermogravimetric kinetic study of solid recovered fuels pyrolysis. Hem. Ind. 72, 99–106. https://doi.org/10.2298/HEMIND171009002R

Rupar-Gadd, K., Forss, J., 2018. Self-heating properties of softwood samples investigated by using isothermal calorimetry. Biomass and Bioenergy 111, 206–212. https://doi.org/10.1016/j.biombioe.2017.04.008

Saeed, M.A., Fernandez-Anez, N., Andrews, G.E., Phylaktou, H.N., Gibbs, B.M., 2017. Steam exploded pine wood burning properties with particle size dependence. Fuel 194, 527–532. https://doi.org/10.1016/j.fuel.2017.01.028

Saldarriaga, J.F., Aguado, R., Pablos, A., Amutio, M., Olazar, M., Bilbao, J., 2015. Fast characterization of biomass fuels by thermogravimetric analysis (TGA). Fuel 140, 744–751. https://doi.org/10.1016/j.fuel.2014.10.024

Shankar, T.J., Wright, C.T., Boardman, R.D., Yancey, N.A., Sokhansanj, S., 2011. A review on biomass classification and composition, co-firing issues and pretreatment methods. 2011 Louisville, Kentucky, August 7 - August 10, 2011. https://doi.org/10.13031/2013.37191

Sronsri, C., Boonchom, B., 2018. Thermal kinetic analysis of a complex process from a solid-state reaction by deconvolution procedure from a new calculation method and related thermodynamic functions of Mn0.90Co0.05Mg0.05HPO4·3H2O. Trans. Nonferrous Met. Soc.

China (English Ed. 28, 1887–1902. https://doi.org/10.1016/S1003-6326(18)64834-4

Star Tribune. Koda Energy invests in safer technology [WWW Document], 2013. . Star Trib. URL http://www.startribune.com/biomass-burner-koda-energy-invests-in-safer-technology/216239441/ (accessed 12.19.19).

Szamosi, Z., Tóth, P., Koós, T., Baranyai, V.Z., Szepesi, G.L., Siménfalvi, Z., 2017. Explosion Characteristics of Torrefied Wheat Straw, Rape Straw, and Vine Shoots Fuels. Energy and Fuels 31, 12192–12199. https://doi.org/10.1021/acs.energyfuels.7b01875

Thrän, D., Witt, J., Schaubach, K., Kiel, J., Carbo, M., Maier, J., Ndibe, C., Koppejan, J., Alakangas, E., Majer, S., Schipfer, F., 2016. Moving torrefaction towards market introduction – Technical improvements and economic-environmental assessment along the overall torrefaction supply chain through the SECTOR project. Biomass and Bioenergy 89, 184–200. https://doi.org/10.1016/j.biombioe.2016.03.004

Uemura, Y., Omar, W.N., Tsutsui, T., Yusup, S.B., 2011. Torrefaction of oil palm wastes. Fuel 90, 2585–2591. https://doi.org/10.1016/j.fuel.2011.03.021

Uzun, H., Yıldız, Z., Goldfarb, J.L., Ceylan, S., 2017. Improved prediction of higher heating value of biomass using an artificial neural network model based on proximate analysis. Bioresour. Technol. 234, 122–130. https://doi.org/10.1016/j.biortech.2017.03.015

Van der Stelt, M.J.C., Gerhauser, H., Kiel, J.H.A., Ptasinski, K.J., 2011. Biomass upgrading by torrefaction for the production of biofuels: A review. Biomass and Bioenergy 35, 3748–3762. https://doi.org/10.1016/j.biombioe.2011.06.023

Zborowska, M., Prądzyński, W., Kusiak, W., Stachowiak-Wencek, A., Roszyk, E., Moliński, W., 2018. A selection of the application of Pinus Sylvestris L. From Puszcza Notecka by chemical analysis. Drewno 61, 39–51. https://doi.org/10.12841/wood.1644-3985.D10.02

DOI: 10.7795/810.20200724

Burning and explosion behaviour of ethanol/water - sucrose mixtures

Maria Mitu [a], Thomas Stolz [b], Elisabeth Brandes [b] and Sabine Zakel [b]

[a] Ilie Murgulescu Institute of Physical Chemistry, Romanian Academy, Bucharest, Romania
[b] Physikalisch-Technische Bundesanstalt (PTB), Braunschweig, Germany

E-mail: Sabine.Zakel@ptb.de

Abstract

This study investigates the influence of sucrose content on fire and explosion protection requirements relevant for the storage and filling of ethanol/water cosolvent mixtures. These mixtures are of particular interest for the alcoholic beverages industry. The aim of this investigation is to determine which reduced requirements (deviating from the technical regulations) for constructional fire protection equipment can be permitted in the safety assessment of such mixtures. The results of the project can be incorporated into the upcoming revision of the regulations referred to.

Keywords: *ethanol, water, sugar, sucrose, flash point, fire point, sustained combustion test, sustained combustibility*

1. Introduction

When storing and filling bottling ethanol/water mixtures, aspects of explosion protection and fire protection defined in existing laws concerning dangerous substances must be considered. TRGS 509 (GMBI, 2014) is the first German technical rule containing the same requirements for the storage and bottling/emptying points of water-soluble flammable liquids as those for other flammable liquids. For liquids with flash points from 21 °C to 55 °C, this situation was different before 2003, as water-soluble flammable liquids were not covered by the regulation titled "Verordnung über brennbare Flüssigkeiten (VbF)", which was the precursor of TRGS 509. Most spirits (distilled alcoholic beverages) belong to this group; before 2003, the spirits industry was largely free of requirements concerning fire and explosion protection. The current requirements are based on the three flash point categories (cat.1 to 3) for flammable liquids given in the regulation on classification, labelling and packaging (CLP) of substances and mixtures (EC, 2008). In this regulation, it is not necessary to classify flammable liquids with a flash point of ≥ 35 °C as category 3 if they do not support sustained combustion.

The test for sustained combustion is carried out in accordance with ISO 9038 (2013) at fixed testing temperatures of 60.5 °C and 75 °C (UN test L.2, 2005). Most flammable liquids with a flash point between 35 °C and 60 °C show sustained combustion as defined in UN test L.2. Only a minority of this group does not support combustion. Of the liquids that do not support combustion, most contain high amounts of components which do not burn, such as water. The fire load then corresponds to the amount of the flammable component, which is ethanol in this study. When the test is carried out at other testing temperatures, it may lead to other ethanol-content threshold values (i.e. the maximum ethanol content at which the test is still negative). As the maximum storage temperature is 40 °C in Europe, a modification of the test might be useful.

Within the scope of TRGS 509, liquids with a flash point of up to 370 °C are regarded as combustible. In order to ease requirements for construction-related fire safety, a differentiated risk assessment is allowed as defined in the Ordinance on Industrial Safety and Health (BetrSichV, 2003; LV 49, 2017). As a prerequisite, the given liquid must not behave like other combustible materials even if its flash point is ≤ 370 °C; a distinction is made between liquids whose burning behaviour is similar to that of non-water-soluble flammable liquids and liquids with significantly reduced fire intensity. Flammable water-soluble liquids with a significantly reduced fire intensity entail reduced construction-related fire protection requirements. With such liquids, the liquid will stop burning by itself when the flammable component has been consumed. Furthermore, a small amount of extinguishing water can stop the liquid from burning. The reduced need for extinguishing water can be considered when determining the extinguishing water retention volumes.

When the results from the ethanol/water model systems are compared with those from commercially available spirit preparations, the influence of sucrose should be considered. Additional compounds such as sucrose can influence the viscosity and solvation capability of the cosolvent mixture, and these factors can have significant impact on the flash point and sustained combustibility.

Sucrose is highly soluble in water, but dissolves poorly in ethanol. Because the sucrose molecule has eight hydroxyl groups and three hydrophilic oxygen atoms, the water molecule interacts easily with it via hydrogen bonding. Ethanol has only one hydroxyl group, and the interaction between molecules of sucrose and alcohol is weak. Mixtures of both solvents (cosolvent mixtures) are generally capable of dissolving sucrose. The solubility of sucrose in the mid-range of water/ethanol mixtures is primarily determined by the amount of water. Nevertheless, at both ends of the composition range, this behaviour is slightly different. Small amounts of ethanol appear to support the solution process of sucrose in water, while with small amounts of water, the ethanol additionally hinders the sucrose from dissolving in the water (Galvao, 2016).

A study on potential explosion hazards due to evaporating ethanol in whisky distilleries was presented in Ledin (2003). Hakkarainen et al. (2017) studied the heat release characteristics of ethanol/water mixtures in small-scale experiments. They observed that a significant fire load is not formed until the ethanol volume fraction in the alcoholic beverage is at least 20 %. Chen et al. (2019) presented an investigation of the fire hazard characteristics of ethanol/water mixtures and Chinese spirits by means of a cone calorimeter and an automatic flash point tester.

The flammability and sustained combustion of ethanol/water mixtures and commercially available alcoholic beverages are examined in detail in this study. The aspect of sugar admixture is given special consideration. Experimental results are presented for the flash point, fire point and sustained combustibility. For the comparison of the current standard methods, the correlation of the flash point with the ethanol content of the cosolvent mixtures was measured beforehand. A method of calculating the flash point of sucrose-containing cosolvent mixtures is also presented.

2. Experiments

All experiments were performed in a laboratory whose ambient temperature and pressure levels varied between 20 °C and 30 °C and between 99.0 kPa and 102.8 kPa. Before testing, the samples were pre-cooled to 5 °C. The results were corrected to a standard pressure of 101.3 kPa and rounded in accordance with the standards.

2.1 Samples

Ethanol/water mixtures containing sucrose were prepared in various compositions with an expanded measurement uncertainty (k=2) at a 95 % confidence level of U= 0.2 % in mass fraction. Ethanol with a purity of 99.9 % by mass was gravimetrically mixed with deionized water and the mass fraction was converted to volume fractions φ_{et} in accordance with equation 1. The density of ethanol at 20 °C was taken as 0.789 g/ml and the density of water as 0.998 g/l. These cosolvent mixtures covered a range from 15 % to 40 % in steps of 5 %. Sucrose with a grade of reag.PhEur. was then dissolved in the cosolvent mixtures in various mass fractions w_{suc} (eq. 2) from 10 % to 40 % in steps of 10 %.

Depending on their alcohol and sugar content, different alcoholic beverages were chosen to represent both sugar-sweetened and unsweetened spirits. These beverages are given in Table 1.

$$\varphi_{\text{et}} = \frac{V_{\text{ethanol}}}{V_{\text{ethanol}} + V_{\text{water}}} \tag{1}$$

$$w_{\text{suc}} = \frac{m_{\text{sucrose}}}{m_{\text{sucrose}} + m_{\text{cosolvent mixture}}} \tag{2}$$

Table 1: *Selected alcoholic beverages*

Sweetened	**φ_{et} in %**	**Concentration of sugar in g/l**
Port	19.5	<100
Peach liqueur	20	<150
Egg liqueur	20	≈150
Herb liqueur	21	≈100
Triple sec	40	≈203
Unsweetened		
Schnapps	32	-
Vodka	38	-
Whisky	40	-
Arak	47	-
Rum	54	-

2.2 *Flash point and fire point tests*

The flash point is defined as the lowest temperature of a flammable liquid corrected to a standard pressure of 101.3 kPa at which the application of a test flame causes the vapour of the test portion to ignite momentarily and the flame to propagate across the surface of the liquid. Methods of measuring the flash point of a liquid are specified in international and national standards (ISO 13736, ISO 3679, ISO 1523, ISO 1516, ISO 2719, ISO 2592, DIN 51755, ASTM D56). They differ primarily in terms of the temperature range and the state of equilibrium the gas phase can reach.

Generally, the closed-cup flash point methods result in lower flash points than the open-cup methods, which makes the results more reliable when used in an explosion risk assessment. Two different closed-cup methods were chosen here in order to compare a non-equilibrium method and an equilibrium method. The non-equilibrium method defined in ISO 13736 (2013) is suitable for most flammable liquids and uses a sample volume of 71 ml, which is slowly heated up and tested at each degree Celsius. This might result in early consumption of part of the flammable vapour at lower temperatures. In order to prevent this, the rapid equilibrium closed-cup method ISO 3679 (2015) uses a fresh 2 ml sample for each test. Both methods can produce very similar results with pure substances. Nevertheless, for some mixtures with a small content of a flammable volatile liquid, the ISO 13736 method results in lower flash points due to its better ability to reach the lower explosion limit in the vapour phase, as the ratio of the liquid bulk phase volume to the volume of the gas phase is higher. On the other hand, because the rapid equilibrium method is fast and requires less material, it is widely used. For this reason, a comparison of both methods was included in this study. The measured values of both methods were corrected to standard pressure and rounded to 0.5 °C. The ISO 13736 tests were performed by means of an automated Petrotest ABA4 device equipped with a Haake WKl 26 cryostat. For the ISO 3679 test, an automated Stanhope-Seta Setaflash 8 device was used. Additionally, the

Cleveland open-cup method for mineral oil products presented in ISO 2592 (2017), which uses a sample volume of about 88 ml, was applied for the determination of the open-cup flash point and fire point. The tests were performed with a semi-automatic device (Walter Herzog). Open-cup flash points were always measured under non-equilibrium conditions. The values were corrected to standard pressure and rounded to 1 °C.

The fire point of a fuel is the lowest temperature corrected to standard pressure at which the vapour of that fuel will continue to burn after ignition by means of an open flame of standard dimension. The fire point may be significantly higher than the flash point measured via the Cleveland method. After reaching the flash point, the sample is therefore additionally heated in such a way that its temperature rises at a rate of 5 K/min to 6 K/min. The test flame is applied every 2 K until the vapour phase of the sample ignites and continues to burn for at least five seconds. The temperature at this point is the fire point determined for the sample, which is then corrected to ambient pressure and rounded to the nearest degree Celsius.

2.3 *Sustained combustibility test*

The test for sustained combustibility was performed to identify whether a given mixture sustains combustion when heated and exposed to a flame. The method is standardized in ISO 9038 (2013) but also referred to in UN Test L.2 (2005) for the transport of dangerous goods. For this purpose, two testing temperatures (60.5 °C and 70 °C) and two different heating times (15 s and 30 s) are defined. The test can be performed to check whether flammable liquids whose flash point is > 35 °C and ≤ 60 °C can be exempted from being classified as flammability category 3 as defined in the CLP directive. If the test is negative, the liquid does not have to be classified as flammability category 3; however, it should be noted that substances that pass this test may still form explosive atmospheres.

A standard testing device was used, as shown in Figure 1. A metal block with a concave sample well was heated to a specified temperature. A hole was drilled into the block and a thermometer inserted into the hole. A 2 ml portion of the liquid was transferred to the well and heated for either 30 s or 60 s at a defined testing temperature. Subsequently, an ignition source was applied to the vapour phase above the liquid for 15 s. If a flame developed at the top of the liquid, it was observed to see whether it continued to burn for at least 15 seconds after removal of the ignition source. The sample undergoes sustained combustion if the following criteria are fulfilled: 1) either the liquid catches fire directly via self-ignition during the heating time or the sample burns for more than 15 s after removal of the ignition source applied for 15 s; 2) at least one of the three tests is positive (Figure 2). In this study, most of the test temperatures were set to 40 °C, 50 °C or 60 °C in order to find the temperature which barely supports the burning duration of 15 s with respect to the mixture composition. The three substances listed in ISO 9038 were measured to verify the apparatus and the performance of this method.

Deviating from the standard, the stop (B in Figure 1) was positioned further away from the cup centre to avoid early ignition without a stable flame. Early ignition consumes fuel and leads to a reduced burning period once the sustained combustion has started. The whole instrument was placed in a box which was then tightly sealed, as preliminary experiments demonstrated that ambient draughts severely reduce the burning period and hinder the formation of a stable flame.

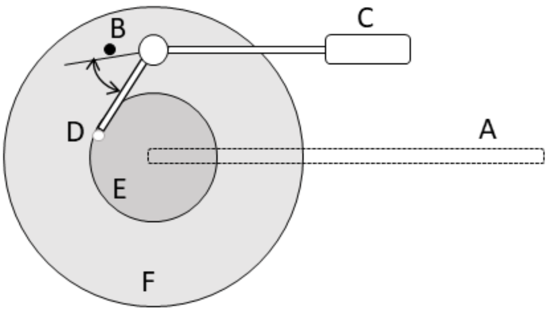

Fig. 1: *Combustibility tester (A: thermometer, B: stop, C: handle, D: test gas jet, E: sample well, F: heated metal block)*

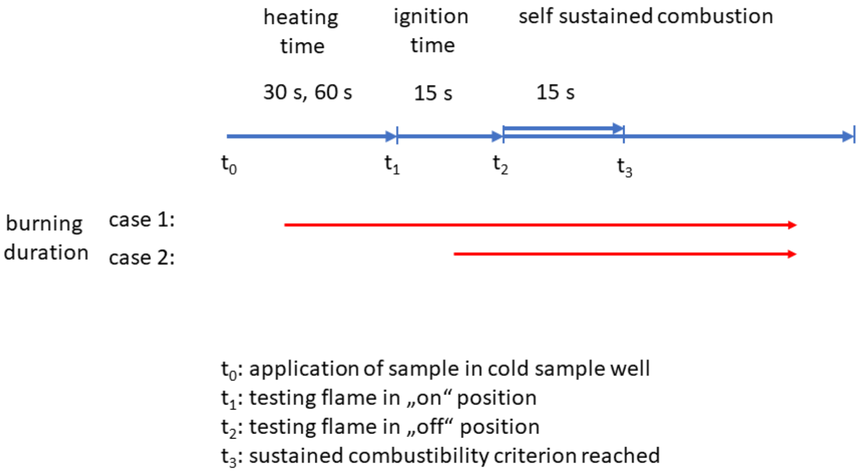

Fig. 2: *Scheme of UN test L.2 and definition of the term "burning duration" as used in this study.*

2.3 Measurement uncertainty of the tests

The flash point methods used in this work are described in the standards listed in table 2 as well as in the conditions of use. The apparatuses were verified beforehand using CRM materials. The repeatability and reproducibility given in the standards together with the expanded measurement uncertainty $\boldsymbol{U}$ are listed in table 3. The expanded measurement uncertainty U (k=2, confidence interval 95 %) was calculated in accordance with equation (3). For each mixture, the flash point was measured three times and the mean value was determined, deviating from the standards which prescribe only a single measurement.

$$U = 2 \cdot R/2.8 \qquad (3)$$

Table 2: *Flash point and fire point methods*

Standard	**Temperature range**	**Heating rate in K/min**	**Testing interval in K**	**Cup type**	**Equilibrium**	**Volume in ml**
ISO 13736	-30 °C to 75 °C	1	0.5	closed	no	71
ISO 3679	-30 °C to 300 °C	none	1	closed	yes	2
ISO 2592	>79 °C	5-6	2	open	no	88

Table 3: *Reproducibility (R) and uncertainty of the applied flash point and fire point methods*

Standard	***R* *in °C***	***U*(*k*=2) *in °C***
ISO 13736 flash point	3.2	2.3
ISO 3679 flash point	0.02561(X+110)	2R/2.8
ISO 2592 flash point	18	12
ISO 2592 fire point	14	10

X: arithmetic mean of the testing results under comparison

3. Results and discussion

3.1 Flash point and fire point of ethanol/water mixtures

Below, the results of the flash point measurements are discussed regarding the CLP classification. Fig. 3 gives a graphical comparison of the former and current regulations. Figure 4 shows the closed-cup flash points of the ethanol/water mixtures; these flash points were obtained using the Abel method (ISO 13763) and compared with values from the Chemsafe database (CHEMSAFE, 2020).

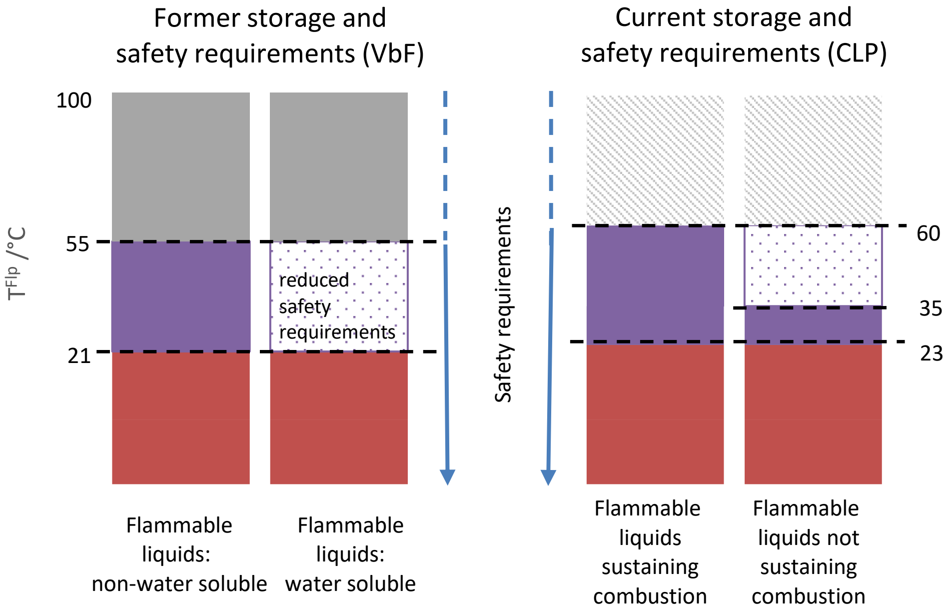

Fig. 3: *Graphical comparison of former and current regulations*

The Chemsafe database provides values measured at PTB in 1963 in accordance with DIN 51755 (Abel Pensky), a method widely used in Germany before ISO 13736 was established in 1997. In DIN 51755, a method is described in which the sample is not stirred during heating. In contrast, ISO 13726 describes stirring the sample during heating, which leads to a more homogeneous temperature distribution over the sample. The stated reproducibility is slightly better adapted to interlaboratory testing. Generally, the values obtained via the different methods cannot be directly compared, as they depend to a large extent on the given apparatus and conditions. Nevertheless, both methods agree very well, as do the values recently published by Chen et al. (2018).

As shown in Figure 4, the flash point decreases with increasing ethanol volume fraction, following a nonlinear curve whose inflection point is around 60 %. Without considering the measurement uncertainty, the flash point limit of 21 °C corresponds to 75 % ethanol, a limit commonly used in safety assessments of ethanol/water mixtures based on the former VbF. Considering the uncertainty indicated in the standards (Table 3) and erring on the side of caution, mixtures with a flash point from 21 °C to 55 °C have a volume fraction range from 58 % to 7 %. The current CLP regulation states that flammable mixtures with a flash point from 23 °C to 60 °C have a volume fraction range from 45 % to 5 %. Consequently, aqueous solutions of ethanol are not considered to be flammable (category 3) as defined in the CLP regulation if the alcohol volume fraction is below 5 % (T^{Flp} = 60 °C). Such solutions do not belong to the group whose flash point is ≤ 55 °C regarding additional fire safety requirements as defined in TRGS 509 if the alcohol volume fraction is below 7 %.

Aqueous solutions of ethanol are flammable (category 3) if the alcohol volume fraction is between 5 % (T^{Flp} = 60 °C) and 45 % (T^{Flp} = 23 °C). Solutions with an ethanol volume fraction between 20 % and 5 % (T^{Flp} = 35 °C to 60 °C) could constitute an exception provided they do not sustain combustion in the L.2 test. Aqueous ethanol solutions with an alcohol volume fraction of more than 45 % are classified as highly flammable (category 2). The shift of the category limit from 58 % (T^{Flp} = 21 °C) to 45 % (T^{Flp} = 23 °C) means that some of the mixtures regarded as “flammable” as defined in the former VbF regulation are now regarded as “highly flammable”. This shift in categorization means that the mixtures will have to either be stored in smaller volumes or be subject to stricter safety requirements. Figure 5 compares the ISO 13763 results with those obtained from the closed-cup rapid test (ISO 3679). The two sets of results agree very well within the range of the measurement uncertainty. Nevertheless, ISO 13763 yields the lowest values, which are 1.5 K lower than those for ISO 3679.

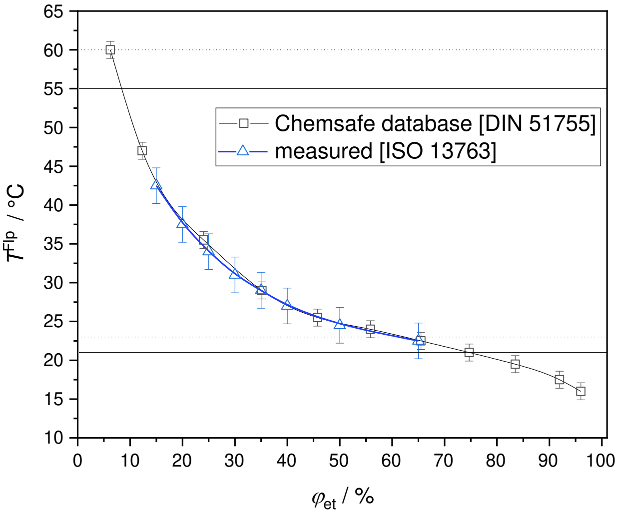

Fig. 4: *Closed-cup flash points obtained from different sources as a function of the ethanol volume fraction in the cosolvent mixture. The classification limits defined in the CLP directive (dotted line) and the withdrawn VbF directive (solid line) have been added to the graph. The values have been corrected and rounded. The error bars show the expanded measurement uncertainty.*

The Cleveland test ISO 2592 was used here in order to get an impression on the temperature for continuous burning of the solutions. The standard was written for mineral oils with flash points of 79 °C to 400 °C. Using this method at lower flash points is accompanied by high measurement uncertainty. This open-cup method produces flash points which are more than 7 K higher than those measured via the Abel method. The fire point also included in the graph is about 10 K higher than the associated flash point and at least 15 K higher than the flash point defined in ISO 13676. This means that the mixture is not able to continuously burn for more than 5 s without the temperature being 15 K above the Abel flash point.

3.2 Flash point and fire point of ethanol/water mixtures containing sucrose

The results of the flash point measurements on ethanol/water mixtures containing sucrose are given in Figure 6. Increasing sucrose content in the ethanol/water mixtures causes a clear decrease in the flash point. Comparison of the results again shows that the Abel flash points are 1 to 2 K lower than the results from ISO 3679. Although the Cleveland flash point method is not suitable for the temperature range found here, a decrease in the flash point was also seen. However, a quantitative result cannot be given.

A more thorough quantitative statement on the continuous burning behaviour of the sample can be made based on the fire point. The fire point measured via the Cleveland method shows a decrease in the sugar content as well. It is higher than the Cleveland flash point and therefore has better reproducibility (Figure 6). Regarding fire safety assessment, the flash point defined in ISO 13736 can be compared with the starting temperature of continuous burning, which is given by the fire point: at 10 K above the Abel flash point, the solution starts to burn for at least 5 s.

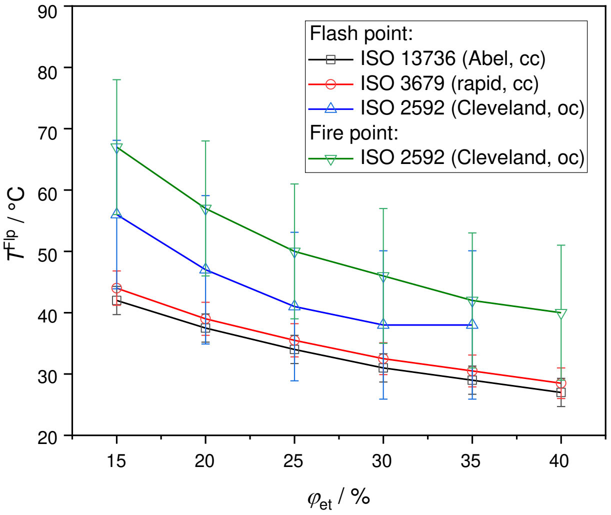

Fig. 5: *Flash points and fire point in dependence on the ethanol volume fraction (cc: closed-cup; oc: open-cup). The values have been corrected and rounded. The error bars show the expanded measurement uncertainty.*

DOI: 10.7795/810.20200724

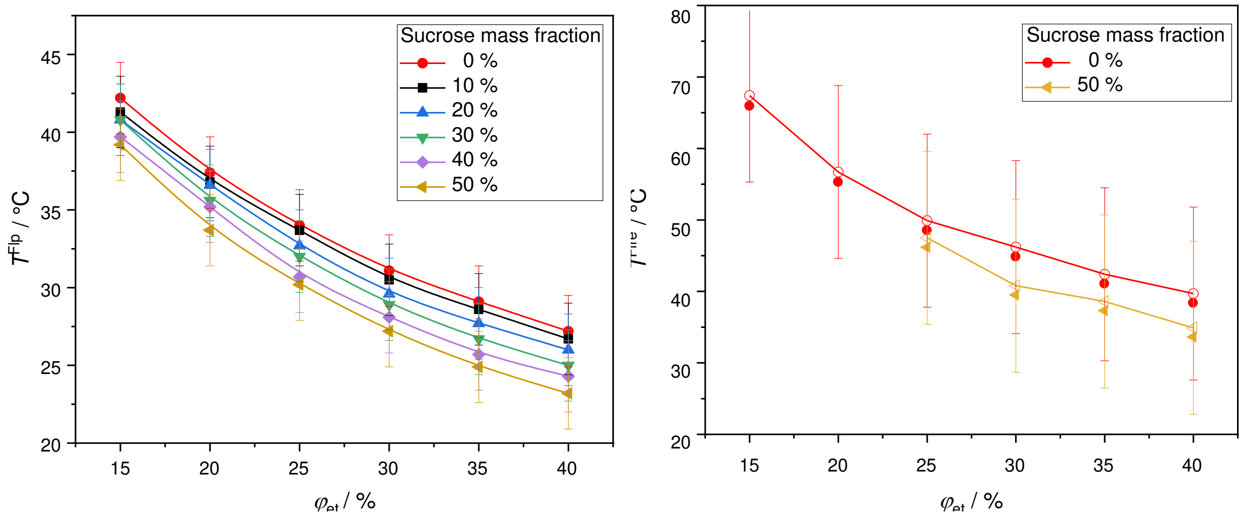

Fig. 6: Left: flash points measured for ethanol/water solutions with various levels of sucrose. The values were not rounded. Right: fire point defined in the Cleveland method.

3.3 Flash point calculation for sucrose containing ethanol/water mixtures

For the compositions investigated, the flash point decreases linearly with increasing sucrose mass fraction when only the sum of the water and the sucrose is considered (Figure 7). For this assessment, the unrounded values after standard pressure correction were used. Linear regression for the various ethanol/water solutions results in an average slope of 0.067 K/mass% ± 0.008 K/mass%. For a specific ethanol/water mixture, it is therefore possible to estimate the flash point with the aid of the pure-mixture flash point without sucrose (T_0^{Flp}) and to subtract 0.7 K per 10 mass% of sucrose in the sucrose plus water fraction:

$$T_{suc}^{Flp} = T_0^{Flp} - (0.07\, K \cdot m_{suc}/(m_{suc} + m_{water})) \quad (3)$$

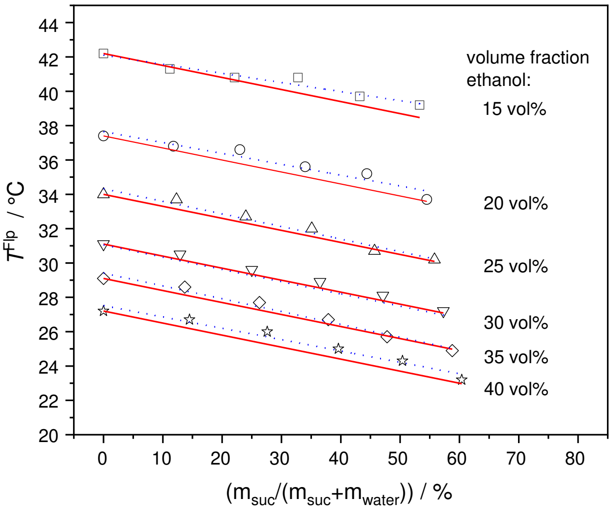

Fig. 7: Linear decrease of the flash point with increasing mass content of sucrose in the water/sucrose mixture for the different ethanol/water cosolvent mixtures. The values have not been rounded. The dotted lines show the linear regressions and the solid lines show the estimation curve with a decrease of 0.7 K per 10 mass% sucrose.

3.3 Alcoholic beverages

Figure 8 shows the results of the flash point measurements of alcoholic beverages as defined in ISO 3679 together with the flash point curve of the ethanol/water mixtures as defined in ISO 13736. The graph shows that the unsweetened spirits follow the curve very closely. The flash point values are slightly lower than the flash points of the model solutions. Apart from the fact that deviations from the alcohol content indicated by the manufacturer are allowed, one reason for this could be the presence of additional flavouring substances, which can be considered as belonging to the flammable volatile component of the spirits. The sugar-sweetened beverages behave differently. Although the exact sugar content is not indicated by the manufacturer, the trend follows the estimated sugar content (table 1). The classification limits in the graphs show that some of the beverages previously classified as “flammable” would now be classified as “highly flammable” in accordance with the CLP regulation, particularly when the uncertainties are considered. Although the alcoholic beverages are considered food and do not fall under the scope of the European chemicals regulation REACH (i.e. the flammability of the beverages does not have to be labelled on the bottle for retail purposes), the recategorization carries with it implications for storage regulations.

3.4 Sustained combustion

The sustained combustibility test was carried out and the burning duration measured at a given test temperature after ignition. It was clear from the nature of this test that the results would show a relatively large scatter. However, this test is the standard test with respect to classification and labelling when the 15 s criterion of sustained burning after removal of the ignition source is applied at testing temperatures of 70 °C and 60.5 °C. Furthermore, the test result is considered positive even if the sample ignites during the heating time regardless of the total burning duration.

It was found in several hundred individual tests on ethanol/water mixtures containing sucrose that the heating time (30 s vs. 60 s) has only a minor influence. If the sample is heated for 60 s, the time to ignition is one second shorter than for the 30 s test; the same was found to be true of the burning duration. This difference is small compared to the standard deviation of the repetition tests. To err on the side of caution (i.e. allowing longer burning times), a heating time of 30 s was found to be appropriate in this study. As the ethanol content increases, ignition takes place sooner, while the amount of sucrose does not seem to have a clear influence on the time to ignition.

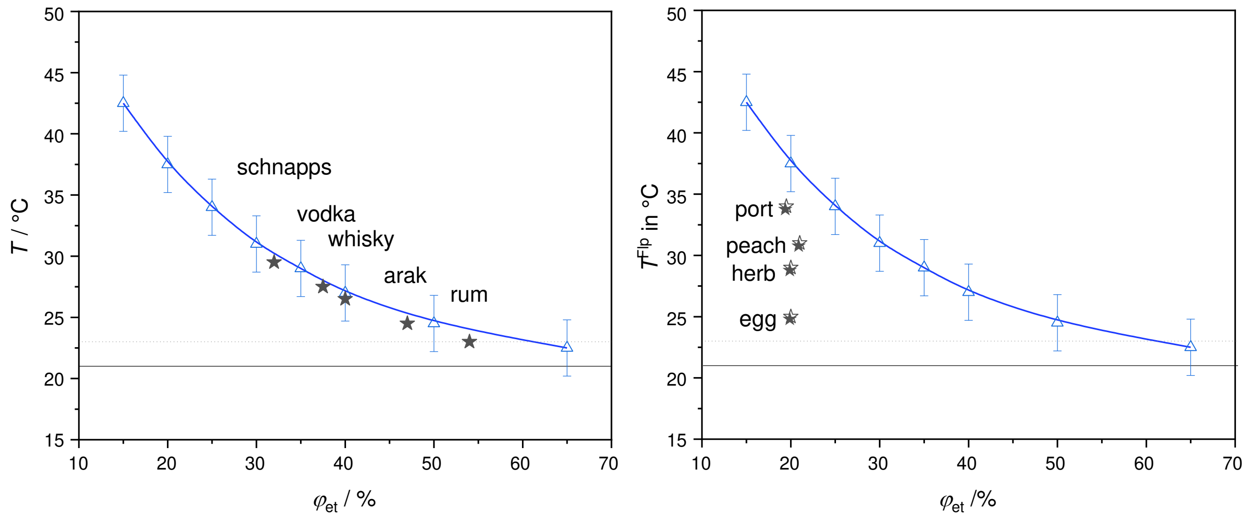

Fig. 8. *Flash points measured as a function of the ethanol volume fraction in water for unsweetened alcoholic beverages (left) and sweetened liqueurs (right). The values have been corrected and rounded.*

Generally, the burning duration itself is highest when a high ethanol content is present in the cosolvent mixture, as shown in Figure 9. Near the standard test temperature (60 °C), there is a clear decrease in the burning duration with increasing sucrose content. This trend indicates that the partial pressure of ethanol is higher when sucrose is present because part of the water dissolves sucrose and because hydrogen bonding between ethanol and water is hindered. This finding is supported by the flash point measurements. The 15 s burning duration given in Figure 9 is not the same as that in UN test L.2 (Figure 10), which considers the burning time only after the ignition source has been applied for 15 s. In some cases, the ethanol flame was stable at a much earlier stage and the total burning duration lasted longer than 15 seconds; however, the test was still negative because the 15 s criterion was not fulfilled. Furthermore, even if only one out of three tests is positive, the result is positive. For this reason, the results for the L.2 test at 60 °C are given separately in Figure 10 and differ from the results in Figure 9, where the average burning duration is given.

UN test L.2 is negative (i.e. combustion is not sustained) for all mixtures with an ethanol volume fraction of 15 % in the cosolvent mixture and a sucrose mass fraction of up to 50 % (Figure 10). These mixtures have flash points of ≥ 35 °C and do not sustain combustion even at a test temperature of 75 °C. Therefore, they do not need to be classified as category 3. This is true for the model solutions given in Figure 6 and for the first two alcoholic beverages from Table 4. All other alcoholic beverages tested and given in Figure 8 had flash points below 35 °C and therefore cannot be excluded from category 3 irrespective of the result of the sustained combustion test. UN Test L.2 matches perfectly with the flash point limit of ≥ 35 °C for aqueous ethanol solutions containing a sucrose mass fraction of up to 50 %.

At an ethanol volume fraction above 25 % in the cosolvent mixtures, the flash points are too low to be exempted from classification. For mixtures with an ethanol volume fraction of 20 %, the test is negative, as the sucrose mass fraction rises to 30 %. Here, the sucrose lowers the flash point to a level near 35 °C but does not lead to sustained combustion. In this individual case, an exemption is appropriate if the measurement uncertainty of the flash point is not considered. Less sucrose sustains combustion, as confirmed by the last three beverages in Table 4, while more sucrose lowers the flash point to below the classification limit.

When the test temperature is lowered, more and more mixtures show burning durations below 15 s. The general decrease in the burning duration with decreasing sucrose content was again observed for mixtures with sucrose mass fractions of more than 20 %. Three different effects are noted:

- Mixtures with sucrose mass fractions of ≤ 20 % or with no sucrose are very sensitive to the test temperature. The burning duration increases when the test temperature rises from 40 °C to 50 °C. This is due to the simple fact that the higher vapour pressure of ethanol delivers more fuel to the vapour phase at higher temperatures. The beverages in Table 4 show the same effect when the temperature rises from 60.5 °C to 75 °C.
- The burning duration of the cosolvent mixtures with an ethanol volume fraction of ≥ 30 % decreases when the temperature is increased from 50 °C to 60 °C. This can be explained by the additional heating of the sample during burning. Cosolvent mixtures with an ethanol volume fraction of > 30 % sustain combustion at test temperatures from 40 °C to 60 °C. Even due solely to their flash point, they must be classified as flammable category 3.
- Cosolvent mixtures with an ethanol volume fraction of < 30 % can show a negative result regarding the 15 s criterion when the test temperature is lowered from 60 °C to 50 °C or even to 40 °C.

The test creates the impression that, because a higher sugar content reduces the burning time, the effects of burning are less dangerous. However, it should be noted that the shorter burning time is due to the increased evaporation of ethanol. The mixture burns off more quickly, which is accompanied by a higher heat release per unit of time.

4. Conclusions

The flash points of ethanol/water mixtures containing sucrose, which were obtained via different methods in accordance with ISO 13763 and ISO 3679, agree very well within the respective measurement uncertainty. However, ISO 13763 leads to lower values by tendency and is therefore preferred. The flash points decrease with increasing ethanol volume fraction in the cosolvent mixtures and with increasing sucrose mass fraction. The fire point of the samples is at least 10 K higher than the flash point defined in ISO 13763 when measurement uncertainties are not considered. It decreases with increasing sucrose content.

Flammable ethanol/water mixtures with a flash point from 23 °C to 60 °C have a volume fraction range from 45 % to 5 %. Consequently, aqueous solutions of ethanol are not considered flammable (category 3) as defined in the CLP regulation if the alcohol volume fraction is below 5 %. These solutions do not belong to the group with a flash point of ≤ 55 °C regarding additional fire safety requirements as defined in TRGS 509 if the alcohol volume fraction is below 7 %. Aqueous ethanol solutions with an ethanol volume fraction of > 45 % must be classified as “highly flammable” (category 2). The shift of the category limit from 21 °C (which corresponds to 58 % ethanol) to 23 °C (which corresponds to 45 % ethanol) means that some mixtures regarded as “flammable” as defined in the former VbF regulation are now to be classified as “highly flammable”. This shift in categorization means that the mixtures will have to either be stored in smaller volumes or be subject to stricter safety requirements. Some of the alcoholic beverages tested which were previously classified as “flammable” will now be classified as “highly flammable” as defined in the CLP regulation, especially when the uncertainties in flash point determination are considered.

The flash point of a given ethanol/water mixture containing sucrose can be interpolated when the flash point of the pure cosolvent mixture is known. There is a direct relation between the amount of sugar and the amount of water in the mixture. The partial pressure of ethanol is higher if sucrose is present. This effect is caused by hydrogen bonding taking place primarily between water and sucrose. This finding was confirmed in the test for sustained combustibility, which showed that the burning duration is shorter with higher sucrose content.

Mixtures and beverages with less than 15 % ethanol in the cosolvent mixture and a sucrose mass fraction of up to 50 % have flash points of ≥ 35 °C and do not sustain combustion even at a test temperature of 75 °C. Therefore, they do not need to be classified as category 3. By contrast, all alcoholic beverages tested which have an ethanol volume fraction of ≥ 15 % had flash points below 35 °C and/or sustained combustion and therefore cannot be excluded from category 3. Only one ethanol/water mixture with an ethanol volume fraction of 20 % and a sucrose mass fraction of 30 % were exempted, as the flash point was still slightly higher than 35 °C; however, due to the sucrose content, the sustained combustion was less than 15 s. It should be noted that the shorter burning time with a higher sucrose content is due to the increased vapour pressure of ethanol. The mixture burns off more quickly than without sucrose, which is accompanied by a higher heat release per unit of time. It is also this effect which makes such mixtures substantially different from other flammable liquids such as petrol.

A distinction was made between the classification and the necessity of the measures. Which measures are necessary depends on how hazardous a given situation is. If, for example, the storage temperature is sufficiently below the flash point, a potentially explosive atmosphere and continued combustibility are not to be expected, even in unforeseen scenarios.

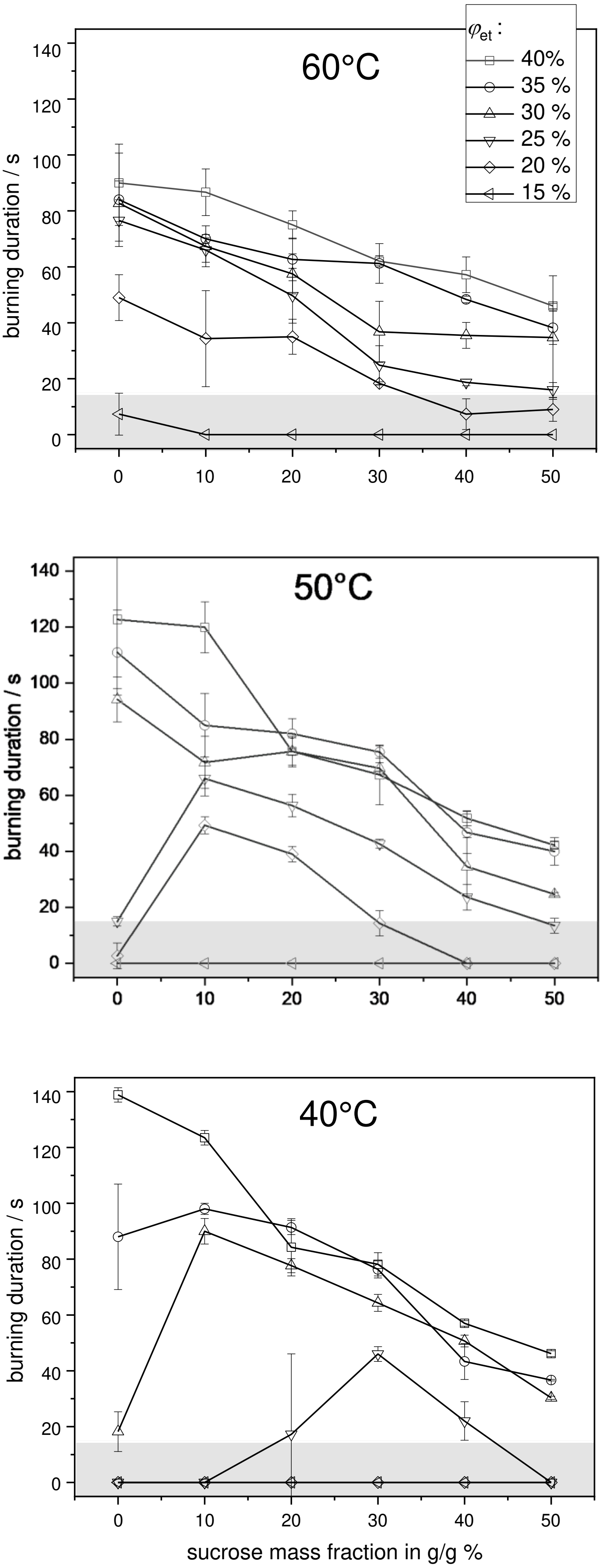

***Fig. 9:** Burning duration starting from stable flame detection on the surface of the liquid mixture for the various test samples at different test temperatures. The 15 s criterion is marked in grey. The error bars show the standard deviation of three test repetitions.*

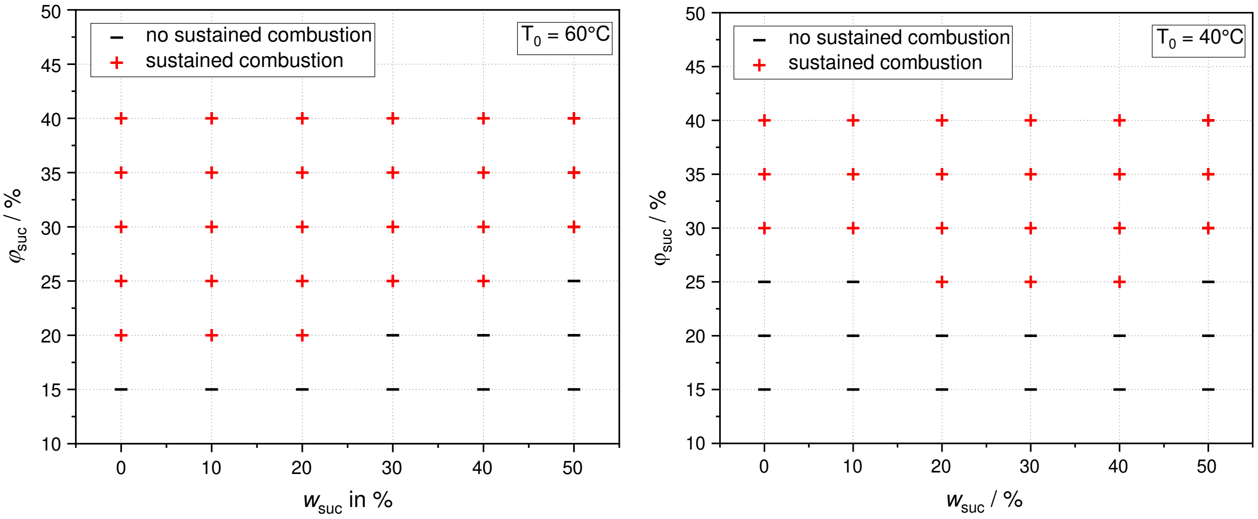

Fig. 10: *Results of UN test L.2 at 60 °C for all ethanol/water mixtures with various levels of sucrose. A testing temperature of 40 °C was applied for comparison.*

Table 4: *Result of UN test L.2 for commercially available beverages (+: sustains combustion)*

Sample	***φ_{et} in %***	***60.5 °C***	***75 °C***
Berry wine	12.5	-	-
Sherry	15	-	-
Vodka preparation	16	-	+
Vodka and orange	17.5	+	+
Port	19.5	+	+
Egg liqueur	20	+	+
Herb liqueur	21	+	+

References

BetrSichV (2003). Verordnung über Sicherheit und Gesundheitsschutz bei der Verwendung von Arbeitsmitteln (Betriebssicherheitsverordnung-BetrSichV). *Bundesgesetzblatt,* 1(4): 49

CHEMSAFE (2020). www.chemsafe.ptb.de, access date 20.02.19

Chen, Q., Wang, X., Zhou, T., Ding, C., Wang, J. (2018). Investigation on the fire hazard characteristics of ethanol-water mixture and Chinese liquor by a con calimeter. *Journal of Thermal Analysis and Calorimetry*, 135: 2297-2308

EC (2008). Regulation (EC) No 1272/2008 of the European parliament and of the council of 16 December 2008 on classification, labelling and packaging of substances and mixtures, amending and repealing Directives 67/548/EEC and 1999/45/EC, and amending Regulation (EC) No 1907/2006. *Official Journal of the European Union*, L353/1.

GMBI (2014). Technische Regeln für Gefahrstoffe (TRGS) 509: Lagern von flüssigen und festen Gefahrstoffen in ortsfesten Behältern sowie Füll- und Entleerstellen für ortsbewegliche Behälter. *Gemeinsames Ministerialblatt* (66-67): 1346-1400.

Hakkarinen, T., Korhonen, T., Vaari, J. (2017). Heat release characteristics of ethanol-water mixtures: Small-scale experiments. *Fire Safety Journal 91* (2017) 174-181.

ISO 13736 (2013). *Determination of flash point - Abel closed-cup method.* International Organization for Standardization, Geneva.

ISO 2592 (2017). *Petroleum and related products - Determination of flash and fire points - Cleveland open cup method.* International Organization for Standardization, Geneva.

ISO 3679 (2015). *Determination of flash no-flash and flash point - Rapid equilibrium closed cup method.* International Organization for Standardization, Geneva.

ISO 9038 (2013). Determination of sustained combustibility of liquids (ISO 9038:2013); Deutsche Fassung EN ISO 9038:2013. Beuth Verlag

Ledin, H.S. (2003). Potential Explosion Hazards due to Evaporating Ethanol in Whisky Distilleries. *Report HSL/2003/08*, Health and Safety Laboratory, Harper Hill, Buxton, England

LV 49 (2017). Länderausschuss für Arbeitsschutz und Sicherheitstechnik: Erläuterungen und Hinweise für die Durchführung der Erlaubnisverfahren nach §18 der Betriebssicherheitsverordnung. *LASI-Veröffentlichung -LV49*, ISBN 978-3-936415-89-6.

UN Test L.2 (2005). Sustained Combustion Test. *Recommendations on the Transport of Dangerous Goods, Manual of Tests and Criteria, Sixth revised edition*, United Nation, New York and Geneva.

DOI: 10.7795/810.20200724

Flammability characteristics of methane enriched with H_2 using CO_2 in the Spark Test Apparatus

Isabel Amez[a], Blanca Castells[a], Ljiljana Medic[a] & Javier Garcia-Torrent[a]
[a] Universidad Politécnica de Madrid & Laboratorio Oficial Madariaga, Spain
E-mail: isabel.amez@upm.es

Abstract

Hydrogen is becoming one of the most important energy vectors for future. Its versatility and the possibility to produce it by renewable energies make hydrogen an excellent alternative to the current fuels. The integration of a hydrogen economy appears to be a large distance solution, but, interestingly, hydrogen can be used as a transition element to cleanest energy production systems. The addition of hydrogen to gas fuels such as natural gas improves the combustion characteristics and reduces greenhouse gases.

Nevertheless, the use of hydrogen implies safety explosion risks that must be taken into account. The flammable nature of hydrogen poses serious safety problems even when is mixed with other gases. Through the study of flammability limits and limiting oxygen concentration, is possible to prevent accidents and to assure a safe environment.

There are numerous experimental studies providing flammability limits of H_2/CH_4 mixtures. However, when comparing literature data, the differences are remarkable, since the method, the apparatus and the test conditions clearly influence the results. The present work proposes an experimental method to obtain the flammability limits and the flammability interval using the Spark Test Apparatus (STA). The fuel varies with the hydrogen content, analysing the mixtures of methane enriched at 10, 20, 30 and 50%. Moreover, the test procedure to determine the flammability interval is also described, through the theoretical representation of the flammability interval in ternary diagrams. The method is validated by means of literature data comparison.

The results in the STA show great alignment with bibliographic and theoretical data. Furthermore, the comparison of the existing data allows generating an empirical curve that resume the influence of hydrogen addition in methane-air mixtures. The theoretical flammability intervals are also presented as a result. Such representations, after the method validation, are the base of the flammability interval test in the STA.

Keywords: *hazards, prevention, inertization, industrial explosions, methane, hydrogen*

1. Introduction

Recently, the potential of hydrogen as an energy vector has aroused great interest due to the necessity to raise new energy systems capable to palliate the current environmental problems (Elsherif et al., 2015). However, hydrogen integration in the conventional energy system still must overcome technological, social, and economic barriers, specifically regarding industrial safety (Acar et al., 2019; Amez et al., 2019). Despite some advantages of hydrogen such as its non-toxicity and the fact that, in the event of a leak its lightness allows a rapid gas dispersion, its use implies a high explosion risk. Hydrogen has a wide range of flammable concentrations when mixed with air and present lower ignition energy than gasoline or natural gas, which means easier ignition (Cashdollar et al., 2000).

Adequate ventilation and leak detection are important elements when designing safe hydrogen systems.

In recent decades, hydrogen has become a potential transition element as technology for a “hydrogen economy” reaches the required mature. The enrichment of some fuels, such as natural gas, with hydrogen is considered an interesting option for the current energy sector since several studies, demonstrate that the hydrogen addition considerably enhances the combustion characteristics of methane (Cellek & Pınarbaşı, 2018; Ge et al., 2019; Hussain et al., 2019; Karlis et al., 2019; Li et al., 2018; Schroeder et al., 2014). Moreover, recent investigations proved that hydrogen addition to the fermentation process of biogas production might increase the methane production yield up to 98% (Abdin et al., 2020).

Flammability characteristics of CH_4 have been widely studied due to its importance in the mining and energy sectors (Gieras et al., 2006; Tian et al., 2017; W. Q. Wang & Sun, 2019). Nevertheless, methane enriched with hydrogen has a completely different behaviour regarding flammability and explosiveness. The understanding of the flammability characteristics of such mixture in the air is a major issue to allow its safe use in industry (X. H. Wang et al., 2017). Hydrogen concentration is a crucial parameter in every flammability and combustion characteristic (Q. Wang et al., 2019). Small percentages of hydrogen improve global efficiency in some combustion processes, while large amounts can change the flame typology causing an incomplete combustion (Benard et al., 2017; Peñaranda et al., 2018). Hence, literature is focused on hydrogen percentages between 0-50% although in practical applications the hydrogen concentration does not exceed 20% (Rajpara et al., 2018; J. Wang et al., 2020).

Despite some authors affirm that the addition of less than 25% of hydrogen not necessarily rises the risk in certain scenarios (Shirvill et al., 2019), the knowledge of the flammability characteristics is essential as they allow to control the safety parameters of fuel gases in industry. Lower and Upper Flammability Limits (LFL and UFL respectively) encompass the set of flammable mixtures and are one of the most important parameters at the time of characterizing and handling flammable gases. LFL, and largely UFL, are affected by pressure and temperature conditions so the tests developed in this study are carried out at atmospheric conditions (Kondo et al., 2011; Pio & Salzano, 2019). The addition of inert gas to the flammable mixture allows avoiding the explosion risk, where the limiting oxygen concentration (LOC) represents the threshold value from which the mixture is not able to generate an explosive atmosphere (Van den Schoor et al., 2009; Zlochower & Green, 2009). Inertization of CH_4-air mixtures decreases both adiabatic and experimental pressure of explosion along with explosion time (Mitu et al., 2016, 2017; D. Wang et al., 2019), but the influence of hydrogen addition needs to be studied experimentally. Specifically, regarding safety measures in the industry since some prevention methods might be affected by hydrogen addition (Wen et al., 2019).

Flammability characteristics are not physical material properties as they depend on the measuring method. The standardization of test methods tries to avoid differences caused by parameters such as direction of flame propagation, ignition energy, heat losses from the gas mixture to the surroundings and isobaric and isochoric conditions of testing since LFL, UFL and LOC are strongly affected by these parameters. The main methods for measuring explosion limits of gases and vapors are (Uber et al., 2019):

- The USBM method: the explosion occurs in a cylindrical vertical tube with an inner diameter of 50 mm and a length of 1500 mm. The ignition is made by an electric spark or a pilot flame passed by at the open lower end of the tube.
- The ATSM 681-98 standard: The explosion occurs in a 5 dm^3 spherical glass; The ignition is made by a central spark igniter of 15 kV.
- The German method according to DIN 51 649: the explosion occurs in a cylindrical vertical glass tube with an inner diameter of 60 mm and a length of 300 mm. The electric spark igniter of 15 kV is located at the tube bottom.

- The determination of the flammability limits and the limiting oxygen concentration is regulated in standard EN 1839 (EN 1839:2017 (E), 2017), wherein the FL and the LOC are obtained through an experimental method consisted on a test vessel (80±2 mm of diameter) with two stainless steel electrodes that produce an electric spark to ignite the gas mixture.

All methods require considering the minimization of heat losses in the burnt gas region. There are also correlations to calculate the flammability limits in an empirical way, considering the parameters such as the heat released by a mole of limiting mixture, normal burning velocity, and adiabatic flame temperature (Saito et al., 1996; Melhem, 1997).

Experimental methods to determine flammability limits or limiting oxygen concentration provide single values of LFL, UFL, and LOC. However, triangular diagrams allow representing all the possible concentrations of a ternary mixture. Indeed, ternary diagrams allow evaluating the mixture from a safety point of view when both, flammable and non- flammable mixtures, are represented. The curve named Flammability Interval (FI) or explosive area, separates both areas by means of a curve. The FI normally has a shape of a parable where the vertex corresponds to LOC. The Spark Test Apparatus (STA) is proposed in this study to obtain the exact parable by means of experimental test. The use of the methodology posed for STA instead of the vessel tests, allows to obtain all the points belonging to the flammability interval and not only the LOC that is just the vertex of the flammability interval.

The STA is described in intrinsic safety standards as an apparatus to control the risk of ignition posed by contact arcs so that, even if the contact arc discharge occurs, the gas mixture does not ignite. The discharges occurring in the STA have been poorly studied. Electrical contact arcs are an electric discharges and are a quite unknown ignition source. Discharges can result when two electrodes get in contact or when the contact is broken (Shekhar et al., 2017). One of the most dangerous aspects of electrical contact arcs is the fact they can occur at voltages significantly below 300V that corresponds with the minimum voltage required for the dielectric breakdown of air according to Paschen's law (Shekhar et al., 2017). Typical conditions for electrical contact arcs are 15-40V, 50-300mA and 30-200μs. The highly flammable nature of hydrogen presents an important risk associated with this kind of ignition source, so the study of the addition of hydrogen to the methane-air mixture in the STA is an important research topic.

In this context, the present study proposes a different method to obtain the flammability limits and the limiting oxygen concentration on the STA. The method is validated through the calculation of the flammability limits evaluating the influence of hydrogen addition. The flammability limits of the methane-air mixture enriched with 10%, 20%, 30% and 50% of hydrogen have been obtained experimentally in the STA. Then, departing on the experimental results and by means of the representation of LFL and UFL over ternary diagrams, a theoretical method is presented to obtain the LOC of the CH_4-H_2-Aire-CO_2 mixture that will be the base for the experimental method to obtain the LOC and the flammability interval in the STA.

2. Experimental and theoretical methodology

According to Le Chatelier law, the flammability limits of a mixture depend on molar fractions and flammability limits of each single component (W. Q. Wang & Sun, 2019). Thus, the addition of a second flammable gas to the methane-air mixture, such as hydrogen, has a direct effect on this parameter. Hydrogen addition has a greater influence on UFL than LFL (Van den Schoor, Verplaetsen, et al., 2008; Van den Schoor & Verplaetsen, 2007), as reflected in numerous studies focused on experimental procedures to obtain the flammability limits of methane-hydrogen mixtures in air, although there are significant discrepancies in the experimental results, depending on the method (Ge et al., 2019).

The sensitivity to electrostatic and electric ignition sources is strongly affected by hydrogen addition as well; the minimum ignition energy (MIE) decreases as the hydrogen content increase (Hankinson et al., 2009). This kind on ignition source is quite interesting since hydrogen installations deal with process automation applications such as actuators, sensors, and displays, where electrical discharges can occur with current values below 1 A and voltages lower than 50 V. Normally, the discharge can be considered as a short arc, however, there are some differences as the discharge present shorter times and lower energies cannot be clearly compared to an arc due to the short times and the small energies (Kammermann et al., 2018). The electrical discharge depends on multiple factors such as the surface characteristics, electrode surface characteristics, cadmium deposits, oxide, and wire length. The correct maintenance of the electrodes is an essential measure in order to ensure the reproducibility of the results.

The experimental methodology presented in this study is based on the use of the Spark Test Apparatus. The flammability limits determined in the STA depend on statistical parameters based on the number of contacts needed to ignite the mixture ("IEC 60079-11, 2011). Indeed, one of the main disadvantages of STA is the poor reproducibility of the results, besides the toxicity of the cadmium electrode (Uber et al., 2019). Some studies show great results of flammability characteristics such as the Minimum Ignition Current (MIC) of hydrogen-methane mixtures in the air in de STA (Janès et al., 2017), parameter that can successfully measure the sensitivity of flammable gas to electrostatic or electric sources. However, the discharges occurring in the STA have been poorly studied despite discharges are crucial phenomena controlling the gas ignition. According to Uber et al., this phenomenon can be explained in four phases. The contact between the electrodes occurs in the first phase. However, the preliminary processes occur when the electrodes begin to separate, in phase two. The grater discharge takes place in phase three releasing the higher energy. Finally, in the fourth phase, the distance between both electrodes is greater so the thermochemical reaction occurs. Hence, the spark test apparatus checks if the gas mixture produces a thermochemical ignition or not.

The experimental determination of the flammability limits and the LOC described in this section provides a methodology to overcome the poor reproducibility and to assure the accuracy with literature data. The method is validated through the flammability limits calculation.

2.1 Experimental development in the STA.

The STA is described in standard EN 60079-11 as an apparatus to measure the capability of a circuit to ignite an explosive atmosphere ("IEC 60079-11, 2011). The extended use of STA for intrinsic safety tests, the possibility to vary the energy of the spark, to check visually the explosion, and the high sensitivity of the pressure sensors make the STA interesting equipment to calculate flammability parameters like FL, LOC, and the FI. However, its use is limited by its disadvantages. The uncontrolled way in which contact arcs occur implies an extremely poor reproducibility of results besides the energy of the spark is not exactly the energy fixed in the external power supply. Moreover, the STA has physical differences comparing with other experimental methods such as, among other factors, the volume and shape of the combustion chamber, the energy of the ignition source, and the sensitivity of the sensors to detect the explosion.

The STA contains a hemispherical chamber with a volume of 250 cm^3 which is smaller than the chambers used in other methods (Miao et al., 2011). The ignition energy is controlled by an external power supply allowing to adjust it depending on the gas tested or the explosive atmosphere conditions. The discharge energy needs to ignite a hydrogen-methane/air mixture with a hydrogen content per volume until 50%. Energies greater than 18μJ are effective for hydrogen percentages of up to 21% (Uber et al., 2019) and, according to the MIE of hydrogen, the ignition energy is fixed at 20 mJ. The electric discharge in the STA occurs by contact and not by dielectric breakdown of air. The first electrode consists of a rotating cadmium disk with two slots that cross it from side to side. The second one is a "thread supporting", constituted by a circle, or square, of brass wherein the four 4 wolfram wires of 0.2 ± 2% mm of diameter are attached. The wolfram wires must be long enough to assure the contact between both electrodes. The rotation speed of the thread holder is fixed at 80 rpm, as established in the standard EN 60079-11.

The mass controller regulates the flow of the three gases setting the inlet pressure of each gas at 2 bar. To ensure the homogenization of the mixture, the experimental set up is composed of a mixer and a gas circuit before entering the ignition chamber. When the STA is used to characterize flammable gasses, the explosion can be double-checked: visually and by means of the high precision pressure sensors. The purge of gases is guaranteed with a filling time of 120 s. Figure 1 describes the experimental setup previously explained.

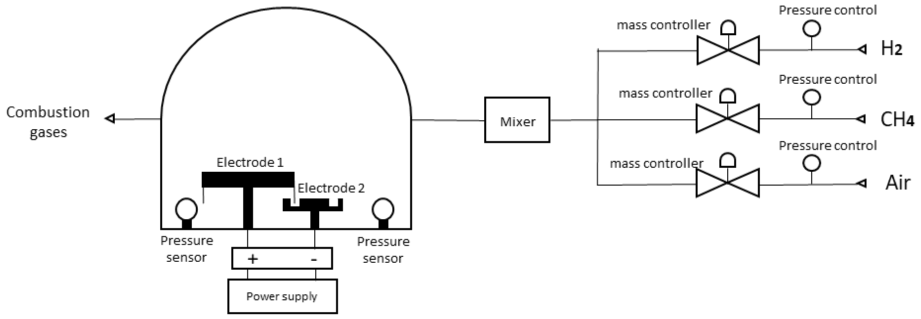

Fig. 1 *Experimental setup in the STA and STA description*

The experimental methodology tries to overcome the reproducibility problems by registering and controlling the number of revolutions needed to ignite the mixture. The STA is an empirical test device that verifies the power limitation where the number of revolutions needed to ignite the mixture is a key parameter in order to determine if the risk of explosion is acceptably low or not (Shekhar et al., 2017). Table 1 exposes the risk assessment criteria to determine the mixture flammability. Each test is repeated four times. If the result is located in the same group of table 1 in all four repetitions, the result can be considered valid, otherwise, it is necessary to repeat it 6 times more. Between 1 to 50 rounds, the mixture is considered as flammable, after the round 51, the probability of ignition is low so the mixture is considered non-flammable, as well as if the mixture does not inflame.

Table 1 *Experimental flammability limits of methane/air mixtures obtained in the STA*

1-20	Very high probability
20-50	High probability
50-100	Low probability
100-200	Very low probability

Considering these criteria, the experimental methodology consists of testing the different concentrations of fuel-air mixtures, from the lower values of air concentration an increasing it until the ignition is observed. This first turning point will correspond to LFL. To obtain the UFL, the inverse procedure is carried out. As the flammability limits are calculated for binary mixtures, the methane and the hydrogen are premixed, maintaining the same proportion of hydrogen in methane, and varying the air concentration. The pressure sensors detect the explosion from 5% differential pressure.

2.2 *Experimental system validation*

The values of the FL of H_2/CH_4 mixtures in air present remarkable differences in the literature (Miao et al., 2011). As this study proposes the use of a different apparatus, it is expected to obtain values with certain misalignment. To ensure the accuracy of the results presented in the present work, the experimental system is validated through the comparison of literature data and experimental results in the STA. Even so, by collecting the existing data and the results of this study is possible to calculate a tendency line to approximate in an empirical way the influence of the hydrogen addition in the flammability limits of methane in the air. This line can provide reliable approximations from where it is possible to estimate the FL of the hydrogen-methane-air mixture.

2.3 *Experimental and theoretical methodology to obtain the flammability intervals in the STA*

Inert gases such as nitrogen and carbon dioxide are used in industry to prevent the explosions (Mendiburu et al., 2018). Nitrogen is normally used due to its low cost despite it has less inert power against hydrogen than carbon dioxide (García Torrent, 2003, Di Benedetto et al., 2009)). However, some processes generate carbon dioxide so it could be used directly to carry out the atmosphere inertization. This is the case of biomethane production, since the addition of hydrogen in the fermentation process enhances the yield of methane conversion, generating CO_2 that can be used for safety controls. Taking advance of this scenario, this study is focused on carbon dioxide inertization.

The representation of the flammability interval or explosive area in ternary diagrams is quite useful and is drawn on European standards (EN 14756, 2007). Graphically, the set of flammable mixtures is delimited by the FL and the LOC. The three points belong to the flammability interval, which can be defined as the curve that contains all the flammable mixtures. The knowledge of the theoretical flammability interval is a valuable approach to get a preliminary idea of the flammability of a ternary mixture. In this section, the theoretical method is explained through the calculation of the flammability interval of the H_2-CO_2-air mixture. Ternary diagrams must refer to pure oxygen first as this method is based on the oxygen stoichiometric point. The LFL of hydrogen in oxygen is 4% and the UFL is 94% (García Torrent, 2003). The stoichiometric point “S” in figure 2 corresponds to the stoichiometric concentration of fuel on pure oxygen needed to complete the combustion reaction, X_{O2}. “S” point results in the stoichiometric line connecting the S point and the inert vertex.

$$C_{\eta_C}H_{\eta_H}O_{\eta_O} + \nu_{O_2}O_2 \longrightarrow \nu_{CO_2}CO_2 + \nu_{H_2O}H_2O$$

$$x_{O_2} = \frac{\nu_{O_2}}{\nu_{fuel} + \nu_{O_2}} = \frac{\eta_C - \frac{\eta_O}{2} + \frac{\eta_H}{4}}{1 + \eta_C - \frac{\eta_O}{2} + \frac{\eta_H}{4}}$$

The stoichiometry of the reaction of the H_2/CH_4 mixture refers to both reactives, considering methane presents the major proportion. In the scenario of 0% of methane (which is the case of this example) the combustion reaction refers to pure hydrogen, where the X_{O2} is 33% (figure 2). The theoretical LOC_{O2} is located approximately in the crossing point between the stoichiometric line and the LFL line which means that LOC occurs at a stoichiometric concentration. Razus et al, measured the LOC for several hydrocarbon-air-nitrogen mixtures determining that LOC occurs at a fuel/air equivalence ratio in the range 1.10 to 1.49 and not at a stoichiometric concentration (Razus et al., 2004). However, as this method is a preliminary approximation intended to use as base for the experimental tests, the deviation is considered acceptable. The LFL line can be approximated as a parallel of the CO_2-O_2 vertex. This hypothesis lies in the lack of fuel gas so there is always an oxidant excess below LFL which means that it can be assumed the independence of LFL of oxygen concentration. Consequently, the line is approximately a parallel of the CO_2-O_2 vertex, drown from UFL. Both lines and the LOC_{O2} referred to oxygen are in figure 2.

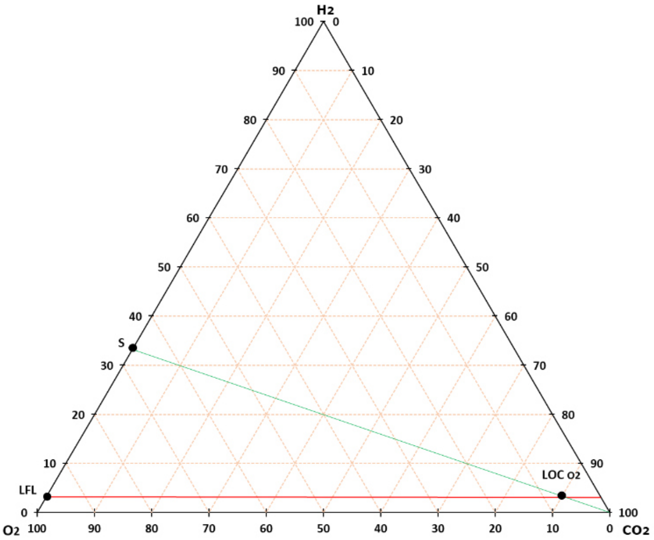

Fig. 2 *Graphical calculation of LOC referred to pure oxygen*

Figure 2 reveals LOC_{O2} is composed of 4% of hydrogen, 8% of oxygen, and 88% of CO_2. Considering that air is composed approximately by 21% of oxygen and that the LFL of hydrogen in the air is also 4%, the LOC is composed of 4% of hydrogen, a 38,1% of air, and a 57,9% of CO_2. Kutcha (Kutcha, 1985) proposed a minimum volume of 57% CO_2 needed to inertize the mixture, which has a great agreement with the theoretical percentage of CO_2 calculated here. LOC differs largely as the theoretical approximation gives a LOC of 8% while normally the oxygen concentration is between

4.6 and 5.2%. Figure 3 represents the flammability interval of hydrogen in the air when it is diluted with CO_2, in the simplest shape, a triangle. Nevertheless, the shape of the FI closes in the form of a parable when reaching the LOC.

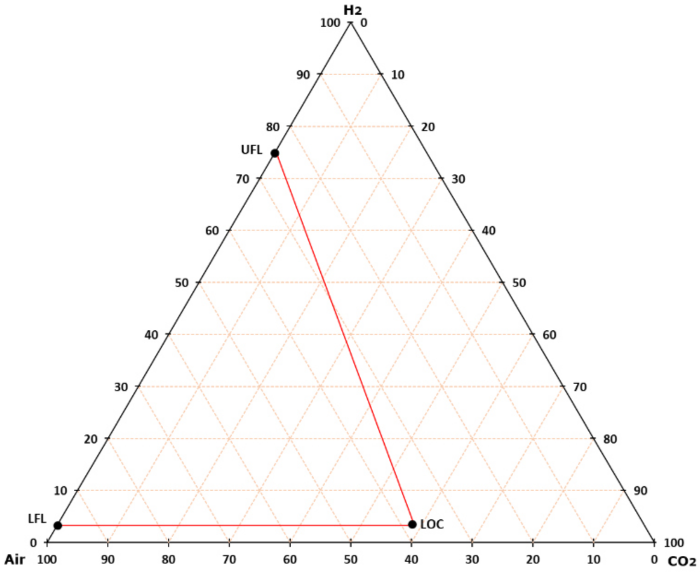

Fig. 3 *Theoretical LOC of hydrogen-air-carbon dioxide mixture*

The experimental methodology to obtain the flammability interval departs from the theoretical FI. Then, at least ten lines are represented, starting in the flammability limits and ending at the inert gas vertex. Each line cross the theoretical flammability limit in one point (blue points in figure 4). These points are the base of the experimental methodology since this method intends to obtain the intersection between the experimental FI and each represented line (lines L1, L2, L3... in figure 4). To do that, it is necessary to represent over the lines at least three points after the intersection point and three before. All these points are tested in the STA to find the last flammable point and the first non-flammable point. The precision of this method depends on the number of lines represented and the distance between points tested.

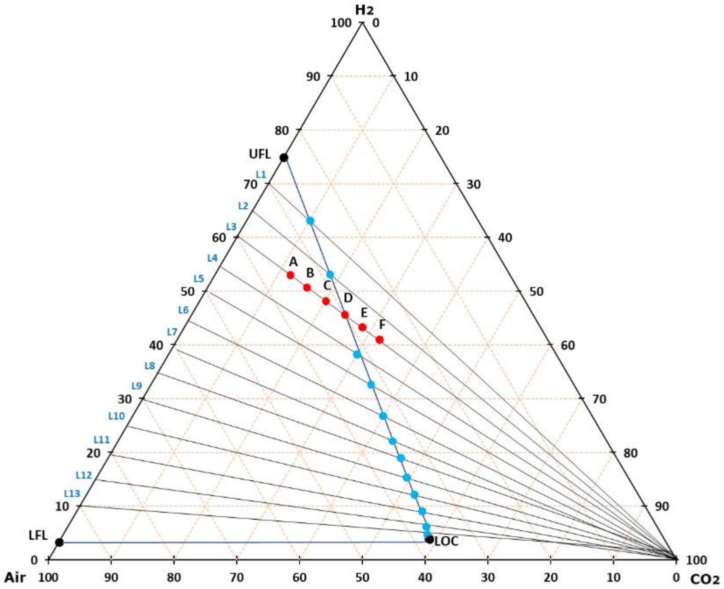

Fig. 4 *Representation of the experimental method to obtain the flammability interval in the STA*

3. Results and discussion

Theoretical flammability limits exposed in table 2 give a preliminary idea of the expected results. Moreover, this data has been also included in the graphical comparison of existing data since Hodges et al. (Hodges et al., 2015) established, that both flammable limits and limiting oxygen concentration of enriched natural gas can be reasonably calculated using the Le Chatelier formula.

Table 2 *Theoretical flammability limits of methane/air mixtures from Le Chatelier equation*

%H_2	**0**	**10**	**20**	**30**	**50**	**100**
LFL	4,69	4,61	4,53	4,46	4,39	4,00
UFL	14,98	16,28	17,83	19,71	22,03	75,00

3.1 Experimental results of the Flammability Limits

Following the methodology described in section 2.1, table 3 presents the flammability limits obtained in the STA. The explosion behaviour was analysed through the translucent window of the STA chamber and the ignition detected by means of pressure sensors. Empirically, the mixtures normally ignite between the round 1 and 5, particularly in mixtures near the flammability limits. In isolated cases, the ignition occurs around the twentieth round. If the mixture does not ignite in the round 40, it can be considered that the mixture does not ignite. This effect is related to the ignition energy as the fixed energy for the test is high enough to ignite the mixture. Besides, the mixture homogeneity plays a key role in explosion risk probability even assuming a high level of the blend. The addition of hydrogen has a direct influence on the explosion behaviour, as it is possible to notice an increment of the explosion luminosity at the same time that the hydrogen concentration increases. The results are given with a standard deviation of 0.25% concentration.

Table 3 *Experimental flammability limits of methane/air mixtures obtained in the STA*

%H_2	**10**	**20**	**30**	**50**
LFL	4,50	4,50	4,50	4,25
UFL	16,25	21,25	23,75	27,50

3.2 Experimental system validation results

This study poses an ignition criterion to standardize the results and to improve the repeatability. Hence, the system validation departs from the comparison between the flammability limits of methane in the STA and bibliographic data. Nominal deviation of methane FL obtained in the STA is compared with bibliographic FL in figure 5 (Miao et al., 2011; Razus et al., 2004; Van den Schoor, Hermanns, et al., 2008). The bibliographic flammability limits of methane have great alignment with the results obtained in the STA. The LFL differs 0.1 points from the average (figure 5, b) while the UFL differs 0.25 points (figure 5, a). Those results allow the validation of the STA method.

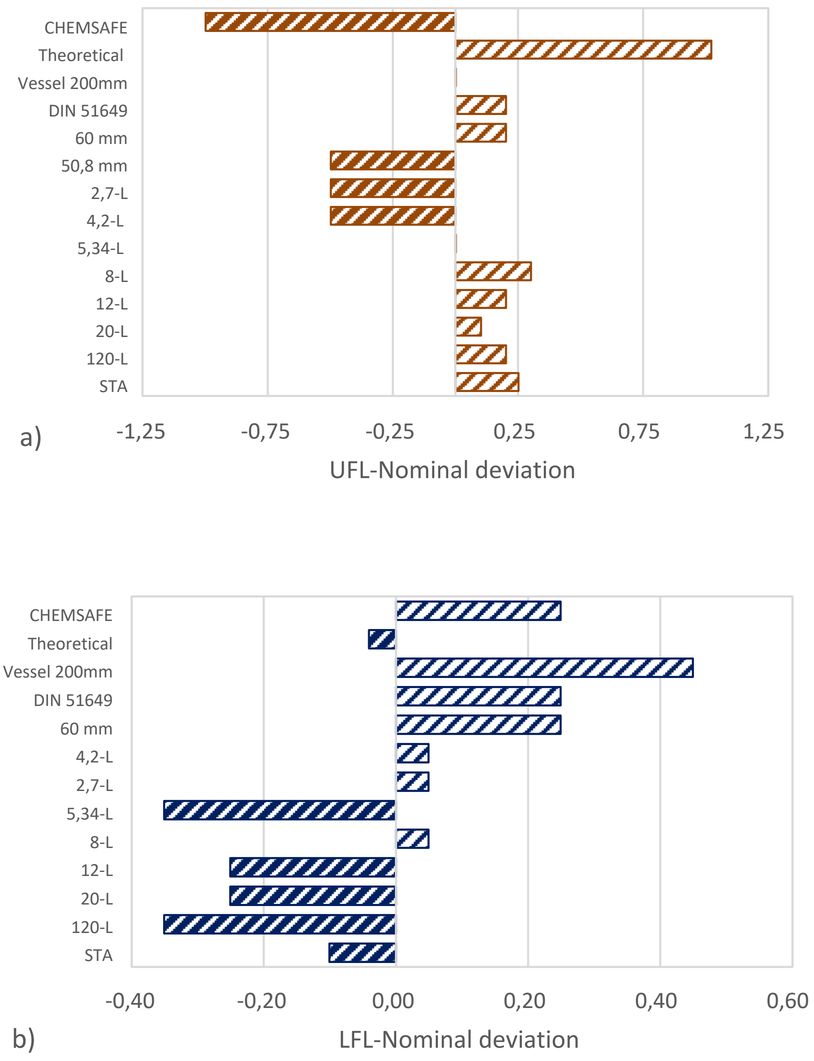

Fig. 5 *Comparison of bibliographic values of methane/air flammability limits for STA method validation; a)Normal deviation of UFL comparing bibliographic and experimental results b) Normal deviation of LFL comparing bibliographic and experimental results*

The methods exposed in figures 6 and 7 consider different combustion chamber volumes being STA the smallest one. However, those methods also have similarities as all of them ignite the mixtures by electric sparks and the criteria to detect explosion is a pressure rise in a range of 2%-10%, typically, fixing the pressure rise at 5% or 7%.

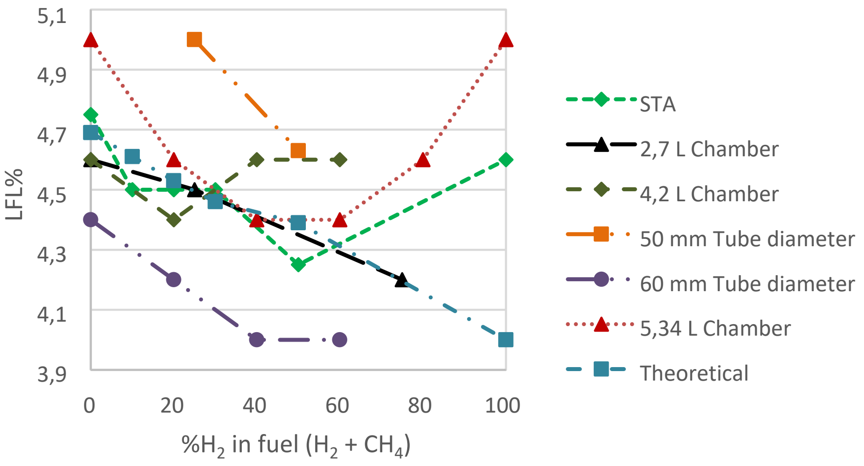

Fig. 6 *LFL comparison between existing data in literature and data from this study (Miao et al., 2011; Razus et al., 2004; Van den Schoor, Hermanns, et al., 2008)*

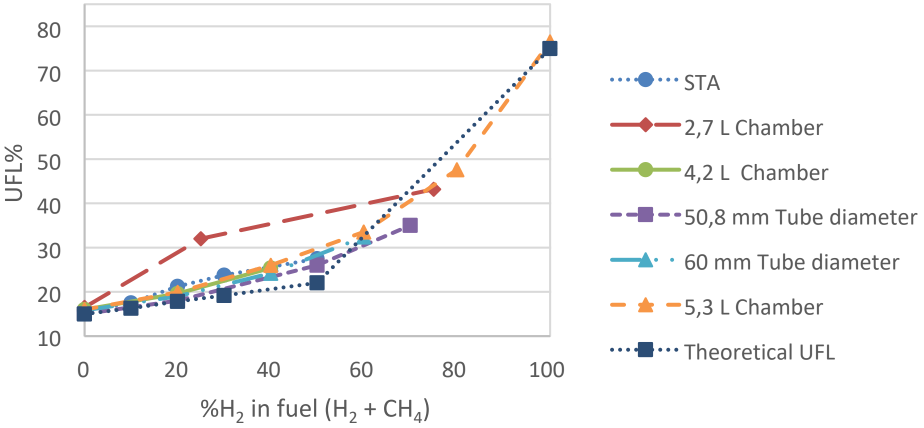

Fig. 7 *UFL comparison between existing data in literature and data from this study(Miao et al., 2011; Razus et al., 2004; Van den Schoor, Hermanns, et al., 2008)*

The method using the 2,7 L chamber shows the FL closer to the theoretical results. Most of the test share the same results, specifically for hydrogen concentrations until 50%. Moreover, both methods using tubes to test the FL are the most desalinated ones. Analysing the STA method, with a volume of 250 cm^3, the results are close enough to theoretical values.

Both figures reveal a clear tendency similar in every experimental study. First, the addition of hydrogen has a low influence in the LFL since all the values vary between 5% to 4% as expected. From an industrial point of view, this comparison is enough to fix the lower flammability limit of the hydrogen-methane mixture in 4,5 ± 0.5% for every concentration of hydrogen, always applying safety coefficients.

However, the addition of hydrogen clearly influences the UFL as it increases as hydrogen concentration in fuel mixture increases. Thanks to several data collected in this study, figure 8 represents a cloud of points from where the tendency equation is obtained. The curve can be used to obtain the UFL for every concentration of hydrogen, taking into account that de results need a safety coefficient to be used under real conditions.

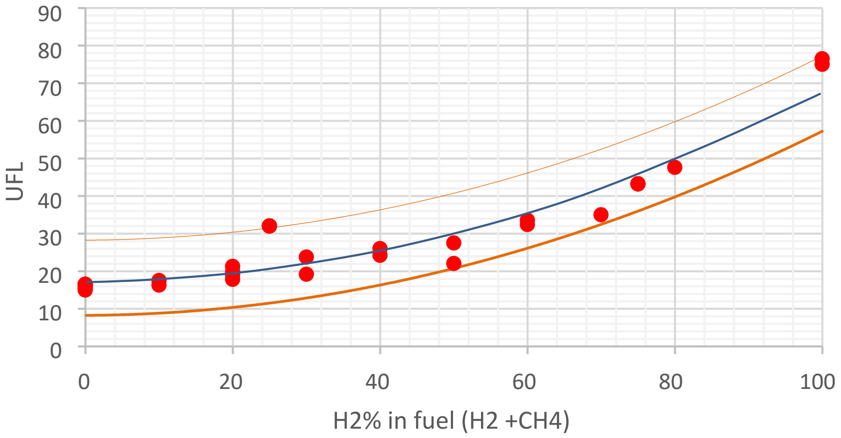

Fig. 8 *Trendline of hydrogen addition influence in the UFL of methane/air mixtures*

As mentioned before, from the experimental data, it is possible to define a trendline that allows the estimation of UFL from hydrogen content as figure 8 explains. However, this trendline does not fit accurately enough the data, as the R^2 is 0.871. The empiric equation that defines the influence of hydrogen addition is:

$$UFL = 0{,}0048 \cdot H_2\%_{\ in\,fuel}{}^2 + 0{,}0097 \cdot H_2\%_{\ in\,fuel} + 18{,}276$$

Such empiric equation has great results between concentrations 10 to 80% of hydrogen, while it has poor results for the flammability limits of pure hydrogen and pure methane. In order to provide a solution, two more curves are defined, the first one 10 points over the trendline and the second one 10 points beneath the trendline. By doing this, the trendline becomes an area, a channel whose error margin has remarkable diminished. All the points located out of both lines can be considered as safety mixtures.

3.2 Theoretical approximation of the FI

The influence of hydrogen addition on the flammability limits directly involves influence in the flammability interval. Then, as the results of table 3 show an increment on the flammability limit when hydrogen is added, the flammability intervals will increase as well. Maria Molnarne et al, (Molnarne & Schroeder, 2019) obtain the flammability interval according to the standard EN 14756 (EN 14756, 2007) that is currently overturned by standard EN 1839 (EN 1839, 2017). This method is focused on LOC calculation, however, the STA allows obtaining all the points belonging to the flammability interval, so safety measures can be assured.

Figure 9 resumes the theoretical flammability intervals calculated in this study. The influence of hydrogen addition looks clear, so it is essential to evaluate it further. The inert gas concentration needed to avoid the explosion seems lower in theoretical calculation than in experimental calculations (Molnarne & Schroeder, 2019). Experimental calculations according to European standards locate the minimum concentration of CO_2 in a 34% for 10% of hydrogen concentration, while theoretical results exposed in figure 9 locate it in 31%. The difference is even greater with the LOC of pure hydrogen and pure methane. The use of theoretical approximations can give a preliminary idea for the control of explosive atmospheres. Naturally, always is needed the application of safety coefficients since the comparison of figure 9 reflects that theoretical flammability intervals are fewer conservatives regarding safety uses of the mixtures. Experimental procedures result essential to adjust the safety measures.

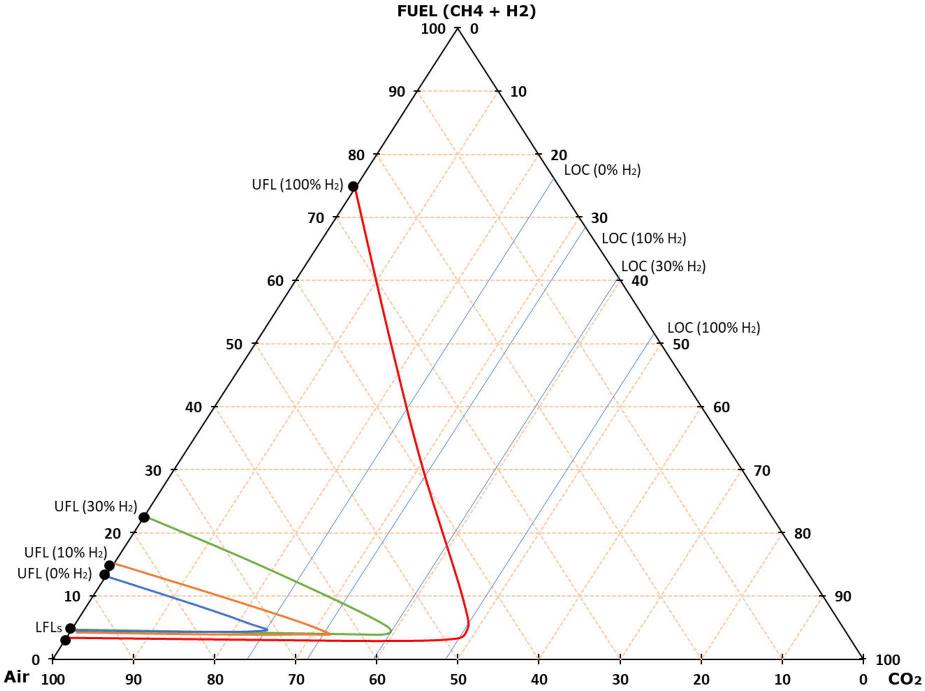

__Fig. 9__ Theoretical flammability interval of different percentages of hydrogen addition

4. Conclusions

The importance of the study of hydrogen-methane mixtures is reflected in literature. Nevertheless, the observed differences presented in literature data confirm the importance of the method and the equipment used to obtain the flammability characteristics of gases. The STA seems to be a valuable method as the results have been validated in this paper. Moreover, the low volume of its combustion chamber allows the reduce the gas consumption of the tests. However, the poor reproducibility of the results obtained in the STA is a crucial issue regarding its utilization to determine the flammability characteristics of gases. The criteria proposed in this study improves the repeatability of the results although it is needed a further investigation in the statistical nature of the STA results.

The LFL of every hydrogen-methane mixture in the air can be fixed, in every case, at 4%, from a conservational point of view. The UFL has greater discordances. However, the great amount of data allows approximating a tendency curve that, by applying a high safety coefficient, can be used as a first approximation. The addition of hydrogen to methane not only has an influence in the FL but also influences the flammability interval when the mixture is inertizated. The addition of hydrogen implies an increase in the concentration of inert gas needed to completely avoid the explosion.

From these results, it is possible to confirm that the use of hydrogen addition on fuel gases such as natural gas or methane involves an increase in the risk when handled. Nevertheless, the risk of the mixtures is lower than the risk associated with pure hydrogen utilization. This fact allows a softer transition to a new energy system.

References

Acar, C., Bicer, Y., Demir, M. E., & Dincer, I. (2019). Transition to a new era with light-based hydrogen production for a carbon-free society: An overview. *International Journal of Hydrogen Energy*, *44*(47), 25347–25364. https://doi.org/10.1016/j.ijhydene.2019.08.010

Amez, I., Castells, B., Garcia-Torrent, J., & Medic, L. (2019). Influence of the addition of hydrogen on the flammability intervals of the methane, air and CO2 mixtures. *Proceedings of the Air and Waste Management Association's Annual Conference and Exhibition, AWMA*, *9*, 8.

Benard, P., Moureau, V., Lartigue, G., & D'Angelo, Y. (2017). Large-Eddy Simulation of a hydrogen enriched methane/air meso-scale combustor. *International Journal of Hydrogen Energy*, *42*(4), 2397–2410. https://doi.org/10.1016/j.ijhydene.2016.11.206

Cashdollar, K. L., Zlochower, I. A., Green, G. M., Thomas, R. A., & Hertzberg, M. (2000). Flammability of methane, propane, and hydrogen gases. *Journal of Loss Prevention in the Process Industries*, *13*(3–5), 327–340. https://doi.org/10.1016/S0950-4230(99)00037-6

Cellek, M. S., & Pınarbaşı, A. (2018). Investigations on performance and emission characteristics of an industrial low swirl burner while burning natural gas, methane, hydrogen-enriched natural gas and hydrogen as fuels. *International Journal of Hydrogen Energy*, *43*(2), 1194–1207. https://doi.org/10.1016/j.ijhydene.2017.05.107

Elsherif, M., Manan, Z. A., & Kamsah, M. Z. (2015). State-of-the-art of hydrogen management in refinery and industrial process plants. *Journal of Natural Gas Science and Engineering*, *24*, 346–356. https://doi.org/10.1016/j.jngse.2015.03.046

EN 1839:2017 (E). (2017).

EN 14756: Determination of the limiting oxygen concentration (LOC) for flammable gases and vapours, (2007).

EN 1839:2017 (E) Determination of the explosion limits and the limiting oxygen concentration (LOC) for flammable gases and vapours, (2017).

García Torrent, J. (2003). *Seguridad Industrial en Atmósferas Explosivas* (J. G. Torrent (Ed.); First).

Ge, B., Ji, Y., Zhang, Z., Zang, S., Tian, Y., Yu, H., Chen, M., Jiao, G., & Zhang, D. (2019). Experiment study on the combustion performance of hydrogen-enriched natural gas in a DLE burner. *International Journal of Hydrogen Energy*. https://doi.org/10.1016/j.ijhydene.2019.03.257

Gieras, M., Klemens, R., Rarata, G., & Wolański, P. (2006). Determination of explosion parameters of methane-air mixtures in the chamber of 40 dm3at normal and elevated temperature. *Journal of Loss Prevention in the Process Industries*, *19*(2–3), 263–270. https://doi.org/10.1016/j.jlp.2005.05.004

Hodges, J., Geary, W., Graham, S., Hooker, P., & Goff, R. (2015). Injecting hydrogen into the gas network – a literature search. *Health and Safety Laboratory*, 1–53. www.nationalarchives.gov.uk/doc/open-government-licence/,%0Ahttp://www.hse.gov.uk/research/rrpdf/rr1047.pdf

Hussain, T., Talibi, M., & Balachandran, R. (2019). Investigating the effect of local addition of hydrogen to acoustically excited ethylene and methane flames. *International Journal of Hydrogen Energy*, *44*(21), 11168–11184. https://doi.org/10.1016/j.ijhydene.2019.02.182

IEC 60079-11 Explosive atmospheres – Part 11: Equipment protection by intrinsic safety “i.” (2011). In *English*.

Janès, A., Lesage, J., Weinberger, B., & Carson, D. (2017). Experimental determination of minimum ignition current (MIC) ratio of hydrogen/methane (H2NG) blends up to 20 vol.% of hydrogen. *Process Safety and Environmental Protection*, *107*, 299–308. https://doi.org/10.1016/j.psep.2017.02.020

Kammermann, T., Kreutner, W., Trottmann, M., Merotto, L., Soltic, P., & Bleiner, D. (2018). Spark-induced breakdown spectroscopy of methane/air and hydrogen enriched methane/air mixtures at engine revelant conditions. *Spectrochimica Acta Part B*, *148*, 152–164. https://doi.org/10.1109/MTAS.2004.1371634

Karlis, E., Liu, Y., Hardalupas, Y., & Taylor, A. M. K. P. (2019). H2 enrichment of CH4 blends in lean premixed gas turbine combustion: An experimental study on effects on flame shape and thermoacoustic oscillation dynamics. *Fuel*, *254*(June), 115524. https://doi.org/10.1016/j.fuel.2019.05.107

Kondo, S., Takizawa, K., Takahashi, A., & Tokuhashi, K. (2011). On the temperature dependence of flammability limits of gases. *Journal of Hazardous Materials*, *187*(1–3), 585–590. https://doi.org/10.1016/j.jhazmat.2011.01.037

Kutcha, J. . (1985). Investigation of fire and explosion accidents in the chemical mining and fuel-related industries- A manual. *United States Department of the Interior, Bureau of Mines, Bulletin 680*, *30*(5), 876–878.

Li, T., Hampp, F., & Lindstedt, R. P. (2018). Experimental study of turbulent explosions in hydrogen enriched syngas related fuels. *Process Safety and Environmental Protection*, *116*, 663–676. https://doi.org/10.1016/j.psep.2018.03.032

Mendiburu, A. Z., de Carvalho, J. A., & Coronado, C. R. (2018). Method for determination of flammability limits of gaseous compounds diluted with N2 and CO2 in air. In *Fuel* (Vol. 226, pp. 65–80). https://doi.org/10.1016/j.fuel.2018.03.181

Miao, H., Lu, L., & Huang, Z. (2011). Flammability limits of hydrogen-enriched natural gas. *International Journal of Hydrogen Energy*, *36*(11), 6937–6947. https://doi.org/10.1016/j.ijhydene.2011.02.126

Mitu, M., Giurcan, V., Razus, D., & Oancea, D. (2017). Inert gas influence on the laminar burning velocity of methane-air mixtures. *Journal of Hazardous Materials*, *321*, 440–448. https://doi.org/10.1016/j.jhazmat.2016.09.033

Mitu, M., Prodan, M., Giurcan, V., Razus, D., & Oancea, D. (2016). Influence of inert gas addition on propagation indices of methane-air deflagrations. *Process Safety and Environmental Protection*, *102*, 513–522. https://doi.org/10.1016/j.psep.2016.05.007

Molnarne, M., & Schroeder, V. (2019). Hazardous properties of hydrogen and hydrogen containing fuel gases. *Process Safety and Environmental Protection*, *130*, 1–5. https://doi.org/10.1016/j.psep.2019.07.012

Peñaranda, A., Martinez Boggio, S. D., Lacava, P. T., Merola, S., & Irimescu, A. (2018). Characterization of flame front propagation during early and late combustion for methane-hydrogen fueling of an optically accessible SI engine. *International Journal of Hydrogen Energy*, *43*(52), 23538–23557. https://doi.org/10.1016/j.ijhydene.2018.10.167

Pio, G., & Salzano, E. (2019). The effect of ultra-low temperature on the fl ammability limits of a methane / air / diluent mixtures. *Hazardous Materials*, *362*(362), 224–229.

Rajpara, P., Shah, R., & Banerjee, J. (2018). Effect of hydrogen addition on combustion and emission characteristics of methane fuelled upward swirl can combustor. *International Journal of Hydrogen Energy*, *43*(36), 17505–17519. https://doi.org/10.1016/j.ijhydene.2018.07.111

Razus, D., Molnarne, M., & Fuß, O. (2004). Limiting oxygen concentration evaluation in flammable gaseous mixtures by means of calculated adiabatic flame temperatures. *Chemical Engineering and Processing: Process Intensification*, *43*(6), 775–784. https://doi.org/10.1016/S0255-2701(03)00078-3

Saito, N., Ogawa, Y., Saso, Y., Liao, C., & Sakei, R. (1996). Flame-extinguishing concentrations and peak concentrations of N2, Ar, CO2 and their mixtures for hydrocarbon fuels. *Fire Safety Journal*, *27*(3), 185–200. https://doi.org/10.1016/S0379-7112(96)00060-4

Schroeder, V., Schalau, B., & Molnarne, M. (2014). Explosion protection in biogas and hybrid power plants. *Procedia Engineering*, *84*, 259–272. https://doi.org/10.1016/j.proeng.2014.10.433

Shekhar, R., Boeck, L. R., Uber, C., & Gerlach, U. (2017). Ignition of a hydrogen–air mixture by low voltage electrical contact arcs. *Combustion and Flame*, *186*, 236–246. https://doi.org/10.1016/j.combustflame.2017.08.006

Shirvill, L. C., Roberts, T. A., Royle, M., Willoughby, D. B., & Sathiah, P. (2019). Experimental study of hydrogen explosion in repeated pipe congestion – Part 2: Effects of increase in hydrogen concentration in hydrogen-methane-air mixture. *International Journal of Hydrogen Energy*, *44*(5), 3264–3276. https://doi.org/10.1016/j.ijhydene.2018.12.021

Tian, H., Wu, M., Shu, G., Liu, Y., & Wang, X. (2017). Experimental and theoretical study of flammability limits of hydrocarbon–CO2mixture. *International Journal of Hydrogen Energy*, *42*(49), 29597–29605. https://doi.org/10.1016/j.ijhydene.2017.10.053

Uber, C., Hilbert, M., Felgner, A., Hüser, D., Kurrat, M., & Gerlach, U. (2019). Electrical discharges caused by opening contacts in an ignitable atmosphere – Part I: Analysis of electrical parameters at ignition limits. *Journal of Loss Prevention in the Process Industries*, *61*, 114–121. https://doi.org/10.1016/j.jlp.2019.06.011

Van den Schoor, F., Hermanns, R. T. E., van Oijen, J. A., Verplaetsen, F., & de Goey, L. P. H. (2008). Comparison and evaluation of methods for the determination of flammability limits, applied to methane/hydrogen/air mixtures. *Journal of Hazardous Materials*, *150*(3), 573–581. https://doi.org/10.1016/j.jhazmat.2007.05.006

Van den Schoor, F., Norman, F., Vandermeiren, K., Verplaetsen, F., Berghmans, J., & Van den Bulck, E. (2009). Flammability limits, limiting oxygen concentration and minimum inert gas/combustible ratio of H2/CO/N2/air mixtures. *International Journal of Hydrogen Energy*, *34*(4), 2069–2075. https://doi.org/10.1016/j.ijhydene.2008.12.038

Van den Schoor, F., & Verplaetsen, F. (2007). The upper flammability limit of methane/hydrogen/air mixtures at elevated pressures and temperatures. *International Journal of Hydrogen Energy*, *32*(13), 2548–2552. https://doi.org/10.1016/j.ijhydene.2006.10.053

Van den Schoor, F., Verplaetsen, F., & Berghmans, J. (2008). Calculation of the upper flammability limit of methane/hydrogen/air mixtures at elevated pressures and temperatures. *International Journal of Hydrogen Energy*, *33*(4), 1399–1406. https://doi.org/10.1016/j.ijhydene.2008.01.002

Wang, D., Changwei Ji, Wang, S., Yang, J., & Tang, C. (2019). Experimental investigation on near wall ignited lean methane/hydrogen/air flame. *Energy*, *168*, 1094–1103. https://doi.org/10.1109/MTAS.2004.1371634

Wang, J., Wu, Y., Zheng, L., Yu, M., Pan, R., & Shan, W. (2020). Study on the propagation characteristics of hydrogen/methane/air premixed flames in variable cross-section ducts. *Process Safety and Environmental Protection*, *135*, 135–143. https://doi.org/10.1016/j.psep.2019.12.029

Wang, Q., Zhao, Y., Wu, F., & Bai, J. (2019). Study on the combustion characteristics and ignition limits of the methane homogeneous charge compression ignition with hydrogen addition in micro-power devices. *Fuel*, *236*(May 2018), 354–364. https://doi.org/10.1016/j.fuel.2018.09.010

Wang, W. Q., & Sun, Z. Y. (2019). Experimental studies on explosive limits and minimum ignition energy of syngas: A comparative review. *International Journal of Hydrogen Energy*, *4*, 5640–5649. https://doi.org/10.1016/j.ijhydene.2018.08.016

Wang, X. H., Sun, Y. F., Wang, Y. F., Li, N., Sun, C. Y., Chen, G. J., Liu, B., & Yang, L. Y. (2017). Gas production from hydrates by CH4-CO2/H2 replacement. *Applied Energy*, *188*, 305–314. https://doi.org/10.1016/j.apenergy.2016.12.021

Wen, X., Wang, M., Su, T., Zhang, S., Pan, R., & Ji, W. (2019). Suppression effects of ultrafine water mist on hydrogen/methane mixture explosion in an obstructed chamber. *International Journal of Hydrogen Energy*, *44*(60), 32332–32342. https://doi.org/10.1016/j.ijhydene.2019.10.110

Zlochower, I. A., & Green, G. M. (2009). The limiting oxygen concentration and flammability limits of gases and gas mixtures. *Journal of Loss Prevention in the Process Industries*, *22*(4), 499–505. https://doi.org/10.1016/j.jlp.2009.03.006

DOI: 10.7795/810.20200724

Do nanostructured materials influence the ignition behavior of combustible dust?

Susanne Hacke

Berufsgenossenschaft Nahrungsmittel und Gastgewerbe (BGN), Mannheim, Germany

E-mail: susanne.hacke@bgn.de

Abstract

Current applications of nanostructured materials are numerous such as silica used as flow aid and anticaking agent for example in food industry. It is well known that nanostructured materials are characterized by a high surface activity caused by the high surface to volume ratio. The influence of these additives on the ignition behavior of combustible powders is still a knowledge gap.

To estimate the ignition behavior experimental investigations have been conducted to determine the safety characteristics like minimum ignition energy of mixtures of combustible with silica.

The investigations resulted in a strong influence of only a small number of additives on the ignition behavior of the mixtures with combustible powders depending on the kind of silica.

Keywords: *Minimum ignition energy, dust explosions, nanostructured materials, occupational risk assessment*

1. Introduction

Industrial applications of mixtures of combustible and inert powders in food and feed industry are numerous. One aspect to apply additives is the improvement of material properties mainly to optimize the processing of raw materials or the product features. Another aspect is to minimize the explosion risk by decreasing the ignition sensitivity of combustible dust using inert materials (e.g. Addai et al., 2016).

The most common food additives are silica (E551) and titanium dioxide (E171) used as flow aid and anticaking agent or food colorant in powdered food items. It is known from literature that these materials are (partly) in nanoscale size (RIKILT & JRC, 2014).

The physical and chemical properties of nanomaterials, typically between 1 and 100 nm (European Commission, 2011) can differ crucial to micro-size materials. It is caused by the high surface to volume ratio, effecting e.g. a higher surface reactivity. This property leads to a strong effect on the flowability of powdered product mixtures adding only a few per cent of nano-silica.

So, the following question arises: Is such a small amount of inert material in nano-size range able to influence the explosion properties like dustiness, ignition energy or explosion behavior of a mixture of combustible with inert dust?

It is well-known, that dust explosions occurring at workplaces are mainly caused by ignition sources like hot surfaces, friction, mechanical and electric sparks and electrostatic discharges as well. The ignition sensitivity of mixtures of combustible with inert dust in air is characterized by the minimum ignition energy (MIE).

One point of interest is the dependence of MIE on mixing ratio of multi-component mixtures (Marx et al., 2017). Furthermore, a lot of scientific work has been done to estimate the influence of nano-size to the micro-size range dust to dust mixtures e.g. to determine the explosion characteristics of micro- and nano-size magnesium or titanium powders (Boilard et al., 2013; Mittal, 2014).

The focus of current research is the influence of noncombustible nano-sized food additives on the ignition sensitivity of micro-size combustible bulk materials used in food items.

2. Experiments

2.1 Materials

The choice of the combustible bulk materials is focused on the minimum ignition energy. As raw materials used in food industry wheat flour (Type 550) is characterized by a rather high minimum ignition energy whereas cornstarch is classified as a particularly highly flammable material dust with low MIE (<10mJ).

To understand the influence of the interactions between silica and the different combustible food powders on the ignition behavior two silica additives (Aerosil®200 and Sipernat®22S) different in size distribution and morphology are applied in a percentage up to 2 by weight in mixtures with wheat flour and cornstarch, respectively.

As delivered from the manufacturing company wheat flour (A) has a moisture content of less than 12% by weight and corn starch less than 3% by weight. To achieve a better comparability to corn starch material, a part of the wheat flour material (B) was prepared referring to ISO/IEC 80079-20-2 (drying).

Table 1: *Selected combustible bulk materials*

Material		**Particle size** (sieving)	**Moisture content**
Wheat flour A	Raw material as used in industrial applications	91% < 125 µm	< 12% by weight
Wheat flour B	Prepared to ISO/IEC 80079-20-2	50% < 63 µm	< 3% by weight
Corn starch	Raw material as used in industrial applications	99% < 32 µm	< 3% by weight

2.2 Sample Preparation

Mixtures with a small content of inert material were prepared (0.25, 0.5, 1.0, 1.5, 2.0% by weight) using a kitchen machine (Bosch MUM 6612/03, 600 W).

To prepare the mixtures, a fixed amount of bulk material (600 g) was added to a premix containing bulk material (100 g) and corresponding amount of inert material (2.5 to 20 g). After 10 minutes mixing, 300 g of the bulk material was added to the mixture and the whole sample was mixed again for another 10 minutes.

Table 2: *Properties of the mixtures of combustible with inert dust*

Sample + inert material	**Moisture content [% by weight]**	
	Bulk material	**Mixtures**
Wheat flour A + Aerosil or Sipernat	< 12	< 12
Wheat flour B + Aerosil or Sipernat	0.6	0.1
Corn starch + Aerosil or Sipernat	0.2	0.1

2.3 *Minimum ignition energy measurement (MIE)*

MIE is defined as “lowest amount of energy (mJ) of an electrical spark that can cause a particulate dispersed in air to explode. Fire and explosion hazard risk usually increases as MIE decreases, as even very weak ignition sources are then capable of causing fire and / or explosion” (Lemkowitz & Pasman, 2014).

According to ISO/IEC 80079-20-2 (2016) the safety characteristic minimum ignition energy (MIE) was determined by a Mike 3 apparatus (TÜV Süd Schweiz AG, Switzerland). MIE characterizes the ignition sensitivity of dust primarily with respect to electric sparks and electrostatic discharges. The discharge values available are 1, 3, 10, 30, 100, 300 and 1000 mJ.

During the test procedure dust concentrations (in a range from 600 to 2400 mg) were explored and ignition time delays (90, 120 and 150 ms) are varied. All measurements were performed with an inductance of 1mH in the discharge circuit.

The minimum ignition energy “(MIE) lies between the highest energy, at which ignition fails to occur in 10 times success attempts to ignite the dust/air mixture *W1* and the lowest energy at which ignition occurs within 10 times success attempts *W2*” (Jaeger & Siwek, 1999):

$$W1 < MIE < W2.$$

Applying the probability of ignition, the statistical value of MIE (Es) can be estimated instead of using an energy range (W1, W2) by equation 1:

$$Es = 10^{\frac{\log W2 - I[W2](\log W2 - \log W1)}{(NI+I)[W2]+1}} \quad (1).$$

Applying to: I[W2] represents the number of tests where ignition occurs for energy W2 and (NI+I)[W2] the total number of tests for energy W2 (Cesana et al., 2010).

For example, an experimental result of the MIE measurements showing boundaries W1 and W2 and the calculated statistical value Es (figure 1).

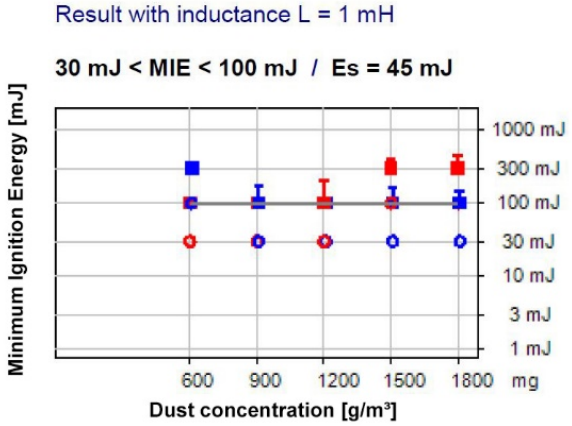

Fig. 1. *MIE of the mixture of wheat flour B with Aerosil (0.25% by weight) at to different ignition time delays (90 and 120 ms). MIE is plotted as a function of dust concentration. The solid squares indicate ignition and the open circles no ignition.*

The investigations in MIE values (Es) of the combustible dusts and the mixtures with silica are summarized in table 3.

3. Results and discussion

Table 3: *MIE tests and results*

Sample	**Inert material**	**MIE values (Es) [mJ]** (* not measured)					
Amount of silica by weight [%]		0	0.25	0.5	1.0	1.5	2.0
Wheat flour A	Aerosil	810	780	540	440	*	190
Wheat flour A	Sipernat	810	660	440	540	440	360
Wheat flour B	Aerosil	82	45	37	14	25	21
Wheat flour B	Sipernat	82	62	60	82	140	170
Corn starch	Aerosil	7	*	12	12	*	12
Corn starch	Sipernat	7	8	8	8	7	8

In case of highly flammable dusts increasing the inert material concentration leads to an increase of the minimum ignition energy. In the context of investigations in nanostructured materials exposure at workplaces in the food and feed industry only a few percentages of silica are applied as additives (Hacke, 2018).

3.1 Effect of silica on MIE of wheat flour

Figure 2 represents the results of the influence of silica on the wheat flour A (untreated raw material). In contrast to the investigations of Addai et al. (2016) even a small percentage of Aerosil shows a strong influence on the MIE of the mixed powders. It is not caused by an effect of inerts but rather by the interactions of the combustible dust with the two silica additives, different in size distribution and morphology.

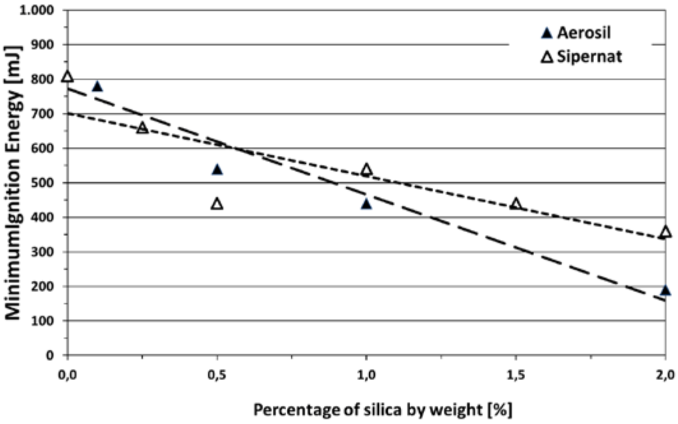

Fig. 2. *MIE of wheat flour A as function of silica concentration [weight-%]*

As not expected, a strong decrease of 77% in MIE value (810 to 190 mJ) for the mixtures of wheat flour A with Aerosil has been obtained. Like the mixtures with Aerosil the mixture with Sipernat shows the same effect but in a less strong decrease of 56% in MIE values (810 to 360 mJ).

Figure 3 demonstrates the results for the influence of silica on wheat flour B (prepared referring to ISO/IEC 80079-20-2).

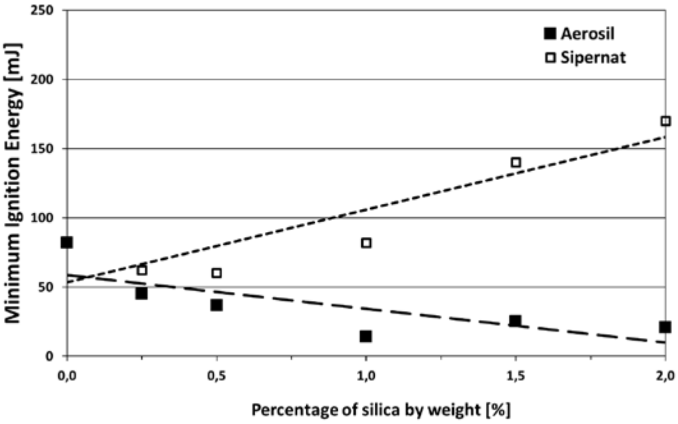

Fig. 3. *MIE of wheat flour B as function of silica concentration [weight-%]*

As shown in figure 2 the mixtures of wheat flour B with Aerosil indicates the same effect with a strong decrease of 74% in MIE value (82 to 21 mJ). As expected, in relation to MIE values of the mixtures of wheat flour B with Aerosil to the mixtures of wheat flour A with Aerosil are ten times higher.

The trends of the mixtures of wheat flour A and B with Aerosil likewise the mixture wheat flour A with Sipernat demonstrate a movement towards more critical MIE values.

In contrast therefor, the mixtures of wheat flour B with Sipernat show a contrary trend to the above-mentioned mixtures. MIE values are increasing slightly by factor two (82 to 170 mJ). This mixture demonstrates a trend to more non-critical values of MIE by adding Sipernat.

3.2 *Effect of silica on MIE of corn starch*

Figure 4 presents the results for the influence of Aerosil and Sipernat on corn starch.

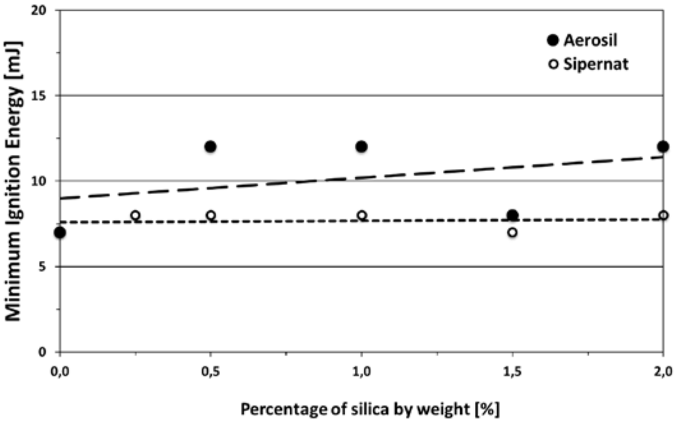

Fig. 4. *MIE of corn starch as function of silica concentration [weight-%]*

In relation to the results of mixing silica to wheat flour (figure 2 and 3) marked differences in MIE values by adding Aerosil or Sipernat are not obtained. In case of mixture corn starch with Sipernat there is quasi no difference in MIE values (7 to 8 mJ). The mixture corn starch with Aerosil shows a very slight tendency to increase in MIE values (7 to12 mJ) but almost no effect.

4. Conclusions

Investigations in mixtures of wheat flour with silica with an increasing amount of Aerosil resulted in a strong decrease of MIE values to more critical values. In contrast as not expected the mixtures of wheat flour B with Sipernat demonstrate a strong increase to more non-critical MIE values.

In relation to the results of mixing silica to wheat flour marked differences in MIE values by adding Aerosil or Sipernat to cornstarch are not obtained. Adding Aerosil results in a an almost no effect and adding Sipernat the mixtures show quasi no difference in MIE values.

Summarizing the experimental investigations, a small amount of silica may have a strong influence on the ignition behavior of combustible dust depending on the kind of silica.

The differences in ignition behavior may be caused by different interactions between the bulk material and the additives. To understand these effects further investigations like dustiness and Scanning Electron Microscopy analyses should be done. Furthermore, the explosion characteristics are another key aspect for the occupational risk assessment.

Acknowledgements

This research was supported by the Research Centre for Applied System Safety and Industrial Medicine (FSA e.V.) under the Project No F05-1402.

References

Addai, E.K., Gabel, D. & Krause, U. (2016). Experimental investigations of the minimum ignition energy and the minimum ignition temperature of inert and combustible dust cloud mixtures. *Journal of Hazardous Materials*, 307: 302-311.

Boilard, S.P., Amyotte, P.R., Khan, F.I., Dastidar, A.G. & Eckhoff, R.K. (2013). Explosibility of micron- and nano-size titanium powders. *Journal of Loss Prevention in the Process Industries*, 26 (6): 1646-1654.

Cesana, C., Kühner, A. & Siwek, R. (2010). Operating Manual MIKE 3.4, Kühner AG: CH-4127 Birsfelden, Switzerland.

European Commission (2011). Commission recommendation of 18 October 2011 on the definition of nanomaterial. *Official Journal of the European Union*, L 275, 20 October 2011.

Hacke, S. (2018). Messtechnische Bestimmung von Nanopartikel-Expositionen an Arbeitsplätzen der Lebens- und Futtermittelindustrie. *Gefahrstoffe - Reinhaltung der Luft* 78 (7/8): 279-286**.**

ISO/IEC 80079-20-2 (2016). Explosive atmospheres - Part 20-2. Material characteristics - Combustible dusts test methods. Edition 1.0 2016-02.

Jaeger, N. & Siwek, R. (1999). Prevent Explosions of Combustible Dusts. *Chemical Engineering Progress*, 95 (6): 25-37.

Lemkowitz, S.M. & Pasman, H.J. (2014). A Review of the Fire and Explosion Hazards of Particulates. *KONA Powder and Particle Journal* 31: 53-81.

Marx, M., Baier, C., Gabel, D., Bloeß, H. & Krause, U. (2017). Minimale Zündenergie von Staubmischungen. *Technische Sicherheit* 7 (6): 25-29.

Mittal, M. (2014). Explosion characteristics of micron- and nano-size magnesium powders. *Journal of Loss Prevention in the Process Industries* 27: 55-64.

RIKILT & JRC (2014). Inventory of Nanotechnology applications in the agricultural, feed and food sector. EFSA supporting publication 2014: EN-621.

DOI: 10.7795/810.20200724

Nex-Hys – Minimum Ignition Temperature of Hybrid Mixtures

Dieter Gabel[a], Paul Geoerg[a], Fabian Franken[a] & Ulrich Krause[a]
[a] Otto-von-Guericke-University, Magdeburg, Germany
E-mail: *dieter.gabel@ovgu.de*

Abstract

Although the minimum ignition temperature is an important safety characteristic and of practically relevance in industrial processes, actually only standard operation procedures are available for pure substances and single-phase values. Nevertheless, combinations of substances or mixtures are used in industrial processes and actually it is not possible to provide a standardised minimum ignition temperature and in consequence to design a process safely with regard to the substances used.

In order to get minimum ignition temperatures for frequently used hybrid mixtures, first, the minimum ignition temperatures and ignition frequencies were determined in the modified Godbert-Greenwald furnace for two single phase solids dusts and a liquid substance. Second, minimum ignition temperatures and ignition frequencies were determined for several combinations as hybrid mixture of dust and liquid.

In parallel to the determination of ignition temperatures a new camera and computer system to differentiate ignition from non-ignition is developed. First results are promising such a system could be much less operator depended.

By a high number of repetitions to classify regions of ignition the base is made to decide about a new procedure to propose for a hybrid standard and updating existing ones, too. This is one of the necessary aims to be reached in the Nex-Hys project.

A noticeable decrease of minimum ignition temperatures below the MIT of the pure solids was observed for the one hybrid mixture tested, yet. Furthermore more widely dispersed area of ignition distributions is shown. In accordance to previously findings, the results demonstrate a strong relationship between likelihood of explosion an amount of the quantity added solvent. In consequence the hybrid mixtures is characterized by a lower minimum ignition temperature than the single dust.

Keywords: *hybrid mixture, dust, gas, vapour, ignition, explosion*

1 Introduction

The impact of mixtures of burnable dusts and liquids (hybrid mixtures) on safety characteristics are important for several industrial processes. Safety characteristics and operational procedures are based on knowledge about the ignition potential and explosion characteristics [1]. Although efforts have been made in recent years by various research groups to generate parameters for hybrid mixtures, most values are often based on the properties of pure substances.

As already emphasized by the fundamental work of Bartknecht, 1981 [2], a two-component mixture of a flammable dust and gas can be ignited below the lower explosion limit of a single component of the mixture. The minimum ignition temperature (MIT) of dust mixture was experimentally addressed by Zunaid, 2013 [3]. A substantial amount of spark formation below the MIT was reported which might be an ignition resource for hybrid mixtures. Dufaud et al. 2008 reported effects of ignitable dust-vapor-mixtures to explosions with a greater severity than the ones of both compounds taken separately [4, 5].

DOI: 10.7795/810.20200724

A substantial increase of knowledge about the behaviour of hybrid mixtures has been made by the research of Addai et al. who has published various experimental results that focused on the lower explosion limits [1, 6–9], the minimum ignition temperature [7, 10, 11], the minimum ignition energy [11, 12] and the minimum explosion concentration [6, 8] of hybrid mixtures respectively.

Gabel and Krause 2019 presented recently findings of minimum ignition temperature for premixed dust-solvent mixtures [13]. They came up with an impact of the phase conditions of the components of the mixture on the MIT outcome.

As the combination of presence of hot surfaces and dealing with ignitable dust clouds is frequently relevant in industrial processes (e.g. sawing, cutting, grinding, drying or heating of particles), the MIT has a high technical relevance to benchmark the probability of an ignition [14]. Summarising the main outcome of previous research activities appears that the effect of hybrid mixture explosion are rather a linear combination of single-substance characteristics than a high influenced ignition frequency by a low amount of a combustible gas to a dust cloud. Therefore it is questionable

1. that the variations and replications specified in the standard for determining the MIT for pure dust clouds can be applied to hybrid mixtures without any adjustments;
2. that the visually determined Boolean operator used in the standard procedure – ignition or non-ignition by visible flame exit from the furnace tube – is applicable to hybrid mixtures; and
3. that the MIT of hybrid mixtures is characterised by a distinct range of reliable ignition/non-ignition frequencies.

The aim of this contribution is to investigate the MIT of the pure substances (Lycopodium, dehumidified maize starch and n-Heptane) and a hybrid combination of maize starch and n-Heptane in a modified Godbert-Greenwald-furnace (GG furnace) with frequent repetitions.

2 Methods

2.1 Tested substances

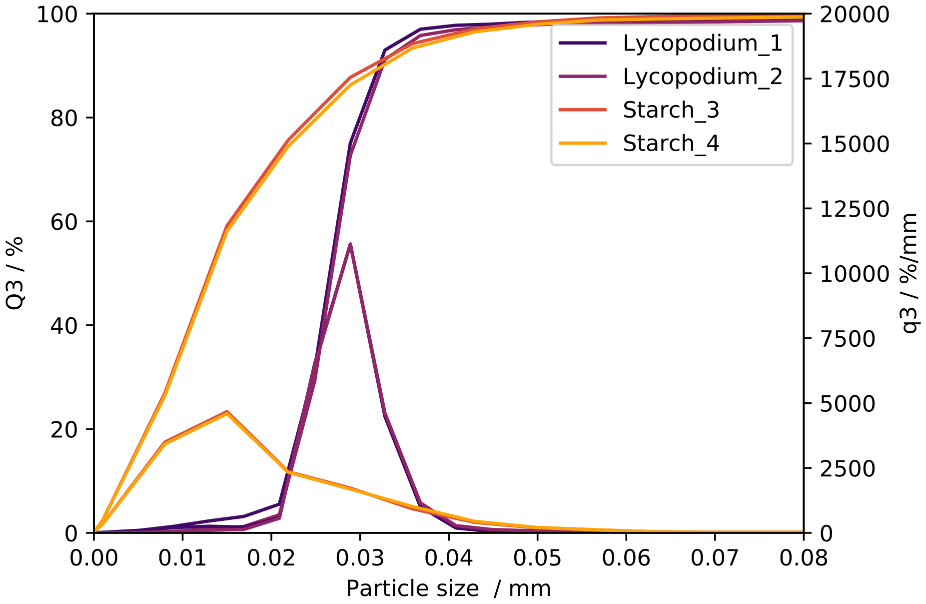

Fig. 1: *Distribution of particle size. Median value at $Q3{=}90\,\%$ of the particle size is* 0.038 mm *for Lycopodium and* 0.042 mm *for dehumidified maize starch.*

Studies with frequent repetition of single measurements were performed for dehumidified maize starch, lycopodium and n-Heptane. Particle size distribution was determined for the two samples for starch and lycopodium by using Camsizer (Retsch Technology) according to ISO 13322-2:2006-11

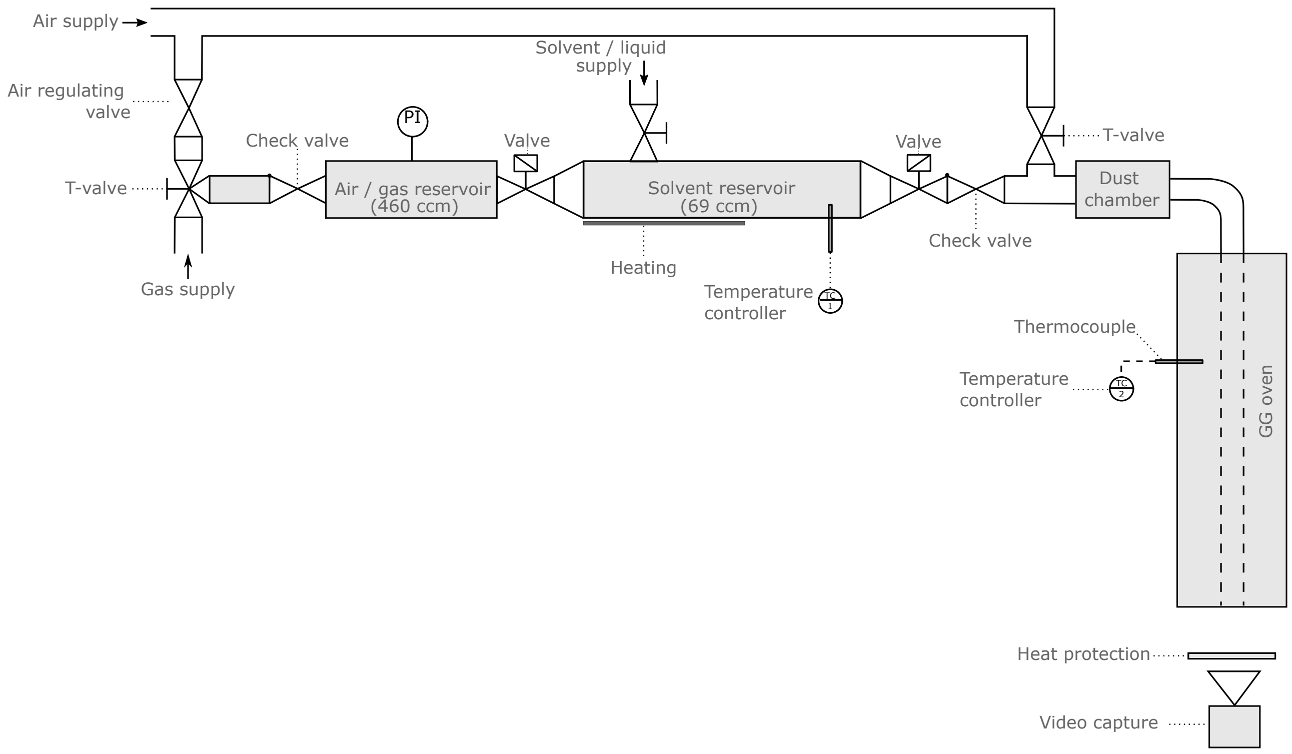

***Fig. 2**: Sketch of the modified Godbert-Greenwald-apparatus.*

[15]. A median particle size of approximately 0.03 mm for lycopodium was determined. The median particle size of the dehumidified starch was approximately 0.02 mm. The particle size distribution a presented in (Fig. 1) showing the repeated measurement for both dust.

The residual moisture of the samples was examined for loss of mass after the sample had been in the drying oven for two and seven hours (Tab 1). The mean residual moisture for Lycopodium was 7.74 wt% after two hours and 7.90 wt% after seven hours respectively. The dehumidified starch dust was characterised by a mean residual moisture 3.16 wt% after two hours and 3.44 wt% after seven hours respectively.

***Table 1**: Moisture content of Lycopodium and Starch determined using drying oven after* 2 h *and* 7 h.

Substance	#	Tare weight [g]	Weight in [g]	Weight out (2 h) [g]	Weight out (7 h) [g]	Moisture (2 h) [wt%]	Moisture (7 h) [wt%]
Lycopodium	01	29.5199	3.6470	32.8860	32.8809	7.70	7.84
	02	28.4109	3.1635	31.3284	31.3229	7.78	7.95
	Mean					7.74	7.90
Starch	01	28.5123	1.6028	30.6446	300599	3.15	3.44
	02	27.4660	1.6185	29.0331	29.0290	3.18	3.43
	Mean					3.16	3.44

2.2 Experimental setup and procedure for dust and hybrid mixture

A modified Godbert-Greenwald furnace (doubled length of the heated oven of 42 cm) was used to determine the minimum ignition temperature according to [16]. A principle of the furnace is presented in Fig 2.

Main modification, as already described in [7, 10, 11], is the double length of the furnace. The influence of the length and thus the residence time of the ignitable substance is currently not known and will be systematically investigated in the further course of the Nex-Hys-project. Therefore, a new GG furnace that completely fulfills the requirements of the standard is already acquired. All results presented here will be remeasured and deliver an answer to the question whether all substance show the same behaviour in both furnaces. To test hybrid mixtures further modification were necessary. To create gas mixtures an additional input was realized to mix other gases to the air in the gas pressurized vessel. Defined gas mixtures will be achieved by the partial pressure method. This only made the replacement of the pressure indicator necessary; now a high precision digital pressure gauge is used instead of the usually installed simple analogues one.

The third modification is the solvent chamber in front of the dust chamber. Here a heated piece of pipe is mounted in between two solenoid valves that operate simultaneously. The reservoir is equipped with a ball valve to enter the solvent. Choosing temperatures of the solvent chamber above the boiling point of the liquids tested ensures a reproducible creation.

Finally, an additional air supply was installed in front of the dust chamber to allow flushing of residues more effectively, as air pressure here is higher as in the air provided to the air chamber. Due to the experience made so far the two check valves will not be necessary in the final setup.

Of cause the arrangement of the different parts will influence the mixture present in the heated tube. Therefore this is an object of interested in the overall Nex-Hys project, too.

The procedure is based on the experimental ignition of a cloud of dust in a furnace at a constant temperature (refereed to as procedure B in the standard) and displayed in Fig 3. First, the tube was heated and fixed at a initial temperature of 410 °C and the defined amount of dust has been introduced in the dust chamber. Second, the air reservoir was filled by compressed air to the defined initial pressure and, third, the dust sample was was injected into the furnace with compressed air. The ignition criterium according to the standard DIN EN 50281-2-1 [16] is defined as the observation of a visible flame at the furnace exit. To achieve the desired reference condition where the ”best’ explosion is observed, both the pressure and the amount of dust was varied. Pressure was varied with increments of 0.1 bar in an interval of [0.1, 0.5]bar (atmospheric overpressure). The mass of dust was varied with increments of 0.1 g in an interval of [0.1, 0.5]g. The furnace temperature was reduced at the reference condition point until the explosion criterion was not met for ten trials. Increments of 20 K for $T \geq 300\,°C$ and increments of 10 °C if $T < 300\,°C$ were used. In order to obtain information about the reliability of the MIT measures and deviating from the standard, the masses of the dust for Lycopodium was increased in the range of [0.5, 1.3]g as well as the injection pressures of [0.5, 1.0]bar. Increments of 0.1 were used for both parameters. Furthermore, in this publication each data point was measured ten times in deviation from the standard.

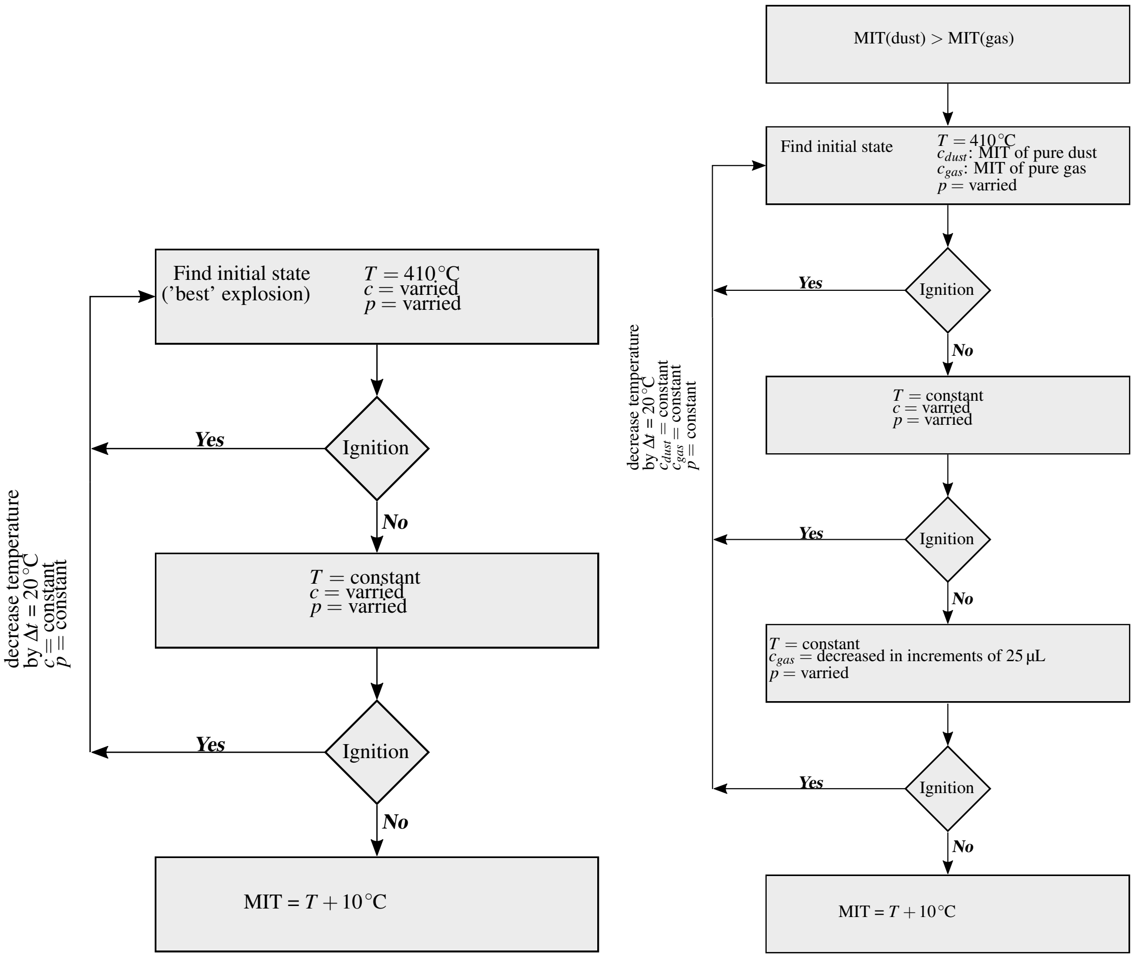

(a) MIT of pure substances *(b) MIT of dust-liquid-mixtures*

***Fig. 3**: Principle of study procedure on measuring the minimum ignition temperature for pure substances and a dust-liquid-mixture (simplified scheme according to [10]).*

The ignition criterion according to the standard is a flame that leaves the tube. For weak explosions the light emitted by the reaction is only visible inside the tube. Therefore, a mirror is placed below the furnace to be able to observe the flame. Nonetheless, it is sometimes hard to decide whether there is an ignition or not. In some experiments only sparks are visible (no ignition); sometimes thick smoke make the flame hard to detect. As an alternative to the mirror used in the standard, a camera was mounted at the bottom of the open furnace (Fig 2) and the dust injection was captured at a framerate of $15\,\mathrm{s}^{-1}$. On the one hand, this simplifies the documentation and the ex-post check-ability of ignition decisions (Fig 4). On the other hand, in future work a detection of ignitions by means of image analysis methods is to be developed. For the results presented here, all three colors of the RGB spectrum were used for the time being to calculate the intensity value of the image (Fig 4d). The intensity value of an image weights the sum of red, yellow and blue and gives a value for the brightness of an image pixel independent of the specific colors. Due to the intensity produced by the substances presented here, the average value of the intensity value of an image section was used in a simplified way.

Further work will include signals in the near infra-red spectrum as well. The aim is to be able to clearly differentiate between ignition and non-ignition based on a measurable parameter. Therefore disturbing factors like sparks and smoke need to be differentiated from the combustion reaction. Further ideas to be realised will be presented in the outlook section .

DOI: 10.7795/810.20200724

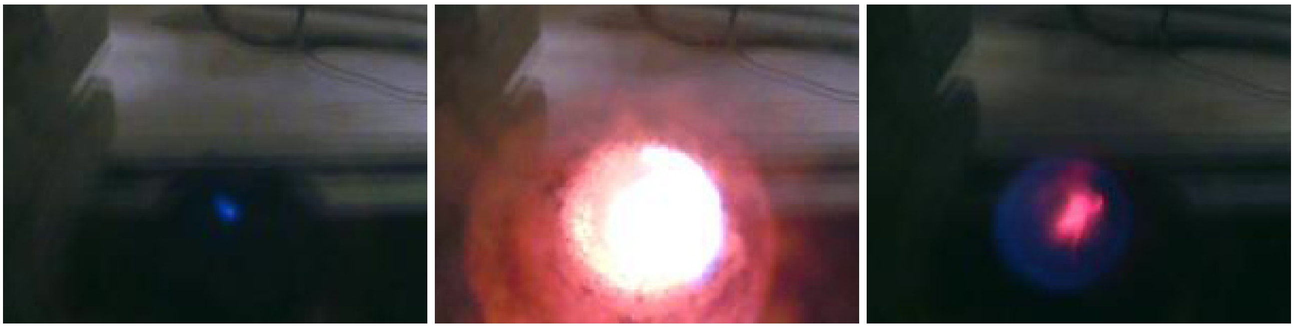

(a) frame 102 *(b) frame* 103 *(c) frame* 107

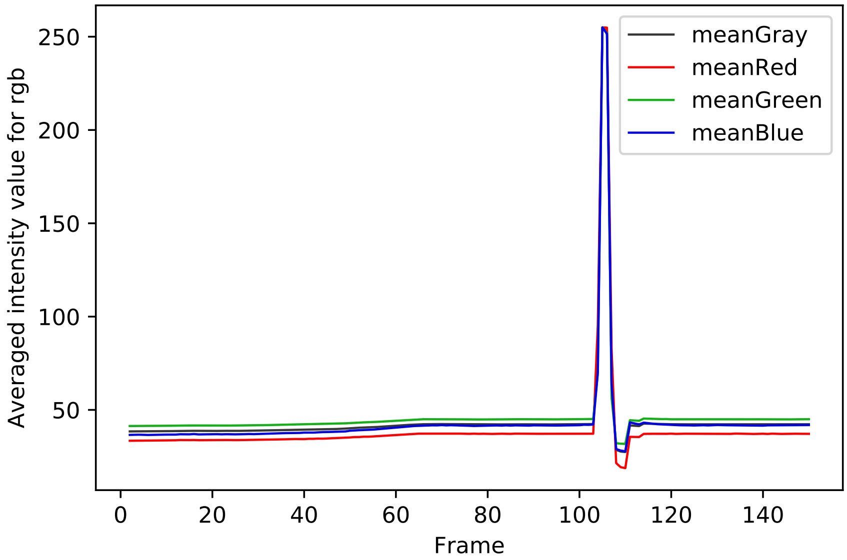

(d) Averaged intensity value

***Fig. 4**: Still images of ignition video capture for n-Heptane (top line) and corresponding averaged intensity values (greyscale value) for rgb (bottom line).*

3 Results and discussion

For this basic research each experimental trial for each point defined by the amount of substance m/g or $V/\mu\mathrm{L}$, temperature of the furnace $T/°\mathrm{C}$ and injection over-pressure p^{+}/bar was repeated ten times. This high amount of repetitions was necessary in order to analyse frequencies of ignitions and to define ranges of transitions. Later investigation will be carried out with a reduced number of trials based on the new procedure proposed according to the primary findings.

Starting with pure Lycopodium the following experimental results were achieved:

- Results of pure Lycopodium (Fig 5a),
- Results of pure maize starch (Fig 5b),
- Results of pure n-Heptane (Fig 5c),
- Results of Starch-n-Heptane-mixture (Fig 6).

3.1 Minimum ignition temperature and ignition frequencies for pure substances

As can be seen in (Fig 5a) most experiments were carried out for pure Lycopodium. The idea was to get a complete map of values of the region of parameters covered by the standard. For the pure dust no clear indicator was found that the limits given in the standard would prevent the user from really identifying the lowest MIT. Altogether 2400 single experiments are represented in the sub-figure for Lycopodium.

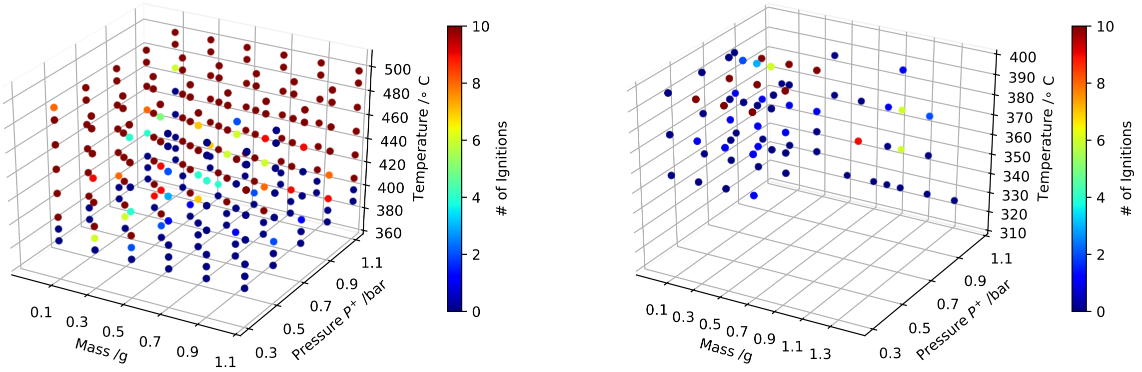

(a) Lycopodium *(b) Starch*

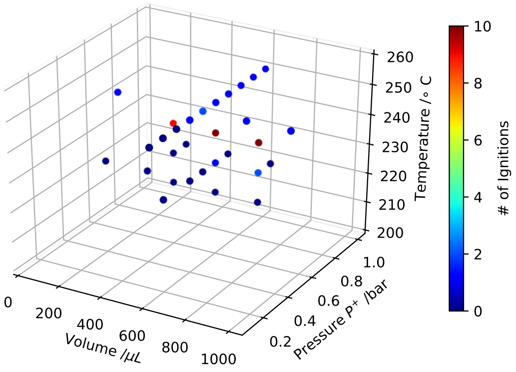

(c) n-Heptane

***Fig. 5**: Frequency of ignitions of pure substances.*

The diagrams for the other two substance show nothing unexpected. In becomes obvious that a probability of 100 % for the ignition does not occur that often. Only at temperatures much higher than the MIT this can be investigated at all. To reduce the number of trials the staring point was closed to the expected MIT what leads to a huge number of non-ignition as can be seen in Figures 5b and5c. As already assumed by previous experiments the MIT of the solvent is relatively closed to it standard value. Other liquids have already been tested and their results will be published as soon as the MITs for the hybrid mixtures for these substances in combination with the two dust have be determined as well. This work is postponed, as the focus is on proposing a experimental setup and a procedure first.

3.2 Minimum ignition temperature and ignition frequencies for hybrid mixtures substances

Up to now only the two hybrid mixtures are tested. In Figure 6 the results for the combination Starch and n-Heptane is presented.

For the tests only volumes of n-Heptane that did not lead to an ignition by itself anymore were used. It can clearly be seen, that the addition of the solvent vapour significantly reduces the hybrid-MIT

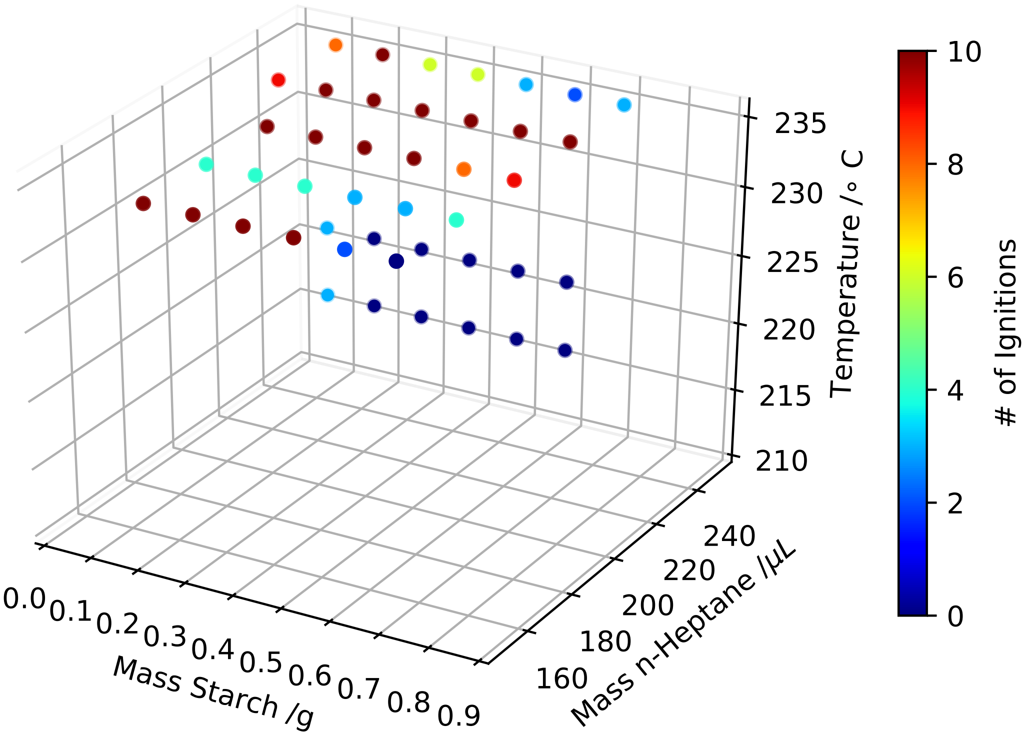

***Fig. 6**: Frequency of ignitions of hybrid mixtures.*

below the MIT of the pure dust. The final temperature practically equals the value for pure n-Heptane. Represented here is only one initial pressure of air used to blow the mixture into the tube. Of cause, the results were obtained under variation of the pressure as well. Testing for all combination is practically not possible. Here the procedure used is oriented at the results achieved before for pure substances. Here the final procedure still has to be discussed and tested.

Consequently, the results for Lycopodium are missing at the moment as they are not complete, yet.

4 Conclusions and Outlook

The experimental setup presented here is capable to determine the MIT of hybrid mixtures. This can be proofed by the data and has already been shown before. The aim to create a setup and procedure that can be standardised increases the effort as the experimental results must be reliable and comprehensible. Consequently, the project started with pure dust to generate a comparable and stable foundation for variation to be tested.

During the Nex-Hys project the following questions need to be answered to later justify the proposed modified equipment and procedure based on scientific data:

1. Considering the great variation of dusts occurring in industry, some of which have challenging properties for optical detection, an alternative test method must be offered.
2. Is the number of trials justified as it is in the standard and can this directly be adopted for hybrid mixtures?
3. Is the step-width to vary the mass and pressure sufficient and what range has to be used for the gas phase of hybrid mixtures.
4. How to define and specify the MIT of a hybrid mixture?
5. What modification to the experimental setup is appropriate to reliably test hybrid mixtures?

The experimental results obtained up to now allow to systematically continue to change settings and continue testing. Next step will be the comparison between the existing modified furnace and the new standard GG furnace. While test are running in the new setup the mixing system in the modified oven will be varied, next.

In parallel the procedural approach for testing will be fixed in order to to reduce the necessary effort and to make the results reliable and repeatable.

Additionally, the camera system is further tested and extended. The final idea is to construct a setup that reduces the operator input as far as possible. This includes the recording of the furnace temperature and used over-pressure by computer programs. Together with the automatic ignition detection a specific code could implement the procedure and suggest the next step to the operator. Such a system would reduce operator errors significantly. Practically, a fully automated system would be possible allowing to test for much more variation as manually possible.

Acknowledgements

This work has been performed within the research program 'Development of standardised determination methods for safety parameters of explosion protection for hybrid mixtures (NEX-HYS)' funded by the German Federal Ministry of Education and Research - BMBF (grant number 03TNH006A). The authors would like to thank SaiLokesh Pinjala, Ajinkya Kunjir and Sinha Shruti for their great effort in carrying out the laboratory experiments.

References

[1] Emmanuel Kwasi Addai, Dieter Gabel, and Ulrich Krause. "Lower explosion limit of hybrid mixtures of burnable gas and dust". In: *Journal of Loss Prevention in the Process Industries* 36 (2015), pp. 497–504. ISSN: 09504230. DOI: `10.1016/j.jlp.2015.02.014`.

[2] Wolfgang Bartknecht. *Explosions: Course, Prevention, Protection*. Berlin, Heidelberg: Springer Berlin Heidelberg, 1981. ISBN: 9783642677496. DOI: `10.1007/978-3-642-67747-2`.

[3] Shaikh Zunaid. "Ignition Temperature of Dust Mixture". Master thesis. Magdeburg: Otto-von-Guericke-University, 2013.

[4] Olivier Dufaud, Laurent Perrin, and Mamadou Traoré. "Dust/vapour explosions: Hybrid behaviours?" In: *Journal of Loss Prevention in the Process Industries* 21.4 (2008), pp. 481–484. ISSN: 09504230. DOI: `10.1016/j.jlp.2007.11.005`.

[5] O. Dufaud et al. "Explosions of vapour/dust hybrid mixtures: A particular class". In: *Powder Technology* 190.1-2 (2009), pp. 269–273. ISSN: 00325910. DOI: `10.1016/j.powtec.2008.04.046`.

[6] Emmanuel Kwasi Addai, Dieter Gabel, and Ulrich Krause. "Explosion characteristics of three component hybrid mixtures". In: *Process Safety and Environmental Protection* 98 (2015), pp. 72–81. ISSN: 09575820. DOI: `10.1016/j.psep.2015.06.013`.

[7] Emmanuel Kwasi Addai et al. "Investigation of the minimum ignition temperature and lower explosion limit of multi-components hybrid mixtures in the Godbert-Greenwald furnace". In: *Process Safety and Environmental Protection* 111 (2017), pp. 785–794. ISSN: 09575820. DOI: `10.1016/j.psep.2017.09.003`.

[8] Emmanuel Kwasi Addai, Dieter Gabel, and Ulrich Krause. "Lower explosion limit/minimum explosible concentration testing for hybrid mixtures in the Godbert-Greenwald furnace". In: *Process Safety Progress* 36.1 (2017), pp. 81–94. ISSN: 10668527. DOI: `10.1002/prs.11825`.

[9] Zaheer Abbas et al. "Theoretical evaluation of lower explosion limit of hybrid mixtures". In: *Journal of Loss Prevention in the Process Industries* 60 (2019), pp. 296–302. ISSN: 09504230. DOI: `10.1016/j.jlp.2019.05.014`.

[10] Emmanuel Kwasi Addai, Dieter Gabel, and Ulrich Krause. "Experimental investigation on the minimum ignition temperature of hybrid mixtures of dusts and gases or solvents". In: *Journal of hazardous materials* 301 (2016), pp. 314–326. DOI: `10.1016/j.jhazmat.2015.09.006`.

[11] Emmanuel Kwasi Addai, Dieter Gabel, and Ulrich Krause. "Experimental investigations of the minimum ignition energy and the minimum ignition temperature of inert and combustible dust

cloud mixtures". In: *Journal of hazardous materials* 307 (2016), pp. 302–311. DOI: `10.1016/j.jhazmat.2016.01.018`.

[12] Emmanuel Kwasi Addai et al. "Minimum ignition energy of hybrid mixtures of combustible dusts and gases". In: *Process Safety and Environmental Protection* 102 (2016), pp. 503–512. ISSN: 09575820. DOI: `10.1016/j.psep.2016.05.005`.

[13] Dieter Gabel and Ulrich Krause. "Minimum ignition temperature of hybrid mixtures". In: *Chemical engineering transactions* 75 (2019), pp. 1–6.

[14] Paul Amyotte. "Myth No. 2 (Fuel): Dust Explosions Happen Only in Coal Mines and Grain Elevators". In: *An Introduction to Dust Explosions*. Ed. by Paul Amyotte. Elsevier, 2013, pp. 17–29. DOI: `10.1016/B978-0-12-397007-7.00003-3`.

[15] International Standards Organisation. *ISO 13322-2:2006-11. Partikelgrößenanalyse - Bildanalyseverfahren - Teil 2: Dynamische Bildanalyseverfahren ISO*. Berlin, 2006.

[16] Deutsches Institut für Normung. *DIN EN 50281-2-1. Elektrische Betriebsmittel zur Verwendung in Bereichen mit brennbarem Staub: Teil 2-1: Untersuchungsverfahren - Verfahren zur Bestimmung der Mindestzündtemperatur von Staub*. November 1999.

Proceedings of the 13th Symposium International Symposium
on Hazards, Prevention and Mitigation of Industrial Explosions
DOI: 10.7795/810.20200724

A Thermal Model for the Minimum Ignition Energy of Dusts

Tengfei Chen [a], Jan Berghmans [b], Jan Degrève [d], Filip Verplaetsen [c,d], Jo Van Caneghem [e] &
Maarten Vanierschot [a]

[a] KU Leuven, Mechanical Engineering Technology TC, Campus Group T, A. Vesaliusstraat 13, B-3000 Leuven, Belgium
[b] KU Leuven, Department of Mechanical Engineering, Celestijnenlaan 300A, B-3001 Heverlee, Belgium
[c] Adinex NV, Brouwerijstraat 11, B-2200 Herentals, Belgium
[d] KU Leuven, Department of Chemical Engineering, Celestijnenlaan 200f, B3001 Leuven, Belgium
[e] KU Leuven, Materials Technology TC, Campus Group T, A. Vesaliusstraat 13, B-3000 Leuven, Belgium

E-mail: tengfei.chen@kuleuven.be & maarten.vanierschot@kuleuven.be

Abstract

In this study, a physical model of the dust cloud ignition process is developed. The model is based on the temporal and spatial distribution of heat coming from the ignition source and heat released by ignited dust particles. Using this model, a numerical algorithm for the calculation of the minimum ignition energy (MIE) is derived. This algorithm can evaluate MIEs of dusts and their mixtures with different dust concentrations and particle sizes. Although the calculated MIE values generally only amount to 20 to 50 % of the experimental results, the algorithm correctly predicts the MIE variation trends against particle diameter and dust concentration. There is a power function relationship between the MIE and particle diameter of the type $MIE \propto d_p^k$ with k being approximately 2. Moreover, the MIE decreases nearly inversely-proportional to dust concentration at fuel-lean concentrations, but generally increases as dust concentration rises beyond the stoichiometric value.

Keywords: *minimum ignition energy, dust clouds, theoretical model*

1. Introduction

The minimum ignition energy of a dust cloud (MIE) is the minimum energy required to ignite a dust cloud, whilst maintaining self-propagation of the flame in a standardized MIKE3 apparatus. MIE is a significant parameter to reflect dust explosion risk and provides the basis for preventive method selection (Ren et al. (2011), Li et al. (2017)). Currently, research on MIEs causing dust explosions mainly focusses on three aspects: effect of different discharge modes on the MIE (Eckhoff et al. (2007)), MIEs of nano and micro meter particle-sized dusts (Randeberg et al. (2007), Wu et al. (2009), Bernard et al. (2012), Boilard et al. (2013) and Mittal et al. (2014)) and influence of mixing and inerting of different combustible dusts (Azhagurajan (2012), Hosseinzadeh et al. (2015), Addai et al. (2016), Choi et al. (2016)).

However, most studies on these subjects are still in data collection phase, mainly focusing on experimentally determining the MIE. Despite some attempts to explore the theoretical calculation method of dust cloud MIE, currently MIEs are mainly calculated based on simple function fitting of experimental MIE values for parameters such as dust concentrations, ignition delay times and pressures during the standard tests (Li et al. (2017), Li et al. (2018)), ignoring the physicochemical characteristics of the dust cloud ignition process. A first attempt of a theoretical analysis of the MIE was undertaken by Kalkert & Schecker (1979). Hosseinzadeh et al. (2019) tried to develop a theoretical model for the calculation of the MIE of a dust cloud, but only considered a hypothetical

DOI: 10.7795/810.20200724

particle in the centre of the ignition field, neglecting the propagation of the combustion from particle to particle.

In the present study, a physical model of the ignition process of a dust cloud is developed, resulting in a set of controlling equations and an algorithm for the calculation of the MIE. Moreover, the accuracy of the calculation procedure is investigated by comparing calculated and experimental data.

2. Physical model of the ignition process of a dust cloud

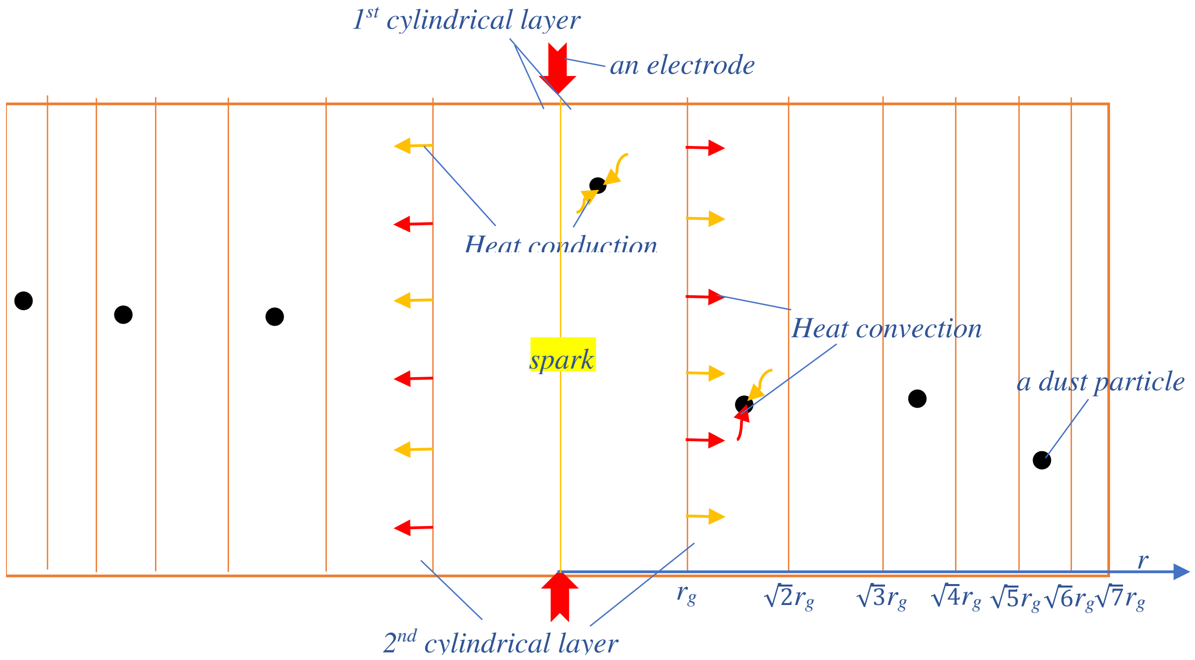

Fig. 1. *Physical model*

The physical model of the ignition process of a uniform dust cloud triggered by a straight-line shaped arc between two electrodes is shown in Fig.1, in which the space around the ignition spark is divided into cylindrical layers. Each layer contains one dust particle and due to a constant concentration of the cloud, has the same volume ($V = \frac{V_s \rho_s}{conc}$, V_s — volume of a single particle, m^3, ρ_s — particle density, kg·m^{-3}, *conc* — dust concentration, kg·m^{-3}). The radius of the first layer is shown in Fig. 1 as r_g ($r_g = \sqrt{\frac{V}{\pi l_g}}$, l_g — distance between the electrodes, m). Ignition of particles is assumed to propagate layer by layer along the radial direction from the central line through heat conduction in the gas (air) and heat convection to the particles. Successful ignition of a particle is assumed to occur when the temperature of the particle reaches its experimental minimum ignition temperature (MIT). After that, the particle will start burning and releasing heat. This heat will be transferred to the air and will contribute to the heating of neighboring particles. When this process continues in the radial direction away from the spark area, the cloud is considered to be ignited. The smallest amount of ignition (spark) energy giving rise to cloud ignition is the minimum ignition energy. The following assumptions are made regarding the dust cloud:

(1) All dust particles are assumed to be spheres of the same size and particle distribution in space is uniform, which means that two regions in the dust cloud space with the same volume contain the same number of dust particles;

(2) The biot number for a dust particle is usually less than 0.2 (Hosseinzadeh et al., 2019), so the temperature distribution in a particle is assumed to be uniform all the time and the ignition temperature of each particle is equal to the experimentally determined minimum ignition temperature of the dust;

(3) Once ignited, a particle would start burning and releasing its heat of combustion instantly;

(4) The composition and properties of each particle and the surrounding air do not change during the combustion process.

3. Governing equations

3.1 Governing equations of air and particle temperatures in the dust cloud

The temperature distribution in the air of the dust cloud due to a line-shaped initial energy input E_0 is determined by heat conduction in the air and heat convection between the air and the particle (if there is one), which is governed analytically by the following equation in cylindrical coordinates (Taler and Duba (2006)):

$$\varepsilon_g \rho_g C_{p\_g} \frac{\partial T_g(r,t)}{\partial t} = \frac{1}{r}\frac{\partial}{\partial r}\left(\varepsilon_g\, k_g r \frac{\partial T_g(r,t)}{\partial r}\right) + \frac{E_0}{l_g}\delta(t)\delta(\vec{r}) - (1-\varepsilon_g) h_s a_p \left(T_g(r,t) - T_s(r,t)\right) \quad (1)$$

With initial conditions: $T_g(r\,,0) = T_i$ and

boundary conditions: $T_g(\infty, t) = T_i$ and

$$\frac{\partial T_g(0,t)}{\partial r} = 0$$

where

ε_g— volume fraction of the air in the dust cloud;

ρ_g— gas density, kg·m^{-3};

C_{p_g}— gas specific heat, J·(kg·K)$^{-1}$;

k_g— thermal conductivity, W·(m·K)$^{-1}$;

a_p —$\frac{S}{V_s} = \frac{6}{d_p}$, 1/m;

V_s —volume of a single particle, $V_s = \frac{4}{3}\pi\left(\frac{d_p}{2}\right)^3$, d_p— particle diameter, m;

h_s— convective heat transfer coefficient, $h_s = \frac{N_u k_g}{d_p}$, N_u— Nusselt number, a dimensionless parameter reflecting the intensity of heat convection, for the use of small particles, the Nusselt number is assumed constant (Nu = 2) (Yarin and Hetsroni, 2004);

S — surface area of a single particle, $S = 4\pi\left(\frac{d_p}{2}\right)^2$, m^2.

$T_g(r,t)$ — air temperature, K;

$T_s(r,t)$ — particle temperature, K

T_i — initial air temperature, 300 K

E_0 — initial line-shaped heat input in the center, J

l_g — distance between the electrodes, m

$\delta(t)$ — the Dirac delta function in time, $\delta(t) = \begin{cases} 1 & t = 0 \\ 0 & t \neq 0 \end{cases}$, 1/s.

$\delta(\vec{r})$ — the Dirac delta function in space, $\delta(\vec{r}) = \begin{cases} 1 & \vec{r} = \vec{0} \\ 0 & \vec{r} \neq \vec{0} \end{cases}$, 1/m^2.

Heat transfer between the air and a particle is through heat convection. Particle temperature is governed by the following equation (Yarin and Hetsroni (2004)):

DOI: 10.7795/810.20200724

$$\rho_s C_{p\_s} \frac{dT_s(r,t)}{dt} = h_s a_p \left(T_g(r,t) - T_s(r,t)\right) \tag{2}$$

With initial condition: $T_s(r,0) = T_i$

where:

ρ_s— particle density, kg·m^{-3};

C_{p_s}— particle specific heat, J·(kg·K)$^{-1}$.

It should be noted that once a particle is ignited, it will start burning and releasing its combustion heat instantly, so at the time and position of the ignition of a particle, another set of conditions should be included. However, due to the difficulties in interpreting these conditions analytically, they are not presented in Eq (1) or (2), but the numerical forms of these conditions will be revealed in the following numerical method.

In this work, first, the space around a line-shaped initial spark is divided into multiple cylindrical layers, each of which containing a single particle assumed to be located on the central line of the layer; then governing equations of heat transfer during the ignition process are derived. Since the equations cannot be solved analytically, finite difference method and energy balance method are adopted to solve the temperature profiles of the air and the particles numerically (Cengel, 2004). Time is divided into small steps with step size Δt, space is divided into small volumes around a node and each node is situated in the central line of each cylindrical layer (Fig.1). As shown in Fig. 2, in each region an energy balance analysis is made to discretise Eq. (1) and (2). Finally, the discrete heat transfer equations are solved node by node and layer by layer to determine whether the dust cloud is successfully ignited.

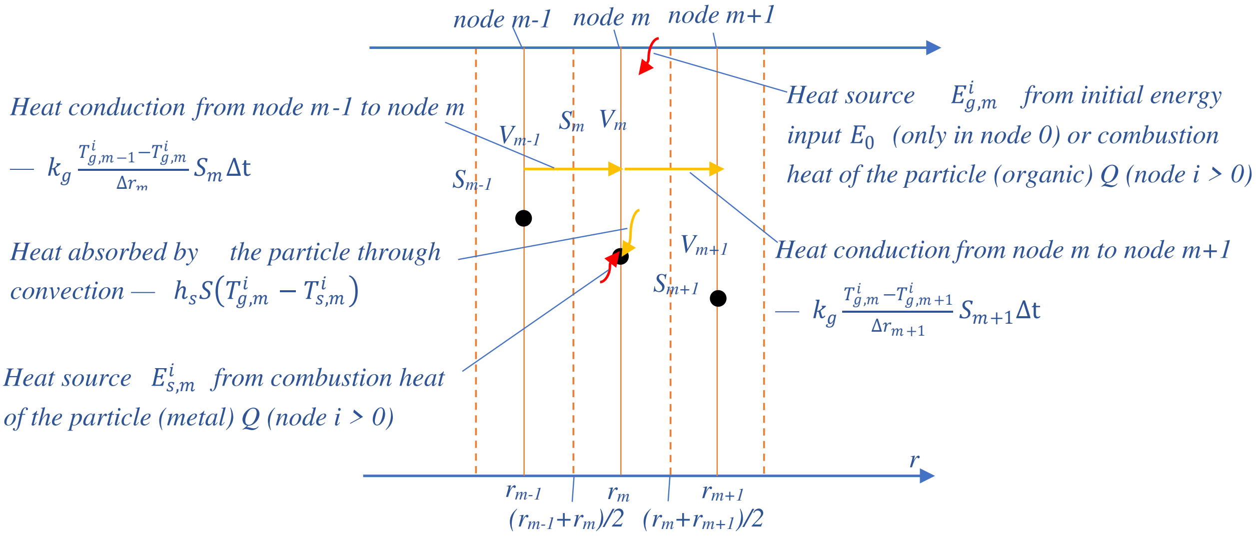

Fig. 2. *Energy balance analysis of layer m*

After the discretisation and the consideration of the heat input from the spark or from the combustion of a particle, the energy balance equations of the air and the particle in layer *m* from time step *i* to time step *i+1* become:

$$\varepsilon_g \rho_g C_{p\_g} V_m \left(T^{i+1}_{g,m} - T^i_{g,m}\right) = \varepsilon_g k_g \left(\frac{T^i_{g,m-1} - T^i_{g,m}}{\Delta r_m} S_m - \frac{T^i_{g,m} - T^i_{g,m+1}}{\Delta r_{m+1}} S_{m+1}\right) \Delta t - h_s S\left(T^i_{g,m} - T^i_{s,m}\right) \Delta t + E^i_{g,m} \tag{3}$$

and

$$\rho_s C_{p\_s} V_s \left(T^{i+1}_{s,m} - T^i_{s,m}\right) = h_s S\left(T^i_{g,m} - T^i_{s,m}\right) \Delta t + E^i_{s,m} \tag{4}$$

where:

Δr_m — distance between node *m-1* and node m, $\Delta r_m = r_m - r_{m-1}$, m; r_m — radium position of node m located in the central line of each cylindrical layer in Fig. 1., $r_m = \frac{\sqrt{m-1}+\sqrt{m}}{2} r_g$, m;

S_m — surface area of the interface between volume *m-1* and volume m located in the middle of node *m-1* and node m, $S_m = \pi l_g (r_m + r_{m-1})$, m^2;

V_m — volume between two interfaces surrounding node m, $V_m = \pi l_g ((\frac{r_{m+1}+r_m}{2})^2 - \left(\frac{r_m+r_{m-1}}{2}\right)^2)$, m^3;

$T^i_{g,m}$ — temperature of air in layer m at time step i, K;

$T^i_{s,m}$ — temperature of the particle in layer m at time step i, K;

$E^i_{g,m}$ — instant energy released in the gas phase, $E^1_{g,0} = E_0$ representing initial energy input from the spark; $E^i_{g,m} = Q$ at node $m > 0$ and the time step i when particle temperature at node m reaches its MIT for organic dust; $E^i_{g,m} = 0$ at node $m > 0$ for metal dust; Q — combustion heat of a particle (for details, see Section 3.2);

$E^i_{s,m}$ — instant energy released in the solid phase, $E^1_{s,0} = 0$; $E^i_{s,m} = Q$ at node $m > 0$ and the time step i when particle temperature at node m reaches its MIT for metal dust; $E^i_{s,m} = 0$ at node $m > 0$ for organic dust.

It should be noted that both Eq (3) and (4) contain heat source term ($E^i_{g,m}$, $E^i_{s,m}$). This is because of the difference between the combustion mechanisms of organic and metal dusts. For organic dusts, the combustion happens in the gas phase, so when a particle is ignited, the combustion heat is released directly into the air ($E^i_{g,m}$ in Eq (3)). However, for metal dusts, the combustion happens on the particle surface, so the combustion heat is assumed to be released first in the particle ($E^i_{s,m}$ in Eq (4)) then transferred into the air through convection. By solving Eq (3) and (4) from layer to layer and step by step, the temperature profiles of air and particles in each layer can be derived numerically.

With the consideration of the same distance between the adjacent central line in each layer Δr, and no heat source or particle existence, Eq. (3) would be simplified into the following form:

$$\rho_g C_{p\_g}\left(T^{i+1}_{g,m} - T^i_{g,m}\right) = k_g\left(\frac{T^i_{g,m-1} - 2T^i_{g,m} + T^i_{g,m+1}}{\Delta r^2} + \frac{T^i_{g,m+1} - T^i_{g,m-1}}{2m\Delta r^2}\right)\Delta t \tag{5}$$

which is exactly the second-order spatial discrete scheme of Eq (2), means that this numerical method has second order accuracy.

3.2 Governing equations for the chemical reactions

Once the temperature of particles in each layer reaches the MIT, ignition is considered to be successful and combustion heat will be released. The chemical reaction is considered as single-step reaction, the only oxidant in the air is oxygen and the reaction rate is infinite. Chemical reactions for metals and hydrocarbon-based materials are as follows:

For metals such as Magnesium:

$$M + x(O_2 + 3.76N_2) = MO_{2x} + 3.76xN_2 \tag{6}$$

For hydrocarbon-based materials such as Lycopodium and Niacin:

$$C_xH_yO_z + \left(x + \frac{y}{4} - \frac{z}{2}\right)(O_2 + 3.76N_2) = xCO_2 + \frac{y}{2}H_2O + 3.76\left(x + \frac{y}{4} - \frac{z}{2}\right)N_2 \tag{7}$$

However, heat released from each particle is affected by the combustion heat of single mass of the particle material and dust concentration. For fuel-lean concentrations, oxygen is present in over stoichiometric amounts so each particle will combust completely once ignited, implying that heat released from each particle Q is constant as dust concentration increases. In fuel-rich conditions with sub stoichiometric oxygen amounts, particles cannot combust completely after being ignited, so Q will decrease with increasing dust concentrations. Heat released by a particle by combustion is calculated as follows:

$$Q = VconcQ_{comb} = \rho_s V_s Q_{comb} \ \ when\ conc\ \leq\ concs \tag{8a}$$

$$Q = VconcsQ_{comb} < \rho_s V_s Q_{comb} \ \ when\ conc\ >\ concs \tag{8b}$$

Where

Q_{comb}—heat of combustion per mass of the dust material, J/kg;

$concs$—the stoichiometric concentration of the dust material in air, kg·m^{-3}.

4. Algorithm for the calculation of the MIE of dusts

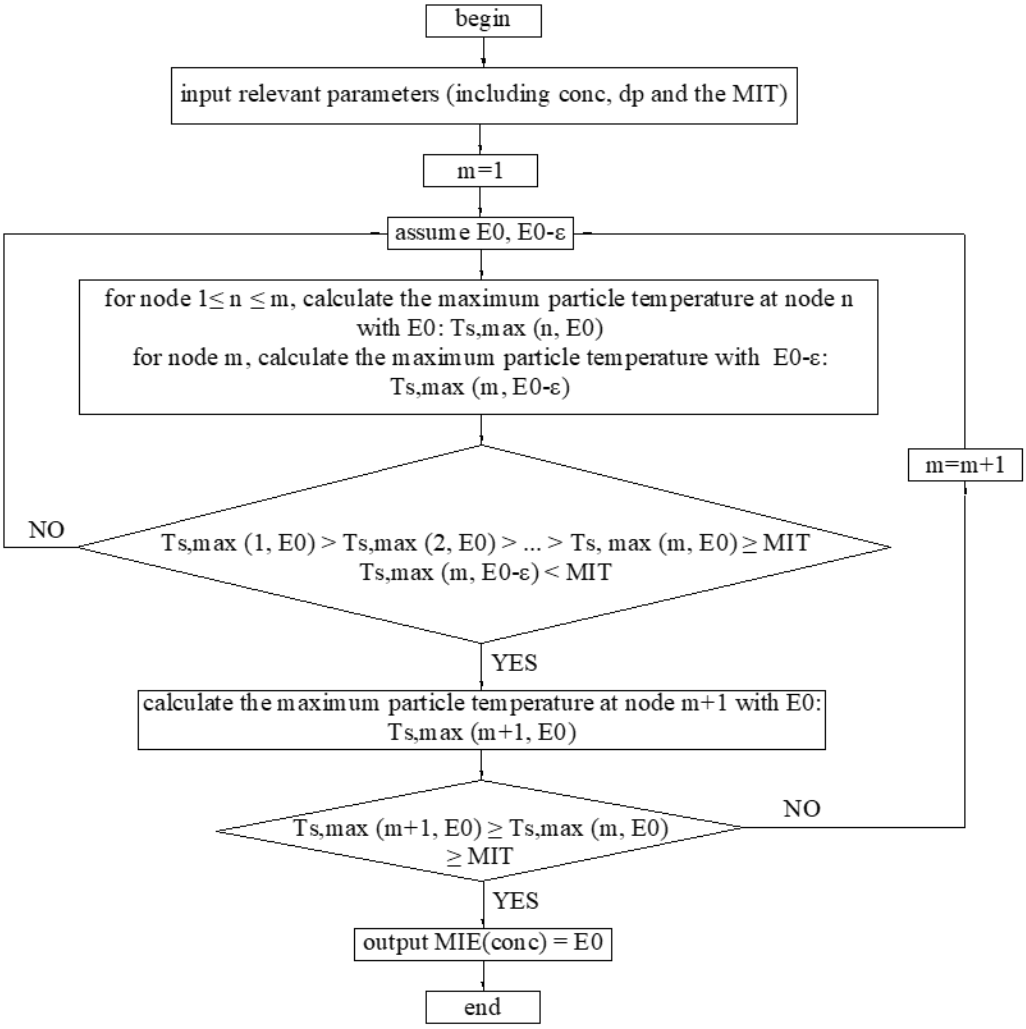

Fig. 3. *Flow chart of the calculation of the MIE of dusts*

The algorithm for the calculation of the MIE of dusts is summarized with a flow chart in Fig. 3. It should be noted that in this study, three significant digits are applied when assuming the initial energy input E_0 and the precision of E_0 is ε. Moreover, here the *MIE(conc)* represents the minimum ignition energy to ignite a dust cloud with a given dust concentration, while the MIE of a dust cloud means the minimum value of the function *MIE(conc)*. $T_{s,max}(m, E_0)$ is the maximum particle temperature at node *m* when ignition of all the particles at its previous nodes are considered with the initial energy input of E_0, but without considering the ignition of the particle at node *m* itself.

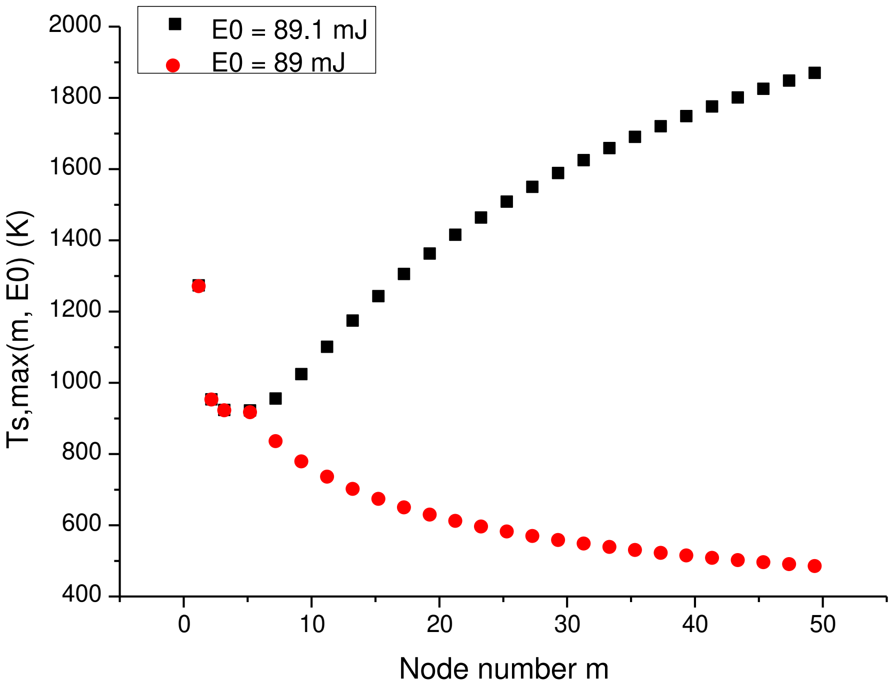

Fig. 4. *Variation of* $T_{s,max}(m, E_0)$ *at each node against node number m (163 µm magnesium dust cloud with 1000 g/m*^{3} *concentration). When* E_0 *= 89.1 mJ, ignition of the dust cloud succeeds; when* E_0 *= 89 mJ, ignition of the dust cloud fails*

Fig. 4 shows the variation trends of $T_{s,max}(m, E_0)$ against node number m when E_0 being fixed as 89.1 mJ and 89 mJ. It implies that when E_0 = 89.1 mJ, ignition of the dust cloud is successful: as node number m increases, $T_{s,max}(m, E_0)$ generally decreases first to a minimum but then starts rising, the combustion of particles can propagate spontaneously in the dust cloud; however, when E_0 drops to $E_0 - \varepsilon$ (89 mJ), $T_{s,max}(m, E_0)$ initially shows similar trend as the case of 89.1 mJ, but will keep dropping as m increases, the combustion of particles is interrupt at a certain node and ignition of the dust cloud fails in this case. Therefore, when E_0 is high enough to ignite the dust cloud, there will always be a minimum value of $T_{s,max}(m, E_0)$ against m; $T_{s,max}(m, E_0)$ usually decreases first but then increases (if it keeps decreasing, sooner or later $T_{s,max}(m, E_0)$ of a particle will drop below the MIT and stop the ignition process), and the minimum value of $T_{s,max}(m, E_0)$ ($min\left(T_{s,max}(m, E_0)\right)$) should be higher than or at least equal to the MIT. The higher E_0 is, the higher $min\left(T_{s,max}(m, E_0)\right)$ will be. In fact, this algorithm attempts to find the MIE which should be a critical value high enough to ignite all particles but low enough to make $min\left(T_{s,max}(m, \text{MIE})\right)$ just reach the MIT value: $min\left(T_{s,max}(m, \text{MIE})\right) = T_{s,max}(l, \text{MIE}) \geq \text{MIT}$ and $T_{s,max}(l, \text{MIE} - \varepsilon) < \text{MIT}$. The ignition of the particle at this node l can be regarded as a symbol of successful ignition of the dust cloud with the MIE, and the time between the release of the MIE and the ignition of the particle at node l is the ignition delay time of the dust cloud t_{ig}.

5. Properties of dusts and experimental settings

The MIEs of different types of dusts were calculated with the above model, and the calculation results are compared with experimental results. Table 1 gives the physical and chemical properties of the combustible dusts used. Most of these data are from the literature survey and online databases. The reason for choosing 5 mm distance between the electrodes for magnesium and 6 mm for the other dusts in the model is to be consistent with the experimental settings in two different references, i.e. Nifukua et al. (2007) with experimental results for magnesium obtained with a distance between the electrodes of 5 mm and Hosseinzadeh et al. (2019) with experimental results for the other dusts obtained with a distance between the electrodes of 6 mm.

Table 1: *Physical and chemical properties of the combustible dusts and the distance between the electrodes*

Dust	**Molecular formula**	**Heat of combustion /kJ·kg^{-1}**	**Median diameter /µm**	**Particle density /kg·m^{-3}**	**Heat capacity /J·(kg. K)$^{-1}$**	**Distance between the electrodes /mm**
Magnesium	Mg	25404 (Rumble, 2018)	10,29,41,60, 90,115,137 and 163 (Nifukua et al., 2007)	1738 ("The Engineering toolBox" n.d.)	1036 (Rumble, 2018)	5 (Nifukua et al., 2007)
Oak wood	$C_{4.13}H_{6.3}O_{2.76}$ ("Chemical composition of wood" n.d.)	18000 (Kim et al., 2016)	62.9 (Hosseinzadeh et al., 2019)	1430 (Kim et al., 2016)	2390 (Hosseinzadeh et al., 2019)	6 (Hosseinzadeh et al., 2019)
Niacin	$C_6H_5NO_2$ (Addai et al., 2016)	20538 (Addai et al., 2016)	17.9 (Hosseinzadeh et al., 2019)	1400 (Hosseinzadeh et al., 2019)	1229 Hosseinzade et al. (2019)	6 (Hosseinzadeh et al., 2019)
Lycopodium	$C_{5.77}H_{9.59}O_{1.23}$ (Addai et al., 2016)	28447 (Addai et al., 2016)	35.9 (Hosseinzadeh et al., 2019)	1096 (Hosseinzadeh et al., 2019)	1381 (Hosseinzadeh et al., 2019)	6 (Hosseinzadeh et al., 2019)

6. Results and discussion

6.1 Comparison between the experimental and calculated results

In table 2 the results of the numerical model are compared with experimental data (Nifukua et al. (2007) and Hosseinzadeh et al. (2019)). The numerical results generally only amount to 20 to 50 % of the experimental values except for 10 µm magnesium, for which the numerical MIE is only 5.48 % of the experimental result possibly due to agglomeration of particles in the experiments. This difference between the calculated and experimental minimum ignition energy can be attributed to two effects: the assumptions made in the model (properties, particle shape…) and losses of the ignition energy input from the MIKE3 apparatus due to various causes (heat radiation, electrode heating, etc.), resulting in an actual heat input into the dust cloud lower than the experimental MIE results.

Table 2: *Comparison between the experimental numerical MIE for different types of dusts*

Dust	**Particle diameter /µm**	**MIT experimental /K**	**MIE experimental / mJ**	**MIE numerical / mJ**	**MIE numerical / MIE experimental**
Niacin	17.9	790	1.6	0.837	52.3 %
Lycopodium	35.9	680	4	2.1	52.5 %
Oak wood	62.9	755	42	19.5	46.4 %
Magnesium	10	786	4	0.219	5.48 %
	29	803	5	1.9	38 %
	41	803	12	3.78	31.5 %
	60	836	42	8.92	21.2 %
	90	848	82	21	25.6 %
	115	851	102	34.7	34 %
	137	858	194	49.7	25.6 %
	163	898	242	77.9	32.2 %

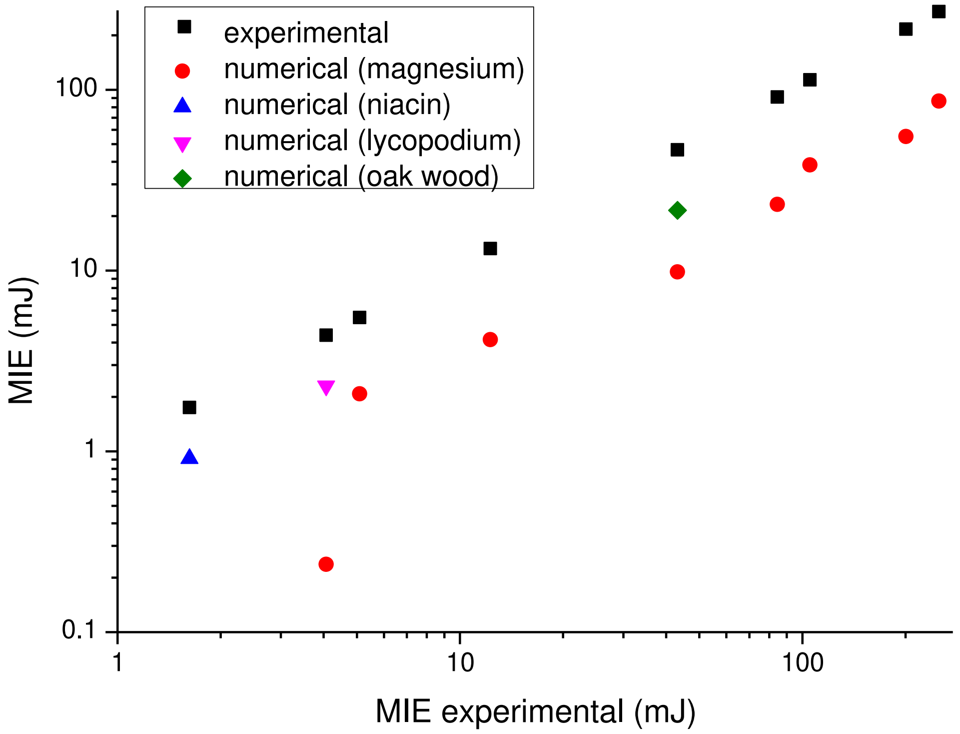

Fig. 5. *Comparison between the experimental numerical MIE for different types of dusts (data from Table 2)*

6.2 The influence of particle diameter and dust cloud concentration on the MIE

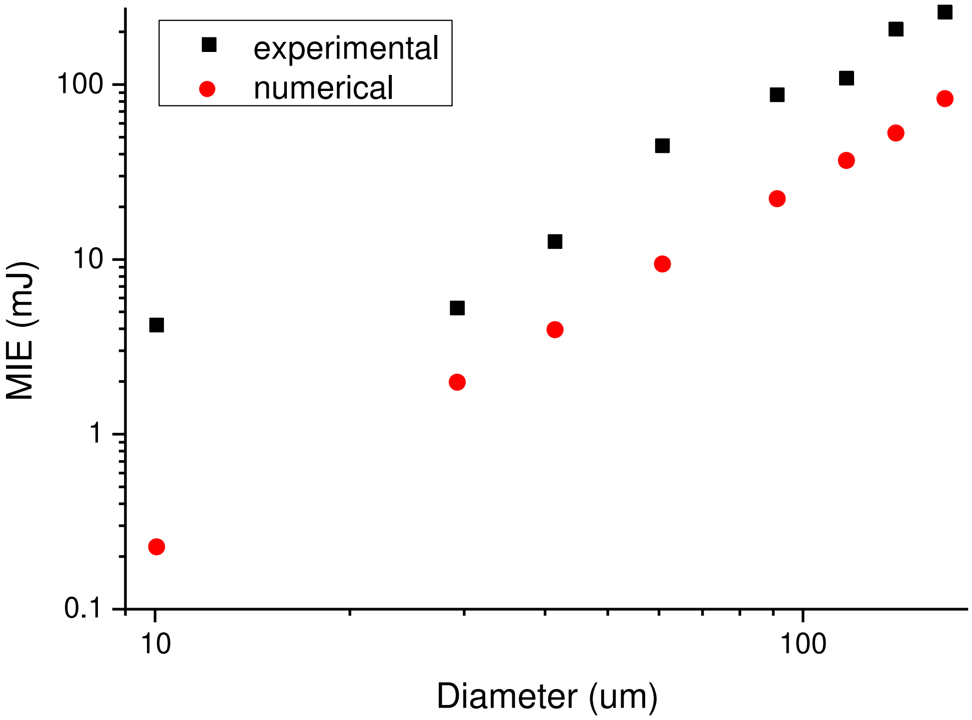

Fig. 6. *Variation of the MIE of magnesium dust against particle diameter*

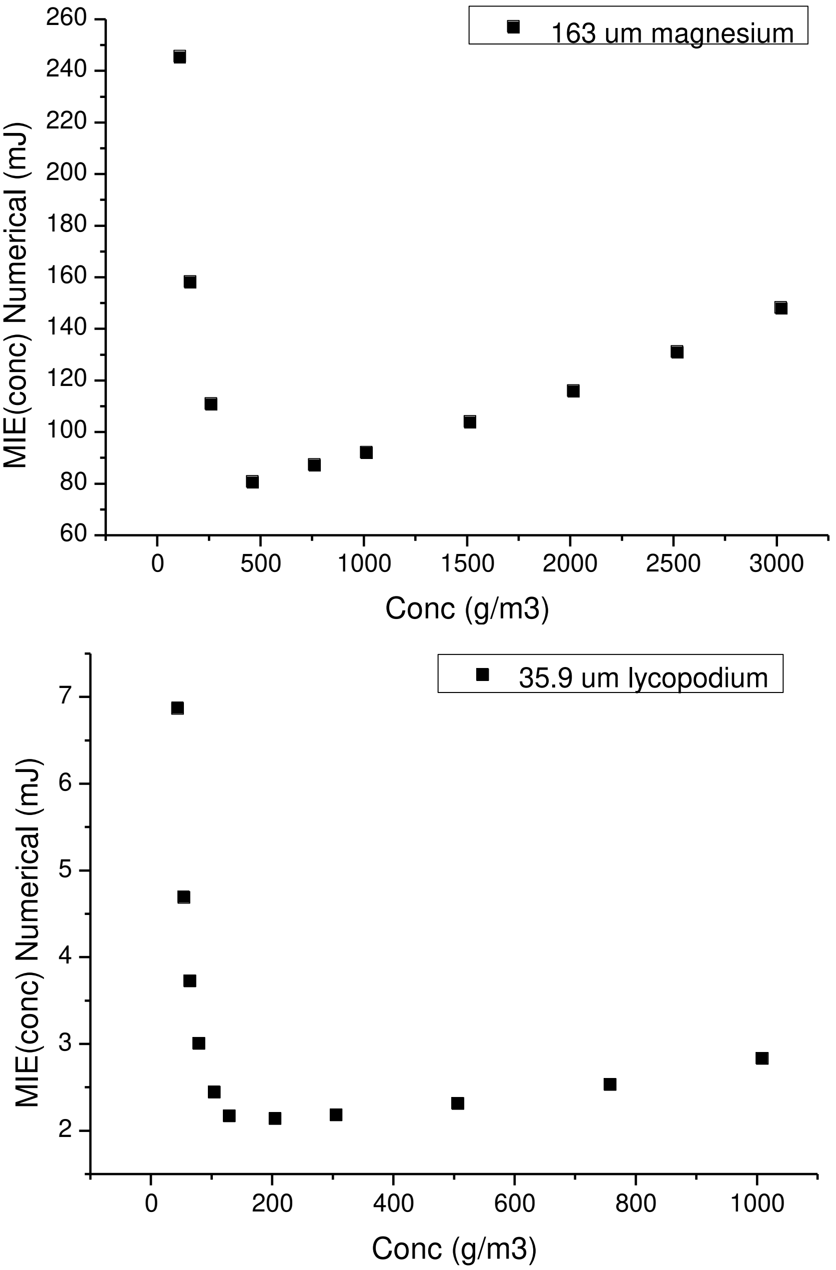

Fig. 7. *Variation of the MIE(conc)s of 163 μm magnesium and 35.9 μm lycopodium dust against dust cloud concentration*

The variation of the MIE of magnesium dust as a function of particle diameter is shown in figure 6. A power function relationship between the calculated MIE and particle diameter can be derived — $MIE \propto d_p^k$. k is approximately 2. The actual energy required to raise the temperature of a particle to its MIT is very small compared with the calculated MIE. For example: The energy for a 163 μm magnesium particle to reach its MIT is only 2.4 mJ, and the ignition of a dust cloud of 163 μm magnesium with 450 g/m^3 only requires to ignite 2 particles (l=2), but the MIE of 163 μm magnesium is as high as 77.9 mJ, meaning that most of the energy input *from the spark* diffuses away in the air and the air temperature profile is almost not affected by the heat conduction process. Therefore, Eq (1) can be approximated by:

$$\rho_g C_{p\_g} \frac{\partial T_g(r,t)}{\partial t} = \frac{1}{r}\frac{\partial}{\partial r}\left(k_g r \frac{\partial T_g(r,t)}{\partial r}\right) \tag{9}$$

The analytical solution of Eq (9) is:

$$T_g(r,t) = T_i + \frac{E_0}{4\pi t k_g l_g} e^{-\frac{r^2}{4\alpha_g t}} \tag{10}$$

where $\alpha_g = \frac{k_g}{\rho_g C_{p\_g}}$.

Eq (2) can be written as:

$$\frac{dT_s(r,t)}{dt} = \frac{6N_u k_g}{\rho_s C_{p\_s} d_p^2}\left(T_g(r,t) - T_s(r,t)\right) \tag{11}$$

This means that the speed to heat up a particle is inversely-proportional to the second power of the particle diameter, so the ignition delay time t_{ig} should be proportional to the second power of the particle diameter: $t_{ig} \propto d_p^2$. The temperature of a particle reaches its maximum when the air temperature is equal to the particle temperature. Therefore, the air temperature around a particle at the moment of ignition has to be equal to the MIT of the particle if E_0 is just enough to raise its temperature to the MIT. Assuming the MIT to be independent of the diameter of the particle, then equation 10 implies that $MIE \propto t_{ig}$, and since $t_{ig} \propto d_p^2$, it can be deduced that $MIE \propto d_p^2$.

Fig. 7 presents the *MIE(conc)* of 163 μm magnesium and 35.9 μm lycopodium dust with different dust cloud concentrations. Generally, the *MIE(conc)* drops approximately inversely-proportional to the concentration as the concentration increases to around the stochiometric concentration. Then the *MIE(conc)* increases as the concentration increases further. For fuel-lean concentrations, the combustion heat of a particle in each layer Q is constant but the distance between the ignition source and the nearest particles decreases with increasing concentration. This results in faster heating up of these particles and thus less required ignition energy. However, when the concentration increases beyond the stoichiometric concentration, decrease of each particle's heat of combustion Q requires the ignition energy to be increased.

7. Conclusions

In this study, a thermal model for the calculation of the MIE of dusts is established and validated. This model first divides the space and time into small grids and steps based on the uniformly distributed particle locations, then solves the heat transfer and heat balance equations numerically with a finite difference method. The following conclusions can be drawn:

(1) the calculated MIEs of various dusts generally lie between 20 to 50 % of the experimental results possibly due to energy loss in the experiment and the assumptions made in the thermal model;

(2) there is a power function relationship between the MIE and particle diameter defined as $MIE \propto d_p^k$ with k being approximately 2;

(3) the *MIE(conc)* decreases nearly inversely-proportional to dust concentration at fuel-lean concentrations, but generally increases as dust concentration rises beyond the stoichiometric value.

Acknowledgements

The authors gratefully acknowledge the financial contribution from China Scholarship Council (No. 201806030181).

References

Addai, E.K., Gabel, D. & Krause, U. (2016). Experimental investigations of the minimum ignition energy and the minimum ignition temperature of inert and combustible dust cloud mixtures. *Journal of Hazardous Materials*, 307: 302-311.

Azhagurajan, A., Selvakumar, N. & Mohammed, Y.M. (2012). Minimum ignition energy for micro and nano flash powders. *Process Safety Progress*. 31(1): 19-23.

Bernard, S., Gillard, P., Foucher, F., et al. (2012). MIE and flame velocity of partially oxidized Aluminum dust. *Journal of Loss Prevention in the Process Industries*, 25(3): 460-466.

Boilard, S.P., Amyotte, P.R., Khan, F.I., Dastidar, A.G. & Eckhoff, R.K. (2013). Explosibility of micron- and nano- size Titanium powders. *Journal of Loss Prevention in the Process Industries*, 26(6): 1646-1654.

Cengel, Y.A. & Afshin J.G., 2015. Heat and Mass Transfer: Fundamentals and Applications 5th Edition. McGraw-Hill Inc., New York.

Chemical composition of wood. (n.d.). Retrieved Feburary18, 2019, from https://akela.mendelu.cz/~xcepl/inobio/nove/Wood_anatomy/WAEF-02-chemical_composition.pdf

Choi, K., Sakasai, H. & Nishimura, K. (2016). Minimum ignition energies of pure Magnesium powders due to electrostatic discharges and Nitrogen's effect. *Journal of Loss Prevention in the Process Industries*, 41: 144-146.

Eckhoff, R.K. & Randeberg, E. (2007). Electrostatic spark ignition of sensitive dust clouds of MIE < 1 mJ. *Journal of Loss Prevention in the Process Industries*, 20(4/6): 396-401.

Hosseinzadeh, S., Berghmans, J., Degrève, J. & Verplaetsen, F. (2019). A model for the minimum ignition energy of dust clouds. *Process Safety and Environmental Protection*, 121: 43-49.

Hosseinzadeh, S., Norman, F., Verplaetsen, F., Berghmans, J. & Van den Bulck, E. (2015). Minimum ignition energy of mixtures of combustible dusts. *Journal of Loss Prevention in the Process Industries*, 36(6): 92-97.

Kalkert, H.G. & Schecker, N. (1979). Theoretische Überlegungen zum Einfluß derTeilchengröße auf die Mindestzündenergie von Stäuben. *Chemie Ingenieur Technik*. 51 (12): 1248–1249.

Kim, Y.H., Lee, M.C. & Rie, D.H. (2016). Explosion characteristics of combustible wood dust in confined system: Analysis using oxygen consumption energy. Journal of Mechanical Science and Technology, 30 (12): 5771-5779.

Li, C., Bu, Y.J., Yuan, C.M., Hao, J.T., & Li, G. (2017). Research status of the minimum ignition energy of dust clouds. *Industrial Safety and Environmental Protection*, 43(3): 14-16.

Li, M.J., Li, X.Q., Ding, L.Y., Liang, L.L. & Wang, F. (2018). Experimental study on minimum ignition energy of Sucrose dust. *Industrial Safety and Environmental Protection*, 44(3): 13-15.

Mittal, M. (2014). Explosion characteristics of micron- and nano- size Magnesium powders. *Journal of Loss Prevention in the Process Industries*, 27(1): 55-64.

Nifuku, M., Koyanaka, S., Ohya, H., Barre, C., Hatori, M., Fujiwara, S., Horiguchi, S. & Sochet, I. (2007). Ignitability characteristics of aluminium and magnesium dusts that are generated during the shredding of post-consumer wastes. *Journal of Loss Prevention in the Process Industries*, 20: 322-329.

Randeberg, E. & Eckhoff, R.K. (2007). Measurement of minimum ignition energies of dust clouds in the MIE < 1 mJ region. *Journal of Hazardous Materials*, 140(1/2): 237-244.

Ren, C. (2011). Experimental investigation and numerical simulation of minimum ignition energy of dust cloud. *Northeastern University, Shenyang*.

Rumble, J.R., ed. (2018). CRC Handbook of Chemistry and Physics (99th ed.). CRC Press. Boca Raton. p.4.61.

Taler, J. & Duba, P. 2006. Approximate analytical methods for solving transient heat conduction problems. In: Solving Direct and Inverse Heat Conduction Problems. Springer Berlin Heidelberg, Berlin, Heidelberg. pp. 587–604.

The Engineering toolBox. (n.d.). Retrieved December 19, 2018, from https://www.engineeringtoolbox.com/metal-alloys-densities-d_50.html

Wu, H.C., Chang, R.C. & Hsiao, H.C. (2012). Research of minimum ignition energy for nano Titanium powder and nano Iron powder. *Journal of Loss Prevention in the Process Industries*, 22(1): 21-24.

Yarin, L.P. & Hetsroni, G., 2004. Dynamics of a Single Particle. In Combustion of Two-Phase Reactive Media. Springer Berlin Heidelberg, Berlin, Heidelberg.

DOI: 10.7795/810.20200724

Safety Related Properties of Tetrafluoroethylene Research on the Explosive Decomposition on an Industrial Scale

C. Liebner [a], V. Schröder [a] & M.J. Shenton [b]

[a] Bundesanstalt für Materialforschung und –prüfung (BAM), Berlin, Germany
[b] PlasticsEurope Fluoropolymers TFE Safety Task Force, UK

E-mail: christian.liebner@bam.de

Abstract

Tetrafluoroethylene (TFE; C_2F_4) is an important industrial chemical. When ignited the chemically unstable TFE gas is able to decompose in an explosive way. Explosions propagating through production plants have led to damage and fatalities, unfortunately only few of them have been published, e.g. by Reza and Christiansen (2007), Klais et al. (2001) and in a decision of the Supreme Court of Florida (2000). Safety related research regarding TFE has been done for decades and revealed the special behaviour of TFE. Different ignition sources were applied in laboratory scale tests. Ferrero et al. (2013) identified local hotspots by polymerisation and compression heat being relevant sources of ignition. Unexpected explosion propagation phenomena were observed.

A comparison of the different experimental apparatus as well as an explanation concerning the identification of the initial hazardous conditions will be given. In the present contribution, a brief summary of laboratory test results is included. Furthermore, recent explosion test results obtained in an industrial scale test apparatus of an ongoing safety research project will be discussed. This also includes geometrical influences. Images from a video depicting the venting process of an explosive decomposition reaction from a 2.5-inch (63 mm) pipe will be analysed.

Keywords: *Tetrafluoroethylene, explosion, safety*

1. Introduction

Every explosion needs an ignition source, i.e. a certain amount of energy released within a time sufficiently short thereafter leading to a self-propagating reaction. Supported by statistical data, see Ferrero et al. (2017), it can be assumed that ignition sources like electrical sparks are not likely to be present in PTFE (Polytetrafluoroethylene is the polymer of TFE) production plants since they are known well enough to be avoided. Spark ignitors and exploding wire igniters are used in the determination of explosion limits. Biryulin et al. (2014) determined the minimum energies required initiating the combustion of gaseous TFE and mixtures thereof with nitrogen, argon, and helium at various initial pressures and temperatures. The lower flammability and detonation limits of TFE–air mixtures under normal conditions were reported to be identical.

TFE is a decomposable substance that needs to be stabilized by an agent inhibiting the start of unwanted oligomerisation, polymerisation and partial oxidation if traces of oxygen being present. Triggering these exothermic reactions must be suppressed since they can be the origin of the energy releases that lead to the ignition source of the TFE decomposition.

According to Ferrero et al. (2017) statistics of TFE accidents revealed unwanted polymerisation, see Babenko et al. (1993), and heat of compression, see Ferrero et al. (2013), to be the two most relevant root causes. When prior to a polymerization reactor the stabilizing agent is removed, unintended polymerisation could take place. In addition to PFTE somewhere in the pipework being produced which may plug the pipe, an exothermic reaction could generate a hotspot that is capable to act as an ignition source. Ignition by hotspots was investigated by Gula (2005). If the temperature of a hotspot in contact with an ignitable gas exceeds a certain value and if at the same time the gas remains that hot, some pre-reactions take place during the Ignition Delay Time (IDT). Reaction heat produced further increases the temperature and reaction rates. As the concentration of reactive intermediate products and temperature is rising further reaction follows. This situation leads to a flame detachment and a self-propagating reaction which is called an explosion.

When the explosion is an oxidation reaction the lowest temperature necessary to start ignition in defined testing apparatus is called the Minimum Ignition Temperature (MIT), sometimes referred to as the Ignition Temperature or Auto Ignition Temperature. In the case of an explosion driven by a decomposition reaction, it is called the Minimum Ignition Temperature of the Decomposition reaction (MITD). Determination of auto ignition phenomena is done in pre-heated closed vessels. The experimental procedures start with flushing in the gas to be tested. Note that standard test procedures, e.g. DIN EN 14522 (2005) and ISO/IEC 80079-20-1-2017 (2017), use open glass flasks and therefore inhomogeneous mixtures of fuel in air. For TFE, experimental MIT data from homogeneous mixtures measured in pre-heated steel vessels described e.g. by Meyer (2009), Teranishi (1958) and Ferrero et al. (2013), as well as MITD data from Gula (2005) and Kluge (2012) is available. A comparison of MIT of TFE-air mixtures with MITD is given by Ferrero et al. (2013). A steel autoclave with an inner volume of 3 dm^3 that could be heated and was strong enough to withstand explosions was developed. Once heated up, TFE and the TFE-air mixtures were charged, and pressure-time histories were recorded. It was found that the ignition temperatures of the stoichiometric TFE-air mixtures were always lower than the corresponding ignition temperatures for the decomposition reaction of the pure TFE.

The other most relevant ignition source, heat of compression, is also related to the ignition temperature. The energy supplying process is compression. The compression temperature necessary for ignition must be higher than the MITD of TFE at the corresponding pressure since the gas will start to cool down immediately after being compressed if its surrounding surfaces are at a lower temperature. The compression ratio Ψ is defined as

$$\Psi = \frac{P_d}{P_r}$$

where P_d is the initial pressure in the donor section and P_r is the initial pressure in the receiving section. Compression is a highly dynamic process that depends on the compression ratio Ψ, the heat capacity c_p of the gases compressed, the opening speed of the separation valve and the heat exchange with the walls. Depending on the initial conditions of the compression process temperature can rise high enough to initiate the explosive decomposition reaction. Initial conditions characterizing hazardous situations have already been investigated by Ferrero et al. (2017) and Kluge et al. (2016) for a straight pipe with an inner diameter of 28 mm.

2. Experiments

Safety related properties of TFE were determined in two compression pipes. The one pipe has an inner diameter of 28 mm and a total length of 22 m, the second pipe provides an inner diameter of 63 mm and a total length of 30 m. Figure 1 depicts the simplified flow chart diagram of this type of setup. A pipe is separated in to two sections by a high-speed ball valve V-12 with typical opening times adjustable from 0.10 to 2.00 s. The left side of the pipe is called the donor pipe since this is where TFE is filled at elevated pressure. There is a burst disc installed at its very left end. The right part of the pipe is called the receiving section. There are open junction thermocouples Type K according to IEC 584 class 1 installed at the right end flange. The initial temperature of the thermally insulated test apparatus is kept between 35 to 40 °C using up to eight microprocessor heating controls from WEST type 6100+, heating bands from Horst and Pt 100 sensors. The receiving section contains air at a technical vacuum grade with an absolute pressure ranging from 1.000 to 0.100 bar(a). Pressure measurement is done with piezo resistive pressure sensors from Keller type PA-10 (PIR 211 and 212) to adjust for the initial conditions and piezo electrical pressure transducers from PCB type 102 (PIR 221 and 223) for the dynamic pressure measurement during the compression. When suddenly the separation valve V-12 is opened, TFE will flow from the donor pipe (left) to the receiving section (right). The place of ignition in the experimental setup is near the right end flange. From this place the decomposition reaction travels through the tube to the left side. The marked field of view (left side in Fig. 1) corresponds to the images from a video recorded during the venting process of an explosion, these are shown in Fig. 2.

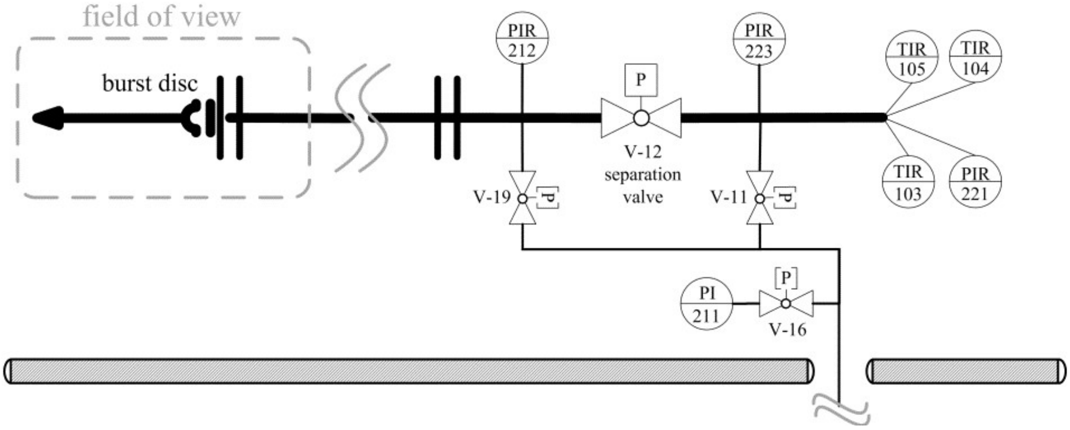

Fig. 1. *Simplified diagram of the compression apparatus*

3. Results and discussion

It is to be distinguished between two different types of experiments. Compression tests with air in both of the two tube sections are performed to understand the temperature levels of air being compressed under polytropic conditions. Those screening tests allow to make predictions for the TFE tests that contain TFE in the donor section. Such a TFE test is depicted in the picture sequence in Fig. 2. After the compression takes place it may take a couple of seconds before the reaction accelerates along the tube and the inner pressure increases to an extent to open the rupture disc. The decomposition reaction gases are vented, then. In the venting process observed in Fig. 2 unburnt TFE is released before the flame and the soot. Therefore, the flame propagation mode in this case is not of a detonative character.

The difference in heat capacity between air $c_p(air)$ = 29 J/(mol·K) and TFE $c_p(TFE)$ = 80 J/(mol·K) leads to a significantly higher compression temperature if air is compressed instead of the receiving section would have been filled with TFE. Air is a commonly identified impurity after maintenance work in TFE plants in past accident's investigations. The high temperature achieved is due to the air or nitrogen present in the receiving section. Heat transfer is one of the critical parameters. Inhibitors used in TFE processing plants partially suppress but they do not perfectly stop the polymerization reaction. Over time a polymer layer may be deposited at the walls. In principle, a hazard scenario in a production plant could take place in a different geometry and at walls that provide a lower heat transfer due to the polymer layer. Compression in pipes with less local heat loss leads to higher compression temperatures. If applying the hazard diagram (Ferrero et al., 2017) it is therefore advisable not to come too close to the warning line, i.e. the reaction threshold line that distinguishes between initial conditions leading to a slow exothermic reaction and such initial conditions where no exothermicity could be observed in the test apparatus. Even though removing deposits is part of the maintenance work in production plants and in the test apparatus, PTFE build-up is known to form over time in production plant conditions. PTFE deposits are known to cause hotspots due to their heat insulating character, see Gula (2005).

Fig. 2. *Venting process of an explosive decomposition from a pipe of 63 mm inner diameter (2.5-inch pipe; L = 30 m); Pd = 10.00 bar(a); Pr = 0.400 bar(a). (a) short before the bust disc opened; (b) release of unburnt TFE; (c) release of some dirt and soot; (d) and (e) flame; (f) release of decomposition reaction products.*

For a better understanding of the dependency of the compression temperature on the initial conditions, screening experiments are carried out with air in both sections of the pipe before verification tests with TFE are performed. In Fig. 3 compression temperature vs. compression ratio from those air-air compression tests is plotted. The compression temperature is not a function of just the compression ratio; if P_d and P_r would be varied at a constant Ψ, the compression temperature would increase with increasing pressure since the heat release increases faster than the heat transfer to the walls. This is a complex issue. The adiabatic temperature line is calculated using GasEQ (Morley, 2005). In Fig. 3, the triangles belong to tests in a receiving section of L_r = 2 m length. The squares belong to compression tests in the 1 m receiving section. Different initial pressure conditions in the receiving pipe could be distinguished by the different shaded symbols. Of course, the data given below is only valid for a straight pipe of a certain diameter. Pipe work in a production plant never meets these boundary conditions. Installations like elbows, tee-pieces, strainers, flame arrestors and valves lead to an increased turbulence in the gas flow. In the case of an accidental compression such installations could be in the receiving section. The circle symbols in Fig. 3 belong to tests with a 2-hole orifice, i.e. a steel plate with two 10 mm bores. This represents a flow meter installed in the middle of a 2 m receiving pipe. It acts as a flow restrictor reducing the flow area by 75 %. Compression temperatures determined with this modified experimental setup were measured at two positions: at the end flange (filled circles ●) and directly in front of the baffle of the orifice (open circles ○). Temperatures determined at the baffle are all slightly below 100 °C.

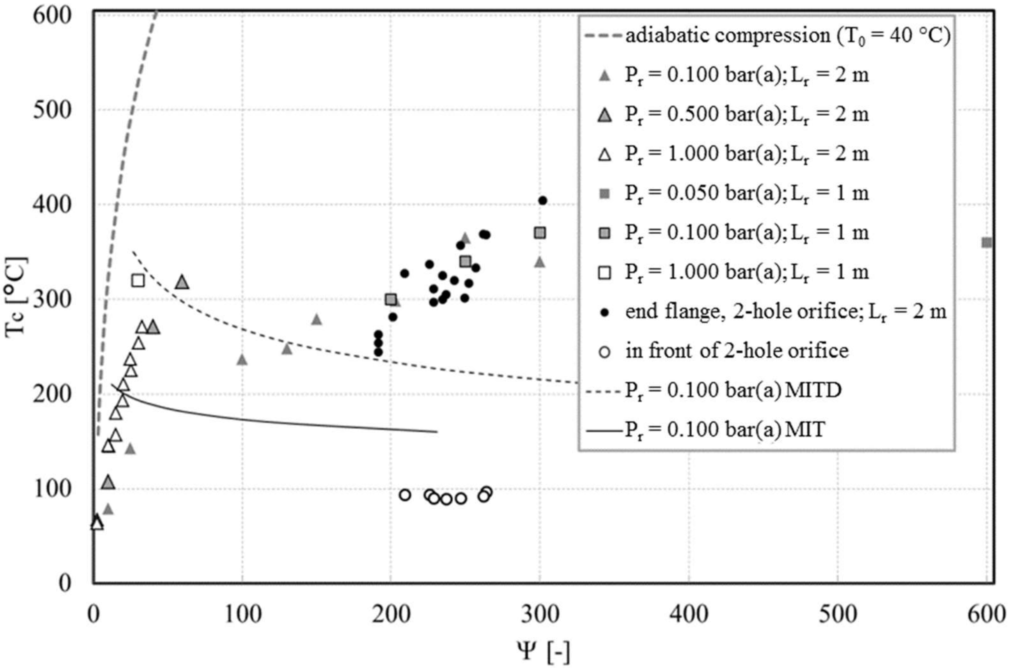

Fig. 3. *Compression Temperature T_c vs. Compression Ratio Ψ in tests where air is compressed with air in a pipe of 28 mm inner diameter (1.1-inch pipe)*

There are two lines in Fig. 3 denoted as 'P_r = 0.100 bar(a) MITD' and 'P_r = 0.100 bar(a) MIT'. Data describing the pressure dependency of MITD [8] and MIT [11] is used to plot these two lines. These lines are safety related properties that are different from compression temperatures but added to the plot for comparison. Initiation of explosion in a compression situation strictly needs a compression temperature that is at least above the corresponding MITD or MIT. Otherwise no explosion can be initiated. Assuming the receiving pressure is P_r = 0.100 bar(a), Eq. (1) is applied to calculate the donor pressure for each compression ratio. Then the MITD and MIT corresponding to P_d are calculated from the literature data.

Basically, the same is done for a pipe providing an inner diameter of 63 mm (2.5-inch-pipe). The so-called Hazard Diagram, Fig. 4, is set up for a straight pipe configuration. Fig. 4 modifies the Hazard Diagram given by Ferrero et al. (2017). The area above the lines plotted in the diagram are found to be safe initial conditions in the corresponding test apparatus. Below the lines explosive decomposition reactions are detected.

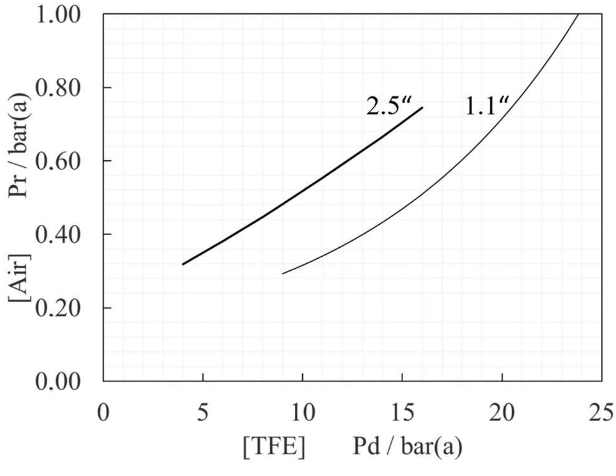

Fig. 4. *Hazard Diagram. Influence of inner diameter (1.1-inch pipe vs. 2.5-inch pipe) is depicted. Below the line compression in the experimental apparatus led to explosive decomposition reaction.*

It is necessary to distinguish between different protective measures when handling TFE. Primary measures should aim at avoiding hazardous initial conditions. As TFE can explosively decompose, this means avoiding conditions above the limiting decomposition concentration, the limiting decomposition pressure and the limiting decomposition temperature. In every part of an apparatus where this is not possible, the secondary protective layer would be to avoid mechanical and electrical ignition sources and to take care the substance will not be heated up above its MITD. In PTFE production plants, it is not always possible to meet these demands in all parts of the apparatus. Therefore, additional protective measures have to be taken, e.g. a pressure resistant design of the apparatus, flame arrestors and pressure release devices. In any case it is advisable that measures capable of extinguishing the explosion flame before it accelerates to a detonation are in place.

In 1989, a research group at BAM intended to determine explosion propagation characteristics of TFE in a tube of 50 mm inner diameter and a length of 6 m; the tube had a pressure resistance of 2 kbar. TFE was filled in at an initial pressure of 20 bar(a). The explosion led to the destruction of the end flange. A lens sealing made from stainless steel ruptured into pieces and the bolts were bent. Those unexpected test results gave reason for further investigation of explosion characteristics of TFE (Hieronymus et al., 1994). Explosions were determined in tube diameters of 40 and 50 mm, tube lengths ranging from 1.9 to 10.1 m and initial pressures from 5 to 25 bar(a). Ignition sources were normally exploding wires although in some cases an incoming detonation from a separated volume filled with an acetylene-oxygen mixture was used. Unusual oscillations driven by reactive shock waves travelling through the tube were observed. It was concluded that in certain cases the resulting pressure of the decomposition process can be about 200 times the initial pressure, i.e., ten times the pressure expected for a steady detonation. This effect was explained by the assumption that the decomposition reaction of TFE on the conditions investigated here is not perfectly detonable or that the run-up distance is very long. In a follow-on project unusual run-up distances of 200 times the inner diameter were measured by Lietze (2001). These investigations gave some insight in what could happen in case of a TFE explosion is propagating but did not answer the question what is the origin of the energy release that could serve as an ignition source in a production plant processing TFE. An observation made running compression tests presently reported is that the decomposition reaction starts slowly in the beginning. From the moment of ignition, i.e. the moment of compression occurs, it is observed that explosion is obtained some seconds later. Acceleration and propagation throughout the volume takes time. Even the deflagrative explosion is relatively slow. Soot may act as a temperature shield that keeps the heat inside the reaction zone. This would explain why the temperature at the thermocouples can be high enough to melt them. Hot reaction intermediate products providing a high reactivity serve for the destruction for seals. Because of the ignition process and the explosion propagation acceleration is slow, the resulting explosion later on is most violent. Long run-up distances could provide an ideal build-up of deflagrative pressure before the detonation sets in.

Before restarting a production plant, it is advised (Ferrero et al., 2017) to flush with nitrogen to remove oxygen and add TFE at a low rate and pressure in order to reduce the possibility of ignition by heat of compression. Furthermore, it is desirable to flush with low pressure TFE before introducing TFE at elevated pressures.

4. Conclusions

Following experts' advice (Ferrero et al., 2017), air has been identified as a common impurity after maintenance work in TFE plants. In many past industrial accidents, heat of compression was found to be the root cause of the ignition. In the present contribution two geometrical influences on gas phase compression temperatures are reported. An investigation approach that is based on the comparison of air-air compression tests with existing MITD and MIT data is useful for a rough estimation of dangerous initial conditions.

Firstly, the pipe diameter of a straight pipe is found to influence the initial conditions that can be foreseen as being hazardous. In a comparison of the initial experimental conditions from the Fig. 2

experiment with the hazard diagram (Ferrero et al., 2017 and Kluge et al., 2016) for a tube with about half of the inner diameter, the situation is reported to be safe in the smaller tube whereas clearly for the larger tube a decomposition has occurred. This is expected when the surface to volume ratio changes.

Secondly, the influence of flow restrictors is discussed. Flow restrictors, the roughness of the walls or the presence of other equipment are likely to generate additional turbulence. Compression temperatures recorded at the baffle of the flow restrictor do not serve as an ignition source. The temperature at the baffle is too low to ignite TFE because the temperature is far below MITD and MIT. Instead, the compressing gas is now a mixture of TFE and air and this compresses the remaining air. This TFE-air mixture is larger and easier to ignite than the situation where there is no additional turbulence. This results in a slightly lower ignition temperature at the end flange after a flow restrictor such as an orifice. Flow restrictors will act as a mixing device. The major part of the compression energy release does not occur at the place of the restriction but at the end flange. Therefore, temperature increase at the place of the restriction will probably not be high enough to ignite the gas but due to turbulences provides an accelerated mixing of the donor gas with the receiving gas. Compression of air with a mixture of TFE and air leads to a mixture that can have a much higher sensitivity and may trigger the explosive decomposition even if it was believed to be safe. The hazard diagram (Ferrero et al., 2017) provides useful data to identify hazardous initial conditions but does not give a guarantee about the safe initial conditions if its boundary conditions are disregarded.

Acknowledgements

Financial support from PlasticsEurope TFE Safety Task Force is gratefully acknowledged. The authors also thank Sven Maurice Hyman for his assistance with the experimental explosion testing.

References

Babenko, Yu. I., Lisochkin, Ya. A., Poznyak, V.I. (1993). Explosion of Tetrafluoroethylene during nonisothermal polymerization. *Combustion Explosion and Shock Waves* 29: 603-609.

Biryulin, Yu. S., Borisov, A. A., Mailkov, A. E., Troshin, K. Ya., Khomik, S. V. (2014). Explosive Characteristics of Tetrafluoroethylene. *Russian Journal of Physical Chemistry* B 8(2): 165-171.

DIN EN 14522 (2005). Determination of the minimum ignition temperature of gases and vapors.

Ferrero, F., Meyer, R., Kluge, M., Schröder, V. Spoormaker, T. (2013). Self-ignition of tetrafluoroethylene induced by rapid valve opening in small diameter pipes. *Journal of Loss Prevention in the Process Industries* 26: 177–185.

Ferrero, F., Meyer, R., Kluge, M., Schröder, V., Spoormaker, T. (2013). Study of the spontaneous ignition of stoichiometric tetrafluoroethylene-air mixtures at elevated pressures. *Journal of Loss Prevention in the Process Industries* 26: 759–765.

Ferrero, F., Shenton, M.J., Bellucci, D., Spoormaker, T. (2017). Guide for the Safe Handling of Tetrafluoroethylene. *PlasticsEurope*.

Gula, M. (2005). Heiße Oberflächen als Zündquelle für den Zerfall von Tetrafluorethylen. *Thesis, Bundesanstalt für Materialforschung und –prüfung (BAM) and TU Berlin, Berlin, Germany.*

Hieronymus, H., Plewinsky, B., Barfuss, S., Kowall, R., Seeger, H.-J. (1994). Shock waves during the explosion of decomposing tetrafluoroethylene in tubes. *Archivum combustionis* 14(3-4): 181-192.

ISO/IEC 80079-20-1-2017 (2017). Explosive atmospheres – Part 20-1: Material characteristics for gas and vapour classification – Test methods and data.

Klais, O., Westphal, F., Killich, A., Staudt, H.-J. (2001). Lesson to learn: The decomposition of Tetrafluoroethylene in a distillation column. *Proceedings of the 10th International Symposium on Loss Prevention and Safety Promotion in the Process Industries, Stockholm*: 493-506.

Kluge, M. (2012). Experimentelle Bestimmung und Modellierung von sicherheitstechnischen Eigenschaften der Zerfallsreaktion von Tetrafluorethen. *Thesis, Bundesanstalt für Materialforschung und –prüfung (BAM) and TU Berlin, Berlin, Germany*.

Kluge, M., Kreißig, M., Liebner, C., Spoormaker, T. (2016). Identifying hazardous conditions for rapid compression scenarios of chemically unstable gases in industrial scaled pipes. *Chemical Engineering Transactions* 48: 607-612.

Lietze, D. (2001). Untersuchungen mit einem Zerfall von Tetrafluorethylen in längeren Rohrleitungen. *Chemie Ingenieur Technik* 73(4): 393-399.

Meyer, R. (2009). Untersuchung des Zündverhaltens des Tetrafluorethens (TFE) durch adiabatische Kompression. *Thesis, Bundesanstalt für Materialforschung und –prüfung (BAM) and TU Berlin, Berlin, Germany.*

Morley, C. (2005). GasEQ V.0.79 b. *http://www.gaseq.co.uk* (accessed 15 January 2020).

Reza, A., E. Christiansen, E. (2007). A Case Study of a TFE Explosion in a PTFE Manufacturing Facility. *Process Safety Progress* 26(1): 77-82.

Supreme Court of Florida (2000). Debra Ann Turner, James Creighton and Lynn Creighton vs. PCR, INC., Corrected Opinion. No. SC94468.

Teranishi, H. (1958). Studies on the Explosions under high pressures, IV The Explosions of Tetrafluoroethylene mixed with oxygen or air. *The Review of Physical Chemistry of Japan* 28: 9-23.

DOI: 10.7795/810.20200724

Influence of thermal shock of piezoelectric pressure sensors on the measurement of explosion pressures

Tim Krause [a], Mirko Meier [b] & Jens Brunzendorf [a]

[a] Physikalisch-Technische Bundesanstalt (PTB), Braunschweig, Germany
[b] Kistler Instrumente AG, Winterthur, Switzerland

E-mail: Tim.Krause@ptb.de

Abstract

Piezoelectric pressure sensors are susceptible to changing temperatures, because resulting mechanical deformations of the sensor membrane and housing may exert a positive or negative force on the piezo crystal, thus changing the reading of this sensor. The consideration and compensation of this influence quantity is a frequent topic of many investigations in the field of combustion chambers, of spark-ignition engines and internal combustion engines. However, this is not the case in the field of the type of protection "flameproof enclosures". Here a peculiarity is the fast temperature rise during a single explosion and the concurrent influence of the temperature gradient, which is often described as thermal shock. The whole event has a typical duration time of the order of seconds and less. Thermal shocks have so far received little attention, as was also a lesson learnt from the evaluation of an interlaboratory comparison between Ex testing laboratories. The laboratories handle thermal shock in a variety of ways, starting from complete ignorance up to various sophisticated coatings. This was a main source of different results within the field of participants. This work evaluates the behavior of different piezoelectric pressure sensor types with respect to thermal shock. Different temperature protection measures are investigated regarding their functionality, practicability and stability. Possible influences on the sensitivity of the sensors due to the used protective measures regarding thermal shock are shown. The transient temperature load of the sensor membrane is estimated by physical calculations as well as numerical analysis based on surface temperature measurements transformed in a surface heat flux density. This work provides guidelines for typical end-users in the field of flameproof enclosures how to handle thermal shock correctly.

Keywords: *flameproof enclosures, explosion pressure, piezoelectric pressure sensor, thermal shock*

1. Introduction

In potentially hazardous locations, equipment and devices of the type of protection "flameproof enclosures" are often used. One of the main parameters which must be determined during the process of conformity assessment is the maximum pressure during the explosion. Besides the pressure rise time, the reference pressure determined from the maximum explosion pressure forms the basis for further type tests of the equipment. The technical requirements and the corresponding type tests are defined internationally in the standard IEC 60079-1 (IEC, 2014). The technical implementation of explosion pressure measurement is undefined except for a few specifications such as fuel-air mixtures and signal filtering. Accordingly, there are many different measurement chains among test laboratories, especially when selecting pressure sensors. The evaluation and analysis of an international interlaboratory comparison between testing laboratories showed that the participants all use piezoelectric pressure sensors (Krause, 2017). A further finding of the analysis was that the missing consideration of the temperature influence on the pressure sensors was one of the main reasons for deviating results and a high variation.

In the field of internal combustion engines for the precise measurement of cylinder pressure traces, there are numerous investigations regarding the thermal influence on the pressure measurement (Higuma, 1999), (Stein, 1987). However, the thermal load of pressure sensors in this field is different. Here the static temperature load due to the frequent number of explosions and the associated high operating temperature is often a problem. The application of the explosion pressure measurement in the field of flameproof enclosures is characterized by single fast explosions. These lead to short-term temperature loads on the pressure sensors. Tichý (1980) describes the effects of this rapid temperature change on the pressure sensor during a measurement as temperature gradient error. Although most users are familiar with the generic term thermal shock, the general understanding of the subject is not very extensive. Therefore, the aim of this work is to investigate the thermal shock and the effects on the pressure sensors and thus also on the explosion pressure measurement to support technical end users.

2. Experimental set-up

The experimental setup used in this work corresponds in its basic structure to the setup usually used by testing laboratories for the determination of explosion pressures in the field of flameproof enclosures. The specific challenge of this setup is to keep as many factors as possible constant (and thus to eliminate them) that influence the explosion pressure. To study the sensors behavior, reproducible explosion events are required. Therefore, a stainless-steel sphere with 10 l volume was chosen as test object. The spherical geometry and central position of the ignition electrodes ensures identical test conditions for all wall-mounted pressure sensors. The test object permits the simultaneous installation of six pressure sensors in the wall at a 45° angle. The fuel-air mixture is purged into the test object by using mass flow controllers. The correct concentration is detected by an oxygen analyzer at the outlet of the test object. After ignition of the fuel-air mixture inside the test object, the pressure curve is recorded with the pressure sensors to be investigated. The protective coating against thermal shock of the sensor membrane is varied depending on the test. The piezoelectric sensors generate a charge signal proportional to the pressure, which is converted into an electrical voltage by a charge amplifier. This voltage is recorded with an oscilloscope or transient recorder. The explosion pressure depends on the pressure and temperature of the fuel-air mixture before ignition (Steen, 2000). For this reason, these two parameters are also measured and kept constant. Afterwards the explosion pressures are converted to reference conditions according to DIN EN 15967 (DIN, 2011). The reference values used are $p_{\text{mix}} = 1$ bar for the pressure and $T_{\text{mix}} = 298.15$ K for the temperature of the fuel-air mixture. The sampling rate used for signal recording is 500 kS/s. Signal filters are not applied. All tests are performed with a fuel air mixture of 31 vol.-% H_2 in air. The schematic experimental setup is shown in Figure 1.

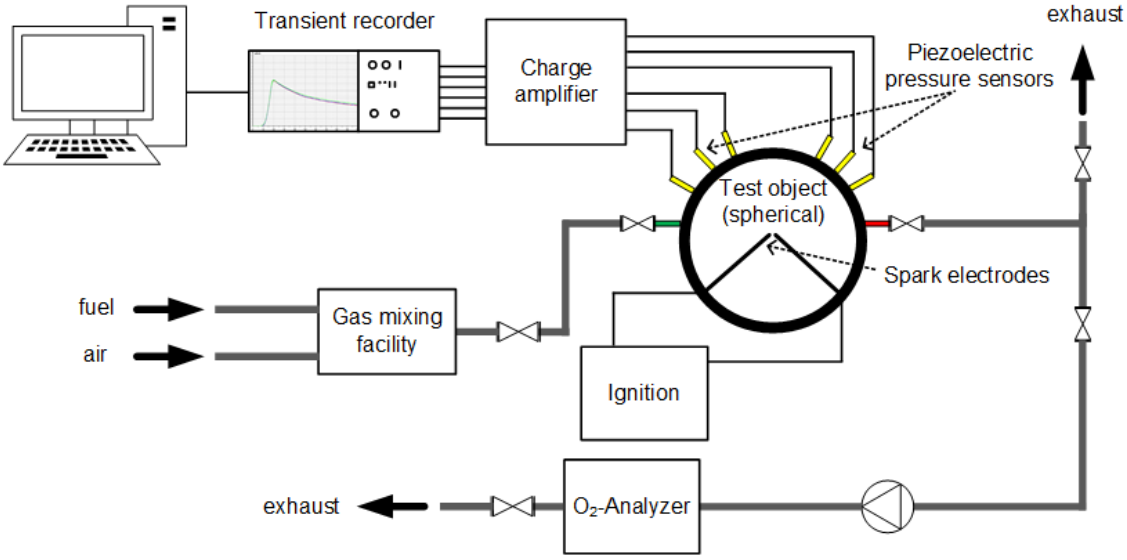

Fig. 1. *Experimental setup for the explosion measurement of the explosion pressure*

3. Thermal shock: The effect of a dynamic temperature gradient on pressure sensors

For piezoelectric pressure sensors, a distinction between static and dynamic temperature loads is advisable. For static temperature loads the focus is on the operating temperature range, the thermal zero shift and the thermal sensitivity drift (Tichý, 1980). These influences become relevant when the sensor undergoes a permanent change in temperature. Dynamic temperature loads due to transient changes in temperature, especially in the sensor membrane, is often called thermal shock. More precisely, this describes a generalized term for the reaction of the sensor to a sudden and rapid positive or negative thermal gradient. This reaction then superimposes the wanted reaction of the sensor caused by a pressure change, in our case the pressure of the explosion. The influence on the pressure signal depends on the sensor design and especially on the structure of the sensor membrane. Figure 2 shows the results of the explosion pressure measurement for a selection of commonly used piezoelectric pressure sensors. This work focuses on the Kistler 6031 and Kistler 601CAA sensors, as these are used very frequently by Ex testing laboratories. The other ones are only shown for overview to demonstrate the variety of the possible sensors to be used and to show the differences in thermal shock behavior. For each sensor type, both the case without a protective coating (w/o TP) and a 1 mm RTV (Room-Temperature-Vulcanizing) silicone layer on the membrane for protection against thermal shock (w/ TP) are considered.

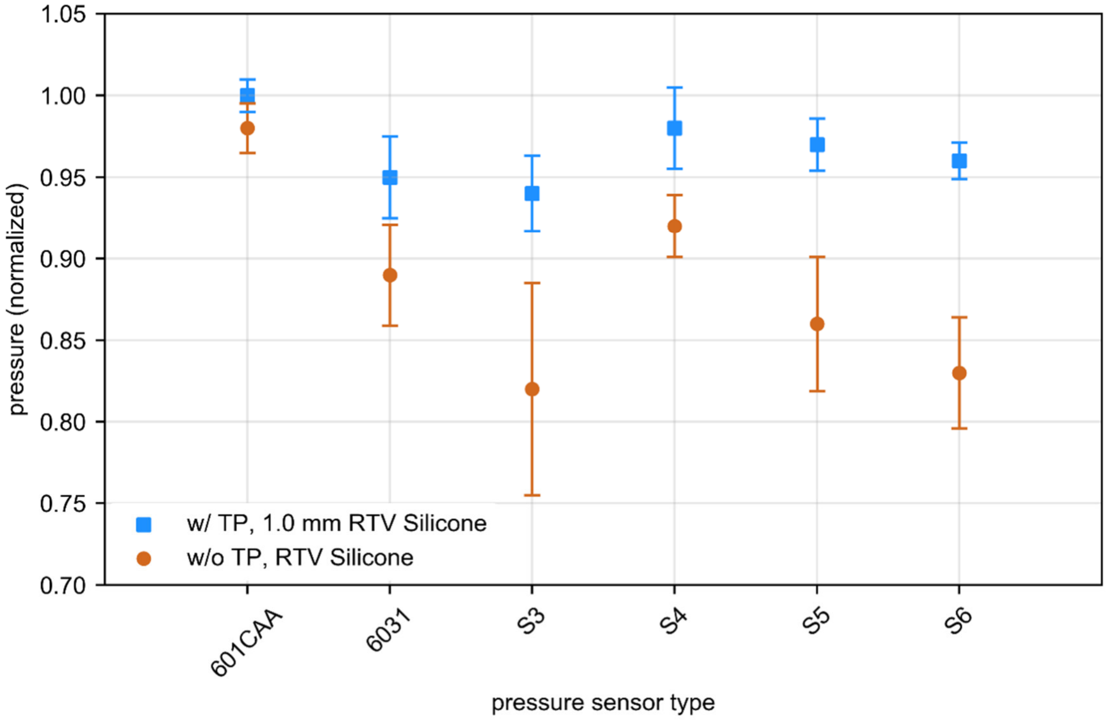

Fig. 2. *Maximum pressures of different pressure sensor types with and without thermal protection, normalized to the maximum value of all measurements.*

The results for each sensor type are mean values of at least two sensors and not less than five explosions each. The pressures are normalized to the maximum measured mean pressure of 7.39 bar by sensor type 601CAA. It can be seen that the measured values using 1 mm RTV silicone for protection against temperature influences are higher compared to the values without protective measures. Furthermore, in five out of six cases the scatter range of the values is higher without using RTV silicone. The maximum deviation results for sensor S6 and is 13 % within the sensor comparison. The minimum deviation results for sensor type 601CAA. Here the values with and without RTV silicone are comparable within the scatter range. Considered as a whole, the sensors without RTV silicone are within a range of 16 %. The sensors with protective layer are within a range of 6 %. Besides the analysis of the maximum values with the assigned scatter ranges (see Figure 2), it is very useful to have a look to the associated pressure curves of the respective sensors. In the field of flameproof enclosures, the decisive criteria are the maximum explosion pressure and the pressure rise time. Nevertheless, these two parameters provide little information about the sensor's behavior with respect to thermal shock. Figure 3 shows the pressure curves of the six sensor types to be investigated for a time range of 500 ms. The mean curve is also formed by at least two sensors per type and at minimum five measurements each.

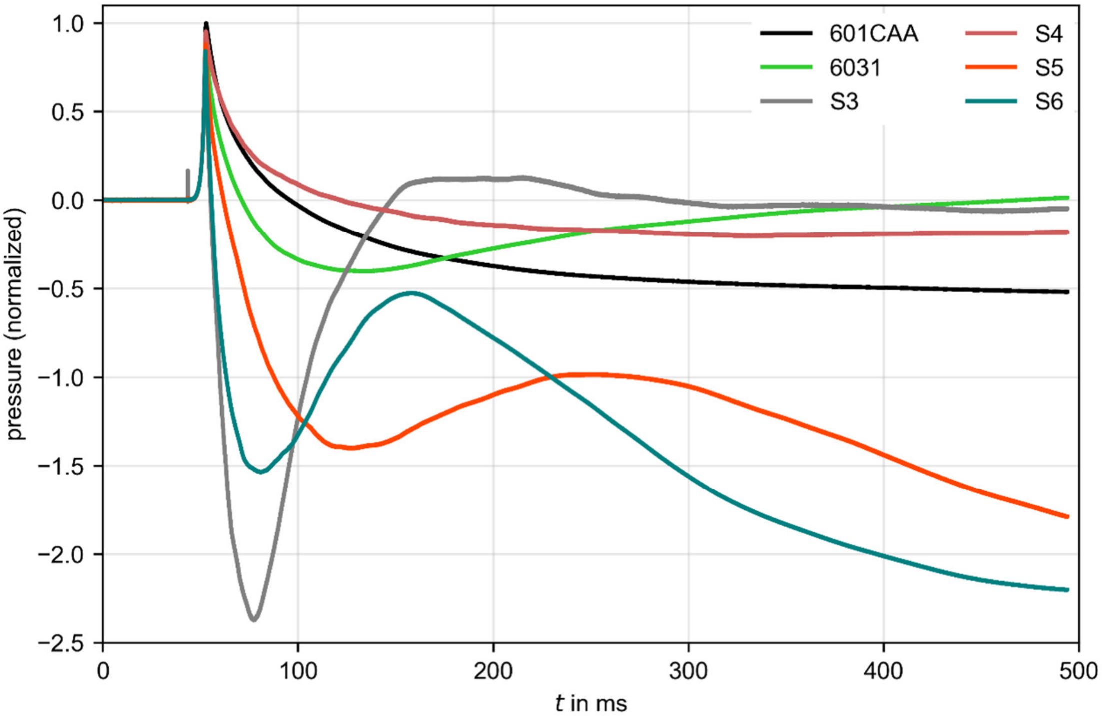

Fig. 3. *Pressure curves of different pressure sensor types without thermal protection, normalized to the maximum value of all measurements.*

It can be observed that the curve progression for the different pressure sensors after reaching the maximum are obviously different. When the respective pressure maximum is reached, the flame front hits the sensor membrane. Depending on the design of the sensor, the pressure curve is influenced differently by the temperature input. While the sensor S4 and 601CAA show a rather moderate drop, the sensors 6031, S3, S5 and S6 react with a significantly steeper drop of the curve. With the curve falling below the zero line, the superimposed influence of the thermal shock is obvious, since it can no longer be a physical pressure. The strong undershoot in the range between the maxima at about 55 ms and the time up to about 80 ms for the sensor S3 and S6 and up to about 130 ms for the sensor S5 shows the reaction of the membrane which deforms against the axial direction due to thermal stress. Thereafter, the thermal expansion on the membrane decreases, which is reflected in an increase in the curve. Finally, the curves drop again, but this is caused by the temperature influence on the piezoelectric elements in the sensor body. The sensors 601CAA and S4 do not show this temperature behavior of the membrane which is because of the different design approach. As a rule of thumb, it can be said that the more the curve shows an undershooting behavior, the more intensely is the effect of a dynamic temperature gradient on the pressure sensor.

Figure 4 shows the region of the maximum explosion pressure in more detail. Depending on the intensity of the undershoot, the sensors have a correspondingly reduced maximum value. Between the sensor 601CAA, which is least sensitive to thermal shock, and the most sensitive sensor S3 the pressure difference of the maximum values is around 16 %.

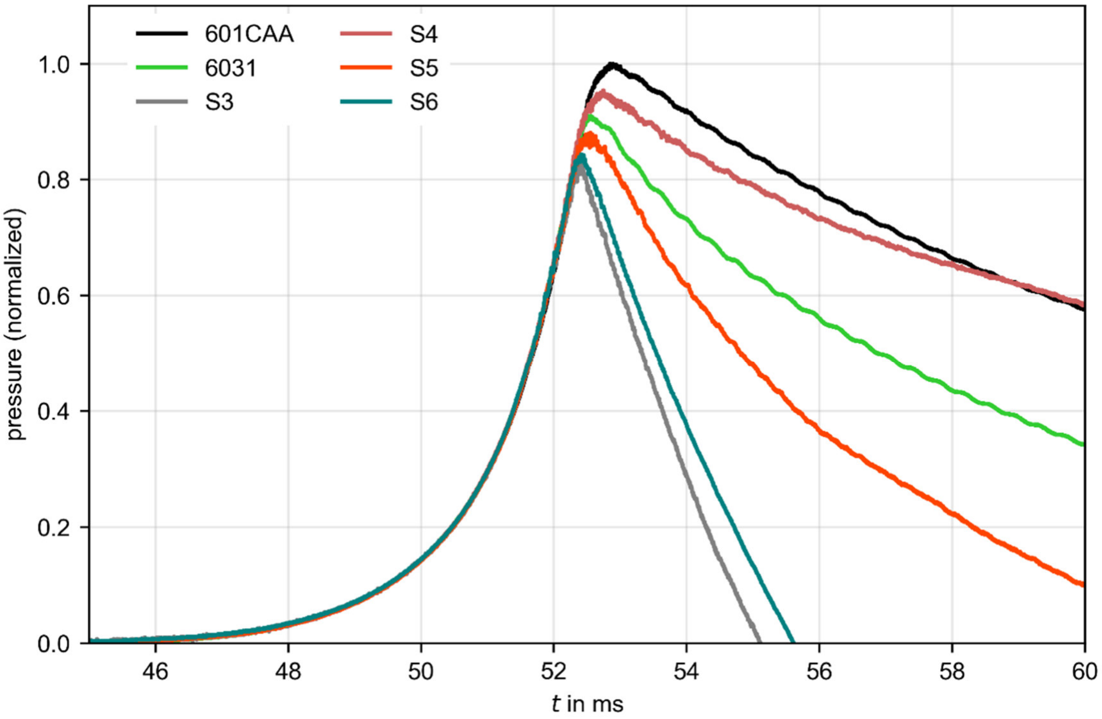

Fig. 4. *Maximum pressure values of different pressure sensor types without thermal protection*

The thermal sensitivity of the same sensors changes significantly, when a protective layer of 1 mm RTV silicone is applied on the sensor membranes. The resulting pressure curves are shown in Figure 5. The differences in the curve progressions compared to the results of the unprotected sensor membranes (see Figure 3), especially in the time range after the pressure maximum, is evident. There is no undershooting, the slope of the curve is more moderate and sensor S6 is the first to drop below the zero line after approx. 420 ms. The pressure curves are much more synchronous and show a similar behavior.

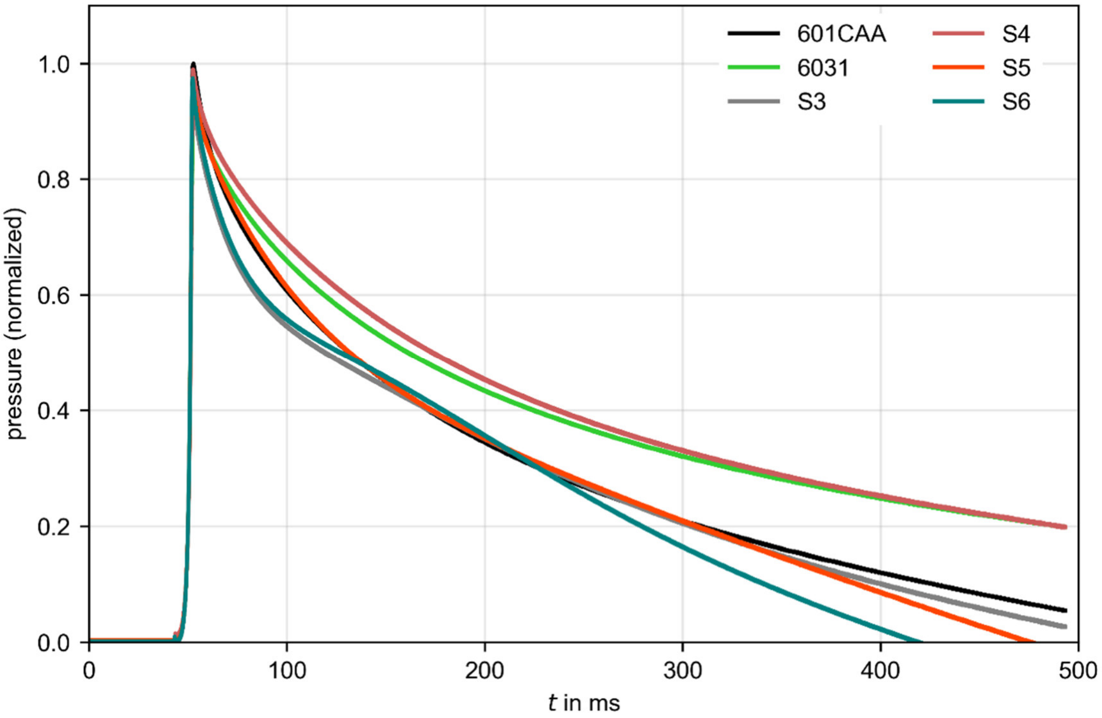

Fig. 5. *Pressure curves of different pressure sensors types with thermal protection (1 mm RTV silicone)*

A detailed view of the maximum pressure values is given in Figure 6. A good overlap of the curves can be seen. The maximum pressure values are in a comparable range.

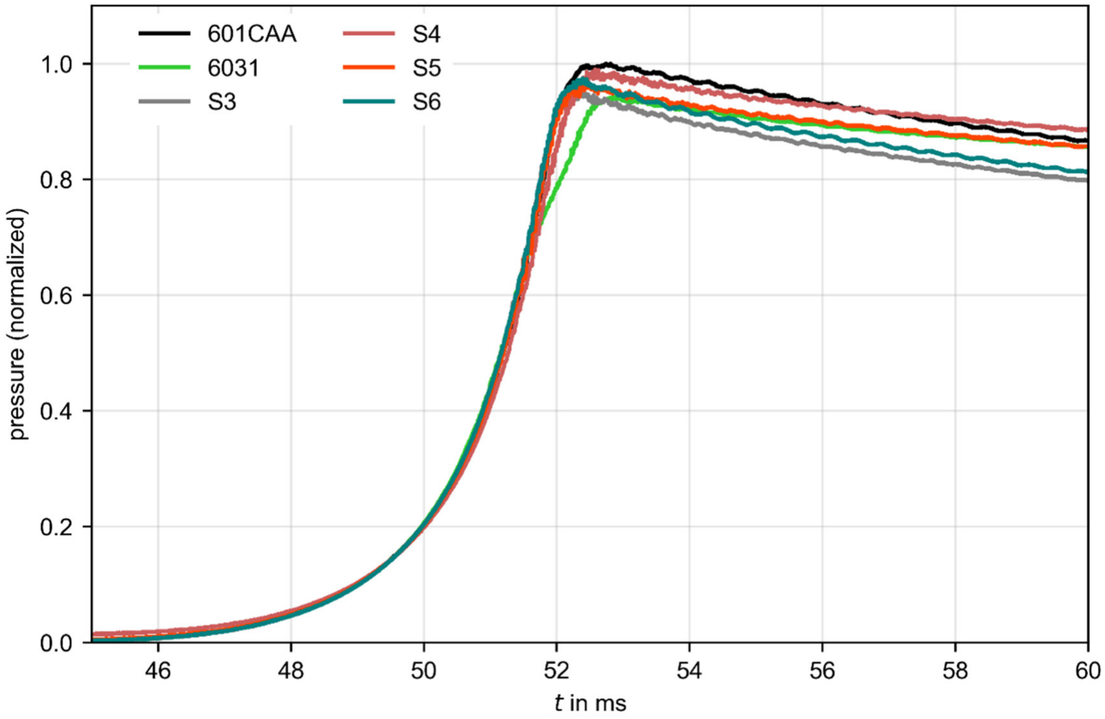

Fig. 6. *Maximum pressure values of different pressure sensor types with thermal protection (1 mm RTV silicone)*

The piezoelectric sensor types examined in this section all respond to thermal shock. However, the extent of the reaction varies significantly. While some of the sensors tend to undershoot strongly with a simultaneous reduction of the maximum value (S3, S5, S6), other sensors are less affected (601CAA). But for all sensors the effect can be clearly seen in the decay behavior of the pressure curves. The use of a protective coating on the sensor membrane causes a time shift of the thermal shock for all sensor types. This leads to an equalization of the maximum values and the pressure curves in the period under consideration.

4. Temperature protection measures in comparison

The results from section 3 demonstrate that the use of a protective coating on the sensor membrane can reduce the influence of temperature on the explosion pressure measurement. The question arises which type of protective coating is most suitable. The further analysis of the interlaboratory comparison together with the feedback from Ex testing laboratories has shown that a large number of different coatings are used in practice. Figure 7 illustrates the results of the mean maximum explosion pressures for a fuel-air mixture of 31 vol.-% H_2 with a pressure sensor of type 601CAA, membranes protected against thermal shock with different common protective coatings: Aluminium foil, vinyl tape (white/black), kapton foil, silicone grease and two types of RTV silicone in different layer thicknesses.

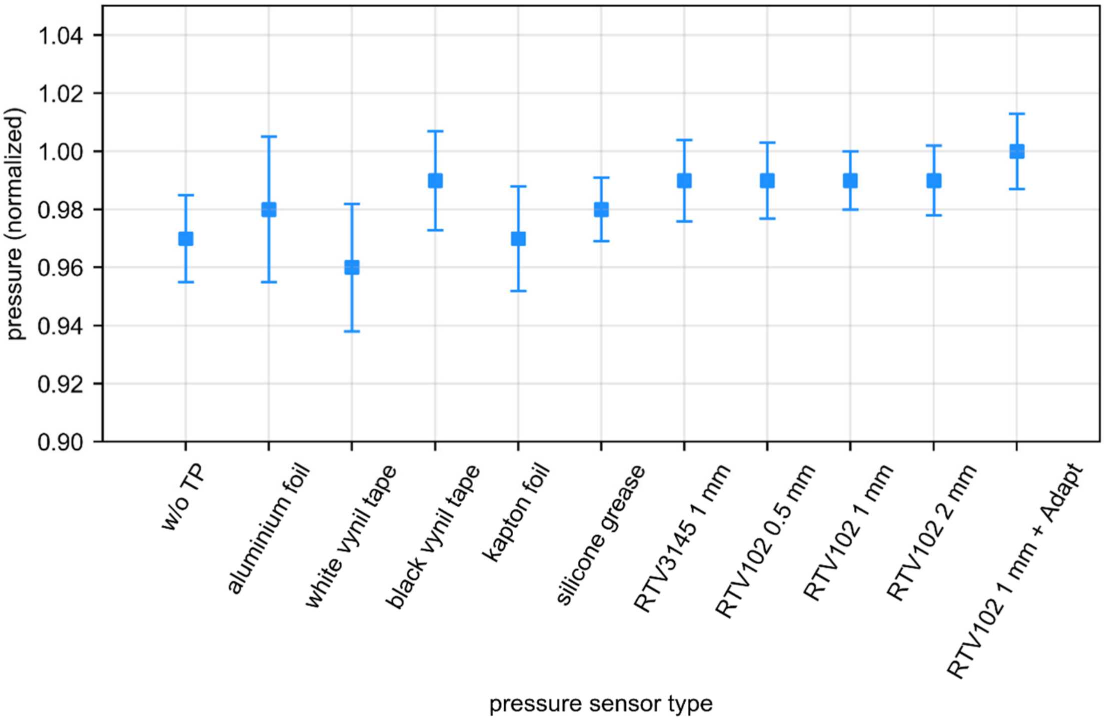

Fig. 7. *Comparison of different protective coatings on the membrane of pressure sensor type 601CAA*

The results from Figure 7 show that the maximum explosion pressures are within a range of 4 %. Considering the variation of the individual results, the values are well comparable. It can be observed that none of the methods used has a significant negative effect on the determination of the maximum explosion pressures. Only with the adhesive protective measures (vinyl tapes, aluminum and kapton foils) the variation increases slightly. The smallest variation is obtained by using a 1 mm RTV silicone layer applied to the sensor membrane. An analysis of the pressure curves for the various protective measures results in more significant differences (see Figure 8). Note that an unprotected sensor membrane causes the steepest drop in the curve which becomes negative about 50 ms after reaching the maximum value. The pressure curves measured with silicone grease and 1 mm RTV silicone do not drop into physically impossible negative pressure values. In between are the pressure curves of the adhesive protective measures, which also drop into the negative range.

It can be concluded from the measurement results that silicone grease and RTV silicone provide the most effective protection against the effects of thermal shock. Compared to the RTV silicone, however, the silicone grease has some decisive disadvantages in practicability and stability. It has been shown during the experiments that it is almost impossible to apply silicone grease in a defined quantity uniformly and reproducibly to the sensor membrane. Depending on the installation position of the pressure sensors, the protective layer changes more or less quickly or disappears completely.

Stability is also a problem during longer series of measurements with frequent explosions. It has been shown that the pressure wave changes the applied structure of the protective layer. Constant conditions during a series of measurements are therefore difficult to realize with silicon grease.

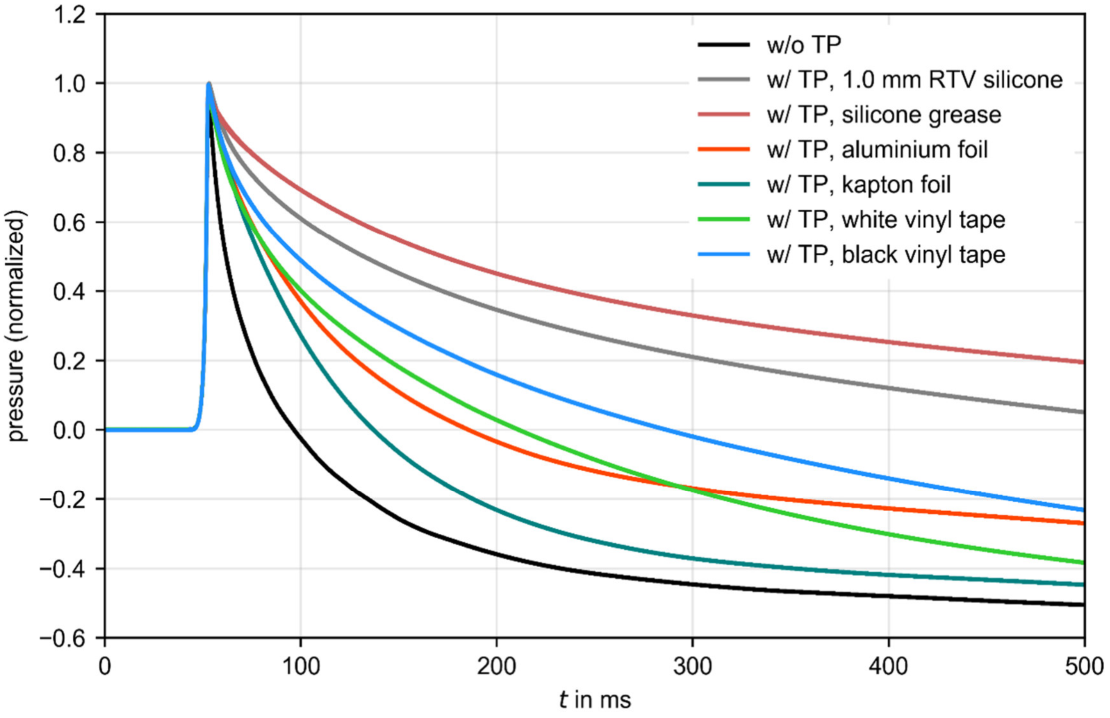

Fig. 8. *Pressure curves for different protective coatings on the membrane of pressure sensor type 601CAA*

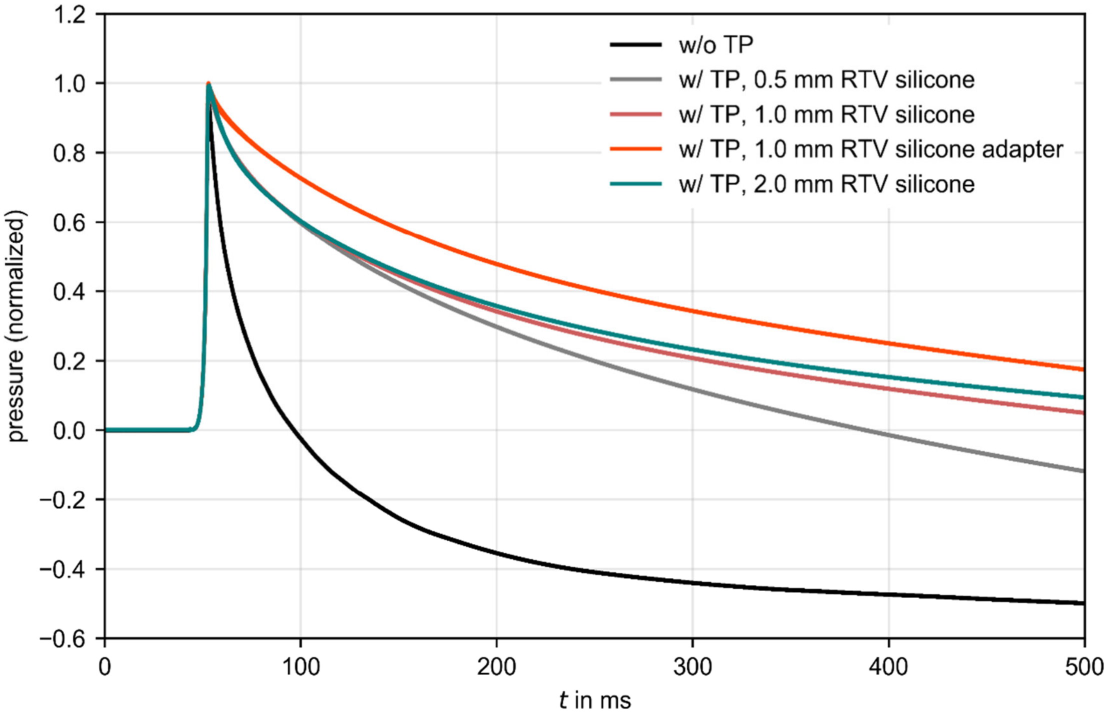

Fig. 9. *Pressure curves for different RTV silicone coatings on the membrane of pressure sensor type 601CAA*

When focusing on RTV silicone as the most suitable method to protect the sensor against thermal shock, further differentiations needs to be made. Figure 9 shows the pressure curves of the preparation of the sensor membrane with different silicone layer thicknesses (0.5 mm, 1.0 mm and 2.0 mm) compared to an unprepared sensor. Furthermore, a configuration is shown where the silicone layer is not only covering the actual sensor membrane, but also the adapter in which the sensor is installed. The latter describes a commonly used case, since the sensor membrane can be simply prepared with this method. The results show again the fast drop of the curve into the negative range for the unprotected sensor membrane (w/o TP). The curves for the three different layer thicknesses of RTV silicone, as well as the maximum values and variations (see Figure 7), are close together and thus show a comparable characteristic. Noticeable, however, is the significantly smooth drop of the curve for the configuration with the 1 mm RTV silicone on membrane and adapter. The assumption that the sensor is simply better protected against thermal shock is not correct. It is rather based on an increase in sensitivity, which is explained in more detail in section 6 of this paper.

Figure 10 shows the application of a 1 mm RTV silicone layer on the sensor membrane in practice.

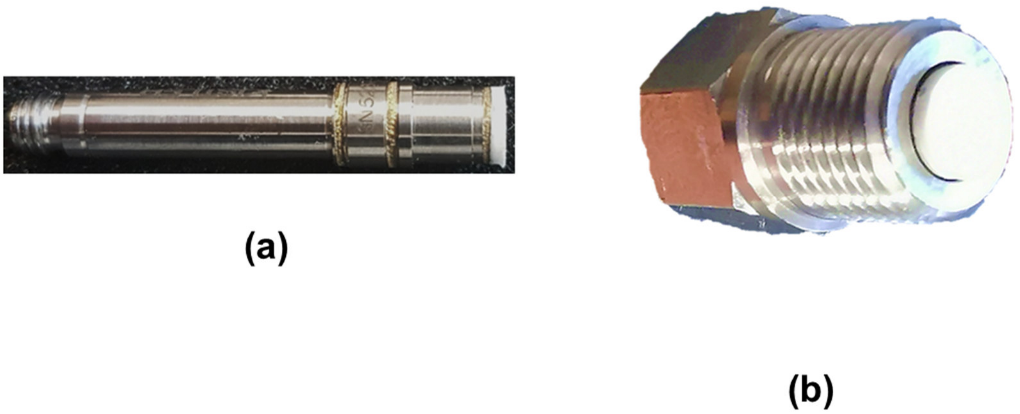

Fig. 10. Illustration of a protective layer on the sensor membrane using 1 mm RTV silicone:
(a): Sensor without adapter, (b): Sensor with adapter

5. Temperature loads on sensor membranes

This chapter deals with influences of temperature on the relationship between the measured value and the output signal of piezoelectric sensors when measuring explosion pressures. In order to understand the thermal shock and the response of the sensors to it, it is essential to investigate the conditions that are present when measuring explosion pressures. Lewis and von Elbe (1987) describe the explosion sequence for an ozone-oxygen mixture (40.06 vol.-% O_3) in a comparable spherical enclosure under simplified assumptions such as adiabatic conditions, a homogeneous fuel-air mixture with constant viscosity and specific heat, and uniform pressure distribution throughout the system. Although the explosive mixture differs from the fuel-air mixture used in our investigations, the basic explosion process with the corresponding temperature characteristics in closed systems are comparable. Here it is indicated that the temperature in front of the wall is still about 70 % of the explosion temperature at the beginning. Transferred to our experiment (adiabatic combustion temperature for H_2 with T_{ad} = 2500 °C) the temperature in front of the wall would be about 1750 °C. This raises the question of what temperature input the sensor or the sensor membrane is exposed to in practice. For this purpose, a first physical estimation is carried out in the following.

The physical laws also apply for our given setup, imposing limits for the membrane and wall temperatures. In particular, the laws of energy conservation, heat transfer and heat capacity must be obeyed. This estimation applies different models with simplified geometries and assumptions to derive upper limits of the maximum membrane temperature. These calculations provide robust estimates. Membrane temperatures outside these limits are physically impossible and to be rejected. Exact calculations require detailed knowledge about the actual membrane construction as well as numerical calculations based on the finite element method (FEM). These FEM-calculations are presented later in this section. Both independent types of calculations –physical limits and numerical calculations – must coincide to be plausible.

Energy release during explosion: In the experiment, the heating of the membrane is triggered by the sudden combustion of 10 l stoichiometric hydrogen/air mixture at room temperature and ambient pressure. With a pressure $p_0 = 1013$ mbar, ambient temperature $T_0 = 293$ K, volume $V = 10$ l, and the ideal gas law

$$pV = nRT \tag{1}$$

(universal gas constant $R = 8.314$ J/mol/K) we obtain the amount of gas being $n = 0.416$ mol. Obeying stoichiometric conditions and the oxygen content of air, the amount of hydrogen in the volume amounts to $n(H_2) = 0.123$ mol. The standard enthalpy H for the formation of 1 mol of water from hydrogen and oxygen is $H = -241.8$ kJ/mol (exotherm). Hence, 100 % combustion of the existing 0.123 mol of hydrogen produce $Q = 29.7$ kJ of heat energy. This value of $Q = 29.7$ kJ is the upper limit of the energy released during the explosion. This energy $Q < 29.7$ kJ is released within some milliseconds and eventually absorbed by the walls within some tens of a second (see Figure 5). In the following, we discuss the resulting upper limits of the maximum wall and membrane temperature. The two cases are also illustrated in Figure 11.

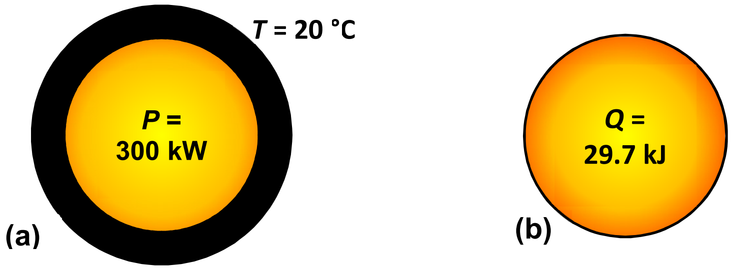

Fig. 11. *Illustration of two extreme cases. Case (a): infinite heating of the inside with P = 300 kW, case (b): wall consists of thin membrane only, whole explosion energy Q is absorbed by membrane*

Case (a) Maximum temperature of the wall – upper limit: The wall of the chamber is simultaneously heated by the contact with the hot gas inside the chamber and cooled by the remaining wall which has ambient temperature (20 °C). Since the heat conductivity of steel is orders of magnitude higher than the one of gas, the inside wall temperature must be dominated by the ambient temperature, not the inside gas temperature. In order to derive an upper limit of the inside wall temperature, an unrealistic worst-case-scenario is discussed: It is assumed that the inside of the wall is constantly heated with a power $P = 300$ kW (see Figure 10, case a). This power P is derived from the simplified assumption that the explosion energy $Q = 29.7$ kJ is released within 0.1 s (thus $P = 300$ kW heating power). The time is a worst-case-assumption based on Fig. 5. The true heating power is always lower than this value and is active for some tens of a second only, hence the true maximum value of the wall temperature must be well below this worst-case scenario.

The maximum possible value of the temperature difference ΔT across the chamber wall is derived from the heat transfer equation

$$P = \frac{kA\Delta T}{d} \tag{2}$$

and the given inner surface $A = 0.224$ m², wall thickness $d = 16.5$ mm, thermal conductivity of steel $k = 50$ W/m²/K, and heating power $P < 300$ kW, resulting in a value of $\Delta T < 440$ K. In other words: Even an infinite heating of the inside wall will not increase the inside wall temperature beyond 460 °C, due to the high thermal conductivity of steel. In reality, the maximum inside wall temperature must be much lower than 460 °C, because thermal equilibrium will not be reached, the heating power is always lower than assumed in this worst-case-scenario, and the total explosion energy Q is by far not sufficient to heat up such a huge amount of steel (see case (b) below).

Case (b) Maximum temperature of the membrane – upper limit: In this extreme case it is assumed that the whole explosion energy Q is absorbed by the membrane only. Of course, the membrane has direct thermal contacts to the piezo crystals, side walls and other mechanical components made of metals with good thermal conductivity, so this simplified model will lead to a vast overestimation of the maximum membrane temperature. However, in terms of an upper limit, this calculation is helpful to limit the interval of reasonable maximum membrane temperatures.

It is assumed that the wall consists of membrane only, i.e. of thin steel with a thickness of $d = 0.08$ mm (membrane thickness), having no thermal contact to the outer world, i.e. all energy is absorbed by the membrane (see Figure 11, case b). The total mass m of the membrane wall is then

$$m = \rho A d \tag{3}$$

with $\rho = 7.9$ g/cm³.

Considering the specific heat capacity of steel $c = 500$ J/kg/K and the specific heat formula

$$Q = cm\Delta T \tag{4}$$

the explosion energy $Q = 29.7$ kJ leads to a temperature increase of $\Delta T < 420$ K. In other words: Even if the whole explosion energy is absorbed by the pressure sensor membrane only, its temperature increase is below 420 K. Higher membrane temperatures are physically impossible.

In a nutshell, these extreme cases prove that the maximum membrane temperatures must be very much lower than 450°C; higher values are physically impossible.

These general physical considerations are backed up by, measurements carried out with a heat flux sensor in the design of a pressure sensor of type 601CAA. The results are shown in Figure 12 below, together with corresponding pressure curves with and without thermal protection.

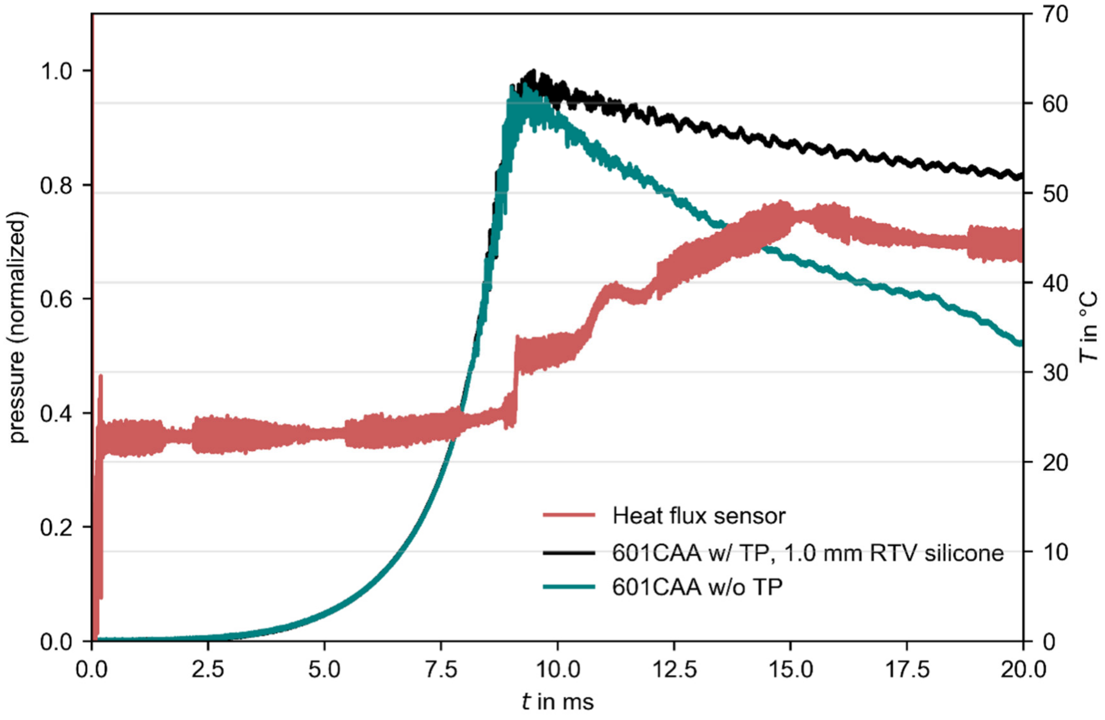

Fig. 12. *Pressure- and temperature curves with and without protective coatings on the membrane of pressure sensor type 601CAA*

DOI: 10.7795/810.20200724

At time 0 ms the ignition impulse can be seen in the curve of the heat flux sensor signal. Subsequently, a slight adiabatic temperature rise begins due to gas compression. The abrupt temperature rise after about 9 ms characterizes the impact of the flame front on the wall and hence on the sensor membrane. The maxima of the pressure sensors are in the same time range. This is followed by a continuous heating of the sensor and the environment, slightly offset due to the thermal inertia of the materials. During this temperature rise, the thermal shock acts on the membrane of the unprotected sensor, which leads to a stronger drop of the pressure curve compared to the prepared sensor. After reaching the temperature maximum of approximately 48 °C after 15 ms, cooling begins after a short phase of equilibrium between thermal in- and outflow.

This temperature curve measured by the heat flux sensor forms the basis for determining the temperatures of the sensor membrane using FEM calculations. For this purpose, the heat flow is calculated from the temperature curve and used on models of the sensor membrane.

Fast surface thermocouples are the essential measuring instruments to determine the heat flux during fast, high energy events. Although they have the disadvantage of measuring the quantity, surface temperature and therefore not directly measuring the heat flux density. The relationship between these two quantities is described by physics and must be determined numerically in a subsequent step. The measurements are performed without an active filter, using a voltage amplifier with a very high sampling rate. This fact is visible in Figure 12, where the surface temperature is shown unfiltered. Physically the surface temperature and the surface heat flux density are a continuous quantity of time. However, the surface temperature is measured as a discrete time signal. Therefore, the measured signal is transformed into a filtered signal, converted into the surface heat flux density in the frequency domain and then retransformed back into a discrete time data set. This data set is used as a thermal boundary condition for numerical analyses. Figure 13 shows the heat flow both for an unprepared membrane (w/o TP) and using a 1 mm RTV silicone layer as thermal protection (w/ TP). Simultaneously, the pressure curves are shown as used in Figure 12.

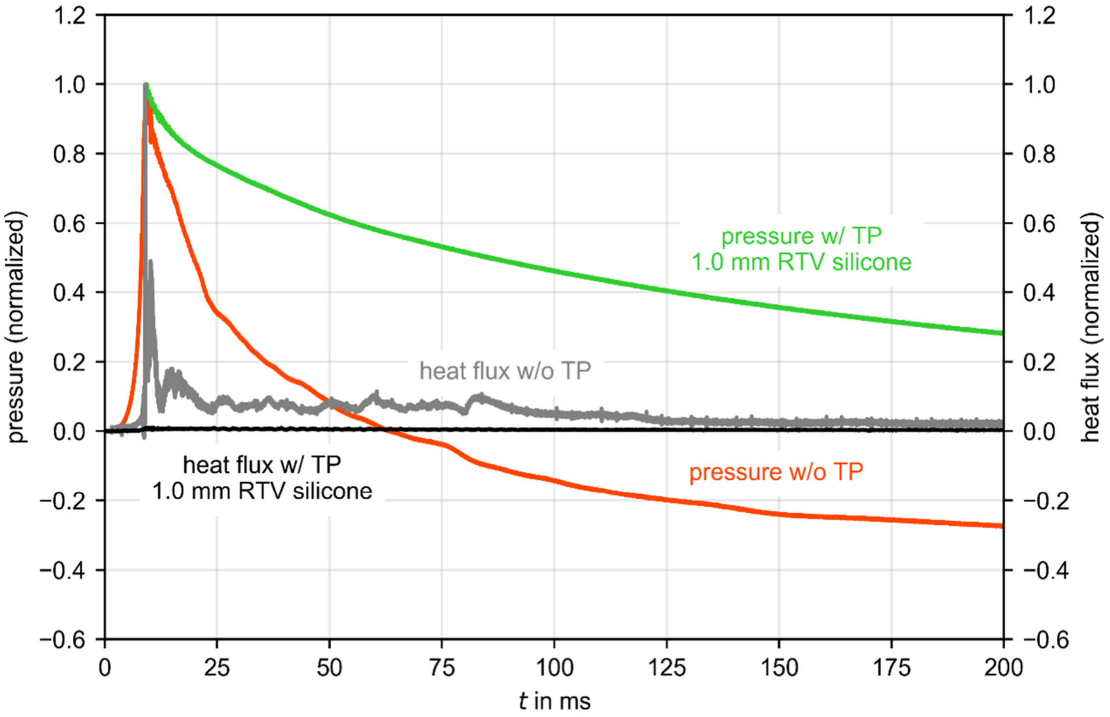

Fig. 13. *Pressure curves and heat flux graphs for sensor 601CAA with and without RTV silicone*

The curves demonstrate that for both considered cases no influence of the thermal load is visible in the area of the pressure increase. The comparison ends when the flame front hits the sensor membrane. In the case without protective coating, the heat flux increases rapidly while the pressure amplitude decreases slightly. The drop of the pressure curve occurs within a short time and ends in the negative pressure range. Only after the heat flux has fallen the further decrease of the pressure measurement value ends. In contrast, no significant heat flux can be measured when using 1 mm RTV silicone as thermal protection.

Transferring the heat flux to the sensor model provides temperature profiles for the different times. Figure 14 shows the temperature profile of a sensor membrane for three time steps. For this type of sensor there is a maximum heating of about 80 °C at the membrane.

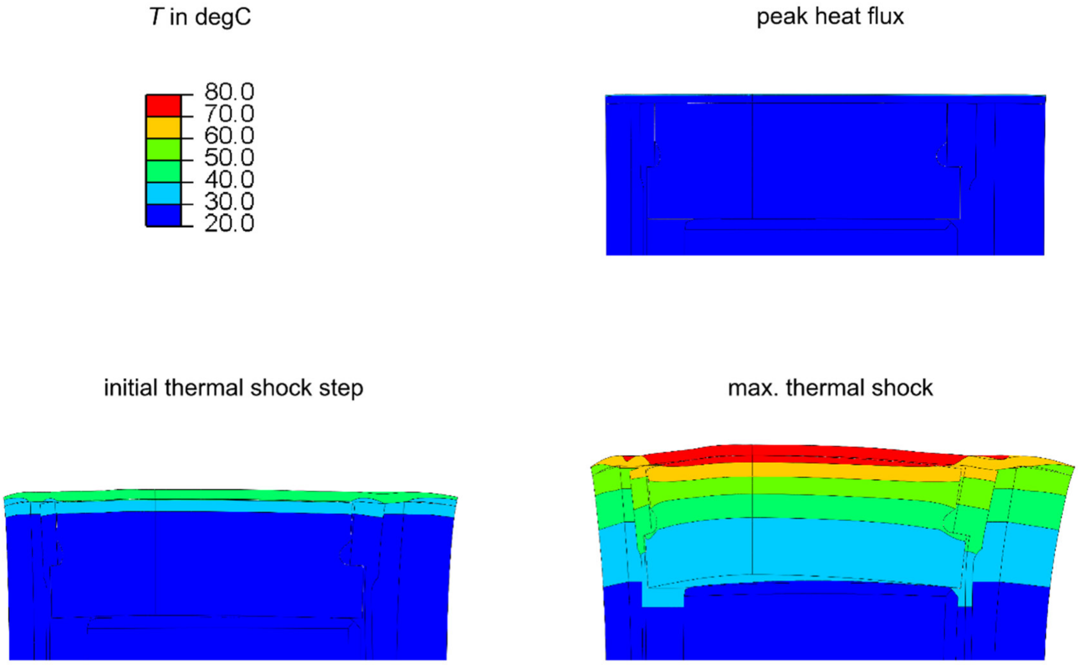

Fig.14. *Temperature profiles of a sensor membrane for three different time steps*

In the upper right corner, the first moment is displayed when the flame front hits the sensor membrane and the heat flow has its maximum. The heat profile shows only a slight warming in a very thin area on the outer membrane. A mechanical deformation is barely noticeable. In the second time step (bottom left) the outside of the membrane has a temperature of about 50 °C. This is the range of the thermal shock and the associated rapid drop in the pressure curve of the unprotected sensors. A mechanical deformation can be observed. The last time step (bottom right) shows the temperature profile during the maximum thermal shock. The membrane has a maximum temperature of about 80 °C on the outside. In addition, a heating of the deeper membrane layers occurs. The mechanical deformation of the membrane in negative axial direction is clearly visible. The deformation counteracts the pressure deformation and leads to a maximum drop of the pressure curve (as shown in Figure 3 as an example for the pressure curve of sensor S3).

DOI: 10.7795/810.20200724

6. Influence of the protective measures against thermal shock on the sensor sensitivity

The results of the previous investigations show that a protective layer of 1 mm RTV silicone is suitable to minimize the effect of a dynamic temperature gradient on the pressure sensor. To quantify the effect of the RTV silicone on the measured pressure amplitude a sensitivity study on five sensors of type 601CAA is conducted. Two different sensor calibration methods are used. The first is the industry wide standard calibration method with oil as calibration medium. With this method, the sensitivity of the sensor can only be determined without a silicone layer, as the silicone would swell otherwise. Therefore, the determination of the sensor sensitivity with coated membranes are carried out with a comparable test setup using air as pressurized medium. The results of the sensitivity study are shown in Figure 15.

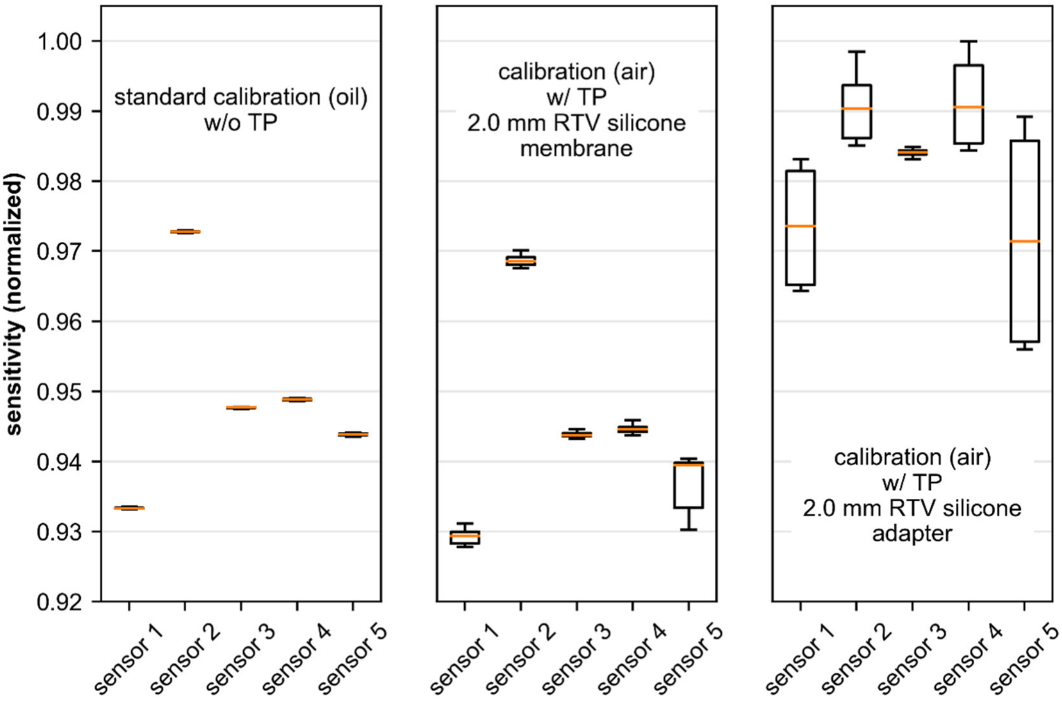

Fig. 15. *Normalized sensitivity of pressure sensors for different protective coatings and with different calibration methods (with oil and air)*

The left diagram in Figure 15 shows the sensor sensitivity, usually expressed as pC/bar, of five pressure sensors without any preparations calibrated with oil. For each sensor 15 measurements are performed. It can be seen that the sensitivity spread for each sensor is negligible. The scattering among the five sensors are common and taken into account with the assignment of the sensitivities in the calibration protocol and the corresponding consideration in the adjustment of the amplifier. The middle diagram shows the sensitivities for the same pressure sensors where the membranes are coated with a 2 mm RTV silicon layer and the sensors are calibrated with air. It can be observed that the absolute sensitivities are comparable. The scattering is marginally larger, pronounced for sensor 5. The diagram on the right shows the same five pressure sensors coated with a 2mm RTV silicone layer covers both the sensor membrane and the front of the adapter. The calibration is performed with air. It is evident, that the sensor sensitivity is increased for all sensors. Furthermore, the scattering within the series of measurements of the individual sensors is clearly more pronounced. A possible reason for this behavior is an undefined artificial enlargement of the membrane which leads to unwanted mechanical coupling with the adapter.

7. Conclusions

When measuring explosion pressures with piezoelectric pressure sensors, the sudden thermal stress onto the sensor - in particular the membrane - can result in mechanical stress onto the piezo crystals, thus altering the reading from the sensor. All pressure sensors respond to this thermal shock, but in different ways depending on the housing and membrane design. The thermal deformation of the membrane and housing interferes with the pressure measurement by the sensor. In effect, incorrect pressure curves and reduced maximum pressures can be measured. The application of protective thermal coating on the sensor membrane can reduce this unwanted behavior or rather delay it, so that it becomes irrelevant for the measurement. During the explosion, the heat flux was measured with a dedicated sensor. Transferring the heat flux to a model of a sensor membrane allows to calculate temperature profiles and the simulation of the thermal expansion of the membrane. The use of RTV silicone as protection against the effects of thermal shock does not lead to a significant change in sensitivity when applied to the membrane. However, inclusion of the adapter changes the sensitivity and increases the variation of the sensor.

Based on the results of this work, the following recommendation can be made in summary: When using piezoelectric pressure sensors to measure explosion pressures, a 1 mm RTV silicone layer should be applied to the membrane of the sensor - but only to the membrane, not the whole adapter. This protection method has shown very good properties in terms of protection against the effect of a dynamic temperature gradient, stability and practicability.

References

International Electrotechnical Commission (2014), IEC 60079-1, Explosive Atmospheres - Part 1: Equipment Protection by Flameproof Enclosures “d”, Edition 7.0

Krause, T, Markus, D. (2017), Herausforderungen bei der dynamischen Messung von Explosionsdrücken, tm - Technisches Messen 84, Heft 2, pp. 101–110 (2017);
doi: https://doi.org/10.1515/teme-2016-0051

Higuma, A., Suzuki, T., Yoshida, M., Oguri, Y., Minoyama, T. (1999), Improvement of Error in Piezoelectric Pressure Transducer, SAE Technical Paper Series, 1999-01-0207

Stein, R.A., Mencik D.Z. and Warren C.C. (1987), Effect of Thermal Strain on Measurement of Cylinder Pressure, SAE Transactions 96, Section 4, pp. 442-449; https://www.jstor.org/stable/44470852

Tichý, J., Gautschi, G. (1980), Piezoelektrische Meßtechnik, Springer-Verlag; ISBN 3-540-09448

Kach, R.A., Adamczyk, A.A. (1985), Effects of thermal loading on pressure measurement in a combustion bomb, *Review of Scientific Instruments* 56, 1274; doi: 10.1063/1.1137991

Steen, H. (2000), Handbuch des Explosionsschutzes, WILEY-VCH Verlag GmbH;
ISBN 9783527298488

Deutsches Institut für Normung (2011), DIN EN 15967:2011-10, Determination of maximum explosion pressure and the maximum rate of pressure rise of gases and vapours doi: https://dx.doi.org/10.31030/1752263

Lewis, B., von Elbe, G. (1987), Combustion, Flames and Explosions of Gases, Elsevier Inc.; ISBN 978-0-12-446751-4

DOI: 10.7795/810.20200724

Modifications of the Standard $1\mathrm{m}^3$ Vessel in Search of Adequate Values of the Maximum Rate of Pressure Rise

Wojciech Adamus[a], Adrian Toman[a]

[a] Central Mining Institute (Katowice, Poland)
E-mail: *w.adamus@gig.eu*

Abstract

Dust explosion hazard identification, quantification and design of prevention means often rely on experimental assessment of explosion and ignition parameters. Among the parameters maximum rate of pressure rise (K_{St} value) plays a very important role as it gives an assessment of the explosion dynamics. Modified $1\mathrm{m}^3$ apparatus was used to assess the rate of dust explosion pressure rise. Appropriate vessel modifications allowed to improve homogeneity of the dust/air mixture and control the turbulence intensity prior to ignition while the vessel's design still fulfills the requirements of the ISO (ISO 6184/1, 1985) and European Standard (EN 14034-2:2006+A1, 2011).

In the paper the correlation between ignition delay time, state of dust/air mixture (turbulence intensity) and $(\mathrm{d}p/\mathrm{d}t)_{max}$ were used to adjust the parameters of apparatus operation. The adjustment should allow to obtained an appropriate assessment of the explosion dynamics. The results suggest that the factor that should be kept constant in the tests is rather turbulence intensity, expressed by u'_{rms} instead the ignition delay time.

Keywords: *dust explosion, 1m^3 explosion vessel, hazard identification*

1 Introduction

Maximum explosion pressure and maximum rate of pressure rise are the most important explosion severity parameters used in the process safety is assessment of dust explosion hazard in industry. Therefore a correct assessment of the parameters are essential for adequate design of protective methods to assure proper control of the dust explosion Eckhoff (2003)). Here the word *parameter* indicates that its assessed value depends not only on properties of the dust tested but also on the method utilized for the assessment. Standards either in Europe (EN 14034-1, 2011 & EN 14034-2, 2011) or in the America (ASTM E1226-12a, 2019) or international (ISO 6184/1, 1985) define the test methodology. The recommended size of the test vessel is 1 m^3 but other experimental vessels are allowed. In practice smaller vessels are used most often. A smaller volume test chamber requires less sample mass per test, it is simpler in operation and therefore allows higher number of test performed. The most widely used is the 20-l sphere manufactured by Kühner AG (lately by TÜV SÜD). However the explosion severity parameters, especially the K_{St}, not always agree with each other when measured in these two vessels (Proust et al., 2007). Among factors that contribute to the difference is different turbulence intensity created inside the test vessel after dispersion of a test sample and different rate of the turbulence decay. The turbulence intensity measured in 20-l explosion sphere by Dahoe (2000) and Pu and Jarosinski (1991) overlap very well. The ignition starts at 60 ms after the injection. At that time the turbulence intensity quantified by root-mean-square of velocity fluctuation is approximately 3 m/s. In 200 ms, this is a time when an explosion usually is completed, the turbulence intensity decays to approximately 0.5 m/s with Rebound Nozzle used for dispersion. In 1 m^3 test vessel the mixture is ignited at 600 ms. The turbulence intensity measured by van der Wel (1993) at that time is 0.5 m/s. Measurements reported by Proust et al. (2007) in his 1 m^3 vessel show fast turbulence decay after injection, however at the time of typical explosion duration, between 600 and 1000 ms, the turbulence intensity levels off at the value of 2 m/s. Hauert et al. (1994) measured both horizontal and vertical components and obtained the values of 1.2 and 5.36 m/s, respectively, after 600 ms. The difference between the measured turbulence intensities in 1 m^3 vessel might be due to differences in engineering factors like shape of the test vessel, dispersion system or dispersion nozzle used.

The paper presents results of turbulence intensity measurement performed in 1 m^3 vessel built and used at Experimental Mine Barbara of Central Mining Institute, Poland. The vessel fulfills the requirements imposed by the European Standards EN 14034. Instantaneous velocity in the vessel generated by an air injection from the dust dispersion system was measured with use of Bi-Directional Velocity Probe BDVP developed by McCaffrey & Heskestad (1976). From the measurements the root-mean-square of velocity fluctuation u'_{rms} was calculated. Then some tests of dusts were carried out at different turbulence intensity.

The tests presented in the paper are continuation of the work described by Dyduch etal (2016). In comparison to previous work the dust dispersion system has been modified. As the fast acting valve a simple ball valve was used driven pneumatically. Bi-Directional Velocity Probe also was modified. Instead of differential pressure transducer that separates two parts of the measuring head a transducer of different type was located right under the measuring head. Also the size of the head was halfed. The length was 2 cm and the diameter of 1 cm.

2 Experiments

In previous work (Dyduch et al., 2016), isotropy and homogeneity of turbulence generated by air release from dust dispersion units were confirmed in 1m^3 explosion vessel. After modification of fast acting valve to quantify turbulence intensity, velocity fluctuation at center of explosion vessel were measured by bi-directional velocity probe. Explosion pressure (p_{max}) and rate of explosion pressure rise ($\mathrm{d}p/\mathrm{d}t$) at different turbulence intensity levels were measured for corn starch, Lycopodium Clavatum dust and Niacin.

2.1 1m^3 explosion vessel

Measurements were performed in explosion vessel designed according to (EN 14034-2:2006+A1, 2011). During all tests two dispersion systems with rebound nozzle dispersers were used. Dust cloud was ignited by two 5 kJ Sobbe pyrotechnic ignitors source located in the center of vessel and pressure changes were measured by piezoresistive pressure transducers. To maintain constant conditions during measurements, temperature of explosion vessel was controlled by cooling system.

2.2 Dust dispersion system

Dispersion unit consists of dust container closed by ball valve and connected to the side of the explosion vessel by one inch connecting tube. Volume and aspect ratio of dust container follows description from (EN 14034-2:2006+A1, 2011). Opening/closing of ball valve is realized by electrically activated pneumatic actuator. Operation of dispersion unit allows to fully discharge dust container (initially pressurized to 20 barg) in time range specified by EU Standard. Pressure in the dust container was measured during discharge and compared with reference curves (EN 14034-2:2006+A1, 2011). Actuation of ball valve used in this work takes about 0.1 s and the dispersion lasts 0.35 s.

As shown in Fig. 1 the time required to start opening of the ball valve is much longer than for the valves required by EU Standard. However the balance between pressure in explosion vessel and in dust container is reached 0.45 s after beginning of valve actuation, practically at the same moment as for all other compared dispersion system. For the tests the initial 0.1 s delay in unimportant. The time $t = 0$ may be set at any point in the interval.

2.3 Measurements of turbulence intensity

Dynamic pressure fluctuations at the center of explosion vessel was measured with bi-directional probe. Its construction is based on McCaffrey Heskestad (1976). Keeping the length-to-diameter ratio of original design, probe with 20 mm length and 10 mm diameter was constructed. Differential pressure transducer mounted directly under the probe head was used to measure the pressure changes. Bi-directional probe operates under the same principles as pitot–static probes so relations dynamic

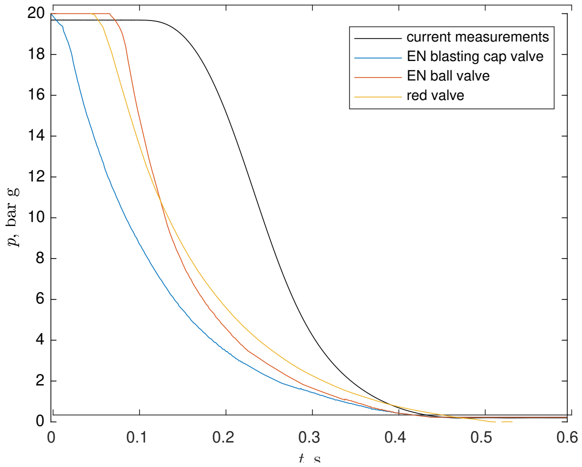

***Fig. 1**: Pressure changes in dust container during discharge*

pressure fluctuations were used to determine flow velocity.
Majority of reported turbulence measurements in 1m^3 vessel refers to dust–less airflow, and only limited information are available on the influence of dust particles on turbulence intensity. The same approach was used to measure u'_{rms} in flow generated by releasing pure air from two dispersion units.

3 Results and discussion

3.1 Root mean square value of fluctuation part of velocity

Reynolds decomposition was used to obtain mean velocity and velocity fluctuations. Measured velocity was split by applying high–pass frequency filter. Fluctuating velocity was divided into 10 ms intervals in which negligible turbulence dissipation was assumed. For each interval root mean square value was calculated. Each point in Fig. 2 represents mean value of u'_{rms} obtained from series of five measurements. For comparison the same type of results obtained in previous work (Dyduch etal (2016)) are included. Those results were obtained when different type of fast acting valve, so called *red valve* was used in the dispersion system.

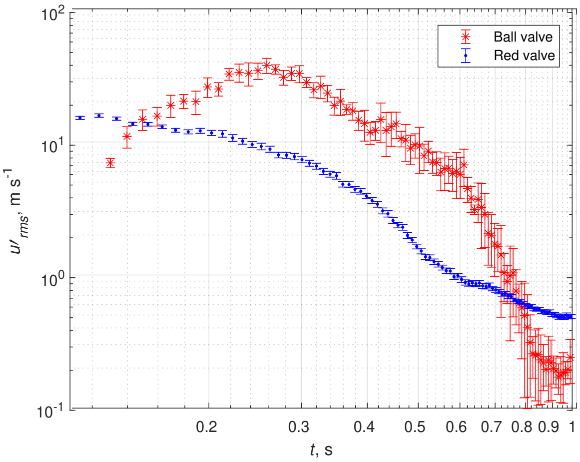

***Fig. 2**: Root mean square of velocity fluctuation*

In the current tests u'_{rms} reaches maximum value of 40 m/s in time between 0.24 and 0.3 s. After that time turbulence decays, firstly relatively slowly then, starting from about 0.6 s much faster. At about 0.9 s u'_{rms} decreases to 0.2 m/s which is the level of noise.
Changes of u'_{rms} when *red valve* was used are different. Maximum value, reached at 0.12 s is less than 20 m/s. Then the turbulence decays slowly. The two sets of data indicate that turbulence, quantified by u'_{rms}, is similar after 0.8 s.

DOI: 10.7795/810.20200724

3.2 Explosion indices of selected dusts

To determine the influence of turbulence intensity on the maximum rate of pressure rise series of test with corn starch and Niacin were carried out. In the tests ignition delay time t_v was varied.

In Fig. 3 results for dry corn starch (moisture content 5%) are presented. Tests were carried out for three values of t_v between 0.6 s and 0.8 s. In that time interval root-mean-square velocity decreases from 7 m/s to 0.6 m/s. Additionally, one test for t_v = 0.5 s was added.

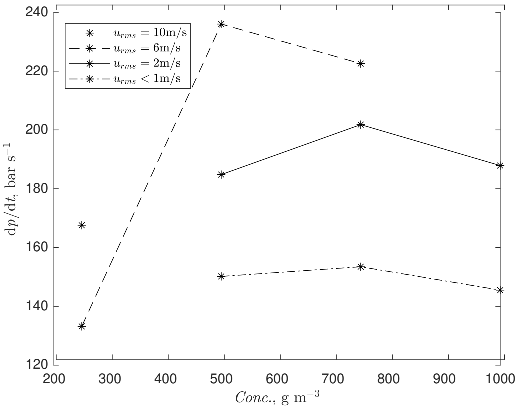

***Fig. 3**: Influence of ignition delay time on* $\left(\frac{\mathrm{d}p}{\mathrm{d}t}\right)$ *for corn starch*

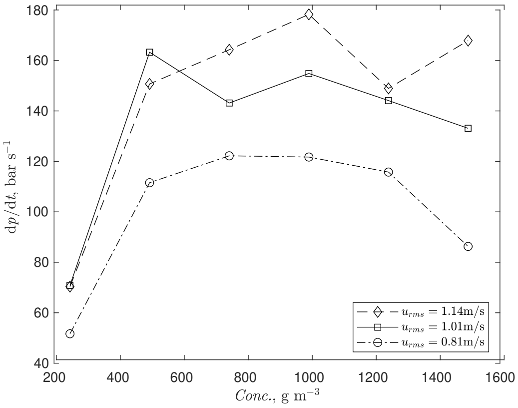

***Fig. 4**: Influence of ignition delay time on* $\left(\frac{\mathrm{d}p}{\mathrm{d}t}\right)$ *masured using red valve as a dispersion system for corn starch*

The results show strong dependence of $\left(\frac{\mathrm{d}p}{\mathrm{d}t}\right)$ on turbulence. An increase of the ignition delay time causes significant decrease of that parameter.

In Fig. 4 measurements of $\left(\frac{\mathrm{d}p}{\mathrm{d}t}\right)$ for corn starch using *red valve* as a dispersion system are presented. Ignition delay times of 550, 600 and 700 ms results in u'_{rms} values of 1.14, 1.01 and 0.81 m/s respectively. Comparison of Fig. 3 and Fig. 4 leads to conclusion that measurements with different dispersion systems resulted in similar values of $\left(\frac{\mathrm{d}p}{\mathrm{d}t}\right)$ at the same u'_{rms} level.

Similar effect may be observed in Fig. 5 for Niacin. Here a few points corresponding to different ignition delay times are plotted together with results obtained with dispersion system equipped with *red valve* and ignition delay time set to 0.6 s. Measured values of $\left(\frac{\mathrm{d}p}{\mathrm{d}t}\right)$ with different dispersion systems are similar when tests were performed at similar turbulent intensity, however reference value of 251 bars^{-1} were obtained when u'_{rms} was 6 ms^{-1}.

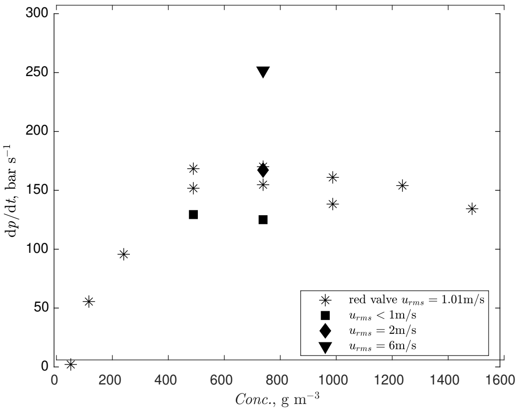

***Fig. 5**: Influence of ignition delay time on* $\left(\frac{\mathrm{d}p}{\mathrm{d}t}\right)$ *for Niacin*

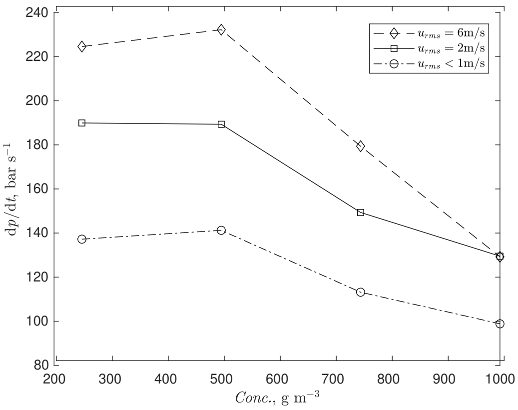

***Fig. 6**: Influence of ignition delay time on* $\left(\frac{\mathrm{d}p}{\mathrm{d}t}\right)$ *for Lycopodium*

In Fig. 6 maximum rate of explosion pressure rise was assessed for Lycopodium. Tests performed at lowest turbulence intensity were in good agreement with referenced values measured in 1m^3 explosion vessel in Bartknecht (1986) and in 20-l sphere (ASTM E1226-12a (2019)).

Table 1 summarize p_{max} and $\left(\frac{\mathrm{d}p}{\mathrm{d}t}\right)_{max}$ measurements for Corn Starch, Lycopodium Clavatum dust and Niacin. Corresponding values of u'_{rms} are also included.

Comparison between reference and measured values of $\left(\frac{\mathrm{d}p}{\mathrm{d}t}\right)_{max}$ suggests that tuning of 1m^3 is possible by changing ignition delay time. Different initial conditions provide agreement with reference data. Similar results were obtained by Addo et al. (2019). They used $\left(\frac{\mathrm{d}p}{\mathrm{d}t}\right)_{max}$ measurements to calibrate $1m^3$ vessel. Ignition at 0.55 s for niacin and 0.6 s for lycopodium showed good correspondence to the reference values. As an explanation of the discrepancy in $\left(\frac{\mathrm{d}p}{\mathrm{d}t}\right)_{max}$ they proposed the differences in dust densities.

4 Conclusions

Presented results indicate that the state of the dust/air mixture in the standard 1 m^3 vessel at the moment when the explosion is initiated plays a crucial role in the assessment of the standard explosion parameter $(\mathrm{d}p/\mathrm{d}t)_{max}$. Turbulence generation and its subsequent decay depend on an apparatus design, specifically on a design of the dispersion system. Ignition delay time seems to be unimportant as long as turbulence intensity is consistent. Therefore, rather than fixing ignition delay time in the definition included in the standards reference turbulence conditions should be specified. The results

***Table 1**: Explosion indices for different ignition delay times*

Sample	u'_{rms}, ms^{-1}	*Conc.* $\mathrm{g/m^3}$	p_{max}, barg	$\left(\frac{\mathrm{d}p}{\mathrm{d}t}\right)_{max}$, $\mathrm{bar\,s^{-1}}$
corn starch	6	750	10.28	222
corn starch	2	750	10.15	201
corn starch	< 1	750	9.92	153
corn starch (*red valve*)	1.14	1000	8.48	178
corn starch (*red valve*)	1.01	500	4.49	163
corn starch (*red valve*)	0.81	750	8.96	122
lycopodium	6	500	8.44	232
lycopodium	2	500	8.75	189
lycopodium	< 1	500	8.52	141
niacin	6	750	8.95	251
niacin	2	750	9.09	167
niacin	< 1	750	9.40	125

suggest that the most important parameter to be defined is root-mean-square velocity. The role of the other parameter that is usually used to describe turbulence, turbulent length scale l_t, seems to be less important. That role was not considered in this paper but its influence on the value of $(\mathrm{d}p/\mathrm{d}t)_{max}$ should also be examined. According Proust (2017) in small volumes, up to about 1 m^3, l_t does not very significantly.

In the tests described in the paper it was not possible to obtain $(\mathrm{d}p/\mathrm{d}t)_{max}$ values coherent with well established values for Lycopodium and Niacin when ignition delay time, e.g. turbulence intensity, was kept constant. Ignition delay time set to 0.6 s for Niacin and slightly over 0.7 s for Lycopodium led to correct results.

The conclusion are based on limited sets of experimental results. Their validity should be confirm by gathering larger set of the data.

References

Addo, A., Dastidar, A. G., Taveau, J. R., Morrison, L. S., Khan, F. I., Amyott, P. R. (2019). *Niacin, lycopodium and polyethylene powder explosibility in 20-l and 1-m^3 test chambers*. Journal of Loss Prevention in the Process Industries, 62.

ASTM E1226-12a (2019). *Standard Test Method for Explosibility of Dust Clouds*.

Bartknecht, W. (1986). *Dust Explosions*. Springer Verlag Berlin Heidelberg.

Dyduch, Z., Toman, A., Adamus, W. (2016). *Measurements of turbulence intensity in the standard 1 m^3 vessel*. Journal of Loss Prevention in the Process Industries, 40:180–187.

Eckhoff, R. K. (2003). *Dust Explosions in the Process Industries*. Gulf Professional Publishing, Amsterdam, third edition.

EN 14034-2:2006+A1 (2011). *Determination of explosion characteristics of dust clouds - Part 2: Determination of the maximum rate of explosion pressure rise $(\mathrm{d}p/\mathrm{d}t)_{max}$ of dust clouds*.

ISO 6184/1 (1985). *ExplosionProtection Systems - Part 1: Determination of Explosion Indices of Combustible Dusts in Air*.

McCaffrey, B. J., Heskestad, G. (1976). *A robust bidirectional low-velocity probe for flame and fire application*. Combustion and Flame, 26:125–127.

Proust, C. (2017). *Turbulent flame propagation in large dust clouds*. Journal of Loss Prevention in the Process Industries, 49:859–869.

DOI: 10.7795/810.20200724

Turbulence in real flammable gas releases

Didier Jamois [a], Christophe Proust [a], Jérôme Hébrard [a], Emmanuel Leprette [a], Helene Hisken [b], Lorenzo Mauri [b], Gordon Atanga [b], Melodia Lucas [b], Kees van Wingerden [b], Trygve Skjold [c], Pierre Quillatre [d], Antoine Dutertre [e], Thibault Marteau [e], Andrzej Pekalski [f], Lorraine Jenney [g], Dan Allason [g], & Mike Johnson [g]

[a] Ineris, Verneuil-en-Halatte, France
[b] Gexcon R&D, Bergen, Norway
[c] University of Bergen, Norway
[d] GRTgaz, Safety and Risk Assessment, France
[e] Total, France
[f] Shell Global Solutions, UK
[g] DNV GL Spadeadam Testing and Research, UK

E-mail: didier.jamois@ineris.fr

Abstract

The research activities in AIRRE project (Assessing the Influence of Real Releases on Explosions) include a unique series of large-scale explosion experiments with ignited high-momentum jet releases of natural gas directed into congested geometries. The primary objective for the AIRRE project is to gain improved understanding of the effect realistic releases and turbulent flow conditions have on the course and consequences of accidental gas explosions in the petroleum industry, and thereby develop and commercialize technology and methodology that can facilitate safe and optimal design of process facilities.

A few tests were performed in open air without any congestion. The mean velocity and turbulence flow fields are presented herein. Flameproof turbulence sensors were purposely designed for the project and calibrated at small scale. These are Pitot probes connected to fast differential pressure sensors. This paper describes the turbulence measurement technique used and highlights the specific issues related to the data post-processing in order to calculate the turbulence intensity and the turbulent length scale. Test results are analysed, and comparisons are made with free jet experiments at small scale, and related jet theories.

Keywords : *realistic releases, large-scale experiments, gas explosions, turbulence*

1. Introduction

Accidental releases of pressurized combustible gas in congested industrial environments generate flammable fuel air clouds with high levels of turbulence. The current practice for estimating the consequences of accidental explosions, for instance as part of quantitative risk assessments, entails the use of the so-called equivalent gas cloud method (Hansen *et al.*, 2013). However, the available concepts for defining equivalent gas clouds do not account for the combined effect of pre-ignition turbulence and explosion-generated turbulence on explosion pressures and critical separation distances. Furthermore, there are very limited data available in the public domain for validating consequence models that describe such scenarios. This may result in either severe over-prediction or severe under-prediction of the consequences of explosions.

Following a detailed review of previous experimental work on the effect of realistic releases on explosions (Skjold *et al.*, 2018), primary objective for the AIRRE project (Assessing the Influence of Real Releases on Explosions) is to gain improved understanding of the effect realistic releases and turbulent flow conditions have on the course and consequences of accidental gas explosions. The experimental program includes a set of tests that investigate the influence of pre-ignition turbulence generated by high-momentum releases on explosion effects and critical separation distances. The goal is to reduce the uncertainty in the estimation of consequences for accidental explosions by developing and validating more accurate models for the physical phenomena involved, in conjunction with improved methodology.

Even if turbulence has been a field of investigation for decades with an important amount of experimental results obtained at lab scale, to our knowledge very few data have been obtained at the industrial scale. This lack was partially filled during AIRRE program. The present work focusses on large free releases performed in open air, equipped with a specific turbulence instrumentation. The specific issues related to the instrumentation and to the data post-processing in order to calculate the turbulence intensity, the turbulent length scale and flow field are described hereafter.

2. Experimental conditions

2.1 Hardware

DNV GL Spadeadam Research and Testing conducted the large-scale experimental campaign in AIRRE project in the Spadeadam test site (UK).

The releases were produced from blowing down a storage reservoir containing approximately 22 Tons of natural gas when charged to its operating pressure of 150 barg. When depleted from 150 barg to 90 barg through a 100 mm orifice, the amount of natural gas expelled is approximately 10 Tons in 100 s meaning 100 kg/s release rate. The release point was flowing horizontally 1.5 m above the ground over a flat area measuring approximately 70 m by 320 m. The releases were oriented along the 320 m axis of the test area (figure 1).

Fig. 1. *AIRRE Experimental area on SPADEADAM test site*

2.2 Test conditions

The AIRRE campaign included 16 tests. Three tests with un-obstructed jet (tests n°1, 2 and 15), and the rest with obstacles located in the central part of the jet. The focus is on the un-obstructed jets, and particularly on test n°2 and 15 for which turbulent data were recorded.

As shown on figure 2 (mass flowrate curves), the jet is allowed to settle for about 30 seconds before ignition (time 0). It takes about 10 seconds for the jet to reach a steady state, knowing that the pressure in the vessel is decreasing from about 120 bar down to about 90 bar at ignition. In the meantime, outside conditions (wind velocity and wind direction) may vary.

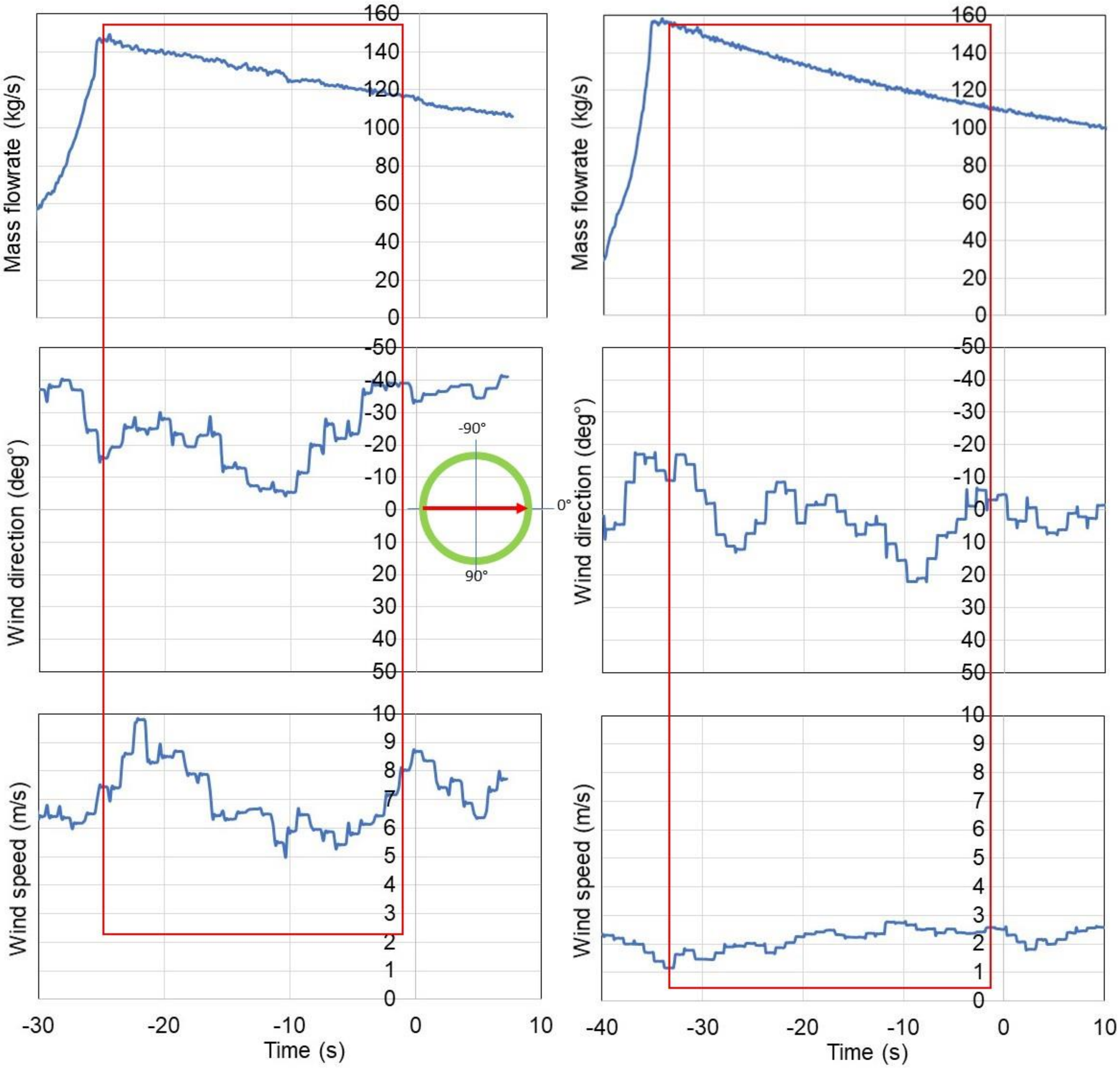

…

Fig. 2. *Mass flow rate and wind conditions during the free jet releases n°2 (left) and 15 (right). Red frames indicate the time window used to process the release data*

2.3 Probes distribution

As shown by Kristen *et al.* (2020), various categories of probes were used: up to 20 pressure transducers, 20 ionisation probes, fluxmeters... and about 20 velocity probes. Only the latter are considered in this paper. The layout is shown on Figure 3. Turbulent probe signals are recorded at a rate of 500 kHz during the entire duration of the release, but only the most stable part of these records is exploited (red frames in figure 2).

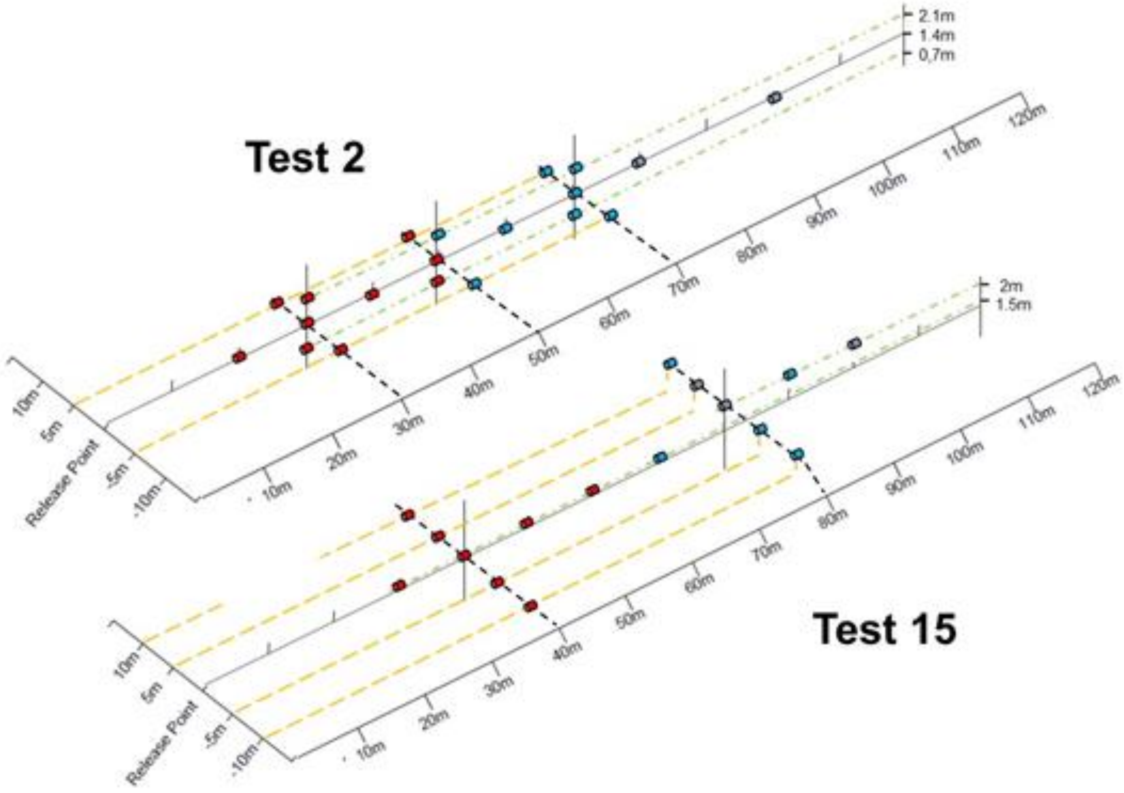

Fig. 3. *turbulent probe layout for the two free jet releases studied. Red symbol corresponds to large range sensors (+/-7000 Pa) and blue one to lower range sensors (+/-1250 Pa)*

Some information about the performances of the probes and about the expected behaviour of the kind of jet produced in AIRRE are given in the next section.

3. Measuring the aerodynamics in the jet

3.1 Bidirectional probes

Experience shows that it may prove difficult to use standard laboratory techniques (LDA, PIV, hot wire) in real scale conditions, especially the one produced in AIRRE where even stone were lifted by the momentum of the jet!

Following the pioneering work of Tamanini (Tamanini, 1990, 1991), the original Mc Caffrey technique (Mc Caffrey, 1976) was progressively adapted to the measurement of the turbulence in such situations. The Mc Caffrey gauge is based on the Pitot tube technique (differential pressure measurement). The ability to measure turbulence with this technique is dependent on the features of the differential pressure sensor used and the way it is mounted to the probe. The gauge (Fig.4) is a head connected via small tube to a differential pressure sensor. The head is a tube facing the flow with a wall in the middle, the pressure difference on both sides of the wall is measured and is close to the dynamic pressure of the flow.

The relevant theory and the performances are detailed elsewhere (Proust *et al.*, 2020). For the present purpose, it should be said that the bidirectional probe measures the modulus of the mean velocity and the fluctuations along the axis of the probe. The cutoff frequency is almost 200 Hz (reported value from the supplier) and the measuring range is 1 m/s to 100 m/s.

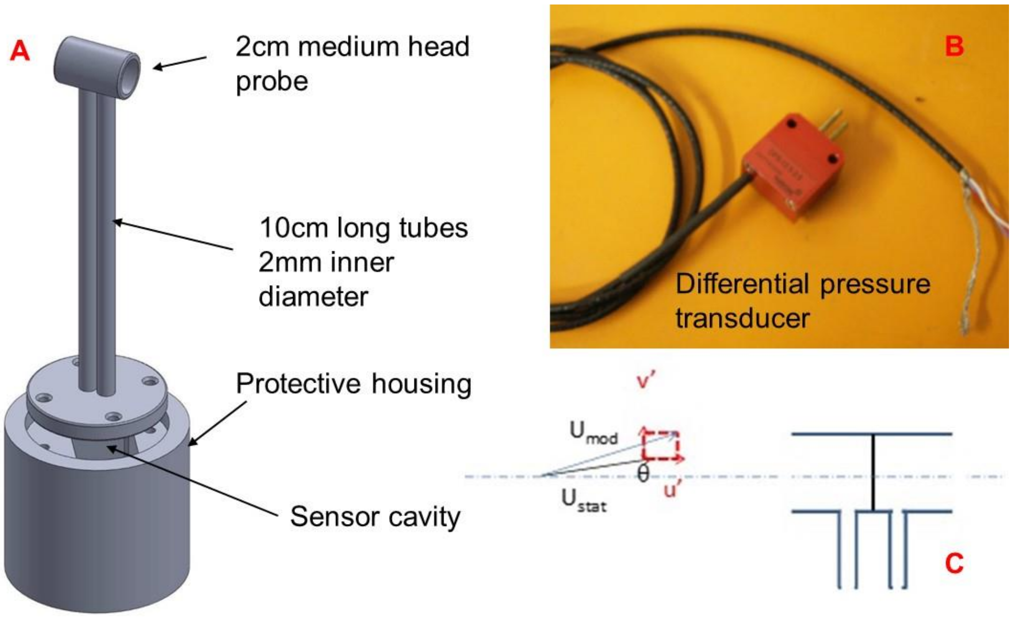

Fig. 4. *A : Drawing of the turbulent probe designed for AIRRE with B : the transducer used. C : U_{mod} is the instantaneous modulus of the velocity vector and U_{stat} is the average of the velocity field as defined in the Reynolds approximation. u' and v' are the velocity fluctuations along the axis of the probe and in the radial direction.*

An example of the performance of this probe is shown on figure 5. The configuration is a free round subsonic jet of air in the open atmosphere and the measurement is performed on the axis of the jet. The instantaneous velocity is extracted from the dynamic pressure, the mean velocity is the time average and the fluctuations are the difference between the instantaneous velocity and the mean one. The space correlation R(x) is approximated using the time autocorrelation curve and the Taylor assumption ($R(x) = R(t) \cdot \overline{U}$).

Given the intensity of the velocity fluctuations this can only be a rough approximation. From this correlation curve the integral scale of the turbulence is derived using the theorical relation:

$$L_{int} = \int_0^{+\infty} R(x) \cdot dx$$

Using the same correlation curve, the "spectral energy" of the turbulence may be obtained using:

$$E(\kappa) = \frac{2}{\pi} \cdot u'^2 \cdot \int_0^{\infty} R(x) \cdot cos(\kappa \cdot x) \cdot dx$$

The spectral energy E(κ) (units m^3/s^2) is the kinetic energy per unit mass and per unit wavenumber of fluctuations around the wavenumber κ (κ = 2π/λ, where λ is the wavelength/size of the eddies). The spectral energy describes the turbulent cascade of a flow and depends on the former parameters u' and L_{int} (Hinze, 1975).

Under the present experimental conditions, the theoretical and measured jet correlations and turbulence spectrum are shown on figure 5. The agreement seems reasonable.

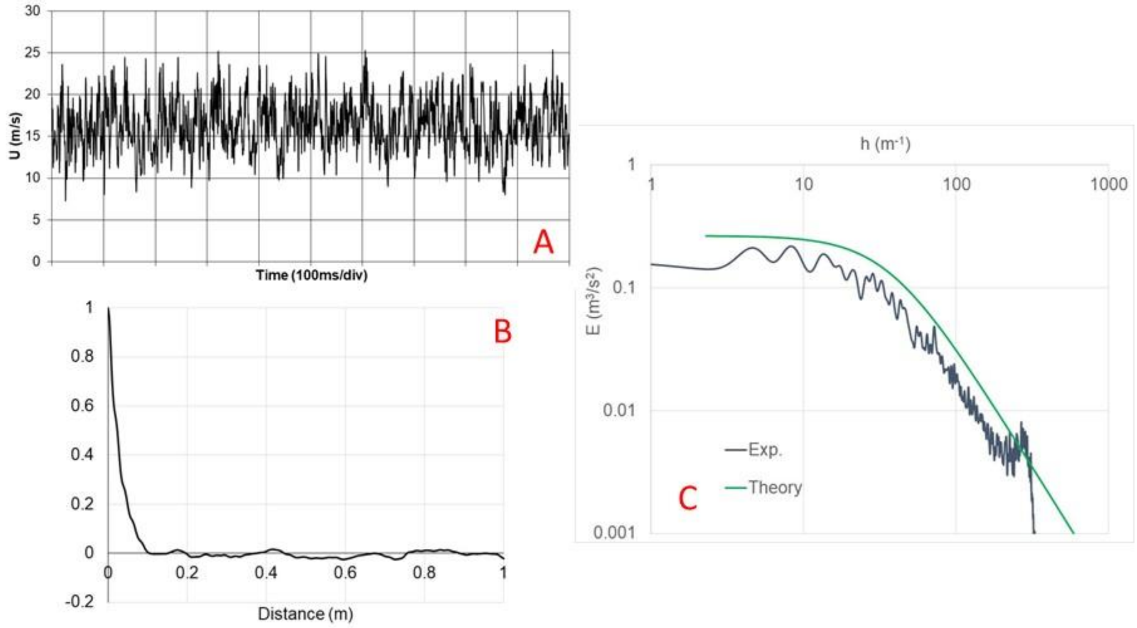

Fig. 5. *A: Velocity raw data. B: Autocorrelation curve R(x) obtained from A. C: Spectral Energy as the Direct Fourier Transform from R(x). The green solid curve represents the theorical expression of* $E(\kappa)$ *for high Reynolds flow following Hinze*

3.2 "Crawling" jet

Large accidental releases have little chance to be round free jets. They rather may be impinging jets, jets in congested zone or "crawling" jets. The latter, which corresponds to the AIRRE configuration investigated in this paper, may be assimilated to the "wall jet theory" which has been studied due to engineering applications such as inlet devices in ventilation, separation control on airfoils and film-cooling of turbine blades (among others: Launder *et al.*- 1983, Hussein *et al.* - 1994, Abrahamsson *et al.*-1996, Sun - 2002, Khritov *et al.*- 2002)

The typical "wall jet" is a turbulent round jet exiting over a flat plate and parallel to it. Investigations have shown that the mean velocity and turbulent stress profiles are self-similar in the far field. The main feature is that the spreading rate parallel to the wall is 5 to 7 time greater than the spreading rate normal to the wall. The mainstream velocity (along x) in the far field is poorly documented and frequently assimilated to that of the free jet. In the near field (up to 50/D, D being the notional release diameter) correlations based on experimental results were proposed by Sun and Khritov.

The experimental program EXJET (INERIS, 2014-2016) aimed to study at a relatively large scale (about 1 kg/s) the physical mechanism of explosion in a flammable jet. The bidirectional probes were used to measure the velocity and the turbulence in the jet prior to ignition (figure 6). Different industrial accidental situations were simulated and in particular the free crawling jet. It was highlighted that the mainstream velocity obeys a self-similar profile and that the turbulence intensity conforms with the free jet theory along the axis.

Fig. 6. *View of an EXJET crawling jet (release diameter: 12mm, flowrate about 1 kg/s)*

It can be convenient to assimilate a crawling jet to a half free jet (or a half cone) neglecting the friction at the wall. It is equivalent to calculate velocity and turbulence profiles along the jet axis using a flowrate twice that of the real crawling jet. This effect would increase the size of the jet. But in reality the presence of the wall increases sharply the lateral spreading (and mixing) as compared to a round free jet so that both effects more or less compensate as noticed by Khritov et al.. These authors suggest that the round free jet correlation might provide a reasonable approximation of the crawling jet properties, along the axis (at least ($U_{max}/U_{exit} = 5.8/(x/D - 4.25)$ for the velocity).

Figure 7 gives an example of velocity measurement along x axis for a crawling jet of methane from an orifice of 12mm located 20cm above the ground and an upstream pressure of 40 bar. On fig. 7, the correlations of Sun and Abrahamsson are indicated (respectively the red and green diamonds) together with the self-similar correlation based on the round free jet correlation (solid orange line). The exit velocity (U_{exit}) is set at 400m/s in this case (sound speed) and the notional diameter D is 42mm (Birch -1984 theory, with a discharge coefficient = 1).

There is a reasonable agreement between the various wall jet correlations and the present data points from EXJET experimental series.

A gap appears between the wall jet near field correlation (Sun) and the EXJET data from about 30 x/D. Since the wall jet experiments conducted by Sun were performed with a release velocity rate of about 40m/s, the results are suspected to be unreliable because lying in the lower range of the instrument (hot wire device in that case).

The turbulence intensity from EXJET is in reasonable agreement with the wall jet correlation for values of x/D between 100 and about 200. Above 200, the means jet velocity is comparable to that of the surrounding atmosphere and the plume may not be aligned with the jet axis anymore (the local axial velocity U drops whereas u' remains constant so that u'/U increases). For x/D below 100, the velocity fluctuations are too fast to be captured by the probe.

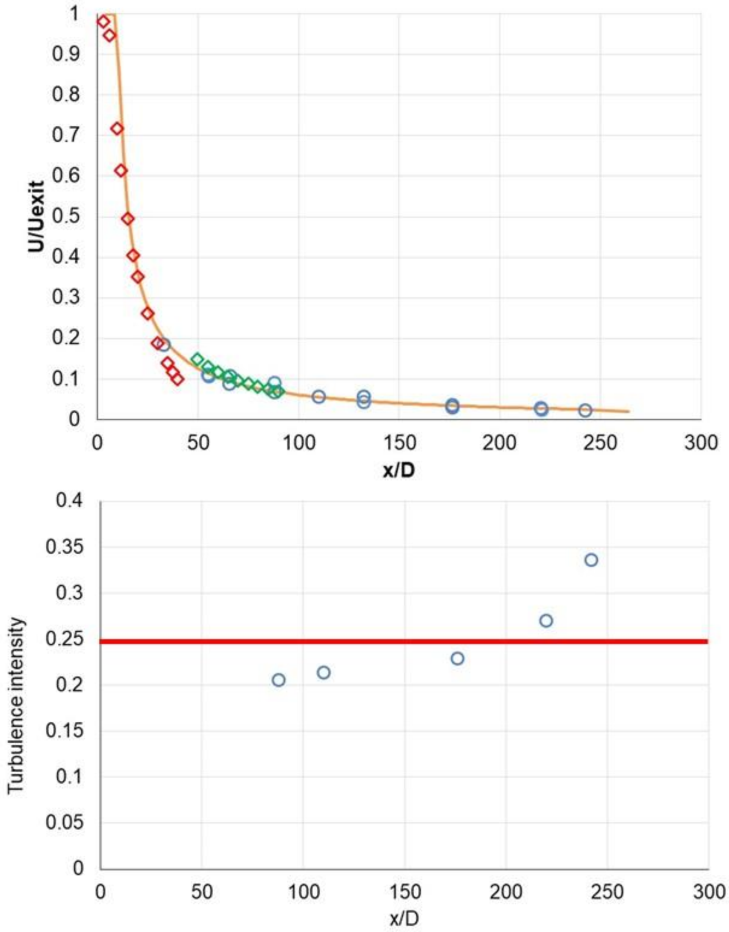

Fig. 7. *Upper diagram - Exjet velocity results for a methane crawling jet (blue circle) together with H. Sun correlation (red diamonds), H. Abrahamsson correlation (green diamonds) and round free jet model (solid curve). Bottom diagram – Measured turbulence intensity along the x axis for the same release*

The free releases studied in AIRRE project can clearly be considered as crawling jets (figure 1). It then may be interesting to compare the velocity measurement to the correlations cited above.

4. Results

4.1 Data selection

AIRRE real scale conditions were particularly harsh since the momentum was so large that even stones were lifted away down to about 50 to 70 m from the release. Often, the measuring masts were impacted and sometimes thrown away. Furthermore, the videos clearly show that an important quantity of dust/mud is raised and blown away until a steady state is reached.

under such circumstances, it is not surprising to find that many of probes were suspected to be clogged with dust and mist, misaligned of even destroyed.

One particularly tricky work was to sort out unreliable data. To do that each raw record was studied, and only realistic ones were selected (uncapped raw data, steady on average, for about 20 seconds, without any disruption or baseline shift).Only about 30% of the probes gave reliable results for tests n°2 and 15. The labelling and the location of the “valid probes” are presented in table 1.

***Table 1**: "valid" probes for tests n°2 and 15 (layout on figure 3)*

Test n°2	TS3	TS7	TS8	TS9	TS10	TS19	TS20
x	30	40	50	50	50	80	100
y	0	0	5	0	0	0	0
z	0.7	1.4	1.4	0.7	1.4	1.4	1.4
Test n°15	TS1	TS3	TS5	TS7	TS11	TS12	TS16
x	30	40	40	50	80	80	100
y	0	3	-3	0	5	0	0
z	1.5	1.5	1.5	1.5	2	2	2

Figure 8 shows a typical velocity record by probe TS10 during release n°2 as function of time. Since the mean velocity evolves during the release, first because the flowrate decreases, but also because the wind is not steady (figure 2), it is necessary to choose a time integration slot sufficiently small as compared to these large scale time evolutions and sufficiently large as compared to the various turbulence time scales to analyse the structure of the locally stable jet. The former time scales are typically seconds or even tens of seconds. The latter are on the order of $L_{int}/U(x)$. Using the free jet approximation proposed by Khritov, U(x) is about 30 m/s at 50 m from the release point and L_{int} is typically 5 m. Hence, the turbulent time scales are on the order of 0.1 s. As shown later during the discussion about the turbulence spectra, it was verified that the calculated flow properties (turbulence intensity, mean velocity) were reliable when the time slot varies between 1 s and 3 seconds. So, the signals were sampled in a series of about 1 s slots and, in each slot, the flow properties were calculated.

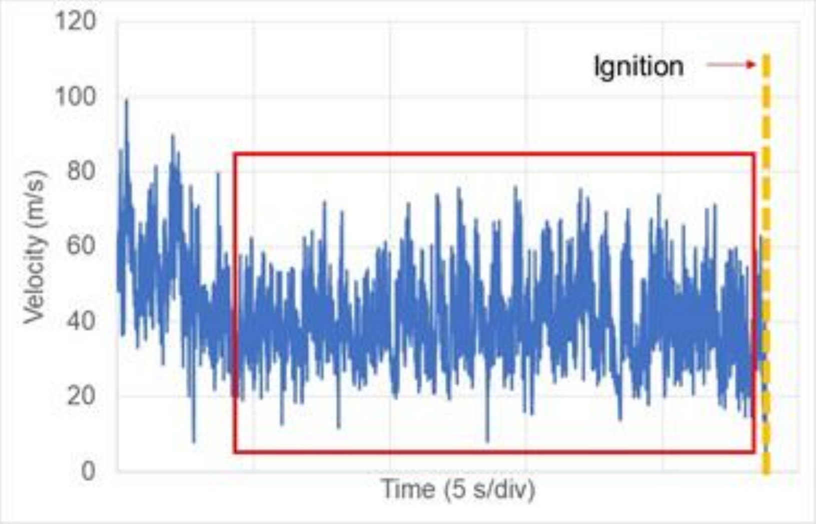

***Fig. 8.** velocity data of probes TS10 (test n°2). The red frame indicates the part of the record which was processed*

4.2 *Mean velocity and turbulence intensity*

The evolution as function of time of the turbulence intensity and of the mean velocity are presented in Fig. 9 for test n°2. Even apparently reliable, some records may be questionable. Consider signal E2-3 (Test °2 sensor TS3) for instance where the turbulence intensity is much too large because the mean velocity is too small (this sensor is the closest from the release point and its velocity signal should stand above the others). Possibly, the probe head of this sensor moved out from the axis of the jet.

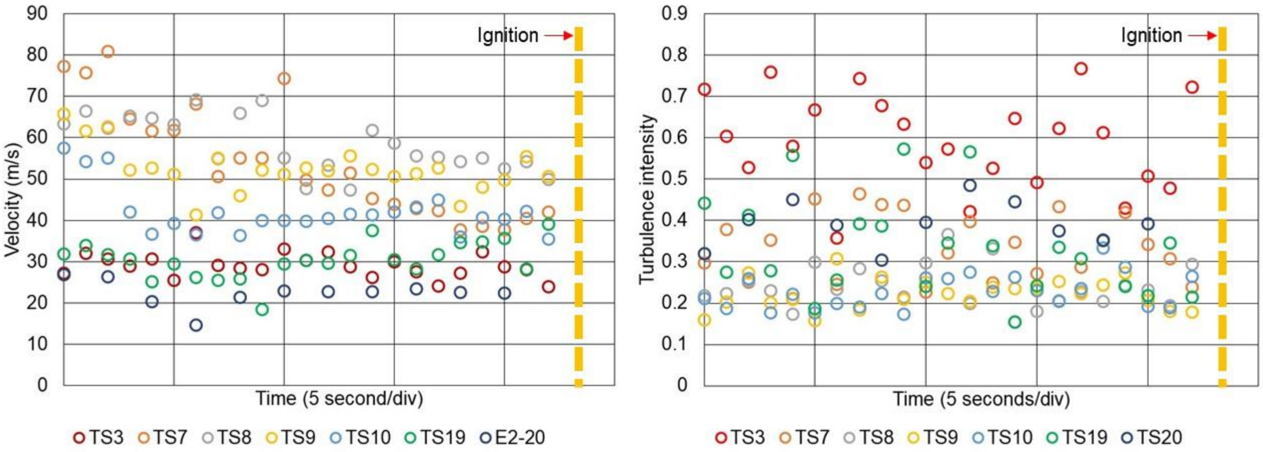

Fig. 9. *Velocity and turbulence intensity averaged over 1 second length data bit for selected sensors of test n°2*

Such aspects considered, the results can be compared to the existing jet theories (Fig. 10) for tests 2 and 15 (E2 and E15). The notional nozzle diameter is 570 mm (Birch, 1984) and the jet velocity is 400 m/s (sound speed).

There is a scattering in the mean velocity whereas the rms of the velocity fluctuations is more stable. This might be due to the lateral movement of the plume since, in jets, the variations on the mean velocity in the radial direction is much more pronounced than for the rms of the velocity fluctuations. The turbulence intensity is in line with the jet theories (free jets and wall jets). The variations of this parameter are due to the scattering of the mean velocity. Contrary to EXJET experimental series, the experimental points are clearly above the wall jet correlations. The best fit hyperbola is: $U_x/U_{exit} = 8.2/(x/D)$. This means that the outward horizontal spreading of the jet due to the presence of the wall does not compensate for the reduced half-space dispersion. Looking at the jet from the top and from the side (figure 11) reveals that the angles of the mixing layers are similar in the vertical plane and in the horizontal plane. This suggest that the first phenomenon (lateral outward increased expansion) is limited and that the jet behaves as a free jet expanding in a half space. This may be modeled using the free jet theory with a double flowrate or, similarly, using a double section for the flow. Doing this, the notional jet diameter should by multiplied by the square root of 2 in the free jet correlation. The reader could easily check that the experimental best fit correlation is retrieved.

DOI: 10.7795/810.20200724

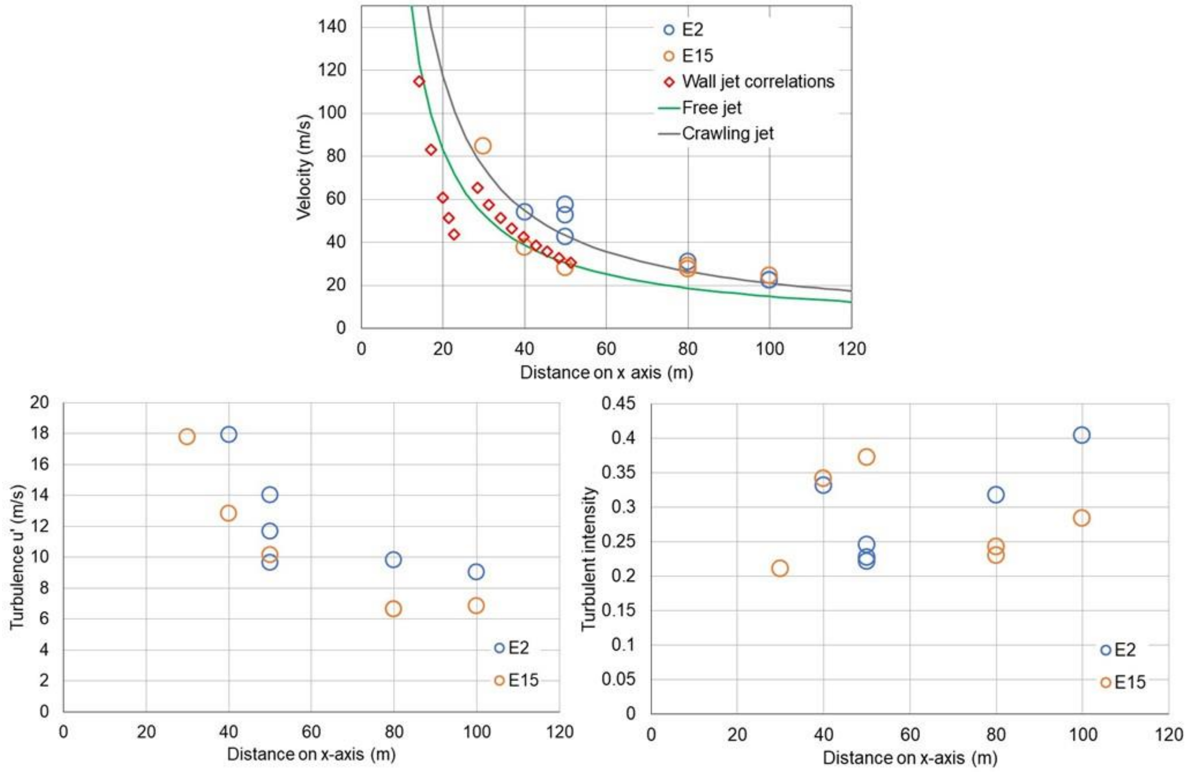

Fig. 10. *Mean velocity, turbulence and turbulence intensity as function of the distance to the orifice.*

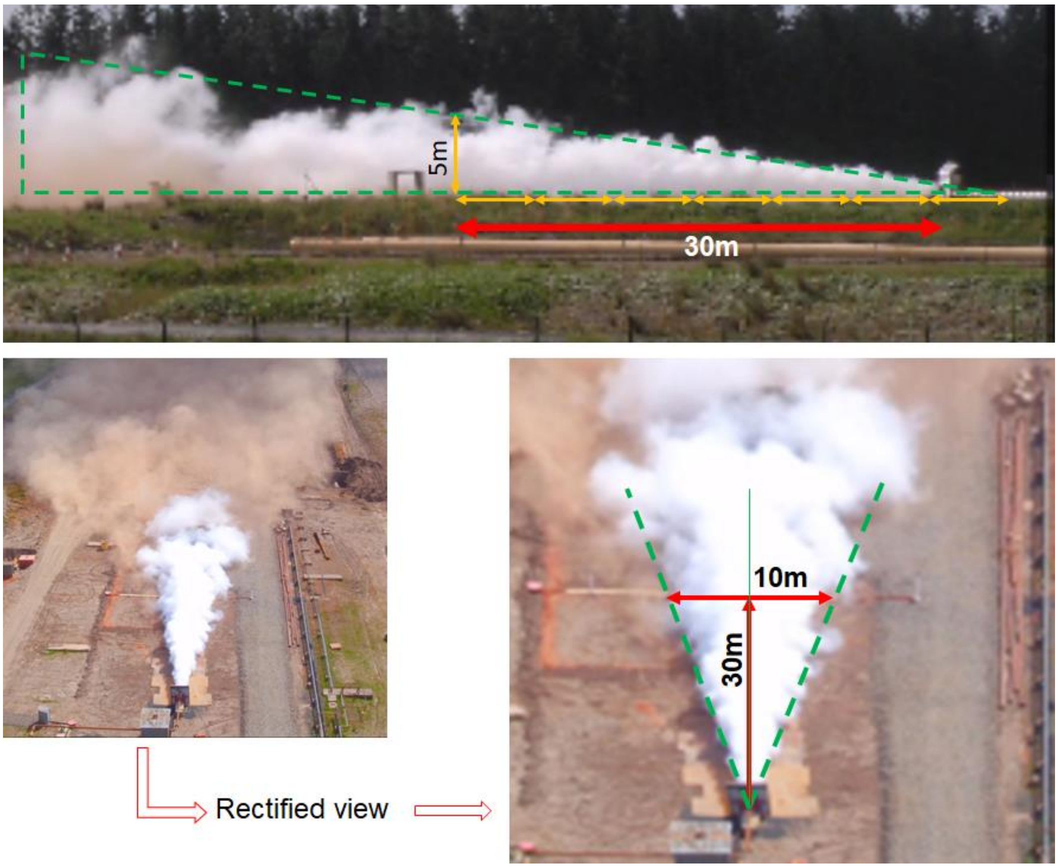

Fig. 11. *Side view and top view (rectified to obtain orthogonal references) of AIRRE release. The vertical angle is about 8/9° and the horizontal wide angle is about 18° (half angle 9°)*

4.3 Integral scale and spectral energy of the turbulence

Assuming the turbulence field is fully developed and stable within the selected time slot (fig. 8), the autocorrelation curve should not change with time provided the duration over which the correlation curve is calculated is larger than the integral time of the turbulence. As explained before the latter is on the order of 0.1 s. The integration time for the autocorrelation time should at least be ten times larger. Once the latter is chosen, the time slot available for the data analysis is divided into N intervals of duration equal to the chosen integration time. The autocorrelation curve is calculated for each interval and the final autocorrelation curve is the average of N raw autocorrelation curves. This procedure, (which is based on Bartlett method: Bartlett M. S., 1948), provides a better accuracy in the correlation process especially when most of the information of the correlation is available in short time scales (typically 0.1 second in the present case). The important point is to choose adequately the integration time.

The influence of the integration time on the final correlation curve is shown on figure 12 left. Clearly the autocorrelation curves look very similar once the integration time is about 1 second. When it is smaller, probably part of the largest structures of the turbulence are lost, the autocorrelation signal changes significantly. When it is much larger (over 3 seconds), noise appearing at large time delays where normally the signals should not be correlated is integrated over all the curve due to the autocorrelation process smearing out the curve and introducing a baseline shift. A more quantitative estimate of the potential influence of the integration time is obtained looking at the integral time of the turbulence, L_t, which is the area under the autocorrelation curve. The evolution of L_t as function of the integration time is shown on figure 12 right. The latter reaches a sort of plateau in the region of 2 s and for larger values seem to diverge due to the integration of the noise. Following, in analyzing the data, the "measuring" time of about 1 s was chosen for all the transducers.

Considering the autocorrelation curve (1.25 or 2 s integration time slot), it is known (Hinze, 1975) that for large Reynolds number flows (fully developed turbulence), as in the present experimental situation, the curve should obey an exponential law: $R(t)=\exp(-t/Lt)$. In the present situation, this baseline exponential decay exists but superimposed on it is a low frequency sinusoidal signal (few Hz). This specificity is addressed later.

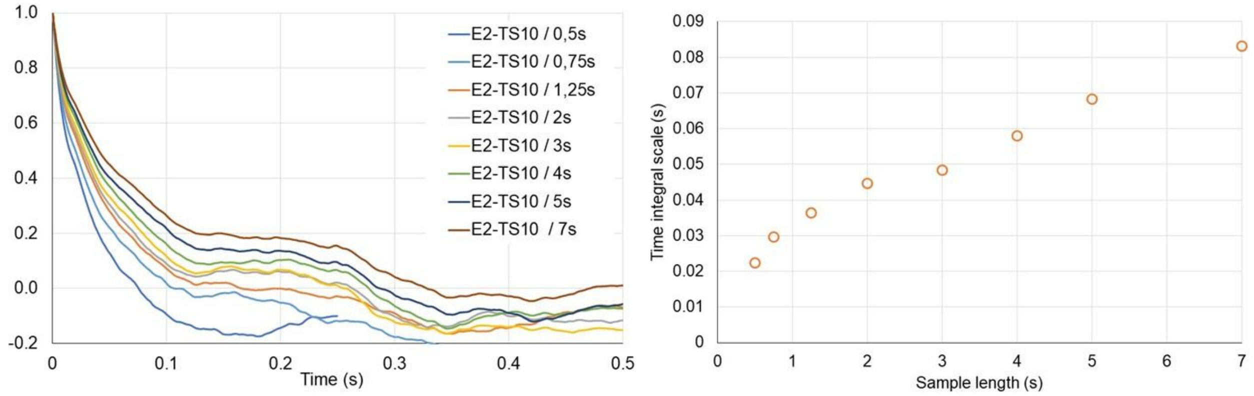

Fig. 12. *Influence of the integration time on the autocorrelation curve (left)and on the integral time of the turbulence L_t (right)*

The other autocorrelation curves are shown on figure 13 for tests n°2 and 15. The same features as described above are retrieved.

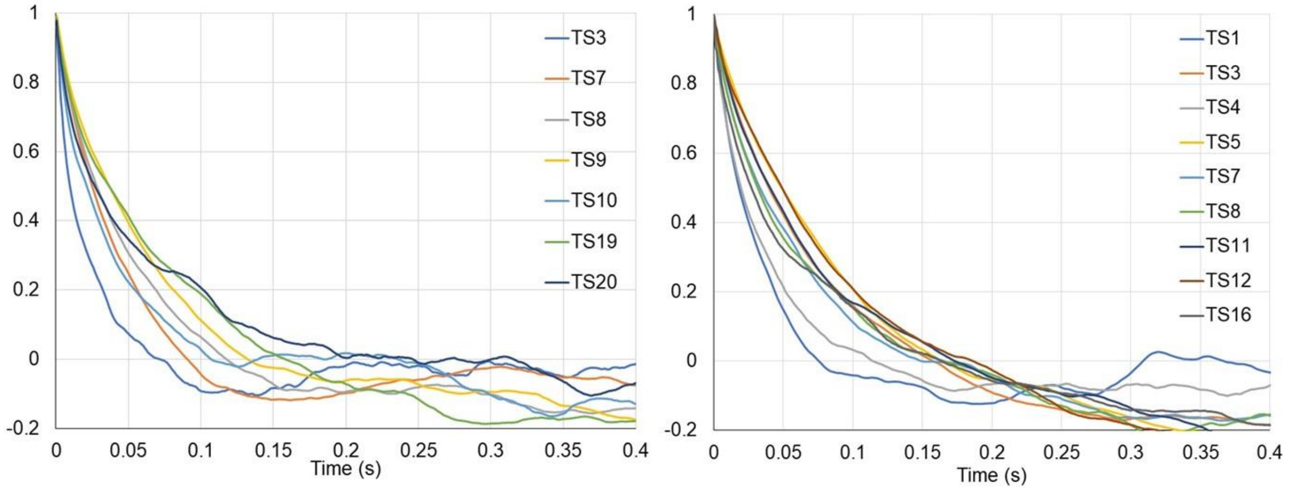

Fig. 13. *Time auto-correlation curves obtained for test n°2 and 15 and various sensors.*

The integral times of the turbulence are calculated and the integral scale are deduced using the Taylor assumption (Figure 14: $L_{int} = L_t \cdot \overline{U}$). It seems that the turbulence scales fit with the free jet theory down to 60 m from the release point and that, further downstream, a significant discrepancy appears. The scales drop to about 1 m or less and do not seems to change with distance anymore. Note this would be coherent with the turbulent scale of a flow along a wall knowing the transducers are located 1.5 m above ground (the integral scale of the turbulence at a distance h from the wall is h/2).

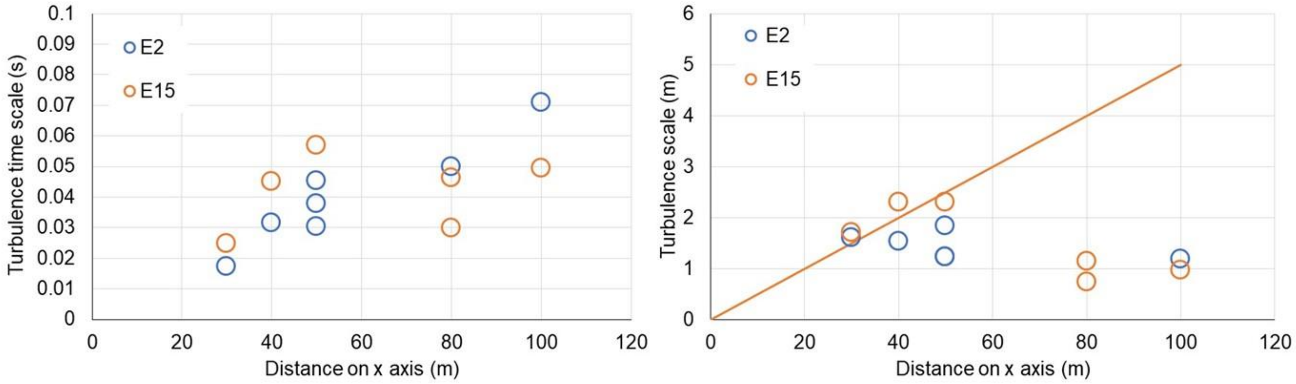

Fig. 14. *Turbulent time scale Lt and integral turbulent scale Lint according to distance on x axis. The solid line corresponds to the standard free jet correlation*

To go further, the turbulence energy spectra can be extracted from the Fourier transform of the autocorrelation curve and by applying the Taylor assumption to switch from the frequency space to the wavenumber space. The experimental distribution obtained for tests n°2 and 15 are shown on figure 15 (full lines) and compared to the free jet theory (dotted lines). The experimental signal fades for wavelengths on the order of 50 m^{-1} meaning a corresponding frequency of a few hundreds of Hz. This is the cutoff frequency of the pressure transducers. The slope of the turbulent cascade is in line with the Kolmogorov theory but the position of the spectra according to the wavenumber coordinate does not correspond to that of the free jet theory. Another difference is that a bump is visible at low wavenumbers, approximately at 0.3 m^{-1}. The corresponding wavelength is roughly 20 m and the corresponding duration (at 50 m from the release point so, close to sensor T10) amounts 0.3s which is the period of the sinusoidal wave superimposed on the exponential decay on the autocorrelation curve of figure 12. It can easily by shown, using the definition of the turbulence spectrum superimposing a cosine function over the traditional exponential decay, that the resulting spectrum resembles those shown on figure 15, with the appearance of the bump, the displacement of the curve towards larger wavenumbers and a drop of the horizontal plateau.

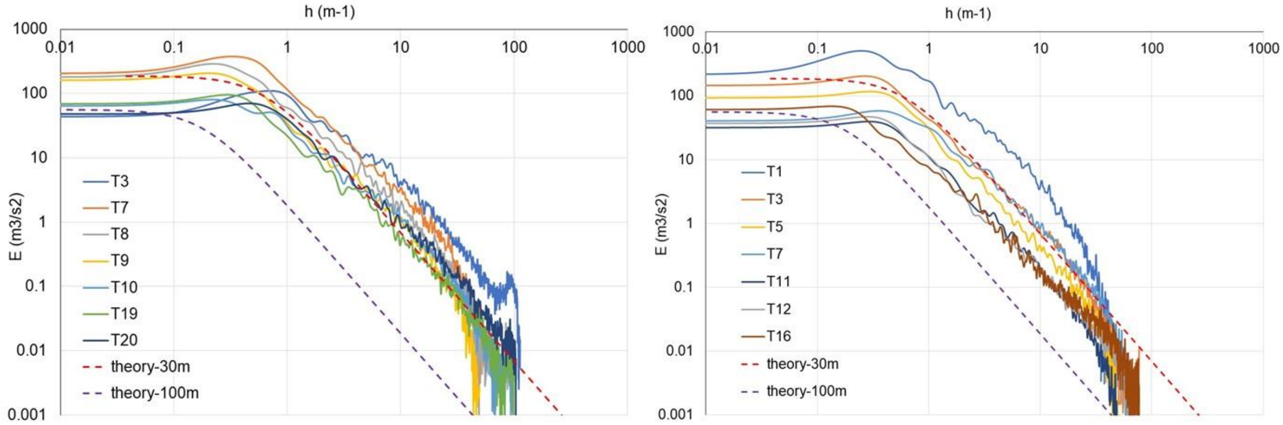

Fig. 15. *Turbulence energy spectra for tests n°2 and 15 (dotted lines: free jet theory)*

This large dynamic phenomenon seems to have a significant influence on the turbulence cascade. Note, it does not appear at small scale (EXJET). It might be visible on the videos under the form of large waves affecting the visible border of the cloud (figure 1). It could be a Kelvin-Helmholtz instability.

Conclusion

Perhaps for the first time, a very large scale under expanded gaseous jet was instrumented with turbulence probes. Free releases of pressurized natural gas performed during the AIRRE project were investigated. The release, under 100 bar and through a 100 mm orifice, was horizontal 1.5 m above the ground. The measuring technique is presented in this paper. It was carefully validated before the implementation of the field. The axial mean velocity, the turbulent velocity fluctuations, the integral scale of the turbulence and the spectra of the turbulence were obtained. The results are compared to tests at a smaller scale (12 mm orifice size).

Whereas small scale jets obey the wall jet theory, large scale jets do not. At least up to 60 m from the release point, the free jet theory would much better fit (apart the mixing occurs only in a half space). At large scale only, large scale pseudo periodic waves appear and interact significantly with the structure of the jet.

The proposed instrumentation proved to be sufficiently robust and can be used to interpret the results of the other tests of the AIRRE program.

References

Abrahamsson H., Johansson B., Löfdahl L. (1996), An Investigation of the Turbulence Field in a Three-Dimensional Wall Jet, Advances in Turbulence VI. Fluid Mechanics and its Applications, vol 36. Springer, Dordrecht

Bartlett M. S. (1948), Smoothing Periodograms from Times Series with Continuous Spectra, Nature (London), Vol. 161, pp 686-687

Birch A.D, Brown D.R., Dodson M.G., Swafield F. (1984), The structure and concentration decay of high-pressure jets of natural gas, Comb. Sci. and Techno., vol. 36, pp. 249-261

Hansen, O. R., Gavelli, F., Davis, S. G., and Middha, P. (2013), Equivalent cloud methods used for explosion risk and consequence studies, Journal of Loss Prevention in the Process Industries, 26(3), pp 511–527

Hinze J.O. (1975), Turbulence, Mc GrawHill, New-York

Hisken H., Mauri L.,Atanga G., Lucas M., Van Wingerden K., Skjold T., Quillatre P., Dutertre A., Marteau T., Pekalski A., Jenney L., Allason D., Johnson M., Leprette E., Jamois D. (2020), Assessing the influence of real releases on explosions: selected results from large-scale experiments, 13th International Symposium on Hazards, Prevention, and Mitigation of Industrial Explosions Braunschweig, Germany

Hussein H. J., Capp S. P., George W. K. (1994), Velocity measurements in a high-Reynolds-number, momentum-conserving, axisymmetric, turbulent jet, J. Fluid Mech., vol 258, pp. 31-75

Khritov K., M. Lyubimov D. A., Maslov V. P., Mineev B. I., Secundov A. N., Birch S. F. (2002), Three-dimensional wall jets - Experiment, theory and application, 40th AIAA Aerospace Sciences meeting and exhibit

Launder B. E., Rodi W. (1983), The turbulent wall jet -measurements and modeling, Annual Review of Fluid Mechanic

Mc Caffrey B. J., Heskestad G. (1976), A robust bidirectional low-velocity probe for flame and fire application, Combustion and Flame, vol. 26, pp125-127

Proust, C., Jamois D. (2020), Measuring the flow and the turbulence in dust air mixtures and in flames using a modified Mc Caffrey gauge. To be published

Sun H. (2002), The Development of Three-dimensional Wall Jet, Thesis, Mc Master University

Tamanini F. (1990), Turbulence effect on dust explosion venting, Plant/Opération Progress, vol. 9

Tamanini F., Chaffee J. L. (1991), Turbulent unvented gas explosions under dynamic mixture injection conditions, 23rd Symp (Int.) on Combustion, The Combustion Institute, Pittsburgh pp. 851-858

Skjold, T., Hisken H., Mauri L., Atanga G., Bernard L., Van Wingerden K., Foissac A., Quillatre P., Blanchetiere V., Dutertre A., Kostopoulos D., Pekalski A., Allason D., Johnson M., Jenney L., Leprette E., Jamois D. (2018), Assessing the influence of real releases on explosions: motivation and previous work, Proceedings of the Twelfth International Symposium on Hazards, Prevention and Mitigation of Industrial Explosions (12 ISHPMIE), Kansas City, 12-17 August 2018: 24 pp. Fike Corporation, Blue Springs, MO, USA.

DOI: 10.7795/810.20200724

Charge-separating processes by spraying water under high pressure

F. Baumann [a], M. Himstedt [a], D. Möckel [a] & Dr. M. Thedens [a]

[a] Physikalisch-Technische Bundesanstalt, 38116 Braunschweig, Germany

E-mail: *florian.baumann@ptb.de*

Abstract

Spraying water under high pressure generates charge-separating processes. While cleaning tanks and vessels in which an explosive atmosphere is present, an explosion may occur in the event of a resulting discharge. Water forms electrical double layers at the phase boundaries. Mechanical separation processes dissolve the water into many drops. This leads to charge separation and the charging of the sprayed water. The mechanical separation processes include water exiting from the nozzle, hydrodynamic instability in the jet and impact with an obstacle. Given that water has many charge carriers, the charge is stronger than with solvents. Whether the charges and the resulting discharges are potentially capable of igniting an explosive atmosphere must be investigated. The aim of this research is to define the quantity and polarity of the electrostatic charges of sprayed water under high pressure. Different measurement techniques and methods are used to enable mutual validation and to generate verified measurement results of the electric field and the potential. Water of different electrical conductivity is sprayed in free space and into a grounded conductive 1 m^3 vessel. Design changes to the vessel allow centric or oblique spraying. The result is intended to extend the scope of application of TRGS 727, which refers to ignition hazards due to electrostatic charging. This project is funded by the DGUV (German Social Accident Insurance) and partners from industry.

Keywords: *electrostatic, high pressure, water jet, field meter*

1. Introduction

As a polar liquid, water has the property of forming electrical double layers with the surrounding air (Krämer, 1983). The negative charge of this double layer is found in the outer layer of a drop. The positive charge points to the inside of the drop. The formation of excess charges occurs when the outer negative layer is torn off the body of a drop. The detached fine drops (aerosol) have a negative excess charge. The remaining body of the drop has a positive excess charge (Lüttgens et al., 2019).

Air, as a gas mixture, does not have its own electrical double layer. It has been shown that there is no charge separation which causes an electrostatic charge of air (Lüttgens et al., 2015). The acceleration of two media of different density (water/air) against each other causes a disturbance in their area of contact. This so-called "hydrodynamic instability" can cause the water drops to tear up and, as a result, may lead to the described charge separation (Krämer, 1983). Detached from the impact on an obstacle, experiments are performed with a free jet. Experiments in a grounded 1 m^3 stainless steel intermediate bulk container (IBC) involve charge separation through the impact of the drops on an obstacle. The "intensity" with which water strikes an obstacle is decisive for the level of charge separation (Lenard, 1892). To investigate this dependence, water is sprayed at pressures of 100 bar to 500 bar. In the real process of vessel cleaning, rotating vessel washing heads and manually guided high-pressure cleaners are used. For this reason, investigations where spraying is carried out in the middle of the vessel are not sufficient for safety considerations. A "worst case" consideration is made by aligning the nozzle in different positions and angles.

Measurements of the electric field strength of a sprayed liquid are used for safety considerations regarding possible ignition hazards (Post et al., 1983; Blum et al., 2015). In TRGS 727 A3.3 (2016), a limit value of 100 kV/m is specified. No brush discharges are to be expected below this limit value, even if field-distorting devices are present in the vessel (TRGS 727, 2016). Field meters have a measuring angle depending on the size of the measuring head (Schierding et al., 2019). Due to this measuring angle, a field meter is not able to measure focused at one point. Instead, the circular measuring area increases with the distance to the measuring object. For measurements of the electric field strength of sprayed liquids, there is currently no known calibration method with which a measurement accuracy can be determined. Usable values can be generated, because the measuring area is usually smaller or equal to the area of the fanned-out spray jet (Baumann et al., 2019). The problem with the measurement is that there are positively and negatively (aerosol) charged drops in the measuring area. The measured value may result from averaging the currently charged drops. To prove this thesis, spatially resolved measurements of the potential in and outside the spray jet are carried out and compared with the measured values of the electric field strength. This shows which maximum and minimum values are generated by the charge separation of the drops.

It is not practical to measure the current at the nozzle. All components of the test stand are conductively connected to each other through the water. The pump, the conductive hoses on the ground and the water tap itself are grounded, which would create an electrical nodal point. Furthermore, only the charge separation at the nozzle can be determined by measuring the current at the nozzle. The charge separation due to hydrodynamic instability and the impact on the vessel wall are not considered, compared to the measurement of the electric field and the potential of the sprayed water.

The aim of this work is to prove that charge separation occurs through the tearing of water drops during high-pressure spraying.

2. Input variable spray jet

The high-pressure cleaner HD 9/50 Ge Cage from Kärcher generates a pressure of 100 bar to 500 bar. A point jet nozzle with a diameter of 1.05 mm is used. The flow rate dependent on the pressure and nozzle diameter is shown in Fig. 1 (left). The temperature of the sprayed water also depends on the pressure (Fig. 1 (right)). Tap water (electrical conductivity from 1.6×10^{-2} S/m to 1.7×10^{-2} S/m, measured at 25 °C) and deionized water (electrical conductivity from 6.8×10^{-5} S/m to 9.7×10^{-5} S/m, measured at 25 °C) are sprayed.

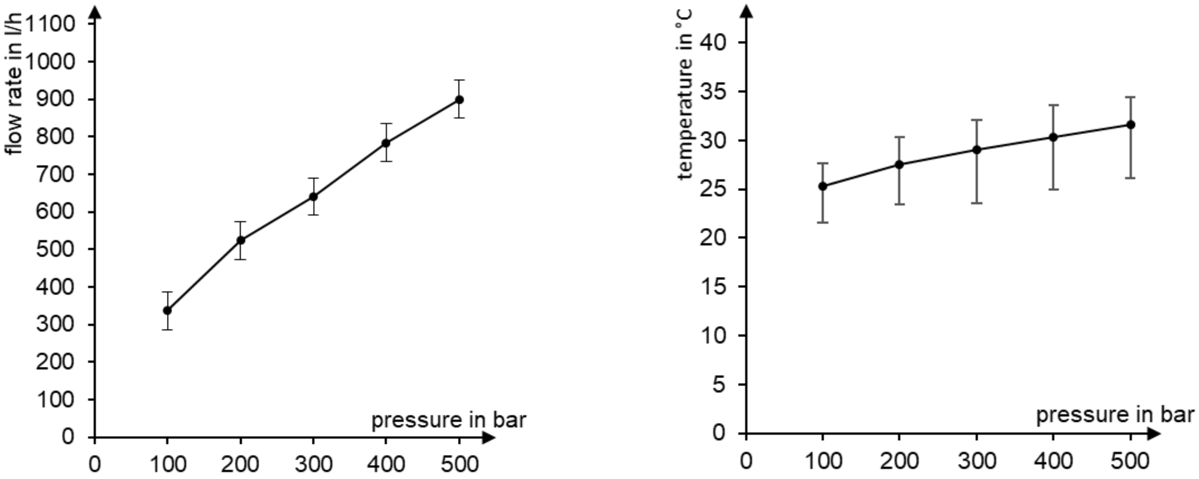

Fig. 1. *Flow rate as a function of the pressure (left), temperature as a function of the pressure (right)*

3. Free jet experiments

Free jet experiments are performed to investigate the charge separation caused by tearing the drops at the nozzle exit and by hydrodynamic instability. Charge separation through an impact with an obstacle does not occur.

3.1. Measurement of the electric field strength

Post et. al (1983) performed measurements of the electric field strength along a horizontally directed free jet of tap water (resting conductivity of 5 x 10^{-2} S/m, measured at 20 °C) at pressures of 100 bar to 400 bar. The nozzle diameter was 1.20 mm. Flow rate specifications are not given. Up to 3 m after the nozzle outlet, positive electric field strengths of up to 0.5 kV/m are measured. From 3 m onwards, the electric field strengths become negative.

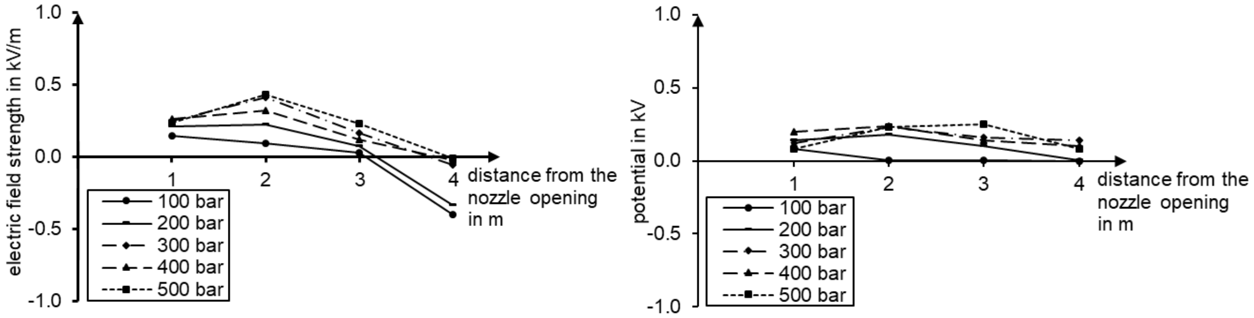

Fig. 2. *Electric field strength (left) and potential (right) along a horizontally directed free jet*

These tests have been performed again within the scope of this project. Measurements of the electric field strength are made along a horizontally directed free jet of tap water at pressures of 100 bar to 500 bar (Fig. 2, left). The nozzle diameter of the point jet nozzle is 1.05 mm. The downwardly directed measuring head of the JCI 131 field meter obtained from the Chilworth Technology Ltd. company is, as in the measurements of Post et al. (1983), positioned at a distance of 0.5 m to the middle of the jet. By means of constant compressed air flushing (3 bar) and the downwardly directed measuring head, the intrusion of water is avoided. Flushing the measuring head with compressed air has no effect on the measuring device. The measuring head is mounted flush in a metal plate with a diameter of 0.4 m. This homogenization reduces the distortion of the electric field caused by the measuring head itself (Lüttgens et al., 2019). The JCI 131 field meter has a measuring angle of (40 ± 5) °. Due to this measuring angle, the field meter is not able to measure in a focused manner at one point. Instead, the circular measuring area increases with the distance to the measurement object. The JCI 131 field meter and the nozzle are grounded.

During high-pressure spraying of tap water, the negatively charged aerosol is volatilized in the surrounding area. This increases the percentage of positively charged drops in the jet. This is measured at a distance from the nozzle of 1 m, 2 m and 3 m. The positively charged drops in the jet are heavier than the negatively charged aerosol. Depending on the pressure and the distance to the nozzle, the larger positively charged drops rain off through gravity. A spatial separation of the oppositely charged drops takes place. From 3 m to the nozzle, the negatively charged aerosol predominates. The electric field strength becomes negative, as in the measurements of Post et al. (1983).

3.2. Measurement of the potential

Spatially resolved potential measurements in the middle of the jet are carried out by a tip electrode (Ø 0.010 m, L = 0.010 m) which is insulated from the ground. Through contact with the drops, the electrode takes on their potential. The electrode is conductively connected with the ± 2 kV voltage measuring head of the EMF58 field meter obtained from the Eltex company. This design allows the load-free measurement of the potentials along the horizontally directed free jet of tap water at pressures of 100 bar to 500 bar (Fig. 2, right). A measuring accuracy of ± 50 V applies. The measured positive potentials of up to +0.3 kV at a distance from the nozzle of 1 m, 2 m and 3 m confirm that the drops in the jet are positively charged. At a distance from the nozzle of 4 m, positive potentials are measured too. The potential is measured spatially resolved and there is no averaging of the predominantly negative aerosol in the surrounding area and the positive drops in the jet as with the field meter. The remaining positive drops that are not rained off and are in the middle of the jet are measured.

4. Measurements in the grounded 1 m^3 stainless steel IBC

During measurements in the grounded horizontal 1 m^3 stainless steel IBC (Ø 1.07 m, length 1.00 m), the spray jet hits the vessel wall. This causes an effective charge separation by tearing the drops. An outlet is mounted at the lowest point of the IBC. Because of this, the filling of the IBC during the tests is avoided. To create an initial situation that is constant, the IBC is dried before each test. The measured values are recorded automatically at 100 samples per second. The measurement time is seven minutes. The measured electric field strength fluctuates strongly around a constant average value depending on each measurement. For this reason, as in the measurements by Post et al. (1983), a range of measured values is given for the electric field strength. The highest value is given for the potentials. The measuring accuracy of the EMF 58 field meter in combination with the ± 40 kV high-voltage gauge head depends on the set measuring range. The measurement accuracy is specified separately for each measurement series.

4.1. Spraying centrally into the vessel

The measurement of the electric field strength and the potential is carried out on a horizontally directed jet of tap water at pressures of 100 bar to 500 bar. The point jet nozzle is located centrally in a cover made of PVC-U. The nozzle does not protrude into the IBC as it is flush with the cover opening. The nozzle is conductively connected to the grounded IBC.

4.1.1 Measurement of electric field strength

The JCI 131 field meter is mounted flush with the shell surface of the IBC (Fig. 3). The distance to the nozzle is 0.50 m. By means of constant compressed air flushing (3 bar) and the downwardly directed measuring head, the intrusion of water is avoided.

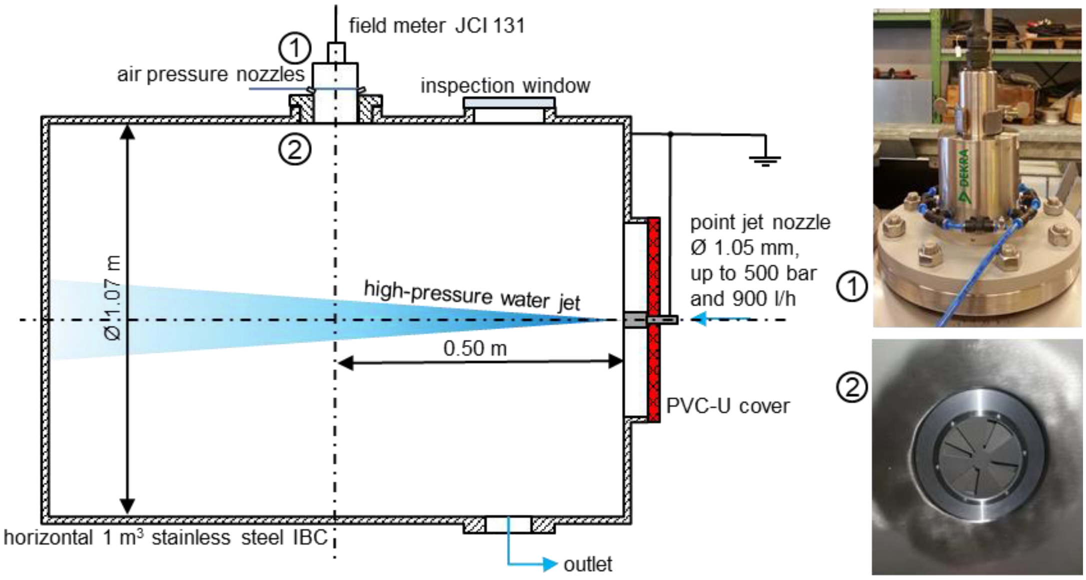

Fig. 3. *Test stand to measure the electric field strength when spraying water centrally into the grounded IBC*

Analogous to the free jet measures, negative electric field strengths are measured inside the grounded IBC (Fig. 4). The tearing of the drops at the impact leads to further charge separations. The positively charged drops of the jet melt on the vessel wall. The negatively charged aerosol is distributed in the IBC. This spatial separation of the oppositely charged drops generates negative electric field strengths in the IBC. In terms of amount, the values are at least one power of ten greater than the values of the free jet. Comparable measurements by Post et al. (1983) in a grounded 1 m^3 vessel show the same order of magnitude (Fig. 4). The pressure increases cause considerably higher electric field strengths of up to -12.4 kV/m at 500 bar. The positive charge of the drops in the jet is not detected by the field meter but must be present. The spatially resolved measurement of the potentials will show this positive charge of the drops in the jet.

DOI: 10.7795/810.20200724

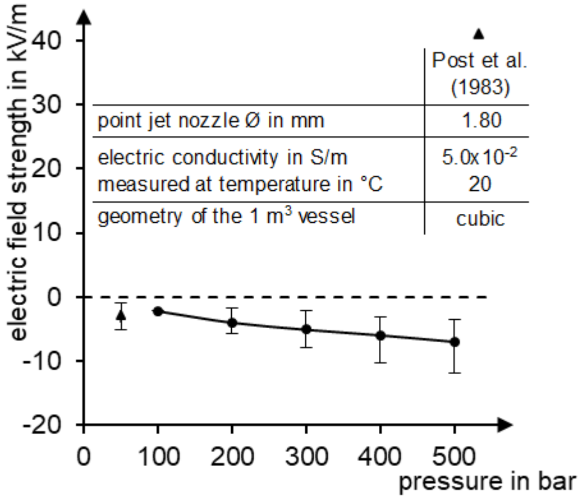

	Post et al. (1983)
point jet nozzle Ø in mm	1.80
electric conductivity in S/m measured at temperature in °C	5.0×10^{-2} 20
geometry of the 1 m^3 vessel	cubic

Fig. 4. *Electric field strength as a function of the pressure when spraying tap water centrally into the IBC*

4.1.2 Measurement of the potential

Measurements of the potential (Fig. 5) are carried out with a tip electrode (Ø 0.010 m, L = 0.010 m) which is insulated from the grounded IBC. The tip electrode is screwed to the end of the insulating rod pointing into the inside of the vessel. Through contact with the surrounding drops, the electrode assumes their potential. The distance of the electrode to the vessel wall is 0.15 m, 0.30 m, 0.45 m or 0.54 m (centre of the IBC). At a distance of 0.54 m, the electrode is directly in the spray jet. A further insulating body is mounted in the shell surface of the IBC. It has a drip edge and eight compressed air nozzles (4 bar). This keeps the insulating rod dry in the area of the measuring hole and prevents water from escaping. The insulating rod has a through hole in which a high-voltage cable is embedded. This high-voltage cable conductively connects the electrode with the ± 40 kV high-voltage gauge head of the EMF58 field meter. Using this construction, the potentials are measured load-free 0.50 m after the nozzle exit. The measuring accuracy is ± 25 V.

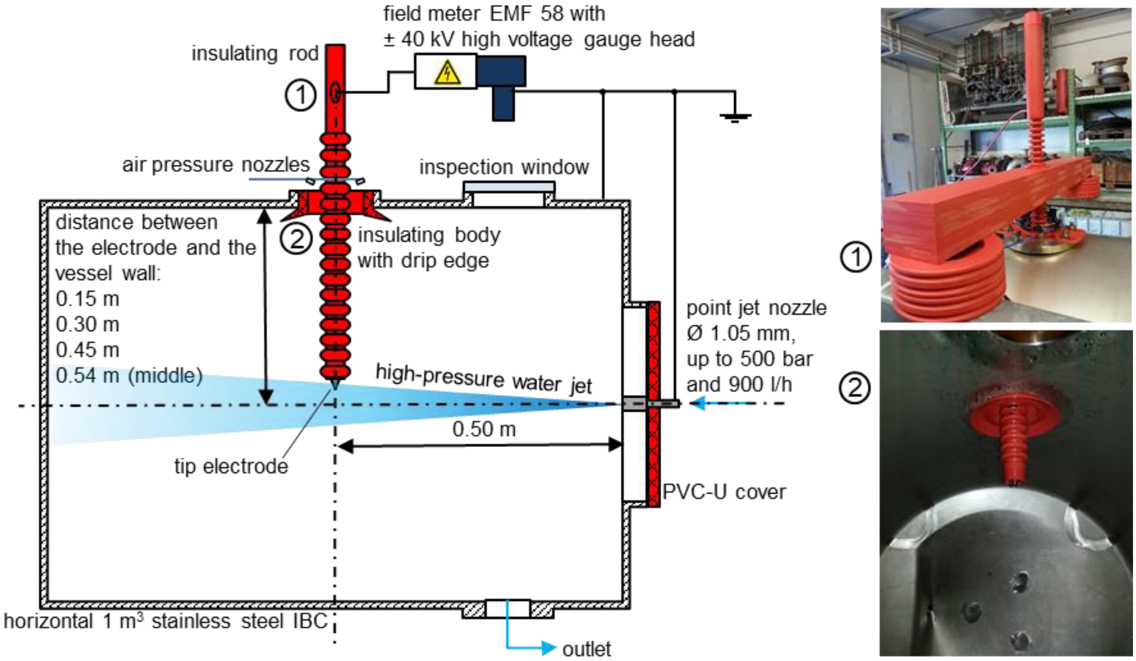

Fig. 5. *Test stand to measure the potential when spraying water centrally into the grounded IBC*

The potentials (Fig. 6) measured in the spray jet (0.54 m) correspond with +0.3 kV in polarity and quantity to the values of the free jet measurements (see Section 3). The positively charged drops of the jet melt on impact and transfer their charge to the grounded IBC. What remains are the small drops (aerosol) with a negative charge. These are measured outside the spray jet at a distance between the electrode and the vessel wall of 0.15 m, 0.30 m and 0.45 m. If this description of the spatial charge separation is correct, no positive potential ought to be measurable at a distance of the electrode to the vessel wall of 0.54 m when positioning the nozzle at an angle (Section 4.2.2.).

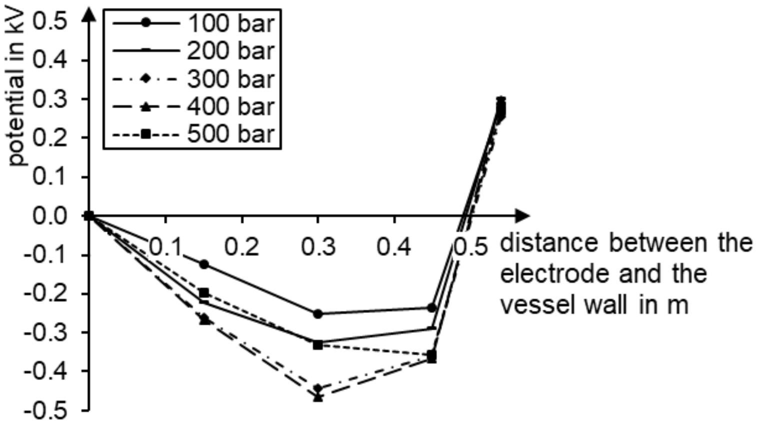

Fig. 6. *Potential as a function of the pressure and the distance between the electrode and the vessel wall when spraying tap water centrally into the IBC*

4.2 Positioning of the nozzle at an angle

The process of vessel cleaning requires positioning the nozzle at an angle (Fig. 7). The nozzle with the associated jet pipe is mounted in an excentrically mounted sphere (Ø 0.1 m) in the cover of the IBC. The distance between the centre of the cover and the sphere is 0.14 m.

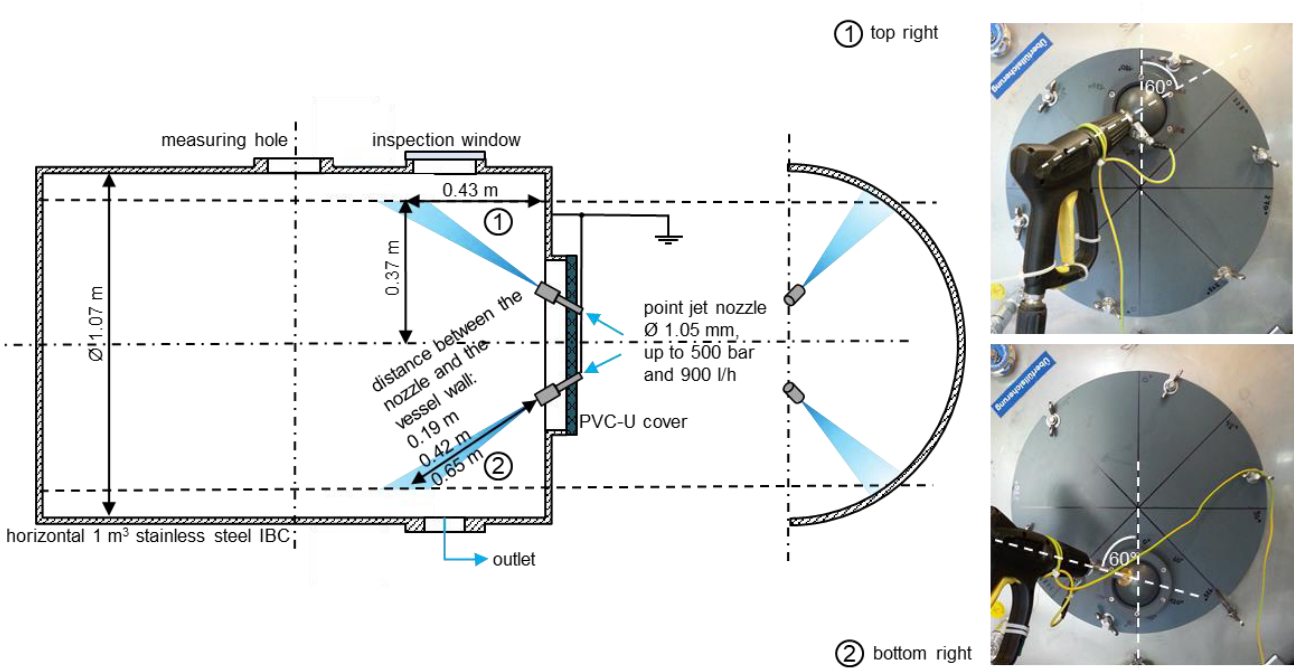

Fig. 7. *Positioning of the nozzle at an angle*

In the "top right" position, the sphere in the cover is oriented upwards. The jet pipe in the sphere is pressed against the lower edge of the sphere holder (view from outside). The sphere is then rotated clockwise along the bolt circle of the sphere holder until the 60° mark is reached. In the "bottom right" position, the sphere in the cover is oriented downwards. The jet pipe in the sphere is pressed against the upper edge of the sphere holder. The sphere is then rotated anticlockwise along the bolt circle of the sphere holder up to the 300° mark. Damage to the measuring instruments by the spray jet is ruled out by the selected positions. The distance between the nozzle and the vessel wall is varied between 0.19 m, 0.42 m and 0.65 m. The nozzle and the jet pipe are conductively connected to the grounded IBC. The measurements of the electric field strength and potential are carried out with tap water at pressures of 100 bar to 500 bar.

4.2.1 Measurement of the electric field strength

As in the case of centrally spraying into the IBC (Section 4.1.1.), the JCI 131 field meter is mounted flush with the shell surface and is constantly flushed with compressed air. The distance between the nozzle and the vessel wall is 0.19 m. When spraying to the "top right" position, large drops fall through the IBC. These either have a positive charge or are electrostatically neutral due to the impact. Small negatively charged drops (aerosol) in the IBC are absorbed by the large drops due to cluster formation. The amount of negatively charged drops is reduced. Due to this fact, the negative values of the "top right" position are reduced by exactly 25 % compared to the measurements of the "bottom right" position in a pressure range from 200 bar to 500 bar (Fig. 8). The increase in pressure causes higher electric field strengths of up to -12.3 kV/m at 500 bar, measured in the "bottom right" position. The values correspond in polarity and quantity to the electric field strengths of centrally spraying tap water into the IBC (Fig. 4). There are differences in the height of fluctuation around the mean value. The JCI 131 field meter has a circular measuring area which increases with the distance to the measurement object. When spraying centrally into the IBC, the positive charge of the drops in the jet and the negative charge of the aerosol are averaged. This leads to large fluctuations. If the nozzle is positioned at an angle, the spray jet hits the vessel wall after 0.19 m. In the IBC, the aerosol with a negative charge predominates. The fluctuations are thus significantly reduced.

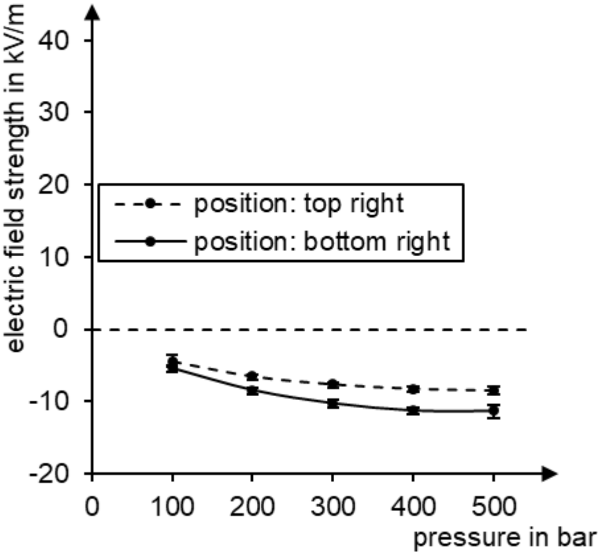

Fig. 8. *Electric field strength by spraying tap water to the "top right" and "bottom right" position into the IBC as a function of the pressure*

4.2.2 Measurement of the potential

The test stand with the insulated electrode for potential measurement is described in Section 4.1.2. A measuring accuracy of ±100 V applies to the following measurements. The distance of the electrode to the vessel wall is initially 0.54 m (centre of the IBC). Spraying is done to the "bottom right" position with a pressure of 500 bar. The distance of the nozzle to the vessel wall is varied between 0.19 m, 0.42 m and 0.65 m. If the smallest distance of the nozzle to the vessel wall of 0.19 m is set, the highest negative potentials of -1.4 kV (Fig. 9) occur. The potential difference is decisive. There are higher potential differences between the negatively charged aerosol and the positively charged drops in the jet than between the negatively charged aerosol and the grounded jet pipe. This fact leads to reduced negative potentials if the distance is increased to 0.42 m or 0.65 m. Furthermore, the "intensity" with which water hits an obstacle is decisive for the level of charge separation (Lenard, 1892). This explains further that the highest potentials are measured at a distance of 0.19 m.

DOI: 10.7795/810.20200724

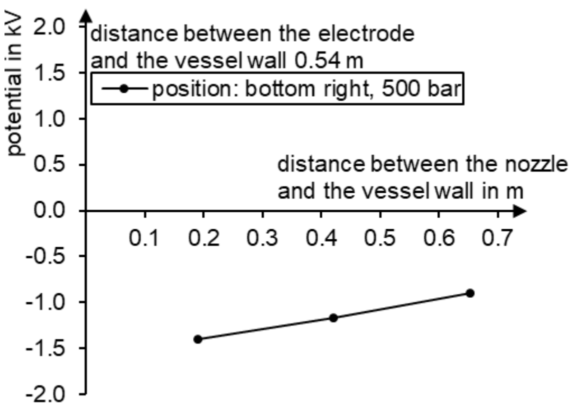

Fig. 9. Potential by spraying tap water in the "bottom right" position into the IBC as a function of the distance between the nozzle and the vessel wall

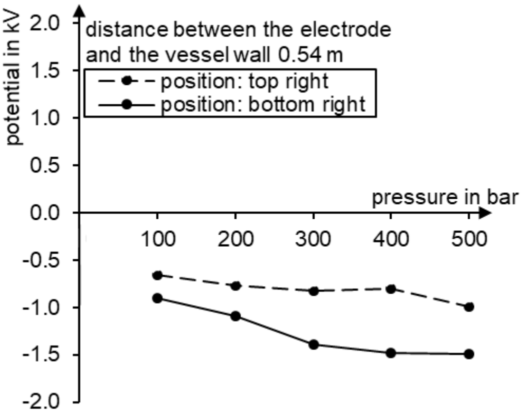

Fig. 10. Potential by spraying tap water in the "top right" and "bottom right" positions into the IBC as a function of the pressure

When spraying to the "top right" position, the negative electric field strengths are reduced by 25 % compared to spraying to the "bottom right" position (Section 4.2.1). To validate this reduction through cluster formation, a measurement of the potentials in the same positions is carried out. The distance of the electrode to the vessel wall is 0.54 m (centre of the IBC). The negative potentials of the "top right" position are also reduced by 25 % to 45 % (Fig. 10).

The distance of the electrode to the vessel wall when spraying in the "bottom right" position is varied between 0.15 m, 0.30 m, 0.45 m and 0.54 m (centre of the IBC). As the nozzle is positioned at an angle, the spray jet hits the vessel wall after 0.19 m. Therefore, the aerosol with a negative charge predominates in the IBC. In the centre of the IBC, the distance to the nearest ground and to the positively charged drops in the jet is greatest. For this reason, the largest negative potentials are measured here (Fig. 11). In comparison to spraying centrally into the IBC, the value of the negative potential is three times higher. The highest negative potential is -1.5 kV, measured at a pressure of 400 bar. Above 300 bar, a further increase in pressure does not lead to significantly higher potentials.

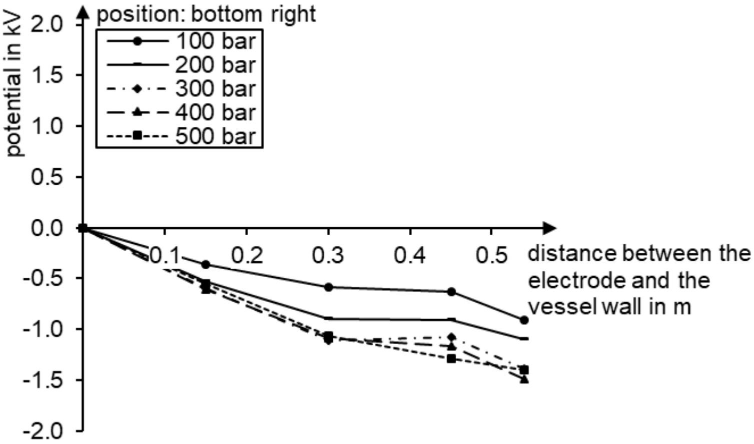

Fig. 11. Potential by spraying tap water in the "bottom right" position into the IBC as a function of the distance between the electrode and the vessel wall

4.3. Deionized water tests

The measurements described when tap water is sprayed centrally into the grounded IBC are repeated with deionized water. For a description of the test stands, see Section 4.1.

4.3.1 Measurement of the electric field strength

When deionized water is sprayed centrally into the grounded IBC, the measured electric field strengths are negative up to a pressure of 200 bar (Fig. 12). An increase of the pressure to over 200 bar leads to positive values. Comparable measurements by Post et al. (1983) and Blum et al. (2015) in a grounded 1 m^3 vessel show the same tendency (Fig. 12). It is assumed that the measured value of Post et al. (1983) is negative.

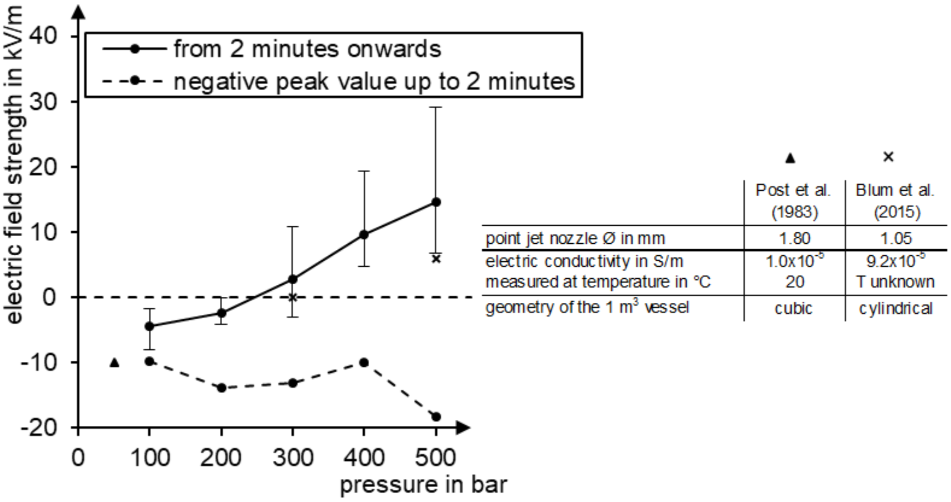

	▲ Post et al. (1983)	× Blum et al. (2015)
point jet nozzle Ø in mm	1.80	1.05
electric conductivity in S/m measured at temperature in °C	$1.0x10^{-5}$ 20	$9.2x10^{-5}$ T unknown
geometry of the 1 m^3 vessel	cubic	cylindrical

Fig. 12. *Electric field strength by spraying tap water centrally into the IBC as a function of the pressure*

The highest positive electric field strength is +29.2 kV/m, measured at a pressure of 500 bar. Negative peak values result up to a measuring time of 2 minutes. The highest values of these negative peaks are shown in Fig. 12 as a function of pressure. This negative peak occurs even if the electric field strength assumes positive values after a measuring time of 2 minutes. In contrast to tap water, the drops in the jet must have a high negative charge. It follows that before the aerosol with a positive charge is sufficiently formed, the negative peak values of the electric field strength are measured.

4.3.2 Measurement of the potential

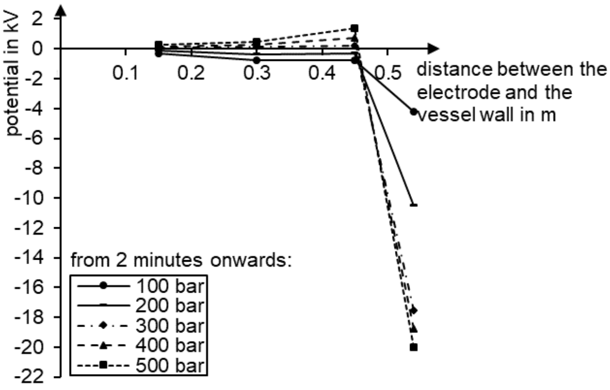

Fig. 13. *Potential from 2 minutes onwards by spraying deionized water centrally into the IBC as a function of the pressure and the distance between the electrode and the vessel wall*

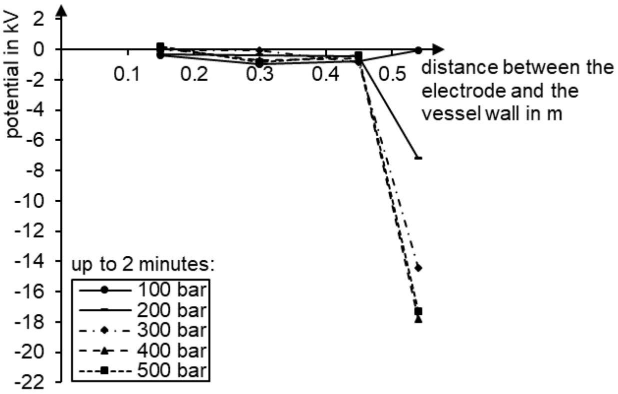

Fig. 14. *Potential up to 2 minutes by spraying deionized water centrally into the IBC as a function of the pressure and the distance between the electrode and the vessel wall*

A measuring accuracy of ±1 kV applies to measurements in the spray jet. For measurements outside the spray jet, it is ±100 V. The potentials measured in the spray jet (0.54 m) are, as assumed by the measurements of the electric field strength, strongly negative with up to -20.0 kV (Fig. 13). The negatively charged drops in the jet transfer most of their negative charge to the grounded IBC during the impact. The "intensity" with which water hits an obstacle is decisive for the level of charge separation (Lenard, 1892). From 300 bar, the charge separation is sufficient to generate positive potentials outside the spray jet at a distance of 0.15 m, 0.30 m and 0.45 m between the electrode and the vessel wall. This change in polarity is also observed during measurements of the electric field strength (Fig. 12). The highest positive potential is +1.4 kV. Up to a measuring time of 2 minutes, only negative values are measured (Fig. 14), which is also true of the measurements of the electric field strength (Fig. 12). A predominantly negatively charged aerosol must be present in the IBC for up to 2 minutes.

5. Discussion of results

5.1 Tap water

The JCI 131 field meter has a circular measuring area that increases with the distance to the measurement object (Schierding et al., 2019). This results in an averaging of the charged drops in the measurement area. In the free jet, parts of the negatively charged aerosol volatilize in the surrounding area. This process leads to a spatial separation of the charges. The drops with a positive charge in the measuring area predominate. A positive electric field strength of up to +0.5 kV/m is measured (Section 3.1). Charge equalization takes place when the spray jet with the positive charge drops hits the vessel wall. On impact, aerosol is also formed with a negative charge. The aerosol cannot volatilize. The positive charge of the drops in the jet and the predominant negative charge of the aerosol are averaged. The electric field strength becomes negative and reaches values up to -12.4 kV/m (Section 4.1.1). The proof of this explanation is provided by the potential measurement. Positive potentials are measured in the spray jet and negative potentials in the aerosol. Further proof is that the fluctuations of the electric field strength are significantly reduced when spraying with a nozzle positioned at an angle (Section 4.2.1). In these measurements, the distance of the nozzle from the vessel wall is only 0.19 m. There is no averaging, because the positive charge of the drops in the jet is not recorded.

The highest potential in the IBC depends on the positioning of the nozzle. In the "bottom right" position and at a minimum distance between the nozzle and the vessel wall, the highest potentials of up to -1.5 kV are measured in the IBC (Section 4.2.2.). The volume in which the aerosol can be distributed with a negative charge is maximum. As a result, the distance to the nearest ground or spray jet is maximized. This defined "worst case" serves as a basis for measurements in vessels which exceed a volume of 1 m^3.

At pressures above 300 bar, no significant increase in values is observed when measuring the electric field strength and potential. It is assumed that an increase in pressure to over 500 bar does not lead to significantly higher values. However, this assumption must be verified by tests at pressures above 500 bar.

In TRGS 727 A3.3 (2016), a limit value of 100 kV/m is specified. No brush discharges are to be expected below this limit value, even if field-distorting devices are present in the vessel (TRGS 727, 2016). This limit value is not exceeded by any of the measurements of the electrical field strength with tap water. The low negative potentials support this statement.

5.2 Deionized water

When deionized water is sprayed centrally into the IBC, negative electric field strengths are measured at a pressure of up to 200 bar. At over 200 bar, the measured values become positive. This pressure-dependent polarity charge also occurred during potential measurements in the aerosol. This indicates that the negative charge is found in the spray jet and the positive charge in the aerosol. Potential measurements in the spray jet show that the negative charge can have potentials of -4.2 kV (100 bar) to -20.0 kV (500 bar) (Section 4.3.2). Negative electric field strengths of up to -9.8 kV/m (100 bar) to -18.3 kV/m (500 bar) are only measured in the first two minutes of the measurement. Measurements taken during the central spraying of tap water into the IBC also give negative electric field strengths of up to -12.4 kV/m (Section 4.1.1). The difference is that, when spraying tap water, the maximum potential in the IBC is -0.5 kV (Section 4.1.2). This impressively demonstrates that the field meter is not capable of measuring the high negative charges of the spray jet. For this reason, the measurement of the electric field strength alone is not sufficient for safety-related considerations.

When measuring the potential, it is important to consider whether charge separation occurs when the spray jet hits the potential measuring electrode or whether the potential is already present in the jet. By measuring the leakage resistance of the jet, it could be shown that the charge does not first arise at the electrode. The leakage path via the spray jet predominates potentially charging processes. Using deionized water, the polarities of the charges are inverse to those of tap water. There is currently no explanation for this effect. The electrical conductivity, the pH value and the salinity are different for tap and deionized water. Further investigations on this topic are planned.

Insulated conductors can be formed by falling coherent water clusters. These insulated conductors can assume the high negative potential of the spray jet. When approaching conductive grounded components or the vessel wall, electrostatic discharges may occur, which could ignite explosive atmospheres (TRGS 727, 2016). The limit value of 100 kV/m specified in TRGS 727 A3.3 (2016) is not exceeded by any measurement of the electric field strength. It must be mentioned, however, that the measured field strength is an average of the positive and negative charged drops of the sprayed water. The local maximum and minimum cannot be measured.

In this paper the first results of the described test stand are presented. Further experiments with different temperatures, nozzle geometries, salinity of the water and to the droplet size distribution will be performed.

6. Conclusion

When water is sprayed at high pressure, the charge is separated through the tearing of the drops. As a result, positive and negative potentials can always be found in the vessel. Measuring the electric field strength alone cannot detect the local maximum or minimum of these spatially separated potentials. For safety considerations, the measurement of the electric field strength alone is not enough. To understand where the spatial separation of the potentials takes place, a spatially resolved measurement of the potentials can be used.

Acknowledgement

The authors would like to take this opportunity to thank the German Social Accident Insurance (DGUV) and the five professional associations involved, BG RCI, BG ETEM, BG HM, BG Verkehr and BG HW, for their financial support. This work was supported by application technology and the necessary know-how provided by Alfred Kärcher SE & Co. KG. The 1 m^3 stainless steel IBC with measuring openings and several 1000 l deionized water were made available by Merck KGaA. Also, a big thank you goes to the PTB working group 3.73.

References

Krämer, H. (1983). Kriterien zur Beurteilung der Zündgefahren infolge elektrostatisch aufgeladener Flüssigkeiten. *Chem.-Ing.-Tech.* 55 No. 6, pp. 419-428.

Lüttgens, G., Schubert, W., Lüttgens, S., von Pidoll, U., Emde, S. (2019). *Statische Elektrizität Durchschauen-Überwachen-Anwenden.* First edition. Wiley-VCH Verlag, Weinheim.

Lüttgens, S., Lüttgens, G., Thulin, A., Thierry, P., Touchard, G. (2015). Electrostatic Charge Measurements of Droplets of Various Liquids Falling over a Large Distance. *Chem. Eng. Technol.*, 38, No. 00, 1-9.

Lenard, P., (1892). Ueber die Electrizität der Wasserfälle. *Annalen der Physik*, Vol. 46, pp. 584-636.

Post, L., Lüttgens, G., Maurer, B., Glor, M. (1983). *Vermeidung von Zündgefahren infolge elektrostatischer Aufladungen beim Versprühen von Flüssigkeiten unter hohem Druck*. Special publication "Die BG" Issue 7/83. Erich Schmidt Verlag, Bielefeld.

Blum, C., Losert, O. (2015). Charge generation associated with liquid spraying in tank cleaning and comparable processes – preliminary experiments. *Journal of Physics: Conference Series* 646, 012024.

TRGS 727 Vermeidung von Zündgefahren infolge elektrostatischer Aufladungen, Ausschuss für Gefahrstoffe -AGS-Geschäftsführung -BAuA (2016).

Schierding, C., Möckel, D., Thedens, M., Beyer, M. (2019). Neueste Erkenntnisse bei der Charakterisierung der berührungslosen Messung elektrostatischer Aufladung mittels Feldmühlen. *15. BAM-PTB-Kolloquium*, DOI: 10.7795/210.20190521C.

Baumann, F., Esslinger, J. Möckel, D., Thedens, M., Losert, O. (2019). Measurement of electric fields of charged spray clouds of conductive liquids in free space and in a conductive vessel. *Journal of Physics: Conf. Series* 1322, 012019.

Presentation of the experimental JIP SPARCLING: Inside and beyond a pressurised LNG release

Lauris Joubert [a], Guillaume Leroy [a], Steven Betteridge [b], Elena Vyazmina [c], Laurence Bernard [c],
Romain Jambut [d] & Jérôme Frindel [e]

[a] INERIS, 60550 Verneuil en Halatte, France,
[b] Shell Global Solutions (UK), Shell Centre, London SE1 7NA,
[c] Air Liquide, Innovation Center Paris, Jouy-en-Josas, France,
[d] GRTgaz, Research and Innovation Center for Energy, Villeneuve la Garenne, France,
[e] Total, Tour Coupole, Place Jean Miller, Paris La Défense, France

E-mail: lauris.joubert@ineris.fr

Abstract

The SPARCLING JIP was launched by TOTAL, AIR LIQUIDE, SHELL, GRTgaz & INERIS. The goal of the project was to produce high-quality experimental data on the size distribution and velocities of the LNG droplets using a dual PDA (Phase Doppler Anemometer), following the pressurized release of LNG. One area of particular concern is the potential for rainout and subsequent pool dispersion. The test programme was managed and run by INERIS at their test site at Verneuil-en-Halatte on behalf of the members of the JIP. The paper describes in detail the testing bench and test protocol, as well as the lessons learned from the use of the bench. The occurrence of rainout is then discussed.

Keywords: *pressurised LNG, two-phase release, rainout, dispersion, experimental set-up*

1. Introduction

The small-scale Liquefied Natural Gas (LNG) economy is expected to continue growing over the foreseeable future and so there is a requirement for further deployment of more delivery points in fluvial and maritime ports, not only along the main road axes, but also in city centres. Therefore, the need for more accurate risk assessment models is becoming essential for the safe deployment of this technology.

Current models used to assess the consequences of hazardous phenomena involving pressurised LNG are quite empirical and mostly based on other fluids, such as Liquefied Petroleum Gas (LPG). In addition, when available, experimental data for LNG are not necessarily fully instrumented. Yet high-quality experimental data are required to check the accuracy of the models, especially for small-scale LNG where the site footprint and distance to public is smaller than traditional major hazard sites.

As recalled by (Webber et al., 2009), "*The dispersion of releases of hazardous fluids through from loss of containment to dilution below hazardous levels can be simply considered as comprising two stages: source term formation and atmospheric dispersion…The earlier source-dominated behaviour has received comparatively less attention both theoretically and experimentally, though its importance in the overall release process is widely recognised. This is probably due to the very complex and variable behaviour during this stage and the difficulty of obtaining definitive experimental data close to the source*".

(Prince, 1983), (Thyer, 2003), (Luketa-Hanlin, 2006) and (Cleaver et al., 2007) identified that most of the experiments previously carried out involved spills of LNG and other cryogens onto water and the data for land spills was very sparse. More recent experiments on pressurized LNG releases from 2 and 3" flexible hoses have been done by Shell to quantify dispersion distances (Betteridge, 2015) , but no measurement of droplet size were made on LNG releases. Most models currently used to predict this parameter are based on correlations deduced from experiments usually involving LPG (Witlox et al., 2013) or non-cryogenic fluids, such as cyclohexane or water (Johnson et al., 1999). As underlined by (Webber et al., 2009), "*with no information about droplet sizes it is not possible to predict any fall-out of liquid from the jet*".

To fill these gaps, the SPARCLING JIP was launched by TOTAL, AIR LIQUIDE, SHELL, GRTgaz & INERIS. The goal of the project was to produce high-quality experimental data on the size distribution and velocities of the LNG droplets using a dual PDA (Phase Doppler Anemometer), following the pressurised release of LNG. The test programme was managed and run by INERIS at their test site at Verneuil-en-Halatte on behalf of the members of the JIP.

The paper describes in detail the testing bench and test protocol, as well as the lessons learned from the use of the bench. The occurrence of rain-out is then discussed.

2. Description of the experimental setup

2.1 Testing site

All releases were performed on the INERIS Fire Platform. Fig. 1 shows an aerial view of this Fire Platform with the testing zone encircled in red. This zone is about 30 m long, is free of obstacles. A fence is positioned on each side of this testing zone to channel the cloud out of the Fire Platform in the last stage of its dispersion. To perform measurements in the close field of the release even when the weather is bad (rain, snow), a tent is positioned above the first meters of the release. The position of the tent (supports, lateral walls) were checked before each test to make sure they did not affect the release.

Fig. 1. *Aerial view of the testing site*

2.2 Bench description

Fig. 2 shows a schematic view of the experimental bench.

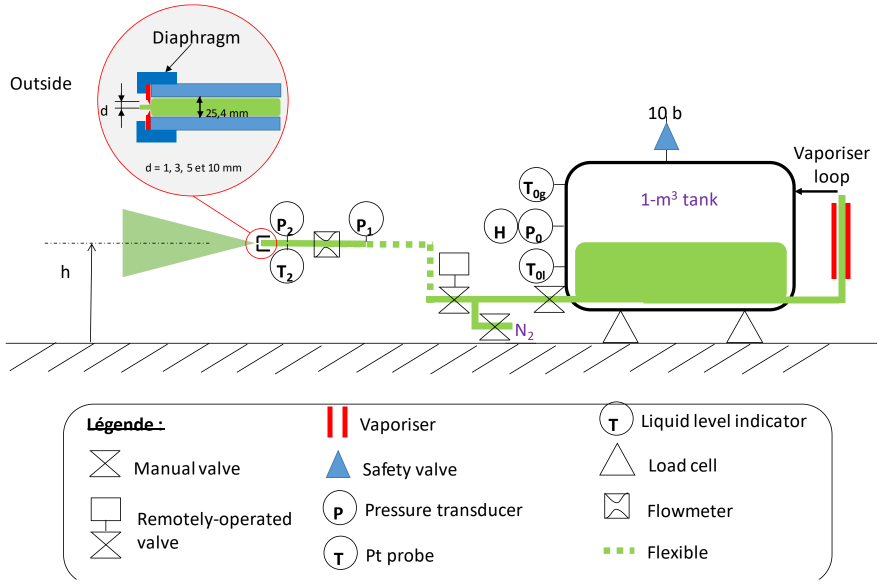

Fig. 2. *Schematic view of the experimental bench*

2.2.1 Storage tank

The tank used to store the cryogenic fluid is cylindrical with its axis of revolution positioned vertically (see Fig. 3). It has a double-wall structure with the inner and outer envelopes respectively made in SA-240 3014 and SA-516 Gr.70 materials. Thermal insulation between these two envelopes was ensured by a vacuum-packed Perlite layer. The volume of the internal envelope is 995 L and its diameter 1150 mm. This storage can operate at temperatures varying between – 190°C and + 50°C. It was equipped with a safety valve set to open when the internal pressure exceeds 10 bar. In addition, to control the internal pressure during the release, the tank was fitted with a vaporiser. The system works (1) by bleeding part of the liquid phase from the tank, (2) by circulating this liquid within the vaporiser and (3) by injecting the vapour hence produced into the top part of the tank.

(Focus on the vaporiser)

Fig. 3. *Storage tank for the cryogenic fluid*

2.2.2 *Release line*

The release line has a nominal diameter of 1'' and an approximate length of 9 m. By following the flow direction from the storage tank, this line was made up of three main elements:

- a remotely-operated valve;
- a flexible hose;
- a release assembly.

Every effort was made to reduce the friction pressure drop within the flow and the heat losses with the environment. This was achieved:

- by keeping the cross-sectional area of the line as constant as possible. There is hardly no singularity in the line;
- by installing already-insulated components and, if not possible, by coating these components with a 13-mm thick layer of Insulfrax S.

The flexible hose was 7.7 m long. It was composed of two tubes made in Inox 304 L. Thermal insulation between these two tubes was provided by vacuum. Fig. 4 shows a picture of the release assembly. This assembly was built using a flowmeter, a 1'' pipe and a diaphragm that could be screwed at the end of the pipe. Different diaphragms, each of them featuring a given opening (2, 3, 5, 7 or 9 mm), were used.

Fig. 4. *Release assembly*

2.3 *Instrumentation*

2.3.1 *Tank*

When delivered, the tank was already instrumented with:

- a pressure transducer (P0 on Fig. 2);
- two Pt100 probes, one located on top of the tank to assess the gaseous phase temperature and the other in the bottom of the tank for the liquid phase (respectively T0g and T0l);
- a level indicator (H). This parameter is determined by measuring the hydrostatic pressure of the cryogenic fluid column. This provided the first method for assessing the released mass flow rate.

In addition, the tank is placed on 4 load cells with a maximal load capacity of 3000 kg. This weight measurement was the second method for assessing the released mass flow rate.

2.3.2 Release line

A Coriolis flowmeter was used, OPTIMASS 6400 C and it was capable of operating at a maximal pressure of 40 bar with a temperature in the range – 200°C / + 40°C (see Fig. 5). Therefore, this apparatus was used as a third method to measure the released mass flow rate. The flowmeter also gave a measure of the volumetric mass and of the fluid temperature since it was equipped with a Pt500 probe. It is worth precising that this possibility of measuring the volumetric mass drove INERIS to install the flowmeter as far as possible from the tank. This was intended to control the flow phase as close as possible to the nozzle orifice.

Fig. 5. *Flowmeter Optimass 6400 C*

Pressure was also measured upstream of the flowmeter and nozzle orifice (respectively P1 and P2 on Fig. 2). Piezoresistive pressure sensors were used (range: 0 – 14 barg). It must be pointed out that these sensors were not particularly suitable for cryogenic applications. To prevent their sensitive membrane from being damaged due to direct coldness exposure, the measurement was not made in situ (i.e. directly in the cryogenic flow) but remotely. This was done by positioning the sensor at the end of a small tube tapped into the pipe of the release assembly. This tube was about 100 cm long (see Fig. 6).

Fig. 6. *Picture of the pressure transducer upstream of the flowmeter*

The temperature was also measured upstream of the nozzle orifice (see T2 on Fig. 2) by means of a Pt100 probe. This probe was flush mounted with the flow to avoid any unduly friction pressure loss. Knowing the pressure and temperature just upstream of the nozzle orifice, it was possible to apply the Bernoulli equation to estimate the mass flow rate, assuming that the outflow was all liquid. This was the fourth method for assessing the released mass flow rate.

2.3.2 PDA system

PDA (Phase Doppler Anemometry) is an optical technique that allows measuring the size and velocity of a moving spherical particle. The PDA technique is based upon on Doppler shift of the light reflected (and/or refracted) from a moving seeding particle. When two laser beams of the same wavelength intersect, they will interfere in the volume of intersection and form fringes. When the particle will move through this volume (also called the measuring volume), the intensity of the light reflected (and/or refracted) by this particle will vary with a frequency proportional to its velocity. Only one photodetector is required to calculate the velocity. Yet the determination of the droplet size requires two photodetectors. Indeed, when the particle passes through the measuring volume, both photodetectors will receive a reflected (and/or refracted) light of the same frequency, but the phases of the two lights will vary with the angular position of the detectors. This phase difference is function of the particle diameter.

The main requirement of the SPARCLING project, a Dual-PDA was used to measure two components of velocity and the diameter of the droplets in the close field of the cryogenic release. The Dual-PDA combines two conventional PDAs. Fig. 7 shows the positioning of the two lenses of the Dual-PDA in the close field of the cryogenic release.

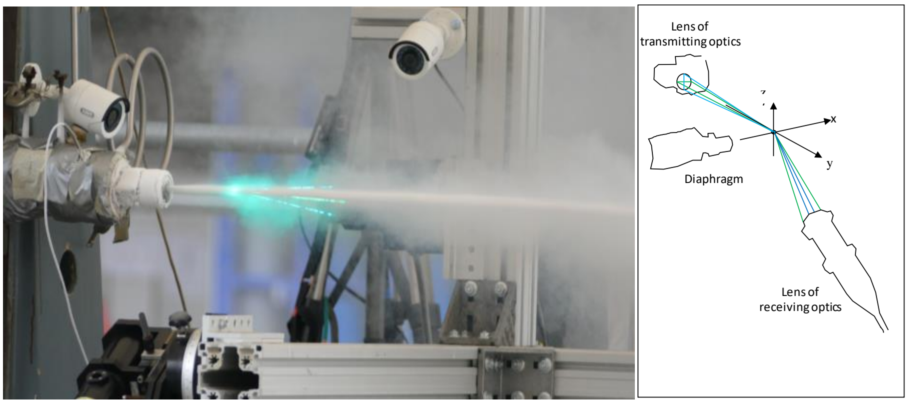

Fig. 7. *Picture of the Dual-PDA*

The two lenses were positioned on a 3-D displacement system that was remotely controlled. This system allowed the PDA measuring volume to be moved to the desired locations within the cryogenic release. The cartography performed for most of the tests is presented in Fig. 8. The x-axis represents the axis along the release direction. The z-axis is vertical.

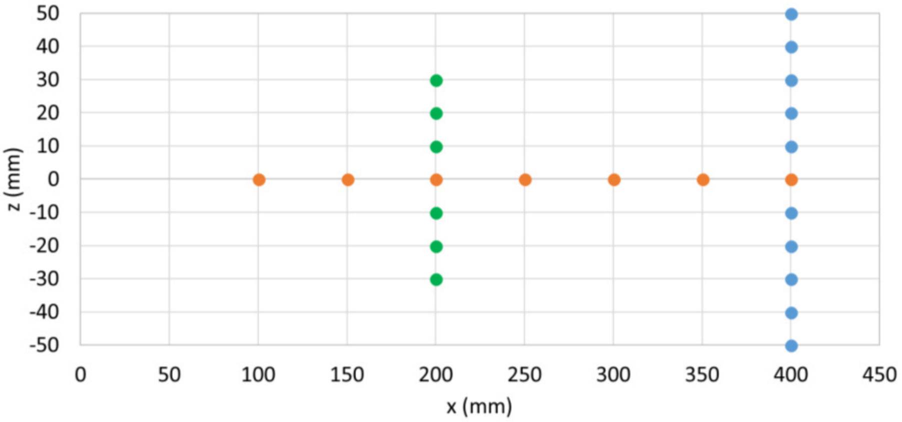

Fig. 8. *PDA cartography used*

3. Experimental campaign

3.1 Testing matrix

18 tests were performed, 16 with LNG and 2 with liquid nitrogen (LN_2). The influence of the orifice diameter and storage conditions were studied. The tests conditions are presented Table 1.

Table 1: *Tests parameters*

Parameter	**Value**
Product	LNG (16) and LN_2 (2)
Orifice diameter	2, 3, 5, 7 and 9 mm
Pressure	Atmospheric to 9 bara
Temperature	Saturated and subcooled (up to 8 bara)

The LNG composition was not available for each delivery. When it was, this composition came from the LNG terminal and was therefore representative of the composition before its transportation. To cope with this lack of information, a method was developed to measure the composition. It entailed allowing a small liquid leak from the bottom of the vessel. The released LNG was diluted with air and homogenized by the air flow. The concentration of methane, ethane and propane were then continuously measured using FTIR spectroscopy after the vaporization of the LNG. The composition was then obtained using a time integration. As expected, it was found that the proportion of methane decreased during the lifetime of a single delivery of LNG as it gradually warmed up.

3.2 Test protocol

The steps of the test protocol developed are described below.

1. Tank conditions setting

Before the test, the pressure and temperature inside the storage tank had to be set considering the test conditions. The LNG storage vessel did not have a heating element, therefore to increase the temperature of the LNG to the targeted value, it was necessary to wait for the LNG temperature to increase as a natural consequence of heat exchange with the environment. To decrease the temperature to the targeted value the pressure was decreased until it reached the corresponding saturation pressure. In the initial experiments, gas was released from the top of the tank at once, which required waiting for the conditions inside the tank to stabilize. Later, to ensure that the product is at equilibrium, a pressure control device was connected to the tank to maintain constantly the pressure inside the tank to the targeted value.

For subcooled releases the vaporiser was used to reach the targeted pressure just before the test.

2. Release line cooling

LN_2 was used to cool down the line before the test. This was achieved by connecting a LN_2 450 L tank to the release line as close as possible of the tank. The line was then cooled until the temperature at the orifice dropped below the liquid phase temperature in the tank.

3. LNG (or LN_2) release test

As soon as the line was cooled, the LNG (or LN_2) release was started. The vaporiser was then manually set.

- For subcooled releases it was set to maintain the pressure steady.
- For saturated releases it was set to slowly increase the pressure inside the tank until the release at the orifice became a liquid.

As soon as the release was liquid the PDA measurements were started. The criterion for the release to be liquid was that the void fraction was less than 10%. The void fraction is calculated using the density measured by the flowmeter:

$$\rho_{flowmeter} = x.\rho_{gas} + (1 - x).\rho_{liquid}$$

where:

- $\rho_{flowmeter}$ is the density measured by the flowmeter,
- ρ_{gas} is the vapour density of the LNG,
- ρ_{liquid} is the liquid density of the LNG,
- x is the void fraction.

Usually the void fraction was found to be zero when the PDA measurements were triggered (especially for subcooled releases). The density measured by the flowmeter reached a plateau when it was fully liquid. It was interesting to note that the release became quiet suddenly when the release turned into liquid. It is then possible to hear the transition on the test site. As soon as the PDA measurement was over, the release was stopped and the release line was purged with LN_2.

4. Rainout

Rainout was only observed for the two tests that were performed with a pressure as close as possible to atmospheric pressure:

- Test 8b (LNG, 7 mm, 1.5 bara)
- Test 15 (LN_2, 7 mm, 1.5 bara)

The release pressures and orifice diameters are the same for the 2 tests (7 mm, 1.5 bar) but the products are different. For higher pressure, even for subcooled tests, no rainout was observed. It is worth noting that for smaller orifice diameters (≤3 mm) it was not possible to reach 100% liquid release for this pressure condition.

A screenshot of the IR camera and a picture of the jet are presented on Fig. 9 for test 8b. It gives a clear view of the jet and reveals the rain-out. The mark left by the rain-out after the release was centered about 3,5 m ahead from the release point. It was about 2 m long and 1 m wide.

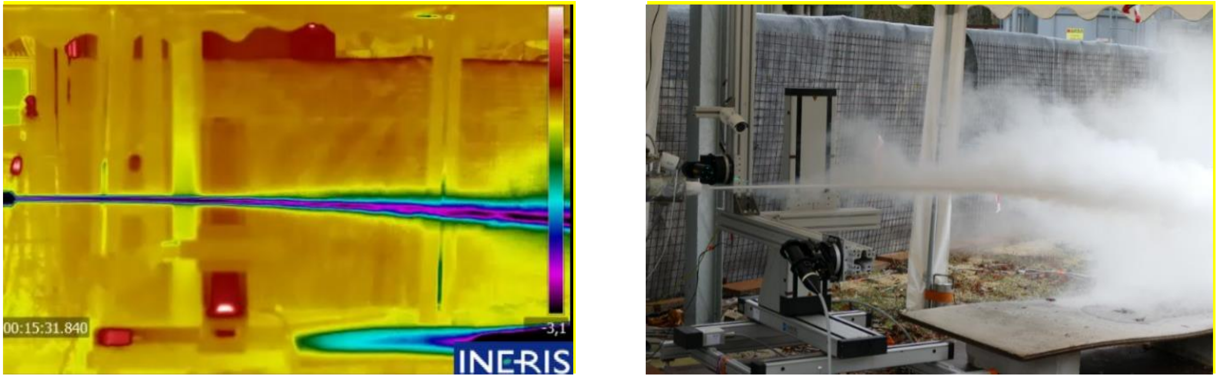

Fig. 9. *Test 8b - Rainout evidence. IR screenshot (left), visible (right).*

Fig. 10 and Fig. 11 present some pictures revealing the rain-out observed during test 15. The mark left by the rain-out after the release was centered about 3.5 m ahead from the release point. It was about 2.5 m long and 1 m wide.

Fig. 10. *Test 15 - Pictures revealing rain-out during the release*

Fig. 11. *Test 15 - Pictures showing the rain-out marks after the end of the release*

5. Conclusions

The SPARCLING JIP was launched by TOTAL, AIR LIQUIDE, SHELL, GRTgaz & INERIS. The goal of the project was to produce high-quality experimental data on the size distribution and velocities of the LNG droplets using a dual PDA (Phase Doppler Anemometer), following the pressurised release of LNG. The test programme was managed and run by INERIS at their test site at Verneuil-en-Halatte.

The testing bench and test protocol developed is presented in detail. 16 pressurised releases of LNG and 2 of LN_2 were performed. The different release conditions parameters are presented below.

Parameter	**Value**
Orifice diameter	2, 3, 5, 7 and 9 mm
Pressure	Atmospheric to 9 bara
Temperature	Saturated and subcooled (up to 8 bara)

Rainout was observed only for the 2 tests that were performed with a pressure as close as possible of the atmospheric pressure:

- Test 8b (LNG, 7 mm, 1.5 bara)
- Test 15 (LN_2, 7 mm, 1.5 bara)

For higher pressure, even for subcooled tests, no rainout was observed.

The analysis of the experimental data produced, especially those with the PDA, is an ongoing work. The influence of the release conditions on the droplets size is being investigated.

References

Betteridge S., “Experimental studies of LNG dispersion”, 55th UKELG One Day Discussion Meeting on Dispersion and Consequences of LNG Releases, 2016

Cleaver P., Johnson M. and Ho B., “A summary of some experimental data on LNG safety”, Journal of Hazardous Material, 140, pp 429-438, 2007.

Johnson D. W. and Woodward J. L., “RELEASE: A model with data to predict aerosol rainout in accidental releases”. Center for Chemical Process Safety of the AICHE., March 1998, ISBN 978-0-8169-0745-8.

Luketa-Hanlin A., “A review of large-scale LNG spills: experiments and modelling”, J. Hazard. Mater, 132, pp 119-140, 2006.

Prince A.J., “Details and Results of spill experiments of cryogenic liquids onto land and water”, Joint HSE and UKAEA, SRD Report, HSE/SRD/PD058/WP4.

Thyer A.M., “Review of data on spreading and vaporisation of cryogenic liquid spills”, J. Hazard. Mater., 99, pp 31-40, 2003.

Webber D.M., Gant S.E., Irvings M.J. and Jagger S.F.,” LNG source term models for hazard analysis: a review of the state-of-the-art and an approach to model assessment”, Health & Safety Laboratory, 2009.

Henk W.M. Witlox, Mike Harper, Two-phase jet releases, droplet dispersion and rainout I. Overview and model validation, Journal of Loss Prevention in the Process Industries, Volume 26, Issue 3, 2013, Pages 453-461.

Proceedings of the 13th Symposium International Symposium
on Hazards, Prevention and Mitigation of Industrial Explosions
DOI: 10.7795/810.20200724

Hydrocarbon aerosol explosion: towards hazardous area classification

Stephanie El - Zahlanieh [a], Augustin Charvet[a] , Alexis Vignes [b] , Benoit Tribouilloy [b] & Olivier Dufaud [a]

[a] Université de Lorraine, CNRS, LRGP, F-54000 Nancy, France
[b] INERIS, Accidental Risks Division, Parc Technologique ALATA, Verneuil-en-Halatte, France

E-mail: olivier.dufaud@univ-lorraine.fr

Abstract

Assessing the risk of formation and ignition of explosive atmosphere (ATEX) associated with the generation of a flammable aerosol is required by European ATEX regulation. However, such risk analysis sometimes proves difficult because of the lack of tools correlating the dispersion conditions of a mist cloud with its flammability and explosivity. This work aims to define objective criteria for assessing the risk related to the hydrocarbon mists explosion within the framework of hazardous area classification. Different fluids were selected according to their industrial interest and their physicochemical characteristics; here, a volatile solvent (ethanol), a lubricating oil and kerosene. Existing experimental set-ups as the 20L sphere and the modified Hartmann tube were adapted to determine the flammability and explosion severity of sprays and mists. A sensitivity study was performed as a function of influential parameters such as the fluid composition, the generation mode, the pressure and the turbulence. The time evolution of droplet size distributions was determined by in situ laser diffraction and APS spectrometry (aerodynamic diameter measurement). The flammability study was focused on the determination of the Lower Explosive Limit and the Minimum Ignition Energy. In parallel, the study of the flame propagation in a semi-open tube was used to qualify the effects of the turbulence/combustion interactions. Some tests were also performed in a standard 20L explosion sphere to determine the maximum explosion pressure and maximum rate of pressure rise of specific mists. Finally, these experimental results could serve as an input for reactive CFD simulations aiming at predicting the consequences of aerosol explosions. From a practical point of view, this study should provide decision support tools for hazardous area classification, especially for the definition of the flammable cloud extent on the basis of a percentage of the lower explosive limit.

Keywords: *aerosol, spray, explosion, flame propagation, hazardous area classification*

1. Introduction

In 2009, an incident survey of the Health and Safety Laboratory, reported 37 mist incidents, among which 9 explosions lead to 29 fatalities (Santon, 2009). In most of the cases, the incidents arose from the ignition of mist or spray at a temperature near or below the liquids' flash point. Similar to what is proposed by Eckhoff (2016), the terms "spray" or "mist" are used arbitrarily in this text as they are both relevant terms in explosion incidents. Sprays are usually produced mechanically from a spray nozzle or an accidental leak whereas mists are clouds of liquid droplets of smaller size, usually generated by condensation of a supersaturated liquid.

Ten years later, Lees et al. (2019) showed that 10% of reported releases on offshore oil and gas installations in the UK involved sprays or mists. Such cases demonstrate the need to acquire full knowledge and ability in order to classify hazardous mist explosive areas. This classification is currently well established for gas and dust explosions (Gant, 2013). Several regulations (Directives 2014/34/EU and 1999/92 CE), standards (e.g. EN 14034 series), and industry codes of practice are already available for use in industries in order to study the conditions of dispersion and explosions of flammable gas or dust releases; however, such standards for mists have not been completely set yet. In fact, some guides such as EI15 underline this lack of knowledge. It is noted in the guide's model code of safe practice on area classification (Energy Institute, 2015) that "there is little knowledge on the formation of flammable mists and the appropriate extents of associated hazardous areas". Also, two pages of qualitative guidance on flammable mists are embodied in the latest version of the relevant IEC standard (IEC 60079-10-1; IEC 2015) (Gant el al., 2016).

Identifying factors and criteria of liquid handling, as well as determining fluids' safety parameters will be helpful to assess the flammability and explosion severity of hydrocarbon mists. The ability to determine the latter, is a stepping stone to the classification of hazardous areas (HAC) and to the improvement of current ATEX standards and regulatory provisions concerning liquid aerosols.

However, the subject of mist ignition/explosion has been under study and investigation for over seventy years. Eichhorn (1955) has notably published an article in the Petroleum Refiner entitled "Careful! Mist can explode". He has introduced the concept that aerosols of flammable liquids at temperatures well below their flash points can explode. Eckhoff (1995) has also written a review of spray and mist explosions, and has defined some conditions under which any combustible liquid aerosol can be explosive. The possibility of a mist ignition/explosion has been studied in an HSE report by Gant (2013). Such a report provides a large background on the physics of spark ignition and flame propagation, the fundamentals of droplet dynamics and pressurized liquid releases, as well as mitigation measures.

Scientifically studying mist formation, ignition and explosion is an object of study that can also be presented as an intermediate case between gases and dusts. The behaviour of liquid sprays or mists differs from that of gases as several phenomena, such as light diffraction, fuel evaporation (Ballal et Lefebvre, 1981) or flame stretching by impacting droplets, occur for mists but not for gases. For instance, Eckhoff (2016) describes explosive mist clouds as less stable than explosive dust clouds due to the collisions between droplets, which gives rise to coalescence and the transformation to fewer and larger droplets. The increase of size leads to a greater sedimentation velocity and perhaps more turbulence and flame disturbance.

By addressing the unknowns and studying the differences between mist, gas and dust explosions, guidelines can be provided to industrialists as well as standardised methods for HAC of liquid mists. In order to illustrate this approach, this paper will be focused on common liquid fuels of different physical properties (ethanol, kerosene, and a lubricating oil). Their dispersion, using spray nozzles, ignition and explosion will be studied to highlight their different behaviours and stress their specificities, notably with regard to gas explosion.

2. Materials and Methods

At first, the fuels selected will be presented according to their industrial interest and their physical properties. The second step encompasses the description of the generation mode and the characterisation of mist properties such as the droplet size distribution and concentration. The third step focuses mainly on the determination of the explosion severity parameters of such mists, i.e. the maximum deflagration pressure P_{max}, the maximum rate of pressure rise dP/dt_{max} and the laminar flame velocity.

2.1 Fuel Selection

A fluid classification system was developed by the Health and Safety Executive (Burrell and Gant, 2017), which divided fluids of industrial interest into four release classes based on their flashpoint and their ease of atomisation represented by the Ohnesorge number Oh. This paper deals with three fuels representing three releases classes.

Ethanol was chosen due to its growing use in our daily lives as an engine fuel, fuel additive for automobiles or marine sector. With the increase of the demand for ethanol-fuel blends, its production and transport increases, which requires to manage the fire and explosion risks. Beside to its physical properties, ethanol was also selected as a calibration fluid as numerous studies were already performed to characterised the ignition sensitivity and explosion severity of its vapours and mists (Timothée, 2017).

Tests were performed on Kerosene, which represents the HSE Release Class I. Kerosene is a combustible hydrocarbon liquid derived from petroleum. It is widely used as a jet fuel and also has a range of household applications. Kerosene mist explosions have been frequently reported throughout the years; for example: an explosion in 1886, UK due to a leak of Russian kerosene as a form of mist ignited by a naked light (Santon, 2009). Various studies, on different types of kerosene, can be found in literature; HSE, for instance, have performed ignition tests on spray releases of Jet A1 kerosene with an ignition source of 1 Joule electric spark and a release pressure ranging from 5 to 20 bars. (Bettis et al. 2017; Vukadinovic et al. 2013; Wu, 2016)

Another fluid tested is the Mobil DTE Heavy Medium VG68, which exemplifies HSE Release Class III. This fluid is a hydraulic oil also tested by HSE at various release pressures. It is a lubricant designed for applications where long lubricant service life is required; such as in gas turbines (Dufaud et al. 2015) and hydraulic pumps.

Table 1 shows some physical properties from the literature for the three liquids tested. Other properties, such as heat capacity and surface tension will be characterised experimentally for these fuels and several others (iso-octane, methyl butanoate as a biodiesel surrogate …) in further studies.

Table 1: *Physical properties of different fluids*

	Ethanol*	**Mobil DTE Heavy Medium****	**Kerosene (jet A1/A) ♣**
Flashpoint (°C)	13	223	> 38°C
Density (kg.m^{-3})	794	860	775 – 840 (ASTM D7566)
Viscosity (cSt)	1.2 (at 20°C)	64.3 (at 40°C)	8
Surface tension (kg.s^{-2})	0.023	0.033♦	0.024
Flammability limits (%)	3.3 - 19	0.9 - 7.0 %	0.7 - 7%
LTL/ UTL (lower temperature limit/ upper temperature limit)	9 - 44°C	-	38 - 83 °C
HSE Release Class♠	Class I or 'unclassified' (Oh ratio ≥ 2, Flashpoint < 125°C)	Class III (Oh ratio < 2, Flashpoint ≥ 125°C)	Class I (Oh ratio ≥ 2, Flashpoint < 125°C)

* (Brandes and Frobese, 2009), ** MSDS from ExxonMobil, ♣ MSDS from Honeywell Fluka, ♦ (Mouzakitis and Giles, 2017), ♠ (Burrell and Gant, 2017)

It should be noted that the influence of temperature on the physical properties of these fluids should always be taken into consideration. As such, the temperature of the fluid may significantly influence its viscosity, hence introducing notable uncertainties in the assessment of risks. In this study, fluids were used at ambient temperatures in order to have a preliminary idea of their behaviour.

2.2 *Mist properties*

Characterising and predicting the behaviour of mist is a challenge. For instance, a rupture or leak in a vessel, due to damage or corrosion, has a very uneven shape and occurs in different conditions. To better predict the behaviour of mist, tests should be performed in the closest conditions possible to that of industrial accidents. Nevertheless, the experimental procedure proposed to characterise the ignition sensitivity and explosion severity of such mists should also be standardized, so that the results can be compared and that generic safety measures can be proposed. It should be noted that characterising properly the mist before its ignition is of great importance since the safety parameters of mists are highly affected by their droplet size distribution, concentration and turbulence (Gant et al., 2013).

2.2.1 *Mist generation mode*

There exist several ways to generate a mist/spray, such as: condensation of saturated vapour, agitation and splashing, air stripping, and spray discharge from a pressurised liquid reservoir. For this paper, mist was generated by using siphon/gravity-fed spray set-ups as shown in Figure 1. These dispersion systems comprise a Venturi junction with 2 inlets: an air inlet and a liquid inlet.

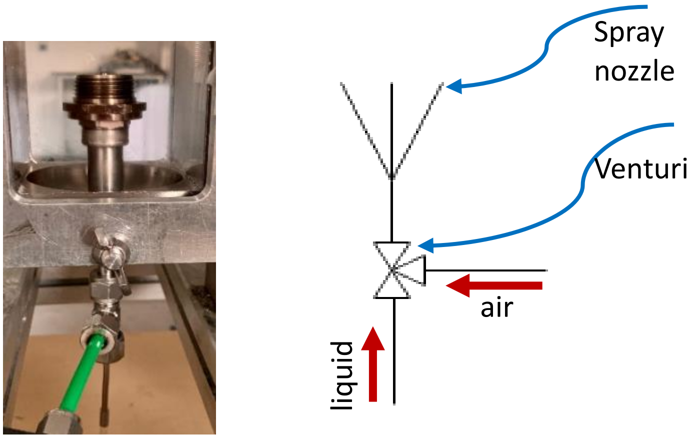

Fig. 1. *Example of a spray nozzle and focus on the generation by Venturi effect*

Mist spray generation was investigated as a function of the relevant parameters stated by Kooij et al. (2018): nozzle type, spraying pressure and fluid properties. The nozzle type was varied as well as the type of air cap (varying between a flat orifice and a round one with different diameters) installed on top of each nozzle. The results presented in this paper in section 3.1 are that of experiments performed using two different sets of air atomizing nozzles from Spraying Systems Co comprising one fluid cap of reference 1650-DF combined with two different air caps: a circular jet air cap (reference: 64-SS-S – Cap 1) and a flat jet air cap (reference: SS.CO-73420 – Cap 2).In addition to the type of nozzle and air cap, the air pressure was varied between 1 and 6 bars according to the maximum pressure tolerance of each type of nozzle.

2.2.2 *Droplet size distribution (DSD)*

The size of a droplet can be defined by a competition between fluid inertia and surface tension (Kooij et al. 2018). The time evolution of droplet size distributions was determined by in situ laser diffraction (Helos/KR-Vario by Sympatec GmbH) and will be supplemented by APS spectrometry (aerodynamic diameter measurement) to quantify the submicron droplets.

The Helos laser sensor is designed to analyse extended aerosols' and sprays' droplet size using 5 high-resolution measuring ranges from 0.5µm to 3500µm. The apparatus measures directly through the transparent walls (borosilicate glass) of the flame propagation tube with adjustable heights (see Figure 2.a.). The R3 lens was used as it covers a range of droplet diameters from 0.5/0.9µm to 175µm.

The acquisition frequency was set at 2 distributions per millisecond. The measurements given by the sensor are notably the volume diameter d_{10}, d_{50}, d_{90} and the $D_{3,2}$ (Sauter Mean Diameter, SMD). In order to have an approximation of the DSD near the kernel spark produced by an ignition source described in more details in Section 2.3, the height of the sensor was adjusted to a height corresponding to the location of the ignition source.

The flame propagation tube is a 1 m long hermetic tube with a 0.07 m^2 cross section. As it can be seen in Figure 2.b the spray nozzle was set at the bottom of the tube. The latter was then closed and equipped by a safety release valve at its upper end.

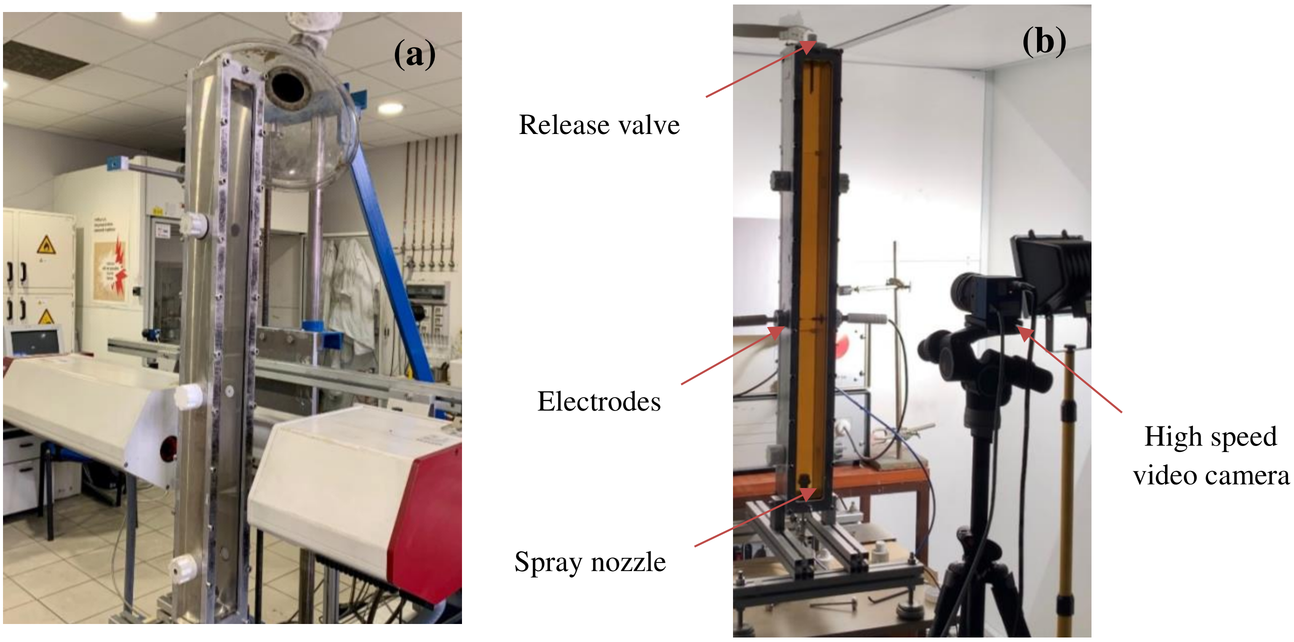

Fig. 2. *(a) Laser diffraction sensor Helos positioned to determine the DSD in the tube, (b)Flame propagation tube equipped with a spray nozzle, positioned for explosion tests*

2.3 Flammability and explosion severity

Both an opened-vessel, i.e. the flame propagation tube (Figure 2b) and a closed-vessel, i.e. the 20 L explosion sphere (Figure 3) were alternately used to test the flammability and explosivity of the mists.

2.3.1. Flame propagation tube

The tests performed on the flame propagation tube enable to evaluate the flammability characteristics of aerosols, i.e. their minimum ignition energies (MIE) and their lower explosivity limits (LEL) as well as an intrinsic safety parameter, the laminar flame speed. This paper focuses primarily on the determination of the laminar flame propagation speed as its knowledge will be useful to calibrate the test procedure and equipment.

To disperse the mist into the tube, KSEP 310 unit (Cesana AG) is used. This gas control unit is usually connected to the 0.6 L dust storage chamber of the standardised 20 L explosion chamber (EN 14034) for controlling the injection of compressed air into the explosion chamber. It was used as an inlet to the spray nozzle in order to have a fixed duration of mist generation. The generation duration is approximately 8.7 seconds, i.e. the pressurized air is injected for about 8.7 seconds simultaneously triggering mist formation by the Venturi effect. To ignite the mists, an ignition system comprised of two fixed electrodes was connected to a KSEP 320 unit, which is a high-voltage transformer supplying power for ignition. An additional control system designed by LRGP is used to control the spark persistence time of the KSEP 320. The latter generates a power of 225 W; therefore, the ignition energy depends on the persistence time of the spark. For example, to give a supply of 20 J, the spark will be generated non-stop for a duration of 89 ms. It should be noted that the sedimentation of the droplets should be taken into consideration, hence, using Stokes law for flows of Re < 1, the ignition duration must be chosen according to the terminal velocity.

Several measurements were carried out for the three tested fluids with an ignition energy of 20 J and an ignition delay time t_v ranging from 100 ms to 1000 ms, i.e. the time between the mist generation and ignition. A new generation unit is currently designed to adjust the various generation and ignition parameters as requested.

After ignition, flame propagations were recorded using a high-speed video camera (the MotionBlitz EoSens mini2 camera which has a resolution of 1,696 x 1,710 pixels and is equipped with an AF NIKKOR 35mm f/2D lens from Nikon). The recorded videos were treated and analysed in order to calculate the laminar flame speed. The procedure used to analyse the flame kernel growth and extract the flame front position and surface area as a function of time is described by Cuervo et al. (2017). Then, assuming a linear relationship between the flame spatial velocity and the Karlovitz factor (stretching factor), the laminar burning velocity S_{u0} can be estimated (Cuervo et al., 2017).

2.3.2. 20L explosion sphere

As for the study of mist ignitability, the standard 20L sphere was used to determine the mis explosion severity (Figure 3.a). The spray nozzle was installed on the bottom entry port of the sphere which is a modification added to the original sphere (Figure 3.b). Before injecting the fuel/air mixture, the sphere was partially vacuumed, so that, when the mist is injected, an atmospheric pressure would be attained. The generation time is adjusted as a function of the desired fuel concentration. The ignition source used for this test was a pyrotechnical chemical igniter of an energy of 100J. The igniters were actuated electrically by a low-voltage electrical signal sent by a KSEP 310 unit (Cesana AG). The ignition delay time can be varied, but it was set to zero for this study, which means that the ignition occurs immediately after the end of the mist injection. It should be noticed that, under industrial conditions, fluids as lube oil or hydraulic oil can be generated at high temperatures, which is not the case here. Two piezoelectric pressure transducers were connected to a KSEP 332 unit to measure the pressure as a function of time. Then, the pressure was acquired in the software package KSEP 7.1 which is also used to allow a safe operation of the test equipment and an optimum evaluation of the explosion results.

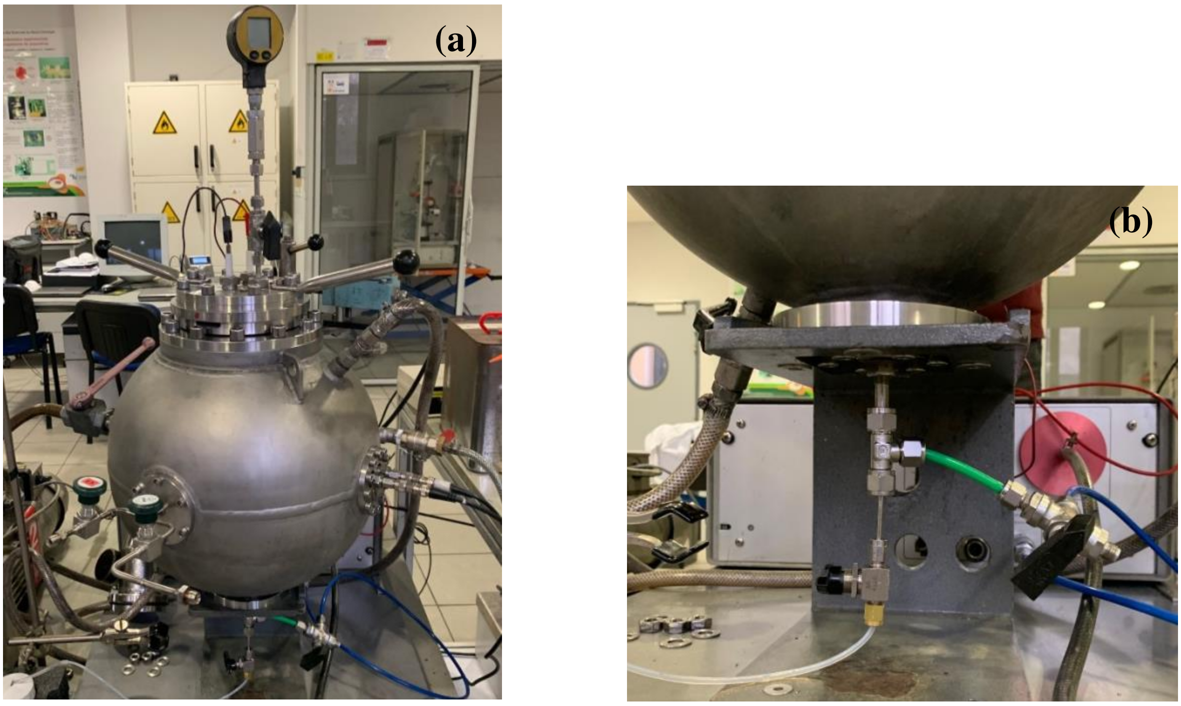

Fig. 3. *(a) the standardized 20L explosion sphere, (b)the nozzle connections to the 20L sphere*

Moreover, in order to visualise the flame propagation and the droplet size distribution of mists in the 20L sphere, several modifications were applied to a similar vessel (Santandrea et al., 2020). Four windows were added to another sphere, as well as a vent. Further studies will show results of tests performed on the open sphere.

3. Results and discussion

3.1 Droplet size distribution and flow rate

As it can be seen in Figure 4, the DSD of the Ethanol mist, generated with Cap 2, can be considered as unimodal with a maximum at about 3.39 µm, which is the Sauter Mean Diameter (SMD). A small second peak appears at about 8-9µm which may be due to the coalescence of some droplets during either the generation phase or the sedimentation phase.

Granulometry tests were also performed on Kerosene and on Mobil DTE Heavy-Medium VG68 and similar distributions were obtained. The DSDs of Kerosene and Mobil oil both showed a unimodal distribution with SMDs of 4.2µm and 2.8µm, respectively.

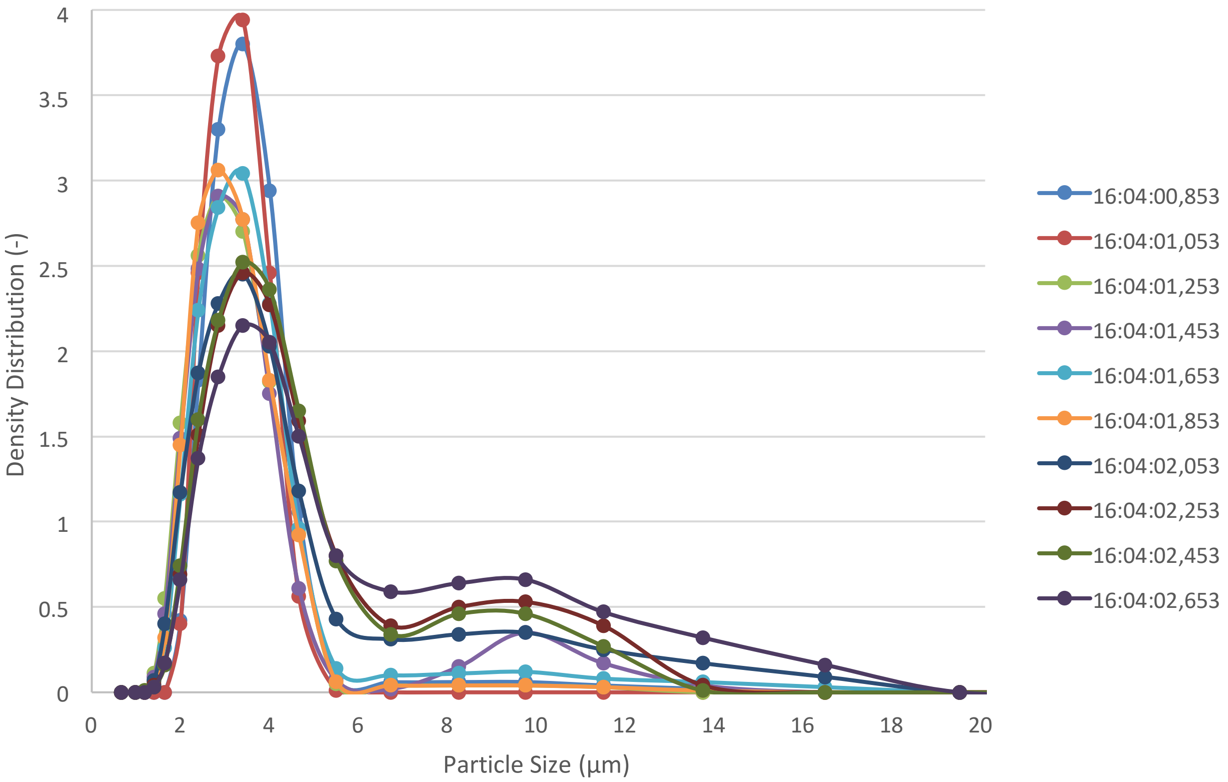

Fig. 4. *Droplet size volume/mass distribution of Ethanol mist generated at P = 4bars (Cap 2) – Time step: 200 ms*

The values shown in Figure 4 represent the droplet size evolution over a 1.8 s period after generation with an interval of 200ms.. It should be stressed that these results were obtained in a semi-open tube. However, even though ignition occurs directly after injection in the sphere, it is possible that a similar DSD could be obtained, neglecting the effect of liquid perspiration on the walls of the tube. Such DSD was also tested in the modified 20 L open sphere for the three fluids generated using various combinations of fluid and air caps with increasing orifice diameters. Moreover, in order to have a clearer look at the particle size distribution of the generated mists right before explosion, and in order to test the evolution of the distribution as a function of time, DSD measurements were also performed after 8.7s of generation. Results showed the presence of droplets of larger size (around 50µm) indicating the presence of coalescence. Moreover, nozzle sets with a larger orifice diameter demonstrated a similar distribution behaviour but with larger values of SMD.

Table 2 shows that the influences of the nozzle and of air pressure on the droplet size distribution of an ethanol mist remain weak. Similar trends were observed for the lubricating oil and kerosene. However, it appears that the flow rate, determined by collecting and weighing the generated mist, changes as a function of the nozzle and ranges from 0.06 mL.s^{-1} to 0.15 mL.s^{-1} for cap 2 and cap 1, respectively.

Table 2: *Mean diameter d_{50} (µm) of ethanol mist after 700 ms generation*

Air pressure (bar)	Cap 1	Cap 2
1	8.0	6.3
4	6.8	7.2

Being able to independently control the flow and DSD is an essential point of any study on the risks associated with mists. This will allow to conduct a sensitivity study on the following parameters: the fuel equivalent ratio, the droplet size distribution and the chemical nature of the fuel, and to determine their impact on the ignition sensitivity and the explosion severity of hydrocarbon mists. In this paper, only the latter parameter will be developed.

3.2 Flame propagation speed

Preliminary tests were performed on ethanol mists in order to calibrate the procedure of laminar flame velocity determination. Experiments were carried out with cap 2 and an ignition energy of 20 J.

First, it should be noted that ignition occurred for both ethanol and kerosene mists with an energy of 20 J, whereas no ignition was observed for the hydraulic oil Mobil DTE Heavy-Medium VG68, even by increasing the ignition energy up to 200 J. This absence of ignition is due to the very high minimum ignition energy of the lubricating oil. Such conclusion is consistent with the results obtained by Dufaud et al. (2015), who studied mists from a lubricating oil used in gas turbines and found that no ignition occurred for energies lower than 2000 J. The flame propagations observed for ethanol and kerosene were expected as their minimum ignition energies are 0.23 and 0.65 mJ (Bane et al., 2013), respectively. It should be noted that the latter parameters are valid for gaseous fuel/air mixtures and do not correspond to the MIE of liquid aerosols. Nevertheless, it would seem that the MIE of a mist is always greater than the MIE of an equivalent gaseous mixture of vapour and air (Gant, 2013); the experimental demonstration of this assertion is part of the objectives of this study. Finally, the high ignition sensitivity of kerosene is not surprising as numerous experiments previously performed on this fuel showed that ignition was possible whatever the injection pressures tested (Bettis et al., 2017).

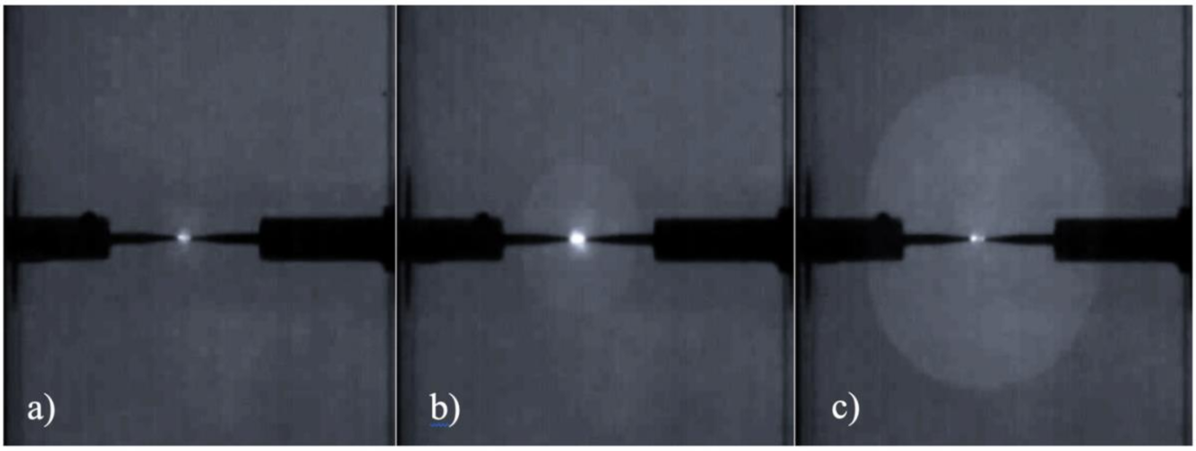

Fig. 5. *Flame propagation in an ethanol mist - ignition energy: 20 J and 500 ms; a) 0.5 ms; b) 4 ms; c) 8 ms*

DOI: 10.7795/810.20200724

The videos recorded by the high-speed video camera were analysed for both ethanol and kerosene at various ignition delay time. The tests carried out at low turbulence levels, i.e. at high t_v, lead to the more stable flame kernels and to ellipsoidal flame surfaces, which makes it easier to determine the normalized increase of flame surface area or flame stretch K. Figure 5 shows the flame propagation in an ethanol mist for a t_v of 500 ms, which corresponds to a root-mean-square velocity u_{rms} lower than 0.1 m.s-1 (Cuervo, 2015). In this case, spatial flame speeds up to 5 m.s-1 were recorded.

Considering the ellipsoidal flame deformation and assuming a linear relationship between the burning velocity and the Karlovitz factor K (Clavin, 1985; Markstein, 1964), laminar burning velocities of 57 cm.s-1 and 31 cm.s-1 were obtained at t_v 500 ms for ethanol and kerosene mists, respectively. It should be underlined that the using such linear relationship requires validating numerous assumptions, such as an unwrinkled, infinitesimally thin and weakly stretched flame, which is impossible in practice, especially when dealing with biphasic combustion.

The results found for the ethanol mist are consistent with literature values, i.e. Liao et al. (2007) found a laminar burning velocity between 54 and 58 cm.s-1 for mixtures of gaseous ethanol and air at elevated temperatures. Bradley et al. (2014) found a laminar speed between 28 and 35 cm.s-1 for ethanol aerosols, with DSD ranging from 5 to 30 µm.

As for ethanol, tests were mainly performed on kerosene vapours, i.e. at least at a temperature of 400K in gas phase. Vukadinovic et al. (2013) found an approximate of 82 cm.s-1 for the laminar flame velocity of kerosene, whereas Wu (2016) obtained velocities ranging between 57 and 78 cm.s-1 for temperatures ranging from 400 to 473K. The experimental value determined for kerosene mist is then much lower than the literature values. Obviously, this difference can be due to the nature of the fuel (liquid droplets or vapour), but before validating this assertion, tests should be performed at various fuel equivalent ratio.

3.3 *Explosion severity*

As presented in section 2.3.2, the 20 L sphere has been modified in order to allow the generation of mists and a test procedure has been validated. Preliminary tests performed on ethanol mists show that maximum explosion pressure reaches 8.8 bar, whereas the dP/dt_{max} is 1553 bar.s-1 (Figure 6).

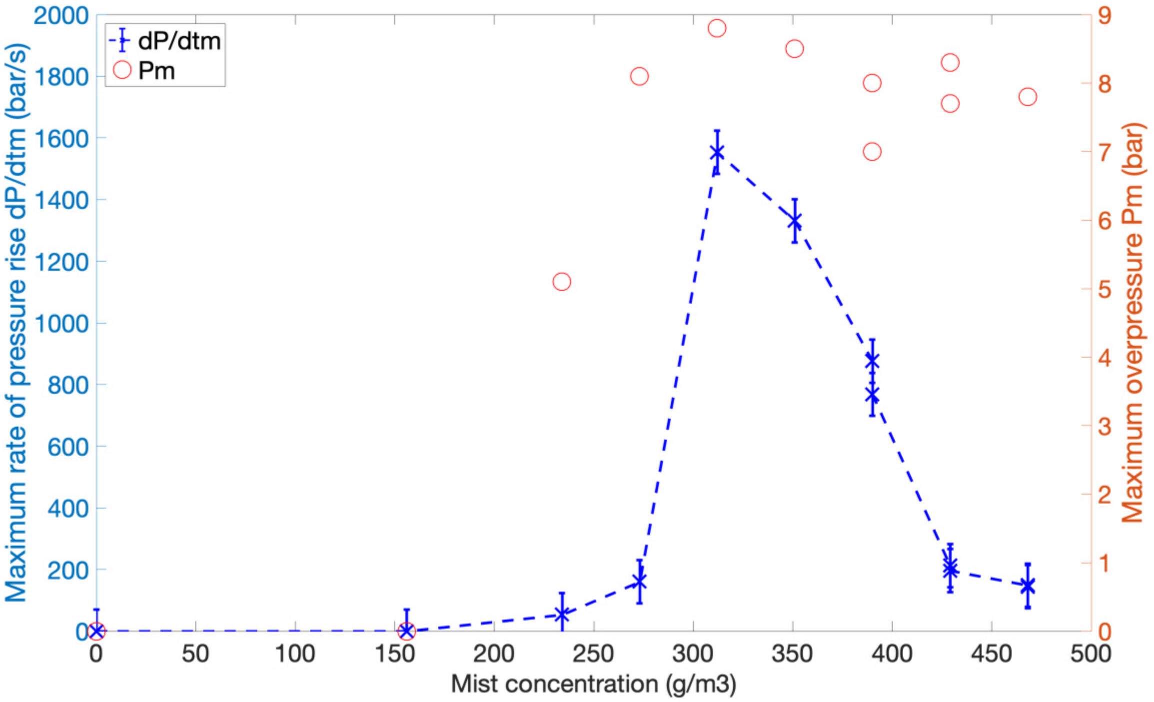

Fig. 6. *Evolution of the maximum overpressure and rate of pressure rise in the 20L sphere as a function of the ethanol mist concentration (7 bars injection pressure, ignition energy: 100 J, t_v: 0)*

If the evolution of the maximum overpressure as a function of the mist concentration is consistent with the explosive behavior of a combustible gas or a dust, showing a lower explosive limit around 160 $g.m^{-3}$ followed by an increase and then a decrease of P_m, the evolution of the dP/dt_m parameter is apparently unusual with a sharp peak around 300 $g.m^{-3}$. A direct visualization of the flame propagation in the open tube (3.2) at different fuel equivalence ratio will help to better interpret the previous evolutions.

In addition, it should be kept in mind that the maximum adiabatic pressure for ethanol vapour is 9.5 bar and that a maximum pressure of 7.7 bar was reached in a 5 L explosion sphere for fuel equivalent ratio of 1 at 293K (Cammarota et al., 2012), which is in rather good agreement with the preliminary tests. Following the first validation tests, it is now necessary to conduct a sensitivity study including the droplet size distribution, the initial turbulence of the mist and the chemical nature of the fuel.

Concerning the latter parameter, Table 3 shows a comparison between the explosivity parameters of ethanol and kerosene mist generated under similar injection conditions. It should be stressed that the ignition energy of kerosene had to be increased as no ignition occurred with 100 J chemical igniters in the sphere, which is different from the results obtained in the flame propagation tube with a different injection set. If the maximum overpressures of kerosene and ethanol mists are rather similar, the maximum rate of pressure rise is of kerosene is much lower than that of ethanol, as well as it sensitivity to ignition.

Table 3: *Explosion severity parameters of ethanol and kerosene mists (7 bars injection pressure, ignition energy: 100 J for ethanol, 5000 J for kerosene, t_v: 0 ms)*

Explosion severity of mists	**Ethanol**	**Kerosene**
P_{max} (bar)	8.8	2.1
dP/dt_{max} ($bar.s^{-1}$)	1553	249

4. Conclusions

This preliminary study aims at developing and proposing new tests procedures in order to determine the ignition sensitivity and explosion severity of hydrocarbon mists. These tests should be performed on simple or/and standard equipment which can be found in industries or laboratories, in order to be able to compare the results and propose adequate solutions for explosion risk management.

Experiments carried out on ethanol, kerosene and lubricating oil have allowed to validate the procedures and setups. Additional tests are currently performed on a larger range of DSD using different types of nozzles and different fuels (iso-octane, methyl butanoate). A sensitivity study is in progress in order to highlight the influences of the fuel equivalent ratio, the DSD, the initial turbulence and the chemical nature of the fuel.

From a practical point of view, this study should provide decision support tools for hazardous area classification. In particular, it should assess if the definition of the flammable cloud extent on the basis of a percentage of the assumed LEL of the vapours is valid or not and should provide simple models linking the mists generation and ignition to the droplet size distribution and fluid properties. These preliminary tests demonstrate that classical standard set-ups, as the 20L sphere, can be modified and used to quantitatively assess the explosion severity of hydrocarbon mists, but also put forward an alternative way based on the estimation of the unstretched/laminar flame velocity of such compounds. Finally, thanks to different nozzles, caps and operating conditions, the impact of the DSD of the flame propagation and explosion severity will be highlighted.

Acknowledgements

The authors gratefully acknowledge the financial support of the French Ministry for the Ecological and Solidary Transition and The French Ministry for Higher Education and Research.

References

Ballal, D.R. & Lefebvre, A.H. (1981). A general model of spark ignition for gaseous and liquid fuel-air mixtures. *Symposium (International) on Combustion, Eighteenth Symposium on Combustion* 18, 1737–1746.

Bane, S.P.M., Ziegler, J.L., Boettcher, P.A., Coronel, S.A. & Shepherd, J.E. (2013). Experimental investigation of spark ignition energy in kerosene, hexane, and hydrogen. *Journal of Loss Prevention in the Process Industries*, 26(2): 290-294.

Bettis, R., Burrell, G., Gant, S. & Coldrick, S. (2017). *Area classification for oil mists - final report of a Joint Industry Project.* RR1107 HSL report, Buxton, UK.

Bradley, D., Lawes, M., Liao, S. & Saat, A. (2014). Laminar mass burning and entrainment velocities and flame instabilities of i-octane, ethanol and hydrous ethanol/air aerosols. *Combustion and Flame*, 161: 1620–1632.

Brandes, E. & Frobese, D.H. (2009). Ethanol-containing automotive fuels - A safety concept for petrol stations in Germany, *Forschung auf dem Gebiete des Ingenieurwesens*, 73(1): 25-32.

Burrell, G. & Gant, S. (2017). *Liquid classification for flammable mists*. RR1108 HSL report, Buxton, UK.

Cammarota, F., Di Benedetto, A., Di Sarli, V. & Salzano, E. (2012). The effect of hydrogen addition on the explosion of ethanol/air mixtures, *Chemical Engineering Transactions*, 26: 405-410.

Clavin, P. (1985). Dynamic behavior of premixed flame fronts in laminar and turbulent flows. *Progress in Energy and Combustion Science*, 11: 1–59.

Cuervo, N. (2015). *Influences of turbulence and combustion regimes on explosions of gas-dust hydrid mixtures* (PhD Thesis). The University of Lorraine, France (in English).

Cuervo, N., Dufaud, O. & Perrin, L. (2017). Determination of the burning velocity of gas/dust hybrid mixtures. *Process Safety and Environmental Protection*, 109: 704–715.

Dufaud, O., Charvet, A., Mougel, G., Molière, M., Luthun, S., Brunello, D., Perrin, L., Delimoges, S. & Couchot, M. (2015). Generation, Characterization and Ignition of Lube Oil Mists, *ASME Turbo Expo 2015, Combustion, Fuels and Emissions*. ASME, Montreal, Canada, Paper No. GT2015-43524, p. V04BT04A039.

Eckhoff, R.K. (2016). *Explosion Hazards in the Process Industries*. Gulf Professional Publishing.

Eckhoff, R.K. (1995). Generation, ignition, combustion and explosion of sprays and mists of flammable liquids in air: a literature survey, *Offshore Technology Report OTN 95 260*, Health and Safety Executive, Bootle, UK.

Eichhorn, J. (1955). Careful! Mist can explode. *Petroleum Refiner*, 34 (11): 194-196.

Gant, S. (2013). *Generation of flammable mists from high flashpoint fluids: Literature review*. Research Report RR980, HSL report, Buxton, UK.

Gant, S., Bettis, R., Coldrick, S., Burrell, G., Santon, R., Fullam, B., Hill, H., Mouzakitis, K., Giles, A. & Bowen, P. (2016). Area classification of flammable mists: summary of joint-industry project findings, *Symposium series n°161*, IChemE Hazards 26, 24-26 May, Edinburgh, UK.

Kooij, S., Sijs, R., Denn, M.M., Villermaux, E. &Bonn, D. (2018). What determines the drop size in sprays?, *Phys. Rev.* X 8, 031019.

Lees, P., Gant, S., Bettis, R., Vignes, A., Lacome, J.L. & Dufaud, O. (2019). Review of recent incidents involving flammable mists. *Symposium series n°166,* IChemE Hazards 29 Conference, Birmingham, UK.

Liao, S.Y., Jiang, D.M., Huang, Z.H., Zeng, K. & Cheng, Q. (2007). Determination of the laminar burning velocities for mixtures of ethanol and air at elevated temperatures. *Applied Thermal Engineering*, 27, 374–380.

Markstein, G.H., (1964). *Non-Steady Flame Propagation*. Pergamon, New York.

Mouzakitis, K. & Giles, A. (2017). *Experimental investigation of oil mist explosion hazards*, Research Report RR1109, HSL report, Buxton, UK.

Santandrea, A., Gavard, M., Pacault, S., Vignes, A., Perrin, L. & Dufaud, O. (2020). 'Knock on nanocellulose': Approaching the laminar burning velocity of powder-air flames. *Process Safety and Environmental Protection*, 134: 247–259.

Santon, R.C. (2009). Mist fires and explosions - an incident survey. *Symposium series,* IChemE Hazards XXI Symposium & Workshop, Manchester, UK.

Thimothée, R. (2017) *Experimental characterization of a laminar flame propagation in a two-phase medium (aerosol) in microgravity conditions*, PhD thesis, Université d'Orléans, France (in French).

Vukadinovic, V., Habisreuther, P. & Zarzalis, N. (2013). Influence of pressure and temperature on laminar burning velocity and Markstein number of kerosene Jet A-1: Experimental and numerical study. *Fuel*, 111: 401–410.

Wu, Y. (2016). *Experimental investigation of laminar flame speeds of kerosene fuel and second generation biofuels in elevated conditions of pressure and preheat temperature*, PhD thesis, INSA de Rouen, France (in English).

DOI: 10.7795/810.20200724

On an Assessment of Dust Explosion Dynamics in the Standard 20-l Sphere

Zdzisław Dyduch
Experimantal Mine Barbara of Central Mining Institute, Mikołów, Poland
E-mail: *zdyduch@gig.eu*

Abstract

Dust explosion dynamics, usually expressed by the parameter K_{St}, plays a key role in an assessment of a dust explosion hazard in industrial installations, particularly in design and choice of explosion protection systems. In practice most often the K_{St} value is assessed in the standard 20-l sphere, e.g. Siwek sphere. Explosion dynamics strongly depends on turbulence intensity in dust/air mixture. Measurements of the turbulence in the standard 20-l sphere (Dahoe (2000), Dyduch et al. (2016)) revealed its fast decay in the time interval when a typical explosion reaches highest intensity – maximum value of $(dp/dt)_{max}$. Therefore when the explosion develops fast, maximum rate of pressure rise occurs at higher turbulence intensity and vice versa, longer time to reach $(dp/dt)_{max}$ should result in conditions of lower turbulence intensity.

In the paper the magnitude of the effect is assessed. Its influence on K_{St} value of different dusts was checked based on experimental results obtained in the standard 20-l sphere. At first, reference level of the turbulence intensity was chosen. Then K_{St} values of several dusts were adjusted to the reference conditions. The results indicate that in extreme cases (very long or very short time to $(dp/dt)_{max}$) the corrected values of K_{St} differ significantly from those obtained the standard way.

Keywords: *dust explosion, explosion dynamics, standard test, industrial explosions*

Nomenclature

K_{St}	Value of maximum rate of pressure rise in each pressure-time history scaled with cube root of the volume
K_{St}^{corr}	Corrected K_{St} value
$K_{St\ max}$	Actual value as defined in the Standards
l_t	Turbulence length scale
l_t^{ref}	Reference value of l_t
S_t	Turbulent burning velocity
S_l	Laminar burning velocity
t_{ex}	Time when $\left(\frac{dp}{dt}\right)_{max}$ is reached
t_v	Ignition delay time
u_{rms}	Root-mean-square velocity
u_{rms}^{ref}	Reference value of u_{rms}
δ	Flame thickness

1 Introduction

Maximum rate of pressure rise converted, if necessary to $K_{St\ max}$, is among the most important explosion severity parameters used in the process safety assessment of dust explosion hazard in industry. Subsequently knowledge of $K_{St\ max}$ parameter is essential for adequate design of a protective method to assure proper control of the dust explosion Pekalski (2005). Standards either in Europe EN-14034-2 (2011) or in North America ASTM-E-1226 (2019) define the test methodology. The recommended apparatus for the test is the standard 1 m^3 vessel but other apparatus are allowed as long as their usage lead to adequate results. In practice vessels of smaller volume are used most often. Such apparatus requires less sample mass per test, it is simpler in operation and therefore allows larger number of test performed. The most widely used is the 20-l sphere previously produced by Kühner A.G. and now by TÜV SÜD Schweiz, so called Siwek sphere. However the $K_{St\ max}$ assessed in the sphere not always agree with the results from the standard 1 m^3 vessel (Proust, 2007). Amongst factors that contribute to the difference is turbulence intensity created inside the test vessel after dispersion of a sample and different rate of the turbulence decay. Measurements of turbulence intensity published by several authors show fast turbulence decay in the 20-l sphere, in the time interval when the dynamics of a typical dust explosion is highest. As the value of $K_{St\ max}$ strongly depends on the turbulence intensity the moment when the explosion dynamics is highest may influence the test results.

In the paper the magnitude of the effect is assessed. Its influence on $K_{St\ max}$ value of different dusts was checked based on experimental results obtained in the standard 20-l sphere. At first, reference level of the turbulence intensity was chosen. Then a method of $K_{St\ max}$ correction was described. Finally $K_{St\ max}$ values of several dusts were adjusted to the reference conditions and compared with the original ones.

2 Correction method

To assess how the explosion dynamics, expressed by K_{St}, is influenced by different turbulence intensity a relationship between K_{St} and turbulence parameters is required. First of all a suitable form of K_{St} dependence on turbulence parameters should be chosen. Then a reference level of turbulence to which all results will be adjusted ought to be defined. Finally, the method of the correction should be developed.

2.1 Suitable form of K_{St} dependence on turbulence

To find a relationship between K_{St} and turbulence parameters it is useful to recall that maximum rate of pressure rise $(dp/dt)_{max}$ and therefore K_{St} is proportional to turbulent burning velocity S_t. Many forms of a relationship that bonds S_t with turbulence parameters have been proposed. Following discussion presented by Proust (2017) the relationship in the form

$$\frac{S_t}{S_l} = 0.6\left(\frac{u_{rms}}{S_l}\right)^{0.75}\left(\frac{l_t}{\delta}\right)^{0.25} \tag{1}$$

has been chosen. Among other advantages the relationship has a form suitable for the correction purposes required here.

2.2 Reference value of turbulence

To perform the adjustment a reference turbulence intensity is required. The reference conditions should reflect the standard conditions, e.i. should lead to correct, well established values of $K_{St\ max}$. There is a general agreement that $K_{St\ max}$ value for Lycopodium clavatum is about 150 bar m/s. This result was obtained both in the standard $1m^3$ vessel and 20-l sphere. Therefore data for Lycopodium has been used to define the reference turbulence intensity in the standard sphere. The data is plotted in Figure 1.

In Figure 1 and further figures three plots are aggregated. The upper plot presents "raw" results directly obtained from the tests. The plot in the middle shows root-mean-square velocities that cor-

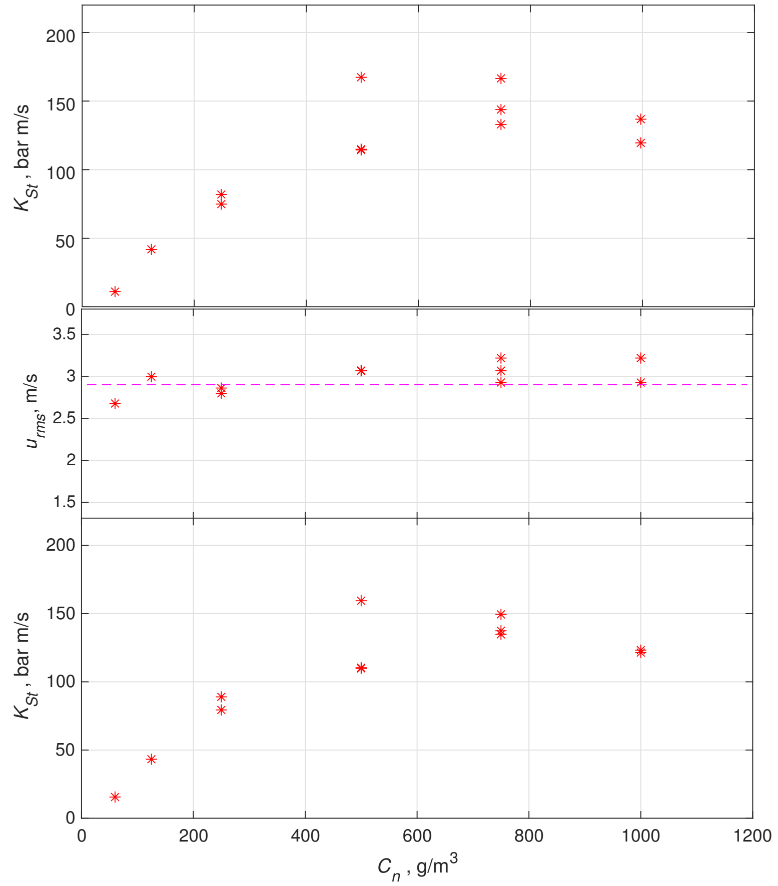

***Fig. 1**: Choice of u_{rms} reference value based on Lycopodium data. $u_{rms}^{ref} = 2.9m/s$*

responds to the time when $(dp/dt)_{max}$ was reached in each test. To simplify further description that time will be identified as t_{ex}. u_{rms} was calculated from the fit to experimental data published in Dahoe (2000). In the lower plot corrected results are shown.

Presented results indicate that time t_{ex} is practically the same for all dust concentrations tested. The average value of the reference root-mean-square velocity is $u_{rms}^{ref} = 2.9m/s$. This value was used in all adjustments done in this paper.

2.3 Correction method

To perform the adjustment to the reference conditions the procedure presented by Dyduch (2013) was applied. The procedure was modified by replacing the Bray's equation with equation (1). The corrected K_{St} value was calculated the following way:

$$K_{St}^{corr} = K_{St} \left(\frac{u_{rms}^{ref}}{u_{rms}} \right)^{0.75} \left(\frac{l_t^{ref}}{l_t} \right)^{0.25} \tag{2}$$

where root-mean-square velocities u_{rms} and turbulence length scales l_t, both reference and actual, were calculated from empirical relationships developed by Dahoe (2000).

Before the main evaluation the performance of the adjustment method was verified. In Figure 2 plots present results of the adjustment method applied to Niacin data obtained in different conditions. The tests were performed in standard conditions (t_v = 60 ms) with use of Rebound nozzle and Mushroom

DOI: 10.7795/810.20200724

nozzle (Dahoe, 2000). Additionally, tests were carried out with Mushroom nozzle and extended ignition delay time $t_v = 80$ ms.

Generally, the correction works satisfactory. Only one point from the tests with longer ignition delay time for the dust concentration 1000 g/m^3 differs significantly from the other two. The rest of the experimental points represent practically the same dependence K_{St} vs. C_n.

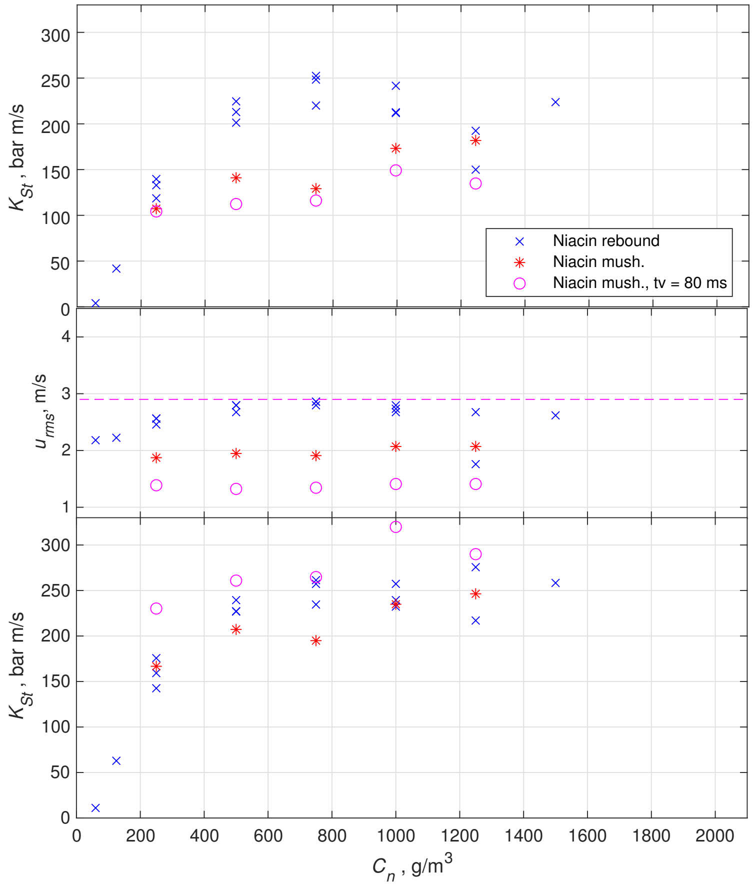

Fig. 2*: Performance of the correction method*

Results in Figure 2 allow to accept the adjustment procedure for the purpose of the intended assessment. Other experimental results, not presented here, also confirm its correctness.

3 Results and discussion

The adjustment procedure was then applied to four sets of experimental results. The sets were chosen such a way that two of them are characterized by very short time t_{ex}, much shorter than typical time and two other by rather large value of t_{ex}. For each set of results, before and after correction, $K_{St\ max}$ value was calculated following the standard method given in European EN-14034-2 (2011) and ASTM-E-1226 (2019) standards.

3.1 Early explosion development

As short t_{ex} time dust an obvious choice is sulphur dust. It is well known that sulphur dust is very easy to ignite and has very small value of minimum ignition energy of a dust cloud MIE. Results of application of the adjustment procedure to results obtained in 20-l sphere for sulphur dust are presented in Figure 3, together with a set of results for Embonian - dust of similar properties.

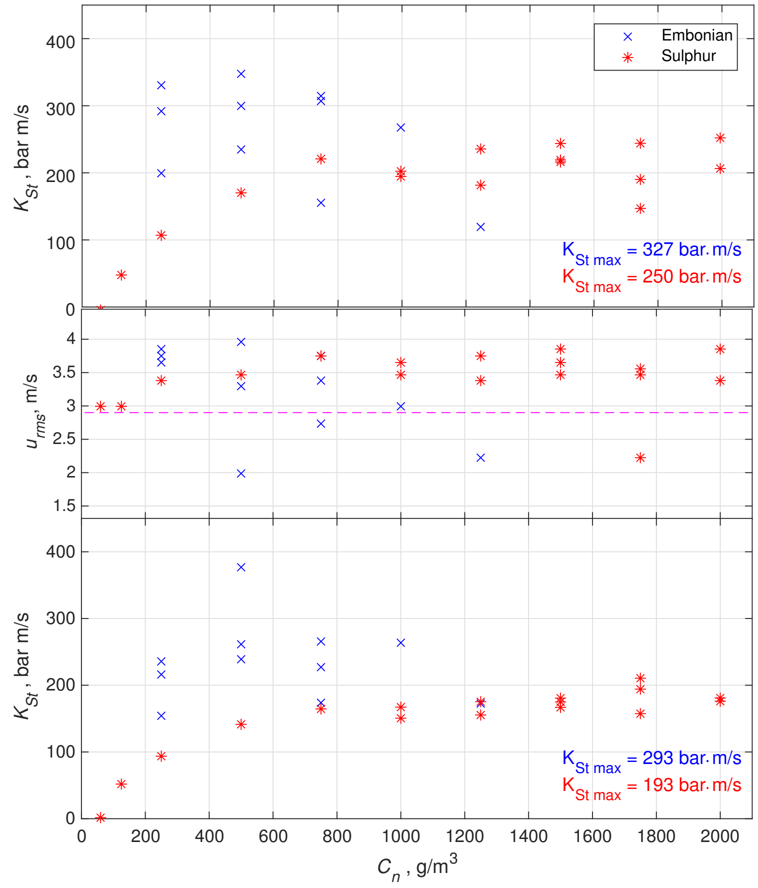

***Fig. 3**: The correction applied to Sulfur and Embonian dusts*

For both dusts the correction has changed the results significantly. The dusts have changed explosibility class. Embonian, according the original results, was St3 class dust while after correction it belongs to St2 class. Similarly, suplhur dust being in the middle of St2 class after correction is in St1 class.

3.2 Delayed explosion development

As dusts with time t_{ex} much longer than typical values diaper fibers and sawdust were chosen. As can be seen in the middle plot in Figure 4 in all tests of the dusts the values of u_{rms} are smaller than 2 m/s, significantly less than u_{rms}^{ref}.

Standard tests result may lead to the conclusion that both dusts may be regarded as marginally explosible dusts. Correction to the standard turbulence conditions causes significant increase of their K_{St} values although they are still dusts of moderate explosive properties. Interestingly, after the adjustment the explosion dynamics of sawdust is assessed as higher than diaper fibers while the conclusion from the original data is opposite.

4 Conclusions

Measurements of turbulence intensity published by several author show fast turbulence decay in the time interval when the dynamics of a typical dust explosion is highest. An application of the correction procedure designed to adjust the results of tests in the standard 20-l sphere to the same, reference conditions of turbulence in case of some dusts leads to significant changes of the original results. When turbulence intensity, expressed by root-mean-square velocity, is large at the moment when the explosion reaches maximal dynamics (dp/dt_{max} and K_{St}) the corrected values of those parameters

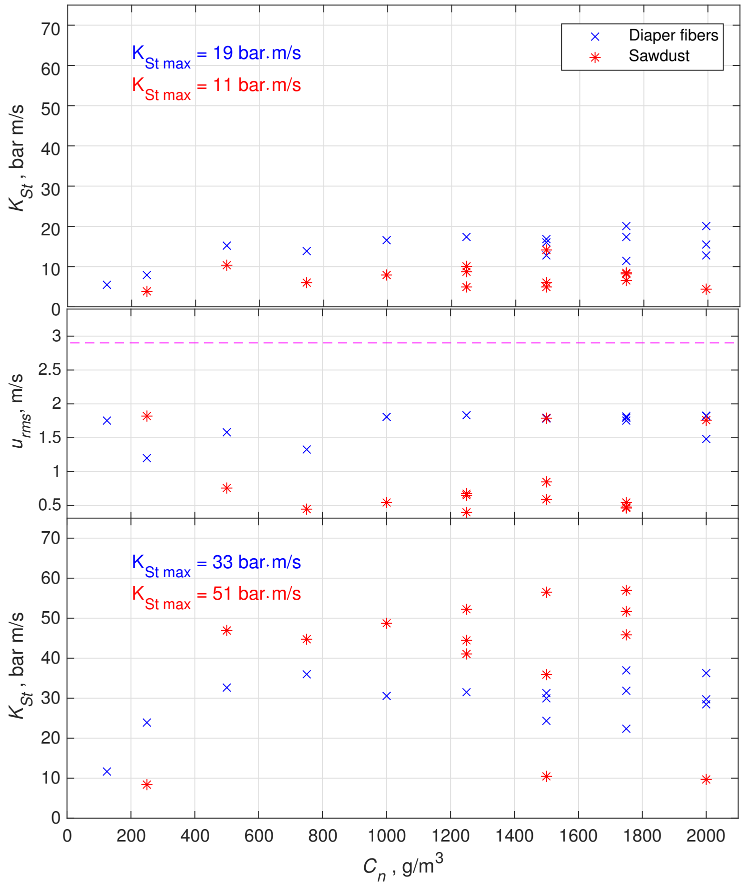

***Fig. 4**: The correction applied to Sawdust and Diapers fibers*

may be significantly smaller. And vice versa, longer time to reach $(dp/dt)_{max}$, at a moment when turbulence intensity is smaller may result in considerable underestimation of that parameter. The results indicate that in extreme cases (very long or very short time to $(dp/dt)_{max}$) the corrected values of $K_{St\ max}$ differ significantly from those obtained the standard way. Such a difference may pose a real hazard.

As $K_{St\ max}$ value is a fundamental parameter used to design protection systems intended to mitigate dust explosion consequences in industrial installations underestimation of $K_{St\ max}$ value lead to hazardous situations. In practice quite often protection systems are not design for exact $K_{St\ max}$ value of the dust present in the installation but rather for dusts of a certain explosibility class. Most often it is for dusts of St1 class. If in standard test in 20-l sphere assessed $K_{St\ max}$ value is near the upper border of an explosibility class and the dust explosions reach maximal dynamics after unusually long time, the protection system designed for that class may be insufficient.

For the evaluation described in the paper the sets of extreme times t_{ex} have been chosen, i.e. with largest and smallest values of that parameter obtained in many tests performed at Experimental Mine *Barbara*. Usually, the values are well inside the range defined by the dusts chosen, somewhere in the middle.

In Figure 5 the scaled differences of K_{St} values for randomly chosen dusts are plotted as a function of the difference $t_{ex} - t_{ex}^{ref}$. Most of the points lay in the range of small differences. Nevertheless it seems a good practice to control the parameter t_{ex} in tests in the standard 20-l sphere.

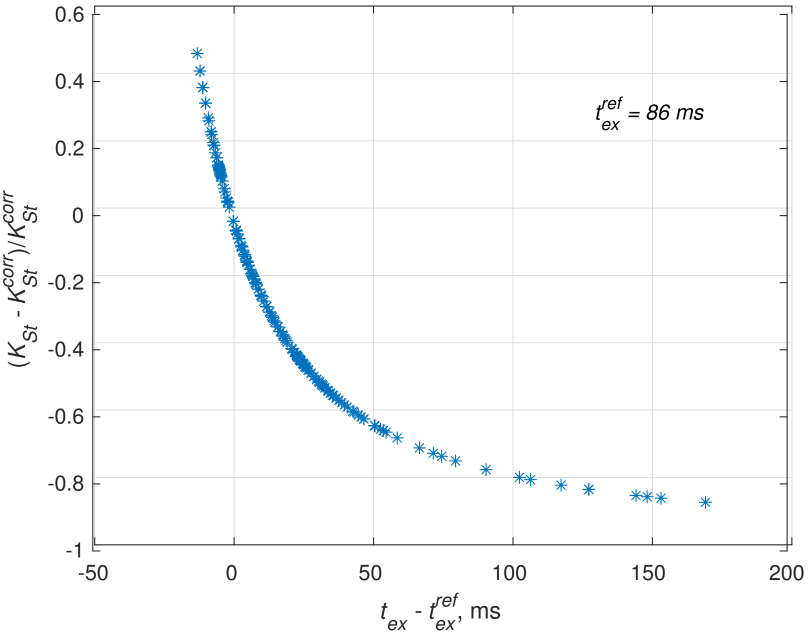

Fig. 5: *Scaled difference of K_{St} values as a function of $t_{ex} - t_{ex}^{ref}$*

References

ASTM-E-1226 (2019). *Standard test method for pressure and rate of pressure rise for combustible dusts.*

Dahoe, A. F. (2000). *Dust Explosions: a Study of Flame Propagation.* Delft University of Technology, Delft, ph.d. thesis edition.

Dyduch, Z. Pekalski, A. (2013). *Methods for more accurate determination of explosion severity parameters.* Journal of Loss Prevention in the Process Industries, 26:1002–1007.

Dyduch, Z., Toman, A., Adamus, W. (2016). *Measurements of turbulence intensity in the standard $1m^3$ vessel.* Journal of Loss Prevention in the Process Industries, 40:180–187.

EN-14034-2 (2011). *Determination of explosion characteristics of dust clouds – Part 2: Determination of the maximum rate of explosion pressure rise $(dp/dt)_{max}$ of dust clouds.*

Pekalski, A. Zevenbergen, J. L. S. P. H. (2005). *A review of explosion prevention and protection systems suitable as ultimate layer of protection in chemical process installations.* Process Safety and Environmental Protection Journal, 83(B1):1–17.

Proust, Ch. Accorsi, A. D. L. (2007). *Measuring the violence of dust explosions with the 20-l sphere and with the standard iso 1 m^3 vessel. systematic comparison and analysis of the discrepancies.* Journal of Loss Prevention in the Process Industries, 20:599–606.

Proust, C. (2017). *Turbulent flame propagation in large dust clouds.* Journal of Loss Prevention in the Process Industries, 49:859–869.

DOI: 10.7795/810.20200724

Ignition Temperatures and Flame Velocities of Metallic Nanomaterials

A. Krietsch [a], M. Reyes Rodriguez [b], A. Kristen [c], D. Kadoke [a], Z. Abbas [b] & U. Krause [b]

[a] Bundesanstalt für Materialforschung und -prüfung (BAM), Berlin Germany
[b] Otto-von-Guericke-Universität, Magdeburg, Germany
[c] Freie Universität, Berlin, Germany

E-mail: *arne.krietsch@bam.de*

The production of materials with dimensions in the nanometre range has continued to increase in recent years. In order to ensure safety when handling these products, the hazard potential of such innovative materials must be known. While several studies have already investigated the effects of explosions (such as maximum explosion pressure and maximum pressure rise) of powders with primary particles in the nanometre range, little is known about the ignition temperatures and flame velocities. Therefore, the minimum ignition temperature (MIT) of metallic nano powders (aluminium, iron, copper and zinc) was determined experimentally in a so called Godbert-Greenwald (GG) oven. Furthermore, the flame velocities were determined in a vertical tube. In order to better classify the test results, the tested samples were characterised in detail and the lower explosion limits of the tested dust samples were determined. Values for the burning velocity of aluminium nano powders are higher compared to values of micrometre powders (from literature). While MIT of nanometre aluminium powders is within the range of micrometre samples, MIT of zinc and copper nano powders is lower than values reported in literature for respective micrometre samples.

Keywords: *Dust explosion, Nanomaterials, Minimum ignition temperature (MIT), Flame velocity*

1. Introduction

Over the past years, the use of nanomaterials in industrial applications has grown, going from pharmaceutical and cosmetics fields, to biomedical, electronics, environment and energy (Vignes, et al. 2012). As the use and production of metallic nano powders increases, measures need to be taken to mitigate accidents (fires, explosions etc.) caused by nanomaterials. The progress in the field of prevention of metal dust explosions has been slow, due to the complexity of extracting the fundamental combustion parameters from laboratories, like ignition sensitivity, burning velocity, flame quenching distance or flame structure (Julien, et al., 2015). However, in terms of nano powders some studies have been performed. Krietsch et al. (2015) have tested metallic nanoparticles in the 20 L-sphere (Siwek chamber) to investigate their explosion behaviour. Sun et al. (2018) measured the flame length, flame height, flame propagation and flame velocity of nano-aluminium clouds in a transparent quartz tube for different atmospheres. Another investigation was carried out by Huang et al. (2007) who studied the combustion processes of nano and micro aluminium particles with a type of Bunsen-burner apparatus. The results showed an increase of the flame speed by adding nanoparticles to the fuel (micrometre particles). Dust explosion in the metal processing industry represents a continuous hazard, it is known that some combustible metals can be as energetic and hazardous as organic fuels. In order to determine if the physical and chemical properties of the nano powders cause an increase in the explosion potential, several parameters that affect the explosivity of metallic nanoparticles have been studied, including the maximum explosion overpressure (p_{max}), the maximum pressure rise $(dp/dt)_{max}$ and the minimum ignition energy (MIE). Nevertheless, research on minimum ignition temperature (MIT) of metal nanoparticles has been limited (Yuan, et al., 2014).

Although several studies have been conducted, there is still a need for more information to better understand the explosion behaviour of nanomaterials. The change in the specific properties of nano powders and the need to develop suitable protective measures against dust explosions lead to the following research questions:

- Does the ignition temperature further decrease when the primary particle size is smaller than one micrometre?
- How does the flame of metallic nano powders propagate?
- How does the laminar burning velocity change for primary particles within the nanometre range?

The aim of this paper is to study the influence of the particle size of metallic nano powders on ignition temperatures and the flame propagation. These characteristics will be assessed by determining the minimum ignition temperature (MIT) and evaluating the flame propagation in a vertical tube. A big challenge when conducting dust explosion tests in general is, that the dust must be dispersed before ignition. In this way, a good distribution of the particles in the corresponding test volume is ensured. This results in high turbulence conditions in standard test apparatuses at the time of ignition. The safety parameters determined are therefore strongly dependent on the respective test conditions. Especially for metallic dusts, the so-called cubic law can often not be applied. Therefore, not only from a scientific point of view, it would be desirable to be able to determine the so-called laminar flame propagation velocity in dust clouds without the influence of initial turbulence. This paper presents results of experiments with different metallic materials and particle size distributions. The aim of these experiments was to minimise the turbulence conditions at the time of ignition by means of a special experimental setup. The flame propagation was experimentally investigated in a vertical tube open at the top side. The tube is placed on a metallic base, which simultaneously holds the dust sample and allows air to enter the tube. A porous plate is located inside the metallic base to minimize turbulence in the air flow. The ignition source is provided by a high voltage spark from two electrodes located on one third of the tube length. The dust concentration is measured optically (by light attenuation) with two concentration probes arranged below and above the electrodes. A high-speed camera is used to record the flame propagation. The burning velocity is calculated considering the ratio between the cross-sectional area and the surface area of the flame zone.

2. Characterisation

According to Krietsch et al. (2015), the increase in the specific surface area of the nano powders increases the ignition sensitivity. On the other hand, oxidation reactions may take place on the surface of the particles before testing. This process is known as “passivation”. This may lead to a decrease in the ignition sensitivity compared to not passivated powders. Furthermore moisture, particle size distribution or agglomeration may influence the reactive properties of nanomaterials. In order to be able to better assess experimental results, a precise characterisation is indispensable. For this reason, the dust samples examined were characterised in detail.

2.1 Particle size distribution

In order to have a better overview of the particle size distribution in the gas phase (during flame propagation testing), the particle size distribution was determined in a “dry dispersion unit”. The purpose of the dry dispersion is to overcome the binding forces between agglomerated particles in the micrometre range, as well as optical dilution of the particle collective, to make them measurable by the sensors. However, dry dispersion is not suitable for very fine particles (< 1 µm), because it is difficult to overcome the high particle binding forces. In this case, a wet dispersion method can be used as validation. The measurement was done using the unit Mastersizer Sirocco 2000 from Malvern Panalytical GmbH. Results from dry and wet dispersion are given in Table 1. D_{10}, d_{50} and d_{90} signify the point in the particle size distribution, up to and including which, 10%, 50% or 90% of the total volume of material in the sample is ‘contained’.

For the "wet dispersion method", a dust sample is suspended in a liquid dispersant. The method is based on laser diffraction measurements which produce volume based particle size distributions. The particle size distribution was measured using Mastersizer 2000 from Malvern Panalytical GmbH in accordance with the ISO 13320 (10/2009) standard. For sample preparation, the nano powders are dispersed in a 3 mmol/l tetrasodium diphosphate solution. For dispersing the zinc sample ethanol is used. An external ultrasonic sonotrode is used to disperse the sample until agglomerates have been destroyed. The finest distribution is then the output as the measurement result. During the measurements, the pre-dispersed suspension is added to the dispersion unit and the samples are stirred. After recording the scattered light data, the particle size distribution is calculated using Mie-theory.

Due to the high surface energy of the nano powders, all particles investigated tend to agglomerate. Although the particles were produced in the nanometre range, they can form structures with diameters of far more than 10 micrometres. Under the selected conditions it was not possible to separate the particles down to the specified primary particle size. The particle size of the agglomerates to be expected is much higher than the information given on the label of the manufacturer.

The measurement results in Table 1 show a large difference between dry and wet dispersion for all samples except iron. For the dry dispersion method, it can be observed that the aluminium samples show bigger agglomerate sizes. However, this feature is not seen on the wet method. Even though the wet dispersion method is more suitable for nanoparticles, the use of both methods is required because the conditions during the flame propagation test are more similar to the dry method. From this evaluation it can be predicted that a homogeneous dispersion of the particles in the vertical tube will be difficult to achieve, as the distribution of the agglomerates varies from less than one micrometre to more than 100 micrometres in the case of aluminium 200 nm.

Table 1: *Particle size distribution measurements*

Sample	**Dry dispersion Particle size distribution [µm]**			**Wet dispersion Particle size distribution [µm]**		
	d_{10}	**d_{50}**	**d_{90}**	**d_{10}**	**d_{50}**	**d_{90}**
Aluminium 18 nm	1.6	7.8	18.6	0.1	0.8	3.5
Aluminium 40–60 nm	0.9	7.2	22.5	0.2	0.4	0.8
Aluminium 50–70 nm	0.7	2.6	10.3	0.2	0.7	3.4
Aluminium 90-110 nm	0.8	6.4	26.2	0.2	0.7	3.6
Aluminium 130 nm	0.7	4.5	24.7	0.2	0.9	5.8
Aluminium 200 nm	0.8	6.5	119.2	0.4	1.9	11.0
Iron 50–70nm	0.4	1.1	8.0	0.5	1.0	3.3
Iron 90-110 nm	0.4	1.2	6.9	0.5	1.3	6.1
Copper 50–70 nm	0.5	2.0	14.7	0.3	1.2	9.3
Zinc 40–60 nm	0.5	1.6	10.2	0.7	3.7	18.5

2.2 *Specific surface area and True density*

The absolute density was determined by helium pycnometer (AccuPyc 1340 II) according to DIN 66137-2(03/2019). A 10 cm^3 stainless steel cup was used. For the sample preparation, drying was carried out in an oven at 80°C for 3 hours. Results are shown in Table 4.

The measurement for the specific surface area was carried on as double determination, using NOVA 2200 from Quantachrome. The method is based on the BET determination (Brunauer, Emmett and Teller), the specific surface area is determined by physical adsorption of a gas on the surface of the particles, and by calculating the amount of adsorbate gas corresponding to a monolayer on the surface. Physical adsorption results from van der Waals forces between the adsorbate gas molecules and the adsorbent surface of the particles. The measurement was carried out based on DIN ISO 9277 (01/2014) and DIN EN ISO 18757 (01/2006). In each case, 5 points of the adsorption isotherm in the range of the relative pressure p/p_0 from 0.05 to 0.3 (BET range) were used for evaluation. The samples were heated in a degasser at 100 °C in nitrogen steam for a period of 2 hours.

Table 2 shows a summary of all measurement results. Aluminium particles have smaller density values than iron, copper and zinc. On the other hand, the specific surface area is bigger. However, the determination shows smaller values than expected. The relatively small specific surface areas of iron, copper and zinc as well as the broader particle size distributions, indicate not only agglomerates but also solid aggregates.

The results show that the samples with the smaller primary particle sizes have the larger specific surface area.

The true density of aluminium samples is close to the values reported in the literature (2.7 g/cm³), except for Al 18 nm and Al 50-70 nm. The increase in the density of the aluminium samples may indicate an oxide layer (Al_2O_3), on the other hand, a lower value can be due to a layer of aluminium hydroxide ($Al(OH)_3$). The density values for iron, copper and zinc are below the respective literature values for the pure metal. From this, the conclusion can be drawn that the particles are surrounded by an oxide layer.

Table 2: *True density and specific surface area (BET)*

Sample	True density [g/cm³]	Specific surface area (BET) [m²/g]	Moisture content [%]
Aluminium 18 nm	2.89	23.53	1.6
Aluminium 40–60 nm	2.67	24.08	2.1
Aluminium 50–70 nm	2.58	14.82	1.8
Aluminium 90-110 nm	2.67	11.92	1.6
Aluminium 130 nm	2.67	14.05	1.2
Aluminium 200 nm	2.69	9.44	0.9
Iron 50–70nm	7.15	5.77	-
Iron 90-110 nm	7.12	5.79	-
Copper 50–70 nm	7.83	6.30	0.7
Zinc 40–60 nm	6.06	5.18	0.2

2.3 *Moisture content*

Moisture content in the metallic nano powders was determined by gravimetric analysis. As it was mentioned before, this parameter has a direct influence on the explosion behaviour. Results are also listed in Table 2. Because the analysis involves drying, it was not possible to determine the moisture content of the iron samples due to the decomposition and burning presented during the test, which resulted in an erroneous measurement. The highest value was determined for aluminium 40-60 nm with a water content of 2.1 %. It is expected that the experimental results are not much influenced by moisture content, since all samples showed values around or below 2%.

3. Experimental

Within the framework of the experimental work, the minimum ignition temperature and flame propagation of the metallic nanomaterials mentioned above were investigated. In the following, the respective experimental setups and the investigation procedures are briefly described.

3.1 Minimum ignition temperature

The MIT of a dust cloud in a hot furnace is defined as "the lowest temperature of a hot surface on which the most ignitable mixture of the dust with air is ignited under specified test conditions" (ISO/IEC 80079-20-2, 2016). At this temperature, the heat produced by a chemical reaction exceeds the loss of heat to the surroundings. The MIT is a useful tool to assess the risk of ignition of a dust cloud from different sources especially like hot surfaces. An overview of the experimental setup is illustrated in Figure 1.

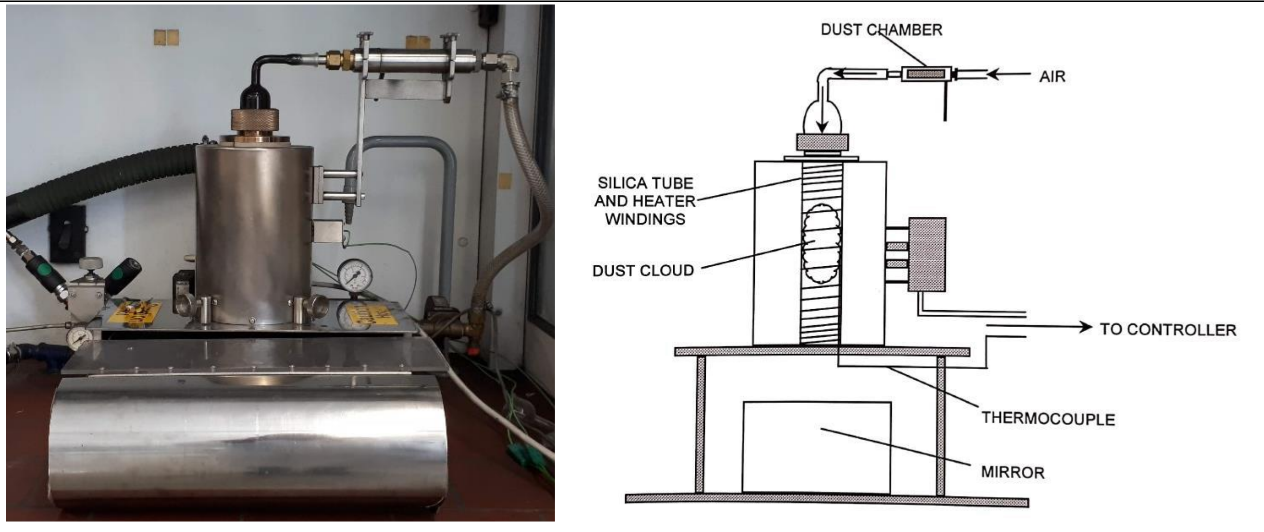

Fig. 1. *GG oven experimental setup*

The determination of the MIT for metallic nano powders was performed in the standardised Godbert-Greenwald (GG) oven. The furnace consists of a vertical silica tube of 23 cm long and 3,6 cm internal diameter. Beneath the furnace, a mirror is located for observation of ignition inside the tube. According to the standardised test method the sample is placed into the storage container and then dispersed into the oven by an air blast through the heated vertical tube and the ignition is detected visually, when a flame is observed (outside the oven). For high-density materials, such as metals, the dust quantity is varied from 1 g to 5 g, and the dust is dispersed with air at different overpressures between 0.1 barg and 0.7 barg (10 kPa to 70 kPa). The MIT is the lowest temperature of the wall furnace at which ignition was observed by the above procedure minus a safety margin of 20 K for temperatures above 300 °C and minus 10 K for temperatures at or below 300 °C. A more detailed description of the test procedure can be found in ISO/IEC 80079-20-2 (2016).

3.2 Vertical tube apparatus

The flame propagation of metallic nano powders was studied in the experimental setup shown in Figure 2. The equipment consists of a vertical tube made of acrylic glass with an inner diameter of 60 mm, an outer diameter of 70 mm and a length of 1 m. The tube is placed on a metallic base that provides support and at the same time it contains the dust sample and allows the air supply into the tube. A porous plate is located inside of the metallic base to reduce the turbulence in the air flow. The ignition source is provided by a high-voltage spark from two electrodes located at one-third of the length of the tube (from the bottom).

The dust concentration is measured optically (by light attenuation) with two concentration probes which are positioned beneath the electrodes (lower) and above them (upper). The distance between the two measurement probes is equal to 10 cm. A pressure reducer connected to a flow meter and a solenoid valve allow the air-flow control. It is worth to mention that the pressurized air is fed into a dryer before to get into the tube. Flame propagation behaviour is observed by the high-speed camera FASTCAM APX RS of 17500 frames per second (FPS). A more detailed description of the experimental setup is presented in Reyes Rodriguez (2019).

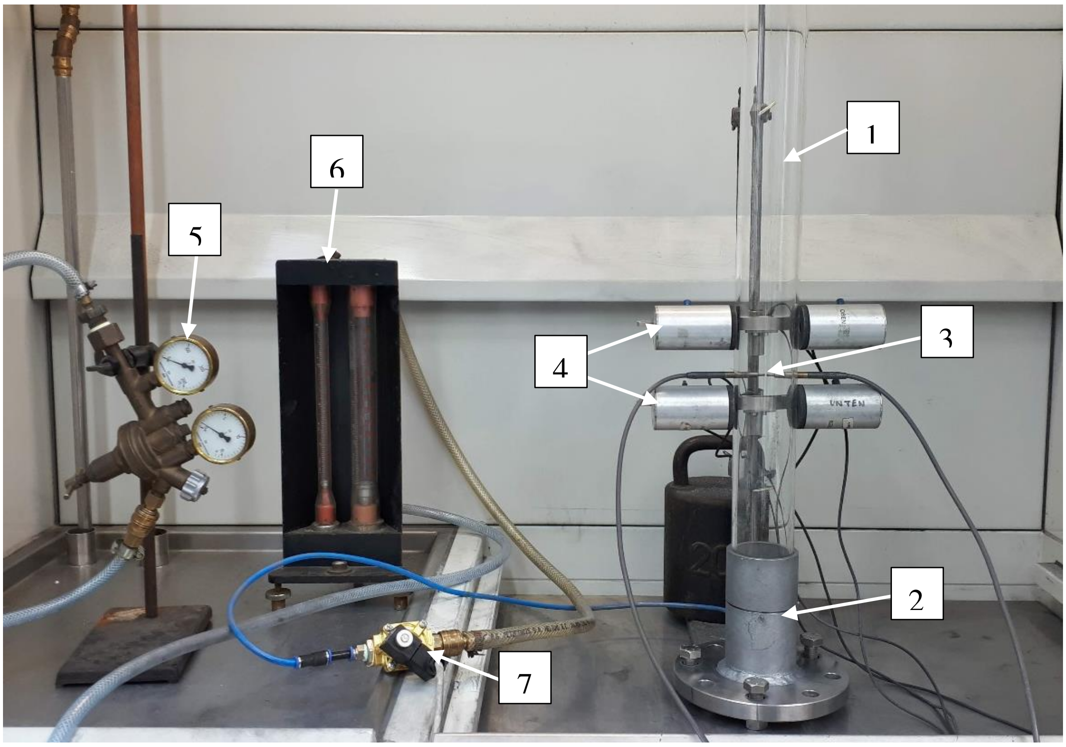

1: Vertical tube
2: Metallic base
3: Electrodes
4: Concentration probes
5: Pressure reducer
6: Flow meter
7: Solenoid valve

Fig. 2. *Vertical tube experimental setup*

Dust concentration has a major impact on the evaluation of the explosion characteristics. Therefore, to analyse the flame propagation, it is crucial to know the concentration of the dust-air mixture at the moment of the ignition. For this reason, two concentration probes (placed above and below the ignition source) were used. The measurement principle is based on the Beer-Lambert law (Eq. 1), which states that the absorbance of the light in a sample is proportional to the concentration of the attenuating species existing.

$$I = I_0 \cdot e^{-klc} \tag{1}$$

Where I is the intensity reduced, I_0 is the initial intensity, k is the extinction coefficient of the material, l is the measurement distance and c is the dust concentration. For the calibration of the concentration probes, a container filled with water is used. Calibration is performed by adding portions of dust to the liquid and mixing with a magnetic stirrer. Since the volume of the liquid and the mass of the dust are known, the concentration can be determined. Each measurement from the concentration probes [mV] is assigned to a specific concentration, then an extinction curve is created for each sample. In order to calculate the concentration at the ignition time, the measurement from the concentration probes is recorded. To make a comparison between each test, it is necessary to linearise the extinction curve using the natural logarithm and expressing it as the proportional change in the light attenuation [%] versus the dust concentration [g/m³]. Figure 3 shows the calibration line and equation for aluminium 90-110 nm.

DOI: 10.7795/810.20200724

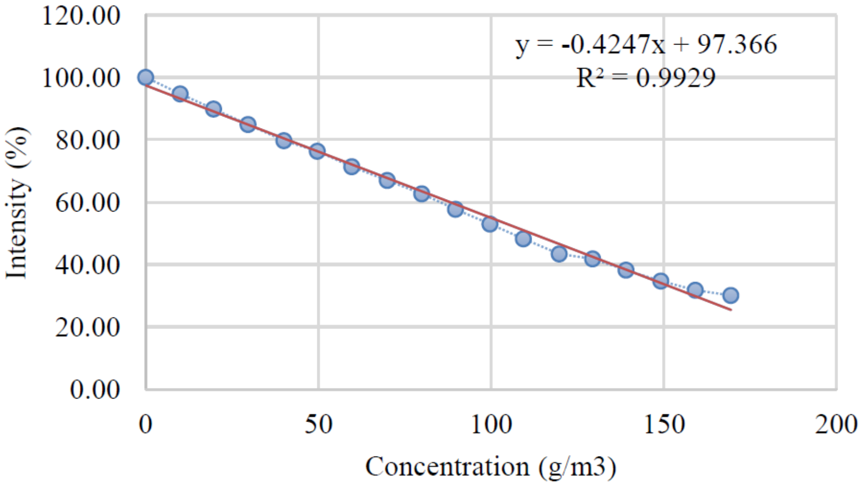

Fig. 3. *Calibration result (lower concentration probe) with aluminium 90-110 nm*

The test procedure starts with the weighing of the sample. Because of the difference in the density between samples, different quantities of dust were required. For instance, aluminium samples required 2–3 g to have an ignition, contrary to iron samples where 5 g were needed. Once the flow rate has been adjusted at the desired value, the sample is placed in the metallic base. After this, the tube is locked onto the base. The concentration probes must remain in the same place and distance for all tests. The test starts with the input of the uniform air flow, whereby the particles are dispersed slowly. For most of the samples, a flow rate of 3000 l/h is sufficient to create a homogenous cloud within the tube. Before the dust cloud reaches the top of the tube (after a few seconds), the flow is stopped and almost simultaneously the ignition source is triggered. Due to the lack of air flow, the particles no longer rise in the tube. At the same time, the sinking process has not yet begun. Ignition therefore occurs at a moment when the particle velocity or turbulence within the tube is almost zero. At the same moment, the camera is started. For a correct concentration record, the values from the concentration probes are monitored. By doing this, the change in the light attenuation can be analysed after each test.

Figure 4 shows the dispersion of a dust cloud of one of the aluminium samples, the moment of the ignition and the flame expansion.

Fig. 4. *Experimental observation of the flame propagation of an aluminium sample*

DOI: 10.7795/810.20200724

3.3 Determination of quasi laminar (unstretched) flame velocities

The flame velocity S_{fl} is calculated from the video recording. After each test, the high-speed camera creates a file with 7000 pictures. Therefore, a computer program is needed in order to determine the flame front propagation. In this study, a self-created program was used. This program is able to scan the pixels from the pictures and recognise the "flame front".

Figure 5 shows the distance in pixels of the image, which goes from 0 to 1022 pixels. In the picture, the flame is recognised at the x-value of 207 pixels.

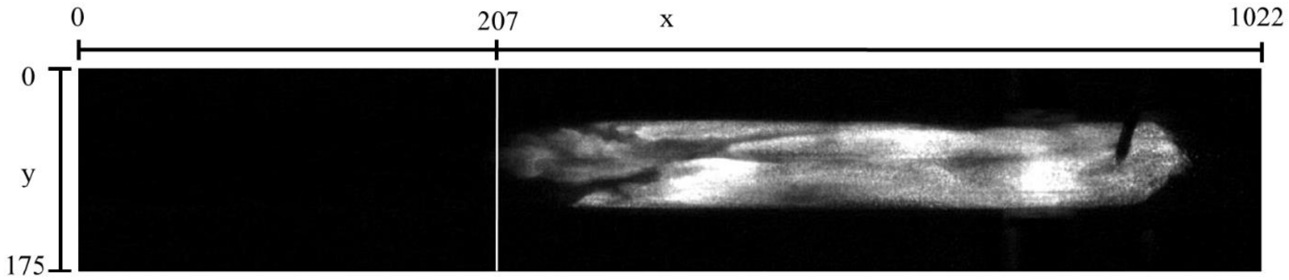

Fig. 5. *Determination of the flame front at a specific time*

The flame velocity S_{fl} is then determined as the distance travelled by the flame in a certain time interval. It is worth to mention that the flame velocity of every test performed varies depending on the concentration. It is also not constant along the tube (see Figure 6). By knowing the change in the distance travelled by the flame front every millisecond, S_{fl} can be monitored and the highest value of S_{fl} during one test can be determined.

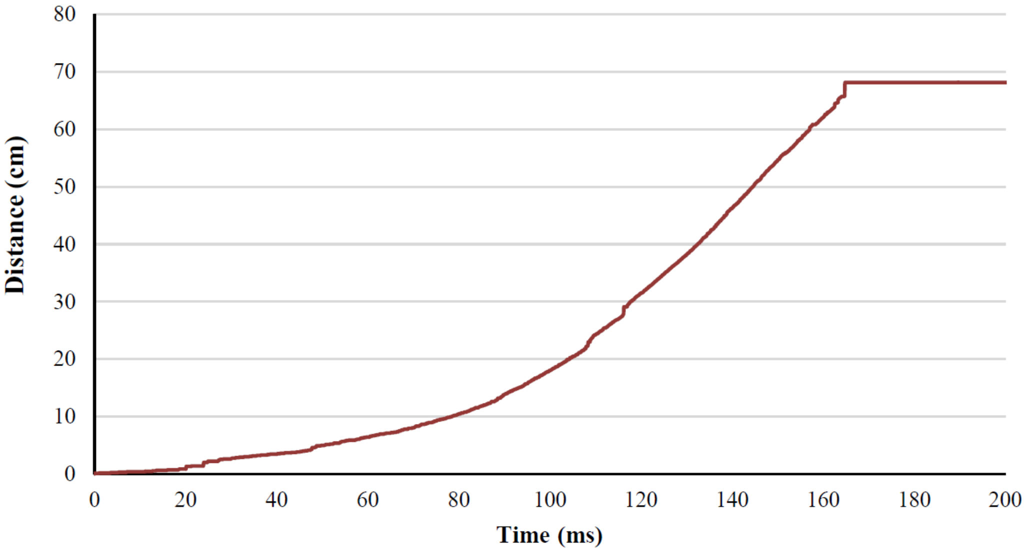

Fig. 6. *Flame propagation during a test with iron 90-110 nm*

As it can be noticed from Figure 6, there is a "jump" of the flame front after about 115 ms. This can be explained with the presence of combustion gases in the middle of the tube which thrust the flame upwards and therefore increase the flame speed. Therefore, it is important to determine the maximum flame speed of every test before the combustion gases are notably present in the system and consequently the flame lifts off. Figure 6 illustrates that the highest flame velocity during this single test (mean concentration of 324 g/m³) was found after 108 ms.

Since the flame velocity is known, the laminar flame velocity could be determined. However, it should be noted that the propagation of the flame upwards within the tube causes turbulence, cooling effects etc. at its walls. The flame only propagates quasi laminar the first milliseconds from time of ignition at the center until the flame hits the tube wall. Therefore, the term unstretched flame velocity would be more appropriate in this case. For a better comparison, however, the term laminar flame velocity is used in the following. To determine the laminar flame velocity (S_L), the model of Andrews and Bradley (1972) is used. They calculate the laminar burning velocity S_L by using Equation 2:

$$S_L = \frac{A\prime}{A_{fl}}(S_{fl} - u) \tag{2}$$

Where S_{fl} is the flame velocity selected at the maximum value reached by the flame front during the test, $A\acute{}$ is the flame section at the bottom of the flame zone, A_{fl} is the surface of the flame zone and u is the flow velocity. In this study u is considered as zero because the air flow stops just before ignition, so that the particle velocity is almost zero. The flame velocity S_{fl} in Equation 2 is valid for states where $S_{fl} > S_L$ and $S_{fl} > u$. When the flame is completely developed along the tube, $A\acute{}$ should correspond to the cross-sectional area of the tube. On the contrary, when the flame does not occupy the entire section, the dead space near to the tube walls should be taken into account. The surface of the flame zone A_{fl} can be considered as a paraboloid of revolution. Figure 7 illustrates the geometry of the flame shape (Di Benedetto, et al., 2011).

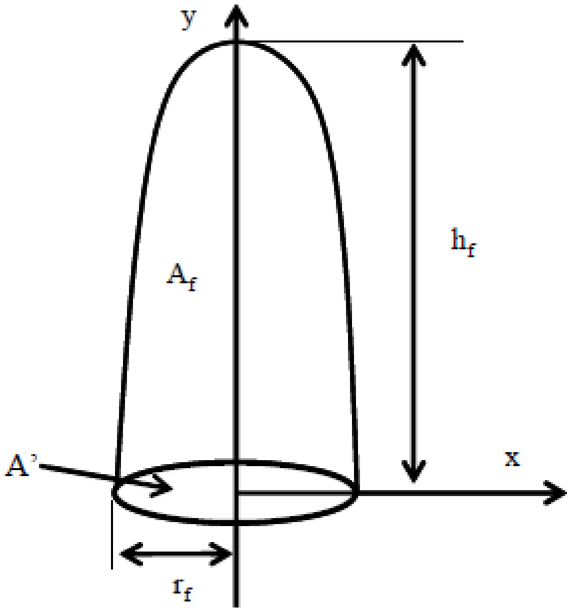

Fig. 7. *Geometry of the flame*

The surface area of the flame can be calculated by Equation 3 (Perry & Green, 2007)

$$A_{fl} = 2\pi \cdot \left(r_f^2 + \frac{r_f \cdot h_f \cdot a}{e}\right) \tag{3}$$

Where r_f is the flame radius and h_f is the flame height, $a = arccos(r_f h_f)$ and $e = sin(a)$.

For the estimation of the height and the radius of the flame, the program *ImageJ* was used. Once the scale has been established, just by selecting both the diameter and the height on the image, the value in distance scale (m or cm) can be found.

It is assumed that S_L is constant over the entire cross section of the tube and at any time for one specific concentration. In order to verify this, the laminar burning velocity was calculated for time steps of 20 ms during a test with one of the iron samples. Table 3 shows the variation of the S_L within a single test. Contrary to the original assumption, the values are not constant, since the values vary between 0.11 m/s and 0.17 m/s.

Table 3: *Calculation of laminar flame velocity during a single test with one of the Iron samples*

Time [ms]	**Diameter [cm]**	**Height [cm]**	**A\` [cm²]**	**A_{fl} [cm²]**	**S_L [m/s]**
60	2.52	7.17	4.99	90.36	0.13
80	3.51	11.68	9.68	204.34	0.11
100	4.35	19.84	14.86	428.24	0.13
120	4.81	30.76	18.17	732.22	0.17
140	4.2	44.27	13.85	918.54	0.12

4. Results and discussion

In addition to the investigations on MIT and flame propagation, the lower explosion limit (LEL) of the nano powders was also determined in the 20 L-sphere (Siwek Chamber) according to EN 14034 part 3 (2006). It is equivalent to the Minimum Explosive Concentration (MEC). The LEL is taken as the highest concentration of the dust at which no ignition occurs in three consecutive tests. Table 4 shows the results of the determination. Notice that copper has a value above 1000 g/m³, which makes it difficult to ignite in the vertical tube.

Table 4: *LEL, explosion behaviour at lower concentrations and MIT*

Sample	**LEL [g/cm³]**	**Concentration [g/m³]**	**p_{ex} [barg]**	**$(dp/dt)_{ex}$ [barg/s]**	**MIT [°C]**
Aluminium 18 nm	60	125 250	1 3.3	11 53	440
Aluminium 40–60 nm	20	125 250	3.7 4.9	106 190	470
Aluminium 50–70 nm	30	125 250	4 5.7	102 304	540
Aluminium 90-110 nm	30	-	-	-	510
Aluminium 130 nm	30	125 250	3.9 5.5	126 286	580
Aluminium 200 nm	30	125 250	4.7 7	141 555	310
Iron 50–70nm	60	125 250	0.4 2.4	9 74	pyrophoric
Iron 90-110 nm	60	125 250	3.9 5.3	89 238	pyrophoric
Copper 50–70 nm	above 1000	-	-	-	250
Zinc 40–60 nm	60	125 250	0.1 1.2	0 27	300

The overpressure (p_{ex}) occurring during the explosion of the metallic nano powders and the rate of the explosion pressure rise $(dp/dt)_{ex}$ were also determined in the 20 L-sphere. The determination was made for two main concentrations similar to those existing during the study of flame propagation in the vertical tube. It should be noted that the determination was made for reference purposes, using two chemical igniters of 1 kJ each (2x1 kJ in total). This is different to the standard procedure for determining the maximum overpressure (p_{max}), for which two chemical igniters of 5 kJ each are used, and tests are conducted over a wide range of concentrations. The idea was to keep the overdriving of the ignition source low and thus possibly better recognize connections between the experiments in the 20 L-sphere (explosion severity) and the vertical tube (flame velocity). Results are shown in Table 4. Copper is excluded from this determination, since its LEL is higher than 1000 g/m³. For nano iron and nano aluminium, it can be observed that p_{ex} and $(dp/dt)_{ex}$ increase as the primary particle size increases from smaller to bigger fractions. In general, aluminium samples created higher pressures, followed by iron.

4.1 Results of the MIT determination

In this research aluminium, copper and zinc nano powders were tested in the GG oven, following the standardised method from ISO/IEC 80079-20-2:2016. The Iron samples sometimes ignited spontaneously at air without any ignition source and have thus not been tested in the GG oven.

The values obtained with nano powders are within the range of lowest values or lower than those for micrometre powders reported in databases. The German GSBL database (GSBL 2019) reports MIT of micrometre aluminium samples from 440-850 °C. The highest MIT value for nano aluminium samples is 580°C (aluminium 130 nm). With decreasing particle size, MIT of nano aluminium is further decreasing. Aluminium 18 nm has a MIT (440 °C) which is equal to the lowest values reported in the database for micrometre aluminium. However, for aluminium 200 nm the MIT is 330 °C and thus the lowest value of all aluminium samples and even lower than all database values for aluminium.

The copper sample has a MIT equal to 250 °C, which seems to be quite low, considering that there is not a single reported MIT for copper (some samples with no ignition up to 850 °C). The reported values for zinc powder with particle size <10 µm is 570 °C and 830 °C for 160 µm. These values are also above the MIT value determined for zinc 40-60 nm (300°C). In the case of the iron powders, the MIT reported in the literature (BIA 1997) for a particle size equal to 12 µm is 580 °C. As mentioned before, in this research the iron powders in the nanometre range showed a pyrophoric behaviour. For this reason, it was not necessary to determine their MIT.

Investigated nano powders clearly show that the ignitability increases further from the micrometre range to the nanometre range as the particle size decreases. Particularly noteworthy, however, are the results obtained with aluminium 200 nm. Both the explosion pressure, pressure rise and MIT are most critical in comparison to the other aluminium samples. A glance at the characterisation of particle sizes (Table 1) shows that this sample has a very large particle size distribution. This might favour such a behaviour.

4.2 Results of the flame propagation tests

Since one of the aims of the study was to compare the influence of the particle size on the burning characteristics, samples with different particle size were chosen for aluminium. The comparison between different metallic nano powders was also of research interest, therefore nano powders of iron, copper and zinc were tested in the vertical tube apparatus. In the case of the copper sample, the LEL is higher than 1000 g/m³, since ignition was not achieved in the vertical tube. For aluminium 18 nm, the ignition of the dust cloud was also not achieved. Even though the particle size distribution is not that wide (see Table 1). The tendency to form big agglomerations while lifting the particles caused that an adequate cloud not be formed within the LEL. In addition, the smaller particles are attracted to the wall due of the tube immediately after switching on the air flow. Thus, ignition could not be realised.

The dust concentration is a key parameter in the determination of the burning characteristics of a dust sample. Therefore, achieving similar concentrations for all samples was one of the first aims. However, neither changing the amount of dust nor adjusting the air flow had a major impact on the concentration of the cloud at the time of ignition. This may be due to measurement errors but moreover due to the wide particle size distribution of all samples, which is one of the characteristics of nano powders. After a lot of failed tests, when ignition was not achieved with all samples at the same concentration, tests were continued with trying to realise at least comparable concentrations for each sample.

The flame velocities were determined using the procedure described in chapter 3.3. As a result of the data analysis, a velocity profile specific for each test was created. As it can be seen in Figure 8, there are "peaks" in the velocity profile that do not correspond to such a drastic velocity increase. There are jumps where the program is not able to correctly detect the flame front in a series of images.

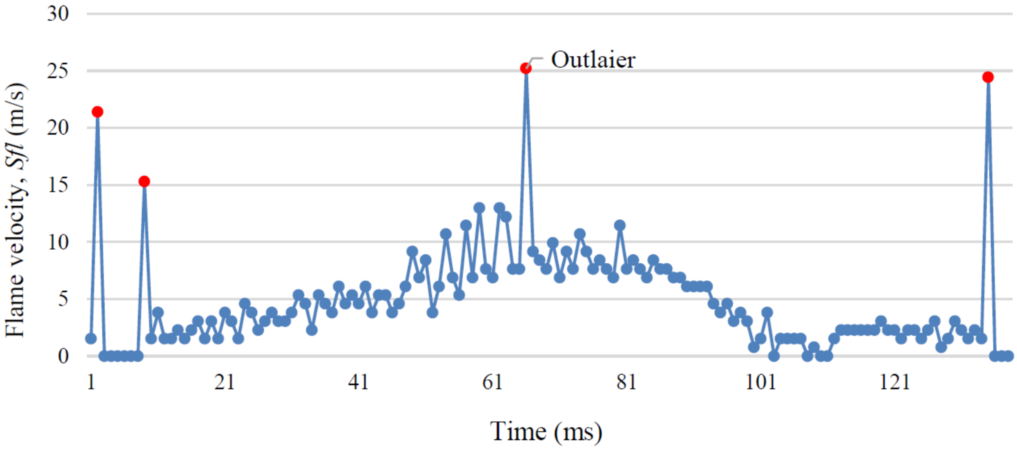

Fig. 8. *Flame velocity profile of one test with iron 90-110 nm*

In order to determine which velocities were abnormal peaks and which were the highest flame velocities, a graphical analysis of the data was performed to rule out the irregular values. A boxplot is a graphical tool that shows the distribution of the data within a sample. By using the median and the range between the first quartile and the third quartile, the boxplot creates an upper and lower whisker. If a normal distribution is considered, 99.3% of the data should be within the whiskers. Thus, any value below or above the whiskers is considered an outlier, meaning, it is not a representable value of the sample. The boxplot in Figure 9 shows that the outlier values correspond to the peaks in the graph of Figure 8.

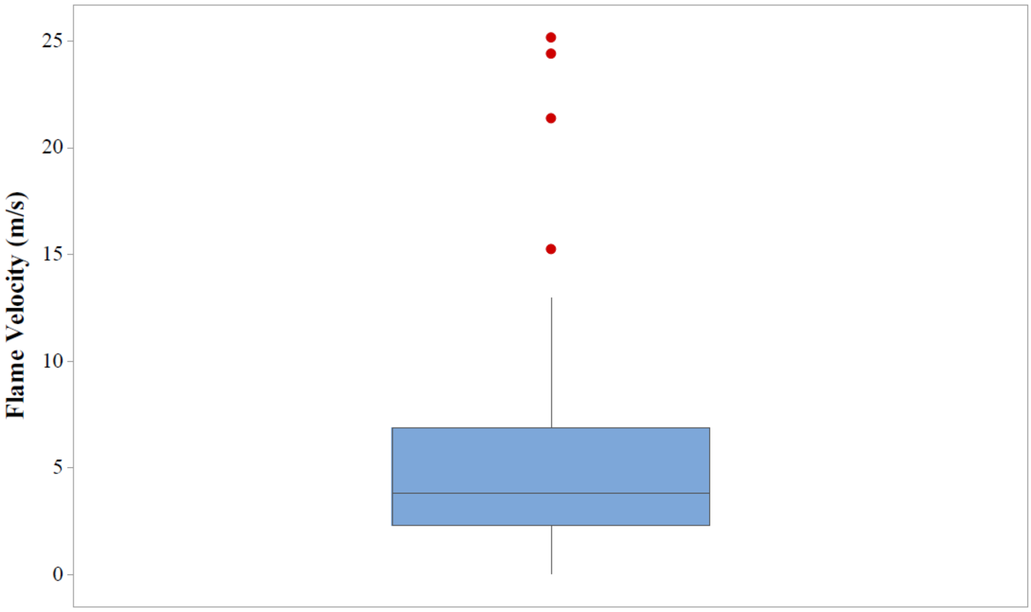

Fig. 9. *Boxplot of the one test with iron sample 90-110*

This procedure was performed for all successful experiments. The boxplot results were summarised, the resulting S_{fl} evaluated and then the S_L calculated according the described procedure. Table 5 shows the results of all successful tests performed with aluminium 200 nm. The highest S_L (Test 16, 0.52 m/s) is twice the lowest value (Test 5, 0.26 m/s). However, this behaviour is not related to the concentration since other tests have a higher concentration and a lower S_L.

Table 5: *Flame velocities of aluminium 200 nm*

Sample	Concentration [g/cm³]	S_{flmax} [m/s]	S_L [m/s]
Test 2	123.9	11.45	0.29
Test 3	146.5	15.26	0.40
Test 5	151.5	11.45	0.26
Test 7	145.6	12.97	0.46
Test 8	162.6	13.74	0.38
Test 9	191.7	7.63	0.27
Test 11	194.8	12.21	0.33
Test 16	141	20.61	0.52
Test 18	142.6	12.21	0.30

The listing of all tables of the values determined with all dusts would go beyond the scope of this article. For this reason, all calculated S_L of the respective successful tests are shown in Figure 10. It displays a comparison of all samples between the laminar burning velocities determined and the corresponding concentration. The zinc sample has higher concentrations, due to the higher density. Therefore, it was necessary to use more material in order to observe the flame propagation in the vertical tube. Despite this, the laminar burning velocity is still in the same range as the other samples.

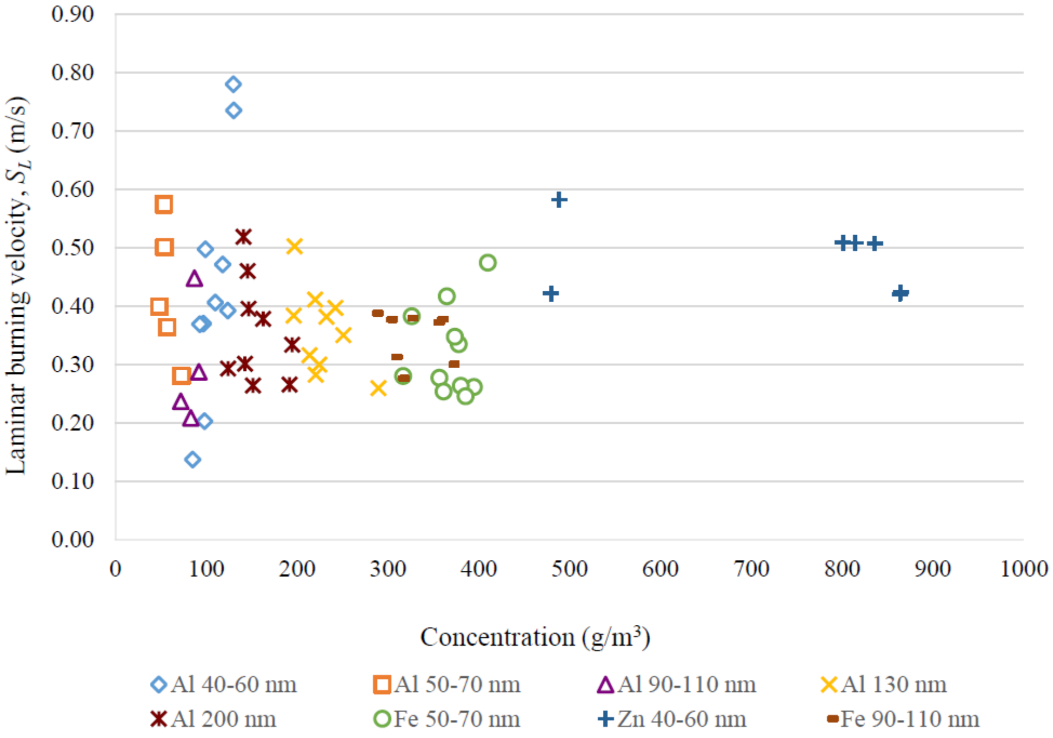

Fig. 10. *Comparison of the quasi laminar flame velocity for different metallic nano powders*

Data dispersion may be caused by the difficulties experienced in obtaining repeatability in experiments and to the accuracy of dust concentration measurement. Aluminium sample 40-60 nm shows the highest variation as well as the highest value for the S_L. This sample also has the largest specific surface area equal to 24 m^2/g and the lowest LEL of 20 g/m^3.

The results of this study can be compared with the data reported in the literature on the combustion of aluminium clouds. Figure 11 shows the results reported by Escot Bocanegra et al. (2010). Experimental results show faster flame propagation in nanoparticle clouds compared to microparticle clouds. The experimental set up was also a vertical tube, with the difference that the cloud was ignited at the top and the flame propagation was observed from top to bottom.

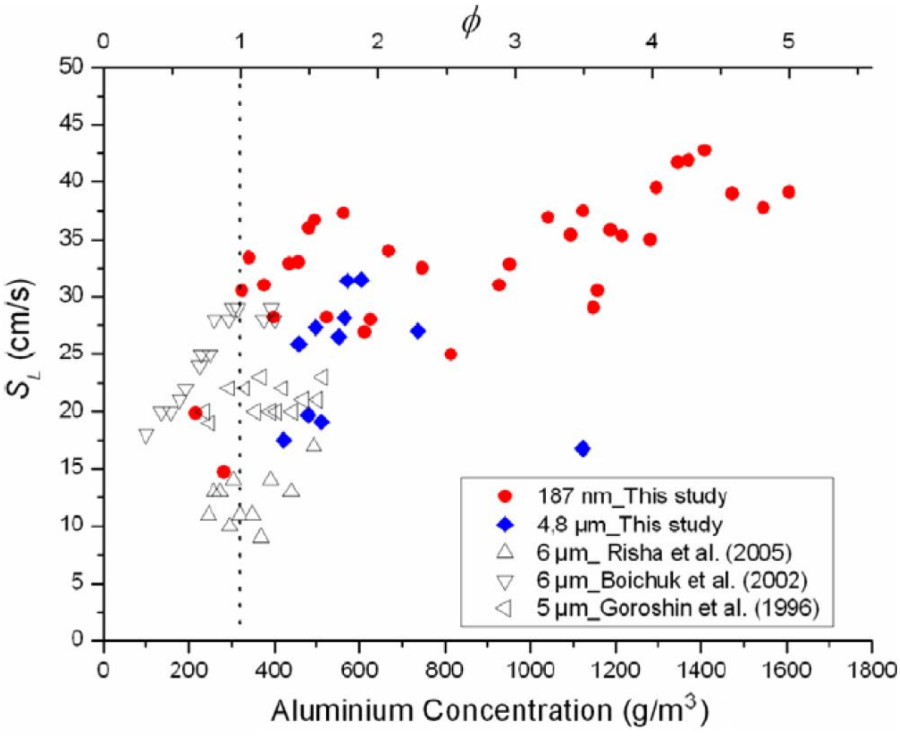

Fig. 11. *Laminar flame velocity versus aluminium concentration (Escot Bocanegra, et al., 2010)*

5. Conclusions

The aim of this work was to study the influence of the particle size of metallic nano powders on ignition temperatures and the flame propagation. Samples of aluminium with different particle sizes were analysed as well as nano powders of iron, copper and zinc. In total 10 samples were investigated. The particle size is an important parameter for the combustion mechanism. The influence of the heat and mass transfer becomes relevant when the combustion reaction takes place on the particle surface. For nanoparticles in a dust cloud, previous studies (e.g. Huang et al. 2007) have shown that the combustion behaves as kinetic-controlled whereas micrometric particles show diffusion-controlled combustion. This can be directly correlated with the results obtained for the flame propagation test in the vertical tube. Aluminium nanoparticles present higher laminar burning velocities in comparison with micrometric particles reported in the available literature like Escot Bocanegra et al. (2010).

The particle size distribution is one of the main parameters to evaluate and compare the results of the flame propagation tests. Two methods were used, a dry dispersion and a wet dispersion. As a result, all samples showed larger particle sizes than the primary particle sizes given by the manufacturer. In addition, the measurements showed a wide particle size distribution, which hindered the homogeneous dispersion in the vertical tube. The determination of the specific surface area yielded lower values than one would theoretically expect for nanoscale particles. This is due to the much larger agglomerates and aggregates.

Furthermore, most of the aluminium samples showed true density values close to the data reported for pure aluminium, which indicates that the samples did not show a high degree of passivation, except for the 18 nm aluminium sample. This feature contributed to the fact that the 18 nm aluminium sample could not be ignited and analysed for the flame propagation test. As a result of the determination of the minimum ignition temperature (MIT), it was observed that the ignition temperature decreases for particles smaller than one micrometre. Results of the measurements in the GG oven were compared with data reported for the same method. The tests show that all nano samples studied can have lower MIT than micrometric samples.

The flame propagation of metallic nano powders was observed in a vertical tube. More than one hundred tests were carried out in order to be able to analyse and compare the results. A high-speed camera was used to record the progress of the flame over time. The flame velocity was obtained from the video recordings, as a measure of the distance travelled by the flame front in a time interval of one millisecond. The quasi laminar (unstretched) burning velocity S_L was then calculated. It was found that the values of S_L obtained for nano powders were higher than the values reported in the literature for larger particles (micrometric). The S_L might be an alternative to assess the explosion severity instead of the so-called dust explosion constant K_{St}, which is strongly influenced by turbulent conditions.

References

Andrews, G. & Bradley, D. (1972). Determination of burning velocities: A critical review. Combustion and flame, 18(1), pp. 133-153.

BIA (1997). Combustion and explosion characteristics of dust, s.l.: HVBG (Federation of the statutory accident insurance institutions of the industrial sector).

Di Benedetto, A. et al. (2011). Flame propagation of dust and gas-air mixtures in a tube. Chia Laguna, Cagliari, Sardinia, Italy, Conference: MCS 7 (Seventh Mediterranean Combustion Symposium).

EN 14034-3, 2006. Determination of explosion characteristics of dust clouds - Part 3: Determination of the lower explosion limit LEL of dust clouds.

Escot Bocanegra, P. et al. (2010). Experimental and numerical studies on the burning of aluminum micro and nanopartcle clouds in air. Experimental thermal and fluid science, Volume 34, pp. 299-307.

GSBL (2019). ChemInfo/Gemeinsamer Stoffdatenpool Bund Länder. www.gsbl.de (13.12.2019)

Huang, Y., Risha, G. A., Yang, V. & Yetter, R. A., (2007). Combustion of bimodal nano/micron - sized aluminum particle dust in air. Proceedings of the combustion institute, pp. 2001-2009.

ISO/IEC 80079-20-2 (2016). International standard: explosive atmospheres- Part 20-2: Material characteristics - Combustible dusts test methods. Geneva: International Electrotechnical Commission.

Julien, P. et al. (2015). Effect of scale on freely propagating flames in aluminum dust clouds. Journal of loss prevention in the process industries, 36 July, pp. 230-236.

Klippel, A., 2015. Investigation into the influence of dustiness on the course of vented dust explosions, Berlin: Bundesanstalt für Materialforschung und -prüfung.

Krietsch, A., Scheid, M., Schmidt, M. & Krause, U. (2015). Explosion behaviour of metallic nano powders. Journal of loss prevention in the process industries, Volume 36, pp. 237-243.

Reyes Rodriguez, M. D. (2019). Investigation on ignition temperatures and flame propagation of metallic nanopowders. Master Thesis at Otto-von-Guericke-Universität Magdeburg and Bundesanstalt für Materialforschung und -prüfung (BAM), Germany.

Sun, Y. et al. (2018). Combustion characteristics on nanoaluminum cloud in different atmospheres. Industrial & engineering chemistry research, pp. 129-138.

Vignes, A. et al. (2012). Risk assessment of the ignitability and explosivity of aluminium nanopowders. Process safety and environmental protection, Volume 90, pp. 304-310.

Yuan, C., Amyotte, P. R., Hossain, M. N. & Li, C. (2014). Minimum ignition temperature of nano and micro Ti powder clouds in the presence of inert nano TiO2 powder. Journal of hazardous materials, Volume 275, pp. 1-9.

DOI: 10.7795/810.20200724

A flame propagation model for nanopowders

Audrey Santandrea [a,b], David Torrado [a], Matteo Pietraccini [a], Alexis Vignes [b], Laurent Perrin [a] &
Olivier Dufaud [a]

[a] Laboratoire Réactions et Génie des Procédés, Université de Lorraine, CNRS, LRGP, Nancy, France
[b] INERIS, Accidental Risks Division, Parc Technologique ALATA, Verneuil-en-Halatte, France

E-mail: olivier.dufaud@univ-lorraine.fr

Abstract

The determination of explosion severity should be made from intrinsic properties of the fuel-air mixture in order to avoid the influence of external parameters, such as the vessel volume or the initial turbulence. To overcome such limitations, the flame propagation of gaseous mixtures is often studied in order to estimate their laminar burning velocity, which is independent of external factors and is a useful input for CFD simulation and for the sizing of protective devices. Experimentally, this parameter is difficult to evaluate when it comes to dust explosion due to the inherent turbulence during the dispersion of the cloud. However, the low inertia of nanoparticles allows performing tests at very low turbulence without sedimentation. Knowledge on flame propagation concerning nanoparticles may then be modelled and, under certain conditions, extrapolated to microparticles, for which an experimental measurement is a delicate task. This work then focused a nanocellulose with primary fiber dimensions of 3 nm width and 70 nm length. A one-dimensional model was developed to estimate the flame velocity of a nanocellulose explosion, based on an existing model already validated for hybrid mixtures of gas and carbonaceous nanopowders similar to soot. Due to the fast devolatilization of organic powders, the chemical reactions considered are limited to the combustion of the pyrolysis gases. The finite volume method was used to solve the mass and energy balances equations and mass reactions rates constituting the numerical system. Finally, the radiative heat transfer was also considered, highlighting the influence of the total surface area of the particles on the thermal radiation. Flame velocities of nanocellulose from 17.5 to 20.8 cm.s^{-1} were obtained numerically depending on the radiative heat transfer, which proves a good agreement with the values around 21 cm.s^{-1} measured experimentally by flame visualization and allows the validation of the model for nanoparticles.

Keywords: *dust explosion, flame propagation, nanoparticles, modeling*

1. Introduction

To mitigate dust explosions, safety barriers such as explosion venting need to be designed by considering the experimental characteristics of the dust explosibility. Such characteristics are routinely determined in a 20 L sphere (Zalosh, 2019) according to well established standards like EN 14034-1 (2004) and EN 14034-2 (2006). This approach only holds by assuming that dust explosibility can be represented by the maximum explosion overpressure value and the Kst. However, such an approach needs to be further questioned as the measurement of dust explosion severity is actually influenced by several parameters such as the initial turbulence (Amyotte et al., 1988; Zhen and Leuckel, 1997), the ignition energy (Zhen and Leuckel, 1997), the moisture content of the powder (Traoré et al., 2009) and the type of nozzle (Dahoe et al., 2001; Murillo et al., 2018; Yao et al., 2020). Beyond these main influential factors, the validity of the so-called ‘cubic law’ (Dahoe et al., 2001) commonly used to extrapolate results obtained in a confined volume to another volume (Eckhoff, 2003) is also questioned.

Standard conditions were initially defined to evaluate the explosion severity of microparticles, but when it comes to nanoparticles, potential discrepancies can arise. Indeed, their small size induces a high specific area and new properties, which can lead to modifications in the combustion kinetics (Bouillard et al., 2010; Dufaud et al., 2011) along with extremely high ignition sensitivity, especially for metallic nanopowders that can spontaneously ignite when exposed to air (Boilard et al., 2013; Krietsch et al., 2015). An evaluation of the adequacy of the current standards for the evaluation of the explosion severity of nanoparticles is then necessary (Santandrea et al., 2019b).

To overcome the identified limitations, direct investigation of the flame propagation could be useful so as to provide fundamental inputs in advanced simulations (CFD or phenomenological approach). The essential parameter is then the laminar burning velocity, which is an intrinsic property of the fuel-air mixture (Belerrajoul, 2019; Dahoe et al., 2002) that can be used in such simulations to evaluate the consequences of an explosion scenario in specific conditions (Skjold, 2003). The existence of a laminar burning velocity of dusts is difficult to define due to the inherent turbulence related to the dispersion of the powder but such an approach was already proposed 30 years ago by Bradley and Lee (1984) though it proved itself challenging when it comes to dusts. Nevertheless, the low inertia and sedimentation rate of nanoparticles enable to investigate flame propagation in very low turbulent conditions (Santandrea et al., 2020).

In this paper, a one-dimensional model initially conceived and validated for hybrid mixtures (Torrado et al., 2018) has been adapted to predict the laminar flame velocity of nanocellulose. Results of simulations are then compared to the experimental values measured on nanocellulose using a flame propagation tube and a vented explosion sphere (Santandrea et al., 2020). The consistency of a correlation established by Silvestrini et al. (2008) to predict laminar flame velocity of micropowders based on the knowledge of their explosion severity was also analyzed for nanocellulose.

2. Material and experimental method

2.1 Flame propagation observation

Nanocellulose powder, or more precisely a cellulose nanocrystals powder NCC (CelluForce), is composed of primary fibers, whose dimensions are 70 nm length and 3 nm width. The flame propagation of nanocellulose was studied at low turbulence by Santandrea et al. (2020) in a flame propagation tube and in a vented visualization 20 L sphere, as summarized in Fig. 1. Due to a difficult visualization of the flame kernel at high concentration, a concentration of 500 $g.m^{-3}$ was chosen, as it is higher than the minimum explosible concentration, i.e. 125 $g.m^{-3}$, to ensure an ignition at low ignition energy, and rather close to the experimental optimal concentration, i.e. 750 $g.m^{-3}$. The particle size distribution of nanocellulose dispersed in both setups was determined using a laser diffraction sensor (Helos - Sympatec). It appears that agglomerates ranging from a few micrometers up to 60 µm are formed in the powder. Explosion were recorded using a high-speed video camera, and the flame kernel growth was analysed in terms of flame front position and surface area using a model developed by Cuervo (2015) in Matlab's Simulink. The equations initially established for gases were then applied to the obtained values, considering that the devolatilization of organic powders is fast and that, under certain concentration and turbulence conditions, the reaction is then limited by the combustion of the pyrolysis gases (Cuervo, 2015; Di Benedetto and Russo, 2007; Dufaud et al., 2012a). Thus, the burning velocity was calculated using the spatial velocity S_u, the estimated cross-section A_s and the flame surface A_f according to Andrews and Bradley (1972), along with the flame stretching factor K, called Karlovitz factor (Karlovitz et al.,1951). Those parameters were then combined to apply a linear relation linking the burning velocity and the Karlovitz factor K to the laminar burning velocity S_{u0} and the Markstein length δ_M, which is a parameter characterizing the stability of the flame (Clavin, 1985; Markstein, 1964).

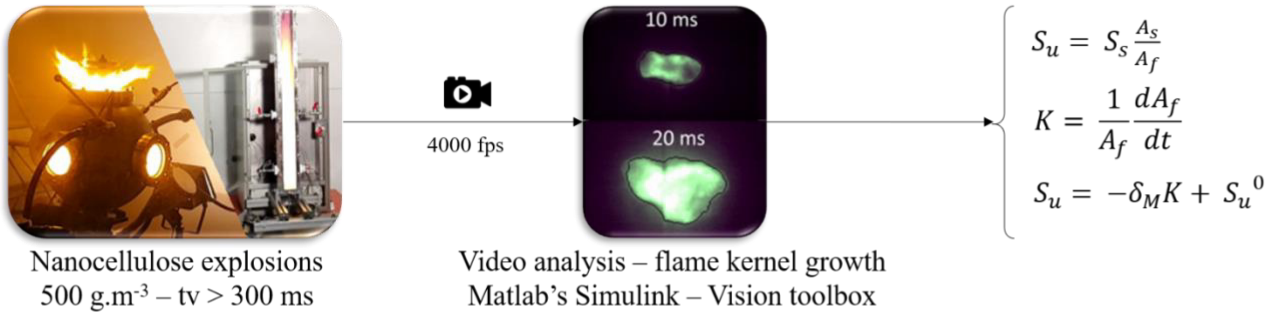

Fig. 1. *Simplified scheme of the experimental determination of the laminar burning velocity by flame visualization used by Santandrea et al. (2020)*

2.2 *Pressure-time evolution interpretation*

In order to take advantage of the standard explosion tests realized in the 20L sphere, some authors such as Silvestrini et al. (2008) developed a correlation between the laminar burning velocity and the parameters P_{max} and K_{St}. Explosions tests were conducted on nanocellulose in the standard 20 L sphere according to international standards (EN 14034-1, 2004; EN 14034-2, 2006), but using chemical igniters of 100 J to avoid an overdriving phenomenon, knowing the minimum ignition energy of the dried nanocellulose is 5 mJ (Santandrea et al., 2019b). Since the values of laminar burning velocity obtained by flame propagation observation are available only at 500 g.m$_{-3}$, only the results obtained for this concentration are discussed in this work. Nevertheless, tests were performed over a wide range of dust concentration (up to 1250 g.m$_{-3}$), and the influence of the dust concentration on the laminar burning velocity is discussed by Santandrea et al. (2020). The laminar burning velocity S_{u0} of starch was then calculated from the knowledge of the explosion overpressure P_m and rate of pressure rise $(dP/dt)_m$, using the correlation established by Silvestrini et al. (2008):

$$S_u{}^0 = 0.11 \frac{\left(\frac{dP}{dt}\right)_m V^{1/3}}{P_m \left(\frac{P_m}{P_0}\right)^{0.14} \left(\frac{P_m}{P_0}\right)^{\left(\frac{1}{\gamma}\right)}} \tag{1}$$

where V is the vessel volume, P_0 the atmospheric pressure and γ the ratio of specific heats. This correlation is based on several assumptions, such as the spherical expansion of the flame, the neglecting of the turbulent length scales and the fact that the burnt gases are trapped behind the expanding flame front (Silvestrini et al., 2008).

3. One-dimensional modelling of flame propagation

Complementary to experiments relying on the flame visualization and the pressure-time evolution, the laminar flame velocity was approached using a one-dimension flame propagation model developed by Torrado et al. (2018) and initially designed to describe gas and hybrid mixtures explosions. The model was then adapted to nanocellulose using the same hypothesis than for flame visualization experiments, i.e. considering a fast devolatilization of the dust and a flame propagation kinetically limited by the combustion of the pyrolysis gases. Moreover, since cellulose and starch are both polymers formed of glucose chains, both compounds are assumed to produce the same pyrolysis gases when tested in the same conditions. Thus, pyrolysis experiments were conducted on wheat starch in a Godbert-Greenwald oven modified according to Dufaud et al. (2012b) to collect the post-pyrolysis gases. The composition obtained for a concentration of approximately 500 g.m$_{-3}$ and a temperature of 973K was then used as the initial composition of the fuel (Fig. 2) in the model for a numerical determination of the laminar flame velocity of nanocellulose.

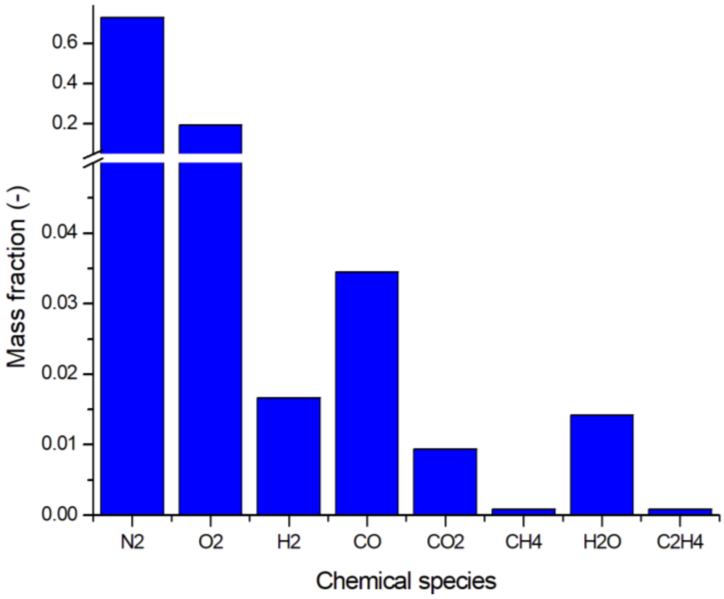

Fig. 2. *Initial composition of the nanocellulose pyrolysis gases/air mixture considered in the flame propagation model for 500 g.m3 of nanocellulose*

The simulation domain is constituted of a horizontal tube with a numerical length of 5 cm involving two parallels walls divided into three distinct zones: preheat, reaction and post-flame, knowing that the flame propagates from the post-flame zone to the preheat zone. Mass, species and energy balances, notably based on the properties of the considered chemical species, were then expressed in the simulation domain. Since the main chemical species constituting the pyrolysis gases of nanocellulose are the same than the species initially considered in the model for the flame propagation of a methane/air flame (Torrado et al., 2018), the same reaction mechanisms were used. However, since the pyrolysis step mainly produced carbon monoxide, a reversible oxidation reaction of this gas to produce carbon dioxide was added (Table 1, reactions 7 and -7).

Table 1: *Reaction mechanisms considered for the combustion of the pyrolysis gases (Units cal, mol, m, s)*

#	Reaction	A_i	β	E_i	Reaction order	Reference
1	$CH_4 + 0.5O_2 \rightarrow CO + 2H_2$	2.45×10^9	0	3×10^4	$[CH_4]^{0.5} [O_2]^{1.25}$	(Jones and Lindstedt, 1988)
2	$CH_4 + H_2O \rightarrow CO + 3H_2$	3×10^5	0	3×10^4	$[CH_4] [H_2O]$	(Jones and Lindstedt, 1988)
3	$CO + H_2O \rightarrow CO_2 + H_2$	2.75×10^6	0	2×10^4	$[CO] [H_2O]$	(Jones and Lindstedt, 1988)
-3	$CO_2 + H_2 \rightarrow CO + H_2O$	9×10^7	0	2.8×10^4	$[CO_2] [H_2]$	(Torrado et al., 2018)
4	$H_2 + 0.5O_2 \rightarrow H_2O$	3.85×10^{13}	-1	4×10^4	$[H_2]^{0.25} [O_2]^{1.50}$	(Jones and Lindstedt, 1988)
-4	$H_2O \rightarrow H_2 + 0.5O_2$	9.27×10^{18}	0.88	9.8×10^4	$[H_2O] [H_2]^{-0.75} [O_2]$	(Andersen et al., 2009)
5	$O_2 \rightarrow 2O\cdot$	1.5×10^9	0	1.13×10^5	$[O_2]$	(Frassoldati et al., 2009)
6	$H_2O \rightarrow H\cdot + OH\cdot$	2.3×10^{22}	-3	1.2×10^5	$[H_2O]$	(Frassoldati et al., 2009)

7	$CO + 0.5O_2 \rightarrow CO_2$	1.26 x 10^4	0	10 x 10^3	$[CO]\ [O_2]^{0.25}\ [H_2O]^{0.5}$	(Andersen et al., 2009)
-7	$CO_2 \rightarrow CO + 0.5O_2$	1.95 x 10^{12}	-0.97	78.4 x 10^3	$[CO_2]\ [H_2O]^{0.5}\ [O_2]^{-0.25}$	(Andersen et al., 2009)

The calculation of the flame velocity then relies on the numerical integration of the differential equations of mass, species and energy. The space derivatives were discretized using the finite volume method with 160 control volumes to obtain a system of ordinary differential equations, which was solved using the integration functions ODE in Matlab. The expression of the mass and species balance, the mass diffusion fluxes and the energy balance, along with the numerical resolution, are properly described by Torrado et al. (2018).

The resolution of the ordinary differential equations requires an initial value of the temperature and mass fractions of all the considered species in every numerical domain. The composition in the preheat zone, which represents 25% of the numerical domain, is defined by the mass fractions of the considered mixture in laboratory conditions. As a first approximation, the mass fractions and temperature are assumed to evolve linearly in the reaction zone, implying those values are known if the initial and final conditions are fixed. To estimate the conditions in the post-flame zone (70% of the considered distance), the adiabatic temperature and mass fraction of the burnt gases for a steady flame were calculated using PREMIX program (Kee et al., 1993). This approach, represented in Fig. 3, was used to reduce the calculation time and to improve the convergence of the program, by initializing all the conditions close to a stable solution. Since this numerical model aims at considering the radiative heat transfer induced by the presence of nanoparticles in the mixture, which is not the case of the PREMIX program, this latter was not considered as a suitable method to determine the laminar burning velocity of nanopowders.

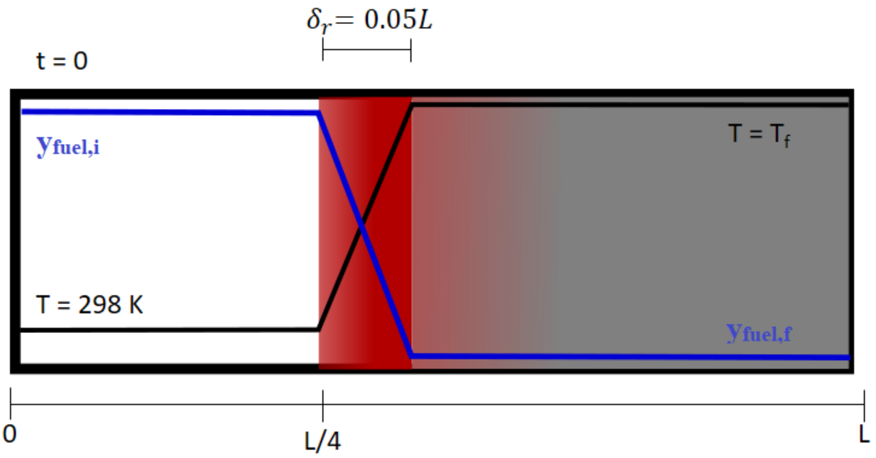

Fig. 3. Schema of the initial conditions of the temperature and fuel fraction in each zone of the flame (adapted from Torrado et al. (2018))

The system previously defined was then analyzed considering a distance L of 5 cm and an integration time of 50 ms. The evolution of the temperature with time is presented in Fig. 4 at different positions to describe each zone, knowing that the preheat zone initially spreads up to 1.25 cm and that the post-flame zone starts at 1.5 cm. It appears that, in the post-flame zone (2.5 and 5 cm), the temperature is constant with time, since the reaction already occurred. Then, a fast increase of the temperature after a few milliseconds is visible in the reaction zone, and progressively shifts toward the preheat zone with time, describing the propagation of the flame.

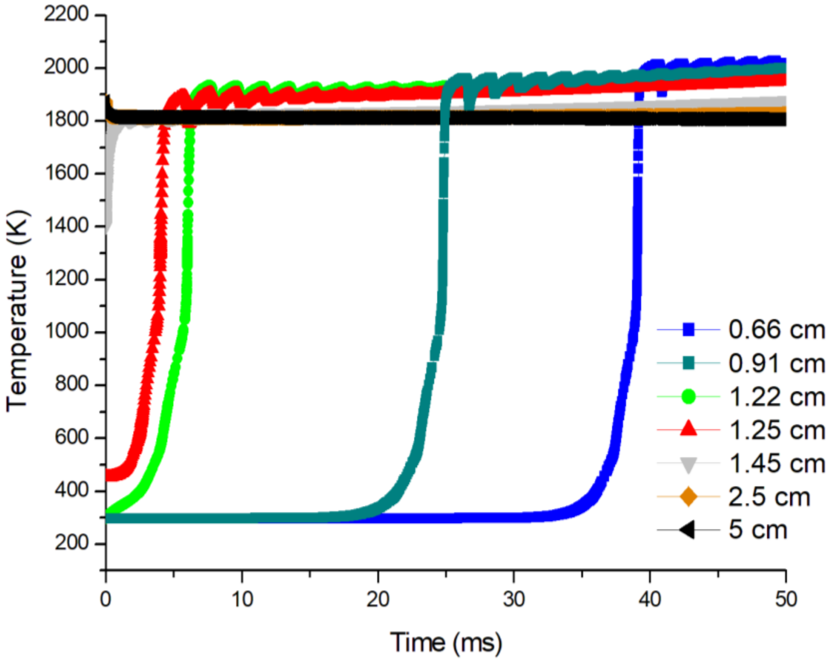

Fig. 4. *Evolution of the temperature with time for different control volumes when modelling the flame propagation of nanocellulose (quiescent conditions, 500 g.m-3)*

4. Results and discussion

4.1 Combustion of the pyrolysis gases

The position of the flame front, assimilated to the position of the highest temperature, was recorded for each integration time and is presented in Fig. *5*. It should be reminded that the reaction zone was initially located between 1.25 cm and 1.5 cm. However, before 1 ms, a very fast displacement of the flame is observed, preventing a clear determination of the flame front position between 1.4 and 1.5 cm. Nevertheless, a linear evolution of the flame position with time can be observed from 1 ms to 50 ms. A laminar flame velocity of 17.5 cm.s-1, represented by the slope of the linear regression, was then obtained for the combustion of nanocellulose. It should be stressed that this value should be viewed with caution as the pyrolysis step has been considered as very fast with regard to the combustion of the pyrolysis gases, which is a strong assumption.

The flame velocity calculated using the flame propagation model was then compared to the values experimentally obtained by Santandrea et al. (2020) (Table 2). The value determined numerically appears to be of the same order of magnitude than the experimental ones, with a maximum difference of 22% with regard to the laminar flame velocity measured in the flame propagation tube. This value is also consistent with laminar flame velocity of “wood gas” at the stoichiometry mentioned in the literature by Mollenhauer and Tschöke (2010) and Przybyla et al. (2008), reaching around 14 cm.s-1 and 20 cm.s-1 respectively. Nevertheless, this difference between experimental and numerical values can come from experimental uncertainties, but can also be due to the neglecting of the contribution of the radiative heat transfer to the flame propagation. Indeed, if the pyrolysis step can decrease the flame velocity due to a kinetic limitation, the fresh or unburnt remaining particles can also improve the flame propagation through a heat transfer modification in the preheat zone. To evaluate this influence, the contribution of the radiative heat transfer, added to the flame propagation model by Torrado et al. (2018) and based on the work of Haghiri and Bidabadi (2010), is now considered during the combustion of the pyrolysis gases of nanocellulose.

DOI: 10.7795/810.20200724

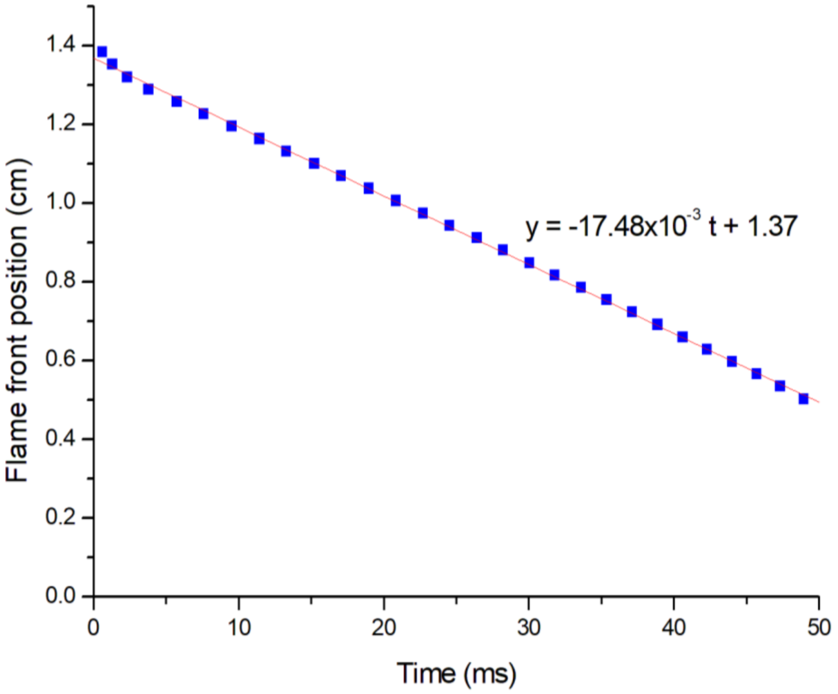

Fig. 5. *Evolution of the flame front position with time during the combustion of nanocellulose pyrolysis gases*

Table 2: *Numerical and experimental values of laminar flame velocity of nanocellulose*

Determination method	**Laminar flame velocity (cm.s-1)**
Flame propagation model	17.5
Flame visualization: propagation tube	21.4 ± 1
Flame visualization: vented sphere	20.5 ± 3
Pressure-time evolution: application of Silvestrini et al. (2008) correlation	19.9 ± 3

4.2 Influence of the radiative heat transfer

Since the pyrolysis of nanocellulose particles and the combustion of the pyrolysis gases happen simultaneously, the unburnt particles can impact the flame propagation by variations of the heat transfer. However, the remaining dust can hardly be quantified and characterized for each integration time without taking the pyrolysis kinetics into account. Thus, several dust concentrations, assumed constant with time, were tested. The dust clouds were supposed to be homogeneous over the simulation domain and constituted of monodispersed spherical particles. Moreover, due to the agglomeration of the nanoparticles, the particle size after dispersion must be considered (Santandrea et al., 2019a). Particle size distribution measurements after dispersion of nanocellulose in the 20L sphere led to a mean value of 10 µm (Santandrea et al., 2020). This value was then chosen as a reference for the calculation, along with 100 nm, to represent the primary particles, and 60 µm, which is the mean diameter of nanocellulose agglomerates before dispersion, i.e. the agglomerates not broken by the dispersion process. In this model, Mie scattering, valid for micron particles, was then used to define the radiative heat transfer. It should be noted that Rayleigh scattering, encountered for particles smaller than 100 nm, do not contribute significantly to the flame expansion due to the emission in every direction (Hong and Winter, 2006). Thus, decreasing the particle size below this size would only decrease the radiative heat transfer contributing to the flame propagation, and so the flame velocity. The concentration of dust that did not react during the combustion of the 500 g.m-3 of nanocellulose was varied from 2.5 g.m-3 to 100 g.m-3, to represent the radiative heat transfer at the beginning and at the end of the reaction. The radiative heat transfer was then added to the energy balance, and the heat capacity of the dust was then taken into account during the calculation of the mean heat capacity of the mixture. Due to the assumption of a fast pyrolysis, the reactions involving the solid particles were not considered in the model. However, it should be noted that Torrado et al. (2018) evidenced that the contribution of the chemical reactions of the powder is negligible with regard to the contribution of the radiative heat transfer at low concentrations (2.5 g.m-3).

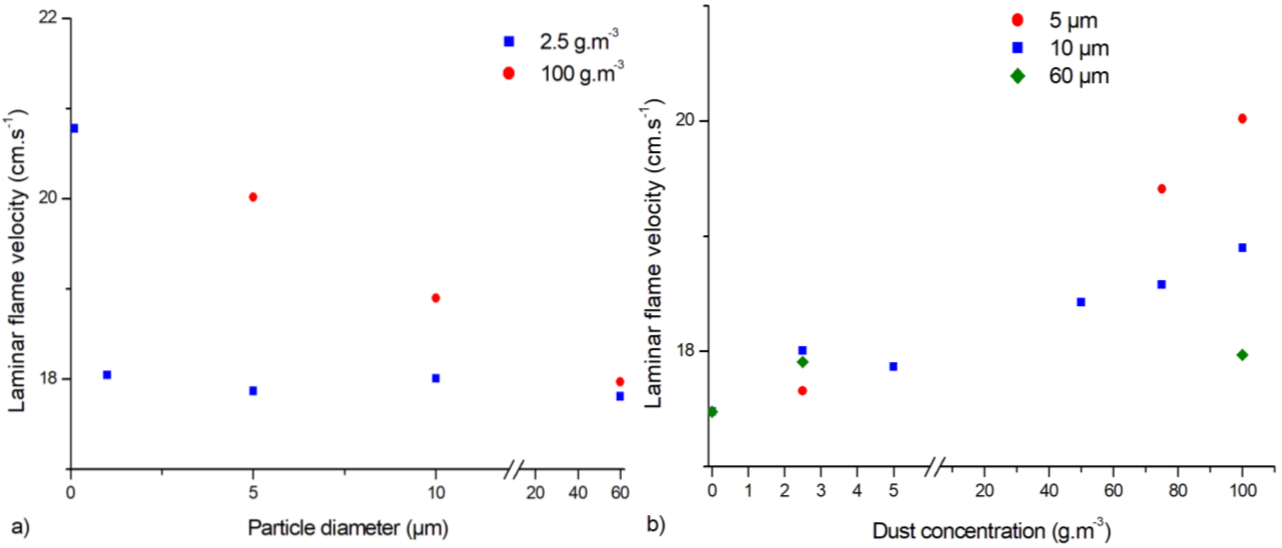

Fig. 6. *Influence of the a) primary diameter and b) of the dust concentration considered for the radiative heat transfer on the laminar flame velocity of nanocellulose (500 g.m-3)*

In Figure 6a, it appears that small particles contribute more to the radiative heat transfer than bigger particles in the micro-range. Indeed, particles of 60 µm bring similar contribution to the flame acceleration, i.e. around 0.5 cm.s-1, at 2.5 g.m-3 and 100 g.m-3, whereas 100 g.m-3 of particles of 5 µm lead to a flame velocity of 20 cm.s-1, i.e. 14% higher than the flame velocity of the pyrolysis gases. It should be underlined that the contribution of particles of 100 nm to the radiative heat transfer may be overestimated since Mie scattering was considered for the calculation whereas Rayleigh scattering is more representative of the heat transfer of nanoparticles. In Figure 6b, it appears that a dust concentration of 2.5 g.m-3 leads to a mean flame velocity of around 17.8 cm.s-1 for particles between 5 and 60 µm. Increasing the concentration then also increases the contribution of the radiative heat transfer to the flame propagation, reaching 20.0 cm.s-1 when considering 100 g.m-3 of particles of 5 µm.

Therefore, both the dust concentration and the particle size are of great importance when considering the radiative heat transfer. Indeed, the absorption coefficient K_a and the scattering coefficient K_s directly depend on the dust concentration, the dust density and the particle size, as follows (Haghiri and Bidabadi, 2010):

$$K_a = \frac{3}{2}\frac{C}{\rho_p\, d_p}\, Q_{abs} \tag{2}$$

$$K_s = \frac{3}{2}\frac{C}{\rho_p\, d_p}\, Q_{sca} \tag{3}$$

where C is the dust concentration, ρ_p the particle density, d_p the particle diameter and Q_{abs} and Q_{sca} respectively the absorption and scattering efficiency.

The absorption and scattering coefficients are then directly proportional to the total surface area (TSA) developed by the particles in the cloud, which can be expressed as follows for spherical particles:

$$TSA = \frac{6\,C}{\rho_p\, d_p} \tag{4}$$

A linear evolution of the calculated flame velocity with the total surface area developed by the particles considered in the radiative heat transfer appears in Fig. . Then, it can be observed that the radiative heat transfer generated by particles developing a total surface area lower than 10 $m^2.m^{-3}$ does not lead to a significant increase of the flame velocity, with values between 17.5 and 18 $cm.s^{-1}$. However, when considering a total surface area of 100 $m^2.m^{-3}$, a flame velocity of 20.8 $cm.s^{-1}$ is reached, thus proving the importance of considering the surface area when analysing dust explosions, instead of focusing only on mass concentration. It should also be noted that increasing the concentration too much would lead to an important increase of absorption, which would limit the heat radiation in the preheat zone.

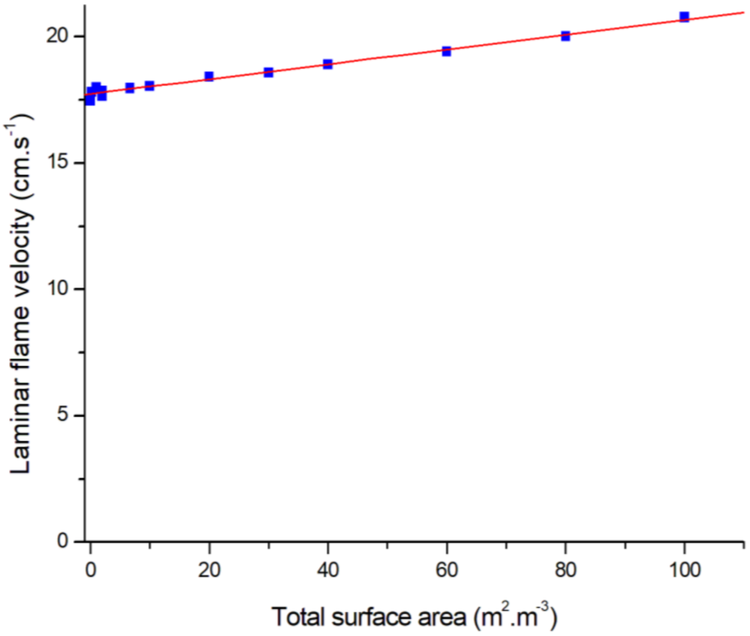

Fig. 7. *Influence of the total surface area of the particles implied in the radiative heat transfer on the flame velocity*

5. Conclusions

The laminar burning velocity of nanocellulose has been determined using a one-dimensional flame propagation model adapted from a model already validated for hybrid mixtures. The numerical system, composed of mass and energy balances equations and of mass reaction rates adapted to the combustion reactions, was solved by the finite volume method. Since the devolatilization of organic powders is fast, the chemical reactions were considered limited to the combustion of the pyrolysis gases. A first value of laminar flame velocity of 17.5 $cm.s^{-1}$ was obtained for 500 $g.m^{-3}$ of nanocellulose, which is close to values experimentally measured in a flame propagation tube or a 20 L sphere, around 21 $cm.s^{-1}$, thus showing a good consistency between the numerical and experimental approaches.

However, since, in practice, the devolatilization of the particles is not instantaneous, the remaining particles can contribute to the radiative heat transfer, which was added to energy balance. Due to the tendency of nanoparticles to agglomerate, different particle diameters and dust concentrations were tested. Thus, although the heat transfer of nanoparticles tends to be neglected due to Rayleigh scattering, which does not contribute to the flame propagation, the contribution of the remaining micro-agglomerates after dispersion must be considered. Indeed, the existence of a linear relation

DOI: 10.7795/810.20200724

between the laminar flame velocity and the total surface area developed by the particles implied in the radiative heat transfer was highlighted. A flame velocity reaching 20.8 $cm.s^{-1}$ for a total surface area of 100 $m^2.m^{-3}$ considered for the radiative heat transfer was then obtained, showing a strong impact of the heat radiation on the flame propagation.

Acknowledgements

This work was supported financially by the French Ministry for the Ecological and Solidary Transition and The French Ministry for Higher Education and Research.

References

Amyotte, P.R., Chippett, S., Pegg, M.J., 1988. Effects of turbulence on dust explosions. Progress in Energy and Combustion Science 14, 293–310. https://doi.org/10.1016/0360-1285(88)90016-0

Andersen, J., Rasmussen, C.L., Giselsson, T., Glarborg, P., 2009. Global Combustion Mechanisms for Use in CFD Modeling under Oxy-Fuel Conditions. Energy & Fuels 23, 1379–1389. https://doi.org/10.1021/ef8003619

Andrews, G.E., Bradley, D., 1972. Determination of burning velocities: A critical review. Combustion and Flame 18, 133–153. https://doi.org/10.1016/S0010-2180(72)80234-7

Belerrajoul, M., 2019. Modélisation multi-échelle de la combustion d'un nuage de particules (PhD Thesis). National Polytechnic Institute of Toulouse.

Boilard, S.P., Amyotte, P.R., Khan, F.I., Dastidar, A.G., Eckhoff, R.K., 2013. Explosibility of micron- and nano-size titanium powders. Journal of Loss Prevention in the Process Industries 26, 1646–1654. https://doi.org/10.1016/j.jlp.2013.06.003

Bouillard, J., Vignes, A., Dufaud, O., Perrin, L., Thomas, D., 2010. Ignition and explosion risks of nanopowders. Journal of Hazardous Materials 181, 873–880. https://doi.org/10.1016/j.jhazmat.2010.05.094

Bradley, D., Lee, J.H.S., 1984. . Proceedings of the first international colloquium on the explosibility of industrial dusts 220–223.

Clavin, P., 1985. Dynamic behavior of premixed flame fronts in laminar and turbulent flows. Progress in Energy and Combustion Science 11, 1–59. https://doi.org/10.1016/0360-1285(85)90012-7

Cuervo, N., 2015. Influences of turbulence and combustion regimes on explosions of gas-dust hydrid mixtures (PhD Thesis). The University of Lorraine, France.

Dahoe, A.E., Cant, R.S., Scarlett, B., 2001. On the Decay of Turbulence in the 20-Liter Explosion Sphere. Flow, Turbulence and Combustion 67, 159–184. https://doi.org/10.1023/A:1015099110942

Dahoe, A.E., Hanjalic, K., Scarlett, B., 2002. Determination of the laminar burning velocity and the Markstein length of powder–air flames. Powder Technology, Special issue i in Honour of Prof Jimbo 122, 222–238. https://doi.org/10.1016/S0032-5910(01)00419-3

Di Benedetto, A., Russo, P., 2007. Thermo-kinetic modelling of dust explosions. Journal of Loss Prevention in the Process Industries, Selected Papers Presented at the Sixth International Symposium on Hazards, Prevention and Mitigation of Industrial Explosions 20, 303–309. https://doi.org/10.1016/j.jlp.2007.04.001

Dufaud, O., Khalili, I., Cuervo-Rodriguez, N., Olcese, R.N., Dufour, A., Perrin, L., Laurent, A., 2012a. Highlighting the Importance of the Pyrolysis Step on Dusts Explosions. Chemical Engineering Transactions 26, 369–374.

Dufaud, O., Poupeau, M., Khalili, I., Cuervo, N., Christodoulou, M., Olcese, R., Dufour, A., Perrin, L., 2012b. Comparing Pyrolysis Gases and Dusts Explosivities: A Clue to Understanding Hybrid Mixtures Explosions? Ind. Eng. Chem. Res. 51, 7656–7662. https://doi.org/10.1021/ie201646s

Dufaud, O., Vignes, A., Henry, F., Perrin, L., Bouillard, J., 2011. Ignition and explosion of nanopowders: something new under the dust. Journal of Physics: Conference Series 304, 012076. https://doi.org/10.1088/1742-6596/304/1/012076

Eckhoff, R.K., 2003. Dust Explosions in the Process Industries - 3rd Edition, 3rd ed. Gulf Professional Publishing.

EN 14034-1, 2004. Determination of explosion characteristics of dust clouds — Part 1: Determination of the maximum explosion pressure □max of dust clouds.

EN 14034-2, 2006. Determination of explosion characteristics of dust clouds — Part 2: Determination of the maximum rate of explosion pressure rise (dp/dt)max of dust clouds.

Frassoldati, A., Cuoci, A., Faravelli, T., Ranzi, E., Candusso, C., Tolazzi, D., 2009. Simplified kinetic schemes for oxy-fuel combustion. 1 st International Conference on Sustainable Fossil Fuels for Future Energy – S4FE 2009.

Haghiri, A., Bidabadi, M., 2010. Modeling of laminar flame propagation through organic dust cloud with thermal radiation effect. International Journal of Thermal Sciences 49, 1446–1456. https://doi.org/10.1016/j.ijthermalsci.2010.03.013

Hong, S.-H., Winter, J., 2006. Size dependence of optical properties and internal structure of plasma grown carbonaceous nanoparticles studied by *in situ* Rayleigh-Mie scattering ellipsometry. Journal of Applied Physics 100, 064303. https://doi.org/10.1063/1.2338132

Jones, W.P., Lindstedt, R.P., 1988. Global reaction schemes for hydrocarbon combustion. Combustion and Flame 73, 233–249. https://doi.org/10.1016/0010-2180(88)90021-1

Karlovitz, B., Denniston, D.W., Wells, F.E., 1951. Investigation of Turbulent Flames. J. Chem. Phys. 19, 541–547. https://doi.org/10.1063/1.1748289

Kee, R.J., Grcar, J.F., Smooke, M.D., Miller, J.A., Meeks, E., 1993. PREMIX: A FORTRAN Program for Modeling Steady Laminar One-Dimensional Premixed Flames.

Krietsch, A., Scheid, M., Schmidt, M., Krause, U., 2015. Explosion behaviour of metallic nano powders. Journal of Loss Prevention in the Process Industries 36, 237–243. https://doi.org/10.1016/j.jlp.2015.03.016

Markstein, G.H., 1964. Non-steady flame Propagation. P22, Pergarmon, New York.

Mollenhauer, K., Tschöke, H., 2010. Handbook of Diesel Engines. Springer Science & Business Media.

Murillo, C., Amín, M., Bardin-Monnier, N., Muñoz, F., Pinilla, A., Ratkovich, N., Torrado, D., Vizcaya, D., Dufaud, O., 2018. Proposal of a new injection nozzle to improve the experimental reproducibility of dust explosion tests. Powder Technology 328, 54–74. https://doi.org/10.1016/j.powtec.2017.12.096

Przybyla, G., Ziolkowski, L., Szlęk, A., 2008. Performance of SI engine fuelled with LCV gas. Poland: Institute of Thermal Technology.

Santandrea, A., Gavard, M., Pacault, S., Vignes, A., Perrin, L., Dufaud, O., 2020. 'Knock on nanocellulose': Approaching the laminar burning velocity of powder-air flames. Process Safety and Environmental Protection 134, 247–259. https://doi.org/10.1016/j.psep.2019.12.018

Santandrea, A., Pacault, S., Perrin, L., Vignes, A., Dufaud, O., 2019a. Nanopowders explosion: Influence of the dispersion characteristics. Journal of Loss Prevention in the Process Industries 62, 103942. https://doi.org/10.1016/j.jlp.2019.103942

Santandrea, A., Vignes, A., Krietsch, A., Perrin, L., Laurent, A., Dufaud, O., 2019b. Some Key Considerations when Evaluating Explosion Severity of Nanopowders. Chemical Engineering Transactions 77, 235–240. https://doi.org/10.3303/CET1977040

Silvestrini, M., Genova, B., Leon Trujillo, F.J., 2008. Correlations for flame speed and explosion overpressure of dust clouds inside industrial enclosures. Journal of Loss Prevention in the Process Industries 21, 374–392. https://doi.org/10.1016/j.jlp.2008.01.004

Skjold, T., 2003. Selected aspects of turbulence and combustion in 20-Litre explosion vessel (Master thesis). University of Bergen, Norway.

Torrado, D., Pinilla, A., Amin, M., Murillo, C., Munoz, F., Glaude, P.-A., Dufaud, O., 2018. Numerical study of the influence of particle reaction and radiative heat transfer on the flame velocity of gas/nanoparticles hybrid mixtures. Process Safety and Environmental Protection 118, 211–226. https://doi.org/10.1016/j.psep.2018.06.042

Traoré, M., Dufaud, O., Perrin, L., Chazelet, S., Thomas, D., 2009. Dust explosions: How should the influence of humidity be taken into account? Process Safety and Environmental Protection, 12th International Symposium of Loss Prevention and Safety Promotion in the Process Industries 87, 14–20. https://doi.org/10.1016/j.psep.2008.08.001

Yao, N., Wang, L., Bai, C., Liu, N., Zhang, B., 2020. Analysis of dispersion behavior of aluminum powder in a 20 L chamber with two symmetric nozzles. Process Safety Progress 39. https://doi.org/10.1002/prs.12097

Zalosh, R., 2019. Dust explosions: Regulations, standards, and guidelines, in: Methods in Chemical Process Safety. Elsevier, pp. 229–282. https://doi.org/10.1016/bs.mcps.2019.03.003

Zhen, G., Leuckel, W., 1997. Effects of ignitors and turbulence on dust explosions. Journal of Loss Prevention in the Process Industries 10, 317–324. https://doi.org/10.1016/S0950-4230(97)00021-1

DOI: 10.7795/810.20200724

Construction of a 4 m long test rig for experimental investigations on flame propagation in combustible dust/air mixtures

Katja Hüttenbrenner [a], Hannes Kern [b], Florian Toth [a], Julian Glechner [a] & Harald Raupenstrauch [a]

[a] Montanuniversitaet Leoben, Leoben, Austria
[b] IRIS - Industrial Risk and Safety Solutions, Vorau, Austria

E-mail: katja@nuculeus.at

Abstract

Currently, safety relevant characterization of combustible dusts strongly depends on testing methods. Therefore, the direct scale up of results and the applicability to larger vessels is discussable. Research in the field of gas explosions shows that one alternative to safety parameters is the use of the laminar flame velocity for the layout of relief systems (NFPA Standard 68 and 69). For dust explosions this might also be more suitable but still has severe flaws. Currently flame velocities are determined through tube methods, which can still not guarantee an adequately low level of turbulence for the measurements. Aim of this paper is to describe the construction of a 4 m long and 800 mm diameter testing tube to be used to investigate the ignition behaviour and the flame propagation in large volumes through a combustible dust/air mixture under conditions of low initial turbulence. After previous investigations on the flame velocity in an explosion tube with a length of 2 m, the motivation for the work on a larger scale was to gain further understanding of flame propagation in larger volumes. Compared to the smaller 2 m combustion tube wall effects and other influencing factors on flame propagation are significantly reduced in the larger setup. Therefore, not only the length, but also the cross-section was extended. The size of the tube and moreover the innovative dust feed enable a state at the bottom of the combustion tube with very low initial turbulence. The movement of the dust particles, inserted into the tube through a specially designed dust feeding device, was simulated using computational fluid dynamics (CFD) models in the open-source software OpenFOAM®. An Euler-Lagrangian approach was chosen to calculate the particle-laden flow regime of the gaseous phase. For measurement purposes photooptical sensors and thermocouples were installed along the length of the tube. Analysis of these sensors give an impression of flame propagation in the investigated dust/air mixture. At the bottom of the tube a continuous spark igniter is used as ignition source. This paper focuses on the construction and start up of the described large scale test rig.

Keywords: *flame propagation, tube method, scale up, CFD simulation*

1. Introduction

Safety relevant characterisation of combustible dust, as well as gas, is done by standardized methods in specially designed and standardized apparatus like the 20-Liter-Siwek chamber. The resulting values are strongly dependent on the testing method. In the field of gas explosions researchers use as one alternative to the K_G value the laminar flame velocity for the layout of relief systems. This method is described in the NFPA Standard 68 and 69 and is a new approach compared to European standards. In the field of dust explosions this approach could also be a way to succeed. But for this purpose, an experimental setup to determine the laminar flame velocity of dust/air mixtures is still missing. Currently, experimental determination of flame velocities in dust/air mixtures is done by the help of the so-called tube method, invented by Mallard and Le Chatelier. The explosion chamber is a tube and the dust/air cloud ignites at one end and propagates to the other. Studies conducted by various authors (Palmer & Tonkin, 1971; Proust & Veyssiére, 1988; Han, 2000; Krause, 2002; Kern, 2013) follow different approaches to achieve low turbulence levels, essential to reach laminar combustion conditions. Aim of these research efforts is to obtain the laminar flame velocity as a parameter for safety equipment layout independent from the testing method. Moreover, the use for calculation purposes in explosion simulation would be a step nearer to tailor-made safety systems. Other possibilities for testing methods can be found in literature, however, often turbulent conditions are produced by these setups (cf. Cao et al. 2014, Skjold et al. 2014). Flame propagation in vertical ducts shows a significant increase in speed along the length of the tube (Krause, 2002). Besides other effects turbulence caused by wall effects is one of the influencing factors leading to this behaviour. A scale up would possibly lead to a reduction of these wall effects especially directly after ignition. Therefore, a 4 m long and 800 mm diameter testing rig was constructed to gain further understanding of the flame propagation. Large-scale tests done by other research teams (cf. Eckhoff et al., 1987; Skjold et al., 2014; Taveau, 2017) often use pressure difference for dust insertion and turbulent conditions are produced for dispersion purposes. To be able to carry out studies on combustion under low turbulence conditions, a new the dust feeding system had to be designed in a way that allows particle feed and dispersion without adding further turbulence during the dust input procedure.

2. Investigations on flame propagation

Flame propagation in a combustible dust/air mixture can be investigated with different measurement devices, depending on the experimental setup. To cover the flame front various methods are known. One possibility is photooptical detection of the emitted light of the front. Another option could be the measurement of the flame temperature. Electrical resistance measurement is also used and for the detection of the burning zone other researchers install ionisation probes in their apparatus.

In the sections below the current experimental setup for investigations on flame propagation is described. It works as a basis and test ground for the development of the larger test rig described in the introduction.

2.1 Combustion tube

Basis for the construction of a larger experimental rig is a smaller explosion tube introduced by Kern (Kern, 2013). This vertical tube with a length of 2,000 mm has an inner diameter of 140 mm and is made of transparent PMMA. With this setup it is possible to determine flame behaviour and flame speed in dust/air mixtures. The bottom section of the apparatus is the closed end and contains a spark ignition system. The middle section consists of the main explosion tube (PMMA) with a photooptical measurement system, the feeding device (screw-conveyor) is arranged at the top section which also holds an explosion flap and a flame arrester. The particle flow is gravity driven and leads to a good dispersion of the dust in the tube after around 500 mm from the feed point. The advantage of this arrangement is to be able to create repeatable conditions of the turbulence and dust dispersion in the combustion chamber (Hüttenbrenner et al., 2016). To be able to compare results with former studies Lycopódium (spore of club moss) and a modified maize starch were used as combustible dusts. Computational fluid dynamics (CFD) simulations of the described apparatus were done by other authors (Spijker, 2015) to receive an idea of the particle flow regime during experimental tests (cf. Fig. 1).

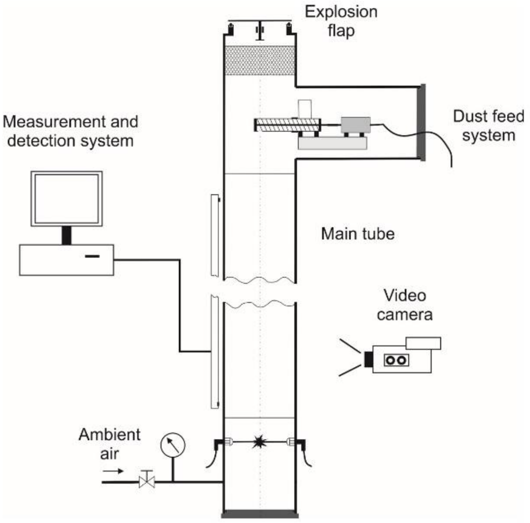

Fig. 1. *Scheme of the explosion tube, introduced by Kern (Kern, 2013)*

2.2 Photooptical measurement device

The flame front propagates along the length of the explosion tube and can be detected with photooptical measurement devices which are mounted along the vertical axis. The flame speed can be calculated (Eq. 2-1) out of the time interval between the offset points of the first and the second signal (Δt) and the distance between the two detection points (Δs).

$$s_f = \frac{\Delta s}{\Delta t} \qquad (2\text{-}1)$$

Photodiodes, which are mounted along the tube, help to detect the flame front and transform the incident light of the flame in an electrical signal, which can be process further. The used photodiode absorbs emitted light between 450 and 1,100 nm, nearly the whole visible light spectrum and parts of the infrared spectrum. Therefore, the photodiodes IF-D91 fit very well to the requirements. The setup is chosen in a way to prevent detection of scattered light. Just the impingement of orthogonal light on the device is detected. The response time is set to 15 ns. The light impulse produces a photocurrent at the photodiode, which gets processed with the help of a transimpedance amplifier. To get an idea of the resulted signal, Fig. 2 can be consulted. To detect the flame front and not scattered light the signal is overdriven for interpretation purpose.

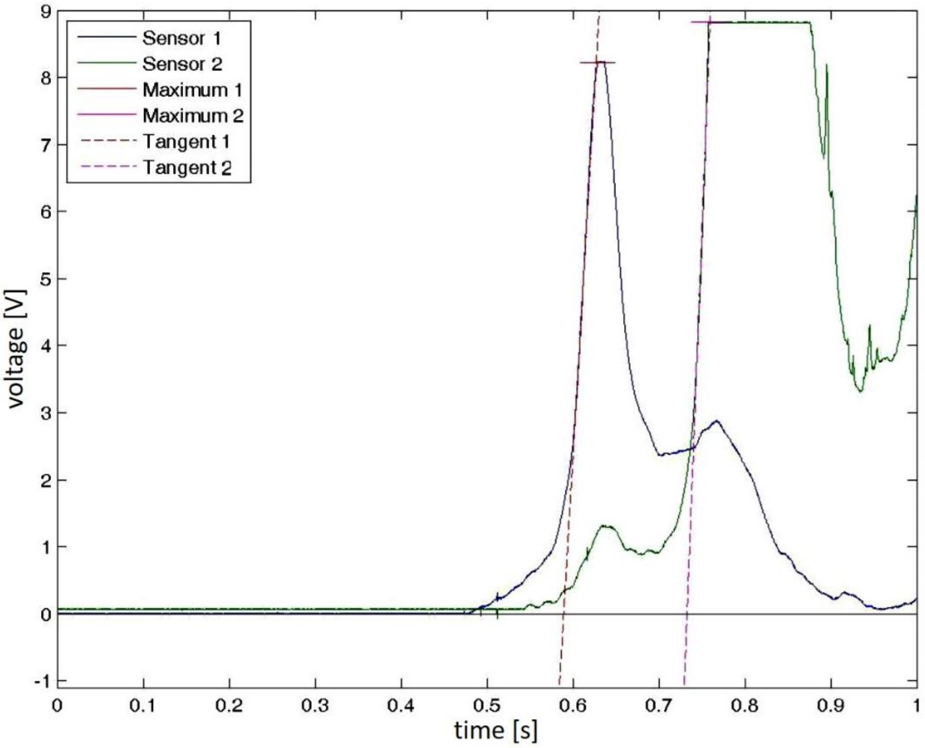

Fig. 2. *Results of flame detection between two measurement points in the explosion tube*

2.3 Flame temperature

For characterisation purpose of the flame front the temperature can be measured at any location in the explosion chamber of the test rig. Therefore, thermocouples with a diameter of 80 µm and a very fast reaction time are installed. The sampling rate is set at 100 Hz.

Experimental studies done by other authors (Smoot et al. 1977, Cashdollar et al. 1983, Veyssiére 1992) show that the displayed values of the thermocouples are lower than theoretical calculated values, caused by heat losses due to thermal radiation. Smoot et al. assume that besides radiative losses, char and ash layers on thermocouples could indicate measurement failures. Cashdollar and Hertzberg suggested a radiation correction factor up to 800 °K and Veyssiére stated that values of thermocouples are 500 to 600 °K lower than by other measuring devices, e.g. infrared pyrometers. Comparison studies done by Cashdollar and Hertzberg between thermocouples and pyrometers show particle temperatures at low dust concentrations 200 °K cooler. They assumed the continuous accretion of endothermically pyrolyzing particles on the thermocouples as explanation for lower values. A graphic of the used software for analysis can be seen in Fig. 3. However, an alternative of temperature values is the use for measuring the flame speed, which can be calculated in the same way as the photooptical method (cf. Eq. 2-1), whereas the time step of the temperature rise has to be detected.

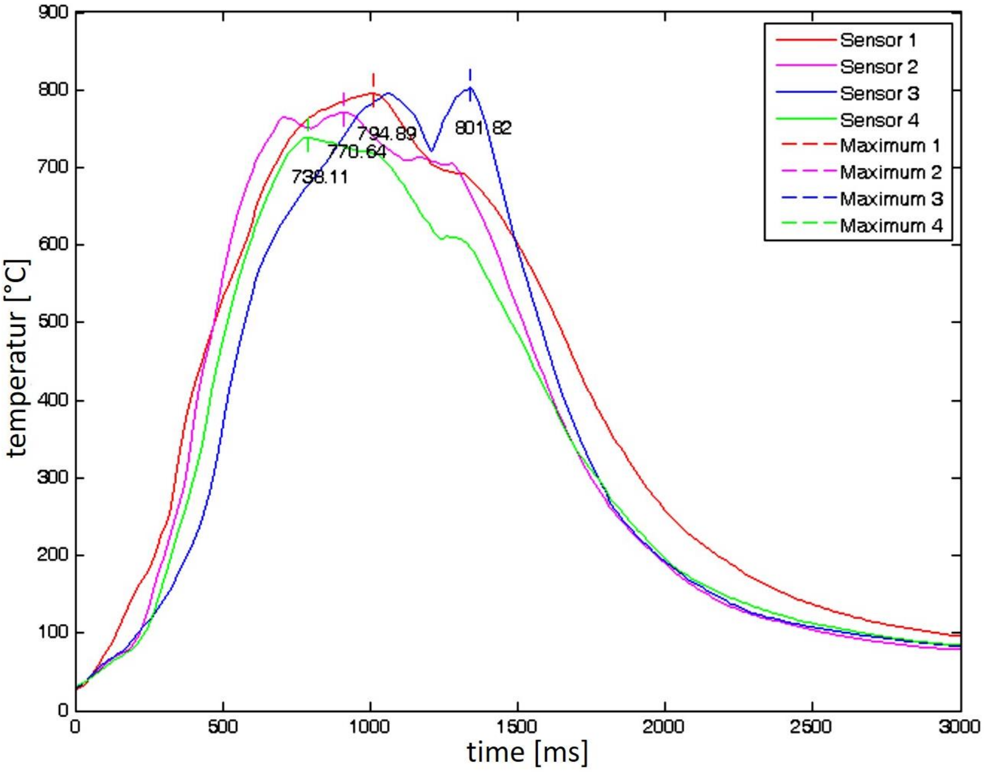

Fig. 3. *Graphic of the measured flame temperature during an experimental test*

3. Scale up and test rig construction

Motivation for the work on a larger scale of the experimental apparatus was to gain further understanding of flame propagation in a larger space with less disturbance by wall effects and other influencing parameters. Therefore, the cross-section of the test setup was extended from 140 mm (laboratory rig) to a diameter of 800 mm. With an ignition source in the middle of the cross-section at the bottom of the tube, the flame front has more time to spread without impacts until it reaches the tube wall. Based on the results obtained from CFD modelling the length of the explosion tube was chosen 4,000 mm, to generate adequate dust particle dispersion with low turbulence conditions. Within this length the dust particle flow from the top has enough time to disperse driven by gravity. The test rig itself is built of steel with several flange connections along the length to be able to insert various sensors for further research purposes. The bottom section of the tube is closed and holds an ignition source 530 mm above the bottom. The middle section of the test rig consists of the main explosion chamber with a volume of about 2.2 m³ and various detection devices, depending on the experimental setup. A balanced explosion flap on the top of the tube prevents impacts of the surrounding conditions during experiments on the one hand and releases the necessary cross-section when the flame front approaches on the other hand. Due to the fine balance of the flap system, a significant pressure increase within the tube can be avoided. A graphic of the test rig can be seen in Fig. 4.

DOI: 10.7795/810.20200724

Fig. 4. *CAD graphic of the constructed explosion tube*

As mentioned above, the ignition source is located at the bottom of the explosion tube. The used ignition spark has an energy level high enough to ignite the dust/air cloud, however, as low as possible to prevent further impact on the flame propagation. For spark generation steel electrodes with a distance of 6 mm are used. Prior to testing the minimum ignition energy and the minimum ignition temperature of the used dust is determined to ensure ignition. As ignition source for the proof of concept a spark with an electrical power amount of 30 W was used. Further experiments with Lycopodium and maize starch will be done with the same ignition spark, because a temperature of 1,200 °C is reached in the spark area.

3.1 Dust feeding device

At the top section of the explosion tube the feeding system is installed to create a dust dispersion in the explosion chamber with very low turbulence condition due to gravity driven flow. Four concentric inlet points were taken to reach an equal distribution of the whole cross-section (cf. Fig. 5). Next to a continuous feed rate to achieve a homogeneous distribution of the dust concentration along the height of fall, a reproduceable feed rate is necessary to ensure the same mass flow at all inlet points (cf. Fig. 6 and Fig. 7). The design of the device is alterable, therefore various dust samples with different particle sizes can be conveyed. Solution for this requirement was a specially designed dust feeding device (cf. Fig. 5), based on a stirrer with soft bristles attached and a changeable sieve in the bottom cap. The dust is transported with this stirrer through the sieve to prevent agglomeration of the dust particles. Due to this design various dust samples can be investigated and brought into the system with very low turbulence. A brushless bipolar hybrid stepper motor is used as actuator. A claw coupling connects the motor with the stirrer and a motor driver board was constructed to control the motor.

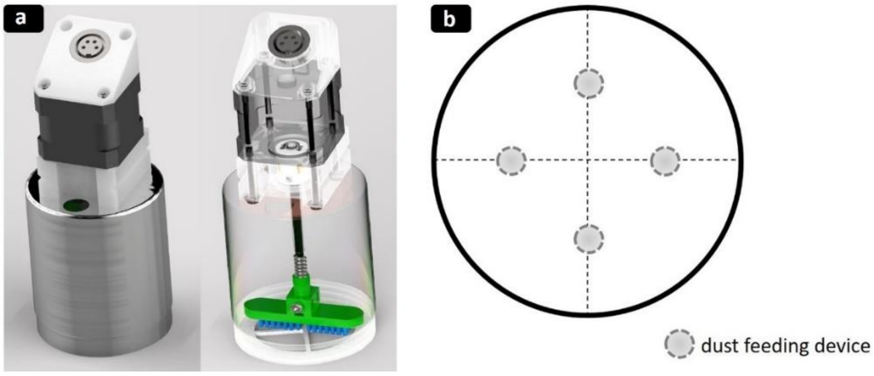

Fig. 5. *Graphic of the designed dust feeding device for the explosion tube (a) and location of the four devices in the cross-section at the top section of the tube (b)*

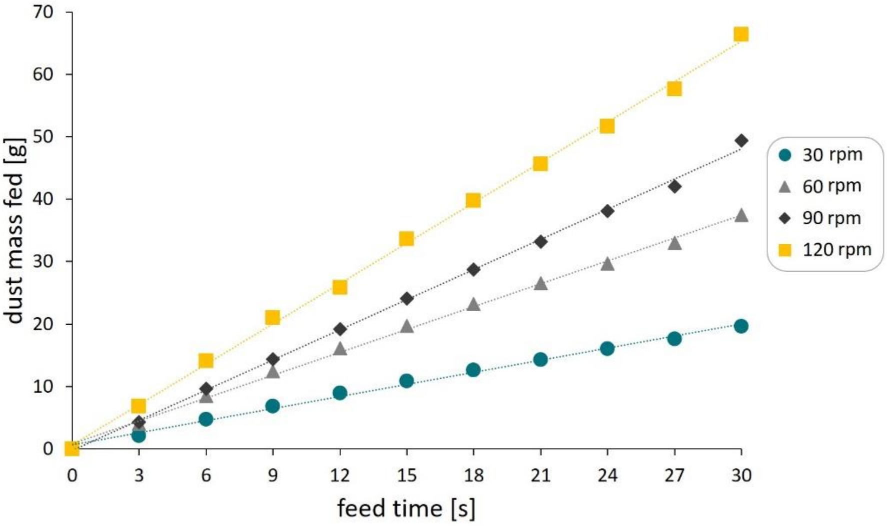

Fig. 6. *Results from preliminary tests of the feed rate in relation to the feed time of the feeding devices (mesh 200 µm)*

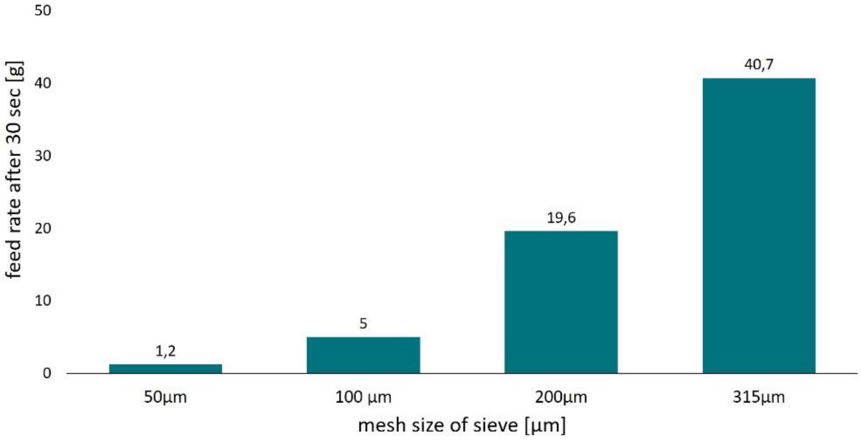

Fig. 7. *Results from preliminary tests of the production rate in relation to the mesh size of the designed feeding devices (30 rpm)*

3.2 *Particle flow in the explosion tube*

In order to get more information about particle movement of the inserted dust particles through the dust feeding device, the particle flow was calculated with the help of computational fluid dynamics (CFD) simulations in the open source software OpenFOAM® (Field Operation and Manipulation). Aim of the numerical model was the description of the particle distribution in a gravity driven two-phase-flow. *Lycopódium Clavátum* was modeled to be able to compare with former studies. Caused by the feeding method no considerable pressure gradient exists in the system, therefore the transient incompressible solver *pimpleFOAM* was used. For the calculation of the gas phase in a three dimensional solution space the finite-volume method was applied to solve the conservation equations for momentum and mass. (The OpenFOAM Foundation, 2015) To describe the particles an Euler-Lagrangian approach was adapted to calculate the particle-laden flow regime of the gaseous phase. In this method the gas phase is modelled a continuum in whose framework dispersed solid particles are tracked. Momentum between the phases were considered through two-way coupling. Caused by the low turbulence conditions the k-ε Launder Sharma turbulence model was suited (Davidson, 2015), a two-equation model which uses an approach that expresses the Reynolds stress with the help of the Boussinesq approximation. The model provides two conservation equations, one for the turbulent kinetic energy k and one for the dissipation energy ε from which the value can be deduced. To depict the influence of the turbulent fluid on the particles the *Discrete Random Walk* was used (Dehbi, 2006). A reduction of solution time of the Lagrangian phase could be achieved through *Particle Clustering*, an opportunity to transfer properties of one calculated particle to a user specified number of particles that are aggregated in a group defined as one *parcel*, which has the same properties as the particle itself. Generation of the finite-volume-mesh was done with the commercial software ICEM CFD through extrusion of a 2D O-mesh. Simulation results of the dust particle concentration in the vertical explosion tube during 15 sec with a continuous dust feed over 10 sec can be seen in Fig. 8.

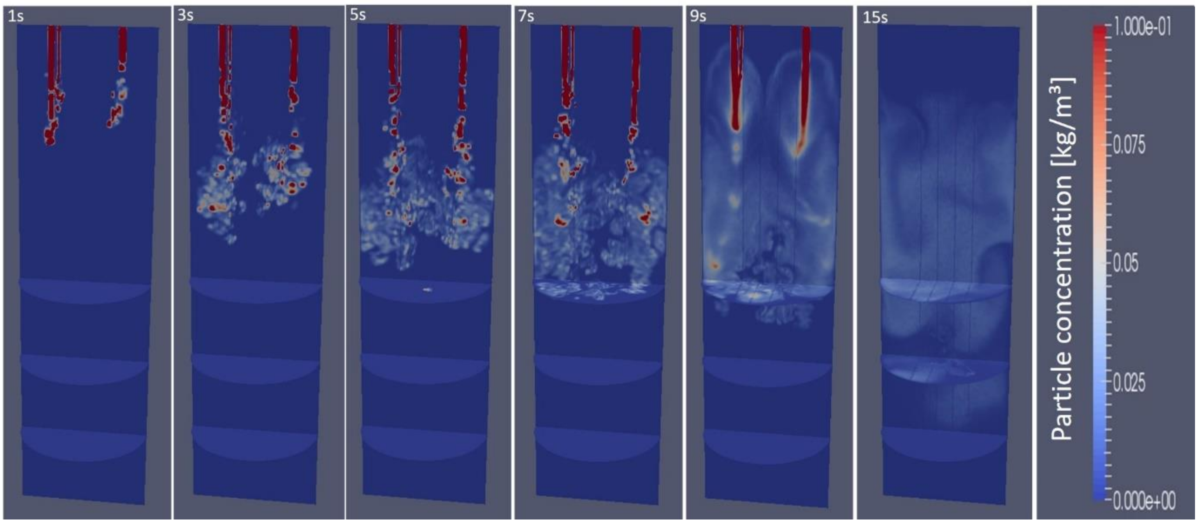

Fig. 8. *Simulation results of the particle concentration [kg/m³] in the vertical test rig (Hüttenbrenner et al, 2019)*

3.3 *Proof of concept and start up*

The first tests with the new experimental rig have already been done to find out if the experimental setup fulfills the requirements. The dust feed device operated for about 20 seconds (steady state according to simulation results), afterwards the dust layer at the bottom was investigated. The bottom plate of the combustion tube was covered evenly with Lycopodium dust. The dust concentration measurement device did not work at this time, however, the dust at the bottom might indicate that a similar distribution over the cross-section could be achieved by the selected dust feeding system. The second run was for testing purposes on the ignition system. After reaching steady state conditions, the ignition source was activated and the spark ignited the dust/air mixture and a flame was formed. The flame front propagated relatively slow from the ignition point upwards to the top of the test rig. However, after ignition the flame front showed serious wrinkling after some seconds and became unsteady. The flame propagated along the explosion tube and at the top end of the tube the explosion flap opened as designed for. No significant pressure rise could be observed. The explosion flap and relief system were tested successfully. Regarding flame wrinkling several influencing factors might be causing this effect. Besides effects originating in the combustion process itself, there might be also effects related to the dust input or the ignition system. Further investigations are necessary to obtain more knowledge about the causing factors.

4. Conclusions

The basis for the design and construction of the described test rig was a smaller combustion tube, that allowed to conduct research on flame propagation in dust/air mixtures. Main advantage of the smaller tube was the dust feed system, which allowed low turbulence dust insertion into the combustion chamber. During the construction of the larger (4 m) test rig, a new dust feed system was designed and tested. Results obtained from CFD simulations indicated that the chosen dust feed system allows to create low turbulence conditions around the ignition spot and within the combustion area. Although accurate dust concentration measurements are still missing, the settling pattern indicates a very homogeneous and even dust distribution within the lower section of the combustion chamber. First ignition tests indicate that the electrical layout and position of the ignition source is adequate to meet the experimental requirements. The visual observation of the combustion process indicates a very low turbulence combustion with very limited pressure build up. In contrary to the smaller combustion tube, flame speed measurements in the larger combustion chamber have to follow a different approach. Whilst the measurement of flame speed by photooptical devices or thermocouples along the tube wall are an adequate choice for the smaller tube, sensor positions have to be redesigned in the larger test tube due to intensive flame wrinkling.

Although measurements on flame speed can be conducted easier in the smaller test rig, the larger setup allows studies on flame propagation in larger volumes and with less influence of wall effects. Future work will focus on dust concentration measurement and the design of adequate sensor systems to measure flame propagation.

References

Binder, A. (2012). *Elektrische Maschinen und Antriebe*, Springer, Heidelberg [u.a.].

Cao, W., Gao, W., Peng, Y., Liang, J., Pan, F., Xu, S. (2014). Experimental and numerical study on flame propagation behaviors in coal dust explosions. *Powder Technology,* 266: 456–462.

Cashdollar, K.L., Hertzberg, M. (1983). Infrared Temperatures of Coal Dust Explosions, *Combustion and Flame*, 51: 23-35.

Davidson, L. (2015). *An Introduction to turbulence models*, Chalmers University of Technology. Göteborg, Sweden.

Dehbi, A. (2006). Assessment of a new FLUENT model for particle dispersion in turbulent flows. *Workshop proceedings on benchmarking of CFD codes for application to nuclear reactor safety (CDF4NRS)*: 703–720.

Dewitte, M., Vrebosch, J., van Tiggelen, A. (1964). Inhibition and Extinction of Premixed Flames by Dust Particles, *Heterogeneous flame inhibition*, 8: 257–266.

Eckhoff, R.K.; Fuhre, K.; Pedersen, G.H. (1987). Dust Explosion Experiments in a Vented 236 m³ Silo Cell. *Journal of Occupational Accidents*, 9: 161-175.

Han, O., Yashima, M., Matsuda, T., Matsui, H., Miyake, A., Ogawa, T. (2000). Behavior of flames propagating through lycopodium dust clouds in a vertical duct. *Journal of Loss Prevention in the Process Industries,* 13: 449–457

Hüttenbrenner, K., Kern, H., Donner, C., Raupenstrauch, H. (2016). Investigations on the influence of the specific surface on the ignition and flame behavior of combustible dust/air-mixtures. *Brochure of 11th International Symposium on Hazards, Prevention, and Mitigation of Industrial Explosions*: 66.

Hüttenbrenner, K., Kern, H., Glechner, J., Raonic, S., Raupenstrauch, H. (2019). CFD-Simulation und Entwicklung eines Staubeintragverfahrens für die Tube-Methode zur Bestimmung der Flammengeschwindigkeit in Staub/Luft-Gemischen, *14. Fachtagung Anlagen-, Arbeits- und Umweltsicherheit - Schloss Köthen*, Köthen, Deutschland.

Kern, H. (2013). *Explosible Dust/Air Mixtures. Investigations on flame propagation under non-atmospheric conditions*, Dissertation, Montanuniversitaet, Leoben.

Krause, U. (2002). *Wärme- und Stofftransportvorgänge bei sicherheitstechnischen Untersuchungsverfahren für Staubbrände und Staubexplosionen.* Shaker Verlag, Aachen.

Palmer, K.N., Tonkin P.S. (1971). Coal Dust Explosions in a Large-Scale Vertical Tube Apparatus. *Combustion and Flame*, 17: 159–170.

Proust, C., Veyssiere, B. (1988). Fundamental Properties of Flames Propagating in Starch Dust-Air Mixtures. *Combustion Science and Technology*, 62: 149–172.

Skjold, T.; Castellanos, D.; Olsen, K.L.; Eckhoff, R.K. (2014). Experimental and numerical investigation of constant volume dust and gas explosions in a 3.5-m flame acceleration tube. *Journal of Loss Prevention in the Process Industries*, 30: 164-176.

Smoot, L.D., Horton, M.D. (1977). Propagation of laminar pulverized coal-air flames, *Prog. Energy Combustion Science*, 3: 235-258.

Spijker, C. (2015). *Numerische Untersuchung der partikelinneren Effekte bei Lykopodiumstaubdeflagrationen*, Dissertation, Montanuniversitaet, Leoben.

Taveau, J. (2017). Dust explosion propagation and isolation. *Journal of Loss Prevention in the Process Industries*, 48: 320-330.

The OpenFOAM Foundation Ltd. Openfoam 2.4.x (2015). URL https://github.com/OpenFOAM/OpenFOAM-2.4.x, 23-01-2020

Veyssiére, B. (1992). Development and propagation regimes of dust explosions. *Powder Technology*, 71: 171-180.

DOI: 10.7795/810.20200724

Self-similar propagation of expanding spherical flames in lean hydrogen-air mixtures

Wookyung Kim [a*], Takumi Namba [a], Tomoyuki Johzaki [a] & Takuma Endo [a]

[a] Hiroshima University, Higashihiroshima, Japan

E-mail: *kimwk@hiroshima-u.ac.jp*

Abstract

The self-similar propagation of expanding spherical flames in lean hydrogen-air mixtures at elevated pressure were experimentally investigated using the dual-chamber apparatus with the quartz windows enabled to a flame radius with up to 110 mm. The flame images of more the fully developed cellular structure were captured, and the large values of r/r_c and Pe for the dual-chamber apparatus were measured. The acceleration exponent, α, corresponding to the fractal dimension in lean hydrogen-air mixtures at elevated pressure were evaluated by plotting the experimental flame radius as a function of time. In the present study, the experimental values of α are α = 1.25–1.43 within a wide range of r/r_c = 2–15. The increasing trends of α with a decrease in ϕ and with an increase in initial pressure, P_i, were observed owing to the effects of the diffusional-thermal as well as Darrieus-Landau instabilities. The value of α increased with an increase in r/r_c and it saturated to α = 1.43 at $r/r_c > 10$, and the saturated values of hydrogen-air flame are within α = 1.4–1.5. The results demonstrated that the flame acceleration was classified as laminar ($r/r_c < 1$), acceleration ($r/r_c > 1$), transition ($1 < r/r_c < 10$), and self-similar regimes ($r/r_c > 10$). Consequently, the practical three-dimensional fractal dimensions for accidental hydrogen-air explosions are D_3 = 2.29–2.33.

Keywords: *hydrogen, flame acceleration, self-similarity, gas explosions*

1. Introduction

Self-acceleration of the hydrogen-air flame caused by the cellular instabilities such as Darrieus-Landau instability and diffusional-thermal instability leads to serious damage by the dramatically increasing blast wave during the accidental hydrogen-air explosions. The development of cellularity on the flame surface at small radius is controlled by the stretch effect. As the flame expands, the flame self-accelerates due to Darrieus-Landau as well as diffusional-thermal instabilities. It is known that the self-accelerating flame reach the self-similar regime, as the flame radius becomes much larger (Gostinsev et al., 1988; Molkov et al., 2007; Kim et al., 2015). Gostinsev et al (Gostinsev et al., 1988) demonstrated that the critical flame radius associated with the onset of self-similar propagation of stoichiometric hydrogen-air flame in the large atmospheric explosions was r = 1.0–1.2 m corresponding to r/r_c = 8.6–10.3, where r_c is a critical flame radius for the onset of flame acceleration. The critical flame radius for the onset of flame acceleration of the stoichiometric hydrogen-air flame was r_c = 0.116 m (Kim et al., 2015). The similar value, r = 1.0 m for the onset of self-similarity is also confirmed in the large-scale near stoichiometric hydrogen-air flame (Molkov et al., 2007). In the previous large-scale experiments, the transition to self-similarity of expanding spherical hydrogen-air flame of equivalence ratio ϕ = 0.7 observed at r/r_c = 7–9 (Kim et al., 2015). It is indicated that the onset of self-similarity of hydrogen-air flame occurred at r/r_c > 7-10. Although such onset of the instabilities (Kwon et al., 2001; Jomaas et al., 2007; Bradley et al., 2000; Matalon et al., 2003), self-accelerating flame (Kim et al., 2015; Wu et al., 2013; Yang et al., 2016; Sun et al., 2012; Liu et al., 2012; Hu et al., 2009) have been extensively studied, the critical condition on transition to self-similarity is still inconclusive. Therefore, further studies on the transition to self-similarity of hydrogen-air flame are merited.

Another important issue for the self-similar propagation is the acceleration exponent, α, corresponding to the fractal excess, $d = (\alpha\text{-}1)/\alpha$, estimated by the power-law expression, $r \sim t^{\alpha}$, where r_c is neglibile for $r >> r_c$. Formerly, Gostinsev et al (Gostinsev et al., 1988) have suggested a value of α for a free turbulent flame in premixed mixtures is $\alpha = 1.5$. However, the smaller values of the exponent in the range of $\alpha = 1.2$–1.4 were found by small-scale high-pressure (Wu et al., 2013; Kim et al., 2018) as well as large-scale filed experiments (Kim et al., 2015; Bauwens et al., 2017). According to the previous study, we found that the value of α increased with an increase in the flame radius and it saturated the limited value corresponding to the fractal dimension. In other words, the transition regime to self-turbulization for large-scale expanding spherical flame existed. The question on the saturated value associated with the fractal dimension still remains. The further studies on this issue are required to estimate the accidental hydrogen-air explosions.

According to substantial earlier studies (Kwon et al., 2001 Wu et al., 2013; Kim et al., 2018; Bauwens et al., 2017), the lean hydrogen-air flames were cellularly unstable, and the values of r_c decreased with a decrease in ϕ owing to Darrieus-Landau instability and diffusional-thermal instability. The lean hydrogen-air flames are Le <1 mixture, where Le is Lewis number defined as the ratio of the thermal diffusivity to mass diffusivity. In addition, the hydrogen-air flames were wrinkled, and the values of r_c decreased with an increase in initial pressure P_i, because of the decrease in the flame thickness, enhancing Darrieus-Landau and diffusional-thermal instabilities. Therefore, the lean hydrogen-air flames at high-pressure enable to extend the range of r/r_c. In view of the above considerations, the objectives of the present study are to investigate experimentally the self-similarity of lean hydrogen-air flames for a wide range of r/r_c, and to estimate the fractal dimension for accidental hydrogen-air explosions.

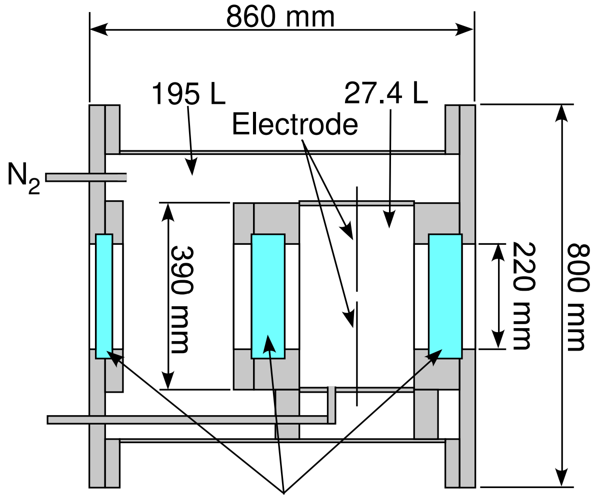

***Fig. 1.** The dual-chamber apparatus.*

2. Experiments

In order to investigate the self-similar propagation of expanding spherical flames in lean hydrogen-air mixtures, we have developed a dual-chamber apparatus enabled to observe a high-pressure spherical flame diameter with up to 220 mm. This apparatus referenced the high-pressure combustion apparatus developed in Princeton University (Tse et al., 2004) and extended the scale of the vessels. Figure 1 shows the two-dimensional schematic drawings of the dual-chamber apparatus. It consists of two cylindrical chambers with three quartz windows. The size of two quartz windows in inner vessel is 260 mm diameter, 70 mm thickness, and the diameter of quartz window in outer vessel is 260 mm with 35 mm thickness. The volume of inner vessel is 27.4 L with 381.5 mm inner diameter, 406.9 mm outer diameter and 462 mm length including three flanges. The volume of outer vessel is 195.5 L with 590.6 mm inner diameter, 609.6 mm outer diameter and 860 mm length including two flanges. The holes with 10 mm diameter in the lateral walls of the inner vessel are pierced. In order to reduce the effect of increasing pressure in the vessel on the propagation behaviors, a thin polyethylene plastic film of 50 μm thickness covered the lateral walls of the inner vessel and ripped by pressure increase.

The lean hydrogen-air mixture initially filled in the inner, and nitrogen supplied to outer vessels at the same pressure. The hydrogen-air mixture at the center of the inner vessel is ignited by two electrodes of 0.5 mm diameter. In the present experiments, the hydrogen-air mixtures with equivalence ratio $\phi = 0.5–1.0$ at initial pressure $P_\mathrm{i} = 0.1$, 0.2 and 0.5 MPa were used. The behaviors of flame propagation were imaged with schlieren photography and recorded using a high-speed camera (Photron, FASTCAM Mini AX 50 and UX100) at 5000 frames per second. In this study, the edge of flame front was detected by a canny edge method using MATLAB. The flame radius is defined as $r = \sqrt{A/\pi}$, where A is the flame area. Details of the image analysis are in (Kim et al., 2018). In this study, the values of laminar burning velocity, S_L, the expansion ratio, σ, the laminar flame thickness, $\delta = (T_\mathrm{f}\text{-}T_\mathrm{i})/(dT/dx)_\mathrm{max}$, where T_f, T_i, and $(dT/dx)_\mathrm{max}$ are the flame temperature, unburned gas temperature, and maximum temperature gradient, respectively, were calculated by using Chemkin-Pro software with the GRI Mech 3.0 reaction model.

3. Results and discussion

3.1 Cellular flame developments

The Schlieren images of outwardly propagating spherical flames for lean hydrogen-air mixture at $P_\mathrm{i} = 0.2$, 0.5 MPa are shown in Fig. 2. In this experiment, the evaluated maximum flame radius was r_max = approximately 100 mm, because the quartz window diameter is 220 mm. In the present study, a fully developed cellular structure of lean hydrogen-air flame that in turn leads to the flame acceleration was observed at the small flame radii. As the flame radius became larger, the flame was more wrinkled owing to the enhancement of the Darrieus-Landau instability. The flame was wrinkled with a decrease in ϕ and P_i due to Darrieus-Landau and diffusional-thermal instabilities. These trends agreed well with previous work (Kim et al., 2018).

The relatively large-scale flames from the present tests (27.4 L) was observed than those from the previous works with the 70 mm diameter quartz window (0.79 L) (Kim et al., 2018), as shown in Fig. 3. The flame images of more and more the fully developed cellular structure in this test were captured. In addition, the values of r/r_c and Péclet number $Pe = r/\delta$ for dual-chamber apparatus were 3–4 times larger than those for small chamber apparatus (Kim et al., 2018). The value of r/r_c for hydrogen-air flame of $\phi = 0.7$ at $P_\mathrm{i} = 0.2$ was $r/r_\mathrm{c} = 9.8$, and that of r/r_c for hydrogen-air flame of $\phi = 0.5$ at $P_\mathrm{i} = 0.5$ was $r/r_\mathrm{c} = 10.5$. The value of $r = 102$ mm at $P_\mathrm{i} = 0.2$ and 0.5 was similar to $r = 1.0–1.2$ m corresponding to $r/r_\mathrm{c} = 8.6–10.3$ corresponding to the onset of self-similarity of large-scale near stoichiometric hydrogen-air flame. The flame images of $\phi = 0.7$ at $P_\mathrm{i} = 0.2$ and $\phi = 0.5$ at $P_\mathrm{i} = 0.5$ indicated the self-similar flame structure.

DOI: 10.7795/810.20200724

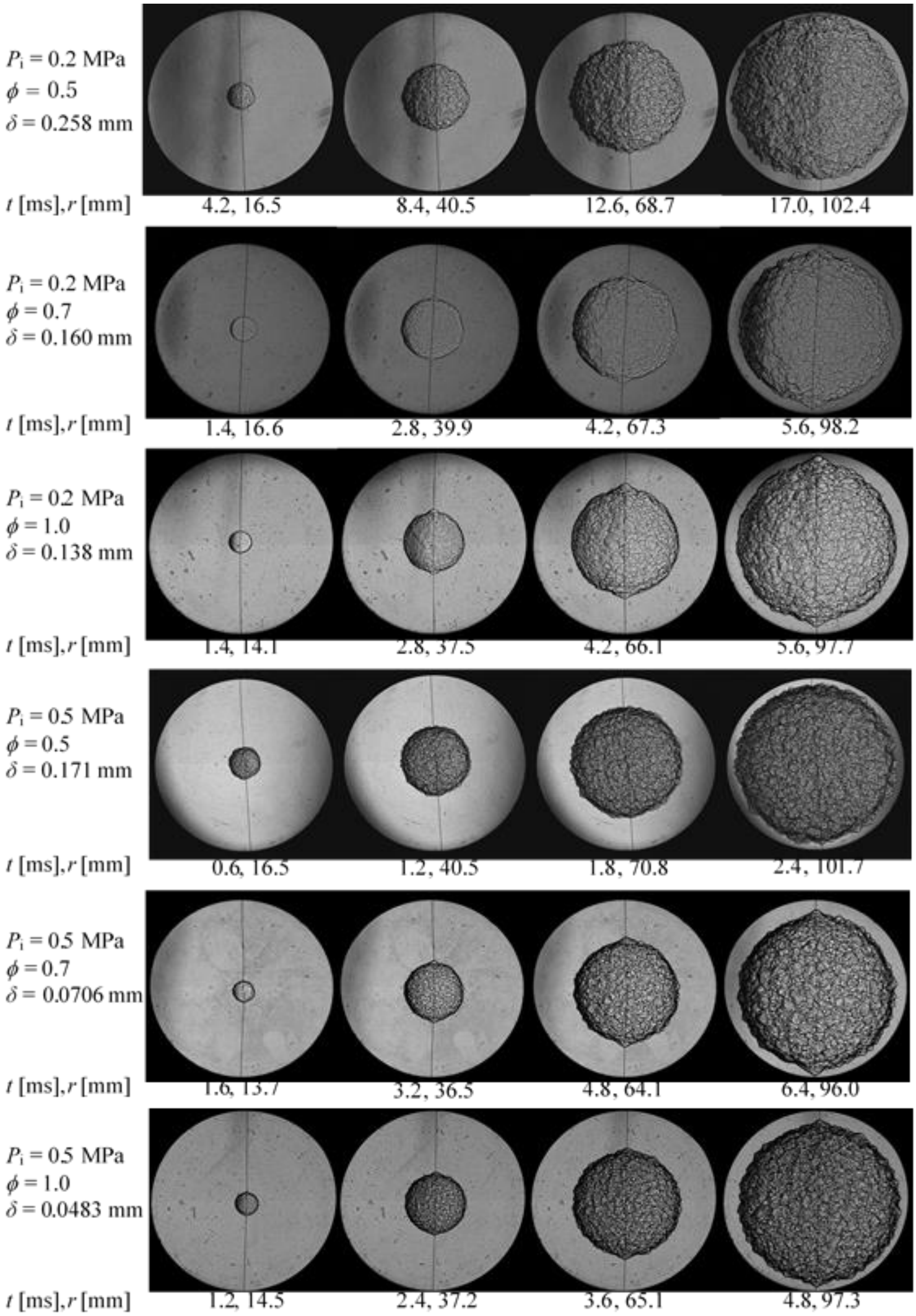

Fig. 2. *Schlieren images of outwardly propagating spherical flames for lean hydrogen-air mixture at* $P_i = 0.2, 0.5$ *MPa.*

(a) Small chamber (0.79 L)

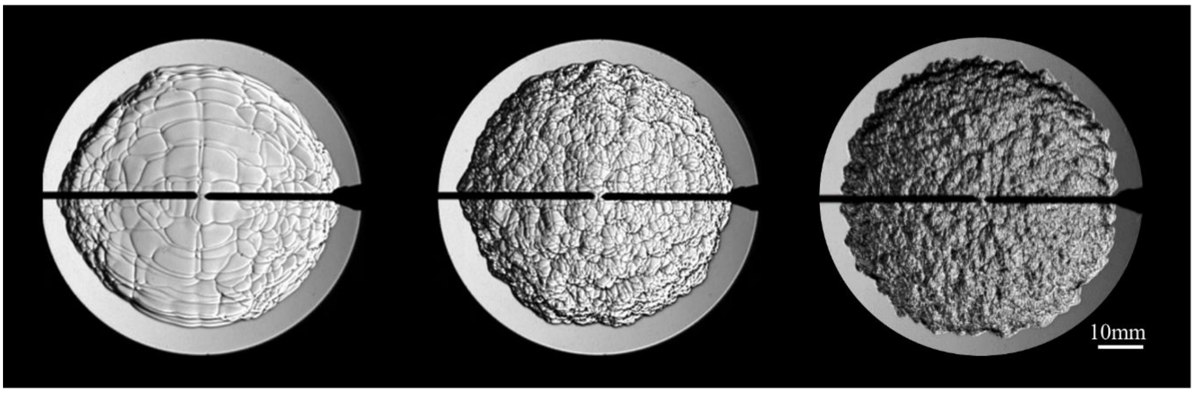

- P_i = 0.1 MPa, ϕ=0.5
- δ = 0.48982 mm
- r = 30.3 mm, r_c = 26 mm
- r/r_c = 1.16
- Pe = 62

- P_i = 0.2 MPa, ϕ=0.7
- δ = 0.15966 mm
- r = 29.4 mm, r_c = 10.4 mm
- r/r_c = 2.83
- Pe = 184

- P_i = 0.5 MPa, ϕ=0.5
- δ = 0.17079 mm
- r = 30.1 mm, r_c = 5.78 mm
- r/r_c = 5.2
- Pe = 176

(b) Dual chamber (27.4 L)

- P_i = 0.1 MPa, ϕ = 0.5
- δ = 0.48982 mm
- r = 102 mm, r_c = 26 mm
- r/r_c = 3.92
- Pe = 208

- P_i = 0.2 MPa, ϕ = 0.7
- δ = 0.15966 mm
- r = 102 mm, r_c = 10.4 mm
- r/r_c = 9.8
- Pe = 639

- P_i = 0.5 MPa, ϕ = 0.5
- δ = 0.17079 mm
- r = 102 mm, r_c = 9.5 mm
- r/r_c = 10.5
- Pe = 597

Fig. 3. *Cellular flame at different scale experiments at elevated initial pressure: (a) Small chamber (0.79 L), (b) Small chamber (27.4 L).*

3.2 *Onset of flame acceleration*

Figure 4 shows the measured flame speed as a function of the flame stretch rate, $K = (2/r)\, dr/dt$, at P_i = 0.5 MPa, ϕ = 1.0. In the early stage, the positive stretch influences on the flame propagation, and thereby the flame propagates with a constant speed, $dr/dt = \sigma S_L$. As the flame expands, the stretch effect progressively decreased, and the flame wrinkled with the enhancement of influence of the cellular instabilities, and consequently the flame speed increased. Because the development of a cellular flame structure owing to the instabilities is suppressed by the flame stretching, in this study, the critical flame radii for the onset of flame acceleration were estimated through the relation between the values of K and dr/dt, as shown in Fig. 4. Figure 5 shows the critical Péclet number for the onset of flame acceleration, $Pe_c = r_c/\delta$, as a function of ϕ. The values of Pe_c increased with ϕ owing to the diffusional-thermal instability. The values compared with the previous results at small-scale chamber (Kim et al., 2018) and the increasing tendency of Pe_c with ϕ agreed well with the previous works.

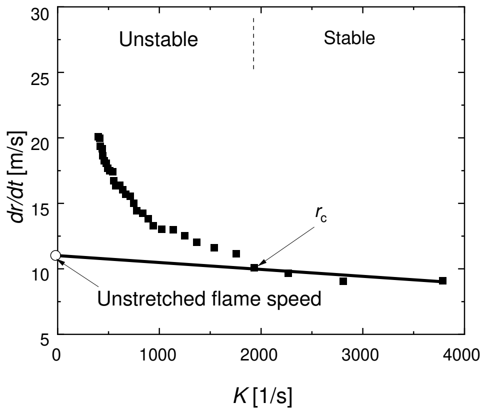

Fig. 4. *Measured flame speed at different flame stretch rate at Pi = 0.5 MPa, $\phi = 1.0$.*

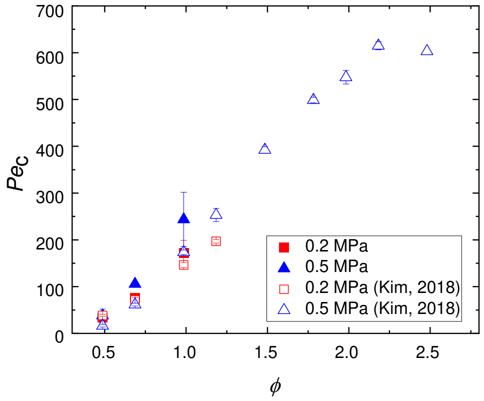

Fig. 5. *Critical Péclet number as a function of ϕ.*

3.3 Acceleration exponent and self-similarity

The experimental acceleration exponent, α, for the flame acceleration was evaluated by plotting the flame radius with time $r \sim t^{\alpha}$. For instance, the logarithmic plot of the experimental flame radius as a function of time at $P_i = 0.5$ MPa, $\phi = 1.0$ is shown in Fig. 6. The slope is the value of α within $r_c < r < r_{max}$ = approximately 100 mm. Figure 7 shows the experimental values of α for hydrogen-air at various initial pressures as a function of ϕ with the references (Kim et al, 2018; Wu et al, 2013). The data taken from references was estimated in the range between r_c and $r_{max} = 20$ mm (Wu et al, 2013), and the range between r_c and $r_{max} = 30$ mm (Kim et al, 2018). The value of r_{max} evaluated through the present test is 3-5 times as large as the previous works (Kim et al, 2018; Wu et al, 2013). In the present test, the experimental values of α for lean hydrogen-air flame are $\alpha = 1.25$–1.43 at $P_i = 0.2$, 0.5 MPa, as seen in Fig. 7. The value of α increased with an increase in P_i owing to the reduction in δ. The increasing trends of α with a decrease in ϕ owing to the effect of diffusional-thermal instability. The values of α in the present experiments were larger than those in the previous works (Kim et al, 2018; Wu et al, 2013), because the present tests further cover the self-acceleration regime. Such result demonstrated that the values of α increased as the flame expand, and the values of α were within the intermediate stage i.e, the transition regime to self-similarity. Therefore, the values of α cannot be expressed as a fractal dimension, because the evaluated values of α have yet to reach the self-similar regime.

DOI: 10.7795/810.20200724

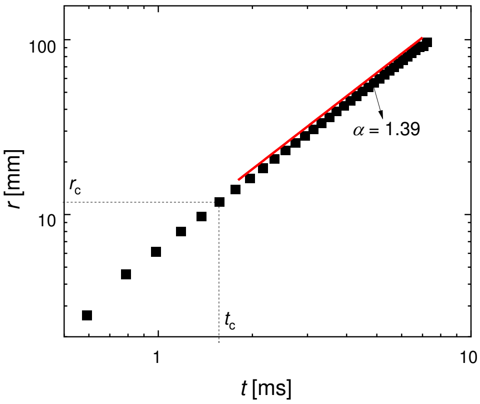

Fig. 6. *Time history of hydrogen-air flame radius at* P_i *= 0.5 MPa,* ϕ *= 1.0.*

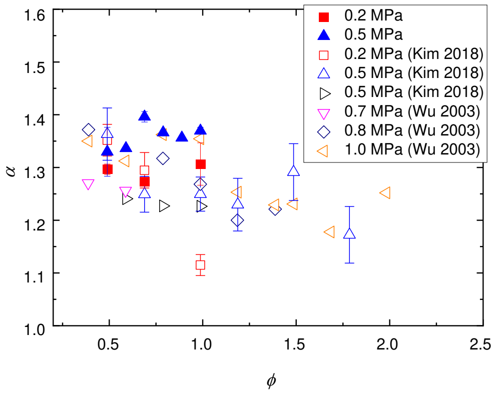

Fig. 7. *Experimental acceleration exponent for hydrogen-air at various initial pressures as a function of* ϕ *with data from the small-chamber experiments.*

The values of r_c decreased, and thereby the value of r/r_c also increased with an increase in initial pressure, because of the decrease in the flame thickness, enhancing Darrieus-Landau and diffusional-thermal instabilities. The estimated range in the present work was extended to $r/r_c = 2–15$. The values of α as a function of r/r_c are shown in Fig. 8. The results demonstrated that the value of α increased with an increase in r/r_c, and it saturated at $r/r_c > 6–10$. The saturated maximum value of $\alpha = 1.43$ agreed well with the experimental value $\alpha = 1.42$ at $r/r_c > 103$ estimated from large-scale near stoichiometric hydrogen-air flame (Molkov et al., 2007), although it is smaller than the critical value $\alpha = 1.5$ for self-turbulization suggested by Gonstinsev (Gostinsev et al., 1988). The results showed that the flame acceleration was classified as laminar, acceleration, transition, and self-similar regimes. The flame propagates smoothly with a constant speed at $r/r_c < 1$, and the flame accelerates with an increase in flame speed at $r/r_c > 1$ as the flame expand. As the flame radius becomes larger, its acceleration transits to self-similar regime, and consequently the values reached the self-similar regime at $r/r_c > 10$. Such results demonstrated that the saturated values of hydrogen-air flame are within $\alpha = 1.4–1.5$. Therefore, the experimental three-dimensional fractal dimensions, $D_3 = 2+d$, are found to be $D_3 = 2.29–2.33$. Mukaiyama et al., (Mukaiyama et al., 2013) numerically investigated the dependences of expansion ratio on the fractal structure using the Sivashinsky equation which derived the asymptotic nonlinear integrodifferential equation for cellular flame front due to the instability (Sivashinsky, 1977). The numerical results indicated that the fractal dimensions increased with an increase in the expansion ratio, σ and the fractal dimensions of hydrogen-air flames were $D_3 = 2.30–2.38$ at $\sigma = 4–8$, as seen in Fig. 9. The practical three-dimensional fractal dimensions for accidental

DOI: 10.7795/810.20200724

hydrogen-air explosions are $D_3 = 2.29$–2.33, although the numerical data are slightly larger than those from the present experiments.

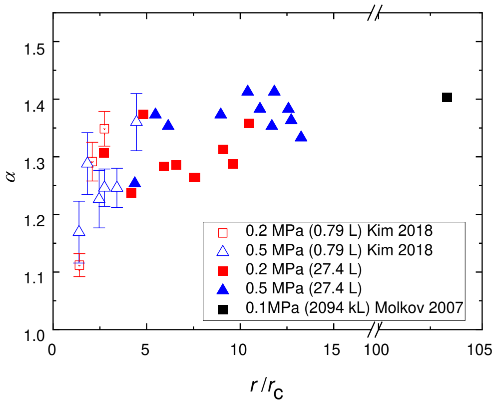

Fig. 8. *Experimental acceleration exponent as a function of* r/r_c.

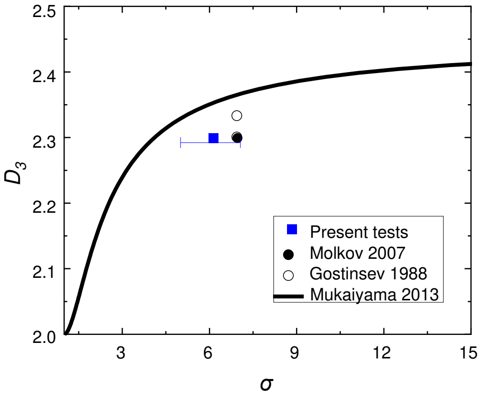

Fig. 9. *Fractal dimension as a function of σ (Solid line: numerical vales).*

4. Conclusions

In the present study, the self-similarity of expanding spherical flames in hydrogen-air mixtures were experimentally investigated. In particular, the lean hydrogen-air flames for $Le < 1$ mixtures at initial pressure $P_i = 0.1$, 0.2 and 0.5 MPa were tested using the dual-chamber apparatus. The dual-chamber experiments enable to measure the fully developed cellular flame. It is indicated that the present tests further cover the transition regime to self-similarity. The value of α increased with an increase in r/r_c and it saturated to $\alpha = 1.43$ at $r/r_c > 10$, and saturated values of hydrogen-air flame are within $\alpha = 1.4$–1.5. The results demonstrated that the flame acceleration was classified as laminar ($r/r_c < 1$), acceleration ($r/r_c > 1$), transition ($1 < r/r_c < 10$), and self-similar regimes ($r/r_c > 10$). The practical three-dimensional fractal dimensions for accidental hydrogen-air explosions are $D_3 = 2.29$–2.33.

Acknowledgements

This study was supported by Suzuki foundation, Electric technology research foundation of chugoku, JSPS KAKENHI Grant Numbers 18H03822, and 18K13958.

References

Bauwens, C., Bergthorson, J., and Dorofeev, SB. (2017). Experimental investigation of spherical-flame acceleration in lean hydrogen-air mixtures, *International Journal of Hydrogen Energy*, 42: 7691-7697.

Bradley, D., Sheppart, C.G.W., Woolley, R., Greenhalgh, D.A., and Lockett, R.D., (2000). The development and structure of flame instabilities and cellularity at low Markstein numbers in explosions, *Combustion and Flame*,122:195-209.

Gostintsev, Y.A., Istratov, A.G., and Shulenin, Y.V., (1988). Self-similar propagation of a free turbulent flame in mixed gas mixtures, *Combust Explosions and Shock Waves*, 24(5): 569–563.

Hu, E., Huang, Z., He, J., Zheng, J., and Miao, H., (2009) Measurements of laminar burning velocities and onset of cellular instabilities of methane–hydrogen–air flames at elevated pressures and temperatures, *International Journal of Hydrogen Energy*,34:5574-5584.

Jomaas, G., Law, C.K., Bechtold, J.K., (2007). On transition to cellularity in expanding spherical flames, *Journal of Fluid Mechanics,* 583:1-26.

Kim, W., Mogi, T., Kuwana, K., and Dobashi, R. (2015). Self-similar propagation of expanding spherical flames in large scale gas explosions. *Proceedings of the Combustion Institute*, 35: 2051–2058.

Kim, W., Sato, Y., Johzaki, T. Endo, T. Shimokuri, D. Miyoshi, A. and Dobashi, R. (2018). Experimental study on self-acceleration in expanding spherical hydrogen-air flames. *International Journal of Hydrogen Energy*, 40: 11087–11092.

Kwon, O.C., Faeth, G.M., (2001). Flame/stretch interactions of premixed hydrogen-fueled flames: measurements and predictions, *Combustion and Flame*, 124:590-610.

Liu, F., Bao, X., Gu, J., and Chen, R., (2012). Onset of cellular instabilities in spherically propagating hydrogen-air premixed laminar flames, *International Journal of Hydrogen Energy*, 37:11458-11465.

Matalon, M., Cui, C., Bechtold, J.K., (2003). Hydrodynamic theory of premixed flames: effects of stoichiometry, variable transport coefficients and arbitrary reaction orders, *Journal of Fluid Mechanics*, 487:179-210.

Molkov, V.V., Makarov, D.V., and Schneider, H., (2007). Hydrogen-air deflagrations in open atmosphere: Large eddy simulationanalysis of experimental data, *International Journal of Hydrogen Energy*, 32(13): 2198–2205.

Mukaiyama, K., Shibayama, S., and Kuwana, K., (2013). Fractal structures of hydrodynamically unstable and diffusive-thermally, *Combustion and Flame*, 160 (11): 2471–2475.

unstable flames

Sivashinsky G.I., (1977). Nonlinear analysis of hydrodynamic instability in laminar flames—I. Derivation of basic equations, *Acta Astronautica*, 4 (11): 1177-1206.

Sun, Z.Y., Liu, F.S., Bao, X.C., and Liu, X.H., (2012). Research on cellular instabilities in outwardly propagating spherical hydrogen-air flames, *International Journal of Hydrogen Energy*, 37:7889-7899.

Yang, S., Saha, A., Wu, F., Law, C.K., (2016) Morphology and self-acceleration of expanding laminar flames with flame-front cellular instabilities, *Combustion and Flame*, 171:112-118.

Wu, F., Jomaas, G., and Law, C.K. (2013). An experimental investigation on self-acceleration of cellular spherical flames. *Proceedings of the Combustion Institute*, 34: 937–945.

DOI: 10.7795/810.20200724

Assessing the influence of real releases on explosions: selected results from large-scale experiments

Helene Hisken [a], Lorenzo Mauri [a], Gordon Atanga [a], Melodia Lucas [a], Kees van Wingerden [a],
Trygve Skjold [b], Pierre Quillatre [c], Antoine Dutertre [d], Thibault Marteau [d], Andrzej Pekalski [e],
Lorraine Jenney [f], Dan Allason [f], Mike Johnson [f], Emmanuel Leprette [g], Didier Jamois [g],
Jérôme Hébrard [g] & Christophe Proust [g]

[a] Gexcon R&D, Bergen, Norway
[b] University of Bergen, Norway
[c] GRTgaz, Research and Innovation Center for Energy, France
[d] Total, France
[e] Shell Global Solutions, UK
[f] DNV GL Spadeadam Research and Testing, UK
[g] Ineris, Verneuil-en-Halatte, France

E-mail: Helene.Hisken@gexcon.com

Abstract

The research activities in the project *Assessing the Influence of Real Releases on Explosions* (AIRRE) included a unique series of large-scale explosion experiments with ignited high-momentum jet releases directed into congested geometries. The primary objective for the AIRRE project was to gain improved understanding of the effect realistic releases and turbulent flow conditions have on the consequences of accidental gas explosions in the petroleum industry, to develop methodology that can facilitate safe and optimal design of process facilities. This paper presents selected results from experiments involving ignition of a highly turbulent gas cloud, generated by a large-scale, pressurised release of natural gas. The paper gives an overview of the effect on maximum explosion overpressures of varying the ignition position relative to the release point of the jet and a congested region placed inside the flammable cloud, with either a high or medium level of congestion. For two of the tests involving a jet release and the medium congestion rig, the maximum overpressures significantly exceeded those obtained in a quiescent reference test. The paper presents detailed results for selected tests in the campaign. The effects on the relevant explosion phenomena from introducing initial turbulence, initial flow momentum and concentration gradients, as generated by the realistic release, are discussed.

Keywords: *realistic releases, large-scale experiments, gas explosions*

1. Introduction

According to Marsh (2018), a majority of the 100 largest property losses in the hydrocarbon industries from 1974 to 2017 involved fires and explosions. In order to assess the potential consequences of such events, and implement effective risk-reducing measures, the industry requires knowledge about the underlying physical phenomena. Accidental gas explosions will typically include loss of containment of gaseous or liquid fuel, dispersion, mixing to form a flammable fuel-air cloud, ignition, turbulent combustion, pressure build-up, and propagation of blast waves in the surroundings (CCPS, 1994). Furthermore, recent incidents such as the vapour cloud explosions in Jaipur in 2009 and Skikda in 2004, as well as the extensive research conducted after the Buncefield incident in 2005, highlight the importance of considering deflagration-to-detonation transition (DDT) in risk assessments (Johnson *et al.* 2015; Oran *et al.*, 2020).

Gas explosions are inherently complex, as they involve physical phenomena on a wide range of spatial and temporal scales. The pressure loads from accidental gas explosions depend strongly on the rate of combustion, which is determined by factors such as degree of congestion, degree of confinement, the reactivity of the fuel-air mixture, and properties of the reactive flow. The primary mechanism for flame acceleration in congested geometries is the positive feedback between expansion of combustion products, turbulence generated in the unreacted mixture, especially in shear and boundary layers from flow past obstacles and walls, and enhanced combustion rates (Schelkin, 1940; Moen *et al.*, 1980; Hjertager, 1984; Bjerketvedt *et al.*, 1997). In a flammable fuel-air cloud generated by a high-pressure release, a certain degree of pre-ignition turbulence will normally be present. Initial turbulence can significantly enhance the rate of flame acceleration in gas explosions (Skjold *et al.*, 2018). Furthermore, if ignition happens while the release is still on-going, the initial mean flow speed can be relatively high. This affects how the flame front propagates in different regions (with or against the flow) as well as the properties of the wakes generated downstream of obstructions prior to ignition. Significant concentration gradients may be present in the cloud, and regions of reduced reactivity of the flammable mixture can produce oscillatory pressure pulses as the flame repeatedly speeds up and slows down (Johnson *et al.*, 2015). Finally, it is likely that pre-ignition turbulence will reduce the run-up distance to DDT (Davis *et al.*, 2016; Davis *et al.*, 2018), and hence increase the likelihood of detonation of a flammable cloud generated by a high-pressure release. It may not be straightforward to assess the combined effect of these factors.

Skjold *et al.* (2018) provided a detailed review of previous experimental work on the effect of realistic releases on explosions from the open literature. For example, as part of the project Blast and Fire Engineering for Topside Structures (BFETS), a range of gas explosion experiments were performed in full-scale or medium-scale offshore modules (Johnson & Cleaver, 2002; Johnson *et al.*, 2002). The campaigns included tests with gas clouds resulting from realistic, high-pressure releases of natural gas. In most tests, the releases generated clouds that were less reactive and/or had a less “optimal” distribution (with respect to explosion pressure generation after ignition) throughout the rigs than near-stoichiometric, homogeneous clouds. However, a few of the realistic release tests produced overpressures that were comparable to or even locally exceeded the pressures recorded in the corresponding reference experiments with homogeneous and quiescent clouds.

Probabilistic explosion studies frequently apply computational fluid dynamics (CFD) simulations where non-homogenous fuel-air clouds, generated by pressurised gaseous releases, are represented by so-called *equivalent clouds* (Hansen *et al.*, 2013; Skjold *et al.*, 2018; Stewart & Gant, 2019). By replacing inhomogeneous and turbulent gas clouds with equivalent homogeneous fuel-air mixtures, that can be moved around and ignited in various positions, risk analysts can investigate numerous explosion scenarios (with comparatively short simulations) based on a relatively limited number of time-consuming release and dispersion simulations. Stewart & Gant (2019) reviewed previous work and the scientific basis for the equivalent cloud concept. GDF SUEZ (currently GRTgaz) compared explosion pressures predicted with FLACS v10.2 in geometries with a medium or high level of congestion for scenarios involving jet releases of methane at flow rates of 1, 10 or 100 kg/s and the corresponding homogeneous and quiescent clouds defined according to the Q9 equivalent-cloud concept (Skjold *et al.*, 2018). When applying the Q9 approach for the scenarios with a *medium* level of congestion, the maximum overpressures were approximately a factor two lower than the maximum overpressures obtained when igniting the clouds from the realistic releases.

Motivated by these results, the goal of the project *Assessing the Influence of Real Releases on Explosions* (AIRRE) was to gain improved understanding of the effect realistic releases and turbulent flow conditions have on the consequences of accidental gas explosions in the petroleum industry. From the open literature, there is limited data available that show the combined effects on gas explosion severity from pre-ignition turbulence generated by jet releases and explosion-generation turbulence. Furthermore, the spatial scales and flow rates for which previous experiments with delayed ignition of pressurised releases have been performed, are rather limited (Skjold *et al.*, 2018). The AIRRE project included an experimental campaign with delayed ignition of natural gas jets with a mass flow in excess of 100 kg/s, either directed into congested regions with two different congestion levels or into an open area. The present paper discusses selected results from this campaign.

2. Experiments

2.1 Experimental setup

DNV GL Spadeadam Research and Testing conducted the large-scale experimental campaign in AIRRE at the Spadeadam test site in the UK. As part of the campaign, transient releases of natural gas were directed into obstructed regions that were placed at various distances from the release. The ignition point was varied relative to the position of the congested regions and the point of release.

The releases in the AIRRE project were fed from a storage reservoir containing approximately 22 metric tonnes of inventory when charged to its operating pressure of 150 bar*g* with natural gas. The storage reservoir is in a nominally flat area of the site measuring approximately 70 m wide by 320 m long. Fig. 1 shows an aerial view of the test site, with the release (blue) directed into two congested regions (red squares).

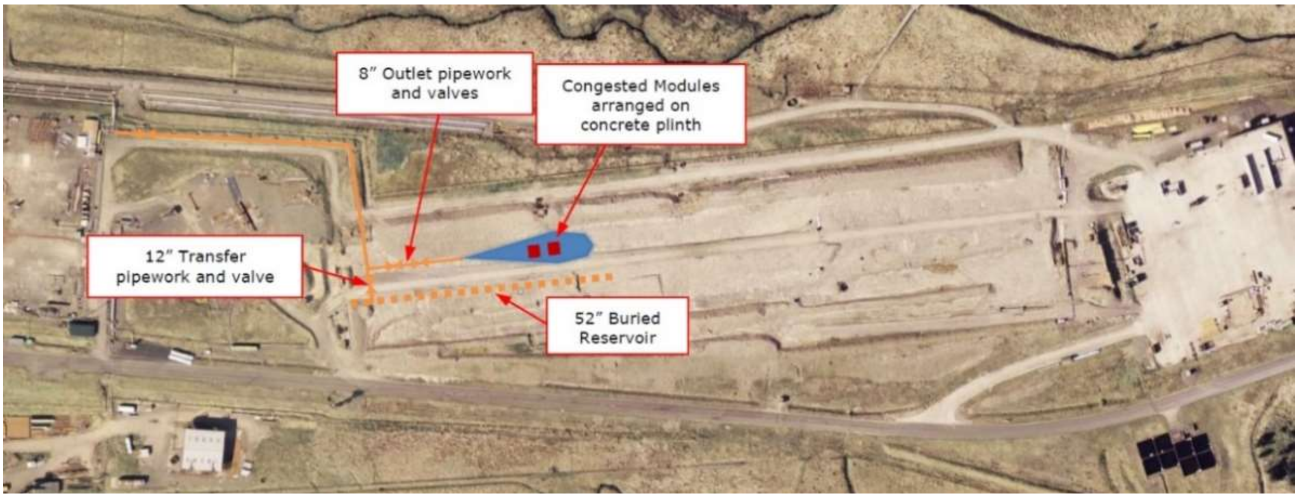

Fig. 1. *Overview of test area.*

The storage reservoir was connected to the 100 mm nozzle at the release point by a pipeline with initial diameter 0.3 m (12-inch), later reduced to 0.2 m (8-inch). The flow rate was calculated from the differential pressure over an orifice plate that was installed in the 8-inch pipework. In each test, a transient flow was driven by a reservoir pressure starting at approximately 132 barg and reducing to 70 barg, and ignition was initiated when the outlet pressure was around 75 barg. Using outlet pressure for timing ignition provided repeatable mass release rates that could be checked by the independent flow measurement. Ignition was accomplished by one of a set of three chemical fuses located in various positions. A backup igniter consisting of an incendiary firework was also installed, to be used if none of the other fuses were able to ignite the cloud. Shutdown of the release was initiated as soon as ignition occurred, however the actuated release valve took around 16 seconds to close, so a jet fire continued through this period.

Two different obstructed regions were used in the AIRRE project, one with a *high* level of congestion (denoted as "rig 7"), and one with a *medium* level of congestion (denoted as "rig 8"). Each obstructed region is constructed from pipes arranged in a three-dimensional mesh. Both rigs have dimensions of approximately 10.0 m × 5.0 m × 2.5 m. The high congestion rig is made from 32 by 16 by 8 pipes with a diameter of approximately 76 mm, while the medium congestion rig is made from 16 by 8 by 4 pipes with a diameter of approximately 168 mm. The volume blockage of the high congestion rig is around 12 %, while the volume blockage for the medium congested rig is around 17 %. Fig. 2 illustrates the congestion level of the two rigs.

One of the tests in the AIRRE project involved a homogeneous, nominally quiescent and near-stoichiometric natural gas-air cloud (i.e. not generated by a jet release). The flammable mixture was contained by a polythene sheet fastened to a 26 m × 6.5 m × 3 m steel angle frame. To achieve a homogenous gas concentration, a system of 600 mm diameter flap valves, a fan and polythene tubing was used to circulate the gas through the test rig. The medium congestion rig was placed inside the flammable cloud during the test. A spark igniter was installed within the test rig at ground level, positioned centrally at the edge of the congestion.

Fig. 2. *The test rigs, with high (left) and medium (right) level of congestion, denoted as rig 7 and rig 8, respectively.*

The composition of the natural gas used in the campaign varied between 91-93 vol.% methane, 5-7 vol.% ethane, 0.6-0.7 vol.% propane, 0.1-0.2 vol.% I-butane, 0.1-0.2 vol.% N-butane, and 0-0.4 vol.% nitrogen.

2.2 Instrumentation

The pressure of the gas in the reservoir and pipework was monitored at four locations: one transducer was placed in the reservoir, one upstream of the metering orifice, one downstream of the metering orifice and one close to the exit orifice. The fluid temperature in the pipework was measured at three locations: one thermocouple in the reservoir, one in the pipe bore near to the metering orifice and one near to the release orifice. The mass flow rate of the gas through the orifice was determined using measurement of static wall fluid pressure, temperature and differential pressure across the orifice plate placed in the outlet pipework, following the method described in ISO 5167-1 (2003) and ISO 5167-2 (2003).

Sensors were installed to measure the fuel concentration, the explosion overpressure and the flame arrival time at several locations distributed throughout the gas plume in every test. The gas concentration in the plume was derived from measurements of oxygen depletion using City Technology AO2 (City Technology, 2017) (or equivalent) electro-chemical sensors. To minimise the effects of pressure and temperature fluctuations, the sensors were mounted in steel enclosures with a pressure-snubbing orifice. The concentration sensors were mounted on steel stands to enable measurement at different elevations from ground level. Section 3 includes further discussion on the concentration measurements.

Explosion overpressure was measured by a total of 20 PCB type M113B26 ICP pressure transducers (PCB Piezotronics, 2020), mounted at ground level in steel boxes. The faces of the pressure transducers were covered with a layer of silicone grease and silver foil in order to reduce thermal effects on the transducer. Measurement of flame arrival time was attempted by using an array of up to 28 ionisation probes. However, in the high-pressure jet release tests, the reliability of the sensors was limited due to the turbulent nature of the flow, the water vapour and the debris that was drawn up from the ground and into the jet release prior to ignition. Therefore, flame speed was instead estimated from high-speed video recordings of each experiment, as explained in Section 3. In one large-scale release test, thermal radiation after ignition was measured in 15 locations, using MEDTHERM® radiometers with a measuring range of 0-200 kW/m^2. The wind speed and direction were measured at 5 and 10 m above the local ground level, at a single location approximately 30 m behind the release point. The relative humidity was also measured 30 m behind the release point. Finally, in selected tests, up to 20 sensors were installed to measure turbulence in the flow prior to flame arrival (Jamois *et al.*, 2020).

Signals from the dynamic pressure sensors, ionisation probes and turbulence sensors in each experiment were recorded at a sample frequency of 500 kHz. In jet release tests the gas concentration, pipework conditions, thermal radiation and ambient conditions were recorded at a rate of 10 Hz. In the quiescent test, the gas concentration and rig conditions prior to ignition was recorded at a rate of 1 Hz. Section 3 includes further details on the setups and measurements for a selection of the large-scale tests performed as part of the AIRRE project.

3. Results and discussion

3.1 Overview of results

The AIRRE campaign included in total 16 tests: three tests with an un-obstructed jet, 8 tests with the medium congestion rig (including the quiescent reference test) and 5 tests with the high congestion rig. Fig. 3 shows the maximum overpressures that were measured in all 16 tests of the AIRRE campaign. The pressure-time traces used to obtain the maximum values in Fig. 3 have been filtered with a 0.1 ms moving average filter.

Fig. 3. *Maximum explosion overpressures from all tests in the AIRRE campaign.*

The significant spread in results for a given level of congestion and ignition annotation in Fig. 3 is partly caused by the fact that the ignition point relative to the release was varied between tests (for example at several different positions upstream of rig 8). Furthermore, in three of the tests with rig 8, the congested region was placed at a distance from the point of release where the resulting fuel-air cloud was found to be fuel-rich. For all other tests, the congested regions were positioned 55 m from the release, where the average fuel-air concentration in the plume was expected to be near-stoichiometric. The presence of the jet release leads to inherent variability in the initial conditions at the time of ignition, due to fluctuations in the concentration and velocity fields.

Regardless of the variations in initial conditions between experiments, certain trends can be discerned from Fig. 3. The overall highest overpressures of the campaign were obtained with the high congestion rig in a test where ignition was initiated upstream of the congested region (the un-filtered peak value exceeded 30 bar). This maximum overpressure value is similar to overpressures obtained in a corresponding test with a homogeneous cloud from a previous campaign. Fig. 3 also shows that for the medium congestion level, the initial conditions generated by the realistic release can cause an explosion event that is significantly more severe than in the corresponding quiescent configuration. For example, this was the case for test 8 of the AIRRE campaign, which involved rig 8 positioned 55 m from the release point. Ignition was initiated upstream of the rig, 100 mm from ground level at the centre of the congested region's edge. The equivalent quiescent, near-stoichiometric natural gas-air experiment, test 16, had the same ignition location relative to the congestion as in test 8.

It may be reasonable to assume that ignition upstream of the congested region would enhance explosion severity compared to the tests with downstream ignition, as the flame front in this situation is pushed towards the obstructions by the mean flow. The flame speed and the shape of the flame front at entry into the congestion can have a significant effect on the explosion severity, cf. the observations by for example Cronin & Wickens (1986), Tomlin & Johnson (2013) and Davis in the RPSEA II project (S. Davis, private communication, 2019). This effect seems to be present in the tests with medium congestion in Fig. 3, while it is less pronounced for the high congestion rigs.

In the following, further results are presented for two of the tests performed as part of the AIRRE project: **test 8** (medium congestion rig, ignition at the upstream edge of the congestion, 55 m from the point of release) and **test 16** (reference test with a quiescent, homogeneous cloud enclosed in polythene tent, ignition at edge of congestion). Reference is also made to results from **test 15** ("free" jet, i.e. without congested regions, ignition at 55 m from the release point).

3.2 Concentration measurements

In each of the large-scale jet release tests, pressurised natural gas was released horizontally, at approximately 1.4 m above ground level, from the 100 mm diameter nozzle. The release rate at ignition time varied between approximately 100 and 120 kg/s between the different tests. Since the outflow of natural gas was not terminated immediately after ignition of the jet, a jet fire developed in the final stage of the experiment. Fig. 4 illustrates the different phases for one of the un-obstructed high-pressure release tests. Radiation measurements from one of the jet fires will be reported elsewhere.

Concentration sensors were placed along the release direction at 10 m intervals from 20 m to 80 m and at 100 m, measured from the release point. The sensors were mounted 1.4 m above the ground on instrumentation stands. Additional sensors were positioned at selected distances from the release point (depending on each test), symmetrically around the centre line along the direction of the release, at 5 m and 10 m from the centre line. At certain distances, the concentration was measured at three different elevations, 0.7 m, 1.4 m and 2.1 m from the ground. In the tests with congested regions, a different layout of sensors was used in the rig area with positions relative to the rig. On the same stands, depending on the position, the instrumentation also included pressure transducers, turbulence sensors and ionisation probes. Fig. 5 shows the layout of the instrumentation for test 8, which had a medium congestion rig placed 55 m from the release point.

The concentration measurements were recorded by sensors that apply the oxygen-depletion principle, i.e. in the large-scale release experiments it is assumed that air is displaced by natural gas (cf. Section 2.2). The time response of the sensors to an oxygen concentration change from 20.9 vol% to 2.1 vol% is quoted by the manufacturer as being below 5 seconds. Since partial pressure diffusion is required to transfer oxygen to the sensing elements, the concentration sensors are sensitive to pressure and temperature fluctuations. In high-velocity flows, this effect results in a reduction in the apparent gas concentration, as the signal from the sensor is directly proportional to the pressure of the fluid. To evaluate the impact of such effects on the results, a set of small-scale commissioning tests were performed prior to the large-scale tests. Based on these results, it is assumed the dynamic pressure generated by flow velocities higher than 25 m/s may underestimate the actual concentration. This can be seen in some of the concentration-time traces (measured close to the release point) as short term 'dips' in measured gas concentration.

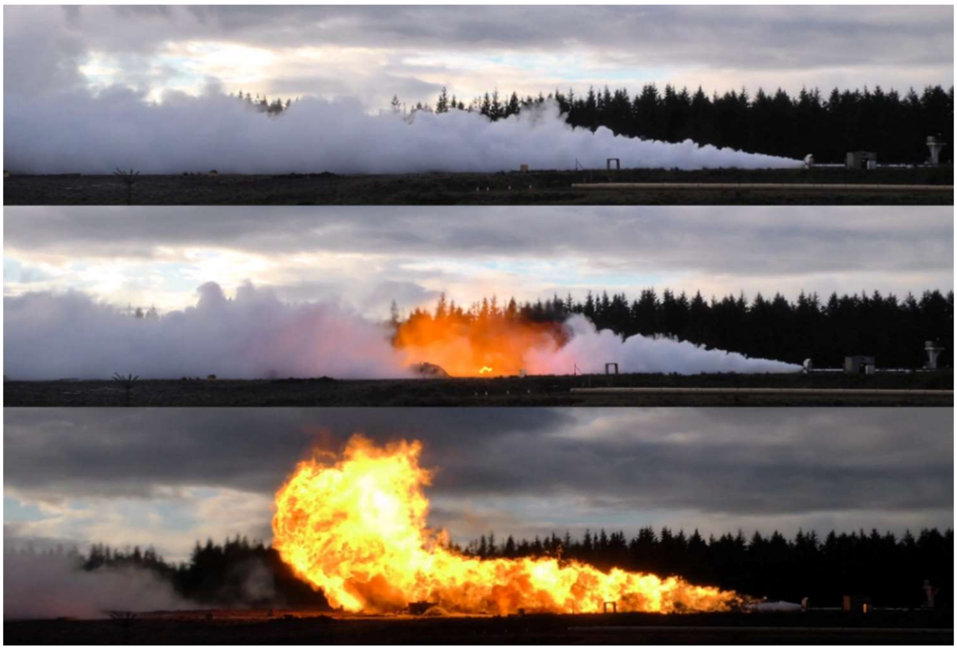

Fig. 4. *Snapshots from different phases of a "free" jet release experiment: unignited jet release phase (top), flame propagation after ignition (middle) and jet fire phase (bottom).*

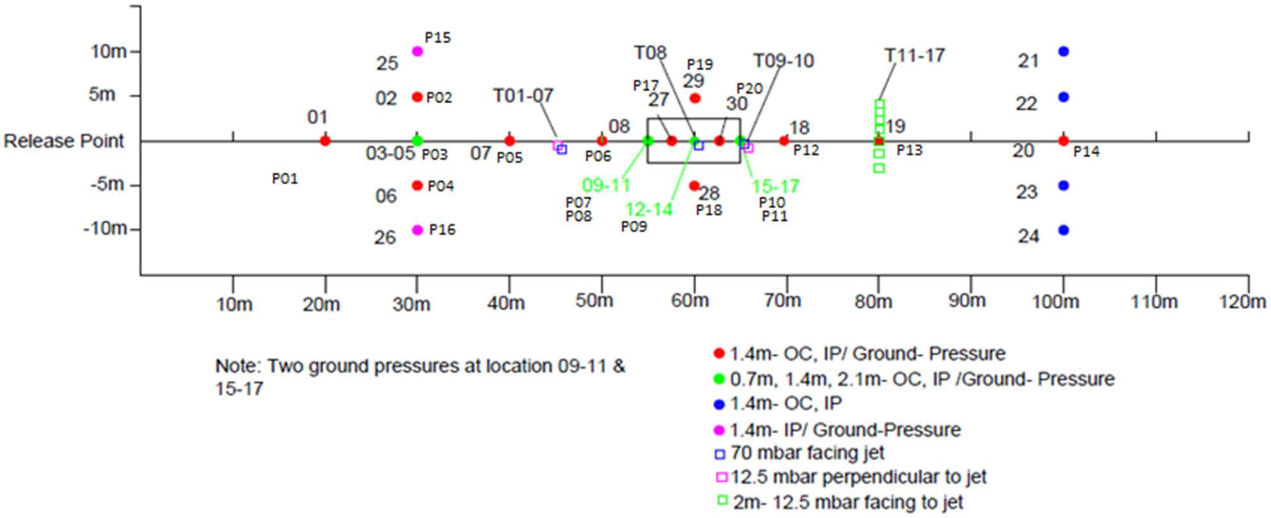

Fig. 5. *Instrumentation layout for test 8. The legend explains the plotting style for each sensor type (OC – Oxygen Cell, IP – Ionisation Probe, T- Turbulence Probe). The square markers denote different types and configurations of turbulence probes.*

In the full-scale experiments, post-processing of turbulence measurements performed by Ineris (Jamois *et al.*, 2020) showed that the jet centreline velocity at 40 m from the point of release was around 50 m/s, thus, concentration measurements at this distance and upstream may be significantly affected by dynamic pressure effects. In the following, concentration measurements upstream of 40 m from the release are therefore not included in the analysis. When interpreting the results for gas concentration at the time of ignition for the remaining sensors, the period maximum value recorded in a certain period before ignition is used. Inside the congested regions, post-processing of the turbulence measurements suggests that flow velocities were reduced to less than 20 m/s. The dynamic pressure effect on these sensors is therefore likely negligible.

Fig. 6 shows the estimated mass flow rate across the orifice plate for tests 15 and 8. The differential pressure signal, from which the rate is calculated, was aligned to zero at the time corresponding to the closure of the valve. The mass flow rates are similar from around 30 s prior to ignition – at this point the jet was likely quasi-steady. Minor variations in the initial pressure and temperature in the reservoir lead to variations of the mass flow rate of less than +/- 10 % between tests.

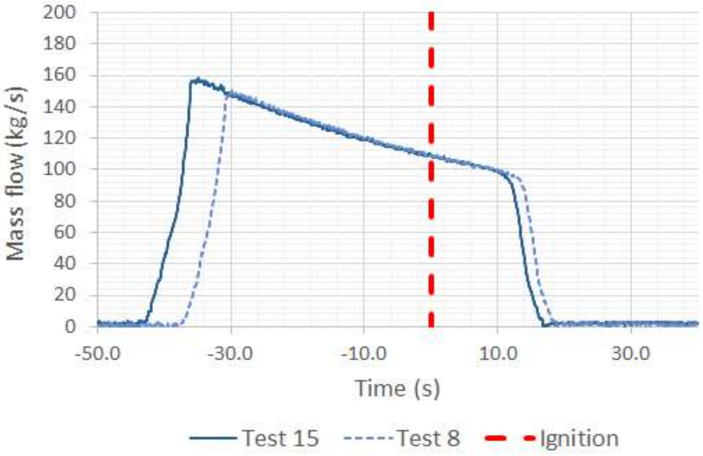

Fig. 6. *Mass flow rate across orifice plate for tests 15 and 8.*

The wind speed and direction were measured before and during each test, at approximately 30 m behind the release point, at both 5 and 10 m above the local ground level. The average wind speed during the last 30 s before ignition, measured at an elevation of 5 m above the ground, varied between approximately 2 and 8 m/s between tests. The effect of wind is likely limited close to the release and in the congested region but may affect the far-field concentrations where flow speeds are low. Humidity and condensation of water may have influenced the temperature of the plume. Similarly, atmospheric stability can change the relative buoyancy of the cloud and the background turbulence level. However, considering the high velocities generated by the jet, it is reasonable to assume that both humidity and atmospheric stability had a minor influence on concentrations above the lower flammability limit.

Fig. 7 shows the period maximum concentration (over 5 s before ignition) measured by selected sensors that were placed at 1.4 m above ground level in test 8. Concentrations measured upstream of 40 m have been excluded, as already described, together with measurements from certain sensors that appeared to be erroneous. Similarly, Fig. 8 shows the maximum concentration measured (over a 5 s period before ignition) on the release centre line (y=0) at different elevations from ground level. The black rectangle marks the position of the rig in both Fig. 7 and Fig. 8.

Fig. 9 shows selected concentration measurements in time from sensors located 1.4 m from the ground level, along the centreline of the release, at various distances from the release orifice. The profile for the 50 m location show that there are still some effects due to the dynamic pressure from the jet on the measurements at this point; there are fewer oscillations and less noise on the traces that were recorded further away from the point of release and within the congested region. The increase in concentration at 62.5 m from the release was measured either slightly before or at the same time as that measured by the three sensors positioned at 60 m from the release (Fig. 9 only shows the sensors at an elevation of 1.4 m). This is likely due to different positioning of the sensors relative to the pipes in the congested region (the same effect was also observed in a test with a similar layout). As the focus in the present work is mainly on the quasi-steady concentrations at ignition time, the time of arrival of the flammable cloud is not considered further here.

At the time of ignition in test 8, Fig. 7 - Fig. 9 show that the measured period maximum concentrations in at least ¾ of the rig length are between 10 – 11.5 vol% natural gas in air. The concentrations are increasing slightly along the centreline up to 62.5 m from the point of release. At the rear end of the rig, in the wake of the jet, concentrations are lower (around 7 vol%). The jet velocity decreases significantly inside the congestion – measurements from the turbulence probes indicate that the mean flow velocity is less than 10 m/s at 60 m from the release (i.e. halfway through the congested region). The velocity was likely further reduced in the region from 60 m to 65 m. Due to low flow velocities, changes in gas concentration require a longer time to propagate through the congestion compared to the "free jet" conditions.

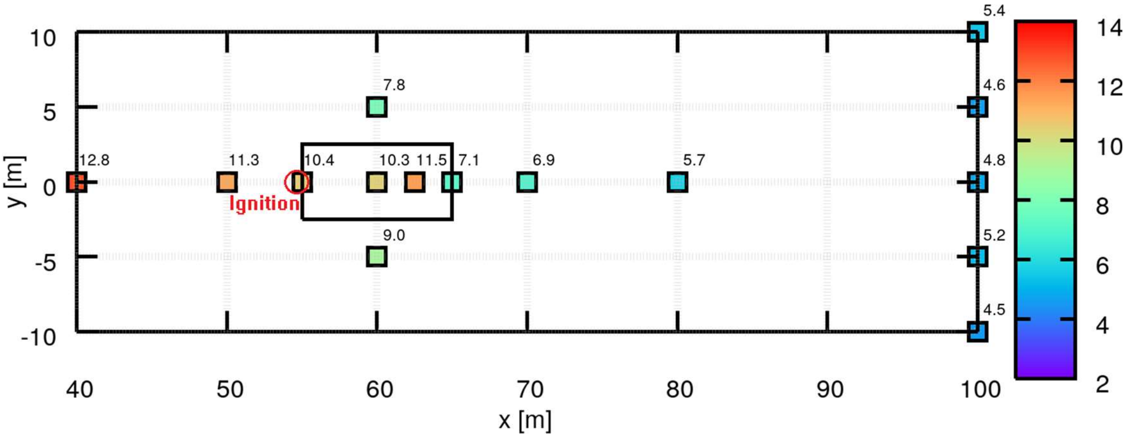

Fig. 7. *Measured mole fractions 1.4 m from ground level in test 8, period maximum over 5 s before ignition. Here, x and y are zero at the release point. The red circle marks the ignition location.*

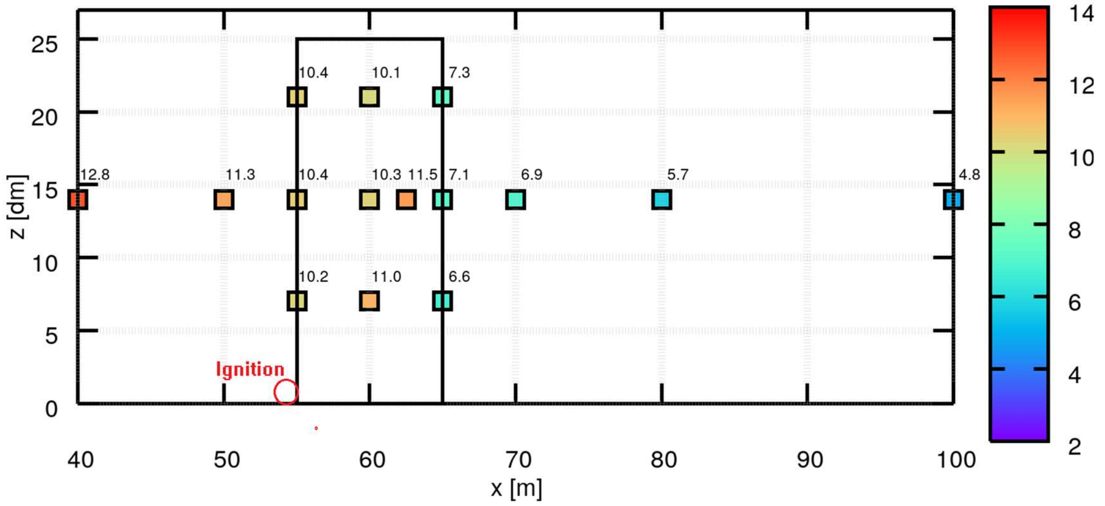

Fig. 8. *Measured mole fractions at release centre line (y=0) at different elevations from ground level in test 8, period maximum over 5 s before ignition. Here, x and y are zero at the release point. The red circle marks the ignition position.*

Fig. 7 indicates that the fuel concentration is near uniform across the jet 100 m downstream of the release point, with slightly higher concentrations on the positive side of the y-axis. Since flow speeds in the jet are low here, this asymmetry may be caused by the ambient wind.

Fig. 10 shows the measured concentrations (maximum over 5 s period before ignition) at the release centreline at different elevations from ground level in the "free jet" test 15 (it is important to note that the location of sensors differ somewhat between test 8 and test 15). In test 15, the concentrations appear to uniformly decrease with increasing distance from the point of release. Mass release rates and atmospheric conditions were similar for test 15 and test 8, however, the measured concentrations upstream of 60 m were somewhat higher in test 8 than in test 15.

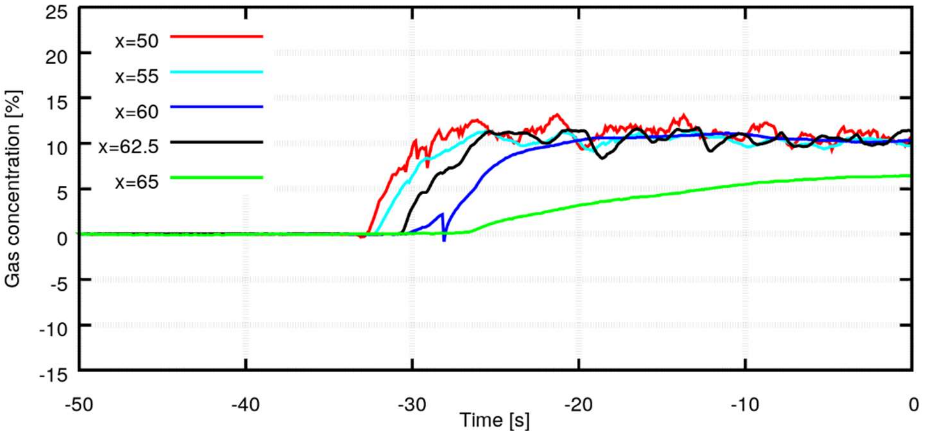

Fig. 9. *Measured mole fractions at release centre line (y=0) at different distances from the release point in test 8. The sensors are placed 1.4 m from the ground. Ignition occurred at 0 s.*

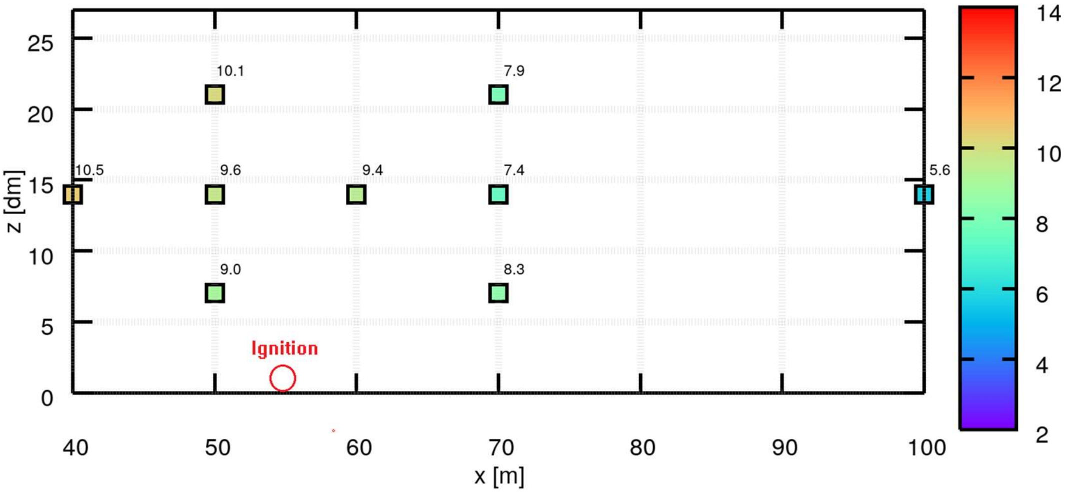

Fig. 10. *Measured mole fractions at release centre line (y=0) at different elevations from ground level in test 15, period maximum over 5 s before ignition. The red circle marks the ignition position.*

Fig. 8 and Fig. 10 indicate that the period maximum concentrations (over 5 s before ignition) are relatively uniform in the vertical direction in the region between 55 m and 65 m from the release – stratification is not observed in either test.

3.3 Turbulence measurements

In some of the large-scale tests in the AIRRE project, up to 20 differential pressure sensors were installed to measure turbulence in the flow. The demanding conditions under which the sensors operated during the tests, i.e. high-velocity flows with excess debris present and instrumentation masts that occasionally fell, caused several sensors to malfunction or the recorded data to be invalid. In addition, the high explosion pressures generated in several of the tests damaged many of the turbulence sensors. It was therefore necessary to replace several sensors after these tests. This effectively limited the number of tests where turbulence measurements could be performed. It was also challenging to obtain reliable recordings for a sufficiently long period to enable the extraction of turbulence velocities. Ineris performed the analysis of the turbulence measurements (Jamois *et al.*, 2020), and retained signals from 14 pressure time series from the unobstructed tests and 50 from the tests with congested regions to evaluate the turbulence fields. Most of the measurements were taken at an elevation of 1.4 m, while a limited number of sensors were placed either at 0.7 m or 2.1 m.

The measured dynamic pressure was used to estimate the velocity in the direction of the jet axis. The integral time scale of turbulent fluctuations was obtained from the autocorrelation function, while the integral length scale was obtained by multiplying the latter by the average velocity at the same point.

In the tests without obstructed regions, the jet mean velocity along the release direction (at y = 0) was around 70-90 m/s at 30 m from the release point, 50-60 m/s at 40 m, 40-60 m/s at 50 m, around 30 m/s at 80 m, and approximately 20 m/s at 100 m. Downstream of 40 m from the release point, the relative turbulence intensity was estimated to vary between 20-40 % along the release centreline. The average turbulent velocity in the region between 40 m to 60 m was estimated to be approximately 12 m/s.

In the tests with rigs installed, the mean velocity was significantly reduced (to below 20 m/s) inside and just downstream of the congested region. Very few probes gave reliable data inside the rig, but the few available results indicated maximum turbulence intensities of around 40 % inside the congestion. Upstream of 5 m from the rig, and downstream of 15 m from the congestion, results seemed to follow the same trend as in the tests with un-obstructed jets. The estimated values for the integral length scale for the tests without obstructed regions were (in line with the free jet theory) between 1 m and 2.5 m up to 60 m from the release point. Further downstream, the integral length scales were reduced to around 1 m or less and appeared to be approximately constant with increasing distance from the release point. Jamois *et al.* (2020) discuss the turbulence measurements in the AIRRE experiments in more detail.

3.4 Pressure-time recordings and flame speeds

Up to 20 pressure sensors were distributed throughout the region of interest in the high-pressure release experiments. During the tests, the transducers were subject to significant mechanical vibration, debris throw and heat post-ignition. Different levels of noise due to electrostatic and mechanical variations in the mounting, cabling and signal conditioning arrangement of each transducer were present, to varying degrees, in many of the pressure-time traces. Where possible, traces were corrected for these effects to leave only the relevant pressure event. To account for velocity head and temperature effects pre-ignition (from the cold jet), the traces were balanced for zero-pressure at the time of ignition.

Due to the highly turbulent, high-velocity nature of the releases, debris from the ground was entrained in the jet. Furthermore, the release produced condensed water droplets that were entrained and transported by the jet flow, significantly affecting the visibility of the region downstream of the release point, see Fig. 4 (top). Debris, water vapour and mechanical vibration can lead to a spurious trigger of the circuitry in the ionisation probes used for flame detection. These issues complicated the analysis of the ionisation probe measurements.

However, the high-speed video recordings provided useful information on the flame speeds. A tailor-made, in-house computer program was used by DNV GL to evaluate the changes in pixel intensities along three lines (at different heights) with respect to time. Fig. 11 illustrates results from the video analysis performed by DNV GL at two flame positions for test 8. The change in pixel intensity for each frame (relative to the initial frame) along the three straight lines (blue, green and red) was evaluated automatically, to produce a flame position and a corresponding time relative to the start of the analysis. This information was used to estimate a flame speed along each of these three lines, using a linear regression fit based on a user-defined set of frames over which to fit. The speed was only recorded if the linear regression showed a maximum error of 10 % or less. However, as the presence of water vapour reduced the visibility of the flame in most tests, the interpretation of this data was not straightforward, as shown in Fig. 11. Where it was not possible to determine a flame speed, it was set to zero in the analysis. Flame speeds were therefore also estimated using manual definition of the flame position on each video frame (illustrated by the magenta line in Fig. 11). This manual approach was found to be more effective and is used in the flame speed estimates presented here. It should be noted that though there are significant uncertainties in measuring flame speeds from frame to frame, the overall view is still useful to consider together with the measurements of explosion pressure.

In Fig. 11 (top), the flame had propagated around 5 m from the edge of the congestion, and the flame speed was still below the speed of sound in the mixture. Fig. 11 (bottom) shows the flame position at the maximum observed flame speed of 821 m/s. At this point, the flame had propagated approximately 9.3 m from the ignition point and had entered the fast deflagration regime (Oran *et al.*, 2020).

Fig. 12 shows the calculated flame speed as a function of distance from the release point, estimated from high-speed video recordings of test 8. The flame speeds in test 8 are plotted together with those from test 16. Due to the presence of excessive water vapour in test 8, the visibility of the flame was poor. Furthermore, the high explosion overpressures that were generated in the test lead to loss of the ionisation probe data. Therefore, significant uncertainty is associated with the flame speed estimates, in particular for the flame propagation through the first 5 m of the rig.

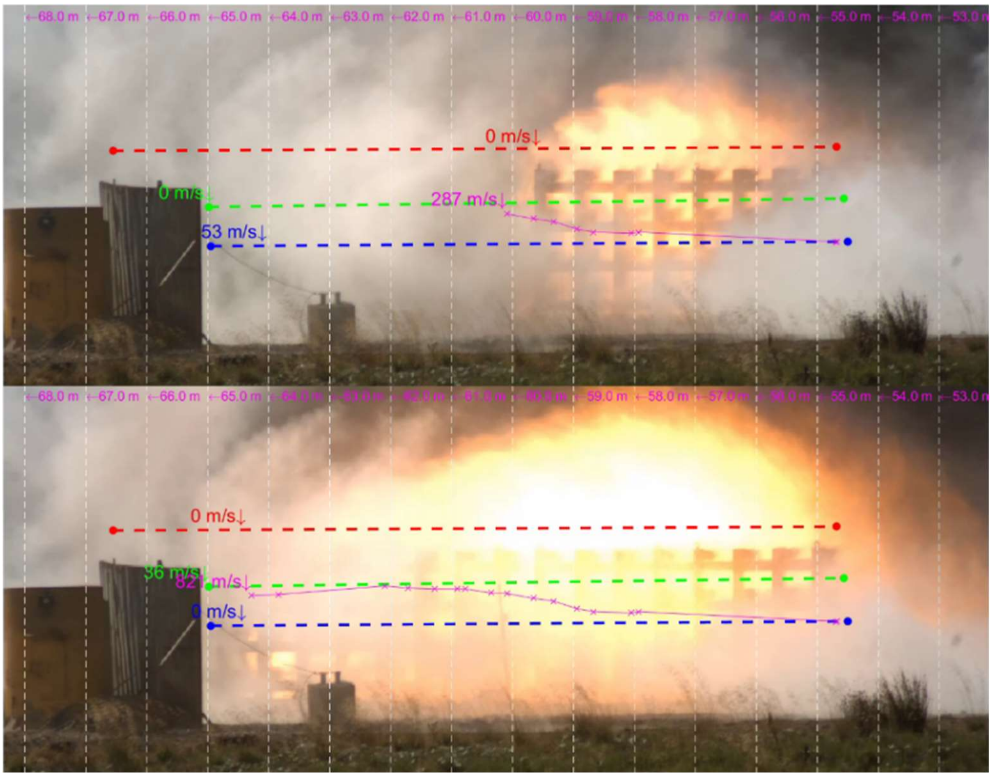

Fig. 11. *Estimated speed of flame front as the flame enters the second half of the congested region (estimated to 287 m/s at 60 m from the release along the manually defined flame path, marked with a magenta line) (top) and as the flame propagates towards the end of the congested region (similarly estimated to 821 m/s at 64.3 m from the release, 10.7 ms later) (bottom) in test 8.*

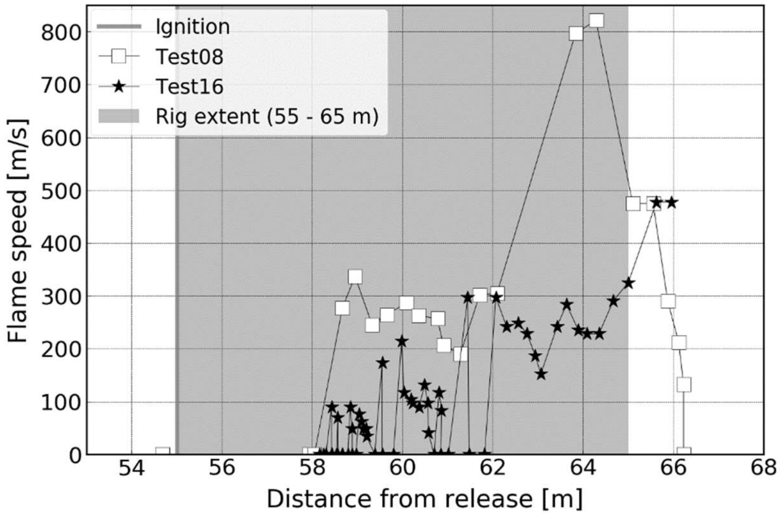

Fig. 12. *Flame speed extracted from high-speed video recordings for tests 8 and 16. Test 16 is plotted for comparison with test 8, so the rig and ignition positions are aligned. The "distance from release" is not applicable to test 16.*

The measurements from the turbulence sensors in the AIRRE tests with rig 8 suggest that the relative turbulence intensities were around 40 % inside the congestion, while the mean flow speeds were strongly reduced when compared to the un-obstructed cases. After the onset of the release, the flow would have generated turbulent wakes downstream of the pipes in the congested region, including turbulent shear layers that would co-exist with more energetic, coherent structures. The wakes likely interacted throughout the rig and formed a complex flow pattern prior to flame arrival. However, from the limited number of turbulence measurements (due to the challenges discussed in Section 3.3) it is not straightforward to obtain a detailed picture of the flow field internal to the rig.

In order to assess the combined effect of pre-ignition turbulence, non-zero mean flows and concentration gradients generated by the high-pressure releases, it is relevant to compare the results from test 8 to those from test 16. Fig. 13 (left) shows the peak pressure values from test 8 as a function of distance from the release point, while Fig. 13 (right) shows the pressure-time traces that were recorded inside the rig during the explosion event. A 0.1 ms moving average filter has been applied to the pressure signals to remove high-frequency noise.

Fig. 13 shows that the highest overpressures in test 8 were recorded at the edge of the congested region, 10 m downstream of the ignition point. The dominating explosion pressure-generating event in test 8 was flame acceleration through the congested region, with the highest flame acceleration occurring in the second half of the congested rig (between 60 m and 65 m from the release point).

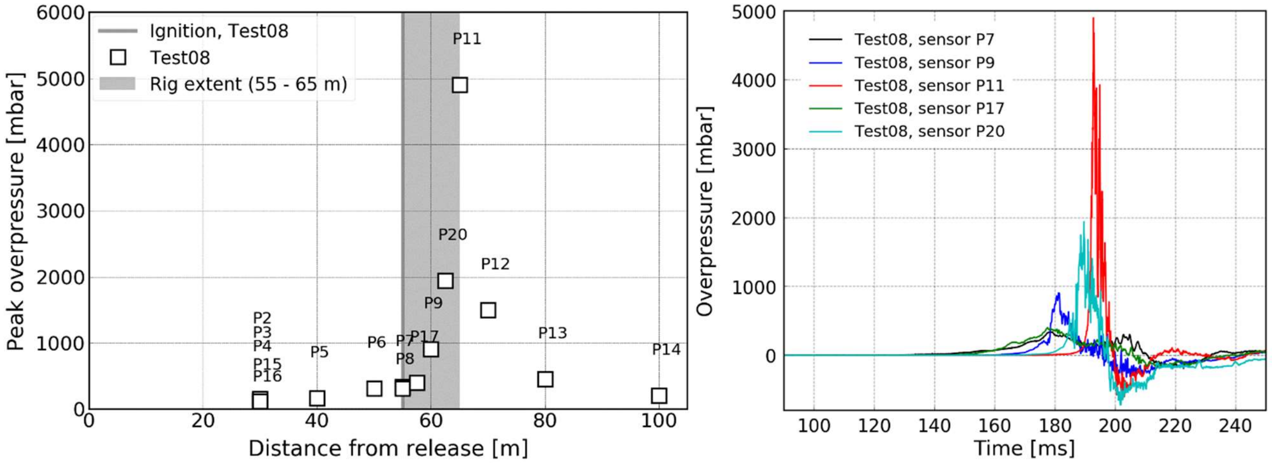

Fig. 13. *Measured peak overpressures (left) and pressure-time traces from selected sensors located inside the rig in test 8 (right).*

For the flammable gas mixture used in the AIRRE experiments, the stoichiometric concentration is approximately 8.9 vol.% natural gas in air, while the top reactivity is expected to occur around 9.7 vol.% natural gas in air (Nilsson *et al.*, 2019). If the concentration measurements prior to ignition are representative of the actual concentrations around the sensors at the time of flame arrival, the concentration measurements in Fig. 7, Fig. 8 and Fig. 9 suggest that the flammable cloud inside of the rig was overall fuel-rich in the upstream ¾ of the rig. Towards the downstream edge of the congested region, the concentrations were reduced quite significantly, i.e. approximately 7 vol.%. It is possible that fuel concentrations in the final ¼ of the rig, where the most significant flame acceleration occurred, were closer to the "optimal" reactivity.

Test 16 was a reference test for the experiments with high-pressure jet releases and the medium congestion level in the AIRRE project. The test was performed with a quiescent mixture with a nominally homogeneous concentration of approximately 9.2 vol.% natural gas in air, and ignition occurred at the edge of the congestion, close to the ground (corresponding to the ignition position in test 8). Fig. 14 illustrates the position of the ignition source and the pressure transducers that were placed inside the rig in test 16, along the rig centreline. Fig. 15 (left) presents the maximum overpressures measured inside the rig, while Fig. 15 (right) shows selected pressure-time traces (corresponding to the same distance from ignition as the sensors plotted in Fig. 13 (right) for test 8).

The flame speeds in both tests are shown in Fig. 12. In test 16, reduced visibility of the flame and lack of ionisation probe data in the first ¼ of the rig lead to difficulties in extracting a reliable flame speed. However, in the first 5 m of the rig, the flame acceleration and generation of overpressure seem to have been modest, with regions where the flame speed was almost constant or even decelerating at times. Significant flame acceleration was observed as the flame propagated into the final ¼ of the rig, at 7-8 m from the ignition point. Flame acceleration seemed to persist after the flame front exited the rig, approximately 10 m downstream of the ignition point, as the region of highly reactive mixture extended past the rig. Despite the differences in initial conditions of the flow, the explosion event in test 16 and test 8 appears to have been qualitatively similar, cf. Fig. 12 and Fig. 15. However, in test 8, the pre-ignition turbulence most likely enhanced the flame acceleration throughout the rig, resulting in a maximum overpressure that is approximately a factor 2.7 higher than that obtained in the quiescent reference. It is worth noting that if it is assumed that the pressure is proportional to the square of flame speed, this equates to an increase in peak flame speed by a factor of approximately 1.6, which corresponds very closely to the ratio of peak flame speeds between tests 8 and 16 (800 m/s and 500 m/s). This suggests that the estimation of peak flame speeds is relatively accurate, despite the issues already described.

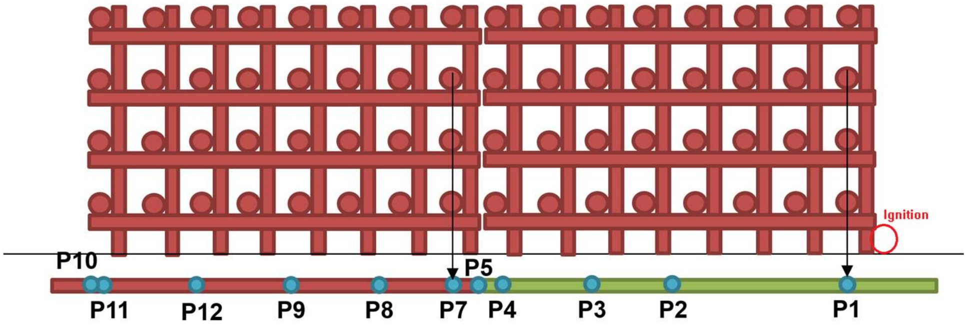

Fig. 14. Positions of pressure transducers and ignition point in test 16.

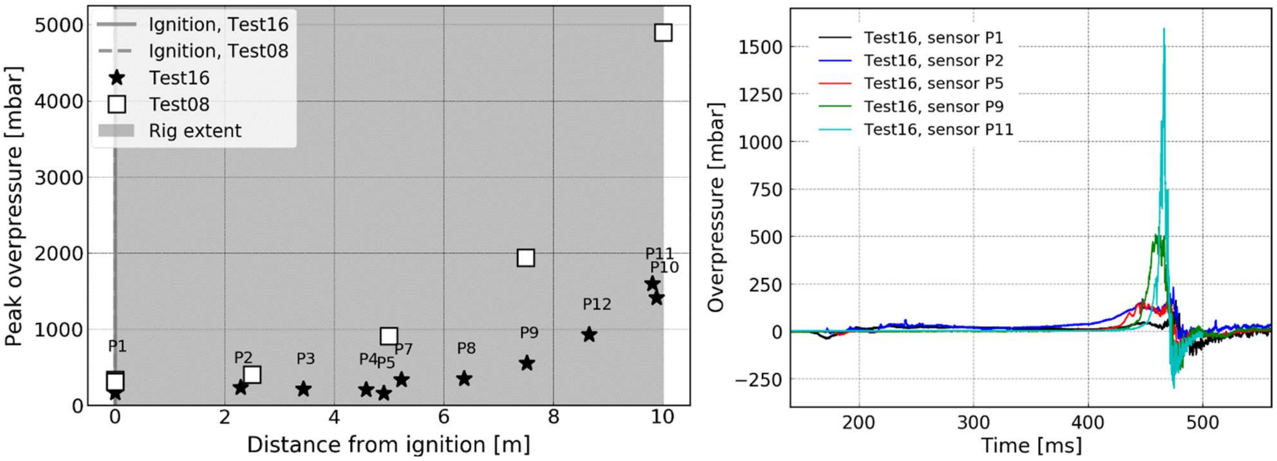

Fig. 15. *Measured peak overpressures in test 16 and test 8 (left) and pressure-time traces from sensors located inside the rig in test 16 (right).*

4. Conclusions

The primary objective for the AIRRE project was to gain improved understanding of the effect of realistic releases on the consequences of accidental gas explosions in the petroleum industry and evaluate the current state-of-the-art methodologies for quantitative risk assessment (QRA) considering the new results. The research activities in the project included a unique series of large-scale explosion experiments with ignited high-momentum jet releases directed into geometries with varying levels of congestion. Selected results from these large-scale experiments are reported in this paper.

The summary of maximum overpressures from the AIRRE campaign shows that explosion severity significantly depends on the congestion level present in each test, the position of the congested region, and the ignition location relative to both the release outlet and the congested rig. The results demonstrated that an explosion propagating through a homogeneous, quiescent and near-stoichiometric (most reactive) cloud that encloses a congested region does not necessarily represent the “worst-case scenario” in terms of generated explosion overpressures. The pre-ignition turbulence generated by the high-pressure release produced higher explosions pressures than the corresponding quiescent reference test in two of the experiments with the medium congestion rig. However, in the present campaign, this only occurred when ignition happened upstream of the medium congestion rig, and the flame front accelerated with the mean flow induced by the release. In the high congestion configurations, the maximum generated overpressure seemed to be less sensitive to the position of the ignition point. However, the limited number of sensors and the variations in initial conditions complicates the analysis. Tests with corresponding configurations typically exhibited variations in period averaged concentrations of ±1-2 vol.%, measured in the same positions. These variations will affect the reactivity of the fuel-air cloud and must be considered when results from different tests are compared.

The large-scale experiments in AIRRE also included measurements of flow velocities, turbulence levels, explosion overpressures and flame arrival times throughout the flammable gas plume. Due to the intense conditions inside the plume caused by the high-velocity jet release (as well as the high explosion pressures generated in several tests) it was challenging to obtain enough measurements to determine the properties of the flammable cloud and the ensuing flame propagation. It would therefore be beneficial to complement the results from the large-scale AIRRE campaign with smaller-scale studies where more extensive measurements of turbulence, concentrations and flame speeds may be feasible, and a higher number of tests can be performed. If possible, experimental work should be combined with CFD simulations using models that are both capable of resolving part of the turbulence spectrum and represent the enhancement in flame surface area from various physical phenomena.

Finally, the modelling work performed as part of the AIRRE project suggests that scenarios that entail flame propagation past obstacles in established, turbulent flow fields, may not be straightforward to represent with the commonly used consequence models. However, to assess whether the present results should affect the current state-of-the-art QRA methodologies requires a thorough treatment – work on modelling and methodology will therefore be reported in subsequent publications.

Acknowledgements

The authors gratefully acknowledge the financial contribution to the AIRRE project from the Research Council of Norway (RCN) under grant agreement no. 269360 in the Demo 2000 program. Gexcon gratefully acknowledges the financial contributions from the sponsors GRTgaz, TOTAL and Shell Global Solutions, as well as the technical contributions from the subcontractors DNV GL Spadeadam Research and Testing and Ineris.

References

Bjerketvedt, D., Bakke, J.R. & van Wingerden, K. (1997). Gas explosion handbook. *Journal of Hazardous Materials*, 52: 1-150.

CCPS (1994). Guidelines for evaluating the characteristics of vapour cloud explosions, flash fires and BLEVEs. Center for Chemical Process Safety (CCPS), New York.

City Technology. (2017). Product Datasheet AO2 Oxygen Sensor. https://www.citytech.com/en-gb/PDF-Datasheets/ao2.pdf. Accessed on 17 Feb. 2020.

Cronin, P. & Wickens, M.J. (1986). A large scale experimental study of the conditions required for sustained high speed flame propagation in a flammable vapour cloud. Report No. MRS I 4348. British Gas Corporation, UK.

Davis, S., Engel, D., Groethe, M. & van Wingerden, K. (2016). Large scale deflagration to detonation testing. Eleventh International Symposium on Hazards, Prevention and Mitigation of Industrial Explosions (11 ISHPMIE), Dalian, 24-29 July 2016, pp. 110-124.

Davis, S.G., Pagliaro, J., Botwinick, D., van Wingerden, K., Allason, D. & Johnson, M. (2018). Don't believe the hype: using case studies and experimental evidence to show why HSE is wrong about exploding DDTs. Proceedings Fourteenth Global Congress on Process Safety (GCPS 2018), Orlando, Florida, 22-25 April 2018, 24 pp.

Hansen, O.R., Gavelli, F., Davis, S.G., Middha, P. (2013). Equivalent cloud methods used for explosion risk and consequence studies. *Journal of Loss Prevention in the Process Industries*, 26: 511-527.

Harris, R.J. & Wickens, M.J. (1989). Understanding vapour cloud explosions – an experimental study. Fifty-fifth autumn meeting of the Institution of Gas Engineers.

Hjertager, B. H. (1984). Influence of turbulence on gas explosions. *Journal of Hazardous Materials*, 9(3): 315-346.

ISO 5167-1:2003. (2003). Measurement of fluid flow by means of pressure differential devices inserted in circular-cross section conduits running full – Part 1: General principles and requirements.

ISO 5167-2:2003. (2003). Measurement of fluid flow by means of pressure differential devices inserted in circular cross-section conduits running full – Part 2: Orifice plates.

Jamois, D., Hébrard, J., Leprette, E., Proust, C., Mauri, L., Hisken, H., Atanga, G., Lucas, M., van Wingerden, K., Skjold, T., Quillatre, P., Dutertre, A., Marteau, T., Pekalski, A., Jenney, L., Allason, D. & Johnson, M. (2020). Turbulence in real flammable gas releases. *Thirteenth International Symposium on Hazards, Prevention and Mitigation of Industrial Explosions (13 ISHPMIE)*, Braunschweig, Germany, 27-31 July.

Johnson, D.M. & Cleaver, R.P. (2002). Gas explosions in offshore modules following realistic releases (PHASE 3B): final summary report. Advantica Technology, UK. Report number: R4853.

Johnson, D.M., Cleaver, R.P., Puttock, J.S. & van Wingerden, C.J.M. (2002). Investigation of gas dispersion and explosions in offshore modules. Offshore Technology Conference (OTC), Houston, Texas, 6-9 May 2002, Paper OTC 14134: 7 pp.

Johnson, D.M., Tomlin, G.B. & Walker, D.G. (2015). Detonations and vapor cloud explosions: Why it matters. Journal of Loss Prevention in the Process Industries, 36: 358-364.

Marsh (2018). *The 100 largest losses 1978-2017 – Large property damage losses in the hydrocarbon industry*. 25th edition.

Moen, I.O., Donato, M., Knystautas, R., Lee, J.H. (1980). Flame acceleration due to turbulence produced by obstacles. Combustion and Flame, 39(1): 21-32.

Nilsson, J.K.E, van Sprang, A., Larfeldt, J. & Konnov, A.A. (2019). Effect of natural gas composition on the laminar burning velocities at elevated temperatures. Fuel, 253: 904-909.

Oran, E.S., Chamberlain, G. & Pekalski, A. (2020). Mechanisms and occurrence of detonations in vapor cloud explosions. Progress in Energy and Combustion Science, 77: 100804. DOI: https://doi.org/10.1016/j.pecs.2019.100804.

PCB Piezotronics. (2020). https://www.pcb.com/products?m=113B26. Accessed on 17 Feb. 2020.

Schelkin, K.I. (1940). Influence of tube roughness on the formation and detonation propagation in gas. Zhurnal Eksperimentalnoi i Teoreticheskoi Fiziki, 10:823–827.

Skjold, T., Hisken, H., Mauri, L., Atanga, G., Bernard, L., van Wingerden, K., Foissac, A., Quillatre, P., Blanchetière, V., Dutertre, A., Kostopoulos, D., Pekalski, A., Allason, D., Johnson, M., Jenney, L., Leprette, E. & Jamois, D. (2018). Assessing the influence of real releases on explosions: motivation and previous work. In *Proceedings of the Twelfth International Symposium on Hazards, Prevention and Mitigation of Industrial Explosions (12 ISHPMIE)*, Kansas City, 12-17 August 2018: 24 pp. Fike Corporation, Blue Springs, MO, USA.

Stewart, J. & Gant, S. (2019). A review of the Q9 equivalent cloud method for explosion modelling. FABIG Newsletter, Issue 75, March 2019: 16-25.

Tomlin, G. & Johnson, D.M. (2013). A large scale study of the venting of confined explosions into unobstructed and congested flammable vapour clouds. Proceedings Seventh International Seminar on Fire and Explosion Hazards (ISFEH), Providence, 5-10 May 2013, Research Publishing, Singapore: 679-688. ISBN: 978-981-07-5936-0.

DOI: 10.7795/810.20200724

Investigations on the effect of particle size on dust dispersion in MIKE 3 apparatus

Yangyue Pan[a], Christoph Spijker[a], Hannes Kern[a] & Harald Raupenstrauch[a]
[a] Chair of Thermal Processing Technology, Montanuniversitaet Leoben, Leoben Austria
E-mail: *yangyue.pan@unileoben.ac.at*

Abstract

Particle size is one of the important factors influencing the dust dispersion when dust explosion experiments are carried out. To observe the influence of particle size on coal dust propagation behaviors, the dispersion experiments were conducted in MIKE 3 apparatus from Kuehner AG. Seven different size classes of coal dust were prepared using a sieve shaker. High-speed photography was used to record the propagation. The videos were processed by MATLAB to track the dust front locations in MIKE 3. By separating and filtering the red, green and blue color components in each frame of the video, the threshold values of the start and end points of dust dispersion can be defined. The result of the video analysis shows that the particles which are smaller than 250 μm move upwards with similar velocities, whereas if they are larger than the critical size, the movement becomes much slower. For a detailed investigation of the fluid flow, OpenFOAM was used to simulate the dispersion of coal dust. A compressible fluid solver rhoPimpleFoam from the package was modified for calculating the movement of Lagrangian particles inside of the flow. Source terms of energy and species for particles were implemented into Eulerian gas phase. Standard k-ε model was used for turbulence modelling. The inlet of continuous air inlet resulted in nearly constant velocity of the coal dust due to high momentum from the continuous pressurized air inlet. Another injection system which has a compressed air tank showed that pressure and velocity field have smaller values in overall than the previous system at the same time.

Keywords: *MIKE 3, dust dispersion, particle size, CFD simulation*

1 Introduction

Dust explosion hazard is an important issue for most industrialized countries due to its disastrous consequences. Although it has been studied for more than 200 years (Eckhoff, 2003), the fundamental aspects concerning to the dust itself are still unknown especially for the new products in process lines.

As one of the most important characters of dust samples, particle size influences not only the dust explosion itself, but also the preparation of the dust samples in laboratory research. Experiments that are conducted for the effects of particle sizes are already available (Eckhoff, 1996). Most of the studies about particle sizes are focusing on the flame characters and propagation patterns (Yuzuriha et al., 2017, Zhang et al., 2017, Cloney et al., 2020). Studies on turbulence of dust clouds in the content of flame propagation and dust explosion still need attention.

Dust dispersion depends highly on the actual conditions of each test, such as air humidity, ambient pressure and each dust sample. Researchers tried to create homogeneous and reproducible dust cloud in the experiments to control the dispersion effects (Klippel et al., 2014). Computational Fluid Dynamic (CFD) tools are a good solution that are able to create same test conditions. Pollhammer (Pollhammer et al., 2016) simulated dust dispersion in a 20 L vessel and found out that at the time of ignition, the dust concentration near wall increased from around 200 g/m^3 to 2000 g/m^3 within 10 mm distance.

The aim of this work is to study the particles dispersion in MIKE 3 apparatus. Simulations have been carried out, in order to assess the ability of the CFD model. The model developed in the current work is based on the openly available OpenFOAM CFD toolkit. The reults of this study provide an assessment of the strengths and limitations of this model to simulate multiphase propagation in dust clouds.

DOI: 10.7795/810.20200724

2 Experimental study on dust dispersion.

2.1 *Experiment set up*

In this study, coal dust dispersion in MIKE 3 apparatus was investigated. In the preparation of the sample, raw coal was firstly smashed and ground in a crusher. Then the coal dust was put into a drying oven with 120 degree for 12 hours. After that, a sieve shaker was used to separate the dusts into seven different classes. The size classes includes: 20-32 μm, 32-45 μm, 45-63 μm, 63-71 μm, 71-125 μm, 125-250 μm, 250-500 μm.

Experimental apparatus is shown in Fig. 1. MIKE 3 apparatus consists of the dispersion tube, dispersion system (nozzle), pneumatic system, measurement and detection system. An additional video camera was set to record the whole experiment. For each class of the dusts, tests were repeated five times to assure consistency of the measurement results. 900 mg of each dust sample was put inside of the dispersion nozzle for testing. All the tests are carried out under ambient pressure and temperature condition. The aim of the study is to investigate the influence of particle size on dust dispersion. Therefore, the spark of the electrodes was turned off to prevent ignition of dust.

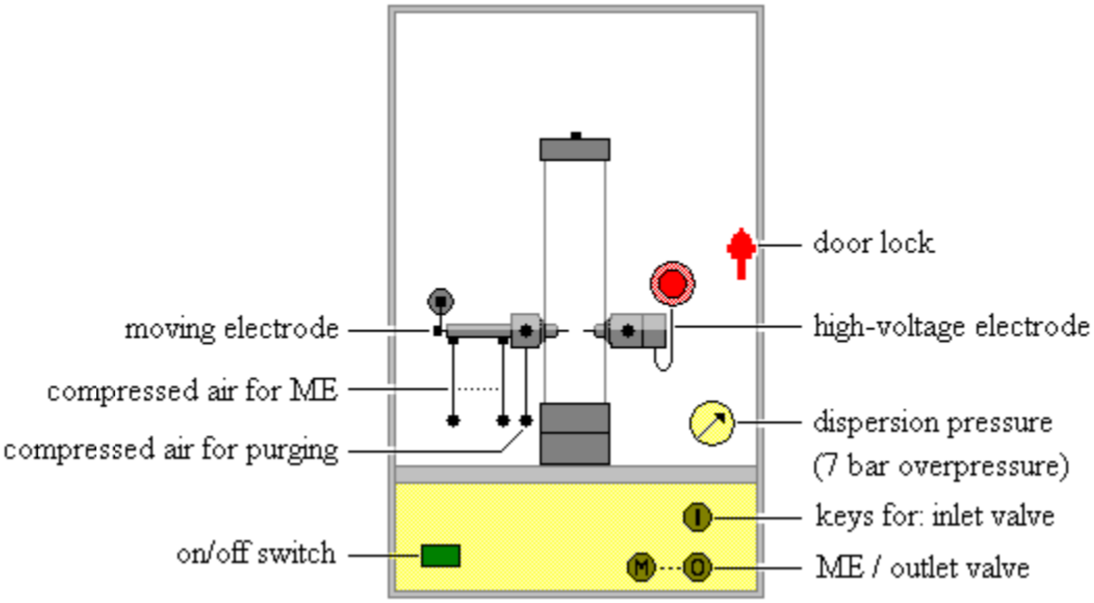

Fig. 1: *MIKE 3-apparatus from Kuehner AG (Cesana and Siwek, 2010).*

2.2 *Experimental results*

Two example pictures from the recorded video is shown in Fig. 2. They illustrate the development of dust dispersion in MIKE 3. As the study focuses on filling up process, the dusts were not ignited as it is designed. The filling up process is very rapid and form a dust cloud inside quickly. When the dust moves inside of the tube, the wall effect from the tube slows down the velocity of near-wall particles and thus distorts the dust front shape. The shape of the dust cloud font starts to form a parabolic shape after it passes the electrodes. The dust front is not a clear curve but blurring because of part of high velocity particles.

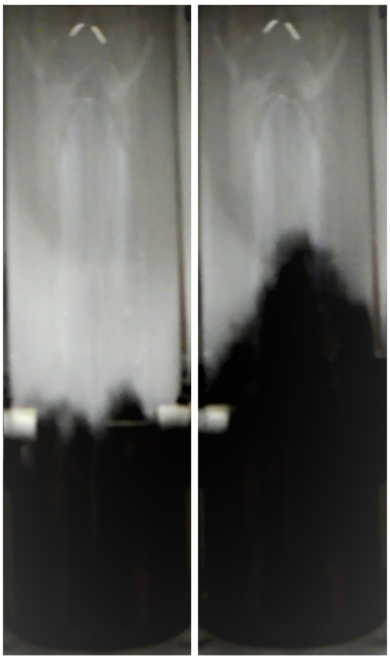

***Fig. 2**: Coal dispersion at different times.*

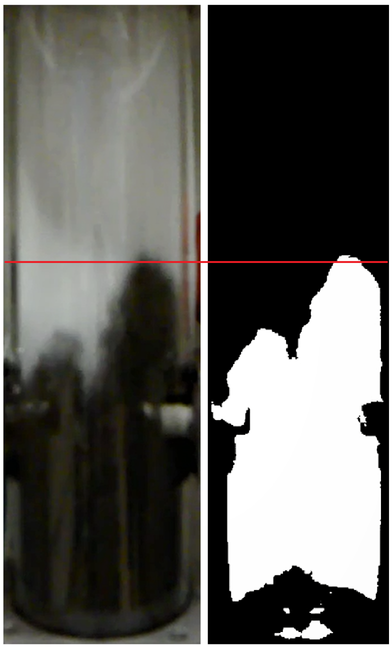

***Fig. 3**: Post-processing using MATLAB.*

To track the dust front positions, MATLAB has been used to post-process the videos. By separating and filtering the red, green, and blue color components in each frame of the video, the threshold values of the start and end points of dust dispersion can be defined. Fig. 3 is the comparison of filtered dispersion picture (right) and the experiment picture at the same time. The edges of the dust front in two pictures are the same. Therefore, the reference value can be used to define the dust front positions. The dust front position data over time is shown in Fig. 4. The movement of each cloud class has similar pattern for all size of particle. Except the 250-500 μm particles, the other dust samples which are under the critical size of 250 μm, have very close time history curves. This could be the reason of particle agglomeration. Especially, the smallest sample does not have the highest velocity and the velocity of 71-125 μm sample prevails a little in the later time of dispersion.

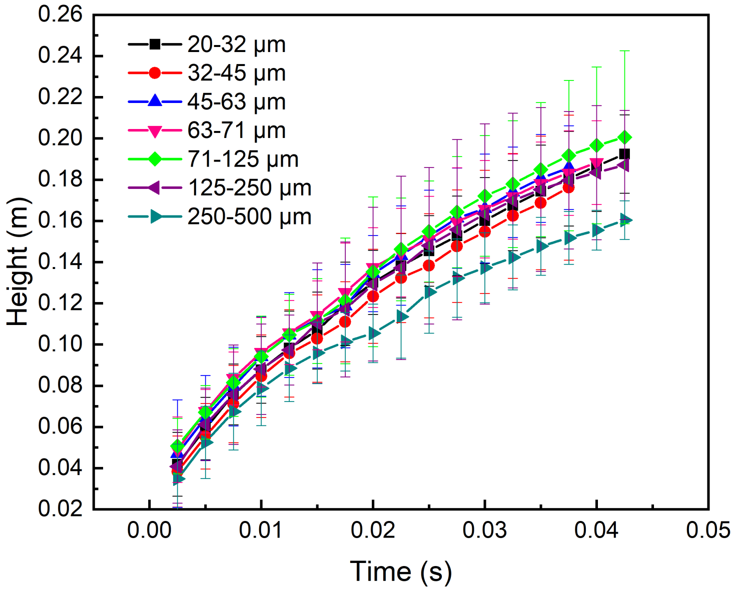

***Fig. 4**: Coal dust front positions over time in different size classes.*

3 Simulation study on inlet air condition

3.1 Simulation cases

The flow domain of MIKE3 was modelled for further investigation. Two air injection methods were considered when the simulation geometries were created. As shown in Fig.5, a simplified inlet system, system 1 has a air inlet where continuous high compressed air was injected into the small pipe until the particle reaches the outlet. System 2 was set with a compressed air tank which would undergo a pressure release when the simulation started. In MIKE 3, the pneumatic system also has a compressed air tank like system 2. Thereby, system 1 has a boundary condition of *inlet* and the compressed air tank is set as *wall*. Except inlet and outlet, all other boundaries are considered as *wall*. Except the inlet, other parts of two systems have same geometry. Both of them consist of dispersion nozzles, dispersion tube and the outlet. There are eight nozzles around the mushroom shape dispersion nozzle. They are designed to spread equally on the rim of the circle. The electrodes were also added to the simulation geometry for the consistency with the experiment tube. System 1 mesh is composed of 509,942 cells, which have been defined with mostly hexahedral cells.

Two simulation cases were carried out using these two systems. System 1 was used to simulate the dispersion of 25 μm coal dust. The result will be compared with the experiment to test the injection system. System 2 was used to simulate the flow field to compare the difference from two inlet systems.

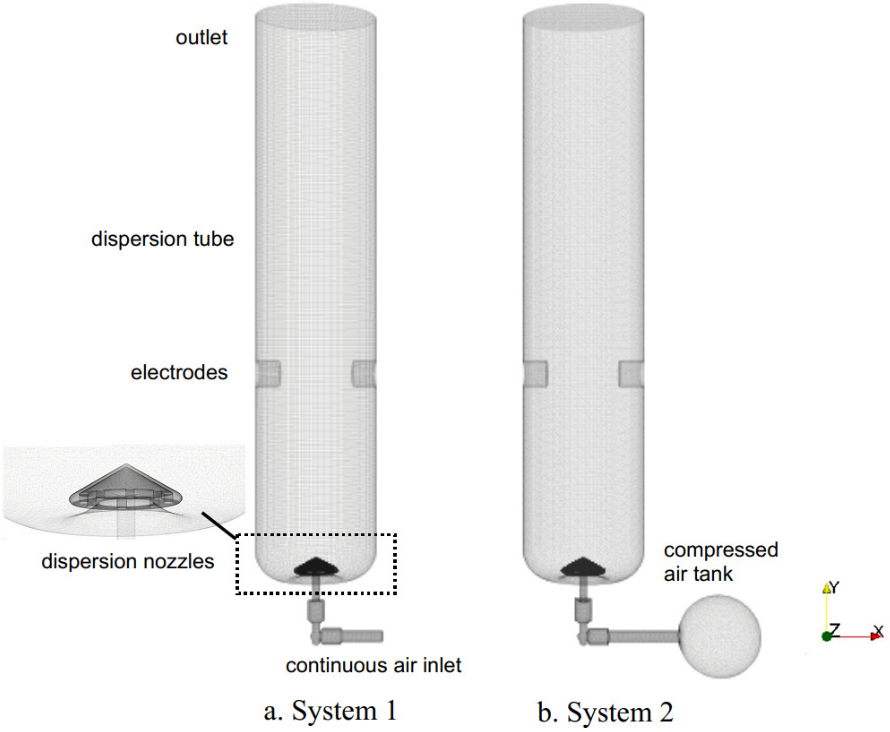

a. System 1 b. System 2

Fig. 5*: Flow domain of two simulation systems.*

In the simulation of dust dispersion, 900 mg coal dust was injected within first time step using *manualInjection* model. Particle size distribution was set as *uniformDistribution*, which means the size of each particle is the same. The dispersionModel is *stochasticDispersionRANS* for the turbulent flow. To set up initial positions of the representative particles (parcels), a MATLAB program was developed to generate the coordinates. As shown in Fig. 6, 2,831 coordinates which are close to the bottom were generated for 25 μm dust cloud. The initial velocity of particles are 0 m/s. The density of coal particles is measured as 1,007 kg/m^3. Sphere drag and gravity of particles are considered in the simulation. Standard *sphereDrag* model was used.

DOI: 10.7795/810.20200724

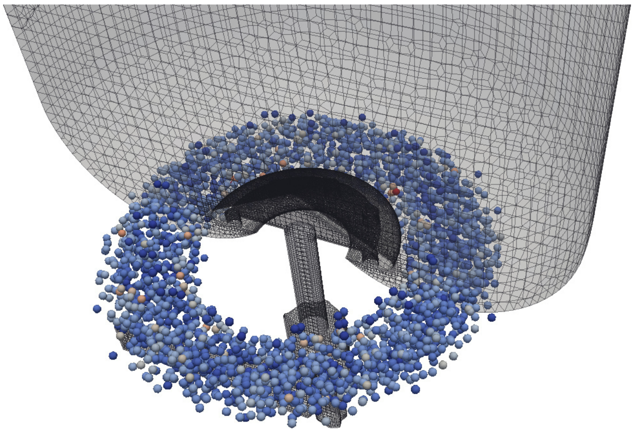

***Fig. 6**: Initial positions for particles in simulation.*

3.2 Solver description

This section describes the models used in this work. To investigate the particle size effect, the Lagrangian approach must be used to discrete the coal particles. The computational methods are based on the rhoPimpleFoam solver from the OpenFOAM toolkit version 5. The solver was modified to include Lagrangian particles. Transport equations for mass and momentum were solved for gas phase and particles. The Eulerian approach was used for the continuous gas phase, and the Lagrangian approach was used for discrete particle phase. In gas transport, standard k-ε model was used to model the turbulence effects. The transport equation for overall mass, momentum are as follow:

$$\frac{\partial \rho}{\partial t} + \nabla \cdot \phi = S_{\rho}^{p}$$

$$\frac{\partial \rho \vec{u}}{\partial t} + \nabla \cdot (\phi \vec{u}) - \nabla^2(\mu_{eff} \cdot \vec{u}) + \nabla \cdot p = S_{\rho \vec{u}}^{p}$$

where ρ is the fluid density (kg/m^3), $\vec{u}$ is the fluid velocity (m/s), ϕ is mass flux ($kg/(m^2 \cdot \mathrm{s})$), and is defined as $\phi = \rho \vec{u}$. μ_{eff} is effective viscosity ($Pa \cdot s$). p is fluid pressure (Pa). S_{ρ}^{p} and $S_{\rho \vec{u}}^{P}$ describes the source term interacting with the Lagrangian phase.

For Lagrangian term, forces from fluid phase act on particles change their momentum. Particle velocity and position are calculated from Newton's second law:

$$m_p \frac{\partial^2 x_p}{\partial t^2} = \Sigma \vec{F}_p$$

where m_p is the mass of a single particle (kg), x_p is the particle position (m), and $\vec{F}_p$ is the sum of the forces which include drag force and gravity force (N).

In the simulation of Lagrangian particles, Discrete Particle Model (DPM) was used since the large amount of coal particles to reduce computing effort. This method uses representative particles (i.e. Parcels), which is a group of particles that has same physical properties, to simulate the particles. The particle-particle interaction is neglected in this work as the particle movement direction is toward one direction.

PIMPLE (Pressure-Implicit Method for Pressure Linked Equations) algorithm was set up for the pressure/velocity coupling. It is a combination of SIMPLE (Semi-Implicit Method for Pressure Linked Equations) algorithm and PISO (Pressure-Implicit with Splitting of Operators) algorithm. In each time step,SIMPLE algorithm is used as the fluid field is considered as a steady state. PIMPLE solver was set up with 22 outer correctors. It was preferred since the time step can be adjusted based on the CFL (Courant-Friedrichs-Lewy) number.

3.3 Simulation results

3.3.1 Particle movement in system 1

Dust dispersion was simulated with the continuous compressed air inlet. Fig. 7 shows the velocity of gas field and position of 25 μm particle at different times. At 0.01 s, the particles are raised up when the velocity field builds up. The highest velocity is at the bottom close to the round wall and the outer rim of the nozzle. Therefore, there are more particles on the two side of the tube than that in the center. The velocity magnitude in the upper part also increases and shows a corrugated appearance because of the turbulence. From 0.02 s to 0.03 s, velocity field near wall changes along the time. High pressure field region near wall increases. Particles scatter evenly over the tube when they surpass the high velocity near wall region. Particles in that region are pushed away at first and result in a distribution of particles along the whole tube. The front of the particles has a round shape from 0.03 s. At 0.05 s, the velocity field is built up fully when most particles leave the bottom part. At the time of 0.06 s, particles have reached the outlet of the tube, while most particles are distributed above the electrodes.

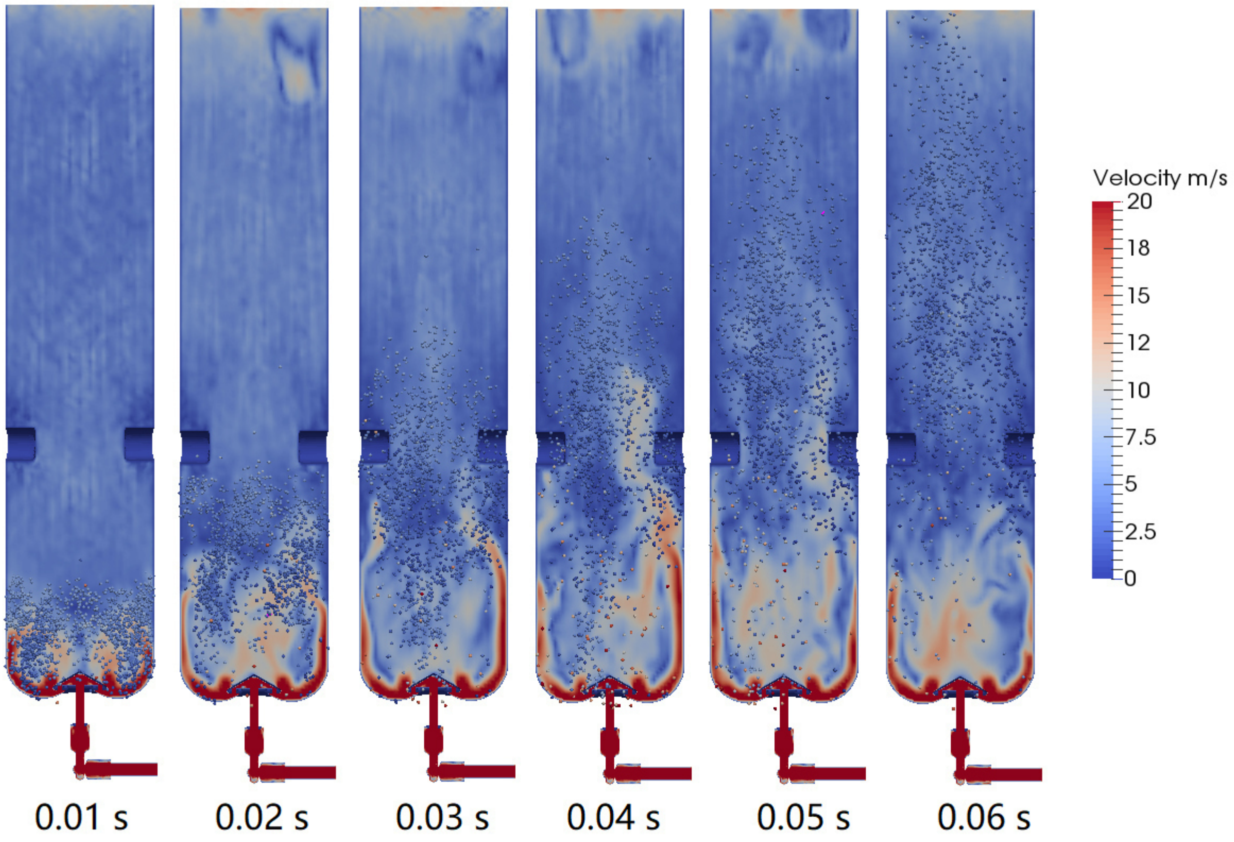

***Fig.** 7: Velocity field of coal dust cloud development at different times (25 μm).*

The particle front positions of 25 μm particles from system 1 simulation is plotted in Fig.8. The data is compared with the experimental results. Due to the strong upward flow near the wall, the top of the particle cloud of the 25 μm particles moves upwards in the geometry with nearly constant velocity, which is contradictory to the experiments. In system 1, the 8 bar compressed air inlet created too much fluid momentum. This simplified inlet caused the inaccuracy of the particle movement. Thus the system 2 which was designed like MIKE3 was tested on the inlet fluid flow.

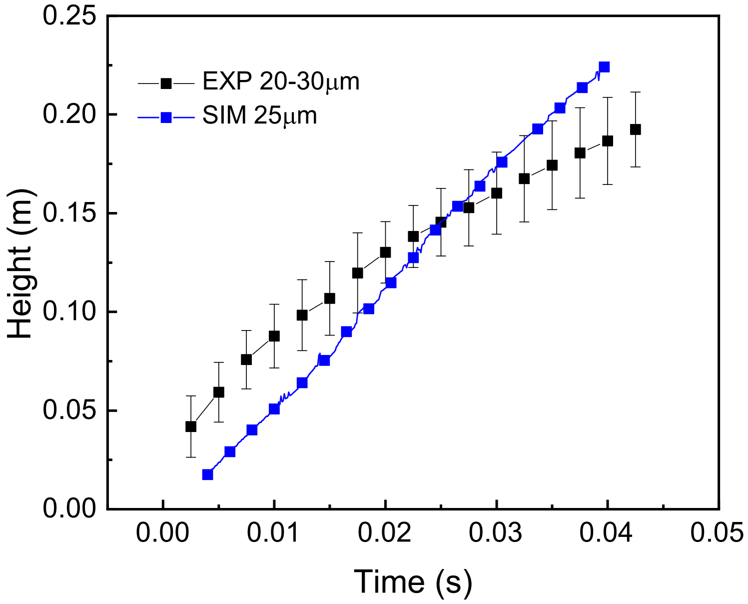

***Fig. 8**: Coal dust front positions over time: comparison between system 1 result and experimental result.*

3.3.2 Influence of inlet air from two systems

The initial pressure field of system 2 is shown in Fig. 9. The inlet was replaced with a 50 ml air tank which was initialized with compressed air (8 bar). When the simulation starts, the pressurized air will be released. Therefore, the pressure and velocity field near the dispersion nozzles would be unsteady.

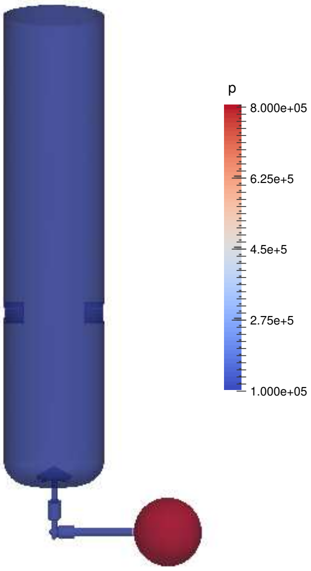

***Fig. 9**: Initial pressure field of system 2.*

Fig.10 illustrates the cloud picture of two geometries at 0.003 s around the inlet pipe. Both systems have pressure drop when air is injected into the pipe. The system 1 has overall larger pressure field than the compressed system due to the high inlet pressure. The pressure in nozzles of system 1 is also larger at the same time. In the velocity field, as shown in Fig. 11, the flow of both systems reach the nozzles at 0.003 s. In the nozzles, the velocity reaches 600 m/s. When the air is released to the dispersion tube, the velocity of the fluid field reduces because of the expansion of the air and the momentum transfer between continuous and discrete phases. At 0.003 s, the velocity around the particles is around 200 m/s in system 1, which is also faster than that in system 2.

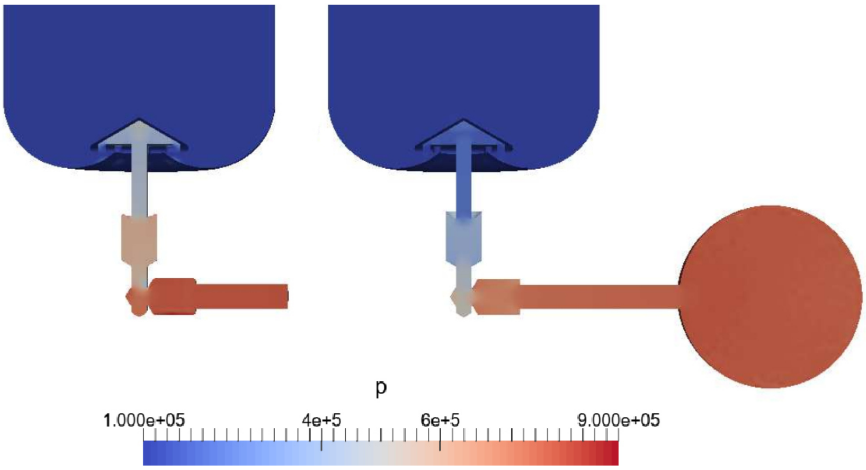

***Fig. 10**: Comparison of pressure field near the nozzle between two simulation systems at 0.003 s.*

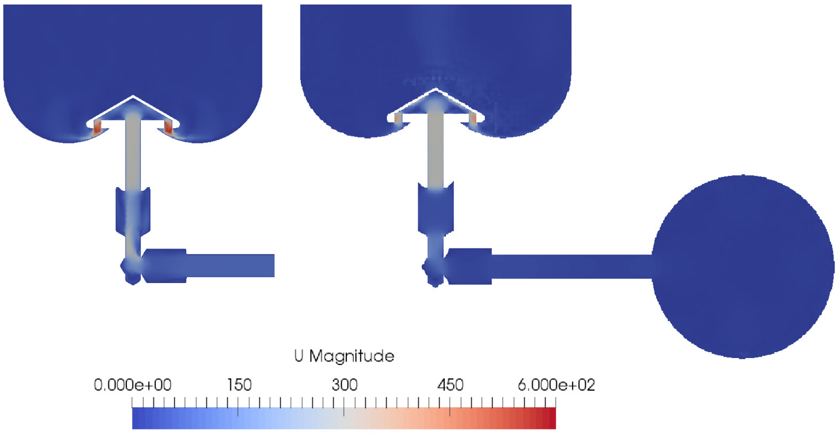

***Fig. 11**: Comparison of velocity field near the nozzle between two simulation systems at 0.003 s.*

4 Conclusion

In this study, experiments using the high-speed photography and image processing by MATLAB allowed a detailed and accurate tracking of the dust front. The dispersion system shows similar results for a large variation in particle size. For detail investigation of the dispersion, such as turbulence flow patterns and particle distribution a simulation model is necessary. Two simulation systems was set up to study the inlet flow effect. System 1 which has a continuous compressed inlet which resulted in a nearly constant velocity for the particles. System 2 which replaced the continuous inlet with a 50 ml compressed air tank showed lower pressure value in the inlet pipe. At 0.003 s, the pressure and velocity field near the dispersion nozzles of system 1 are higher. The Lagrangian approach for discrete phase required very large computation effort. Further work will be continued on the particle size effect.

References

Cesana, C., Siwek, R. (2010). *Manual MIKE 3 apparatus*. Kuehner AG, Switzerland.

Cloney, C. T., Ripley, R. C., Pegg, M. J., Amyotte, P. R. (2020). *Role of particle diameter in laminar combustion regimes for hybrid mixtures of coal dust and methane gas*. Powder Technology, 362:399–408. ISSN 00325910. doi:10.1016/j.powtec.2019.11.106.

Eckhoff, R. K. (1996). *Prevention and mitigation of dust explosions in the process industries: A survey of recent research and development*. Journal of Loss Prevention in the Process Industries, 9(1):3–20. ISSN 09504230. doi:10.1016/0950-4230(95)00044-5.

Eckhoff, R. K. (2003). *Dust Explosions in the Process Industries*. Gulf Professional Publishing, Amsterdam, third edition.

Klippel, A., Schmidt, M., Muecke, O., Krause, U. (2014). *Dust concentration measurements during filling of a silo and cfd modeling of filling processes regarding exceeding the lower explosion limit*. Journal of Loss Prevention in the Process Industries, 29:122–137. ISSN 09504230. doi: 10.1016/j.jlp.2014.02.006.

Pollhammer, W., Spijker, C., Kern, H., Raupenstrauch, H. (2016). *Development of a dust dispersion system for investigation on reduced pressure conditions in the 20-liter siwek apparatus using openfoam*. In Gao, W., editor, *Proceedings of the 11th International Symposium of Hazards, Prevention, and Mitigation of Industrial Explosions*, pages 275–286. Dalian University of Technology, Dalian. ISBN 9787894371652.

Yuzuriha, Y., Gao, W., Mogi, T., Dobashi, R. (2017). *Effects of particle size distributions on flame propagation behavior through dust clouds of pmma*. Journal of Loss Prevention in the Process Industries, 49:852–858. ISSN 09504230. doi:10.1016/j.jlp.2017.06.011.

Zhang, H., Chen, X., Zhang, Y., Niu, Y., Yuan, B., Dai, H., He, S. (2017). *Effects of particle size on flame structures through corn starch dust explosions*. Journal of Loss Prevention in the Process Industries, 50:7–14. ISSN 09504230. doi:10.1016/j.jlp.2017.09.002.

DOI: 10.7795/810.20200724

Numerical investigation of overdriving in the 20-L Siwek chamber

Martin P. Clouthier,[a,b] Damilare Ogungbemide,[a] Chris Cloney,[c]
Robert G. Zalosh,[d] Robert C. Ripley,[e] & Paul R. Amyotte [b]

[a] Jensen Hughes, Halifax, Canada; [b] Dalhousie University, Halifax, Canada; [c] DustEx Research Ltd., Halifax, Canada; [d] Firexplo, Wellesley, USA; [e] Lloyd's Register, Halifax, Canada
E-mail: *mclouthier@jensenhughes.com*

Abstract

Overdriving in the 20-L chamber has been attributed to the relatively high igniter energy-to-volume ratio compared to the ISO one cubic-meter vessel. However, the many aspects associated with the use of 10-kJ igniters to which overdriving can be attributed (e.g., distributed ignition, temperature increase, pressure increase, etc.) have not been systematically investigated. Numerical modelling using OpenFOAM was used to gain insight into the mechanism by which overdriving in the 20-L chamber occurs. A model of an initially quiescent methane deflagration was developed and validated against literature data. The model was then adapted to simulate coal dust combustion. The results of the investigation show that the approximate 450 K temperature increase caused by a 10-kJ ignition may be a key factor that influences overdriving. The higher initial temperature caused by the igniters result in lower values for P_{max} and higher values for K_{St} for some dust cloud concentrations.

Keywords: *dust explosion, 20-L Siwek chamber, overdriving, OpenFOAM, numerical modelling*

1 Introduction

Several studies have been undertaken to investigate dusts considered to be "marginally explosible" in terms of their explosion behaviour. These materials pose a unique challenge when designing dust explosion prevention and mitigation measures; while they may appear to explode during laboratory-scale tests, their explosion characteristics in industrial-size facilities can be less certain. For example, uncertainties have been found in the results for some materials as determined in different-size vessels and in accordance with standardized test protocols (Cashdollar and Chatrathi, 1993, Proust et al., 2007, Cloney et al., 2013, Thomas et al., 2013). In particular, Proust et al. (2007) surmised that a dust having a value of $K_{\mathrm{St}} < 45\,\mathrm{bar\,m\,s^{-1}}$ measured in a standard 20-L sphere might not be explosible in a 1-m^3 chamber. Most studies have attributed this behavior largely to the phenomenon of over-driving leading to false positives in smaller explosion chambers (Cashdollar and Chatrathi, 1993, Going et al., 2000, Rodgers and Ural, 2011, Kuai et al., 2011, 2013, Thomas et al., 2013).

Variables that affect overdriving have not been explored (i.e., temperature rise, increase in initial pressure, distributed ignition, radiation, turbulence, etc.). The research described in this paper investigates whether the explosion behaviour of marginally explosible dusts observed in the 20-L Siwek chamber can mostly be attributed to over-driving, that is, increase in temperature caused by the powerful igniters used in the sphere. The tested hypothesis is that temperature increase plays the greatest role in overdriving in the 20-L Siwek chamber. A methane flame model, using the OpenFOAM CFD Toolkit, was developed and validated by experimental data from the literature. Afterwards, similar simulations and validation were performed for coal dust. This work is built on previous CFD modelling work at Dalhousie University, and it is hoped that it would provide a viable starting point for future intermediate-scale modelling. The research described in this paper is part of a larger body of work aimed at enabling safer operation of industrial enterprises worldwide with respect to the processing and handling of combustible particulate. Clouthier et al. (2016) have given a comprehensive review of "marginally explosible" dusts.

The model developed in the current work is based on the coalChemistryFoam solver in the freely available OpenFOAM CFD toolkit. The results of this study provide an assessment of the strengths and limitations of this model to simulate multiphase, laminar flame propagation in monodisperse, homogeneously suspended dust clouds. The results also provide a baseline, which is missing in the literature, that more comprehensive modeling approaches can be compared to moving forward.

2 Methodology

This section describes the computational domain, case set up, multiphase discretization, and numerical solution methods used in the simulations.

2.1 Model description

The computational methods used in this study are based on the coalChemistryFoam solver from the OpenFOAM toolkit version 5.0.1. The rectilinear geometry of the "Siwek chamber" tutorial that came prepackaged with the coalChemistryFoam solver was replaced with a sphere to better replicate the actual 20-L sphere. The 20-L sphere (Siwek chamber) is typically used to determine the maximum explosion pressure ($P_{\max}$), maximum rate of pressure rise $(dP/dt)_{\max}$ (from which the deflagration index, K_{St} or K_{G}, can be computed), lower explosion limit (LEL) and limiting oxygen concentration (LOC). Measurements are performed in accordance with ASTM E1515 and E1226. The 20-L sphere consists of a hollow sphere made of stainless steel with an internal volume of 20 litres (Fig. 1). It is equipped with a jacketed cooling system, a vacuum pump for evacuating the chamber, distribution systems for gases and dusts, an ignition source at the center of the sphere, a pressure measurement device, and a data recording system (Kuhner KSEP-Software). An ignition source is placed at the center of the sphere through a flange located on the top of the combustion chamber. International standards require ignition energies of 10 kJ (2 x 5 kJ) for testing dusts, 10 J for gases and 2 kJ (2 x 1 kJ) for hybrid mixtures. The electrical spark electrodes are two round tungsten rods with ends ground to a point whose tips are spaced 6 mm apart. They are supplied with power from a high voltage transformer (KSEP 320) and produce a permanent spark (15 kV, 30 mA).

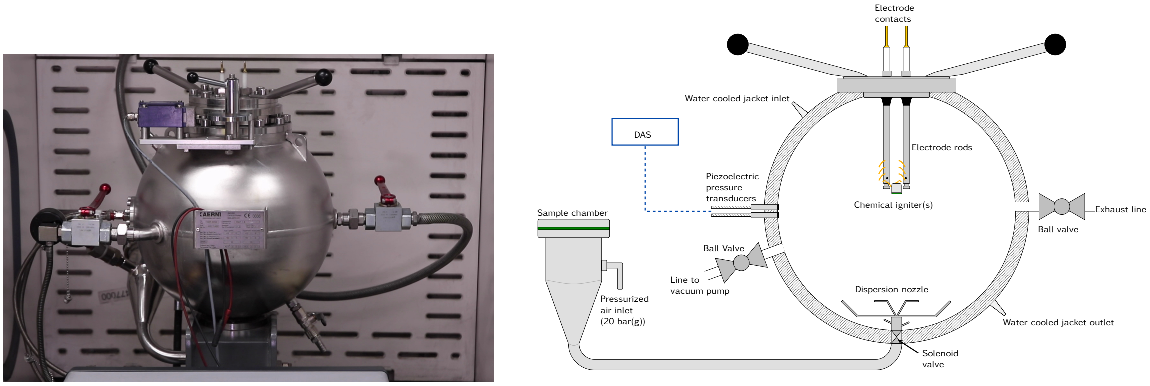

***Fig. 1**: The 20-L Siwek chamber.*

The geometry was modelled and meshed using the Salome CAD and meshing software. The radius of the 20-L sphere is ~ 0.162 m; however, due to computational resource constraint, a quarter scale of the sphere geometry was used, reducing the radius of the sphere to 0.042 m. Furthermore, due to the symmetry of the sphere, one-eighth section of the scaled-down sphere geometry was used for the simulations. Two sets of simulations were performed: the first set was performed with the sphere geometry filled with methane gas, while the second set was performed with the sphere filled with a coal dust-air mixture.

The three-dimensional, multi-species, reactive transport equations for mass, momentum, and enthalpy are solved in this work. The fluid viscosity is calculated using Sutherland's Law. Multicomponent specific heat and enthalpies are calculated based on polynomial fits to the NASA JANAF tables provided with the GRI-Mech 3.0 reaction mechanism. Similar to Cloney et al. (2018), in the current model particle diameter is held constant and density is reduced from devolatilization and surface reaction. Heat is removed from the particle due to devolatilization, which is described by a single-step Arrhenius expression. Momentum exchange is calculated based on drag force for a spherical particle. Gravity is used in the model. Energy exchange is calculated by heating at the particle surface and heterogeneous surface reactions.

The gas-phase chemistry reaction mechanism used in the current work is the MP1 mechanism which has five species and one reaction (Table 1). Though there are other more comprehensive chemistry reaction mechanisms, the MP1 mechanism was selected for the simulations to further simplify modelling complexity and reduce computational requirements.

***Table 1**: Single-step global reaction model parameters.*

Name	Reaction	A_r	n_r	$E_{a,r}/R$ (K)	Reaction Order
MP1	$CH_4 + 2\,O_2 \longrightarrow CO_2 + 2\,H_2O$	3.48×10^8	0.0	10063.8	$[CH_4]^1[O_2]^{0.5}$

The overall rate of any specific reaction ($\dot{\omega}_r$, $\mathrm{mol\,m^{-3}\,s}$) is determined based on a general Arrhenius expression for the forward and backward reaction coefficients:

$$\dot{\omega}_r = k_r^f \prod_{k=1}^{N_k} \eta_k^{\nu'_{k,r}} - k_r^b \prod_{k=1}^{N_k} \eta_k^{\nu''_{k,r}}$$

$$k_r = A_r T^{n_r} e^{\left(-\frac{E_{a,r}}{RT}\right)}$$

where A_r is the Arrhenius pre-exponential factor, n_r is the temperature coefficient, and $E_{a,r}$ is the activation energy ($\mathrm{J\,kg^{-1}}$).

Following the work of Bradley et al. (1994) and Cloney et al. (2018), the particle composition is assumed to be 40% methane and 60% carbon in this work. Heterogeneous combustion is specified based on a single surface reaction between oxygen molecules and carbon in the coal particle. A comprehensive model description for the OpenFOAM coalChemistryFoam solver can be found in Cloney et al. (2018).

2.2 Numerical domain

The simulation domain for the current model is shown schematically in Fig. 2. The three-dimensional domain represents one-eighth of a quarter-scale 20-L sphere. At the start of the simulation, an initial flame profile including temperature, velocity, and species distribution, is specified for the geometry.

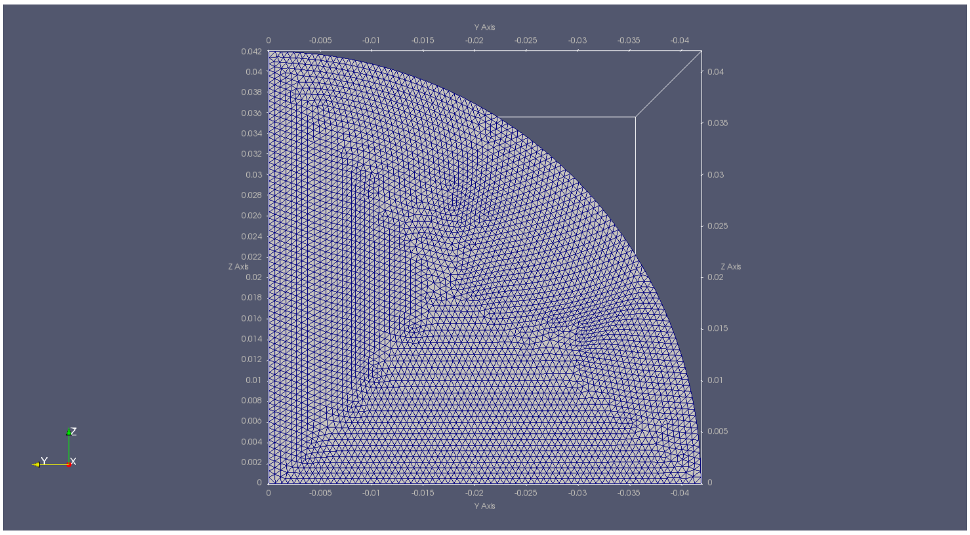

***Fig. 2**: Mesh of the one-eighth of a quarter-scale sphere used in the simulations.*

For the methane gas simulations, the gas flame profile used to initialize the simulations was calculated using the Cantera Package (Goodwin et al., 2009) with the MP1 gas reaction mechanism. This allowed the initial temperature and species profiles to be determined faster than if determined natively in OpenFOAM. The Cantera solution was mapped to OpenFOAM using Python scripts. For the coal dust simulations, ignition was initiated directly in OpenFOAM at 2 ms after start of simulation and continued throughout the entire simulation period. The boundary conditions of the shell (wall) and the three symmetric faces of the geometry are given in Table 2. The flame was set to propagate towards the wall as an initially quiescent gas and particle mixture. Pressure, temperature and velocity were measured by probes positioned at three locations within the geometry (one at the centre, and one each at 1 cm and 2 cm from the centre).

***Table 2**: Boundary conditions for flame simulation.*

Variable	Shell boundary	Side boundaries	Value
Pressure	zeroGradient	symmetry	1×10^5 Pa
Temperature	fixedValue: uniform	symmetry	300 K, 400 K
Velocity	fixedValue: uniform	symmetry	$0\,\mathrm{m\,s^{-1}}$
Mass fractions	zeroGradient	symmetry	Calculated

For the coal dust simulations, the cellZone Injection model was used to place the dust within the geometry. A mass parcel basis type and fixed-value particle size distribution of 33 µm were used. To ensure that all mixtures could actually ignite, the modelled ignition source was set to a value of 1500 K. A summary of the simulation parameters used in the present study is shown in Table 3.

***Table 3**: Simulation parameters used in the model.*

Parameter	Value
Fluid (gas simulation)	methane
Fluid (particle simulation)	air
Solid	coal dust
Particle size (µm)	33
Coal volatile content (%)	40
Methane equivalence ratio at 300 K (ϕ)	0.6, 0.8, 1.0
Methane equivalence ratio at 400 K (ϕ)	0.6, 0.8, 1.0
Dust concentration at 300 K ($\mathrm{g\,m^{-3}}$)	100, 150, 300, 450, 600
Dust concentration at 400 K ($\mathrm{g\,m^{-3}}$)	100, 150, 300, 450, 600
Coal particle density ($\mathrm{kg\,m^{-3}}$)	1300
Ambient pressure (Pa)	100 000
Temperature (fluid) (K)	300 & 400 (500 & 600)
Temperature (particles) (K)	300
Ignition temperature (K)	1500
Cell (tets) size (µm)	600
Simulation time (ms)	30 (methane) & 400 (coal dust)
Start of ignition, coal (ms)	2

In this work the coal particles are discretized using the Discrete Particle Model (DPM) Lagrangian approach. Particle-wall interaction was taken into consideration, but particle–particle interaction was neglected. Interaction between the gas and particle phase is modelled using a particle-source-in-cell method (Christ, 2013, Migdal and Agosta, 1967) where the particles act as point sources and sinks within the cell that their center resides.

The gas phase conservation equations were solved using a segregated approach where each equation is discretized over all cells with the finite volume method. The convective terms were discretized using a bounded Gaussian upwind interpolation scheme, the diffusion terms were discretized using Gaussian linear interpolation, and the time-derivative terms were discretized with an Euler scheme.

DOI: 10.7795/810.20200724

Preconditioned Conjugate Gradient (PCG) was used for symmetric matrices (pressure) and Preconditioned Bi-Conjugate Gradient (PBiCG) for asymmetric matrices (velocity). The Diagonal-based Incomplete Cholesky (DIC) preconditioner was used with the PCG solver, while the Diagonal-based Incomplete LU preconditioner (DILU) was used with the PBiCG solver. Pressure-velocity coupling is achieved using the PIMPLE algorithm, which is a combination of PISO (Pressure Implicit with Splitting of Operator) and SIMPLE (Semi-Implicit Method for Pressure-Linked Equations). The simulation was treated as transient but used the SIMPLE (steady-state) treatment to find the steady-state solution for each time step. An advantage of using the PIMPLE algorithm is that it generally achieves better stability over PISO algorithm and allows the Courant number to be larger than one; however, the Courant number was kept at a maximum of 0.75 for all the simulations.

The Lagrange solution method includes a fractional timestep approach as described by Macpherson et al. (2009). At each timestep, the numerical scheme loops through all Lagrange particles, updates their properties, calculates new velocities, positions, temperature, and densities, and calculates the gas phase source terms. If the particle residence time in a cell is smaller than the overall timestep, all variables are updated using the state in that cell. However, if the particle transfers to an adjacent cell, it takes a fractional timestep to the cell face, and then a second timestep within the adjacent cell. This process occurs repeatedly until the overall outer timestep is complete. The Lagrange momentum and energy exchange equations are integrated analytically. This is completed based on the fractional timestep, where a semi-implicit Euler formulation is used to solve for velocity and an explicit exponential Euler scheme is used to solve for temperature. The particle density is updated explicitly based on the fractional timestep, and the devolatilization and surface reaction models.

The combustion model is a Partially Stirred Reactor (PaSR) model. In the PaSR approach, a computational cell is split into two different zones. In one zone all the reactions occur, while in the other one there are no reactions. Thus, the composition changes due to mass exchange with the reacting zone. The reaction zone is treated as a perfectly stirred reactor (PSR), in which all reactants are assumed to be perfectly mixed with each other. This allows us to neglect any fluctuations when calculating the chemical source terms. A set of ordinary differential equations (ODEs) are constructed from the species and energy solution vectors, along with the details of the chemistry reaction model. A robust solver is required to integrate this stiff system of equations, and the Rosenbrock34 algorithm was used in this work due to the constant failure of the default Seulex algorithm. Coupling between the gas phase, Lagrange particles, and chemistry solutions is also completed using a segregated approach. At the start of the timestep the Lagrange position, velocity, temperature, and density are updated along with the respective gas phase source terms. The fluid velocity is calculated based on the momentum transport equation, followed by calculation of the combustion reaction source terms. The species mass fraction and energy transport equations are then solved with the updated source terms and velocity.

3 Results

This section discusses the results of parametric analyses performed to investigate the effect of concentration and initial temperature on explosion overpressure, rate of pressure rise and temperature profile of methane and coal dust combustion. This also allows comparison to previous experimental and simulation results from the literature. Prior to that, the section discusses the results of sensitivity analyses performed to investigate the sensitivity of the simulations to grid cell resolution and ignition source size.

3.1 Sensitivity analysis

Analyses performed to evaluate the sensitivity of simulation results to the grid cell resolution (grid independence study) and ignition source size are discussed in this section.

DOI: 10.7795/810.20200724

3.1.1 Grid independence study

As grid dependency is a known problem in computational fluid dynamics, a grid independence study was performed to ensure the grid size selected for the simulations was fine enough to capture the parameters of interest. Grid dependency was assessed by repeating simulations with various grid cell sizes. Three grid cell sizes of 450 µm, 600 µm and 1 mm were used. The results are shown in Fig. 3 for methane gas at an equivalence ratio of 1.0. Although the slope for the 1 mm cell resolution is the steepest of the cell resolutions used, the difference does not appear to have a significant impact on the simulated temperature and pressure. For all three resolutions, the general trends of pressure and temperature rise in a fully enclosed vessel appear to be similar. A computational mesh resolution of 600 µm was used for all methane simulations presented in this work.

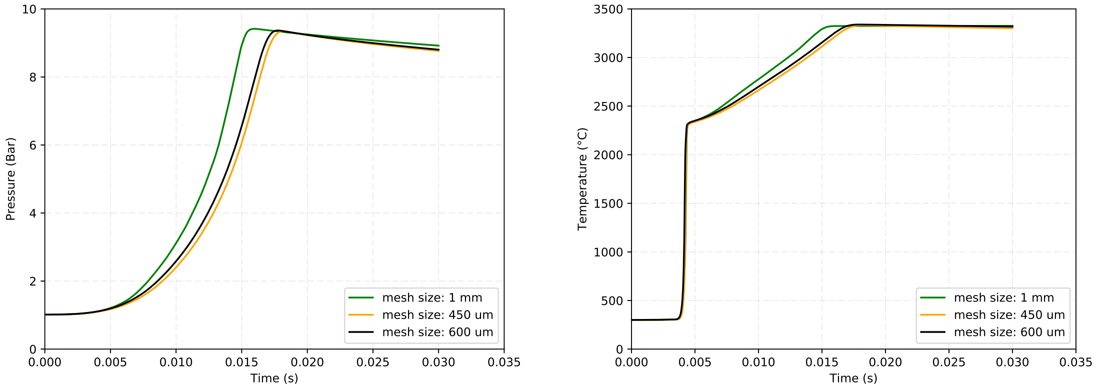

(a) Pressure *(b) Temperature*

***Fig. 3**: Pressure and temperature profiles at various grid cell resolutions for methane combustion at equivalence ratio of 1.0.*

A similar grid independence study was performed for the coal dust simulations using three grid cell sizes of 450 µm, 600 µm and 1 mm. The results are shown in Fig. 4 for a dust cloud concentration of 300 $\mathrm{g\,m^{-3}}$ and temperature of 300 K. Here, the differences are even less noticeable for the pressure profiles. Thus, it appears that the coal dust simulations were less sensitive to cell resolution than the methane simulations. In contrast, the temperature profiles for coal appear to be more sensitive to cell resolution than the methane simulations. The 1 mm cell resolution appears to underestimate the temperature relative to the other two resolutions; still, the difference does not appear to be significant. For all three resolutions, the general trends of pressure and temperature rise in a fully enclosed vessel appear to be similar. A computational mesh resolution of 600 µm was used for all coal dust simulations presented in this work.

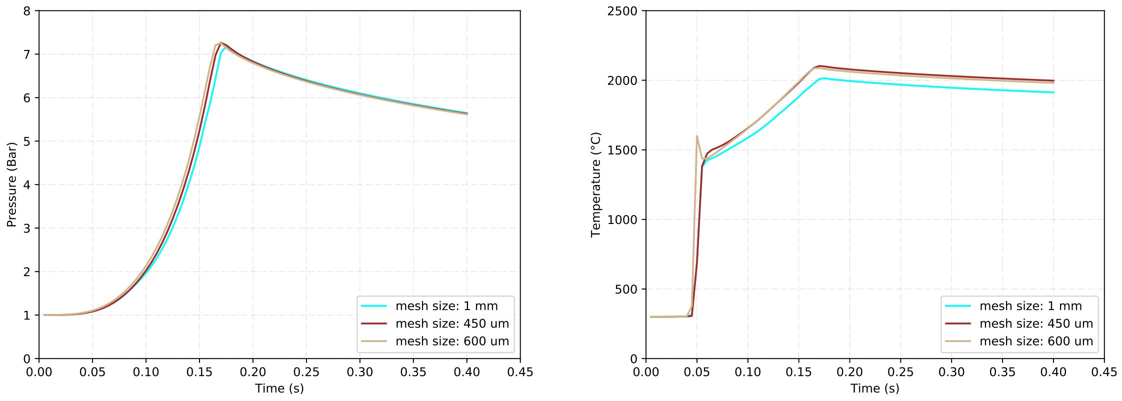

(a) Pressure *(b) Temperature*

***Fig. 4**: Pressure and temperature profiles at various grid cell resolutions for coal dust combustion at a dust cloud concentration of* 300 $\mathrm{g\,m^{-3}}$.

3.1.2 Effect of ignition sizes

Simulations were performed to determine the impact of varying the number of ignition cells on the explosibility parameters of interest for coal dust combustion. This is important as many experimental and theoretical studies assume a point-source ignition. However, for CFD simulations, using too few ignition cells may not initiate the combustion of the dust cloud as desired. It was, therefore, important to know whether the choice of ignition size would impact the simulation results. Three ignition sizes named "original," "halved," and "doubled" were used in the simulations for coal dust. The simulation results are shown in Fig. 5. There was no significant difference in the simulation results due to doubling or halving the ignition size. Thus, there appears to be some leeway in the choice of ignition source size to ensure that ignition is initiated. It seems that the ignition temperature is more important than the size of the ignition source for OpenFOAM CFD simulations.

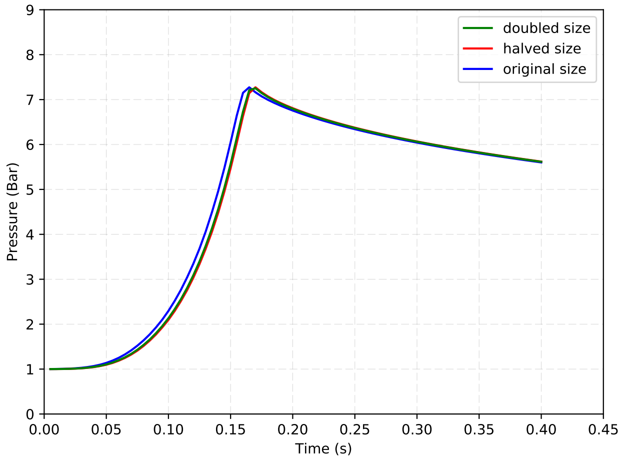

Fig. 5: *Pressure profiles at various grid cell resolutions for coal dust combustion.*

The combined results for all sensitivity simulations performed in this study are presented in Fig. 6. The plots demonstrate that there was no significant difference in the simulation results due to changing the grid cell size or the ignition size.

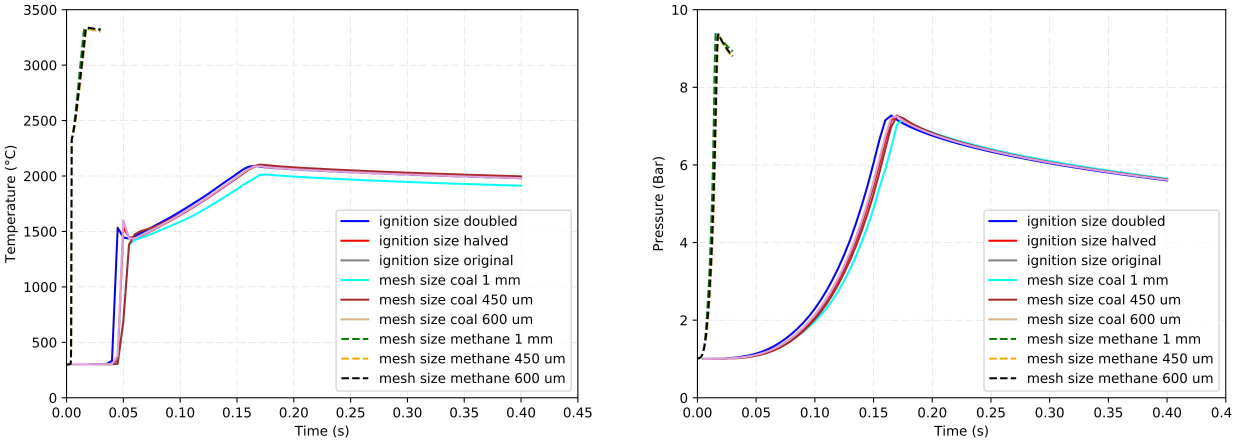

(a) Temperature for all sensitivity simulations *(b) Pressure for all sensitivity simulations*

Fig. 6: *Summary of all grid cell size and ignition size sensitivity analyses performed for methane and coal combustion.*

3.2 Parametric analysis: methane combustion

This section discusses the results of the parametric analysis performed for methane combustion.

3.2.1 Effect of equivalence ratio

The pressure profiles and rates of pressure rise for methane combustion with equivalence ratios of 0.6, 0.8 and 1.0 at an initial temperature of 300 K are shown in Fig. 7. The unadjusted maximum pressure (P_{ex}) increases as the equivalence ratio increases. For example, the P_{ex} at the equivalence ratio of 1.0 is approximately 40% higher than the P_{ex} reported for the equivalence ratio of 0.6. Another observation from Fig. 7 is that the pressure profiles shift to the left as equivalence ratio increases, indicating that the time to reach peak pressure decreases as the equivalence ratio increases. For instance, the time to reach peak pressure decreased from 0.058 ms to 0.018 ms as the equivalence ratio was increased from 0.6 to 1.0. In contrast, the rate of pressure rise increases with equivalence ratio. The rate of pressure rise increased from 367 bar s^{-1} to 1400 bar s^{-1} when the equivalence ratio was increased from 0.6 to 1.0. The effect of increasing the equivalence ratio on the deflagration index, K_{G} is also shown in Fig. 7. As expected, K_{G} increases with equivalence ratio.

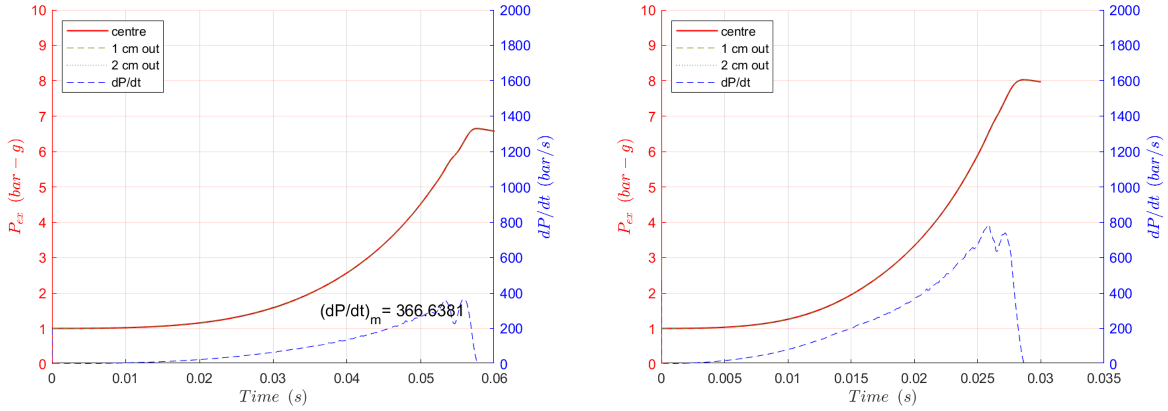

(a) Pressure profile for simulation at 300 K *and equivalence ratio of 0.6.*

(b) Pressure profile for simulation at 300 K *and equivalence ratio of 0.8.*

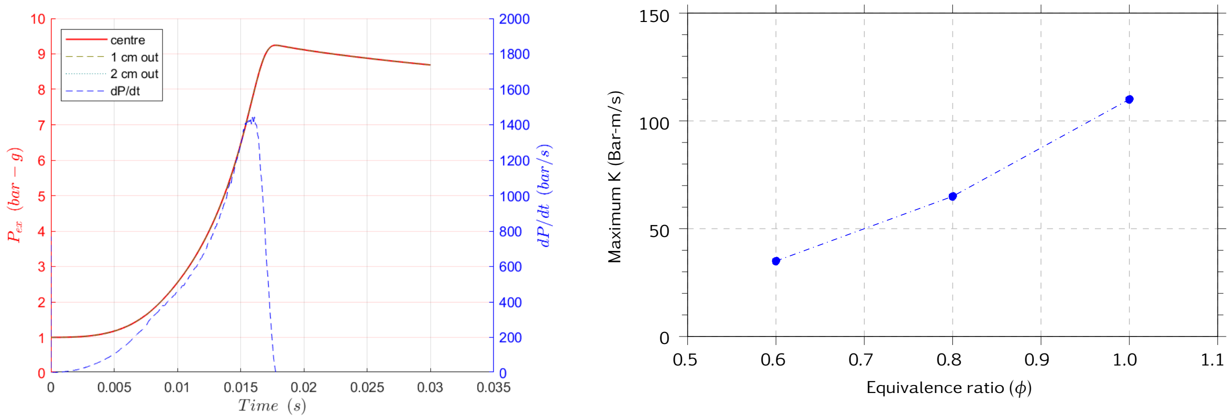

(c) Pressure profile for simulation at 300 K *and equivalence ratio of 1.0.*

(d) K_G *at* 300 K *and various equivalence ratios.*

Fig. 7*: Pressure profiles and* K_G *for simulations at* 300 K *and various equivalence ratios.*

DOI: 10.7795/810.20200724

3.2.2 Effect of initial temperature

As shown in Fig. 8, generally, K_G increased as the temperature was increased from 300 K to 400 K. However, increasing the temperature from 300 K to 400 K did not appear to have a significant impact on K_G until the equivalence ratio reached 1.0. The K_G at 400 K is 20% higher than that recorded at 300 K. A major takeaway from Fig. 8 is that although equivalence ratio is a strong driver of the increase in the rate of pressure rise, temperature also has a substantial role to play, and its impact becomes more prominent as the equivalence ratio increases. Furthermore, temperature has a significant impact on the time to reach the peak $\mathrm{d}P/\mathrm{d}t$. The time to reach peak $\mathrm{d}P/\mathrm{d}t$ decreases with increasing temperature.

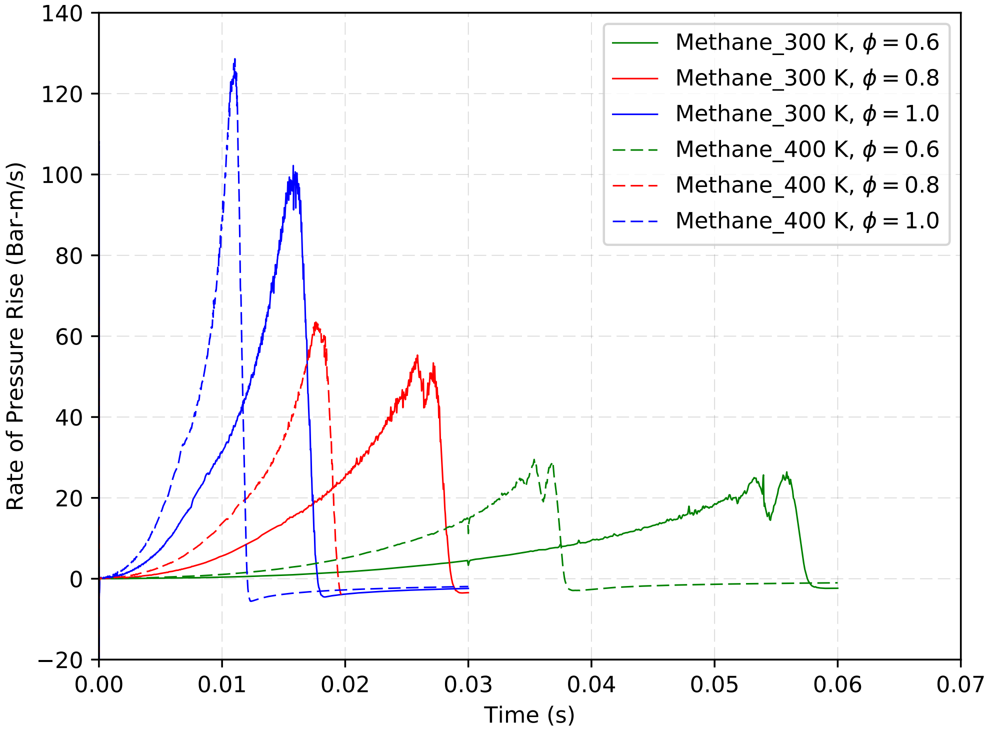

Fig. 8: *Rate of pressure rise at different equivalence ratios and temperature for methane combustion.*

3.2.3 Comparison with experimental data and calculated values

Simulation results for the maximum pressure (P_m) computed at various equivalence ratios and temperatures for pure methane are summarized in Fig. 9. The results comprise experimental data from Cashdollar (1996) indicated as open squares, data from Nagy (1983) as solid squares, calculated theoretical adiabatic pressure at 300 K as a broken line, and the current simulation results are represented by closed and open circles. Cashdollar (1996) performed his experiments in a 20-L (0.02 m^3) vessel, whereas Nagy (1983) performed his experiments in a 25 m^3 vessel.

For the simulations performed at an intial temperature of 400 K, the current model slightly underpredicted P_m, compared to the experimental data from Cashdollar (1996), except at the equivalence ratio of 0.6. In contrast, the model slightly overpredicted P_m for simulations performed at an intial temperature of 300 K. Nagy (1983) reported P_m only at the equivalence ratio of 1.0, for which the model overpredicted P_m for simulations performed at both 300 K and 400 K. The simulated results at 300 K are in almost perfect agreement with the calculated theoretical curve, except at the equivalence ratio of 1.0. Overall, the simulated P_m and K_G for methane are in good agreement with the literature data and the calculated theoretical adiabatic pressure.

DOI: 10.7795/810.20200724

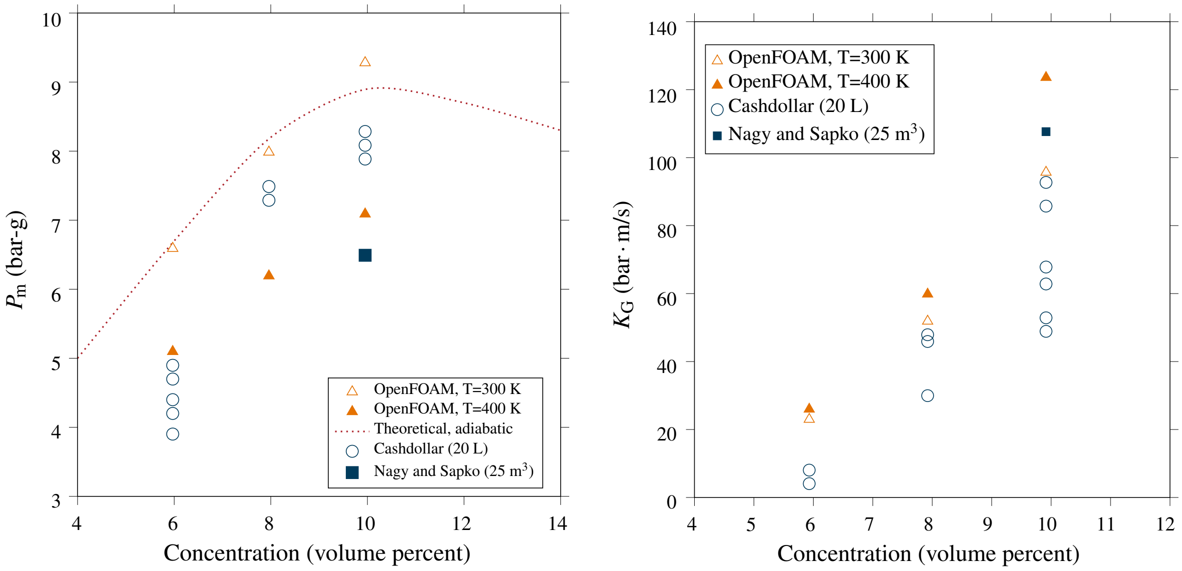

(a) At 400 K *and equivalence ratio of 0.6.* *(b) At* 400 K *and equivalence ratio of 0.6.*

Fig. 9*: P_m and K_G for methane from current study compared with values from the literature and calculated theoretical adiabatic pressure. The literature data is from Cashdollar (1996) and Nagy (1983).*

3.3 Parametric analysis: coal dust combustion

This section discusses the results of the parametric analysis performed for the simulation of the coal dust explosion. A typical timeline of coal dust explosion observed for the simulations is shown in Fig. 10.

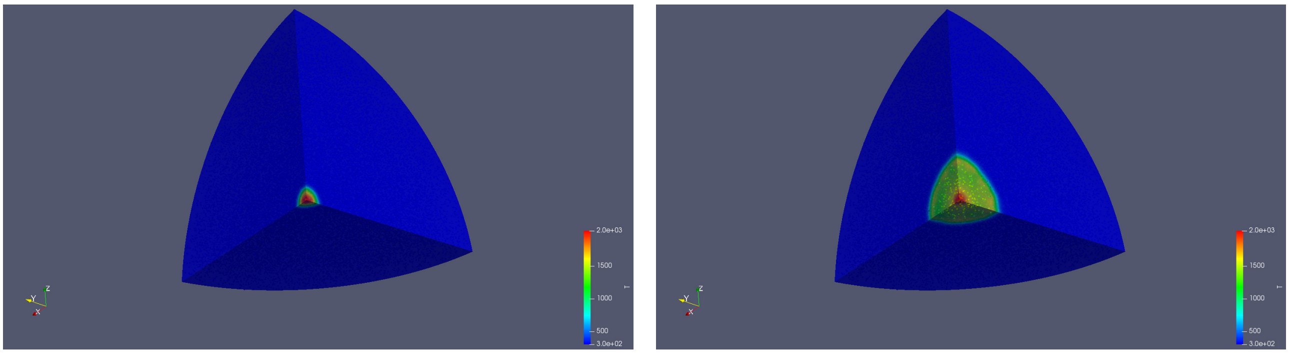

(a) 5 ms from start time. *(b) 25 ms from start time.*

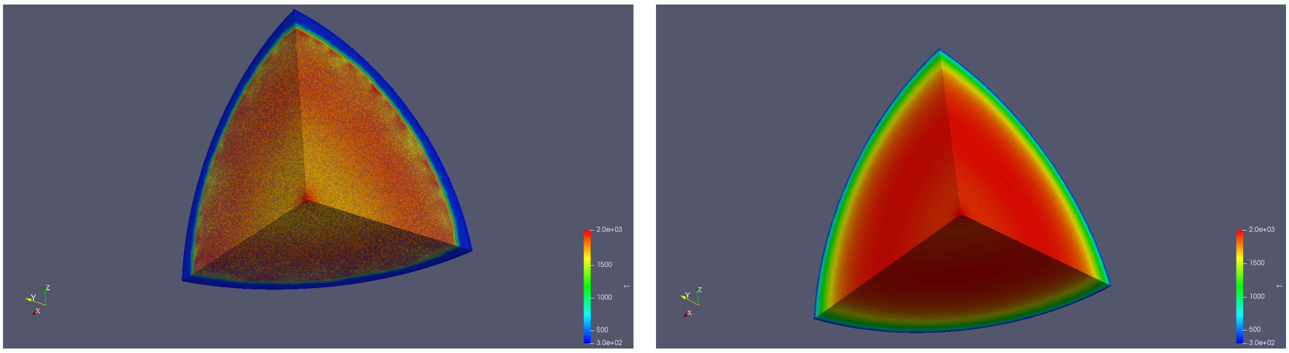

(c) 125 ms from start time (with particles shown). *(d) 400 ms from start time.*

Fig. 10*: Timeline of coal dust explosion simulation.*

3.3.1 Effect of dust cloud concentration

Pressure profiles at different dust cloud concentrations and temperature are shown in Fig. 11. The unadjusted maximum pressure (P_{ex}) increases as concentration decreases. For example, the P_{ex} at $100\,\text{g}\,\text{m}^{-3}$ is 62% higher than the P_{ex} at $600\,\text{g}\,\text{m}^{-3}$. Thus, it appears that of all the coal dust cloud concentrations used in the simulations, $100\,\text{g}\,\text{m}^{-3}$ was the optimum concentration. Another observation from Fig. 11 is that the pressure profiles shift to the right as concentration decreases, indicating that the time to reach peak pressure increases as the concentration decreases. For instance, at 300 K, the peak pressure for $600\,\text{g}\,\text{m}^{-3}$ occurred at 210 ms while that of $100\,\text{g}\,\text{m}^{-3}$ occurred at 270 ms.

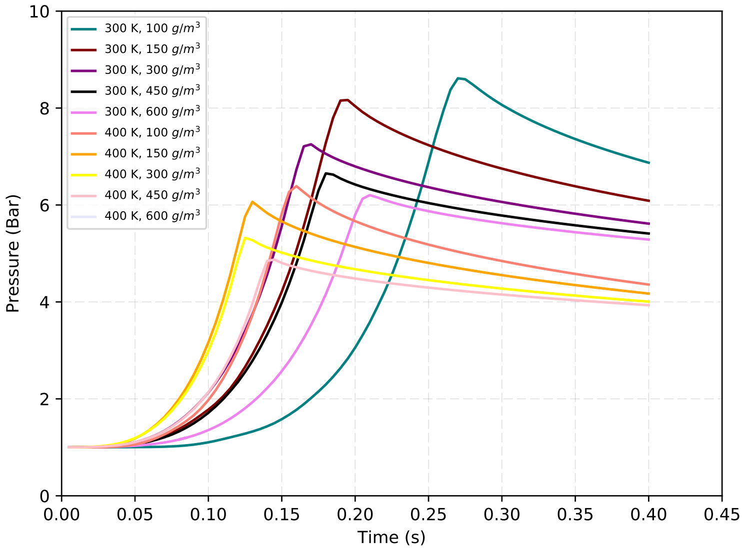

Fig. 11: *Pressure profiles for coal dust explosions at different dust cloud concentrations.*

3.3.2 Effect of initial temperature

Simulated maximum pressure (P_{m}) recorded for different dust cloud concentrations at the initial temperature of 300 K, 400 K, 500 K and 600 K are shown in Fig. 12.

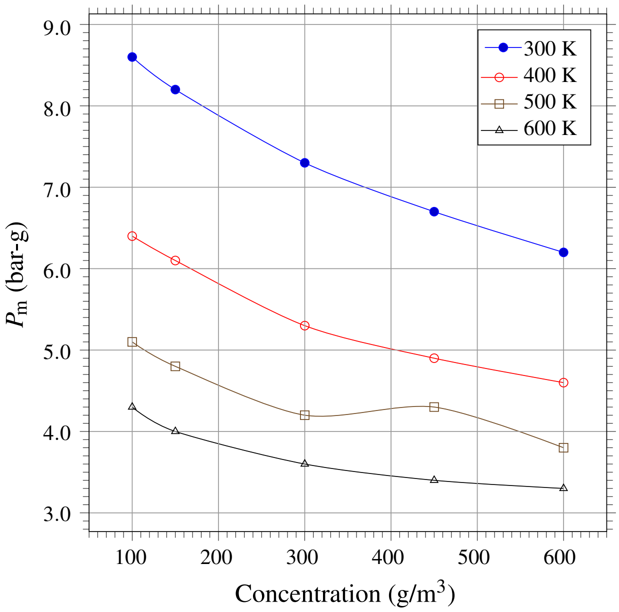

Fig. 12: *Maximum pressures for coal dust explosions at different dust cloud concentrations and temperature.*

Maximum pressure clearly decreases proportionally with increasing initial temperature in the system. Generally, reducing the initial temperature by a factor of two doubled the maximum pressure. At first, this may appear counter-intuitive; however, it is a reasonable outcome. As the temperature of the system was increased, the initial energy in the system increased such that the igniters (with fixed energy) had a lower net effect on the system than when it was at the lower temperature. Consequently, a lower P_{m} was observed at the higher temperature.

3.4 Overdriving in the 20-L Sphere

The pressure profiles for all simulations performed for this study are shown in Fig. 13. The steeper curves at the extreme left of the plot represent the results of the methane combustion, while the curves to the right represent the coal dust combustion.

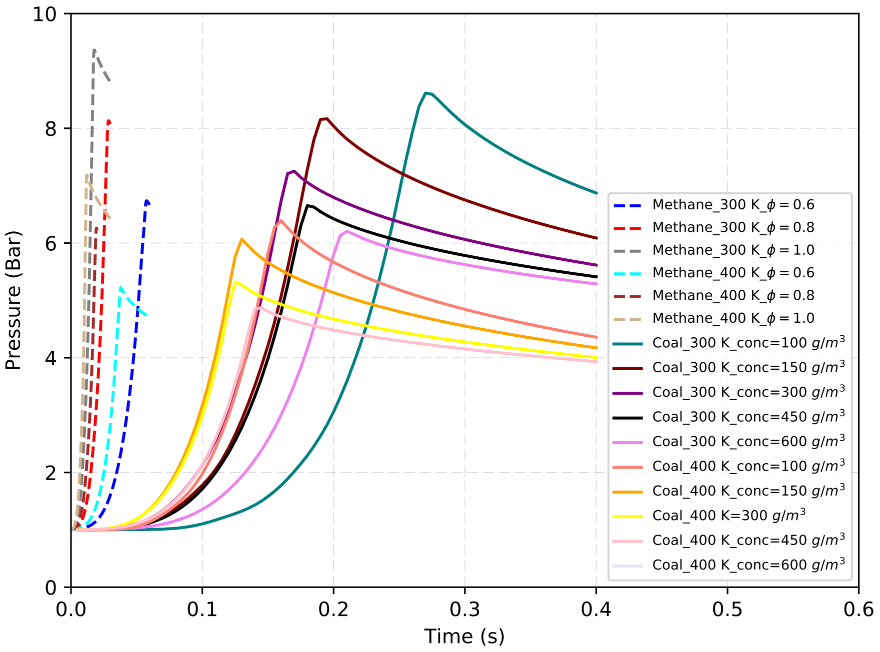

Fig. 13*: Pressure profiles for all methane and coal dust combustion simulations.*

Though Fig. 13 clearly demonstrates that increase in temperature by 100 K reduced the maximum pressure, simulation results for K_{St} were more complicated. K_{St} increased substantially with increase in temperature at low dust cloud concentrations; however, at higher concentrations, the trend is not definitive. Hence, the discussion will focus on the increase in K_{St} induced by the 100 K rise in temperature at the low dust cloud concentrations.

A 10 kJ ignition source is typically used in the 20-L chamber, which could cause a temperature increase of approximately 450 K. This elevated initial temperature would increase the energy-to-volume ratio in the 20-L chamber compared to the ISO one cubic-meter vessel; thus, contributing significantly to the overdriving observed in the 20-L chamber. This does not rule out other potential contributory factors such as distributed ignition sources and pressure increase. Nonetheless, the simulation results have demonstrated that, for low dust cloud concentrations, increase in the initial temperature in the chamber has a significant impact on increasing the K_{St} and may explain the discrepancy observed in the so-called "marginally explosible" dust which may be explosible in the 20-L chamber but not in the ISO one cubic-meter vessel.

4 Conclusion

The current work tested the hypothesis that temperature increase plays a major role in overdriving in the 20 L Siwek chamber. Methane and coal dust flame models, using OpenFOAM CFD Toolkit, were developed and validated by experimental data from the literature. The methane simulations were performed at various initial temperature and equivalence ratios, while the coal dust simulations were performed at various initial temperature and dust cloud concentrations. CFD modelling appears to support the notion that "overdriving" in the 20 L chamber can be attributed (at least in part) to the temperature rise caused by the igniters. Moreover, the current work has provided a comprehensive set of simulation data for methane and coal dust explosions which can form a baseline for further research on the subject matter. Thus, though the preliminary results support the hypothesis that temperature contributes significantly to the overdriving observed in the 20-L chamber, further studies will be conducted to explore the trend in K_{St} as the dust cloud concentration increases.

Acknowledgements

The authors gratefully acknowledge financial contributions from (i) the Natural Sciences and Engineering Research Council of Canada (NSERC) in the form of a Collaborative Research & Development (CRD) Grant, (ii) Fauske & Associates, LLC, (iii) Fike Corporation, and (iv) PLC Fire Safety Solutions.

References

Bradley, D., Chen, Z., El-Sherif, S., Habik, S. E.-D., John, G., Dixon-Lewis, G. (1994). *Structure of laminar premixed carbon methane-air flames and ultrafine coal combustion*. Combustion and flame, 96(1-2):80–96.

Cashdollar, K. L. (1996). *Coal dust explosibility*. Journal of loss prevention in the process industries, 9(1):65–76.

Cashdollar, K. L., Chatrathi, K. (1993). *Minimum explosible dust concentrations measured in 20-l and 1-m3 chambers*. Combustion Science and Technology, 87(1-6):157–171.

Christ, D. M. (2013). *The effect of char kinetics on the combustion of pulverized coal under oxyfuel conditions*.

Cloney, C. T., Ripley, R. C., Amyotte, P. R., Khan, F. I. (2013). *Quantifying the effect of strong ignition sources on particle preconditioning and distribution in the 20-L chamber*. Journal of Loss Prevention in the Process Industries, 26(6):1574–1582.

Cloney, C. T., Ripley, R. C., Pegg, M. J., Amyotte, P. R. (2018). *Laminar burning velocity and structure of coal dust flames using a unity lewis number cfd model*. Combustion and Flame, 190:87–102.

Clouthier, M. P., Zalosh, R. G., Ripley, R. C., Amyotte, P. R., Khan, F. I. (2016). *Marginally explosible dust: A critical review*. In *Proceedings of the 11th International Symposium on Hazards, Prevention, and Mitigation of Industrial Explosions*, pages 372–382.

Going, J. E., Chatrathi, K., Cashdollar, K. L. (2000). *Flammability limit measurements for dusts in 20-l and 1-m3 vessels*. Journal of Loss Prevention in the Process Industries, 13(3-5):209–219.

Goodwin, D. G., Moffat, H. K., Speth, R. L. (2009). *Cantera: An object-oriented software toolkit for chemical kinetics, thermodynamics, and transport processes*. Caltech, Pasadena, CA.

Kuai, N., Huang, W., Du, B., Yuan, J., Li, Z., Gan, Y., Tan, J. (2013). *Experiment-based investigations on the effect of ignition energy on dust explosion behaviors*. Journal of Loss Prevention in the Process Industries, 26(4):869–877.

Kuai, N., Huang, W., Yuan, J., Du, B., Li, Z., Wu, Y. (2011). *Experimental investigations of coal dust-inertant mixture explosion behaviors*. Procedia Engineering, 26:1337–1345.

Macpherson, G. B., Nordin, N., Weller, H. G. (2009). *Particle tracking in unstructured, arbitrary polyhedral meshes for use in cfd and molecular dynamics*. Communications in Numerical Methods in Engineering, 25(3):263–273.

Migdal, D., Agosta, V. (1967). *A source flow model for continuum gas-particle flow*.

Nagy, J. (1983). *Development and control of dust explosions*, volume 8. CRC Press.

Proust, C., Accorsi, A., Dupont, L. (2007). *Measuring the violence of dust explosions with the "20l* *sphere" and with the standard "ISO 1* m^3 *vessel"*. Journal of Loss Prevention in the Process Industries, 20(4-6):599–606.

Rodgers, S. A., Ural, E. A. (2011). *Practical issues with marginally explosible dusts—evaluating the real hazard*. Process Safety Progress, 30(3):266–279.

Thomas, J. K., Kirby, D. C., Going, J. E. (2013). *Explosibility of a urea dust sample*. Process Safety Progress, 32(2):189–192.

Proceedings of the 13th Symposium International Symposium
on Hazards, Prevention and Mitigation of Industrial Explosions DOI: 10.7795/810.20200724

Prenormative Study on the Safety Characteristics of Explosion Protection for Hybrid Mixtures of Dusts and Vapours

Vanessa Heilmann [a], Adeyemi Taiwo [a], Werner Hirsch [a], Holger Großhans [a], Sabine Zakel[a]
& Ulrich Krause [b]

[a] Physikalisch-Technische Bundesanstalt (PTB), Braunschweig, Germany
[b] Otto-von-Guericke Universität (OVGU), Magdeburg, Germany

E-mail: Vanessa.Heilmann@ptb.de

Abstract

The present work is part of a joint project, initiated to develop standardized methods to evaluate the safety characteristics of flammable hybrid mixtures. It focuses on the dust/vapour/air systems. The safety characteristics to be measured comprise the maximum explosion pressure (p_{max}), the maximum rate of pressure rise $(\mathrm{d}p/\mathrm{d}t)_{\mathrm{max}}$ and the lower explosion limit (LEL). From previous investigations on dust/gas/air mixtures it is known, that these values cannot be evaluated by a simple linear combination of the respective values of the pure substances. In some cases, this would lead to an underestimation of the explosion risk and severity.

The standard 20L-sphere for dusts was used for the experiments. Some modifications of the set-up were required to allow experiments with dust/vapour/air mixtures. Verification of the modified apparatus was done for dust and vapour separately in order to ensure accuracy of the results even for the individual components. The different testing procedures used for gases or vapours on the one hand and dust on the other hand are quite different. While vapour characteristics are measured in a quiescent atmosphere with moderate-energy electrical sparks, turbulence and high-energy chemical igniters are intended to determine these values for dust. Prior to performing the hybrid mixture tests, the quantitative change in the safety characteristics for turbulent vapour/air mixtures was investigated as well as the influence of the ignition source and energy. The concentration related p_{ex}, $(\mathrm{d}p/\mathrm{d}t)_{\mathrm{ex}}$, and LEL were quantified for 2-propanol under different states of turbulence. Additionally, the process of mixture formation is studied in a numerical simulation and first results presented. These investigations serve as the starting point for measurement series on the safety characteristics of hybrid dust/vapour/air systems.

Keywords: *hybrid mixtures, explosions, safety characteristics, standardization*

1. Introduction

A hybrid explosive mixture is a multi-phase system consisting of a fuel gas or vapour, air, and combustible dust. Such mixtures are encountered regularly in industry, for example in the pharmaceutical industries, drying processes or in painting plants. To assess the safety risks when running a process, it is necessary to know about the behavior of the flammable substances and their safety characteristics. For flammable gases, vapours and dusts, there are already standards that define procedures for determining the relevant characteristics such as DIN EN 14034-1 (EN 14034-1:2004+A1:2011); DIN EN 14034-2 (EN 14034-2:2006+A1:2011); DIN EN 15967 (EN 15967:2011). Standards ensure the comparability of the measured values between different laboratories. However, these standards treat gaseous and solid flammable substances separately due to their different explosion properties. For example, the design of the ignition vessels, the ignition sources and the test procedure for fuel gases and dusts differ considerably. For hybrid mixtures, however, the safety parameters cannot be determined according to the existing standards. The studies found in the literature use different experimental procedures and often the results are not comparable. This study is part of a joint project (NEX-HYS), in which standardized measurement methods for hybrid mixtures are developed. The results will be published in a final report and as a pre-standard of the German Institute for Standardization (DIN). This pre-standard enables test institutes and industry to assess explosion hazards when operating technical plants with hybrid mixtures and thus to control processes both more safely and more efficiently. Standardization at the international level is supposed to be initiated based on this pre-standard.

While a large body of data on safety characteristics exists both for gases and dusts separately, the number of investigations for hybrid mixtures is much smaller. This is true especially for mixtures of dusts with the vapour of liquids. It is known from previous research that some of these mixtures are more sensitive to ignition, have wider explosion ranges and that the effects of explosions can be more severe (Hesener und Beck 2016). The maximum explosion pressure increases when only a small amount of vapour or gas is added to the dust (Amyotte P. et al. 2010). In a comparison of mathematical models with experimental values it was shown, that the calculated safety characteristics are not reliable for all kinds of hybrid mixtures (Addai et al. 2019). An attempt to measure safety characteristics of vapour containing hybrid mixtures in the 20L-sphere was already made (Dufaud et al. 2009). The influence of vapours was distinct for the maximum rate of pressure rise and the maximum explosion pressure of dusts. Therefore, for the purpose of a hazard assessment with hybrid mixtures it is not enough to rely on the safety-related characteristic parameters of the individual components.

Furthermore, there is a strong influence of the ignition source on the determination of the individual parameters tested. The current standard ignition sources for vapours supply energies < 10 Joule, for dusts the energies are higher by three orders of magnitude. The measured safety characteristics could be falsified if the ignition source is over initiated. (Amyotte P. et al. 2010).

The time interval between the entering of the pressure blast to the 20L-sphere and the moment of ignition is denoted as the ignition delay time. In the testing of dusts, the ignition delay time is fixed in the standard. In finding the optimum ignition delay in testing dusts, the velocities inside the sphere play a big role (Dahoe et al. 2001; Bartknecht 1980). If the ignition delay time is to large the dust settles down before ignition (Klippel et al. 2015). The Hydraulic conditions before and during the ignition have a big influence of the correctness of the safety characteristics (Scheid et al. 2006). For this reason, the mixture formation in the test apparatus is investigated in this study and a procedure for further tests is developed.

The present paper has a focus on the verification of the testing equipment after some modifications from the commercially available standard set-up were applied. The influence of the time to ignition on the safety characteristics of vapours was measured and numerical simulations were compared with the experimental results. Over the last years, several studies have been performed on this topic. The effect of dust diameters on the dispersion and the effect of the dust concentration on flow patterns in the 20-L-sphere was investigated via CFD (DiSarli et al. 2014; Di Sarli et al. 2013) and the effect of ignition times on the fluid flow of dust with air in the 20L-sphere was studied. A CFD simulation was done and compared with experimental results of the flow patterns established with a particle image velocimetry (PIV). It was found that the local concentration of dusts can vary significantly. In this paper the homogeneity of mixing with vapours and the effect of turbulence on the safety characteristics was investigated (Vizcaya et al. 2018).

2. Experiments

2.1 Explosion testing in the 20L-sphere

The standard 20L-sphere was used throughout the testing of the different explosive mixtures (Figure 1). It is described in DIN EN 14034-1 (DIN EN 14034-1:2004+A1:2011) for measuring safety characteristics of dusts and fulfills the requirements of DIN EN 15967 (DIN EN 15967:2011)) for gases and vapours. It consists of the steel sphere itself, which is kept at a temperature of 20 °C by water cooling of the double-walled jacket, a dust container with fast-acting valve at the inlet, and an outlet for the reaction products. The dynamic pressure inside the sphere is monitored by two pressure transducers at the side of the sphere. The combustible dust sample is turbulently dispersed by a rebound nozzle when introduced by a pressure blast. The electrode stands, which carry the igniters, are mounted to the removable lid and located at the center of the sphere. At these stands, either electrodes or chemical igniters can be mounted. An additional liquid injection unit was assembled, which doses a defined mass of a combustible liquid with a syringe pump inside the evacuated sphere before the dust enters. All components of the set-up are remotely controlled by the user via software programmed in LabVIEW. Compressed air according to EN12021 (DIN EN 12021:2014-07) is used for mixture preparation.

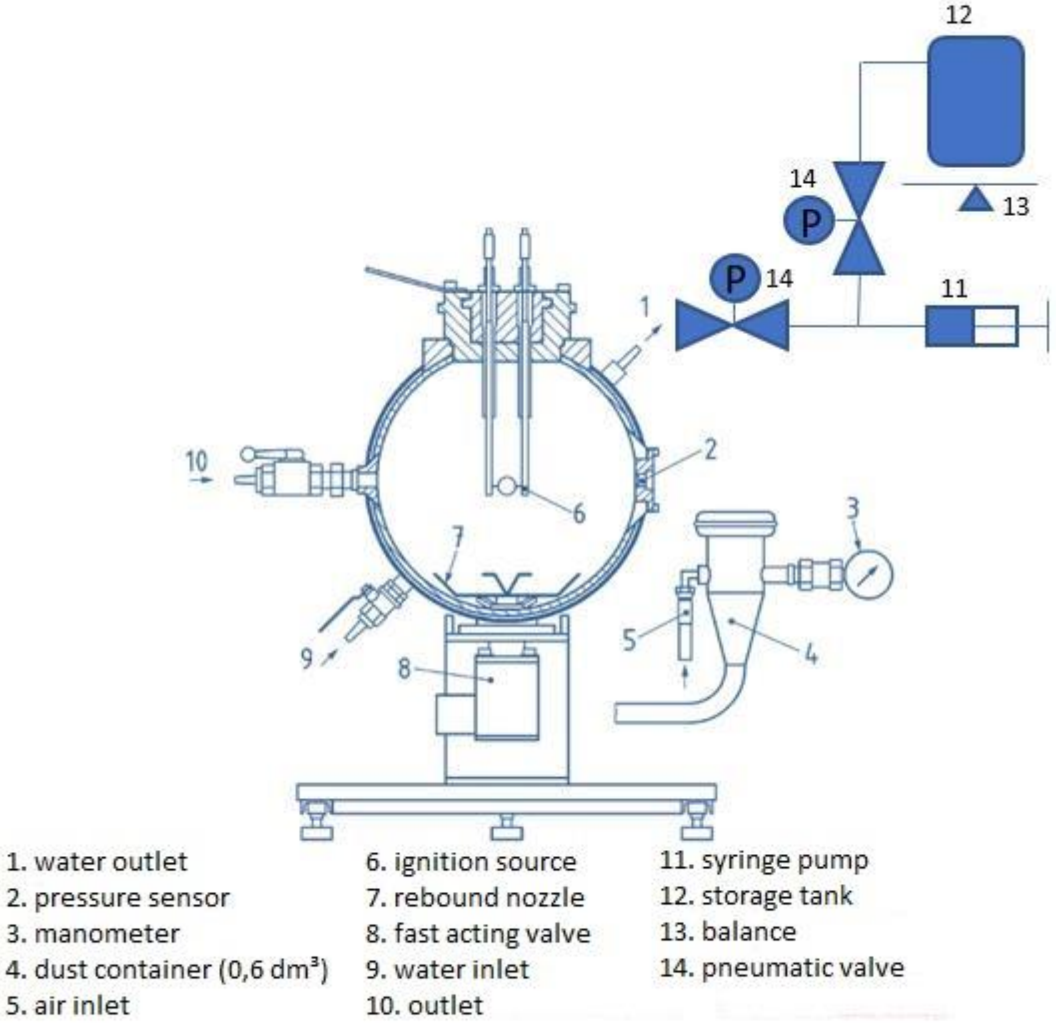

Fig. 1: *20l-sphere with liquid injection (DIN EN 14034)*

2.2 Measurement procedure for flammable dusts

At the beginning of each experiment the sphere was evacuated to 0.2 bar and filled again with air to a pressure of 0.4 bar. A defined mass of the dust sample was filled to the dust chamber, the chamber was closed and then pressurized to 20 bar. The initial pressures were checked by two static pressure sensors, one inside the sphere and one inside the dust container. When the ignition sequence was started, the dust was inducted into the sphere by the pressure blast. After an ignition delay time of 60 ms, during which the dust is distributed inside the sphere, two chemical igniters with 5 kJ each were activated for the determination of p_{max} and $(\mathrm{d}p/\mathrm{d}t)_{\mathrm{max}}$. The apparatus was verified with Niacin from an international round robin (CaRo, 2013) (Cesana-AG 2013). Each concentration was measured three times and the result was calculated according to the standard and the testing manual. The results were within the tolerance range of the certified reference value from the interlaboratory test and the apparatus and method were therefore verified.

The model dust, which was chosen to test the set-up with hybrid mixtures was corn starch, supplied to the project partners by INBUREX. It is well known in the explosion testing of combustible dusts that particle size distribution and humidity are of major influence on the result. The median particle size distribution determined by using a laser diffraction analyzer was 41 µm as median with 80,4 % with a size distribution of 0-63 µm. The humidity was determined by the standard procedure for measuring humidity for starches (DIN EN ISO 1666 (ISO 1666:1998-01)) to be 6 % by mass fraction. To be sure that the humidity was constant throughout the testing series, it was checked several times: 5 g of the cornstarch were dried for 45 minutes at a temperature of 130 °C, cooled down over drying resin for 30 minutes and then weighted. The mass loss gives the absolute water content of the starch.

2.3 Measurement procedure for flammable vapours

The standard procedure for the measurement of vapour explosion characteristics was adapted to the 20L-sphere. The sphere was evacuated to 0.01 bar and afterwards a defined mass of the liquid was injected by a syringe pump. The sphere was filled with air to 0.4 bar subsequently. As with the dust experiments, the empty dust chamber was pressurized with air to 20 bar and the fast-acting valve was opened to let the air blast inside the sphere. The final pressure inside the sphere was then at the standard condition of 1 bar. The air pressure blast mixes the vapour and air to form a homogeneous mixture A two-minute settling time is needed to make sure that the ignition could take place under quiescent conditions. All experiments were performed at a temperature of 20°C.

The flammable liquid chosen for the model system was 2-propanol (99% by mass fraction). The development of pressure before, during and after ignition was recorded regarding different concentrations. The lower explosion limit (LEL) the maximum explosion pressure ($p_{\max}$) and the maximum rate of pressure rise $(\mathrm{d}p/\mathrm{d}t)_{\max}$ were determined this way. The apparatus was verified by comparison with literature values for 2-propanol.

2.4 Ignition sources

One of the main objectives of the study it to find a suitable ignition source for hybrid mixtures which avoids over-initiation. Chemical igniters supply too much energy and therefore, an exploding wire igniter with adjustable energy will be developed as the project proceeds. In the present investigation, an electrical spark of 10 W power and 200 ms duration in the centre of the sphere was used as ignition source. Its effective spark energy used in the experiments was confirmed to be 2 J by a calorimetric method developed by the BAM to be 2 J. This corresponds very well to the 10 W electrical spark with a duration of 0.2 s mentioned in the standard.

2.5 Numerical simulations

Simulations of the turbulent flow in the vessel were conducted using the open-source toolbox OpenFoam (OpenCFD Ltd 2019) . The different geometries were created using the Salome software (Salome 2019) considering the dimensions of the sphere from the standard. The geometry was meshed through SnappyHexMesh (OpenCFD Ltd 2014) ensuring a high resolution in regions where high gradients are expected. The PIMPLE is applied which is a combination of the pressure-implicit split-operator (PISO) and the semi-implicit method for pressure-linked equations (SIMPLE) algorithms. This algorithm is an iterative procedure for coupling equations for momentum and mass conservation. The rhoPimpleFOAM solver was selected where density is as a varying quantity.

Turbulence is modeled via the Large Eddy Simulations (LES) methodology, i.e. large energetic flow scaled are resolved on the grid and smaller ones are accounted for by a turbulence model. This model is based on the eddy-viscosity concept. Thus, the governing equations are the filtered Navier-Stokes equations which comprise mass conservation for compressible flows (equation (1)) and momentum conservation (equation (2)). The variables in both equations have the following meaning: $\bar{\rho}$: average density, t: time, x: general spatial coordinate with dimension indices i und j, u: velocity, $\bar{\tau}_{ij}$:mean shear-rate tensor and $\bar{p}$: average pressure.

$$\frac{\partial \bar{\rho}}{\partial t}+\frac{\partial}{\partial x_i}(\bar{\rho}\tilde{u}_i)=0 \qquad (1)$$

$$\rho\frac{\partial \bar{u}_i}{\partial x_t}+\rho\bar{u}_j\frac{\partial \bar{u}_i}{\partial x_j}=-\frac{\partial \bar{p}}{\partial x_i}+\frac{\partial \bar{\tau}_{ij}}{\partial x_j}-\rho\frac{\partial\left(\overline{u_i u_j}-\bar{u}_i\bar{u}_j\right)}{\partial x_j} \qquad (2)$$

3. Results and discussion

3.1. Data acquisition and evaluation

Pressure traces we recorded with two piezoelectric pressure transducers with a rise time of < 2µs at a sampling rate of 4 kHz to meet the requirements of (DIN EN 14034-1:2004+A1:2011). The commercially available set-up discards a major part of the measured values and proposes for $(dp/dt)_{ex}$ a tangent to the pressure curve that can be corrected by the eye of the user. In this study the procedure for finding p_{ex} and $(dp/dt)_{ex}$ was fully automated.

The explosion pressure p_{ex} could be taken from the maximum of the pressure trace without any further treatment because of a low noise of the raw pressure signals. However, to evaluate the rate of pressure rise smoothing was necessary. A 3rd degree Savitzky-Golay smoothing with a window of 6 ms was found to reduce the noise efficiently without visible distortion of the main signal. For calculation of trace curvature, a much stronger smoothing with wider windows had to be used. Here signal distortion was of minor importance as only the difference in positions of two peaks had to be used.

For p_{ex} it is necessary to account for the influence of vessel size and of the energy of the igniters. Note that for dusts explosion pressures are commonly given as gauge pressure p_g.

For a 20L-sphere the following relations are given in the standard (DIN EN 14034-1 (EN 14034-1:2004+A1:2011)). With E_i is the meaning of the ignition energy.

If $p_{g,ex,20l} \geq 5{,}5$ bar: $$p_{g_{ex}} = 0{,}775 \cdot p_{g_{ex,20l}}^{1{,}15} \qquad (3)$$

If $p_{g,ex,20l} < 5{,}5$ bar: $$p_{g_{ex}} = \frac{5{,}5\left(p_{g_{ex,20l}}-p_{Ci}\right)}{5{,}5-p_{Ci}} \qquad (4)$$

where $$p_{Ci} = \frac{1{,}6\cdot E_I}{10000}$$

The volume-corrected value of the maximum rate of pressure rise $(dp/dt)_{max}$ is called K_D and can be calculated from the vessel volume V by the cubic law given in eq. (5):

$$K_D = V^{\frac{1}{3}} \cdot \left(\frac{dp}{dt}\right)_{max} \qquad (5)$$

For each experiment the higher of the two values for p_{ex} and $(dp/dt)_{ex}$ was reported as the final result. For every dust concentration the experiments were repeated three times. For reliable results it is necessary to check the correctness of the ignition delay time for every experiment. The ignition delay time is defined in this study as the period from the start of valve opening to the pressure rise caused by the ignition source. These points were determined by finding the maxima in the curvature of the pressure trace. This procedure is shown as the green curve in Figure 2.

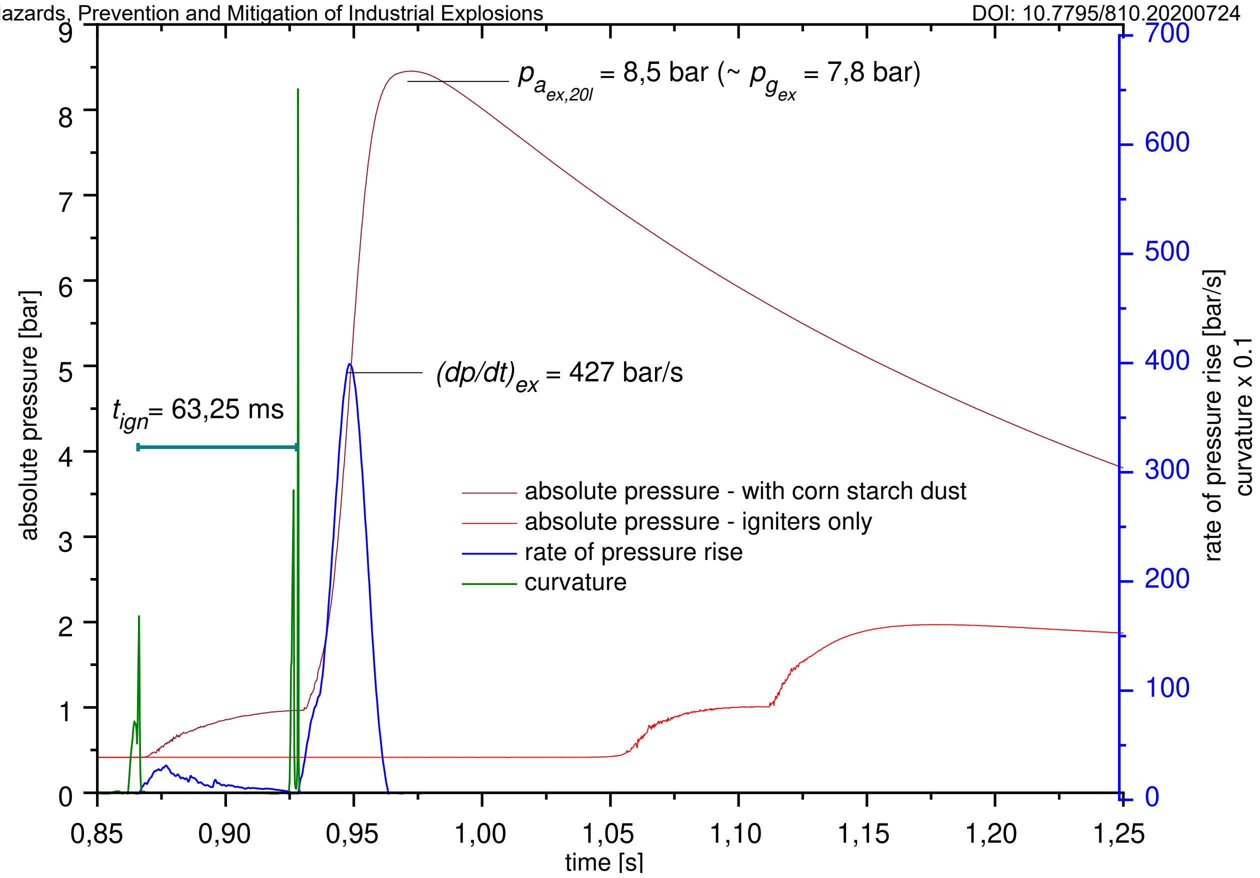

Fig. 2: *Evaluation of a single experiment of ignition of corn starch (751g/m³) and comparison with an ignition of two 5 kJ igniters in pure air. The trace of only one of the pressure transducers is shown.*

Figure 2 also shows that the 10 kJ energy released by firing of the igniters leads to a substantial increase of the pressure inside the sphere. For weak explosions this must be accounted for, which is done by application of eq. (4). Data acquisition for the vapour experiments was basically the same as for the dusts. To comply with the vapour standards the sampling rate was increased to 10 kHz. For vapours the explosion pressures are given as absolute presures without the index g.

3.2. Experiments with corn starch

The measured explosion pressures p_{ex} and pressure rise rates $(dp/dt)_{ex}$ for the corn starch sample are presented in Figure 3. The maximum explosion pressure was found to be p_{max} =7,9 bar ± 10% and the maximum explosion pressure rise rate is $(dp/dt)_{max}$=520 bar/s ±10%. Application of the cubic law leads to a K_D-value of 140 bar·m/s ± 10%. These values are in good agreement with the literature (Chemikalieninformationssystem des Bundes und der Länder).

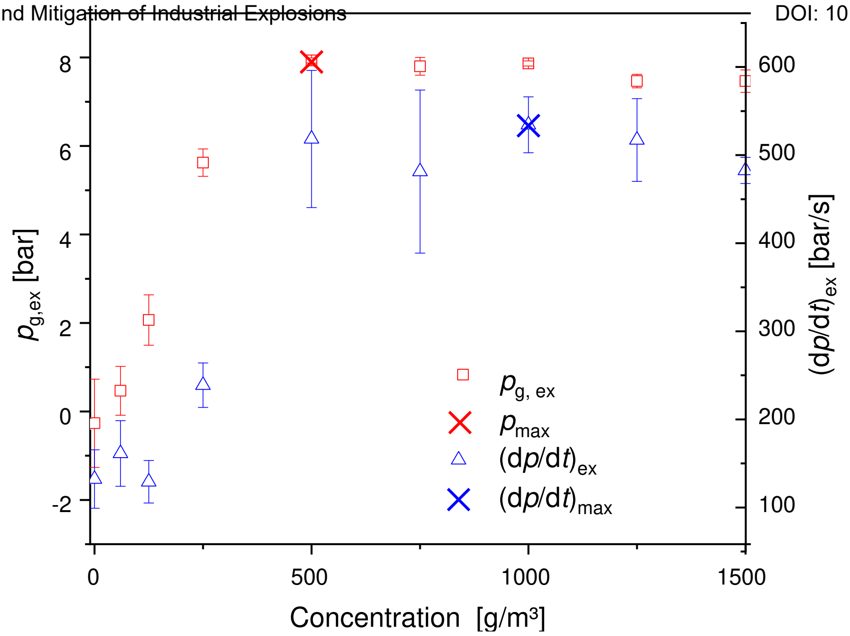

Fig 3: *Measured explosion pressure (p_{ex}) and pressure rise rate $(dp/dt)_{ex}$ in dependence on the concentration of corn starch in mixture with air*

3.3. Experiments with 2-propanol

The results of the tests on 2-propanol are shown in Figure 4. The concentration step size was 0.2 % by volume fraction. The lowest concentration at which ignition occurred was 2.8 % by volume fraction and therefore the highest non-ignition was at 2.6 % by volume fraction. The lower explosion limit (*LEL*) at 2.2 % by volume fraction measured according to DIN EN 1839 which is found in the Chemsafe database (PTB). Both values agree because the LEL is given after subtraction of the measurement uncertainty as the lowest value found for five non-ignitions.

With flammable liquids $p_{\max}$ und $(dp/dt)_{\max}$ are normally found at a concentration slightly higher than the stoichiometric composition. This is just not possible for 2-propanol at 20°C because the vapour pressure of 2-propanol at 20°C is 43 mbar (PTB) and the stoichiometric concentration is 4.4 % in volume fraction. Nevertheless, the overall intention of this study on hybrid mixtures is to qualify the influence of low amounts of solvent vapour on the dust explosion characteristics. For this reason, the measurements on 2-propanol were carried out with lower concentrations than stoichiometric as shown in Figure 4. The temperature dependence of the maximum explosion pressure is described to be (Brandes and Möller 2008):

$$p_{\max}(T_2) = p_{\max}(T_1) \cdot \frac{T_1}{T_2} \tag{6}$$

where T_1 and T_2 denote thermodynamic temperatures of state 1 and 2 in Kelvin. A value of p_{max}(50°C)=8.6 bar is found in the Chemsafe database (E. Brandes et al.). The value of p_{max}(20°C) would be 9.5 bar according to equation 4. Explosion pressures up to 8.6 bar were measured with the maximum possible concentrations close to the stoichiometric concentration which is in good agreement with the calculated value. The measured K_G-value is 88 bar·m/s, which is nearly equal to the literature value of 80 bar·m/s measured at higher temperatures (M. Mitu und E. Brandes 2013), however there is no simple relation for the temperature dependence of K_G.

When the influence of small amounts of flammable solvent vapour on the safety characteristics of dust is investigated, it is essential to quantify the influence of turbulence on the less conservative safety characteristics of the vapours first. A hybrid mixture explosion cannot be studied under the quiescent conditions normally applied for gas and vapour testing as the dust has to be dispersed in the gas phase by a turbulent pressure blast. For this reason, the 2-propanol/air mixtures were not only studied at the standard ignition delay time for vapours of 2 minutes but also at the reduced delay times used for dust explosions in order to quantify the influence of inhomogeneous mixing and turbulence.

In Figure 5 the influence of the ignition delay time on the rate of pressure rise nearly the lower explosion limit of 2-propanol/air mixture is depicted. Turbulence is known to increase pressure rise rates and one would expect the *(dp/dt)*$_{ex}$-value to decrease with increasing settling time. However, such a decrease is found only for long settling times of more than 1 s while for small settling times *(dp/dt)*$_{ex}$ is nearly constant. This is explained by the way the turbulence is generated within the explosion chamber. The pure air is blown into a quiescent fuel/air atmosphere thus generating not only turbulence, but also a high degree of inhomogeneity.

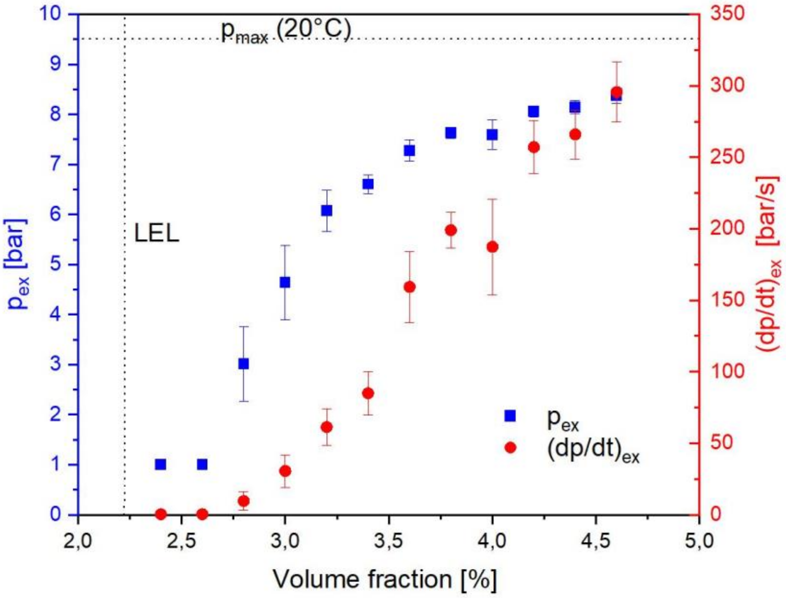

***Fig. 4:** Explosion characteristics of 2-propanol in quiescent mixture*

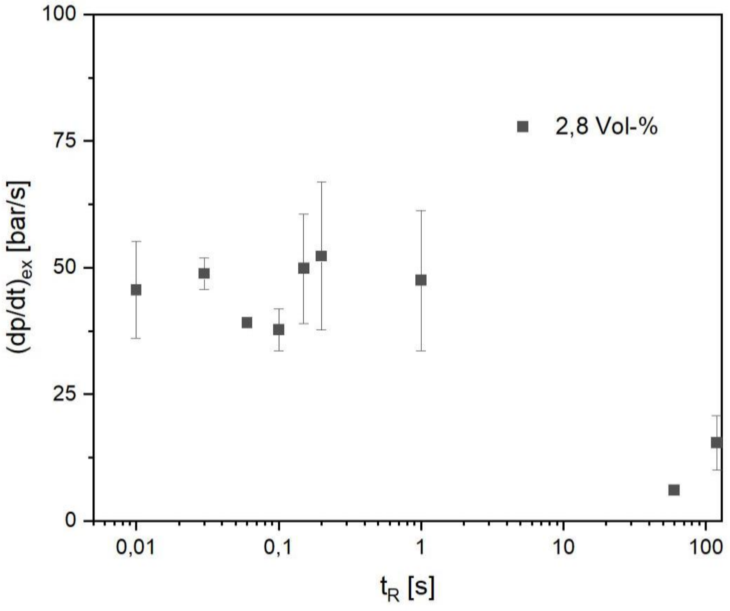

***Fig.5:** Pressure rise rate of 2-propanol against ignition delay time at 2,8Vol-%.*

3.4 Numerical simulations

From the experiments with 2-propanol it was assumed, that pure air blown into a quiescent fuel/air atmosphere is generating not only turbulence, but also a high degree of inhomogeneity. To establish a numerical simulation a pressure difference of 0.7 bar to 1.0 bar was chosen and the ignition delay times were limited to 10 ms. Figure 6 and Figure 7 show the streamlines of the air blast which enters at the bottom. A nozzle at the bottom of the sphere causes the entering air and the already present vapour/air mixture in the sphere to swirl. The streamlines show, that the swirls are localized, and the distribution is not homogeneous after 10 ms, which is also seen in the experiments.

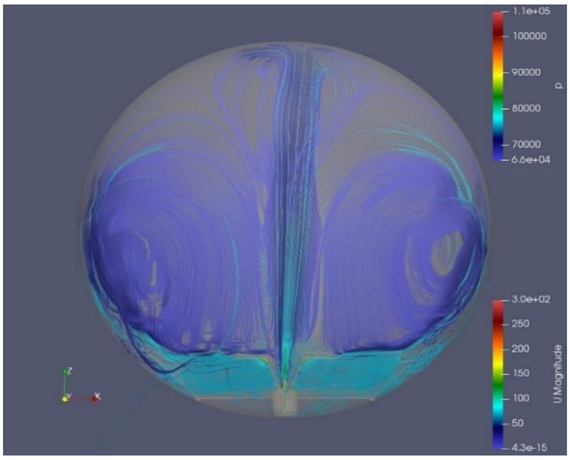

Fig. 6: *Streamline front view after 10 ms*

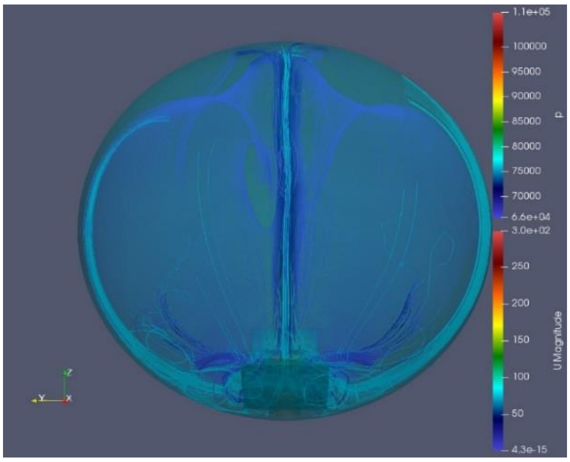

Fig. 7: *Streamline side view after 10 ms*

The flow velocities (Figure 8) are highest at the nozzle itself. The introduced air causes a local increase in flow velocity at the nozzle blades and in the centre of the nozzle, at the injection holes. The flow lines and the flow velocities result in turbulence fields, which are shown in Figure 9. The introduced air is first of all accelarated by the nozzles geometry and forms turbulences. The turbulence fields are located at the ball wall and in the centre of the ball. It can be assumed that a turbulence steam mixture is present in the area around the igniter at the time of ignition. However, the current statement is not true for all areas, so the status is very inhomogeneous after 10 ms within the sphere.

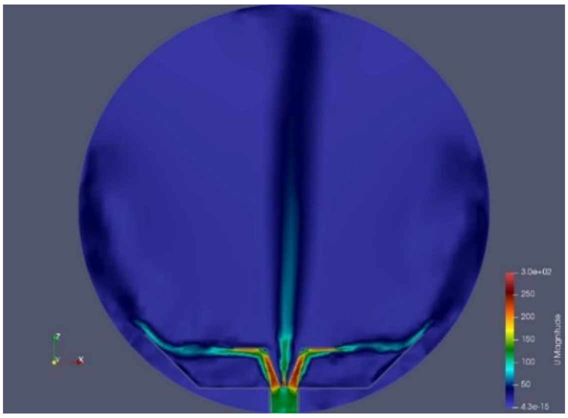

Fig.8: *Velocity Profile after 10 ms*

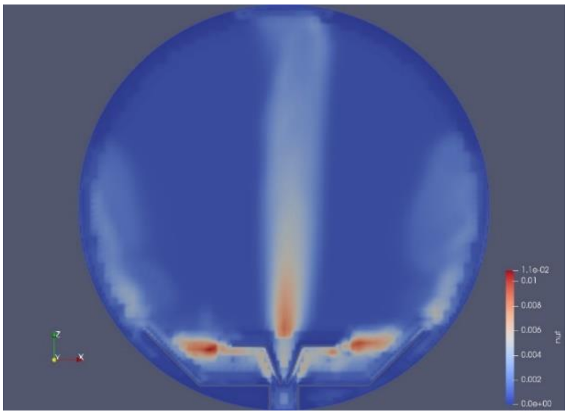

Fig. 9: *Turbulence viscosity after 10 ms*

4. Conclusions

The experimental set-up described in this paper is verified for use with the individual components and therefore ready to start measurement series on hybrid mixtures. The flow conditions inside the sphere have an enormous influence on the determination of K_G and K_D for both dusts and vapours.

Experiments show that the flow conditions during injection of the dust may influence the results of hybrid explosions not only by the generated turbulence but also by the incomplete mixing of the injected air with the fuel/air mixture already in the vessel.
The numerical simulation shows local turbulence fields, which on the one hand could provide a faster mixing within the sphere and on the other hand could keep the dust dispersed long enough to form a hybrid mixture for the determination of K_{HYB}. The increased flow velocity directly at the nozzle ensures that the dust is whirled up, while the turbulence fields distribute the vapour in the sphere. They show that after 10 ms the local turbulence fields necessary for distribution of the dust and for mixing of the fuel vapour with air have developed only in a part of the volume. It will be necessary to extend the simulations to longer dispersion times and to study the flow fields of vapours and hybrid mixtures in more detail.
Further simulations at different pressure steps are useful to characterize the flow fields of vapours and later of hybrid mixtures in more detail. In order to validate the fluid mechanic calculations measurements of the flow velocities inside the sphere will be done in a next step.

Acknowledgements

The project is funded by the Federal Ministry of Economy as part of the WIPANO frame program, which promotes knowledge and technology transfer through patents and standards. The authors would like to thank S. Spitzer of the Bundesanstalt für Materialforschung und -prüfung (BAM) for the determination of the effective spark energy.

Literaturverzeichnis

Addai, E. K.; Ali, H.; Amyotte P.; Krause, U. (2019): Experimental and theoretical investigation of the lower explosion limit of multiphase hybrid mixtures. In: *process safety progress*, S. 1–13.

Amyotte P.; Lindsay, M.; Domaratzki, R.; Marchand, N.; Di Benedetto, A.; Russo, P. (2010): Prevention and mitigation of dust and hybrid mixture explosions. In: *process safety progress* 29 (1), S. 17–21.

DIN EN 12021:2014-07: Atemgeräte-Druckgase für Atemschutzgeräte.

Bartknecht, W. (1980): Explosionen. Ablauf und Schutzmaßnahmen. 2. Aufl. Berlin, Heidelberg: Springer Verlag.

DIN EN 14034-1 (EN 14034-1:2004+A1:2011): Bestimmung der Explosionskenngrößen von Staub/Luft-Gemischen.

DIN EN 14034-2 (EN 14034-2:2006+A1:2011): Bestimmung der Explosionskenngrößen von Staub/Luft-Gemischen.

Cesana-AG (2013): Kalibrier-Ringversuch CaRo 18 Schlussbericht. Bettingen, Schweiz.

Chemikalieninformationssystem des Bundes und der Länder: gsbl. Online verfügbar unter https://gsbl.de/index.html, zuletzt geprüft am 28.02.2020.

Dahoe, A. E.; Cant, R. S.; Scarlett, B. (2001): On the decay of turbulence in the 20-Liter Explosion Sphere. In: *Flow, Turbulence and Combustion* (67), S. 159–184.

Di Sarli, V.; Russo, P.; Sanchirico, R.; Di Benedetto, A. (2013): CFD Simulations of the effect of dust diameter on the dispersion in the 20 l bomb. In: *Chemical Engineering Transactions* (31), S. 727–732.

DiSarli, V.; Russo, P.; Sanchirico, R.; Di Benedetto, A. (2014): CFD simulations of dust dispersion in the 20 l vessel: Effect of nominal dust concentration. In: *Journal of Loss Prevention in the process industries* (27), S. 8–12.

Dufaud, O.; Perrin, L.; Traore, M.; Chazelet, S.; Thomas, D. (2009): Explosions of vapour/dust hybrid mixtures: A particular class. In: *Powder Technology* (190), S. 269–273.

E. Brandes; D. Pawel; J. Alpers; J. Scheffler: Safety characterisitic data at non-atmospheric conditions: reduced pressures; elevated temperatures. In: Loss Prevention and safety promotion in the process industries 9 th international symposium, Proceedings 2, S. 590–598.

Hesener, U.; Beck, M. (2016): Sicherheitstechnische Kenngrößen von hybriden Gemischen. Forschungsbericht. Dekra Exam GmbH.

Klippel, Alexander; Schmidt, Martin; Krause, Ulrich (2015): Dustiness in workplace safety and explosion protection- Review and outlook. In: *Journal of Loss Prevention in the process industries* (34), S. 22–29.

M. Mitu; E. Brandes (2013): Sicherheitstechnische Kenngrößen von Alkohol/Luft-Gemischen-Explosionsdruck, zeitlicher Druckanstieg, Verbrennungsgeschwindigkeit (13. BAM-PTB-Kolloqium zur chemischen und physikalischen Sicherheitstechnik) (269. PTB Seminar), S. 178–186.

OpenCFD Ltd (2014): Snappy Hex Mesh. Online verfügbar unter https://openfoam.org/release/2-3-0/snappyhexmesh/.

OpenCFD Ltd (2019): OpenFoam. Version 7. Online verfügbar unter https://www.openfoam.com/.

PTB (Hg.): Chemsafe. Online verfügbar unter www.chemsafe.ptb.de, zuletzt geprüft am 21.02.2020.

Salome (2019). Online verfügbar unter https://www.salome-platform.org/.

Scheid, Marc; Geißler, Andreas; Krause, Ulrich (2006): Experiments on the influence of pre-ignition turbulence on vented gas and dust explosions. In: *Journal of Loss Prevention in the process industries* (19), S. 194–199.

DIN EN ISO 1666 (ISO 1666:1998-01): Stärke - Bestimmung des Feuchtegehaltes.

DIN EN 15967 (EN 15967:2011): Verfahren zur Bestimmung des maximalen Explosionsdruckes und des maximalen zeitlichen Druckanstiegs für Gase und Dämpfe.

Vizcaya, D.; Pinilla, A.; Amin, M.; Ratkovich, R.; Munoz, F. (2018): CFD as an approach to understand flammable dust 20 l standard test: effect of the ignition time on the fluid flow. In: *AIChE Journal* 64 (1), S. 48–54.

E: Brandes, W. Möller: Safety Characteristic Data, vol. 1: Flammable Liquids and Gases, 2nd ed.; Wirtschaftsverlag NW Verlag für neue Wissenschaft 2008, p. 33

E. Brandes, D. Pawel, J. Alpers, J. Scheffler, Safety characterisitic data at non-atmospheric conditions: reduced pressures; elevated temperatures, in: Loss Prevention and safety promotion in the process industries 9 th international symposium, pp. 590–598.

M. Mitu, E. Brandes, Sicherheitstechnische Kenngrößen von Alkohol/Luft-Gemischen-Explosionsdruck, zeitlicher Druckanstieg, Verbrennungsgeschwindigkeit 13. BAM-PTB-Kolloqium zur chemischen und physikalischen Sicherheitstechnik, 2013, pp. 178–186

DOI: 10.7795/810.20200724

The Explosion of Non-nano Iron Dust Suspension in the 20-l Spherical Bomb

Enrico Danzi [a], Gianmaria Pio [b], Luca Marmo [a] & Ernesto Salzano [b]

[a] Politecnico di Torino, Dip. di Scienza Applicata e Tecnologia, Torino (IT)
[b] Università di Bologna, Dip. di Ingegneria Civile, Chimica, Ambientale e dei Materiali, Bologna (IT)

E-mail: *ernesto.salzano@unibo.it*

The understanding of dust explosion is still incomplete because of the lack of reliable data and accurate models accounting for all the physic-chemical aspects. Besides, most of the experimental data available in the current literature has been accumulated on the 20-l spherical bomb tests, which gives coarse results for the pressure history that cannot be easily converted into fundamental combustion parameters. Nevertheless, the large amount of experimental data available in the spherical bomb is attractive.

In this work, the explosion of non-nano iron dust in the standard spherical vessel is analysed, aiming at evaluating the burning velocity from the theoretical point of view and from the simple experiments performed by the standard explosion tests. The choice of iron is of relevance because its adiabatic flame temperature is below the boiling temperature of both the reactants and oxidized gaseous, liquid, or solid (intermediate and final) products and for the negligible porosity with respect to organic substances. Therefore, a non-nano iron dust explosion can be reconducted to a reduced mechanism since heterogeneous (surface) combustion may be considered, exclusively, and the diffusion mechanism for oxygen is the only relevant. The laminar burning velocity is strongly dependant on the particle diameter and tends asymptotically to about 8 cm/s for larger particle diameters, whereas little effects are due to the dust concentration.

Keywords: *dust explosions, iron dust, burning velocity, heterogeneous combustion*

Introduction

The prevention and the mitigation of dust explosions are essential for process safety and for the proper design of safety barriers. To this aim, several international standards and regulations are established worldwide. Most of them refer to data obtained using a spherical or quasi-spherical explosion reactor, which is essentially based on a solid injection system, an ignition device (either chemical or electrical) and two low-frequency pressure transducers. The reactor is in principle that of 1 m^3 volume, but most of the standards consider the well-known spherical bomb as well of 20-l.

The large success of this procedure, which is simple and relatively cheap, is confirmed by the several design equations, e.g. suppression systems or venting devices, shown in the literature and in the current normative and standards, and by the huge amount of data for organic and metallic dust which can be retrieved from literature (Marmo et al., 2017, Clouthier et al., 2019).

Nowadays, several detailed experimental and modelling study in the spherical bomb include the effects of humidity, particle diameter, time delay to ignition and other important physical and technical parameters, e.g. suspension system design (Amyotte, 2013, Taveau et al., 2018)

Besides, the possibility of describing the actual kinetic and thermo-physical processes involved in the fast oxidation of solid suspension in air in the standard test is hindered by the contemporary occurrence of several complex phenomena at either micro or macro scale. Indeed, the understanding of the entire phenomena is still unclear, because the data obtained by the pressure history measured in the 20-l sphere cannot be easily converted into fundamental combustion parameters due to the unknown flame temperature to the low-frequency pressure recording, to the inhomogeneous combustion caused by the dispersion device (Kalejaiye et al., 2010, Sanchirico et al., 2015), by the ignition device (often a detonator, see Proust et al., 2007 and Cloney et al., 2013) and due to the non-adiabatic conditions (Goroshin et al., 1996).

Nevertheless, the very large database composed by experimental data obtained in the spherical bomb is quite attractive for further insight into the explosion physics. Hence, in our opinion, any effort addressed to the use of the 20-l data into more fundamental comprehension is positive and useful because the understanding of the mechanisms controlling flame propagation in suspensions of non-volatile particles is crucial to obtaining efficient combustion of metallized propellants, powdered metals as carbon-free chemical energy carriers other than the above-cited safety issues (Soo et al., 2017).

In this work, the explosion of non-nano, non-volatile iron dust is studied in the 20lt bomb by running standard test using air and by substituting helium instead of nitrogen for the analysis of the oxygen diffusion effects, which are prevalent for the chosen dust.

Methodology

The pre-mixed combustion of micro-sized dust suspension (i.e. dust explosion) can be represented by the synergistic phenomena of the heterogeneous combustion over the solid surface and by the homogeneous combustion of the gases and vapours formed alternatively or jointly through pyrolysis, gasification, and vaporization (or even sublimation) of the condensed phase.

Reproducing the details of these effects is *de facto* a very complex issue if also including the particle size dependence, the complex fluid-dynamic effects (turbulence) related to the necessity of producing the suspension, the ignition modality and the oxidant variability, as the humidity and the presence of inert gases as argon and pollutants either in the solid or in the gas phase.

For the combustion models, quite often a continuum assumption is considered, which underlines the fact that the inter-particle spacing l_p is smaller than the flame width l_f (Tang et al., 2012) This concept is also expressed in terms of a regime of propagation by using a dimensionless combustion time τ_c defined as:

$$\tau_c = \frac{t_r \cdot \alpha}{l_p^2} \qquad [1]$$

where t_r is the characteristic reaction time of the burning particle and α is the thermal diffusivity of the gas mixture. A continuum regime is then observed for $\tau_c > 1$. In this case, which is typical for nano and sub-micron dust, particles react at nearly the same temperature as the surrounding gas in the flame zone (Tang et al., 2011) and the chemical kinetic mechanics at the surface become relevant. Furthermore, the kinetics of surface reactions are independent of the particle size.

In the case of non-nano iron dust, the formation of a continuous flame is unlikely because it requires the accumulation of a substantial amount of iron vapour in a preheat zone, which is hindered by the high boiling temperature ($Fe, T_b = 3130\ K$), and due to the high rate of reaction of iron vapour with oxygen. Furthermore, no intermediated gaseous sub-oxides are formed, as demonstrated by thermogravimetric analyses which show, at higher temperature, the absence of hematite ($Fe_2O_3, T_b = 1870\ K$) or magnetite ($Fe_3O_4, T_b = 2896\ K$ (Lysenko et al., 2014), as only wüstite ($FeO, T_b = 3687\ K$) is formed through the reaction (Ogle, 2016):

$$Fe + 0.5\ O_2 \rightarrow FeO \qquad [2]$$

For $\tau_c \ll 1$, which is the case here analysed, the flame exhibits a discrete characteristic and the propagation of the flame front is dominated by the interactions between neighbouring particles and/or by the low thermal diffusion. Also, the heat release becomes dependent on the spatial distribution of the particles.

For micro-scale particles, the rate of the chemical reaction (as described by the kinetic rate constant) is much faster than the rate of oxygen diffusion to the particle surface or towards a gas flame zone that envelopes each particle close to its surface. Hence the gas-phase diffusion of the oxidant becomes the rate-limiting process. This behaviour is already confirmed for aluminium dust flames with a diameter as small as 5 μ. Indeed, the burning particles exhibit greater temperatures than the surrounding gas, hence consistently with the particles burning in a diffusive regime.

These effects are described by the Damköhler number Da, i.e., the ratio of the surface reaction rate to the rate of oxygen diffusion. For most of the industrial non-nano dust forming suspension (hence diameters ranging from few μm to more than 200 μm), the Da number is much larger than unity so that the diffusive regime is confirmed. Quite clearly, for the lower values, alternate regions of kinetic and diffusion particle combustion modes may co-exist within the same flame.

In the case of a lean mixture of non-nano iron dust, oxygen is in excess. Hence, the burning rate of the dust in the flame front is equivalent to the burning rate ω_p of a single particle. Following the approach of Frank-Kamenetskii (Soo et al., 2017), the overall reaction rate per unit surface area of a particle A_p in an oxidizing gas, accounting for both kinetic and diffusion resistances can be then written as:

$$\omega_p = \frac{1}{A_p}\frac{dm_p}{dt} = \nu \frac{k \cdot \beta}{k+\beta} c_{O_2} \qquad [4]$$

where m_p is the mass of the particle, t is the time, ν is the stoichiometric coefficient for the oxygen, c_{O_2} is the molar fraction of oxygen at the bulk of the oxidant, and k is the overall Arrhenius surface reaction rate. The term β is the mass transfer coefficient between the particle and the gas at the given temperature, and can be calculated as:

$$\beta = \frac{Sh \cdot \mathcal{D}}{\theta} \qquad [4]$$

where Sh is the Sherwood number, θ is the particle diameter and $\mathcal{D}$ is the diffusion coefficient of the oxidant at the particle-gas interface. The term beta can be obtained by Damköhler number Da, which is defined as:

$$Da = k \cdot \beta^{-1} \qquad [5]$$

Hence, by using a normalized Da^*:

$$Da^* = \frac{Da}{1+Da} = \frac{k}{k+\beta} \qquad [6]$$

we obtain:

$$\omega_p = \nu \cdot Da^* \cdot \beta \cdot c_{O_2} \qquad [7]$$

For a purely diffusive regime $Da^* \approx 1$ as $k \gg \beta$. Furthermore, for a spherical particle that is stationary relative to the gas, the exact solution to the steady-state spherical diffusion equation yields a Sherwood number Sh equal to 2. Hence:

$$\omega_p = 2 \cdot \nu \cdot \frac{\mathcal{D}}{\theta} \cdot c_{O_2} \qquad [8]$$

The term ω_p is related to the unit surface of the particle suspension. Being the concentration of the particle c_p:

$$c_p = \frac{m_p}{V} = \frac{\rho_p V_p}{V} = \frac{\rho_p \theta A_p}{V} \qquad [9]$$

It is then, for the overall volumetric reaction rate r_p:

$$r_p = \frac{1}{V}\frac{dm_p}{dt} = \frac{A_p}{V}\omega_p = \frac{c_p}{\rho_p}\frac{\omega_p}{\theta} = \frac{c_p}{\rho_p}\frac{\omega_p}{\theta} = \frac{2 \cdot \nu \cdot \mathcal{D} \cdot c_{O_2} \cdot c_p}{\rho_p \cdot \theta^2} \qquad [10]$$

which is equivalent, in terms of dependency with the square of the particle diameter, to the equation reported by Glassman and Yetter (2008) for particles burning in the diffusion-controlled mode, if considering the inverse of the burn time for the single particle as:

$$r_p = \frac{8 \cdot \rho \cdot \mathcal{D} \cdot \ln\left(1 + \nu \cdot c_{O_2}\right)}{\rho_p \cdot \theta^2} \qquad [11]$$

where ρ is the density of the bulk mixture. Following the classical Mallard-Le Chatelier theory and the modifications of Lewis-von Elbe, an apparent laminar burning velocity can be then calculated as (Glassman):

$$S_u^2 = \alpha \frac{(T_f - T_i)}{(T_f - T_u)} \frac{r_p}{\rho} \qquad [12]$$

where the subscripts f, i and u refer to the adiabatic flame, ignition and initial temperature of the mixture, respectively.

As for gases, the laminar burning velocity increases with the fuel and oxidant concentration. The dependency on the concentration is essentially related to the adiabatic flame temperature and ignition temperature, which brings some difficulties in the case of dust explosions. To this aim, this work assumes that, as for typical dust explosion analysis, the ignition temperature and the adiabatic flame temperature follow the same ratio as the pressure in the 20 lt bomb:

$$\frac{(P_f - P_i)}{(P_f - P_u)} = \frac{(T_f - T_i)}{(T_f - T_u)} \qquad [13]$$

where the ignition temperature (and pressure) are dependent on the pure dust only.

Finally, the obtained laminar burning velocity can be used for the sake of comparison with the classical equation for the rate of pressure rise:

$$\frac{dp}{dt}=\frac{3(p_{max}-p_0)}{r_{flame}}\left[1-\left(\frac{p_0}{p}\right)^{\frac{1}{\gamma}}\frac{p_{max}-p}{p_{max}-p_0}\right]^{\frac{2}{3}}\left(\frac{p}{p_0}\right)^{\frac{1}{\gamma}}S_u \qquad [14]$$

where the value of p_{max} is that recorded in the 20-l sphere (or calculated through thermodynamic), r_{flame} is the flame radius at the instant corresponding to the pressure p. For each dust diameter and concentration, considering the maximum pressure, assuming unity for the initial pressure and for γ, under the simplified assumption that the maximum pressure corresponds to the flame arrival to the spherical wall of the reactor (r_{flame}=R_{vessel}), the equation can be further reduced to:

$$S_{u,20lt}=k\cdot\left(\frac{dp}{dt}\right)_{max}\cdot R_{vessel} \qquad [15]$$

where k is a constant.

Experimental

In this work, a commercial iron powder (Sigma-Aldrich, FE006020) has been tested following the UNI EN 14034:2011 standard to measure P_{max} and K_{St}. The iron dust has a density of 7860 g/m^3. The granulometric distribution has been obtained by laser diffractometry using a Malvern MASTERSIZER E1000. The Particle Size Distribution is given in Figure 1, which shows an average volume median diameter of about 45 µ.

Explosion tests were conducted in the 20-l sphere according to the UNI EN 14034: 2011 standard procedure used to measure K_{St} (hence using 2 x 5 kJ Sobbe chemical igniters and 60 ms delay time at ignition). A wide range of concentrations was tested, from 250 g/m^3 up to 2000 g/m^3. According to the UNI EN 14034, the maximum measured explosion pressure P_{ex} must be corrected to a final explosion pressure P_m as follows:

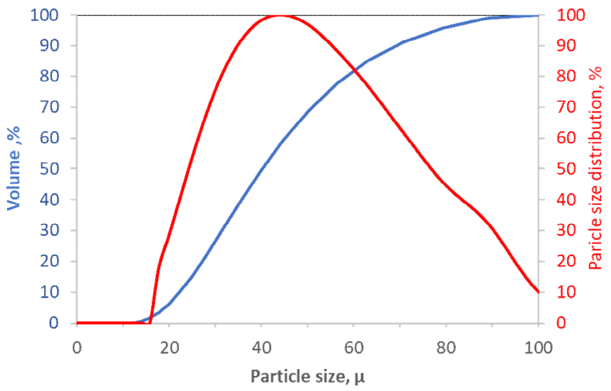

Fig. 1. Distributive and cumulative particle size distribution for the analysed iron dust.

P_{ex} > 5.5 bar $$P_m=0{,}775\cdot P_{ex}^{1{,}15} \qquad [16]$$

P_{ex} < 5.5 bar $$P_m=\frac{5.5\cdot(P_{ex}-\Delta P_{ignitor})}{(5.5-\Delta P_{ignitor})} \qquad [17]$$

where:

DOI: 10.7795/810.20200724

$$\Delta P_{ignitor} = \frac{1.6 \cdot E_i}{10000} \qquad [18]$$

where E_i is the ignitor energy [J] and $\Delta P_{ignitor}$ [bar] is the pressure rise caused by the chemical igniters. Average P_{ign} is about 1.07 bar (Taveau et al., 2017).

Results and Discussion

A typical dust-type pressure history for the metallic powder is shown in Fig. 2 (Danzi & Marmo, 2019). In the plot, several phases can be observed, showing that only a small fraction of the iron dust explodes at high rates. The first rise of pressure is due to igniters; hence a steep rate of pressure rise is observed, thus showing a fast combustion regime for the smallest particles with full oxygen availability. Then the rate of pressure rise decreases possibly indicating that diffusive effects may limit the combustion rate. Finally, the presence of non-adiabatic effects is observed after the maximum pressure, as the value decreases slowly as some heat losses occurs.

The experimental maximum pressure P_{max} and the maximum rate of pressure rise $(dP/dt)_{max}$ are given in Fig. 3. Results show a value of $(dP/dt)_{max}$ = 300 bar/s at 1000 g/m^3, hence a K_{St} = 80 bar m/s. The value of P_{max} is about 2.1 bar$_g$ at the same concentration, which indicates that only partial combustion of the iron occurs. The value of K_{St} clearly reflects low reactivity of the dust, which is typical of a diffusive flame.

Figure 4 shows the laminar burning velocity calculated for the equivalent diameter of dust and concentration between 500 g/m^3 and 1500 g/m^3 by the model reported above.

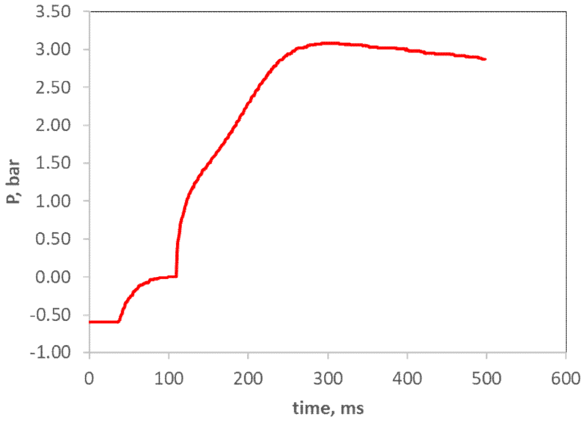

Fig. 2. *Explosion pressure measured in the 20lt sphere for dust concentration of 1000 g/m^3.*

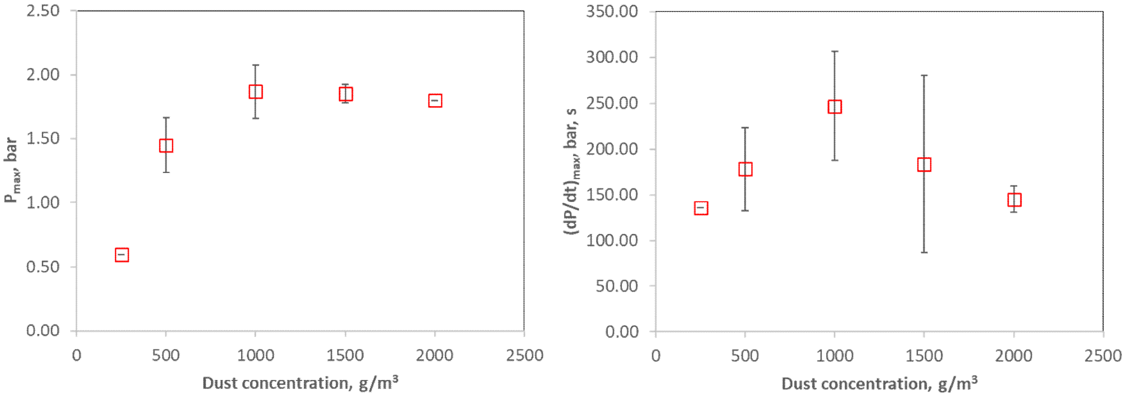

Fig. 3. *Experimental P_{max} and $(dP/dt)_{max}$ vs iron dust concentration.*

In the same figure, the average values (no error bars are shown, concentration between 900 and 1200 g/m^3) obtained by Tang et al. (2009; 2012) and Sun et al. (2017) for iron dust suspension are given.

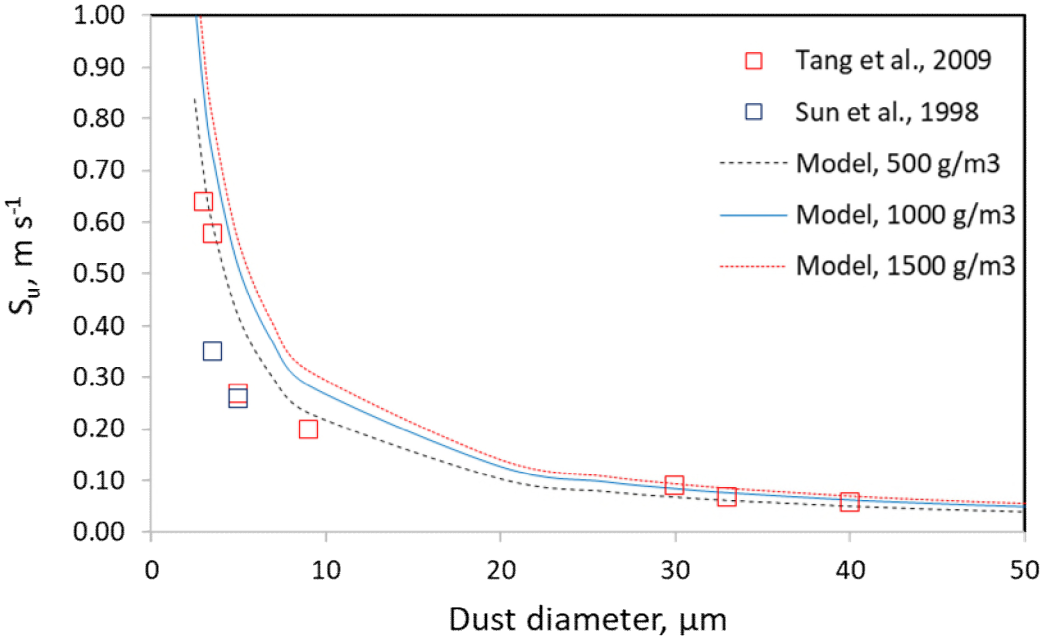

Fig. 4. *Laminar burning velocity for the iron dust to the dust diameter, average particle concentration of 1000 g/m^3. Experimental data from Tang et al. (2009) and Sun et al. (1998).*

The quality of the model for the particle size range where the combustion kinetic is controlled by diffusion (dust diameter larger than 5 µm) is clearly shown. The laminar burning velocity can be obtained from the maximum pressure and maximum rate of pressure rise as measured in the 20-l. Quite clearly, non-adiabatic conditions and turbulence effects affect the result. A best-fitting value is obtained for k = 7x10^{-4}. The results are in Figure 5.

Conclusions

A methodology for the prediction of laminar burning velocity in a purely diffusive regime has been defined. The maximum pressure and rate of pressure rise of non-nano iron dust in the 20-l explosion bomb have been measured, under the purely diffusive regime. The laminar burning velocity calculated directly from the experimental rate of pressure rise can be compared to the experimental data provided a proportional factor which is likely dependent on the hydrodynamics of the 20-l sphere. Further studies are ongoing to clarify its nature by using helium instead of nitrogen as inert.

Acknowledgement

This paper is dedicated to the memory of our mentor prof. Gennaro Russo, who recently passed away.

DOI: 10.7795/810.20200724

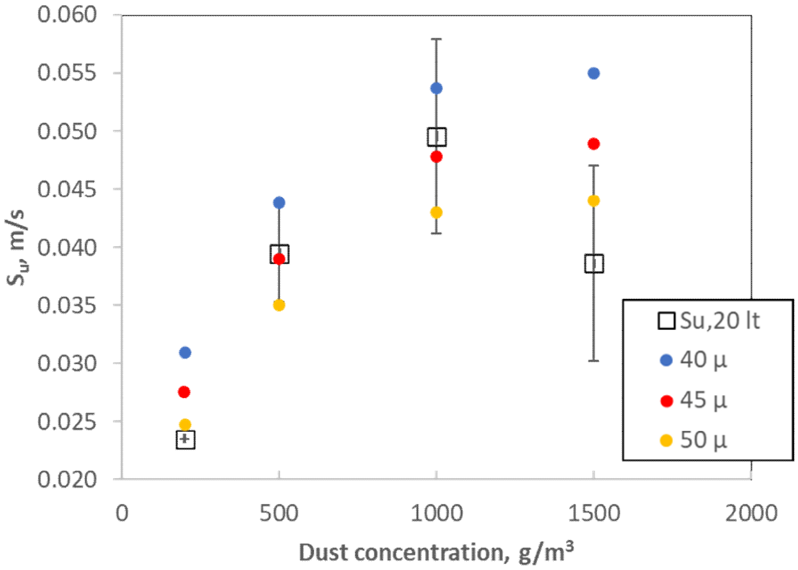

Fig. 5. *Comparison of the laminar burning velocity calculated through the theoretical equation shown in this work (Eqs. 14,15) by varying the dust concentration and the particle diameter, and the experimental value calculated from the measurement of (dP/dt)*$_{max}$ *in the 20lt sphere.*

References

Amyotte, P., 2013. An Introduction to Dust Explosions-Understanding the Myths and Realities of Dust Explosions for a Safer Workplace. Butterworth–Heinemann (Elsevier), Waltham MA, US, pp. 9–16.

Cashdollar, K. L., & Zlochower, I. A. (2007). Explosion temperatures and pressures of metals and other elemental dust clouds. Journal of Loss Prevention in the Process Industries. https://doi.org/10.1016/j.jlp.2007.04.018

Cloney, C. T., Ripley, R. C., Amyotte, P. R., & Khan, F. I. (2013). Quantifying the effect of strong ignition sources on particle preconditioning and distribution in the 20-L chamber. Journal of Loss Prevention in the Process Industries, 26(6), 1574–1582. https://doi.org/10.1016/j.jlp.2013.08.010

Clouthier, M. P., Taveau, J. R., Dastidar, A. G., Morrison, L. S., Zalosh, R. G., Ripley, R. C., … Amyotte, P. R. (2019). Iron and aluminum powder explosibility in 20-L and 1 m3 chambers. Journal of Loss Prevention in the Process Industries, 103927.

Danzi, E., & Marmo, L. (2019). Dust explosion risk in metal workings. Journal of Loss Prevention in the Process Industries, 61, 195–205.

Glassman, I., Yetter, R.A. (2008) Combustion, Elsevier Inc.

Goroshin, S., Fomenko, I. & Lee, J.H.S., Burning velocities in fuel-rich aluminum dust clouds (1996). Proceedings of the Combustion Institute, 1961–1967.

Julien, P., Whiteley, S., Goroshin, S., Soo, M.J., Frost, D.L., Bergthorson Jeffrey M. (2015) Flame structure and particle-combustion regimes in premixed methane–iron–air suspensions, Proceedings of the Combustion Institute, 35, 2431-2438.

Kalejaiye, O., Amyotte, P. R., Pegg, M. J., Pegg, M. J., & Cashdollar, K. L. (2010). Effectiveness of dust dispersion in the 20-L Siwek chamber, 23, 46-59.

Kenneth L. Cashdollar & Kris Chatrathi (1993) Minimum Explosible Dust Concentrations Measured in 20-L and 1-M3 Chambers, Combustion Science and Technology, 87:1-6, 157-171, DOI: 10.1080/00102209208947213

Lysenko, E. N., Surzhikov, A. P., Zhuravkov, S. P., Vlasov, V. A., Pustovalov, A. V., & Yavorovsky, N. A. (2014). The oxidation kinetics study of ultrafine iron powders by thermogravimetric analysis. Journal of Thermal Analysis and Calorimetry, 115, 1447–1452.

Marmo, L., Riccio, D., & Danzi, E. (2017). Explosibility of metallic waste dusts. Process Safety and Environmental Protection, 107.

Ogle, R.A., (2016) Dust Explosion Dynamics, Elsevier Science.

Proust, C., Accorsi, A., Dupont, L., 2007. Measuring the violence of dust explosions with the 20-L sphere and with the standard ISO 1m3 vessel. J. Loss Prev. Process Ind. 20, 599–606

Sanchirico, R., Di Sarli, V., Russo, P., & Di Benedetto, A. (2015). Effect of the nozzle type on the integrity of dust particles in standard explosion tests. Powder Technology, 279, 203–208.

Soo, M.J., Kumashiro, K., Goroshin, S., Frost, D.L., Bergthorson J.M., Thermal structure and burning velocity of flames in non-volatile fuel suspensions, Proceedings of the Combustion Institute, 36, 2017, 2351-2358.

Sun, J.-H., Dobashi, R., Hirano, T. (1998) Structure of flames propagating through metal particle clouds and behavior of particles, Proceedings of the Combustion Institute, 27, 2405–2411.

Tang, F. D., Goroshin, S., Higgins, A., & Lee, J. (2009). Flame propagation and quenching in iron dust clouds. Proceedings of the Combustion Institute, 32 (2009) 1905–1912.

Tang, F.-D., Goroshin, S. & Higgins, A.J. (2011). Modes of particle combustion in iron dust flames, Proceedings of the Combustion Institute, 33, 1975-1982.

Tang, F.-D., Goroshin, S., & Higgins, A.J. (2012). Propagation Regime of Iron Dust Flames. Retrieved from https://ntrs.nasa.gov/search.jsp?R=20120015602

Taveau, J. R., Going, J. E., Hochgreb, S., Lemkowitz, S. M., & Roekaerts, D. J. E. M. (2017). Igniter-induced hybrids in the 20-l sphere. Journal of Loss Prevention in the Process Industries, 49, 348–356.

Taveau, J., Lemkowitz, S., Roekaerts, D. (2018). Scaling up metal dusts deflagrations severity. In: Proceedings of the Twelfth International Symposium on Hazards, Prevention, and Mitigation of Industrial Explosions, Kansas City, USA, August 12-17.

Wright, A., Goroshin S., Higgins A. (2015). Combustion Time and Ignition Temperature of Iron Particles in Different Oxidizing Environments, 25th ICDERS, Leeds, UK

DOI: 10.7795/810.20200724

An investigation of micron and nano scale of aluminium dust explosion

Po-Jul Chang [a], Toshio Mogi [a] & Ritsu Dobashi [a]

[a] Department of Chemical System Engineering (The University of Tokyo, Tokyo, Japan)

E-mail: changpojul@chemsys.t.u-tokyo.ac.jp

Abstract

A series of dust explosion were conducted to compare the flame structure between nano and micron aluminium dusts. Two-color pyrometer technique is applied to have qualitative observation of flame development. Measurement of temperature indicates that explosion in micron aluminium dust clouds start in a single spot at 3000 K, in contrast, explosion in nano aluminium dust clouds start when hot powder accumulated to a certain amount at lower temperature of 2600 K. For micron aluminium dust clouds, flame at leading edge has the highest temperature and propagates in all directions. On the other hand, flame in nano aluminium dust clouds propagate only upward with the hottest part left behind at the downside. As flame propagates, the temperature at top edge gradually decreases from 2600 K to finally 2000 K, but temperature at bottom edge maintains in 3000 K with no significant displacement. The unevenness of flame structure is considered as the consequence of different particle densities, which suggests that the reaction of nano aluminium particles stays in molten state, meanwhile, the high surface area also leads to unignorable heat loss.

Keywords: *dust explosion, nano aluminium particle, temperature measurement*

1. Introduction

Up to now, the potential risks of dust explosion are generally characterized following standard analytical procedures, such as JIS standard (JIS Z 8818, 2002) and ASTM (ASTM E1515, 2006). For example, minimum explosible concentration (MEC), minimum ignition energy (MIE), and maximum explosion pressure (P_{max}) give an immediate idea to the explosion characteristics (Cashdollar and Zlochower, 2007). On the other hand, Bazyn et al. (2007) has reported that dominant reaction transits from detached diffusional gas reaction to kinetical surface reaction as Al particle decreases from micron to nano scale, but reported MECs does not reflected in the fact of mechanism transition (Cashdollar and Zlochower, 2007; Wu et al., 2010). The normal way of analytics seems not enough for nanomaterials. Therefore, more detailed investigations are necessary for considering the potential risks of dust explosion.

In previous work, to explain the transition process of dominant reaction from diffusional gas reaction to kinetical surface reaction, Gao et al. (2015) found that the transition can be categorized by Damköhler number. Chang et al. (submitted) proposed a heterogeneous model to describe the oxidation of Al particle in the preheating zone for micron and nano scale aluminium. Burning of particle was assumed into two extreme conditions: whether the metal oxide film was involved in the reaction or not. For micron Al, since it is naturally covered by metal oxide, the reaction rate is assumed to be determined by the diffusion rate of oxygen through alumina shell, which is considered as diffusion controlled reaction. For nano-Al, the influence of metal oxide on the surface reaction is ignored, and it is considered as kinetically controlled reaction. The model provides a way to predict the reacted amount as the particle is heated up from ambient temperature. The results indicate that the reacted amount is insignificant for a micron scale aluminium as particle below 2000 K. On the other hand, it is completely burned out in case of nano-scale aluminium. Because particle is barely left before gasifying, the results suggest that gas phase reaction does not occur in nano-Al and surface reaction dominates the combustion.

So far, the studies were focused on the observation of luminous zone where chemical reaction rates are growing fast. For example, Dobashi and Senda (2005) found that leading flame of stearic acid dust clouds is close to the behavior of premixed flame as particle gets vaporized. Several evidences also indicate that flame temperatures of aluminium are limited to its boiling point. (Bazyn et al., 2007; Sundaram et al., 2015). Micron aluminium combustion has been widely accepted as gas phase reaction at leading flame due to the emission of gaseous product AlO (Beckstead, 2004). On the other hand, the domination of surface reaction on nano Al is still uncertain due to lack of evidence. Furthermore, most reports were limited in the discussion of individual isolated particle, which may not represent the flame behavior in dust clouds. Therefore, two-color pyrometer technique is applied in current work to have a whole picture of flame structure during dust explosion.

2. Experiments

2.1 Aluminium particles

Experiments were conducted using three Al particle sizes. Micron size Al (High Purity Chemicals, Japan) was sieved to the range between 20~30 μm, and 3 μm Al (High Purity Chemicals, Japan) and 100 nm Al (uncoated, Alex) were used as received from the makers.

2.2 Experimental apparatus

Dust explosions were performed with an open space system as illustrated in Fig. 1. The dispersion procedures of powders follow the JIS standard (JIS Z 8818, 2002) as for the procedure of minimum explosible concentration (MEC) measurement. Initially, the sample powders were placed on the bottom of tube (ϕ=70 mm, length=293 mm), and then a blast of air (from a 0.0013 m^3 tank at pressure 0.07~0.09MPa) dispersed the sample forming a dust cloud in the tube. At first, the movable tube was closed to prevent dust cloud from going out. After 0.3 sec delay from blast, the center part of tube dropped down, and the dust cloud was exposed to the environment in an open space. After 0.5sec delay from blast, a 15kV neon transfer was arcing for 0.2 sec to generate an ignition spark (around 60J). The advantage of this apparatus is to create a dust cloud with estimable concentration, and the open space is easier for observation during dust explosion. The dust clouds were under fuel-rich condition at concentration of 840 g/m^3 (ϕ=2.7) for all experiments.

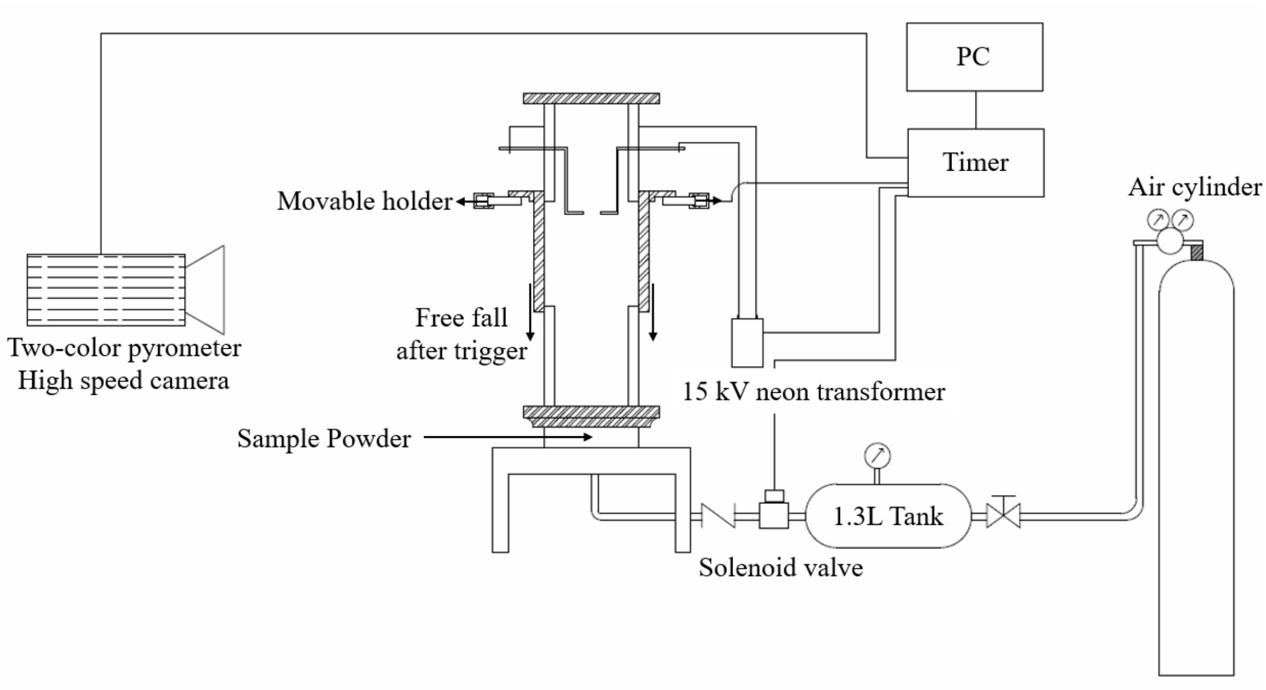

Fig. 1. *Schematic of the experimental apparatus*

2.3 *Two-color pyrometer*

A broadband two-color ratio was measured by a high-speed camera (Photron, FASTCAM SA2). Bandpass filter 450~690nm (Asahi Spectra VIS 690nm 50x50) and ND filter were set in front of lens to prevent signal from saturation. The unprocessed raw data were recorded in 8bits Bayer filter as RGGB pattern as shown in Fig 2. Due to relative weak intensity of blue (B) light in the current work, red (R) and green (G) were chosen for temperature measurement. The average G/R ratio at each pixel was calculated from the surrounding 3x3 matrix. Temperatures were calibrated by Tungsten Halogen lamp (Newport, QTH 20w) from 1000~2500 K as shown in Fig. 3. Emissivity is assumed to be constant at the detection range of wavelength (Gray body assumption), and temperature can be measured as the function of two-color ratio (Goulay et al., 2010; Densmore et al., 2011; Draper et al., 2012). A computer code (python 3.8) was written to solve for the temperature in 2048x2048 pixel pictures.

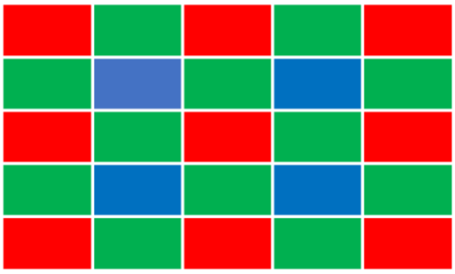

Fig. 2. *The Bayer filter of RGGB pattern*

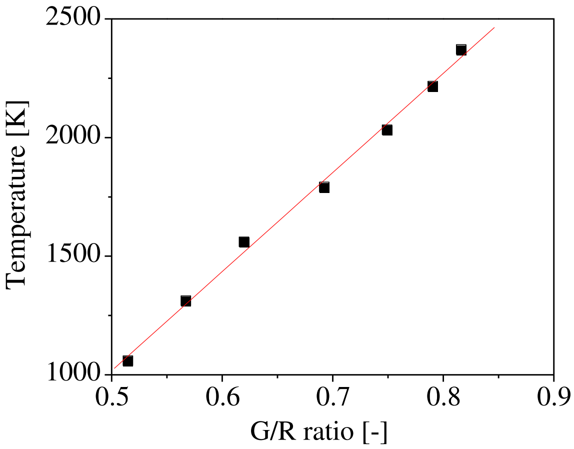

Fig. 3. *Temperature calibration result*

3. Results and discussions

3.1 Ignition of dust clouds

Typical results for the ignition of three particle sizes are shown in Fig. 4. For micron Al dust clouds, the initially stable light emission can be observed after ~20 msec of high voltage arcing, and the average starting temperatures are above 3000 K within a small spot. For nano Al dust clouds, the powder took ~120 msec to be ignited at average temperature 2600K. Based on the high-speed camera, the heated-up nano powder continuously falling downward, and the explosion started as hot powder accumulated to a certain amount. Even though nano aluminium particles have much lower minimum ignition energy (<1mJ for 100 nm) than micron aluminium (59.7mJ for 40μm) (Wu et al., 2010), the results imply that nano aluminium has higher rate of heat loss, which has been suggested by Ballal (1983) due to the high surface area. In other words, if the heat loss on nano aluminium can be limited, the MIE could be lower. Bazyn et al. (2007) has indicated that the combustion of nano aluminium without the "shields" of diffusion flame structure leads to a strong dependence of ambient temperature. For higher ambient temperature, nano aluminium shows shorter particle burning time and higher flame temperature.

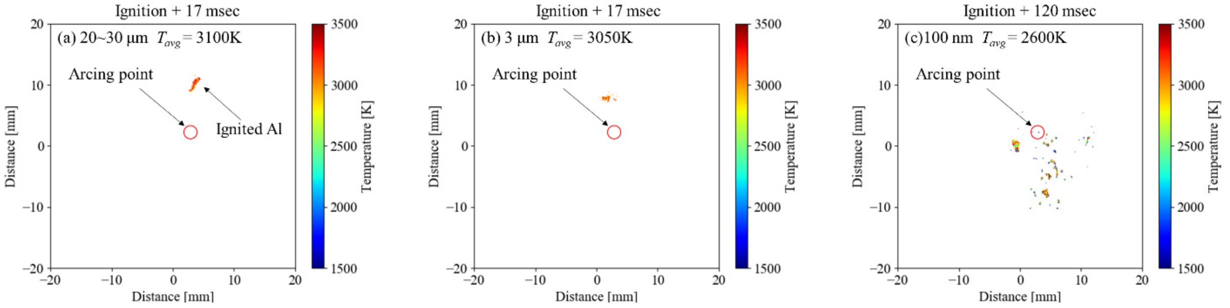

Fig. 4. *Ignition of aluminium clouds*

3.2 Flame temperature developments

The temperature development of flame through dust clouds are shown in Fig. 5. For micron sizes, the shapes of flames show good symmetricity as a spherical fire ball during propagation. The hottest regime is at the flame leading edge of ~3000K and observed flame thickness is in the range of 2~5

DOI: 10.7795/810.20200724

mm with no significant change in all propagating directions as shown in Fig. 6. Bazyn et al. (2007) has reported that the flame temperatures of micron aluminium particles are around 3100K by pyrometer or by the AlO emission (486 nm) correlation, which is in good agreement with the current work. On the other hand, the temperatures within the fire ball are not always clear, because leading flame also propagates toward the camera.

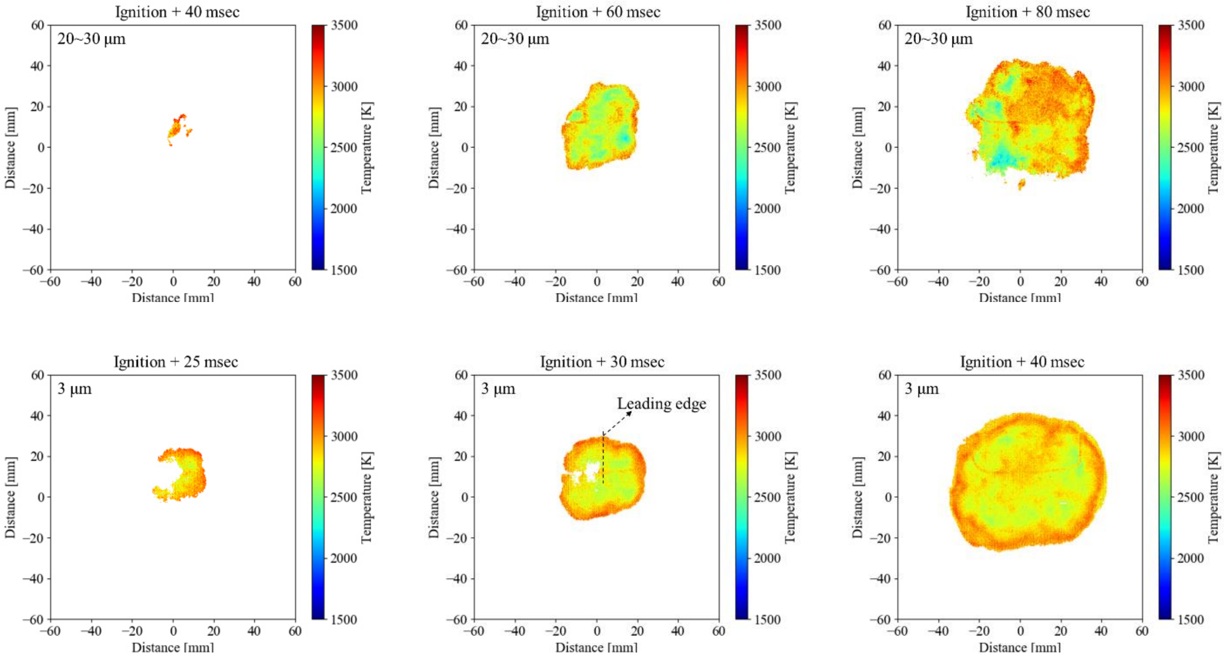

Fig. 5. Flame development in micron aluminium dust clouds

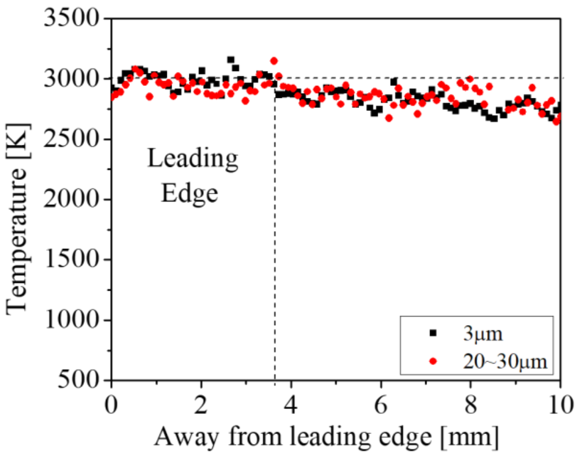

Fig. 6. Flame structure at leading edge in micron aluminium dust clouds

In contrast, the flame in nano aluminium dust clouds propagated upward with the hottest part left behind at the downside. As flame propagates, the temperature at leading edge gradually decreases.

Figure 7 shows that the leading edge of temperature ~2500K at 200 msec decreased to ~2000K at 230 msec. A cross section temperature distribution is shown in Fig. 8. The unevenness of flame structure from top to down is considered as the consequence of different particle densities; i.e., ρ=3.99 g/cm^3 for alumina and ρ=2.4 g/cm^3 for aluminium. The results suggest that reaction of nano aluminium was stayed in molten state, and the bottom part was the suspension of residues. Again, the heat loss is significant either at the moment of ignition or during flame propagation.

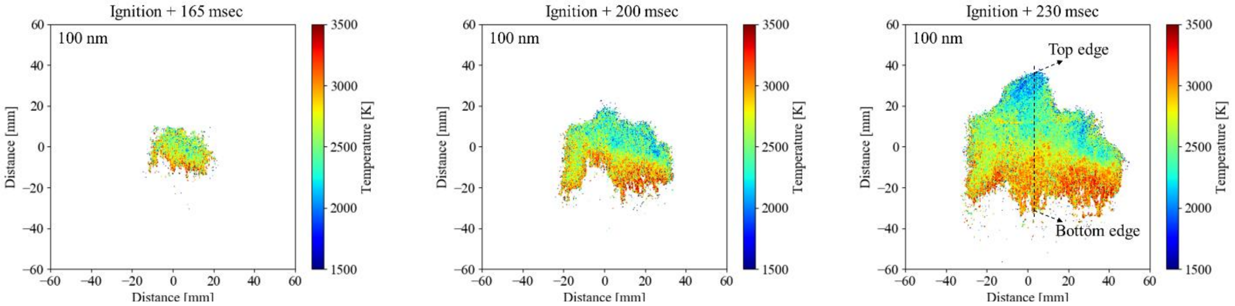

Fig. 7. *Flame development in nano aluminium dust clouds*

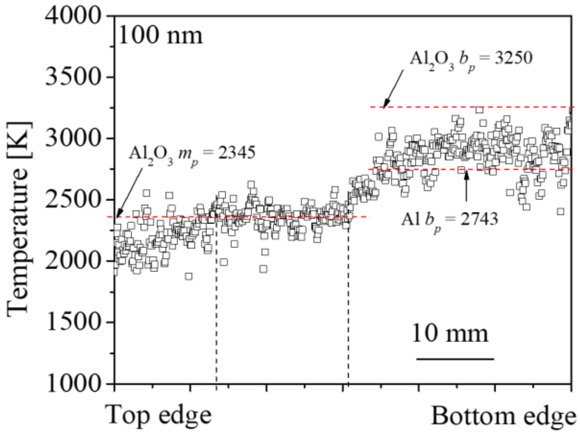

Fig. 8. *Temperature distribution in nano aluminium dust clouds*

3.3 Flame propagating speed

Flame propagating speeds were calculated by measuring the horizontal displacement of leading flame to minimize the influence of buoyancy as shown in Fig. 9. The flame in 3 μm aluminium dust clouds show the speed of 3.6 cm/s which is three times faster than that in 20~30 μm aluminium dust clouds of 1.2 cm/s. It is interesting to note that the leading edge of flame in micron aluminium dust clouds (3 and 20~30 μm) are at the hottest regime. Even though nano aluminium dust clouds have comparable flame speed to the 3 μm aluminium in horizontal direction, the bottom edge is under highest temperature of 3000 K with no significant displacement.

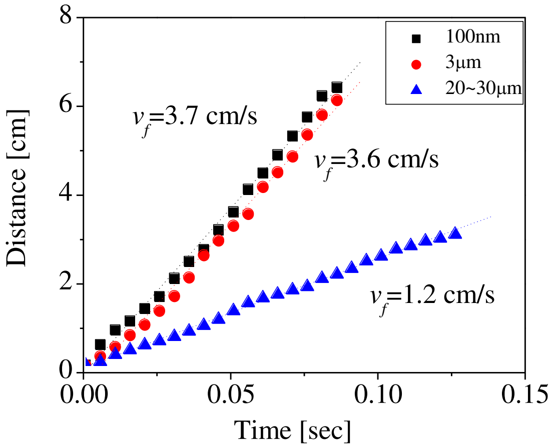

Fig. 9. *Flame propagation speed*

4. Conclusions

Temperature structures in aluminium dust explosion has been obtained by two-color pyrometer. Based on the measurement, there are several observations in sharp contrast between micron and nano aluminium particles.

(1) For micron aluminium dust clouds, explosion starts in a single spot at 3000 K. For nano aluminium dust clouds, explosion starts when hot powder accumulated to a certain amount with lower temperature at 2600 K.

(2) Flame at leading edge has highest temperature and propagates in all directions in micron aluminium dust clouds.

(3) In contrast, flame in nano aluminium dust clouds propagate upward with the hottest part left behind at the downside. As flame propagates, the temperature at top edge gradually decreases, but temperature at bottom edge maintains in 3000K with no significant displacement.

(4) The unevenness of flame in nano aluminium dust clouds is considered as the consequence of different particle densities, which suggests that the reaction of nano aluminium stays in molten state, meanwhile, the high surface area also leads to unignorable heat loss.

Acknowledgements

The authors would like to thank Prof. Keiichi Hori of Japan Aerospace Exploration Agency (JAXA)/ Institute of Space and Astronautical Science (ISAS) for his comments and assistance in conducting experiments.

References

ASTM International, 2006. Standard test method for minimum explosible concentration of combustible dusts, E1515-03. In Annual book of ASTM standards, Vol. 14.02, 480-488.

Ballal, D.R., 1983. Flame Propagation Through Dust Clouds of Carbon, Coal, Aluminium and Magnesium in an Environment of Zero Gravity. Proc. R. Soc. A Math. Phys. Eng. Sci. Vol. 385, Issue 1788, 21-51.

Bazyn, T., Krier, H., Glumac, N., 2007. Evidence for transition from the diffusion-limit in aluminum particle combustion. Proc. Combust. Inst. 31, 2021-2028.

Beckstead, M. W., 2004. A Summary of aluminum combustion. NATO Report RTO-EN-23. Bringham Young University Provo, Utah, USA.

Cashdollar, K. L., Zlochower, I. A., 2007. Explosion temperatures and pressures of metals and other elemental dust clouds. *Journal of Loss Prevention in the Process Industries*, 20: 337-348.

Chang, P. J., Mogi, T., Dobashi, R., Flame propagation through dust clouds of nano and micron scale aluminum, *Journal of Loss Prevention in the Process Industries*, (submitted)

Densmore, J.M., Homan, B.E., Biss, M.M., McNesby, K.L., 2011. High-speed two-camera imaging pyrometer for mapping fireball temperatures. Appl. Opt. 50, 6267-6271.

Draper, T.S., Zeltner, D., Tree, D.R., Xue, Y., Tsiava, R., 2012. Two-dimensional flame temperature and emissivity measurements of pulverized oxy-coal flames. Appl. Energy 95, 38-44.

Gao, W., Mogi, T., Yu, J., Yan, X., Sun, J., Dobashi, R., 2015. Flame propagation mechanisms in dust explosions. *Journal of Loss Prevention in the Process Industries*, 36, 186-194.

Goulay, F., Schrader, P.E., Michelsen, H.A., 2010. Effect of the wavelength dependence of the emissivity on inferred soot temperatures measured by spectrally resolved laser-induced incandescence. Appl. Phys. B Lasers Opt. 100, 655-663.

Japanese Industrial Standard, 2002. Test method for minimum explosible concentration of combustible dusts. JIS Z 8818.

Sundaram, D.S., Yang, V., Zarko, V.E., 2015. Combustion of nano aluminum particles (Review). *Combust. Explos. Shock Waves* 51, 173-196.

Wu, H. C., Ou, H. J., Hsiao, H. C., Shih, T. S., 2010. Explosion characteristics of aluminum nanopowders. Aerosol Air Qual. Res. 10, 38-42.

DOI: 10.7795/810.20200724

Minimum Ignition Energy of Coal Dust Clouds in air and O_2/CO_2 Atmospheres with Small Amount of CH_4/H_2

Dejian Wu [a, c, *], Arne Krietsch [a], Frederik Norman [b] & Martin Schmidt [a, *]

[a] Division 2.1 ‘‘Explosion Protection Gases and Dusts’’, BAM Federal Institute for Materials Research and Testing, Unter den Eichen 87, D-12205 Berlin, Germany

[b] Adinex NV, Brouwerijstraat 5/3, B 2200 Noorderwijk, Belgium

[c] State Key Laboratory of Fire Science, University of Science and Technology of China, Hefei 230026, PR China

E-mail: dejian.wu@bam.de ; martin.schmidt@bam.de

Abstract

MIKE 3 apparatus tests were conducted to investigate the minimum ignition energy (MIE) of coal dusts in air and O_2/CO_2 atmospheres with CH_4/H_2 below the gas lower explosion limit. Two coal dusts: Indonesian Sebuku (IS) coal and South African (SA) coal were tested. The O_2 mole fraction in the gas mixtures varied from 21% to 50% with the CH_4/H_2 mole fraction from 0 to 2%. Experimental results showed that the dust explosion risk increases significantly with increasing O_2 mole fraction by dramatically reducing the MIE for the tested coal dust clouds, and the presence of CH_4/H_2 further decreases the MIE, even by three orders of magnitude in mJ. For instance, The MIE of SA coal decreased from >1000 mJ in air to 1.7 mJ in the gas mixture of 50% O_2 in CO_2 with 2% H_2. Compared with the conventional combustion in air, the inhibiting effect of CO_2 was found to be even larger than the promoting effect of 2% CH_4/H_2 on the both coal samples by replacing the N_2 in air by CO_2. However, this inhibiting effect was comparatively small compared with 9% increase of O_2 mole fraction in oxy-fuel combustion atmosphere. This is the first time to study the ignition behaviour of hybrid mixtures in the O_2-enriched ambient and the oxy-fuel combustion system, thus helping to understand the ignition behaviour and the explosion risk of coal dust clouds in O_2/CO_2 atmospheres with the presence of flammable gases.

Keywords: *Ignition energy; Hybrid mixture; Oxygen rich; O_2/CO_2 ambient; MIKE 3 apparatus*

Introduction

Oxy-fuel combustion as one of the most promising technologies for carbon capture and storage has generated noticeable interests for newly built and retrofitted coal-fired power plants [1]. Instead of using air as the oxidizer, oxy-fuel combustion uses pure oxygen or a mixture of O_2 and recycled flue gas (mainly CO_2) to generate high-concentration CO_2 gas products for carbon capture and storage [1, 2]. Considering the ignition of combustible dust is of interest in the fields of industrial safety and a fundamental issue in combustion science and technology [3-7], attentions on safety concerns have also been drawn in this unconventional combustion system, including minimum ignition temperature of dust cloud (MITC) [2] and the self-ignition characteristics [8-13]. For instance, Wu *et al.* [2] investigated the ignition temperature of coal dust in oxy-fuel combustion atmospheres via the horizontal BAM apparatus and found that the MITC substantially decreases (even by 100 °C) with increasing oxygen mole fraction (X_{O_2}), but slightly increases by replacing N_2 in air with CO_2. Self-ignition and subsequent smouldering combustion behaviours of coal dust in this unconventional atmosphere were also systematically conducted by both experimental and numerical studies, including dust samples in the hot-oven basket [8-11] and dust layers on the hot-plate [8, 12, 13] scenarios. The key conclusions showed that ambient atmosphere has a significant influence on the self-ignition and smouldering characteristics of coal dusts, and the smouldering front as a hotspot, as

DOI: 10.7795/810.20200724

well as some flammable gases or pyrolysis gases (e.g., CH_4 and H_2) in the smouldering gas may pose a higher dust explosion risk in oxy-fuel combustion atmospheres. The gas and dust explosions caused by smouldering combustion was also pointed out by Eckhoff [14] and Dufaud *et al.* [15].

The ignition and explosion behaviours of the hybrid mixtures of flammable gas and combustible dust have attracted the attentions in the industrial safety community because of its potential fire and explosion hazards, i.e., the explosion can still occur when both dust and gas concentrations are lower than their own lower explosion limit values. The coupling ignition mechanism of hybrid mixtures has not been well studied. Most of the studies focused on the experimental observations of the ignition and explosion characteristics of the hybrid mixtures with different dusts, such as oil shale dust [16], biomass dust [17-19], metal dust [20-23], coal dust [24-29], and some other chemical dusts [30-31]. The general results revealed that hybrid mixture might have lower explosion sensitivities (including minimum ignition energy (MIE), MITC, lower explosion limit (LEL) and limiting oxygen concentration (LOC)) and higher explosion severities (including maximum explosion pressure, maximum rate of explosion pressure rise, as well as flame propagation velocity). Moreover, 5 different explosion regimes based on the concentration of each components in hybrid mixtures were proposed by Agrida *et al.* [30], i.e., dust driven explosion, dual fuel explosion, gas driven explosion, synergic explosion and no explosion. Bartknecht's curve [3] and Le Chatelier's line [32] were also extensively used to classify the synergic explosion region and no explosion region. Notes that except for the hot surface or hotspot ignition [33] and chemical ignitors, spark discharge [33, 34] including static spark, electrical spark and mechanical spark, is the most common ignition source used in the above literatures. The MIE is a key parameter to evaluate the explosion risk of combustible substances posed by the spark discharge. Extensive experiments have been performed to investigate the effects of test conditions on the MIE, including particle size [35], inert material [36, 37] and blend substances [38]. Randeberg *et al.* [35] found that MIE can be lower than 1 mJ for some nano dust particles, posing a technical challenge for dust explosion preventions. For instance, MIE of nano Ti powder was still as low as 2.1 mJ even with mixed with 90% Nano TiO_2 powder [36].

In the oxy-fuel combustion system, neither the increased risk of fires and dust explosions with increasing oxygen mole fraction posed by spark discharge, nor the effect of additional flammable gas from smouldering has been well studied. To fill this gap, this work thus aims to investigate the critical ignition characteristics of coal dusts posed by spark discharge in oxy-fuel combustion environments with presence of small amount of flammable gas. Firstly, MIKE 3 apparatus is used to determine the minimum ignition energy (MIE) of coal dust samples in air and O_2/CO_2 atmospheres with presence of small amount of CH_4 or H_2. By varying the ambient conditions (X_{O_2} , diluent gas and flammable gas) and test conditions (ignition delay and dust concentration), the MIEs were measured. Then based on the determined experimental data, empirical models are used to estimate the MIE of hybrid mixture of coal dust and flammable gas.

1. Experiments

1.1 Experimental materials

Two coal samples with different volatile matters: a sub-bituminous Indonesian Sebuku (IS) coal and a medium-volatile bituminous South African (SA) coal were tested in this study. Prior to each test, the dusts were first milled or sieved in order to obtain dust particles with a diameter < 63 μm, and then dried in a vacuum oven at 50 °C and pressure 0.1 bar until the moisture content was no more than 3% in mass basis. The particle size distributions of the prepared dusts are quite similar as shown in Fig. 1. The median values (d_{50}) of the particle size are 14.9 μm (IS coal) and 15.0 μm (SA coal), respectively. Table 1 shows the results of the proximate and ultimate analyses for these two coal samples. In general, the SA coal has more fixed carbon (FC) and less volatile matter (VM) (i.e. more mature or higher rank) than the IS coal on a dry basis. Moreover, their ash content, bulk densities, and heating values are similar.

DOI: 10.7795/810.20200724

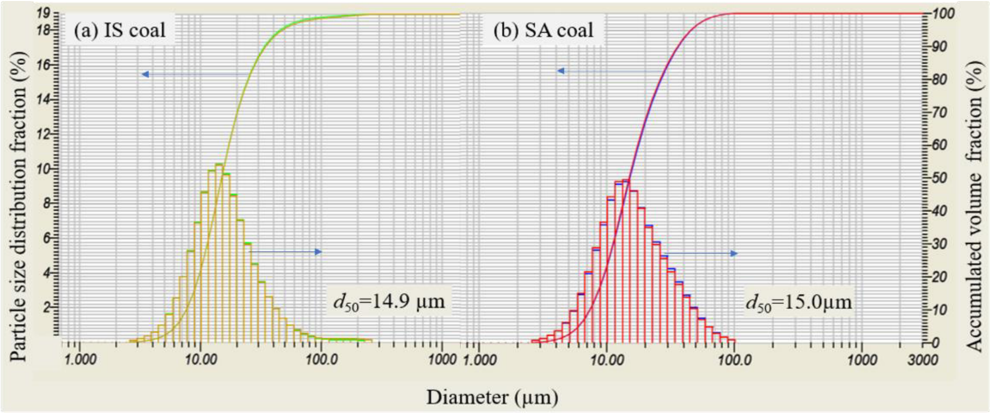

Fig.1. Particle size distributions of the tested coal samples: (a) IS coal; (b) SA coal.

Table 1 Properties of three coal dust samples.

Properties	Coal dust samples	
	IS (sub-bituminous)	SA (medium-volatile bituminous)
Proximate analysis		
Fixed carbon (%) (by diff.)	47.0	56.3
Volatile matter (%)	38.2	26.9
Moisture content (%)	3.0	2.7
Ash (%)	11.8	14.1
Ultimate analysis (on a dry basis)		
Carbon (%)	65.7	67.5
Hydrogen (%)	5.22	4.26
Nitrogen (%)	1.58	1.76
Sulphur (%)	0.31	0.44
Ash (%)	10.6	14.9
Oxygen (%) (by diff.)	16.59	11.58
Gross heating value (MJ/kg)	27.65	27.37
Bulk density of dry fuel (kg/m^3)	645±5	600±5

In this experiment, both air and O_2/CO_2 mixtures with various O_2 mole/volume fractions, X_{O_2} = 21, 30, 40 and 50 ± 1%, were used as ambient gases. To address the effect of small amount of flammable gases on the ignition behaviours of coal dusts, two flammable gases (i.e., methane and hydrogen) were used. These gases are the main components of the typical smouldering gas due to the self-ignition [9-12], and the properties of them are summarised in Table 2.

Table 2. Properties of flammable gas at 25°C and 1atm standard atmospheric conditions [6, 39, 40].

Properties	CH_4	H_2
In air		
Density, ρ (g/m^3)	660.0	89.9
Molecular weight, M (g/mol)	16	2
Stoichiometric coefficient, C_{stoi} (vol. %)	9.51	29.59
Adiabatic temperature rise, T_{ad} (K)	2225	2345
Laminar burning velocity	0.45	3
Thermal conductivity, λ (W/m/K)	0.035	0.186
Heat of combustion, ΔH (kJ/mol)	890.3	285.5
Specific heat capacity, c_p (kJ/kg·K)	2.238	14.440
Explosion range (vol. %)	4.4~17.0	4.0~77.0
Minimum ignition energy, MIE (mJ)	0.3	0.017
In pure oxygen		
Minimum ignition energy, MIE (mJ)	0.00027	0.0013

1.2 MIKE 3 apparatus test

The MIKE 3 apparatus was used to determine MIEs of the coal dusts with small amount of flammable gases in air and oxy-fuel combustion atmospheres. The experimental apparatus and procedure are according to the test procedures [41] and were similar with the description in Yuan *et al*. [36] and Hosseinzadeh *et al*. [38]. The explosion chamber contains of a vertical and cylindrical glass tube with inner diameter, height and volume of 68 mm, 300 mm and 1.2 L as shown schematically in Fig. 2. The dust dispersion system at the base of the tube is of the "mushroom-shaped" type around which the sample is loosely scattered. A blast of compressed air at 7-bar overpressure is used to disperse the dust samples to form a dust cloud in the glass cylinder where it is ignited by a spark between two electrodes with 6 mm as the gap space. The discharge energy initiating from a high voltage for the MIKE 3 tests can be performed at 1000, 300, 100, 30, 10, 3 and 1 mJ. The ignition delay (t_v) is defined as the time between the onset of dispersion of the dust sample into a cloud and the occurrence of the spark discharge, and it can be adjusted as 60, 90, 120, 150 and 180 ms. Inductance can be set at 0 or 1 mH. Considering the most conservative or lowest ignition energy is determined with inductance, 1 mH was used in this work. According to the recommendation in manual of MIKE 3, the amount of dust samples (m) 300, 600, 900, 1200, 1500, 1800, 2400 and 3000 mg were used. The approach of how the MIE of both single dust and gas-dust hybrid mixtures was referred by Addai's work [37].

For a given dust sample in a certain ambient atmosphere with a fixed amount of flammable gas, the lowest electrical energy can be obtained by varying the amount of the dust sample and the ignition delay. In other words, the MIE (E_s) lies between the energy (E_1) at which in at least 10 successive tests with no ignition and the lowest energy value (E_2) at which ignition occurred at least once for each concentration and each ignition delay, i.e., E_1 < MIE < E_2. Fig. 3 gives examples of the MIE determination for IS coal in 30% O_2 in CO_2 with 2% H_2 and SA coal in 40% O_2 in CO_2 with 2% CH_4. It shows that 900 mg IS coal and 1500 mg SA coal ignited with ignition delay of both 90 ms and 120 ms, but MIEs of the two dust samples fell in the lower range with ignition delay of 90 ms: 30 mJ < MIE <100 mJ for IS coal (see Fig. 3a) and 3 mJ < MIE <10 mJ for SA coal (see Fig. 3b). Therefore, 90 ms was taken as the correpsonding ignition delay obtained the MIEs for both dust samples.

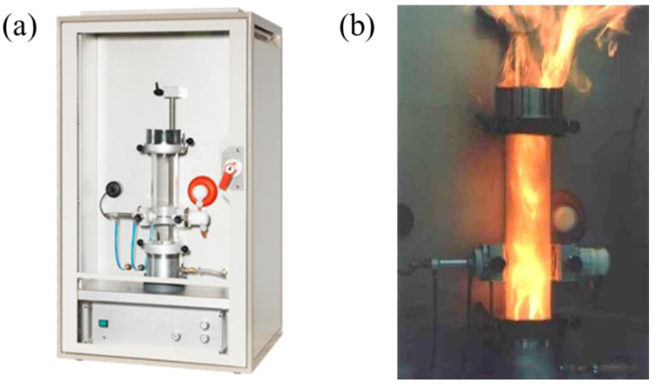

Fig. 2. The MIKE III apparatus: (a) schematic diagram, and (b) instant of ignition.

The MIE is usually stated as a range of values rather than a single value. But for the convenience of comparison the MIE determined at the different conditions, a single value of MIE is used. This value can be roughly estimated using the probability of ignition as expressed below [41]:

$$\mathrm{lgMIE} = \lg E_2 - I[E_2] \cdot \frac{(\lg E_2 - \lg E_1)}{(NI+I)[E_2]+1} \tag{1}$$

where $I[E_2]$ represents the number of runs with successful ignition at E_2 and $(NI+I)[E_2]$ stands for the total number of tests at the energy level of E_2. At least 5 concentrations need to be investigated to calculate the probability of ignition. For instance, the MIEs were measured and estimated as 55 mJ for IS coal in 30% O_2 in CO_2 with 2% H_2 and 8 mJ SA coal in 40% O_2 in CO_2 with 2% CH_4 as shown in Fig. 3.

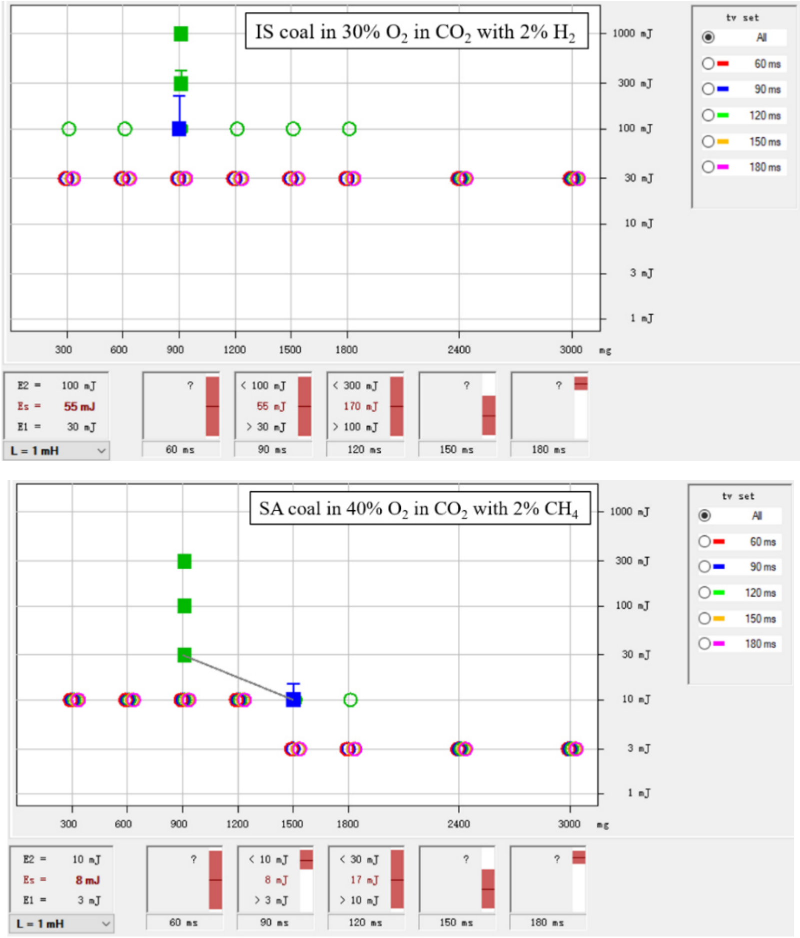

Fig. 3. Determination of the MIE for: (a) IS coal in 30% O_2 in CO_2 with 2% H_2, and (b) SA coal in 40% O_2 in CO_2 with 2% CH_4.

2. Theories for spark ignition and MIE of hybrid mixtures

2.1 Spark ignition

Ignition from a spark or an arc between two metallic electrodes can be caused by two methods [6]: (1) by applying a sufficiently large voltage across electrodes held a fixed distance apart, usually used in the research studies; (2) by switching on or off and electric contact, which extensively exists in actual industrial ignition scenarios. Minimum ignition energy as one of the most important safety parameters for explosion prevention, is defined as the lowest energy value of a high-voltage capacitor discharge that is capable to ignite a combustible cloud. The flame kernel has been introduced to explain how spark can lead to an ignition. A spark raises a small volume of gas to a very high temperature so that the fuel (e.g., gas or dust) within the volume can be burned. This flame kernel will proceed to grow if the heat that is released from fuel combustion exceeds the heat losses from this volume. As a consequence, there exists a minimum size of kernel flame to maintain the self-sustained propagation, i.e., heat release/loss ratio is equal to 1. The heat release is proportional to the volume of the kernel, but the heat losses are proportional to its surface area. Obviously, the higher spark energy, the bigger size of the initial flame kernel is. More details about spark ignition theory can be found in Lewis and von Elbe [42].

2.2 Ignition kinetics of hybrid dust-gas mixtures

Ignition of coal dust particles is a complex interaction phenomenon among different mechanisms including heat and mass transfer, evaporation, devolatilization, heterogeneous oxidation on the particle surface, and volatiles oxidation in the gas-phase [4]. The presence of flammable gas may make this ignition process more complex and uncertain. The possible reaction pathways for the ignition of dust clouds are proposed in Fig. 4 based on the heterogenous ignition of hydrocarbon solid

DOI: 10.7795/810.20200724

fuels [9, 29]. With increasing ignition temperature or spark energy, both the rates of heterogeneous reactions on the particle surface and the homogenous reactions in the gas phase are increased. In general, the combustion process of dried hydrocarbon dust undergoes four steps as shown in Eqs. (2) ~ (5). These parallel and competitive equations are critical steps of the ignition process and thus the MIE, affected by the dust physico-chemical properties and ambient conditions. For instance, the addition of extra flammable gases may have a strong impact on the ignition kinetics according to Eqs. (6) & (7). The combustion of flammable gases in the gas-phase is faster than that of dust on the particle surface [15], i.e., combustion timescale in gas-phase is smaller, so the concentration and type of the flammable gas may also affect the ignition process of dust. Moreover, the increased oxygen mole fraction in oxy-fuel combustion atmospheres can directly or indirectly promote all the reactions listed from Eqs. (2) ~ (7).

$$C_xH_yO_z \cdot H_2O \cdot \text{Ash} + O_2 \rightarrow CO_2 + CO + H_2O + \text{Ash} \tag{2}$$

$$C_xH_yO_z \cdot H_2O \cdot \text{Ash} \xrightarrow{\text{heating}} \text{Char} \cdot \text{Ash} + \text{Volatile}\ (CH_4,\ H_2\ \text{etc.}) \tag{3}$$

$$\text{Char} \cdot \text{Ash} + O_2 \rightarrow CO_2 + CO + \text{Ash} \tag{4}$$

$$\text{Volatile} + O_2 \rightarrow CO_2 + CO + H_2O \tag{5}$$

$$CH_4 + 2O_2 + 7.52N_2 \rightarrow CO_2 + 2H_2O + 7.52N_2 \tag{6}$$

$$H_2 + 0.5O_2 + 1.88N_2 \rightarrow H_2O + 1.88N_2 \tag{7}$$

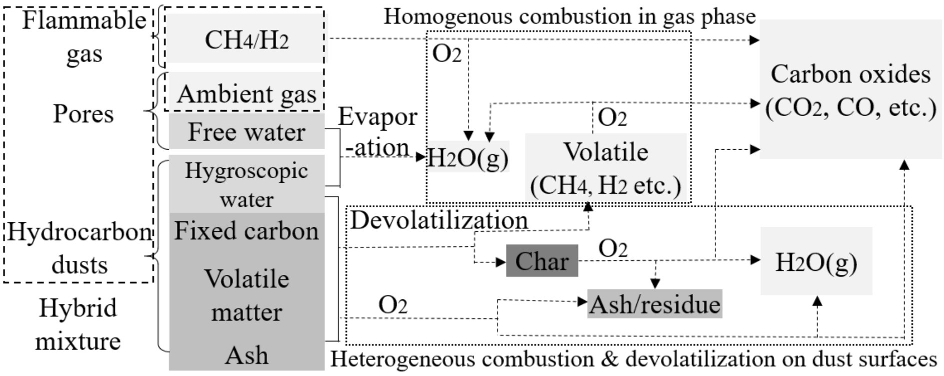

Fig. 4. Proposed reaction pathways proceeding in the combustion of hydrocarbon dust clouds with the presence of CH_4/H_2.

3. Results and discussion

3.1 Effect of O_2 mole fraction and diluent gas

Fig. 5 shows the influence of the oxygen mole fraction on the MIE for the coal samples (hereinafter, solid dot denotes ignition, hollow dot denotes no ignition and cross represents no ignition for all. The MIE value is supposed to be > 1000 mJ, when not ignition is found at 1000 mJ). Clearly, the determined MIE is classified into 8 different regions by the spark energy of 1, 3, 10, 30, 100, 300 and 1000 mJ. Notes that in this work no MIE data have been found in the <1 mJ region that was not shown in Fig. 5. The details of the point MIE data based on Eq. (1) under different atmosphere conditions are summarized in Table 3. The results indicate that the mole fraction of oxygen has a strong influence on the MIE, showing an asymptotic function correlation with arbitrarily exponential fittings. As X_{O_2} increases from 21% to 30%, the MIEs sharply decrease from the range of no ignition (MIE >1000 mJ) to ignition range for the both coal dusts, while this trend becomes moderate and smooth as further X_{O_2} increasing from 40% to 50%. It was visually observed that the deflagration in the glass tube (see Fig. 2b) was more violent with brighter flame, faster flame propagation and shorter ignition delay at elevated oxygen mole fractions. Similar phenomena were also observed in our previous MITC test in BAM apparatus [2]. The above observations suggest both ignition sensitivity and explosion severity

DOI: 10.7795/810.20200724

of coal dusts strengthen in elevated oxygen atmospheres. In addition, the MIE of IS coal is always lower than SA coal under the same test conditions, agreeing with the determined MITC results in [2]. The reason is probably that IS coal has a higher percentage of volatile matter (see Table. 1) which facilitates homogeneous ignition, which was verified in our previous work [2]. Fig. 5 also shows that the effect of the oxygen mole fraction on the MIE of SA coal is stronger when the O_2 mole fraction in CO_2 increases from 30% to 40%, because it has a three-level decrease, i.e., from the range between 300 to 100 mJ decreasing to the range between 10 to 30 mJ. However, the maturity of coal or volatile matter plays a little role when X_{O_2} is higher than 40%. This finding is supported by the experimental work of Zhang *et al.* [43, 44].

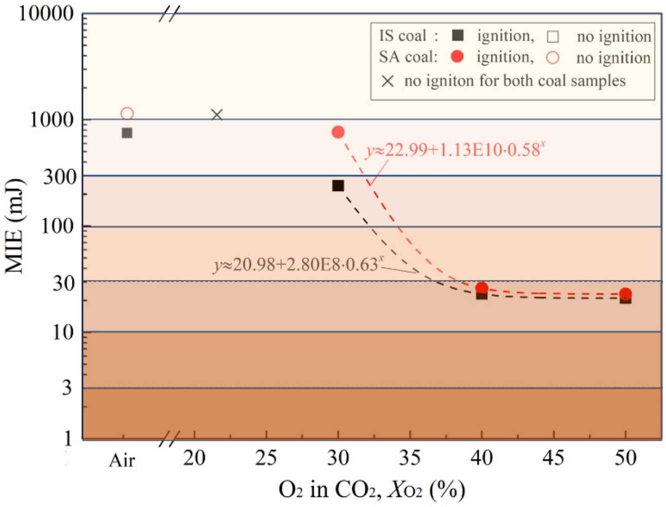

Fig. 5. MIEs of two samples at different atmospheres with various oxygen mole fractions.

Table 3 Measured MIEs (mJ) in the MIKE III apparatus for two coal dusts under different ambient conditions.

Ambient condition				IS					SA				
				Flammable gas concentration					Flammable gas concentration				
	X_{O2} (%)	X_{CO2} (%)	X_{N2} (%)	0	CH_4		H_2		0	CH_4		H_2	
					1%	2%	1%	2%		1%	2%	1%	2%
Air	21	0	79	740	173	74	87	66	>1000	>1000	240	>1000	256
O_2/CO_2	21	79	0	>1000									
Mixture	30	70	0	240	81	78	208	87	768	548	261	740	79
	40	60	0	23	21	17	21	9	26	21	8	23	7
	50	50	0	21	8	7	8	5	23	5	2.6	2.5	1.7

On the other hand, as the ambient condition was shifted from air to 21% O_2 /79% CO_2, the MIE of IS coal increase from ignition region to non-ignition region. The result implies that the effect of CO_2 is stronger than that of N_2 as a diluent gas or an inert gas for coal dusts. Similar phenomena were observed for other ignition sensitivities including the LOC [5] and MITC [2]. This is probably because the O_2 diffusivity in CO_2 is lower than in N_2 and CO_2 has a larger heat capacity than N_2 [1]. Unlike the finding of MITCs, the MIEs in 30% O_2/70% CO_2 are distinctly lower than the values in air for both IS and SA coals. This suggests that the inhibiting effect of CO_2 is lower than the promoting effect of 9% increment of X_{O_2} for the spark ignition, but they are comparable for the hot surface ignition.

3.2 Effect of small amount of flammable gas

Table 3 also lists the MIE data of the two coal samples under different ambient conditions with the presence of small amount of CH_4 and H_2 (1% and 2%). The corresponding dust mass (m) and spark ignition delay (t_v) used to obtain the MIEs summarised in Table 3 for IS and SA coal are listed in Table 4 and Table 5, respectively. Fig. 6 presents an example of effect of the presence of small amount CH_4 on the MIEs for SA coal in 40% O_2 /60% CO_2 atmosphere. It clearly shows that not only the value of determined MIEs, but also both the corresponding ignition delay and the dust concentration vary with varying the mole fraction of addition flammable gas. Table 4 and 5 show that most of the MIEs obtained at 900 mg (or 1200 mg) dust and 120 ms ignition delay for the both coal samples, but there are several exceptional data (in *italic*). The variation of m and t_v is probably caused by the ignition mechanism of the hybrid dust-gas mixtures. Generally, the ignition mechanism of combustible dusts is synergistically controlled by the properties of dust samples (e.g., particle size and volatile content), ambient conditions (e.g., oxygen mole fraction, diluent gas and temperature rise rate). Furthermore, the introduction of flammable gas makes it more complicated due to the parallel and competitive reactions in gas phase and their subsequent effects (see Fig. 4). The ignition mechanism will be further studied in future works.

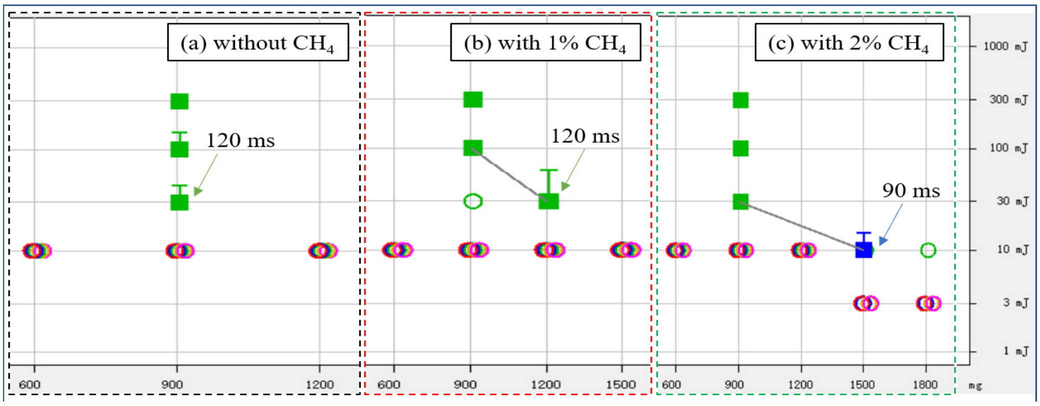

Fig. 6. SA coal dust in 40% O_2 /60% CO_2 atmosphere with/without small amount of CH_4.

Table 4 The corresponding amount of dust (m, mg) and spark ignition delay (t_v, ms) at the measured MIEs in Table 3 for IS coal under different ambient conditions.

Ambient condition				Flammable gas mole fraction										
	X_{O2} (%)	X_{CO2} (%)	X_{N2} (%)	without flammable gas		CH_4				H_2				
						1%		2%		1%		2%		
				m	t_v	m	t_v	m	t_v	m	t_v	m	t_v	
Air	21	0	79	-	-	900	120	900	120	900	90	900	180	
O_2/CO_2 Mixture	21	79	0					-						
	30	70	0	900	120	*2400*	*90*	900	120	1200	120	900	90	
	40	60	0	1200	120	1200	120	900	120	1200	120	*3000*	*180*	
	50	50	0	900	120	1500	90	900	120	900	120	900	150	

Table 5 The corresponding amount of dust (m, mg) and spark ignition delay (t_v, ms) at the measured MIEs in Table 3 for SA coal under different ambient conditions.

Ambient condition				Flammable gas mole fraction										
	X_{O2} (%)	X_{CO2} (%)	X_{N2} (%)	without flammable gas		CH_4				H_2				
						1%		2%		1%		2%		
				m	t_v	m	t_v	m	t_v	m	t_v	m	t_v	
Air	21	0	79	-	-	-	-	900	120	-	-	900	60	
O_2/CO_2 Mixture	21	79	0					-						
	30	70	0	1200	60	900	120	900	120	900	120	1200	120	
	40	60	0	900	120	1200	120	*1500*	*90*	1200	120	1200	90	
	50	50	0	900	120	900	120	*2400*	*150*	*1800*	*150*	1200	150	

Figs. 7 and 8 show the trend of MIEs under different ambient conditions with the presence of CH_4/H_2 (0~2%) for IS and SA coal, respectively. At first, the addition of flammable gas significantly lowers the MIE of both coal samples as a general trend, and this trend becomes more distinct with a higher mole fraction of both CH_4 and H_2. For example, no ignitions were found for the SA coal until the mole fraction of the additional flammable gases reach 2% as shown in Fig. 8 and Table 3. Moreover, when air was replaced by the atmosphere of 21% O_2 /79% CO_2, no ignitions could be found at all for all the mixtures of both coal samples even with 2% CH_4 or H_2 (see the sign of "×" in Figs. 7 and 8). This suggests that the inhibition effect of CO_2 is stronger than the promotion effect of the presence of flammable gas. In fact, the MIE of flammable gas is also strongly influenced by CO_2 as the diluent gas, due to its higher specific heat capacity and the lower diffusivity of O_2 and CH_4 or H_2 in CO_2.

DOI: 10.7795/810.20200724

However, with increasing O_2 mole fraction, all the MIEs decrease dramatically following the similar asymptotic function trend. Notes that at the atmosphere of 30% O_2 in CO_2, all the mixtures with the 1% or 2% flammable gas ignited for the both coal samples, might suggesting that the effect on MIEs follows: 10% increment of X_{O_2} (promotion) > diluent gas CO_2 (inhibition) > the present of 1% (or 2%) CH_4 or H_2 (promotion).

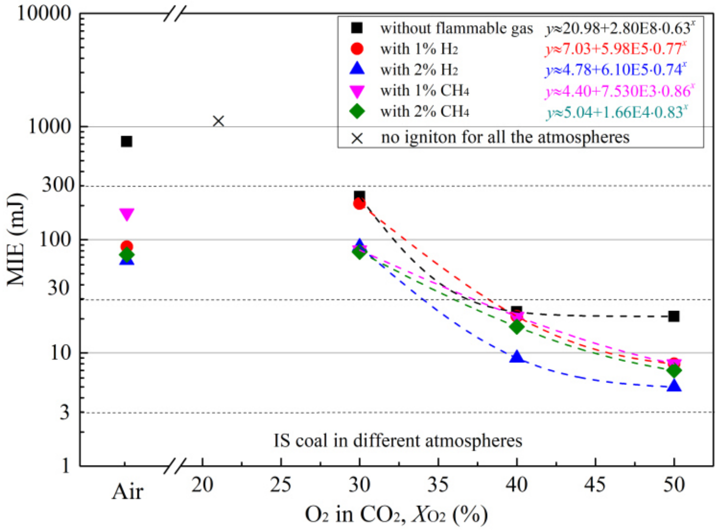

Fig. 7. MIEs of IS coal dust in air and O_2/CO_2 atmospheres with/without flammable gas.

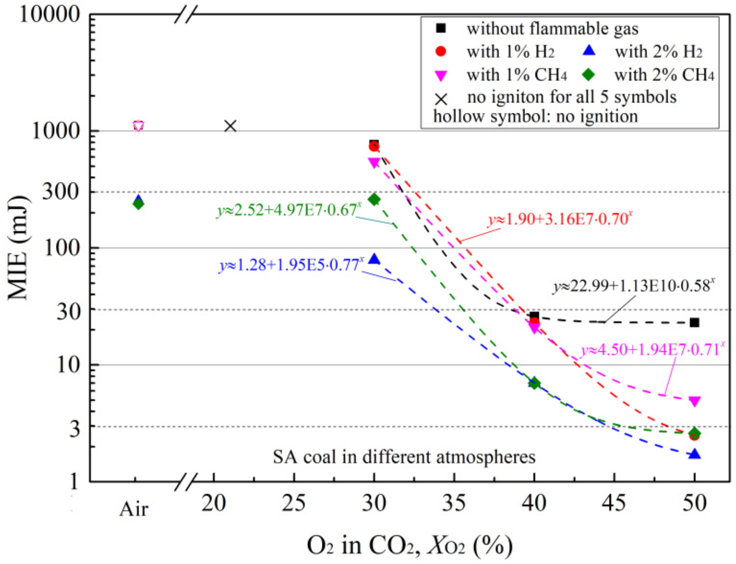

Fig. 8. MIEs of SA coal dust in air and O_2/CO_2 atmospheres with/without flammable gas.

As we discussed above, the effect of volatile content reduces with increasing X_{O_2}, and the MIE of IS coal is always lower than the MIE of SA coal under the same conditions in the most of cases (see Table 3). Interestingly, there are clear reversions of the MIE at the atmosphere of 50% O_2 in CO_2 with CH_4 or H_2, i.e., the MIE of SA coal is abnormally lower than the MIE of IS coal, falling in the region between 1 and 3 mJ. There are reasons more likely to contribute this unconventional phenomenon. On the one hand, with further increasing of X_{O_2}, the direct oxidation on the particle surface Eq. (2) is substantially strengthened, while the devolatilization reaction Eq. (3) is independent with X_{O_2}, but depends on heating rate. The following reactions Eqs. (4) and (5) are limited or controlled by Eq. (3) as shown in Fig. 4. Therefore, the heterogenous reaction dominants the dust ignition. On the other hand, the gas phase reaction rate of Eqs. (6) or (7) increases with higher X_{O_2}, releasing heat faster to heat up the dust particle, then promoting the Eqs. (2) and (3). The diluent and the diffusion effects of

CH_4 or H_2 are ignorable, and the flammable gas itself cannot be ignited directly considering the amount of them is very low. Thus, the main promotion effect of flammable gas is heating effect during the ignition process of dust clouds. Normally, the characteristic reaction time in gas phase is much shorter than the heterogenous reaction on the surface of dust particle, the synergetic effects of increasing X_{O_2} and addition of flammable gas may change the scenario that the coal with higher volatile has a lower MIE. In addition, the volatile (mainly CH_4) can be ignited soon, especially with the adding of H_2, i.e., the presence of H_2 not only has the above-mentioned heating effect, but also has the promoting effect on CH_4 combustion. This is probably the reason why at high X_{O_2} (40% or 50%), the presence of H_2 has a lower MIE for both coal samples as summarised in Table 3.

4. Conclusions

In this work, a series of experimental investigation of the minimum ignition energy (MIE) of two coals in air and O_2/CO_2 atmospheres with addition of CH_4/H_2 was systematically performed via MIKE 3 apparatus. Experimental results of the MIEs under different conditions were presented to provide data and an experimental basis for the evaluation and prevention of coal dust explosion risks resulting from spark discharge. The Results showed that the dust explosion risk increases dramatically with increasing O_2 mole fraction from 21% to 50% for the two coal samples due to substantial reductions of MIEs: shifting from >1000 mJ region to 10 mJ< MIE <30 mJ region. Moreover, the present of CH_4/H_2 further decreased the MIE even falling in the region between 1 mJ and 3 mJ for SA coal sample, suggesting a very high dust explosion hazard with spark discharge. Compared with N_2, CO_2 had a comparatively large retardation effect for the ignition behaviour coal dusts in the spark ignition apparatus, and this effect was found to be even larger than 2% promoting effect of CH_4/H_2. This insight is of high value for the assessment and prevention of dust explosions in oxy-fuel combustion systems, as well as for fundamental studies on the ignition behaviour of combustible solid dust clouds, especially considering the presence of small amount of flammable gas.

Acknowledgements

The authors gratefully acknowledge Mr. Alexander Przybilski (BAM) for assistance running the experiments and Dr. Enis Askar (BAM) for mixture gas installations. D. Wu gratefully acknowledge the financial support from the opening project of State Key Laboratory of Fire Science (No. HZ2019-KF04), University of Science and Technology of China and the opening project of State Key Laboratory of Explosion Science and Technology (No. KFJJ19-14M), Beijing Institute of Technology.

References

[1] L. Chen, S.Z. Yong, A.F. Ghoniem. Oxy-fuel combustion of pulverized coal: Characterization, fundamentals stabilization and CFD modelling, Prog. Energy Combust. Sci, 38(2012) 156-214.
[2] D. Wu, F. Norman, F. Verplaetsen, E. Van den Bulck. Experimental study on the minimum ignition temperature of coal dust clouds in oxy-fuel combustion atmospheres, J. Hazard. Mater. 307(2016) 274-280.
[3] W. Bartknecht, Dust Explosions: Course Prevention Protection, Springer, 1989.
[4] R.H. Essenhigh, M.K. Misra, D.W. Shaw. Ignition of coal particles: a review, Combust. Flame. 77(1989) 3-30.
[5] R. Eckhoff, Dust Explosions in the Process Industries, third ed., Gulf Professional Publishing, Amsterdam, 2003.
[6] V. Babrauskas, Ignition Handbook, Fire Science Publishers, Washington, 2003.
[7] T. Abbasi, S.A. Abbasi, Dust explosions – Cases, causes, consequences and control, J. Hazard. Mater. 140(2007) 7-44.
[8] D. Wu, X. Huang, F. Norman, F. Verplaetsen, J. Berghmans, E. Van den Bulck, Experimental investigation on the self-ignition behaviour of coal dust accumulations in oxy-fuel combustion system, Fuel, 160(2015) 245-254.
[9] D. Wu, M. Schmidt, X. Huang, F. Verplaetsen. Self-ignition and smouldering characteristics of coal dust accumulations in O_2/N_2 and O_2/CO_2 atmospheres, Proc. Combust. Inst. 36(2017) 3195-3202.
[10] D. Wu, F. Norman, M. Vanierschot, F. Verplaetsen, J. Berghmans, E. Van den Bulck. Self-heating characteristics of coal dust deposits by a hot gas flow in oxy-fuel atmospheres, Appl. Therm. Eng. 131(2018) 947-957.
[11] D. Wu, F. Norman, M. Schmidt, M. Vanierschot, F. Verplaetsen, J. Berghmans. Numerical investigation on the self-ignition behaviour of coal dust accumulations: the roles of oxygen, diluent gas and dust volume, Fuel 188(2017) 500-510.

[12] D. Wu, M. Vanierschot, F. Verplaetsen, J. Berghmans, E. Van den Bulck. Numerical study on the self-ignition behaviour of coal dust layers in O_2/CO_2 atmospheres, Appl. Therm. Eng. 109(2016) 709-7147.
[13] D. Wu, Z. Song, M. Schmidt, Q. Zhang, X. Qian. Theoretical and numerical study on ignition behaviour of coal dust layers on a hot surface with corrected kinetic parameters, J. Hazard. Mater. 368(2019) 156-162.
[14] Eckhoff R.K. Gas and Dust Explosions Caused by Smouldering Combustion in Powder Layers and Deposits, Explosion Hazards in the Process Industries, 2nd Edition, 2016.
[15] O. Dufaud, L. Perrin, M. Traoré. Dust/vapour explosions: hybrid behaviours? J. Loss Prev. Process Ind. 21(2008) 481-484.
[16] L. Yu, G. Li, W. Liu, J. Yu, C. Yuan. Experimental investigations on ignition sensitivity of hybrid mixtures of oil shale dust and syngas, Fuel 210(2017) 1-7.
[17] I. Khalili, O. Dufaud, M. Poupeau, L. Perrin. Ignition sensitivity of gas-vapor/dust hybrid mixtures, Powder Tech. 217 (2012) 199-206.
[18] R. Sanchirico, A.D. Benedetto, G.A. Agreda, P. Russo. Study of the severity of hybrid explosions and comparison to pure dust-air and vapour-air explosions, J. Loss Prev. Process Ind. 24 (2011) 648-655.
[19] Q. Zhang, R. Tan. Effect of aluminum dust on flammablility of gaseous epoxypropane in air, Fuel 109(2013) 647-652.
[20] R. Sanchirico, P. Russo, A. Saliva, A. Doussot, V. D. Sarli, A. D. Benedetto. Explosion of lycopodium-nicotinic acid–methane complex hybrid mixtures, J. Loss Prev. Process Ind. 36 (2015) 505-508.
[21] Denkevits, A., Hoess, B. Hybrid H_2/Al dust explosions in Siwek sphere, J. Loss Prev. Process Ind. 36(2015) 509-521.
[22] Y. Cheng, S. Song, H. Ma, J. Su, T, Han, Z. Shen, X. Meng. Hybrid H_2/Ti dust explosion hazards during the production of metal hydride TiH_2 in a closed vessel, Int. J. Hydrogen Eng. 44(2019)11145-52.
[23] X. Yu, J. Yu, X. Zhang, W. Ji, X. Lv, Y. Hou, Z. Li, X. Yan. Combustion behaviours and residues characteristics in hydrogen/aluminium dust hybrid explosions, Process Saf. Environ. 134 (2020) 343-352.
[24] E.K. Addai, D. Gbel, M. Kamal, U. Krause. Minimum ignition energy of hybrid mixtures of combustible dusts and gases, Process Saf. Environ. 102(2016) 503-512.
[25] Amyotte P., Mintz. K., Pegg M., Sun Y. The ignitability of coal dust/air and methane/coal dust/air mixtures, Fuel 72(1993) 671-679.
[26] E.K. Addai, M. Clouthier, P. Amyotte, M. Safdar, U. Krause. Experimental investigation of limiting oxygen oncentration of hybrid mixtures, J. Loss Prev. Process Ind. 57(2019) 120-130.
[27] Y. Song, Q. Zhang. Multiple explosions induced by the deposited dust layer in enclosed pipeline, J. Hazard. Mater. 371(2019) 423-432.
[28] P. Zhao, X. Tan, M. Schmidt, A. Wei, W. Huang, X. Qian, D. Wu. Minimum explosion concentration of coal dusts in air with small amount of $CH_4/H_2/CO$ under 10-kJ ignition energy conditions, Fuel 260(2020), 116401.
[29] X. Tan, M. Schmidt, P. Zhao, A. Wei, W. Huang, X. Qian, D. Wu. Minimum ignition temperature of carbonaceous dust clouds in air with $CH_4/H_2/CO$ below the gas lower explosion limit, Fuel 263(2020)116811.
[30] A. Agreda, A. Benedetto, P. Russo, E. Salzano, R. Sanchirico. Dust/gas mixtures explosion regimes, Powder Tech. 205(2011) 81-86.
[31] O. Dufaud, L. Perrin, M. Traore, S. Chazelet, D. Thomas, Explosions of vapour/dust hybrid mixtures: a particular class, Powder Tech. 190(2009) 269-273.
[32] I. Glassmann, R. Yetter. Combustion, Elsevier Inc. 2008.
[33] Y. Bu, C. Yuan, P. Amyotte, C. Li, J. Cai., G. Li. Ignition hazard of non-metallic dust clouds exposed to hotspots versus electrical sparks, J. Hazard. Mater. 365(2019) 895-904.
[34] Y. Song, Q. Zhang. Criterion and propagation process of spark-induced dust layer explosion, Fuel 367(2020) 117205.
[35] E. Randeberg, R. Eckhoff. Measurement of minimum ignition energies of dust clouds in the <1 mJ region, J. Hazard. Mater. 140 (2007), 237-244.
[36] C. Yuan, P.R. Amyotte, M.N. Hossain, C. Li. Minimum ignition energy of nano and micro Ti powder in the presence of inert nano TiO_2 powder, J. Hazard. Mater. 274(2014) 322-330.
[37] E.K. Addai, D. Gbel, U. Krause. Experimental investigations on the minimum ignition energy and the minimum ignition temperature of inert and combustible dust cloud mixtures, J. Hazard. Mater. 307 (2016) 303-311.
[38] S. Hosseinzadeh, F. Norman, F Verplaetsen, J. Berghmans, E. Van den Bulck. Minimum ignition energy of mixtures of combustible dusts, J. Loss Prev. Process. Ind., 36(2015) 92-97.
[39] E. Brandes, W. Möller. Safety Characteristic Data, Volume 1: Flammable Liquids and Gases, Wirtschaftsverlag NW, Bremerhaven (2008).
[40] Transport properties calculator, http://navier.engr.colostate.edu/~dandy/code/code-2/.
[41] CEN, 2003. Potentially Explosive Atmospheres, Explosion Prevention and Protection, Determination of Minimum Ignition Energy of Dust/air Mixtures, European Standard EN 13821. European Committee for Standardization, Brussel.
[42] B. Lewis, G. von Elbe. Combustion, flames and explosions in gases, 3rd ed., Academic Press, Orlando 1987.
[43] D. Zhang, T. Wall, D. Harris, I. Smith, J. Chen, B. Stanmore. Experimental studies of ignition behaviour and combustion reactivity of pulverized fuel particles, Fuel 71(1992) 1239-1246.
[44] D. Zhang, T.F. Wall. An analysis of the ignition of coal dust clouds, Combust. Flame. 92(1993) 475-480.

DOI: 10.7795/810.20200724

Modelling of detonation flows in inhomogeneous gas particle suspensions within the framework of the reduced kinetics

Tatyana Khmel & Sergei Lavruk

Khristianovich Institute of Theoretical and Applied Mechanics SB RAS,

630090, Novosibirsk, Russia

E-mail: khmel@itam.nsc.ru

Abstract

A physical and mathematical model of the reduced kinetics is presented describing heterogeneous detonation in suspensions non-uniform in particle concentration. The model is based on the heterogeneous media approaches, semi-empirical laws of ignition and combustion, and data on the dependence of the detonation velocity on particle concentration. Formation of suboxides and incomplete combustion of aluminum are taken into account integrally. The dependence of the heat release of chemical reactions and the fraction of unburnt particles on the initial composition is determined from the solution of the stationary problem of the structure of the detonation wave. In the calculations of unsteady detonation flows, it is supposed to solve an additional equation for the spatial distribution of initial concentrations. The problems of initiation and development of cellular detonation in suspensions of micron-sized and submicron aluminum particles in flat channels in the presence of particle concentration gradients are considered. The flow patterns of cellular structures, the forms of the leading front, and the propagation velocities are analyzed.

Keywords: *detonation, gas particle suspensions, reduced kinetics, concentration gradients, numerical modelling*

1. Introduction

Investigation of the explosive characteristics of reactive particle powders is of interest both in terms of safety and in connection with the development of detonation technologies. Aluminum powders are widely used in industry, and ultrafine aluminum particles represent great prospects for use as part of mixed fuels in detonation combustion devices.

Theoretical and numerical studies of detonation processes in gas suspensions, supplementing experimental observations, are of great importance, since experiments are expensive and their possibilities are limited. In nature and in industrial facilities, dangerous accumulations of solid particles, formed, in particular, as a result of the lifting of particles and dispersion of dense layers, are inhomogeneous. The problems of combustion and detonation of inhomogeneous gas mixtures were analyzed by Fomin et al. (2001), Li et al. (2015), Chengken et al. (2017), Prokhorov (2017), Boulal et al. (2016). For two-phase dispersed media, these problems were considered in a very few works on combustion and detonation in aerosols (Smirnov et al. (2007), Smirnov et al. (2015)) and in the problems of lifting, ignition, and detonation-like combustion of dust layers (Korobeinikov et al. (2002), Semenov et al. (2013), Houim & Oran (2015), Kei & Matsuo (2019)). The spatial heterogeneity of the inert discrete component was taken into account in works by Kratova & Fedorov (2014) and Fedorov & Kratova (2015) when studying problems of suppressing detonation by clouds of particles.

In theoretical studies of heterogeneous detonation various kinetic models are used to describe chemical interactions. The main factors hindering the development of detailed kinetics models are the difficulties of their implementation, in particular, due to the presence of physical features (finite particle size, the presence of an oxide film) that do not allow the use of these models directly. For example, a detailed model of kinetic combustion of aluminum particles is presented by Starik et al. (2015), but its use is limited by particle sizes up to 20 - 40 nanometers.

Semi-empirical models based on the reduced kinetics are based on the experimental data available in the literature on the combustion of single particles or a combination of particles under various conditions, including behind shock waves, as well as on experimental data or thermodynamic calculations of equilibrium detonation parameters.

Models of heterogeneous detonation of suspensions of aluminum particles in oxygen, air, and reactive gas media were developed by Fedorov (1992), Veyssiere & Khasainov (1991), Fedorov et al. (1999), Zhang et al. (2009). Khmel & Fedorov (2018) and Khmel et al. (2018) expanded the model of detonation of aluminum suspensions in oxygen to the submicron and nanometer range of particle sizes. The constants of the reduced kinetics model of detonation in aluminum nano-sized particle suspensions were determined from experimental data presented by Sundaram et al. (2015) and Bazyn et al. (2006). The dependences of the burning time on the pressure and temperature of the surrounding gas, the fraction of the oxidizing agent, and the particle diameter were taken into account. Khmel & Fedorov (2018) analyzed stationary detonation structures in particle suspensions of 50 nm - 250 nm, which showed some differences from similar structures in micron-sized mixtures, in particular, very short zones of thermal and velocity relaxation with respect to the combustion zone. A strong dependence of the combustion zone on the amplitude of the leading shock wave was also established. Khmel (2019) showed that these properties cause an increase in the irregularity of cellular structures. Khmel et al. (2018) proposed interpolation formulas for constants in the intermediate interval of particle diameters from 200 nm to 1 μm: the activation energy, the power degree in the dependence of the reaction rate on the pressure of the surrounding gas, and the pre-exponent factor. Such an approach describes the transition regime of combustion of aluminum particles from the diffusion-limited regime of large micro-sized particles to the kinetic regime of combustion of nanoparticles. Zhang et al. (2009) proposed a different approach for describing the ignition and combustion of submicron aluminum particles based on the use of the equation of hybrid kinetics, including both reactions: diffusion combustion and kinetic Arrhenius reaction. This model was applied in aluminum detonation studies by Briand et al. (2010), Khasainov et al. (2013), Teng & Jiang (2013), Hosoda et al. (2013).

Fedorov & Khmel (2005), Briand et al. (2010) Benkewicz & Hayashi (2003), Hosoda et al. (2013) performed a numerical simulation of two-dimensional flows of cellular detonation in mixtures of aluminum particles with oxygen or air within the framework of reduced kinetics models. Fedorov et al. (2010), Kratova et al. (2016), Fedorov et al. (2018) obtained data on the critical propagation conditions of heterogeneous detonation in volumes of varying geometry. Kratova & Fedorov (2014), Fedorov & Kratova (2015) determined the modes and conditions for suppressing detonation in oxygen suspensions of aluminum particles by clouds of inert particles. In the above detonation studies, mixtures of particles uniformly distributed throughout the volume were considered. However, the problems of explosion safety and analysis of the behavior of powders in dynamic conditions cannot be limited only to models of homogeneous gas suspensions.

Known experimental dependences of the detonation velocity on the initial particle loading indicate a different degree of particle burning and differences in the equilibrium composition at different initial particle concentrations. Vasil'ev et al. (1980) presented data on thermodynamic calculations of the equilibrium composition during detonation combustion of various substances, in particular, aluminum particles in air. According to these data, aluminum combustion can occur both with the formation of oxide Al_2O_3 and with the formation of suboxides AlO, AlO_2, Al_2O. Models of detonation combustion of aluminum, which take into account the formation of suboxides in various ways, are discussed in a review by Fedorov & Khmel (2019). Schloffel et al. (2010) noted the possibility of the formation of AlO during particle combustion directly behind the shock wave, which is not associated with the lack of an oxidizing agent. The problems of modeling the deflagration combustion of aluminum with an oxidizer deficiency were discussed by Kryukov and Malinin (2018).

Fedorov (1992) and Fedorov et al. (2006) used the detonation velocity data by Strauss (1968) to determine the integral heat release in aluminum – oxygen mixtures in a certain range of near stoichiometric concentrations. The Fedorov model (1992) was applied further in Fedorov et al. (1999) and subsequent works for the stoichiometric composition. Veyssiere et al. (2008) presented the dependence of the detonation velocity on the mass loading of aluminum particles in an oxygen medium, obtained on the basis of thermodynamic calculations of the propagation of non-ideal detonation in pipes and the data of Strauss experiments (1968). Within the range of experimental results, these data are consistent with each other. A characteristic feature is the displacement of the maximum detonation velocity towards lean mixtures of aluminum with oxygen, while its value correlates with the detonation velocity of air suspensions of aluminum.

The aim of this work is to expand the model of detonation of oxygen suspensions of aluminum to a wide range of concentrations and its application for studying detonation processes in suspensions that are inhomogeneous in composition. The problems of the propagation of cellular detonation in channels with longitudinal or transverse concentration gradients will be considered.

2. Physical and mathematical model

Two-dimensional detonation flows are described within the framework of the mechanics of interpenetrating continua by the Euler equations for the gas phase and particles.

$$\begin{gathered}
\frac{\partial \rho_1}{\partial t}+\frac{\partial \rho_1 u_1}{\partial x}+\frac{\partial \rho_1 v_1}{\partial y}=J \\
\frac{\partial \rho_1 u_1}{\partial t}+\frac{\partial (\rho_1 u_1^2+p)}{\partial x}+\frac{\partial (\rho_1 u_1 v_1)}{\partial y}=-f_x+Ju_2 \\
\frac{\partial \rho_1 v_1}{\partial t}+\frac{\partial (\rho_1 u_1 v_1)}{\partial x}+\frac{\partial (\rho_1 v_1^2+p)}{\partial y}=-f_y+Jv_2\,, \\
\frac{\partial \rho_1 E_1}{\partial t}+\frac{\partial \rho_1 u_1 (E_1+p/\rho_1)}{\partial x}+\frac{\partial \rho_1 v_1 (E_1+p/\rho_1)}{\partial y}=-q-f_x u_2-f_y v_2+JE_2\,, \\
\frac{\partial \rho_2}{\partial t}+\frac{\partial \rho_2 u_2}{\partial x}+\frac{\partial \rho_2 v_2}{\partial y}=-J \\
\frac{\partial \rho_2 u_2}{\partial t}+\frac{\partial (\rho_2 u_2^2)}{\partial x}+\frac{\partial (\rho_2 u_2 v_2)}{\partial y}=f_x-Ju_2 \\
\frac{\partial \rho_2 v_2}{\partial t}+\frac{\partial (\rho_2 u_2 v_2)}{\partial x}+\frac{\partial (\rho_2 v_2^2)}{\partial y}=f_y-Jv_2\,, \\
\frac{\partial (\rho_2 E_2)}{\partial t}+\frac{\partial (\rho_2 u_2 E_2)}{\partial x}+\frac{\partial (\rho_2 v_2 E_2)}{\partial y}=q+f_x u_2+f_y v_2-JE_2\,, \\
\frac{\partial (\rho_2 \zeta)}{\partial t}+\frac{\partial (\rho_2 u_2 \zeta)}{\partial x}+\frac{\partial (\rho_2 v_2 \zeta)}{\partial y}=-J\zeta\,,
\end{gathered} \tag{1}$$

Here p is pressure, $\rho_i, u_i, v_i, T_i, E_i, c_{v,i}$ are mean density, longitudinal and transversal velocity components, temperature, total energy per mass unit and heat capacity of the i -th phase (1,2 indicate gas and particles, respectively). Mass concentrations of gas and particles are defined as $\xi_i = \rho_i / \rho$, $\rho = \sum_i \rho_i$, $\rho_i = \rho_{ii} m_i$, m_i is the volume concentration of the i -th phase.

The function $\zeta(x, y)$ shows the spatial distribution of the initial (at start of combustion) mass concentration of particles in a moving volume. Accordingly, the thermal effect of the reaction Q and the proportion of unburned particles ξ_k at each point in space are different and depend on what was the initial concentration of the volume of particles that arrived at this point in space. To do this, the function $\zeta(x, y)$ is introduced as follows: the initial distribution is $\zeta_0(x, y) = \xi_0(x, y)$, and as the mixture moves, it is determined from the equation $D\zeta / Dt_2 = 0$, which, taking into account the equation for ρ_2 gives the last equation in the system (1). This approach is justified for suspensions of fairly small particles (less than 1 μm), for which the zone of velocity nonequilibrium corresponds to the ignition delay zone, and the combustion proceeds practically under conditions of the phase velocity equilibrium.

The system is closed by the equations of state and relations describing the interphase exchange of masses, momentum and energy. The interphase interaction processes are represented by the parameters J (mass transfer), $\vec{f}$ (interphase interaction force), and q (heat transfer).

$$\vec{f} = \frac{\rho_2}{\tau_u}(\vec{u}_1 - \vec{u}_2) \ , \ q = \frac{\rho_2 c_{v,2}}{\tau_T}(T_1 - T_2) \ . \tag{3}$$

Particle combustion is described in the framework of the simplest model of one-stage kinetics, taking into account incomplete particle burning (the presence of residual concentration of unburned particles) and the transitional regime from diffusion-limited to kinetically-controlled combustion for particles with a diameter of less than 1 micron (Khmel' & Fedorov (2018), Khmel' et al. (2018)). The dependence of the characteristic burning time of aluminum particles in the submicron range from 300 nm to 1 μm is taken as:

$$J = \frac{\rho_2}{\tau_\xi}[\xi - \xi_k(\zeta)] \ \text{at} \ T_2 \geq T_{ign},\ \xi > \xi_k\ ;\ J = 0,\ \text{at}\ T_2 < T_{ign}\ \text{or}\ \ \xi \leq \xi_k\ .$$

$$\tau_\xi = \tau_0 (d / d_0)^{0.3} \exp(E_a / RT_1)(p / p_*)^{-m} \tag{4}$$

where $m = -0.25 \ln d[\mu\text{m}]$, $E_a = 0.5\{E_{\text{micro}}(2 + \ln d[\mu\text{m}] - E_{\text{nano}} \ln d[\mu\text{m}]\}$, and E_{micro} is the activation energy for micron particles (32 kJ/mol), E_{nano} is the activation energy for nanoparticles (60 kJ/mol), p is pressure, and d is the particle diameter. According to numerous experimental data on aluminum particle ignition presented by Sundaram et al. (2015), and previous studies by Fedorov & Khmel (2005), we take the ignition temperature equal to the melting point $T_{ign} = T_{\text{melt}}$ =930 K.

Since for suspensions of particles with a diameter of more than 250 nm, the effects of free molecular flow and heat transfer are insignificant (Khmel' & Fedorov (2018)) to describe interfacial interactions, we use the formulas presented earlier (Fedorov & Khmel' (2005)).

$$\tau_u = 4d\rho_{22} / 3c_D \rho_{11} |\vec{u}_1 - \vec{u}_2|. \tag{5}$$

The drag coefficient c_D is determined similar to micron-sized particle detonations with regard for supersonic flow around particle in detonation structure using the formula proposed by Boiko et al. (1996), which provide correlations of numerical and experimental data on particle trajectories behind shock waves

$$c_D(\text{Re}, M_{12}) = \left(1 + \exp(-\frac{0.43}{\text{M}_{12}^{4.67}})\right)\left(0.38 + \frac{24}{\text{Re}} + \frac{4}{\sqrt{\text{Re}}}\right), \tag{6}$$

DOI: 10.7795/810.20200724

$$\mathrm{Re} = \frac{\rho_{11} d \left|\vec{u}_1 - \vec{u}_2\right|}{\mu_1}, \ \mathrm{M}_{12} = \frac{\left|\vec{u}_1 - \vec{u}_2\right| \sqrt{\rho_{11}}}{\sqrt{\gamma_1 p}},$$

where μ_1 is the gas dynamic viscosity and γ_1 is the adiabatic exponent. The heat exchange between the gas and particles have a form

$$\tau_T = d^2 \rho_{22} c_{v2} / 6\lambda_1 \mathrm{Nu}\ , \ \mathrm{Nu} = 2 + 0.6 \mathrm{Re}^{\,1/2} \mathrm{Pr}^{1/3}\,. \tag{7}$$

Here Nu, Pr are the Nusselt and Prandtl numbers (usually, Pr=0.7), λ_1 is the gas heat conductivity. The equations of state have a form.

$$p = \rho_{11} R T_1\,, \ E_1 = 0.5(u_1^2 + v_1^2) + c_{v1} T_1, \ E_2 = 0.5(u_2^2 + v_2^2) + c_{v2} T_2 + Q(\zeta)\,. \tag{8}$$

In the framework of the simplest model of one-stage kinetics $Q(\zeta)$ includes the integral thermal effect of the particle combustion reaction, excluding the cost of heat for melting and evaporation of the particle material. According to experimental observations and data of thermodynamic calculations, the detonation velocity of gas particle suspensions D depends on the initial concentration of particles ξ_0 (Veyssiere et al. (2008)). The CJ velocity in numerical calculations can be determined by two ways. In the problem of the detonation initiation the self-sustained propagation of the detonation structure in conjugation with a rarefaction wave establishes at the CJ velocity. Also, the CJ velocity is an eigenvalue parameter in the problem of the structure of a stationary wave, which is reduced to solving a system of ordinary differential equations (ODE) resulting from (1) when moving to a coordinate system associated with the wave front. If this parameter corresponds to the CJ velocity in a two-phase mixture, the solution of an ODE system has either an internal sonic point (with respect to the frozen sound velocity) or a finite equilibrium state, which is sonic with respect to the equilibrium sound velocity (Fedorov et al. (1999)). In the pre-stoichiometric range, according to experimental data by Strauss (1968), we take $\xi_k = 0.1$. For superstoichiometric compositions we assume $Q(\zeta) = Q(\zeta_{st})$ and determine ξ_k, which provide correspondence with data from Veyssiere et al. (2008) on the detonation velocity. Figure 1a shows the corresponding dependence of the detonation velocity on the mass concentration of particles. The calculated values $\theta = Q(\zeta)/Q_*$ (Q_*=20 MJ/kg) and $\xi_k(\zeta)$ are presented in Fig. 1b.

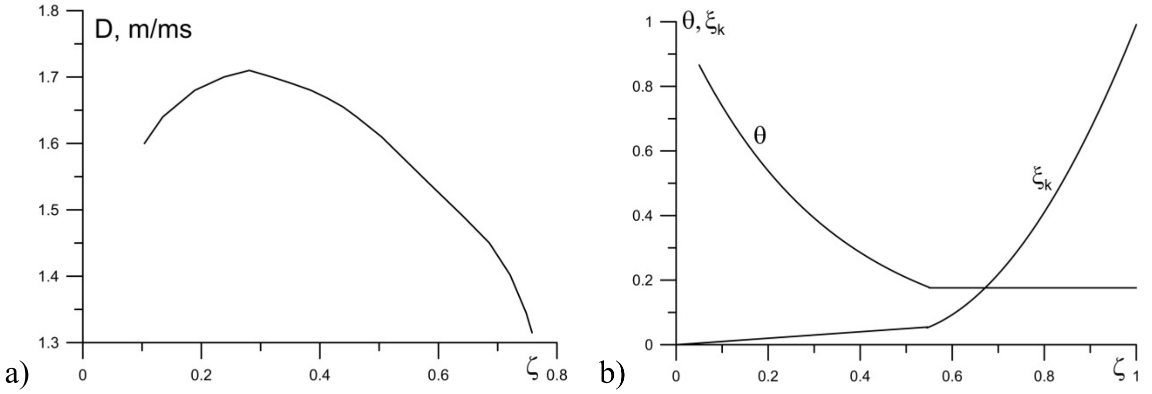

Fig. 1. *Dependences of detonation velocity and model parameters on particle concentration*

The numerical study is performed for the problem of initiation and propagation of cellular detonation in a flat channel, similarly to the work by Fedorov & Khmel (2005), Khmel (2019).

The numerical technique is based on the conservative flux-splitting schemes: the TVD scheme by Harten for gas and the Gentry-Martin-Daly scheme for particles. The numerical method has been tested earlier and applied for 2-D numerical simulations of the shock wave and detonation flows. The step of the finite-difference grid was determined according to the scale of the relaxation zones, varied in the test calculations. An example of calculations with varying grid spacing will be given below.

3. Results and discussion

3.1 Detonation structures in homogeneous mixtures of various concentrations

The correspondence of the detonation velocity in numerical calculations was verified on the problem of initiation of plane detonation in a one-dimensional formulation. Figure 2 shows the pressure profiles with time interval 0.04 ms at various initial particle concentrations. In the concentration range from 0.1 to 0.8 (which corresponds to the initial particle density range from approximately 140 g/m^3 to 5.2 kg/m^3), a self-sustaining Chapman-Jouguet structure associated with a rarefaction wave is established (Fig. 2b, Fig. 2c).
Beyond these limits at ξ_0 =0.07 (96.5 g/m^3) and ξ_0 = 0.82 (5.83 kg/m^3) calculations show the destruction of the detonation structure and the disruption of detonation (Fig. 2a, Fig 2d). Thus, the lower concentration limit is fully consistent, and the upper is outside the limits of the figure presented by Veyssiere et al. (2008). The detonation velocity at ξ_0 =0.1 is determined as 1.45 km/s, which is much lower than the corresponding to this concentration value 1.58 km/s in the work of Veyssiere et al. (2008). For the upper concentration limit ξ_0 =0.8, the calculated detonation velocity is 1.2 km/s and corresponds to the curve smoothly extended to the region of higher concentrations.

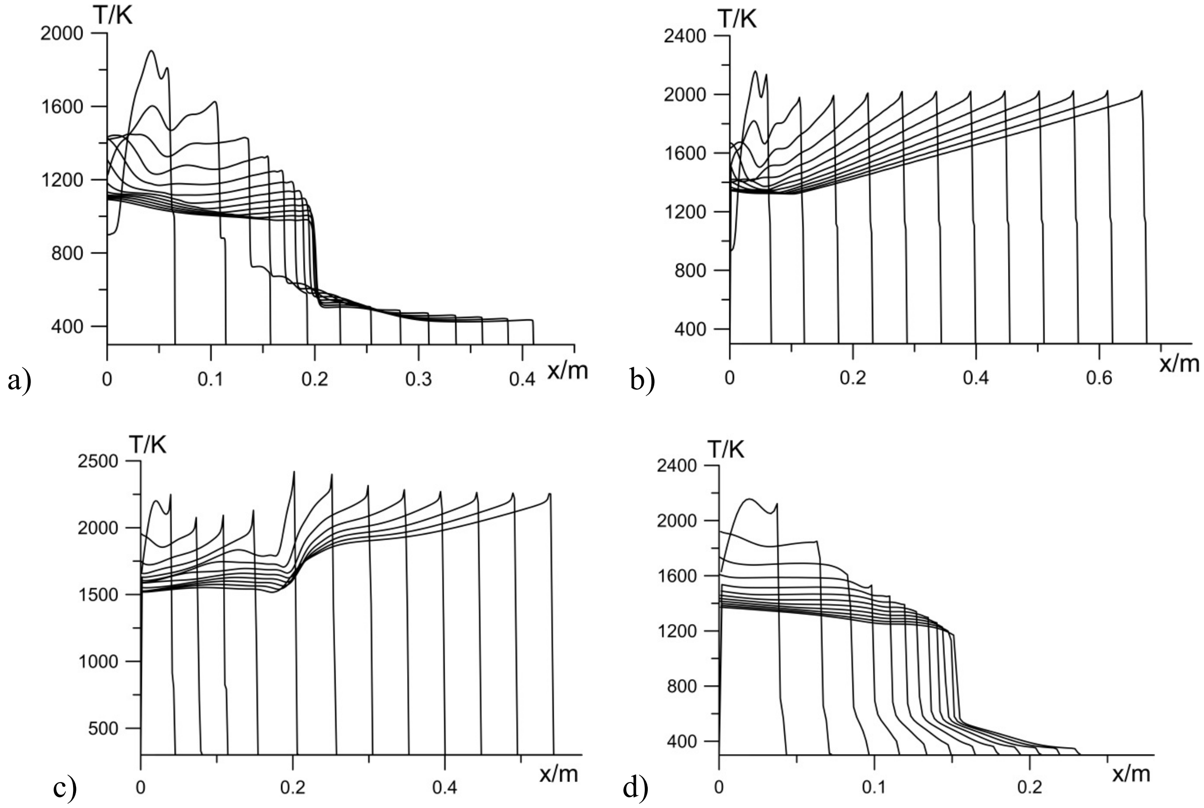

Fig. 2. *Scenarios of initiation of plane detonation near the concentration limits (gas temperature profiles,* Δ*t*=0.04 *ms)*: ξ_0 =0.07 (*a*); ξ_0 =0.1 (*b*); ξ_0 =0.8 (*c*); ξ_0 =0.82 (*d*).

Detonation flows in aluminum suspensions are characterized by the development of cellular structures. Fedorov & Khmel (2005) found that for particles larger than 1 µm, detonation cells are regular, which made it possible to determine the dependence of their size on the particle diameter and to analyze the relationship between the cell scales and the scales of relaxation processes. Khmel (2019) and Khmel & Tolkacheva (2019) obtained regular cells for non-stoichiometric concentrations of particle suspensions 1 μm in size. It turned out that, despite significant differences in the detonation velocity and average and peak values of parameters such as particle density, gas density and pressure, the cell size in uniform suspensions weakly depends on the initial concentration.

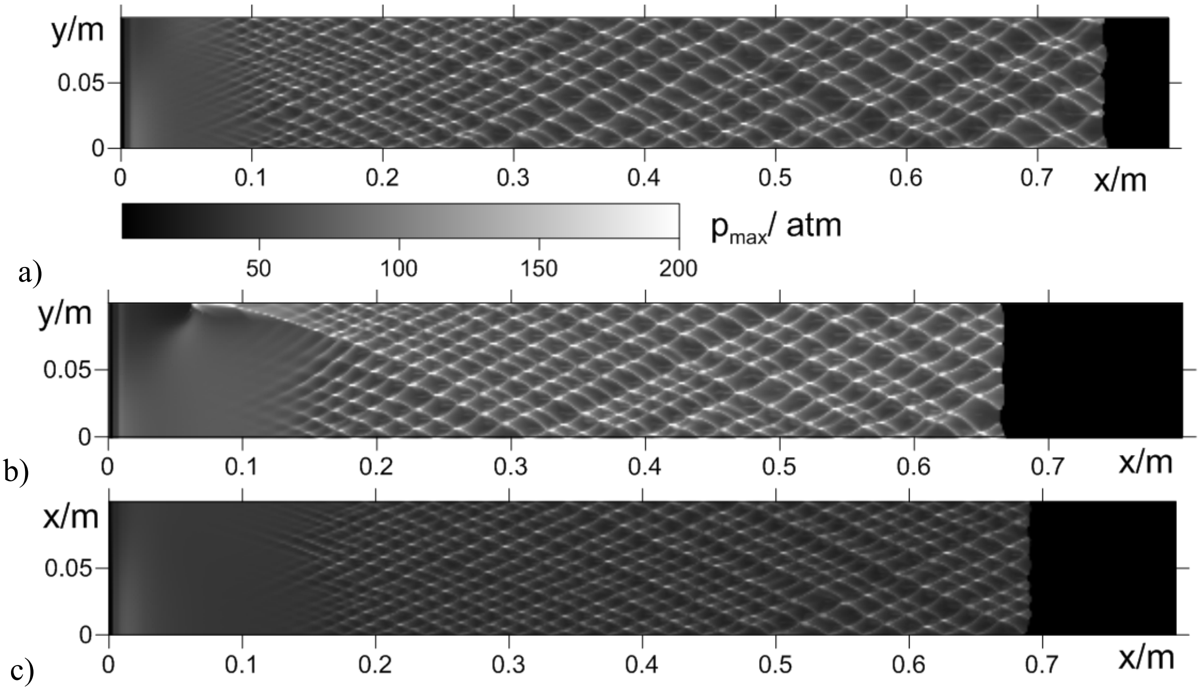

Fig. 3. *Cellular detonations in oxygen mixtures of 300-nm particles(maximal pressure histories):* $\xi_0 = 0.55$ *(a),* $\xi_0 = 0.7$ *(b) u* $\xi_0 = 0.25$ *(c).*

A decrease in the particle size of monodisperse mixtures in the region of the submicron and nanometer ranges shows a violation of the regularity of the cells. For stoichiometric mixtures, this was demonstrated by Khmel (2019). Figure 3 shows examples of calculations of cellular detonation of suspensions of particles with a size of 300 nm of three different concentrations. Pictures are constructed at the time 0.48 ms in Fig. 3a and 3b and at the time 0.4 ms in Fig. 3c. From the position of the front, it can be established that the average propagation velocity corresponds to the dependence shown in Fig. 1a. By the nature of the cells, it can be seen that the initially formed small cells enlarge as detonation propagates, and a tendency toward irregularity also manifests itself. In a steady flow in the region 0.6 m < x < 0.7 m, the number of transverse waves is approximately the same in Fig. 3a and 3b and somewhat more in Fig. 3c. The average and peak pressure values directly depend on the initial particle density, which can be seen from the brightness of the patterns, which are built in a single shadow scale.

3.2 Detonation propagation in channels with a longitudinal gradient of particle concentrations

The detonation propagating through a mixture with a longitudinal gradient of particle concentration changes its propagation velocity. In the region of low concentrations (not exceeding 0.3) with a negative gradient, the detonation velocity decreases, and with a positive gradient it increases accordingly to the data in Fig. 1. On the contrary, in the range of particle concentrations from 0.3 and higher with a positive gradient, the detonation front slows down, and with a negative one it accelerates. In one-dimensional calculations, this property was demonstrated by Khmel & Tolkacheva (2019). In two-dimensional calculations of cellular detonation, the leading front, interacting with transverse waves, propagates irregularly. Therefore, the trend of acceleration or deceleration can be seen only with a rather sharp gradient of particle concentration.

Figure 4 shows the calculation data for the propagation of detonation in a gas suspension of particles with a size of 2 μm in a 6 cm channel with a linear law of a change in the concentration of particles from 0.7 in the left part of the channel to 0.3 in its right part. As can be seen in Fig. 3a, a structure with three transverse waves (one and a half cells per channel width) is formed in the channel. The development of cellular detonation determines the pulsation behavior of the parameters of the gas phase: density (Fig. 4b) and temperatures (Fig. 4c). A change in the initial particle concentration is well demonstrated on particle density profiles, where both a change in the initial density and a corresponding decrease in the peak density values in the ρ - layer are visible (Fig. 4d). According to the change in the distance between the peaks in Fig. 4d, we can conclude that the average front propagation velocity increases.

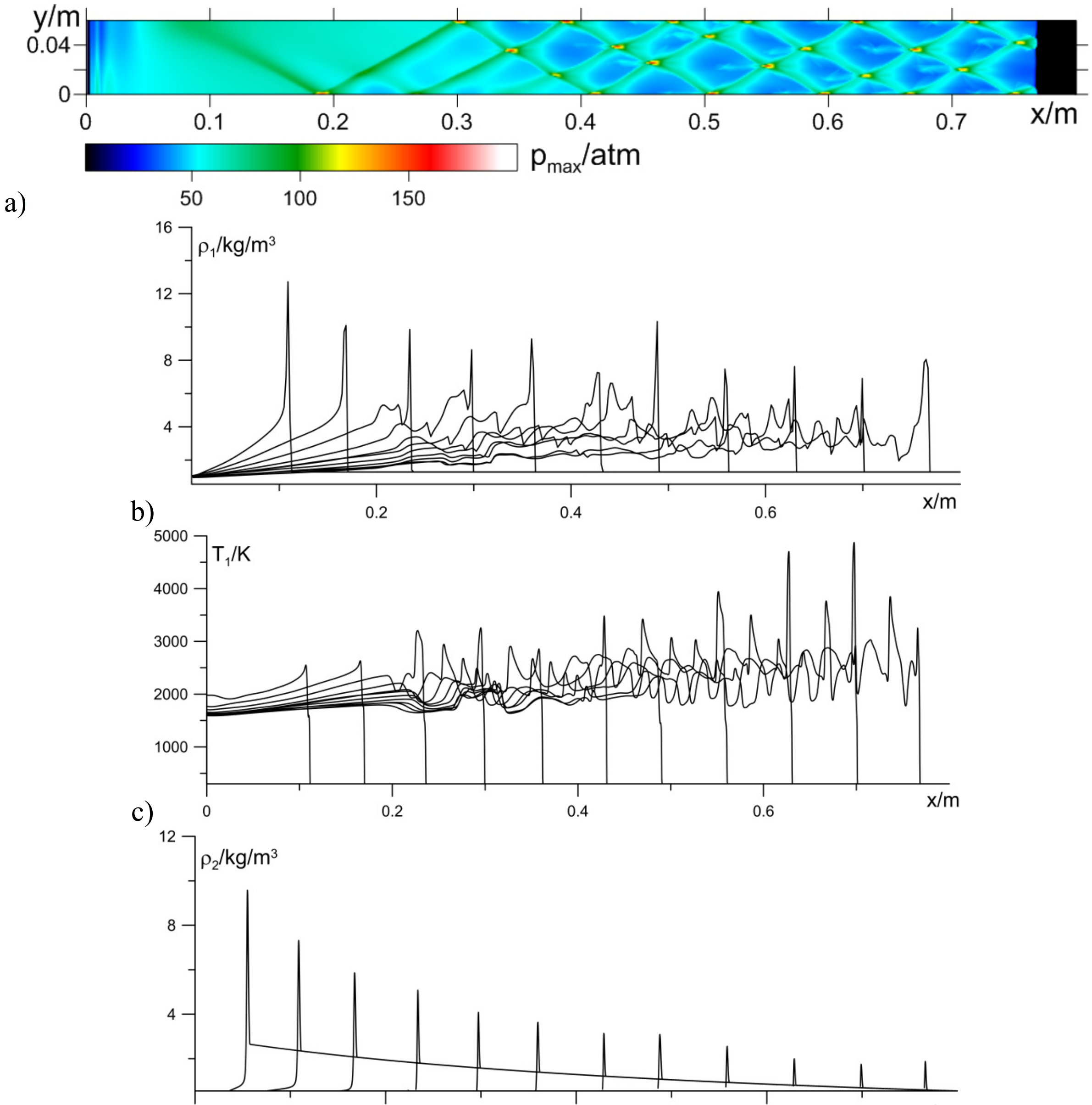

Fig. 4. *Detonation propagation in a channel with longitudinal inhomogeneity (ξ_0 =0.7 left, ξ_0 =0.3 right), d=2 μm: maximal pressure field (a); parameter profiles at y=0, Δt=0.04 ms (b)-(d).*

3.3 Detonation propagation in a gas suspension with a transverse particle concentration gradient

When detonation propagates through a mixture with a transverse concentration gradient, the leading wave front is curved. There is a tendency to accelerate the front in areas of concentration where the detonation velocity is higher and slowdowns in the region where the detonation velocity is lower.

At the same time, the transverse waves develop and interact with the leading front. As a result, detonation cells become oblique and are characterized by significant non-uniformity. Figure 5 shows the calculation data in a 6 cm channel for a suspension of 1 μm with a linearly varying concentration of particles from $\xi_0 = 0.3$ near the lower wall to $\xi_0 = 0.75$ near the upper wall. As can be seen in the figures, a detonation structure with an inclined leading wave is formed in the channel. In this case, a system of transverse waves is formed, the distance between which is different. Whereas in homogeneous mixtures of the same dispersion, the distance between the transverse waves weakly depends on the initial concentration (Khmel (2019), Khmel & Tolkacheva (2019)). To confirm that the result is not related to numerical effects, in Fig. 5 shows the calculation data on two grids: Δx =0.2 mm (300 mesh nodes per channel width) and Δx =0.1 mm (600 mesh nodes).

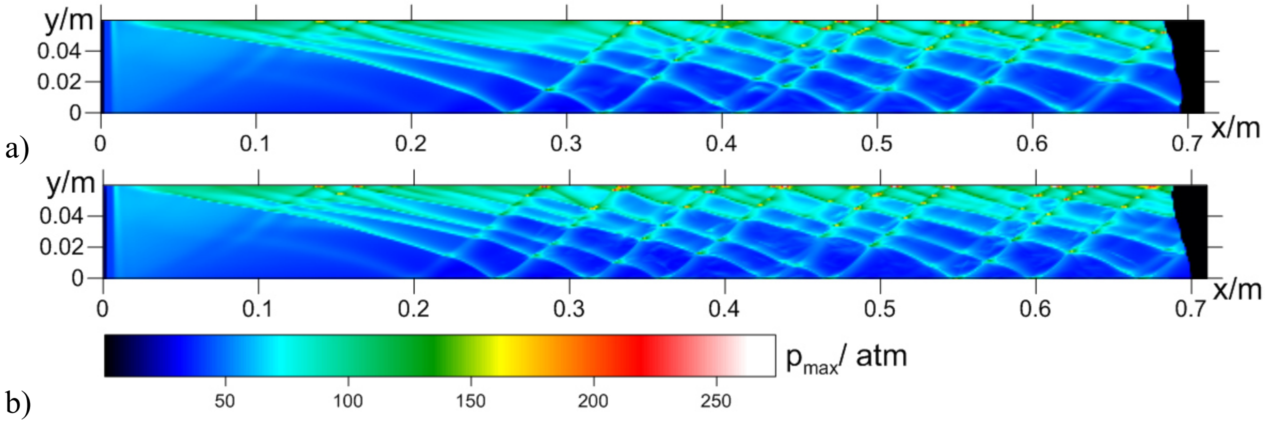

Fig. 5. *Cellular detonation in a mixture with a transverse concentration gradient, d=1 μm. Comparison of calculation results on two grids: Δx =0.2 mm (a) and Δx =0.1 mm (b).*

The detonation velocity averaged over a time interval of 0.04 ms is determined at 1.612 km/s on the grid Δx =0.1 mm and 1.610 km/s on the grid Δx = 0.2 mm. This value lies between the values characteristic of the maximum and minimum particle concentrations (1.7 km/s at ξ_0 = 0.3 and 1.33 km/s at ξ_0 = 0.75) and corresponds to a velocity in a homogeneous mixture of a certain average concentration (ξ_0 = 0.50).

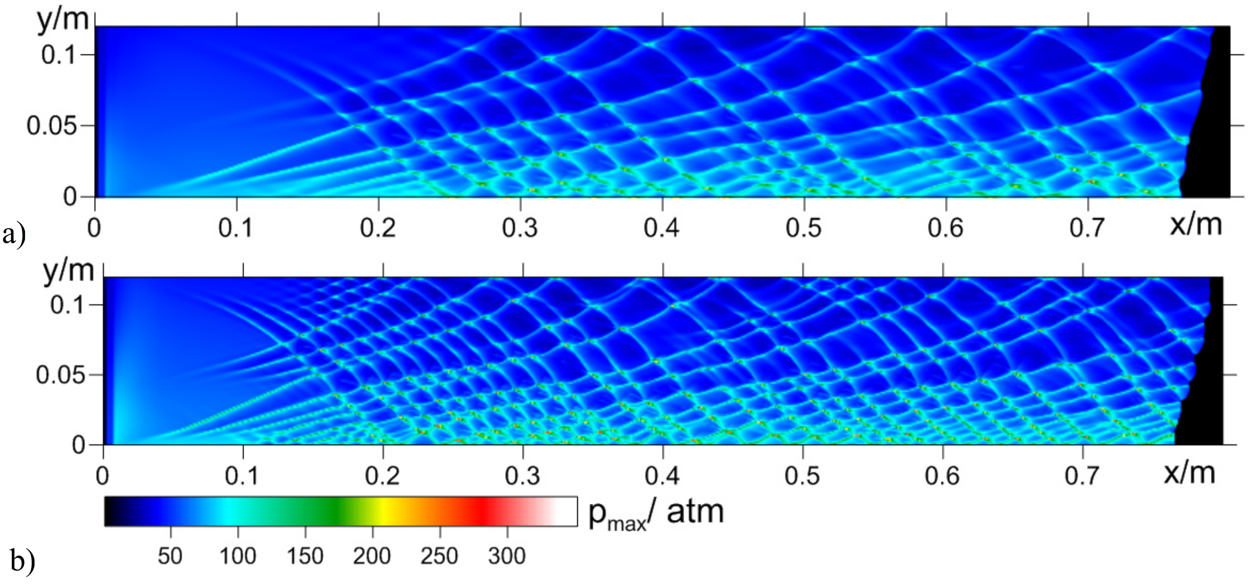

Fig. 6. *The propagation of cellular detonation in a channel with a transverse concentration gradient in submicron suspensions: d=600 nm (a); d=300 nm (b);*

Figure 6 shows the calculation results for a mixture of particles with a size of 600 nm in a wider channel (12 cm) with a concentration change from 0.7 (on the lower wall) to 0.25 (on the upper wall). As can be seen, the pattern of cellular detonation is similar to Fig. 5. The average detonation velocity in the interval 0.12 ms is 1.61 km/s in a mixture of 300 nm and 1.62 km/s in a mixture of 600 nm. A certain discrepancy is associated both with averaging errors and, possibly, with the fact that initially overdriven detonation is formed in the initiation problem, and the period of establishment of a self-sustaining normal mode in a suspension of 600 nm is longer than in a suspension of 300 nm.

Thus, oblique cells are formed in channels with a transverse particle concentration gradient. The distance between the transverse waves is minimal in the region of high concentrations and maximally in the region of low concentrations for both micron-sized and submicron suspensions. Note that the oblique shape of the leading front and oblique cell were previously obtained by Fomin et al. (2001) in the calculations of cellular gas detonation in a narrow channel (with one cell per width).

4. Conclusions

The paper presents a physical and mathematical model for describing detonation processes in inhomogeneous gas suspensions of reacting particles. The model is based on the approaches of mechanics of heterogeneous media and simple semi-empirical kinetic models that integrally describe the chemical reactions occurring in the mixture. The total heat release is determined by a function that is determined from the known data on the dependence of the normal detonation velocity on the particle concentration based on the solution of the problem of stationary structures or the analysis of one-dimensional solutions of steady-state detonation waves. For micro-sized and submicron suspensions of aluminum particles, the dependences of the integral heat release and the fraction of unburned particles are obtained, which ensure compliance with the data of Veyssiere et al. (2008).

The results of one-dimensional calculations of the initiation and propagation or disruption of plane detonation waves have shown compliance with the concentration limits of detonation of oxygen suspensions of aluminum. The upper concentration limit is outside the range presented by Veyssiere et al. (2008) data, with the detonation velocity corresponding to extrapolation of the curve. The lower concentration limit corresponds, although near it, the calculated values of the detonation velocity are lower than those indicated by Veyssiere et al. (2008). Perhaps this is due to a calculation error caused by significant gradient of the detonation velocity function in this particle concentration region.

Two-dimensional calculations showed the development of cellular detonation in homogeneous microdispersed and submicron suspensions of various concentrations with a tendency to cell irregularity with a decrease in particle size to 300 nm.

In channels with a longitudinal concentration gradient of microdispersed particles, an acceleration (deceleration) of the front occurs, while the cellular structures change only slightly.

In channels with a transverse particle concentration gradient, oblique cells form. The distance between the transverse waves is minimal in the region of high concentrations and maximally in the region of low concentrations for both microdispersed and submicron suspensions. The results are in qualitative agreement with the calculations of cellular gas detonation by Fomin et al. (2001).

Acknowledgements

The reported study was funded by RFBR, project number 20-08-00295.

References

Bazyn, T., Krier, H. & Glumac, N. (2006). Combustion of nanoaluminum at elevated pressure and temperature behind reflected shock waves. *Combustion and Flame,* 145: 703–713.

Benkewicz, K. & Hayashi, A.K. (2003). Two-dimensional numerical simulations of multi-headed detonations in oxygen-aluminum mixtures using an adaptive mesh refinement. *Shock Waves*, 12(5): 385-402.

Boulal, S., Vidal, P. & Zitoun, R. (2016) Experimental investigation of detonation quenching in non-uniform compositions. *Combustion and Flame*, 172: 222-233.

Briand, A., Veyssiere, B. & Khasainov, B.A. (2010). Modelling of detonation cellular structure in aluminium suspensions. *Shock Waves,* 20(6): 521–529.

Chengken, Q., Peng, D., Hao, Yu. & Zheng, C. (2017) Different modes of reaction front propagation in n-heptane/air mixture with concentration non-uniformity. *Proceedings of the Combustion Institute,* 36(3): 3633-3641.

Fedorov, A.V. (1992). Structure of the heterogeneous detonation of aluminum particles dispersed in oxygen, *Combustion, Explosion and Shock Waves,* 28 (3): 277–286.

Fedorov, A.V., Fomin, V. M. & Khmel', T.A. (2006) Theoretical and numerical study of detonation processes in gas suspensions with aluminum particles. *Combustion, Explosion and Shock Waves,* 42(6), 735–745.

Fedorov, A.V. & Khmel', T.A. (2005). Numerical simulation of formation of cellular heterogeneous detonation of aluminum particles in oxygen. *Combustion, Explosion, and Shock Waves,* 41(4): 435-448.

Fedorov, A.V. & Khmel', T.A. Problems of closing models that describe detonation of gas suspensions of ultrafine aluminum particles (review). (2019). *Combustion, Explosion and Shock Waves,* 53(5): 585-595.

Fedorov A.V., Khmel' T.A. & Fomin V.M. (1999) Non-equilibrium model of steady detonations in aluminum particles - oxygen suspensions. *Shock Waves* 9(5): 313-318.

Fedorov, A.V., Khmel T.A. & Kratova Y.V. (2010) Cellular detonation diffraction in gas-particle mixtures. *Shock Waves,* 20(6): 509-519.

Fedorov, A.V., Khmel, T.A. & Lavruk, S.A. (2018). Exit of a heterogeneous detonation wave into a channel with linear expansion. II. Critical propagation condition. *Combustion, Explosion and Shock Waves*. 54(1): 72-81.

Fedorov, A.V. & Kratova, Yu.V. (2015). Influence of non-reactive particle cloud on heterogeneous detonation propagation. *Journal of Loss Prevention in the Process Industries*, 36: 404-415.

Fomin, P.A., Kash, T., Trotsyuk, A.V. & Hieronymus, H. (2001) Modeling of film and surface detonation. *Internal Flows (Proc. 5th Int. Symp. on Experimental and Computational Aerothermodynamics of Internal Flows, Gdansk, Poland, 2001, September 4-7),* Piotr Doerffer (Ed.), (IFFM Publishers), 2: 935-943.

Houim, R.W. & Oran E.S. (2005). Numerical simulation of dilute and dense layered coal-dust explosions. *Proceedings of the Combustion Institute*, 35(2): 2083-2090.

Hosoda, H., Hayashi, A. K. & Yamada, E. (2013) Numerical analysis on combustion characteristics of nano aluminum particle-oxygen two-phase detonation. *Science and Technology of Energetic Materials,* 74(2): 34-39.

Kei, S. & Matsuo A. (2019) Using an extended CFD–DEM for the two-dimensional simulation of shock-induced layered coal-dust combustion in a narrow channel. *Proceedings of the Combustion Institute* 37: 3677–3684.

Khasainov, B., Virot, F. & Veyssiere, B. (2013). Three-dimensional cellular structure of detonations in suspensions of aluminium particles. *Shock Waves*, 23: 271–282.

Khmel' T.A. & Fedorov A.V. (2018) Modeling of plane detonation waves in a gas suspension of aluminum nanoparticles. *Combustion, Explosion and Shock Waves,* 54 (2), 189–199.

Khmel', T.A., Fedorov, A.V. & Lavruk, S.A. (2018) Modeling of heterogeneous detonation propagation in variable cross-section channels with consideration of transient combustion of aluminum. *AIP Conference Proceedings,* 1939: 020024.

Khmel', T.A. (2019) Modeling of cellular detonation in gas suspensions of submicron and nano-sized aluminum particles. *Combustion, Explosion and Shock Waves,* 55(5): 580-588.

Khmel, T.A. & Tolkacheva, S.I. (2019). Model of reduced kinetics for describing heterogeneous detonation in gas particle mixtures with non-uniform concentration distribution. *Journal of Physics: Conference Series,* 1382: 012102.

Korobeinikov, V.P. Semenov, I.V. Markov, V.V. Menshov, I.S. Klemens, R. Wolanski, P. et al. (2002) Modelling of flow and combustion behind shock waves propagating along dust layers in long ducts. *Journal de Physique IV France*, 12 (7): 113-115.

Kratova, Yu.V. & Fedorov, A.V. (2014). Interaction of a heterogeneous detonation wave propagating in a cellular regime with a cloud of inert particles. *Combustion, Explosion and Shock Waves,* 50 (2): 183-191.

Kratova, Yu.V., Khmel, T.A., & Fedorov, A.V. (2016). Axisymmetric expanding heterogeneous detonation in gas suspensions of aluminum particles. *Combustion, Explosion and Shock Waves,* 52(1): 74-84.

Kryukov, A.Yu. & Malinin, V.I. (2018). Mathematical modeling of the combustion of an overfueled aluminum–air mixture based on the nonequilibrium thermodynamics of the process. *Combustion, Explosion, and Shock Waves,* 54 (1): 35–46.

Li, J., Mi, X. & Higgins, A.J. (2015) Effect of spatial heterogeneity on near-limit propagation of a pressure-dependent detonation. *Proceedings of the Combustion Institute*, 35(2): 2025-2032.

Prokhorov E.S. (2017) Mean detonation velocity in poorly mixed gas mixtures. *Combustion, Explosion, and Shock Waves*, 53(6): 705-710.

Semenov, I., Utkin, P., Markov V. (2013). Numerical modelling of dust-layered detonation structure in a narrow tube. *Journal of Loss Prevention in the Process Industries*, 26(2): 380-386.

Schloffel G., Eichhorn, A., Albers, H., Mundt, Ch., Seiler, F. & Zhang, F. (2010) The effect of a shock wave on the ignition behavior of aluminum particles in a shock tube. *Combustion and Flame,* 157: 446–454.

Smirnov, N.N., Nikitin, V.F., Dushin, V.R., Filippov, Yu.G., Nerchenko, V.A. & Khadem J.. (2015) Combustion onset in non-uniform dispersed mixtures. *Acta Astronautica,* 115: 94-101.

Smirnov, N.N., Nikitin, V.F., Khadem J. & Alyari-Shourekhdeli, Sh. (2007) Onset of detonation in polidispersed fuel-air mixtires. *Proceedings of the Combustion Institute*, 31(2): 2195-2204.

Starik, A.M. Savel'ev, A.M. & Titova N.S. (2015). Specific features of ignition and combustion of composite fuels containing aluminum nanoparticles (Review), *Combustion, Explosion and Shock Waves,* 51(2): 197–222.

Strauss, W.A. (1968). Investigation of the detonation of aluminum powder-oxygen mixtures. *AIAA Journal,* 6(12): 1753-1761

Sundaram, D., Yang, V. & Zarko, V.E. (2015) Combustion of nano aluminum particles (Review). *Combustion, Explosion, and Shock Waves*, 51(2): 173–196.

Teng, H. & Jiang, Z. (2013). Numerical simulation of one-dimensional aluminum particle-air detonation with realistic heat capacities. *Combustion and Flame*. 160(2): 463–472.

Vasil'ev, V.M., Vol'pert, A.I., Klychnikov, L.V., Petrov, Yu.M., Salakatova, L.S. & Stesik, L.N. (1980). *Combustion, Explosion and Shock Waves,* 16(3): 354–360.

Veyssiere, B. & Khasainov, B. (1991) A model for steady, plane, double-front detonations (DFD) in gaseous explosive mixtures with aluminum particles in suspension. *Combustion and Flame*, 85 (1, 2): 241-25.

Veyssiere, B., Khasainov, B.A. & Briand, A. (2008) Investigation of detonation initiation in aluminum suspensions. *Shock Waves,* 18(4): 307-315.

Zhang, F., Gerrard, K.B. & Rypley, R. (2009) Reaction Mechanism of Aluminum Particles – Air Detonation. *Journal of Propulsion and Power*, 25(4): 845-858.

DOI: 10.7795/810.20200724

Numerical investigation of propagation of heterogeneous detonation in nanodispersed aluminum particle suspensions in expanding channels

Sergey Lavruk, Tatyana Khmel

Khristianovich Institute of Theoretical and Applied Mechanics SB RAS,
630090, Novosibirsk, Russia

E-mail: lavruks@mail.ru

Abstract

Regimes of detonation propagation in channels with linear expansion filled with monodisperse mixtures of oxygen and submicron or nano-sized aluminum particles are studied by methods of numerical simulations. The detonation combustion of submicron and nano aluminium particles is described within the semi-empirical model taking into account transition from diffusion regime to kinetic one. As the initial conditions, waves of both planar and cellular detonation were considered. The characteristics of the main flow regimes were obtained and described: subcritical (detonation failure), critical (detonation failure in some part of the channel) and supercritical (continuous detonation propagation). Maps of flow regimes were constructed for particles of 200 nm and 400 nm in the plane of parameters: channel width, expansion angle. The obtained critical conditions are closing to those observed in gas detonation. The expansion angle linearly depends on the critical channel width to a first critical value, after a second critical value the expansion angle is independent of the channel width. At that, there is a certain region of nonmonotonicity similar to the detonation of micro-sized suspensions of aluminum particles.

Keywords: *detonation, aluminium gas suspensions, expansion channels, critical conditions.*

1. Introduction

Industrial technologies using micro- and nano-sized aluminum powders have been extensively developed and widely used. Studies of detonation propagation in complex volumes are of interest for different applications. On the one hand, they are related with problems of detonation prevention and suppression in cases of man-made disasters. On the other hand, channel configurations with variable cross-sections are typical for devices, which are the working part of detonation engines. The fundamental problem is to analyze the mechanisms of propagation of detonation waves (DW) in heterogeneous mixtures of gas and particles in channels of various geometries.

The properties of aluminum particle combustion and characteristics of detonation in aluminum dust suspensions have been studied in great number of works. There are several theoretical models of detonation of aluminum dust in air, detonation products of gaseous mixtures, and oxygen presented by Medvedev et al. (1984), Veyssiere et al. (1991) and Zhang et al. (2009). In Fedorov (1992) and Fedorov et al. (1999), a model of heterogeneous detonation of stoichiometric aluminum – oxygen suspensions verified by experimental data from Strauss et al. (1968) was developed. Agreements with known experimental data on reaction zone length, initiation energy, and detonation cell size was obtained in calculations within the framework of the model for micron-sized aluminum particles. The data on the propagation of cellular detonations in monodisperse and polydisperse suspensions were obtained in Fedorov et al. (2005) and Fedorov et al. (2008). In micron-sized suspensions the trajectories of triple points show a nearly regular cellular structure in Fedorov et al. (2005), the detonation cell size correlates with acoustic prediction by the method offered by Barthel (1974).

The behavior of detonation waves behind a rectangular step in a heterogeneous mixture of micron-sized aluminum particles and oxygen has been studied by Fedorov et al. (2008), Kratova et al. (2009), Fedorov et al. (2010), Kratova et al. (2011) and Kratova et al. (2016). Diffraction patterns have been analyzed for two types of initial conditions of the problem: a flat detonation wave (Chapman–Jouguet flow) and cellular detonation. In paper Fedorov et al. (2008), wave patterns of the diffraction of plane DWs on a backward-facing step are described and the main regimes of detonation propagation are classified as subcritical, critical, and supercritical. Fedorov et al. (2010) demonstrate that even with a flat detonation wave as the initial conditions, the flow with transverse waves proper to cellular detonations develops in the wide part of the channel. The behaviour of detonation in channels with sudden expansion is discussed by Kratova et al. (2011), together with questions of detonation re-initiation. Kratova et al. (2011) studied the diffraction of cellular detonation behind a backward-facing step, and the flow rearrangement. An overview of the criteria for the propagation of detonation for a mixture of oxygen and aluminum is presented by Kratova et al. (2011) and Kratova et al. (2016). It has been found that the critical number of cells is 3 for a cylinder and less than 1 for a planar channel, which is very different from the critical conditions for similar processes in gaseous detonation. In studies Fedorov et al. (2017) and Fedorov et al. (2018) the detonation diffraction in the channel with the linear expansion are investigated. The main regimes of detonation propagation are found analogous to propagation on backward facing step. Maps of detonation regimes are presented in coordinate system: the critical width of the channel – the extension angle.

In recent years, interest in research in the field of nanodispersed media has increased and a significant number of works on combustion characteristics of nano- aluminum particles have been performed. A comprehensive review of new experimental data on the ignition, melting, heat transfer, and combustion of submicron and nanoscale aluminum particles is given by Sundaram et al. (2015). Numerous experimental data of recent years have shown that in the submicron and nanometer range of particle sizes, the aluminum particles combustion properties vary accordingly to the transition from the diffusion to the kinetic regime of combustion. Respectively, both the dependence of the characteristic burning time on the particle diameter and the value of the activation energy of the combustion reaction differ from that for micron-sized particles. The data on the dependence of the burning time of submicron and nanoscale aluminum particles on the diameter Sundaram et al. (2015) show that in a wide range of sizes, the power dependence is valid with a significantly lower exponent than for microparticles. Also the specific feature of nanoscale aluminum particle burning is much higher value of the activation energy of the combustion reaction that presented in Bazyn et al. (2006).

A semi-empirical physical and mathematical model of detonation of nanoscale aluminum particles in oxygen was developed in Fedorov et al. (2018) on the base of new experimental data on ignition and combustion of nano-sized aluminum particles presented in Sundaram et al. (2015) and in Bazyn et al. (2006). The model takes into account the free-molecular effects in the description of the flow around and heat transfer of nanoscale particles with gas. The simplest analysis of stationary detonation structures in Fedorov et al. (2018) showed that in the nanoscale range of particle diameters the burning times are much longer (order of magnitude more for 100-nm particles) than the times of thermal and velocity relaxation. It means that the combustion proceeds essentially in equilibrium mixture with respect to the velocities and temperatures of the phases. The comparative analysis of the Chapman-Jouguet, strong detonation waves and decayed detonations reveals strong dependence of the detonation structure length on the amplitude of the leading shock wave. This may be significant for the regularity character of the cellular detonation regimes.

The purpose of the present study is to obtain the properties of detonation propagation in submicron or nanoparticle aluminum suspensions in oxygen in channels with linear expansion with big angles on the base of numerical simulations of 2-D detonation flow.

2. Physical and mathematical model

The Euler equations for two-dimensional flow in dilute gas particle suspensions follow from conservation laws for mass, momentum, and energy that firstly was offered in Fedorov (1992) and Fedorov et al. (1999). 2-D equations for conservation laws are presented in Fedorov et al. (2017). The value of heat effect of particle combustion in the frame of reduced chemical kinetics (*Q*) for stoichiometric composition has been determined to agree with experimental data by Strauss (1968) on detonation velocity. Since weak dependence of detonation velocity on particle diameter for micro-sized and nano-sized aluminum particles by Zhang et al. (2006) we use the same universal value *Q*= 3.5 MJ/kg as in Fedorov et al. (2005) – (2018) and Kratova et al. (2011) – (2016).

The processes of velocity relaxation and heat transfer in gas-laden nanoscale particles are characterized by a transition from a continual to a free-molecular regime of particle interaction with gas molecules. If the particle size is comparable with the mean free path of gas molecules, then the particle drag force in the gas flow is determined with regard for the Cunningham correction factor by Sundaram et al. (2015):

$$\tau_u = 4d\rho_{22}C_c / 3c_D\rho_{11}\left|\vec{u}_1 - \vec{u}_2\right|,\ C_c = 1 + 2\mathrm{Kn}[1.257 + 0.4\exp(-1.1/2\mathrm{Kn})]\ . \qquad (1)$$

Here $\mathrm{Kn} = RT_1/(\sqrt{2}\pi d_g^2 N_A p d_2)$ is the Knudsen number that is the ratio of the mean free path of the molecular in gas to the particle diameter, d_g, m_g are the gas molecular size and mass, N_A is the Avogadro number. The drag coefficient c_D is determined similar to micron-sized particle detonations with regard for supersonic flow around particle in detonation structure using the formula by Fedorov et al. (2005)

$$c_D(\mathrm{Re}, M_{12}) = \left(1 + \exp\left(-\frac{0.43}{\mathrm{M}_{12}^{4.67}}\right)\right)\left(0.38 + \frac{24}{\mathrm{Re}} + \frac{4}{\sqrt{\mathrm{Re}}}\right), \qquad (2)$$

$$\mathrm{Re} = \frac{\rho_{11} d\left|\vec{u}_1 - \vec{u}_2\right|}{\mu_1},\ \mathrm{M}_{12} = \frac{\left|\vec{u}_1 - \vec{u}_2\right|\sqrt{\rho_{11}}}{\sqrt{\gamma_1 p}},$$

where μ_1 is the gas dynamic viscosity and γ_1 is the adiabatic exponent.

The heat exchange between the gas and particles for submicron and nano-sized particles is determined following to changing the flow regime of particles from the continuum at Knudsen numbers below 0.01 to the free-molecular one at $\mathrm{Kn} > 10$ in Sundaram et al. (2015). Presentations for the characteristic times of heat relaxation in the regimes mentioned have a different form

$$\tau_T^{\ cont} = d^2\rho_{22}c_{v2} / 6\lambda_1\mathrm{Nu}\ ,\ \mathrm{Nu} = 2 + 0.6\mathrm{Re}^{\ 1/2}\mathrm{Pr}^{1/3}\ , \qquad (3)$$

$$\tau_T^{\ fm} = \frac{d\rho_{22}c_{v2}}{6\alpha p}\sqrt{\frac{8\pi m_g T_1}{k_B}}\left(\frac{\gamma_1 - 1}{\gamma_1 + 1}\right). \qquad (4)$$

Here Nu, Pr are the Nusselt and Prandtl numbers (usually, Pr=0.7), λ_1 is the gas heat conductivity, k_B is the Boltzman constant, α is the accommodation coefficient. In the particle size range 10 nm -

1 μm, the Knudsen number varies from about 0.01 to about 10, respectively, the flow regime is transitional. For the transition region we suggest a logarithmic interpolation formula Fedorov et al. (2018).

$$\tau_T{}^{tr} = [(\log \mathrm{Kn}{+}2)\,\tau_T{}^{fm} + (1-\log \mathrm{Kn})\,\tau_T{}^{cont}]\,/\,3 \qquad (5)$$

The processes of ignition and combustion of nanoscale aluminum particles are described using the known empirical data given in Sundaram et al. (2015) and Bazyn et al. (2006). A temperature criterion is adopted as in previous works Fedorov et al. (2005) – (2010) and Kratova et al. (2011) – (2016). According to numerous experimental data on aluminum nanoparticle ignition presented in Sundaram et al. (2015), we take the ignition temperature equal to the melting point $T_{ign} = T_{\mathrm{melt}}$ =930 K.

Aluminum particle combustion is described with regard for transition from the diffusion regime of coarse particle combustion to the kinetic regime for ultrafine particles. Model for burning of aluminum nanoparticles is presented in Khmel 2019 and developed based on data from Sundaram et al. (2015) and in Bazyn et al. (2006). Experimental result for aluminum nanoparticles detonation presented in Zhang et al. (2006). Also numerical model for simulation of nanoparticles detonation presented in Hosoda et al. (2013). Hosoda et al. (2013) used the model of nano-sized aluminum particle combustion by Zhang et al (2006) with Arrhenius-type equation and $d^{0.3}$ law for the burning time dependence on the particle diameter.

We use the Arrhenius type kinetics $\tau_\xi = \tau_0 (d/d_0)^n (p/p^*)^m \exp(E_a/RT_2)$, n=0.3. In the range 150 nm ≤ d ≤ 1 μm here a smooth approximating functions for m and E_a are accepted as follows: $m = -0.25 \ln d[\mu\mathrm{m}]$, $E_a = 0.5\{E_{\mathrm{micro}}(2+\ln d[\mu\mathrm{m}]) - E_{\mathrm{nano}} \ln d[\mu\mathrm{m}]\}$. $E_{\mathrm{micro}} = 32$ kJ/mol $E_{\mathrm{nano}} = 60$ kJ/mol as was proposed by Khmel et al. (2018).

3. The problem formulation

The geometry of channel with a linear expansion is presented in Fig. 1. The channel is filled with stoichiometric monodisperse suspension of fine (submicron or nano-sized) aluminum particles in oxygen. L₁ is the location of the detonation front at the initial moment; L₂ is the location of the inclination angle. The inclined wall is considered to be a straight line. We analyze the influence of the width of the narrow part of the channel H₁, the inclination angle α, and the particle size d on the flow patterns at the detonation wave propagation into the expanding section of the channel.

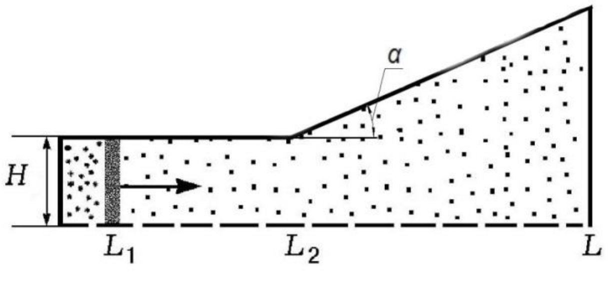

Fig. 1. Flow pattern in a channel with linear expansion

The boundary conditions on the inclined wall are set in accordance with the conditions of non-penetration and thermal isolation: $\partial\phi`/\partial n = 0$, $\rho_i u_{ni} = 0$, where n is the normal to the inclined wall,

$\phi` = \{\rho_i,\ \rho_i u_{si}, \rho_i E_i\}$, normal u_n and tangential u_s with respect to the wall velocity components are found as:

$$\begin{cases} u_n = u_y \cos\alpha - u_x \sin\alpha \\ u_s = u_x \cos\alpha + u_y \sin\alpha \end{cases},$$

where u_x, u_y are the projections on axes X и Y. On the right side of the of computation domain the conditions relate to undisturbed flow, on the left side the outflow conditions are posed. For more exact realization of boundary conditions the mesh is organized in such way that the nodes coincide with the wall. Thus, the ratio between the longitudinal and transverse mesh size depends on the inclination angle.

The numerical technique is based on the conservative flux-splitting schemes: the TVD scheme by Harten for gas and the Gentry-Martin-Daly scheme for particles. The numerical method has been tested earlier and applied for 2-D numerical simulations of the shock wave and detonation flows in Fedorov et al. (2005) – (2018) and Kratova et al. (2011) – (2016). For modelling of detonations in nano-sized aluminum suspensions the step of the finite-difference grid was determined according to the scale of the relaxation zones, varied in the test calculations. Some results of test calculations are presented in Khmel (2017), where also the properties of cellular detonations in nano-sized suspensions are obtained.

4. Detonation modes in channels with linear expansion

Detonation propagation in channels with linear expansion in micron-sized aluminum mixtures was studied in Fedorov et al. (2017) – (2018). It was found that three regimes of detonation propagation in expanded channel are possible: supercritical regime (continuous propagation of detonation), critical regime (with partial failure of detonation and its re-initiation), and subcritical regime (with detonation failure). These regimes are analogous to gaseous detonations and were identified previously in Fedorov et al. (2008), Kratova et al. (2009) for the problem of heterogeneous detonation wave diffraction on a backward-facing step.

Similar to the flow behind a backward-facing step, secondary transverse waves on the front form a cellular structure in the expanding channel. At small expansion angles, this structure is close to regular in the vicinity of the plane of symmetry. Since the cellular detonation in nano-sized suspensions is characterized by irregularities it is of interest to analyze the flow in all regimes of propagation or failing in the expanding channels. The calculations were performed for mixtures of 200 nm and 400 nm particles (corresponding values of the activation energy are E_a=54.53 kJ/mol and E_a=44.82 kJ/mol respectively).

4.1 Subcritical regime (detonation failing)

The subcritical regime is realized in a monodisperse mixture of 200-nm particles at H = 0.02 m and the inclination angle α = 45°. The Schlieren images show that after the detonation wave passing the inclination angle the combustion fronts and the shock wave are separated in the region near the inclined wall (Fig. 2a). At the same time transverse waves develop in the plane of symmetry (Fig. 2a). At the moment of 0.21 ms (Fig. 2c), the combustion front is separated from the shock wave over the entire section. The surface of the combustion front is considerably curved due to the action of transverse waves and the development of Richtmyer-Meshkov instability. The traces of the transverse waves are visible in the maximal pressure fields (Fig. 2c) near the plane of symmetry at $x \approx 0.15$ m. However, re-initiation of detonation does not occur and the transverse waves decay rather rapidly. The same pattern can be seen for the case when cellular detonation wave goes out the plane channel and detonation failure occurs (Fig. 2d). There are two transverse waves which do not provide re-initiation on the inclined wall.

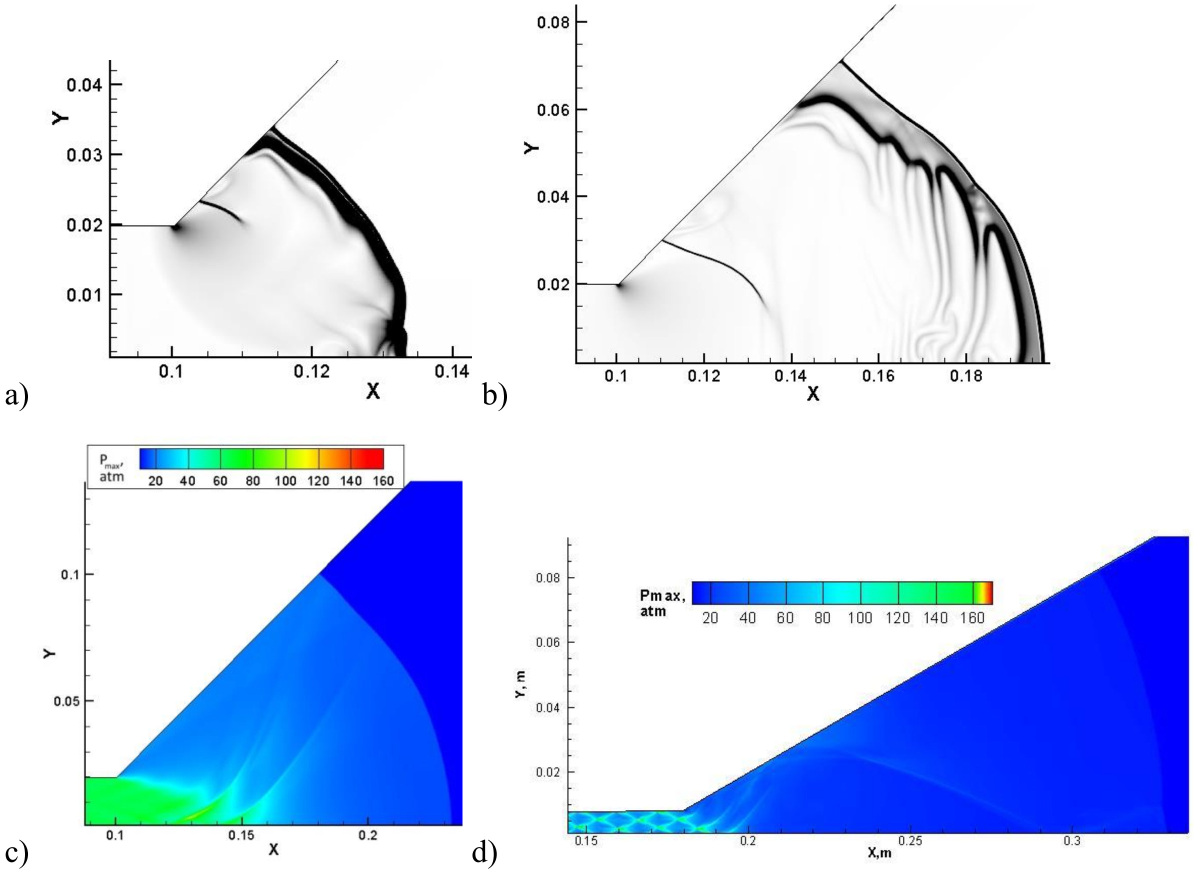

Fig.2. *Subcritical regime (detonation failing) in the expanded channel H=0.02 m, α=45° in mixture with d=200 nm. Schlieren images at different time moments: t=0.08 ms (a), 0.21 ms (b). Maximal pressure fields at t=0.3 ms (c) Maximal pressure fields H=0.008 m, α=30° d=200 nm (d).*

4.2 Critical regime (partial detonation failure with subsequent re-initiation)

In mixture of 400-nm particles in channel with the same parameters as above H=0.006 m, α=45° the regime with detonation re-initiation is realized. The corresponding flow patterns are presented in Fig. 3. In this case three domains of local detonation failures occur: in the plane of symmetry (Fig. 3a), near the wall and in the plane of symmetry (Fig. 3b), and two domains in the central part between the wall and plane of symmetry (Fig. 4c). The traces prints of the separation of the combustion front and the leading shock wave are visible in Fig. 4d as dark blue areas where the pressure falls down to 25 – 30 atm. The detonation re-initiation occurs in transverse waves and is characterized by irregularity of cellular structure and high amplitude of pressure pulsations. The maximal pressures at triple point collisions reach values higher than 200 atm (Fig. 5d, $x \approx 0.32$).

The results presented in Figs. 2-3 reveal the property which is opposite to that for micron-sized particles where increase in particle diameter promotes earlier failure of a detonation. The one reason is that the relaxation zones in nano-sized aluminum detonations are very short with respect to the combustion zone and do not play a decisive role in the processes. The other reason is that the activation energy of the combustion reaction increases with decrease in particle size that does a detonation more sensitive and close to gaseous detonation.

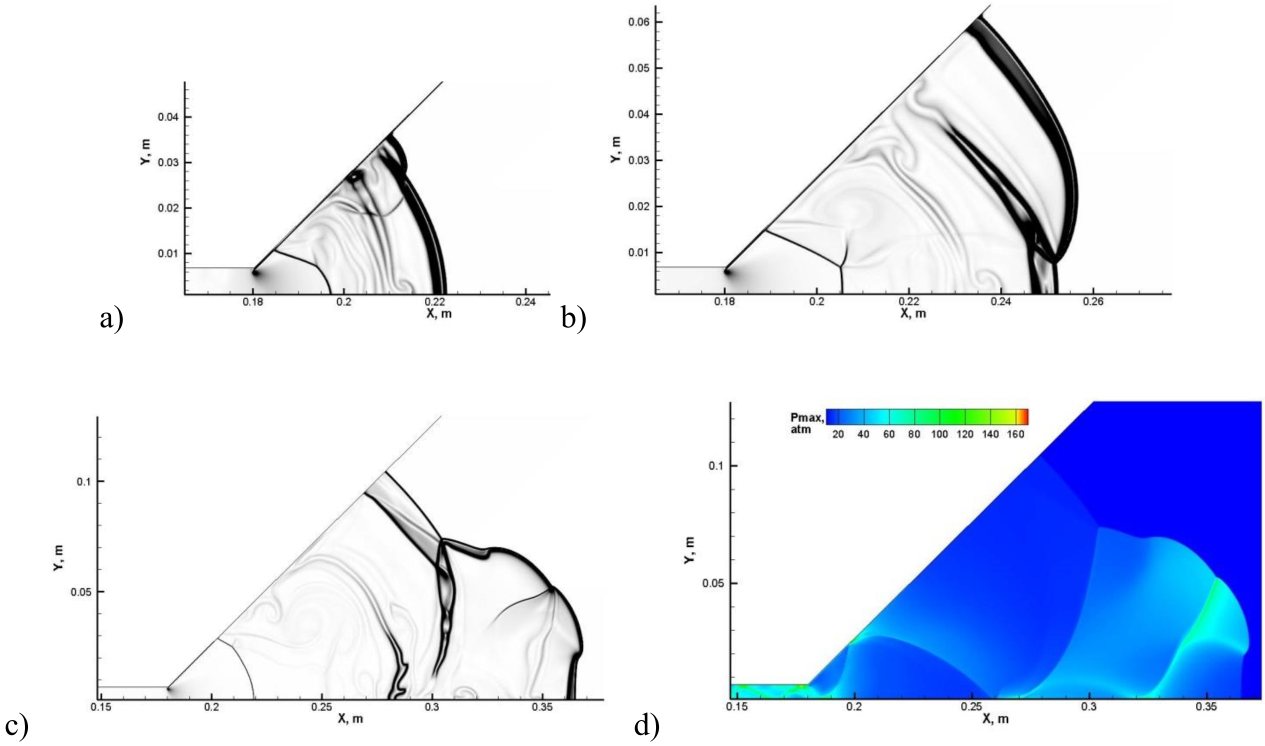

Fig. 3. *Critical regime (partial detonation failing and re-initiation) in the expanded channel H=0.006 m, α=45º in mixture with d=400 nm. Schlieren images at different time moments: t=0.08 ms (a), 0.16 ms (b), 0.26 ms (c). Maximal pressure fields at t=0.26 ms (d).*

Figure 4 shows maximal pressure fields for two cases of critical regimes in mixture of 200-nm particles in wider channels and different inclination angles. In the channel with *H*=0.05 m, α=30º the detonation re-initiation at first occurs near the plane of symmetry (Fig. 4a, 0.15 m < *x* < 0.2 m) where two transverse waves are traced and reflected. The disappearing traces of the secondary transverse waves formed in the central part of the channel (0.13 < *x* < 0.2) indicate significant attenuation of the leading front. The only first transverse wave reaches the inclined wall and the secondary re-initiation takes place in its reflection from the wall (*x* ≈ 0.23). In wider channel *H*=0.1 m, with greater inclination angle α=60º the critical regime is characterized by formation of cellular-like structure in the central part of the channel (Fig. 4b). Here the transverse waves remain and their collisions provide the detonation propagation. The peak pressures in the points of re-initiation or triple point collisions in both cases presented in Fig. 4 exceed 160 atm.

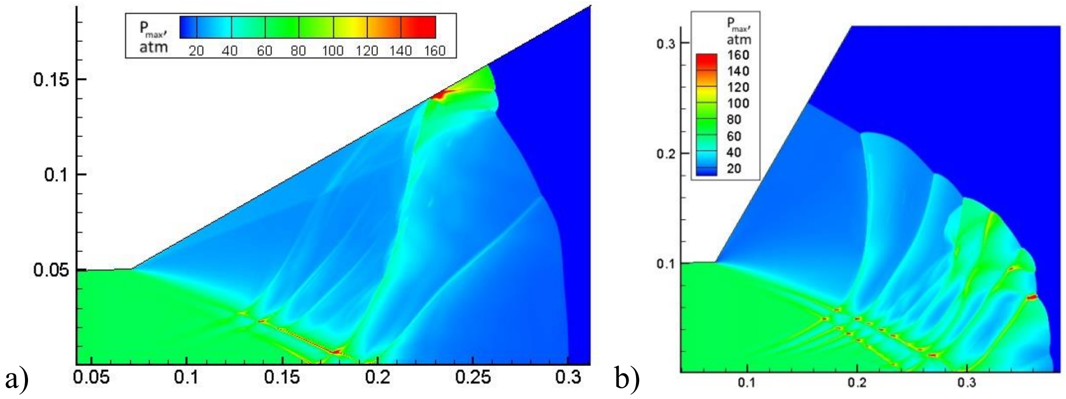

***Fig. 4.** Critical regimes in the expanded channels in mixture with d=200 nm: H=0.05 m, α=30° (a); H=0.1 m, α=60° (b). Maximal pressure fields at t=0.19 ms (a); 0.25 ms (b).*

4.3 Supercritical regime (continuous detonation propagation)

In mixtures of nano-sized particles the supercritical regimes analogous to that obtained in Fedorov et al. (2008), Kratova et al. (2009), Fedorov et al. (2017) – (2018) are not observed. In wide channels or with small values of the inclination angle the modes with local detonation failures and its re-initiation in the transverse waves all the same are implemented. Some regimes close to supercritical are realized in the channel with *H*=0.02 m and α=15° in the 200-nm aluminum suspension and in the channel with *H*=0.04 m and α=45° in the 400-nm mixture. Figure 5 presents the corresponding maximal pressure fields which reveal areas of the local detonation failure with pressure values lower than 40 atm and sufficiently developed cellular structure in the expanded channel with set of the transverse waves along the front.

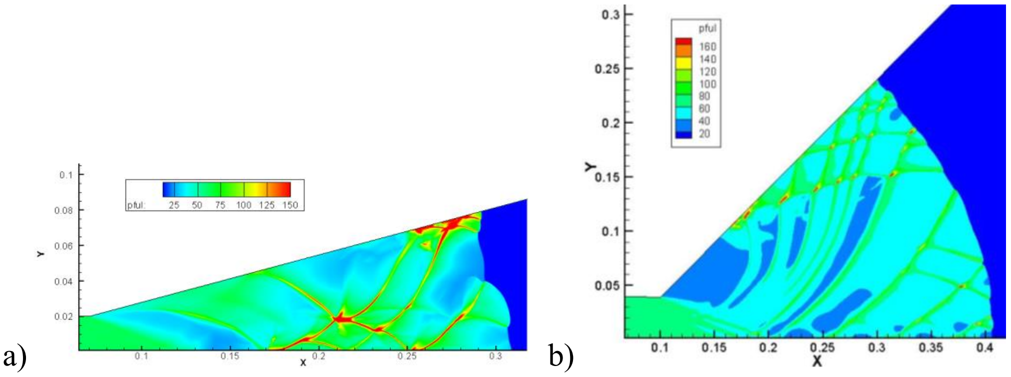

***Fig. 5.** Regimes close to supercritical in the expanded channels (maximal pressure fields): d=200 nm, H=0.02 m, α=15°, t=0.23 ms (a); d=400 nm, H=0.04 m, α=45°, t=0. 3 ms (b).*

5. Critical conditions of detonation propagation in channels with linear expansion

Critical conditions of heterogeneous detonations propagation in plane channels or cylindrical tubes with abrupt expansions for mixtures of micron-sized aluminum particles are discussed in Kratova et al. (2016). The conditions relate the channel width (tube diameter) and the particle diameter. The plane and cylindrical geometric criteria differ by a factor of 2–2.5, which is close to the results for gas detonation. Also the results are consistent with the theoretical curves constructed on the basis of the Mitrofanov–Soloukhin criterion applying to heterogeneous detonations. At the same time, the critical number of the cells is several times smaller than that in gas mixtures, which is caused by principal differences in the particle ignition mechanisms and influence of the thermal and velocity relaxation processes.

The critical conditions of detonation propagation in mixtures of micron-sized aluminum particles in channels with linear expansion were analyzed in Fedorov et al. (2018). The non-monotonic dependence of the critical channel width on the inclination angle was obtained. A possible explanation for this fact is related with qualitative reconstruction of the vortex flow and formation of hanging shocks. This factor also has been discussed for problem of gaseous detonation diffraction from circular tube to cone in Khasainov et al. (2005) where monotonic function consisting in two sections was obtained: linear dependence at angles less than some critical and constant at angles more than critical.

The critical conditions of detonation propagation in terms the critical channel width – the angle of expansion are presented on Fig. 6 for particles 200 nm (Fig. 6a) and 400 nm (Fig. 6b). There are two cases of detonation propagation presented on graphics. In first case cellular detonation does not occur after propagation in plane channel and planar detonation wave exits to the expansion channel (stars – detonation failure for planar DW, squares – detonation propagation for planar DW, solid line – critical conditions for planar DW). In second case in plane channel cellular detonation propagates and detonation front with transverse waves exits in expansion channel (circles - detonation failure for cellular DW, diamonds - detonation propagation for cellular DW, dashed dotted line - critical conditions for cellular DW). Common to both cases is that for angles less 40º for 200 nm and 35º for 400 nm particles, critical conditions are close to each other. In area from 40º to 50º for flat DW it can be seen non-monotonous behavior of critical conditions line that is similar to conditions in Fedorov et al. (2018) for micron particles. For angles greater than 50º critical width of the channel does not depend on the angle of expansion. For cellular detonation case critical conditions are similar to conditions described at Fedorov et al. (2010) paper where detonation failure occurs under condition of half a detonation cell on plane channel. In the range from 40º to 50º for cellular detonation propagation critical line is close to conditions described by Khasainov et al. (2005) for gas detonation.

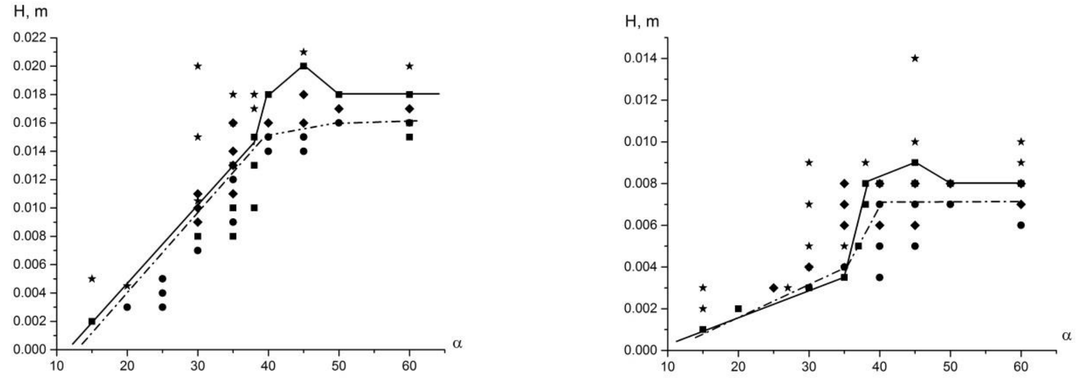

a) b)

Fig. 6. *Map of detonation regimes in the mixture of 200-nm particles (a) and 400-nm particles(b). Stars – detonation failure for planar DW, squares – detonation propagation for planar DW, solid line – critical conditions for planar DW, circles - detonation failure for cellular DW, diamonds - detonation propagation for cellular DW,* dashed dotted line - *critical conditions for cellular DW.*

6. Conclusions

Formation of cellular detonation structures in monodisperse submicron and nanosized aluminum particle suspensions in oxygen in channels with linear expansion is studied by methods of numerical simulations of two-dimensional detonation flows.

The detonation combustion are described within the semiempirical model developed earlier which takes into account transition regime of aluminum particle combustion from diffusion for micro-sized to kinetic for nanosized particles. The free-molecular effects are considered in the processes of heat and velocity relaxation of the phases.

In the problem of detonation propagation in channels with linear expansion tree regimes similar to analogous problem in micron-sized particle suspensions are obtained: subcritical regime (detonation failure), critical regime (partial failing with consequent re-initiation) and supercritical regime (continuous detonation propagation). In nano-sized suspensions the Richtmyer-Meshkov instability develops on the combustion front which is separated and lagging behind the leading shock wave in subcritical regimes. The critical regimes are characterized by existence of extended zones of the detonation failure with re-initiation in transverse waves. In the supercritical regimes multiple separations of the leading front and the combustion front are observed which make them close to critical regimes.

The critical conditions of detonation propagation are determined in terms the channel width – the angle of expansion. The linear dependence takes place to angle 40° for 200-nm particles and 35° for 400-nm particles. Under planar DW as initial condition there is non-monotonous area (from 40º to 50º) similar to micron particles. For angles greater than 50º the critical width does not depend on the angle. With the propagation of cellular detonation in a plane channel, the patterns qualitatively coincide with those presented by Khasainov et. al. (2005).

Acknowledgements

The research was carried out within the framework of the Program of Fundamental Scientific Research of the state academies of sciences in 2013-2020 (project No. AAAA-A17-117030610139-4).

References

Barthel H.O. (1974). Predicted spacings in hydrogen-oxygen-argon detonations. *Phys. Fluids*. 17 (8): 1547–1553.

Bazyn, T., Krier, H. & Glumac, N. (2006). Combustion of nanoaluminum at elevated pressure and temperature behind reflected shock waves. *Combustion and Flame,* 145: 703–713.

Benkewicz, K. & Hayashi, A.K. (2003). Two-dimensional numerical simulations of multi-headed detonations in oxygen-aluminum mixtures using an adaptive mesh refinement. *Shock Waves*, 12(5): 385-402.

Briand, A., Veyssiere, B. & Khasainov, B.A. (2010). Modelling of detonation cellular structure in aluminium suspensions. *Shock Waves,* 20(6): 521–529.

Fedorov, A.V. (1992). Structure of the heterogeneous detonation of aluminum particles dispersed in oxygen, *Combustion, Explosion and Shock Waves,* 28 (3): 277–286.

Fedorov A.V., Khmel' T.A. & Fomin V.M. (1999) Non-equilibrium model of steady detonations in aluminum particles - oxygen suspensions. *Shock Waves* 9(5): 313-318.

Fedorov, A.V. & Khmel', T.A. (2005). Numerical simulation of formation of cellular heterogeneous detonation of aluminum particles in oxygen. *Combustion, Explosion, and Shock Waves,* 41(4): 435-448.

Fedorov A.V., Khmel T.A. (2008). Cellular detonations in bi-dispersed gas-particle mixtures. *Shock Waves*, 18: 277-80.

Fedorov A.V., Khmel T.A., Kratova Y.V. (2008). Shock and detonation wave diffraction at a sudden expansion in gas–particle mixtures. *Shock Waves*, 18: 280-290.

Fedorov A.V., Khmel'T.A., Lavruk S.A. (2017) Exit of a heterogeneous detonation wave into a channel with linear expansion. I. Propagation regimes. *Combust. Expl. Shock Waves*. 53(5): 585-595.

Fedorov, A.V., Khmel, T.A. & Lavruk, S.A. (2018). Exit of a heterogeneous detonation wave into a channel with linear expansion. II. Critical propagation condition. *Combustion, Explosion and Shock Waves*. 54(1): 72-81.

Fedorov A.V., Khmel T.A. (2018) Modeling of plane detonation waves in a gas suspension of nano-sized aluminum particles. *Combust. Expl. Shock Waves,* 52 (2): 74–84.

Hosoda, H., Hayashi, A. K. & Yamada, E. (2013) Numerical analysis on combustion characteristics of nano aluminum particle-oxygen two-phase detonation. *Science and Technology of Energetic Materials,* 74(2): 34-39.

Khasainov, B., Virot, F. & Veyssiere, B. (2013). Three-dimensional cellular structure of detonations in suspensions of aluminium particles. *Shock Waves*, 23: 271–282.

Khasainov B., Presles H.N., Desbordes D., Demontis P., Vidal P. (2005). Detonation diffraction from circular tubes to cones. *Shock Waves,* 14: 187–192.

Khmel T.A.(2017). Cellular detonations in nano-sized aluminum particle gas suspensions. *J. Phys.: Conf. Ser.*

Khmel', T.A., Fedorov, A.V. & Lavruk, S.A. (2018) Modeling of heterogeneous detonation propagation in variable cross-section channels with consideration of transient combustion of aluminum. *AIP Conference Proceedings,* 1939: 020024.

Khmel', T.A. (2019) Modeling of cellular detonation in gas suspensions of submicron and nano-sized aluminum particles. *Combustion, Explosion and Shock Waves,* 55(5): 580-588.

Kratova Yu.V., Fedorov A.V. and Khmel' T.A. (2009). Diffraction of a plane detonation wave on a back-facing step in a gas suspension. *Combust. Expl. Shock Waves*, 45(5): 591–602.

Kratova Yu.V., Fedorov A.V., Khmel' T.A. (2011). Propagation of detonation waves in gas suspensions in channels with a backward-facing step. *Combust. Expl. Shock Waves*. 47(1): 70–80.

Kratova, Yu.V., Khmel, T.A., & Fedorov, A.V. (2016). Axisymmetric expanding heterogeneous detonation in gas suspensions of aluminum particles. *Combustion, Explosion and Shock Waves,* 52(1): 74-84.

Medvedev A.E., Fedorov A.V., Fomin V.M. (1984). Description of ignition and combustion of gas mixtures with solid particles by methods of the mechanics of continuous media. *Combust. Expl. Shock Waves*, 20 (2): 127-133.

Sundaram D.S., Yang V., Zarko V.E. (2015). Combustion of nano aluminum particles (Review). Combust. Expl. *Shock Waves*, 51(2): 173–196.

Strauss, W.A. (1968). Investigation of the detonation of aluminum powder-oxygen mixtures. *AIAA Journal,* 6(12): 1753-1761

Veyssiere, B. & Khasainov, B. (1991) A model for steady, plane, double-front detonations (DFD) in gaseous explosive mixtures with aluminum particles in suspension. *Combustion and Flame*, 85 (1, 2): 241-25.

Veyssiere, B., Khasainov, B.A. & Briand, A. (2008) Investigation of detonation initiation in aluminum suspensions. *Shock Waves,* 18(4): 307-315.

Zhang F., Murray S.B., Gerrard R.B. (2006). Aluminum particle-air detonation at elevated pressures. *Shock Waves.* 15: 313-324.

Zhang, F., Gerrard, K.B. & Rypley, R. (2009) Reaction Mechanism of Aluminum Particles – Air Detonation. *Journal of Propulsion and Power*, 25(4): 845-858.

A Simple Dust Combustion Model for Characterizing Reactivity in Large-Scale Experiments

C. Regis L. Bauwens, Lorenz R. Boeck & Sergey B. Dorofeev
FM Global, Research Division, Norwood, USA
E-mail: carl.bauwens@fmglobal.com

Abstract

Dust explosions present a major hazard in many facilities where combustible dusts are handled, and a range of protection and mitigation strategies have been developed to address these hazards. Assessing the ability of these approaches to successfully mitigate the risk, however, typically requires large-scale testing to ensure their effectiveness. These tests are performed in various facilities with different vessel geometries and injection characteristics, and their reactivity is typically only characterized using an effective large-scale K_{st}, referred to as K_{eff}. This reactivity measure is limited, however, as it only characterizes the maximum rate of pressure rise at a single time and it does not consider when in the process the maximum occurs. To address this limitation, a simple dust combustion model is developed to provide a representative rate of pressure rise generated during a confined dust explosion. This model considers two parameters, a characteristic turbulent burning velocity, and a characteristic reaction time. In this study, it is shown how the model can reasonably reproduce the rate of pressure rise as a function of time for different dust mixtures in different vessel volumes, and how these reactivity parameters can be used to provide a basis for quantifying the overall effective dust reactivity in a large-scale experimental setup.

Keywords: *dust explosions, dust reactivity, large-scale testing*

1. Introduction

Dust explosions can present a severe hazard to property and personnel in a wide range of process industries. To protect against the hazard posed by dust explosions, various protection measures, such as explosion venting, suppression, and isolation, are commonly used to minimize the consequences of these events. In order to adequately protect an enclosure, however, these protection measures must be properly designed to the severity of the dust hazard present. Large-scale explosion testing is commonly used to assess the performance of these protective devices and develop the guidelines for how much explosion venting needed to protect a specific enclosure.

It is well known that different dusts can present significantly different hazards, due to their inherent reactivity (Eckhoff, 2003). The main parameter used to assess the reactivity of a combustible dust is its deflagration index, K_{st}, which is related to the maximum rate of pressure rise during dust combustion in a specific volume. Unlike flammable gases, where the reactivity can be defined independently of a specific test apparatus, using the laminar burning velocity, the deflagration index of a dust is an empirical parameter that is characterized for a specific standard test apparatus. This is because the level of turbulence at the time of ignition is an integral factor that determines the propagation velocity of a dust flame and the severity of the explosion (Amyotte et al., 1988). As a result, for a given dust, the delay between dust injection and ignition is one of the primary factors that determines the severity of the event.

When large-scale testing is performed, it is common practice to calibrate the ignition delay to reproduce the value of K_{st} obtained at smaller scales in standard tests. While the use of K_{st} may be effective for assessing the relative hazard presented by different dusts, it can be easily shown that it is inadequate to describe the behavior of a large-scale dust explosion (Eckhoff, 2015), as it characterizes the reactivity at a late time, and experiments performed with consistent values of K_{st} can produce significantly different rates of pressure rise at the early times when explosion protection devices would activate.

Models have been developed to approximate the rate of pressure rise observed during a confined explosion, (Bradley and Mitcheson, 1976, Tamanini, 1993, Dahoe et al., 1996), but thus far these models lack critical components of dust reactivity, such as a proper treatment of turbulence, are more applicable to gas combustion, and/or are more complex than can be readily deployed. As a result, there is a need for new simple models describing dust combustion to develop a consistent reactivity measure between large-scale experimental setups.

This study demonstrates the fundamental issue of using K_{st} as a parameter to describe the effective dust reactivity in large-scale experiments and develops a new simple method for estimating the pressure rise during dust combustion in a closed vessel. This method is then compared with large-scale experiments performed in an 8-m^3 vessel, where ignition delay and dust concentration were varied, as well as existing experimental data from a 2.5-m^3 and a 25-m^3 vessel.

2. Model

2.1 Model Description

In this study, dust combustion is modeled assuming turbulent dust flame propagation, with a finite reaction time for the dust within the flame region. For fuel rich dust explosions, typical of practical applications, the reaction time represents the consumption time of oxidizer in the flame region. The model assumes that the leading edge of the flame front propagates by turbulent mixing, and that a mixture of unburned dust/air enters the flame or burning region. The unburned mixture is not consumed immediately, however, and within the effective flame radius, r_f, a mixture of burned and unburned dust is present. This model follows formulations for mass and energy conservation consistent with previously developed models (Chao et al., 2015, Boeck et al., 2018) for gas flames where the flame progress is tracked on a mass basis (Boeck et al., 2018). In this model, a simple mass balance of the oxidizer is considered, where its mass in three states is tracked; the unburned mass upstream of the flame, m_u the unburned mass within the flame region, $m_{f,u}$, and the mass of oxidizer contained within the combustion products of the flame region, $m_{f,b}$. The total mass of oxidizer, m_T, is conserved in a closed volume and is given by:

$$m_T = m_u + m_{f,u} + m_{f,b}. \tag{1}$$

Assuming spherical flame propagation, the rate at which unburned mass enters the flame region is given by:

$$\frac{dm_u}{dt} = -4\pi r_f^2 S_T \rho_u, \tag{2}$$

where, r_f is the flame radius, S_T is the turbulent propagation velocity of the leading edge of the flame, and ρ_u is the unburned gas density of the oxidizer. The propagation velocity of the leading edge of the flame is assumed to be governed by turbulent mixing and the scale of the flame radius, proportional to the turbulent fluctuation velocity at this scale. For a Kolmogorov cascade, this yields an increase of S_T with flame radius due to the increase in turbulent length scales present as the flame grows:

$$S_T = ku' \left(\frac{r_f}{R}\right)^{\frac{1}{3}}, \tag{3}$$

where u' is the turbulent fluctuation velocity at an integral scale, R, and k is a proportionality coefficient. As both the level of initial turbulence and the proportionality factor k are not typically known for a specific experimental apparatus, a characteristic turbulent burning velocity $S_{T,0} = ku'$ is used to combine the two values into a single effective reactivity parameter that is specific to a given dust and experimental setup.

The accumulation of unburned mass within the flame region is the balance of the rate at which upstream gas enters the flame region, and the rate unburned gas within the flame region is consumed:

$$\frac{dm_{f,u}}{dt} = 4\pi r_f^2 S_T \rho_u - \frac{dm_{f,b}}{dt}. \tag{4}$$

The rate of gas consumption within the flame region is given by the diffusive transport of oxidizer to burning dust particles. Since the Kolmogorov scale of turbulence is typically larger than the particle size in dust explosions, one can assume that molecular diffusion limits the rate of gas transport. Then, the consumption of the oxidizer is assumed to be proportional to its mass fraction in the flame region, and the molecular diffusion coefficient, yielding:

$$\frac{dm_{f,b}}{dt} = \frac{P_0}{P}\left(\frac{T_f}{T_0}\right)^{1.75} \frac{\rho_0 V}{\tau}\left(\frac{m_{f,u}}{m_{f,u}+m_{f,b}}\right), \tag{5}$$

where τ is a characteristic burning time, which is dependent on dust properties such as particle size distribution (Di Benedetto et al., 2010), turbulence intensity, and the scale of the vessel. The pressure and temperature dependence in Eq. (5) is taken as that of the diffusion coefficient, where P is the vessel pressure, P_0 is the initial vessel pressure, and T_f is the average temperature within the flame region, approximated as:

$$\frac{T_f}{T_0} \approx \frac{\sigma m_{f,b}+m_{f,u}}{m_{f,b}+m_{f,u}}, \tag{6}$$

where σ is the ratio of unburned to burned gas density at ambient pressure. For the purpose of this study a value of $\sigma = 8$ is assumed.

Assuming isentropic compression, the unburned and burned gas densities at a given pressure are:

$$\rho_u = \rho_0\left(\frac{P}{P_0}\right)^{\frac{1}{\gamma_u}}, \quad \rho_b = \frac{\rho_0}{\sigma}\left(\frac{P}{P_0}\right)^{\frac{1}{\gamma_b}} \tag{7}$$

where γ_u and γ_b are the unburned and burned specific heat capacity ratios respectively. As these values are poorly defined for a dust/air mixture, and to simplify the calculation, it is assumed that $\gamma_u = \gamma_b = \gamma^*$, where γ^* is an effective specific heat ratio. A value of γ^* is selected to yield the correct constant volume explosion pressure, $P_{\max}$, and expansion ratio at low pressure, and is calculated using the following expression (Boeck et al. 2018):

$$\gamma^* = \frac{\log(P/P_{\max})}{\log(1/\sigma)}. \tag{8}$$

To evaluate the vessel pressure from the mass balance within the enclosure, we first note that the total vessel volume is constant:

$$V = \frac{m_{f,b}}{\rho_b} + \frac{m_u+m_{f,u}}{\rho_u}, \tag{9}$$

and Eq. (7) and (9) can be combined to yield the following expression for pressure:

$$P = P_0\left((\sigma - 1)\frac{m_{f,b}}{m_T} + 1\right)^{\gamma^*}. \tag{10}$$

The flame radius is then obtained from the flame volume, $V_f = \frac{m_{f,b}}{\rho_b} + \frac{m_{f,u}}{\rho_u}$:

$$r_f = \left(\frac{3V}{4\pi}\left(1 - \frac{m_u}{(\sigma-1)m_{f,b}+m_T}\right)\right)^{1/3}. \tag{11}$$

To obtain the model results, Eqs. (2) and (5) are then solved numerically.

2.2 Model Results

Figure 1 illustrates the model results by showing the effect of varying τ. Here, the rate of pressure rise is compared with a dimensionless pressure $P^* = (P - P_0)/(P_{\max} - P_0)$, which is analogous to a completeness of combustion, and eliminates the effect of time shifts due to ignition and the effect of scale. For all of the curves, the early rate of pressure rise converges as the unburned mass within the flame region takes a finite time to accumulate. These results also illustrate that, as τ approaches zero, the model approaches that of a thin flame assumption, where dP/dt achieves a maximum when the flame reaches the enclosure walls. Note that heat losses are not included in the model, and the observed decrease in dP/dt is due to the decrease in reaction rate as the remaining oxidizer is depleted. For small values of τ, a sharp change in slope in the rate of pressure rise is observed when the flame reaches the vessel walls, as unburned mixture is no longer entering the flame region. As τ increases, it is found that the maximum rate of pressure rise occurs at lower dimensionless pressures, and a smoother transition is seen when the flame reaches the vessel walls, as a larger quantity of unburned fuel is present in the flame region at that time.

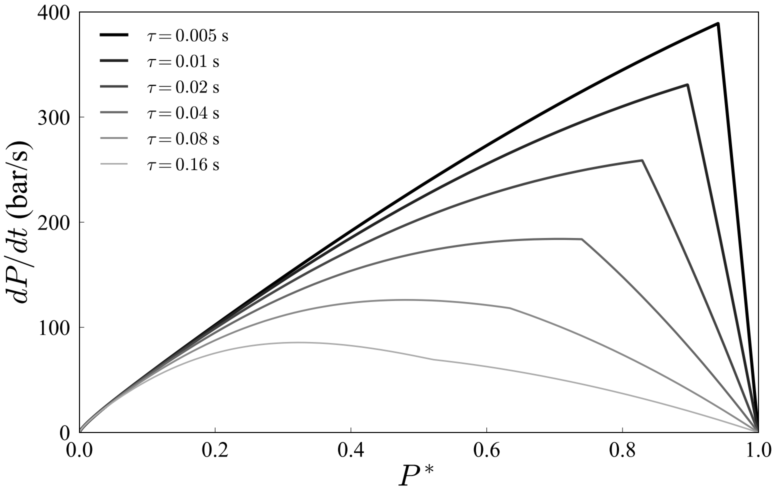

Fig. 1. *Effect of varying* $\boldsymbol{\tau}$ *on model results for* $S_{T_0} = 4$ *m/s in an 8* m^3 *vessel.*

When the value of τ is held constant and the characteristic turbulent burning velocity is varied, as shown in Fig. 2, the rate of pressure rise converges after the flame reaches the vessel walls. This is to be expected, because the reaction rate only depends on τ after all of the upstream oxidizer has entered the flame region. As S_{T_0} increases, the peak pressure occurs earlier in time and at a lower value of the dimensionless pressure.

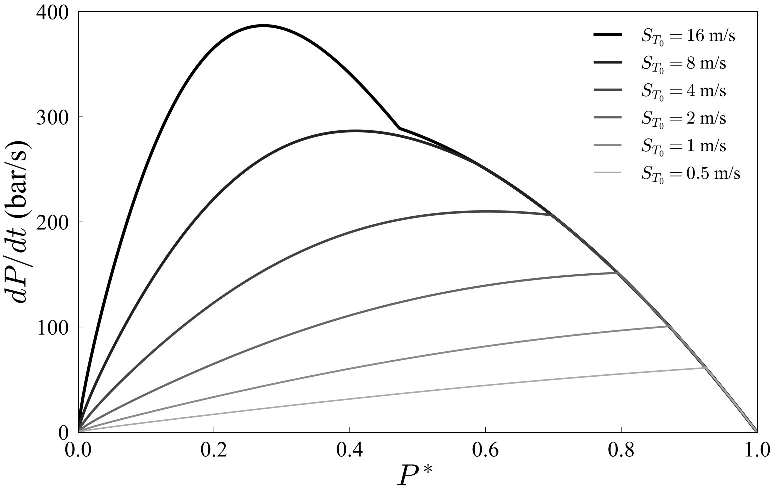

Fig. 2. *Effect of varying S_{T_0} on model results for $\tau = 0.04$ s in an 8-m^3 vessel.*

Figures 1 and 2 show that the maximum rate of pressure rise increases both as S_{T_0} increases and as τ decreases, but each effect shifts the dimensionless pressure at which this occurs in different directions. This behavior suggests a self-similarity of the shape of the pressure rise curve. It was found that a dimensionless shape factor, χ, in the form $\chi = \frac{S_{T_0}\tau}{V^{1/3}}$ can characterize the shape of the curves. The effect of χ on the rate of pressure rise is shown in Fig. 3, where the rate of pressure rise is normalized by its maximum value. Furthermore, it should be noted that the maximum rate of pressure rise varies with $V^{1/3}$, for a given value of S_{T_0} and χ, which is consistent with the scaling assumed for K_{st}.

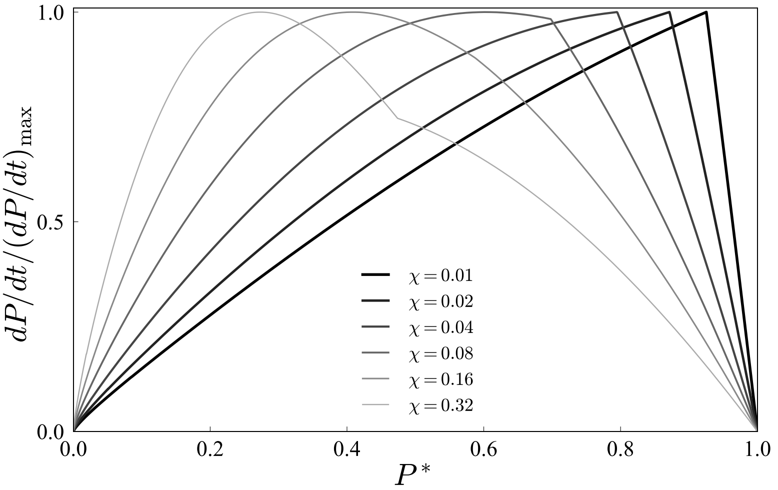

Fig. 3. *Effect of varying the shape factor, χ, on the model results.*

3. Experiments

To support the development of the new simple dust combustion model, a series of closed volume dust explosion experiments were performed in an 8-m^3 vessel, with a height-to-diameter ratio of 1.45, as described in previous studies (Chao and Dorofeev, 2015, Boeck et al. 2018). For this work, cornstarch dust explosion tests were performed, where the ignition delay, t_{d}, defined as the time between the start of injection and ignition, and the dust loading, ρ_{d0}, were varied. Three dust loadings were examined, $\rho_{d_0} = 750$, 1150, and 1500 g/m^3 and the ignition delay was varied between 0.6 and 1.0 s.

DOI: 10.7795/810.20200724

Fig. 4. *Image of the 8-m^3 test vessel showing the location of two dust injectors.*

Dust was injected into the vessel using four independent dust injectors. The injectors were oriented in two counter-flow pairs, with each pair located roughly 1/3 of the vessel height from the top and bottom of the vessel respectively, as shown in Fig. 4. Each injector was driven by a 150-L air cannon operating at 8.2 barg, which forces compressed air through a dust hopper followed by a 4-inch diameter dispersion nozzle into the vessel. Pressure within each air cannon was measured during injection to ensure consistent discharge and confirm ignition delays. Before each test, the dust was conditioned to reduce the moisture content to below 1% by mass, and the dust was loaded into the hoppers in a humidity-controlled environment. After the hoppers were loaded into the dust injectors, they were only opened immediately prior to injection to ensure a stable dust moisture content.

Prior to dust injection the vessel was evacuated to an initial pressure, on the order of 0.5 bar, such that the final pressure after dust injection was 1 bar. Following dust injection, the mixtures were ignited using a single 10 kJ-Sobbe ignitor located at the center of the vessel, and each dust injector was sealed using a fast-acting explosion isolation valve to prevent combustion products from entering the dust injection system during the test, and to allow for short ignition delays. The pressure rise during each test was measured at three locations using Kistler 4260A 0-10 bar piezo-resistive pressure transducers. Throughout the experiments, the measurements obtained between the different transducers were effectively identical and only the results obtained from a transducer at the mid-height of the vessel, filtered using an 80-Hz low-pass filter, were used in this study.

4. Results and Discussion

To examine the ability of the model to reproduce the profiles observed in each test, values for the parameters S_{T_0} and τ were fitted to each experimental curve. For the purpose of this study, it was assumed that $P_{\text{max}} = 9$ bar, and $\sigma = 8$ for all mixtures and test parameters.

4.1 Effect of Vessel Volume

To examine the effect of vessel volume, experiments performed in the 8 m^3-vessel are compared with experimental data previously collected in geometrically similar 2.5- and 25-m^3 vessels for test configurations that produced similar values of K_{eff} for cornstarch with a dust loading $\rho_{d0} = 750$ g/m^3.

While geometrically similar, these experiments were performed with a substantially different injection system, equivalent to that used in a previous study (Chao and Dorofeev, 2015).

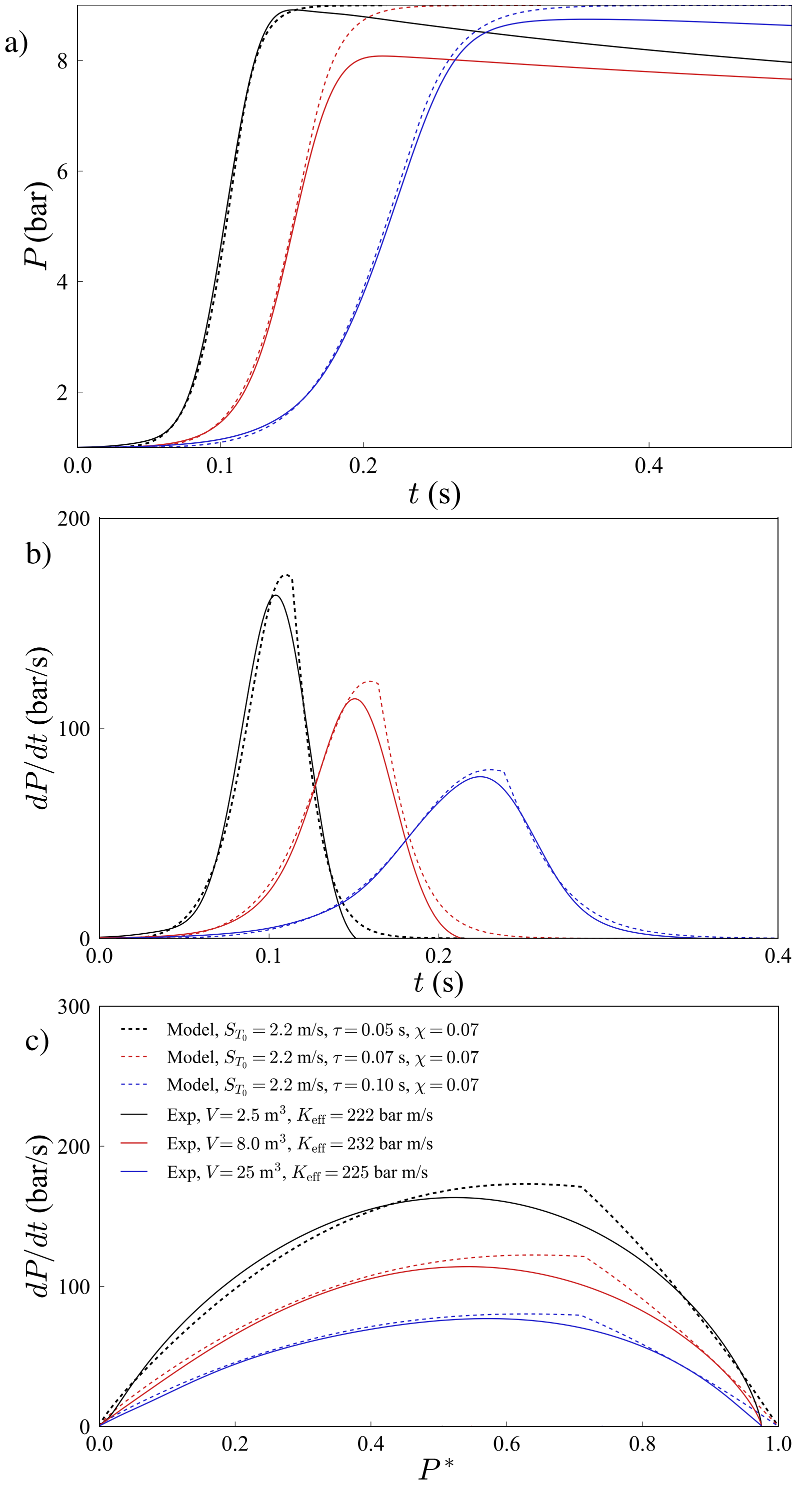

Fig. 5. *Effect of vessel volume on cornstarch dust explosions with a dust loading of* ρ_{d0} *=750 g/m*^{3} *and nominal* K_{eff} *≈225 bar m/s*

It can be seen that good agreement is obtained between the simple model and experimental results for all three vessel volumes, Fig. 5. In dimensional terms, Fig. 5a shows vessel pressure as a function of time, where the model curves were shifted in time to match the overall shape of the curve to eliminate ignition effects, resulting in good qualitative agreement. When examining the rate of pressure rise,

Fig. 5b, it can be seen that the model results overshoot the experiments. This can be partially explained by the effect of heat loss when the flame front reaches the vessel walls, which is an not considered by the model. It is interesting to note that, while τ increased with volume, the best fit prodices values of χ that remain constant between the different volumes, as shown in Fig. 5c, despite the different dust injection systems used. Furthermore, S_{T_0} is also equivalent between tests. These results suggest that there is some universality of the shape factor for a given dust reactivity and that the volume scaling obtained using this method is compatible with that currently used for K_{eff}.

4.2 Effect of Ignition Delay and Dust Type

In the cornstarch dust explosions where ignition delay was varied, Fig. 6, it was found that χ also does not vary strongly with ignition delay. Instead, virtually all of the difference in reactivity can be attributed to differences in the turbulence intensity. The model captures this behaviour, and it is seen that the characteristic turbulent burning velocity increases significantly as ignition delay decreases.

To examine this effect on another type of dust, existing experimental data from experiments performed in the 8-m^3 vessel with powdered sugar is used. While it should be noted that the previous injection system, (Chao and Dorofeev, 2015), was used, the results from the volume comparison demonstrate that the injection system did not have a strong effect on the results for cornstarch in the 2.5-m^3 and 25-m^3 vessel experiments.

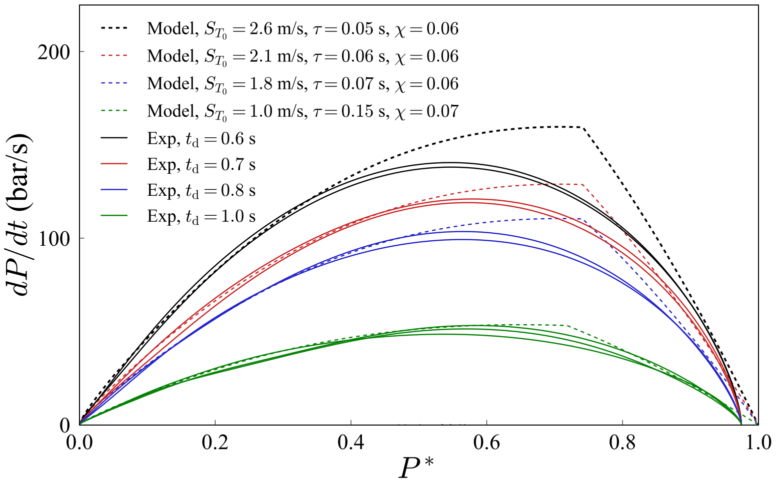

Fig. 6. *Varying ignition delay for* ρ_{d0} = *750 g/m*^{3} *of cornstarch in the 8-m*^{3} *vessel.*

When compared to the results for cornstarch in the 8-m^3 vessel, the model requires significantly higher values of τ and χ to capture the shape of powdered sugar pressure profiles. This suggests much slower reaction rates and, as a result, the maximum rate of pressure rise occurs at much lower normalized pressures. Using these parameters, the model reproduces the overall shapes of these pressure rise curves.

These curves have a distinctively different profile compared to the cornstarch experiments. They demonstrate how significantly different rates of pressure rise at lower pressures can occur in tests that produce the same K_{eff}, which would have significant implications on the performance of explosion protection devices and the pressures that would be achieved for a specific venting configuration.

DOI: 10.7795/810.20200724

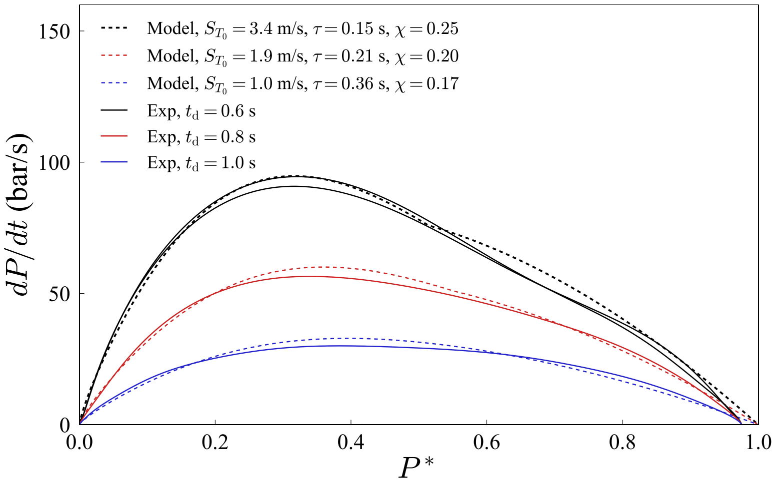

Fig. 7. *Varying ignition delay for ρ_{d0} = 750 g/m^3 of powdered sugar in the 8-m^3 vessel.*

4.3 Effect of Dust Loading

When the effect of elevated dust loading was examined, Figs. 8 - 9, it was found that a higher dust loading increased χ and decreased S_{T_0}. This is to be expected, as the increased mass of dust being injected will significantly affect the development of turbulence within the enclosure, resulting in a drop in turbulence intensity and a reduction in the characteristic turbulent burning velocity. Furthermore, the increased dust loading may also increase the characteristic burning time τ, and correspondingly χ, by both reducing the bulk concentration of oxidizer in the flame region and increasing the thermal mass of the unburned mixture. This is seen for both an ignition delay of t_d = 0.7 s, and t_d = 0.8 s, where, for a given dust loading, an increase in ignition delay only reduces S_{T_0}, while χ remained constant.

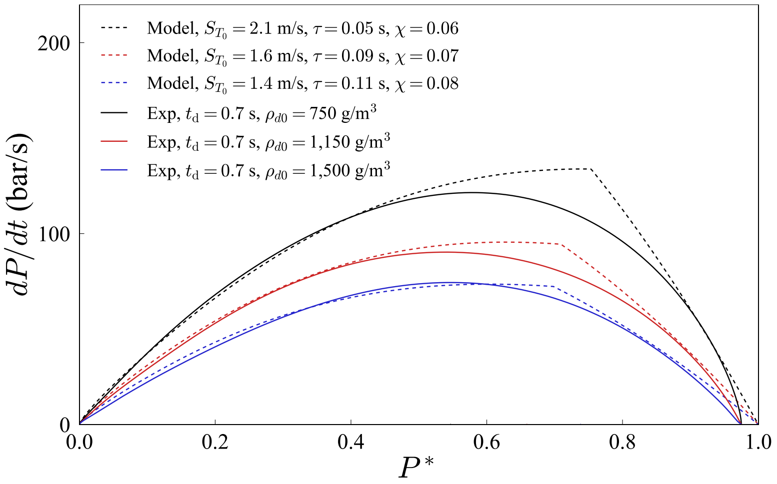

Fig. 8. *Varying dust loading, ρ_{d0}, of cornstarch in the 8-m^3 vessel with an ignition delay, t_d = 0.7 s.*

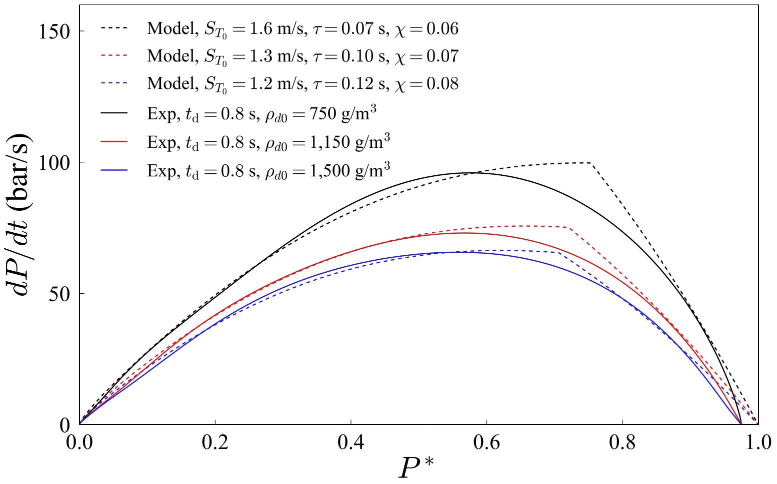

Fig. 9. *Varying dust loading, ρ_{d0}, of cornstarch in the 8-m^3 vessel with an ignition delay, $t_d = 0.8$ s.*

4.4 Discussion

The simple model demonstrates how a larger portion of a pressure-time history can be incorporated to assess the overall dust reactivity observed in a large-scale experiment using only two parameters. The fact that the value of χ for cornstarch only varies slightly, in the range of 0.06 - 0.08, across all of the ignition delays, volumes, and dust loadings examined in this study provides interesting insight. This suggests some universality of the value of χ for a given dust at a specified dust loading over a range of concentrations. The significantly higher values of χ observed in powdered sugar experiments, and its variation with ignition delay, may have been the result of the relatively low reactivity of powdered sugar (K_{st} = 60 bar m/s) relative to that of cornstarch (K_{st} = 160 bar m/s). The high level of turbulence needed to force powdered sugar to behave like a dust with a significantly higher K_{st} is likely responsible for much of the difference. Nevertheless, the powdered sugar test performed with the longest ignition delay had a K_{eff} equivalent to its K_{st}, i.e. $K_{\mathrm{eff}} = K_{\mathrm{st}} = 60$ bar m/s, yet still required a significantly higher value of χ, suggesting differences in dust also plays a strong role.

For a given value of χ, the model attributes the change in the rate of pressure rise to changes in S_{T_0}, and this value alone can be used as a parameter to assess overall reactivity. Furthermore, if the values of S_{T_0} and χ are reproduced between different experimental setups, the rate of pressure rise, as a function of vessel pressure, will also be reproduced. This method can be used to ensure test consistency over range of pressures/flame radii, rather than at a single point like the current K_{eff} methods by only specifying target values of S_{T_0} and χ. The model can also be tuned to focus on the specific part of the curve of interest, to characterize tests performance during early flame transients, which is of critical importance in applications examining the activation of explosion protection devices.

Further work is still needed to improve the model. First, the effect of vessel geometry/aspect ratio still needs to be assessed through a comparison of data from different experimental setups. In addition, data from different injection systems and different dusts should be examined to ensure no additional parameters need to be added to the model. Finally, the addition of heat loss to the model may also be incorporated to improve its behaviour at late times.

5. Conclusions

In this work, a simple dust flame combustion model is developed based on two parameters, a characteristic turbulent burning velocity and a characteristic reaction time. If was found that the model can reproduce the experimental rate of pressure rise observed in a wide range of experiments where ignition delay, dust loading, vessel volume, and dust composition were varied. The model suggests that, for a given shape of the pressure rise curve, the maximum rate of pressure rise scales with $V^{1/3}$, which is consistent with the scaling currently used to evaluate the effect of volume on K_{st} and K_{eff}.

By comparing cornstarch dust explosion tests with those performed using powdered sugar, it was shown how the shape of the rate of pressure rise curve can vary significantly and the maximum rate of pressure rise can occur at considerably lower pressures. This has significant implications when assessing the performance of explosion protection devices and demonstrates how only using a single value of K_{eff} is insufficient to characterize the behavior of a large-scale explosion test.

By specifying target values of S_{T_0} and χ for a given test, this model can provide a rigorous methodology through which equivalency can be ensured between different experimental setups, dusts, and dust loadings and can also provide a starting point for creating models describing the pressure development during dust explosions in more complex configurations.

Acknowledgements

The work presented in this paper was funded by FM Global and performed within the framework of the FM Global Strategic Research Program on Explosions and Material Reactivity. The technical assistance of Kevin Mullins, Thomas Lapierre, and Joseph Marte in preparing and conducting the tests is greatly appreciated.

References

Amyotte, P. R., Chippett, S., & Pegg, M. J. (1988). Effects of turbulence on dust explosions. *Progress in Energy and Combustion Science*, 14(4), 293-310.

Boeck, L.R., Bauwens, C.R., & Dorofeev, S.B. (2018). A physics-based model for explosions in vented vessel-pipe systems. *12th International Symposium on Hazards, Prevention, and Mitigation of Industrial Explosions*, Kansas City, USA.

Bradley, D., & Mitcheson, A. (1976). Mathematical solutions for explosions in spherical vessels. *Combustion and Flame*, 26, 201-217.

Chao, J., Lee, J. H., Bauwens, C. R., & Dorofeev, S. B. (2015). Laminar burning velocities of various silanes. *Journal of Loss Prevention in the Process Industries*, 36, 471-477.

Chao, J., & Dorofeev, S. B. (2015). Evaluating the overall efficiency of a flameless venting device for dust explosions. *Journal of Loss Prevention in the Process Industries*, 36, 63-71.

Dahoe, A. E., Zevenbergen, J. F., Lemkowitz, S. M., & Scarlett, B. (1996). Dust explosions in spherical vessels: the role of flame thickness in the validity of the ‘cube-root law’. *Journal of Loss Prevention in the Process Industries*, 9(1), 33-44.

Di Benedetto, A., Russo, P., Amyotte, P., & Marchand, N. (2010). Modelling the effect of particle size on dust explosions. *Chemical Engineering Science*, 65(2), 772-779.

Eckhoff, R.K. (2003). *Dust explosions in the process industries*. Third edition. Gulf Professional Publishing, Amsterdam.

Eckhoff, R. K. (2015). Scaling of dust explosion violence from laboratory scale to full industrial scale–A challenging case history from the past. *Journal of Loss Prevention in the Process Industries*, 36, 271-280.

Tamanini, F. (1993). Characterization of mixture reactivity in vented explosions. *14th International Colloquium on the Dynamics of Explosions and Reactive Systems* (pp. 1-6). Coimbra, Portugal: University of Coimbra.

DOI: 10.7795/810.20200724

Quasi-static dispersion of dusts for the determination of lower explosion limits of hybrid mixtures

Zaheer Abbas[a], Olivier Dufaud[b], Dieter Gabel[a], Arne Krietsch[c] & Ulrich Krause[a]

[a] Institut für Apparate- und Umwelttechnik, Otto-von-Guericke Universität, Magdeburg, Germany
[b] Laboratoire Réactions et Génie des Procédés, Université de Lorraine, Nancy, France
[c] Bundesanstalt für Materialforschung und -prüfung, Berlin, Germany

E-mail: zaheer.abbas@ovgu.de

Abstract

Knowledge of explosion limiting concentration of explosible materials is necessary for the design of explosion protection measures. Currently employed methods of testing MEC of a dust cloud or LEL of a hybrid mixture are based on arbitrary assumptions and possess technical limitations that often lead to values of MEC/LEL, which are unrealistically low or poorly reproducible.

This contribution presents an improved method for experimental determination of MEC of a combustible dust cloud or LEL of a flammable gas or hybrid mixture. The new set-up operates under laminar conditions and allows a uniform suspension of dust particles in an open top acrylic glass tube. Dust concentration is measured with the help of infrared sensors installed a few centimeters above and below the ignition source.

In order to evaluate the dependence of MEC on flow front velocity, MEC of lycopodium was determined at four flow velocities. The results show that the flow field intensity does not significantly influence the MEC of lycopodium for the flow ranges tested in this work. Moreover, LEL of hybrid mixtures of lycopodium and methane was also tested at flow velocities of 4.7 cm/s, 5.8 cm/s, 7 cm/s and 11 cm/s and compared with the values obtained from other sources. The results suggest that the requirement of high energy pyrotechnical igniter may be relinquished, provided that a truly homogeneous suspension of dust particles could be achieved.

Moreover, the effect of relative amount of dust and gas, on the course of ignition and flame propagation in hybrid mixtures at their LEL, was studied by the help of high speed videos. For hybrid mixtures of carbonaceous dusts (like lycopodium) at their LEL, ignition occurs in the gas phase, however, flame propagation is only possible through a two-way interaction of dust and gas during the course of combustion.

Keywords: *Lower Explosion Limits, Hybrid mixtures, Flame propagation*

1. Introduction

Protection systems against dust, gas or hybrid mixture explosions are commonly designed based on characteristic data, which describe the explosion sensitivity and explosion severity of the material under consideration. One of these characteristic parameters is the explosion limiting concentration of the combustible material, referred to as minimum explosible concentration (MEC) for particulate materials and lower explosion limit (LEL) in case the combustible material is a gas or a mixture of dust and gas, also known as hybrid mixtures.

According to the EN standard, MEC of a dust cloud is measured in standard 1 m^3 sphere. Annex C of DIN EN 14034-3 (2011) quotes “an alternative type of test equipment, for which the conformity has been proven, is the 20 l sphere”. Over past few decades, the use of 20-l sphere has gained more popularity than the 1 m^3 vessel because of its cost effectiveness and relatively easier and quicker operation. However, the wide use of 20-l sphere is accompanied by a number of sources of uncertainties related to device configurations, experimental procedure and data treatment protocol, which lead to values of MEC or LEL that are either too low or poorly reproducible (Babrauskas and Britton, 2018). A classic example in this regard is the MEC of corn starch in air, with the reported values ranging from 8 g/m^3 to 400 g/m^3 (Eckhoff, 2003; Makris, 1988). This contribution analyses the sources of errors that lead to the discrepancies in the experimentally determined MEC of a dust cloud or LEL of a hybrid mixture and presents an improved method for their determination.

DIN EN 14034-3, 2011 defines MEC of a dust cloud as the lowest concentration of dust (or other combustible/flammable material) in mixture with air at which an explosion will occur. The same standard in Annex C.4 states that the highest concentration of a combustible dust at which no explosion occurs in three consecutive tests shall be taken as the lower explosion limit. Moreover, the test procedure is designed in a way that the highest non explosible concentration is always 50% of the lowest explosible concentration. This means that if, for a given dust, there was an explosion recorded at 125 g/m^3 and a no-explosion at 60 g/m^3 (i.e. ≈50% of the preceding concentration) in three consecutive tests, according to the standard protocol the reported LEL/MEC would be 60 g/m^3. Best guess of the true LEL/MEC for this particular dust, however, would be an arithmetic mean of 125 g/m^3 and 60 g/m^3, yielding ≈90 g/m^3 as MEC value. This induces an apparent uncertainty of 50% of the reported MEC value, which does not agree with the information included in the test report stating that the results might deviate up to 10% (DIN EN 14034-3, 2011).

As part of the standard reporting protocol, particle size distribution of the tested dust shall be measured before the commencement of experiments and shall be included in the test report. It is globally agreed upon that the MEC of a dust cloud varies with changes in the particle size distribution of the tested powder (Amyotte, 2013; Baker and Tang, 1991; Bartknecht, 1989; Dufaud et al., 2012; Eckhoff, 2003; Ogle, 2016). Several studies have been performed to investigate the impact of high pressure air blast dispersion, during the explosion experiments, on the particle integrity. The work of Bagaria et al., Du et al. and Kalejaiye et al. is of prime importance in this regard (Bagaria et al., 2017; Du et al., 2015; Kalejaiye et al., 2010). Kalejaiye et al. (2010) investigated the effect of dust dispersion system on particle breakage in 20-l sphere by measuring particle size distribution before and after dispersion. They performed a total of 540 tests at different nominal concentrations of three dusts, namely, Gilsonite, purple K and Pittsburgh coal using the rebound and perforated annular dispersion nozzles and reported that the size after dispersion was about 50%, 80% and 40% of the original size for Gilsonite, purple K and Pittsburgh coal dust respectively. They attributed the particle size reduction to the unique design of the outlet (dispersion) valve and dispersion nozzle, which impose a strong shearing effect on the dust particles as they flow through. The effect of dust concentration on the extent of particle size reduction was found to be negligible. Bagaria et al. (2017) and Du et al. (2015) reported similar data in terms of particle size reduction during dispersion, however, contrary to the findings of Kalejaiye et al. (2010), they observed that there was a decrease in the particle breakage with increasing dust concentration, owing to the decreased probability of impact per particle. This suggests a maximum particle breakage at the concentrations near the MEC of the dust. Concluding this discussion, it could be attested that the specimen tested in the 20-l sphere has a notably smaller diameter distribution than the original specimen, which consequently results in overly conservative values of MEC.

One fundamental flaw in the design of the 20-l sphere test procedure is the use of pyrotechnical igniters. DIN EN 14034-3 (2011) recommends using two chemical igniters each having an energy of 1 kJ, whereas (ASTM 2014) advises measuring the MEC at 2.5 and 5 kJ. LEL/MEC, by definition is the lowest concentration at which a self-sustained flame propagation is achieved. The activation of pyrotechnical igniters, irrespective of their energy content, creates a fireball of burning particles that is way bigger than the size of the sphere and practically covers the whole available space (Taveau et al., 2017). A self-sustained flame propagation through dust air mixture cannot be achieved under these conditions and, as a consequence, each test is rather an igniter induced flame propagation.

Other sources of unreliability of the reported MEC values of dusts include errors due to database abridgment and differences in the definition of an explosion or ignition (visual flame propagation or a certain pressure rise), dust cloud non uniformity and the consideration of nominal concentration, and constant ignition delay time for all types of dusts and highly fluctuating turbulence levels, which are discussed in detail by Babrauskas and Britton in their recent work (Babrauskas and Britton, 2018). Sources of discrepancies between data of a same compound can also be found in the variations of the moisture content, the standard deviation of the particle size distribution or the powder shape factor.

For hybrid mixture LEL testing, no standard device or protocol has been defined so far. Most common experimental apparatus used for this purpose is 20-l sphere, following same protocol as for the MEC determination with an addition of introduction of flammable gas in the system. This is usually done by partial pressure method. Results reported in literature for the LEL of hybrid mixtures also possess inconsistencies (Cloney, Ripley et al. 2018). An example is useful.

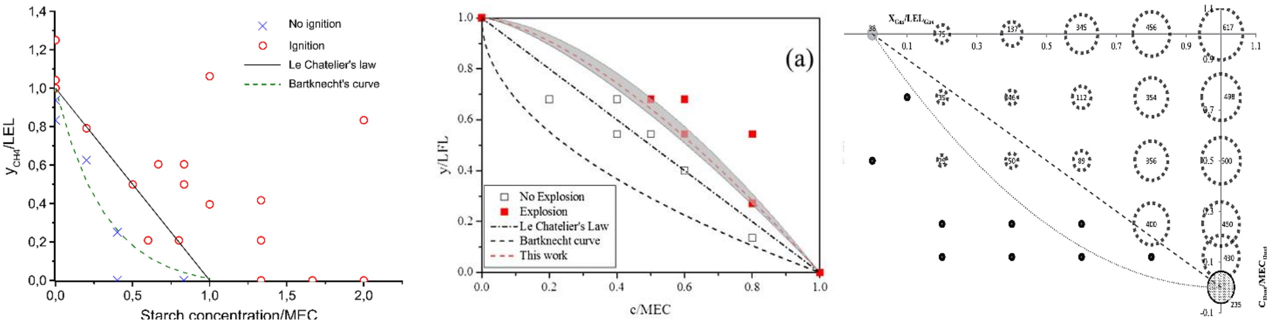

Fig. 1: LEL of hybrid mixture of starch and methane from left to right (Khalili et al., 2012), (Jiang et al., 2014) and (Addai et al., 2015a)

Hybrid mixture of starch and methane is one of the most commonly tested hybrid mixture. Figure 1 provides a comparison of decrease in starch concentration in hybrid mixture with addition of small amounts of methane, measured experimentally at three laboratories. Although the difference in the median particle size (d_{50}) of all three starch samples lied in a narrow range of ± 6 µm, conflicting conclusions were deduced. Jiang et al. (2014) claimed that amount of dust required to render the hybrid mixture of starch and methane explosible is higher than the one predicted by Le Chatelier's law or the Bartknecht's curve. Khalili et al. (2011), on the other hand, highlighted that the explosible concentration of dust in a hybrid system is less, in comparison to the theoretically calculated value using Le Chatelier's law, however, more than the concentration of dust predicted by Bartknecht's curve. In contrast to the findings of Jiang et al. (2014) and Khalili et al. (2011), Addai et al. (2015a) concluded in their research that hybrid mixture of starch and methane is explosible in the concentration ranges even below the Bartknecht's curve. The reason behind these contradictory findings is the inherent sources of uncertainties or errors that make the results of these experiments stochastic in nature and consequently lead to poor reproducibility.

Taken together, above discussion implicates the need for an improvement in the design of standard experimental apparatus and procedure as well as in the data analysis protocol in order to improve the MEC/LEL data quality and achieve better reproducibility. The focus of this research work is to develop a new and improved method for experimental determination of MEC of a dust cloud and LEL of a hybrid mixture. Achieved experimental results are then to be compared with the experimental as well as theoretical results of other authors, accompanied by a discussion on validation and scientific justification of the presented results. Furthermore, this paper explores the contribution of dust and gas on the ignition step and flame propagation mechanism in hybrid mixtures at their lower explosion limit.

2. Materials and Methods

2.1.Material characterisation

Hybrid mixtures of lycopodium and methane, were selected for the experimental investigations of this work. Moisture content was determined using a thermogravimetric moisture analyser (Satorius® MA100) in compliance with ISO 5071:1996. In order to define the LEL of hybrid mixtures in molar units, average molecular mass lycopodium must be defined. This has been established by analysing the quantitative elemental analysis data, collected in-house by using CS230 (LECO®) for Sulphur and CHN628 (LECO®) for carbon, hydrogen, oxygen and nitrogen, in accordance with ISO 29541 and ISO 19579:2002 respectively. Moreover, heat of combustion or calorific value was systematically determined by employing a combustion calorimeter (IKA®, C 200). The measured values were validated according to DIN 51900, ISO 1928 and ASTM D5865.

Table 1: *Properties of lycopodium and methane*

Dust sample	**Moisture Content**	**Calorific Value**	**Elemental analysis (%wt.)**					**Av. M.wt**	**Particle Size distribution**		
			C	**H**	**O**	**S**	**N**		**d_{32}(μm)**	**d_{50}(μm)**	**d_{90}(μm)**
Lycopodium	3 %wt.	30.1 MJ/kg	68	9.6	21	0.3	1	76 g/mol	30.3	31.7	37.9

Gas	**M.wt (g/mol)**	**Density (g/m^3)**	**Heat Capacity (J/mol.K)**	**Calorific Value (kJ/mol)**
Methane	16	675.2	35.52	891.2

According to ASTM and European standards, particle size distribution of the dust material must be determined before the commencement of explosion experiments. This was measured by using a multi-wavelength laser diffraction particle size analyser (Beckman Coulter LS 13320 CAMSIZER®) according to ISO 13319:2007. The samples were characterized by the d_{32}, d_{50} and d_{90} quantiles of the volumetric distribution as indicated in Table 1. Due to the narrow particle size distribution, the particle segregation during the dust dispersion could be neglected. Dust particles were also examined under scanning electron microscope (SEM), to reveal their surface structure (Figure 2).

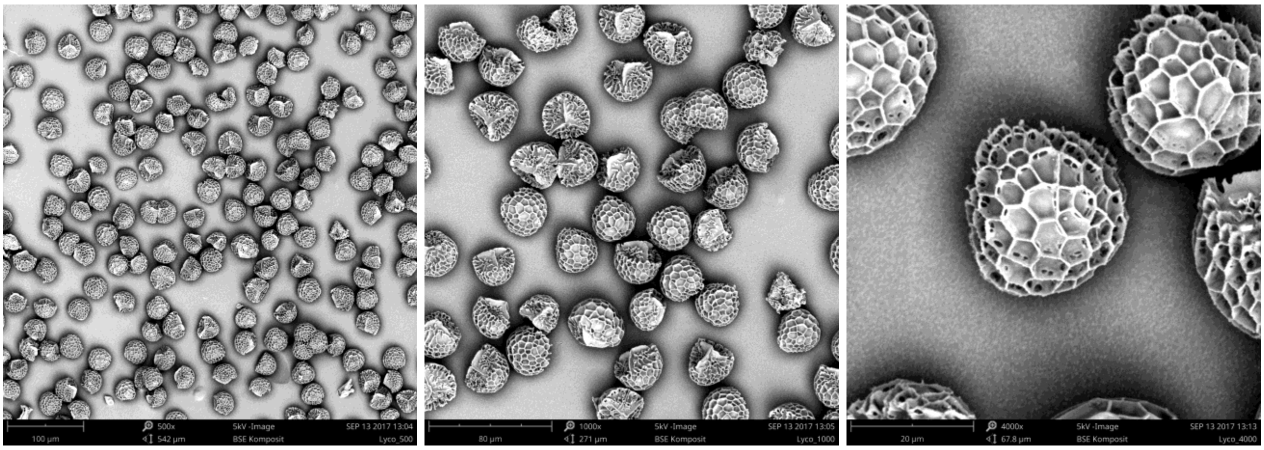

Fig. 2: *SEM images of lycopodium*

2.2.Experimental setup and procedure

For experimental purposes of this research work, a special stand has been designed and constructed, enabling a reliable measurement of MEC/LEL of dust and hybrid mixtures in a non-turbulent environment. The conceptual design of the experimental device is based on an open-tube apparatus, first introduced by Krause et al., in 1996 to investigate the influence of flow field intensity and turbulence on flame propagation through dust-air mixtures. The set-up consists of a vertically mounted acrylic glass tube of 1000 mm length, with an internal diameter of 60 mm and a wall thickness of 5 mm. The upper end of the tube remained open to allow for venting of gaseous combustion products and to ensure constant pressure conditions during the reaction. The bottom end of the tube is closed with a filter paper, resting on a sintered glass filter (diameter 70 mm, thickness 5.5 mm and 40-100 µm pore size) and a bed of steel wool. The filter disc together with the steel wool acts as a flow rectifier, facilitating a uniform profile of the flow velocity. The tube is equipped with two brass electrodes, installed at a height of 330 mm from the bottom end and connected to a high voltage transformer, producing a permanent electrical spark of 10J for a duration of 50ms.

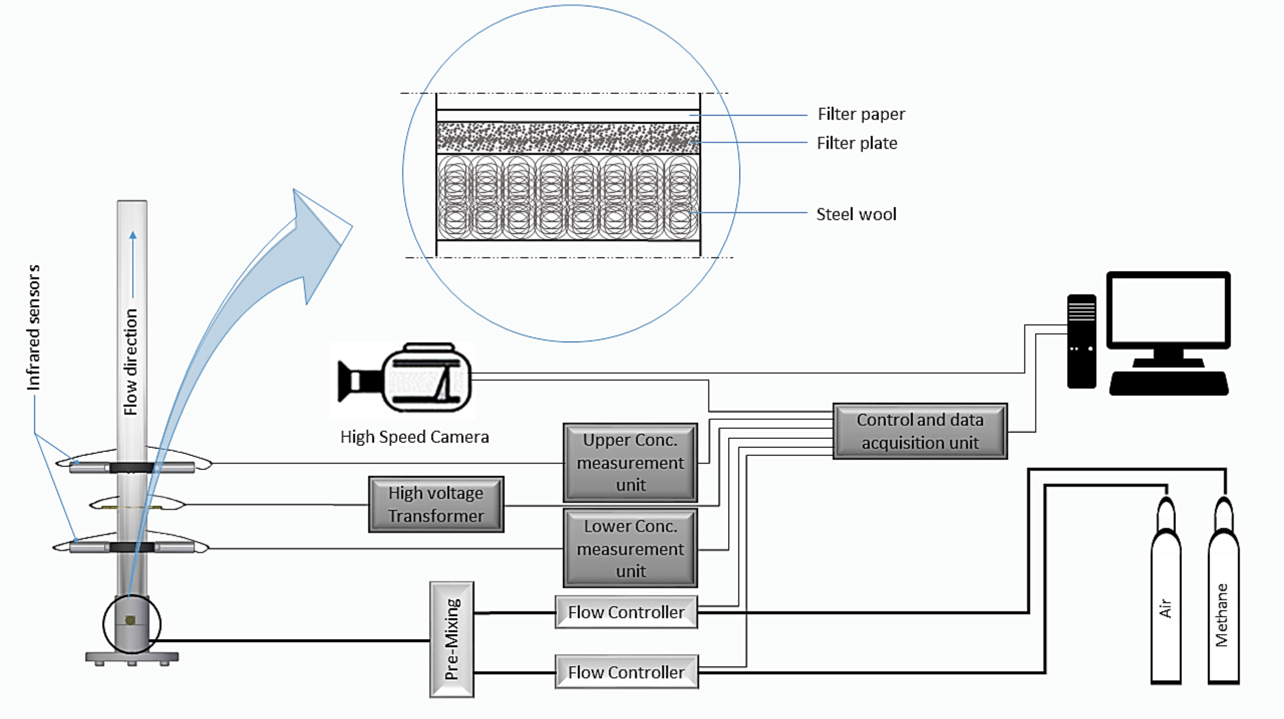

Fig. 3: *Schematic diagram of the experimental set-up*

The device is equipped with the possibility of reliable in-situ measurement of dust concentration, using infrared light attenuation technique, with the help of two concentration measurement probes, mounted a few centimetres above and below the spark. Flow velocity and composition of flammable gas (in case of hybrid mixtures) was controlled using thermal mass flow controllers. Furthermore, a high speed camera is integrated into the set-up, which enables visual observation of the flame, supporting the ignition or no ignition decision.

In order to ensure good reproducibility of results, a precise protocol was followed throughout the experiments. At the beginning of each experiment, a known mass of dust material was layered on the filter paper at the bottom of the tube. A constant and steady stream of flammable gas-air mixture (for measurement of MEC of dust only air) was inserted from the bottom for a predefined time, depending on the flow velocity, until the flow front reached the top of the tube. At this point, the tube was filled with a homogenous non turbulent column of hybrid mixture, the gas flow was stopped and spark was initiated with a specific delay time, corresponding to the moment when the dust particles are in a quasi-static state, after decelerating under the action gravitational force. Ignition delay time was calculated for different flow velocities assuming that all the particles in the cloud move upwards with a constant velocity equivalent to flow front velocity. Spark energy was controlled by regulating the duration of the spark, keeping the voltage and current at a constant value (5kV and 40mA). An electrode gap of 5 mm was used through the complete course of experiments. High speed camera was triggered automatically upon application of the spark and the concentration value at the time of ignition/no ignition was recorded. Visual flame detachment from the electrodes, as defined by DIN 51649-1, was used as the ignition criteria. In case of an ignition, concentration of dust was decreased by decreasing the inserted mass and the process was repeated, until no ignition was possible for at least five test trials with dust concentrations in the range of ±5 g/m^3 of the average value. The lowest concentration of dust, where ignition occurred, was recorded as the MEC of dust. The experimental scheme was controlled by a control and data acquisition unit and a software module developed in LabVIEW.

3. Results and discussions

3.1.Concentration reproducibility and MEC of lycopodium

A number of experiments were performed to check the reliability and reproducibility of the concentration data. A known mass of dust was dispersed in the tube and at the time the flow front reached the top end of the tube, concentration values in the upper and lower sensor were recorded. For all the concentration values, where the difference between the readings of two sensors was less than 10% of the average value, were considered valid. The process was repeated 10 times by keeping all the parameters (mass of dust, flow front velocity, flow time) constant and average value was taken as concentration at that particular flow velocity (Figure 4 (a)).

The error bars here present the percentage uncertainty in the concentration values for each flow velocity. Good reproducibility of dust concentration (uncertainty 8.5% - 4.8%) was found for all the four tested flow velocities, with 5.8 cm/s being the most reliable value (uncertainty 4.8%). This is understandable considering that the intensity of flow field has inverse relation with the homogeneity of dust suspension. However, the flow velocity of 4.7 cm/s seems to show the opposite result than what would be expected. An explanation to this could be that the flow velocity of 4.7 cm/s was too low to get all the dust suspended in the tube and as a consequence more mass of dust was required to produce a certain concentration of dust cloud. Because of this added mass of dust, the cloud in the upper part of the tube became denser than the lower part, contributing to a larger difference between the values of upper and lower sensors and hence higher uncertainty.

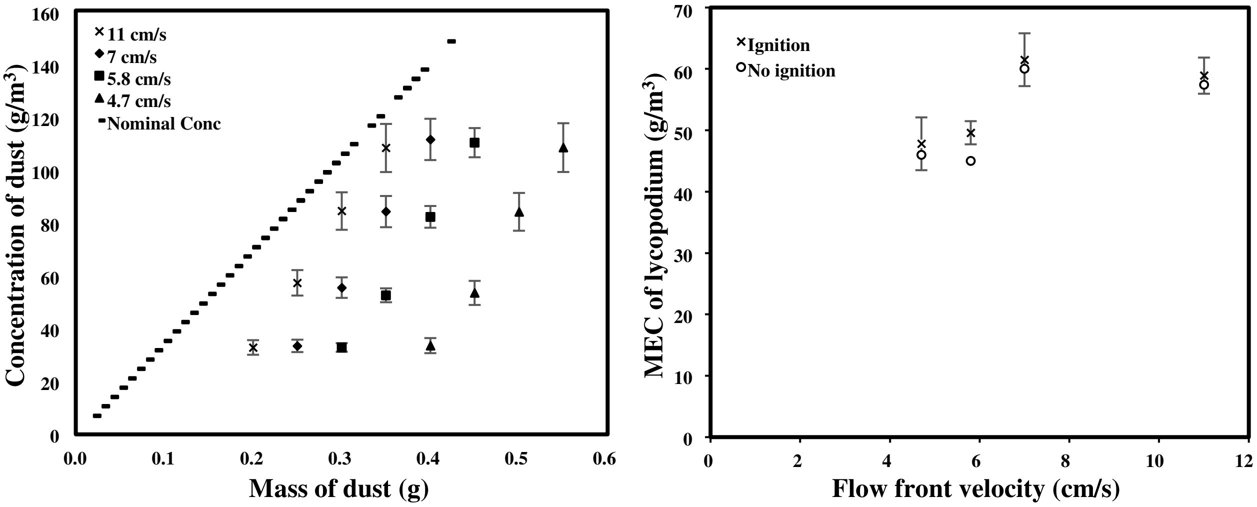

Fig. 4 (a): *Reproducibility of dust concentration* ***(b):*** *MEC of lycopodium*

A series of experiments were conducted to examine the dependence of MEC of lycopodium on the intensity of flow field (Figure 4 (b)). Considering the uncertainty involved, it can be stated that the MEC of lycopodium does not significantly change by changing the flow velocity. This statement might not be valid in general, however holds true for the flow velocity range considered for the scope of this paper.

Table 2 shows a comparison of the MEC of lycopodium along with the measurement apparatus, median particle size and elemental composition. MEC value measured with the open tube apparatus seems to be more conservative than the ones measured in 20-l sphere (using permanent spark) and in GG furnace, however, higher than ones quoted in GESTIS-DUST-EX database. The later states that, for obtaining MEC data, a sphere shaped vessel of 20-l or 1 m^3 in combination with 2 kJ or 10kJ pyrotechnical igniters was used.

GESTIS-DUST-EX database reports an exceptionally low MEC value of <15 g/m^3 for lycopodium, although the median particle size is almost the same as the other five source listed in Table 2.

***Table 2:** Comparison of MEC of lycopodium*

Source	**Median particle size (µm)**	**Elemental analysis (%wt.)**					**Ignition source**	**Apparatus**	**MEC (g/m^3)**
		C	**H**	**O**	**N**	**S**			
Addai, 2016	32	69	9.6	19.6	1.3	---	10 J permanent spark	20-l sphere	125
Addai et al., 2016	32	69	9.6	19.6	1.3	---	Hot surface at 420 °C	GG furnace	108
Sanchirico et al., 2015	32	59	8.1	21.9	2.4	---	10 J permanent spark	20-l sphere	125
Abbas et al., 2019	31.7	68	9.6	20.7	1	0.3	10 J permanent spark	20-l sphere	93
GESTIS-DUST-EX	30	---	---	---	---	---	2 kJ/10 kJ chem. igniter	20-l/1-m^3 sphere	<15
Present work	31.7	68	9.6	20.7	1	0.3	10 J permanent spark	Open tube apparatus	49.6

Considering that there are only two organic vapors with MEC values below 30 g/m^3, it is physically implausible that dust clouds would be more prone to ignition than vapors (Babrauskas and Britton, 2018). Combustion of dust clouds have all of the types of heat losses that occur as with the burning of vapour clouds, but have additional sources of heat losses, e.g. particulate radiation and endothermic pyrolysis, not present for vapors.

3.2. LEL of hybrid mixtures

Before commencement of hybrid mixture explosion experiments, LEL of methane was measured in the 20-l sphere and the open tube apparatus with their resulting values of 4.6% and 5% respectively. The difference between these values could be attributed to the different ignition criteria. 20-l sphere operates on the pressure rise criteria which is electronically detected, whereas, in the open tube apparatus the ignition/no ignition decision is made based on the visual observation of the flame. Since methane flame near its lower explosion limit is very weak and nearly impossible to visualize under normal light conditions, a higher value was recorded. It must be mentioned here that also at 5% methane, no visual observation of the flame was possible and ignition was detected by the deposition of a thin layer of steam on the tube wall, which was generated as a result of the combustion reaction.

To have a comprehensive demonstration of the impact of relative amount of mixture constituents on the LEL of hybrid mixtures, results are presented by adopting the commonly used representation proposed by Bartknecht and a recent representation in molar units suggested by the author of this paper (Abbas et al., 2018)

3.2.1.Effect of flow velocity on LEL of hybrid mixtures

Amount of dust required to support a self-propagating flame in hybrid mixtures at their LEL decreases with the addition of a small amount of flammable gas. This decrease tends to become smaller as the concentration of gas increases in the mixture (Figure 5(a)). The maximum decrease in the dust concentration was observed, when the gas concentration was in the range of 0 - 20% of its LEL (i.e. ≤ 1% vol.). This could be because, the presence of small amount of flammable gas together with the pyrolysis gases (produced by the dust particles that are caught in the spark) increases the local gas concentration and temperature near the ignition source to the level that a self-supporting flame propagation becomes possible (See section 3.3). However, if a small amount of lycopodium (approx. <10 g/m^3) was added to methane at its LEL, the amount of gas required for combustion to prevail through the system did not decrease. The reason behind could be that at low dust concentration, particles are relatively more distant from each other and the hot pyrolysis gases, released from the particles caught in the spark, are not in sufficient amount to either increase the local gas concentration or decrease the LEL of local gas cloud (near the ignition source) by increasing the temperature of the gas mixture.

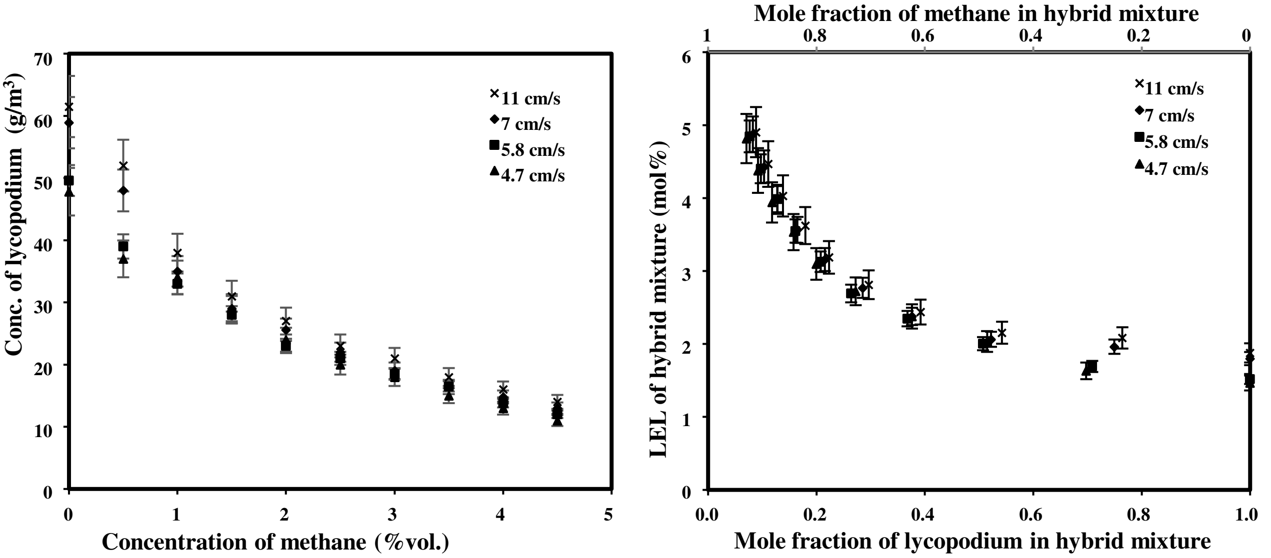

Fig. 5: *Dependence of flow velocity on LEL of hybrid mixture of lycopodium and methane a) mass per unit volume units b) molar units*

The effect of flow field intensity on the LEL of hybrid mixtures was investigated at four flow front velocities (Figure 5). Considering the uncertainty associated with the experimental values, it can be deduced that LEL of hybrid mixture of lycopodium and methane does not change significantly by changing the flow velocity. An explanation to this behaviour could be the design of the experimental scheme, aimed at igniting the dust particles in a quasi-static state by changing the ignition delay time with respect to the flow front velocity.

3.2.2. Comparison and validation

LEL of hybrid mixtures of lycopodium and methane is compared with previously published results of Abbas et al. and Addai et al., both measured in 20-l sphere using 10 J permanent electrical spark. Moreover, three models for the theoretical evaluation of LEL of hybrid mixtures, namely Le Chatelier's law, Bartknecht's curve and the equation suggested by Abbas et al. (2019), have been plotted. Based on quantifiable errors in the experimental system, an average uncertainty of ±5% (Figure 6 (a)) and ±4.2% (Figure 6 (b)) for the open tube apparatus and ±12% for the results of 20-l sphere (Abbas et al., 2019; Addai et al., 2015b) was considered and consequently added to the respective experimental values. For calculation of theoretical values using Abbas et al.'s equation (2019), a constant temperature rise (ΔT) of 1000 K was used as an ignition criteria for all the hybrid mixtures.

It can be seen at a first glance that the LEL values measured with the new setup are essentially lower and more reliable (lower uncertainty) than the ones determined in 20-l sphere, which operates under very high turbulence, hindering the growth of flame, especially when the concentration of fuel is close to its LEL. High turbulence when coupled with a 10 J electrical spark leads to a higher value of LEL in 20-l sphere. This effect is presumably eliminated by the use of strong pyrotechnical igniters of 2 kJ. However, in reality, the use of strong chemical igniters may cause combustion of dust, even if the concentration is below that required for self-sustained flame propagation at constant pressure, resulting in ultra conservative values of the LEL or MEC (Eckhoff, 2003). The need for highly energetic igniters is supposedly because of the potential of encountering high-energy ignition source in industrial accidents, however, apart from the work of Kauffmann, no information evidently exists on this important question (Eckhoff, 2003; Kauffmann, 1982). Furthermore, in 20-l sphere the local dust concentration in the region of ignition is not measured, rather it is assumed that the dust particles are homogeneously distributed in the sphere. The concentration value reported as LEL practically refers to the mass of dust equally distributed through the whole volume of the vessel. The effect of turbulence intensity and non-homogeneity of dust distribution is controlled and (supposedly) eliminated by selection of an appropriate ignition delay time, corresponding to the moment, when the dust is equally distributed in the sphere. DIN EN 14034-3, 2011 quotes a constant ignition delay time of 60 ms (20-l sphere), regardless of the size and density of the dust being tested. However, particles with higher density and/or larger particle size (e.g. iron, zirconium) would tend to settle faster than the ones with lower density and/or smaller particle size (lycopodium, polyethylene). These suppositions make the results of 20-l sphere stochastic in nature and quantitatively unrealistic.

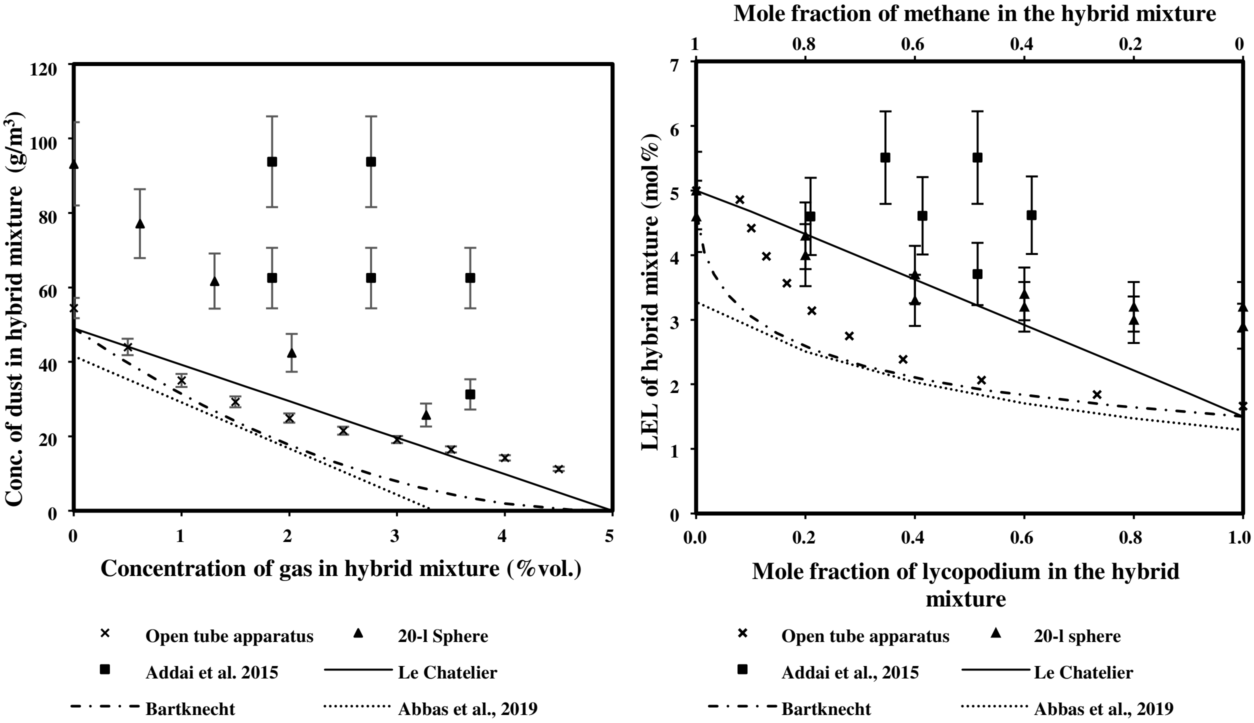

***Fig. 6:** LEL of hybrid mixture of lycopodium and methane a) mass per unit volume units b) molar units*

Basic requirement, as highlighted by Buksowicz and Wolanski (1983) is that "ignition energy must be strong enough to ignite the mixture, but it should not affect the ensuing process of flame propagation. This is especially important at concentration limits, where too strong ignition can support a flame which otherwise would have been extinguished. Furthermore, ignition must be activated at a proper time to match local concentration fluctuations" (Buksowicz and Wolanski, 1983). This prerequisite is achieved in the open tube apparatus by the application of 10 J ignition energy, which is sufficient to ignite the fuel mixture at its LEL without impeding flame propagation.

Summarizing above discussion, one could affirm that the requirement of high energy pyrotechnical igniter could be relinquished, provided that a truly homogeneous and non-turbulent suspension of dust particles is achievable.

3.3.Ignition initiation and flame propagation mechanism in hybrid mixtures

Methane flames at its explosion limits are invisible under normal light conditions. In order to visualize the gas phase combustion, high speed flame/ignition propagation videos were post-processed using an open source image processing package called Fiji. The colours are related to the radiation intensity with red and blue representing maximum and minimum values respectively. Images were extracted from these post-processed videos to investigate the interaction between dust and gas in the hybrid mixture explosion (Figure 7 and 8).

Apart from investigating the LEL of hybrid mixtures, this research work attempts to answer the question, *"what is the contribution of individual components of a hybrid mixture on the course of ignition initiation and the flame propagation, when the concentration of hybrid mixture in air is at its LEL?"*

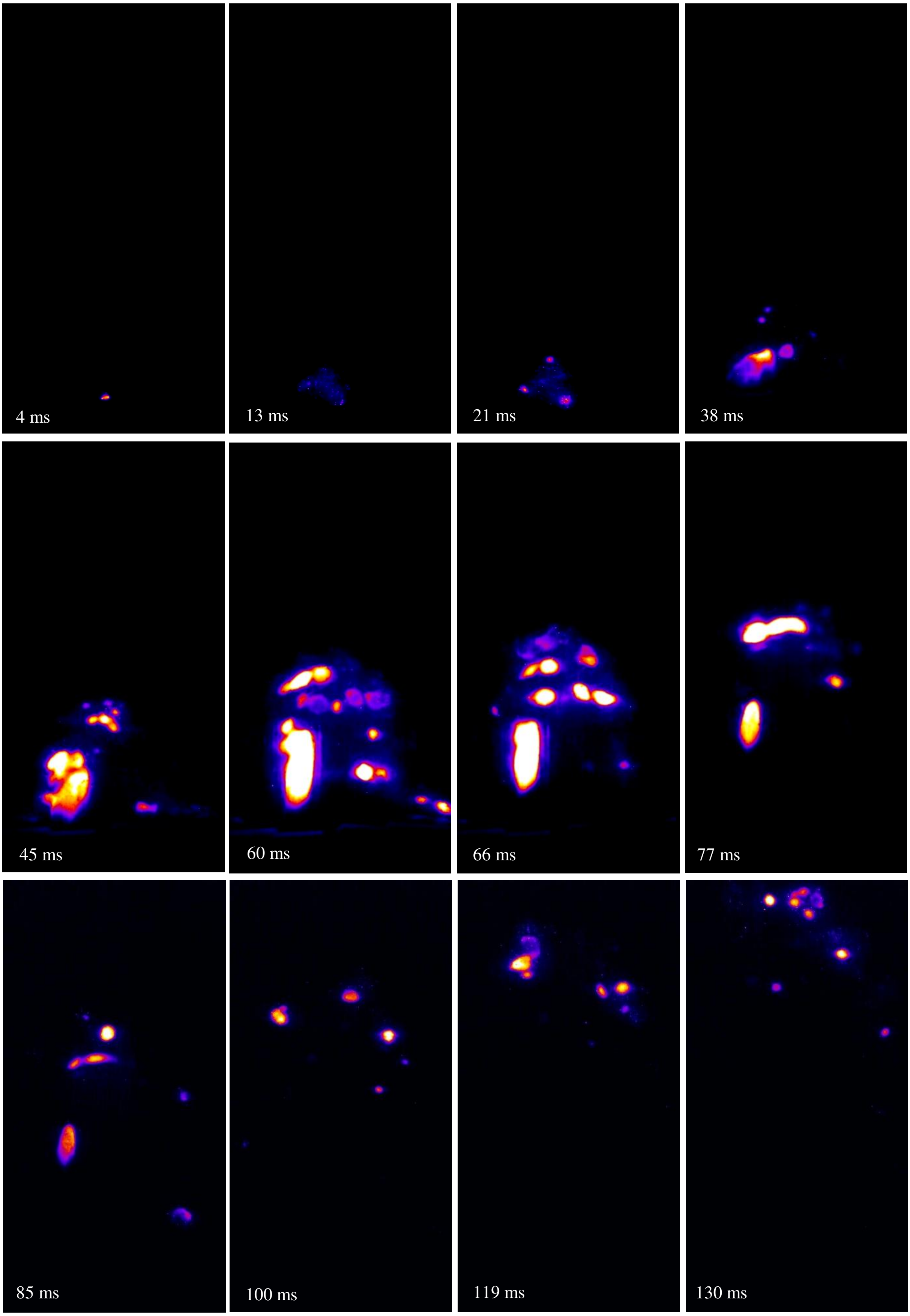

Fig. 7: *Ignition initiation and flame propagation in hybrid mixture of 3% methane and 19 g/m^3 lycopodium*

Ignition initiation and flame propagation in dust clouds may follow one or both of the two types of combustion mechanisms, namely homogeneous and heterogeneous. In general, carbonaceous and higher volatile content dusts undergo homogenous combustion, while metal dusts burn through heterogeneous surface oxidation (Bind et al., 2011; Cloney, Ripley et al. 2017; Di Benedetto et al., 2010; Fumagalli et al., 2016; Kuai et al., 2013).

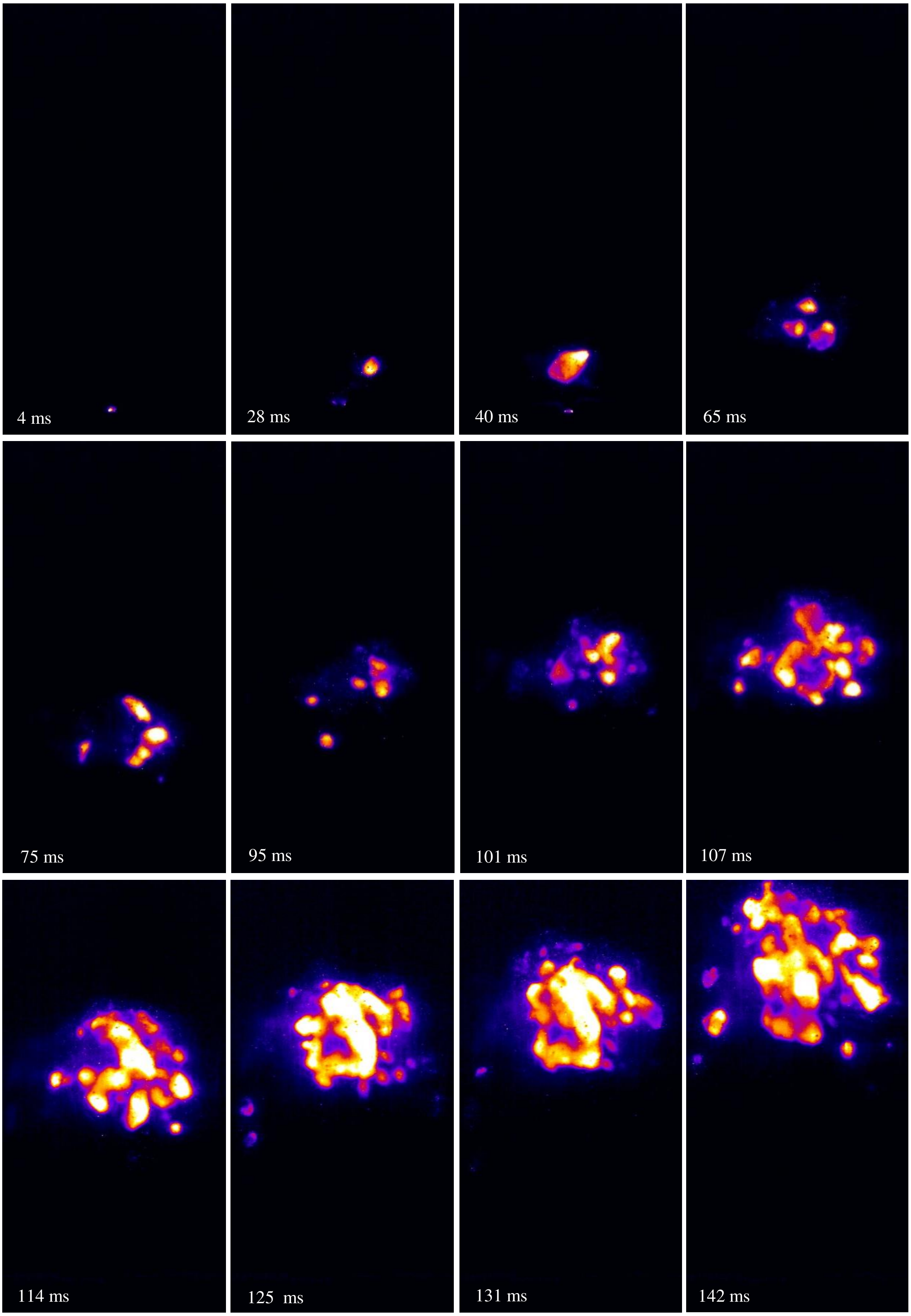

Fig. 8: *Ignition initiation and flame propagation in hybrid mixture of 1.5% methane and 30 g/m^3 lycopodium*

Flame propagation behaviour (in carbonaceous dusts) depends on a number of successive steps during the oxidation process of the combustible fraction. These include devolatilization of the volatiles (also called pyrolysis), mixing of volatiles with air, combustion of volatiles and combustion of the remaining solid fraction. It is evident and has been proven that the combustion of solid particles is mainly controlled by the heat and mass transfer in the reaction zone (Buksowicz and Wolanski, 1983; Eckhoff, 2003; Krause and Kasch, 2000).

Hybrid mixture of a dust and gas/vapour at its LEL refers to a system where the individual concentration of both dust and gas is below their respective MEC/LEL, which implies that there must be two-way interaction between the particles and flammable gas, in order for combustion to prevail through the system. This phenomenon was confirmed within the scope of this investigation (Figure 7 and 8).

In a hybrid mixture at its LEL, combustion starts with the pyrolysis of the particles that are caught in the spark, as is evident from the blue spot in Figure 7 (frame at 13 ms). These pyrolysis gases, in case there is no flammable gas present in the system and the concentration of dust is below its MEC, are not in sufficient amount to ignite the system. Presence of a flammable gas increases the local gas concentration near the ignition source. Since the pyrolysis gases are at higher temperature than ambient, concentrations even lower than the respective LEL of the gas mixture (at ambient conditions) are able to ignite, consequently creating a hot-spot near the igniter. Pyrolysis of the dust particles is accompanied by the particle size reduction. The energy released from this hot-spot causes the heterogeneous combustion of the particles (which already underwent size reduction and are easier to ignite), trapped within the boundaries of the high temperature zone. As a result more energy is released, which heats up the next group of particles releasing more pyrolysis gases in the surrounding and therefore forming new hot-spots. This two way coupling of the radiating particle clusters and burning gas zones enables combustion to prevail through the system.

Regarding the impact of relative amount of dust and gas in hybrid mixtures, it was noticed that increase in the dust concentration lead to a slower combustion propagation in comparison to the mixture compositions where the gas was in relatively higher amount. The term "combustion propagation" has been used here instead of flame propagation because at composition where dust was in relatively less amount, a smooth and continuous flame was not observed rather many discrete burning spot flames. As the fraction of the dust was increased in the fuel mixtures, the gap between these burning fragments decreased and eventually, at sufficiently higher concentration of particles, a proper flame front could be observed.

4. Conclusions

Within the context of experimental determination of MEC of a dust cloud or LEL of a hybrid mixture, a number of sources of discrepancies, inherent to the standard experimental apparatus, protocol and data treatment procedure, have been identified. It has been pointed out that as a combined effect these flaws, some of the reported MEC values are physically implausible, which accentuates the necessity for improvements since compliance with the explosion protection measures based on unrealistically low values of MEC/LEL might be extravagant.

A new and improved method for experimental determination of MEC of combustible dust cloud or LEL of a hybrid mixture has been presented. Instead of the impulse dispersion of a known mass of dust in a fixed volume and assuming homogeneous dispersion, the new set up allows a smooth and uniform suspension of the dust cloud in an open top acrylic glass tube, equipped with the possibility of a reliable in-situ measurement of the dust concentration. Furthermore, a high speed camera is integrated into the setup, which enables visual observation of the flame, supporting the ignition and no ignition decision, instead of relying on an arbitrary pressure rise criterion.

To examine the dependence of MEC on flow field intensity, MEC of lycopodium was measured at four flow front velocities. Within the flow front velocity range tested for the scope of this paper (4.7 cm/s – 11 cm/s), MEC did not change significantly by changing the flow velocity. 49.6 g/m^3 was considered as the MEC of lycopodium and compared with values reported by other authors and the German database GESTIS-DUST-EX, which quotes an exceptionally low MEC value of <15 g/m^3 for lycopodium, although the median particle size is almost the same as the other five source. Such a low value of MEC for an organic dust is physically implausible since there are only two organic vapours with MEC below 30 g/m^3**.**

LEL of hybrid mixtures of lycopodium and methane was also tested at four flow front velocities and the average value was compared with experimental and theoretical values from other sources measure in 20-l sphere. It has been demonstrated that the requirement of high energy pyrotechnical igniter may be abandoned, provided that a truly homogeneous suspension of dust particles could be achieved.

Moreover, the effect relative amount of dust and gas on the course of ignition and flame propagation was studied. For hybrid mixtures of carbonaceous dusts (like lycopodium) at their LEL, ignition occurs in the gas phase, however, flame propagation is only possible through a two-way interaction between the dust and gas.

Acknowledgments

The authors gratefully acknowledge the IND EX® (Intercontinental association of experts for industrial explosion protection) for providing financial support for this research work.

References

Abbas, Z., Gabel, D., Silva, V., Zinke, R., Darbanan, A., Krause, U., 2018. Modelling the Lower Explosion Limit of hybrid mixtures : A thermochemical approach, in: 12th International Symposium on Hazards, Prevention and Mitigation of Industrial Explosions Kansas City, USA. pp. 170–182.

Abbas, Z., Zinke, R., Gabel, D., Addai, E.K., Darbanan, A.F., Krause, U., 2019. Theoretical evaluation of lower explosion limit of hybrid mixtures. J. Loss Prev. Process Ind. 60, 296–302.

Addai, E.., Gabel, D., Krause.U, 2016. Lower Explosion Limit/Minimum Explosible Concentration Testing for Hybrid Mixtures in the Godbert-Greenwald Furnace. Process Saf. Prog. 36, 81–94.

Addai, E.K., 2016. Investigation of Explosion Characteristics of Multiphase Fuel Mixtures with Air Dissertation.

Addai, E.K., Gabel, D., Krause, U., 2015a. Lower explosion limit of hybrid mixtures of burnable gas and dust. J. Loss Prev. Process Ind. 36, 10–14.

Addai, E.K., Gabel, D., Krause, U., 2015b. Lower explosion limit of hybrid mixtures of burnable gas and dust. J. Loss Prev. Process Ind. 36.

Amyotte, P., 2013. An Introduction to Dust Explosions: Understanding the Myths and Realities of Dust Explosions for a Safer Workplace, An Introduction to Dust Explosions: Understanding the Myths and Realities of Dust Explosions for a Safer Workplace.

ASTM, E. (2014). "1515-14." Standard Test Method for Minimum Explosible Concentration of Combustible Dusts.

Babrauskas, V., Britton, L.G., 2018. Errors in the Compilations of Minimum Explosion Concentration Values for Dust Clouds. Fire Technol. 54, 37–55.

Bagaria, P., Zhang, J., Mashuga, C., 2017. Effect of dust dispersion on particle breakage and size distribution in the minimum ignition energy apparatus. J. Loss Prev. Process Ind. 1–6.

Baker, W.E., Tang, M.J., 1991. Gas, dust and hybrid explosions. https://doi.org/10.1016/0950-4230(92)80049-e

Bartknecht, W., 1989. Dust explosions: course, prevention, protection. Springer Science & Business Media.

Bind, V.K., Roy, S., Rajagopal, C., 2011. CFD modelling of dust explosions: Rapid combustion in a 20L apparatus. Can. J. Chem. Eng. 89, 663–670.

Buksowicz, W., Wolanski, P., 1983. Flame propagation in dust-air mixtures at minimum explosive concentration. Prog Astronaut Aeronaut 87, 414–425.

Cloney, C. T., R. C. Ripley, M. J. Pegg and P. R. Amyotte (2017). "Evaluating regime diagrams for closed volume hybrid explosions." Journal of Loss Prevention in the Process Industries 49: 912-918.

Cloney, C. T., R. C. Ripley, M. J. Pegg, F. Khan and P. R. Amyotte (2018). "Lower flammability limits of hybrid mixtures containing 10 micron coal dust particles and methane gas." Process Safety and Environmental Protection 120: 215-226.

Di Benedetto, A., Russo, P., Amyotte, P., Marchand, N., 2010. Modelling the effect of particle size on dust explosions. Chem. Eng. Sci. 65, 772–779.

DIN 51649-1, 1986. Bestimmung der Explosionsgrenzen von Gasen und Gasgemischen in Luft.

DIN EN 14034-3, 2011. Bestimmung der Explosionskenngrößen von Staub/Luft-Gemischen.

Du, B., Huang, W., Liu, L., Zhang, T., Li, H., Ren, Y., Wang, H., 2015. Visualization and analysis of dispersion process of combustible dust in a transparent Siwek 20-L chamber. J. Loss Prev.

Process Ind. 33, 213–221.

Dufaud, O., Khalili, I., Cuervo, N., Olcese, R., Dufour, A., Perrin, L., Laurent, A., 2012. Highlighting the importance of the pyrolysis step on dust explosions. Chem. Eng. Trans. 26, 369–374.

Eckhoff, R.K., 2003. Dust explosions in the process industries: identification, assessment and control of dust hazards. Elsevier.

Fumagalli, A., Derudi, M., Rota, R., Copelli, S., 2016. Estimation of the deflagration index KSt for dust explosions: A review. J. Loss Prev. Process Ind. 44, 311–322.

GESTIS-STAUB-EX, n.d. Datenbank mit Brenn- und Explosionskenngrößen von Stäuben, https://www.staubex.ifa.dguv.de visited on 20.02.2020.

Jiang, J., Liu, Y., Mannan, M.S., 2014. A correlation of the lower flammability limit for hybrid mixtures. J. Loss Prev. Process Ind. 32, 120–126.

Kalejaiye, O., Amyotte, P.R., Pegg, M.J., Cashdollar, K.L., 2010. Effectiveness of dust dispersion in the 20-L Siwek chamber. J. Loss Prev. Process Ind. 23, 46–59.

Kauffmann, C.., 1982. Agricultural dust explosions in grain handling facilities, in: International Conference on Fuel-Air Explosions. University of Waterloo Press, Canada, McGill University 4-6 November 1981, pp. 305–347.

Khalili, I., Dufaud, O., Poupeau, M., Cuervo-Rodriguez, N., Perrin, L., 2012. Ignition sensitivity of gas-vapor/dust hybrid mixtures. Powder Technol. 217, 199–206.

Krause, U., Kasch, T., 2000. The influence of flow and turbulence on flame propagation through dust-air mixtures. J. Loss Prev. Process Ind. 13, 291–298.

Krause, U., Kasch, T., Gebauer, B., 1996. Velocity and concentration effects on the laminar burning velocity of dust-air mixtures. Arch. Combust. 16, 159–176.

Kuai, N., Huang, W., Du, B., Yuan, J., Li, Z., Gan, Y., Tan, J., 2013. Experiment-based investigations on the effect of ignition energy on dust explosion behaviors. J. Loss Prev. Process Ind. 26, 869–877.

Le Chatelier, H., 1895. Estimation of firedamp by flammability limits. Ann. Mines 19, 388–395.

Makris, A., 1988. Lean flammability limits of dust--air mixtures.

Ogle, R.A., 2016. Dust Explosion Dynamics, Dust Explosion Dynamics.

Sanchirico, R., Russo, P., Di Sarli, V., Di Benedetto, A., 2015. On the explosion and flammability behavior of mixtures of combustible dusts. Process Saf. Environ. Prot. 94, 410–419.

Taveau, J.R., Going, J.E., Hochgreb, S., Lemkowitz, S.M., Roekaerts, D.J.E.M., 2017. Igniter-induced hybrids in the 20-l sphere. J. Loss Prev. Process Ind. 49, 348–356.

DOI: 10.7795/810.20200724

Testing of dust clouds for the electrostatic-spark ignition hazard in industry. Need for a modified approach?

Rolf K. Eckhoff

University of Bergen, Dept. physics & technology, Bergen, Norway

E-mail: rolf.eckhoff@uib.no

Abstract

In order to minimize measured minimum ignition energies (MIEs) of dust clouds in air by current standard test methods, inclusion of a series inductance of at least 1-2 mH in the electrical-spark discharge circuit is a compulsory requirement.

However, when assessing the minimum energy for ignition by accidental electrostatic-spark discharges, current testing standards require that the series inductance of 1-2 mH be removed from the spark discharge circuit. No other changes of apparatus and test procedure are required. The present paper questions whether this simple approach is adequate.

The pioneering experimental investigations of Boyle and Llewellyn (1950) and Line et al. (1959) in fact provided sufficient experimental evidence for asking the question even at that time. However, it appears that for some reason the question was never asked untill now. Both studies showed that the minimum electrostatic energy $\frac{1}{2}CU^2$ required for igniting a given dust cloud in air can drop substantially if an appreciable series resistance R_s, in the range 10^4 to 10^7 Ω, is introduced in the discharge circuit. Boyle and Llewellyn worked mainly with metal powders, whereas Line et al. worked with the natural organic powder *lycopodium*. By means of high-speed movie recordings, Line at al. disclosed that the increased spark discharge duration, caused by the added large R_s, produced a marked reduction of the mechanical disturbance of the dust cloud by the blast wave emitted by the discharge. With sparks of $\frac{1}{2}CU^2$ energies of the order of 1 J and durations of just a few µs, the blast wave from the spark channel blew the dust particles far away from the hot spark channel before an ignition process could have started. This blowing-away phenomenon was explored further by Eckhoff (1970, 2017), Eckhoff and Enstad (1976) and Enstad (1981).

Accidental electrostatic-spark discharge circuits in industry may contain large ohmic resistances due to corrosion, poor electrical grounding connections, poorly electrically conducting construction materials etc. Therefore, testing for min. $\frac{1}{2}CU^2$ for ignition by accidental electrostatic spark discharges not only requires removal of the series inductance of 1-2 mH from the standard MIE spark discharge circuit. Additional tests may be required with one or more quite large series resistances R_s included in the spark discharge circuit. Unless this is done the electrostatic-spark ignition hazard, in terms of min. $\frac{1}{2}CU^2$ for ignition, can be grossly underestimated. This is definitely the case when the min. $\frac{1}{2}CU^2$ for ignition without added R_s is large, of the order of at least 0.1 J. For dust clouds of min. $\frac{1}{2}CU^2$ for ignition below about 10 mJ without added R_s, the mechanical disturbance of the cloud by the blast wave from the sparks of short discharge times is small. Then adding an appreciable R_s may in fact increase the measured min. $\frac{1}{2}CU^2$ for ignition due to the energy loss in R_s.

The present paper proposes that a modified standard test procedure for measurement of the min. electrostatic-spark ignition energy of dust clouds should account for these effects.

Keywords: *Dust clouds, dust explosions, ignition sources, electrostatic sparks, minimum ignition energy (MIE), laboratory-scale test methods*

DOI: 10.7795/810.20200724

Prologue

Without any knowledge whatsoever about the topic of his research project the present writer embarked on his postgraduate studies, on ignition of dust clouds by electric sparks, at King's College, University of London, in the autumn of 1966. In fact, he did not even know that the phenomenon of dust explosions existed. His first urgent task, therefore, was to collect and read relevant information. To give him an effective start, his supervisor, professor H.E. Rose, advised him to pay a visit to Fire Research Station (FRS), at Borehamwood, just north of central London. There Ken Palmer, later director of FRS, gave him a copy of the excellent literature survey by Brown and James (1962). The young Norwegian student could then read about the pioneering works of Boyle end Llewellyn (1950) and Line et al. (1959). By visiting the unique Patent Office Library in Chancery Lane in the City of London he obtained copies of their papers. Then more than 50 years elapsed before he realized that these two publications could in fact provide the point of departure for preparing the present paper for the 13th ISHPMIE.

1. Introduction

1.1 General background

As reviewed by Eckhoff (2003, 2016), explosible dust clouds in industry can be ignited by a variety of ignition source categories. One of these is accidental electrostatic spark discharges. Eckhoff (2019) reported that experiments more than a century ago had confirmed that electric sparks and arcs can ignite clouds of combustible dust in air. Later it was established that the minimum spark ignition energy (MIE) of dust clouds in air varies considerably with the chemistry of the dust. Other parameters influencing MIE include the size distribution of the primary particles in the dust, the degree of particle agglomeration in the dust cloud, the dust concentration, and the cloud turbulence. The spatial and temporal distributions of energy in the electric spark/arc channel also play important roles.

Up to about 1970 it was assumed by many that minimum electric spark energies needed for igniting dust clouds in air were generally much higher, by one or two orders of magnitude, than typical minimum ignition energies for gases and vapours in air. However, it is now accepted that clouds in air of many dusts can be ignited by spark energies in the range 1–10 mJ, and with some dusts even in the range 0.1–1 mJ, i.e. the range typical of minimum ignition energies of many gases and vapours in air. Glor (2003) presented a summary of the state-of-the-art at that time on the hazard of ignition of explosible dust clouds by accidental electrostatic discharges in industry.

The review by Eckhoff (2019) has provided most of the references to previous research required for producing the present paper.

1.2 Inductive and capacitive spark discharges

There are two quite different categories of electric sparks/arcs. The first is *inductive sparks/arcs*. These are generated when live electric circuits are broken, either accidentally or intentionally (e.g. in switches). The second is *capacitive sparks* caused by release to earth, across a spark gap, of accumulated electrostatic charge on electrically conducting unearthed objects.

In the *inductive* case, if the points of rupture are separated at a high speed, a transient spark is formed across the air gap generated by the rupture. If the current in the circuit prior to rupture is i and the circuit inductance is L, the theoretical spark energy, neglecting external circuit losses, but including heat losses to the electrodes across which the spark passes, will be $\frac{1}{2}Li^2$.

Capacitive electrostatic spark discharges typically occur in industrial plant when excess electrostatic charge that has accumulated on some electrically conducting, unearthed plant item, discharges to earth across some small air gap. With dusts of very low minimum ignition energies even electrostatically charged persons can generate sparks discharges capable of initiating dust explosions.

The theoretical spark energy, neglecting external circuit losses, of a capacitive spark discharge equals $\frac{1}{2}CU^2$, where C is the capacitance of the un-earthed, charged object with respect to earth, and U is the initial voltage difference between the charged object and earth.

In process industries producing and/or handling powders, electrostatic charging is tribo-electric. Then negative electric charge is transferred between objects of different electron affinities when they make contact. By subsequent separation of the objects the charge difference remains. This occurs whenever the powder/dust and process equipment make contact and are subsequently separated.

Lüttgens and Glor (1989) estimated typical approximate capacitances to earth for various objects encountered in the process industry, as shown in Table 1.

Table 1. *Examples of possible combinations of capacitances and voltages, and resulting stored electrostatic energies in industrial plants. From Lüttgens and Glor (1989)*

Charged plant item	**Assumed capacitance to earth C (pF)**	**Assumed voltage to earth U(kV)**	**Stored electro-static energy ½CU² (mJ)**
Single screw	1	5	0.01
Flange (100 mm nominal diam.)	10	10	0.5
Hand held shovel	20	15	2
Small container (50 liter drum, bucket etc.)	50	8	2
Funnel	50	15	6
Person	300	10	15
Large drum (200 liter)	200	20	40
Road tanker	1000	15	110

It seems reasonable to assume that capacitances to earth of large un-earthed metal storage silos for powders in industry can be considerably larger than the largest capacitance (road tanker) in Table 1. An anonymous internet source gave a further capacitance value of 5000 pF for a silo truck. This would yield stored electrostatic energies of 250 mJ and 2250 mJ at voltages of 10 and 30 kV respectively. The nomogram in Fig. 1 gives the charged electrostatic energy $\frac{1}{2}CU^2$ as a function of the capacitance C and the voltage U to which C has been charged.

Capacitive electrostatic spark discharges in air can only take place if the two objects at different electrical potential are sufficiently close to each other at some point to allow electrical breakdown of the air gap between them there to take place. On the other hand, the spark gap distance must be sufficiently long to permit the required voltage difference for ignition to build up before break-down.

Boyle and Llewellyn (1950a) described some experiments where various quantities of various metal powers (Al, Fe-Mn, Mg, Si and Zn) were passed through a sieve cloth of copper or silk, into a metal pan of known capacitance with respect to earth. The aim of the experiments was to determine the min. mass of the various powders that had to be passed through the sieve to produce a stored electrostatic energy in the pan equal to the minimum electrostatic-spark ignition energies of clouds in air of the various powders. The largest required mass varied with the type of powder, the capacitance of the pan, the min. ign. energy of the dust cloud etc., but none of them exceeded 5-6 kg.

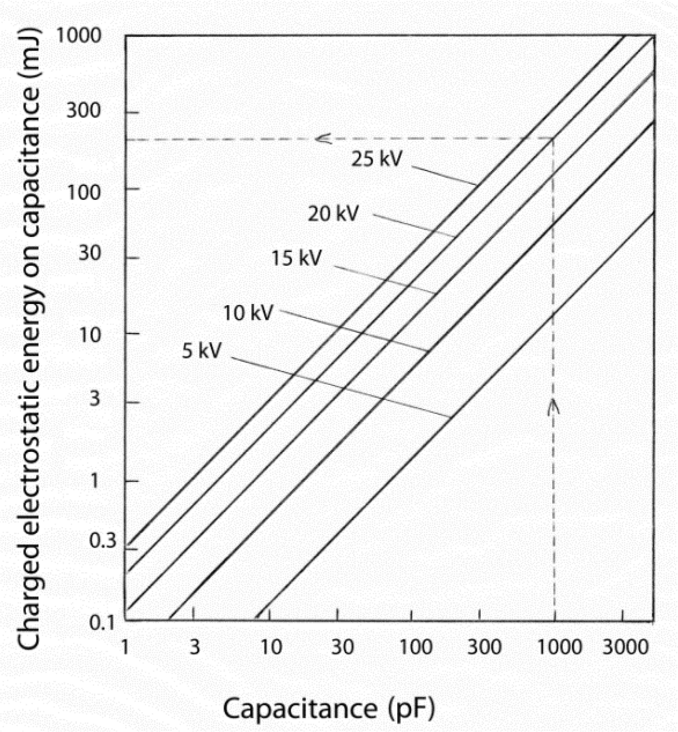

Fig. 1. *Nomogram giving the charged electrostatic energy ½CU^2 on a process item as a function of the capacitance C of the item and the voltage U to which C has been charged. The dotted lines give an example: A capacitance of 1000 pF charged to a voltage of 20 kV gives a charged electrostatic energy ½CU^2 of about 200 mJ*

1.3 Current standard methods for measurement of MIEs of dust clouds

ISO/IEC (2016) and ASTM (2015) describe the essential requirements to test apparatuses and methods currently approved for laboratory determination of minimum ignition energies (MIEs) of dust clouds internationally. Cesana and Siwek (2016) describe the commercially available and widely used MIKE 3 apparatus for this purpose.

The main features of such apparatuses are illustrated in Fig. 2. The main steps of the experimental procedure are as follows: At first an appropriate quantity of the dust to be tested is placed in the ring-shaped dispersion cup at the bottom of the about 1.2 L cylindrical explosion vessel made of glass or transparent plastic. Then this dust is dispersed, by means of a blast of air, to form a dust cloud throughout the vessel volume. To facilitate the dust dispersion process, the upwards flow of dispersion air into the vessel is deflected downwards onto the dust sample by means of a conical 'hat' as indicated in Fig. 2. Then a capacitive electric spark of a selected energy ½CU^2 is passed across the gap between the two electrodes. This passage has to occur synchronously with the appearance of the transient dust cloud in the spark gap region. Various synchronization techniques are in use, as reviewed by Eckhoff (2019). However, in general these do not work for spark energies below 1-2 mJ.

During an experiment with apparatuses as illustrated in Fig. 2 it is observed by the eye if ignition of the dust cloud takes place. The entire experiment is repeated, varying the quantity of dust, the delay between onset of dust dispersion and spark discharge, and the strength of the air blast, until the lowest spark energy for ignition of clouds in air of the dust under test has been found. When the optimal test conditions for ignition have been identified, MIE is defined as the lowest spark energy at those test conditions that gives at least one ignition in a series of apparently identical trials, typically 10 or 20.

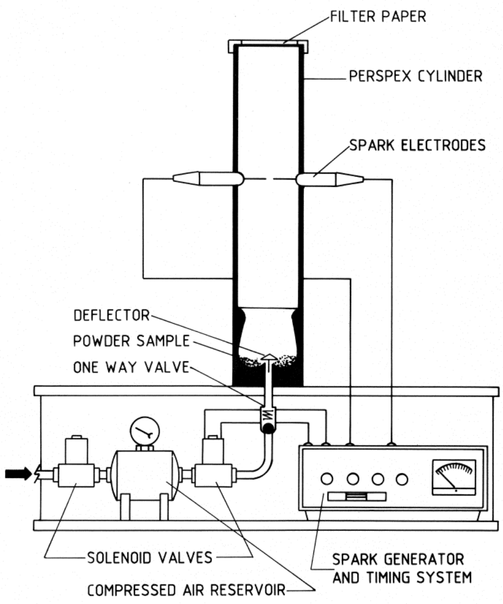

Fig. 2. *Illustration of a typical apparatus for experimental determination of minimum electric spark ignition energies (MIEs) of explosible dust clouds in air. From Eckhoff (2016).*

1.4 Influence of spark discharge duration on MIE

As discussed by Eckhoff (2003, 2019) there can be a strong influence of the spark discharge duration on MIE of dust clouds, in particular with large spark energies of the order of 1 J and more. In standard MIE testing according to ISO/IEC (2016) and ASTM (2015) it is assumed that optimal discharge times for ignition are achieved by introducing a series inductance of at least 1-2 mH in the discharge circuit.

1.5 Range of MIEs for dust clouds

Minimum electric spark energies (MIE) for ignition of dust clouds vary with dust material, particle size, and other factors. Right up to the 1970-s it was thought that the absolute lower limit of MIEs of dust clouds in air was of the order of 10 mJ, i.e. about two orders of magnitude larger than the typical MIE range most gases and vapours in air. However, it is now generally accepted that clouds of many dusts in air have lower MIEs in air that 1 mJ. Bartknecht (1993) showed that MIEs of clouds of various dusts in air span over at least 7-8 decades, from perhaps 10 μJ in the lower energy end to beyond 1kJ in the upper. This is illustrated in Fig. 3.

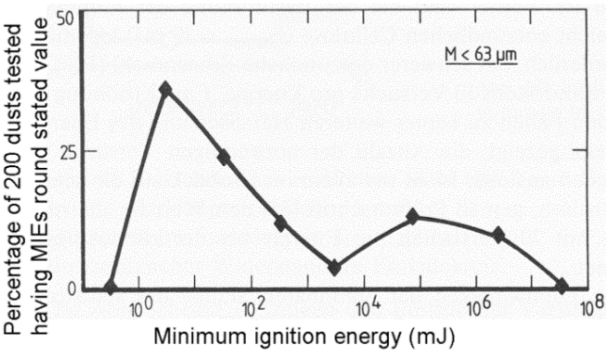

Fig. 3. *Broad spectrum of MIE values obtained with 200 different dusts as reported by Bartknecht (1993). Each diamond point represents the percentage of the 200 tested dusts having MIEs in an interval around the diamond point value. Hence, the sum of all the 7 percentages given in the figure amounts to 100. Bartknecht (1993) did not clarify the exact meaning of "M < 63μm"*

Current standard test apparatuses for determining MIEs of dust clouds cannot produce synchronized electric sparks of energies lower than about 1 mJ. This is because of limitations in the various methods currently used for synchronizing the spark discharge with the appearance of the transient experimental dust cloud in the test apparatus. Efforts have been made, therefore, to develop special spark generators that can produce synchronized sparks of energies down to the order of 0,1 mJ. One possible solution was presented by Olsen et al. (2015).

2. Pioneering research on the effect of a series resistance on min. electrostatic energy for dust cloud ignition

2.1 Boyle and Llewellyn (1950b)

The earliest detailed study traced of the effect of series resistance on the min. capacitor energies $\frac{1}{2}CU^2$ for ignition of dust clouds is the one by Boyle and Llewellyn (1950). Some of their results are reproduced in Fig. 4. As the figure shows, Boyle and Llewellyn found that the minimum capacitor energy $\frac{1}{2}CU^2$, C being the capacitance and U the capacitor voltage before discharge, capable of igniting clouds in air of a wide range of dusts, decreased substantially when a large series resistance was introduced in the discharge circuit. Fig. 4 shows that the min. $\frac{1}{2}CU^2$ for ignition of clouds in air of both a fine Al powder and a fine Mg powder decreased by a factor of about 10 when a series resistance in the range 10^4 - 10^5 Ω was introduced in the discharge circuit.

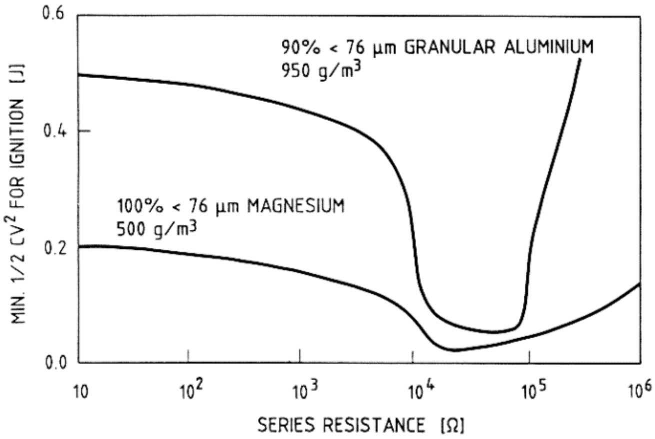

Fig. 4. *Ignition of dust clouds in air by capacitive electric sparks when including large an additional series resistance in the discharge circuit. From Eckhoff (2003) based on Boyle and Llewellyn (1950b)*

Boyle and Llewellyn (1950b) also reported similar trends for dust clouds in air of ferromanganese, zinc, silicon, and sulphur. Table 2 summarizes the main findings. In their paper Boyle and Llewellyn (1950b) did not specify the level of ignition probability to be associated with their quoted minimum ignition $\frac{1}{2}CU^2$ values, whether 50% or some lower value.

Table 2. *Summary of data given in Tables I and Tables IV-VIII of Boyle and Lewellyn (1950b).*

Powder/dust type	Min. $\frac{1}{2}CU^2$ for ign. without added R_s [mJ]	Min. $\frac{1}{2}CU^2$ for ign. with optimal added R_s [mJ]	Value of optimal added R_s [kΩ]
Granular Al (Table I)	> 490	47	75
Mg (Table I)	200	25	45
FeMn (Table IV)	3300	280	250-1000
Zn (Table IV)	No data in Table IV	170	75
Si (Table IV)	> 4300	2500	35-50
Tetryl (Table V) C=1-3 nF	23-38	12-16	50-1000
Acaroid resin (Table VI)	60	30	25
PMMA (Table VII)	27	17	50
S (Table VIII) C=0.55-2 nF	45	9-24	50-250

DOI: 10.7795/810.20200724

Table 2 shows that for some materials the min. $\frac{1}{2}CU^2$ for ignition varied somewhat with the value of the capacitance C, both with and without added series resistance. It is not clear why this is so. Probably there was some influence of the time constant $R \bullet C$ of the discharge circuit. However, three overall conclusions seem so emerge from the data in the table: Firstly, for most of the metal powders the min. $\frac{1}{2}CU^2$ for ignition dropped by a factor of about 10 when an optimal series resistance was added to the spark discharge circuit. Secondly, the optimal series resistance for ignition varied considerably, from 25 kΩ to 1 MΩ. Thirdly, the influence on the min. $\frac{1}{2}CU^2$ for ignition seems to be less pronounced with organic powders/dusts than with metal powders/dusts. Boyle and Llewellyn (1950b) commented on the third point as follows:

> *"The inclusion of a series resistance in the discharge circuit increases the incendiary power of an electrostatic spark so far as ignition of metal powder dust clouds is concerned. This principle, however, cannot be extended 'ad hoc' to all other dust clouds since we have established cases, e.g. dust clouds of some organic materials, where it does not appear to be applicable; further the resistance which corresponds to the lowest igniting energy is not always 50,000 ohms."*

Boyle and Llewellyn (1950b) expressed their results in terms of stored capacitor energy $\frac{1}{2}CU^2$. However, during a spark discharge with a large series resistance in the discharge circuit, a major part of the initial capacitor energy is absorbed by the series resistor. Therefore, as discussed by Eckhoff (1970, 2017) the energy actually delivered in the spark gap, and hence available for igniting the dust clouds, was considerably lower than the corresponding $\frac{1}{2}CU^2$ values. When relating their findings to practical conditions in industrial plants, Boyle and Llewellyn (1950b) stated as follows:

> "*The hazard, reduced to its simplest terms, therefore consists merely in the discharge of a condenser through an airborne dispersion of the inflammable powder. The discharge may either occur directly to earth or to another conductor of a different potential, when it will be noisy and luminous, or through a resistance, e.g. an operative or a piece of wood, when it will be less obvious, but nevertheless more incendiary."*

Most of the data in Table 2 are reproduced graphically in Fig. 5.

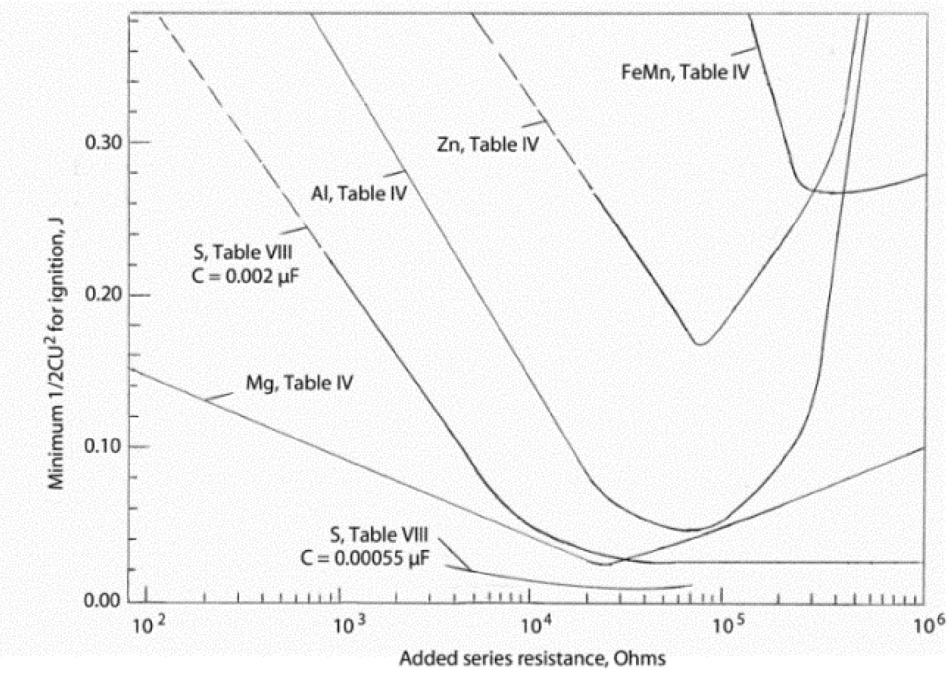

Fig. 5. *Ignition of dust clouds in air by capacitive sparks, including large additional series resistances in the discharge circuit. Graphs constructed from data in tables in the paper by Boyle and Llewellyn (1950b)*

2.2 *Line et al. (1959)*

Line *et al.* (1959) followed up Boyle and Llewellyn's pioneering research. However, they limited their investigation to one dust only, viz. the naturally occurring organic dust *lycopodium*, i.e. the spores of the plant *club moss*. Furthermore, instead of working with transient dust clouds generated by exposing a small sample of the dust to a blast of air, they worked with stationary quasi-laminar columns of dust settling in air. Some results for both wall free and wall confined 25 mm columns, are reproduced in Fig. 6. The inclusion of a series resistance of 100 kΩ in the spark discharge circuit in fact reduced the min. $½CU^2$ for ignition by a factor of about 10 even for the organic dust lycopodium. As can be seen for both wall free and wall confined dust columns, the min. capacitor energies $½CU^2$ required for producing a given probability of ignition, decreased by a factor of roughly 10 if a series resistance of 10^5 Ω was included in the discharge circuit. Both the magnitude of the maximum decrease and the order of magnitude of the series resistance giving this decrease, agree with the corresponding figures found by Boyle and Llewellyn for various metal powders/dusts (Figs. 4 and 5).

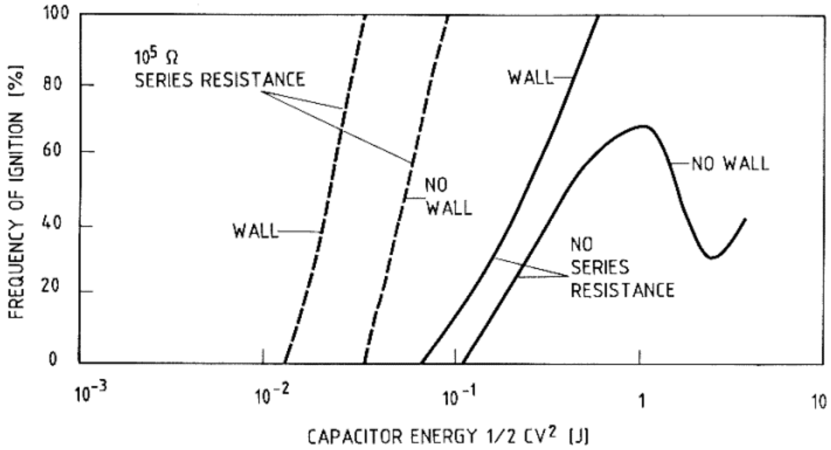

Fig. 6. *Frequency of ignition of a 25 mm diameter laminar column of 80 g/m^3 of lycopodium dust in air, as a function of capacitor energy. Effect of an additional 10^5 Ω series resistance in the discharge circuit, and of wall confinement of the dust cloud. From Eckhoff (2003) based on Line et al. (1959)*

It is interesting to note that the min. $½CU^2$ for ignition of clouds in air of lycopodium responded more strongly to adding a large R_S into the discharge circuit than did the organic powders/dusts tested by Boyle end Llewellyn. The unique surface topography of lycopodium particles may offer a possible reason for this. One side of the particle surface is covered by a thin-walled honey-comb structure with the walls oriented perpendicularly to the main, rather smooth particle surface. The other half of the main particle surface is covered by three plane "foils", also perpendicularly oriented at the surface with approximately 120 degrees between them. It may appear that this special surface structure causes very efficient transport of lycopodium particles by an air flow, including the blast wave emitted by a spark discharge.

2.3 *Research at King's College London (1970)*

During his experimental research at King's College London, Eckhoff (1970) studied the ignition of clouds in air of lycopodium (*clavatum)* by capacitor sparks of comparatively high energies (range about 1-10 J) and quite short discharge times (a few µs). Some results are given in Fig. 7.

A comparison of Fig. 7 with Line et al.'s data in Fig. 6 shows that with no added series resistance, the probability of ignition was between 0 and 100% over an appreciable range of comparatively high spark energies in both investigations. Even with very high min. $½CU^2$ values of nearly 10 J, the ignition probability was lower than 100%. Nearly 50 years after the appearance of Eckhoff's 1970 thesis, his original results were eventually published in an international journal (Eckhoff, 2017).

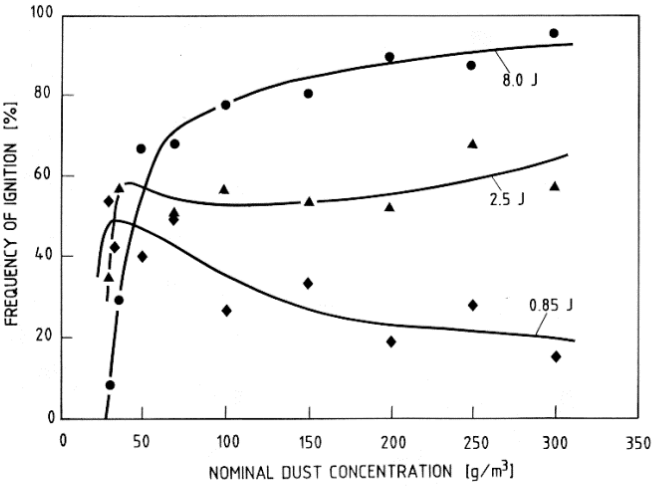

Fig. 7. Probability of electric spark ignition of clouds of lycopodium in air as a function of dust concentration, for three different spark energies. Spark discharge duration 5–10 μs. External circuit resistance 0.01 Ω. Circuit inductance 2 μH. Spark gap length 2.7 mm. From Eckhoff (2003), based on Eckhoff (1970)

Based on the high-speed movie records by Line et al. (1959) Eckhoff (1970, 2017) assumed that the poor incendivity of "short" energetic sparks was the result of a "knife edge" competition between the two processes illustrated in Fig.8.

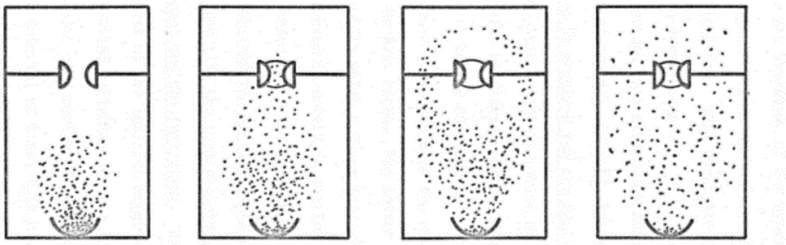
THE DISPERSION OF THE DUST IN THE CUP HAS BEEN INITATED

STRAY PARTICLES AT THE FRONT OF THE RAISING DUST CLOUD ENTERS THE SPARK GAP AND TRIGGER THE SPARK DISCHARGE

THE DUST IN THE SPARK GAP ZONE IS BLOWN AWAY FROM THE SPARK BY THE PRESSURE WAVE EMITTED BY THE SPARK DISCHARGE

IGNITION OF THE DUST CLOUD WILL OCCUR IF THE CONTACT BETWEEN THE SPARK AND THE DUST CLOUD IS RE-ESTABLISHED AND LASTS LONGER THAN A MINIMUM PERIOD

Fig. 8. Qualitative conception of process of ignition of explosible dust clouds by electrostatic spark discharges of high energies and short discharge times.
From Eckhoff (1970, 2017)

The first process is transfer of heat from the hot spark channel to the surrounding dust cloud, which clearly promotes ignition. However, this energy transfer is counteracted by a competing process, viz. very fast mechanical separation of the dust from the very hot high-pressure spark channel by the blast wave emitted from the channel when it expands, which counteracts ignition because the dust particles are blown away from the spark. This existence of this separation process was actually confirmed by high-speed film recordings performed by Line et al. (1959). The "knife edge" nature of the competition between these two processes is illustrated by Line et al.'s results in Fig. 6 for the wall free case and no series resistance. The probability of ignition in fact dropped as the discharged energy $\frac{1}{2}CU^2$ was increased from 1 J to 3 J.

In his experiments as illustrated in Fig. 8, Eckhoff (1970, 2017) synchronized the appearance of the dust cloud at the spark gap with the appearance of the spark discharge in a way that may also occur accidentally in industry. Before dispersing the dust sample in the dispersion cup, the voltage across the spark gap was raised to slightly below the natural breakdown voltage in air for the hemispherical electrode gap used (about 10 kV). Then the air blast was for dust dispersion was activated. As soon as the front of the raising dust cloud entered the spark gap, electrical breakdown of the gap occurred.

More recently further experiments demonstrating ignition of dust clouds in this way were presented by Eckhoff and Randeberg (2005) and Randeberg and Eckhoff (2006).

2.4 Research at CMI (Chr. Michelsen Institute), Bergen, Norway

In a later study Eckhoff (1975) worked with a spark discharge circuit containing a 1 mH series inductance as an inherent part of the system used for synchronizing spark discharge with dust dispersion. Because of the resulting comparatively long spark discharge durations, very low MIEs were measured for clouds in air of a fine sulphur powder and a fine aluminium powder.

Inspired by the high-speed film recordings by Line at al. (1959) Eckhoff and Enstad (1976) conducted a simple experiment demonstrating the “blowing away” effect of strong short spark discharges. They found that the blast wave from capacitive discharges of durations about 1 μs and energies of up to 0.3 J could push a 4 × 5 mm piece of very thin paper, supported by thin threads, and initially hanging very close to the spark gap, an appreciable distance away from the spark. Table 3 gives the actual figures.

Table 3. *Displacement of a 4 × 5 mm paper piece, initially hanging close to a spark gap, by the blast waves from capacitive electric sparks of short and long discharge times. From Eckhoff and Enstad (1976)*

Spark energy [mJ]	**Length of spark gap [mm]**	**Displacement distance [mm]**	
		‘short’ spark	**‘long’ spark**
10	0.1	< 0.5	0
25	0.2	2.5	0
100	1.0	12	< 0.5
300	2.0	35	1

As the spark energy increased beyond 25 mJ, the displacement of the paper piece by ‘short’ spark discharges was appreciable.

On the other hand, with decreasing spark energies below 10 mJ, the displacement was practically negligible even for the ‘short’ sparks. This probably means that the minimum ignition energy may not necessarily increase with decreasing discharge duration in the range of spark energies below the order of 10 mJ. At such low spark energies, the influence of the shock wave from the spark discharge is small. Adding a series resistance to the spark discharge circuit, in this case may in fact increase the ½CU^2 required for ignition, rather than reducing it.

Enstad (1981) investigated the particle displacement caused by the blast wave from the spark discharge theoretically. His “bench marks” were the high-speed-movie-record data of Line et al. (1959). Enstad’s results for a 1.5 J spark discharge in a cloud of lycopodium in air are summarized graphically in Fig. 9. The assumptions made are listed in Eckhoff (2003). Each solid curved line in Fig. 9 gives the calculated distance of a dust particle (lycopodium) away from the spark centre as a function of the time after spark discharge and the initial position of the particle. Beyond about 10^4 μs (10 ms) after spark discharge the settling velocity of the particles in quiescent air dominates.

Enstad’s theoretical calculations agree well with the experimental high-speed-film observations reported by Line et al. (1959). A dust free zone, separating the dust cloud from the hot gas core, was established. The zone radius at 2 ms after spark discharge is in close agreement with the experimental value of about 10 mm observed by Line *et al.* (1959) for the same spark energy, dust type and instant after spark discharge.

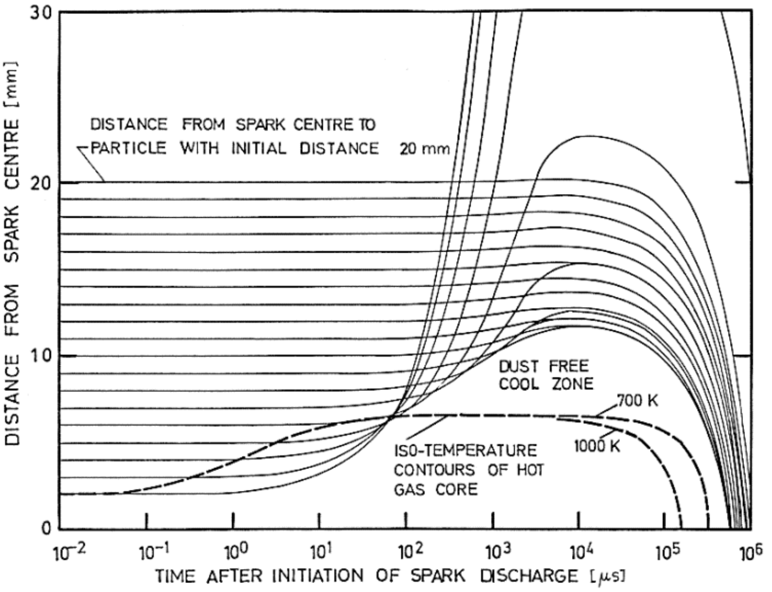

Fig. 9. *Summary of theoretical prediction of positions of dust particles and surface contours of the hot-gas core following a 'short' spark discharge (discharge time about 1 µs) of 1.5 J stored capacitor energy, inside a cloud of lycopodium particles in air. From Enstad (1981)*

Fig. 9 also gives the 1000 K and 700 K radii of the hot gas sphere resulting from the spark as functions of time. The minimum ignition temperature of lycopodium clouds in air, as determined in the standard Godbert-Greenwald furnace, is about 700 K. From Fig. 9 it thus follows that a dust free zone separating the dust cloud from the incendive part of the hot gas core of the spark channel, is gradually formed from 100 µs after the spark discharge and onwards, making ignition of dust particles impossible. Fig. 9 indicates that from less than 1 µs to about 100 µs after the spark discharge, particles with initial positions 2 to 5 mm from the spark centre will be trapped in the spark. However, this is unlikely to cause ignition, because the induction period for 'long' spark ignition of lycopodium clouds in air, as shown by high speed photography by Line *et al.* (1959), is of the order of 1 ms.

3. Proposal for a modified test method for assessing min. ½CU^2 for ignition by accidental electrostatic spark discharges

3.1 Current standardized test circuit

Fig. 10 illustrates the basic structure of capacitive spark discharge circuits prescribed by current standards (ISO, IEC, ASTM) for assessing the min. ½CU^2 for ignition by accidental electrostatic spark discharges in industry. As reviewed by Eckhoff (2019) various types of switches are in current use.

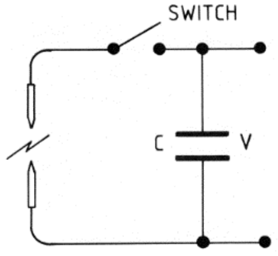

Fig. 10. *Basic spark discharge circuit used currently for determining MIEs of dust clouds for assessing the ignition hazard by electrostatic spark discharges.*

3.2 Proposed modified test circuit and test method

Fig. 11 illustrates the modification of the test circuit suggested in the present paper, viz. addition of an appreciable series resistance R_s to the discharge circuit.

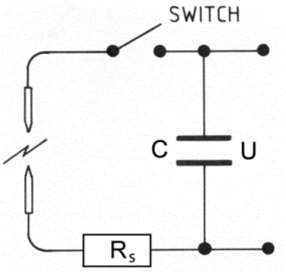

Fig. 11. *Proposed modified basic spark discharge circuit, with an added series resistance, for assessing the ignition hazard by accidental electrostatic spark discharges*

A first provisional outline of a revised test method could be as follows: If the min. $½CU^2$ for ignition without added R_s is >10 mJ an additional test series is to be carried out with R_s = 50 kΩ. It is then assumed that spark discharges of $½CU^2$ >10 mJ emit blast waves of sufficient strength to displace dust particles close to the spark channel to an extent that will inhibit ignition significantly. If then the min. $½CU^2$ for ignition with added R_s is lower than without R_s, further tests are to be carried out with other values of R_s in order to detect the very min. $½CU^2$ for ignition. This value of min. $½CU^2$ for ignition will then be the result of the test. If, on the other hand, the min. $½CU^2$ for ignition without added R_s is <10 mJ, no further tests will be required.

A revised test method along these lines necessarily implies that the modified test method will be more laborious than the present one. However, this seems to be a necessity if one aims at a realistic assessment of the true min. $½CU^2$ values for ignition.

It is clear that the revised method indicated above can by no means be the final method. For example, further research and testing with various dust types is required for identifying the max. $½CU^2$ values without added R_s that do not to any significant extent blow away the dust particles close to the spark channel. Also, this max value will probably vary from dust to dust. The optimal R_s for yielding the very lowest min. $½CU^2$ for ignition will probably also vary with type of dust, as indicated by Fig. 5.

4. Conclusion

Accidental electrical circuits in industry that can accumulate electrostatic charges may contain large ohmic resistances e.g. due to corrosion or construction materials of comparatively low electrical conductivity. Such large resistances can prolong the spark discharge time substantially and thereby reduce the blast wave emitted from the spark channel. This, in turn, will significantly reduce the blowing-away of dust particles adjacent to the spark channel and hence reduce the min. $½CU^2$ for ignition.

Therefore, current standard test methods for min. $½CU^2$ for ignition by accidental electrostatic spark discharges should not only require removal of the series inductance of 1-2 mH from the standard MIE spark discharge circuit. Additional tests with one or more selected added series resistances R_s in the spark discharge circuit are required. The purpose will then be to detect the very lowest min. $½CU^2$ for ignition as a function of added series resistance. Unless this is done the electrostatic-spark ignition hazard can be grossly underestimated. This is definitely so when the min. $½CU^2$ values for ignition without added R_s are from the order of 100 mJ and upwards. On the other hand, for dusts of min. $½CU^2$ values for ignition without added R_s, from 10 mJ and downwards, the mechanical disturbance of the dust cloud by the spark discharge without added R_s becomes negligible.

The details of a final experimental test procedure have to be clarified through further research. Tentatively it seems reasonable to start with $R_s = 0$, as in the current standard test procedure. If the min. $½CU^2$ for ignition is then large (say > 100 mJ, further tests should be performed with an agreed value of R_s, e.g. 50 kΩ. If the min. $½CU^2$ for ignition is then significantly lower than with $R_s = 0$, tests with R_s both smaller and larger than 50 kΩ may have to be conducted to detect the absolute min. $½CU^2$ for ignition.

Further systematic research with various dust types is required to resolve the influence on the min. $½CU^2$ values for ignition of both R_s and other apparatus parameters, e.g. the shape of the electrodes for both symmetrical and asymmetrical spark gaps.

Acknowledgement

As a professor emeritus at the Department of physics and technology at the University of Bergen, the author wishes to express his indebtedness to this Department for so generously allowing him to keep an office there and for providing him with the infrastructure that makes it possible for him to carry on with his writing.

References

ASTM (2015): *Standard test method for minimum ignition energy of a dust cloud in air*, Test No. E2019, Annual Book of ASTM Standards, Volume 14.02, pp.711-719, ASTM International, 100 Barr Harbor Drive, West Conshohocken, PA, USA

Bartknecht, W. (1993): *Explosionsschutz*, Springer-Verlag, Berlin, ISBN: 3-540-55464-5

Boyle, A. R., and Llewellyn, F. J. (1950a): The electrification of metal dusts. *J. Soc. Chem. Ind.,* Vol. 69, pp. 45-49

Boyle, A. R., and Llewellyn, F. J. (1950b): The electrostatic ignitability of dust clouds and powders. *J. Soc. Chem. Ind. Trans.*, Vol. 69, pp. 173–181

Brown, K.C. and James G.J. (1962): *Dust explosions in factories: A review of the literature*, Safety in Mines Research Establishment, Research Report No. 201, H.M. Factory Inspectorate, Ministry of Labour, June 1962

Cesana, C. and Siwek, R. (2016): *Handbuch zu Mike 3.5* (A manual for Mike 3.5), issued by Cesana AG, Bettingen, Switzerland, the successor of the previous Adolf Kühner AG in Switzerland

Eckhoff, R.K. (1970): *The energy required for the initiation of explosions in dust clouds by electric sparks*, M.Phil. thesis, University of London

Eckhoff, R.K. (1975): Towards absolute minimum ignition energies of dust clouds? *Combustion & Flame*, Vol. 24, pp. 53-64

Eckhoff, R.K. and Enstad, G.G. (1976): Why are "Long" electric sparks more effective dust explosion initiators than "short" ones? *Combustion and Flame*, Vol. 27, pp. 129-131

Eckhoff, R.K. (2003): *Dust explosions in the process industries*, 3rd edition, Gulf Professional Publishing (an imprint of Elsevier Science), ISBN 0-7506-7602-7

Eckhoff, R.K. and Randeberg, E. (2005): A plausible mechanism for initiation of dust explosions by electrostatic spark discharges in industrial practice, *VDI Berichte* Nr. 1873, Verein Deutscher Ingenieure, Düsseldorf, Germany

Eckhoff, R.K. (2016): *Explosion hazards in the process industries*, 2nd edition, Gulf Professional Publishing, an imprint of Elsevier, Amsterdam, ISBN: 978-0-12-803273-2

Eckhoff, R.K. (2017): Ignition of combustible dust clouds by strong capacitive electric sparks of short discharge times, *Z. Phys. Chem.*, Walter de Gruyter GmbH

Eckhoff, R.K. (2019): Measurement of Minimum Ignition Energies (MIEs) of Dust Clouds – History, present, future. *J. Loss Prev. Proc. Ind.,* Vol. 61, pp. 147-159

Enstad, G.G. (1981): *Effect of shock wave emitted from electric spark discharges on the energy required for spark ignition of dust clouds*, Report No.813101-2, dated February 1981, from Chr. Michelsen Institute, Bergen Norway (presently: GexCon AS, Bergen , Norway

Glor, M. (2003): Ignition hazard due to static electricity in particulate processes, *Powder Technology*, Vol. 135-136, pp. 223-233

ISO/IEC (2016) standard: ISO/IEC 80079, Part 20.2 Material characteristics-Combustible dusts test methods, Edition 1.0. IEC Central Office, Geneva, Switzerland

Laar, G.F.M. van (1980): Minimum ignition energy of lycopodium under several experimental conditions, Report No. G9548/G0093, Prins Maurits Laboratorium tno

Line, L. E., Rhodes, H. A., and Gilmer, T. E. (1959): The spark ignition of dust clouds. *Journal of Physical Chemistry,* Vol. 63, pp. 290–294

Lüttgens, G. and Glor, M. (1989): *Understanding and controlling static electricity,* Expert Verlag, Ehningen bei Böblingen, ISBN 3-8169-0510-2

Olsen, W. Arntzen B.J., Eckhoff, R.K.: Electrostatic dust explosion hazards – towards a < 1 mJ synchronized-spark generator for determination of MIEs of ignition sensitive transient dust clouds, *J. Electrostatics,* Vol. 74, pp. 66-72

Randeberg, E. and Eckhoff, R.K. (2006): Initiation of dust explosions by electric spark discharges triggered by the explosive dust cloud itself, *Journal of Loss Prevention in the Process Industries,* Vol. 19, pp.154-160

DOI: 10.7795/810.20200724

Self-ignition tendency of solid fuels: a gas emissions approach for early detection

Nieves Fernandez-Anez[a], Blanca Castells-Somoza[b], Isabel Amez-Arenillas[b] & Javier Garcia-Torrent[b]

[a] Department of Safety, Chemistry and Biomedical Laboratorio Sciences, Western Norway University of Applied Sciences, Haugesund, Norway
[b] Department of Energy and Fuels & Laboratorio Oficial Madariaga, Universidad Politécnica de Madrid, Spain

E-mail: *Nieves.Fernandez@hvl.no*

Abstract

Self-ignition of solid fuels storage is one of the main causes of human and economic losses. Additionally, each fire caused by this phenomenon emits an amount of toxic gases that contributes on the development of climate change. Nowadays, several methodologies are used in order to detect the self-ignition tendency of solid fuels, but they have as main disadvantages the amount of money and time that they require. The aim of this study is to propose a methodology of detection of incipient self-ignition of solid fuels through the measurement of gas emissions. With this methodology, it is possible to determine this process in advance with the equipment currently available in every industrial facility, reducing costs and improving efficieny.

Keywords: *self-ignition; storage; biomass; gas emission*

1. Introduction

Nowadays, climate change is the most dangerous environmental problem affecting all regions over the world ("Climate Change" 2015; European Union, n.d.; Nasa Earth Observatory, n.d.), clearly related to the emission of greenhouse gases. A greenhouse gas is defined as "any gas that absorbs infrared radiation in the atmosphere". This definition includes carbon dioxide, methane, nitrous oxide, ozone and fluorinated gases (chlorofluorocarbons, hydrochlorocarbons, hydrofluorocarbons, perfluorocarbons and sulfur hexafluoride) (Agency, n.d.) However, the primary gas emitted through human activities is carbon dioxide (Metz et al. 2007).

Carbon dioxide is naturally present in the atmosphere as part of the Earth's carbon cycle, but human activities are altering this cycle, increasing the CO_2 emissions primarily since the industrial revolution. The main human activity that emits this gas is the combustion of fossil fuels for energy and transportation ("Climate Change" 2015), and the amount of emitted CO_2 related with these fuels is continuously increasing.

This problem may be partially reduced by the use of biomass sources. It has been considered that the net CO_2 emissions of biomasses are almost null, due to the amount of gases emitted during their processing and use are almost the same as the CO_2 absorption they have while they are alive.

However, the use of biomass presents some disadvantages and risks that are still under research. Self-ignition of dust materials is one of the most dangerous phenomenon that can occur during the storage of coal, carbonaceous material and of course biomass materials, and it can be an important source of CO_2 emissions. Burning of coal waste piles and accidental fires in biomass stockpiles can be developed as a result of a self-heating process leading to the ignition of the organic material (Ribeiro, da Silva, and Flores 2010). Besides the loss of raw materials and gas emissions, these accidents represent an important safety problem.

These associated risks have been evaluated for several materials, as agricultural products (Ramírez, García-Torrent, and Tascón 2010) or thermally dried sewage sludge (Medic Pejic et al. 2016). Several experimental techniques can be used to characterize the thermal behaviour of materials (Raemy, Hurrell, and Löliger 1983)(Gil et al. 2010). The self-ignition temperature can be determined in samples of different volumes in an isothermal oven that reproduces environmental temperatures (García-Torrent et al. 2012), but this technique needs a large amount of sample and a long time for testing. On the other hand, self-ignition properties can be determined by thermogravimetry and differential scanning calorimetry techniques (Doyle 1961)(Jones et al. 1998), which need less amount of sample and provides more information about the combustion process (Magdziarz and Wilk 2013).

Also numerical simulations can be used to study the combustion processes of dust materials (Everard et al. 2014). However, the combustion process starts even before the point detected by these analyses, and the first indicator of this combustion is the gas emissions associated to their heating processes. In fact, in the very beginning stage of a self-combustion process, the heating starts to break some chemical bonds in the solid structure, releasing molecules of gases.

Due to this conviction, experimental research has been carried out in order to develop a new methodology for the detection of the incipient self-ignition processes in solid fuels (Fernandez Anez et al. 2015), and it has been implemented in several fuels to study their self-ignition tendency. Here, we compare different compactions and particle size, and describe the best methodology to define the incipient self-ignition temperature for detecting the process in advance.

2. Materials and methods

2.1 Materials

Fourteen samples have been selected including biomass (7), sewage sludge (4) and fossil fuels (3) with the objective of comparing a wide range of solid fuels. Their main granulometric parameters, determined by laser diffraction with a Mastersizer 3000 in the fine cases and by sieving in the coarse ones, are shown in Table 1, representing d10, d50 and d90 the grain diameter where 10 %, 50 % and 90 % of the distribution has a smaller particle size, respectively. Samples received as bulk material (SAM-1, 2, 3, 5, 6, 9 and 14) were milled and sieved through a 180-µm mesh, and tested in both sizes when possible. SAM-4 was milled and sieved through a 1-mm mesh due to its high ignition tendency when milled. The rest of the samples were received as powdery substances and tested as received.

Table 1. *Particle size specifications of the studied samples*

Sample		**Material**	**d10 (µm)**	**d50 (µm)**	**d90 (µm)**
SAM-1	Fine	Wood chips	46.5	146.6	404.1
	Coarse		400	1100	1800
SAM-2		Wood pellets	43.4	152.9	379.0
SAM-3	Fine	Torrefied wood pellets	22.3	104.0	327.0
	Coarse		2300	3500	6400
SAM-4		Stubble	160.00	800.00	1750.00
SAM-5		Straw	43.7	171.2	474.5
SAM-6	Fine	Olive pit	20.5	68.2	196.7
	Coarse		800	1300	1800
SAM-7		Almond shell	14.8	44.3	143.0
SAM-8		Sewage sludge	290.5	638.2	1209.7
SAM-9	Fine	Sewage sludge	24.5	98.1	204.3
	Coarse		1000	1500	2000
SAM-10		Sewage sludge	29.6	92.0	193.7
SAM-11		Sewage sludge	17.7	94.7	205.3
SAM-12		Coal	8.2	45.9	116.1
SAM-13		Coal	4.4	26.8	68.2
SAM-14	Fine	Coke	8.8	77.4	194.9
	Coarse		500	1200	3600

Their proximate analyses, determined following Standards EN 14775 (“EN 14775. Solid Biofuels. Determination of Ash Content” 2009), EN 15148 (“EN 15148. Solid Biofuels. Determination of the Content of Volatile Matter” 2009) and EN 14774 (“EN 14774. Solid Biofuels. Detemrination of Moisture Content. Oven Dry Method” 2009) for samples SAM-1 to SAM-7, and Standards UNE 32004 (“UNE 32004. Solid Mineral Fuels. Determination of Ash” 1984), UNE 32019 (“UNE 32019. Hard Coal and Coke - Determination of Volatile Matter Content” 1984) and UNE 32002 (“UNE 32002. Solid Mineral Fuels. Determination of Moisture in the Analysis Sample” 1995) for samples SAM-8 to SAM-14, are represented in a triangular diagram with volatiles (top), ash (bottom right) and fixed carbon (bottom left) in the three vertices as can be seen in Figure 1, where the differentiation among the different studied groups is shown. Biomasses present higher percentage of volatiles and lower ash content, while fossil fuels present a higher percentage of fixed carbon. Sewage sludge samples present almost the same volatiles than ash contents, while their fixed carbon content is the smallest of the studied groups.

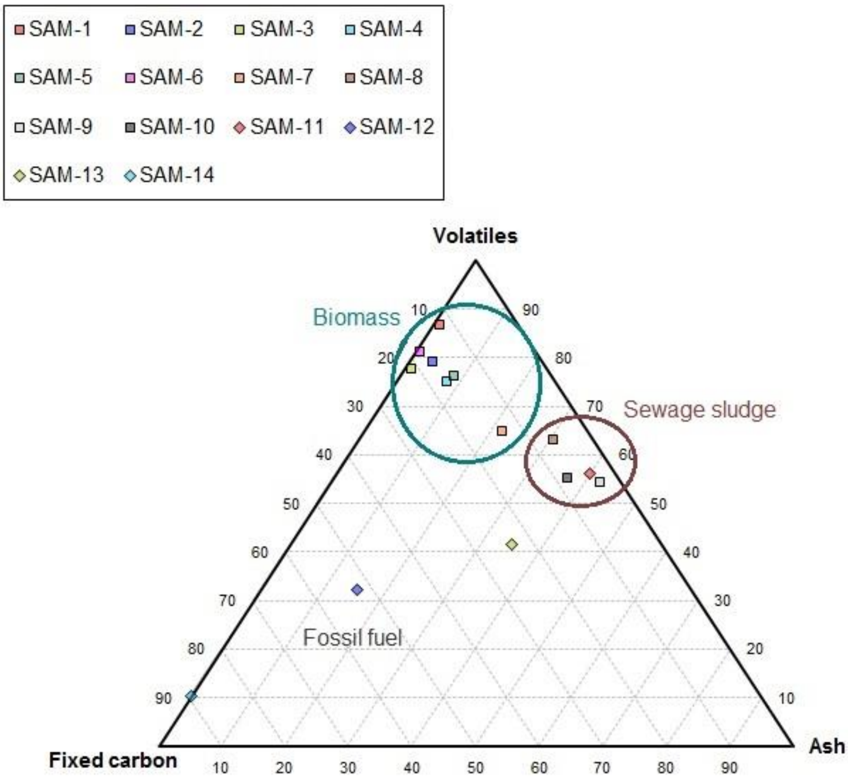

Fig. 1. *Triangular diagram of proximate analyses of the studied samples, with the three vertices been volatiles (top), ash (right) and fixed carbon (left).*

2.2 Methods

2.2.1. Gas emissions test

This test was carried out through the equipment schematically represented on Figure 2, composed by a 10 L sealed cylindrical container, an isothermal oven P-Selecta, a Type K thermocouple, a digital temperature display Testo 925, a suction pump, two 1-litre Tedlar sampling bags Sigma-Aldrich and a gas analyser Rosemount Analytical NGA-2000.

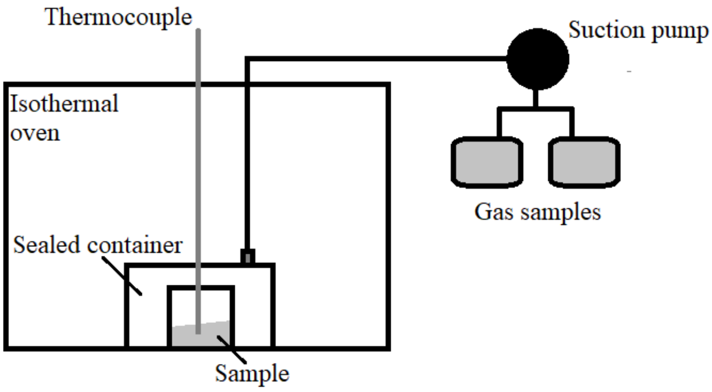

Fig. 2. *Schematic of the used experimental device.*

50 grams of the analysed sample were introduced inside a 1000 cm^3 basket without tapping or compacting, and the basket was placed inside the sealed container and closed. This container had a narrow fitting 3 millimetres diameter that connected the inside of the container with the suction pump through a plastic tube closed with a Mohr wrench. The thermocouple was located in the middle point of the sample in order to detect the temperature of the sample in every moment during the experiment, through the connection with the temperature display. The container was closed and introduced inside the isothermal oven, previously preheated at the tested temperature.

Once the desired temperature inside the sample was reached, the gas accumulated inside the container was stored inside the Tedlar bags through the plastic tube by opening the Mohr wrench. Due to the small volume of the tested samples, temperature quickly stabilizes and it is considered constant during the sampling time. When the bags were full, they were disconnected from the plastic tub and connected to the analysers. CO and CO_2 emitted during combustion were measured, starting at the connection between bag and analyser, until gas emission was back to zero. The value of the concentration of emitted gas was considered as the maximum value that was achieved during the measuring process.

This methodology was repeated for all the studied temperatures, from 40 to 200 ºC each 20 K, replacing the sample for each test. CO and CO_2 emissions were plotted on a diagram vs temperature as the one shown on Figure 3 for wood chips, where the dots represent the values experimentally determined, and the lines are approximation of the expected behaviour on the middle values.

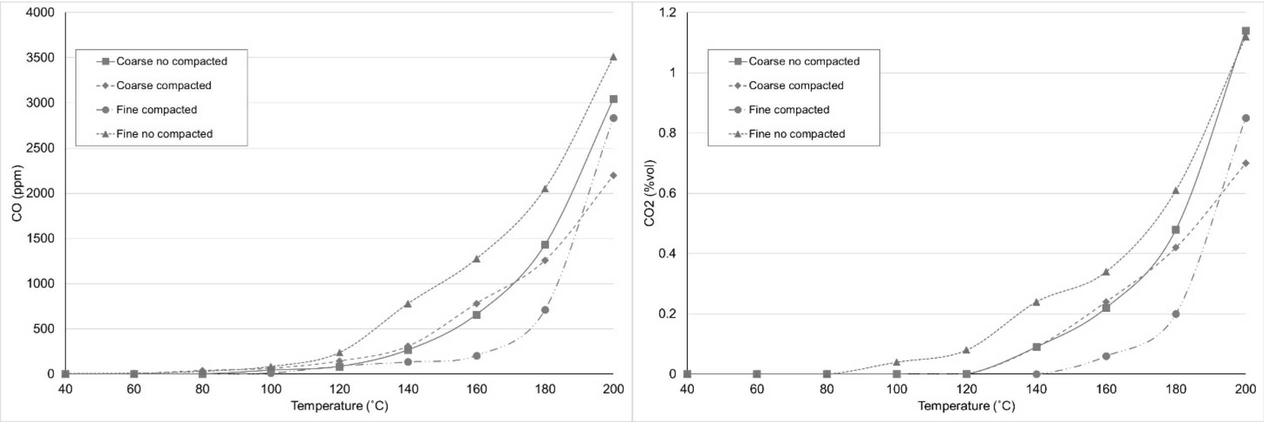

***Fig. 3**. CO and CO_2 emissions during the heating process of wood chips. Dots are the experimentally determined values, lines are approximations of the expected behaviour in the middle values.*

2.2.2. Thermogravimetric and differential scanning calorimetric analysis

Thermogravimetric (TG) and differential scanning calorimetric (DSC) analyses have been widely used to study the thermal behaviour of solids and to determine their self-ignition tendency. These analyses have been carried out with a Mettler Toledo TG 50 apparatus. The procedure followed in this case has been detailed in previous publications (Fernandez Anez et al. 2015). We have used this data in order to compare the studied procedure with methodologies that are commonly used in the field.

3. Results

The goal of this research is to determine the initial point of self-heating process through the detection of the gases emitted during the heating process of solid materials. With this knowledge, prevention and protection measurements can be designed to act on an early measure to minimize the consequences of an incident or accident. Additionally, we studied different particle sizes and compaction to understand their behaviour and differences in terms of gas emissions.

Figure 4 shows the results experimentally obtained in the lab. We have divided the samples in two groups in order to make easier-to-see graphs. One group is formed by biomass and the other one is formed by sewage sludge and fossil fuels. In these graphs, the data obtained in the lab are represented by dots, while the lines are approximations of the expected behaviour for intermediate temperatures. Both CO (top graphs) and CO_2 (bottom graphs) emissions were studied.

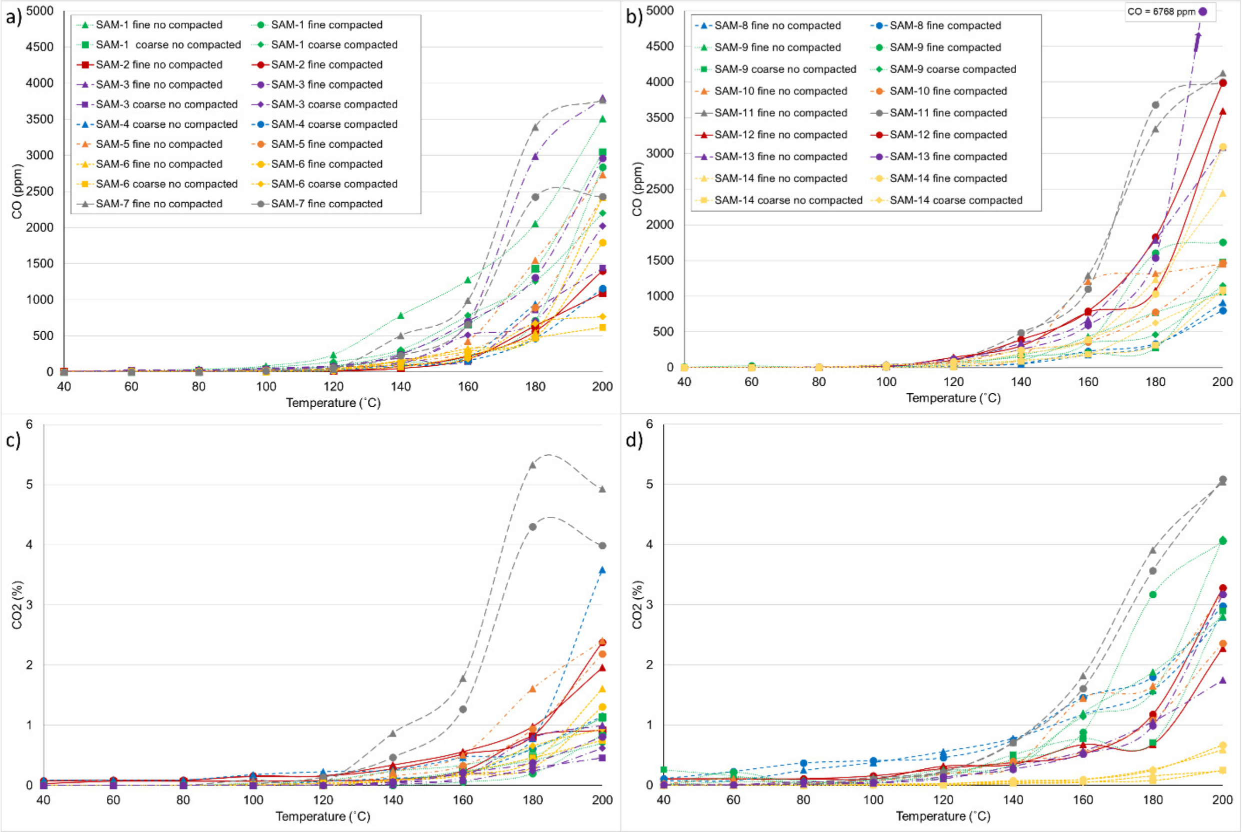

Fig. 4. *CO and CO_2 emissions vs temperature of all the studied samples: a) CO emissions of biomass, b) CO_2 emissions of biomass, c) CO emissions of sewage sludge and fossil fuels, and d) CO_2 emissions of sewage sludge and fossil fuels.*

Here, we can observed how both granulometry and compaction affect the emission of gases during the heating process of biomass. However, the observed dependency is not similar in all the studied samples, and does not fit our previous expectations.

The first hypothesis that we worked with was that in all cases coarse particles were going to emit less gases than fine particles due to the increase on specific surface area for finer particles, which implies an increase on the reaction rate. However, when looking at the five samples that we studied for both granulometries, this behaviour was not always observed. Two of the samples (SAM-1 and SAM-9) do not follow this, emitting more amount of gases for coarse particles than for fine. There is an influence of the compaction that needs to be taken into account, but in SAM-9 the fine non-compacted sample is the one emitting the least amount of gases, while expectations were just the opposite.

The second hypothesis was that compacted samples were going to emit less gases than the same non-compacted ones, based on the oxygen access and supported by the fact that compacting samples has been a way of avoiding self-ignition in storages for a long time. Several of the studied samples supported this hypothesis, but not all of them.

The differences between our pre-established hypotheses and the obtained results show that both the heating and the emission processes are not the same for all the materials, and their composition is key when studying their self-ignition tendency.

These two lines together show the importance of new methodologies and techniques to be used to determine the starting point of self-heating. To this end, focusing on the graphs in Figure 4, the point at which the heating starts needs to be determined, being the point at which the slope of the graphs starts increasing. We obtained that point using four different methodologies that are detailed in the following subsections.

3.1. Relative percentage of emissions

In first procedure consists on determining the relative percentage of emissions for each 20 K – interval using Eq. 1.

$$RP = \frac{\dfrac{(e_{T2} - e_{T1})}{e_{T1}}}{\sum_i \left(\dfrac{(e_{T2} - e_{T1})}{e_{T1}}\right)_i} \cdot 100$$

Where e_{T1} means the emissions at the lowest temperature of the interval and e_{T2} are the emissions at the highest temperature of the interval, it represents each interval.

We consider that the emissions start to significantly increase when the relative percentage is larger than 15%.

3.2. Inflexion point

The second procedure consists on determining the inflexion point of a third degree curve that has been previously obtained from the numerical results of the test (Figure 5). The inflexion point is the point in which the curve changes from a concave form to a convex one, or vice versa. It can be determined by calculating the second derivative of the curve and equate it to zero.

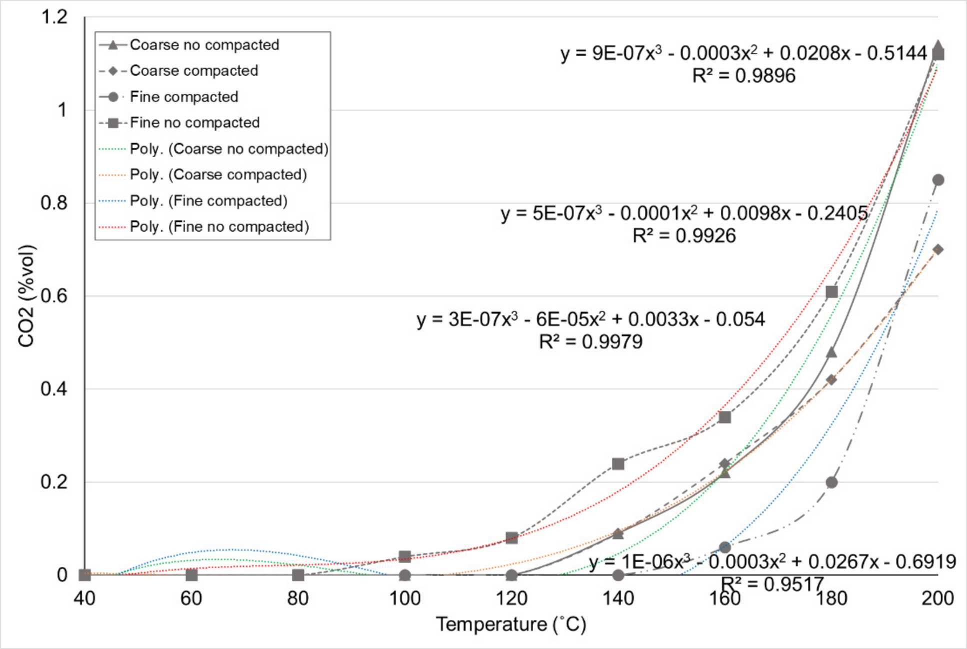

Fig. 5. *Inflexion point methodology for CO₂ emissions of wood chips, with the third degree curves approximated to the experimental curves.*

DOI: 10.7795/810.20200724

3.3. Environmental limits

This procedure aims to be a quick and easy to understand way of determining a common threshold for all the available materials. It is based on the environmental limits that have been stablished for this pollutants. The emission temperature is determined as the temperature at which these limits are achieved, revealing that the process is already underway. These limits are 25 ppm for CO and 0.5 %vol for CO2.

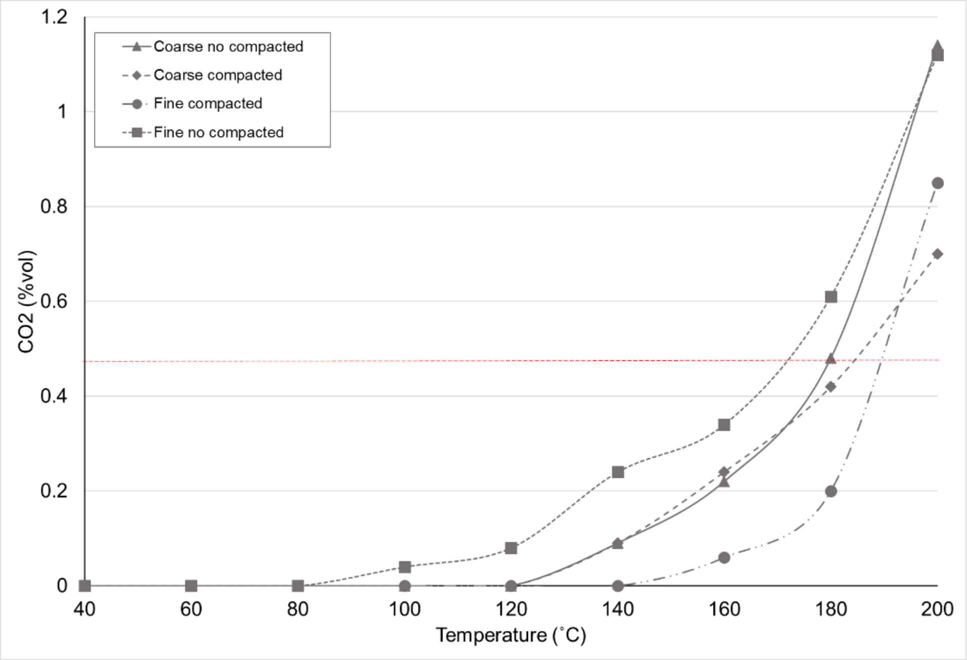

Fig. 6. *Environmental limits methodology for CO_2 emissions of wood chips, represented by the red horizontal line.*

3.4. Baselines

Once the RP are calculated, the first one greater than 15% is considered the critical interval as it represents the precise moment where the combustion-related gas emissions rise. The interval will be defined by its lower temperature (Tl) and its higher temperature (Th). As the record is not constant, and the data is discrete, it is necessary to fit a curve to the data. The fit type curve selected in this method is Piecewise Cubic Hermite Interpolating Polynomial (PCHIP), which is a cubic Hermite spline. From now on, the considered data will be the curve points, instead of the experimental data.

A straight line that approximates data from starting temperature to Tl, and a second straight line from Th to the ending temperature are calculated. The crossing point of both lines would be the represents the initial gas-emission temperature (IET), and it is always within the critical interval.

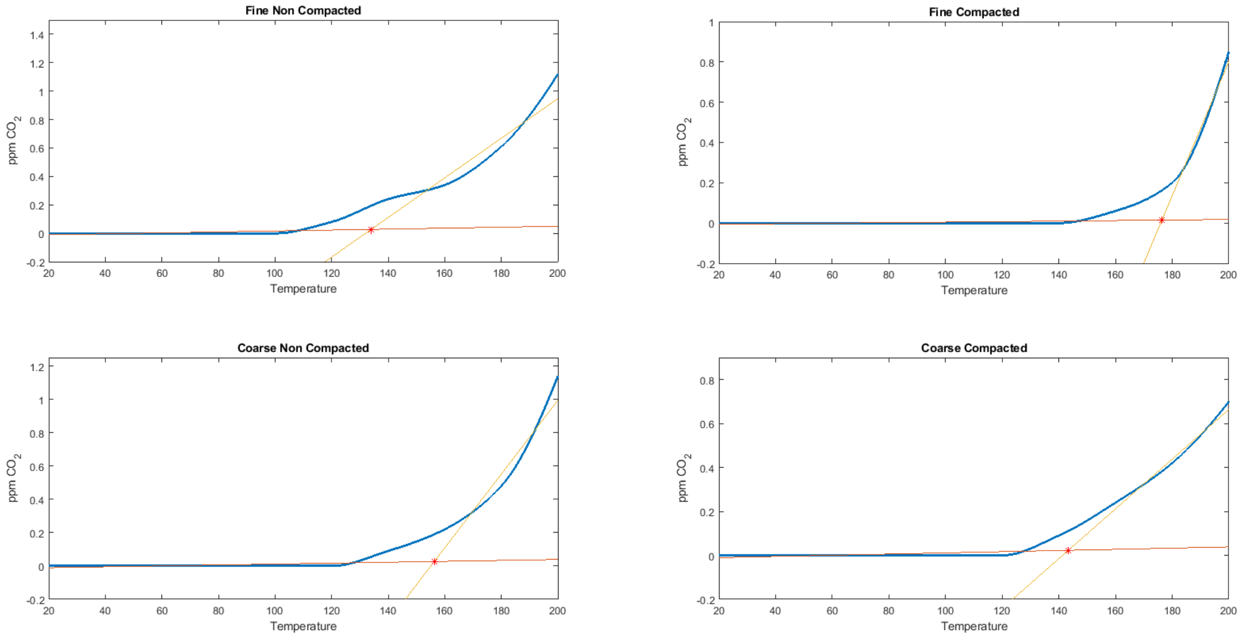

Fig. 7. Baselines methodology for CO_2 emissions of wood chips

4. Discussion

Gas emissions tests have been used to measure CO and CO_2 emissions, and the point at which these emissions start to be significant has been determined by four methodologies, as showed in Table 2 In order to discuss the obtained results, we compare them with the thermogravimetric and differential scanning calorimetric results, common methodologies used to this end.

Table 2. *Gas emissions results for solid fuels*

Sample	Method				
	Interval (˚C)	Inflexion (˚C)	Limits (˚C)	Baselines (˚C)	DSC (˚C)
SAM-1	70	62	75	102	83.9
SAM-2	90	98	123	121	94.2
SAM-3	90	76	84	103	90.3
SAM-4	90	100	118	123	105.3
SAM-5	90	67	105	123	93.0
SAM-6	110	92	110	134	116.7
SAM-7	130	93	93	136	81.3
SAM-8	70	96	113	92	109.8
SAM-9	50	42	104	105	103.6
SAM-10	50	83	102	103	107.2
SAM-11	90	33	92	131	107.1
SAM-12	90	50	80	119	104.1
SAM-13	70	83	102	131	100.0
SAM-14	130	95	94	158	72.0

We defined the temperature at which self-ignition starts as the lowest of the values obtained for CO or CO_2 for each methodology. In the case of the intervals methodology, and in order to make it comparable with the other methods, we have put the middle value of the range in the table. The minimum values of all the compared methodologies is highlighted in Table 2. When comparing the five methods (including DSC), we can see that the inflexion point methodology is the one providing the lower temperatures, meaning that it would be the first one detecting the incipient process of self-heating.

Furthermore, we compared these numerical results with the information provided by the susceptibility graph Tcharact vs Ea, both parameters obtained or derived from TG analyses. In this graph (Figure 8) 10 of the 14 studied samples are located on the high self-ignition risk area, one in the very high (sewage sludge), and the other three in the medium area (wood chips, wood pellets and coke). The activation energy does not seem to be an important parameter in this study, since the only samples that present a value of more than 79 kJ/mol are the coals and the coke.

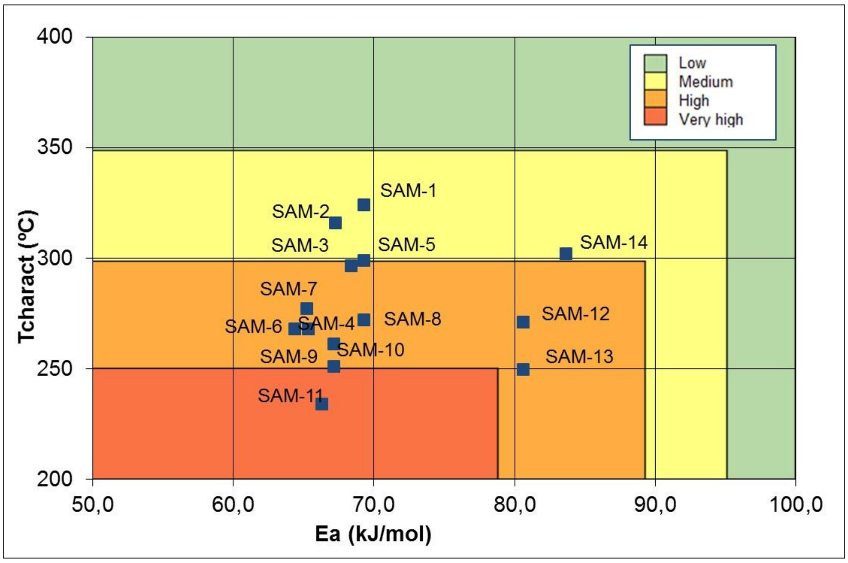

Fig. 8. *Susceptibility graph of the studied samples.*

When comparing these locations with the results obtained from the emissions of gases experiments, it is observed that the only sample located in the very high-risk area is the one with the lowest temperature of incipient self-ignition, and the one with the highest temperature is one of the samples located in the mid-risk area. Therefore, both methodologies agree on the main outcome, while the provided information is complementary and, together, could give a general view of the risk.

5. Conclusions

Different methodologies for the detection of incipient self-ignition and its risk of occurrence are currently in use all over the wold. TG and DSC tests provide important information about combustion processes, and about the self-ignition risk of dust materials. However, the starting point at which this self-ignition will take place can be detected in advance by studying the emissions of gases of the samples.

CO and CO_2 are gases that are measured in many industrial facilities due to environmental policies. If the self-ignition tendency of dust samples can be detected in advance by these emissions, it is an easy-to-implement and cheap way of increasing the safety in solid fuel storage and handling processes. Three different methods to study these emissions in relation to the self-ignition of solid substances are presented. One of them is based on reaching environmental safety limits of CO and CO2 to detect the phenomenon and it provides higher temperatures than the other methods studied. The interval method allows to detect the incipient combustion process in advance, while the inflexion point method is more consistent and provides more accurate results.

References

Agency, United States Environmental Protection. n.d. “Glossary of Climate Change Terms.” https://19january2017snapshot.epa.gov/climatechange/glossary-climate-change-terms_.html#G.

“Climate Change.” 2015. 2015. mso-bidi-language:AR-SA%22%3Ehttp://www3.epa.gov/climatechange/ghgemissions/gases/co2.html.

Doyle, C D. 1961. “Kinetic Analysis of Thermogravimetric Data.” *Journal of Applied Polymer Science* 5 (15): 285–92.

“EN 14774. Solid Biofuels. Detemrination of Moisture Content. Oven Dry Method.” 2009.

“EN 14775. Solid Biofuels. Determination of Ash Content.” 2009.

"EN 15148. Solid Biofuels. Determination of the Content of Volatile Matter." 2009.

European Union. n.d. "Climate Change Consequences." http://ec.europa.eu/clima/change/consequences/index_en.htm.

Everard, Colm D, Martin Schmidt, Kevin P McDonnell, and John Finnan. 2014. "Heating Processes during Storage of Miscanthus Chip Piles and Numerical Simulations to Predict Self-Ignition." *Journal of Loss Prevention in the Process Industries* 30: 188–96.

Fernandez Anez, N., J. Garcia Torrent, L. Medic Pejic, and C. Grima Olmedo. 2015. "Detection of Incipient Self-Ignition Process in Solid Fuels through Gas Emissions Methodology." *Journal of Loss Prevention in the Process Industries* 36. https://doi.org/10.1016/j.jlp.2015.02.010.

García-Torrent, J, Á Ramírez-Gómez, E Querol-Aragón, C Grima-Olmedo, and L Medic-Pejic. 2012. "Determination of the Risk of Self-Ignition of Coals and Biomass Materials." *Journal of Hazardous Materials* 213: 230–35.

Gil, Mar\'\ia Victoria, D Casal, C Pevida, J J Pis, and F Rubiera. 2010. "Thermal Behaviour and Kinetics of Coal/Biomass Blends during Co-Combustion." *Bioresource Technology* 101 (14): 5601–8.

Jones, J C, K P Henderson, J Littlefair, and S Rennie. 1998. "Kinetic Parameters of Oxidation of Coals by Heat-Release Measurement and Their Relevance to Self-Heating Tests." *Fuel* 77 (1): 19–22.

Magdziarz, Aneta, and Małgorzata Wilk. 2013. "Thermogravimetric Study of Biomass, Sewage Sludge and Coal Combustion." *Energ Convers Manage* 75: 425–30.

Medic Pejic, L., N. Fernandez Anez, J. Garc?a Torrent, and A. Ram?rez-G?mez. 2016. "Determination of Spontaneous Combustion of Thermally Dried Sewage Sludge." *Journal of Loss Prevention in the Process Industries* 36. https://doi.org/10.1016/j.jlp.2015.01.013.

Metz, Bert, Ogunlade R Davidson, Peter R Bosch, Rutu Dave, and Leo A Meyer. 2007. "Contribution of Working Group III to the Fourth Assessment Report of the Intergovernmental Panel on Climate Change."

Nasa Earth Observatory. n.d. "The Effects of Climate Change." https://climate.nasa.gov/effects/.

Raemy, A, R F Hurrell, and J Löliger. 1983. "Thermal Behaviour of Milk Powders Studied by Differential Thermal Analysis and Heat Flow Calorimetry." *Thermochimica Acta* 65 (1): 81–92.

Ramírez, Álvaro, Javier García-Torrent, and Alberto Tascón. 2010. "Experimental Determination of Self-Heating and Self-Ignition Risks Associated with the Dusts of Agricultural Materials Commonly Stored in Silos." *Journal of Hazardous Materials* 175 (1): 920–27.

Ribeiro, J, E Ferreira da Silva, and D Flores. 2010. "Burning of Coal Waste Piles from Douro Coalfield (Portugal): Petrological, Geochemical and Mineralogical Characterization." *International Journal of Coal Geology* 81 (4): 359–72.

"UNE 32002. Solid Mineral Fuels. Determination of Moisture in the Analysis Sample." 1995.

"UNE 32004. Solid Mineral Fuels. Determination of Ash." 1984.

"UNE 32019. Hard Coal and Coke - Determination of Volatile Matter Content." 1984.

Proceedings of the 13th Symposium International Symposium
on Hazards, Prevention and Mitigation of Industrial Explosions

DOI: 10.7795/810.20200724

Behaviour of smouldering fires during periodic refilling of wood pellets into silos

Nieves Fernandez-Anez [a], Anita Katharina Meyer [a], Javier Elio Medina [a], Gisle Kleppe [a],
Bjarne Christian Hagen [a] & Vidar Frette [a]

[a] Western Norway University of Applied Sciences. Bjørsonsgate 45, 5528, Haugesund, Norway
E-mail: Nieves.Fernandez@hvl.no

Abstract

Severe accidents in biomass storage units, including explosions and large flaming fires, are often preceded by smouldering fires. We report laboratory experiments on the evolution of smouldering fires in biomass stored in silos. Specifically, we study the effects on smouldering processes of supplying additional fuel material. The direct consequences on the sample of the material added are: cooling, enhanced thermal isolation, and facilitation of more intense combustion at a later stage. We find that the effects these mechanisms have are highly dependent on the stage of the smouldering process.

Keywords: *wood pellets, silo, smouldering*

1. Introduction

Biomass represents a way to harvest solar energy that is technological simple. The use of biomass has continuously increased during the last 15 years and this rise is expected to continue. Within this group of fuels, forestry accounts for more than 60% of all EU domestic supplied for energy purposes (The European Comission's Knowledge Centre for Bioeconomy 2019). In the EU, *wood pellets have become an important energy carrier traded on a large scale and over long distances, due to their high energy density and stable characteristics* (The European Comission's Knowledge Centre for Bioeconomy 2019). On the other hand, there are concerns that production of wood pellets directly from the main stems (instead of from wood wastes) may harm the climate (Searchinger et al. 2018). Irrespectively of the raw material used, large quantities of wood pellets are produced and need to be handled and stored. A common way of storing biomass is in vertical silos with roofs that prevent moisture absorption. With this configuration, large amount of material can be stored in a limited plant area.

However, storing organic materials in such a configuration leads to high-risk situations as self-heating (Guo 2013; Larsson et al. 2012). During self-heating, temperatures increase spontaneously in the stored material due to (exothermal) oxidation processes. Part of this heat accumulates in the material, accelerating the oxidation process, eventually leading to combustion of the material, a phenomenon known as self-ignition. One of the most common consequences of self-ignition is smouldering fires, a slow, low-temperature, and flameless form of combustion (Rein 2016).

Consequences of smouldering in silos include loss of stored material, fires and dust explosion, causing both human and material losses. Smouldering fires are difficult to predict, detect and control. They occur deep inside the material, releasing low quantities of gases, and reaching only moderate temperatures (Lohrer, Krause, and Steinbach 2005). Attempts to extinguish these fires using water are often unsuccessful, even if significant amounts are applied, making the best solution in many situation to let the content of the silo burn (Mikalsen et al. 2019).

However, materials are not always feed into silos in a continuous mode, but often in batches after being processed. This refilling process involves several risks: the generation of dust clouds due to the perturbation of the stored bulk material is an example. A not-yet-answered question is what happens if these refills are made when smouldering combustion is already ongoing. The introduction of fresh material will on one hand lower the temperature of the stored sample, while it also increase the potential for more intense combustion at a later point. We have investigated these two opposing effects experimentally in a laboratory-scale silo geometry. The time scales are well separated: the cooling leads to an almost instantaneous reduction in the combustion rate – followed by a much slower increase, in part facilitated by the additional fuel material. We focus on the cooling phase and obtain a master curve for the reduction in combustion rate as a function of the amount of added material.

2. Methodology

2.1 Materials

We have tested wood pellets that hast the characteristics detailed in Table 1.

Table 1. *Material properties of the wood pellets used in the experiments. Columns 1-4: Determined using Thermogravimetric Analyzer and Carbon/Hydrogen/Nitrogen determinator. Column 5: Determined using Thermogravimetric Analyzer and Moisture Analyzer. Columns 6-7: Determined using Thermogravimetric Analyzer. Defined as the amount of the material which undergoes pyrolysis and primary oxidation to form char. Columns 8-9: Determined using bomb calorimetry.*

C (%)	H (%)	N (%)	S (%)	Moisture (%)	Volatiles (% d.b.)	Ash (% d.b.)	Upper calorific value (kJ/kg)	Lower calorific value (kJ/kg)
47.91	6.42	0.03	0.10	6.76	82.13	0.49	18 834	17 433

2.2. Experimental set-up and procedure

Wood pellets have been studied in the experimental set-up shown schematically in Figure 1. It consists of a steel cylinder, 15 cm diameter, surrounded by 6 cm thick isolation along the side walls. This cylinder is on top of an aluminium plate that homogeneously distributed the heat from a hotplate below it, set at 320 to 340 ˚C. A thin steel ladder containing 30 Type-K thermocouples was placed in the middle of the cylinder. Thermocouples were separated 2 cm vertically and 3.7 cm horizontally. These components were placed on a scale that registered changes in the sample mass as the experiment evolved. Temperatures and mass were recorded every 15 s.

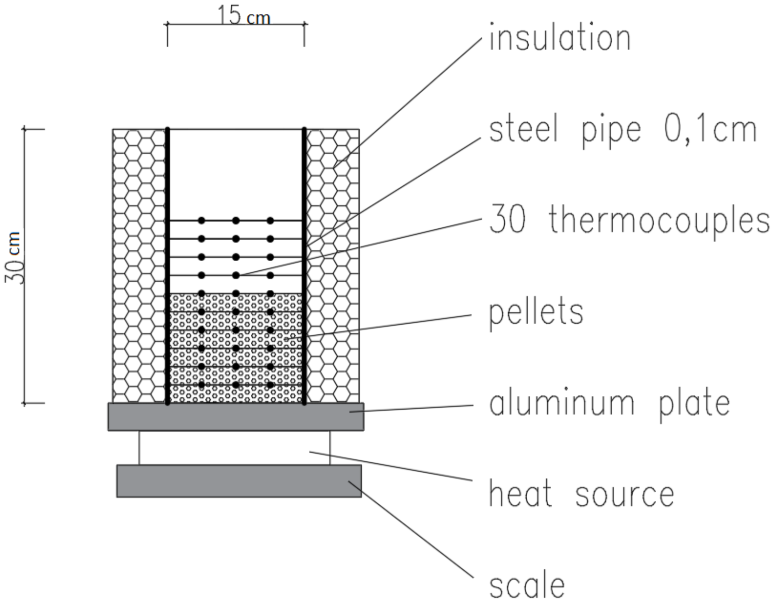

Fig. 1. *Experimental set-up. Main components (top to bottom): cylindrical sample holder with positions where temperatures were measured, hotplate and scale. Further details are described in the main text.*

Once the ladder was placed in the cylinder, wood pellets were slowly filled in, until the sample height reached a predetermined value. It was not possible to further compact the sample. Smouldering was initiated by switching on the hotplate for a given time. After the hotplate had been switched off, the sample evolved independently of external disturbances, with one exception:

Additional wood pellets were added to the sample at 8 h intervals. The amount of wood pellets was adjusted in each case, so that the sample mass after refilling reached its initial value. Thus, the refilled amount of material varied – reflecting the combustion during the preceding 8 h period.

Typical results from the experiments are shown in Figure 2, for a 14-cm-height sample, with recorded mass (top) and temperatures (bottom). Focusing on the mass vs time graph, it has a characteristic saw-tooth shape, with the vertical portions corresponding to the refill. During much of the process, the mass-loss rate is relatively low. Occasionally, however, the smouldering combustion gets more intense, with larger mass losses up to 50%. The cooling from the refilled material stops this intense combustion. Each of these peaks of intense combustion has a corresponding peak of high temperatures (middle part of Figure 2). Figure 2 bottom shows where the maximum temperatures were recorded (red areas). For the experiment in figure 2, the highest temperatures are mainly in the core of the sample (between 6 and 12 cm), and when the intense combustion periods occur, high temperatures are recorded near the upper surface of the sample.

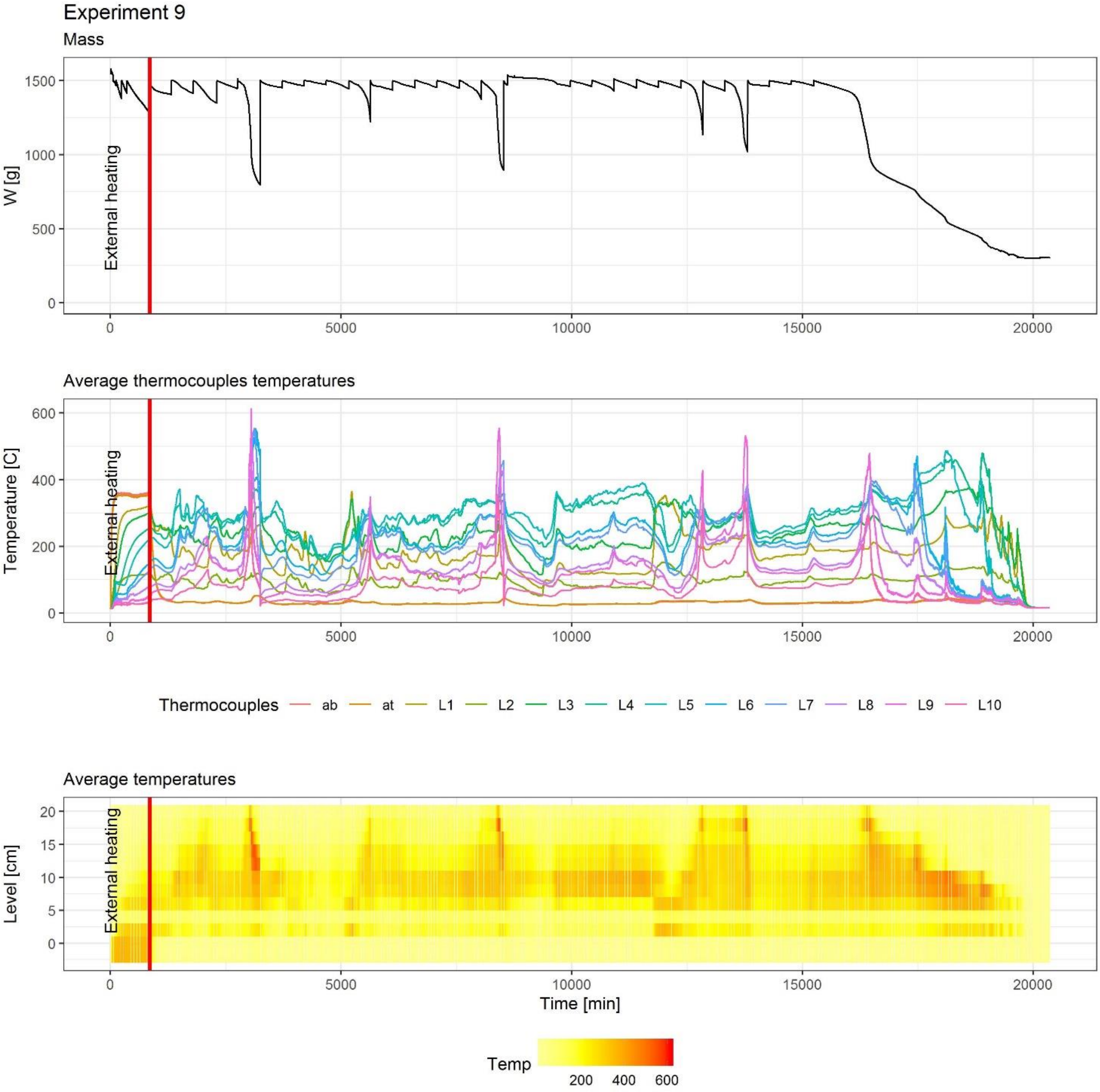

Fig. 2. *A typical experiment. Upper part: sample mass as function of time. Middle part: temperature as functions of time-measured at a number of positions in and above the sample (as shown in figure 1). Lower part: temperatures recorded at the different heights at different times.*

In previous studies with the same experimental set-up, there seemed to be a lower threshold for inducing self-sustained smouldering using the protocol described above, at a sample height of 6 cm. We therefore decided to start these experiments at a sample height 10 cm, and have explored 10, 12, 14, 16 and 20 cm. We observed that for the three first heights smouldering occurred in a similar manner that we will discuss later in this manuscript. However, 16-cm-height samples did not smoulder, while smouldering was observed again for larger samples (20 cm), but a different behaviour than for the smaller sizes was observed.

2.3 Data analysis

Statistical tools were developed to characterise the behaviour observed in the experiments. A linear prediction (i.e. R: zoo::na.approx, (Team and others 2013)(Zeileis and Grothendieck 2005)) was carried out to estimate values in points where there were no recorded data (i.e. fall-out in the data logging). Then, the mass data was smoothed to further investigate the characteristic features of the mass curve with time (Figure 3). We have used a Local Polynomial Regression fitting (LOESS). The fitting is done locally, which means that a value in a point X_i is estimated based on the value of its neighbourhood, weighted by their distance from X_i. The size of the neighbourhood is controlled by the span, and the larger it is, the smoother the results are. In our case, we have used a span which covers 100 measurements and a polynomial degree of 1.

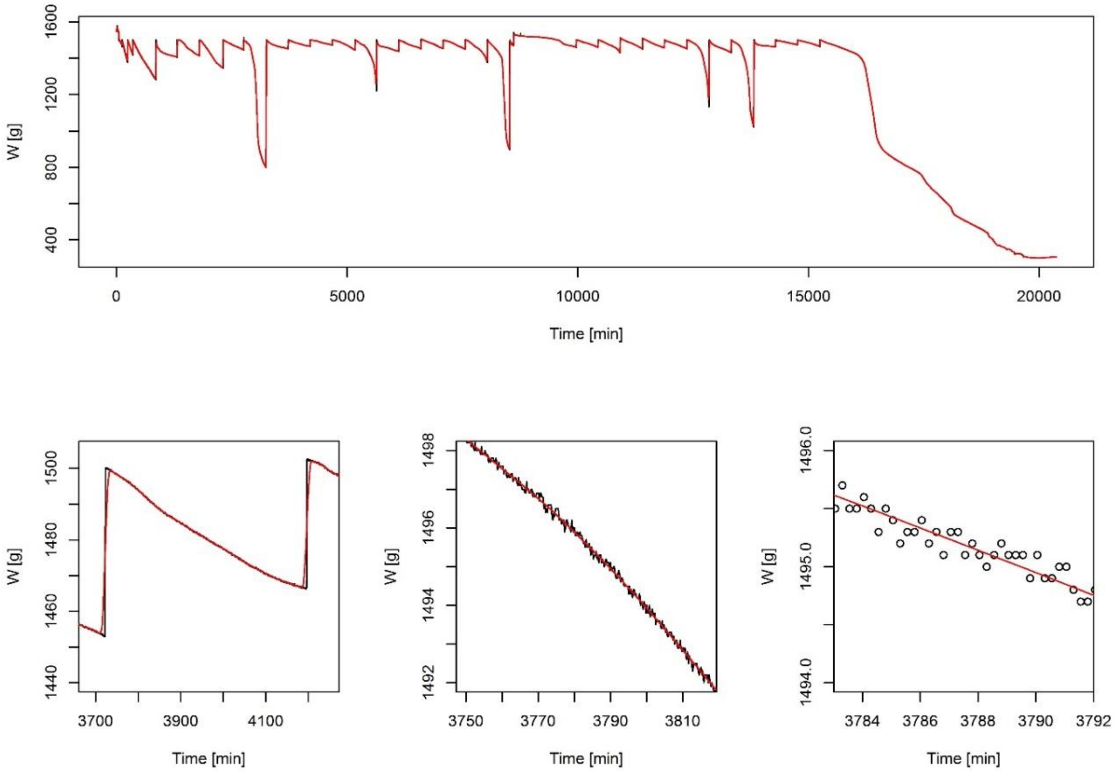

Fig. 3. *Recorded sample mass (black) and filled (smoothed) curves using LOESS approach described in the main text (red). The upper part shows the entire experiment, while the lower part displays a sequence of magnifications (zooms). This is the same experiment as shown in Figure 2.*

We predicted the mass variation by intervals of 1 second (h = 1 s), and then calculated the first derivative numerically using a centred difference approximation (Eberly 2008).

$$F'(X) = \frac{(F[x+h] - F[x-h])}{2h}$$

At each refill point (i.e. points where new material was added to take the sample back to its initial mass; Figure 3) we calculated the refilled mass and the difference of the combustion rates before and after refilling, defining the combustion rate (the mass-loss rate) as the negative of the derivative of the sample mass curve. The refilled mass is the difference between the mass at the beginning (W_i) and at the end (W_f) of the refill, while the difference in the combustion rates is obtained from the first derivative of the adjusted curve (i.e. LOESS prediction) at 15 min before (CR_i) and 15 min after (CR_f) the refilling point. There are two reasons for this choice. First, the smoothed curve does not fit well near the refilling point (compare red and black in vertical parts of the left plot in lower line of Figure 3). Second, it also allows the system to stabilize after the disturbance from the refill (Figure 4).

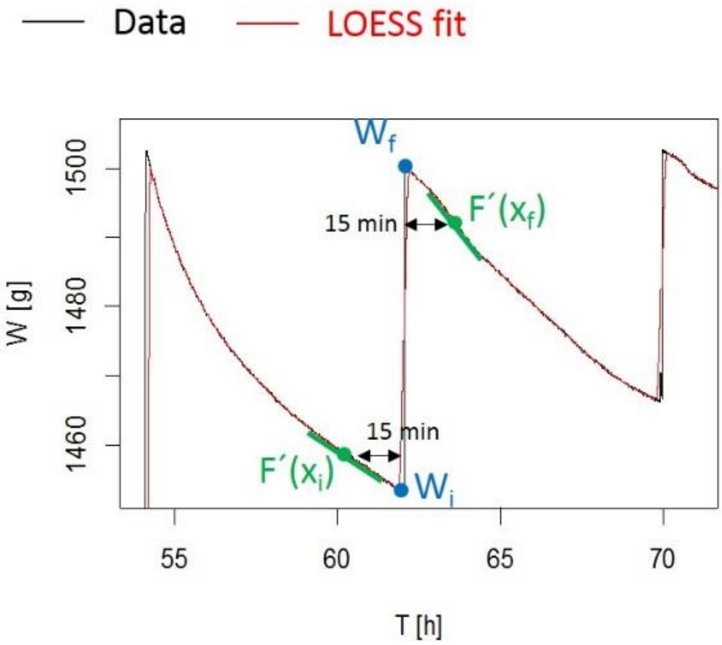

Fig. 4. Important quantities used to calculate the amount of refilled material and the combustion rate directly before and directly after the refill. See further explanation in the main text.

3. Results and discussion

Following the procedure described in Section 2.2.1, we analysed each peak of the mass vs time curve (each refill), as shown in Figure 5 upper part, where the refills are marked with consecutive numbers from 1 to 28. We also plot the difference in combustion rates vs the mass of the refill (Figure 5 lower part).

For small refills, the change in combustion rate (mass-loss rate) is small, but increases for large refills More surprisingly, for the largest refills, the change in combustion rate is again close to zero.

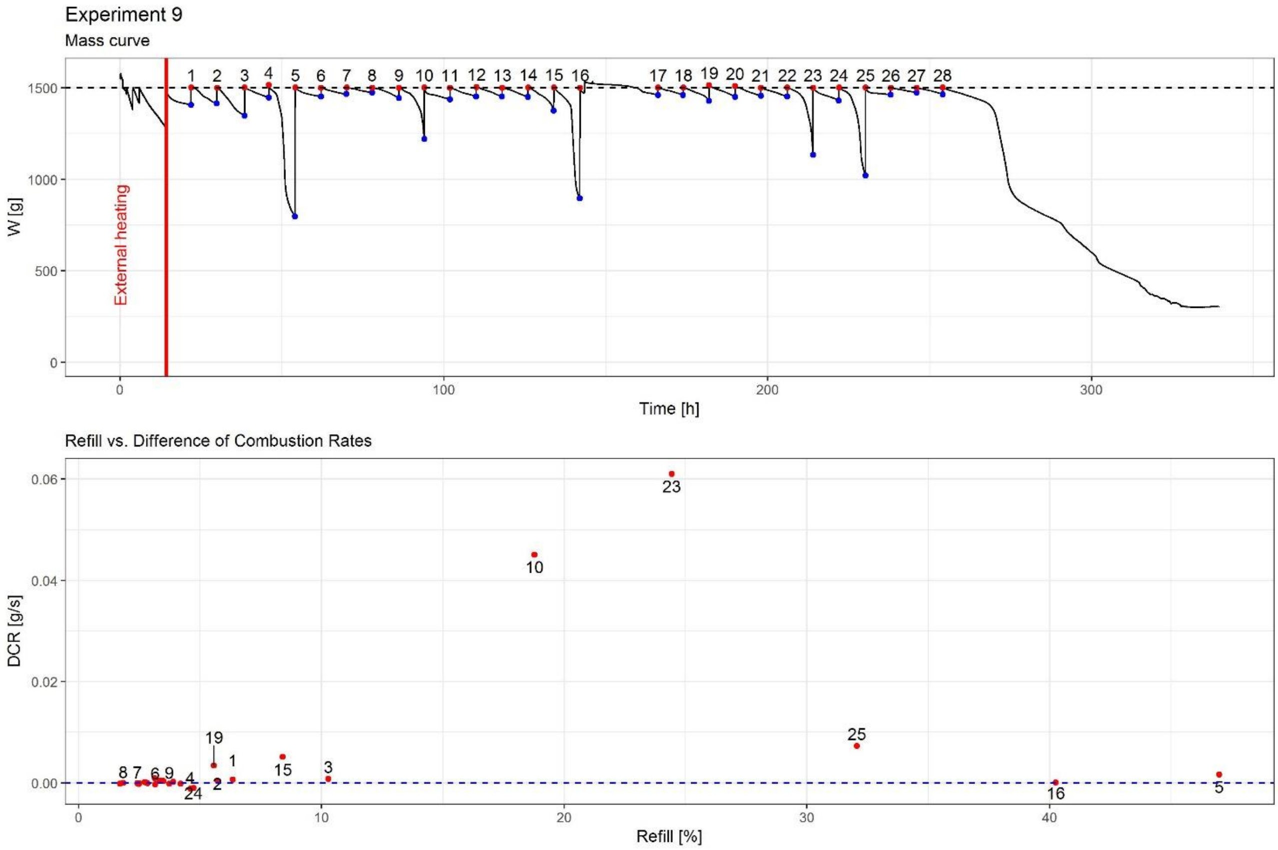

Fig. 5. *Results from analysing the same experiment as shown in Figures 2 and 3. The upper part in the present figure shows again the smoothed data, with refills numbered. The analysis has been carried out from the red vertical line on. Thus, the initial period with external heating (hotplate on) has been excluded from the analysis. The lower part shows results, in terms of the difference in combustion rate (mass-loss rate) from directly before to directly after the refill – as a function of the refilled amount of wood pellets (as fraction of initial sample mass).*

Repeating this analysis for all experiments, results follow a similar trend for all sample heights, as observed in Figure 7 where the difference in combustion rates versus refill (as fraction of initial sample mass) is plotted. Three graphs are displayed: i) the combustion rate before the refill (top left); ii) the combustion rate after the refill (top right); and iii) the difference in the combustion rate with the refill (bottom). A LOESS fit (span = 0.25, and degree = 2) was used for plotting trends in the data for each sample height (i.e. colour lines). Four regimes may be observed in the graph (as indicated by vertical lines):

a) Up to 10 % refills: the combustion rates before refills increase linearly, and the refill does not affect it. The difference in the combustion rates is close to 0. Thus, the refill do not influence the smouldering process

b) From approx. 10 % to 25 % refills: there is a rapid increase in the combustion rate before refill, which is halted when we add more fuel material (i.e. combustion rates after refill are much lower). In this regime, the smouldering processes are more intense and occur at higher temperatures. Consequently, the mass-loss is larger and so is the refilled amount of wood pellets. A large refill leads to a stronger cooling of the sample and a larger reduction in the combustion rate. The nonlinear curve shapes in Figure 6, parts A and C is reasonable in view of the highly nonlinear dependency of the combustion rate on temperature (Arrhenius expression).

c) From 25 % to 50 %: the combustion rates before refills level off and start to decrease, In this regime, the large refilled amounts of wood pellets indicate a relatively long period of intense (high temperature) smouldering before the refill occurred. During this period, the sample has lost significant amounts of heat through convection and radiation. Thus, the cooling effect of the added material is less pronounced.

d) Refills higher than 50 %: the combustion rate before refills are low and similar to the values after refills (i.e. differences close to 0). In this regime, the sample has lost heat to an even larger degree than in the previous regime. The added fuel material, when the refill finally occurs, have close to no cooling effect.

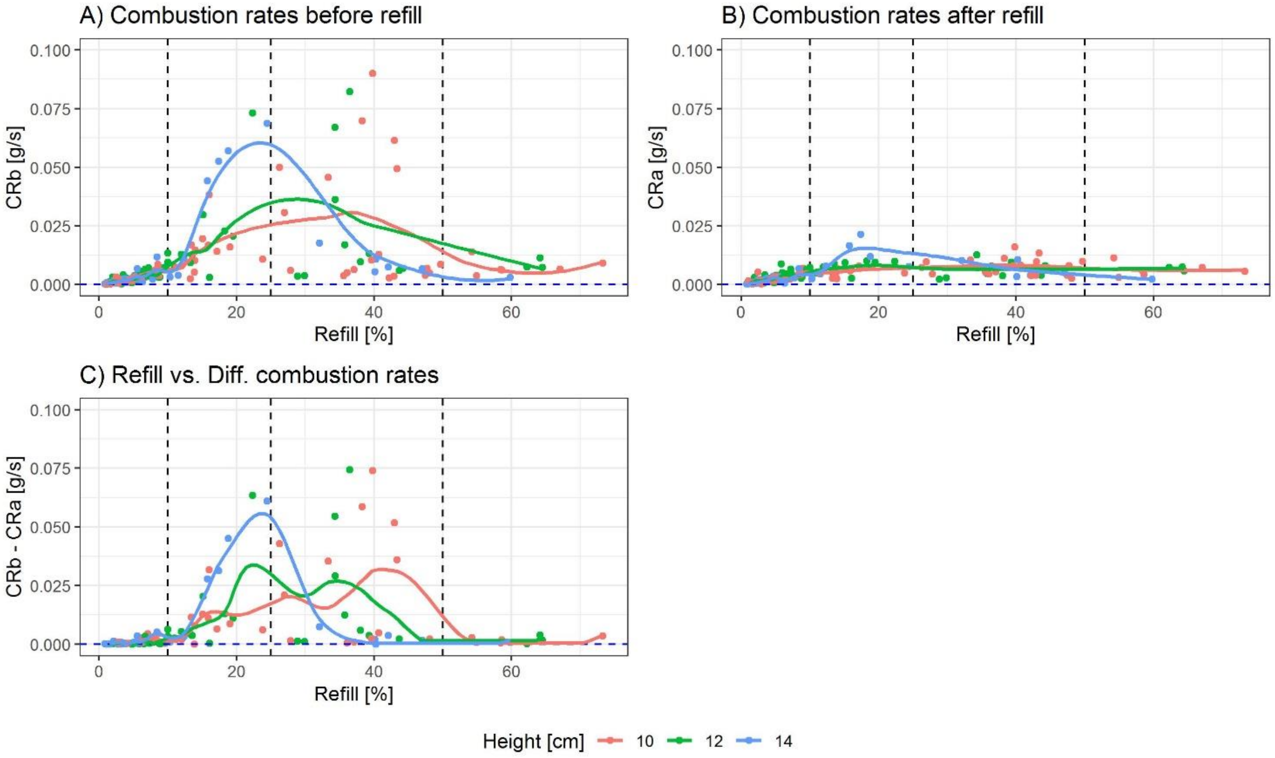

Fig. 6. Refill vs. diff combustion rate for all experiments

4. Conclusions

Storage of biomass as wood pellets is and will continue being key in a renewable-energy future. In order to secure the availability of these materials, a safe storing system should be ensured. Self-heating, self-ignition and smouldering combustion in silos have previously been widely studied due to its high frequency of occurrence. A specific situation is refilling of these silos when a smouldering process is already ongoing. This process has been studied by long-run experiments at different sample heights (10, 12 and 14 cm) in a 15 cm diameter silo, and the influence of the refill size was studied. If the refill is small or large, it does not influence the behaviour of the smouldering fire, and we observe the same combustion rate before and after the refill. However, if the refill is intermediate in size, the smouldering process is normally ongoing under a high combustion rate, and by refilling the laboratory-scale silo these rates decrease, slowing down the combustion process.

Acknowledgements

The authors gratefully acknowledge funding from the Research Council of Norway, project 238329: Emerging Risks from Smoldering Fires (EMRIS).

References

Eberly, David. 2008. “Derivative Approximation by Finite Differences.” *Magic Software, Inc*.

Guo, Wendi. 2013. “Self-Heating and Spontaneous Combustion of Wood Pellets during Storage.” University of British Columbia.

Larsson, Sylvia H., Torbjörn A. Lestander, Dave Crompton, Staffan Melin, and Shahab Sokhansanj. 2012. “Temperature Patterns in Large Scale Wood Pellet Silo Storage.” *Applied Energy* 92: 322–27. https://doi.org/10.1016/j.apenergy.2011.11.012.

Lohrer, C, U Krause, and J Steinbach. 2005. “Self-Ignition of Combustible Bulk Materials under Various Ambient Conditions.” *Process Safety and Environmental Protection* 83 (2): 145–50.

Mikalsen, Ragni Fjellgaard, Bjarne Christian Hagen, Anne Steen-Hansen, Ulrich Krause, and Vidar Frette. 2019. “Extinguishing Smoldering Fires in Wood Pellets with Water Cooling: An Experimental Study.” *Fire Technology* 55 (1): 257–84. https://doi.org/10.1007/s10694-018-0789-9.

Rein, Guillermo. 2016. “Smouldering Combustion.” In *SFPE Handbook of Fire Protection Engineering*, 581–603. https://doi.org/10.1007/978-1-4939-2565-0_19.

Searchinger, Timothy D., Tim Beringer, Bjart Holtsmark, Daniel M. Kammen, Eric F. Lambin, Wolfgang Lucht, Peter Raven, and Jean Pascal van Ypersele. 2018. “Europe’s Renewable Energy Directive Poised to Harm Global Forests.” *Nature Communications* 9 (1): 10–13. https://doi.org/10.1038/s41467-018-06175-4.

Team, R Core, and others. 2013. “R: A Language and Environment for Statistical Computing.”

The European Comission’s Knowledge Centre for Bioeconomy. 2019. “Brief on Biomass for Energy in the European Union.”

Zeileis, Achim, and Gabor Grothendieck. 2005. “Zoo: S3 Infrastructure for Regular and Irregular Time Series.” *ArXiv Preprint Math/0505527*.

DOI: 10.7795/810.20200724

Effect of particle size distribution, drying and milling technique on explosibility behaviour of olive pomace waste

Matteo Pietraccini [a], Enrico Danzi[a], Luca Marmo[a], Albert Addo[b] & Paul Amyotte[b]

[a] Politecnico di Torino, Dipartimento di Scienza Applicata e Tecnologia, Torino (IT)
[b] Department of Process Engineering & Applied Science, Dalhousie University, Halifax, NS, Canada

E-mail: luca.marmo@polito.it

Abstract

The Mediterranean area is responsible for about 98% of the olive oil world-wide production, with 900 million of olive trees occupying 10 million of hectares. However, the manipulation of 100 kg of olives leads to the production of 40 kg of wastes, mainly constituted by olive pomace, which is potentially recoverable as energetic or material source. In general, in the past 20 years, the exploitation of olive pomace has increased, but along with it the need of further information about its chemical-physical characterization and the related hazard in industry. Thus, a risk analysis assessment (RAS) was made. When pelletized or in chunks, olive pomace does not pose any greater hazard than a pile of woody material, but when pulverized, it might become dangerous. Two parallel series of experiments were carried out at Dalhousie University (Lab 1) and at Polytechnic of Turin (Lab 2), according to slightly different experimental procedures. Olive pomace dust explosibility and flammability parameters were measured: minimum ignition energy (MIE), minimum ignition temperature (MIT), maximum pressure rise rate ((dP/dt)max and KSt), maximum pressure (Pmax) and minimum explosible concentration (MEC). Moreover, the chemical and physical characterization of olive pomace was carried out: moisture content, particle size analysis, Scanning Electronic Microscope (SEM) investigation, thermo-gravimetric analysis (TGA), solid-state Nuclear Magnetic Resonance (NMR), mass spectrometry, calorific value and bulk density estimation. Different thermal behavior was observed in function of the sieving/grinding pretreatment. As concern flammability tests, samples seemed not to be sensitive to electric arc ignition (a value of MIE could not be measured) while coarser samples demonstrated higher ignition sensitivity to hot environment sources (MIT furnace) than finer ones. On the opposite, explosion violence parameters were enhanced by decreasing the particles size (KSt), while peak pressures were significantly influenced by the heat of combustion and the moisture content. Finally, a new test was developed to quantify the propensity of the raw material to produce fines by abrasion. The properties of the fines produced were measured as well.

Keywords: *dust explosions, olive pomace, moisture effect, particle size distribution effect, milling, grinding*

1. Introduction

The Mediterranean Sea area is responsible for the production of about 98% of the olive oil worldwide produced, which counts 900 million of olive trees occupying 10 million of hectares, as reported by Barbanera et al. (2016). From each 100 kg of olive it is possible to produce about 60 kg of olive oil, which makes its production an important economic, cultural and political resource for the countries which look out on the Mediterranean Sea, as well as, unfortunately, 40 kg of waste, which needs to be treated or recovered. Current extraction technology passed from the traditional pressing to a continuous centrifugation process, which could be realized in two or three phase flow. A wet solid phase is obtained as waste, with a moisture content of about 55-70%, which could be reduced afterwards with a drying phase, and a little fraction of oil, which is recovered with solvent extraction. The resulting solid residue, made predominantly of olive skin, pit and pulp, is called olive pomace or olive mill waste (as in Christoforou & Folkaides, 2016). According to today's need of an ecological transition, this waste may be introduced in a circular-economy-based supply chain. Energetic characteristics, combustion behavior and densification properties made these biomass feedstock usable to generate energy through different processes (Eliche-Quesada & Costa, 2016, Yucel, 2011 and Akar et al. 2009): olive pomace could be feed to thermochemical processing (combustion, pyrolysis, gasification) or biochemical processing (Christoforou & Folkaides, 2016). The first, implying high temperatures ambiances, do present several hazardous situations involving olive pomace handling and conveying, silos storing, gasification and pyrolysis in reactors or undesirable deposits in milling and/or grounding systems. In order to respond to a lack of information concerning the safety of these operations, this work aims to conceive a physical-chemical characterization method for olive pomace, as well as a risk assessment analysis, focused on its explosibility and flammability as a dust and on the comprehension of its behavior in the above-mentioned possible situations.

2. Experiments

This work was carried out with the same olive pomace sample but in two different laboratories, in order to enlighten eventual differences concerning the equipment, the methods and the standards. The laboratories were the Dust Explosion and Process Safety Laboratory at Dalhousie University (Halifax, Canada) and the dust Explosion Laboratory of the Applied Science and Technology Department of Polytechnic of Turin (Turin, Italy). From here on, they will be referred as Lab 1 and Lab 2, respectively.

2.1 Characterization analysis

The olive pomace sample came from a Spanish olive mill that uses a 2-phase extraction method (as depicted in Figure 1), with a final pelletizing step. Different milling techniques and tools were used in the two laboratories involved in this work, as to obtain information in a quite wide range of PSD (coarse, intermediate and fine particles). For samples A, B, C and D a complete conditioning process was performed, leaving the samples with a residual moisture content between 1.1 and 0.6% in weight, whereas samples from Lab 2 were not conditioned and were tested as received. Moisture content of these samples was between 5 and 7% in weight. This differentiation was thought to compare the explosivity behaviour of the samples and investigate moisture effect. These characteristics are synthetized in Table 1, while the appearance of the samples is shown in Fig. 2.

Different sieves were used to obtain fractions, according to ASTM mesh numbers, Particle size distribution was measured through granulometric diffraction with a laser granulometer, coupled with a dry dispersion system.

The SEM was used to describe the particle shape and the eventual presence of peculiar structures or agglomerates. The coating was made using a Low Vacuum Coater Leica EM ACE200 (current intensity of 20 mA, exposition time of 260 s, pressure of 0.04-0.08 bar). At the end, particles were coated with a 20 nm gold-palladium layer. The SEM investigation was carried out with a Hitachi S4700 Field Emission Scanning Electron Microscope, using a potential of 10 kV.

The thermal behavior of the samples was determined through a thermo-gravimetric analysis (TGA). Having the results from both the under-air and under-nitrogen test, it is possible to determine the moisture content (MC), the volatile matter (VM), the fixed carbon (FC) and the ash content of the sample. Both VM and FC influence the combustion behavior and can be used as indicator of the biomass reactivity. In fact, high VM and low FC means higher reactivity of the biomass (Garcia et al., 2013).

The analysis was performed in a Q600 SDT (Simultaneous Differential Technique), with a heating rate of 10°C/min, a final temperature of 1000°C, under air and argon atmosphere.

Table 1: *Characterization of the different samples tested for this work.*

	Lab 1	Lab 2
Particle size distribution (fraction, range in µm)	D : < 45	IV : < 75
	C : 75 - 45	III : < 250
	B : 212 - 75	II : 500 - 250
	A : 425 - 212	I : 1000 - 500
Conditioning	24 hours @ 110°C	NO
Milling/Grinding method	Hammer mill	Knife mill

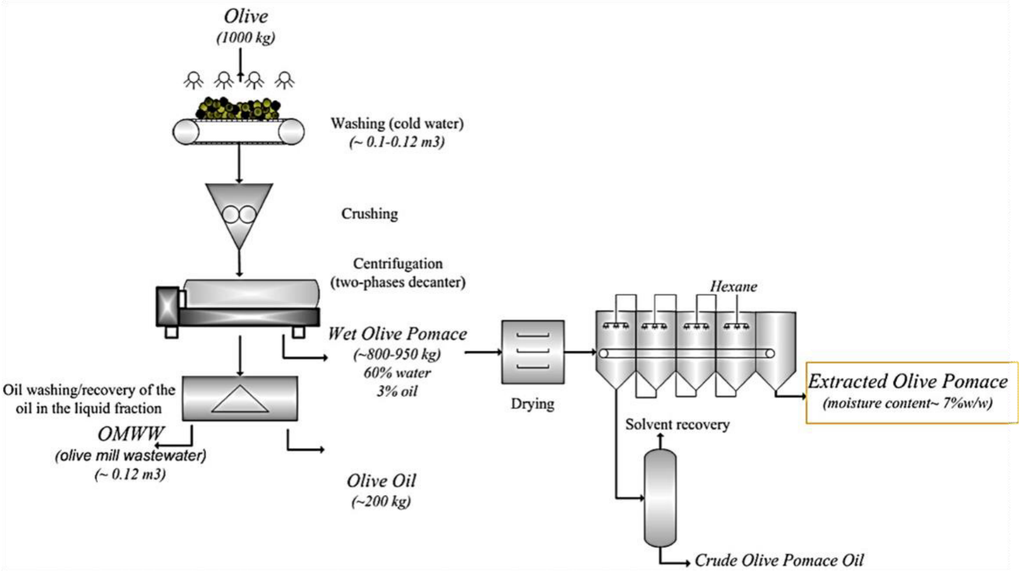

Fig. 1. *Two-phase continuous centrifugation process to extract oil from olives.*

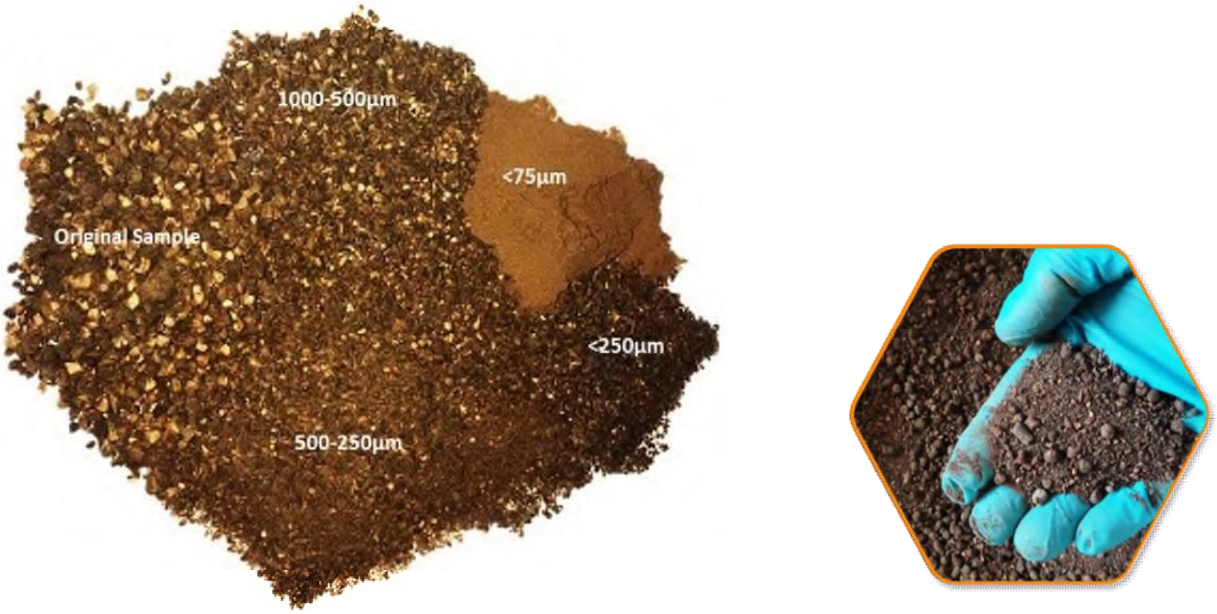

Fig. 2. *Appearance of the olive pomace sample: as it were (to the right) and compared to the sieving outcomes (to the left).*

Through a solid-state NMR it is possible to obtain information about the sample's chemical composition. In this case, since the material has a ligneous-cellulosic matrix, the main goal is to estimate its chemical composition in terms of lignin, cellulose and hemicellulose contents. Carbohydrates, aromatics, carboxylic and aliphatic species classes were adopted to identify cellulose, hemicellulose and lignin, respectively. Each of them has a specific maximum peak which can be used for the characterization: carboxyl groups have maxima around 173 ppm (integral range 191 - 164 ppm); aromatic groups (integral range 164 - 112 ppm) have maxima around 154 ppm (aromatic containing oxygen atoms), 144 ppm (aromatics bonded each other), 129-116 ppm (aliphatic-substituted or non-substituted aromatics); carbohydrates have maxima typically around 104 ppm, 72 ppm, 64 ppm, 56 ppm (integral range 112 - 45 ppm); aliphatic (CHn where n=1-3) have not specific maxima (integral range 45 - 3 ppm) (Cory & Ritchey, 1988, Harris et al., 2001) Hence, 1H and 13C were chosen as nuclei. This analysis was carried out in a Bruker Avance DSX NMR spectrometer with a 9.4 T magnet (Larmor frequencies: 400.24 MHz for 1H, 100.64 MHz for 13C) using a probe head for rotors of 4 mm diameter.

Calorific value allows to know the amount of thermal energy released by tested sample complete combustion and thus the maximal thermal energy potentially available for an explosive-like behavior. The analysis was made with a Parr oxygen calorimetric bomb.

2.2 Explosibility and flammability parameters

Explosibility parameters were measured on all the samples A to D and I to IV separately. Methods and results are described hereafter.

2.2.1 Minimum Ignition Energy

The apparatus used to determine the MIE was a MIKE 3, equipped with a 1,2 L glass tube as explosion vessel and generally following the ASTM E2019-03 standard procedure. The dispersion occurs with a 7 bar pressurized air pulse. The analysis was carried out (according to the ASTM E2019-03 standard procedure) with different amounts of dust (900, 1200, 1500, 1800, 2400 and 3000 mg), different delay time (90, 120 and 150 ms) and with inductance (1 mH) for each sample. The spark energy ranged between 1 and 1000 mJ.

2.2.2 Minimum Ignition Temperature, in cloud

As for samples A, B, C and D the MIT measurement was made with a 0.35 L BAM Oven generally following the ASTM E1419-06 standard procedure. A test was considered positive if the ignition occurs within 5 seconds from the dust injection. MIT of samples analyzed in Lab 2 were obtained with a Godbert-Greenwald Furnace, according to ISO 80079-20-2:2016.

2.2.3 Minimum Ignition Temperature, in layer

Sample III was also subjected to a layer ignition tests; Chilworth Hot-plate apparatus was used for this purpose and the procedure followed the ISO 80079-20-2:2016. The layer height was 5 mm.

2.2.4 Minimum Explosible Concentration

To determine the MEC, a Siwek 20L spherical vessel was used with a butterfly-shaped rebound nozzle. Lab 1 made the measurements following ASTM E1515-07 standard procedure, using one 2.5 kJ chemical igniter as ignition source. Lab 2 measured MEC in a 20 L sphere according to UNI EN 14034-3:2011, using two 1 kJ chemical igniters.

2.2.5 Explosion parameters

KSt and Pmax are the explosion parameters which were determined. The measurements were undertaken by Lab 1 generally following ASTM E1226-12a standard procedure. The software that was used for the measurements was the KSEP 6.0. Similarly, in Lab 2 explosion parameters were measured by means of the same apparatus, according to UNI EN 14034-1 and 2.

3. Results and discussion

3.1 Characterization analysis

Sample granulometric distributions are shown in Fig. 3. They are all unimodal, except for sample C, which shows a little (and negligible) mode centred in 18.5 µm. Furthermore, there are no isolated groups of coarse particles (as it happens in a bimodal distribution with one of the mode-values in the coarse particles range), which may act like a heat sink during the explosion (Saeed et al., 2018).

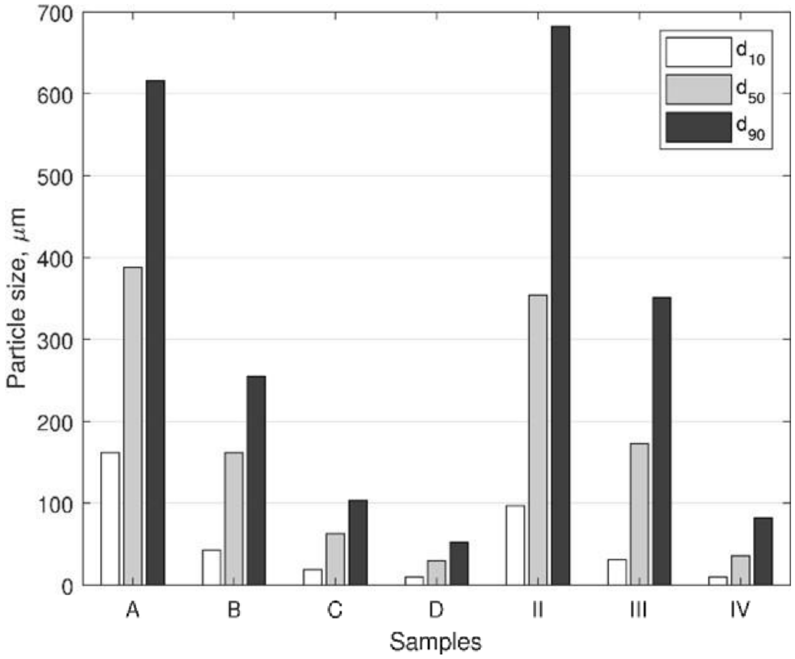

Fig. 3. *Particle size distribution (d10, d50 and d90) for the samples tested.*

The proximate analysis (Table 3) was obtained by TG analysis. The samples had different behavior when slowly heated up. The pellets showed some irregularity compared to the others, it was still possible to identify three characteristic peaks: the first wide one is associated to water loss (A, B, C, D do not show such a peak because they passed through an air-oven-drying step before); the second one, between about 180 and 370°C is associated to some thermal degradation reaction; the third one, between 370 and 520°C, is associated to the oxidation of the char (Xie et al., 2018a, Guizani et al., 2016, Di Blasi, 2008, Xie et al., 2018b, Vecchio et al., 2009). The peak associated to the hemicellulose and cellulose degradation reactions are rather narrow and centered respectively around 250 and 290°C, while the lignin one is wider, centered around 350-400°C and covering the range 200-450°C. The samples showed a slightly different behavior in the char combustion step, where sample D (the finest one) stands out with its sharp peak. Furthermore, the peak temperature seems to follow a decreasing trend as the particle size increases. The results from the TG analysis were used to determine the proximate analysis, whose results are reported in Table 3, together with the moisture content and the calorific value. The samples presented different volatile matter to fixed carbon ratio (VM/FC) when heated up: sample B showed the highest value, samples C and D similar values, while sample A showed the lowest one.

The different thermal behavior did not come from a difference in the chemical composition. In fact, the signals resulting from the solid-state NMR are in almost the same for all samples, with some relatively important changes only for the pelletized sample.

The SEM investigation was useful to understand how the particles are shaped and whether it was possible to identify some characteristic structures, related to olive pit, skin, pulp or kernel, which could possibly explain any difference observed in the flammability tests of the samples. Pictures are shown in Fig. 4.

Table 2 : *Proximate analysis results. VM, FC and HHV were calculated on a dry-ash-free basis, ash content was calculated on a dry-basis.* [a] *Calculated from the TG analysis.* [b] *From Miranda et al., 2008.*

Sample	Moisture (before drying) %wt	Moisture (after drying) %wt	Volatile Matter %wt	Fixed Carbon %wt	VM/FC	Ash %wt	HHV MJ/kg
Pellets	6.1	-	72.8	11.7	6.2	15.5	23.7
A	5.4	0.6	66.0	25.5	2.3	8.5	22.9
B	5.0	1.0	79.3	6.7	11.8	14.0	24.4
C	6.4	1.0	76.0	13.3	5.7	10.7	23.7
D	6.0	1.1	74.5	17.1	4.4	8.3	22.6
Olive pit	9.0 - 10	-	80.9	18.5	4.3	0.6	20.7
Olive pulp	6.0 - 6.5	-	79.1	15.3	5.2	5.6	24.4
Residual olive cake	5.5 - 6.0	-	77.8	17.9	4.3	4.3	23.3

Samples A and B showed a variety of particle shapes, more than the other two, but also particles with smoother surface, while the two finest samples seemed to have more jagged surfaces. Main structures identified are indicated here as: broken pills, wrap, blunt particles, cylinders, smooth particles and agglomerates. Broken pills are present in coarser samples (A, B) and present a honeycomb-like morphology, which could be attributed to olive cells in the endocarp, as in Marsilio et al. (2000). Wrap structures are quite irregular and appear only for sample A; they could be associated to olive skin, epicarp (see Lanza et al. (2015)). Blunt particles are present in all samples, as they likely constitute the softer fraction, the olive pulp, or mesocarp (Lammi et al., 2018). Cylinders are very different from any other particle shapes and could be part of some olive tree inflorescences or fractionated tranches (wooden, and so fragile material). Flat particles could be found in all samples, except A, and they seem to come from the inner layer of olive endocarp, as in Marinova et al., 2011. Smooth particles (C and D samples) are derived from the crushing of olive endocarp layer, the most resistant part. Agglomerates are made by finer particles which stick together, the majority could be found in finer fractions, C and D.

3.1 Explosibility and flammability

Explosibility and flammability analysis results are shown in Table 4.

As regards the MIE test, it was found that the olive pomace dusts were not sensitive to be ignited by an electrical spark with energy lower than 1 J.

The explosion parameters and the MEC values showed how the explosibility of olive pomace dust is likely related to the chemical composition (affecting the energetic content) and the particle size distribution (affecting the flame propagation rate). This dependence is shown in Fig. 5 and in Fig. 6. As expected, the (dP/dt)max (and also KSt) followed an increasing trend as the particle size decreased, while Pmax showed a maximum for sample B, which had the maximum HHV and the maximum VM/FC ratio (respectively, higher energetic content and higher volatile matter over fixed matter). As the particle size decreases, in fact, the surface area increases and in turn also the reaction rate does and consequently the KSt, as well-known from literature (as reference Cashdollar, 2000), and specifically for biomass dust, as in Semenova et al (2006) with pine bark dust, Huescar Medina et al. (2015). Finest samples, thus, needed also a lower concentration to ignite, while the coarsest samples registered higher MEC values. Conclusively, (dP/dt)max, KSt and MEC were mainly influenced by the particle size, while Pmax was mainly influenced by energetic content and chemical reactivity (VM/FC). The moisture content has had an important role in determining the explosion

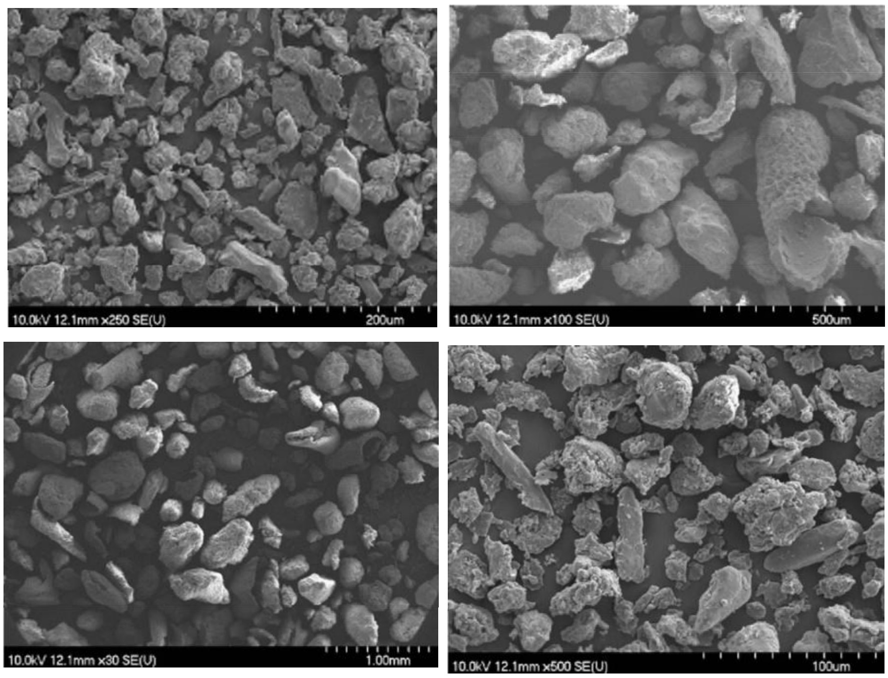

Fig. 4. *SEM images of the four samples: sample A (upper-left); sample B (upper-right); sample C (lower-left); sample D (lower-right). The images were chosen in order to be as much representative as possible*

parameters of olive pomace dust as can be seen comparing the results obtained from samples II and II, which did not undergo conditioning.

Higher moisture content in the samples led to a rather important decreasing of Pmax, mainly influenced by the energetic content of the dust (a 20% decrease of HHV is observed), whereas the slight differences in KSt are mainly due to the different particle size distribution.

MIT values showed the two finest samples were more thermally stable than the coarsest two, thus needing a higher temperature to reach the ignition point. It was noticed using the BAM oven, that for temperatures above 510°C the two coarsest samples showed an instantaneous ignition, while as the temperature was around 500°C, the flame coming out the metal flap was weaker and slower (result of the ignition of the off-gases). As regards of the two finest samples, the flame was never as instantaneous as in the case of the two others, but it was probably due to the ignition of the off-gases released by the settled dust and the excess of particulate matter. This analysis confirmed the hypothesis of low thermal reactivity of the two finest samples, as well as the higher thermal reactivity of the other two. Sample B registered the lowest MIT, as similarly high Pmax was obtained, attesting a dependence of the two values on specific characteristics of this sample, different from PSD (i.e. chemical and physical of singular particles, as reported in the conclusions). Although the fractions analyzed were not the same the lowest MIT value was the one relative to sample III, quite close to size range of sample B. A similar trend was observed in the MIT evolution with particle size for the two Labs, as in Fig. 7, where for both a minimum was registered (samples III, B). MIT of non-conditioned samples were higher than conditioned ones (so directly correlated to higher moisture content), while the difference could be also explained by the adoption of the two different measuring devices, since the BAM furnace gives slightly higher temperatures than the GG furnace (Echkoff, 2003). In the GG furnace, the combustion chamber containing the hot surface is vertical: this allows to eliminate the effect of the off-gases, which can ignite instead of the dust. An ignition in the GG furnace is, then, only attributable to the ignition of the dust cloud.

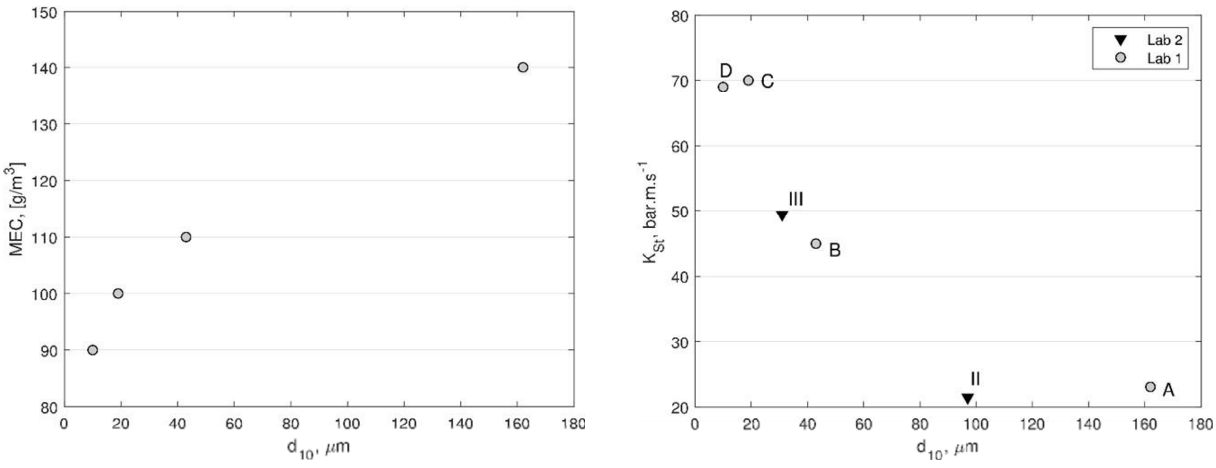

Fig. 5. *Influence of particle size (tenth percentile, d10) on the maximum explosion concentration (MEC) and on the* K_{St}, *for samples A to D.*

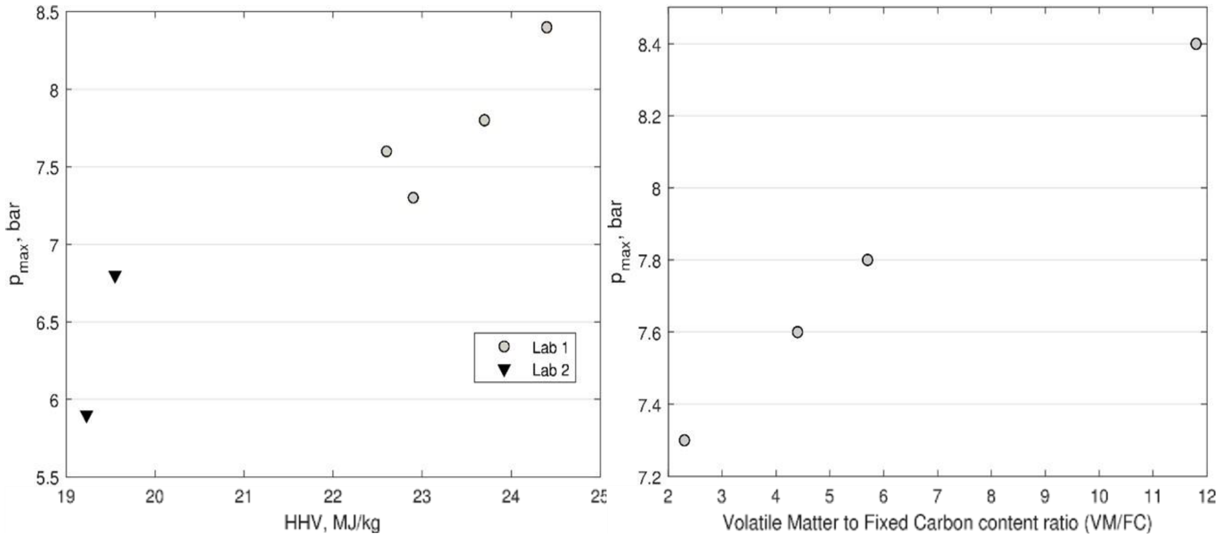

Fig. 6. *Influence of calorific value (left) and VF/MC (right) on the maximum explosion pressure,* P_{max}. *determined in the Lab 1 and 2*

Table 3*: Results from the MIE, MIT, MEC and explosion parameters study. The MIE apparatus highest spark energy which could be studied was 1000 mJ; thus a negative test obtained at 1000 mJ means the MIE is higher; ND stands for not determined values.*

Sample	**A**	**B**	**C**	**D**	**I**	**II**	**III**	**IV**
MIE, mJ	>1000	>1000	>1000	>1000	ND	ND	ND	ND
MIT, °C	500	480	540	550	740	660	490	590
P_{max}, bar(g)	7.3	8.4	7.8	7.6	ND	5.9	6.8	ND
$(dP/dt)_{max}$, bar/s	84	166	258	255	ND	78.8	182.1	ND
K_{St}, bar/m/s	23	45	70	69	ND	21	49	ND
MEC, g/m³	140	110	100	90	ND	>1250	200	ND

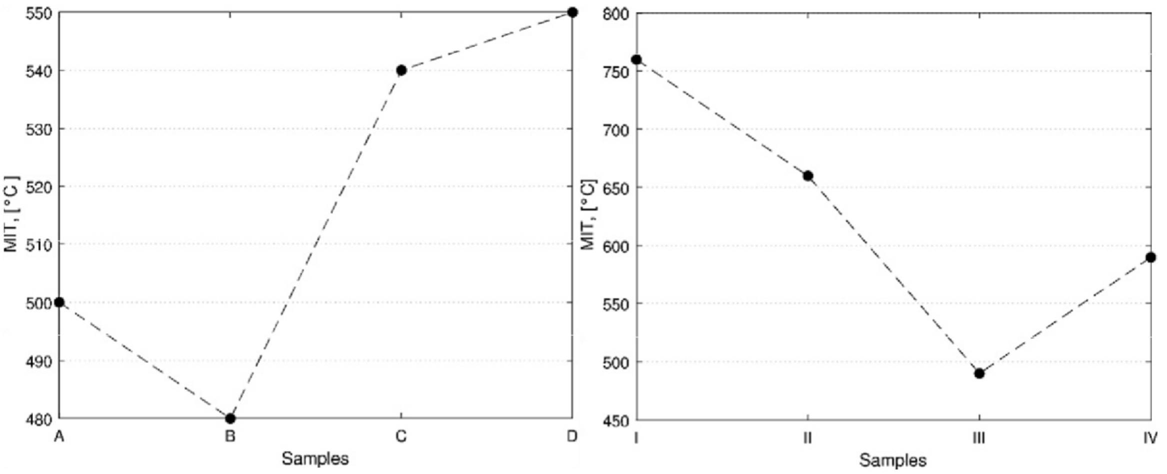

Fig. 7. *MIT trend for the samples: Lab 1 (left) and Lab 2 (right).*

3.2 Influence of grinding and sieving

The samples behaved differently from each other, even though they only went through a grinding-sieving step. Olive pomace is constituted by particles coming from the olive tissues: exocarp (skin), mesocarp (pulp), endocarp (pit) and kernel. Each of them has different mechanical resistances and thus they might show different behavior to a grinding treatment. As a result, particles coming from the softer parts of the olive (pulp and skin) will be more easily ground than the harder part (pit and kernel, mainly). Then, with a further sieving step, these two types of particles are separated from each other, generating two fractions with different mechanical, physical and chemical behavior. In fact, Lammi et al (2018) performed a dry fractionation by following a flowchart-procedure based only on mechanical processes, to obtain stone-rich and pulp-rich fractions from olive pomace, using various types of mill (knife, impact and ball mills) and a sieving system. Then, it is possible to assume that the grinding and sieving step of olive pomace led to A, B, C and D powders with potentially different physical and chemical behaviors. Beside this, the differentiation in the milling tool used in the two labs is likely to affect the particle shape and size, since knife mill used to obtain samples I to IV do apply a shear stress, while hammer mill (samples A to D) impact differently on the pellets.

3.3 Role of the chemical composition

A chemical composition variation among the different samples is not straightforward observable. The solid-state NMR did not enlighten any important differences in terms of aromatics, carbohydrates, carboxyl-group or aliphatic compounds. The main cause of these different explosivity behaviors among the samples may be a change in the specific areas associated to different particles. It is well known that as the particle size decreases, the surface specific area of particles increases, so that the overall reactivity of the sample increases. However, if the sample is made of particles with different mechanical-resilience (as in the case of olive pomace) and the grinding-sieving step has been proved to be influencing the sample behavior, then it is possible to assume that each particle comes from a different tissue of the olive, which has peculiar characteristics, such as specific area, porosity and heat transfer coefficient. Even though the overall composition did not change so much, certain characteristics may have changed from particle to particle, leading to some different thermal behaviors. This could be the key to explain the observed differences in the samples' thermal behavior.

3.4 Fine particles generation: cause and effects

As to understand the magnitude of fines generation by abrasion with respect to material manipulation and handling, a simple test was developed in Lab 2. Pelletized olive pomace was put inside of a cylindrical box and then left for 48 hours on a rolling mixer device (those typically used for powder mixing in laboratories). This device was thought to recreate the actual stresses to which a granulated/pelletized biomass, as olive pomace waste, is subjected when conveyed to storage or to furnace in biomass plants.

The sample was sieved under 250 μm and the explosibility parameters of the fines measured. This sample is defined as "Sample V" in the followings. As depicted in Fig. 8 (to the right), the fines generated by milling contains a greater fraction of fine particles (<100 um about 25% against 7%). Sample V has been tested for its explosibility and it revealed to be, as expected, less hazardous than sample III (see Fig. 8, to the left), with a KSt lower by about 40%, while its explosion is slightly more severe with respect to that of Sample II. As Pmax is considered, a decrease of about 16% is observed between milling and rolling sample, while same values are measured between rolling sample and sample II.

These results underline the degree of uncertainties in term of explosible parameters values, when different sampling procedure or material preparation to test are chosen. Sample III seems to be a conservative choice as reference for pomace dust, while actually sample V does represent better the manipulation effect on this material, in its processing plant. A clear view of the issue must consider all those factors, if a reliable risk assessment is required and where a detailed approach is needed to go beyond mere KSt and Pmax measurements.

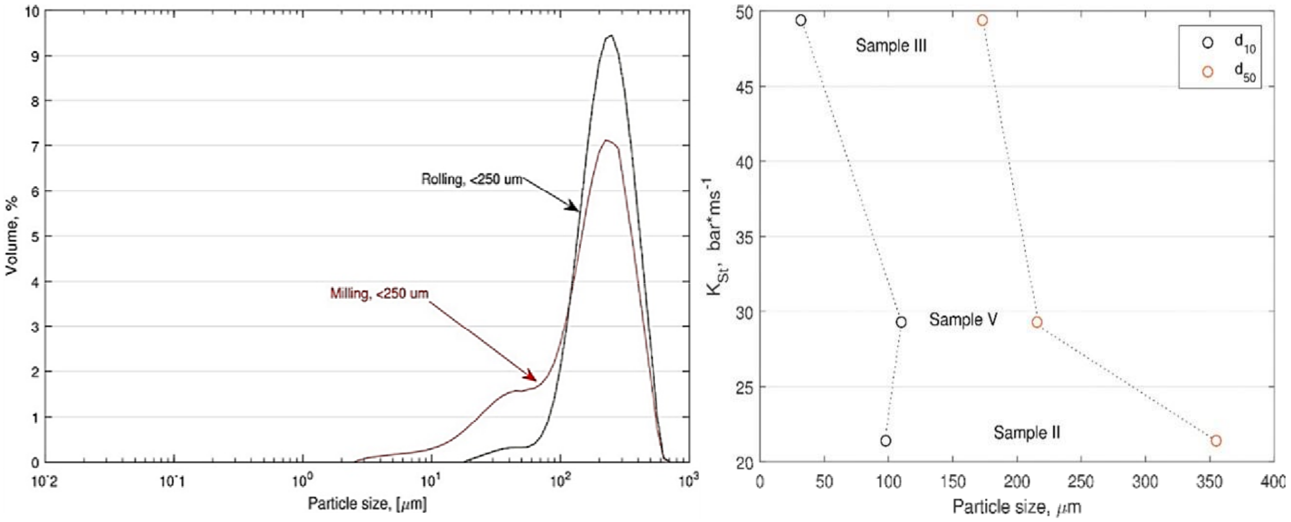

Fig. 8. *To the left, PSD curve for Sample III (milling) and V (rolling). To the right, the influence of the milling/rolling procedure to generate fine particles on the* K_{St} *values.*

4. Conclusions

The hazard related to the handling of olive pomace and potential formation of olive pomace dust has been estimated studying its explosibility and its flammability when dispersed in air, forming dust clouds. Particle size did not have the major and absolute role in determining the explosion characteristics of the samples (Pmax and KSt), but it seemed to be co-ruling over it with the heterogeneous nature of the sample itself. It seems the grinding-sieving step had a deep influence on the behavior of the samples, in terms of thermal behavior, explosibility and flammability. Nonetheless, particle size was the most influencing factor on the MEC. Olive pomace dust clouds showed to be rather sensitive to be ignited by hot surfaces, causing fire classifiable as flashfire. These results were quite in line with the VM/FC values, which allowed to estimate the thermal reactivity of the samples. Actually, some other factor did contribute to give the MIT rise for finer samples (as occurred in both Labs test, see Fig. 7), such as chemical or physical differentiation of the material, as explained before. Samples did not show sensitivity to be ignited by an electric spark with an associated energy of 1000 mJ. Moreover, a 5%wt difference in the moisture content may potentially lead to a 20% reduction of the Pmax, though leaving the KSt almost unaltered.

This work would need to be filled with further information, in order to have an overall comprehension of which factors are significant in olive pomace dust risk analysis and which ones are not. PSD, chemical nature, morphology and moisture content will be relevant factors to investigate further, by testing samples with a broader range of these parameters. Furthermore, a dry fractionation of olive pomace to obtain a pulp- and a pit-rich fraction might illuminate on the different behavior of the two main tissues of olives and thus on the olive pomace dust behavior during explosion and fire, and coherently give targeted indications on the explosion risk level, according to the waste fraction processed in different operations or the different oil extraction method, generating the pomace.

Acknowledgements

This work was developed during an exchange program between Polytechnic of Turin (Turin, Italy) and Dalhousie University (Halifax, Canada). We would like to thank Gaëlle Ducom and Mathieu Gautier from the DEEP Laboratory (Laboratoire Déchets Eaux Environnement Pollutions) of INSA Lyon for providing the olive pomace sample used in this work, as well as Daniel Chevalier and his team from the Minerals Engineering Centre of Dalhousie University for their fundamental help with the preparation of the sample. We acknowledge Dr. Ulrike Werner-Zwanziger from the NMR-3 at the Chemistry Department at Dalhousie University and the Institute for Research in Materials for the acquisition and analysis of the NMR data.

References

Addo, A., Dastidar, A. G., Taveau, J. R., Morrison, L. S., Khan, F. I., & Amyotte, P. R. (2019). Niacin, lycopodium and polyethylene powder explosibility in 20-L and 1-m3 test chambers. Journal of Loss Prevention in the Process Industries, 103937.

Akar, T., Tosun, l., Kaynak, Z., Ozkara, E., Yeni, O., Sahin E. N. and Tunali Akar S. (2009). An attractive agro-industrial by-product in environmental cleanup: Dye biosorption potential of untreated olive pomace, Journal of Hazardous Materials 166, 1217-1225

Amyotte P., 2013, An introduction to dust explosions. Understanding the myths and realities of dust explosions for a safer workplace, Elsevier – Butterworth-Heinemann, Oxford, UK

Bagaria, P., Li, Q., Dastidar A. and Mashuga, C. (2019). Classification of particle breakage due to dust dispersion, Powder Technology 342, 204–21\3

Bagaria, P., Zhang, J., Yang, E., Dastidar, A. and Mashuga, C. (2016). Effect of dust dispersion on particle integrity and explosion hazards, Journal of Loss Prevention in the Process Industries 44, 424-432

Barbanera, M., Lascaro, E., Stanzione, V., Esposito, A., Altieri R. and Bufacchi, M. (2016). Characterization of pellets from mixing olive pomace and olive tree pruning. Renewable energy 88, 185-191.

Braadbaart, E. Marinova and A. Sarpaki (2016), Charred olive stones: experimental and archaeological evidence for recognizing olive processing residues used as fuel, Veget Hist Archaeobot 25, 415–430

Cashdollar, K. L. (2000). Overview of dust explosibility characteristics. Journal of Loss Prevention in the Process Industries, 13(3–5), 183–199.

Chawla, N., Amyotte, P. R. and Pegg, M. J. (1996), A comparison of experimental methods to determine the minimum explosible concentration of dusts, Fuel 75, 654-658

Christoforou, E., & Fokaides, P. A. (2016). A review of olive mill solid wastes to energy utilization techniques. Waste Management 49, 346–363.

Cory, D. G. and Ritchey, W. M. (1988). Suppression of signals from the probe in Blochdecay spectra. J.Mag.Res.(80), 128-132.

Di Blasi, C. (2008). Modeling chemical and physical processes of wood and biomass pyrolysis, Progress in Energy and Combustion Science 34, 47–90

Di Sarli, V., Sanchirico, R., Russo, P. and Di Benedetto, A. (2015). CFD modeling and simulation of turbulent fluid flow and dust dispersion in the 20-L explosion vessel equipped with the perforated annular nozzle, Journal of Loss Prevention in the Process Industries 38, 204-213

Eliche-Quesada D. and Leite-Costa, J. (2016). Use of bottom ash from olive pomace combustion in the production of eco-friendly fired clay bricks, Waste Management 48, 323-333.

García, R., Pizarro, C., Lavín, A. G., Bueno, J. L. (2013). Biomass proximate analysis using thermogravimetry, Bioresource Technology 139, 1–4

Guizani, C., Haddad, K., Jeguirim, M., Colin B. and Limousy, L. (2016). Combustion characteristics and kinetics of torrefied olive pomace, Energy 107, 453463

Harris, R. K., Becker, E. D., Cabral De Menezes, S. M., Goodfellow, R. and Granger, P. (2001) NMR nomenclature. Nuclear spin properties and conventions for chemical shifts (IUPAC Recommendations 2001) Pure Appl. Chem. (73), 1795-1818.

Huéscar Medina, C., Maccoitir, B., Sattar, H., Slatter, D. J. F., Phylaktou, H. N., Andrews, G. E., & Gibbs, B. M. (2015). Comparison of the explosion characteristics and flame speeds of pulverised coals and biomass in the ISO standard 1 m3dust explosion equipment. Fuel, 151, 91–101.

Lammi, S., Le Moigne, N., Djenane, D., Gontard N. and Angellier-Coussy H. (2018), Dry fractionation of olive pomace for the development of food packaging, Bio-composites, Industrial Crops & Products 120, 250-261

Lanza B. and Di Serio M. G. (2015), SEM characterization of olive (Olea europaea L.) fruit epicuticular waxes and epicarp, Scientia Horticulturae 191, 49–56

Marinova, E., van der Valk, M. A., Maria Valamoti S. and Bretschneider J. (2011), An experimental approach for tracing olive processing residues in the archaeobotanical record, with preliminary examples from Tell Tweini, Syria, Veget Hist Archaeobot 20, 471–478

Marsilio, V., Lanza, B., Campestre C. and De Angelis M. (2000), Oven-dried table olives: textural properties as related to pectic composition, Journal of the Science of Food and Agriculture 80, 1271-1276

Miranda, T., Esteban, A., Rojas, S., Montero I. and Ruiz, A. (2008). Combustion Analysis of Different Olive Residues, International Journal of Molecular Sciences, 9, 512-525

Saeed M. A., Andrews G. E., Phylaktou, H. N. and B. M. Gibbs, 2017, Flame speed and Kst reactivity data for pulverized corn cobs and peanut shells, Journal of Loss Prevention in the Process Industries 49, 880-887

Saeed, M. A., Andrews, G. E., Phylaktou H. N. and Gibbs, B. M. (2018) Burning Properties and Flame Propagation of varying size Pulverized Rice Husks. 12th International Symposium on Hazards, Prevention and Mitigation of Industrial Explosions (ISHPMIE), Kansas City, USA August 12-17/2018

Semenova, O., Pilão R. and Pinho C. (2006). Influence of concentration and particle size on the explosibility of air pine bark dust mixtures, 11th Brazilian Congress of Thermal Sciences and Engineering, Curitiba, Brazil Dec 5-8

Silva Durán M. A. (2019). Characterization of the deflagration parameters of the dust deriving from processing of the olive pomace, Master Thesis, Polytechnic of Turin, Turin, Italy

Vecchio, S., Cerretani, L., Bendini A. and Chiavaro, E. (2009). Thermal Decomposition Study of Monovarietal Extra Virgin Olive Oil by Simultaneous Thermogravimetry/Differential Scanning Calorimetry: Relation with Chemical Composition, Journal of Agricultural and Food Chemistry 57, 4793–4800

Watkins, D., Nuruddin, Md., Hosur, M. Tcherbi-Narteh, A. Jeelani, S. (2015), Extraction and characterization of lignin from different biomass resources, Journal of Materials Research and Technology 4, 26-32

Xie, C., Liu, J., Xie, W., Kuo, J., Lu, X., Zhang, X., He, Y., Sun, J., Chang, K., Xie, W., Liu, C., Sun, S., Buyukada M. and Evrendilek, F. (2018). Quantifying thermal decomposition regimes of textile dyeing sludge, pomelo peel, and their blends, Renewable Energy 122, 55-64

Xie, W., Huang, J., Liu, J., Zhao, Y., Chang, K., Kuo, J., He, Y., Sun, J., Zheng, L., Xie, W., Sun, S., Buyukada M. and Evrendilek, F. (2018). Assessing thermal behaviors and kinetics of combustion of textile dyeing sludge and sugarcane bagasse, Applied Thermal Engineering 131, 874–883

Yücel, Y. (2011). Biodiesel production from pomace oil by using lipase immobilized onto olive pomace, Bioresource Technology 102, 3977-3980.

DOI: 10.7795/810.20200724

Pressure peaking phenomena: Large-scale experiments of ignited and unignited hydrogen releases

Agnieszka Lach [a,], André Vagner Gaathaug [a]

[a] University of South-Eastern Norway, Porsgrunn, Norway

E-mail: *Agnieszka.Lach@usn.no*

Abstract

This work aims to validate the pressure peaking phenomenon occurring in constant hydrogen releases, which is important for the safety of enclosures and human beings during accidental releases of ignited and unignited hydrogen. Rapid hydrogen discharge from a tank in confined spaces leads to high overpressures that can cause property damage. This pressure peaking phenomenon (PPP) is defined as an impermanent pressure rise in an enclosure with limited ventilation. PPP is a specific phenomenon for gases lighter than air, especially when a lighter gas is released at a relatively high mass flow rate into an enclosure filled with a denser gas with a relatively small vent area.

The experiments were performed in a large-scale setup consisting of a steel-reinforced container with volume 14.9 m^3 and a ventilation area sized from 0.0006 m^2 to 0.0165 m^2. The hydrogen was released through a 4 mm round nozzle with varying mass flow rates ($\dot{m}$), and the overpressure was measured within the enclosure. The aim was to choose parameters that result in a pressure lower than 10–20 kPa, which is accepted as a safe overpressure limit. Experiments were controlled by a pulse generator (a central timing unit), and all data were stored on two oscilloscopes. The $\dot{m}$ was measured during the experiments by a Coriolis-type mass flow meter, and a Kulite pressure transducer (XTM-190) was used to measure the overpressure inside the enclosure. Two different cases were investigated, one with unignited releases of hydrogen and the second with ignited releases. Hydrogen concentration sensors (XEN-5320) were installed on the enclosure walls to measure the hydrogen concentration and temperature change during unignited experiments. For ignited releases, thermocouples were used for temperature measurements. The experimental setup assured no air ingress into the enclosure, a constant ventilation area, and almost constant hydrogen inflow. All the experiments proved the phenomenon and the hazards of hydrogen releases in confined spaces. The maximum pressure occurs at the beginning of the hydrogen release. For unignited releases, the hydrogen concentration continues to increase after the pressure peak. This considerably increases the risk of ignition and thus explosion hazards as well as oxygen depletion leading to asphyxiation. The ignited releases result in much higher overpressures. In this case, the ventilation area had to be increased a minimum of 28 times to keep the pressure below the 10 kPa limit.

Keywords: *hydrogen safety, pressure peak phenomenon, hazards, passive ventilation, large-scale experiments.*

1. Introduction

Hydrogen fuel vehicles are becoming a valuable and attractive zero-emission alternative. Two types of tanks are used for hydrogen storage: 350 bar and 700 bar, each with mandatory mounted pressure relief devices (PRD) (European Parliament, 2010). The PRD provides fast hydrogen release from the tank in the case of a car accident where high temperatures are present. The role of PRDs is to keep the tanks safe from explosion when exposed to fire for extended amounts of time (Sunderland, 2008).

The regulation codes and standards (RCS) do not specify safety orifice diameters for PRDs. The orifice presently used has diameter of 5.08 mm, which results in high mass flow rates (Brennan et al., 2019).

The hydrogen releases from a thermally activated pressure release device (TPRD) with the mentioned diameter will likely be acceptable in open-air scenarios. Nevertheless, the rapid discharge of hydrogen in confined spaces presents additional hazards and must be considered by automobile manufacturers and regulated by the RCS.

The pressure peaking phenomenon occurs for both ignited and unignited releases. Nevertheless, the overpressure reaches different ranges (ignited releases result in much higher overpressures due to the combustion process), and the two cases must be investigated separately. The environmental conditions have an influence on the results; thus, it is worth noting that the unignited release experiments in this work were performed in the summer and the ignited release experiments in the autumn.

The consequences of indoor hydrogen releases differ significantly from outdoor releases and can affect people, structures, and the environment. Many European research projects have focused on those consequences by investigating hydrogen energy systems and related safety issues. Releases in an enclosure with insufficient ventilation can result in the formation of explosive clouds (Papanikolaou et al., 2010). The final report of one of the projects (HyIndoor; Fuster et al., 2017) presented existing knowledge gaps including ventilation solutions. Leakage from the hydrogen fuel tank inside a small enclosure was studied by Gupta et al. (2009) with non-catastrophic conditions. The relationship between the hydrogen discharge ratio and the enclosure ventilation is a crucial parameter to avoid or significantly reduce the risk of the enclosure's collapse. For the safety development of hydrogen applications, those knowledge gaps need to be closed. Consequently, an engineering tool must be developed and distributed among hydrogen safety engineers.

The high mass flow rates of hydrogen releases in confined spaces result in high overpressures. This may create hazards and cause property damage and injury. The rising pressure is called the pressure peaking phenomenon (PPP) and can be defined as "a transient process of pressure change in vented enclosure with a characteristic peak exceeding the steady-state pressure" (Makarov et al., 2018). PPP occurs when introducing a gas with lower density into an enclosure filled with a heavier gas (e.g., hydrogen into air). The phenomenon is pronounced for hydrogen and occurs when the released hydrogen mass flow rate is relatively high and the vent area is relatively small (Makarov et al., 2018). Under those conditions, the molar flow at the vent will consist of a mixture of the gases inside the enclosure. The inflow will only be hydrogen. At the beginning of the hydrogen release, the flow rate at the nozzle is higher than that at the vent area. This will lead to molar accumulation and hence increased pressure inside the enclosure. The overpressure will grow until the molar flows at both openings become equal. Then pressure peak will be reached and the molar flow at the vent area starts to increase, hence the pressure will decrease.

A previous study (Hussein et al., 2018) affirmed that the vent size and hydrogen mass flow rates are major parameters that determine the overpressure in an enclosure. Brennan and Molkov (2018) investigated hydrogen releases with constant and blowdown mass flow rates. The results of their work showed hazards with the TPRD diameters used presently. Their study provided a model that was used to prepare the experiments described in this work. Their study presented a relationship between TPRD diameter, overpressures, concentration, and vent area. Larger orifice diameters result in higher overpressures. Increasing the vent area decreases the maximum overpressure but increases the hydrogen concentration inside the enclosure, hence creating a higher hydrogen concentration at the maximum overpressure. A high level of hydrogen concentration creates hazards of asphyxiation and ignition. The hydrogen tanks designed for cars that are currently in use are type 4 (Stephenson, 2005), with the limitation of being exposed to high temperatures. The exposure time increases with decreasing PRD diameter, which must be taken under consideration. The PPP validation study was made for the first time by Makarov et al. (2018). Their study developed a model for ignited releases

DOI: 10.7795/810.20200724

from the TPRD and revealed the risk of much higher overpressures compared to unignited releases. The model consists of the volumetric mass balance of introduced, generated, and combusted gases under the perfect mix assumption based on a stoichiometric evaluation. The adiabatic temperature was included in calculations for the temperature change inside the enclosure. The results from laboratory-scale experiments presented the possibility of a new hazard for garage-like enclosures, as they showed that, in few seconds during ignited hydrogen releases, the enclosure will be destroyed by the overpressure. This issue must be addressed in order to avoid too high pressures from hydrogen releases in confined spaces.

The following study considers hydrogen releases in a confined space with a limited ventilation area. Residential garages and underground parking are the main focus. In Norway, passenger ferries and ships play a significant role in transport traffic, and their use of hydrogen systems and fuel cells provide a promising alternative that reduces greenhouse gas emissions. A risk assessment of a hydrogen-fueled high-speed ferry (Aarskog et al., 2020) showed the need for adjustments to keep risks within acceptable limits. The PPP is relevant for maritime applications as well as any confined space where hydrogen releases may occur. Specifically, proper ventilation systems must be investigated as a part of a risk evaluation. The investigation of hazards from unignited and ignited hydrogen releases at the mentioned conditions is part of the pre-normative research for the safety of hydrogen fuel vehicles and transport through tunnels and similar confined spaces (HyTunnel-CS, project founded by HFC, Horizon2020).

2. Experiments

The experiments were performed in a steel-reinforced container of volume 14.9 m^3, shown in Fig. 1. The steel-reinforced container has five vents with 80 mm diameter in total, each located at the front and back wall. Four of them are in the lower corners, and the fifth is located in the middle of the front wall (Fig. 1) to the inside of the chamber floor. The fifth vent was used for the hydrogen inlet from a crate of 12x50 l bottles at 200 bar. For the case of ignited releases, a propane pipe was used as an ignition system, described in Section 2.2.

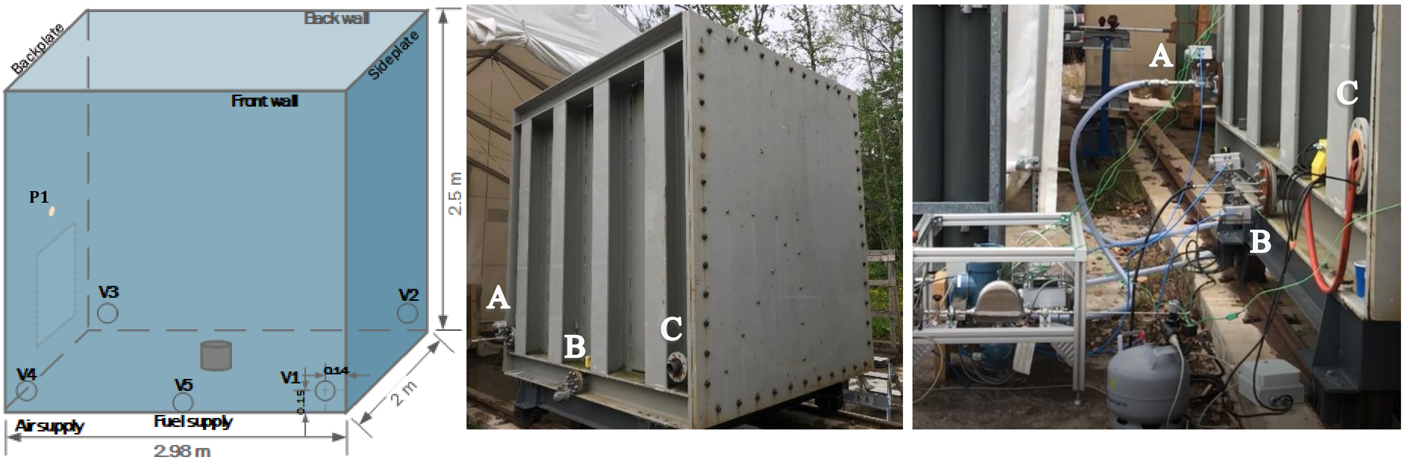

Fig. 1. The steel-reinforced container of volume 14.9 m^3. (A) Air inlet, (B) hydrogen inlet, (C) ventilation area.

A valve at the bottle crate was used to control the hydrogen pressure. A stainless steel pipe with ID 4 mm connected the bottle crate with the mass flow meter. From the mass flow meter, the pipe was connected to a ball valve before it was connected to the 4 mm release nozzle. The nozzle was placed in the center of the steel-reinforced container's floor to vertically discharge hydrogen inside the chamber. An oscilloscope (Sigma; Fig. 3 and Fig. 5) was used to record the hydrogen mass flow data obtained from the Coriolis-type mass flow meter. The mass flow rates of hydrogen discharge were narrow due to the maximum operating pressure of the mass flow meter (110 bar) and a continuously reducing hydrogen pressure in the bottle stack. The explosion chamber was equipped with a pressure transducer, thermocouples (ignited), and hydrogen sensors (unignited). To measure the overpressure, the Kulite pressure transducers XTM-190-10A (unignited) and -50A (ignited) were used, mounted 1.5 m above the floor in the middle of the back-plate (P1 in Fig. 1). The overpressure was logged at 25 kHz, which gave a measurement precision of $\sigma = 0.07\ kPa$. The accuracy was calibrated with a Fluke pressure calibrator. The pressure transducer was connected to an oscilloscope (HBM Gen3i) with a transient recording. A pulse generator was used to control all instrumentation. It was programmed to send the trigger at the same time to both oscilloscopes and the hydrogen release valve. An air fan (Fig. 1, A) was activated after the release of hydrogen was closed. This was done to dilute the hydrogen inside the enclosure after unignited releases and to flush out the hot air after ignited releases.

2.1 Unignited experiments

For unignited releases, only one vent was used for ventilation (V1 in Fig. 1), located 15 cm above the floor. To place the ventilation outlet 20 cm from the ceiling, a 75 mm diameter vertical PVC pipe was installed inside the steel-reinforced container. The cover with the diameter of the desired ventilation area was placed at the end of the PVC pipe (outside the explosion chamber) (Fig. 2).

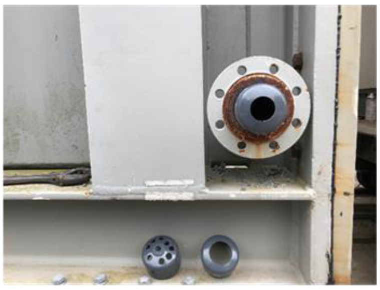

Fig. 2. *The vent with variable area.*

Hydrogen concentration measurements were carried out continuously with two wireless XEN-3520 concentration sensors, placed inside the steel-reinforced container during experiments. Due to technical problems for Experiments 6–11, a USB cable was used instead of the wireless connection (measurements at 3 Hz were stored by the laptop computer). One sensor was mounted in the middle of the front wall, 1.24 m above the floor. The second sensor was mounted in the middle of the back plate, 2.85 m above the floor (Fig. 3).

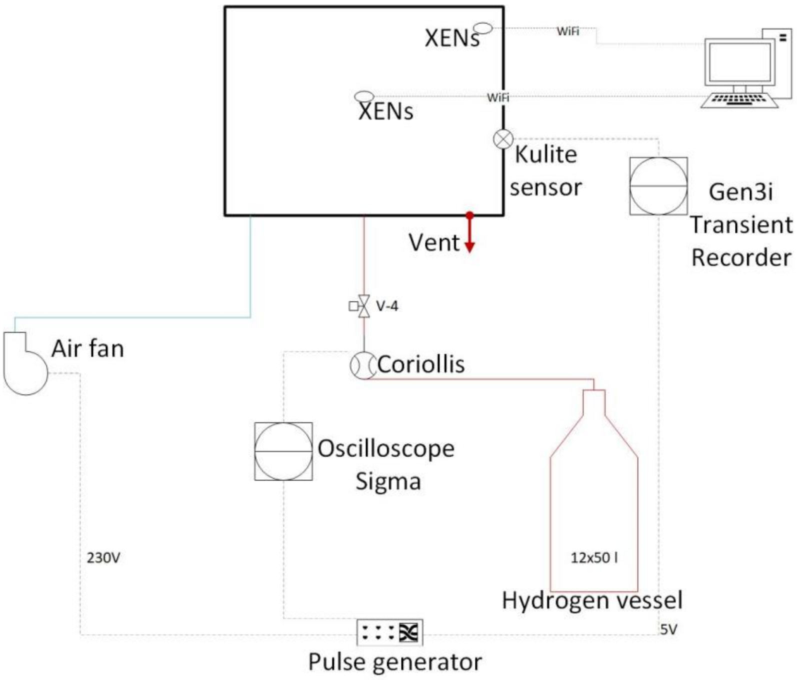

Fig. 3. *Unignited setup: Simplified piping and instrumentation diagram (P&ID).*

The hydrogen concentration (after the hydrogen discharge was stopped) in the steel-reinforced container reached 13%–62% (depending on the experiment). To ensure the same initial conditions for each experiment, air from the fan was introduced to reduce the hydrogen concentration to less than 2% (without interfering with the applied sealing).

2.2 Ignited experiments

For the ignited releases, a propane pilot flame with a 10 kV spark ignition source controlled by a pulse generator (Fig. 4) was mounted on the hydrogen nozzle. The propane was supplied through a stainless steel pipe with ID 4 mm. The potential pressure increase due to the propane pilot flame was measured to be lower than the precision of the sensor.

Fig. 4. *The ignition pilot, located together with hydrogen nozzle.*

The ignited hydrogen releases were carried out without hydrogen concentration sensors. The temperature was measured continuously with four thermocouples (Type K Autek-TD20H-KP). Teflon cables were used between the thermocouples and amplifiers, and a PVC-insulated compensation cable was used between oscilloscope and amplifiers. Each thermocouple had a 20 mm compression fitting plug mounted in the chamber walls. Sensors were mounted 0.06 m from the wall to avoid boundary layers. They were mounted at heights 0.035 m, 1.24 m, 1.85 m, and 2.85 m.

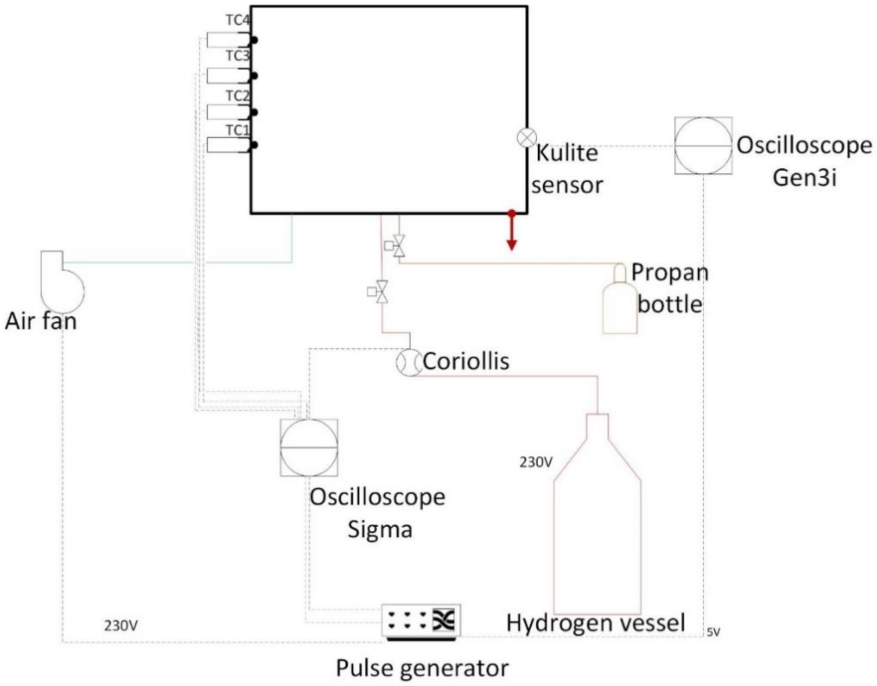

Fig. 5. *Ignited setup: A simplified piping and instrumentation diagram (P&ID).*

3. Results and discussion

In this chapter, the experiments from unignited and ignited releases will be presented and analyzed.

3.1 Unignited releases

Table 1 lists the measured overpressures (pressure peaks) and maximum concentrations. The pressure peaking phenomenon was observed during all experiments. Due to the limitation of hydrogen discharge described in Section 2, observations of PPP required the implementation of small ventilation areas (Table 1, column 4). The ventilation area was assured constant by applied sealing. The initial pressure in the enclosure was equal to the ambient pressure. Due to technical issues with the XENsensors, no data were stored for Experiments 4 and 5. For Experiments 2 and 3, the temperature data used a format rounding to unity, resulting in large uncertainty. Therefore, the initial temperature for those experiments was assumed to be 293 K. The hydrogen concentration increased until the H_2 discharge was stopped, resulting in maximum values at the end of the H_2 inflow.

Table 1. *Results of measured maximum overpressures and hydrogen concentrations for Experiments 2–11. Vertically discharged unignited hydrogen through 4 mm nozzle.*

Setup					Measured	
Exp. no.	T_0 in enclosure [K]	H_2 release time [s]	Vent area [m^2]	Mass flow rate [g/s]	Experimental overpressure [kPa]	Experimental max H_2 conc. [%]
2	293.00^{*}	*90*	*0.0012*	*1.90*	**0.42**	13
3	293.00^{*}	*120*	*0.0020*	*3.50*	**0.51**	28
4	293.00^{*}	*120*	*0.0020*	*9.05*	**2.86**	-
5	293.00^{*}	*120*	*0.0014*	*9.90*	**6.45**	-
6	*296.00*	*120*	*0.0014*	*10.1*	**6.74**	62
7	*292.34*	*180*	*0.0006*	3.05	**4.07**	35
8	*291.94*	*180*	*0.0006*	3.05	**3.96**	35
9	*293.12*	*200*	*0.0006*	*4.75*	**8.05**	53
10	*289.71*	*200*	*0.0006*	*4.20*	**6.70**	47

DOI: 10.7795/810.20200724

11	*293.57*	*1000*	*0.0006*	*blowdown*	**7.00**	34

**Assumed values*

The last experiment was performed with a continuously decreasing mass flow rate (blowdown) from a maximum value of 4.85 g/s. The mass flow rate decreased due to the falling pressure inside the hydrogen bottles. This experiment had the longest duration of hydrogen inflow, but the hydrogen concentration data was only stored until 122 s (due to a technical issue). Nevertheless, H_2 concentration data were captured at the time of maximum pressure t(p_{max}) (Table 2). The H_2 concentration changes depended on the experimental conditions ($\dot{m}$ and A_v). From Table 2, it can be seen that the concentration at t(p_{max}) is higher with higher $\dot{m}$ at the same A_v.

Table 2. *Measured hydrogen concentration at max pressure.*

Exp. No.	***2***	***3***	***6***	***7***	***8***	***9***	***10***	***11***
$\dot{m}$ *[g/s]*	*1.90*	*3.50*	*10.10*	*3.05*	*3.05*	*4.75*	*4.20*	*4.85*$_{blowdown}$
A_v *[m^2]*	*0.0012*	*0.0020*	*0.0014*	*0.0006*	*0.0006*	*0.0006*	*0.0006*	*0.0006*
H_2 *% at* p_{max}	1.5%	0.2%	24.0%	15.4%	16.0%	25.0%	22.0%	21.5 %
t(p_{max}) [s]	10 s	10 s	37 s	80 s	77 s	89 s	89 s	64 s

When $\dot{n}_{in} = \dot{n}_{out}$, the maximum overpressure (p_{max}) is reached. Then, the molar flow at the vent ($\dot{n}_{out} = \dot{m}_{out}/M_{en}$) continues to increase, as it is higher than the molar flow at the nozzle ($\dot{n}_{in} = \dot{m}_{in}/M_{H_2}$). This leads to a decrease in the overpressure. The enclosure volume does not affect the time of maximum overpressure t(p_{max}) at a given ventilation area, but $\dot{n}_{in}$ does have an affect (Brennan and Molkov, 2018). As an obvious outcome based on a model description (Lach, 2019), with the same ventilation area and constant enclosure volume, p_{max} will be higher for higher $\dot{n}_{in}$. Higher $\dot{m}$ increases the time needed to reach the maximum pressure (Fig. 6). This result can be used to estimate the evacuation time and also provides a design criterion for the TPRD diameter.

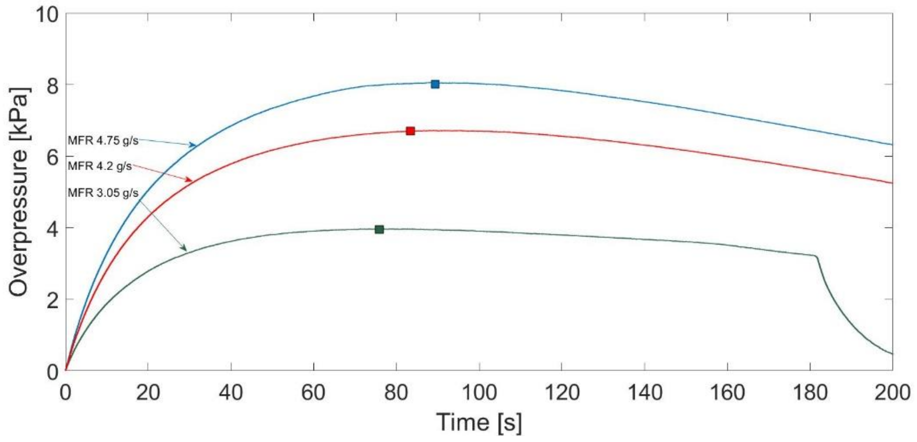

Fig. 6. *Experimental overpressures for different* $\dot{m}$ *at the same ventilation area (*$A_v = 0.0006\ m^2$*); pressure peak occurrence (rectangle).*

All the experiments showed that the maximum overpressure occurred before the hydrogen concentration reached its maximum (Fig. 7). Increasing the hydrogen concentration increases ignition risks and depletes the oxygen in the container, which is hazardous to human life.

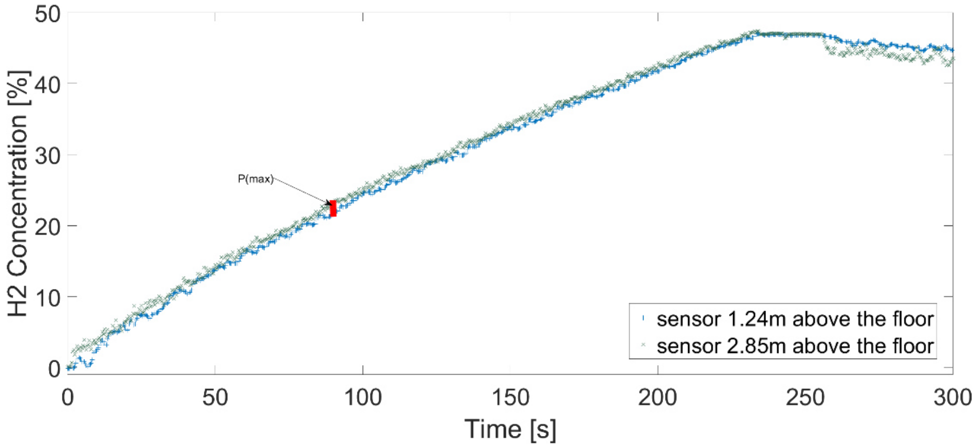

Fig. 7. *Hydrogen concentration for Experiment 10. Inflow duration is 200 s, $\dot{m}$ is 4.2 g/s.*

As expected, the results showed that higher $\dot{m}$ results in higher p_{max} and a higher hydrogen concentration for the same ventilation area. Experiment 9 had the highest pressure peak among the experiments with Av=0.0006 m^2. It also had the highest hydrogen concentration at that point (Table 2).

3.2 Ignited releases

Table 3 lists the results from 31 tests of ignited hydrogen releases in the same steel-reinforced container. The pressure peak phenomenon was successfully demonstrated for hydrogen jet fires. The tests were conducted with different and approximately constant mass flow rates and a combination of three possible vents. Each vent has an area of 0.0055 m^2. Steel flanges were used to blind the vents to get the desired total ventilation area. The initial pressure in the enclosure was equal to ambient pressure. The temperature and pressure were measured continuously; Table 4 provides the maximum values for overpressures and underpressures and the maximum values for each thermocouple. The initial temperature is the volume-weighted average temperature, measured with thermocouples at the beginning of the experiment. For the first 10 experiments, the air fan was used to flush out hot air and water from the enclosure after the hydrogen jet flame was shut down. This was done prior to opening the door to the enclosure. Due to the observed underpressure after the H_2 release was closed, the air fan was disconnected for the rest of the experiments. This was done to investigate the possible underpressures in the experiments.

Table 3. *Experimental results: 31 tests of H_2 releases through a 4 mm nozzle with varying $\dot{m}$ and ventilation area. One open vent = 0.0055 m^2, two open vents = 0.0109 m^2, three open vents = 0.0164 m^2.*

Setup					Measured					
Exp no.	T_0 in enclosure [K]	H_2 release time [s]	Open vent	Mass flow rate [g/s]	Experimental overpressure [kPa]	Experimental underpressure [kPa]	Temperature [°C]			
							T1	T2	T3	T4
1	*8*	*5.0**	*1*	*1.45*	4.8	-0.1	9	45	86	85
2	*9*	*10.0**	*1*	*1.37*	4.5	-0.3	14	81	128	125
3	*10*	*5.0**	*1*	*3.38*	16.7	-0.6	69	119	171	164
4	*12*	*10.0**	*1*	*3.15*	15.8	-2.8	141	175	251	225
5	*15*	*10.0**	*2*	*3.14*	5.3	-1.1	93	175	270	230
6	*15*	*10.0**	*2*	*3.04*	5.0	-1.1	86	176	258	223
7	*3*	*6.0**	*2*	*7.90*	22.0	-2.5	166	209	353	319
8	*4*	*6.0**	*2*	*7.50*	20.6	-2.3	142	207	348	287
9	*6*	*6.0**	*3*	*8.37*	13.9	-2.9	194	242	403	345

DOI: 10.7795/810.20200724

10	*6*	*6.0**	*3*	*8.35*	13.7	-2.8	192	243	389	332
11	*7*	*7.5*	*3*	*8.63*	14.7	-3.3	204	249	416	358
12	*9*	*6.0*	*3*	*8.90*	15.1	-2.3	176	215	372	322
13	*8*	*6.0*	*3*	*11.72*	21.7	-4.3	244	288	458	408
14	*4*	*6.0*	*3*	*11.37*	21.1	-3.8	241	274	430	352
15	*4*	*6.0*	*3*	*4.00*	4.3	-0.5	40	129	202	194
16	*4*	*6.0*	*3*	*4.07*	4.5	-0.5	45	130	209	190
17	*5*	*6.0*	*2*	*11.52*	33.3	-3.2	211	263	415	367
18	*5*	*6.0*	*2*	*11.47*	33.0	-3.4	205	267	414	367
19	*5*	*6.0*	*1*	*8.62*	48.1	-5.7	194	205	359	300
20	*5*	*7.5*	*1*	*8.50*	46.5	-8.2	243	247	383	332
21	*7*	*6.0*	*2*	*8.52*	23.7	-2.0	166	223	333	294
22	*7*	*6.0*	*2*	*2.60*	4.1	-0.3	12	98	142	139
23	*6*	*15.0*	*2*	*2.36*	3.5	-1.1	87	174	275	238
24	*7*	*25.0*	*3*	*2.38*	1.8	-1.0	195	240	368	331
25	*5*	*25.0*	*3*	*3.87*	4.1	-2.2	315	339	481	435
26	*9*	*20.0*	*3*	*6.70*	10.1	-4.6	384	467	603	568
27	*8*	*10.0*	*3*	*6.65*	9.9	-2.7	213	259	433	391
28	*9*	*10.0*	*2*	*6.56*	16.8	-3.5	219	247	419	369
29	*8*	*20.0*	*2*	*6.55*	16.7	-8.7	375	474	578	531
30	*10*	*10.0*	*1*	*6.65*	35.9	-14.1	246	259	392	349
31	*9*	*20.0*	*1*	*6.56*	35.3	-25.3	366	444	556	522

* The air fan was used after hydrogen release (duration time).

The obtained overpressures show the dependency (with high sensitivity) of hydrogen mass flow rates and ventilation areas (Fig. 8), as was expected based on previous unignited experiments and other PPP studies. The model developed for ignited releases in enclosures (Makarov et al., 2018) simulated overpressures from a 700 bar tank through a 2 mm nozzle in the 1 m^3 enclosure. The model showed that overpressures from ignited hydrogen releases of 107 g/s can be 100 kPa higher with only one brick difference and will destroy the enclosure in less than 10 s.

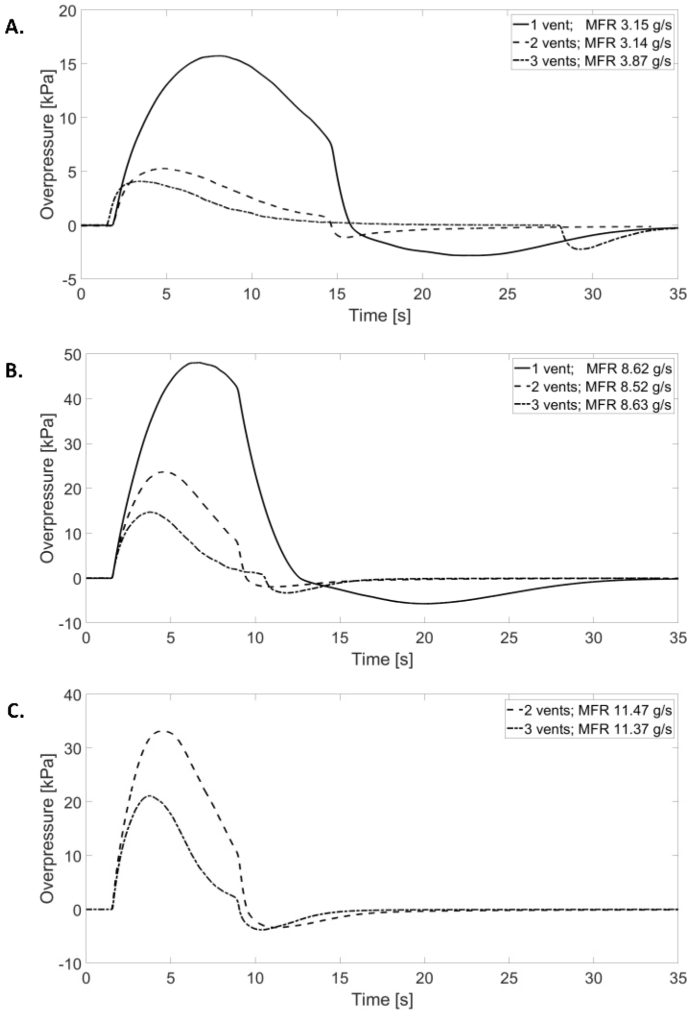

Fig. 8. *Overpressures for (A) 3.1–3.9 g/s, (B) ~8.6 g/s, and (C) ~11.4 g/s $\dot{m}$s at three different ventilation areas, where one open vent = 0.0055 m^2, two open vents = 0.0109 m^2, and three open vents = 0.0164 m^2.*

The experiments from this study showed that, with a higher ventilation area, the overpressures reach lower values and the time of pressure peak (t(pmax)) occurs earlier (Fig. 8). The accepted safe overpressure in enclosures has a threshold of 10–20 kPa (Brennan and Molkov, 2018). During experiments with $\dot{m}$ not higher than 4 g/s, the safe overpressures were obtained with all three ventilation areas ($P_{max} < 20\ kPa$); see Fig. 8(A). The ventilation area with two and three open vents gives a pressure below the threshold ($P_{max} < 10\ kPa$). For $\dot{m}$ = 8–9 g/s, only three open vents gave overpressures below 20 kPa; see Fig. 8(B). The ventilation area with one open vent showed overpressure over 45 kPa, double the threshold, and further experiments with only one open vent for $\dot{m}$ ~11.5 g/s have not been performed. For $\dot{m}$ ~11.5 g/s, the obtained overpressures were over 21 kPa, which is above the thresholds with both ventilation areas (two and three open vents). The pressure peak occurred about 2 to 6 seconds after the hydrogen releases (for unignited experiments, it was 75 to 90 seconds).

For higher ventilation areas, the value of the pressure peak is lower but occurs faster (Fig. 8). This is opposite the results from the unignited experiments, where a higher $\dot{m}$ resulted in a later time for the pressure peak.

In the 14.9 m^3 steel-reinforced container with a ventilation area of 0.0165 m^2 (three open vents), the pressure peak occurs no later than 3 s for each value of tested $\dot{m}$. This means that the time of maximum pressure (t(pmax)) can be estimated based on ventilation area and enclosure volume (independent of $\dot{m}$). The pressure drop takes longer than its rise but is still relatively short. The fast pressure drop may cause enclosure collapse and is a danger to the enclosure, surroundings, and human lives.

The comparison of overpressures with hydrogen releases from unignited (Experiment 8) and ignited releases (Experiment 4) are presented in Fig. 9. The hydrogen was released into the same enclosure volume with approximately the same $\dot{m}$ but with different ventilation areas. The hydrogen jet fire resulted in four times higher overpressure than occurred from unignited releases with nine times larger ventilation area.

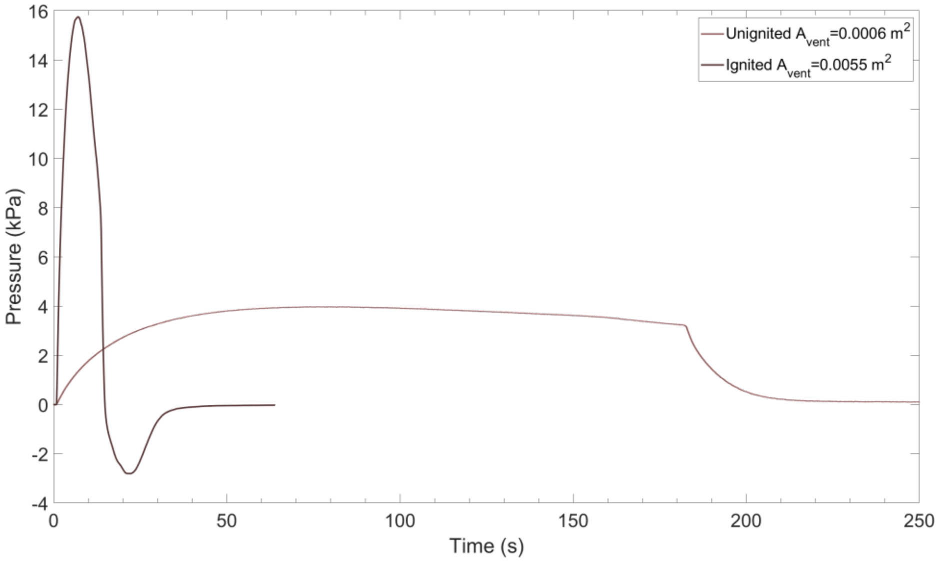

Fig. 9. *Pressure peak phenomenon for unignited and ignited releases with $\dot{m}$~3.1 g/s through a 4 mm nozzle.*

Hydrogen jet fires cause high overpressure due to the large amount of energy (from the chemical reaction) released in a very short time. Water vapor is the only combustion product. The energy of water formation has the highest influence on the temperature inside the enclosure, hence the overpressure.

The temperature depends on the total amount of energy from combustion and heat loss in the enclosure (as well as the ventilation area):

- The heat loss in the enclosure is the sum of the convective heat loss and the heat loss from vapor condensation at the walls/ceiling. The condensing water increases the heat transfer to the walls. The temperature of the walls is an important factor affecting the condensation rate (Jia et al., 2001) and, at the beginning, was assumed to be equal to the ambient temperature (~4°C for a Norwegian autumn).
- The longer combustion occurred, the higher the maximum temperatures that were obtained (last six experiments).

The pressure peak does not depend on the total amount of burnt hydrogen. It occurs at the beginning of the release of jet fires and drops to a value close to ambient pressure. While combustion continues, the temperatures increase inside the enclosure. After closing the hydrogen release (no jet fire), a rapid decline in the temperature was observed. As a consequence, an underpressure was measured inside the enclosure. This depended on the total energy released during combustion (total amount of burnt hydrogen) and the change in density inside the enclosure as air from the outside flowed into the enclosure.

The last six experiments investigated the relationship between overpressure and underpressure from the total time of combustion and ventilation area (for the same mass flow rates). The experiments showed that, for the same ventilation area, the pressure peak was the same, independent of the total time of hydrogen combustion (Fig. 10). The underpressure, on the other hand, showed a large dependency on the ventilation area, as also occurred for overpressures and the duration of hydrogen combustion. With a longer combustion duration, the absolute values of the underpressure increased.

Fig. 10 presents the pressure data from the last six experiments. The red curves show the data from the experiments with one open vent, the black curves represent two open vents, and the blue curves are for three open vents. Dashed lines are the short combustion duration experiments (10 s), while the solid line indicates the longer combustion duration (20 s). If we investigate the difference between the overpressures, we see that there is no significant difference between the short and long combustion times. However, the combustion time influences the peak underpressure. In general, longer combustion duration results in a lower absolute pressure in the negative phase.

The two experiments with three open vents show that the difference in underpressure was 1.9 kPa. For the two experiments with two open vents, the difference was 5.2 kPa, and with one open vent, it was 11.2 kPa.

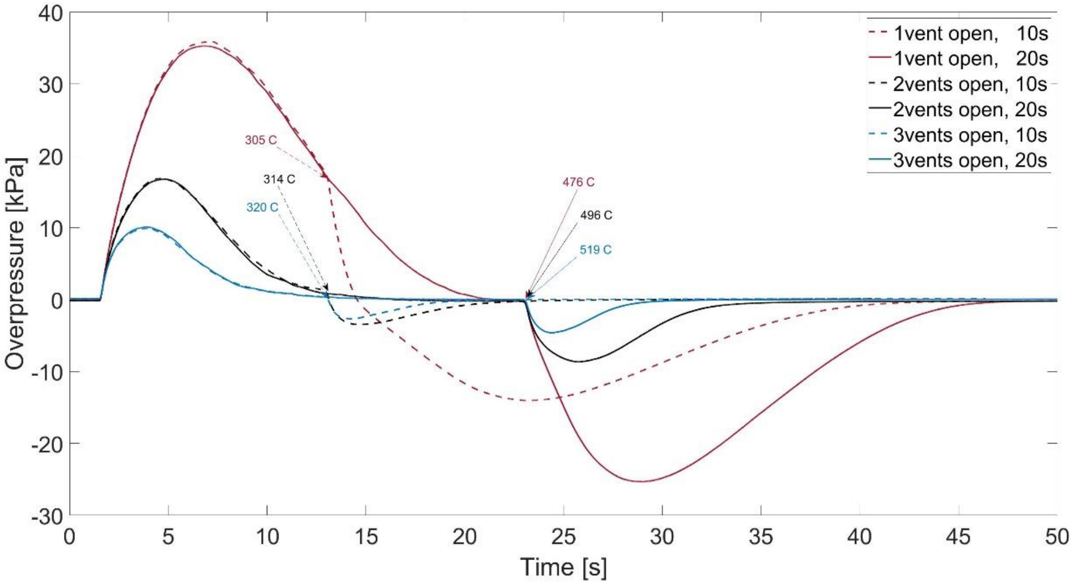

Fig. 10. *Overpressures in the 14.9 m^3 enclosure during hydrogen releases of 10 s and 20 s with three different ventilation areas at the same $\dot{m}$~6.6 g/s. One open vent = 0.0055 m^2, two open vents = 0.0109 m^2, three open vents = 0.0164 m^2. Experiments 26–31.*

4. Conclusions

The pressure peaking phenomenon was validated in large-scale experiments for two cases: ignited and unignited releases:

- Ignited releases result in much higher overpressures, and a larger ventilation area has to be applied.
- With increasing $\dot{m}$, the value of pressure peak is higher. For ignited releases, it occurs earlier. The opposite results are shown for the unignited experiments, where a higher $\dot{m}$ resulted in a later occurrence for the pressure peak.
- The heat loss is a significant factor and cannot be neglected when designing an engineering tool.

- Ignited releases result in underpressure after closing the hydrogen discharge, creating additional hazards to the enclosure, surroundings, and human lives.

Further investigations into hydrogen releases (ignited and unignited) with a blowdown mass flow type from a 700-bar tank are scheduled for later this year (2020). The heat loss investigation and detailed modeling will be an integral focus of further studies.

Acknowledgments

The authors wish to acknowledge funding from the Fuel Cells and Hydrogen 2 Joint Undertaking (JU) under grant agreement No 826193. The JU receives support from the European Union's Horizon 2020 research and innovation programme and United Kingdom, Germany, Greece, Denmark, Spain, Italy, Netherlands, Belgium, France, Norway, Switzerland.

This work was performed within MoZEES, a Norwegian Centre for Environment-friendly Energy Research (FME), co-sponsored by the Research Council of Norway (project number 257653) and 40 partners from research, industry, and the public sector.

References

Aarskog, Fredrik G, Olav R Hansen, Trond Strømgren, and Øystein Ulleberg. 2020. "Concept Risk Assessment of a Hydrogen Driven High Speed Passenger Ferry." *International Journal of Hydrogen Energy* 45(2): 1359–72. http://www.sciencedirect.com/science/article/pii/S0360319919319846.

Brennan, S. et al. 2019. "Pressure Effects of an Ignited Release from Onboard Storage in a Garage with a Single Vent." *International Journal of Hydrogen Energy* 44(17): 8927–34. https://www.sciencedirect.com/science/article/pii/S0360319918323541 (April 5, 2019).

Brennan, Sile, and Vladimir Molkov. 2018. "Pressure Peaking Phenomenon for Indoor Hydrogen Releases." *International Journal of Hydrogen Energy* 43(39): 18530–41. https://www.sciencedirect.com/science/article/pii/S0360319918326375 (April 3, 2019).

European Parliament. 2010. "COMMISSION REGULATION (EU) No 406/2010 of 26 April 2010 Implementing Regulation (EC) No 79/2009 of the European Parliament and of the Council on Type-Approval of Hydrogen-Powered Motor Vehicles." *Official Journal of the European Union* (2).

Fuster, Béatrice et al. 2017. "Guidelines and Recommendations for Indoor Use of Fuel Cells and Hydrogen Systems." *International Journal of Hydrogen Energy* 42(11): 7600–7607.

Gupta, Sanjeev, Jerome Brinster, Etienne Studer, and Isabelle Tkatschenko. 2009. "Hydrogen Related Risks within a Private Garage: Concentration Measurements in a Realistic Full Scale Experimental Facility." *International Journal of Hydrogen Energy* 34(14): 5902–11. https://www.sciencedirect.com/science/article/pii/S0360319909003759 (March 27, 2019).

Hussein, H.G. et al. 2018. "Numerical Validation of Pressure Peaking from an Ignited Hydrogen Release in a Laboratory-Scale Enclosure and Application to a Garage Scenario." *International Journal of Hydrogen Energy* 43(37): 17954–68. https://www.sciencedirect.com/science/article/pii/S0360319918323784 (April 3, 2019).

Jia, L. et al. 2001. "Effects of Water Vapor Condensation on the Convection Heat Transfer of Wet Flue Gas in a Vertical Tube." *International Journal of Heat and Mass Transfer* 44(22): 4257–65. https://www.sciencedirect.com/science/article/pii/S0017931001000825 (January 28, 2020).

Lach, Agnieszka Weronika. 2019. *Pressure Peaking Phenomena-Unignited Releases. Report Experiments*. USN

Makarov, D., V. Shentsov, M. Kuznetsov, and V. Molkov. 2018. "Pressure Peaking Phenomenon:

Model Validation against Unignited Release and Jet Fire Experiments." *International Journal of Hydrogen Energy* 43(19): 9454–69. https://www.sciencedirect.com/science/article/pii/S0360319918309911 (April 11, 2019).

Papanikolaou, E.A. et al. 2010. "HySafe SBEP-V20: Numerical Studies of Release Experiments inside a Naturally Ventilated Residential Garage." *International Journal of Hydrogen Energy* 35(10): 4747–57. https://www.sciencedirect.com/science/article/pii/S0360319910002715 (April 1, 2019).

Stephenson R. 2005. "Fire Safety of Hydrogen-Fueled Vehicles : System-Level Bonfire Test." *Ichs* (September).

Sunderland, P. 2008. "Pressure Relief Devices for Hydrogen Vehicles." *3rd european summer school in hydrogen safety, Belfast, UK*: 1–29.

DOI: 10.7795/810.20200724

Investigation of the correlation between the electrical power and flame front of a discharge caused by a slow contact opening in a H_2/air mixture

Carsten Uber[a], Bogdan Barbu[b], Michael Hilbert[a], Frank Berger[b], Frank Lienesch[a]

[a] Physikalisch-Technische Bundesanstalt, Braunschweig, Germany
[b] Technische Universität Ilmenau, Germany

E-mail: carsten.uber@ptb.de

Abstract

Contact-opening discharges from electrical equipment in potentially explosive atmospheres typically generated at low voltages below 30 V and low currents between 30 mA and 100 mA are a relevant ignition source. The electrical characteristics of these discharges, which are dominated by metal vapor, have been presented in previous works (Uber et al. , 2019). However, the transition phase from a discharge to a thermochemical ignition has not yet been properly analyzed. This fact prevents a multiphysical model from being developed and evaluation criteria from being defined for the non-ignition or ignition of a discharge. Here, the correlation between the electrical power of the discharge and the ignition is analyzed and determined with the aim of correcting this shortcoming. In these investigations, discharges are systematically generated by using a constant voltage source with an electronic current limitation circuit in order to maintain a constant current value throughout the entire experimental procedure. Depending on the electrical power input and its temporal and spatial distribution, the development of the discharge and its ignition is monitored and data for the ignition limit is determined. Initial estimations are made for the ignition limit with and without thermochemical ignition in accordance to the energy conservation law.

Based on previous work and present results, an initial estimation is made here for an evaluation of the ignition energy. However, more detailed investigations are necessary in order to ensure statistical significance for the results presented here.

Keywords: contact-opening discharges, ignition limit, thermochemical ignition, spark test apparatus, metal vapor discharge, intrinsic safety

1. Introduction

For the evaluation of contact discharges in electric circuits in the field of explosion protection, the so-called spark test apparatus described in IEC 60079-11 (2012) and the ignition limit characteristics defined in IEC 60079-11 (2012) are used. These curves are also based on the spark test apparatus. For a rough estimation of the ignitability of such discharges generated during contact-making operations, a simplified calculation model of the effective energy was developed by Johannsmeyer (1983). For contact-breaking operations, such a simple assessment method is not yet available.

Calculations for contact-breaking operations, such as those presented by Zborowski & Cotugno (1974), have not yet provided useable results. Ignitable discharges from make-contact processes are also shorter than break discharges and last typically 2 µs. More comprehensive examinations exist for discharges near the ignition limit with significantly higher voltages and a fixed position of the electrodes with a gap of several millimeters (Bane, 2010; Essmann, 2018). These discharges are significantly shorter, being in the range of nanoseconds. Many other publications treat this subject but disregard the thermochemical ignition. They often analyze the “electrical discharge” process in the field of electrical engineering.

For ignitable high-voltage discharges with fixed electrode gaps, Eckhoff & Olsen (2010) described the elements of the energy flow as follows: losses in the circuit, losses of the discharge due to electromagnetic radiation, heat conduction into the electrodes, shock wave and expansion of the gas core and thermochemical ignition. In order to calculate the ignitability of discharges via slow contact opening processes using the energy balance, the process must also include the mechanical contact opening during the breaking operation and the energy transfer from the discharge into the gas mixture. The correlation between the mechanical contact opening and the discharge development was investigated in Uber (2019). An essential element in this process is the transition of the discharge energy into the volume required for the ignition and its influences (e.g. flow), as the quenching distance is much larger than the maximum discharge length. The quenching distance and critical radius for other conditions are described in various publications (Lewis & von Elbe, 1987; Warnatz & Maas, 1993; Glassman & Yetter, 2008; Ballal & Lefebvre, 1977; Bradley & Lung, 1987). According to Lintin & Wooding (1959), the ignition of the flammable gas occurs in a layer on the surface of the discharge that is reduced by the electrode’s surfaces during the contact opening process investigated here.

For the experimental validation of the processes and correlations described, it must be specified that, for a discharge of the type examined here created by a slow contact opening a specific determination of each individual effect is not possible.

2. Setup and Experiments

In the experimental setup presented here, a tungsten wire with a diameter of 200 µm is used as an anode. The cathode consists of a rough, preconditioned cadmium block. The preconditioned surface was prepared by carrying out several thousand contact operations. The contact opening process that takes place during the breaking operation is shown in Fig. 1.

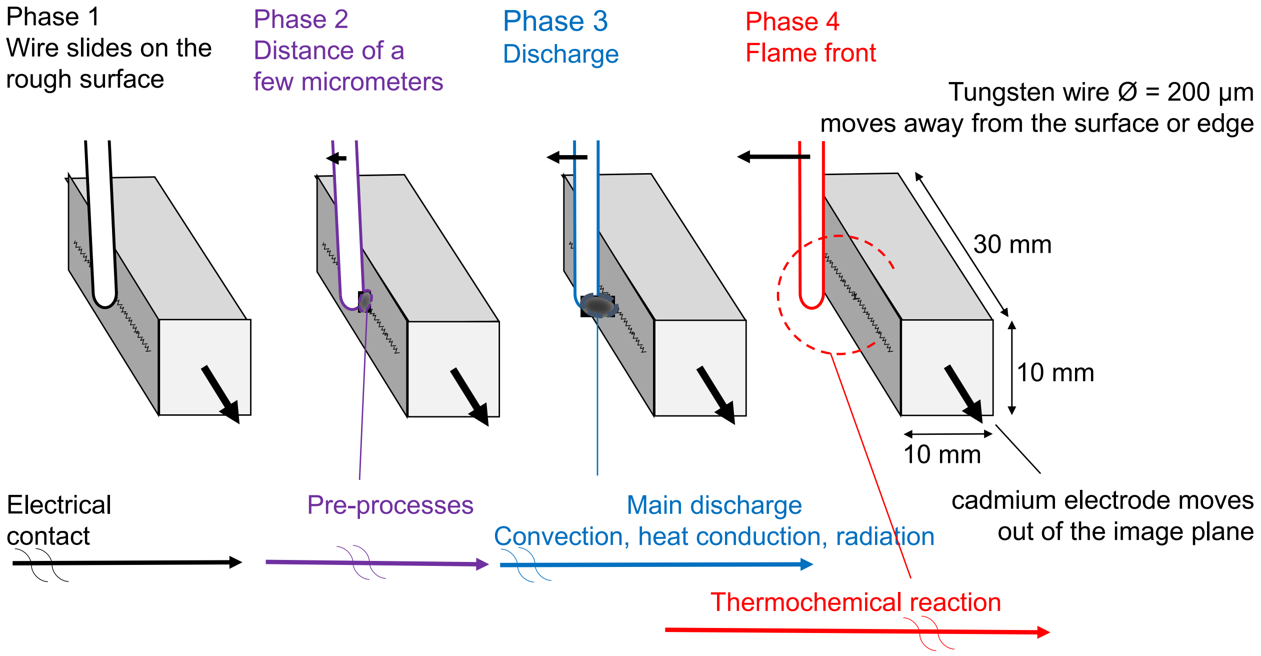

Fig. 1. General schematic procedure of the processes and duration of a slow contact opening in the experimental contact apparatus

In the first phase of the slow contact breaking operation, the tungsten wire slides over the moving cadmium surface (cathode). In this time interval, the cadmium block moves out of and into the image plane. During this phase, there is always an electrical contact between the tungsten wire and the cadmium block. As the tungsten wire is moved away, pre-processes (small discharges, which are considered to influence the probability of ignition) take place at a very small electrode distance (phase 2). As the wire slowly moves aside, the distance between the electrodes increases; after approx. 1 ms, a distance of approx. 150 µm is reached. When this point is reached, electrical discharges with typical lengths of approx. 150 µm are generated (phase 3). The discharge generates a temperature field with a hot gas core whose changes over time are influenced by the local conditions (geometry, flow, etc.) Uber (2019).

According to Eckhoff & Olsen (2010), the discharge generates a shock wave and the gas core expands. This can result in a flame front (phase 4). A more precise estimation of the temperature field around the discharge, the expansion of the gas core and the influence of the electrodes are the objectives of the investigations presented here.

3. Experiments

An experimental contact device was specially designed for the investigation of the above-mentioned discharge processes. For the optical investigations, the experimental contact device was placed in an explosion chamber (12 liter volume) with windows made of quartz glass. The hydrogen-air mixture (φ (H_2) = 21 %) fed into the explosion chamber was controlled by a mass flow controller. The contact device is connected to a constant current source with a voltage limitation in order to be able to carry out specific, systematic experiments with fixed parameters (see Uber, 2019).

The schlieren photography was performed with a schlieren system following the experiments of Toepler with two lenses and a knife edge (Schardin, 1942). A far-field microscope (Questar QM1), an image intensifier (Hamamatsu C10880) and a high-speed camera (Photron Fastcam SA5) were used for the optical imaging. The images were taken at a frame rate of 10 000 fps as a compromise between the radiation intensity and the temporal resolution. The electrical values were recorded with an oscilloscope (Yokogawa type DL9040L) and corresponding probes. More detailed information regarding the experimental setup can be found in Uber (2019).

4. Modelling approach

By including the above-mentioned contact discharge characteristics and conditions, the following mathematical models for the ignitable discharges and their corresponding ignition criteria can be derived (See table 1 and 2).

Table 1: *Mathematical models used for the ignition of the hydrogen-air mixture (φ(H2) = 21 %)*

Equation	Annotation	Reference
$W_{dis} = \int_0^{\mathrm{t}} \left(V_{\mathrm{sup}}(\mathrm{t}) - V_{\mathrm{los}}\right) \cdot I_{\mathrm{dis}}(\mathrm{t})\mathrm{dt}$ (01) $P_{dis}(t) = \left(V_{sup}(t) - V_{los}\right) \cdot I_{dis}(t)$ (02)	Make discharges $V_{los} = 11\ \mathrm{V}$ Duration typ. approx. 2 µs	Johannsmeyer (1983)
$P_{dis} = \frac{\left(V_{sup,max} - 10\ \mathrm{V}\right)^2}{4R}$ (03) $\bar{P}_{dis,max} > 350\ \mathrm{mW}$ for an ignition	Resistive circuits	Johannsmeyer et al. (2010)

Table 2: *Ignition characteristics for a hydrogen-air mixture (φ(H2) = 21 %)*

Characteristics	**Reference**
Min. ignition energy (MIE) 17 µJ Autoignition temp. 560 °C Max. exp. safe gap (MESG) 290 µm (spark between flat plates)	Brandes & Möller (2008)
Min. ignition volume approx. 0.1 mm³ (r ≈ 350 µm) Quenching distance (flame in a tube) $d_p = 0.65 \cdot d_z \quad d_z \approx 450\ \mu m$	Steen (2000)
$MIE = 0.07\, {d_q}^2$ $d_q = \sqrt{\frac{MIE}{0{,}07}} = \sqrt{\frac{17\ \mu J}{0.07}} = 490\ \mu m$	Lewis & van Elbe (1987), Babrauskas, V. (2003).
$Min.\,ignition\ energy = c_p \rho \Delta T_{ad} \left(\frac{1}{6}\pi\right) {d_q}^3$	Ballal & Lefebvre (1977).
Min. ignition energy 17 µJ with 0.5 mm electrode distance Min. ignition energy 38 µJ with 0.45 mm electrode distance	Wähner et al. (2010)

Equation 1, originally presented by Johannsmeyer (1983), refers to normally make contact discharges that occur in combination with capacitive circuits. Compared to contact break discharges, these are significantly shorter (typically with 1-2 µs discharge duration), occur at an electrode gap of approx. 60 µm and have significantly higher current and power values. The resulting energy value corresponds to the minimum energy of 17 µJ obtained by Brandes & Möller (2008), with an ignition probability of 10^{-3} (see Table 2).

Equation 3 in table 1 and the power value required for an ignition originally presented by Johannsmeyer et al (2010) are empirically determined for resistive circuits and were measured using the spark test apparatus.

Table 2 shows relevant ignition criteria such as the minimum ignition energy and volumes required for successful ignition. Values for these parameters have already been mentioned but used fixed electrodes, high voltage and no contact break. Wähner et al. (2010) also mentioned a dependence of the energy required for the ignition on the electrode gap. There, the optimum electrode gap for an ignition is 500 µm, which is larger than the maximum experimental safe gap and smaller than the quenching diameter.

For the estimation of the ignition limit for a contact break discharge, the above-mentioned relationships and criteria do not offer suitable results. Therefore, in the following sections, a selection of findings and the resulting conclusions necessary for an initial estimation of this specific situation are presented.

The general characteristics of a discharge leading to an ignition are presented in Fig. 2. In order to achieve this discharge, a voltage limited constant current source with 60 mA and an adjustable voltage source generating a voltage on the order of 30 V were used. The curves presented in Fig. 2 show the different discharge phases discussed in the previous chapter. A contact opening is created in which pre-processes are generated for approx. 240 µs (t_1 to t_2); here, the wire touches the micro-tips of the rough surface. A voltage of approx. 8 – 12 V can be measured in this phase because of the explosively collapsing micro-tips. Then, the wire is moved slowly from the surface (t_2); after 1 ms, a distance of approx. 150 µm is reached (past t_4) in order to allow better examinations. The distance-time characteristic of the tungsten wire is shown in Fig. 2 as well.

DOI: 10.7795/810.20200724

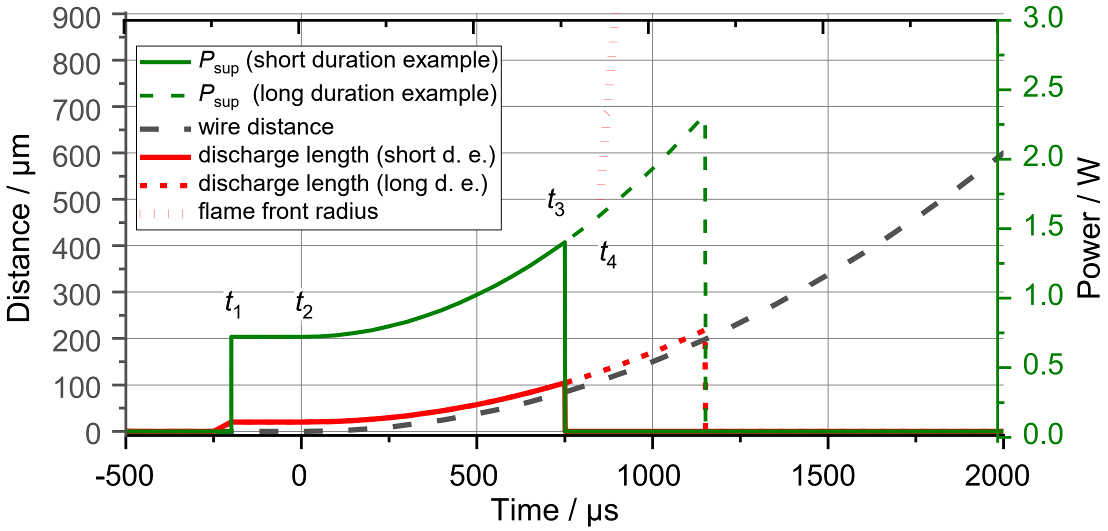

Fig. 2. *Schematic sequence of the wire distance, electrical power supplied and flame front*

The electrical power supplied (green, t_1 to t_3) is calculated from the product of the constant current (60 mA) and the length-dependent voltage of this discharge form, according to the equation presented in Uber (2019).

Also shown in this diagram is the curve of the radius of the temperature threshold (t_4) of the flame front as a rough estimation. For the first estimation presented here, this was determined from schlieren photographs (Uber et al. ,2016) taken with a faster contact opening but in a comparable situation with adapted time steps. In the context of the scattering of measurement results, this is the first practical approach as an applicable estimation. The schlieren images are shown in Fig. 3.

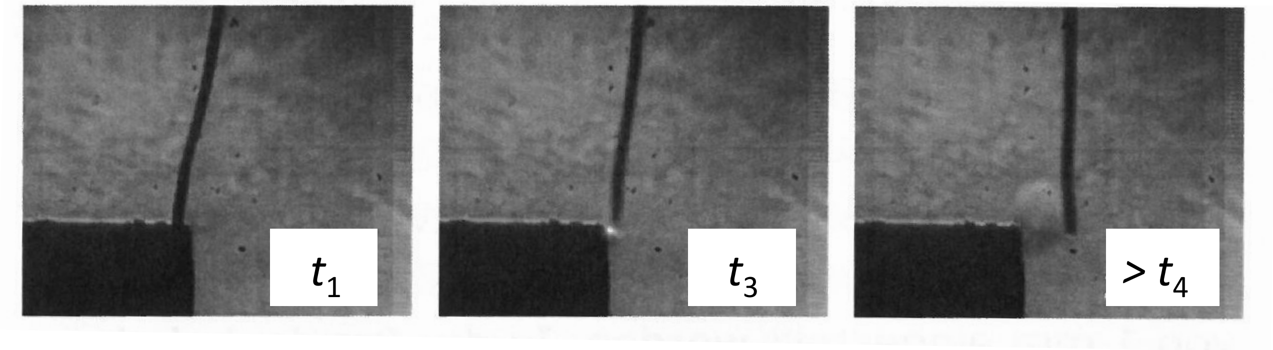

Fig. 3. *Schlieren images for a contact break with the experimental contact apparatus (Uber et al., 2016)*

In the sequence of images presented in Figure 3, starting from the left, the wire is on the surface and there is electrical contact. In the following image, the discharge is formed at the outer edge of the cadmium block. This leads to the propagation of the hot gas kernel (flame front), as depicted in the right image. A schematic representation of these physical processes as they are applied to the test situation presented here is shown in Fig. 4:

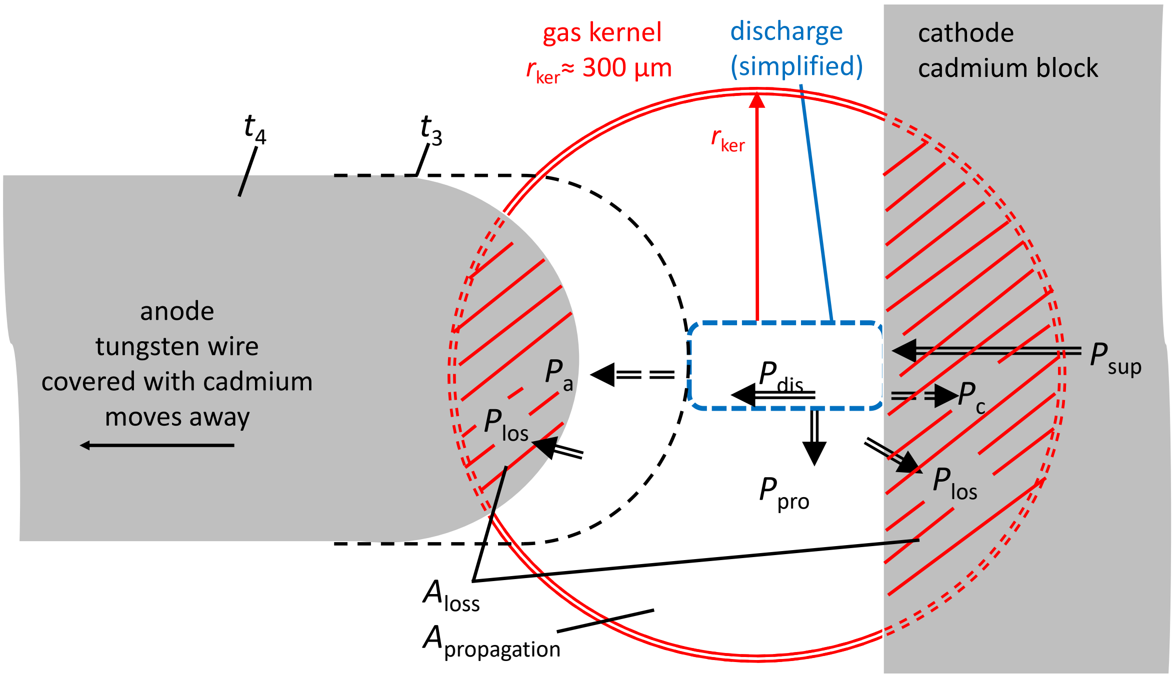

Fig. 4. *Geometric correlations of the electrodes, the discharge and the gas kernel (2D)*

In Fig. 4, the discharge generated between the cathode (right) and the anode (dashed line, left, t_1) is shown in the middle in a simplified form. The length of the smallest ignitable discharge measured is 110 µm. In this schematic representation, the power transferred to the discharge column is determined following Capp (1972). The power stored in the plasma column is estimated by subtracting the cathode sheath voltage drop from the measured discharge voltage drop. The remaining voltage drop, which is over only the discharge column, is multiplied by the discharge current, resulting in the total discharge power input. Only part (44 %) (Capp, 1972) of the total input power will be used to heat up and expand the surrounding gas. This part is considered to be 44 % of the total input power. The mathematical system of equations used to compute this power (P_{dis}) is presented in Eq. (4) and (5).

$$V_{dis}(t) = \left(V_{sup}(t) - 8.6\,V\right) \cdot 0.44 \qquad (4)$$

$$P_{dis}(t) = \left(V_{sup}(t) - 8.6\,V\right) \cdot 0.44 \cdot I_{\mathrm{dis}}(t) \qquad (5)$$

For a successful ignition, the hot gas kernel must propagate to at least the size at which the self-sustaining thermochemical ignition and the flame front can occur. This size was determined by Wähner et al. (2010) to be 500 µm for the radius with the lowest required energy; this value is used in the estimation presented here. Based on our images, we estimated that a radius of approximately 500 µm is reached after 200 µs. This time interval is therefore used for the calculation presented in this paper.

In Fig. 3, the gas kernel is quenched, most likely due to the electrode geometry. Here, it is assumed that the power losses via heat conduction into the electrode surface increase due to the large metallic surface surrounding the discharge. A shock wave common at high current values is not visible here. The effective power P_{pro} for the expansion of the gas kernel was estimated in accordance with fig. 4 via the ratio of the 2D areas $A_{\mathrm{propagation}}$ and A_{loss} (see equation 6) based on the schlieren images of Uber et al. (2016).

$$\frac{(P_{los} + P_{pro})}{P_{los}} = \frac{(A_{loss} + A_{propagation})}{A_{propagation}} \qquad (6)$$

DOI: 10.7795/810.20200724

According to these estimations, the power estimated for the expansion P_{exp} of the gas kernel using the area is estimated to be 55 % of the power stored in the discharge column P_{dis}. The criterion for estimating the beginning of the expansion is the point in time at which a power P_{dis} of 190 mW is reached. This value is a reference to the 350 mW (net) of Johannsmeyer (2010). Thus, the energy in the gas kernel is

$$t_0 < t < t_3\text{: } W_{gas\ kernel} = 0 \quad \text{for } P_{\mathrm{dis}}(t_3) < 190\ \text{mW} \qquad (7)$$

$$t_3 > t > t_4\text{: } W_{gas\ kernel} = \int_{t_3}^{t_4} (P_{dis}(t) - P_{los}(t))\ dt \quad \text{with } t_4 - t_3 = 200\ \mu\text{s} \qquad (8)$$

This correlation is assumed for 200 µs since, in the schlieren images in Fig. 3, this is the length of time required for the kernel to grow to the estimated 500 µm. If no electrical power is supplied in the period of 200 µs, a reduction in energy must be taken into account, which is estimated here to be 45 % of the last power P_{dis} according to equation 6. For purposes of simplification, this value is assumed here to be constant, in spite of the fact that it depends, among other things, on the geometry, the electrode distance and the energy level.

These equations yield the following curves for the above-mentioned power and energy in the gas kernel result (see Fig. 5)

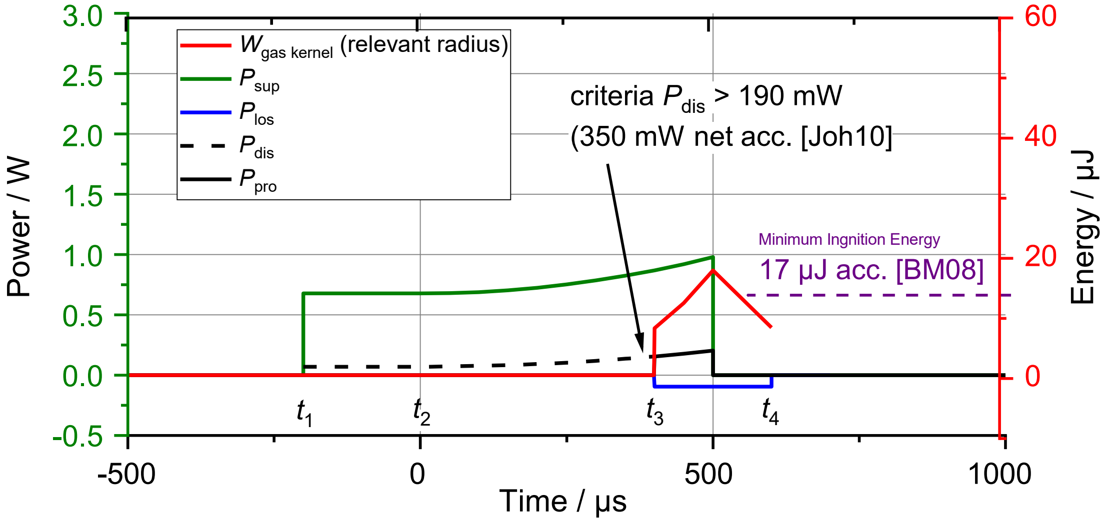

Fig. 5. *General example of the curves of the different power and energy in the gas kernel*

The example chosen is a typical discharge that, in our tests, resulted in an ignition probability of less than 10^{-3} – statistically, one ignition in over 1000 discharges. Therefore, given similar conditions, many discharges take place in the experiment without an ignition; this is assumed to be due to the influence of other effects such as surface structure and flow. A typical measured curve including the power and energy curve in the gas core of a discharge with an ignition is shown in the following diagram.

DOI: 10.7795/810.20200724

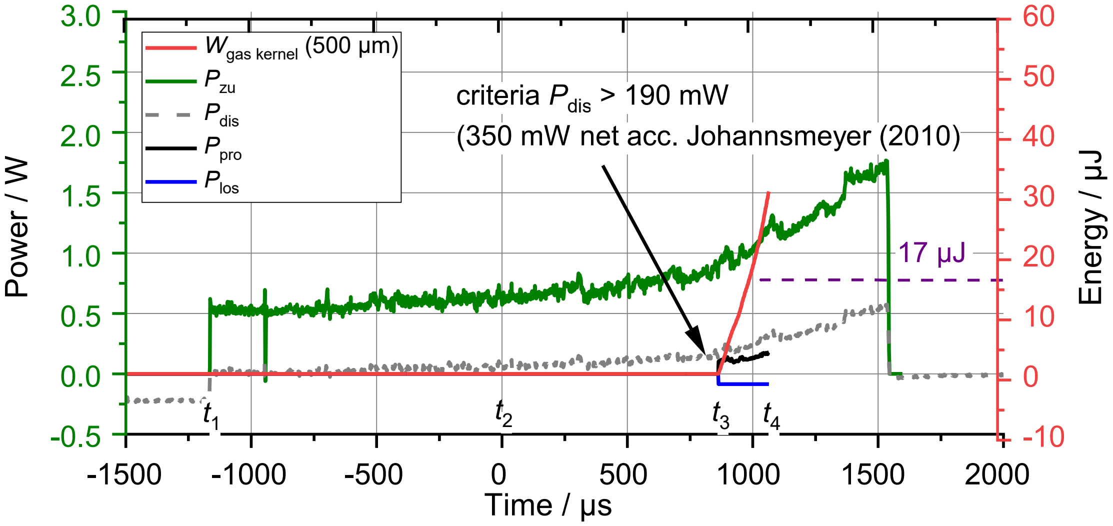

Fig. 5. *Curves of the different power and energy in the gas kernel of a measured discharge*

In Figure 5, an energy of approx. 30 µJ in the relevant gas kernel is estimated for the time at which the gas kernel reaches the estimated relevant radius of 500 µm. Compared to Figure 4, a longer energy input can be seen for other parameters, as in practice, the discharges can exist longer than the example in Fig. 4 up to the spatial (and thus temporally given) length limited by the maximum source voltage.

The energies of the gas core with 500 µm of further example discharges show energies of 30 µJ to 60 µJ, which are in the same range as the values of Wähner et al. (2010). However, these have only been developed under very imprecise and rough assumptions. For an application, a detailed analysis of the relationships and values is necessary.

5. Discussion and Conclusion

The results presented here offer an initial estimation of the comprehensive interrelationships of an ignition created by a discharge with a slow contact opening. Due to the assumptions and influences that can currently only be approximately determined, this is only a rough estimation. More precise information must be determined by means of schlieren investigations or comparable methods with a higher temporal and local resolution. In addition, the detailed relationships present at the transition from the discharge to the ignition with the combustion zone must also be checked, determined and understood. A numerical model able to physically describe the discharge may also be able to support this.

Additional investigations with a variation of the electrical circuit parameters, the opening speed of the wire and the speed of the cadmium block or the electrode geometry would provide further information for the slow contact break discharge. Investigations on faster contact-opening discharges must also take place.

Acknowledgements

The authors thank Niklas Schüler, Mattis Vogt, Rilana Rohde, Rebecca Diethelm, Robin Herman, Sönke Niemann and Thomas Uehlken for their experimental work. Financial support by the Deutsche Forschungsgemeinschaft (DFG) is gratefully acknowledged.

References

Bane, S. (2010). Spark Ignition: Experimental and Numerical Investigation with Application to Aviation Safety, PhD thesis, California Institute of Technology, Pasadena, California.

Babrauskas, V. (2003). Ignition handbook. Fire Science Publishers, Issaquah (WA, USA).

Ballal, D. R. & Lefebvre, A. H. (1977). Ignition and flame quenching in flowing gaseous mixtures. *Proceedings of the Royal Society of London*, Series A, Mathematical and Physical Sciences 357, P. 163-181. DOI: 10.1098/rspa.1977.0161.

Brandes, E & Möller, W. (2008). Flammable liquids and gases, Vol 1 Safety characteristic data, Wirtschaftsverl. NW, Bremerhaven.

Bradley, D. & Lung, F. K.-K. (1987). Spark ignition and the early stages of turbulent flame propagation. *Combustion and Flame* 69, P. 71–93. DOI: 10.1016/0010-2180(87)90022-8.

Capp, B. (1972). The power balance in electrode-dominated arcs with a tungsten anode and a cadmium or zinc cathode in nitrogen. *Journal of Physics D: Applied Physics*, Vol. 5, P. 2170.

Eckhoff, R. & Olsen, W. (2010). A new method for generation of synchronized capacitive sparks of low energy, *Journal of Electrostatics*, 2010, Vol. 68, P. 73 -78.

Essmann, S. (2018). Experimentelle Untersuchung der Zündung durch elektrostatische Entladungen geringer Energie, Dissertation Karlsruher Institut für Technologie (KIT).

Glassman, I. & Yetter, R. A. (2008). Combustion. Academic Press, Amsterdam, Boston.

Litin, D.R. & Wooding, E.R. (1959). Investigation of the ignition of a gas by an electric spark, *British Journal of Applied Physics*, Vol. 10, No. 4, P. 159 -166, DOI: 10.1088/0508-3443/10/4/302.

Lewis, B.; van Elbe, G (1987). Combustion, flames and explosion of gases. Academic Press, Orlando (FL, USA), 1987, DOI: doi.org/10.1016/C2009-0-21751-X.

IEC 60079-11:2011 Corr 2012, (2012). Explosive Atmospheres Part 11: Equipment Protection by Intrinsic Safety "i".

Johannsmeyer, U. (1984). Zündung explosionsfähiger Gemische durch kurzzeitige Schließfunken in kapazitiven Stromkreisen für die Zündschutzart Eigensicherheit, Dissertation TU Braunschweig.

Johannsmeyer, U.; Gerlach, U.; Uehlken, T. (2010): Sicherheitsrelevante Parameter. "Netto"-Betrachtung von maximalen Funkenleistungen. Contribution to IEC60079-11 Maintenance Team Meeting, Seattle, USA.

Schardin, H. (1942). Die Schlierenverfahren und ihre Anwendungen. Ergebnisse der exakten Naturwissenschaften. Eds. Trendelenburg, F., Hund, F., Springer, Berlin P. 303 – 439.

Steen, H. (2000), Handbuch des Explosionsschutzes. Wiley-VCH, Weinheim.

Uber, C. (2019). Charakterisierung elektrischer Kontakt-Entladungen im Bereich niedriger Spannungen im Zündgrenz-Bereich von Wasserstoff-Luft-Gemisch, Dissertation TU Ilmenau.

Uber, C., Hilbert, M., Felgner, A., Hüser, D., Kurrat, M., Gerlach, U. (2019). Electrical discharges caused by opening contacts in an ignitable atmosphere – Part I: Analysis of electrical parameters at ignition limits, *Journal of Loss Prevention in the Process Industries*, Vol. 61, P. 114-121, https://doi.org/10.1016/j.jlp.2019.06.011.

Uber, C.; Shekhar, R.; Gerlach, U. (2016). Ansatz zur Modellierung von Zündfunken durchelektrische Kontaktvorgänge für die Zündschutzart Eigensicherheit. *14.BAM-PTB-Kolloquium zur chemischen und physikalischen Sicherheitstechnik*, P.76–83.

Warnatz, J.; Maas, U. (1993): Technische Verbrennung. Physikalisch-Chemische Grundlagen, Modellbildung, Schadstoffentstehung. Springer-Verlag, Berlin, Heidelberg, DOI:10.1007/978-3-662-10266-4.

Wähner, A., Gramse, G., Langer, T., Beyer, M. (2013): Determination of the minimum ignition energy on the basis of a statistical approach. *Journal of Loss Prevention in the Process Industries*, Vol. 26, P.1655–1660, doi.org/10.1016/j.jlp.2013.06.002.

Zborovszky, Z. & Cotugno. L. A. (1974): Evaluation of the Cadmium Disc Breakflash in Testing Electrical Circuits. A Comprehensive Study of Intrinsic Safety Criteria, Denver.

DOI: 10.7795/810.20200724

Spectroscopic investigations of the correlation between the discharge caused by a slow contact opening and the flame front in a H_2/air mixture

Carsten Uber[a], Steffen Franke[b], Jens Brunzendorf[a], Michael Hilbert[a], Dirk Uhrlandt[b],
Frank Lienesch[a]

[a] Physikalisch-Technische Bundesanstalt (PTB), Braunschweig, Germany
[b] Leibniz Institute for Plasma Science and Technology (INP), Greifswald, Germany

E-mail: carsten.uber@ptb.de

Abstract

Electrical contact break discharges are a potential ignition source for combustible gas mixtures. Therefore, electrical equipment in which electrical contact discharges may occur must meet safety requirements when used in explosive atmospheres. The electrical discharges generated by slow contact openings have been characterized in previous articles of the authors. The relevant discharges near the minimum ignition energy (17 µJ for hydrogen-air mixture) typically occur at voltages lower than 30 V and currents higher than 30 mA. These discharges are dominated by metal vapor, which can be deduced from the optical radiation. Processes that operate on different time scales (nano-, micro- and milliseconds) as well as on different spatial scales (micro- and millimeter) pose a considerable challenge for optical investigations. In this article, the relevant electrical and spectroscopic parameters of the discharge and the mechanical parameters of the contact opening are compared. The data obtained serves as the basis for modeling and as support for standardization.

Keywords: Electrical discharge, optical emission spectroscopy, cadmium, temperature determination

1. Introduction

An assessment for the safe operation of electrical equipment in explosive atmospheres in which contact break discharges can occur can be carried out using the so-called spark test apparatus according to the international standard IEC 60079-11 (6th Ed.) (2012). In this device, electrical discharges are generated in a gas mixture, but the results scatter and their reproducibility is poor. For the development of an alternative to the spark tester with more reproducible results, the physical relationships are currently being analyzed and a multiphysical model is being developed.

In explosion protection, the ignition behavior of electrical discharges, which can occur due to high voltages, has been investigated (Essmann, 2018; Eckhoff & Olsen, 2010; Bane, 2010; Brabrauskas, 2003). Ignitions due to electrical discharges in the low-voltage range can occur during contact openings and closures and have only been partially investigated to date (Johannsmeyer, 1984; Zborovszky & Cotugno, 1974; Babrauskas, 2003; Uber, 2019a). These investigations are not sufficient for modeling ignitable discharges by means of contact processes. The electrical discharges described in this article at slow contact openings have been characterized by Uber (2019a). The relevant discharges near the minimum ignition energy (17 µJ for hydrogen-air mixture $\varphi(H_2) = 21$ %, Brandes & Möller, 2008) typically occur at voltages lower than 30 V and currents higher than 30 mA. These discharges are dominated by metal vapor. However, the transition from the discharge dominated by metal vapor to the thermo-chemical ignition has not yet been sufficiently analyzed to derive a model and evaluation criteria for the ignition or non-ignition of a discharge.

To understand the transition from the electrical contact break discharge to the ignition processes, spectroscopic investigations can be carried out. Spectroscopic investigations of electrical discharges do exist, but were performed under different conditions such as the use of high voltage

(Essmann, 2018). First investigations on contact break discharges with low voltage have been presented in Uber (2019c).

In this article, the procedure for determining the relevant electrical and spectroscopic measured variables of the discharge, the mechanical characteristics of the contact opening and the resulting propagation of the flame front are presented. A model contact apparatus developed for this purpose is based on the components of the above-mentioned spark test apparatus but allows systematic investigation and separation of effects (Uber, 2019a). The basic data obtained serves as a basis for modeling and as support for standardization.

2. Experimental methods

For the investigation of parameters and physical effects of slow contact-opening discharges, a model contact apparatus has been developed and put into operation. During the contact opening, the following processes can be observed (Fig. 1).

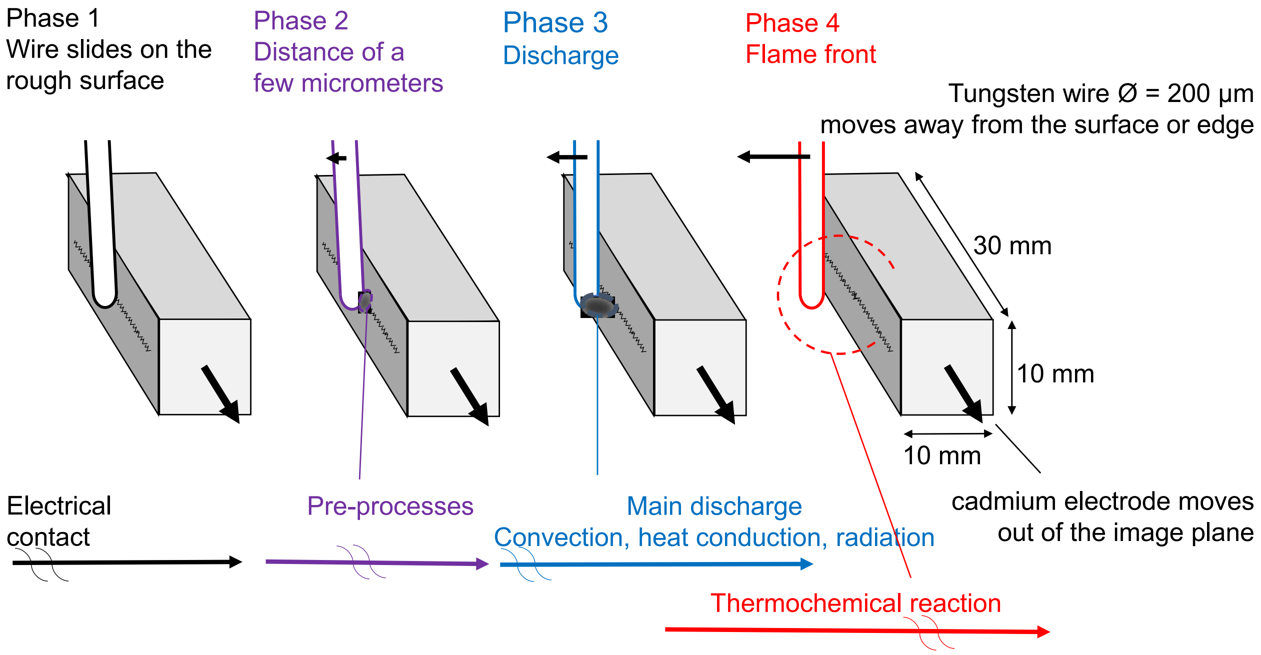

Fig. 1. *General schematic sequence of processes of a slow contact opening in the model contact apparatus (cf. Uber (2020))*

First, the tungsten wire (anode) slides along the surface of a solid cadmium block (cathode). Whenever there is a gap between the anode and the cathode due to the surface topology, the pre-processes will be initiated. These micro-discharges occur sporadically, have a spatial dimension of at most a few tens of micrometers, and have a duration of some microseconds. If the wire is released to more than 100 µm, the main discharge is established and an ignition usually follows. More details can be found in Uber (2020) and Uber (2019a).

For experimental investigations, the model contact apparatus was placed in an explosion chamber (12-liter volume) equipped with quartz windows for optical access. Prior to each experiment, the chamber was flushed with ambient air three times the chamber volume. Then, the hydrogen-air mixture ($\varphi(H_2) = 21\ \%$) was added via a mass flow controller. The model contact apparatus was operated by means of a constant current source with maximum voltage limitation in order to be able to carry out targeted and systematic experiments with fixed parameters (see Uber, 2019a).

Optical emission spectroscopy was performed with a grating spectrometer Acton Research Cooperation Type SpectraPro 300. A grating with 150 lines/mm was used, leading to a spectral window of about 500 nm that was observed by the detector. The discharge was imaged onto the entrance slit of the spectrometer by means of a Questar QM1 far-field microscope and recorded by a

Photron Fastcam SA5 high-speed camera utilizing a Hamamatsu C10880 image intensifier. The spectroscopic images were taken at a frame rate of 10,000 fps as a compromise between radiation intensity and temporal resolution. The electrical values were recorded with a Yokogawa oscilloscope type DL9040L and corresponding probes. More detailed information is given in Uber (2019a).

3. Results and discussion

The voltage and current characteristic of the model discharge investigated in this article is shown in Fig. 2.

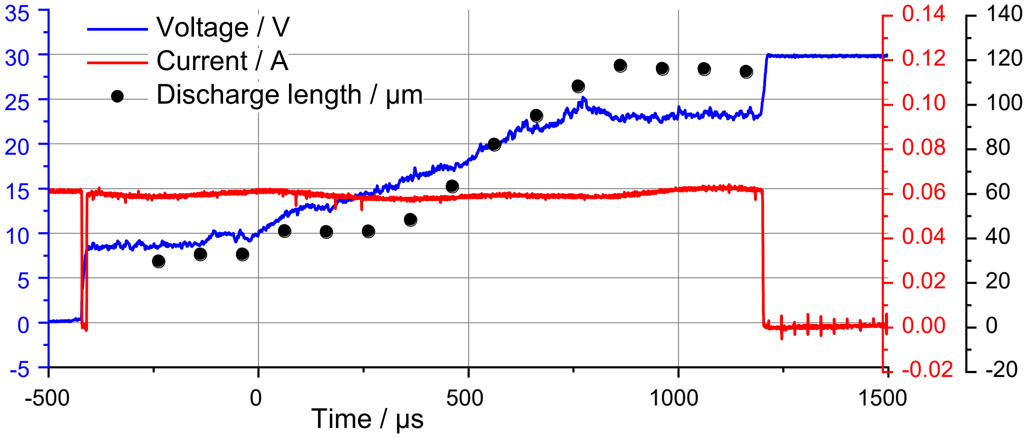

Fig. 2. Voltage and current characteristics of a contact break discharge with 60 mA constant current and 30 V (voltage limited) with a following ignition (cf. Uber (2019c)

The current is set at 60 mA by a current source. The length of the discharge was determined using half the maximum value of the intensity (Uber, 2019a). The discharge starts with pre-processes characterized by a discharge length shorter than 50 µm (≈-450 µs <t< ≈450µs) and a voltage level of less than 10 V. When the contacts are separated with a speed of around 0.15 m/s, the voltage required to drive the current is increased. A zero point in time is set to the trigger signal for contact separation. The discharge lasts about 1.5 ms and is interrupted when the required voltage exceeds the supplied voltage. Therefore, the duration of the discharge depends on the contact opening speed. The higher the opening speed is, the shorter the maximum discharge duration will be.

The temperature of the discharge over time using the electrical conductivity as well as the excitation temperature for the area of greatest intensity close to the electrodes was determined in Uber et al. (2019c). Here, a more detailed analysis is performed to evaluate the spatial distribution of excitation temperatures depending on the location between the anode and the cathode. Fig. 3 presents spectra taken at different instants in the discharge evolution showing the axial intensity distribution.

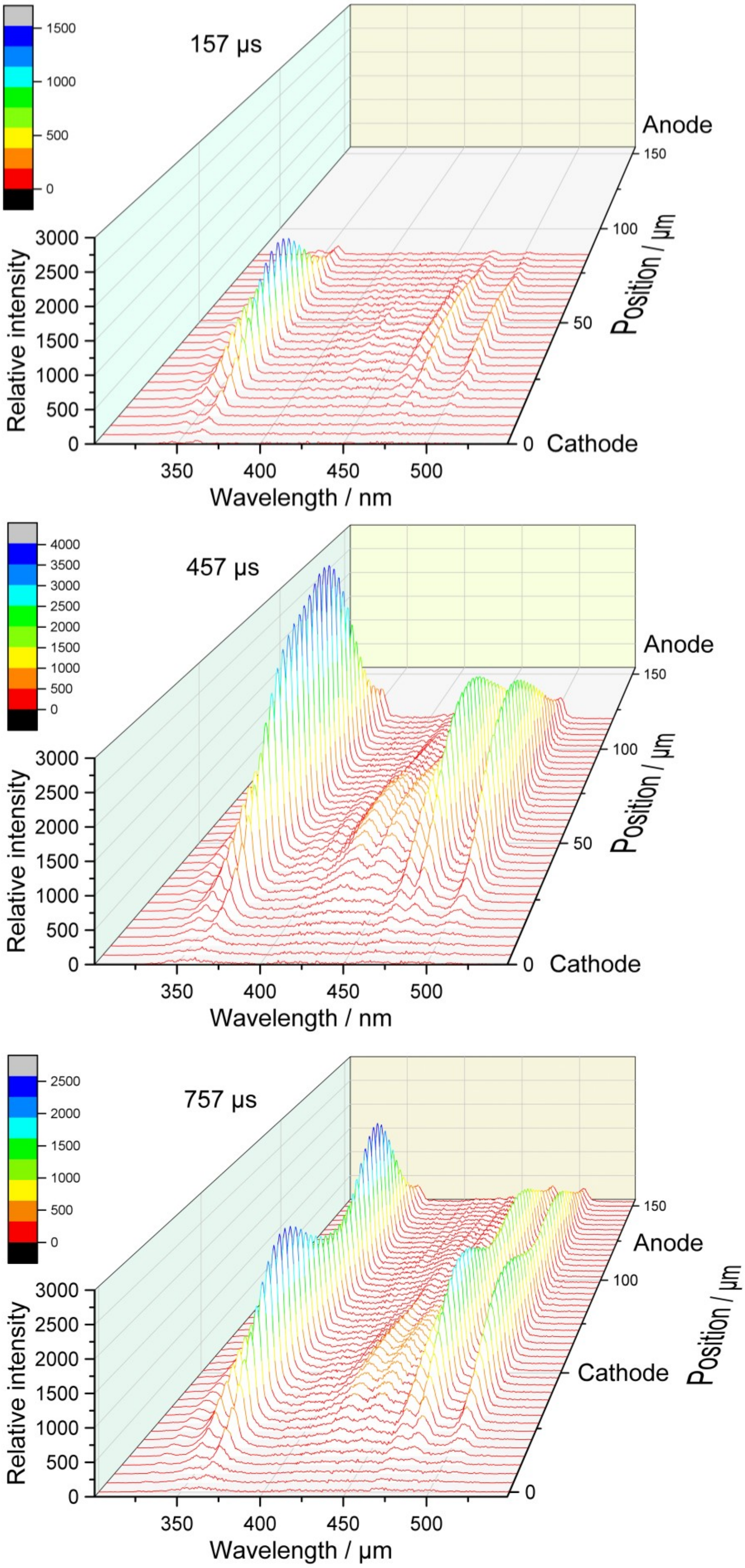

Fig. 3. Spectra of the sample discharge for three representative points in time 157 µs (top), 457 µs (center) and 757 µs (bottom).

The discharge spectrum at 157 µs (Fig. 3 top) corresponds to a distance between the electrodes of less than 50 µm and is dominated by one spatial peak of low intensity. In addition, cadmium lines are visible. In the spectrum of the discharge after 457 µs, only one spatial peak is visible, but the intensity of the discharge is higher and the region is larger. In the spectrum after 757 µs, the discharge has increased even more: two peaks can now be seen in front of the electrodes that can be clearly identified as an anode and cathode glow. The intensity values in between are about 40 % lower. The prominent lines of cadmium can also be seen in the further spectra.

For each spectrum, a linear regression was performed in a Boltzmann plot taking into account Cd atomic lines at 326 nm, 347 nm, 361 nm, 468 nm, 480 nm and 508 nm. This allowed the excitation temperature per time step along the axial coordinate to be estimated.

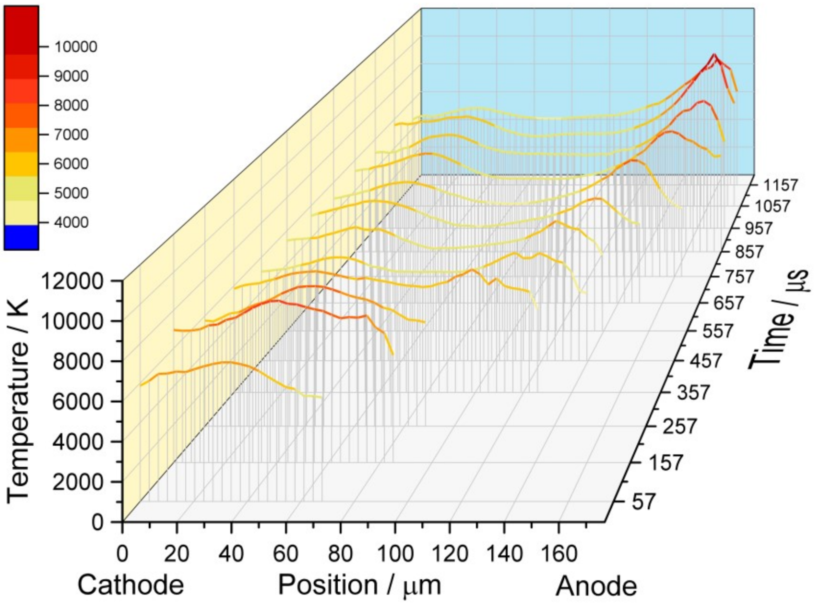

Fig. 4. Estimation of the spatio-temporal excitation temperature distribution between the anode and cathode.

The discharge in the H_2/air mixture in Fig. 4 shows maximum excitation temperatures between 5500 K and 10500 K that are also located at the positions of the intensity maxima directly in front of the electrodes. These values are comparable to earlier results at the position with the highest intensity and in a similar time range (Uber et al., 2019c). However, this figure reveals that temperatures in front of the anode are higher than in front of the cathode. This behavior cannot be explained directly because higher electric fields are expected in the cathode sheath while stronger heat flux into the electrode via the electron inrush is expected for the anode, which might also affect the energy deposited into a space charge sheath in front of the anode. Furthermore, conclusions drawn from the maximum temperatures according to the overall electrical conductivity are of limited accuracy, as extended regions of the discharge exist at lower excitation temperatures. Here, the temperature drops to values around 4600 K.

From this figure, it is also obvious that the limited spatial resolution, which is expected to be around 20 µm, hinders interpretation of the first 300 µs because spatial blurring cannot be distinguished from the interaction of the cathode sheath and the anode sheath. Blurring might also explain a slight shift of the local maximum in front of the cathode towards the anode up to 10 µm. Hence, conclusions must be drawn carefully. The fact that there is just one spatial maximum for the first time points does not mean that there the cathode and anode sheaths are not well separated.

Although it is highly reasonable that non-equilibrium effects are to be expected during initiation of the discharge and in the electrode sheaths, as already concluded in Shekhar et al. (2019), a detailed analysis shows excitation temperature in the column of around 4600 K, which is very close to previously estimated temperatures from electrical conductivities, which are about 5000 K (Shekhar et al. (2019)). Associated with the information that an ignition takes place starting from 350 mW net according to Johannsmeyer et al. (2010) and Uber (2019a), the relevant value is in the range of the discharge length from 80 to 100 µm. From this discharge length with two peaks, a larger extension can be seen at comparable temperatures. The challenge is to verify which part of the ohmic heating is invested in the enthalpy of the flammable gas. Initial steps in this direction are detailed in Uber (2020) (at this conference).

Another topic addressed in this investigation is the spectral emission of a flame front and its relation to the discharge. By means of optical emission spectroscopy utilizing a far-field microscope, a region of about 300 µm x 300 µm is imaged onto the entrance slit of the spectrometer. Discharges leading to an explosive ignition show an additional spectral feature that can be found around 450 nm in Fig. 3. To date, it has not been possible to identify this spectral feature by means of an atomic spectral line nor by means of molecular emission of known constituents of the plasma. In addition, no further spectral emission is observed during the discharge that is clearly identifiable for the emission of the flame front and the thermo-chemical reaction.

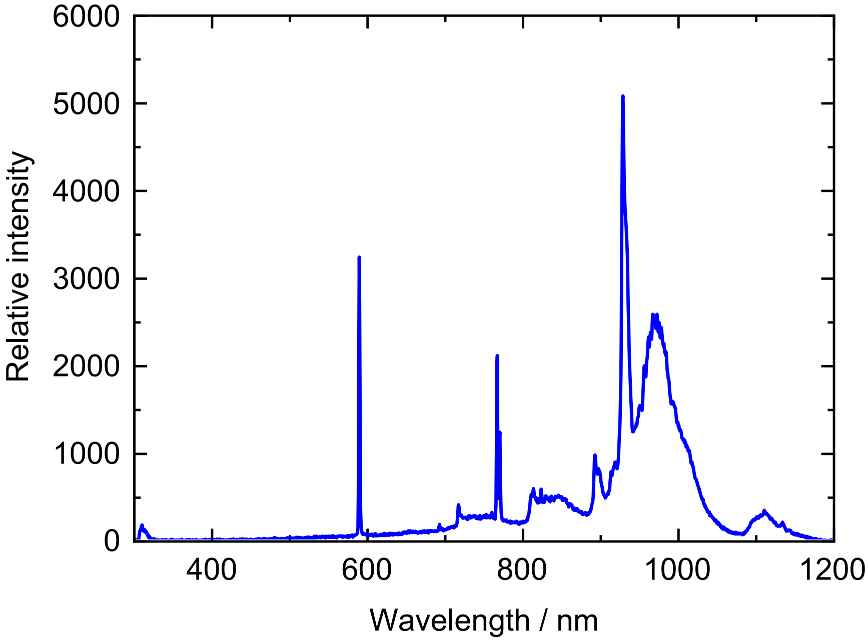

Fig. 5. *Overview of spectrum obtained with compact spectrometer during ignition including contact break discharge (100 ms exposure).*

However, examining the plasma by means of a bare fiber connected to a compact spectrometer (Avantes ULS2048-EVO) during the explosion yields the spectrum presented in Fig. 5. The fiber collects radiation from a cone covering a significant part of the whole volume of the explosion chamber (approx. Ø ≈ 250 mm, h ≈ 250 mm). All the Cd lines including the additional spectral feature mentioned above disappear from this spectrum, although the exposure time includes the contact break discharge as well. Nevertheless, some spectral features starting at 600 nm have not been observed for the Cd discharge. These features must be examined in terms of the thermo-chemical reaction of H_2 and O_2 and the radiation emitted during this reaction. Furthermore, a typical OH band (around 310 nm) is observed in the flame front spectrum of Fig. 5 but not in the spectrum of the discharge in Fig. 3. Moreover, none of the atomic spectral lines of H, O or N is identified in the spectrum of Fig. 5, as the gas is assumed to be too cold for these emissions. Nevertheless, it is reasonable to argue that the radiation from the thermo-chemical reaction is much more intense and lasts much longer than the initial discharge, which is why no Cd lines are observed here.

4. Conclusion

The spectra obtained in this investigation provide detailed information on discharges that ignite flammable gas mixtures. From the axial distribution of excitation temperatures, it can be concluded that temperatures in front of electrodes are significantly higher compared to the bulk discharge. Moreover, temperatures in the bulk volume are very close to the temperatures estimated from electrical conductivities in previous investigations (Uber, 2019a). Hence, the investigations form a solid basis for further estimations of the energy dissipation of discharges that are capable of igniting hydrogen-air mixtures. The results presented here do not support the hypothesis that the physical properties of the individual discharges promote an ignition. Further questions to be investigated concern the overall energy balance and heat transfer to the flammable medium and possible quenching effects due to geometrical boundary conditions. In the future, additional spectroscopic investigations of the discharge as well as schlieren measurements of the flame front will help to address these questions.

Acknowledgements

The authors thank Niklas Schüler, Markus Sinnigen, Rilana Rohde, Rebecca Diethelm, Robin Herman, Sönke Niemann and Thomas Uehlken for their experimental work. Financial support by the Deutsche Forschungsgemeinschaft (DFG) is gratefully acknowledged.

References

Bane, S. (2010). Spark Ignition: Experimental and Numerical Investigation with Application to Aviation Safety, PhD thesis, California Institute of Technology, Pasadena, California.

Babrauskas, V. (2003). Ignition handbook. Fire Science Publishers, Issaquah (WA, USA).

Brandes, E. & Möller, W. (2008). Flammable liquids and gases, Safety characteristic data. Bremerhaven: Wirtschaftsverl. NW.

Eckhoff, R. & Olsen, W. (2010). A new method for generation of synchronized capacitive sparks of low energy, *Journal of Electristatics*, 2010, Vol. 68, P. 73 -78.

Essmann, S. (2018). Experimentelle Untersuchung der Zündung durch elektrostatische Entladungen geringer Energie, Dissertation Karlsruher Institut für Technologie (KIT).

IEC 60079-11:2011 Corr. hydrogen-air mixture 2012, (2012). Explosive Atmospheres Part 11: Equipment Protection by Intrinsic Safety “i”.

Johannsmeyer, U. (1984). Zündung explosionsfähiger Gemische durch kurzzeitige Schließfunken in kapazitiven Stromkreisen für die Zündschutzart Eigensicherheit, Dissertation TU Braunschweig.

Johannsmeyer, U.; Gerlach, U.; Uehlken, T. (2010): Sicherheitsrelevante Parameter. „Netto“-Betrachtung von maximalen Funkenleistungen. Contribution to IEC60079-11 Maintenance Team Meeting, Seattle, USA.

Shekhar, R., Gortschakow, S., Grosshans, H., Gerlach, U. & Uhrlandt, D. (2019). Numerical investigation of transient, low-power metal vapor discharges occurring in near limit ignitions of flammable gas. *Journal of Physics D-Applied Physics*, 52(4).

Uber, C. (2019a). Charakterisierung elektrischer Kontakt-Entladungen im Bereich niedriger Spannungen im Zündgrenz-Bereich von Wasserstoff-Luft-Gemisch, Dissertation TU Ilmenau, urn:nbn:de:gbv:ilm1-2019000239.

Uber, C., Hilbert, M., Felgner, A., Hüser, D., Kurrat, M., Gerlach, U. (2019b). Electrical discharges caused by opening contacts in an ignitable atmosphere – Part I: Analysis of electrical parameters at ignition limits, *Journal of Loss Prevention in the Process Industries*, Vol. 61, P. 114-121, doi.org/10.1016/j.jlp.2019.06.011.

Uber, C., Runge, T., Brunzendorf, J., Kurrat, M. Gerlach, U. (2019c). Electrical discharges caused by opening contacts in an ignitable atmosphere – Part II: Spectroscopic investigation and estimation of temperatures. *Journal of Loss* Prevention *in the Process Industries*, Vol. 61, 213-219, doi.org/10.1016/j.jlp.2019.05.010.

Uber, C., Barbu, B., Hilbert, M., Berger, F., Lienesch, F. (2020). Investigation of the correlation between the electrical power and flame front of a discharge caused by a slow contact opening in H_2/air mixture, in preparation for the *13th International Symposium on Hazards, Prevention, and Mitigation of Industrial Explosions (ISHPMIE),* Braunschweig, July 27-31, 2020.

Zborovszky, Z. & Cotugno. L. A. (1974): Evaluation of the Cadmium Disc Breakflash in testing Electrical Circuits. A Comprehensive Study of Intrinsic Safety Criteria, Denver.

DOI: 10.7795/810.20200724

New aspects of the ignition of burnable gas mixtures by low-energy electrical discharges

Stefan Essmann[a], Johann-Robert Kummer[a], Holger Grosshans[a], Detlev Markus[a] & Ulrich Maas[b]

[a] Physikalisch-Technische Bundesanstalt (PTB), Bundesallee 100, Braunschweig, Germany
[b] Karlsruhe Institute of Technology, Institute of Technical Thermodynamics, Karlsruhe, Germany

E-mail: *stefan.essmann@ptb.de*

Abstract

The ignition of combustible gas mixtures by electrical discharges can lead to catastrophic consequences. While this potential ignition source needs to be considered regularly, the prediction of ignitions by electrical discharges by numerical models is not yet feasible for practical systems. This study gives an overview of recent experimental work by means of optical emission spectroscopy, schlieren imaging, and laser-induced fluorescence of OH. Based on the results, a qualitative analysis of the energy balance in the ignition kernel is performed. Further, one-dimensional numerical simulations considering detailed chemical kinetics and detailed transport processes are performed. Through the combination of these techniques, a detailed view of the ignition process by electrical discharges close to the MIE is obtained.

Keywords: *ignition, electrical discharge, minimum ignition energy, optical emission spectroscopy, schlieren, laser-induced fluorescence, numerical simulation*

1 Introduction

The ignition of combustible gas mixtures by electrical discharges poses a risk to the safe operation of electrical equipment in hazardous areas as well as to safety-relevant processes in the chemical industry and can lead to catastrophic consequences (Hattwig & Steen, 2004). To avoid such events, explosion-protected devices must be designed according to certain standards. However, the background of these standards is, in parts, experience-based rather than scientifically sound. Despite numerous experimental and theoretical studies, the ignition by electrical discharges can be predicted only for simple systems. For accurate predictions concerning practical systems, an even more detailed comprehension of all sub-processes governing the ignition and their implementation in numerical models is required.

The main parameter influencing the outcome of an ignition test at energies close to the minimum ignition energy (MIE) is, obviously, the ignition energy E. Increasing the energy will yield a higher probability of ignition (Eckhoff et al., 2010, Bane, 2010, Wähner et al., 2013) as well as a faster transition of the hot kernel into a self-sustaining flame (Lim et al., 1987, Kono et al., 1989, Ko et al., 1991, Essmann et al., 2020). However, the exact pathway that turns a higher discharge energy into a more probable ignition event was not the focus of these papers. A common perception seems to be that a higher discharge energy leads to an increased temperature of the kernel which, in turn, will lead to a more probable ignition. In this study, we contend that this view may be only partially correct. In general, at some point during the evolution of the kernel, the heat released by chemical reactions needs be larger than the heat losses, mainly due to conduction, in order to sustain a flame (Sloane, 1990b).

For this purpose, we combine results from different experimental techniques and numerical simulations to elucidate the role of the parameter *ignition energy*. In particular, optical emission spectroscopy (OES) yielded information about the diameter and temperature of the discharge (Essmann et al., 2017). Further, we consider phase-resolved schlieren measurements of the expansion of the hot gas kernel and the pressure wave resulting from the discharge at times 10^{-9} s to 10^{-5} s after the discharge (Essmann et al., 2016, Korytchenko et al., 2018). In the 10^{-5} s to 10^{-3} s range, time-resolved schlieren data of the early flame propagation was collected (Essmann et al., 2020). Finally, planar laser-induced fluorescence of the OH radical (OH-LIF) was carried out for times 10^{-6} s to 10^{-3} s after the discharge (Essmann et al., 2018a). Details on these experiments are presented in the referenced papers. Thus, only a brief outline will be given in the following section and the results will not be discussed in depth.

***Table 1**: Gas mixtures*

Burnable gas	Concentration in air	MIE (Brandes & Möller, 2008)	Electrode distance
Hydrogen	23.3 vol. %	17 µJ	0.5 mm
Ethene	8.0 vol. %	82 µJ	1.2 mm
Propane	5.2 vol. %	240 µJ	1.7 mm

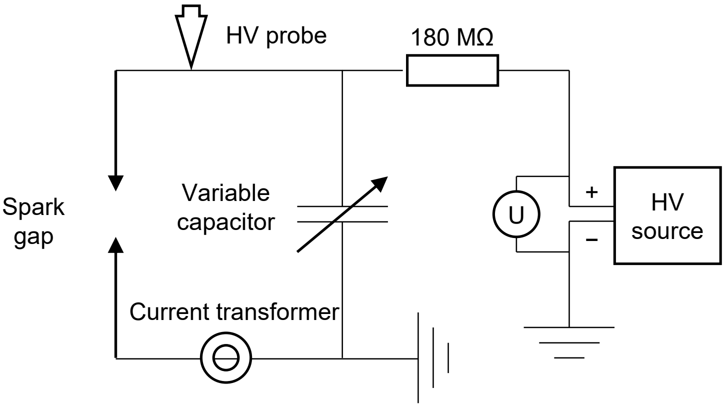

***Fig. 1**: Electrical set-up (Essmann et al., 2016)*

Based on the experimental results, we qualitatively analyse the energy balance in the discharge volume. Moreover, we investigate the ignition process numerically and compare the simulation results with the experiments. The combination of these approaches yields insights concerning the role of the ignition energy and temperature.

2 Experiments

Electrical discharges were generated between two tungsten electrodes (2.4 mm diameter rods with rounded tips) which were placed in a stainless steel explosion chamber. The cylindrical chamber (140 mm diameter, 110 mm height) was equipped with four flanges to allow for optical access. Mixtures of combustible gases with air were generated by means of mass flow controllers (table 1). The electrode distance was selected according to previous research (Wähner et al., 2013). The discharge energy was chosen close to the respective MIE of the mixture and was varied systematically during the experiments. To achieve this, the capacitance of the set-up was varied while the voltage across the gap was kept constant (cf. fig. 1). The discharge energy was estimated as $E = \frac{1}{2}CU^2$, where C is the capacitance of the set-up, including stray capacitances, and U is the breakdown voltage (measured with a high voltage probe). Ultraviolet light from a frequency quadrupled Nd:YAG laser at 266 nm was used to trigger the discharge at the desired time instance to allow for synchronization with the measurement equipment (Essmann et al., 2018b). All experiments were carried out at ambient conditions ($T = 21.5 \pm 1.0\,°\mathrm{C}$, $p = 1000 \pm 40\,\mathrm{mbar}$). Details regarding the experimental set-up may be found in the paper by Essmann et al. (2020).

2.1 Optical emission spectroscopy

We recorded emission spectra of the discharge with a temporal resolution of 10 ns (Essmann et al., 2017). In particular, the emission bands in the second positive system of nitrogen at 360 nm to 410 nm were analysed. The experimental spectra were compared with a database of numerically simulated spectra (software *Specair*) (Laux et al., 2003). From the best fit, the rotational and vibrational temperature of the plasma, T_{rot} and T_{vib}, were determined. At atmospheric pressure, T_{rot} is a good estimate for the gas temperature (Laux et al., 2003).

2.2 Schlieren measurements

Different schlieren set-ups were used to investigate different temporal regimes of the experiment. Both set-ups consisted of a light source, two field lenses (500 mm focal length), a schlieren stop, and a camera. The spatial resolution was determined via a target printed on transparent foil.

A single-shot set-up was utilised to investigate very fast processes with characteristic speeds of several 100 m/s (Essmann et al., 2016). Therefore, a flash lamp with a very short pulse (< 25 ns) was used to freeze the image. A knife edge oriented parallel to the electrode axis was employed as the schlieren stop. The images were recorded on a CCD camera.

For the high-speed set-up an intense green LED in combination with a pinhole was taken as the light source (Essmann et al., 2020). Another pinhole served as the schlieren stop. A high-speed CMOS camera registered the images at 62.5 kHz.

2.2.1 Laser-induced fluorescence of OH

Single-shot OH-LIF was performed for different times after the discharge. Laser light at 532 nm from an Nd:YAG laser pumped a Rhodamine 6G dye laser whose frequency doubled output was tuned to 283.6 nm to excite the $Q_1(8)$ transition of the OH radical (Essmann et al., 2018a). The resulting laser beam was formed into a thin sheet and cut in the perpendicular direction to match the electrode distance. The laser sheet was positioned centred in between the electrodes. A CCD camera in combination with an image intensifier registered the fluorescence at a 90° angle.

3 Numerical simulations

We performed numerical simulations with the program INSFLA (Maas & Warnatz, 1988), which employs a one-dimensional formulation of unsteady laminar flames. The conservation equation for mass, momentum, energy and species mass are solved using the method of lines. This method uses a time integration for the differential-algebraic equations resulting from the spatial discretisation by the finite difference method. Adaptive grid refinement ensures the accurate resolution of the smallest flow scales. INSFLA includes a detailed transport model and chemical kinetics. The simulations were performed for the fuel ethene (C_2H_4) using a mechanism containing 32 species and 206 elementary reactions (Luo et al., 2012). The electrical discharge is modeled by adding a source term to energy conservation equation (Dreizler et al., 2000). A cylindrical shape was considered for the source in the simulations. The values for the parameters of the source term and the energies are specified in table 2.

4 Results and discussion

4.1 Characteristics of the discharge

Results from the OES experiment show that a typical duration of the discharge light emission is 50 ns. In the investigated range of discharge energies and electrode distances, this duration depends neither on the discharge energy E nor on the energy density $D = E/V$, where V is the volume of the discharge.

Determination of the rotational and vibrational temperature of the plasma showed no clear trend concerning E, D, or the time after the discharge, either. However, the plasma obviously is non-thermal, since $T_{\text{vib}} = 4000 \pm 625\,\text{K}$ was much greater than $T_{\text{rot}} = 525 \pm 125\,\text{K}$ (Essmann et al., 2017). The temperature rise of the gas is around 230 K and not as strong as could be expected. Nevertheless, OES can only yield data while the discharge volume is emitting a sufficient amount of light. At the end of this observation interval ($t = 50\,\text{ns}$), a substantial amount of energy is stored in the vibrational excitation of the gas molecules. Eventually, vibrational relaxation will transfer this energy to heat and increase the (translational) gas temperature further.

Further, we found that the discharge diameter is $130 \pm 10\,\mu\text{m}$ and is also independent of E and D. This quantity and its relation with other radii than can be measured will be discussed at the end of section 4.2.

***Table 2**: Parameters for the numerical simulations. Bold values indicate the parameter which was held constant for a set of simulations. For all simulations the source time (discharge duration) was kept constant at 50 ns and the spark length (electrode distance) was 1.2 mm. SE – source energy, SW – source width, ST – source time, E/MIE – discharge energy normalized by minimum ignition energy, V – discharge volume, D – energy density.*

Input parameters			Derived parameters		
$SE/(J/m)$	SW/m	ST/s	E/MIE	V/m^3	$D/(J/m^3)$
$\mathbf{1.333\cdot10^{-1}}$	$9.000\cdot10^{-5}$	$5.000\cdot10^{-8}$	2.00	$3.05\cdot10^{-11}$	$5.24\cdot10^{6}$
$\mathbf{1.333\cdot10^{-1}}$	$1.000\cdot10^{-4}$	$5.000\cdot10^{-8}$	2.00	$3.77\cdot10^{-11}$	$4.24\cdot10^{6}$
$\mathbf{1.333\cdot10^{-1}}$	$1.250\cdot10^{-4}$	$5.000\cdot10^{-8}$	2.00	$5.89\cdot10^{-11}$	$2.72\cdot10^{6}$
$\mathbf{1.333\cdot10^{-1}}$	$1.500\cdot10^{-4}$	$5.000\cdot10^{-8}$	2.00	$8.48\cdot10^{-11}$	$1.89\cdot10^{6}$
$8.920\cdot10^{-2}$	$8.500\cdot10^{-5}$	$5.000\cdot10^{-8}$	1.34	$2.72\cdot10^{-11}$	$\mathbf{3.93\cdot10^{6}}$
$1.000\cdot10^{-1}$	$9.000\cdot10^{-5}$	$5.000\cdot10^{-8}$	1.50	$3.05\cdot10^{-11}$	$\mathbf{3.93\cdot10^{6}}$
$1.235\cdot10^{-1}$	$1.000\cdot10^{-4}$	$5.000\cdot10^{-8}$	1.85	$3.77\cdot10^{-11}$	$\mathbf{3.93\cdot10^{6}}$
$1.494\cdot10^{-1}$	$1.100\cdot10^{-4}$	$5.000\cdot10^{-8}$	2.24	$4.56\cdot10^{-11}$	$\mathbf{3.93\cdot10^{6}}$
$1.929\cdot10^{-1}$	$1.250\cdot10^{-4}$	$5.000\cdot10^{-8}$	2.89	$5.89\cdot10^{-11}$	$\mathbf{3.93\cdot10^{6}}$
$2.778\cdot10^{-1}$	$1.500\cdot10^{-4}$	$5.000\cdot10^{-8}$	4.17	$8.48\cdot10^{-11}$	$\mathbf{3.93\cdot10^{6}}$
$4.938\cdot10^{-1}$	$2.000\cdot10^{-4}$	$5.000\cdot10^{-8}$	7.41	$1.51\cdot10^{-10}$	$\mathbf{3.93\cdot10^{6}}$
$1.000\cdot10^{-1}$	$\mathbf{1.000\cdot10^{-4}}$	$5.000\cdot10^{-8}$	1.50	$3.77\cdot10^{-11}$	$3.18\cdot10^{6}$
$1.333\cdot10^{-1}$	$\mathbf{1.000\cdot10^{-4}}$	$5.000\cdot10^{-8}$	2.00	$3.77\cdot10^{-11}$	$4.24\cdot10^{6}$
$1.933\cdot10^{-1}$	$\mathbf{1.000\cdot10^{-4}}$	$5.000\cdot10^{-8}$	2.90	$3.77\cdot10^{-11}$	$6.15\cdot10^{6}$

4.2 Expansion of the hot kernel and pressure wave

Schlieren images depicting the gas-dynamic processes following a discharge are shown in fig. 2. Here, the experiment was carried out in the propane/air mixture several times and the time at which the schlieren image was taken was varied. A rapid growth of the kernel occurs during 1 µs following the discharge. After 0.5 µs to 1 µs, a pressure wave detaches from the expanding kernel. Its initially cylindrical shape changes to a nearly spherical shape during its propagation. The bottom row of fig. 2 (7.5 µs to 1000 µs) illustrates how the flow induced by the discharge interacts with the kernel.

Figure 3 shows the kernel radius and the reduced pressure wave radius extracted from schlieren images similar to those in fig. 2 for the case of discharges in air at a constant electrode distance of 0.5 mm and varying discharge energy. Here, the reduced pressure wave radius $r_{\mathrm{PW,\,red}}$ is the difference of the pressure wave radius r_{PW} to the radius of a sound wave traveling at speed c, thus $r_{\mathrm{PW,\,red}} = r_{\mathrm{PW}} - ct$. Figure 3a confirms the two-step expansion of the gas kernel with a rapid growth for 1 µs and a much slower growth afterwards (note the logarithmic time axis). Increasing the discharge energy yields a faster expansion of the kernel and an increased kernel radius even at very early time steps. For higher energies, a temporary reduction of the radius is evident between 1 µs and 10 µs. This is due to the gas flow which constricts the kernel in the centre (cf. fig. 2). When the energy density is varied while the discharge energy is kept constant, no significant effect on the expansion of the gas kernel and the pressure wave is found (Essmann et al., 2016).

Figure 4 depicts the initial radius of the hot gas kernel yielded from schlieren images for a range of electrode distances and discharge energies. Here, the initial radius was defined as the mean value of radii measured at up to 200 ns after the discharge. During this time interval, the radius in the schlieren images is nearly constant (cf. fig. 3a). Clearly, there is a dependency of the initial radius on the discharge energy. The series of measurements represented as green triangles was performed to examine the influence of the energy density. Here, the energy was kept constant and the electrode distance was varied. The energy density changed accordingly. All data points within this subset overlap considering

DOI: 10.7795/810.20200724

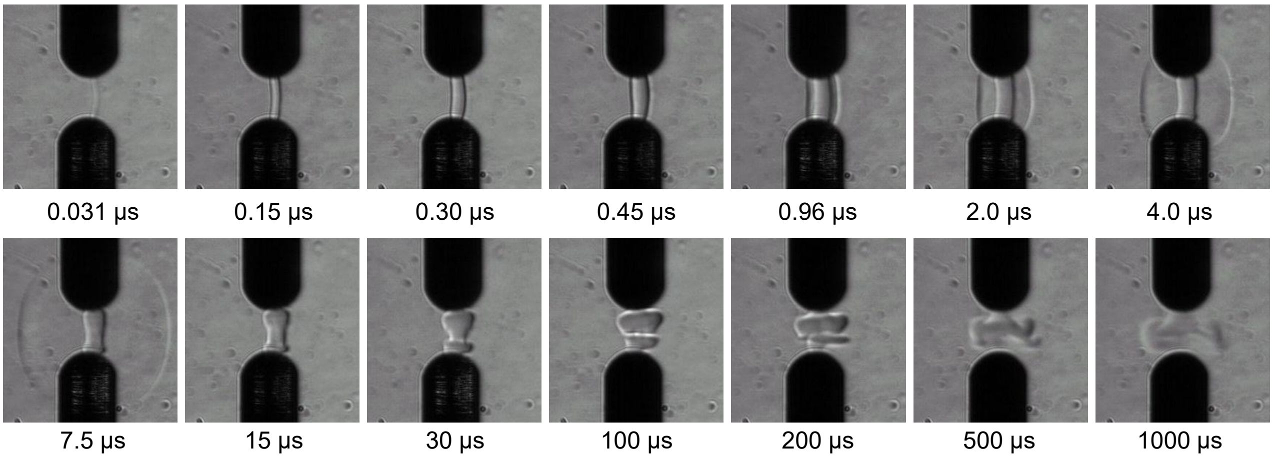

***Fig. 2**: Series of single-shot schlieren images showing the expansion of the hot gas kernel and the pressure wave after an electrical discharge ($E = 241\,\mu J$) in a 5.2 vol. % propane/air mixture (Essmann et al., 2016). The electrode distance is 1.7 mm.*

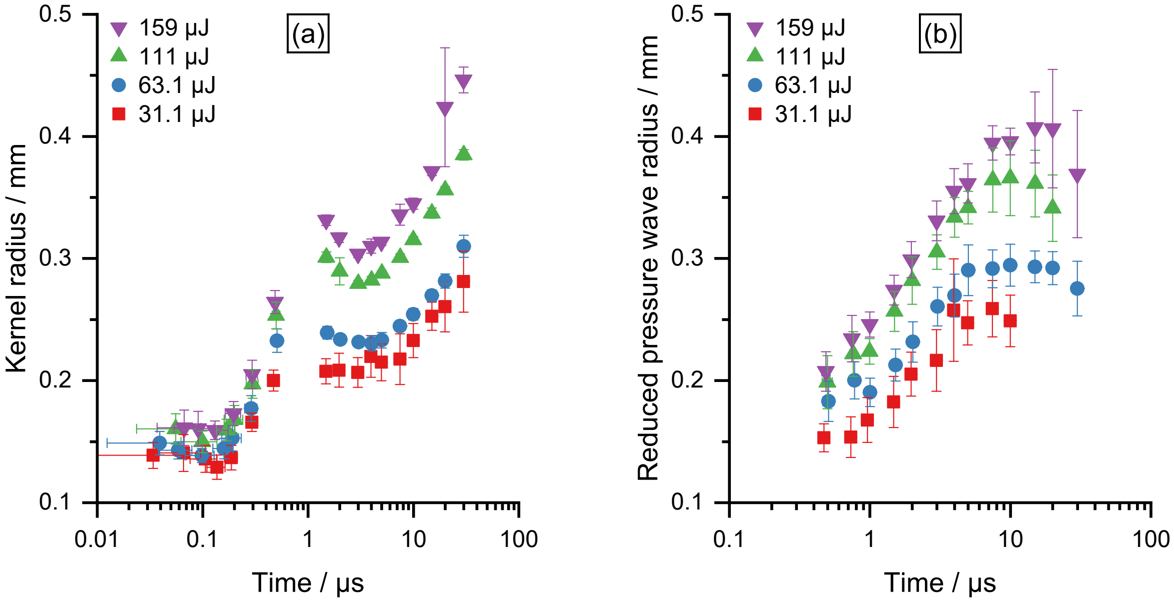

***Fig. 3**: Expansion of the hot gas kernel and the pressure wave following an electrical discharge in air (0.5 mm electrode distance). (a) Kernel radius, (b) reduced pressure wave radius (Markus et al., 2017).*

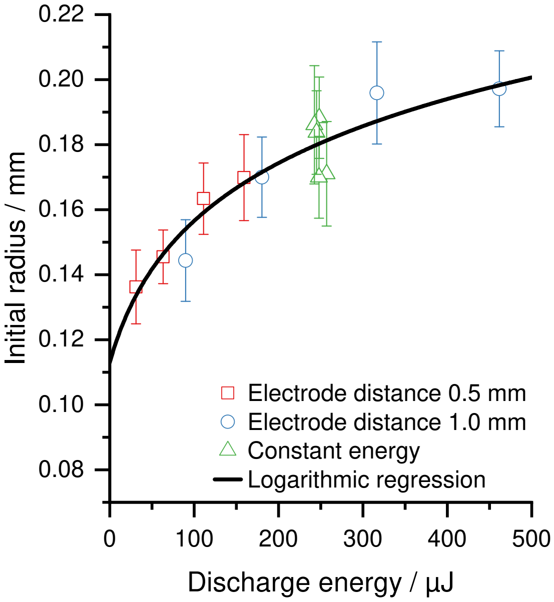

Fig. 4: *Initial radius of the hot kernel after a discharge in air, measured at times up to 200 ns after the discharge (Markus et al., 2017).*

the margin of error. Thus, the initial radius is a function of the discharge energy, but not of the energy density.

At first glance, these results are contradictory to the measurements of the discharge radius via OES. However, the measurement quantity is not the same: OES measurements yield the radius of the light emitting plasma channel while the schlieren signal is based on the temperature gradient (assuming constant pressure). The width of the radial temperature distribution corresponds to the heavy particles and can be much wider than the width of the electron density distribution (Leipold et al., 2000). For ignition processes, the gas temperature is the appropriate parameter to consider, though radical generation in the plasma column has been shown to play an important role in some cases (Langer et al., 2011, Castela et al., 2016).

4.3 Energy balance in the discharge volume

Combining the results from OES and schlieren, we analyse the energy balance in the discharge volume qualitatively. We assume that the energy input phase by the discharge is finished. Further, we assume there is a cylindrical volume $V_0 = L\pi r_0^2$ heated to a spatially uniform temperature T_0, where L is the length of the spark (equal to the electrode distance) and r_0 is the initial radius (corresponding to the temperature profile). We are interested in the change in temperature over time. In terms of rate of heat transfer, there is a loss term due to heat transfer to the electrodes and the cold gas surrounding the hot channel. For the sake of simplicity, these rates of heat transfer are combined to a term $\dot{Q}$. Its magnitude is proportional to the temperature difference to the surrounding ΔT and the surface area of the gas kernel A, $\dot{Q} \sim A \cdot \Delta T$. On the other hand, there is a heat production term stemming from the combustion, $\dot{R}$. It depends on the temperature in the hot volume in a non-linear fashion described by the Arrhenius relation. In practice, the reaction speed and thus the heat release rate will increase substantially with T. Radiation is neglected since absolute temperatures are not high during the flame initiation process. The sum of these rates of heat transfer leads to a temperature change in the heated gas volume which is inversely proportional to the heat capacity c_p and the mass $m = \rho V$.

We now consider the evolution of temperature in two such gas kernels following discharges at different energies. This is shown schematically in fig. 5. Here, the discharge energy of the upper kernel was larger than that of the lower kernel ($E_1 > E_2$). From the experimental results we know that at the end of the energy input the temperature in both gas kernels is similar, as indicated by the red colouring. The experimental results also showed that the radius and thus the volume is not equal: the upper kernel

DOI: 10.7795/810.20200724

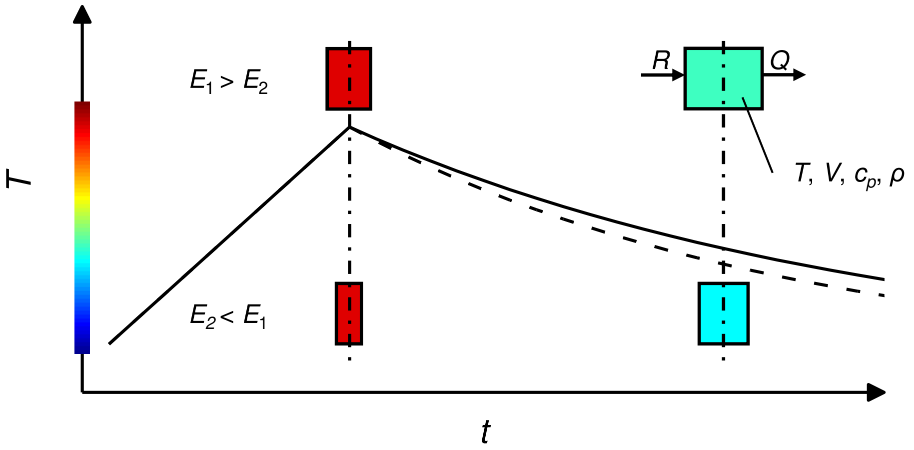

***Fig. 5**: Qualitative evolution of the temperature in two gas kernels following discharges with different energies, E_1 (upper kernel) and E_2 (lower kernel), where $E_1 > E_2$. The kernels are coloured according to their temperature as indicated by the colourbar.*

has a larger volume than the lower kernel. Thus, the rates of heat transfer due to chemical reactions and heat transfer to the surrounding are also similar for both kernels.[1] Therefore, when estimating the change in temperature, all inputs are equal except for the volume. Hence, the lower kernel will cool faster than the upper kernel, as indicated in fig. 5. In the further process, the heat release rate due to chemical reactions will be larger in the upper kernel. There will also be a higher rate of heat transfer to the surrounding. Nevertheless, $\dot{R}$ grows more strongly with temperature than $\dot{Q}$ and, eventually, the temperature will rise. Meanwhile, the radius of both kernels will increase further over time (as sketched in fig. 5); yet, the upper kernel will always be larger than the blue one (cf. fig. 3a).

An important aspect is that the energy in both cases is near the MIE. If the energy were much higher, for instance ten times the MIE, then ignition would occur during the energy deposition phase. This is the ignition regime that is intended in internal combustion engines. In addition, the spark duration of widely-used spark plugs is longer by orders of magnitude. Hence, this kind of treatment would not be adequate for a spark ignition engine.

To sum up, an increase in discharge energy will lead to a more probable ignition. However, this is not directly due to a higher temperature of the produced kernel. Instead, the kernel volume is increased while the temperature stays approximately equal (cf. fig. 4). The larger kernel volume leads to a slower temperature decrease and consequently to faster chemical reactions, facilitating an ignition. In the following section, this qualitative analysis is complemented by numerical simulations so as to gain a quantitative understanding.

4.4 Numerical simulation of the ignition process

Using the numerical model described in section 3, simulations of the ignition process in an 8.0 vol. % ethene/air mixture were carried out. The input parameters were chosen in a range according to the experiment. We systematically varied the the discharge energy E, initial radius r_0, and the energy density D as laid out in table 2. Figures 6 to 8 show the maximum OH mole fraction as an indicator of the progress of the chemical reaction and the maximum temperature in the domain, both as a function of time.

The results for constant energy are displayed in fig. 6. Here, the initial radius was varied and the energy density changed accordingly. A decrease of the initial radius results in a higher energy density. Therefore, the temperature increase is faster and a higher maximum value is reached. After 50 ns, the energy deposition stops and the gas begins to cool. The cooling rate is higher for the smaller radii

---

[1] This is not entirely true, as the heat loss term also depends on the surface area of the kernel which is larger for the higher-energy kernel. However, the change in temperature due to Q is larger for the smaller kernel since its ratio of surface area to volume is larger.

DOI: 10.7795/810.20200724

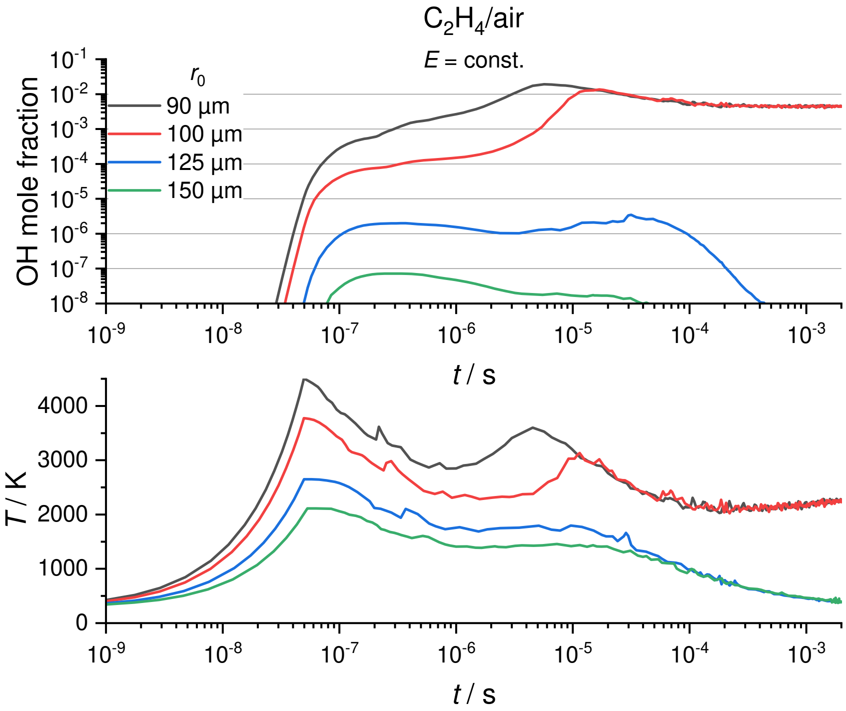

Fig. 6*: Simulation results for constant energy. Top: Maximum OH mole fraction in the domain. Bottom: Maximum temperature in the domain.*

due to the increased temperature difference to the surrounding. However, the absolute temperature is still increased. For smaller initial radii, the onset of OH production occurs at an earlier time. Due to the increased temperature, the OH mole fraction increases faster and to a higher level. After approximately 10^{-5} s, a peak in the OH mole fraction and a second peak in the temperature is observed for $r_0 = 90\,\mu\text{m}$ and $100\,\mu\text{m}$, indicating that ignition has taken place. For $r_0 = 125\,\mu\text{m}$ and $150\,\mu\text{m}$, the temperature and OH mole fraction decline and no ignition occurs. After 10^{-4} s, the source has no more influence on the temperature in the system.

Figure 7 shows the results for constant initial radius and varying discharge energy. This case is straightforward: A higher discharge energy results in a faster temperature rise and an increased maximum temperature. Also, the OH mole fraction increases earlier and reaches a higher maximum value. Thus, ignition becomes more likely when the energy is increased at constant initial radius. While the case $E = 1.5\,\text{MIE}$ does not show ignition, the other cases exhibit two dissimilar modes of ignition: At $E = 2.9\,\text{MIE}$ the energy is sufficient to ignite the mixture immediately. At $E = 2.0\,\text{MIE}$, on the other hand, ignition is delayed to 10^{-6} s to 10^{-5} s. This indicates that the heat flux from the hot kernel to the outside is similar in magnitude to the heat release due to chemistry.

The case of constant energy density is presented in fig. 8. Here, the initial radius was varied and the discharge energy was changed accordingly to keep the energy density constant. First, the time evolution of the maximum temperature is analysed. During the energy input phase, the temperature is equal for all cases. From 10^{-7} s to 10^{-6} s the temperature decreases. This decrease is similar for all cases, but there is a tendency that cooling is stronger for cases with smaller initial radii. At $2 \cdot 10^{-6}$ s to $5 \cdot 10^{-6}$ s the temperature rises again. Now, large differences become visible. The temperature rise is stronger and occurs earlier when the initial radius is large. The plot of OH mole fraction aids in explaining this behaviour. Starting from 10^{-7} s, the OH mole fraction is higher for larger r_0. This correlates with the slightly higher temperature and results in faster heat release from the chemical reactions. This process is self-enforcing, so the differences grow quickly. Between 10^{-6} s to 10^{-5} s a rapid rise of OH indicates the ignition. The ignition takes place at an earlier time for large r_0. There appears to be a critical radius between $r_0 = 85\,\mu\text{m}$ and $90\,\mu\text{m}$ where the behaviour changes dramatically. For the smallest initial radius shown, the OH production is minuscule, accordingly the heat release is low and the temperature drops to the ambient value – no ignition occurs.

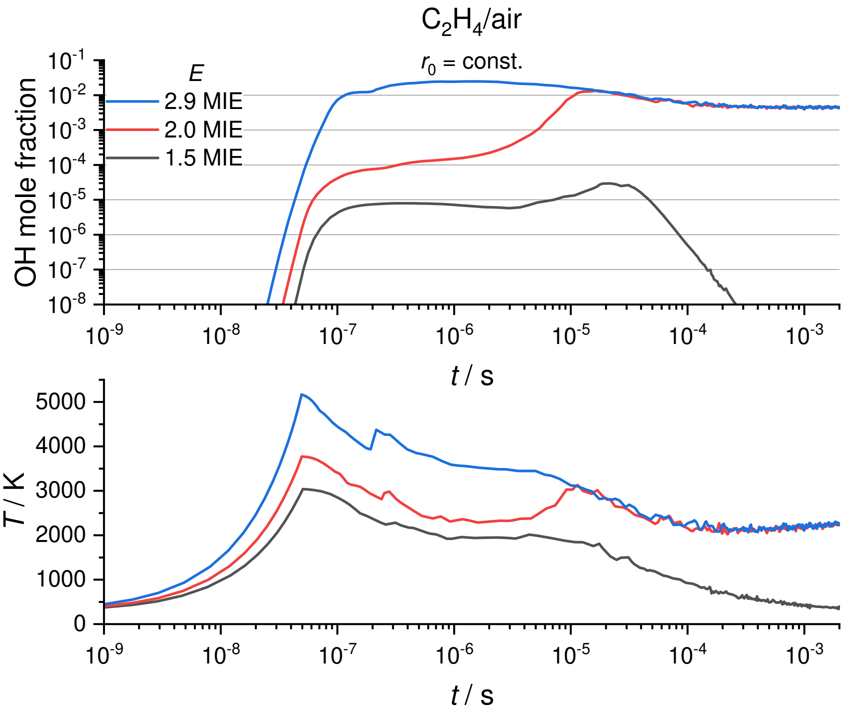

Fig. 7*: Simulation results for constant initial radius. Top: Maximum OH mole fraction in the domain. Bottom: Maximum temperature in the domain.*

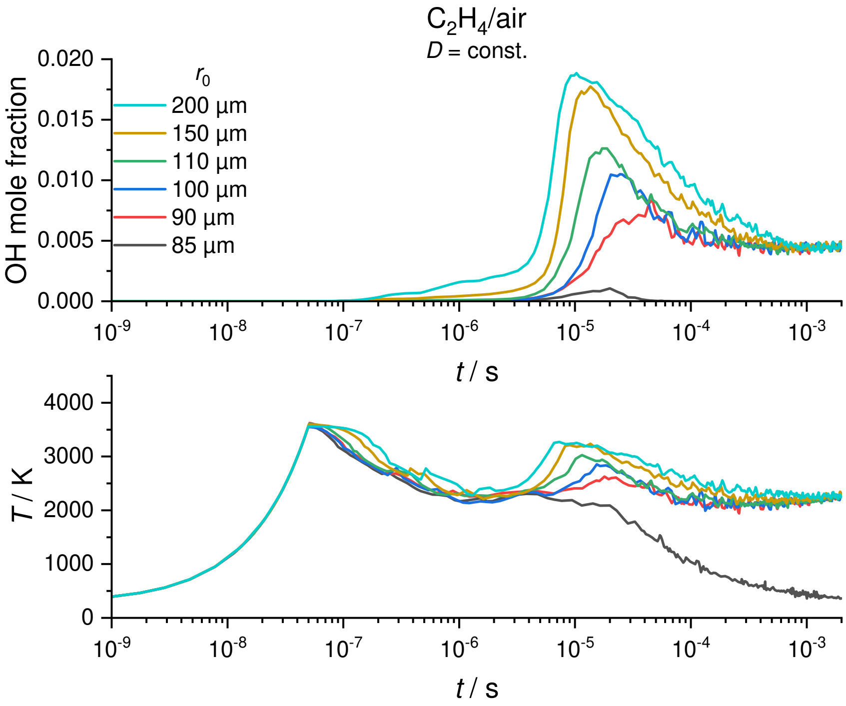

Fig. 8*: Simulation results for constant energy density. Top: Maximum OH mole fraction in the domain. Bottom: Maximum temperature in the domain.*

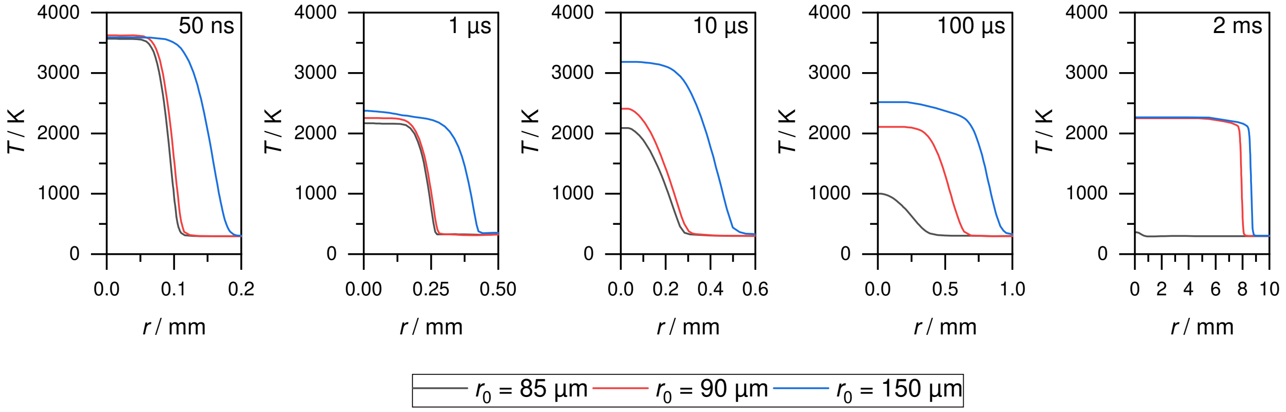

***Fig. 9**: Radial temperature profiles for simulations with constant energy density and different initial radii at several time instances*

Recalling the experimental results, the case of constant energy density seems to be one that is most likely applicable. Here, the energy increase is compensated by an accompanying increase of the initial radius. Thus, the temperature at the end of the discharge is not a function of the discharge energy. The greater volume-to-surface-area-ratio of larger kernels reduces the heat loss to the surrounding, allowing more time at a higher temperature for the chemical reactions to generate a sufficient rate of heat release for the kernel to transition to a self-sustained flame.

The case of constant energy density will be analysed in more detail using the radial temperature profiles shown in fig. 9. For three initial radii, corresponding to a case just below the ignition threshold ($r_0 = 85\,\mu\text{m}$), one just above ($r_0 = 90\,\mu\text{m}$) and one well above this threshold ($r_0 = 150\,\mu\text{m}$), such profiles are shown for five time steps during the evolution of the kernel:

1. $t = 50\,\text{ns}$ marks the end of energy input. The maximum temperature is equal for all cases (minor deviations are due to slightly different time instances actually output during the simulation) and the radius is, in essence, still the initial radius.
2. $t = 1\,\mu\text{s}$ is near the time when cooling and heat production from the chemical reactions are equal in magnitude (cf. fig. 8). The temperature difference between $r_0 = 85\,\mu\text{m}$ and $90\,\mu\text{m}$ is about $90\,\text{K}$ and the difference of the kernel radius is still about $5\,\mu\text{m}$.
3. $t = 10\,\mu\text{s}$ is close to the second temperature maximum in fig. 8. While the temperature in the $r_0 = 85\,\mu\text{m}$ case is reduced by a small amount, there is an appreciable temperature rise for $r_0 = 90\,\mu\text{m}$. Also, the radius difference has become larger.
4. $t = 100\,\mu\text{s}$ is a point in time during the transition to a self-sustained flame. By now, the initially small differences have amplified to totally different outcomes between the three case.
5. $t = 2\,\text{ms}$ marks the end of the simulation with a fully-developed flame. The profiles for $r_0 = 90\,\mu\text{m}$ and $150\,\mu\text{m}$ are similar, but the radius difference is now $700\,\mu\text{m}$, much larger than the $60\,\mu\text{m}$ in the beginning. In the $r_0 = 85\,\mu\text{m}$ case, the temperature has nearly returned to the ambient temperature.

Sloane (1990a) performed a similar simulation for methane-air mixtures. He likewise found that a non-ignition case could be turned into an ignition-case by depositing the same energy density over a larger region. Sloane argued that the H radical is an important parameter to consider: The “temperature falls more slowly and the rate of build-up of H atoms is faster. The H atoms are lost more slowly by diffusion because of the smaller concentration gradient near the centre of the larger ignition kernel” (Sloane, 1990a). However, no experimental data was available at this time to compare the results regarding this specific issue.

Figure 10 shows radial profiles of the H molar fraction for the same simulations as in fig. 9. Overall, the profiles tell the same story as the temperature profiles in fig. 9. Clearly, the temperature and H molar fraction are closely linked quantities. On the other hand, it is not immediately clear whether the H concentration follows temperature or vice versa.

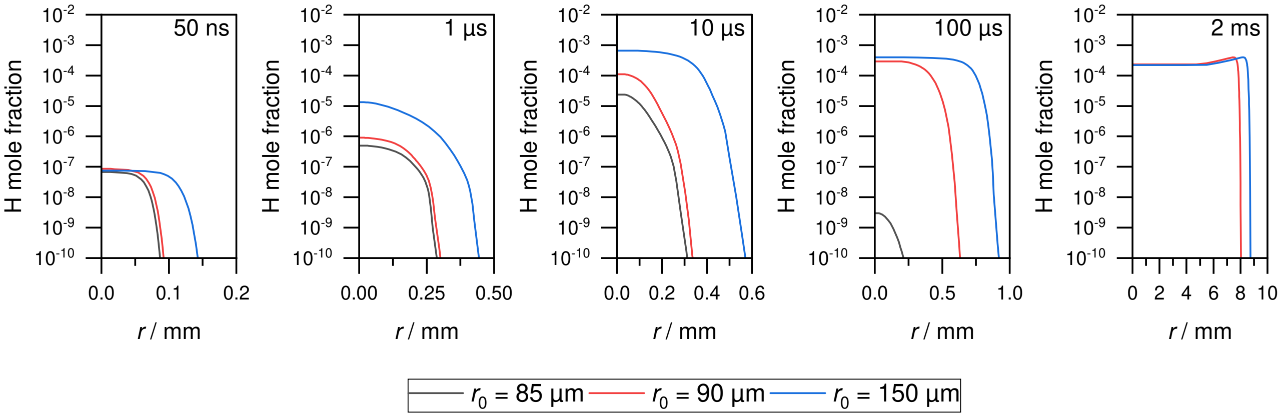

***Fig. 10**: Radial profiles of the H molar fraction for simulations with constant energy density and different initial radii at several time instances*

4.5 Early phase of flame propagation

After the kernel has been ignited, it expands spherically. The early phase of propagation of ethene/air flames was analysed via high-speed schlieren imaging and single-shot OH-LIF. The kernel radius extracted from schlieren images is shown in fig. 11a. For each discharge energy (expressed here in terms of the MIE) several ignition experiments were performed. The dashed lines indicate data from single experiments and the average values for each energy are plotted as solid, bold lines. The effect of energy is clearly visible: an increase leads to a faster kernel growth, especially within the first 100 µs. Also, the ignition process becomes more repeatable, as can be seen by the large scatter between individual experiments at $E/\mathrm{MIE} = 1.5$. The scatter reduces as the energy is increased. Figure 11b shows the temporal derivative of the average curves in fig. 11a plotted over the kernel radius. Three phases of flame propagation can be identified. First, an over-driven phase where the propagation speed is dominated by the electrical discharge, second, a transitional phase, and third, a phase where the propagation speed is independent of the ignition source and only determined by chemistry and flame stretch. The first phase – termed *spark-assisted flame propagation* by Bradley & Lung (1987) – affirms once more that the discharge energy is not consumed solely for heating the gas volume but also contributes to the kernel growth by means of gas-dynamic expansion.

While the high-speed schlieren images are useful to investigate the time-dependent evolution of the kernel, their information is limited to the kernel radius. The radial distribution of OH in the kernel yields information about its internal structure. Figure 12 shows the radial intensity profile of single-shot OH-LIF experiments for two discharge energies at three time steps. The first time step ($t = 40\,\mu\mathrm{s}$) corresponds to the rapid growth phase of the cylindrical kernel before detachment of the pressure wave; the second one ($t = 130\,\mu\mathrm{s}$) is near the end of the first phase of flame propagation (spark-assisted regime); and the third one ($t = 580\,\mu\mathrm{s}$) is in the transitional phase where the propagation speed is still influenced by the ignition source. At $t = 40\,\mu\mathrm{s}$ the profiles appear bell-shaped. The maximum intensity and the radius of the distribution are enhanced at larger discharge energy. This suggests faster production of OH radicals and a faster expansion of the kernel which matches the previously discussed experimental data and the results from the numerical simulations. At $t = 130\,\mu\mathrm{s}$, the difference in flame radius is further increased. The maximum OH intensity of the lower-energy case approaches that of the higher-energy case. At $t = 580\,\mu\mathrm{s}$, the difference in flame radius does not change by a large amount with respect to the previous time step. The radial OH profiles start to appear like those of a fully-developed laminar flame with steep gradients at the flame front and a gentle decay in the centre region (Berglind & Sunner, 1986, Dreizler et al., 2000). However, at least the data for $E/\mathrm{MIE} = 2.0$ must be viewed with caution since it is single-shot data from different realizations of the experiment. As fig. 11 shows, the amount of variation is significant in this case. Still, this data provides important insights as to the structure of the flame kernels at different energies.

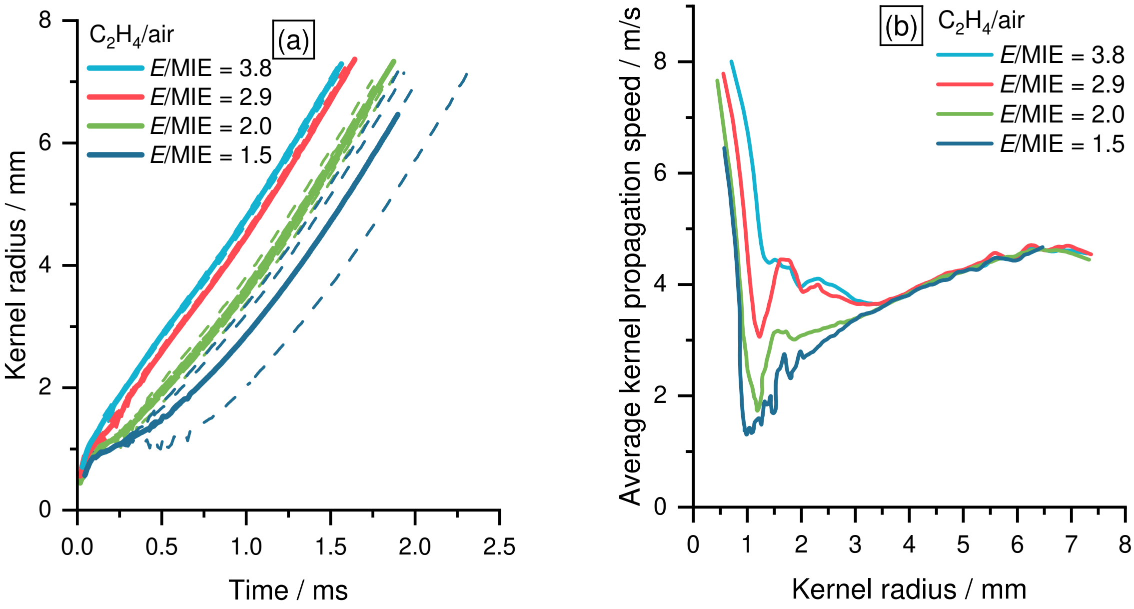

***Fig. 11**: Expansion of the kernel in an 8.0 vol. % ethene/air mixture after ignition by an electrical discharge for several ignition energies close to the minimum ignition energy. (a) Kernel radius as a function of time after discharge, extracted from schlieren images. The dashed lines indicate individual experiments; solid, bold lines indicate the respective average values. (b) Average kernel propagation speed as a function of the kernel radius, based on the average values (Essmann et al., 2020).*

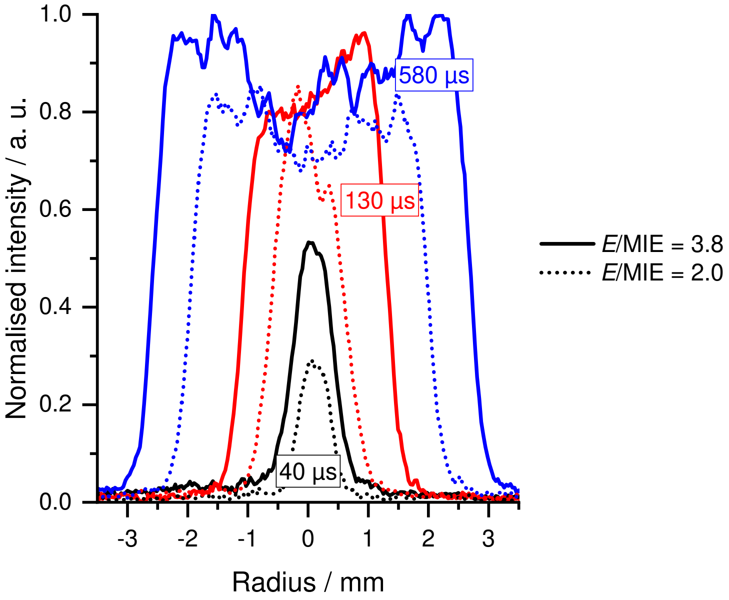

***Fig. 12**: OH-LIF signal intensity in flame kernels in 8.0 vol. % ethene/air for two ignition energies*

5 Conclusions

The ignition of combustible gas/air mixtures by electrical discharges at energies close to the MIE was investigated experimentally and numerically. Optical emission spectroscopy was employed to study the discharge diameter and the temperatures of the plasma. Here, no clear dependency on the discharge energy were found. Schlieren measurements of the gas-dynamic expansion of the hot kernel and the pressure wave created by the discharge evidenced that higher discharge energies lead to a faster expansion of the kernel. Also, the kernel radius at very early time steps is influenced by the energy. Based on these results, a qualitative analysis of the energy balance and the temperature evolution inside the kernel was performed. The analysis is able to explain how an increase in energy yields a higher chance of ignition even though the temperature after the discharge is not increased. To further study this process, we performed numerical simulations assuming cylindrical symmetry while considering detailed transport processes as well as detailed chemical kinetics. The simulation parameters were chosen according to the experiment. Systematic variation of the energy, the initial radius, and the energy density was carried out. The results indicate that in the experiments, an increase in energy is accompanied by an increase of the initial radius in such a way that the energy density stays approximately constant. However, the larger kernel cools down more slowly and is more likely to ignite the mixture. Finally, experimental results concerning the early phase of flame propagation after an ignition were presented. Data from high-speed schlieren imaging revealed the limited repeatability at low energy and the propagation of the kernel in three phases. Radial profiles of the OH-LIF intensity allowed for an analysis of the kernel structure at several time steps during this early stage.

In combination, our results present a detailed analysis of the ignition process by electrical discharges close to the MIE. Further research will target the time-resolved temperature field induced by the discharge. This will be achieved via background oriented schlieren (BOS). In addition, OH-LIF experiments will be carried out at 50 kHz to account for the variation of the ignition process at low energies.

Acknowledgements

The authors gratefully acknowledge the financial contribution from the Deutsche Forschungsgemeinschaft (DFG) through grant FOR 1447.

References

Bane, S. P. M. (2010). *Spark ignition: experimental and numerical investigation with application to aviation safety*. Ph.D. thesis, California Institute of Technology.

Berglind, T., Sunner, J. (1986). *The temporal development of OH-concentration profiles in ignition kernels studied by single-pulse laser induced fluorescence*. Combustion and Flame, 63:279–288.

Bradley, D., Lung, F. K.-K. (1987). *Spark ignition and the early stages of turbulent flame propagation*. Combustion and Flame, 69:71–93.

Brandes, E., Möller, W. (2008). *Flammable liquids and gases: Brennbare Flüssigkeiten und Gase*, volume 1 of *Safety characteristic data*. Wirtschaftsverl. NW, Bremerhaven, 2 edition. ISBN 978-3-86509-811-5.

Castela, M., Fiorina, B., Coussement, A., Gicquel, O., Darabiha, N., Laux, C. O. (2016). *Modelling the impact of non-equilibrium discharges on reactive mixtures for simulations of plasma-assisted ignition in turbulent flows*. Combustion and Flame, 166:133–147.

Dreizler, A., Lindenmaier, S., Maas, U., Hult, J., Aldén, M., Kaminski, C. F. (2000). *Characterisation of a spark ignition system by planar laser-induced fluorescence of OH at high repetition rates and comparison with chemical kinetic calculations*. Applied Physics B: Lasers and Optics, 70:287–294.

Eckhoff, R. K., Ngo, M., Olsen, W. (2010). *On the minimum ignition energy (MIE) for propane/air*. Journal of Hazardous Materials, 175:293–297.

Essmann, S., Kummer, J.-R., Markus, D., Maas, U. (2018a). *Experimental and numerical investigation of the ignition by electrical discharges close to the minimum ignition energy*. In *12th International Symposium on Hazards, Prevention, and Mitigation of Industrial Explosions*. Kansas City.

Essmann, S., Markus, D., Grosshans, H., Maas, U. (2020). *Experimental investigation of the stochastic early flame propagation after ignition by a low-energy electrical discharge*. Combustion and Flame, 211:44–53.

Essmann, S., Markus, D., Maas, U. (2016). *Investigation of the spark channel of electrical discharges near the minimum ignition energy*. Plasma Physics and Technology, 3:116–121.

Essmann, S., Markus, D., Maas, U. (2017). *Investigation of the Flame Kernel Propagation after Ignition by a Low Energy Electrical Discharge*. In *26th International Colloquium on the Dynamics of Explosions and Reactive Systems (ICDERS)*, page Paper 1006. Boston.

Essmann, S., Spörhase, S., Grosshans, H., Markus, D. (2018b). *Precise triggering of electrical discharges by ultraviolet laser radiation for the investigation of ignition processes*. Journal of Electrostatics, 91:34–40.

Hattwig, M., Steen, H. (2004). *Handbook of explosion prevention and protection*. Wiley-VCH, Weinheim. ISBN 978-1-28123-928-0.

Ko, Y., Anderson, R. W., Arpaci, V. S. (1991). *Spark ignition of propane-air mixtures near the minimum ignition energy: Part I. An experimental study*. Combustion and Flame, 83:75–87.

Kono, M., Niu, K., Tsukamoto, T., Ujiie, Y. (1989). *Mechanism of flame kernel formation produced by short duration sparks*. Symposium (International) on Combustion, 22:1643–1649.

Korytchenko, K. V., Essmann, S., Markus, D., Maas, U., Poklonskii, E. V. (2018). *Numerical and experimental investigation of the channel expansion of a low-energy spark in the air*. Combustion Science and Technology.

Langer, T., Markus, D., Maas, U. (2011). *Repetitive streamer discharges leading to Ignition of hydrogen/air mixtures*. Science and Technology of Energetic Materials, 72:51–56.

Laux, C. O., Spence, T. G., Kruger, C. H., Zare, R. N. (2003). *Optical diagnostics of atmospheric pressure air plasmas*. Plasma Sources Science and Technology, 12:125–138.

Leipold, F., Stark, R. H., El-Habachi, A., Schoenbach, K. H. (2000). *Electron density measurements in an atmospheric pressure air plasma by means of infrared heterodyne interferometry*. Journal of Physics D: Applied Physics, 33:2268–2273.

Lim, M. T., Anderson, R. W., Arpaci, V. S. (1987). *Prediction of spark kernel development in constant volume combustion*. Combustion and Flame, 69:303–316.

Luo, Z., Yoo, C. S., Richardson, E. S., Chen, J. H., Law, C. K., Lu, T. (2012). *Chemical explosive mode analysis for a turbulent lifted ethylene jet flame in highly-heated coflow*. Combustion and Flame, 159:265–274.

Maas, U., Warnatz, J. (1988). *Ignition processes in hydrogen-oxygen mixtures*. Combustion and Flame, 74:53–69.

Markus, D., Essmann, S., Kummer, J.-R., Shekhar, R., Uber, C., Gerlach, U., Maas, U. (2017). *Ignition by electrical discharges*. Zeitschrift für Physikalische Chemie, 231:1655–1682.

Sloane, T. M. (1990a). *Energy requirements for spherical ignitions in methane-air mixtures at different equivalence ratios*. Combustion Science and Technology, 73:351–365.

Sloane, T. M. (1990b). *Numerical simulation of electric spark ignition in atmospheric pressure methane-air mixtures*. Combustion Science and Technology, 73:367–381.

Wähner, A., Gramse, G., Langer, T., Beyer, M. (2013). *Determination of the minimum ignition energy on the basis of a statistical approach*. Journal of Loss Prevention in the Process Industries, 26:1655–1660.

DOI: 10.7795/810.20200724

Determination of the ignition temperature of flammable liquids under different initial conditions

Libor Ševčík [a], Ondřej Suchý [a]

[a] Technical Institute of Fire Protection in Prague, Fire Rescue Service of the Czech Republic

E-mail: libor.sevcik@tupo.izscr.cz, ondrej.suchy@tupo.izscr.cz

Abstract

The determination of ignition temperature under non-atmospheric conditions provides a new view on the behavior of flammable liquids under the conditions in which they are present usually today. The study of flammable substances under increased initial pressures should be studied to ensure safety in operation, equipment and other areas where flammable substances occur. In contrast to the determination of the ignition temperature in an open cup under atmospheric conditions, the determination of the ignition temperature under non-atmospheric condition is performed in a closed vessel at a constant volume without air exchange with the surroundings. These ignition temperature determinations also differ in the way of determination. Papp, et al. (2012) describes an ignition criterion in a closed vessel as a temperature increase of at least 50 °C and a pressure increase of at least 10 %.

This article describes the determination and evaluation of ignition temperatures of two commonly used flammable liquids, on which the effect of initial pressure and oxygen concentration was tested. On these two parameters, the test equipment developed by us was tested and verified by comparing selected values with literature and with results from our cooperating organization PTB Braunschweig. Our test equipment is made of stainless steel, which is a suitable material to guarantee the safety of operation in the test vessel. During the tests, we confirmed the effect of increased initial pressures on the ignition temperatures. In our experiments, we also found under what non-atmospheric conditions flammable liquids can cause fire, loss of life, personal injury and property damage. There is currently no standard to determine the ignition temperature of flammable liquids in a closed vessel.

Keywords: *ignition temperature, non-atmospheric condition, closed vessel, pressure, oxidant*

1. Introduction

Many industrial processes are now operated under increased pressures. It is known that the ignition temperature of a mixture of flammable liquids and air decreases with increasing pressure.

Brandes et. al. (2005) wrote that according to Semenoff's theory, the dependence between the pressure of the mixture and the ignition temperature is expressed in relation (1):

$$p = k.T^{\left(\frac{2}{n}+1\right)}.exp\left(\frac{E_A}{RT}\right) \tag{1}$$

where	p	is pressure fuel/air mixture
	T	is autoignition temperature fuel/air mixture
	E_A	is an apparent activation energy
	n	is the overall reaction order (usually assumed to be 2).
	k	is speed constant
	R	is gas constant

The ignition delay time is expressed by the reaction value according to the following Arrhenius-like relation (2):

$$\tau \sim \frac{k}{p^n} .exp\left(\frac{E_A}{RT}\right) \tag{2}$$

where τ is ignition delay time

At higher pressures the expected ignition temperature is lower and the ignition time is longer. In some cases, the determinated ignition temperatures in a closed vessel are significantly lower at a pressure of 100 kPa compared to the determinated ignition temperatures by standardised methods (e.g. EN 14 522, IEC 60079-20-1). These methods use an open cup, and therefore the ambient pressure is constant. As an ignition criterion, they use a visible flame. For our determination in a closed vessel, the ignition criterion is a sharp increase in temperature and a sharp increase in pressure. Series of substances have ignition temperature in an open cup between (300 to 450) °C. Especially esters and ketones show a significant decrease of the ignition temperature in closed vessel compared to an open vessel (Papp, et al., 2012).

2. Experiments

2.1 Test vessel

The Technical Institute of Fire Protection has a 1 dm^3 test vessel. The test vessel allows measuring of the ignition temperature of flammable liquids up to an initial pressure of 5 MPa and is designed to a maximum operating temperature up to 450 °C and a maximum pressure of 44.5 MPa. This vessel was structurally modified after initial experiments, when some deficiencies were detected. We have based these adjustments on the experience and knowledge of foreign and domestic partners. The design modifications consisted of adjusting the input opening for the liquid dosage using an HPLC pump and creating two holes for thermocouples that scan the temperature in the middle and top of the pressure vessel. This design modification is apparent from the following Figure 1 (Ševčík, et al., 2018).

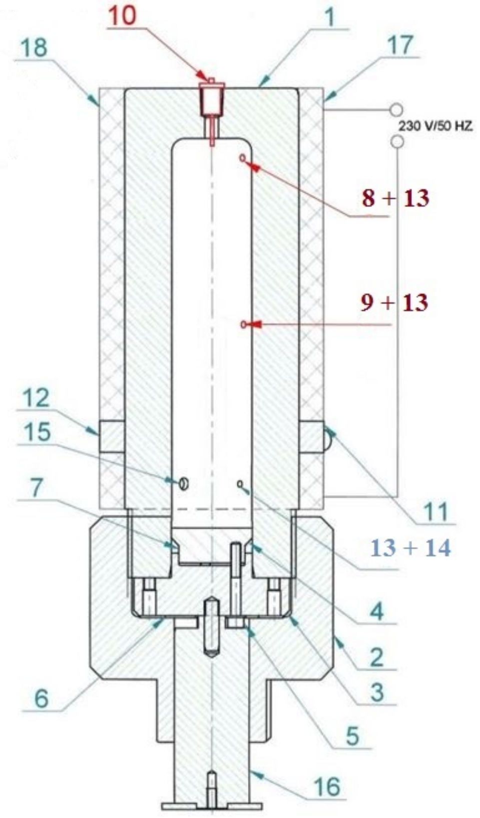

Fig. 1. *Drawing of the test vessel in the cut*

Legend: *1 - test vessel, 2 - collar nut, 3 - flat cover, 4 - internal lid, 5 - screws, 6 - duplicator in a central section, 7 - graphite trapezium gasket, 8 - thermocouple No. 1, 9 - thermocouple No. 2, 10 - armature for HPLC pump, 11 - burst membrane, 12 - valve, 13 - thermocouple pocket, 14 - thermocouple No. 3, 15 - sensor for pressure measuring, 16 - plunger, 17 - heating jacket, 18 - thermally insulating sheath, 19 - extender of the internal lid*

The temperature in the closed vessel is indicated by three thermocouples with a diameter of 1 mm, which are evenly spaced in the test vessel. The furnace is horizontally divided and consists of a fixed top and a flip bottom, which allows the mounting of a collar nut, see Figure 2. Temperature control is ensured by two programmable regulators, see Figure 3.

***Fig. 2.** Test vessel placed in the furnace*

***Fig. 3.** Temperature control*

2.2 Ignition temperature determination procedure

The determination is carried out by heating the vessel to the required temperature and subsequently by evacuating to 3 kPa. A mixture of a flammable liquid and air is dosed into the test vessel. First, the air is dispensed into the test vessel from a pressure cylinder. This is followed by spraying of the exact amount of a flammable liquid using the HPLC pump. After spraying of the flammable liquid, the ignition is determined. The time when the ignition occurs is normally within 180 seconds, therefore the interval of 300 s is sufficient to determine whether the ignition occurs or not. The lowest temperature is determined as the ignition temperature, at which the substance with air ignites. To determine the ignition temperature, it is necessary to determine at least five different concentrations of a flammable liquid. Between the measurements, the vessel is released, repeatedly evacuated and refilled with a mixture of air with a liquid after the test. Measurements with different concentrations are carried out because not all concentrations of the mixture ignite at a given temperature.

3. Results and discussion

3.1 Comparison of measurements in closed vessels

We first verified the accuracy of our measurement by comparing the set ignition temperature values for heptane at different initial pressures, see Table 1. The measured values of the Technical Institute of Fire Protection and PTB can be found a good match of the measured results. Differences are due to the size of the vessel, the shape of the test vessel, the thermocouples used, the dosing method, the amount of the spraying mixture of a flammable liquid with air, etc. Our test equipment has a volume of 1 dm^3, three thermocouples with a diameter of 1 mm and we use a three-way hand valve for dosing flammable liquid. Brandes et. al. (2005) describes the equipment of PTB, which has a volume of 0,5 dm^3, has only 2 thermocouples with a diameter of 0,5 mm and uses a pneumatic valve to dosing a flammable liquid. PTB dosed the amount of flammable liquid in the range (15 to 40) % vol., we in the range (10 to 50) % vol.

***Table 1:** Comparison of heptane ignition temperatures with PTB* (Brandes et. al., 2005)

Initial pressure p_0 [kPa]	T_{ign} [° C] (1 l vessel TÚPO)	T_{ign} [° C] (0,5 l vessel PTB)
100	218	220
200	207	201
500	203	197

We also compared our test results with the results calculated according to the equation (1). The calculated apparent activation energies under different initial pressure for heptane and pentane were in the range from 140 kJ/mol to 230 kJ/mol. We also compared our calculated results with the calculated results of Brandes et. al. (2005). Their calculated results from experimental values for pure substances (not only heptane and pentane) were in the range from 100 kJ/mol to 350 kJ/mol.

3.2 Effect of test pressure on ignition temperature

We did measurements on two flammable liquids (heptane, pentane) at different initial pressures. For our own experiments, we chose three different initial pressures of 100 kPa, 200 kPa and 500 kPa. The test samples were selected because heptane is used as a comparison liquid for methods that use an open cup. Both samples do not have such high ignition temperatures as to get to the maximum allowed temperature of our test vessel. For both flammable liquids, the ignition temperature decreased when the initial pressure increased.

***Table 2:** Comparison of ignition temperatures for heptane and pentane at different initial pressures*

Initial pressure p_0 [kPa]	T_{ign} (heptane) [° C]	T_{ign} (pentane) [° C]
100	218	258
200	207	247
500	203	232

3.3 Effect of oxygen concentration on ignition temperature

In these experiments we reduced the oxygen content in the test vessel from 21 % vol. (oxygen content in the air) to lower values. This was performed by filling the vessel first with air and refilling it with pure nitrogen. This filling was carried out by the partial pressure method. For example, at the initial pressure of 100 kPa, when 10 % vol. of a liquid was injected into the vessel, the vessel was first filled with a mixture of air and nitrogen at 90 kPa and then the liquid was injected to achieve an increase in initial pressure to 100 kPa.

We examined the minimum oxygen concentration, which still ignites the flammable mixture in the vessel. The experiments were carried out at initial pressures of 100 kPa, 200 kPa and 500 kPa. The minimum oxygen concentrations were verified by further reducing the oxygen concentration and increasing the initial temperature in the closed vessel. Under these conditions, there has been no more ignition of the test samples, see Tables 3 and 4. We didn´t carry out so many experiments for pentane, because the behavior of these two flammable liquids was similar.

The determination of the ignition temperature of flammable liquids at increased oxygen concentrations wasn´t measured because of the safety.

DOI: 10.7795/810.20200724

Table 3: *Effect of oxygen concentration on ignition temperature in heptane*

Test conditions	**100 kPa**	**200 kPa**	**500 kPa**
Vol. fraction O_2		**T_{ign} (heptane) [°C]**	
21 %	218	207	203
18 %	219	*	*
15 %	220	213	203
12 %	224	213	203
11 %	226	*	*
10 %	264 (no ignition)	*	*
9 %	-	214	209
8 %	-	217	209
7 %	-	225	215
6 %	-	231	215
5 %	-	231	220
4 %	-	270 (no ignition)	228
3 %	-	-	270 (no ignition)

Table 4: *Effect of oxygen concentration on ignition temperature in pentane*

Test conditions	**100 kPa**	**200 kPa**	**500 kPa**
Vol. fraction O_2		**T_{ign} (pentane) [°C]**	
21 %	258	247	232
18 %	259	*	*
15 %	259	251	232
12 %	264	*	*
11 %	265	*	*
10 %	293 (no ignition)	*	*
9 %	283 (no ignition)	256	233
8 %	-	*	*
7 %	-	*	*
6 %	-	257	243
5 %	-	283 (no ignition)	244
4 %	-	-	251
3 %	-	-	269 (no ignition)

Explanatory notes:

*	*non-determination*
-	*non-ignition*

DOI: 10.7795/810.20200724

4. Conclusions

The results of the measurements confirmed that the ignition temperature of flammable liquids decreases with increasing pressure in the closed vessel. It can also be noted that in the event of a decrease in the oxygen content of the air, the ignition temperature increases. We have been able to determine the minimum oxygen concentration in the air that is necessary to ignite the test samples. This concentration decreases with the pressure increases in the test vessel.

Acknowledgements

The equipment was developed as part of the research project No. VF20112015020 “Research and development of progressive methods for determinnation fire technical characteristics of flammable substances and materials under specific technological conditions” (Suchý, et al., 2015).

References

Pappp, Ch., Brandes, E., Hirsch, W., Marx, M. (2012), *Autoignition temperatures of flammable liquids in closed vessels*, IX th ISPHMIE, Cracow.

Brandes, E., Hirsch, W., Stolz, T. (2005), *Autoignition Temperature for Mixtures of Flammable Liquids with Air at Elevated Pressure*, Proceedings of the European Combustion Meeting.

Ševčík, L., Suchý, O. (2018), Method for determination of the ignition temperature of liquid substances under specific technological conditions, *Magazine 112,* (5): 8-9.

Suchý, O. et al. (2015), Research Project No. VF20112015020: Research and development of progressive methods for determination of fire technical characteristics of flammable substances and materials under specific technological conditions, Partial research task No. 1: Research and development of test methods determination and calculation estimation of the ignition temperature of solid flammable substances and flammable liquids under pressure, overpressure in the air, oxygen or other gaseous oxidant, *Final Research Report*, Prague.

DOI: 10.7795/810.20200724

Comparative study on standardized ignition sources used for explosion testing

Stefan Spitzer, Enis Askar, Arne Krietsch & Volkmar Schröder
Bundesanstalt für Materialforschung und -prüfung, Berlin, Germany
E-Mail: stefan.spitzer@bam.de

Abstract

For the determination of safety characteristics of gases, vapors and dusts different types of ignition sources are used in international standards and guidelines. Table 1 compares technical relevant ignition sources with their main features. The paper presents test results of a comparative calorimetric and visual study between four different types of ignition sources. The ignition procedures were analyzed visually with a high-speed camera and electric recordings. In addition to that, the influence of the electrode-orientation, -distance as well as ignition energy on the reproducibility of the exploding wire igniter was tested.

The exploding wire is already in use for standardized determination of safety characteristics of gases [1], first tests on the suitability of the exploding wire igniter for dust testing have been carried out by Scheid et al. [2]. Using the exploding wire, the ignition energy can be varied from 2 to 10 000 J (2 x 5 000 J) and thus it could be used for gases, vapors, dusts and hybrid mixtures. Moreover it can be used at high initial pressures and it is the only ignition source with an easily measurable ignition energy release. Furthermore, it does not introduce another chemical reaction into the system.

Finally, a proposal for a standard ignition source for explosion tests on hybrid mixtures is derived from the test results.

Keywords: *Ignition source, Exploding Wire, hybrid mixtures, safety characteristics determination*

***Table 1:** Technical relevant ignition sources*

Ignition source	Energy range [J]	Adjustable Energy	Application (example)	Used/Found in	Affecting chemical reaction	Suitable for high pressures
Exploding wire	Low to high, 2 – 5 000	Yes	Determination of LEL and UEL of gases and vapors	EN 1839 B, ASTM E918, EN ISO 10156	No	Yes, Tested up to 100 bar
Chemical igniter	Moderate to high, 100 – 10 000	No, Stepwise	Determination of LEL, p_{max}, $(dp/dt)_{max}$, (K_{St}) of dusts	EN 14034 series	Yes	Yes
Induction spark	Low, < 10 J	Yes	Determination of LEL and UEL of gases vapors	EN 1839, ASTM E681	No	No, Just up to 5 bar
Surface-gap spark	Low, 10 – 40	Yes	Determination of LOC of gases and vapors under non-atmospheric conditions	ASTM 2079	No	No, Just up to 25 bar

1. Introduction

Safety characteristics of gases, vapors and dusts are often investigated without considering the influence of the ignition source in more detail, even though it is found to have an impact on them [3, 4]. Other standards say, that the "delivered ignition energy" (= net energy) must be specified in the test report but don't give a hint how to measure it [5]. This is caused by the fact, that for most ignition sources it is hard to measure the real energy and burning duration under laboratory conditions and almost impossible during tests. Rough estimates such as the gross energy for all electrical igniters based on capacitors ($E[J] = 0.5 * C[F] * U[V]^2$ with E: Energy (Joule), C: Capacitance (Farad) and U: Voltage (Volts)) are known to be unprecise [3, 6] but are still widely used. The net energy therefore is, because of the dependence on cable resistance and length, burning duration and other technical parameters, unknown and varies between 20% to 80% of the gross energy for electrical igniters [3].

Additionally to the ignition energy that is actually introduced into a system, there are several other specifications of the ignition source that might influence the effectivity of an ignition source, particularly the ignition duration and the initial volume that is affected by the ignition source, which is also dependent from the distance and the orientation of the electrodes.

For explosion tests on dusts mainly chemical igniters are used [7]. There are standardized chemical igniters with defined energies varying from 100 J up to 10 000 J but with them the energy cannot be adjusted fluently, and the net energy that is introduced into the system (and their variation) as well as the burning duration are unknown.

For gas explosion tests, typical ignition sources are the induction spark and the exploding wire [1]. The spark ignition is probably the most common ignition source for gas explosions. It is characterized by a rather low ignition energy (< 10 J) and long ignition duration of (200 – 400) ms. Measuring the actual net ignition energy of the spark igniter is not directly possible. Contrary to the exploding wire igniter it can only be used at atmospheric or slightly elevated pressure. Using the exploding wire igniter much higher ignition energies can be realized and it is possible to calculate the actual net ignition energy in each test by measuring the ignition current and voltage, whereas the ignition duration of around 5 ms is much shorter compared to the spark ignition. The surface gap spark is another alternative ignition source mainly for gas explosion tests [5]. Considering the ignition energy, that can be realized, it is stronger, than the spark ignition, but not as strong as the exploding wire igniter. However, the ignition duration is much shorter than all other ignition sources that are considered. In this work the four types of ignition source mentioned above should be characterized experimentally. The net ignition energy introduced into the system as well as the reproducibility was compared by calorimetric measurements. The burning duration has been compared by high-speed-recordings. Finally, the influence of the orientation of the electrodes was studied for the exploding wire igniter. Based on the test results a standardized ignition source for the determination of safety characteristics of hybrid mixtures of gases and dusts is proposed.

DOI: 10.7795/810.20200724

2. Experiments

The induction spark (Fig. 1) is the most common ignition source for gas testing. It consists of a high voltage transformer with an open-circuit voltage of 15 kV and a short circuit current of 30 mA. The electrodes have a distance of 5 ± 1 mm and the burning duration is set to 200 ms [1].

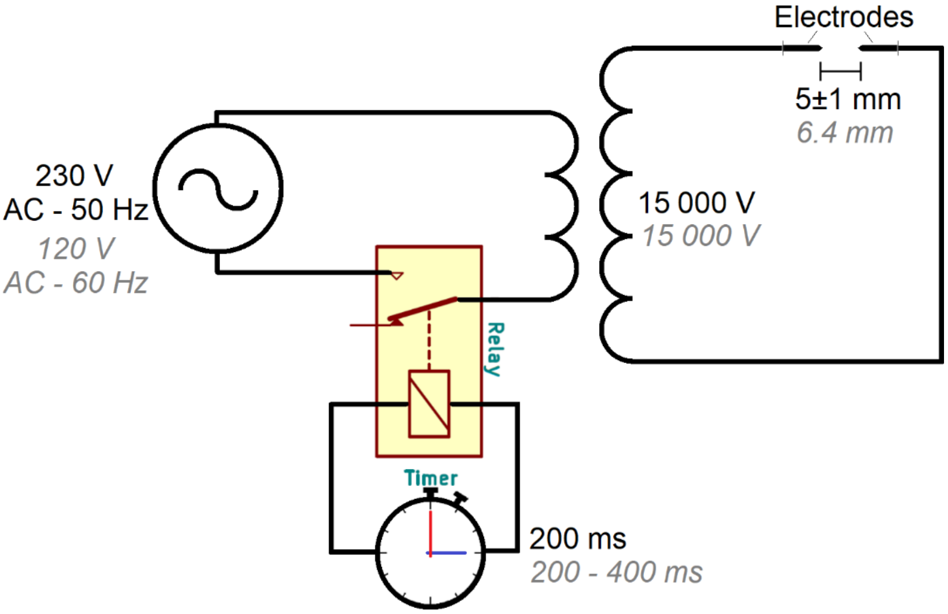

Fig. 1. *Schematic if the Induction spark with specifications according to DIN 1839:2017 [1] and ASTM E-681 [8] in italic*

The chemical igniters (Fig. 2) consist of small plastic or aluminum buckets filled with a firing charge of 40% zirconium, 30% barium nitrate and 30% barium peroxide. A sealing cap keeps the firing charge inside. An electrical fuse head is connected to two wires for a precise electrically controlled ignition from the outside of the apparatus.

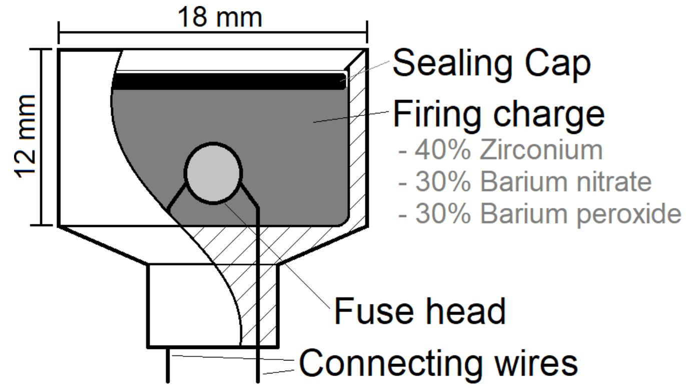

Fig. 2. *Structure of a chemical igniter*

The surface-gap spark (Fig. 3) is made of two electrodes, separated by a pencil lead mainly consisting of graphite with 6 to 10 mm in length and an electrical power supply. The emerging discrete spark is a surface discharge on the outside of the pencil lead.

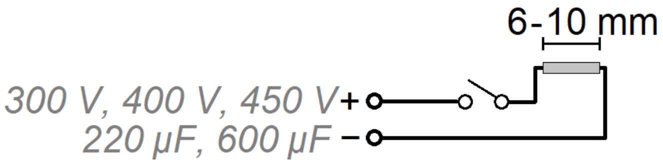

Fig. 3 *Schematic of the surface-gap spark, listed values in italic are typical but not specified*

The exploding wire consists of a copper nickel manganese alloy (CuNi30Mn) wire that is mounted between two metal rods and a power supply. An electric current is passed through the wire, melting it and generating an electric arc. Typical values specified in standards for the determination of safety characteristics of gases are an electrode diameter greater than 3 mm and an electrode distance of (5 ± 1) mm. The diameter of the connecting alloy wire shall be between 0.05 mm and 0.2 mm (typical: 0.12 mm). The electrical power for melting the wire and generating the arc is typically supplied by an alternating current isolating transformer with a power of 700 VA to 3 500 VA and a secondary voltage 230 V. The secondary winding of the transformer shall be switched by thyristors to control the time the voltage passes through the rods and the wire for adjustment of the ignition energy between 10 J and 20 J [1, 9].

For higher delivered energies of up to 2 000 J capacitors with an operating voltage of 450 V and a capacity of up to 21 000 µF are used. To achieve a comparable burning duration of 4 – 10 ms an inductor is introduced to the circuit (see Fig. 4).

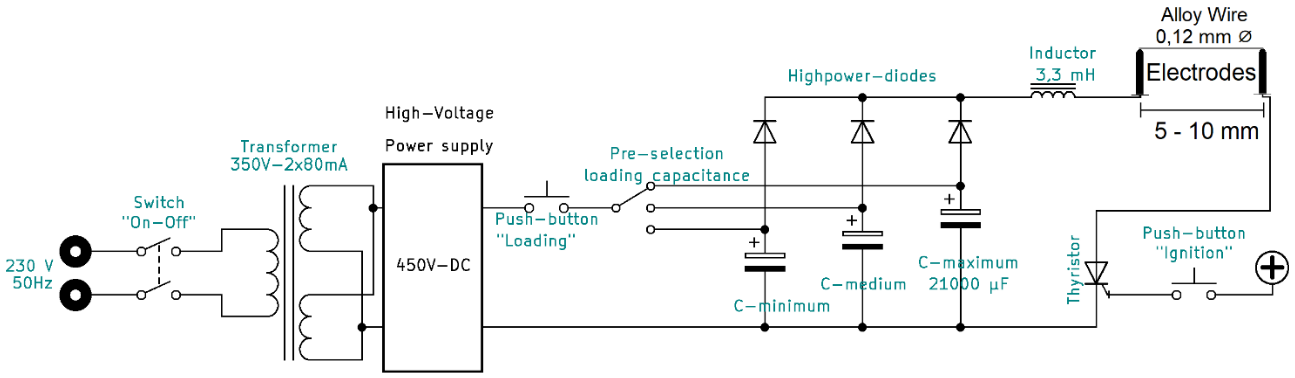

Fig. 4. Schematic of a high-energy exploding wire ignition source

Two test set-ups were built for the results presented in this paper. The first was a quasi-adiabatic calorimeter to measure the net energy and comparing it to the specified values and the electrical recordings (if available). The second was a fire-proof chamber equipped with different high-speed cameras and electrical measurement devices to capture the ignition procedures on video and measure the burning duration and net energy.

2.1 Calorimetric measurements of the net energy of different ignition sources

The calorimeter is made of brass and has an inner diameter of 2 cm, outer diameter of 6.5 cm and a total height of 7 cm. It was isolated by foamed polystyrene with a thickness of at least 90 mm. The temperature increase of the calorimeter was measured with a high precision semiconductor thermistor, TS-NTC-203, Hygrosens Instruments GmbH, and a self-designed circuit board transferring the changing resistance into a changing voltage. The recorded voltage signal is proportional to the temperature increase and thus to the released energy (see Fig. 6).

The calorimeter was calibrated with a 100 Watt lamp, a 12.5 Volt DC power source adjusted to an output of 8 Ampere and a timed relay that was set to several switching times to get a calibration curve according to the formula $E[J] = U[V] * I[A] * t[s]$ (E: Energy (Joule), U: Voltage (Volts), I: Current (Ampere), t: time (seconds)). By means of the calibration a sensitivity of 0.0698 mV/J and a mean variation of 1.63% (max 4%) was obtained. In Fig. **5** the calibration curve is shown together with the results of several validation tests.

DOI: 10.7795/810.20200724

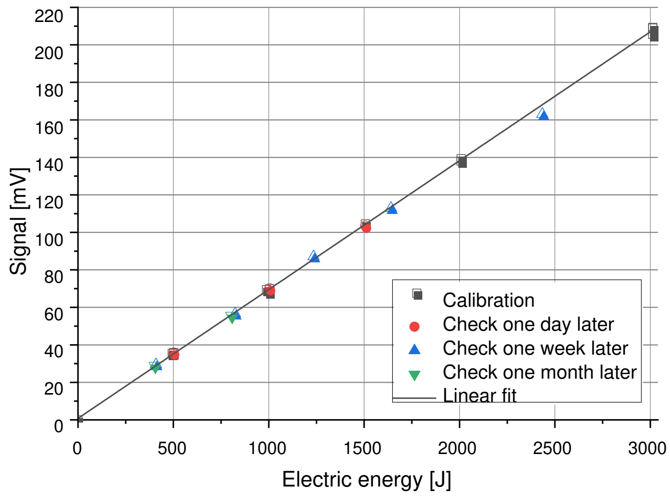

Fig. *5. Calibration line and three verification tests with a variation of less than 4%*

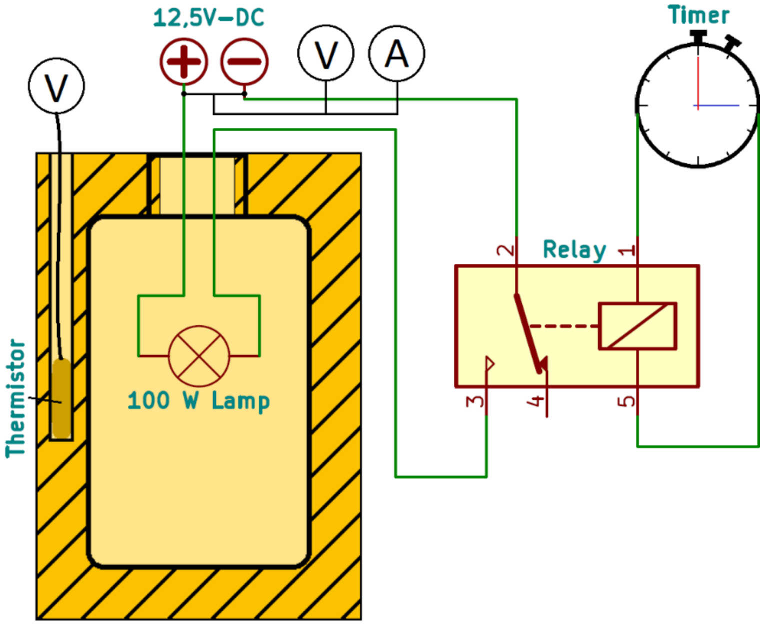

Fig. 6. *Adiabatic brass calorimeter in the calibration set-up*

2.2 Highspeed camera and electrical recordings

Three different high-speed cameras (MotionCorder Analyzer Model SR-1000 from Kodak, FASTCAM APX RS from Photron and HPV-1 from Shimadzu) were used for filming with maximum framerates of 1 000, 20 000 and 1 000 000 frames per second. The electrical recordings of the ignition current and ignition voltage of the exploding wire were measured with a frequency of 30 kHz.

3. Results and discussion

3.1 Results of the calorimetric measurements

Ten tests with different ignition times of the induction spark and an electrode distance of 6 mm showed a power of 11.9 W with a mean variance of 4.4%. This matches DIN EN 1839 in which the power of this ignition source is specified with circa 10 W. In the standard gas explosion tests the burning duration is adjusted to 200 ms [1] or respectively 200 – 400 ms [8] so the net energy released by the induction spark is between 2.2 J and 5.0 J (E(J)=P(W)*t(s); variance included). Other standards that included the same ignition source with 15 kV and 30 mA differ by specifying a delivered energy instead of power of 10 J in 200 – 500 ms [9]. The energy can only be increased by a longer burning duration. Higher energies for dust explosions of at least a few hundred joules cannot be provided in a reasonable time span.

Twenty-two tests with a surface-gap spark igniter were carried out. The energy was provided by capacitors with a operating voltage of 450 V and a capacitance of 220 µF. In the tests an average net ignition energy of 7.9 J with a mean variance of 4.5% was measured. The efficiency in this set-up is 35% compared to the gross energy of 22.75 J.

Another test with a capacitance of 600 µF and different loading voltages led to the results shown in the following diagram (see Fig. 7). The efficiency was between 41% and 29% with the trend of decreasing with higher voltages.

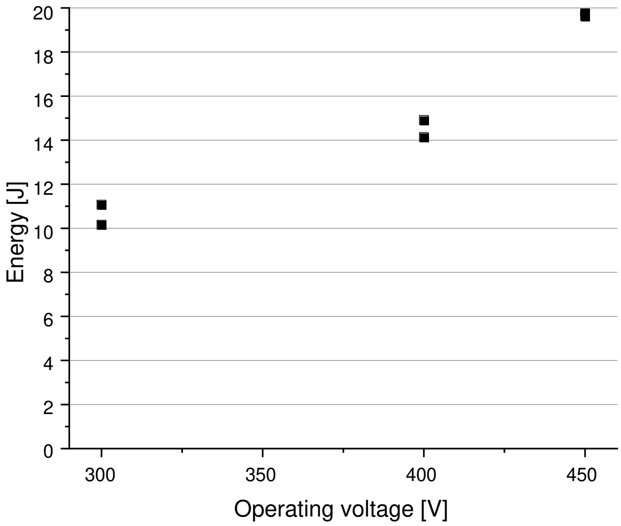

Fig. 7. *Calorimetric measurements of a surface-gap spark igniter with a capacitance of 600 µF, calorimetric measured energy against operating voltage*

The influence of the cable length was also measured with two cables of the same cross section of 4 mm² and a length of 3.2 m and 21,7 m. The efficiency decreased with the longer cable from 40% on average to 32% on average. Another influencing factor is the number of the ignitions carried out with one pencil lead mainly consisting of graphite. In the first few ignitions the released energy is decreasing from test to test, then after about 5 ignitions the released net energy is constant (see Fig. 8). This may be because of the lacquer or something else that is burned from the surface at the first ignition. The resistance of the pencil lead was measured in an additional test showing the dropping resistance over the first three ignitions.

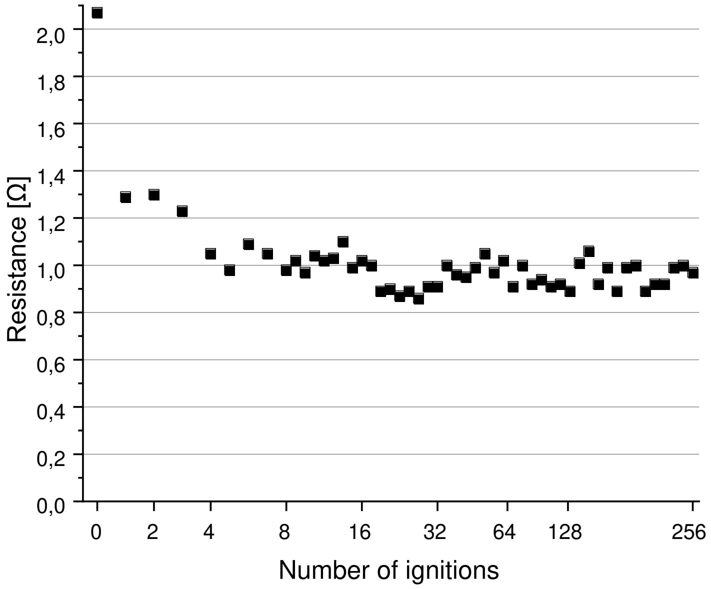

Fig. 8. *Resistance of the 10 mm (length) * 2 mm (Ø) pencil lead against the number of ignitions*

The surface-gap spark has many parameters influencing the energy and the efficiency. For every set-up, calorimetric tests should be made or the set-up conditions (cable length, cable cross-section, number of ignitions, resistance and length of pencil lead) should be described precisely to have a chance to check the net energies in subsequent tests.

Three tested chemical igniters with a specified energy of 1 000 J had a calorimetric energy of 1 090 J ± 24 J. For the igniters with smaller specified energies (three tests each) the difference between the specified and the measured ignition energy was higher. The calorimetric measured energies were 660 J ± 32 J instead of 500 J, 477 J ± 35 J instead of 250 J and 425 J ± 51 J instead of 100 J. The chemical igniters consist of an explosive and an igniting pill. It was assumed, that the weight of the explosive is adjusted, and the igniting pill is disregarded. To prove this, chemical igniters of different specified energies were disassembled, and the explosive weight measured. Afterwards the ignition pills were ignited in the calorimeter without explosive.

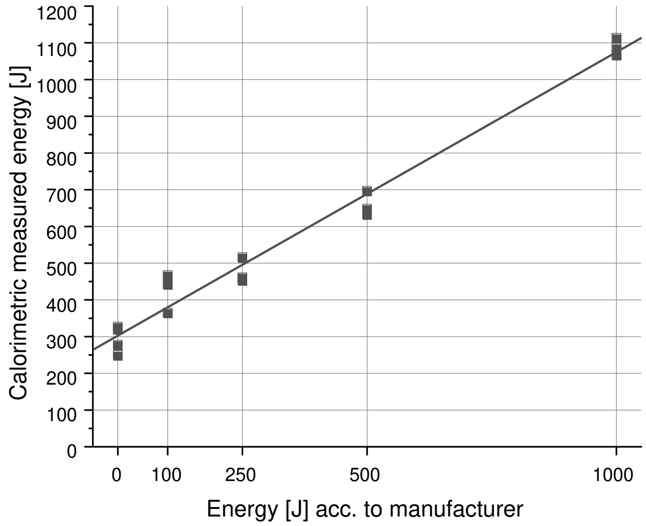

Fig. 9. *Calorimetric measured energy of the chemical igniters against specified energy according to the manufacturer, three tests each except "0 Joule" with four tests*

The weights are shown in Table 2 and the calorimetric values are plotted in Fig. 9 under "0 Joule" leading to values of 288 J ± 38 J, lying exactly around the extrapolated linear fit of the other tests.

Table 2: *Weights of the chemical igniters, with and without explosive and difference (mass of explosive without ignition pill)*

Sample number	Specified energy [J]	Gross weight, filled [g]	Gross weight, empty [g]	Difference/mass of explosive [g]	Ratio to 1.000 J
1	1 000	5.23	5.01	0.22	-
2	1 000	5.28	5.05	0.23	-
3	1 000	5.25	5.01	0.24	-
4	500	5.11	4.98	0.11	~ ½ of the mass
5	500	5.09	4.98	0.11	~ ½ of the mass
6	500	5.10	4.97	0.13	~ ½ of the mass
7	100	5.01	4.98	0.02	~ ⅒ of the mass
8	100	4.99	4.96	0.02	~ ⅒ of the mass
9	100	5.02	5.00	0.02	~ ⅒ of the mass

The exploding wire showed a low variation in the efficiency and in overall energy with the same set-ups: All the tests were carried out twice over a range from 6.6 J to 1 400 J. The comparison between the calorimetric and the electrical measurements showed, that the calorimetric values were 7% higher on average (see Fig. 10). This may be because of an insufficient calibrating method of the calorimeter or the ignition device, but it is still smaller than any variation of the other ignition sources and the only one, that could be with two methods at the same time.

DOI: 10.7795/810.20200724

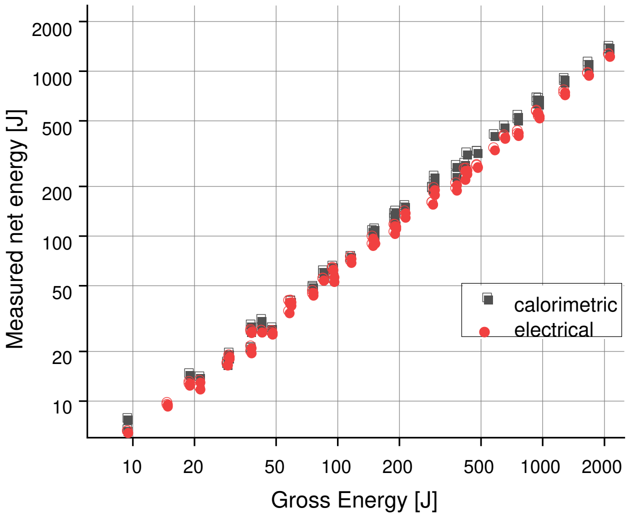

Fig. 10. *Calorimetric measurements of exploding wire, calorimetric and electrical measured energy against the gross energy of the loaded capacitors (double-logarithmic scale)*

3.2 Results of highspeed camera recordings

The surface-gap spark igniter is too fast for electrical measurements. To achieve an idea of the ignition procedure a camera with up to 1 000 000 fps was used, the cable length to the electrodes was 1,6 m with a cross-section of 4 mm², the capacitance was 220 µF, loading voltage 450 V and the pencil lead had a length of 10 mm and a diameter of 2 mm. It turned out, that the whole burning duration is less than 170 µs long, with a core-time (where one can clearly see a light) of about 60 µs (see Fig. 11). For gases the burning duration is not very crucial but for dusts this might be too short to ignite leading to the experimental determination of wrong safety characteristics.

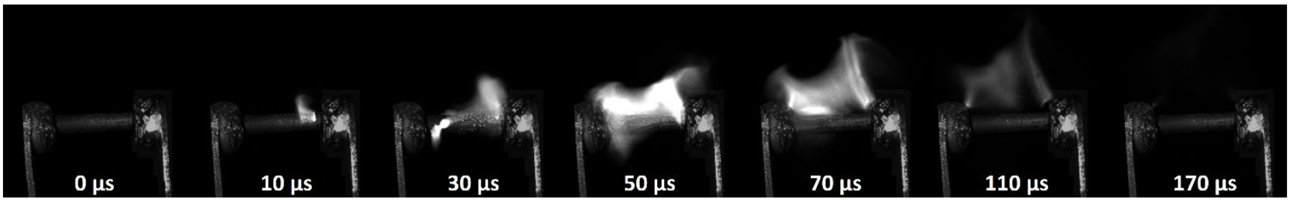

Fig. 11. *Full ignition procedure of a surface-gap spark, burning duration of less than 0.17 ms*

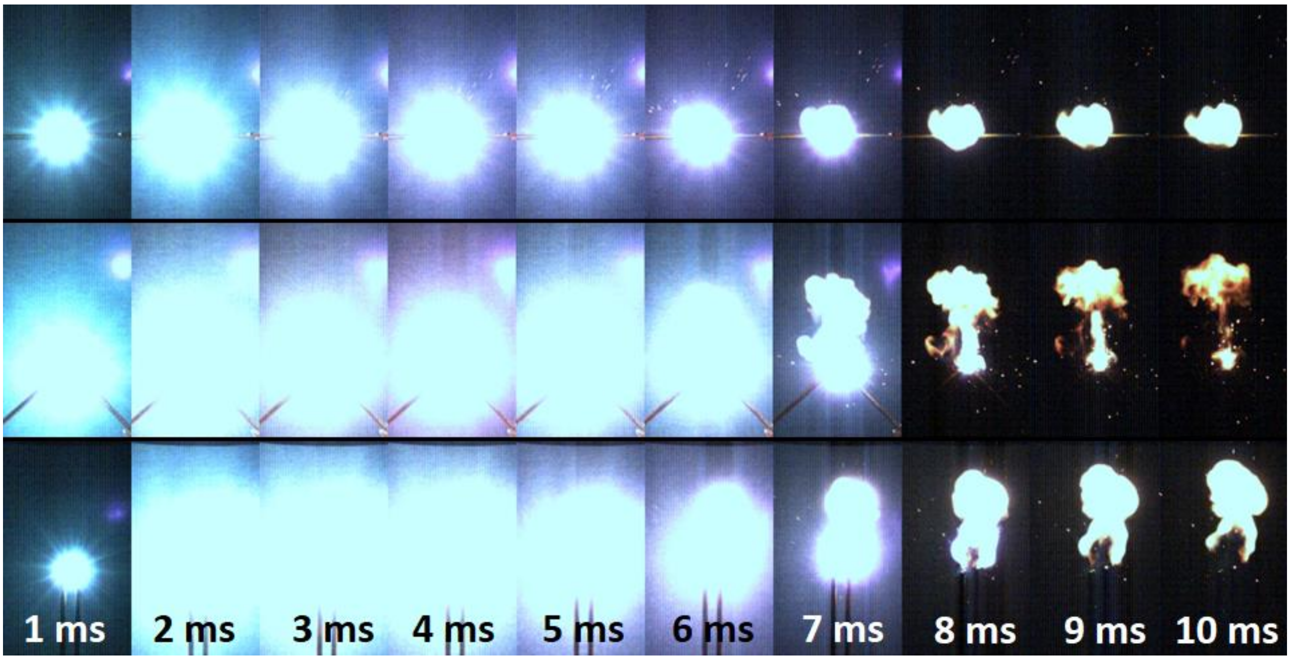

Fig. 12. *Three different ignition procedures of the exploding wire with different electrode angles; 180° (adjacent) with 20.5 J in top row, 90° in the middle with 26.5 J and 0° (parallel) in the bottom row with 29.5 J*

Fig. 12 is a slideshow of three ignition procedures with different angles of the electrode. One can clearly see the well-controlled ignition with adjacent (180°) electrodes staying in one place and light arcs pushed away from the electrodes if the angle varies. This leads to a higher variation of the net energy and the burning duration with increasing angles (see Fig. 13).

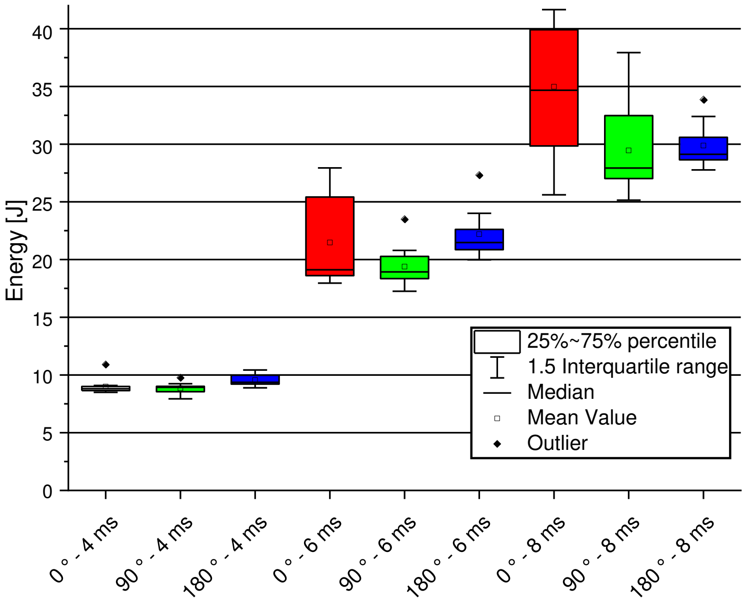

Fig. 13. *Electrically measured ignition energy against ignition time and angle of the electrodes, ten tests were carried out for each set-up*

The variation of the ignition energy changes clearly with different angle; parallel electrodes show a variation of 11.2% (max. 30.1%), orthogonal electrodes of 7.0% (max. 28.8%) and adjacent electrodes of 5.4% (max. 23.1%). There is another trend, that decreasing electrode angles increase the efficiency of the ignition system, otherwise identical set-ups cause a higher net energy with parallel electrodes than with adjacent ones.

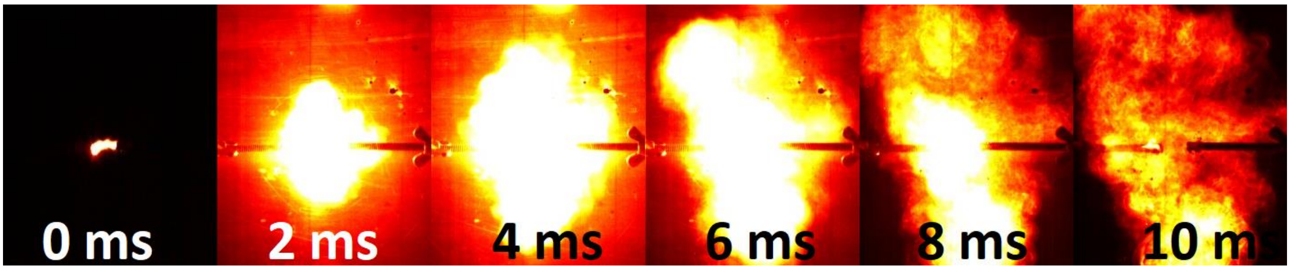

Fig. 14. *Ignition procedure of an exploding wire with 820 J and an electrode angle of 180° (adjacent)*

The above described correlation between increasing angle and decreasing variation does not apply for energies above ~50 J. Parallel electrodes show a variation of 3.0% (max. 12.1%), orthogonal electrodes of 3.2% (max. 13.9%) and adjacent electrodes of 2.6% (max. 11.5%).

The cause for this may be, that the energy amount is too big to last between the two electrodes and is pushed besides due to thermal and electromagnetic effects (see slideshow in Fig. 14). This causes a higher turbulence and therefore a higher variation, comparable to the variation of parallel electrodes. The trend with the efficiency is clearer with increasing energies; parallel electrodes show higher net energies with otherwise identical set-ups of the ignition system (see Fig. 15).

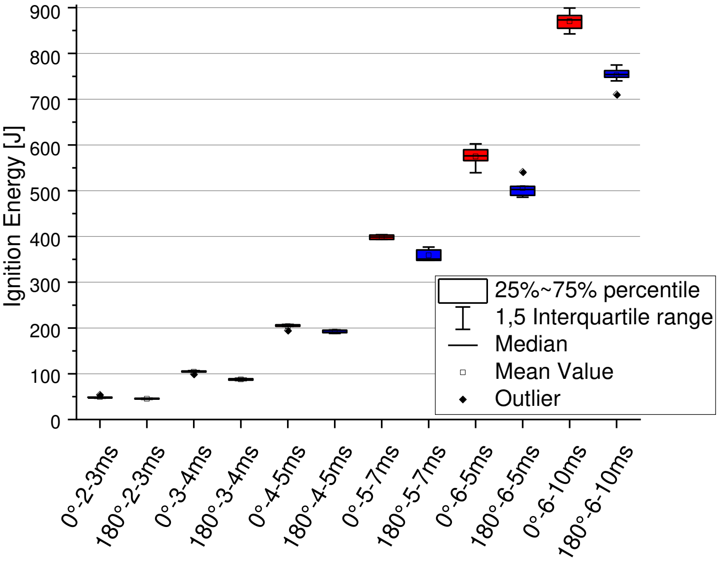

Fig. 15. *Electrically measured ignition energy against angle of the electrodes, capacitance value (2 ≙ 940 µF, 3 ≙ 1880 µF, 4 ≙ 4700 µF, 5 ≙ 9400 µF, 6 ≙ 20680 µF) and ignition time, unvaried loading voltage of 450 V*

4. Conclusions

The exploding wire igniter has several advantages compared to the other common ignition sources used for explosion testing. Particularly the burning duration and the ignition energy can be adjusted fluently. The lower mean variance and measurable ignition energy in each ignition are another two features that make the exploding wire suitable for a standardized ignition source for hybrid mixtures. The angle of the electrodes can be varied to achieve a lower mean variation, but this causes much more effort and does only make sense for ignition energies below 50 J. The distribution of the ignition energy in space (ignition volume) is higher with parallel electrodes what might be an advantage, however the ignition volume is of different ignition sources under examination and will be published in the near future.

The burning duration of the surface-gap spark is probably too short for a dust explosion. Two other disadvantages of the surface-gap spark are that it is not possible to measure the net energy while in use and the many parameters influencing it.

Because of the unspecified ignition energies of the chemical igniter under 1.000 J it is not suitable for the determination of safety characteristics for gas explosions. With 1.000 J the energy is likely to drive the hybrid mixture into over-ignition in the gas-driven regions. For the dust-driven hybrid mixtures it may be suitable.

The induction spark does probably not provide enough energy for determining safety characteristics for explosion of hybrid mixtures with energies of around 10 J per second.

Acknowledgements

The authors would like to thank Daniel Kadoke from 8th division of BAM and Peter Löwe from 5th division of BAM for providing us with highspeed-cameras and supporting us with their long-term knowledge in highspeed-filming.

References

[1] DIN EN 1839:2017 - Determination of the explosion limits for flammable gases and vapours, Beuth-Verlag, Berlin

[2] Scheid, M., Kusche, C., Schröder, V., Barth, U. (2013). Tests on Suitability of the Ignition Source “Exploding Wire” for the Determination of Explosion Characteristics of Combustible Dusts in the 20-L-Sphere. *CHEMICAL ENGINEERING TRANSACTIONS VOL. 31, 2013*

[3] Franke, H. (1978) - Bestimmung der Mindestzuendenergie von Kohlenstaub/Methan/Luft-Gemischen, VDI-Berichte Nr. 304

[4] Askar, E., Schröder, V. (2019) - The influence of strong ignition sources on the explosion and decomposition limits of gases, Chemical Engineering Transactions Vol.75

[5] ASTM E 2079-00 - Standard Test Methods for Limiting Oxygen (Oxidant) Concentration in Gases and Vapors, ASTM International, West Conshohocken

[6] Cashdollar, K., Zlochower, I., Green, G., Thomas, R., Hertzberg, M., (2000). Flammability of methane, propane, and hydrogen gases. Journal of Loss Prevention in the Process Industries 13 (2000) 327–340

[7] DIN EN 14034:2006 - Determination of explosion characteristics of dust clouds, Beuth-Verlag, Berlin

[8] ASTM 681-09 - Standard Test Method for Concentration Limits of Flammability of Chemicals (Vapors and Gases), ASTM International, West Conshohocken

[9] DIN EN ISO 10156:2017 - Gas cylinders – Gases and gas mixtures – Determination of fire potential and oxidizing ability for the selection of cylinder valve outlets, Beuth-Verlag, Berlin

Spontaneous combustion behaviour of solids: Validation of extrapolation of laboratory tests by means of semi-technical tests up to 1 m³ and advanced thermoanalytical methods

Martin Schmidt [a], René Erdt [a], Markus Gödde [b] & Steffen Salg [b]

[a] Bundesanstalt für Materialforschung und –prüfung (BAM),
Division 2.1 „Explosion Protection Gases and Dusts“, Berlin
[b] BASF SE, Safety Engineering, Ludwigshafen

E-mail: martin.schmidt@bam.de

Abstract

Several analytical methods are used for the determination of reaction kinetic data of solid bulk materials and to predict the self-ignition behaviour of large storages. These are thermal analyses such as differential scanning calorimetry DSC, simultaneous thermal analysis STA as well as microcalorimetry for high-precision measurement of heat flows. Very small sample quantities are used for the above methods.

Normally, the self-ignition behaviour is determined with the aid of isoperibolic or adiabatic hot storage tests; the sample volumes here are usually in the range of approx. 100 cm³ to several litres. The extrapolation to technically relevant volumes holds, however, considerable uncertainties.

The main objective of a research project launched in 2018 is to identify and to reduce these uncertainties. This is to be done primarily by setting up a test stand for the investigation of sample sizes of up to 1000 dm³. The suitability (or unsuitability) of the established methods is to be demonstrated and influencing variables that cannot be measured on a laboratory scale are to be determined. First results of the project confirm that the determination of the self-ignition behaviour of dusts and bulk materials and in particular the determination of reaction kinetic data are subject to considerable uncertainties. Both hot storage tests on a laboratory scale and thermoanalytical methods evaluated with the aid of various methods allow only partially reliable conclusions about the self-ignition behaviour of large bulk materials. Complete test series using all mentioned test methods will be presented and - depending on the sample material - conclusions regarding the applicability of the extrapolation methods will be discussed.

Keywords: *self-ignition, extrapolation methods, large scale tests, kinetic data, thermoanalytical methods*

1. Introduction

The storage and transport of flammable bulk materials poses the risk of fire by spontaneous combustion. The risk of spontaneous combustion increases with both the quantities of the stored flammable material and the duration of storage.

To assess the self-ignition behaviour of a bulk material, so-called isoperibolic hot storage tests in accordance to prEN15188 (2019) are frequently used to determine self-ignition temperatures (T_{SI}) for various sample volumes on a laboratory scale. An extrapolation of the results obtained at laboratory scale is based on the theory of thermal explosion. As a result of these experiments, conditions can be derived which ensure safe storage or safe transport of the different materials. This can be achieved by limiting both the storage temperatures and quantities as well as the duration of storage.

The extrapolation to technically relevant volumes holds, however, considerable uncertainties. These are based on:

- extrapolation over several orders of magnitude of volume,
- limitations of the extrapolation method used (restricted start and boundary conditions),
- the different temperature levels of the laboratory experiments compared to the technical storage, in particular the influence of the water contained,
- unclear criteria for ignition/non-ignition,
- influence of different extrapolation methods,
- reactions not detectable by laboratory tests (low temperature oxidation, decomposition, autocatalysis etc.),
- scattering of the test results.

The main objective of the research presented is to identify and to reduce these uncertainties. By means of a combination of semi-technical hot storage test up to a volume of 1 m³ as well as thermoanalytical methods, the following questions are to be addressed:

- a general review of the methods of extrapolation listed in prEN15188 (2019),
- the verification of the suitability or unsuitability of extrapolation procedures for materials with complex reaction kinetics and/or mechanisms, such as autocatalytic processes, inhibited systems, multi-step reaction systems or processes with limited mass transport,
- derivation of decision criteria for the applicability of extrapolation methods,
- testing the applicability of (new) screening methods based on microcalorimetric methods,
- the improvement of the measurement uncertainty by investigations in the volume range between laboratory tests and practical conditions,
- the examination of further influences such as product moisture or low temperature reactions of highly reactive components to the spontaneous ignition process,
- Influence of convection-dominated transport processes in large deposits with the aim of verification and validation of test methods and simulation models.

2. Current situation

One common approach to transfer results from laboratory experiments to practical conditions is the so-called theory of thermal explosion, developed by Frank-Kamenetzkii. Based on this theory, a correlation results from the characteristic length of a deposit (e.g. radius of a cylinder) and its critical storage temperature T_{SI} (self-ignition temperature).

Fig. 1 shows the extrapolation of critical storage temperatures to larger volumes in the so-called Arrhenius plot with δ_{cr} – critical Frank-Kamenetzkii-parameter, T_{SI} – self-ignition temperature, r – characteristic length.

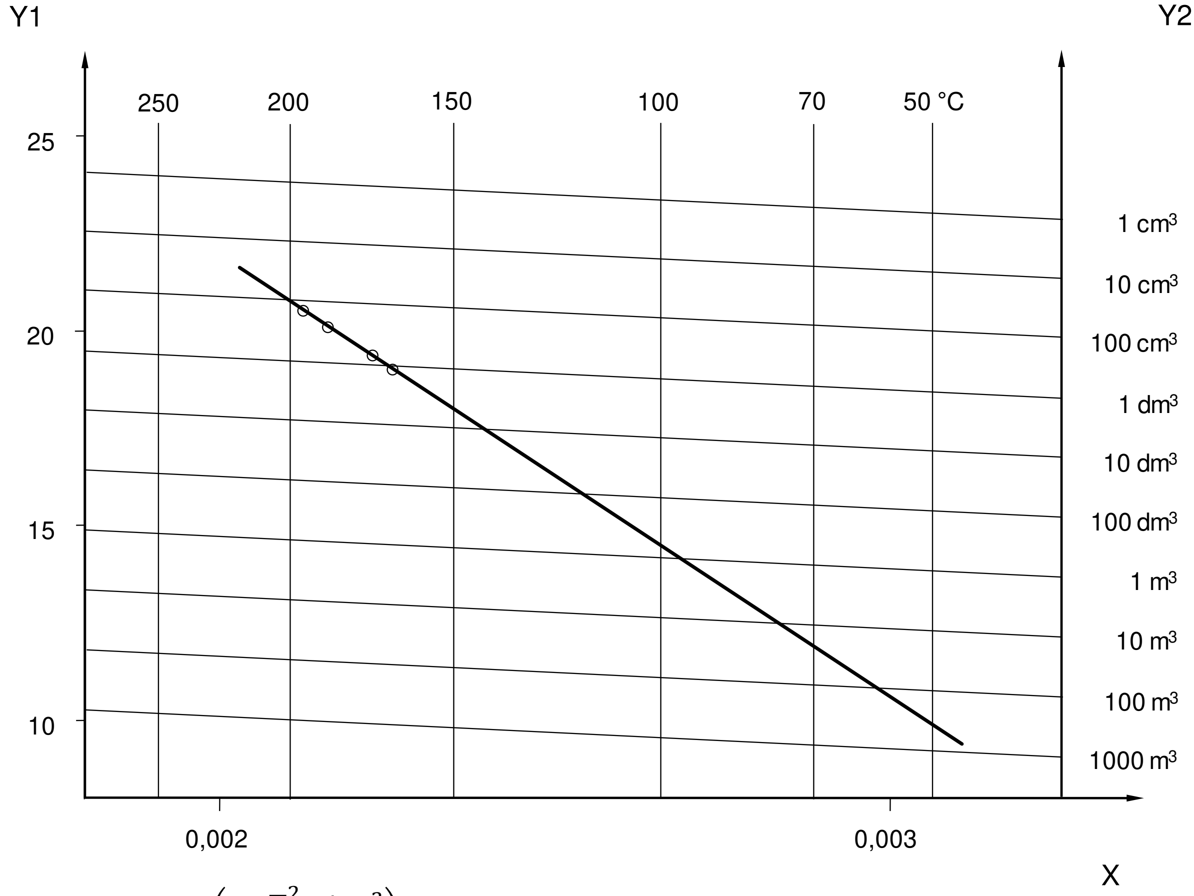

$$\text{Y1: } \ln\left(\delta_{cr}\frac{T_{SI}^2\ /1K^2}{r^2\ /1m^2}\right) \qquad \text{Y2: volume (cube)} \qquad \text{X: reciprocal } T_{SI} \text{ in } K^{-1}$$

***Fig. 1.** Arrhenius plot according to prEN15188 (2019)*

This procedure represents the current state of the art. For a simplified fast extrapolation, the so-called Pseudo-Arrhenius plot is often used where the volume to surface ratio of the sample (V/A) is plotted against the reciprocal self-ignition temperature ($1/T_{SI}$), see Annex A.5 of prEN15188 (2019). This method is used in section 3.2.3 to illustrate the results of the performed isoperibolic test series.
However, experience from incidents has shown that the data obtained on a laboratory scale are often only transferable to real-scale applications to a limited extent and with an uncertainty that cannot be quantified. If reaction processes not covered by this method can be taken into account, in particular using detailed mathematical models, self-ignition processes can be predicted much more accurately on a real scale and better parameters can be derived for safer operation of process plants and during storage and transport. This requires laboratory tests as well as numerical methods to be verified by means of large-scale experiments on a semi-industrial scale. Systematic large-scale experiments with volumes far above the laboratory quantities normally used in the past have not yet been carried out.

Spontaneous combustion of flammable materials can occur during both process engineering applications and the transport or storage of bulk materials. An overview of the methods for determining the spontaneous ignition behaviour is given by Fei and Liang (2011), for example. Various parameters (e.g. material properties, storage conditions and the geometry of the bulk solid) influence the spontaneous ignition process. For this reason, efforts have already been made in the past to better describe these processes through systematic laboratory experiments in combination with suitable model approaches and to transfer the results of the laboratory experiments to real scale with the aid of numerical methods, e.g. Fierro et al. (1999), Lohrer et al. (2005), Krause et al. (2006), Ferrero et al. (2009), Zhu et al. (2013), Everard et al. (2014), Degenkolbe et al. (2016), Wu et al. (2017) and Wu et al. (2019). Some of the work carried out so far also includes large-scale experiments. In this context, investigations of the spontaneous combustion processes in bulk materials on a real scale were carried out, such as coal stockpiles (Fierro, 1999) and wood chip stockpiles (Ferrero, 2009). However, these studies did not involve the systematic determination of critical storage conditions, as would be necessary for checking the extrapolation, but rather the investigation of selected scenarios.

The basic prerequisite for the successful application of numerical calculation methods, however, is the knowledge of reaction-kinetic data of the processes taking place during the spontaneous ignition processes. These data are in turn determined from the laboratory tests already described and are thus subject to the uncertainties listed above.

3. Experiments

3.1 Materials tested

A wide range of materials have been investigated including wood pellets, petroleum coke, vitamine mixture, crosslinked polyvinyl-pyrrolidone (PVP) and a sterol mixture. A detailed description can be found in Schmidt et al. (2020).

3.2 Isoperibolic hot storage tests

3.2.1 Large scale test setup

The setup for carrying out tests on a semi-industrial scale consists of four heating chambers with an internal volume of about 3 m³ each, designed to store four 200 L barrels or containers up to a volume of 1 m³, see Fig. 2, left. The air in the heating chamber is permanently circulated by means of a fan. Holes drilled in the rear wall ensure a four- to fivefold air exchange per hour. For safety reasons, it is planned to stop the tests at a point in time when an ignition could be clearly detected. For this purpose, a system has been installed which allows the oven (heating, fan) to be switched off automatically and the oven chamber to be purged with nitrogen.

Wire mesh baskets with volumes of approx. 125 dm³ and 1000 dm³ are available as sample containers, see Fig. 2, right. Each oven is equipped with a system to measure temperatures at up to 16 points in and around the sample. If necessary, it is possible to detect fire gases generated during the test. A mobile FT-IR spectrometer and oxygen analyser are available for this purpose.

Fig. 2. *Weather protection tunnel with 4 ovens (heat chambers, left) and equipped sample container (125 dm³) with petroleum coke sample (right)*

3.2.3 Test results

3.2.3.1 Wood pellets

In order to determine the self-ignition behaviour of wood pellets, isoperibolic hot storage tests up to a volume of 1000 dm³ were carried out.

Fig. 3 shows the determined T_{SI} in the Pseudo-Arrhenius plot. The extrapolation of test results in laboratory scale (red) show a good agreement with tests performed with volumes of 125 dm³ and 1000 dm³. The self-ignition temperatures determined for larger volumes deviate only slightly from the extrapolation of the laboratory values and are within the measuring uncertainty of extrapolation defined in prEN15188 (2019). Extrapolation over all investigated volumes results in slightly higher critical temperatures for technical storage volumes.

However, in the tests with 125 dm³ and 1000 dm³ convective effects are observed within the deposit. In Fig. 4 the temperature curves over time are plotted for two tests (1000 dm³ sample) at storage temperatures of 113 °C (black) and 111 °C (orange). The temperature in the sample center (solid curves) and the temperature 25 cm above the sample center (dashed curves) are shown. While the first self-heating in both experiments takes place in the sample center, the ignition at a storage temperature of 113 °C occurs above the sample center. The reason for this is probably a convective effect (mass and heat transport) in the bulk material, which has a comparatively large gap volume. These observed effects require further investigations.

DOI: 10.7795/810.20200724

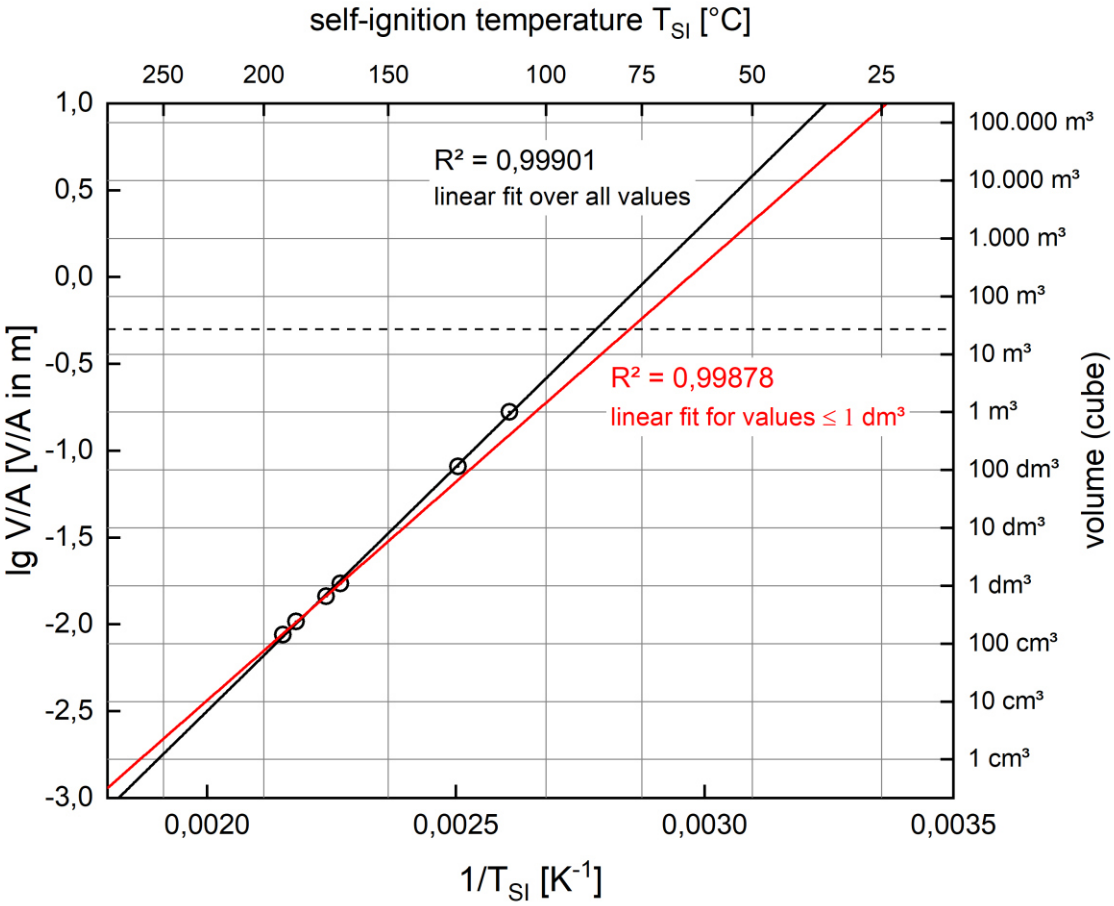

Fig. 3. *Pseudo-Arrhenius plot wood pellets*

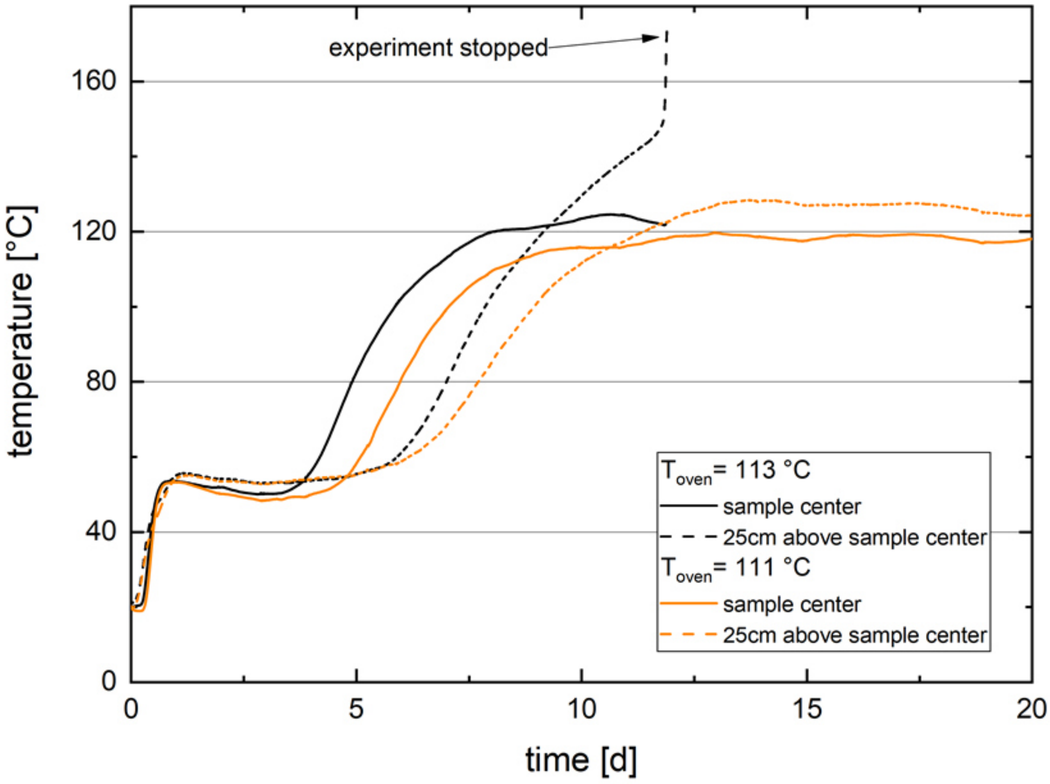

Fig. 4. *Temperature-time plots at the center of a 1 m³ sample and 25 cm above*

3.2.3.2 Petroleum coke

Fig. 5 shows temperature curves of the isoperibolic hot storage tests with petroleum coke at four different sample volumes.

According to prEN15188 (2019) a test is evaluated as having ignited if one of two criteria is fulfilled:

a) when the temperature-time-curve, measured at the center of the sample, shows an inflection point during the heating phase at a temperature above the oven temperature;

or

b) when the temperature at the center of the sample rises at least 60 K above the oven temperature (ΔT > 60 K).

Usually, both criteria occur at an identical oven (storage) temperature, i.e. in case of non-ignition no inflection point occurs and the temperature difference between the oven and the sample is less than 60 K. In case of ignition, a temperature rise of more than 60 K occurs, combined with an inflection point and a significant mass loss due to burning.

In Fig. 5 (top left) tests with 137 cm³ of petroleum coke at oven temperatures of 206 °C to 265 °C are shown. The temperature in the center of the sample increases by more than 60 K above the oven temperature at all oven temperatures above 206 °C and must therefore be regarded as ignition according to prEN15188 (2019). The maximum temperature reached in the center of the sample rose successively with the increase of the oven temperature. However, an inflection point as well as a burn-up with significant mass loss occurred only at oven temperatures above 265 °C. The critical temperature determined by the different criteria thus deviates by 59 K. The question therefore arises whether the 60 K criterion defined in prEN15188 (2019) is actually a suitable ignition criterion.

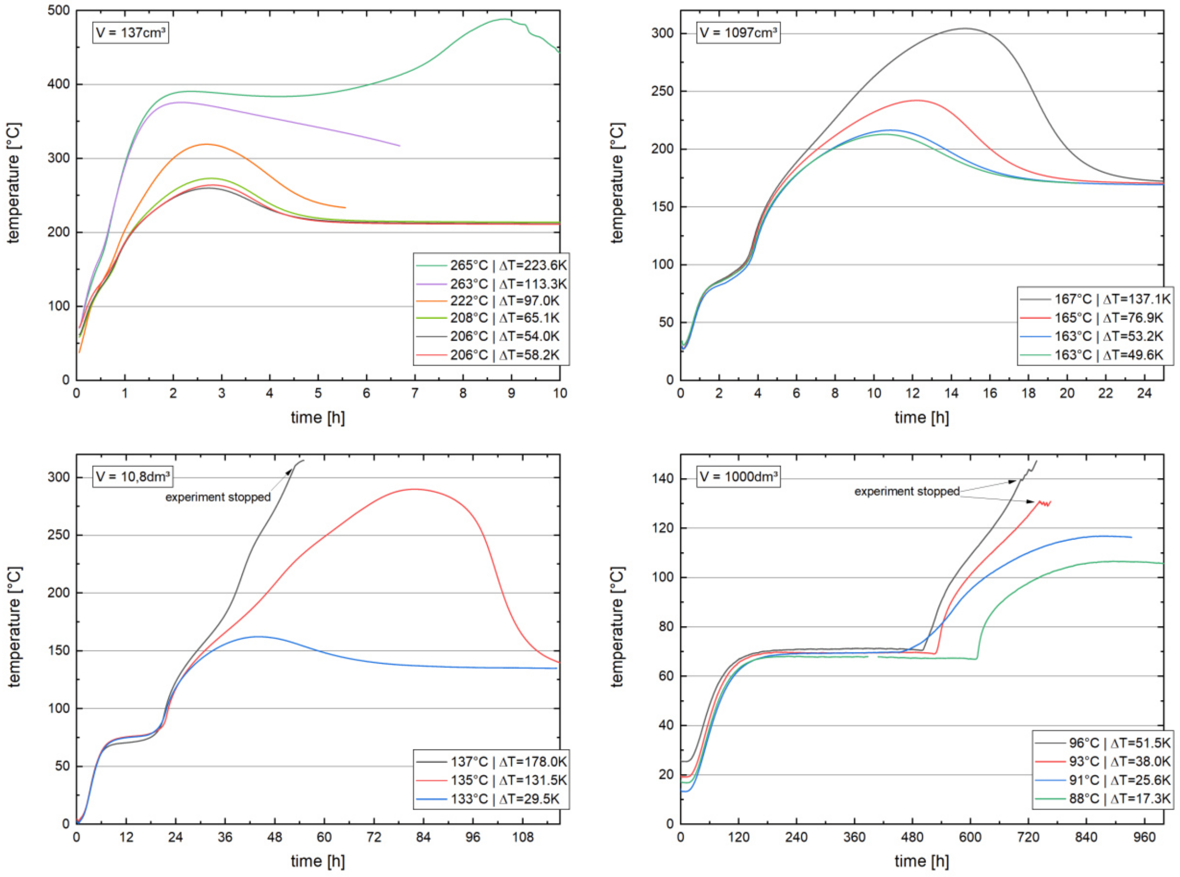

Fig. 5. *Temperature-time curves of hot storage tests of petroleum coke at different sample volumes*

If the sample volume is increased, this deviation decreases gradually. In tests with 1097 cm³ of petroleum coke, the 60 K criterion is reached at a storage temperature of 165 °C, a first inflection point can be seen at 167 °C. If the experiments are carried out with larger sample volumes (10.8 dm³ and larger), both ignition criteria mentioned in prEN15188 (2019) occur at the same storage temperature; e.g. at 135 °C for a 10.8 cm³ sample.

The Pseudo-Arrhenius plot in Fig. 6 clearly shows that the extrapolation of laboratory scale tests using the 60 K ignition criterion deviate significantly from critical temperatures observed for larger volumes. The application of the 60 K criterion for laboratory scale tests with petroleum coke overestimates the proneness to spontaneous combustion.

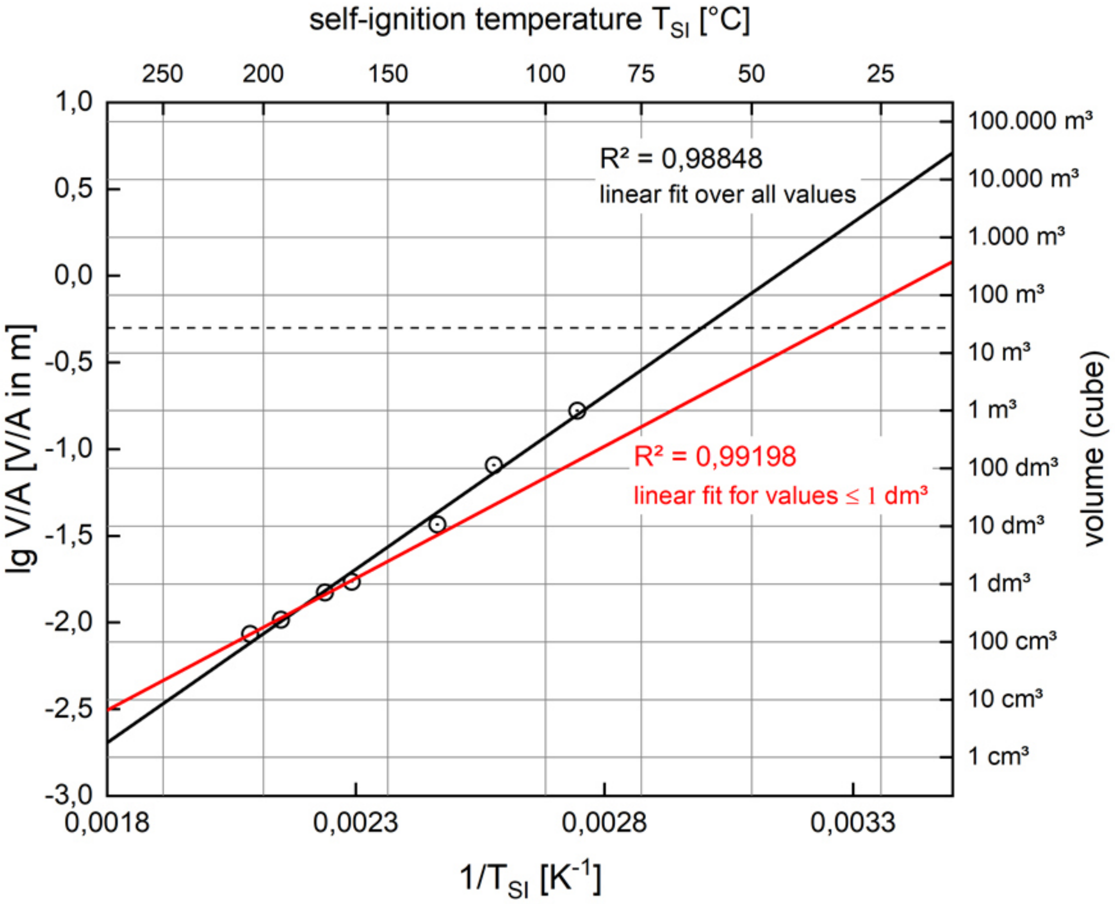

Fig. 6. *Pseudo-Arrhenius plot petroleum coke*

3.3 Adiabatic hot storage tests

In adiabatic tests, the ambient (oven) temperature is adjusted to correspond to the temperature in the center of the sample. Under these conditions, the Fourier heat equation is simplified in that way that no heat conduction in the sample and heat transfer from the sample to the surrounding occur and hence, the reaction kinetics may be determined from a single test. Adiabatic hot storage tests are described in Annex D of prEN15188 (2019). The results of adiabatic measurements of the vitamine mixture and of the sterol mixture are shown in Fig. 8. The apparent activation energies obtained from adiabatic measurements are discussed in section 4.

3.4 Thermoanalytical investigations

3.4.1 Differential Scanning Calorimetry (DSC)

Four samples - i.e. petroleum coke, the vitamine mixture, PVP and the sterol mixture - were chosen to perform kinetic analyses. Their thermograms are shown in Fig. 7.

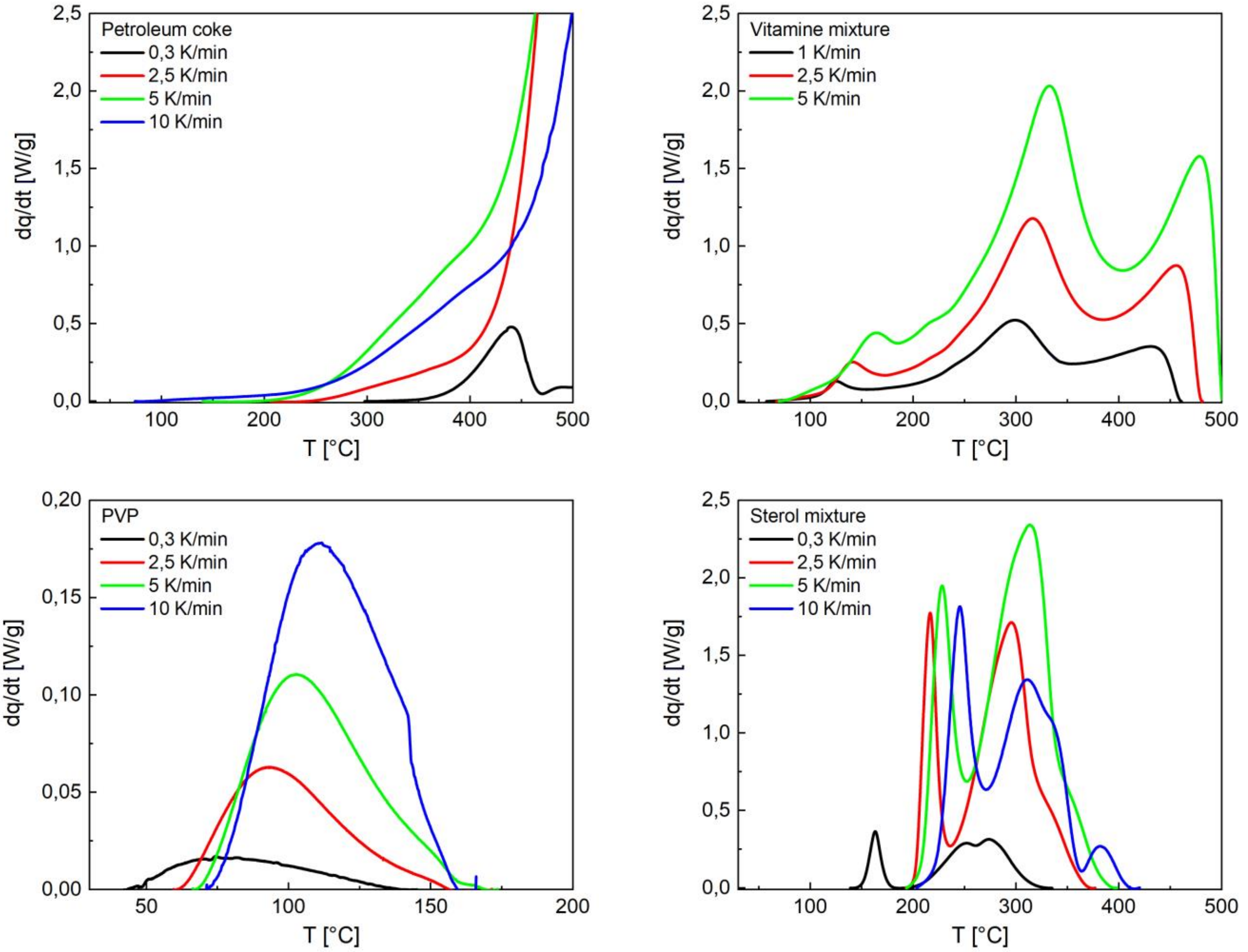

Fig. 7. *Thermograms of petroleum coke (top left), vitamine mixture (top right), polyvinyl-pyrrolidone (PVP, bottom left) and sterol mixture (bottom right) with different heating rates*

3.4.2 Model free estimation methods

The results of thermoanalytical investigations had been presented in a previous paper by Schmidt et al. (2020). In these investigations, the degree of thermal conversion α is the basis for kinetic calculations. The rate of conversion $\frac{d\alpha}{dt}$ can be calculated as

$$\frac{d\alpha}{dt} = k(T) \cdot f(\alpha) = A \cdot \exp\left(-\frac{E_a}{R \cdot T}\right) \cdot f(\alpha) \qquad (1)$$

whereas $f(\alpha)$ refers to the reaction model and $k(T)$ is the rate constant which depends on temperature T. With Arrhenius equation, $k(T)$ can be calculated using the preexponential factor A, the apparent activation energy E_a and the universal gas constant R (Vyazovkin, S. et al., 2011).

Model free methods such as Friedmann (1964), Ozawa (1965)/Flynn/Wall (1966), Kissinger (1957) and determination of initial slope had been used to estimate kinetic parameters and to discover if a reaction follows rather complex or simple mechanisms. One part of the investigations was to estimate the apparent activation energy of the first reaction step and to check if the results are suited for predicting the reaction behaviour on a larger scale. These results are summarized in Table 2 and discussed in section 4.

3.4.3 Microcalorimetry

Microcalorimetry is based on the differential heat flow principle like DSC. It is distinguished by very high measurement sensitivity in the range from 1 mW/kg to 10 mW/kg and in a high baseline stability. This enables the measurement of low heat fluxes and thus an assessment of reactions at low temperatures. In this way, the heat production rate of self-heating processes can be measured directly in the temperature range, which is relevant for an industrial scale. The type of microcalorimeter used is a Thermal Activity Monitor (TAM III) from TA Instruments. Within this device, a so-called perfusion cell is applied to measure oxidative self-heating processes. This enables air flow through the sample during the measurement in order to ensure a sufficient supply of oxygen. The results of microcalorimetric measurements of the vitamine mixture and of the sterol mixture are shown in Fig. 8. The advantages of microcalorimetric measurements are outlined in section 4.

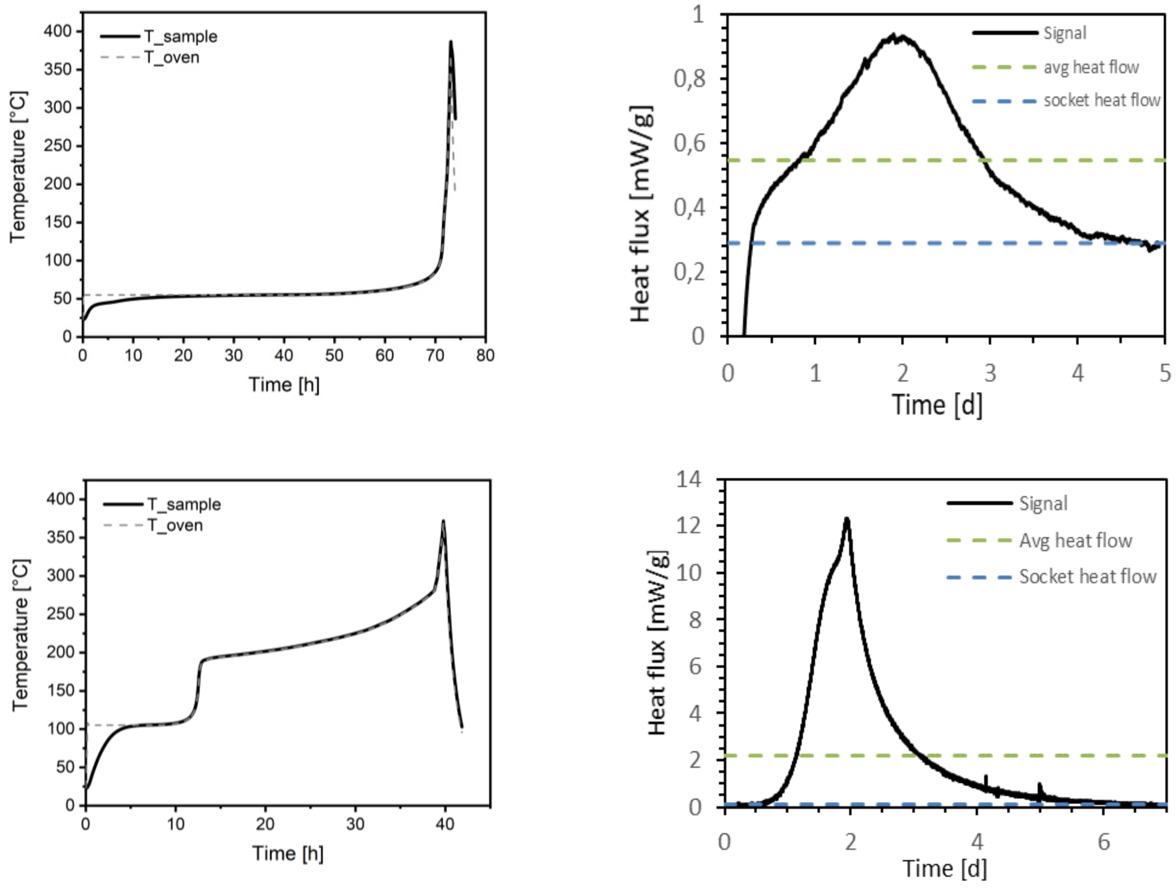

Fig. 8. *Vitamine mixture: adiabatic hot storage test at an initial temperature of 55 °C (top left) and isothermal TAM measurement at 60 °C (top right); sterol mixture: adiabatic hot storage test at an initial temperature of 105 °C (bottom left) and isothermal TAM measurement at 90 °C (bottom right)*

3.5 Evaluation and extrapolation of test results (kinetic data)

The reaction behaviour of bulk materials can be described with the theory of thermal explosion by Frank-Kamenetzkii (1969). According to this, the dimensionless and geometry-independent reaction rate δ_c can be described as

$$\delta_c = \frac{E_a \cdot r^2 \cdot \rho \cdot Q \cdot A}{\lambda \cdot R \cdot T_{SI}^2} \cdot \exp\left(-\frac{E_a}{R \cdot T_{SI}}\right) \tag{2}$$

or, in a linearized way as

$$\ln\left(\frac{\delta_c \cdot T_{SI}^2}{r^2}\right) = ln\left(\frac{E_a \cdot \rho \cdot Q \cdot k_0}{\lambda \cdot R}\right) - \frac{E_a}{R} \cdot \frac{1}{T_{SI}}. \tag{3}$$

The parameter δ_c is also called the Frank-Kamenetzkii parameter. It is a maximum value for a certain geometry which just fulfills the stationary thermal equilibrium criteria. For an equicylinder, meaning diameter equals height, $\delta_c = 2{,}76$, for cubes $\delta_c = 2{,}52$ (prEN15188, 2019).

Equation (3) is the basis for extrapolation of results from lab-scale to technical scale. However, the Frank-Kamenetzkii model does not take into account the real behaviour of small sample volumes like in lab-scale. In this case, the model's assumption that only thermal conduction within the bulk is determining the heat transport to ambience is not appropriate. For such volumes, heat transfer at the boundaries of the bulk is also relevant. Therefore, the model from Thomas provides a better description of the reaction behaviour. This model considers the ratio of heat transfer at the boundaries and heat conduction within the bulk. This ratio can be expressed as Biot number:

$$Bi = \frac{h}{\lambda} L\,. \tag{4}$$

h refers to the heat transfer coefficient and can be approximated with $h = 5\ \frac{W}{m^2K}$ (BASF test setup) and $h = 10\ \frac{W}{m^2K}$ (BAM test setup). λ refers to the heat conductivity of the bulk material and was measured using the Hot Disk method. The resulting values of λ for different samples are listed in Table 1. L is the characteristic length of a geometry. In the case of a cylindrical volume, it is the radius of the cylinder, for cubes half the edge length, see prEN15188 (2019). Using the Biot number, the critical Frank-Kamenetzkii parameter for equicylinders and cubes can be calculated as described in prEN1588 (2019). Both models, Frank-Kamenetzkii and Thomas, are used and compared within the present paper for determination of kinetic data (apparent activation energy E_a), see section 4.

Table 1: *Property data of the samples*

Sample	**λ [W/(m*K)]**	**c_p [J/(g*K)]**
Petroleum coke	0,15874	1,47
Vitamine mixture	0,08954	1,71
Polyvinyl-pyrrolidone (PVP)	0,07207	1,51
Sterol mixture	0,06163	1,85

4. Discussion

Despite thermoanalytical methods, classical hot storage tests in wire baskets provide kinetic parameters of the oxidative self-heating reaction. Adiabatic experiments as well as isoperibolic experiments with different sample volumes were used to determine the apparent activation energy. In the case of isoperibolic experiments, both extrapolation models, Frank-Kamenetzkii (FK) and Thomas (Thom), were used. The resulting apparent activation energy determined with different experiments and calculation methods is given in Table 2.

Table 2: *Overview of apparent activation energies resulting from different experiments and calculation methods*

Sample	E_a **Friedman [kJ/mol]**	E_a **Ozawa, Flynn, Wall [kJ/mol]**	E_a **Kissinger [kJ/mol]**	E_a **initial slope [kJ/mol]**	E_a **adiabatic exp. [kJ/mol]**	E_a **isoperibol. exp. (FK/Thom) [kJ/mol]**
Petroleum coke	n.a.	n.a.	n.a.	n. a.	64-73 [a, 1] 66 [b]	83/72 [a] 91/85 [a, 2]
Vitamine mixture	89 ± 5	99 ± 7	56 ± 4	80 ± 24	101-118 [a, 1] 89 [b]	108/89 [a]
Polyvinyl-pyrrolidone	104 ± 4	101 ± 3	99 ± 5	150 ± 69	99 [b]	102/90 [a] 99/76 [b]
Sterol mixture	72 ± 1	76 ± 9	74 ± 6	528 ± 157	61 [b]	62/54 [a] 60/47 [b]

[a] measurements BAM, [b] measurements BASF

[1] result depend on start temperature, sample volume or both

[2] only sample volume of 10 dm³ and above considered

The vitamine mixture and the sterol mixture were additionally stored isothermally in the microcalorimeter at different temperatures, see Fig. 8. In Fig. 9 and Fig. 10 the maximum as well as the average and socket heat flow during storage is plotted against the reciprocal sample temperature together with the heat flow determined from an adiabatic hot storage test shown in Fig. 8. The heat flow of the hot storage test was calculated from the measured temperature gradient and with the specific heat capacities given in Table 1.

For petroleum coke, the exothermic signal does not fall back to the baseline at the end of the measuring range at 500 °C, which means that the entire reaction was not observable. Therefore, model free estimation methods are not applicable on the basis of the available data.

The estimated values of the apparent activation energy for the vitamine mixture fluctuate between 56 kJ/mol and 118 kJ/mol. The results of the isoconversional methods Friedman and Ozawa, Flynn, Wall as well as adiabatic and isoperibolic results variate within a range of ± 15 kJ/mol. The Kissinger method and initial slope deliver results deviating more from the spread of the beforementioned methods. The results of an adiabatic hot storage experiment and results of microcalorimetric measurements are shown in Fig. 9. There is a relatively large part of a linear temperature gradient in a $\ln \dot{q}$-$\frac{1}{T}$-plot. In this way, the apparent activation energy can be determined with high certainty and it seems like rather a n-th order reaction is ongoing. An Arrhenius-extrapolation of the measured temperature gradient indicates a good match with the socket heat flow measured in isothermal microcalorimetric experiments at 45 °C and 60 °C.

In the case of crosslinked polyvinyl-pyrrolidone, there is very good agreement between the values determined by the estimation methods and the values measured in the hot storage tests. Although the reaction appears to follow an autocatalytic mechanism, the estimation methods provide very good predictions of the apparent activation energy.

For the sterol mixture, the analyzes according to Friedman, Ozawa, Flynn, Wall and Kissinger provide a good match between the apparent activation energy. The correct interpretation of the measurements is challenging, since the reaction proceeds in several stages and the first step is apparently autocatalytically activated. This can be recognized, for example, through the steep course of the temperature gradient in a $\ln \dot{q}$-$\frac{1}{T}$-plot, see Fig. 10. In such cases, it is hard to find the true apparent activation energy without further investigation. This is a good example where microcalorimetric experiments provide valuable additional information. Especially isothermal measurements at lower temperatures than such, where heat flows in adiabatic hot storage tests are detectable, contribute in checking kinetic data required for extrapolation. In the present example, the microcalorimetric results at 75 °C and 90 °C in combination with adiabatic data indicate an apparent activation energy of 61 kJ/mol. Further investigations will be done to validate this interpretation.

Comparing the model free estimation methods, it has to be stated that the determination of the initial slope is the weakest method. It delivers rather poor prediction results in all examples and the values themselves contain a high uncertainty. The value determined for the sterol mixture is unrealistically high at 528 kJ/mol.

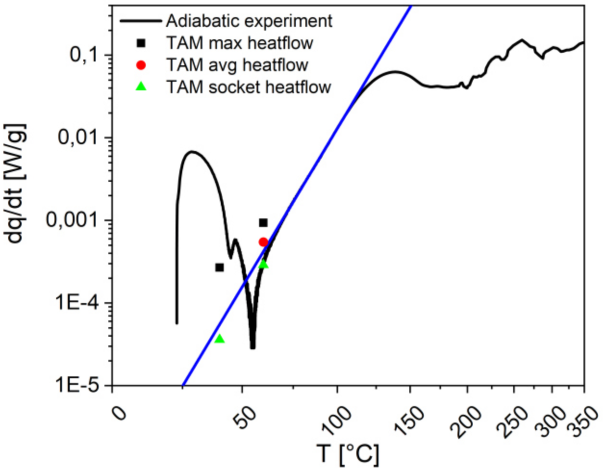

Fig. 9. *Results from adiabatic test (derivative of T-t curve as given in Fig. 8) and isothermal TAM measurements at 45 °C and 60 °C for the vitamine mixture*

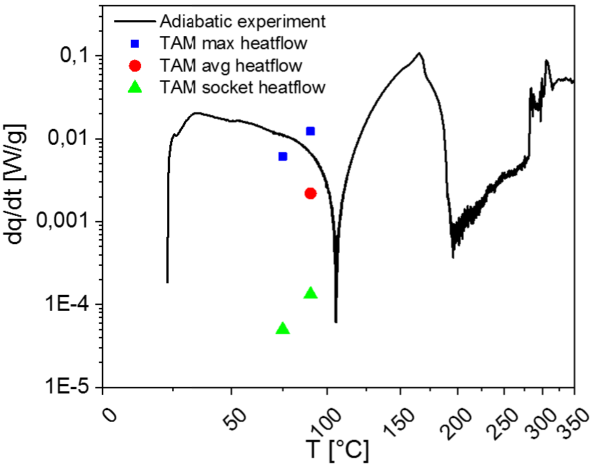

Fig. 10*. Results from adiabatic test (derivative of T-t curve as given in Fig. 8) and isothermal TAM measurements at 75 °C and 90 °C for the sterol mixture*

DOI: 10.7795/810.20200724

5. Conclusions

The determination of the self-ignition behaviour of combustible substances is subject to uncertainties. Tests on a semi-technical scale can help to improve the accuracy of extrapolation of laboratory data to technical conditions. This is particularly the case where laboratory-scale tests show ignition behaviour which is difficult to evaluate. For the materials investigated so far up to a volume of 1 m³, the critical storage temperatures of technically relevant volumes shifted towards higher values compared to the extrapolations from tests on laboratory scale.

Isoperibolic hot storage tests can be usefully supplemented by model-free estimation methods based on thermoanalytical investigations. In particular, the methods according to Fiedman and Ozawa, Flynn, Wall show a good agreement with the kinetic data obtained from hot storage tests. These methods are therefore suitable for the approximate assessment of a possible risk of spontaneous combustion. The evaluation of kinetic data from adiabatic experiments can be difficult or lead to incorrect results, e.g. in the presence of multi-step reactions. Microcalorimetric tests, which can be used to determine heat release rates at comparatively low temperatures, can provide valuable additional information for the interpretation of hot storage tests.

References

prEN 15188:2019 (2019), Determination of the spontaneous ignition behaviour of dust accumulations. *DIN Deutsches Institut für Normung e.V. Berlin*. Beuth Verlag GmbH.

Degenkolbe, S. and Witt, W. (2016), Self-ignition in structured packed columns, fundamentals of methodology development. *Journal of Loss Prevention in the Process Industries* 40: 437-448.

Everard, C. D., Schmidt, M., McDonnell, K. P., and Finnan, J., (2014), Heating processes during storage of Miscanthus chip piles and numerical simulations to predict self-ignition. *Journal of Loss Prevention in the Process Industries* 30: 188-196.

Fei, F. and Liang, D. (2011). Research Progress and Comparison of Methods for Testing Self Ignition Materials. *Procedia Engineering* 11: pp 91-99.

Ferrero, F., et al. (2009), A mathematical model to predict the heating-up of large-scale wood piles. *Journal of Loss Prevention in the Process Industries* 22: 439–448.

Fierro, V., et al. (1999), Prevention of spontaneous combustion in coal stockpiles – Experimental results in coal storage yard. *Fuel Processing Techn.* 59: 23–34.

Flynn, J.H. and Wall, L.A., (1966), General treatment of the thermogravimetry of polymers. *Journal of Research of the National Bureau of Standards Section A: Physics and Chemistry*, 70A: 487 ff.

Frank-Kamenetzkii, D.A. (1969), Diffusion and heat transfer in chemical kinetics. *Plenum Press,* New York, London.

Friedman, H.L. (1964), Kinetics of thermal degradation of char-forming plastics from thermogravimetry. Application to a phenolic plastic. *Journal of Polymer Science Part C: Polymer Symposia* 6: 183.

Kissinger, H.E. (1957), Reaction Kinetics in Differential Thermal Analysis. *Analytical Chemistry,* 1957. 29: 1702-1706.

Krause, U., Schmidt, M., Lohrer, C., (2006), A numerical model to simulate smouldering fires in bulk materials and dust deposits. *Journal of Loss Prevention in the Process industries* 19: 218-226.

Lohrer, C., Schmidt, M. and Krause, U., (2005), A study on the influence of liquid water and water vapour on the self-ignition of lignite coal-experiments and numerical simulations. *Journal of Loss Prevention in the Process Industries* 18(3): 167-177.

Ozawa, T. (1965), A New Method of Analyzing Thermogravimetric Data. *Bulletin of the Chemical Society of Japan*, 38(11): 1881-1886.

Schmidt, M., Erdt, R., Gödde, M., Salg, S. and Ittemann, L. (2020), Selbstentzündungsverhalten von Feststoffen: Validierung der Extrapolation von Labortests mit Hilfe halbtechnischer Versuche bis 1 m³. PTB-Mitteilungen 130(1): 9-18.

Vyazovkin, S., et al. (2011), ICTAC Kinetics Committee recommendations for performing kinetic computations on thermal analysis data. *Thermochimica Acta,* 520(1): 1-19.

Wu, D., Norman F., Schmidt, M., Vanierschot, M., Verplaetsen, F., Berghmans, J. and Van den Bulck, E., (2017), Numerical investigation on the self-ignition behaviour of coal dust accumulations: The roles of oxygen, diluent gas and dust volume. *Fuel* 188: 500-510.

Wu, D., Schmidt, M., Berghmans, J. (2019), Spontaneous ignition behaviour of coal dust accumulations: A comparison of extrapolation methods from lab-scale to industrial-scale. *Proceedings of the Combustion Institute* 37: 4181-4191.

Zhu, H., et al. (2013), Numerical investigation and theoretical prediction of self-ignition characteristics of coarse coal stockpiles. *Journal of Loss Prevention in the Process Industries* 26: 236-244.

DOI: 10.7795/810.20200724

Low Temperature Autoignition of Jet A and Surrogate Jet Fuels

Conor Martin & Joseph Shepherd

Graduate Aerospace Laboratories, California Institute of Technology, Pasadena, CA, U.S.A
E-mail: *cdmartin@caltech.edu*

Abstract

An experimental study of the low-temperature and low-pressure autoignition of Jet A and surrogate fuels was conducted using the ASTM-E659 standardized test method. Two surrogate fuels (Aachen and JI mixtures), their individual components and two batches (POSF-4658 and POSF-10325) of standardized Jet A were tested using the ASTM-E659 method for a range of fuel concentrations and temperatures. The ignition behaviors were categorized into four distinct ignition modes. The individual hydrocarbon components had a wide range of ignition behaviors and AIT values depending on the molecular structure. The two Jet A batches showed similar ignition behavior with measured AITs of 229°C ± 3°C and 225°C ± 3°C respectively. Both surrogates exhibited similar ignition behavior to Jet A with comparable AITs of 219°C ± 3.1°C (Aachen) and 228°C ± 3°C (JI) with the JI mixture proving to be a more suitable surrogate to Jet A in the low-temperature thermal ignition regime.

Keywords: *Thermal Ignition, Autoignition, Surrogate Fuel, Jet Fuel*

1 Introduction

1.1 Autoignition Background

The study of thermal ignition has been of interest to the combustion community for over a century with initial motivation arising from areas like process safety where the use, storage and shipment of combustible liquids was rapidly becoming commonplace in many areas of the world economy. This led to the development of standardized methods for determining minimum autoignition (AIT) or self ignition temperature (SIT) criteria for spontaneous thermal ignition of a given substance in air at atmospheric pressure.

A comprehensive summary of the early efforts to create an AIT test was given by Setchkin (1954). His studies led him to develop what would become the forerunner to the modern day ASTM-E659 standardization for determination of the AIT (ASTM, 2005). In this test, a small quantity of liquid fuel (0.05 to 0.5 mL) is injected into a preheated flask containing hot air with ignition determination made by visual observations and temperature measurements. Setchkin's study found that the minimum AIT is typically decreased as combustion chamber size is increased. Depending on the substance, this can have a large effect ($50 - 100$°C) on the measured AIT. From this and other details uncovered in these early studies it became clear that the AIT is not a fundamental property of a substance alone but is rather highly dependent on the method and apparatus used in its determination. More recent work at PTB has further illustrated this fact through studies on the influence of increased pressure, nitrogen dilution levels, and combustion vessel volume on AIT (Hirsch and Brandes, 2005, Brandes and Hirsch, 2017a,b).This makes it crucial to fully understand the methodology used in obtaining an AIT value if it is to be of any use in practical analysis and engineering design applications where conditions may differ significantly from the standard tests.

A similar test was also proposed by Zabetakis et al. (1954) in the same year as Setchkin (1954), with the major differences being the use of a 200 mL Erlenmeyer flask in place of the larger spherical flask and the use of the flask temperature instead of the gas temperature to report the test condition. This apparatus seems to also have been the forerunner of a separate AIT standardization, ASTM-D2155, which was discontinued in 1978 in favor of the E659 standard (ASTM, 1976), as well as the current international standard (ISO/IEC, 2017).

Although the ASTM-E659 is the now the widely accepted standard in North America for AIT determination, literature sources rarely specify this as the method used in obtaining their reported AIT's. Many safety data sheets (SDS) and chemical databases cite the origin of reported AIT numbers, but in almost all cases these sources are simply other chemical databases or property handbooks which do not claim to have performed any testing themselves or have cited a different test method for AIT determination, e.g., Sax (1957), Zabetakis (1965), CRC (1983), NFPA (1991), USCG (1999), Zakel et al. (2019). As a consequence, it is challenging to determine the origin of reported AIT numbers or the details of the testing method. This lack of consistency in the literature complicates the comparison of AIT values of different fuels or the same fuels tested by different research groups.

The nature of the data also hampers the development of models for the prediction of the AIT based on molecular properties alone. Affens et al. (1961) used the same apparatus as Setchkin (1954) in an effort to correlate ignition behavior to chemical structure for various classes of alkane and aromatic substances. They noted some correlations between a decrease in chain length, methyl groups, unsaturation, and chain branching with an increase in the minimum AIT for aliphatic hydrocarbons as well as a correlation between existing side chains and side chain length and increased AIT for alicyclic compounds and aromatics (Affens et al., 1961). More recently, a study by Tsai et al. (2012) attempted to fit a model to the AIT of 820 compounds reported in the DIPPR database based on a set of molecular descriptors. This approach was moderately successful (36°C mean absolute error) in reproducing experimental AIT values. Given the manual nature of the injection process and the wide range of fuel viscosity and vapor pressure examined in these studies, it is not surprising that there are significant discrepancies between test data and predictions based solely on molecular structure.

A significant issue in interpreting and modeling the ASTM-E659 test is the lack of characterization or control of the mixing processes between the fuel and hot air. The formation of droplets, vaporization and diffusion of the fuel into the air, convective motion and the potential impingement of the fuel on the hot flask surface make this a very challenging situation to measure and model. The fuel-air mixture is likely to be highly nonuniform as is the temperature distribution due to the cooling effects of fuel vaporization. Despite the widespread use of ASTM-E659 and related test methods, the inherent variability and complexity has inhibited scientific investigations and modeling efforts. A brief summary and discussion of some of these issues related modeling and theoretical treatment of AIT is presented in Hattwig and Steen (2004).

Although widely used in safety assessment and setting design criteria, it is apparent that the ASTM-E659 test is not always an appropriate method for evaluating industrial thermal ignition hazards. In the particular case of aircraft, most of the hot surfaces encountered are metals (steel, nickel and titanium alloys, and aluminum) rather than glass as in ASTM-E659 testing. Heating transients and ignition events can also occur over much longer times than the 10 minutes examined in ASTM-E659 testing. These are important considerations since the surface material can have a significant effect on the ignition thresholds for a given fuel ($>$ 100°C variation) and longer duration experiments can lead to significant fuel decomposition (Smyth, 1990) as well as unusual ignition transients (Boettcher et al., 2012) without any obvious rapid energy release. Even more important than surface material are the differences between the confined flow within the vessel used in ASTM-E659 testing and unconfined or partially confined external flows that occur in many industrial situations. The heated surface geometry and residence time in the thermal layer (Jones and Shepherd, 2020) can be significantly different in actual hazards than in ASTM-E659 testing. This is important because fuel decomposition and the formation of the ignition kernel has been observed to take place preferentially close to the heated surface (Coronel et al., 2019).

Studies of autoignition behavior of commodity fuels have been conducted using heated shock tubes and rapid compression machines (RCMs) to measure ignition delay times. In comparison to ASTM-E659 testing, these studies have well-controlled conditions and instrumentation that enables validation of chemical reaction models of ignition. However, the test gas temperatures are significantly higher than those relevant to low temperature thermal hazards and the minimum AIT conditions examined in ASTM-E659 testing. These ignition studies (Vasu et al., 2008, Wang and Oehlschlaeger, 2012, Liang et al., 2012, Zhukov et al., 2014, De Toni et al., 2017) have also mainly been conducted at elevated pressures (8-51 atm) which are uncharacteristic of thermal ignition hazards in aircraft and industrial hazards associated with accidental releases. These studies examined kerosene fuels (including Jet A) however with the typical wide variation in composition found in commodity supplies (Edwards, 2017). The variability in commodity fuels and the associated uncertainty in the experimental results has motivated the development of surrogate fuels as well as standardized batches of Jet A to facilitate comparison between experimental studies.

1.2 Surrogate Fuels

Commodity fuels like gasoline, diesel or Jet A typically consist of hundreds of different hydrocarbon species in imprecise and varying quantities, even between different batches of the same fuel. This complexity makes it difficult both to accurately reproduce experimental results across distinct fuel batches and to model the reaction mechanisms leading to ignition. As an alternative, suitably representative mixtures of hydrocarbons, called surrogate fuels, can be developed to mimic a few important commodity fuel characteristics such as laminar flame speed, ignition delay time, cetane number and distillation curve while consisting of only a handful of species in well controlled concentrations (Mueller et al., 2012, Chen et al., 2016, Kim and Violi, 2018). This makes surrogates much more amenable to experimental reproducibility as well as numerical modeling because the species and reaction pathways to consider are both far fewer in number and typically much better understood than they are for many components of the commodity fuel. Several surrogate fuels have been developed in the literature to mimic Jet A ignition behavior at high pressures and a range of temperatures similar to the studies previously mentioned (T=645-1750 K at 8.5-20 atm). These surrogate fuel studies have used the existing shock tube and RCM data from the previously mentioned studies as sources of validation of their proposed surrogate blends (Dean et al., 2007, Dooley et al., 2010, Chen et al., 2016). Few if any of these detailed surrogate studies have been performed in the very low-temperature (<600 K) and low pressure regime of autoignition likely due to the scarcity of data available in this regime for model validation. Some simple fuels like n-Hexane have been studied extensively at these conditions (Mével et al., 2019) but these studies have not yet been performed on larger hydrocarbon molecules that are more characteristic of Jet A. For this reason, it is unclear if the previously developed surrogates are relevant to autoignition of Jet A at low pressure and temperature conditions.

Two Jet A surrogates from the literature have been identified in this study for their relevance to matching ignition behavior as well as for their simplicity in composition. These surrogates are: (1) the Aachen surrogate (Honnet et al., 2009): n-Decane/1,2,4-Trimethylbenzene, (80/20 wt%), and (2) the JI surrogate (Chen et al., 2016): n-Dodecane/Isocetane/Trans-decalin/Toluene, (0.3/0.36/0.246/0.094 mol%). These surrogates were formulated in an effort to match high-temperature and high-pressure autoignition behavior of Jet A so it is crucial to determine if their usefulness can be extended to Jet A studies focused on the low temperature and low pressure regime of thermal ignition. This is indeed one of the main goals of the present study. To validate these surrogates' ignition behavior in the regime of interest, two well-controlled and extensively studied (Edwards, 2017) blends of Jet A were also examined: POSF-4658 and POSF-10325. These fuel blends also provide a quantifiable baseline for comparison with the surrogate samples on a chemical level which is shown in Table 1.

Table 1: Comparison between composition of Jet A blends and surrogate fuels

		% by Weight			
		POSF-4658	**POSF-10325**	**Aachen Surrogate**	**JI Surrogate**
Alkanes	n-Alkanes	19	19.98	80	29.17
	iso-Alkanes	31.34	29.69	-	46.53
	cyclo-Alkanes	28.42	31.79	-	-
	Total	78.76	81.46	80	75.7
Aromatics	Alkylbenzenes	13.69	12.9	20	4.94
	Alkylnapthalenes	1.76	2.34	-	-
	Cycloaromatics	5.79	3.29	-	19.41
	Total	21.24	18.53	20	24.35
Avg. Molecular Formula		$C_{11.69}H_{22.62}$	$C_{11.4}H_{22.1}$	$C_{9.77}H_{19.7}$	$C_{12.49}H_{25.22}$
H/C ratio		1.935	1.939	2.016	2.019

In studying multi-component liquid fuels like these surrogates and Jet A, there are several difficulties one must be aware of. The major challenge in performing experiments in particular is the discrepancy between the gas phase and liquid phase compositions owing to differences in vapor pressure of the individual species. This is especially important in this work as all ignition takes place in the vapor phase. Therefore in order to appropriately match the Jet A ignition behavior with a surrogate, it is the vapor phase composition that must be matched. This approach is taken in the literature with the computational formulation of the JI surrogate which was designed to match the distillation curve of Jet A in order to match both droplet evaporation and ignition behavior (Chen et al., 2016). Other surrogate studies like that of the Aachen surrogate instead simply attempted to reduce to as few representative components as possible and to roughly capture the properties of the alkanes and aromatics with one compound of each without a comprehensive analysis of the physical chemistry at play in the mixture (Honnet et al., 2009).

2 Experiments

The procedure and testing apparatus employed in this study was the same as that described in the ASTM-E659 standardized test specification for the determination of the AIT and so the test method is only briefly discussed. The test apparatus is shown in Fig. 1 along with a schematic representation of the combustion vessel contained within the furnace. A small liquid sample of the fuel to be tested was injected via syringe into a uniformly heated 500mL flask containing room air and left open to the atmosphere. The lights were turned out and the sample was observed via a mirror mounted above the flask opening using a Phantom VR3746 high speed camera which was manually triggered upon ignition of the sample. The gas temperature within the flask was also recorded and monitored during each test in order to determine the extent of self heating occurring in the sample and to provide a secondary indication of ignition via the presence of a sharp temperature spike. This was also used to obtain a measure of ignition delay time, τ_{ign} which was defined as the time between fuel injection and ignition. Typically these events were very easily distinguished in the temperature profile with the injection corresponding to a steep temperature drop by a few degrees and the ignition evidenced by a sharp temperature rise. However, as will be discussed in section 3.1, some temperature profiles did not exhibit such a sharp spike in temperature which led to the classification of multiple distinct ignition modes.

Each test was limited to no more than 10 minutes, at which point if ignition had not yet been observed then a non-ignition case was recorded. If instead a flame appeared or the temperature profile indicated some steep temperature increase then an ignition or cool flame event was recorded. However, in many cases it would become clear that the sample was not going to ignite long before the 10 minute limit as self heating typically only lasted for 4-5 minutes after injection for the substances studied here. After the gas temperature leveled off, it was usually evidence that a limit had been reached and the temperature would begin to decay. In these cases, the sample was observed for an extra 1-2 minutes after the level off and if the decay continued then the test was considered as a non-ignition case and preparation for the next test would begin. Preparation for the next test included the use of a hot air gun or blow dryer applied to the top of the apparatus for up to 30 seconds in order to purge the flask of any remaining ignition products or unburnt fuel. Following purging, temperature adjustments were made via a temperature controller and the furnace was allowed to return to equilibrium at the new set temperature.

2.1 Equipment

The furnace used was a Mellen CV12 crucible furnace with a 13.3 cm diameter by 20 cm deep cylindrical heated volume capable of achieving temperatures up to 1250°C. A PID controller (Love Controls series 16B) system was used to set the furnace at the desired temperature and was accurate to 1°C. A schematic cross section of the apparatus is shown in Fig. 1 which illustrates the location of the 500 mL round bottom borosilicate flask within the heated volume along with the four thermocouples used to monitor the temperature evolution during a test. The flask was suspended and secured in the furnace by means of an insulating ceramic holder fabricated using a fused silica casting compound.

The location of the four type K thermocouples are also shown in the schematic in Fig. 1 with the gas temperature being read from T_4 which was suspended approximately in the center of the flask volume. Preliminary tests to characterize the apparatus showed that the location of the gas phase thermocouple within the volume had little effect on the reading ($\pm 0.5^\circ$C) providing indication of temperature uniformity within the flask at elevated temperatures. The thermocouples were constructed from 36 gauge (0.127 mm diameter) wire and sheathed in stainless steel for protection. The temperatures at the bottom, side, and neck of the flask's outer wall were monitored via T_1,T_2,and T_3 respectively. The temperature of the flask wall was much less uniform than the gas, with typical variations of up to 5°C when set near 250°C or 10-15°C above 400°C.

Temperature profiles were recorded from the time of injection through any self heating or ignition event using an OMEGA HH520 four channel data logger calibrated to the nearest 0.1°C up to 600°C and 1°C for higher temperatures. All channels were sampled at 1 Hz as per the ASTM-E659 specification. Reported experimental errors were estimated based on both the standard error limits for type K thermocouple probes and the reported error of the HH520 datalogger itself.

2.2 Surrogate Fuel Preparation

An early attempt at mixing the surrogates was made using a Tree Model HRS3100 scale calibrated to the nearest 0.001 g to weigh out the individual compounds, but this method proved unreliable as shown by GC-FID (Gas Chromatography with Flame Ionization Detector) measurements (Sund, 2019). The first batch of surrogate used a mixture of Trans- and Cis-decalin (the AITs of these isomers are similar) and the mixture is much easier to obtain in larger quantities than either isomer individually. The second batch of the surrogate which was used for the AIT testing used only the Trans-decalin isomer. The mass fractions obtained in the GC-FID analysis as well as target values are shown in Table 2.

The results showed that for the JI surrogate, two of the four components had relatively large percent errors in their measured mass fractions (Toluene and Decalin). These two components also both happened to have the smallest target mass fractions and Toluene in particular had the highest vapor pressure by far at room temperature. As a result, it was determined that there were two possible factors at play in producing such larger errors, (1) inaccurate mixing and (2) poor sealing/storage of the fuel batch. To address these issues, two changes were made in mixing the second batch of JI, namely (1) the use of pipettes to measure out the components volumetrically, and (2) the

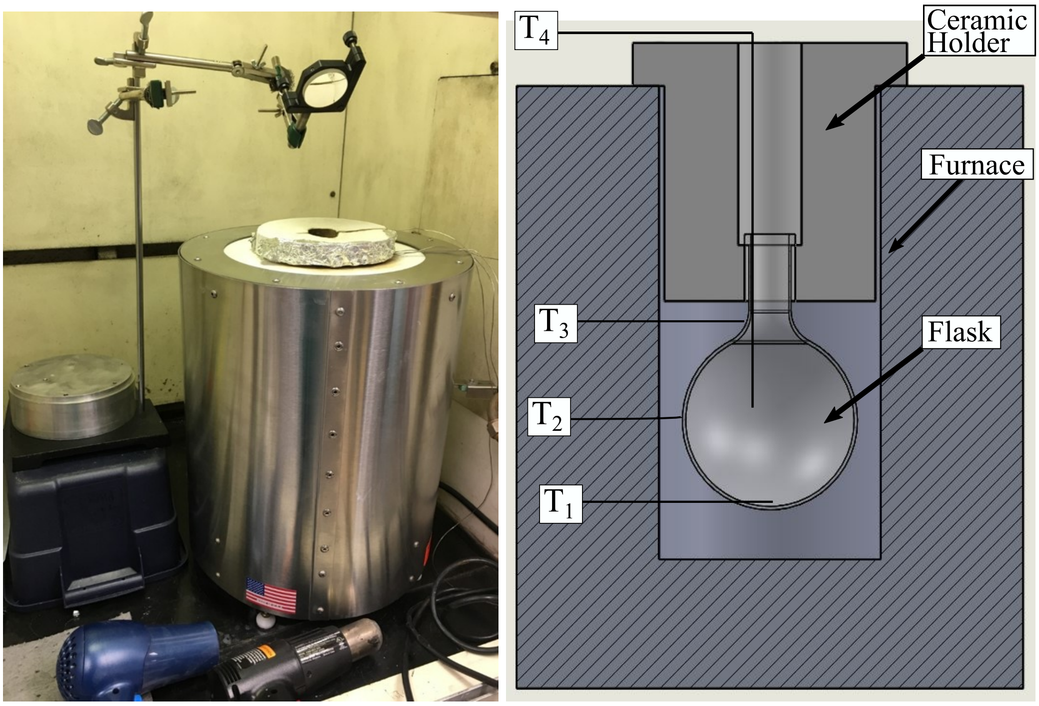

***Fig. 1**: (left) ASTM-E659 test apparatus (right) Cross section of internal heated region with thermocouple locations highlighted*

use of higher quality storage vessels (PTFE lined caps) and a chemical refrigerator to maintain the batch at a low temperature in order to lower the vapor pressure of the entire mixture and mitigate the preferential loss of lighter compounds over time. The second batch was mixed on a volumetric basis using graduated pipettes into a large 146 mL total batch in order to minimize volume measurement errors especially in the more dilute components. This batch was then stored in an ABS flammable storage refrigerator maintained at 3°C and smaller quantities were extracted for use in the autoignition experiments.

Table 2: JI surrogate (Batch 1) results from GC-FID analysis

	Mass fraction			**Vapor Pressure[a] (T=20°C) [kPa]**
Fuel	**Target**	**Measured**	**% Error**	-
n-Dodecane	0.2915	0.2980	2.24	0.012
Isocetane	0.4651	0.4643	0.15	0.004
Decalin	0.1940	0.2066	6.49	0.116
Toluene	0.0494	0.0310	37.2	2.903

[a] Sund (2019)

3 Results and discussion

3.1 Classifications

Throughout the range of ignition tests conducted here, there were 4 distinct ignition modes observed along with non-ignition cases. These ignition behaviors were classified as (I) Ignition, (II) Cool Flame, (III) Non-Luminous Cool Flame and (IV) Rapid Reaction. These were distinguished using a combination of visual evidence as well as the reading of the gas phase thermocouple (T_4). Qualitatively the differences between these modes are summarized in Table 3. This classification is limited mainly to qualitative descriptors since the temperature rises and timescales for the same ignition mode can vary substantially between two different fuels or even different compositions of the same fuel. For instance mode III ignition events for n-Decane were seen to produce a temperature rise of 50-200°C on timescales of 1.5-3.5 minutes for various fuel volumes while for Jet A these events were only capable of 25-70°C temperature increases on similar timescales. A representative series of images showing the time progression of each of the first three ignition modes

Table 3: Classifications of various ignition behaviors observed in ASTM-E659

Ignition Mode	**Name**	**Luminosity**	**Temperature Rise (ΔT)**	**Timescale for reaction**
I	Ignition	Large	Large	5 sec - 2.5 mins
II	Cool Flame	Small	Small	15 sec - 4 mins
III	Non-Luminous Cool Flame	None[a]	Large	1 - 5 mins
IV	Rapid Reaction	None	Small	30 sec - 2 mins
-	Non-Ignition	None	<15°C	> 4 - 5 mins

[a] Faint glow only visible to naked eye and small puff of smoke

is shown in Fig. 2. In events classified as mode I, the images show that the initial explosion progresses rapidly and the flame quickly expands out the top opening of the flask before burning out. For mode II events, it was typically observed that the ignition event is less energetic and the flame remains confined to the interior of the flask indicative of a low pressure rise which is consistent with the measured low temperature rise. Mode II was primarily observed in compounds with high ignition temperatures ($> 400°\text{C}$) including the aromatics and Isocetane. Mode III ignition events were more prevalent in heavier hydrocarbon species and were indicated by a brief and very dim glow visible to the naked eye only in complete darkness. Alternatively, a puff of smoke escaping from the flask could also be observed in these cases and was much easier to record with the current setup as shown by the series of images for mode III in Fig. 2. Mode IV was similarly non-luminous but was distinguished by a much smaller temperature rise and shorter timescale for the peak temperature to be reached as compared to mode III. These events were observed primarily for multi-component mixtures including the Jet A blends and surrogate fuels.

The thermocouple traces accompanying each of these ignition cases are shown in Fig. 2. The difference between the initial gas temperature and the peak temperature measured by T_4 is defined as the peak temperature rise. In some cases the visual evidence alone was not sufficient to distinguish between ignition modes I and II so the thermocouple trace was used for classification. Mode II ignition was always characterized by a longer ignition delay time as well as a lower peak temperature as compared to mode I events for the same fuel. Mode III also had a far longer timescale than the other modes which further distinguished it from the other modes. Mode IV was unique in that the reaction delay occurred on a similar timescale as that of a normal mode I ignition but resulted in a very small temperature spike, in some cases comparable to non-ignition cases.

The results of the ASTM-E659 ignition testing are presented here for each of the Jet A batches and surrogates studied. These data are summarized for each fuel by separate plots containing each ignition test as a data point in the temperature-composition space. Also plotted are the reported AIT values from the literature sources discussed in section 1.1. However, these numbers are always reported as a global minimum with no associated composition given so these values are plotted as constant lines across the compositional domain. The peak temperature rise during each test (ΔT) was also recorded and is shown here for two fuels. Tests were also performed with the molecular components of each surrogate as well as n-Hexane but complete results are not presented here.

A global equivalence ratio (ϕ) was defined in order to more easily compare results from fuels of different structure and molecular weight by putting the seemingly arbitrary fuel volumes into context. This ϕ is defined based on the vapor space for each fuel sample as if the fuel mass were fully vaporized and mixed homogeneously with air and is calculated by the equation

$$\phi = \frac{m_{fuel}/(\rho_{air} V_{flask})}{(F/A)_{stoich}} \tag{1}$$

where m_{fuel} is the fuel mass, V_{flask} is the flask volume, ρ_{air} is the air density, and $(F/A)_{stoich}$ is the stoichiometric fuel to air mass ratio. Using this parameter, it is much easier to see what the effect of having a fuel rich ($\phi > 1$) or fuel lean ($\phi < 1$) mixture is on the ignition behavior and to interpret the different ignition modes.

3.2 Alkanes & Aromatics

Three normal alkanes (n-Hexane, n-Decane, and n-Dodecane) and three aromatic compounds (1,2,4-Trimethylbenzene(TMB), Toluene, Trans-decalin) were studied along with one branched

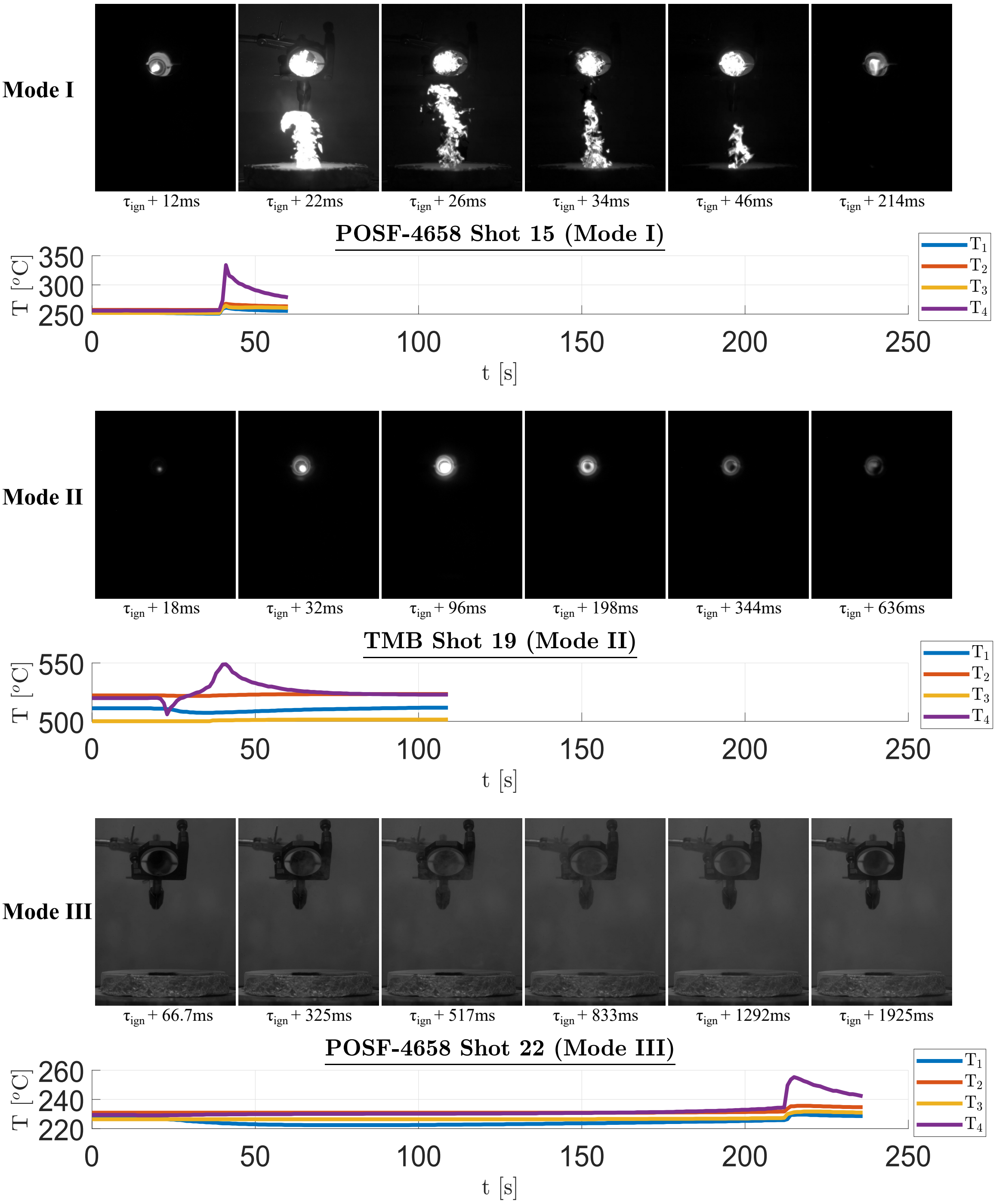

***Fig. 2**: Representative ignition events for 3 distinct ignition modes: (I) Ignition, (II) Cool flame, (III) and Non luminous cool flame (Note these correspond to POSF-4658 Shot 15, TMB Shot 19, and POSF-4658 Shot 22)*

DOI: 10.7795/810.20200724

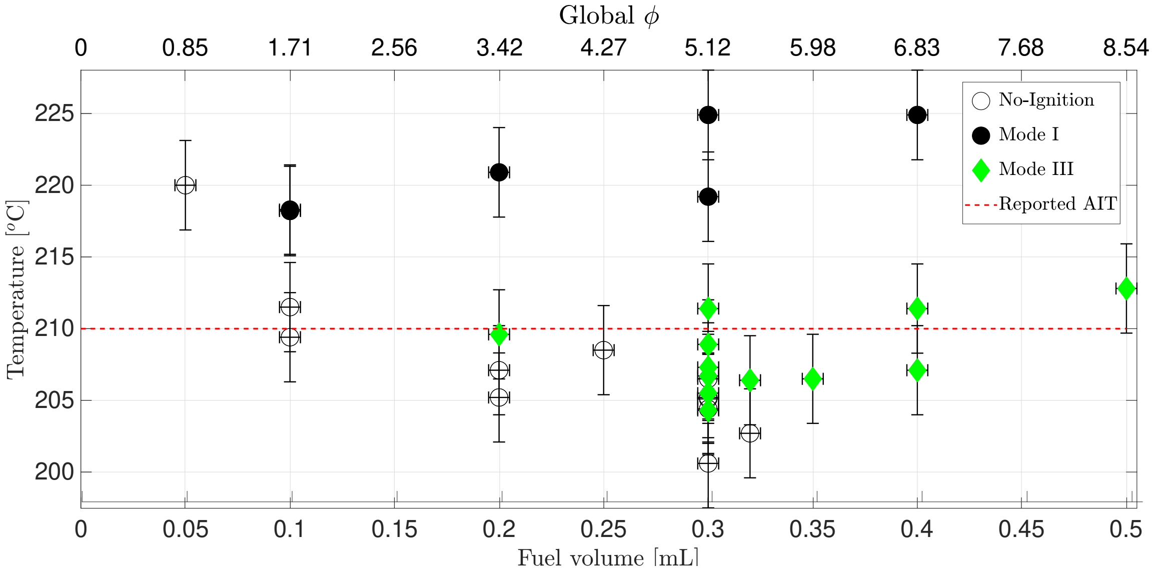

***Fig. 3**: n-Alkane representative ignition test results (n-Decane)*

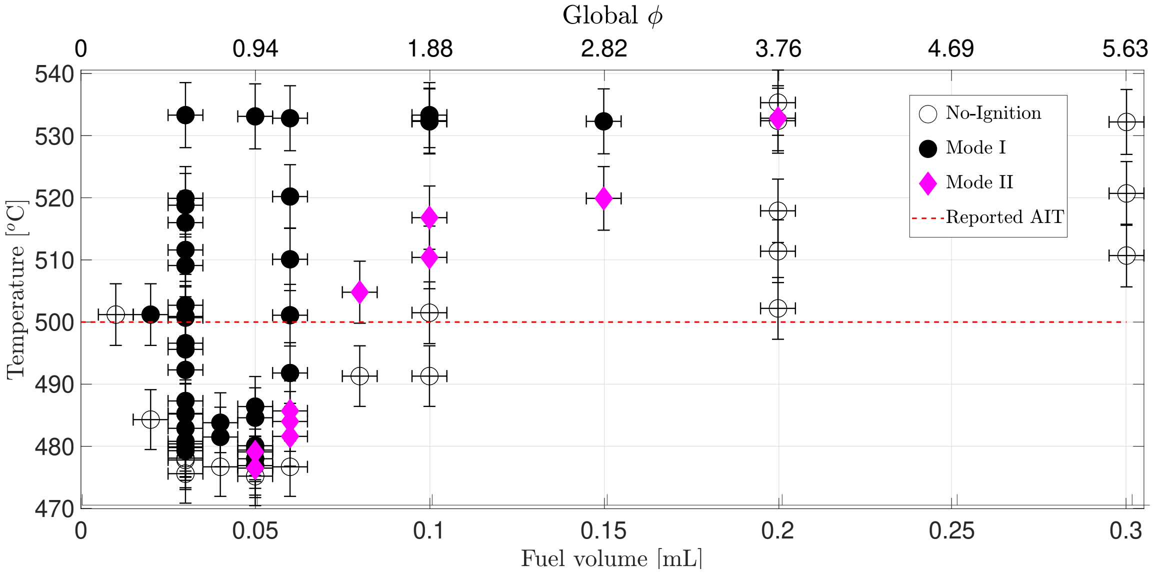

***Fig. 4**: Aromatic representative ignition test results (1,2,4-Trimethylbenzene)*

alkane (2,2,4,4,6,8,8-heptamethylnonane, more commonly known as Isocetane). These compounds were chosen for study because they are the molecular components for both of the surrogate fuels (Aachen and JI). n-Hexane was also chosen for study due to extensive previous work from our group on n-Hexane ignition in various test conditions, see Boettcher et al. (2012, 2013), Mével et al. (2014), Coronel et al. (2018), Mével et al. (2019). Some representative results of n-alkane and aromatic ignition results are shown in Fig. 3 and Fig. 4 respectively. The influence of fuel volume on AIT seen in these figures is a result of the complex dynamics associated with the fuel injection, vaporization and mixing processes which can create an inhomogeneous mixture within the combustion chamber with pockets that may be beyond the rich or lean flammability limits. These effects require further study in the present geometry in order to fully understand the influ-

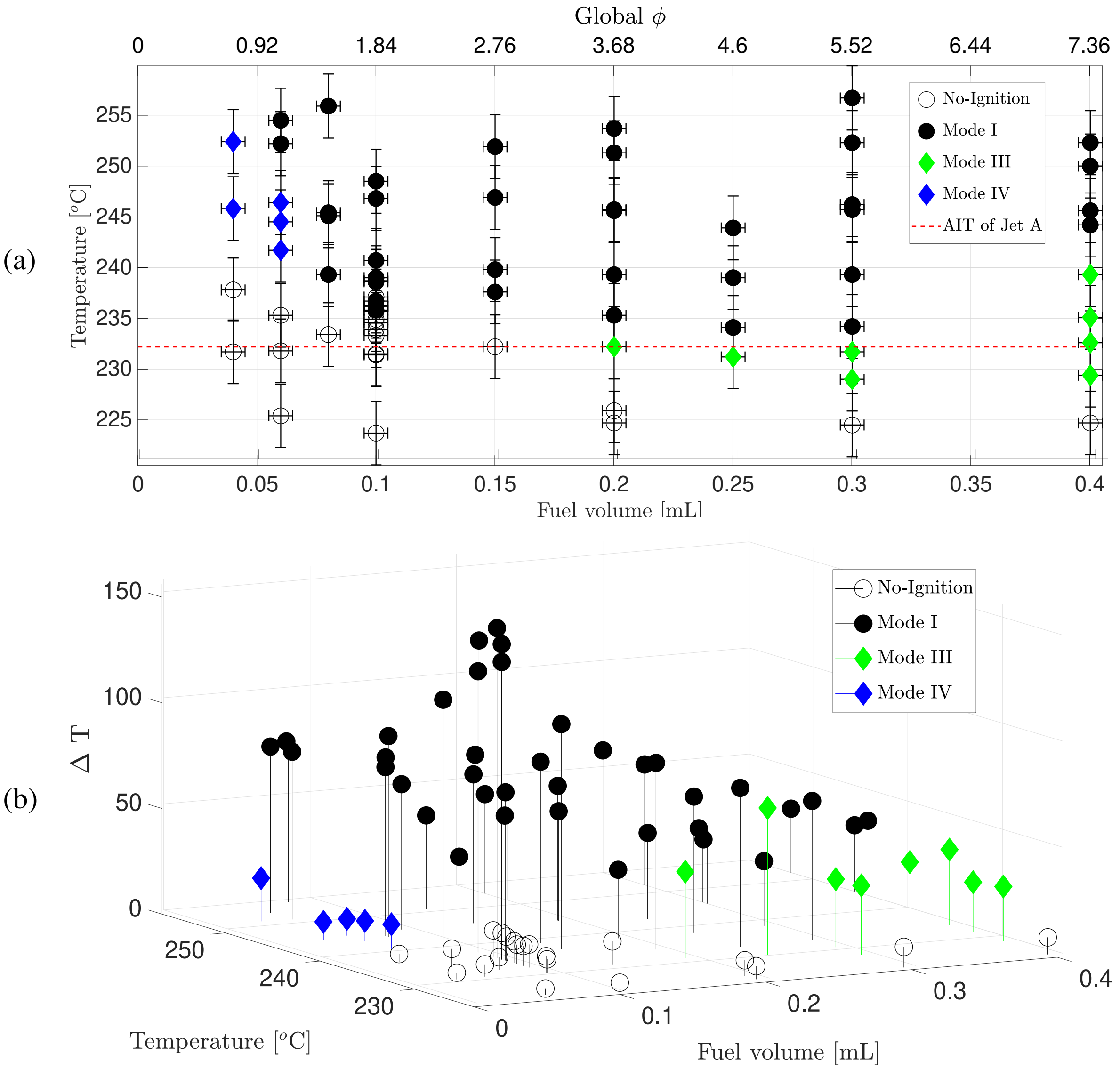

***Fig. 5**: (a) POSF-4658 (Jet A) ignition testing results (b) Peak temperature rise*

ence of these processes on AIT. The global minimum AIT measured from each of the fuels as well as the corresponding test conditions are also summarized in Table 4 for convenience. The n-alkanes studied showed generally lower AITs than Isocetane and the aromatics which is consistent with the connections made between chemical structure (branching, unsaturation) and AIT as laid out in Affens et al. (1961). The n-alkanes also generally exhibited lower ignition temperatures at more fuel rich conditions where mode III ignition events became dominant. Isocetane also followed this trend but with mode II ignition becoming dominant at fuel rich conditions. The TMB and Toluene showed an opposite trend in that the minimum AIT was generally observed at near stoichiometric or slightly lean conditions with increasingly great difficulty igniting at rich conditions. Additionally mode II ignition rapidly became dominant at even slightly rich conditions for both of these aromatics. The exception to these trends for the aromatic fuels was the Trans-decalin which became more easily ignited at rich conditions with a far lower AIT around 240°C. In addi-

DOI: 10.7795/810.20200724

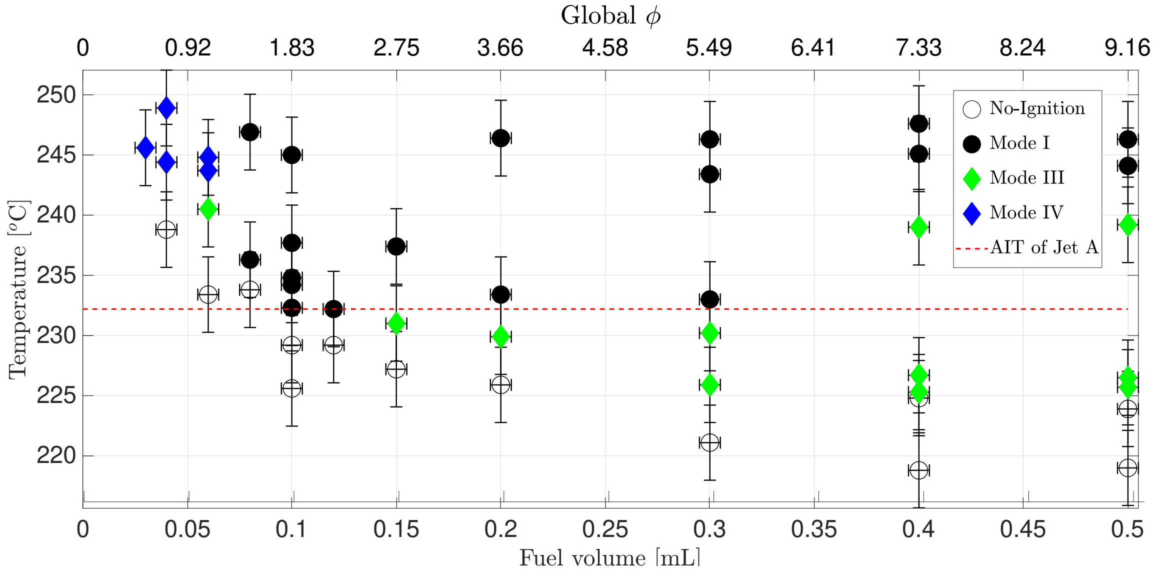

***Fig. 6**: POSF-10325 (Jet A) ignition testing results*

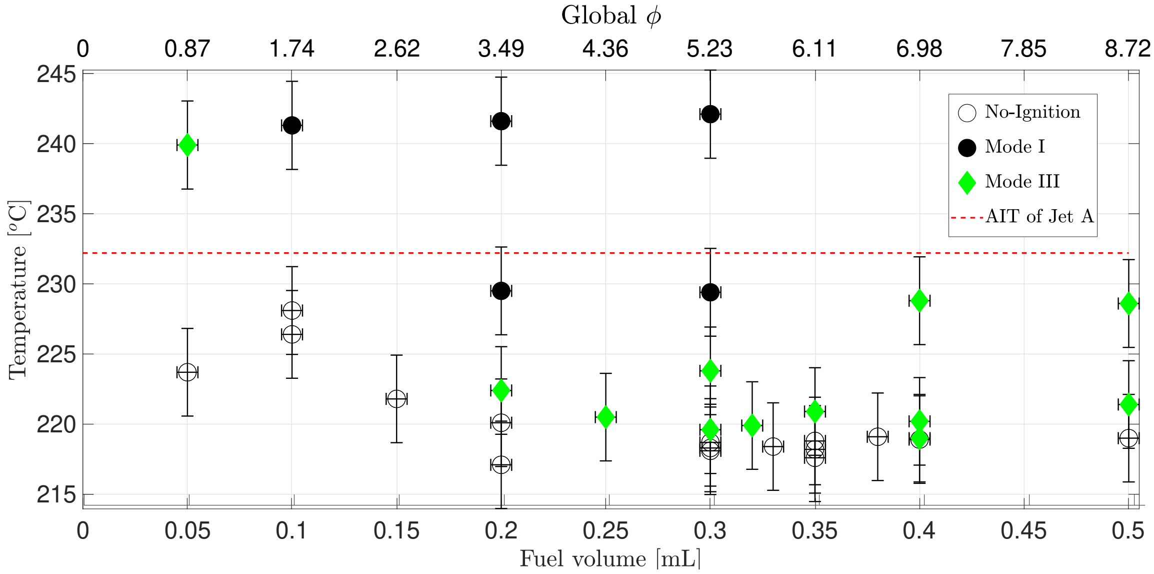

***Fig. 7**: Aachen surrogate ignition testing results*

tion Trans-decalin exhibited all four ignition modes with mode II and III both becoming dominant at rich conditions and mode IV ignition being observed only at lean conditions near the ignition threshold. The temperature rises measured were also far higher for the n-alkanes than Isocetane or any of the aromatics.

3.3 Multi-component fuels

The multi-component fuels examined in this study were Jet A fuel standards (POSF-4658 and POSF-10325) and surrogate jet fuels from the literature (Aachen and JI). Some of the observed ignition behaviors of these fuels can be attributed to characteristics of their molecular components.

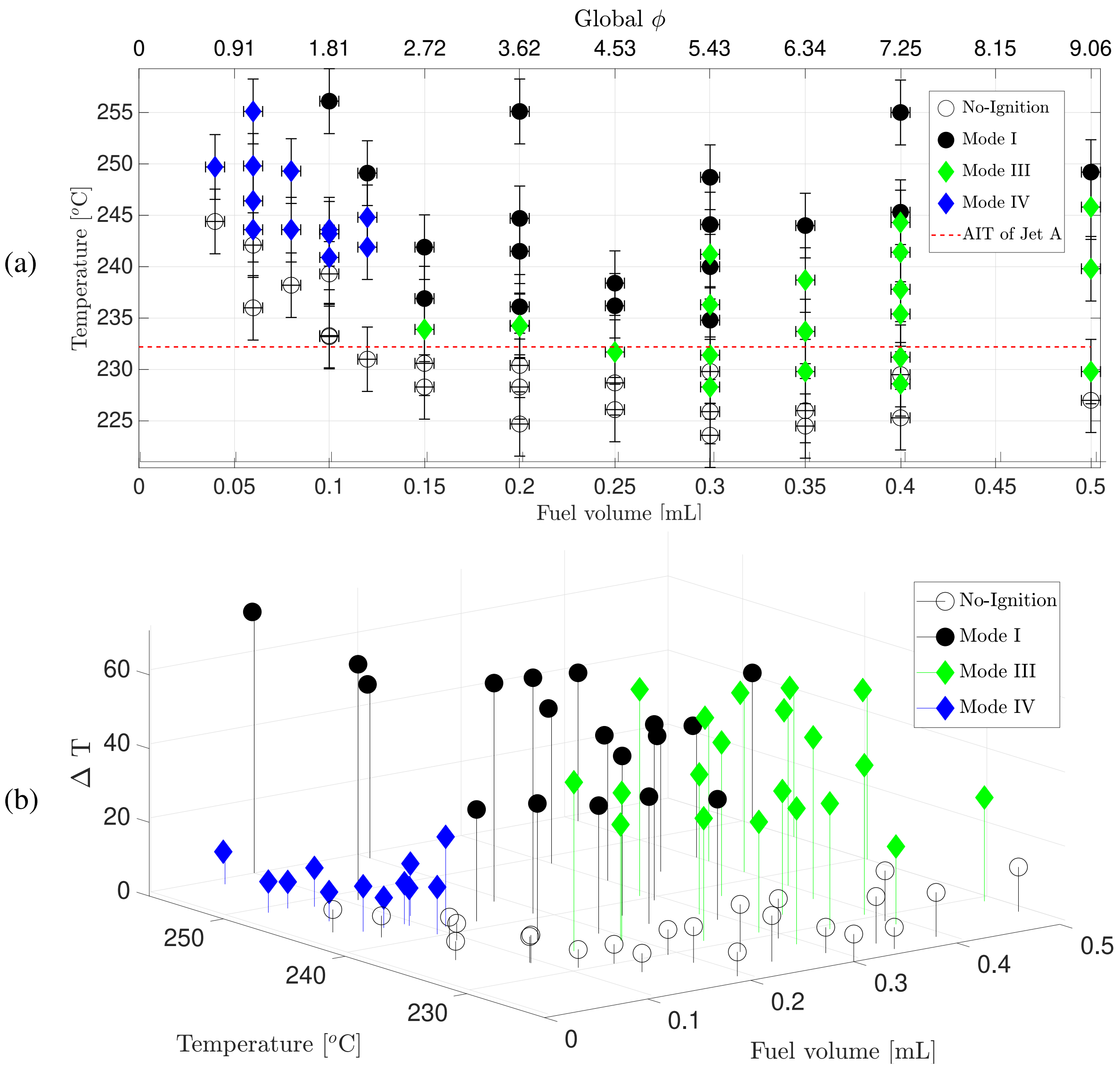

***Fig. 8**: (a) JI surrogate ignition testing results (b) Peak temperature rise*

As summarized in Table 1, these fuels are effectively entirely composed of alkanes and aromatic compounds with the alkanes being present in much larger proportions than the aromatics (approximately 3-4 to 1) so the alkane ignition behavior is expected to dominate.

POSF-4658 is a Jet A blend which has been examined extensively by a number of researchers, see Edwards (2017). Fig. 5 (a) shows the ignition results obtained in this study for this blend. Mode III and mode IV events are observed in the rich and lean regimes respectively which is similar to the behavior of the simple fuels. There is a good agreement between these experimental results and the reported Jet A AIT value ($T = 229.0°\mathrm{C} \pm 3.1°\mathrm{C}$ vs 232°C). This relatively low AIT can likely be attributed to the alkane dominant composition of Jet A since alkanes generally exhibit AITs in this range while aromatic compounds tend to be much higher. Fig. 5 (b) shows temperature rises around 100°C while the mode III and IV events exhibit far lower temperature increases.

POSF-101325 shows substantially similar ignition behavior to POSF-4658, which is consistent

Table 4: Summary of measured minimum AIT values and corresponding test conditions

		Measured			Literature
	Fuel	**Fuel Volume [mL]**	**Global ϕ**	**Minimum AIT [°C]**	**Reported AIT [°C]**
Alkanes	n-Hexane	0.10	1.56	235.3 ± 3.1	225[a] (236[b])
	n-Decane	0.30	5.12	204.3 ± 3.1	210[ab]
	n-Dodecane	0.30	5.24	202.2 ± 3.1	203[a]
	Isocetane	0.40	7.36	395.2 ± 4.1	-
Aromatics	1,2,4-Trimethylbenzene	0.05	0.94	476.5 ± 4.8	500[ab]
	Trans-decalin	0.25	5.04	239.5 ± 3.1	255[a]
	Toluene	0.06	1.09	508.2 ± 5.0	480[ab]
Multi component	POSF-4658	0.30	5.52	229.0 ± 3.1	232[c]
	POSF-10325	0.40	7.33	225.3 ± 3.1	232[c]
	Aachen Surrogate	0.40	6.98	219.0 ± 3.1	-
	JI Surrogate	0.30	5.43	228.3 ± 3.1	-

[a] NFPA (1991) ; [b] USCG (1999) ; [c] FAA (2018)

with the modest differences in composition between the two fuel blends (Table 1). The POSF-10325 ignition data shown in Fig. 6 is similar to Fig. 5 (a) but has a few minor differences. One of these differences is in the lean regime where the mode IV ignition occurs at slightly lower temperatures than for the POSF-4658. Peak temperature rises for all ignition modes are also similar to those seen for POSF-4658 so are not included here. The minimum AIT is also similar to that found for POSF-4658.

The Aachen surrogate is a simple two component blend which seems to capture the general trends from the Jet A batches while missing some details like mode IV events in the lean regime as seen in Fig. 7 (a). Mode III events are generally well captured in the rich regime with this mode extending to higher temperatures for richer compositions as was seen for Jet A. The Aachen surrogate also exhibits relatively lower ignition temperatures than those seen for Jet A samples as well as the reported value ($T = 219.0°\text{C} \pm 3.1°\text{C}$ vs 232°C). The peak temperature rises (not shown) are also quite similar to that of the two Jet A batches.

The more complex JI surrogate consisting of 4 components does a much better job at reproducing the ignition behaviors found in the Jet A samples. Fig. 8(a) shows the existence of mode IV events in the near stoichiometric regime along with the mode III events being maintained in the rich regime. However, these mode IV events occur at slightly richer compositions than observed for Jet A. Fig. 8(b) shows another difference in that the temperature rises measured for JI are much lower than those seen in either of the Jet A samples as shown by Fig. 5(b). The minimum AIT measured here is also much more consistent with the reported value as well as that measured for the Jet A samples ($T = 228.3°\text{C} \pm 3.1°\text{C}$ vs 232°C).

The global minimum AIT measured from each of the fuels as well as the corresponding test conditions are summarized in Table 4 and compared to some values reported in the literature. The differences between present results and literature values range from 1 to 7%, comparable to or larger than the estimated uncertainty of ±1%.

DOI: 10.7795/810.20200724

4 Conclusions

The very low-temperature thermal ignition regime is important to industrial safety for commodity fuels but presents many challenges for combustion experimenters and modelers. In concert with related efforts in our laboratory, we have examined the potential for using surrogate fuels with simple and well-controlled composition rather than samples of Jet A which can have wide variability in properties. As a first step in determining the applicability of surrogates for very low temperature Jet A thermal ignition studies, we have examined the ignition behavior in the ASTM-E659 apparatus for two Jet A surrogates, and two standardized batches of Jet A.

Four distinct ignition modes were observed near the AIT threshold and were characterized using the limited diagnostic tools possible in the ASTM-E659 test. Experimental results were compared with reported minimum AIT numbers from literature sources with some data obtained showing significant discrepancies with reported AIT numbers. The multi-component fuels exhibited ignition characteristics that appear to be dominated by n-alkanes which is consistent with the predominance of alkane components in these fuels. The two Jet A batches studied showed very similar ignition behavior across the parameter space while both the Aachen and JI surrogates were able to reasonably replicate most of the Jet A ignition trends with composition and temperature. The JI surrogate did however exhibit much better agreement for ignition thresholds in comparison with Jet A than the Aachen surrogate and was even able to reproduce the existence of mode IV ignition events which the Aachen surrogate could not.

Acknowledgements

This work was carried out in the Explosion Dynamics Laboratory of the California Institute of Technology and was partially supported by The Boeing Company (CT-BA-GTA-1). Conor Martin was also supported by the Department of Defense (DoD) through the National Defense Science & Engineering Graduate Fellowship (NDSEG) Program. The GC-FID measurements were made in the Caltech Environmental Analysis Center with the guidance of Dr. Nathan Deleska.

References

Affens, W. A., Johnson, J. E., Carhart, H. W. (1961). *Effect of Chemical Structure on Spontaneous Ignition of Hydrocarbons.* Journal of Chemical & Engineering Data, 6(4):613–619.

ASTM (1976). *ASTM-D2155:Test Method for Determination of Fire Resistance of Aircraft Hydraulic Fluids by Autoignition Temperature.*

ASTM (2005). *ASTM-E659: Standard Test Method for Autoignition Temperature of Liquid Chemicals.*

Boettcher, P. A., Menon, S. K., Ventura, B. L., Blanquart, G., Shepherd, J. E. (2013). *Cyclic flame propagation in premixed combustion.* Journal of Fluid Mechanics, 735:176–202.

Boettcher, P., Mével, R., Thomas, V., Shepherd, J. (2012). *The effect of heating rates on low temperature hexane air combustion.* Fuel, 96:392–403.

Brandes, E., Hirsch, W. (2017a). *Zündtemperaturen In Anderen Oxidationsmitteln Als Luft.* Technical report, PTB Braunschweig.

Brandes, E., Hirsch, W. (2017b). *Zündtemperaturen In Großen Behältern.* Technical report, PTB Braunschweig.

Chen, X., Khani, E., Chen, C. (2016). *A unified jet fuel surrogate for droplet evaporation and ignition.* Fuel, 182:284–291.

Coronel, S. A., Lapointe, S., Shepherd, J. E. (2019). *Boundary Layer Ignition Modeling.* In *11th*

U.S. National Combustion Meeting, page 10. Pasadena, California.

Coronel, S. A., Melguizo-Gavilanes, J., Mével, R., Shepherd, J. E. (2018). *Experimental and numerical study on moving hot particle ignition*. Combustion and Flame, 192:495–506.

CRC (1983). *Handbook of Aviation Fuel Properties*. Technical report, Coordinating Research Council.

De Toni, A., Werler, M., Hartmann, R., Cancino, L., Schieß l, R., Fikri, M., Schulz, C., Oliveira, A., Oliveira, E., Rocha, M. (2017). *Ignition delay times of Jet A-1 fuel: Measurements in a high-pressure shock tube and a rapid compression machine*. Proceedings of the Combustion Institute, 36(3):3695–3703.

Dean, A., Penyazkov, O., Sevruk, K., Varatharajan, B. (2007). *Autoignition of surrogate fuels at elevated temperatures and pressures*. Proceedings of the Combustion Institute, 31(2):2481–2488.

Dooley, S., Won, S. H., Chaos, M., Heyne, J., Ju, Y., Dryer, F. L., Kumar, K., Sung, C.-J., Wang, H., Oehlschlaeger, M. A., Santoro, R. J., Litzinger, T. A. (2010). *A jet fuel surrogate formulated by real fuel properties*. Combustion and Flame, 157(12):2333–2339.

Edwards, J. T. (2017). *Reference Jet Fuels for Combustion Testing*. In *55th AIAA Aerospace Sciences Meeting*. American Institute of Aeronautics and Astronautics, Grapevine, Texas.

FAA (2018). *FAA AC 25.981-1D: Fuel Tank Ignition Source Prevention Guidelines*.

Hattwig, M., Steen, H. (2004). *3.1.6.2 Autoignition Temperature (AIT)*. In *Handbook of Explosion Prevention and Protection*, pages 301–304. Wiley-VCH Verlag GmbH & Co. KGaA, Weinheim, FRG.

Hirsch, W., Brandes, E. (2005). *Zündtemperaturen Binärer Gemische Bei Erhöhten Ausgangsdrücken*. Technical report, PTB Braunschweig and Berlin.

Honnet, S., Seshadri, K., Niemann, U., Peters, N. (2009). *A surrogate fuel for kerosene*. Proceedings of the Combustion Institute, 32(1):485–492.

ISO/IEC (2017). *ISO/IEC 80079-20-1: Explosive atmospheres – Part 20-1: Material characteristics for gas and vapour classification – Test methods and data*.

Jones, S., Shepherd, J. E. (2020). *Thermal ignition of n-hexane mixtures by vertical cylinders*. In *13th International Symposium on Hazards, Prevention and Mitigation of Industrial Explosions (ISHPMIE)*. Braunschweig, Germany.

Kim, D., Violi, A. (2018). *Hydrocarbons for the next generation of jet fuel surrogates*. Fuel, 228:438–444.

Liang, J., Wang, S., Hu, H., Zhang, S., Fan, B., Cui, J. (2012). *Shock tube study of kerosene ignition delay at high pressures*. Science China Physics, Mechanics and Astronomy, 55(6):947–954.

Mével, R., Chatelain, K., Boettcher, P., Dayma, G., Shepherd, J. (2014). *Low temperature oxidation of n-hexane in a flow reactor*. Fuel, 126:282–293.

Mével, R., Rostand, F., Lemarié, D., Breyton, L., Shepherd, J. (2019). *Oxidation of n-hexane in the vicinity of the auto-ignition temperature*. Fuel, 236:373–381.

Mueller, C. J., Cannella, W. J., Bruno, T. J., Bunting, B., Dettman, H. D., Franz, J. A., Huber, M. L., Natarajan, M., Pitz, W. J., Ratcliff, M. A., Wright, K. (2012). *Methodology for Formulating Diesel Surrogate Fuels with Accurate Compositional, Ignition-Quality, and Volatility Characteristics*. Energy & Fuels, 26(6):3284–3303.

NFPA (1991). *Fire Protection Guide to Hazardous Materials*. National Fire Protection Association, Quincy, Ma, tenth edition.

Sax, N. I. (1957). *Dangerous Properties of Industrial Materials*. Reinhold Publishing Corporation, New York, first edition.

Setchkin, N. (1954). *Self-ignition temperatures of combustible liquids*. Journal of Research of the National Bureau of Standards, 53(1):49.

Smyth, K. C. (1990). *Short-duration autoignition temperature measurements for hydrocarbon fuels*. Technical Report NIST IR 4469, National Institute of Standards and Technology, Gaithersburg, MD.

Sund, S. M. (2019). *Thermal Ignition of Surrogate Jet Fuels*. Master's Thesis in Process Technology, University of South-Eastern Norway.

Tsai, F.-Y., Chen, C.-C., Liaw, H.-J. (2012). *A Model for Predicting the Auto-ignition Temperature using Quantitative Structure Property Relationship Approach*. Procedia Engineering, 45:512–517.

USCG (1999). *CHEMICAL HAZARD RESPONSE INFORMATION SYSTEM (CHRIS)*. United States Coast Guard.

Vasu, S. S., Davidson, D. F., Hanson, R. K. (2008). *Jet fuel ignition delay times: Shock tube experiments over wide conditions and surrogate model predictions*. Combustion and Flame, 152(1-2):125–143.

Wang, H., Oehlschlaeger, M. A. (2012). *Autoignition studies of conventional and Fischer–Tropsch jet fuels*. Fuel, 98:249–258.

Zabetakis, M. G. (1965). *Flammability characteristics of combustible gases and vapors*. Technical Report BM–BULL-627, 7328370, Bureau of Mines, Washington D.C.

Zabetakis, M. G., Furno, A. L., Jones, G. W. (1954). *Minimum Spontaneous Ignition Temperatures of Combustibles in Air*. Industrial & Engineering Chemistry, 46(10):2173–2178.

Zakel, S., Brandes, E., Schröder, V. (2019). *Reliable safety characteristics of flammable gases and liquids – The database CHEMSAFE*. Journal of Loss Prevention in the Process Industries, 62:103914.

Zhukov, V. P., Sechenov, V. A., Starikovskiy, A. Y. (2014). *Autoignition of kerosene (Jet-A)/air mixtures behind reflected shock waves*. Fuel, 126:169–176.

DOI: 10.7795/810.20200724

Influence of gap length on re-ignition by hot free jets

Franziska Seitz[a,b,c], Jens Brunzendorf[a], Robert Schießl[b] & Detlev Markus[a]

[a] Physikalisch-Technische Bundesanstalt (PTB), Bundesallee 100, 38116 Braunschweig, Germany
[b] Karlsruhe Institute of Technology (KIT), ITT, Engelbert-Arnold-Str. 4, 76131 Karlsruhe, Germany
[c] Hagen Ingenieurgesellschaft für Brandschutz mbH, Keekener Straße 98a, 47533 Kleve, Germany

E-mail: *Seitz.Franziska@posteo.de*

Abstract

Hot exhaust gas jets impinging into a surrounding combustible atmosphere are a potential source of accidental ignition in certain technical appliances. The hot gas jet might provide the high temperatures that are necessary to allow fast chemical reactions in the ambient gas to take place; this can cause auto-ignition and subsequent flame propagation into the surrounding mixture. In our study, the mixing processes at a hot free jet impinging into a hydrogen-air mixture are investigated experimentally. The setup comprises two gas-filled chambers which are connected by a thin nozzle; it can be used to create transient hot gas jets impinging into an initially quiescent, combustible, cold hydrogen-air mixture. The interaction between jet and ambient gas and in particular the mixing process and the occurrence or non-occurrence of flame initiation by the jet are monitored by high-speed Schlieren image sequences as well as by high-resolution 2D NO-PLIF imaging. By repeating the experiment with different parameters, the frequency as well as the spatial and temporal position of the re-ignition is obtained as a function of nozzle length, nozzle diameter and pressure ratio across the nozzle. Subsequent statistics on the re-ignition frequency as well as the location of a spreading flame front, as an estimation of the re-ignition position, are presented. It was found that long nozzles may cause a significantly higher re-ignition frequency than short nozzles of the same diameter, in contrast to common belief. Also, re-ignition occurred at larger distances from the nozzle for the longer 70 mm long nozzle compared to a 25 mm nozzle. This unexpected behaviour is attributed to different re-ignition processes for longer gaps, where re-ignition occurs later (hence at a higher pressure ratio and jet flow speed) and at much larger distances from the gap.

Keywords: *Laser-induced Fluorescence, NO-LIF, free jet, mixing, gap, flameproof enclosure*

1 Introduction

Hot exhaust gas jets constitute a significant hazard, even without flame propagation, because they represent a potential ignition source when impinging into a combustible atmosphere. To prevent an explosion, flameproof enclosures can be used when operating electrical devices in areas where explosive atmospheres are present. These enclosures are designed to confine accidental explosions to a pressure-resistant housing, thus preventing the propagation of a flame into a combustible surrounding. However, hot burned gas can escape through inevitable gaps as a hot free jet into the surroundings due to the pressure rise inside the housing. This jet may ignite the surroundings and cause flame propagation into the ambience. This re-ignition involves the turbulent mixing of the gas jet with the ambient gas, driven by pressure gradients, flow and molecular transport, as well as chemical reactions triggered by radicals transported with the jet stream. The interaction and the coupling of these processes complicates the understanding and the prediction of jet-induced ignition hazards.

Due to the much higher temperature of the burned gas compared to the surrounding fuel-air mixture at ambient temperature, there is a strong difference in the fluid densities. Such variable-density turbulent jets show a very specific mixing behaviour. Accurate consideration of the relevant effects like turbulent flows, molecular diffusion and chemical reactions is crucial for this type of ignition (Zheng, X. and Law, C. (2004), Sadanandan et al. (2011)). It is, for instance, unclear to which extent the ignition is controlled by low-temperature chemistry, chemical radicals from the burned gas or dominated by the rate at which hot gas is mixed with the fuel-air mixture. Even if a local auto-ignition takes place, the interaction of turbulence and chemistry may later lead to extinction, thus preventing further flame propagation (Sadanandan et al. (2007), Sadanandan et al. (2011), Ghorbani et al. (2015)).

Throughout the literature, studies report that the longer and the narrower a gap, the less likely re-ignition by hot free jets becomes (e.g. Beyer (1997) and references therein). This virtually obvious conclusion is plausibly substantiated by the stronger cooling-down of the hot gas in a long and narrow gap compared to a short and wide one. However, in this paper some contradicting evidence is presented, which is based on experimental studies of re-ignition events by hot jets impinging into an unburned, cold H_2-air mixture at well-defined initial and boundary conditions. The experiment offers optical access, thus allowing observation of the transient mixing and possible reaction process at the jet. Time-resolved Schlieren imaging and Laser-Induced Fluorescence (LIF) of nitric monoxide (NO) seeded to the jet gas flow is employed to monitor the process with spatial and temporal resolution. From the observed dependency of the experimental outcome on the initial and boundary conditions (nozzle geometry, jet speed), some conclusions on the underlying processes controlling the re-ignition process by hot jets are drawn.

2 Experiments

Schlieren imaging as well as planar laser-induced fluorescence (LIF) were applied in this study as optical diagnostic methods. They are both non-invasive and provide two-dimensional measurements at high spatial and temporal resolution. The re-ignition frequencies and the location of the first flame front were determined using the Schlieren method. LIF was used in order to determine information on mixing along the jet axis as well as perpendicular to the jet penetration.

2.1 Free jet generation and experimental parameters

The hot free jets were generated in a specially designed test chamber, the hot jet re-ignition facility. It is designed to model specific properties of a flameproof enclosure: a pre-ignition chamber with an explosion, an outer ambient combustible atmosphere, and an adjustable gap between both chambers through which the hot free jet escapes. This facility allows to generate and investigate reproducible hot jets resulting from an explosion in a pre-ignition chamber at well defined boundary conditions.

A scheme of the facility is shown in Fig. 1. It consists of two chambers: a small pre-ignition chamber representing the flameproof enclosure (cf. Fig. 1 no. 2) that is located on top of a larger, main (explosion) chamber (cf. Fig. 1 no. 4), where re-ignition by the hot jet might occur. The chambers are interconnected by an idealised gap in the form of an exchangeable nozzle tube (cf. Fig. 2). The pre-ignition chamber measures a volume of 267 ml with an inner diameter of 70 mm. For a hydrogen-air mixture, the volume of the pre-ignition chamber does not affect the re-ignition process as it is well within the range determined by Redeker (1981) to have no effect on the maximum experimental safe gap (MESG) value for a hydrogen-air mixture.

In order to keep the optical paths unchanged when the nozzle length is varied, the vertical position of the pre-ignition chamber can be adjusted using spacers (cf. Fig. 1 no. 7). Pre-ignition is initiated by a spark plug (cf. Fig. 1 no. 1). Its location can be varied vertically within the pre-ignition chamber. During the explosion, the pressure rise is recorded in the pre-ignition as well as the main chamber by two dynamic pressure transducers (cf. Fig. 1 no. 5) that are located at the top plates of both chambers. Further specifications of the nozzles, the pressure transducers and the test chamber have been published in Seitz (2020).

To study worst-case jet ignition scenarios, a H_2-air mixture with 28 vol.-% hydrogen was used as a representative of explosion group IIC with maximum experimental safe gap (MESG) values < 0.5 mm. A concentration of 27 % vol hydrogen results in the smallest MESG values of 0.29 mm (Bartknecht and Zwahlen (1993)).

The location of the spark plug was varied with respect to the nozzle inlet to investigate this influencing quantity. The effect of the gap width and gap length was studied by varying the nozzle length and diameter. The nozzle lengths tested were 25 mm and 70 mm, as there exist various studies throughout

DOI: 10.7795/810.20200724

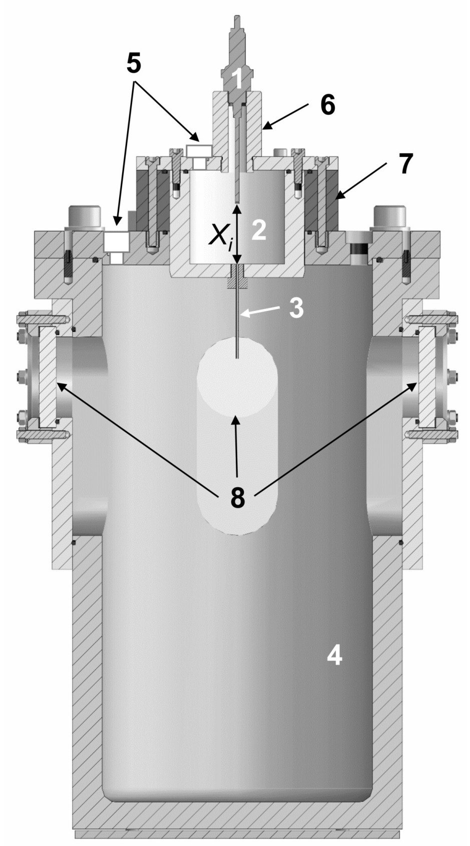

Fig. 1: Test chamber for reactive hot free jet experiments. X_i - Distance spark plug to nozzle. 1 - Spark plug, 2 - Pre-ignition chamber, 3 - Nozzle, 4 - Main chamber, 5 - Dynamic pressure sensor, 6 - Spark plug X_i positioning, 7 - nozzle positioning, 8 - Quartz glass windows. This figure has previously been published in Seitz et al. (2017).

the literature that have investigated 25 mm nozzles. The inner diameter of the nozzle tubes was varied within a range of 0.6 mm to 1.2 mm.

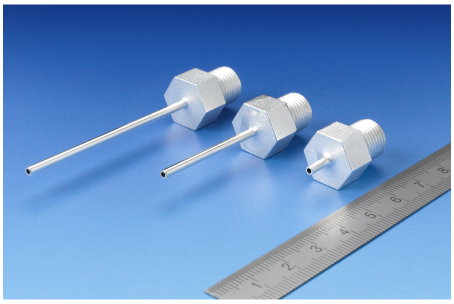

***Fig. 2**: Picture of nozzles that served as idealised gaps to connect the pre-ignition chamber with the main chamber. The stainless steel tubes were silver-plated to minimise reflections of the UV laser light and attached to an M 10 screw. Seitz et al. (2017)*

2.2 *Explosion pressure in a closed chamber with simple geometry*

When the hydrogen-air mixture in the pre-chamber is ignited, the temperature as well as the pressure in the pre-chamber increase, resulting in a pressure difference to the main chamber. At first, unburned hydrogen-air mixture is pushed through the nozzle into the main chamber. However, when the flame front in the pre-ignition chamber reaches the nozzle, this jet is replaced by hot burned exhaust gas. As the flame speed is much smaller than the speed of sound, the pressure inside the pre-ignition chamber at any given time is spatially practically uniform (Maas and Warnatz (1988)). Hence, the pressure ratio between the pre-ignition chamber and the main chamber is a well-defined quantity, and equal to the pressure ratio across the nozzle tube.

This pressure ratio will in the following be referred to by the variable Π_{nozzle}. It determines the flow velocity as well as the mass flow of the hot exhaust gas jet (Beyer (1997)). If Π_{nozzle} is large

DOI: 10.7795/810.20200724

enough and the nozzle is narrow, the gas inside the nozzle can be accelerated to reach velocities that are as fast as the speed of sound. At this point, the pressure ratio is called critical pressure ratio $\Pi_{\text{nozzle}_\text{crit}} = \left({}^{p_\text{ex}}/{}_{p_1}\right)_\text{crit}$. In general, p_ex denotes the absolute pressure, i.e. the explosion pressure inside the pre-ignition chamber. This value can be a theoretical one as it is in case of determining the critical pressure ratio, but can also be measured at the instant in time, when the jet exits from the nozzle, as it is the case for Π_nozzle. The variable p_1 refers to the pressure conditions in the main chamber which correspond to the ambient pressure $p_1 = p_\text{amb}$.

For most common gases at standard pressure and ambient temperature, the critical pressure ratio is in the range of $1.78 < \Pi_{\text{nozzle}_\text{crit}} < 1.89$ (Beyer (1997)). As a result, the flow inside the nozzle reaches supercritical conditions, if ${}^{p_\text{ex}}/{}_{p_1} > \Pi_{\text{nozzle}_\text{crit}}$, leading to flow velocities inside the nozzle that are in the range of the speed of sound. For the experimental conditions within this study, the average critical pressure ratio $\Pi_{\text{nozzle}_\text{crit}} = 1.81 \pm 0.02$.

2.3 *Schlieren imaging*

Schlieren imaging is frequently used as it is quite straightforward and relatively easy to implement into any setup. But at the same time it is a very versatile technique that gives valuable insights into the combustion process. In the current study, a two collecting lens schlieren setup with an extended light source and a 2.0 mm pinhole as a knife edge was used. For further information on the exact setup, the reader is referred to Seitz (2020).

2.4 *Laser-induced fluorescence*

Planar LIF is used to visualize the jet and its interaction with the ambient gas. For this, the hot jet is seeded with nitric monoxide (NO), which can be excited to emit strong LIF signals, and which can also exist at the high temperatures of the burned jet. The setup is outlined in Fig. 3, a detailed description can be found in Seitz et al. (2017) and Seitz (2020).

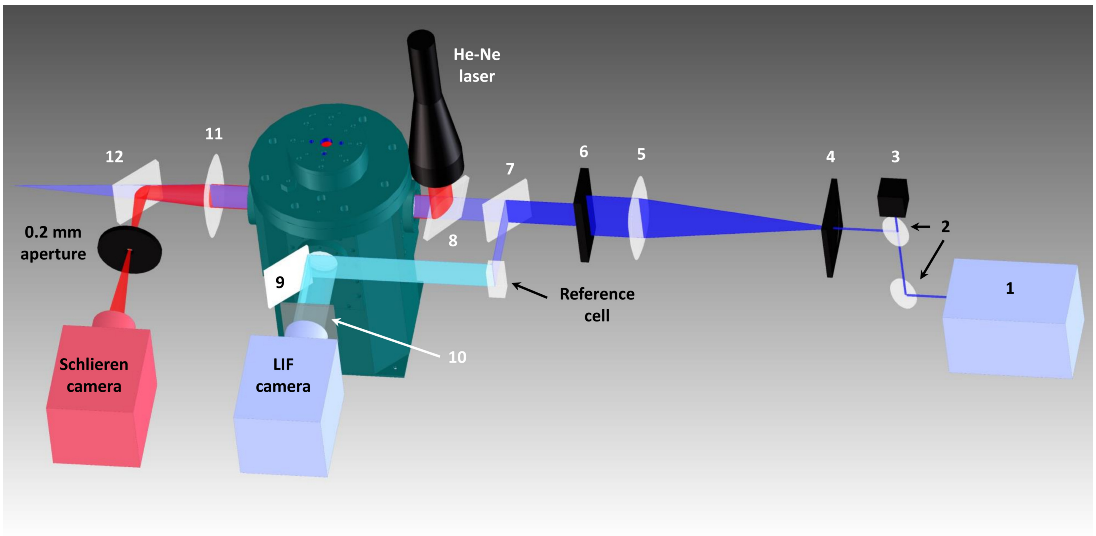

***Fig. 3**: Planar LIF-setup (blue beam) with implemented schlieren setup (red beam) with the main components named. The LIF sheet is formed by a cylindrical lens (5) and a slit aperture (6), it is then split into two by a semi-transparent mirror (7); one part illuminates the NO reference cell which produces the reference light. The UV laser beam for LIF images and the red laser beam for schlieren images are combined and separated by dielectric mirrors (8 and 12). Further components are: 1-UV-Laser, 2-Mirror, 3- Photodiode, 4 and 5- Sheet forming optics, 9-UV mirror, 10- UG5 filter, 11-Collecting lens.*

2.5 *Experimental procedure*

Prior to each experiment, residual components such as water and exhaust gas were removed from both chambers by evacuation of the test chamber or scavenging with dry air at a flow rate of 30 l/min for 10 minutes. Then, both chambers were scavenged with the test gas mixture of 28 vol. % hydrogen in dry air for at least 4 minutes; the total gas volume used for scavenging was more than ten times the complete gas exchange. For the LIF-measurements, the pre-ignition chamber was additionally filled with 2000 ppm of the LIF-tracer molecule nitric monoxide (NO). All valves were then closed. Here, the inlet valves were closed first, the outlet valves a few seconds later and the experiment was started within ten seconds. In this way, it can be ensured, that the NO concentration in the pre-ignition chamber is indeed 2000 ppm and has not been reduced as a result of chemical reactions with oxygen. Detailed information on the experimental procedure have been published in Seitz (2020).

3 Results and discussion

3.1 *Re-ignition frequencies*

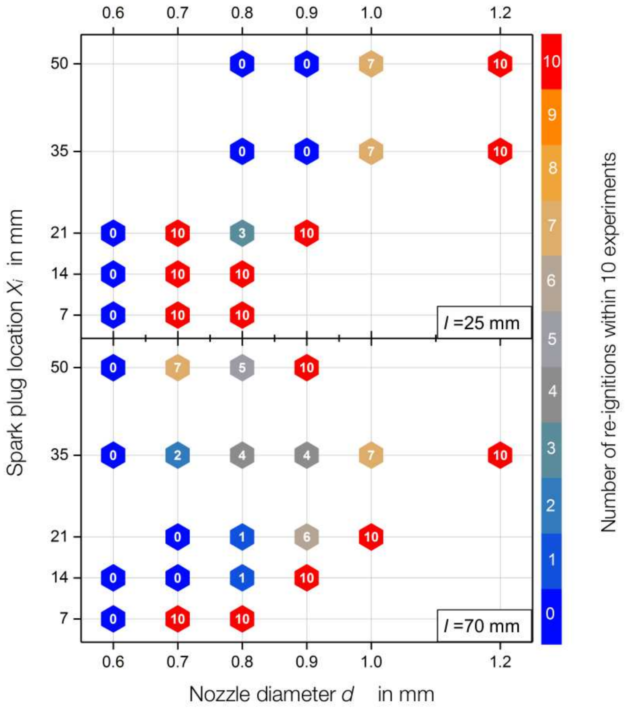

***Fig. 4**: Re-ignition frequencies for various nozzle lengths and diameters as a function of the location of pre-ignition X_i. The color bar denotes the number of re-ignitions per ten repetitions of the same experiment. Contents of this figure have previously been published in Seitz et al. (2017).*

The influence of the nozzle length, its inner diameter and the spark plug location on the re-ignition frequency is shown in Fig. 4. The number of re-ignitions per 10 experiments is colour-encoded from blue (0 = no re-ignition) to red (10 = 100% re-ignition rate). For a nozzle diameter d of 0.6 mm, re-ignition never occurred. In general, the re-ignition frequency increases with the nozzle diameter. As the jet width scales with the nozzle diameter, resulting in a larger hot core region and a larger mass flow rate. As a result, the impact of the shear generated turbulence on the hot gas in the jet axis decreases and less heat is dissipated from the hot core region in the centerline of the jet (cf. Ghorbani et al. (2015)). This observation is in good agreement with the literature. However, the behaviour of the $l = 70$ mm nozzles at a spark plug location of 50 mm cannot be explained by this common model. The same applies to the higher re-ignition rate of the $l = 70$ mm nozzle compared to the $l = 25$ mm nozzle at large spark plug distances. The higher re-ignition frequency of the $l = 25$ mm nozzle with 0.7 mm diameter compared to the one with 0.8 mm diameter at a spark plug distance of 21 mm is diametrical to the standard model that the re-ignition frequency increases with gap width. These results are all statistically significant, as the number of repetitions per experiment was always above 10 and exceeded 80 in contradicting cases like the 0.7/0.8 mm nozzle case. Note that in all these experiments Schlieren videos confirmed that no flame front traveled through the gap, re-ignition was always initiated by the hot jet.

For the further investigation of these phenomena, the pressure trace information were evaluated. The pressure ratio across the nozzle at the time of jet exit is listed in Table 1 for three relevant experimental configurations. In all three cases, the re-ignition frequency of the short $l = 25$ mm nozzle is compared with the long $l = 70$ mm nozzle of the same diameter at (almost) the same pressure ratios Π_{nozzle}.

The pressure ratio across the nozzle at time of jet exit increases, the further away the spark plug location is from the nozzle. In the first case, the pressure ratio $\Pi_{\text{nozzle}} \approx 1.4$ is well below the critical pressure ratio, i.e. the jet speed is well below the speed of sound. Pre-ignition was initiated 14 mm away from the nozzle in the pre-chamber. Here, re-ignition takes place significantly more often (ten times out of ten experiments) for the short 25 mm nozzle compared to the long nozzle, where re-ignition was observed only once. The other two cases compare the situation when the jet enters the main chamber with super-sonic speed, i.e. the pressure ratios are above the critical value. Here, the opposite tendency can be seen: re-ignition is favoured for longer nozzle lengths, at otherwise nominally identical experimental conditions.

***Table 1**: Re-ignition frequency as function of nozzle length and pressure ratio across the nozzle at time of jet exit. For high pressure ratios Π_{nozzle} the longer nozzle has a higher re-ignition rate than the shorter one*

$x_{\mathbf{i}}$	$\Pi_{\mathbf{nozzle}}$	**Nozzle length l**	**Nozzle diameter d**	**No. of re-ignitions within 10 experiments**
14 mm	1.4	25 mm 70 mm	0.8 mm	10 1
35 mm	3.3	25 mm 70 mm	0.8 mm	0 4
50 mm	5.5	25 mm 70 mm	0.9 mm	0 10

This behaviour can be caused by the dependency of the initial flow conditions of the hot jet on the nozzle length, in particular the jet gas temperature at the nozzle exit. To investigate this finding more in detail, further experiments were conducted, which will be discussed in the next section.

3.2 Location of earliest visible flame front from schlieren images

For all experimental configurations tested, re-ignition was observed very close to the nozzle as well as more than 60 diameters downstream of the nozzle. With the respect to the jet axis, re-ignition occurred within the jet axis in the head vortex of the jet as well as in the shear layer. Here, a first flame front was visible downstream of the jet (cf. Figure 5, upper row) but also in one or more isolated areas close to the nozzle (cf. Figure 5, bottom row.)

The location of the re-ignition region was measured via high-speed high-resolution Schlieren videos. Fig. 6 depicts the location of the earliest visible flame front x_{f} with respect to the nozzle as a function of the nozzle diameter d and the nozzle length l (top row: $l = 25$ mm, bottom: $l = 70$ mm). The pressure ratio across the nozzle at the time of the jet exit Π_{nozzle} is colour-encoded.

The observed distribution is rather complex and contradicts common explanations. When the nozzle length is increased from 25 mm (cf. Fig. 6 top row) to 70 mm (cf. Fig. 6 bottom row), re-ignition tends to occur closer to the nozzle. The 0.7 mm nozzle has two prominent distances at which re-ignition can take place: either close to the nozzle or at large distances up to 60 times the nozzle diameter. The similar 0.8 mm nozzle, however, shows a different behaviour. For the 0.9 mm nozzles, the difference between both lengths are particularly remarkable: the short 25 mm nozzle shows re-ignitions far away from the nozzle (at distances of about 40 nozzle diameters) at low pressure ratios, whereas the long 70 mm nozzle of the same diameter shows re-ignitions close to the nozzle at high pressure ratios, corresponding to super-sonic jets.

A plausible explanation can be that a larger nozzle diameter leads to a bigger hot core region in the jet axis and a lower mixing rate, as suggested in the literature (e.g. Ghorbani et al. (2015)). Thus, conditions for re-ignition are reached earlier after the jet emerges from the nozzle. According to Fig. 4 a larger nozzle diameter increases also the re-ignition frequency.

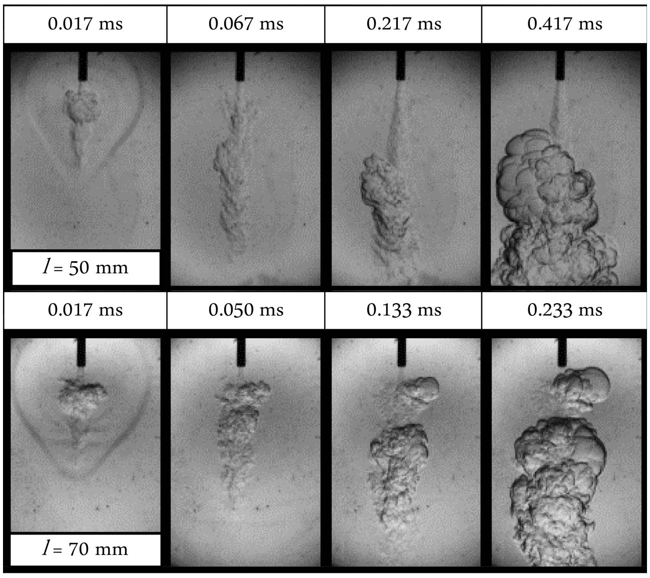

***Fig. 5**: Schlieren images of temporal development of free jets for nozzle lengths of 50 mm and 70 mm. The time designations refer to the instant in time, when the jet exits from the nozzle. A similar figure was previously published by one of the autors in (Seitz, 2020).*

3.3 Axial mixing profiles from LIF-images

In the following, a mixture fraction related quantity named ${F^*_{\mathrm{LIF}}}^{S}$ is introduced in order to investigate the mixing process, which is derived from NO-LIF images which are corrected for background, sensor-sensitivity and laser sheet inhomogeneities and normalized to a reference light beam through a vial with 2000 ppm NO reference gas. Detailed information on the calculation method of this quantity is beyond the scope of this work. For further information on how to determine ${F^*_{\mathrm{LIF}}}^{S}$ from raw LIF images, the reader is referred to the the publication of Seitz (2020). Within this work, the focus is mainly on the re-ignition process in the centreline of the jet axis. Therefore, axial profiles of the mixing field (as represented from LIF-images) in free jets at varying time instances after start of jet penetration are shown in Fig. 7. These ${F^*_{\mathrm{LIF}}}^{S}$ profiles are from different experimental runs, but are phase-resolved with respect to the first visible occurrence of jet at the nozzle tip in simultaneously recorded time-resolved schlieren image sequences.

The two diagrams show data from two different nozzle lengths, namely 25 mm (Fig. 7 (a)) and 70 mm (Fig. 7 (b)). For all experiments that are presented in the following, the experimental conditions were nominally identical, with only the nozzle length being varied. The pressure ratio across the nozzle at time of jet exit was $\Pi_{\mathrm{nozzle}} > 3$ (i.e., the jet exit speed is super-sonic) and the nozzle diameter was $d = 0.8$ mm.

At first, the signal at the nozzle exit first is temporally nearly constant for times of up to 0.18 ms. After that an increase is noticeable for both nozzle lengths tested. This increase becomes prominent after 1 ms, in particular for the 70 mm nozzle.

The red curve in diagram (b) is for a case where re-ignition was observed at 0.3 to 0.6 ms after the jet emerged from the nozzle; the time of ignition is well behind the time ($\Delta\tau_{\mathrm{exit}} = 0.05$ ms) where this profile was recorded. At early stages of jet development, the axial profiles of the LIF fields do not show any clear indication of whether the jet would finally lead to ignition or not; the pre-ignition profiles from experiments where re-ignition occurs (like the red curve) did not differ significantly from cases where no re-ignition took place (grey curve). This is an indication that ignition or non-ignition is, under nominally identical initial conditions, not related to the early development of the jet, but is linked to the interaction of chemical reaction with turbulence on a larger timescale.

DOI: 10.7795/810.20200724

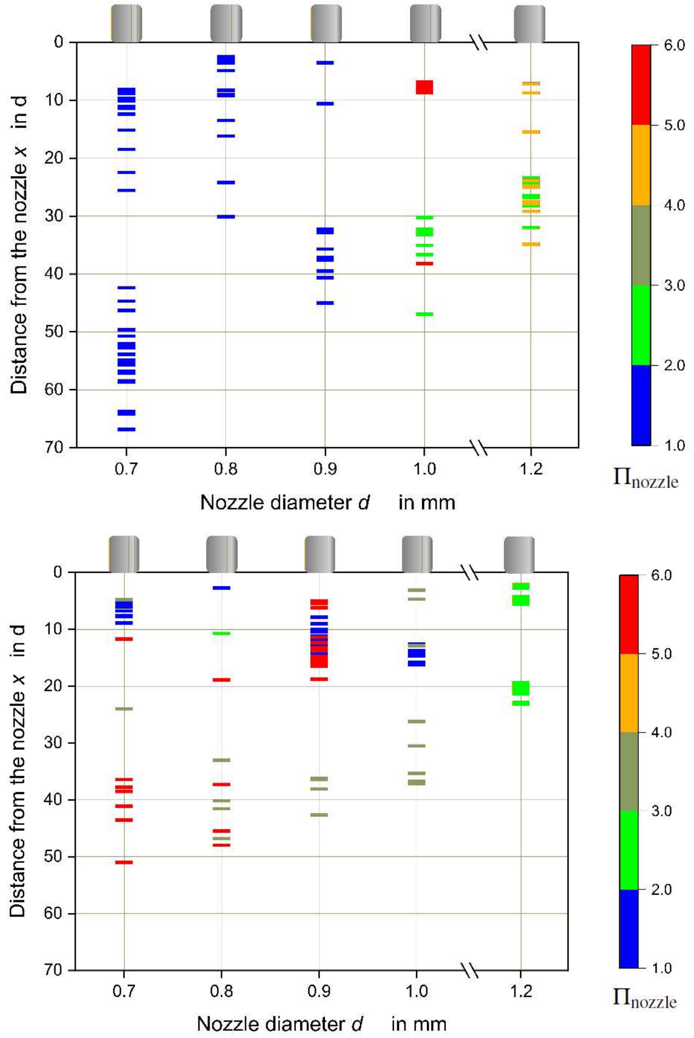

Fig. 6: *Distance between the earliest visible flame front and the nozzle end in units of the nozzle diameter d for different nozzle diameters d. The pressure ratio across the nozzle at time of jet exit* Π_{nozzle} *is colour-coded as indicated by the vertical color bar. Top Figure:* $l = 25\,\text{mm}$ *nozzle, bottom:* $l = 70\,\text{mm}$ *nozzle. A similar figure was previously published by one of the authors in Seitz (2020).*

4 Summary and Conclusions

In this study, re-ignition of a hydrogen-air mixture by impinging hot exhaust gas jets emerging from flameproof enclosures was investigated experimentally. A dedicated experiment allows studying the process systematically under well-defined conditions. It creates hot gas jets by spark-igniting a hydrogen-air mixture in one chamber. Hot exhaust gases then flow through a nozzle into the larger main chamber. In a systematic series of experiments, the probability of a successful re-ignition was tested in dependence of the gap length, gap diameter and pressure ratio between the two chambers. The results show that there is a complex, in part non-monotonic dependence of the re-ignition probability on the parameters. The results indicate that long gaps are not necessarily safer (i. e., have lower ignition probability) than short gaps. If the pressure ratio between the flameproof enclosure and the ambience at time of jet exit is larger than the critical pressure ratio (i.e. when the jet speed is higher than the speed of sound in the ambient gas), re-ignition was observed to become more likely if the nozzle length is increased from 25 mm to 70 mm. At the same time, the safe diameter decreases as well by 0.3 mm. Detailed spatially resolved investigations of the mixing field at these jets were also performed. Neither axial nor radial profiles of the mixing ratio show a correlation between profile and later re-ignition frequency. This is an indication that re-ignition or non-ignition is, under nominally identical initial conditions, not related to the early development of the jet, but is linked to the interaction of chemical reaction with turbulence on a larger timescale.

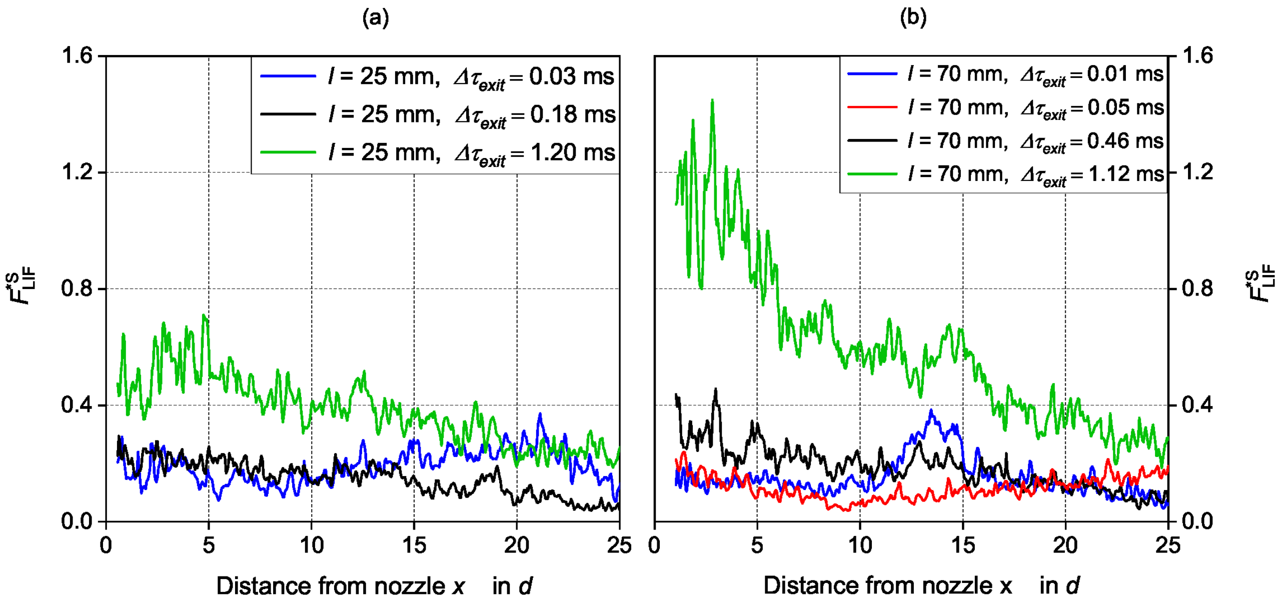

***Fig.** 7: Profiles of the signal fraction along the jet axis at experimental conditions of* $\Pi_{\text{nozzle}} = 3.3$ *and* $d = 0.8\,\text{mm}$*. Left: Nozzle length* $l = 25\,\text{mm}$*, Right:* $l = 70\,\text{mm}$*.*

Acknowledgements

The authors kindly acknowledge the funding of this project as part of the research group FOR 1447 *Physicochemical-based Models for the Prediction of safety-relevant Ignition Processes* by the DFG (German Research Foundation).

References

Bartknecht and Zwahlen (1993). *Explosionsschutz: Grundlagen und Anwendung*. Springer, Berlin.

Beyer, M. (1997). *Über den Zünddurchschlag explodierender Gasgemische an Gehäusen der Zündschutzart "druckfeste Kapselung"*. Fortschritt-Berichte VDI / 21: Elektrotechnik. VDI-Verlag. ISBN 978-3-1832-2821-8.

Ghorbani, A., Steinhilber, G., Markus, D., Maas, U. (2015). *Ignition by transient hot turbulent jets: An investigation of ignition mechanisms by means of a PDF/REDIM method*. Proceedings of the Combustion Institute, 35(2):2191–2198.

Maas and Warnatz (1988). *Ignition processes in hydrogen-oxygen mixtures*. Combustion and Flame, 74(1):53–69.

Redeker, T. (1981). *Classification of flammable gases and vapours by the flameproof safe gap and the incendicity of electrical sparks*. Technical Report PTB-W-18.

Sadanandan, R., Markus, D., Schießl, R., Maas, U., Olofsson, J., Seyfried, H., Richter, M., Aldén, M. (2007). *Detailed investigation of ignition by hot gas jets*. Proceedings of the Combustion Institute, 31(1):719 – 726. ISSN 1540-7489. doi:https://doi.org/10.1016/j.proci.2006.08.027.

Sadanandan, R., Schießl, R., Markus, D., Maas, U. (2011). *2D mixture fraction studies in a hot-jet ignition configuration using no-lif and correlation analysis*. Flow, turbulence and combustion, 86(1):45–62. doi:https://doi.org/10.1007/s10494-010-9285-0.

Seitz, F. (2020). *Characterization of the re-ignition process by hot free jets with the focus on mixing -An experimental investigation -*. Shaker Verlag.

Seitz, F., Schießl, R. A., Markus, D. (2017). *Ignition by Hot Free Jets*. Zeitschrift für Physikalische Chemie, 231(10):1737–1771.

Zheng, X. and Law, C. (2004). *Ignition of premixed hydrogen/air by heated counterflow under reduced and elevated pressures*. Combustion and Flame, 136(1-2):168–179.

DOI: 10.7795/810.20200724

Combustion characteristics and kinetic analysis of pine sawdust based on deconvolution and isoconversional method

Xiaomeng Sun[a], Depeng Kong[a],

[a] Center for Offshore Engineering and Safety Technology, China University of Petroleum (East China), Qingdao 266580, China

E-mail: kongdepeng@upc.edu.cn (D. Kong)

With the rapid consumption of non-renewable resources such as oil and ceaseless environmental pollution, it is urgent to find a kind of efficient renewable energy. In recent years, as the only renewable carbon source, the energy conversion of biomass by combustion and pyrolysis have become one of the most important topics. Typically, biomass resources consist of crops, wood, aquatic plants, animal waste and other organic waste, in which wood biomass is now widely used. Wood biomass contain cellulose, hemicellulose and lignin. For the sake of improving and advancing the combustion requirement and efficiency, it is needed to comprehend the combustion principle of biomass.

In this paper, the combustion characteristics of pine, a kind of common used biomass, were studied by the thermos-gravimetric analysis (TGA) and differential scanning calorimeter (DSC) tests. The combustion process can be split into two periods according to the activation energy gained by using the isoconversional method. The average activation energy was 140.45363 kJ/mol and 239.76526 kJ/mol. Because the combustion of wood biomass is a complex and continuous process, the DSC curves may have overlapping peaks under the cover of a single peak, which affected the characterization of thermal behaviour. The deconvolution method was used to divide the overlapping peaks to obtain three separate peaks with reaction activation energy was 24.43 kJ/mol, 123.37 kJ/mol, and 80.61 kJ/mol respectively. As the heating rate increases, the entire combustion process moved to higher temperatures.

The study of kinetic parameters provided a theoretical basis for improving the combustion efficiency of wood biomass particles.

Keywords: *kinetic parameters, thermal behaviour, isoconversional method, deconvolution, TG-DSC*

1. Introduction

With the rapid consumption of oil and other non-renewable resources and the aggravation of environmental pollution, it is urgent to find renewable energy. As the fourth largest energy resource, biomass energy solves approximately 14% of global energy requirement, particularly in developing countries, where biomass provides about 35% of energy demand (Kerolli-Mustafa *et al.*, 2015). By 2050, biomass is estimated to offer approximately 38%of the world's original fuel and 17% of electric power. Potential biomass fuels include wood and wood waste, agricultural garbage and a host of other materials. The high volatility of the biomass and the high reactivity of the char it produces give it an advantage as a fuel. As far as environment is concerned, Biomass fuels absorb carbon dioxide in the procedure of growth and emit carbon dioxide in the procedure of combustion, so the use of biomass fuels is conducive to the carbon dioxide cycle without exacerbating the greenhouse effect (Demirbas, 2004). Studies have shown that the combustion rate and efficiency of pulverized biomass fuel are higher than that of coal. However, it is worth noting, that biomass has less carbon, more oxygen and a lower calorific value than solid fossil fuels. Therefore, some physical, chemical and biological transformation methods are often used to convert bulky, low-energy-concentration biomass into liquid, gas, and solid fuels that are more convenient to store and transport and have better combustion performance. Pyrolysis, gasification, densification, anaerobic digestion and alcohol production have been widely used in biomass conversion (Pham *et al.*, 2015). Gasification and combustion are the most effective energy utilization methods, both of which involve the oxidation of biomass. In order to improve combustion efficiency and better control the gasification process, the kinetic parameters of combustion need to be analyzed.

Experimental data obtained from thermogravimetric analysis (TGA) and differential scanning calorimeter (DSC) is needed for the kinetic and thermodynamic evaluation(Grønli *et al.*, 2002; Gao *et al.*, 2013; Gu *et al.*, 2013; Owen *et al.*, 2015; Yu *et al.*, 2016). Common methods for calculating dynamic parameters can be divided into the model-fitting method (Vlaev *et al.*, 2003) and the model-free method(Budrugeac and Segal, 2007; Burnham and Dinh, 2007; Sánchez-Jiménez *et al.*, 2008; Cai *et al.*, 2018). The experimental information at a single heating rate are used to obtain the optimal model by fitting different mechanism functions, so as to obtain the dynamic parameters. Vlaex et al. (Vlaev *et al.*, 2003) studied the kinetics of pyrolysis of rice husk based on the means of Coats–Redfern and fourteen kinetic equations. As the results show that the laboratorial information was best characterized by the function of Ginstling–Brounshtein. However, studies have shown that there are significant differences in the values gained from dynamic techniques using a unitary heating rate. One the other hand, model-free or isoconversional methods calculate kinetic parameters by using data obtained from multiple heating rates, avoiding the selection of reaction mechanism functions, thus eliminating errors caused by different assumptions of mechanism functions. Burnham et al. (Burnham and Dinh, 2007) compared the accuracy and suitability of model-fitting model and isoconversional method for distinct kinds of chemical reactions and found that model fitting and isoconversional methods have accuracy for extrapolation outside the scope of calibration. But isoconversional method is usually more accurate. The common isoconversional methods involve Flynn-Wall-Ozawa integral method (Ding *et al.*, 2017), Friedman differential method (Gogoi *et al.*, 2018), Kissinger differential method (Budrugeac and Segal, 2007) and so on.

Nonetheless, it is challenging to describe the thermodynamic and kinetic behaviours of biomass exactly because of the overlapping reactions in the process of biomass combustion, which are shown by the overlapping peaks in the DTG and DSC profiles. The deconvolution method as an impactful mathematical method which is often used to split the overlapped peaks to gain the different peaks and comprehensive information of these separated peaks (Kong *et al.*, 2019; Yao *et al.*, 2019).

Pine, as a common wood, produces a lot of sawdust during processing. At present, the common utilization ways of pine sawdust are as bedding, cultivation base and biomass pellet fuel (Sikkema *et al.*, 2011). In this paper, the TG-DSC was used to test pine sawdust under air condition, and the dynamics and thermodynamic parameters, such as heat of reaction, apparent activation energy and pre-exponential factor, were gained by deconvolution method and isoconversional method. The effect of different heating rate on the burning procedure of pine sawdust was also discussed. The preliminary study on the combustion kinetic characteristics of pine sawdust has a guiding role in the study of the direct combustion and gasification process of pine sawdust.

2. Experiments

2.1 Materials

The natural pine sawdust was bought from an agricultural product processing plant in Lianyungang. The particle size of pine chips used for testing is 80 mesh. The industrial composition analysis results of the used sample are listed in Table 1.

Table 1: *Proximate analysis of the pine sawdust*

Moisture/%	Ash/%	Fixed carbon/%	Volatile matter/%
4.64	0.46	15.13	79.77

2.2 TGA-DSC experiment

In this experiment, the thermosgravimetric analysis was carried out by the TG-DAC system (NETZSCH STA 449T5, Germany). For each test, approximately 5mg samples were tested under air and nitrogen atmosphere at flow rate of 50ml/min. For study the influence of diverse heating rate on combustion of pine chips, diverse heating rates were used for experiments. The sample with different particle sizes were heated up to 700 ℃ at heating rate of 5 ℃/min, 10℃/min, 20℃/min and 40℃/min respectively and the detailed experimental scheme are shown in Table 2. The curves of heat flux and mass loss rate with time and temperature can be presented by experiments. Meanwhile the differential thermogravimetric (DTG) curves can be gained by differentiating the TG curves.

Table 2： *Experimental conditions of samples under air*

No.	Sample mass/mg	Particle size/mesh	heating rate/℃ $\cdot$ min^{-1}
1	5.116	80	5
2	5.043	80	10
3	5.244	80	20
4	5.092	80	40

2.3 The deconvolution method

A common mathematical technique to separate individual peaks from overlapping peaks is the deconvolution method (Kong *et al.*, 2019). For the heat flux profiles obtained from experiments, it can be presumed that the gained signal *f(t)* is a convolution of the “true” signal *g(t)* with the appliance response function *I(t)*, i.e.:

$$f(t) = g(t) \otimes I(t) \tag{1}$$

In which, $\otimes$ means convolution. The equation (1) can be expressed as follows:

$$f(t) = g(t) \otimes I(t) = \int_{-\infty}^{+\infty} g(t-x)I(x)dx = \int_{-\infty}^{+\infty} g(t)I(\mathrm{t}-x)dx \tag{2}$$

According to the convolution theorem, the product of the Fourier transforms of two functions gives the Fourier transform of the convolution of the two functions, that is:

$$\mathbf{F}[g(t) \otimes I(t)] = \mathbf{F}[g(t)] \times \mathbf{F}[\mathrm{I(t)}] \tag{3}$$

And then

$$\mathbf{F}[g(t)] = \mathbf{F}[g(t) \otimes I(t)] / \mathbf{F}[I(t)] = \mathbf{F}[f(t)] / \mathbf{F}[I(t)] \tag{4}$$

Where, **F** represents the arithmetic of Fourier transform:

$$\begin{aligned} \mathbf{F}[f(t)] &= \int_{-\infty}^{+\infty} f(t) e^{-i\omega t} dt \\ \mathbf{F}^{-1}[F(x)] &= \frac{1}{2\pi} \int_{-\infty}^{+\infty} F(x) e^{i\omega x} dx \end{aligned} \tag{5}$$

In the above equation (5), $\mathbf{F}^{-1}$ expresses the opposite Fourier transform.

Inverse Fourier transform operation on both sides of the equation (4), the function $f(t)$ can be deconvoluted with $I(t)$, and the true signal $g(t)$ is received:

$$g(t) = f(t)[\otimes^{-1}]I(t) = \mathbf{F}^{-1}\{\mathbf{F}[g(t)]\} = \mathbf{F}^{-1}\{\mathbf{F}[f(t)] / \mathbf{F}[I(t)]\} \tag{6}$$

Where, $\otimes^{-1}$ means deconvolution.

A great deconvolution of the overlapped peaks in molecular spectroscopy and scanning microcalorimetry of protein solutions can be gained by using a Gaussian function as the function $I(t)$ (Elsabee and Prankerd, 1992):

$$f(x) = a_0 \exp\left[-\frac{1}{2} \left(\frac{x - a_1}{a_2} \right)^2 \right] \tag{7}$$

Where, x indicates the temperature, $f(x)$ is the calculated heat flux, a_0 represents the range of peak, a_1 is the abscissa corresponding to the midpoint of the peak and a_2 means the peak width.

For the peaks with asymmetric figure, the exponentially modified Gaussian (EMG) function can be used to take the place of the Gaussian function:

$$f(x) = \frac{a_0}{2a_3} \exp\left(\frac{a_2^2}{2a_3^2} + \frac{a_1 - x}{a_3} \right) \left[\operatorname{erf}\left(\frac{x - a_1}{\sqrt{2} a_2} - \frac{a_2}{\sqrt{2} a_3} \right) + \frac{a_3}{|a_3|} \right] \tag{8}$$

Where, a_3 is an asymmetric constant and erf( ) is a mistake function. The overlapping peaks in the heat flux curves were deconvolved by the EMG function.

The overlapped curves could be divided into any single peaks by the deconvolution technique. The multiple reaction of pine biomass combustion can be split into several parts and the kinetics and thermal dynamics parameter of each period could be studied, which will be shown in Section 2.4.

2.4 kinetic parameter calculation

The conversion rate α can be expressed by equation (9):

$$\alpha = \frac{m_0 - m_t}{m_0 - m_\infty} \tag{9}$$

Where m_0、m_t、m_∞ indicate the initial mass of the pine sample, the mass at time t and the final mass respectively . Kinetic equation is shown in equation (10):

$$\frac{d\alpha}{dt}=kf(\alpha) \tag{10}$$

Where, k is Arrhenius constant, $f(\alpha)$ refer to differential mechanism function. The relationship between rate constant and temperature was proposed by Arrhenius:

$$k=A\exp(-\frac{E}{RT}) \tag{11}$$

Combine the equations (10) and (11), the expression of the reaction rate can be obtained as follows:

$$\frac{d\alpha}{dt}=A\exp(-\frac{E}{RT})\,\mathrm{f}(\alpha) \tag{12}$$

Where, the A indicates the pre-exponential factor; E means the activation energy; R represents ideal gas constant. In non-isothermal conditions, the heating rate is known and the relationship between temperature and time is shown below:

$$\mathrm{T_t}=\mathrm{T_0}+\mathrm{bt} \tag{13}$$

$$\beta=\frac{dT}{dt} \tag{14}$$

Where, T_t is sample temperature at time t; T_0 indicates the initial temperature; β is the heating rate. The equation (15) can be obtained by combining equation (12) and (14):

$$\frac{d\alpha}{dT}=\frac{A}{\beta}\exp(-\frac{E}{RT})\,\mathrm{f}(\alpha) \tag{15}$$

And then, integrate both sides of equation (14)：

$$\int_0^\alpha \frac{d\alpha}{f(\alpha)}=\frac{A}{\beta}\int_{T_0}^{T}\exp(-\frac{E}{RT})dT \tag{16}$$

Owing to $\int_0^{T_0}\frac{A}{\beta}\exp(-\frac{E}{RT})\,\mathrm{dT}=0$, So the integral can be rewritten as：

$$G(\alpha)=\frac{A}{\beta}\int_0^{T}\exp(-\frac{E}{RT})dT \tag{17}$$

The equation (15) has not adetailed solution. Hence, a number of approximate solutions were studied in the past (Fernandez-Lopez *et al.*, 2016). The methods of dynamic analysis of thermal analysis curves can be divided into integral method and differential method, among which the integral method includes Coats-Redfern method, Flynn-Wall-Ozawa method, etc. The differential method includes Kissinger method, Friedman-Reich-Levi method, Starink method and Borchardt-Daniels method, etc. The solution method involving mechanism function can be split into model-free method and model-fitting method. The model-fitting method need to find a suitable reaction mechanism function. In contrast to the model-fitting method, model-free method obtains the kinetic parameter by iso-conversion method. Therefore, the error caused by the different choice of mechanism function is avoided.

2.4.1 Calculation of the kinetic and thermodynamics parameters

Assuming that the combustion processes complies with Arrhenius's law, the mass loss rate of the oxidation process as follows:

$$-\frac{dM}{dt}=A\exp(-\mathrm{E}_a/\mathrm{RT})\mathrm{M}^n \tag{18}$$

In which, M indicates the mass at time of *t,* g; T is the temperature, K; n means the order of reaction.

multiply ΔH on both sides of the equation (18), the rate of heat flow can be expressed as:

$$\frac{dH}{dt}=\Delta HM^nA\exp(-\mathrm{E}_a/\mathrm{RT}) \tag{19}$$

The reaction heat per unit mass sample could be obtained by integrating equation (19):

$$\Delta H=\frac{1}{M_0}\int_{t_0}^{t_{end}}\frac{dH}{dt}dt \tag{20}$$

where, M_0 indicates the initial sample mass, g; t_0 and t_{end} represent the starting and terminal time of reaction, s.

Some scholars found that when the pyrolysis reaction order of biomass equal to 1, the experimental value and the calculated value were in good agreement (Burnham and Dinh, 2007). Thus, assume the reaction order is 1, the equation (19) can be converted into the equation (21):

$$\frac{dH/dt}{\Delta H\cdot M_0}=A\exp(-\mathrm{E}_a/\mathrm{RT}) \tag{21}$$

Taking a natural logarithm of equation (21):

$$\ln\left(\frac{dH/dt}{\Delta H\cdot M_0}\right)=-\frac{E_a}{RT}+\ln A \tag{22}$$

So the E_a and A can be gained by slope and intercept, respectively.

2.4.2 Flynn-Wall-Ozawa method

Define $u=\frac{E}{RT}$,

$$G(\alpha)=\frac{AE}{\beta R}\int_{\frac{E}{RT}}^{+\infty}\frac{e^{-u}}{u^2}du \tag{23}$$

Replace $\int_{\frac{E}{RT}}^{+\infty}\frac{e^{-u}}{u^2}du$ with $P(\mathrm{u})$,

$$G(\alpha)=\frac{AE}{\beta R}P(\mathrm{u}) \tag{24}$$

And then take the logarithm of both sides of the equation (24), and get the following equations according to the Doyle approximation:

$$\lg\beta=\lg\frac{AE}{RG(\alpha)}-2.315-0.4567\frac{E}{RT} \tag{25}$$

Or

$$\ln\beta = \ln\frac{AE}{RG(\alpha)} - 5.3308 - 1.0516\frac{E}{RT} \tag{26}$$

3. Results and discussion

3.1 Influence of Experimental factors on combustion process

TG-DSC tests were performed at diverse heating rates and the TG and DTG profiles at diverse heating rates are shown in Fig. 1. It can be observed from the curves that the combustion process of pine sawdust can be split into three periods. The first part is about ambient temperature to about 142 ° C, and the mass loss is not obvious. It can be inferred that this stage is the evaporation of water in pine sawdust. The second stage ranges from 170℃ to 416℃ and is accompanied by significant mass loss, which may be related to combustion of volatile components (Aghamohammadi *et al.*, 2011). The third stage occurs between 420℃ and 600℃, which may be due to the oxidation of char. The tendency and temperature range is similar to previous research (Gil *et al.*, 2010).

As TG curve show that the profiles at various heating rates have similar trends, which represents that the pine sawdust combustion undergoes similar processes at different heating rates. In addition, as the heating rate increases, the entire combustion process moves to higher temperatures. This may be due to the excessively rapid heating rate, resulting in a large temperature gradient inside the particles, which raises the minimum temperature that the pyrolysis process may proceed, so that the whole reaction presents a lagged state.

As the TG and DTG profiles show, with the heating rate increases, the remaining proportion of the sample mass increases. This is because the sample reaches the same temperature at diverse heating rates, the faster the heating rate, the shorter the reaction time, the lower the reaction degree. Thus, combustion at higher heating rates is insufficient at the same temperature, especially for biomass containing highly volatile components (Ma et al., 2015)。

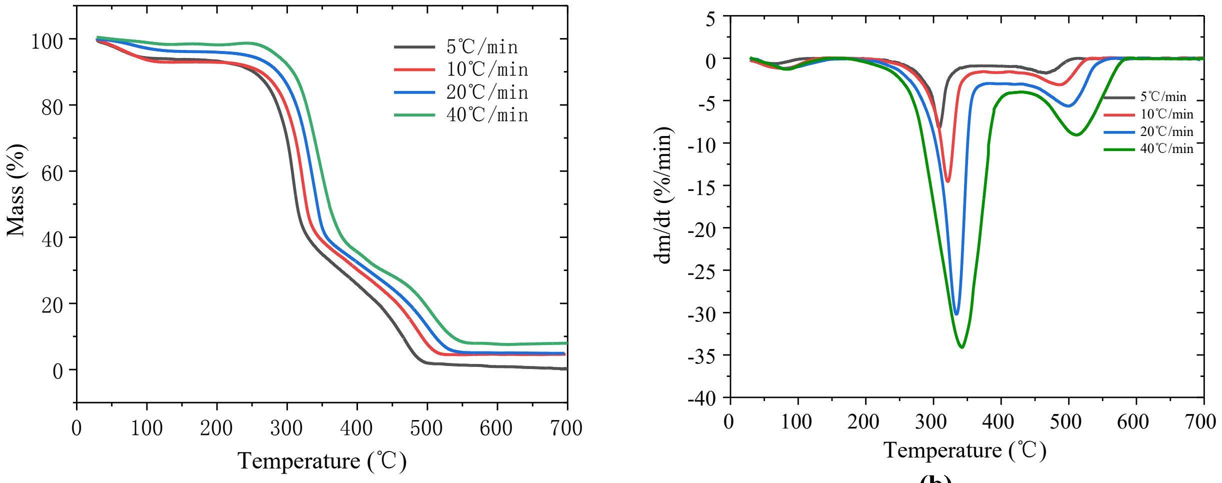

(a) **(b)**

Fig. 1 *(a)TG profiles at different heating rates (b)DTG curves at different heating rates*

3.2 Kinetic analysis based on FWO method

In this paper, the TG curves were further analysed by the FWO method to evaluate the reaction kinetic parameters, the reaction conversion rate was selected as 0.1-0.95 and make a logarithmic plot of the five groups of heating rate curves, as shown in Fig. 2.

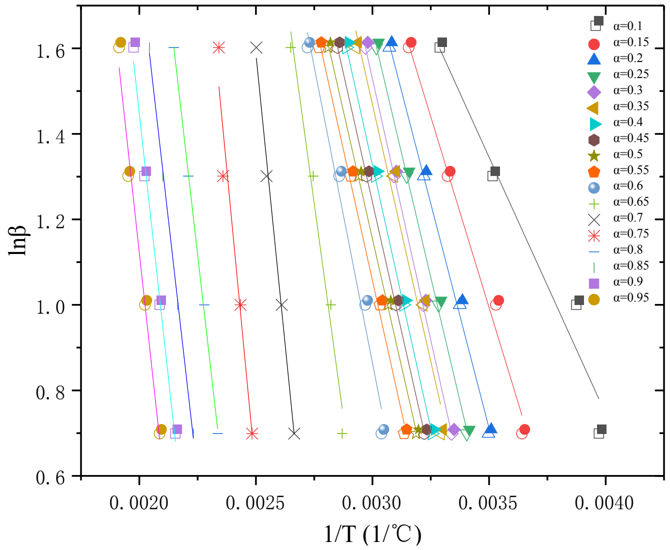

***Fig. 2** FWO plots for different conversion*

The obtained straight line was fitted, and the reaction activation energy *E* can be calculated from the slope. Assuming that the reaction order was 1, the reaction mechanism function was $g(\alpha) = -\ln(1-\alpha)$, and the pre-exponential factor *A* can be obtained. The calculation results were shown in Table 3.

***Table 3:** Calculation results of activation energy (E) and pre-exponential factors (A) by the FWO method*

α	*E*/kJ mol^{-1}	lg*A*/min^{-1}	*R*^{2}
0.1	86.50181	10.15792	0.93618
0.15	120.48544	13.19503	0.97822
0.2	137.28287	14.65768	0.99429
0.25	148.20175	15.59618	0.99802
0.3	153.98529	16.07624	0.99934
0.35	149.0865	15.66324	0.95299
0.4	151.56864	15.81194	0.99946
0.45	147.34375	15.42128	0.99918
0.5	144.06758	15.11261	0.99762
0.55	145.70094	15.2206	0.99144
0.6	160.76529	16.41572	0.9653
0.65	223.30541	21.40317	0.96466
0.7	287.20415	25.88429	0.99275
0.75	286.08752	24.87523	0.93098
0.8	224.80924	19.41273	0.99769
0.85	218.2724	18.48949	0.99908
0.9	220.72257	18.3827	0.99219
0.95	217.95552	17.97642	0.98177

In order to observe the change trend of the activation energy directly, the change trend of the activation energy with the conversion rate was shown in Fig. 3. The activation energy can be roughly segmented into two stages. When the conversion rate was between 0.1-0.6, the activation energy rose from 86.5 to 160.7 kJ/mol, and when the conversion rate was between 0.65-0.95, the activation energy was 217.9- 287.2 kJ / mol. Taking the conversion rate of 0.65 as the boundary, the entire combustion process can be divided into two periods. The average activation energy of the first period (conversion rate below 0.65) was 140.4 kJ/mol, and the average activation energy of the second stage (conversion rate above 0.6) was 239.8 kJ/mol.

The activation energy is the minimum energy requirement for starting the reaction. From Figure 3, we can see that the activation energy in the second period had large fluctuations, which indicated that the second stage may include some complex reactions, such as parallel reactions, continuous reactions, and so on (Ma et al., 2015).

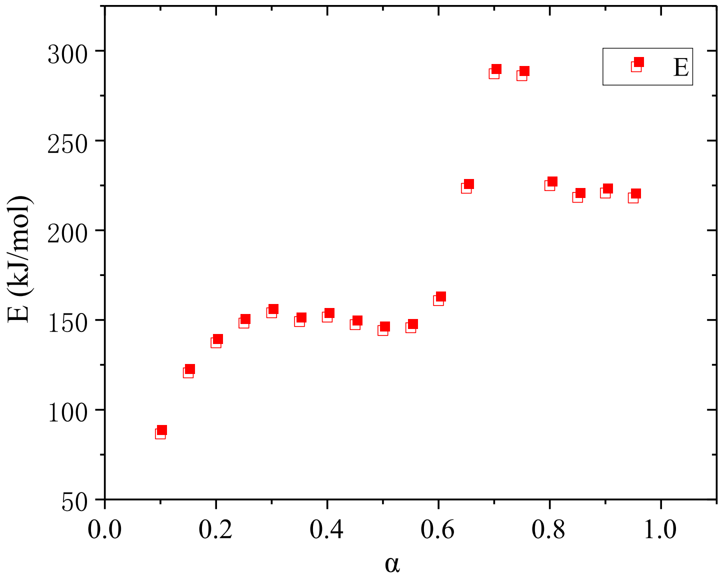

Fig. 3 *Distribution of activation energy at different conversion rates*

3.3 Thermal behavior analysis based on the deconvolution technique

The TG and heat flow curve of pine sawdust at a heating rate of 10 ℃ / min was shown in Fig. 4. From the curve, it can be seen that the burning process of pine sawdust was roughly split into three parts. First of all, it was an endothermic phase from room temperature to 101 ℃, and the mass loss is about 7.5% of the total weight, which may be caused by the evaporation of water. Two distinct exothermic peaks can be observed between 100-500 ℃, the heat of reaction was 17289 kJ/kg, and the peak temperatures were 341 and 489 ℃ respectively. This stage experienced two consecutive mass losses, which accounted for about 57% and 31% of the total sample, respectively, which may be due to the combustion of volatile components and char.

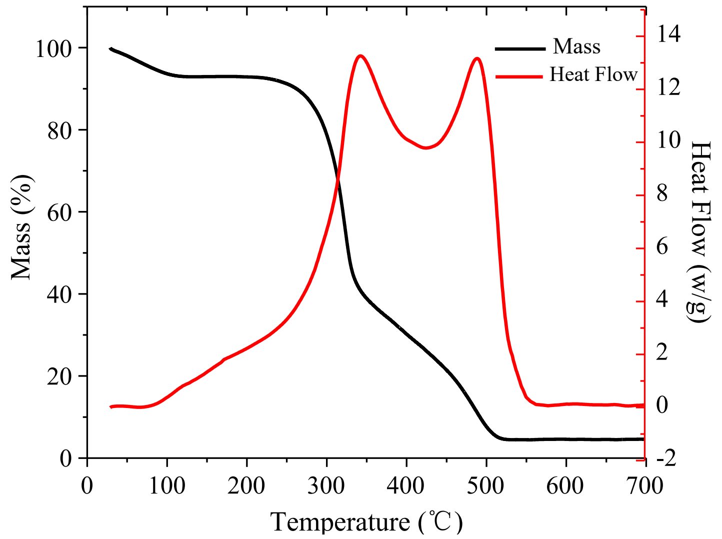

Fig. 4 TG and DSC curves of pine biomass

However, the activation energy obtained by the FWO method indicated that the combustion of pine sawdust is a complex reaction, and the obtained curves may have overlapping peaks, and it was hard to establish a clear boundary for these reaction stages (Zheng and Koziński, 2000). Deconvolution is a common mathematical technique that can separate overlapping peaks to obtain individual peak curves.

In this paper, the deconvolution method was used to transform the heat flow curve with heating rate of 10 ℃/min, as shown in Fig. 5. It can be observed that the two curves had a higher degree of fit. The original curve showed two peaks. After deconvolution, three peaks can be obtained, namely peak a, peak b, and peak c.

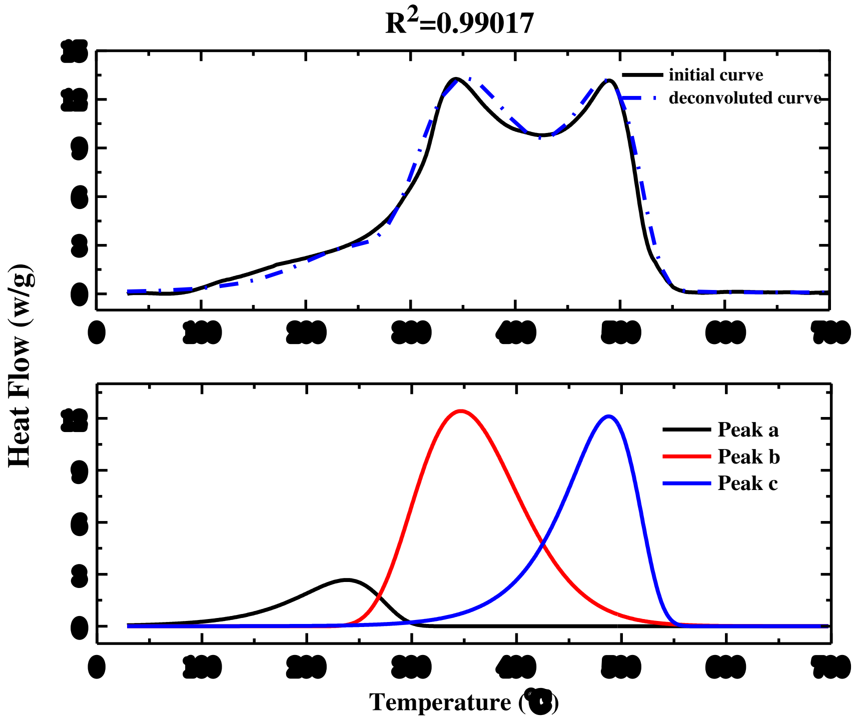

***Fig. 5** Initial and deconvoluted DSC curves of pine biomass at 10 ℃/min heating rate.*

The kinetic and thermodynamic parameters can be obtained by analysing the different peaks, as shown in Table 4. Peak a and peak b corresponded to the pyrolysis volatiles combustion of hemicellulose and cellulose, while peak c was caused by the combustion of lignin after carbonization. This was because when the heat input was slow, there were two exothermic peaks of volatiles and char combustion in pine sawdust combustion. Therefore, the combustion of volatiles was the starting point of the burning process of pine sawdust which restricts the burning of pine sawdust. The heat generation of these three separate peaks was 17828 kJ/kg in total, which was similar to the heat of reaction of the original curve, 17289 kJ/kg, which indicated that the deconvolution method was reasonable and reliable.

Table 4: *Thermal dynamic and kinetics of Pine chips combustion process based on deconvolution technique*

	Onset temperature/℃	**Peak temperature/℃**	ΔH **/kJ · kg^{-1}**	***E*/kJ • mol^{-1}**	**ln*A*/s^{-1}**	***R*^{2}**
Initial	66.71	341.22,488.85	17288.56	87.22	7.16	0.99585
Peak a	83.82	239.27	1716.64	24.43	-0.80	0.98042
Peak b	232.17	346.73	9220.92	123.37	18.28	0.99001
Peak c	279.30	487.55	6890.32	80.61	6.5583	0.99776
Total	-	-	17827.88	-	-	-

The results showed that the activation energy and pre-finger factors first increased and then decreased. At higher temperature ranges, the activation energy was lower, which is consistent with the results observed by Gao et al (Gao *et al.*, 2013). This may be because during the low-temperature oxidation, the char oxidized by pine sawdust covered the surface of the sample, forming a barrier, which affected the heat transfer rates, reduces the reactivity, and requires more energy for the reaction. However, with increasing temperature, the char covering the surface burned, the barrier disappeared, the main reactions of the remaining samples changed, and the activation energy decreased.

Conclusions

In this paper, the combustion kinetics of pine sawdust was studied according to the application needs, which has a guiding role. The TG-DSC experiment, FWO method and deconvolution method were used to analyse the combustion process of pine chips. The relevant kinetic parameters and the influence of heating rate on the combustion process were obtained. The main results are as follows:

At different heating rates, the combustion of pine sawdust went through a similar process. However, the faster the heating rate, the shorter the heating time, the shorter the reaction time experienced by the sample, and the lower the reaction degree. As the heating rate increases, the temperature gradient formed inside the particles intensifies, and the entire reaction moved to high temperatures. The influence of the heating rate on the initial combustion temperature of volatiles can provide an important basis on improving the burning efficiency of pine sawdust.

The whole combustion process can be separated into two parts according to the activation energy. The average activation energy was 140.45363 kJ/mol and 239.76526 kJ/mol, respectively. The results showed that the activation energy had a large fluctuation, which indicated that the burning process of pine chips may include some parallel reactions or continuous reactions and so on.

The overlapped exothermic peaks were separated by deconvolution method. After separation, three separate peaks, peak a, peak b, peak c, whose reaction heat was 1717 kJ/kg ,9221 kJ/kg and 6890 kJ/kg respectively and the reaction activation energy was 24.43 kJ/mol, 123.37 kJ/mol, and 80.61 kJ/mol respectively. The sum of the reaction heats of the three individual peaks was similar to that obtained from the original curve, which indicated that the deconvolution method was reasonable and effective. Peak a and peak b corresponded to the pyrolysis volatiles combustion of hemicellulose and cellulose, while peak c was caused by the combustion of lignin after carbonization. This has reference value for industrial process to obtain the target product.

Acknowledgements

The work studied in this paper is supported by the National Natural Science Foundation of China (Nos. 51874344 and 51604297), as well as the Key Research and Development Program of Shandong Province (2018GSF120011). All the researchers are grateful for contribution of the above institutions.

References

Aghamohammadi, N., N.M.N. Sulaiman and M.K. Aroua, (2011). Combustion characteristics of biomass in southeast asia. Biomass and bioenergy, 35(9): 3884-3890.

Budrugeac, P. and E. Segal, (2007). Applicability of the kissinger equation in thermal analysis. Journal of thermal analysis and calorimetry, 88(3): 703-707.

Burnham, A.K. and L. Dinh, (2007). A comparison of isoconversional and model-fitting approaches to kinetic parameter estimation and application predictions. Journal of Thermal Analysis and Calorimetry, 89(2): 479-490.

Cai, J., D. Xu, Z. Dong, X. Yu, Y. Yang, S.W. Banks and A.V. Bridgwater, (2018). Processing thermogravimetric analysis data for isoconversional kinetic analysis of lignocellulosic biomass pyrolysis: Case study of corn stalk. Renewable and Sustainable Energy Reviews, 82: 2705-2715.

Demirbas, A., (2004). Combustion characteristics of different biomass fuels. Progress in energy and combustion science, 30(2): 219-230.

Ding, Y., O.A. Ezekoye, S. Lu, C. Wang and Z. Ru, (2017). Comparative pyrolysis behaviors and reaction mechanisms of hardwood and softwood. Energy Conversion & Management, 132: 102-109.

Elsabee, M. and R.J. Prankerd, (1992). Solid-state properties of drugs. Ii. Peak shape analysis and deconvolution of overlapping endotherms in differential scanning calorimetry of chiral mixtures. Int. J. Pharm., 86(92): 211–219.

Fernandez-Lopez, M., G. Pedrosa-Castro, J. Valverde and L. Sanchez-Silva, (2016). Kinetic analysis of manure pyrolysis and combustion processes. Waste management, 58: 230-240.

Gao, N., A. Li, C. Quan, L. Du and Y. Duan, (2013). Tg–ftir and py–gc/ms analysis on pyrolysis and combustion of pine sawdust. Journal of Analytical and Applied Pyrolysis, 100: 26-32.

Gil, M.V., D. Casal, C. Pevida, J. Pis and F. Rubiera, (2010). Thermal behaviour and kinetics of coal/biomass blends during co-combustion. Bioresource Technology, 101(14): 5601-5608.

Gogoi, M., K. Konwar, N. Bhuyan, R.C. Borah, A.C. Kalita, H.P. Nath and N. Saikia, (2018). Assessments of pyrolysis kinetics and mechanisms of biomass residues using thermogravimetry. Bioresource Technology Reports, 4: 40-49.

Grønli, M.G., G. Várhegyi and C. Di Blasi, (2002). Thermogravimetric analysis and devolatilization kinetics of wood. Industrial & Engineering Chemistry Research, 41(17): 4201-4208.

Gu, X., X. Ma, L. Li, C. Liu, K. Cheng and Z. Li, (2013). Pyrolysis of poplar wood sawdust by tg-ftir and py–gc/ms. Journal of Analytical and Applied Pyrolysis, 102: 16-23.

Kerolli-Mustafa, M., V. Lajqi-Makolli, S. Berisha–Shala, LetafeteLatifi and IlirMorina, (2015). Biomass and biofuel overview: A global sustainability challenge. Journal of Environmental Protection & Ecology, 16(1): 222-232.

Kong, D., R. Peng, X. Sun, J. Zhang, P. Ping and J. Du, (2019). Study of the influence of crude oil on the spontaneous combustion risk of sulfurized rust in crude oil tanks. Fuel, 255: 115816.

Ma, Z., D. Chen, J. Gu, B. Bao and Q. Zhang, (2015). Determination of pyrolysis characteristics and kinetics of palm kernel shell using tga–ftir and model-free integral methods. Energy Conversion and Management, 89: 251-259.

Owen, K., O. Fasina, S. Taylor and S. Adhikari, (2015). Thermal decomposition behavior of loblolly pine stemwood, bark, and limbs/foliage using tga and dsc techniques. Transactions of the Asabe, 58(2): 509-518.

Pham, T.P.T., R. Kaushik, G.K. Parshetti, R. Mahmood and R. Balasubramanian, (2015). Food waste-to-energy conversion technologies: Current status and future directions. Waste management, 38: 399-408.

Sánchez-Jiménez, P.E., J. Criado and L.A. Pérez-Maqueda, (2008). Kissinger kinetic analysis of data obtained under different heating schedules. Journal of thermal Analysis and calorimetry, 94(2): 427-432.

Sikkema, R., M. Steiner, M. Junginger, W. Hiegl, M.T. Hansen and A. Faaij, (2011). The european wood pellet markets: Current status and prospects for 2020. Biofuels, Bioproducts and Biorefining, 5(3): 250-278.

Vlaev, L.T., I.G. Markovska and L.A. Lyubchev, (2003). Non-isothermal kinetics of pyrolysis of rice husk. Thermochimica Acta, 406(1): 1-7.

Yao, X., L. Ni, J. Jiang, J. Huang, J. Yang and G. Yang, (2019). Thermal hazard and kinetic study of 5-(2-pyrimidyl) tetrazole based on deconvolution procedure. Journal of Loss Prevention in the Process Industries, 61: 58-65.

Yu, Y., X. Fu, L. Yu, R. Liu and J. Cai, (2016). Combustion kinetics of pine sawdust biochar. Journal of Thermal Analysis and Calorimetry, 124(3): 1641-1649.

Zheng, G. and J. Koziński, (2000). Thermal events occurring during the combustion of biomass residue. Fuel, 79(2): 181-192.

DOI: 10.7795/810.20200724

Pyrolysis and Pilot Ignition of PMMA Dust by Constant Conduction

Lei Huang [a], Wei Gao [a*]

[a] State Key Laboratory of Fine Chemicals, Department of Chemical Machinery and Safety Engineering,
Dalian University of Technology, 2 Linggong Rd., Dalian 116024, China

E-mail: gaoweidlut@dlut.edu.cn

Abstract

In this work, three particle sizes (100 nm, 5 μm, 30 μm) of poly methyl methacrylate (PMMA) dust were selected to analyse the influence of particle size, dust layer thickness and heating temperature on pyrolysis and pilot ignition behavior. The histories of the in-depth sample temperature as well as ignition time had been measured for various heating temperature. Ignition occurred as the heating temperature reached a critical value (an ignition temperature). For 20 mm thick dust layer, the ignition temperature of PMMA dust increased with increasing particle size. The ignition temperatures of 100 nm PMMA, 5 μm PMMA, and 30 μm PMMA were 340℃, 350℃, and 360℃. As the thickness of the dust layer increased from 20 mm to 30 mm, the ignition temperature of 100 nm PMMA, 5 μm PMMA, and 30 μm PMMA increased by 20℃, 50℃, 70℃. The ignition time of dust increased as the dust layer thickness and the dust particle size increased. A 2D numerical model and theoretical analysis were utilized to describe temperature distribution of PMMA dust layers, the numerical results of in-depth temperature agreed well with the experimental data. Thermal and kinetic parameters including thermal conductivity (K), activation energy (E), pre-exponential factor (A) and specific heat (c_p) were estimated based on experimental data and TG-DSC analysis for model. These results improve our understanding of the ignition behaviour and provide guidance for fire accident prevention and mitigation.

Keywords: *pyrolysis, pilot ignition, PMMA, ignition temperature, ignition time*

1. Introduction

Ignition of dust layer is one of the most common causes of dust explosions in industry. There is a risk of fire when combustible dust accumulates on hot surfaces of equipment and facilities. Many studies have discussed the problem of dust layer ignition for different materials. Chunmiao and Dezheng et al.(2013) studied the ignition behavior of magnesium powder layers. A numerical model was established to determine the temperature distribution in the dust layer and the subsequent ignition process. Wu and Song et al.(2019) proposed an improved analogy method considering the effect of oxygen diffusion to correct the kinetic parameters so that the minimum ignition temperature of the coal dust layer can be predicted more accurately. El-Sayed and Mostafa (2016) developed a method to determine the thermal and kinetic parameters of sugarcane bagasse and cotton stalks dust layers from hot surface ignition tests. Most of the previous studies were about the problem of self-ignition of dust, and lack of investigation on other ignition methods.

For some combustible materials, especially high-molecular polymers, the pyrolysis reaction will occur under the external heat flow. Even if there is no flaming combustion, a large amount of flammable gas will be generated. Flammable gases from pyrolysis pose fire hazards under the ignition source. Many studies have discussed the pilot ignition behavior of solid materials. Reszka and Borowiec et al.(2012) developed a method to estimate the ignition times of Nylon and PMMA by pilot ignition tests, the time to ignition was proportional to the squared time integral of the incident heat flux. Fang and Meng et al.(2018) studied the ignition behaviour of thermally thick PMMA through experiments, numerical calculations and theoretical analysis. They analyzed the effects of the on-off cycle irradiation on the surface and in-depth specimen temperatures, the mass flux and the ignition time. Vermesi and Roenner et al.(2016) studied the process of pyrolysis and ignition of PMMA by transient irradiation experiments and a 1D pyrolysis model Gpyro (Lautenberger and Fernandez-Pello, 2009). The results of simulations were compared with the transient irradiation experiments. Finally, they assessed the ignition criteria with respect to both constant and transient irradiation. Among them, PMMA was the most common experimental material. This was because PMMA had excellent transparency, strength and chemical stability. It was often made of organic glass and was widely used in industry.

The previous studies on the pilot ignition of combustible materials were all about bulk materials, there was no related investigation on powder materials. At the same time, previous studies on the risk of dust accumulation on hot surfaces had not considered the influence of external ignition sources. In this paper, we conducted a series of constant temperature heating experiments using the ignition electrode as the ignition source to investigate the pilot ignition behavior of PMMA dust layer. In addition, the effect of various dust particle sizes, dust layer thicknesses and heating temperature on ignition characteristic parameters were investigated. Dust with a smaller particle size had a larger specific surface area (Jiang and Bi et al., 2020), which mean that the finer particle had higher reactivity than coarser particle. Therefore, in order to make this research more valuable, three nano- and micro-scale PMMA dusts were selected as experimental materials.

We developed a 2D numerical model to investigate the temperature distribution in the dust layer, and a sensitivity analysis of the thermodynamic parameters in the model was conducted. The heat and mass transfer processes in the heating of the dust layer and the ignition process were investigated as the theoretical basis for the analysis of experimental results.

2. Experiments

2.1 *Experimental setup*

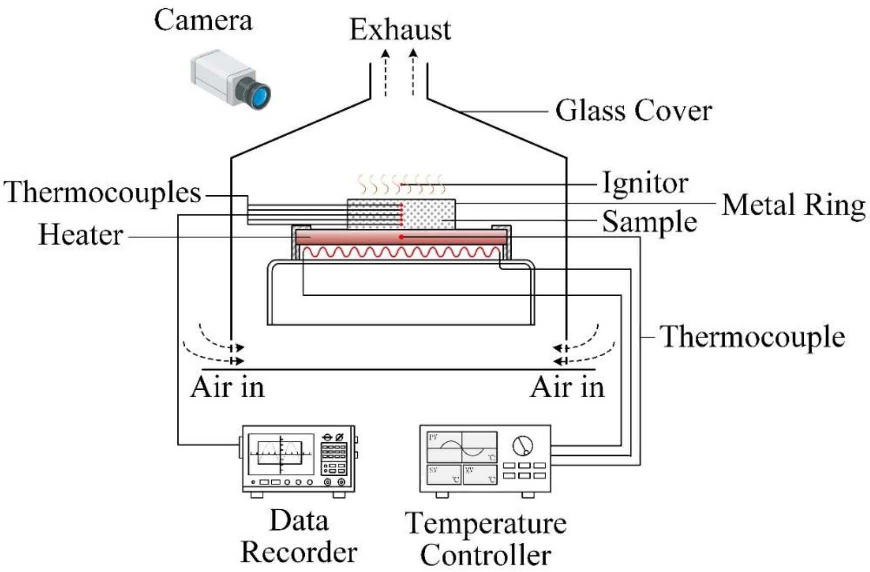

Fig. 1. *Semi-closed dust layer heating and pilot ignition apparatus*

A schematic of the experimental set-up is provided in Fig. 1. Conduction was provided by a plate heated at constant temperature. Heating performance of the hot-plate in accordance with the standard of ASTM E 2020-06 (2006). Hot-plate surface temperature was set by temperature controller (Xiamen Yudian Automation Technology Co., Ltd. accuracy: ±3℃). A metal ring was fixed on the hot-plate to contain the dust layer. The inner diameter (*D*) of the metal ring was 50 mm, and the wall thickness was 1.5 mm. This study used two height (*L*) metal rings: 20 mm and 30 mm. Some 0.25 mm diameter K-type bare thermocouples (Omega CHAL-010-BW, accuracy: ±2.2℃) were inserted into the center of the dust layer. Because the direct contacted between the thermocouple and the metal ring will reduce the accuracy of reading, a ceramic tube was placed between the thermocouple and the metal ring wall for insulation. Thermocouples were positioned 2 mm, 5 mm, 10 mm, 15 mm, 18 mm in height for 20 mm high metal ring. Similarly, thermocouples were positioned 2 mm, 5 mm, 10 mm, 15 mm, 20 mm, 25 mm, 28 mm in height for 30 mm high metal ring.

An ignition electrode with 15 kV voltage and 0.04 A current was situated 20 mm (Fang and Meng et al., 2018) above the sample as a pilot source. The effect of the heat flow generated during the ignition electrode discharge on the dust layer was ignored (Vermesi and Roenner et al., 2016; Fang and Meng et al., 2018).

To ensure good air circulation, the experimental apparatus was placed in a glass cover with a fan. A gap under the chamber wall allowed the ingress of ambient air. The air flow generated by the fan was very weak and would not affect the natural diffusion of the gas produced by pyrolysis and oxidation. At the same time, due to the existence of the glass cover, the external air flow would not affect the accuracy of experiment data.

The temperature data was recorded by a data acquisition instrument (Yokogawa DL850E). Time step for data recording was set as 0.1 s. The heating process of the dust layer was recorded by a digital video camera (Canon-G20, 30fps). The ignition time was determined from the data recorded by the camera.

In order to reduce the agglomeration of dust particles, before experiment, the experimental materials were dried in a drying oven at 35℃ for at least 24 hours (Zhou and Li et al., 2019). The experimental procedures were as follows: (1) heated the hot-plate to a stable temperature; (2) weighted a certain amount of PMMA dust; (3) turned on the digital video camera and the data acquisition instrument; (4) filled the metal ring with PMMA dust and gently scraped the upper surface within two minutes; (5) data measurement started after energizing the ignition electrode. Tests were run until either the layer temperature reached a steady state for no less than 30 min or clear thermal runaway was observed. If the dust layer was not ignited at the pre-set temperature (T_p), increased it by 10℃ until the dust layer was ignited. Resolution of 10℃ was adopted for all tests.

2.2 *Sample preparation*

The experimental materials (Soken Chemical Co., Ltd. of Japan Ministry) were 100 nm (MP-300), 5 μm (SX-500H), 30 μm (MZ-30H) PMMA dust. The particle size distribution of PMMA dust measured by the Malvern Mastersizer (AWM 2000) was shown in Fig. 2. Table 1 listed the volume average diameter D[4,3], the Sauter diameter D[3,2] and the quantiles of the volumetric distribution Dv (10), Dv (50) and Dv (90). The particle size distribution range of 100 nm PMMA dust particles was wide from 0.448 to 89.337 μm. Volume average diameter and Sauter diameter of 100 nm PMMA were 24.877 μm and 10.486 μm, so there was a serious agglomeration effect of 100 nm PMMA dust particles. The characteristic diameters of 5 μm PMMA and 30 μm PMMA were closer to the nominal value.

The micrographs of dust particles shown in Fig. 3 were observed by scanning electron microscopy (FEI Nova NanoSEM 450). It could be seen from Fig. 3 that 100 nm, 5 μm and 30 μm PMMA were regular spherical structures. 5 μm PMMA and 30 μm PMMA particles had good dispersibility. As with the results of the particle size distribution of PMMA, 100 nm PMMA had obvious agglomeration.

DOI: 10.7795/810.20200724

Table 1. *Characteristic diameters of 100 nm, 5 μm, and 30 μm PMMA particles (Zhang and Yu et al., 2017)*

Characteristic diameters	MP- 300 (100 nm)	SX- 500H (5 μm)	MZ- 30H (30 μm)
D[4,3] (μm)	24.877	5.149	28.974
D[3,2] (μm)	10.486	3.284	24.080
*D*v (10) (μm)	6.151	1.186	16.509
*D*v (50) (μm)	22.543	5.294	24.523
*D*v (90) (μm)	46.764	7.428	43.186

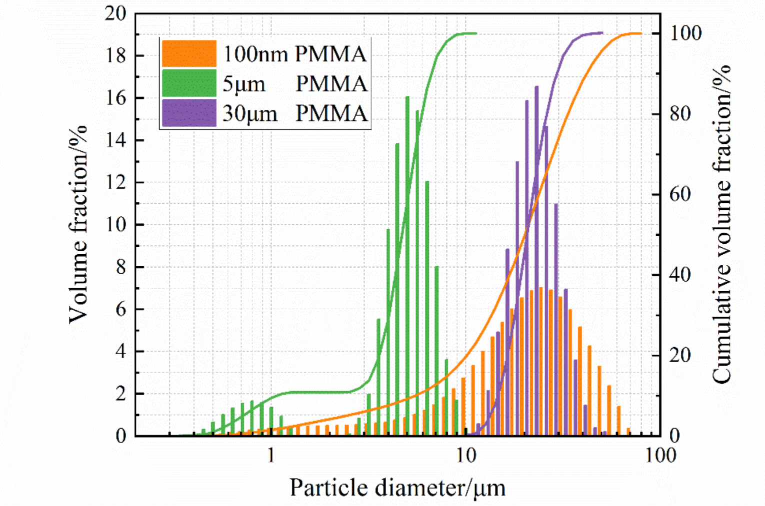

Fig. 2. *Particle size distribution of PMMA dust*

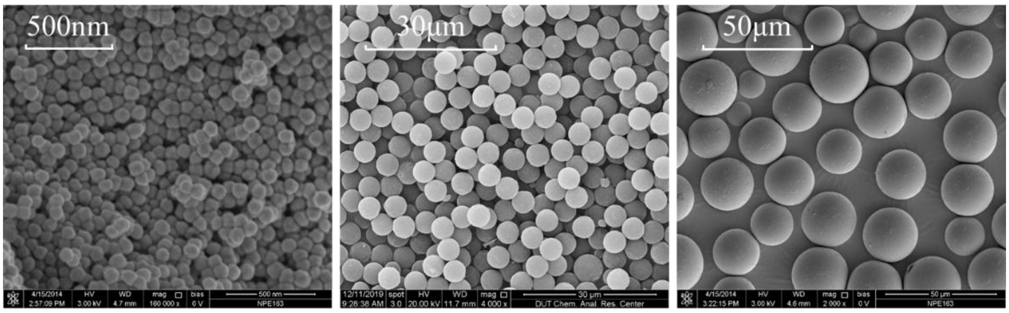

(a) 100 nm (b) 5 μm (c) 30 μm

Fig. 3. *SEM photographs of 100 nm, 5 μm and 30 μm PMMA dust particles*

3. Theoretical method

3.1 Governing equations

In order to understand the temperature distribution in the dust layer under constant temperature heating, we investigated the heat and mass transfer process in the dust layer. The PMMA dust layer could be regarded as a porous medium. Figure 4 showed the heat absorption and loss of PMMA dust layer during pyrolysis. After the sample was placed on the hot-plate surface, heat entered the dust layer through heat conduction, and at the same time, heat was lost on the upper surface of the dust layer due to convection and radiation. For simplicity, the following assumptions were made:

- since the experimental material was sufficiently dried before the experiment, the effect of the moisture content was not considered;
- the effects of gas conditions on heat and mass transfer coefficients and stoichiometric coefficients were ignored;

- the parameters such as the bulk porosity, thermal conductivity and specific heat capacity of PMMA dust and gas mixture were independent of time and temperature.

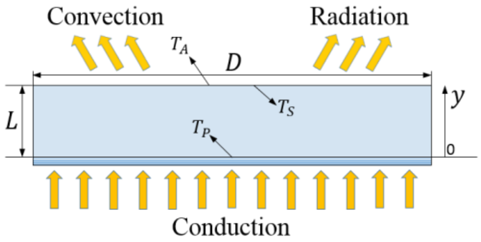

Fig. 4. *Absorption and loss of heat during PMMA pyrolysis*

A one dimensional equation of energy balances for the dust layer in Fig. 4 could be simplified to (Wu and Vanierschot et al., 2016):

$$\left((1-\varepsilon_b)\rho_s c_s+\varepsilon_b\rho_{air}c_{air}\right)\frac{\partial T}{\partial t}=\nabla\cdot\left(k_e\nabla T\right)+Q \tag{1a}$$

The heat of oxidation reaction could be formulated by the Arrhenius law as:

$$Q=\left(1-\varepsilon_b\right)\rho_s A\exp\left(\frac{-E}{RT}\right)\Delta H_s \tag{1b}$$

Where k_e is the effective thermal conductivity of a dust layer (W m^{-1} K^{-1}), T is temperature (K), ρ_s, ρ_{air} are the density of PMMA and air (kg m^{-3}), c_s and c_{air} are the specific heat of PMMA and air (J kg^{-1} K^{-1}), ε_b is the bulk porosity of dust layer, ΔH_s is heat of reaction (J kg^{-1}) of PMMA, A is Arrhenius pre-exponential factor (s^{-1}), E is activation energy (J mol^{-1}) and R is the universal gas constant (8.314J mol^{-1} K^{-1}).

3.2 Boundary and initial conditions

A Neumann boundary condition was considered for the temperature filed of the PMMA dust layer. At the upper surface of the dust layer (y=L):

$$-k_e\left(\frac{\partial T}{\partial y}\right)=h\left(T_S-T_A\right)=h_c\left(T_S-T_A\right)+\varepsilon\sigma\left(T_S^4-T_A^4\right) \tag{2}$$

Where h=h_c+h_r is total heat transfer coefficient (W m^{-2} K^{-1}), h_c is convective heat transfer coefficient (W m^{-2} K^{-1}), h_r is radiant heat transfer coefficient (W m^{-2} K^{-1}), T_S is the upper surface temperature of the dust layer (K), T_A is ambient temperature (K), σ is the Stefan–Boltzmann constant (5.67×10^{-8}W m^{-2} K^{-4}), and ε is the emissivity of the layer surface.

The convective heat transfer coefficient of the sample was determined using Eq. (3). (Park and Rangwala et al., 2009).

$$h_c=\frac{0.54Ra^{0.25}k_a}{l}\quad \text{for}\ (10^5\le Ra\le 10^7) \tag{3}$$

Convective heat transfer coefficient h_c was a time-dependent parameter. It depended on T_A and T_S, and it could determine the value through the COMSOL Multiphasics software.

At the lower surface of the dust layer (y=0):

$$T=T_P \tag{4}$$

Where T_p is the hot-plate temperature (K).

The dust layer was contained in a metal ring made of stainless steel with a wall thickness of 1.5 mm. Because the metal ring was thin enough, it could be regarded as thermally thin material. The metal ring could be heated by the hot-plate. Heat conduction occurred between the cylindrical surface of the dust layer and the metal ring.

Before the dust layer was heated, the temperature in the dust layer was approximately regarded as ambient temperature (16℃), so at time t=0:

$$T = T_A \tag{5}$$

3.3 Solution method

The numerical solution of Eqs. (1) -(5) could be obtained by COMSOL Multiphasics software. The bulk density (ρ_b) of the dust layer could be obtained through experiments, it could be expressed as Eq. (6a), and the bulk porosity (ε_b) could be obtained by Eq. (6b)

$$\rho_b = (1-\varepsilon_b)\rho_s + \varepsilon_b \rho_{air} \tag{6a}$$

$$\varepsilon_b = 1 - \frac{\rho_b - \rho_{air}}{\rho_s - \rho_{air}} \approx 1 - \frac{\rho_b}{\rho_s} \tag{6b}$$

Simulations were performed through heat transfer in solids interface and irreversible transformation subfeature. Effective material properties need to be defined in the model, such as effective density and effective specific heat capacity, which could be obtained by Eq. (7) and Eq. (8). The oxidation reaction took place in an isobaric environment, and the enthalpy change was considered equal to the heat of reaction of PMMA .

$$\rho_{eff} = \rho_b \tag{7}$$

$$(\rho c_p)_{eff} = (1-\varepsilon_b)\rho_s c_s + \varepsilon_b \rho_{air} c_{air} \tag{8}$$

The time step was set to 10 s and the calculation termination time was set to 1800 s

3.4 Parameter estimation

According to Fourier's law, the effective thermal conductivity k_e had an effect on the temperature distribution in the dust layer and it could be estimated by assuming that heat generation at low temperature is negligible (Park and Rangwala et al., 2009). Therefore, at a lower temperature, some tests were performed to determine the value of the parameter using the method described by Park and Rangwala et al.(2009) before the formal experiment began. In this paper, the effective thermal conductivity of PMMA dust layer was obtained by heating the dust layer with a thickness of 10 mm.

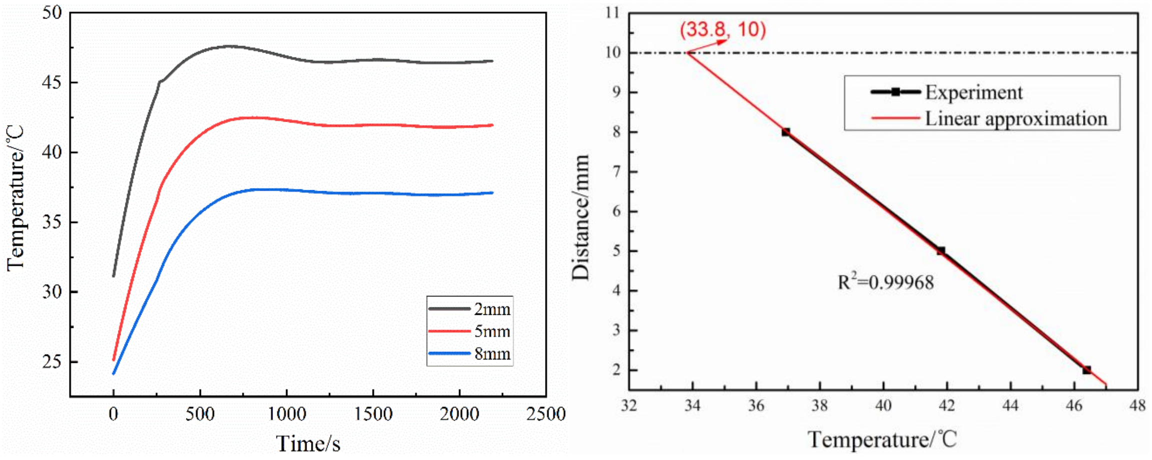

(a) (b)

Fig. 5. *30 μm PMMA dust layer temperature distribution when exposed to a hot-plate surface of 50 ℃ (a), and steady state temperature distribution in the dust layer and its linear trend line (b)*

For 30 μm PMMA dust, the temperature distribution obtained by exposing a dust layer with a thickness of 10 mm on a hot-plate at a temperature of 50℃ was shown in the Fig. 5(a). Linear extrapolation from the three temperature curves yields T_S of 33.8℃ as shown in Fig. 5(b). The ambient temperature T_A was 16℃. The estimated effective thermal conductivity of 0.13 W $m^{-1}K^{-1}$ was obtained with T_A=16℃ and T_S=33.8℃. Different thermal conductivity could be obtained by performing the same test on other particle sizes. For 100 nm PMMA and 5 μm PMMA, the effective thermal conductivity was 0.108 W $m^{-1}K^{-1}$ and 0.122 W $m^{-1}K^{-1}$ respectively.

Activation energy (E) and pre-exponential factor (A) were important parameters about the hazard of thermal runaway of dust materials and they could be obtained by using thermogravimetric analysis (TGA) at three heating rates (10 K min^{-1}, 20 K min^{-1}, 30 K min^{-1}) (Tian and Shen et al., 2016). Activation energy could be obtained by FWO method (Sharara and Holeman et al., 2014) and KAS method (Starink, 2003). Thus, E could be obtained by the slope of the straight line plotted by Eq (9) and Eq (10). Where β is the heating rate of the sample (K min^{-1}), α is conversion rate of the sample.

$$\ln\beta = \ln\frac{A\cdot E}{R\cdot g(\alpha)} - 5.335 - \frac{1.0516E}{RT} \tag{9}$$

$$\ln\frac{\beta}{T^2} = \ln\frac{AR}{E\cdot g(\alpha)} - \frac{E}{RT} \tag{10}$$

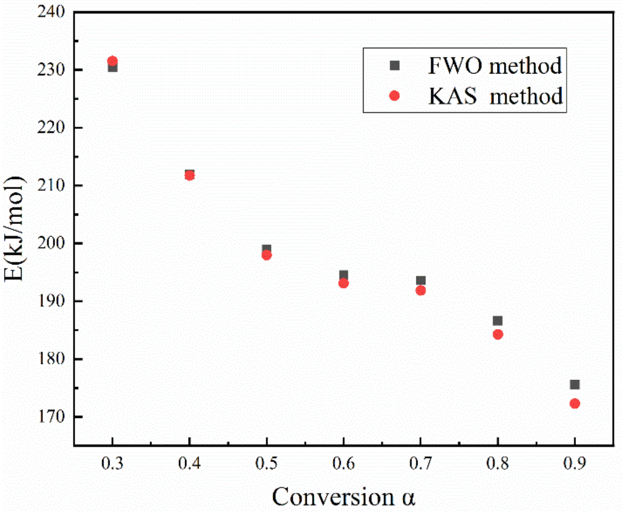

Fig. 6. *Activated energy of 30 μm PMMA by FWO method and KAS method at different α.*

Pre-exponential factor could be obtained by Coats-Redfern method (Tian and Shen et al., 2016).

$$\ln\left(\frac{g(\alpha)}{T^2}\right) = \ln\frac{AR}{\beta E} - \frac{E}{RT} \tag{11}$$

The values of activation energy, pre-exponential factor and correlation coefficient (R^2) obtained by Coats-Redfern method were listed in Appendix A. Several solid-state pyrolysis mechanisms were listed in Appendix B.

It could be seen from Fig. 6 that the activation energy obtained by the two methods has the same trend with the conversion rate. Since the activation energy value was approximately unchanged when α was in the range of 0.6 < α < 0.7, the activation energy could be averaged as the final value, approximately 195.7 kJ mol^{-1}. It was known that the activation energy values obtained by the FWO method and KAS method were considered reasonable (Moriana and Zhang et al., 2014). The activation energy and correlation coefficients obtained under different pyrolysis mechanisms were shown in Appendix A, it shown that the value of activation energy obtained by mechanism A1/2 was similar to that obtained by FWO method and KAS method and the correlation coefficient was higher than 95%, which proved that mechanism A1/2 was the most suitable mechanism for the pyrolysis process. The value of the pre-exponential factor was determined to be 3.55×10^{14} by mechanism A1/2 when $\beta = 10$ K min^{-1}. The activation energy and pre-exponential factor of 100 nm PMMA and 5 μm PMMA were considered to be the same as 30 μm PMMA.

The following Eq. (12) allowed the calculation of the specific heat (c_s) for 30 μm PMMA (Collazo and Pazó et al., 2012). The TG and DSC curves were shown in Fig. 7. The heating rate was 20℃ min^{-1} and 10.766 mg of sample was used. The TG and DSC results were obtained under a flow of nitrogen at a rate of 100 ml min^{-1} to avoid oxidation of the sample. It could be known from the DSC curve that there was an endothermic peak between 330℃ and 516℃. The specific heat calculated in this interval was 1924 J kg^{-1} K^{-1}. The specific heat of 100 nm PMMA and 5 μm PMMA were considered to be the same as 30 μm PMMA.

$$\frac{dH}{dt} = mc_s \frac{dT}{dt} \tag{12}$$

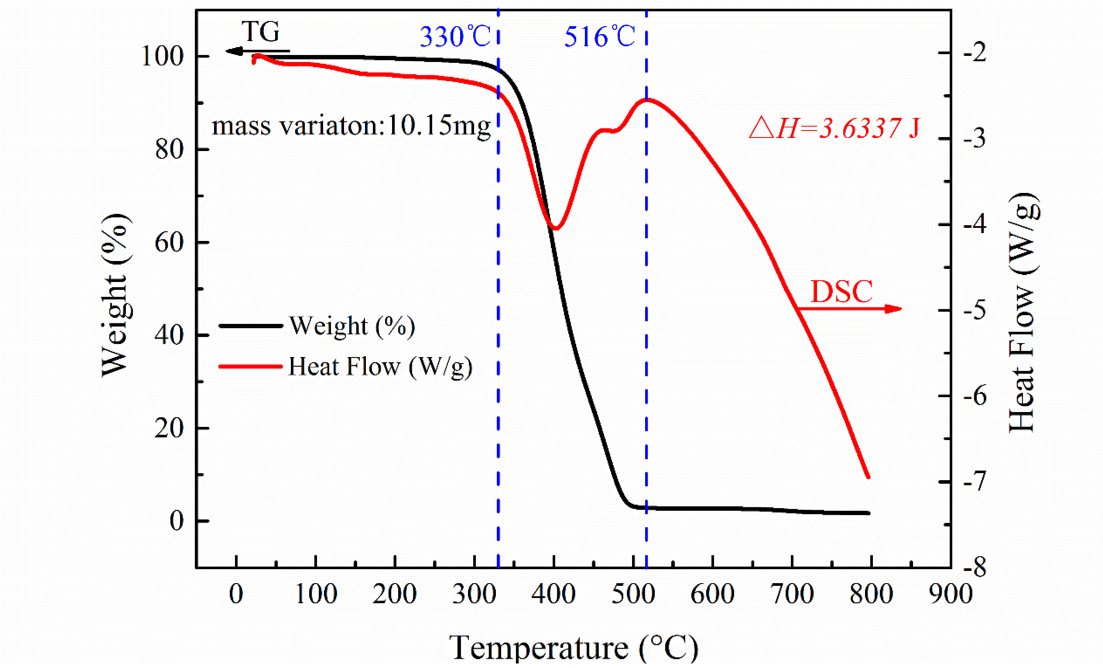

Fig. 7. *The TG and DSC curves for 30 μm PMMA.*

Table 2 showed the parameters obtained through experiments and theoretical calculations, other parameters obtained through references were shown in Table 3.

Table 2. *Summary of experimentally determined parameters.*

parameter	100 nm	5 μm	30 μm
ε_b	0.72	0.70	0.46
ρ_b / kg m^{-3}	332.57	363.64	641.20
k_e / W m^{-1}K^{-1}	0.108	0.122	0.13
E / kJ mol^{-1}	195.7	195.7	195.7
A / s^{-1}	3.55E+14	3.55E+14	3.55E+14
c_s / J kg^{-1} K^{-1}	1924	1924	1924

Table 3. *Summary of parameters obtained by references (Fang and Meng et al., 2018) (Wu and Vanierschot et al., 2016)*

name	symbol	value	unit
density of PMMA	ρ_s	1180	kg m^{-3}
density of air	ρ_{air}	1.293	kg m^{-3}
specific heat capacity	c_{air}	1013	J kg^{-1} K^{-1}
surface emissivity	ε	0.9	—
heat of reaction	ΔH_s	540	kJ kg^{-1}

4. Results and discussion

4.1 Ignition mechanism and behaviour

The dust layer was placed on a constant temperature hot-plate. Due to external energy, pyrolysis and slow smouldering occurred in the dust layer. The multi-step reaction of PMMA occurred during pyrolysis (Wenru and Shufen, et al., 2003). First, PMMA was thermally degraded to MMA (Equation 13.1), and then MMA continued to decompose to generate free radicals R_1 and R_2 (Equation 13.2). R_2 could continue to split to produce carbon monoxide and carbon dioxide, and the methoxy and methyl produced at the same time could combine with hydrogen free radicals to produce methanol and methane (Equation 13.3-13.6). R_1 could combine with hydrogen free radicals and methyl to form propylene and 2-methyl propene (Equation 13.7-13.8).

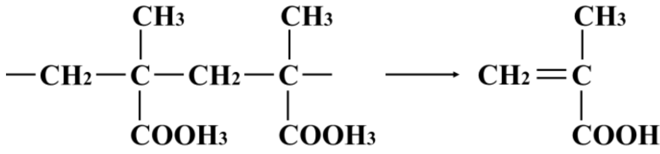

$$-\mathrm{CH_2}-\underset{\mathrm{COOH_3}}{\overset{\mathrm{CH_3}}{\mathrm{C}}}-\mathrm{CH_2}-\underset{\mathrm{COOH_3}}{\overset{\mathrm{CH_3}}{\mathrm{C}}}- \longrightarrow \mathrm{CH_2}=\underset{\mathrm{COOH_3}}{\overset{\mathrm{CH_3}}{\mathrm{C}}} \tag{13.1}$$

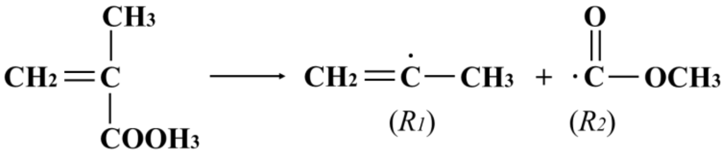

$$\mathrm{CH_2}=\underset{\mathrm{COOH_3}}{\overset{\mathrm{CH_3}}{\mathrm{C}}} \longrightarrow \underset{(R_1)}{\mathrm{CH_2}=\dot{\mathrm{C}}-\mathrm{CH_3}} + \underset{(R_2)}{\cdot\overset{\mathrm{O}}{\overset{\|}{\mathrm{C}}}-\mathrm{OCH_3}} \tag{13.2}$$

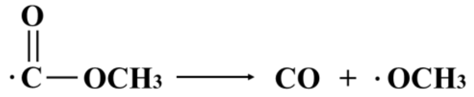

$$\cdot\overset{\mathrm{O}}{\overset{\|}{\mathrm{C}}}-\mathrm{OCH_3} \longrightarrow \mathrm{CO} + \cdot\mathrm{OCH_3} \tag{13.3}$$

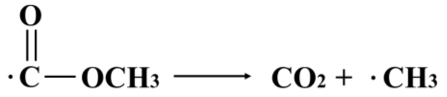

$$\cdot\overset{\mathrm{O}}{\overset{\|}{\mathrm{C}}}-\mathrm{OCH_3} \longrightarrow \mathrm{CO_2} + \cdot\mathrm{CH_3} \tag{13.4}$$

$$\cdot\mathrm{OCH_3} + \cdot\mathrm{H} \longrightarrow \mathrm{CH_3OH} \tag{13.5}$$

$$\cdot\mathrm{CH_3} + \cdot\mathrm{H} \longrightarrow \mathrm{CH_4} \tag{13.6}$$

$$\mathrm{CH_2}=\dot{\mathrm{C}}-\mathrm{CH_3} + \cdot\mathrm{H} \longrightarrow \mathrm{CH_2}=\mathrm{CH}-\mathrm{CH_3} \tag{13.7}$$

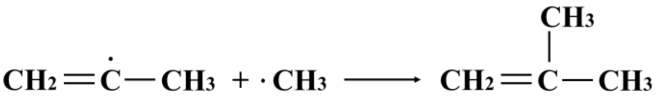

$$\mathrm{CH_2}=\dot{\mathrm{C}}-\mathrm{CH_3} + \cdot\mathrm{CH_3} \longrightarrow \mathrm{CH_2}=\overset{\mathrm{CH_3}}{\overset{|}{\mathrm{C}}}-\mathrm{CH_3} \tag{13.8}$$

In addition to the main products such as methanol, methane, propylene and 2-methyl propene, a small amount of acetone, formaldehyde and methyl pyruvate were also produced during the pyrolysis of PMMA (Wenru and Shufen, et al., 2003). Propylene reacted with oxygen molecules to form acetone (Equation 13.9). At higher temperature. MMA reacted with oxygen and water to form intermediates

R$_3$ and *R*$_4$, then *R*$_3$ and *R*$_4$ dehydrated to form formaldehyde and methyl pyruvate (Equation 13.10-13.12). Methyl pyruvate could also remove ester groups at high temperature to generate acetone (Equation 13.13).

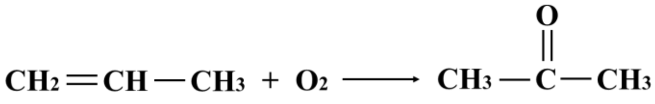

$$CH_2{=}CH{-}CH_3 + O_2 \longrightarrow CH_3{-}\overset{\overset{O}{\|}}{C}{-}CH_3 \qquad (13.9)$$

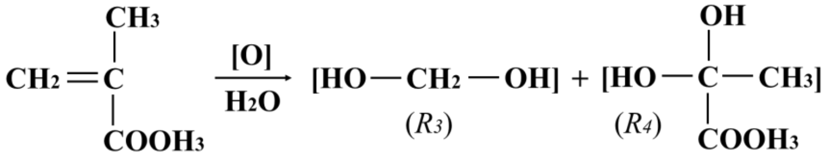

$$CH_2{=}\underset{\underset{COOH_3}{|}}{\overset{\overset{CH_3}{|}}{C}} \xrightarrow[H_2O]{[O]} \underset{(R_3)}{[HO{-}CH_2{-}OH]} + \underset{(R_4)}{[HO{-}\underset{\underset{COOH_3}{|}}{\overset{\overset{OH}{|}}{C}}{-}CH_3]} \qquad (13.10)$$

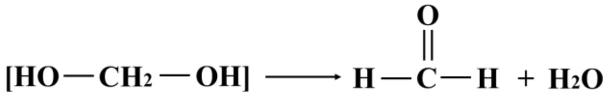

$$[HO{-}CH_2{-}OH] \longrightarrow H{-}\overset{\overset{O}{\|}}{C}{-}H + H_2O \qquad (13.11)$$

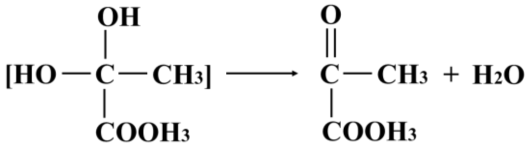

$$[HO{-}\underset{\underset{COOH_3}{|}}{\overset{\overset{OH}{|}}{C}}{-}CH_3] \longrightarrow \underset{\underset{COOH_3}{|}}{\overset{\overset{O}{\|}}{C}}{-}CH_3 + H_2O \qquad (13.12)$$

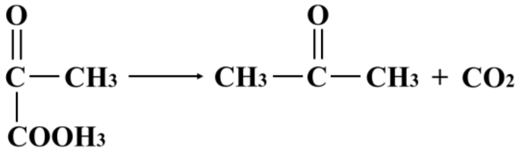

$$\underset{\underset{COOH_3}{|}}{\overset{\overset{O}{\|}}{C}}{-}CH_3 \longrightarrow CH_3{-}\overset{\overset{O}{\|}}{C}{-}CH_3 + CO_2 \qquad (13.13)$$

The small molecule flammable gas generated during the pyrolysis of PMMA would diffuse upward into the air through the tiny voids in the dust layer and the air would diffuse downward into the dust through the tiny voids too. Part of the flammable gas reacted with oxygen in the dust layer, and the rest of flammable gas would diffuse to the ambient through the dust layer surface and mix with oxygen. As time went on, the concentration of flammable gas mixture in the ambient gradually increased and it would be ignited by the ignition electrode when the concentration was between the Lower Flammability Limit (LFL) and the Upper Flammability Limit (UFL).

The images of the PMMA dust layer being ignited were shown in Fig. 8. As shown in Fig. 8, a blue flash (flash point) appeared on the surface of the dust layer multiple times before ignition, and then, as the concentration of flammable gas increased, a small yellow flame (fire point) appeared. Due to the buoyancy effect, the yellow flame gradually became larger and constantly oscillated. The critical time for the dust layer to ignite was equal to the moment when the yellow flame was obviously visible and sustained, which was determined as the ignition time. Then the yellow flame continued to grow and spread throughout the surface of the dust layer.

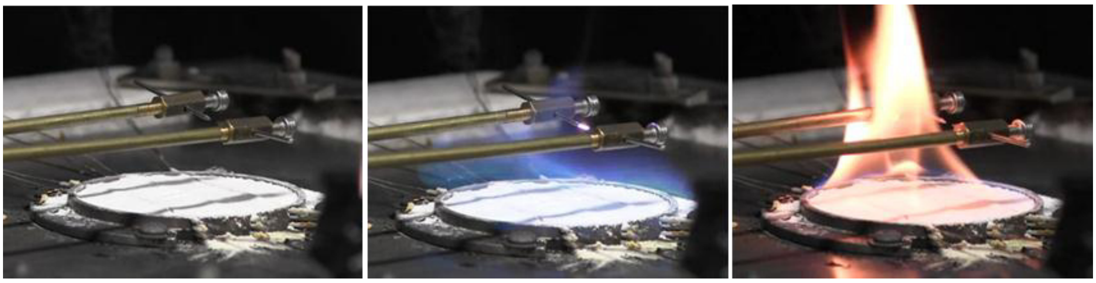

Fig. 8. *The process of PMMA dust layer being ignited*

Fig. 9 showed the typical temperature profile of the dust layer during heating when the dust layer thickness was 20 mm and the PMMA dust particle size was 100 nm. The dust layer was not ignited when the hot-plate was set to a temperature of 340℃. Fig. 9(a) showed the two-dimensional temperature distribution after the temperature in the dust layer had stabilized (1800s). Fig. 9(b) showed that the temperature at different heights in the center of the dust layer increased with time. As the heating time increased, the temperature at different heights in the dust layer continued to rise and eventually stabilized while there was a temperature gradient in the dust layer. The stabilized temperature at different height in the dust were below that of the hot-plate temperature. Fig. 9(b) showed that the simulation and experimental data demonstrated a close agreement.

Fig. 10 showed the evolutions of temperature distribution at different T_p for the 20 mm thick 100 nm PMMA dust layer, t_{ig} represented the experimental ignition time, which meant the time from the start of heating to the ignition of the dust layer. As the temperature of the hot-plate increased, the ignition time of the dust layer decreased, and the temperature rose rate at different heights of the dust layer increased. The temperature at the y=2 mm in the dust layer significantly higher than the temperature at other positions. It indicating that y=2 mm in the dust layer was the most sensitive position for the dust layer and the temperature at y=2 mm in the dust layer could represent the risk of the dust layer after heating in this paper.

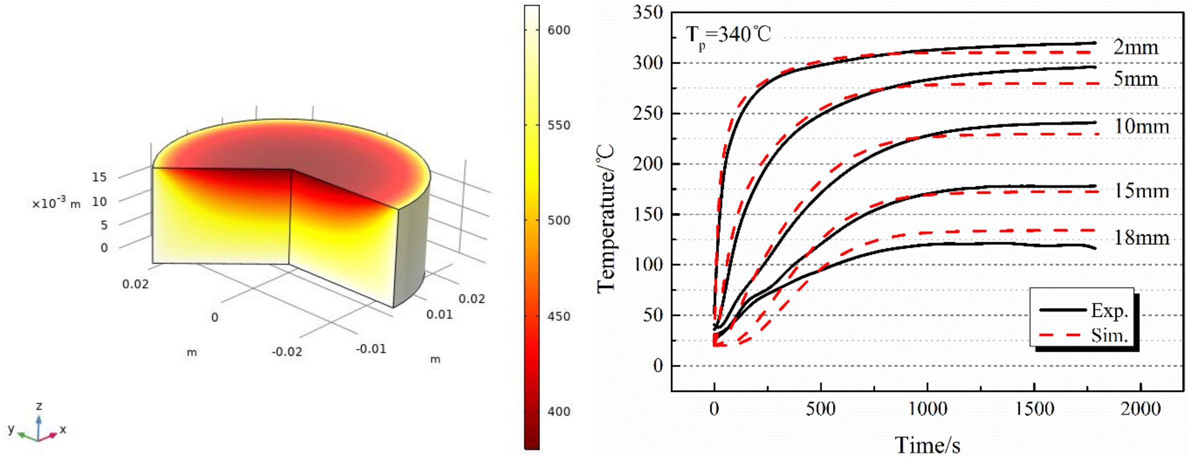

(a) (b)

Fig. 9. *The typical temperature profile of the dust layer*

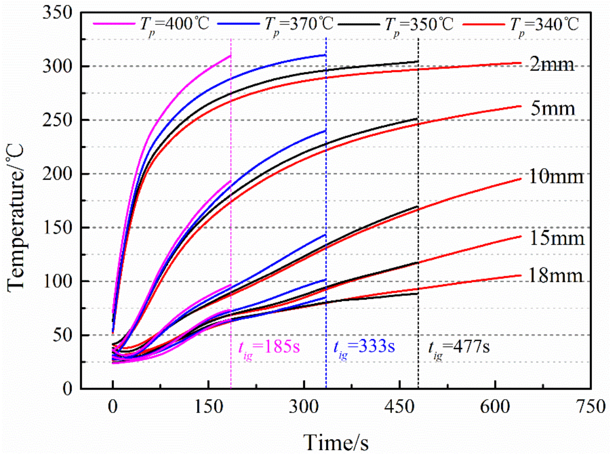

Fig. 10. *Temperature distribution at different T_p for the 20 mm thickness dust layer*

4.2 Effect of particle size and thickness

The ignition behavior of the dust in the accumulation state was controlled by the heat transfer of the geometric surface of the dust particles and the oxygen diffusion in the dust layer. Fig. 11 and Fig. 12 showed the ignition time of three different PMMA dusts at different heating temperatures when the dust layer thickness were 20 mm and 30 mm. At the same heating temperature, ignition time increased as particle size increased. As the heating temperature increased, the ignition time of the dust layer decreased.

Fig. 13 showed the heat transfer and mass transfer inside the PMMA dust layer. The arrangement of dust particles would generate a large number of tiny voids, and the flammable gas would diffuse upward into the air through these tiny voids and the oxygen would diffuse downward into the dust through these tiny voids too. Reactions occurred on the surface of the particles. The transfer of combustion intermediates and products from the inside of the particle was an important process to control the rate of the chemical reaction. For particles with a large particle size, it took a longer time to heat throughout, gaseous products took longer to diffuse outward. The chemical reaction rate was also controlled by the diffusion of oxygen to the reactive centre of the particle (Miron and Lazzara, 1988; Li and Li et al., 2020). PMMA dust with a smaller particle size had a larger specific surface area (Jiang and Bi et al., 2020), which mean that the finer particle had more intensive oxidation reaction than coarser particle, thus dust particle with a smaller particle size had a larger value of the chemical reaction rate, which made the pyrolysis and oxidation reaction faster.

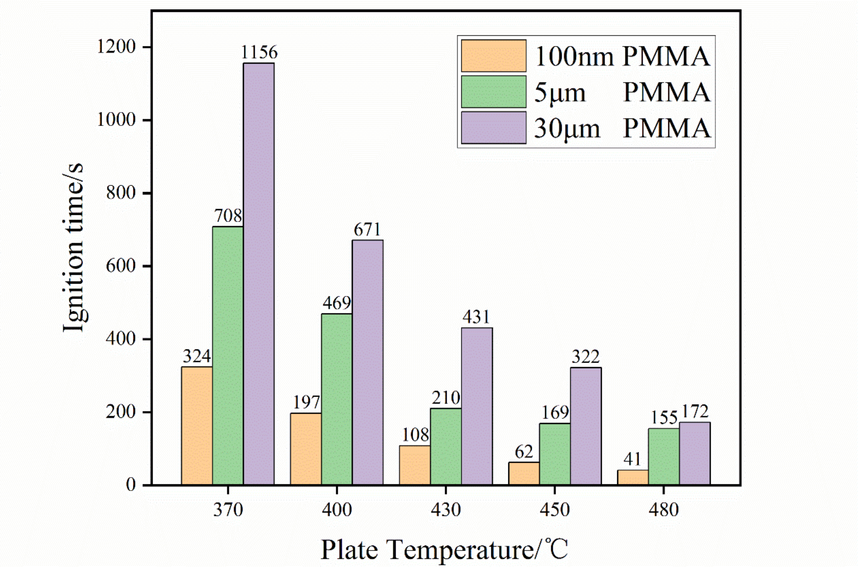

Fig. 11. *Ignition time with plate temperature for 20 mm thickness dust layer*

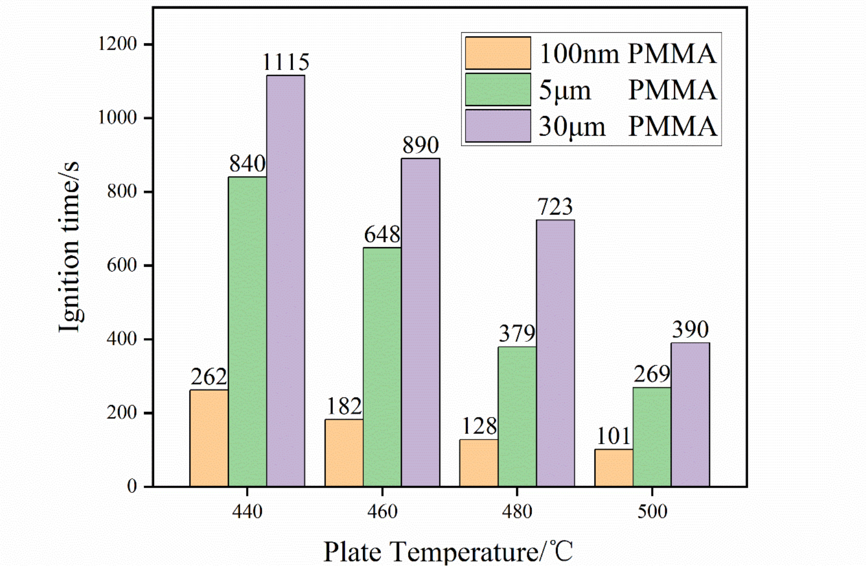

Fig. 12. *Ignition time with plate temperature for 30 mm thickness dust layer*

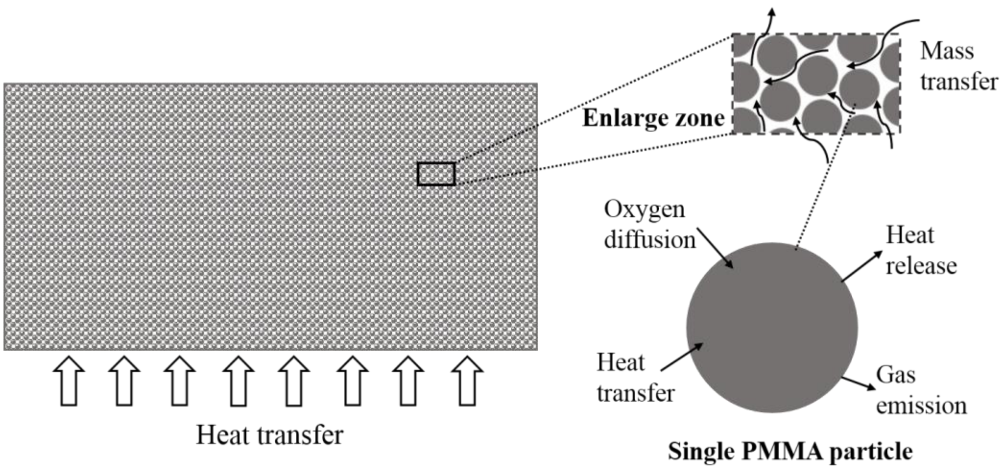

Fig. 13. *Heat transfer and mass transfer inside the PMMA dust layer.*

The source term of the exothermic rate of chemical reaction per unit volume in Eq. (1) could be rewritten as Eq. (14). (Chunmiao and Chang et al., 2017)

$$Q_E(T)=\Delta H_s \cdot \rho_b \cdot \frac{6Z_s}{\rho_s \cdot d_p} \cdot \exp\left(\frac{-E}{RT}\right) \tag{14}$$

Where Z_s is another form of the pre-exponential factor (A), ρ_s is the density of PMMA, d_p is the diameter of the dust particles. Z_s and ρ_s of the three samples was considered to be the same. The three samples differ only in ρ_b and d_p. The other parameters are the same, so the exothermic rate of chemical reaction per unit volume was a function of ρ_b and d_p. For 100 nm PMMA, 5 μm PMMA and 30 μm PMMA, $Q_{E\text{-100 nm}} > Q_{E\text{-5 μm}} > Q_{E\text{-30 μm}}$.

The agglomeration of 100 nm PMMA dust particles was mainly due to the strong interaction forces between the particles, such as Van der Waals force, electrostatic force and Inter-particle force due to liquid (Eckhoff, 2012), of which Van der Waals force was the main force. The stronger interaction force between the particles could suppress the gravity sedimentation and loosen the particle accumulation (Chunmiao and Chang et al., 2017). Therefore, compared with 5 μm PMMA and 30 μm PMMA, 100 nm PMMA had a lower packing density and greater bulk porosity, so 100 nm PMMA was more likely to react with oxygen. For the above reasons, the ignition time of the PMMA dust layer increased as the particle size increased.

As the temperature of the hot-plate increased, the ambient temperature around the hot-plate increased. According to Eq. (15), the LFL(T) decreased as the ambient temperature increased (LYON and QUINTIERE, 2007). At the same time, according to the Arrhenius law, the reaction rate of PMMA increased as temperature increased, therefore, as the temperature of the hot-plate increased, the flammable gas concentration in the air was more likely to reach the LFL, so the ignition time decreased.

$$\frac{LFL(T)}{LFL_0} = 1 - \frac{\Delta T}{T_f - T_a} \tag{15}$$

Table 4 showed the ignition temperature of 100 nm PMMA, 5 μm PMMA and 30 μm PMMA at different layer thicknesses. As the thickness of the dust layer increased from 20 mm to 30 mm, the ignition temperatures of 100 nm PMMA, 5 μm PMMA, and 30 μm PMMA increased by 20℃, 50℃, and 70℃, respectively. Oxygen and pyrolysis gases diffused through tiny voids created by dust accumulation. As the thickness of the dust layer increased, the gravity sedimentation of the dust layer increased, the width of the tiny voids decreased, and the viscous resistance of the gas during the diffusion process increased, so the ignition temperature of the dust layer increased. Similarly, as shown in Fig. 14. As the thickness of the dust layer increased from 20 mm to 30 mm, the ignition time of dust layers with different particle sizes increased to a certain extent, where the change of 100 nm PMMA was significantly less than 5 μm PMMA and 30 μm PMMA because the strong interaction force between the particles of 100 nm PMMA could suppress the enhancement of gravity settlement.

Table 4. *The measured ignition temperature of the three PMMA dusts at different layer thicknesses*

Samples	Ignition temperature /℃	
	20mm	30mm
100nm PMMA	340	360
5μm PMMA	350	400
30μm PMMA	360	430

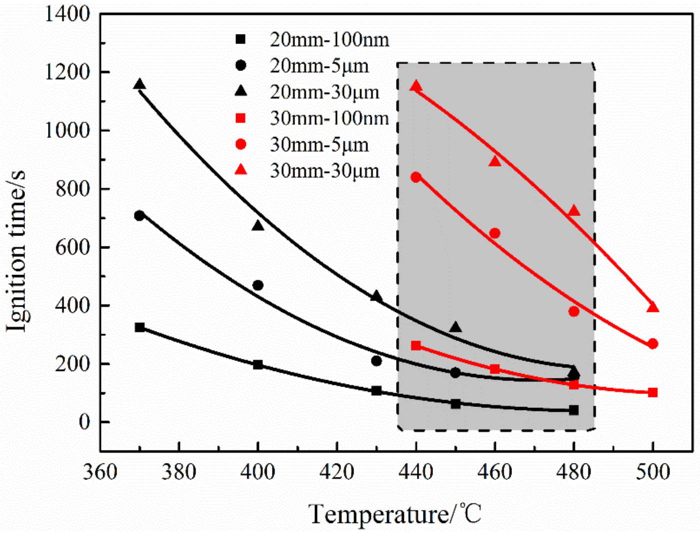

Fig. 14. *Ignition time of dust layer under different thickness.*

4.3 Sensitivity analyses

The simulation required input of many thermodynamic parameters, and all parameters could be obtained through experiments and references. Due to the differences in experimental materials and conditions, which led to uncertainties of the thermodynamic parameters entered in the model, it was necessary to quantitatively analyze the effects of thermodynamic parameters on the simulation results.

For repeated tests in the same situation, you would get a similar temperature distribution and ignition time, so for a certain experimental conditions, we approximated that if a certain position in the dust layer reached a constant temperature, it could be ignited.

Fig. 15(a) showed the temperature change at a height of 2 mm in the center of the dust layer with time under a typical experimental condition. It could be seen from the experimental data that the ignition time was 477 s and the temperature reached 304.16 ℃, and the same temperature could be reached by 430 s through simulation calculation. Fig. 15(b) described the impact of variations of the thermodynamic parameters on the ignition time. Because according to Fourier's law, the thermal conductivity directly affected the heat transfer in the dust layer, the results showed that the change in the effective thermal conductivity k_e of the dust layer had a significant effect on the ignition time. Varying it by only -7.9 %, from 0.108 W $m^{-1}K^{-1}$ to 0.1 W $m^{-1}K^{-1}$, the ignition time could be accurately predicted. The effect of other thermodynamic parameters on ignition time was less than the effect of effective thermal conductivity on it, where the reaction heat had little effect on ignition.

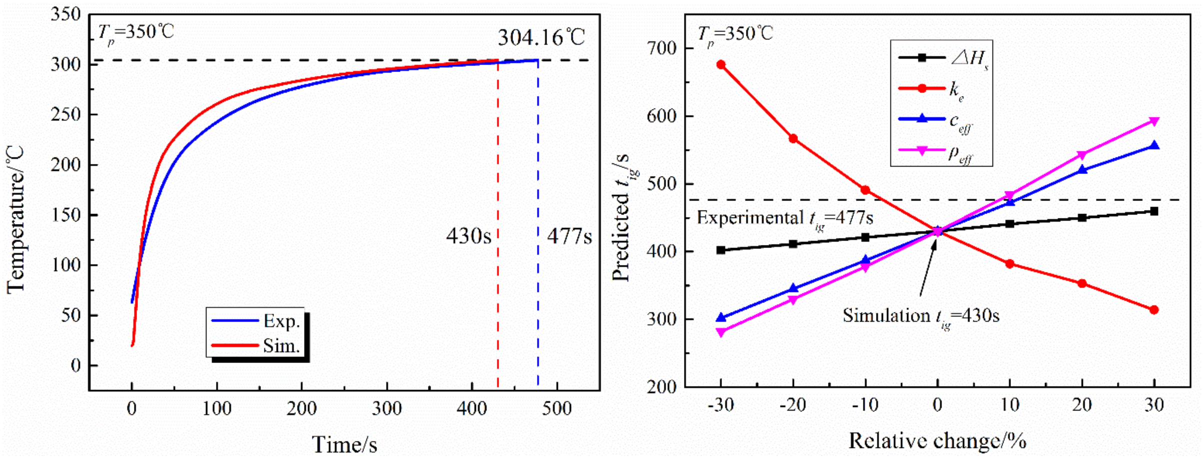

(a) (b)

Fig. 15. *Sensitivity analysis based on the base case; (a) 100 nm PMMA, L=20 mm, T_p=350 ℃;(b) Dependence of T_{ig} on the relative change of thermodynamic parameters.*

5. Conclusions

In this paper, We developed a 2D numerical model to investigate the temperature distribution in the dust layer, the numerical results of in-depth temperature agreed well with the experimental data. This showed that the thermodynamic parameters obtained through experimental data and TG-DSC analysis in this paper were effective and reliable.

When the dust layer was heated, a slow smoldering occurred in the dust layer and the temperature rose with time until it reached stability. There were temperature gradients at different heights in the dust layer. After the temperature in the dust layer had stabilized, no mutation will occur.

Dust particle size had a vital effect on the ignition behavior of the PMMA dust layer. The ignition time and ignition temperature of the PMMA dust layer increased as the particle size increased.

When the thickness of the dust layer was 20 mm, ignition temperature for 100 nm PMMA, 5 μm PMMA and 30 μm PMMA were 340℃, 350℃ and 360℃. As the thickness of the dust layer increased from 20 mm to 30 mm, the ignition temperatures of 100 nm PMMA, 5 μm PMMA, and 30 μm PMMA increased by 20℃, 50℃, and 70℃, respectively. It means that the effect of the thickness of the dust layer on the ignition temperature increased with the increasing of the particle size of the dust. Due to the strong interaction force between the particles of 100 nm PMMA, the enhancement of the gravity sedimentation caused by the increase of the thickness of the dust layer was suppressed. Therefore, when the thickness of the dust layer increased from 20 mm to 30 mm, the ignition temperature of 100 nm PMMA increases less than 5 μm PMMA and 30 μm PMMA.

Acknowledgements

The authors gratefully acknowledge the financial support from the National Natural Science Foundation of China (No. 51922025 and No. 51874066).

References

Chunmiao, Y. and H. Dezheng, et al. (2013). Ignition behavior of magnesium powder layers on a plate heated at constant temperature. Journal of Hazardous Materials 246-247: 283-290.

Wu, D. and Z. Song, et al. (2019). Theoretical and numerical study on ignition behaviour of coal dust layers on a hot surface with corrected kinetic parameters. Journal of Hazardous Materials 368: 156-162.

El-Sayed, S. A. and M. E. Mostafa (2016). Estimation of Thermal and Kinetic Parameters of Sugarcane Bagasse and Cotton Stalks Dust Layers from Hot Surface Ignition Tests. Combustion Science and Technology 188 (10): 1655-1673

DOI: 10.7795/810.20200724

Reszka, P. and P. Borowiec, et al. (2012). A methodology for the estimation of ignition delay times in forest fire modelling. Combustion and Flame 159 (12): 3652-3657.

Fang, J. and Y. Meng, et al. (2018). Experimental, numerical and theoretical analyses of the ignition of thermally thick PMMA by periodic irradiation. Combustion and Flame 197: 41-48.

Vermesi, I. and N. Roenner, et al. (2016). Pyrolysis and ignition of a polymer by transient irradiation. Combustion and Flame 163: 31-41.

Lautenberger, C. and C. Fernandez-Pello (2009). Generalized pyrolysis model for combustible solids. Fire Safety Journal 44 (6): 819-839.

ASTM E 2020-06: Standard Test Method for Hot-Surface Ignition Temperature of Dust Layers

Zhou, J. and B. Li, et al. (2019). Suppression of nano-polymethyl methacrylate dust explosions by ABC powder. Process Safety and Environmental Protection 122: 144-152.

Zhang, X. and J. Yu, et al. (2017). Effects of particle size distributions on PMMA dust flame propagation behaviors. Powder Technology 317: 197-208.

Park, H. and A. S. Rangwala, et al. (2009). A means to estimate thermal and kinetic parameters of coal dust layer from hot surface ignition tests. Journal of Hazardous Materials 168 (1): 145-155.

Tian, L. and B. Shen, et al. (2016). Thermal behavior of waste tea pyrolysis by TG-FTIR analysis. Energy 103: 533-542.

Sharara, M. A. and N. Holeman, et al. (2014). Pyrolysis kinetics of algal consortia grown using swine manure wastewater. Bioresource Technology 169: 658-666.

Starink, M. J. (2003). The determination of activation energy from linear heating rate experiments: a comparison of the accuracy of isoconversion methods. Thermochimica Acta 404 (1-2): 163-176.

Moriana, R. and Y. Zhang, et al. (2014). Thermal degradation behavior and kinetic analysis of spruce glucomannan and its methylated derivatives. Carbohydrate Polymers 106: 60-70.

Collazo, J. and J. A. Pazó, et al. (2012). Determination of the specific heat of biomass materials and the combustion energy of coke by DSC analysis. Energy 45 (1): 746-752.

Wenru, Z. and l. Shufen, et al. (2003). Study of the combustion mechanism of poly (methyl methacrylate). Poymer Materials Science and Engineering 19 (6): 183-186.

Eckhoff, R. K. (2012). Does the dust explosion risk increase when moving from µm-particle powders to powders of nm-particles? Journal of Loss Prevention in the Process Industries 25 (3): 448-459.

Miron, Y. and C. P. Lazzara (1988). Hot‐surface ignition temperatures of dust layers. Fire and Materials 12 (3): 115-126

Li, B. and M. Li, et al. (2020). Effects of particle size on the self-ignition behaviour of a coal dust layer on a hot plate. Fuel 260: 116269.

Chunmiao, Y. and L. Chang, et al. (2017). Ignition and Explosion of Metal Dusts: Modeling and Experiments. First edition. China Science Publishing & Media Ltd, Beijing.

Wu, D. and M. Vanierschot, et al. (2016). Numerical study on the ignition behavior of coal dust layers in air and O2/CO2 atmospheres. Applied Thermal Engineering 109: 709-717.

LYON, R. and J. QUINTIERE (2007). Criteria for piloted ignition of combustible solids. Combustion and Flame 151 (4): 551-559.

Jiang, H. and M. Bi, et al. (2020). Suppression mechanism of Al dust explosion by melamine polyphosphate and melamine cyanurate. Journal of Hazardous Materials 386: 121648.

Appendix A
The parameters of different pyrolysis mechanisms by Coats-Redfern method

mechanism	10K/min			20K/min			30K/min		
	E kJ mol^{-1}	A s^{-1}	R^2	E kJ mol^{-1}	A s^{-1}	R^2	E kJ mol^{-1}	A s^{-1}	R^2
P1	7.00	5.28E-02	0.5461	7.19	1.06E-01	0.5371	4.72	6.59E-02	0.5470
P2	25.19	3.99E+00	0.8022	25.76	8.08E+00	0.7950	20.86	3.93E+00	0.8645
P3	13.07	2.72E-01	0.7063	13.38	5.46E-01	0.6976	10.10	3.36E-01	0.7638
P4	97.96	3.03E+06	0.8751	100.07	6.44E+06	0.8697	85.39	5.34E+05	0.9263
R1	61.58	4.31E+03	0.8608	62.92	8.94E+03	0.8551	53.12	1.82E+03	0.9152
R2	75.34	3.75E+04	0.9168	77.01	7.90E+04	0.9122	64.83	1.04E+04	0.9589
R3	80.61	7.36E+04	0.9324	82.42	1.56E+05	0.9282	69.30	1.73E+04	0.9699
F1	92.25	2.35E+06	0.9581	94.35	5.08E+06	0.9550	79.16	3.82E+05	0.9864
F1.5	112.48	1.37E+08	0.9828	115.10	3.04E+08	0.9811	96.25	1.17E+07	0.9975
F2	135.87	1.42E+10	0.9930	139.09	3.28E+10	0.9926	115.96	5.72E+08	0.9957
F3	190.29	6.22E+14	0.9890	194.93	1.56E+15	0.9907	161.76	4.30E+12	0.9746
A1.5	57.77	3.56E+03	0.9522	59.11	7.45E+03	0.9487	48.97	1.41E+03	0.9837
A2	40.53	1.23E+02	0.9451	41.48	2.53E+02	0.9412	33.88	7.57E+01	0.9803
A3	23.29	3.46E+00	0.9258	23.86	7.05E+00	0.9207	18.78	3.25E+00	0.9698
A4	14.67	4.83E-01	0.8956	15.05	9.78E-01	0.8891	11.23	5.40E-01	0.9504
D1	134.34	1.84E+09	0.8815	137.22	4.00E+09	0.8763	117.65	1.34E+08	0.9311
D2	150.96	2.57E+10	0.9107	154.24	5.70E+10	0.9062	131.83	1.13E+09	0.9534
D3	172.41	4.01E+11	0.9410	176.22	9.16E+11	0.9373	150.02	9.01E+09	0.9749
D4	158.00	2.31E+10	0.9220	161.46	5.18E+10	0.9178	137.80	8.16E+08	0.9617
J1	32.07	1.35E+01	0.8864	32.81	2.77E+01	0.8807	26.71	1.09E+01	0.9377
J2	161.86	1.12E+11	0.9278	165.42	2.52E+11	0.9237	141.07	3.49E+09	0.9659
J3	34.71	1.99E+01	0.9090	35.52	4.07E+01	0.9038	28.95	1.47E+01	0.9552
J4	120.07	1.07E+07	0.8624	122.63	2.30E+07	0.8570	105.28	1.16E+06	0.9164
D5	221.93	6.74E+15	0.9790	227.01	1.65E+16	0.9770	191.91	3.16E+13	0.9961
A5/2	30.19	1.50E+01	0.9365	30.91	3.07E+01	0.9320	24.82	1.19E+01	0.9758
A4/3	66.39	1.84E+04	0.9543	67.92	3.89E+04	0.9509	56.52	5.87E+03	0.9847
A2/3	143.97	3.09E+10	0.9615	147.22	6.99E+10	0.9586	124.45	1.30E+09	0.9879
A1/2	195.69	3.55E+14	0.9631	200.09	8.37E+14	0.9602	169.73	3.83E+12	0.9886
A1/3	299.13	3.85E+22	0.9646	305.83	9.95E+22	0.9618	260.30	2.74E+19	0.9892
A1/4	66.39	1.84E+04	0.9543	67.92	3.89E+04	0.9509	56.52	5.87E+03	0.9847
R4	83.38	9.72E+04	0.9395	85.26	2.07E+05	0.9356	71.65	2.09E+04	0.9748
N3	80.61	2.21E+05	0.9324	82.42	4.69E+05	0.9282	69.30	5.18E+04	0.9699
N2	75.34	7.50E+04	0.9168	77.01	1.58E+05	0.9122	64.83	2.07E+04	0.9589
R1/2	41.71	1.22E+02	0.7256	42.59	2.47E+02	0.7185	36.09	9.30E+01	0.7954
R1/3	28.82	9.84E+00	0.5854	29.41	1.97E+01	0.5781	24.90	1.07E+01	0.6569
R1/4	20.08	1.56E+00	0.4520	20.49	3.11E+00	0.4453	17.22	2.11E+00	0.5131

Appendix B

Commonly used solid-state reaction models.

No.	Symbol	Name of function	f(α)	g(α)
1	P1	Power law	$4\alpha^{3/4}$	$\alpha^{1/4}$
2	P2	Power law	$3\alpha^{2/3}$	$\alpha^{1/3}$
3	P3	Power law	$2\alpha^{1/2}$	$\alpha^{1/2}$
4	P4	Power law	$2/3\alpha^{-1/2}$	$\alpha^{3/2}$
5	R1	Zero-order (Polany-Winger equation)	1	α
6	R2	Phase-boundary controlled reaction	$2(1-\alpha)^{1/2}$	$[1-(1-\alpha)^{1/2}]$
7	R3	Phase-boundary controlled reaction	$3(1-\alpha)^{2/3}$	$[1-(1-\alpha)^{1/3}]$
8	F1	First-order	$(1-\alpha)$	$-\ln(1-\alpha)$
9	F3/2	Three-halves order	$(1-\alpha)^{3/2}$	$2[(1-\alpha)^{-1/2}-1]$
10	F2	Second-order	$(1-\alpha)^{2}$	$(1-\alpha)^{-1}-1$
11	F3	Third-order	$(1-\alpha)^{3}$	$(1/2)[(1-\alpha)^{-2}-1]$
12	A1.5	Avrami–Eroféev (n=1.5)	$(3/2)(1-\alpha)[-\ln(1-\alpha)]^{1/3}$	$[-\ln(1-\alpha)]^{2/3}$
13	A2	Avrami–Eroféev (n=2)	$2(1-\alpha)[-\ln(1-\alpha)]^{1/2}$	$[-\ln(1-\alpha)]^{1/2}$
14	A3	Avrami–Eroféev (n=3)	$3(1-\alpha)[-\ln(1-\alpha)]^{2/3}$	$[-\ln(1-\alpha)]^{1/3}$
15	A4	Avrami–Eroféev (n=4)	$4(1-\alpha)[-\ln(1-\alpha)]^{3/4}$	$[-\ln(1-\alpha)]^{1/4}$
16	D1	One-dimensional diffusion	$1/(2\alpha)$	α^{2}
17	D2	Two-dimensional diffusion	$1/[-\ln(1-\alpha)]$	$(1-\alpha)\ln(1-\alpha)+\alpha$
18	D3	Three-dimensional diffusion	$3/2[1-(1-\alpha)^{1/3}]^{1/2}$	$[1-(1-\alpha)^{1/3}]^{2}$
19	D4	Three-dimensional diffusion	$3/2[(1-\alpha)^{-1/3}-1]^{-1}$	$(1-2\alpha/3)-(1-\alpha)^{2/3}$
20	J1	Jander equation	$4(1-\alpha)^{1/2}[1-(1-\alpha)^{1/2}]^{1/2}$	$[1-(1-\alpha)^{1/2}]^{1/2}$
21	J2	Jander equation	$(1-\alpha)^{1/2}[1-(1-\alpha)^{1/2}]^{-1}$	$[1-(1-\alpha)^{1/2}]^{2}$
22	J3	Jander equation	$6(1-\alpha)^{2/3}[1-(1-\alpha)^{1/3}]^{1/2}$	$[1-(1-\alpha)^{1/3}]^{1/2}$
23	J4	Anti-Jander equation	$3/2(1+\alpha)^{2/3}[(1+\alpha)^{1/3}-1]^{-1}$	$[(1+\alpha)^{1/3}-1]^{2}$
24	D5	Z.-L.-T. equation	$3/2(1-\alpha)^{4/3}[(1-\alpha)^{-1/3}-1]^{-1}$	$[(1-\alpha)^{-1/3}-1]^{2}$
25	A5/2	Avrami–Eroféev (n=5/2)	$5/2(1-\alpha)[-\ln(1-\alpha)]^{3/5}$	$[-\ln(1-\alpha)]^{2/5}$
26	A4/3	Avrami–Eroféev (n=4/3)	$4/3(1-\alpha)[-\ln(1-\alpha)]^{1/4}$	$[-\ln(1-\alpha)]^{3/4}$
27	A2/3	Avrami–Eroféev (n=2/3)	$2/3(1-\alpha)[-\ln(1-\alpha)]^{-1/2}$	$[-\ln(1-\alpha)]^{3/2}$
28	A1/2	Avrami–Eroféev (n=1/2)	$1/2(1-\alpha)[-\ln(1-\alpha)]^{-1}$	$[-\ln(1-\alpha)]^{2}$
29	A1/3	Avrami–Eroféev (n=4/3)	$1/3(1-\alpha)[-\ln(1-\alpha)]^{-2}$	$[-\ln(1-\alpha)]^{3}$
30	A1/4	Avrami–Eroféev (n=4/3)	$4/3(1-\alpha)[-\ln(1-\alpha)]^{1/4}$	$[-\ln(1-\alpha)]^{3/4}$
31	R4	Reaction order (n=4)	$4(1-\alpha)^{3/4}$	$1-(1-\alpha)^{1/4}$
32	N3	n=3 (three dimension)	$(1-\alpha)^{2/3}$	$3[1-(1-\alpha)^{1/3}]$
33	N2	n=2 (two dimension)	$(1-\alpha)^{1/2}$	$2[1-(1-\alpha)^{1/2}]$
34	R1/2	Reaction order (n=1/2)	$1/2(1-\alpha)^{-1}$	$1-(1-\alpha)^{2}$
35	R1/3	Reaction order (n=1/3)	$1/3(1-\alpha)^{-2}$	$1-(1-\alpha)^{3}$
36	R1/4	Reaction order (n=1/4)	$1/4(1-\alpha)^{-3}$	$1-(1-\alpha)^{4}$

Proceedings of the 13th Symposium International Symposium
on Hazards, Prevention and Mitigation of Industrial Explosions
DOI: 10.7795/810.20200724

Thermal ignition of n-hexane air mixtures by vertical cylinders

Silken Jones & Joseph Shepherd

Graduate Aerospace Laboratories, California Institute of Technology, Pasadena, CA, U.S.A
E-mail: *smjones@caltech.edu*

Abstract

An experimental study of thermal ignition of stoichiometric n-hexane and air mixtures by vertical cylinders is performed. Five cylinders were tested with surface areas ranging from 50 to 200 cm^2. Limited variation of igntion temperature with surface area was observed with ignition temperatures from 1019 to 1117 K; this is approximately 200 to 500 K higher than previous studies with similar surface areas. Quantitative temperature fields from the experiments were extracted via interferometry and the profile of the thermal layer agreed well with temperature results from numerical similarity solutions to the boundary layer equations. The ignition results are compared to relevant literature and the importance of a change in surface size versus a change in flow type is discussed.

Keywords: *combustion, thermal ignition, natural convection, aircraft safety*

1 Introduction

Accidental thermal ignition events caused by a hot surface represent a significant industrial safety hazard. It is important to understand the effect that a change in flow configuration or surface size has on ignition behavior. Current safety standards often do not account for such variation. For example, current Federal Aviation Administration (2018) regulations limit the maximum allowable temperature in a flammable leakage zone to 477 K (Federal Aviation Administration, 2018). This regulation does not consider the size or flow type of the hazard region. Flows can be internal or external, and subject to natural or forced convection.

Available literature does account for some variation in size or flow configuration. Previous studies by Kuchta et al. (1965) show a dependence of the ignition temperature on the surface area of the ignition source for surface areas from less than 1 cm^2 to 200 cm^2 for a variety of fuels including n-hexane. Surfaces less than 40 cm^2 in area are subject to external forced convection around a cylindrical rod or wire while the largest surfaces studied (greater than 40 cm^2) are heated vessels subject to internal natural convection. White (1967) studied thermal ignition by vessels filled with kerosene vapor mixtures subject to internal natural convection ranging from 250 to 6000 cm^2 in area. Ono et al. (1976) studied thermal ignition by vertical flat plates in propane, methane, ethaniol, and diethyl ether fuel mixtures with areas from 1.5 to 9 cm^2, subject to external natural convection. Smyth and Bryner (1997) investigated thermal ignition of many fuel mixtures including n-hexane by a flat plate 25 cm^2 in area, inclined at a number of angles to an external forced convection flow. Boettcher (2012) studied the effect of pressure, composition, and heating rate on ignition of n-hexane mixtures inside a vessel (380 cm^2) subject to internal natural convection flow. Melguizo-Gavilanes et al. (2016) studied thermal ignition by external natural convection of n-hexane mixtures over a glowplug (approximately a vertical cylinder) with a surface area of 1.5 cm^2. Boeck et al. (2017) studied thermal ignition of n-hexane by a small cylinder (3.14 cm^2) in horizontal and vertical orientations subject to external natural convection.

The purpose of the present work is to examine the effect of surface area on ignition by surfaces subject to external natural convection flows only. There is a particular scarcity of literature available for thermal ignition by external natural convection flows over surfaces larger than 10 cm^2. The surfaces investigated here are vertical cylinders ranging in size from 50 to 200 cm^2.

DOI: 10.7795/810.20200724

2 Experiments

2.1 Experimental Design

The surfaces studied are vertical cylinders made of stainless steel tubes with a wall thickness of 0.05 cm. The experiments are conducted in a cylindrical combustion vessel 30.4 cm in diameter by 66.0 cm tall filled with a reactive gas mixture. A cylinder is held in place inside the vessel with a copper support structure, which also provides a path for up to 375 A of current to flow to resistively heat the cylinder. A natural convection flow develops on the exterior as the cylinder heats up; the ends of the cylinder are sealed and the interior is filled with air. Water cooling is implemented at the ends of the cylinders to force a 298 K constant temperature in the support structure. This prevents the support structure from significant heating due to conduction and preserves the axisymmetry of the experiments. Axisymmetry is key for proper operation of the interferometer. The temperature of the cylinder is measured via two-color pyrometer and thermocouple, and quantitative temperature field measurements are taken via interferometer. Heating is achieved by applying constant current until within 10% of the preset temperature, at which point a temperature based feedback control system drives the cylinder to that temperature until ignition occurs or 300 seconds have elapsed. Figure 1 includes a schematic of the experimental setup.

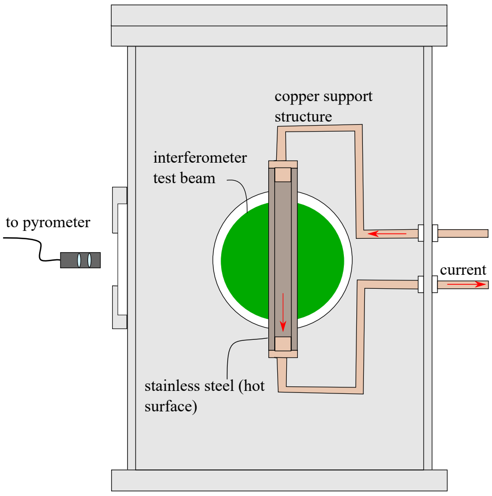

Fig. 1*: Experimental setup schematic, including combustion vessel, test cylinder, support structure, and diagnostics. Water cooling not shown.*

Five different cylinders are investigated in this work. Table 1 includes the measurements of all cylinders investigated.

Table 1*: Measurements of all five test cylinders*

Cylinder tag	**Surface area, cm^2**	**Length, cm**	**Diameter, cm**
50A	50	25.4	0.635
50C	50	12.7	1.27
75B	75	19.1	1.27
100A	100	25.4	1.27
100C	100	12.7	2.54
200A	200	25.4	2.54

2.2 Diagnostics

Two main diagnostics are used in these experiments. A two-color pyrometer takes non-contact surface temperature measurements of the cylinder, and an interferometer takes optical measurements of the temperature of the gas surrounding the cylinder.

2.2.1 Pyrometer

A two-color pyrometer takes non-contact measurements of surface temperature at a rate of 1 kHz. The benefit of the pyrometer is that it does not disturb the natural convection flow, enabling direct measurement of surface temperature at the location along the cylinder where ignition occurs.

The pyrometer collects light from the surface being measured. Light is split around 1800 nm by a longpass dichroic mirror. One narrow bandpass filter is used for each beam, one centered at 1700 nm and the other at 1940 nm to further filter the light. Finally, the light is projected onto a photodetector, one for each wavelength, which converts light intensity to a voltage reading. The ratio of bandpass-filtered radiation intensities, I_1/I_2, correlates with the surface temperature T_S. The advantage of a two color pyrometer is that it does not need to account for the value of surface emissivity when using the assumptions of gray-body emission, i.e. wavelength-independent emissivity, from the hot surface and narrow filter bandwidths. T_S is determined by equation 1:

$$T_S = \frac{A}{\ln(\frac{I_1}{I_2}) - B} \tag{1}$$

Constants A and B are determined by calibration with a blackbody radiation source (Process Sensors BBS1200). The spot size of the pyrometer is determined during calibration to be approximately 0.32 cm in diameter.

Initial characterization of the cylinders shows that a large central portion of a cylinder reaches a uniform high temperature. Approximately the last two centimeters at each end of a cylinder are cooler due to conduction to the water cooled end. To test the pyrometer operation immediately before ignition testing, a cylinder is heated up in air and allowed to oxidize until a thick oxide layer develops and subsequent oxidation is very slow. During this oxidation period, pyrometer measurements of the central hot region of the cylinder are checked against thermocouple measurements taken in the same region. Additionally, a thermocouple is placed at the top of the cylinder in the cooler edge region. This is above the location where ignition occurs and should not disturb natural convection flow development in the ignition region. Heating tests are performed to construct a polynomial fit by which the temperature of the central hot region can be extrapolated from the temperature reading of the top thermocouple. The central thermocouple is removed before ignition testing, while the top thermocouple remains to provide a double check for the pyrometer reading. Figure 2 shows a schematic of this situation.

2.2.2 Interferometer

Interferometry has a long history as a technique to make gas temperature measurements. Coronel et al. (2018) presents a detailed account of the exact postprocessing techniques used in our laboratory to extract temperature field measurements of a gas from interferometry. A new interferometer design is implemented for this set of experiments and is briefly described here.

The surfaces under investigation in this work are much larger in size than those in Coronel et al. (2018) so an interferometer with a much larger test beam is constructed. The design chosen is a modified Mach-Zehnder interferometer, with the test beam expanded to 101.6 mm diameter at the focal plane and the reference beam transmitted through an optical fiber. Figure 3 shows a schematic of the

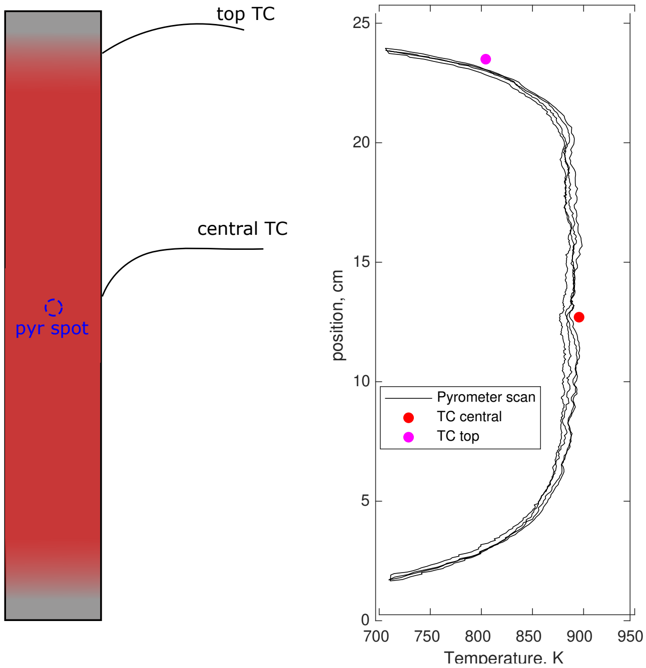

***Fig. 2**: (Left) Placement of thermocouples and pyrometer during heating tests. The central hot region is indicated in red, fading to the cooler edge region in gray. (Right) Temperature distribution along cylinder length from cylinder characterization compared with thermocouple measurements.*

interferometer.

532 nm light from a Coherent Sapphire laser at emerges at the laser head with a 0.7 mm diameter. It is expanded once by a 5X beam expander to a 3.5 mm diameter. The light is then split by a 50:50 unpolarized cubic beamsplitter into a test beam and a reference beam. The test beam is expanded again by a factor of 5X to 17.5 mm diameter and a focusing lens and a concave mirror are used to collimate the light at a diameter of 101.6 mm. This matches the aperture of the windows on the combustion vessel and maximizes the amount of information that the interferometer can collect at the focal plane. After the test beam passes through the combustion vessel it is condensed to a 17.5 mm beam diameter by an identical concave mirror and focusing lens pair. It then passes through the second beamsplitter to recombine with the reference beam.

After splitting from the test beam the reference beam couples into a single mode polarization preserving fiber with the use of an 18 mm focal length collimation package. The collimation package is compatible with the 3.5 mm diameter of the test beam. The fiber is routed to the other side of the interferometer. An identical collimation package is used at the fiber output to return the reference beam to a 3.5 mm diameter. A third 5X beam expander is used to match the reference beam diameter to the test beam. The two beams recombine at the second beam splitter. The combined beams pass through a final focusing lens to ensure the the focal plane coincides with the center of the test cylinder. A Phantom V711 camera is used to record the interferometer at frame rates in excess of 10,000 fps. The method described by Coronel et al. (2018) is used to post process the recorded interference patterns.

The new interferometer design was checked for validity by placing a well-characterized hot surface (Autolite glowplug from Boettcher (2012) and Melguizo-Gavilanes et al. (2016)) in the focal plane. The surface was heated in nitrogen while interferometer recordings were taken, and the post-processed temperature fields were compared against previous temperature field results validated for the glowplug heating configuration. Temperature fields extracted from this new interferometer compared very well with previous results, indicating the accuracy of the new interferometer.

DOI: 10.7795/810.20200724

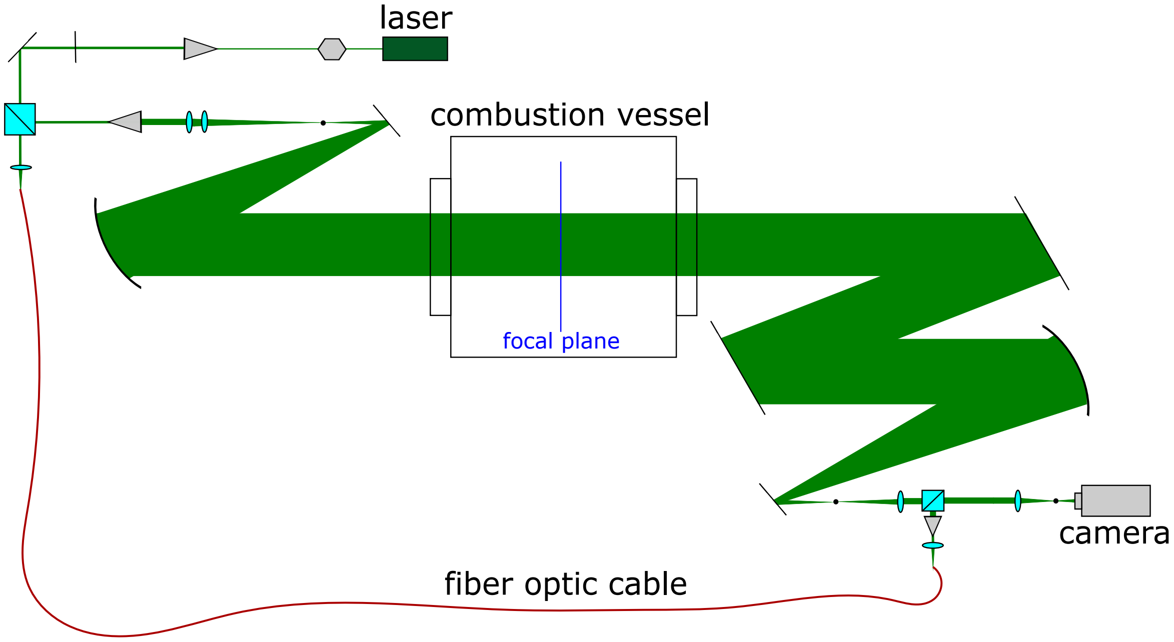

***Fig. 3**: Schematic of Mach-Zehnder interferometer with fiber optic reference beam. Focal plane of interferometer is inside the test section/combustion vessel and is shown in dark blue.*

3 Numerical methods

To gain an understanding of how the natural convection flow develops, a suitable numerical method is implemented. The goal for this numerical method is to make predictions of the thermal layer development that can then be compared with experimental tempertature fields from interferometry.

The similarity solution developed by Cairnie and Harrison (1982) presents a numerical method for solving the boundary layer equations over a vertical flat plate with a high temperature difference between wall and ambient conditions. Gas properties such as density, viscosity, heat capacity, and thermal conductivity are highly variable due to the large temperature difference. The dependency of these properties on temperature is accounted for in the numerical method (Cairnie and Harrison, 1982). Capturing this dependency is key to getting accurate results for large temperature differences. The implementation in MATLAB is checked for validity by using the conditions presented in Cairnie and Harrison (1982) and comparing the output to their original results. The numerical method is subsequently used to predict development of natural convection over flat plates of the same length as the cylinders studied experimentally.

4 Results and discussion

Experiments are conducted as described in Section 2.1 with a stoichiometric n-hexane and air mixture. N-hexane is chosen as a fuel because it is a simple surrogate for aviation kerosene and because of its legacy use within the laboratory which enables direct comparison with previous work. Boeck et al. (2017) show little variation in ignition temperature of n-hexane mixtures with composition up to the flammability limits so only one mixture composition is investigated in this work. More than 20 tests are conducted for each cylinder with the exception of 100C. It is important to note that the power supply used (Magna Power XR5-375/208) is not powerful enough to heat cylinder 100C to ignition temperatures. The maximum temperature achieved over five tests of 100C is 1013 K and no ignition is observed.

The independent variable in these tests is surface temperature, T_S, at trigger time. The trigger is caused by a pressure spike in tests with ignition and the time to ignition ranges from approximately 30 to 260

s. The triggering is done manually after 300 seconds of test time for non ignition tests. The test time is limited to 300 s because preliminary tests with longer test times did not exhibit change in behavior. The dependent variable is a binary outcome of 0 or 1 representing a non-ignition and ignition result respectively. The data pairs of (T_S, binary ignition variable) are plotted in Figure 4 for cylinders 50A and 50C as examples. These data pairs can also be used to generate a logistic regression model for the probability of achieving ignition as a function of T_S. The temperature set points are chosen to span the range of interest such that both ignition and non ignition events will be observed to provide both the number and quality of data points to enable useful statistics from the logistic regression. Bane et al. (2011) discuss set point picking methods and provide a detailed description of the procedure used to generate the probability model. This probability function is represented in Figure 4 by a solid black line.

4.1 *Ignition temperatures and overlap behavior*

Table 2 shows the ignition temperature (T_S at which there is a 50% probability of ignition) for all cylinders investigated. It also indicates if a cylinder demonstrated any sign of overlap behavior. Overlap occurs when there are T_S at which both ignition and non ignition results are observed. Overlap can be seen first in the raw data points in Fig. 4 (left). There is a non ignition case with higher T_S than two of the lowest temperature ignition cases. Overlap is also indicated by a more gradual rise in the probability function and indicates increasing variability in the results. Cylinders 50A, 75B, 100A and 200A demonstrate overlap behavior, while no overlap is seen in cylinder 50C. Overlap occurs with longer cylinder lengths (19.1 and 25.4 cm), indicating that there is more scatter in ignition results with longer cylinders. Overlap can also be examined in the context of aspect ratio; cylinder 50C exhibits no overlap behavior with an aspect ratio of 0.1 while 200A has the same aspect ratio and does demonstrate overlap behavior. Consequently, cylinder length is a more appropriate variable to indicate overlap behavior versus aspect ratio. Future work planned with a wider range of cylinder lengths and aspect ratios will further inform the role of these variables in overlap behavior.

The uncertainty in the ignition temperatures can be quantified in two ways. The first is to look at the width of the 95% confidence limits on the probability function at fifty percent probability of ignition. This produces an uncertainty of ±8 K for cylinder 50A, ±5 K for cylinder 75B, ±6 K for cylinder 100A, and ±5 K for cylinder 200A. The confidence limits cannot be calculated for cylinders that do not exhibit overlap behavior. The other way to quantify uncertainty is to use the uncertainty of pyrometer measurements which is calculated during calibration to be ± 30 K. The pyrometer uncertainty is larger than that from the confidence limits on the probability function and applies to all cylinders investigated. The pyrometer uncertainty is therefore used in all subsequent discussion of uncertainty on ignition temperatures.

***Table 2**: Ignition Temperature Results*

Cylinder tag	T_{ign}, K	L, cm	Aspect Ratio, D/L	Overlap?
50A	1085	25.4	0.025	1
50C	1117	12.7	0.1	0
75B	1078	19.1	0.066	1
100A	1055	25.4	0.05	1
100C	1013 (max T, no ign)	12.7	0.2	–
200A	1019	25.4	0.1	1

4.2 *Gas temperature fields*

The numerical results from Section 3 are presented in Figure 5 for a plate 25.4 cm long. Results for a shorter plate can be obtained by truncating the numerical results at the desired total height of the plate.

DOI: 10.7795/810.20200724

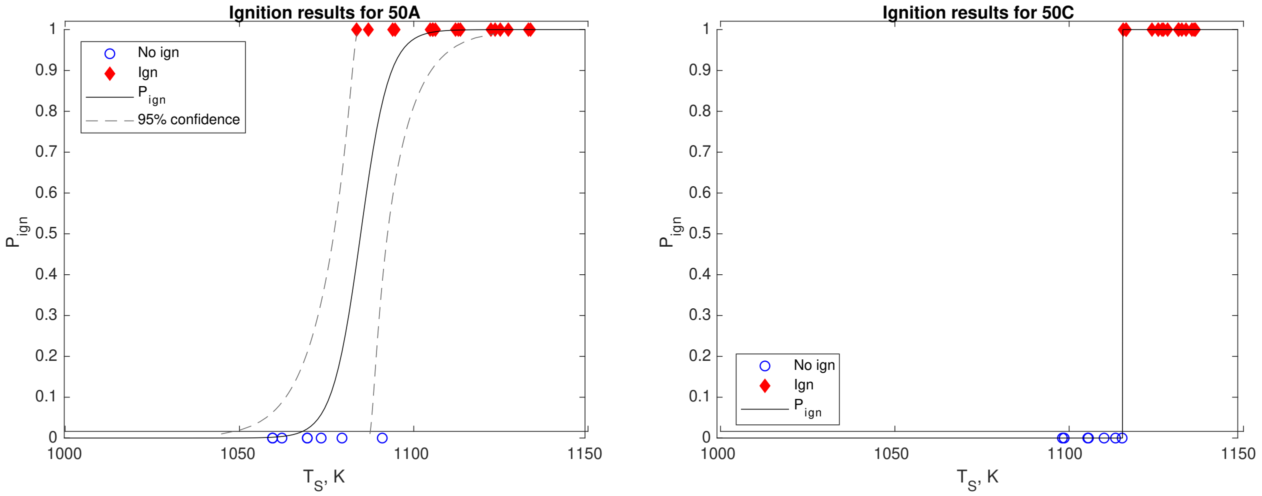

***Fig. 4**: Left: Ignition data for cylinder 50A. Test results show overlap in temperatures for ignition (red filled diamonds) and non-ignition (empty blue circles) results. Right: Ignition data for cylinder 50C. Test results show no overlap in temperatures for ignition and non-ignition results. The black line shows the probability of ignition as a function of temperature and the gray dashed lines show the 95% confidence limits on the probability function where applicable.*

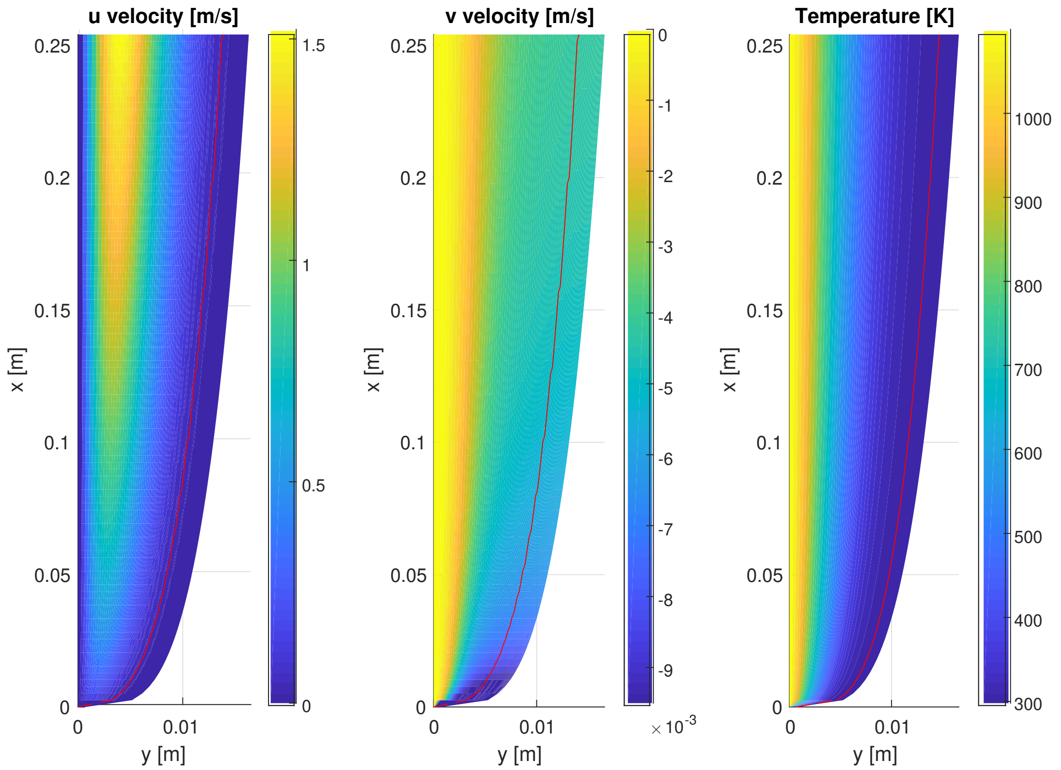

***Fig. 5**: Results from numerical method presented in Section 3. Fields of velocity parallel to wall (u), velocity perpendicular to wall (v), and temperature (T) are presented. The red line shows where numerical results are within 1% of ambient conditions.*

Velocity fields parallel and perpendicular to the wall and temperature fields are presented. The wall parallel velocity takes the expected structure for a natural convection flow: no-slip creates a velocity of zero next to the wall. Buoyancy forces increase the velocity as distance from the wall increases, reaching a maximum before velocity drops again to zero at the edge of the momentum layer to match ambient conditions. Similarly, wall perpendicular velocity appears as expected for a natural convection flow. The velocity is largest and negative at the leading edge of the cylinder as gas is entrained into the natural convection flow. The entrainment effect becomes less pronounced along the outer edge of the momentum layer as distance from the leading edge increases. The perpendicular velocity next to the wall is zero. Temperature results show the gas matches wall temperature immediately next to the surface and then gas temperature drops off exponentially until ambient temperature is matched at the edge of the thermal layer. Additionally, the width of the thermal layer increases very quickly in approximately the first centimeter along the plate, after which there is a much more gradual increase in the width of the thermal layer as the distance from the leading edge increases.

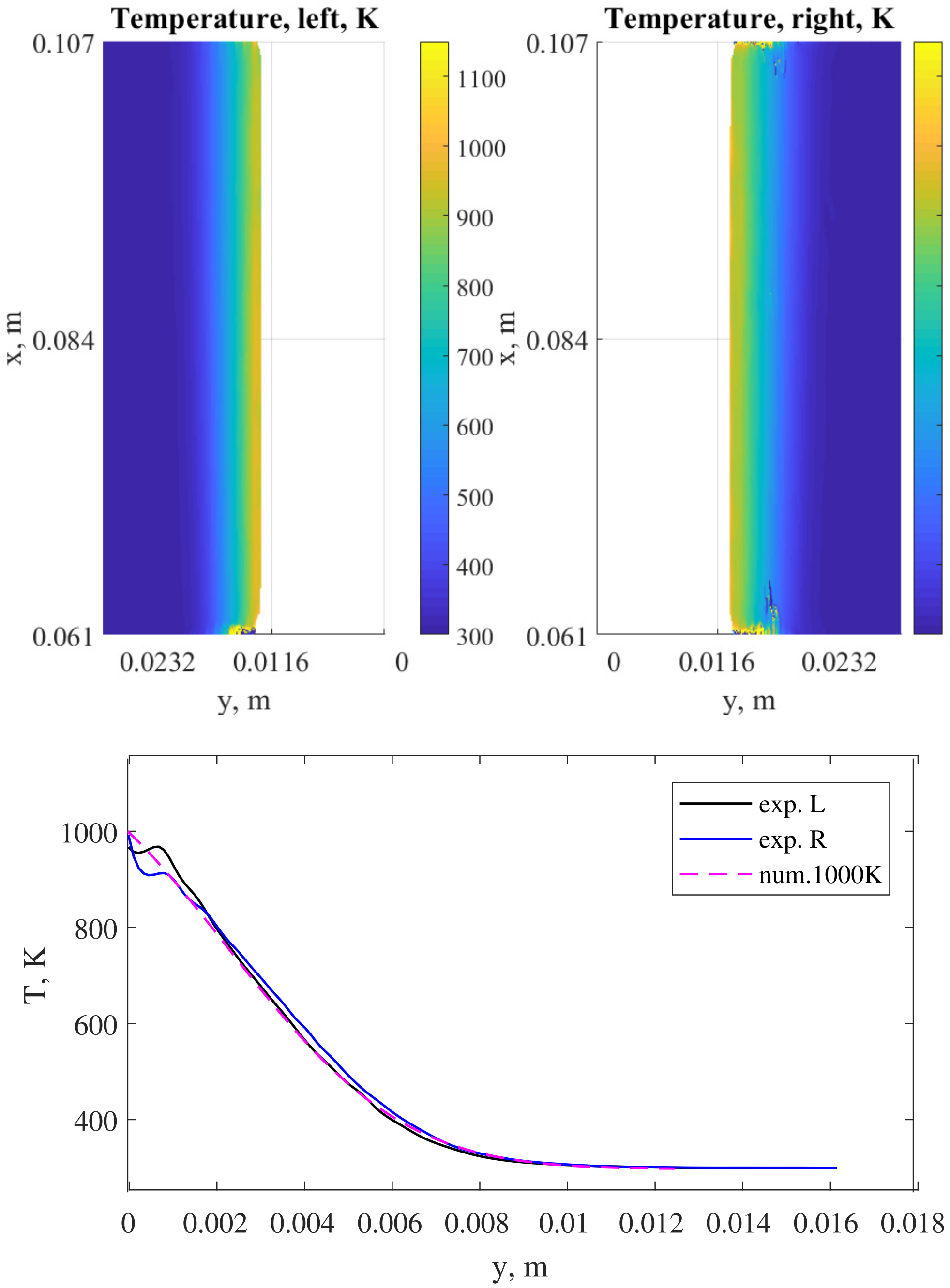

Fig. 6: *Processed interferometer results for cylinder 100C in pure N_2, T_S = 1001 K. Top: experimental temperature fields from interferometery for both sides of cylinder averaged over 100 s of steady-state T_s. Bottom: Comparison of thermal layer profiles at 8.4 cm along cylinder for left and right sides of experimental temperature fields as well as for numerical results.*

These numerical results can be compared directly with experimental results. Fig. 6 shows the experimental temperature fields for cylinder 100C in pure nitrogen with a wall temperature of 1000 K. It also compares the thermal layer profile on both sides of the cylinder with the numerical results 8.4 cm from the leading edge. The experimental temperature fields are symmetrical, indicating good axisymmetry in the experiments. There are artifacts visible 0.001 m from surface; these are due to errors in the postprocessing methods including errors from subpixel inaccuracies in picking the centerline of the surface which results in errors accumulating towards the center of the processed image. Despite these artefacts from postprocessing, comparing the thermal layer profile for both sides of the cylinder with the numerical results shows that the numerical method accurately predicts the thermal layer observed experimentally with less than 6% error.

The agreement between both sides of the post-processed interferometer results and the numerical results indicates that experimental temperature fields are accurately reconstructed, and that the numerical method from Section 3 is useful for predicting the natural convection flow. There are some limitations to the numerical method presented in Section 3. First, the similarity solution developed by Cairnie and Harrison (1982) is developed for flat plates and the experiments are conducted on vertical cylinders. The numerical method does not account for effects of curvature of the surface. Approximating a vertical cylinder as a vertical flat plate with less than 5% error is assumed valid so long as Equation 2 holds.

$$\frac{D}{L} \geq \frac{35}{Gr_L^{0.25}} \tag{2}$$

Where D is the diameter of the cylinder, L is the height of the cylinder, and Gr_L is the Grashof number based on the height of the cylinder. This approximation comes from Sparrow and Gregg (1956). None of the cylinders satisfy the inequality, but for cylinder 100C the right and left hand sides of Equation 2 are within the same order of magnitude. Since there is an excellent comparison with the numerical prediction of the thermal layer in this case we conclude that this cylinder can still be approximated as a flat plate with reasonable accuracy despite not meeting the limit posed by Sparrow and Gregg (1956). Additionally, the numerical method only considers inert gases; there is no consideration of reaction effects. Despite these limitations, the numerical results for temperature compare well with experimental temperature fields from interferometry prior to the onset of significant visible reaction, as shown by Fig. 6.

4.3 Comparison with literature results

The ignition results from Section 4.1 can also be compared with results from the literature. First, the results are compared with those from Kuchta et al. (1965) for internal natural convection of n-hexane mixtures with similar surface areas, as show in Fig. 7. The mixture composition of the data points from Kuchta shown in Fig. 7 is not reported in the original text but the range of mixture compositions investigated varied from 0.05 to 0.5 fuel-air weight ratio with little effect of composition. There is a significant change in ignition temperature between internal and external natural convection flows with similar surface areas. The ignition temperatures for external natural convection flows investigated here are approximately 200 to 500 K higher than the ignition temperatures for internal natural convection (Kuchta et al., 1965).

This can be explained by the difference in confinement between these two flow configurations. An internal natural convection flow is confined inside a heated vessel and the reactive mixture continuously recirculates within that vessel, getting exposed to the heated surface many times. The significant confinement and recirculation causes a long residence time. Long residence times generally lead to lower ignition temperatures as fuel is able to decompose and slower low-temperature chemistry can occur. For external natural convection flows in unconfined geometries the reactive mixture is only exposed to the hot surface once as it moves through the thermal layer. The gas does not recirculate and the

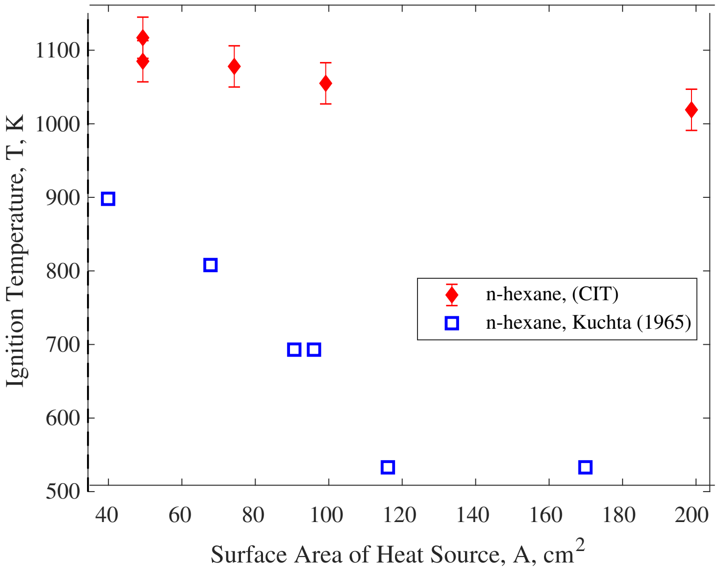

***Fig. 7:** Ignition results from this work (red filled diamonds) compared with those from Kuchta (1965) (blue empty squares) for a similar range of surface areas.*

residence time is shorter. If the external flow is confined in some manner (e.g. inside a vessel), it is possible the flow recirculates and thus increases the residence time. In such situations it is important to understand if there is recirculation of the flow.

Because the hot cylinder in the present study is confined within a closed vessel, there is the potential for recirculation of gas through the thermal layer. The natural convection around the cylinder acts a pump with cold gas entering from the bottom, accelerating upward and exiting the top of the thermal layer. The total mass flow rate induced by this process can be estimated from the model of natural convection presented in Section 3. Using the numerical results presented in Section 4.2, the wall parallel velocity and density are numerically integrated to estimate the mass flow rate. Wall perpendicular velocity is neglected as it is two orders of magnitude smaller than wall parallel velocity.

$$\dot{m} = \int_V \rho u dV = \int_0^L \int_0^{2\pi} \int_{R_c}^{R'} \rho(r,z) u(r,z) r dr d\theta dz \qquad (3)$$

Where L is the length of the cylinder, R_c is the radius of the cylinder, and R' is the outer radius of the flow as determined by the point at which conditions are within one percent of ambient values. The shortest estimated recirculation time, estimated as $M/\dot{m}$ where M is the total mass of gas in the vessel, is 460 seconds and corresponds to cylinder 200A. This is 50% more than the test time of the experiments. Therefore it is reasonable to assume there is no significant recirculation in these experiments and any given portion of the reactive mixture is heated only once.

Comparisons can also be made with the wider body of literature. Starting with results on external natural convection, Melguizo-Gavilanes et al. (2016) report ignition temperatures of n-hexane with an equivalence ratio of 0.9 at 1275 ± 45 K for a glowplug (approximately a vertical cylinder) with 1.5 cm^2 surface area. Boeck et al. (2017) report ignition temperatures of 1270 K for stoichiometric n-hexane air mixtures for a vertical cylinder 3.14 cm^2 in area and Ono et al. (1976) report an ignition temperature of approximately 1250K for stoichiometric propane-air and vertical plates 9 cm^2 in area. Data from all cited studies are compared against results from this work in Fig. 8. Two conclusions are drawn when literature data is compared with the results found in this work. Ignition temperatures for external natural convection are consistently much higher than ignition temperatures for internal

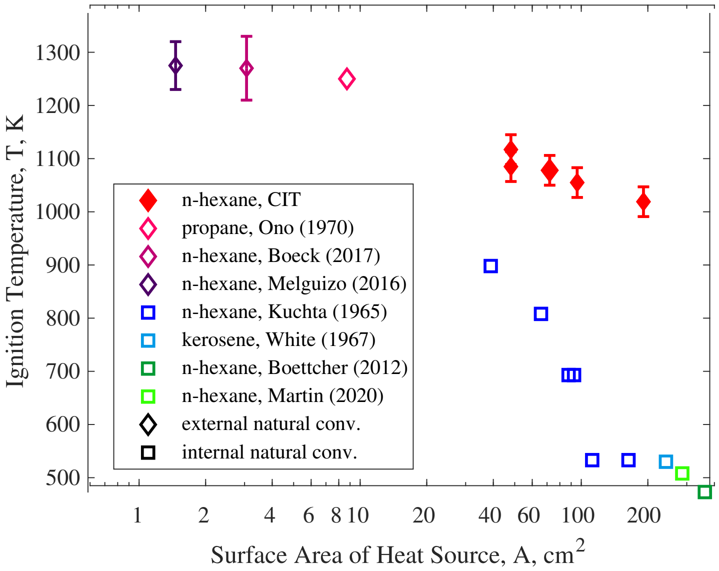

***Fig. 8**: Ignition results from this work (red filled diamonds) compared with results from literature. External natural convection represented by diamonds and internal natural convection represented by squares.*

natural convection flows. Additionally, there is a significant difference in the trend of ignition temperature with surface area. Kuchta et al. (1965) report ignition temperature dropping from 898 K at 40.5 cm^2 to 533 K at 171 cm^2 which amounts to a 365 K decrease in ignition temperature over 130 cm^2 of area change. For a similar area change the ignition temperature of the cylinders drops from 1117 K at 50 cm^2 to 1019 K at 200 cm^2. This is a difference of 98 K over a 150 cm^2 area change and shows a much more modest depended of ignition temperature on surface area in comparison to Kuchta et al. (1965).

Additional literature on thermal ignition from internal natural convection gives points of comparison for the results of Kuchta et al. (1965). White (1967) reports ignition temperatures of 530 K for a vessel approximately 250 cm^2 in area with an air-fuel ratio from 0.85 to 40 for kerosene-air mixtures. Boettcher (2012) reports ignition temperatures of 473 K for a 380 cm^2 vessel with n-hexane fuel at an equivalence ratio of 1.2. Martin and Shepherd (2020) followed the autoignition testing procedure prescribed by ASTM E659 (ASTM International, 2015) and found an ignition temperature of 508 ± 3 K for hexane in a 300 cm^2 vessel. These results further demonstrate the large difference in ignition temperatures between internal and external natural convection flows. This indicates that a change from internal to external flow has much more impact on ignition temperature than a change in surface area for the range investigated here.

5 Conclusions

Thermal ignition of stoichiometric n-hexane and air mixtures by vertical cylinders from 50 to 200 cm^2 is investigated experimentally. Five out of six of the tested cylinder geometries achieve ignition. Ignition thresholds are found to range from 1019 to 1117 ± 30 K. Surface temperatures at which both ignition and non ignition results are observed, e.g. overlap behavior, are found for cylinders with longer lengths (19.1 to 25.4 cm) but are not observed with a cylinder length of 12.7 cm. This indicates that a longer cylinder and thus a longer residence time leads to more scatter in ignition results.

For inert mixtures, a simple similarity-type solution accurately predicts the thermal layer formed by natural convection over a vertical cylinder. Temperature fields from interferometry compare well with

DOI: 10.7795/810.20200724

numerical results from a similarity solution adapted from Cairnie and Harrison (1982). This indicates that the similarity solution is useful for predicting momentum and thermal layers as long as the right and left hand sides of Equation 2 are of the same order of magnitude.

Finally, cylinder ignition results are compared to published values obtained by previous researchers. The ignition temperatures from this work are overall consistent with ignition temperatures for other external natural convection flows. Examination of ignition temperature data from external natural convection flows shows a modest decrease in ignition temperature as surface area increases for a total of 220 K decrease between 1275 K at 1.5 cm^2 and 1019 K at 200 cm^2. The present study demonstrates that external natural convection over hot surfaces results in ignition temperatures which are significantly higher and much less dependent on surface area than previous studies that used natural convection inside heated vessels.

Acknowledgements

This work was carried out in the Explosion Dynamics Laboratory of the California Institute of Technology, and was supported by The Boeing Company through a Strategic Research and Development Relationship Agreement CT-BA-GTA-1. The authors gratefully acknowledge the contributions of Esmir Mesic on initial characterization of the cylinders.

References

ASTM International (2015). *ASTM E659-15, Standard Test Method for Autoignition Temperature of Chemicals*.

Bane, S., Shepherd, J., Kwon, E., Day, A. (2011). *Statistical analysis of electrostatic spark ignition of lean $H_2/O_2/Ar$ mixtures*. International Journal of Hydrogen Energy, 36:2344–2350.

Boeck, L., Meijers, M., Kink, A., Mével, R., Shepherd, J. E. (2017). *Ignition of fuel-air mixtures from a hot circular cylinder*. Combustion and Flame, 185:265–277.

Boettcher, P. (2012). *Thermal Ignition*. Ph.D. thesis, California Institute of Technology.

Cairnie, L. R., Harrison, A. J. (1982). *Natural Convection Adjacent to a Vertical Isothermal Hot Plate with a High Surface to Ambient Temperature Difference*. International Journal of Heat and Mass Transfer, 25(7):925–934.

Coronel, S., Melguizo-Gavilanes, J., Jones, S., Shepherd, J. (2018). *Temperature field measurements of thermal boundary layer and wake of moving hot spheres using interferometry*. Experimental Fluid and Thermal Science, 90:76–83.

Federal Aviation Administration (2018). *Advisory circular 25.981-1D*.

Kuchta, J., Bartkowiak, A., Zabetakis, M. (1965). *Hot surface ignition temperatures of hydrocarbon fuel vapor-air mixtures*. Journal of Chemical Engineering Data, 10(3):282–288.

Martin, C., Shepherd, J. (2020). *Low temperature autoignition of jet a and surrogate jet fuels*. 13th International Symposium on Hazards, Prevention, and Mitigation of Industrial Explosions.

Melguizo-Gavilanes, J., Nove-Josserand, A., Coronel, S., Mevel, R., Shepherd, J. E. (2016). *Hot surface ignition of n-hexane mixtures using simplified kinetics*. Combustion Science and Technology, 188(11–12):2060–2076.

Ono, S., Kawano, H., Niho, H., Fukuyama, G. (1976). *Ignition in a free convection from vertical hot plate*. Bulletin of the JSME-Japan Society of Mechanical Engineers, 19(132):676–683.

Smyth, K., Bryner, N. (1997). *Short-duration autoignition temperature measurements for hydrocarbon fuels near heated metal surfaces*. Combustion Science and Technology, 126(16):225–253.

Sparrow, E. M., Gregg, J. L. (1956). *Laminar-Free-Convection Heat Transfer From the Outer Surface of a Vertical Circular Cylinder*. Transactions of the ASME, 78:1823–1829.

White, R. (1967). *Spontaneous ignition of kerosene/avtur/vapour - the effect of the ratio, vessel surface area to volume (effect of vessel surface area on minimum spontaneous ignition temperature of kerosene)*. Technical Report 67107, Royal Aircraft Establishment.

Ignition delay times of methane/diethyl ether (DEE) blends measured in a rapid compression machine (RCM)

Simon Drost, Marc Werler, Robert Schießl & Ulrich Maas

Institute of Technical Thermodynamics, Karlsruhe Institute of Technology, KIT, Kaiserstraße 12,
76131 Karlsruhe, Germany

E-mail: *simon.drost@kit.edu*

Abstract

Diethyl ether (DEE) is an interesting species for combustion for at least two reasons: On the one hand, it is used as a kind of "worst case" reference substance for studies concerned with the prevention of accidental ignition events. On the other hand, it is also a candidate bio-fuel. For this reason, in this work, auto-ignition of two different CH_4/DEE-mixtures (90/10 and 95/5 mol-% CH_4/DEE) are studied in a rapid compression machine (RCM). In the RCM, the gas mixture is compressed in a piston-cylinder device up to 20 bar and held under isochoric conditions at top dead center. Auto-ignition occurs after an ignition delay time (IDT). IDTs are measured for compression temperatures ranging between 515 and 925 K, for both, stoichiometric and fuel-rich mixtures (equivalence ratio $\phi = 2$). The experimental data are compared to results of simulations involving detailed chemistry, as well as to other fuels investigated in the same RCM (results from literature).

Keywords: *Ignition delay times, Diethyl ether, DEE, Rapid compression machine, methane*

1 Introduction

Diethyl ether (DEE, $CH_3{-}CH_2{-}O{-}CH_2{-}CH_3$) is an interesting fuel. With respect to safety engineering, it is extremely flammable, and its vapour/air mixtures can be highly explosive (International Labour Organization, 2002). DEE is therefore often employed as a kind of worst case substance for explosion safety considerations.

Moreover, in compression ignition (CI) engines, the operation range can be extended operating them in a dual fuel mode with DEE as an ignition enhancer (Polat, 2016). As a fuel component, DEE can have several beneficial effects: In CI engines, a wider operation range in comparison to methane (CH_4) only is observed, as well as a positive effect concerning efficiency and pollutants. For example, hydrogen with DEE (Dhanasekaran and Mohankumar, 2016), as well as bio-gas and DEE (Sudheesh and Mallikarjuna, 2010) are used to promote the auto-ignition. Further, the interest in bio-fuels is growing, and with this, the safety aspect becomes more important as well, such as the auto-ignition behavior (Rajesh Kumar and Saravanan, 2016).

Compared to more conventional fuels or fuel components like e.g. alkanes, there are many studies available investigating the auto-ignition properties: There are studies investigating CH_4/air-mixtures in shock tubes (ST) and in rapid compression machines (RCM) (Burke et al., 2015b, Gersen et al., 2008, Petersen et al., 1999). Furthermore, there are studies investigating the ignition delay time (IDT) of DEE (Werler et al., 2015a, Inomata et al., 1991). However, there is only little data available combining both, CH_4 and DEE, as a dual fuel, such as (Herzler et al., 2019). As mentioned above, according to engine operation, dual fuel operation has its benefits. For this reason, we investigate mixtures of CH_4/DEE in a RCM to understand the ignition enhancing effect of DEE on CH_4 in an engine like apparatus. These data can also serve for development and validation of reaction mechanisms.

This work investigates two CH_4/DEE mixtures, namely a 95/5 and a 90/10 (mol/mol) mixture in a range of end-of-compression temperature from $T_C = 515\,\mathrm{K}$ to 925 K, and an end-of-compression pressure range of $p_C = 10\,\mathrm{bar}$ to 20 bar. Both mixtures are investigated under stoichiometric and fuel-rich ($\phi = 2$, fuel-air equivalence ratio) conditions. The experimentally obtained data is used for comparison with two reaction mechanisms developed to describe DEE chemistry, published by Eble

***Table 1**: Mixture compositions (mole-fractions in %)*

No.	Fuel	Equivalence ratio	CH_4	DEE	O_2	Inert species
1	95/5 CH_4/DEE	$\phi = 1$	8.28	0.436	19.17	72.12
2	90/10 CH_4/DEE	$\phi = 1$	7.24	0.805	19.31	72.64
3	95/5 CH_4/DEE	$\phi = 2$	15.23	0.802	17.63	66.34
4	90/10 CH_4/DEE	$\phi = 2$	13.40	1.489	17.87	67.24

et al. (2017) and Sakai et al. (2017).

This work outlines the experimental procedure; then, we present the measured IDTs. The results are discussed in terms of the promoting effect of DEE on methane auto-ignition. Predicted IDTs from numerical simulations based on detailed reaction mechanisms are tested against the experimental data; it is assessed in which regimes the mechanisms can reproduce the IDT, despite the fact that they were originally developed for auto-ignition of stoichiometric DEE/air mixtures (Eble et al. (2017): 500 to 900 K / 3 to 5 bar and 900 to 1300 K / 10 to 40 bar; Sakai et al. (2017): 500 to 1300 K / 1 to 40 bar), and not for the CH_4/DEE/air-mixtures presented in this work with a very small ratio of DEE/CH_4.

Furthermore, the experimental data are compared to results for other ignition enhancing fuels investigated in the same RCM (results from literature). These fuels are Dimethyl ether (DME), two polyoxymethylene dimethyl ether fuels (OME_2 and OME_3) and n-heptane (C_7H_{16}). The comparison highlights the strong ignition enhancing effect of DEE, which is significantly larger than for the other fuels.

2 Experimental Setup

The auto-ignition behavior of the investigated CH_4/DEE/air-mixtures is studied in a rapid compression machine (RCM). This machine has been described in detail in previous publications (Drost et al., 2019, Werler et al., 2015a). For this reason, only a brief description of the experimental setup is given in this work.

The RCM is a piston-cylinder device which allows to achieve high temperatures and pressures in a fuel/air mixture by rapid compression, thereby also stimulating chemical reactions. Therefore, the operation is similar to a CI engine, but the RCM allows better defined initial conditions with respect to temperature, pressure, mixture composition and flow field. The volume- and pressure history during and after the compression event is tracked in each experiment; the pressure measurement is split into a measurement of the static/initial pressure and the time dependent in-cylinder pressure measurement. The static initial pressure p_0 is measured with an absolute pressure transducer (MKS Baratron type 121A) with an accuracy of $U_{p0} = \pm 0.5\%$ of reading (MKS, 2008), whereas the time dependent pressure trace $p(\tau)$ is monitored by a quartz pressure transducer (Kistler 6061 B) with a linearity of $U_{p(\tau)} = 0.5\%$ (full scale output, adjusted to 10 bar) (Kistler, 2013). This pressure transducer is optimized against thermo-shocks with a double diaphragm. For reciprocating internal combustion engines with 1500 revolutions per minute (approximately a similar speed as the presented RCM; compression time of 20 - 40 ms) and an indicated mean effective pressure of 9 bar, the thermo shock causes a pressure fluctuation of $\Delta p = \pm 0.2$ bar (Kistler, 2013).

The time-resolved position of the piston is measured with a potentiometric position sensor (Burster type 8712), which is connected to the piston rod with a non-linearity of $U_S = 0.1\%$ of full scale (Burster, 2020).

Before a series of RCM-experiments is performed, the mixture is prepared in a mixing vessel by filling in the desired mole fractions of the pure components, as given by their partial pressures. The mixing vessel contains gas for about 10 - 100 RCM experiments, depending on the detailed conditions. The mixtures investigated in this work are summarized in Table 1.

In an experiment, the gas mixture is filled into the initially evacuated RCM combustion chamber. After this, the piston is driven into the cylinder within a compression time of about $\tau_C = 20$ to 40 ms, depending on the compression pressure p_C in the combustion chamber. After reaching top dead center (TDC), the piston is held in fixed position, granting isochoric conditions till the experiment ends. After some ignition delay time (IDT), auto-ignition occurs; the IDT is counted relative to the end of compression (the time when the piston first reaches TDC).

To assign a temperature and pressure to an ignition event and its IDT, the conditions at the end of compression are chosen. The temperature at this time is calculated from the measured pressure ($p(\tau)$), and the initial values of pressure/temperature and the temperature-dependent heat capacities of the investigated gas-mixture, using an isentropic relation.

3 Simulations

The simulations in this work are performed with the in-house code HOMREA (Maas and Warnatz, 1988) using a homogeneous reactor model. HOMREA has been extended over years by its functions (Golda et al., 2019, Yu et al., 2019) and by its input algorithm for reading new reaction mechanisms and their functions.

Characterising the RCM and its specific heat losses, an effect volume is calculated and serves as an input for the simulations (described below in more detail). The initial temperature, pressure, and chemical composition of the mixture are defined by the corresponding experimental conditions.

Detailed reaction mechanisms from Sakai et al. (2017) (341 species and 1867 reactions) and from Eble et al. (2017) (133 species and 792 reactions) are used.

In RCM experiments, an adiabatic core is assumed in the center of the combustion chamber. However, the whole combustion chamber is affected by heat losses. Combining the idea of this adiabatic core and the heat losses of the surrounding gas layers, an effective volume model, as described by Goldsborough et al. (2017) and Sung and Curran (2014), can be used to perform IDT simulations taking the facility effects into account.

To obtain this effective volume, a RCM experiment with an inert mixture is used. Hereby, for each mixture in Table 1, the oxygen (O_2) is substituted by the same molar amount of nitrogen (N_2). N_2 has a similar molar heat capacity as O_2; however, in the range of conditions it is considered here, there is practically no reaction of the fuel as shown by (Vin et al., 2016). The unreactive experiments are performed with compression temperatures below 830 K to prevent thermal decomposition/pyrolysis of DEE (Vin et al., 2016). Further, gas chromatography analysis has shown that there was no thermal decomposition (pyrolysis) of the inert gas mixture. This means that the pressure trace is only affected by the volume change and the heat losses.

Thus, at isochoric conditions, a pressure drop is directly linked to heat losses and the corresponding drop in temperature caused by heat losses. The time-dependent effective volume $V(\tau)$ is calculated from

$$\ln\left(\frac{p_0}{p(\tau)}\right) = \int_{V_0}^{V(\tau)} \frac{c_p(T)}{c_v(T)} \frac{1}{V^*} \mathrm{d}V^*. \tag{1}$$

Here, p_0 and V_0 are the initial pressure and volume, respectively, $p(\tau)$ is the pressure trace over time and $V(\tau)$ the effective volume over time. Moreover c_p and c_v are the temperature-dependent heat capacities at isobaric and isochoric conditions.

As a result of the heat losses, the effective compression ratio used in the simulation is lower than the geometric one defined by the experimental apparatus. Furthermore, after reaching TDC, the effective volume expands slightly over time.

4 Results and discussion

4.1 Ignition delay times of stoichiometric CH_4/DEE mixtures

In this section, the IDT of the stoichiometric CH_4/DEE mixtures of Table 1 are presented (mixture #1 and #2). Figure 1a shows the behaviour of different CH_4/DEE mixtures vs. CH_4. Comparing the 95/5 vs. 90/10 CH_4/DEE mixture, three effects are notable:

First, at a given temperature, the ignition of 90/10 CH_4/DEE mixtures is about one order of magnitude faster than for the 95/5 mixture. Second, with the higher amount of DEE, the gas mixture can be ignited at lower temperatures. Here the DEE chemistry becomes more dominant. Third, comparing the 95/5 CH_4/DEE mixture to CH_4 one observes that the small addition of DEE already has a significant effect.

Adding 5 mol-% DEE, there is ignition at lower temperatures, a lower apparent activation energy is observed and ignition delay times above $\tau_I \approx 60\,\mathrm{ms}$ can be measured. Comparing 95/5 CH_4/DEE to CH_4 by the temperature with an IDT of $\tau_I = 55\,\mathrm{ms}$, the required temperature is lowered from $T_C \approx 1045\,\mathrm{K}$ (CH_4) to $T_C \approx 925\,\mathrm{K}$ (95/5 CH_4/DEE).

Comparing the experimental results with the simulation in Figure 1a, the reaction mechanism of Sakai et al. (2017) agrees better with the experimental results than the reaction mechanism of Eble et al. (2017). Further, both reaction mechanisms show a better agreement with the 90/10 CH_4/DEE mixture than with the 95/5 CH_4/DEE mixture. A reasonable explanation at this point is, that both reaction mechanisms were developed for auto-ignition of DEE.

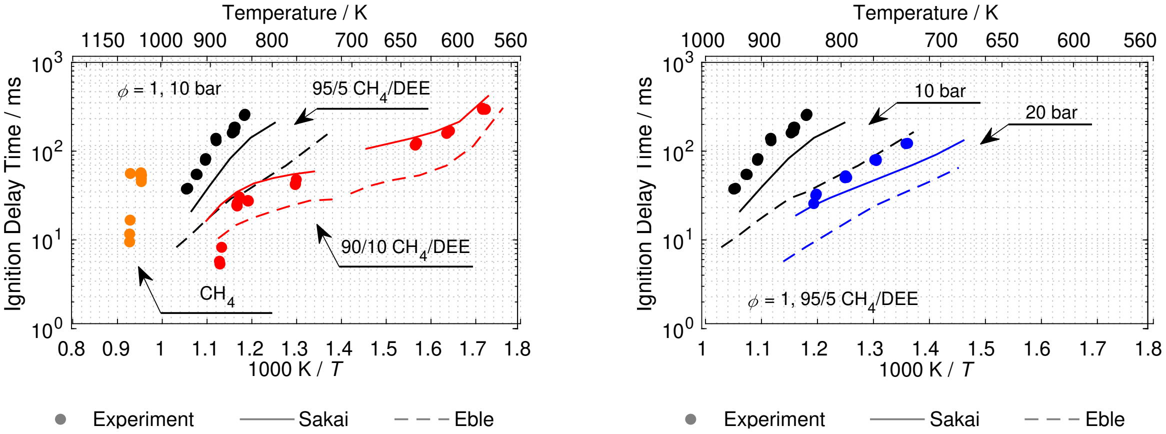

*(a) Comparison of different CH_4/DEE ratios and CH_4 at constant pressure (*10 bar*).*

(b) Comparison of two compression pressures at constant 95/5 CH_4/DEE ratio.

Fig. 1*: Stoichiometric 95/5 CH_4/DEE and 90/10 CH_4/DEE mixtures at two different compression pressures. Simulations (lines) are performed with the reaction mechanism of Eble et al. (2017) and Sakai et al. (2017)*

Figure 1b compares the stoichiometric 95/5 CH_4/DEE mixture at two different compression pressures ($p_C = 10$ vs. 20 bar). The increased compression pressure results in a shorter IDT. Furthermore, ignition is detected at lower compression temperatures. For the 95/5 CH_4/DEE mixture, both reaction mechanisms predict a shorter IDT than the experiments, however, at higher pressure, the experiments and simulations agree better than for the 10 bar case.

The C0-C4 base-reaction mechanism of Sakai et al. (2017) is based on the reaction mechanism from Burke et al. (2014, 2015a) (Part of AramcoMech 2.0). Replacing this C0-C4 base-reaction mechanism with its newer C0-C4 base-reaction mechanism of the AramcoMech 3.0 (Zhou et al., 2018) resulted in almost the same IDTs (for this reason the result is not shown). However, one can argue, that the differences in IDTs cannot be attributed to the base-reaction mechanism of small alkanes such as CH_4.

4.2 Ignition delay times of fuel rich CH_4/DEE mixtures

To investigate the behavior of fuel rich mixtures, the presented mixtures with the same CH_4/DEE ratio are mixed with O_2/inert species to reach an overall equivalence ratio of $\phi = 2$ (Table 1 mixture #3 and #4). The results for these mixtures are shown in Fig. 2 with an end of compression pressure of 10 bar.

In Fig. 2a, a comparison of the fuel rich 90/10 CH_4/DEE to its stoichiometric mixture is shown. Overall, at low temperatures, the IDT of the $\phi = 2$ fuel rich mixture is approximately one order of magnitude shorter than that of the stoichiometric ones.

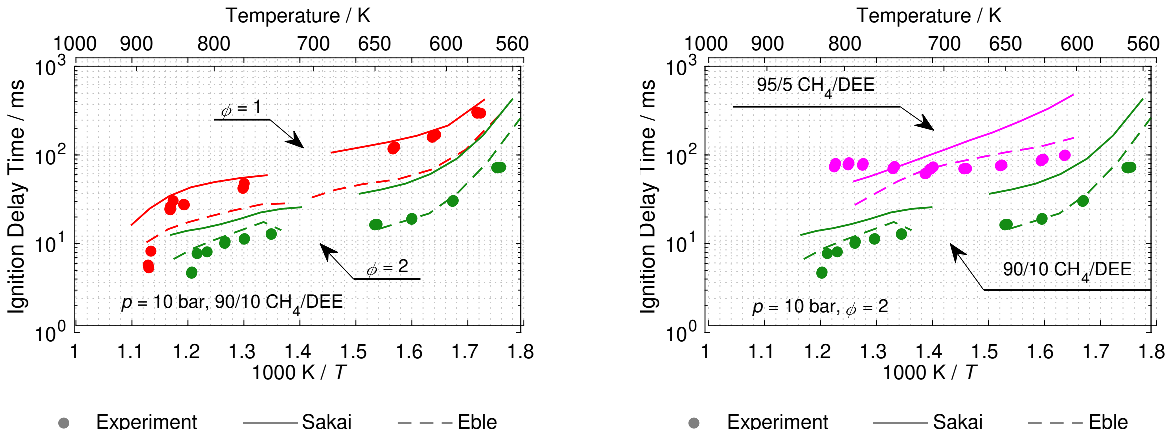

(a) Comparison of 90/10 CH_4/DEE mixtures at stoichiometric and fuel rich conditions, respectively.

(b) Influence of DEE in CH_4 at fuel rich conditions ($\phi = 2$).

***Fig. 2**: Effect of fuel rich mixtures at a compression pressure of* 10 bar. *Simulations (lines) are performed with the reaction mechanism of Eble et al. (2017) and Sakai et al. (2017).*

Since DEE ignites faster than CH_4, the ignition process is controlled by DEE. Further, stoichiometric mixtures ignite faster than (ultra) lean mixtures (Yasunaga et al., 2010). By comparing the equivalence ratio of only DEE in O_2 (by ignoring CH_4), the overall stoichiometric mixture #2 has a DEE-equivalence ratio of $\phi_{DEE} = 0.25$ and the overall fuel rich mixture #4 has a DEE-equivalence ratio of $\phi_{DEE} = 0.5$. This is probably one reason for the ignition promoting effect of the fuel rich conditions. At this point, this behaviour is not investigated in this work. However, alkanes with an equivalence ratio of $\phi = 2$ ignite fast than the stoichiometric ones (Healy et al., 2008).

Both reaction mechanisms show a similar trend in shortening the IDT for the transition from stoichiometric to fuel rich conditions. However, in the experiments, another trend is observed. At a given temperature, the IDT for a fuel mixture is reduced more by changing the equivalence ratio from $\phi = 1$ to 2 than in the simulations.

Figure 2b compares the different CH_4/DEE mixtures at an equivalence ratio of $\phi = 2$ and 10 bar. Again, the higher amount of DEE enhances auto-ignition. Both reaction mechanisms predict the trend of the fuel rich conditions. Here, the Eble et al. (2017) reaction mechanism results predict the results of the experiments better.

4.3 Difference of the reaction mechanisms

Comparing both reaction mechanisms and the experimental results, it is observed that especially at a low amount of DEE, the reaction mechanism of Eble et al. (2017) overestimates the IDT. Investigating this behavior in more detail, IDT simulations (homogeneous reactor, adiabatic and isochoric conditions) are performed for different initial temperatures and different amounts of DEE in the fuel. The first observation is that for the cases with CH_4, both reaction mechanisms result in the same IDT. Starting from CH_4 and increasing the amount of DEE in the fuel, especially at low temperatures (besides 700 K), there is an increasing difference in the predicted IDT by both reaction mechanisms in the range between 5 to 10 mol − % DEE in the fuel.

Understanding the difference between both reaction mechanisms at low amounts of DEE more, sensitivity analysis according to the OH radical are performed for an adiabatic and homogeneous reactor, for both, the Eble et al. (2017) and the Sakai et al. (2017) reaction mechanisms. According to mentioned IDT simulations, an initial temperature of 800 K and an initial pressure of 10 bar is taken for a stoichiometric 95/5 (molar) CH_4/DEE mixture. Under these conditions, for both reaction mechanisms, the reaction

$$\mathrm{DEE} + \mathrm{CH_3O_2}\cdot \rightleftharpoons \mathrm{CH_3{-}CH{\cdot}{-}O{-}CH_2{-}CH_3} + \mathrm{CH_3O_2H} \qquad \text{(R1)}$$

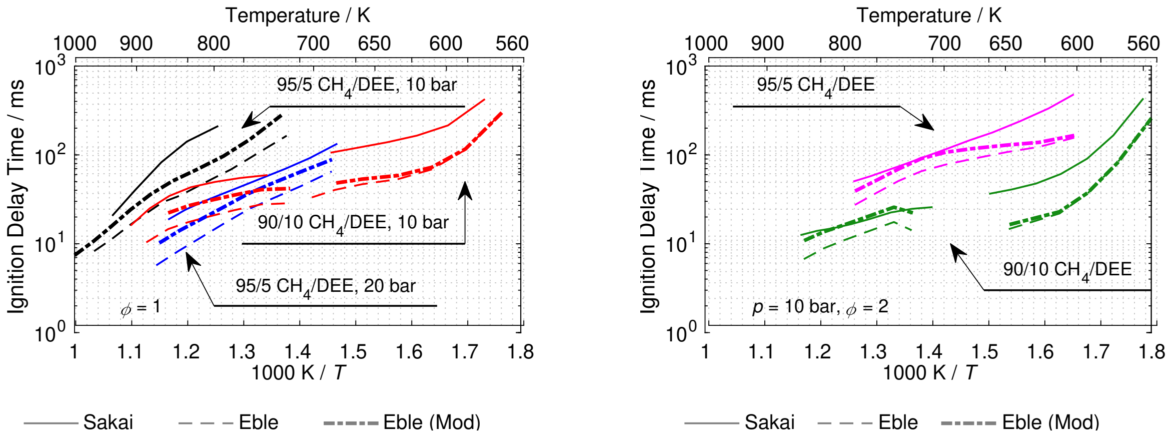

(a) Stoichiometric conditions, different pressures and mixtures.

(b) Fuel rich conditions ($\phi = 2$) and a constant pressure (10 bar).

***Fig. 3**: Comparison between simulations (experiments are not shown for better readability) with the reaction mechanism of Eble et al. (2017), Sakai et al. (2017) and the modified reaction mechanism of Eble et al. (2017).*

is most sensitive at the time $\tau = 0.9\tau_I$. Analyzing this reaction, the parameters of the modified Arrhenius equation are summerized in Table 2.

***Table 2**: Coefficients from reaction (R1) for the Arrhenius equation $k = AT^{\beta}\exp(-E/(RT))$.*

Reaction Mechanism	A	β	E / (cal/mol)
Eble et al. (2017)	$1.176 \cdot 10^{14}$	0	17700
Sakai et al. (2017)	$7.240 \cdot 10^{-01}$	3.980	9058.0

Updating the mentioned reaction (R1) in the reaction mechanism of Eble et al. (2017) by the values of Sakai et al. (2017), an improved IDT is found for higher temperatures (closer results to the experimental data and the predicted IDT of Sakai et al. (2017)) for the stoichiometric mixtures as shown in Fig. 3a.

Fig. 3b shows the comparison between the reaction mechanisms for fuel rich conditions. The IDTs at higher temperatures are too long with a similar result obtained with the reaction mechanism of Sakai et al. (2017). At lower temperatures, the result is similar to the original reaction mechanism of Eble et al. (2017).

The sensitivity analysis was performed for an initial temperature of 800 K, which refers to the upper limit of the investigated temperature regime. Furthermore, the mentioned modification has a higher impact at higher temperatures. On the other side, at lower temperatures the original reaction mechanism (thin dashed lines) and the modified one (thick dashed lines) show a similar result.

For this reason, a sensitivity analysis is performed at an initial temperature of 600 K as well. Both reaction mechanisms show reaction R2 (positive sensitivity) and reaction R3 (negative sensitivity) to be the most sensitive reactions.

$$\mathrm{DEE + OH \rightleftharpoons H_2O + CH_3{-}CH\cdot{-}O{-}CH_2{-}CH_3} \tag{R2}$$

$$\mathrm{CH_4 + OH \rightleftharpoons CH_3 + H_2O} \tag{R3}$$

However, R2 has similar Arrhenius parameters in both reaction mechanisms. For this reason, adapting the Arrhenius parameters shows just a minor change in IDT. Furthermore, reaction R3 has the same values of the Arrhenius equation.

The second most sensitive reactions (R4 and R5) include those DEE molecules for which the first O_2 addition already took place. The second O_2 addition, reaction R4, has a positive sensitivity. In contrast to this, the chain branching reaction R5 of this molecule has a negative sensitivity.

$$CH_3{-}CH(OOH){-}O{-}CH\cdot{-}CH_3 + O_2 \rightleftharpoons CH_3{-}CH(OOH){-}O{-}CH(OO\cdot){-}CH_3 \qquad \text{(R4)}$$

$$CH_3{-}CH(OOH){-}O{-}CH\cdot{-}CH_3 \rightleftharpoons OH + CH_3CHO + CH_3CHO \qquad \text{(R5)}$$

Reactions R4 and/or R5 in the reaction mechanism of Eble et al. (2017) can be adjusted by adapting the Arrhenius parameters from Sakai et al. (2017), as described above. However, by changing reaction R4 and/or R5, the IDTs predicted by the modified reaction mechanism are too long and the IDT is depending on both reactions (R4 and R5). Since there is a too strong effect by changing the Arrhenius parameters, this modification is not recommended.

For an initial temperature of 600 K, a further sensitive reaction is found in both reaction mechanisms, namely reaction R1. This reaction is found most sensitive for an initial temperature of 800 K for both reaction mechanisms and was already adjusted.

Further sensitive reactions related to DEE molecules, are not found in both reaction mechanisms. For example, in the reaction mechanism of Eble et al. (2017) a reaction of DEE and CH_3O is the third most sensitive reaction, however, under the investigated conditions, this reaction has a minor sensitivity in the reaction mechanism of Sakai et al. (2017).

Other sensitive reactions are reactions of intermediates and radicals and are not directly linked to the fuel structure of DEE (C−C−O−C−C) or are reactions which are sensitive just in one reaction mechanism.

4.4 Comparison of CH_4/DEE mixtures with other fuels

Highlighting the effect of even small amounts of DEE in fuel, Fig. 4 compares the IDT of the present study against IDT of previous studies obtained in the same RCM. The selected fuels are known as reference fuel (n-Heptane, C_7H_{16}), potential bio fuels for CI engines (oxygenated fuels) or as a reference for this study (DEE). The fuels are summarized in Table 3. Fig. 4 shows, DEE auto-ignites at the lowest temperature and CH_4 at the highest temperatures. By adding already 10 mol-% DEE to CH_4, at low temperature the IDT of this 90/10 CH_4/DEE mixture is of the same order of magnitude as the IDT of C_7H_{16}.

***Table 3**: Mixture compositions in mol-% fractions*

No.	Fuel	Chemical formula	Pressure / bar	Literature
E1	DEE	$H_3C{-}CH_2{-}O{-}CH_2{-}CH_3$	$p_C = 10.5 - 11.5\,\text{bar}$	Werler et al. (2015a)
E2	DME	$H_3C{-}O{-}CH_3$	$p_C = 10 - 11\,\text{bar}$	Werler et al. (2015b)
E3	OME_2	$H_3C{-}O{-}(CH_2{-}O)_2{-}CH_3$	$p_C \approx 10\,\text{bar}$	Drost et al. (2019)
E4	OME_3	$H_3C{-}O{-}(CH_2{-}O)_3{-}CH_3$	$p_C \approx 10\,\text{bar}$	Drost et al. (2019)
E5	n-Heptane	$H_3C{-}(CH_2)_5{-}CH_3$	$p_C \approx 10\,\text{bar}$	Drost et al. (2019)

However, in the investigated pressure regime, the 90/10 CH_4/DEE mixture shows a weaker temperature dependence (reduced IDT by increased temperature) than the other oxygenated fuels. For this reason, the IDT does not drop as fast as for example for OME_3 (slope in the Arrhenius diagram).

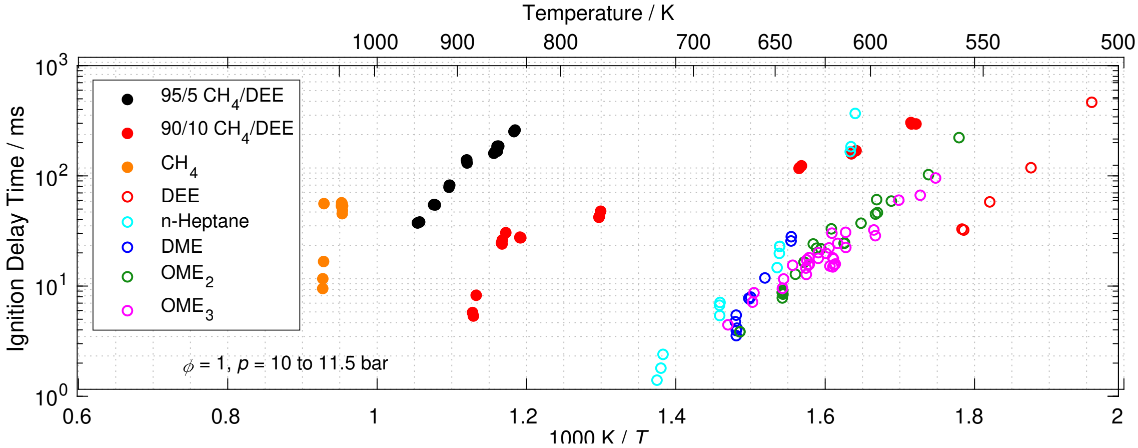

***Fig. 4**: Comparison of CH_4/DEE mixtures with other potentially bio fuels and CH_4. Full symbols represent data from this work, opened symbols represent data from literature with the references in Table 3.*

One reason for this observation is the negative temperature coefficient (NTC) behaviour of DEE. Werler et al. (2015a) showed that DEE has a pronounced NTC behaviour. The IDT data of DEE in Fig. 4 does not show this NTC behaviour since the IDT at 10 bar and above 600 K is too short in relation to the compression time. Thus, the DEE data (red circles) show here only the IDT at low temperatures below the NTC behaviour. The IDT data of DEE show a steeper slope and a strong dependence on temperature change in comparison to 90/10 CH_4/DEE. One can argue, that the 90/10 CH_4/DEE mixture is affected by the NTC behaviour of DEE. In comparison to this, due to lower DEE concentration, the 95/5 CH_4/DEE mixture is affected less.

5 Conclusions

Ignition delay times of CH4/DEE/air mixture have been investigated in a Rapid Compression Machine. Two different CH_4/DEE ratios, both at stoichiometric and fuel-rich conditions ($\phi = 2$) are investigated, in a temperature range of 515 to 925 K and a pressure range of 10 to 20 bar. The ignition delay times are compared to predictions from simulations based on detailed chemistry, using two reaction mechanisms. Further, the two reaction mechanisms are compared to each other, using a homogeneous reactor model and different fuel compositions as well as a sensitivity analysis. Experimental IDTs of the DEE/CH4 mixtures are also compared to other fuels. The main results are:

1. By adding 5 mol% of DEE to the fuel CH_4, the ignition delay is strongly decreased. For instance, to obtain an IDT shorter than 55 ms requires a temperature of at least about 1045 K for CH_4; with 95/5 CH4/DEE (molar), the required temperature is reduced to about 925 K.
2. Throughout the investigated temperature and pressure-range, the ignition delay time decreases by a factor of about 10 by doubling the amount of DEE from 5 mol-% to 10 mol-%.
3. For the investigated conditions, the reaction mechanisms from Eble et al. (2017) and Sakai et al. (2017) predict the trend in IDT change over temperature well, expect for the mixture 95/5 CH_4/DEE at fuel rich conditions.
4. For a temperature of $T = 600$ K and a stoichiometric 95/5 (molar) CH_4/DEE mixture, the reaction of DEE with OH and the reaction of CH_4 and OH are most sensitive (positive and negative).
5. For temperature $T = 800$ K and low amounts of DEE in CH_4, the reaction of DEE + $CH_3O_2\cdot \rightleftharpoons C_4H_9O\cdot + CH_3O_2H$ is most sensitive.
6. In the investigated conditions, updating the reaction DEE + $CH_3O_2\cdot \rightleftharpoons C_4H_9O\cdot + CH_3O_2H$ in the reaction mechanism of Eble et al. (2017) with the values of Sakai et al. (2017) results in IDTs closer to the experimental IDTs and closer to IDTs predicted by the reaction mechanism of Sakai et al. (2017).

Acknowledgements

Financial support by the Deutsche Forschungsgemeinschaft within the framework of the DFG research group FOR 1993 "Multi-functional conversion of chemical species and energy" (No. SCHI647/3-2) is gratefully acknowledged.

References

Burke, S. M., Burke, U., Mc Donagh, R., Mathieu, O., Osorio, I., Keesee, C., Morones, A., Petersen, E. L., Wang, W., DeVerter, T. A., Oehlschlaeger, M. A., Rhodes, B., Hanson, R. K., Davidson, D. F., Weber, B. W., Sung, C.-J., Santner, J., Ju, Y., Haas, F. M., Dryer, F. L., Volkov, E. N., Nilsson, E. J., Konnov, A. A., Alrefae, M., Khaled, F., Farooq, A., Dirrenberger, P., Glaude, P.-A., Battin-Leclerc, F., Curran, H. J. (2015a). *An experimental and modeling study of propene oxidation. Part 2: Ignition delay time and flame speed measurements*. Combustion and Flame, 162(2):296–314. ISSN 0010-2180. doi:10.1016/J.COMBUSTFLAME.2014.07.032.

Burke, S. M., Metcalfe, W., Herbinet, O., Battin-Leclerc, F., Haas, F. M., Santner, J., Dryer, F. L., Curran, H. J. (2014). *An experimental and modeling study of propene oxidation. Part 1: Speciation measurements in jet-stirred and flow reactors*. Combustion and Flame, 161(11):2765–2784. ISSN 0010-2180. doi:10.1016/J.COMBUSTFLAME.2014.05.010.

Burke, U., Somers, K. P., O'Toole, P., Zinner, C. M., Marquet, N., Bourque, G., Petersen, E. L., Metcalfe, W. K., Serinyel, Z., Curran, H. J. (2015b). *An ignition delay and kinetic modeling study of methane, dimethyl ether, and their mixtures at high pressures*. Combustion and Flame, 162(2):315–330. ISSN 15562921. doi:10.1016/j.combustflame.2014.08.014.

Burster (2020). *Potentiometric Displacement Sensors. Models 8712, 8713*. burster Praezisionsmesstechnik GmBH & Co KG, Gernsbach, Germany.

Dhanasekaran, C., Mohankumar, G. (2016). *Dual fuel mode DI diesel engine combustion with hydrogen gas and DEE as ignition source*. International Journal of Hydrogen Energy, 41(1):713–721. ISSN 03603199. doi:10.1016/j.ijhydene.2015.10.028.

Drost, S., Schießl, R., Werler, M., Sommerer, J., Maas, U. (2019). *Ignition delay times of polyoxymethylene dimethyl ether fuels (OME2 and OME3) and air: Measurements in a rapid compression machine*. Fuel, 258. ISSN 00162361. doi:10.1016/j.fuel.2019.116070.

Eble, J., Kiecherer, J., Olzmann, M. (2017). *Low-Temperature Autoignition of Diethyl Ether/O2 Mixtures: Mechanistic Considerations and Kinetic Modeling*. Zeitschrift fur Physikalische Chemie, 231(10):1603–1623. ISSN 09429352. doi:10.1515/zpch-2016-0959.

Gersen, S., Anikin, N. B., Mokhov, A. V., Levinsky, H. B. (2008). *Ignition properties of methane/hydrogen mixtures in a rapid compression machine*. International Journal of Hydrogen Energy, 33(7):1957–1964. ISSN 03603199. doi:10.1016/j.ijhydene.2008.01.017.

Golda, P., Blattmann, A., Neagos, A., Bykov, V., Maas, U. (2019). *Implementation problems of manifolds-based model reduction and their generic solution*. Combustion Theory and Modelling, pages 1–30. ISSN 17413559. doi:10.1080/13647830.2019.1682198.

Goldsborough, S. S., Hochgreb, S., Vanhove, G., Wooldridge, M. S., Curran, H. J., Sung, C. J. (2017). *Advances in rapid compression machine studies of low- and intermediate-temperature autoignition phenomena*. Progress in Energy and Combustion Science, 63:1–78. ISSN 03601285. doi:10.1016/j.pecs.2017.05.002.

Healy, D., Curran, H., Simmie, J., Kalitan, D., Zinner, C., Barrett, A., Petersen, E., Bourque, G. (2008). *Methane/ethane/propane mixture oxidation at high pressures and at high, intermediate and low temperatures*. Combustion and Flame, 155(3):441–448. ISSN 00102180. doi: 10.1016/j.combustflame.2008.07.003.

Herzler, J., Sakai, Y., Fikri, M., Schulz, C. (2019). *Shock-tube study of the ignition and product formation of fuel-rich CH 4 /air and CH 4 /additive/air mixtures at high pressure*. Proceedings of the Combustion Institute, 37(4):5705–5713. ISSN 15407489. doi:10.1016/j.proci.2018.05.120.

Inomata, T., Griffiths, J. F., Pappin, A. J. (1991). *The role of additives as sensitizers for the spontaneous ignition of hydrocarbons*. Symposium (International) on Combustion, 23(1):1759–1766.

International Labour Organization (2002). *ICSC 0355 - DIETHYL ETHER*.

Kistler (2013). *Kistler Gruppe: ThermoCOMP®-Quarz-Drucksensor, Typ 6061B*. 8408 Winterthur, Swiss.

Maas, U., Warnatz, J. (1988). *Ignition processes in hydrogen-oxygen mixtures*. Combustion and Flame, 74(1):53–69. doi:10.1016/0010-2180(88)90086-7.

MKS (2008). *MKS Instruments Inc.: Pressure Measurement & Control Baratron ® Manometer*. Andover, MA 01810, USA.

Petersen, E. L., Davidson, D. F., Hanson, R. K. (1999). *Kinetics modeling of shock-induced ignition in low-dilution CH4/O2 mixtures at high pressures and intermediate temperatures*. Combustion and Flame, 117(1-2):272–290. ISSN 00102180. doi:10.1016/S0010-2180(98)00111-4.

Polat, S. (2016). *An experimental study on combustion, engine performance and exhaust emissions in a HCCI engine fuelled with diethyl ether-ethanol fuel blends*. Fuel Processing Technology, 143:140–150. ISSN 03783820. doi:10.1016/j.fuproc.2015.11.021.

Rajesh Kumar, B., Saravanan, S. (2016). *Use of higher alcohol biofuels in diesel engines: A review*. Renewable and Sustainable Energy Reviews, 60:84–115. ISSN 18790690. doi: 10.1016/j.rser.2016.01.085.

Sakai, Y., Herzler, J., Werler, M., Schulz, C., Fikri, M. (2017). *A quantum chemical and kinetics modeling study on the autoignition mechanism of diethyl ether*. Proceedings of the Combustion Institute, 36(1):195–202. ISSN 15407489. doi:10.1016/j.proci.2016.06.037.

Sudheesh, K., Mallikarjuna, J. M. (2010). *Diethyl ether as an ignition improver for biogas homogeneous charge compression ignition (HCCI) operation - An experimental investigation*. Energy, 35(9):3614–3622. ISSN 03605442. doi:10.1016/j.energy.2010.04.052.

Sung, C. J., Curran, H. J. (2014). *Using rapid compression machines for chemical kinetics studies*. Progress in Energy and Combustion Science, 44:1–18. ISSN 03601285. doi: 10.1016/j.pecs.2014.04.001.

Vin, N., Herbinet, O., Battin-Leclerc, F. (2016). *Diethyl ether pyrolysis study in a jet-stirred reactor*. Journal of Analytical and Applied Pyrolysis, 121:173–176. ISSN 01652370. doi: 10.1016/j.jaap.2016.07.018.

Werler, M., Cancino, L., Schiessl, R., Maas, U., Schulz, C., Fikria, M. (2015a). *Ignition delay times of diethyl ether measured in a high-pressure shock tube and a rapid compression machine*. Proceedings of the Combustion Institute, 35(1):259–266. doi:10.1016/J.PROCI.2014.06.143.

Werler, M., Schießl, R., Maas, U. (2015b). *A Rapid Compression-Expansion Machine : The experimental setup and first results with DME-air mixtures*. In *Proceedings of the European Combustion Meeting – 2015*, pages P1–71. Budapest, Hungary.

Yasunaga, K., Gillespie, F., Simmie, J. M., Curran, H. J., Kuraguchi, Y., Hoshikawa, H., Yamane, M., Hidaka, Y. (2010). *A multiple shock tube and chemical kinetic modeling study of diethyl ether pyrolysis and oxidation*. Journal of Physical Chemistry A, 114(34):9098–9109. ISSN 10895639. doi:10.1021/jp104070a.

Yu, C., Minuzzi, F., Bykov, V., Maas, U. (2019). *Methane/Air Auto-Ignition Based on Global Quasi-Linearization (GQL) and Directed Relation Graph (DRG): Implementation and Comparison*. Combustion Science and Technology, pages 1–23. ISSN 1563521X. doi: 10.1080/00102202.2019.1625337.

Zhou, C. W., Li, Y., Burke, U., Banyon, C., Somers, K. P., Ding, S., Khan, S., Hargis, J. W., Sikes, T., Mathieu, O., Petersen, E. L., AlAbbad, M., Farooq, A., Pan, Y., Zhang, Y., Huang, Z., Lopez, J., Loparo, Z., Vasu, S. S., Curran, H. J. (2018). *An experimental and chemical kinetic modeling study of 1,3-butadiene combustion: Ignition delay time and laminar flame speed measurements*. Combustion and Flame, 197:423–438. ISSN 15562921. doi:10.1016/j.combustflame.2018.08.006.

DOI: 10.7795/810.20200724

Simulation of the Flow of an Explosive Atmosphere Exposed to a Hot Hemisphere

Subrahmanyeswara Velagala[a,b], Priyank Raval[a,b], Sai Charan Singh Chowhan[a,b], Ghazaleh Esmaeelzade[a], Michael Beyer[a], Holger Grosshans[a,b]

[a] Physikalisch-Technische Bundesanstalt (PTB), Bundesallee 100, 38116 Braunschweig, Germany
[b] Institute of Apparatus- and Environmental Technology, Otto von Guericke University Magdeburg, Germany

E-mail: *holger.grosshans@ptb.de*

Abstract

The accidental ignition of combustible atmospheres by hot surfaces is of great concern for the safety of industrial processes. In this paper, we present our research regarding the evolution of thermal plumes originating from hot hemispheres. In particular, we focus on the effect of the orientation of the surface on the ignition process. The auto-ignition temperatures and ignition locations were studied experimentally. To get further insight, we conducted detailed numerical simulations and validated our model with measurements. Three-dimensional simulations were performed for hemispheres of orientations ranging from 0° to 180°. The solver employs a transient, implicit scheme which is based on the coupled heat transfer and flow equations. The mesh in the vicinity of the hot surfaces is refined to resolve the steep temperature gradients and to capture the boundary layer separation. The influence of the orientation on critical hot spots in the gas mixture is analyzed by examining the flow structures and the temperature evolution of the buoyancy-driven flow. Using the obtained results, we discuss the change of the onset and location of the ignition.

Keywords: *Simulation, thermal flow, hot surface*

1 Introduction

The accidental ignition of combustible atmospheres by hot surfaces which causes disastrous fires or explosions is a great concern in many industries (Eckhoff and Thomassen, 1994). For this reason, it is important to understand the underlying physics of the heat transfer from a hot surface towards the flammable mixture. A measure to characterize the ignition hazard of an atmosphere in the absence of a spark or flame is the auto-ignition temperature (AIT). The AIT is defined as the maximum acceptable surface temperature in a particular area to prevent fires and explosions (Chen et al., 2010, Eckhoff and Thomassen, 1994). Typically, the AIT is measured by placing the substance in a half-liter vessel and inside a temperature-controlled oven, where the rate of heating is not relevant. At first, the fuel/air mixture in the vicinity of the hot surface heats up and the surrounding air remains at the ambient temperatures. The resulting temperature gradient and, thus, the density gradient near the surface induces buoyant forces acting on the gas. Then, the affected gas acquires velocity and convects in the opposite direction to the gravity vector away from the high-temperature region. In order to ignite, a heated fuel/air packet needs to obtain a sufficiently high temperature for a certain amount of time which is called the residence time. However, the concept of the AIT is defined assuming the fuel/air packet to remain in a specific condition for an indefinitely long period. Therefore, ignition in real applications requires a higher temperature than the AIT in an environment where because of buoyancy the gas is constantly accelerated (Raval, 2019, Babrauskas, 2008)

The earliest experimental study by Coward and Guest (1927) concerned the effect of the material of the hot surface on ignition. Through the years a range of researchers shed light on different aspects of the topic: Ashman and Büchler (1961) conducted investigations using a cylindrical wire located in the combustible atmosphere and heated it until the mixture ignited. The ignition of gases through a suddenly heated circular rod has been examined by Adomeit (1965) for different equivalence ratios and gas pressures. Then, the influence of the hot surface area and the diameter of the hot sphere were studied experimentally by Laurendeau (1982). More recently, Babrauskas (2008) concluded that the actual surface temperature required for ignition does highly depend on the degree of enclosedness. More specifically, higher temperatures are needed to start the ignition process as the degree of enclosedness is increased. Another recent experimental work on hot hemispheres by Raval (2019) and Chowhan et al. (2020) investigated the effect of the orientation on the auto-ignition temperatures and ignition locations of carbon disulfide and Diethyl ether. It was observed that the ignition location changes with the orientation of the hot surface and the highest values of the hot surface ignition temperature were observed for an orientation of 180°. The precise reasons for this behavior and the ignition location remain to date unclear.

Due to the development of numerical tools and the increase of computational power, simulations represent today an attractive approach to study ignition-related processes (for example Esmaeelzade et al. (2019), Shekhar et al. (2018)). As regards hot surfaces, Griffiths and Barnard (2012) analyzed the influence of the size of the surface on the ignition temperature. The influence of the surface temperature to ignite the ethylene-air mixture by horizontal and vertical cylinders was the focus of the computations of Melguizo-Gavilanes and Shepherd (2017). Further, the influence of viscosity and buoyancy on transient natural convection over a sphere was examined by Jia and Gogos (2007). The ignition of a cold combustible mixture of propane/air has been investigated for the stagnation region of a hot projectile by Sharma and Sirignano (2007).

Nevertheless, little attention has been paid so far on spherical surfaces and their orientation effects on the ignition and ignition locations. In the present study, three-dimensional numerical simulations of thermal plumes originating from hot hemispheres of five different orientations are discussed. The effects of the orientation on critical hot spots are presented by examining flow structures and the temporal evolution of the temperature and velocity fields. Also, the results are validated against experimental data.

2 Description of the Computational Fluid Dynamics (CFD) model

The examination of the complex buoyancy-driven gas flow and heat transfer inside the combustion chamber is performed using the *BuoyantPimpleFoam* solver which is part of the OpenFOAM toolbox. The mathematical model and techniques to solve the equations are detailed in the following.

2.1 Governing equations and numerical methods

The mathematical model to predict the evolution of thermal hot spots inside the combustion chamber couples the transient heat transfer to the laminar flow. To account for stratification, the gas mixture is considered to be quasi-compressible, including density as an explicit variable in the calculation. Thus, the physics of the flow is described by the governing equations of CFD, namely the continuity, momentum, and energy equations. In Cartesian coordinates, these equations read

$$\frac{\partial \rho}{\partial t} + \nabla \cdot (\rho \boldsymbol{u}) = 0 \,, \tag{1}$$

$$\frac{\partial (\rho \boldsymbol{u})}{\partial t} + \nabla \cdot (\rho \boldsymbol{u}\boldsymbol{u}) = -\nabla p + \rho \boldsymbol{g} + \mu \left(\nabla^2 \cdot \boldsymbol{u}\right) . \tag{2}$$

The pressure gradient and gravity force in the momentum equation (Eq. (2)) are rearranged as

$$\nabla p + \rho \boldsymbol{g} = \nabla p_{\mathrm{rgh}} - (\boldsymbol{g} \cdot \boldsymbol{r}) \nabla \rho \,, \tag{3}$$

were p_{rgh} is the dynamic pressure which is given by

$$p_{\mathrm{rgh}} = p - \rho \boldsymbol{g} \cdot \boldsymbol{r} \,. \tag{4}$$

In the above equations, $\boldsymbol{u}$ is the fluid velocity, ρ is the density, p is the static pressure, $\boldsymbol{g}$ is the gravitational acceleration, μ is the dynamic viscosity, and $\boldsymbol{r}$ is the position vector.

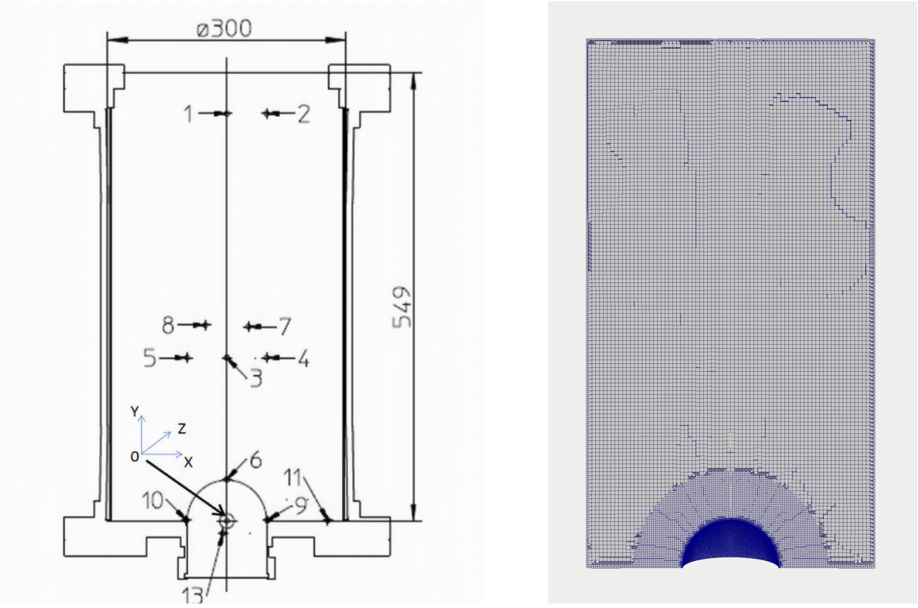

(a) (b)

***Fig. 1**: (a) Schematic representation of the experimental setup and the location of thermocouples (reprinted from Raval (2019)) and (b) numerical grid for the simulations.*

The thermal energy transport is described through the enthalpy equation

$$\frac{\partial(\rho h)}{\partial t} + \nabla\cdot(\rho\boldsymbol{u}h) + \frac{\partial(\rho K)}{\partial t} + \nabla\cdot(\rho\boldsymbol{u}K) - \frac{\partial p}{\partial t} = \nabla\cdot(\alpha\nabla h) + \rho\boldsymbol{u}\cdot\boldsymbol{g}\,, \tag{5}$$

where K and h are the kinetic energy and enthalpy per unit mass, respectively. The thermal diffusivity, α, is estimated based on the ratio of viscosity and Prandtl number, i.e.

$$\alpha = \frac{\mu}{Pr}\,. \tag{6}$$

Finally, to close the system of equations the ideal gas law is solved, which reads

$$p = \rho RT\,, \tag{7}$$

where the specific gas constant is $R = 287$ J/(kg K).

As regards the boundary conditions, no-slip velocity and zero pressure gradient are assumed at all surfaces, i.e. both the hot surface and the chamber walls. Initially, the temperature at the hot surface is set to room temperature, 293.65 K. Then, it is gradually and uniformly increased with time according to the procedure applied in the experiments. At the walls of the combustion chamber, a uniform fixed temperature of 293.65 K is applied.

2.2 Geometry and mesh generation

The geometry is created using the open-source CAE software Salome based on the experimental setup which is sketched in Fig. 1(a). The geometry consists of a cylinder of a height of 549 mm and a diameter of 300 mm and contains a hot surface at the bottom. Then, the geometry is discretized to a computational mesh on which the governing equations are solved. The meshing of the geometry is done using the blockMesh and SnappyHexMesh utilities provided in OpenFOAM. In most of the domain, hexahedral elements are generated. The mesh near the hot surfaces is refined in order to capture the thermal and velocity boundary layers, see Fig. 1(b).

3 Results

3.1 *Set-up*

In the present study, extensive numerical simulations of transient laminar natural convection of a carbon disulfide/air mixture from a gradually heated spherical convex surface were carried out. Hereby, a volume fraction of 2% of CS_2 was considered as working fluid. In the previous experiments, it was observed that the start of ignition time in the combustion chamber changes with orientation and also with the kind of hot surface being used. Thus, the main focus was on answering the questions of why the ignition location changes with the orientation of the surface and at which location ignition initiates. The simulations were performed for five different orientations ranging from 0° to 180° with an interval of 45°. The temperature of the hot surface was gradually increased with time at the same rate as that of experiments. All the simulations are run until the time instance when, according to the experiments conducted by Raval (2019), ignition takes place. The simulations were performed using the Linux high-performance computing cluster at Physikalisch-Technische Bundesanstalt (PTB), Berlin. Each case was distributed on 12 processors.

3.2 *Validation of the simulation model*

The major contributors to the numerical error of our simulation results are the truncation error of the employed spatial discretization schemes and the possible inaccuracies in describing the real physical problem through our mathematical model. As regards the former, the truncation error diminishes with the successive refinement of the mesh. Thus, we first carried out a grid refinement study for a representative flow case. The tested meshes consisted of 0.25 million to 2.28 million cells. The maximum observed difference in the results between the cases of 1.17 million and 2.28 million cells is depending on the spatial location between 0.009% and 0.34% in terms of the temperatures at the locations of the thermocouples. Thus, we can safely assume that the results obtained from our simulations conducted on a grid of 1.17 million cells are grid-independent.

Further, we use the experimental data of Raval (2019) to validate our mathematical model. This data represents the temporal evolution measured by the thermocouples at the locations depicted in Fig. 1(a). The transient CFD model was validated for the 0° orientation of the hemisphere surface.

Figure 2 plots the temperature evolution obtained from simulations and experiments considering five chosen thermocouple locations, namely numbers 1, 2, 3, 6, and 8. Comparing these curves demonstrates that the maximum difference is 1.66% which is observed at thermocouple 6. Thus, the simulations are in very close agreement with the experiments and our model was judged to be suitable for

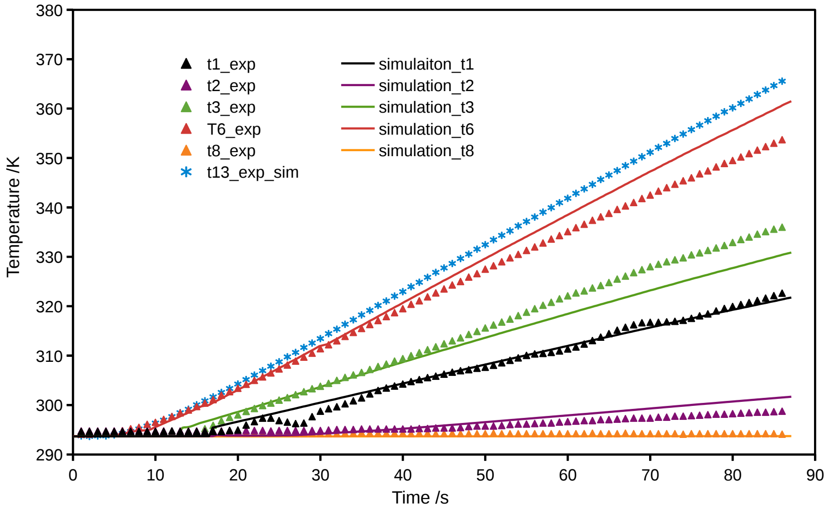

***Fig. 2**: Comparison of the simulation results with experimental data by Raval (2019).*

carrying out a detailed analysis. It is noted that thermocouple number 13 is directly located on the hot surface. The temperature evolution measured at this position was applied as boundary condition to the simulations.

3.3 Analysis of the thermal flow field

In the following, we discuss the flow and thermal field induced by a hot hemisphere of the orientations $\phi = 0°$, 45°, 90°, 135°, and 180°. The magnitude of the flow velocity for each case is depicted in Fig. 3. We are mainly interested in the precise conditions which lead to the ignition of the explosive atmosphere. Thus, each snapshot corresponds to the time instance were ignition was observed in the experiments. For further visualization of the flow field, the streamlines of the flow at the same time instances are given in Fig. 4. Moreover, the resulting thermal plumes are shown in Fig. 5.

As it can be observed in these figures, the buoyancy induced by the heat transfer from the hemisphere results in thermal and velocity boundary layers. In the experiments, it was found that the ignition location for the case of $\phi = 0°$ is always directly above the hemisphere. In the early stage of the simulation the buoyancy induced motion is restricted along the hot surface. Afterward, a steady velocity boundary layer is formed that propagates towards the top of the sphere. Then the separation of the boundary layer takes place at the top of the sphere creating a stagnation zone, as can be seen in Fig. 3(a). Also, the thermal boundary merges where the velocity separation takes place resulting in a relatively thick thermal flow over the sphere. Here, the heat accumulates and a high-temperature region (hot spot) as shown in see Fig. 5(a). Further, the streamlines in Fig. 4(a) visualize the hot gas continuing to rise to the top of the chamber as it was already observed by Turner (1973). The heated fluid moves up in a plume and forms a stagnation zone at the top of the vessel. From there the cooled fluid moves further upward within the boundary layer and then falls downward in the outer region. Thus, in the case of $\phi = 0°$, the highest temperatures are reached remote from the hot surface inside the stagnation zone. In this region, the conditions are favorable for a possible ignition of the explosive atmosphere.

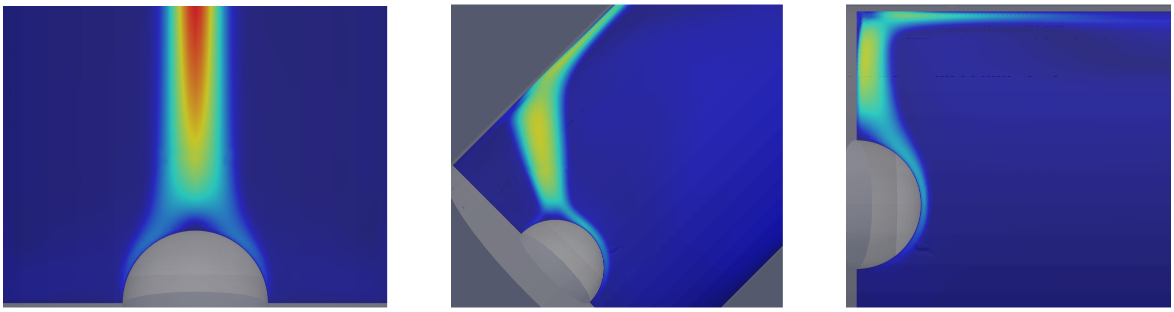

(a) $\phi = 0°, t = 183.0$ s (b) $\phi = 45°, t = 187.0$ s (c) $\phi = 90°, t = 182.5$ s

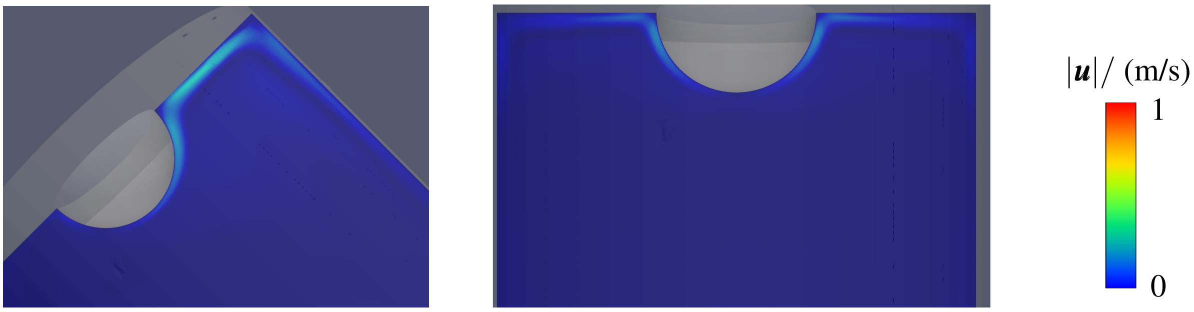

(d) $\phi = 135°, t = 216.5$ s (e) $\phi = 180°, t = 225.0$ s

***Fig. 3**: Magnitude of the velocity of the buoyant flow induced by the hot hemisphere. The depicted instantaneous snapshots correspond for each case to the time instance of ignition as observed in the experiments.*

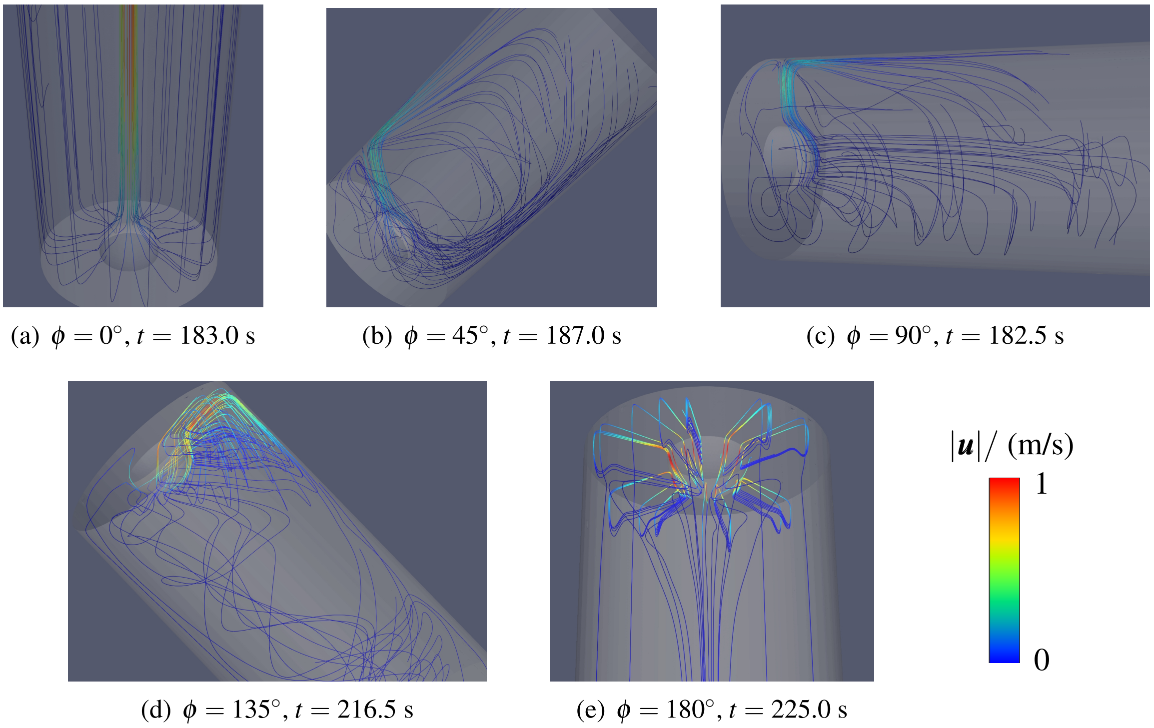

(a) $\phi = 0°, t = 183.0$ s
(b) $\phi = 45°, t = 187.0$ s
(c) $\phi = 90°, t = 182.5$ s
(d) $\phi = 135°, t = 216.5$ s
(e) $\phi = 180°, t = 225.0$ s

***Fig. 4**: Streamlines of the buoyant flow induced by the hot hemisphere, colored by the magnitude of the velocity. The depicted instantaneous snapshots correspond for each case to the time instance of ignition as observed in the experiments.*

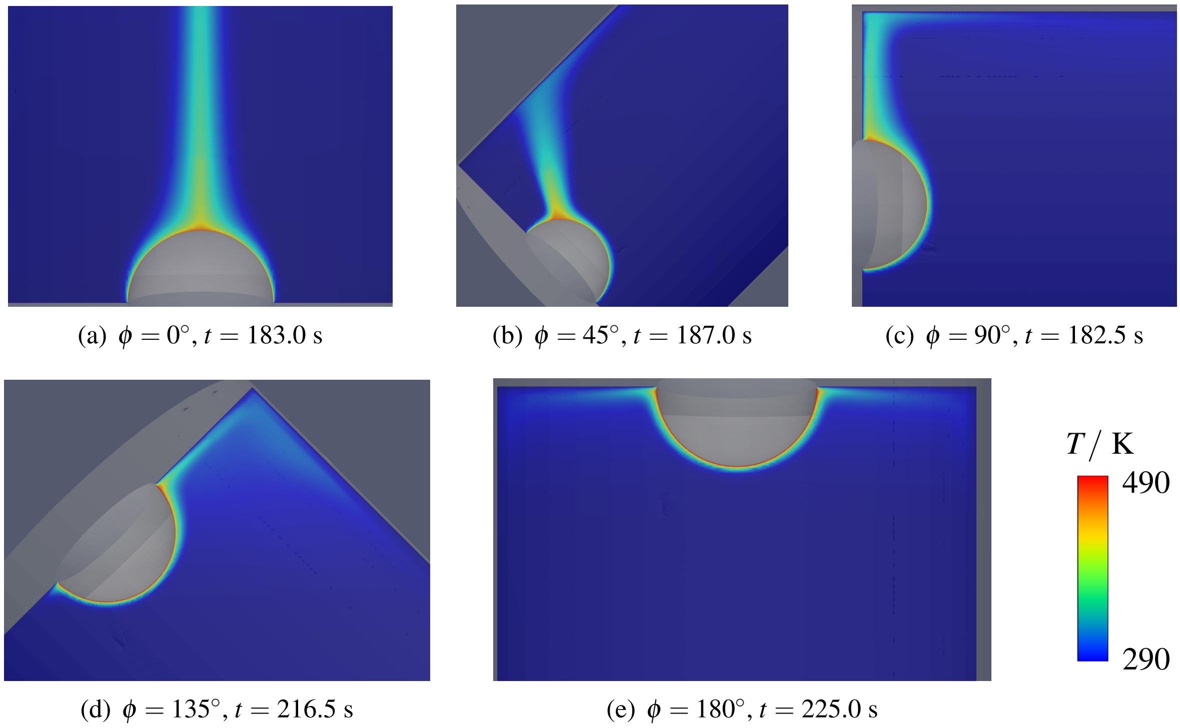

(a) $\phi = 0°, t = 183.0$ s
(b) $\phi = 45°, t = 187.0$ s
(c) $\phi = 90°, t = 182.5$ s
(d) $\phi = 135°, t = 216.5$ s
(e) $\phi = 180°, t = 225.0$ s

***Fig. 5**: Temperature field of the thermal plumes induced by the hot hemisphere. The depicted instantaneous snapshots correspond for each case to the time instance of ignition as observed in the experiments.*

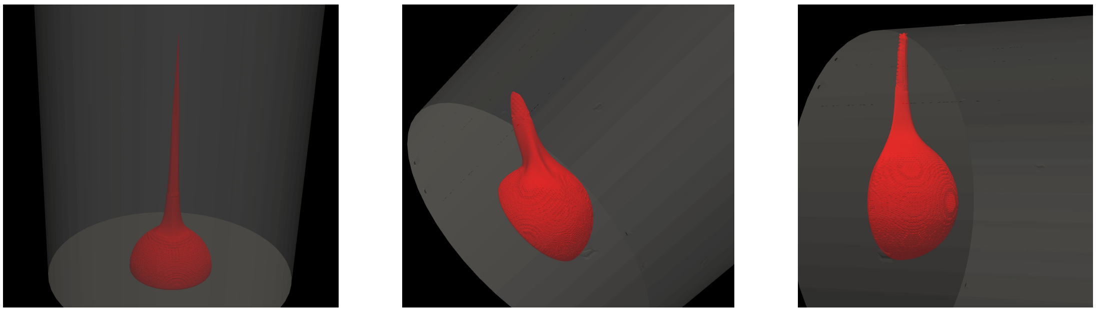

(a) $\phi = 0°, t = 183.0$ s (b) $\phi = 45°, t = 187.0$ s (c) $\phi = 90°, t = 182.5$ s

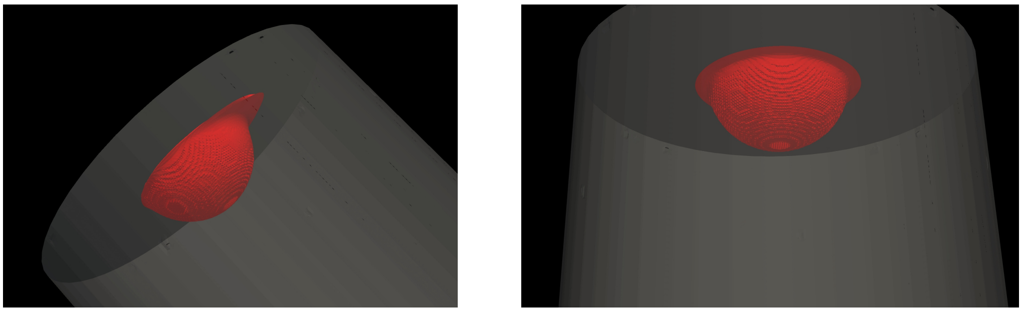

(d) $\phi = 135°, t = 216.5$ s (e) $\phi = 180°, t = 225.0$ s

Fig. 6*: Fluid volume which is above the AIT of CS_2 of 363 K. The depicted instantaneous snapshots correspond for each case to the time instance of ignition as observed in the experiments.*

For the remaining orientations, namely $\phi = 45°$, $90°$, and $135°$, the thermal plumes (Figs. 5(b)–5(e)) do not grow along the symmetry line but follow the direction of the flow (Figs. 3(b)–3(e)). The stagnation zone is shifted towards the left on the hemisphere surface with respect to the orientation. This shifting occurs since the boundary layer separates at the hemisphere's surface always in the direction of buoyancy. This, in turn, leads to the shifting of the hot spot from the top of the hemisphere to the left of the combustion chamber. Comparison with the experiments ascertains that the ignition locations for the above-mentioned orientations of the hemisphere coincide with the location of hot spots from simulations.

Remarkably, the flow fields of the cases of $\phi = 0°$ and $\phi = 180°$ (Figs. 4(a) and 4(e)) are nearly completely inverse to each other. It can be seen that for $\phi = 180°$ the velocity boundary layer forms at the top of the hemisphere. Then, it moves upwards towards the base of the hemisphere and separates in the corner where the hemisphere connects with the wall of the combustion chamber. This leads to the formation of a narrow ring-shaped stagnation zone around the base of the hemisphere. In this region also the thermal boundary layer is a thick ring around the base that exhibits the highest temperature in the whole domain. In the experiments, it was observed that the ignition takes place in a ring similar to that is observed in simulations.

Next, the volume occupied by fluid of high temperature is analyzed. More specifically, in Fig. 6 the volume of the fluid which temperature, at the time instance of ignition, is higher than the AIT is visualized. The AIT of CS_2 is 362.15 K.

It is apparent from Fig. 6(a) that the volume occupied by the hot gas mixture for $\phi = 0°$ is larger than for the other orientations (Figs. 6(b)–(6(e)). The volume of hot gas that is accumulated in the chamber is assumed to be a major parameter of influence on the ignition times. Interestingly, it was observed in the experiments that the ignition duration for $\phi = 0°$ is less compared to the other orientations. In contrast, the case of $\phi = 180°$ that exhibits the second largest volumes of hot gas is found to have a longer ignition duration than the remaining orientations. Also, for the remaining orientations, there was no obvious correlation found between the hot gas volume and the ignition time. As a final remark, it is noted that ignition and combustion are not considered in the present simulations.

4 Conclusion

In this paper, the thermal flow fields originating from a hot hemispherical surface of different orientations were investigated numerically through three-dimensional simulations. The computational results agree well with experimental data obtained from thermocouples. A total of five different orientations was considered ranging from $0°$ to $180°$. The numerical data allowed a detailed explanation of the formation of the thermal hot spots. It was observed that the critical hot spot location changes with the orientation of the hemisphere. More precisely, the location shifts towards the left of the hemisphere with increasing orientation angle ϕ in clock-wise direction. For the case of $\phi = 180°$, the critical hot spot forms a ring around the base of the hemisphere. In general, the location of the hot spots in simulations was in good agreement with the ignition location found in the experiments.

Acknowledgements

The authors gratefully acknowledge the financial contribution from the Berufsgenossenschaft Rohstoffe und chemische Industrie (BG RCI).

References

Adomeit, G. (1965). *Ignition of gases at hot surfaces under nonsteady-state conditions*. In *Int. Symp. Combust.*, volume 10, pages 237–243. Elsevier.

Ashman, L., Büchler, A. (1961). *The ignition of gases by electrically heated wires*. Combust. Flame, 5:113–121.

Babrauskas, V. (2008). *Ignition of gases, vapors, and liquids by hot surfaces*. Int. Symp. Fire Invest. Sci. Technol., (July):4–14.

Chen, C.-C., Liaw, H.-J., Shu, C.-M., Hsieh, Y.-C. (2010). *Autoignition temperature data for methanol, ethanol, propanol, 2-butanol, 1-butanol, and 2-methyl-2,4-pentanediol*. J. Chem. & Eng. Data, 55(11):5059–5064.

Chowhan, S. C. S., Raval, P. K., Velagala, S., Hau, M., Grosshans, H., Beyer, M. (2020). *Ignition at plane and convex hot surfaces at different spatial orientation*. In *13th International Symposium on Hazards, Prevention and Mitigation of Industrial Explosions*. Braunschweig, Germany.

Coward, H. F., Guest, P. G. (1927). *Ignition of natural gas-air mixtures by heated metal bars*. Journal of the American Chemical Society, 49(10):2479–2486. doi:10.1021/ja01409a017.

Eckhoff, R. K., Thomassen, O. (1994). *Possible sources of ignition of potential explosive gas atmospheres on offshore process installations*. J. Loss Prev. Proc. Ind., 7(4):281 – 294. ISSN 0950-4230.

Esmaeelzade, G., Moshammer, K., Fernandes, R., Markus, D., Grosshans, H. (2019). *Numerical study of the mixing inside a jet stirred reactor using large eddy simulations*. Flow Turbul. Combust., 102:331–343.

Griffiths, J. F., Barnard (2012). *Thermal ignition*, volume 2012. CRC Press.

Jia, H., Gogos, G. (2007). *Transient laminar natural convection heat transfer from isothermal spheres*. Numerical Heat Transfer, Part A: Applications, 29(1):83–101.

Laurendeau, N. M. (1982). *Thermal ignition of methaneair mixtures by hot surfaces: A critical examination*. Combust. Flame, 46(C):29–49.

Melguizo-Gavilanes, J., Shepherd, J. (2017). *Effect of orientation on the ignition of stoichiometric ethylene mixtures by stationary hot surfaces*. In *26th Int. Colloquium on the Dynamics of Explosions and Reactive Systems (ICDERS), Boston, USA*.

Raval, P. (2019). *Ignition Temperature of explosive atmosphere in dependence on spatial orientation of the hot surface*. Master's thesis, University of Magdeburg.

Sharma, O. P., Sirignano, W. A. (2007). *Ignition of Stagnation Point Flow by a Hot Body*. Combust. Sci. Technol., 2202(May).

Shekhar, R., Gortschakow, S., Grosshans, H., Gerlach, U., Uhrlandt, D. (2018). *Numerical investigation of transient, low-power metal vapour discharges occurring in near limit ignitions of flammable gas*. J. Phys. D: Appl. Phys., 52:045202.

Turner, J. S. (1973). *Buoyancy Effects in Fluids*. Cambridge Monographs on Mechanics. Cambridge University Press.

DOI: 10.7795/810.20200724

Ignition by low energy electrical discharges - Interference of self-generated vortices with the hot gas kernel

Johann-Robert Kummer[a], Stefan Essmann[a], Holger Grosshans[a], Detlev Markus[a] & Ulrich Maas[b]

[a] Physikalisch-Technische Bundesanstalt (PTB), Braunschweig, Germany
[b] Karlsruhe Insitute of Technology, Institute of Technical Thermodynamics, Karlsruhe, Germany

E-mail: *johann-robert.kummer@ptb.de*

Abstract

Ignition by electrical discharges in explosive atmospheres represents a serious safety risk in certain industrial applications. A characteristic parameter is the minimum ignition energy (MIE). Near the MIE, chemical and physical processes including flow effects interfere with the successful transition to a self-sustaining flame, leading to a statistical nature of the ignition process for a given fuel. In this work, we use numerical investigations to determine particular flow effects interacting with physiochemical processes leading to the ignition of hydrogen/air and methane/air mixtures close to the respective MIE. The results show that the hot gas kernel formed by the electrical discharge is influenced by generated vortices. The use of higher energy impacts the intake of cool gas towards the hot gas kernel by vortices significantly in case of methane. This outcome stresses the influence of flow phenomena especially on the early phase of ignition by low-energy discharges.

Keywords: *minimum ignition energy, ignition process by electrical discharges, flow effects*

1 Introduction

The possible ignition of combustible gas/air mixtures by electrical discharges is a serious safety hazard in various industries. A relevant characteristic of the fuel in this context is the minimum ignition energy (MIE). At discharge energies close to the respective MIE the ignition process becomes highly stochastic (Bane et al., 2011). Essmann et al. (2020) showed that not only the qualitative outcome (ignition or no ignition) is subject to variation, but the outcome of ignition qualitatively varies due to differences in the early phase of flame propagation. Investigations of the development of a stable flame kernel in methane/air and in hydrogen/air were conducted by Thiele et al. (2000) emphasizing the influence of the electrode geometry. Further work with this set-up dealt with the ignition of lean hydrogen/air mixtures (Thiele et al., 2002). The effect of the electrode geometry on the ignition process was analyzed and compared to experiments. Satisfactory agreement of the 2D numerical simulations with the experimental results was achieved. However, the energy input was larger, over a much longer time period and with compelling higher temperatures between the electrodes. Bane et al. (2015) showed the impact of the electrode shape for a non-reactive medium and hydrogen/air, depicting the formed vortex close to the electrode tip. They kept the energy input constant at a much higher level than the respective MIE for hydrogen/air. This shows that the influence by generated flow fields is important. We assess, the generated flow fields at energies close to the respective MIE for a short time of energy input. Since the outcome in experiments also differs quantitatively, we compare the outcome of 1D and 2D simulations and investigate the results of the temperature distribution and the velocity field from the two-dimensional calculations for the identical electrode shape at energy levels close to the respective MIE for H_2/air and CH_4/air mixture to determine the impact of the gas flow on the ignition.

Table 1*: Parameters of the used fuels*

Burnable gas	Concentration in air	MIE
Hydrogen	23.3%	17 µJ
Methane	9.5%	290 µJ

2 Numerical simulations

The one-dimensional simulations of unsteady flames in laminar flow were performed by the program INSFLA (Maas and Warnatz, 1988) for quiescent gas at standard condition for pressure and temperature of 25 °C. It solves the conservation equation for mass, momentum, energy and species mass with adaptive griding. The spark is represented by a source term in the energy conservation equation. Heat loss to the electrodes is not implemented.

The two-dimensional calculations were carried out by employing an in-house tool for the simulation of two-dimensional transient ignition and combustion processes including detailed transport and chemical kinetics models (Thiele, 1999). The conservation equations for total mass, species mass and momentum and energy are solved by the method of lines and a following time-integrating approach for the resulting algebraic-differential equation system. The grid is fixed with 36 lines in radial direction and 32 lines in axial direction. The minimal grid resolution is 80 µm for three grid point in x direction located at the outer boundary. The highest radial resolution is between the electrodes up to 74 µm for three grid points. In y direction the minimal grid resolution is 140 µm for three grid points at the bottom of the computational domain and the highest resolution near the radial center line with 33 µm for three grid points. Thus, the steep gradients are accounted for by three grid points in radial direction. The initial profile for the 2D calculations starts at 50 ns after the energy input ended, i.e. no additional energy input in the 2D simulation is present. In this initial profile, the profiles for the radial grid lines between the electrodes are the results from 1D calculations when the energy input ended. Both velocity components are set to zero for a quiescent gas mixture in the 2D simulation. The profiles on the other radial grid lines is set to a homogeneous, quiescent mixture at 25 °C and ambient pressure. The heat loss to the electrodes is switched off in order to account only for the flow effects in the 2D calculations in difference to the 1D simulations.

The reaction mechanism for hydrogen/air contains nine species and 38 reactions (Warnatz et al., 1996). For methane/air a reduced mechanism with 15 species and 84 reactions is used (Smooke et al., 1986). The gas is assumed to be quiescent and ambient pressure is applied. The source time is set to 50 ns according to Essmann et al. (2017). The spark geometry is assumed to be cylindrical and in conjunction with utilizing the rotational symmetry of the electrode along the vertical axis and symmetry along the horizontal axis the computational cost is reduced. The computational domain is displayed in fig. 1. The domain is 2.5 mm long and wide. The electrode is implemented as a wall. The electrode has a radius of 0.5 mm at the bottom and of 0.3 mm at the top. It is 2 mm long with a distance of 0.5 mm to the radial center line.

The fuel/air compositions and the minimum ignition energies are shown in table 1.

3 Results and discussion

3.1 Hydrogen/air mixture

In fig. 2 the maximum profiles for temperature and OH mass fraction are taken from the 1D and 2D simulation in case of hydrogen/air at 55 µJ and displayed, respectively, along the radial center line. For the 2D case, the radial center line is depicted in fig. 1. As stated in section 2, the 2D simulations starts after the energy input ended at $t = 50$ ns with the same radial profile as the 1D simulation except that the velocity components are set to zero. Thus, the temperature is in fig. 2a at 4000 K at $t = 50$ ns in both cases. Afterwards the gas cools down; slower for the 2D case since the gas is quiescent here. This explains the higher OH mass fraction for the 2D simulation between $t = 60$ ns and $t = 90$ ns,

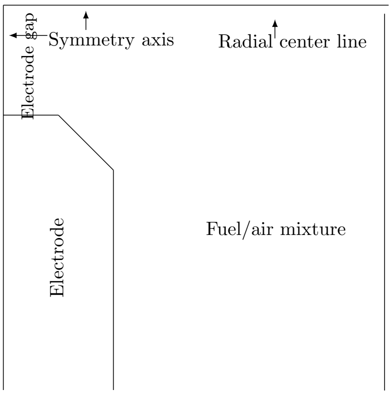

***Fig. 1**: Layout of the domain for the simulations*

see fig. 2b. The hydrogen/air mixture ignites at the end of the energy input due to the steep rise in the maximum OH mass fraction. For the 2D case the maximum temperature and maximum OH mass fraction decrease faster at $t = 500\,\mathrm{ns}$. Due to the transition to a self-sustaining flame front, the temperature in both cases is similar and nearly constant after 5 µs.

In fig. 3 the velocity vectors for hydrogen/air from 2D calculations are displayed at three time instances. At 2 µs (fig. 3a) a distinct flow to the right around the center line for $x = 1\,\mathrm{mm}$ is formed after the shock wave detached and the flame front propagates to the outside. Such detachment of the shock wave can also be observed for a different electrode shape in experiments via Schlieren imaging (Korytchenko et al., 2018). Minor vortices at the outer corner of the electrode, contributed by its shape, are present leading to certain intake of cold ambient gas along the electrode. At $t = 9\,\mu\mathrm{s}$, this is still the case (fig. 3b). At this time instance the flow away from the electrode is weaker except for the domain of the electrode gap. In fig. 3c, the flow is slower but additional small vortices are formed at $x = 0\,\mathrm{mm}$ and at $x = 0.6\,\mathrm{mm}$ between the electrodes due to the initial flow along the radial center line and the followed inflow along the electrode. The vortices in fig. 3c contribute to the divergence after 55 µs in temperature and OH mass fraction between the 1D and 2D calculations (fig. 2b) by mixing with cold ambient gas.

For the hydrogen/air case, the influence by self-generated flow on the ignition process is limited. Due to the short ignition delay time, chemical processes lead fast to an ignition of this fuel/air mixture before forming significant vortices, which take in cold gas to the electrode gap and have an effect on the ignition.

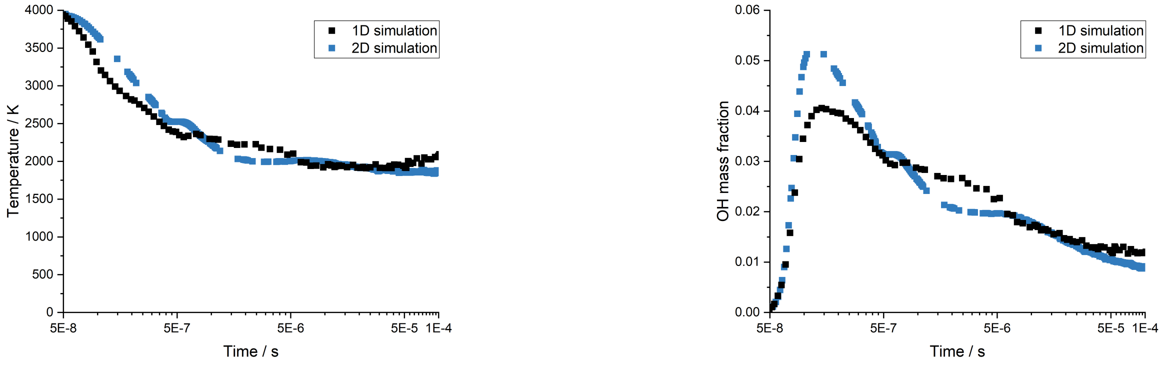

(a) Maximum temperature profile

(b) Maximum OH mass fraction profile

***Fig. 2**: Comparison of results from one-dimensional and two-dimensional calculations for hydrogen after end of energy input*

DOI: 10.7795/810.20200724

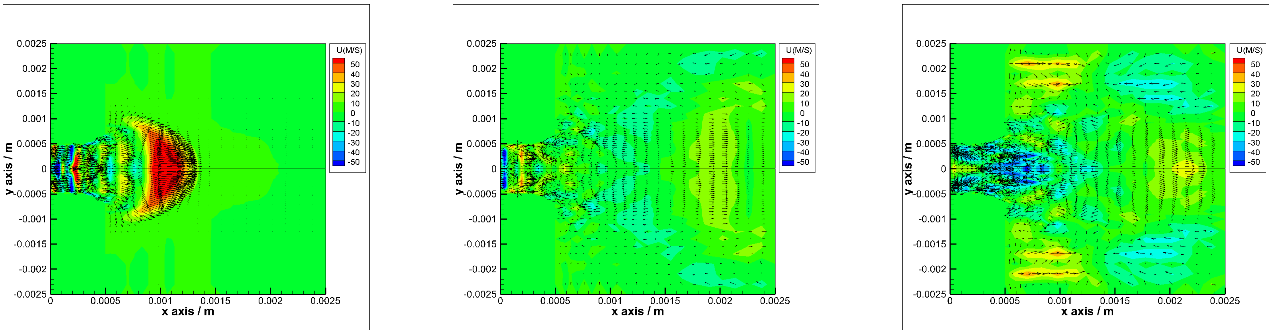

(a) $t = 2\,\mu s$ *(b)* $t = 9\,\mu s$ *(c)* $t = 55\,\mu s$

Fig. 3*: Velocity vectors and velocity in x direction as contour plot of hydrogen/air with* 58 µJ *(*3.4 MIE*) energy input*

3.2 Methane/air mixture

Fig. 4 shows for the methane/air mixture the maximum temperature and maximum OH mass fraction profile along the center line from 1D and 2D calculations with an energy input of 1740 µJ. At $t = 50$ ns the values are identical for fig. 4a and fig. 4b due to same profile at this time instance. The maximum temperature drops until 0.8 µs since no more energy is supplied and is constant until 6 µs. From this point forward the temperature decreases faster in the 2D simulation below 2000 K. The perturbation results from the shock wave on the small computational domain in this case. The maximum OH mass fraction differs significantly after 2 µs in the 2D results from the 1D calculations with even larger differences after $t = 6$ µs due to quiescent gas mixture. The further decrease after $t = 6$ µs is perturbed by the pressure wave as the maximum temperature for the 2D case. The velocity and temperature distribution in the 2D simulation (fig. 5) indicate processes leading to the deviation of 1D and 2D results of the maximal temperature and maximum OH mass fraction profile. Fig. 5 shows the temperature distribution and the velocity field from the 2D calculations in detail for three time steps. At 2 µs the gas flows strongly to the outside in radial direction over a significant width at $x = 1.2$ mm (fig. 5d). The flow field at this time instance is stronger going outward and is more homogeneous between the inclining electrode edges than for hydrogen/air, see fig. 3a. Close to the outer corner of the inclined edge, small vortices are present. The flow of cool gas towards the electrode gap between vortex and electrode edge influences nearly the entire electrode gap. The intake of cool gas is stronger at $t = 9$ µs, see fig. 5e, and at the center line the gas flow going outwards is faster than at the earlier time instance, so that the vortex is stronger. As a consequence the pocket of hot gas is constricted (fig. 5b). As displayed in fig. 5f, a strong flow outwards is formed, starting at $x = 0.3$ mm, $y = 2.5$ mm and broadens in y direction. This leads to the cut off and cooling down of the gas pocket, as displayed in fig. 5c, and the gas temperature between the electrodes decreases further. After 55 µs the pocket of hot gas is narrower and further cooled down at the axial symmetry line.

The ignition delay time is smaller for hydrogen/air than for methane/air and the flow is stronger in the latter case. Thus, the influence of the flow field leading to differences in temperature and OH mass fraction profiles along the radial center line between 1D and 2D calculations by inflow of cool ambient gas towards the electrode gap is indicated. It contributes therefore to the interference with the ignition process of the methane/air mixture close to the MIE.

4 Conclusions

We investigated the influence of self-generated vortices on the ignition process by electrical discharges for two different fuel/air mixtures at conditions close to the respective MIE using numerical simulations with constant electrode geometry. While in case of hydrogen/air no significant effect is visible, there is a strong impact of vortices generated by the electrical discharge on the ignition in case of methane/air. For methane/air, significant flow of cold gas towards the electrode cooling the hot gas channel is shown. This influences the chemical process inside the hot gas between the electrodes

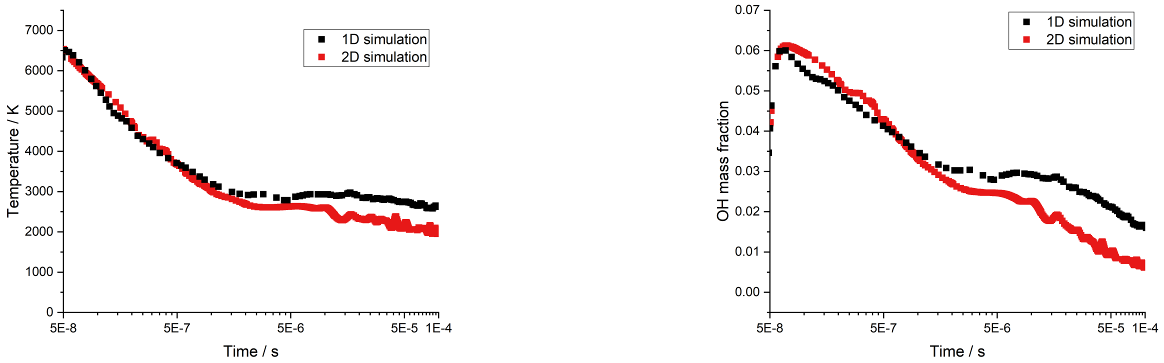

(a) Maximum temperature profile *(b) Maximum OH mass fraction profile*

***Fig. 4**: Comparison of results from one-dimensional and two-dimensional calculations for methane/air after end of energy input*

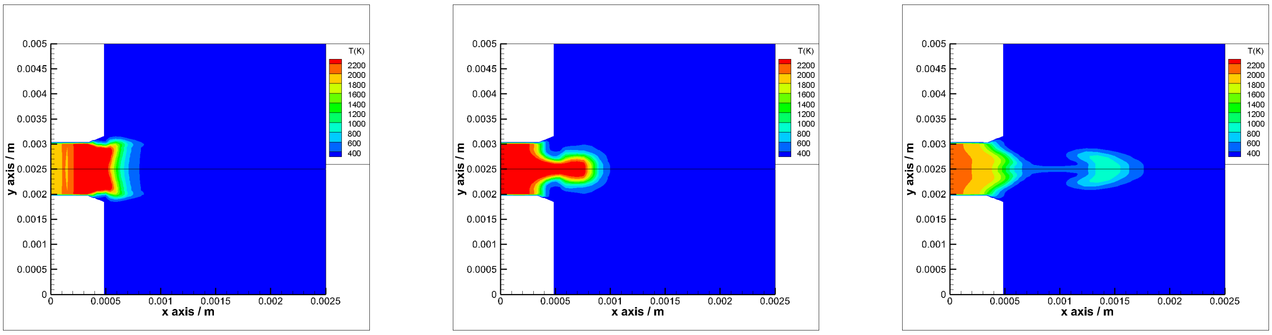

(a) $t = 2\,\mu s$ *(b)* $t = 9\,\mu s$ *(c)* $t = 55\,\mu s$

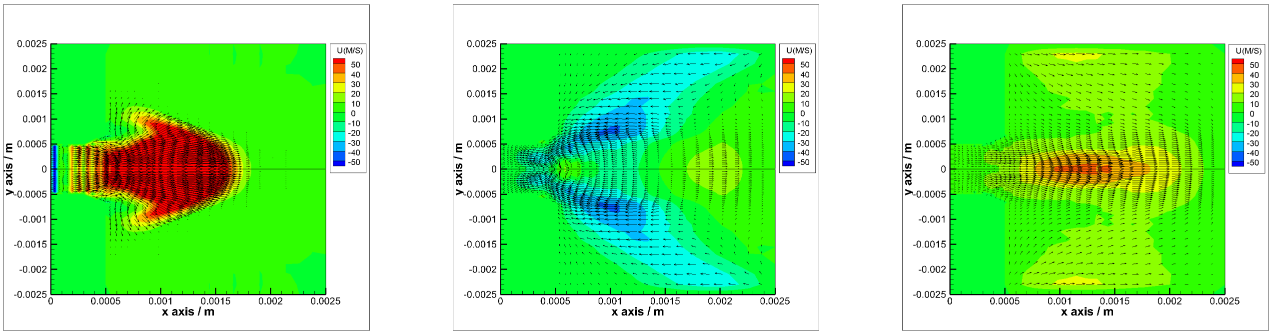

(d) $t = 2\,\mu s$ *(e)* $t = 9\,\mu s$ *(f)* $t = 55\,\mu s$

***Fig. 5**: Temperature distribution and velocity field with velocity component in x direction as contour plot of methane/air with* $1740\,\mu J$ *(*$6.0\,MIE$*) energy input*

hindering a successful ignition for the used energy due to the larger ignition delay time. The results emphasize the importance of the generated flow field of the gas.

In future work, we will extend the investigations to the additional influence of heat loss to the electrodes on the generated flow field at these energy levels, include ions in the calculations and assess this for different energy levels of each fuel/air mixture. Furthermore, we will adjust the electrode shape in the simulation for comparison with experimental results (Essmann et al. (2018, 2020)).

References

Bane, S. P. M., Ziegler, J. L., Boettcher, P. A., Coronel, S. A., Shepherd, J. E. (2011). *Experimental investigation of spark ignition energy in kerosene, hexane, and hydrogen*. Journal of Loss Prevention in the Process Industries, 26(2):290–294. doi:10.1016/j.jlp.2011.03.007.

Bane, S. P. M., Ziegler, J. L., Shepherd, J. E. (2015). *Investigation of the effect of electrode geometry on spark ignition*. Combustion and Flame, 162(2):462–469. doi: 10.1016/j.combustflame.2014.07.017.

Essmann, S., Kummer, J.-R., Markus, D., Maas, U. (2018). *Experimental and numerical investigation of the ignition by electrical discharges close to the minimum ignition energy*. 12th International Symposium on Hazards, Prevention, and Mitigation of Industrial Explosions (ISHPMIE). Kansas City, 2018-08-12/2018-08-17.

Essmann, S., Markus, D., Grosshans, H., Maas, U. (2020). *Experimental investigation of the stochastic early flame propagation after ignition by a low-energy electrical discharge*. Combustion and Flame, 211:44–53. doi:10.1016/j.combustflame.2019.09.021.

Essmann, S., Markus, D., Maas, U. (2017). *Investigation of the flame kernel propagation after ignition by a low energy electrical discharge*. In:. 26th International Colloquium on the Dynamics of Explosions and Reactive Systems (ICDERS). Boston, 2017-07-30/2017-08-04, page Paper 1006.

Korytchenko, K. V., Essmann, S., Markus, D., Maas, U., Poklonskii, E. V. (2018). *Numerical and experimental investigation of the channel expansion of a low-energy spark in the air*. Combustion Science and Technology. doi:10.1080/00102202.2018.1548441.

Maas, U., Warnatz, J. (1988). *Ignition processes in hydrogen-oxygen mixtures*. Combustion and Flame, 74(1):53–69. doi:10.1016/0010-2180(88)90086-7.

Smooke, M. D., Mitchell, R. E., Keyes, D. E. (1986). *Numerical solution of two-dimensional axisymmetric laminar diffusion flames*. Combustion Science and Technology, 67(4-6):85–122. doi: 10.1080/00102208908924063.

Thiele, M. (1999). *Simulation von Zündfunken*. Doctoral thesis, Ruprecht-Karls-Universität, Heidelberg.

Thiele, M., Warnatz, J., Dreizler, A., Lindenmaier, S., Schießl, R., Maas, U., Grant, A., Ewart, P. (2002). *Spark ignited hydrogen/air mixtures: Two dimensional detailed modeling and laser based diagnostics*. Combustion and Flame, 128(1-2):74–87. doi:10.1016/S0010-2180(01)00333-9.

Thiele, M., Warnatz, J., Maas, U. (2000). *Geometrical study of spark ignition in two dimensions*. Combustion Theory and Modelling, 4(4):413–434. doi:10.1088/1364-7830/4/4/303.

Warnatz, J., Maas, U., Dibble, R. W. (1996). *Combustion: physical and chemical fundamentals, modeling and simulation, experiments, pollutant formation*. Springer, Berlin, 1 edition. doi: 10.1007/978-3-642-97668-1.

DOI: 10.7795/810.20200724

Ignition at plane and convex hot surfaces at different spatial orientation

Sai Charan Singh Chowhan[a,b], Priyank Raval[a,b], Subrahmanyeswara Velagala[a,b], Michael Hau[a], Holger Grosshans[a], Michael Beyer[a]

[a] Physikalisch-Technische Bundesanstalt (PTB), Bundesallee 100, 38116 Braunschweig, Germany
[b] Department of System Design and Plant Safety, Otto von Guericke University Magdeburg, Germany

E-mail: michael.beyer@ptb.de

Abstract

Ignition temperatures of explosive gas-air mixtures at hot surfaces of equipment and process technology systems are usually above the safety characteristic auto ignition temperature (AIT). The actual ignition temperatures depend very much on the heat transfer and on the flow conditions at the hot surface. Without forced external flow, these in turn are very much determined by the shape and geometrical arrangement of the ignition source as well as the convective flow. The aim of the work is to investigate the development of the ignition at real hot surfaces in natural convection and to measure the specific ignition temperatures of the explosive mixtures by ignition sources in different spatial orientations. The influence of the orientation on critical hot spots in gas mixtures of carbon disulfide and diethyl ether are investigated in a cylindrical vessel with a heating body at the bottom. The vessel is rotated in steps of 45° to the top to analyse the ignition and the convective flow in different orientations. Temperature measurements at the heating body and in the free volume show the temporal evolution of the temperature distribution. The place of the ignition is recorded by a high-speed camera. We discuss the change of the onset, temperature and location of the ignition. The results are used as a basis for the validation of numerical simulations.

Keywords: *ignition source, ignition temperature, hot surface*

1. Introduction

The hot surface can be present as a potential ignition source during normal operation of mechanical and electrical equipment, gas pipeline, fuel tanks, in case of malfunction of pump, turbine and overheated bearing. So, the study of ignition of flammable and combustible gases by a hot surface is very crucial for many different industries like process and chemical industries, aviation and automobile industries to identify the potential ignition hazard and ensure the safe operation (Shyam et al., 2013; Duarte et al., 1998 and Davis et al., 2010). For design aspects, it is crucial to know the dependence of the ignition temperature on the hot surface geometry and size since limiting space restrictions will make design solutions as unfeasible (Boettcher, 2012). A term associated with hot surface ignition is safety characteristic auto ignition temperature (AIT). Currently, ISO/IEC 80079-20-1:2017 standard procedure is used to determine AIT. As this standard procedure uses an almost closed Erlenmeyer flask with an almost uniform temperature of the gas mixture, the ignition temperature of real hot surfaces (HSIT) is always higher than the standard AIT. So, it is significant to know the actual ignition temperature by hot surfaces for practical industrial situations (Bothe et al., 1989 and Üngüt, 2001). The autoignition temperature of a mixture of gases is affected by pressure (Menon et al., 2016), shape and volume of the vessel, hot surface dimension (Beyer et al., 2012), surface activity, contaminants, flow rate, reaction rate, droplet and mist formation, gravity, and reactant concentration (Babrauskas, 2003 and Warnatz et al., 2012).

Previously a lot of work has been carried out to find hot surface ignition temperature for different substances with different heating sources like a cylinder, glow plug, wire, and pipe and at different orientations of the heating sources (Ott et al., 2010 and Melguizo-Gavilanes et al., 2017). An experiment was done to find the ignition temperature of a CS_2-air mixture with a heated wire wound resistor *(L = 20 mm, D = 6.5 mm)*. The ignition temperature was 250 °C at 1 vol% and 365 °C at 9 vol%. It shows that the ignition temperature increased with increasing fuel concentration of CS_2. The ignition temperature of a diethyl ether-air mixture decreased with increasing concentration for 6-15% and a plateau region was found for 15-30% (Babrauskas, 2003). Experiments on ethers and hydrocarbon vapours (n-heptane and n-hexane) ignition by hot plates and hot pipes made of stainless steel *(D = 10 to 52 mm)* and quartz *(D = 21 mm)* in a vessel *(V = 35 l, D = 300 mm)* have shown that HSIT is around 20 °C higher than the AIT for diethyl ether and the HSIT is approximately 70 °C higher than the AIT for hydrocarbons, and very low influence of the diameter of the tube on the HSIT is observed (Bothe et al., 1989 and Gosda et al., 1989). In another experiment, the hot surface ignition of a hydrogen-air mixture by glow plug *(H = 9.3 mm, D = 5.1 mm)* was investigated to show the effect of heating rate on the ignition location (Melguizo-Gavilanes et al., 2016 and 2019). In most of the previous experiments, HSIT was found by using the small heating bodies and considered the effects of only horizontal and vertical positions on HSIT. There is a lack of data available for HSIT of the large heating bodies as they may seem in mechanical or electrical equipment. So, we will use the plane and convex shaped heating bodies of diameter 100 mm at five different orientations (0°, 45°, 90°, 135°, and 180°). The results from present experiments can be used to develop a numerical simulation model that studies the buoyancy- driven flow inside the vessel for different positions of heating bodies (Velagala et al., 2020).

2. Experimental procedure

Flammable substances like carbon disulfide (CS_2) and diethyl ether ($C_4H_{10}O$) are taken and their HSIT is measured at different concentrations. We prefer these substances because of its low boiling temperature, low AIT and lower minimum ignition energy. The safety characteristics of these substances are obtained from the CHEMSAFE database. They are given in table 1. AIT is auto ignition temperature; BPT is boiling point temperature; FP is flash point; LEL is lower explosion limit; Stoi. mix. means stoichiometric mixture; MIE is minimum ignition energy and T class is temperature class.

Table 1: *Safety characteristic data of carbon disulfide and diethyl ether (CHEMSAFE).*

Substance	AIT (°C)	BPT (°C)	FP (°C)	LEL (vol%)	UEL (vol%)	Stoi. mix. (vol%)	MIE (mJ)	T Class	Explosion Group
Carbon disulfide (CS_2)	95	46	< -20	0.6 ± 10	60.0 ± 5	6.5	0.01	T6	IIC
Diethyl ether ($C_4H_{10}O$)	175	35	< -20	1.7 ± 10	39.2	3.4	0.19	T4	IIB

The cylindrical vessel *(V = 37 l, D = 300 mm and L = 599 mm)* is made up of borosilicate glass as it is transparent enough to record the ignition process. The schematic diagram of the experimental vessel and its angle of rotation is shown in figure 1. A heating body is mounted on the bottom of the vessel and the bottom is attached with the lines of the water-cooling system. The vessel is rotated in steps of 45° to the top to analyse the ignition and the convective flow in different orientations. The vessel can withstand only 1 bar pressure. So, a quick pressure relief rupture disc made of Aluminium foil is used to cover the top of the vessel. The necessary diameter of this rupture disc is calculated according to EN 14994.

For the temperature measurement, we used 13 k-type (nickel-chromium) thermocouples *($D = 0.13$ mm)*. To measure the temperature variation of a gas-air mixture during the experiment, we used 11 thermocouples inside the vessel. 12th thermocouple is placed outside the vessel to measure the ambient temperature. 13th thermocouple is placed inside the heating body to measure the heating body temperature and this temperature is treated as the hot surface ignition temperature (HSIT) during the ignition process as shown in figures 1(a) and 1(b).

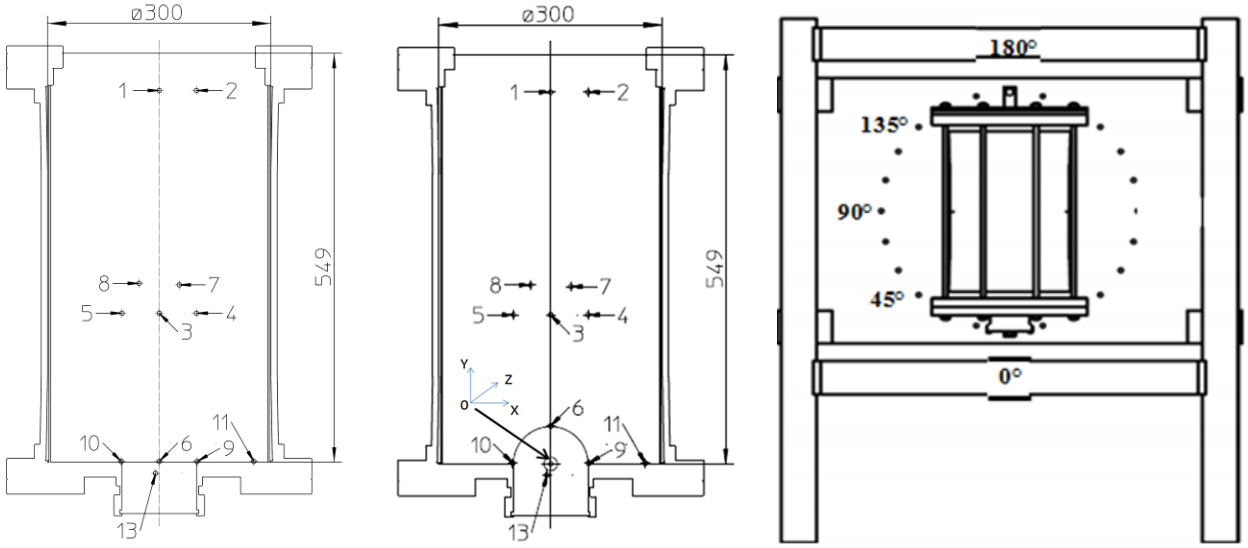

(a) (b) (c)

Fig. 1. *(a) Position of thermocouples inside a cylindrical vessel with plane heating element; (b) Position of thermocouples inside a cylindrical vessel with a hemispherical(convex shaped) heating element; (c) Rotation of the cylindrical vessel in five different orientations (0°, 45°, 90°, 135°, and 180°).*

For a cylindrical vessel with a plane heating body, the position of thermocouples is given in table 2 and figure 1(a). For a cylindrical vessel with a hemispherical heating body, the position of thermocouples is similar to table 2, except for thermocouples T6, T9 and T10 as these thermocouples positioned 1 mm above the radius of the hemispherical heating body as shown in figure 1(b). Therefore, thermocouple T6 is +51 mm on y-axis. Thermocouple T9 is +51 mm and T10 is -51 mm on x-axis.

Table 2: *Position of the thermocouples inside the cylindrical vessel with plane heating body (x-axis is along the symmetry axis of the vessel; the bottom of the vessel is zero; y and z-axis form the plane parallel to the bottom of the vessel; y and z are exchangeable in the symmetric cylindrical configuration.)*

Coordinate	T1	T2	T3	T4	T5	T6	T7	T8	T9	T10	T11
x (mm)	+000	+050	+000	+050	-050	+000	+027	-027	+050	-050	+127
y (mm)	+499	+499	+200	+200	+200	+001	+238	+240	+001	+001	+001
z (mm)	+000	+000	+000	+000	+000	+000	+147	+147	+000	+000	+000

These thermocouples are connected with temperature measurement modules NI-9213 and NI-9174 (National Instruments) combined with a C-DAQ (Compact data acquisition) chassis which controls the timing, synchronization and data transfer. LabVIEW software is used for controlling the data acquisition, for the graphical representation and for the storage of the Measurement results. The heating body is made up of copper due to its high thermal conductivity. Gold layer is coated on the copper surface to avoid the oxidization of the copper metal when it interacts with the fuel-air mixture. It will minimize the radiation and suppress the catalytic effects. As shown in figure 2, the dimension of a heating cartridge is 12.5 mm * 40 mm. The heat is uniformly distributed around the heating body by heating cartridges of power up to 2800 watts, voltage of 230 V and maximum operating temperature up to 750 °C. The heating body is surrounded by an insulating ring (IBF- Fiberboard 120B) to reduce the heat loss from the heating body to the bottom plate.

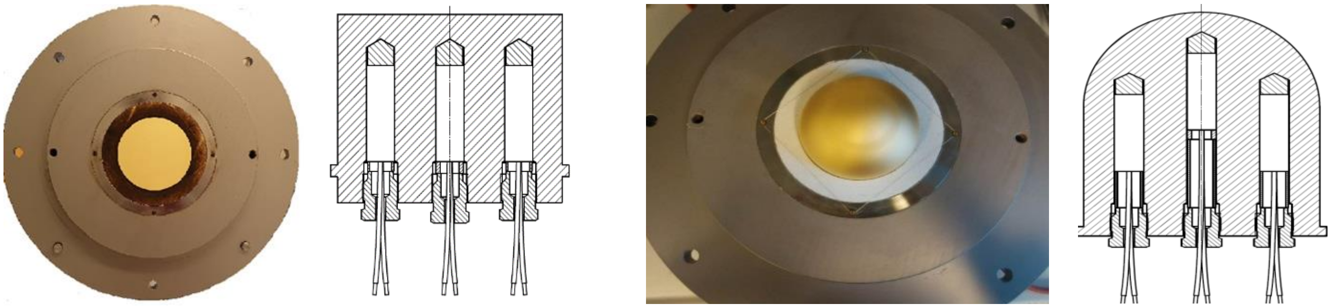

(a) (b) (c) (d)

Fig. 2. *(a) Plane heating body with insulation ring and base plate; (b) Plane heating body with heating cartridge; (c) Convex heating body with insulation ring and base plate; (d) Convex heating body with heating cartridge.*

We need to calculate the air supply rate and pump rate of the substance to get the required composition of the flammable gas-air mixture inside the vessel. The total flow rate is taken as 19.5 l/min. The calculated values of flow rates for different concentrations is given in table 3. The experiments are conducted at atmospheric conditions (P = 1 bar and T = 21 °C). The KP2000 liquid pump with a pumping rate (V_{pump}) 1 to 2000 ml/h is used to supply the flammable liquid into the heating coil. It is maintained at a temperature above the boiling point of the flammable substance. So, flammable liquid converts into gaseous form inside the heating coil. Compressed air obtained from a compressor passes through a drying cartridge (tube filled with silica gel to absorb moisture) to get dry air as a product. This dry air is passed through the heating coil and then it mixes with the flammable gas inside the heating coil. Volume of dry air (V_{air}) is controlled by a digital control unit (Bronkhorst) with attached flow meters (Bronkhorst EL- Flow). After that, the flammable gas-air mixture enters into the cylindrical vessel.

Table 3: *Volume flow rates of flammable gases at different concentrations*

Concentration (% by volume)	1.4% CS_2	1.7% CS_2	2% CS_2	3% CS_2	4% CS_2	5% $C_4H_{10}O$	6.5% $C_4H_{10}O$	8% $C_4H_{10}O$
V_{gas} (l/min)	0.27	0.33	0.39	0.58	0.78	0.98	1.56	1.56
V_{air} (l/min)	19.23	19.17	19.11	18.92	18.72	18.52	17.94	17.94
V_{pump} (ml/h)	44.18	53.65	63.12	94.68	126.25	272	436	436

The mixture composition inside the vessel is measured by a gas analyser (Oxymat) which works on the paramagnetic oxygen principle. After obtaining the required concentration inside the vessel, a variable transformer (maximum output = 230 V) is switched on to heat the ignition source. It is heated until the ignition of flammable mixture is detected inside the vessel. The ignition temperature is noted, and the ignition process is recorded with a high-speed camera (Mini UX50/100). After the experiment, the heating body with bottom plate is cooled until it reaches atmospheric temperature with the help of a cooling system. It has a double flushing water channel. The experimental setup is placed in a closed fume hood with a continuous ventilation system to ensure safety during the work.

3. Results and discussion

HSIT values of CS_2 and diethyl ether at different concentrations for five different orientations (0°, 45°, 90°, 135° and 180°) are given in table 4. The measurement uncertainty of HSIT is ± 3 K and mixture composition uncertainty is ± 0.05% by volume. The values of the HSIT raises with the rise in the concentration of CS_2. The minimum HSIT values of CS_2 are on the fuel lean mixture side which is near to the lower explosion limit (LEL). In contrast to it, as the concentration of the diethyl ether increases, a decrease in HSIT values is observed and the lowest HSIT values of diethyl ether are seen in the fuel rich mixture side.

Table 4: *Results of CS_2 and diethyl ether for a plane and convex shaped heating surface at different concentrations of the flammable mixture and different orientations of the heating body.*

Concentration (% by volume)		HSIT 0° (°C)	HSIT 45° (°C)	HSIT 90° (°C)	HSIT 135° (°C)	HSIT 180° (°C)
1.4% of CS_2	Plane	146	194	Cold flame	Cold flame	Cold flame
	Convex	159	159	156	184	190
1.7% of CS_2	Plane	153	198	211	204	153
	Convex	166	167	166	193	200
2% of CS_2	Plane	166	212	223	210	164
	Convex	174	177	175	202	210
3% of CS_2	Plane	198	234	251	240	192
	Convex	200	200	197	232	238
4% of CS_2	Plane	223	259	272	266	221
	Convex	222	221	219	252	259
6.5% of CS_2	Plane	273	301	Not measured	Not measured	Not measured
	Convex	272	270	Not measured	Not measured	Not measured
5% of diethyl ether	Plane	245	274	289	279	273
	Convex	237	Cold flame	234	Cold flame	Cold flame
6.5% of diethyl ether	Plane	242	270	279	274	264
	Convex	236	236	232	250	257
8% of diethyl ether	Plane	241	257	274	266	260
	Convex	235	235	232	248	256
18% of diethyl ether	Plane	235	Not measured	Not measured	Not measured	Not measured
	Convex	232	Not measured	Not measured	Not measured	Not measured

The lowest HSIT of CS$_2$ (1.4% by volume) is 146 ± 3 °C for the plane heating body and 156 ± 3 °C for the convex shaped heating body. The lowest HSIT of diethyl ether (18 % by volume) is 235 ± 3 °C for the plane heating body and 232 ± 3 °C for the convex shaped heating body. In both cases, the difference between lowest HSIT and standard AIT is more than 50 K. When the change in the concentration and orientation of the heating body is considered simultaneously, then there is a difference of more than 150 K for CS$_2$ and 100 K for diethyl ether. It clearly shows that change in orientation has a significant effect on HSIT values. For 1% by volume and 1.4% by volume of CS$_2$, and for 5% by volume of diethyl ether, a cold flame has been generated as selected concentrations are close to their LEL. These cold flames are formed because of the degenerating branching chain mechanism. For diethyl ether, two-stage ignition is also possible in which first cold flame is generated and later converts into hot flames. Experiments with higher concentrations than 6.5% of CS$_2$ and 8% of diethyl ether are not performed with this setup for safety reasons.

The graph between HSIT (°C) and concentration (% by volume) of different flammable gases like CS$_2$ and diethyl ether for plane and convex shaped heating surfaces at different orientations is given in figure 3. For CS$_2$ in figure 3(a), when the plane heating surface is considered as an ignition source, the HSIT values for 0° and 180° orientation are almost similar. The HSIT values for 45° orientation are slightly similar to 135° orientation but higher than 0° orientation. The highest HSIT values are recorded for the 90° orientation. HSIT difference between 0° and 90° orientation at a given concentration has remained above 50 K. When the convex shaped heating surface is considered as an ignition source, the HSIT difference between 0°, 45°, and 90° has an insignificant variation of 1 to 2 K only. The HSIT difference between 0° and 180° orientation has remained above 30 K. For both the heating bodies, as the concentration of the CS$_2$ increases, a rise in HSIT values is observed and the highest HSIT values are observed near the stoichiometric concentration. At a particular orientation, there is a difference of more than 100 K from 1.4% to 6.5% by volume of CS$_2$.

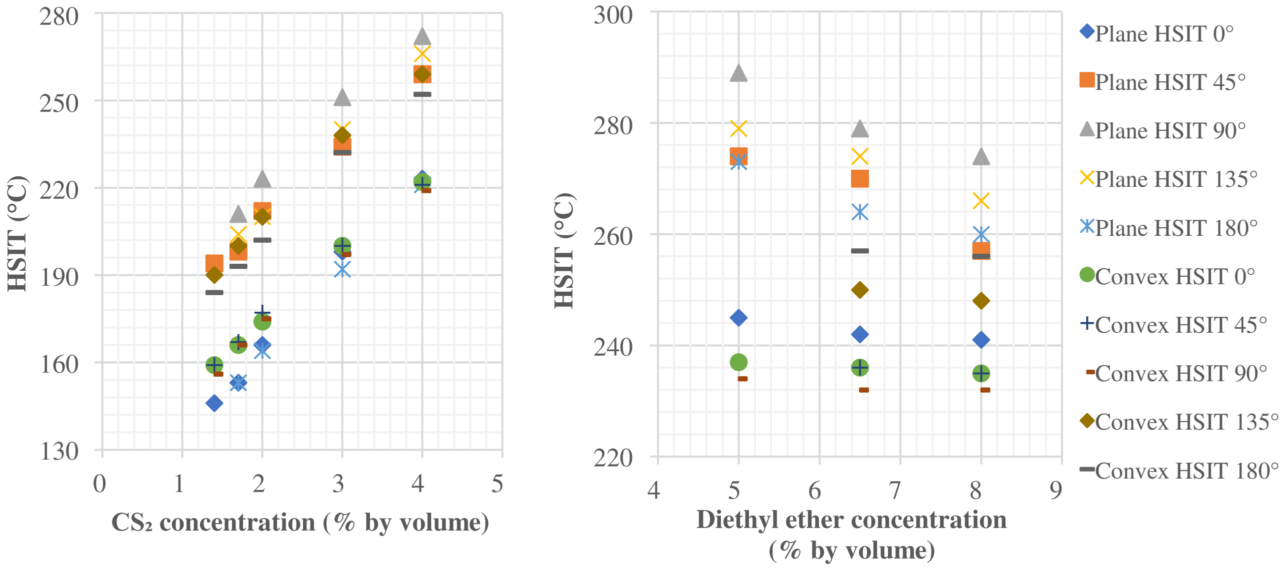

(a) (b)

Fig. 3. *HSIT (°C) vs Concentration (% by volume) diagram for plane and convex shaped heating surfaces at different orientations for (a) CS$_2$; (b) Diethyl ether.*

For diethyl ether in figure 3(b), when plane heating surface is considered as an ignition source, the lowest HSIT values are seen at 0° orientation and highest values are seen at 90° orientation. The HSIT difference between 0° and 90° orientation is more than 40 K. When convex shaped heating surface is considered as an ignition source, the HSIT values at 0°, 45°, and 90° is almost similar and the HSIT difference between 90° and 180° has remained above 20 K. For both the heating bodies, the change in concentrations of diethyl ether has less influence on HSIT because for a large range of concentrations (3.4% to 18% by volume) the HSIT vary less than 10 K. In our experiments, ignition was difficult to occur below the stoichiometric mixture (3.4% by volume) of diethyl ether. We observed HSIT values slightly decrease from 3.4% to 10% by volume. For later concentration from 10% to 18% by volume, the plateau region is formed. HSIT of both the flammable gases at any particular concentration and orientation for the plane heating surface is higher than the convex shaped heating surface due to change in the pattern of convective flow on the heating surface and change in the area of the stagnation zone.

A graph is drawn to study the effect of the orientation of the plane and convex shaped heating surface at a particular concentration for CS_2 (2% by volume) and diethyl ether (6.5% by volume) as given in figure 4. The curves are of fifth order polynomial. For a plane heating surface, lowest HSIT values are obtained at 0° position and when the angle of rotation of the heating surface gradually increased from 0° to 90° position, an increase in the HSIT value is observed and as the heating body is further rotated from 90° position to 180° position, a decrease in the HSIT is observed. So, it is concluded that the highest HSIT values are obtained at 90° orientation of the plane heating surface. For a convex shaped heating surface, the HSIT value of 0°, 45°, and 90° is slightly look alike, and then, HSIT increases from 90° to 180° orientation. So, the highest HSIT values are observed at 180° orientation of the convex shaped heating surface.

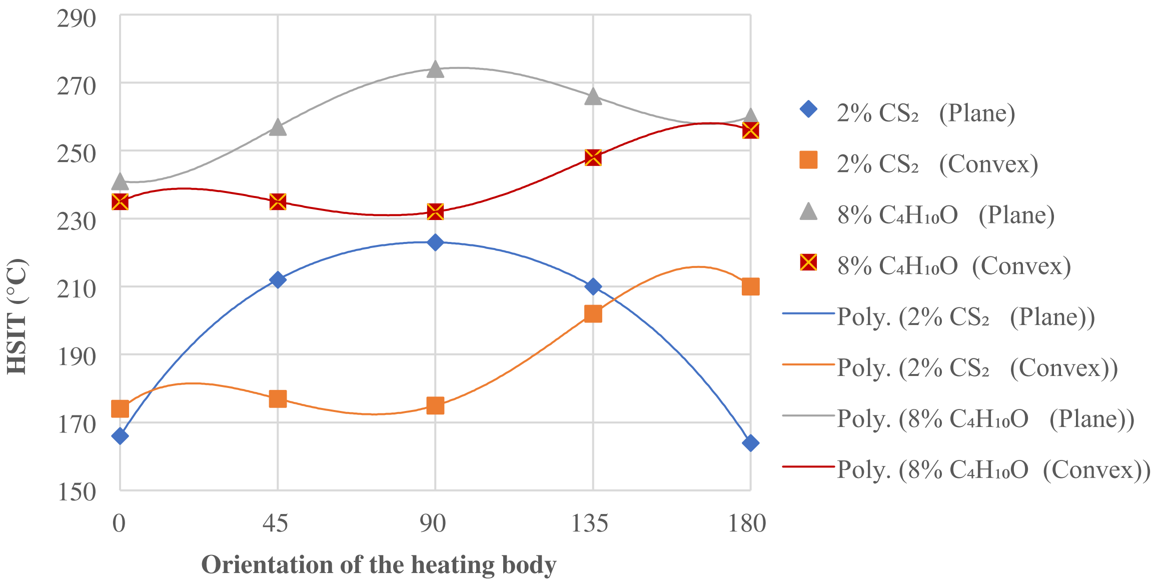

Fig. 4. *HSIT (°C) vs Orientation of the heating body (0°, 45°, 90°, 135°, and 180°) for 2% concentration of* CS_2 *and 8% concentration of diethyl ether (*$C_4H_{10}O$*) for plane and convex shaped heating bodies.*

The temperature-time curve for 2% by volume of CS_2 for 0° orientation of the convex shaped heating body is given in figure 5. The total time of ignition is 2.64 s. Ignition occurs on the top of the heating body and it is detected firstly by thermocouple 6 which is 1 mm above the heating surface. Thermocouples 1, 3, and 6 lies in the convective flow field during the ignition process. So, a rise at these thermocouple temperatures is observed. The stagnation zone and residence time is higher for 0° orientation of the convex shaped heating surface. So, we observe the lowest HSIT values at this orientation. Temperature-time curve for 6.5% by volume of diethyl ether for 90° orientation of the plane heating body is given in figure 6.

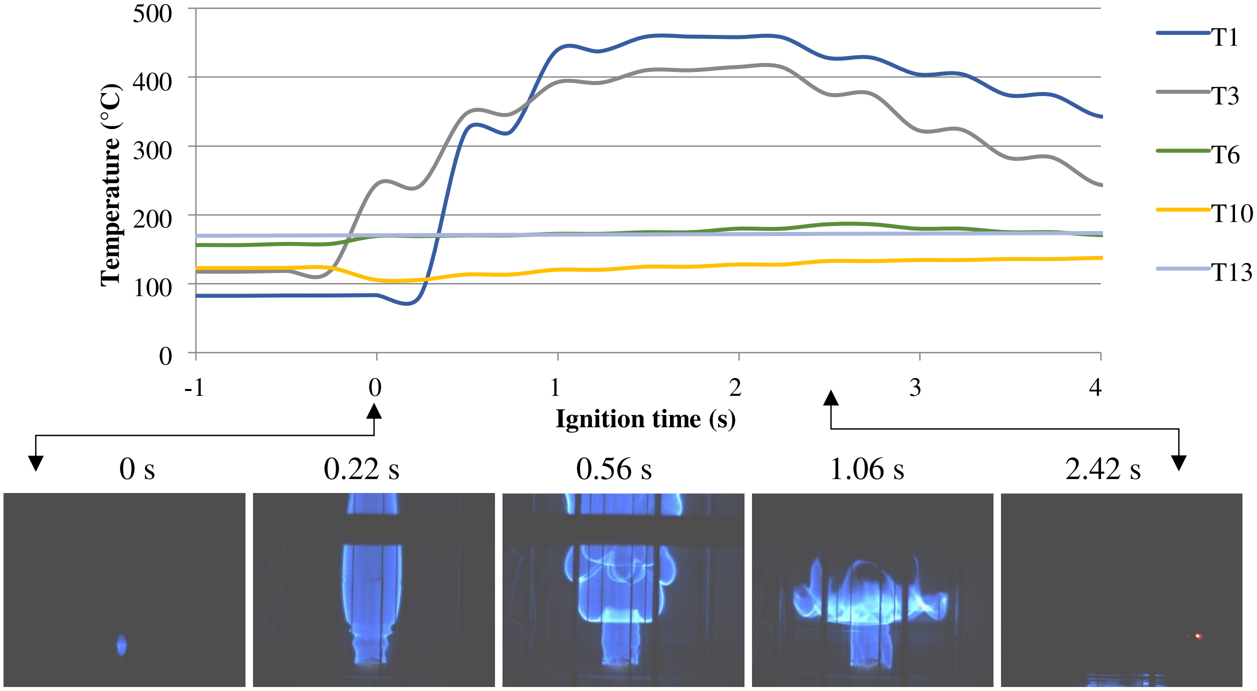

Fig. 5. *Temperature (°C) vs Ignition time (s) diagram of 2% by volume of CS_2 with synchronized films for 0° orientation of the convex shaped heating body.*

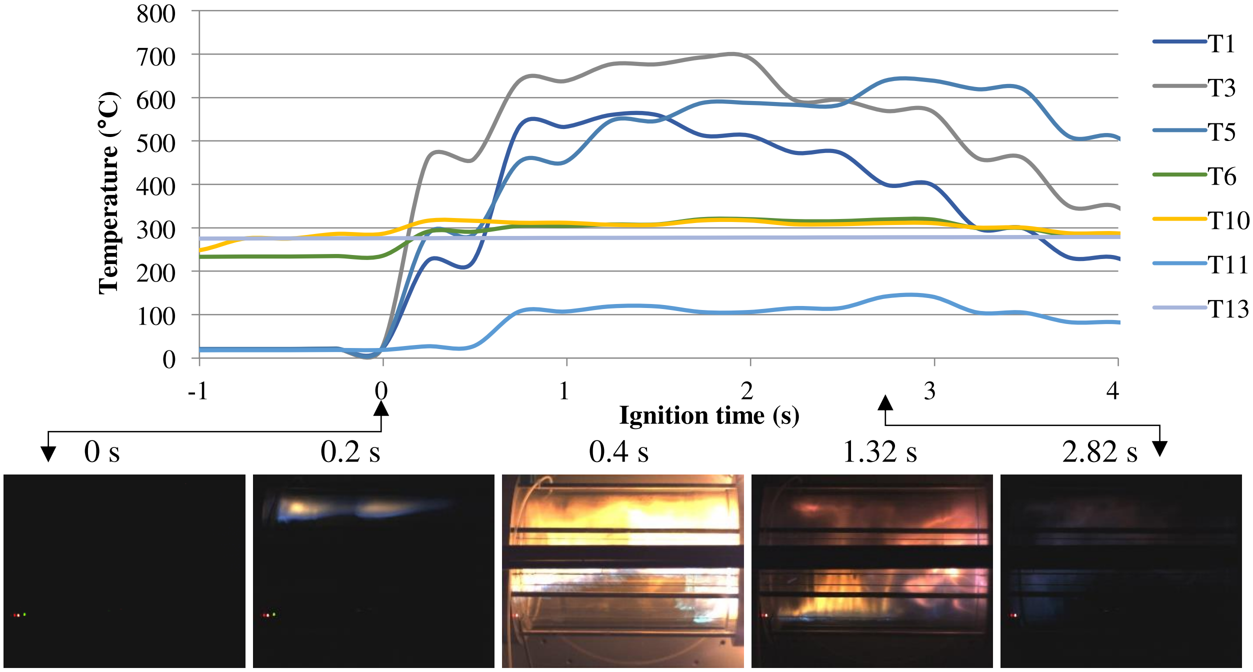

Fig. 6. *Temperature (°C) vs Ignition time (s) diagram of 6.5% by volume of diethyl ether with synchronized films for 90° orientation of plane heating body.*

The total time of ignition is 3.28 s. The flow is similar to 0° position but interrupted by the vessel walls. Therefore, the flow changes its direction and flows along the wall from left to right side of the vessel. The start of ignition is detected at thermocouple 10 which is located at the upper left end of the heating surface. The stagnation zone area is least for 90° position of plane heating surface than any other position. So, it requires a high temperature to start the ignition process. Hence, higher HSIT values are recorded for 90° orientation of the plane heating body. In contrast to it, lower HSIT values are obtained at 90° orientation of the convex shaped heating body due to the formation of a larger thermal stagnation zone at the upper left side of the convex heating body.

4. Conclusions

The outcomes of this experimental work are very helpful to know the hot surface ignition temperature (HSIT) of CS_2 and diethyl ether at five different orientations (0°, 45°, 90°, 135° and 180°) of the plane and convex heating body. The effect of orientation on the HSIT values and the effect of convective flow inside the vessel is investigated. The lowest HSIT of CS_2 (1.4 % by volume) is 146 ± 3 °C and the lowest HSIT of diethyl ether (18 % by volume) is 232 ± 3 °C. In both cases, the difference between the lowest HSIT and standard AIT is more than 50 K. The minimum HSIT values are on the fuel lean mixture side for CS_2 and fuel rich mixture side for diethyl ether. When 90° orientation is considered, the highest HSIT values are obtained for a plane heating surface and the lowest HSIT values are obtained for a convex heating surface than any other orientation. So, this drastic change in HSIT shows the significance of the natural convective flow pattern inside the vessel with the change in heating surface shape. In most cases, when the plane heating surface is considered as an ignition source, it has higher HSIT values than the convex shaped heating surface. So, it is better to prefer plane surfaces over convex surfaces for the equipment in industries to avoid accidental ignition at low temperatures.

References

Babrauskas, V. (2003). *Ignition Handbook*, Fire Science Publishers: 13-128 and 182-227, ISBN 0-9728111-3-3.

Beyer M., Markus D. (2012). Ignition of explosive atmospheres by small hot particles: Comparison of experiments and simulations. *Sci. Tech. Energetic Materials*, 73(1).

Boettcher, Philipp Andreas. (2012). *Thermal Ignition. Dissertation* (Ph.D.), California Institute of Technology: 63-113, DOI:10.7907/H2W9-ZK95.

Bothe, H., Steen, H. (1989). The ignition of flammable vapours by hot pipes and plates. Proc. of the 6th Int. Symp. *"Loss Prevention and Safety Promotion in the Process Industries",* Oslo, Norway, Vol. III: 85.1 – 85.13.

CHEMSAFE: Data base for safety characteristics in explosion protection (*chemsafe.ptb.de*; open access)

Davis, S., Kelly, S., Somandepalli, V. (2010). Hot Surface Ignition of Performance Fuels. Fire Technology, 46(2): 363–374.

Duarte, D., Rohatgi, J. (1998). Mechanics of Ignition by hot surfaces. *Journal of Applied Fire Science*, 7(2): 165-180.

EN 14994:2007. *Gas explosion venting protective systems.*

Gosda, G., Oelmeyer, R., Schacke, H., Walther, C.-D. (1989). Hot pipeline ignition source or not? Proc. of the 6th Int. Symp. *"Loss Prevention and Safety Promotion in the Process Industries"*, Oslo, Norway, Vol. IV: 13.1 – 13.19.

ISO/IEC 80079-20-1. "*Explosive Atmospheres-Part 20-1: Material characteristics for gas and vapor classification - Test methods and data* (ISO/IEC FDIS 80079-34:2017)".

Melguizo-Gavilanes, J., Boeck, L.R., Mével, R., Shepherd, J. E. (2019). Experimental and numerical study of the ignition of hydrogen-air mixtures by a localized stationary hot surface. *International Journal of Heat and Fluid Flow*, 76: 154-169.

Melguizo-Gavilanes, J., Boeck, L.R., Mével, R., Shepherd, J. E. (2016). Hot surface ignition of stoichiometric hydrogen-air mixtures. *International Journal of Hydrogen Energy*. DOI: 10.1016/j.ijhydene.2016.05.095.

Melguizo-Gavilanes, J., Shepherd, J. E. (2017). Effect of orientation on the ignition of stoichiometric ethylene mixtures by stationary hot surfaces. *26th Int. Colloquium on the Dynamics of Explosions and Reactive Systems (ICDERS)*, Boston, USA.

Menon, S. K., Boettcher, P. A., Ventura, B., Blanquart, G. (2016). Hot surface ignition of n-hexane in air. *Combustion and flame*, 163: 42-53.

Ott, T., Beyer, M. (2010). Thermische Zündung von Dampf-Luft Gemischen durch heiße Oberflächen – Simulation und Experiment im Vergleich. *12. Koll. zu Fragen der chemischen und physikalischen Sicherheitstechnik, Bundesanstalt für Materialforschung und –prüfung*, Berlin: 50-54.

Shyam K. Menon, Philipp A. Boettcher, Brian Ventura, Guillaume Blanquart. (2016). Hot surface ignition of n-hexane in air. *Combustion and Flame*,163: 42-53.

Üngüt, A. (2001). CFD simulation and detailed chemical modelling of alkane autoignition near a heated metal surface. Shell Global Solutions (UK) for the Health and Safety Executive, Report 352/2001.

Velagala, S., Raval, P., Chowhan, S. C. S., Esmaeelzade, G., Beyer, M., Grosshans, H., (2020). Simulation of the Flow of an Explosive Atmosphere Exposed to a Hot Hemisphere. In *13th International Symposium on Hazards, Prevention and Mitigation of Industrial Explosions*. Braunschweig, Germany.

Warnatz, J., Maas, U., Dibble, R.W. (2012). *Combustion, Physical and Chemical Fundamentals, Modelling and Simulation, Experiments, Pollutant Formation*. Springer Science & Business Media: 148-149, ISBN-10 3-540-25992-9.

DOI: 10.7795/810.20200724

Numerical Studies on Minimum Ignition Energies in Methane/Air and Isooctane/Air Mixtures

Chunwei Wu [a], Robert Schießl [a] & Ulrich Maas [a]

[a] Institute of Technical Thermodynamics, Karlsruhe Institute of Technology, Karlsruhe, Germany

E-mail: *chunwei.wu@kit.edu*

Abstract

In this study, the dependence of minimum ignition energies (MIE) on ignition geometry, ignition source radius and mixture composition is investigated numerically for methane/air and isooctane/air mixtures. Methane and isooctane are both important hydrocarbon fuels, but differ strongly with respect to their Lewis numbers. Lean isooctane air mixtures have particularly large Lewis numbers. The results show that within the flammability limits, the MIE for both mixtures stays almost constant, and increases rapidly at the limits. The MIEs for both fuels are also similar within the flammability limits. Furthermore, the MIEs of isooctane/air mixtures with a small spherical ignition source increase rapidly for lean mixtures. Here the Lewis number is above unity, and thus, the flame may quench because of flame curvature effects. The observations show a distinct difference between ignition and flame propagation for iso-octane. The minimum energy required for initiating a successful flame propagation can be considerably higher than that required for initiating an ignition in the ignition volume. For iso-octane with a small spherical ignition source, this effect was observed at all equivalence ratios. For iso-octane with cylindrical ignition sources, the phenomenon appeared at lower equivalence ratios only, where the mixture's Lewis number is large. For methane fuel, the effect was negligible. The results highlight the significance of molecular transport properties on the decision whether or not an ignitable mixture can evolve into a propagating flame.

Keywords: *Ignition energy, spark ignition, detailed chemistry*

1. Introduction

Flame initiation is one of the essential problems in combustion processes. It is either desired, e.g., in gasoline engines, or one seeks to prevent it, like in explosion-critical environments. In both cases, understanding details of the flame initiation and early flame propagation can help for improving processes. In IC engines, this understanding allows for improved designs with better fuel efficiency and lower emission. Thus, the investigation of flame initiation is especially important for combustion engines.

It is well known that for a successful induced ignition, a minimum ignition energy (MIE) is needed to achieve high temperatures of the fuel-air mixture in the ignition volume to allow fast chemical reactions to commence. This leads to the formation of a flame kernel, which then might give rise to further propagation of a self-sustained flame. In the past, the dependence of MIE on the pressure, initial temperature, mixture stoichiometry and ignition source volume for different fuels has been investigated (see e.g. Maas et al., 1988, Frendi et al., 1990, Lewis et al., 1987). There are two possibilities after a certain amount of external energy is deposited: the spherical flame propagates outwardly and finally becomes a planar flame or the flame quenches.

The flame initiation and early propagation of the simpler fuels like hydrogen or methane is well studied. For isooctane, an important component and model fuel for gasoline, less studies are available. Beside its practical significance, the case of induced ignition in iso-octane/air mixtures is also interesting from a more fundamental viewpoint, because at least two physical or chemical aspects of this fuel are more complicated than for CH_4. The Lewis number (see e.g. Mills et al., 1993) of isooctane/air mixtures is very different from that of methane/air mixtures: while the Lewis number for methane/air mixtures is overall close to 1 at atmospheric pressure and room temperature (Clarke, 2002), the Lewis number of isooctane/air mixtures varies from under unity at rich condition to 3 for lean mixtures (Takashi et al., 2006, Abdel-Gayed et al., 1985). Also, iso-octane as a higher hydrocarbon features a more complicated chemistry during its oxidation compared methane; also in this behavior, iso-octane is closer to most practical gasoline-type fuels than methane.

This work aims to investigate the MIEs for methane and isooctane with different fuel compositions (throughout the flammable range), different ignition source geometries (spherical and cylindrical) and different ignition source sizes (0.5 mm to 3 mm) at 1 bar and 298K, in order to find out the ignition properties of the two fuels, and to better understand how the interplay of chemical reaction and transport effects (in particular, species diffusion and heat conduction) affect the ignition process. It uses numerical simulations, involving a detailed treatment of chemical reactions and molecular transport effects, for this.

2. Numerical Method

Model simulations of flame initiation were performed using the in-house code INSFLA (Maas et al., 1988). This code computes the temporal evolution of combustion processes in one-dimensional geometries, considering detailed chemistry and detailed molecular transport.

The simulations use a domain which depends on one spatial variable *r*; this can describe cylindrically symmetric domains with infinite extent in axial direction and spherically symmetric domains. Simulations are initialized with a compositionally and thermally homogeneous fuel/air mixture at some predefined initial conditions. The combustion processes are calculated based on the assumption of constant pressure (1 bar), and the initial temperature was set to a homogeneous profile with 298 K. The air used in this study has a composition of 21% O_2 and 79% N_2 by mole. The investigated fuel compositions are varied within an interval that includes the flammability limits (from $\Phi = 0.46$ to $\Phi = 1.86$ for methane/air mixtures and from $\Phi = 0.77$ to $\Phi = 4.57$ for isooctane/air mixtures).

Starting from $t = 0$, an energy source term is applied for a duration (ignition duration) of 10^{-4} s in a region (whose size is defined by the ignition radius r_s) at the inner domain boundary ($r = 0$). In the following, this region will be referred to as *ignition kernel*. We considered both spherical and cylindrical ignition kernels. For each ignition geometry, several ignition radii (ranging from $r = 0.5$ mm to $r = 3$ mm) were investigated.

In order to compare the MIE between different ignition geometries and ignition radii, the minimum ignition energy density q is used, defined as

$$q = \frac{E}{V_S}$$

Here E is the ignition energy and V_S is the ignition kernel volume.

For spherical geometry, E is the total energy deposited at the center of the gas mixture, E is in J. The energy density is

$$q = \frac{E_{sph}}{\frac{4}{3}\pi {r_s}^3}.$$

For cylindrical geometry (infinite cylinder, Maas et al. 1988), E is the deposited energy per length of the infinite cylinder, and has a unit of J/m. So we only need to divide E by the circle area in order to calculate the energy density

$$q = \frac{E_{cyl}}{\pi {r_s}^2}.$$

The computational domain size for $r_s \leq 1$ mm was set to 0.01 m, while for $r_s > 1$ mm, it was set to 0.05 m. Thus, there was sufficient space to make sure the outer boundary of the domain did not affect the ignition process and early phase of flame propagation.

Premixed methane/air mixtures and isooctane/air mixtures were used as fuels in this present study. We used the GRI 3.0 mechanism with 53 species and 325 reactions to describe the detailed chemical kinetics of methane (Smith et al., 2004). A semi-detailed chemical kinetics model for Toluene Reference Fuels (TRF) with 137 species and 633 reactions is used, which also contains chemistry for iso-octane (Andrae et al., 2008).

Running the code delivers spatiotemporal profiles of temperature and species. Temperature profiles are analysed to decide between flame propagation and flame extinction. For example, fig.1 shows the temperature profiles for the case of a successful ignition (diagram (a)), and also for an ignition failure (diagram (b)). As can be seen, in a successful ignition, the temperature in the center of the mixture rises and a flame kernel is formed; after some time, a self-sustaining flame starts to propagate outwards. On the other hand, in an ignition failure, the heat is conducted to the surroundings, and the the temperature at the center finally decreases back to 298 K.

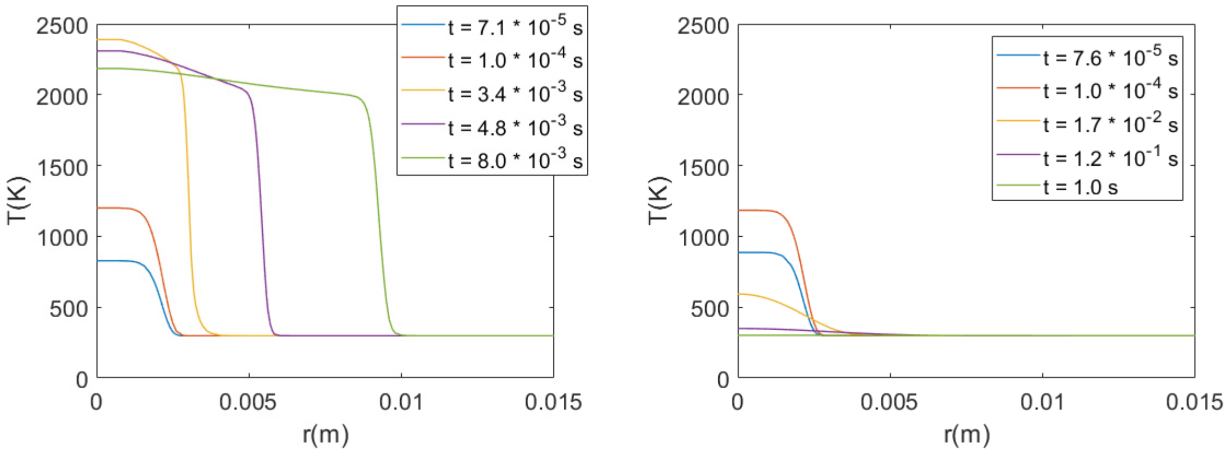

Isooctane, $\Phi = 1.6$, spherical geometry, $r_s = 2$ mm

(a) The temperature history for the case of a successful ignition. (Isooctane/air mixture, $\Phi = 1.60$, spherical geometry, $r_s = 2$ mm, $q = 5.74\times10^5$ J/m^3)

(b) The temperature history of an ignition failure. (Isooctane/air mixture, $\Phi = 1.60$, spherical geometry, $r_s = 2$ mm, $q = 5.77\times10^5$ J/m^3)

***Fig.1** The temperature history of a successful ignition and an ignition failure*

3. Results and discussion

3.1 Minimum ignition energies for methane/air mixtures and isooctane/air mixtures

Fig. 2 shows the results of minimum ignition energies in dependence on the equivalence ratio ϕ, with spherical ignition source for both fuels. In the diagrams, a normalized equivalence ratio ϕ_n was used, which allows showing the rich ($\phi > 1, \phi_n > .5$) and lean ($\phi < 1, \phi_n < .5$) side of the flammable range in a nearly symmetric fashion (Law, 2010):

$$\phi_n = \frac{\phi}{1+\phi}.$$

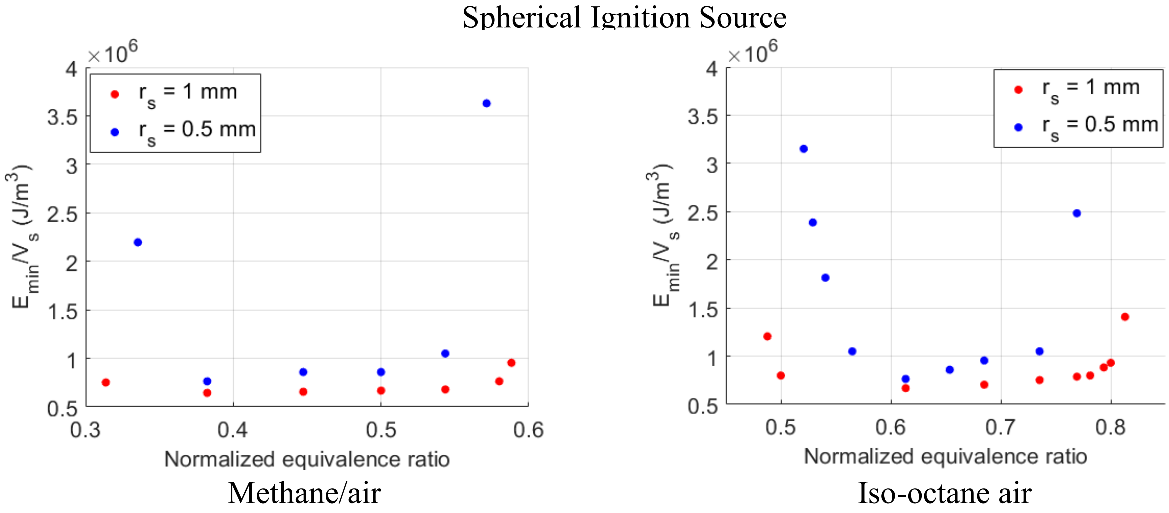

Methane/air

Iso-octane air

***Fig. 2.** Minimum ignition energy densities in dependence on the equivalence ratio with a spherical ignition source for two ignition radii (r_s = 0.5 mm and r_s = 1 mm) for methane/air and isooctane/air mixtures.*

Within the flammability limits, the minimum ignition energy densities are comparable for both mixtures. This agrees with the results from Moorhouse (1974). For both mixtures, with a relatively large spherical ignition source (r_S = 1 mm), the minimum ignition energy density is almost constant within the flammability limits. It increases rapidly near the upper and lower flammability limits. This "U-shape" ignition energy density agrees with former studies (see e.g. Moorhouse et al., 1974). For both fuels, the ignition energy densities for smaller ignition radii r_S are higher than for large r_S. For smaller radii, we observe a notable dependence of MIE on the equivalence ratio also within the flammable range; compare the essentially "flat" curve described by the red points ($r_S = 1$ mm) in Fig. 2 with the more variable dependence outlined by the blue points ($r_S = 0.5$ mm).

For isooctane/air mixtures, the MIE increases slightly with increasing equivalence ratio from ϕ_n = 0.62 to $\phi_n = 0.8$ (ϕ = 1.60 to ϕ = 4), after that, the MIE increases faster when it approaches the upper flammability limit. On the other hand, at the lean side, the MIE starts to increase from ϕ_n = 0.6 (ϕ = 1.5). Here the effective Lewis number is above unity, and the Lewis number increases when the equivalence ratio decreases, which makes the minimum ignition energy density especially sensitive to the equivalence ratio. The spherical flame is positively stretched by the outward propagation, the heavy molecules will diffuse to the region with lower temperature. Thus the flame is weakened and perhaps eventually quenches by the stretch effect (Law, 2010, Xin et al., 2012, Han et al., 2015). It is also observed that stoichiometric isooctane/air mixtures with a small spherical ignition source cannot be ignited no matter how large the ignition energy is. This phenomenon will be further discussed in section 3.2.

The results of the minimum ignition energy densities in dependence on the equivalence ratio with a cylindrical ignition source, shown in fig. 3, are similar to the case of spherical ignition: the minimum ignition energy density is nearly independent of the equivalence ratio within the flammability limits and increases near the limits. The minimum ignition energy densities are higher for smaller ignition radius. Some differences are observed, though. The increase of minimum ignition energy at the flammability limit is lower with cylindrical geometry than with the spherical geometry. The rapidly increasing minimum ignition energy for lean isooctane/air mixture is less pronounced for the cylindrical geometry. This can be attributed to the effect of strongly different diffusivities of the fuel and oxidizer, like it is present for iso-octane/air mixtures, in conjunction with different stretch rates for spherical and cylindrical flames.

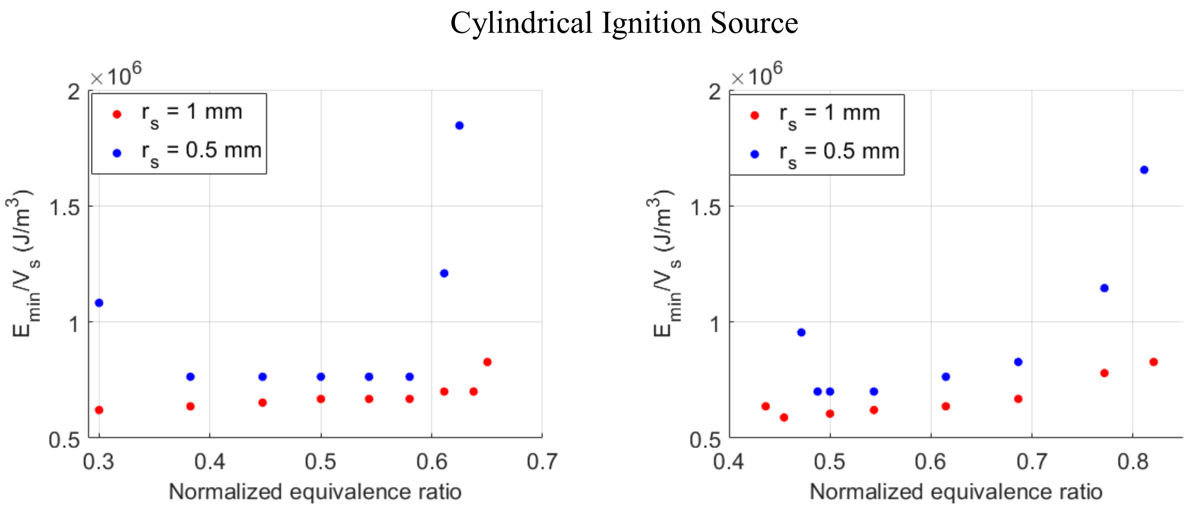

Methane/air
Iso-octane air

Fig. 3. *Minimum ignition energy densities in dependence on the equivalence ratio with a cylindrical ignition source for two ignition radii (r_s = 0.5 mm and r_s = 1 mm) for methane/air and isooctane/air mixtures.*

The stretch rate is defined as the ratio of the time derivation of the area of an infinitesimal element of the flame surface to the area itself. For outwardly propagating spherical flames (spherical flames that propagate in direction of larger radii), the stretch rate is

$$\kappa = \frac{2}{R_f}\frac{dR_f}{dt}$$

,

and for outwardly propagating cylindrical flames, it is

$$\kappa = \frac{1}{R_f}\frac{dR_f}{dt}$$

where R_f is the flame radius (Law, 2010). This indicates a smaller stretch rate for cylindrical flames than for spherical flames, and thus a less pronounced influence of flame front curvature.

3.2 The curvature effect on minimum ignition energy for isooctane/air mixture

To further understand the rapid increase of minimum ignition energy density for isooctane/air mixtures from $\phi = 1.5$ ($\phi_n = 0.6$) to lean mixtures with spherical geometry, the profiles of CO_2 and CHO are investigated. The values of CHO (CO_2) in Fig.4 are given as specific mole numbers, i.e., as the ratio of mass fraction w_i and molar mass M_i of the species:

$$Y_i = \frac{w_i}{M_i}, \qquad i = \mathrm{CHO}, \mathrm{CO_2}.$$

The profiles of CO_2 are used to assess to which extent the gas mixture in the ignition volume is already burned; CO_2 is thus used as a kind of reaction progress indicator. Note that the temperature, which in other situations can serve as a reaction progress marker, is unsuitable for the purpose here because it is affected not only by reaction, but also by the external energy source. The profiles of CHO are used as representatives for the heat release rate. Large values of CHO indicate regions of large chemical reaction rates, thereby outlining the approximate position of the flame front (Paul et al., 1998).

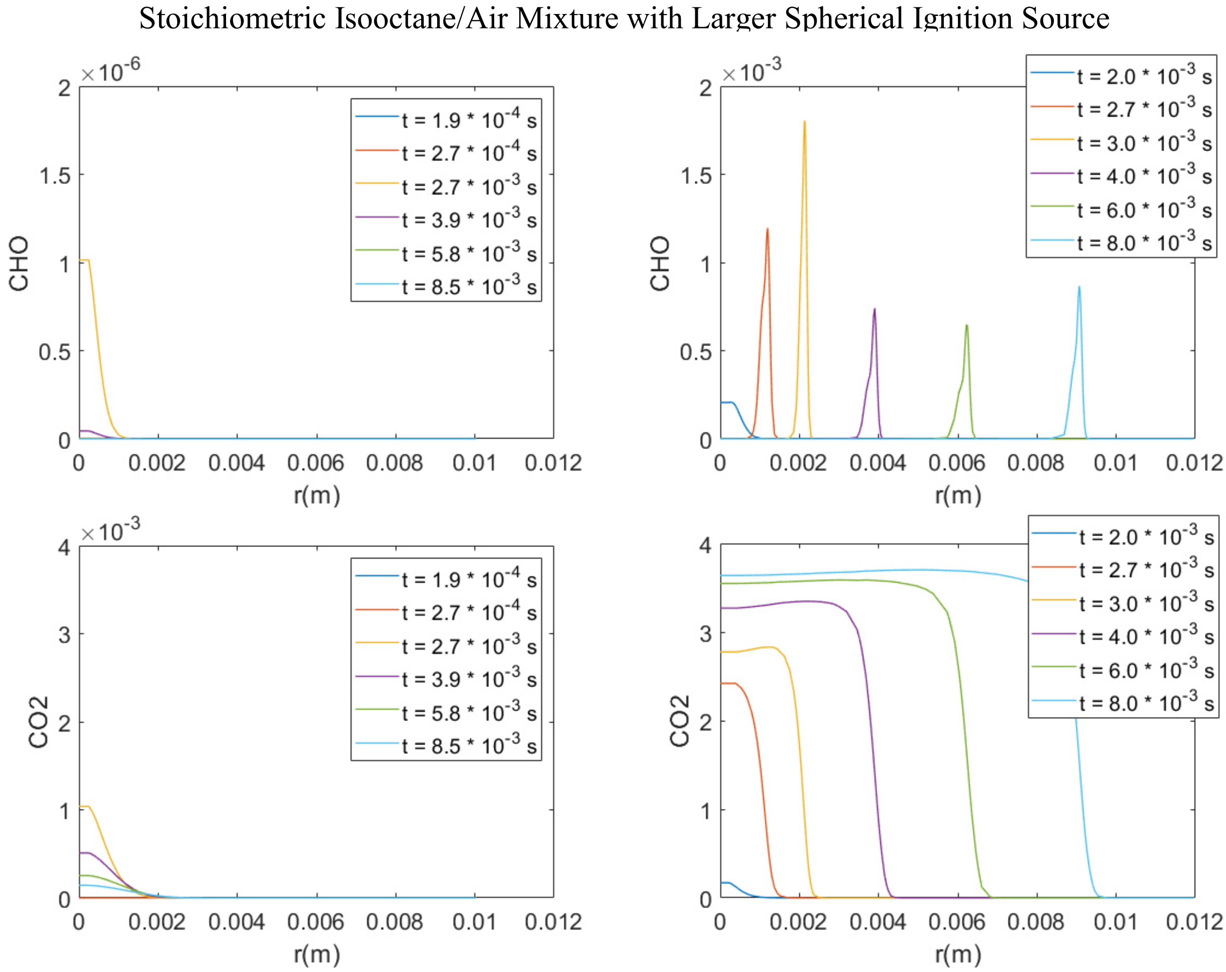
Stoichiometric Isooctane/Air Mixture with Larger Spherical Ignition Source

$q = 5.37\times10^5$ J/m^3 , $E = 18.00$ mJ

$q = 5.39\times10^5$ J/m^3, $E = 18.05$ mJ

Fig. 4. *CHO and CO_2 profiles for stoichiometric isooctane/air mixture with spherical ignition source (r_s = 2 mm), with no successful ignition (left) and successful ignition (right). Note the different scales on the y-axis for both CO_2 and CHO on the left vs. right side.*

For the mixture shown in Fig. 4, the minimum ignition energy density is $q = 5.39\times10^5$ J/m^3. It is clearly seen that with an ignition energy density $q = 5.37\times10^5$ J/m^3 only a very limited amount of CO_2 is formed (about 10^{-3}, which means the mass fraction of CO_2 is about 0.0044%), which means the energy is not enough to ignite the mixture in the ignition volume. However, with $q = 5.39\times10^5$ J/m^3, we can see the formation of CO_2 and the propagation of the flame.

On the other hand, the stoichiometric isooctane/air mixture with an ignition source r_s = 1 mm behaves differently, as is shown in Fig.5.

Stoichiometric Isooctane/Air Mixture with Smaller Spherical Ignition Source

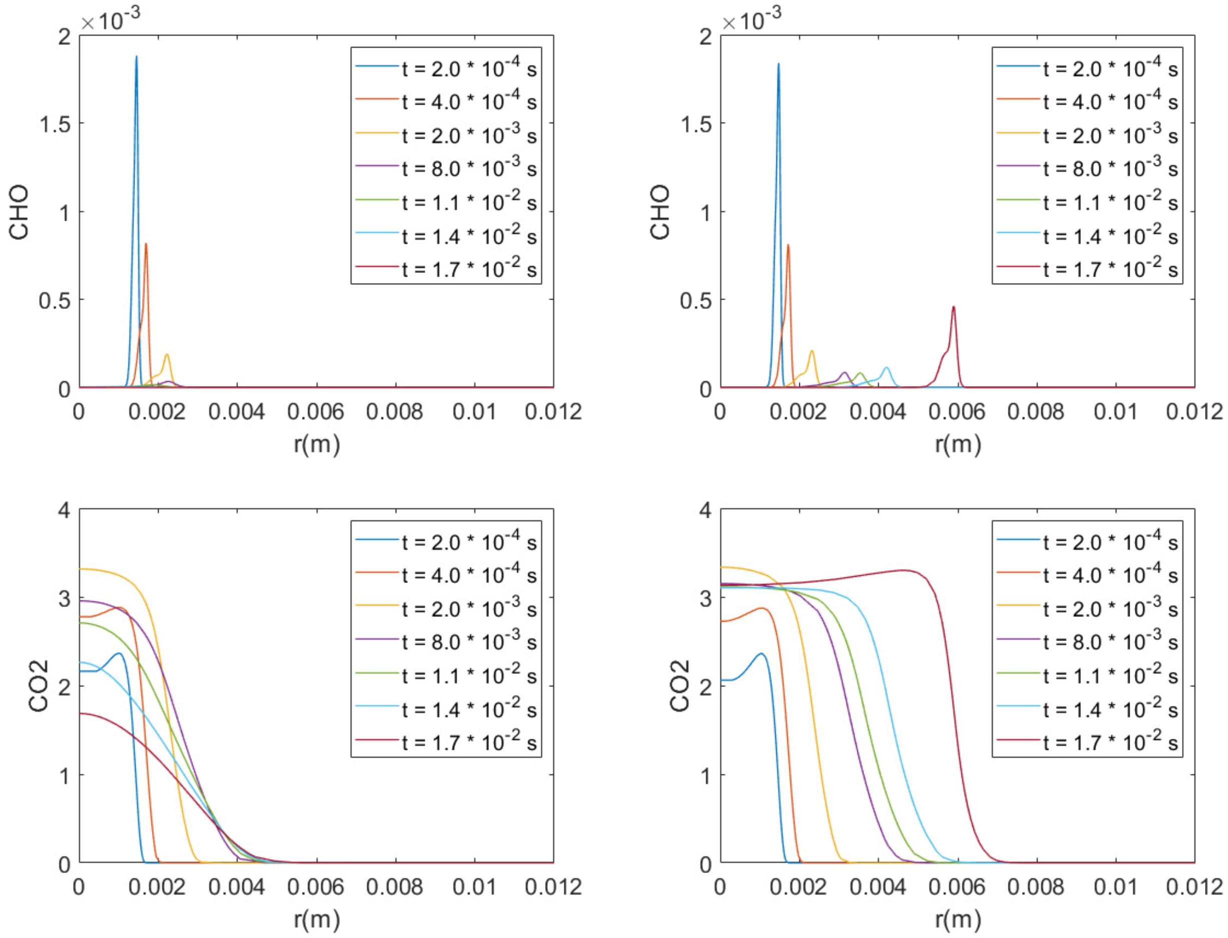

(a) (b)

Fig. 5. *The CHO and CO_2 profiles for stoichiometric isooctane/air mixture with spherical ignition source ($\boldsymbol{r_s}$ = 1 mm) with source energy of: (a)* $q = 7.88\times10^5$ J/m^3 *(E = 3.25 mJ), no flame propagation and (b)* $q = 8.00\times10^5$ J/m^3 *(E = 3.35 mJ), flame propagation*

Here the minimum ignition energy density is 8.00×10^5 J/m^3. In contrast to the results of r_S **=** 2 mm, where no ignition was found below the minimum ignition energy, here, even when the source energy density is 7.88×10^5 J/m^3 (below the MIE), the mixture in the ignition volume is still ignited. During the first 2 ms, the CO_2 formation and the propagation of the peak of CHO are very similar. But when the reaction front (as identified by the peak of CHO) has moved about 2 mm away from the ignition source, the flame quenches. The ignition energy density $q = 7.88 \times 10^5$ J/m^3 is therefore enough to generate a flame kernel, but the flame cannot further propagate.

We define the distance between the CHO peak and the left boundary of the calculation domain (r = 0) as the flame radius. The evolution of this for the different cases is shown in fig. 6. The propagation and extinction of the flame is clearly seen in Fig. 6. For the ignition source radius r_s = 2 mm, when the ignition energy density increases, the temperature in the center also increases, when there's enough energy for the ignition of the mixture in the ignition volume, the flame is formed and can propagate. On the other hand, for the ignition source radius r_s = 1 mm, even if the mixture in the ignition volume can be ignited and a flame is formed, the flame will quench if the ignition energy is not high enough.

DOI: 10.7795/810.20200724

r = 2 mm

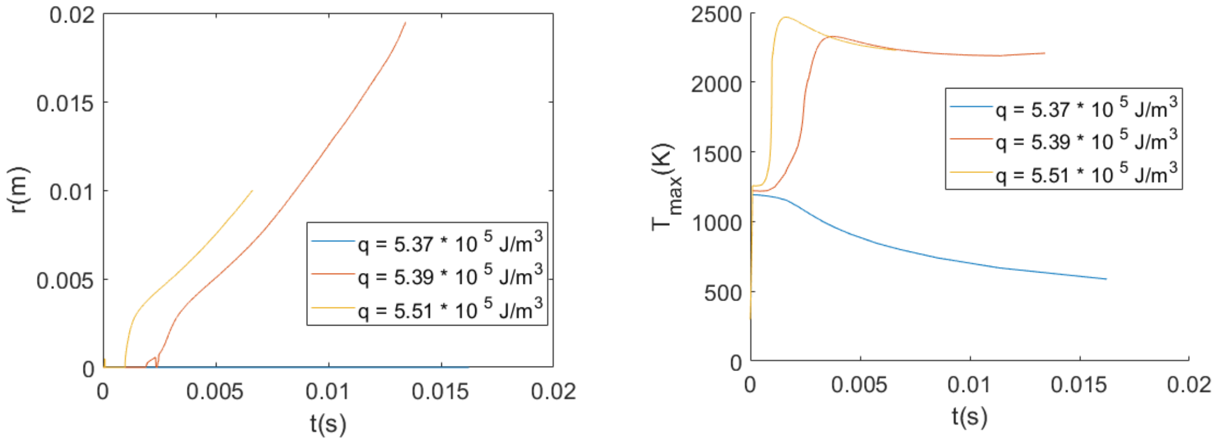

r = 1 mm

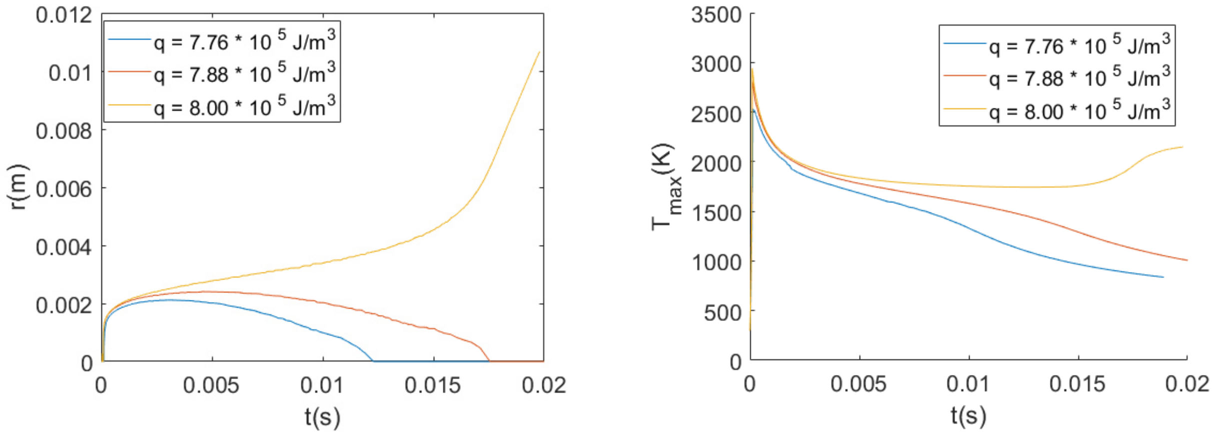

r = 0.5 mm

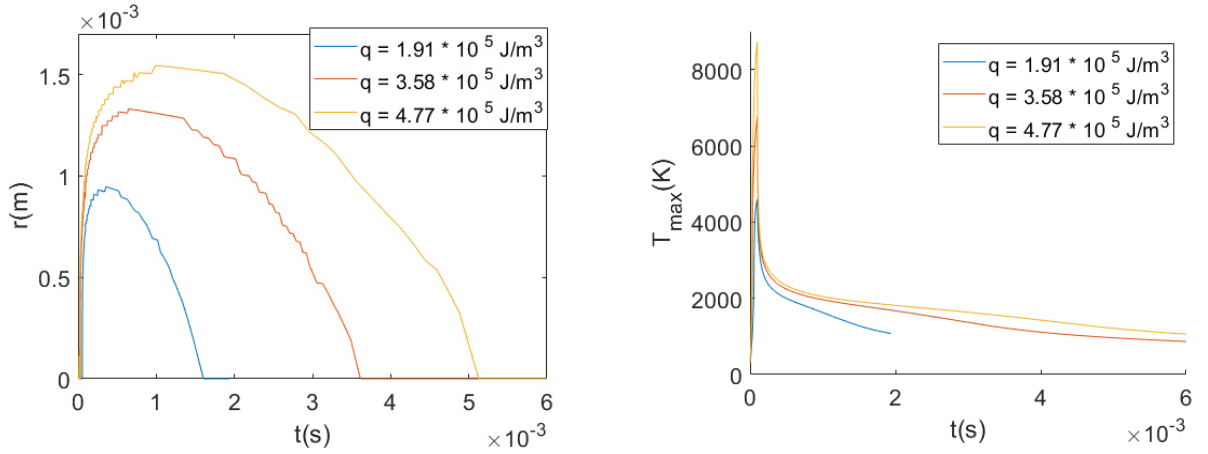

Fig. 6. *Temporal development of the flame radius and of the maximal temperature for stoichiometric isooctane/air mixtures with a spherical source* $r_s = 2$ *mm (top)* $r_s = 1$ *mm (middle) and* $r_s = 0.5$ *mm (bottom).*

According to He (2000) and Kelley et al. (2008), a critical flame radius exists. For a positively stretched spherical flame, if the flame can reach this critical radius, then the flame can further propagate. Otherwise the flame quenches. Hence for smaller ignition radii, more energy is needed to reach the critical radius.

In Fig.6, we can clearly see this critical radius (about 0.0025 m) for smaller ignition sources. For r_s = 1 mm, if the ignition energy density q is 7.88 × 10^5 J/m^3, the flame will propagate to a radius about 2.2 mm, which is smaller than the critical radius, and then quenches. If the ignition energy density q is even smaller than 7.88 × 10^5 J/m^3, the flame quenches at even smaller radii. On the other hand, if the ignition energy density is a little bit higher and reach the minimum ignition energy density, the flame can reach the critical radius and further propagate.

This can also explain why the stoichiometric isooctane/air mixture cannot be ignited with a spherical source r_s = 0.5 mm. As is shown in Fig.6, the temperature in the center increases up to 8000K, and the initiated flame still cannot reach the critical flame radius for stoichiometric isooctane/air mixture. As a result, the flame quenches and the rest of the mixture remains unignited.

3.3 The dependence of minimum ignition energies on the ignition radius for isooctane/air mixtures

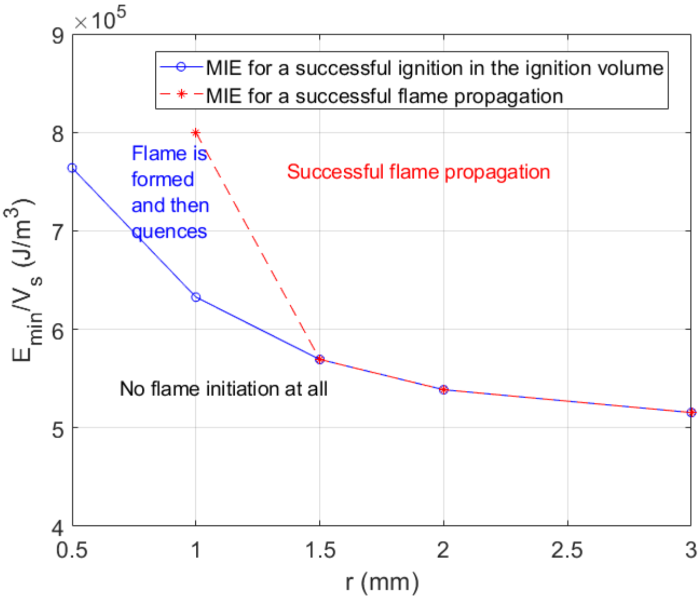

Fig. 8. *The dependence of minimum ignition energy on ignition radius for stoichiometric isooctane/air mixture with spherical ignition source*

Fig. 8 shows the dependence of minimum ignition energy densities on the ignition radius for stoichiometric isooctane/air mixtures with spherical ignition sources. As discussed in section 3.2, for mixtures like stoichiometric isooctane/air with Le>1, the flame kernel must reach a certain radius for a successful flame propagation (He, 1999, Kelley et al. 2008). Results show that if $r_s > 1.5$ mm, the minimum ignition energy densities for the flame initiation in the ignition volume and for a successful flame propagation are the same, and it decreases slightly when the ignition radius increases due to heat conduction becoming less important. This means that either the mixture can be ignited and the flame can propagate, or the energy is not enough to ignite the mixture at all. However, as $r_s < 1.5$mm, a third region becomes more significant, where the energy is enough to ignite the mixture ignition kernel, but not enough for the flame to propagate to the critical radius. The flame quenches because of the curvature effect at small flame radius.

4. Conclusions

In this study, the dependence of the minimum ignition energies (MIEs) on the fuel composition, the ignition source geometry and the ignition source size for methane/air mixtures and isooctane/air mixtures is investigated.

The MIE vs. equivalence ratio diagrams for both fuels show “U”-shaped curves. Within the flammability limits, the MIE stays almost constant, and it increases rapidly at the limits. The MIEs for both fuels are also similar within the flammability limits.

However, for isooctane/air mixture with $\Phi < 1.5$, where the Lewis number is above 1 and further increases when the mixture gets leaner, the MIE is very sensitive to the change of equivalence ratio. For $r_s = 0.5$ mm, even a stoichiometric mixture of isooctane/air cannot be ignited. The main reason for this is related to the curvature of the reaction zone: For small flame radii and the resulting large stretch rates, molecular diffusion has a strong effect on the evolution of the system. Strong gradients at the reaction zone cause large fluxes of species. The isooctane molecule cannot diffuse into the reaction zone at the same rate like oxygen; this leads to a local lack of fuel at the reaction zone, which in turn reduces the chemical source terms. This impedes a sufficiently fast propagation. This phenomenon is less pronounced for a cylindrical ignition kernel, because the stretch rate for a cylindrical flame is smaller and thus the curvature effect is smaller as in the spherical case.

In contrast, for methane/air mixtures, even with small ignition radii this phenomenon mentioned above is not observed: if the energy is large enough for an ignition in the center, then the flame is also able to propagate. The curvature effect for methane/air mixture is negligible.

Furthermore, we investigated the flame front propagation for spherical isooctane/air flames. Results show that for larger ignition sources, the mixture can either be ignited in the center and the flame is able to propagate, or the mixture cannot be ignited at all. On the other hand, with a smaller ignition source, it is possible that a flame is formed but then quenches.

For $r_s > 1.5$ mm, the minimum ignition energy densities for a flame initiation in the ignition volume and for a successful flame propagation are the same. Bur for $r_s < 1.5$mm, there’s a difference between the two minimum ignition energy densities. The difference becomes larger for smaller ignition radii.

Acknowledgements

The authors gratefully acknowledge the financial contribution from the Deutsche Forschungsgemeinschaft (DFG) under the project MA1205/26-1.

References

Abdel-Gayed, R.G., Bradley, D., Hamid, M.N., Lawes, M. (1985). Lewis number effects on turbulent burning velocity, *Symposium (International) on Combustion,* 20(1): 505-512

Andrae, J.C.G., Brinck, T., & Kalghatgi, G.T. (2008). HCCI experiments with toluene reference fuels modeld by a semidetailed chemical kinetic model. *Combustion and Flame*, 155(4): 696-712

Chen, Z. & Ju, Y. (2007) Theoretical analysis of the evolution from ignition kernel to flame ball and planar flame, *Combustion Theory and Modelling*, 11:3, 427-453.

Clarke, A. (2002). Calculation and Consideration of the Lewis Number for Explosion Studies. *Process Safety and Environmental Protection*. 80(3): 135-140

Frendi, A. & Sibulkin, M. (1990). Dependence of minimum ignition energy on ignition parameters. *Combustion Science and Technology.* 73: 395-413.

Han, W. & Chen, Z. (2015). Effects of Soret diffusion on spherical flame initiation and propagation. *International Journal of Heat and Mass Transfer*. 82: 309-315

He, L. (2000) Critical conditions for spherical flame initiation in mixtures with high Lewis numbers. *Combustion Theory and Modelling*. 4(2): 159-172

He, L. & Law, C.K.(1999). On the Dynamics of Transition from Propagating Flame to Stationary Flame Ball. *AlAA* 99-0325.

Kelley, A.P., Jommas, G. & Law, C.K. (2008). Critical radius for sustained propagation of spark ignited spherical flames. *Combustion and Flame.* 156(5): 1006-1013

Law, C.K. (2010). *Combustion physics.* Cambridge University Press.

Lewis, B., Von Elbe, G. (1987). *Combustion, Flames and Explosions of Gases*, Third Edition. Academic Press

Maas, U. & Warnatz, J. (1988). Ignition processes in hydrogen-oxygen mixtures, *Combustion and Flame*, 74(1): 53-69.

Mills, I., Cvitas, T., Homann, K., Kallay, N., Kuchitsu, K., Quantities (1993), *Units and Symbols in Physical Chemistry*. Second Edition. Blackwell Schience.

Moorhouse, J., Williams, A. & Maddison, T.E. (1974). An investigation of the minimum ignition energies of some C1 to C7 hydrocarbons, *Combustion and Flame*, 23(2): 203-213

Paul, P.H. & Najm, H.N. (1998), Planar laser-induced fluorescence imaging of flame heat release rate, *Symposium (International) on Combustion*. 27(1):43-50

Takashi, H. & Kimitoshi, T. (2006). Lamina flame speeds of ethanol, n-heptane, isooctane air mixtures.

Smith, G.P., Golden, D.M., Frenklach, M., Moriarty, N.W., Eiteneer, B., Goldenberg, M., Bowman, C.T., Hanson, R.K., Song, S., Gardiner, W.C., Jr., Lissianski, V.V., & Qin, Z. (2004) *GRI-MECH 3.0* http://www.me.berkeley.edu/gri_mech/

Warnatz, J., Maas, U. & Dibble, R.W. (2006), *Combustion – Physical and chemical fundamentals, modeling and simulation, experiments, pollutant formation.* Fourth edition. Springer.

Williams, F. A. (1975). Recent advances in theoretical descriptions of turbulent diffusion flames. In *Turbulent mixing in nonreactive and reactive flows*. Springer.

Xin, Y., Sung, C. & Law, C.K. (2012). A mechanistic evaluation of Soret diffusion in heptane/air flames. *Combustion and Flame.* 159(7): 2345-2351

Herausgeber:

Physikalisch-Technische Bundesanstalt
ISNI: 0000 0001 2186 1887
Bundesallee 100
38116 Braunschweig, Germany

Dr. Michael Beyer
Dr. Arnas Lucassen
3.7 | Fundamentals of Explosion Protection

phone: +49 531 592-3700
e-mail: michael.beyer@ptb.de

ishpmie2020.ptb.de
ishpmie2020@ptb.de

DOI: 10.7795/810.20200724

As of: 08/20